Seventh Symposium

NAVAL HYDRODYNAMICS

UNSTEADY PROPELLER FORCES

FUNDAMENTAL HYDRODYNAMICS

UNCONVENTIONAL PROPULSION

DR-148

Office of Naval Research
Department of the Navy

J H Thomson
July 1972
Lynn, Mass

Seventh Symposium

NAVAL HYDRODYNAMICS

UNSTEADY PROPELLER FORCES

— — —

FUNDAMENTAL HYDRODYNAMICS

— — —

UNCONVENTIONAL PROPULSION

sponsored by the

OFFICE OF NAVAL RESEARCH

the

MARINA MILITARE ITALIANA

and the

ISTITUTO NAZIONALE PER STUDI ED ESPERIENZE
DI ARCHITETTURA NAVALE DI ROMA

August 25-30, 1968
Rome, Italy

RALPH D. COOPER
STANLEY W. DOROFF
Editors

OFFICE OF NAVAL RESEARCH—DEPARTMENT OF THE NAVY
Arlington, Va.

PREVIOUS BOOKS IN THE NAVAL HYDRODYNAMICS SERIES

"First Symposium on Naval Hydrodynamics," National Academy of Sciences—National Research Council, Publication 515, 1957, Washington, D.C.; PB133732, paper copy $3.00, 35-mm microfilm 95¢.

"Second Symposium on Naval Hydrodynamics: Hydrodynamic Noise and Cavity Flow," Office of Naval Research, Department of the Navy, ACR-38, 1958; PB157668, paper copy $10.00, 35-mm microfilm 95¢.

"Third Symposium on Naval Hydrodynamics: High-Performance Ships," Office of Naval Research, Department of the Navy, ACR-65, 1960; AD430729, paper copy $10.00, 35-mm microfilm 95¢.

"Fourth Symposium on Naval Hydrodynamics: Propulsion and Hydroelasticity," Office of Naval Research, Department of the Navy, ACR-92, 1962; AD447732, paper copy $10.00, 35-mm microfilm 95¢.

"The Collected Papers of Sir Thomas Havelock on Hydrodynamics," Office of Naval Research, Department of the Navy, ACR-103, 1963; AD623589, paper copy $10.00, microfiche 95¢.

"Fifth Symposium on Naval Hydrodynamics: Ship Motions and Drag Reduction," Office of Naval Research, Department of the Navy, ACR-112, 1964; AD640539, paper copy $15.00, microfiche 95¢.

"Sixth Symposium on Naval Hydrodynamics: Physics of Fluids, Maneuverability and Ocean Platforms, Ocean Waves, and Ship-Generated Waves and Wave Resistance," Office of Naval Research, Department of the Navy, ACR-136, 1966; AD676079, paper copy $10.00, microfiche 95¢.

NOTE: The above books are available from the National Technical Information Service, Operations Division, Springfield, Virginia 22151. The catalog number and the price for paper copy and for microform copy are shown for each book.

For sale by the Superintendent of Documents, U.S. Government Printing Office
Washington, D.C. 20402 - Price $13

PREFACE

The Seventh Symposium on Naval Hydrodynamics continues the policy, initiated in the first of the series in 1956, of providing an international forum for the presentation of research results and the exchange of scientific information in that portion of hydrodynamics especially of naval and marine interest.

In this spirit three major themes were selected for the technical program of the Seventh Symposium: (a) unsteady propeller forces, a concentrated presentation of the latest theoretical and experimental research results dealing with time-dependent forces generated by marine propellers, (b) fundamental hydrodynamics, a sampling of advanced analytical results emphasizing numerical techniques for solving a variety of basic hydrodynamic problems, and (c) unconventional propulsion, a wide-ranging discussion of a number of different propulsion schemes and devices other than conventional marine propellers.

The international aspects of the symposium are reinforced by the distribution of nationalities among the authors and chairmen of the technical sessions, by its location in the beautiful city of Rome, and by the joint sponsorship of the Office of Naval Research, the Marina Militare Italiana, and the Istituto Nazionale per Studi ed Esperienze di Architettura Navale with the collaboration of the Consiglio Nazionale delle Ricerche. To these Italian organizations the Office of Naval Research extends its gratitude and appreciation for their long and arduous efforts which resulted in such superb arrangements for the Symposium. In particular, the encouragement and support of Gen. Isp. Giovanni Di Mento, Ten. Gen. Alberto Alfano, and Ten. Gen. Antonio Siena are gratefully acknowledged. To Col. Angelo Ferrauto and T. Col. Pier Giacomo Maioli, who bore the primary responsibility for the detailed management of the Symposium and for the resolution of the innumerable day-to-day problems, go our limitless admiration, respect, and appreciation for a demanding task magnificently executed. Our gratitude is similarly extended to Dr. Umberto Berni for his efficiency in managing the fiscal aspects of the symposium. We are also deeply indebted to Gen. Isp. Italo Battigelli, who, prior to his retirement from the Marina Militare Italiana, initiated the discussions which led to the organization of the Seventh Symposium on Naval Hydrodynamics. Mr. Stanley Doroff of the Office of Naval Research, one of the principal contributors to the organization and management of this series of Symposia almost from its inception, provided invaluable assistance in his usual efficient and effective manner.

Ralph D. Cooper

RALPH D. COOPER
Fluid Dynamics Program
Program Director

CONTENTS

FUNDAMENTAL HYDRODYNAMICS

UNCONVENTIONAL PROPULSION

UNCONVENTIONAL PROPULSION

PANEL DISCUSSIONS

WELCOME (Translation)

Gen. Isp. G. N. G. Di Mento
Navalcostarmi
Rome, Italy

Yesterday you were welcomed to Italy on the banks of the Tiber; today the work of the Symposium begins, preceded by this opening ceremony, at which we see present a large number of lovely ladies whom we thank for the note of brightness which they bring.

In expressing his displeasure at not being able to take part in this opening ceremony, the President of the Republic has granted his esteemed patronage to this Seventh Symposium and has given me the pleasant duty of passing on to you his cordial salutation and his good wishes.

The participants in the symposium number more than 260; they are accompanied by about 105 ladies and represent as many as 24 nations. The participation puts into relief the ever-growing interest which studies on naval hydrodynamics are gaining in all the world—studies which even in times long past have fired the minds of outstanding men who, for their insight, can be defined as the precursors of modern science. One member of the organizing committee has managed to discover among the innumerable works of Leonardo Da Vinci a passage which might be considered one of the first specific studies in this branch of science and which you will find reproduced in the central pages of your program as a reminder of this symposium.

The papers to be presented at the general session in the mornings are many in number and of high scientific value. In the afternoons panel discussions have been organized in order to permit the various participants interested in specific studies to exchange their ideas, their opinions, and the results of tests they have carried out. The interest in these discussions is stressed by the large number of participants by which each one is to be attended. And I hope that between one general session and the next panel discussion you may also find the time to go around and to admire the beauties of Rome.

WELCOME (Translation)

Senator Donati
Sotto Segretano della Difesa
Rome, Italy

As he has found it impossible to participate at this opening ceremony, the Honorable Luigi Gui, Minister of the Defense, has given me the responsibility of offering to you his welcome and his appreciation of your work as scholars and research workers.

The continual development of sea transport, entailing ever-increasing demands on performance, emphasizes the usefulness and stresses the importance of these meetings at which the results of continuous and intense research work in a branch of science which is of basic importance for the progress of naval constructions can be presented and discussed.

The abundantly rich technical program of this Seventh Symposium includes, among other topics, a look toward tomorrow and at future prospects for propulsion and confirms the vitality of this important sector of naval science.

The Italian Government, which is particularly sensitive to all problems regarding naval construction and therefore supports any activity which contributes to scientific and technological progress, is highly pleased not only that Rome is the hostess to this symposium and to such a large number of scholars from all parts of the world, but also that the symposium's organization has been shared in together by the United States Office of Naval Research, the Marina Militare Italiana, which has a long and meritable tradition in the field of scientific activity, the Istituto Nazionale per Studi ed Esperienze di Architettura Navale, and the Consiglio Nazionale delle Ricerche.

With best wishes that your work may be profitable and rich with interest, and the hope that the present meeting may help to strengthen or to create personal ties and reciprocal acquaintanceships, I have the pleasure and the honor of declaring open the Seventh Symposium on Naval Hydrodynamics.

OPENING REMARKS

Emilio Castagneto
University of Naples
Naples, Italy

It is for no merit or for any particular talents of my own that I have the privilege of being the first to take the floor upon the opening of this symposium, but it is in the name of and on behalf of Professor Vincenzo Caglioti, President of the Italian National Research Council, that I am here to offer greetings and a welcome from the council itself to the authorities, to the ladies, and to all the participants who have come to this meeting in such large numbers from all parts of the world.

I am delighted to have been entrusted with this charge and thus to have the opportunity of expressing all my regard and admiration to you of my friends whom I met for the first time over 35 years ago, to you who have joined them over the years, and especially to you in the ranks of young men who, in a certain sense, I have seen grow and mature and give a great impetus to the studies of naval hydrodynamics.

The Italian National Research Council, which came into being under the initiative and direction of Guglielmo Marconi, is the Italian center which promotes and coordinates studies and research work in all fields of pure and applied science, and above all in those of physics and engineering, guiding the trends of their technical development. To achieve its goals the Italian National Research Council depends on its own laboratories and staff and to a greater extent on University and private institutes with which it draws up contracts for research. In addition, it maintains close collaboration with the technical state departments and their related laboratories, especially those under military administration. In particular, for its research on naval hydrodynamics the Italian National Research Council relies on the Rome Towing Tank, and in addition it collaborates with the Hydrodynamic Center of The Navy and in general with the technical boards of that department.

In their method of operating with respect to this particular naval branch, there is a close resemblance between the Italian National Research Council and the Office of Naval Research, which, together with the Italian Navy and the Rome Towing Tank, was a promoter of this conference. It is also for these very reasons that the Research Council is particularly pleased to act as a collaborator for the symposium. The broadmindedness of ONR in basing its policies, the practicability

of its criteria in choosing the themes and in allotting the funds, and the simplicity of the contractual procedure are well-known and appreciated here in Italy.

In the certainty of portraying the sentiments of Professor Caglioti, I should like to voice the wish that the relations which are established today between ONR and the National Research Council will become closer and closer, and more and more fruitful, as a result of the exchange of their reciprocal experience in the organization of research.

Our country's principle means of communication is the sea, while on the seacoast are found its principle sources of activity and life. Therefore our interest in all problems which concern the sea and progress in the art of navigation cannot be thought other than logical and natural. This is borne witness to by the fact that the first naval basin on the mainland of Europe, and at that time the largest in the world, was erected at La Spezia in 1888 under the initiative of Guiseppe Rota, and it is proved by the fact that a new large hydrodynamic center is now being constructed in Rome. Italy's sensitiveness in this field is also shown by its being perhaps the only nation where experiments with models are compulsory by law for every new passenger ship and for every new cargo ship with a displacement of over 2000 tons.

Thus stems our interest in these meetings and our satisfaction that Rome has chosen as the site for the seventh one, the themes of which look so decidedly to the future.

The ancient Romans sought an omen for the good or bad outcome of an enterprise or event by consulting the flight of birds. Now, without doubt, the flight of the large, winged vehicles which have brought here so many eminent experts and have brought together in one effort of collaboration theorists and designers, mathematicians and physicists, and engineers and constructors, cannot be other than an excellent omen for the Seventh Symposium and, even more than for the symposium, for the future.

OPENING REMARKS

Capt. C. T. Froscher
United States Office of Naval Research Branch Office
London, England

It is my pleasant duty to represent Admiral Owen, the Chief of Naval Research, at this opening ceremony of the Seventh Symposium on Naval Hydrodynamics. These symposia, sponsored primarily by ONR, have been one way for ONR to fulfill its mission: ensuring maximum contributions of basic science to naval effectiveness.

I believe it particularly appropriate to note the new and increasing scope of hydrodynamics. Hydrodynamics is today truly a dynamic field of science and technology. Not too many years ago the naval architect could feel relatively secure working in a realm that had changed little for decades. His world went from a few meters above the surface to a few decameters below and to a speed that seldom exceeded 40 knots. Today, through renewed basic research, you are finding much that is new, even in that realm.

At the same time a revolution in marine vehicles is taking place. They run deeper and hover higher. They go faster and in some applications (such as data gathering platforms like FLIP) require better stability at rest. Their dynamics below, on, and above the water's surface today involve scientific disciplines not traditionally associated with marine applications. It is therefore most appropriate that two of your sessions at this symposium will be devoted to unconventional propulsion. Yes, hydrodynamics is on the move; and in a very real sense previous meetings in this series have led the way.

The first symposium, held in Washington in 1956, was devoted to general surveys of various fields, covering critical reviews of the state of the art, and interpretation of results for design applications. Even then, however, emphasis was on ideas for new research in order to stiumlate increased interest in hydrodynamics, particularly in the United States. The future international character of these gatherings was forecast in this first symposium, it being notable for reviews on hydrodynamics by Professor Milne-Thomson of the Royal Naval College, England, and on the contribution of ship theory to the seaworthiness problem by Professor Weinblum of the University of Hamburg.

Subsequent symposia, held at 2-year intervals, have each had a theme selected either to stimulate important and needed research or to disseminate the results

of significant progress in a field. The second symposium, in 1958, was marked by original contributions in fully cavitating flows, when Marshal Tulin showed the possibility of obtaining good lift-drag properties from specially designed sections, and A. J. Tachmindji and W. B. Morgan applied the idea to the design of fully-cavitating propellers for high-speed craft, with a reduction of blade erosion and possibly beneficial effects on noise emission.

The third symposium, in 1960, introduced a new feature, that of holding alternate meetings in countries outside the United States, which has been continued up to the present time and culminates in our presence here in Rome today. The third symposium was co-sponsored by ONR and the Netherlands Ship Model Basin, and had as its theme High-Performance Ships. It was dedicated to Sir Thomas Havelock, a world-famous figure in ship hydrodynamics, the dedication speech being made by Theodore von Karman. This present occasion is an additional opportunity to pay tribute to Havelock, who died a few weeks ago at the age of 91 after a long life dedicated very largely to the subject of these symposia.

The papers at the third symposium covered all types of craft—hydrofoil boats, hovercraft, deep-diving submarines, and submarine cargo ships and tankers. Mister Tulin underlined the severe problems which the designer faces in hydrofoil craft, including power plants, power transmission, structural strength, and propeller design, pointing out that the wing loadings are much higher than in aircraft and that such craft operate in a very hostile environment.

High-speed submarines introduced many critical control problems, and this symposium was marked by the description of new experimental techniques for carrying out research on models and new methods of analysis. A planar-motion mechanism, devised by Morton Gertler and Alex Goodman at the Taylor Model Basin, was described by Mister Goodman. That development enables coefficients to be measured which can then be applied in mathematical models to explore different maneuvers and arrangements of control surfaces. Replicas of this instrument are now in use in a number of towing tanks in Europe as well as in the United States.

In Washington in 1962 the themes were Propulsion, covering new theories of propeller design and fundamental differences in the method of operation of non-cavitating and fully cavitating propellers, and Hydroelasticity, dealing with forces on hydrofoils and control surfaces in fully cavitating and ventilated flow.

The fifth symposium, co-sponsored by ONR and the Norwegian Model Basin in Bergen, in 1964, was dedicated to a study of Ship Motions and Drag Reduction. Important papers dealt with the prediction of ship motions in waves, the application of seakeeping research results to design, and a new "force-pulse" testing technique for ship models in waves which made possible a great reduction in model testing time. Some of the problems of hydrofoil ships and hovercraft in waves were also discussed. Other papers described the results of original research in methods of reducing ship resistance by the use of additives to the water, by boundary layer suction, and by designing the hull form to ensure low wave-making resistance.

Interest in drag-reducing polymers was continued at the sixth symposium in 1966, together with discussion of problems in cavitation, maneuvering, and the effect of ocean waves on ship resistance and the towing of ocean platforms.

It is submitted that these symposia have been significant factors in contributing to the progress of hydrodynamics and have become patterns of the type of international scientific interaction that is so greatly needed in today's world of exploding technology.

It has long been recognized that—as then Foreign Minister Fanfani stated in his address to NATO on the Technology Gap—"on both sides of the Atlantic there exist discoveries that are officially of the public domain which cannot be usefully put to profit...due to a lack of complete information." These symposia and the outstanding proceedings which have resulted from them are significant contributions to the "efficient system for the exchange of information and knowledge" that the Foreign Minister called for.

The United States Office of Naval Research is proud to have long supported and contributed to effective exchange of scientific knowledge wherever and whenever possible. Science, of course, is mainly concerned with the secrets of nature which are revealed to and by the researcher. Today the relentless attack on nature's secrets goes on simultaneously in thousands of laboratories and research centers throughout the world. These numerous research programs are based on an extensive, freely available bank of knowledge, developed and verified through the ages.

It is, therefore, no surprise that a current line of research undertaken at one laboratory may be concurrently explored elsewhere or that the process in both instances can and will profit from timely exchange of findings. I believe it is also demonstrable that all parties benefit from such exchanges. When an investigator works in the dark, whether it be because of imposed secrecy or because of lack of adequate flow of information, the quality of his research is bound to decline. Free critical discussion and exposure to new ideas are powerful catalysts to creativity.

But research in itself is not sufficient; the results must be developed by engineering skills to the point where they can influence the design of new ships and weapons. Moreover, the needs in the application field can and must in their turn influence future research. In a gathering such as the one assembled here today, containing research workers, naval architects, and engineers, there is a wonderful opportunity for an exchange of views which cannot but exert a beneficial influence on the future.

As Commanding Officer of the Office of Naval Research Branch Office, London, I have observed and appreciated the enthusiasm and encouragement generated by the spirited exchanges between our liaison scientists and their European colleagues. Ours at ONR London is but a small effort but one which pays big dividends in improving scientific knowledge and in building mutual respect and lifelong friendships between scientists of many nations.

In fact, the Office of Naval Research, to a large extent, exists primarily in recognition of the catalysis provided through just such scientific interaction. This was a basic goal of the Act of Congress in 1946 that established the Office of Naval Research and charged ONR with covering worldwide trends in science and technology. Certainly, no better example can be found of an area of international and naval interest than hydrodynamics. We are, therefore, proud to have participated in each of these symposia and particularly happy to be able to welcome today so many outstanding attendees from so many countries to this Seventh Symposium in Rome.

Each of us here today has an opportunity to benefit personally from the new ideas that will be aired and the personal contacts that will be made. I trust that we will all take maximum advantage of our good fortune. The scheduled papers, the panel discussion periods, the coffee breaks, and the social program all promise stimulating activity.

It is extremely gratifying to Admiral Owen that this symposium is being sponsored by the Marina Militare Italiana and the Istituto Nazionale per Studi ed Esperienze di Architettura Navale di Roma, with the collaboration and under the auspices of the Consiglio Nazionale delle Richerche (National Council of Research).

The arduous tasks of organization, scheduling, ensuring that our fine authors get their papers in on time, and the myriad of other logistic details have fallen to our local hosts. By every indication they have been eminently successful. We of ONR are most appreciative of their labors and take pride in sharing their product.

On behalf of The Office of Naval Research and the United States Navy, I extend best wishes for a successful Seventh Symposium here in beautiful Rome and hope that this one will be followed by many more.

Monday, August 26, 1968

Morning Session

UNSTEADY PROPELLER FORCES

Chairmen: Ten. Gen. G. N. A. Siena

Ministero Difesa, Marina
Rome, Italy

and

W. P. A. Van Lammeren

Netherlands Ship Model Basin
Wageningen, The Netherlands

PRESSURE FIELD AROUND A PROPELLER OPERATING IN A SPATIALLY NONUNIFORM FLOW

V. F. Bavin, M. A. Vashkevich, and I. Y. Miniovich
Kryloff Ship Research Institute
Leningrad, U.S.S.R.

ABSTRACT

The theory for determining the pressures generated by a ship propeller is extended by deriving the relation between propeller-induced pressures and the circulation around the blade of a propeller operating in a wake.

Expressions are presented which make it possible to compute the amplitudes of blade-frequency pressure harmonics.

The calculations and experimental results show that an increase of 20 to 60 percent is possible over the maximum pressures generated by a propeller operating in a uniform flow.

INTRODUCTION

A number of theoretical and experimental studies concerned with the pressures induced by the propeller in the ambient fluid have been carried out in the past decade. An extensive bibliography and a review of the principal works on this subject published before 1964 have been given by Breslin (1,2). A comparison of theoretical and experimental results for the pressure generated by a ship propeller in a uniform flow (2) showed good agreement if the blade thickness contribution to the pressure field, as well as that of the blade loading, was taken into account.

In 1966 an investigation treating the pressure in the neighborhood of a propeller in uniform flow as a function of propeller geometry was completed in the Soviet Union. In this work a more consistent mathematical model was used than in earlier works by Breslin (1), Babaev (3), and Pohl (4); i.e., the propeller blade was replaced by a suitable distribution of vortices and sources over the part of a helical surface bounded by the blade contour, whereas in Ref. (1), for example, load-associated pressure was calculated in the usual lifting-line theory manner and the effect of blade thickness was estimated on the assumption of a zero-pitch propeller.

By using a more consistent mathematical model it became possible to study the influence of such propeller characteristics as blade area ratio and pitch

ratio on the fluctuating pressure amplitude; their influence turned out to be rather small. Experiments carried out in the Soviet Union confirmed the aforementioned conclusion about good agreement of experimental and theoretical values of pressures generated by a propeller in a uniform flow.

The effect of nonuniform inflow conditions on the propeller-induced pressure was first taken into account by Babaev (3). However, later experiments showed his equation to overestimate the nonuniformity contribution, due to some shortcomings in the underlying assumptions. A more general expression for the pressure generated by a propeller operating in a nonuniform flow is given in Ref. 5. It is based on the quasi-steady assumption; i.e., at a given circulation value the pressure induced by a propeller blade in a nonuniform flow is considered to be the same as in the case of a uniform flow. In 1963 Tsakonas, Breslin, and Jen concluded from their study (6) that the effect of a nonuniform inflow on the vibratory pressure is negligible at the propeller location and increases with distance from the propeller. The unsteady blade loading distribution was determined in this work approximately by applying results of unsteady two-dimensional airfoil theory.

In the present report the relation between fluctuating pressure and nonstationary circulation around the blade of a propeller operating in a nonuniform flow will be obtained. It will be shown that within linearized theory this relation remains the same as in the case of a uniform flow. Thus the abovementioned assumption made in Ref. 5 is proved to be valid. Equations will be given which make it possible to compute the amplitudes of the blade-frequency pressure harmonics for the propeller operating in a wake, provided the circulation on the blade is known.

Calculations performed by the authors indicate that maximum pressure values in a nonuniform inflow may increase to 1.6 times those in a uniform flow. The results of the blade-frequency pressure measurements are available.

PRESSURE FIELD AROUND A PROPELLER OPERATING IN A WAKE

Let us consider a z-bladed propeller advancing in the positive direction of the x axis and rotating at constant angular velocity around the x axis in a nonuniform flow (Fig. 1). The relative inflow velocity at the propeller location is equal to $(-V_p \cdot \mathbf{i} + \Delta v)$, where V_p is the mean axial velocity and Δv is the perturbation velocity induced by a ship hull. The perturbation velocity Δv is assumed to be a function of position only (i.e., independent of time) and small compared to V_p.

Nonuniform flow at the propeller leads to variation of the relative velocity and the angle of incidence of a blade section during propeller rotation. Hence, both constituents of the pressures produced by a propeller in nonuniform flow should differ from those attending propeller operation in uniform flow. However, it is evident from the equations for the blade-thickness constituents of the propeller-induced pressures (e.g., see Ref. 1) that for such thin bodies as propeller blades the effect of the nonuniform inflow conditions on the pressure

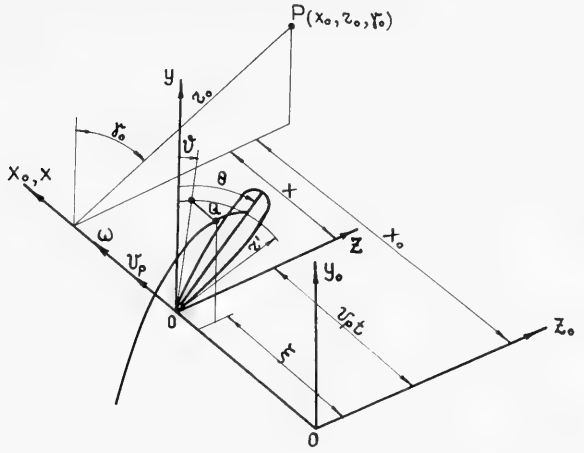

Fig. 1 - Coordinate systems and notations

arising from blade thickness is negligibly small. Therefore, only the influence of flow nonuniformity on the pressure due to loading will be treated.

Disregarding the physical effects which contribute to the origin of the nonuniform flow, we assume the fluid to be ideal. In addition we assume that the propeller-induced flow is potential. The vortex system of a propeller can be represented by: z radial bound vortices whose strength $\Gamma(r',t)$ depends on radial coordinate r' and time t; z helicoidal free vortex surfaces formed by helicoidal and radial vortices arising due to radial and temporal variation of Γ respectively. Propeller-induced velocities are assumed to be small compared to V_p and the pitch of helicoidal surface is taken to be constant and equal to $2\pi V_p/\omega$.

We define a cylindrical coordinate system x_0, r_0, γ_0 fixed in space and a system x, r, γ advancing along the x axis with a speed V_p (Fig. 1). The angular coordinate γ is measured in the direction of the propeller rotation.

The velocity potential of a single propeller blade can be written in terms of a distribution of doublets whose axes are perpendicular to the helicoidal surface swept out by the advancing lifting line. The strength of the doublets is equal to the discontinuity of the potential $[\Phi_L]$ between the upper and lower sides of the helical surface, so that one is led to

$$\Phi_L(x_0, r_0, \gamma_0, t) = -\frac{1}{4\pi} \int_0^{R_0} \int_0^{\infty} [\Phi_L] \sqrt{V_p^2 + (\omega r')^2} \frac{\partial}{\partial n} R^{-1} \, d\tau \, dr' ,$$

where

$$R = [(x_0 - V_p t + V_p \tau)^2 + r_0^2 + r'^2 - 2 r_0 r' \cos(\gamma_0 - \omega t + \omega\tau)]^{1/2}$$

is the distance between the field point $P(x_0, r_0, \gamma_0)$ and the point of helical surface Q whose coordinates are $\xi = V_p(t-\tau)$, r', and $\vartheta = \omega(t-\tau)$; τ is the time during which the lifting line has moved from point Q to its position at time t (Fig. 1); and n is the normal direction at point Q.

The magnitude of the potential discontinuity $[\Phi_L]$ at point Q equals the circulation around the circuit ℓ embracing the part of the helical surface between this point and the bound vortex (Fig. 2). If the surface on which the circuit ℓ lies is taken to cross the helicoidal surface along a helical line passing through the point Q, then the circulation in the circuit ℓ will be equal to the sum of the bound vortex strength $\Gamma(r', t)$ at time t and the total strength of all the free vortices distributed between the bound vortex and the point Q, i.e., radial free vortices shed by the blade during the time τ. But according to Thomson's theorem the aforementioned sum is equal to the strength of the bound vortex at time $(t-\tau)$ when the latter was at the point Q. Then $[\Phi_L] = \Gamma(r', t-\tau)$ and

$$\Phi_L = -\frac{1}{4\pi} \int_0^{R_0} \int_0^{\infty} \Gamma(r', t-\tau)\, D(x_0, \gamma_0)\, R^{-1}\, d\tau\, dr', \tag{1}$$

where (1)

$$D(x_0, \gamma_0) = \left(\omega r' \frac{\partial}{\partial x} - \frac{V_p}{r'} \frac{\partial}{\partial \gamma}\right).$$

In terms of the linearized theory the pressure at an arbitrary point of the field (exclusive of any hydrostatic increments) is

$$p_L = -\rho \frac{\partial \Phi_L}{\partial t}, \tag{2}$$

where ρ is the density of the fluid. Then

$$p_L = \frac{\rho}{4\pi} \frac{\partial}{\partial t} \int_0^{R_0} \int_0^{\infty} \Gamma(r', t-\tau)\, D(x_0, \gamma_0) \frac{1}{R(x_0, r_0, \gamma_0, t-\tau)}\, d\tau\, dr'$$

$$= -\frac{\rho}{4\pi} \int_0^{R_0} \int_0^{\infty} \frac{\partial}{\partial \tau} \left[\Gamma(r', t-\tau)\, D(x_0, \gamma_0)\, R^{-1}\right] d\tau\, dr'$$

$$= \frac{\rho}{4\pi} \int_0^{R_0} \Gamma(r', t) \frac{-\omega r'(x_0 - V_p t) + V_p r_0 \sin(\gamma_0 - \omega t)}{R^3_{\tau=0}}\, dr'.$$

Introduction of the coordinates $x = x_0 - V_p t$, $r = r_0$, and $\gamma = \gamma_0$ yields

$$p_L = \frac{\rho}{4\pi} \int_0^{R_0} \Gamma(r', \theta) \frac{-\omega r' x - V_p r \sin(\gamma - \theta)}{[x^2 + r^2 + r'^2 - 2rr' \cos(\gamma - \theta)]^{3/2}}\, dr', \tag{3}$$

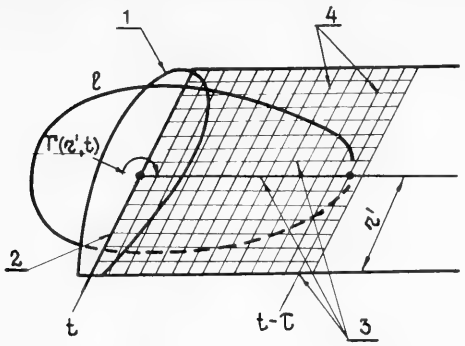

Fig. 2 - Propeller blade vortex system: 1, propeller blade; 2, bound vortex; 3, helicoidal free vortices; 4, radial free vortices

where $\theta = \omega t$.

Thus in the case of a lightly loaded propeller the pressure generated by a propeller blade in a nonuniform flow is related to the circulation in the same manner as in uniform-inflow conditions. The only difference lies in the fact that the constant circulation $\Gamma(r')$ is replaced by its instantaneous value $\Gamma(r',t)$. The latter in general should be determined taking into account the nonstationary flow conditions.

For a z-bladed propeller one obtains

$$p_L = \frac{\rho}{4\pi} \sum_{j=0}^{z-1} \int_0^{R_0} \Gamma\left(r', \theta + \frac{2\pi}{z} j\right) \frac{-\omega r' x + V_p r \sin\left(\gamma - \theta - \frac{2\pi}{z} j\right)}{\left[x^2 + r^2 + r'^2 - 2rr' \cos\left(\gamma - \theta - \frac{2\pi}{z} j\right)\right]^{3/2}} dr' .$$

Let us express the pressure in the dimensionless form:

$$\bar{p} = \frac{p}{\frac{P_0}{(\pi R_0^2)}} = \frac{p}{\frac{\rho V_p^2}{2} b_p},$$

where P_0 is the mean propeller thrust and $b_p = P_0/(\rho V_p^2/2)\pi R_0^2$ is the propeller loading coefficient; and let us nondimensionalize all lengths with respect to the propeller radius R_0.

Then we may write the expression for the propeller vibratory pressure due to loading:

$$\bar{p}_L(x,r,\gamma,\theta) = \frac{1}{2}\sum_{j=0}^{z-1}\int_0^1 \bar{\Gamma}\left(r',\ \theta+\frac{2\pi}{z}j\right) \times \frac{\left[-r'x+\frac{\lambda_p}{\pi}r\sin\left(\gamma-\theta-\frac{2\pi}{z}j\right)\right]}{\left[x^2+r^2+r'^2-2rr'\cos\left(\gamma-\theta-\frac{2\pi}{z}j\right)\right]^{3/2}}dr', \quad (4)$$

where $\lambda_p = \pi V_p/\omega R_0$ (advance ratio) and $\bar{\Gamma} = \Gamma/(2P_0/\rho\omega R_0^2)$.

The blade frequency content of the pressure can be determined (1) by making use of the relation

$$\frac{1}{R} = \frac{1}{\pi\sqrt{rr'}}\sum_{m=0}^{\infty}\varepsilon_m\theta_{m-1/2}(z)\cos m(\gamma-\theta),$$

where $\varepsilon_0 = 1$ and $\varepsilon_m = 2$; $Q_{m-(1/2)}(z)$ is the Legendre function of the second kind, of order $m-(1/2)$; and $z = (x^2+r^2+r'^2)/2rr'$.

The dimensionless circulation may be written in the form

$$\bar{\Gamma}(r',\theta) = \sum_{n=0}^{\infty}\left[A_n(r')\cos n\theta + B_n(r')\sin\theta\right].$$

Then for the nondimensional pressure after lengthy manipulations one obtains

$$\begin{aligned}\bar{p}_L = -\frac{z}{4\pi\sqrt{r}}\sum_{m=0}^{\infty}\sum_{n=0}^{\infty}\varepsilon_m\Bigg\{&\left(\frac{m\lambda_p N^A_{mn}}{\pi}-\frac{xK^B_{mn}}{r}\right)\sin\left[(m+n)\theta-m\gamma\right]\\ &-\left(\frac{m\lambda_p N^B_{mn}}{\pi}+\frac{xK^A_{mn}}{r}\right)\cos\left[(m+n)\theta-m\gamma\right]\\ &+\left(\frac{m\lambda_p N^A_{mn}}{\pi}+\frac{xK^B_{mn}}{r}\right)\sin\left[(m-n)\theta-m\gamma\right]\\ &-\left(-\frac{m\lambda_p N^B_{mn}}{\pi}+\frac{xK^A_{mn}}{r}\right)\cos\left[(m-n)\theta-m\gamma\right]\Bigg\}, \quad (5)\end{aligned}$$

where

$$N^A_{mn} = \int_0^1 \frac{A_n(r')\,\theta_{m-(1/2)}(z)}{r'^{3/2}}\,dr',$$

$$K^{B}_{mn} = \int_{0}^{1} \frac{B_n(r')\,\theta'_{m-(1/2)}(z)}{r'^{1/2}}\,dr' ,$$

and N^{B}_{mn} and K^{A}_{mn} are defined by analogous expressions. In the above formulas n and m have to satisfy the relations

$$\left.\begin{matrix} m + n \\ m - n \end{matrix}\right\} \pm \ell z$$

where $\ell = 1, 2, 3, \ldots$ is the harmonic number.

Although Eq. (4) is derived on the basis of lifting line theory, it can be easily extended for the case of a lifting surface propeller representation. However, in this case, to calculate the vibratory pressure one should know the chordwise distribution of the bound vorticity on the blade of a propeller operating in a wake.

NUMERICAL RESULTS AND COMPARISON WITH EXPERIMENTAL DATA

Calculations of the loading-induced pressure have been made by means of Eq. (4) to evaluate quantitatively the effect of inflow nonuniformity on the vibratory pressure generated by a propeller under different inflow conditions. Numerical computations have been performed with a digital computer. Nonstationary circulation around the blade section has been determined by the (3/4)-line method.

The calculations have shown that the most pronounced effect of the flow nonuniformity on the pressure amplitude is felt in the points of the hull with angular coordinates corresponding to the position of the blade under maximum loading conditions. Furthermore, the calculations confirmed the conclusion drawn in Ref. 6 that the influence of nonuniform inflow conditions on the pressure amplitude increases with distance from the propeller plane. This is explained by the fact that in nonuniform flow a propeller-induced pressure decays with distance from the propeller much more slowly than in the uniform flow.

The results of calculations of the pressure amplitudes generated by a five-bladed propeller on the hull of a single-screw ship are shown in Fig. 3. The amplitudes of the first and second harmonics of the blade-frequency pressure were calculated at the points immediately above the propeller, i.e., at the region of maximum blade loading. The calculated pressures were doubled to account for the hull surface effect. The amplitudes of the first harmonic were also computed assuming the propeller to operate in a circumferentially uniform flow with the radial distribution of velocities corresponding to that of a real wake (line 3 in Fig. 3). It is evident from Fig. 3 that in this particular case the effect of nonuniformity causes an increase of 40 to 60 percent over the pressures corresponding to the propeller operating in a circumferentially uniform flow.

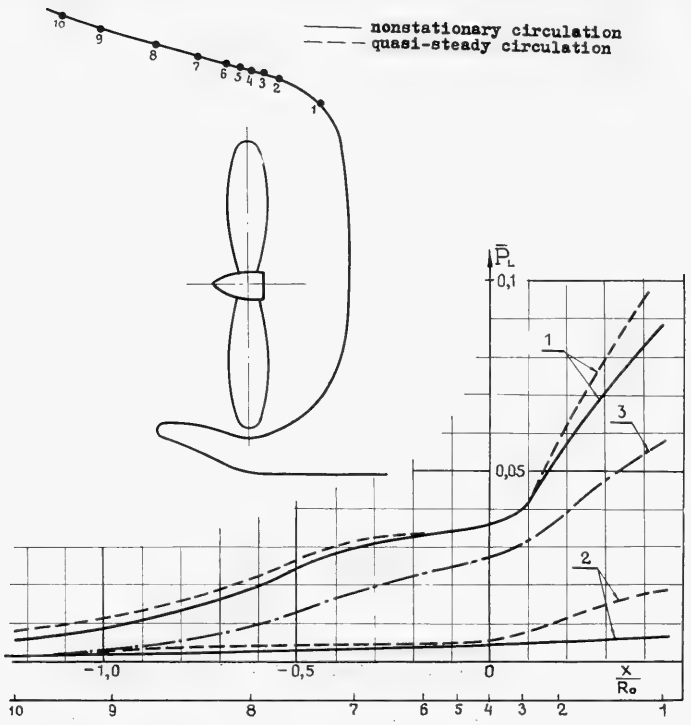

Fig. 3 - Effect of flow nonuniformity on pressures due to loading: 1, first harmonic; 2, second harmonic; 3, first harmonic for the case of a circumferentially uniform flow

The dashed lines in Fig. 3 correspond to the case when circulation around the blade of a propeller operating in a wake was calculated by means of the quasi-steady theory. It can be seen that percentagewise this method gives overestimated values of second-harmonic amplitudes, whereas the amplitudes of the first harmonic of the pressure remain almost the same as those corresponding to the nonstationary circulation. The conclusion that the amplitudes of higher pressure harmonics are overestimated when making use of quasi-steady circulation was confirmed by some other calculations.

It should be noted that for lightly and moderately loaded propellers the effect of nonuniform inflow conditions on the total pressure (both loading and thickness constituents) should be less pronounced than that on the loading-associated pressures only. For higher propeller loadings ($b_p > 1$) the total pressure practically is equal to its loading component.

Calculations of propeller-induced pressures for different wakes have shown that the maximum pressure amplitudes at some points of the hull surface can be

1.2 to 1.6 times greater than those calculated under the uniform inflow assumption. The lower limit corresponds to the case of a moderately nonuniform flow behind the hull of a twin-screw ship; the upper one corresponds to the case of a significantly nonuniform wake of a single-screw ship. These values are in agreement with the corresponding evaluations mentioned in Ref. 2.

A special experiment was carried out (by B. A. Biskup) in the cavitation tunnel to check the theoretically predicted effect of flow nonuniformity on the propeller-induced pressures. The amplitudes of pulsating pressures were measured with a three-bladed propeller operating both in the free stream and behind a screen generating a significantly nonuniform velocity field. The propeller geometry was: blade area ratio $A/A_d = 0.5$, pitch ratio $H/D = 1.2$, and thickness ratio $t_0/D = 0.05$. Measurements were made at a fixed radial distance $r = 1.2R_0$ and various axial distances from $-0.4R_0$ to $0.4R_0$. In the case of nonuniform flow, pressures were measured at two angular positions $\gamma = 0$ and $\gamma = \pi/2$, corresponding to the regions of maximum and minimum wake respectively. The results are presented in Fig. 4 (pressure amplitudes having been made dimensionless by division with $P_0/\pi R_0^2$). The dashed lines in Fig. 4 correspond to the calculated amplitudes of the first harmonic of the blade-frequency pressure. Loading-associated pressures were computed according to the equation given in the present report, whereas pressures due to the thickness effect were computed by means of a corresponding equation for a propeller operating in uniform flow.

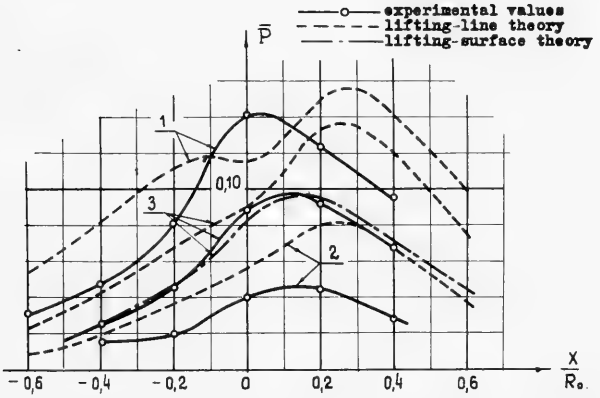

Fig. 4 - Effect of flow nonuniformity on pressures generated by a propeller operating behind a screen: 1, maximum wake; 2, minimum wake; 3, uniform inflow

It can be seen that the lifting-line representation of the propeller leads to overestimated (as compared with the experimental data) values of pressure amplitudes for the case of both nonuniform and uniform flow. Actually if the loading-associated pressure for the case of uniform flow is calculated according

to the equations for a wide-bladed propeller, the calculated pressure amplitudes are in perfect agreement with the experimental ones (see the dash-dot curve in Fig. 4). Corresponding calculations for the case of a propeller operating in a wake cannot be made at present because of the lack of precise knowledge of the chordwise distribution of the loading on the blade of a propeller operating in a nonuniform flow.

The curves in Fig. 5 show the relative effect of flow nonuniformity on pressure amplitudes for a propeller behind a screen. It can be seen that for this particular case the theory underestimates the relative effect as compared with the experimental data.

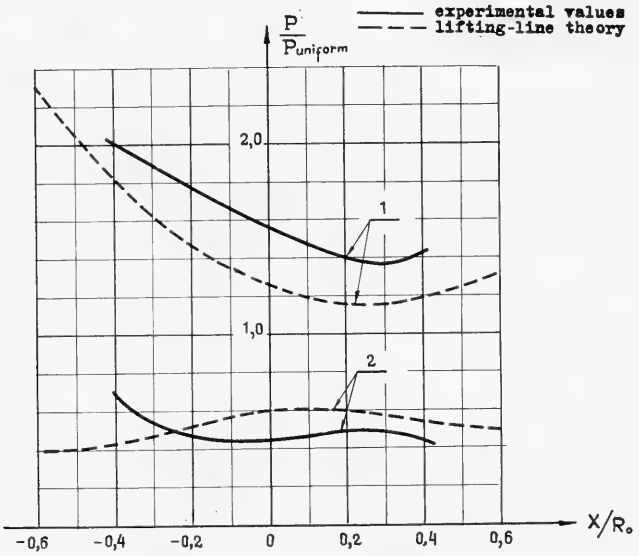

Fig. 5 - Relative effect of flow nonuniformity for a propeller behind a screen: 1, maximum wake; 2, minimum wake

A more complete experimental investigation of the effect of nonuniformity on vibratory pressures should be carried out in the future with propellers having various geometrical elements.

CONCLUSIONS

1. The equations derived in this paper make it possible to compute the amplitudes of the blade-frequency harmonics of the pressures generated by a ship propeller operating in a wake. It is shown that within linearized theory the relation between induced pressure and nonstationary circulation around the propeller blade remains the same as in the case of uniform flow conditions.

2. On the basis of the calculations made it is seen that the space-variable wake increases the pulsating pressures on a ship hull surface generated by a propeller. The magnitude of this increase depends upon the degree of nonuniformity of the inflow at the propeller location. The maximum pressure amplitudes at some points of the hull surface can be 1.2 to 1.6 times greater than those calculated under the uniform inflow assumption. The lower limit corresponds to the case of moderately nonuniform flow behind the hull of a twin-screw ship; the upper limit corresponds to the case of a significantly nonuniform wake behind a single-screw ship.

Calculations made by the authors confirm the conclusion of earlier work by Breslin and his colleagues that the space-variable inflow velocities are of greater relative importance as the distance from the propeller increases.

3. For a given wake distribution over the screw disk the smaller the propeller loading is, the more pronounced will be the pressure amplitude increase due to nonuniformity.

4. When calculating the pressures generated by a propeller in nonuniform flow one may use the quasi-steady values of circulation instead of nonstationary ones. The error involved by this substitution will be within the range of accuracy of the method based on the lifting-line representation of the propeller.

5. To calculate the pressures generated by a ship propeller in a nonuniform flow with greater accuracy it would be necessary to develop the method of calculation based on the nonstationary lifting-surface theory of propellers.

REFERENCES

1. Breslin, J. P., "Review and Extension of Theory for Near-Field Propeller-Induced Vibratory Effects," Fourth Symposium on Naval Hydrodynamics, Washington, 1962

2. Breslin, J. P., "Review of Theoretical Predictions of Vibratory Pressures and Forces Generated by Ship Propellers," Proceedings of the International Ship Structure Congress, Vol. 4, Delft, 1964

3. Babaev, N. N., and Lentjakov, V. G., "Some Aspects Concerning General Ship Vibration," Sudpromgiz, 1961

4. Pohl, K. H., "Das instationäre Druckfeld in der Umgebung eines Schiffspropellers und die von ihm auf Benachbarten Platten erzeugten periodischen Kräfte," Schiffstechnik, Vol. 32, June 1959

5. Basin, A. M. and Miniovich, I. Y., "Theory and Design of Ship Propellers," Sudpromgiz, 1963

6. Tsakonas, S., Breslin, J. P., and Jen. N., "Pressure Field Around a Marine Propeller Operating in a Wake," J. Ship Research 6, No. 4, 1963

DISCUSSION

G. G. Cox
Naval Ship Research and Development Center
Washington, D.C.

The excellent agreement between experimental measurements and lifting-surface calculations with uniform inflow shown in Fig. 4 is very encouraging, and the authors are thanked for their fine work. This result will surely stimulate continuing efforts to develop lifting-surface theory and numerical procedures for the varying wake situation.

Do the authors intend to study this problem where the wake contains tangentially varying components in addition to axially varying components? This would, of course, imply experimental measurements behind a ship model rather than a wake screen.

It has been our experience at the Naval Ship Research and Development Center that the theory for the freestream pressure field gave good results forward of the propeller but not aft. This is outside the slipstream and was traced to the loading effects. The thickness effects correlated very well.

* * *

DISCUSSION

J. P. Breslin
Davidson Laboratory, Stevens Institute of Technology
Hoboken, New York

This paper by Mr. Bavin and his colleagues is a welcome addition to the growing literature related to the excitation developed by propellers operating in nonuniform inflow. We at Stevens Institute have been devoting considerable effort on this problem. About 1960 I first became aware of the interesting coupling between the blade loading and the dipole propagation function in the propeller pressure field integral. The significance of this is that in principle all of the wake harmonics play a role in the makeup of the total blade frequency pressure. For example in the case of a single-screw ship with a three-bladed propeller the strong first, second, and fourth shaft harmonics of the wake will contribute in addition to the mean loading arising from the zero shaft harmonics. Thus these strong harmonics of the wake will contribute to the surface forces. In contrast the shaft forces and torques arise only from the second, third, and fourth harmonics of shaft frequency.

To give some idea of the importance of the various harmonics I have recently calculated the lateral form induced on a cylindrical hull by a propeller in a wake. Here the loading is taken from the solution by unsteady lifting surface theory carried out by S. Tsakonas and W. Jacobs.

I have only one question regarding the application of a factor of 2.0 to account for the effect of the ship model boundary, I am sure that Mr. Bavin well appreciates that this represents a rough approximation when the surface is not flat. Were all the data obtained on a stern frame line or on a flat boundary in the case of data with screens?

I agree with Mr. Bavin that the pressure field of a propeller in a wake requires the application of unsteady lifting surface theory. I wish the authors further successes in this work.

* * *

REPLY TO DISCUSSION

V. F. Bavin
Kryloff Ship Research Institute
Leningrad, U.S.S.R.

The authors are grateful to the contributors to the discussion for their interest in this work.

Replying to Mr. Cox we must note that when calculating vibratory pressures we took into account the tangential wake components as well as the axial ones (with the exception of the propeller behind the screen, because there was no tangential wake in that case).

Mr. Breslin draws attention to the fact that in principle all of the wake harmonics play a role in the makeup of the total blade frequency pressure. The authors are fully aware of this fact.

The authors agree with Mr. Breslin that the factor 2 is only a rough approximation in the case of an actual ship hull surface. It was used due to the lack of precise knowledge of the magnitude of the boundary surface effect.

In the case of the propeller operating behind the screen the pressures were measured in the free stream around the propeller and not on the hull surface.

* * *

THEORY OF UNSTEADY PROPELLER FORCES

Ryusuke Yamazaki
Kyushu University
Fukuoka, Japan

ABSTRACT

As the simplest example of the problem of unsteady propeller forces, a treatment is presented for a ship or a submarine with a single propeller and a single rudder being moved straight with a constant speed in unrestricted still water by rotating the propeller with a constant angular velocity. The velocity field is represented hydrodynamically by a potential due to distributions of sources, doublets, and vortex systems so as to satisfy the boundary conditions on the hull, the rudder, and the propeller in which mutual interactions among these three parts are generally taken into account. The unsteady propeller forces are subdivided into bearing forces, surface forces, and impulse forces, for which general mathematical expressions are obtained. Finally numerical examples are presented for the effects of propeller forms on the bearing forces.

INTRODUCTION

When a ship is being moved straight with an almost constant speed on or under still water by rotating the propeller steadily, the flow surrounding it fluctuates with respect to time, since the propeller with a finite number of blades is rotating in the nonuniform wake flow behind the hull. The unsteady forces and moments of water acting on the hull, rudder, and propeller caused by the rotating propeller are called unsteady propeller forces. The forces can be divided into two parts: one is the mean value of the forces with respect to time and is connected mainly with the propulsion characteristics of the ship, and the other is the fluctuating part of the forces whose magnitudes and periods are related mainly to the vibration of the ship. These unsteady propeller forces are transmitted to the ship hull either directly through a shaft bearing of the propeller or indirectly through surfaces of the hull, rudder, etc., in the form of water pressure. The former are called bearing forces, and the latter are called surface forces. In particular the forces and moments acting on bodies such as a rudder placed in the fluctuating propeller race may be called impulse forces (1). In the existing papers about the unsteady propeller theories (2-6) some examples of the bearing forces were calculated for given propellers in given nonuniform flows without taking into account the interactions with the hull and rudder. However, the surface forces on the hull were calculated for the case where the velocity field generated by the propeller replaced with simplified vortex lines satisfied the boundary condition on the hull surface (7). Accordingly, both forces

have not yet been obtained for the case where the velocity field around the ship satisfies the boundary conditions on the hull, rudder, and propeller simultaneously.

In my previous paper (8) a general hydrodynamical theory was developed for propulsion of a ship with a single propeller and a single rudder in which the mutual interactions among the hull, rudder, and propeller are generally taken into account. We will now develop this theory further for the computation of the unsteady propeller forces. At first we shall employ the following assumptions:

1. The field of fluid flow around the ship can be represented by an incompressible inviscid irrotational flow superposed linearly on a flow caused by viscosity such as the viscous wake behind the ship hull.

2. A discontinuous flow such as a flow containing a free vortex or cavity is not produced at the ship hull.

3. No cavitation is produced at the propeller and the rudder.

Then the ship speed can be assumed to be kept almost constant, because the inertia of the ship is very large and the periods of vibratory forces generated by the rotating propeller are very small. Similarly, the angular velocity of the propeller is assumed to be almost constant. Further, since the influence of the free water surface on the flow field around the ship can be generally represented by the velocity potentials due to appropriate distributions of singular points in the upper half space of unlimited still water (8), we may safely treat the problem of the ship moving on the surface of still water by replacing it with that of a submarine moving in unlimited water modified by superposing a flow field due to the added singular points. Thus, we can define clearly the unsteady propeller forces including both the surface and the bearing forces. Therefore, we will consider the submarine with a single propeller and a single rudder being moved straight with a constant speed by rotating the propeller with a constant angular velocity in unlimited still water as the simplest example and then derive a mathematical expression for the unsteady propeller forces in this case. Finally numerical examples will be presented to determine the effects of skew and chord length of the propeller on the bearing forces under a given nonuniform flow.

FUNDAMENTAL THEORY

Consider a submarine with a single propeller and a single rudder being moved straight with a constant velocity by rotating the propeller with a constant angular velocity in unlimited still water, for which the hydrodynamical theory presented in the previous paper (8) can be applied. We will use the term ship instead of submarine in the following for convenience.

At first we define a rectangular coordinate system $O - xyz$ fixed in space and a cylindrical coordinate system $O - xr\theta$ by the relations

$$x = x , \quad y = r \cos \theta , \quad z = r \sin \theta , \tag{1}$$

where the x and y axes are chosen so as to coincide with the axis of rotation of the propeller and with the upward vertical line respectively (Fig. 1). The ship is assumed to be advancing straight along the x axis in the negative direction with a constant velocity V as the result of rotating the propeller around the x axis with a constant angular velocity Ω in the negative direction of θ. Further we define another rectangular coordinate system $O_1 - x_1y_1z_1$ fixed to the ship satisfying the relations

$$x = x_1 - Vt \ , \quad y = y_1 \ , \quad z = z_1 \ , \tag{2}$$

where t is time and the origin O_1 is set at the representative point on the propeller axis. From Eq. (1) and (2), it follows that

$$x_1 = x_1 \ , \quad y_1 = r \cos\theta \ , \quad z_1 = r \sin\theta \ . \tag{3}$$

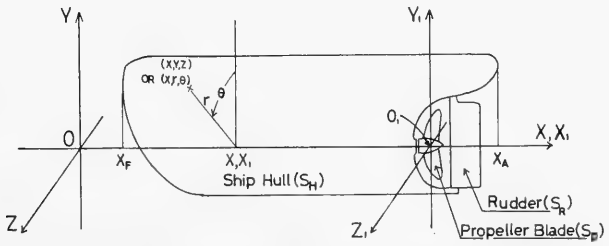

Fig. 1 - The ship with a propeller and rudder and the coordinate systems

Next let us consider the geometrical presentations of positions and shapes of the ship hull, propeller, and rudder. The hull, propeller, and rudder are assumed to be set roughly in order from the front. Generally the ship hull containing the propeller hub and bossing or strut is symmetrical with respect to the x_1y_1 plane, and the rudder is set in the vicinity of the x_1y_1 plane. The propeller consists of a set of identical, symmetrically spaced blades attached to the hub, having number of blades N, radius r_0, and hub radius r_B. Accordingly, the surface S_H of the ship hull can be expressed by

$$z_1 = (-1)^{\kappa-1} z_0(x_1, y_1) \ , \tag{4}$$

where

$$y_b(x_1) \le y_1 \le y_d(x_1) \ , \quad x_F \le x_1 \le x_A \ , \quad z_0(x_1, y_1) \ge 0 \ , \quad \kappa = 1, 2 \ .$$

The mean surface S_P of the kth blade of the propeller can be expressed by using the parameters r and v as follows:

$$x_1 = x_b(r, v) \ , \quad r = r \ , \quad \theta = \theta_M(r) + \bar{\theta}(r)\, v + 2\pi(k-1)/N - \Omega t \ , \tag{5}$$

where

$$-1 \le v \le 1 , \quad r_B \le r \le r_0 , \quad \bar{\theta}(r) \ge 0 , \quad k = 1, 2, \ldots, N ,$$

and $\bar{\theta}(r)$ and $\theta_M(r)$ are respectively the quantities related to the half chord length and the skew of the blade. The mean surface S_P can be approximated by a helical surface with pitch $2\pi a(r)$ and rake angle ε, that is, we have

$$x_b(r,v) \approx a(r) [\theta_M(r) + \bar{\theta}(r) v] + r\varepsilon , \tag{6}$$

where the more precise designation of $2\pi a(r)$ will be noted later on. Further the blade thickness at the point (r,v) on S_P is denoted by $t(r,v)$. Then the mean surface S_R of the rudder is expressed by using the parameters y_1 and u as follows:

$$x_1 = x_M(y_1) + \bar{x}(y_1) u , \quad y_1 = y_1 , \quad z_1 = z_R(y_1,u) , \tag{7}$$

where

$$-1 \le u \le 1 , \quad y_\ell \le y_1 \le y_u , \quad \bar{x}(y_1) \ge 0 , \quad x_M(y_1) - \bar{x}(y_1) > 0 ,$$

and $\bar{x}(y_1)$ and $x_M(y_1)$ are respectively the half chord length of the rudder and the distance between the propeller and the rudder. We can get approximately

$$z_R(y_1,u) \approx 0 , \quad \text{i.e.,} \quad \theta \approx 0 \quad \text{or} \quad \pi . \tag{8}$$

Further the rudder thickness at the point (y_1,u) on S_R is denoted by $t_R(y_1,u)$. Then the lines v or $u = 1$ and -1 on S_P or S_R indicate the trailing and leading edges of the propeller blade or rudder respectively. Equation (4) may be considered to represent either the original hull form or the hull form modified so as to include the effect of the boundary layer thickness, and in this paper, for simplicity, we carry forward the former.

Since no lift acts on the ship hull under the assumptions of the Introduction, the hull form can be represented hydrodynamically by source distribution on the surface S_H. We denote the strength of sources at time t in the elemental area on S_H, whose projection on the x_1y_1 plane is dx_1dy_1 by $m_\kappa(x_1,y_1,t)\, dx_1dy_1$, where the subscript κ refers to Eq. (4) and the value of $m_1(x_1,y_1,t)$ is not always equal to that of $m_2(x_1,y_1,t)$ because of the presence of the propeller. Thus the velocity potential ϕ_H due to the hull can be obtained from the source distributions. The propeller can be represented hydrodynamically by appropriate vortex systems and chordwisely distributed doublets. The former consist of the bound and free vortices, and the later represent the effect of the thickness of blade sections. The bound vortex is arranged approximately along the line v = constant over all the surface S_P, and the free vortex shed from the bound vortex flows with the velocity of the water at its position. However, as the result of observations on the experiments in cavitation tunnels, the geometrical form of the free vortex is not greatly disturbed by the presence of the hull and rudder, so that the free vortex can be assumed to extend rearward in a helicoid without contraction retaining

the pitch $2\pi h(r)$. Denoting the strength of the bound vortex in the elemental area at point (r,v) at time t by $\gamma_k(r,v,t)\,dvdr$, we can set

$$\gamma_k(r,v,t) = \gamma_1[r,v,t - 2\pi(k-1)/(N\Omega)] , \tag{9}$$

because the hydrodynamic state of flow field has the periodicity of period $2\pi/(N\Omega)$. The doublets representing the blade thickness are distributed on S_P in the chordwise direction, and their strengths are approximately proportional to the product of the blade thickness $t(r,v)$ and the chordwise component of the mean velocity, where the mean velocity is the velocity averaged over the chord of the blade section. The similar procedure can be applied for the rudder. That is, the bound vortex of the rudder is arranged approximately along the line u = constant on the x_1y_1 plane instead of the surface S_R, and its strength in the elemental area at point (y_1,u) at time t is denoted by $\gamma_R(y_1,u,t)\,dudy_1$. The free vortex shed from it extends straight rearward in the x_1y_1 plane. Further the rudder thickness can be represented by doublets distributed on the x_1y_1 plane in the x direction, whose strengths are approximately proportional to the product of the thickness $t_R(y_1,u)$ and the mean velocity component along the chord. Thus, denoting the velocity potentials due to the propeller and the rudder by ϕ_P and ϕ_R respectively, they can be obtained from the vortex systems and doublet distributions. By using subscripts ℓ and t for the vortex systems (load) and the doublet distributions (thickness) respectively, the total velocity potential ϕ at point (x,y,z) or (x,r,θ) at time t due to the ship hull, propeller, and rudder is

$$\phi = \phi_H + \phi_P + \phi_R , \quad \phi_P = \phi_{P\ell} + \phi_{Pt} , \quad \phi_R = \phi_{R\ell} + \phi_{Rt} . \tag{10}$$

Then denoting the velocity components induced by ϕ in the x, y, z, r, and θ directions by w_x, w_y, w_z, w_r, and w_θ respectively, we get

$$w_x = \frac{\partial\phi}{\partial x} , \quad w_y = \frac{\partial\phi}{\partial y} , \quad w_z = \frac{\partial\phi}{\partial z} , \quad w_r = \frac{\partial\phi}{\partial r} , \quad w_\theta = \frac{\partial\phi}{r\partial\theta} , \tag{11}$$

and the following relations among them are obtained:

$$w_r = w_y \cos\theta + w_z \sin\theta , \quad w_\theta = -w_y \sin\theta + w_z \cos\theta . \tag{12}$$

On the other hand we cannot neglect the effect of viscous velocity on the flow field around the actual ship, where the viscous velocity, i.e., the velocity caused by viscosity, is equal to the remainder obtained by subtracting the velocity induced by the velocity potential from the actual velocity; the viscous velocity appears in the boundary layer and wake of the hull. We denote the components of viscous velocity in the x, y, z, r, and θ directions by v_{1x}, v_{1y}, v_{1z}, v_{1r}, and $v_{1\theta}$ respectively and get the following relations among them:

$$v_{1r} = v_{1y} \cos\theta + v_{1z} \sin\theta , \quad v_{1\theta} = -v_{1y} \sin\theta + v_{1z} \cos\theta . \tag{13}$$

Further the condition of continuity must be satisfied as follows:

$$\frac{\partial v_{1x}}{\partial x} + \frac{\partial v_{1y}}{\partial y} + \frac{\partial v_{1z}}{\partial z} = \frac{\partial v_{1x}}{\partial x} + \frac{\partial v_{1r}}{\partial r} + \frac{v_{1r}}{r} + \frac{\partial v_{1\theta}}{r\partial\theta} = 0 . \tag{14}$$

To calculate these viscous velocity components we must require full knowledge of the three-dimensional turbulent boundary layer and turbulent wake, but we will not further refer to the problems in this paper. Moreover, if both the velocity induced by ϕ and the viscous velocity are small compared with the ship speed V, these velocities should approximately be superposed on each other.

For convenience, defining the nondimensional quantities

$$s = \Omega t, \quad \zeta = x/r_0, \quad \zeta_1 = x_1/r_0, \quad \eta = y/r_0, \quad \eta_1 = y_1/r_0, \quad z^* = z/r_0, \quad z_1^* = z_1/r_0,$$

$$\xi = r/r_0, \quad \zeta_A = x_A/r_0, \quad \zeta_F = x_F/r_0, \quad \eta_b(\zeta_1) = y_b(x_1)/r_0, \quad \eta_d(\zeta_1) = y_d(x_1)/r_0,$$

$$z_0^*(\zeta_1,\eta_1) = z_0(x_1,y_1)/r_0, \quad \xi_B = r_B/r_0, \quad \textcircled{\nu}(\xi) = a(x)/r_0, \quad \nu(\xi) = h(x)/r_0,$$

$$x_b^*(\xi,v) = x_b(r,v)/r_0, \quad \theta_M(\xi) = \theta_M(r), \quad \bar{\theta}(\xi) = \bar{\theta}(r), \quad t^*(\xi,v) = t(r,v)/r_0,$$

$$\delta_k = 2\pi(k-1)/N - \Omega t, \quad \eta_u = y_u/r_0, \quad \eta_\ell = y_\ell/r_0, \quad \zeta_M(\eta_1) = x_M(y_1)/r_0,$$

$$\bar{\zeta}(\eta_1) = \bar{x}(y_1)/r_0, \quad z_R^*(\eta_1,u) = z_R(y_1,u)/r_0, \quad t_R^*(\eta_1,u) = t_R(y_1,u)/r_0,$$

$$\nu_0 = V/(\Omega r_0), \quad m_\kappa^*(\zeta_1,\eta_1,s) = m_\kappa(x_1,y_1,t)/(\Omega r_0), \quad g_k(\xi,v,s) = \gamma_k(r,v,t)/(\Omega r_0^2),$$

$$g_R(\eta_1,u,s) = \gamma_R(y_1,u,t)/(\Omega r_0^2), \quad \phi^* = \phi/(\Omega r_0^2), \quad \phi_H^* = \phi_H/(\Omega r_0^2), \quad \phi_P^* = \phi_P/(\Omega r_0^2),$$

$$\phi_R^* = \phi_R/(\Omega r_0^2), \quad w_x^* = w_x/(\Omega r_0), \quad w_y^* = w_y/(\Omega r_0), \quad w_z^* = w_z/(\Omega r_0), \quad w_r^* = w_r/(\Omega r_0),$$

$$w_\theta^* = w_\theta/(\Omega r_0), \quad v_{1x}^* = v_{1x}/(\Omega r_0), \quad v_{1y}^* = v_{1y}/(\Omega r_0), \quad v_{1z}^* = v_{1z}/(\Omega r_0),$$

$$v_{1r}^* = v_{1r}/(\Omega r_0), \quad v_{1\theta}^* = v_{1\theta}/(\Omega r_0), \tag{15}$$

we obtain from Eqs. (2), (3), (12), and (13)

$$\zeta = \zeta_1 - \nu_0 s, \quad \eta = \eta_1 = \xi\cos\theta, \quad z^* = z_1^* = \xi\sin\theta,$$

$$w_r^* = w_y^*\cos\theta + w_z^*\sin\theta, \quad w_\theta^* = -w_y^*\sin\theta + w_z^*\cos\theta,$$

$$v_{1r}^* = v_{1y}^*\cos\theta + v_{1z}^*\sin\theta, \quad v_{1\theta}^* = -v_{1\theta}^*\sin\theta + v_{1z}^*\cos\theta. \tag{16}$$

The surface S_H of the ship hull is expressed from Eq. (4) as

$$\zeta = \zeta_1 - \nu_0 s, \quad \eta = \eta_1, \quad z^* = z_1^* = (-1)^{\kappa-1} z_0^*(\zeta_1,\eta_1), \tag{17}$$

where

$$\eta_b(\zeta_1) \le \eta_1 \le \eta_d(\zeta_1), \quad \zeta_F \le \zeta_1 \le \zeta_A, \quad z_0^*(\zeta_1,\eta_1) \ge 0, \quad \kappa = 1, 2,$$

and the mean surface S_P is represented from Eqs. (5) and (6) by

$$\zeta = \zeta_1 - \nu_0 s\,, \quad \zeta_1 = x_b^*(\xi, v) \approx \textcircled{\nu}(\xi)[\theta_M(\xi) + \bar{\theta}(\xi)\, v] + \xi\varepsilon\,,$$

$$\theta = \theta_M(\xi) + \bar{\theta}(\xi)\, v + \delta_k\,, \tag{18}$$

where

$$-1 \le v \le 1\,, \quad \xi_B \le \xi \le 1\,, \quad \bar{\theta}(\xi) > 0\,, \quad k = 1, 2, \ldots, N\,.$$

From Eqs. (7) and (8) the mean surface S_R is expressed as

$$\zeta = \zeta_1 - \nu_0 s\,, \quad \zeta_1 = \zeta_M(\eta_1) + \bar{\zeta}(\eta_1)\, u\,, \quad \eta = \eta_1\,, \quad z^* = z_1^* = z_R^*(\eta_1, u) \approx 0\,, \tag{19}$$

where

$$-1 \le v \le 1\,, \quad \eta_\ell \le \eta_1 \le \eta_u\,, \quad \bar{\zeta}(\eta_1) \ge 0\,, \quad \zeta_M(\eta_1) - \bar{\zeta}(\eta_1) > 0\,.$$

Since the thickness at the leading and trailing edges of the propeller blades and the rudder are zero, we get

$$t^*(\xi, \pm 1) = 0\,, \quad t_R^*(\eta_1, \pm 1) = 0\,, \tag{20}$$

and using Eqs. (15), Eq. (9) is rewritten as

$$g_k(\xi, v, s) \equiv g_1(\xi, v, -\delta_k)\,. \tag{21}$$

Further, the bound vortices must vanish on the trailing edge lines of the propeller blades and the rudder, since the extended Kutta's conditions must be satisfied there. They are assumed to vanish at the tips and roots of the propeller blades and at the upper and lower ends of the rudder. Thus the following relations are obtained:

$$g_k(\xi, 1, s) \equiv g_1(\xi, 1, -\delta_k) = 0\,, \quad g_R(\eta_1, 1, s) = 0\,, \tag{22}$$

$$g_k(1, v, s) = g_k(\xi_B, v, s) = 0\,, \quad g_R(\eta_u, u, s) = g_R(\eta_\ell, u, s) = 0\,. \tag{23}$$

Since the surface S_H is closed, the nondimensional source distributions representing the hull must satisfy the relation

$$\int_{\zeta_F}^{\zeta_A} d\zeta_1 \sum_{\kappa=1}^{2} \int_{\eta_b(\zeta_1)}^{\eta_d(\zeta_1)} m_\kappa^*(\zeta_1, \eta_1, s)\, d\eta_1 = 0\,. \tag{24}$$

The nondimensional velocity potential ϕ^* at point (ζ, η, z^*) or (ζ, ξ, θ) at nondimensional time s is obtained from Eq. (10) by using the results of the previous paper (8) as follows:

$$\phi^* = \phi^*_H + \phi^*_P + \phi^*_R , \quad \phi^*_P = \phi^*_{P\ell} + \phi^*_{Pt} , \quad \phi^*_R = \phi^*_{R\ell} + \phi^*_{Rt} , \tag{25}$$

where

$$\phi^*_H = - \frac{1}{4\pi} \int_{\zeta_F}^{\zeta_A} d\zeta'_1 \sum_{\kappa'=1}^{2} \int_{\eta_b(\zeta'_1)}^{\eta_d(\zeta'_1)} \frac{m^*_{\kappa'}(\zeta'_1, \eta'_1, s)}{\sqrt{(\zeta'_1 - \zeta - \nu_0 s)^2 + (\eta'_1 - \eta)^2 + [(-1)^{\kappa'-1} z^*_0(\zeta'_1, \eta'_1) - z^*]^2}} d\eta'_1 ,$$

$$\phi^*_{P\ell} = \frac{1}{4\pi} \int_{\xi_B}^{1} d\xi' \int_{-1}^{1} dv' \sum_{k'=1}^{N} \int_{0}^{\infty} g_1[\xi', v', -\delta_{k'} - \varphi/\varphi_0(\xi')] \left\{ \left[\xi' \frac{\partial}{\partial \zeta} - \frac{\nu(\xi')}{\xi'} \frac{\partial}{\partial \theta} + B^* \frac{\partial}{\partial \xi'_f} \right] \frac{1}{R^*} \right\}_{\xi'_f = \xi'} d\varphi ,$$

$$\phi^*_{Pt} = \frac{1}{4\pi} \int_{\xi_B}^{1} \bar{\theta}(\xi') \, d\xi' \int_{-1}^{1} t^*(\xi', v') \sum_{k'=1}^{N} W^*_1(\xi, -\delta_{k'}) \left[\frac{\partial}{\bar{\theta}(\xi') \partial v'} \frac{1}{R^*} \right]_{\xi'_f = \xi', \varphi = 0} dv' ,$$

$$\phi^*_{R\ell} = \frac{1}{4\pi} \int_{\eta_\ell}^{\eta_u} d\eta'_1 \int_{-1}^{1} du' \int_{0}^{\infty} \frac{g_R[\eta'_1, u', s - \varphi/\nu_x(\eta'_1)] \, z^*}{\sqrt{[\varphi + \zeta_M(\eta'_1) + \bar{\zeta}(\eta'_1) u' - \zeta - \nu_0 s]^2 + (\eta'_1 - \eta)^2 + z^{*2}}^3} d\varphi ,$$

$$\phi^*_{Rt} = - \frac{1}{4\pi} \int_{\eta_\ell}^{\eta_u} V^*_{Rx}(\eta'_1, s) \, \bar{\zeta}(\eta'_1) \, d\eta'_1 \int_{-1}^{1} \frac{t^*_R(\eta'_1, u')[\zeta_M(\eta'_1) + \bar{\zeta}(\eta'_1) u' - \zeta - \nu_0 s]}{\sqrt{[\zeta_M(\eta'_1) + \bar{\zeta}(\eta'_1) u' - \zeta - \nu_0 s]^2 + (\eta'_1 - \eta)^2 + z^{*2}}^3} du' ,$$

$$R^* = \sqrt{(\zeta'_f - \zeta)^2 + \xi'^2_f + \xi^2 - 2\xi'_f \xi \cos(\theta'_f - \theta)} ,$$

$$\zeta'_f = \nu(\xi) \varphi + \textcircled{\nu}(\xi') [\theta_M(\xi') + \bar{\theta}(\xi') v'] + \xi' \varepsilon - \nu_0 s , \quad \theta'_f = \varphi + \theta_M(\xi') + \bar{\theta}(\xi') v' + \delta_{k'} ,$$

$$B^* = \xi' \{ [\varphi + \theta_M(\xi') + \bar{\theta}(\xi') v'] d\nu(\xi')/d\xi' + \varepsilon \} , \quad \bar{\theta}(\xi) [\textcircled{\nu}(\xi)/\nu(\xi) - 1] < 2\pi/N . \tag{26}$$

From Eq. (11) the nondimensional components of the induced velocity are expressed by

$$w_x^* = \frac{\partial \phi^*}{\partial \zeta}, \quad w_y^* = \frac{\partial \phi^*}{\partial \eta}, \quad w_z^* = \frac{\partial \phi^*}{\partial z^*}, \quad w_r^* = \frac{\partial \phi^*}{\partial \xi}, \quad w_\theta^* = \frac{\partial \phi^*}{\xi \partial \theta}. \tag{27}$$

Then defining the nondimensional relative velocities of water to the propeller blade and the rudder as

$$V_x^* = \nu_0 + w_x^* + v_{1x}^*, \quad V_r^* = w_r^* + v_{1r}^*, \quad V_\theta^* = \xi + w_0^* + v_{1\theta}^*,$$

$$V_y^* = w_y^* + v_{1y}^*, \quad V_z^* = w_z^* + v_{1z}^*, \tag{28}$$

the quantities $\varphi_0(\xi)$, $\textcircled{\nu}(\xi)$, $W_k(\xi, s)$, $\nu_x(\eta_1)$, and $V_{Rx}^*(\eta_1, s)$ in Eqs. (26) are

$$V_{kx}^* = \frac{1}{\pi} \int_{-1}^{1} \sqrt{\frac{1-v}{1+v}} \left[V_x^*\right]_{(SP)} dv, \qquad V_{kr}^* = \frac{1}{\pi} \int_{-1}^{1} \sqrt{\frac{1-v}{1+v}} \left[V_r^*\right]_{(SP)} dv,$$

$$V_{k\theta}^* = \frac{1}{\pi} \int_{-1}^{1} \sqrt{\frac{1-v}{1+v}} \left[V_\theta^*\right]_{(SP)} dv, \quad V_{RX}^*(\eta_1, s) = \frac{1}{\pi} \int_{-1}^{1} \sqrt{\frac{1-u}{1+u}} \left[V_x\right]_{(SR)} du,$$

$$\nu_x(\eta_1) = \frac{1}{2\pi} \int_0^{2\pi} V_{Rx}^*(\eta_1, s)\, ds, \qquad \varphi_0 = \frac{1}{2\pi\xi} \int_0^{2\pi} V_{k\theta}^*\, ds,$$

$$\textcircled{\nu}(\xi) = \frac{1}{2\pi} \int_{-1}^{1} \sqrt{\frac{1+v}{1-v}} \frac{\partial x_b^*(\xi, s)}{\bar{\theta}(\xi)\, \partial v}\, dv,$$

$$W_k^*(\xi, s) \equiv W_1^*(\xi, -\delta_k) \approx \sqrt{V_{kx}^{*2} + V_{k\theta}^{*2}}, \tag{29}$$

and the quantity $\nu(\xi)$, which represents the nondimensional pitch of helical free vortex of the propeller, is

$$\nu(\xi) \approx \frac{1}{2} \left[\textcircled{\nu}(\xi) + \frac{1}{2\pi^2} \int_0^{2\pi} ds \int_{-1}^{1} \sqrt{\frac{1-v}{1+v}} \left[\nu_0 + \frac{\partial (\phi_H^* + \phi_R^*)}{\partial \zeta} + v_{1x}^* \right]_{(SP)} dv \Big/ \frac{1}{2\pi^2 \xi} \int_0^{2\pi} ds \int_{-1}^{1} \sqrt{\frac{1-v}{1+v}} \left[\xi + \frac{\partial (\phi_H^* + \phi_R^*)}{\xi \partial \theta} + v_{1\theta} \right]_{(SP)} dv \right], \tag{30}$$

where the symbols $[\ ]_{(SP)}$ and $[\ ]_{(S_R)}$ indicate that the quantities in the brackets at point (ζ, ξ, θ) on the surface S_P are represented by Eqs. (18) and at point (ζ, η, z^*) on the surface S_R are represented by Eqs. (19) respectively (9, 10). Further we may set approximately

$$\nu(\xi) \approx \text{(face pitch at } 0.7\, r_0)/2\pi \text{ or an appropriate constant.} \tag{31}$$

It is found from Eqs. (29) that the quantity $\pi\textcircled{\nu}(\xi)$ represents the pitch ratio of the zero lift line of the blade section at ξ.

Then we consider the boundary conditions satisfied on the hull surface S_H the mean surface S_P of the kth blade of the propeller, and the mean surface S_R of the rudder (8). Since the thickness of the boundary layer on the hull is considered to be very thin compared with the breadth of the hull, the viscous velocity may be neglected on the surface S_H. Thus we obtain the boundary condition on S_H as

$$\frac{m_k^*(\zeta_1,\eta_1,s)}{2} + (-1)^{\kappa-1}\left[w_z^*\right]_{(SH)} - \frac{\partial z_0^*(\zeta_1,\eta_1)}{\partial\zeta_1}\left[w_x^*\right]_{(SH)} - \frac{\partial z_0^*(\zeta_1,\eta_1)}{\partial\eta_1}\left[w_y^*\right]_{(SH)} = \nu_0\frac{\partial z_0^*(\zeta_1,\eta_1)}{\partial\zeta_1}, \tag{32}$$

where the symbol $[\ ]_{(SH)}$ indicates the quantity in the brackets at point (ζ,η,z^*) on the surface S_H are expressed by Eqs. (17). The viscous velocity, however, cannot be generally neglected in the wake behind the hull, so that the boundary conditions on the mean surfaces S_P and S_R are

$$\left[w_x^* + v_{1x}^*\right]_{(SP)} - \frac{\textcircled{\nu}(\xi)}{\xi}\left[w_\theta^* + v_{1\theta}^*\right]_{(SP)} - \left\{\left[\theta_M(\xi) + \bar{\theta}(\xi)v\right]\frac{d\textcircled{\nu}(\xi)}{d\xi} + \varepsilon\right\}$$

$$\left[w_r^* + v_{1r}^*\right]_{(SP)} = \frac{\partial x_b^*(\xi,v)}{\bar{\theta}(\xi)\partial v} - \nu_0, \tag{33}$$

$$\left[w_z^* + v_{1x}^*\right]_{(SR)} - \frac{\partial z_R^*(\eta_1,u)}{\bar{\zeta}(\eta_1)\partial u}\left[w_x^* + v_{1x}^*\right]_{(SR)} - \left\{\frac{\partial z_R^*(\eta_1,u)}{\partial\eta_1} - \left[\frac{d\zeta_M(\eta_1)}{d\eta_1} + \frac{d\bar{\zeta}(\eta_1)}{\partial\eta_1}u\right]\frac{\partial z_R^*(\eta_1,u)}{\bar{\zeta}(\eta_1)\partial u}\right\}\left[w_y^* + v_{1y}^*\right]_{(SR)} = \nu_0\frac{\partial z_R^*(\eta_1,u)}{\bar{\zeta}(\eta_1)\partial u}, \tag{34}$$

The nondimensional viscous velocity components v_{1x}^*, v_{1y}^*, v_{1z}^*, v_{1r}^*, and $v_{1\theta}^*$ are mainly produced by the hull, so that they can be assumed to be functions of ζ_1, η, and z^* and explicitly independent of s. And their vorticities are assumed to be very small. We denote the density of water, the water pressure, and the ambient pressure due to only the viscous velocity by ρ, p, and p_0 respectively and define the nondimensional pressures p^* and p_0^* as

$$p^* = p/(\rho\Omega^2 r_0^2), \quad p_0^* = p_0/(\rho\Omega^2 r_0^2). \tag{35}$$

We shall assume in this paper that the pressure p^* at any point at any time is given by the approximate equation

$$p^* \approx p_0^* + \nu_0 v_{1x}^* + \frac{1}{2}\left(v_{1x}^{*2} + v_{1y}^{*2} + v_{1z}^{*2}\right) - \frac{\partial \phi^*}{\partial s}$$

$$- \frac{1}{2}\left[\left(w_x^* + v_{1x}^*\right)^2 + \left(w_y^* + v_{1y}^*\right)^2 + \left(w_z^* + v_{1z}^*\right)^2\right] - \nu_0 v_{1x}^* \,. \tag{36}$$

In this equation the pressure near the hull is equal to that due to Bernoulli's theorem because of the absence of viscous velocity, and the pressure in the wake behind the hull is considered to be independent of the viscous velocity when the potential flow is negligibly small, because p_0 is almost constant according to the boundary layer and wake theory. However, strictly speaking, this pressure p_0 is not always a constant independent of time and position. Using Eq. (36) we can calculate the pressure on the surfaces of the hull, rudder, and propeller and, consequently, the forces and moments acting on the hull, rudder, and propeller.

We first consider the force and moment acting on the hull (8). Denoting for the x_1, y_1, and z_1 directions the components of the force due to pressure by F_{Hx0}, F_{Hy0}, and F_{Hz0} respectively, denoting the components of the moment due to pressure about the x_1, y_1, and z_1 axes by M_{Hx0}, M_{Hy0}, and M_{Hz0} respectively, defining nondimensional coefficients as

$$K_{HFx0} = F_{Hx0}/(\rho n_r^2 D^4) \,, \quad K_{HFy0} = F_{Hy0}/(\rho n_r^2 D^4) \,, \quad K_{HFz0} = F_{Hz0}/(\rho n_r^2 D^4) \,,$$

$$K_{HMx0} = M_{Hx0}/(\rho n_r^2 D^5) \,, \quad K_{HMy0} = M_{Hy0}/(\rho n_r^2 D^5) \,, \quad K_{HMz0} = M_{Hz0}/(\rho n_r^2 D^5) \,, \tag{37}$$

where

$$n_r = \Omega/2\pi \tag{38}$$

(revolutions per unit time) and $D = 2r_0$ (diameter), the nondimensional coefficients are expressed as follows:

$$K_{HFx0} = -\frac{\pi^2}{4}\int_{\zeta_F}^{\zeta_A} d\zeta_1 \sum_{\kappa=1}^{2} \int_{\eta_b(\zeta_1)}^{\eta_d(\zeta_1)} \left\{ m_\kappa^*(\zeta_1,\eta_1,s)\left[\nu_0 + \left[w_x^*\right]_{(SH)}\right] + \zeta_1 \partial m_\kappa^*(\zeta_1,\eta_1,s)/\partial s \right\} d\eta_1 \,,$$

$$K_{HFy0} = -\frac{\pi^2}{4}\int_{\zeta_F}^{\zeta_A} d\zeta_1 \sum_{\kappa=1}^{2} \int_{\eta_b(\zeta_1)}^{\eta_d(\zeta_1)} \left[m_\kappa^*(\zeta_1,\eta_1,s)\left[w_y^*\right]_{(SH)} + \eta_1 \partial m_\kappa^*(\zeta_1,\eta_1,s)/\partial s \right] d\eta_1 \,,$$

$$K_{HFz0} = -\frac{\pi^2}{4}\int_{\zeta_F}^{\zeta_A} d\zeta_1 \sum_{\kappa=1}^{2} \int_{\eta_b(\zeta_1)}^{\eta_d(\zeta_1)} \left[m_\kappa^*(\zeta_1,\eta_1,s)\left[w_z^*\right]_{(SH)} + (-1)^{\kappa-1} z_0^*(\zeta_1,\eta_1)\, \partial m_\kappa^*(\zeta_1,\eta_1,s)/\partial s \right] d\eta_1 \,, \tag{39}$$

(Cont)

$$K_{HMx0} = -\frac{\pi^2}{8}\int_{\zeta_F}^{\zeta_A} d\zeta_1 \sum_{\kappa=1}^{2} \int_{\eta_b(\zeta_1)}^{\eta_d(\zeta_1)} \Big\{ m_\kappa^*(\zeta_1,\eta_1,s)\Big[\eta_1\big[w_z^*\big]_{(SH)} - (-1)^{\kappa-1} z_0^*(\zeta_1,\eta_1)\big[w_y^*\big]_{(SH)}\Big] + \big[\partial\phi^*/\partial s\big]_{(SH)} (-1)^\kappa\big[\eta_1 + z_0^*(\zeta_1,\eta_1)\,\partial z_0^*(\zeta_1,\eta_1)/\partial\eta_1\big]\Big\} d\eta_1 ,$$

$$K_{HMy0} = -\frac{\pi^2}{8}\int_{\zeta_F}^{\zeta_A} d\zeta_1 \sum_{\kappa=1}^{2} \int_{\eta_b(\zeta_1)}^{\eta_d(\zeta_1)} \Big\{ m_\kappa^*(\zeta_1,\eta_1,s)\Big[(-1)^{\kappa-1} z_0^*(\zeta_1,\eta_1)\,\nu_0 + \big[w_x^*\big]_{(SH)} - \zeta_1\big[w_z^*\big]_{(SH)}\Big] + \big[\partial\phi^*/\partial s\big]_{(SH)} (-1)^{\kappa-1}\big[z_0^*(\zeta_1,\eta_1)\,\partial z_0^*(\zeta_1,\eta_1)/\partial\zeta_1 + \zeta_1\big]\Big\} d\eta_1 ,$$

$$K_{HMz0} = -\frac{\pi^2}{8}\int_{\zeta_F}^{\zeta_A} d\zeta_1 \sum_{\kappa=1}^{2} \int_{\eta_b(\zeta_1)}^{\eta_d(\zeta_1)} \Big\{ m_\kappa^*(\zeta_1,\eta_1,s)\Big[\zeta_1\big[w_y^*\big]_{(SH)} - \eta_1\big(\nu_0 + \big[w_x^*\big]\big)_{(SH)}\Big] + \big[\partial\phi^*/\partial s\big]_{(SH)}\Big[\zeta_1\,\partial z_0^*(\zeta_1,\eta_1)/\partial\eta_1 - \eta_1\,\partial z_0^*(\zeta_1,\eta_1)/\partial\zeta_1\Big]\Big\} d\eta_1 . \tag{39}$$

On the other hand, we must take account of the friction drag caused by viscosity in addition to the water pressure. So that, denoting the nondimensional components of the force and moment due to friction drag by K_{HFxD}, K_{HFyD}, K_{HFzD}, K_{HMxD}, K_{HMyD}, and K_{HMzD} similarly as in Eqs. (37), the nondimensional components K_{HFx}, K_{HFy}, K_{HFz}, K_{HMx}, K_{HMy}, and K_{HMz} of the total force and moment acting on the hull are given as

$$K_{HFx} = K_{HFx0} + K_{HFxD}, \quad K_{HFy} = K_{HFy0} + K_{HFyD}, \quad K_{HFz} = K_{HFz0} + K_{HFzD},$$
$$K_{HMx} = K_{HMx0} + K_{HMxD}, \quad K_{HMy} = K_{HMy0} + K_{HMyD}, \quad K_{HMz} = K_{HMz0} + K_{HMzD}. \tag{40}$$

Next we consider the force and moment acting on the rudder (8). The nondimensional bound vortex $g_R(\eta_1,u,s)$ can be expanded in the series of the appropriate functions of u as

$$g_R(\eta_1,u,s) = a_0^*(\eta_1,s)\sqrt{\frac{1-u}{1+u}} + a_1^*(\eta_1,s)\sqrt{1-u^2} + a_2^*(\eta_1,s)\,u\sqrt{1-u^2} + \cdots , \tag{41}$$

where $a_0^*(\eta_1,s)$, $a_1^*(\eta_1,s)$, etc., are functions of η_1 and s. Then we have

$$a_0^*(\eta_1,s) = \frac{1}{\sqrt{2}} \lim_{u\to -1} g_R(\eta_1,u,s)\sqrt{1+u} . \tag{42}$$

We denote the x_1, y_1, and z_1 components of the force by F_{Rx}, F_{Ry}, and F_{Rz} respectively, we denote the components of the moment about the x_1, y_1 and z_1 axes by M_{Rx}, M_{Ry}, and M_{Rz} respectively, and then we define the nondimensional coefficients as

$$K_{RFx} = F_{Rx}/(\rho n_r^2 D^4) , \quad K_{RFy} = F_{Ry}/(\rho n_r^2 D^4) , \quad K_{RFz} = F_{Rz}/(\rho n_r^2 D^4) ,$$

$$K_{RMx} = M_{Rx}/(\rho n_r^2 D^5) , \quad K_{RMy} = M_{Ry}/(\rho n_r^2 D^5) , \quad K_{RMz} = M_{Rz}/(\rho n_r^2 D^5) . \tag{43}$$

The total drag coefficient K_{RFx} is composed of four terms: the term due to the pressure difference between both sides of the mean surface K_{D1}, the term due to viscous drag K_{D2}, the term caused by the rudder thickness K_{D3}, and the term of the suction force at the leading edge K_S. Thus we get

$$K_{RFx} = K_{D1} + K_{D2} + K_{D3} - K_S , \tag{44}$$

where

$$K_{D1} = -\frac{\pi^2}{4} \int_{\eta_\ell}^{\eta_u} d\eta_1 \int_{-1}^{1} g_R(\eta_1, u, s) \left\{ \left[V_x^*\right]_{(SR)} - \left[\frac{d\zeta_M(\eta_1)}{d\eta_1} - \frac{d\bar{\zeta}(\eta_1)}{d\eta_1} u \right] \right.$$

$$\left. \left[V_y^*\right]_{(SR)} \right\} \frac{\partial z_R^*(\eta_1, u)}{\bar{\zeta}(\eta_1)\, \partial u} du ,$$

$$K_{D2} = \frac{\pi^2}{4} \int_{\eta_\ell}^{\eta_u} C_{RD} V_{Rx}^*(\eta_1, s)^2 \bar{\zeta}(\eta_1)\, d\eta_1 ,$$

$$K_{D3} = \frac{\pi^2}{4} \int_{\eta_\ell}^{\eta_u} V_{Rx}^*(\eta_1, s)\, d\eta_1 \int_{-1}^{1} t_R^*(\eta_1, u) \frac{\partial \left[V_x^*\right]_{(SR)}}{\partial u} du ,$$

$$K_S = \frac{\pi^3}{8} \int_{\eta_\ell}^{\eta_u} \frac{a_0^*(\eta_1, s)^2}{\bar{\zeta}(\eta_1)} d\eta_1 , \tag{45}$$

in which C_{RD} is the section viscous drag coefficient of the rudder. The section lift coefficient $C_{RL}(\eta_1, s)$ is expressed approximately as

$$C_{RL}(\eta_1, s) \approx \frac{1}{\bar{\zeta}(\eta_1)\, V_{Rx}^*(\eta_1, s)} \int_{-1}^{1} g_R(\eta_1, u, s)\, du . \tag{46}$$

Then we can set the coefficient C_{RD} in the form

$$C_{RD} = C_{RD0}(\eta_1) + a_R(\eta_1)[C_{RL}(\eta_1, s) - b_R(\eta_1)]^2 , \tag{47}$$

where $C_{RD0}(\eta_1)$, $a_R(\eta_1)$, and $b_R(\eta_1)$ are constants to be determined experimentally depending on the section shape and the surface roughness of the rudder. The nondimensional components of the force and moment acting on the rudder except K_{RFx} can be expressed approximately by only the terms due to the pressure difference of both sides of the mean surface S_R, since the terms caused by viscosity can be negligibly small. That is, we have, for example,

$$K_{RFz} \approx \frac{\pi^2}{4} \int_{\eta_\ell}^{\eta_u} d\eta_1 \int_{-1}^{1} g_R(\eta_1, u, s) \left\{ \left[V_x^*\right]_{(SR)} - \left[\frac{d\zeta_M(\eta_1)}{d\eta_1} + \frac{d\bar{\zeta}(\eta_1)}{d\eta_1} u \right] \left[V_y^*\right]_{(SR)} \right\} du ,$$

$$K_{RMx} \approx \frac{\pi^2}{8} \int_{\eta_\ell}^{\eta_u} \eta_1 d\eta_1 \int_{-1}^{1} g_R(\eta_1, u, s) \left\{ \left[V_x^*\right]_{(SR)} - \left[\frac{d\zeta_M(\eta_1)}{d\eta_1} + \frac{d\bar{\zeta}(\eta_1)}{d\eta_1} u \right] \left[V_y^*\right]_{(SR)} \right\} du . \quad (48)$$

Finally we consider the force and moment acting on the propeller (6, 8). Since the magnitude of the suction force at the leading edge of the propeller blade is considered to be much smaller or at most the same order compared with the section viscous drag, we may safely neglect it or take it to be included formally in the viscous drag in this paper. Since the blade surface is closed and the blade thickness is very thin, the direct effect of blade thickness on the forces is negligibly small. Thus the force and moment acting on the propeller are generated mainly by the vortex systems. We denote the components of the force in the x_1, y_1, and z_1 directions by F_x, F_y, and F_z respectively, we denote the components of the moment about the x_1, y_1, and z_1 axes by M_x, M_y, and M_z respectively, and we define the nondimensional coefficients as

$$K_{Fx} = F_x/(\rho n_r^2 D^4) , \quad K_{Fy} = F_y/(\rho n_r^2 D^4) , \quad K_{Fz} = F_z/(\rho n_r^2 D^4) ,$$

$$K_{Mx} = M_x/(\rho n_r^2 D^5) , \quad K_{My} = M_y/(\rho n_r^2 D^5) , \quad K_{Mz} = M_z/(\rho n_r^2 D^5) . \quad (49)$$

Then these coefficients are expressed as

$$K_{Fx} = \int_{\xi_B}^{1} d\xi \int_{-1}^{1} \sum_{k=1}^{N} K_x \, dv , \quad K_{Fy} = \int_{\xi_B}^{1} d\xi \int_{-1}^{1} \sum_{k=1}^{N} (K_r \cos\theta_b - K_\theta \sin\theta_b) \, dv ,$$

$$K_{Fz} = \int_{\xi_B}^{1} d\xi \int_{-1}^{1} \sum_{k=1}^{N} (K_r \sin\theta_b + K_\theta \cos\theta_b) \, dv , \quad K_{Mx} = \frac{1}{2} \int_{\xi_B}^{1} d\xi \int_{-1}^{1} \sum_{k=1}^{N} K_\theta \, \xi \, dv ,$$

$$K_{My} = \frac{1}{2} \int_{\xi_B}^{1} d\xi \int_{-1}^{1} \sum_{k=1}^{N} [K_x \xi \sin\theta_b - (K_r \sin\theta_b + K_\theta \cos\theta_b) \, x_b^*(\xi, v)] \, dv ,$$

$$K_{Mz} = \frac{1}{2} \int_{\xi_B}^{1} d\xi \int_{-1}^{1} \sum_{k=1}^{N} [-K_x \xi \cos\theta_b + (K_r \cos\theta_b - K_\theta \sin\theta_b) \, x_b^*(\xi, v)] \, dv , \quad (50)$$

where

$$x_b^*(\xi,v) \approx \textcircled{\nu}(\xi)[\theta_M(\xi)+\bar{\theta}(\xi)v] + \xi\varepsilon\,, \quad \theta_b = \theta_M(\xi) + \bar{\theta}(\xi)\,v + \delta_k\,,$$

$$K_x = K_{x0} + K_{xD}\,, \quad K_r = K_{r0} + K_{rD}\,, \quad K_\theta = K_{\theta 0} + K_{\theta D}\,,$$

$$K_{x0} = -\frac{\pi^2}{4}\, g_1(\xi,v,-\delta_k)\left\{\left[V_\theta^*\right]_{(SP)} - \xi\left[\frac{d\theta_m(\xi)}{d\xi} + \frac{d\bar{\theta}(\xi)}{d\xi}\,v\right]\left[V_r^*\right]_{(SP)}\right\}\,,$$

$$K_{r0} = \frac{\pi^2}{4}\, g_1(\xi,v,-\delta_k)\left\{\frac{\partial x_b^*(\xi,v)}{\partial\xi}\left[V_\theta^*\right]_{(SP)} - \xi\left[\frac{d\theta_M(\xi)}{d\xi} + \frac{d\bar{\theta}(\xi)}{d\xi}\,v\right]\left[V_x^*\right]_{(SP)}\right\},$$

$$K_{\theta 0} = \frac{\pi^2}{4}\, g_1(\xi,v,-\delta_k)\left[\left[V_x^*\right]_{(SP)} - \frac{\partial x_b^*(\xi,v)}{\partial\xi}\left[V_r^*\right]_{(SP)}\right],$$

$$K_{xD} = \frac{\pi^2}{8}\, C_{PD}\left\{1+\left[\textcircled{\nu}(\xi)/\xi\right]^2\right\}V_{k\theta}^*\, V_{kx}^*\,\xi\,\bar{\theta}(\xi)\,,$$

$$K_{rD} = \frac{\pi^2}{8}\, C_{PD}\left\{1+\left[\textcircled{\nu}(\xi)/\xi\right]^2\right\}V_{k\theta}^*\, V_{kr}^*\,\xi\,\bar{\theta}(\xi)\,,$$

$$K_{\theta D} = \frac{\pi^2}{8}\, C_{PD}\left\{1+\left[\textcircled{\nu}(\xi)/\xi\right]^2\right\}V_{k\theta}^{*2}\,\xi\,\bar{\theta}(\xi)\,, \tag{51}$$

and C_{PD} is the section viscous drag coefficient. The section lift coefficient $C_{kL}(\xi,s)$ of the kth blade can be obtained approximately as

$$C_{kL}(\xi,s) \equiv C_{1L}(\xi,-\delta_k) \approx \frac{1}{\bar{\theta}(\xi)\, W_1^*(\xi,-\delta_k)\sqrt{\xi^2+\textcircled{\nu}(\xi)^2}}\int_{-1}^{1} g_1(\xi,v,-\delta_k)\,dv\,. \tag{52}$$

Similarly as in Eq. (47) we can set the coefficient C_{PD} as

$$C_{PD} \approx C_{PD0}(\xi) + a_P(\xi)[C_{kL}(\xi,s) - b_P(\xi)]^2\,, \tag{53}$$

where $C_{PD0}(\xi)$, $a_P(\xi)$, and $b_P(\xi)$ are constants to be determined experimentally depending on the section shape and surface roughness. Denoting respectively the thrust and torque of propeller by T and Q, we get

$$T = -F_x\,, \quad Q = M_x\,. \tag{54}$$

Then defining the thrust coefficient C_T and torque coefficent C_Q as

$$C_T = T/(\rho n_r^2 D^4)\,, \quad C_Q = Q/(\rho n_r^2 D^5)\,, \tag{55}$$

we can obtain from Eqs. (52) and (47)

$$C_T = -K_{Fx}\,, \quad C_Q = K_{Mx}\,. \tag{56}$$

In calculating the integrals in the equations presented we must take finite parts or principal values for the improper integrals at the singular points or surfaces.

The angular velocity Ω of the propeller is to be determined for a given velocity V of the ship so as to satisfy the relation that the difference between the mean thrust of the propeller and the total mean resistance acting on the hull and rudder is equal to zero or to the external force acting on the ship through ropes, etc. On the other hand the nondimensional velocity components v_{1x}^*, v_{1y}^*, and v_{1z}^* are assumed to be given in this paper, though they are to be obtained experimentally or theoretically by using some other procedure. In actual calculations, first substituting Eqs. (25), (26), and (27) into Eqs. (32), (33) and (34), we can obtain the simultaneous equations for $m_\kappa(\zeta_1,\eta_1,s)$, $g_1(\xi,v,-\delta_k)$, and $g_R(\eta_1,u,s)$ and solve these equations by reference to Eqs. (28) and (29). Then by substituting these solutions into Eqs. (25), (26), and (27) the quantities $\partial\phi^*/\partial s$, w_x^*, w_y^*, and w_z^* are obtained at an arbitrary point (ζ,η,z^*) at an arbitrary nondimensional time s. Accordingly, we can get the pressure p^* in the water at (ζ_1,η,z^*) at s from Eq. (36). Further we can calculate the forces and moments acting on the hull, rudder, and propeller by using Eqs. (37) through (56).

SURFACE FORCES AND BEARING FORCES

In this section, by applying the theory developed in the previous section, the characteristics of a flow around a ship with a propeller and a rudder will be compared with those around a ship from which the propeller is taken off, and then the mathematical expressions will be derived for the unsteady propeller forces. In the following we shall omit, for the sake of simplicity, the adjective nondimensional for the nondimensional quantities defined in the previous section.

Let us first consider the case of a ship without a propeller, i.e., a ship composed of a hull and a rudder. Then the quantities in this case are distinguished from those for the ship with the rudder and the rotating propeller by using the superscript 0. Further, we can omit time s, since the quantities are independent of time. For example, $m_\kappa^*(\zeta_1,\eta_1,s)$, ϕ_H^*, K_{RFx}, etc., are expressed as $m_\kappa^{*0}(\zeta_1,\eta_1)$, ϕ_H^{*0}, K_{RFx}^0, etc., for a ship without a propeller. Thus we have

$$\phi_P^{*0} = 0\,, \quad \left[v_{1z}^{*0}\right]_{(SR)} = 0\,. \tag{57}$$

Hence, from Eqs. (25) and (26),

$$\phi^{*0} = \phi_H^{*0} + \phi_{R\ell}^{*0} + \phi_{Rt}^{*0}\,, \tag{58}$$

where

$$\phi_H^{*0} = -\frac{1}{4\pi}\int_{\zeta_F}^{\zeta_A} d\zeta_1' \sum_{\kappa'=1}^{2} \int_{\eta_b(\zeta_1)}^{\eta_d(\zeta_1)} m_{\kappa'}^{*0}(\zeta_1',\eta_1')\,\frac{1}{R_H^*}\,d\eta_1'\,, \tag{59}$$

(Cont)

$$\phi^{*0}_{R\ell} = -\frac{1}{4\pi}\int_{\eta_\ell}^{\eta_u} d\eta_1' \int_{-1}^{1} du' \int_0^\infty g_R^0(\eta_1', u') \frac{\partial}{\partial z^*}\frac{1}{R_R^*}\, d\varphi ,$$

$$\phi^{*0}_{Rt} = \frac{1}{4\pi}\int_{\eta_\ell}^{\eta_u} V^{*0}_{Rx}(\eta_1')\,\bar{\zeta}(\eta_1)\, d\eta_1' \int_{-1}^{1} t_R^*(\eta_1', u')\left[\frac{\partial}{\partial X_R^*}\frac{1}{R_R^*}\right]_{\varphi=0} du' ,$$

$$R_H^* = \sqrt{(\zeta_1' - \zeta - \nu_0 s)^2 + (\eta_1' - \eta)^2 + \left[(-1)^{\kappa'-1} z_0^*(\zeta_1', \eta_1') - z^*\right]^2} ,$$

$$X_R^* = \varphi + \zeta_M(\eta_1') + \bar{\zeta}(\eta_1')\, u' - \zeta - \nu_0 s , \quad R_R^* = \sqrt{X_R^{*2} + (\eta_1' - \eta)^2 + z^{*2}} , \tag{59}$$

and from Eqs. (26), (27), and (28) we get

$$V^{*0}_{Rx}(\eta_1) = \frac{1}{\pi}\int_{-1}^{1}\sqrt{\frac{1-u}{1+u}}\left(\nu_0 + \left[\frac{\partial \phi_H^{*0}}{\partial \zeta} + v^{*0}_{1x}\right]_{(SR)}\right) du . \tag{60}$$

Neglecting small quantities of higher orders, the boundary conditions of Eqs. (32) and (34) are rewritten

$$\frac{m_\kappa^{*0}(\zeta_1, \eta_1)}{2} + (-1)^{\kappa-1}\left[\frac{\partial \phi^{*0}}{\partial z^*}\right]_{(SH)} - \frac{\partial z_0^*(\zeta_1, \eta_1)}{\partial \zeta_1}\left[\frac{\partial \phi^{*0}}{\partial \zeta}\right]_{(SH)}$$

$$- \frac{\partial z_0^*(\zeta_1, \eta_1)}{\partial \eta_1}\left[\frac{\partial \phi^{*0}}{\partial \eta}\right]_{(SH)} = \nu_0 \frac{\partial z_0^*(\zeta_1, \eta_1)}{\partial \zeta_1} , \tag{61}$$

$$\left[\frac{\partial \phi^{*0}}{\partial z^*} + v^{*0}_{1z}\right]_{(SR)} - \frac{\partial z_R^*(\eta_1, u)}{\bar{\zeta}(\eta_1)\,\partial u}\left[\frac{\partial \phi^{*0}}{\partial \zeta} + v^{*0}_{1x}\right]_{(SR)} = \nu_0 \frac{\partial z_R^*(\eta_1, u)}{\bar{\zeta}(\eta_1)\,\partial u} . \tag{62}$$

Then the pressure p^{*0} is obtained from Eq. (36) by

$$p^{*0} = p_0^* + \frac{1}{2}\left(v^{*0\,2}_{1x} + v^{*0\,2}_{1y} + v^{*0\,2}_{1z}\right) - \frac{\partial \phi^{*0}}{\partial s} - \frac{1}{2}$$

$$\left[\left(\frac{\partial \phi^{*0}}{\partial \zeta} + v^{*0}_{1x}\right)^2 + \left(\frac{\partial \phi^{*0}}{\partial \eta} + v^{*0}_{1y}\right)^2 + \left(\frac{\partial \phi^{*0}}{\partial z^*} + v^{*0}_{1z}\right)^2\right] . \tag{63}$$

Here, of course, we can substitute theoretically

$$\frac{\partial \phi^{*0}}{\partial s} = \nu_0 \frac{\partial \phi^{*0}}{\partial \zeta} . \tag{64}$$

From Eqs. (39) the components of force and moment caused by water pressure acting on the hull surface are

$$K^0_{HFx0} = -\frac{\pi^2}{4}\int_{\zeta_F}^{\zeta_A} d\zeta_1 \sum_{\kappa=1}^{2} \int_{\eta_b(\zeta_1)}^{\eta_d(\zeta_1)} m^{*0}_{\kappa}(\zeta_1,\eta_1)\left(\nu_0 + \left[\frac{\partial \phi^{*0}}{\partial \zeta}\right]_{(SH)}\right) d\eta_1 ,$$

$$K^0_{HFy0} = -\frac{\pi^2}{4}\int_{\zeta_F}^{\zeta_A} d\zeta_1 \sum_{\kappa=1}^{2} \int_{\eta_b(\zeta_1)}^{\eta_d(\zeta_1)} m^{*0}_{\kappa}(\zeta_1,\eta_1)\left[\frac{\partial \phi^{*0}}{\partial \eta}\right]_{(SH)} d\eta_1 ,$$

$$K^0_{HFz0} = -\frac{\pi^2}{4}\int_{\zeta_F}^{\zeta_A} d\zeta_1 \sum_{\kappa=1}^{2} \int_{\eta_b(\zeta_1)}^{\eta_d(\zeta_1)} m^{*0}_{\kappa}(\zeta_1,\eta_1)\left[\frac{\partial \phi^{*0}}{\partial z^*}\right]_{(SH)} d\eta_1 ,$$

$$K^0_{HMx0} = -\frac{\pi^2}{8}\int_{\zeta_F}^{\zeta_A} d\zeta_1 \sum_{\kappa=1}^{2} \int_{\eta_b(\zeta_1)}^{\eta_d(\zeta_1)} m^{*0}_{\kappa}(\zeta_1,\eta_1)\left[\eta_1\left[\frac{\partial \phi^{*0}}{\partial z^*}\right]_{(SH)} + (-1)^{\kappa} z^*_0(\zeta_1,\eta_1)\left[\frac{\partial \phi^{*0}}{\partial \eta}\right]_{(SH)}\right] d\eta_1 ,$$

$$K^0_{HMy0} = -\frac{\pi^2}{8}\int_{\zeta_F}^{\zeta_A} d\zeta_1 \sum_{\kappa=1}^{2} \int_{\eta_b(\zeta_1)}^{\eta_d(\zeta_1)} m^{*0}_{\kappa}(\zeta_1,\eta_1) \left[(-1)^{\kappa-1} z^*_0(\zeta_1,\eta_1)\left(\nu_0 + \left[\frac{\partial \phi^{*0}}{\partial \zeta}\right]_{(SH)}\right) - \zeta_1\left[\frac{\partial \phi^{*0}}{\partial z^*}\right]_{(SH)}\right] d\eta_1 ,$$

$$K^0_{HMz0} = -\frac{\pi^2}{8}\int_{\zeta_F}^{\zeta_A} d\zeta_1 \sum_{\kappa=1}^{2} \int_{\eta_b(\zeta_1)}^{\eta_d(\zeta_1)} m^{*0}_{\kappa}(\zeta_1,\eta_1) \left[\zeta_1\left[\frac{\partial \phi^{*0}}{\partial \eta}\right]_{(SH)} - \eta_1\left(\nu_0 + \left[\frac{\partial \phi^{*0}}{\partial \zeta}\right]_{(SH)}\right)\right] d\eta_1 . \tag{65}$$

Further, since the flow streaming into the rudder is parallel to the xy plane, we have in Eq. (44)

$$K^0_{D1} - K^0_s = 0 . \tag{66}$$

Hence, from Eqs. (44), (45), and (48) we get

$$K^0_{RFx} = K^0_{D2} + K^0_{D3} ,$$

$$K^0_{RFz} = \frac{\pi^2}{4} \int_{\eta_\ell}^{\eta_u} d\eta_1 \int_{-1}^{1} g_R^0(\eta_1,u) \left(\nu_0 + \left[\frac{\partial \phi^{*0}}{\partial \zeta} + v^{*0}_{1x} \right]_{(SR)} \right) du ,$$

$$K^0_{RMx} = \frac{\pi^2}{8} \int_{\eta_\ell}^{\eta_u} \eta_1 d\eta_1 \int_{-1}^{1} g_R^0(\eta_1,u) \left(\nu_0 + \left[\frac{\partial \phi^{*0}}{\partial \zeta} + v^{*0}_{1x} \right]_{(SR)} \right) du , \tag{67}$$

where

$$K^0_{D2} = \frac{\pi^2}{4} \int_{\eta_\ell}^{\eta_u} C^0_{RD} V^{*0}_{Rx}(\eta_1)^2 \bar{\zeta}(\eta_1)\, d\eta_1 ,$$

$$K^0_{D3} = \frac{\pi^2}{4} \int_{\eta_\ell}^{\eta_u} V^{*0}_{Rx}(\eta_1) \bar{\zeta}(\eta_1)\, d\eta_1 \int_{-1}^{1} t^*_R(\eta_1,u) \left[\frac{\partial^2 \phi^{*0}_H}{\partial \zeta_1^2} \quad \frac{\partial v^{*0}_{1x}}{\partial \zeta_1} \right]_{(SR)} du . \tag{68}$$

To compare the performance characteristics of a ship with a propeller and rudder with those of a ship without a propeller, we define the quantities

$$\Phi = \phi^* - \phi^{*0} = \Phi_H + \Phi_{R\ell} + \Phi_{Rt} + \phi^*_P ; \quad \Phi_H = \phi^*_H - \phi^{*0}_H , \quad \Phi_{R\ell} = \phi^*_{R\ell} - \phi^{*0}_{R\ell} , \quad \Phi_{Rt} = \phi^*_{Rt} - \phi^{*0}_{Rt} ,$$

$$\tilde{m}^*_\kappa(\zeta_1,\eta_1,s) = m^*_\kappa(\zeta_1,\eta_1,s) - m^{*0}_\kappa(\zeta_1,\eta_1) , \quad \tilde{g}_R(\eta_1,u,s) = g_R(\eta_1,u,s) - g^0_R(\eta_1,u) ,$$

$$\tilde{a}^*_0(\eta_1,s) = a^*_0(\eta_1,s) - a^{*0}_0(\eta_1) , \quad \tilde{V}^*_{Rx}(\eta_1,s) = V^*_{Rx}(\eta_1,s) - V^{*0}_{Rx}(\eta_1) , \quad \tilde{C}_{RD} = C_{RD} - C^0_{RD} ,$$

$$\tilde{v}^*_{1x} = v^*_{1x} - v^{*0}_{1x} , \quad \tilde{v}^*_{1y} = v^*_{1y} - v^{*0}_{1y} , \quad \tilde{v}^*_{1z} = v^*_{1z} - v^{*0}_{1z} , \quad \tilde{v}^*_{1r} = v^*_{1r} - v^{*0}_{1r} , \quad \tilde{v}^*_{1\theta} = v^*_{1\theta} - v^{*0}_{1\theta} . \tag{69}$$

Then, from Eq. (42) we have

$$a^{*0}_0(\eta_1) = \frac{1}{\sqrt{2}} \lim_{u \to -1} g_R^0(\eta_1,u) \sqrt{1+u} , \quad \tilde{a}^*_0(\eta_1,s) = \frac{1}{\sqrt{2}} \lim_{u \to -1} \tilde{g}_R(\eta_1,u,s) \sqrt{1+u} . \tag{70}$$

Assuming for simplicity that the pitch of the helical free vortex shed from the propeller is constant radially, and considering that the period of variation of its strength with respect to time s is 2π, we can set

$$\textcircled{\nu}(\xi) \approx \nu(\xi) \approx \nu , \quad \varphi_0(\xi') \approx 1 . \tag{71}$$

Then Eqs. (18) are rewritten as

$$\zeta_1 = x^*_b(\xi,v) \approx \nu[\theta_M(\xi) + \bar{\theta}(\xi) v] + \xi\varepsilon , \quad \theta = \theta_M(\xi) + \bar{\theta}(\xi) v + \delta_k , \tag{72}$$

where

$$-1 \le v \le 1\,, \quad \xi_B \le \xi \le 1\,,$$

and we get from Eqs. (25) and (26)

$$\phi_P^* = \phi_{P\ell}^* + \phi_{Pt}^*\,, \tag{73}$$

where

$$\phi_{P\ell}^* = -\frac{1}{4\pi}\int_{\xi_B}^{1} d\xi' \int_{-1}^{1} dv' \sum_{k'=1}^{N} \int_0^{\infty} g_1(\xi', v', -(\varphi + \delta_{k'}))\left(\xi' \frac{\partial}{\partial X^*} - \frac{\nu}{\xi'}\frac{\partial}{\partial \Theta^*}\right)\frac{1}{R^*}\, d\varphi\,,$$

$$\phi_{Pt}^* = \frac{1}{4\pi}\int_{\xi_B}^{1} \bar{\theta}(\xi')\, d\xi' \int_{-1}^{1} t^*(\xi', v') \sum_{k'=1}^{N} W_1^*(\xi', -\delta_{k'})\left[\left(\nu\frac{\partial}{\partial X^*} + \frac{\partial}{\partial \Theta^*}\right)\frac{1}{R^*}\right]_{\varphi=0} dv'\,,$$

$$X^* = \nu[\varphi + \theta_M(\xi') + \bar{\theta}(\xi')\, v'] - \zeta - \nu_0 s\,,$$

$$\Theta^* = \theta_f' - \theta\,, \quad \theta_f' = \varphi + \theta_M(\xi') + \bar{\theta}(\xi')\, v' + \delta_{k'}\,,$$

$$R^* = \sqrt{X^{*2} + \xi'^2 + \xi^2 - 2\xi'\xi\cos\Theta^*}\,. \tag{74}$$

Further, from Eqs. (25), (26), (29), and (69),

$$\Phi_H = -\frac{1}{4\pi}\int_{\zeta_F}^{\zeta_A} d\zeta_1' \sum_{\kappa'=1}^{2} \int_{\eta_b(\zeta_1')}^{\eta_d(\zeta_1')} \tilde{m}_{\kappa'}^*(\zeta_1', \eta_1', s)\frac{1}{R_H^*}\, d\eta_1'\,,$$

$$\Phi_{R\ell} = -\frac{1}{4\pi}\int_{\eta_\ell}^{\eta_u} d\eta_1' \int_{-1}^{1} du' \int_0^{\infty} \tilde{g}_R(\eta_1', u', s - \varphi/\nu_x(\eta_1'))\frac{\partial}{\partial z^*}\frac{1}{R_R^*}\, d\varphi\,,$$

$$\Phi_{Rt} = \frac{1}{4\pi}\int_{\eta_\ell}^{\eta_u} \tilde{V}_{Rx}^*(\eta_1', s)\,\bar{\zeta}(\eta_1')\, d\eta_1' \int_{-1}^{1} t_R^*(\eta_1', u')\left[\frac{\partial}{\partial X_R^*}\frac{1}{R_R^*}\right]_{\varphi=0} du'\,,$$

$$\tilde{V}_{Rx}^*(\eta_1, s) = \frac{1}{\pi}\int_{-1}^{1}\sqrt{\frac{1-u}{1+u}}\left[\tilde{v}_{1x}^* + \frac{\partial(\phi_P^* + \Phi_H)}{\partial\zeta}\right]_{(SR)} du\,,$$

$$\nu_x(\eta_1) = V_{Rx}^{*0}(\eta_1) + \frac{1}{2\pi}\int_0^{2\pi} \tilde{V}_{Rx}^*(\eta_1, s)\, ds\,. \tag{75}$$

Then from Eqs. (27), (28), and (69) Eqs. (29) and (30) are rewritten

$$V^*_{kx} = \frac{1}{\pi}\int_{-1}^{1}\sqrt{\frac{1-v}{1+v}}\left(\nu_0 + \left[\frac{\partial\phi^{*0}}{\partial\zeta} + \frac{\partial\Phi}{\partial\zeta} + v^{*0}_{1x} + \tilde{v}^*_{1x}\right]_{(SP)}\right)dv ,$$

$$V^*_{k\theta} = \frac{1}{\pi}\int_{-1}^{1}\sqrt{\frac{1-v}{1+v}}\left(\xi + \left[\frac{\partial\phi^{*0}}{\xi\partial\theta} + \frac{\partial\Phi}{\xi\partial\theta} + v^{*0}_{1\theta} + \tilde{v}^*_{1\theta}\right]_{(SP)}\right)dv ,$$

$$W^*_1(\xi,-\delta_k) = \sqrt{V^{*2}_{kx} + V^{*2}_{k\theta}} , \quad \textcircled{v}(\xi) = \frac{1}{\pi}\int_{-1}^{1}\sqrt{\frac{1+v}{1-v}}\frac{\partial x^*_b(\xi,v)}{\bar{\theta}(\xi)\,\partial v}dv ,$$

$$\nu \approx \frac{1}{2}\left[\textcircled{v}(\xi) + \frac{1}{2\pi^2}\int_0^{2\pi}ds\int_{-1}^{1}\sqrt{\frac{1-v}{1+v}}\left\{\nu_0 + \left[\frac{\partial\phi^{*0}}{\partial\zeta} + \frac{\partial(\Phi_H+\Phi_{R\ell}+\Phi_{Rt})}{\partial\zeta} + v^{*0}_{1x} + \tilde{v}^*_{1x}\right]_{(SP)}\right\}dv\right.$$

$$\left.\frac{1}{2\pi^2\xi}\int_0^{2\pi}ds\int_{-1}^{1}\sqrt{\frac{1-v}{1+v}}\left\{\xi + \left[\frac{\partial\phi^{*0}}{\xi\partial\theta} + \frac{\partial(\Phi_H+\Phi_R+\Phi_{Rt})}{\xi\partial\theta} + v^{*0}_{1\theta} + \tilde{v}^*_{1\theta}\right]_{(SP)}\right\}dv\right]_{\xi=\sqrt{(1+\xi_B^2)/2}} . \tag{76}$$

By reference to Eqs. (69), (61), and (62), the boundary conditions of Eqs. (32) and (34) are rewritten

$$\frac{\tilde{m}^*_\kappa(\zeta_1,\eta_1,s)}{2} + (-1)^{\kappa-1}\left[\frac{\partial\Phi}{\partial z^*}\right]_{(SH)} - \frac{\partial z^*_0(\zeta_1,\eta_1)}{\partial\zeta_1}\left[\frac{\partial\Phi}{\partial\zeta}\right]_{(SH)} - \frac{\partial z^*_0(\zeta_1,\eta_1)}{\partial\eta_1}\left[\frac{\partial\Phi}{\partial\eta}\right]_{(SH)} = 0 , \tag{77}$$

$$\left[\frac{\partial\Phi}{\partial z^*} + \tilde{v}^*_{1z}\right]_{(SR)} - \frac{\partial z^*_R(\eta_1,u)}{\bar{\zeta}(\eta_1)\,\partial u}\left[\frac{\partial\Phi}{\partial\zeta} + \tilde{v}^*_{1x}\right]_{(SR)} = 0 . \tag{78}$$

And the boundary condition of Eq. (33) on the propeller blade is rewritten

$$\left[\frac{\partial\Phi}{\partial\zeta} + \frac{\partial\phi^{*0}}{\partial\zeta} + v^{*0}_{1x} + \tilde{v}^*_{1x}\right]_{(SP)} - \frac{\nu}{\xi}\left[\frac{\partial\Phi}{\xi\partial\theta} + \frac{\partial\phi^{*0}}{\xi\partial\theta} + v^{*0}_{1\theta} + \tilde{v}^*_{1\theta}\right]_{(SP)} = \frac{\partial x^*_b(\xi,v)}{\bar{\theta}(\xi)\,\partial v} - \nu_0 . \tag{79}$$

The difference of water pressure between the case of the ship with a propeller and rudder and that of the ship without a propeller, which is denoted by Δp^*, is expressed from Eqs. (36), (63), and (69) as

$$\tilde{p}^* \equiv p^* - p^{*0}$$

$$= -\frac{\partial \Phi}{\partial s} - \left[\left(\frac{\partial \phi^{*0}}{\partial \zeta} + v^{*0}_{1x}\right)\left(\frac{\partial \Phi}{\partial \zeta} + \tilde{v}^*_{1x}\right) + \left(\frac{\partial \phi^{*0}}{\partial \eta} + v^{*0}_{1y}\right)\left(\frac{\partial \Phi}{\partial \eta} + \tilde{v}^*_{1y}\right)\right.$$

$$\left. + \left(\frac{\partial \phi^{*0}}{\partial z^*} + v^{*0}_{1z}\right)\left(\frac{\partial \Phi}{\partial z^*} + \tilde{v}^*_{1z}\right)\right]$$

$$- \frac{1}{2}\left[\left(\frac{\partial \Phi}{\partial \zeta} + \tilde{v}^*_{1x}\right)^2 + \left(\frac{\partial \Phi}{\partial \eta} + \tilde{v}^*_{1y}\right)^2 + \left(\frac{\partial \Phi}{\partial z^*} + \tilde{v}_{1z}\right)^2\right] + v^{*0}_{1x}\,\tilde{v}^*_{1x} + v^{*0}_{1y}\,\tilde{v}^*_{1y} + v^{*0}_{1z}\,\tilde{v}^*_{1z}$$

$$+ \frac{1}{2}\left(\tilde{v}^{*2}_{1x} + \tilde{v}^{*2}_{1y} + \tilde{v}^{*2}_{1z}\right). \tag{80}$$

Substituting Eqs. (69), (74), and (75) into Eq. (80) we get

$$\tilde{p}^* = \frac{1}{4\pi}\int_{\zeta_F}^{\zeta_A} d\zeta_1' \sum_{\kappa'=1}^{2} \int_{\eta_b(\zeta_1')}^{\eta_d(\zeta_1')} \frac{\partial \tilde{m}^*_\kappa(\zeta_1', \eta_1', s)}{\partial s} \frac{1}{R^*_H}\, d\eta_1'$$

$$+ \frac{1}{4\pi}\int_{\eta_\ell}^{\eta_u} d\eta_1' \int_{-1}^{1} du' \int_0^\infty \frac{\partial \tilde{g}_R(\eta_1', u', s - \varphi/\nu_x(\eta_1'))}{\partial s} \frac{\partial}{\partial z^*}\frac{1}{R^*_R}\, d\varphi$$

$$+ \frac{1}{4\pi}\int_{\xi_B}^{1} d\xi' \int_{-1}^{1} dv' \sum_{k'=1}^{N} \int_0^\infty \frac{\partial g_1[\xi', v', -(\varphi + \delta_{k'})]}{\partial s}\left(\xi' \frac{\partial}{\partial x^*} - \frac{\nu}{\xi'^2}\frac{\partial}{\partial \Theta^*}\right)\frac{1}{R^*}\, d\varphi$$

$$- \frac{1}{4\pi}\int_{\eta_\ell}^{\eta_u} \frac{\partial \tilde{V}^*_{Rx}(\eta_1', s)}{\partial s}\,\bar{\zeta}(\eta_1')\, d\eta_1' \int_{-1}^{1} t^*_R(\eta_1', u')\left[\frac{\partial^2}{\partial x^{*}_R}\, R^*_R\right]_{\varphi=0} du'$$

$$- \frac{1}{4\pi}\int_{\xi_B}^{1} \bar{\theta}(\xi')\, d\xi' \int_{-1}^{1} t^*(\xi', v') \sum_{k'=1}^{N} \frac{\partial W^*_1(\xi', -\delta_{k'})}{\partial s}\left[\left(\nu \frac{\partial}{\partial x^*} + \frac{\partial}{\partial \Theta^*}\right)\frac{1}{R^*}\right]_{\varphi=0} dv'$$

$$- \frac{\partial(\phi^*_{P\ell} + \phi^*_{Pt})}{\partial \theta} - \left[\left(\nu_0 + \frac{\partial \phi^{*0}}{\partial \zeta} + v^{*0}_{1x}\right)\left(\frac{\partial \Phi}{\partial \zeta} + \tilde{v}^*_{1x}\right) + \left(\frac{\partial \phi^{*0}}{\partial \eta} + v^{*0}_{1y}\right)\left(\frac{\partial \Phi}{\partial \eta} + \tilde{v}^*_{1y}\right)\right.$$

$$\left. + \left(\frac{\partial \phi^{*0}}{\partial z^*} + v^{*0}_{1z}\right)\left(\frac{\partial \Phi}{\partial z^*} + \tilde{v}^*_{1z}\right)\right] - \frac{1}{2}\left[\left(\frac{\partial \Phi}{\partial \zeta} + \tilde{v}^*_{1x}\right)^2 + \left(\frac{\partial \Phi}{\partial \eta} + \tilde{v}^*_{1y}\right)^2 + \left(\frac{\partial \Phi}{\partial z^*} + \tilde{v}^*_{1z}\right)^2\right]$$

$$+ \left[(\nu_0 + v^{*0}_{1x})\,\tilde{v}^*_{1x} + v^{*0}_{1y}\,\tilde{v}^*_{1y} + v^{*0}_{1z}\,\tilde{v}^*_{1z}\right] + \frac{1}{2}\left(\tilde{v}^{*2}_{1x} + \tilde{v}^{*2}_{1y} + \tilde{v}^{*2}_{1z}\right). \tag{81}$$

Then, subtracting Eqs. (65) from Eqs. (39) and referring to Eq. (69) the differences of the components of force and moment due to water pressure acting on the hull, which are denoted by $\tilde{K}_{HFx0}$, $\tilde{K}_{HFy0}$, $\tilde{K}_{HFz0}$, $\tilde{K}_{HMx0}$, $\tilde{K}_{HMy0}$ and $\tilde{K}_{HMz0}$, are as follows:

$$\tilde{K}_{HFx0} \equiv K_{HFx0} - K^0_{HFx0}$$

$$= -\frac{\pi^2}{4}\int_{\zeta_F}^{\zeta_A} d\zeta_1 \sum_{\kappa=1}^{2} \int_{\eta_b(\zeta_1)}^{\eta_d(\zeta_1)} \left[m^{*0}_{\kappa}(\zeta_1,\eta_1)\left[\frac{\partial\Phi}{\partial\zeta}\right]_{(SH)} + \tilde{m}^{*}_{\kappa}(\zeta_1,\eta_1,s)\left(\nu_0 + \left[\frac{\partial\phi^{*0}}{\partial\zeta} + \frac{\partial\Phi}{\partial\zeta}\right]_{(SH)}\right) + \zeta_1 \frac{\partial\tilde{m}^{*}_{\kappa}(\zeta_1,\eta_1,s)}{\partial s}\right] d\eta_1 ,$$

$$\tilde{K}_{HFy0} \equiv K_{HFy0} - K^0_{HFy0}$$

$$= -\frac{\pi^2}{4}\int_{\zeta_F}^{\zeta_A} d\zeta_1 \sum_{\kappa=1}^{2} \int_{\eta_b(\zeta_1)}^{\eta_d(\zeta_1)} \left[m^{*0}_{\kappa}(\zeta_1,\eta_1)\left[\frac{\partial\Phi}{\partial\eta}\right]_{(SH)} + \tilde{m}^{*}_{\kappa}(\zeta_1,\eta_1,s)\left[\frac{\partial\phi^{*0}}{\partial\eta} + \frac{\partial\Phi}{\partial\eta}\right]_{(SH)} + \eta_1 \frac{\partial\tilde{m}^{*}_{\kappa}(\zeta_1,\eta_1,s)}{\partial s}\right] d\eta_1 ,$$

$$\tilde{K}_{HFz0} \equiv K_{HFz0} - K^0_{HFz0}$$

$$= -\frac{\pi^2}{4}\int_{\zeta_F}^{\zeta_A} d\zeta_1 \sum_{\kappa=1}^{2} \int_{\eta_b(\zeta_1)}^{\eta_d(\zeta_1)} \left[m^{*0}_{\kappa}(\zeta_1,\eta_1)\left[\frac{\partial\Phi}{\partial z^*}\right]_{(SH)} + \tilde{m}^{*}_{\kappa}(\zeta_1,\eta_1,s)\left[\frac{\partial\phi^{*0}}{\partial z^*} + \frac{\partial\Phi}{\partial z^*}\right]_{(SH)} + (-1)^{\kappa-1} z^{*}_{0}(\zeta_1,\eta_1) \frac{\partial\tilde{m}^{*}_{\kappa}(\zeta_1,\eta_1,s)}{\partial s}\right] d\eta_1 ,$$

$$\tilde{K}_{HMx0} \equiv K_{HMx0} - K^0_{HMx0}$$

$$= -\frac{\pi^2}{8}\int_{\zeta_F}^{\zeta_A} d\zeta_1 \sum_{\kappa=1}^{2} \int_{\eta_b(\zeta_1)}^{\eta_d(\zeta_1)} \left\{ m^{*0}_{\kappa}(\zeta_1,\eta_1)\left[\eta_1\left[\frac{\partial\Phi}{\partial z^*}\right]_{(SH)} + (-1)^{\kappa} z^{*}_{0}(\zeta_1,\eta_1)\left[\frac{\partial\Phi}{\partial\eta}\right]_{(SH)}\right] + \tilde{m}^{*}_{\kappa}(\zeta_1,\eta_1,s)\left[\eta_1\left[\frac{\partial\phi^{*0}}{\partial z^*} + \frac{\partial\Phi}{\partial z^*}\right]_{(SH)}\right. \right. \quad (82)$$

(Cont)

$$\tilde{K}_{HMx0} \equiv K_{HMx0} - K^0_{HMx0}$$

$$+ (-1)^{\kappa} z_0^*(\zeta_1,\eta_1)\left[\frac{\partial \phi^{*0}}{\partial \eta} + \frac{\partial \Phi}{\partial \eta}\right]_{(SH)}\Bigg] + (-1)^{\kappa}\left[\frac{\partial \Phi}{\partial s}\right]_{(SH)}$$

$$\left[\eta_1 + z_0^*(\zeta_1,\eta_1)\ \frac{\partial z_0^*(\zeta_1,\eta_1)}{\partial \eta_1}\right]\Bigg\}\, d\eta_1 ,$$

$$\tilde{K}_{HMy0} \equiv K_{HMy0} - K^0_{HMy0}$$

$$= -\frac{\pi^2}{8}\int_{\zeta_F}^{\zeta_A} d\zeta_1 \sum_{\kappa=1}^{2} \int_{\eta_b(\zeta_1)}^{\eta_d(\zeta_1)} \Bigg\{ m_\kappa^{*0}(\zeta_1,\eta_1)\left[(-1)^{\kappa-1} z_0^*(\zeta_1,\eta_1)\left[\frac{\partial \Phi}{\partial \zeta}\right]_{(SH)}\right.$$

$$\left. - \zeta_1\left[\frac{\partial \Phi}{\partial z^*}\right]_{(SH)}\right] + \tilde{m}_\kappa^*(\zeta_1,\eta_1,s)\left[-\zeta_1\left[\frac{\partial \phi^{*0}}{\partial \zeta} + \frac{\partial \Phi}{\partial \zeta}\right]_{(SH)}\right.$$

$$\left. + (-1)^{\kappa-1} z_0^*(\zeta_1,\eta_1)\left(\nu_0 + \left[\frac{\partial \Phi^{*0}}{\partial \zeta} + \frac{\partial \Phi}{\partial \zeta}\right]_{(SH)}\right)\right]$$

$$+ (-1)^{\kappa-1}\left[\frac{\partial \Phi}{\partial s}\right]_{(SH)}\left[z_0^*(\zeta_1,\eta_1)\ \frac{\partial z_0^*(\zeta_1,\eta_1)}{\partial \zeta_1} + \zeta_1\right]\Bigg\}\, d\eta_1 ,$$

$$\tilde{K}_{HMz0} \equiv K_{HMz0} - K^0_{HMz0}$$

$$= -\frac{\pi^2}{8}\int_{\zeta_F}^{\zeta_A} d\zeta_1 \sum_{\kappa=1}^{2} \int_{\eta_b(\zeta_1)}^{\eta_d(\zeta_1)} \Bigg\{ m_\kappa^{*0}(\zeta_1,\eta_1)\left(\zeta_1\left[\frac{\partial \Phi}{\partial \eta}\right]_{(SH)} - \eta_1\left[\frac{\partial \Phi}{\partial \zeta}\right]_{(SH)}\right)$$

$$+ \tilde{m}_\kappa^*(\zeta_1,\eta_1,s)\left[\zeta_1\left[\frac{\partial \phi^{*0}}{\partial \eta} + \frac{\partial \Phi}{\partial \eta}\right]_{(SH)} - \eta_1\left(\nu_0 + \left[\frac{\partial \phi^{*0}}{\partial \zeta} + \frac{\partial \Phi}{\partial \zeta}\right]_{(SH)}\right)\right]$$

$$+\left[\frac{\partial \Phi}{\partial s}\right]_{(SH)}\left[\zeta_1\ \frac{\partial z_0^*(\zeta_1,\eta_1)}{\partial \eta_1} - \eta_1\ \frac{\partial z_0^*(\zeta_1,\eta_1)}{\partial \zeta_1}\right]\Bigg\}\, d\eta_1 . \qquad (82)$$

The presence of the roating propeller can be considered to have a small influence on the local viscous drag on the hull surface, so that the vibrating parts of this viscous drag, which are contained in the components generated by the propeller, can be considered to be negligibly small compared with those caused by normal pressure. Hence, the differences of the components of total force and moment acting on the hull can be expressed by $\tilde{K}_{HFx0}$, $\tilde{K}_{HFy0}$, etc., approximately. Next,

using Eqs. (44), (45), and (48) and neglecting the small quantities of higher order the differences of the components of force and moment of water acting on the rudder, which are denoted by $\tilde{K}_{RFx0}$, $\tilde{K}_{RFy0}$, $\tilde{K}_{RFz0}$, $\tilde{K}_{RMx0}$, $\tilde{K}_{RMy0}$, and $\tilde{K}_{RMz0}$, are

$$\tilde{K}_{RFx} \equiv K_{RFx} - K^0_{RFx} = K_{D1} + (K_{D2} - K^0_{D2}) + (K_{D3} - K^0_{D3}) - K_S ,$$

$$\tilde{K}_{RFz} \equiv K_{RFz} - K^0_{RFz}$$

$$= \frac{\pi^2}{4} \int_{\eta_\ell}^{\eta_u} d\eta_1 \int_{-1}^{1} \left[g_R^0(\eta_1, u) \left[\frac{\partial \Phi}{\partial \zeta} + \tilde{v}^*_{1x} \right]_{(SR)} \right.$$

$$\left. + \tilde{g}_R(\eta_1, u, s) \left(\nu_0 + \left[\frac{\partial \phi^{*0}}{\partial \zeta} + \frac{\partial \Phi}{\partial \zeta} + v^{*0}_{1x} + \tilde{v}^*_{1x} \right]_{(SR)} \right) \right] du ,$$

$$\tilde{K}_{RMx} \equiv K_{RMx} - K^0_{RMx}$$

$$= \frac{\pi^2}{8} \int_{\eta_\ell}^{\eta_u} \eta_1 d\eta_1 \int_{-1}^{1} \left[g_R^0(\eta_1, u) \left[\frac{\partial \Phi}{\partial \zeta} + v^*_{1x} \right]_{(SR)} \right.$$

$$\left. + \tilde{g}_R(\eta_1, u, s) \left(\nu_0 + \left[\frac{\partial \phi^{*0}}{\partial \zeta} + \frac{\partial \Phi}{\partial \zeta} + v^{*0}_{1x} + \tilde{v}^*_{1x} \right]_{(SR)} \right) \right] du , \qquad (83)$$

where

$$K_{D1} = -\frac{\pi^2}{4} \int_{\eta_\ell}^{\eta_u} d\eta_1 \int_{-1}^{1} [g_R^0(\eta_1, u) + \tilde{g}_R(\eta_1, u, s)]$$

$$\left(\nu_0 + \left[\frac{\partial \phi^{*0}}{\partial \zeta} + \frac{\partial \Phi}{\partial \zeta} + v^{*0}_{1x} + \tilde{v}^{*0}_{1x} \right]_{(SR)} \right) \frac{\partial z^*_R(\eta_1, u)}{\bar{\zeta}(\eta_1)\, \partial u} du ,$$

$$K_{D2} - K^0_{D2} = \frac{\pi^2}{4} \int_{\eta_\ell}^{\eta_u} \left\{ C^0_{RD} \tilde{V}^*_{Rx}(\eta_1, s) [2 V^{*0}_{Rx}(\eta_1) + \tilde{V}^*_{Rx}(\eta_1, s)] \right.$$

$$\left. + \tilde{C}_{RD} \left[V^{*0}_{Rx}(\eta_1) + \tilde{V}^*_{Rx}(\eta_1, s) \right]^2 \right\} d\eta_1 , \qquad (84)$$
(Cont)

$$K_{D3} - K^*_{D3} = \frac{\pi^2}{4}\int_{\eta_\ell}^{\eta_u} d\eta_1 \int_{-1}^{1} t^*_R(\eta_1,u)\left[V^{*0}_{Rx}(\eta_1)\left[\frac{\partial^2\Phi_H}{\partial\zeta_1^{\,2}} + \frac{\partial^2\phi^*_P}{\partial\zeta_1^{\,2}} + \frac{\partial\tilde{v}^*_{1x}}{\partial\zeta_1}\right]_{(SR)}\right.$$

$$\left. + \tilde{V}^*_{Rx}(\eta_1,s)\left[\frac{\partial^2\phi^{*0}_H}{\partial\zeta_1^{\,2}} + \frac{\partial v^{*0}_{1x}}{\partial\zeta_1} + \frac{\partial^2\Phi_H}{\partial\zeta_1^{\,2}} + \frac{\partial^2\phi^*_P}{\partial\zeta_1^{\,2}} + \frac{\partial\tilde{v}^*_{1x}}{\partial\zeta_1}\right]_{(SR)}\right] du\,,$$

$$K_S = \frac{\pi^3}{8}\int_{\eta_\ell}^{\eta_u} \frac{\left[a^{*0}_0(\eta_1) + \tilde{a}^*_0(\eta_1,s)\right]^2}{\bar{\zeta}(\eta_1)}\, d\eta_1\,. \tag{84}$$

Further, since $[V^*_r]_{(SP)}$ is negligibly small compared with $[V^*_x]_{(SP)}$ and $[V^*_\theta]_{(SP)}$ (11), referring to Eqs. (69), (27), and (28) the components of force and moment acting on the propeller expressed by Eqs. (50) and (51) are rewritten

$$\begin{aligned} &K_{Fx} = K_{Fx0} + K_{FxD}\,, \quad K_{Fy} = K_{Fy0} + K_{FyD}\,, \quad K_{Fz} = K_{Fz0} + K_{FzD}\,, \\ &K_{Mx} = K_{Mx0} + K_{MxD}\,, \quad K_{My} = K_{My0} + K_{MyD}\,, \quad K_{Mz} = K_{Mz0} + K_{MzD}\,, \end{aligned} \tag{85}$$

where

$$[V^*_x]_{(SP)} = \nu_0 + \left[\frac{\partial\phi^{*0}}{\partial\zeta} + \frac{\partial\Phi}{\partial\zeta} + v^{*0}_{1x} + \tilde{v}^*_{1x}\right]_{(SP)}\,,$$

$$[V^*_\theta]_{(SP)} = \xi + \left[\frac{\partial\phi^{*0}}{\xi\partial\theta} + \frac{\partial\Phi}{\xi\partial\theta} + v^{*0}_{1\theta} + \tilde{v}^*_{1\theta}\right]_{(SP)}\,,$$

$$V^*_{kx} = \frac{1}{\pi}\int_{-1}^{1}\sqrt{\frac{1-v}{1+v}}\,[V^*_x]_{(SP)}\,dv\,, \quad V^*_{k\theta} = \frac{1}{\pi}\int_{-1}^{1}\sqrt{\frac{1-v}{1+v}}\,[V^*_\theta]_{(SP)}\,dv\,,$$

$$K_{Fx0} = -\frac{\pi^2}{4}\int_{\xi_B}^{1} d\xi \int_{-1}^{1}\sum_{k=1}^{N} g_1(\xi,v,-\delta_k)\,[V^*_\theta]_{(SP)}\,dv\,,$$

$$K_{Fy0} = -\frac{\pi^2}{4}\int_{\xi_B}^{1} d\xi \int_{-1}^{1}\sum_{k=1}^{N} g_1(\xi,v,-\delta_k)\,[V^*_x]_{(SP)}\,\sin\left[\theta_M(\xi) + \bar{\theta}(\xi)\,v + \delta_k\right] dv\,,$$

$$K_{Fz0} = \frac{\pi^2}{4}\int_{\xi_B}^{1} d\xi \int_{-1}^{1}\sum_{k=1}^{N} g_1(\xi,v,-\delta_k)\,[V^*_x]_{(SP)}\,\cos\left[\theta_M(\xi) + \bar{\theta}(\xi)\,v + \delta_k\right] dv\,,$$

$$K_{Mx0} = \frac{\pi^2}{8}\int_{\xi_B}^{1} d\xi \int_{-1}^{1}\sum_{k=1}^{N} g_1(\xi,v,-\delta_k)\,[V^*_x]_{(SP)}\,\xi\; dv\,, \tag{86 (Cont)}$$

$$K_{My0} = -\frac{\pi^2}{8}\int_{\xi_B}^{1} d\xi \int_{-1}^{1} \sum_{k=1}^{N} g_1(\xi, v, -\delta_k)\left([V_\theta^*]_{(SP)}\,\xi\,\sin[\theta_M(\xi) + \bar{\theta}(\xi)v + \delta_k]\right.$$

$$\left. + [V_x^*]_{(SP)}\cos[\theta_M(\xi) + \bar{\theta}(\xi)v + \delta_k]\left\{\nu[\theta_M(\xi) + \bar{\theta}(\xi)v] + \xi\varepsilon\right\}\right) dv\,,$$

$$K_{Mz0} = \frac{\pi^2}{8}\int_{\xi_B}^{1} d\xi \int_{-1}^{1} \sum_{k=1}^{N} g_1(\xi, v, -\delta_k)\left([V_\theta^*]_{(SP)}\,\xi\,\cos[\theta_M(\xi) + \bar{\theta}(\xi)v + \delta_k]\right.$$

$$\left. - [V_x^*]_{(SP)}\sin[\theta_M(\xi) + \bar{\theta}(\xi)v + \delta_k]\left\{\nu[\theta_M(\xi) + \bar{\theta}(\xi)v] + \xi\varepsilon\right\}\right) dv\,,$$

$$K_{FxD} = \frac{\pi^2}{4}\int_{\xi_B}^{1} \sum_{k=1}^{N} C_{PD}[1 + (\nu/\xi)^2]\,V_{k\theta}^*\,V_{kx}^*\,\bar{\theta}(\xi)\,\xi\,d\xi\,,$$

$$K_{FyD} = -\frac{\pi^2}{4}\int_{\xi_B}^{1} \sum_{k=1}^{N} C_{PD}[1 + (\nu/\xi)^2]\,V_{k\theta}^{*2}\sin\bar{\theta}(\xi)\sin[\theta_M(\xi) + \delta_k]\,\xi\,d\xi\,,$$

$$K_{FzD} = \frac{\pi^2}{4}\int_{\xi_B}^{1} \sum_{k=1}^{N} C_{PD}[1 + (\nu/\xi)^2]\,V_{k\theta}^{*2}\sin\bar{\theta}(\xi)\cos[\theta_M(\xi) + \delta_k]\,\xi\,d\xi\,,$$

$$K_{MxD} = \frac{\pi^2}{8}\int_{\xi_B}^{1} \sum_{k=1}^{N} C_{PD}[1 + (\nu/\xi)^2]\,V_{k\theta}^{*2}\,\bar{\theta}(\xi)\,\xi^2\,d\xi\,,$$

$$K_{MyD} = \frac{\pi^2}{8}\int_{\xi_B}^{1} \sum_{k=1}^{N} C_{PD}[1 + (\nu/\xi)^2]\,V_{k\theta}^*\left(V_{kx}^*\,\xi\,\sin\bar{\theta}(\xi)\sin[\theta_M(\xi) + \delta_k]\right.$$

$$- V_{k\theta}^*\left\{[\nu\theta_M(\xi) + \xi\varepsilon]\sin\bar{\theta}(\xi)\cos[\theta_M(\xi) + \delta_k]\right.$$

$$\left.\left. - \nu\sin\bar{\theta}(\xi)\sin[\theta_M(\xi) + \delta_k] + \nu\,\bar{\theta}(\xi)\cos\bar{\theta}(\xi)\sin[\theta_M(\xi) + \delta_k]\right\}\right)\xi\,d\xi\,,$$

$$K_{MzD} = -\frac{\pi^2}{8}\int_{\xi_B}^{1} \sum_{k=1}^{N} C_{PD}[1 + (\nu/\xi)^2]\,V_{k\theta}^*\left(V_{kx}^*\,\xi\,\sin\bar{\theta}(\xi)\cos[\theta_M(\xi) + \delta_k]\right.$$

$$+ V_{k\theta}^*\left\{[\nu\theta_M(\xi) + \xi\varepsilon]\sin\bar{\theta}(\xi)\sin[\theta_M(\xi) + \delta_k]\right.$$

$$\left.\left. + \nu\sin\bar{\theta}(\xi)\cos[\theta_M(\xi) + \delta_k] - \nu\,\bar{\theta}(\xi)\cos\bar{\theta}(\xi)\cos[\theta_M(\xi) + \delta_k]\right\}\right)\xi\,d\xi\,. \quad (86)$$

The unsteady propeller forces are classified into "surface forces" and "bearing forces," and the former contains "impulse forces" as mentioned earlier. In the above expressions, Eqs. (82) and (83) represent the surface forces, Eqs. (85) represent the bearing forces, and Eqs. (83) particularly represent the impulse forces respectively.

According to the result of a previous paper (6) the chordwise mean velocity component $W_1^*(\xi, -\delta_k)$ flowing on the propeller blade can be assumed to be approximately independent of s, and so we can express

$$W_1^*(\xi, -\delta_k) \approx \sqrt{v_{x0}^*(\xi)^2 + v_{\theta 0}^*(\xi)} \equiv W_1^*(\xi) . \tag{87}$$

Taking into account that the mean surface of the rudder passes through many helical trailing vortices shed from the propeller blades at the same time, the chordwise mean velocity component $V_{Rx}^*(\eta_1, s)$ flowing on the rudder surface can be approximated to be independent of time, so that we can assume

$$V_{Rx}^*(\eta_1, s) \approx \nu_x(\eta_1) . \tag{88}$$

Thus, substituting Eqs. (87) and (88) into Eqs. (74) and (75), the velocity potentials ϕ_{Pt}^* and ϕ_{Rt}^* can be obtained as

$$\begin{aligned} \phi_{Pt}^* &= \frac{1}{4\pi} \int_{\xi_B}^{1} \bar{\theta}(\xi') \, d\xi' \int_{-1}^{1} t^*(\xi', v') \, W_1^*(\xi') \sum_{k'=1}^{N} \left[\left(\nu \frac{\partial}{\partial x^*} + \frac{\partial}{\partial \Theta^*} \right) \frac{1}{R^*} \right]_{\varphi = 0} dv' , \\ \Phi_{Rt} &= \frac{1}{4\pi} \int_{\eta_\ell}^{\eta_u} \bar{\zeta}(\eta_1') \, d\eta_1' \int_{-1}^{1} t_R^*(\eta_1', u') \left[\nu_x(\eta_1') - V_{Rx}^{*0}(\eta_1') \right] \left[\frac{\partial}{\partial x_R^*} \frac{1}{R_R^*} \right]_{\varphi = 0} du' . \end{aligned} \tag{89}$$

It is convenient in actual calculations to use Eqs. (89) instead of ϕ_{Pt}^* and Φ_{Rt} in Eqs. (74) and (75).

Let us reduce further the preceding equations to convenient forms for performing the actual calculations. Since the viscous velocity components $[v_{1x}^*]_{(SP)}$ and $[v_{1\theta}^*]_{(SP)}$ are expressed by periodic functions of s, they are expanded in the series

$$\begin{aligned} \nu_0 + \left[v_{1x}^* \right]_{(SP)} &= \nu_0 + \left[v_{1x}^{*0} + \tilde{v}_{1x}^* \right]_{(SP)} = \sum_n v_{xn}^*(\xi) \, e^{in[\theta_M(\xi) + \bar{\theta}(\xi) v + \delta_k]} , \\ \xi + \left[v_{1\theta}^* \right]_{(SP)} &= \xi + \left[v_{1\theta}^{*0} + \tilde{v}_{1\theta}^* \right]_{(SP)} = \sum_n v_{\theta n}^*(\xi) \, e^{in[\theta_M(\xi) + \bar{\theta}(\xi) v + \delta_k]} , \end{aligned} \tag{90}$$

where $[v_{1x}^*]_{(SP)}$ and $[v_{1\theta}^*]_{(SP)}$ are approximately independent of ζ_1. The viscous velocity components $[\tilde{v}_{1x}^*]_{(SR)}$, $[\tilde{v}_{1y}^*]_{(SR)}$ and $[\tilde{v}_{1z}^*]_{(SR)}$ are independent of time s. Then, it is found physically that $\tilde{m}_k^*(\zeta_1, \eta_1, s)$, $\tilde{g}_R(\eta_1, u, s)$, and the induced

velocities on S_H and S_R are periodic functions of period $2\pi/N$ with respect to time s and that $g_1(\xi, v, -\delta_k)$ and the induced velocity on S_P are periodic functions of period 2π. Thus the quantities $g_1(\xi, v, -\delta_k)$, $\tilde{m}^*_\kappa(\zeta_1, \eta_1, s)$, and $\tilde{g}_R(\eta_1, u, s)$ can be expanded formally as

$$g_1(\xi, v, -\delta_k) = \sum_n g_n(\xi, v)\, e^{in\delta_k}\,, \quad \tilde{m}^*_\kappa(\zeta_1, \eta_1, s) = \sum_m m^*_{\kappa m}(\zeta_1, \eta_1)\, e^{-imNs}\,, \tag{91}$$

$$\tilde{g}_R(\eta_1, u, s) = \sum_m g_{Rm}(\eta_1, u)\, e^{-imNs}\,,$$

where

$$g_n(\xi, v) = g_{n0}(\xi)\sqrt{\frac{1-v}{1+v}} + g_{n1}(\xi)\sqrt{1-v^2} + g_{n2}(\xi)\, v\sqrt{1-v^2} + \cdots\,,$$

$$g_{Rm}(\eta_1, u) = g_{Rm0}(\eta_1)\sqrt{\frac{1-u}{1+u}} + g_{Rm1}(\eta_1)\sqrt{1-u^2} + g_{Rm2}(\eta_1)\, u\sqrt{1-u^2} + \cdots\,,$$

$$g^0_R(\eta_1, u) = g^0_{R0}(\eta_1)\sqrt{\frac{1-u}{1+u}} + g^0_{R1}(\eta_1)\sqrt{1-u^2} + g^0_{R2}(\eta_1)\, u\sqrt{1-u^2} + \cdots\,, \tag{92}$$

and $g_{n0}(\xi)$, $g_{Rm0}(\eta_1)$, $g^0_{R0}(\eta_1)$, etc., are functions of ξ or η_1. From Eqs. (70) we get the relations

$$g^0_{R0}(\eta_1) = a^{*0}_0(\eta_1)\,, \quad \sum_m g_{Rm0}(\eta_1)\, e^{-imNs} = \tilde{a}^*_0(\eta_1, s)\,. \tag{93}$$

We define the following functions:

$$-e^{-imNs}\left[\frac{\partial}{\partial\zeta}\frac{1}{R^*_H}\right]_{(SH)} = H_{\kappa,xH\kappa}\, e^{-imNs}, \quad -e^{-imNs}\left[\frac{\partial}{\partial\eta}\frac{1}{R^*_H}\right]_{(SH)} = H_{\kappa,yH\kappa}\, e^{-imNs}\,,$$

$$-e^{-imNs}\left[\frac{\partial}{\partial z^*}\frac{1}{R^*_H}\right]_{(SH)} = H_{\kappa,zH\kappa}\, e^{-imNs}\,,$$

$$-\left[\frac{\partial}{\partial\zeta}\int_0^\infty e^{imN[\varphi/\nu_x(\eta_1')-s]}\frac{\partial}{\partial z^*}\frac{1}{R^*_R}\,d\varphi\right]_{(SH)} = R_{LxH\kappa m}\, e^{-imNs}\,,$$

$$-\left[\frac{\partial}{\partial\eta}\int_0^\infty e^{imN(\varphi/\nu_x(\eta_1')-s)}\frac{\partial}{\partial z^*}\frac{1}{R^*_R}\,d\varphi\right]_{(SH)} = R_{LyH\kappa m}\, e^{-imNs}\,,$$

$$-\left[\frac{\partial}{\partial z^*}\int_0^\infty e^{imN[\varphi/\nu_x(\eta_1')-s]}\frac{\partial}{\partial z^*}\frac{1}{R^*_R}\,d\varphi\right]_{(SH)} = R_{LzH\kappa m}\, e^{-imNs}\,, \tag{94}$$

(Cont)

$$\left[\frac{\partial^2}{\partial\zeta\,\partial X_R^*}\frac{1}{R_R^*}\right]_{\substack{\varphi=0\\(SH)}} = R_{TxH\kappa}\,,\quad \left[\frac{\partial^2}{\partial\eta\,\partial X_R^*}\frac{1}{R_R^*}\right]_{\substack{\varphi=0\\(SH)}} = R_{TyH\kappa}\,,$$

$$\left[\frac{\partial^2}{\partial z\,\partial X_R^*}\frac{1}{R_R^*}\right]_{\substack{\varphi=0\\(SH)}} = R_{TzH\kappa}\,,$$

$$-\left[\frac{\partial}{\partial\zeta}\sum_{k'=1}^{N}\int_0^\infty e^{in(\varphi+\delta_{k'})}\left(\xi'\frac{\partial}{\partial X^*}-\frac{\nu}{\xi'}\frac{\partial}{\partial\Theta^*}\right)\frac{1}{R^*}\,d\varphi\right]_{(SH)} = \sum_m P_{LxH\kappa nm}\,e^{-imNs}\,,$$

$$-\left[\frac{\partial}{\partial\eta}\sum_{k'=1}^{N}\int_0^\infty e^{in(\varphi+\delta_{k'})}\left(\xi'\frac{\partial}{\partial X^*}-\frac{\nu}{\xi'}\frac{\partial}{\partial\Theta^*}\right)\frac{1}{R^*}\,d\varphi\right]_{(SH)} = \sum_m P_{LyH\kappa nm}\,e^{-imNs}\,,$$

$$-\left[\frac{\partial}{\partial z^*}\sum_{k'=1}^{N}\int_0^\infty e^{in(\varphi+\delta_{k'})}\left(\xi'\frac{\partial}{\partial X^*}-\frac{\nu}{\xi'}\frac{\partial}{\partial\Theta^*}\right)\frac{1}{R^*}\,d\varphi\right]_{(SH)} = \sum_m P_{LzH\kappa nm}\,e^{-imNs}\,,$$

$$\left[\frac{\partial}{\partial\zeta}\sum_{k'=1}^{N}\left(\nu\frac{\partial}{\partial X^*}+\frac{\partial}{\partial\Theta^*}\right)\frac{1}{R^*}\right]_{\substack{\varphi=0\\(SH)}} = \sum_m P_{TxH\kappa m}\,e^{-imNs}\,,$$

$$\left[\frac{\partial}{\partial\eta}\sum_{k'=1}^{N}\left(\nu\frac{\partial}{\partial X^*}+\frac{\partial}{\partial\Theta^*}\right)\frac{1}{R^*}\right]_{\substack{\varphi=0\\(SH)}} = \sum_m P_{TyH\kappa m}\,e^{-imNs}\,,$$

$$\left[\frac{\partial}{\partial z^*}\sum_{k'=1}^{N}\left(\nu\frac{\partial}{\partial X^*}+\frac{\partial}{\partial\Theta^*}\right)\frac{1}{R^*}\right]_{\substack{\varphi=0\\(SH)}} = \sum_m P_{TzH\kappa m}\,e^{-imNs}\,, \qquad (94)$$

$$-e^{-imNs}\left[\frac{\partial}{\partial\zeta}\frac{1}{R_H^*}\right]_{(SR)} = H_{\kappa' xR}\,e^{-imNs}\,,\quad -e^{-imNs}\left[\frac{\partial}{\partial z^*}\frac{1}{R_R^*}\right]_{(SR)} = H_{\kappa' zR}\,e^{-imNs}$$

$$-\left[\frac{\partial}{\partial\zeta}\int_0^\infty e^{imN[\varphi/\nu_x(\eta_1')-s]}\frac{\partial}{\partial z^*}\frac{1}{R_R^*}\,d\varphi\right]_{(SR)} = R_{LxRm}\,e^{-imNs} = 0\,,$$

$$-\left[\frac{\partial}{\partial z^*}\int_0^\infty e^{imN[\varphi/\nu_x(\eta_1')-s]}\frac{\partial}{\partial z^*}\frac{1}{R_R^*}\,d\varphi\right]_{(SR)} = R_{LzRm}\,e^{-imNs}\,, \qquad (95)\ (\text{Cont})$$

$$\left[\frac{\partial^2}{\partial\zeta\partial X_R^*}\frac{1}{R_R^*}\right]_{\substack{\varphi=0\\(SR)}} = R_{TxR}\,, \qquad \left[\frac{\partial^2}{\partial z^*\partial X_R^*}\frac{1}{R_R^*}\right]_{\substack{\varphi=0\\(SR)}} = R_{TzR} = 0\,,$$

$$-\left[\frac{\partial}{\partial\zeta}\sum_{k'=1}^{N}\int_0^\infty e^{in(\varphi+\delta_{k'})}\left(\xi'\frac{\partial}{\partial X^*}-\frac{\nu}{\xi'}\frac{\partial}{\partial\Theta^*}\right)\frac{1}{R^*}\,d\varphi\right]_{(SR)} = \sum_m P_{LxRnm}\,e^{-imNs}\,,$$

$$-\left[\frac{\partial}{\partial z^*}\sum_{k'=1}^{N}\int_0^\infty e^{in(\varphi+\delta_{k'})}\left(\xi'\frac{\partial}{\partial X^*}-\frac{\nu}{\xi'}\frac{\partial}{\partial\Theta^*}\right)\frac{1}{R^*}\,d\varphi\right]_{(SR)} = \sum_m P_{LzRnm}\,e^{-imNs}\,,$$

$$\left[\frac{\partial}{\partial\zeta}\sum_{k'=1}^{N}\left(\nu\frac{\partial}{\partial X^*}+\frac{\partial}{\partial\Theta^*}\right)\frac{1}{R^*}\right]_{\substack{\varphi=0\\(SR)}} = \sum_m P_{TxRm}\,e^{-imNs}\,,$$

$$\left[\frac{\partial}{\partial z^*}\sum_{k'=1}^{N}\left(\nu\frac{\partial}{\partial X^*}+\frac{\partial}{\partial\Theta^*}\right)\frac{1}{R^*}\right]_{\substack{\varphi=0\\(SR)}} = \sum_m P_{TzRm}\,e^{-imNs}\,, \qquad (95)$$

$$-e^{-imNs}\left[\frac{\partial}{\partial\zeta}\frac{1}{R_H^*}\right]_{(SP)} = \sum_n H_{\kappa' xPmn}\,e^{in\delta_k}\,,$$

$$-e^{-imNs}\left[\frac{\partial}{\xi\partial\theta}\frac{1}{R_R^*}\right]_{(SP)} = \sum_n H_{\kappa'\theta Pmn}\,e^{in\delta_k}\,,$$

$$-\left[\frac{\partial}{\partial\zeta}\int_0^\infty e^{imN[\varphi/\nu_x(\eta_1')-s]}\frac{\partial}{\partial z^*}\frac{1}{R_R^*}\,d\varphi\right]_{(SP)} = \sum_n R_{LxPmn}\,e^{in\delta_k}\,,$$

$$-\left[\frac{\partial}{\xi\partial\theta}\int_0^\infty e^{imN[\varphi/\nu_x(\eta_1')-s]}\frac{\partial}{\partial z^*}\frac{1}{R^*}\,d\varphi\right]_{(SP)} = \sum_n P_{L\theta Pmn}\,e^{in\delta_k}\,,$$

$$\left[\frac{\partial^2}{\partial\zeta\partial X_R^*}\frac{1}{R_R^*}\right]_{\substack{\varphi=0\\(SP)}} = \sum_n R_{TxPn}\,e^{in\delta_k}\,, \qquad \left[\frac{\partial^2}{\xi\partial\theta\partial X_R^*}\frac{1}{R_R^*}\right]_{\substack{\varphi=0\\(SP)}} = \sum_n P_{T\theta Pn}\,e^{in\delta_k}\,,$$

$$-\left[\frac{\partial}{\partial\zeta}\sum_{k'=1}^{N}\int_0^\infty e^{in(\varphi+\delta_{k'})}\left(\xi'\frac{\partial}{\partial X^*}-\frac{\nu}{\xi'}\frac{\partial}{\partial\Theta^*}\right)\frac{1}{R^*}\,d\varphi\right]_{(SP)} = P_{LxPn}\,e^{in\delta_k}\,, \qquad (96)\ \text{(Cont)}$$

$$-\left[\frac{\partial}{\xi\partial\theta}\sum_{k'=1}^{N}\int_0^{\infty} e^{in(\varphi+\delta_{k'})}\left(\xi'\frac{\partial}{\partial X^*}-\frac{\nu}{\xi'}\frac{\partial}{\partial\Theta^*}\right)\frac{1}{R^*}\,d\varphi\right]_{(SP)} = P_{L\vartheta Pn}\,e^{in\delta_k},$$

$$\left[\frac{\partial}{\partial\zeta}\sum_{k'=1}^{N}\left(\nu\frac{\partial}{\partial X^*}+\frac{\partial}{\partial\Theta^*}\right)\frac{1}{R^*}\right]_{\substack{\varphi=0\\(SP)}} = P_{TxP},\quad \left[\frac{\partial}{\xi\partial\theta}\sum_{k'=1}^{N}\left(\nu\frac{\partial}{\partial X^*}+\frac{\partial}{\partial\Theta^*}\right)\frac{1}{R^*}\right]_{\substack{\varphi=0\\(SP)}} = P_{T\vartheta P}, \tag{96}$$

where $H_{\kappa',xH\kappa}$, $R_{LxH\kappa m}$, etc., are independent of time s and can be reduced to the forms convenient for the actual calculations. Then by using Eqs. (94), (95), and (96) the induced velocity components

$[\partial\Phi/\partial\zeta]_{(SH)}$, $[\partial\Phi/\partial\eta]_{(SH)}$, $[\partial\Phi/\partial z^*]_{(SH)}$, $[\partial\Phi/\partial\zeta]_{(SR)}$, $[\partial\Phi/\partial z^*]_{(SR)}$,

$[\partial\Phi/\partial\zeta]_{(SP)}$, $[\partial\Phi/\xi\partial\theta]_{(SP)}$, $[\partial\phi^{*0}/\partial\zeta]_{(SH)}$, $[\partial\phi^{*0}/\partial\eta]_{(SH)}$, $[\partial\phi^{*0}/\partial z^*]_{(SH)}$,

$[\partial\phi^{*0}/\partial\zeta]_{(SR)}$, $[\partial\phi^{*0}/\partial\zeta]_{(SP)}$, $[\partial\phi^{*0}/\xi\partial\theta]_{(SP)}$, $[\partial^2\Phi_H/\partial\zeta^2+\partial^2\phi_P^*/\partial\zeta^2]_{(SR)}$,

and

$[\partial^2\phi^{*0}/\partial\zeta^2]_{(SR)}$,

which are derived from Eqs. (69), (58), (59), (73), (74), and (75), can be reduced to harmonic series with respect to time. Some examples of them are

$$\left[\frac{\partial\Phi}{\partial\zeta}\right]_{(SH)} = \sum_m e^{-imNs}\left[\frac{1}{4\pi}\int_{\zeta_F}^{\zeta_A} d\zeta_1'\sum_{\kappa'=1}^{2}\int_{\eta_b(\zeta_1')}^{\eta_d(\zeta_1')} m^*_{\kappa',m}(\zeta_1',\eta_1')\,H_{\kappa',xH\kappa}\,d\eta_1'\right.$$

$$+\frac{1}{4\pi}\int_{\eta_\ell}^{\eta_u} d\eta_1'\int_{-1}^{1} g_{Rm}(\eta_1',u')\,R_{LxH\kappa m}\,du'$$

$$+\frac{1}{4\pi}\sum_n\int_{\xi_B}^{1} d\xi'\int_{-1}^{1} g_n(\xi',v')\,P_{LxH\kappa nm}\,dv'$$

$$\left.+\frac{1}{4\pi}\int_{\xi_B}^{1}\bar{\theta}(\xi')\,d\xi'\int_{-1}^{1} t^*(\xi',v')\,W_1^*(\xi')\,P_{TxH\kappa m}\,dv'\right]$$

$$+\frac{1}{4\pi}\int_{\eta_\ell}^{\eta_u}\bar{\zeta}(\eta_1')\,d\eta_1'\int_{-1}^{1} t_R^*(\eta_1',u')\,[\nu_x(\eta_1')-V_{Rx}^{*0}(\eta_1')]\,R_{TxH\kappa}\,du', \tag{97}$$

(Cont)

$$\left[\frac{\partial \Phi}{\partial \zeta}\right]_{(SR)} = \sum_m e^{-imNs}\left[\frac{1}{4\pi}\int_{\zeta_F}^{\zeta_A} d\zeta_1' \sum_{\kappa'=1}^{2} \int_{\eta_b(\zeta_1')}^{\eta_d(\zeta_1')} m^*_{\kappa',m}(\zeta_1',\eta_1')\, H_{\kappa',xR}\, d\eta_1'\right.$$

$$+ \frac{1}{4\pi}\sum_n \int_{\xi_B}^{1} d\xi' \int_{-1}^{1} g_n(\xi',v')\, P_{LxRnm}\, dv'$$

$$\left. + \frac{1}{4\pi}\int_{\xi_B}^{1} \bar{\theta}(\xi')\, d\xi' \int_{-1}^{1} t^*(\xi',v')\, W_1^*(\xi')\, P_{TxRm}\, dv'\right]$$

$$+ \frac{1}{4\pi}\int_{\eta_\ell}^{\eta_u} \bar{\zeta}(\eta_1')\, d\eta_1' \int_{-1}^{1} t_R^*(\eta_1',u')\,[\nu_x(\eta_1') - V_{Rx}^{*0}(\eta_1')]\, R_{TxR}\, du' ,$$

$$\left[\frac{\partial \Phi}{\partial \zeta}\right]_{(SP)} = \sum_n e^{in\delta_k}\left\{\frac{1}{4\pi}\sum_m \int_{\zeta_F}^{\zeta_A} d\zeta_1' \sum_{\kappa'=1}^{2} \int_{\eta_b(\zeta_1')}^{\eta_d(\zeta_1')} m^*_{\kappa',m}(\zeta_1',\eta_1')\, H_{\kappa',xPmn}\, d\eta_1'\right.$$

$$+ \frac{1}{4\pi}\sum_m \int_{\eta_\ell}^{\eta_u} d\eta_1' \int_{-1}^{1} g_{Rm}(\eta_1',u')\, R_{LxPmn}\, du'$$

$$+ \frac{1}{4\pi}\int_{\xi_B}^{1} d\xi' \int_{-1}^{1} g_n(\xi',v')\, P_{LxPn}\, dv'$$

$$\left. + \frac{1}{4\pi}\int_{\eta_\ell}^{\eta_u} \bar{\zeta}(\eta_1')\, d\eta_1' \int_{-1}^{1} t_R^*(\eta_1',u')\,[\nu_x(\eta_1') - V_{Rx}^{*0}(\eta_1')]\, R_{TxPn}\, du'\right\}$$

$$+ \frac{1}{4\pi}\int_{\xi_B}^{1} \bar{\theta}(\xi')\, d\xi' \int_{-1}^{1} t^*(\xi',v')\, W_1^*(\xi')\, P_{TxP}\, dv' ,$$

$$\left[\frac{\partial \phi^{*0}}{\partial \zeta}\right]_{(SH)} = \frac{1}{4\pi}\int_{\zeta_F}^{\zeta_A} d\zeta_1' \sum_{\kappa'=1}^{2} \int_{\eta_b(\zeta_1')}^{\eta_d(\zeta_1')} m_{\kappa'}^{*0}(\zeta_1',\eta_1')\, H_{\kappa',xH\kappa}\, d\eta_1'$$

$$+ \frac{1}{4\pi}\int_{\eta_\ell}^{\eta_u} d\eta_1' \int_{-1}^{1} g_R^0(\eta_1',u')\, R_{LxH\kappa 0}\, du'$$

$$+ \frac{1}{4\pi}\int_{\eta_\ell}^{\eta_u} \bar{\zeta}(\eta_1')\, d\eta_1' \int_{-1}^{1} t_R^*(\eta_1',u')\, V_{Rx}^{*0}(\eta_1')\, R_{TxH\kappa}\, du' ,$$

(97) (Cont)

$$\left[\frac{\partial^2 \phi_H^{*0}}{\partial \zeta^2}\right]_{(SR)} = \frac{1}{4\pi}\int_{\zeta_F}^{\zeta_A} d\zeta_1' \sum_{\kappa'=1}^{2} \int_{\eta_b(\zeta_1')}^{\eta_d(\zeta_1')} m_{\kappa'}^{*0}(\zeta_1', \eta_1') \frac{\partial H_{\kappa' xR}}{\partial \zeta} d\eta' , \tag{97}$$

and the rest are omitted. Thus, the integral equations, which are derived by substituting Eqs. (97), etc., into the boundary conditions of Eqs. (77), (78), and (79), hold irrespective of time s, so that each component of the harmonic series with respect to e^{-ims} or $e^{in\delta_k}(m, n = 0, \pm 1, \pm 2, \ldots)$ in these equations must vanish. Hence, the following equations are obtained for each harmonic number n or m:

$$\begin{aligned}
&\frac{1}{2} m_{\kappa m}^*(\zeta_1, \eta_1) + \frac{1}{4\pi}\int_{\zeta_F}^{\zeta_A} d\zeta_1' \sum_{\kappa'=1}^{2} \int_{\eta_b(\zeta_1')}^{\eta_d(\zeta_1')} m_{\kappa m}^*(\zeta_1', \eta_1') H_{\kappa' H\kappa} d\eta_1' \\
&\quad + \frac{1}{4\pi}\int_{\eta_\ell}^{\eta_u} d\eta_1' \int_{-1}^{1} g_{Rm}(\eta_1', u') R_{LH\kappa m} du' \\
&\quad + \frac{1}{4\pi}\sum_n \int_{\xi_B}^{1} d\xi' \int_{-1}^{1} g_n(\xi', v') P_{LH\kappa nm} dv' \\
&\quad + \frac{1}{4\pi}\int_{\xi_B}^{1} \bar{\theta}(\xi') d\xi' \int_{-1}^{1} t^*(\xi', v') W_1^*(\xi') P_{TH\kappa m} dv' \\
&= \begin{cases} 0 , & \text{for } m \neq 0 , \\ -\frac{1}{4\pi}\int_{\eta_\ell}^{\eta_u} \bar{\zeta}(\eta_1') d\eta_1' \int_{-1}^{1} t_R^*(\eta_1', u') [\nu_x(\eta_1') - V_{Rx}^{*0}(\eta_1')] R_{TH\kappa} du' , & \text{for } m = 0 , \end{cases}
\end{aligned} \tag{98}$$

$$\begin{aligned}
&\frac{1}{4\pi}\int_{\zeta_F}^{\zeta_A} d\zeta_1' \sum_{\kappa'=1}^{2} \int_{\eta_b(\zeta_1')}^{\eta_d(\zeta_1')} m_{\kappa' m}^*(\zeta_1', \eta_1') H_{\kappa' R} d\eta_1' + \frac{1}{4\pi}\int_{\eta_\ell}^{\eta_u} d\eta_1' \int_{-1}^{1} g_{Rm}(\eta_1', u') R_{LRm} du' \\
&\quad + \frac{1}{4\pi}\sum_n \int_{\xi_B}^{1} d\xi' \int_{-1}^{1} g_n(\xi', v') P_{LRnm} dv' \\
&\quad + \frac{1}{4\pi}\int_{\xi_B}^{1} \bar{\theta}(\xi') d\xi' \int_{-1}^{1} t^*(\xi', v') W_1^*(\xi') P_{TRm} dv'
\end{aligned} \tag{99}$$
(Cont)

$$
= \begin{cases} 0, & \text{for } m \neq 0, \\ -\left[\tilde{v}^*_{1z}\right]_{(SR)} + \dfrac{\partial z^*_R(\eta_1, u)}{\bar{\zeta}(\eta_1)\,\partial u}\left[\tilde{v}^*_{1x}\right]_{(SR)} \end{cases}
$$

$$
- \frac{1}{4\pi}\int_{\eta_\ell}^{\eta_u} \bar{\zeta}(\eta_1')\, d\eta_1' \int_{-1}^{1} t^*_R(\eta_1', u') \left[\nu_x(\eta_1') - V^{*0}_{Rx}(\eta_1)\right] R_{TR}\, du', \quad \text{for } m = 0, \tag{99}
$$

$$
\frac{1}{4\pi}\sum_m \int_{\zeta_F}^{\zeta_A} d\zeta_1' \sum_{\kappa'=1}^{2} \int_{\eta_b(\zeta_1')}^{\eta_d(\zeta_1')} m^*_{\kappa',m}(\zeta_1', \eta_1')\, H_{\kappa',Pmn}\, d\eta_1'
$$

$$
+ \frac{1}{4\pi}\sum_m \int_{\eta_\ell}^{\eta_u} d\eta_1' \int_{-1}^{1} g_{Rm}(\eta_1', u')\, R_{LPmn}\, du'
$$

$$
+ \frac{1}{4\pi}\int_{\xi_B}^{1} d\xi' \int_{-1}^{1} g_n(\xi', v')\, P_{LPn}\, dv'
$$

$$
+ \frac{1}{4\pi}\sum_m \int_{\eta_\ell}^{\eta_u} \bar{\zeta}(\eta_1')\, d\eta_1' \int_{-1}^{1} t^*_R(\eta_1', u')\, \nu_x(\eta_1')\, R_{TPn}\, du'
$$

$$
+ \frac{1}{4\pi}\int_{\zeta_F}^{\zeta_A} d\zeta_1' \sum_{\kappa'=1}^{2} \int_{\eta_b(\zeta_1')}^{\eta_d(\zeta_1')} m^{*0}_{\kappa}(\zeta_1', \eta_1')\, H_{\kappa Pon}\, d\eta_1'
$$

$$
- \frac{1}{4\pi}\int_{\eta_\ell}^{\eta_u} d\eta_1' \int_{-1}^{1} g^0_R(\eta_1', u')\, R_{LPon}\, du'
$$

$$
= \begin{cases} \left[\dfrac{\nu(\xi)}{\bar{\zeta}}\, v^*_{\theta n}(\xi) - v^*_{xn}(\xi)\right] e^{in[\theta_M(\xi)+\bar{\theta}(\xi)v]}, & \text{for } n \neq 0 \\ \left[\dfrac{\partial x^*_b(\xi, v)}{\bar{\zeta}\,\bar{\theta}(\xi)\,\partial v}\, v^*_{\theta 0}(\xi) - v^*_{x0}(\xi)\right] \\ \quad - \dfrac{1}{4\pi}\displaystyle\int_{\xi_B}^{1} \bar{\theta}(\xi')\, d\xi' \int_{-1}^{1} t^*(\xi', v')\, W^*_1(\xi')\, P_{TP}\, dv', \quad \text{for } n = 0, \end{cases} \tag{100}
$$

where

$$H_{\kappa' H\kappa} = (-1)^{\kappa-1} H_{\kappa' zH\kappa} - \frac{\partial z_0^*(\zeta_1,\eta_1)}{\partial \zeta_1} H_{\kappa' xH\kappa} - \frac{\partial z_0^*(\zeta_1,\eta_1)}{\partial \eta_1} H_{\kappa' yH\kappa},$$

$$H_{\kappa' R} = H_{\kappa' zR} - \frac{\partial z_R^*(\eta_1,u)}{\bar{\zeta}(\eta_1)\,\partial u} H_{\kappa xR},$$

$$R_{LH\kappa m} = (-1)^{\kappa-1} R_{LzH\kappa m} - \frac{\partial z_0^*(\zeta_1,\eta_1)}{\partial \zeta_1} R_{LxH\kappa m} - \frac{\partial z_0^*(\zeta_1,\eta_1)}{\partial \eta_1} R_{LyH\kappa m}, \quad R_{LRm} = R_{LzRm},$$

$$P_{LH\kappa nm} = (-1)^{\kappa-1} P_{LzH\kappa nm} - \frac{\partial z_0^*(\zeta_1,\eta_1)}{\partial \zeta_1} P_{LxH\kappa nm} - \frac{\partial z_0^*(\zeta_1,\eta_1)}{\partial \eta_1} P_{LyH\kappa nm},$$

$$P_{LRnm} = P_{LzRnm} - \frac{\partial z_R^*(\eta_1,u)}{\bar{\zeta}(\eta_1)\,\partial u} P_{LxRnm},$$

$$R_{TH\kappa} = (-1)^{\kappa-1} R_{TzH\kappa} - \frac{\partial z_0^*(\zeta_1,\eta_1)}{\partial \zeta_1} R_{TxH\kappa} - \frac{\partial z_0^*(\zeta_1,\eta_1)}{\partial \eta_1} R_{TyH\kappa},$$

$$R_{TR} = -\frac{\partial z_R^*(\eta_1,u)}{\bar{\zeta}(\eta_1)\,\partial u} R_{TxR},$$

$$P_{TH\kappa m} = (-1)^{\kappa-1} P_{TzH\kappa m} - \frac{\partial z_0^*(\zeta_1,\eta_1)}{\partial \zeta_1} P_{TxH\kappa m} - \frac{\partial z_0^*(\zeta_1,\eta_1)}{\partial \eta_1} P_{TyH\kappa m},$$

$$P_{TRm} = P_{TzRm} - \frac{\partial z_R^*(\eta_1,u)}{\bar{\zeta}(\eta_1)\,\partial u} P_{TxRm},$$

$$H_{\kappa' Pmn} = H_{\kappa' xPmn} - (\nu/\xi) H_{\kappa' \theta Pmn}, \quad R_{LPmn} = R_{LxPmn} - (\nu/\xi) R_{L\theta Pmn},$$

$$P_{LPn} = P_{LxPn} - (\nu/\xi) P_{L\theta Pn}, \quad R_{TPn} = R_{TxPn} - (\nu/\xi) R_{T\theta Pn}, \quad P_{TP} = P_{TxP} - (\nu/\xi) P_{T\theta P}. \tag{101}$$

By solving simultaneously Eqs. (98), (99) and (100) we get the solutions $m_{\kappa m}^*(\zeta_1,\eta_1)$, $g_{Rm}(\eta_1,u)$, and $g_n(\xi,v)$. Substituting Eqs. (97), etc., and these solutions into the expressions from Eqs. (82) through (86) we can obtain the forces and moments acting on the hull, rudder, and propeller. Of course the steady components, i.e., the values for $m = 0$, correspond to the mean values, and the unsteady components, i.e., the values for $m \neq 0$, represent the vibrating parts.

Finally, let us consider the velocity induced by $\phi_{P\ell}^*$. Letting $\varphi = \bar{\theta}(\xi')(v_1 - v')$, $\phi_{P\ell}^*$ defined in Eq. (74) is rewritten as

$$\phi_{P\ell}^* = -\frac{1}{4\pi} \int_{\xi_B}^{1} d\xi' \sum_{k'=1}^{N} \int_{0}^{\infty} g_1^*(\xi', v_1, -\delta_{k'})\, \bar{\theta}(\xi') \left(\xi' \frac{\partial}{\partial X^*} - \frac{\nu}{\xi'} \frac{\partial}{\partial \Theta^*} \right) \frac{1}{R^*}\, dv_1, \tag{102}$$

where

$$X^* = \nu[\theta_M(\xi') + \bar{\theta}(\xi')v_1] - \zeta - \nu_0 s\,, \quad \Theta^* = \theta_M(\xi') + \bar{\theta}(\xi')v_1 - \theta + \delta_{k'}\,,$$

$$R^* = \sqrt{X^{*2} + \xi'^2 + \xi^2 - 2\xi'\xi\cos\Theta^*}\,,$$

$$g_1^*(\xi', v', -\delta_{k'}) = \int_{-1}^{v_1} g_1\{\xi', v', -[\bar{\theta}(\xi')(v_1 - v') + \delta_{k'}]\}\,dv'\,,$$

$$g_1(\xi', v', -\delta_{k'}) = 0\,, \quad \text{for } v' \geq 1 \text{ or } v' < -1\,. \tag{103}$$

From Eqs. (22) and (23) we get

$$g_1^*(\xi', -1, -\delta_{k'}) = 0\,, \quad g_1^*(\xi_B, v_1, -\delta_{k'}) = g_1^*(1, v_1, -\delta_{k'}) = 0\,. \tag{104}$$

The velocity components induced by $\phi_{P\ell}^*$ in the x, r, and θ directions, which are denoted by $w_{P\ell x}^*$, $w_{P\ell r}^*$, and $w_{P\ell\theta}^*$ respectively, are obtained by differentiating partially with respect to ζ, ξ, and θ; then integrating them by parts, referring to Eqs. (104), the following expressions are obtained:

$$w_{P\ell x}^* \equiv \frac{\partial\phi_{P\ell}^*}{\partial\zeta} = -\frac{1}{4\pi}\int_{\xi_B}^{1} d\xi' \sum_{k'=1}^{N} \int_{-1}^{\infty}\left[\frac{\partial g_1^*(\xi', v_1, -\delta_{k'})}{\partial\xi'}\,\frac{\xi'(\xi' - \xi\cos\Theta^*)}{R^{*3}}\,\bar{\theta}(\xi')\right.$$

$$\left. + \frac{\partial g_1^*(\xi', v_1, -\delta_{k'})}{\partial v_1}\,\frac{\xi\sin\Theta^* - \xi'(\xi' - \xi\cos\Theta^*)\,\partial\Theta^*/\partial\xi'}{R^{*3}}\right]dv_1\,,$$

$$w_{P\ell r}^* \equiv \frac{\partial\phi_{P\ell}^*}{\partial\xi} = -\frac{1}{4\pi}\int_{\xi_B}^{1} d\xi' \sum_{k'=1}^{N} \int_{-1}^{\infty}\left[\frac{\partial g_1^*(\xi', v_1, -\delta_{k'})}{\partial\xi'}\right.$$

$$\frac{\xi'\sin\Theta^*\,\partial X^*/\bar{\theta}(\xi')\,\partial v_1 - \xi' X^*\cos\Theta^*}{R^{*3}}\,\bar{\theta}(\xi') + \frac{\partial g_1^*(\xi', v_1, -\delta_{k'})}{\partial v_1}$$

$$\left.\frac{X^*\sin\Theta^* - \xi'\sin\Theta^*\,\partial X^*/\partial\xi' + \xi' X^*\cos\Theta^*\,\partial\Theta^*/\partial\xi'}{R^{*3}}\right]dv_1\,,$$

$$w_{P\ell\theta}^* \equiv \frac{\partial\phi_{P\ell}^*}{\xi\,\partial\theta} = -\frac{1}{4\pi}\int_{\xi_B}^{1} d\xi' \sum_{k'=1}^{N} \int_{-1}^{\infty}\left[\frac{\partial g_1^*(\xi', v_1, -\delta_{k'})}{\partial\xi'}\right.$$

$$\frac{(\xi - \xi'\cos\Theta^*)\,\partial X^*/\bar{\theta}(\xi')\,\partial v_1 - \xi' X^*\sin\Theta^*}{R^3}\,\bar{\theta}(\xi') + \frac{\partial g_1^*(\xi', v_1, -\delta_{k'})}{\partial v_1}$$

$$\left.\frac{-X^*\cos\Theta^* - (\xi - \xi'\cos\Theta^*)\,\partial X^*/\partial\xi' + \xi' X^*\sin\Theta^*\,\partial\Theta^*/\partial\xi'}{R^{*3}}\right]dv_1\,. \tag{105}$$

Here, in each component of the induced velocity, the first term of the right-hand side represents the velocity component induced by the trailing vortex along the helix, and the second term represents the velocity component induced by the bound and shed vortices arranged in the radial direction. The function $\partial g_1^*(\xi', v_1, -\delta_{k'})/\partial v$ $(-1 \le v_1 \le 1)$ is sometimes called "the bound vortex." Moreover, for $v_1 \ge 1$, we can get

$$
\begin{aligned}
g_1^*(\xi', v_1, -\delta_{k'}) &= \int_{-1}^{1} g_1\{\xi', v', -[\bar{\theta}(\xi')(v_1 - v') + \delta_{k'})]\}\, dv' \\
&= \int_{-1}^{1} g_1\{\xi', v', -[\bar{\theta}(\xi')(v_1 - 1) + \delta_{k'} + \bar{\theta}(\xi')(1 - v')]\}\, dv' \\
&= g_1^*\{\xi', 1, -[\bar{\theta}(\xi')(v_1 - 1) + \delta_{k'}]\} \\
&= g_1^*\{\xi', 1, \theta_M(\xi') + \bar{\theta}(\xi') - [\theta_M(\xi') + \bar{\theta}(\xi')\, v_1 + \delta_{k'}]\},
\end{aligned}
\tag{106}
$$

and this function is rewritten as $g^*(\xi', \theta')$, where $\theta' = \theta_M(\xi') + \bar{\theta}(\xi')\, v_1 + \delta_{k'}$. That is, the function $g^*(\xi, \theta)$ represents the strength of the helical trailing vortex at the point

$$
\zeta = \nu[\theta_M(\xi) + \bar{\theta}(\xi)\, v_1] - \nu_0 s, \quad \xi = \xi, \quad \theta = \theta_M(\xi) + \bar{\theta}(\xi)\, v_1 + \delta_k. \tag{107}
$$

Next we consider the velocity potential and the induced velocity in the domain of a propeller wake, i.e., $\xi_B \le \xi \le 1$ and $v_1 > 1$. In this domain the velocity potentials and velocity components except $\phi_{P\ell}^*$, $w_{P\ell x}^*$, $w_{P\ell r}^*$, and $w_{P\ell\theta}^*$ are continuous. The quantities $\phi_{P\ell}^*$, $w_{P\ell x}^*$, $w_{P\ell r}^*$, and $w_{P\ell\theta}^*$ are discontinuous at any point on the surfaces of trailing vortices which satisfies Eqs. (107) and are continuous at all remaining points in the domain of propeller wake. In general, the closed vortex can be replaced hydrodynamically by doublet distributions. Accordingly the helical surfaces of trailing vortices are equivalent to the surfaces of doublet distributions. We denote the increments of values of $\phi_{P\ell}^*$, $w_{P\ell x}^*$, $w_{P\ell r}^*$, and $w_{P\ell\theta}^*$ at the discontinuous surfaces when a point passes through the point (ζ, ξ, θ) of Eqs. (107) so as to increase θ keeping ζ constant or decrease ζ maintaining θ constant by $\Delta\phi_{P\ell}^*$, $\Delta w_{P\ell x}^*$, $\Delta w_{P\ell r}^*$, and $\Delta w_{P\ell\theta}^*$ respectively. Then using the classical potential theory we get

$$
\begin{aligned}
&\Delta\phi_{P\ell}^* = g^*(\xi, \theta), \quad \Delta w_{P\ell x}^* = \frac{\nu}{\xi^2 + \nu^2} \frac{\partial g_1^*(\xi, \theta)}{\partial \theta}, \quad \Delta w_{P\ell r}^* = \frac{\partial g^*(\xi, \theta)}{\partial \xi}, \\
&\Delta w_{P\ell\theta}^* = \frac{\xi}{\xi^2 + \nu^2} \frac{\partial g^*(\xi, \theta)}{\partial \theta}.
\end{aligned}
\tag{108}
$$

We must take Eqs. (108) into account in the actual calculations of $w_{P\ell x}^*$, $w_{P\ell r}^*$, and $w_{P\ell\theta}^*$ in the domain of the propeller wake.

A METHOD TO CALCULATE BEARING FORCES

The mathematical expressions of unsteady propeller forces for a ship with a propeller and a rudder were introduced in the previous section. It is further necessary to reduce them to forms suitable for numerical calculations. However, it seems laborious as shown in the previous section to calculate the surface and bearing forces simultaneously by using a high-speed digital computer. Hence, for simplicity, the results presented in the previous section will be reformulated for bearing forces in this section. Let us denote the components of inflow velocity to the propeller in the x, r, and θ directions by v_x^*, v_r^*, and v_θ^* respectively, which are composed of the viscous velocities and the potential velocities induced by the hull and rudder and are expressed as

$$v_x^* = \frac{\partial(\phi_H^* + \phi_R^*)}{\partial\zeta} + v_{1x}^* = \frac{\partial\phi^{*0}}{\partial\zeta} + v_{1x}^{*0} + \frac{\partial(\Phi_H + \Phi_{R\ell} + \Phi_{Rt})}{\partial\zeta} + \tilde{v}_{1x}^* ,$$

$$v_r^* = \frac{\partial(\phi_H^* + \phi_R^*)}{\partial\xi} + v_{1r}^* = \frac{\partial\phi^{*0}}{\partial\xi} + v_{1r}^{*0} + \frac{\partial(\Phi_H + \Phi_{R\ell} + \Phi_{Rt})}{\partial\xi} + \tilde{v}_{1r}^* ,$$

$$v_\theta^* = \frac{\partial(\phi_H^* + \phi_R^*)}{\xi\partial\theta} + v_{1\theta}^* = \frac{\partial\phi^{*0}}{\xi\partial\theta} + v_{1\theta}^{*0} + \frac{\partial(\Phi_H + \Phi_{R\ell} + \Phi_{Rt})}{\xi\partial\theta} + \tilde{v}_{1\theta}^* . \qquad (109)$$

We shall consider that the propeller is operating in a nonuniform flow with inflow velocity components v_x^*, v_r^*, and v_θ^* which are not influenced directly by the presence of the propeller. Further, since the effect of blade thickness on the performance characteristics of the propeller is known to be negligibly small (11), we may neglect this factor in the calculation of bearing forces, i.e., we set

$$\phi_{Pt}^* \approx 0 . \qquad (110)$$

Then the following expression for the potential is obtained from Eqs. (74) and (76):

$$\phi_{P\ell}^* = -\frac{1}{4\pi}\int_{\xi_B}^{1} d\xi' \int_{-1}^{1} dv' \sum_{k'=1}^{N} \int_{0}^{\infty} g_1[\xi', v', -(\varphi + \delta_{k'})] \left(\xi' \frac{\partial}{\partial X^*} - \frac{\nu}{\xi'^2}\frac{\partial}{\partial\Theta^*}\right)\frac{1}{R^*} d\varphi , \qquad (111)$$

where

$$X^* = \nu[\varphi + \theta_M(\xi') + \bar{\theta}(\xi')v'] - \zeta - \nu_0 s ,$$

$$\Theta^* = \varphi + \theta_M(\xi') + \bar{\theta}(\xi')v' - \theta + \delta_{k'} ,$$

$$R^* = \sqrt{X^{*2} + \xi'^2 + \xi^2 - 2\xi'\xi\cos\Theta^*} , \qquad (112)$$

(Cont)

$$V^*_{kx} = \frac{1}{\pi}\int_{-1}^{1}\sqrt{\frac{1-v}{1+v}}\left(\nu_0 + \left[\frac{\partial\phi^*_{P\ell}}{\partial\zeta}\right]_{(SP)} + [v^*_x]_{(SP)}\right)dv \ ,$$

$$V^*_{k\theta} = \frac{1}{\pi}\int_{-1}^{1}\sqrt{\frac{1-v}{1+v}}\left(\xi + \left[\frac{\partial\phi^*_{P\ell}}{\xi\partial\theta}\right]_{(SP)} + [v^*_\theta]_{(SP)}\right)dv \ ,$$

$$W^*_1(\xi, -\delta_k) = \sqrt{V^{*2}_{kx} + V^{*2}_{k\theta}} \ , \quad \textcircled{\nu}(\xi) = \frac{1}{\pi}\int_{-1}^{1}\sqrt{\frac{1+v}{1-v}}\frac{\partial X^*_b(\xi,v)}{\bar{\theta}(\xi)\,\partial v}\,dv \ ,$$

$$\nu \approx \frac{1}{2}\left[\textcircled{\nu}(\xi) + \frac{1}{2\pi^2}\int_0^{2\pi} ds \int_{-1}^{1}\sqrt{\frac{1-v}{1+v}}(\nu_0 + [v^*_x]_{(SP)})\right.$$

$$\left. dv \Big/ \frac{1}{2\pi^2\xi}\int_0^{2\pi} ds \int_{-1}^{1}\sqrt{\frac{1-v}{1+v}}(\xi + [v^*_\theta]_{(SP)})\,dv\right]_{\xi=\sqrt{(1+\xi_B^2)/2}}$$

or

$$\approx (\text{face pitch})/2r_0 \ . \tag{112}$$

Since the velocity components $\nu_0 + [v^*_x]_{(SP)}$ and $\xi + [v_\theta]_{(SP)}$ can be assumed to be independent of ζ, they can be expanded similarly to Eqs. (90) as

$$\begin{aligned} \nu_0 + [v^*_x]_{(SP)} &= \sum_n v^*_{xn}(\xi)\, e^{in[\theta_M(\xi)+\bar{\theta}(\xi)v+\delta_k]} \ , \\ \xi + [v^*_\theta]_{(SP)} &= \sum_n v^*_{\theta n}(\xi)\, e^{in[\theta_M(\xi)+\bar{\theta}(\xi)v+\delta_k]} \ , \end{aligned} \tag{113}$$

where

$$\begin{aligned} v^*_{xn}(\xi) &= \frac{1}{2\pi}\int_0^{2\pi}(\nu_0 + [v^*_x]_{\zeta=-\nu_0 s})\, e^{-in\theta}\,d\theta \ , \\ v^*_{\theta n}(\xi) &= \frac{1}{2\pi}\int_0^{2\pi}(\xi + [v^*_\theta]_{\zeta=-\nu_0 s})\, e^{-in\theta}\,d\theta \ , \end{aligned} \tag{114}$$

in which $[\ ]_{\zeta=-\nu_0 s}$ indicates the value of $[\ ]$ at the representative plane of the propeller disk. With account taken of the characteristics of a two-dimensional unsteady airfoil in sinusoidal gusts the bound vortex $g_1(\xi, v, -\delta_k)$ in Eqs. (91) and (92) can be approximated by

$$g_1(\xi, v, -\delta_k) \approx \frac{1}{\pi} \sum_n G_n(\xi) \sqrt{\frac{1 - v}{1 + v}}\, e^{in\delta_k} \quad , \tag{115}$$

where $G_n(\xi)$ is the circulation with a harmonic number n around the blade section. Then referring to Eqs. (86), (69), (109), (110), (111), (113), and (96), we get

$$\begin{aligned} [V_x^*]_{(SP)} &= \nu_0 + \left[\frac{\partial \phi^*_{P\ell}}{\partial \zeta}\right]_{(SP)} + [v_x^*]_{(SP)} = \sum_n V_{xn} e^{in\delta_k} \quad , \\ [V_\theta^*]_{(SP)} &= \xi + \left[\frac{\partial \phi^*_{P\ell}}{\xi \partial \theta}\right]_{(SP)} + [v_\theta^*]_{(SP)} = \sum_n V_{\theta n} e^{in\delta_k} \quad , \end{aligned} \tag{116}$$

where

$$\begin{aligned} V_{xn} &= v^*_{xn}(\xi)\, e^{in[\theta_M(\xi) + \bar{\theta}(\xi)v]} + \frac{1}{4\pi^2} \int_{\xi_B}^1 G_n(\xi')\, d\xi' \int_{-1}^1 \sqrt{\frac{1 - v'}{1 + v'}}\, P_{LxPn}\, dv' \quad , \\ V_{\theta n} &= v^*_{\theta n}(\xi)\, e^{in[\theta_M(\xi) + \bar{\theta}(\xi)v]} + \frac{1}{4\pi^2} \int_{\xi_B}^1 G_n(\xi')\, d\xi' \int_{-1}^1 \sqrt{\frac{1 - v'}{1 + v'}}\, P_{L\theta Pn}\, dv' \quad , \end{aligned} \tag{117}$$

We substitute Eqs. (109), (110), (111), (113), and (115) into Eq. (79), i.e., the boundary condition on S_P, and multiply this equation by the weight operator

$$\frac{1}{\pi} \int_{-1}^1 dv \sqrt{\frac{1 + v}{1 - v}} \quad . \tag{118}$$

Then, since the equation obtained in this way is to be independent of δ_k, the following equation is obtained for each n similarly to Eqs. (100):

$$\begin{aligned} &\frac{1}{4\pi^3} \int_{\xi_B}^1 G_n(\xi)\, d\xi \int_{-1}^1 \sqrt{\frac{1 + v}{1 - v}} \int_{-1}^1 \sqrt{\frac{1 - v'}{1 + v'}} \left(P_{LxPn} - \frac{\nu}{\xi} P_{L\theta Pn}\right) dv' \\ &= \left[\frac{\textcircled{\nu}(\xi)}{\xi} v^*_{\theta n}(\xi) - v^*_{xn}(\xi)\right] \frac{1}{\pi} \int_{-1}^1 \sqrt{\frac{1 + v}{1 - v}}\, e^{in[\theta_M(\xi) + \bar{\theta}(\xi)v]}\, dv \quad , \end{aligned} \tag{119}$$

where

$$\begin{aligned} P_{LxPn} &= \sum_{k'=1}^N \int_0^\infty e^{in[\varphi + 2\pi(k'-1)/N]}\, A_{xk'1}(\xi', \xi, \nu; \varphi + \psi_0)\, d\varphi \quad , \\ P_{L\theta Pn} &= \sum_{k'=1}^N \int_0^\infty e^{in[\varphi + 2\pi(k'-1)/N]}\, A_{\theta k'1}(\xi', \xi, \nu; \varphi + \psi_0)\, d\varphi \quad , \end{aligned} \tag{120}$$

(Cont)

$$A_{xk'1}(\xi',\xi,\nu;\psi) = -\frac{\xi'}{\sqrt{\nu^2\psi^2+\xi'^2+\xi^2-2\xi'\xi\cos[\psi+2\pi(k'-1)/N]^3}}$$

$$+\frac{3\nu^2\psi\{\xi'\psi-\xi\sin[\psi+2\pi(k'-1)/N]\}}{\sqrt{\nu^2\psi^2+\xi'^2+\xi^2-2\xi'\xi\cos[\psi+2\pi(k'-1)/N]^5}},$$

$$A_{\theta k'1}(\xi',\xi,\nu;\psi) = \frac{\nu\cos[\psi+2\pi(k'-1)/N]}{\sqrt{\nu^2\psi_1^2+\xi'^2+\xi^2-2\xi'\xi\cos[\psi+2\pi(k'-1)/N]^3}}$$

$$+\frac{3\nu\xi'\sin[\psi+2\pi(k'-1)/N]\{\xi'\psi-\xi\sin[\psi+2\pi(k'-1)/N]\}}{\sqrt{\nu^2\psi^2+\xi'^2+\xi^2-2\xi'\xi\cos[\psi+2\pi(k'-1)/N]^5}},$$

$$\psi_0 = \theta_M(\xi') - \theta_M(\xi) + \bar{\theta}(\xi')\,v' - \bar{\theta}(\xi)\,v\,. \tag{120}$$

Substituting Eqs. (116) and (117) into Eqs. (112) we get

$$V^*_{xn} = \frac{1}{\pi}\int_{-1}^{1}\sqrt{\frac{1-v}{1+v}}\,V_{xn}\,dv\,,\quad V^*_{\theta n} = \frac{1}{\pi}\int_{-1}^{1}\sqrt{\frac{1-v}{1+v}}\,V_{\theta n}\,dv\,,\quad V^*_{kx} = \sum_n V^*_{xn}\,e^{in\delta_k}\,, \tag{121}$$

$$V^*_{k\theta} = \sum_n V^*_{\theta n}\,e^{in\delta_k}\,,\quad W_1(\xi,-\delta_k) = \sqrt{V^{*2}_{kx}+V^{*2}_{k\theta}}\,.$$

Hence, from Eqs. (52) and (53) we get the section lift coefficient $C_{kL}(\xi,s)$ and the section viscous drag coefficient C_{PD}:

$$C_{kL}(\xi,s) = \frac{\sum_n G_n(\xi)\,e^{in\delta_k}}{\bar{\theta}(\xi)\,W^*_1(\xi,-\delta_k)\sqrt{\xi'^2+\nu^2}}\,,\quad C_{PD} = C_{PD0}(\xi) + a_P(\xi)[C_{kL}(\xi,s) - b_P(\xi)]^2\,. \tag{122}$$

Substituting Eqs. (109), (110), (114), and (116) into Eqs. (85) and (86), and referring to Eqs. (121), we obtain the force and moment acting on the propeller as

$$K_{Fx} = K_{Fx0} + K_{FxD}\,,\quad K_{Fy} = K_{Fy0} + K_{FyD}\,,\quad K_{Fz} = K_{Fz0} + K_{FzD}\,,$$
$$K_{Mx} = K_{Mx0} + K_{MxD}\,,\quad K_{My} = K_{My0} + K_{MyD}\,,\quad K_{Mz} = K_{Mz0} + K_{MzD}\,, \tag{123}$$

where

$$K_{Fx0} = -\frac{\pi}{4}\int_{\xi_B}^{1}\sum_{k=1}^{N}\sum_{n,n'}G_n(\xi)\,e^{i(n+n')\delta_k}\,d\xi\int_{-1}^{1}\sqrt{\frac{1-v}{1+v}}\,V_{\theta n'}\,dv\,, \tag{124}$$

(Cont)

$$K_{Fy0} = -\frac{\pi}{4}\int_{\xi_B}^{1}\sum_{k=1}^{N}\sum_{n,n'} G_n(\xi)\, e^{i(n+n')\delta_k}\, d\xi \int_{-1}^{1}\sqrt{\frac{1-v}{1+v}}\, V_{xn'}$$

$$\sin\left[\theta_M(\xi) + \bar{\theta}(\xi)\, v + \delta_k\right] dv \ ,$$

$$K_{Fz0} = \frac{\pi}{4}\int_{\xi_B}^{1}\sum_{k=1}^{N}\sum_{n,n'} G_n(\xi)\, e^{i(n+n')\delta_k}\, d\xi \int_{-1}^{1}\sqrt{\frac{1-v}{1+v}}\, V_{xn'}$$

$$\cos\left[\theta_M(\xi) + \bar{\theta}(\xi)\, v + \delta_k\right] dv \ ,$$

$$K_{Mx0} = \frac{\pi}{8}\int_{\xi_B}^{1}\sum_{k=1}^{N}\sum_{n,n'} G_n(\xi)\, e^{i(n+n')\delta_k}\, \xi d\xi \int_{-1}^{1}\sqrt{\frac{1-v}{1+v}}\, V_{xn'}\, dv \ ,$$

$$K_{My0} = -\frac{\pi}{8}\int_{\xi_B}^{1}\sum_{k=1}^{N}\sum_{n,n'} G_n(\xi)\, e^{i(n+n')\delta_k}\, d\xi \int_{-1}^{1}\sqrt{\frac{1-v}{1+v}}$$

$$\left(V_{\theta n'}\, \xi \sin\left[\theta_M(\xi) + \bar{\theta}(\xi)\, v + \delta_k\right]\right.$$

$$\left. + V_{xn'}\left\{\nu\left[\theta_M(\xi) + \bar{\theta}(\xi)\, v\right] + \xi\varepsilon\right\} \cos\left[\theta_M(\xi) + \bar{\theta}(\xi)\, v + \delta_k\right]\right) dv \ ,$$

$$K_{Mz0} = \frac{\pi}{8}\int_{\xi_B}^{1}\sum_{k=1}^{N}\sum_{n,n'} G_n(\xi)\, e^{i(n+n')\delta_k}\, d\xi \int_{-1}^{1}\sqrt{\frac{1-v}{1+v}}$$

$$\left(V_{\theta n'}\, \xi \cos\left[\theta_M(\xi) + \bar{\theta}(\xi)\, v + \delta_k\right]\right.$$

$$\left. - V_{xn'}\left\{\nu\left[\theta_M(\xi) + \bar{\theta}(\xi)\, v\right] + \xi\varepsilon\right\} \sin\left[\theta_M(\xi) + \bar{\theta}(\xi)\, v + \delta_k\right]\right) dv \ ,$$

$$K_{FxD} = \frac{\pi^2}{4}\int_{\xi_B}^{1}\sum_{k=1}^{N} C_{PD}\left[1 + (\nu/\xi)^2\right] V^*_{k\theta}\, V^*_{kx}\, \bar{\theta}(\xi)\, \xi d\xi \ ,$$

$$K_{FyD} = -\frac{\pi^2}{4}\int_{\xi_B}^{1}\sum_{k=1}^{N} C_{PD}\left[1 + (\nu/\xi)^2\right] V^{*2}_{k\theta} \sin\left[\theta_M(\xi) + \delta_k\right] \sin\bar{\theta}(\xi)\, \xi\, d\xi \ ,$$

$$K_{FzD} = \frac{\pi^2}{4}\int_{\xi_B}^{1}\sum_{k=1}^{N} C_{PD}\left[1 + (\nu/\xi)^2\right] V^{*2}_{k\theta} \cos\left[\theta_M(\xi) + \delta_k\right] \sin\bar{\theta}(\xi)\, \xi\, d\xi \ ,$$

(124)
(Cont)

$$K_{MxD} = \frac{\pi^2}{8} \int_{\xi_B}^{1} \sum_{k=1}^{N} C_{PD}[1 + (\nu/\xi)^2] V_{k\theta}^{*2} \bar{\theta}(\xi) \xi^2 d\xi ,$$

$$K_{MyD} = \frac{\pi^2}{8} \int_{\xi_B}^{1} \sum_{k=1}^{N} C_{PD}[1 + (\nu/\xi)^2] V_{k\theta}^{*}(V_{kx}^{*} \sin[\theta_M(\xi) + \delta_k] \xi \sin\bar{\theta}(\xi)$$

$$+ V_{k\theta}^{*}\{\sin[\theta_M(\xi) + \delta_k] \nu [\sin\bar{\theta}(\xi) - \bar{\theta}(\xi) \cos\bar{\theta}(\xi)]$$

$$- \cos[\theta_M(\xi) + \delta_k][\nu\theta_M(\xi) + \xi\varepsilon] \sin\bar{\theta}(\xi)\}) \xi d\xi ,$$

$$K_{MzD} = -\frac{\pi^2}{8} \int_{\xi_B}^{1} \sum_{k=1}^{N} C_{PD}[1 + (\nu/\xi)^2] V_{k\theta}^{*}(V_{kx}^{*} \cos[\theta_M(\xi) + \delta_k] \xi \sin\bar{\theta}(\xi)$$

$$+ V_{k\theta}^{*}\{\cos[\theta_M(\xi) + \delta_k] \nu [\sin\bar{\theta}(\xi) - \bar{\theta}(\xi) \cos\bar{\theta}(\xi)]$$

$$+ \sin[\theta_M(\xi) + \delta_k][\nu\theta_M(\xi) + \xi\varepsilon] \sin\bar{\theta}(\xi)\}) \xi d\xi . \tag{124}$$

From Eqs. (56) we get the thrust coefficient C_T and torque coefficient C_Q:

$$C_T = -K_{Fx} , \quad C_Q = K_{Mx} . \tag{125}$$

Further, denoting the components of K_{Fx}, K_{Fy}, etc., for a harmonic number ℓ by $K_{Fx}^{(\ell)}$, $K_{Fy}^{(\ell)}$, etc., respectively, assuming that C_{PD} is a constant independent of k and s instead of the expression in Eqs. (122), and using the formula

$$\sum_{k=1}^{N} e^{i\ell\delta_k} = \begin{cases} Ne^{-imNs} , & \text{for } \ell = mN , \\ 0 , & \text{for } \ell \neq mN , \end{cases} \tag{126}$$

then Eqs. (122) and (123) are reduced to

$$K_{Fx} = \sum_m K_{Fx}^{(mN)} e^{-imNs}, \quad K_{Fy} = \sum_m K_{Fy}^{(mN)} e^{-imNs}, \quad K_{Fz} = \sum_m K_{Fz}^{(mN)} e^{-imNs},$$

$$K_{Mx} = \sum_m K_{Mx}^{(mN)} e^{-imNs}, \quad K_{My} = \sum_m K_{My}^{(mN)} e^{-imNs}, \quad K_{Mz} = \sum_m K_{Mz}^{(mN)} e^{-imNs}, \tag{127}$$

where

$$K_{Fx}^{(mN)} = K_{Fx0}^{(mN)} + K_{FxD}^{(mN)}, \quad K_{Fy}^{(mN)} = K_{Fy0}^{(mN)} + K_{FyD}^{(mN)}, \quad K_{Fz}^{(mN)} = K_{Fz0}^{(mN)} + K_{FzD}^{(mN)},$$

$$K_{Mx}^{(mN)} = K_{Mx0}^{(mN)} + K_{MxD}^{(mN)}, \quad K_{My}^{(mN)} = K_{My0}^{(mN)} + K_{MyD}^{(mN)}, \quad K_{Mz}^{(mN)} = K_{Mz0}^{(mN)} + K_{MzD}^{(mN)}, \tag{128}$$

$$K_{Fx0}^{(mN)} = - \sum_n \frac{\pi}{4} \int_{\xi_B}^{1} NG_n(\xi)\, d\xi \int_{-1}^{1} \sqrt{\frac{1-v}{1+v}}\, V_{\theta,mN-n}\, dv ,$$

$$K_{Fy0}^{(mN)} = - \sum_n \frac{\pi}{4} \int_{\xi_B}^{1} NG_n(\xi)\, d\xi \int_{-1}^{1} \sqrt{\frac{1-v}{1+v}}\, \frac{1}{2i} \left\{ V_{x,mN-n-1}\, e^{i[\theta_M(\xi)+\bar{\theta}(\xi)v]} - V_{x,mN-n+1}\, e^{-i[\theta_M(\xi)+\bar{\theta}(\xi)v]} \right\} dv ,$$

$$K_{Fz0}^{(mN)} = \sum_n \frac{\pi}{4} \int_{\xi_B}^{1} NG_n(\xi)\, d\xi \int_{-1}^{1} \sqrt{\frac{1-v}{1+v}}\, \frac{1}{2} \left\{ V_{x,mN-n-1}\, e^{i[\theta_M(\xi)+\bar{\theta}(\xi)v]} + V_{x,mN-n+1}\, e^{-i[\theta_M(\xi)+\bar{\theta}(\xi)v]} \right\} dv ,$$

$$K_{Mx0}^{(mN)} = \sum_n \frac{\pi}{8} \int_{\xi_B}^{1} NG_n(\xi)\, \xi\, d\xi \int_{-1}^{1} \sqrt{\frac{1-v}{1+v}}\, V_{x,mN-n}\, dv ,$$

$$K_{My0}^{(mN)} = - \sum_n \frac{\pi}{8} \int_{\xi_B}^{1} NG_n(\xi)\, d\xi \int_{-1}^{1} \sqrt{\frac{1-v}{1+v}} \left(\frac{1}{2i}\, \xi \left\{ V_{\theta,mN-n-1}\, e^{i[\theta_M(\xi)+\bar{\theta}(\xi)v]} - V_{\theta,mN-n+1}\, e^{-i[\theta_M(\xi)+\bar{\theta}(\xi)v]} \right\} + \frac{1}{2} \{\nu[\theta_M(\xi) + \bar{\theta}(\xi)\, v] + \xi\varepsilon\} \left\{ V_{x,mN-n-1}\, e^{i[\theta_M(\xi)+\bar{\theta}(\xi)v]} + V_{x,mN-n+1}\, e^{-i[\theta_M(\xi)+\bar{\theta}(\xi)v]} \right\} \right) dv ,$$

$$K_{Mz0}^{(mN)} = \sum_n \frac{\pi}{8} \int_{\xi_B}^{1} NG_n(\xi)\, d\xi \int_{-1}^{1} \sqrt{\frac{1-v}{1+v}} \left(\frac{1}{2}\, \xi \left\{ V_{\theta,mN-n-1}\, e^{i[\theta_M(\xi)+\bar{\theta}(\xi)v]} + V_{\theta,mN-n+1}\, e^{-i[\theta_M(\xi)+\bar{\theta}(\xi)v]} \right\} - \frac{1}{2i} \{\nu[\theta_M(\xi) + \bar{\theta}(\xi)\, v] + \xi\varepsilon\} \left\{ V_{x,mN-n-1}\, e^{i[\theta_M(\xi)+\bar{\theta}(\xi)v]} - V_{x,mN-n+1}\, e^{-i[\theta_M(\xi)+\bar{\theta}(\xi)v]} \right\} \right) dv ,$$

$$K_{FxD}^{(mN)} = \sum_n \frac{\pi^2}{4} \int_{\xi_B}^{1} NC_{PD}[1 + (\nu/\xi)^2]\, V_{\theta n}^{*}\, V_{x,mN-n}^{*}\, \bar{\theta}(\xi)\, \xi\, d\xi , \qquad \text{(129) (Cont)}$$

$$K_{FyD}^{(mN)} = - \sum_n \frac{\pi^2}{4} \int_{\xi_B}^{1} NC_{PD}[1 + (\nu/\xi)^2] \; V_{\theta n}^* \; \frac{1}{2i}\left[V_{\theta, mN-n-1}^* \; e^{i\theta_M(\xi)} - V_{\theta, mN-n+1}^* \; e^{-i\theta_M(\xi)}\right] \sin\bar{\theta}(\xi) \; \xi \, d\xi ,$$

$$K_{FzD}^{(mN)} = \sum_n \frac{\pi^2}{4} \int_{\xi_B}^{1} NC_{PD}[1 + (\nu/\xi)^2] \; V_{\theta n}^* \; \frac{1}{2}\left[V_{\theta, mN-n-1}^* \; e^{i\theta_M(\xi)} + V_{\theta, mN-n+1}^* \; e^{-i\theta_M(\xi)}\right] \sin\bar{\theta}(\xi) \; \xi \, d\xi ,$$

$$K_{MxD}^{(mN)} = \sum_n \frac{\pi^2}{8} \int_{\xi_B}^{1} NC_{PD}[1 + (\nu/\xi)^2] \; V_{\theta n}^* \; V_{\theta, mN-n}^* \; \bar{\theta}(\xi) \; \xi^2 \, d\xi ,$$

$$\begin{aligned} K_{MyD}^{(mN)} = \sum_n \frac{\pi^2}{8} \int_{\xi_B}^{1} NC_{PD}[1 + (\nu/\xi)^2] \; V_{\theta n}^* \Bigg\{ & \frac{1}{2i}\left[V_{x, mN-n-1}^* \; e^{i\theta_M(\xi)} - V_{x, mN-n+1}^* \; e^{-i\theta_M(\xi)}\right] \xi \sin\bar{\theta}(\xi) \\ & - \frac{1}{2}\left[V_{\theta, mN-n-1}^* \; e^{i\theta_M(\xi)} + V_{\theta, mN-n+1}^* \; e^{-i\theta_M(\xi)}\right] [\nu\theta_M(\xi) + \xi\varepsilon] \sin\bar{\theta}(\xi) \\ & + \frac{1}{2i}\left[V_{\theta, mN-n-1}^* \; e^{i\theta_M(\xi)} - V_{\theta, mN-n+1}^* \; e^{-i\theta_M(\xi)}\right] \\ & \nu \, [\sin\bar{\theta}(\xi) - \bar{\theta}(\xi) \cos\bar{\theta}(\xi)] \Bigg\} \xi \, d\xi , \end{aligned}$$

$$\begin{aligned} K_{MzD}^{(mN)} = - \sum_n \frac{\pi^2}{8} \int_{\xi_B}^{1} NC_{PD}[1 + (\nu/\xi)^2] \; V_{\theta n}^* \Bigg\{ & \frac{1}{2}\left[V_{x, mN-n-1}^* \; e^{i\theta_M(\xi)} + V_{x, mN-n+1}^* \; e^{-i\theta_M(\xi)}\right] \xi \sin\bar{\theta}(\xi) \\ & + \frac{1}{2i}\left[V_{\theta, mN-n-1}^* \; e^{i\theta_M(\xi)} - V_{\theta, mN-n+1}^* \; e^{-i\theta_M(\xi)}\right] [\nu\theta_M(\xi) + \xi\varepsilon] \sin\bar{\theta}(\xi) \\ & + \frac{1}{2}\left[V_{\theta, mN-n-1}^* \; e^{i\theta_M(\xi)} + V_{\theta, mN-n+1}^* \; e^{-i\theta_M(\xi)}\right] \\ & \nu \, [\sin\bar{\theta}(\xi) - \bar{\theta}(\xi) \cos\bar{\theta}(\xi)] \Bigg\} \xi \, d\xi . \end{aligned} \tag{129}$$

The frequency of bearing forces is represented by $mN\Omega/2\pi = mn_rN$. Therefore, denoting the components of forces and moments for frequency $mn_rN > 0$ by K_{Fxm}, K_{Fym}, etc., we can get

$$K_{Fxm} = K_{Fx}^{(mN)} e^{-imNs} + K_{Fx}^{(-mN)} e^{imNs}, \quad K_{Fym} = K_{Fy}^{(mN)} e^{-imNs} + K_{Fy}^{(-mN)} e^{imNs}, \ldots . \tag{130}$$

From Eqs. (127), (128), and (129) the complex functions $K_{Fx}^{(-mN)}$, $K_{Fy}^{(-mN)}$, etc., are the conjugate complex functions of $K_{Fx}^{(mN)}$, $K_{Fy}^{(mN)}$, etc., respectively. Consequently, for $mn_rN > 0$, denoting the amplitudes of K_{Fxm}, K_{Fym}, etc., by A_{Fxm} A_{Fym}, etc., respectively, they are equal to twice the absolute values of $K_{Fx}^{(mN)}$, $K_{Fy}^{(mN)}$, etc., respectively. That is, we get for $m \geq 1$

$$\begin{aligned} A_{Fxm} &= 2|K_{Fx}^{(mN)}|, \quad A_{Fym} = 2|K_{Fy}^{(mN)}|, \quad A_{Fzm} = 2|K_{Fz}^{(mN)}|, \\ A_{Mxm} &= 2|K_{Mx}^{(mN)}|, \quad A_{Mym} = 2|K_{My}^{(mN)}|, \quad A_{Mzm} = 2|K_{Mz}^{(mN)}|. \end{aligned} \tag{131}$$

With the particular values of a propeller $\theta_M(\xi)$, $\bar{\theta}(\xi)$, $x^*(\xi,\nu)$, and ε, the inflow velocity components v_x^*, v_r^*, and v_θ^*, and the advance coefficient ν_0 given, let us calculate the bearing forces by using the preceding equations. That is, calculating $\nu(\xi)$, $v_{xn}^*(\xi)$, $v_{\theta n}^*(\xi)$, and $\textcircled{\nu}$ by using Eqs. (112) and (113), we obtain $G_n(\xi)$ by solving Eq. (119) and then calculate V_{xn} and $V_{\theta n}$ from Eqs. (117), V_{xn}^*, $V_{\theta n}^*$, V_{kx}^*, $V_{k\theta}^*$, and $W_1(\xi, -\delta_k)$ from Eqs. (121), and $C_{kL}(\xi, s)$ from the first of Eqs. (122). On the other hand, when the values of $C_{PD0}(\xi)$, $a_P(\xi)$, and $b_P(\xi)$ are assumed to be known for each blade section, C_{PD} can be obtained from the second of Eqs. (122). Substituting the resulting values of $G_n(\xi)$, V_{xn}, $V_{\theta n}$, V_{kx}^*, $V_{k\theta}^*$, and C_{PD} into Eqs. (123) and (124) we can calculate K_{Fx}, K_{Fy}, K_{Fz}, K_{Mx}, K_{My}, and K_{Mz}. Thus the bearing forces can be obtained. The detailed procedure to calculate K_{Fx} and K_{Mx}, i.e., C_T and C_Q was presented in the appendix of Ref. 6. The components of force and moment acting on the propeller other than K_{Fx} and K_{Mx} can be calculated according to a similar method as for K_{Fx} and K_{Mx}. Similarly, by substituting $G_n(\xi)$, V_{xn}, $V_{\theta n}$, V_{xn}^*, and $V_{\theta n}^*$ into Eqs. (128), (129), and (130), and further assuming C_{PD} to be constant, we can calculate the amplitudes A_{Fxm}, A_{Fym}, etc., of vibratory forces and moments for frequency mn_rN (>0).

NUMERICAL EXAMPLES OF BEARING FORCES

As numerical examples, propeller M of Ref. 6 is adopted as a parent propeller, whose principal parameters N, ξ_B, $\textcircled{\nu}(\xi)$, ε, etc., are shown in Table 1. Then the variations from propeller M are as follows: $\theta_M(\xi)$ and $\bar{\theta}(\xi)$ of any given propeller are respectively α and β times as much as those of propeller M. The values of the particular magnification factors α and β used here are summarized in Table 2. For propellers M_{12}, M_{22}, M_{32}, M, and M_{52}, we take $\alpha = 1$ and $\beta = -0.5$, 0, 0.5, 1.0, and 2 respectively, and this group is employed to determine the effect of skew on bearing forces. When we take $\alpha = 1$ and $\beta = 0.75$, 1.00, and 1.25 for propellers M_{41}, M, and M_{43} respectively and also $\alpha = 0$ and $\beta = 0.75$, 1.00, and 1.25 for propellers M_{21}, M_{22}, and M_{23} respectively, these two groups determine the effect of the blade area ratio on the bearing forces. The blade area ratios of the given propellers are also shown in Table 2.

Table 1
Parameters of Propeller M (Diameter D = $2r_0$ = 215.67 mm; Face Pitch $2\pi r$ = 205.85 mm; N = 4; ξ_B = 0.1765; Blade Area Ratio = 0.5748; Pitch Ratio = 0.9546; $\varepsilon = 8° = 0.1396$; $\nu = 0.276$)

i	$\xi = \xi_i$	$\theta_M(\xi)$	$\bar{\theta}(\xi)$	$\textcircled{\nu}(\xi)$	α_{g1}	Thickness-to-Chord Ratio
0	0.176500	-0.1537	0.6627	0.33122	-	-
1	0.260818	-0.1498	0.6518	0.33191	0.0446	-
2	0.415976	-0.1151	0.5816	0.33660	0.0495	-
3	0.574626	-0.0665	0.4875	0.34069	0.0494	-
4	0.718036	-0.0117	0.3954	0.33505	0.0362	0.0491
5	0.837232	0.0417	0.3020	0.33078	0.0280	0.0378
6	0.926346	0.0864	0.2085	0.32506	0.0207	0.0317
7	0.981390	0.1136	0.1029	0.32130	0.0153	0.0279
8	1.000000	0.1222	0.0000	-	-	-

Table 2
Magnification Factors of $\theta_M(\xi)$ and $\bar{\theta}(\xi)$

Blade Area Ratio	β	Magnification Factor				
		α = -0.5	α = 0	α = 0.5	α = 1.0	α = 2.0
0.4310	0.75	-	M_{21}	-	M_{41}	-
0.5748	1.00	M_{12}	M_{22}	M_{32}	M	M_{52}
0.7184	1.25	-	M_{23}	-	M_{43}	-

The inflow velocity components $v^*_{xn}(\xi)$ and $v^*_{\theta n}(\xi)$ of Ref. 6 are also used in this section and are:

$$v^*_{xn}(\xi) = \begin{cases} \nu_0 a_n(\xi), & \text{for } n = 0, \pm1, \pm2, \ldots, \pm8, \\ 0, & \text{for } n = \pm9, \pm10, \ldots, \end{cases}$$

$$v^*_{\theta n}(\xi) = \begin{cases} \xi, & \text{for } n = 0 \\ 0, & \text{for } n = \pm1, \pm2, \ldots, \end{cases} \qquad (132)$$

and $a_{-n}(\xi) = a_n(\xi)$. The values of $a_n(\xi)$ are shown in Table 3. Figure 2 shows the given longitudinal inflow velocity components

$$1 + v^*_x/\nu_0 = \sum_{n=-8}^{8} a_n(\xi)\, e^{in\theta}$$

versus angle θ. The symbol i as expressed by $\xi = \xi_i (i = 1, 2, \ldots, 7)$ in the figures and tables of this section designates the blade section, and the relation between i and ξ_i is defined in Table 1. Denoting the advance coefficient by standard notation and the circulation about a blade section by J and $G_k(\xi, s)$ respectively we get

$$J = \pi\nu_0 , \quad G_k(\xi, s) = G_1(\xi, -\delta_k) = \sum_{n=-\infty}^{\infty} G_n(\xi)\, e^{in\delta_k} . \tag{133}$$

Further we adopt 0.276 as a convenient approximate value of ν in the numerical calculation. Following the procedure in the previous section the values of $G_n(\xi)$ for various values of J, and also V_{xn}, $V_{\theta n}$, V^*_{xn}, $V^*_{\theta n}$, V^*_{kx}, $V^*_{k\theta}$, $W_1(\xi, -\delta_k)$, $G_k(\xi, s)$, $C_{kL}(\xi, s)$, etc., can be calculated. Then, denoting the zero lift angle of the blade section in radians by α_{g1} and using the relations

$$C_{PD0}(\xi) = 0.0080 , \quad a_P(\xi) = 0.08315 , \quad b_P(\xi) = 6.283\, \alpha_{g1} - 0.1097 \tag{134}$$

in accordance with Kerwin (6), the values of C_{PD} and consequently the bearing forces K_{Fx}, K_{Fy}, K_{Fz}, K_{Mx}, K_{My}, and K_{Mz} can be calculated numerically. Then, denoting the mean values of K_{Fx}, K_{Fy}, etc., with respect to time s by $\bar{K}_{Fx}$, $\bar{K}_{Fy}$, etc., respectively and denoting the magnitudes of the vibrating parts of K_{Fx}, K_{Fy}, etc., with time s by ΔK_{Fx}, ΔK_{Fy}, etc., respectively, the mean values can be obtained by

$$\bar{K}_{Fx} = \frac{N}{2\pi} \int_0^{2\pi/N} K_{Fx}\, ds , \quad \bar{K}_{Fy} = \frac{N}{2\pi} \int_0^{2\pi/N} K_{Fy}\, ds , \quad \text{etc.} ,$$

$$\Delta K_{Fx} = \max_s K_{Fx} - \min_s K_{Fx} , \quad \Delta K_{Fy} = \max_s K_{Fy} - \min_s K_{Fy} , \quad \text{etc.} \tag{135}$$

Further, assuming that C_{PD} is a constant and equal to 0.01 instead of using Eqs. (134), we can calculate the aplitudes A_{Fxm}, A_{Fym}, etc., for m = 1, 2, 3, 4.

We will apply the method of comparing the bearing forces of propellers on the basis of the idea of thrust identity. With the propeller diameter D, the ship speed V, and the mean thrust $\bar{T}$ given in common, we will compare the number of revolutions of the propellers per unit time and the other characteristics of the bearing forces. We will take two propellers M_1 and M_2 and will use the subscripts 1 and 2 referring to propellers M_1 and M_2 respectively. Then, from the requirement of constant thrust, we obtain

$$\bar{T} = -\rho D^2 V^2 J_1^{-2} \bar{K}_{Fx1}(J_1) = -\rho D^2 V^2 J_2^{-2} \bar{K}_{Fx2}(J_2) , \tag{136}$$

where

$$J_1 = V/(n_{r1} D) , \quad J_2 = V/(n_{r2} D) \equiv J_1/\mu , \quad \mu = n_{r2}/n_{r1} , \tag{137}$$

and $K_{Fx1}(J_1)$ and $K_{Fx2}(J_2)$ means that $\bar{K}_{Fx1}$ and $\bar{K}_{Fx2}$ are respectively functions of J_1 and J_2. Hence, from Eqs. (137) we get

Table 3
Values of $a_n(\xi)$ for a Given Inflow Velocity ($a_n(\xi) = a_{-n}(\xi)$)

i	$a_0(\xi)$	$a_1(\xi)$	$a_2(\xi)$	$a_3(\xi)$	$a_4(\xi)$	$a_5(\xi)$	$a_6(\xi)$	$a_7(\xi)$	$a_8(\xi)$
1	0.63209	0.07094	-0.08118	-0.01419	-0.02940	-0.01599	-0.01966	-0.01058	-0.01336
2	0.70250	0.07417	-0.09785	0.00783	-0.03975	-0.01589	-0.02216	-0.01412	-0.01549
3	0.75104	0.05637	-0.09343	0.01564	-0.04760	-0.01194	-0.02831	-0.01571	-0.02053
4	0.77992	0.05304	-0.08451	0.01208	-0.04633	-0.01060	-0.02992	-0.01534	-0.02324
5	0.79241	0.05726	-0.07828	0.01445	-0.04139	-0.00625	-0.02764	-0.01258	-0.02083
6	0.79512	0.05865	-0.07800	0.01377	-0.04115	-0.00601	-0.02761	-0.01245	-0.02057
7	0.79423	0.05833	-0.07915	0.01293	-0.04147	-0.00683	-0.01299	-0.01291	-0.02086

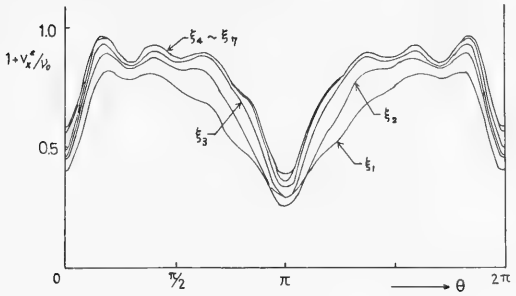

Fig. 2 - Longitudinal component of a given inflow velocity

$$\bar{K}_{Fx1}(J_1) = \mu^2 \bar{K}_{Fx2}(J_2) , \quad J_2 = J_1/\mu . \tag{138}$$

From Eqs. (138) we can calculate μ or J_2 of propeller M_2 for a given value of J_1 of propeller M_1. Thus we get the ratios of the bearing forces of propeller M_2 to those of propeller M_1 as follows:

$$\bar{R}_{Fy} = \frac{\mu^2 \bar{K}_{Fy2}(J_2)}{\bar{K}_{y1}(J_1)} , \quad \bar{R}_{Fz} = \frac{\mu^2 \bar{K}_{Fz2}(J_2)}{\bar{K}_{z1}(J_1)} ,$$

$$\bar{R}_{Mx} = \frac{\mu^2 \bar{K}_{Mx2}(J_2)}{\bar{K}_{mx1}(J_1)} , \quad \bar{R}_{My} = \frac{\mu^2 K_{My2}(J_2)}{\bar{K}_{My1}(J_1)} , \quad \bar{R}_{Mz} = \frac{\mu^2 \bar{K}_{Mz2}(J_2)}{\bar{K}_{Mz1}(J_1)} ,$$

$$\Delta R_{Fx} = \frac{\mu^2 \Delta K_{Fx2}(J_2)}{\Delta K_{Fx1}(J_1)} , \quad \Delta R_{Fy} = \frac{\mu^2 \Delta K_{Fy2}(J_2)}{\Delta K_{Fy1}(J_1)} , \quad \Delta R_{Fz} = \frac{\mu^2 \Delta K_{Fz2}(J_2)}{\Delta K_{Fz1}(J_1)} ,$$

$$\Delta R_{Mx} = \frac{\mu^2 \Delta K_{Mx2}(J_2)}{\Delta K_{Mx1}(J_1)} , \quad \Delta R_{My} = \frac{\mu^2 \Delta K_{My2}(J_2)}{\Delta K_{My1}(J_1)} \quad \Delta R_{Mz} = \frac{\mu^2 \Delta K_{Mz2}(J_2)}{\Delta K_{Mz1}(J_1)} . \tag{139}$$

First let us calculate the bearing forces of the parent propeller M. The values of the bearing forces K_{Fx}, K_{Fy}, K_{Fz}, K_{Mx}, K_{My}, and K_{Mz} for J = 0.70, 0.85, 1.00, and 1.15 are periodic functions of period $2\pi/N \equiv \pi/2$ and are shown in Fig. 3. The mean values of the bearing forces $\bar{K}_{Fx}$, $\bar{K}_{Fy}$, $\bar{K}_{Fz}$, $\bar{K}_{Mx}$, $\bar{K}_{My}$, and $\bar{K}_{Mz}$ and the magnitudes of the vibrating parts of the bearing forces ΔK_{Mx}, ΔK_{Fy}, ΔK_{Fz}, ΔK_{Mx}, ΔK_{My}, and ΔK_{Mz} are presented in Table 4, in which the values of their components caused by viscous drag are shown in parentheses. As shown in Table 4, the ratios of components caused by viscous drag to the total bearing forces are 10% at most. The mean values of the bearing forces and the magnitudes of the vibrating parts of the bearing forces versus J are shown in Fig. 4 and Fig. 5 respectively. From Figs. 4 and 5 the absolute values of $\bar{K}_{Fx}$ and $\bar{K}_{Mx}$ decrease with increase of J, and the absolute values of $\bar{K}_{Fy}$, $\bar{K}_{Fz}$, $\bar{K}_{My}$, $\bar{K}_{Mz}$,

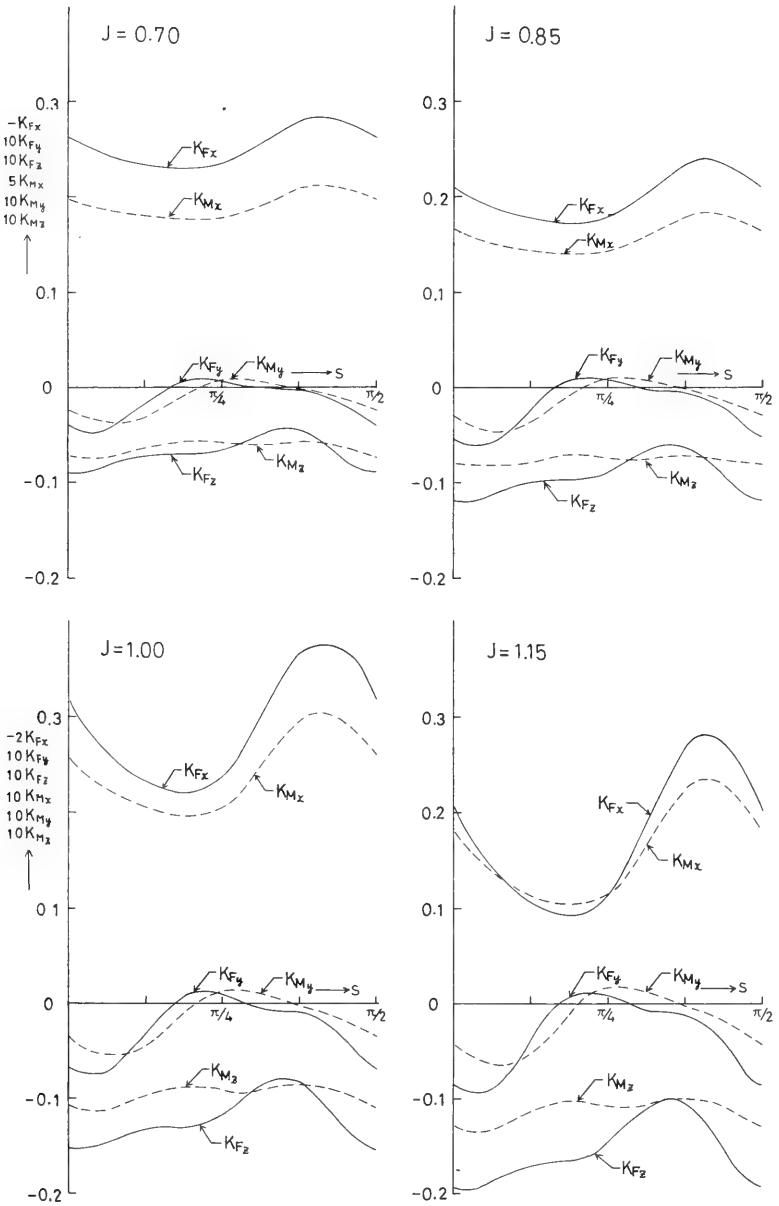

Fig. 3 - Bearing forces of propeller M fluctuating with time s

Table 4
Bearing Forces Acting on Propeller M

J	$\bar{K}_{Fx}$	$\bar{K}_{Fy}$	$\bar{K}_{Fz}$	$\bar{K}_{Mx}$	$\bar{K}_{My}$	$\bar{K}_{Mz}$
0.70	-0.25289 (0.00445)*	-0.00139 (0.00006)	-0.00678 (-0.00101)	0.03822 (0.00356)	-0.00123 (0.00010)	-0.00631 (0.00012)
0.85	-0.19977 (0.00393)	-0.00192 (0.00005)	-0.00927 (-0.00088)	0.03165 (0.00308)	-0.00148 (0.00009)	-0.00787 (0.00010)
1.00	-0.14444 (0.00381)	-0.00253 (0.00003)	-0.01214 (-0.00066)	0.02423 (0.00286)	-0.00171 (0.00007)	-0.00952 (0.00007)
1.15	-0.08687 (0.00412)	-0.00323 (0.00000)	-0.01540 (-0.00034)	0.01594 (0.00290)	-0.00194 (0.00004)	-0.01124 (0.00001)

J	ΔK_{Fx}	ΔK_{Fy}	ΔK_{Fz}	ΔK_{Mx}	ΔK_{My}	ΔK_{Mz}
0.70	0.05026 (0.00130)	0.00519 (0.00057)	0.00443 (0.00074)	0.00623 (0.00087)	0.00447 (0.00013)	0.00183 (0.00011)
0.85	0.06271 (0.00121)	0.00666 (0.00055)	0.00533 (0.00107)	0.00812 (0.00081)	0.00559 (0.00011)	0.00220 (0.00015)
1.00	0.07579 (0.00097)	0.00827 (0.00058)	0.00718 (0.00133)	0.01022 (0.00067)	0.00676 (0.00011)	0.00270 (0.00021)
1.15	0.08949 (0.00057)	0.01000 (0.00080)	0.00877 (0.00159)	0.01253 (0.00047)	0.00800 (0.00011)	0.00325 (0.00028)

*The values in parentheses are the values of components caused by viscous drag.

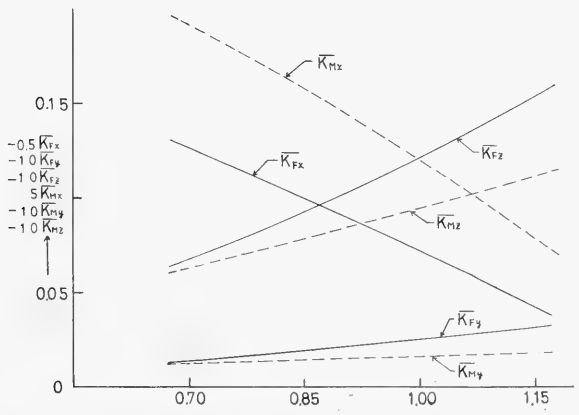

Fig. 4 - Mean values of the bearing forces of propeller M

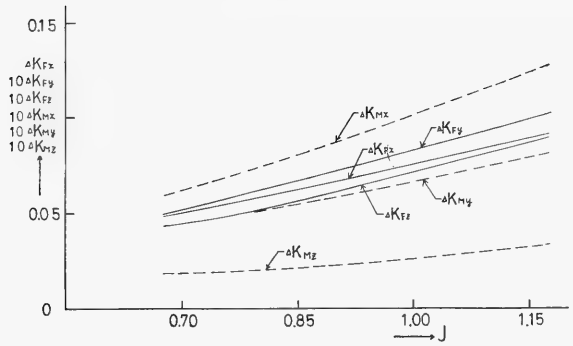

Fig. 5 - Magnitudes of the vibrating parts of the bearing forces of propeller M

ΔK_{Fx}, ΔK_{Fy}, ΔK_{Fz}, ΔK_{Mx}, ΔK_{My}, and ΔK_{Mz} increase with increase of J, or with decrease of the mean thrust coefficient $-K_{Fx}$.

The mean values and the magnitudes of the vibrating parts of the bearing forces of propellers M_{12}, M_{22}, M_{32}, M_{52}, M_{41}, M_{43}, M_{21} and M_{23} versus J are shown respectively in Figs. 6 through 13.

Let us examine the effect of skew on the bearing forces. It is found from Figs. 6, 7, 8, 4, and 9 that the mean values of the bearing forces of the propellers with a blade area ratio of 0.5748 have almost the same value for each J independent of the skews. Let us compare the magnitudes of the vibrating parts of the bearing forces for each J. The values of ΔK_{Fx}, ΔK_{Fy}, ΔK_{Fz}, ΔK_{Mx}, ΔK_{My}, and ΔK_{Mz} versus α for J = 0.85 and 1.00 are taken from Figs. 6, 7, 8, 5, and 9 and are shown in Fig. 14. It is found in Fig. 14 that all the magnitudes of the vibrating parts of the bearing forces of the propellers with a constant blade area ratio decrease with increase of backward skew. Similar results are obtained in the cases of propellers M_{21} and M_{41} and in the cases of propellers M_{23} and M_{43}.

We will next examine the effect of the blade area ratio on the bearing forces. To compare propellers M_{41}, M, and M_{43} on the basis of idea of thrust identity, we use Figs. 10, 4, 5, and 11 and we calculate the ratios $\bar{R}_{Fy}$, $\bar{R}_{Fz}$, $\bar{R}_{Mx}$, $\bar{R}_{My}$, $\bar{R}_{Mz}$, ΔR_{Fx}, ΔR_{Fy}, ΔR_{Fz}, ΔR_{Mx}, ΔR_{My}, and ΔR_{Mz} of propellers M_{41} and M_{43} to propeller M as shown in Fig. 15. Similarly we calculate the ratios of propellers M_{21} and M_{23} to propeller M_{22} as shown in Fig. 16. It is found from Figs. 15 and 16 that the mean values and the magnitudes of the vibrating parts of the bearing forces vary within 10% for blade area ratios between 0.43 and 0.72, excepting $\bar{R}_{Fy}$ and ΔR_{Fz}, which vary about 15%.

Finally let us consider the amplitudes of the bearing forces for the frequency mn_rN. The amplitudes A_{Fxm}, A_{Fym}, A_{Fzm}, A_{Mxm}, A_{Mym}, and A_{Mzm} of propeller M for $m > 0$ are shown in Table 5. Since the harmonic numbers n of the inflow velocity are ± 8 at most as shown in Eqs. (132) and Table 3, the amplitudes of the bearing forces for m = 3 and 4 are negligibly small compared with those for m = 1 and 2. The characteristics of the amplitudes versus J for m = 1 and 2 are similar in tendency to the characteristics of the magnitudes of the vibrating parts versus J.

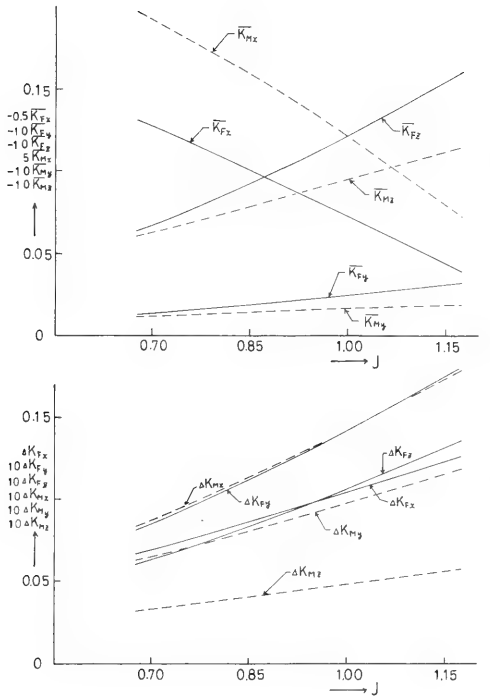

Fig. 6 - Mean values of the bearing forces (top) and the magnitudes of the vibrating parts of the bearing forces (bottom) of propeller M_{12}

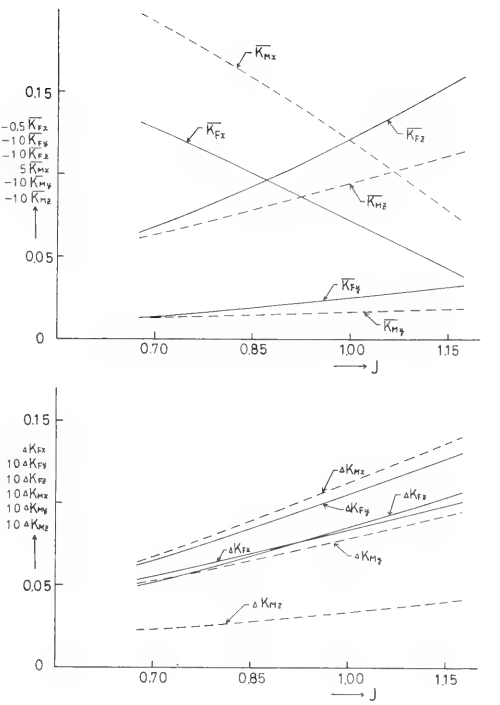

Fig. 7 - Mean values of the bearing forces (top) and the magnitudes of the vibrating parts of the bearing forces (bottom) of propeller M_{22}

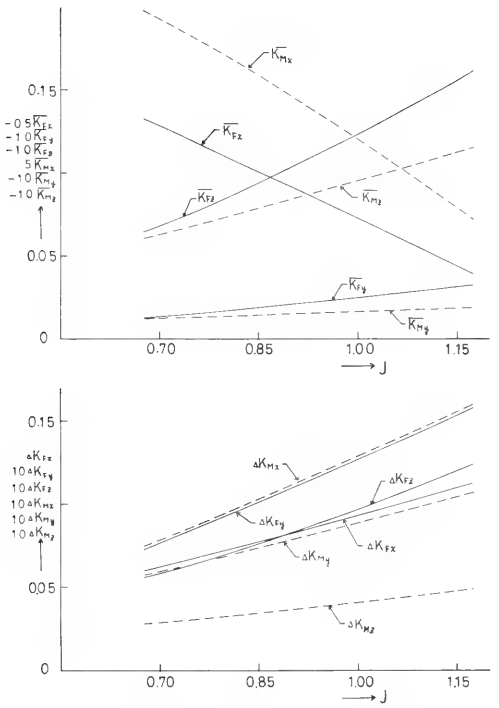

Fig. 8 - Mean values of the bearing forces (top) and the magnitudes of the vibrating parts of the bearing forces (bottom) of propeller M_{32}

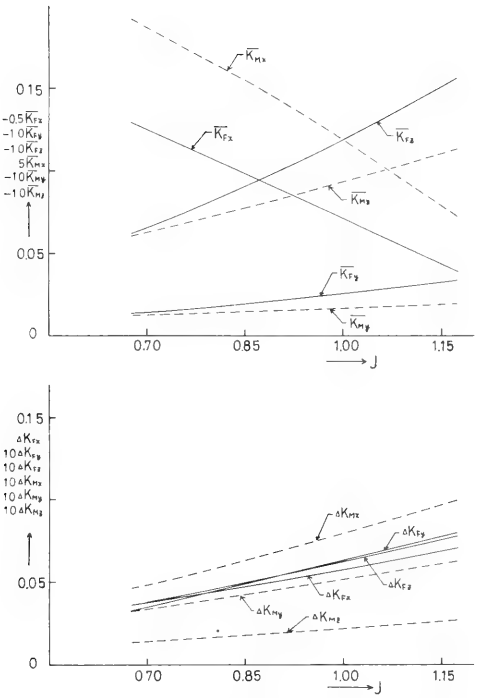

Fig. 9 - Mean values of the bearing forces (top) and the magnitudes of the vibrating parts of the bearing forces (bottom) of propeller M_{52}

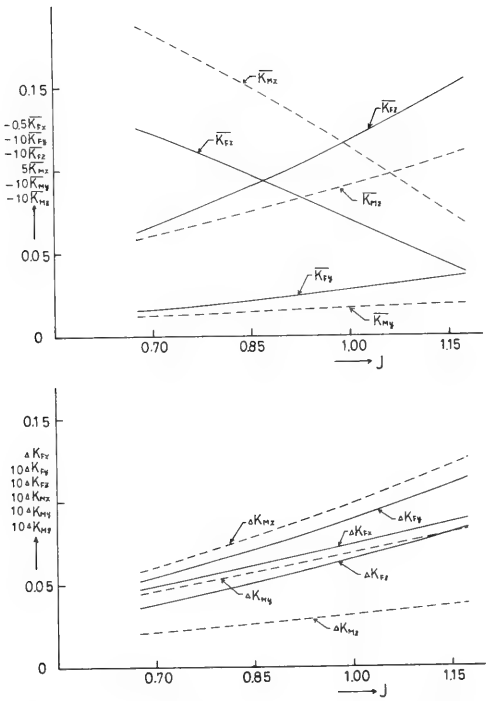

Fig. 10 - Mean values of the bearing forces (top) and the magnitudes of the vibrating parts of the bearing forces (bottom) of propeller M_{41}

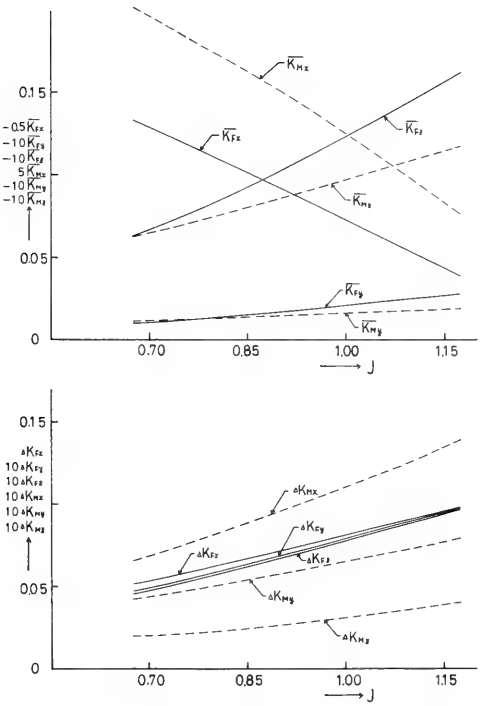

Fig. 11 - Mean values of the bearing forces (top) and the magnitudes of the vibrating parts of the bearing forces (bottom) of propeller M_{43}

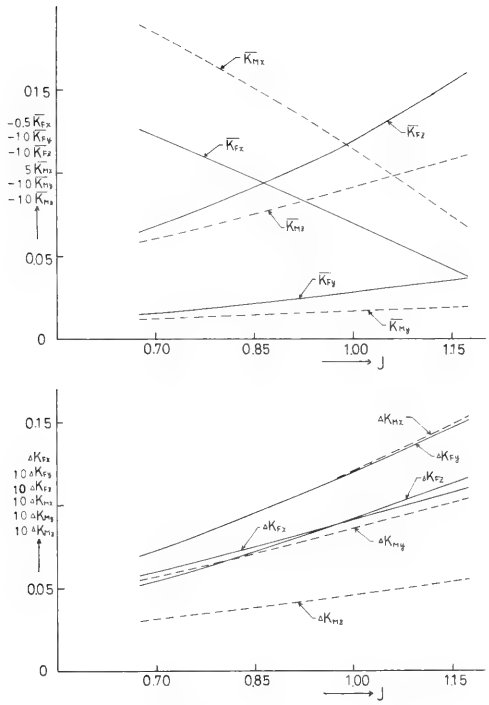

Fig. 12 - Mean values of the bearing forces (top) and the magnitudes of the vibrating parts of the bearing forces (bottom) of propeller M_{21}

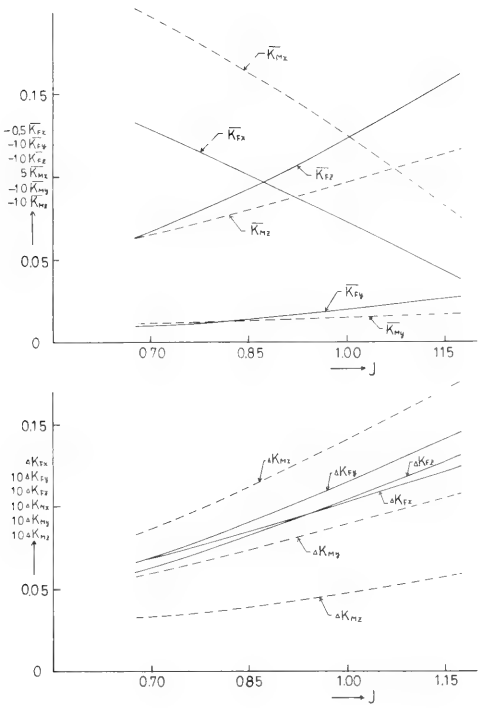

Fig. 13 - Mean values of the bearing forces (top) and the magnitudes of the vibrating parts of the bearing forces (bottom) of propeller M_{23}

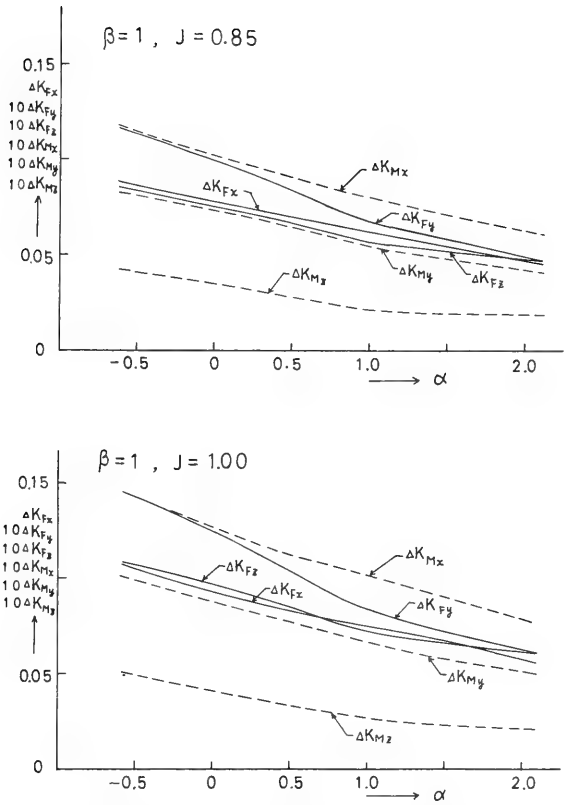

Fig. 14 - Magnitudes of the vibrating parts of the bearing forces versus skew

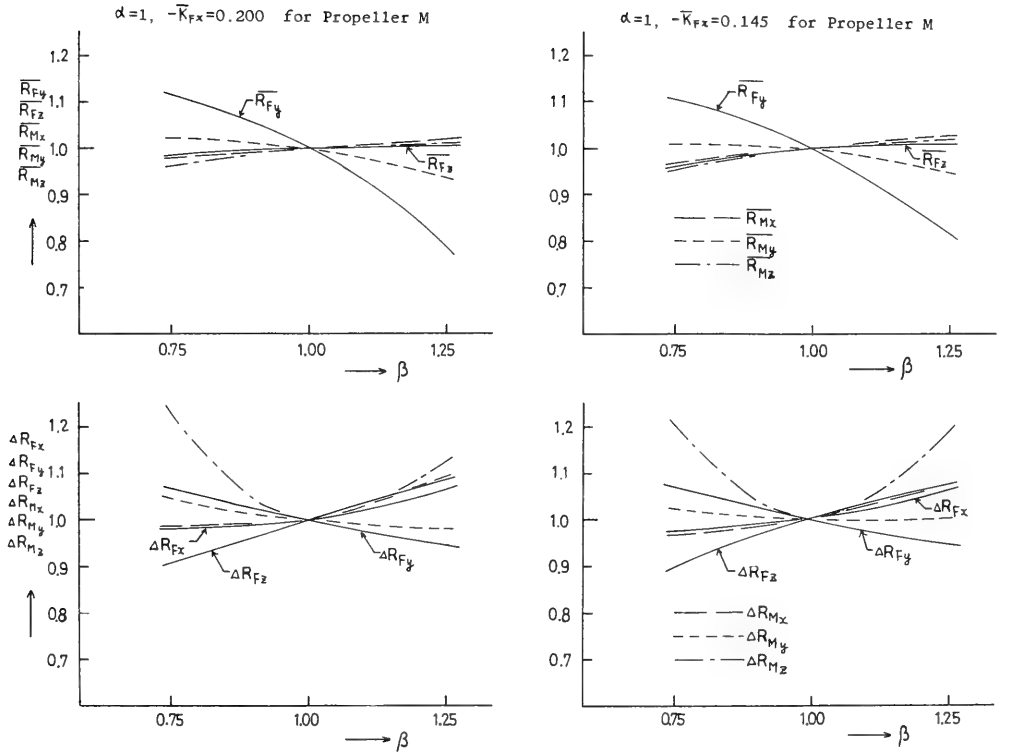

Fig. 15 - Ratios of the bearing forces versus the blade area ratio for $\alpha = 1$

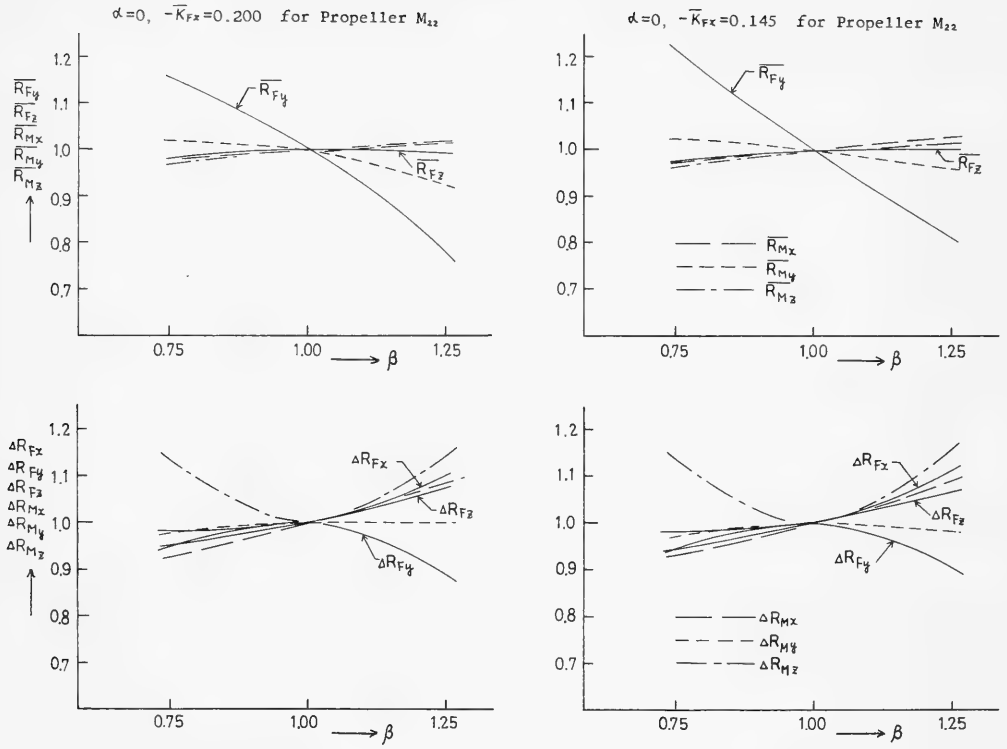

Fig. 16 - Ratios of the bearing forces versus the blade area ratio for $\alpha = 0$

CONCLUSION

In the case of a ship with a single propeller and a single rudder being moved straight with a constant velocity by rotating the propeller with a constant angular velocity in unlimited still water, a general theory was developed for the flow field around the ship and then the forces and moments acting on the hull, rudder, and propeller on the basis of ideal fluid dynamics, in which the mutual interactions among these parts were taken into account generally. The flow field around the ship was determined so as to satisfy the boundary conditions on the surfaces of the three parts simultaneously and was assumed to be composed of the irrotational velocity field and the viscous velocity field. The viscous velocity field and its interaction with the irrotational velocity field were assumed in appropriate forms not to contradict with the boundary layer and wake theory. Then, by comparing the characteristics of the flow around a ship with a propeller and a rudder with those around a ship from which the propeller was taken off, we derived the general mathematical expressions for the differences of the forces and moments acting on the hull, rudder, and propeller between these two ships. Thus we obtained the unsteady propeller forces, which were subdivided into the surface

Table 5
Amplitudes of the Vibrating Parts of the Bearing Forces

J	m	A_{Fx}	A_{Fy}	A_{Fz}	A_{Mx}	A_{My}	A_{Mz}
0.70	1	0.02648	0.00216	0.00178	0.00273	0.00223	0.00068
	2	0.00493	0.00095	0.00089	0.00065	0.00052	0.00051
	3	0.00001	0.00000	0.00003	0.00001	0.00000	0.00000
	4	0.00001	0.00001	0.00001	0.00001	0.00000	0.00000
0.85	1	0.03291	0.00293	0.00248	0.00373	0.00277	0.00083
	2	0.00602	0.00123	0.00114	0.00084	0.00063	0.00062
	3	0.00002	0.00001	0.00004	0.00001	0.00000	0.00000
	4	0.00001	0.00001	0.00001	0.00001	0.00000	0.00000
1.00	1	0.03960	0.00381	0.00329	0.00487	0.00334	0.00099
	2	0.00712	0.00154	0.00141	0.00103	0.00075	0.00073
	3	0.00002	0.00001	0.00006	0.00001	0.00000	0.00000
	4	0.00002	0.00002	0.00002	0.00002	0.00000	0.00000
1.15	1	0.04656	0.00479	0.00422	0.00617	0.00393	0.00116
	2	0.00823	0.00187	0.00171	0.00125	0.00087	0.00084
	3	0.00003	0.00001	0.00008	0.00002	0.00000	0.00000
	4	0.00003	0.00002	0.00002	0.00002	0.00000	0.00000

forces and the bearing forces. Then, for the numerical calculations, we reformulated the expressions of the bearing forces of a propeller placed in a given nonuniform flow, which was assumed to coincide with the measured hull wake of the ship without a propeller.

Finally, numerical calculations were performed for nine examples of four-bladed propellers with a constant pitch ratio which have various skews and blade area ratios to examine their effect on the characteristics of bearing forces. The results obtained are as follows. The absolute mean values and the magnitudes of the vibrating parts of the bearing forces decrease with decrease of the advance coefficient, excepting the thrust and torque coefficients, which increase with decrease of the advance coefficient. We compared the bearing forces of various propellers on the basis of the idea of thrust identity. For a given value of the blade area ratios the mean values of the bearing forces are independent of the skew, while the magnitudes of the vibrating parts of the bearing forces in general decrease with increase of backward skew. For the case of a constant skew the bearing forces vary a little with the variations of blade area ratio.

The numerical calculations for the effects of the number of blades and the pitch ratio on the bearing forces and also on the surface forces are left to later works.

ACKNOWLEDGMENT

The author expresses his cordial gratitudes to Prof. K. Kitajima, Kyushu University, for his kind discussions, and to Mr. K. Ueda and Mr. K. Nakatake, Kyushu University, for their assistances in computer programming and drafting of the figures.

REFERENCES

1. Schwanecke, H., "State of Art on Propeller-Excited Vibrations," Proc. of 11th ITTC, Tokyo, 1966

2. Greenberg, M.D., "The Unsteady Loading on a Propeller in Nonuniform Flow," Therm Advanced Research, Inc., TAR-TR6404, 1964

3. Brown, N.A., "Periodic Propeller Forces in Non-Uniform Flow," MIT, Dept. of Naval Architecture and Marine Engineering, Report 64-7, 1964

4. Tsakonas, S. and Jacobs, W., "Unsteady Lifting Surface Theory for a Marine Propeller of Low Pitch Angle with Chordwise Loading Distribution," SIT, Davidson Laboratory, Report 994, 1964; Tsakonas, S., Breslin, J., and Miller, M., "Correlation and Application of an Unsteady Flow Theory for Propeller Forces," Preprint 5 presented at the Annual Meeting of SNAME, New York, N.Y., Nov. 15-18, 1967

5. Lerbs, H.W. and Schwanecke, H., "Ansatze einer instationaren Propellertheorie," Shiff und Hafen 17 (1965); Lerbs, H.W., "Einige Gesichtspunkte beim Entwurf von Propellern grösserer Leistung," Jahrbuch der Schiffbautechnischen Gesellschaft 60 (1966)

6. Yamazaki, R., "On the Theory of Screw Propellers in Non-Uniform Flows," Memoirs of the Faculty of Engineering, Kyushu University, Vol. 25 No. 2 (1966)

7. Breslin, J.P., "Estimation of Propeller-Induced Blade-Frequency Pressures and Forces on Simple Boundaries and Ships," Naval Engineers Journal 78 (1966)

8. Yamazaki, R., "On the Propulsion Theory of Ships on Still Water — Introduction," Memoirs of the Faculty of Engineering, Kyushu University, Vol. 27, No. 4, 1968

9. Gersten, K., "Nichtlineare Tragflächen Theorie, insbesondere für Tragflügel mit Kleinem Seitenverhältnis," Ingenieur-Archiv 30 (1961)

10. Yamazaki, R., "On the Theory of Screw Propellers," in "Fourth Symposium on Naval Hydrodynamics," 1962, and Memoirs of the Faculty of Engineering, Kyushu University, 23, No. 2 (1963)

11. Yamazaki, R. and Nishiyama, S., "On the Velocity Field Near a Propeller Working Steadily in Still Water," Journal of the Society of Naval Architecture of West Japan, No. 31 (1966)

* * *

DISCUSSION

P. C. Pien
Naval Ship Research and Development Center
Washington, D.C.

This paper is another important contribution of the author to the field of propeller hydrodynamics. It is a very comprehensive paper in which the author has given a complete expression of the velocity potential of a single-screw hull-propeller-rudder configuration. As shown by Eqs. (25) and (26) it is written in terms of the source and the vorticity distributions which are determined by satisfying simultaneously the unsteady boundary conditions on the hull surface, propeller-blade surface, and rudder surface. Once the velocity potential is obtained, it is a relatively easy matter to compute the vibratory forces on either the hull, the propeller, or the rudder. However, it seems extremely difficult to calculate these time-dependent source and vorticity distributions. Would the author care to suggest a practical numerical procedure to obtain these distributions?

Concerning the computation of the periodic blade loading, I would like to make one remark related to the geometry of a trailing vortex sheet in the behind condition. As shown in Eqs. (112) the geometry of the free-vortex sheet is a function of ν, which is a function of the inflow velocity as well as the blade loading. It is convenient to make the usual assumption that the free-vortex sheet lies on a helical surface with the pitch the same as the blade-face pitch. However, this assumption also implies that there is no circumferential inflow variation, otherwise the free-vortex sheet cannot possibly lie on a helical surface. Hence, such an assumption may not be proper, especially when the inflow to the propeller is highly nonuniform and the blade is heavily loaded. Under such circumstances, it may be necessary to keep the actual slip-stream geometry intact. However, as shown by Eqs. (112), the problem becomes extremely difficult if no simplification is made on the slip-stream geometry. A long tedious iterative procedure becomes necessary. This makes one wonder whether the vortex representation of a blade loading is an appropriate approach in solving an unsteady propeller problem under a heavily loaded condition. I would like to know the author's view on this point.

* * *

DISCUSSION

William B. Morgan
Naval Ship Research and Development Center
Washington, D.C.

This paper is very interesting and ambitious. We at the Naval Ship Research and Development Center have followed the work of Prof. Yamazaki with interest for many years. Studies at the Naval Ship Research and Development Center indicate that the influence of the propeller on the hull is mainly potential in origin and the influence of the hull on the propeller is mainly viscous in origin. These conclusions are based on theoretical work confirmed by tests in the Naval Ship Research and Development Center. The influence of the propeller on the separation point, especially on single-screw ships, is very important, and I wonder if Prof. Yamazaki has plans to include the viscous effects in a more rational manner. It seems to me that the vorticity in the wake of the ship must be considered to make the solution practical.

* * *

DISCUSSION

V. F. Bavin
Kryloff Ship Research Institute
Leningrad, U.S.S.R.

I wish to compliment the author on the considerable amount of work he has done in formulating the problem of the hull-propeller-rudder interaction in its most general aspect. Being also involved in this field I agree with the author that the rigorous solution of this problem is a very difficult task.

Therefore it seems to be quite reasonable first to investigate each aspect of the problem separately. The evaluation of the effect of blade width and skew on the amplitudes of bearing forces made by the author is very valuable. I was a little surprised to find the theoretically predicted influence of the blade area ratio to be rather small. This conclusion is not consistent with the results obtained by Krohn and Miller.

It would be very interesting to compare in the future the magnitude of the surface and bearing forces for some typical hull forms and to evaluate the influence of the afterbody configuration on the magnitude of the surface forces.

* * *

REPLY TO DISCUSSION

Ryusuke Yamazaki

I would like to express my gratitude to Dr. Pien, Dr. Morgan, and Mr. Bavin for their useful discussions and valuable comments. I have intended in this paper to find a theoretical clue to calculate the unsteady propeller forces including the propulsion performance of a ship on the basis of my present knowledge, and so the theory in it is not a completed closed system mainly because of an imperfection in the treatment of the viscous flow which holds vorticity. I agree with Dr. Morgan's opinion about the interaction of the ship hull and the propeller. I have formed a plan as follows. By using the method developed in this paper, we can calculate the stream line, the flow velocity, and the pressure near the hull surface, and then, applying the two-dimensional boundary layer theory to the flow along each stream line, we can obtain the frictional resistance of the hull, the separation point of the boundary layer, and the wake velocity behind the hull and can correct numerically the equations of the boundary conditions on the hull, propeller, and rudder and the balance of the forces acting on these three parts. By repeating the procedure the precise values of the unsteady propeller forces are expected to be obtained.

On the other hand, the flow state of the three-dimensional boundary layer surrounding such a three-dimensional body as a ship is generally different from that obtained by means of the above-mentioned two-dimensional process, even in the case of steady condition. Therefore, as described in this paper, to solve the problem of fluid flow near the hull, especially viscous flow, we must apply the three-dimensional turbulent boundary layer and turbulent wake theory, which is not yet completed. For example, at present we cannot calculate numerically the exact values of the pressure in a laminar flow with vorticity for high Reynolds numbers. In the future I want to study further the viscous flow near the hull, which contains the boundary layer, its separation point, and the wake.

In reply to Dr. Pien and Mr. Bavin, I plan to carry on the numerical calculation of the bearing and surface forces for the typical ship simultaneously. However, it seems very difficult, because the velocity components induced by the velocity potential contain infinite series of improper integrals of Bessel functions. In the examples of this paper the influence of the blade area ratio on the bearing forces is rather small compared with the results obtained by Krohn and Miller, as Mr. Bavin said, and I consider the reason to be the differences of the wake distributions and the geometrical shapes of propeller blades except for the blade area ratio.

On the basis of the unsteady lifting surface theory with higher order terms, the general theory to calculate hydrodynamic performance characteristics of a heavily loaded propeller working unsteadily in a nonuniform flow was developed in the beginning of Ref. 6, in which exact expressions were obtained for calculating the spatial and temporal distortion of the geometrical shape of the free vortex sheet with the fluctuating strength from a regular helical surface with a constant pitch. However, in the numerical examples of this paper and Ref. 6, I calculated

the bearing forces by adopting only the first term of the Birnbaum's series as the chordwise distribution of the bound vortex and the regular helical surface with a constant pitch as the geometrical shape of the free vortex to simplify programming the numerical calculation. Accordingly I agree with Dr. Pien's opinion about the procedure to calculate numerically the path of the free vortex practically. I doubt the need of an exact solution for the path of the free vortex, because the hydrodynamical performance characteristics obtained theoretically do not agree exactly with the experimental results even in a case where the propeller is working steadily in a uniform flow.

A GENERAL THEORY FOR MARINE PROPELLERS

Pao C. Pien and J. Strom-Tejsen
Naval Ship Research and Development Center
Washington, D. C.

ABSTRACT

Based on the concept of an acceleration potential, a general lifting surface theory for marine propellers has been developed. It is applicable to propellers with rake, skew, arbitrary pitch distribution, arbitrary blade contour outline, etc. Also the propeller loading can be steady or unsteady, light or heavy.

A numerical technique for the evaluation of the kernel function is discussed, and some preliminary results from a computer program are given.

INTRODUCTION

A screw propeller is a very simple, rugged, efficient marine propulsive device. However, it has shortcomings. When propeller loading is heavy, it may induce severe hull vibration. Erosion and noise may also become serious problems in many instances. Theoretical studies on marine propellers have attempted to eliminate or minimize these shortcomings, and in recent years several papers dealing with propeller theory have been published, e.g., Refs. 1 through 10. Unfortunately, existing propeller theories have many limitations because of the assumptions made to facilitate development of the theory or to shorten the numerical analysis. Generally speaking, these limitations involve three areas: propeller geometry, propeller loading, and propeller operating conditions. Such geometrical features as radial pitch variations, skew, and rake are not always properly dealt with by existing theories. Most propeller theories are applicable only to lightly or moderately loaded propellers. Moreover, unsteady propeller theory is still in its infancy. In many instances, it is advantageous to operate in fully cavitated condition, but the present methods of designing a supercavitating propeller are not entirely satisfactory.

In view of the present situation, it appears that there is a need for a general lifting-surface theory for marine propellers which is applicable to a practical propeller under any operating condition. This paper represents an attempt toward developing such a theory.

It may seem appropriate to select one of the existing propeller theories and attempt to generalize it, but this is not a realistic approach. If an existing

vortex-propeller theory is chosen as a point of departure, it is difficult to take contraction of the slipstream into account. Such an attempt has been made in the hope of developing a theory for heavily loaded propellers, but so far it has not been successful. Propeller theory based on vortex representation has been extended to cover unsteady operation, e.g., Refs. 11 through 18. Despite many simplifications having been made in such unsteady propeller theories, the numerical analysis is still so complicated that hours of computing time on a high-speed computer would be needed. Therefore, it is not practical to generalize such a theory any further.

To overcome some of the difficulties inherent in a vortex-propeller theory, theories based on the concept of acceleration potential have been developed recently, e.g., Refs. 1 and 19 through 21. The starting point is the Euler equations of motion; the concept states that the pressure gradient at any point divided by the fluid density gives the acceleration of the fluid element at that point. Strictly speaking, the pressure field of a fluid is not a potential function. Hence, such propeller theories are viewed as linearized theories and are applicable only to lightly loaded propellers. Unless the acceleration potential itself is modified, there is not much room for generalization.

It seems imperative to take a fresh look at the problem before attempting to develop a general lifting-surface theory for marine propellers. When a propeller blade is moving through a fluid, the fluid motion in a fixed space is unsteady. Various fluid particles experience certain accelerations. The acceleration of a moving fluid particle $d\mathbf{q}/dt$ consists of two parts:

$$\frac{d\mathbf{q}}{dt} = \frac{\partial \mathbf{q}}{\partial t} + (\mathbf{q}\nabla)\,\mathbf{q} \quad . \tag{1}$$

The first part, $\partial \mathbf{q}/\partial t$, is due to the unsteadiness of the velocity field or the acceleration at a fixed space. The second part $(\mathbf{q}\nabla)\,\mathbf{q}$ is due to the motion of the fluid particle. It is more convenient if we consider these two parts separately. As a matter of fact the time integration of the acceleration at a fixed space plus the initial velocity field yields the velocity field at any time:

$$\mathbf{q} = \mathbf{q}_0 + \int_{t=t_0}^{t} \frac{\partial \mathbf{q}}{\partial t}\, dt \quad . \tag{2}$$

Then the second part of the acceleration of a moving fluid particle can be obtained from the velocity field at that time. The fluid-particle acceleration due to the movement of the particle can be left out in the calculation of the velocity field at any time. Therefore it is logical to define a new acceleration potential, whose gradient will yield an acceleration field in a fixed space. The general theory of marine propellers described herein is based on this concept.

The amount of numerical work involved in any propeller theory is always a practical concern. A propeller theory is useful only if the computer time required is within a reasonable limit. The kernel function involved in a propeller theory is quite complicated, and the usual practice is to evaluate it numerically. In some cases, modification of the kernel function is made for convenience in

evaluation. However, if the modification is too drastic, the solution obtained may no longer be related to the problem to be solved.

The main difficulty in attempting to functionally carry out the integration involved in a propeller theory is the cosine factor in the integrand. In the past, efforts have been made to find an approximating expression for either the whole integrand or the distance factor in the denominator of the integrand, but no satisfactory expression has been obtained, because the range of integration extends to negative infinity. On the other hand, it is well known that a cosine function within a small range of the argument can be accurately approximated by a second-degree polynomial. Hence by dividing the range of integration into steps and replacing the cosine factor of the integrand by an appropriate second-degree polynomial the integration can be carried out functionally within each step. This approach greatly reduces the required computing time compared to the usual tedious numerical integration. Based on this numerical technique a very efficient computing program can be developed. Such a development is now under way, and some preliminary results are included in this paper.

BASIC CONCEPT

When a propeller blade advances through a fluid, a pressure field is moving with the blade. As a result, an unsteady motion is created throughout the fluid. As was stated in the Introduction, the acceleration of a fluid particle of any unsteady flow consists of two parts:

$$\frac{d\mathbf{q}}{dt} = \frac{\partial \mathbf{q}}{\partial t} + (\mathbf{q}\nabla)\,\mathbf{q} \quad , \tag{1}$$

where $\mathbf{q}$ is a velocity vector. The first part, $\partial \mathbf{q}/\partial t$, is due to the time rate of change of velocity in a fixed space. The second part, $(\mathbf{q}\nabla)\,\mathbf{q}$, is due to the movement of the fluid particle.

For an inviscid fluid, in the absence of an external force field, we have the equations of motion

$$\rho_f \frac{d\mathbf{q}}{dt} = -\nabla p \quad , \tag{3}$$

where ∇p is the gradient of the pressure field p, and ρ_f is the fluid density. Combining Eqs. (1) and (3) we write

$$\frac{\partial \mathbf{q}}{\partial t} = -\frac{1}{\rho_f}\nabla p - (\mathbf{q}\nabla)\,\mathbf{q}$$

or

$$\frac{\partial \mathbf{q}}{\partial t} = -\frac{1}{\rho_f}\nabla p - \nabla\left(\frac{1}{2}q^2\right) + \mathbf{q} \times \bar{\xi} \quad , \tag{4}$$

where $\bar{\xi}$ is a vorticity vector.

In front of the moving blade there is no vorticity, and the cross product in Eq. (4) is zero. Our first conclusion was that in the wake, vortex lines are parallel to the streamlines, and the cross product is again zero. Later we realized this conclusion is not true, but for the reasons discussed in the appendix we still feel justified in assuming the simplification that the cross product is zero in the wake. With this simplification the following equation is valid through the space except on the blade surface:

$$\frac{\partial \mathbf{q}}{\partial t} = -\frac{1}{\rho_f}\nabla p - \nabla\left(\frac{1}{2}q^2\right) \tag{5}$$

For incompressible fluid ρ_f is a constant, and we have

$$\frac{\partial \mathbf{q}}{\partial t} = -\nabla\left(\frac{p}{\rho_f} + \frac{1}{2}q^2\right) \tag{6}$$

We introduce a function Φ as follows:

$$\Phi = \frac{p}{\rho_f} + \frac{1}{2}q^2 \ . \tag{7}$$

Then

$$\frac{\partial \mathbf{q}}{\partial t} = -\nabla\Phi \ . \tag{8}$$

For later convenience we also define an induced pressure p_i as follows

$$p_i = \rho_f \Phi = p + \frac{1}{2}\rho_f q^2 \ . \tag{9}$$

From the continuity equation

$$\nabla\left(\frac{\partial \mathbf{q}}{\partial t}\right) = \frac{\partial}{\partial t}(\nabla \mathbf{q}) = 0 \ , \tag{10}$$

and Φ consequently satisfies the Laplace equation

$$\nabla^2 \Phi = 0 \ . \tag{11}$$

The function Φ is defined as an acceleration potential, the negative gradient of which according to Eq. (8) yields an acceleration field. Since it satisfies the Laplace equation, it is an "exact" acceleration potential. It should be noted that Φ is not the same as defined in Refs. 1 and 19 through 21, in which the acceleration potential is based on the linearized equations of motion. The exact acceleration potential differs from the linearized one by a second-order term $q^2/2$.

The exact acceleration potential is the foundation for developing a general theory for marine propellers. Since the acceleration potential is analogous to the velocity potential, it is helpful to discuss very briefly how the velocity

potential is used in developing a vortex propeller theory. After this has been done, it will be easy to understand how the acceleration potential is used in developing our theory for marine propellers.

For a velocity potential we may (22) write

$$\phi_P = -\frac{1}{4\pi}\iint\frac{1}{r}\left(\frac{\partial\phi}{\partial n}+\frac{\partial\phi'}{\partial n'}\right)dS+\frac{1}{4\pi}\int\int(\phi-\phi')\frac{\partial}{\partial n}\left(\frac{1}{r}\right)dS\ , \qquad (12)$$

where ϕ_P is the value of the velocity potential ϕ at a field point P, ϕ is the velocity potential value on one side of the boundary surface, ϕ' is that on the other side, and $\partial/\partial n$ is equal to $-\partial/\partial n'$.

The first term is due to a surface distribution of simple sources of density

$$-\left(\frac{\partial\phi}{\partial n}+\frac{\partial\phi'}{\partial n'}\right).$$

It gives the discontinuity of the normal velocities on the two sides of the boundary. The second term is due to a surface distribution of dipoles of density $\phi - \phi'$. It gives the discontinuity of the tangential velocities across the boundary.

In applying Eq. (12) to a propeller problem the discontinuity of the normal velocities is due to the blade thickness. Hence the simple source distribution at the boundary can be derived from the thickness. In a propeller problem we are concerned with the lift distribution produced by the discontinuity of the tangential velocities. Hence for the sake of convenience we specify the circulation distribution on the boundary directly rather than specify the discontinuity of the velocity potential across the boundary. The boundary surface, in the case of a propeller blade, extends from the leading edge to infinity behind, since there is a discontinuity of the tangential velocities across the trailing free-vortex sheet as well as across the blade surface.

The discussion about the velocity potential can be repeated for the acceleration potential, except for replacing the word velocity by the word acceleration. We may write in analogy with Eq. (12),

$$\Phi_P = -\frac{1}{4\pi}\int\int\frac{1}{r}\left(\frac{\partial\Phi}{\partial n}+\frac{\partial\Phi'}{\partial n'}\right)dS+\frac{1}{4\pi}\int\int(\Phi-\Phi')\frac{\partial}{\partial n}\left(\frac{1}{r}\right)dS\ . \qquad (13)$$

In applying Eq. (13) to a propeller problem, the first term is again due to the blade thickness. However, the pressure source distribution at the boundary is derived from the blade-section curvature on both sides of the blade rather than from the thickness. The second term is also due to the blade-load distribution.

For the sake of convenience in the following discussion let us temporarily approximate Φ by p/ρ_f. As shown by Eq. (7) they differ only by a second-order quantity $q^2/2$. The pressure dipoles in the second term of Eq. (13) then correspond to the pressure jump across the boundary or the blade-load distribution.

Since no singularity exists except at the blade surface, the complexity of a propeller problem is greatly reduced.

It may be noted that the concept of the acceleration potential may be used for supercavitating propeller problems. A cavity can be taken as the blade thickness as far as viewed from the fluid, but the geometry of the cavity is unknown before the problem is solved. Hence we cannot specify the simple source distribution in Eq. (12) a priori if we base our analysis on the velocity potential. This situation makes the problem extremely difficult. However, if the acceleration potential is used in our analysis, the pressure-source distribution in the first term of Eq. (13) can be determined from the blade loading and the cavitation number σ. This is shown as follows, beginning with

$$p^u = p_0 - \frac{1}{2} \Delta p \ , \qquad (14)$$

where p^u is the pressure on the upper or suction side of the blade, p_0 is the ambient pressure in the absence of the blade, and Δp is the pressure jump across the boundary or the lift. The cavity pressure p_c is

$$p_c = p_0 - \frac{1}{2} \rho_f \sigma V^2 \ , \qquad (15)$$

where V is the speed used in defining the cavitation number σ. Subtracting Eq. (14) from Eq. (15) we have

$$F = \frac{1}{2} (\Delta p - \rho_f \sigma V^2) \ , \qquad (16)$$

where F is the required additional pressure distribution to make the pressure on the suction side equal to the cavity pressure.

It has been observed that the curvature of the cavity wall may be very large at the leading edge, depending upon the angle of attack. However, the curvatures are small near the trailing edge and become large again near the end of the cavity. Since there is no pressure discontinuity across the cavity wall, the singularity distribution required to represent that portion of the cavity which is trailing the blade is small to begin with and becomes appreciable at the end of the cavity. It has been found that various models of the cavity closure condition does not affect the loading significantly if the cavity is sufficiently long. Therefore, at least as a first approximation, we may ignore the singularity of the acceleration potential beyond the blade surface and consider the blade surface as the only boundary where the pressure dipole Δp and the pressure source p_s are distributed. The pressure dipole is derived directly from the specified blade-load distribution. The pressure-source distribution is obtained by solving the integral equation

$$F = -\frac{1}{4\pi} \int\int \frac{1}{r} p_s \, dS \ . \qquad (17)$$

Once the pressure dipoles and pressure-source distributions at the blade surface are determined, Eq. (13) is used to obtain the acceleration field from which the velocity field is obtained. If a higher order solution is required, an iterative procedure may be tried.

It is not our intention here to show how to design a supercavitating propeller. Our discussion is merely to indicate how the acceleration potential may be conveniently used in such problems.

Let us return to the general propeller problem. For a thin blade with a zero thickness, only the second term of Eq. (13) exists on the boundary. We want to find the relationship between the jump in $\rho_f \Phi$ and the jump in pressure p across the blade surface. From Eqs. (7) and (9) we have

$$\Delta p_i = \Delta p + \frac{1}{2} \rho_f (q_L^2 - q_U^2) , \tag{18}$$

where Δp_i and Δp denote the jump across the blade of $\rho_f \Phi$ and p respectively, and q_L and q_U are the absolute velocities of the fluid at the lower and the upper blade surfaces respectively. The velocity squared is equal to the sum of the square of the normal velocity and the square of the tangential velocity. Since the normal velocity is continuous across the blade due to zero thickness, the contribution to $q_L^2 - q_U^2$ must be from the difference in the tangential velocities across the blade. The magnitude of the tangential velocities on both sides of the boundary are nearly equal but with opposite signs. Hence, the difference between the square of the tangential velocities is negligible, and the approximation of Δp by Δp_i is correct to the second order of the induced velocity. If the blade thickness is not zero, the thickness distribution produces continuous tangential and discontinuous normal velocity components across the blade. Hence there may be some differences of $q_L^2 - q_U^2$, depending on the relative magnitudes of the induced velocities due to blade loading and blade thickness respectively. In a performance prediction, Δp_i instead of Δp is determined from the boundary condition, and Δp is then computed from Eq. (18). In a design problem the Δp_i distribution can be taken equal to the specified Δp distribution as a first approximation. If their differences are found to be appreciable, Δp_i can be corrected accordingly and the computation repeated.

The feature of any propeller theory is to obtain the changes in fluid velocity in the vicinity of the blade due to the direct action of the propeller. This can be done quite conveniently by using the acceleration potential. Let us assume that the time history of singularity distributions of pressure sources and dipoles are specified on the blade surface and that the blade position in the past relative to the present position is also known. By taking the negative gradient of Eq. (13) the acceleration at any point relative to the present blade position is known from t equal to $-\infty$ to the present time. The time integration of the acceleration plus the initial fluid velocity at the point under consideration, in the absence of the propeller, gives the fluid velocity at the present time. This procedure is much simpler than that involved when the velocity potential is used.

In a vortex theory based on the velocity potential a trailing vortex sheet extends to infinity, and its geometry is not only a function of the blade loading but also a function of the fluid flow when the propeller is absent. For an unsteady

operating condition the geometry of the free vortex sheet as well as the vorticity-strength distribution on this sheet becomes almost immanageable unless drastic simplification and assumptions are made.

When the acceleration potential is used, the blade position is determined by the advance velocity and the angular velocity and is independent of the blade loading. Hence, the induced fluid velocity at the point under consideration is proportional to the blade loading, and the principle of superposition can be applied. The contribution to the induced fluid velocity from each of the blade-loading components can be computed separately.

Furthermore, no limitation is needed on blade loading, blade geometry, or blade motion. As long as the total time history of the blade loading and blade position are known during any time period, the change in fluid velocity during that time period at any point relative to the present position of the blade can be computed. Therefore, the unsteady propeller problem can be dealt with in a straightforward manner.

If a propeller has several blades, or if several propellers or other lifting surfaces operate simultaneously in the same vicinity, the computational work may increase, but the basic concept of using an acceleration potential is the same.

In summary it can be stated that a useful tool, the exact acceleration potential, has been developed which greatly facilities development of a general theory for marine propellers. However in this paper we shall limit ourselves to the discussion of periodic propeller loading in the noncavitating condition only.

Even though it is possible with the approach mentioned to include all the details of a blade element section in the formulation of our general propeller theory, there is no reason to unduly complicate our problem beyond the practical engineering necessity. For instance a great deal of computing time can be saved if the pressure source or dipole distribution can be placed along a chord rather than along a meanline. To find out whether such simplification will impair the practical usefulness of our theory, information on airfoils as given in Ref. 23 have been studied with care. Figure 1 (taken from this reference) compares theoretical and experimental pressure distributions on both sides of the foil. The theoretical curves are computed on the assumption that the velocity distribution about the foil is composed of three separate and independent components:

1. The distribution corresponding to the velocity distribution over the basic thickness form at zero angle of attack.

2. The distribution corresponding to the load distribution of the meanline at its ideal angle of attack.

3. The distribution corresponding to the additional load distribution associated with the angle of attack.

Items 2 and 3 are computed on the basis of a thin foil theory where the aerodynamic singularities are distributed along a chord rather than along the meanline.

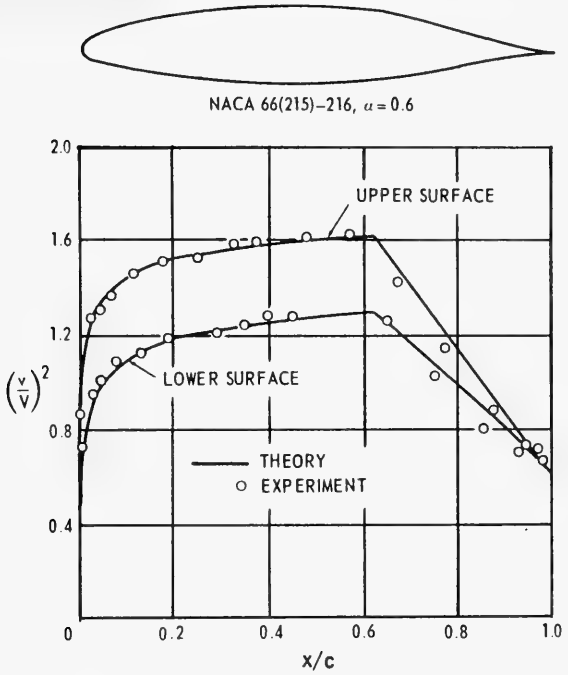

Fig. 1 - Comparison of theoretical and experimental pressure distributions for the NACA 66(215)-216 airfoil; c_L = 0.23 (from Ref. 23)

In view of the fact that the lift coefficient c_L of 0.23 is relatively large compared with that of a propeller blade and that the agreement between the theoretical and the experimental pressure distribution is excellent from a practical viewpoint, it seems permissible to place the pressure source and pressure dipole distributions along a chord line.

Another interesting point to be drawn from this comparison is that the viscosity effect does not significantly influence the normal force on the blade. This important fact greatly simplifies the task of computing the viscous drag of the blade. By examining the drag coefficient curves of various foil sections as plotted against the section lift coefficient c_L, as given in the same reference, it clearly indicates that the viscous drag is greatly influenced by the pressure distribution. With the same basic section at the same lift coefficient, the viscous drag coefficient differs depending on whether the lift is produced by camber or by angle of attack. This means that the viscous drag cannot be accurately computed unless the lift or pressure distribution over the blade has been obtained. Since the pressure distribution is not affected by the viscosity within the range of lift coefficient of interest, no iteration between the lift and drag is necessary. The viscous effect on propeller thrust and torque can be analyzed after the potential problem has been solved first.

Based on these considerations, it is logical to first develop a general theory for marine propellers in inviscid fluid. Since the induced velocity due to blade loading is independent of that due to blade thickness, a propeller with zero blade thickness will be considered here as a first step.

DEVELOPMENT OF THE THEORY

Derivation of Kernel Functions

It is assumed that the propeller blade thickness is zero and that the fluid is inviscid. The steady case of a propeller operating in open water is considered first; the propeller operating in the behind condition is discussed.

Figure 2 defines a cylindrical coordinate system. The position of a moving blade at time t equal to zero is also shown. The essential part of our problem is to calculate the induced velocity at any point $P(x,r,\phi)$ due to the action of the blade. It is convenient in our discussion to introduce three equations:

$$u(x,r,\phi) = \int_S\int L(\xi,\rho,\theta)\ K_1(x,r,\phi;\xi,\rho,\theta)\ d\rho d\theta\ , \tag{19a}$$

$$v(x,r,\phi) = \int_S\int L(\xi,\rho,\theta)\ K_m(x,r,\phi;\xi,\rho,\theta)\ d\rho d\theta\ , \tag{19b}$$

$$w(x,r,\phi) = \int_S\int L(\xi,\rho,\theta)\ K_n(x,r,\phi;\xi,\rho,\theta)\ d\rho d\theta\ , \tag{19c}$$

where $u(x,r,\phi)$, $v(x,r,\phi)$, and $w(x,r,\phi)$ are respectively the axial, tangential, and radial induced velocity components at $P(x,r,\phi)$, $L(\xi,\rho,\theta)$ is the blade load distribution, and $K_1(x,r,\phi;\ \xi,\rho,\theta)$ represents the contribution to the axial component of the induced velocity at $P(x,r,\phi)$ of a unit blade loading at $Q(\xi,\rho,\theta)$, etc.

Our first objective is to derive expressions for the kernel functions K_1, K_m, and K_n. In the case of zero blade thickness the blade loading $L(\xi,\rho,\theta)$ can be represented by the induced pressure jump Δp_i as discussed in the previous chapter, and the field value of the acceleration potential Φ at $P(x,r,\phi)$ due to a unit pressure dipole at $Q(\xi,\rho,\theta)$ is

$$\Phi(x,r,\phi) = \frac{1}{4\pi\rho_f}\frac{\partial}{\partial n'}\left(\frac{1}{R}\right)\ , \tag{20}$$

where n' is the normal of the blade surface at $Q(\xi,\rho,\theta)$ and R is the distance from point $Q(\xi,\rho,\theta)$ to $P(x,r,\phi)$.

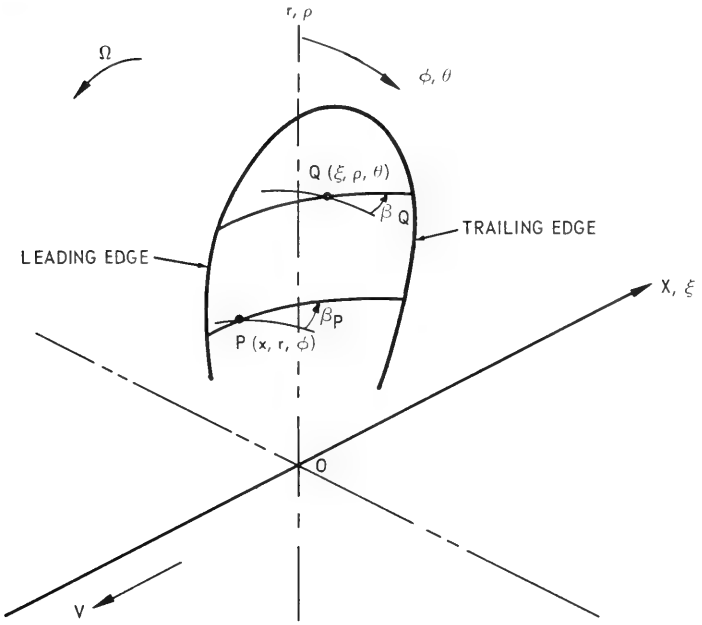

Fig. 2 - Coordinate system and notation

When t is zero, we have

$$\xi = \rho \tan \gamma + \rho \theta \tan \beta_Q \ , \tag{21}$$

where γ is the rake angle and β_Q is the blade element pitch angle at radius ρ. When t is not zero, we have

$$\xi = \rho \tan \gamma + \rho \theta \tan \beta_Q - \rho \Omega t \tan \beta \ . \tag{22}$$

The last term of this equation relates to the fact that the point $Q(\xi, \rho, \theta)$ is moving along a helical line with a pitch angle of β. From this equation

$$\xi = \rho \tan \gamma + \rho s \theta + \rho \theta' \tan \beta \ , \tag{23}$$

where $s = \tan \beta_Q - \tan \beta$ and $\theta' = \theta - \Omega t$ is the angular coordinate of $Q(\xi, \rho, \theta')$ at time t.

If $P(x, r, \phi)$ is on the lifting surface when t is zero, we have

$$x = r \tan \gamma + r \phi \tan \beta_P \ , \tag{24}$$

where β_P is the blade element pitch angle at radius r. Then

$$x - \xi = -(\rho - r) \tan \gamma - \phi \, (\rho \tan \beta - r \tan \beta_P)$$

$$-\rho(\theta' - \phi) \tan \beta - \rho s\theta$$

or

$$x - \xi = -[d + \rho(\theta' - \phi) \tan \beta] \ , \tag{25}$$

where

$$d = (\rho - r) \tan \gamma + \rho s \, (\theta - \phi) + \phi (\rho \tan \beta_Q - r \tan \beta_P) \ , \tag{26}$$

and

$$R = [(x - \xi)^2 + \rho^2 + r^2 - 2\rho r \cos (\theta' - \phi)]^{1/2} \ . \tag{27}$$

When the propeller pitch varies with radius, the normal to the blade surface will have a radial component corresponding to a force in the radial direction. However, the radial component of the pressure dipole is ignored, since it is usually very small and since a pressure dipole in a radial direction produces very small downwash compared with a pressure dipole normal to the radial vector with the same strength. Hence $\cos \beta_Q$ and $\sin \beta_Q$ become the axial and tangential components of the unit pressure dipole at $Q(\xi, \rho, \theta)$. We break the tangential component further into $\sin \beta_Q \cos (\theta' - \phi)$ and $\sin \beta_Q \sin (\theta' - \phi)$ corresponding to the tangential and radial directions at point $P(x, r, \phi)$, respectively. We denote these components by l, m, and n as follows:

$$l = \cos \beta_Q \ , \tag{28a}$$

$$m = \sin \beta_Q \cos \lambda \ , \tag{28b}$$

$$n = \sin \beta_Q \sin \lambda \ , \tag{28c}$$

where $\lambda = (\theta' - \phi)$. Likewise we have the three components of the distance vector from $Q(\xi, \rho, \theta')$ to $P(x, r, \phi)$ parallel to l, m, and n respectively as follows:

$$R_l = x - \xi = -(d + \rho\lambda \tan \beta) \ , \tag{29a}$$

$$R_m = \rho \sin \lambda \ , \tag{29b}$$

$$R_n = r - \rho \cos \lambda \ . \tag{29c}$$

By taking the gradient of both sides of Eq. (20) we obtain the acceleration components A_l, A_m, and A_n at point $P(x, r, \phi)$ in the axial, tangential, and radial directions respectively:

$$A_l = \frac{1}{4\pi\rho_f} \left(- \frac{1}{R^3} + \frac{3R_l M}{R^5} \right), \tag{30a}$$

$$A_m = \frac{1}{4\pi\rho_f}\left(-\frac{m}{R^3} + \frac{3R_mM}{R^5}\right), \tag{30b}$$

$$A_n = \frac{1}{4\pi\rho_f}\left(-\frac{n}{R^3} + \frac{3R_nM}{R^5}\right), \tag{30c}$$

where

$$\begin{aligned} M &= lR_1 + mR_m + nR_n \\ &= -\cos\beta_Q(d + \rho\lambda\tan\beta) + r\sin\beta_Q\sin\lambda\ . \end{aligned} \tag{31}$$

Then we have

$$K_1 = \int_{-\infty}^{0} A_1\,dt\ ,$$

$$K_m = \int_{-\infty}^{0} A_m\,dt\ ,$$

$$K_n = \int_{-\infty}^{0} A_n\,dt\ .$$

Since

$$\lambda = \theta' - \phi = \theta - \phi - \Omega t\ ,$$

$$d\lambda = -\Omega\,dt\ ,$$

$$\lambda = \theta - \phi\ , \quad \text{when} \quad t = 0\ ,$$

$$\lambda = \infty\ , \quad \text{when} \quad t = -\infty\ ,$$

then

$$K_1 = \frac{1}{4\pi\rho_f\Omega}\int_{\theta-\phi}^{\infty}\left(-\frac{1}{R^3} + \frac{3R_1M}{R^5}\right)d\lambda\ , \tag{32a}$$

$$K_m = \frac{1}{4\pi\rho_f\Omega}\int_{\theta-\phi}^{\infty}\left(-\frac{m}{R^3} + \frac{3R_mM}{R^5}\right)d\lambda\ , \tag{32b}$$

$$K_n = \frac{1}{4\pi\rho_f\Omega}\int_{\theta-\phi}^{\infty}\left(-\frac{n}{R^3} + \frac{3R_nM}{R^5}\right)d\lambda\ . \tag{32c}$$

For later convenience, the range of integration is divided into two and K_1 is written

$$K_1 = K_{1_1} + K_{1_2} \tag{33}$$

with

$$K_{1_1} = \frac{1}{4\pi\rho_f \Omega} \int_{\theta-\phi}^{0} \left(-\frac{1}{R^3} + \frac{3R_1 M}{R^5} \right) d\lambda \ , \tag{34a}$$

$$K_{1_2} = \frac{1}{4\pi\rho_f \Omega} \int_{0}^{\infty} \left(-\frac{1}{R^3} + \frac{3R_1 M}{R^5} \right) d\lambda \ . \tag{34b}$$

Similarly we also define K_{m_1}, K_{m_2} and K_{n_1}, K_{n_2}.

Evaulation of Kernel Functions

The preceding integrations cannot be carried out functionally. To avoid a long tedious numerical procedure, we approximate $\sin \lambda$ and $\cos \lambda$ as follows: Let

$$\lambda = k\alpha + y \ ,$$

where y varies from 0 to α and k is an integer varying from 0 to ∞. Then we have

$$\cos \lambda = \cos k\alpha \cos y - \sin k\alpha \sin y \ , \tag{35a}$$

$$\sin \lambda = \sin k\alpha \cos y + \cos k\alpha \sin y \ . \tag{35b}$$

If α is chosen small enough, we can approximate $\cos y$ and $\sin y$ as follows:

$$\cos y = 1 + a_1 y + a_2 y^2 \ , \tag{36a}$$

$$\sin y = y + a_3 y^2 \ , \tag{36b}$$

where a_1, a_2, and a_3 are so chosen that the best approximation can be made within the range of y. From Eqs. (35) and (36),

$$\sin \lambda = s_0 + s_1 y + s_2 y^2 \ , \tag{37a}$$

where $s_0 = \sin k\alpha$, $s_1 = a_1 \sin k\alpha + \cos k\alpha$, and $s_2 = a_2 \sin k\alpha + a_3 \cos k\alpha$, and

$$\cos \lambda = c_0 + c_1 y + c_2 y^2 \ , \tag{37b}$$

where $c_0 = \cos k\alpha$, $c_1 = a_1 \cos k\alpha - \sin k\alpha$, and $c_2 = a_2 \cos k\alpha - a_3 \sin k\alpha$. Equations (28) become

$$1 = \cos \beta_Q \ , \tag{38a}$$

$$m = c_0 \sin \beta_Q + c_1 \sin \beta_Q \, y + c_2 \sin \beta_Q \, y^2 \ , \tag{38b}$$

$$n = s_0 \sin \beta_Q + s_1 \sin \beta_Q \, y + s_2 \sin \beta_Q \, y^2 \ . \tag{38c}$$

Equations (29) become

$$R_1 = -(d + \rho\lambda \tan \beta) = -d - \rho k\alpha \tan \beta - \rho \tan \beta \, y$$

$$= x_0 + x_1 y, \quad \text{with} \quad x_0 = -(d + \rho k\alpha \tan \beta), \ x_1 = -\rho \tan \beta \ , \tag{39a}$$

$$R_m = \rho s_0 + \rho s_1 y + \rho s_2 y^2 \tag{39b}$$

$$R_n = r - \rho c_0 - \rho c_1 y - \rho c_2 y^2 \ . \tag{39c}$$

From Eqs. (31), (37b), and (38)

$$M = M_0 + M_1 y + M_2 y^2 \ , \tag{40}$$

where

$$M_0 = x_0 \cos \beta_Q + r s_0 \sin \beta_Q \ , \tag{41a}$$

$$M_1 = r s_1 \sin \beta_Q + x_1 \cos \beta_Q \ , \tag{41b}$$

$$M_2 = r s_2 \sin \beta_Q \ . \tag{41c}$$

Equation (27) becomes

$$R = (ay^2 + 2by + c)^{1/2} \ , \tag{42}$$

where

$$a = \rho^2 \tan^2 \beta - 2\rho r c_2 \ , \tag{43a}$$

$$b = \rho \tan \beta \, (d + \rho k\alpha \tan \beta) - 2\rho r c_1 \ , \tag{43b}$$

$$c = (d + \rho k\alpha \tan \beta)^2 + \rho^2 + r^2 - 2\rho r c_0 \ . \tag{43c}$$

Now within each interval, say from $k\alpha$ to $(k+1)\alpha$, we define K_{1k} as

$$K_{1k} = \frac{1}{4\pi\rho_f\Omega}\int_{k\alpha}^{(k+1)\alpha}\left(-\frac{1}{R^3}+\frac{3R_1M}{R^5}\right)dy \quad . \tag{44}$$

From Eqs. (38), (39), and (42)

$$K_{1k} = \frac{1}{4\pi\rho_f\Omega}\int_{k\alpha}^{(k+1)\alpha}\frac{-\cos\beta_Q}{(ay^2+2by+c)^{3/2}}dy$$

$$+\frac{3}{4\pi\rho_f\Omega}\int_{k\alpha}^{(k+1)\alpha}\frac{M_0x_0+(M_1x_0+M_0x_1)y+(M_1x_1+M_2x_0)y^2+M_2x_1y^3}{(ay^2+2by+c)^{5/2}}dy$$

$$=-\frac{\cos\beta_Q}{4\pi\rho_f\Omega}I_3^0 \quad \frac{3M_0x_0}{4\pi\rho_f\Omega}I_5^0+\frac{3(M_1x_0+M_0x_1)}{4\pi\rho_f\Omega}I_5^1$$

$$+\frac{3(M_1x_1+M_2x_0)}{4\pi\rho_f\Omega}I_5^2+\frac{3M_2x_1}{4\pi\rho_f\Omega}I_5^3 \quad , \tag{45}$$

where

$$I_3^0 = \int_{k\alpha}^{(k+1)\alpha}\frac{dy}{(ay^2+2by+c)^{3/2}} = \frac{1}{ac-b^2}\frac{ay+b}{\sqrt{ay^2+2by+c}}\Bigg|_{k\alpha}^{(k+1)\alpha} \quad , \tag{46a}$$

$$I_5^0 = \int_{k\alpha}^{(k+1)\alpha}\frac{dy}{(ay^2+2by+c)^{5/2}}$$

$$=\frac{1}{3(ac-b^2)}\frac{ay+b}{(ay^2+2by+c)^{3/2}}\Bigg|_{k\alpha}^{(k+1)\alpha}+\frac{2a}{3(ac-b^2)}I_3^0 \quad , \tag{46b}$$

$$I_5^1 = \int_{k\alpha}^{(k+1)\alpha}\frac{y\,dy}{(ay^2+2by+c)^{5/2}}$$

$$=-\frac{1}{3a}\frac{1}{(ay^2+2by+c)^{3/2}}\Bigg|_{k\alpha}^{(k+1)\alpha}+\frac{b}{a}I_5^0 \quad , \tag{46c}$$

$$I_5^2 = \int_{k\alpha}^{(k+1)\alpha}\frac{y^2\,dy}{(ay^2+2by+c)^{5/2}}$$

$$=-\frac{1}{2a}\frac{y}{(ay^2+2by+c)^{3/2}}\Bigg|_{k\alpha}^{(k+1)\alpha}-\frac{b}{2a}I_5^1+\frac{c}{2a}I_5^0 \quad , \tag{46d}$$

$$I_5^3 = \int_{k\alpha}^{(k+1)\alpha} \frac{y^3\,dy}{(ay^2+2by+c)^{5/2}}$$

$$= -\frac{y^2}{a(ay^2+2by+c)^{3/2}}\Bigg|_{k\alpha}^{(k+1)\alpha} + \frac{b}{a} I_5^2 + \frac{2c}{a} I_5^1 \,. \tag{46e}$$

We also need I_3^1 and I_3^2 for calculating K_{mk} and K_{nk}. They are

$$I_3^1 = \int_{k\alpha}^{(k+1)\alpha} \frac{y\,dy}{(ay^2+2by+c)^{3/2}} = -\frac{1}{ac-b^2}\frac{by+c}{\sqrt{ay^2+2by+c}}\Bigg|_{k\alpha}^{(k+1)\alpha}, \tag{47a}$$

$$I_3^2 = \int_{k\alpha}^{(k+1)\alpha} \frac{y^2\,dy}{(ay^2+2by+c)^{3/2}} = \frac{1}{a} I_1^0 - \frac{2b}{a} I_3^1 - \frac{c}{a} I_3^0 \,, \tag{47b}$$

where

$$I_1^0 = \int_{k\alpha}^{(k+1)\alpha} \frac{dy}{\sqrt{ay^2+2by+c}}$$

$$= \frac{1}{\sqrt{a}} \log\left(\frac{ay+b}{\sqrt{a}} + \sqrt{ay^2+2by+c}\right)\Bigg|_{k\alpha}^{(k+1)\alpha}, \quad \text{for } a > 0 \,, \tag{48a}$$

$$I_1^0 = \frac{-1}{\sqrt{-a}} \arcsin\left(\frac{ay+b}{\sqrt{b^2-ac}}\right)\Bigg|_{k\alpha}^{(k+1)\alpha}, \quad \text{for } a < 0 \,, \tag{48b}$$

$$I_1^0 = \frac{1}{\sqrt{a}} \log(ay+b)\Bigg|_{k\alpha}^{(k+1)\alpha}, \quad \text{for } b^2 - ac = 0 \,. \tag{48c}$$

Theoretically speaking, in computing K_{1_2} of Eq. (34b), k takes values from zero to infinity. However for engineering purposes, only a few turns of the path of Q are necessary. Within the range where Q is near to P, and α value of one-half radian can give very good accuracy. This value can be increased while Q is moving away from the point P. By integration stepwise, K_{1_2} can quite easily be obtained to the desired accuracy.

In Eq. (34a), the expression for K_{1_1}, the lower integration limit $\theta - \phi$ corresponds to the difference between the angular coordinates of the control point and the field point on the blade Q. The number of integration steps required to obtain the same degree of accuracy for K_{1_1} as for K_{1_2} depends on the blade area ratio. Unless the area ratio is very large, one step is sufficient to obtain a desired accuracy. K_{m_1}, K_{m_2}, K_{n_1}, and K_{n_2} are computed similarly.

This concludes our discussion on kernel functions for the case of steady blade loading such as in the open water condition. The case of periodic blade loading such as in the behind condition is discussed in the next subsection.

Kernel Functions for Periodic Blade Loading

Whenever a ship changes speed or course, the velocity or wake field becomes time dependent. Although it is feasible to analyze such problems within the framework of our basic approach, we have chosen here a much simpler example of the unsteady case, that of a periodic blade loading.

When a ship is maintained on a steady course, we assume that the wake field behind is time independent. Since wake strength varies spatially, a rotating propeller blade experiences a periodic inflow variation. As a result the blade loading also becomes periodic. Since the induced velocity is proportional to the blade loading if everything else is kept the same, we can use the principle of superposition. A periodic loading is first broken into its harmonic contents. By summing up induced velocity due to each loading harmonic, we obtain the total induced velocity due to the total periodic loading. Therefore, our problem is essentially to obtain new kernel functions $\tilde{K}_l$, $\tilde{K}_m$, and $\tilde{K}_n$, similar to those defined by Eqs. (32), due to a pressure dipole with a periodic varying strength $e^{iq\Omega t}$ at a point $Q(\xi,\rho,\theta-\Omega t)$ on the moving blade, where q is the order of the loading harmonic. Now $\tilde{K}_l$, $\tilde{K}_m$, and $\tilde{K}_n$ are complex functions with a real and an imaginary part, which can be expressed as

$$\tilde{K}_l = K_{la} + iK_{lb} , \tag{49a}$$

$$\tilde{K}_m = K_{ma} + iK_{mb} , \tag{49b}$$

$$\tilde{K}_n = K_{na} + iK_{nb} . \tag{49c}$$

Since the load variation over the blade area may not be in phase, we write the load distribution as

$$\tilde{L}(\xi,\rho,\theta) = L(\xi,\rho,\theta)_a + iL(\xi,\rho,\theta)_b . \tag{50}$$

Now we may write

$$\tilde{u}(x,r,\phi) = \int_S\int \tilde{L}(\xi,\rho,\theta)\, \tilde{K}_l \, d\rho d\theta , \tag{51a}$$

$$\tilde{v}(x,r,\phi) = \int_S\int \tilde{L}(\xi,\rho,\theta)\, \tilde{K}_m \, d\rho d\theta , \tag{51b}$$

$$\tilde{w}(x,r,\phi) = \int_S\int \tilde{L}(\xi,\rho,\theta)\, \tilde{K}_n \, d\rho d\theta , \tag{51c}$$

The induced fluid velocity components given by these equations also have a real and an imaginary part.

To find the expressions for the complex kernel functions for the qth order of the loading harmonic, for instance, we start with the following equation, corresponding to Eq. (20),

$$\tilde{\Phi}(x, r, \phi) = \frac{1}{4\pi\rho_f} \frac{\partial}{\partial n'} \left(\frac{e^{iq\Omega t}}{R} \right) . \tag{52}$$

Instead of Eqs. (28) we obtain the following expressions for the axial, tangential, and radial components of the pressure dipole:

$$\tilde{l} = l \cdot e^{iq\Omega t} , \tag{53a}$$

$$\tilde{m} = m \cdot e^{iq\Omega t} , \tag{53b}$$

$$\tilde{n} = n \cdot e^{iq\Omega t} . \tag{53c}$$

From Eq. (31)

$$\begin{aligned} \tilde{M} &= \tilde{l} R_1 + \tilde{m} R_m + \tilde{n} R_n \\ &= (l R_1 + m R_m + n R_n) e^{iq\Omega t} \\ &= M e^{iq\Omega t} . \end{aligned} \tag{54}$$

By replacing l, m, n, and M by $\tilde{l}$, $\tilde{m}$, $\tilde{n}$, and $\tilde{M}$ respectively in Eqs. (32) we obtain

$$\tilde{K}_1 = \frac{1}{4\pi\rho_f \Omega} \int_{\theta-\phi}^{\infty} e^{iq\Omega t} \left(-\frac{1}{R^3} + \frac{3R_1 M}{R^5} \right) d\lambda , \tag{55a}$$

$$\tilde{K}_m = \frac{1}{4\pi\rho_f \Omega} \int_{\theta-\phi}^{\infty} e^{iq\Omega t} \left(-\frac{m}{R^3} + \frac{3R_m M}{R^5} \right) d\lambda , \tag{55b}$$

$$\tilde{K}_n = \frac{1}{4\pi\rho_f \Omega} \int_{\theta-\phi}^{\infty} e^{iq\Omega t} \left(-\frac{n}{R^3} + \frac{3R_n M}{R^5} \right) d\lambda . \tag{55c}$$

Since $\Omega t = \theta - \phi - \lambda$,

$$\begin{aligned} e^{iq\Omega t} &= \cos q(\theta-\phi-\lambda) + i \sin q(\theta-\phi-\lambda) \\ &= \cos q(\theta-\phi) \cos q\lambda + \sin q(\theta-\phi) \sin q\lambda \\ &\quad + i[\sin q(\theta-\phi) \cos q\lambda - \cos q(\theta-\phi) \sin q\lambda] . \end{aligned} \tag{56}$$

From Eqs. (49), (55), and (56) we have

$$K_{1a} = \frac{\cos q(\theta-\phi)}{4\pi\rho_f\Omega}\int_{\theta-\phi}^{\infty}\cos q\lambda\left(-\frac{1}{R^3}+\frac{3R_1M}{R^5}\right)d\lambda + \frac{\sin q(\theta-\phi)}{4\pi\rho_f\Omega}\int_{\theta-\phi}^{\infty}\sin q\lambda\left(-\frac{1}{R^3}+\frac{3R_1M}{R^5}\right)d\lambda \ , \tag{57a}$$

$$K_{1b} = \frac{\sin q(\theta-\phi)}{4\pi\rho_f\Omega}\int_{\theta-\phi}^{\infty}\cos q\lambda\left(-\frac{1}{R^3}+\frac{3R_1M}{R^5}\right)d\lambda - \frac{\cos q(\theta-\phi)}{4\pi\rho_f\Omega}\int_{\theta-\phi}^{\infty}\sin q\lambda\left(-\frac{1}{R^3}+\frac{3R_1M}{R^5}\right)d\lambda \ . \tag{57b}$$

Let

$$K_{1c} = \int_{\theta-\phi}^{\infty}\cos q\lambda\left(-\frac{1}{R^3}+\frac{3R_1M}{R^5}\right)d\lambda \ , \tag{58a}$$

$$K_{1s} = \int_{\theta-\phi}^{\infty}\sin q\lambda\left(-\frac{1}{R^3}+\frac{3R_1M}{R^5}\right)d\lambda \ . \tag{58b}$$

Then

$$K_{1a} = \frac{\cos q(\theta-\phi)}{4\pi\rho_f\Omega}K_{1c} + \frac{\sin q(\theta-\phi)}{4\pi\rho_f\Omega}K_{1s} \ , \tag{59a}$$

$$K_{1b} = \frac{\sin q(\theta-\phi)}{4\pi\rho_f\Omega}K_{1c} - \frac{\cos q(\theta-\phi)}{4\pi\rho_f\Omega}K_{1s} \ . \tag{59b}$$

Since $\sin q\lambda$ and $\cos q\lambda$ can be expressed in terms of $\sin\lambda$ and $\cos\lambda$, and since $\sin\lambda$ and $\cos\lambda$ are given by Eqs. (37a) and (37b) respectively, we may write

$$\sin q\lambda = \sum_{i=0}^{2q} g_i y^i \ , \tag{60a}$$

$$\cos q\lambda = \sum_{i=0}^{2q} h_i y^i \ , \tag{60b}$$

where g_i and h_i are functions of s_0, s_1, s_2, c_0, c_1, and c_2. From Eqs. (39), (40), and (60)

$$3R_1M \cos q\lambda = 3(x_0 + x_1 y)(M_0 + M_1 y + M_2 y^2)(h_0 + h_1 y + h_2 y^2 + \cdots + h_{2q} y^{2q})$$

$$= r_0 + r_1 y + r_2 y^2 + \cdots + r_{2q+3} y^{2q+3} , \tag{61}$$

where

$$r_0 = 3 x_0 M_0 h_0 ,$$

$$r_1 = 3(x_0 M_0 h_1 + x_0 M_1 h_0 + x_1 M_0 h_0) ,$$

$$r_2 = 3(x_0 M_0 h_2 + x_0 M_1 h_1 + x_0 M_2 h_0 + x_1 M_0 h_1 + x_1 + M_1 h_0) , \quad \text{etc.}$$

Then

$$K_{1c} = -\cos \beta_Q \sum_{i=0}^{2q} \int_{\theta-\phi}^{\infty} h_i \frac{y^i}{R^3} dy + \sum_{i=0}^{2q+3} \int_{\theta-\phi}^{\infty} r_i \frac{y^i}{R^5} dy . \tag{62}$$

By comparing Eq. (58a) with Eq. (32a) it is clear that the evaluation procedure for K_{1c} is just the same as that shown in Eq. (45), for K_1, except that there are more terms in K_{1c} than in K_1. In the steady case we have I_3^n and I_5^m, where n ranges from 0 to 2 and m ranges from 0 to 4. In the case of K_{1c} we have n ranging from 0 to $2q + 2$ and m ranging from 0 to $2q + 4$.

After K_{1c} and K_{1s} have been found, we obtain the expression of $\tilde{K}_1$ by Eqs. (59) and (49a). Likewise we obtain $\tilde{K}_m$ and $\tilde{K}_n$.

In the evaluation of $\tilde{K}_1$, $\tilde{K}_m$, and $\tilde{K}_n$ we need the following expressions to obtain the additional I_3^n and I_5^m:

$$I_3^n = \int_{k\alpha}^{(k+1)\alpha} \frac{y^n \, dy}{(ay^2 + 2by + c)^{3/2}} = \frac{1}{(n-2)a} \frac{y^{n-1}}{\sqrt{ay^2 + 2by + c}} \Bigg|_{k\alpha}^{(k+1)\alpha}$$

$$- \frac{(2n-3)}{(n-2)} \frac{b}{a} I_3^{n-1} - \frac{(n-1)}{(n-2)} \frac{c}{a} I_3^{n-2} , \quad \text{for } n > 2 , \tag{63a}$$

$$I_5^m = \int_{k\alpha}^{(k+1)\alpha} \frac{y^m \, dy}{(ay^2 + 2by + c)^{5/2}} = \frac{1}{(m-4)a} \frac{y^{m-1}}{(ay^2 + 2by + c)^{3/2}} \Bigg|_{k\alpha}^{(k+1)\alpha}$$

$$- \frac{(2m-5)}{(m-4)} \frac{b}{a} I_5^{m-1} - \frac{(m-1)}{(m-4)} \frac{c}{a} I_5^{m-2} , \quad \text{for } m > 4 . \tag{63b}$$

We have developed expressions of kernel functions for a pressure dipole that has a strength of $e^{iq\Omega t}$ at a point $Q(\xi, \rho, \theta - \Omega t)$ which moves along a helical line with a constant speed and with its axis normal to the blade element but with no radial component. Furthermore we have shown a step-by-step procedure for evaluating these kernel functions. In each step the evaluation is done functionally. This concludes our discussion of the kernel functions and their evaluations.

Blade Loading Function

For a two-dimensional lifting surface it is advantageous to express the chordwise loading distribution by a Birnbaum series, because there is a one-to-one correspondence between the loading and downwash terms. In a three-dimensional-propeller problem, however, there is no such advantage. On the other hand, since the kernel functions are expressed in terms of $\theta - \phi$, it is possible to carry out the chordwise integration over the blade functionally if the chordwise loading variation can also be expressed in terms of $\theta - \phi$. This is done as follows:

On the propeller blade ξ is a function of ρ and θ, and the pressure jump Δp_i representing the blade loading is a function of ρ and θ only. Since a given function can be approximated by a polynomial, we write

$$\Delta p_i(\rho,\theta) = \sum_{n=0}^{N} a_n(\rho) \left(\frac{\theta - \theta_L}{\theta_T - \theta_L} \right)^n , \tag{64}$$

where θ_T and θ_L are the angular coordinates of the trailing and leading edge respectively and are functions of ρ. The distance along the chord from the leading edge normalized by the chord length is used as the chordwise variable.

Since $(\theta - \theta_L)^n = [\theta - \phi - (\theta_L - \phi)]^n$, Eq. (64) can be expressed as

$$\Delta p_i(\rho,\theta) = \sum_{n=0}^{N} b_n(\rho)(\theta - \phi)^n . \tag{65}$$

To include the unsteady case we write a general loading function as

$$\Delta \tilde{p}_i(\rho,\theta) = \Delta p_i(\rho,\theta)_a + i\Delta p_i(\rho,\theta)_b , \tag{66}$$

where $\Delta p_i(\rho,\theta)_a$ and $\Delta p_i(\rho,\theta)_b$ are the real and imaginary components of the loading amplitude distribution.

Replacing $\tilde{L}(\xi,\rho,\theta)$ in Eq. (51a) by $\Delta \tilde{p}_i(\rho,\theta)$ of Eq. (66) we obtain

$$\tilde{u}(x,r,\phi) = \iint_S [\Delta p_i(\rho,\theta)_a + i\Delta p_i(\rho,\theta)_b][K_{1a} + iK_{1b}] \, d\rho d\theta$$

$$= \iint_S [\Delta p_i(\rho,\theta)_a K_{1a} - \Delta p_i(\rho,\theta)_b K_{1b}] \, d\rho d\theta$$

$$+ i \iint_S [\Delta p_i(\rho,\theta)_a K_{1b} + \Delta p_i(\rho,\theta)_b K_{1a}] \, d\rho d\theta$$

or

$$\tilde{u}(x,r,\phi) = u(x,r,\phi)_a + iu(x,r,\phi)_b \quad , \tag{67}$$

where

$$u(x,r,\phi)_a = \iint_S [\Delta p_i(\rho,\theta)_a K_{1a} - \Delta p_i(\rho,\theta)_b K_{1b}] \, d\rho d\theta \quad , \tag{68a}$$

$$u(x,r,\phi)_b = \iint_S [\Delta p_i(\rho,\theta)_a K_{1b} + \Delta p_i(\rho,\theta)_b K_{1a}] \, d\rho d\theta \quad . \tag{68b}$$

Likewise we have

$$\tilde{v}(x,r,\phi) = v(x,r,\phi)_a + iv(x,r,\phi)_b \tag{69}$$

with

$$v(x,r,\phi)_a = \iint_S [\Delta p_i(\rho,\theta)_a K_{ma} - \Delta p_i(\rho,\theta)_b K_{mb}] \, d\rho d\theta \quad , \tag{70a}$$

$$v(x,r,\phi)_b = \iint_S [\Delta p_i(\rho,\theta)_a K_{mb} + \Delta p_i(\rho,\theta)_b K_{ma}] \, d\rho d\theta \tag{70b}$$

and

$$\tilde{w}(x,r,\phi) = w(x,r,\phi)_a + iu(x,r,\phi)_b \tag{71}$$

with

$$w(x,r,\phi)_a = \iint_S [\Delta p_i(\rho,\theta)_a K_{na} - \Delta p_i(\rho,\theta)_b K_{nb}] \, d\rho d\theta \quad , \tag{72a}$$

$$w(x,r,\phi)_b = \iint_S [\Delta p_i(\rho,\theta)_a K_{nb} + \Delta p_i(\rho,\theta)_b K_{na}] \, d\rho d\theta \quad . \tag{72b}$$

In the steady case, the expressions for the velocity components can, of course, be reduced. For instance, considering the expressions for $\tilde{u}(x,r,\phi)$ in the steady case, $\Delta p_i(\rho,\theta)_b$ and K_{1b} are zero. Hence $u(x,r,\phi)_b$ is zero. Also since q is zero, K_{1a} is reduced to K_1 and Eq. (68a) is reduced to Eq. (19a) with $L(\xi,\rho,\theta)$ equal to $\Delta p_i(\rho,\theta)_a$. As a result in the steady case, there is only one surface integration to perform instead of four as in the case of periodic loading.

The four surface integrations of Eqs. (68) are all similar. Hence, the induced fluid velocity for the case of periodic loading is found in just the same way as for the steady case, except that more computational work is involved.

Equations (67) through (72) constitute the main body of our results. They relate the induced absolute fluid velocity components to the blade loading, which can be steady or periodic. Even though these equations are derived only for time t being equal to zero at a fixed space, they actually relate the induced absolute fluid velocity component to the blade loading at all times in the space relative to the blade position. This is because whatever is valid in the steady case as observed on the blade for t being equal to zero is valid for t being equal to any value. It is also true for periodic blade loading. The amplitude of a sinusoidal function determined from the real and the imaginary values at any time is the same.

Within our scheme of evaluating kernel functions and representing the loading function components the surface integration involved in Eqs. (68), (70), and (72) can be conveniently carried out since the integration in the chordwise direction can also be performed functionally. The next section gives the details of such surface integration.

Integration Over the Lifting Surface

The surface integrals as discussed in the previous section are all alike. The integrand of each of the surface integrals involves a product of a loading function and an appropriate kernel function. Since each of the kernel functions is a linear combination of I_3^n, I_5^m, and I_1^0, and since the loading function is expressed as a polynomial of $\theta - \phi$ in the chordwise direction, the results of the chordwise integration of the product of a kernel function and a loading function is a linear combination of the quantities

$$J_{1\log}^{n} = \int_{\theta_L}^{\theta_T} (\theta - \phi)^n \log\left[\frac{a(\theta - \phi)}{\sqrt{a}} + \sqrt{a(\theta - \phi)^2 + 2b(\theta - \phi) + c}\right] d\theta , \qquad (73a)$$

where $n = 0, 1, 2, \ldots,$

$$J_1^m = \int_{\theta_L}^{\theta_T} \frac{(\theta - \phi)^m \, d\theta}{\sqrt{a(\theta - \phi)^2 + 2b(\theta - \phi) + c}} , \qquad (73b)$$

where $m = 0, 1, 2, \ldots,$ and

$$J_3^m = \int_{\theta_L}^{\theta_T} \frac{(\theta - \phi)^m \, d\theta}{[a(\theta - \phi)^2 + 2b(\theta - \phi) + c]^{3/2}} , \qquad (73c)$$

where $m = 0, 1, 2, 3, \ldots .$

If the difference between β_Q and β is neglected, a, b, and c in Eqs. (73) are independent of $\theta - \phi$, and these integrations can be carried out functionally. Since recurrence formulas are available to express J_3^m in terms of J_3^{m-1} and J_3^{m-2} for $m > 2$, J_3^m can be obtained rapidly after J_3^0, J_3^1, and J_3^2 have been computed. Likewise it is necessary to obtain only a few terms of J_1^m or $J_{1_{log}}^n$ by integration. The remaining can be obtained by recurrence formulas.

If the difference between β_Q and β is taken into account, a is independent of $\theta - \phi$, but b and c are functions of $\theta - \phi$. However, the expression of the distance factor R in K_{1_1}, K_{m_1}, and K_{n_1} can still be expressed as the square root of a second degree polynomial of $\theta - \phi$. After substituting $\theta - \phi$ for y we have from Eq. (42)

$$R = [a(\theta-\phi)^2 + 2b(\theta-\phi) + c]^{1/2} . \tag{74}$$

From Eq. (26) we write

$$d = d_0 + d_1(\theta-\phi) , \tag{75}$$

where

$$d_0 = (\rho - r) \tan \gamma + \phi (\rho \tan \beta_Q - r \tan \beta_P) \tag{76a}$$

$$d_1 = \rho s = \rho (\tan \beta_Q - \tan \beta) . \tag{76b}$$

From Eqs. (43) and (75)

$$a = \rho^2 \tan^2 \beta - 2\rho r c_2 , \tag{77a}$$

$$b = b_0 + b_1(\theta-\phi) , \tag{77b}$$

$$c = e_0 + e_1(\theta-\phi) + e_2(\theta-\phi)^2 , \tag{77c}$$

where

$$b_0 = \rho^2 k\alpha \tan^2 \beta - 2\rho r c_1 + d_0 \rho \tan \beta ,$$

$$b_1 = d_1 \rho \tan \beta ,$$

$$e_0 = \rho^2 + r^2 - 2\rho r c_0 + (\rho k\alpha \tan \beta)^2 + d_0^2 + 2d_0 \rho k\alpha \tan \beta ,$$

$$e_1 = d_0 d_1 + d_1 \rho k\alpha \tan \beta ,$$

$$e_2 = d_1^2 .$$

Substituting the previous expressions of a, b, and c into Eq. (74) we obtain

$$R = [a'(\theta-\phi)^2 + 2b'(\theta-\phi) + c']^{1/2} ,$$

where

$$a' = a + 2b_1 + e_2 ,$$

$$b' = b_0 + e_1/2 ,$$

$$c' = e_0 .$$

Also

$$ac - b^2 = a[e_0 + e_1(\theta - \phi) + e_2(\theta - \phi)^2] - [b_0 + b_1(\theta - \phi)]^2$$

$$= f_0 + f_1(\theta - \phi) + f_2(\theta - \phi)^2 , \qquad (78)$$

where

$$f_0 = ae_0 - b_0^2 ,$$

$$f_1 = ae_1 - 2b_1 b_0 ,$$

$$f_2 = ae_2 - b_1^2 .$$

With these expressions it is clear that the chordwise integration over the blade can be carried out easily with I_3^n or I_5^m as the integrand, except for I_3^0, I_3^1, and I_5^0, where the factor $ac - b^2$ is also involved in the denominator of the integrand. It is possible to obtain functional solutions even for these special cases. However the functional solution is so complicated in each case that it is easier to carry out the integration numerically.

The last integration in the radial direction with respect to ρ is carried out numerically. A computer program is in preparation for computing at any time the induced velocity components at point $P(x,r,\phi)$ from the action of a moving blade. The total induced velocity due to the action of a propeller is, of course, the sum of the contributions from all the blades. This program can be used either for propeller design or for propeller performance prediction or simply for computing the induced velocity in the field.

APPLICATION OF THE THEORY

Propeller Design Problem

In a design problem, the blade contour is chosen from consideration of cavitation and blade strength. The path of the propeller is known from the propeller forward speed and the angular velocity. The lift distribution depends upon the specified thrust distribution over the blade and the orientation of the blade in space. With the blade contour orientation which defines the blade pitch distribution not known, the pressure dipole distribution is not known. Therefore, an iterative procedure is necessary. To start with, the advance angle β at each

radius, or the β_i angle obtained from a lifting line computation, can be taken as the blade pitch angle. After the first computation the nose-tail line obtained at each radius gives a new blade contour orientation from which pressure dipole distribution is obtained and a second computation can be carried out. This iterative procedure is continued until a convergence is obtained.

It is appropriate to consider the design of a propeller working in the behind condition, since it constitutes one of the problems which has motivated the development of the present theory. However, for the sake of clarity the open-water design problem is discussed first. The design conditions are as follows:

Thrust	T
Diameter	D
Propeller velocity	V
Angular velocity	Ω
Radial thrust distribution	
Chordwise load distribution	
Blade contour	
Number of blades	

Our objective is to obtain the cambered surface which will produce the specified load distribution over the blade in the design condition. We picture the propeller starting from far behind with the blades carrying a specified lift distribution $\Delta p_i(\rho,\theta)$. This lift distribution is derived from the desired thrust distribution and the blade contour and its orientation; these are supposedly known when the computation in each iteration is started. Far ahead of the propeller we choose a number of points along a line corresponding to the leading edge of the blade at time t equal to zero when the blade reaches there. These are starting points for a streamline tracing which defines the blade orientation and chamber. Equations (19) can be used to compute the absolute velocity of the tracing at any time for any point relative to the moving propeller reference axes. Thus the streamline tracing in the propeller reference axes is equivalent to solving the following first-order differential equations:

$$\frac{dx}{u(x,r,\phi) - V} = \frac{r\,d\theta}{v(x,r,\phi) - r\Omega} = \frac{dr}{w(x,r,\phi)} \quad . \tag{79}$$

The streamlines so traced define the cambered surface of the propeller blade.

Before discussing the general case of a propeller behind a surface ship, we will mention briefly the case of a propeller working behind a body of revolution where the flow to the space yet to be occupied by the propeller has a symmetry with respect to the propeller axis of rotation. However, the flow has radial as well as axial variations. Again we picture the propeller moving to a fixed space from far behind. The only difference between this and the open-water case is that the fluid velocity field already exists even when the propeller is still infinitely far behind. Hence, in addition to the induced velocity components calculated by using Equations (19), the velocity components existing in this space must be accounted for to obtain the absolute fluid velocity in that space at any time. After this is done, the streamline tracing is exactly the same as the open-water case (Eq. (79)). If the radial velocity component in the space induced by

the body of revolution is appreciable in comparison with the blade rotating speed, the streamlines will become spiral lines.

After the two cases discussed, it is relatively easy to discuss the general case with the propeller working behind a surface ship, where the wake field does not have axial symmetry. In this condition, the blade loading is periodic. However, from the viewpoint of ship powering, we are only interested in designing a propeller which will produce the required total circumferential average thrust or torque. Hence, we can replace the wake field behind a surface ship by an "equivalent" wake field having an axial symmetry where the wake strength at any radius is equal to the circumferential average of the original wake field. The propeller is then designed as in the case behind a body of revolution. Hence, in this case, the propeller operating condition is quite different from the condition for which it is designed. The actual performance of the propeller has to be calculated after the propeller has been designed, as described in the next section.

If the performance is not satisfactory with regard to alternating propeller forces and pressure distribution over the blade, then such design conditions as number of blades, amount of rake or skew, blade area, and blade contour may require changes.

Propeller Performance Prediction

The previous section discussed the design of a propeller in the behind condition and indicated that the performance in a circumferentially varying wake field is not fully known. In this section we will describe how to calculate such performance. The purpose of the calculation is twofold: to obtain assurance that no operating trouble will arise from propeller cavitation or propeller-induced hull vibration, and to gain more insight regarding such factors as relative rotative efficiency and effective wake.

Information on the pressure distribution over the blade at various blade positions is vital if we are to determine the possibility of propeller cavitation or propeller-induced hull vibration for the particular hull-propeller combination. If the load variation is too severe, the propeller under consideration may have to be redesigned. Perhaps the average radial load distribution needs revision or the radial blade area distribution and the area ratio should be changed. Also, the rake or skew might not be the optimum as viewed in the light of the particular wake distribution at hand. All these questions can be answered by conducting a performance prediction computation.

It is assumed that the wake field in the absence of the propeller is known. Usually this information is obtained by a wake survey in the propeller plane. For an accurate prediction, however, it is very desirable to have a wake survey carried out in three different planes — one near the blade leading edge, one near the blade trailing edge, and one in between these two planes. If the wake suvey is carried out in one plane only, we are compelled to assume that there is no variation of wake velocity in the axial direction.

Let us assume that an harmonic analysis of the circumferential wake velocity variation has been done; for the qth harmonic we may write

$$\tilde{u}_0(x,r,\phi) = u_0(x,r)_a \cos q\phi + iu_0(x,r)_b \sin q\phi \ , \tag{80a}$$

$$\tilde{v}_0(x,r,\phi) = v_0(x,r)_a \cos q\phi + iv_0(x,r)_b \sin q\phi \ , \tag{80b}$$

$$\tilde{w}_0(x,r,\phi) = w_0(x,r)_a \cos q\phi + iw_0(x,r)_b \sin q\phi \ , \tag{80c}$$

where $u_0(x,r)_a$, $v_0(x,r)_a$, and $w_0(x,r)_a$ are the amplitudes of the real or cosine parts and $u_0(x,r)_b$, $v_0(x,r)_b$, and $w_0(x,r)_b$ are the imaginary or sine parts of the three wake velocity components respectively.

For this qth-harmonic wake velocity a qth-harmonic load distribution is induced over the blade to assure that the fluid velocity relative to the blade will always be tangent to the cambered surface. Figure 3 shows an elementary cambered surface at $P'(x',r,\phi')$. The relative fluid velocity there must be tangent to the cambered surface. Let us first ignore the radial fluid velocity component. Then we must have

$$\tan\psi = \frac{u_0(x',r)_a \cos q\phi + u(x',r,\phi')_a}{v_0(x',r)_a \cos q\phi + v(x',r,\phi')_a} \tag{81a}$$

and

$$\tan\psi = \frac{u_0(x',r)_b \sin q\phi + u(x',r,\phi')_b}{v_0(x',r)_b \sin q\phi + v(x',r,\phi')_b} \ . \tag{81b}$$

Equation (81a) states that the real part of the resultant fluid velocity must be in the direction of $P'D$ and Eq. (81b) states the same fact for the imaginary part. The propeller blade velocity does not enter these equations, since the propeller rotates with a constant angular velocity Ω and advances with a constant velocity V. There is no harmonic content in Ω and V, except for q equal to zero. For q equal to zero we have

$$\tan\psi = \frac{u_0(x',r)_a + u(x',r,\phi') - V}{v_0(x',r)_a + v(x',r,\phi') - r\Omega} \ . \tag{81c}$$

The induced fluid velocity at $P'(x',r,\phi')$ due to a load distribution over the cambered surface can be approximated by the induced velocity at $P(x,r,\phi)$ on the chord due to the same loud distribution along chord lines rather than mean lines. Since the distance PP' is very small, the wake velocity at P' can also be approximated by the wake velocity at P. Then we have for $q \neq 0$

$$\tan\psi = \frac{u_0(x,r)_a \cos q\phi + u(x,r,\phi)_a}{v_0(x,r)_a \cos q\phi + v(x,r,\phi)_a} \ , \tag{82a}$$

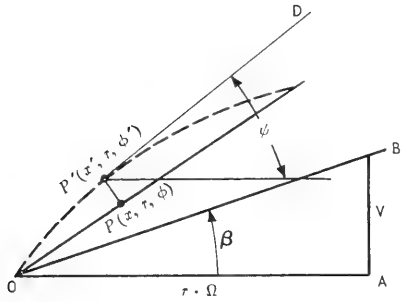

Fig. 3 - Propeller blade element with camber and chord line

$$\tan \psi = \frac{u_0(x,r)_b \sin q\phi + u(x,r,\phi)_b}{v_0(x,r)_b \sin q\phi + v(x,r,\phi)_b} , \tag{82b}$$

where $x = r \tan \gamma + r\phi \tan \beta_P$. For $q = 0$ we have

$$\tan \psi = \frac{u_0(x,r)_a + u(x,r,\phi)_a - V}{v_0(x,r)_a + v(x,r,\phi)_a - r\Omega} , \tag{82c}$$

where $u_0(x,r)_a$ and $v_0(x,r)_a$ are the circumferential average, zero harmonic, wake velocity components.

In Eqs. (82a) and (82b) $u(x,r,\phi)_a$, $u(x,r,\phi)_b$, $v(x,r,\phi)_a$, and $v(x,r,\phi)_b$ are related to the two unknown loading functions $\Delta p_i(\rho,\theta)_a$ and $\Delta p_i(\rho,\theta)_b$ by Eqs. (68) and (70). Hence Eqs. (82a) and (82b) are two simultaneous integral equations to be satisfied over the whole cambered surface. Various techniques are available for solving such equations. A most appropriate method will be investigated in the immediate future. For the case of q being equal to zero, only Eq. (82c) needs to be solved.

The total qth harmonic blade loading is obtained by integrating the loading distribution over the whole lifting surface. We have

$$L_{qa} = \iint_S \Delta p_i(\rho,\theta)_a \, d\rho d\theta , \tag{83a}$$

$$L_{qb} = \iint_S \Delta p_i(\rho,\theta)_b \, d\rho d\theta , \tag{83b}$$

and

$$\tilde{L}_q = L_{qa} + iL_{qb} = Ae^{i\phi} , \tag{83c}$$

where $A = \sqrt{L_{qa}^2 + L_{qb}^2}$ and $\phi = \arctan (L_{qb}/L_{qa})$. When these computations are carried out for all the harmonics of the wake field, the resultant blade loading will be the sum of all the loading harmonics. The resultant load distribution over the blade area is the sum of all the load distribution harmonics.

So far we have ignored the radial fluid velocity component. After the load distribution functions $\Delta p_i(\rho,\theta)_a$ and $\Delta p_i(\rho,\theta)_b$ have been obtained, Eqs. (72) can be used to obtain the radial induced velocity component. The resultant radial velocity component is the sum of the radial wake component and the propeller-induced radial velocity component. If the resultant radial velocity component at each point P′ is large, the mean-line segment shown in Fig. 3 must be taken as the projection of the mean-line segment as traced by a fluid particle through the control point P′. A new value of $\tan \psi$ at each control point is taken accordingly, and the whole computation is repeated. For practical purposes such refined computations may not be necessary.

SOME PRELIMINARY NUMERICAL RESULTS

Based on the theory and the numerical technique outlined in the previous sections, a computer program is being developed for the problem of designing a propeller and predicting its performance. Some preliminary results will be given for (a) an open-water propeller design with constant chordwise load distribution and (b) the inverse calculation for predicting propeller performance in the steady design condition.

For the time being the computer program neglects the difference between β_Q and β in the integration over the lifting surface (as discussed following Eqs. (73)), and in this case the chordwise integration over the blade is readily carried out functionally.

Integration in the radial direction is carried out numerically following an integration procedure similar to that described in Ref. 24 for the spanwise integration of a wing. The propeller blade is divided into three regions, as indicated in Fig. 4. Region II extends a short radial distance on each side of the control point $P(x,r,\phi)$, region I fills the gap between the root section of the blade and region II, and region III extends from region II to the tip of the blade.

The integrand of Eqs. (19) contains a second-order singularity $1/(r-\rho)^2$ in region II; hence the division into the three regions is intended to facilitate the evaluation of the finite part of the improper integral in this region. The integrands in regions I and III are not singular and can readily be evaluated by numerical integration methods.

Propeller Design Example

The design example chosen is a propeller with a symmetrical blade outline and constant chordwise load distribution; the specification is similar to that chosen by Pien in Ref. 3 and by Cheng in Ref. 6.

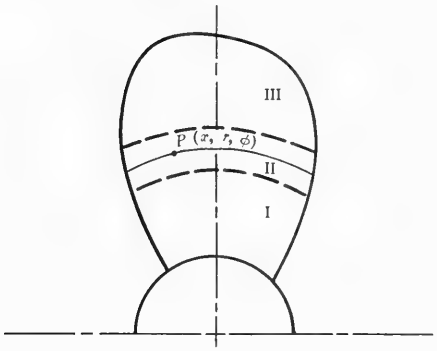

Fig. 4 - Division of the propeller blade into three regions for numerical integration in the radial direction

As discussed previously, without the pitch distribution the dipole distribution is not known prior to the design calculation, and an iterative procedure is necessary. Both the β angle and the β_i angle obtained from the lifting line results of Cheng (6) were used in our design example as starting values in two independent calculations. To obtain accurate camber and pitch distributions with the β-angle required three iterative steps, whereas only two were necessary for the design calculation starting with the β_i angle. Camber values were calculated for ten positions on the chord and for nine radial sections.

Some results of this design example are shown in Figs. 5 and 6. Figure 5 gives the pitch distribution and Figure 6 the maximum camber as function of radius. In both figures the results are compared with those obtained by Cheng (6).

Example of Inverse Calculation

In predicting propeller performance in the steady condition, we are supposed to determine the steady blade loading. The blade loading is presently represented by an expression similar to Eq. (64):

$$\Delta p_i = \sum_{n=0}^{N-1} \sum_{m=0}^{M-1} a_{nm} \left(\frac{\theta - \theta_L}{\theta_T - \theta_L} \right)^n \cos my \qquad (84)$$

with

$$\cos my = \frac{1 + r_h - 2\rho}{1 - r_h} ,$$

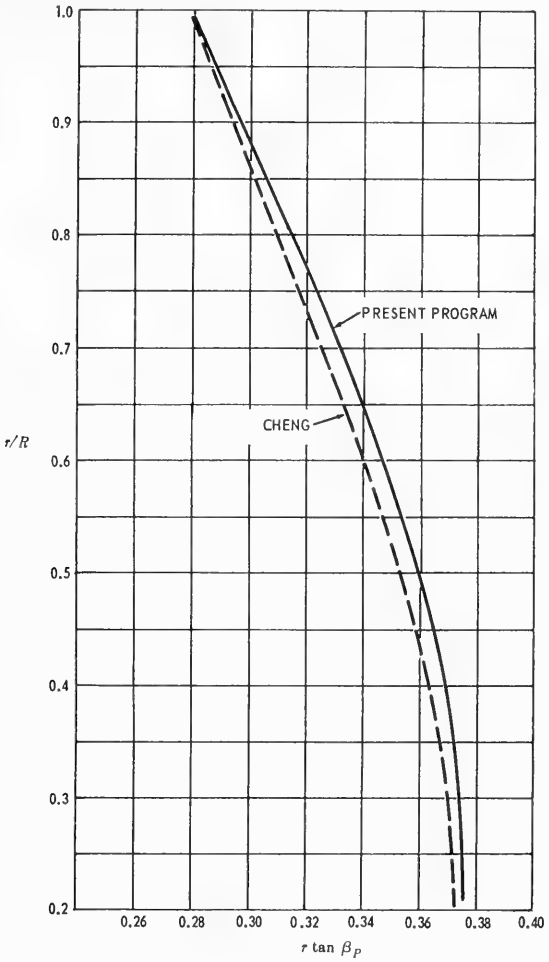

Fig. 5 - Comparison of the pitch distribution from the present design program and Cheng's data from Table 1 of Ref. 6

where r_h is the nondimensional hub radius. N times M is taken to be the same as the number of control points on the propeller blade, so that N corresponds to the number J of control points on each blade section and M to the number K of sections on the propeller blade.

Establishing for each control point $P(r_k, \phi_j)$ the angle of the tangent to the cambered surface, we obtain according to Eq. (82c)

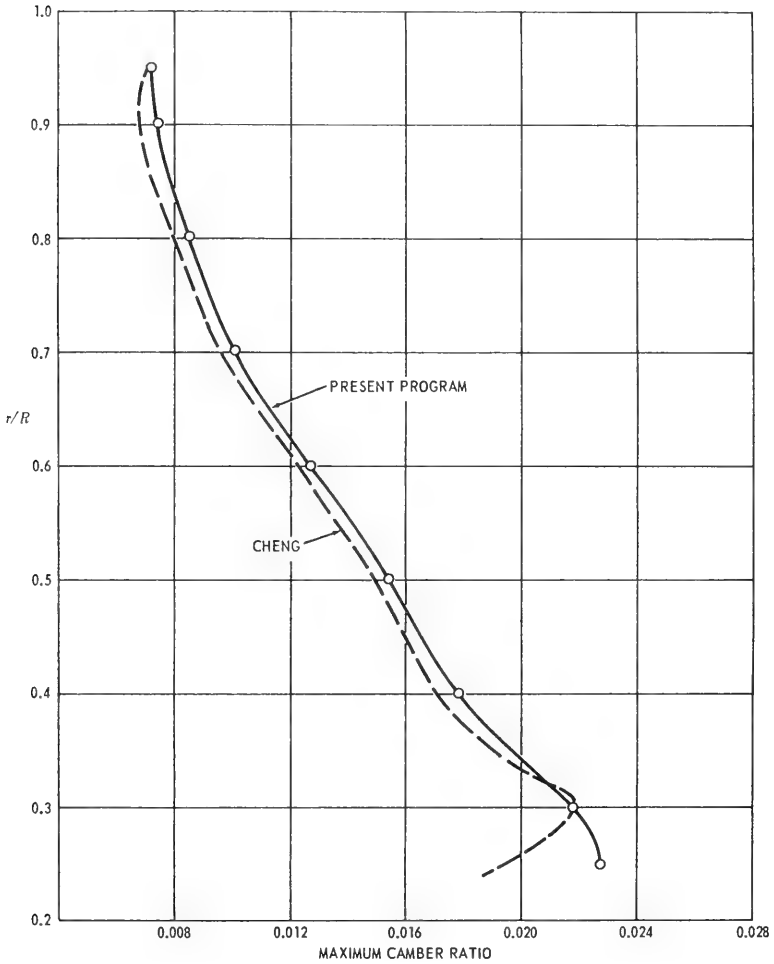

Fig. 6 - Comparison of the maximum camber ratio from the present design program and Cheng's data from Table 1 of Ref. 6

$$\tan \psi(r_k, \phi_j) = \frac{u(r_k, \phi_j) - V}{v(r_k, \phi_j) - r_k \Omega} , \tag{85}$$

where

$$u(r_k, \phi_j) = \sum_{n=0}^{N-1} \sum_{m=0}^{M-1} a_{nm} \cdot u(r_k, \phi_j)_{nm} , \tag{86a}$$

$$v(r_k,\phi_j) = \sum_{n=0}^{N-1} \sum_{m=0}^{M-1} a_{nm} \cdot v(r_k,\phi_j)_{nm} \ , \qquad (86b)$$

in which $u(r_k,\phi_j)_{nm}$ and $v(r_k,\phi_j)_{nm}$ are induced velocities as obtained from Eqs. (19a) and (19b) for the various modes of the load functions, with the load coefficient a_{nm} equal to unity.

Combining Eqs. (85) and (86) we can establish a set of J times K linear equations as follow:

$$\sum_{n=0}^{N-1} \sum_{m=0}^{M-1} -a_{nm}[u(r_k,\phi_j)_{nm} - v(r_k,\phi_j)_{nm} \tan\psi(r_k,\phi_j)]$$

$$= r_k\Omega \tan\psi(r_k,\phi_j) - V \ , \quad \text{for} \quad j = 1, J \quad \text{and} \quad k = 1, K \ . \qquad (87)$$

Consequently, the unknown load distribution coefficients a_{nm} can be obtained by solving the J times K equations with a_{nm} as the corresponding number of unknowns.

As an example of a performance prediction, the simple case of the inverse calculation of the propeller design example is considered. It is felt that this example provides a check on the numerical accuracy of the method.

Five points on each of nine radial sections were used as control points. Table 1 shows the output from the computer program. Figure 7 gives the radial load distribution compared with the load distribution used in the design. Figure 8 shows chordwise load distributions for four of the nine radial sections.

The results from the computer program obtained so far have confirmed that an efficient computer program can be developed on the basis of the theory and the numerical technique. Less than 10 minutes of computer time was required on the IBM 7090 at the Naval Ship Research and Development Center for both the design example and the inverse calculation.

CONCLUDING REMARKS

1. The general theory for marine propellers outlined in the paper is based on an exact acceleration potential. There is no linearization of the equations involved; it is a higher order theory. It imposes no limit on loading of a propeller under normal practical operating conditions.

2. The theory is derived from the equations of motion and the equation of continuity. An irrotational fluid motion has not been assumed. Therefore, the theory can be applied to a propeller operating behind another propeller or another lifting surface where free vortex distribution exists.

3. The theory uses information about the moving propeller blades and their load distributions and positions, whereas it is not required that the fluid flow induced by the propeller be established beforehand.

Table 1
Results From the Inverse Propeller Calculation Showing the Input Data to the Computer Program

PROPELLER DATA FROM SECOND ITERATION OF DESIGN PROGRAM 20 MAY 1968

INVERSE PROPELLER CALCULATION BASED ON ACCELERATION POTENTIAL

INPUT DATA

DIAMETER	0.667 FT	
SPEED OF ADVANCE	0.592 KNOTS	1.000 FT/SEC
ANGULAR VELOCITY	106.855 RPM	1.781 RPS
ADVANCE COEFFICIENT	0.842	
HUB RADIUS XH/R	0.200	
NUMBER OF BLADES	5	

RX/R	0.2000	0.2500	0.3000	0.4000	0.5000	0.6000	0.7000	0.8000	0.9000	0.9500	1.0000
TAN(BO)	1.8320	1.5138	1.2570	0.9258	0.7255	0.5799	0.4735	0.3931	0.3326	0.3059	0.2516
CHORD/R	0.6160	0.6803	0.7440	0.8600	0.9240	0.9280	0.8700	0.7400	0.5360	0.3736	0.0800
SKEW/R	0.	0.	-0.	-0.	-0.	-0.	-0.	-0.	-0.	0.	-0.
RAKE/R	0.	0.	-0.	-0.	-0.	-0.	-0.	-0.	-0.	0.	-0.

CAMBER RATIO AT CONTROL POINTS

RX/R		0.2500	0.3000	0.4000	0.5000	0.6000	0.7000	0.8000	0.9000	0.9500	
X/CHORD											
		0.2000	0.2000	0.2000	0.2000	0.2000	0.2000	0.2000	0.2000	0.2000	
		0.4000	0.4000	0.4000	0.4000	0.4000	0.4000	0.4000	0.4000	0.4000	
		0.6000	0.6000	0.6000	0.6000	0.6000	0.6000	0.6000	0.6000	0.6000	
		0.8000	0.8000	0.8000	0.8000	0.8000	0.8000	0.8000	0.8000	0.8000	
		1.0000	1.0000	1.0000	1.0000	1.0000	1.0000	1.0000	1.0000	1.0000	
CAMBER RATIO											
		0.0160	0.0153	0.0124	0.0110	0.0090	0.0072	0.0060	0.0053	0.0051	
		0.0231	0.0218	0.0174	0.0154	0.0123	0.0099	0.0082	0.0073	0.0069	
		0.0230	0.0218	0.0175	0.0154	0.0122	0.0098	0.0082	0.0073	0.0069	
		0.0158	0.0153	0.0125	0.0110	0.0086	0.0070	0.0059	0.0053	0.0050	
		0.	0.	0.	0.	0.	0.	0.	0.	0.	

OUTPUT - PREDICTION OF PROPELLER PERFORMANCE AND LOAD DISTRIBUTION

THRUST LOADING COEFFICIENT (NONVISCOUS)	CTH	0.5639
POWER LOADING COEFFICIENT (NONVISCOUS)	CP	0.7138
IDEAL PROPELLER EFFICIENCY		0.7899
ADVANCE COEFFICIENT	J	0.8423
THRUST COEFFICIENT (NONVISCOUS)	KT	0.1571
TORQUE COEFFICIENT (NONVISCOUS)	KQ	0.0267

RX/R	0.2000	0.2500	0.3000	0.4000	0.5000	0.6000	0.7000	0.8000	0.9000	0.9500	1.0000
RADIAL LOAD DISTRIBUTION											
	0.0155	0.0428	0.0710	0.1267	0.1753	0.2037	0.2048	0.1806	0.1285	0.0880	0.0201
CHORDWISE LOAD DISTRIBUTION											
X/CHORD											
0.		0.0469	0.0679	0.1211	0.1705	0.1986	0.1991	0.1719	0.1175	0.1090	
0.10		0.0417	0.0686	0.1238	0.1723	0.2007	0.2023	0.1769	0.1259	0.0871	
0.20		0.0398	0.0694	0.1255	0.1739	0.2023	0.2045	0.1800	0.1279	0.0824	
0.30		0.0401	0.0700	0.1266	0.1751	0.2034	0.2060	0.1818	0.1314	0.0834	
0.40		0.0417	0.0708	0.1273	0.1759	0.2043	0.2068	0.1829	0.1318	0.0900	
0.50		0.0435	0.0717	0.1279	0.1765	0.2050	0.2071	0.1834	0.1318	0.0921	
0.60		0.0451	0.0727	0.1284	0.1768	0.2055	0.2069	0.1834	0.1317	0.0904	
0.70		0.0457	0.0734	0.1286	0.1768	0.2056	0.2062	0.1830	0.1311	0.0859	
0.80		0.0450	0.0732	0.1283	0.1765	0.2053	0.2050	0.1817	0.1291	0.0820	
0.90		0.0427	0.0715	0.1273	0.1760	0.2043	0.2031	0.1790	0.1244	0.0845	
1.00		0.0387	0.0675	0.1250	0.1752	0.2022	0.2004	0.1743	0.1150	0.1020	
LOAD COEFFICIENTS (PLOG)											
0	0.0524	0.0469	0.0679	0.1211	0.1705	0.1986	0.1991	0.1719	0.1175	0.1090	0.0439
1	-0.2825	-0.0384	0.0057	0.0168	0.0104	0.0127	0.0134	0.0314	0.0564	-0.1680	-0.2253
2	0.6442	0.0784	-0.0123	-0.0257	-0.0064	-0.0152	-0.0140	-0.0467	-0.1116	0.4641	0.5881
3	-0.6054	-0.0561	0.0232	0.0251	0.0011	0.0141	0.0100	0.0404	0.1115	-0.5220	-0.6465
4	0.2067	0.0119	-0.0136	-0.0106	-0.0002	-0.0067	-0.0037	-0.0164	-0.0434	0.2049	0.2540

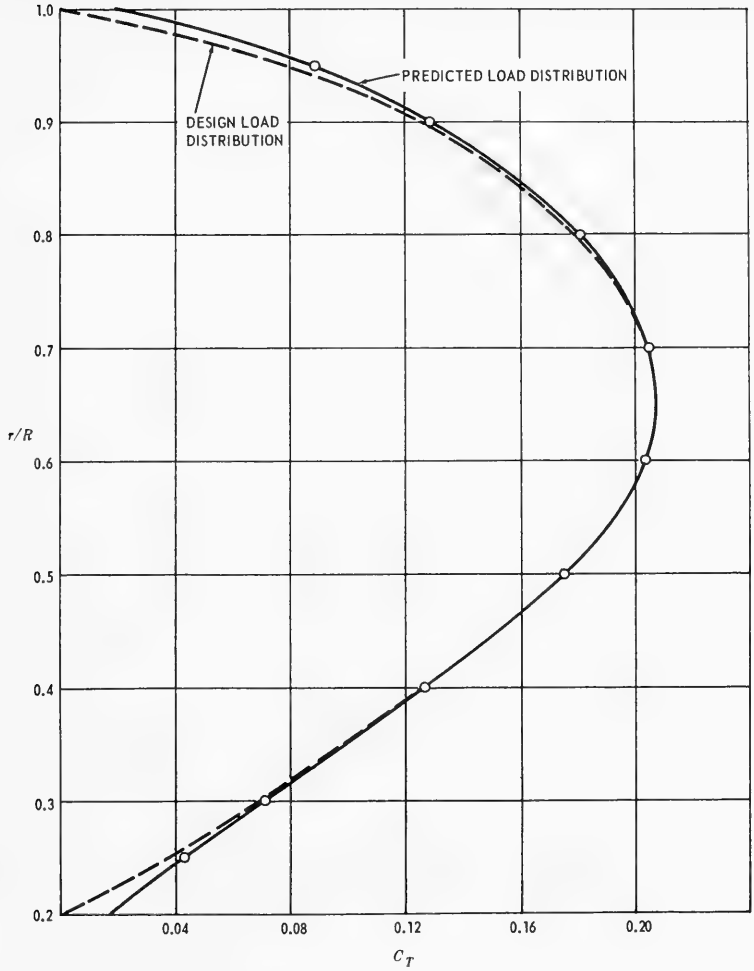

Fig. 7 - Radial load distribution from the inverse calculation as compared with the design load distribution

4. Since the theory does not depend on the induced fluid flow but only on information about the blades, as mentioned in item 3, we need not be concerned with whether the free vortex sheet is going to contract or roll up.

5. The theory is used essentially to obtain the change in fluid velocity in a chosen fixed space due to the direct propeller blade action. Whether, in the absence of the propeller, the fluid in that space is already in motion makes no difference. Therefore the theory is applicable to a propeller in either the open water or the behind condition.

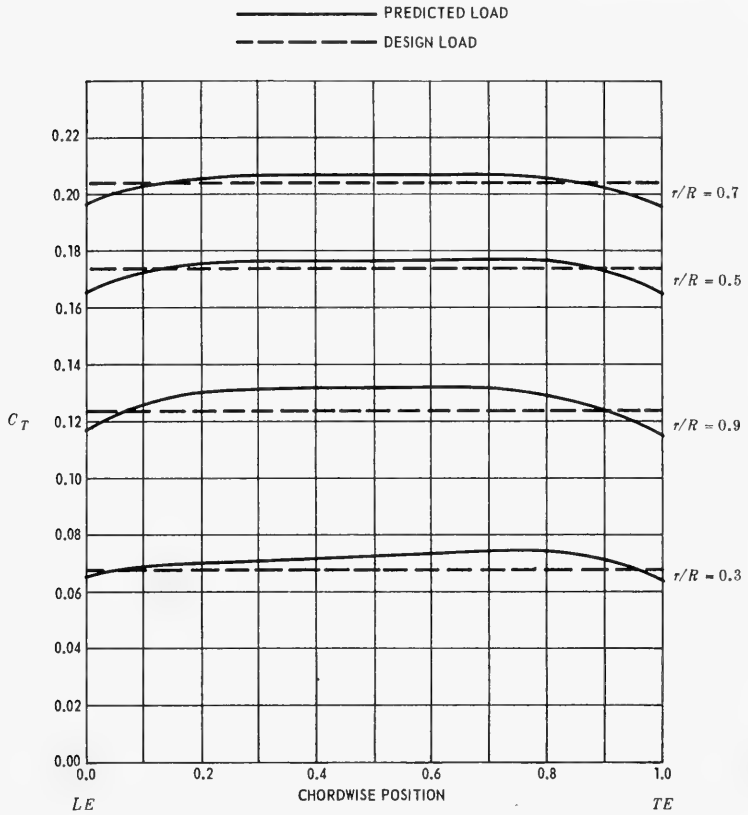

Fig. 8 - Chordwise load distribution from the inverse calculation as compared with the design load distribution

6. Since the camber ratio involved in a practical marine propeller is only a few percent, especially at the outer radii where most of the loading is carried, the load distribution is placed on the chord rather than on the meanline. This saves computer time without losing the accuracy required for engineering purposes. However, the theory takes into account the difference between the blade element pitch angle β_Q and the advance angle β. The former is a function of blade geometry, and the latter is a function of operating condition. They are independent of each other and may differ appreciably.

7. All geometrical features of a propeller blade are incorporated in the theory. Therefore, it is applicable to any practical propeller as far as propeller geometry is concerned.

8. In view of item 2 the present theory can be easily extended to cover multiple propeller systems such as overlapping and contrarotating propellers.

9. It is planned to extend the theory to take the thickness effect into account. Supercavitating propellers with arbitrary blade contours and arbitrary σ values will also be investigated.

10. The effect of viscosity has been ignored in the present work. However since the theory can accurately predict the load distribution along various chords, it paves the way for investigating the effect of viscosity.

11. Preliminary results have indicated that an efficient computer program can be developed on the basis of the numerical technique discussed in the paper.

ACKNOWLEDGMENT

This work was carried out under the Naval Ship Research and Development Center Foundation Research Project.

The authors express their thanks to Mr. J. B. Hadler, Head of the Ship Powering Division, NSRDC, for his encouragement and support. Thanks are due to Mr. H. M. Cheng and Dr. B. Yim for their interest and many stimulating discussions in the development of the basic concept of the theory.

REFERENCES

1. Sparenberg, J.A., "Application of Lifting Surface Theory to Ship Screws," International Shipbuilding Progress 7 (No. 67), 99-106 (1960)

2. Cox, G.G., "Corrections to the Camber of Constant Pitch Propellers," Royal Inst. Naval Architects 103, 227-243 (1961)

3. Pien, P.C., "The Calculation of Marine Propellers Based On Lifting-Surface Theory," J. Ship Research 5 (No. 2), 1-14 (1961)

4. Kerwin, J.E., "The Solution of Propeller Lifting-Surface Problems by Vortex Lattice Methods," Massachusetts Institute of Technology, Dept. of Naval Architecture and Marine Engineering, June 1961

5. Lerbs, H.W., Alef, W., and Albrecht, K., "Numerische Auswertungen zur Theorie der Tragenden Flache von Propellern," Jahrbuch der Schiffbautechnische Gesellschaft 58, 295-318 (1964)

6. Cheng, H.M., "Hydrodynamic Aspect of Propeller Design Based on Lifting Surface Theory, Part I — Uniform Chordwise Load Distribution," David Taylor Model Basin Report 1802, 1964.

7. Cheng, H.M., "Hydrodynamic Aspect of Propeller Design Based on Lifting Surface Theory, Part II — Arbitrary Chordwise Load Distribution," David Taylor Model Basin Report 1803, 1965

8. Kerwin, J.E., and Leopold, R., "A Design Theory for Subcavitating Propellers," Trans. SNAME 72, 294-335 (1964)

9. Isay, W.H. and Armonat, R., "Zur Berechnung der potentialtheoretischen Druckverteilung am Flügelblatt eines Propellers," Schiffstechnik 13 (No. 67), 75-89 (June 1966)

10. Murray, M.T., "Propeller Design and Analysis by Lifting Surface Theory," International Shipbuilding Progress 14 (No. 160), 433-451 (1967)

11. Yamazaki, R., "On the Theory of Screw Propellers in Non-Uniform Flows," Kyushu University, Memoirs of the Faculty of Engineering 25 (No. 2), 107-174 (1966)

12. Yamazaki, R., "On the Theory of Screw Propellers," pp. 3-28 in Fourth Symposium on Naval Hydrodynamics, Propulsion and Hydroelasticity," Washington, D.C., Aug. 1962, Office of Naval Research, Department of the Navy, ACR-92

13. Brown, N.A., "Periodic Propeller Forces in Nonuniform Flow," Massachusetts Institute of Technology, Dept. of Naval Architecture and Marine Engineering, June 1964

14. Brown, N.A., "The Lifting Surface Vortex Sheet Representation of the Propeller in Non-Uniform Flow," Massachusetts Institute of Technology, Dept. of Naval Architecture and Marine Engineering, Oct. 1966

15. Bjorklund, F.R., "Computation of Periodic Propeller Forces in Non-Uniform Flows using a Lifting Surface Model," Massachusetts Institute of Technology, Dept. of Naval Architecture and Marine Engineering, Jan. 1968

16. Greenberg, M.D., "The Unsteady Loading on a Marine Propeller in a Nonuniform Flow," J. Ship Research 8 (No. 3), 27-38 (1964)

17. Lerbs, H.W., and Schwanecke, H., "Ansätze einer instationären Propellertheorie," Schiff and Hafen 17, 797-801 (1965)

18. Laudan, J., "Numerical Calculations on Non-Steady Propeller Forces," Hamburgishe Schiffbau-Versuchsanstalt Report F35/67, Sept. 1967

19. Hanoaka, T., "Hydrodynamics of an Oscillating Screw Propeller," pp. 79-124 in Fourth Symposium on Naval Hydrodynamics, Propulsion and Hydroelasticity," Washington, D.C., Aug. 1962, Office of Naval Research, Department of the Navy, ACR-92

20. Tsakonas, J., Jacobs, W.R., and Rank, P.H., "Unsteady Propeller Lifting-Surface Theory with Finite Number of Chordwise Modes," Stevens Institute of Technology, Davidson Laboratory Report 1133, Dec. 1966

21. Tsakonas, S., Breslin, J., and Miller, M., "Correlation and Application of an Unsteady Flow Theory for Propeller Forces," Trans. SNAME 75, 158-193 (1967)

22. Lamb, H., "Hydrodynamics," Sixth Edition, Dover, New York, p. 60

23. Abott, I.R., and von Doenhoff, A.E., "Theory of Wing Sections," Dover, New York, 1958, p. 79

24. Watkins, C.E., Woolston, D.S., and Cunningham, H.J., "A Systematic Kernel Function Procedure for Determining Aerodynamic Forces on Oscillating or Steady Finite Wings at Subsonic Speeds," NACA Report R-48, 1959

Appendix

SUPPLEMENTAL DISCUSSIONS ON THE BASIC CONCEPT SECTION

During informal discussions with Prof. J. Weissinger, a point was raised as to the general applicability of our preliminary conclusion that the term $\mathbf{q} \times \xi$ in Eq. (4) was zero and could be omitted in the subsequent mathematical development of the basic concept for the marine propeller problem. After a closer examination, we found that our conclusion $\mathbf{q} \times \xi$ is zero in the wake was apparently an error. In this appendix we would like to rectify our error by reasoning that we can assume as a simplification that $\mathbf{q} \times \xi$ is zero and offering the following discussion to supplement our reasoning and to bridge the gap in the formulation.

We shall begin with the general equation of motion for an inviscid fluid particle under the influence of an external force field,

$$\frac{d\mathbf{q}}{dt} = -\frac{1}{\rho_f} \nabla p + \mathbf{F} \ , \tag{A1}$$

where $\mathbf{q}$ is the velocity vector, $\triangle p$ is the gradient of the pressure field p, ρ_f is the fluid density, and $\mathbf{F}$ is the external force per unit mass. The left-hand term represents the acceleration of the fluid particle which may be expressed in two parts, namely, a term representing the local acceleration at a fixed space and a convective term due to the movement of the fluid particle as follows:

$$\frac{d\mathbf{q}}{dt} = \frac{\partial \mathbf{q}}{\partial t} + (\mathbf{q}\nabla)\ \mathbf{q} \ . \tag{1}$$

Combining Equations (A1) and (1) we obtain

$$\frac{\partial \mathbf{q}}{\partial t} = -\frac{1}{\rho_f} \nabla p - (\mathbf{q}\nabla)\ \mathbf{q} + \mathbf{F} \ . \tag{A2}$$

Since

$$(\mathbf{q}\nabla)\ \mathbf{q} = \frac{1}{2} \nabla q^2 - \mathbf{q} \times \xi \ ,$$

where ξ is a vorticity vector, it follows that

$$\frac{\partial \mathbf{q}}{\partial t} = -\frac{1}{\rho_f} \nabla p - \frac{1}{2} \nabla q^2 + \mathbf{q} \times \xi + \mathbf{F} . \tag{A3}$$

For an incompressible fluid, ρ_f being a constant, we have

$$\frac{\partial \mathbf{q}}{\partial t} = -\nabla \left(\frac{p}{\rho_f} + \frac{1}{2} q^2 \right) + (\mathbf{q} \times \xi + \mathbf{F}) . \tag{A4}$$

Applying the continuity equation, i.e., $\nabla q = 0$, Eq. (A4) yields

$$\nabla^2 \left(\frac{p}{\rho_f} + \frac{1}{2} q^2 \right) = \nabla (\mathbf{q} \times \xi + \mathbf{F}) . \tag{A5}$$

We introduce a function Φ and a generalized force vector $\mathbf{k}$ such that

$$\Phi = \frac{p}{\rho_f} + \frac{1}{2} q^2 \tag{7}$$

and

$$\mathbf{k} = \mathbf{q} \times \xi + \mathbf{F} . \tag{A6}$$

Equation (A5) becomes

$$\nabla^2 \Phi = \nabla \mathbf{k} . \tag{A7}$$

This is a general governing equation for an incompressible inviscid fluid flow subjected to an external force field.

Now we shall attempt to discuss the physical significance of this equation and its solution as applied to a propeller problem.

Like an airfoil or wing, a propeller blade is considered to be a lifting surface on which forces are distributed, and this surface distribution of forces may be considered to be a limiting case of volume distribution by reducing one of the dimensions of the volume to zero while increasing the force intensity so that the total force is the same. It can be shown that the action of such external forces upon a fluid will produce vortex motion, and specifically, the curl of the force vector represents the time rate of change of the vorticity generated. It can therefore be said that a lifting surface such as a propeller blade is a vorticity generator. When the blade advances in the fluid, it imparts vorticity to the fluid particles along its path as it passes, i.e., vorticity is left in its wake.

Hence, the entire fluid field may be conveniently divided into three regions, the lifting surface, the wake, and the remaining field, and each region may be described by an appropriate equation based on the previously described general governing equation as follows:

1. Lifting surface where the general equation applies:

$$\nabla^2 \Phi = \nabla(\mathbf{q} \times \xi + \mathbf{F}) \ .$$

2. Wake:

$$\nabla^2 \Phi = \nabla(\mathbf{q} \times \xi) \tag{A8}$$

since the force **F** does not exist in the wake, and

3. Remaining field where both forces and vorticity are zero:

$$\nabla^2 \Phi = 0 \ . \tag{A9}$$

In the text we have discussed the significance of the last equation and briefly how a solution might be obtained. Also, we made a gross simplification, applying this equation to the wake region as well as neglecting the term $\mathbf{q} \times \xi$ in the wake. Now we shall proceed to discuss the implication of such a simplification.

In developing a theory for wings with finite span, von Karman and Burgers (Aerodynamic Theory edited by Durand, Vol, 2, Chapters III and V) presented a thorough treatise on the solution of the general governing equation similar to Equation (A7). They pointed out the difficulties encountered toward an exact solution to the real problem; they also showed that an approximate solution to the real problem might be obtained by neglecting in the wake the generalized force term which they referred to as the induced "second order" forces compared with either the k forces or the F forces and that the influence of the corrections to be deduced from these second order forces is only of the third order of magnitude. Hence, the resulting solution is correct to the second order of magnitude, the reason being that "notwithstanding their smallness, they will have a certain influence on all quantities considered; pressure, potential, and vortex motion. As a force, however, can never produce vortex motion at a point upstream from it, the distribution of the vorticity within the region of lifting surface is not affected." They also showed how a higher order solution could be obtained by iteration based on the blade path rather than the slip-stream geometry.

Thus, the general theory for propellers developed in this paper, neglecting the $\mathbf{q} \times \xi$ term in the wake region, is considered to be a second order theory which is consistent with the definition of the "exact acceleration potential" in the text.

On a lifting surface the vorticity ξ is always tangential to the surface since the velocity discontinuity is in the tangential direction only. If we denote $\mathbf{q}_t$ and $\mathbf{q}_n$ to be the tangential and normal components of $\mathbf{q}$, respectively, we have on the lifting surface the components of the generalized force:

$$\mathbf{k}_t = \mathbf{q}_n \times \xi \tag{A10}$$

$$\mathbf{k}_n = \mathbf{q}_t \times \xi + \mathbf{F} \ . \tag{A11}$$

The tangential force component k_t has an order of magnitude of q^2 because ξ is the difference in q on both sides of the surface. In general, a tangential force cannot produce a normal velocity component on the tangent plane. However, if the lifting surface has some curvature in it, as it usually does, the tangential component of the generalized force k_t would have some effect on the lift distribution but the effect is also of the third order. Therefore, consistent with a second order accuracy, it is only necessary to consider the normal component of the singularity distribution k_n on the lifting surface. This conclusion is significant because it is on the basis of this conclusion that the detailed theory has been developed. Of course, a higher than second order result can be obtained by taking all the neglected small quantities into account with an iterative procedure.

In practice we encounter two different types of problems: performance predictions of a given propeller geometry and design for a specified load requirement. In a performance prediction problem, we choose a proper expression for k_n with a number of relevant parameters. Then Φ can be expressed in terms of these parameters. The acceleration at a field point P is $-\nabla\Phi$. The time integration of $-\nabla\Phi$ gives the velocity q at P. By choosing P to be on the surface presently occupied by the lifting surface, we obtain q on the lifting surface in terms of these parameters. These parameters are determined by the boundary condition on the lifting surface. Subsequently the lift distribution F is calculated from Equation (A11). In a design problem an iterative procedure is necessary since the orientation of the lifting surface is not known. It has been found that the convergence is very rapid in such iterations.

Any of the existing propeller theories based on a linearized acceleration potential can be applied only to lightly loaded propellers since the accuracy of the computed induced velocity on a lifting surface suffers from two possible sources of error. These are (1) the linearization of the governing equation, the equation of motion; (2) the assumption that the lift distribution is perpendicular to the velocity of the lifting surface rather than perpendicular to the relative velocity between the fluid and the lifting surface.

In the case of a propeller theory based on vorticity distribution, effort can be made to have the bound vorticity properly oriented in space. However, a long iterative procedure is necessary in a performance-prediction problem even in a steady case because the geometry of the slipstream is not known. It is extremely difficult to use such a theory to analyze an unsteady propeller problem.

It is felt that the theory developed here not only has the advantage of better accuracy but also has its simplicity in its application, especially to unsteady propeller problems.

* * *

DISCUSSION

T. Y. Wu
California Institute of Technology
Pasadena, California

After we have worked for a number of years on a difficult subject such as the general theory of propellers, with more and more untractable problems accumulating in practice, it is always refreshing, and sometimes rewarding, to lean back and take a new look or try a new approach. This paper, I think, offers such a refreshing point of view. It is encouraging to hear the authors' experience that their theory, equipped with the simplifying assumptions they introduced, has made the numerical calculations noticeably simpler than the other existing methods.

In the case of the linearized theory the difference between the method of velocity potential and that of the Prandtl acceleration potential is nothing more than a personal preference, since they always yield the same result. I believe that another linearized theory in terms of a different function, such as the linearized version of the present theory, must bear a definite correspondence with the former two. It should be valuable if Dr. Pien and Dr. Strom-Tejsen could clarify further these correspondences, including the boundary conditions.

It is in the context of the authors' claim of the exactness and completeness of this theory that I wish to make a minor observation here. If I may put the formulation in a little different way, the relationship between the "exact acceleration potential" $\Phi = p/\rho + q^2/2$ defined by the authors and the velocity potential χ, $\mathbf{q} = \nabla\chi$ is simply

$$\frac{\partial\chi}{\partial t} + \Phi = \text{const.},$$

which is the Bernoulli equation for inviscid, irrotational flows. For steady flows in particular, Φ must be identically a constant and hence cannot be represented by a distribution of singularities. This situation may be changed if the calculation is based on a perturbation of the linear quantities caused by a weak disturbance of a moving body, which may be replaced by a force system. Since this theory is new, its potential usefulness can be greatly enhanced when the exact significance of the approximations introduced here is fully understood.

* * *

REPLY TO DISCUSSION

Pao C. Pien and J. Strom-Tejsen

We would like to thank Dr. Wu for his penetrating comments. In introducing the exact acceleration potential, we discussed a simple case of a lifting surface moving forward with a constant velocity V. Our objective was to obtain the perturbation velocity caused by the action of the lifting surface in a coordinate frame F, fixed to the lifting surface. In our basic concept we used another reference frame F', in which an exact acceleration potential could be found as the two frames approached each other. Then the time integration of the negative gradient of the acceleration potential could yield the perturbation velocity in frame F'.

When frame F' coincides with frame F, the velocity field in frame F differs from that in frame F' by the known relative velocity between F and F'. Dr. Wu has commented that if the flow is steady in frame F, $p/\rho_f + q^2/2$ is a constant, and there is no possible singularity in that frame. This is in accordance with our definition of the exact acceleration potential Φ. However it does not imply that there is no possible singularity distribution for Φ when referred to other frames. To facilitate our discussion we introduce the pressure equation with respect to a moving frame F' as given by L. M. Milne-Thomson in "Theoretical Hydrodynamics" as follows:

$$\frac{p}{\rho_f} + \frac{1}{2} q_r^2 + \Omega - \frac{\partial \phi}{\partial t} - \frac{1}{2} U^2 = C(t) ,$$

where q_r is the magnitude of the fluid velocity in frame F' and U is the translation speed of frame F'. If there is no force field Ω, we may write

$$\frac{p}{\rho_f} + \frac{1}{2} q_r^2 = \frac{\partial \phi}{\partial t} + \frac{1}{2} U^2 + C(t) .$$

By taking the gradient on both sides of the equation we obtain

$$-\nabla\left(\frac{p}{\rho_f} + \frac{1}{2} q_r^2\right) = \frac{\partial \mathbf{q}_r}{\partial t} ,$$

which shows that in any reference frame, the sum of the pressure divided by the fluid density and half of the velocity squared gives an exact acceleration potential. This is the foundation of our approach. The body frame F is a particular case in which the acceleration potential is a constant. It simply means that we should not choose it as our reference frame for an acceleration potential. If a frame fixed in space far ahead of the lifting surface is chosen as our reference frame, q_r becomes the perturbation velocity w. Therefore $p/\rho_f + w^2/2$ is an exact acceleration potential in that frame. It is up to us to choose whichever reference frame is the most convenient one to use.

Dr. Wu has also asked how the linearized version of the present theory compares with other linearized theories. In a lifting-surface theory based on acceleration potential, the governing equation is the equation of motion

$$\frac{\partial \mathbf{q}}{\partial t} + (\mathbf{q}\nabla)\,\mathbf{q} = -\nabla \frac{p}{\rho_f} .$$

This equation is commonly linearized by dropping the nonlinear term $(\mathbf{q}\nabla)\mathbf{q}$. In our approach we simply move it to the right side as follows:

$$\frac{\partial \mathbf{q}}{\partial t} = -\nabla\left(\frac{p}{\rho_f} + \frac{1}{2}\,q^2\right) + \mathbf{q} \times \xi = -\nabla\left(\frac{p}{\rho_f} + \frac{1}{2}\,q^2\right) ,$$

which equation is valid in the whole fluid region where the vorticity is absent. We achieve a linear governing equation by a substitution of variable Φ for $p/\rho_f + q^2/2$. We have only a linear equation to begin with; hence we cannot in a meaningful manner define a linearized version of our theory.

* * *

MODEL TESTS ON CONTRAROTATING PROPELLERS

J. D. van Manen and M. W. C. Oosterveld
Netherlands Ship Model Basin
Wageningen, The Netherlands

ABSTRACT

This paper presents the results of open-water tests with a systematic series of contrarotating propellers, consisting of a four-bladed forward screw and a five-bladed aft screw.

Based on the open-water test results, contrarotating propeller systems were designed for a tanker and a cargo liner. Comparative tests have been carried out with the tanker and the cargo liner both equipped with contrarotating propellers and with a conventional screw. The propulsive efficiencies, the cavitation characteristics, the propeller induced vibratory forces, and the stopping abilities are dealt with.

INTRODUCTION

During the past years the trend of most ship designs has been toward higher speeds (cargo liners) and/or larger displacement (tankers or carriers) and therefore toward high-powered ships. As a result the problems of propeller cavitation and propeller induced vibration became matters of great concern.

In an attempt to provide merchant ships with propulsion devices with superior cavitation and propeller induced vibration characteristics in addition to a high propulsive efficiency, the application of contrarotating propellers have been the subject of several investigations [1-3]. This paper presents the results of investigations on contrarotating propellers performed at the Netherlands Ship Model Basin during the past five years.

These investigations covered the following details. A systematic series of contrarotating propeller systems was designed and manufactured. These systems, consisting of a four-bladed forward screw and a five-bladed aft screw, were designed for equal power absorption by the forward and the aft screw. Tests were carried out in the towing tank to determine the open-water characteristics of this series of contrarotating propellers.

Based on these open-water test results, contrarotating propellers were designed for a tanker and a cargo liner. Comparative tests have been carried out with both ships equipped with a contrarotating propeller system and with a conventional single screw arrangement. In Fig. 1 the contrarotating propeller arrangement on the stern of the tanker model is shown. The propulsive efficiencies,

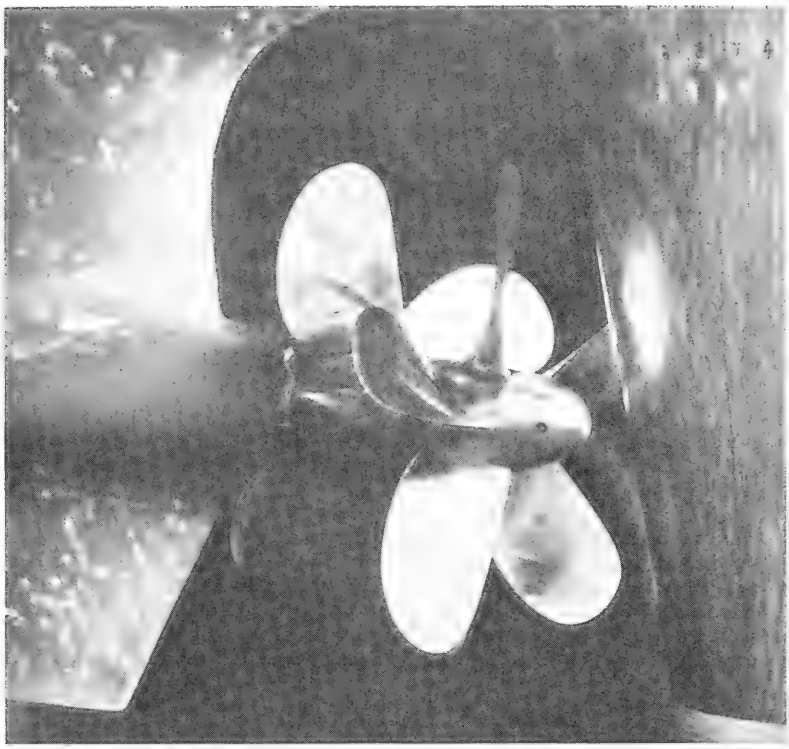

Fig. 1 - Arrangement of contrarotating propellers for a cargo liner model

the cavitation characteristics, the propeller induced vibratory forces, and the stopping abilities were dealt with.

The investigations on contrarotating propellers were given in detail in Refs. 4 through 8; a recapitulation of the results is given here.

TEST RESULTS WITH SYSTEMATIC SERIES OF CONTRAROTATING PROPELLERS

An important method of screw design is that which is based on the results of open-water tests with systematically varied series of screw models [9,10].

According to the lifting line theory, as described in Ref. 11, a systematic series of contrarotating propellers, consisting of a four-bladed forward propeller and a five-bladed aft propeller, was designed. A problem which may occur on contrarotating propellers is that the cavitating tip vortices generated by the blades of the forward propeller may impinge on the blades of the aft propeller

and cause damage there. This problem was avoided by reducing the diameter of the aft propeller. This reduction was based on the expected slipstream contraction at design condition. In addition, this reduction is attractive with regard to efficiency, because for equal screw loadings a five-bladed propeller has a smaller optimum diameter than a four-bladed propeller with equal blade area ratio. The sets of contrarotating propellers were designed in such a way that one set is representative for tanker application and another set for cargo liner application. Three additional sets complete the systematic series. The particulars of the propeller models are given in Table 1 and in Fig. 2.

Table 1
Principal Characteristics of Table 1 Screw Models
of the Contrarotating Propeller Series

Set	Diameter, D (mm)		Number of Blades		Pitch Ratio at 0.7R		Expanded Blade Area Ratio		$\frac{D_{aft}}{D_{forward}}$
	Forward	Aft	Forward	Aft	Forward	Aft	Forward	Aft	
1	210	179.34	4	5	0.627	0.957	0.432	0.507	0.854
2	208	182.72	4	5	0.779	1.034	0.432	0.515	0.878
3	210	191.01	4	5	0.931	1.110	0.432	0.523	0.910
4	217.50	203.33	4	5	1.083	1.196	0.432	0.531	0.935
5	210	198.90	4	5	1.235	1.306	0.432	0.539	0.947

Tests were carried out in the towing tank to determine the open-water characteristics of the series. The open-water test results were faired and plotted in the conventional way using the coefficients $K_T = T/\rho n^2 D^4$, $K_Q = Q/\rho n^2 D^5$, and $\eta_0 = (J/2\pi)K_T/K_Q$ as functions of the advance coefficient $J = V_a/nD$. The diagram is given in Fig. 3. In this diagram each set of contrarotating propellers is considered as one propulsion unit; the thrust T and the torque Q are based on the sum of the thrusts and torques respectively of the forward and aft screw. The diameter D denotes the tip diameter of the forward propeller. In addition, the ratio of the aft propeller thrust to the total thrust T_{aft}/T and the ratio of the aft propeller torque to the total torque Q_{aft}/Q are presented in Fig. 3.

For design purposes, various practical results can be derived from Fig. 3. In the case where the power P and V_e and n are given, the determination of the optimum diameter from a point of view of efficiency of the contrarotating propeller system can be solved by plotting η_0 and δ ($\delta = 101.27/J$) as functions of the coefficient B_p ($B_p = 33.08\ K_Q^{1/2}/J^{5/2}$).

As a comparison the optimum curves for efficiency η_0 and diameter coefficient δ of the contrarotating propeller series and the B 4-70 screw series are given in Fig. 4. Screws of the B 4-70 screw series are usually applied behind single-screw ships [10,12].

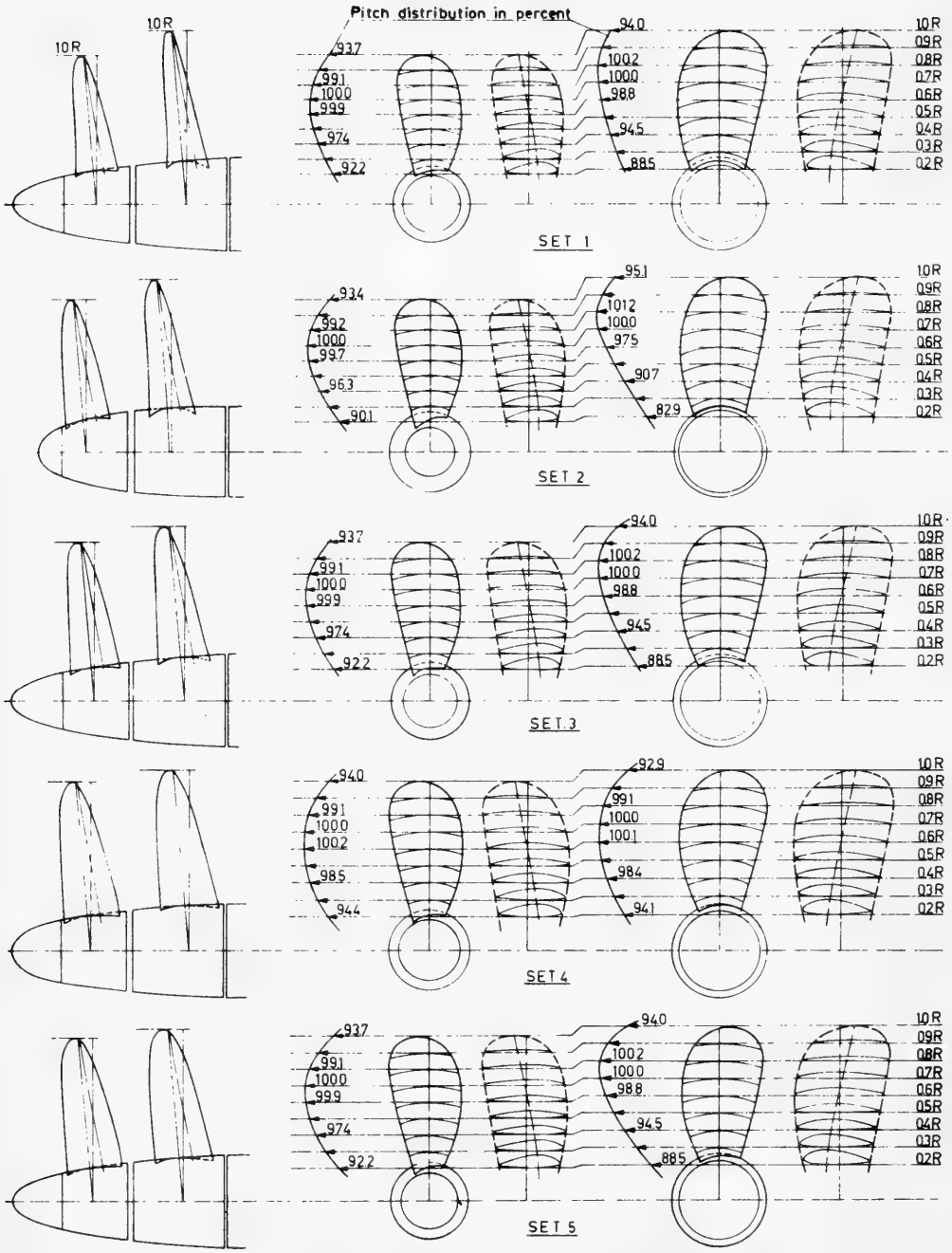

Fig. 2 - Particulars of the propeller models in the contrarotating propeller series

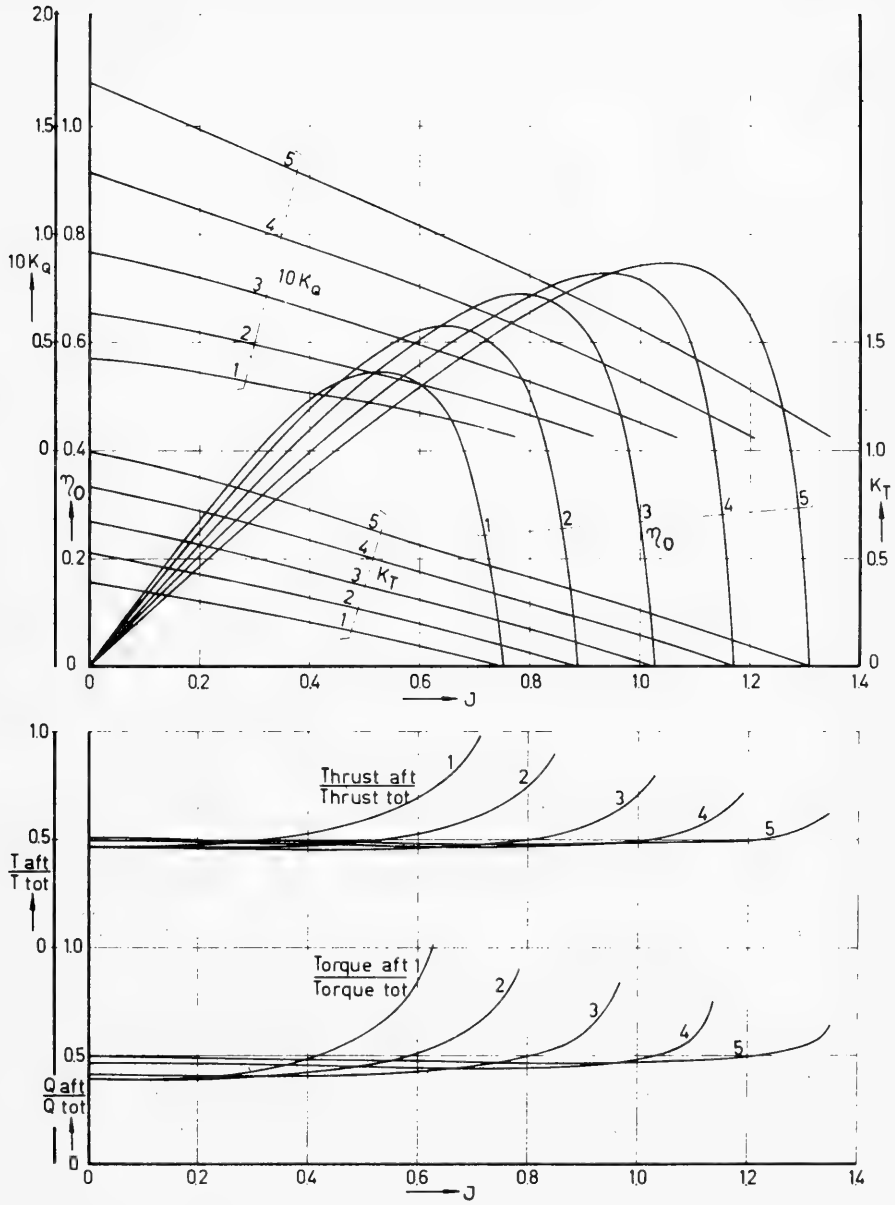

Fig. 3 - Open-water test results of contrarotating propellers (the numbers on the curves are the set numbers given in Table 1)

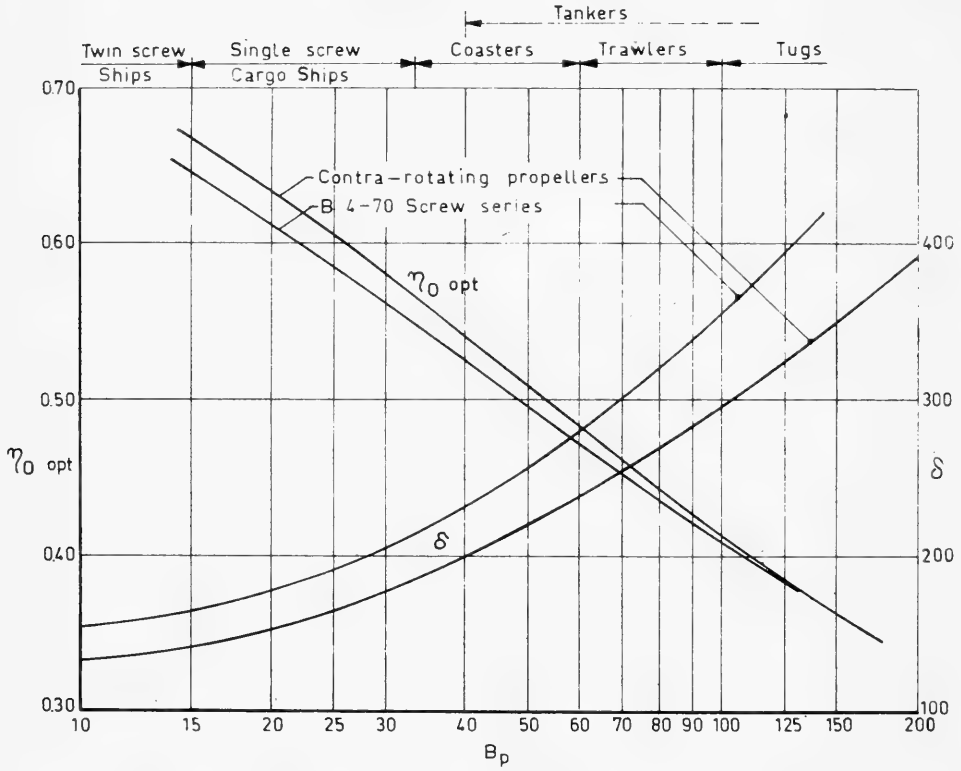

Fig. 4 - Comparison of optimum values for the contrarotating propellers with B 4-70 screws

At the top of Fig. 4 the different ship types are indicated for which the B_p values are typical. The lightly loaded screws of fast ships are at the left, and the heavily loaded propellers for towing vessels are at the right. This diagram gives quick information which type of propeller will be the best with regard to efficiency for a certain ship type. For fast ships (cargo liners) contrarotating propellers appear to give a higher efficiency than conventional screws. It must be noted, however, that by application of a conventional screw behind a ship, the rudder partly removes the rotational velocity from the propeller jet and hence improves the efficiency of the propulsion device. It is obvious that this improvement in efficiency will not be found by application of contrarotating propellers behind a ship.

It can be seen from Fig. 4 that the optimum diameter of the contrarotating propeller series is considerably smaller than the optimum diameter of the conventional screw series.

COMPARATIVE TESTS WITH SHIP MODELS EQUIPPED WITH CONVENTIONAL AND CONTRAROTATING PROPELLERS

Description of Hull Forms and Propellers

Comparative tests have been carried out with a 32,500-DWT tanker model and a cargo liner model both equipped with successively a conventional screw propeller and contrarotating propellers. The principal dimensions of these ships are given in Table 2; the hull forms and the stern arrangements are given in Figs. 5 and 6.

Table 2
Principal Dimensions of Tanker (Fig. 5) and Cargo Liner (Fig. 6)

Ship	Loading Condition	Length Between Perpendiculars (m)	Breadth Molded (m)	Draft Molded (m)			Displacement Mld. (metric tons)
				On F.P.	On A.P.	Mean	
32,500-DWT Tanker	Loaded	195.07	25.91	10.331	10.331	10.331	42,905
	Ballast	195.07	25.91	6.401	6.706	6.554	26,210
Cargo Liner	Loaded	158.50	22.40	8.839	8.839	8.839	19,023

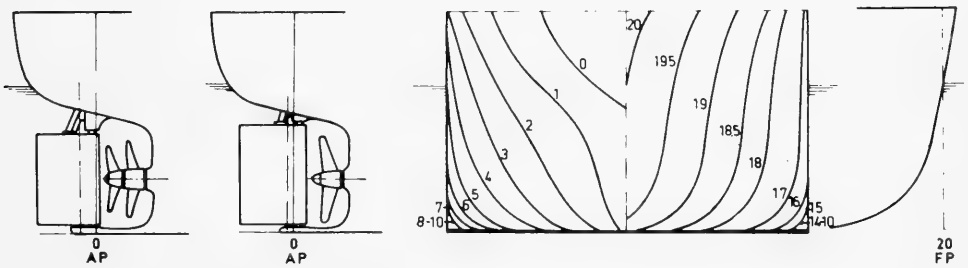

Fig. 5 - Body plan and stern arrangement of tanker

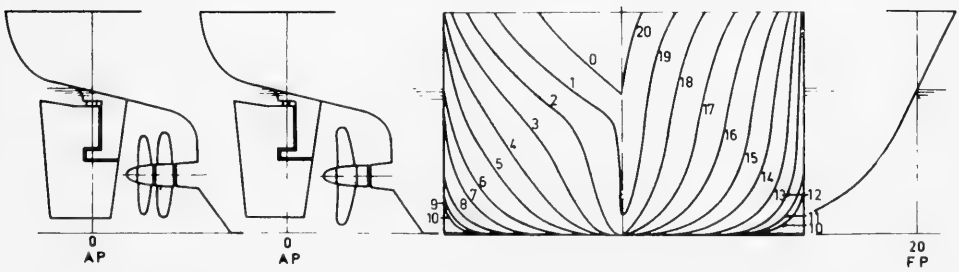

Fig. 6 - Body plan and stern arrangement of cargo liner

The propeller designs for both ships were based on 16,000 metric DHP at 120 rpm, and with ship speeds of 16.5 knots for the tanker and 20.5 knots for the cargo liner. The conventional screws were designed according to the circulation theory for wake adapted propellers. The principal full-scale characteristics of the propellers are given in Table 3; further details of the conventional screw propellers for the tanker and the cargo liner are presented in Figs. 7 and 8. The particulars of the contrarotating propellers for the tanker (set 2) and the cargo liner (set 4) were already presented in Fig. 2.

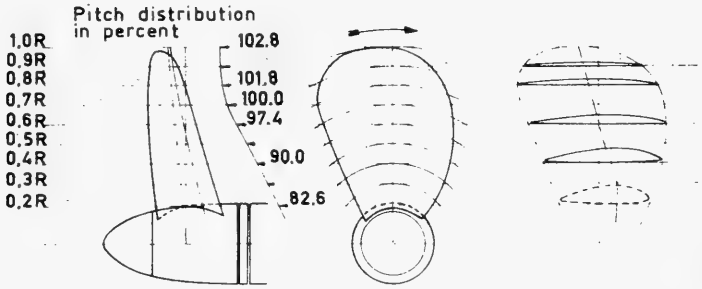

Fig. 7 - Particulars of single screw for tanker

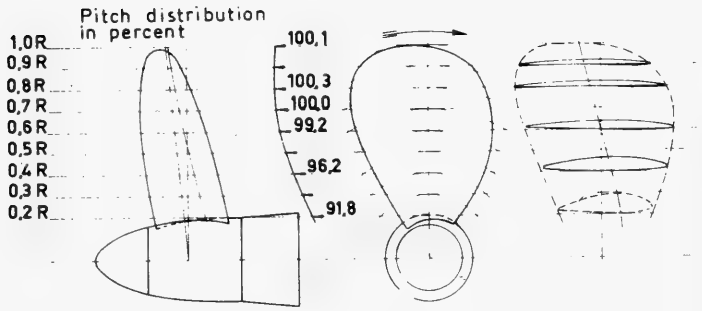

Fig. 8 - Particulars of single screw for cargo liner

Model Resistance and Self-Propulsion Tests

Model tests have been carried out to obtain a comparison of the propulsive quality of the tanker and the cargo liner both equipped with successively contrarotating propellers and a conventional screw propeller. Resistance and self-propulsion tests were conducted in the deep-water basin of the Netherlands Ship Model Basin, in accordance with established procedures. All model data were extrapolated to full-scale ship values using Schoenherr's friction coefficients with an addition of 0.00035 for correlation allowance. For turbulence stimulation, a trip wire of 1-mm diameter was fitted to girth each model at a section

Table 3
Principal Full-Scale Characteristics of Tanker and Cargo Liner Propellers

Ship	Propeller Type	Diameter D (mm)	Number of Blades	Pitch at Blade Root (mm)	Pitch at Blade Tip (mm)	Pitch at 0.7R (mm)	Blade Area Ratio	Direction of Turning	$\frac{D_{aft}}{D_{forward}}$
32,500-DWT Tanker	Single Screw	6400	4	3875	4825	4696	0.624	Right	—
	Contrarotating:								
	Forward	5720	4	3775	4240	4455	0.432	Left	0.878
	Aft	5025	5	4655	4850	5195	0.515	Right	
Cargo Liner	Single Screw	6000	4	5284	5799	5796	0.621	Right	—
	Contrarotating:								
	Forward	5220	4	5383	5251	5652	0.432	Left	0.935
	Aft	4880	5	5513	5488	5838	0.531	Right	

5 percent LBP at aft FP. The tanker model was tested at the loaded and the ballast condition; the cargo liner model was tested only at the loaded condition.

The results of the resistance and self-propulsion tests are presented in Tables 4 through 6. Figs. 9 and 10 show the performance predictions for the tanker and the cargo liner. Table 7 compares the results of the propulsion tests with the ship models equipped with the conventional screws and the contrarotating propellers. Table 7 shows that application of contrarotating propellers on both ships gives a significant reduction in DHP. The DHP of the tanker model with contrarotating propellers is about 4.5 percent less in the loaded condition, and 8 percent less in the ballast condition, when compared to the model with the conventional screw propeller. The contrarotating propellers behind the cargo liner require about 6.5 percent less DHP than the conventional screw propeller in the loaded condition of the ship. The gain in trial speeds, due to application of contrarotating propellers, is at maximum power absorption (16,000 DHP):

tanker in loaded condition, 0.12 knot;
tanker in ballast condition, 0.30 knot;
cargo liner in loaded condition, 0.21 knot.

The tanker with the conventional screw arrangement suffered from air sucking into the propeller plane in the ballast condition, whereas this phenomenon did not occur when the contrarotating propellers were fitted to the model. This must be attributed to the smaller diameters of the contrarotating propellers.

An analysis of the various propulsion factors shows that the wake fraction was larger for the contrarotating propellers than for the conventional screws. This is due to the smaller diameters of the contrarotating propellers. In the case of the tanker the thrust deduction factor did not differ very much. This factor was somewhat larger for the cargo liner with contrarotating propellers than with the conventional screw. For the tanker, the increase in propulsive efficiency due to contrarotating propeller application was principally obtained by a better hull efficiency, whereas for the cargo liner this increase was obtained by both a better hull efficiency and a higher open-water efficiency of the contrarotating propellers. More detailed data must be made available, however, to give a complete explanation of the obtained reduction in DHP.

Cavitation Tests

Cavitation tests were conducted in the 40-cm-diameter slotted wall cavitation tunnel with flow regulator of the Netherlands Ship Model Basin (13,14), simulating the full-load operating conditions. The axial wake distributions behind the two models, as measured in the deep-water basin by means of a pitot-tube were simulated in the tunnel. The results of the velocity surveys in the way of the propeller are described in Fig. 11 for the tanker and the cargo liner.

The results of the cavitation tests are presented in Figs. 12 and 13. From an examination of the various test results it can be concluded that the conventional screw and the forward propeller of the contrarotating propellers are quite comparable as far as blade cavitation is concerned. This holds as well for both

Table 4
Results of Resistance and Self-Propulsion Tests with the Tanker Model in the Loaded Condition

Propeller Arrangement	Speed (knots)	Resistance Tests		Self-Propulsion Tests			Coefficients						DHP		Thrust	
		EHP (metric)	Resistance (tons)	DHP (metric)	RPM	Thrust (tons)	η_D	t	w	η_H	η_0	η_R	Forward Propeller	Aft Propeller	Forward Propeller	Aft Propeller
Conventional screw	14	5273	54.91	7574	92.8	74.50	0.696	0.263	0.396	1.221	0.536	1.063				
	14.5	5986	60.18	8689	97.1	81.64	0.689	0.263	0.393	1.215	0.534	1.063				
	15	6813	66.22	9972	101.4	89.64	0.683	0.261	0.392	1.215	0.531	1.060				
	15.5	7839	73.73	11473	105.8	98.91	0.683	0.255	0.393	1.227	0.527	1.057				
	16	9125	83.15	13206	110.5	109.46	0.691	0.240	0.396	1.258	0.521	1.056				
	16.5	10685	94.41	15343	115.7	122.15	0.696	0.227	0.395	1.278	0.516	1.056				
	17	12474	106.97	18138	121.9	137.81	0.688	0.224	0.392	1.277	0.509	1.059				
Contrarotating propellers	14	—	—	7193	90.5	75.57	0.733	0.273	0.465	1.358	0.512	1.055	3667	3526	40.40	35.17
	14.5	—	—	8246	94.5	82.82	0.726	0.273	0.483	1.359	0.508	1.051	4224	4022	44.24	38.58
	15	—	—	9445	98.6	90.98	0.721	0.272	0.466	1.364	0.504	1.050	4844	4601	50.78	50.20
	15.5	—	—	10914	103.2	100.40	0.718	0.266	0.464	1.371	0.500	1.046	5634	5280	53.92	46.47
	16	—	—	12647	108.1	111.38	0.722	0.253	0.462	1.387	0.496	1.048	6558	6089	60.11	51.27
	16.5	—	—	14805	113.6	124.28	0.722	0.240	0.459	1.405	0.492	1.045	7700	7105	67.36	56.92
	17	—	—	17371	119.6	139.84	0.718	0.235	0.455	1.404	0.486	1.051	9062	8309	76.10	63.74

Table 5
Results of Resistance and Self-Propulsion Tests with the Tanker Model in the Ballast Condition

Propeller Arrangement	Speed (knots)	Resistance Tests		Self-Propulsion Tests			Coefficients						DHP		Thrust	
		EHP (metric)	Resistance (tons)	DHP (metric)	RPM	Thrust (tons)	η_0	t	w	η_H	η_0	η_R	Forward Propeller	Aft Propeller	Forward Propeller	Aft Propeller
Conventional screw	14.5	4941	49.68	6508	90.1	66.30	0.759	0.251	0.399	1.247	0.557	1.093				
	15	5578	54.21	7560	94.4	73.33	0.738	0.261	0.397	1.226	0.554	1.087				
	15.5	6346	59.69	8775	98.8	81.32	0.723	0.266	0.399	1.221	0.549	1.080				
	16	7253	66.08	10176	103.4	90.17	0.713	0.267	0.396	1.213	0.546	1.077				
	16.5	8333	73.63	11890	108.5	100.40	0.701	0.267	0.393	1.208	0.541	1.072				
	17	9610	82.41	14009	114.6	112.02	0.686	0.264	0.378	1.184	0.541	1.072				
	17.5	11160	92.97	16773	122.2	125.77	0.665	0.261	0.347	1.132	0.546	1.077				
Contrarotating propellers	14.5	—	—	6083	85.1	66.51	0.812	0.253	0.518	1.550	0.508	1.031	3010	3073	34.32	32.19
	15	—	—	6940	88.8	72.80	0.804	0.255	0.518	1.547	0.505	1.030	3445	3495	37.52	35.28
	15.5	—	—	8040	93.0	80.76	0.789	0.261	0.516	1.528	0.502	1.028	4005	4035	41.64	39.12
	16	—	—	9352	97.5	89.64	0.776	0.263	0.515	1.518	0.497	1.028	4476	4676	46.15	43.49
	16.5	—	—	10967	102.5	99.98	0.760	0.264	0.512	1.508	0.492	1.024	5488	5479	51.59	48.39
	17	—	—	12858	107.9	111.81	0.747	0.263	0.507	1.498	0.486	1.029	6464	6394	57.88	53.93
	17.5	—	—	15151	113.8	125.45	0.737	0.259	0.500	1.481	0.482	1.031	7669	7482	65.34	60.11

Table 6
Results of Resistance and Self-Propulsion Tests with the Cargo Liner in the Loaded Condition

Propeller Arrangement	Speed (knots)	Resistance Tests		Self-Propulsion Tests			Coefficients						DHP		Thrust	
		EHP (metric)	Resistance (tons)	DHP (metric)	RPM	Thrust (tons)	η_D	t	w	η_H	η_0	η_R	Forward Propeller	Aft Propeller	Forward Propeller	Aft Propeller
Conventional screw	18	6889	55.79	9437	99.7	66.24	0.730	0.158	0.248	1.120	0.632	1.032				
	18.5	7537	59.40	10366	103.0	70.85	0.727	0.162	0.246	1.111	0.632	1.035				
	19	8156	62.58	11324	106.1	75.38	0.720	0.170	0.243	1.097	0.632	1.038				
	19.5	8848	66.15	12435	109.3	80.70	0.712	0.180	0.242	1.083	0.631	1.041				
	20	9766	71.19	13821	112.9	87.14	0.707	0.183	0.243	1.079	0.629	1.041				
	20.5	11109	79.00	15705	117.2	95.72	0.707	0.175	0.243	1.090	0.625	1.038				
	21	12805	88.89	18072	122.0	106.48	0.709	0.165	0.243	1.104	0.619	1.037				
Contrarotating propellers	18	—	—	8997	99.2	72.05	0.766	0.226	0.303	1.110	0.650	1.060	4654	4343	37.48	34.57
	18.5	—	—	9788	102.1	76.09	0.770	0.219	0.298	1.112	0.652	1.063	5059	4729	39.60	36.49
	19	—	—	10600	105.0	80.27	0.769	0.220	0.297	1.110	0.652	1.063	5477	5123	41.80	38.47
	19.5	—	—	11584	107.9	85.44	0.764	0.226	0.300	1.106	0.650	1.063	5979	5605	44.49	40.95
	20	—	—	12927	111.6	92.46	0.755	0.230	0.298	1.097	0.648	1.063	6654	6273	48.18	44.28
	20.5	—	—	14743	116.1	101.95	0.754	0.225	0.296	1.101	0.643	1.065	7581	7162	53.21	48.74
	21	—	—	17163	121.5	113.92	0.746	0.220	0.289	1.097	0.638	1.066	8833	8330	59.72	54.20

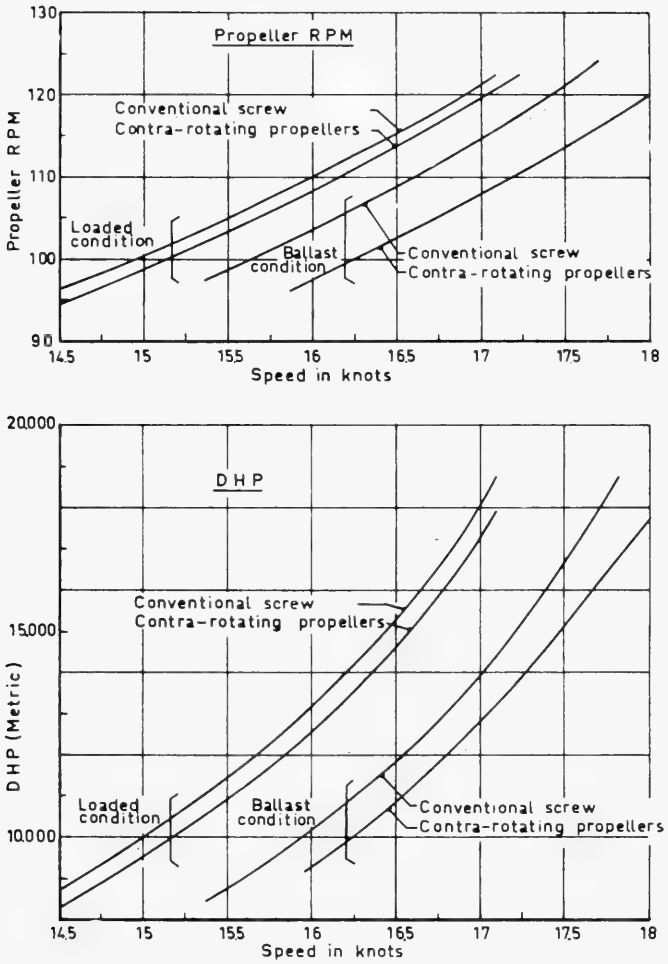

Fig. 9 - Power and rpm curves for the tanker

the tanker and the cargo liner. The extent of sheet cavitation on the back of the aft propeller of the contrarotating propellers was for both ship types considerably smaller than that on the forward propeller. Apparently the forward propeller smoothes the peripheral irregularities in the flow behind the ship and consequently in the inflow to the aft propeller.

From the test results it can be seen that with regard to the strength of the tip-vortex cavitation, the contrarotating propellers were slightly better than the conventional screws. This was to be expected, since the nine blades of the contrarotating propellers were less loaded than the four blades of the individual screws.

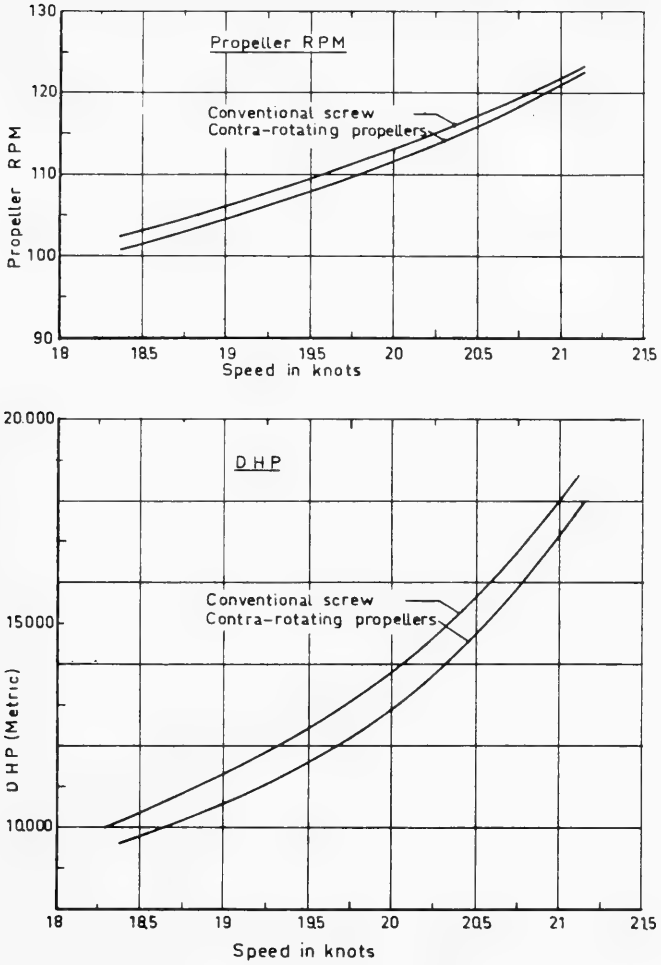

Fig. 10 - Power and rpm curves for the cargo liner

In the upper and lower part of the aperture, the tip-vortex of the forward propeller of the contrarotating propellers interfered with the blades of the aft propeller, especially for the cargo liner propellers, which led periodically to unfavorable cavitation phenomena. The chance for the appearance of these phenomena depends on the angular conjunction of the blades of the forward and the aft propeller. To avoid these phenomena it may be useful to reduce the diameter of the aft propeller slightly more.

Table 7
Extent to which the Contrarotating Propellers are Better (+) or Worse (-) than the Conventional Screw Propellers

Speed (knots)	Tanker		Cargo Liner in the Loaded Condition
	Loaded Condition	Ballast Condition	
14	+5.1%	—	—
14.5	+5.1%	+6.5%	—
15	+5.3%	+8.2%	—
15.5	+4.8%	+8.4%	—
16	+4.2%	+8.2%	—
16.5	+3.4%	+7.8%	—
17	+4.2%	+8.2%	—
17.5	—	+9.6%	—
18	—	—	+4.6%
18.5	—	—	+5.4%
19	—	—	+6.4%
19.5	—	—	+6.8%
20	—	—	+6.6%
20.5	—	—	+6.2%
21	—	—	+5.1%

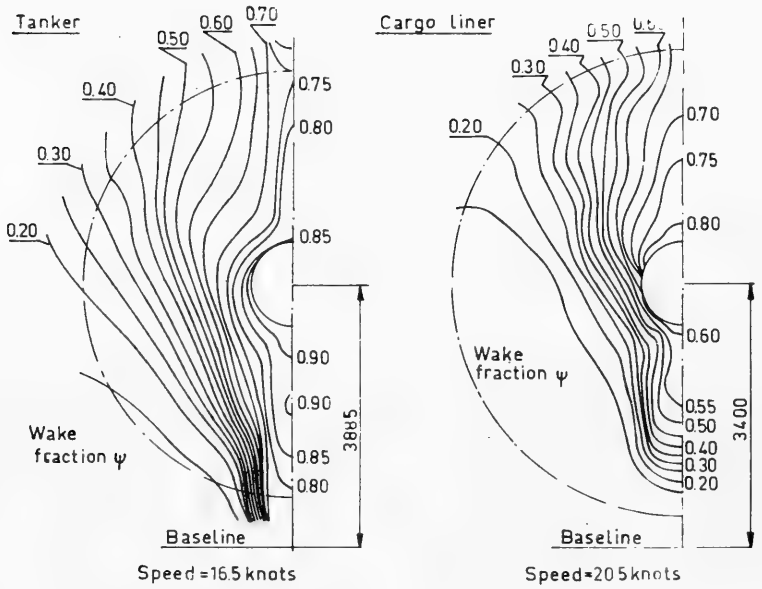

Fig. 11 - Wake distributions in way of the propeller of tanker and of cargo liner in the loaded condition.

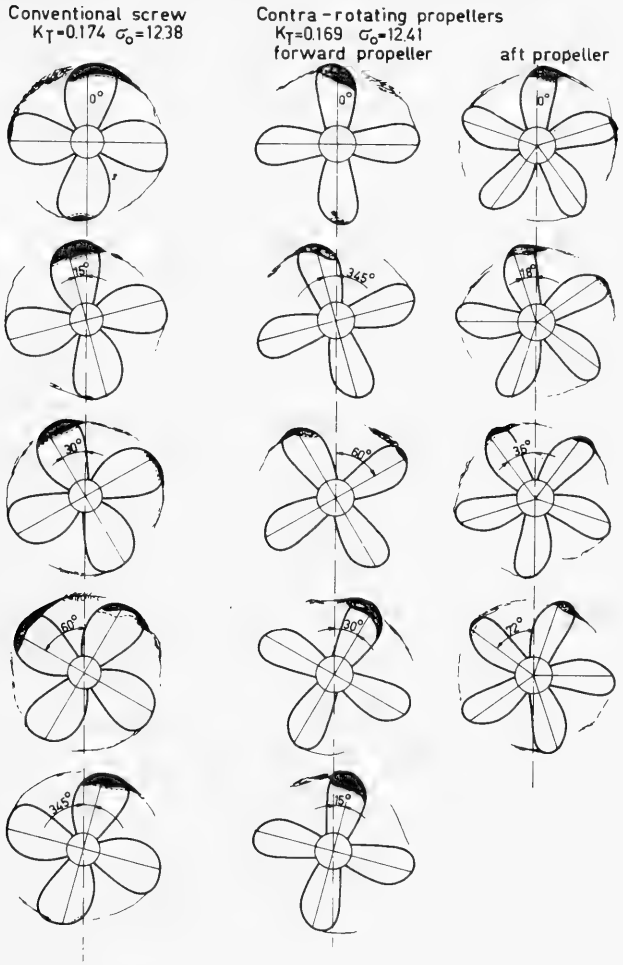

Fig. 12 - Cavitation patterns of conventional and contrarotating propellers behind tanker

Measurements of Propeller-Induced Vibratory Forces

Comparative tests on propeller induced vibratory forces have been carried out on the cargo liner model equipped with successively the conventional screw propeller and the contrarotating screw propellers. To measure these forces, a special arrangement had to be made in the case of the contrarotating propellers to use the existing measuring equipment (15). The forward propeller was driven by the normal dynamometer, installed in the ship model. The aft propeller was driven by a dummy dynamometer. This dummy dynamometer was installed in an open-water test boat, mounted behind the ship model. A stiff coupling shaft

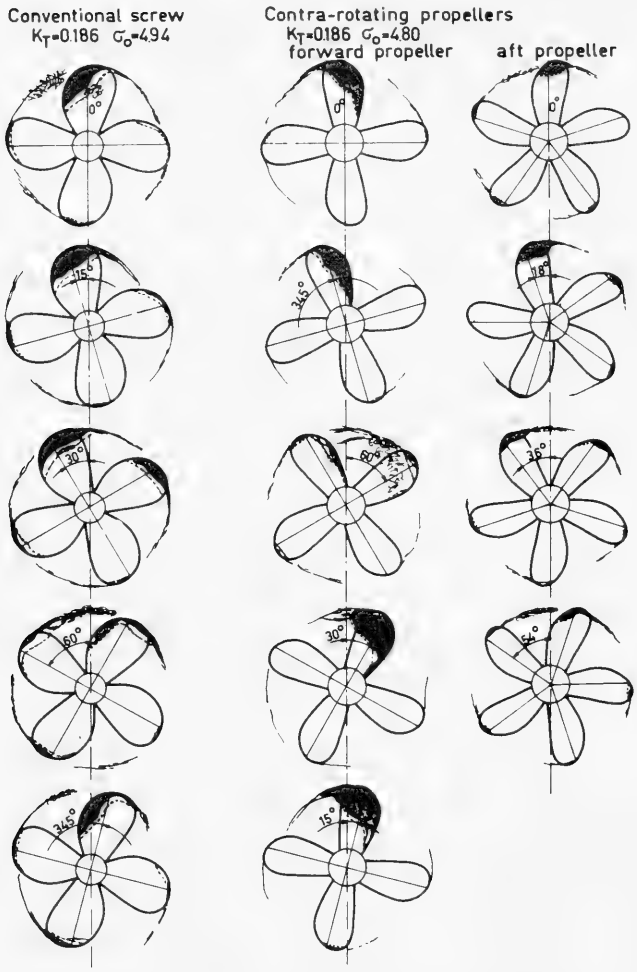

Fig. 13 - Cavitation patterns of conventional and contrarotating propellers behind cargo liner

synchronized the combination. By exchanging the real dynamometer and the dummy dynamometer, the vibratory outputs of both propellers were determined.

The results of the measurements of the propeller induced vibratory forces are given in Figs. 14 through 17. Samples of the instantaneous torque and thrust of the conventional screw and of the forward and aft propeller of the contrarotating propellers are shown in Figs. 14 and 15. The instantaneous thrust eccentricity for the different propellers is given in Fig. 16, and the instantaneous transverse forces are presented in Fig. 17.

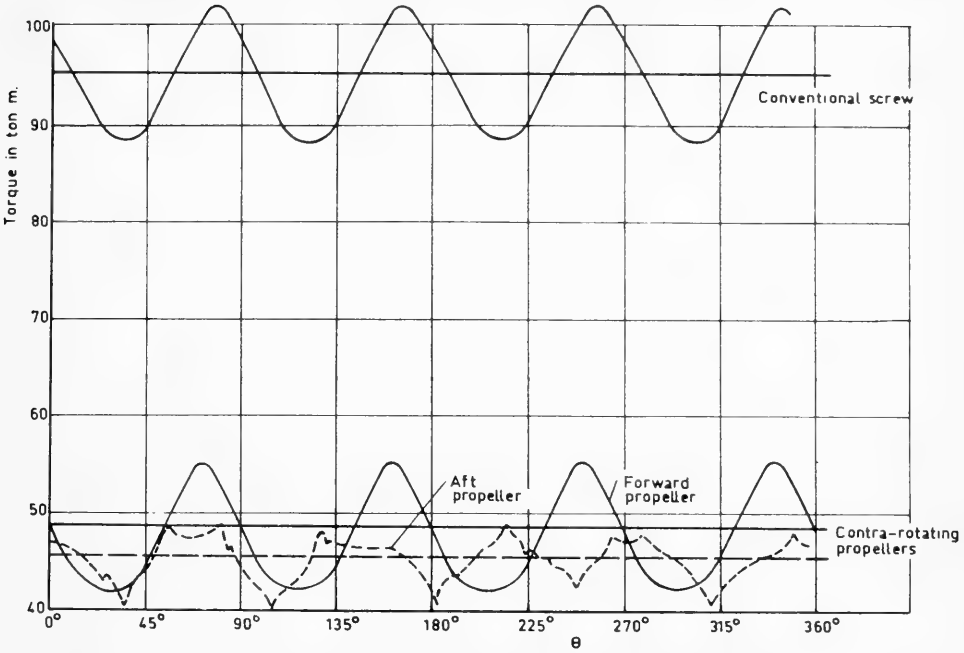

Fig. 14 - Instantaneous torque of cargo liner propellers

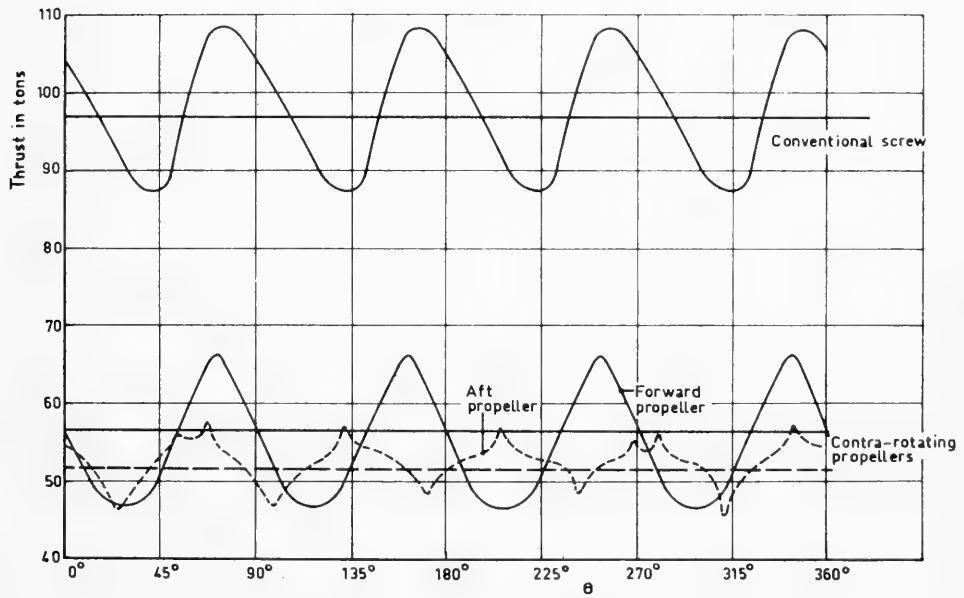

Fig. 15 - Instantaneous thrust of cargo liner propellers

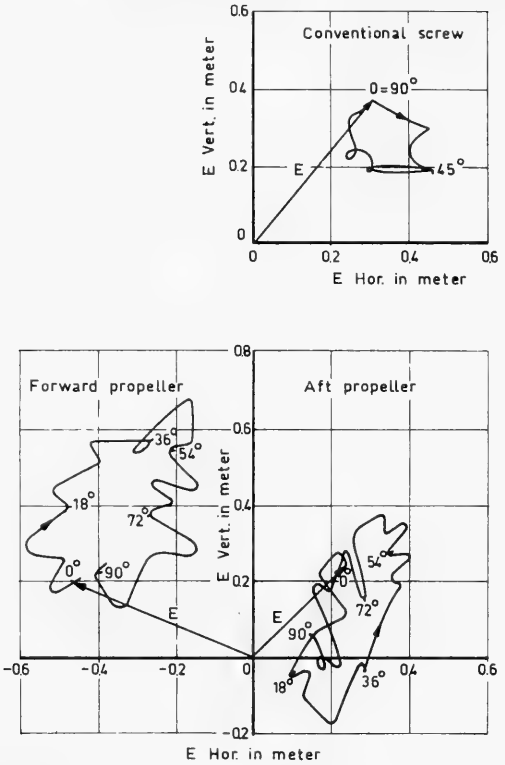

Fig. 16 - Instantaneous thrust eccentricity of cargo liner propellers

Figs. 14 and 15 show clearly that the variations in torque and thrust of the forward screw of the contrarotating propellers are about the same in magnitude as those of the conventional screw, which implies that these variations, expressed in percentages of the mean values, are about twice as large for the forward screw of the contrarotating propellers as those of the conventional screw. The variations of the aft screw are lower than those of the forward screw of the contrarotating propellers. Apparently the forward propeller smoothes the peripheral irregularities of the flow in the way of the aft propeller, as was also evident from the cavitation tests.

It appears from Fig. 16 that the thrust eccentricity of the forward screw of the contrarotating propellers is considerably larger than that of the conventional screw. However, the thrust of this forward screw is about half as large as that of the conventional screw, so that the maximum bending moments due to the eccentricity of the thrust will not change very much. This implies that the stresses due to these bending moments must be almost equal, if the diameter of the outer shaft is the same as that of the shaft of the conventional screw. Since the inner shaft diameter is smaller, possibly the loading of this shaft increases, since its

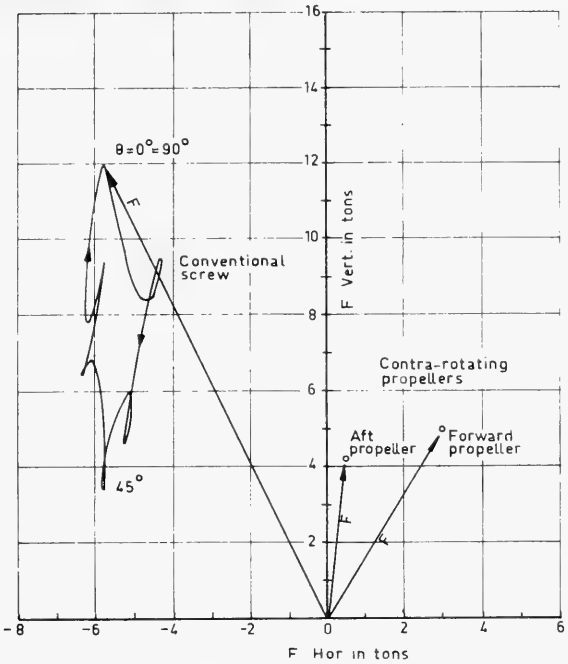

Fig. 17 - Instantaneous transverse forces of cargo liner propellers

stiffness against bending is only about a fourth part of that of the conventional propeller shaft, whereas the moments are about half of those of the conventional propeller.

Figure 16 shows that in many cases the eccentricities for the contrarotating propellers are in opposite direction, so that the bending moment on the forward screw may be reduced by that on the aft screw. The variations in thrust and torque of the forward and aft screw, however, may reinforce each other.

It can be seen from Fig. 17 that the transverse force variations of the conventional screw are large, whereas those of the contrarotating propellers are negligible both in quantity and in direction.

Additional measurements were conducted to determine the effect of a change of the angular positions of the mutual blade encounter of the contrarotating propellers. From these tests it was concluded that no significant differences occur for different angular positions of the mutual blade encounter.

Determination of Stopping Abilities

Investigations have been carried out to compare the contrarotating propellers and the conventional screw with respect to their ability to stop the

32,500-DWT tanker. The propelling machinery was supposed to be a steam turbine or Diesel engine, each capable of developing 16,000 DHP at 120 rpm.

The comparison of the stopping abilities of the contrarotating propellers and the conventional screw is based on a stopping maneuver as illustrated in Fig. 18. This maneuver is divided into four phases:

I. Steam or fuel supply to the engine is shut, the propeller is running slack and the ship speed decreases due to the hull resistance until the propeller rpm is sufficiently low to enable reversing of the engine rotation.

II. The ship is further slowed down by running the propeller system full astern, until a forward speed of about 6 knots is achieved. At this speed the ship will loose steerability, and tugs will have to render assistance.

III. The propeller is stopped, and tugs make fast.

IV. With the propeller slowly turning astern the stopping maneuver is completed. In this phase the ship is steered by tugs.

For a comparison of the conventional screw and the contrarotating propellers, the characteristics for phases I, II, III, and IV of the stopping maneuver were derived from the results of model tests. During these tests the total braking force (hull resistance and propeller force) was measured at different speeds of the model and at different propeller rpm. The speed of the model was kept constant during a test. For the calculation of the head reach it was assumed that the ship's speed changes so slowly during the stopping maneuver that the values of the total braking force, as measured during the stationary tests, were correct. Thus a quasi-steady approach (as described in Refs. 12 and 16) has been used for analyzing the stopping maneuvers. This approach is correct for large ships having relatively low powers installed, so that long stopping times occur (16). To determine the added mass of the ship during the stopping maneuver additional dynamic stopping tests were performed.

A comparison between the stopping abilities of the conventional screw and the contrarotating propellers can be made from the results presented in Figs. 19 through 21. Figure 19 shows the head reaches of the turbine tanker to be almost equal for the conventional screw and the contrarotating propellers. For the Diesel engine tanker (Figs. 20 and 21) the contrarotating propeller reduced the head reach in comparison with the conventional screw. The rpm at which the Diesel engine is reversed affects the head reach of the tanker considerably.

CONCLUSIONS

As a result of these investigations the following conclusions can be made:

- Contrarotating propellers have an open-water efficiency which is slightly higher (about 2 percent) than that of conventional screw propellers; the optimum diameter of contrarotating propellers is less (about 15 percent) than that of conventional screws.

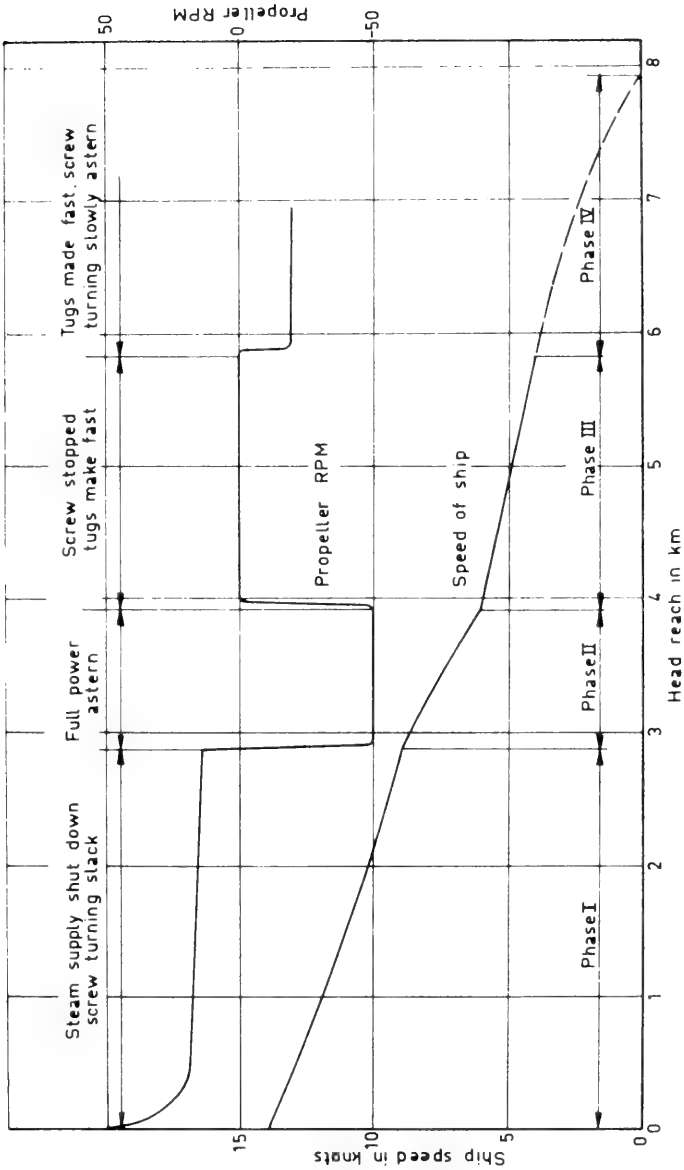

Fig. 18 - Stopping maneuver of a large ship

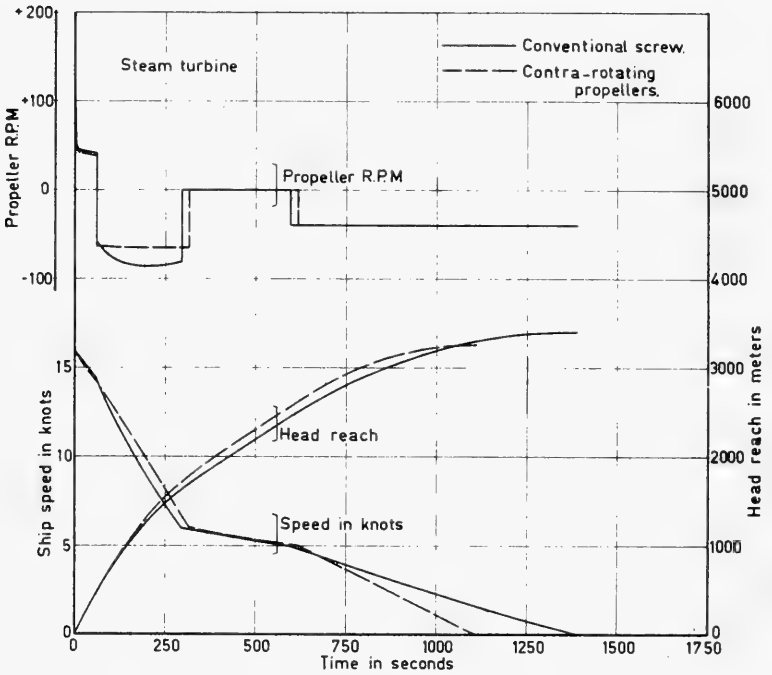

Fig. 19 - Comparison of the stopping abilities of conventional and contrarotating propellers for a steam turbine tanker

• Contrarotating propellers offer a means of improving the propulsive efficiency of ships. The reduction in DHP due to application of the contrarotating propellers for a tanker was about 4.5 percent in the loaded condition and 8 percent in the ballast condition of the ship if compared with the ship with conventional screw. The contrarotating propellers behind the cargo liner compared with the conventional screw requires about 6.5 percent less DHP.

• Conventional screws and the forward propeller of the contrarotating propellers are quite comparable as far as blade cavitation is concerned. The extent of sheet cavitation on the back of the aft propeller of the contrarotating propellers is relatively small. With regard to the strength of tip-vortex cavitation the contra-rotating propellers were slightly better than the conventional screws.

• With regard to the propeller induced vibratory forces the thrust and torque variations as well as the thrust eccentricity of conventional screws and contrarotating propellers did not differ very much, although the average thrust and torque of each of the contrarotating propellers are about half of that of a comparable conventional screw. The application of contrarotating propellers causes a considerable reduction in transverse forces compared to a conventional

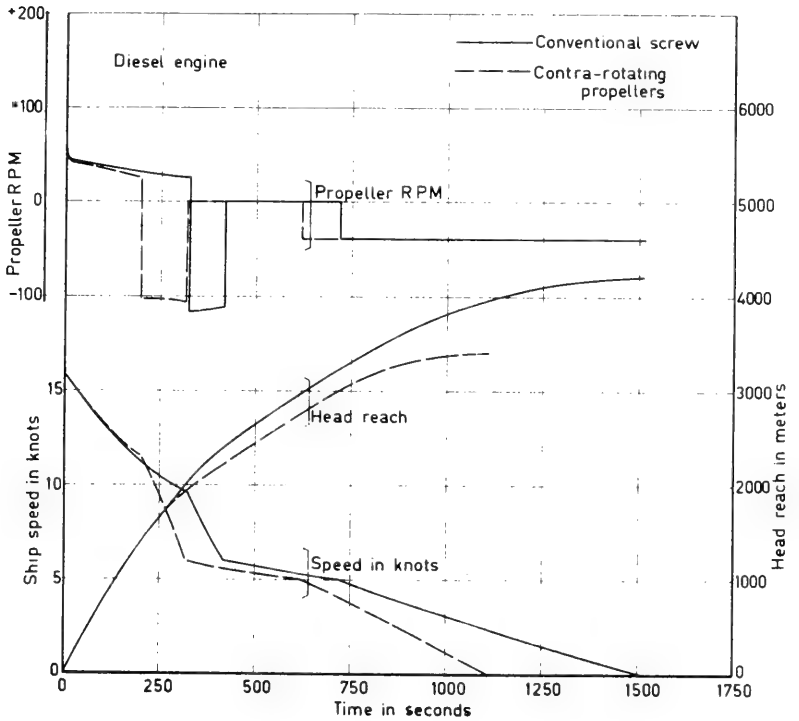

Fig. 20 - Comparison of the stopping abilities of conventional and contrarotating propellers for a tanker with a Diesel engine which can be reversed at 20 rpm

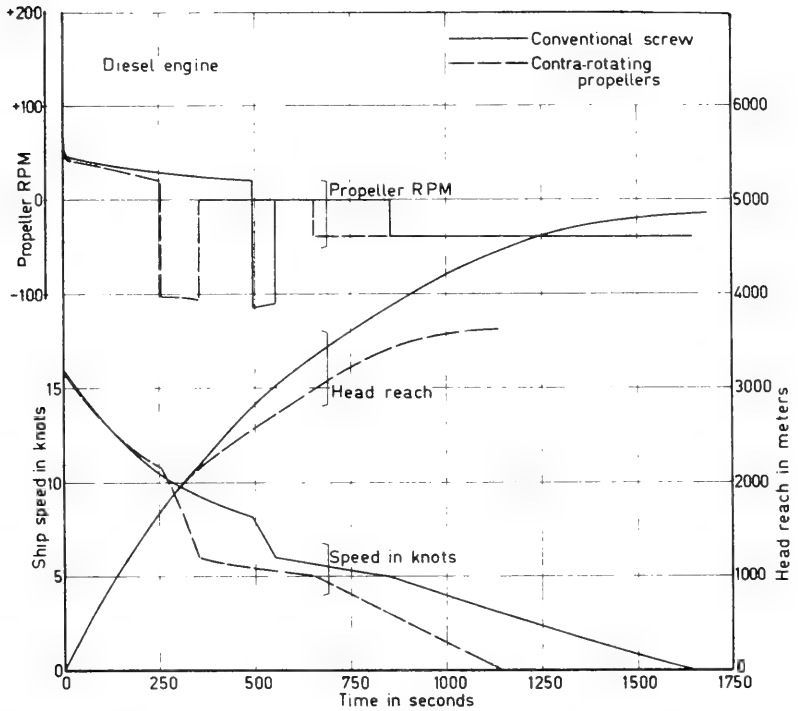

Fig. 21 - Comparison of the stopping abilities of conventional and contrarotating propellers for a tanker with a Diesel engine which can be reversed at 15 rpm

screw. These forces are practically constant both in quantity and in direction for the contrarotating propellers.

• When stopping a ship with steam turbine machinery, the head reaches corresponding to the conventional and the contrarotating propeller are nearly equal. For a ship with Diesel machinery the application of a contrarotating propeller leads to a decrease in head reach.

ACKNOWLEDGMENTS

This investigation was carried out under the auspices of the Royal Netherlands Navy, the shipyards that make up the Netherlands United Shipbuilding Bureaux, Ltd., and Lips N. V. Propeller Works. The permission for the publication of the results of these investigations is gratefully acknowledged. We wish to express our appreciation to Mr. J. auf'm Keller for his valuable assistance in designing the contrarotating propeller series.

REFERENCES

1. Hadler, J.B., Morgan, W.B. and Meyers, K.A., "Advanced Propeller Propulsion for High-Powered Single-Screw Ships," Trans. SNAME, 1964

2. Lindgren, H., Jung, I., and Hillander, H., "Contra-rotating Propellers," "Analysis and Overall Arrangement," Stal-Laval, Technical Information Letter 5/67, 1967

3. Glover, E.J., "Contra-rotating Propellers for High Speed Cargo Vessels: A Theoretical Design Study," Trans. NECI, 1966-1967

4. Auf 'm Keller, W.H., "Comparative Tests with Various Propellers for a Tanker and for a Cargo Liner," NSMB Towing Tank Test Report 217, June 1965

5. Esveldt, J., "Comparative Tests with Various Propellers for a Tanker and for a Cargo Liner," NSMB Cavitation Tunnel Test Report 615, June 1965

6. Wereldsma, J, "Investigation into the Propeller Excited Vibratory Forces for Various Propulsion Devices," NSMB Report 67-210-AS, July 1968

7. Hooft, J.P., "Onderzoek naar de Stopeigenschappen van drie Soorten Voortstuwers," NSMB Report 66-021-BT, Apr. 1966

8. Hooft, J.P., and Manen, J.D. van, "The Effect of Propeller Type on the Stopping Abilities of Large Ships," RINA 1967; De Ingenieur, 1967; Intern. Shipb. Progr., 1967

9. Manen, J.D. van, "Fundamentals of Ship Resistance and Propulsion; Part B, Propulsion," Intern. Shipb. Progr., 1967

10. "Principles of Naval Architecture," Society of Naval Architects and Marine Engineers, New York, 1967

11. Manen, J.D. van, and Sentié, A., "Contra-rotating Propellers," Trans. I.N.A., 1956; Intern. Shipb. Progr., 1956

12. Manen, J.D. van, "The Choice of the Propeller," Marine Technology, 1966

13. Lammeren, W.P.A. van, "Testing Screw Propellers in a Cavitation Tunnel with Controllable Velocity Distribution over the Screw Disc," Trans. SNAME, 1955; Intern. Shipb. Progr., 1955

14. Manen, J.D. van, "On the Usefulness of a Test with a Propeller Model in a Cavitation Tunnel with a Simulated Non-uniform Flow," Symposium on Testing Techniques in Ship Cavitation Research, Trondheim 1967; Intern. Shipb. Progr., 1967

15. Wereldsma, J., "Some Aspects of the Research on Propeller-Induced Vibrations," Intern. Shipb. Progr., 1967

16. Jaeger, H.E., "Le freinage de grands navires (V) corrélation entre navire et modèle en ce qui concerne l'arrêt par le propulseur," ATMA, 1967

* * *

DISCUSSION

Hans B. Lindgren
Swedish State Shipbuilding Experimental Tank
Göteborg, Sweden

This paper is very similar to the paper I will present in the final session on Friday with C. A. Johnson and G. Dyne as coauthors. Unfortunately the paper has not been available in printed version so that we could have made any quantitative comparisons. As our paper has been available for a long time, it would be interesting to know if the authors have made such a comparison. With regard to Mr. Oosterveld's presentation I should like to ask two questions.

First, Mr. Oosterveld mentioned that there is a danger that the tip vortex cavity of the forward propeller causes erosion on the aft propeller. He also mentioned that this could be avoided by decreasing the diameter of the aft propeller in relation to the forward. I should like to know how big a decrease has been adopted and if the result was satisfying. At the Swedish State Shipbuilding Experimental Tank we use in our theoretical design method the hypothesis that

the tips of the two propellers lay on the same mean streamtube. This is not sufficient to avoid the problem mentioned, and a further decrease is necessary.

My second question is related to the figures Mr. Oosterveld gave on the possible power gains with contrarotating propellers for the two different ship projects. Do the figures given refer to the same rpm for the contrarotating and the conventional propeller, or which assumption was adopted?

* * *

DISCUSSION

William B. Morgan
Naval Ship Research and Development Center
Washington, D.C.

In the David Taylor Model Basin at the Naval Ship Research and Development Center we have run a large number of experiments on contrarotating propellers. We have found that in general the hull efficiency, and relative rotating efficiency of the ship model are different from that of the same model with a single propeller. Also, we have shown that for best performance the design of the propellers should be based on their particular application. For these two reasons it is not clear to me how a series of open-water tests of contrarotating propellers can be used to pick the best performing propellers.

* * *

DISCUSSION

C. A. Johnsson
Swedish State Shipbuilding Experimental Tank
Göteborg, Sweden

I notice that the authors, when discussing the different propulsion coefficients, do not mention one of particular interest in this context: the relative rotative efficiency. When we analyzed our self-propulsion data, we found that in some cases most of the gain when using contrarotating propellers could be traced to an increase in the relative rotative efficiency, for which values of 1.05 to 1.10 were obtained. Such figures of this coefficient always makes the practical designer suspicious and often results in discussion of the accuracy of the instrumentation, etc. We were therefore glad to find that test results from NSRDC showed similar figures, and we also got support from some theoretical calculations. I should like to ask the authors what their values of the relative rotative efficiency look like.

The question of this efficiency is rather important. Our values seem to show an increase in the relative rotative efficiency with decreasing thrust coefficient K_T. This indicates that the optimum diameter could be smaller than that obtained from open water tests.

* * *

REPLY TO DISCUSSION

J. D. van Manen and M. W. C. Oosterveld

It was a great privilege to obtain at the final moment the opportunity to present the NSMB-results on contrarotating propellers at this symposium.

The investigations performed at the NSMB were confined to efficiency, cavitation, vibratory forces, and stopping abilities of a contrarotating propeller system consisting of a four-bladed propeller forward and a five-bladed propeller aft. Our final conclusion is that we see a future for application of contrarotating propellers on fast cargo liners, since the power will increase so much that two propellers are needed to absorb the required power.

Our future research will be concentrated on propeller induced vibratory forces for well-selected combinations of the blade numbers fore and aft. In our opinion the problem of propeller induced vibratory forces will be the most critical one in future discussions about the application of contrarotating propellers. The other qualities such as efficiency, cavitation, and stopping are no longer a serious point to delay a possible application.

With regard to Mr. Lindgren's remarks concerning the diameter reduction of the aft propeller, it should be noted that for the tanker and the cargo-liner contrarotating propeller sets these reductions were 12.4 and 6.5 percent respectively. Especially of the cargo liner the tip vortex of the forward propeller interfered with the blades of the aft propeller in the upper and lower part of the aperture and caused unfavorable cavitation phenomena.

Therefore it may be useful to reduce the diameter of the aft propeller slightly more. In regard to Mr. Lindgren's second question it must be emphasized that the propeller designs for both ships were based on given DHP, rpm, and speed and that for the determination of the optimum diameter of the contrarotating propeller sets and the conventional screws, use was made of open-water test results with the contrarotating propellers and conventional screw series. If the propeller designs were based on given DHP, speed, and diameter (for instance the maximum allowable propeller diameter), and if the optimum rpm's with regard to efficiency were chosen, then it can be expected that the reduction in DHP due to contrarotating propeller application in comparison with conventional screws will be larger than by comparing systems with equal rpm.

We agree with Dr. Morgan that for best performance the design of a contrarotating propeller set should be based on a particular application, as was still the case in our contrarotating propeller investigations. However, for the determination of the optimum diameter or rpm of the contrarotating propeller system, the results of open-water tests with a systematic series of contrarotating propellers are very useful.

With regard to Mr. Johnsson's comments it is interesting to note that for the tanker and the cargo liner in the case of contrarotating propeller application the relative rotative efficiencies were 1.050 and 1.065 respectively. These values are of the same order of magnitude as found by tests performed at the Naval Ship Research and Development Center and at the Swedish State Shipbuilding Experimental Tank.

* * *

Monday, August 26, 1968

Afternoon Session

UNSTEADY PROPELLER FORCES

Chairmen: Ten. Gen. G. N. A. Siena

Ministero Difesa, Marina
Rome, Italy

and

W. P. A. Van Lammeren

Netherlands Ship Model Basin
Wageningen, The Netherlands

EXPERIMENTAL AND ANALYTICAL STUDIES OF PROPELLER-INDUCED APPENDAGE FORCES

August F. Lehman and Paul Kaplan
Oceanics, Inc.
Plainview, New York

ABSTRACT

During the past several years experiments involving unsteady forces induced on an appendage by a propeller have been carried out at Oceanics, Inc. Most of these experiments concerned a propeller downstream of an appendage, although certain measurements were made with the propeller upstream (rudder case). An associated theoretical analysis to predict the influence of various physical parameters on the magnitude of the induced forces was also developed, based upon two-dimensional flow considerations. Two-, three-, and four-bladed propellers were studied, with blades of two thicknesses. The effects of spacing distance between the appendage and the propeller, appendage asymmetry, and the appendage attack angle on the induced forces were of primary interest. This paper presents the more pertinent results of these investigations and discusses a technique of using a single-bladed propeller to predict multibladed propeller induced forces. Limited comparisons between the developed theory and the experimental data are also presented.

INTRODUCTION

In evaluating the vibratory characteristics of naval vessels, knowledge of the appendage forces induced by a propeller is important. By the early 1960's theoretical work (1-5) had for the most part preceded any experimental evaluation of this problem, primarily because of the difficulties of satisfactory unsteady measurements. In 1960 Lewis (6) reported on the first successful experimental measurements of the transverse or side forces induced on an appendage upstream of a propeller. This initial work was amplified by further published data in 1963 (7).

In 1964 Oceanics, Inc., was supported by the Naval Ship Research and Development Center on the first of a series of model studies to obtain certain propeller-appendage test data. This first study involved a measurement of both the axial and transverse induced forces; and a series of investigations covering various aspects of this problem followed. The present paper summarizes the pertinent results of those investigations.

The basic measurements were unsteady axial and transverse fluctuating forces induced on an upstream appendage by a propeller at blade-rate frequency

(the number of blades of the propeller times the propeller rotational speed) and higher harmonic frequencies. Specifically, the propeller-induced appendage forces were examined as a function of propeller-appendage spacing for variations in the propeller blade thickness, number of blades comprising the propeller, appendage asymmetry, appendage attack angle, and appendage location (downstream or upstream of the propeller).

An associated theoretical analysis that predicts the influence of the various physical parameters on the magnitudes of the induced forces was also developed, based on two-dimensional flow characteristics. Limited comparisons between this theory and the experimental data are also presented in this paper.

TEST FACILITIES

All of the testing was performed in the Oceanics Water Tunnel. This tunnel is a recirculating, closed-jet-type tunnel having both the water velocity and the test section static pressure as controllable variables. The test section is approximately 20 in. on a side (with rounded corners) and about 7 ft long. The water velocity is controllable to about 40 ft/sec, and the static pressure can be independently controlled from about 0.1 to 2 atmospheres absolute. For the majority of these tests the water velocity in the tunnel was 5.23 ft/sec. This rather low free-stream velocity was required for low speeds of propeller rotation along with acceptable levels of thrust while still allowing the frequencies of interest to be in a range adequately covered by the dynamic response of the balance-appendage system.

An external dynamometer can be placed at either end of the upper horizontal leg of the tunnel; thus propellers can be driven from either their upstream or downstream side. For these tests, the propellers were driven from their downstream side. The axial position of the propeller in the test section can be easily changed, as the dynamometer and propeller drive shaft are connected as a unit which rests on a bed similar to that employed on lathes. The propeller is positioned axially by a lead screw which is independently powered.

In the settling section just ahead of the nozzle there is a honeycomb to improve the flow conditions before the water enters the nozzle and passes through the test section. At the entrance to the test section, screens can be inserted to create the desired profile of a particular wake (axial components only). For the investigations discussed here, no screens were used, and a uniform flow approached the appendage-propeller system. A drawing of the tunnel circuit is shown in Fig. 1.

PROPELLERS

The two propeller designs used in most of these tests were selected from a series with eight variations of blade thickness which received extensive study at the National Physical Laboratory (8). The propellers selected are identified in Ref. 8 as BT-1 and BT-2. The same identification nomenclature is used in this report. The propellers were manufactured as individual blades fastened to a common hub. This permitted testing as one-, two-, three-, and four-bladed units.

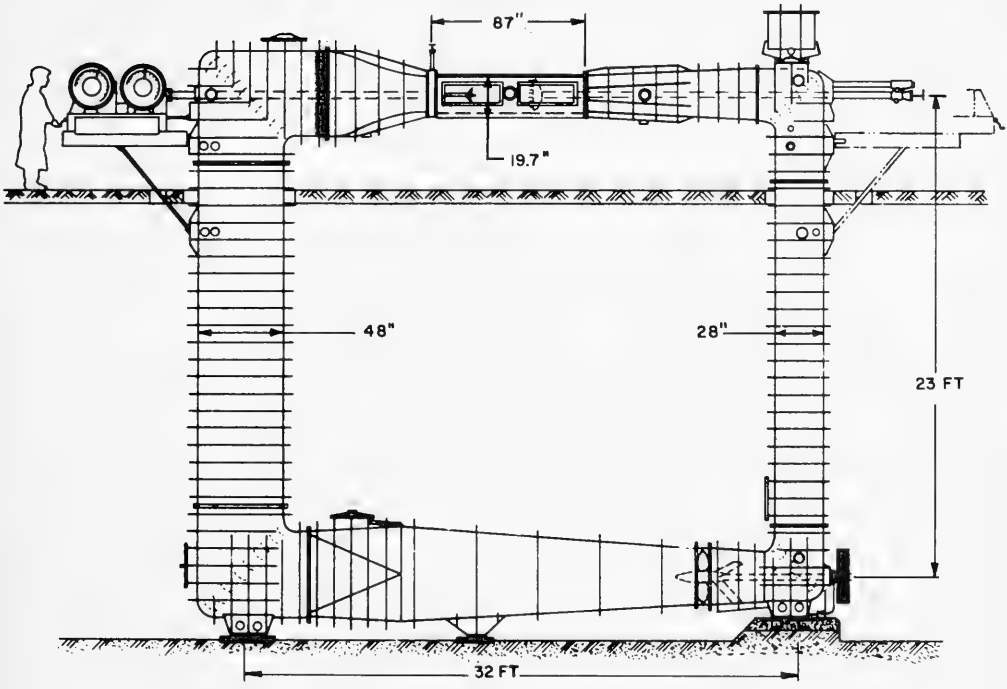

Fig. 1 - Tunnel

The BT-2 propellers had a 100% increase in blade section thickness over BT-1, together with a pitch reduction of 7.5%. Detailed characteristics of the propellers are shown in Fig. 2. The four-bladed propellers are shown in Fig. 3. All test propellers had a diameter of 8 in.

APPENDAGE-BALANCE SYSTEM

The success of an experiment involving dynamic measurement involves a satisfactory sensing or balance system, a stiff (high-resonant-frequency) balance-appendage system, and an adequate dynamic calibration technique. For completeness, each of these components will be discussed in some detail.

Dynamic Balances

The basic balance element consists of a strain-gaged force unit designed on the flexure plate principle with one balance unit mounted on each end of the appendage. The use of flexure plates is a common approach in instrumentation design wherein sensitivity to forces in only one direction are desired. The flexure plate unit consists of extremely stiff top and bottom plates separated by two very thin side members. The upper and lower plates can move parallel to

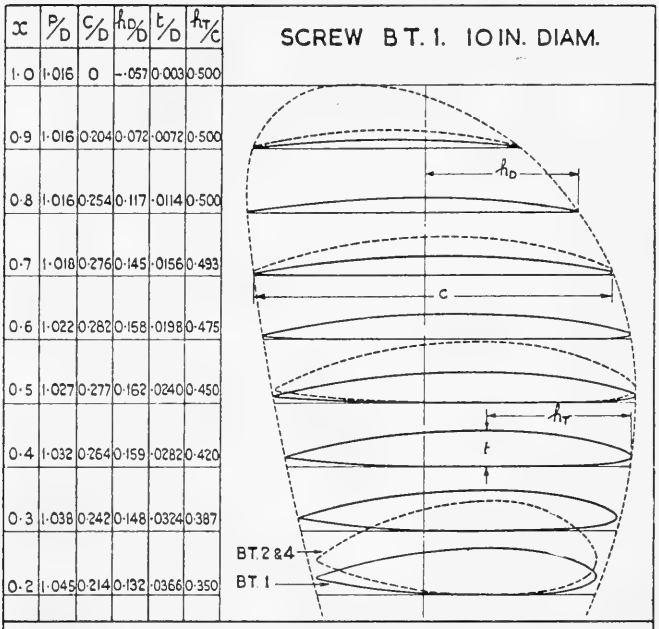

x	P/D	C/D	h_D/D	t/D	h_T/C
1·0	1·016	0	−·057	0·003	0·500
0·9	1·016	0·204	0·072	·0072	0·500
0·8	1·016	0·254	0·117	·0114	0·500
0·7	1·018	0·276	0·145	·0156	0·493
0·6	1·022	0·282	0·158	·0198	0·475
0·5	1·027	0·277	0·162	·0240	0·450
0·4	1·032	0·264	0·159	·0282	0·420
0·3	1·038	0·242	0·148	·0324	0·387
0·2	1·045	0·214	0·132	·0366	0·350

SCREW BT 1. CYLINDRICAL SECTION OFFSETS FROM PITCH LINE. % MAX t

RAD x		FROM MAX. t TO T.E. T.E	80	60	40	20	MAX t	% DISTANCE FROM MAX. THICKNESS TO L.E 20	40	60	70	80	85	90	95	L.E	RAD x
0·95	BACK	19·6	48·6	71·0	87·2	96·8	100	96·8	87·2	71·0	60·6	48·6	41·9	34·9	27·4	19·6	0·95
	FACE	0					0									0	
0·90	BACK	13·9	44·9	69·0	86·2	96·5	100	96·5	86·2	69·0	57·8	44·9	37·8	30·3	22·3	13·9	0·90
	FACE	0					0									0	
0·80	BACK	8·8	41·6	67·2	85·4	96·3	100	96·3	85·4	67·2	55·3	41·6	34·1	26·1	17·7	8·8	0·80
	FACE	0					0									0	
0·70	BACK	10·8	42·4	68·6	86·3	96·5	100	96·8	86·7	69·7	59·0	46·3	39·2	30·6	21·1	10·5	0·70
	FACE	4·4	1·2	0	0	0	0	0	0	0	0	0	0·2	0·4	1·2	4·5	
0·60	BACK	17·4	48·5	71·8	87·5	97·0	100	97·7	89·0	74·7	65·9	54·5	48·2	40·6	31·0	18·0	0·60
	FACE	12·4	5·5	1·6	0	0	0	0	0	0	0·2	1·2	2·1	3·6	6·1	12·2	
0·50	BACK	23·9	53·0	74·8	89·4	97·5	100	97·8	90·7	78·7	70·6	60·8	54·9	48·1	39·6	24·9	0·50
	FACE	19·7	11·0	4·8	1·6	0·3	0	0	0·3	0·9	1·8	3·2	4·3	6·3	9·4	18·7	
0·40	BACK	29·2	56·5	76·9	90·3	97·7	100	98·0	91·6	80·8	73·3	64·3	59·0	52·6	44·7	30·9	0·40
	FACE	25·6	14·5	6·9	2·5	0·5	0	0·2	1·2	3·0	4·5	6·7	8·4	10·8	14·5	23·9	
0·30	BACK	34·0	59·8	78·7	91·1	97·9	100	98·2	92·4	82·6	75·8	67·6	62·7	56·7	49·3	36·4	0·30
	FACE	31·0	17·8	8·7	3·3	0·7	0	0·4	2·0	4·8	7·0	10·0	12·1	14·9	19·1	28·6	
0·20	BACK	38·9	63·0	80·5	91·9	98·1	100	98·4	93·2	84·4	78·3	70·8	66·3	60·8	53·8	41·6	0·20
	FACE	36·1	21·0	10·5	4·1	0·9	0	0·6	2·8	6·6	9·5	13·2	15·7	19·0	23·6	33·4	

SCREW BT. 2. AS BT. 1. WITH t INCREASED 100 % P REDUCED 7½ %

SCREW BT. 3 AS BT. 1 WITH t INCREASED 50 % } P UNALTERED

SCREW BT. 4 AS BT. 1 WITH t INCREASED 100 % }

Fig. 2 - Test propellers

one another very easily if a force is applied to either plate in a direction normal to the weak sides of the unit. Forces applied in any other direction result in extremely small deflections of one plate relative to the other because of the increased stiffness of the unit in all other directions.

In certain instrumentation application the weak sides of the sensing elements are strain gaged; in other applications the coil of a linear differential transformer is attached to one plate and the core to the other plate. Either of these

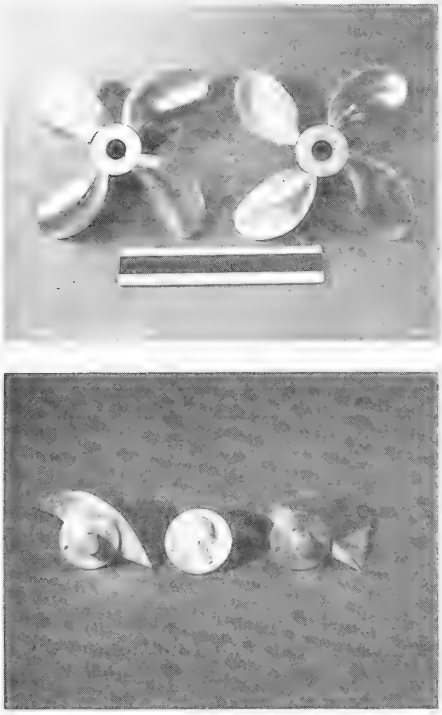

Fig. 3 - Four-bladed test propellers; the BT-1 blades are at the right, and the BT-2 blades are at the left

techniques permits the motion of one plate relative to the other to be calibrated as a function of applied force. While this approach is satisfactory for most steady-state force measurements, it is of little value in sensing dynamic force fluctuations as the deflection of one plate relative to the other is quite large and thus the resonant frequency is quite low.

To overcome this defect a system was employed using the advantage of a flexure plate sensing element while limiting the deflections to extremely small increments, thereby producing a system which is quite stiff. This technique uses pretensioned strain-gaged beams. In this application a thin strip of metal having four strain gages mounted upon it is attached to an opening in one plate of the element (Fig. 4). This opening (as well as the strain-gaged strip of metal) is located perpendicular to the weak sides of the element. This strain-gaged strip of metal is then placed in tension between its end-clamping members by stretching it before tightening the end clamps. To the bottom plate of the sensing element is attached a very rigid massive member, which in turn is then clamped to the center of the strain-gaged strip of metal. In this manner, while the two stiff plates of the element still retain their capability of easily moving relative to

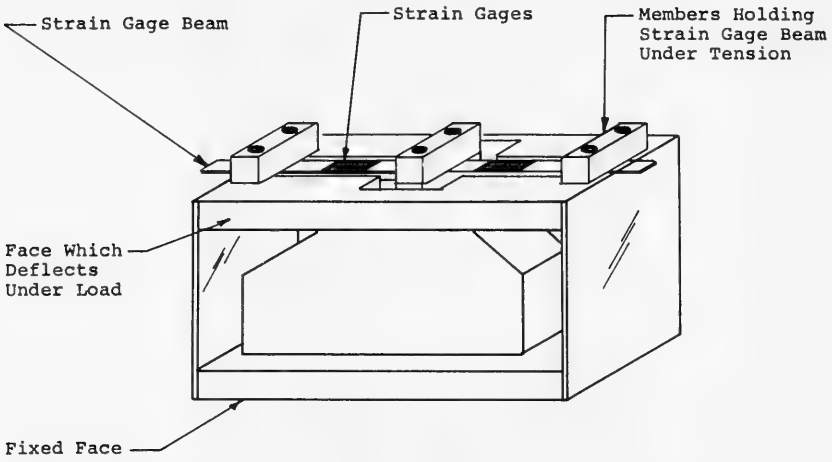

Fig. 4 - Pretensioned strain-gaged flexure element

each other when a force is applied normal to the thin sides of the unit, the strain gaged strip of metal permits only as much motion as the force is capable of additionally stretching the metal strip. Thus deflections are very small, and the unit has a relatively high resonant frequency. The wiring of the strain gage bridges is shown in Fig. 5.

Any number of such basic elements as shown in Fig. 4 can be fastened together so that forces in the desired directions can be sensed (and determined). The interaction of such systems is extremely low, somewhat under 0.5% for all forces or moments except those about an axis perpendicular to both stiff plates, where the interaction is approximately 1.0% (9).

Appendage-Balance Arrangement

The initial propeller appendage investigations (10) had the appendage completely spanning the test section. In this arrangement the appendage was not as stiff in the transverse direction as might be desired for obtaining data at frequencies above the blade rate. The appendage design was therefore modified, based on the suggestions of Dr. Murray Strasberg of the Naval Ship Research and Development Center. This design, used for most of the tests reported here, consisted of having the test appendage perpendicular to the support members. A sketch of this test arrangement with a two-bladed propeller is shown in Fig. 6. It can be noted that the appendage was held in place by two support bars extending through the holes in the mounting windows and then fastened into the dynamic balances. Using the pretensioned strain-gaged force balances discussed, the motion of the support bar under an induced force loading is less than 0.001 in.; thus radial-lip shaft seals can be employed without introducing significant seal reaction forces on the support bars. Consequently the forces introduced on the appendage by propeller action are not affected by seal dynamics. The support

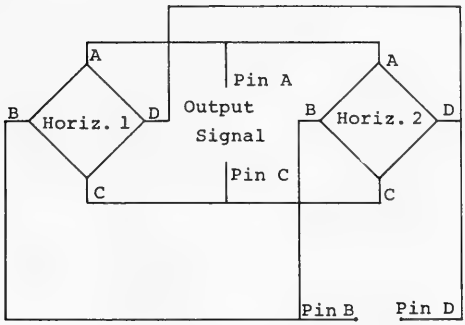

Excitation Voltage
5.2 Volts ac at 20 K.C.

Horizontal Bridges Wired for Summing

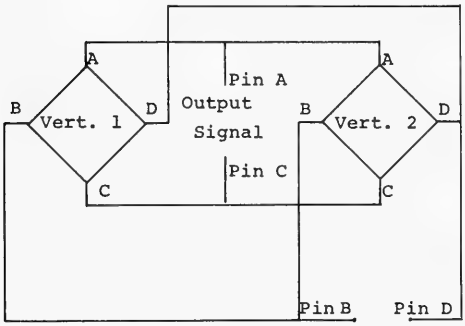

Excitation Voltage
5.2 Volts ac at 20 K.C.

Vertical Bridges Wired for Summing

Fig. 5 - Schematic of balance gages wired for summing

bars themselves are covered with streamlined fairings fastened to the tunnel wall, thus preventing water flow forces from influencing the measured appendage forces. However, it should be pointed out that the propeller is operating in the wake of a cruciform appendage arrangement with measurements made only on the vertical appendage.

Asymmetry of the appendage was introduced by adding extensions to one semispan of the basic symmetrical appendage. The basic appendage had an ogival cross section with a chord of 8 in., a span of 8 in., and a maximum thickness of 1 in. The basic appendage extended 1/2 propeller diameter; i.e., 4 in., to either side of the propeller center line. Extensions having a span of 2 in. were then added to one semispan of the basic appendage to produce the desired

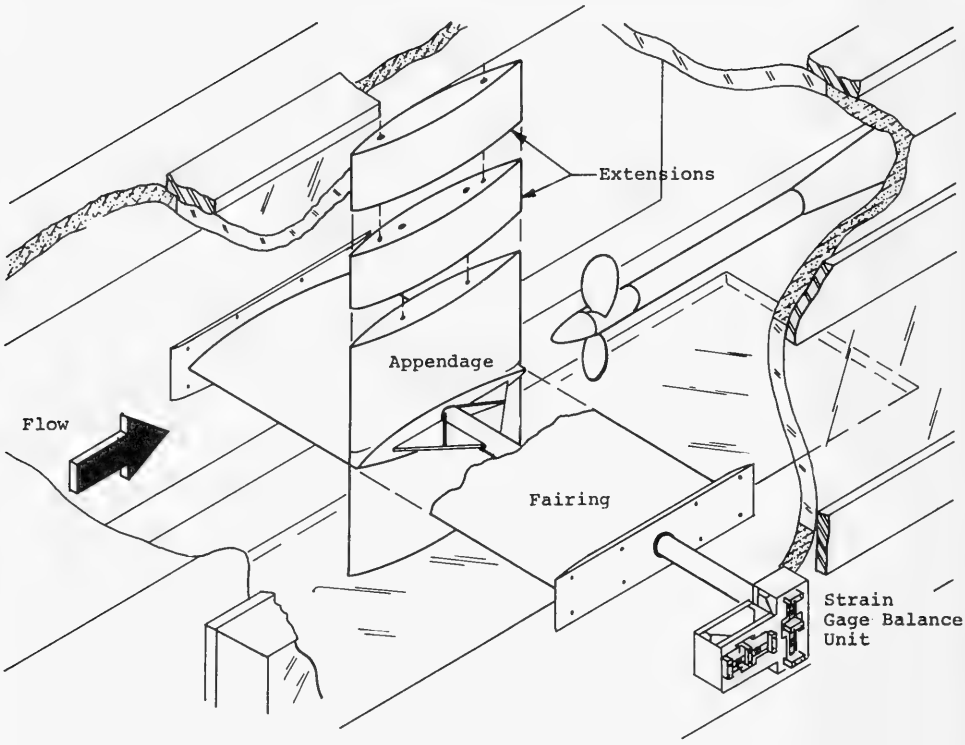

Fig. 6 - Test arrangement

asymmetry. In this manner, one extension resulted in an appendage extending 1/2 propeller diameter below and 3/4 propeller diameter above the propeller center line. Two extensions resulted in an appendage extending 1/2 propeller diameter below and 1 propeller diameter above the propeller center line. Photographs of the appendage, fairings, and dynamic force balance are shown in Figs. 7 and 8. This appendage is considered three-dimensional, as the ends are rather far from the tunnel walls.

Dynamic Calibration of Appendage-Force Sensing System

In calibrating the appendage force sensing system a constant force was applied to the system by a small electrodynamic shaker monitored by a force gage in a small impedance head. The output from the force sensing element (dynamic strain gage balances) was read on the meter of a Hewlett-Packard wave analyzer.* The wave analyzer readings thus permitted plotting the response of the

*A capacitor was installed in parallel across the meter terminals to produce a smooth signal. The bandwidth of the analyzer is 7 Hz for 3 dB attenuation.

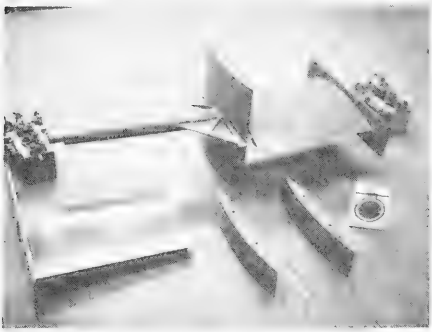

Fig. 7 - Test appendage, extensions, and balance unit

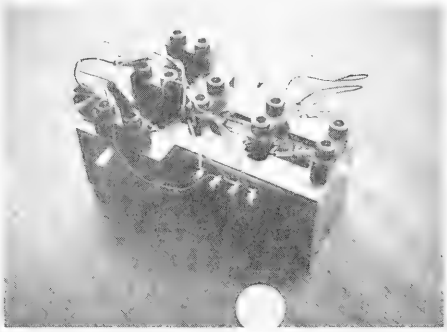

Fig. 8 - Dynamic balance

system in terms of millivolts per pound of applied force as a function of the frequency at which the shaker was operating. Figure 9 is a block diagram of the dynamic calibration setup and wiring of the electronic instrumentation.

The dynamic balance calibrations during this series of investigations were undertaken in the following ways. In the earlier studies the foil was completely submerged during the transverse calibration as the shaker was attached to one end of the support rod which extended outside of the tunnel. However for the axial calibration the shaker was attached to the center of the foil and the calibration undertaken in air. The response of the system in the axial direction as a function of frequency was then plotted. The foil was then completely submerged, and with the output of the dynamic balances fed to an optical galvanometer the foil was struck a sharp blow in the axial direction. The resonant frequency was then determined by examining the optical galvanometer record of the response trace. The calibration curve which had been obtained in air was then shifted by this slight change in the resonant value to obtain the curve used for data evaluation.

During the later studies the transverse calibration was performed in the same way as for the earlier investigations, but for the axial calibration the transducer was encapsulated in a rubber protective cover so that this calibration was also performed while the foil was submerged. Thus all calibration data were obtained with the foil completely submerged in the operating medium.

The system was calibrated for each test condition prior to taking data. This technique permitting establishment of the exact calibration (± 0.02 Hz) at the subsequent desired frequency of interest. By calibrating each system prior to testing, any change in the system response due to foil extension attachment, etc., was included. Flow background levels were also taken at this time. A typical plot of system calibration and flow background levels is shown in Fig. 10.

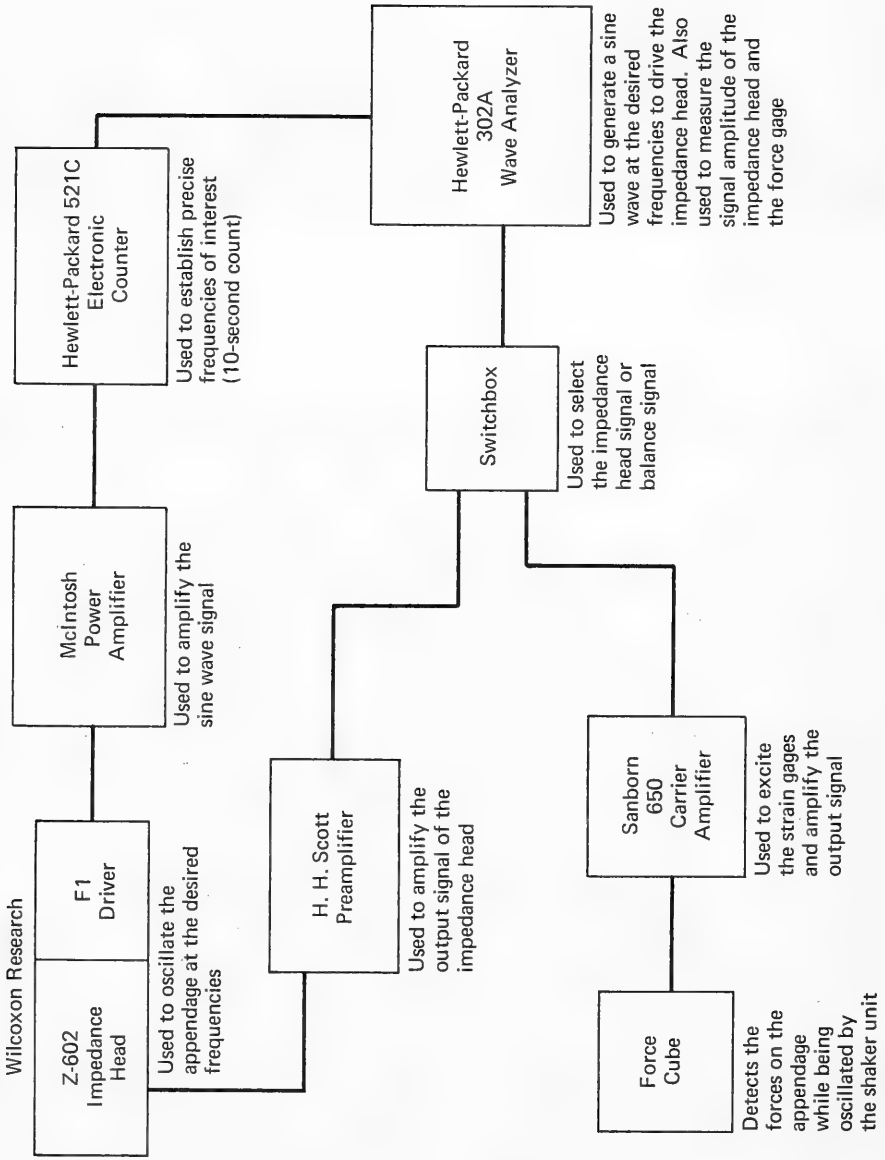

Fig. 9 - Dynamic calibration system

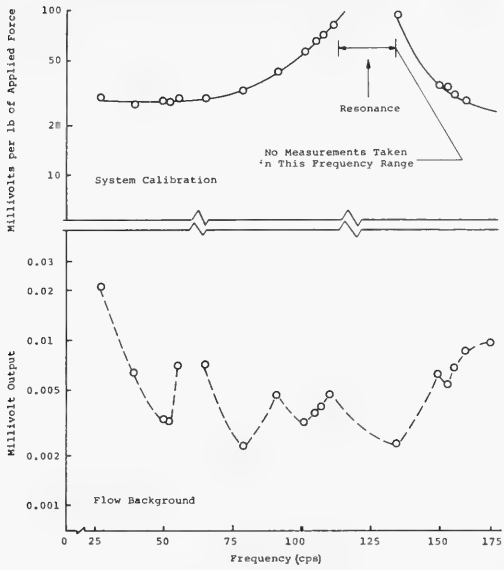

Fig. 10 - Dynamic calibration of the symmetrical appendage system, and flow background levels

TEST PROCEDURES

In undertaking a test run the desired appendage was mounted in the tunnel and the balance-appendage system was calibrated using the technique just described. The propeller was then moved into the proper position, since it was located approximately 6 propeller diameters downstream during the determination of the calibration and flow background levels. The desired tunnel velocity and propeller rotational speeds were established, and then for each propeller-appendage spacing ratio the induced force, as indicated by the output of the strain gage balance system, was recorded at specific frequencies of interest. The test arrangement was then changed and the entire procedure repeated. As was mentioned, most of these tests were undertaken at a free stream velocity of 5.23 ft/sec and a normal rotational speed of 13 rps; thus the advance ratio for most of the tests was 0.603.

DATA EVALUATION

The initial test readings consisted of millivolt levels from the wave analyzer and propeller thrust readings from the dynamometer. The thrust value was corrected for the tare load determined by operating at test conditions without the propeller on the dynamometer shaft. The net thrust value was determined by adjusting the measured value by the tare influence.

The millivolt value recorded from the wave analyzer was converted into pounds of induced force in the following manner. The initial value was adjusted for the influence of the "flow background" by taking the square root of the difference of the squares, a procedure implying an uncorrelated test condition. As noted in Fig. 10 the flow background was extremely small and resulted in a meaningful change in the adjusted millivolt value in very few cases. The adjusted millivolt value was converted into pounds of force by dividing this value by the millivolts-per-pound calibration value existing for that particular frequency and the particular arrangement undergoing test. The final data form was obtained by dividing the "true" induced force by the net propeller thrust value, and this ratio is employed for most of the data presented.

DATA PRESENTATION AND DISCUSSION

Before discussion of the propeller induced appendage forces which existed at specific blade rate harmonics, it is perhaps of value to clarify two points which are raised most often after presenting unsteady appendage data.

The first clarification is to demonstrate that propeller induced appendage forces exist only at the blade rate and its harmonics. During a test the entire frequency range encompassed by the blade rate harmonics is scanned to insure that the induced appendage forces occurring at specific frequencies (corresponding to certain blade rate harmonics) are larger than any force values measured at other frequencies. However, only those values occurring at blade-rate frequencies are normally recorded. Figure 11 illustrates that this contention is true. This figure is a plot of the measured force level ratio as a function of frequency. The data on this figure present the axial induced appendage forces associated with a four-bladed propeller (double-thickness blades) when operating behind a symmetrical appendage. Data taken over the entire frequency range of interest are shown. The information is presented for two spacing ratios. From this figure it can be noted that the induced appendage forces do exist only at frequencies corresponding to specific blade-rate harmonics and that the induced force magnitudes decrease rapidly with an increase in spacing ratio (this latter observation will be illustrated more fully in other figures).

The second point of clarification concerns the relationship between the number of blades on a propeller and the nature of the induced appendage forces. Theory (5) states that a propeller with an even number of blades should induce only axial unsteady forces and that a propeller with an odd number of blades should induce only transverse unsteady forces. All experimental data verify this contention except at extremely close appendage-propeller spacing ratios. For close spacing ratios a propeller with an even number of blades induces some transverse force on the appendage and a propeller with an odd number of blades induces some axial force. An investigation of the effect that the appendage attack angle has on the unsteady propeller induced appendage forces supplied a clue as to the reason for this apparent inconsistency between experiment and theory.

During an investigation involving appendage attack angle (11) it was observed that the appendage attack angle has a significant effect on the nature of the induced appendage forces. Very slight appendage attack angles resulted in the

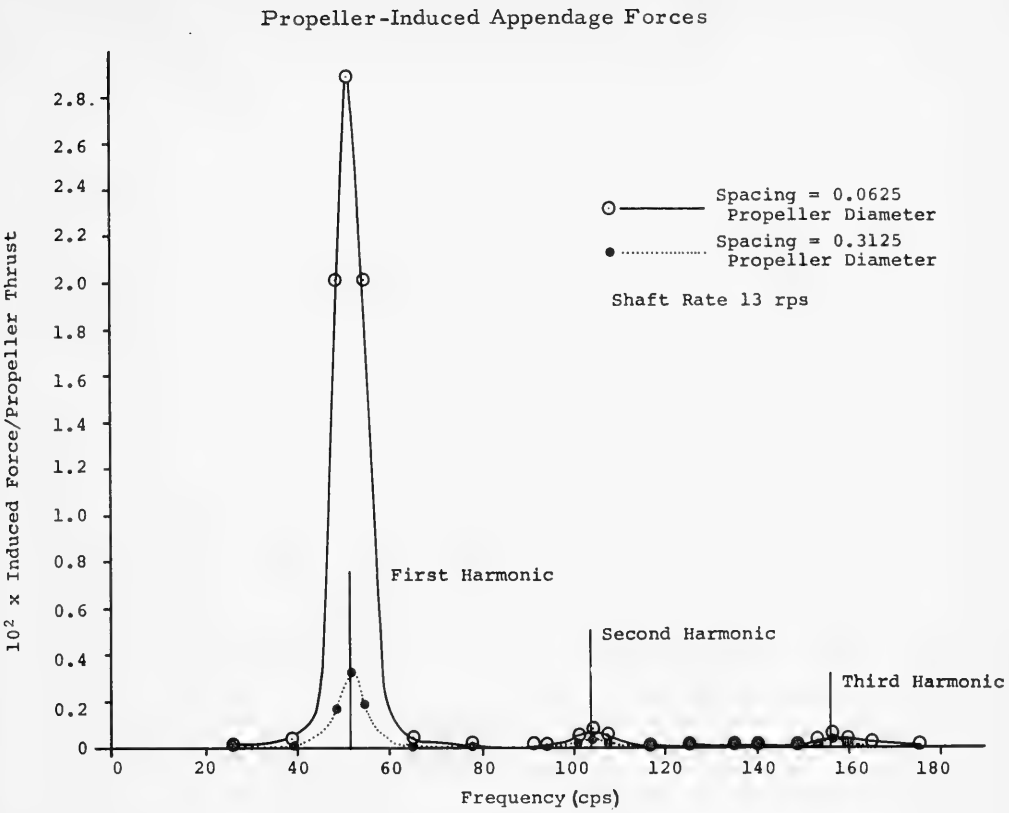

Fig. 11 - Axial induced appendage force levels as a function of scanned frequency for a double-thickness four-bladed propeller and a symmetrical appendage

introduction of both axial and transverse forces regardless of whether there was an even or odd number of blades on the propeller. It therefore seems reasonable to conjecture that with extremely close propeller-appendage spacings the action of the propeller on the flow about the appendage is such as to result in an effective angle of attack of the appendage. This contention is further strengthened by the fact that these "inconsistent" induced appendage forces completely disappear with slight increases in the spacing ratio, and it also follows that the effect of the propeller on the flow field about the appendage does decay rapidly. An example of the magnitude of the "contradictory" transverse force associated with four-bladed propeller tests is shown in Fig. 12.

With those two points clarified the following discussions which involve an appendage at a zero attack angle will be restricted to comments relating only to the appropriate propeller-appendage induced force; i.e., axial induced forces will be discussed with even-bladed propellers and transverse induced forces will be discussed with odd-bladed propellers.

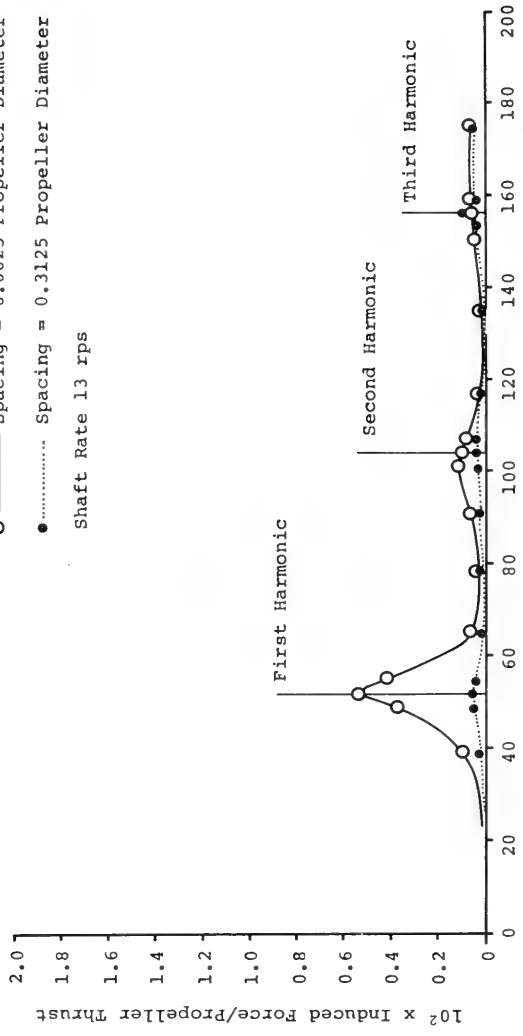

Fig. 12 - Transverse induced appendage force levels as a function of scanned frequency for a double-thickness four-bladed propeller and a symmetrical appendage

Zero Appendage Attack Angle

The first case considered is that of the four-bladed propeller. Figure 13 illustrates the influence of blade thickness on the induced appendage forces for the first, second, and third harmonics of the blade rate for a symmetrical appendage. From this figure it can be noted that blade thickness is an important factor in determining the magnitude of the axial induced appendage force. However appendage asymmetry has little effect, as is shown in Fig. 14. In this same figure, blade-rate (or first-harmonic) data are presented for two propeller blade thicknesses and three appendage asymmetries. This plot reinforces the observation that the blade thickness has the dominant effect and appendage asymmetry has minimal effect. The minimal effect of appendage asymmetry is also shown in Fig. 15, where the unsteady axial induced appendage forces associated with the first, second, and third harmonics of the blade rate are shown for a four-bladed propeller having double-thickness blades. This figure shows that the induced appendage forces associated with the first harmonic of the blade rate are 30 to 40 times as large as those associated with the second and third harmonics of the blade rate.

For transverse induced appendage forces and operations with a three-bladed propeller and a symmetrical appendage, Fig. 16 illustrates the effect of propeller blade thickness on the induced appendage forces for the first, second, and third harmonics of the blade rate. In this case, as for the case of the axial induced unsteady appendage forces, blade thickness is an important factor in determining the magnitude of the forces associated with the first harmonic of the blade rate, but the second and third harmonics of the blade rate are not as strongly influenced by propeller blade thickness as for the case with axial induced appendage forces.

Appendage asymmetry has a much more dominant effect on the transverse induced appendage forces than on the axial induced forces. Figure 17 illustrates the first harmonic data for both of the propeller blade thicknesses and three cases of appendage arrangement. Compare this figure with Fig. 14 to note the different effect appendage asymmetry has on the magnitude of induced axial and transverse appendage forces. The effect of appendage asymmetry on the unsteady induced appendage forces associated with the first, second, and third harmonics of the blade rate are shown in Fig. 18. It is shown that the effect of appendage asymmetry and the propeller blade rate harmonic condition both have a strong influence on the transverse induced appendage forces.

Single-Bladed Propeller Tests

During this series of investigations, data were obtained with a two-bladed propeller as well as with three- and four-bladed units. The information obtained with the two-bladed propeller, coupled with that obtained with the three- and four-bladed units, was then used to verify a test technique developed during these studies which establishes a basic relationship between the unsteady induced appendage force and the propeller thrust. This technique involves testing a particular propeller as a single-bladed unit and from this information then determining the induced appendage forces for a multibladed propeller. Using this technique, it was found that the unsteady force induced on an appendage by a

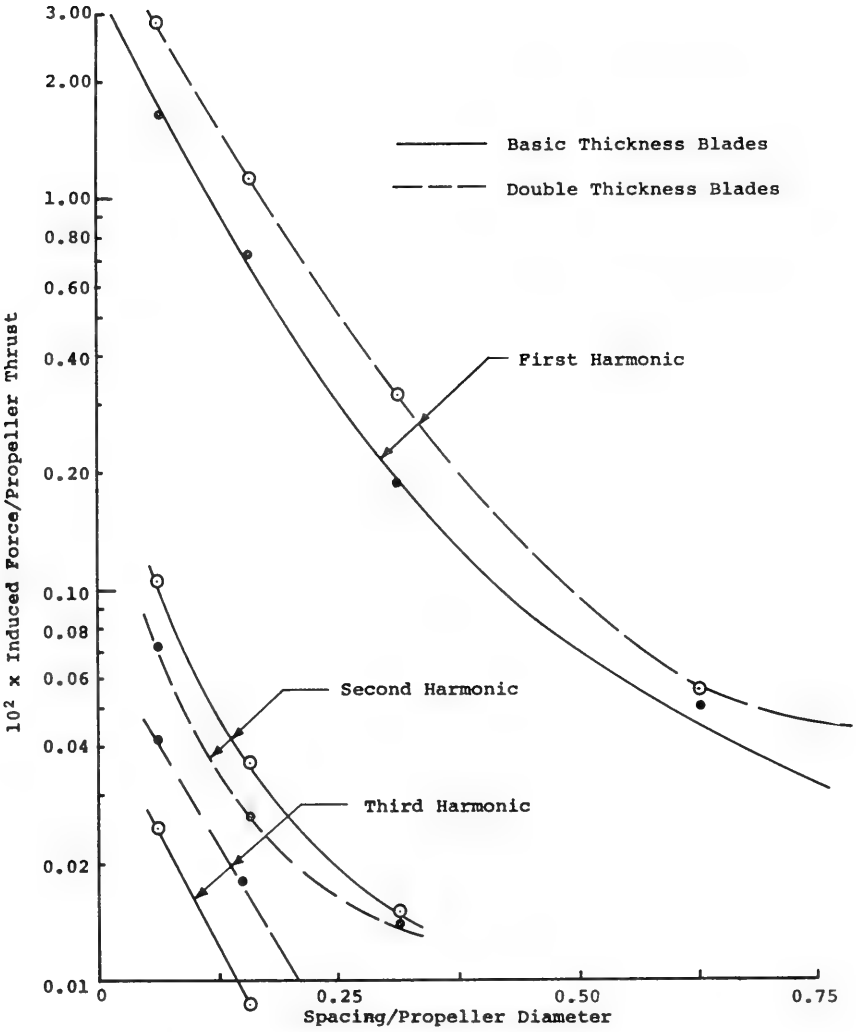

Fig. 13 - Blade-thickness effects on axial measurements at various propeller harmonics with a four-bladed propeller and a symmetrical appendage

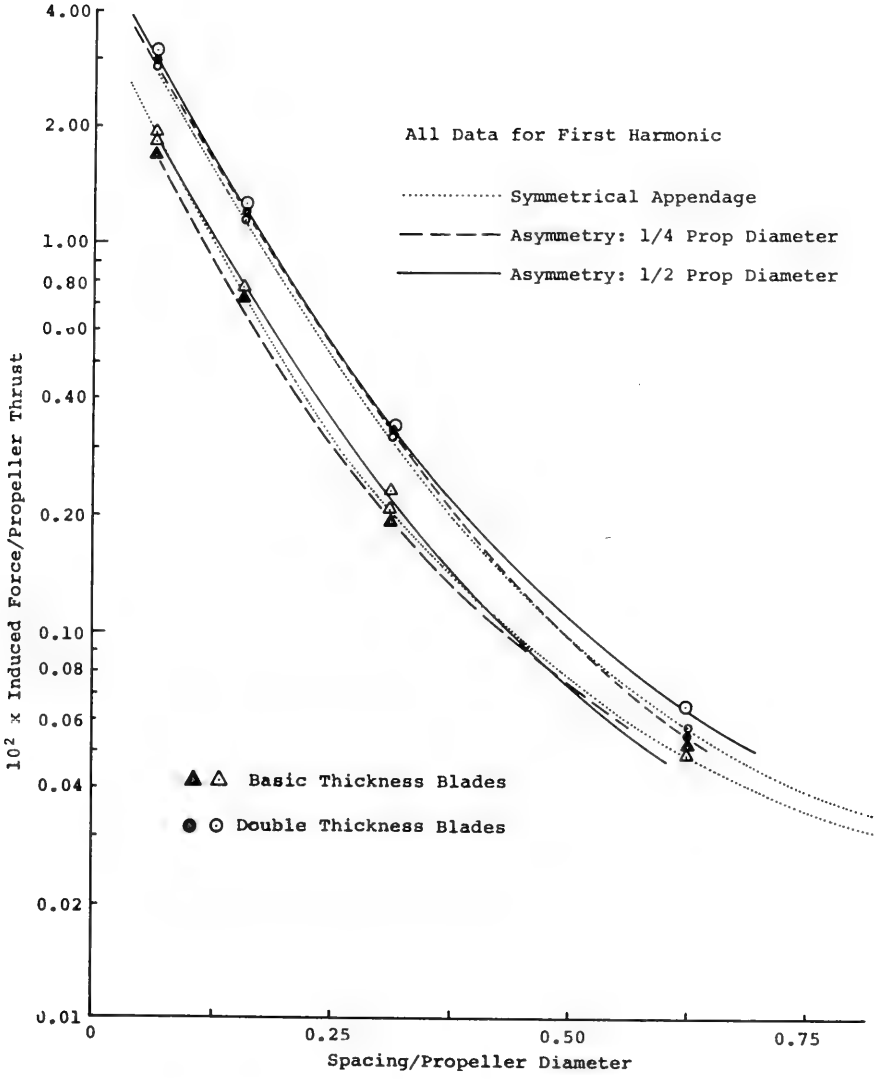

Fig. 14 - The effects of blade thickness and appendage asymmetry on the axial forces associated with a four-bladed propeller

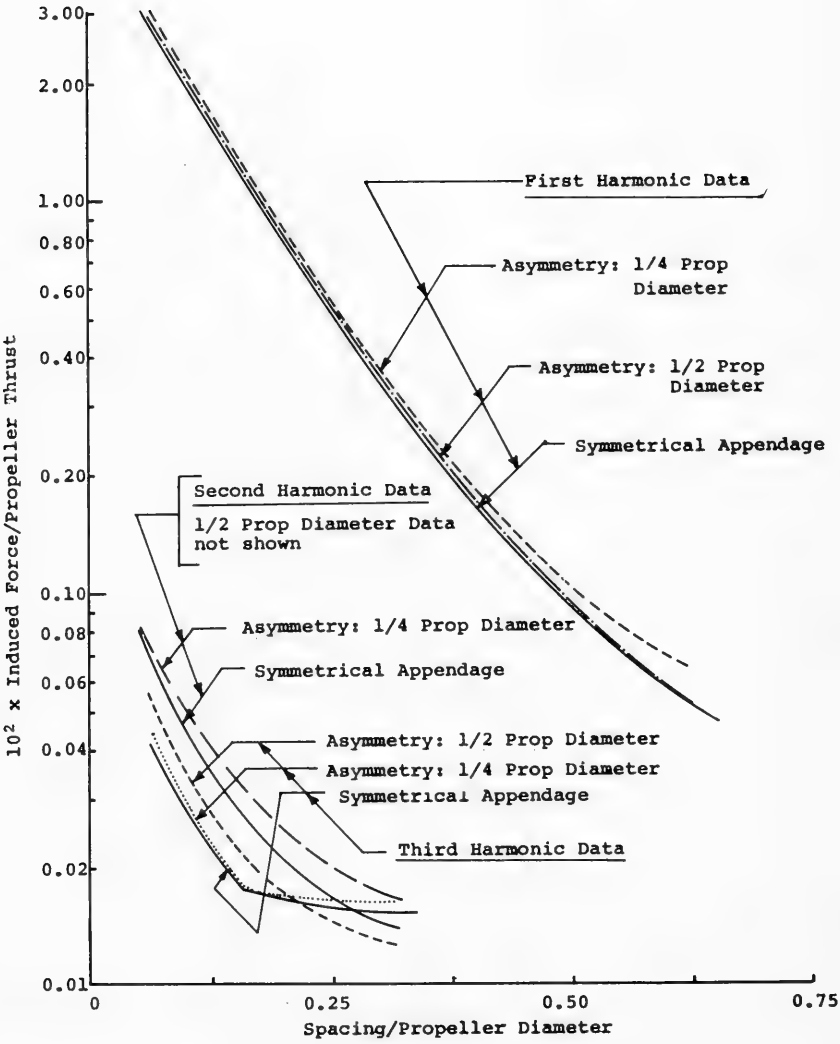

Fig. 15 - Appendage asymmetry effects on axial forces for a double-thickness, four-bladed propeller

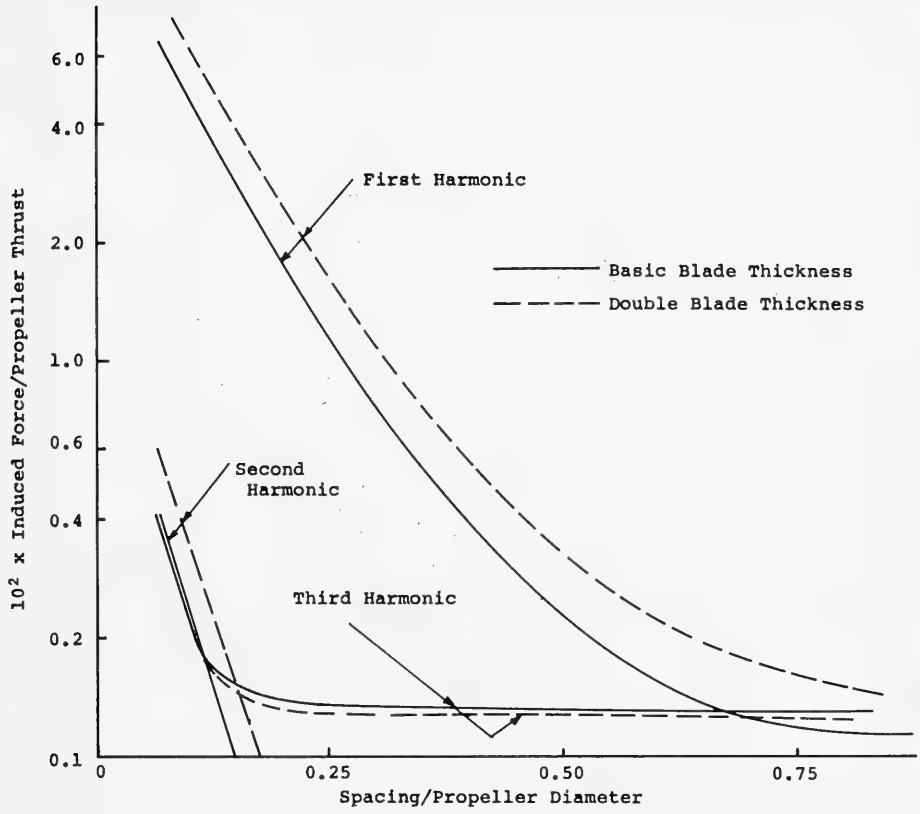

Fig. 16 - The effect of propeller blade thickness on the transverse forces for a three-bladed propeller with a symmetrical appendage

single-bladed propeller, when examined in terms of the ratio of the induced appendage force divided by the single-bladed propeller thrust, resulted in good agreement when compared with the same induced force/thrust ratio associated with a propeller composed of more than one blade. Comparisons must naturally be made at the same frequency. For a three-bladed propeller the first harmonic of blade rate is three times the shaft rate; thus the single-bladed propeller data must also be examined at a frequency corresponding to three times the shaft rate to make a valid comparison.

Using the single-bladed-propeller technique, the ratio of the induced appendage force and the propeller thrust of a multibladed propeller can be determined quite accurately once reasonable propeller thrusts (or K_T operating values) are employed. The inaccuracy of this method arises when extremely light propeller loadings are employed, since the induced appendage force is actually composed of two components: one due to propeller loading and one due to propeller blade thickness. The thickness of the propeller should contribute a certain amount to

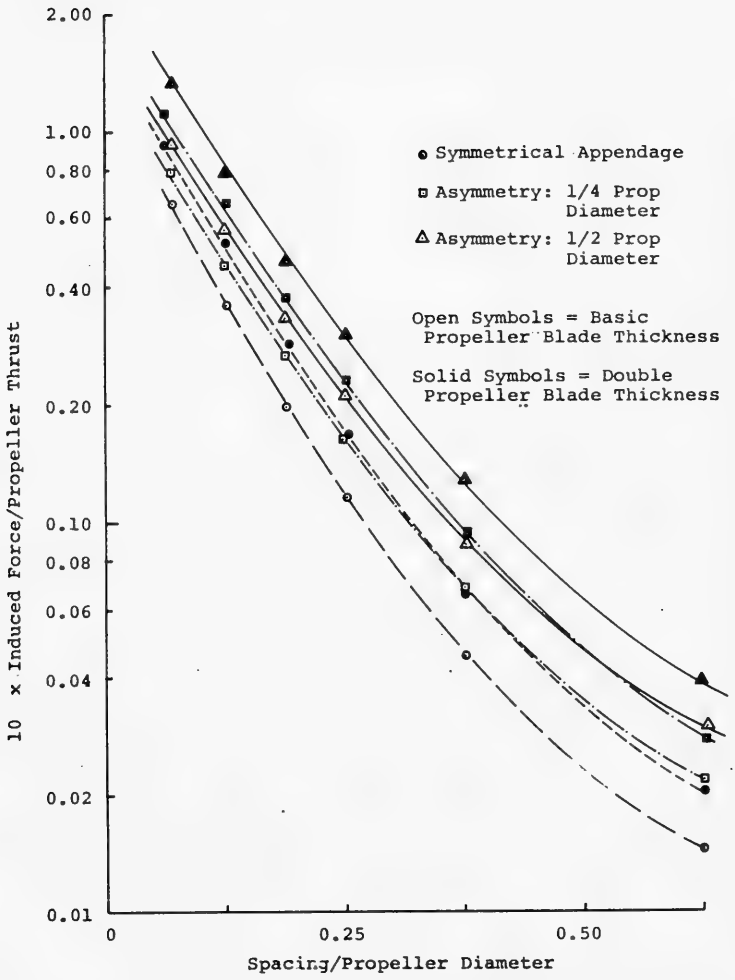

Fig. 17 - Effects of propeller blade thickness and appendage asymmetry on transverse measurements with a three-bladed propeller

the induced force which is independent of the propeller thrust coefficient, but the percentage of the induced force attributed solely to the thickness term becomes larger as the absolute thrust of the propeller decreases. In other words, at a condition of zero propeller thrust there would still be a force induced on the appendage due to the thickness of the passing propeller blade.

The technique proposed here of presenting the induced appendage force as a ratio solely dependent on propeller thrust is thus recognized as not representative of a true scaling parameter, as the thickness contribution is lumped together with the loading contribution. However it does seem that the ratio

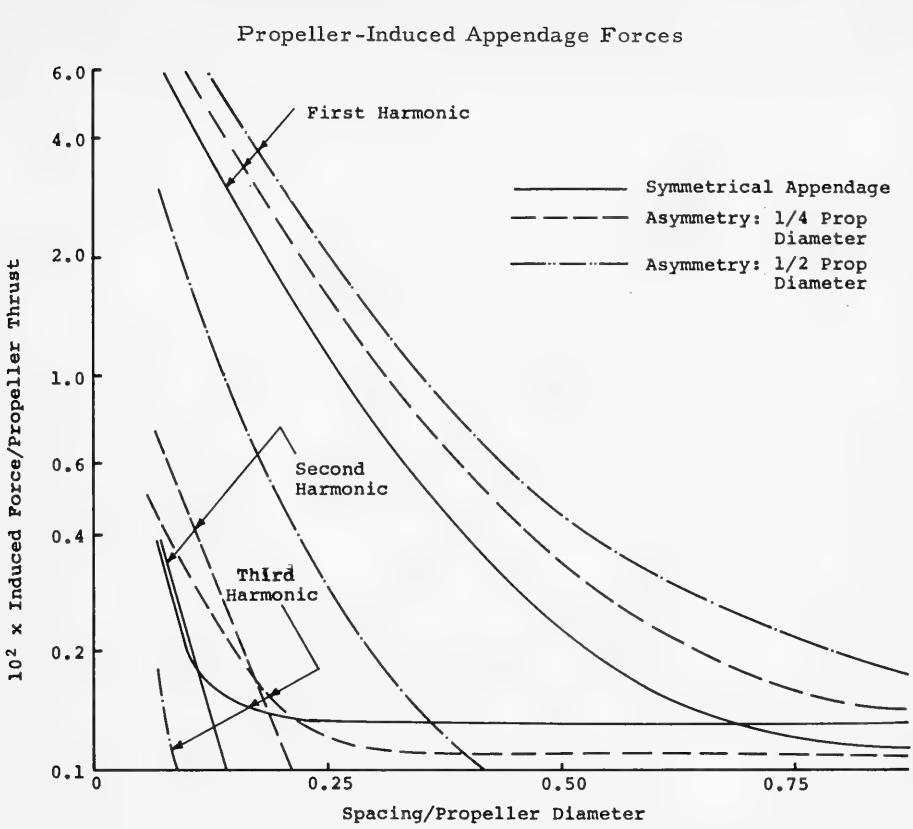

Fig. 18 - Effect of appendage asymmetry on transverse forces for a three-bladed propeller with the basic blade thickness

presented here is valid for engineering purposes when the thrust coefficient of the propeller is representative of actual propeller designs.

An example of the results of this test technique is shown in the following figures. Figure 19 presents the axial induced appendage force, as determined from single-bladed propeller operation, compared with forces induced by propellers having two and four blades. Of interest on this figure is the fact that the induced force associated with the second harmonic of a two-bladed propeller is about as large as that induced by the first harmonic of a two-bladed propeller. This is somewhat contrary to what might be expected, but it is verified from both the single-bladed and two-bladed measurements for these propellers. Figure 20 presents a comparison of the induced force ratios associated with single-bladed and three-bladed propeller units. These data are shown for both the first and second harmonics of the blade rate. From the preceding figures, as well as other data obtained during different test programs, it appears as if this technique is well suited for experimentally evaluating the induced appendage forces of a particular propeller design. It requires the manufacture of only one blade, and

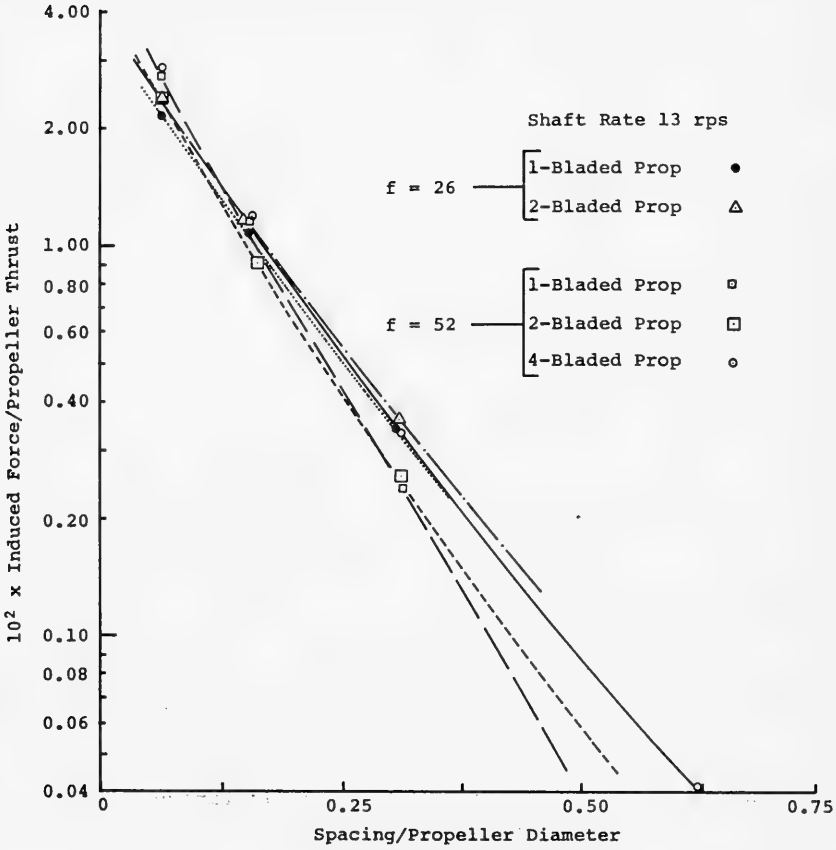

Fig. 19 - Comparison of axial induced appendage forces for single- and multibladed, double-thickness propellers with a symmetrical appendage

from this one blade all induced forces associated with a propeller having a multiple number of blades can be determining for engineering purposes.

Effect of Appendage Thickness and Span

The effect of appendage thickness and span on the induced appendage force magnitude was also investigated for the case involving axial induced forces. For these studies the test arrangement was as shown in Fig. 21. (The propellers employed in this particular study and in the remainder of the discussion of experiments were commercial outboard-motor propellers. They were two- and three-bladed propellers, both having a diameter of 8 in. and a pitch of 6 in., and are shown in Fig. 22.) The appendage span varied from one extending completely across the tunnel test section (19.56 in.) to smaller spans of 14 and 8 in.

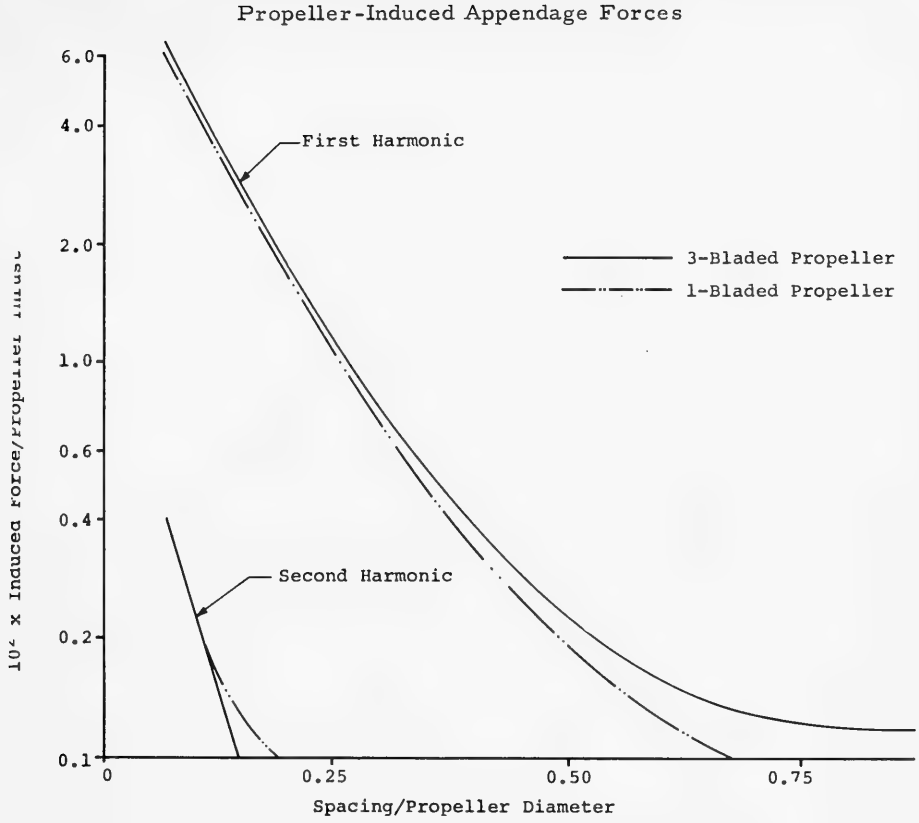

Fig. 20 - Comparison of three-bladed and single-bladed operation with transverse induced forces and a symmetrical appendage

For the smaller span appendages, fairings having the same cross section as the appendage itself were attached to the tunnel walls. All appendages had a ogival cross section and a chord length of 8 in. One foil had a maximum thickness of 1.0 in., and the other had a maximum thickness of 0.5 in. Figure 23 illustrates the effect of foil thickness and span on the axial induced forces associated with the two-bladed propeller.

Appendage Attack Angle

The effect of appendage attack angle on induced appendage forces is of considerable interest, since the appendage attack angle significantly changes the induced appendage forces compared to the case with a zero appendage attack angle. Figures 24 and 25 present the axial induced forces with a two-bladed propeller at appendage attack angles of 0° and 10°. A comparison of the data contained on these two figures is shown in Fig. 26. This figure shows that the induced appendage forces associated with both the first and second harmonics of the blade rate increase with appendage attack angle, with the second harmonic value

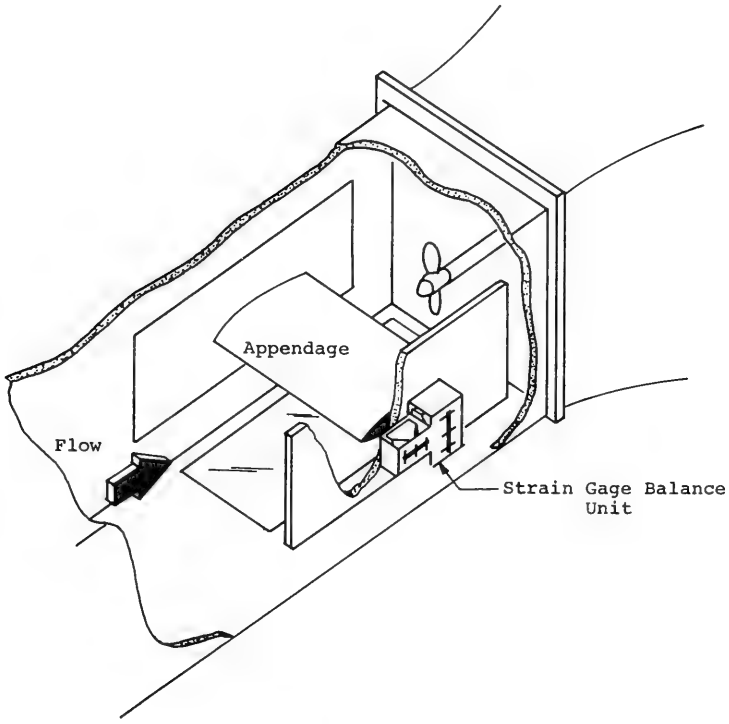

Fig. 21 - Test arrangement for appendage thickness and span studies

Fig. 22 - Commercial 8-in.-diameter propellers used in the arrangement of Fig. 21

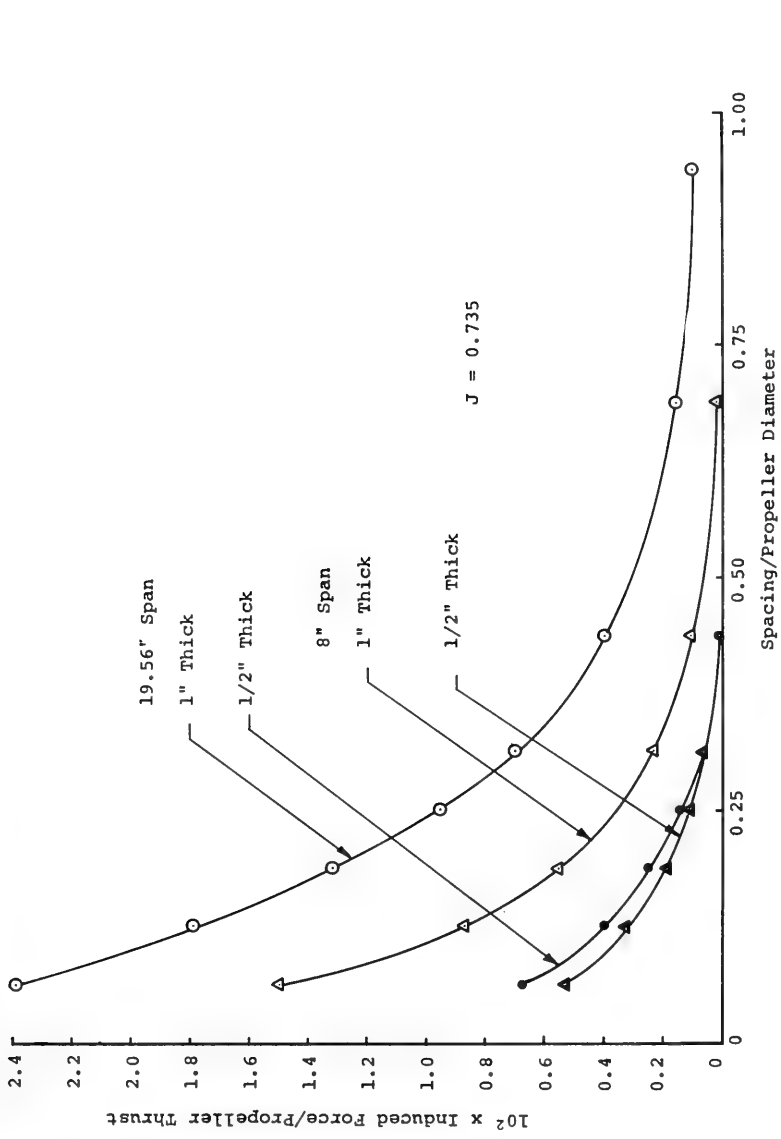

Fig. 23 - Effects of appendage thickness and span on axial induced forces with a two-bladed propeller

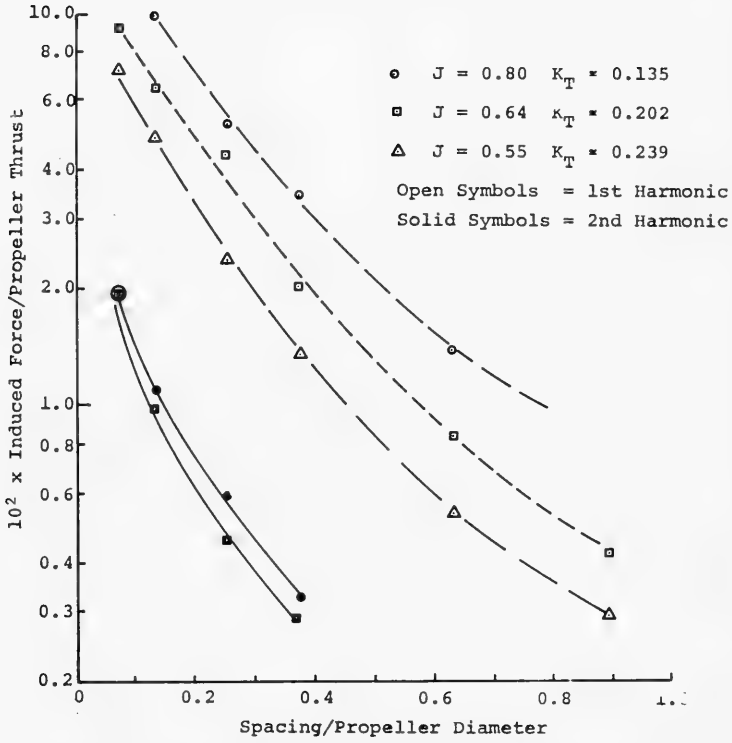

Fig. 24 - Induced force ratio vs spacing ratio for a two-bladed propeller downstream of an appendage, axial measurements, and an appendage angle of 0°

approaching that associated with the first harmonic value for the condition of zero appendage attack angle. It must be remembered in this discussion that the direction of the axial and transverse forces remains referred to the free stream velocity vector and not the appendage chord.

The transverse induced appendage forces associated with a two-bladed propeller are zero for the case of zero appendage attack angle (except for very close spacing ratios, as noted earlier), but with the introduction of an attack angle of 10° the transverse induced forces exceed the axial induced values, as shown in Fig. 27.

For the case of the three-bladed propeller, Fig. 28 presents the transverse induced appendage forces for a 0° appendage attack angle and Fig. 29 presents the forces for a 10° appendage attack angle. A comparison of these figures again shows the strong influence that appendage attack angle has on the induced forces; the force ratios are decreased by about a factor of 2 when the appendage is at an

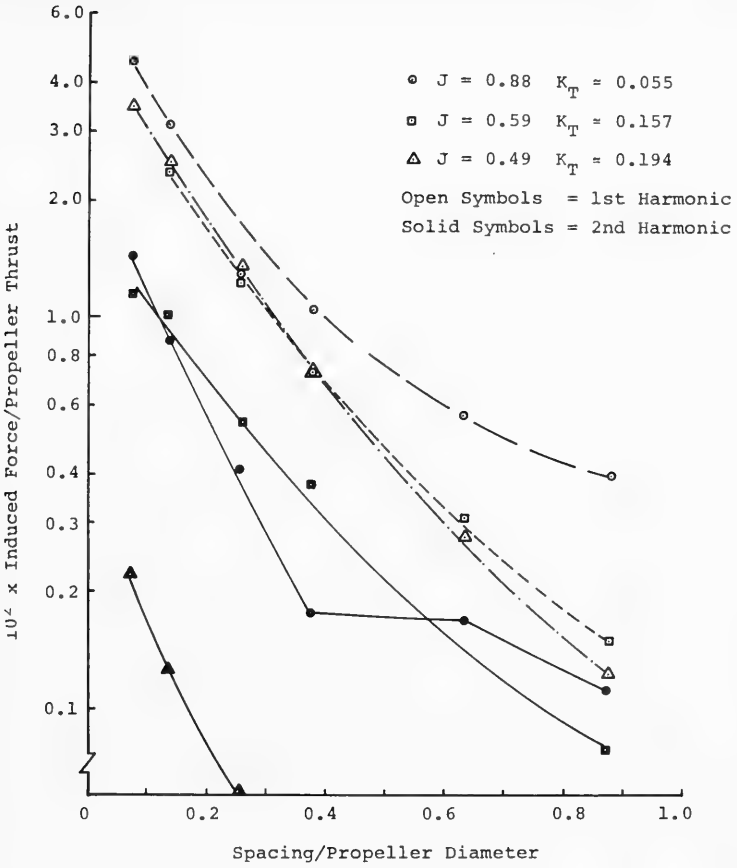

Fig. 25 - Induced force ratio vs spacing ratio for a two-bladed propeller downstream of an appendage, axial measurements, and an appendage angle of 10°

attack of 10°. With a three-bladed propeller, the axial induced force is essentially zero when the appendage attack angle is zero, but with an appendage attack angle of 10° the induced force becomes significant. Data supporting this result are shown in Fig. 30.

Rudder Case

A few cases involving the unsteady forces induced on an appendage downstream of a propeller, i.e., the rudder case, are presented in this discussion to illustrate the complexity of the unsteady propeller induced forces for the arrangement. At the time of this reporting, only some initial studies have been completed, but additional studies are being carried out.

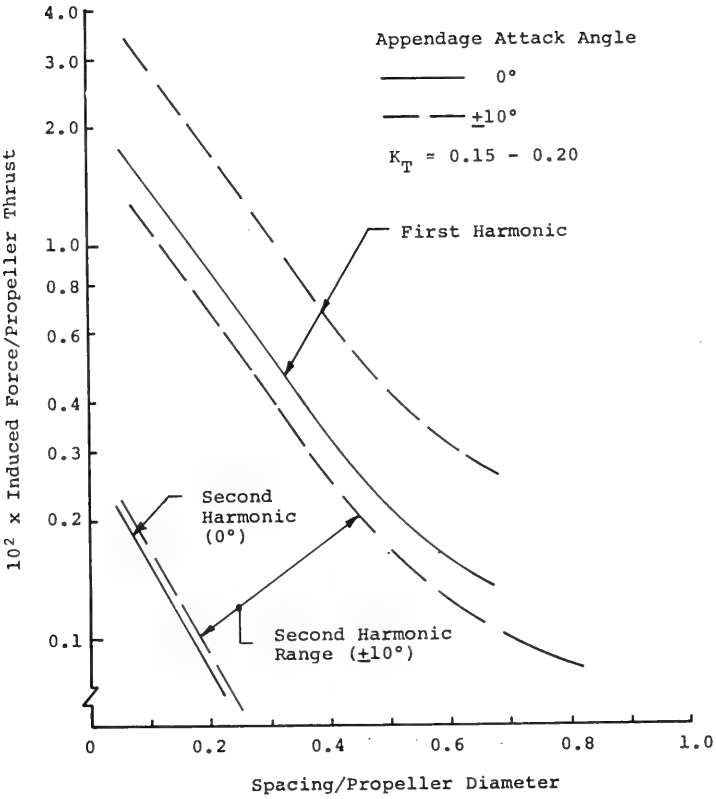

Fig. 26 - Comparison of axial induced appendage force ratios with a two-bladed propeller downstream from the appendage for the first and second propeller blade harmonics over a range of appendage attack angles

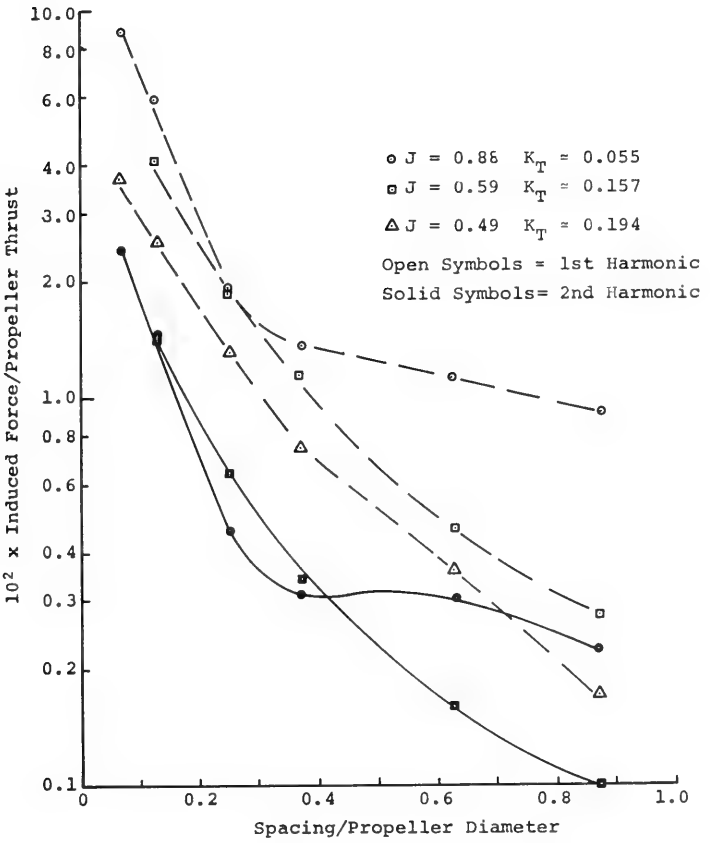

Fig. 27 - Induced force ratio vs spacing ratio for a two-bladed propeller downstream of an appendage, transverse measurements, and an appendage angle of 10°

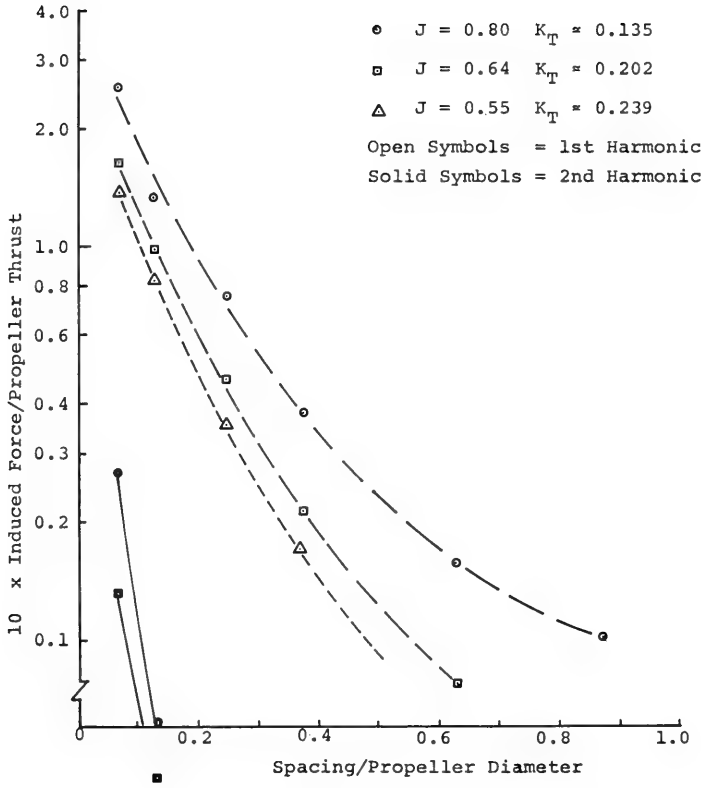

Fig. 28 - Induced force ratio vs spacing ratio for a three-bladed propeller downstream of an appendage, transverse measurements, and an appendage angle of 0°

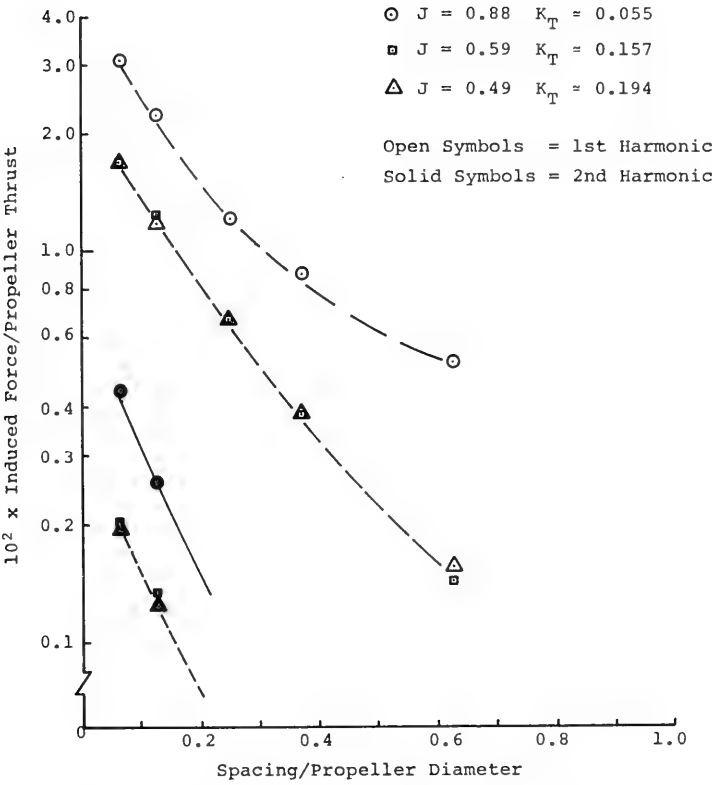

Fig. 29 - Induced force ratio vs spacing ratio for a three-bladed propeller downstream of an appendage, transverse measurements, and an appendage angle of 10°

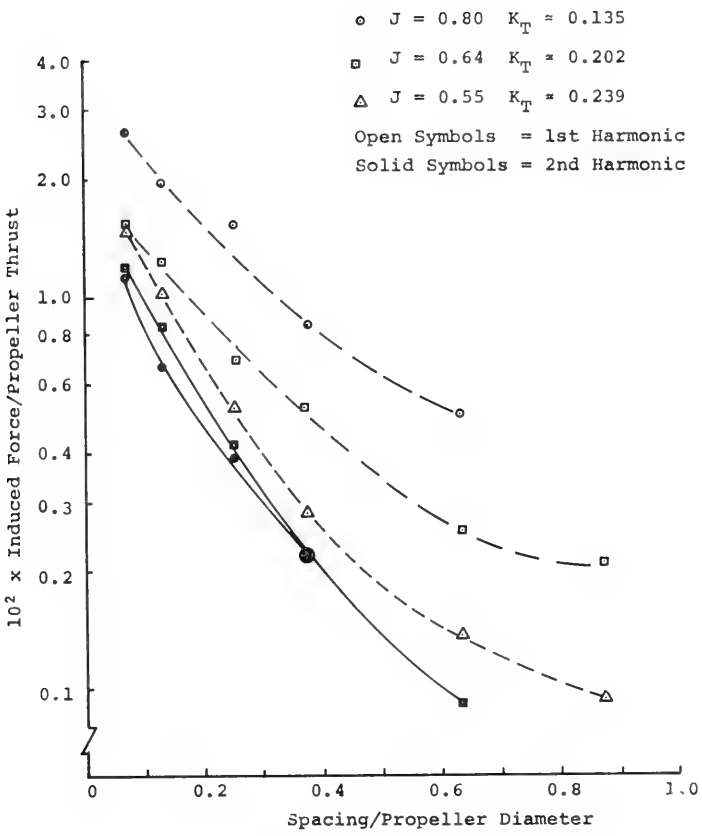

Fig. 30 - Induced force ratio vs spacing ratio for a three-bladed propeller downstream of an appendage, axial measurements, and an appendage angle of -10°

Two interesting observations were made during this study. The first concerned the introduction of both axial and transverse appendage forces by either an even-bladed or odd-bladed propeller as soon as the appendage was at an attack angle, similar to the case of an upstream appendage discussed previously. The second observation, and one which was perhaps more unusual, concerns the undulatory variation of the induced force ratio as a function of propeller-rudder spacing. While this variation of the force ratio would not be expected, particularly in view of the test results associated with the case of a propeller downstream of an appendage, Sugai (12) has hypothesized that such force variations could exist. The present initial experimental data support that hypothesis.

Figure 31 shows the axial induced rudder force ratio for a two-bladed propeller at a 0° rudder angle. Figure 32 shows the induced rudder force ratios with the rudder at an attack angle. The data on these figures show that the undulatory variation of the induced force ratio with axial distance exists both with and without rudder angle. Figure 33 illustrates the transverse induced rudder forces associated with a two-bladed propeller. This figure shows that even-bladed propellers induce transverse forces when the rudder is at an attack angle and that the undulatory nature of the force occurs for this case also.

For the case of transverse induced rudder forces with a three-bladed propeller Fig. 34 shows the force ratios associated with a 0° rudder angle and Fig. 35 presents data for a 10° rudder angle. These figures again illustrate the undulatory nature of the induced rudder force. Figure 36 presents the axial induced rudder force associated with a three-bladed propeller. Here once again the existence of an axial force associated with a three-bladed propeller is shown, together with the persistent undulatory variation with distance of the induced force ratio.

SUMMARY OF EXPERIMENTAL RESULTS

Since a detailed listing of the many implications which can be derived from the data would be very lengthy, only generalized key observations will be presented here.

1. Induced appendage forces are associated with only blade harmonic frequencies.

2. Propeller blade thickness is a major factor influencing both the axial and transverse appendage forces. An increase in blade thickness produces significant increases in the induced force ratios.

3. Appendage asymmetry has a strong influence on the magnitude of the induced force ratio for the case of transverse forces (odd-bladed propellers) but only a minor influence on the axial induced force (even-bladed propellers).

4. Even-bladed propellers induce axial forces and odd-bladed propellers induce transverse forces on an appendage at a zero attack angle. Discrepancies at close propeller spacings can be logically explained as a result of propeller-induced "steady" attack angle changes.

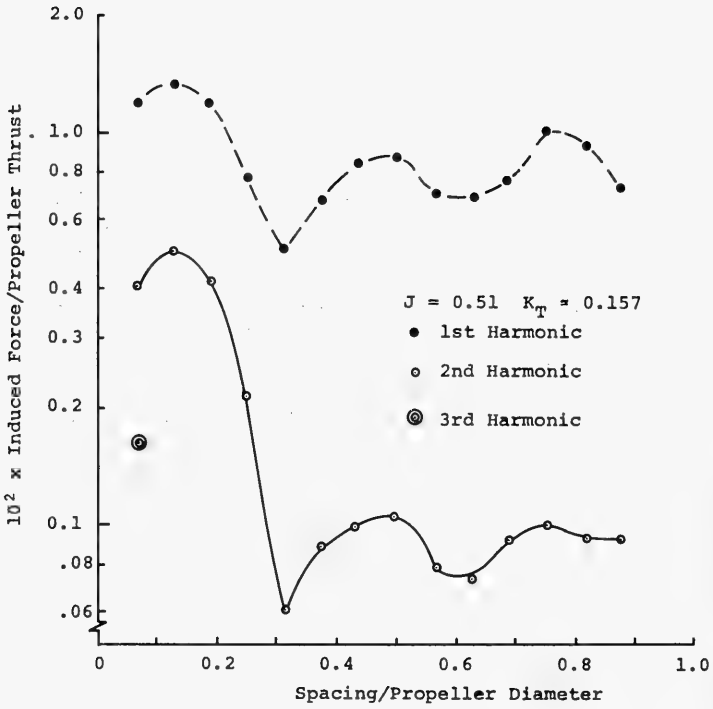

Fig. 31 - Induced force ratio vs spacing ratio for a two-bladed propeller upstream of an appendage, axial measurements, and an appendage angle of 0°

5. All induced forces on an upstream appendage decrease rapidly with an increase in propeller spacing. This holds whether the appendage is at an attack angle or not. In general, once the spacing has approached a propeller radius, the induced force is less than 1% of the propeller thrust.

6. Generally, the induced force values associated with the second and third harmonics of blade rate are well below those associated with the blade rate, but there are certain exceptions, such as the axial induced forces with the two-bladed propeller.

7. The force ratio defined by the unsteady induced appendage force divided by the operating propeller thrust is recognized as not being a proper scaling factor in that both the thickness and loading contributions are lumped together. However, its use for conventional propeller loadings seem valid.

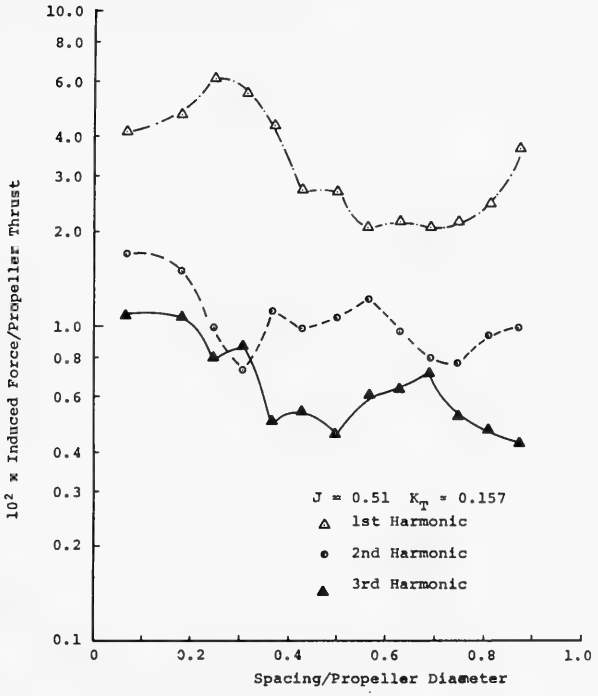

Fig. 32 - Induced force ratio vs spacing ratio for a two-bladed propeller upstream of an appendage, axial measurements, and an appendage angle of 10°

8. Single-bladed-propeller tests can be used to predict the induced appendage force levels associated with multibladed propellers. This technique can be employed for determining both the axial and transverse appendage forces. Comparisons have been made between single-bladed and two-, three-, and four-bladed propeller units. This is perhaps one of the more useful unsteady induced force test techniques developed to date.

9. Introducing an attack angle to an appendage results in both axial and transverse forces for both even- and odd-bladed propellers.

10. With an appendage attack angle of 10° the induced force ratio associated with a two-bladed propeller approximately doubles for the blade rate harmonic. The value for the second harmonic of the blade rate approaches that for the blade rate harmonic at a 0° appendage attack angle.

11. With an appendage attack angle of 10° the induced transverse force ratio associated with a three-bladed propeller decreases to about 1/2 the value associated with the 0° appendage attack angle.

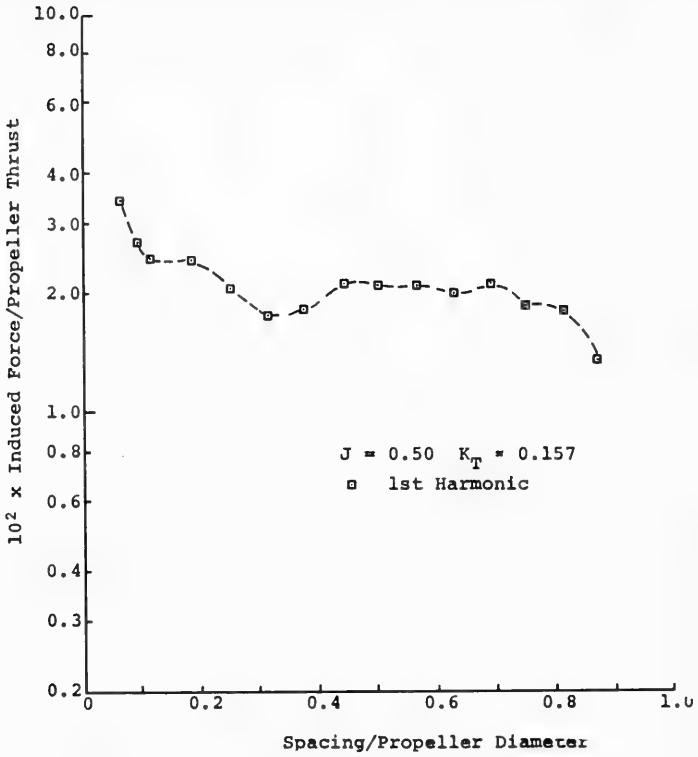

Fig. 33 - Induced force ratio vs spacing ratio for a two-bladed propeller upstream of an appendage, transverse measurements, and an appendage angle of 10°

12. For the rudder case the most important observation is the undulatory variation of both the axial and transverse forces with an increase in propeller spacing. This condition holds for all cases, both with and without attack angles.

13. For the rudder case and a two-bladed propeller the axial induced force at a 10° rudder angle reduces to about 20 to 25% of that existing at a 0° rudder angle. At 10° the transverse force approaches 50 to 60% of the axial force at a 0° angle.

14. For the rudder case and a three-bladed propeller the transverse force generally reduces with the introduction of attack angle. Little axial force is induced with a 0° rudder angle, but with a 10° rudder angle the axial force is about 1/2 the transverse force.

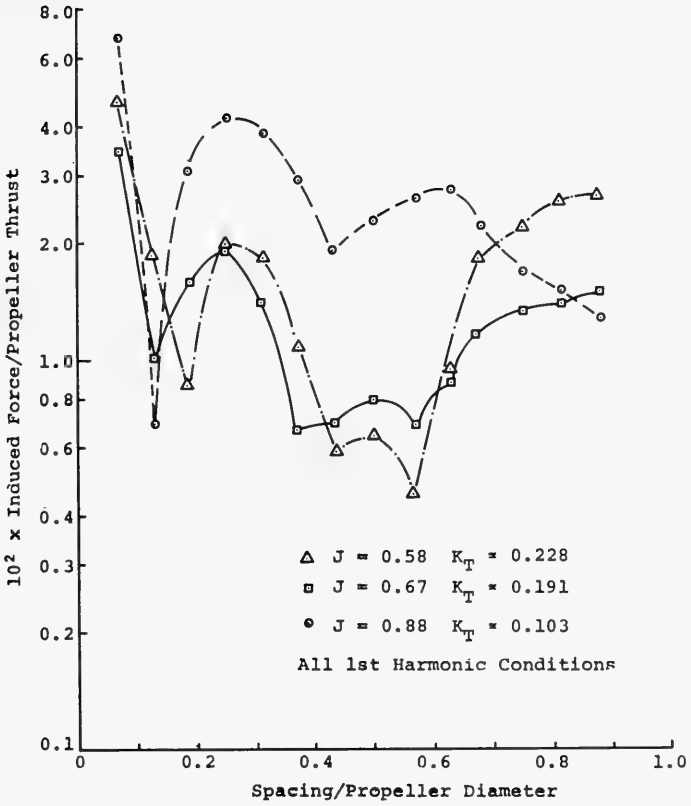

Fig. 34 - Induced force ratio vs spacing ratio for a three-bladed propeller upstream of an appendage, transverse measurements, and an appendage angle of 0°

THEORETICAL STUDIES

At the start of this overall program it was recognized that measurements would be made of relatively small interaction effects, and since the work was exploratory it would be important to have a guide as to the expected relative magnitude and character of the various force components. Thus a coordinated approach of combined theory and experiment was carried out, so that comparisons could establish a predictive tool for future studies. The theoretical study described herein (abstracted from Ref. 5) is intended to determine the relative magnitude of the transverse and axial forces acting on upstream appendages in the presence of a rotating propeller without considering (for this present work) the changing forces on the propeller blades due to the interaction. The mathematical analysis of the flow problem is based on two-dimensional ideal nonviscous flow for which potential theory is applicable, similar to the work on this problem described in Refs. 1 through 4.

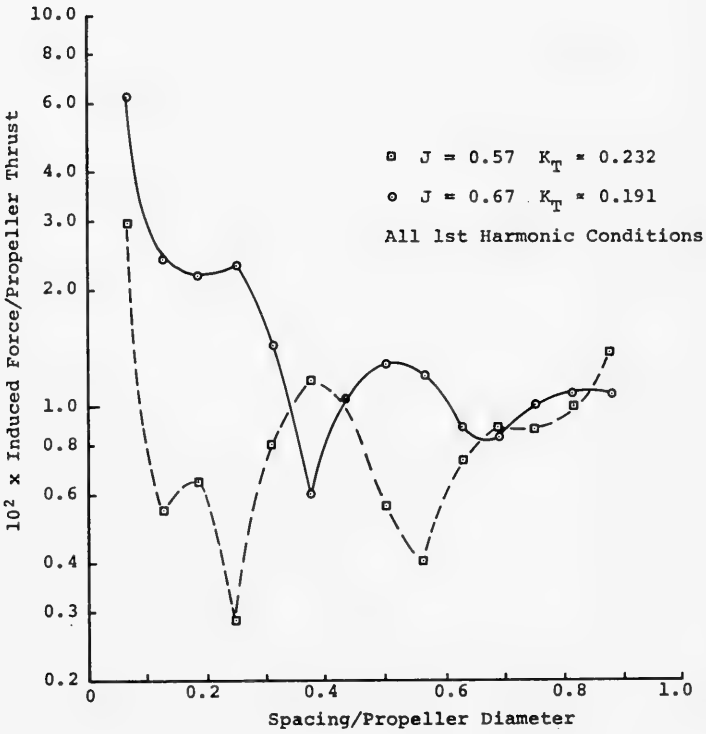

Fig. 35 - Induced force ratio vs spacing ratio for a three-bladed propeller upstream of an appendage, transverse measurements, and an appendage angle of 10°

The propeller blade will be represented by a vortex distribution, and an infinite cascade of propeller blades will be considered to pass the appendage, thereby introducing periodicity effects. In addition to the vortex representation the thickness of the propeller blades will be represented by a source distribution. Similar concepts of cascade theory will be used for this source distribution, in the same manner as for the vortex representation. This inclusion of propeller thickness will allow a relative separation of the force effects on the appendage due to the propeller thrust and due to the pressure field arising from the propeller thickness effects. Neither propeller thickness nor periodicity effects have been considered in any of the previous theoretical studies of propeller-appendage interaction.

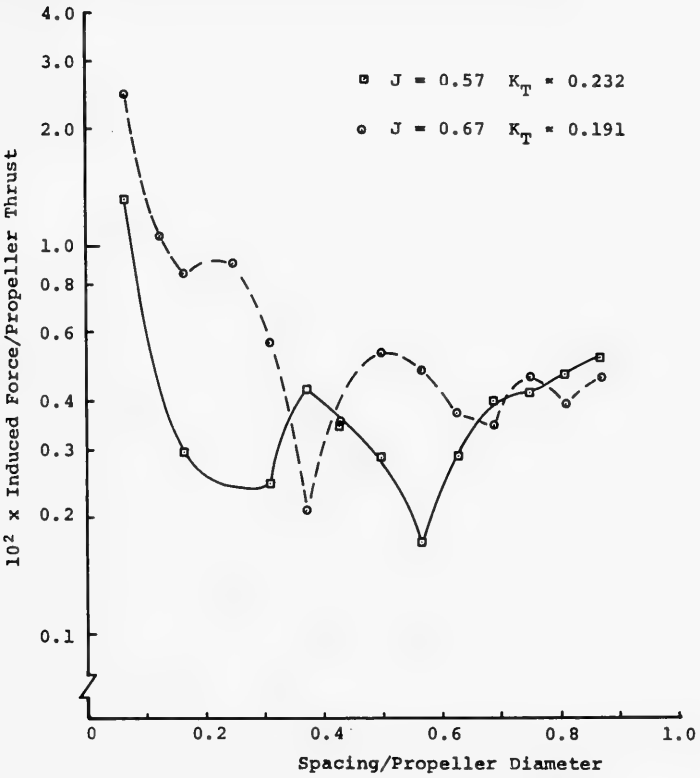

Fig. 36 - Induced force ratio vs spacing ratio for a three-bladed propeller upstream of an appendage, axial measurements, and an appendage angle of 10°

The hydrofoil appendage will be represented initially as a source distribution in a uniform flow, thereby accounting for the appendage thickness problem. The effect of the velocity field induced by the cascade of propeller blades will be used for determining the lateral crossflow on the foil and the longitudinal velocity field superposed on the oncoming uniform flow, both of which are non-uniform and nonsteady.

The normal velocity induced at the appendage results in a vorticity distribution on the appendage, and a nonsteady distribution of axially oriented dipoles along the chord line of the appendage is used to cancel the effect of the longitudinally induced velocity component. The various hydrodynamic singularities that represent the flow around a propeller blade and the appendage is represented in Fig. 37. The periodic lateral and longitudinal forces acting on the appendage are determined by application of fundamental hydrodynamic theories for the forces acting on singularities in oncoming flows, and illustrations of the derivation of particular force components are presented in the following discussion.

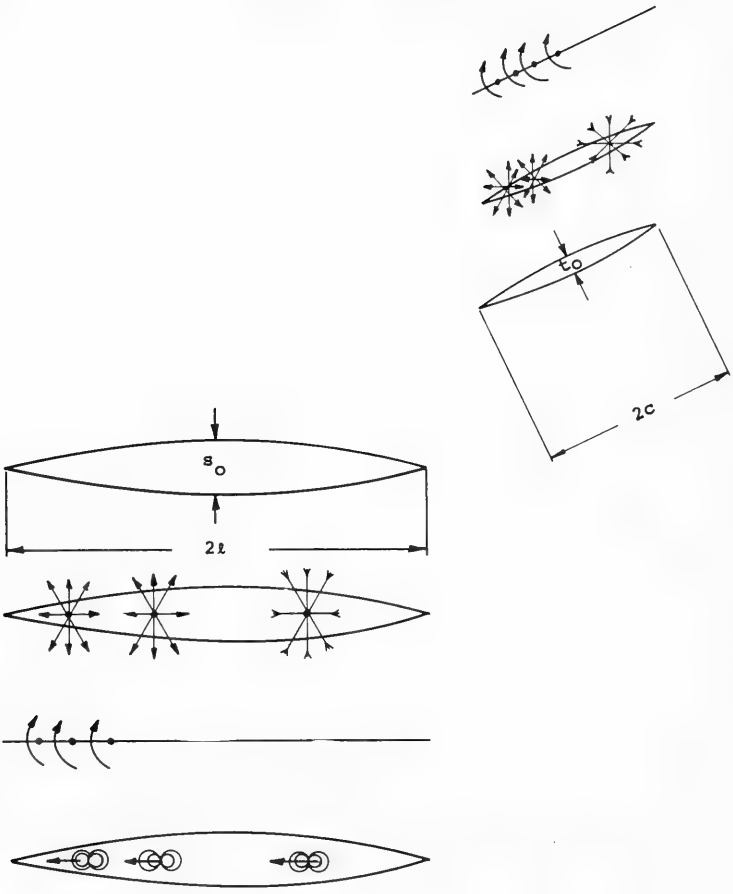

Fig. 37 - Hydrodynamic singularities representing a propeller blade and an appendage

The problem of a propeller rotating in the vicinity of an appendage is formulated in terms of the geometric arrangement indicated in Fig. 38, where the propeller blades are represented as an infinite cascade of finite chord foil sections moving with a velocity $V = \omega R_e$ in the negative y direction past another finite chord foil section representing the appendage, with the entire system in a uniform free stream velocity U in the x direction. It can be shown that the complex velocity on the appendage due to a cascade of concentrated vortices of strength Γ' on the line $x = x_0$ spaced a distance d apart is given by

$$- \left.\frac{dW_v'}{dZ}\right|_{Z=x} = - \frac{i\Gamma'}{2d} \coth \frac{\pi}{d} (x_0 + iy_0 - x) , \quad -\ell \leq x \leq \ell .$$

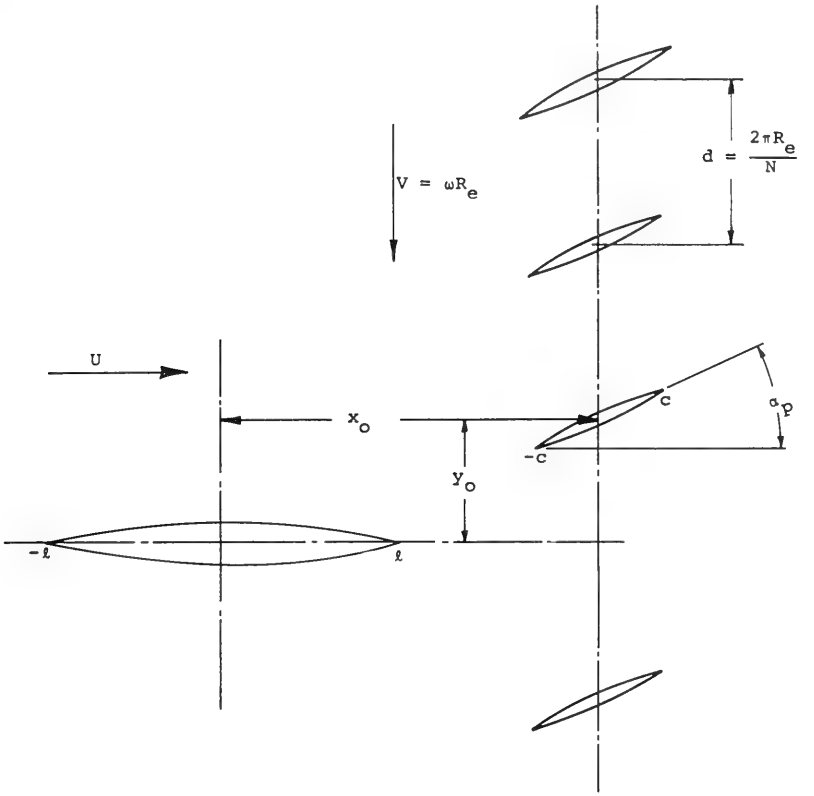

Fig. 38 - Geometric relations between an appendage and a propeller blade cascade

For $|x_0 + iy_0 - x| > 0$ the coth function can be represented in a series whose nonsteady portion is given by

$$-\left.\frac{dW_v'}{dZ}\right|_{Z=x} = -\frac{i\Gamma'}{d}\sum_{m=1}^{\infty} e^{-(2\pi m/d)(x_0+iy_0-x)} .$$

This expression is now generalized to a distribution of vorticity of magnitude $\gamma_p(x_p)\,dx_p$ over each propeller blade chord of length $2c$, with the quantities x_0 and y_0 chosen as the coordinates of the reference propeller blade centroid:

$$\begin{aligned} x_0 &= \ell\,(1 + 2\beta) , \\ y_0 &= -\omega R_e t - c \sin \alpha_p , \end{aligned} \qquad (1)$$

where R_e is the effective radius of the propeller, assumed to be $0.7R$, and the angle $\alpha_p = \tan^{-1}(V/U)$.

With the definition

$$\Gamma_p = \int_{-c}^{c} \gamma_p(x_p)\, dx_p ,$$

and making the substitution $x_p = c \cos \theta$, the vorticity distribution is

$$\gamma_p = 2V_p \left[\frac{A_0(1 - \cos\theta)}{\sin\theta} + 2A_1 \sin\theta \right] , \qquad (2)$$

where

$$V_p = U \cos\alpha_p + V \sin\alpha_p = \sqrt{U^2 + V^2} .$$

This choice of steady propeller vorticity distribution includes the effect of angle of attack on a flat plate airfoil (represented by the A_0 term) and a circular arc camber (represented by the A_1 term).

Using the definition $\sigma = 2c/d$, which is the blade solidity, where the propeller blade spacing $d = 2\pi R_e/N$, with N the number of propeller blades, the complex velocity induced at the appendage is

$$- \left.\frac{dW_v}{dZ}\right|_{Z=x} = - \frac{i\Gamma_p}{2\pi\ell} \sum_{m=1}^{\infty} G_m^v\, e^{Nmx/R_e}\, e^{im\nu_p t} ,$$

where $\nu_p = N\omega$ and

$$G_m^v = \frac{\sigma\pi\ell}{c}\, e^{-\sigma\pi m[(x_0/c) - i \sin\alpha_p]}\, H_m , \qquad (3)$$

in which

$$H_m = \frac{A_0}{A_0 + A_1}(J_0 + iJ_1) + \frac{A_1}{A_0 + A_1}\left(\frac{2ie^{-i\alpha_p}}{\sigma\pi m} J_1\right) ,$$

where the argument of the Bessel functions is

$$\sigma\pi m e^{-i[(\pi/2) - \alpha_p]} .$$

The velocity field induced by the propeller blade thickness can be accounted for by a source distribution along the chord line of each propeller blade, given by

$$M(x_p) = \frac{V_p}{\pi} f'(x_p) ,$$

where $f(x_p)$ is the propeller profile function, chosen for the present purposes as a symmetric blade with a parabolic profile given by

$$f(x_p) = \frac{t_0}{2}\left[1 - \left(\frac{x_p}{c}\right)^2\right] .$$

Following the same procedure as for the vorticity distribution, the complex velocity induced at the appendage by the source distribution of the propeller blades can be found, and the total nonsteady complex velocity induced at the appendage by the propeller blades, including both the vorticity and the thickness effects, can be expressed as

$$-\left.\frac{dW}{dZ}\right|_{Z=x} = \sum_{m=1}^{\infty} \psi_m \, e^{mNx/R_e} \, e^{im\nu_p t} , \tag{4}$$

where

$$\psi_m = -\frac{i\Gamma_p}{2\pi\ell} G_m^v + V_p \frac{\left(\frac{t_0}{c}\right)\left(\frac{R_e}{c}\right)}{\pi N} G_m^t ,$$

with G_m^v defined in Eq. (3) and

$$G_m^t = \frac{1}{m^2} e^{-i2\alpha_p - \sigma\pi m[(x_0/c) - \sin\alpha_p]} \left[e^{\sigma\pi m e^{i\alpha_p}}\left(1 - \sigma\pi m e^{i\alpha_p}\right)\right.$$

$$\left. - e^{-\sigma\pi m e^{i\alpha_p}}\left(1 + \sigma\pi m e^{i\alpha_p}\right)\right] .$$

Using the expressions for the complex velocity induced at the appendage, the normal velocity is given by

$$v(x,t) = -\mathrm{Im} \sum_{m=1}^{\infty} \psi_m \, e^{mNx/R_e} \, e^{im\nu_p t} ,$$

so that it is expressed as an infinite sum of components, each of which is of the form

$$v_m = \psi_m \, e^{-i\mu_m x/U} \, e^{im\nu_p t} ,$$

where

$$\mu_m = \frac{imNU}{R_e} .$$

Using the results of unsteady airfoil theory (13), the nonsteady transverse force (lift) on the appendage due to the propeller blade vorticity and thickness is represented by a sum of two terms: Y_1^v due to the propeller blade vorticity and Y_1^t due to propeller blade thickness. These terms are given by

$$Y_1^v = \mathrm{Re}\,\frac{\Gamma_p}{2\pi\ell}\sum_{m=1}^{\infty} G_m^v\, K_L(m\omega', m\lambda)\; e^{im\nu_p t}$$

and

$$Y_1^t = -\mathrm{Im}\; V_p \frac{\left(\frac{t_0}{c}\right)\left(\frac{R_e}{c}\right)}{\pi N}\sum_{m=1}^{\infty} G_m^t\, K_L(m\omega', m\lambda)\; e^{im\nu_p t}\,,$$

where

$$K_L(\omega', \lambda) = J(\lambda)\, C(\omega') + i\,\frac{\omega'}{\lambda}\, J_1(\lambda)$$

is the Theodorsen function, in which

$$J(\lambda) = J_0(\lambda) - iJ_1(\lambda)\,, \qquad \lambda = \frac{iN\ell}{R_e}\,, \qquad \omega' = \frac{\nu_p \ell}{U}\,,$$

and

$$C(\omega') = \frac{K_1(i\omega')}{K_0(i\omega') + K_1(i\omega')}\,.$$

Forces also arise due to the induced flow field of the propeller interacting with the source distribution representing the finite thickness appendage, where the source distribution for that profile is given by

$$M_a(x) = -\frac{U}{\pi}\left(\frac{s_0}{\ell}\right)\left(\frac{x}{\ell}\right)\,,$$

in which s_0 is the maximum thickness of the appendage and it is assumed that the appendage profile is also parabolic. By application of Lagally's theorem (14) the forces arising due to this interacting are represented by

$$X_2 - iY_2 = 2\pi\rho \int_{-\ell}^{\ell} M(x)\left(-\left.\frac{dW}{dZ}\right|_{Z=x}\right) dx\,,$$

where the total complex velocity induced at the appendage by the propeller is given by Eq. (4).

The nonsteady distribution of axially oriented dipoles induced within the appendage has a strength given by

$$\mu(x,t) = -\frac{1}{\pi}\, u(x,t)\, \frac{s_0}{2}\left[1 - \left(\frac{x}{\ell}\right)^2\right]\,,$$

where $u(x,t)$ is obtained as the real part of Eq. (4). The forces on the appendage due to this dipole distribution are determined from the unsteady Lagally theorem, which includes a quasisteady term and a nonsteady term. The resulting forces are given by

$$X_3 - iY_3 = -2\pi\rho \int_{-\ell}^{\ell} \mu(x,t) \left.\frac{d^2W}{dZ^2}\right|_{Z=x} dx$$

for the quasisteady term and

$$X_4 + iY_4 = -2\pi\rho \int_{-\ell}^{\ell} \frac{\partial}{\partial t} \mu(x,t)\, dx \tag{5}$$

for the unsteady term, which is found in this case to be only an axial force on the appendage.

Examination of the expression for the quasisteady dipole term shows that the force magnitudes are expected to be small and to produce higher harmonics, since the dipole strength is proportional to the induced complex velocity and it is multiplied by the velocity gradient. Thus this term will be deleted from further consideration, since numerical evaluation has also shown that it provides a negligible contribution. The unsteady axial force term arising from the dipole, given by Eq. (5), can be expressed as

$$X_4 = \mathrm{Re}\, \frac{i2\rho s_0 \nu_p}{\ell^2} \left(\frac{R_e}{N}\right)^3 \sum_{m=1}^{\infty} \frac{1}{m^2} \psi_m \left[e^{Nm\ell/R_e} \left(\frac{Nm\ell}{R_e} - 1\right) + e^{-Nm\ell/R_e} \left(\frac{Nm\ell}{R_e} + 1\right) \right] e^{im\nu_p t},$$

from which it is possible to separate the effects of propeller vorticity and thickness as in the previously derived force expressions.

Since the appendage is also represented by an unsteady vorticity distribution, a leading-edge axial suction force will arise. This term will also be small, since it is proportional to the square of the induced vorticity, and hence the induced velocity field, as well as contributing only higher harmonics. Therefore it will be neglected when considering numerical evaluations.

To apply the previous results to an actual three-dimensional propeller-appendage combination, it is necessary to include two infinite cascades of blades. Thus, as the blades on one side of the vertical plane through the propeller axis are moving down past the appendage, the blades on the other side of the plane are moving up. The previous expressions will hold if the directions of certain velocities, angles, etc., are reversed; and an analysis was made in terms of the effects of the different velocities when separately considering odd-bladed and even-bladed propellers. The details of the required analysis are presented in Ref. 5, and the conclusions obtained by considering the effects of the two cascades are summarized as follows:

N even: m odd or even: $Y_i(t) = 0$,

$X_i(t) \neq 0$, $i = 1, \ldots, 4$,

N odd: m even: $Y_i(t) = 0$,

$X_i(t) \neq 0$, $i = 1, \ldots, 4$,

m odd: $Y_i(t) \neq 0$,

$X_i(t) = 0$, $i = 1, \ldots, 4$.

Thus it is seen that the number of blades, odd or even, determines the nature of the induced forces. In the case of a symmetrically disposed appendage the previous results show that even-bladed propellers induce only axial forces and odd-bladed propellers produce only transverse forces for the fundamental blade rate frequency. Odd-numbered harmonics for an odd number of blades result in only transverse forces, whereas any condition where the product Nm is even results in only axial forces.

With the vorticity distribution on the propeller given by Eq. (2) the two-dimensional lift on each propeller blade is

$$L = 2\pi\rho c V_p^2 (A_0 + A_1) .$$

Assuming equal contributions to the lift from the angle of attack and camber terms $(A_0 = A_1)$ the total thrust on the propeller is given by

$$T = 4\pi\rho c_e V_p^2 A_0 NR \sin \alpha_p ,$$

where c_e is the effective half-chord length at 0.7R. The thrust coefficient C_T is then found in terms of the advance ratio J, defined by $J = U/nD = U/2nR$, with n the number of shaft revolutions per second, where

$$C_T = \frac{T}{\rho U^2 \pi R^2/2} .$$

A graph of C_T vs J is given in Fig. 39, where the value of NA_0 is chosen to correspond to the particular operating condition $C_T = 1.0$ for $J = 0.7$, for the value $c_e/R = 0.1875$. These conditions are selected as an appropriate range for calculations that would illustrate the nature of the results of the theoretical study.

The variation of the forces, as functions of the parameters characterizing this physical problem, is determined from numerical computations for the following set of conditions:

propeller diameter, $2R = 16$ ft,

propeller chord at 0.7 radius, $2c_e = 3$ ft,

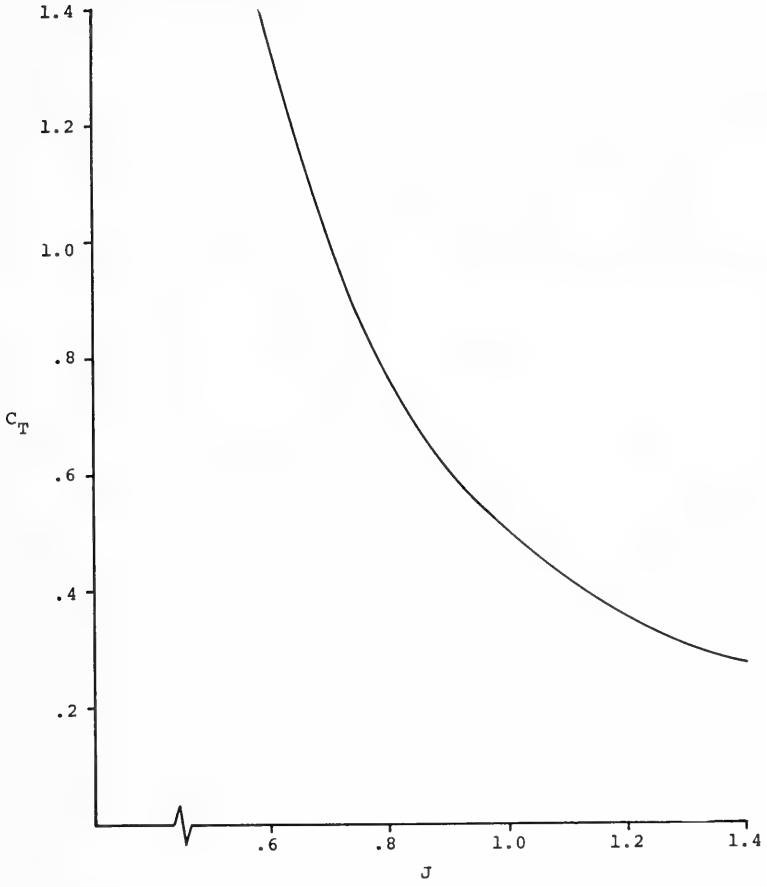

Fig. 39 - Propeller thrust coefficient as a function of advance ratio

appendage chord, 2ℓ = 14 ft,

appendage thickness ratio, $s/2\ell$ = 0.15,

appendage span = propeller diameter = 16 ft.

Since the theory developed herein is two-dimensional, the total force on the appendage is therefore proportional to the total span, and the present set of computations are appropriate to the conditions described above. The parameters that will be varied in the numerical computations are the number of blades N, the propeller advance ratio J, the propeller thickness ratio $t_0/2c_e$, and the separation distance between the propeller and the appendage, represented by the parameter β defined in Eq. (1).

An example of the results obtained from the present theory is shown in Fig. 40 for the fundamental blade rate transverse force on an appendage for a three-bladed propeller, at a spacing corresponding to $\beta = 0.05$. The total force amplitude and the separate contributions of the propeller loading (vorticity) and propeller thickness amplitudes, assuming each acted separately, are shown in this figure, and no phase information between the vorticity and thickness terms is given. The force is nondimensionalized on the basis of forward speed and propeller disk area ($\rho U^2 \pi R^2/2$) and plotted as a function of the advance ratio J. Since the thrust coefficient C_T is defined in the same way, the ratio of the induced force to the propeller thrust can be obtained to compare with experimental data presented in that manner.

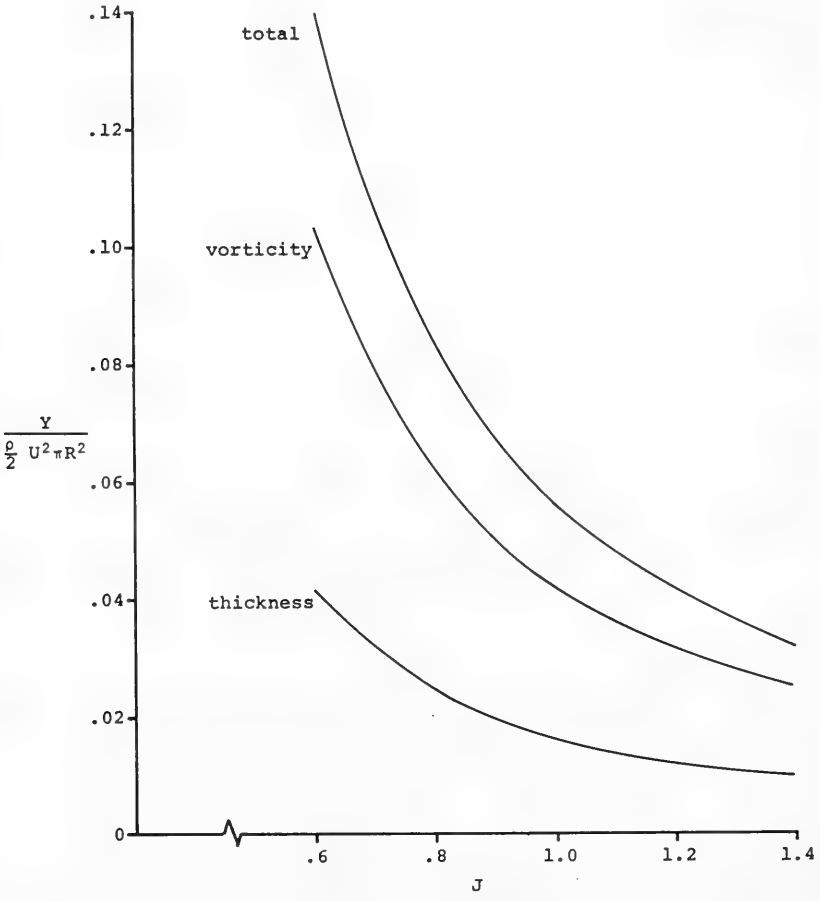

Fig. 40 - Transverse force as a function of the advance ratio for a three-bladed propeller, showing the influence of the propeller thickness and loading (vorticity): $\beta = 0.05$, N = 3, $t_0/2c = 0.05$

Figure 41 presents similar results with the thickness ratio of the propeller doubled; it can be seen that the thickness contribution per se has also been doubled but that the total force is not increased in proportion to the increase in propeller thickness. Thus it is seen that the phase difference between the vorticity and thickness contributions is a significant factor in determining the total force magnitude.

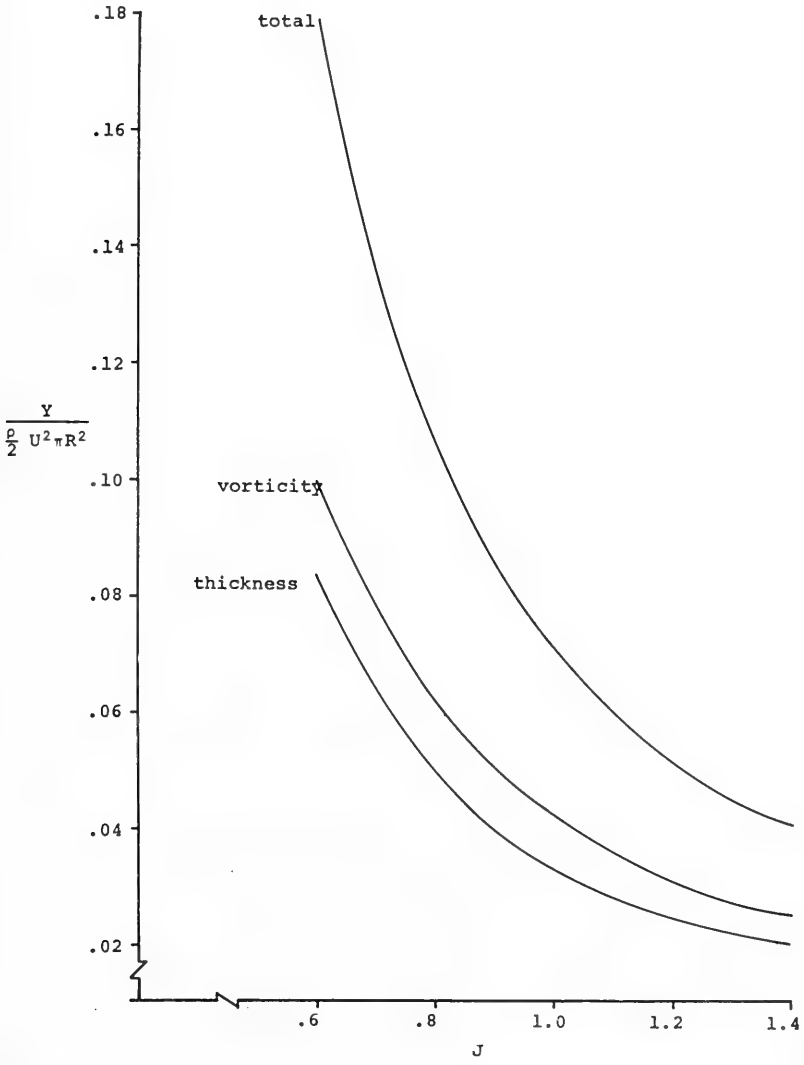

Fig. 41 - Transverse force as a function of the advance ratio for a three-bladed propeller: $\beta = 0.05$, $N = 3$, $t_0/2c = 0.10$

For the axial induced force the relative effects of vorticity and thickness of the propeller are shown for a two-bladed propeller in Figs. 42 and 43, where the effect of doubling the propeller thickness is shown to be smaller as compared with the transverse force results. The blade rate results for the case of a four-bladed propeller are shown in Fig. 44, where the influence of the propeller thickness increase, relative to the magnitude of the total force, is greater. Thus the influence of propeller thickness for both the transverse and axial appendage forces is significant in determining their total amplitude.

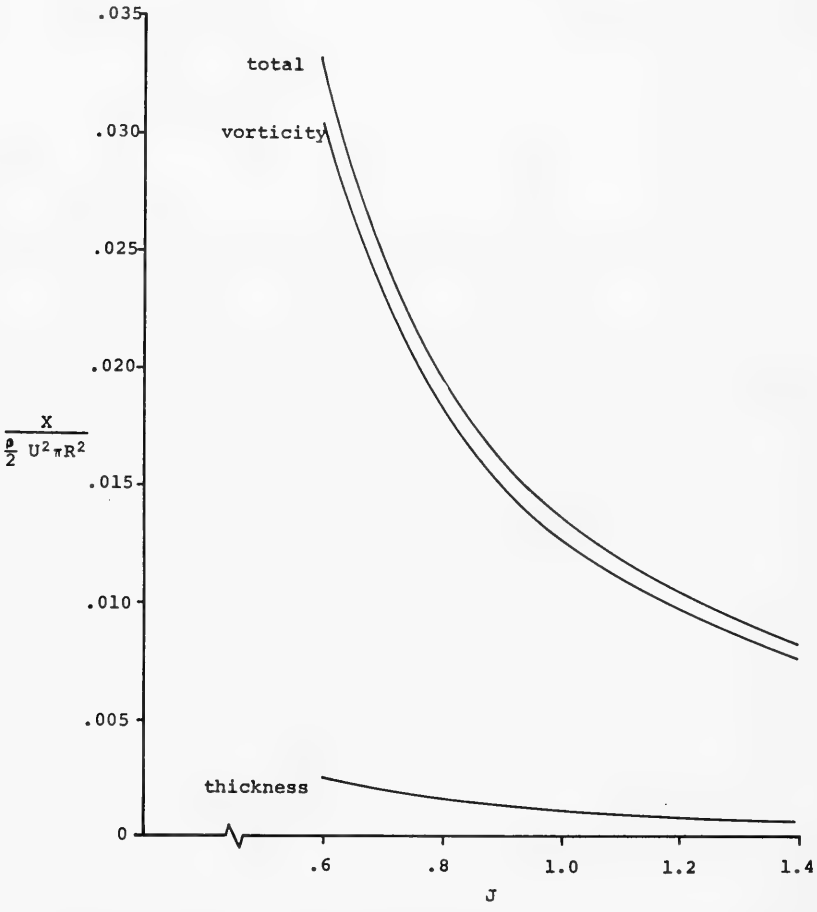

Fig. 42 - Axial force as a function of the advance ratio for a two-bladed propeller: β = 0.05, N = 2, $t_0/2c$ = 0.05

The present theory includes expressions for forces at higher harmonics of the blade rate. The variation of the second-harmonic axial force for a two-bladed propeller is shown in Fig. 45, and the values for the blade-rate axial force for a four-bladed propeller are shown in Fig. 46. The total force, as well

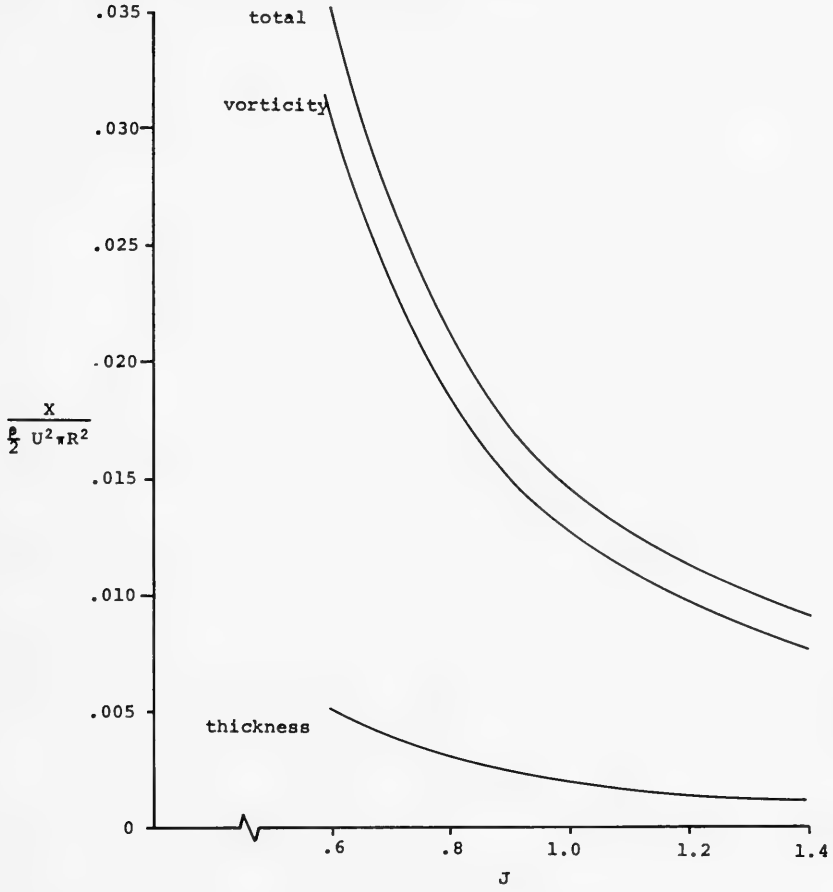

Fig. 43 - Axial force as a function of the advance ratio for a two-bladed propeller: $\beta = 0.05$, $N = 2$, $t_0/2c = 0.05$

as the constituent elements due to propeller vorticity and propeller thickness, are seen to be almost exactly the same for these two cases. An examination of the various theoretical expressions shows that the existence and magnitude of a force depend on the product mN. Thus the first-harmonic blade-rate axial force amplitude of a four-bladed propeller should be the same as the second-harmonic amplitude of a two-bladed propeller, with all other parameters being equal (same value of J, β, propeller thickness, etc.), and this equivalence is exhibited in Figs. 45 and 46.

The main contributors to the axial force are the terms denoted X_2 and X_4, where X_2 arises from the sources that describe the form of the appendage in a free stream and X_4 is due to the dipole that corrects for the axial induced flows. Computations were carried out to determine their separate magnitudes, as well

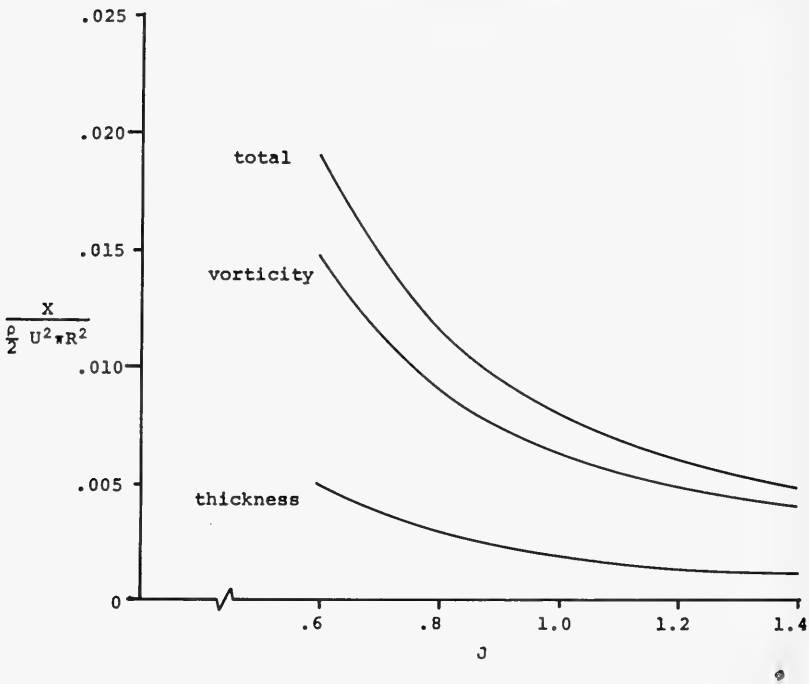

Fig. 44 - Axial force as a function of the advance ratio for a four-bladed propeller: β = 0.05, N = 4, $t_0/2c$ = 0.10

as the total axial force, for a number of conditions. Typical results are given in Fig. 47, where it is shown that the dipole term is the predominant term, and the same effect is true for the higher harmonics of the axial force. Thus it is essential to include this particular induced singularity effect to obtain the major component of the total axial force caused by a rotating propeller.

The theoretical expressions show that the forces decay exponentially with the distance between the propeller and the appendage, with this variation of the form e^{-mNx_0/R_e}, so that there is a faster decay with distance for the higher harmonics and more blades. The exponential variation with distance holds for both the terms due to the propeller vorticity and propeller thickness, so that the total also varies in this manner. The variation with distance between the propeller and appendage is shown by Figs. 48 and 49 for both the axial and transverse force blade-rate components for the particular case where J = 1.0. The variation for a larger number of blades, and for the higher harmonics, is in accordance with the exponential form indicated above. Since there is no dependence on the advance ratio J in the expression for variation with distance, the theory implies that the same decay rate will occur for all advance ratios.

Another theoretical result is the proportionality of the axial force to the appendage thickness. The computations illustrated in the figures are carried out for only one value of appendage thickness, and the axial force due to any other

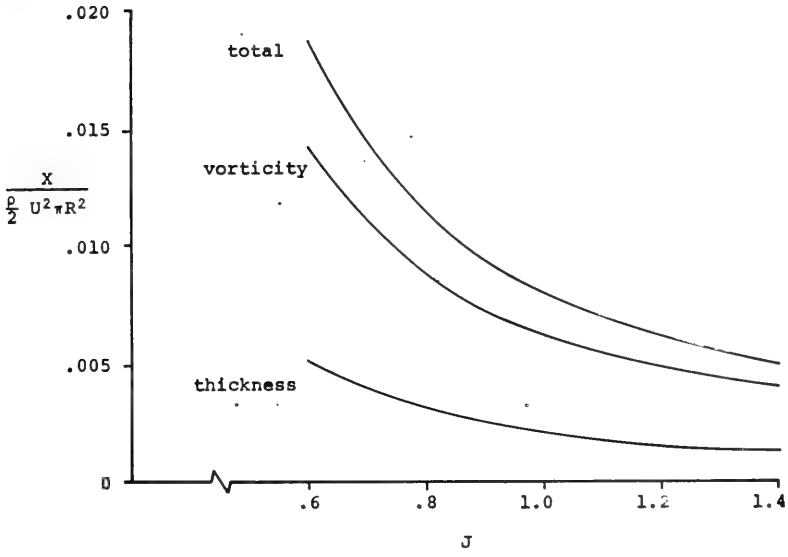

Fig. 45 - Second-harmonic axial force as a function of the advance ratio for a two-bladed propeller: $\beta = 0.05$, $N = 2$, $m = 2$

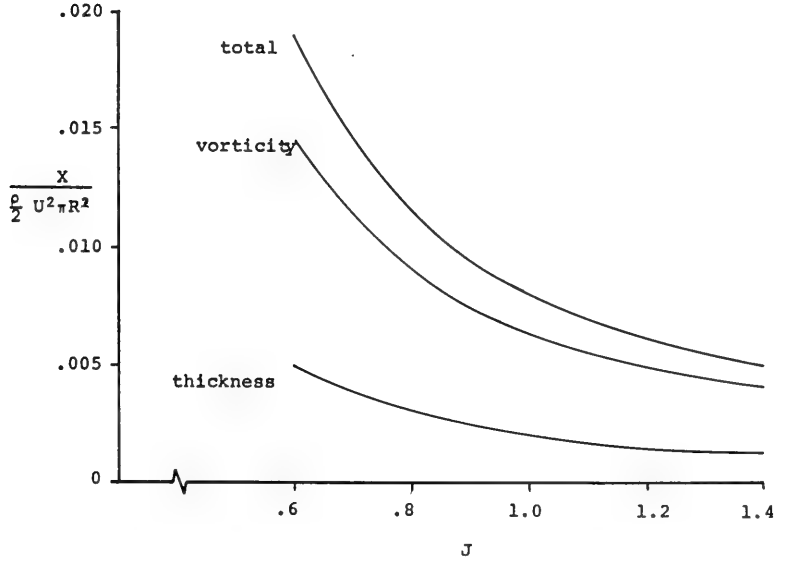

Fig. 46 - Blade-rate axial force as a function of the advance ratio for a four-bladed propeller: $\beta = 0.05$, $N = 4$, $m = 1$

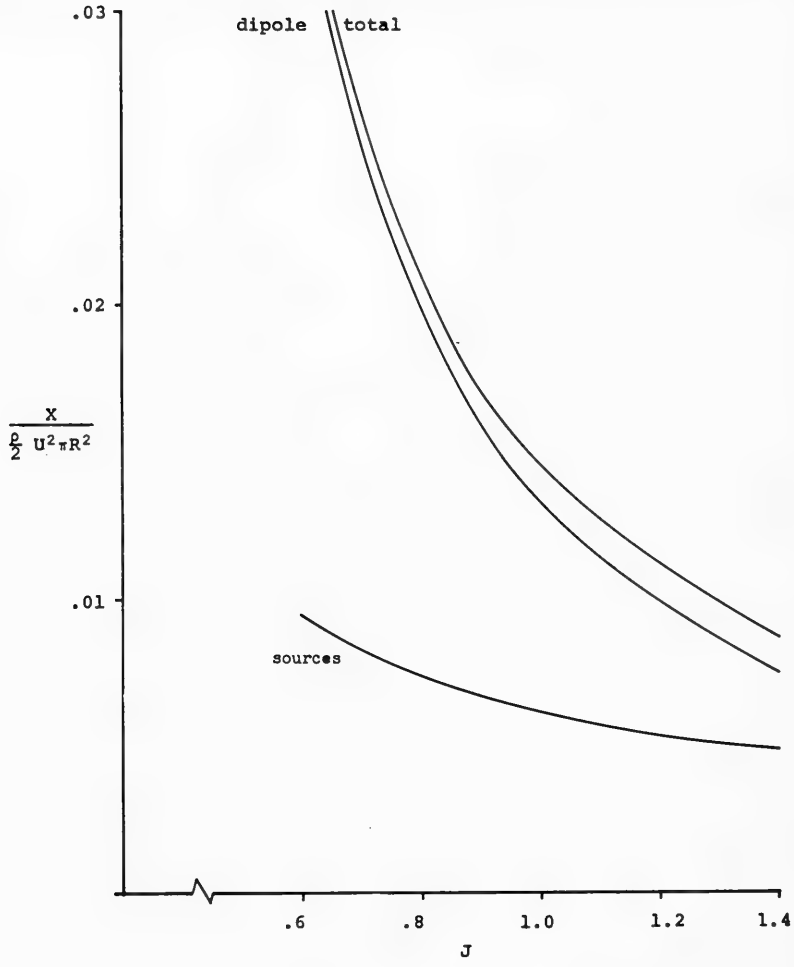

Fig. 47 - Axial force as a function of the advance ratio for a two-bladed propeller, showing the separate contributions from sources in the appendage and the correcting dipole: $\beta = 0.05$, N = 2

appendage thickness can be obtained by simple proportionality relations in accordance with this theory.

Another result indicated by the present theory is shown in Fig. 50, where the ratios of the induced blade-rate axial and transverse forces to the propeller thrust are plotted against the advance ratio J. This presentation shows that there is only a small dependence of these force ratios on the advance ratio, which implies a small influence of the propeller loading characteristics on the induced forces (when they are presented in this way). Since the variation with

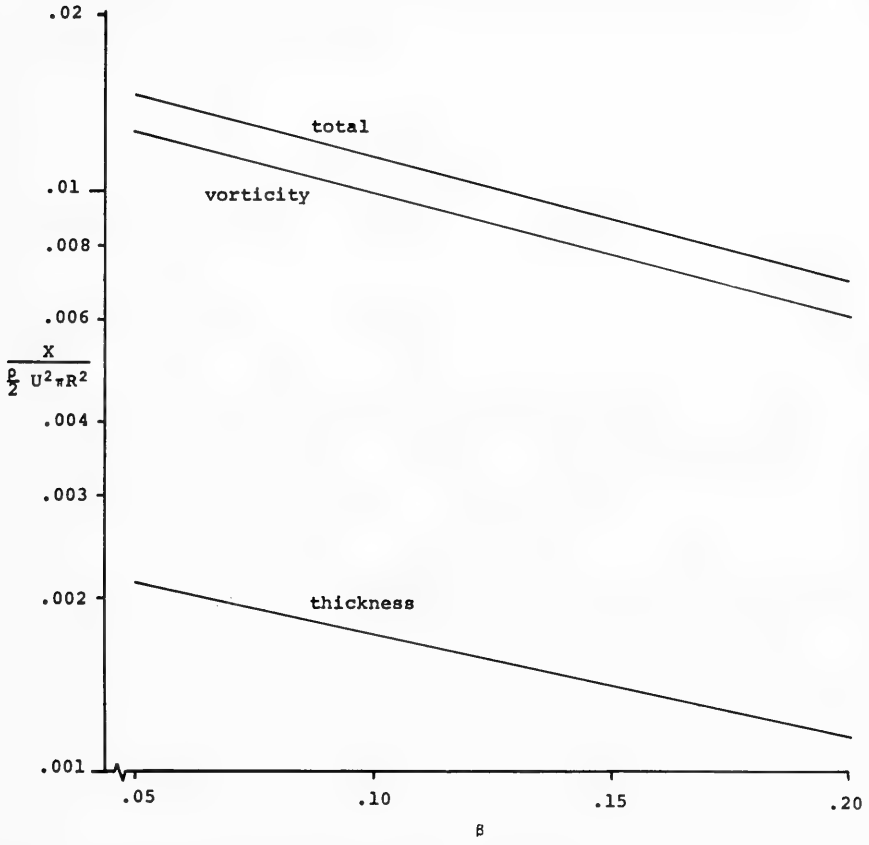

Fig. 48 - Blade-rate axial force as a function of the spacing distance for a two-bladed propeller: $J = 1.0$, $N = 2$, $m = 1$, $t_0/2c = 0.10$

spacing distance between the propeller and the appendage does not depend on J, the same results hold true for other spacings.

SUMMARY OF THEORETICAL RESULTS

The various conclusions obtained from the theory are summarized in the following.

1. The induced appendage forces occur only at blade-rate and higher harmonic frequencies.

2. The number of blades and whether they are odd or even determines the nature of the induced appendage forces; even-bladed propellers produce axial

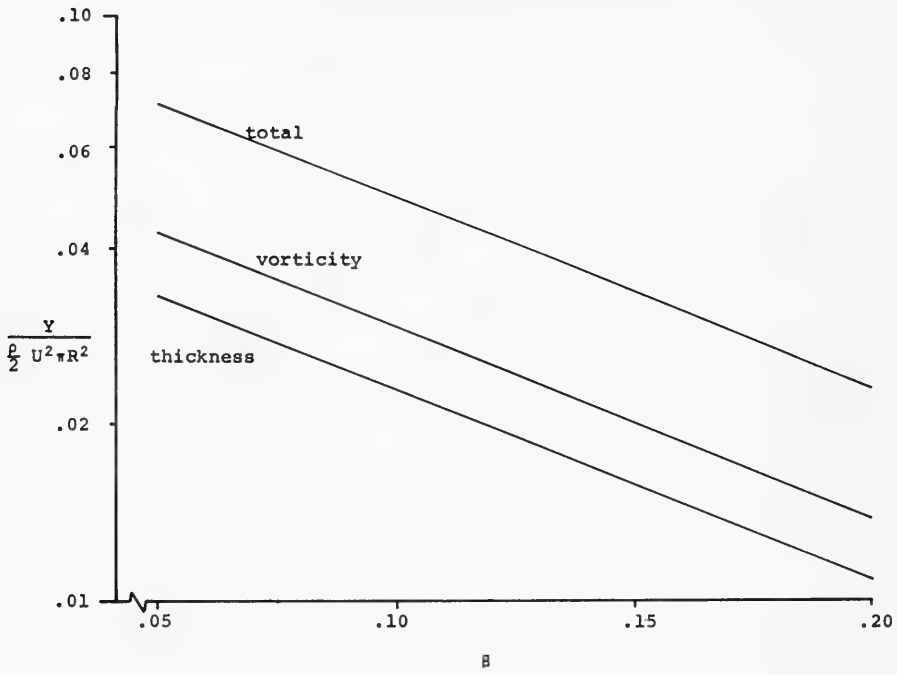

Fig. 49 - Blade-rate transverse force as a function of the spacing distance for a three-bladed propeller: J = 1.0, N = 3, m = 1, $t_0/2c$ = 0.10

forces and odd-bladed propellers produce transverse forces as the fundamental-blade-rate effects on a symmetrical appendage. The existence of a particular force depends upon whether the product (Nm) of the harmonic number and the number of blades is even or odd.

3. The influence of propeller thickness is significant in determining the total amplitude for both the transverse and axial appendage forces. The force amplitudes for a propeller with a particular number of blades are a function of the product Nm, so that higher-harmonic force amplitudes for a propeller will be the same as those for the blade-rate amplitude of a propeller with a larger number of blades but the same Nm.

4. The axial forces are proportional to the appendage thickness.

5. All induced forces on an upstream appendage decrease exponentially with an increase in propeller spacing, with a faster decay for the higher harmonics and for an increased number of blades. This decay with distance exhibits no dependence on the advance ratio, implying the same decay rate for all advance ratios.

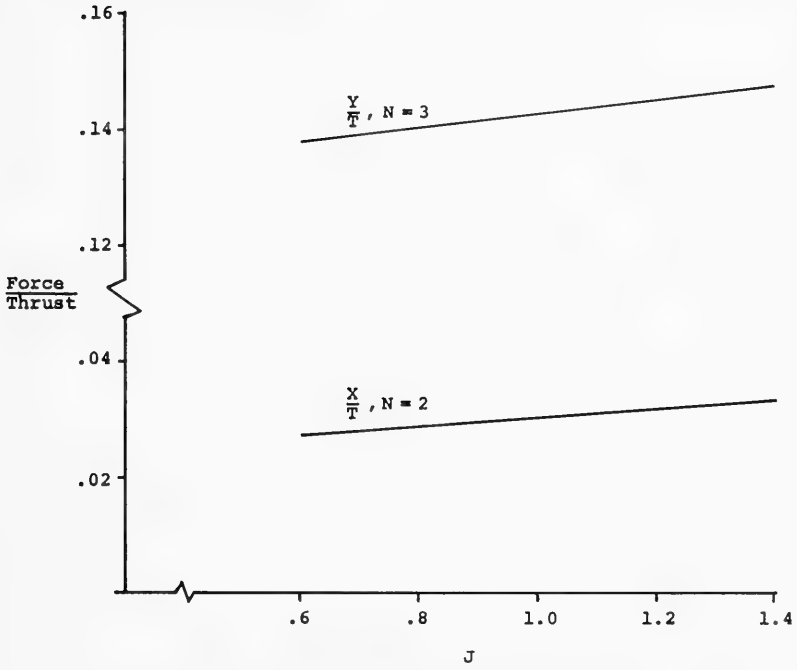

Fig. 50 - Ratios of the induced axial and transverse forces to the propeller thrust as a function of the advance ratio: $\beta = 0.05$

6. The induced forces at the higher harmonics are less than those at blade rate, for propellers with the same number of blades.

7. The induced forces at blade rate decrease as the number of blades is increased, for the same value of thrust coefficient.

8. The ratios of the induced appendage forces to the propeller thrust show only a small dependence on the advance ratio.

COMPARISON OF THEORY AND EXPERIMENT

With the availability of the experimental results that have been presented herein, comparisons can be made to determine if the experimental data verify the conclusions indicated by this theory. Only limited data from Ref. 10 were available at the inception of the theoretical study, for which certain limited comparisons could be obtained, and the additional work in Refs. 15 and 16 provided more data for comparison purposes. Since the values of propeller thickness, chord, loading, etc., were selected as representative for purposes of computation and illustration, no direct comparison can be made with the data in the

references cited above, which are also included in the present paper. However, comparison of trends and indicated behavior can be made and will be described.

The influence of propeller thickness on both the axial and transverse induced forces acting on an appendage is shown by the experimental results described earlier in this paper, and is illustrated by results such as those in Figs. 13 and 16. The theoretical verification of the lack of blade-rate axial forces for odd-bladed propellers, and the similar lack of transverse forces for even-bladed propellers, is shown in the experimental results cited earlier for the case of a symmetrically disposed appendage. Since the present theory is two-dimensional, the total force of a symmetrical appendage is proportional to the span of the appendage for a fixed propeller diameter. As a result the induced forces will vary linearly with the appendage span for a particular separation distance, and this behavior is verified, in a limited sense, by the data in Ref. 10. Thus, the agreement indicated for these particular characteristics supports the qualitative predictions of the theory.

The exponential decay with distance for the induced forces is indicated by the experimental results with the exception of data at large separations, where very small force magnitudes (with possible errors in measurement, noise effects, etc.) occur. Thus the exponential variation appears to be a plausible representation for the decay with increasing separation distance. Since no dependence on the advance ratio is indicated by this exponential form, the variation should be the same for all values of J and depend only on the number of blades. Although only limited data are available and precise comparison cannot be made, it appears that this result is plausible, as illustrated by the data in Figs. 24 and 28 for the range of significant thrust values.

The data in Ref. 10 consider the variation in axial force brought about by changing the appendage thickness, and it is shown there that the axial force is not linearly proportional to thickness. The present theory predicts proportional values, and a possible explanation for this disagreement is the influence of the wake of the appendage through which the propeller must operate. However no evaluation of this particular hypothetical influence can be obtained from the present theory, since wake effects and any interaction of the appendage in altering the propeller thrust characteristics have been neglected in the theoretical development. Further experimental and/or theoretical work will be necessary to determine the influence of this primarily viscous effect.

The theory shows that the ratios of the induced axial and transverse forces to the propeller thrust have only a small dependence on the advance ratio, as indicated by Fig. 50. Experimental results in Ref. 16, as illustrated in Fig. 51, indicate this lack of significant dependence of the force ratios upon the propeller loading, thereby supporting the theoretical contention. The data in Fig. 51 indicate this agreement in the range where significant thrust values occur; departure from this behavior occurs only in the range of higher J values.

While precise comparisons cannot be made because of the particular selected conditions for computation, it can be seen that the general magnitudes of the induced forces inferred by the theory are of the same order as the actual values experienced in the experiments. The spacing distance is defined in the

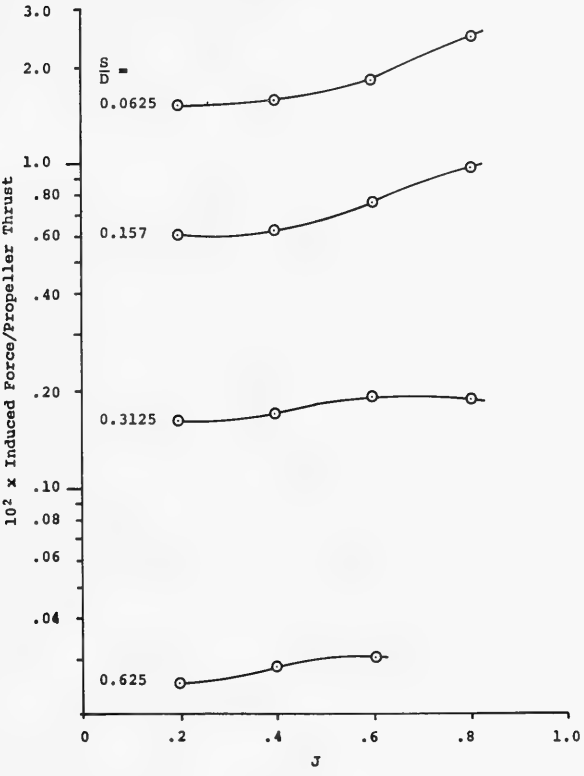

Fig. 51 - Blade-rate axial appendage forces as a function of the advance ratio and the spacing for a four-bladed propeller and a symmetrical appendage

theory by the parameter $\beta = 0.05$, corresponding to the spacing ratio $S/D = 0.02$, while $\beta = 0.10 \rightarrow S/D = 0.063$ and $\beta = 0.20 \rightarrow S/D = 0.107$, where this correspondence was evaluated at $J = 0.6$. The relation between the theoretical and experimental values can then be examined in terms of these particular distances, leading to the conclusion of good qualitative agreement.

A significant consequence of the theory is the dependence of the magnitude of a particular force component on the product of the number of blades N and the particular harmonic term m, so that the product Nm determines the nature of the force. The equivalence of the second-harmonic amplitude for a two-bladed propeller with the blade-rate term for a four-bladed propeller, as illustrated in Figs. 45 and 46, demonstrates this feature of the theory. This same effect occurs in the interpretation of the behavior of a single-bladed propeller, where examination of appropriate harmonics of the propeller shaft rate provides data for a multibladed propeller. The present theory was evaluated for conditions wherein the thrust coefficient given in Fig. 39 was constant for all the different

propeller configurations evaluated herein. Thus the ratio of the induced forces to the thrust of the propeller, under these conditions, would be expected to be the same for the particular case of the two-bladed and four-bladed propellers referred to. Similarly the theory would then produce the same values of the ratios of the forces to the propeller thrust for a single-bladed propeller, when examining the output at the higher harmonics, i.e., for $N = 1$ and $m =$ the corresponding harmonic number that will include the effect of the number of blades. Thus some indication of the reasons for the predictive capability of single-bladed propeller testing is provided by the present theory, although it is considered under the constraint of requiring constant thrust characteristics. While no precise proof of this technique is provided by the present theory for arbitrary conditions, and more conditions should be evaluated analytically with greater care in determining the actual thrust characteristics of propellers with different numbers of blades, there is indication that a theoretical basis does exist for the method of single-bladed propeller testing described in the experimental section.

As a result of the general agreement between the present theory and available experiments a number of possibilities exist for extending the present computations to other cases to obtain further fundamental information on this phenomenon of propeller-induced forces. The theoretical procedures can then be applied to a number of varied operating conditions and thus used to provide useful insight into the important factors that determine the blade-rate forces and their harmonics. The theoretical results will guide particular experimental programs that seek ways of reducing the vibratory input excitation to naval vessels from these propeller-induced effects.

CONCLUSIONS

The previously described experimental and theoretical studies have provided a number of significant results for the problem of propeller-induced forces on nearby appendages. The emphasis in this work has been devoted to appendages upstream of the propeller, and most of the conclusions obtained from this work are concerned with that particular arrangement. However certain consequences due to other geometric and/or hydrodynamic influences were found, and their features also provide signficant information.

Considering the case of appendages parallel to an oncoming stream and upstream of the propeller, the main conclusions derived from this study are the occurrence of a force in accordance with the number of propeller blades and whether that number is odd or even, the importance of propeller thickness in determining the magnitude of both transverse and axial appendage forces, and the nature of the decay with distance between the propeller and the appendage. All of these features have been illustrated by the experimental results, and the theoretical model also predicts the same effects.

An important experimental technique for this arrangement is the use of the single-bladed propeller to determine induced appendage forces in terms of the ratio of the induced force to the thrust of the tested propeller system, with predictions obtained for a multibladed propeller. The small dependence of the ratios of the induced appendage forces to the propeller thrust on the advance

ratio J, for the range of significant thrust values, allows a scaling of model results for estimation of full-scale characteristics. A theoretical basis for both the single-bladed experimental technique and the limited dependence on propeller loading (advance ratio) is given by the present theory, thereby providing basic correlation between theory and experiment.

The present investigations have also demonstrated a significant difference in the behavior of the forces measured on an appendage downstream of the propeller as compared with an upstream appendage, especially in regard to the decay of the forces with respect to increasing distance between the propeller and the appendage. Another difference exists between the case of major interest, an appendage parallel to the stream, and the case of an appendage at an angle relative to the stream. Definite differences in magnitude and behavior of the forces in regard to their variation with number of blades, effects of asymmetry, etc., are found when the appendage is at an angle of attack, whether the appendage is ahead of or behind the propeller.

The foregoing results indicate progress in understanding and predicting unsteady induced forces on appendages due to a propeller rotating nearby. Certain main features have been observed and correlated with theory, while other effects require further investigation. Some work involving wake effects is presently being studied, and those results as well as others that should be pursued in this area will provide the necessary information and guidelines for design application.

REFERENCES

1. Breslin, J.P., "The Unsteady Pressure Field Near a Propeller and the Nature of the Vibratory Forces Produced on an Adjacent Surface," Davidson Laboratory, Stevens Institute of Technology, Report 609, June 1956

2. Pinkus, O., Lurye, J.R., and Feit, D., "The Unsteady Forces Due to Propeller-Appendage Interaction," TRG, Inc., Report TRG-146-FR, Mar. 1962

3. Breslin, J.P., "Review and Extension of Theory for Near-Field Propeller-Induced Vibratory Effects," in "Fourth Symposium on Naval Hydrodynamics: Propulsion and Hydroeleasticity," Aug. 27-31, 1962, Office of Naval Research Report ACR-92

4. Pinkus, O., Lurye, J.R., and Karp, S., "Interaction Forces Between an Appendage and a Propeller," in Fourth Symposium on Naval Hydrodynamics, Propulsion and Hydroelasticity," Aug. 27-31, 1962, Office of Naval Research Report ACR-92

5. Kaplan, P., Feit, D., and Myers, M.K., "A Theoretical Study of Propeller-Excited Forces on Nearby Appendages," Oceanics, Inc., Report 67-40, June 1967

6. Lewis, F.M., "Vibratory Hydrodynamic Forces on Struts Located Forward of a Propeller," MIT DSR 5-7851, June 1960

7. Lewis, F.M., "Propeller-Vibration Forces," Trans. SNAME 71 (1963)

8. O'Brien, T.P., "Some Effects of Blade Thickness Variation on Model-Screw Performance," North-East Coast Institute of Engineers and Shipbuilders Trans. 73 (1957)

9. Gurney, G.B., "An Analysis of Force Measurements," Pennsylvania State Univ., Ordnance Research Laboratory Report TM 19.8841-24, Apr. 1963

10. Lehman, A.F., "An Experimental Investigation of Propeller-Appendage Interaction," Oceanics, Inc., Report 64-11, Jan. 1964

11. Lehman, A.F., "An Experimental Study of Propeller Induced Appendage Forces as Influenced by Appendage Attack Angle and Propeller Position," Oceanics, Inc., Report 68-44, Jan. 1968

12. Sugai, K., "On Vibratory Forces Induced on the Rudder Behind a Propeller," Eleventh International Towing Tank Conference, The Society of Naval Architects of Japan, Tokyo, Oct. 1966

13. Kemp, N.H., and Sears, W.R., "Aerodynamic Interference Between Moving Blade Rows," J. Aero. Sci. 20 (Sept. 1953)

14. Milne-Thomson, L.M., "Theoretical Hydrodynamics," third edition, MacMillan, New York, 1957

15. Lehman, A.F., "An Experimental Investigation of Propeller Blade Thickness and Appendage Asymmetry on Propeller-Appendage Interaction," Oceanics, Inc., Report 66-24, July 1966

16. Lehman, A.F., "Further Experimental Studies of Propeller Blade Thickness and Appendage Asymmetry Effects on Propeller-Appendage Interaction," Oceanics, Inc., Report 67-35, May 1967

* * *

DISCUSSION

R. Wereldsma
Netherlands Ship Model Basin
Wageningen, The Netherlands

The authors made an interesting investigation of propeller induced appendage forces, particularly interesting is the undulatory variation of the appendage

force with increasing propeller spacing. This is important for optimizing the rudder location.

Their statement that the forces are significant only at the blade rate and its harmonics is valid only for a noncavitation condition. When cavitation occurs, appreciable nondeterministic phenomena can be expected. Therefore these measurements should be extended to cavitation conditions to gain more knowledge about these effects.

* * *

DISCUSSION

Jerome H. Milgram
Massachusetts Institute of Technology
Cambridge, Massachusetts

Two effects related to this paper require further examination. The first is that the spatial rate of decay of a hydrodynamic disturbance due to a body should follow an inverse power law in the far field. The authors stress the prediction and observation of an exponential decay for their studies. As regards theoretical studies, exponential decay could be obtained for certain configurations of infinite cascades of hydrofoils. However, in interpreting such results for an application in which infinite cascades do not exist, an interpretation that leads to power-law decay would be correct. The authors interpretation of their experimental observations is not justified on the basis of the limited data available. It is easy to fit an exponential curve closely to a few data points. If more data were available, a more accurate fit to the spatial decay rate would be obtained by an inverse power law.

The second effect is that of force measurements on a foil spanning a tunnel of rectangular cross section. Although the geometry appears two-dimensional at first glance, the flow is not two-dimensional, due to the boundary layers on the side walls of the tunnel. These boundary layers reduce the lift on the foil and increase the drag on the foil. The change in lift is usually very small, but the induced drag due to the boundary layer has about the same magnitude as the friction drag of the foil.

* * *

DISCUSSION

J. P. Breslin
Davidson Laboratory, Stevens Institute of Technology
Hoboken, New York

Figure 51 reveals that the two-dimensional cascade representation of a propeller leads to forces on the appendage some 8 to 10 times that measured. The velocity and pressure fields of a propeller are roughly three-dimensional. Their blade frequency components are strongly three-dimensional, having very rapid decays in all directions. Thus it is not surprising that the two-dimensional theory provides gross overestimates in magnitude and errors in phase.

Mr. Lehman's data provides one of the first opportunities to make comparisons with a three-dimensional propeller-rudder interaction theory recently developed by Dr. Tsakonas and Miss Jacobs at the Stevens Institute of Technology. To obtain results for the experimental configuration it will be necessary to modify the computer program in a straightforward manner. Hopefully when support is found for such calculations, much closer agreement between measurement and theory may be expected. More importantly the character of the force decay with increase of axial clearance should be well predicted.

* * *

REPLY TO DISCUSSION

August F. Lehman and Paul Kaplan

We appreciate the interest in our work and the comments made. With regard to the comment by Dr. Wereldsma, we are definitely interested in the influence of cavitation on propeller-induced forces, although we did state that our conclusions were applicable only to the case where no cavitation occurred in the system. We recognize that fluctuating cavitation on a propeller will contain a broad spectrum of pressure disturbances, since such a force on the appendage will occur at frequencies other than those corresponding to the blade rate and its harmonics, but we still also expect to have large discernible blade rate force signals. The problem of the influence of a cavitating propeller is certainly one in which we have definite interest, and for which we can obtain measurements of induced forces by the same basic techniques described in our paper. Thus we would welcome the opportunity of extending our work to such conditions.

The comment by Dr. Milgram can be answered by recognizing that the mathematical model used in our work was based on an infinite cascade, and the exponential rate of spatial decay directly follows from the analysis, similar to the treatment of aerodynamic compressor blades in the work of Kemp and Sears.

This form manifested itself in nearly all the data obtained in an extensive series of tests, but it is possible to expect a power-law decay in an asymptotic sense for large spacing distances. In that case, at large distances, the magnitudes of the forces would be extremely small and it is not expected that any useful information could be obtained if such a power law was adhered to in the evaluation and interpretation of the results. The other comment by Dr. Milgram is concerned with the effects of boundary layers on the walls of the water tunnel and how they influence our experimental results. All of our data are the values of the amplitudes of oscillatory dynamic forces induced on the foil appendages by the action of a propeller. Boundary layer effects, as mentioned by Dr. Milgram, will influence only the steady lift and drag forces, which are of no concern in this study. It is not expected that the influence of the boundary layers on our water tunnel will affect the dynamic forces of concern in this program.

Dr. Breslin's comment concerning the magnitude of the theoretical forces, as compared to the experimental measured forces, must be examined in greater detail before assuming that the two-dimensional theory has no applicability to force prediction in the present case. The axial forces are predicted in a much closer fashion than the transverse forces, as illustrated in our figures. It is optimistic to expect the very simple blade element treatment for the propeller thrust, assuming an equivalent single vortex, lack of interference between blades, equivalent contributions of angle of attack and camber, etc., to provide a useful model of the disturbance strength provided by the propeller. Since the magnitude of the relative contribution of various components to the total force depends upon the strength of a single vortex derived from the simplified thrust representation, it can be seen that it is difficult to expect good agreement under those circumstances. A more sophisticated two-dimensional treatment of the propeller representation would be expected to lead to better agreement.

The use of our data as a means of comparison with the extensive theoretical work that has been carried out at the Davidson Laboratory and other organizations is an important aspect of our work. We certainly look forward to the results of a comparison with the theoretical work at the Davidson Laboratory so that a rational explanation of the variation of the forces with separation distance, especially for the rudder problem, will be available.

* * *

THE VIBRATORY OUTPUT OF CONTRAROTATING PROPELLERS

R. Wereldsma
Netherlands Ship Model Basin
Wageningen, The Netherlands

ABSTRACT

For high-powered ships unconventional propulsion arrangements such as contrarotating propellers have proved efficient. The fluctuating forces generated by this propeller combination were determined experimentally. The wake has a dominant influence on thrust as well as torque fluctuations of both propellers. The fluctuations, expressed as a percentage of their respective mean values, are comparable with the fluctuating output of single propellers. The lateral forces are considerably reduced. The thrust eccentricity shows a high-frequency disturbance introduced by the mutual blade encounter of the propellers.

Guidelines are given for the dynamic analysis of the axial and torsional vibrations of the shafting for two types of gearings in combination with a turbine engine: conventional and epicyclic gearing. For the epicyclic gearing it is expected that the frequency modulation, introduced by load variations due to ship motions and orbital water motions, is stronger than for a conventional gearing. For the high-frequency analysis a number of unknown coefficients describing the mutual propeller interaction have to be estimated to determine whether they are significant.

NOMENCLATURE

A = gear ratio

A_p = aft perpendicular

A_D = developed blade area

A_0 = disk area of propeller

B = gear ratio

CWL = construction waterline

D = disturbing torque

F = torque-rpm characteristic of propeller

F_p = forward perpendicular

I = moment of inertia

M = mass

P = pitch of propeller

Q = torque, torque of propeller

R = propeller radius

T = propeller thrust

Z = mechanical impedance

n = speed of rotation

x = axial vibratory motion of the propeller

z = blade number of the propeller

θ = angular position

φ = rotational vibratory motion of the propeller

Subscripts

A refers to aft propeller

F refers to forward propeller

T refers to turbine

1 refers to aft propeller shafting system

2 refers to forward propeller shafting system

Superscripts

G refers to gearing

INTRODUCTION

During the past decade much knowledge has been gained about the vibratory effects of ship propellers operating in the wake of a hull. Theoretical as well as experimental techniques have been developed for the study of propeller-generated vibrations.

From this experience it is possible to give indications about changes in the fluctuating forces to be expected due to changes in important parameters such as blade number and hull shape (1,2). Also the effect of propeller geometry has been studied, and guidelines for a favorable vibration level can be given in the design stage. All this information, however, refers to conventional single-screw propulsion systems and moderate power absorption.

Since the general line of ship development tends toward larger units with increased power, efforts have been made to overcome practical difficulties such as limited propeller diameter, which restricts the efficiency and maximum power absorption of single-screw ships. To maintain a favorable propeller efficiency and to prevent cavitation damage for these high-powered units, ducted propellers and contrarotating propellers are seriously considered and have proved to be beneficial (3,4).

For vibration analysis of these type of propulsion systems, however, it is unacceptable to extrapolate knowledge and insight about the dynamic aspects of conventional propellers. Therefore, instantaneous force measurements have been carried out on a set of contrarotating propellers operating behind a fast cargo liner. In this paper the results of this investigation are reported and introductory considerations on the dynamic analysis of "contrarotating-propeller-shaft-engine systems" are given.

THE SHIP AND PROPELLERS AND THE MEASURING TECHNIQUE

The combination of two contrarotating propellers has proved efficient when operating behind a fast cargo liner. The measurements were performed with a model of that ship type (scale 1:24). The body plan of the ship is given in Fig. 1. The particulars of the ship are as follows: the length at DWL is L_D = 160 m, the ratio of L_D to the molded breadth B is L_D/B = 7.13, the ratio of B to the draft T is B/T = 2.53, and displacement/L_DBT = 0.5879.

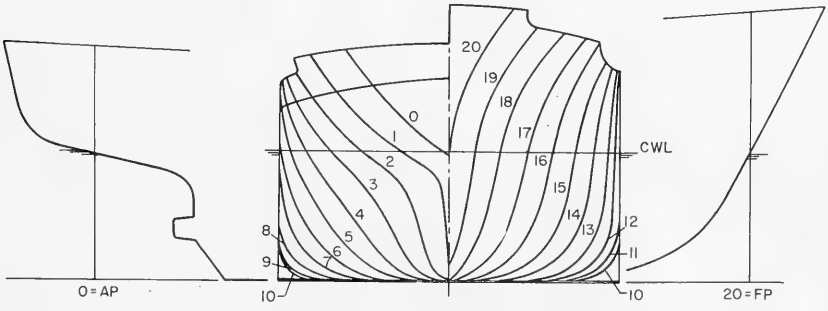

Fig. 1 - Body plan of the investigated ship

The choice of the propeller combination is based on efficiency considerations and on expected favorable vibrational behavior. A four-bladed propeller was chosen for the forward propeller. To avoid impinging of cavitating tip vortices of the forward propeller on the blades of the aft propeller the diameter of the aft propeller was reduced. This reduction is based on the expected slipstream contraction at the design condition of the system. It was decided to have a five-bladed aft propeller. The particulars of both propellers are given in Fig. 2.

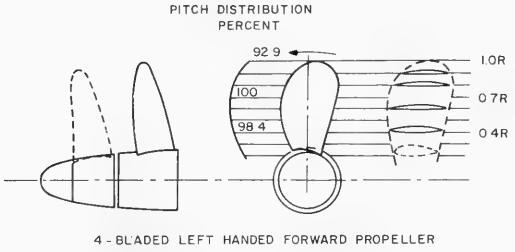

	FORWARD PROPELLER	AFT PROPELLER
DIA	5.22 m	4.88m
Z	4	5
$P_{0.7R}/D$	1.083	1.196
A_D/A_0	0.432	0.531

Fig. 2 - Plan of the pair of contrarotating propellers

This combination is expected to have a reduced vibratory output. The lateral effects, mainly generated by the five-bladed propeller, are expected to be reduced due to the more uniform inflow, being the wake of the forward propeller. Also the total axial excitation, mainly generated by the forward propeller, is expected to be relatively small, due to the distribution of the power between two propellers.

The measurements have been carried out for the following condition:

ship speed	20.78 knots,
propeller speed	121 rpm,

draft	8.839 m,
absorbed power:	16,000 SHP,
forward propeller	8,200 SHP,
aft propeller	7,800 SHP.

To measure the vibratory output, a special arrangement had to be made to use the existing measuring equipment. Because it was not possible to have the usual hollow-shaft combination for the measurements, the two propellers were driven by two synchronized separated systems. The forward propeller was driven by the normal dynamometer, installed in the wooden model of the ship under investigation. The aft propeller was driven by a dummy dynamometer. The dummy dynamometer was installed in an open-water boat mounted behind the ship model in such a way that both propellers were properly positioned relative to the hull. A stiff coupling shaft synchronized the combination. By exchanging the real dynamometer and the dummy dynamometer the vibratory outputs of both propellers were determined. Figure 3 shows the combination of the ship model and the open-water boat.

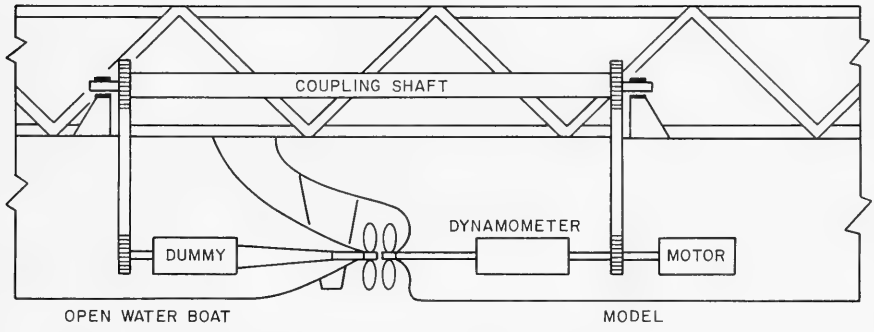

Fig. 3 - Schematic view of the ship model and open-water boat

Due to the vibratory interaction of the two propellers an exact synchronism was required to avoid a nonsynchronous signal that could not be reduced properly by the correlation equipment. Different positions of mutual blade encounters relative to the hull can be characterized by the angular positions of the mutual blade encounters. In Fig. 4 the angular positions and the sequence of the mutual blade encounters are shown for the case when the first blade encounter is vertically upward. The angular position of the nth encounter θ_n is then given by

$$\theta_n = \frac{9}{40} (n-1)\, 2\pi \text{ radians} .$$

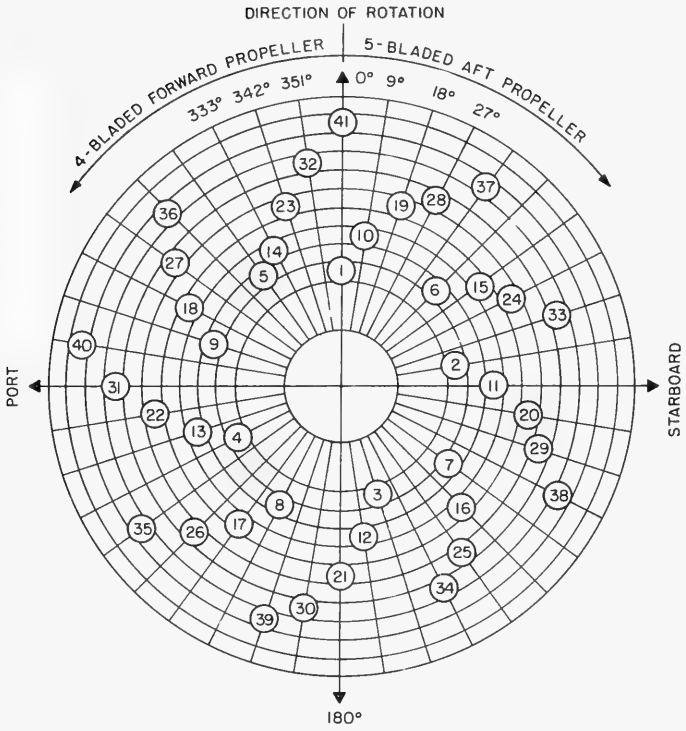

Fig. 4 - Angular position and numbered sequence of mutual blade encounters of a four-bladed and five-bladed contrarotating propeller combination with synchronous drive and equal rpm. The 1st, 21st, and 41st encounters are made by the same two blades.

The angular position of the 41st encounter coincides with the first encounter and occurs after one revolution of each propeller.

A completely different angular position of the two propellers occurs when the angular positions of the mutual blade encounters are between the radial lines shown in Fig. 4. That means

$$\theta_n = \frac{9}{40}(n-1)\,2\pi + \frac{2\pi}{80} \,. \qquad (1)$$

It is expected that this small difference of the relative angular position does not result in a significant change in the vibratory output of the combination.

Since the periodicity of the propeller combination equals one revolution due to the unequal blade numbers, the fundamental frequency of the signals equals the speed of rotation of the propellers (number of revolutions per second). The

frequencies below blade frequency being lower multiples of the rps can be defined as low-frequency interaction of both propellers. The frequencies of mutual blade encounter are high-frequency interactions.

RESULTS OF THE MEASUREMENTS

The frequencies generated by the propeller combination can be estimated as follows. The four-bladed propeller will generate blade frequencies and its multiples, i.e., 4 × rps, 8 × rps, etc. The five-bladed propeller will generate in a similar way 5 × rps, 10 × rps, etc. From previous experience it is reasonable to neglect the wake-generated components, having frequencies higher than 3 × blade frequency. Also very low frequencies from the low-frequency interaction can be expected as well as very high frequencies due to the mutual blade encounter.

The records of the thrust and torque fluctuations of the forward and the aft propeller are shown in Figs. 5 and 6. The peak-to-peak values of the thrust fluctuations of the four-bladed forward propeller amounts to 36% of the mean thrust. The peak-to-peak values of the torque fluctuations amounts to 28% of the mean torque. For the five-bladed propeller the peak-to-peak thrust fluctuations amount to approximately 23% of the mean thrust. The peak-to-peak torque variations equal 20% of the mean torque. These percentages for both propellers are not unusual for four-bladed and five-bladed propellers behind this ship type, which has sharp wake peaks.

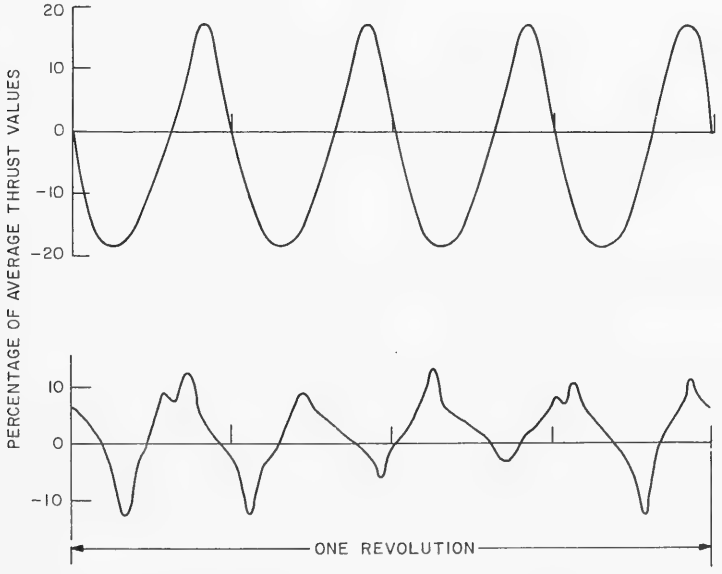

Fig. 5 - Recording of the thrust fluctuations of (top) the four-bladed forward propeller and (bottom) the five-bladed aft propeller

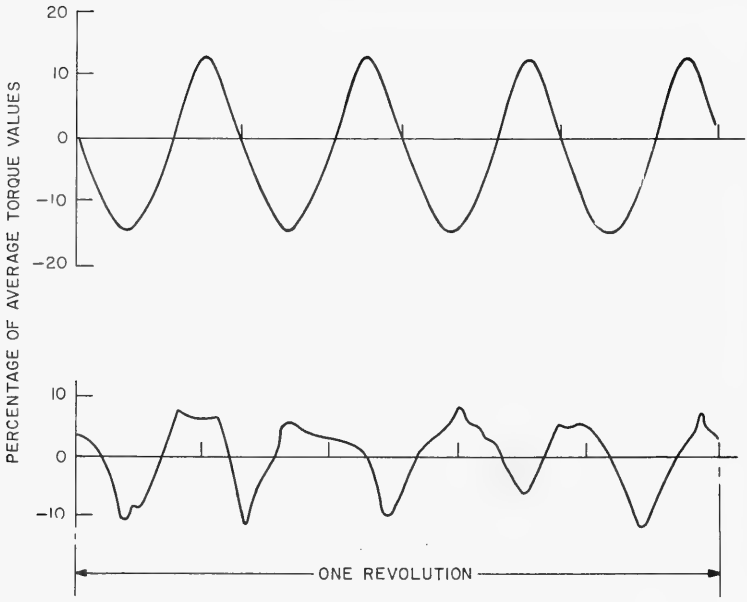

Fig. 6 - Recording of the torque fluctuations of (top) the four-bladed forward propeller and (bottom) the five-bladed aft propeller

The high frequencies of mutual blade encounter cannot be distinguished in the records. The influence of the wake dominates for the forward as well as aft propeller. For the five-bladed propeller a small irregularity has been recorded, probably caused by the interaction with the four-bladed propeller.

The records of the horizontal and vertical bending moments of the four-bladed and the five-bladed propeller are shown in Figs. 7 and 8. From these records the mutual blade encounter can be detected. Forty time per revolution a disturbance occurs. Due to the fact that one blade at a time encounters another, the effect in lateral direction is much greater than in axial direction.

The peak-to-peak variations at blade frequency of the vertical as well as the horizontal bending moment of the four-bladed propeller expressed as a percentage of the mean thrust times the propeller radius amounts to approximately 10%. On these blade frequency fluctuations a high-frequency disturbance due to the mutual blade encounter is superimposed. The peak to peak amplitude of this high frequency output equals from 1% to 2.5% of the mean thrust times the propeller radius. (These figures are corrected for dynamic amplification, as described in the next section.) For the five-bladed propeller the vertical bending moment fluctuations at blade frequency amount to 15% peak-to-peak and the horizontal bending moment to 10%. Superimposed on these blade frequency fluctuations there is an extra ripple of approximately 1 to 2.5% due to the blade encounter.

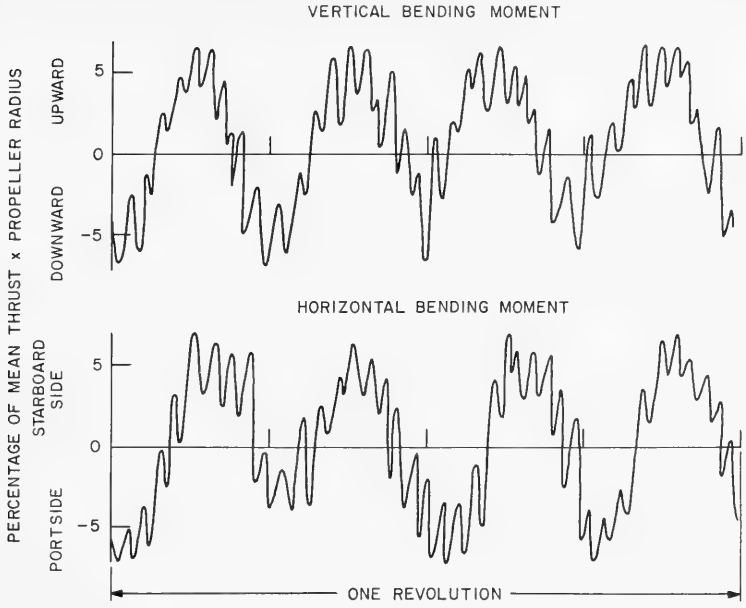

Fig. 7 - Recording of the vertical and horizontal bending moment variations of the four-bladed propeller

For a proper evaluation of the thrust eccentricity, the lateral forces have to be determined with an additional recording. It appears, however, that the fluctuating lateral forces for the forward as well as the aft propeller were not measurable in an accurate way. Apparently the amplitudes are reduced considerably and are hidden by the noise of the measuring system. For further evaluation of the results (determination of the thrust eccentricity) it is assumed that the fluctuations of the lateral forces are negligible for both propellers.

A vectorial summation of the horizontal and vertical thrust eccentricity for both propellers is presented in Fig. 9. To keep the figure readable only about 1/4 of a revolution is presented (blade encounters Nos. 1 through 10 (Fig. 4)). Besides the normal thrust eccentricity and its modulation due to the finite number of blades, again we can distinguish the high-frequency modulations due to the mutual blade encounter.

Additional measurements were conducted to measure the effect of a change of the angular positions of the mutual blade encounter. The new angular positions of mutual blade encounter follow from Eq. (1). The results of these tests are reviewed in Table 1 and compared with the results of the first tests. From this table it can be concluded that no significant differences occur for both conditions.

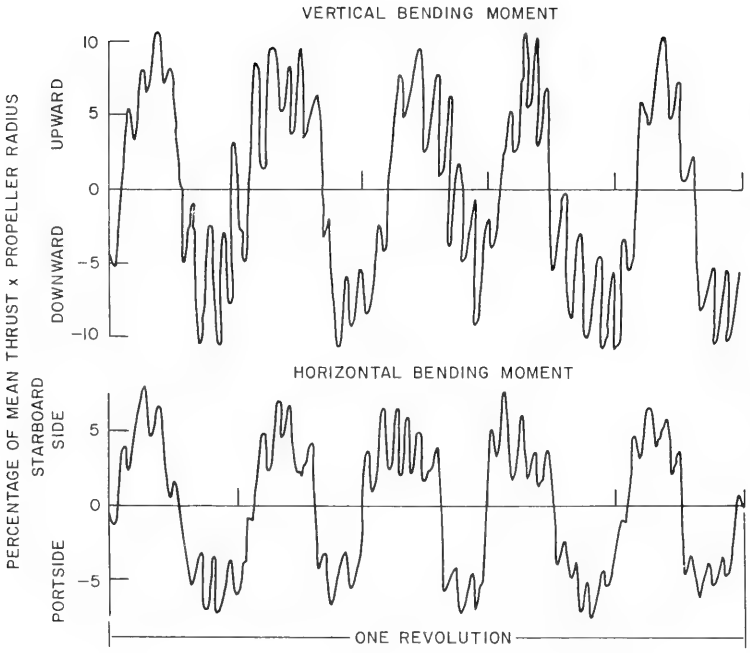

Fig. 8 - Recording of the horizontal and vertical bending moment variations of the five-bladed propeller

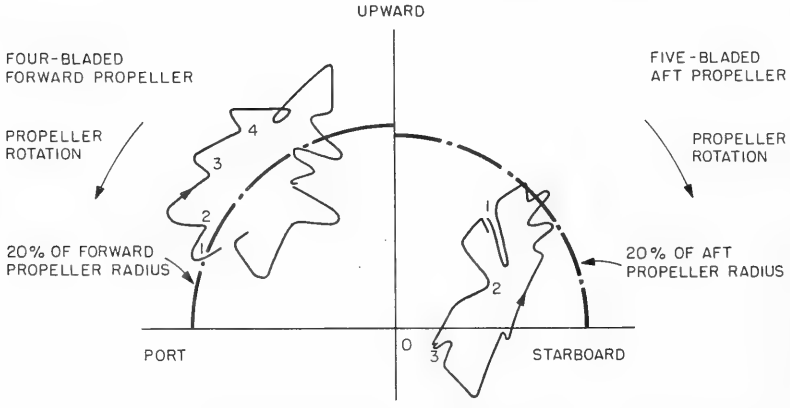

Fig. 9 - Instantaneous thrust eccentricity of (left) the four-bladed propeller and (right) the five-bladed propeller

Table 1
Comparison of Vibratory Propeller Forces of a Synchronized Pair of Contrarotating Propellers for Two Different Angular Positions

Angular Position of the First Blade Encounter (degrees)	Thrust (tons)			Torque (ton-m)			Horizontal Bending Moment, Positive in the Starboard Direction (ton-m)			Vertical Bending Moment, Positive Upward (ton-m)			Horizontal Transverse Force, Positive in the Starboard Direction (tons)	Vertical Transverse Force, Positive Upward (tons)
	Mean Value	Fluctuations		Mean Value	Fluctuations		Mean Value	Fluctuations		Mean Value	Fluctuations			
		Absolute	Percent		Absolute	Percent		Absolute	Percent		Absolute	Percent		
Forward Propeller														
0	56.66	20.2	36	43.50	13.4	27.7	-10.6	20.0	13.6	31.4	19.2	13.0	2.69	4.55
4.5	56.66	20.9	37	48.50	14.1	29.1	-10.6	17.9	12.2	32.9	27.1	18.4	2.55	4.77
Aft Propeller														
0	51.59	12.8	24.8	45.61	9.0	19.7	-11.7	18.4	14.6	-3.55	27.4	21.7	0.35	3.56
4.5	51.59	11.7	22.7	45.61	9.16	20.1	-11.3	22.9	18.2	-4.25	17.7	14.1	0.64	2.84

DISCUSSION OF RESULTS

Since the natural frequency of the measuring system amounts to approximately 600 Hz, the high frequency of blade encounter (approximately 400 Hz) cannot be recorded without unacceptable dynamic error.

The internal stiffness of the propeller influences the measurement significantly when the natural frequencies of the individual propeller blades come closer to the excitation frequency. Therefore the records of these high-frequency phenomena must be seen as indicative rather than accurate. From previous calculations (5) a dynamic amplification of the measuring system of 2.5 times can be estimated for this frequency. This figure must be taken into account for the evaluations of the records of Fig. 7 and 8. It can be concluded that the blade encounter excitation is small compared to the wake excitation. Also the low-frequency interaction is small compared to the blade frequency signals, as is illustrated in Figs. 5 through 8.

The unequal wake is still the dominating input for both propellers, and the interaction of both propellers is shown to be less significant. The relative amplitudes of excitation are comparable with those of single propellers. Since the total propulsive power is divided between the two propellers, the absolute value of the excitations is favorable. The sum of the absolute excitations of both propellers, in the axial direction as well as in the lateral direction, is shown to be a compromise between the behavior of a single four-bladed and five-bladed propeller having the same power absorption.

For this combination of a four-bladed and a five-bladed propeller it appears that the high-frequency interaction is negligible in the axial direction and detectable in the lateral direction. It can be expected that for a combination of propellers with an equal blade number this interaction is negligible in the lateral direction and relatively large in the axial direction, due to the simultaneous blade encounter of all the blades.

FURTHER STEPS FOR THE DYNAMIC ANALYSIS OF CONTRAROTATING PROPULSION SYSTEMS

To obtain insight into the vibratory behavior of a contrarotating propulsion system as installed aboard a ship, indications will be given about the dynamic analysis of the shafting. The analysis will be split in two parts: (a) the low-frequency behavior in the torsional direction, taking into account the modulation of the propeller speed, due to the fluctuating propeller loading caused by ship motions and orbital water motions, and (b) the high-frequency behavior in the torsional and axial directions, describing the propeller vibrations resulting from the fluctuating propeller loading due to the unequal ship's wake. For both types of analysis it is assumed that a turbine engine is installed.

Low-Frequency Behavior

For the analysis of the low-frequency behavior the internal elasticities of the shafting and gearing system are neglected.

It is interesting to compare the dynamics of a conventional gearing and an epicyclic gearing, since the latter may lead to a simple and less expensive installation (6).

Conventional Gearing — The turbine installation with a twin reduction gear and two contrarotating propellers is shown in Fig. 10. The block diagram shown in this figure describes the dynamics of the system. The two propellers are represented by a single inertia I_1 or I_2, each being the sum of the mechanical and hydrodynamical inertia effects. Additional feedback signals represent the static characteristics of the propellers. It is assumed that one torque-rpm relation exists, without mutual interactions of both propellers. This assumption is acceptable when the ship speed and the ratio between the speed of both propellers have a constant value. The following equation can be derived:

$$[I_T + A^2(I_1^G + I_2) + B^2(I_2^G + I_2)]\frac{dn_T}{dt} + [A^2F_1(n_1) + B^2F_2(n_2)]n_T = Q_T - AD_1 - BD_2 .$$

This equation gives the dynamic relation between the torque generated in the turbine, the propeller load fluctuations D_1 and D_2 generated by ship motions and orbital water motions, and the rotational speed of the engine and propellers.

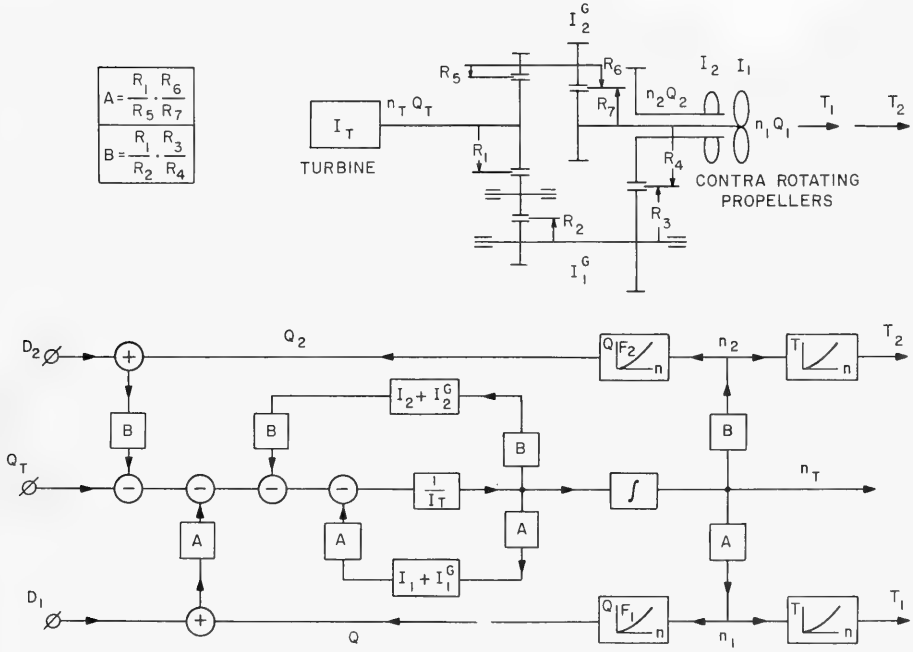

Fig. 10 - Low-frequency analysis of contrarotating propeller arrangement with conventional gearing

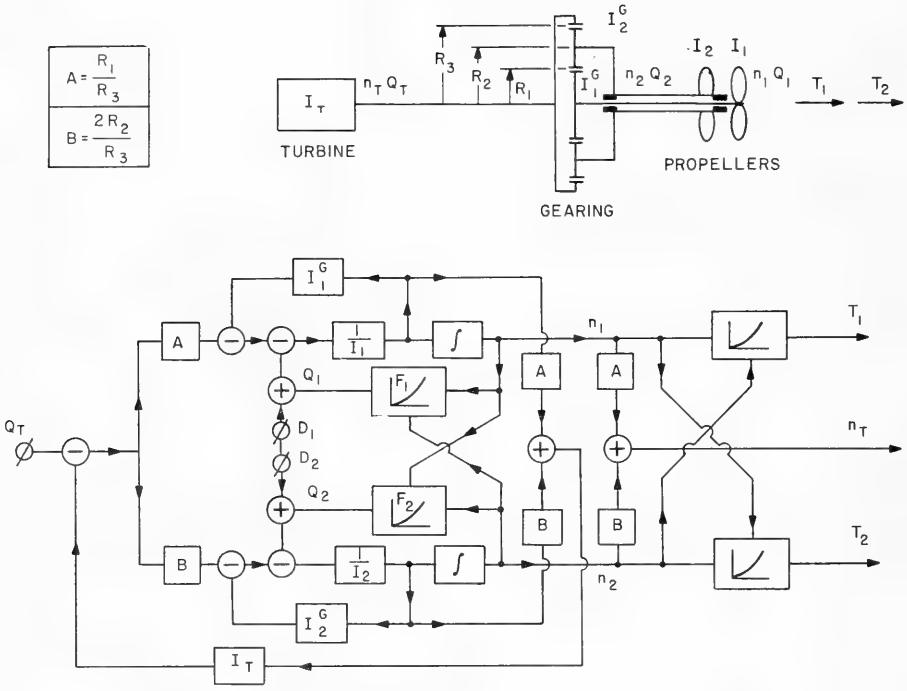

Fig. 11 - Low-frequency analysis of contrarotating propeller arrangement with epicyclic gearing

Epicyclic Gearing — The basic construction of an epicyclic gearing and its block diagram for the low-frequency behavior are shown in Fig. 11. The sum of both propeller rpm's multiplied by their specific gear ratios equals the turbine rpm under all conditions. The ratio between the rpm's of both propellers, however, is not predetermined, as in the case of a conventional gearing, but depends on the characteristics and absorbed torques of both propellers. Therefore, the propeller characteristics F_1 and F_2 are functions of n_1 and n_2, as shown in the diagram. The equations of motions of both propellers are

$$(I_1 + I_1^G + A^2 I_T)\frac{dn_1}{dt} + AB\, I_T \frac{dn_2}{dt} + F_1(n_1, n_2)\, n_1 = AQ_T - D_1 , \qquad (2)$$

$$(I_2 + I_2^G + B^2 I_T)\frac{dn_2}{dt} + AB\, I_T \frac{dn_1}{dt} + F_2(n_2, n_1)\, n_2 = BQ_T - D_2 . \qquad (3)$$

In addition,

$$A\, n_1 + B\, n_2 = n_T . \qquad (4)$$

Comparison of Both Systems — We assume that the turbine rpm is constant, which is reasonable from a practical viewpoint, due to the large moment of inertia of the turbine. For the conventional gearing it follows simply that also both propeller rpm's are constant. No excessive differences between single or contrarotating propeller turbine installations can be expected. For the epicyclic gearing, however, it follows from Eq. (2)

$$\frac{dn_2}{dt} = -\frac{A}{B}\frac{dn_1}{dt} \tag{5}$$

and, for small deviations from the nominal rpm,

$$n_2 = -\frac{A}{B} n_1 . \tag{6}$$

Combining Eqs. (2) through (6) we obtain for epicyclic gearing the following relations between the disturbances D_1 and D_2 and the speed of the propellers:

$$\left[I_1 + I_1^G + \left(\frac{A}{B}\right)^2 (I_2 + I_2^G)\right] \frac{dn_1}{dt} + \left[F_1(n_1,n_2) + \left(\frac{A}{B}\right)^2 F_2(n_2,n_1)\right] n_1 = -D_1 + \frac{A}{B} D_2 \tag{7a}$$

$$\left[\left(\frac{B}{A}\right)^2 (I_1 + I_1^G) + (I_2 + I_2^G)\right] \frac{dn_2}{dt} + \left[\left(\frac{B}{A}\right)^2 F_1(n_1,n_2) + F_2(n_2,n_1)\right] n_2 = D_2 + \frac{B}{A} D_1 . \tag{7b}$$

From these equations follows, in contrast to conventional gearing, that rpm fluctuations of both propellers will still occur, due to disturbances from seawaves, even if the turbine rpm is kept constant. Therefore, it is expected that, in comparison with the conventional gearing, larger deviations from the nominal rpm of both propellers will occur. From Eq. (7) follows additionally

$$B\left[(I_1 + I_1^G)\frac{dn_1}{dt} + F_1(n_1,n_2) n_1 + D_1\right] = A\left[(I_2 + I_2^G)\frac{dn_2}{dt} + F_2(n_2,n_1) n_2 + D_2\right] .$$

This formula shows that the low-frequency torque variations of both propellers are their mutual reactions. For the steady state conditions without disturbances D_1 and D_2,

$$B[F_1(n_1,n_2) n_1] = A[F_2(n_2,n_1) n_2] .$$

This relation also follows from the equilibrium conditions of the planet wheels of the gearing.

Remarks

1. In general it can be concluded that, in comparison with the conventional gearing, for the epicyclic gearing stronger frequency modulations of the fluctuating forces can be expected and as a consequence stronger requirements have to be fulfilled to avoid critical shaft vibrations.

2. For the epicyclic gearing a disturbed action of one of the two propellers will be mechanically reflected in the operation of the other propeller, as distinct from conventional gearing, where both propellers are driven independently.

3. The important advantage of epicyclic gearing, however, is its simple, less-expensive construction, well adapted to the shafting problems of contrarotating propellers.

High-Frequency Behavior

For an analysis of the axial and torsional vibrational behavior of the two propellers, four degrees of freedom have to be taken into consideration, namely, the axial and torsional vibratory motion of both propellers. Also the individual elasticities and inertias of both propeller shafts and gearing systems need to be taken into account (Fig. 12).

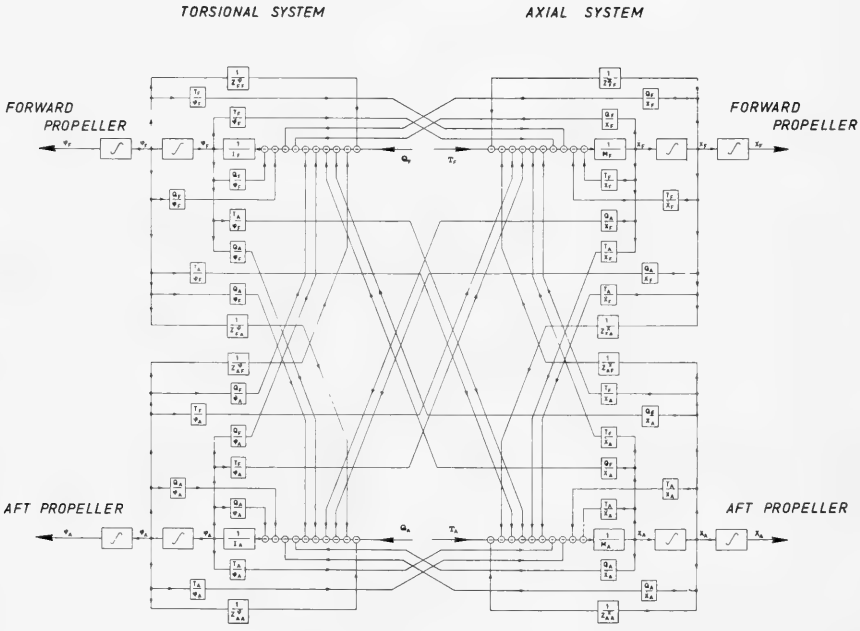

Fig. 12 - High-frequency analysis of a contrarotating propeller arrangement

The individual and mutual coupling effects of both propellers are shown in Fig. 12, and the corresponding equations of motion are given in Fig. 13. Four driving-point impedances can be distinguished, indicated by Z^{x}_{FF}, Z^{φ}_{FF}, Z^{x}_{AA}, and Z^{φ}_{AA}, representing the dynamic behavior of the shafting, gearing, and turbine. Four transfer impedances Z^{x}_{AF}, Z^{x}_{FA}, Z^{φ}_{AF}, and Z^{φ}_{FA}, representing the mechanical

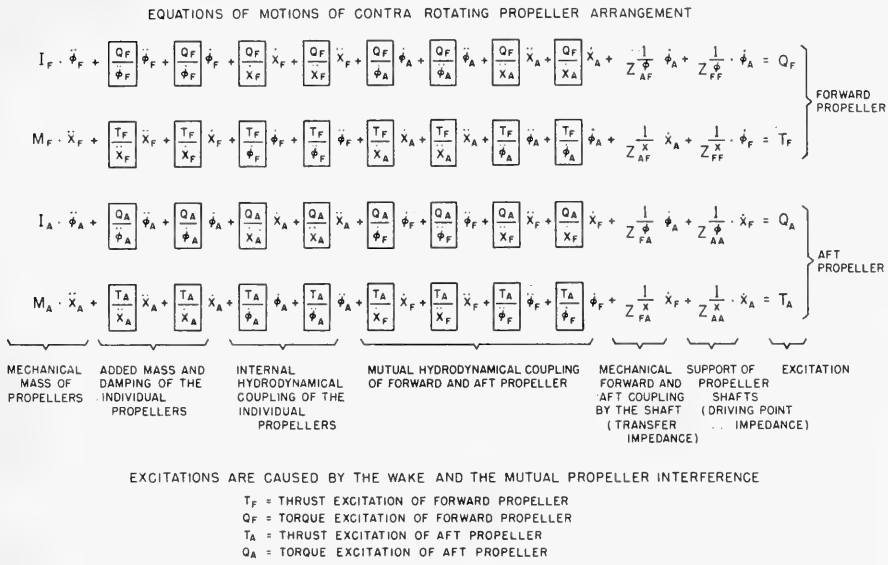

Fig. 13 - Equations of motions for high-frequency analysis of a contrarotating propeller arrangement

coupling of both propeller shafts and introduced by the gearing and turbine, are taken into account.

For both propellers the normal added mass, damping, and individual coupling coefficients can be distinguished. In addition 16 coefficients, representing the mutual hydrodynamic propeller interactions, are introduced. Further investigations are required to estimate the importance or negligibility of the coefficients, before calculations of the forced vibrations resulting from the experimentally determined excitations of the propellers can be started.

CONCLUSIONS

1. The unequal inflow of the ship's hull is still the dominating cause of the unsteadiness in the operation of both propellers of a set of contrarotating propellers. The fluctuating thrust and torque, expressed as a percentage of their mean values, amount to about the same value as for single-propeller arrangements. The lateral effects show a reduced amplitude. The absolute excitations reduced by the division of the total power over two propellers, may result in advantages.

2. The number of blades of both propellers is an essential parameter in the vibratory interaction problem. For the case of a four-bladed and five-bladed propeller the interaction can be divided into a low-frequency and a high-frequency range (respectively below blade frequency and above 3 times the blade frequency).

The low-frequency interaction is of reduced significance. The high-frequency interaction (mutual blade encounter) results in a lateral excitation. Critical conditions of shaft whirling and propeller blade resonance have to be avoided. For the case of a propeller combination with equal blade numbers the interaction is expected to be important in torsional and axial directions, having frequencies equal to the sum of the blade frequencies of both propellers and its multiples.

3. For a proper determination of the resulting vibratory propeller motions and accompanying forces the mutual hydrodynamic interaction coefficients of both propellers have to be estimated in addition to the normal hydrodynamic propeller coefficients. For the high-frequency excitations generated by the mutual blade encounter the internal elasticity of the propellers affects the hydrodynamic coefficients (propeller blade elasticity).

4. Compared with the conventional gearing of a turbine installation the epicyclic gearing will result in a broader range of excitation frequencies as a result of a stronger rpm modulation due to seawave disturbances.

REFERENCES

1. Report of the ITTC Propeller Committee 1966, Tokyo

2. Wereldsma, R., "Some Aspects of the Research on Propeller-Induced Vibrations," International Shipbuilding Progress, 1967

3. Manen, J.D.V., "The Choice of the Propeller," Marine Technology, New York, 1966

4. O'Brien, T.P., "Contra-Rotating Propellers for Large Tankers," International Marine Design Equipment, London, 1967

5. Wereldsma, R., "Dynamic Behaviour of Ship Propellers," Publication 255 of the Netherlands Ship Model Basin, 1965

6. Jung, I., "Swedish Marine Turbine and Gear Development," SNAME Symposium on Marine Power Plants, Philadelphia 1966

* * *

DISCUSSION

J. Strom-Tejsen
Naval Ship Research and Development Center
Washington, D.C.

Dr. Wereldsma's paper is most interesting and timely. According to his measured results, the fluctuating thrust and torque of either of the contrarotating propellers are roughly the same with or without the presence of the other propeller, since the dominating cause of propeller fluctuation forces is the spatial variation of the wake field behind a ship. I would like to ask Dr. Wereldsma whether such an interesting result also would be valid for the overlapping propeller arrangement?

Since the development of the overlapping propeller arrangement at the Naval Ship Research and Development Center a few years ago, several towing tanks in the United States and in Europe have conducted powering tests with this arrangement. However, to my knowledge no investigation of the vibratory forces similar to Dr. Wereldsma's has been conducted.

In most cases it has been anticipated that the two overlapping propellers would be driven with exactly the same rpm through the same gear box. By proper phase adjustment of the propellers, any of the three vibratory forces can be eliminated.

At the present time, however, consideration is being given to installation of an overlapped propeller arrangement, using two power plants independent of each other. This would, for instance, be the case when using two Diesel engines without any phasing of the two propellers. This configuration would, in principle, be very similar to the contrarotating propeller arrangement from a vibratory point of view. It would be of great interest if Dr. Wereldsma would extend his investigation to such an overlapping propeller arrangement.

* * *

REPLY TO DISCUSSION

R. Wereldsma

It is difficult to extrapolate from one extraordinary case to another, particularly in the field of propeller vibrations. If neglect of the interaction of both overlapping propellers is allowed, the relative vibratory shaft output will be comparable to that of the single screw. The bending moments in the individual blades, however, will be considerably increased because of the increased lower

harmonics encountered by the blades of propellers having eccentric location. Of course these statements have to be verified by measurements.

A couple of questions were also raised by Mr. J. B. Hadler of the Naval Ship Research and Development Center which I will comment on. We did not make measurements of the wake of the ship combined with the open-water boat. It was assumed that the effect of the open-water boat on the fluctuating propeller output was negligible. From the point of view of vibrations I do not expect considerable differences when the design is changed to a five-bladed forward propeller and a four-bladed aft propeller. Still the wake will have a dominant influence. These statements of course have to be confirmed by additional investigations.

* * *

EXPERIMENTAL DETERMINATION OF UNSTEADY PROPELLER FORCES

Marlin L. Miller
Naval Ship Research and Development Center
Washington, D. C.

ABSTRACT

Unsteady propeller forces were measured on propellers in a water tunnel in a nonuniform flow produced by wire screens. In order to make these measurements, dynamometers, instrumentation, and testing techniques had to be developed. The effect of blade width and skew of single propellers and the effect of changing the angle between the propellers of a tandem set on the unsteady forces were determined.

INTRODUCTION

One of the principal causes of vibration of ships is the unsteady hydrodynamic action of the propeller. Due to its periodic structure, the propeller can excite severe vibrations in the ship's structure in two ways. The nonuniform pressure field of the propeller rotating past nearby portions of the ship's hull will excite them into vibration and the propeller moving through the spatially nonuniform flow behind the ship will produce unsteady forces that are transmitted to the hull through the propeller shaft and bearings. Since it is usually more convenient to measure these forces separately, it is important that phase angles, as well as amplitudes, be considered, since the net excitation is the vector sum of these two types of forces. In this paper, only the experimental determination of the unsteady forces and moments and their phase angles that the propeller transmits through the shaft will be considered.

In order to be able to reduce these vibratory forces to a minimum, it is necessary to know how they are related to the propeller design parameters and the characteristics of the flow into the propeller. A number of theoretical methods for calculating these forces have been developed, ranging from simple quasi-steady methods based on open-water characteristics to highly sophisticated methods using three-dimensional unsteady propeller theory. Application of these theories produce widely differing results, and, in order to evaluate them, it is necessary to have experimental results for comparison. A number of propeller dynamometers for unsteady forces have been developed at NSRDC and elsewhere (1-8). The early ones measured only thrust, or thrust and torque, and had questionable dynamic characteristics or were limited to low frequencies. Some more recently developed dynamometers have highly improved characteristics, and some are able to measure the six components of the propeller forces and moments. At NSRDC three unsteady — propeller dynamometers are in current use. The MK-III dynamometer, for thrust only, uses a capacitance-type gage between the propeller and an inertial mass [8]. The "Bass" six-component dynamometer was developed for use with ship models in the towing

basin. It uses a six-component strain-gaged balance similar to the string-mounted balances used for wind-tunnel testing. Its design, construction, and calibration are described in detail in Ref. (8). A third dynamometer was developed for use with propellers in the 24-inch water tunnel. Its design, operation, and some typical results will be described here.

DESIGN OF THE WATER-TUNNEL DYNAMOMETER

In order to be useful over the range of test conditions used in the water tunnel, a dynamometer must have a relatively flat frequency response extending from the lowest shaft frequency to several times the highest propeller blade frequency. This range extends from about 10 Hz to at least 400 Hz. It should also be able to measure the steady components of the forces and moments. To simplify calibration, it would be desirable to have a flat response through the working range and extending continuously to zero. The system must be isolated from the vibrations of the tunnel and must be small enough so as not to cause too much disturbance of the tunnel flow. A preliminary examination of these requirements showed that it would be impossible to avoid some resonances well below the upper limit of the desired working range. For isolation, it was decided to mount the propeller and measuring elements on a stiff, heavy shaft rotating in soft mounted bearings and driven through a soft coupling. For each of the six components to be measured, at low frequencies, this propeller, balance, and shaft assembly can be considered as a one-degree-of-freedom system with the natural frequency being determined by the stiffness of the supports and coupling and the mass or moment of inertia of the system. Simple calculations showed that it would be possible to keep the axial, torsional, heaving, and pitching resonances below 8 Hz. In order to reduce the diameter without increasing the torsional frequency, it was decided to construct a substantial portion of this assembly of tungsten. A schematic of this system is shown in Fig. 1. It can be contained in a housing about 4 feet long with a maximum diameter of 7 inches tapering to 2 inches at the propeller.

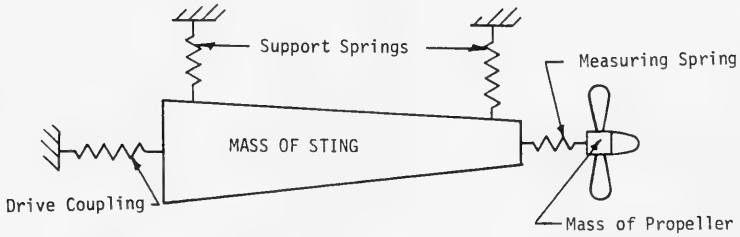

Fig. 1 - Simple schematic of two-degree-of-freedom system

The next problem was to make all the higher vibrational modes fall at frequencies above the operating range. The lowest of these is determined by the mass or moment of inertia of the propeller and the stiffness of the measuring

elements and to some extent, particularly for lateral modes, by the characteristics of the sting. Starting with a preliminary design, a number of progressive changes were made in the sting and balance until the system was free of resonances within the working range. In order to evaluate these design changes, the system was represented by lumped parameters as shown in Fig. 2. The values of these parameters were put into a computer program (9) to calculate the strains in the gaged elements for a unit force applied to the propeller. Very little trouble was experienced in obtaining a good frequency response for thrust and torque. However, 36 modifications had to be made and computed before an acceptable response was obtained for lateral excitation. The computed response of the final design for lateral excitation is shown in Fig. 3. The resonance at about 6 Hz is due to the sting and balance assembly vibrating as a rigid mass on the soft bearing supports. The next resonance, at 465 Hz, is the first bending mode. The region between these resonances is the useful working range. The response curves for thrust and torque were similar except that the useful range extended to higher frequencies for thrust.

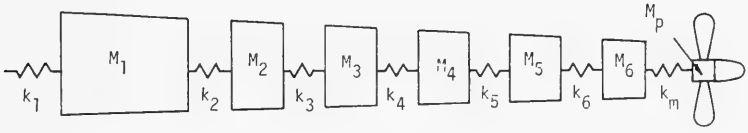

Fig. 2 - Lumped constant system

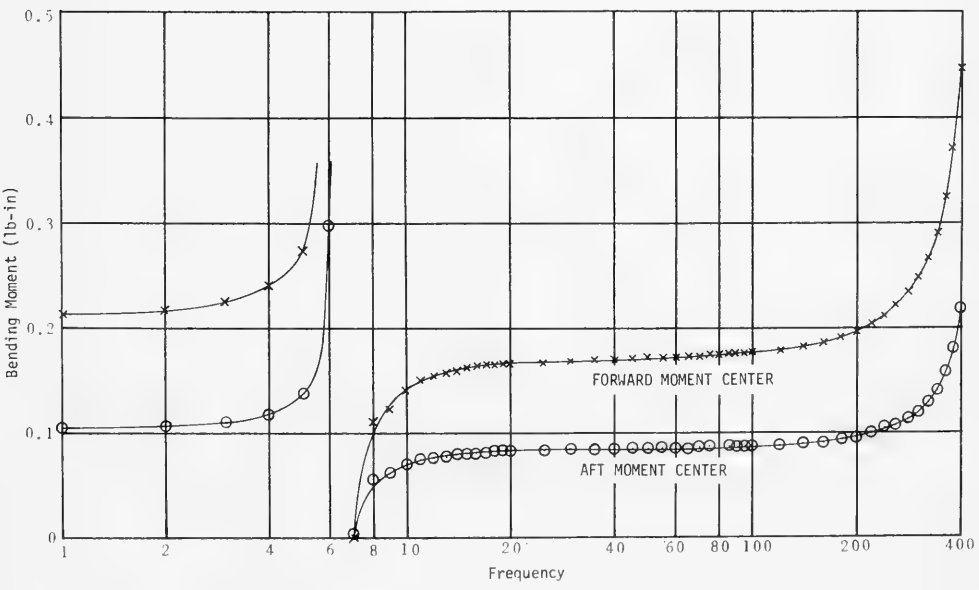

Fig. 3 - Computed response to lateral excitation

The final assembly is shown in Fig. 4. The flywheel, sting, and balance assembly weighs 160 pounds and is supported by rubber-mounted bearings on either side of the tungsten flywheel. This assembly is connected to the main tunnel drive shaft by a rubber coupling. Electrical signals from the balance are transmitted through a cable in the shaft and the unsteady signals are amplified before passing through the sliprings and brushes to the analysis and recording instrumentation.

A simplified drawing of the balance is shown in Fig. 5. It has the form of a steel cylinder with two thin-walled sections on which semiconductor strain gages are mounted. The balance fits a taper socket in the end of the sting and the propeller mounts on the taper on the other end. Figure 6 shows a developed diagram of the gaging and wiring diagrams of the bridges for measuring the six components of force and moment. After gaging, the balance was waterproofed using wax covered with a protective coating of soft epoxy. The completed balance is shown in the photograph of Fig. 7.

Although semiconductor gages are more temperature-sensitive than metallic gages, no difficulties have been experienced with them. This is probably due to the relatively small changes in temperature in the laboratory and the tunnel water and the four-arm bridge arrangement of the gages. There is a considerable drift in the zero readings, but this would only affect the steady measurements and they are made immediately after the bridges are balanced.

CALIBRATIONS

Both static and dynamic calibrations were made for the completed dynamometer. The static calibrations were made for the balance alone outside the tunnel. The dynamic calibrations were made with the balance on the flywheel and sting assembly and supported on rubber mounts. The calibrations were also repeated after installation in the tunnel and with the tunnel filled with water.

For the static calibrations, pure torque and thrust were applied in a conventional manner. Since the axial position of the side force determines its influence on the bending-moment reading and an applied pure moment produced some side force reading, it was necessary to obtain the side force and moment calibrations for the particular axial position that the center of the propeller would occupy. Instead of making individual calibrations for each propeller position, a general calibration was obtained by fitting a cylindrical sleeve to the propeller end of the balance and hanging weights at several measured axial locations. This is a method commonly used for calibrating sting-mounted wind-tunnel balances. This procedures yields enough information to determine side force and bending moment for any axial position of the propeller. The results of this calibration showed that, aside from the effect of side forces on the bending-moment readings inherent in this type of balance design, the only significant interactions were a small effect of torque on the thrust readings and some effect of bending moment on the output of the side-force gages in the same plane.

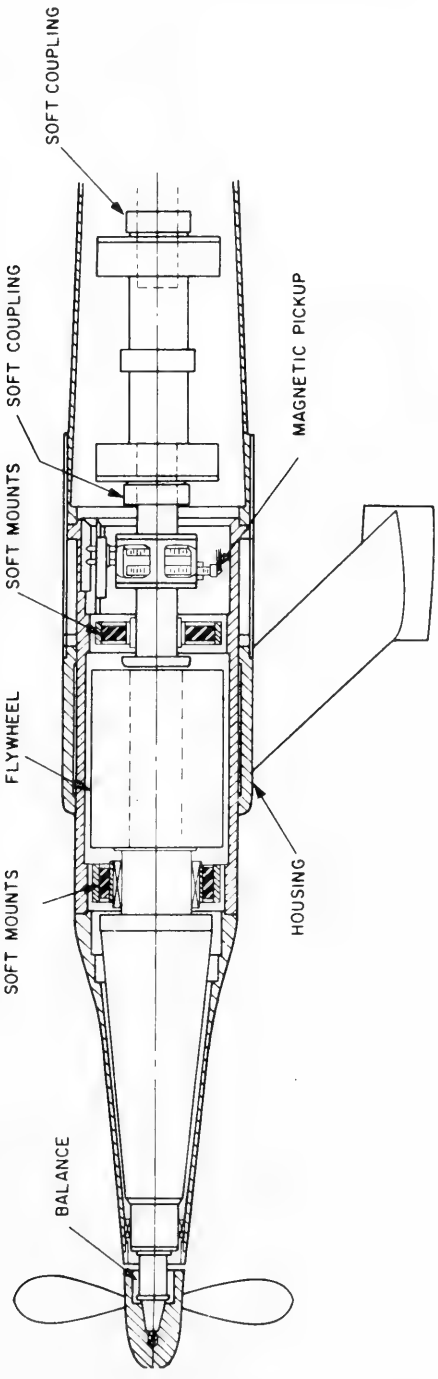

Fig. 4 - Six-component propeller dynamometer assembly

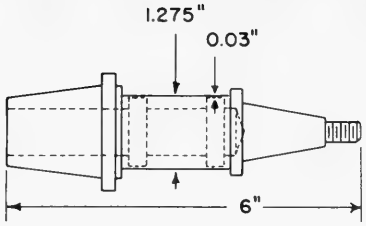

Fig. 5 - Simplified drawing of balance

Dynamic forces and moments were applied to the assembled system with electrodynamic shakers and measured with piezoelectric force gages. The gages were attached to a metal block on the end of the balance in positions determined by the force or moment to be applied. The force was transmitted to the gage through a thin rod in order to avoid any lateral excitation which had been found to affect the calibration of the force gages. Care had to be taken to distinguish resonances in the driving rod from those of the dynamometer. Driving-rod resonances were eliminated by changing its length or by clamping weights to the rod. Preliminary calibrations were made in air, but after it was found that the shakers would operate in water and the force gages were waterproofed, the final calibrations were made with the tunnel filled with water. The results are shown in Figs. 8-11. Figure 8 includes a calibration made in air, which shows very little difference from the one made in water. The calibrations showed good repeatability except for the horizontal bending moment, where three separate calibrations showed considerable spread at the lower frequencies, although the side-force calibrations obtained with the same loading showed excellent agreement. These frequency response curves are in good agreement with the theoretical curves that were computed for the final design, except for the small resonances in bending moment and side force at approximately 230 Hz. The cause of these resonances has not been determined, and attempts to eliminate them have been unsuccessful. The outputs shown in these figures are in relative units. The values used for reducing the test data were derived from these curves at blade frequency. The calibration was put into the computer program in the form of a 6x6 matrix. When the instantaneous readings in millivolts of the six channels are multiplied by this matrix, the thrust, torque, side forces, and bending moments are obtained in pounds or pound-feet.

A typical calibration for one propeller position follows as a coefficient matrix of a set of equations giving the forces and moments as functions of the millivolt output of the six strain-gage bridges:

$$T = 1.75\, e_t + 0.029\, e_q + 0 + 0 + 0 + 0,$$

$$Q = 0 + 0.076\, e_q + 0 + 0 + 0 + 0,$$

$$F_1 = 0 + 0 - 1.96\, e_{f_1} + 0.137\, e_{m_1} + 0 + 0,$$

$$M_1 = 0 + 0 + 0.072\, e_{f_1} + 0.086\, e_{m_1} + 0 + 0,$$

$$F_2 = 0 + 0 + 0 + 0 - 1.89\, e_{f_2} + 0.098\, e_{m_2},$$

$$M_2 = 0 + 0 + 0 + 0 - 0.069\, e_{f_2} - 0.085\, e_{m_2}.$$

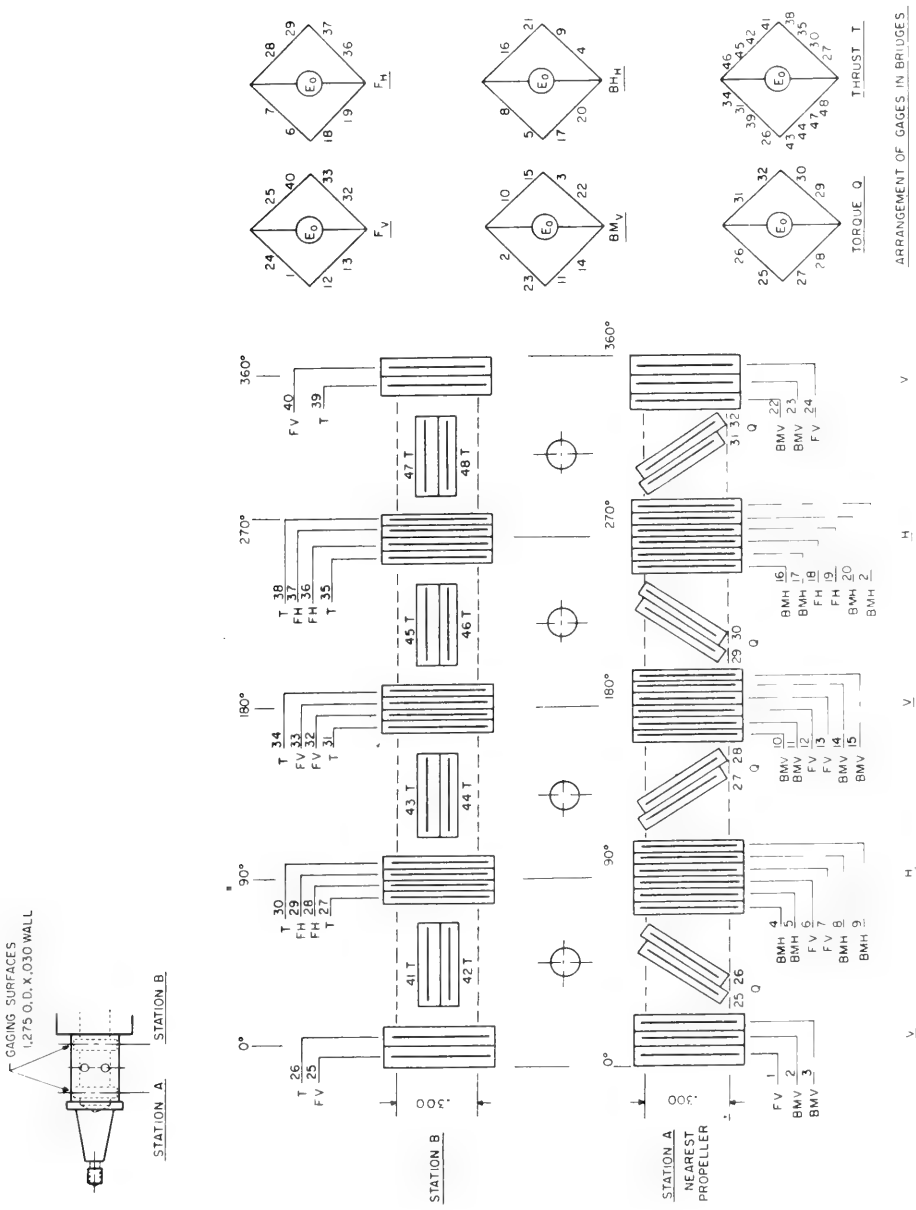

Fig. 6 - Developed diagram of gaging

The zero terms in the above equations represent interactions that were not measurable or were too small to be significant. Only the (T, e_q), (M_1, e_{f_1}), and the (M_2, e_{f_2}) terms are due to inaccuracies in the balance. The (F_1, e_{m_1}) and (F_2, e_{m_2}) terms are inherent to the design and due to the fact that the center of the propeller is displaced axially from the moment center of the balance. The remaining terms, on the diagonal, are of course the principal responses of the balance to the six components.

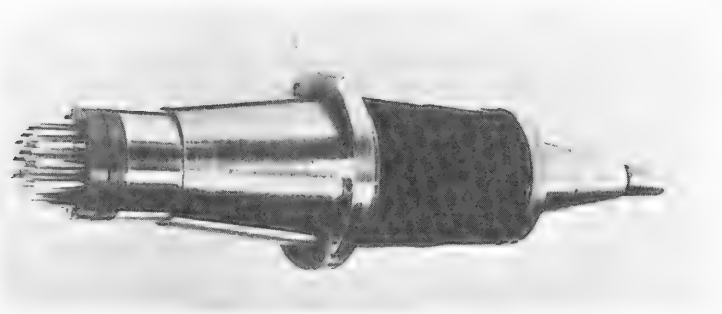

Fig. 7 - Six-component balance

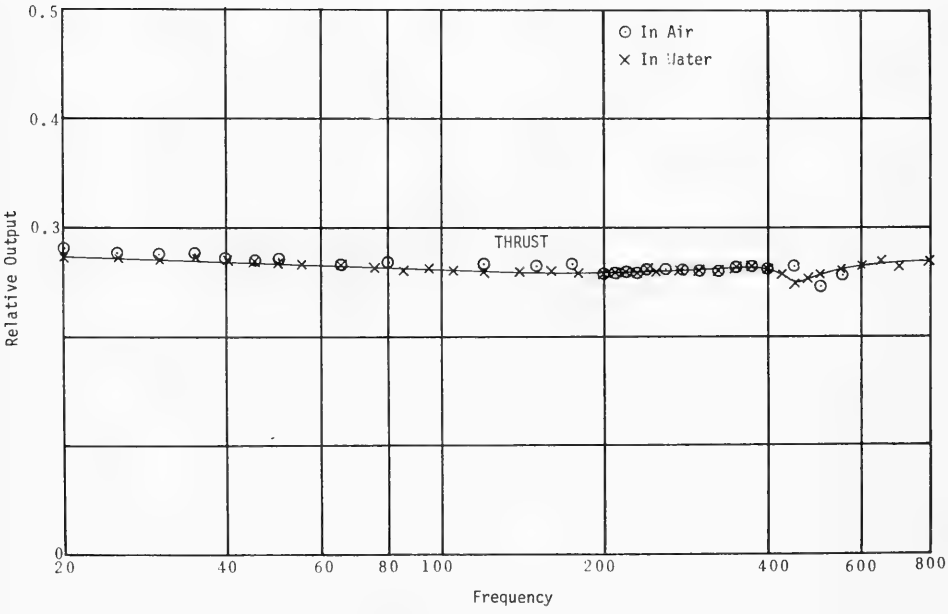

Fig. 8 - Dynamic calibration of thrust

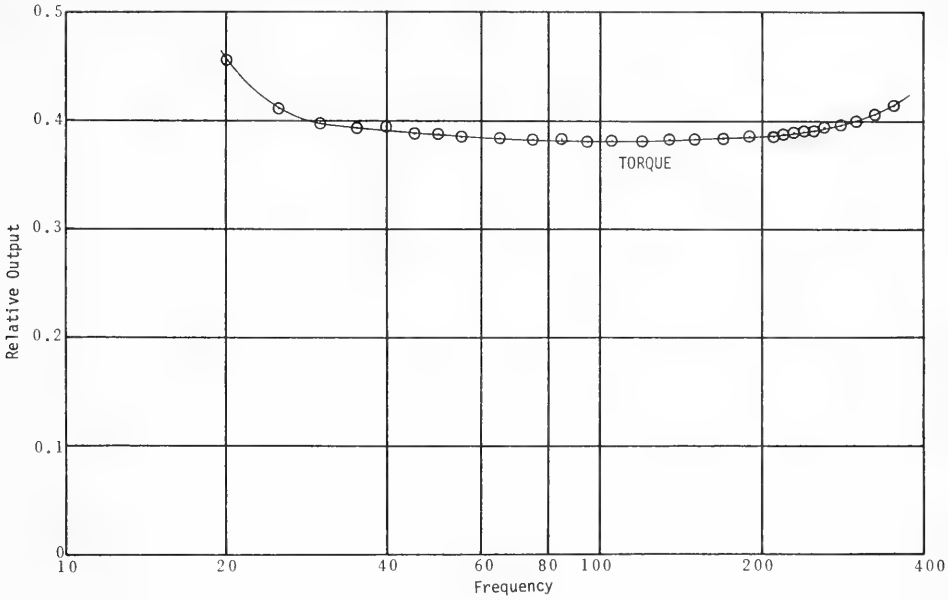

Fig. 9 - Dynamic calibration of torque

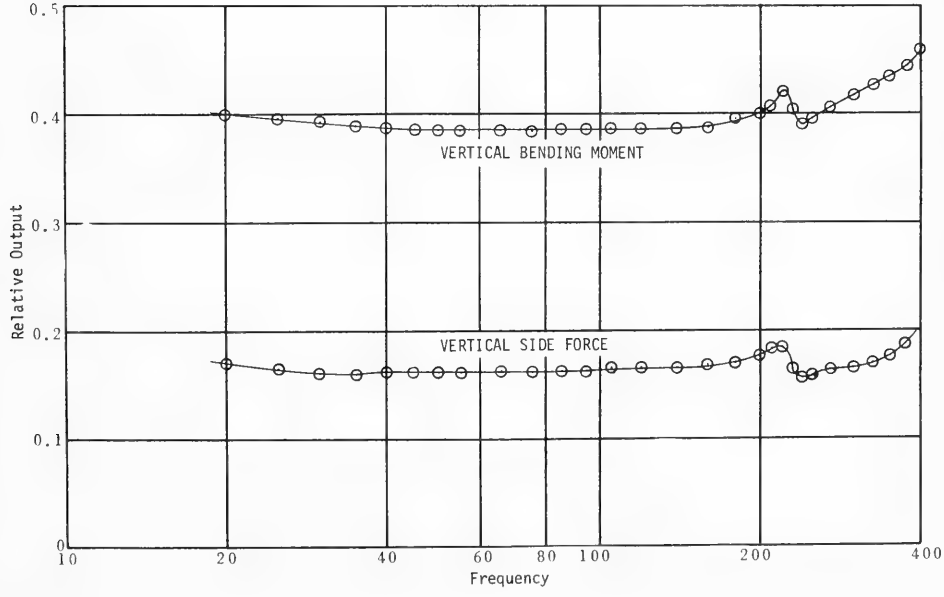

Fig. 10 - Dynamic calibration of vertical side force and bending moment

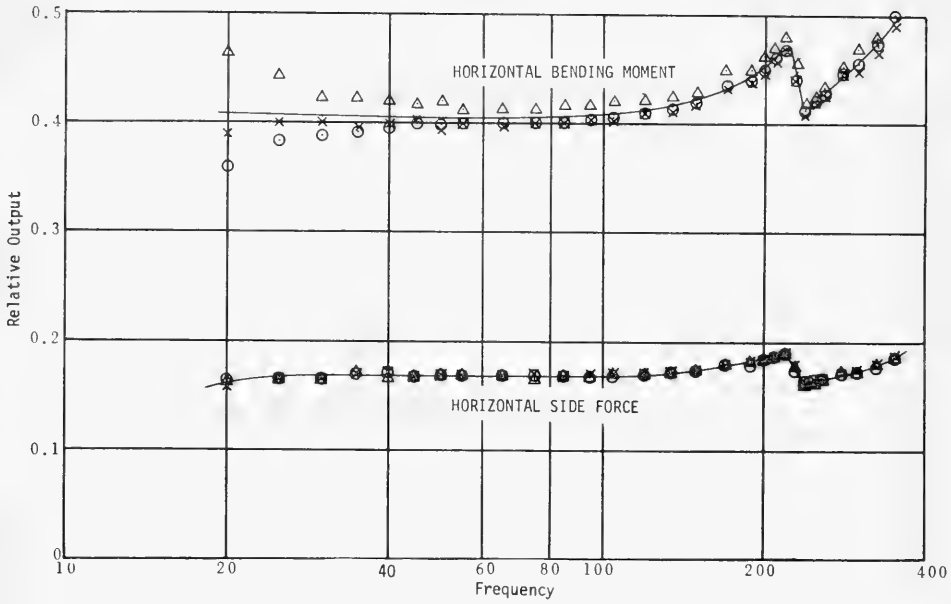

Fig. 11 - Dynamic calibration of horizontal side force and bending moment

The overall accuracy of the system is approximately ±5% for blade frequency and harmonics up to about 200 Hz when values from the calibration curves at blade frequency are used in the calibration matrix. Thrust measurements will retain this accuracy up to 600 Hz and torque measurements can be used to 400 Hz with corrections. Side forces and bending moments are limited to 200 Hz, due to the resonance at 230 Hz.

INSTRUMENTATION

The instrumentation was designed for both obtaining a record on magnetic tape and for making an on-the-spot analysis of the signals directly from the dynamometer during the tests.

Figure 12 shows a block diagram of the system. Power is supplied to the thrust, torque, side-force, and bending-moment strain-gage bridges by four separate power supplies. These supplies are adjustable between 5 and 24 V, and the excitation for each channel is set to a value that will produce a strong signal but will not overload the amplifiers. The output of the gages goes directly through the sliprings and brushes to zero balancing circuits and then to a dc microvoltmeter for measuring the steady components of the propeller forces. The signals also go to ac amplifiers contained in the drive shaft and then through sliprings and brushes to ac recording and analysis instrumentation. The dc output circuit is also used to introduce a measured ac calibration signal to the output of the strain-gage bridges in order to measure the gain of the ac system.

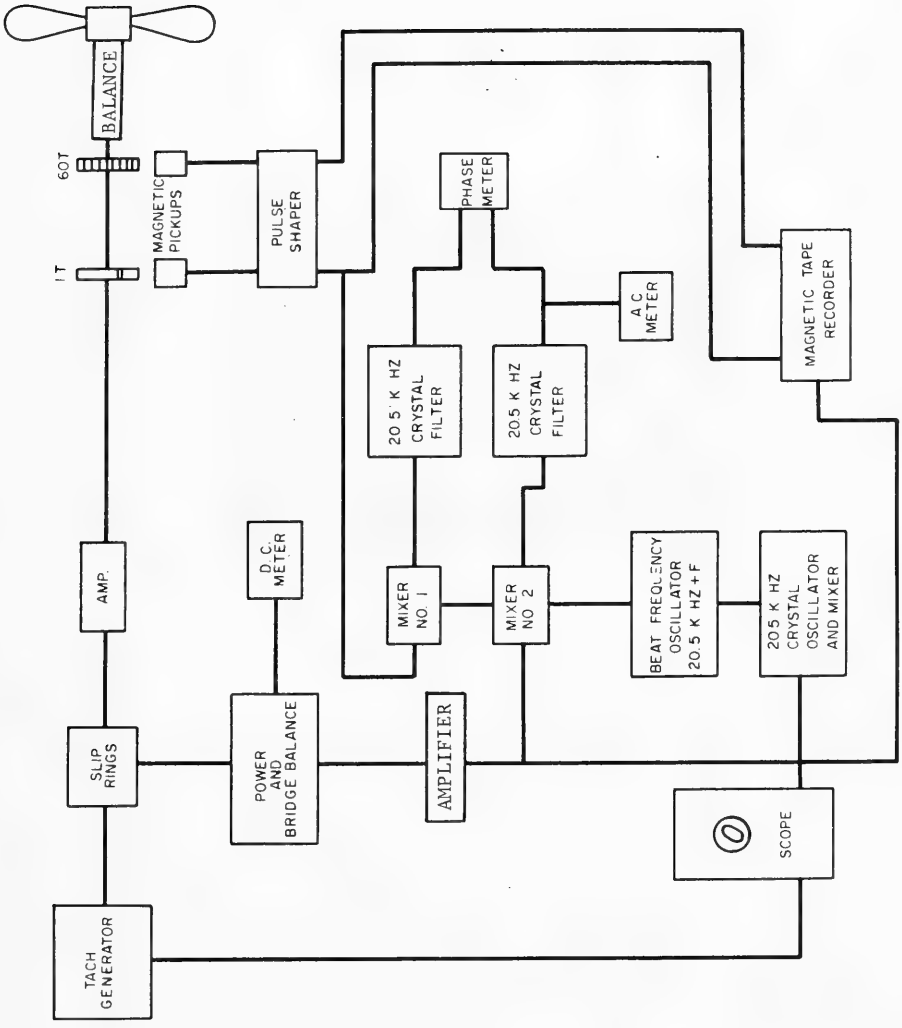

Fig. 12 - Block diagram of instrumentation

The ac outputs are passed through adjustable-gain amplifiers, where the signal levels are set to the optimum level for magnetic-tape recording. Near the flywheel are two toothed wheels that generate 1 and 60 pulses per shaft revolution. Figure 13 shows these pulses for a portion of a revolution before and after passing through a pulse-shaper. The 60 Hz square wave controls the digitalization of the signals, and the single pulse acts as a start signal and as a phase reference. These pulses are recorded on the magnetic tape, along with the six channels of data from the propeller. A digital time code is recorded on the tape to identify the data and to permit the use of an automatic tape-search unit during digitalization. A voice announcement is also used to record additional information concerning the tests. Each of the six data signals is also photographically recorded from an oscilloscope screen, along with the single reference pulse.

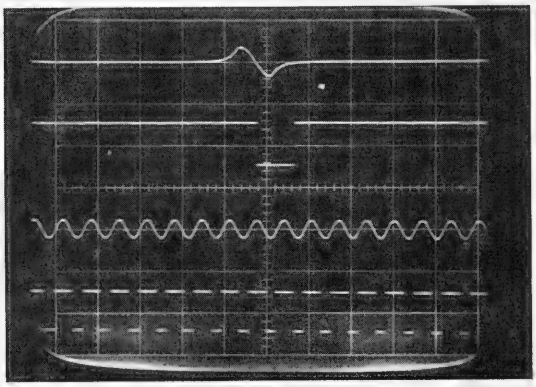

Fig. 13 - Reference pulses before and after shaping

For on-the-spot analysis, a two-channel constant-bandwidth wave analyzer and a phase meter are used. The analyzer consists of a common local oscillator, two mixers, and two 20.5-kHz crystal filters. These filters have a bandwidth of 5 Hz and are matched for frequency and phase. One channel is connected to the phase reference pulse. Since this is a narrow symmetrical pulse, it contains many strong harmonics of shaft frequency that are in phase with each other. Whenever the analyzer is tuned to one of the unsteady signals, there will be a reference signal that has a fixed phase relationship to the angular position of the propeller. The phase meter is connected to the two outputs of the analyzer to measure their phase angle, and the signal channel is connected to a voltmeter to measure the amplitude. The input of the analyzer can be switched to analyze any of the six components. To simplify setting the analyzer to the desired signal frequency, the local oscillator frequency is mixed with that of a 20.5-kHz crystal oscillator to obtain the frequency component being analyzed. This frequency is compared with that of a sine-wave generator connected to the drive motor. Since all the frequencies of interest are simple multiples of shaft frequency, it is easy to tune the local oscillator by setting it for a stationary pattern on the oscilloscope.

DIGITAL ANALYSIS

A digital analysis of the recorded data is performed using an IBM-7090 computer. Each of the data channels is digitized at intervals corresponding to 6 degrees of shaft rotation for 200 shaft revolutions. These values are then averaged to obtain an average cycle for one revolution and calibration signals on the tape are used to scale these average values to represent the input to the recorder in volts. The photographic record made from the oscilloscope can be compared directly with this output from the computer. These average values are then divided by the gain of the amplifiers, which has to be entered into the computer program for each test. The result is the output of each strain-gage bridge in millivolts. Each set of six voltage values, for each 6° increment of shaft rotation is now multiplied by the 6x6 calibration matrix to obtain the propeller forces and moments in pounds and pound-feet. Since the gages are rotating with the propeller, the side forces and bending moments are relative to a rotating reference frame. To obtain vertical and horizontal forces and moments, they are resolved by using trigonometric relationships. A harmonic analysis of these results gives the amplitudes and phase angles of any desired number of harmonics of the shaft rotation frequency.

TYPICAL TEST RESULTS

The unsteady forces produced by a propeller have frequencies determined by the blade frequency and the frequency components in the wake. Unsteady thrust and torque are present only if the wake has frequency components equal to the blade frequency or any of its harmonics. Unsteady side forces and bending moments are present only if the wake has frequency components equal to the blade frequency or a harmonic plus or minus one. The forces relative to the rotating shaft will have this frequency. However, when resolved into vertical and horizontal forces relative to a fixed reference frame, these frequencies become equal to the blade frequency or its harmonics.

Figures 14 and 15 show the outputs of the thrust and moment gages for a three-bladed propeller in a three- and four-cycle wake. These wakes were approximately sinusoidal with only a little harmonic content. Figure 14 shows that in the three-cycle wake a strong three-cycle thrust signal was produced, but the moment signal was rather complex and actually much weaker than indicated by the photographs, since the gain of this channel was greater. Figure 15 shows that in the four-cycle wake the thrust was complex and weak, while the moment shows a strong four-cycle component. When resolved into vertical and horizontal moments, they will become three-cycle or blade frequency signals. These are the unfiltered electrical signals and must be corrected for the gain of each channel and multiplied by the calibration matrix to obtain values in the mechanical units of force and moment. The pulses seen on each record represent shaft revolutions and are used as the phase reference for both the digital and the on-the-spot analysis.

The three- and four-cycle wakes were produced by screens using the method developed by McCarthy (10). Figure 16 shows a drawing of the three-cycle screen. Figures 17 and 18 show the harmonic analysis of the longitudinal velocity component in the propeller plane as measured with a pitot rake.

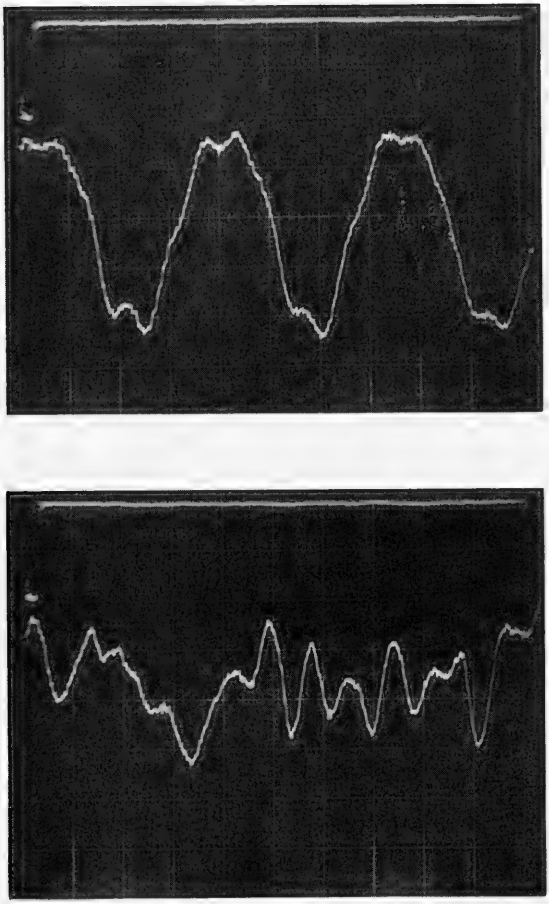

Fig. 14 - Three-bladed propeller in three-cycle wake

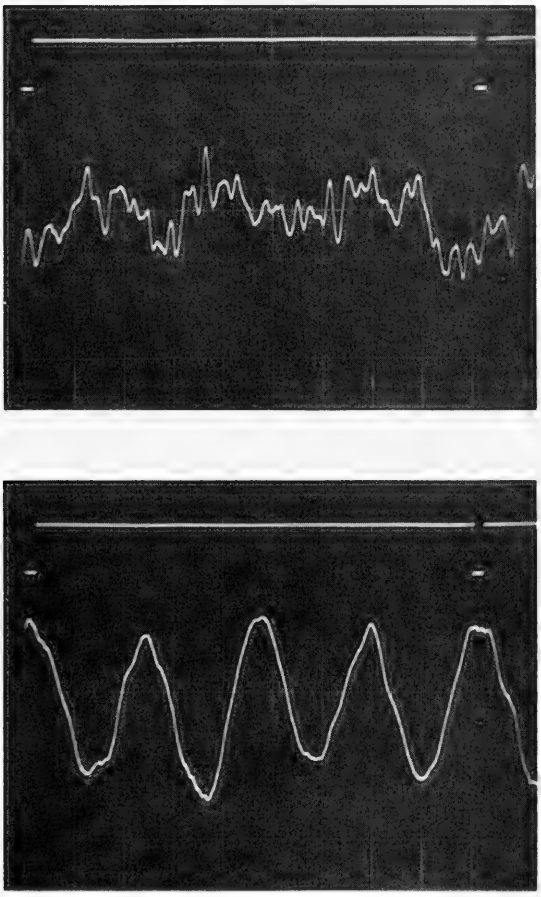

Fig. 15 - Three-bladed propeller in four-cycle wake

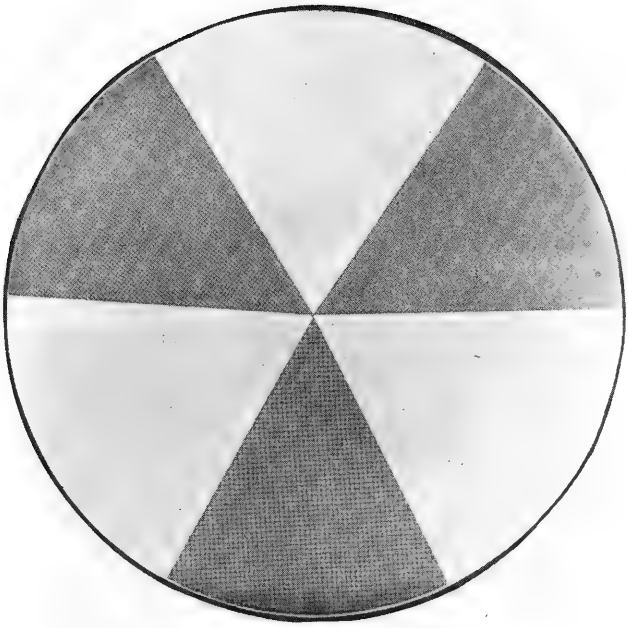

Fig. 16 - Three-cycle screen

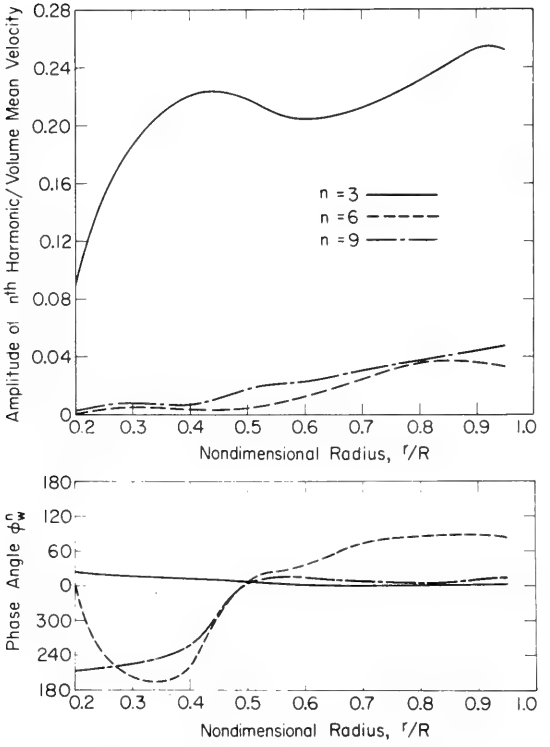

Fig. 17 - Harmonic analysis of three-cycle wake

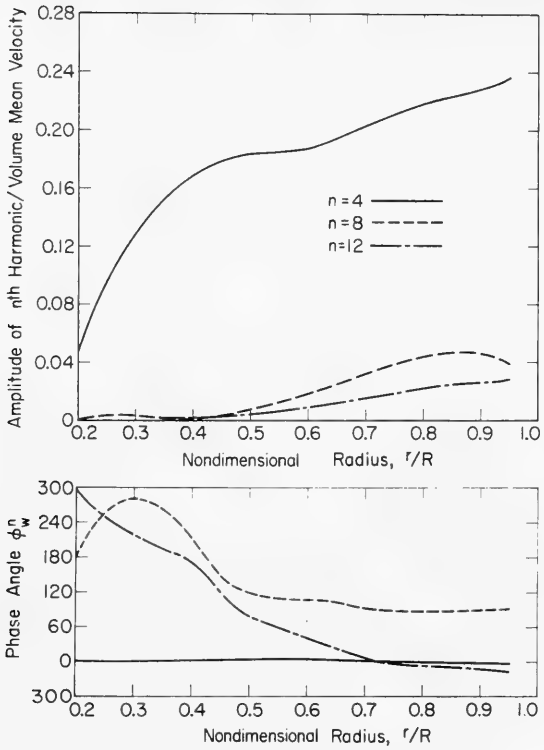

Fig. 18 - Harmonic analysis of four-cycle wake

These simple wakes were used in all the water-tunnel tests because the objective was to obtain a better understanding of the influence of the parameters affecting unsteady forces rather than to model full-scale conditions and determine unsteady full-scale vibratory forces as is usually done in the unsteady tests conducted with models in the towing basin.

Two series of tests have been completed in the water tunnel. The first was an investigation of the effects of blade width and skew on the unsteady forces and moments of three-bladed propellers when operating in three- and four-cycle wakes. Some of these results have been used in Refs. (11) and (12) for comparison with theoretical methods. The propellers (Fig. 19) had expanded area ratios of 0.30, 0.60, and 1.20 with no skew and 0.60 with skew equal to the blade spacing. All were designed for the same operating conditions. The second series of tests used the tandem set of two three-bladed propellers shown in Fig. 20. Each propeller of the set had an expanded area ratio of 0.30 and the set was tested in the three-cycle wake with the blades set at a series of different angles relative to each other. All propellers were 12 inches in diameter. Unsteady forces and moments and their phase angles were determined over a range of loading extending from zero thrust to about twice design thrust.

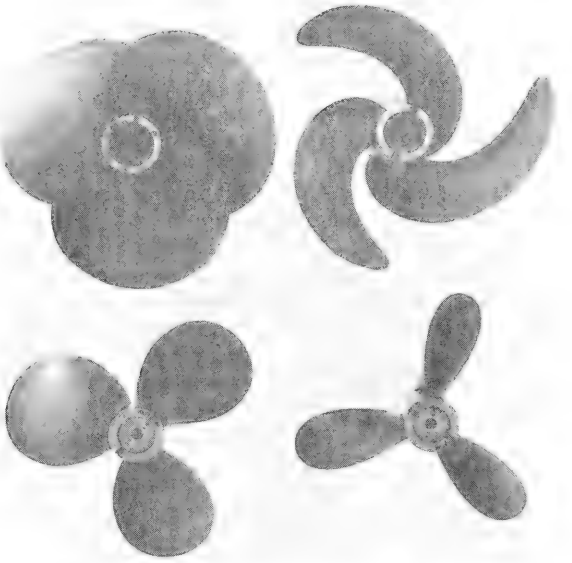

Fig. 19 - Three-bladed single propellers

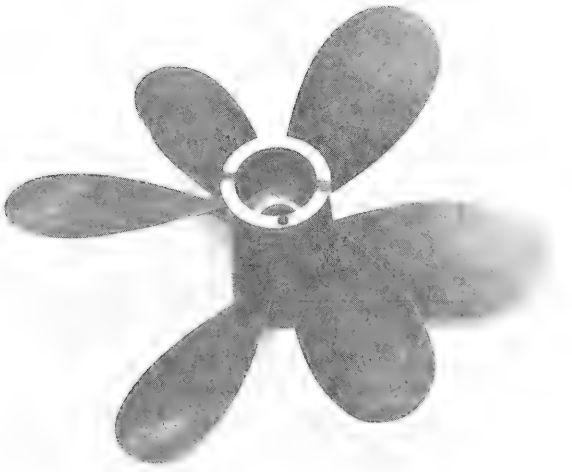

Fig. 20 - Tandem propellers set at 60° angle

The variation of blade frequency thrust, torque, side forces, and bending moments with mean propeller loading for the single propellers is shown in Figs. 21, 22, 23, and 24, respectively. The directions of these forces and moments are defined in Fig. 25. The unsteady thrust and torque were obtained in the three-cycle wake, where they were dominant, while the side forces and bending moments were obtained in the four-cycle wake. The thrust and side forces are nondimensionalized on design thrust, and the torque and bending moments on the torque measured at design thrust. As the loading decreased with increasing advance coefficient, all six blade frequency components increased for the unskewed propellers. This is apparently due to the increased amplitude of the velocity variations as the mean velocity was increased. The decrease in these components at the higher velocities for the skewed propeller is not understood. The largest unsteady forces were obtained with the expanded area ratio of 0.60, although with only three blade widths the value for the maximum cannot be determined accurately. The skewed propeller showed a considerable reduction of the unsteady forces over those of the unskewed propeller. The blade frequency thrust and torque were only about 10% and the side forces and moments about 50% of those for the unskewed propeller of the same blade width.

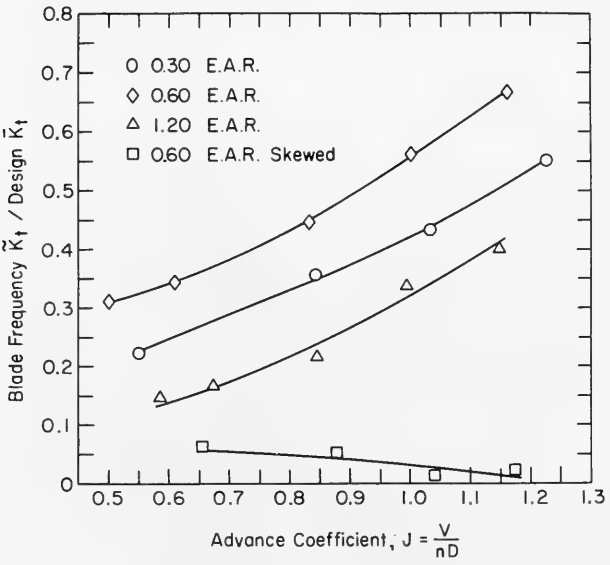

Fig. 21 - Blade-frequency thrust

Phase angles are shown in Figs. 26-28. The angles given are those by which the sinusoidal components of propeller loading lead the same frequency components of the longitudinal velocity at the radial line through the midchord of the root section of a propeller blade. The thrust is assumed to be in the direction for normal propulsion of a ship, i.e., in phase with the torque and opposite to the direction shown in Fig. 25. With this assumption, and from steady theory, the

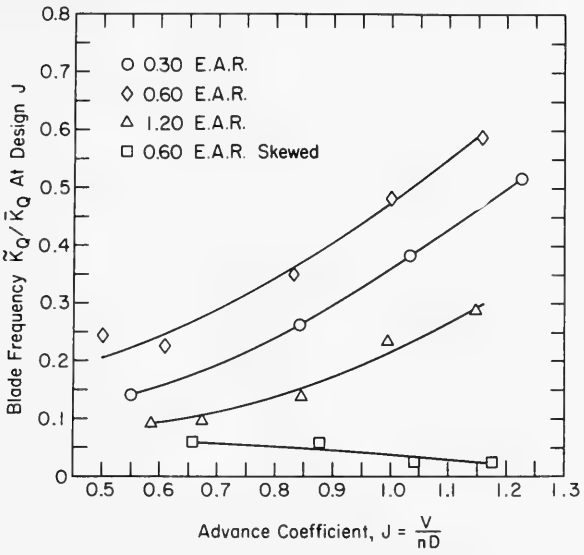

Fig. 22 - Blade-frequency torque

thrust and torque should lead the velocity by 180° for a narrow-bladed propeller. The effect of blade width shown on these figures is apparently due to the effective line of encounter being shifted forward for the wider blades and aft for the skewed blades.

The tandem set was tested in the three-cycle wake, so that the only significant unsteady components were thrust and torque. Titoff and Biskup (13) have reported bending moments for tandem propellers. The type of flow they used was apparently more complex and included frequency components that excited these moments.

Figure 29 shows the unsteady thrust developed by the tandem propellers in the three-cycle wake at design loading. When the blades of the two propellers are aligned with each other, a strong blade-frequency thrust component is produced. As the angle between the two propellers is changed, the blade-frequency thrust is reduced and has a minimum value when the forward propeller lags the after by approximately 60° or half the blade spacing of one propeller. The higher harmonics of blade frequency also show an effect of blade position. This blade-position effect is mostly due to the fact that the three-cycle wake also has small sixth-, ninth-, and twelfth-harmonic components. This figure also shows the blade-frequency thrust component for the single three-bladed propeller, which has an EAR of 0.60, equal to the total EAR of the tandem set which was designed for the same operating conditions. The curves in this figure have been drawn through the points obtained from the computer analysis. They are considered more reliable than the on-the-spot analysis, since they represent averages for 200 shaft revolutions. Also, the values read from the on-the-spot

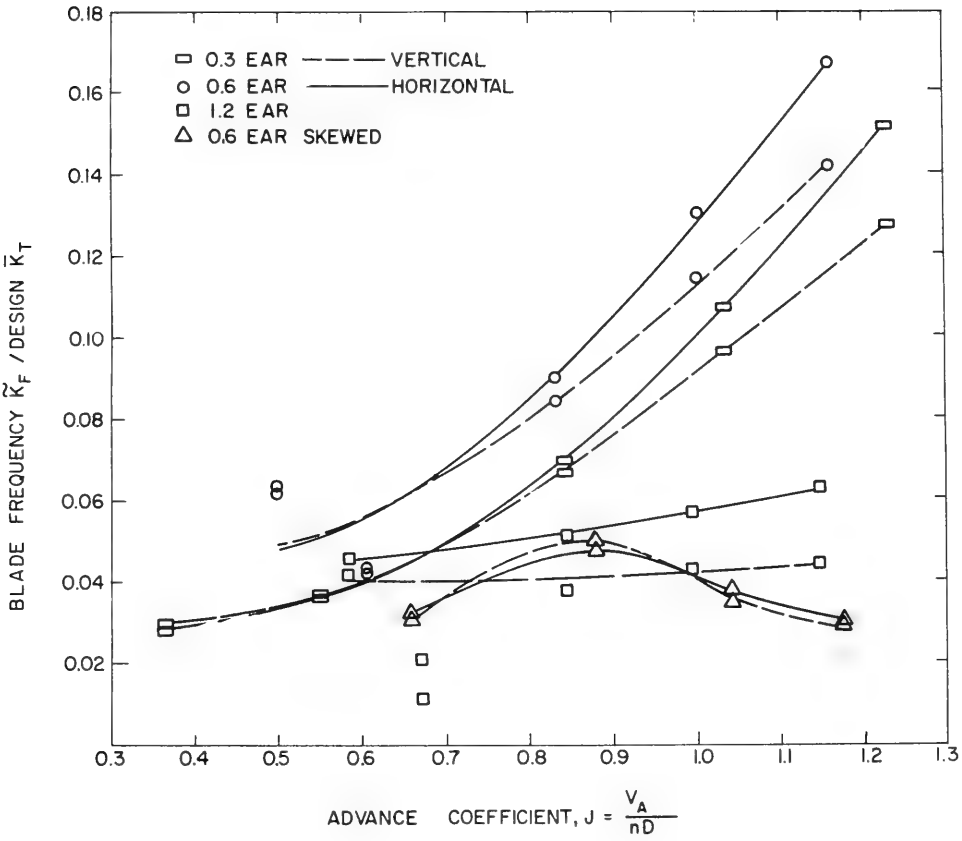

Fig. 23 - Blade-frequency side forces

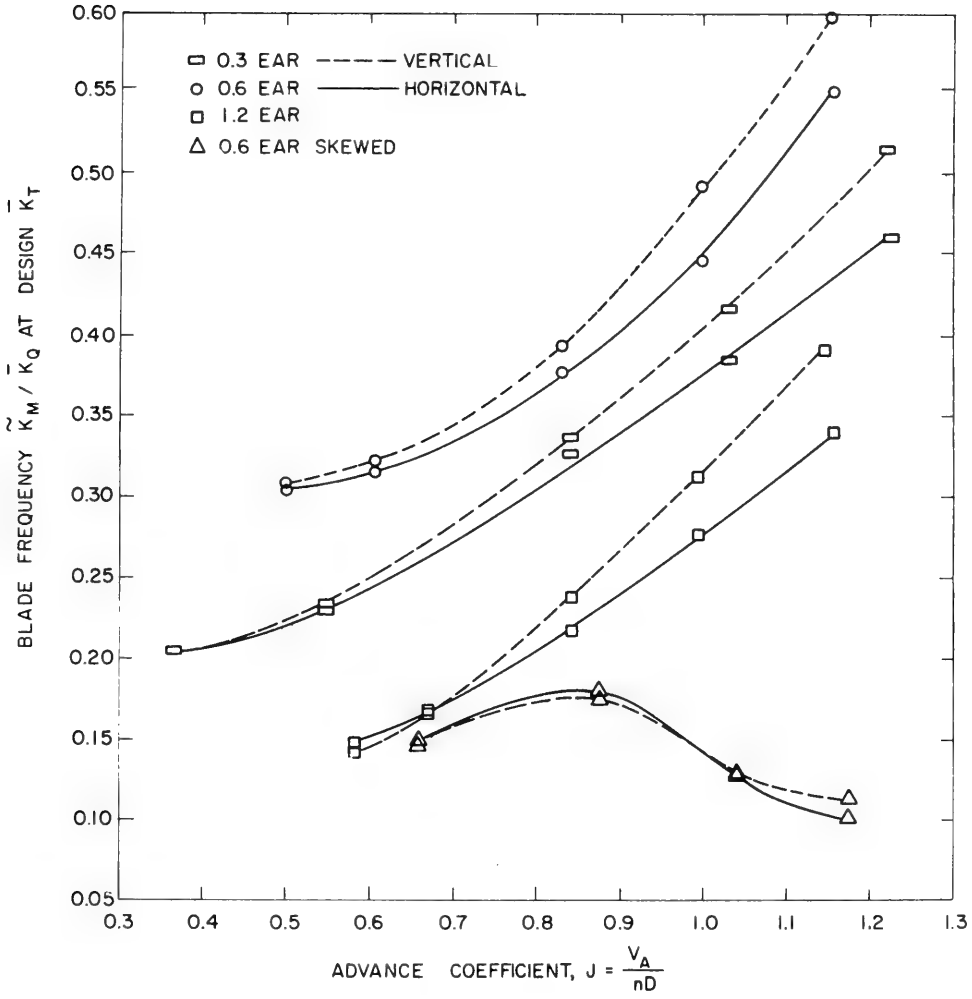

Fig. 24 - Blade-frequency bending moments

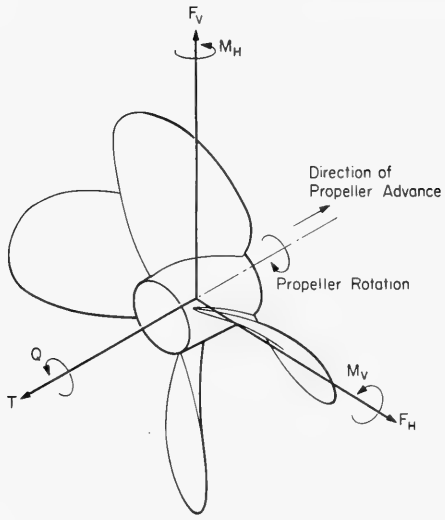

Fig. 25 - Forces and moments acting on propeller

instrumentation are shown for blade frequency and are in good agreement. The agreement is equally good for the higher frequencies. Figure 30 shows similar results for blade-frequency torque.

The effect of the relative angle between the two propellers on the phase angle of the blade-frequency thrust is shown in Figure 31. The curve is drawn through the values obtained from the computer analysis, and again the on-the-spot values are in good agreement. The phase reference is the centerline of the aft propeller blade. It is seen that as the lag of the forward propeller position is increased, the lead of the phase angle is decreased. The phase angles for torque are essentially identical and the agreement of the on-the-spot results is even better.

Figure 32 shows how the waveform of the thrust changes as the angle between the propeller is changed from 0° to 100° in increments of 20° as recorded from the oscilloscope.

CONCLUSIONS

Several dynamometers having high accuracy and good frequency response characteristics are available to obtain reliable measurements of unsteady propeller forces both in the towing basins and in the water tunnel. Experimental results can be obtained which are required for evaluating the sophisticated theories that are being developed, and parametric studies can be made to explore the details of propeller geometry for their effects upon performance. Evaluation tests can also be made to determine the characteristics of specific propeller and hull combinations.

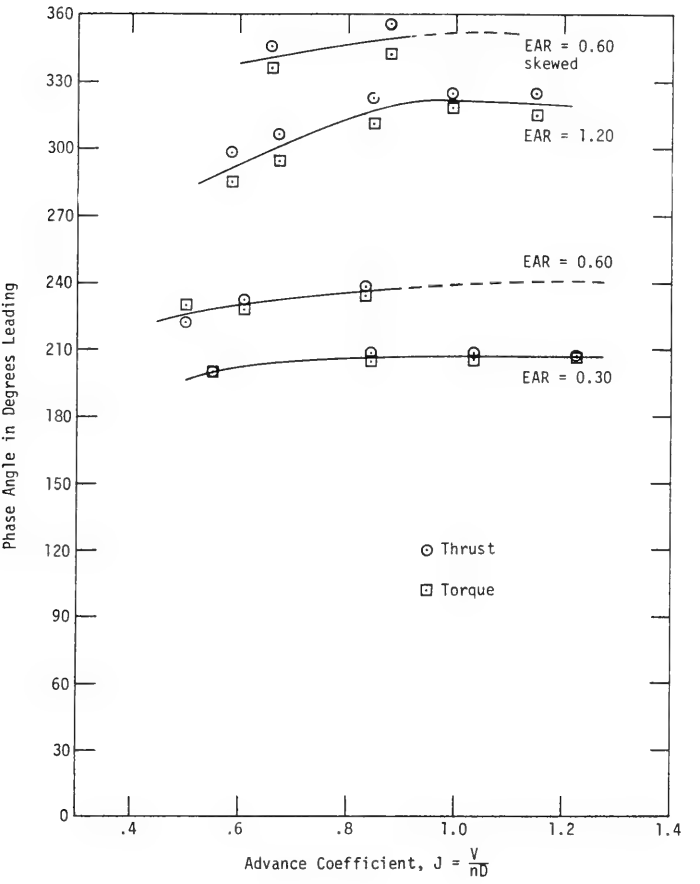

Fig. 26 - Phase angles of thrust and torque

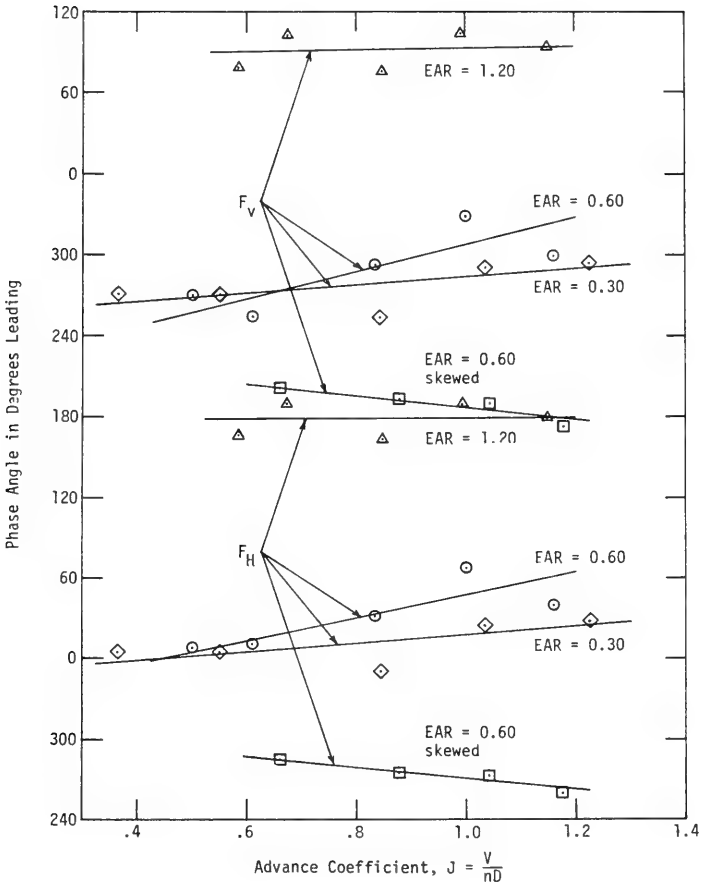

Fig. 27 - Phase angles of vertical and horizontal side forces

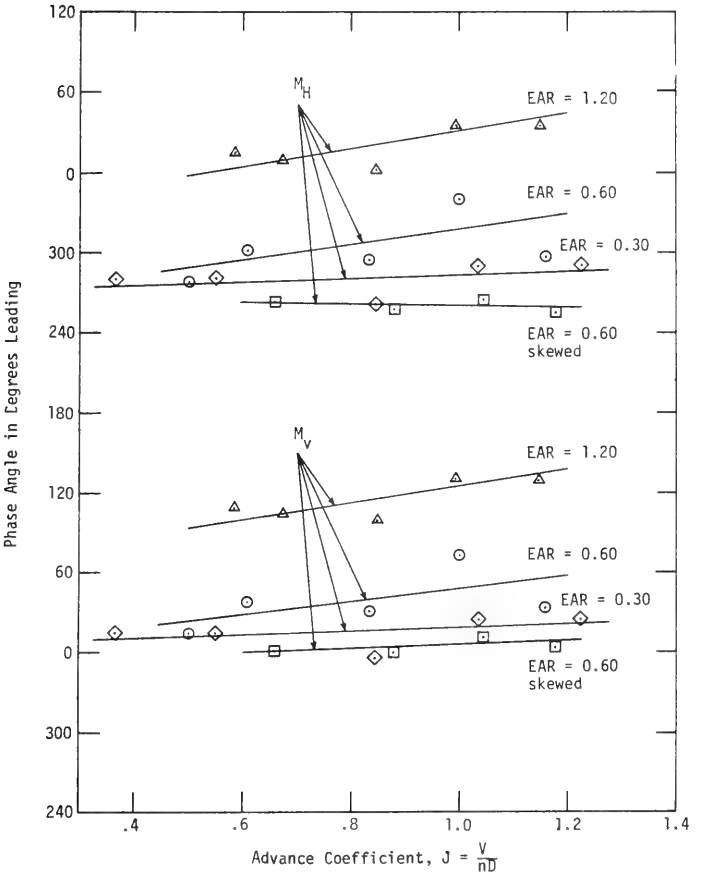

Fig. 28 - Phase angles of vertical and horizontal bending moments

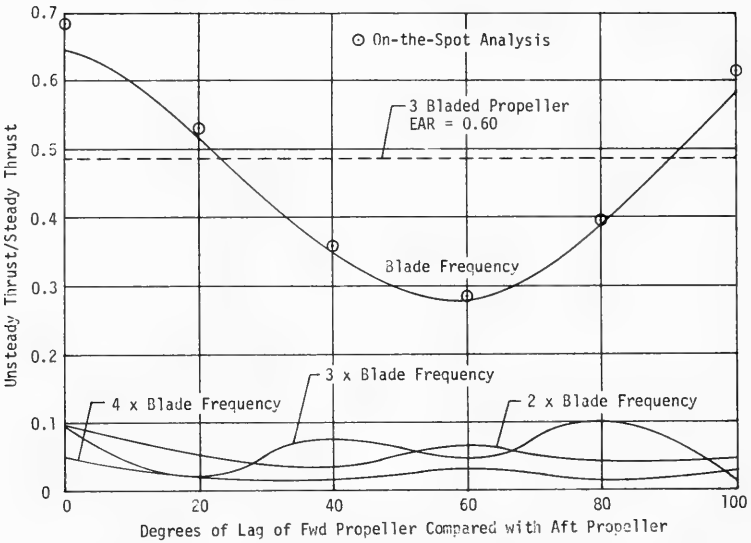

Fig. 29 - Ratio of unsteady thrust to steady thrust at design K_T

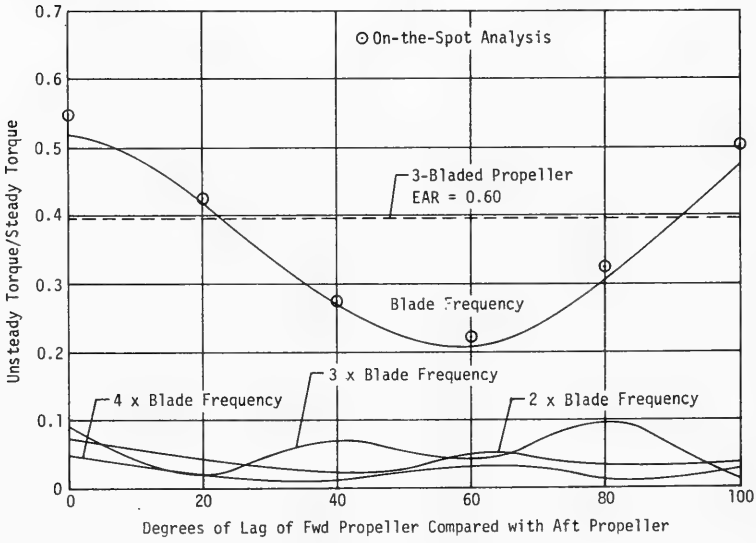

Fig. 30 - Ratio of unsteady torque to steady torque at design K_T

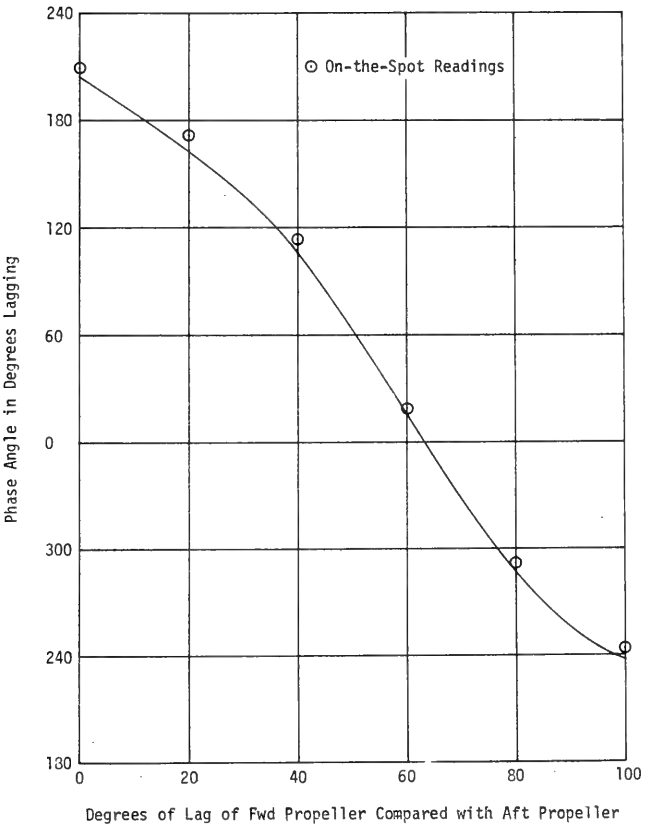

Fig. 31 - Phase angles of blade-frequency thrust

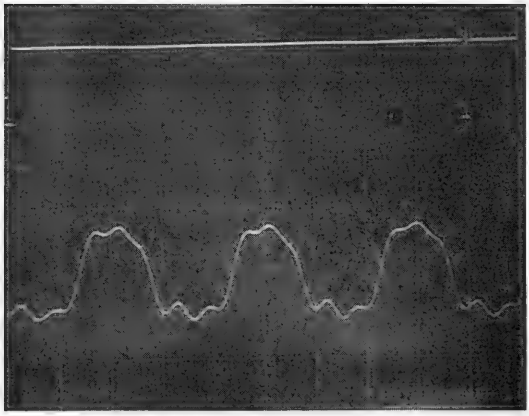

(a) Propellers in phase

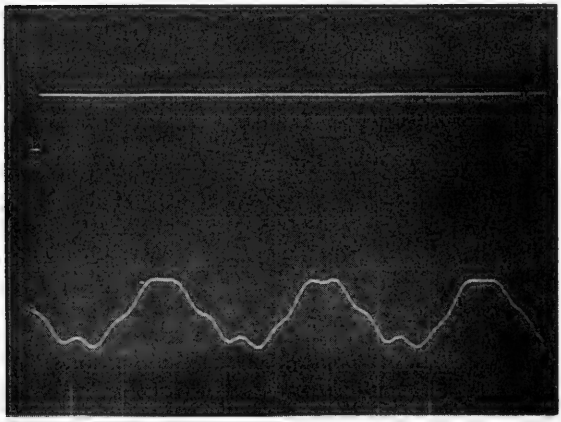

(b) Forward propeller lags 20 degrees

Fig. 32 - Waveforms of unsteady thrust

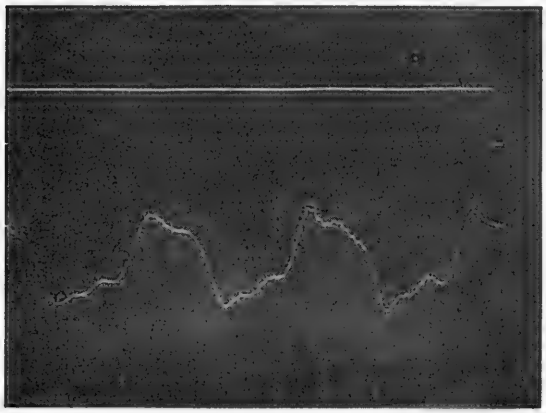

(c) Forward propeller lags 40 degrees

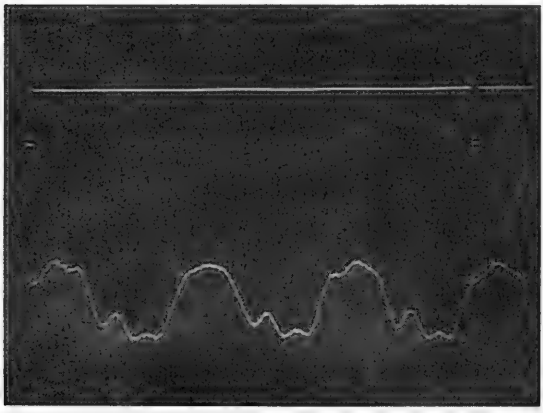

(d) Forward propeller lags 60 degrees

Fig. 32 - Waveforms of unsteady thrust (Continued)

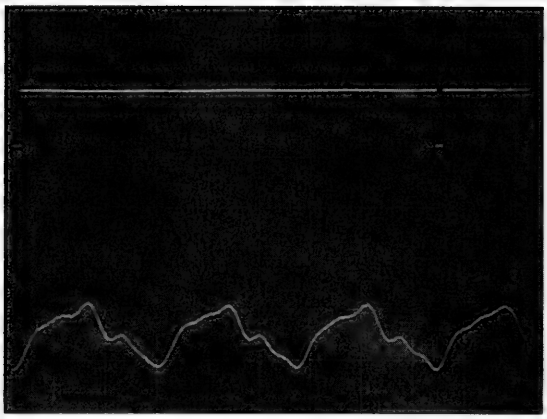

(e) Forward propeller lags 80 degrees

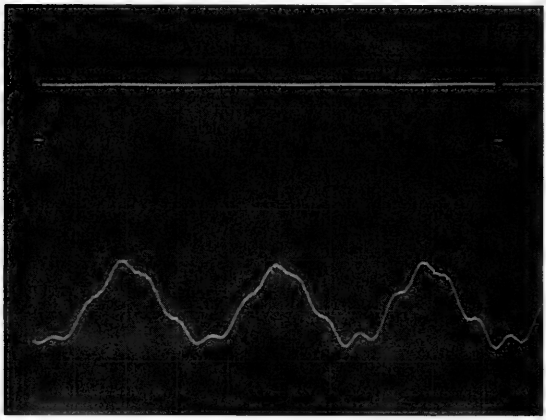

(f) Forward propeller lags 100 degrees

Fig. 32 - Waveforms of unsteady thrust (Continued)

The water-tunnel dynamometer was designed theoretically, using a computer analysis to obtain the dynamic characteristics. The dynamic calibrations of the completed system agreed quite well with the predicted frequency response curves, except for a small resonance in bending moment and side force. Analog instrumentation for obtaining on-the-spot measurements of amplitudes and phase angle of the harmonic frequency components was developed for the water-tunnel tests. Both amplitude and phase values obtained from this instrumentation agree very well with those computed from the digitized tape recordings.

Water-tunnel tests of propellers with three blade widths showed the unsteady forces to be maximum for an expanded area ratio of 0.60. A propeller having extreme skew and the same blade width had only 10% of the thrust and torque and 50% of the side forces and moments on the unskewed propeller. Tests of a set of tandem propellers showed that the phase angle between the two sets of blades has a considerable effect on the unsteady forces. For any given application, the vibratory forces can be reduced by proper adjustment of the angle between the two sets of blades.

Future work will include determinations of the effect of pitch ratio and skew and studies of contrarotating and tandem propellers. Propellers for specific applications will be designed and their performance will be evaluated experimentally.

ACKNOWLEDGMENTS

The author gratefully acknowledges the assistance of Robert Boswell and Mrs. Mary Dickerson in conducting the tests and analyzing the experimental data, Garnell Belt and Dusan Lysey in preparing the figures, and Shirley Childers in preparing the manuscript.

REFERENCES

1. Tachmindji, A.J. and Dickerson, M.C., "The Measurement of Thrust Fluctuations and Free Space Oscillating Pressures for a Propeller," David Taylor Model Basin Report 1107 (Jan. 1957)

2. van Manen, J.D. and Wereldsma, R., "Dynamic Measurements on Propeller Models," International Shipbuilding Progress, Vol. 6, No. 63 (Nov. 1959)

3. Krohn, J.K., "Numerical and Experimental Investigations of the Dependence of the Fluctuations of Thrust and Torque on the Blade Area Ratios of Four-Bladed Ship Propellers," HSVA Report 1236 (May 1961), prepared under ONR Contract No. N62558-2223

4. Norrie, D.H., "Research in Propulsion Vibration at the University of Adelaide," Transactions of Royal Institute of Naval Architects, Vol. 106 (1964), p. 81

5. Wereldsma, R., "Experimental Determination of Thrust Eccentricity and Transverse Forces, Generated by a Screw Propeller," International Shipbuilding Progress, Vol. 9, No. 96 (July 1962)

6. Hadler, J.B., Ruscus, P., and Kopko, W., "Correlation of Model and Full-Scale Propeller Alternating Thrust Forces on Submerged Models," paper presented at the Fourth Symposium on Naval Hydrodynamics, ONR, Washington (Aug. 1962)

7. Brown, N.A., "Periodic Propeller Forces in Nonuniform Flow," Massachusetts Institute of Technology Report 64-7 (June 1964)

8. Brandau, J.H., "Static and Dynamic Calibration of Propeller Model Fluctuating Force Balances," Naval Ship Research and Development Center Report 2350 (Aug. 1967)

9. Strand, S. and Cuthill, E., "General Vibration Code," David Taylor Model Basin AML Report 139 (Sept. 1961)

10. McCarthy, J.H., "Steady Flow Past Nonuniform Wire Grids," Journal of Fluid Mechanics, Vol. 19, Part 4 (1964), pp. 491-512

11. Tsakonas, S., Breslin, J., and Miller, M., "Correlation and Application of an Unsteady Flow Theory for Propeller Forces," Presented at the Annual Meeting, Society of Naval Architects and Marine Engineers, New York (Nov. 1967)

12. Boswell, R.J., "Measurement, Correlation with Theory, and Parametric Investigation of Unsteady Propeller Forces and Moments," M.S. Thesis, Department of Aerospace Engineering, The Pennsylvania State University, University Park, Pennsylvania (1967)

13. Titoff, I.A. and Biskup, B.A., "Investigation into the Possibilities of Tandem Propeller Applications with the Aim of Decreasing the Variable Hydrodynamic Loads Transmitted to a Propeller Shaft," Eleventh International Towing Tank Conference, Tokyo, Japan (1966)

* * *

DISCUSSION

R. Wereldsma
Netherlands Ship Model Basin
Wageningen, Netherlands

My first question refers to the dynamic calibration of the six-component balance: Did the author take into consideration the hydrodynamic effects of the propeller, being a part of the complete system?

When these effects are considered, it is not possible to measure thrust fluctuations having frequencies higher than the terminal natural frequency of the system, due to the hydrodynamic interaction of the thrust and the torque system.

A second question refers to the extremely skewed propeller, showing opposite trends of vibratory output versus advance ratio, as compared to regular propellers. Is the dynamic response of the propeller blades probably the cause of this phenomenon?

* * *

REPLY TO THE DISCUSSION

Marlin L. Miller

The dynamic calibrations were made in water with a mass approximately equal to a propeller mounted on the balance. This did not provide the coupling between the thrust and torque that is present when a propeller is being tested. With a propeller, the thrust response will be limited by the torsional resonance of the system. However, the frequencies measured have been well below this limit, so that the results have not been affected by this coupling.

The resonant frequencies of the blades of the skewed propeller have been measured in water. The hub of the propeller was driven by a shaker and the resonant frequency of each blade determined with a hydrophone held close to the blade. The average resonant frequency was found to be 97 Hz. This is close to the second harmonic of blade frequency, which was 90 Hz for the tests reported in this paper. An examination of the test data has shown an unusually large second-harmonic component of thrust and torque and a somewhat more complex harmonic distortion of the side force and moment signals at the two highest values of advance coefficient for the skewed propeller. Therefore, these values, shown in Figs. 21, 22, 23, and 24, are not reliable. However, little or no harmonic response was observed for the two lower values of advance coefficient, and these values are considered reliable.

* * *

THE RESPONSE OF PROPULSORS TO TURBULENCE

Maurice Sevik
Ordnance Research Laboratory, the Pennsylvania State University
University Park, Pennsylvania

ABSTRACT

The response of a propulsor to random velocity fluctuations has been analyzed. As a special case the theory has been used to predict the force fluctuations on a propeller of low solidity having blades of high aspect ratio and operating in a homogeneous, isotropic turbulence field. The response depends critically on two functions which involve the ratios of the propeller diameter and of the chord of the blades to a characteristic length scale of the energy-containing eddies. The power spectrum peaks at the origin and drops off rapidly with increasing frequency. Experiments performed in a water tunnel with a free-stream propeller placed downstream of grids of various mesh sizes indicate good agreement between theoretical predictions and experimental results.

INTRODUCTION

It is well-known that the fluid-dynamic forces on the blades of turbomachines are unsteady. These unsteady forces may cause a number of undesirable effects such as fatigue failures, high vibration levels, or objectionable acoustic radiation.

In many applications the spectrum of the time-dependent forces exhibit strong lines which generally correspond to harmonics of the blade frequency. These lines are created by effects which are periodic over one revolution of the machine such as mutual interactions between rows of blades or spatial nonuniformities in the inflow velocity field. Kemp and Sears (1,2) were the first to contribute to our understanding of the fundamental unsteady flow phenomena which occur in compressors and turbines by analyzing the aerodynamic interference between rows of blades in relative motion. In the naval field Lewis (3) pioneered theoretical and experimental investigations as early as 1936 in connection with unsteady propeller forces which often cause severe vibrations in ships. Recently Tsakonas (4) developed a lifting surface theory which predicts the time-dependent forces acting on marine propellers possessing numerous, low-aspect-ratio blades. Good agreement between Tsakonas' predictions and test results were observed by Boswell (5).

The studies mentioned, as well as numerous other investigations which have been published from time to time, are all concerned with nonuniformities in the

flow which are deterministic and periodic in nature. However numerous cases exist in which the blades of turbomachines are subjected to random fluctuations of a flow field. A common example is the fan of a household air conditioner operating behind an ornamental grill. Another example is a marine propeller immersed in the turbulent boundary layer of a ship.

In this paper a theoretical analysis of the response of a propulsor to random velocity fluctuations is given. As a special example the theory has been used to predict the force fluctuations on a propeller of low solidity with blades of relatively high aspect ratio operating in a homogeneous, isotropic turbulence field. It is reasonable to expect that the response of the propeller will depend on two parameters, namely, the ratio of propeller diameter and the ratio of blade chord to a characteristic turbulent eddy size. It is shown that the power spectrum peaks at the origin and drops off rapidly with increasing frequency.

THEORETICAL CONSIDERATIONS

The statistical properties of the force fluctuations experienced by a propulsor operating in a turbulent flow can readily be related to those of the random velocity fluctuations, if the response of the propulsor is linear. Imagine the propulsor to be subdivided into an arbitrarily large number of small surface elements, and consider one such element located at y_i (Fig. 1). Steady and unsteady fluid velocities are measured with respect to a Cartesian coordinate system $\alpha'(\alpha' = 1', 2', 3')$ which is fixed in space. An unprimed system $\alpha(\alpha = 1, 2, 3)$ rotates with the propeller and is oriented so that one of its axes coincides with the axis of symmetry of the propeller.

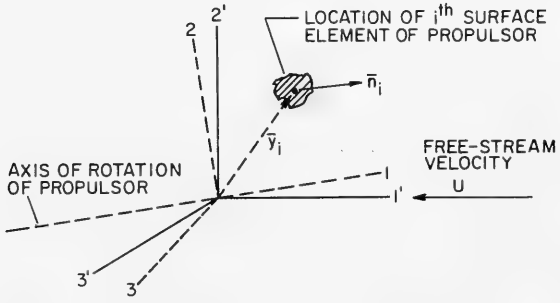

Fig. 1 - Coordinate systems. The primed coordinate system is fixed in space, and the unprimed coordinate system rotates with the propulsor.

The fluctuating aerodynamic forces acting on the various surface elements are interdependent by virtue of induction effects as well as by virtue of spatial and temporal correlation of the turbulent velocity fluctuations. Since the quantities involved in this problem are tensors, the index notation, including the summation convention in the case of repeated indices, constitutes the most convenient choice.

Directions are denoted by superscripts, whereas subscripts denote the propulsor elements involved. For example $u_k^{\beta}(\tau')$ denotes the component of the fluctuating velocity at time τ' in the direction β of the rotating reference frame at the element k. Similarly, $F_{ik}^{\alpha\beta}(t,\tau')$ denotes the aerodynamic force acting on the ith element in the direction α at the instant of time t caused by a velocity fluctuation of unit magnitude in the direction β to which the kth element was subjected at the instant of time τ'. Finally, $\ell_i^{\alpha}(t)$ indicates the aerodynamic force acting on the ith element at time t in the direction α. In terms of these quantities and neglecting higher order terms, the lift force is given by

$$\ell_i^{\alpha}(t) = \int_{-\infty}^{t} F_{ik}^{\alpha\beta}(t,\tau')\, u_k^{\beta}(\tau')\, d\tau' \ , \tag{1}$$

where

$$\alpha, \beta = 1, 2, 3 \ ,$$

$$i, k = 1, 2, \ldots, m \ ,$$

$$\tau' \leq t \ .$$

In most cases the aerodynamic force tensor is time invariant and Eq. (1) can be written as a convolution integral:

$$\ell_i^{\alpha}(t) = \int_{0}^{\infty} F_{ik}^{\alpha\beta}(t)\, u_k^{\beta}(t-\tau)\, d\tau \ , \tag{2}$$

where

$$\tau = t - \tau' \geq 0 \ .$$

The force acting on the entire propulsor at the instant of time t in direction α of the roating reference frame is given by the sum of the the lift forces acting on each individual element:

$$L^{\alpha}(t) = \sum_{i}^{m} \ell_i^{\alpha}(t) \ . \tag{3}$$

Since $L^{\alpha}(t)$ is a random function, it is determined statistically by the complete system of joint-probability distributions of the values of the function at any n values of t, where n may take any integral value. Fortunately, from an

engineering standpoint the correlation tensor $\langle L^{\alpha}(t)\, L^{\beta}(t+\tau)\rangle$ and its Fourier transform are the most significant quantities; consequently only a knowledge of the second-order two-point-product mean values of the turbulence is required.

In Eq. (2) u represents the velocity of the fluid relative to a rotating element of the propulsor. Referring to Fig. 1, let y_i denote the location of the ith element relative to the unprimed reference frame. As was stated this unprimed reference frame is fixed to the propeller and rotates with it.

Suppose that at time t the fixed and rotating frames coincide momentarily; then the position vector of a fluid particle will be the same in both frames. If Ω denotes the angular velocity vector of the rotating frame, the velocity components of the fluid relative to the propulsor element considered are given by

$$u_i^{\beta} = a^{\beta\alpha}\, u_i'^{\alpha} - \varepsilon^{\beta\alpha\gamma}\, \Omega^{\alpha}\, y_i^{\gamma} \ , \tag{4}$$

where ε is the permutation symbol.

Note that all terms in Eq. (4) are time dependent: Ω could, for instance, represent fluctuations in angular velocity resulting from a torsional vibration of the propeller shaft. If the propulsor rotates at a steady speed, we obtain

$$u_i^{\beta} = a^{\beta\alpha}\, u_i'^{\alpha} \ .$$

In forming average values of the forces and fluid velocities we assume that the random processes are stationary and ergodic. The mathematical expectation

$$E[L^{\alpha}(t)\, L^{\beta}(t+\tau)] = \lim_{T\to\infty} \frac{1}{T} \int_0^T L^{\alpha}(t)\, L^{\beta}(t+\tau)\, dt = \Phi^{\alpha\beta}(\tau) \tag{5}$$

is equal to the sum of the auto- and crosscorrelation functions of the forces acting on the constituent segments of the propulsor. This can be shown by substituting Eq. (3) in Eq. (5):

$$\Phi^{\alpha\beta}(\tau) = \lim_{T\to\infty} \frac{1}{T} \int_0^T \sum_i \sum_j \ell_i^{\alpha}(t)\ \ell_j^{\beta}(t+\tau)\, dt = \sum_i \sum_j \Phi_{\ell_i \ell_j}^{\alpha\beta}(\tau) \ .$$

The crosscorrelation tensor $\Phi_{\ell_i \ell_j}^{\alpha\beta}(\tau)$ can be expressed in terms of the aerodynamic force functions and the velocity correlation tensor:

$$\Phi_{\ell_i \ell_j}^{\alpha\beta}(\tau) = \lim_{T\to\infty} \frac{1}{T} \int_0^T \ell_i^{\alpha}(t)\ \ell_j^{\beta}(t+\tau)\, dt$$

$$= \int_0^{\infty} F_{ik}^{\alpha\gamma}(\tau_1)\, d\tau_1 \int_0^{\infty} F_{jr}^{\beta\delta}(\tau_2)\, d\tau_2 \ \lim_{T\to\infty} \frac{1}{T} \int_0^T u_k^{\gamma}(t-\tau_1)\, u_r^{\delta}(t+\tau-\tau_2)\, dt \tag{6}$$

(Cont)

$$\Phi_{\ell}{}^{\alpha\beta}{}_{i\ell_j}(\tau) = \int_0^\infty F_{ik}^{\alpha\gamma}(\tau_1)\, d\tau_1 \int_0^\infty F_{jr}^{\beta\delta}(\tau_2)\, d\tau_2\, R_{kr}^{\gamma\delta}(\tau) \,, \tag{6}$$

where $R_{kr}^{\gamma\delta}(\tau)$ is the velocity correlation tensor for the points located at y_k and y_r respectively.

The spectrum tensor of the forces acting on the propulsor is the Fourier transform of the force correlation tensor $\Phi^{\alpha\beta}(\tau)$. It consists of the sum of the spectral and cross-spectral densities of the forces acting on the individual segments of the propulsor. The spectrum tensor is given by

$$\begin{aligned} G^{\alpha\beta}(\omega) &= \frac{1}{\pi}\int_{-\infty}^{\infty} \Phi^{\alpha\beta}(\tau)\, e^{-i\omega\tau}\, d\tau \\ &= \frac{1}{\pi}\int_{-\infty}^{\infty} \sum_i \sum_j \Phi_{\ell}{}^{\alpha\beta}{}_{i\ell_j}(\tau)\, e^{-i\omega\tau}\, d\tau \\ &= \sum_i \sum_j G_{\ell}{}^{\alpha\beta}{}_{i\ell_j}(\omega) \,, \end{aligned} \tag{7}$$

where $i = \sqrt{-1}$. It is convenient to express the spectrum tensor in terms of the frequency response functions of the individual segments of the propulsor. From Eq. (6) we obtain

$$\begin{aligned} G_{\ell i\ell_j}^{\alpha\beta}(\omega) &= \frac{1}{\pi}\int_{-\infty}^{\infty} \Phi_{\ell}{}^{\alpha\beta}{}_{i\ell_j}(\tau)\, e^{-i\omega\tau}\, d\tau \\ &= \int_0^\infty F_{ik}^{\alpha\gamma}(\tau_1)\, e^{i\omega\tau_1}\, d\tau_1 \int_0^\infty F_{jr}^{\beta\delta}(\tau_2)\, e^{-i\omega\tau_2}\, d\tau_2\, \frac{1}{\pi}\int_{-\infty}^{\infty} R_{kr}^{\gamma\delta}(\tau)\, e^{-i\omega\tau}\, d\tau \\ &= \left[H_{ik}^{\alpha\gamma}(\omega)\right]^* \left[H_{jr}^{\beta\delta}(\omega)\right] G_{kr}^{\gamma\delta}(\omega) \,, \end{aligned} \tag{8}$$

where the frequency response function $H(\omega)$ is given by

$$H_{jr}^{\beta\delta}(\omega) = \int_0^\infty F_{jr}^{\beta\delta}(\tau_2)\, e^{-i\omega\tau_2}\, d\tau_2$$

and where the * denotes the complex conjugate of the quantity. The spectrum tensor of the turbulence has the form

$$G_{kr}^{\gamma\delta}(\omega) = \frac{1}{\pi}\int_{-\infty}^{\infty} R_{kr}^{\gamma\delta}(\tau)\, e^{-i\omega\tau}\, d\tau \,.$$

APPLICATION TO A PROPELLER

As an illustration consider a propeller of low solidity with blades of high aspect ratio operating in a turbulent flow. The turbulence considered is homogeneous and isotropic. The unsteady aerodynamic forces correspond to two-dimensional theory applied to stripwise elements of the blades.

When the turbulence is homogeneous and isotropic, the velocity correlation tensor adopts a simple form. In terms of the distance r between two points and the mean square value of the velocity fluctuations u^2 it is given by

$$R_{kr}^{\alpha\beta}(r) = u^2\left[-\frac{1}{2r}\, r^{\alpha} r^{\beta}\frac{\partial f}{\partial r} + \left(f + \frac{r}{2}\frac{\partial f}{\partial r}\right)\delta^{\alpha\beta}\right] . \tag{9}$$

The function $f(r)$ has been measured by Stewart and Townsend (6) and is shown in Fig. 2 together with its approximate representation used in this paper, namely,

$$f(r) = e^{-\lambda/M} ,$$

where $\lambda = 2.5$ and M is the mesh size of the grids producing the turbulence. The symbol δ in Eq. (9) represents the Kroenecker delta.

As for the aerodynamic response function our analysis is restricted to two-dimensional theory applied to stripwise element of semichord b with spanwise width R. The appropriate form of this function has been given by Sears (7) as

$$H_j(\omega) = 2\pi\rho V_j b_j \delta R_j \{C(k_j)[J_0(k_j) - iJ_1(k_j)] + iJ_1(k_j)\} .$$

where

V_j = the resultant velocity at the jth propulsor element,

J_0, J_1 = Bessel functions,

$C(k)$ = Theodorsen's function,

$k_j = \omega b_j / V_j$ = reduced frequency.

The relationships established so far permit the calculation of the response of a propeller to turbulence by numerical means. Clearly it is desirable to obtain a relatively simple expression for the rms thrust coefficient and the spectrum tensor in terms of readily available propeller parameters. For this purpose, we make some approximations and assumptions:

1. The axis of rotation of the propeller is colinear with the free stream velocity vector.

2. The resultant velocity and chord of the various propulsor elements may be represented by those of a single "typical section" located at some fraction of

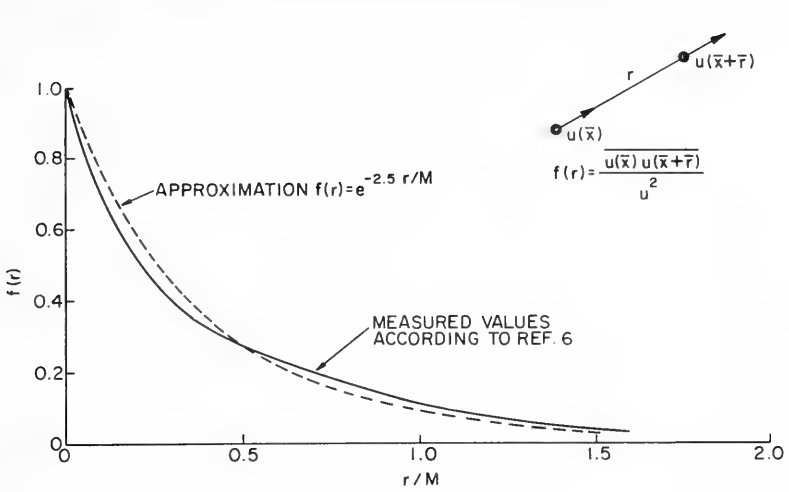

Fig. 2 - Correlation curve for isotropic turbulence. The measurements were made at 30M downstream, where M is the mesh size of the grid producing the turbulence

the span of a blade and denoted by the subscript T. A good choice would be the section exerting the largest steady lift force.

3. The velocity correlation tensor is approximately represented by

$$R_{kr}^{\alpha\beta}(\tau) = e^{-\lambda q/M} R_{kk}^{\alpha\beta}(\tau) \ .$$

where q represents the distance between the elements k and r of the propeller. As a consequence we obtain the following components:

$$R_{kr}^{11}(\tau) = u^2 \, e^{-\lambda[(U_\tau+q)/M]} \ ,$$

$$R_{kr}^{22}(\tau) = u^2 \left\{1 - \frac{\lambda}{2}\frac{U_\tau}{M}\right\} e^{-\lambda[(U_\tau+q)/M]} \ ,$$

$$R_{kr}^{12}(\tau) = R_{kr}^{21}(\tau) = 0 \ .$$

We can now obtain an expression for the mean square thrust coefficient. Consider the geometry of a propeller element, as shown in Fig. 3. We approximate the angle β by

$$\tan \beta \approx \frac{U}{\Omega R}$$

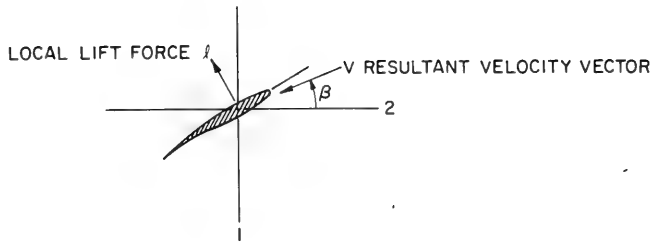

Fig. 3 - Geometry of a propeller element

From Eq. (7) and (8) we obtain an expression for the spectrum tensor of the fluctuating thrust force:

$$G^{11}(\omega) = \sum_i \sum_j \left[H_i^*(\omega)\, H_j(\omega) \cos^2 \beta_i \cos^2 \beta_j\, G_{ij}^{11}(\omega) + \frac{1}{4} H_i^*(\omega)\, H_j(\omega) \sin 2\beta_i \sin 2\beta_j\, G_{ij}^{22}(\omega) \right], \tag{10}$$

where

$$G_{ij}^{11}(\omega) = \frac{2}{\pi} \int_0^\infty R_{ij}^{11}(\tau)\, e^{-i\omega\tau}\, d\tau = \frac{2}{\pi} \int_0^\infty u^2 e^{-\lambda[(U_\tau + q)/M]}\, e^{-i\omega\tau}\, d\tau$$

$$= \frac{2u^2}{\pi} \left[\frac{\frac{\lambda U}{M} - i\omega}{\left(\frac{\lambda U}{M}\right)^2 + \omega^2} \right] e^{-\lambda q/M} \tag{11}$$

and

$$G_{ij}^{22}(\omega) = \frac{2}{\pi} \int_0^\infty R_{ij}^{22}(\tau)\, e^{-i\omega\tau}\, d\tau = \frac{2}{\pi} \int_0^\infty u^2 \left\{ 1 - \frac{\lambda}{2} \frac{U_\tau}{M} \right\} e^{-\lambda[(U_\tau + q)/M]}\, e^{-i\omega\tau}\, d\tau$$

$$= \frac{2u^2}{\pi} \left[\frac{\frac{\lambda U}{M} - i\omega}{\left(\frac{\lambda U}{M}\right)^2 + \omega^2} \right] \left\{ 1 + \frac{1}{2} \frac{\lambda U}{M} \left[\frac{\frac{\lambda U}{M} - i\omega}{\left(\frac{\lambda U}{M}\right)^2 + \omega^2} \right] \right\} e^{-\lambda q/M}. \tag{12}$$

We now introduce the concept of a "typical section" as was mentioned in assumption 2. A simple expression for the product of the aerodynamic response functions is then obtained:

$$H_i^*(\omega)\, H_j(\omega) \approx H_T^*(\omega)\, H_T(\omega) = |H_T(\omega)|^2 \approx (2\pi\rho V_T b_T)^2 \left(\frac{1}{1 + 2\pi \frac{\omega b_T}{V_T}}\right) \delta R_i \delta R_j \ . \tag{13}$$

At this stage the major steps of the theory have been stated. The remainder consists of formal mathematical operations. We substitute Eqs. (11), (12) and (13) in (10) and obtain an expression for the real part of the thrust force spectrum. After some algebraic manipulation this reduces to

$$\text{Re}\ G^{11}(\Gamma) = a \left(\frac{1}{1 + e\Gamma}\right)\left(\frac{\lambda}{\lambda^2 + \Gamma^2}\right)\left[c + \frac{\lambda^2 - \Gamma^2}{\lambda^2 + \Gamma^2}\right] g(M/R,\lambda) \ , \tag{14}$$

where

$$\Gamma = \frac{\omega M}{U} \ ,$$

$$a = \pi R^2 u^2 U M \left(2 b_T \rho \frac{R}{R_T}\right)^2 \left[\frac{1}{1 + \left(\frac{J}{\pi} \frac{R}{R_T}\right)^2}\right] \ ,$$

$$e = 2\pi \frac{b_T}{M} \frac{U}{V_T} \ ,$$

$$c = 2\left[1 + \left(\frac{\pi}{J} \frac{R_T}{R}\right)^2\right] \ ,$$

$J = \pi U/\Omega R$ = advance ratio ,

R = tip radius of the propeller .

The function $g(M/R,\lambda)$ relates two characteristic length scales of our problem and is given by

$$g(M/R,\lambda) = \iint e^{-\lambda q/M} R_i R_j \, dR_i \, dR_j \ , \tag{15}$$

where the integration is applied over all the elements of the propeller. In the case of a two-bladed propeller this function can be readily integrated; we obtain

$$g_2(M/R,\lambda) = \frac{4}{3}\left(\frac{M}{\lambda R}\right)\left[1 - 3\, e^{-\lambda R/M} \left(\frac{M}{\lambda R}\right)\left(1 + \frac{M}{\lambda R}\right)\left(\cosh \frac{\lambda R}{M} - \frac{M}{\lambda R} \sinh \frac{\lambda R}{M}\right)\right] .$$

For propellers containing a larger number of blades Eq. (15) has been evaluated numerically and the results are plotted in Fig. 4.

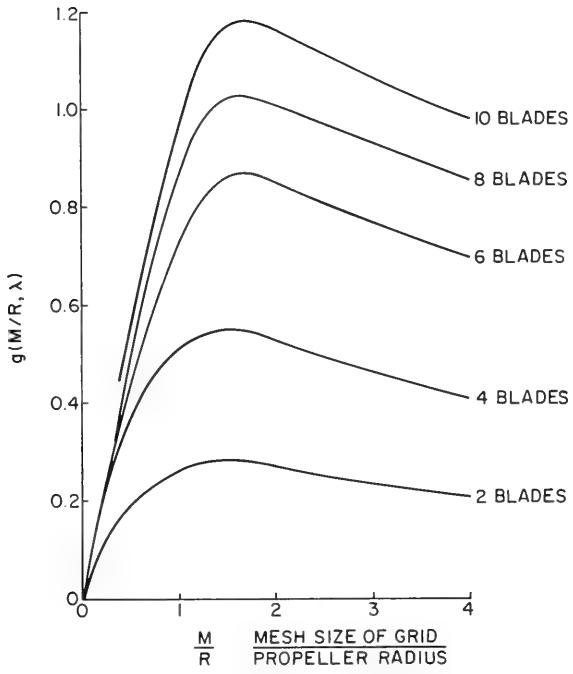

Fig. 4 - Results of numerical evaluation of Eq. (15)

The mean square of the fluctuating thrust force is obtained by integrating Eq. (14) over all frequencies:

$$\langle T^2 \rangle = \frac{U}{M} \int_0^\infty G^{11}(\Gamma)\, d\Gamma .$$

Three general functions emerge from the integration:

$$f_1(\lambda, e) = \int_0^\infty \left(\frac{\lambda}{1 + e\Gamma}\right)\left(\frac{1}{\lambda^2 + \Gamma^2}\right) d\Gamma , \tag{16a}$$

$$f_2(\lambda, e) = \int_0^\infty \left(\frac{\lambda^3}{1 + e\Gamma}\right)\left(\frac{1}{\lambda^2 + \Gamma^2}\right)^2 d\Gamma , \tag{16b}$$

$$f_3(\lambda, e) = \int_0^\infty \left(\frac{\lambda}{1 + e\Gamma}\right)\left(\frac{\Gamma}{\lambda^2 + \Gamma^2}\right)^2 d\Gamma . \tag{16c}$$

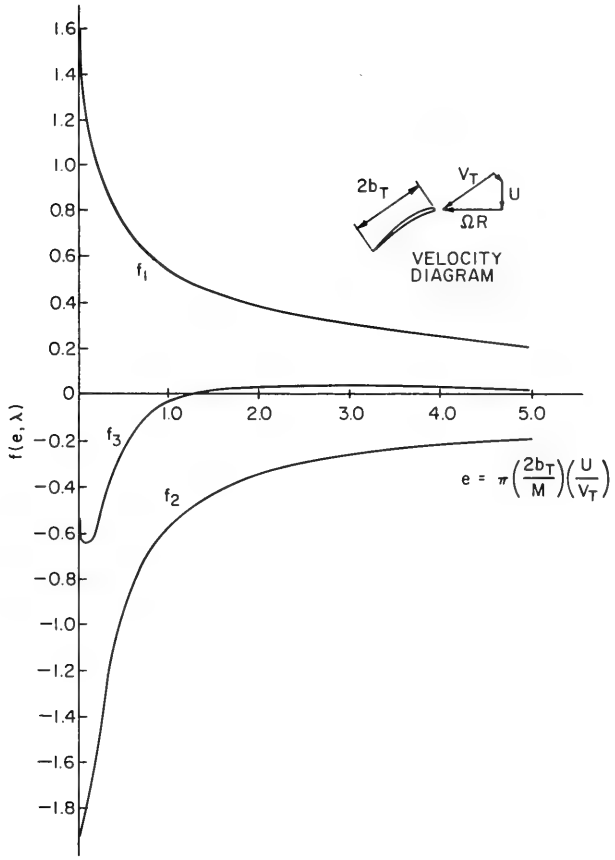

Fig. 5 - Functions f_1, f_2, and f_3 according to Eqs. (16)

These integrals, which can readily be evaluated, are plotted in Fig. 5. In terms of these functions the mean square of the fluctuating thrust force is given by

$$\langle T^2 \rangle = \frac{U_a}{M} \left(c f_1 + f_2 + f_3 \right) g(M/R, \lambda) \ . \tag{17}$$

A fluctuating thrust coefficient can now be obtained by dividing Eq. (17) by $(\rho U^2 \pi R^2/2)^2$:

$$\langle c_T^2 \rangle = \frac{16}{\pi} \left(\frac{u}{U} \right)^2 \left(\frac{b_T}{R_T} \right)^2 \left[\frac{1}{1 + \left(\frac{J}{\pi} \frac{R}{R_T} \right)^2} \right] \left[c f_1 + f_2 + f_3 \right] g(M/R, \lambda) \ .$$

The conclusions which may be drawn from this analysis can be summarized as follows:

1. The rms thrust coefficient is directly proportional to the turbulence level u/U.

2. The rms thrust coefficient depends on the ratios b/M and R/M, namely, the ratio of chord to grid mesh size and radius to grid mesh size.

3. The dependence on the advance ratio J is not very pronounced.

4. The spectrum tensor $\sqrt{\mathrm{Re}\, G^{11}(\Gamma)}$ varies as $\Gamma^{-3/2}$ for large values of the frequency parameter $\Gamma = \omega M/U$. Most of the energy is concentrated at the low-frequency end of the spectrum.

EXPERIMENTAL INVESTIGATIONS

To verify the theory experiments were conducted in the water tunnel of the Ordnance Research Laboratory at the Pennsylvania State University (8). This tunnel has a test section 4 feet in diameter and 14 feet long. Velocities as high as 80 ft/sec can be achieved, and the static pressure can be varied from 3 psia to 60 psia. A honeycomb of large ratio of length to diameter in the settling section of the tunnel reduces the turbulence level in the test section to about 0.1%.

The propeller used for this investigation had ten blades with a constant chord length of 1 inch and a radius of 4 inches. By means of hub inserts the number of blades can be changed and the propeller can be operated with two or five blades. The design static thrust coefficient based on propeller disk area is 0.183, and the advance ratio at the design thrust coefficient is 1.17. The propeller, and its installation in the water tunnel, is shown in Fig. 6.

A special balance was designed for measuring the unsteady propeller thrust force. These measurements require an instrument having a high sensitivity, a low noise level, and a natural frequency much greater than the range of frequencies of interest. Figure 7 illustrates the arrangement used. A piezoelectric crystal is mounted in a steel cup at the end of the propeller shaft. After assembly the cup is positioned by set screws until the hemispherical ball bonded to the crystal lies exactly on the centerline of the shaft, thus minimizing the crystal's response to bending distortions of the shaft caused by hydrodynamic moments acting on the propeller.

The frequency response and the linearity of the balance are shown in Fig. 8. These measurements, made in air, indicate that the useful range of the balance is approximately 600 Hz in water. As shown in Fig. 8 the frequency response was measured by means of an electromagnetic exciter whose force output was monitored by a calibrated force gage. The propeller was driven by a 20-hp dc motor housed in a streamlined enclosure. It was mounted as far downstream as possible in the test section and was carefully aligned so that the propeller shaft was concentric with the center line of the tunnel.

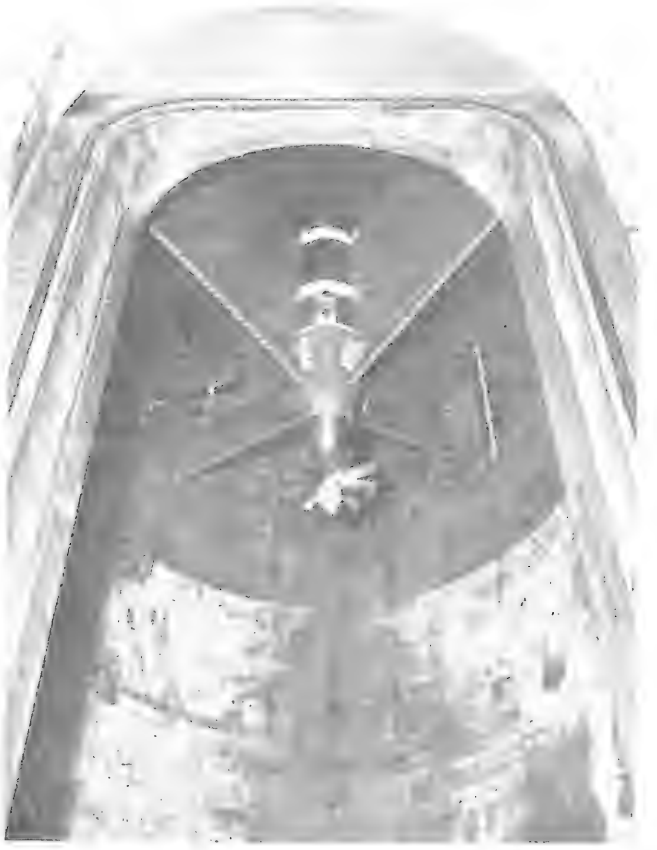

Fig. 6 - Free-stream propeller and balance housing mounted in the water tunnel test section

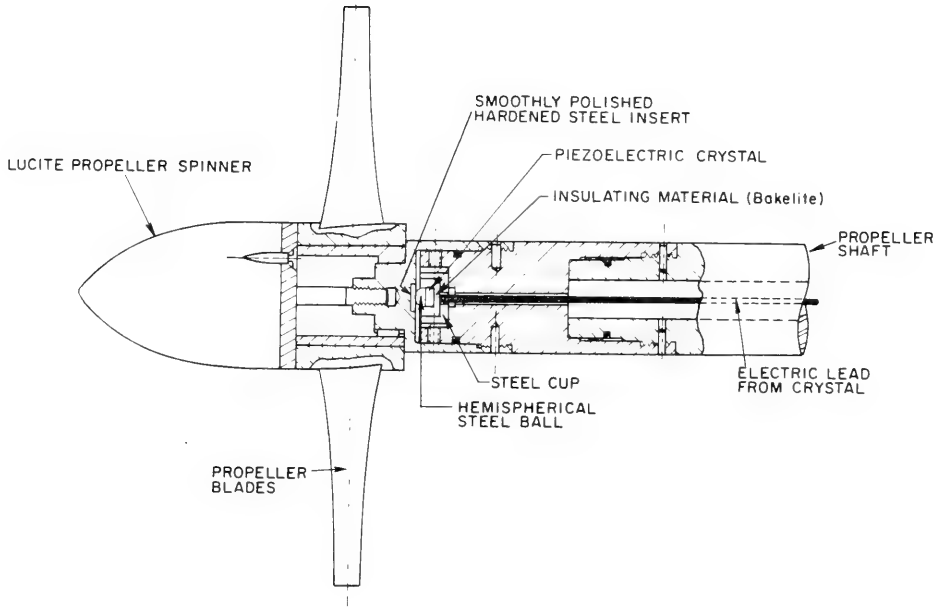

Fig. 7 - Unsteady-force balance

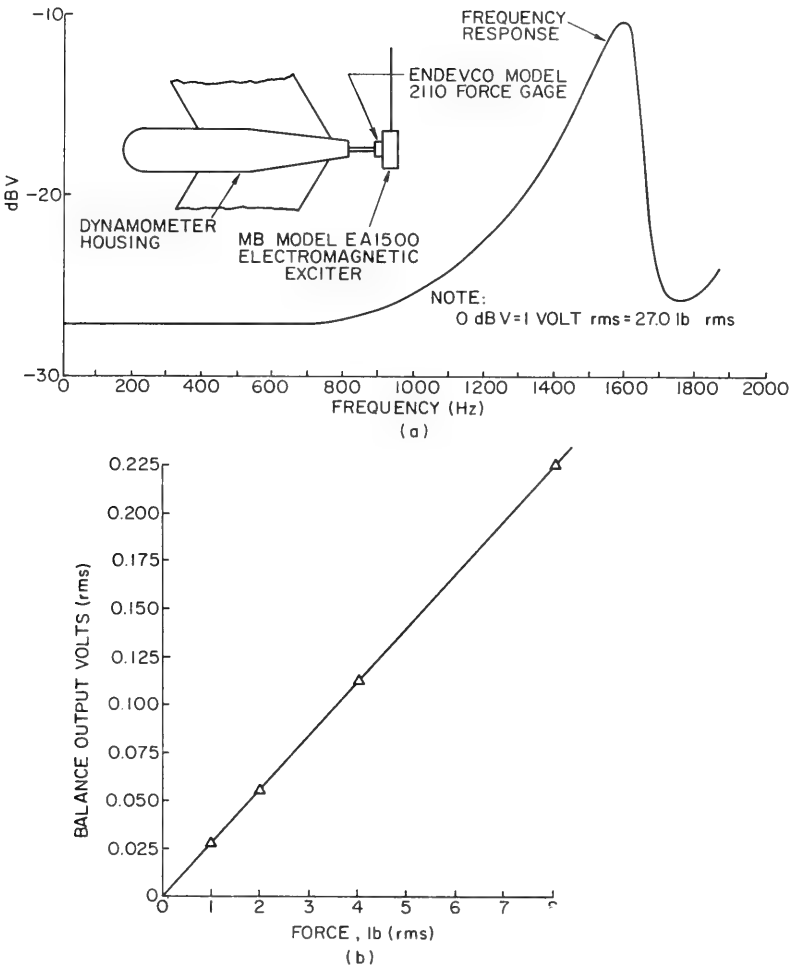

Fig. 8 - Linearity and frequency response of the dynamic-force balance shown in Fig. 7

During the tests turbulence was generated by grids mounted 20 mesh sizes upstream of the propeller. Two grids were used with mesh sizes of 4 inches and 6 inches respectively. The first had a solidity of 0.34 and was fabricated with 3/4-inch-diameter rods. The second had a solidity of 0.27 and consisted of 7/8-inch-diameter rods. Figure 9 shows the propeller photographed from upstream of the 4-inch grid in the water tunnel.

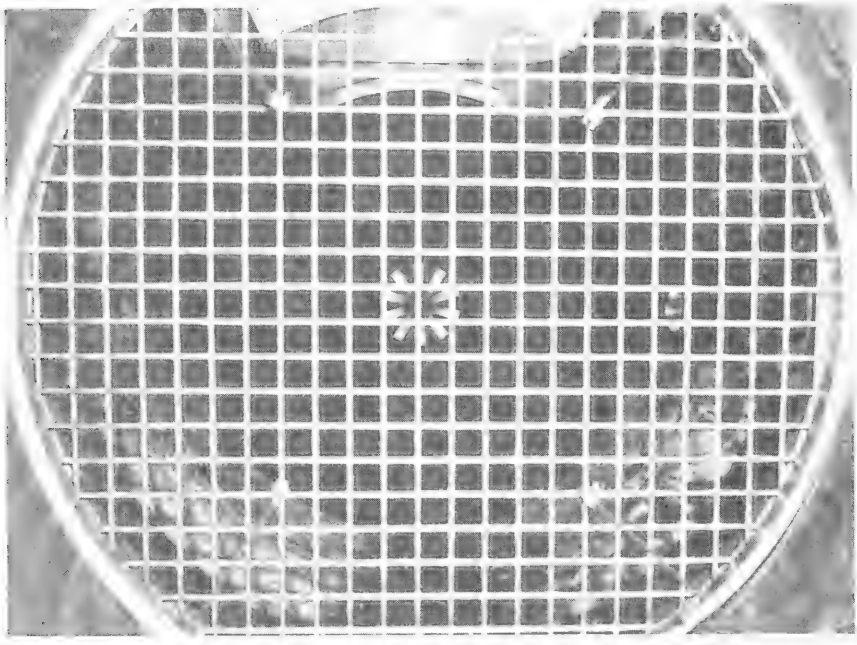

Fig. 9 - Propeller as seen through a 4-inch grid upstream of the propeller

The test were performed at a velocity of 15 ft/sec and at two advance ratios. Initially, runs were made without grids in order to establish the noise level of the balance and of the electronic data acquisition system. The grids were then mounted in the tunnel, and the measurements were repeated. During the entire test program the tunnel pressure was maintained at 20 psia, which ensured absence of cavitation. At the completion of the program the balance was recalibrated, and it was established that its characteristics were unaltered.

The circuitry used for data acquisition is shown in Fig. 10. Three SKL Model 308A variable electronic filters were set up as a bandpass filter. Two, used as high-pass filters, were cascaded to produce a 48-dB-per-octave rejection rate below the cutoff frequency. These filters eliminated the strong balance output at a frequency corresponding to the shaft rps. The cutoff frequency of the high-pass filters were varied with the rps of the propeller shaft. For the

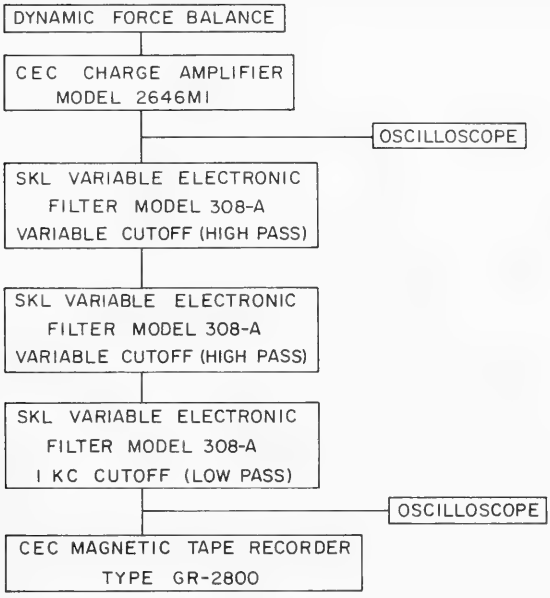

Fig. 10 - Circuitry for data acquisition

data presented here this frequency was 29 Hz. The third filter was used as a low-pass filter with the cutoff frequency fixed at 1 kHz.

After the signal was filtered, it was recorded on a CEC Type GR2800 magnetic tape recorder. The force balance signal was monitored and compared on an oscilloscope at several points in the circuitry as well as from the magnetic tape immediately after being recorded. This was done to detect and prevent any signal distortion in the data acquisition system.

The data were analyzed by means of the instruments indicated in Fig. 11. The signal was played back from the magnetic tape and passed through a Hewlett-Packard Model 302A wave analyzer. This has a constant bandwidth of 7 Hz between the half-power points. The filtered signal was then squared by a Ballantine Model 320 true rms voltmeter and finally integrated for 60 seconds with a Dymec Model 2401C integrating digital voltmeter. All voltage outputs were then converted to forces by using the measured calibration factors.

The data are shown in Figs. 12 and 13. As mentioned before, the low-frequency end of the spectrum had to be filtered to eliminate a strong line component corresponding to the shaft frequency. Consequently it was not possible to determine experimentally the rms thrust coefficients. However, Figs. 12 and 13 indicate good agreement between the theoretically predicted and the measured power spectral densities, except where the measurements show a hump. The reason for this discrepancy is at present not clear.

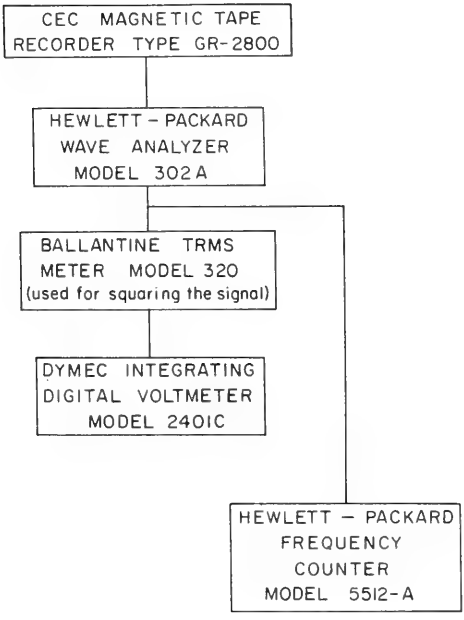

Fig. 11 - Circuitry for data reduction

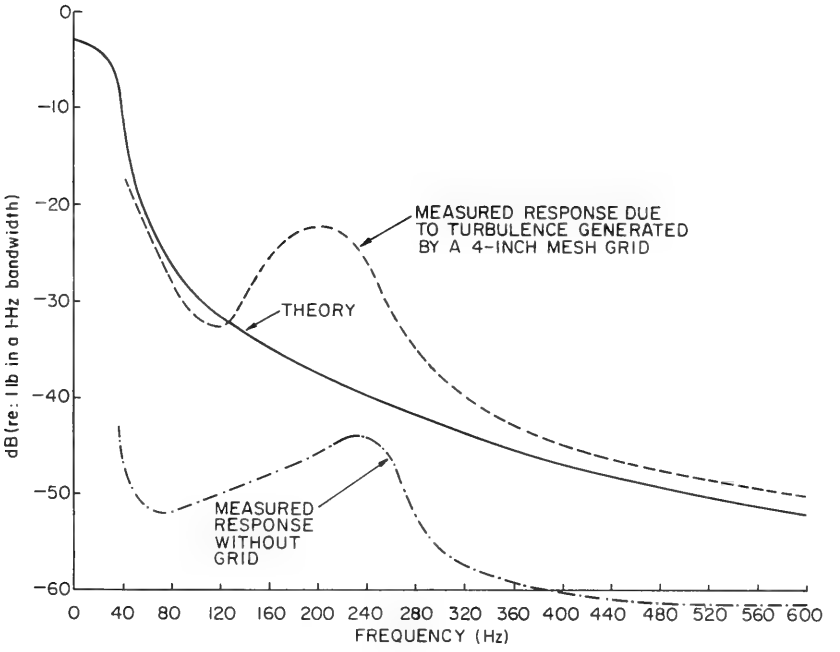

Fig. 12 - Power spectral density of the response of a ten-bladed, 8-inch-diameter propeller to turbulence (Test 5531, Run 2: distance between the grid and the propeller = 20M = 80 inches; measured water-tunnel turbulence level without the grid $u = 0.0011U$; turbulence level at the propeller due to the grid $u = 0.03U$; tunnel velocity $U = 15.4$ ft/sec; propeller advance ratio $J = 1.22$)

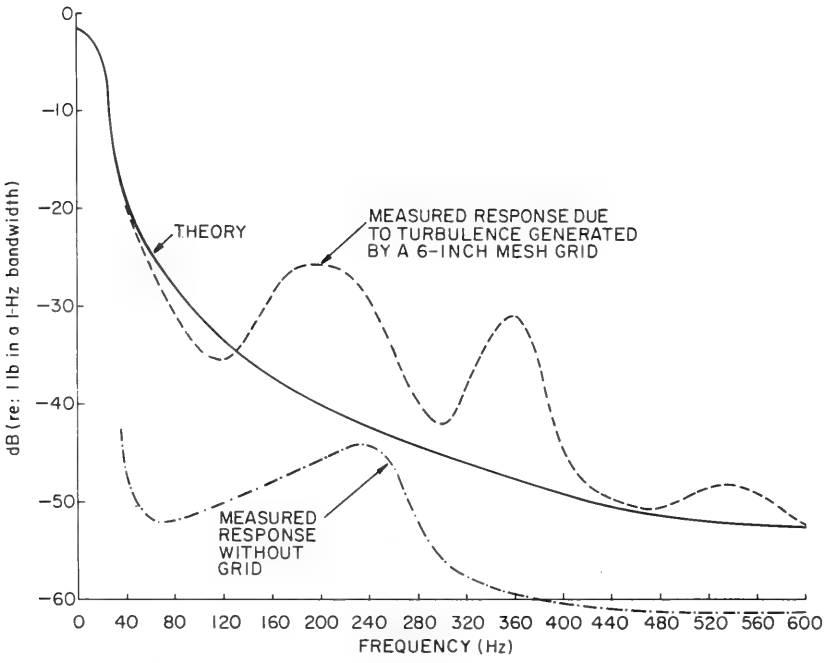

Fig. 13 - Power spectral density of the response of a ten-bladed, 8-inch-diameter propeller to turbulence (Test 5530, Run 2: distance between the grid and the propeller = 20M = 120 inches; measured water-tunnel turbulence level without the grid u = 0.0011U; turbulence level at the propeller due to the grid u = 0.03U; tunnel velocity U = 15.1 ft/sec; propeller advance ratio J = 1.22)

In the case of the 4-inch-grid the theory predicts an rms thrust coefficient of 0.0234, which is equal to 12.8% of the steady-state thrust coefficient. In the case of the 6-inch grid the corresponding values are 0.0250 and 13.6%. In view of the good agreement of the power spectral density at low frequencies, these values appear to be reliable.

REFERENCES

1. Kemp, N.H., and Sears, W.R., "Aerodynamic Interference Between Moving Blade Rows," J. Aeronautical Sciences 20, 585-598 (1953)

2. Kemp, N.H., and Sears, W.R., "The Unsteady Forces Due to Viscous Wakes in Turbomachines," J. Aeronautical Sciences 22, 478-483 (1955)

3. Lewis, F.M., and Tachmindji, A.J., "Propeller Forces Exciting Hull Vibration," Trans. SNAME 62, 1954

4. Shioiri, J. and Tsakonas, S., "Three-Dimensional Approach to the Gust Problem for a Screw Propeller," Stevens Institute of Technology, Davidson Laboratory Report 940, Mar. 1963

5. Boswell, R., "Measurement, Correlation with Theory, and Parametric Investigation of Unsteady Propeller Forces and Moments," M.S. Thesis, Department of Aerospace Engineering, The Pennsylvania State University, Dec. 1967

6. Stewart, R.W., and Townsend, A.A., "Similarity and Self-Preservation in Isotropic Turbulence," Trans. Royal Soc. 243, 359-386 (1951)

7. Sears, W.R., "Some Aspects of Non-Stationary Air Foil Theory and Its Practical Application," J. Aeronautical Sciences 8(No. 3) (Jan. 1941)

8. Lehman, A.F., "Garfield Thomas Water Tunnel," Ordnance Research Laboratory Report NOrd 16597-56, The Pennsylvania State University, Sept. 1959

* * *

DISCUSSION

Paul Kaplan
Oceanics, Inc.
Technical Industrial Park, New York

This paper presents an aspect of unsteady propeller forces that differs from those discussed earlier: it covers a stochastic influence rather than a regular

periodic effect. However it is possible that there is a relation between the two that shows up in the present results, in particular which is concerned with the discrepancy in the figures exemplified by the hump in Fig. 12. Simple calculations indicate that the propeller rotational speed in that case was 19 rps, and the blade rate associated with this case for a ten-bladed propeller would then correspond to 190 Hz. The appearance of the hump in the spectral density presented in Fig. 12 could possibly be due to the existence of a periodic blade-rate signal, which would be obtained via a wave analyzer with the bandwidth characteristics of the equipment used in this study. It is thus possible that the blade-rate signal occurs, since the fluctuations in the propeller thrust force should be due to velocity fluctuations about a steady value, corresponding to the inflow speed, which should be constant circumferentially at any radius. Even though the grid is assumed to be symmetric, and also the tunnel as well, it would be best to survey the flow field that is entering the propeller disk to be certain that no harmonics of blade rate are present in the oncoming flow. A detailed consideration of this point is essential if any random process is analyzed, since the analysis must always refer to a base reference, and the characteristics of that reference should be known and used in analyzing the characteristics of any random response. It is suggested that careful consideration of these points may eliminate spurious results in the future.

* * *

REPLY TO DISCUSSION

Maurice Sevik

The hump in Fig. 12 was a matter of concern, and the reason for its presence was investigated after completion of the experiments. It was felt that vibrations of the propeller blades might be the cause. The first two natural frequencies of the propeller blades were established by calculation and verified experimentally. The fundamental frequency occurred at 127 Hz; the associated mode shape is shown in Fig. D1. The second mode occurred at 231 cps and its modal shape was essentially torsional. The hump in Fig. 12 is located at about 220 Hz, and it appears that it is due to the second mode of vibration of the individual blades, whose resonances are spread in the vicinity of this frequency.

However, I agree that Dr. Kaplan's explanation is also a reasonable one. It is unfortunate that the blade-rate frequency and the natural frequency mentioned above fall so close together that a separation of the two effects is not possible.

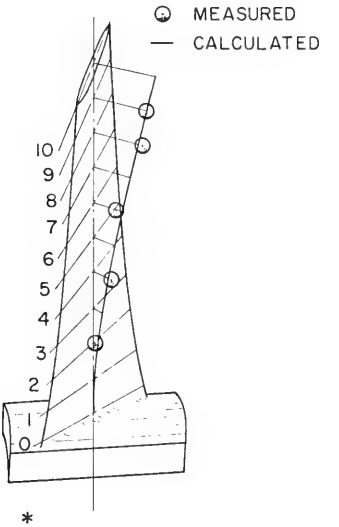

Fig. D1 - Mode shape associated with the fundamental natural frequency of vibration of a typical propeller

* * *

Tuesday, August 27, 1968

Morning Session

FUNDAMENTAL HYDRODYNAMICS

Chairmen: Dr. I. Stakgold

Office of Naval Research Branch Office
London, England

and

Dr. K. Wieghardt

Institut für Schiffbau der Universität Hamburg
Hamburg, Germany

RECENT PROGRESS IN THE CALCULATION OF POTENTIAL FLOWS

A. M. O. Smith
Douglas Aircraft Division, McDonnell Douglas Corp.
Long Beach, Calif.

ABSTRACT

Since about 1954, work has been underway at Douglas Aircraft on the problem of calculating flow about arbitrary bodies by means of a surface source-sink treatment that leads to solution of a Fredholm integral equation of the second kind. The method has been quite successful, and a general review of this work was published in 1966. The present paper describes work done since about 1965, the latest year reported in the published review, and begins with a review of the basic method. Then attention is directed to the principal topics dealt with since 1965. They are:

1. Nonlinear, unsteady airfoil and hydrofoil theory, including two-body problems.

2. Compilation of a report containing extensive flow-field charts for a variety of two-dimensional and axisymmetric bodies.

3. Numerical integration of oscillating functions having nonlinear arguments. This problem arises in wave resistance theory.

4. The dynamics of a three-dimensional floating body subject to simple harmonic motion in any of the six modes (heave, roll, etc.) but otherwise at rest.

5. Some remarks about Laplace problems that do not necessarily deal with fluid flows.

Several interesting results from work on these topics are available and are presented as supporting material.

INTRODUCTION

The subject of this paper is a very general method of flow calculation about arbitrary bodies. A broad review of the work up to 1965 can be found in Ref. 1, which was issued late in 1966. This work has continued to be active, and it is timely to report on the developments that have occurred since 1965. As many readers are not familiar with the work, we shall begin by presenting a short description of the basic method, as well as some examples. We will follow with descriptions of the new work, which includes unsteady-airfoil theory, flow fields,

several problems of naval hydrodynamics, and other problems stemming from Laplace's equation.

A preliminary idea of the power and of the state of development of the method of analysis will be conveyed by an example. Studies supported by NASA (e.g., "Study and Development of Turbofan Nacelle Modifications to Minimize Fan-Compressor Noise Radiation," Contract NAS1-7130) are underway to reduce the noise of jet engines. Figure 1 illustrates one type of inlet that has been designed. It was tested on the ground at full scale under full-power conditions. The two ring airfoils have a double purpose; first, to block passage of noise to the exterior from the fan blades, and second, to provide more area for sound-absorbing material, because the vanes are constructed of such material. The ring airfoils have outwardly directed lift to keep them in tension. As the sketch shows, the inlet consists of four separate bodies; the outer cowl, the two ring airfoils, and the centerbody. The problem further consists of mixed internal and external flows. The vanes as well as the basic inlet were all analyzed as a unit, so that mutual interferences would be properly accounted for. The vanes were shaped and positioned so as to obtain minimum disturbance to the flow by selecting a total configuration, calculating the flow, finding bad pressure distribution features, and correcting them by changes in shape, recalculation, etc., until all the pressures appeared to be the best that could be expected. Boundary layer calculations went hand in hand with the potential flow calculations. The design and analysis were performed by John Hoehne, who is strictly a routine user of the computing program as a design tool, without any need for assistance from those such as John Hess, who has done most of the development. As a matter of fact, while the author was aware of the NASA noise reduction project, he was quite unaware of this particular work until told of the successful ground tests. These tests showed a large reduction in sound level and a barely measurable loss in thrust.

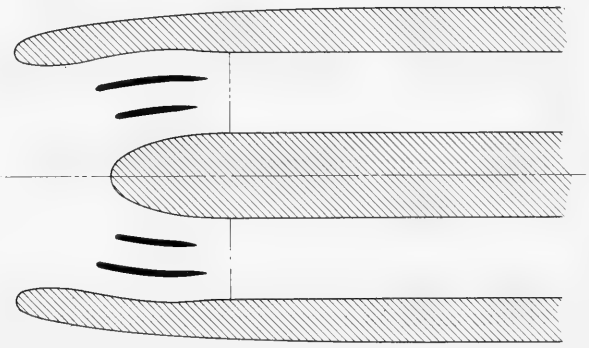

Fig. 1 - An experimental "quiet" turbojet inlet designed by means of the present method of potential-flow calculation.

A SHORT DESCRIPTION OF THE BASIC METHOD

General Remarks

In this section a general description of the basic method will be given, using a minimum of mathematical formulas. All the basic equations and formulas can be found in Ref. 1. If a maximum amount of detail is desired the reader is referred to the various reports and papers listed in (1). Three classes of shapes are treated: two-dimensional bodies, axisymmetric bodies, and truly three-dimensional bodies that may or may not have planes of symmetry.

Mathematical Statement of the Problem

The problem considered is the irrotational flow of an inviscid, incompressible fluid about an arbitrary body surface or surfaces on which the normal velocity of the fluid is either zero or a known quantity. Furthermore, the geometry itself may vary with time. Except at the known body surface, the fluid is unbounded, and the onset flow, i.e., the velocity field that would exist in the fluid if the body were removed, is prescribed. This is a so-called Neumann problem for Laplace's equation and can be formulated mathematically in the following way.

Let the surface of the body be denoted by S, and let the velocity field that would exist in the fluid if the body were removed be denoted by $\mathbf{V}_\infty$. In most cases the onset flow is a uniform stream, and hence $\mathbf{V}_\infty$ is a constant vector. The situation is sketched in Fig. 2 for the case of a fully three-dimensional flow about a single body surface S. For more than one body surface, the situation is not essentially different. The disturbance velocity field due to the presence of the body surface is assumed to be irrotational, and thus it may be expressed as the negative gradient of a potential function φ. This function must satisfy three conditions: It must satisfy Laplace's equation in the region R' exterior to S, must approach zero at infinity, and must have a normal derivative on the surface S equal but opposite to the normal component of the onset flow. (The last condition is where the total normal velocity on the body surface is prescribed as zero. If it is prescribed as nonzero, there is no essential change.) These three conditions may be expressed symbolically as

$$\nabla^2 \varphi = 0 \quad \text{in region } R' , \tag{1}$$

$$|\text{grad } \varphi| \to 0 \quad \text{for} \quad (x^2 + y^2 + z^2) \to \infty , \tag{2}$$

$$\left.\frac{\partial \varphi}{\partial n}\right|_S = \left. + \mathbf{n} \cdot \mathbf{V}_\infty \right|_S , \tag{3}$$

where $\mathbf{n}$ is the unit outward normal vector on the surface as shown in Fig. 2 and n denotes distance along this normal. The Laplacian operator is denoted by ∇^2. The plus sign in Eq. (3) is because the normal velocity due to the body is $-\partial\varphi/\partial n$.

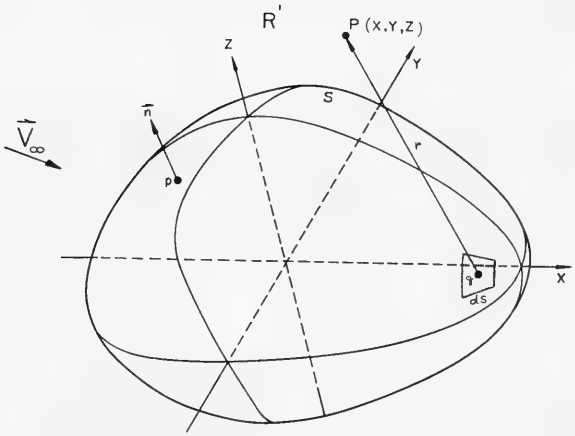

Fig. 2 - Flow about a three-dimensional body

Representation of the Solution by a Surface-Source Distribution

In the present method, the solution is expressed as the potential of a source distribution over the body surface. The potential at a point P due to a point source of unit strength at q is $1/r(P,q)$, where $r(P,q)$ is the distance between two points (Fig. 2). Accordingly, the potential at a point P with coordinates x,y,z due to a source distribution σ over the surface S is

$$\varphi(x,y,z) = \iint_S \frac{\sigma(q)}{r(P,q)}\, dS \,, \qquad (4)$$

where q is a point on the surface S, and dS is an elemental surface area as shown in Fig. 2. Reference 2 has shown that the function satisfying Eqs. (1), (2), and (3) can indeed be represented in the form given Eq. (4). The function φ as given by Eq. (4) satisfies Eqs. (1) and (2) identically for any function σ. This is true simply because the function $1/r(P,q)$ satisfies these conditions. The function σ is determined from the boundary condition on S, Eq. (3). Applying Eq. (3) requires the evaluation of the limit of the normal derivative Eq. (4) as the field point P approaches a point p on the surface S. The derivatives of $1/r(P,q)$ now become singular as P approaches p, and care is required in evaluating the limit.

The limiting process is discussed in detail in Ref. 2. The results are stated here without proof. The limit of the normal derivative of the integral of Eq. (4) consists of two terms. One is the expected term, which is the integral of the normal derivative of the integrand of Eq. (4) evaluated on the surface, i.e., $P = p$. This integral is an ordinary integral, not a principal value, because its integrand is integrable. The other term is something of a surprise. It is a "local effect" term that expresses the fact that an infinitesimal neighborhood of the point p has a finite contribution to the normal derivative there. As is shown in Ref. 2, the "local effect" term is $-2\pi\sigma(p)$. Finally, the result of applying Eq. (3) to φ as given by Eq. (4) is

$$2\pi\sigma(p) - \iint_S \frac{\partial}{\partial n}\left[\frac{1}{r(p,q)}\right]\sigma(q)\,dS = -\mathbf{n}(p)\cdot\mathbf{V}_\infty \,, \tag{5}$$

where the unit outward normal vector has been written $\mathbf{n}(p)$ to show explicitly its dependence on location. The onset flow velocity $\mathbf{V}_\infty$ may or may not vary with position. Equation (5) is seen to be a Fredholm integral equation of the second kind, over the body surface S. Once this equation is solved for the source density distribution σ, the potential φ may be evaluated from Eq. (4) and the disturbance velocity components from the derivatives of Eq. (4) in the three-coordinate directions.

This method of solution is very general. The body surface S is not required to be slender, analytically defined, or even simply-connected; that is, there may be several bodies, as in the example of Fig. 1. The only restriction is that S must have a continuous normal vector $\mathbf{n}(p)$, which means that the method cannot be guaranteed to give correct results for bodies with corners. In practice, this difficulty can be avoided by rounding off any corners with a small radius. Trial calculations show that the method does however give correct results for convex corners, but there may or may not be significant errors near unrounded concave corners. The onset flow $\mathbf{V}_\infty$ is not restricted to being a uniform stream. It may be any flow consistent with the assumption that the perturbation velocity field due to the body is irrotational. This is satisfied if the onset flow has a constant vorticity — a uniform shear, for example — since it can be shown that the perturbation velocity is irrotational.

The efficiency of the method is that only the body surface itself needs to be considered, not the entire exterior flow-field. Thus the dimensionality of the problem is reduced by one: from three to two in three-dimensional problems, and from two to one in axisymmetric and two-dimensional problems; for in these cases the double integral of Eq. (5) can be reduced to a single integral by performing one integration analytically. The area of interest is also shifted from the infinite to the finite.

General Description of the Method of Solution

The central problem of the present method of flow calculation is the numerical solution in Eq. (5). The integral equation is replaced by a set of linear algebraic equations in the following way.

The body surface is approximated by a large number of surface elements, each of which is small in comparison to the characteristic dimensions of the body. Over each surface element the value of the surface source density is assumed constant. That assumption reduces the problem of determining the continuous source density function σ to the problem of determining a finite number of values of σ, one for each of the surface elements. The contribution of each element to the integral in Eq. (5) can now be obtained by taking the constant but unknown value of σ on that element out of the integral and then performing the indicated integration of known geometrical quantities over the element. Requiring Eq. (5) to hold at one point of the approximate body surface, i.e., requiring the normal velocity to vanish (or to take on a prescribed value) at one point, gives a linear

relation between the values of σ on the elements. On each element one point is selected where Eq. (5) is required to hold; i.e., one point is selected where the normal velocity is required to vanish. That requirement gives a number of linear equations equal to the number of unknown values of σ. Once they are solved, flow velocities may be calculated at any point, on or off the body surface, by summing the contributions of the surface elements and the contribution of the onset flow. Usually, velocities and pressures on the body surface are of greatest interest. Because of the way in which the body surface is approximated, these must be evaluated at the same points where the normal velocity was made to vanish.

Approximation of the Body Surface

Figure 3 shows the surface elements used to approximate various types of bodies. Three-dimensional body surfaces are approximated by plane quadrilateral elements, axisymmetric bodies by frustums of cones, and two-dimensional bodies by infinite plane strips. In three-dimensional cases, the body is specified by the coordinates of a set of points distributed over the body surface. These points are used to form quadrilateral elements. For two-dimensional or axisymmetric bodies, only a single-profile curve is specified by points. These points are connected by straight-line segments, which are then the traces of the infinite plane strips or the frustums of cones in the plane of the profile curve.

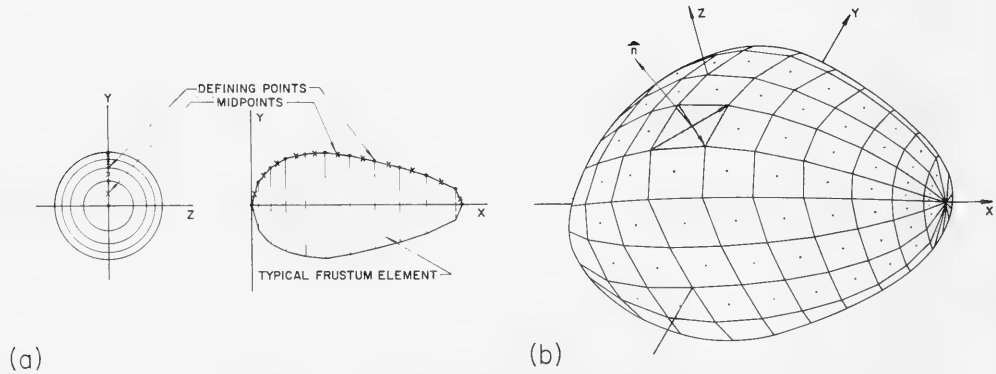

Fig. 3 - Approximation of the body surface by elements (a) two-dimensional and axisymmetric bodies, (b) three-dimensional bodies

If the body surface is axisymmetric, it is not necessary that the flow itself also be symmetric about the same axis. If the flow is axisymmetric, it is independent of circumferential location about the axis of symmetry, and thus the surface source density is truly constant over each frustum element. It is only necessary that the flow vary with the circumferential location in a known way. The

source density is then constant over each frustum only in the axial direction and varies in a prescribed manner circumferentially. This is the situation, for example, when there is flow over a body of revolution at angle of attack. As Ref. 1 shows, this problem may be solved without resort to fully three-dimensional techniques.

For two-dimensional and axisymmetric bodies, the edges of adjacent elements are coincident, but this is not necessarily so for three-dimensional bodies. In general, a three-dimensional body cannot be approximated by plane quadrilaterals in such a way that the edges of adjacent elements are coincident. Any errors due to these gaps are of a higher order than, and negligible with respect to, the errors due to the approximation of the body by plane elements in the first place. Nevertheless, the fact that small gaps exist between the elements is sometimes disturbing to people hearing about the method for the first time. It should be kept in mind that the elements are simply devices for finding the surface source distribution and that the polyhedral body shown in Fig. 3 has no direct physical significance, in the sense that the flow eventually calculated is not that about the polyhedral body. Even if the edges of adjacent elements are coincident (as, for example, can be arranged for any body of revolution), the normal velocity is zero at only one point of each element and there is flow through the remainder of the element. Also, the computed velocities will be infinite on the edges of the elements whether these are coincident or not, as long as there is a break in slope or in source density. The unimportance of the gaps has been further demonstrated by calculating axisymmetric bodies with element distributions that had coincident edges and then recalculating with slight gaps. The two types of element distributions gave essentially identical results. The gaps between the elements can be eliminated by the use of plane triangular elements. This procedure, however, results in no increase in accuracy — in fact may cause a loss of accuracy — and so greatly complicates the input to the digital computer program as to impair its usefulness as a design tool. On many bodies of technical importance such as ships, wings, and hydrofoils, approximation of the shape by quadrilaterals is much more natural than approximation by triangles. However, the triangle is merely a special case of a quadrilateral, and the present method can, in fact, handle triangular approximation, if that is desirable.

This method of geometric representation has been used without modification as a basis for analyzing complicated shapes in hypersonic flow. Figure 4 is taken from some of this work to give an impression of the accuracy of the method. The figure was made by an SC4020 plotter (3).

Induced Velocities

On each element one point is selected at which velocities and pressure are to be evaluated. For two-dimensional and axisymmetric bodies, the point selected is the midpoint of the line segment that is the trace of the element in the plane of the profile curve, i.e., the average of two successive points that were used to define the profile curve (Fig. 3). This is the obvious choice for two-dimensional bodies and probably a reasonable selection for axisymmetric

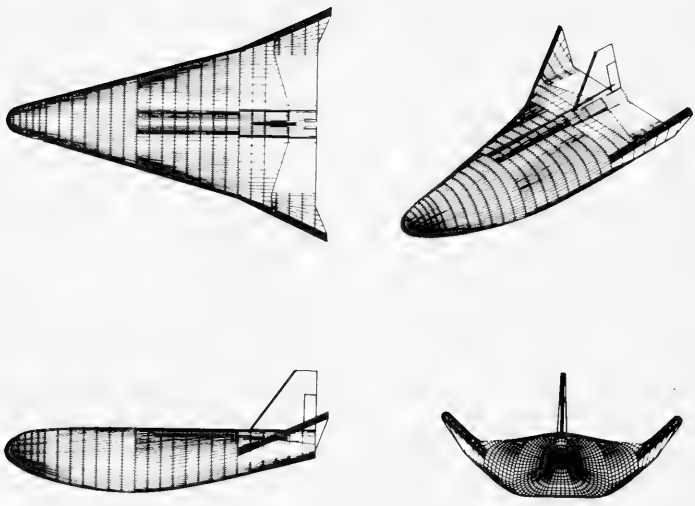

Fig. 4 - Geometric representation of the NASA HL-10 reentry vehicle. Each half is represented by 1278 quadrilateral elements

bodies, although not as obvious for the latter. For the plane quadrilateral elements used with truly three-dimensional bodies, the proper point to use is not obvious at all. For rectangular elements, it seems evident that the point should lie at the center, but there are many possible definitions which reduce to the center for these elements. On each quadrilateral element there is one point where a constant source density on that element gives rise to no velocity in its own plane, i.e., there is a point where the effect of the element is entirely normal to itself. It was decided to evaluate velocities and pressures at this point. For elements that are nearly rectangular this point is located near the centroid of the area of the quadrilateral, but for certain types of quadrilaterals the two points may be a significant distance apart. For all types of body surfaces the point on an element where velocities and pressures are evaluated is designated as the control point of that element.

Once the body surface has been approximated by elements of the appropriate type, the elements are ordered sequentially and numbered from 1 to N, where N is the total number of elements. The exact order of the sequence is immaterial. It is simply a logical device for keeping track of the elements during the computational procedure. Reference will accordingly be made to the ith element and the jth element, where the integers i and j denote the position of the elements in the sequence.

Assume for the moment that the surface source density on the jth element has a constant value of unity. Denote by $\mathbf{V}_{ij}$ the vector velocity at the control point of the ith element that is induced by a unit source density on the jth element. The formulas for the induced velocity $\mathbf{V}_{ij}$ are the basis of the present method of flow calculation. They are obtained by integrating the formulas for the velocity induced by a point source over the element in question, and thus depend on the geometry of the element and the location of the point where the velocity is being evaluated. Since there is no restriction on the location of the control point of the ith element with respect to the jth element, the formulas for $\mathbf{V}_{ij}$ are those for the velocity induced by an element at an arbitrary point in space. The dependence of the induced velocity on the geometry of the element means that there are three completely distinct sets of formulas for $\mathbf{V}_{ij}$, corresponding to the three different types of elements that are needed. Different kinds are used according to whether the bodies are two-dimensional, axisymmetric, or three-dimensional. The axisymmetric situation is further subdivided into the case where the flow is also axisymmetric (i.e., the source density is independent of circumferential location), and the case where the flow is not axisymmetric but is due to a uniform stream perpendicular to the axis of symmetry of the body (i.e., the source density varies with circumferential location in a known way). The induced-velocity formulas (1) are rather lengthy and will not be given explicitly here. A brief discussion of their nature follows.

In two-dimensional and three-dimensional cases the elements are those of a plane, and the integration over an element may be performed analytically to obtain explicit expressions for $\mathbf{V}_{ij}$ in terms of logarithms and inverse tangents. (Obviously, the two-dimensional formulas can be obtained as limiting cases of the three-dimensional formulas, but this is not a computationally efficient procedure.) In three-dimensional cases, so many elements are required to approximate adequately the body surface, that the use of the rather complicated induced-velocity formulas obtained by direct integration is quite time-consuming. Accordingly, these formulas are used only when the control point of the ith element is within a few element dimensions of the jth element. For points farther away, approximate formulas based on a multiple expansion are used. If the point in question is farther from the centroid of the element than four times the maximum dimension of the element, the actual quadrilateral source element may be replaced by a point source of the same total strength located at its centroid, with no loss in the overall accuracy of the method and with a very large saving in computation time. In both two-dimensional and three-dimensional cases, the computation is not significantly complicated by the condition $i = j$; i.e., the velocity induced by an element at its own control point is calculated without undue difficulty, because the integration is analytic. This velocity has a magnitude of 2π and a direction normal to the element [see the discussion preceding Eq. 5)].

For axisymmetric bodies the surface element is a frustum of a cone, and the integration over the element of the velocity induced by a point source cannot be performed analytically. First, the integration in the circumferential direction is accomplished, to give the velocity induced by a ring source, which is expressed in terms of the complete elliptic integrals. The resulting expressions are then integrated numerically over the line segment that is the trace of the element in the plane of the profile curve, as shown in Fig. 3. The number of coordinates used in the numerical-integration scheme decreases with increasing distance of the control point from the element in question. Thus, a saving in computation

time is effected with no loss of overall accuracy. The case of $i = j$, i.e., the calculation of the velocity induced by an element at its own control point, requires special handling for axisymmetric elements. Here the result cannot be predicted in advance, as it can be for the two-dimensional and three-dimensional elements, because of the complicated nature of the ring-source formulas. The procedure is described in detail in Ref. 1. Basically, it consists of a series expansion of the integrand about the singularity at the control point. In the case of axisymmetric flow, the induced velocities have two components, one parallel to the axis of symmetry of the body and one radially outward from or inward to this axis. In the case of flow due to a uniform stream perpendicular to the axis of symmetry, the circumferential variation of the surface source density gives rise to an additional circumferential component of induced velocities.

The Set of Linear Equations for the Values of Surface Source Density

A complete set of N^2 induced-velocities $\mathbf{V}_{ij}$ is computed, to give the velocities induced by all elements at each other's control points. (It will be recalled that N denotes the total number of elements used to approximate the body surface.) In this calculation a constant unit-value of source density is assumed on each element. The quantity

$$A_{ij} = \mathbf{n}_i \cdot \mathbf{V}_{ij} \ , \tag{6}$$

obtained by taking the dot product of $\mathbf{V}_{ij}$ with the unit normal vector $\mathbf{n}_i$ of the ith element, is thus the normal velocity induced at the control point of the ith element by a unit source density on the jth element. Multiplying A_{ij} by the constant but unknown value of σ_j of the source density on the jth element then gives the actual normal velocity at the control point of the ith element due to the jth element. This is the contribution of the jth element to the integral of Eq. (5), where that equation is being required to hold at the control point of the ith element. Summing the normal velocities due to all elements at the control point of the ith element, setting the result equal to the negative of the normal component of the onset flow at that point, and repeating the process for the control points of all elements will give a set of linear algebraic equations for the values of the source density on the elements. Specifically

$$\sum_{j=1}^{N} A_{ij}\sigma_j = -\mathbf{n}_i \cdot \mathbf{V}_{\infty_i} \ , \quad i = 1, 2, \ldots, N, \tag{7}$$

where $\mathbf{V}_{\infty_i}$ is the onset flow evaluated at the control point of the ith element. The set of equations in Eq. (7) is the approximation of Eq. (5).

The set of linear equations in Eq. (7) is solved by an elimination procedure, the method of successive orthogonalization, if the order N is less than 275. This number of elements is sufficient for good accuracy in most two-dimensional and axisymmetric cases. For N greater than 275, the capacity of the computer does not permit solution by direct elimination, and an iterative procedure must be used. In practice, this means iterative solutions are used for three-dimensional bodies and elimination for two-dimensional and axisymmetric bodies. Many conventional matrix-iteration techniques are not efficient in this case,

because the matrix A_{ij} is neither symmetric nor sparse. In fact, none of the terms of A_{ij} need iteration by zero in general. The matrix does, however, have a dominant main diagonal. It will be recalled that the diagonal terms A_{ii} are exactly 2π in two-dimensional and three-dimensional cases. They are fairly close to this value in axisymmetric cases. To a first approximation, the sum of all diagonal terms equals the sum of all off-diagonal terms, and thus on the average each diagonal term equals the sum of the other term in its row. For convex bodies all terms are positive, and thus similar statements hold for the absolute values of the terms. Because of the dominance of the main diagonal, the Gauss-Seidel iterative procedure has been found to be quite effective in the solution of the set of equations in Eq. (7). It has converged in all cases. Usually, convergence is quite rapid, although for certain extreme types of bodies this may not be true. Unfavorable cases typically require as many as 200 iterations, but normal cases converge in about 16 iterations or, more precisely, 4 iterations per decimal place in σ. Methods of accelerating the convergence have been studied and found effective, but have not been incorporated into the method. A great deal more information about convergence rates is given in Ref. (1).

Calculation of Velocities

Once the set of equations in Eq. (7) has been solved, the velocities at the control points of the elements are calculated from

$$\mathbf{V}_i = \sum_{j=1}^{N} \mathbf{V}_{ij}\sigma_j + \mathbf{V}_{\infty_i}, \quad i = 1, 2, \ldots, N. \tag{8}$$

Potentials can also be calculated, using similar types of formulas, if desired. The pressure coefficient C_p is computed by means of Bernoulli's formula. For unsteady flow, it is

$$\frac{p}{\rho} = P(t) - \frac{1}{2}|\mathbf{V}|^2 + \frac{\partial \varphi}{\partial t}, \tag{9}$$

where $P(t)$ is independent of position in the field. For steady flow, Eq. (9) leads to the well-known formula for pressure coefficient,

$$C_{p_i} = \frac{p_i - p_\infty}{(\rho V_\infty^2/2)} = 1 - \left(\frac{V_i}{V_\infty}\right)^2. \tag{10}$$

Velocities and pressures at points off the body are calculated from Eqs. (8) and (10) after sets of $\mathbf{V}_{ij}$ appropriate to the points in question have been calculated. This method is well suited to the simultaneous calculation of several onset flows at once, since the induced velocities $\mathbf{V}_{ij}$ do not depend on the onset flow as long as the basic form of the source density is not affected, which is always true for two-dimensional and three-dimensional cases. This feature has been found

useful for calculating unsteady flows at successive instants of time and for the frequently occurring application of flow about a two-dimensional lifting airfoil.

Maximum Element Number and Computation Times

The maximum number of elements that may be used to approximate a body surface has been largely a matter of arbitrary decisions made during programming and does not represent any true limit. In two-dimensional and axisymmetric cases, the maximum number of elements N is 400. Such a large number has rarely proved necessary in practice. As was stated previously, most cases of interest can be handled satisfactorily with less than 275 elements. Recently, the old machine language program for three-dimensional flows has been replaced by a FORTRAN IV program (20X). With it, up to 1000 unknown values of σ can be used to approximate the body, i.e., if the body has no plane of symmetry it can be approximated by 1000 elements. Provision is made in the program to account for planes of symmetry. Therefore, if there is one plane, the body can in effect be approximated by 2000 elements. For two and three planes, the effective element numbers become 4000 and 8000 respectively. Most applications have at least one symmetry plane. Since the entire surface — not just a single curve as in two-dimensional and axisymmetric cases—must be approximated by elements, the element limits are somewhat lower than is desirable. Very satisfactory results are obtained for single bodies if the shape is not too extreme, but for interference problems the number of available elements is marginal. It is desirable to double the number of elements; beyond this, little need for anything greater can be envisioned.

Computing times are somewhat variable and depend on the geometry of the body as well as on the number of elements. As a rough approximation, the computing time is divided evenly between the calculation of the induced velocities V_{ij} and the solution of the linear equations in Eq. (7). In axisymmetric cases the calculation of induced velocities requires a somewhat greater fraction of the time, and in two-dimensional cases requires somewhat less. The above division of computing time varies considerably with changes in computing equipment.

For the IBM 7094 computer, the following rough estimates of total computation time are useful for 100-element cases: two-dimensional bodies 1.6 minutes; axisymmetric bodies in axisymmetric flow, 2.6 minutes; and axisymmetric bodies at angle of attack (including the axisymmetric flow), 4 minutes. These estimates assume that only surface velocities are required. If the flow at a large number of points off the body in the flow field is required, computing times are increased. Of course, three-dimensional cases take much longer. Typical computing times for cases of 650 elements are 1.5 hours on the IBM 7094. For certain applications it is possible to reduce drastically the element number. Useful results have been obtained in as little as 15 minutes.

UNSTEADY TWO-DIMENSIONAL FLOWS

General Remarks

Because the method just described can handle nearly any kind of boundary condition with great accuracy*, it is quite capable of treating unsteady flows, which involve unusual boundary conditions. One major complication develops if the bodies are capable of developing lift — airfoils, for example. In the process of changing its lift, the body must shed vorticity equal and opposite to that gained on the body itself. If the fluid is originally at rest, the fluid has no vorticity; if the fluid is inviscid, vorticity is conserved no matter what the motion of the body may be. Any positive vorticity developed on the body or bodies must therefore be balanced by equal but opposite vorticity off the bodies, so that the total remains zero. Hence vortex sheets are shed. Now since they are likely to distort with time, their position is unknown in advance, and our problem takes on a new aspect — nonlinearity. J. P. Giesing has been working on problems of unsteady two-dimensional flow since about 1965, and I wish to describe here briefly his method and some of his results. Work on the one-body problem was published in Ref. 4 and work on the two-body problem in Ref. 5.

Description of the Method

Because the two-body problem is more complicated, our description will be of this type of the method. The one-body problem is a great deal simpler and allows many time-saving specializations, especially if the body never changes its shape, because influence coefficients can be calculated once and for all. As will be seen, the treatment is a step-by-step process. Therefore it is at its best in handling transients, although steady periodic motion can also be analyzed, but at greater expense in computer time. In the two-body problem the bodies are assumed to be moving in an inviscid, incompressible fluid. In the existing computer programs the bodies may move relative to each other in arbitrary paths with arbitrary velocities. It would not be very difficult to extend the method to solve problems involving bodies whose shape changes with time. A vibrating plane flap on a hydrofoil or the swimming of a two-dimensional "fish" are examples solvable by an extended program.

If certain fundamental facts are not forgotten, the concept upon which the analysis is founded appears rather simple, although the execution is difficult. These facts are:

1. The flow is potential.

2. No fluid particle can have a rotation if it did not originally rotate.

*An independent assessment of the accuracy of this and several other airfoil methods has recently been compiled in England (D. N. Foster, "Note on Methods of Calculating the Pressure Distribution over the Surface of Two-Dimensional Cambered Wings," Royal Aircraft Establishment Technical Report 67095, April 1967). Of the truly general methods considered, the present was found to be the most accurate.

3. Fluid particles that at any time are part of a vortex line always belong to that same vortex line.

Statements 2 and 3 are two of the Helmholtz vortex theorems.

4. Slip is permitted because of the inviscid character of the fluid, but if the walls of the bodies are impervious, fluid at any point is displaced in a direction normal to the surface with a velocity equal to the velocity of the surface along that normal. If $\mathbf{V}_s$ is the vector velocity of any point of the surface and $\mathbf{n}$ the unit normal vector, this kinematic condition can be stated very compactly as

$$\frac{\partial \varphi}{\partial n} = \mathbf{V}_s \cdot \mathbf{n} \ . \tag{11}$$

An obvious and easily handled modification of Eq. (11) would accomodate mass — transfer types of problems.

5. If pressures are desired, the unsteady Bernoulli equation must be used.

From the unsteady Bernoulli equation the following formula for the pressure coefficient C_p can be derived for a translating and rotating frame of reference fixed in a particular body:

$$C_p = \frac{p - p_\infty}{(\rho\, U_\infty^2/2)} = \left(\frac{V_r}{U_\infty}\right)^2 - \left(\frac{V_c}{U_\infty}\right)^2 - \frac{2}{U_\infty^2}\,\frac{\partial \varphi}{\partial t} \ . \tag{12}$$

Here V_r is the magnitude of velocity of any point on the body, U_∞ is the reference velocity, and V_c is the relative velocity of the fluid. In steady flow, V_r is constant at all points on the body, and it is natural that the reference velocity U_∞ becomes V_r. Then the first term reduces to 1. Also, in steady flow $\partial\varphi/\partial t = 0$, and so one recovers the common formula $C_p = 1 - (V_c/U_\infty)^2$.

Implementation of the method involves solution of boundary-value problems that fall into three classes with respect to computing procedure. Figure 5 shows them. The two bodies are assumed to be moving in some sort of path, and leave vortex wakes as sketched. We must find a total solution that meets the condition of no-flow through the walls (if impervious), satisfies Kutta conditions if required, and accounts for wake and interaction effects. The total solution can be built up from those shown. The first solution is called the quasi-steady flow φQ. Here, the bodies may be considered as translating and rotating, each in its own way, along separate paths, with arbitrary velocities. Then every point on each of the bodies must satisfy the fundmental boundary condition Eq. (11). The φQ solution is the nonhomogeneous solution because $\partial\varphi/\partial n$ is not zero. In this solution no attempt is made to satisfy the Kutta condition.

The other two basic flows are the ones needed to satisfy the Kutta conditions and the conservation of vorticity. If the bodies are changing their lift, vorticity is shed in a continuous sheet. For practical computing purposes, the continuous sheet is approximated by a series of discrete vortices as indicated in the middle sketch of Fig. 5. Each one produces its own onset flow on both bodies,

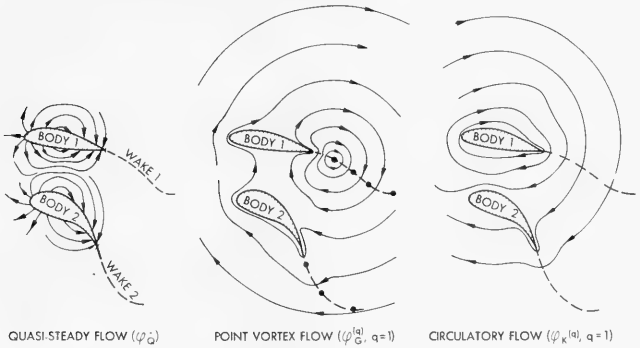

Fig. 5 - Shematic of streamlines associated with quasi-steady, point vortex, and circulatory flow fields

and the total onset flow is due to the total effect of all the lumped point vortices in both wakes. Strengths of these vortices is determined by the basic facts that total vorticity of the system remains equal to zero and that the Kutta condition must hold. These wake-flow influences create additional onset flows. However, the airfoils are now considered to be at rest, so that the boundary condition over all the surfaces is $\partial\varphi/\partial n = 0$. This condition means that the normal velocity due to the surface source distribution is equal and opposite to that created by the vortices in the wake. Hence, since $\partial\varphi/\partial n = 0$, the solution may be called a homogeneous solution. It is called φG, in which G denotes gamma (Γ). It is identified as a different solution because of the details of the calculation procedure. The method of solving the basic Neumann boundary-value problem is no different, however, because in the end the only difference between it and the method of solving for φQ is the column matrix, which amounts to no more than a different set of numbers.

A vortex moves along with the flow. Hence, if there is an array of vortices like that of the middle sketch of Fig. 5, it is evident that the vortices will move as a result of the influences of all the other vortices and the influence of the bodies. Therefore, calculation of the effect of the wake requires knowledge of where the wake is. Differential equations for the motion of the vortices can be written and integrated to find the position of each lumped vortex point. The interaction of the vortices can be violent, as will be seen in some of the examples.

The flows φQ and φG account for motion of the bodies and effects of the wakes, but the Kutta conditions are not satisfied. The third basic flow is used to satisfy these conditions. It is called φK, in which K denotes Kutta. As can be seen in the figure, it is a circulatory flow; and in the process of meeting the Kutta conditions, two circulatory flows must be used, one for body 1 and one for body 2. The circulation about an airfoil is generated by a constant vortex sheet of unit strength covering all the surface of the airfoil. (This known vortex sheet is in addition to the unknown source distribution used to satisfy boundary conditions.) This method of covering the surface with a constant strength vortex

sheet is far from being the only procedure, but it has great practical advantages in computing speed and accuracy. The vortex sheet generates a third type of onset flow, which again generates a set of values of $\partial\varphi/\partial n$, so that the third flow, like the second, has homogeneous boundary conditions; i.e., the body is treated as stationary. The Kutta conditions are then satisfied by the proper linear combination of circulatory flows φK with flows φQ and φG. A proper linear combination will satisfy all the boundary conditions, the Kutta conditions, and the vorticity-conservation condition.

Space is not available to enter into computational details, which in fact are considerable. Both the single-body and two-body problems are programmed on the IBM 7094. For the single-body problem, the body can be defined by as many as 100 coordinate points and 100 time steps can be taken. Often in practical calculations, pressures, forces, and moments are not needed at every time step. Trial runs show that the computing time is given approximately by the following formula, if 72 defining elements are used:

$$T_{minutes} = 2.70\ \frac{(NT)}{20} + 5.15\ \frac{(NPT)}{20} + 1.0\ , \tag{13}$$

where NT is the number of time steps taken and NPT is the number of times at which pressures, forces, and moments are wanted. For example, if $NT = 60$ and $NPT = 20$, the computing time is 14.25 minutes. For the two-body problem, each body can be defined by up to 50 elements, and up to 250 time steps can be taken. Core capacity determines these limits. About 1 minute is required for each time step. Hence, on an IBM 7094, computations can become quite lengthy. A maximum-capacity problem would take over 4 hours.

Examples of Single-Body Problems

An Airfoil Whose Angle of Attack is Suddenly Changed- Figure 6 shows what happens to the wake when the angle of attack is suddenly changed. An 8.4 percent-thick symmetric von Mises airfoil first moves at zero angle of attack. Then, after traveling 0.6 chord lengths, the airfoil is suddenly pitched to 10°. It remains at this position until total travel is 3.05 chords, at which point it returns to $\alpha = 0°$. The motion was broken up into steps of length 0.05c, where c is the chord. The figure shows the motion of the wake and the rollup of vortices. It is interesting to note that each vortex carries the other downward, so that there is a net downward flow. This behavior is consistent with momentum considerations, which require a definite downward displacement of some fluid if lift is developed for a period of time.

Wake Shape - A question can be raised regarding the accuracy of the wake shape. Since no exact solutions are available for reference, assessment was made by using different step lengths in the calculation of the motion. In one case, step lengths differing by a factor of 3 gave nearly the same wake shape. J. B. Bratt, Ref. 6, has determined wake shapes behind an oscillating NACA 0015 airfoil by using smoke. The airfoil oscillated up and down with an amplitude of 0.018c without pitch. Test conditions were duplicated as well as possible. A comparison of calculation and experiment is shown in Figure 7 for the same amplitude at

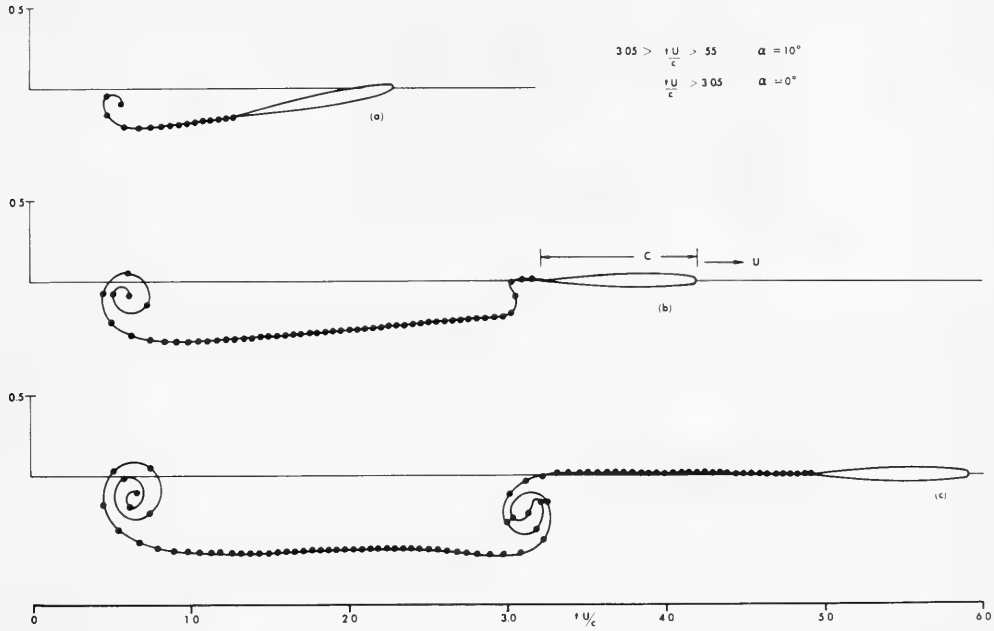

Fig. 6 - Shape of the vortex wake (at three separate times) generated by a symmetric 8.4-percent-thick von Mises airfoil, that has been given a sudden increase (10°) in angle of attack at time 0.55 U/c and a sudden decrease (10°) at time 3.05 U/c

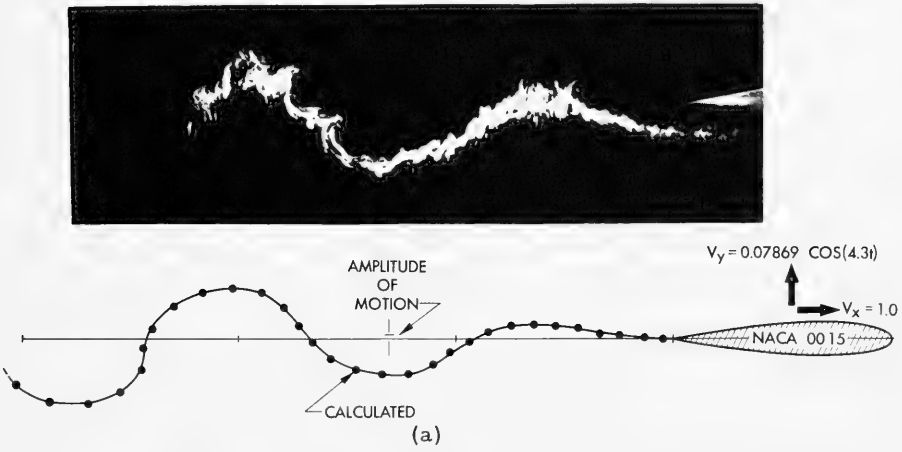

Fig. 7 - Shape of the vortex wake generated by an NACA 0015 airfoil vibrating in a simple harmonic manner with an amplitude of 0.018c (a) frequency = 4.3 U/c.

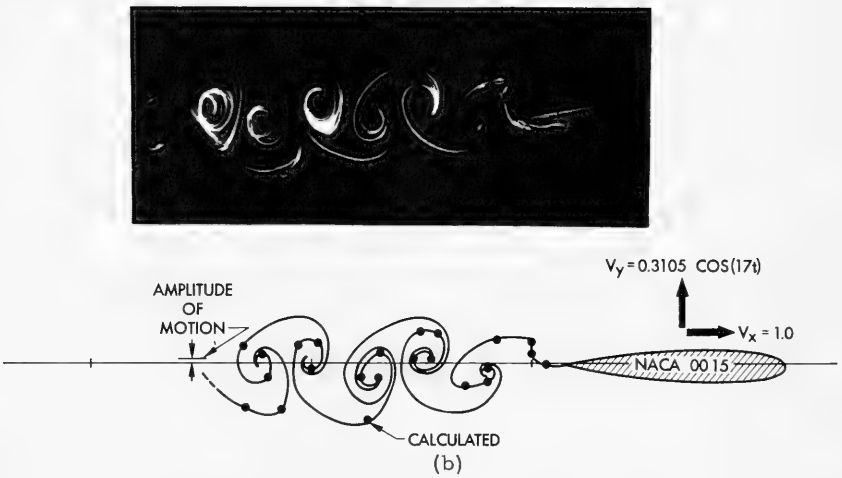

Fig. 7 - (Continued) (b) frequency = 17.0 U/c

two different frequencies. The close agreement between the experiment and the prediction of the effect of frequency are encouraging.

Küssner, Wagner, and Theodorsen functions were calculated by the exact step-by-step procedure for airfoils of several thicknesses, thus identifying the effects of thickness on the Küssner, Wagner, and Theodorsen functions. The effect of thickness is significant. Results for thin airfoils indicated good agreement with classical results derived from flat-plate theory (4).

Comparison of Theoretical and Experimental Forces on an Oscillating Airfoil - Spurk (7) has experimentally measured forces on several airfoils oscillating symmetrically as shown in Fig. 8, which presents the results for one test. Reduced lift and moment coefficients are used; the imaginary part represents phase lag, and the real part, amplitude ratio. At low reduced frequencies rather good agreement occurs, but as frequencies increase, theory and experiment diverge considerably. Because many more studies in addition to those presented here indicate that the present method has great accuracy for a perfect fluid, the failure to agree with experiment can probably be attributed to viscous effects, i.e., the boundary layer, although it should not be forgotten that experimental determination of dynamic effects is difficult and not highly accurate.

Examples of Two-Body Problems

Two Airfoils Passing Each Other in Opposite Directions - Two airfoils passing each other in opposite directions is an exciting problem, if it is thought of as two airplanes passing each other close-by in opposite directions. Two 8.4-percent-thick von Mises airfoils at angles of attack of 5.73° (Fig. 9) are initially at rest with noses spaced one chord length apart. They are impulsively moved, and the motion is traced. Figure 9a shows the wake shape after the airfoils have each traveled 1.5 chord lengths. Figure 9b shows the lift history as the airfoils

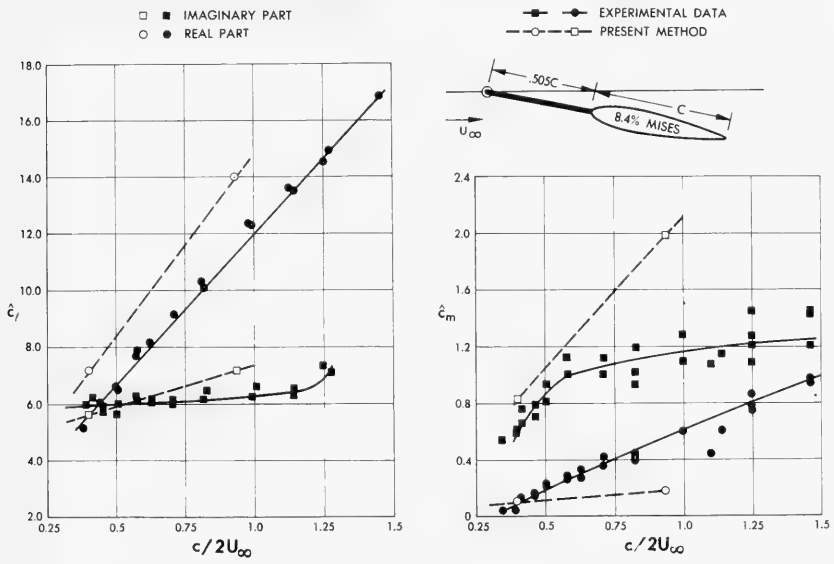

Fig. 8 - Comparison of calculated and experimental reduced circulatory lift and moment coefficients for a symmetrical 8.4-percent-thick von Mises airfoil oscillating in a simple harmonic manner with an amplitude of 0.06. $\hat{C}_\ell$ = lift coefficient (less the added mass terms proportional to accelerations) divided by quarter chord amplitude. $\hat{C}_m$ = moment coefficient analogous to C_ℓ.

pass each other. The general level of the lift is low because the airfoils have not moved far enough to develop steady-state lift. As can be seen, the lift is generally consistent with isolated flat-plate theory. When the airfoils are directly over each other ($tU_\infty/c = 1.0$), the two airfoils have a tendency to be drawn into each other. It would be interesting to see results with a longer run before the airfoils passed each other, in which they would more nearly reach the steady state ($C_\ell/C_{\ell_Q} = 1$). Expensive computer time has, so far, prevented such an experiment.

An Airfoil with an Oscillating Flap - A second example is given in Fig. 10. In this case the flap of an NACA 23012 airfoil is given a simple-harmonic rotational motion (angular range $0° \rightarrow 45°$). The flap was moved from its original position ($\Delta x = -0.047c$, $\Delta y = -0.02c$) before the motion was initiated (Fig. 10b). Figure 10a shows the wake shed from the main section and the flap at two different times. The flap deflection in one case is 45° and 0° in the other. The pressure distribution over the airfoil and flap system when the flap is at its maximum deflection (45°) is given in Fig. 10b. The configuration is shown at the upper left in the figure. The flap is shown undeflected beneath the pressure plot. For comparison, Fig. 10b includes the steady-state pressure distribution.

A Rotor Blade Passing a Stator Blade - As a final example, we consider a rotor blade and a stator blade of a compressor stage, both of chord length c.

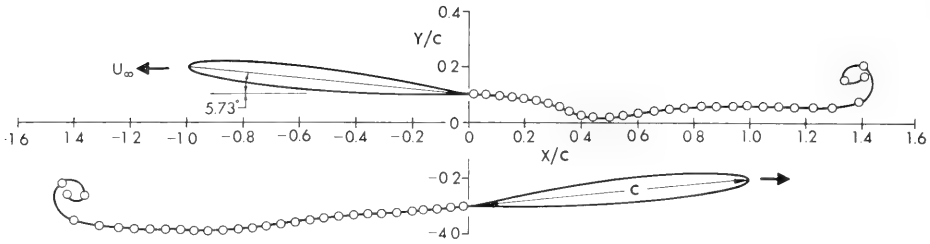

(a) shape of vortex wakes

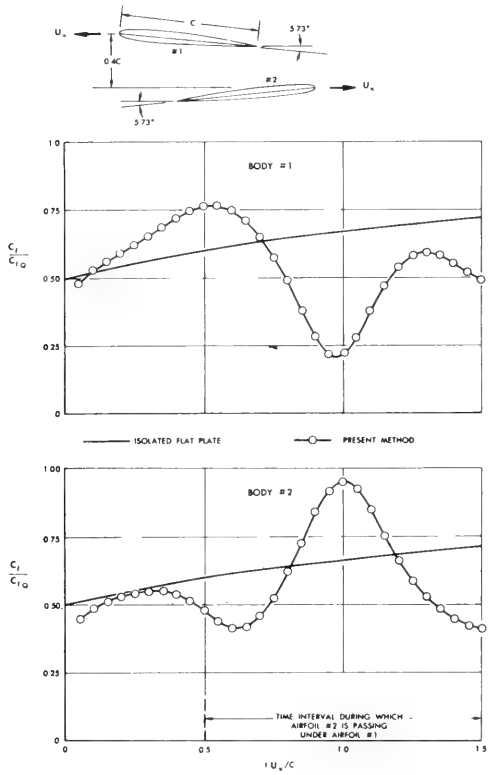

(b) Normalized lift-coefficient-time histories

Fig. 9 - Calculated Results for two 8.4-percent-thick von Mises airfoils moving past each other at an angle of attack

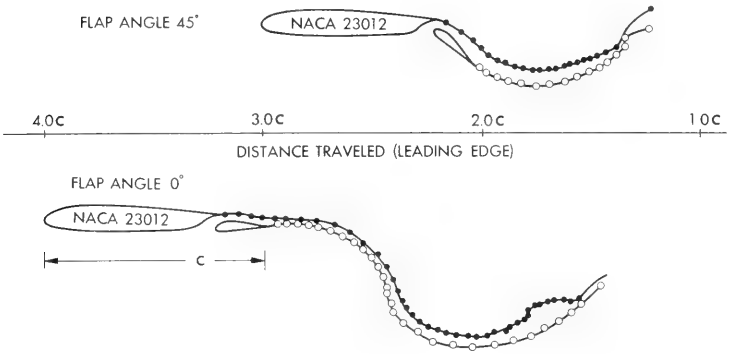

(a) Wake shapes at two different times

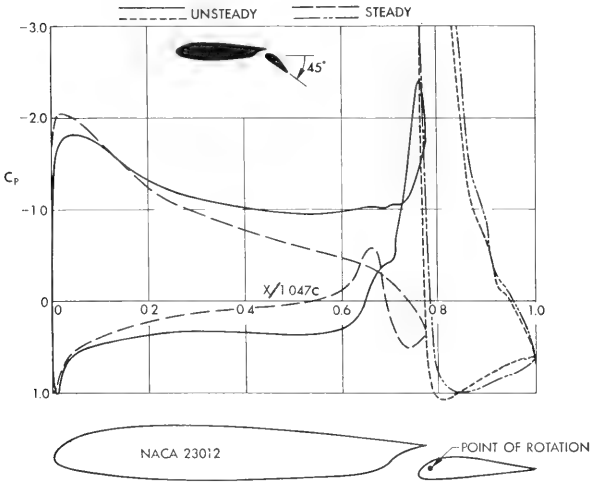

(b) Calculated pressure distribution when the flap is at maximum deflection (45°). The steady-state result is also shown in (b). Rearward movement of flap has increased chord by 4.7%.

Fig. 10 - Calculated results for an NACA 23012 airfoil with a flap undergoing simple-harmonic rotational motion of angular-range amplitude 45°.

The stator blade is an 8.4-percent-thick von Mises symmetrical airfoil and the rotor blade is a cambered 11.4-percent-thick airfoil obtained by conformal transformation. When the trailing edge of the rotor blade is immediately in front of the leading edge of the stator blade, the gap is 0.412c. The stator blade is aligned with the remote onset flow U_∞. The problem is illustrated in Fig. 11a. The figure includes wake shapes shortly after the rotor blade has passed in front of the stator blade. The rotor wake opens up to pass around the stator as it is carried downstream by the general flow U_∞. Figure 11b shows a very highly loaded blade. Here the deflections of the wakes are much greater. The vorticity shed from the rotor is so great that rolling-up instability is developing. Reference 5 presents pressure-distribution and time-history information on the blade force coefficients that is not repeated here. It is interesting to note that the present method can solve exactly a two-dimensional simplification of a Voith-Schneider propeller having either one or two blades.

FLOW-FIELD CHARTS

Charts of flow fields are a rarity; that is why they are mentioned here, even though they represent no advance in basic capability. Reference 8 has been written with the primary objective of providing a set of charts and formulas by which one may conveniently estimate perturbation velocities at any point in the field around some arbitrary shape. In many problems of design, such information is needed. Both two-dimensional flows and flows about bodies of revolution are treated.

Two-Dimensional Flows

A two-dimensional lifting flow can be resolved into three subflows: a uniform onset flow parallel to a chord line, a uniform onset flow perpendicular to a chord line, and a purely circulatory flow (Fig. 12). If there is no lift, of course, the third flow is zero. Now for each flow the body induces perturbations that can be resolved into components parallel and perpendicular to the chord line. Hence to cover all cases of a lifting two-dimensional flow, six charts are needed, which present the following quantities, all of which are perturbations:

$$\frac{V_x}{V_{\infty_x}} - 1\,, \quad \frac{V_x}{V_{\infty_y}}\,, \quad \frac{V_x}{V_\infty C_L}\,, \quad \frac{V_y}{V_{\infty_x}}\,, \quad \frac{V_y}{V_{\infty_y}} - 1, \quad \frac{V_y}{V_\infty C_L}\,.$$

The first line is the set of V_x perturbations, and the second the set of V_y perturbations. The velocity V_∞ is the entire onset velocity, which equals $(V_{\infty_x}^2 + V_{\infty_y}^2)^{1/2}$. By reading the charts, V_x and V_y perturbations can be figured quickly by means of the following formulas, if the surface is at an angle of attack α:

$$\frac{V_{xp}}{V_\infty} = \left(\frac{V_x}{V_{\infty_x}} - 1\right)\cos\alpha + \left(\frac{V_x}{V_{\infty_y}}\right)\sin\alpha + \left(\frac{V_x}{V_\infty C_L}\right)C_L\,, \tag{14}$$

$$\frac{V_{yp}}{V_\infty} = \left(\frac{V_y}{V_{\infty_y}}\right)\cos\alpha + \left(\frac{V_y}{V_{\infty_y}} - 1\right)\sin\alpha + \left(\frac{V_y}{V_\infty C_L}\right)C_L\,. \tag{15}$$

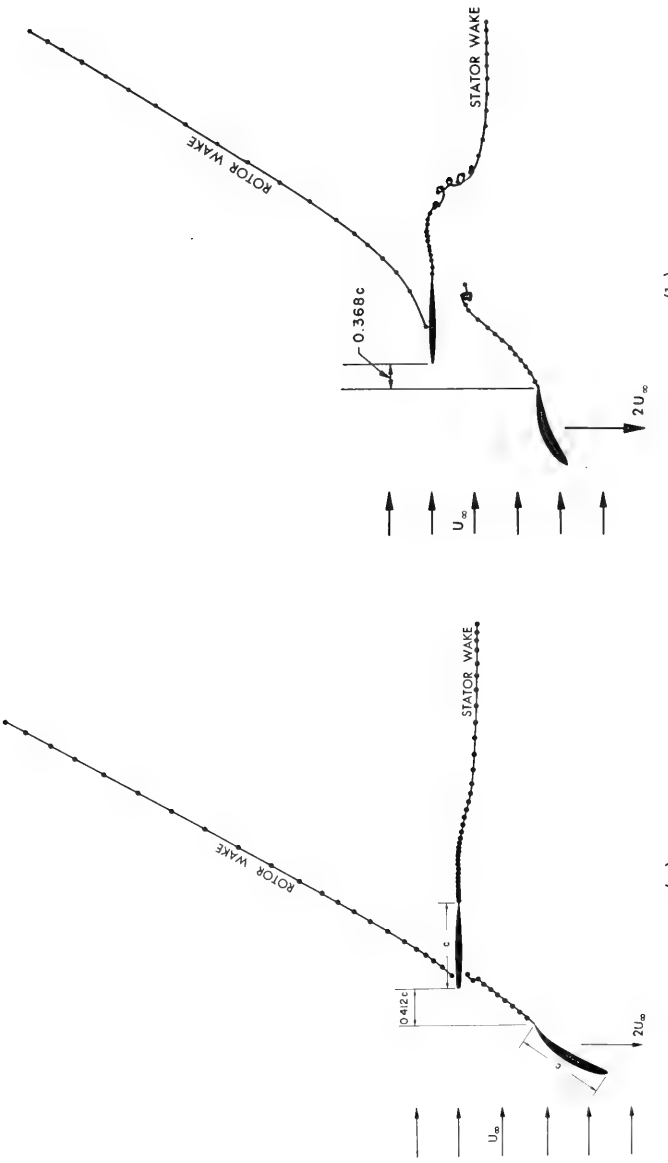

Fig. 11 - Calculated results for the case of a rotor blade passing a stator blade. (a) Wake shapes for a lightly loaded rotor blade. Relative angle of attack of the rotor is 6.2°; trailing-edge, leading-edge gap is 0.412c. (b) Wake shapes for a heavily loaded rotor blade. Relative angle of attack of the rotor is 34.4°; trailing-edge, leading-edge gap is 0.368c.

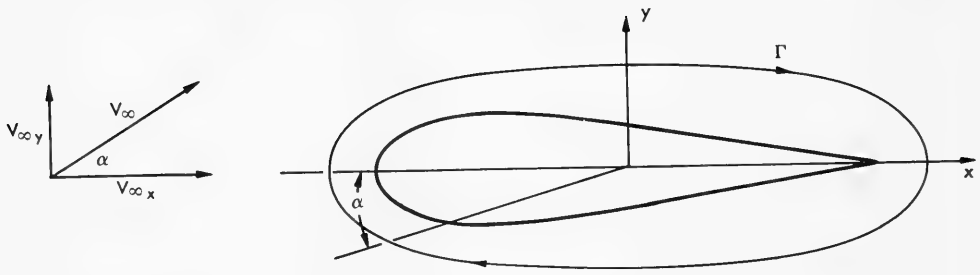

Fig. 12 - Resolution of a flow into V_{∞_x}, V_{∞_y}, and circulatory components

Flows About Bodies of Revolution

If x is the distance parallel to the axis, θ the angular measure around the body starting from the top, and r the radial distance from the axis, it is clear that a body of revolution will have three velocity-perturbation components V_{xp}, $V_{\theta p}$, and V_{rp}. Again referring to Fig. 12, it is clear that for the general angle-of-attack condition we will have two basic onset flows V_{∞_x} and V_{∞_y}, but no circulation. The V_{∞_x} flow is parallel to the axis and generates radial and axial perturbations. The crossflow component V_{∞_y} generates perturbations in all three directions, x, r, and θ. According to crossflow theory, there are then five velocity perturbation components, as follows:

$$\frac{V_x}{V_{\infty_x}} - 1\,, \quad \frac{V_x}{V_{\infty_y} \cos\theta}\,, \quad \frac{V_r}{V_{\infty_x}}\,, \quad \frac{V_r}{V_{\infty_y} \cos\theta} - 1\,, \quad \frac{V_\theta}{V_{\infty_y} \sin\theta} - 1\,.$$

The combined perturbation velocities in the three directions are:

$$\frac{V_{xp}}{V_\infty} = \left(\frac{V_x}{V_{\infty_x}} - 1\right) \cos\alpha + \left(\frac{V_x}{V_{\infty_y} \cos\alpha}\right) \cos\theta \sin\alpha\,, \tag{16}$$

$$\frac{V_{rp}}{V_\infty} = \left(\frac{V_r}{V_{\infty_x}}\right) \cos\alpha + \left(\frac{V_r}{V_{\infty_y} \cos\alpha} - 1\right) \cos\theta \sin\alpha\,, \tag{17}$$

$$\frac{V_{\theta p}}{V_\infty} = \left(\frac{V_\theta}{V_{\infty_y} \sin\theta} - 1\right) \sin\theta \sin\alpha\,. \tag{18}$$

For this problem only five charts are needed. Provided the bodies are not too close together, the charts can be used to work out interference effects. An example would be the determination of the effect of two hydrofoil struts upon each other. The report (8) is written as a sort of manual.

Charts

Charts have been drawn for the shapes listed in Tables 1 and 2. The double wedge was chosen to provide a low block coefficient and the semicircle-flat body to provide a high block coefficient. The ellipse is a natural intermediate case. The same three profile families were used in the axisymmetric problem. A total of 111 charts are required to cover the configurations listed in the tables. Two sets are presented, Figs. 13 and 14, one for the NACA 65(1)-412 airfoil and the other for the 12-percent-thick hemisphere-cylinder body of revolution. The fields for the NACA 65(1)-412 airfoil are defined by 2632 points. For the bodies having double symmetry about 1/4 this number were used. It is informative to compare the two sets and see how much less the disturbances at some distance from the body are for the body of revolution.

Table 1 Two-Dimensional Bodies for Which Flow-Field Charts Have Been Computed

Body Type	Thickness Ratio t/c	Body Profile
Elliptic cylinder	0.06	
	0.12	
	0.18	
Double wedge	0.06	
	0.12	
	0.18	
Double semicircle-flat body	0.06	
	0.12	
	0.18	
NACA 65(1)-012 Airfoil		

Table 1 (Continued) Two-Dimensional Bodies for Which Flow-Field Charts Have Been Computed

Body Type	Thickness Ratio t/c	Body Profile
NACA 65(1)-412 Airfoil		
Prolate spheroid	0.06	
	0.12	
	0.18	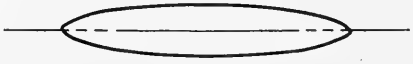
Double Cone	0.06	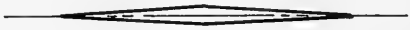
	0.12	
	0.18	
Double hemisphere cylinder	0.06	
	0.12	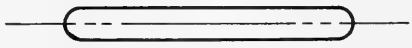
	0.18	

NUMERICAL INTEGRATION OF AN OSCILLATING FUNCTION OCCURRING IN THE THEORY OF WATER WAVES

Background

The function under consideration is Havelock's source function, and it is our purpose to report some progress on its rapid calculation. One part, corresponding to the near-field term, involves evaluation of the complex exponential integral. A good working formula that is valid for all Froude numbers has been developed and is described in Ref. 1 in connection with hydrofoil theory. A second problem, which amounts to evaluation of functions of the form

$$\int f(x) \begin{matrix} \sin \\ \cos \end{matrix} g(x)\, dx \ , \tag{19}$$

occurs in connection with the far-field term.

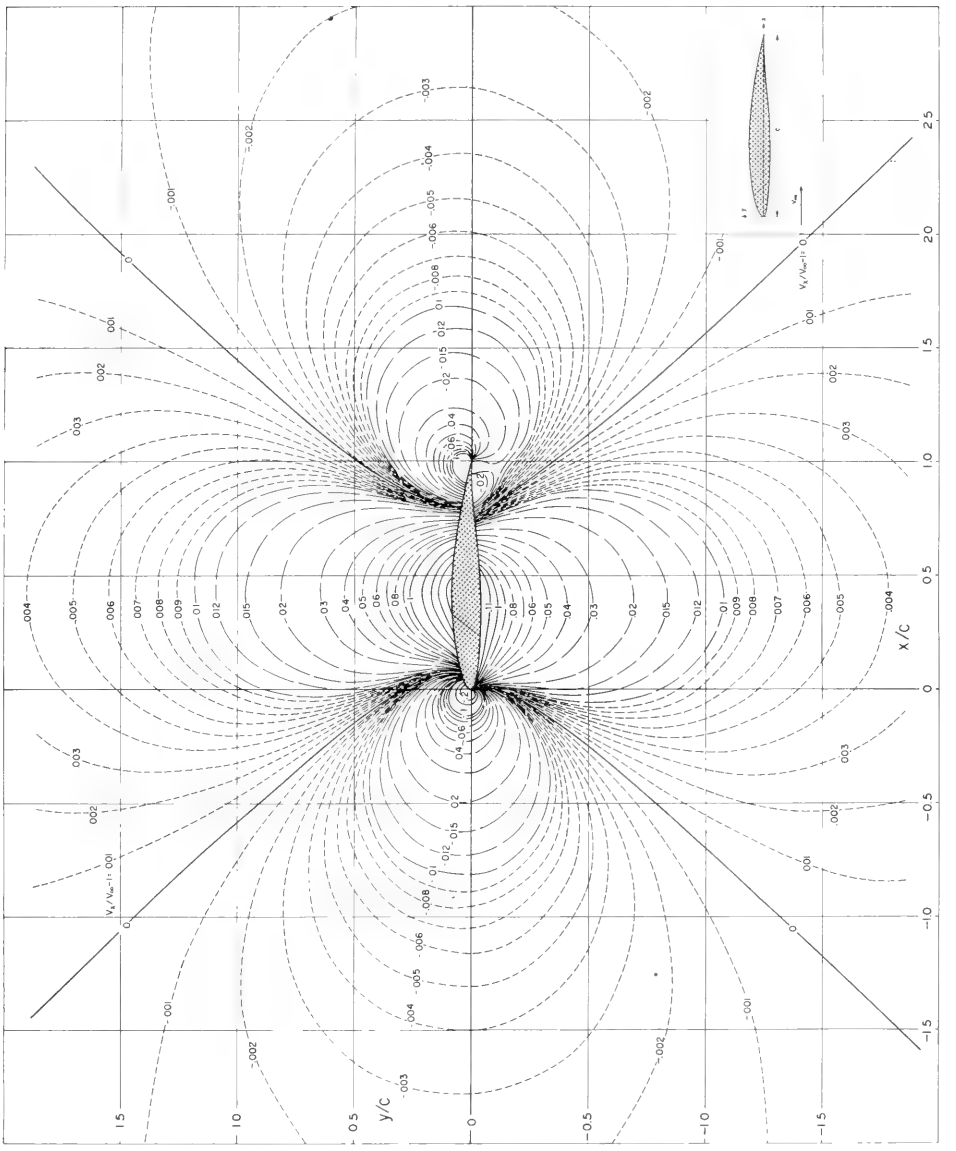

Fig. 13 - Flow-field charts for the NACA 65(1)-412 airfoil. (a) - x onset flow, v_x perturbation

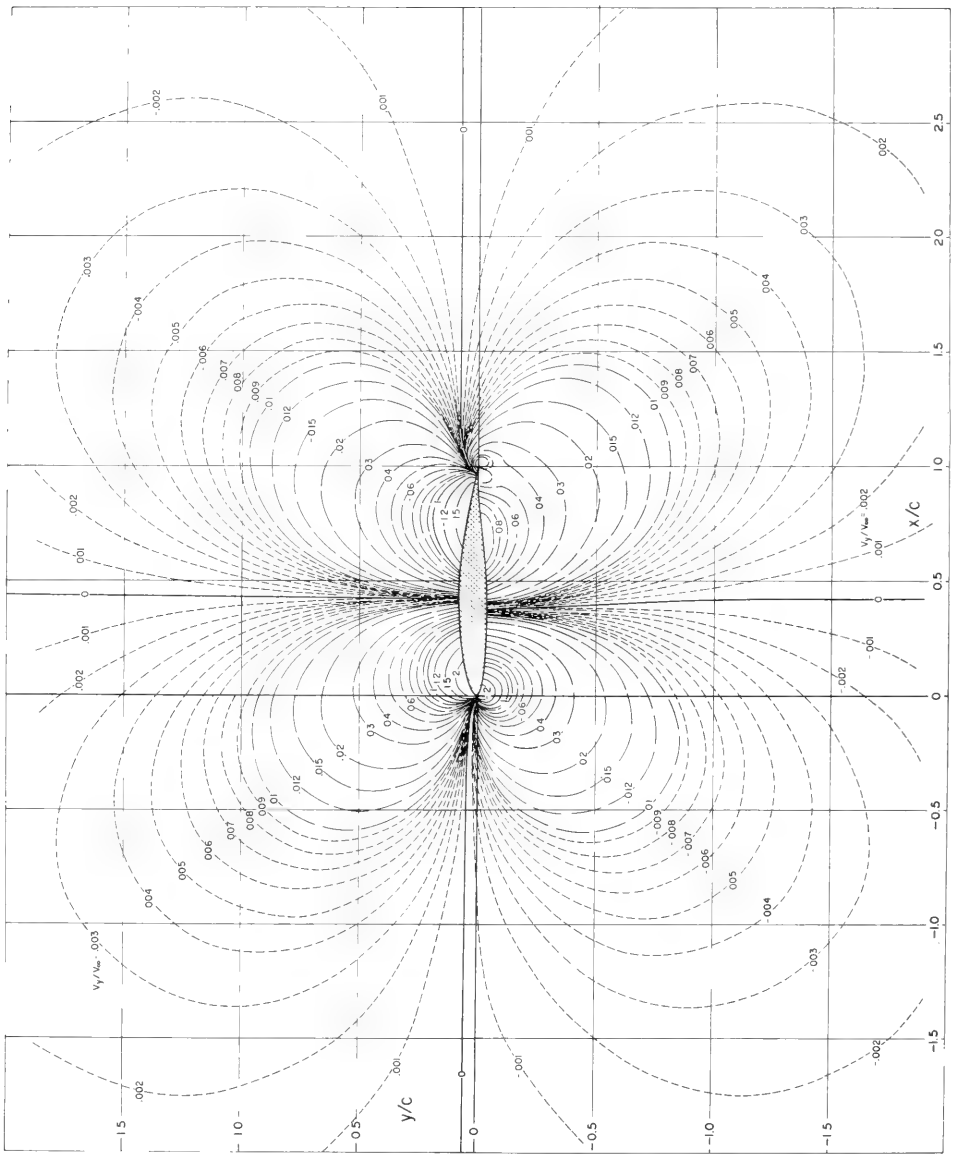

Fig. 13 (Continued). (b) - x onset flow, v_y perturbation

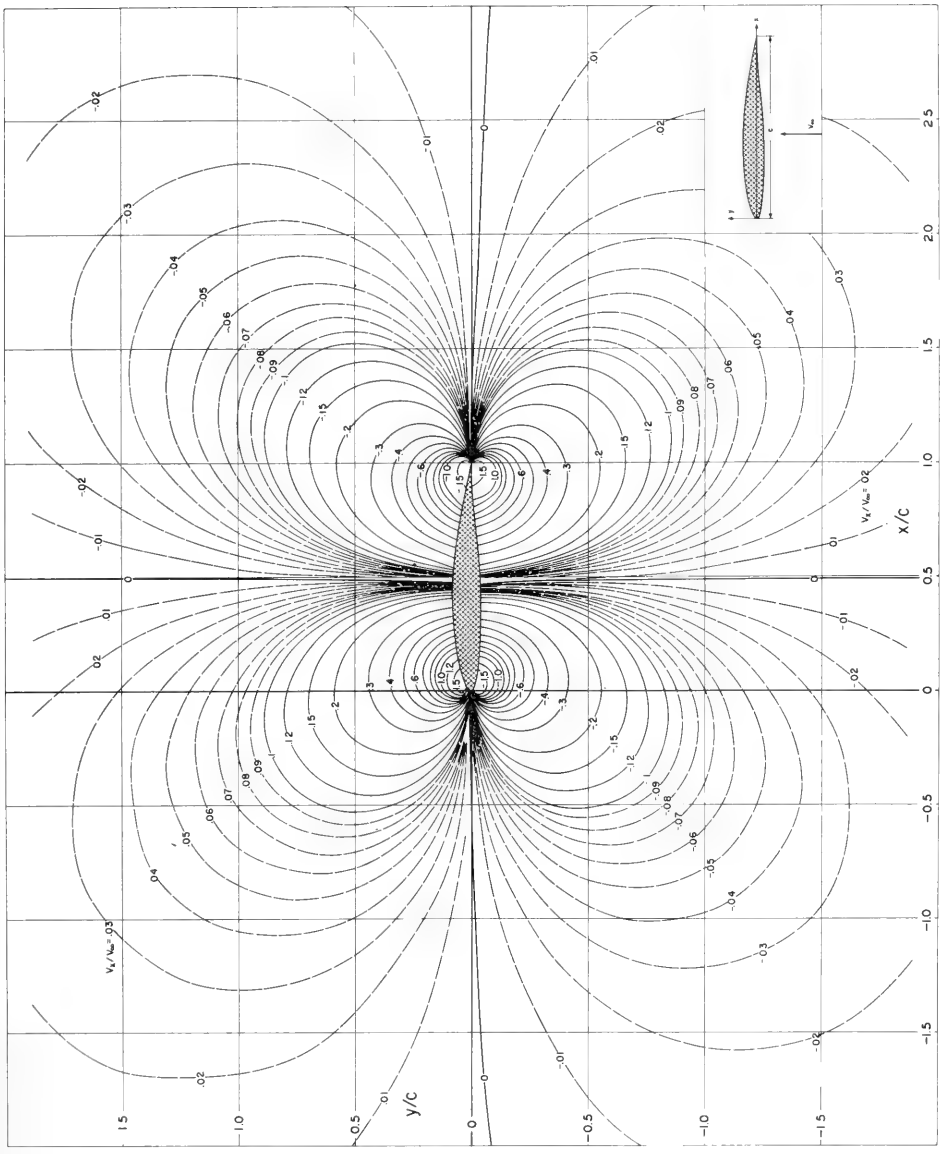

Fig. 13 (Continued). (c) - y onset flow, V_x perturbation

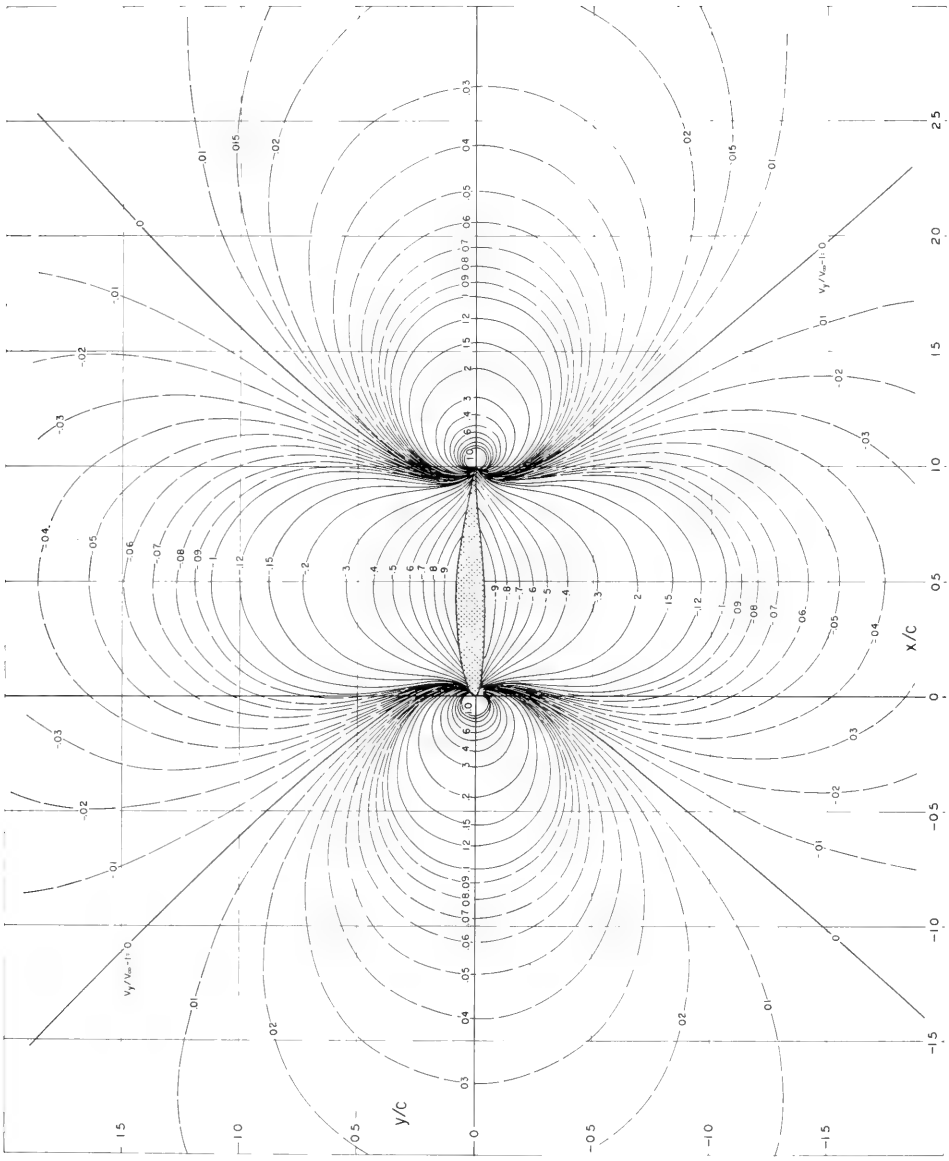

Fig. 13 (Continued). (d) - y onset flow, v_y perturbation

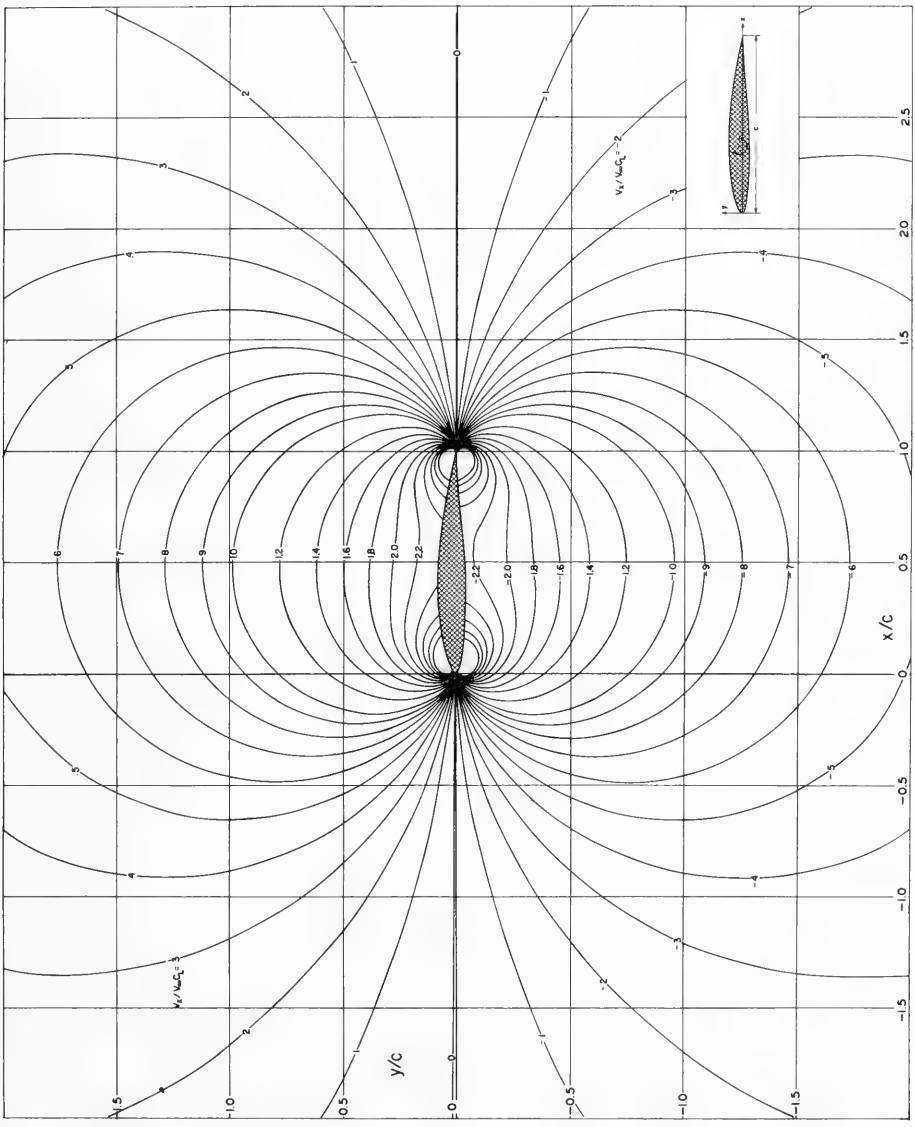

Fig. 13 (Continued). (e) - Circulatory flow, V_x component (the values of $V_x/V_\infty C_L$ are in error and should be divided by 2π)

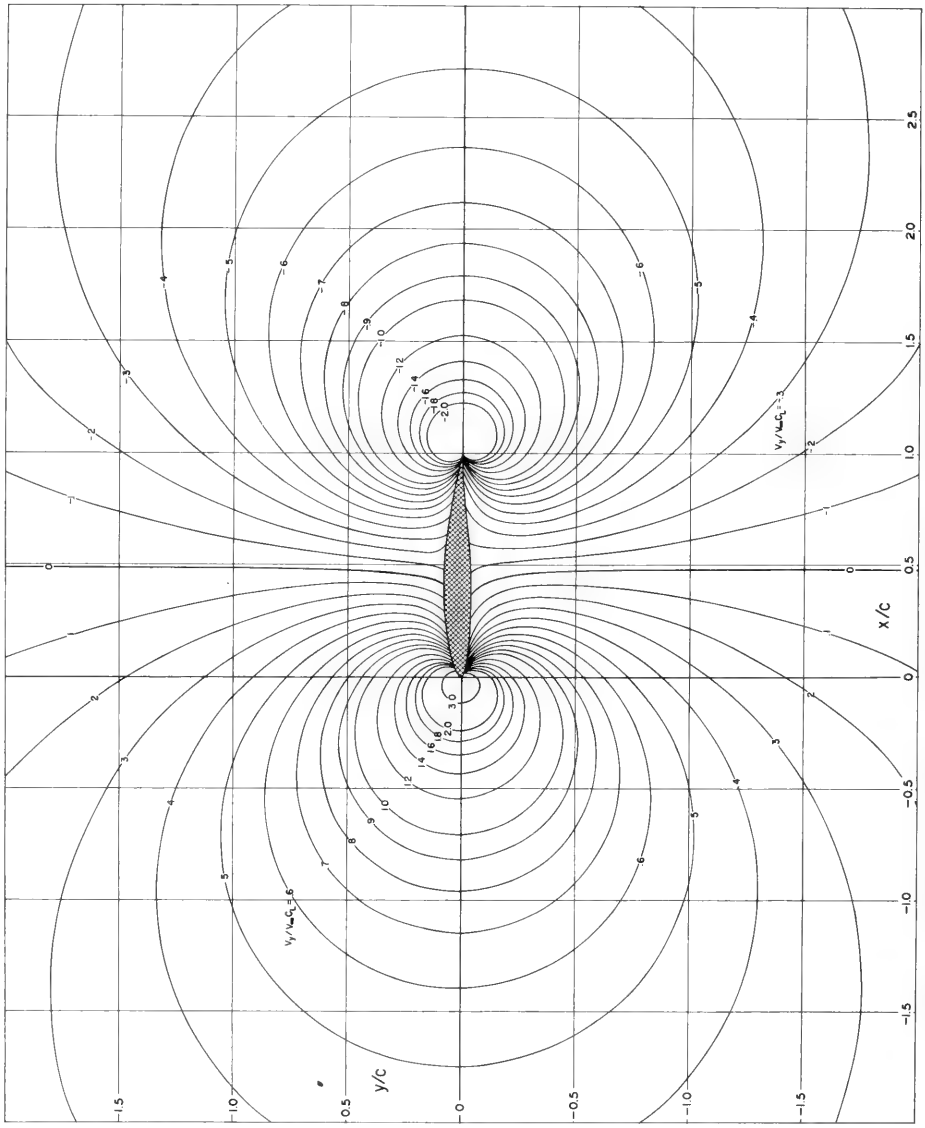

Fig. 13 (Continued). (f) - Circulatory flow, v_y component (the values of $v_y/v_\infty c_L$ are in error and should be divided by 2π)

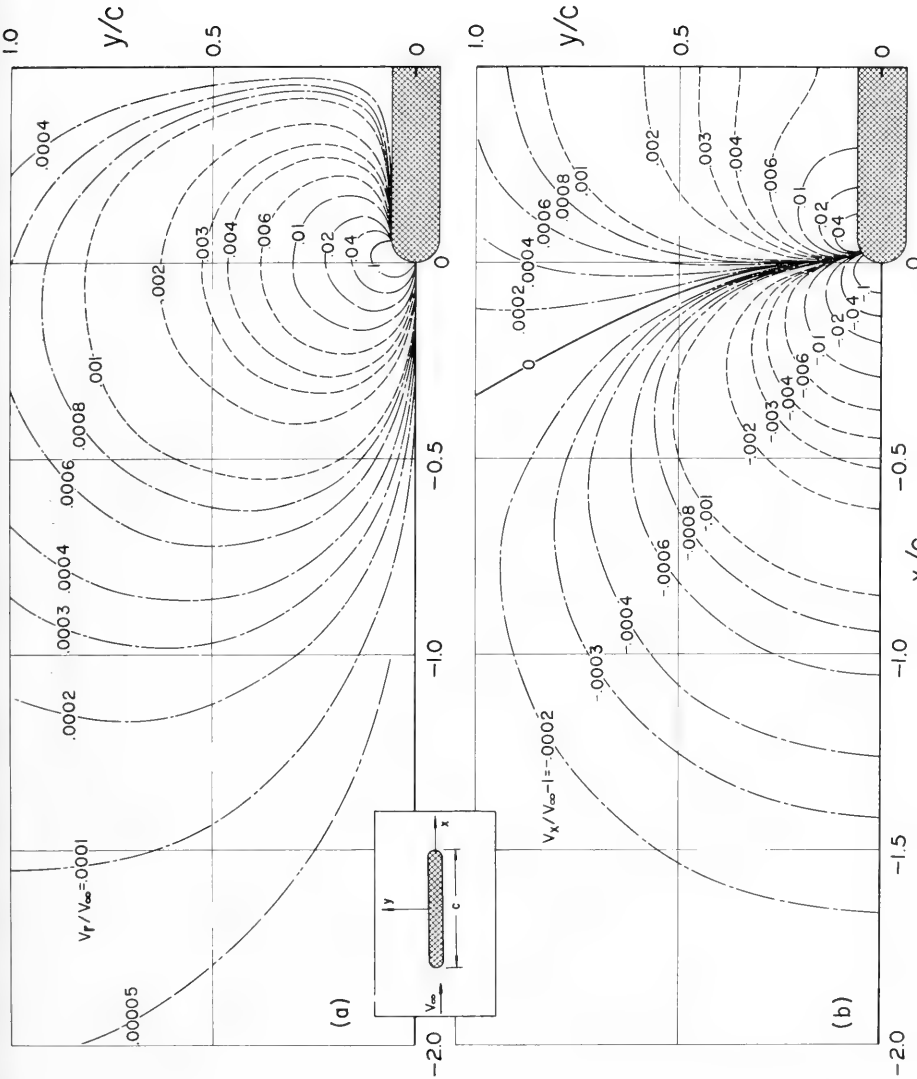

Fig. 14 - Flow-field charts for a hemisphere-cylinder body of revolution. (a) Axial - x onset flow, V_r perturbation. (b) Axial - x onset flow, V_x perturbation.

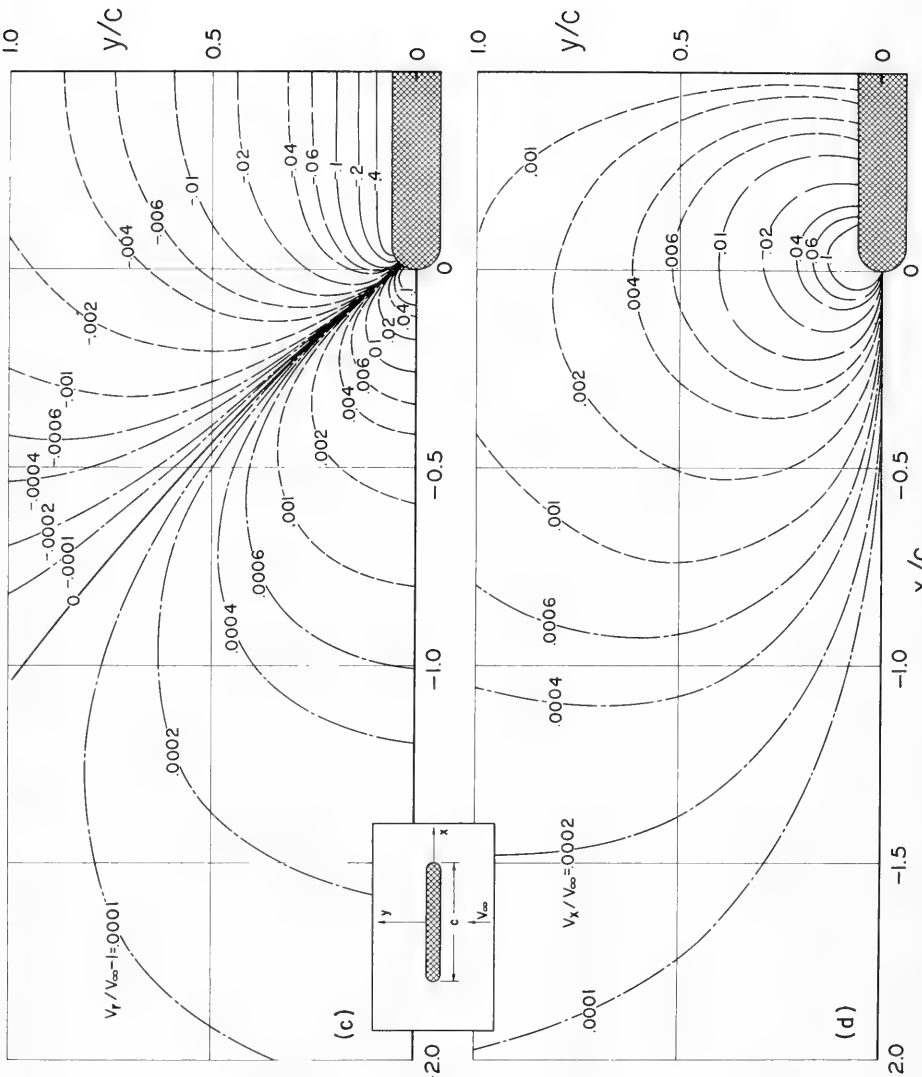

Fig. 14 (Continued). (c) Radial - y onset flow, v_r perturbation.
(d) Radial - y onset flow, v_x perturbation.

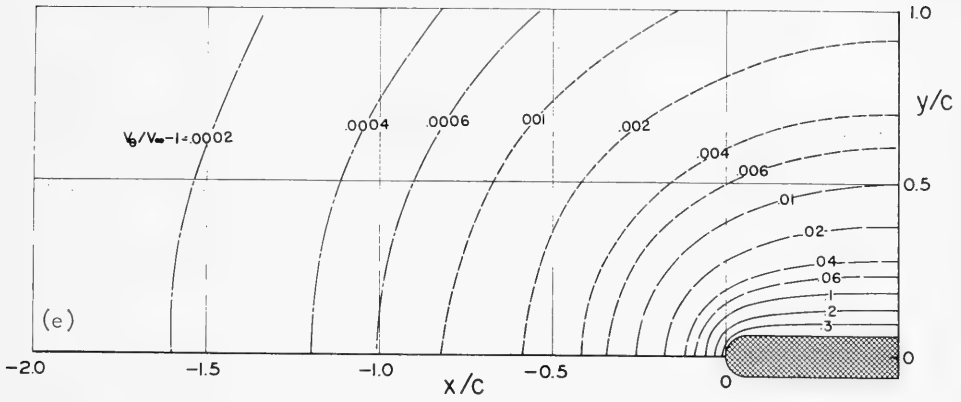

Fig. 14 (Continued). (e) Radial - y onset flow, V_θ perturbation

If our method of attack were applied to the problem of the wave resistance of three-dimensional bodies, such as ships, and if a linearized free-surface boundary condition were used, we would replace our simple source distribution by a distribution of Havelock sources (Wehausen and Laitone, Ref. 9). The source function can be written as

$$\varphi_T(x,y,z) = \frac{1}{r} - \frac{1}{r_1} + \varphi(x,y,z) \ , \tag{20}$$

where

$$\varphi(x,y,z) = \lim_{\mu \to 0} \mathrm{Re}\left[\frac{-\nu}{\pi}\int_{-\pi}^{\pi} \sec^2\theta \int_0^\infty \frac{e^{k(R+i\omega)}dk}{k - (\nu \sec^2\theta - i\mu\sec\theta)}\, d\theta\right] .$$

Some familiarity with this formula is assumed; therefore the terms will not be defined. To evaluate this integral in a rapid and accurate manner, it is desirable to approximate the integrand with functions that can be integrated analytically. With that in mind, we see that the integral presents two difficulties: first, the integral over the variable k develops a singularity as $\mu \to 0$; second, there is the fact that the exponential is complex and does not lend itself to a polynomial approximation. Both difficulties can be overcome if a contour integration is performed in the complex k-plane. This process leads to the following transformed equation:

$$\varphi(x,y,z) = \frac{-2}{\pi}\int_0^{+\pi} \nu\sec^2\theta\ e^{\nu\sec^2\theta(y+b)} \int_{\substack{\nu\sec^2\theta \\ (y+b)}}^\infty \frac{u e^{-u}\, du}{u^2 + [\nu\sec^2(\theta)\rho\cos(\theta-\alpha)]^2}\, d\theta \tag{21}$$
(Cont)

$$\varphi(x,y,z) = +4 \int_{\frac{\pi}{2}}^{\frac{\pi}{2} + \alpha} \nu \sec^2\theta \; e^{\nu \sec^2\theta (y+b)} \sin \left[\nu \sec^2\theta \; \rho \cos (\theta - \alpha)\right] d\theta \; . \tag{21}$$

The exponential integral in u can be evaluated with great accuracy by means of a relatively simple algebraic formula, as mentioned previously. The purpose of the present section is to describe a quadrature technique capable of evaluating the monstrosity on the second line, known as the far-field term.

When the substitution $t = \tan \theta$ is introduced, the far-field can be reduced to an expression of the type

$$2\nu e^{-\alpha} \int_{-\infty}^{\infty} e^{-\alpha t^2} \sin \left[(\beta + \gamma t) \sqrt{1 + t^2} \; dt\right], \tag{22}$$

where α, β, and γ are measures of distance in the y-, x-, and z-directions, respectively. The quantities β and γ may vary from less than 1 to more than 10,000 in practical calculations, and hence under some conditions the integrand in Eq. (22) is a wildly oscillating nonlinear function. It falls within the class of functions covered by Eq. (19).

Description

The essential feature of the method of numerically evaluating Eq. 19 is replacement of the nonlinear function $g(x)$ by a linear function plus an increment $\delta(x)$. If step lengths in the x-direction are chosen so that δ does not vary greatly over the interval of integration, then sin δ or cos δ can be approximated satisfactorily by low-order polynomials, and quadrature of Filon's type can be performed. A detailed description of the development will now be given.

The quantities f and g are arbitrary functions such as those sketched in Fig. 15, which is drawn to illustrate specifically the five-point quadrature treatment, i.e., $n = 2$. For simplicity, we can assume without loss of generality that the origin of x is at the center of the range of integration. At equally spaced steps of length h, the quantities f and g have values as indicated. We now approximate g in the range of interest by a line segment plus an increment $\delta(x)$. Numerous treatments are possible, but the following appears to be as simple as any: A straight line AB is passed through the two values of g at the extremes of the integration range. In Fig. 15 the line passes through the points $(-2h, g_{-2})$ and $(2h, g_2)$. Next, we construct the line CD parallel to AB and passing through the origin. Then we can write

$$g(x) = \lambda x + \delta(x) \; , \tag{23}$$

where δ is the difference between g and the line CD, and λ is the slope of line CD. It is useful to observe that $\delta(0)$ is just the value g_0 and that $\delta(2h) = \delta(-2h) = (g_2 + g_{-2})/2$. The quantity δ can have any magnitude; but d (Fig. 15) should never exceed about one radian, because d measures the extent of the sine or

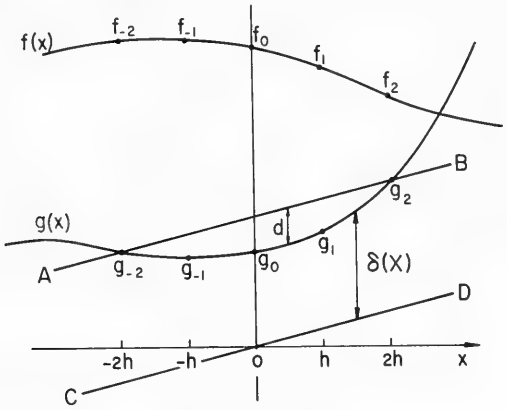

Fig. 15 - The approximation treatment

cosine function that must be approximated by a polynomial. The step length must be chosen so that d is kept reasonably small.

Now by means of Eq. (23), Eq. (19) can be written as

$$\int_{-nh}^{nh} f(x) \begin{matrix} \sin \\ \cos \end{matrix} (\lambda x + \delta)\, dx \ . \tag{24}$$

Next, we expand the trigonometric expression and designate the sine form of integral by S_n and the cosine form by C_n, where the index n corresponds to that specifying the range of integration. We obtain

$$S_n = \int_{-nh}^{nh} f(x)\, [\sin \lambda x \cos \delta + \cos \lambda x \sin \delta]\, dx \tag{25}$$

and a similar form for C_n. These expressions can be written as

$$S_n = \int_{-nh}^{nh} [G(x) \sin \lambda x + H(x) \cos \lambda x]\, dx \ , \tag{26a}$$

and

$$C_n = \int_{-nh}^{nh} [G(x) \cos \lambda x - H(x) \sin \lambda x]\, dx \ , \tag{26b}$$

where $G(x) = f(x) \cos \delta(x)$, and $H(x) = f(x) \sin \delta(x)$.

If the variation of δ is such that d is always less than about one radian, and if f is a not too rapidly varying function, then G and H are both sufficiently smooth to be approximated by low-order polynomials. It should be emphasized that it is

the variation, d, in δ that is important. Shifting the line CD up and down in Fig. 15 merely represents a phase shift, but the variation of δ gives a measure of the number of radians that are involved in the polynomial approximation of the sine and cosine functions.

Each of the terms in the integrands of Eqs. (26a) and (26b) is of the form first treated by Filon. Quadrature formulas with $\sin \lambda x$ or $\cos \lambda x$ as weighting functions are readily constructed, since the terms $x^p \sin \lambda x$ and $x^p \cos \lambda x$ can be integrated analytically. The details are presented in Ref. 10, which gives both three- and five- point formulas. We shall be content to present here only the three-point formulas. They are

$$S_1 = h\left[-k_1(f_1 - f_{-1}) \cos \frac{g_1 + g_{-1}}{2} + 2(k_0 + k_2) f_0 \sin g_0 \right.$$

$$\left. - k_2(f_1 + f_{-1}) \sin \frac{g_1 + g_{-1}}{2}\right], \tag{27}$$

and

$$C_1 = h\left[2(k_0 + k_2) f_0 \cos g_0 - k_2(f_1 + f_{-1}) \cos \frac{g_1 + g_{-1}}{2}\right.$$

$$\left. + k_1(f_1 - f_{-1}) \sin \frac{g_1 + g_{-1}}{2}\right]. \tag{28}$$

For these formulas: step length = h; complete interval = 2h; $\theta = g_1 - g_{-1}/2$; and k_0, k_1, and k_2 are defined in terms of θ, which may be large or small.

Two sets of formulas for the k values are given, for if θ is small the first set loses accuracy because of roundoff.

Formulas for k_0, k_1, and k_2 for large values of θ:

$$k_0 = \frac{\sin \theta}{\theta}, \quad k_1 = \frac{-1}{\theta}(k_0 - \cos \theta), \quad k_2 = \frac{-1}{\theta}(2k_1 + \sin \theta).$$

Formulas for k_2, k_1, and k_0 for small values of θ;

$$k_2 = -\frac{1}{3} + \frac{\theta^2}{5 \cdot 2!} - \frac{\theta^4}{7 \cdot 4!} + \frac{\theta^6}{9 \cdot 6!} - \frac{\theta^8}{11 \cdot 8!} + \frac{\theta^{10}}{13 \cdot 10!} - \cdots,$$

$$k_1 = -\frac{1}{2}(\theta k_2 + \sin \theta), \quad k_0 = -(\theta k_1 - \cos \theta).$$

Because the k-factors must be evaluated in terms of $\sin \theta$ and $\cos \theta$, practical use of the quadrature formula requires a computer. The cosine formula in Eq. (28) reduces to Simpson's rule as $\theta \to 0$, as it should. Integration over an extended range is accomplished by repeated application of the formula.

Figure 16 indicates the formula's accuracy. For this problem, steps can be about 10 times as long as those required by Simpson's rule for the same accuracy.

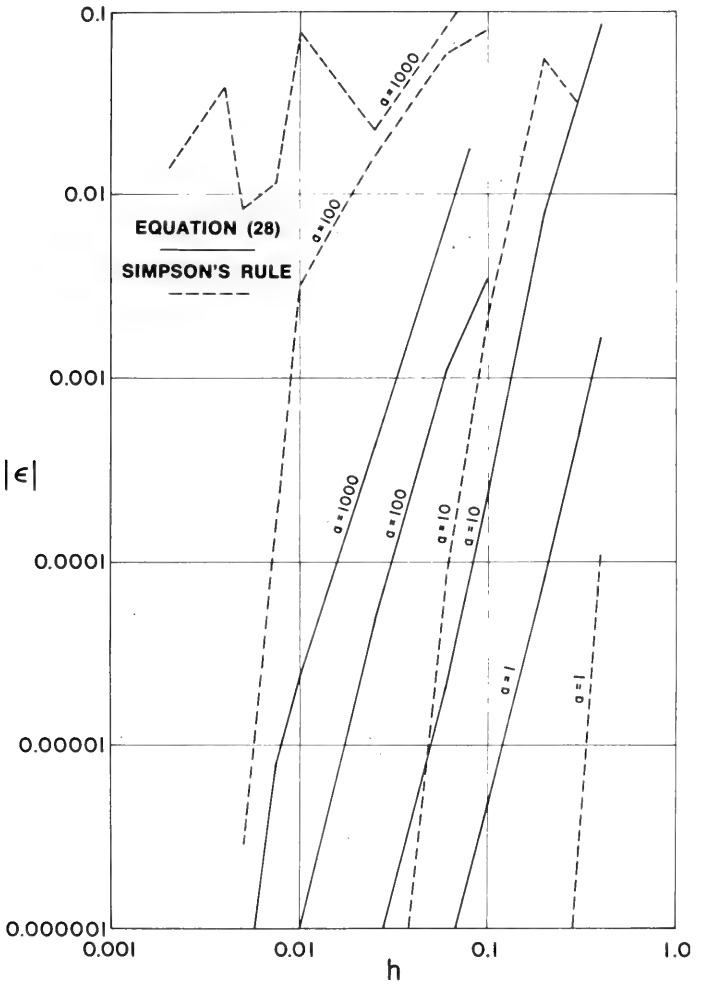

Fig. 16 - Effect of step length h on errors in evaluation of

$$\int_0^\infty e^{-x^2} \cos ax^2 \, dx$$

by Eq. (28) and Simpson's rule, for a = 1, 10, 100, and 1000.

When $a = 1000$, Simpson's rule fails entirely. Unfortunately, when the oscillations are rapid, many short steps must still be taken to obtain reasonable accuracy.

A THREE-DIMENSIONAL BODY OSCILLATING IN THE PRESENCE OF A FREE SURFACE

The previous sections have dealt with work considered as completed. Here we consider some work that is in progress. The problem is that of solving the motion of a true three-dimensional body oscillating with small amplitude in the presence of a free surface. It is the key to the solution of very general problems of motion of a body, according to Ogilvie, Ref. 11, whom we quote:

> "If we can find velocity potentials for the six problems corresponding to the sinusoidal oscillations of a ship in calm water, we can evaluate these potentials far away from the ship (effectively at infinity) and from the resulting simplified functions determine some of the damping coefficients. From the same asymptotic forms of the potentials we can also find the forces on a ship due to sinusoidal incident waves from any direction, without having to solve the problem of determining the diffracted waves around the ship. In both problems we avoid the necessity of integrating the pressure over the ship hull. It is only necessary to integrate over a simplified mathematical surface far away from the ship. Finally, in any case for which we know the damping coefficients we can find the corresponding added-mass coefficients."

Furthermore, if these six problems can be solved, the force and moment on a ship restrained in incident waves can be computed.

A straightforward and very general attack on this problem is to use the basic method described at the beginning of this paper, but to replace the simple, steady 1/r-type of distribution with an oscillating source distribution that will satisfy the linearized free-surface condition. Wehausen and Laitone present equations for this type of source (9). The general approach is consequently unchanged, except that the Fredholm integral equation acquires a new kernel. The six kinds of motion, rolling, heaving, pitching, surging, etc., are all solvable by the same method. The only difference is in the boundary conditions on the body, which amounts to no more than different numbers in the column matrix of Eq. (7).

The Oscillating Source Potential

Let an oscillating point source be located at the point whose Cartesian coordinates are a, b, c. The potential of this source at a field point with coordinates x, y, z may be written

$$\varphi_p = \frac{1}{r} + \frac{1}{r_1} - 2\nu \int_0^\infty \frac{e^{-\nu u}\, du}{\sqrt{R^2 + (u+y+b)^2}} + 2\pi i \nu e^{\nu(y+b)} H_o^{(1)}(\nu R) \,, \qquad (29)$$

where

$$r^2 = (x-a)^2 + (y-b)^2 + (z-c)^2 , \tag{30a}$$

$$r_1^2 = (x-a)^2 + (y+b)^2 + (z-c)^2 , \tag{30b}$$

$$R^2 = (x-a)^2 + (z-c)^2 , \tag{30c}$$

$$\nu = \frac{\omega^2}{g} , \tag{30d}$$

and where $H_o^{(1)} = J_o + iY_o$ is the Hankel function of the first kind and g is the acceleration of gravity. The term u is the vertical distance measured from the image point. It is assumed in this formula that the free surface is the plane $y = 0$ and that the region of interest is the half space $y < 0$. The y-direction may thus be considered vertical and the x- and z-directions horizontal. In particular, R is the horizontal distance between the oscillating point source and the field point. It is evident that the first two terms of Eq. (29) are the potentials of two $1/r$-type point sources - one at the location of the oscillating point source and one at the image of this point in the free surface. The integration of these two terms over a quadrilateral can be accomplished by the basic method described early in this paper and described in detail in Ref. 1. It is the other two terms that concern us.

The third term of Eq. 29 is the potential of a $1/r$-type line-sink of exponentially decaying strength which starts at the image point $(a, -b, c)$ and runs vertically downward through the free surface to minus infinity. This term is denoted the line-source term. The fourth of Eq. (29), which involves a Hankel function, is called the Bessel function term. For large values of νR, it is known that this term oscillates with increasing horizontal distance R at a circular frequency of ν. Thus ν denotes the spatial circular frequency, and its relation to the temporal circular frequency ω is given in Eq. (30d). Rapid evaluation of Eq. (29) over a quadrilateral element is the heart of the problem, for otherwise there is no change in the formation of the basic integral equation.

The basic method chosen for evaluating the line-source term is the Laguerre-Gauss quadrature. However, accuracy becomes poor when the horizontal distance between the oscillating point source and the field point is small. Here, an expansion valid for this condition is developed. A large amount of computing has been done to determine the number of terms required in the Laguerre-Gauss quadrature to meet the specified accuracy. Systematic studies have been made to determine the range of validity of the special expansion. Details of the formulas, as well as tables presenting the accuracy studies are contained in Ref. 12, which is in the nature of a progress report to the Naval Ship Research and Development Center on this work.

The field due to the oscillating source of constant strength distributed over a plane quadrilateral element is found by the multipole expansion method. This method is applied to the last two terms of Eq. (29). Evaluation of the Hankel function term in Eq. (29) is no particular problem, because standard Bessel function subroutines for the computer are available. Several tables in Ref. 12 present the results of error studies in evaluating the field of a square element.

Once the entire procedure for determining the influence function for an element covered by sources of this type has been established, it should be a relatively minor problem to modify the existing three-dimensional computer program. Exactly the same kind of modification procedure has already been accomplished for hydrofoils. It appears that the present work is producing a practical method of evaluating this special source, although whether or not it is the best possible procedure is open to question. A full report on evaluation of this source function is expected in late 1968.

DIRICHLET AND OTHER PROBLEMS

Problems of fluid mechanics are normally Neumann-type problems. Therefore, in our work, we have been concerned with first boundary-value problems. Although the computing programs have the inherent capability of solving a wide variety of these problems, only a few of these have been run, so that we are unable to make such definite statements about their accuracy and ability to obtain solutions as those we can make for fluid problems. A few studies have been made of a temperature distribution in solids for which analytic solutions exist, and the accuracy was found to be good. Our principal reason for mentioning Dirichlet problems is to remind the reader that the basic procedure encompasses that capability. To know this may be useful to someone who finds himself faced with a problem that falls into the Dirichlet class, as was the case with a missiles engineer who was studying the problem of cooling reentry bodies. The basic type of problem will be described to show the Dirichlet capability. John Hess conducted preliminary studies to ascertain our capability, and the following is taken chiefly from his memo which summarizes the work.

> As part of a reentry study program, we were asked to perform certain calculations with our axisymmetric-potential-flow program. The problem of interest is the cooling of a reentry body by forcing liquid from a reservoir in the interior of the body through a porous medium to the surface. See Fig. 17. As is well known, the flow of liquid through a porous medium is governed approximately by Laplace's equation in the pressure for incompressible flow or in the square of the pressure for compressible flow. The boundary conditions are that the pressure equal the constant reservoir pressure on the interior surface of the porous medium and that the pressure equal the surface pressure of the exterior flow (as obtained from hypersonic theory) on the exterior surface of the porous medium. This is thus a Dirichlet problem in the "thick shell" region between the reservoir and the exterior.
>
> As part of a study of added-mass effects sponsored by the Naval Ordnance Test Station in Pasadena, program 50D had previously been modified to handle axisymmetric Dirichlet problems. This capability had been verified by comparison with analytic solutions for exterior problems. Past experience had indicated that an interior problem often leads to considerably more calculational difficulties than the corresponding exterior problem, especially when, as in the present case, a surface source distribution is used to obtain the solution. Accordingly, a test case was set up and run for several boundary conditions for which simple analytic solutions are available. The configuration is shown in Fig. 17. It consists of two concentric spherical shells. The outer one has a radius of unity and the inner one has a radius of 0.8. Four boundary conditions were considered for the potential Φ. They are:

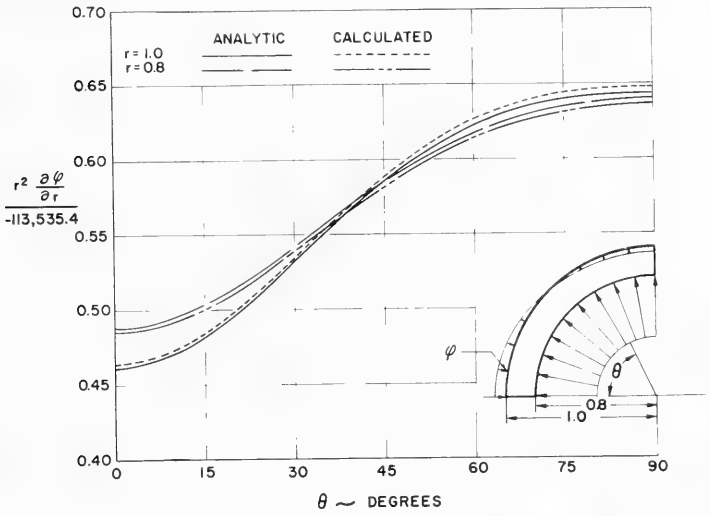

Fig. 17 - External boundary condition approximates that obtained from hypersonic flow theory

1. $\varphi(0.8) = 1,\ \varphi(1) = 0$

2. $\varphi(0.8) = 0,\ \varphi(1) = 1$

3. $\varphi(0.8) = 0,\ \varphi(1) = P_2(\cos\theta) = 1/2\ (3\cos^2\theta - 1)$

4. $\varphi(0.8) = 0,\ \varphi(1) = P_4(\cos\theta) = 1/8\ (35\cos^4\theta - 30\cos^2\theta + 3)$.

Here θ is the angular coordinate measured from the symmetry axis as shown in the figure. The Legendre polynomials P_2 and P_4 are defined above. Two element numbers were used. In the smaller case each element on each sphere had a 3° angular extent. For an exterior problem this is certainly adequate. However, the element length on the outer sphere is longer than one-fourth the 0.2 distance between the spheres. In the larger case the elements were simple halved to give a 1-1/2° angular spacing and an element length of about one-eighth the distance between the spheres. Calculations were compared with analytic solutions for the values of the radial (normal) derivative of the potential on the sphere surfaces. The maximum errors in the calculated derivative are shown in Table 3 as percents of the maximum value of the derivative on the surface for each case. The accuracy is quite good even for the smaller (large element) case. For all boundary conditions halving the element size halves the error, so accuracy is linear in element number. Computing time is quadratic in element number, and thus it is advisable to use small-point number cases.

Table 3

Maximum Percent Errors Obtained for Values of the Surface Normal Derivatives for the Case of Dirichlet Conditions on Concentric Spheres

	3° Elements-Element Length Equals 1/4 Distance Between Spheres		1-1/2° Elements-Element Length Equals 1/8 Distance Between Spheres	
	r = 0.8	r = 1.0	r = 0.8	r = 1.0
$\varphi(0.8) = 1,\ \varphi(1) = 0$	0.60	0.56	0.30	0.30
$\varphi(0.8) = 0,\ \varphi(1) = 1$	0.74	0.56	0.36	0.30
$\varphi(0.8) = 0,\ \varphi(1) = P_2(\cos\theta)$	0.52	0.95	0.27	0.47
$\varphi(0.8) = 0,\ \varphi(1) = P_4(\cos\theta)$	0.53	1.12	0.28	0.51

By suitably combining the above solutions, it is possible to obtain the solution to a problem typical of those of the reentry body application. The boundary conditions are:

$$\varphi(0.8) = 16900$$

$$\varphi(1) = 618.06\ P_4(\cos\theta) + 2793.14\ P_2(\cos\theta) - 133.60\ .$$

Figure 17 compares analytic values of $r^2\ \partial\varphi/\partial r$ with those calculated by using the smaller element number. Agreement is good. The quantity $\partial\varphi/\partial r$ is weighted by r^2 to correct for the difference in surface area of the inner and outer walls. If there were no circumferential flux in the porous material the two curves would coincide. The fact that they do not is evidence of appreciable flux in the circumferential direction. The corresponding curve for the larger element number case lies exactly halfway between the two in the figure (half the error).

In summary, the ability of the existing surface source density program to calculate accurate solutions to the interior Dirichlet problem using reasonable element numbers has been demonstrated. The present application is an unusual one.

Presumably, since the method is not configuration--limited, it could solve similar problems for general shapes with about the same accuracy.

I will close by citing an instrument problem that is especially interesting because Laplace's equation applies so rigorously. That is not the case with fluid flows, because of the effects of viscosity. In fluid flows the Navier-Stokes equation applies rigorously; what we are doing now is approximating it by using Laplace's equation.

The problem is that of a superconducting bearing suspended in a magnetic field. Because the bearing is superconducting the field is unable to penetrate

the bearing, and this inability to penetrate leads to the condition $\partial\varphi/\partial n = 0$ over the surface. Here again we find a classical Neumann problem. Roger Bourke studied such a bearing at Stanford University for his Ph.D. dissertation (13). It is a body of revolution and is shown in Fig. 18. By using the methods of this paper he first calculated the relation between the current and the displacement. A comparison of theory and experiment is included in Fig. 18. Agreement is within experimental accuracy. He then studied the stability problem by analyzing other displacements (rotational and sideways) and obtained the same good agreement between theory and experiment.

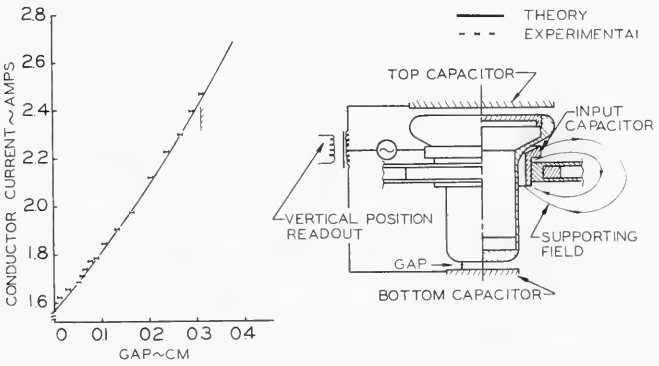

Fig. 18 - A superconducting bearing suspended in a magnetic field. The graph on the left compares theory and experiment for displacement in the axial direction.

REFERENCES

1. Hess, J. L., and Smith, A. M. O., "Calculation of Potential Flows About Arbitrary Bodies," Progress in the Aeronautical Sciences, Vol. 8, New York: Pergamon Press, 1966

2. Kellogg, O. D., "Foundations of Potential Theory," New York: Ungar, 1929 (also available through Dover Publications, New York)

3. Gentry, A. E., "Aerodynamic Characteristics of Arbitrary Three-Dimensional Shapes at Hypersonic Speeds," Aerospace Proceedings 1966, Vol. 1, New York and Washington, D. C.: Spartan Books

4. Giesing, J. P., "Nonlinear Two-Dimensional Unsteady Potential Flow with Lift," J. Aircraft 5(No. 2), 135-143 (Mar.-Apr. 1968)

5. Giesing, J. P., "Nonlinear Interaction of Two Lifting Bodies in Arbitrary Unsteady Motion," ASME Paper 68-FE-22 (to be published in J. Basic Engineering

6. Bratt, J. B., "Flow Patterns in the Wake of an Oscillating Airfoil," British ARC, R and M 2773 (1953)

7. Spurk, J., "Measurement of the Aerodynamic Coefficients of Oscillating Airfoils in the Wind Tunnel and Comparison with Theory," Max Planck Institute Report 29, Gottingen, 1963 (also available as translation by G. de Montalvo, Report LB 31959, Douglas Aircraft Co., Nov. 1964

8. Faulkner, S., Hess, J. L., Smith, A. M. O., and Liebeck, R. C., "Charts and Formulas for Estimating Velocity Fields in Incompressible Flow," McDonnell-Douglas Report 32707, July 1968

9. Wehausen, J. V., and Laitone, E. V., "Surface Waves," Encyclopedia of Physics, Vol. IX, Berlin: Springer Verlag, 1960

10. Smith, A. M. O., "Numerical Integration of Oscillating Functions having a Non-linear Argument," Douglas Aircraft Co. Engineering Paper 3373, (1967)

11. Ogilvie, T. F., "Recent Progress Toward the Understanding and Prediction of Ship Motions," in "Fifth Symposium on Naval Hydrodynamics: Ship Motions and Drag Reduction," Bergen, Norway, Sept. 1964, Office of Naval Research, Department of the Navy, ACR-112

12. Hess, J. L., and Wilcox, D. C., "Solution of the Problem of a Body Oscillating in the Presence of a Free Surface," Douglas Aircraft Co. Report DAC 33739, May 1967

13. Bourke, R. D., "A Theoretical and Experimental Study of a Superconducting Magnetically-Supported Spinning Body," Stanford University, Dept. of Aeronautics and Astronautics, SUDAER 189, May 1964

* * *

DISCUSSION

George P. Weinblum
Institut für Schiffbau der Universität Hamburg
Hamburg, Germany

The paper by Hess and Smith, "Calculation of Potential Flows About Arbitrary Bodies," has become within a short time a classical chapter in ship theory. A more difficult special problem has been treated independently by

H. Nowacki - the interaction between a simplified shipform and the propeller pictured by a sink disc (JSTG 1963). This latter method is based on an iteration procedure; the results are valuable notwithstanding a minor slip in a boundary condition.

It appears that a large number of problems in ship hydrodynamics will be solved by properly extending Dr. Smith's method, following the lines indicated by himself - the flow around bodies in the presence of a bottom, tank walls etc; i.e., the determination of shallow water and blockage effects, which so far have been treated by approximate procedures only.

Valuable fluid charts of the pressure field around general ellipsoids have been treated earlier by Maruhn (Jahrbuch der Luft-fahrtforschung, 1941) before computers had been developed.

Of special interest are the author's remarks on two-body problems as a foundation for determining the interaction forces of passing or overtaking ships.

* * *

DISCUSSION

Louis Landweber
Institute of Hydraulic Research
University of Iowa
Iowa City, Iowa

I wish to discuss the integral equation applied in the paper to obtain surface distributions of sources, viz

$$\sigma(p) = f(p) + \int_S K(P,Q)\,\sigma(Q)\,dS_Q\ , \quad K(P,Q) = \frac{1}{2\pi}\frac{\partial}{\partial n_Q}\left(\frac{1}{r_{PQ}}\right),$$

where $f(p)$ is a given function and P and Q are points on the given surface S. This integral equation, which formulates the Neumann problem for the surface, has the well-known properties that the eigenvalues λ of the kernel $K(P,Q)$ are real, that $\lambda = -1$ is the eigenvalue of smallest absolute value, and that $\lambda = +1$ is not an eigenvalue. Then, according to the fundamental theorem of Fredholm integral equations, a solution of (1) exists.

If we write, instead of (1)

$$\sigma_{i+1}(p) = f(p) + \lambda \int_S K(P,Q)\,\sigma_i(Q)\,dS_Q\ ,$$

and take $\sigma_1(p) = f(p)$, we obtain a sequence of functions

$$\sigma_{i+1} = f + \lambda \int K_1 f + \lambda^2 \int K_2 f + \cdots + \lambda^i \int K_i f \ .$$

As $i \to \infty$, this gives for $\sigma(p)$ an infinite series in λ with a radius of convergence equal to the distance from the origin to the nearest eigenvalue $\lambda = -1$ in the complex λ-plane. Since $\lambda = +1$ also lies on this circle of convergence, the convergence of the sequence σ_i is not assured when $\lambda = +1$; it converges conditionally, if at all.

The slow convergence of the iteration formula reported in the paper is attributable to this property. By analogy with the Gershgorin integral equation for conformal mapping, in which the identical properties occur, I believe, however, that the functions $\bar{\sigma}_i = 1/2\ (\sigma_{i+1} + \sigma_i)$, or some modified version of successive pairs of approximations, may converge much more rapidly, and I would suggest that such a modification be tried by the author.

* * *

DISCUSSION

L. Mazarredo
Asociación de Investigación de la Construcción Naval
Madrid, Spain

I want to ask whether an analytical solution has not been attempted for three-dimensional bodies. Although not essentially needed, it might be of great help in obtaining an efficient, rapid, and accurate way of preparing formal data. We found this out when we began to work on the potential flow around a three-dimensional body that approximated a ship. Our approach was based on the classical relaxation method, but this makes no difference.

In this case, an analytical definition might help in finding the boundary condition. Since the speed induced by a source (q) on a point (p) varies as $(\overline{pq})^{-2}$, an element may be replaced by any other, provided it is parallel, has the same solid angle - as seen from p- and the same intensity of the original one. The original element can also be approximated by a spherical surface element inside the same solid angle and center in p, if we increase its intensity in order to maintain σS.

If we know the equations for the boundary lines of the original elements, a change of coordinates in order to move the origin to p and the z axis-to-the-normal to S_p would not present any difficulty. The unit vectors of these curves would give spherical elements whose projections on the xy plane, when multiplied by $\sigma(q)/\cos \widehat{qr}$!, will give the normal component of the speed. Thus, the integrations are reduced to surfaces on a plane. Of course, this idea, which is very similar to one currently used in radiation transfer, would require small

elements in the neighborhood of p, to limit the solid angles to small values. But the elements can easily be divided around the point calculated (maintaining σ for the subelements), if the analytical definition is known.

Finally, I want to congratulate Dr. Smith for his achievements in this study, which opens many possibilities.

* * *

REPLY TO DISCUSSION

A. M. O. Smith

I wish to thank Dr. Weinblum for his complimentary remarks. I am glad to be reminded of the work by Karl Maruhn on flow fields about ellipsoids. About the time of World War II, I was aware of his work, but it had since gradually faded from my memory. The report (Ref. 1) mentioned in my paper, covering velocity fields, includes the ellipsoid family, but of course, it also covers many more shapes.

With regard to Dr. Landweber's comments, I wish to say that the present paper is restricted to a very brief discussion of various aspects of the method. A more complete analysis of iterative solutions of this problem is contained in section 5.4 of Ref. 1.

The analytical procedure mentioned by Dr. Landweber is numerically approximated by the point-Jacobi iterative matrix method. Indeed, for exterior flows this method has a negative convergence factor slightly less than unity in absolute value. This means that once the procedure has steadied out, successive iterates oscillate about the true solution with slow convergence. Clearly, in this circumstance the averaging of two successive iterates produces a much improved result. The only problem is how many iterations are required before the iterative procedure becomes steady. For single smooth bodies only a few iterations are required, but multiple-body problems require a large number. Averaging is not effective for interior flows. For these the convergence factor is positive and thus the iterates form a monotonic sequence.

Reference 1 states that the iterative procedure actually used is the Gauss-Seidel, which is always superior to the point-Jacobi. For typical exterior flows this procedure requires only four iterations per decimal place of accuracy - a very fast convergence. For interior flows it requires about half as many iterations as the point-Jacobi method. The convergence factor is always positive. Tables summarizing the detailed results may be found on pages 78 and 80 of Ref. 1.

Recent experience has shown that direct-matrix solution is efficient at higher element numbers than had been supposed. Eventually a direct solution, whose computing effort varies as the cube of the matrix order, must be slower

than an iterative solution, whose computing effort varies as the square of the order. However, the direct solution is faster for matrices of the order 500, and is particularly efficient in cases where solutions are required for several onset flows.

I have no comment to make on Dr. Mazarredo's discussion.

NAVAL HYDRODYNAMIC PROBLEMS SOLVED BY RHEOELECTRIC ANALOGIES

L. Malavard
Faculté des Sciences (Chaire d'Aviation)
Université de Paris
Paris, France

INTRODUCTION

For the past 10 years the Centre de Calcul Analogique of the Centre National de la Recherche Scientifique has made various contributions to the study and solution of a large number of naval hydrodynamic problems. These contributions are significant, because they have been made by a small team of research scientists using very simple computing equipment which would seem inadequate to people who are accustomed to using large, sophisticated computers.

It is not feasible to consider these studies of naval hydrodynamics in complete isolation from the context of rheoelectric analogy which has made possible important developments in the various fields of mathematical physics. In this connection, it is convenient to recall that the first studies carried out in France using electric analogy techniques for solving some hydrodynamic problems (flows around bodies with or without circulation — Oseen flows (1, 2), flows with jetstream lines (3), etc.), gave promise of future development. This development has been realized intensively since 1958 because of the experience gained by the Centre de Calcul Analogigue in the study of problems in incompressible aerodynamics, thin foils, lifting lines, lifting surfaces, cascades, simple helicoidal machines, etc. (Refs. 4 through 6), and because of the introduction by Tulin and Burkart (7) in 1955 of the linearized theory of cavitating flows.

One of the assets which has assured the success of rheoelectric analogy since its early beginnings has been its ability in solving Laplace field equations. This computing capacity, together with the experimental character of the technique employed, makes rheoelectric analogy ideal for the practical worker, engineer, or physicist, who remains in contact with a model on which his controlling action may be exercised without any restraint. Nevertheless, for an intensive and complete use of the method, *analog simulation* often requires turning to certain methods of theoretical formulation familiar to the mathematician. It is in this way, for example, that the knowledge of elementary analytical solutions, the use of conformal mapping, the analysis of singularities, etc., allow the solution of each problem in the most efficient way.

From these three elements — experience acquired in incompressible aerodynamics, the linearized theory of cavitations, and auxiliary analytical data — naval hydrodynamic studies have been developed, as outlined below and illustrated in Fig. 1.

Two-Dimensional Problems

In 1958, Luu carried out studies on the solution of the direct problems of supercavitating hydrofoils (8, 9). These studies were the continuation of important research devoted to the problem of thin jetstreams in aerodynamics (Refs. 8 and 10 through 12) and came within the framework of linearized free boundaries.

In 1960, a research program was envisaged concerning the effects of the free surface on slightly immersed sub- and supercavitating hydrofoils. In the case of small Froude numbers, where there is a considerable influence of the gravity-field effect, it was possible to proceed easily to hydrofoil design for imposed pressure distribution *(inverse problem)* (13, 14). These studies took into account the gravity effect on the free surface and on the finite cavity, which, to our knowledge, had not yet been treated. The *direct problem* in the case of the immersed flat plate was also solved and allowed a useful comparison with analytical results (13, 15).

In the case of high Froude numbers and zero cavitation number, Luu and Fruman published, in 1963, a rheoelectric method permitting the design of ventilated hydrofoils with arbitrary local pressure distribution (16). The results obtained agreed with those of Auslaender (17), published shortly before, and extended them by the definition of shapes with larger lift-drag ratios. It was proved that the drag of supercavitating hydrofoils is related to the angle of the spray far downstream, and it seems natural that these studies led to the design of base-vented hydrofoils with zero drag (13).

Subcavitating cascades had been thoroughly studied earlier by Malavard, Siestrunck, and Germain, Refs. 18 through 22, within the framework of the foil theory. The linearization used by Luu in the case of thin-jet flap on the trailing edge of cascades (8) was easily extrapolated to supercavitating cascades (23) which were liable to be used in certain types of pumps and turbines.

Three-Dimensional Problems

Hydrofoils — The two-dimensional studies on supercavitating hydrofoils led Luu to carry out an analog simulation with finite-span wings (24). The experience gained in lifting-surface problems, published in the work of Malavard, Duquenne, Granjean, and Enselme, Refs. 25 through 28, allowed a very rapid implementation of the supercavitating problem in an unbounded flow field, by the introduction of an ingenious decomposition of the potential. This will be examined in detail later in this paper.

The method used also permitted the design of supercavitating wings at zero cavitation number near the free surface (29). The optimal vortex distribution over the span was obtained by using the properties of the potential in the Trefftz

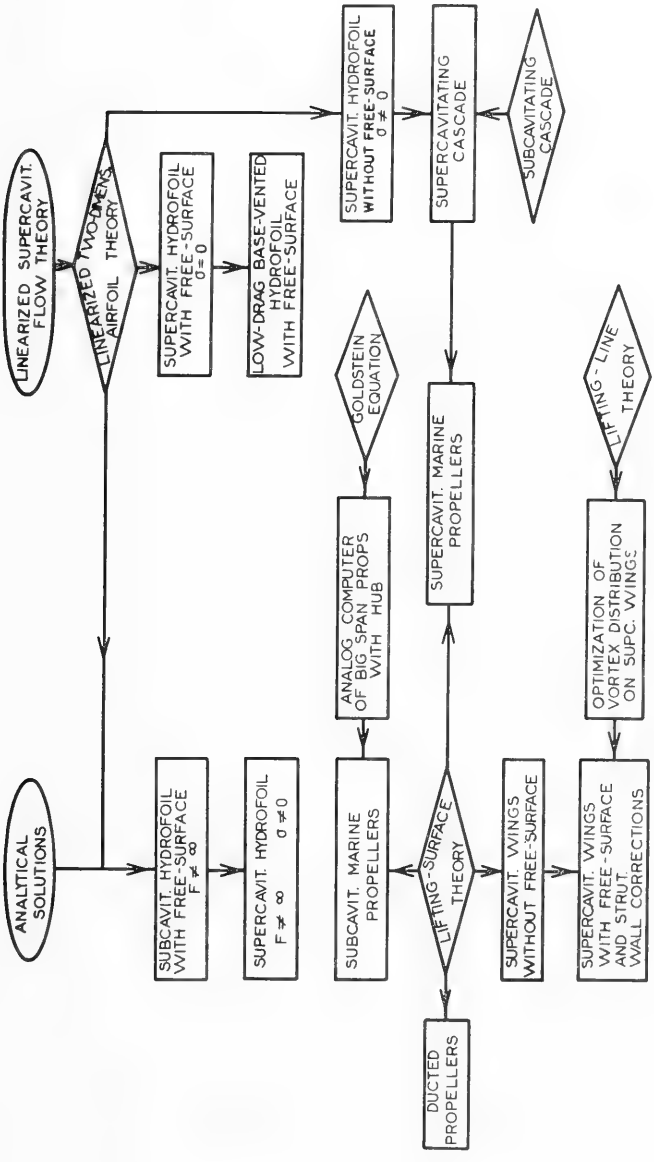

Fig. 1 - Development of analog studies

plan (30) and by transposing the analog simulation used in the principle of the "lifting-line computer" (31). Finally, in order to compare analog results and experiments in a small high-speed hydrodynamic channel, a special simulation device permitted the design of supercavitating wings with strut and wall effects (32, 33), and calculation of the hydrodynamic characteristics of *flat* supercavitating wings.

Screw Propellers — On the same principle as the "lifting-line computer," Siestrunck had conceived, in 1944, an "analog propellers computer" for large-aspect ratio blades. This realization was taken up again in 1959 by Sulmont, who improved it by introducing a resistance network, thus making it easier to use. He also adapted it to simulate hub effects easily (34).

Because of the small span ratio of their blades, naval propellers can be calculated from aeronautical theories only by introducing more or less justified empirical correction coefficients. It was only in 1959 that our first efforts were made to apply the theory of lifting surface to helical flows. The many difficulties in solving this problem by analytical and numerical methods are well known; they are caused mostly by the complexity of the flow field to be considered.

The rheoelectric method allows the representation of this flow field, and thus the design of small-span ratio blades becomes possible by means of techniques similar to those perfected for wings of arbitrary shapes (35). The boundary conditions corresponding to supercavitating blades can also be imposed without major difficulty and lead to a correct definition of the lower surface for the imposed pressure distribution (34, 36). This problem has not yet received any numerical treatment, and accordingly the studies being made at present at the Centre de Calcul Analogique are attempting to transpose the analog method into a program that could be used on large computers.

In the same framework, Sulmont has studied the problem of ducted propellers; by making some assumptions of the propeller's nature (infinite number of blades), he has been able to define adapted duct forms which seem to promise high propulsion efficiency.

To complete this account we must mention the studies being carried out at the Centre de Calcul Analogique. At present, our attention is directed towards the solution of the problem of immersed or semi-immersed bodies which may be so thick that the linearized boundary conditions relative to the obstacle are no longer applicable, although the linearized free surface is preserved. A two-dimensional study (37) has permitted us to test the validity of a new theoretical scheme (38), and in forthcoming studies results in the three-dimensional area should be obtained very soon. At that point, the calculation of the wave resistance of a thick hull will be undertaken.

It would be difficult to sum up completely here all the publications which have been referenced above. We can only present some of the most significant examples of the rheoelectric method and the most outstanding results of its use.

THE HYDRODYNAMIC PROBLEM

General Equations and Boundary Conditions

Consider the permanent and irrotational flow of an inviscid, incompressible, and heavy fluid with density ρ past a supercavitating hydrofoil located at a depth d beneath the free surface, the velocity far upstream being V_0. A set of Cartesian coordinates, x', y', and z' is chosen in such a way that the positive directions of the x' and z' axes are respectively those of V_0 and of the upward direction. Because the plan-form of the wings is generally symmetrical, the field simulation can be limited to a quarter of the space.

The movement is described by the perturbation velocity potential ϕ', which must fulfill the following boundary conditions (Fig. 2):

1. On the *free surface*, $z = 0$, the pressure p_0 is constant, and thus the equilibrium condition gives

$$\frac{\partial^2 \phi}{\partial x^2} = F^{-2} \frac{\partial \phi}{\partial n} , \tag{1a}$$

which is a Poisson condition for ϕ; where $F = V_0/\sqrt{gd}$ is the Froude number, g the gravity force, n the inward normal, and where $\phi = \phi'/V_0 d$, $x = x'/d$, and $n = -z/d$ are nondimensional magnitudes.

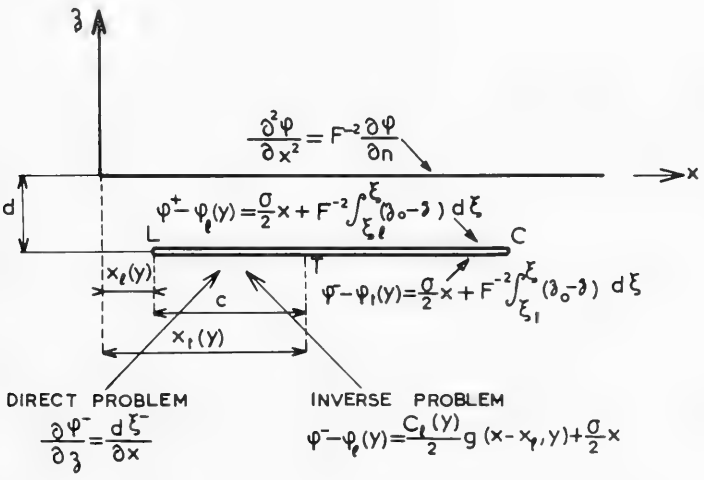

Fig. 2 - Boundary conditions for a supercavitating wing at $y = c_t$

2. Inside the cavity where $p = p_c$ the equilibrium of its boundary requires that

$$\frac{\partial \phi}{\partial x} = \frac{\sigma}{2} + F^{-2}(z_0 - z) \ , \tag{2a}$$

which becomes after integration

$$\phi^{\pm} = \phi_0(y) + \frac{\sigma}{2} x + F^{-2} \int_{\xi_0}^{\xi} (z_0 - z) \, d\xi \ , \tag{3}$$

where ϕ_0 is the value of the perturbation velocity potential at point ξ_0, z_0, (for example, the velocity potential of the leading edge), and where the signs + and - relate to the upper and lower surface of the cavity. The cavitation number σ is defined as

$$\sigma = \frac{p_0 - p_c}{(\rho V_0^2/2)} \ .$$

3. On the lower surface of the hydrofoil the boundary condition can be given in two ways:

A. *Direct problem.* The geometric form of the wing $\zeta^-(x,y)$ is given, then the velocity tangential condition permits us to write

$$\frac{\partial \phi}{\partial z} = \frac{d\zeta^-}{dx} \ , \tag{4a}$$

which is the classical Neumann condition.

B. *Inverse problem.* The pressure distribution over any local chord $\Delta p' = p - p_c$ is given. The boundary condition may be written

$$\frac{\partial \phi^-}{\partial x} = F^{-2}(z_0 - z) + \frac{\sigma}{2} - \frac{1}{2} \frac{\Delta p'}{(\rho V_0^2/2)} = \frac{\sigma}{2} - \frac{1}{2} C_p(x,y) + F^{-2}(z_0 - z) \ .$$

This equation can be integrated to obtain a Dirichlet condition

$$\phi^- = \phi_\ell(y) + \frac{1}{2} C_\ell(y) \, g(x - x_\ell, y) + \frac{\sigma}{2} x + F^{-2} \int_{\xi_\ell}^{\xi} (z_0 - z) \, d\xi \ , \tag{5a}$$

where $C_\ell(y) = 2\Gamma(y)/V_0 C(y)$ is the local lift coefficient at a given section $y = cte$ with chord $C(y)$, $\Gamma(y)$ is the circulation around this section,

$$\Gamma(y) = \phi_\ell - \phi_t = \frac{1}{\rho V_0} \int_{x_\ell}^{x_t = x_\ell + C} \Delta p' \, dx' \ , \tag{6}$$

and $x_\ell = x_\ell(y)$ is the position of the leading edge at the same section. The function g should be such as $g(x_\ell, y) = 0$ and $g(x_t, y) = -1$.

4. On the trailing edge of the wing the Kutta-Joukowski condition must be respected

$$\left(\frac{\partial \phi}{\partial x}\right)_{x = x_t} = 0 \ , \tag{7}$$

with $x_t = x_\ell + C$ as the position of the trailing edge.

5. On the plane $y = 0$, by the symmetry of the flow, the normal velocity is

$$\left(\frac{\partial \phi}{\partial n}\right)_{y=0} = 0 \ , \tag{8}$$

and at infinity upstream the gradient of ϕ also is

$$\text{grad } \phi = 0 \ . \tag{9a}$$

6. The cavitation pocket must be closed, i.e., in a section $y = \text{cte}$, on a closed contour surrounding the foil and the cavity

$$\oint \frac{\partial \phi}{\partial z} \, dx = \oint \frac{\partial \phi}{\partial n} \, ds = 0 \ . \tag{10a}$$

7. The boundary value problem defined by the conditions of Eqs. (1a), (3), (7), (8), (9a), and (4a) or (5a) is not yet determined because the distributions of the potentials on the lower and upper surface of the cavity remain arbitrary. This does not, however, constitute an indetermination, for they are connected in the inverse problem by the known value of $C_\ell(y)$ in Eq. (5a). In the direct problem it may be considered as the unknown of the problem which fulfills the condition of Eq. (7). We shall not discuss this question in detail, but rather insist on the methods used for its solution.

8. In the two-dimensional case there is an associated harmonic function ψ, perturbation stream function, defined by the transformation of conditions in Eqs. (1a), (3), (7), (8), (9a), and (10a):

On the free surface

$$\frac{\partial \psi}{\partial n} = F^{-2}(\psi - \psi_0) \ , \tag{1b}$$

on the upper and lower surface of the cavity

$$\pm \frac{\partial \psi^{\pm}}{\partial n} = \frac{\sigma}{2} + F^{-2}(\psi - \psi_0) \ , \tag{2b}$$

on the lower surface of the foil in the direct problem

$$\psi^{-} = \psi_0 - \zeta^{-} \ , \tag{4b}$$

in the inverse problem

$$- \frac{\partial \psi^{-}}{\partial n} = C_L g(x) + \frac{\sigma}{2} + F^{-2}(\psi - \psi_0) \ , \tag{5b}$$

at the infinity upstream of the field

$$\text{grad } \psi = 0 \ , \tag{9b}$$

so that the closure cavity condition is now written

$$\psi_c^{-} = \psi_{c'}^{+} \ , \tag{10b}$$

where c and c' are two points placed at the downstream top of the cavity on both sides of the slit.

The symbols have the same signification as in the three-dimensional case, except C_L, the global lifting coefficient, and $g(x)$, the function which should now fulfill the conditions $g(x_\ell) = 0$, $g(\xi) < 0$ for $x_\ell < \xi < x_t$, and

$$\int_{x_\ell}^{x_t} g(\xi) \, d\xi = 1 \ .$$

RHEOELECTRIC ANALOGIES — PRINCIPLES

The principles of rheoelectric analogies are classical and various publications on this subject (5, 6, 39) give sufficient information on the special technology required. It may be helpful, however, to recall some of these principles, in a general way.

An analogy can be made between the Laplacian of the velocities potential (or of the stream function) and the Laplacian of the electric potential, created in a homogeneous and isotropic conductor. The latter is generally comprised of a liquid contained in a *rheoelectric tank* and confined by boundaries where electrodes are placed, of judiciously determined form and disposition. The boundary conditions are introduced in a generally discontinuous way, by means of suitable electric setups. The two most simple conditions which are very often found in the problem are those of either the constant potential, which is the condition of Eq. (1a) for $F = \infty$, or the zero normal derivative, which is the condition of Eq. (8), on one or several boundaries. They are conveyed respectively by conductor or insulating surfaces.

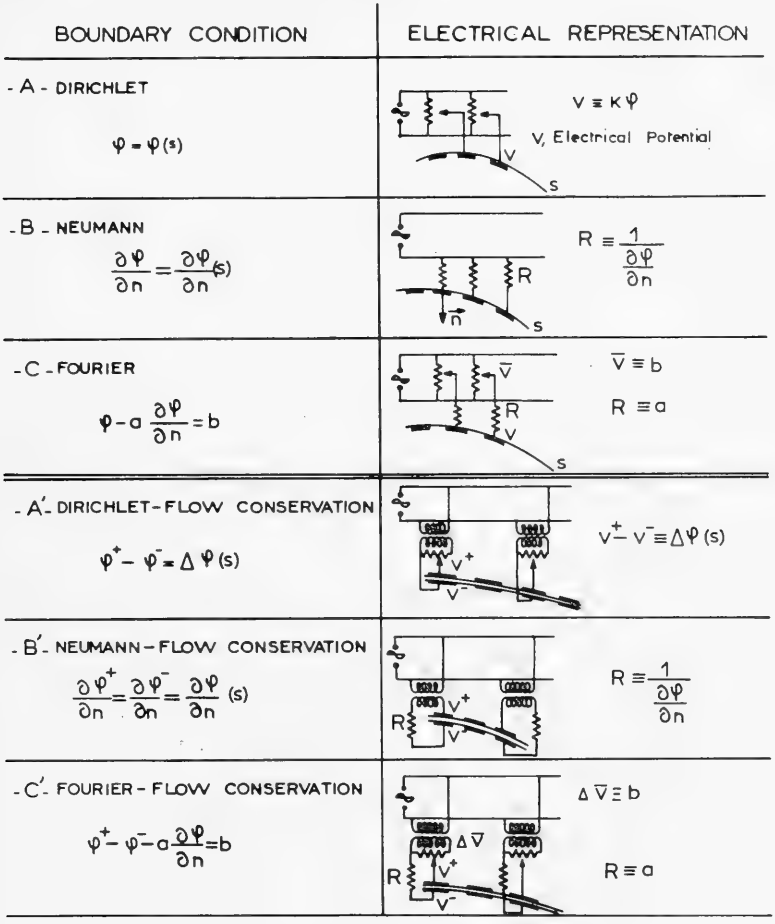

Fig. 3 - The three boundary conditions and their electric analogs

Figure 3 shows the three types of boundary conditions — Dirichlet, Neumann, and Fourier — and the corresponding analog setups. The Dirichlet condition, potential given on a boundary, Eq. (5a), is easily given by the use of potentiometers or of voltage dividers. The Neumann condition of the Eq. (4a) type is realized using resistances of a high value $\mathcal{R}$, so that, in feeding by a unity reference potential, the potential on the electrode is equal or inferior to 0.05. Thus is found

$$\frac{\partial V}{\partial n} \approx -\frac{1}{\sigma_{\mathcal{R}} \Delta s \mathcal{R}} \approx -K\frac{\partial \phi}{\partial n},$$

where Δs, represents the surface of an electrode and K an analog constant. The values of $\mathcal{R}$ are determined by $\Delta s\,\mathcal{R} \approx 1/\sigma_{\mathcal{R}} K(\partial\phi/\partial n)$, where $\sigma_{\mathcal{R}}$ is the conductivity

of the conducting fluid. The Fourier condition, linear relation between the potential and its normal derivative, is frequent in heat problems and thin-jet flap problems (8) or lifting-line problems (2). Considering block C of Fig. 3, the Kirchhoff law permits us to write

$$V - \Re \sigma_{\Re} \Delta s \frac{\partial V}{\partial n} = V ,$$

which is comparable to

$$\phi - a \frac{\partial \phi}{\partial n} = b ,$$

provided that $\Re = a/\sigma_{\Re} \Delta s$ and $V = b$.

For these three conditions, it is sometimes necessary to impose the conservation of the flow between the two sides of a slit. In this case, the electric setups are similar to those of A, B, and C, but additionally they require a transformer which automatically assures this supplementary condition (blocks A', B', and C' of Fig. 3).

It is evident that the precision of the analog representation of a problem depends fundamentally on the electric transposition of the boundary conditions. To describe in detail the techniques applied to make the boundary systems as accurate as possible would go beyond the limits of this paper. Nevertheless, it is interesting to note that, even in the most difficult cases, the elements inserted into the electric circuit are passive, i.e., resistances, potentiometers, and transformers. This process of simulation contrasts with that used elsewhere (40), in which active elements, of intricate electronics, are incorporated in rheoelectric experiments which are in themselves of great simplicity.

TWO-DIMENSIONAL PROBLEMS

Subcavitating Hydrofoil Near the Free Surface

Although the study of the subcavitating hydrofoil is not chronologically the first naval hydrodynamic problem to be treated at the Centre de Calcul Analogique, we believe it is interesting to begin the review of two-dimensional problems with this study.

Solution of the Direct Problem — Consider an immersed foil represented by its mean line, $\zeta = \zeta(\xi)$, near the free surface. The hydrodynamics characteristic of the hydrofoil are determined in solving the following boundary value problem: on the free surface we have the condition of Eq. (1b), on the slit LT representing the foil, $\psi^+ = \psi^- = -\zeta$, on the trailing edge, $\partial\psi^+/\partial n + \partial\psi^-/\partial n = 0$. The electrical simulation of the condition in Eq. (1b) is performed by the use of negative resistors (40), but their use is not easy and sure. We preferred to use an indirect method which allows the replacement of the Poisson condition by a Dirichlet condition. It takes into account the fact that for each vortex distribution connected to the lifting foil, the ordinates of the free surface, which is in fact

induced by the vortices, may be computed numerically by the composition of known (41) elementary perturbations.

The solution of the problem may be obtained for a given shape of the hydrofoil by a series of operations, each consisting of two stages. First, for arbitrary values of ψ in the linearized free surface, the vortex distribution over the chord of the foil is computed, by rheoelectric analogy, which fulfills Joukowski's condition on the trailing edge, without, however, complying with the constant pressure condition at the free surface. Second, the ordinates of the free surface, which would in reality induce the preceding vortex, are determined numerically. This allows a new distribution of potentials on the z-axis and a new analog computation of the connected vortex. The cycle of operations is continued until the potentials on the free surface and the vortex distribution converge simultaneously towards functions which represent the solution of this boundary value problem. A few approximations are generally sufficient. Instead of introducing an arbitrary free surface into the first analogical approximation, it is easy to introduce the boundary conditions corresponding to zero or infinite Froude numbers.

The accuracy of this method was verified by comparison of analog results to those obtained by Isay (42) in the case of a flat plate with incidence (Fig. 4). The application of the rule of reverse flows to free-surface flows and finite Froude number (15) permits the useful exploitation of results obtained in the case of the flat plate and the rapid determination of the influence of the free surface on foils of arbitrary shapes (Fig. 5). An interesting example of the possibilities of the method is given in Fig. 6 which shows for different Froude numbers the distribution of perturbation velocities on the lower and upper surfaces of a flat plate with flap slightly immersed.

Design of Subcavitating Foils Near the Free Surface — The same method may be used to design hydrofoils with given load and thickness distributions. Two effects must be then considered separately; the first corresponding to the distribution of the connected vortex $\gamma(\xi)$, i.e., the lifting effect, and the second to the equivalent distribution of sources and sinks, i.e., the thickness effect. The boundary value problem is now completely defined and the rheoelectric simulation is very simple.

Figure 7 shows, for different Froude numbers, the mean lines obtained for the NACA 65 pressure distribution. From the linearized theory results and in order to verify them, a hydrofoil and the corresponding free surface were represented in a rheoelectric tank. By considering the streamlines of this flow as shown in Fig. 8 it is possible to verify how the Joukowski condition on the trailing edge and the free-entry shock condition at the leading edge are fulfilled. The lift coefficient computed from the value of the circulation, corresponding to the electric results, is 0.3% higher than that chosen to design the hydrofoil.

Supercavitating Hydrofoils Near the Free Surface

Small Froude Numbers — In the case of small Froude numbers the gravity field effects on the free surface and on the boundaries of the cavity may be considered. The rheoelectric method enables us to take them into account with

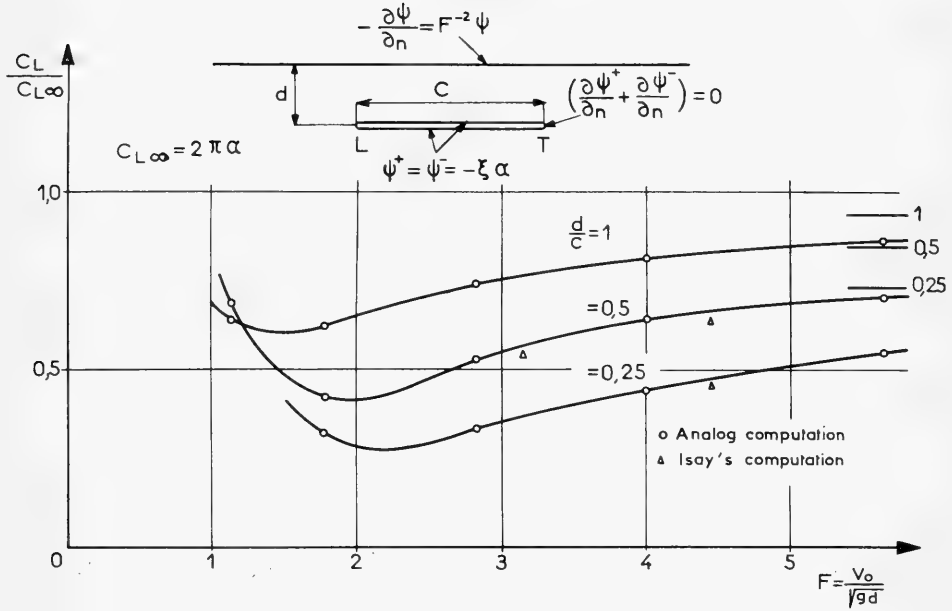

Fig. 4 - Comparison of analog results with Isay's computation, using flat plate with incidence

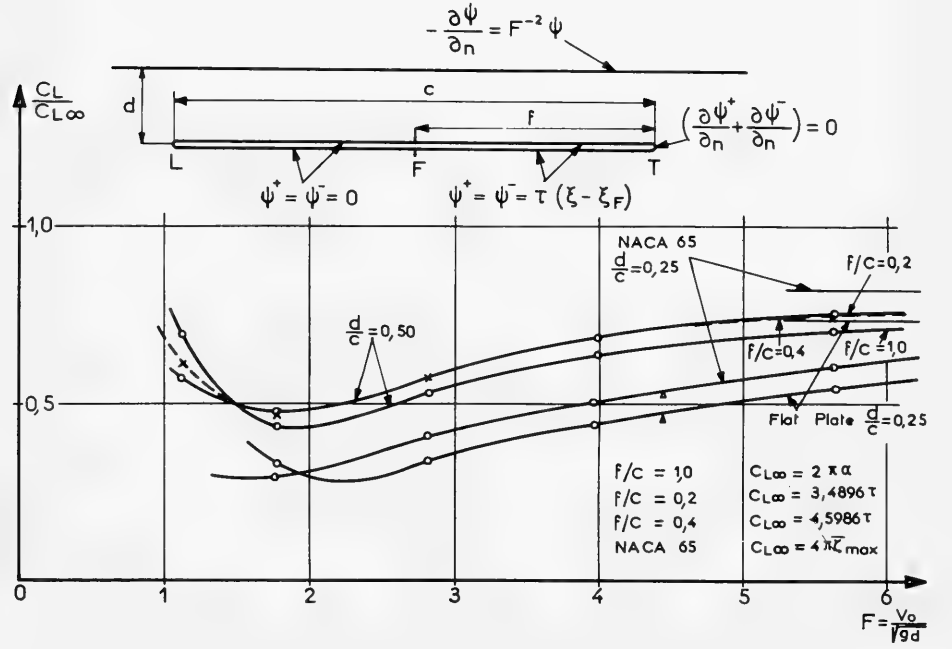

Fig. 5 - Determination of the free surface on foils of arbitrary shapes from results obtained with the flat plate

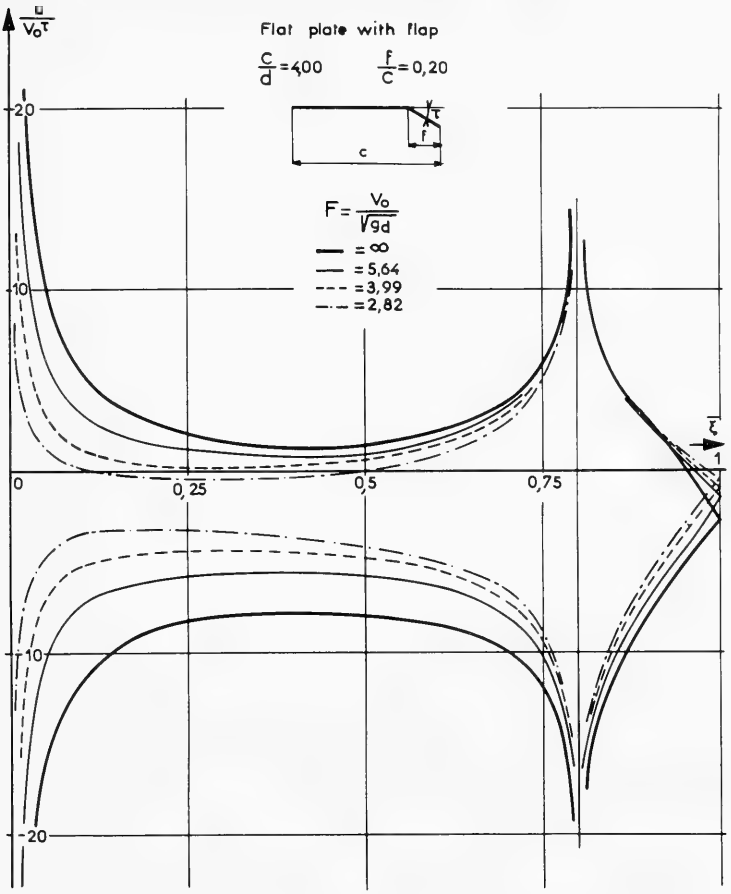

Fig. 6 - Distribution of perturbation velocities for different Froude numbers on the lower and upper surfaces of a flat plate with flap slightly immersed

precision and without complicating the computing process. An important simplification is obtained by introducing two auxiliary functions ψ_1 and ψ_2, defined by the following boundary conditions:

On the cavity

$$\pm \frac{\partial \psi_1^{\pm}}{\partial n} = \frac{\sigma}{2} + F^{-2}(\psi_1 - \psi_{1_0}) , \quad \text{and} \quad \pm \frac{\partial \psi_2^{\pm}}{\partial n} = F^{-2}(\psi_2 - \psi_{2_0}) .$$

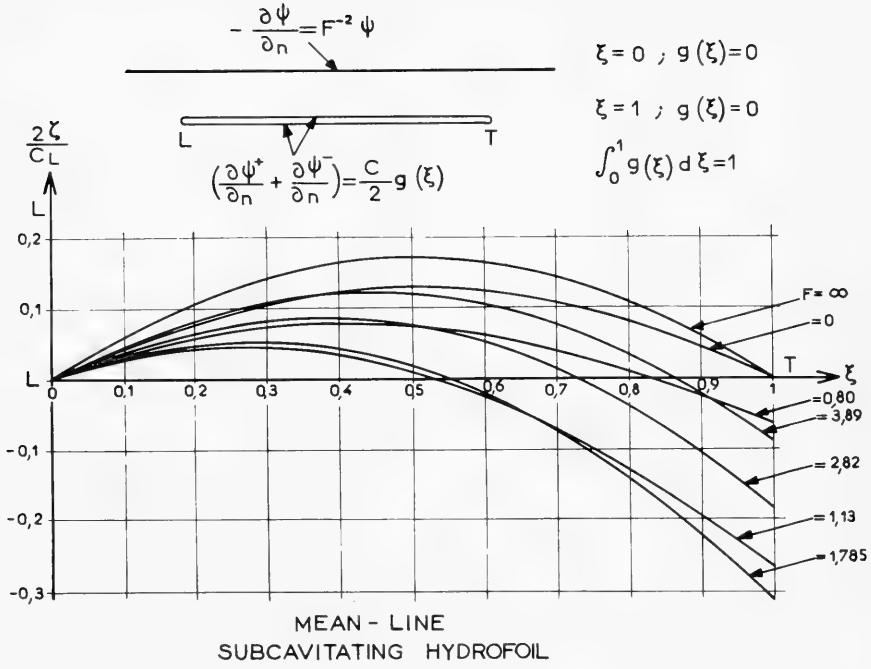

Fig. 7 - Mean lines obtained for the NACA pressure distribution for different Froude numbers

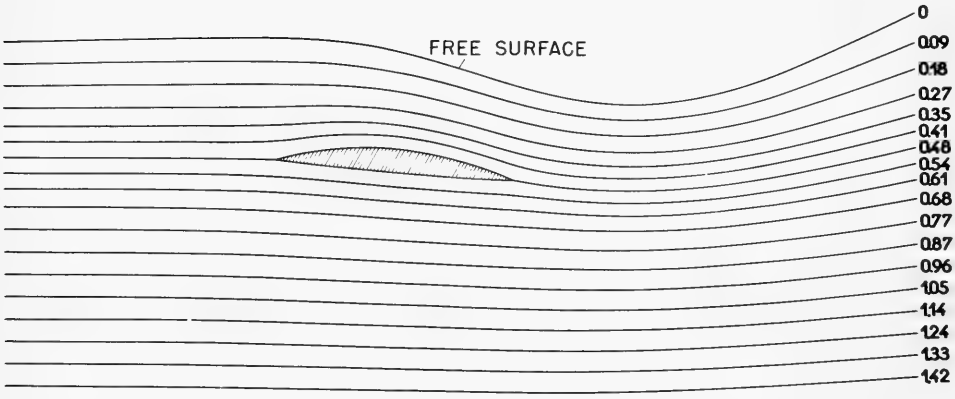

Fig. 8 - Flowlines about a hydrofoil with a corresponding free surface in a rheoelectric tank

On the lower surface of the foil, taking into account the gravity effect,

$$-\frac{\partial \psi_1^+}{\partial n} = \frac{\sigma}{2} + F^{-2}(\psi_1 - \psi_{1_0}),$$

and

$$-\frac{\partial \psi_2^-}{\partial n} = C_L\, g(x) + F^{-2}(\psi_2 - \psi_{2_0}) .$$

The first function corresponds to a nonlifting and free-of-wave-resistance effect, as has already been shown (13). The second function represents the lifting effect connected with the expression of the local pressure distribution. The calculation is made by starting with the solution for $F = \infty$, which is of an easy analog determination because at the free surface $\partial\phi/\partial n = 0$, and the above conditions are of the Neumann type, with flow continuity (Fig. 3B). From this first solution it is easy to define distributions of sources and sinks and of vortices induced by the cavity, so that we can now calculate numerically the free surfaces for finite Froude numbers. The iterations are then carried out as described previously in the subsection Solution of the Direct Problem.

Figure 9 shows the form of foils for the same immersion depth, at the same cavity length, and for Froude numbers infinity and 3.99, as a function of the parameter C_L/σ. The results for the infinite Froude number are given as a means of comparison; it is evident that in this case the hypothesis of a finite cavity is no longer valid, since the cavitation number tends to zero in both instances.

Infinite Froude Number — On the free surface, the upper and lower surfaces of the cavity, we have $\partial\psi/\partial n = 0$; on the lower surface of the foil a Neumann condition is imposed, $-\partial\psi^-/\partial n = C_L\, g(x)$. This makes rheoelectric simulation easy. Figure 10 is a comparison of foils computed for different linear pressure distributions with a foil fulfilling the two-term law of Tulin-Burkart. The comparison of the lift-drag ratio is favorable in the former and shows the advantage of the rheoelectric method in the exploitation of pressure distribution which is hardly accessible to analytical treatment.

If a convenient pressure distribution over the upper surface of the foil is imposed, it is possible to design base-vented hydrofoils with zero spray-jet drag. The depressions thus imposed should be such that the cavitation formation is excluded upstream of the trailing edge. For this purpose a number σ_i must be defined, which is a function of the physical characteristics of the fluid, the vapor pressure, the degree of air dissolved, etc. Three foils, obtained for different pressure distributions and presenting the same value of C_L/σ_i, are shown in Fig. 11.

Hydrodynamic Characteristics of Supercavitating Hydrofoils in Unbounded Flow

These studies were intended to test the feasibility of analog representation of the singularities which arise in the solution of the direct problem of supercavitating

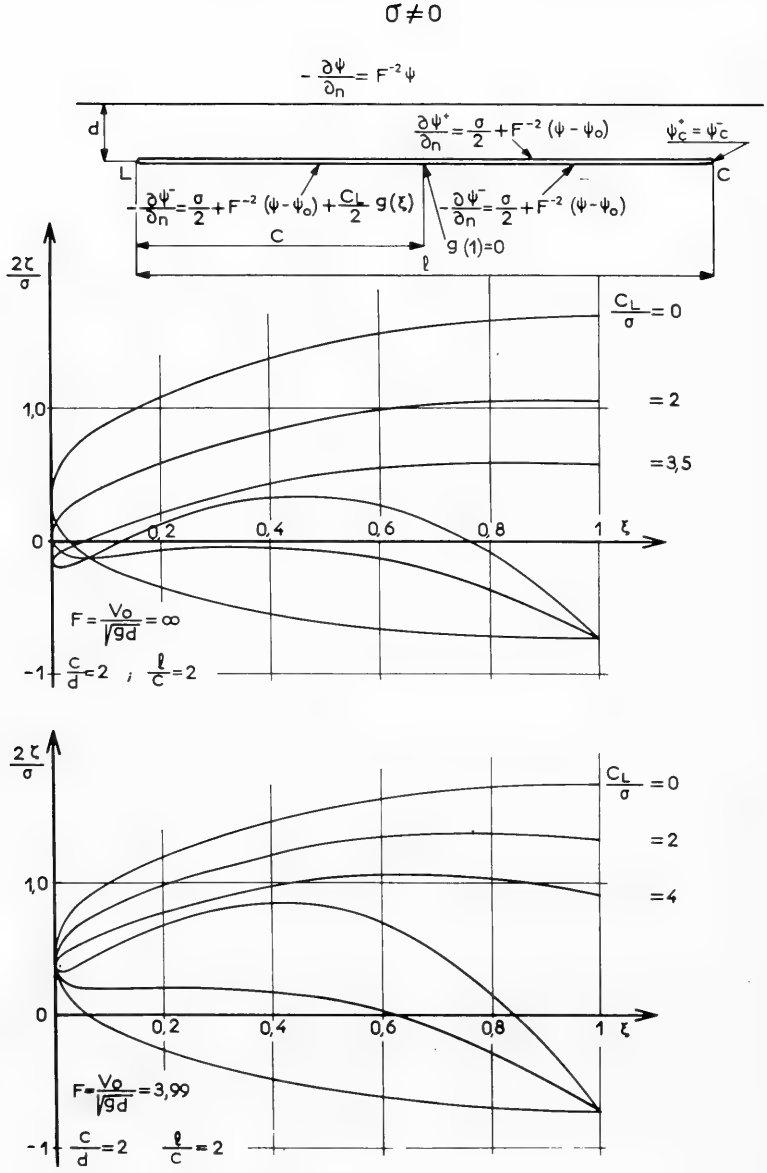

Fig. 9 - Supercavitating hydrofoil near the free surface for a small Froude number in comparison with infinity

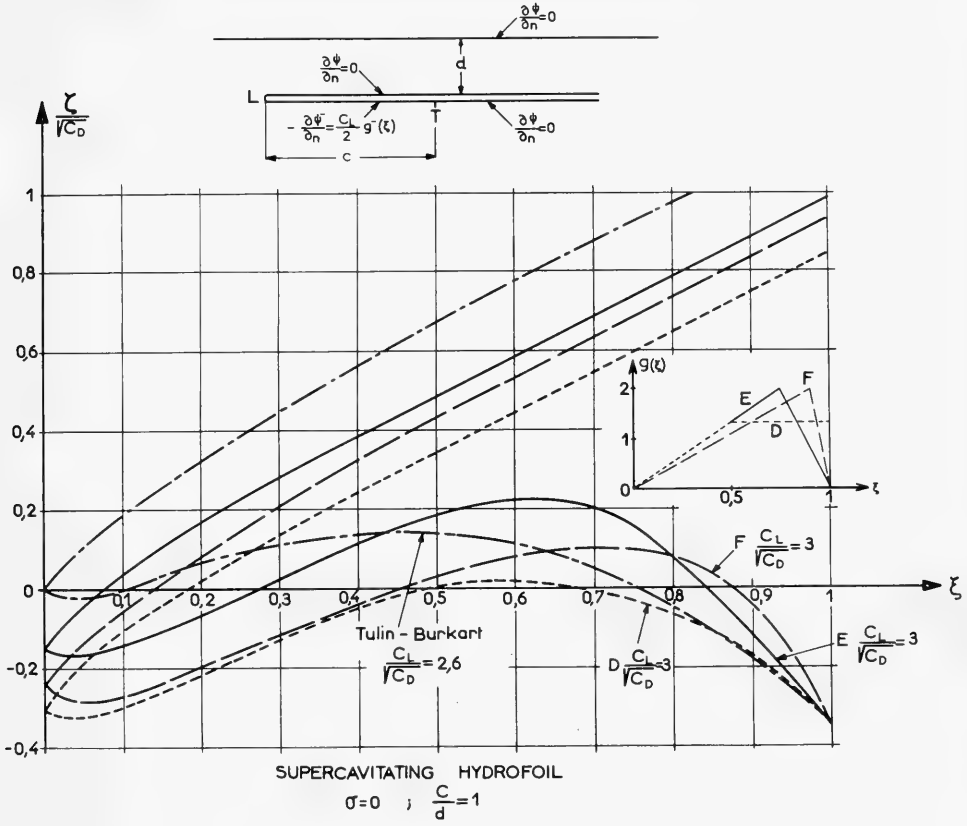

Fig. 10 - Comparison of foils of different linear pressure distributions with a foil fulfilling the two-term law of Tulin-Burkart

foils. It is known that near the leading edge of a hydrofoil, if the slope is finite at the lower surface and the pressure constant at the upper surface, the complex perturbation potential $\phi + i\psi$ gives a singularity of $-ikz^{3/4}$ which corresponds to a complex perturbation velocity $u - iv = -ikz^{-1/4}$. The pattern of the singularity is given in Fig. 12a, where it is seen that the equipotential line from the upper surface of the slit is bending in the leading edge, forming an angle of 240°. Analogically this can be obtained by means of an apparatus shown in the Fig. 12b. The electrode representing the upper surface of the cavity is extended by a small conductor plate placed at an angle of 240°. In the prolongation of this plate a probe is installed, by means of which the correct configuration of the equipotential line can be controlled by adjustment from the potentiometer.

This setup is successful only in two-dimensional problems. It cannot be used in three-dimensional situations because of the complexity encountered.

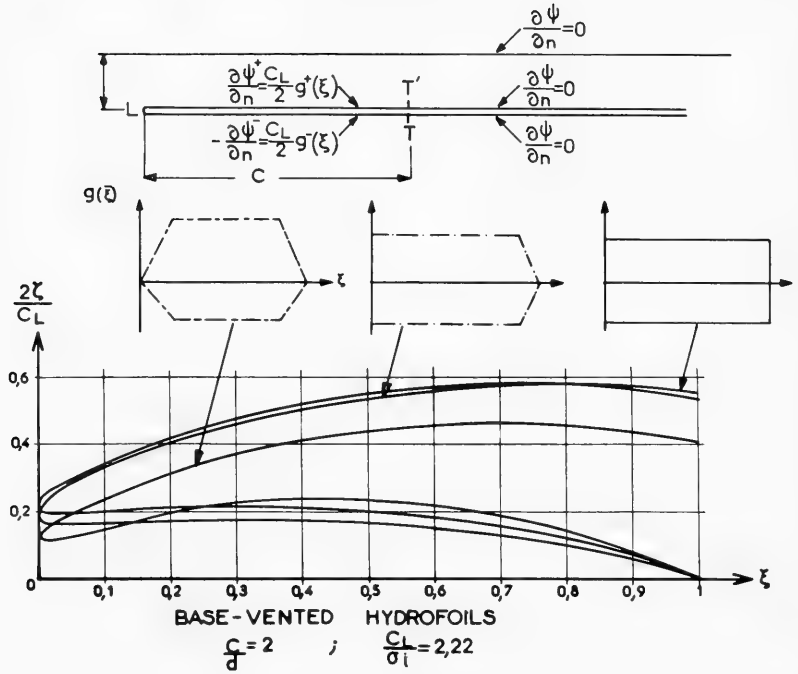

Fig. 11 - Comparison of three base-vented foils of different pressure distributions

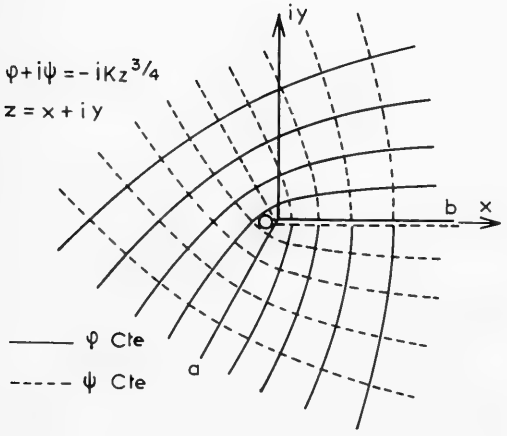

Fig. 12a - Supercavitating foil in unbounded flow

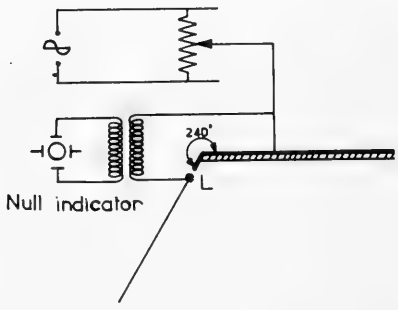

Fig. 12b - Control apparatus

Another method must be used, which will be described in the section on Three-Dimensional Problems.

Supercavitating Cascades

The study of supercavitating cascades is of practical interest in the field of hydraulic machines such as pumps and turbines. It has been possible to design convergent or divergent cascades constituted by supercavitating foils which support imposed pressure distribution. Here, the rheoelectric method shows the possibilities open to the design of supercavitating propellers.

Suppose that the foil camber is small. It is possible to consider, as in the case of isolated profiles, the linearized flow with respect to the velocity far upstream. The periodicity of the velocity field allows the study of the function ϕ in a bounded strip (Fig. 13). The boundary conditions are defined, no longer on a slit as in the preceding cases, but on the two surfaces limiting the strip. The flow is supposed independent of the gravity field, and the boundary conditions are given by Eqs. (3), (5a), (7), and (10a). A supplementary condition which takes into account the periodicity of the field is conveyed by $\phi_B = \phi_{B'}$, where B and B′ are two points periodically apart upstream of the foils.

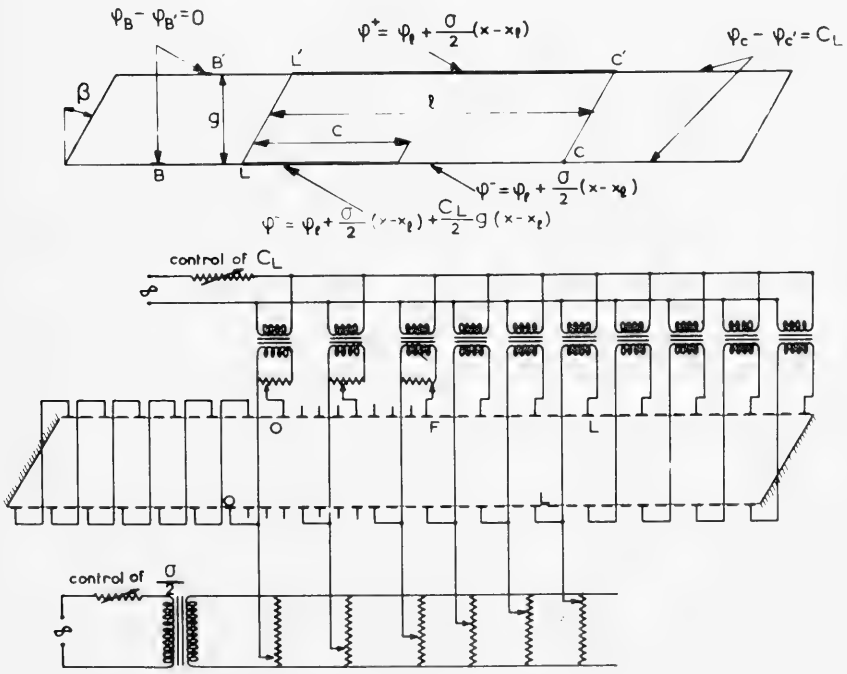

Fig. 13 - Supercavitating cascade: function of ϕ in a bounded strip

The analog representation of these conditions is extremely simple, as can be seen in Fig. 13. The law of potentials on the cavity as well as the potential differences between the lower surface of the foil and the upper surface of the cavity are obtained by means of potentiometers. The closure cavity condition is fulfilled automatically, owing to the transformers which insured the conservation of the current.

Figure 14 shows the form of the lower surface and of the cavities obtained for a uniform load distribution over the foil. The configurations depend on the length of the cavity and the value of the lift coefficient imposed on each foil. The highest limit of $C_L/2\sigma$ is dictated by the degree of thickness tolerance which may be allowed.

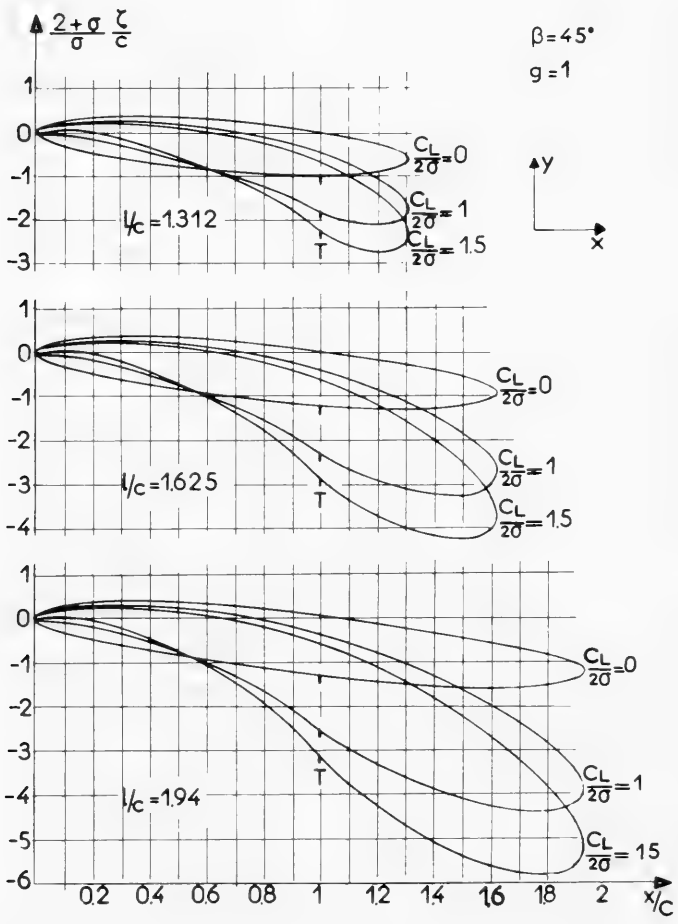

Fig. 14 - Configurations of the lower surface and of the cavities for a uniform load distribution over the foil

THREE-DIMENSIONAL PROBLEMS

We will consider first the problems involved in the calculation of supercavitating wings. Sub- and supercavitating screw propeller problems will then be considered next.

Supercavitating Hydrofoil with Non-Zero Cavitation Number in Unbounded Flow

The inverse problem was defined earlier in the section on the Hydrodynamic Problem (paragraph 3B). To simplify the analog representation, the velocity potential may be written in the form

$$\Phi(x,y,z) = x + \frac{\sigma}{2} x + \phi(x,y,z) \ .$$

The perturbation velocity potential ϕ is then defined by boundary conditions slightly different from those corresponding to the function $\phi = \Phi - x$. These conditions are: on the upper and lower surface of the cavity, $\partial\phi/\partial x = 0$; on the lower surface of the wing the pressure is higher than or at least equal to the cavitation pressure. We thus have the condition $\partial\phi/\partial x \geq 0$, and to define the distribution of ϕ we will have, according to Eq. (5a),

$$\phi^{-} = \phi_0(y) + \frac{1}{2} C_\ell(y)\, g(x - x_\ell, y) \ , \qquad (5c)$$

where g is given and fulfills the conditions indicated in paragraph 3B. At infinity we should find the velocity of the undisturbed flow; hence

$$\left(\frac{\partial\phi}{\partial x}\right)_\infty = - \frac{\sigma}{2} \ . \qquad (9c)$$

The closure cavity condition is conveyed in any section $y = cte$, by $\oint (\partial\phi/\partial x)\, dx = 0$. With the overall boundary conditions we have just established, the ordinates of the lower surface of the wing and of the contour of the cavity are given, if we take, as Tulin suggested, the tangential velocities condition in the form $dz/dx = v/(V_0 + u)$ instead of $dz/dx = v/V_0$, by

$$\zeta = \frac{2}{2 + \sigma} \int_{-\infty}^{x} \frac{\partial\phi}{\partial z}\, dx \ .$$

The rheoelectric simulation can be simplified still more if the potential ϕ is subdivided into three parts

$$\phi = \phi_{E1} + \phi_{E2} + \phi_{OD} \ ,$$

where ϕ_{E1} and ϕ_{E2} represent two even-potential functions characterizing the cavity thickness effect. ϕ_{OD} represents an odd potential function corresponding to the general camber effect. The representation of these functions is extremely

simple analogically, since it amounts to imposing on the plane of the wing, and outside the wing, the cavity, and the wake, a zero normal derivative condition for an even function, or a constant potential condition for an odd function. These three potentials are defined by their boundary conditions so that their sum on each boundary is equal to the condition of the potential ϕ. Thus, for example, on the lower surface of the wing and cavity we will have

$$\phi_{E1} = A(y) ,$$

$$\phi_{E2} = B(y) + \frac{C_\ell(y)}{4} g(x - x_\ell, y) ,$$

$$\phi_{OD}^{\pm} = \pm \frac{C_\ell(y)}{4} [1 - g(x - x, y)] ,$$

The constants $A(y)$ and $B(y)$ are connected according to the above expressions by

$$A(y) + B(y) = \phi_0(y) + \frac{C_\ell(y)}{4} .$$

Figures 15 and 16 show the shape of two supercavitating wings: one of rectangular planform with a span ratio of 4, and the other having an elliptical leading edge and a straight trailing edge, with a span ratio of 4.5. The chosen pressure distribution following the chord of each section is of the Tulin-Burkart type; that of the span circulation is elliptical. The maximum length of the cavity, in the median section, is three times the chord. Especially notable are the difference between the sections of the two hydrofoils and the thickening of the rectangular wing at the wingtip.

Supercavitating Hydrofoils with Zero Cavitation Number

In the case of high Froude numbers the flow around the wing is similar to that already studied for two-dimensional bodies in the subsection on Infinite Froude Number. However, the solution of the optimum distribution of span circulation should precede the design of supercavitating wings.

Luu (3) has shown that this problem is reducible to that of the optimum vortex distribution of the finite span biplane, i.e., constant induced velocity over the span, as treated in (43) and (44). In these publications are found only global results concerning the lift-drag ratio, and not the vortex distribution on the span which is the most interesting feature. Although it is possible to obtain a solution to this problem by analytical methods, it is appropriate to indicate that the rheoelectric method can be utilized advantageously. Consider the flow observed in the Trefftz plan. The potential ϕ_Γ, which is the harmonic function in y, z, is defined by the following boundary conditions:

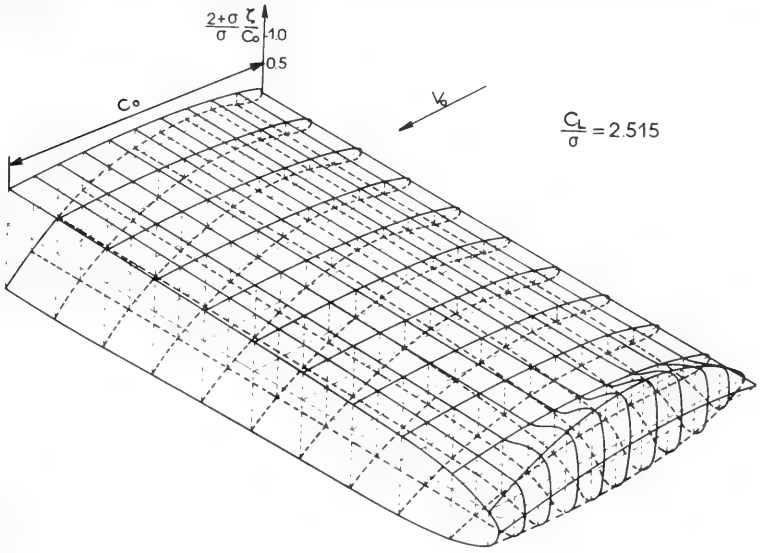

Fig. 15 - Supercavitating rectangular wing with a span ratio of 4

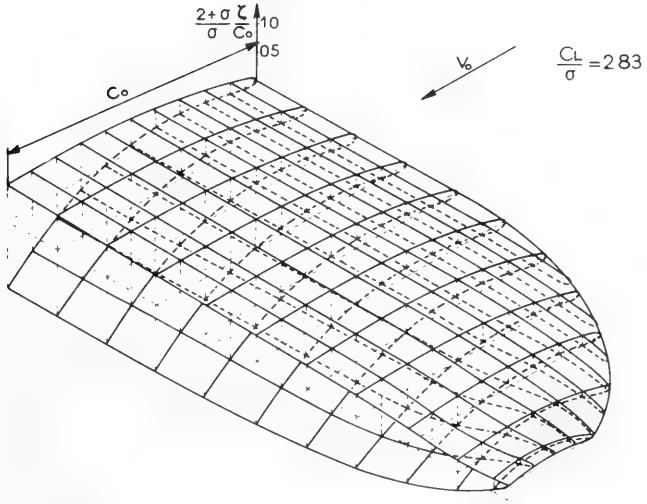

Fig. 16 - Supercavitating wing having an elliptical leading edge and straight trailing edge, with a span ratio of 4.5

(a) $\phi_\Gamma = 0$, on $z = 0$, the free surface

(b) $\partial\phi_\Gamma/\partial z = w_\infty = Ct$, on the wake $(z = -d, -s \leq y \leq s)$ (11)

(c) $\partial\phi_\Gamma/\partial n = 0$, for $y = 0$, by symmetry.

We can see that these are classical conditions; Dirichlet on the free surface, Neumann with flow continuity on the wake, and Neumann on the symmetry axis — the analog simulation is immediate. Figure 17 shows the distribution of Γ/sw_∞ thus obtained, where Γ is the circulation, s the half-span of the wing, and w_∞ the induced velocity, versus y/s for different values of the parameter d/s. These results permit us to approach efficiently the solution of the inverse problem for a supercavitating wing near the free surface.

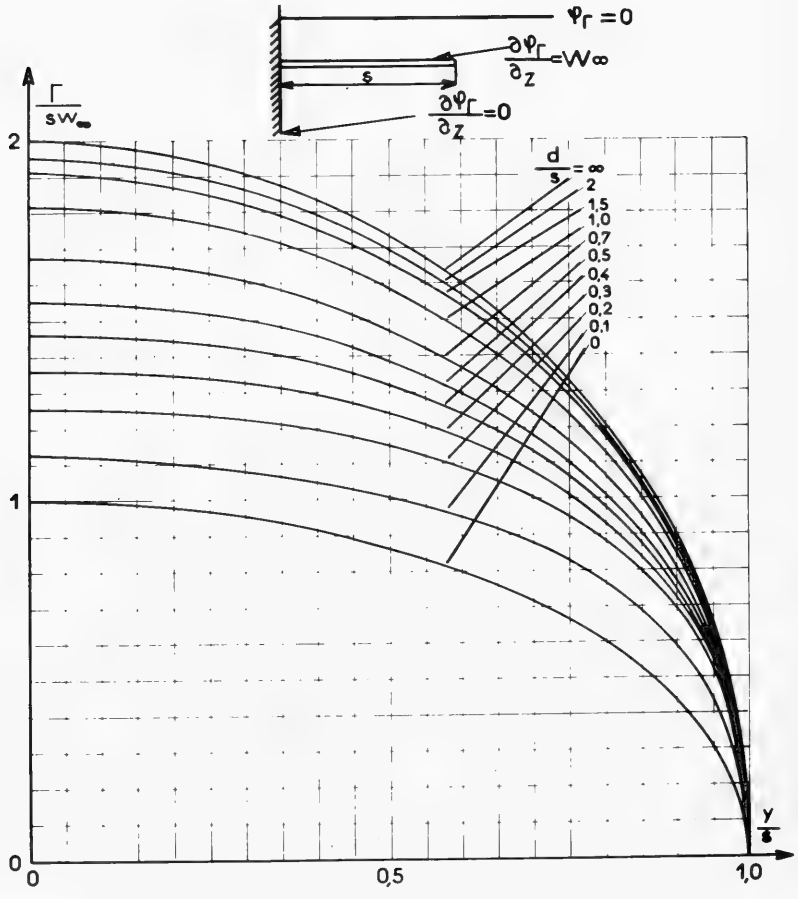

Fig. 17 - Distribution of Γ/sw_∞

Design of a Supercavitating Wing — The boundary conditions on a section $y = cte$ are the following:

$$
\begin{aligned}
&(a)\ \phi = 0, \text{ on } z = 0 \\
&(b)\ \phi^{+} = \phi_{\ell}(y), \text{ on } z^{+} = -d, \ x_{\ell} < x < \infty \\
&(c)\ \phi^{-} = \phi_{t}(y), \text{ on } z^{-} = -d, \ x_{t} < x < \infty \\
&\qquad \phi^{-} = \phi_{\ell}(y) + \frac{C_{\ell}(y)}{2}\, g(x - x_{\ell}, y), \text{ on } z^{-} = -d, \ x_{\ell} < x < x_{t} \\
&(d)\ \lim_{x \to \infty} \int_{x_{\ell}}^{x} \left(\frac{\partial \phi^{+}}{\partial n} + \frac{\partial \phi^{-}}{\partial n} \right) dx \to 0 \ .
\end{aligned}
\tag{12}
$$

When σ is zero, the growth of the cavity thickness is simulated by a source distribution over the wing and the cavity with a density $q(x,y)$, defined by

$$
q(x,y) = \frac{\partial \phi^{+}}{\partial n} + \frac{\partial \phi^{-}}{\partial n} = \frac{\partial \zeta^{+}}{\partial x} - \frac{\partial \zeta^{-}}{\partial x} \ .
$$

Far downstream, q is reduced to a function which depends only on y. However, for the inverse problem we have a certain latitude in the choice of the source distribution. In fact, the boundary conditions (a), (b), and (c) allow that on each line parallel to the x-axis, within the limits defined by the wingspan, the potential ϕ is fixed at an arbitrary level. If we indicate by $k(y)$ the mean value of ϕ_{ℓ} and ϕ_{t}, we have

$$
k(y) = \phi_{\ell}(y) - \frac{C_{\ell}(y)}{4} \ .
$$

It is evident that the distribution of q over the surface of the wing and the cavity, i.e., the cavitation shape, is directly influenced by the choice of the law attributed to $k(y)$.

In order to facilitate analysis of the problem, the potential ϕ is subdivided into two parts, defined by the following boundary conditions:

$$
\begin{aligned}
&(a')\ \phi_{1} = 0 \ , \ \phi_{2} = 0 \ , \ \text{on} \ \ z = 0 \\
&(b')\ \phi_{1}^{+} = \phi_{1_{\ell}}(y) \ , \ \phi_{2}^{+} = k_{2}(y) \ , \ \text{on} \ \ z^{+} = -d \ , \ x_{\ell} < x < \infty \\
&(c')\ \phi_{1}^{-} = \phi_{1_{t}}(y) \ , \ \phi_{2}^{-} = k_{2}(y) \ , \ \text{on} \ \ z^{-} = -d \ , \ x_{t} < x < \infty \\
&\qquad \phi_{1}^{-} = \phi_{1_{\ell}}(y) + C_{\ell}(y)\, g, \ \phi_{2}^{-} = k_{2}(y) \ , \ \text{on} \ \ z^{-} = -d \ , \ x_{\ell} < x < x_{t} \\
&(d')\ \lim_{x \to \infty} \int_{x_{\ell}}^{x} \left(\frac{\partial \phi_{1}^{+}}{\partial n} + \frac{\partial \phi_{1}^{-}}{\partial n} \right) dx \to 0 \ , \quad \lim_{x \to \infty} \int_{x_{\ell}}^{x} \left(\frac{\partial \phi_{2}^{+}}{\partial n} + \frac{\partial \phi_{2}^{-}}{\partial n} \right) dx \to 0 \ .
\end{aligned}
\tag{12 (Cont)}
$$

Following the decomposition of the movement, the function $k(y)$ is also split into two parts: k_1 and k_2. We see that the arbitrary choice of this function is supported by ϕ_2, and that ϕ_1 is completely defined by its overall boundary conditions. The solution of the boundary value problem of ϕ_2 depends on the choice of $k_2(y)$, which finally amounts to the choice of the thickness distribution of the hydrofoil. In the most general way, the choice of $k_2(y)$ is essentially dictated by the structural point of view. The drag coefficient is available by considering the kinetic energy on the Trefftz plane.

An example of the possibilities offered by this method is presented in Figs. 18a and 18b. The planform of the two wings is trapezoidal, the aspect ratio is $\lambda = 4$, the taper ratio is 1/3, and the swept angle back of the line situated at 25% of the chord is 15°30'. The local distribution chosen is constant along the chord and optimal over the span for the immersion depth $d/s = 0.2$. The calculations were made so that in each section the thickness relative to the local chord should not be lower than 1.6% at 10% from the leading edge. The choice of a lower C_L, 0.3 instead of 0.5, led, in the case of Fig. 18b, to a higher lift-drag ratio, 9.52 instead of 6.9.

Design of a Supercavitating Wing with Strut and Walls Effect — This special study was carried out in order to verify analog experimental results. The configuration of the testing channel (Fig. 19a) is taken into account in the calculations by considering the strut and walls effects. The latter are easily represented by rheoelectric analogy, since the zero normal velocity on the walls is conveyed by a zero normal derivative of the potential. The introduction of the strut does not complicate the problem, which is devoid of lifting effect. The strut sections are obtained by the introduction of an appropriate distribution of potential on the projection of the strut and the cavity of its sections on the $y = 0$ plane. The method of solution is similar to that described in the Design of a Supercavitating Wing, above.

Figures 19b and 19c show clearly the influence of the strut on two wings of the same planform with the same load distribution. In the first case, where the length of the strut is equal to that of the central chord, considerable thickening of the sections near it can be noted. In the second case, the width of the strut is imposed to 70% of that of the central chord, the central section is thinner, and this permits a lift-drag ratio 25% higher than that of the preceding illustration.

Hydrodynamic Characteristics of a Flat Wing with Strut and Walls Effect — We have already indicated the difficulties involved in the solution of the direct problem. In the subsection on the Hydrodynamic Characteristics of Supercavitating Hydrofoils in Unbounded Flow, a method applicable to two-dimensional cases was described. In three-dimensional situations at $\sigma = 0$ it seems possible, granting a plausible approximation, to remove these difficulties. With this object, consider the expression of the drag coefficient C_D

$$C_D = \frac{\Lambda}{4 V_0^2 s^2} \oint \phi \left(\frac{\partial \phi}{\partial n} \right) ds \ ,$$

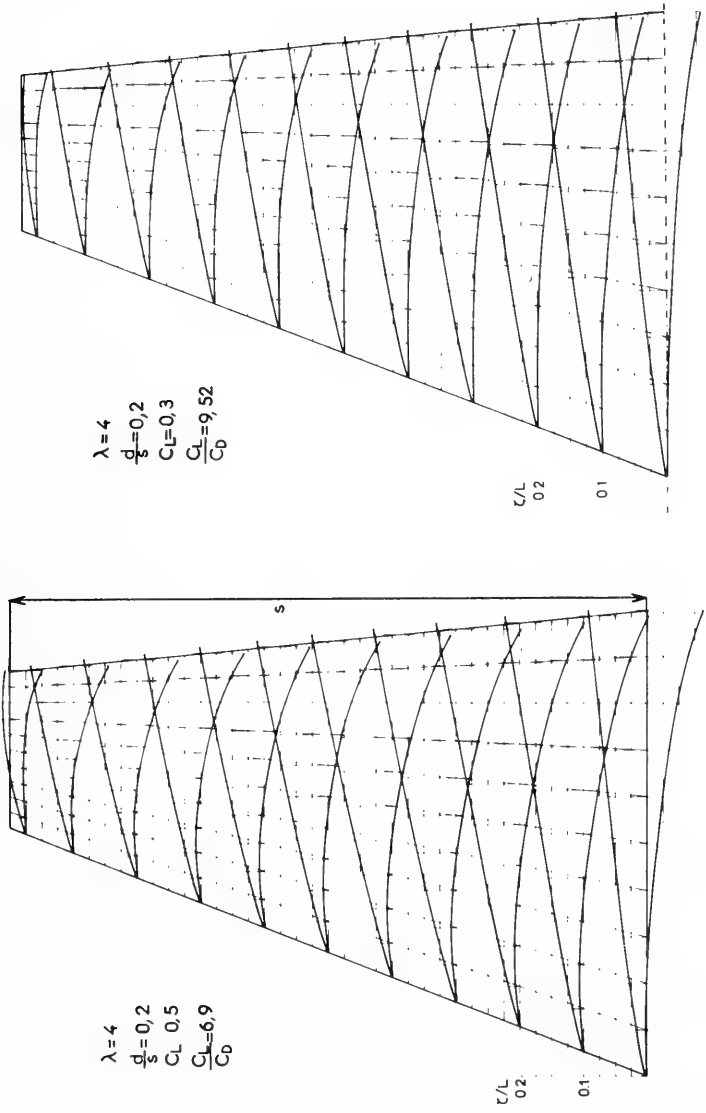

Fig. 18 - Design of a supercavitating wing (a) with C_L 0.5, (b) with C_L 0.3

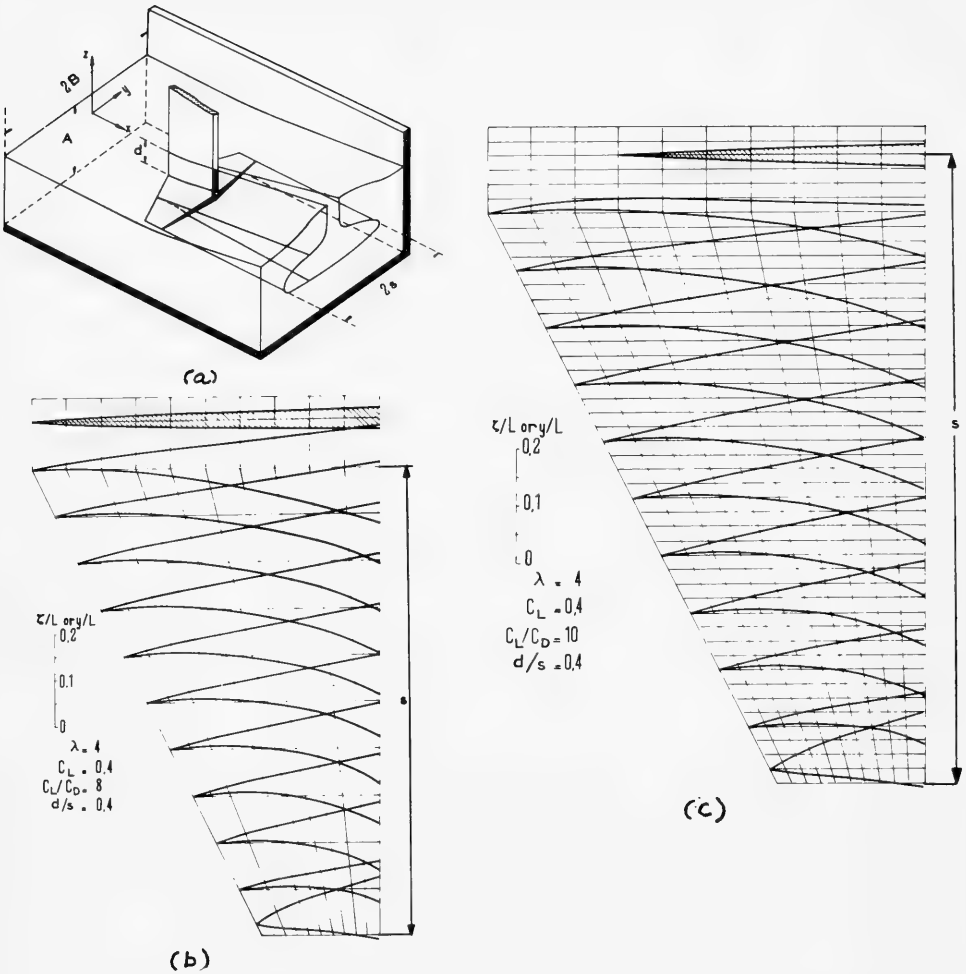

Fig. 19 - Design of a supercavitating wing with strut and walls effect. (a) configuration of the testing channel, (b) length of the strut is equal to that of the central chord, and (c) width of the strut is 70% of that of the central chord.

where the integral is applied to the slit representing the wake of the wing with strut. Because the leading edge of the wing is supposed sharp, the suction drag is here zero. This equation, as applied to the wing only, represents the resistance due to the pressure being exerted on the lower surface. We can thus assume that the resistance of a section of the lower surface is equal to the contribution of the preceding integral, at points corresponding to this section in the Trefftz plan; i.e.,

$$\int_{x_\ell}^{x_t} \left(\frac{\partial \phi}{\partial x}\right)\left(\frac{d\zeta}{dx}\right) dx = \frac{1}{2}\left(\phi^+ \frac{\partial \phi^+}{\partial n} + \phi^- \frac{\partial \phi^-}{\partial n}\right).$$

This property, accurate in two-dimensional situations, is only approximative in three-dimensional cases. In adopting it for the latter, we are at least assured that the balance of the total resistance will always be respected. For a flat wing placed at incidence α the above expression becomes even more simple, since $d\zeta/dx = \alpha$:

$$C_\ell(y) = \frac{1}{\alpha}\left(\phi^+ \frac{\partial \phi^+}{\partial n} + \phi^- \frac{\partial \phi^-}{\partial n}\right).$$

The solution of the problem is then to impose the overall boundary conditions of the function ϕ, as indicated in Fig. 20. Because of the function of the transformer, the zero-flow condition is automatically fulfilled; the potentiometer P_1 allows the Joukowski condition on the trailing edge, and the potentiometer P_2 regulates, by successive approximations, the condition of equality between the potential difference $C_\ell(y) = \phi_\ell(y) - \phi(y)$ and the value of the resistance calculated at the same section in far downstream.

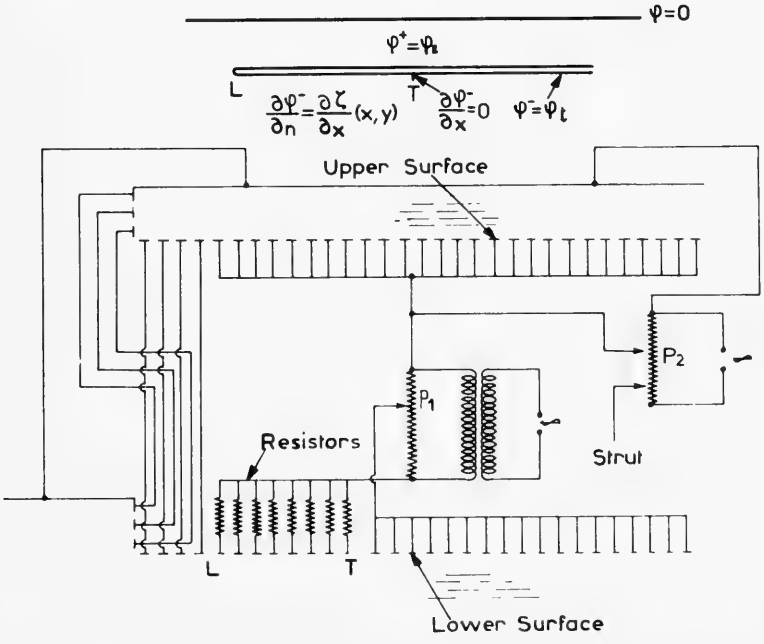

Fig. 20 - Overall boundary conditions of the function ϕ

Figure 21 shows the shape of the cavity thus obtained for a flat wing of trapezoidal planform, with a strut of the same width as the central chord, for incidence $\alpha = 5°$. The calculated lift coefficient is $C_L = 0.12$ and the lift-drag ratio $L/D = 11.5$, for a reduced immersion $d/s = 0.4$. The high value of the

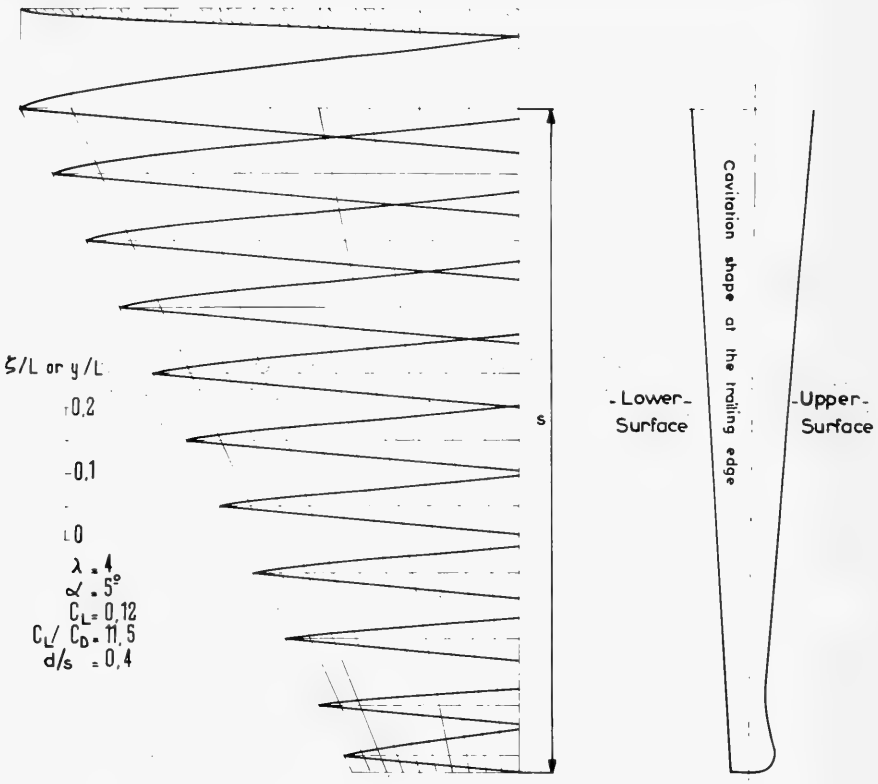

Fig. 21 - Cavity shape for a flat wing of trapezoidal planform, with a strut of the same width as the central chord, for incidence $\alpha = 5°$

lift-drag ratio with respect to the foils designed according to given pressure distribution is not surprising, as the C_L corresponding to $\alpha = 5°$ for the flat wing is very low.

Marine Screw Propellers

The usual aerodynamic theories of screw propellers are particularly effective for airscrews. They do not solve satisfactorily the problems presented by the marine propeller, nor do they permit the analysis of two important factors; one is geometric and concerns the low aspect ratio of the blades, and the other is hydrodynamic and concerns cavitation phenomena. Indeed, the first factor has destroyed the fundamental simplification of the classic theory in which the blade section could be substituted conveniently by an equivalent lifting line. The second factor requires a precise knowledge of pressure distributions on the blades — the only means of foreseeing or avoiding cavitation — which a too general theory

is unable to provide. Only the theory of the lifting surface, applied to the marine propeller, is able to solve these two problems.

Theory of the Lifting Surface of the Screw Propeller— The linearized lifting surface theory, often used in the case of wings, can easily be adopted for the screw propeller.

Assume that the propeller's blades are infinitely thin, inducing only a small perturbation in the relative flow resulting from the uniform velocity V_0 in the negative direction of the z-axis and the angular velocity ω around this axis, and that the blades lie on a helicoidal flow-surface of the nondisturbed flow (Fig. 22). For a p-bladed propeller with maximum radius R, the perturbation velocity field is periodical in space and the study is thus confined to a region between two helicoidal surfaces deduced from one another by a rotation of a $2\pi/P$ angle. The flow field is defined by the following boundary conditions of the perturbation velocities potential ϕ'.

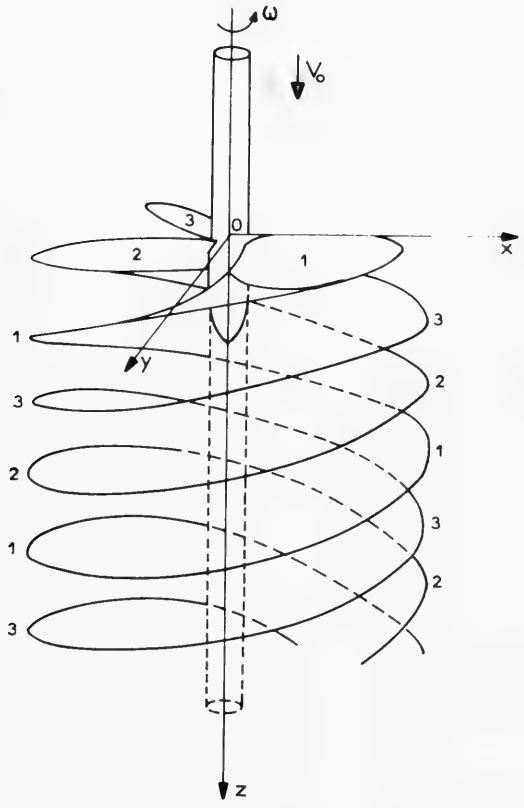

Fig. 22 - Screw propeller blades on a helicoidal flow-surface of nondisturbed flow

1. On the blade surface, the zero normal velocity condition for radius r is

$$\frac{\partial \phi^{\pm}}{\partial n} = \sqrt{\lambda^2 + \xi^2}\; i^{\pm}(\xi,\tau) \ , \tag{13}$$

where $\phi = \phi'/\omega R^2$, $\lambda = V_0/\omega R$, $\xi = r/R$, and $i^{\pm}$ is respectively the slope of the upper or lower surface of the blade at a given reduced radius, ξ, and the curvilinear abscissa along a chord, τ, n the normal directed towards the fluid.

The tangential velocities are connected to the pressure by

$$\frac{\partial \phi^{+}}{\partial \tau} - \frac{\partial \phi^{-}}{\partial \tau} = \frac{1}{\sqrt{\lambda^2 + \xi^2}}\, C_P(\xi,\tau) \ , \tag{14}$$

where $C_P(\xi,\tau) = (p^{-} - p^{+})/(\rho\omega^2 R^2/2)$ is the local pressure coefficient.

This expression can be integrated with respect to τ, which brings us to a condition similar to that of paragraph 3B in the Hydrodynamic Problem section of this paper. As in that paragraph, there are here two problems:

Direct problem: $i\,(\xi,\tau)$ is given, which is equivalent to giving the form of the blade, or —

Inverse problem: $C_P(\xi,\tau) = C\,(\xi)\; g\,(\xi, \tau - \tau_\ell)$ is given.

2. On the trailing edge the Joukowski condition is conveyed by

$$\left(\frac{\partial \phi}{\partial \tau}\right)_{\gamma = \tau_t} = 0 \ .$$

3. The pressure continuity in the wake is conveyed, according to the linearized Bernouilli equation, by a potential difference $\delta\phi(\xi) = \phi_t^{+} - \phi_t^{-}$, which depends only on ξ, between the two sides of the helicoidal free vortex sheet.

4. At far downstream, the potential presents, as in the lifting line theory, the helicoidal symmetry of p-order. The blowing of the propeller implies the existence of induced velocities in the axial and tangential directions. If, then, the reproduction of the field is limited at infinity by a surface perpendicular to the axis, conditions on the normal derivative to this surface must be respected.

According to the conditions in Eqs. (13) and (14), it is evident that the function ϕ is defined in the present case by conditions resembling those in paragraph 3B, except for the factor $\sqrt{\lambda^2 + \xi^2}$, which is taken into account here. It is easy to see that the equilibrium condition of a cavity with constant pressure p_c is given by

$$\frac{\partial \phi}{\partial \tau} = \frac{\lambda^2}{\sqrt{\lambda^2 + \xi^2}} \left(\frac{\sigma}{2}\right), \tag{15}$$

where $\sigma = (P_0 - P_c)/(\rho V_0^2/2)$ is the usual cavitation number. Having this, there is no difficulty in expressing boundary conditions corresponding to a supercavitating blade.

Analog Solution — The rheoelectric solution of this problem requires the construction of a special tank. The electrolyte is contained within the volume between two helicoids. The tank is thus made up of two helicoidal surfaces (Fig. 23) covered with electrodes, the radial angle between them being $2\pi/P$. One surface represents the lower surface of the blade as well as the lower surface of the cavity and/or the lower side of the free vortex sheet; the other surface represents the upper surface of the blade and/or the upper surface of the cavity as well as the upper side of the wake of the adjacent blade. The two helicoidal surfaces are elongated and follow a radial direction to a radius sufficiently large that the perturbations are negligible. Small electrodes placed on these surfaces and symmetrically short-circuited assure the potential continuity. Upstream of the blade the symmetry can be assured more simply by constructing two surfaces a period apart and passing through the axis. A central core and a flat sector perpendicular to the axis complete the tank.

The tank comprises 160 small helicoidal components moulded in resin, each one containing 20 electrodes. Certain of these components are removable for better presentation of the geometry of the blades and cavities. A total of 3600 electrodes is required for each calculation. For this purpose there is an electric setup which consists of about 250 transformers, 200 potentiometers or voltage dividers, and interconnecting units which allow information to be collected at about 250 points on the lower and upper surfaces of the blade.

The geometry of the helicoid is characterized by the speed ratio V_0/ω, which here is equal to 6.6 cm/rad (or 4.8 cm per revolution).

Subcavitating Propellers — The rheoelectric installation just described is especially useful for the solution of the inverse problem, because of the possibility of regulating and controlling precisely the pressure distribution on each section of the blade. To illustrate this, we shall describe the different stages of a complete propeller design that permitted a useful experimental verification in free water and in a cavitation tunnel.

The characteristics of the propeller were the following:

Advance velocity	$V_0 = 7.25$ m/sec
Number of revolutions	$n = 3.75$ t/sec ($\omega = 25.36$ rad/sec)
Blade radius	$R = 1.20$ m
Advance coefficient	$\lambda = \dfrac{V_0}{\omega R} = 0.256$, $\lambda = \dfrac{V_0}{nD} = 0.805$
Thrust	$T = 7200$ kg

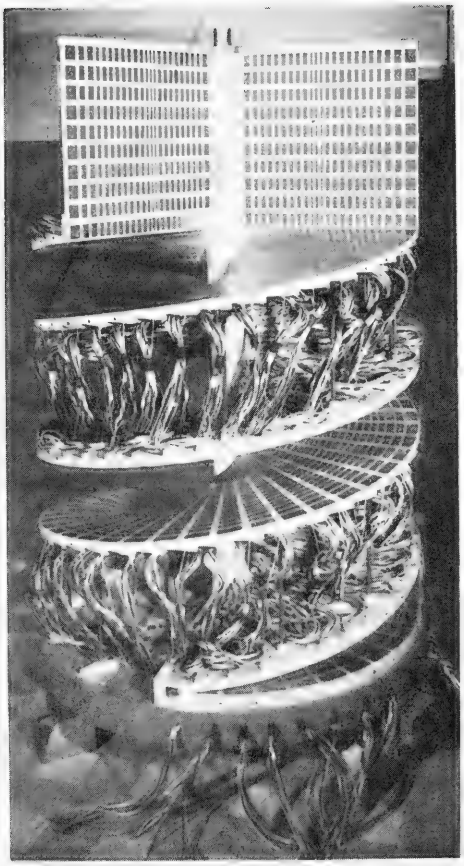

Fig. 23 - Tank model for the rheoelectric solution of the hydrodynamics of the screw propeller

Thrust coefficients

$$C_T = \frac{2T}{\rho\omega^2 R^4} = 0.119$$

$$K_T = \frac{T}{\rho n^2 D^4} = 0.147$$

Developed area ratio 0.40

Number of blades 3.

The conditions imposed were of two kinds: (a) Hydrodynamic — pressure distribution on the blades was as regular as possible and higher than the value

of the saturated vapor pressure; optimal span circulation distribution. (b) Mechanical – span thickness distribution that ensured everywhere a sufficient mechanical resistance. These conditions can be ensured independently, because it is possible, as in the case of wings, to divide the problem into two parts; one referring to the determination of the lifting effect of an infinitely thin surface, and the other to the calculation of the thickness effect while entirely free of lifting.

For the first part, the load distribution, a constant on eight-tenths of the chord and decreasing to zero at the leading and trailing edges, together with optimal span circulation distribution are chosen. The shape of each section and the distribution of velocities on the lower and upper surfaces are then determined. If the depression created by the velocities is considered significant, it is possible to change the load distribution until acceptable levels are reached. For the thickness effect, the calculation process is similar. The form of the lower and upper surfaces corresponding to a nonlifting foil in a helicoidal flow and the distribution of velocities on them, are determined. Once these two operations are completed, the blade sections are deduced by comparison of the lifting and thickness effects. Figure 24 shows the forms of different blade sections according to the parameters just described. Table 1 gives the expected values of the drag and torque coefficient and the values obtained in a test in free water carried out at the Bassin des Carênes, Paris.

Table 1
Expected Values of the Drag and Torque Coefficient and the Values Obtained in a Test in Free Water at the Bassin des Carènes, Paris

	K_T	K_Q	η
Expected values	0.147	0.0258	0.730
Measured values	0.148	0.0268	0.706

It will be seen that the agreement between these values is satisfactory except for the propeller efficiency, which is lower than estimated. The difference seems due to an underestimation of the friction resistance in consideration of the Reynolds number imposed by the test conditions. The experiments in a cavitation tunnel show, as was expected, that for the design value of λ the propellers function without cavitation on the upper surface of the blades, except very near the blade tip $(0.95 < \xi < 1)$ where the end vortex is attached.

These satisfactory observations seem to prove that two important objectives have been attained – control of pressure and a condition of adaptation – and that analog calculation is likely to provide an effective solution to the theory of the lifting surface of propellers.

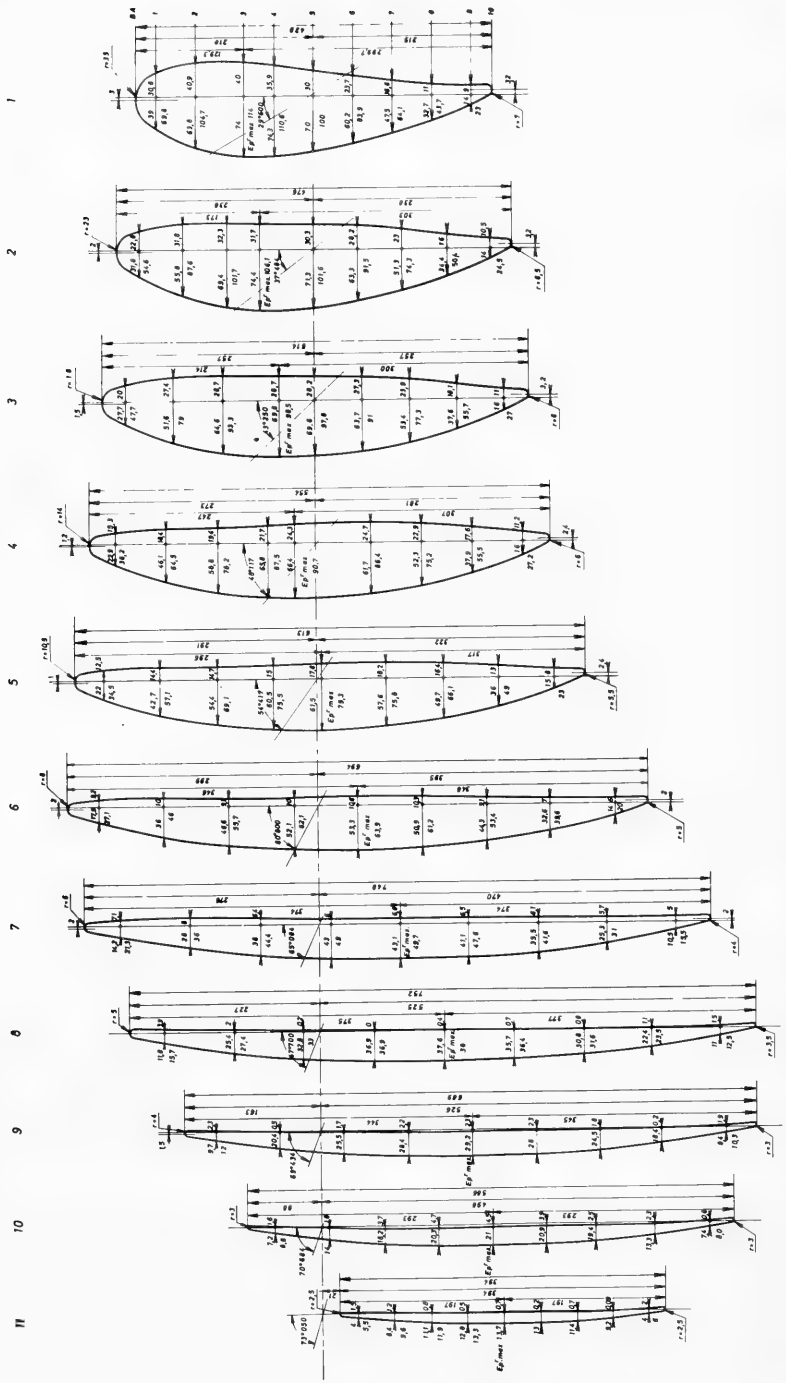

Fig. 24 - Forms of different blade sections according to the parameters of lifting and thickness effects ("Ep. max." means maximum thickness)

Supercavitating Propellers — The boundary conditions and the analog equipment necessary for this study have already been taken into account in Eq. (15) and in the subsection on Supercavitating Cascades. The boundary conditions will now be imposed in the intersection of the straight cylinders $\xi = Ct$, for the helicoids.

Notice, however, the advantages of the lifting surface method as applied to supercavitating propellers when it is compared with the approximate calculation methods in use at the present time. First, the blade and cavity contours are correcting represented, which allows, for a given blade form, the study of the influence of the cavity form on the performance of the propeller. Second, the cascade phenomenon and that of the interaction of the cavities are taken into account during the calculation without having to introduce corrective terms.

Various propellers have been designed by this method. The first propeller calculated was tested in the cavitation tunnel of the Bassin des Carènes, Paris. The results obtained did not confirm the theoretical estimates. This discordance does not seem to be due to a fault in the theory, verified in the subcavitating case, but to an unrealistic choice of speed coefficient. Three propellers have recently been calculated and one of them should be tested very soon at the U.S. Naval Ship Research and Development Center. Figure 25 shows one of these propellers, designed for an optimal span circulation distribution and pressure distribution on each section of the blade such that, at the leading edge a very localized infinite pressure encourages the starting of cavitation (behavior of the flat-plate foil), and the most heavily loaded part of the foil is near the trailing edge (high lift-drag ratio criteria in the two-dimensional case). The characteristics of these three propellers are summed up in Table 2, not taking into account the friction resistance. The figures in the table are for an advance coefficient $\lambda = V_0/\omega R = 0.261$, a cavitation number $\sigma = 2(P_0 - P_c)/\rho V_0^2 = 0.4$, and various blade and cavity forms.

Table 2
Characteristics of Three Supercavitating Propellers Calculated by the Lifting Surface Method

	Propeller Number		
	1	2	3
C_T	0.0855	0.0868	0.0579
C_Q	0.0357	0.0338	0.0225
η	62.3%	67.1%	67.1%

Ducted Propellers — The advantages of ducted propellers over ordinary propellers, for certain speed coefficients, have long been known. However, very little study has been devoted to improvement of the functioning of the nozzle and to increasing the efficiency of the propeller-nozzle system. The analog method (11,45) offers calculation possibilities for this type of device which promise a

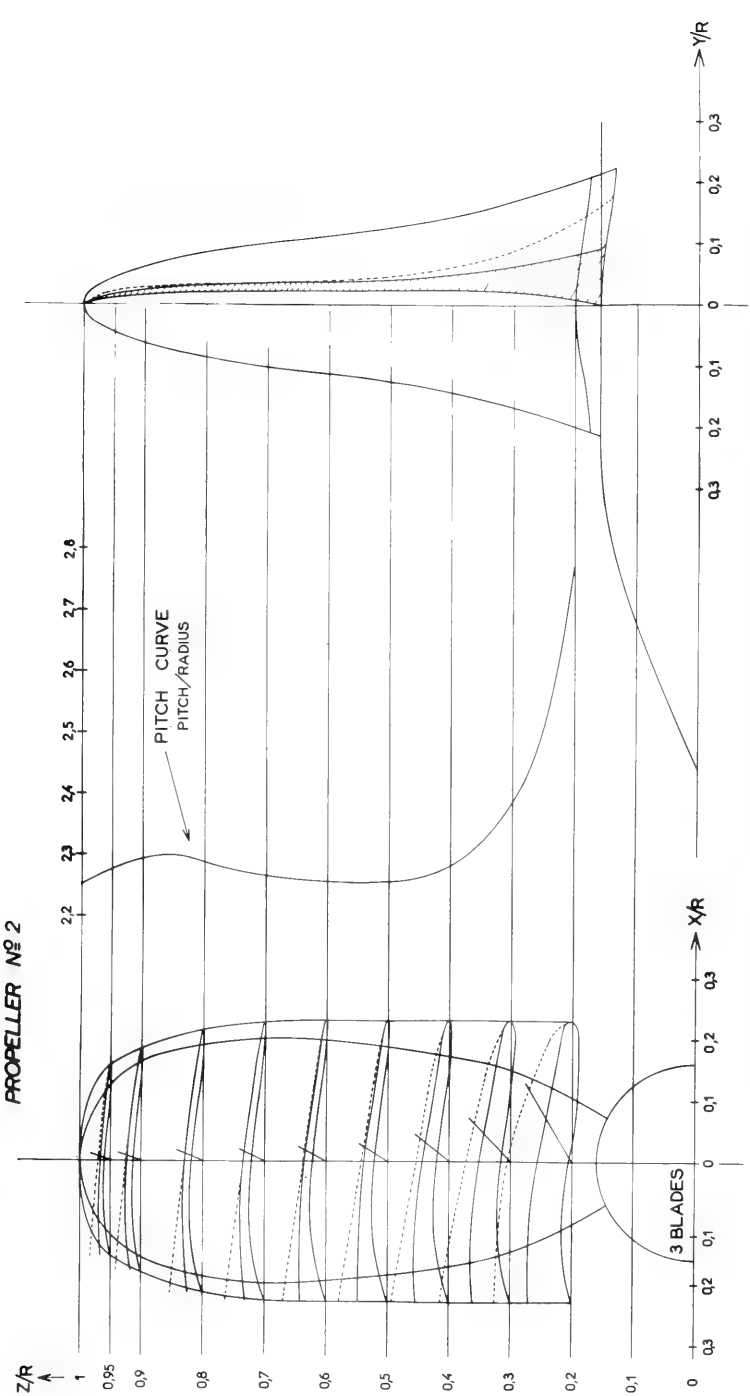

Fig. 25 - Supercavitating propeller calculated by the lifting surface method and designed for an optimal span circulation and pressure distribution on each blade

considerable improvement of its efficiency in performing the functions required of it.

To conduct this study, we are obliged to admit certain hypotheses. We shall assume that: the downstream flow is made axial by straighteners, the propeller is approximated by an actuator disc (infinite-number-of-blades hypothesis) with a discontinuity of constant pressure during its passage (constant circulation hypothesis). Consequently the flow is axisymmetric and its study can be limited to a demiplan meridian. Although this first simplification is necessary, it is not ultimately sufficient, because if we are to represent the flow correctly we must know the discontinuity surface of the velocities which escapes from the trailing edge of the duct; i.e., we must know the free-boundary-with-equilibrium condition which imposes equality between the pressure jump and the difference of the square of the velocities on each side of the jetstream. The difficulty in representing such a condition requires the use of a linearized schema wherein the boundary conditions are imposed on a straight semi-indefined cylinder of generators parallel to the unperturbed velocity, and on an image of the duct and of the discontinuity surface. The flow can then be defined by means of the perturbation-velocities-potential harmonic revolution function, which is easily represented by the electric potential of a tank with an inclined bottom.

Because of the many conditions which must be satisfied in order to improve the hydrodynamic functioning and efficiency of the nozzle, it seemed useful to take as a starting point a given duct form, which is then redefined during the calculation on the basis of the results obtained. The process is greatly facilitated by consideration of several elementary potentials which have in the past revealed the interactions of the propeller and hub on the duct.

This method permits us to show the role played in the increasing of efficiency by two effects; the downstream divergence of the mean line of the duct in connection with the increase of velocity in the plane of the actuator disc, which facilitates and improves the functioning of the latter; and the "adaptation" condition, imposed during the design on the nose of the duct, which reduces the risks of flow separation on the inner surface of the nozzle, and consequently encourages its efficiency, as well as that of the propeller. We must point out nevertheless that the widening effect of the nozzle can be obtained by the blowing effect on the trailing edge, an effect also studied by rheoelectric analogy by means of analog hypotheses (11).

This method has been used for the calculation of a combined propeller-rectifier-nozzle with the following characteristics:

Thrust	$T = 19{,}000$ Kgr
Diameter of the propeller	$D = 2.58$ m
Length of the nozzle	$L = 1.87$ m
Advance coefficient	$\Lambda = V_0/nD = 0.696$
Thrust coefficient	$K_T = T/\rho n^2 D^4 = 0.258$,

of which 0.056 corresponds to the thrust provided by the nozzle and 0.202 to that of the propeller.

A model of the ducted propeller given in Fig. 26 has been tested at the Bassin des Carènes, Paris. The results obtained were very encouraging, since the thrust of the nozzle corresponded well to what was expected, as did the efficiency of the overall propeller. The conclusions drawn were 66% experimental instead of 70% theoretical. The total thrust, however, was only attained to within 16%. In any case, with regard to the so-called nozzle itself, the study showed the advantage of the method of calculation used: if improvements should be sought, they ought to be concerned with the calculation of the fan and of the straighteners. To support this argument it may be noted further that the comparison of the efficiency of this nozzle with a Wageningen no. 9 nozzle fitted with a K 4.55 propeller, which was considered to give the best performance, resulted in a preference for the former. With a practically equal diameter, the gain in efficiency of the first nozzle is about 5 to 13% higher depending on the power.

STUDY OF FLOW AROUND THICK BODIES

In most studies already described the bodies are supposed very thin. In this case the linearization hypotheses are valid. Nevertheless, when the relative thickness of the bodies is important it is not possible to simplify the boundary conditions over their surface. Thus, if we consider the perturbation velocities potential $\phi = \Phi - x$, with a harmonic function in x, y, and z, it is convenient to write, for the whole surface Σ limiting the body, the tangential velocity condition as

$$\frac{\partial \phi}{\partial n} = f(x_i, y_i, z_i) \ ,$$

where $f(x_i, y_i, z_i)$ is a known function of points $M(x_i, y_i, z_i)$ over the surface Σ. This function depends on the local slope of the body and its motion.

The body can be slightly immersed beneath, or can traverse, the free surface. In general, it is possible to simplify the equilibrium condition of this surface by supposing that the perturbation induced by the body is not very important. The linearized boundary condition on the free surface still holds good and can be written in the same form that in the General Equations subsection, described earlier

$$\frac{\partial^2 \phi}{\partial x^2} + K_0 \frac{\partial \phi}{\partial z} = 0 \ .$$

Far upstream we have the condition

$$\lim_{x \to -\infty} \mathbf{grad}\ \phi = 0 \ .$$

This problem can then be solved according to the method described in the subsection on Subcavitating Hydrofoils. The ϕ function, which is the solution of

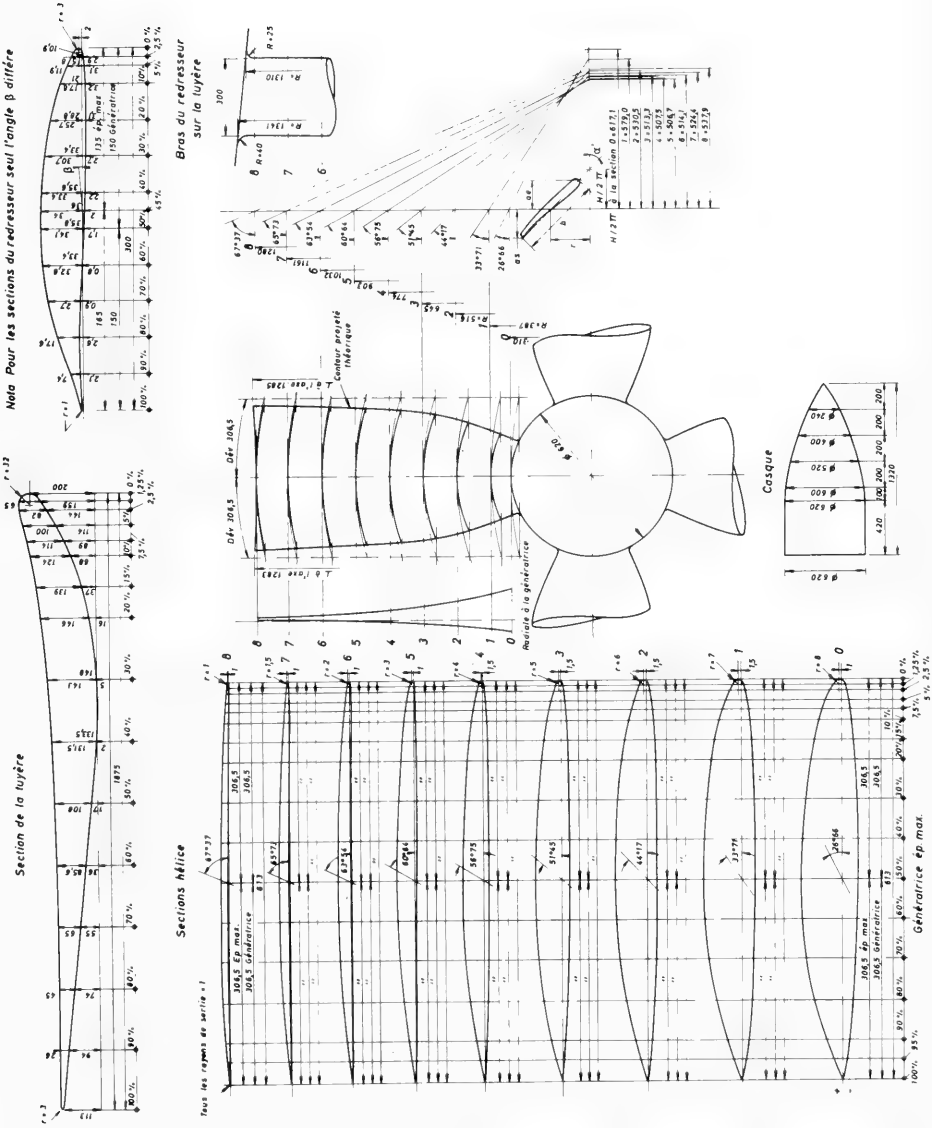

Fig. 26 - Model specifications of a ducted propeller tested at the Bassin des Carènes, Paris

the given boundary value problem, can be considered as the sum of elementary potentials induced in the field by a convenient source distribution. We can then write

$$\phi = \int_{\Sigma} q(x_i, y_i, z_i)(\Omega_s + \Omega_r)\, d\sigma ,$$

where q is the singularity density of the simple layer potential at points (x_i, y_i, z_i) of the surface Σ, $d\sigma$ is an elemental surface around this point, and Ω_s and Ω_r are the *singular and regular parts* of the potential of an immersed source of unit strength. In the two-dimensional case, these two parts are given by the following classical expressions

$$\Omega_s = \mathrm{Re}\, \frac{1}{2\pi} [\log(\zeta - \zeta_i) + \log(\zeta - \bar{\zeta}_i)]$$

$$\Omega_r = \mathrm{Re}\, \frac{1}{\pi} \left[\mathrm{PV} \int_0^{\infty} \frac{e^{-iK(\zeta - \bar{\zeta}_i)}}{K - K_0}\, dK - i\pi e^{-iK_0(\zeta - \bar{\zeta}_i)} \right] ,$$

where $\zeta = x + iz$, $\zeta_i = x_i + iz_i$, and $K_0 = g/V_0^2$.

The ϕ function is also in two parts: ϕ_s and ϕ_r

$$\phi = \phi_s + \phi_r ,$$

where ϕ_s corresponds to the singular part of Ω_s, i.e.,

$$\int_{\Sigma} q\Omega_s d\sigma .$$

Its value is the same on both sides of Σ, while its normal derivatives are discontinuities. The difference between its normal derivatives $(\partial\phi_s^+/\partial n - \partial\phi_s^-/\partial n)$ represents the source flow q. In the present case the superscripts + and - correspond to the *external and internal domains* defined by Σ.

The potential function ϕ_s must then satisfy the following boundary conditions

$$\begin{aligned} &\text{(a) on } z = 0 , \quad \frac{\partial \phi_s}{\partial n} = 0 \\ &\text{(b) for } |x| \to \infty , \quad \mathbf{grad}\, \phi_s = 0 \\ &\text{(c) on } \Sigma , \quad \left(\frac{\partial \phi_s^+}{\partial n} - \frac{\partial \phi_s^-}{\partial n} \right) = q(x_i, y_i, z_i) , \end{aligned} \tag{16}$$

with the external normal derivative given by

$$\frac{\partial \phi_s^+}{\partial n} = f(x_i, y_i, z_i) - \int_\Sigma \mathbf{grad}\ \Omega_r \mathbf{n} q d\sigma . \tag{17}$$

Computation Procedure

The analog simulation of the above boundary condition is very simple. Nevertheless, two different rheoelectric tanks are necessary, one to represent the actual *flow field outside* the body, and the other to represent the *field inside* the body.

The computation procedure is as follows:

1. For the initial iteration it is supposed that $\partial \phi_s^+/\partial n = f(x_i, y_i, z_i)$, i.e., that the regular part ϕ_r of ϕ is neglected. The computation corresponds to the solution of the external field problem for a zero Froude number. The potential distribution $\phi_s^+(x_i, y_i, z_i)$ on each point of Σ is then obtained.

2. These values are then introduced on the corresponding points of the *internal* domain. The measure of the normal derivatives $\partial \phi_s^-/\partial n$ gives a first plausible distribution of $q(x_i, y_i, z_i) = (\partial \phi_s^+/\partial n - \partial \phi_s^-/\partial n)$. With these values it is possible to compute numerically, for a given Froude number, the normal derivatives over Σ due to the regular part, i.e., the normal derivatives induced by the free surface

$$\int_\Sigma \mathbf{grad}\ \Omega_r \mathbf{n} q d\sigma .$$

3. Introducing this integral into Eq. (17) gives a new corrected distribution of $\partial \phi_s^+/\partial n$, which is then imposed on the surface Σ of the external flow field. Hence, a new distribution of the ϕ_s^+ potential is obtained and permits us to continue the procedure by step 2. This iteration procedure is repeated until the convergent values of ϕ_s^+ are obtained.

Application of the Method

To test the validity of this method the above computation procedure was applied to the case of an immersed circular cylinder beneath the free surface. The results obtained were in good agreement with those computed from the analytical solution by Havelock (46) (Fig. 27).

At the present time, the work carried on at the Centre de Calcul Analogique concerns the study of three-dimensional flow fields with free surface. The studies will permit us to obtain the pressure distribution over a thick hull and the wave drag attached to it, over a wide range of Froude numbers. The proposed hull is represented in the rheoelectric tank by 240 electrodes, i.e., the velocity tangential condition is satisfied on 240 control points over its surface. To compute this problem numerically it was necessary to solve a 240×240 matrix at

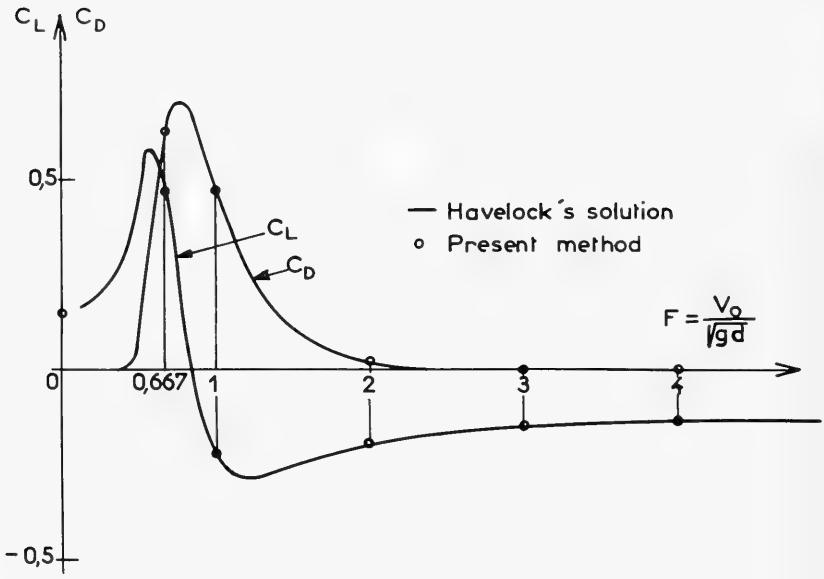

Fig. 27 - Comparison of analogic computation of flow around thick bodies with Havelock's solution

each iteration. We hope these studies will be a valuable contribution to the problem of thick hulls and wave resistance, which is one of the most important aspects of naval hydrodynamics.

CONCLUSION

The purpose of this paper was to give a glimpse of the possibilities of rheoelectric analogies in the field of theoretical naval hydrodynamic problems. The examples given were chosen to illustrate these possibilities and may be summed up as: sub- and supercavitating hydrofoil problems, with or without free-surface effect; supercavitating cascade design; hydrodynamic characteristics and optimum design of finite-span wings, with or without free-surface, strut, and wall effects; design of sub- and supercavitating marine screw propellers; and finally, a tentative method for solving the problem of thick hulls.

Rheoelectric analogy is a very suitable method of study for these hydrodynamic problems, because most of them can be considered as potential flows defined by the Laplace equation. The rheoelectric tank is, indeed, a practical and effective method of simulation of these harmonic functions. The knowledge of their boundary conditions is sufficient for realizing the simulation. Therefore it is not necessary hereafter to look for an explicitly analytical formulation of the problems.

Some of the examples given show that to obtain the best results from the rheoelectric method, it is convenient, very often, to modify the theoretical statement of the problem with a view to simplifying the electrical setups of the boundary conditions and still obtain a good workability. This approach may suggest to some a new way of constructing theoretical models for hydrodynamic problems in order to simplify the analogy. On the contrary, these models would prohibitively complicate the task of the mathematicians who may try to solve hydrodynamic problems by analytical or numerical methods. Rheoelectric methods utilize the possibilities of both numerical analysis and computers to facilitate the preparation of data and to exploit their results. Numerical and computer analysis is also employed in the establishment of new hybrid analog-digital methods. The solution of the thick hull problem shows clearly this interconnection between numerical and analog computation.

Many kinds of problems can be treated directly numerically, but our experience shows that before any extensive programming is undertaken, it is useful to check the validity of the theoretical model by rheoelectric simulation. The physical nature of the analogy often allows a good criterion for disclosing the difficulties of the proposed mathematical model.

Finally, it should be observed that specialists in rheoelectric analogy are convinced of the usefulness of large computers. The analog point of view when applied to numerical solutions, often permits us to obtain conventional yet effective methods.

ACKNOWLEDGMENTS

The author wishes to thank the Office of Naval Research, Department of the Navy — U.S.A., who partially supported, under contract numbers 62558-2545, 62558-2997, 62558-1861, 62558-3645, 62558-4113, 62558-4483, and 62558-4998, numerous studies described in this paper. He would like also to thank Dr. D. H. Fruman of the Centre de Calcul Analogique for his most efficient assistance in the preparation of this paper.

REFERENCES

1. Peres, J. and Malavard, L., "Sur les Analogies Électriques en Hydrodynamique," CRAS*, 18 avril 1932

2. Malavard, L., "Application de l'Analogie Électrique à la Solution de Quelques Problèmes d'Hydrodynamique," Publ. Sc. et Tech. du Min. de l'Air, fasc. 57, 18 décembre 1934

3. Peres, J. and Malavard, L., "Réalisations Analogiques d'Écoulements avec Lignes de Jet," CRAS, 7 janvier 1938

*Comptes-rendus de l'Académie des Sciences — Paris.

4. Malavard, L., "The Use of Rheoelectrical Analogies in Certain Aerodynamical Problems," J. Roy. Aeron. Soc. 51(No. 441), Sept. 1947

5. Malavard, L., "Use of Electrolytic Plotting Tank," High-Speed Aerodynamics and Jet Propulsion, Vol. VII, Art. H. 2, Princeton University, 1951

6. Malavard, L., "The Use of Rheoelectrical Analogies in Aerodynamics," AGARD-ograph, No. 18, Aug. 1956

7. Tulin, M.P. and Burkart, M.P., "Linearized Theory for Flow about Lifting Foils at Zero Cavitation Number," David Taylor Model Basin Report C-638, Feb. 1955

8. Luu, T.S., "Contribution à la Théorie Linéarisée des Effets de Jets Minces et de Cavitations: Calcul des Ecoulements par Analogie Rhéoélectrique," Publ. Sc. et Tech. du Min. de l'Air, No. 389, 1962

9. Luu, T.S., "Contribution à l'Etude des Effets de Volet dans les écoulements Supercavitants à Nombre de Cavitation non Nul," J. de Mécanique, vol. I (No. 2), Paris, juin 1962

10. Luu, T.S., "Méthode d'Analogie Rhéoélectrique dans l'Etude des Problèmes Concernant les Phénomènes de Soufflage," 2èmes Journées Int. de Calcul Analogique, Strasbourg, Septembre 1958 (Proceedings, 1959)

11. Luu, T.S., "Hélice Carénée, Théorie et Calcul Analogique de l'Effet d'un Jet Mince Annulaire au bord de Fuite," CRAS, 16 novembre 1959

12. Luu, T.S., "Soufflage au bord de Fuite des Profils d'un Distributeur," CRAS, 28 mars 1960

13. Fruman, D., "Problèmes de Profils Sub- et Supercavitants près de la Surface Libre. Résolutions Rhéoélectriques," Thèse, Université de Paris, 28 juin 1965

14. Fruman, D., "Calcul Analogique de la Forme des Profils Immergés en présence de la Surface Libre en Régimes Subcavitant et Supercavitant," Col. Int. des Tech. de Calcul Analogique et Numérique en Aéronautique, Liège, 9-12 septembre 1963 (Proceedings, 1964)

15. Fruman, D., "Obtention des Caractéristiques Hydrodynamiques de Profils Immergés près de la Surface Libre au moyen de l'Analogie Rhéoélectrique," Soc. Hydrotech. de France, 6èmes Journées de l'Hydraulique, Question VI (rapport No. 2), Paris, 1-3 juin 1966

16. Fruman, D. and Luu, T.S., "Sur une Méthode de Tracé de Profils Supercavitants en présence de la Surface Libre," CRAS, 17 juin 1963

17. Auslaender, J., J. Ship Res. 6 (No. 2), Oct. 1962

18. Malavard, L. and Siestrunck, R., "Méthode d'Etude des Grilles Rectilignes Indéfinies de Profils Quelconques," 1er Cong. de l'Aviation française, mai 1945

19. Malavard, L. and Siestrunck, R., "Sur l'Etude par Expérimentation Analogique des Grilles Rectilignes de Profils Quelconques," CRAS, 4 juin 1945

20. Malavard, L. and Siestrunck, R., "Application de la Théorie des Grilles de Segments Rectilignes à l'Etude Théorique et Expérimentale des Grilles d'Aubes," CRAS, 12 juin 1946

21. Malavard, L. and Siestrunck, R., "Diverses Méthodes Analogiques pour le Calcul des Grilles d'Aubes," 6ème Cong. Int. de Mécanique Appliquée, septembre 1946

22. Malavard, L., Siestrunck, R., and Germain, P., "Calcul des Répartitions de Vitesse sur les Profils des Grilles Planes," La Rech. Aéronautique, No. 4, juillet 1948

23. Luu, T.S., "Tracé des Profils d'une Grille Supercavitante," CRAS, 23 mai 1966

24. Luu, T.S., "Hydrofoils Supercavitants d'Envergure Finie. Simulation rhéoélectrique," Col. Int. des Tech. de Calcul Analogique et Numérique en Aéronautique, Liège, 9-12 septembre 1963 (Proceedings, 1964)

25. Malavard, L. and Duquenne, R., "Etude des Surfaces Portantes par Analogies Rhéoélectriques," La. Rech. Aéronautique, No. 23, septembre 1951

26. Duquenne, R., "Sur le Calcul Analogique des Surfaces Portantes," CRAS, 26 mai 1952

27. Duquenne, R. and Granjean, C., "Calcul par Analogie Rhéoélectrique de l'Effet d'Epaisseur sur des Ailes Symétriques à la Portance Nulle," CRAS, 12 avril 1954

28. Malavard, L., Duquenne, R., Enselme, M., and Granjean, C., "Propriétés Calculées d'Ailes en Delta Echancré ou non. (Calcul par Analogies Electriques)," ONERA, N.T. No. 25, 1955

29. Luu, T.S., "Méthode de Calcul et Tracé des Hydroptères Supercavitants d'Envergure Finie," Ass. Tech. Maritime et Aéronautique, Paris, 21-28 avril 1967

30. Luu, T.S., "Recherche de la Répartition Tourbillonnaire Optimale sur l'Envergure d'un Hydroptère Supercavitant Fonctionnant près de la Surface Libre," J. de Mécanique, vol. 6 (No. 3), 1967

31. Malavard, L., "Etude de Quelques Problèmes Techniques Relevant de la Théorie des Ailes. Application à leur Solution de la Méthode Rhéoélectrique," Publ. Sc. et Tech. du Min. de l'Air, No. 153, juillet 1939

32. Luu, T.S. and Offner, B., "Projet d'Hydroptères Supercavitants Munis d'un Mât et Destinés au Fonctionnement en Soufflerie Hydrodynamique," CRAS, t. 266, pp. 160-163 (1967)

33. Luu, T.S., Offner, B., and Tsen, L.F., "Etude Théorique et Expérimentale des Hydroptères Ventilés d'Envergure Finie Munis d'un Mât," Ass. Tech. Maritime et Aéronautique, Paris, session 1968

34. Sulmont, P., "Application de la Théorie des Surfaces Portantes au Calcul des Hélices Marines Sub- et Supercavitantes," Thèse, Université de Paris, 25 janvier 1966

35. Sulmont, P., "Détermination Analogique du Potentiel de Perturbation autour d'une Surface Portante en Mouvement Hélicoïdal," CRAS, 5 juin 1963

36. Sulmont, P., "Calcul et Tracé d'Hélices Supercavitantes," Ass. Tech. Maritime et Aéronautique, Paris, session 1968

37. Dong, N.T., Fruman, D., and Luu, T.S., "Sur une Méthode de Calcul des Ecoulements Bidimensionnels avec Surface Libre autour des Corps Immergés," CRAS, t. 266, pp. 382-385 (1967)

38. Luu, T.S. and Fruman, D., "Sur la Résolution des Problèmes du Champ Faisant Intervenir des Conditions aux Limites de Poisson," 5ème Cong. Int. de Calcul Analogique, Lausanne, 28 août-2 Septembre 1967

39. Malavard, L and Renard, G., "La Technique des Analogies Rhéoélectriques," Techniques générales du Laboratoire de Physique, vol. II, CNRS, 1962

40. Strandhagen, A.G. and Welsh, C.A., Proc. of the 7th Midwestern Mechanics Conference, 613-622 (1961)

41. Wehausen, J.V. and Laitone, E.V., "Handbuch der Physik," 489-491 (1961)

42. Isay, W.H., Ingenieur-Archiv 27, 295-313 (1960)

43. Durand, W.F., "Aerodynamic Theory," Vol. II, 208 (1935)

44. Thwaites, B., "Incompressible Aerodynamics," 523 (1960)

45. Malavard, L. and Hacques, G., "Problemes de l'Aile Annulaire Résolus par Analogie Rhéoélectrique," Advances in the Aeronautical Sciences, Vol. 2, 1959

46. Havelock, "The Forces on a Circular Cylinder Submerged in a Uniform Stream," Proc. Roy. Soc., London, 1936

* * *

THE NUMERICAL SIMULATION OF VISCOUS INCOMPRESSIBLE FLUID FLOWS

C. W. Hirt
Los Alamos Scientific Laboratory
University of California
Los Alamos, New Mexico

ABSTRACT

This paper describes an Eulerian finite-difference technique for solving the complete nonlinear Navier-Stokes equations. The technique is applicable to transient flows of viscous, incompressible fluids with free surfaces. The basic features of the finite-difference method are first explained in terms of a simple linear convection equation. The discussion covers questions of accuracy and computational stability. These results are then applied to the solution of the complete time-dependent Navier-Stokes equations. Techniques are also described for incorporating free-surface stress conditions, as well as other boundary conditions. The complete numerical scheme that is developed is referred to as the Marker-and-Cell (MAC) method (1). Two applications of the MAC method are discussed in detail. The first application is to the flow of water under a sluice gate. This example illustrates how the MAC method is kept computationally stable. The second application deals with the formation of a hydraulic jump. This example reveals several important aspects of the numerical treatment of boundary conditions. The hydraulic jump example also illustrates an attempt of the numerical method to simulate fluid turbulence. This leads to a discussion of a new method for obtaining the numerical solution of time-dependent fully turbulent flows.

INTRODUCTION

The Marker-and-Cell (MAC) technique is an Eulerian finite-difference method for solving the complete nonlinear Navier-Stokes equations (1). The MAC method is applicable to transient flows of viscous, incompressible fluids with free surfaces. Examples are the surge of water under a sluice gate, the splashing of liquid drops, and the formation of hydraulic jumps.

In this paper the method is presented for arbitrary two-dimensional flows. Three-dimensional calculations are not treated here since they are impractical with the speed and size of today's computers. Special considerations are given to the conditions for computational stability and accuracy, and to the derivation of boundary conditions, especially at free surfaces. Finally, a brief discussion is presented of a new method for studying fully turbulent flows.

The paper is divided into several sections. In the first section a simple linear difference equation is used to demonstrate several important features of finite-difference equations that we shall use in developing the MAC equations. The following sections develop the basic MAC difference equations and subsidiary details. The next-to-last section presents two applications involving free-surface flows, while the final section makes several comments on the application of high-speed computers to the study of turbulence.

A LINEAR EQUATION

We begin by investigating the properties of a simple finite-difference equation. Many results derived here are directly applicable to the Navier-Stokes equations.

Consider the differential equation

$$\frac{\partial \rho}{\partial t} + u \frac{\partial \rho}{\partial x} = \nu \frac{\partial^2 \rho}{\partial x^2} , \tag{1}$$

which describes the convection and diffusion of a scalar function $\rho(x,t)$. The convection velocity u and positive diffusion coefficient ν are assumed constant. A simple, explicit, finite-difference approximation to Eq. (1) is

$$\frac{\rho_j^{n+1} - \rho_j^n}{\delta t} + \frac{u}{2\delta x}(\rho_{j+1}^n - \rho_{j-1}^n) = \frac{\nu}{\delta x^2}(\rho_{j+1}^n - 2\rho_j^n + \rho_{j-1}^n) \tag{2}$$

where $\rho_j^n = \rho(j\delta x, n\delta t)$, δx is the space increment, and δt is the time increment. The simplicity of Eq. (2) does not guarantee that it is a good approximation to Eq. (1). Equation (2) may have solutions that exhibit computational instabilities or other inaccuracies making it useless.

Equation (1) is stable in the sense that its solutions are bounded and otherwise well behaved. The stability properties of Eq. (2) can be determined by the Fourier method proposed by von Neumann (2). Equation (2) has exponentially growing solutions that oscillate in sign if $(2\nu\delta t/\delta x^2) > 1$, and nonoscillating exponentially growing solutions if $\nu < (u^2\delta t/2)$. In either case these growing solutions in no way approximate the bounded solutions of Eq. (1). Thus, the inequalities

$$\frac{2\nu\delta t}{\delta x^2} \leq 1 , \quad \nu \geq \frac{1}{2} u^2 \delta t \tag{3}$$

are stability conditions for the difference Eq. (2). For specified values of ν, δx, and u these conditions define a range of δt values that do not lead to exponentially growing solutions.

Stability conditions in Eq. (3) can be determined in another way. The alternative method we shall describe is more useful for our purposes than the linear Fourier method, because it is also applicable to the nonlinear Navier-Stokes

equations. The method is based on an examination of truncation errors. Each term in Eq. (2) is expanded in a Taylor series about the point $x = j\delta x$, $t = n\delta t$, e.g.,

$$\rho^{n}_{j+1} = \rho(x,t) + \delta x \frac{\partial \rho}{\partial x} + \frac{\delta x^2}{2} \frac{\partial^2 \rho}{\partial x^2} + \ldots , .$$

Collecting terms, Eq. (2) becomes

$$\frac{\partial \rho}{\partial t} + u \frac{\partial \rho}{\partial x} - \nu \frac{\partial^2 \rho}{\partial x^2} = - \frac{\delta t}{2} \frac{\partial^2 \rho}{\partial t^2} + O(\delta x^2, \delta t^2) , \tag{4}$$

where all second and higher order terms in δx and δt are represented by the order symbol $O(\delta x^2, \delta t^2)$. The zero-order terms on the left-hand side of Eq. (4) are the original differential Eq. (1). All terms on the right-hand side of Eq. (4) are called *truncation errors*. These terms are responsible for the difference between solutions of the difference Eq. (2) and solutions of the differential Eq. (1). This observation is important, because it suggests that the stability conditions in Eq. (3) might be obtained directly from the truncation errors. That this is indeed possible, at least approximately, has been shown in Ref. 3. The prescription developed there is to keep only the lowest order even and odd derivative terms with respect to each independent variable. As applied to Eq. (4), this means keeping the first and second derivative terms with respect to both x and t. After a slight rearrangement of terms, we have

$$\frac{\delta t}{2} \frac{\partial^2 \rho}{\partial t^2} - \nu \frac{\partial^2 \rho}{\partial x^2} + \frac{\partial \rho}{\partial t} + u \frac{\partial \rho}{\partial x} = 0 , \tag{5}$$

which is not identical to Eq. (1), the equation we set out to approximate. Equation (5) is a hyperbolic equation with characteristic lines whose slopes are $(dx/dt) = \pm(2\nu/\delta t)^{1/2}$.

Similarly, difference Eq. (2) propagates information into a region of the x-t plane bounded by lines whose slopes are $(dx/dt = \pm \delta x/\delta t)$. If difference Eq. (2) is to have a solution approximating the solution of its counterpart in Eq. (5), then its "region of influence" must at least include the region of influence of Eq. (5), i.e.,

$$\left(\frac{\delta x}{\delta t}\right)^2 \geq \frac{2\nu}{\delta t} . \tag{6}$$

Courant et al. (4) have shown that a violation of this type of region-of-influence condition leads to oscillating and exponentially growing solutions for the difference equation. This is also true in our case, since Eq. (6) is exactly the first stability condition in Eq. (3).

The condition in Eq. (6) can be given a physical interpretation. It states that a wave disturbance must not travel more than one space increment δx in one time step δt. We would expect this condition to be necessary for accuracy, since difference Eq. (2) relates space location j only to neighboring locations

$j \pm 1$. On the other hand, implicit finite-difference equations can avoid this type of instability, since they require all space locations to be dependent on one another. The region-of-influence condition will be called the *wave propagation condition* for stability.

The second stability condition in Eq. (3) is also obtainable from Eq. (4) if the term proportional to δt is expressed in terms of space derivatives. Using Eq. (4), we have

$$\frac{\partial^2 \rho}{\partial t^2} = u^2 \frac{\partial^2 \rho}{\partial x^2} - 2\nu u \frac{\partial^2 \rho}{\partial x^3} + \nu^2 \frac{\partial^4 \rho}{\partial x^4} + O(\delta t) \ . \tag{7}$$

Inserting Eq. (7) into Eq. (4) yields

$$\frac{\partial \rho}{\partial t} + u \frac{\partial \rho}{\partial x} = \left(\nu - \frac{1}{2} u^2 \delta t\right) \frac{\partial^2 \rho}{\partial x^2} + \delta t \, \nu u \frac{\partial^2 \rho}{\partial x^3} - \frac{1}{2} \delta t \nu^2 \frac{\partial^4 \rho}{\partial x^4} + O(\delta t^2, \delta x^2) \ . \tag{8}$$

Keeping the lowest order even and odd derivative terms with respect to each independent variable gives us

$$\frac{\partial \rho}{\partial t} + u \frac{\partial \rho}{\partial x} = \left(\nu - \frac{1}{2} u^2 \delta t\right) \frac{\partial^2 \rho}{\partial x^2} \ . \tag{9}$$

This truncated equation is similar to Eq. (1), except that it has a different diffusion coefficient. If δt is too large, the diffusion coefficient in Eq. (9) is negative, and Eq. (9) then has exponentially growing solutions. For bounded solutions, the diffusion coefficient must remain positive:

$$\nu \geq \frac{1}{2} u^2 \delta t \ . \tag{10}$$

The condition in Eq. (10) is the second stability condition in Eq. (3). It states that some ν diffusion is necessary to keep the difference equation stable.

Equation (9) also has a bearing on the accuracy of Eq. (2). For a given value of ν the effective diffusion coefficient is, to the terms of order δx^2 and δt^2, $\nu - (u^2 \delta t/2)$, which increases as δt decreases. Solutions of Eq. (2) are smoother as δt decreases, but for finite values of δt, solutions of Eq. (2) are subject to less diffusion than solutions of Eq. (1).

All observations made about the linear difference equation can be applied to difference equations in general. We shall make use of the wave propagation and positive diffusion coefficient conditions to establish stability conditions for the MAC method. Some important comments also will be made about diffusion-like truncation errors in the MAC equations.

THE MAC DIFFERENCE EQUATIONS

The discussion in the previous section showed the futility of applying explicit finite-difference methods, designed for compressible flows, to the solution of incompressible flow problems. Time increments must be chosen very small to limit the distance which sound waves travel in one time step to less than one space increment. The incompressible limit assumes, however, that sound speeds are much larger than fluid speeds, so that it would be necessary to calculate an enormous number of time steps to see a significant flow change. Thus, the wave propagation stability condition precludes the use of purely explicit finite-difference methods. An implicit method is needed that will adjust the flow field simultaneously at all space locations to maintain fluid incompressibility.

The MAC technique accomplishes this task in a fast and novel way. We begin with the incompressible Navier-Stokes equations

$$\frac{\partial u}{\partial x} + \frac{\partial v}{\partial y} = 0 \tag{11a}$$

$$\frac{\partial u}{\partial t} + \frac{\partial u^2}{\partial x} + \frac{\partial uv}{\partial y} = -\frac{\partial \varphi}{\partial x} + g_x + \nu\left(\frac{\partial^2 u}{\partial x^2} + \frac{\partial^2 u}{\partial y^2}\right) \tag{11b}$$

$$\frac{\partial v}{\partial t} + \frac{\partial uv}{\partial x} + \frac{\partial v^2}{\partial y} = -\frac{\partial \varphi}{\partial y} + g_y + \nu\left(\frac{\partial^2 v}{\partial x^2} + \frac{\partial^2 v}{\partial y^2}\right), \tag{11c}$$

where φ is the ratio of pressure to constant density, g_x and g_y are the components of a body acceleration, and ν is the kinematic viscosity.

Finite-difference approximations for Eqs. (11) require a finite set of points on which to specify local values of the field variables. In MAC, this is accomplished by covering the flow region with a mesh of stationary rectangular cells. The region actually occupied by fluid is further covered by a set of marker particles (Fig. 1). These particles move with the fluid and are used to locate free surfaces, but they do not otherwise influence the flow dynamics. More is said about marker particles in the section on Corrective Procedure. In each cell of the stationary mesh, flow variables are specified at the positions indicated in Fig. 2. By not recording all variables at the center of the cell it is possible to obtain more compact finite-difference approximations. It also makes it easier to satisfy boundary conditions at rigid walls, if the walls are assumed to coincide with the cell boundaries.

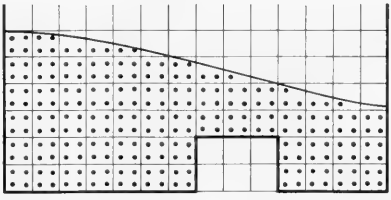

Fig. 1 - Schematic of a typical cell and marker particle layout

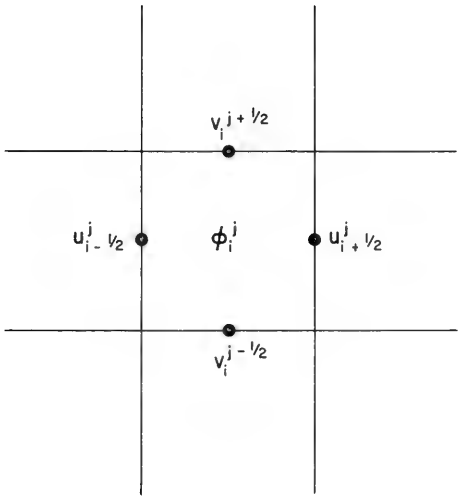

Fig. 2 - Location of flow variables in a cell

Equations (11) are statements of the conservation of mass and momentum. Our finite-difference approximations should likewise maintain these conservation properties. The horizontal-momentum equation is approximated with the explicit-difference equation thus

$$\frac{1}{\delta t}\left({}^{n+1}u_{i+1/2} - {}^{n}u_{i+1/2}^{j}\right) = \frac{1}{\delta x}\left[\left(u_i^j\right)^2 - \left(u_{i+1}^j\right)^2\right]$$

$$+ \frac{1}{\delta y}\left[(uv)_{i+1/2}^{j-1/2} - (uv)_{i+1/2}^{j+1/2}\right]$$

$$+ \frac{1}{\delta x}\left(\varphi_i^j - \varphi_{i+1}^j\right) + g_x$$

$$+ \nu\left[\frac{1}{\delta x^2}\left(u_{i+3/2}^j - 2u_{i+1/2}^j + u_{i-1/2}^j\right)\right.$$

$$\left. + \frac{1}{\delta y^2}\left(u_{i+1/2}^{j+1} - 2u_{i+1/2}^j + u_{i+1/2}^{j-1}\right)\right] \qquad (12)$$

A similar approximation is used for the vertical-momentum equation,

$$\frac{1}{\delta t}\left({}^{n+1}v_i^{j+1/2} - {}^{n}v_i^{j+1/2}\right) = \frac{1}{\delta x}\left[(uv)_{i-1/2}^{j+1/2} - (uv)_{i+1/2}^{j+1/2}\right]$$

$$+ \frac{1}{\delta y}\left[\left(v_i^j\right)^2 - \left(v_i^{j+1}\right)^2\right] \qquad (13)$$

(Cont)

$$+ \frac{1}{\delta y}\left(\varphi_i^j - \varphi_i^{j+1}\right) + g_y$$

$$+ \nu\left[\frac{1}{\delta x^2}\left(v_{i+1}^{j+1/2} - 2v_i^{j+1/2} + v_{i-1}^{j+1/2}\right)\right.$$

$$\left. + \frac{1}{\delta y^2}\left(v_i^{j+3/2} - 2v_i^{j+1/2} + v_i^{j-1/2}\right)\right] \qquad (13)$$

the notation used here is, e.g., $n_{u_i}^j \equiv u(i\delta x, j\delta y, n\delta t)$. All quantities on the right-hand side of Eqs. (12) and (13) are evaluated at time $n\delta t$. Several quantities in Eqs. (12) and (13) are located at positions other than those indicated in Fig. 2. In each case a simple average is implied; for example,

$$u_i^j = \frac{1}{2}\left(u_{i+1/2}^j + u_{i-1/2}^j\right),$$

or

$$v_{i+1/2}^{j+1/2} = \frac{1}{2}\left(v_i^{j+1/2} + v_{i+1}^{j+1/2}\right).$$

For a product, each factor is first averaged and then the product is formed, i.e.,

$$(uv)_{i-1/2}^{j+1/2} = \left(u_{i-1/2}^{j+1/2}\right)\left(v_{i-1/2}^{j+1/2}\right)$$

$$= \left(u_{i-1/2}^{j+1} + u_{i-1/2}^{j}\right)\left(v_{i-1}^{j+1/2} + v_i^{j+1/2}\right).$$

Equations (12) and (13) conserve momentum exactly. A sum over consecutive i and j in either equation leads to a cancellation in pairs of terms on the right-hand side. The only momentum changes occurring in a group of cells are caused by surface fluxes.

The momentum equations are completed by specifying the pressure. The pressure must then be determined to make the velocity field satisfy the conservation-of-mass condition, the first equation of Eqs. (11). For this purpose we need the finite-difference expression for the velocity divergence in cell (i,j),

$$D_i^j = \frac{1}{\delta x}\left(u_{i+1/2}^j - u_{i-1/2}^j\right) + \frac{1}{\delta y}\left(v_i^{j+1/2} - v_i^{j-1/2}\right). \qquad (14)$$

Then, the conservation-of-mass or incompressibility condition is

$${}^{n+1}D_i^j = 0 \qquad (15)$$

for every (i,j). Inserting Eqs. (12) and (13) for the values of u and v at $(n+1)\,\delta t$, into Eqs. (14) and (15) yields the following equations for φ_i^j

$$\frac{1}{\delta x^2}\left(\varphi_{i+1}^{j} - 2\varphi_i^{j} + \varphi_{i-1}^{j}\right) + \frac{1}{\delta y^2}\left(\varphi_i^{j+1} - 2\varphi_i^{j} + \varphi_i^{j-1}\right) = -R_i^{j}\,, \tag{16a}$$

where

$$R_i^{j} = -\frac{{}^{n}D_i^{j}}{\delta t} - \nu\left[\frac{1}{\delta x^2}\left(D_{i+1}^{j} - 2D_i^{j} + D_{i-1}^{j}\right),\ \frac{1}{\delta y^2}\left(D_i^{j+1} - 2D_i^{j} + D_i^{j-1}\right)\right.$$

$$+ \frac{1}{\delta x^2}\left[\left(u_{i+1}^{j}\right)^2 - 2\left(u_i^{j}\right)^2 + \left(u_{i-1}^{j}\right)^2\right]$$

$$+ \frac{1}{\delta y^2}\left[\left(v_i^{j+1}\right)^2 - 2\left(v_i^{j}\right)^2 + \left(v_i^{j-1}\right)^2\right]$$

$$\left. + \frac{2}{\delta x \delta y}\left[(uv)_{i+1/2}^{j+1/2} + (uv)_{i-1/2}^{j-1/2} - (uv)_{i+1/2}^{j-1/2} - (uv)_{i-1/2}^{j+1/2}\right]\right. . \tag{16b}$$

Equations (16) are the approximation for a Poisson equation for the pressure. These equations must be solved by matrix inversion or an iteration process. The necessity for solving a set of coupled equations arises because of the fluid incompressibility. Each finite-difference cell containing fluid influences every other cell containing fluid. This is the implicit part of the difference approximations needed for incompressible flows.

It is very important to note the presence of D_i^{j} terms in Eq. (16b). The D_i^{j}-type term is the source term for the Poisson equation. These terms are so important that we will digress here to consider them in more detail.

CORRECTIVE PROCEDURE

Let us assume Eqs. (16) are solved by an iteration method (matrix inversions are too time-consuming). Every iterative solution of Eq. (16a) must be terminated with some error. Thus, ${}^{n+1}D_i^{j}$ will not be exactly zero. An error in the velocity divergence, however, means an error in mass conservation. To maintain the accuracy of a MAC calculation, in which Eqs. (16) are repeatedly solved at each time step, the accumulated value of D_i^{j} must be kept as small as possible. This could be accomplished, for example, by iterating the pressure equation to a high degree of accuracy at each time step. Unfortunately, the computing time needed to solve sets of linear equations like Eq. (16a) increases very rapidly as the convergence criterion is refined. Another means of preventing a significant accumulation of D error is used in MAC. The D terms retained in Eq. (16b) act as a self-correcting mechanism. An error in D at time step n is automatically corrected at time step $n+1$, since the difference equations are set up to make ${}^{n+1}D$ zero, regardless of the value of ${}^{n}D$. Therefore, a relatively crude iteration solution of Eq. (16a) can be tolerated at each time step without leading to a disastrous accumulation of error after many time steps. Enormous savings in computer time are realized with this technique.

An additional advantage is that initial conditions for a calculation do not have to satisfy the incompressibility conditions. After one cycle of calculation the condition is automatically satisfied. A complete discussion and generalization of this corrective procedure can be found in Ref. 5.

WALL BOUNDARY CONDITIONS

Boundary conditions are needed to complete the basic MAC difference Eqs. (12), (13), and (16). Free boundaries introduce special problems and will be considered later. Here we are deriving conditions for rigid, input, and output boundaries.

Rigid boundaries are assumed to coincide with cell boundaries, otherwise cells would have variable dimensions and this would require additional computer storage. Boundary conditions are imposed by specifying the appropriate values for field variables located in fictitious cells immediately outside the boundary.

For the purposes of illustration, suppose that a vertical boundary coincides with the right-hand side of cell (i,j), and that cell $(i+1,j)$ is outside the boundary. Rigid boundaries are further classified as free-slip or no-slip. At a free-slip boundary, the normal component of velocity is zero, and no tangential shear is allowed:

$$u^{j}_{i+1/2} = 0 , \quad v^{j\pm 1/2}_{i+1} = v^{j\pm 1/2}_{i} . \tag{17}$$

At a no-slip boundary, both the normal and tangential velocity vanish:

$$u^{j}_{i+1/2} = 0 , \quad v^{j\pm 1/2}_{i+1} = -v^{j\pm 1/2}_{i} . \tag{18}$$

The one velocity component of the fictitious cell still undetermined, $u^{j}_{i+3/2}$, is chosen to make D^{j}_{i+1} zero. If this D is not zero, it will diffuse into the flow region through Eqs. (16).

The necessity for a condition on D in the fictitious cell arises from the form chosen for the differential equations in Eqs. (11) and the cell layout in Fig. 2. We might just as well have written the viscous terms in Eqs. (11), which are components of the vector

$$\nu \nabla\cdot\nabla \mathbf{u} , \tag{19}$$

as components of the equivalent vector

$$\nu \nabla\times\nabla\times \mathbf{u} . \tag{20}$$

When Eq. (20) is used as a starting point for making finite-difference approximations, the D diffusion terms will not appear in Eq. (16b) and the fictitious cell velocity $u^{j}_{i+3/2}$ will not otherwise be required. Equation (20), therefore, is preferred, but we have chosen to describe Eq. (19), since it was used in the original MAC development.

For both free-slip and no-slip walls, boundary conditions on the pressure are derived directly from the difference equations. Since $u^j_{i+1/2}$ is identically zero, Eq. (12) relates φ^j_{i+1} to $\varphi_i{}^j$ and other known quantities in the wall vicinity. Remembering that D^j_{i+1} is zero,

$$\varphi^j_{i+1} = \varphi_i{}^j + g_x \delta x + \frac{2\nu}{\delta x} u^j_{i-1/2} \ . \tag{21}$$

Similar conditions can easily be derived when the rigid wall coincides with a different side of cell (i,j).

This completes the necessary boundary conditions for rigid walls. Conditions for prescribed input boundaries are straightforward and can be found in detail in Ref. 1. For output boundaries, there are no unique prescriptions. The investigator is free to choose conditions consistent with whatever flow he imagines to exist outside the region being studied. One choice that has worked quite well for many applications is described in Ref. 1.

FREE-SURFACE BOUNDARY CONDITIONS

With various combinations of rigid-wall, input, and output boundaries, it is possible to simulate a great variety of confined flows. Many interesting incompressible flows, however, involve free boundaries. Waves, jets, and splashing drops are good examples. To treat these free surface flows we must have some means of locating the free surface and of satisfying the surface boundary conditions.

Marker particles are used to solve the first of these problems. They represent selected points whose coordinates are calculated to move with the fluid. An analogy may be drawn with the hydrogen bubbles often used in laboratory experiments as a means of visualizing a flow. Any cell that contains a marker particle is assumed to contain fluid. If such a cell is next to a cell containing no marker particles, then it is designated as a surface cell, i.e., it contains the free surface.

Free-surface boundary conditions are applied at each surface cell. The correct boundary conditions are the vanishing of the normal and tangential surface stresses. If the curvature of the surface is small, the stress conditions in two dimensions can be approximated by

$$\varphi - 2\nu \frac{\partial u_n}{\partial n} = \varphi_a \tag{22}$$

$$\nu \left(\frac{\partial u_n}{\partial m} + \frac{\partial u_m}{\partial n} \right) = 0 \ , \tag{23}$$

where n refers to the outward normal direction to the surface and m to the tangential direction. Allowance is made for an applied surface pressure φ_a, which can be useful on occasion.

To correctly satisfy the conditions in Eqs. (22) and (23), and the conservation of mass requires a knowledge of the exact location and slope of the surface within a surface cell. This information is not available in MAC. Instead, several approximations are introduced which have been found to work quite well, except at very low Reynolds numbers.

The quantities to be determined in each surface cell by the boundary conditions are the pressure and the velocities at each cell boundary adjacent to an empty cell. Conservation of mass is approximated by choosing the velocities to make D vanish in each surface cell. This is just an approximation, since D should be zero only in that part of the cell which is filled with fluid. If the cell has more than one side adjacent to an empty cell, the vanishing of D does not uniquely determine all the velocities. In this case the finite-difference forms of $\partial u/\partial x$ and $\partial v/\partial y$ are individually required to vanish. Other possibilities can be envisioned, but this particular choice seems to work well.

Tangential velocities needed in empty cells at the surface are chosen to make the normal derivative of the tangential velocity zero $\partial u_m/\partial n = 0$. The tangential stress condition in Eq. (23) is approximately satisfied by this choice.

Once the surface velocities are determined, it is easy to satisfy the normal stress condition in Eq. (22). Complete details are given in Ref. 6, where it is shown that the tangential stress condition and the viscous contribution to the normal stress condition are important only at Reynolds numbers less than about 10.

STABILITY AND ACCURACY

To use the MAC equations effectively, it is necessary to know their stability properties. We have already seen that with an incorrect choice for δt, the simple difference Eq. (2) has very misbehaved solutions. Similar solutions develop in MAC. Analogous to the example in the Linear Equation section, there are two kinds of stability conditions for MAC: wave propagation, and the positive diffusion coefficient.

Wave propagative instabilities occur for two reasons. First, in free-surface flows, surface waves may develop with wave speed

$$C = \left[\frac{g}{k} \tanh (hk)\right]^{1/2}, \tag{24}$$

where k is the wave number, h the depth of fluid, and g the downward acceleration of gravity, $g_y = -g$. The first wave propagation condition, therefore, limits the distance surface waves travel in a single time step. Second, in two dimensions the condition is

$$C\,\delta t < \frac{2\delta x \delta y}{\delta x + \delta y}. \tag{25}$$

The second wave condition is analogous to that needed for Eq. (2). For two dimensions,

$$2\nu\delta t < \frac{\delta x^2\, \delta y^2}{\delta x^2 + \delta y^2} . \tag{26}$$

The necessary diffusion coefficient conditions are derived by collecting all truncation errors in the MAC equations that contribute to diffusions of u and v. Keeping only these terms through order δt and δx^2,

$$\begin{aligned}
\frac{\partial u}{\partial t} + \frac{\partial u^2}{\partial x} + \frac{\partial uv}{\partial y} &= -\frac{\partial \varphi}{\partial x} + g_x + \left(\nu - u^2\frac{\delta t}{2} - \frac{\delta x^2}{2}\frac{\partial u}{\partial x}\right)\frac{\partial^2 u}{\partial x^2} \\
&\quad + \left(\nu - v^2\frac{\delta t}{2} - \frac{\delta y^2}{4}\frac{\partial v}{\partial y}\right)\frac{\partial^2 u}{\partial y^2} , \\
\frac{\partial v}{\partial t} + \frac{\partial uv}{\partial x} + \frac{\partial v^2}{\partial y} &= -\frac{\partial \varphi}{\partial y} + g_y + \left(\nu - u^2\frac{\delta t}{2} - \frac{\delta x^2}{4}\frac{\partial u}{\partial x}\right)\frac{\partial^2 v}{\partial x^2} \\
&\quad + \left(\nu - v^2\frac{\delta t}{2} - \frac{\delta y^2}{2}\frac{\partial v}{\partial y}\right)\frac{\partial^2 v}{\partial y^2} .
\end{aligned} \tag{27}$$

Several remarks can be made about the diffusion coefficients appearing in Eq. (27). First, the MAC equations are always unstable if $\nu = 0$. Second, neglecting the δx^2 terms, the diffusion coefficients are positive if

$$\nu > \frac{u^2\delta t}{2} , \quad \nu > \frac{v^2\delta t}{2} . \tag{28}$$

These conditions are approximately the stability conditions obtained from a linear Fourier analysis (7). However, the δx^2 terms cannot be ignored, which requires

$$\nu > \frac{\delta x^2}{2} u' , \tag{29}$$

where u' is a typical velocity derivative in the direction of flow. Instabilities do occur when Eq. (29) is violated, and they are quite insidious, since a reduction in δt cannot cure them. Furthermore, they are more likely to occur when ν is small, i.e., in high Reynolds number flows. Therefore, it is extremely important to recognize the condition Eq. (29), and to distinguish these numerical instabilities from physical instabilities.

The relationship between diffusion-like truncation errors and computational stability is applicable to all finite-difference approximations. It should now be clear why it is so difficult to perform high Reynolds number calculations. Occasionally an investigator claims to calculate at very high Reynolds numbers, but a check on truncation errors most often reveals positive diffusion terms much larger than the real viscosity.

APPLICATIONS

The surge of water under a sluice gate is an example of a complicated nonlinear fluid flow. Figure 3 shows the marker particle configuration obtained in a MAC calculation of such a flow. Fluid falls under the influence of gravity and jets under the gate into a stagnate pool. A surge wave is formed moving to the left. A velocity vector plot, Fig. 4, shows a large eddy at the back of the wave. Each line segment in Fig. 4 characterizes the velocity magnitude and direction for a single computing cell.

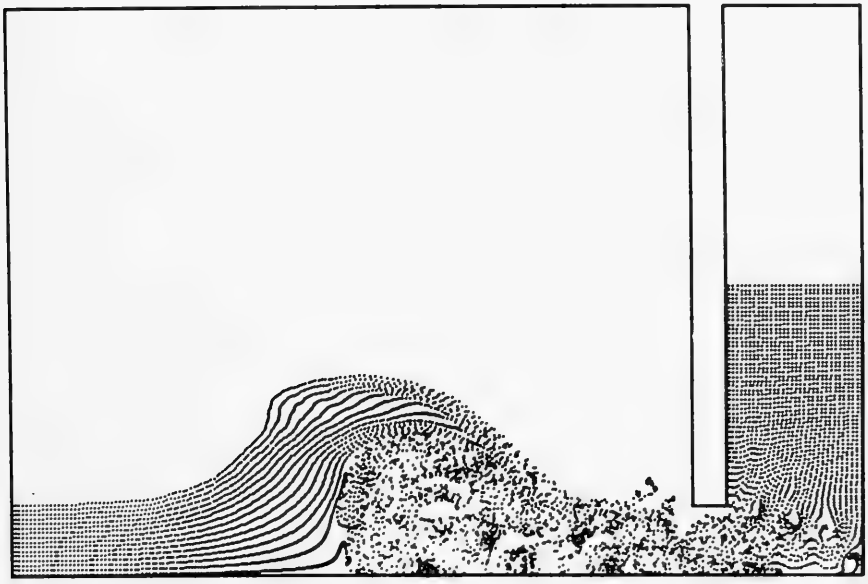

Fig. 3 - Marker particle configuration of a sluice gate calculation

It is evident from the velocity plot that some difficulty is developing along the bottom of the flow region. The irregular appearance of the velocities indicates a computational instability. Although many stable sluice gate problems have been calculated and have given excellent agreement with experimental data, we have purposely chosen a bad example to illustrate an instability.

There are, in fact, two instabilities in this calculation. One is behind the sluice gate and the other is under the surge wave. A decrease in δt by a factor of 20 eliminates the instability under the wave, but produces no significant changes behind the gate. A decrease in δx (and δy which is equal to δx) eliminates the latter instability also. The instability under the surge wave is due to a violation of the condition in Eq. (28), and the other instability to a violation of the condition in Eq. (29). With sufficiently small space and time increments, or a sufficiently large value of ν, the sluice gate calculation is stable.

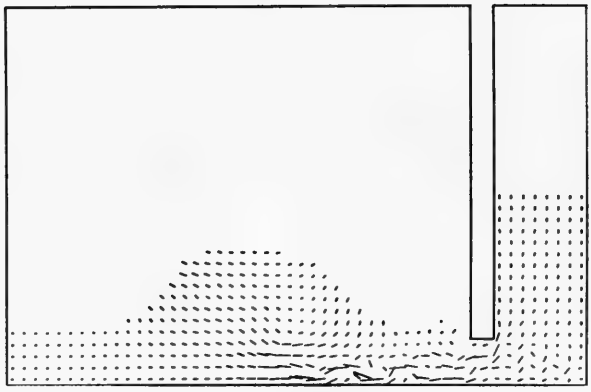

Fig. 4 - Velocity vector plot for the sluice gate calculation shown in Fig. 3

Another interesting flow occurs when fluid piles up against a rigid wall and forms a hydraulic jump. The jump conditions relating uniform states of flow on either side of a hydraulic jump are easy to derive — they are conservation of mass and momentum. Kinetic energy decreases in the transition. The lost energy usually reappears as fluid turbulence. At very low Reynolds numbers, however, there can be enough viscous dissipation in a *laminar* transition to preclude the development of turbulence. Figure 5 shows a laminar jump at Reynolds number 4.33 (based on incoming fluid depth and speed relative to the jump). Fluid is input at the right-hand boundary and piles up at the left boundary, which is a rigid wall. A hydraulic jump is traveling back to the right. Clearly, the flow is laminar. The overshoot in elevation and a slightly low jump speed are believed to be caused by a failure to satisfy correctly the tangential stress condition of Eq. (23). When the Reynolds number exceeds about 10, the free-surface approximations discussed in the section on Free-Surface Boundary Conditions are satisfactory.

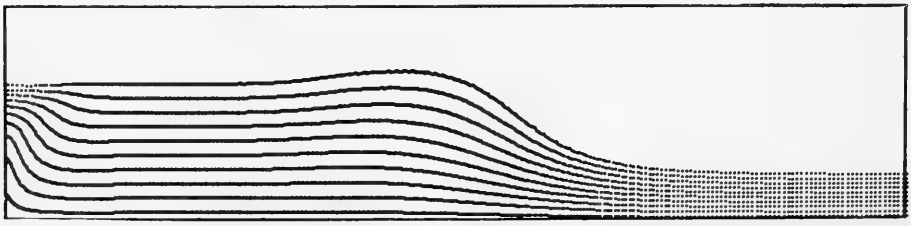

Fig. 5 - A hydraulic jump calculation at Reynolds number 4.33

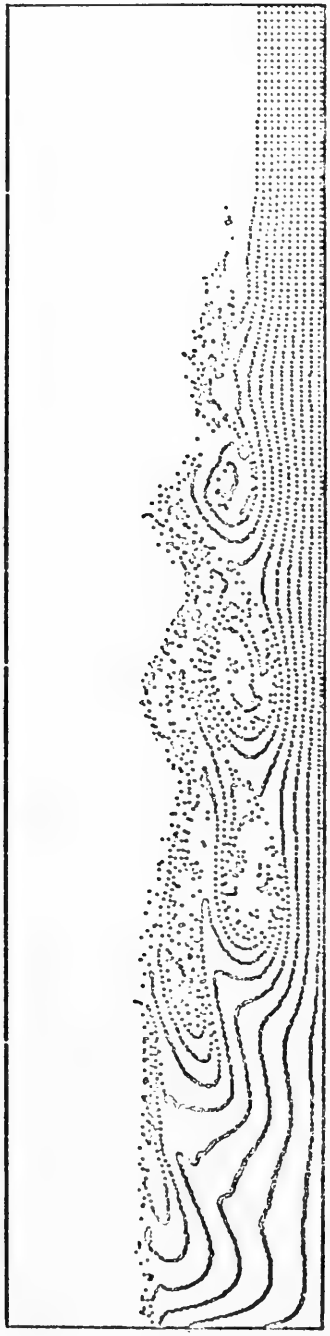

Fig. 6 - A hydraulic jump calculation at Reynolds number 79.25

Figure 6 shows a hydraulic jump at Reynolds number 79.25. The flow in this case is no longer laminar. Large eddies have developed in the transition region in an attempt to simulate turbulence. The calculations do not represent true turbulence, because of the course resolution and the restriction to two-dimensional flow.

TURBULENCE

It is interesting to speculate on the contributions that high-speed computing can make to the understanding of turbulence. Three directions appear open to numerical studies. The first is to use existing computing techniques to make detailed studies of the breakdown and growth of laminar instabilities. Some work on the stability of Poiseville flow has already been undertaken (8). Success in these investigations will continue as the ability to calculate high Reynolds number flows increases.

The second approach is to calculate the detailed structure of a turbulence flow. Such calculations will be extremely difficult, however, because they must be done in three dimensions and require high resolution. Computers are too slow and memory is too limited to permit much progress in this direction.

The third possibility is to develop a capability to calculate the mean motion of turbulent fluid, without regard to its detailed structure. In this approach the turbulence is characterized by a small number of field variables. The variables are postulated to satisfy transport equations that account for the processes of production, decay, convection, and diffusion. A mean flow is influenced by an exchange of energy with the turbulence and by turbulent diffusion of mean momentum.

Although it is too soon to assess the full potential of this last approach, it does appear highly promising. For further details, reference may be made to the work of Harlow and Nakayama (9).

ACKNOWLEDGMENT

This work was performed under the auspices of the United States Atomic Energy Commission.

REFERENCES

1. Harlow, F.H., Welch, J.E., Shannon, J.P., and Daly, B.J., Los Alamos Scientific Laboratory Report LA-3425 (1965); Harlow, F.H., and Welch, J.E., Phys. Fluids 8, 2182 (1965), and 9, 842 (1966)

2. O'Brien, G.G., Hyman, M.A., and Kaplan, S., J. Math. Phys. 29, 223 (1950)

3. Hirt, C.W., J. Computational Phys. 2 (No. 4), 1968

4. Courant, R., Friedricks, K.O., and Lewy, H., Math. Ann. 100, 32 (1928)

5. Hirt, C.W., and Harlow, F.H., J. Computational Phys. 2, 114 (1967)

6. Hirt, C.W., and Shannon, J.P., J. Computational Phys. 2 (No. 4), 1968

7. Daly, B.J., and Pracht, W.E., Phys. Fluids 11, 15 (1968)

8. Dixon, T.N., and Hellums, J.D., "A Study on Stability and Incipient Turbulence in Poiseville and Plane-Poiseville Flow by Numerical Finite Difference Simulation," unpublished

9. Harlow, F.H., and Nakayama, P.I., Phys. Fluids 10, 2323 (1967); Harlow, F.H., and Nakayama, P.I., Los Alamos Scientific Laboratory Report LA-3854 (1968)

* * *

DISCUSSION

M. T. Murray
Admiralty Research Laboratory
Teddington, England

I should like to ask Dr. Hirt the following questions:

1. What computer was used?

2. What running-time did the examples require?

3. What limit does computational feasibility place on the complexity of problems which can be dealt with?

* * *

DISCUSSION

A. M. O. Smith
Douglas Aircraft Company
Long Beach, California

Dr. Hirt and the Los Alamos group certainly deserve congratulations for their pioneering efforts in this field.

Now I have two questions.

1. In most aeronautical and marine applications the surfaces are curved. Have you any comments about methods for handling such boundaries?

2. I understand that Professor Roache at Notre Dame has developed a finite-difference method for the same problems as yours that is stable. Do you know about it and do you have any comments about it?

* * *

REPLY TO DISCUSSION

C. W. Hirt

REPLY TO COMMENTS BY M. T. MURRAY

The computer used was the IBM 7030 (STRETCH) machine. This is a 98,000 (base 10) word machine, which was programed for the MAC method directly in machine language.

The 7030 machine can handle a maximum of 4440 cells with 12,500 marker particles. If fewer cells are used more particles can be included because there is some tradeoff in storage space. Typical problems usually involve on the order of 2000 cells and several thousand particles. For example, the hydraulic jump calculation used 100×25 or 2500 cells and approximately 2700 particles (not all cells contain particles), and the sluice gate calculation used 47×32 or 1504 cells with approximately 6200 particles.

The computer time needed for a problem depends crucially on the number of cells and particles used. The sluice gate calculations, as a typical example, required approximately 12 seconds per cycle. This is not unreasonable considering that one cycle consists of the solution of a Poisson equation for pressure, advancement of all velocity components, and the movement of particles. The loss and gain of surface cells must also be recorded during each cycle.

REPLY TO COMMENTS BY A. M. O. SMITH

Curved boundaries are generally a problem, but not an insurmountable one. It is certainly possible to think of a MAC technique that uses a mesh of irregular polyagonal cells. Assuming that a curved boundary can be approximated by a set of short-line segments, the fluid region could be covered by a mesh of polyagonal cells extending out from the boundary. In this way problems with curved boundaries could be solved. We have not yet attempted this approach with the MAC method, but we are investigating a similar method for compressible flow calculations.

THEORETICAL STUDIES ON THE MOTION OF VISCOUS FLOWS

PREFACE

These studies are in six parts, comprising six papers on various aspects of the motion of viscous flows, prepared by Paul Lieber of the University of California, Berkeley. Two of the papers were prepared in collaboration with Kirit Yajnik, who is now at the Indian Institute of Technology, Kanpur, India. One paper each was prepared in collaboration with Shrikant Desai of the University of California, Berkeley; and with Lionel Rintel, who is now at William and Mary College, Williamsburg, Virginia.

* * *

I—Fundamental Properties of Eddies

Kirit Yajnik
Institute of Technology
Kanpur, India

and

Paul Lieber
University of California
Berkeley, California

ABSTRACT

A new concept of eddy is rigorously introduced here, by stating it in precise mathematical definition. This definition originated in a description of certain general differential-geometrical features of flows which are based on a rotation tensor of the third rank. It is used here to investigate mathematically some fundamental and general properties of eddies. Because any criterion based on the distribution of vorticity alone does not distinguish eddies from other regions (rigid-body rotation and plane Couette flow, for example), new descriptions of rotation having more information than vorticity are needed. The definition presented here is formulated in terms of angular velocities of differential elements of material curves and surfaces. A characteristic kinematic property of an eddy is the positive value of a certain invariant of the velocity gradient. Although vorticity cannot be zero in an eddy, examples show that nonzero vorticity is not sufficient and that concentration of vorticity need not occur in eddies of a real fluid. Other kinematic properties include connections of whirling or closed streamlines with the presence of eddies in plane flows or axisymmetric flows without tangential component of velocity, and with the presence of convex streamlines within the eddies. The connection of eddies of Newtonian fluids of constant properties with low-pressure regions is indicated by the characteristic dynamic property that $\nabla^2 p - \rho \nabla \cdot \bar{F}$ is greater than a certain datum determined by the local three-dimensional character of the flow. The values of the datum for plane flows and axisymmetric flows without tangential component of velocity are zero and $-(3\rho/2)(u_r/r)^2$. The no-slip condition on a stationary solid boundary is shown to lead to large interference of even thin rods with eddies, and experimental evidence given here and elsewhere supports this conclusion. A highly effective method of vortex control can be devised from the conclusion.

INTRODUCTION

Eddies have been extensively investigated on account of their role in fluid motion. The earliest model of an eddy was a potential vortex and its study led to many conclusions about the dynamical behavior of rectilinear vortices and vortex rings. The stability of the vortex street and its associated drag received considerable attention following the successes of the pioneering work of von

Kármán in 1911 and 1912 (1). Despite its successes, certain limitations of the model were recognized. The physical impossibility of velocities being arbitrarily large, and associated difficulties such as infinite angular momentum and kinetic energy led to the modification of Rankine which requires a rigidly turning core with a matching potential flow outside. The new model of steady flow was still not suitable for describing the diffusive and dissipative action of viscosity, particularly near solid boundaries. The unsteady exact solutions of Navier-Stokes equations obtained by G. I. Taylor in 1918 (2), Oseen in 1911 (3), Hamel in 1916 (4), and Rouse and Hsu in 1951 describe the growth and decay of a rectilinear vortex away from a solid boundary and in the absence of neighboring vortices. The three-dimensional behavior of certain eddies has also been described by the exact solutions of N. Rott in 1958 (5) and others.

The picture of an eddy or vortex which has emerged from these studies is that it is essentially a region of concentrated vorticity surrounded by a region of negligible vorticity (Küchmann, 1965) (6). The axisymmetric or two-dimensional character of some of the exact solutions is a mathematically convenient assumption meant to render tractable the problem of integration of Navier-Stokes equations.

The conceptual difficulties created by this picture are many. The picture refers to vorticity distribution, with the inference that if two flows have identical distribution of vorticity and one flow can be called a vortex, the other can be also. But the vorticity distribution of a rigidly turning fluid is the same as the plane Couette flow, so that if a rigidly rotating core of a Rankine vortex is called an eddy, so should the plane Couette flow. However, it is clear that the plane Couette flow does not possess the same whirling character as the rigidly rotating fluid.

Another dilemma created by the picture is that there can be no eddy in a fluid undergoing creeping motion for which vorticity satisfies Laplace's equation, since vorticity or its magnitude cannot be a maximum at any interior point. However, Moffatt in 1964 (7) obtained such flows possessing whirling regions as indicated by closed streamlines.

Even the area of vortex streets is not free from difficulties (Wille, 1960) (8). The earlier model of a line vortex of ideal fluid led to a constant spacing ratio, whereas it was observed that the street becomes wider downstream from the bluff body. Second-order analysis always predicted instability, whereas the vortices preserve their regular pattern for a considerable distance. Theories based on superposition of the vortices of Oseen and Hamel lead to the conclusion that the street becomes narrower downstream.

The work of Michalke in 1964 (9) reveals that the interval between regions of closed streamlines is half that between the locations of maximum vorticity in the case of an unstable free-jet boundary.

These anomalies have led the authors to question whether the whirling property can in principle be described by vorticity distribution. The whirling property is identified by the common operational test of closed streamlines in two-dimensional flows. Hence the authors questioned whether there existed any

connection between maxima of vorticity (or its magnitude) and closed streamlines. It was simple to construct two flows satisfying a continuity equation in such a way that closed streamlines existed in the absence of maxima of vorticity in one flow, while in the other flow, maxima of vorticity occurred in the absence of closed streamlines. These flows are given by the stream functions

$$\psi_1 = -(x^2 + y^2)\,[1 + (x^2 + y^2)/4]/4$$

and

$$\psi_2 = y(x - y + x^2 y)/2 \ ,$$

and associated vorticity fields are given by

$$\xi_1 = [1 + (x^2 + y^2)]$$

and

$$\xi_2 = [1 - (x^2 + y^2)] \ .$$

In the first flow, streamlines are concentric circles and vorticity is minimum at the origin. In the second flow (Fig. 1), there are no closed streamlines, although vorticity is maximum at the origin. Thus if there exists at all a one-to-one connection between concentration of vorticity and closed streamlines, it cannot be on the basis of kinematics or conservation of mass alone. However, hydrodynamics does not provide such a connection, as the computations of Hung and Macagno (1966, 1967) (10,11) show that the regions of closed streamlines in two-dimensional and axisymmetric flows of a Newtonian fluid in a channel or pipe with a sudden expansion do not possess interior points of maximum vorticity.

This paper is devoted to the formulation of a new concept of an eddy related to closed streamlines and to the study of its fundamental properties. The new results obtained are summarized in the following paragraphs.

The angular velocities of elements of material curves and surfaces are defined and are shown to be determined by two tensors of third rank. The tensors bring out the connection between these angular velocities, the vorticity, and the dissipation in a Newtonian fluid of constant properties. The tensors have more information about rotation than the average measure vorticity.

The curvature and torsion of streamlines are shown to be determined by the angular velocities and the velocity. The whirling behavior of streamlines near a point of zero velocity is also shown to be determined by the angular velocities.

General conclusions regarding closed or spiralling streamlines in plane flows are established in terms of the product of maximum and minimum angular velocities of an element of material curve in the plane of motion. It is shown that if the product is positive at a point of zero velocity, the streamlines spiral around the point, and conversely, if the streamlines spiral around a point, the product cannot be negative. Also if the product is positive, the curvature of the

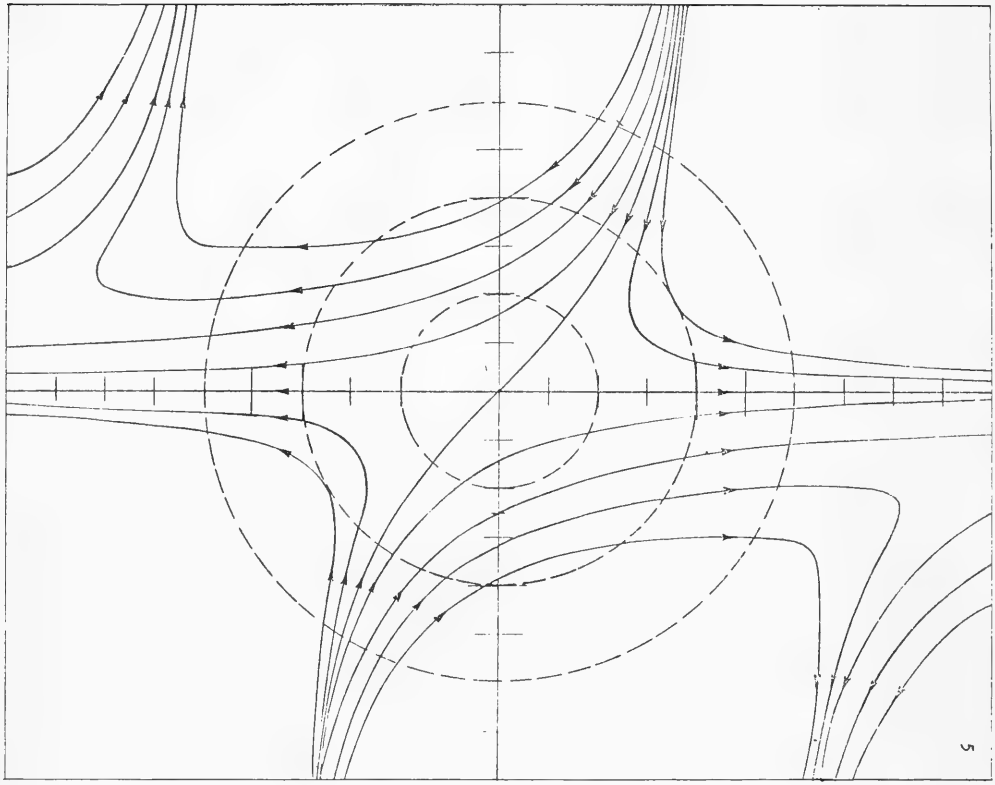

Fig. 1 - Absence of closed streamlines (——) near a point of maximum vorticity (lines of equal vorticity are shown by ---)

streamline at the point cannot be zero. Similar conclusions are valid for axisymmetric flows without tangential component.

A precise and general definition of an eddy is given in terms of the angular velocities and it is shown to be a region of positive discriminant of the characteristic equation of the deviatoric part of velocity gradient $\nabla\bar{u} - (\nabla \cdot \bar{u})\,\bar{\bar{I}}/3$. The definition implies that an eddy in one inertial frame is also an eddy in any other inertial frame. Although vorticity cannot be zero in an eddy, presence of vorticity is not sufficient to make a region of fluid an eddy. Also, since the discriminant is zero for a viscous fluid on a stationary solid surface, even thin rods can cause a large interference with eddies. This conclusion is supported by photographic evidence presented here. It is shown that if $\nabla^2 p$ is positive at a point, in the flow of a Newtonian fluid of constant properties in absence of body forces, the point is in an eddy. The converse is also true in plane flows. Hence the characteristic feature of the stress field in plane eddies is superharmonic character of pressure. It is also shown that the streamlines in plane eddies are convex and that velocity can be zero at, at most, one point in a convex

eddy. In the case of incompressible fluids, if at least one streamline is closed around a point of zero velocity in each of its neighborhoods, and if all the derivatives of velocity do not vanish, the point is in an eddy. Furthermore, if a point of zero velocity is in a plane eddy, there is at least one closed streamline around it in each of its neighborhoods. Similar properties of axisymmetric eddies are also discussed.

These results thus describe the properties of eddies in terms of angular velocities, vorticity, spiralling or closed streamlines, and the convexity of streamlines and low-pressure spots on the basis of the new concept of eddy which differs essentially from the prevailing notion of concentrated vorticity.

ANALYSIS OF ROTATION

Angular velocities of elements of material curves and surfaces are defined and their properties are presented in this section. Let the location of a material filament at time t be given by $\bar{x} = \bar{x}(h,t)$, the parameter h remaining unchanged for a given particle during the motion. The rate of change of a differential element $d\bar{x} = (\partial \bar{x}/\partial h)\, dh$ is then given by

$$\dot{d\bar{x}} = (\partial^2 \bar{x}/\partial h \partial t)\, dh = (\partial \bar{u}/\partial h)\, dh = d\bar{x} \cdot \nabla \bar{u} \ , \tag{1}$$

where a superposed dot indicates a material derivative and $\bar{u}$ is the velocity field. The rates of change of the length ds and the unit tangent vector $\bar{t}$ of the line element are then governed by

$$\dot{ds}\ \bar{t} + ds\ \dot{\bar{t}} = ds\ \bar{t} \cdot \nabla \bar{u} \ , \tag{2}$$

where

$$d\bar{x} = ds\ \bar{t} \ , \quad \bar{t} \cdot \bar{t} = 1, \ \bar{t} \cdot \dot{\bar{t}} = 0 \ . \tag{3}$$

The rotation of the element is most conveniently described by the angular velocity $\bar{w}$ given by $\bar{t} \times \dot{\bar{t}}$, since it can be seen from Eq. (3) that

$$\dot{\bar{t}} = \bar{w} \times \bar{t} \ . \tag{4}$$

One can verify that the angular displacement in time interval t is equal to the magnitude of $w\Delta t$ to the first order of t.

The angular velocity $\bar{w}$ can be evaluated from Eqs. (2) and (3) as

$$\bar{w} = \bar{t} \times (\bar{t} \cdot \nabla \bar{u}) = \bar{t} \times (\bar{\bar{V}} \cdot \bar{t}) \ , \tag{5}$$

where the deviatoric part of the velocity gradient is given by

$$\bar{\bar{V}} = [\nabla \bar{u} - (\nabla \cdot \bar{u})\, \bar{\bar{I}}/3]^{tr} \tag{6}$$

and $\bar{\bar{I}}$ is the identity diadic.

We will briefly depart from the vector-diadic notation to introduce a tensor of third rank. Rewriting Eqs. (5) and (6) in the tensor notation, we have

$$w_i = e_{ij\ell}\, u_{\ell,k}\, t_j\, t_k = e_{ij\ell}\, v_{\ell k}\, t_j t_k, \tag{5a}$$

where

$$v_{ij} = u_{i,j} - u_{k,k}\, \delta_{ij}/3. \tag{6a}$$

To exploit the symmetry in $t_j t_k$, we define

$$\begin{aligned} R_{i:jk} &= (e_{ij\ell}\, u_{\ell,k} + e_{ik\ell}\, u_{\ell,j})/2 \\ &= (e_{ij\ell}\, v_{\ell k} + e_{ik\ell}\, v_{\ell j})/2 \end{aligned} \tag{7}$$

so that

$$w_i = R_{i:jk}\, t_j t_k. \tag{8}$$

Each component of the angular velocity of the line element is thus a quadratic form in its direction cosines, and the coefficients of the quadratic form constitute a tensor of third rank. The tensor $R_{i:jk}$ is symmetric in j and k and will be called the rotation tensor. Note that the rotation tensor and hence the angular velocity are independent of dilation $\nabla\cdot\bar{u}$.

To analyze the rotation of a material surface, let its location at time t be given by $f(\bar{x}, t) = 0$. Note that $\dot{f}$ will be zero on the surface. If $\bar{n}$ is a unit normal at a given particle,

$$\bar{n} = \lambda\, \nabla f, \quad \bar{n}\cdot\bar{n} = 1, \quad \bar{n}\cdot\dot{\bar{n}} = 0 \tag{9}$$

for some λ, and

$$\dot{\bar{n}} = \dot{\lambda}\, \nabla f + \lambda\, \nabla \dot{f} - (\nabla \bar{u})\cdot \bar{n}. \tag{10}$$

Defining the angular velocity $\bar{w}^*$ of the normal as

$$\bar{w}^* = \bar{n} \times \dot{\bar{n}}, \tag{11}$$

we get

$$\dot{\bar{n}} = \bar{w}^* \times \bar{n},$$

and

$$\bar{w}^* = [(\nabla \bar{u})\cdot \bar{n}] \times \bar{n} = (\bar{n}\cdot\bar{\bar{V}}) \times \bar{n}. \tag{12}$$

Note the conjugate character of Eqs. (5) and (12). Rewriting Eq. (12) below in tensor notation, we have

$$w_i^* = e_{\ell ji}\, u_{k,\ell}\, n_j n_k = e_{\ell ji}\, v_{k\ell}\, n_j n_k. \tag{12a}$$

We define

$$R^*_{i:jk} = (e_{\ell ji}\, u_{k,\ell} + e_{\ell ki}\, u_{j,\ell})/2$$

$$= (e_{\ell ji}\, v_{k\ell} + e_{\ell ki}\, v_{j\ell})/2, \tag{13}$$

so that

$$w^*_i = R^*_{i:jk}\, n_j n_k \ . \tag{14}$$

Thus each component of the angular velocity of the normal can also be written as a quadratic form in the direction cosines of the normal and the coefficients constitute a tensor of third rank. The tensor $R^*_{i:jk}$ will be called the adjoint rotation tensor for reasons which will become apparent shortly. This tensor and the angular velocity is also independent of expansion $\nabla \cdot \bar{u}$.

For brevity, we will call $\bar{w}^*$ the angular velocity of a surface element, although it is the angular velocity of the normal.

Vorticity w_i can be readily expressed in terms of the rotation tensors from Eqs. (7) and (13) as

$$w_i = R_{i:jj} = R^*_{i:jj} \ . \tag{15}$$

It is now easy to show that vorticity is an average measure of the angular velocities. In terms of the spherical polar angles θ and ϕ ($t_1 = \cos\theta\cos\phi$, $t_2 = \sin\theta\sin\phi$, and $t_3 = \cos\phi$), the average overall direction is

$$\frac{\int_0^{\pi}\int_{-\pi}^{\pi} w_i \sin\phi\, d\theta\, d\phi}{\int_0^{\pi}\int_{-\pi}^{\pi} \sin\phi\, d\theta\, d\phi} = (R_{i:jk}/4\pi)\int_0^{\pi}\int_{-\pi}^{\pi} t_j t_k \sin\phi\, d\theta\, d\phi \tag{16}$$

$$= R_{i:jk}\,\delta_{jk}/3 = w_i/3 \ .$$

A similar computation can be made for w^*_i . Vorticity is therefore three times the average of the angular velocities of line or surface elements taken over all possible directions. It is well-known that vorticity is proportional to different types of averages, such as the average over three mutually normal directions or all directions in a plane (Cauchy, 1841, and Truesdell, 1954) (12,13).

Let us now consider a line element in the direction of t or a surface element normal to n such that the angular velocity of the line or surface element is zero. Then from Eqs. (5) and (12)

$$\bar{t} \times (\bar{\bar{V}} \cdot \bar{t}) = 0, \quad (\bar{n} \cdot \bar{\bar{V}}) \times \bar{n} = 0,$$

or

$$(\lambda\bar{\bar{I}} - \bar{\bar{V}}) \cdot \bar{t} = 0, \quad \bar{n} \cdot (\lambda\bar{\bar{I}} - \bar{\bar{V}}) = 0 \tag{17}$$

for some real λ . The above conditions are necessary and sufficient for the angular velocity of a line or surface element to be zero. The first condition was essentially the contribution of Thomson and Tait in 1867 (14), and the second

that of Bertrand in 1868 (15). (See also, Truesdell in 1954 (13), and Ericksen in 1955 (16).) As with Eqs. (5) and (12), the two equations here are conjugate.

The number of possible directions of line elements of zero angular velocity and of normals to surface elements of zero angular velocity at a given point is influenced by the characteristic equation

$$\det |\bar{I} - \bar{V}| = 0,$$

or

$$\lambda^3 + M\lambda - N = 0, \tag{18}$$

where

$$M = -V: V/2, \quad N = \det |\bar{\bar{V}}|, \quad t_r \bar{\bar{V}} = 0.$$

The quantity $4M^3 + 27N^2$ is proportional to the discriminant of the cubic equation. It will be called "whirlicity," as it has an important role in deciding the whirling character of streamlines.

We will recall the following theorem which is mainly in accordance with Thomson and Tait (1867), Bertrand (1868), and Truesdell (1954). At any point and time, there is at least one line element and one surface element with zero angular velocity. The number of distinct directions of such line elements or normals of surface elements are: (a) three; or (b) one, two, or infinity; or (c) a number determined according to whether the whirlicity is negative, zero, or positive. A direction refers to a vector $\bar{a}$ or $-\bar{a}$. The details of the proof can be found elsewhere (Yajnik, 1964) (17).

Next we examine the behavior near a point of zero velocity. Suppose that a streamline approaches it in such a way that the unit tangent vector $\bar{t} = \bar{x}'$ approaches to a limit, say $\bar{a}$. Suppose further that the length parameter increases as the point of zero velocity is approached. Then for any given $\epsilon > 0$, there is some s_1 such that

$$|\bar{t} - \bar{a}| < \epsilon = s \geq s_1 . \tag{19}$$

As $\bar{t}$ and $\bar{a}$ are unit vectors, we then obtain

$$\left(1 - \frac{\epsilon^2}{2}\right) \leq \bar{t} \cdot \bar{a} \leq 1,$$

and, by integration, we find

$$\left(1 - \frac{\epsilon^2}{2}\right)(s - s_1) \leq (\bar{x} - \bar{x}_1) \cdot \bar{a} \leq (s - s_k),$$

where $\bar{x}_1$ is the position vector at $s = s_1$. Since the central term in the above inequality approaches to a limit as the point of zero velocity is approached, s

cannot increase indefinitely but must approach a finite value, say s_0 . Applying the mean value theorem to each component of

$$\bar{x} - \bar{x}_0 = \int_{s_0}^{s} \bar{t}\, ds$$

separately, and using Eq. (19), we get

$$|(\bar{x} - (s - s_0)\,\bar{a}| < 3\,\epsilon\,(s_0 - s) \text{ for } s_0 \geq s \geq s_1, \tag{20}$$

since

$$u\bar{t} = \bar{u}, \tag{21}$$

The expansion of velocity into a Taylor series and the use of Eq. (21) leads to

$$\lim_{s \to s_0} \left[|\bar{a} \cdot (\nabla \bar{u})|\, t \right] = \lim_{s \to s_0} \bar{a} \cdot \nabla \bar{u} ,$$

or

$$\bar{a} \cdot (\nabla\, \bar{u}) = \lambda\, \bar{a},$$

where

$$\lambda = |\bar{a} \cdot \nabla\, \bar{u}|.$$

Hence we see by using Eq. (5) that the angular velocity of a line element in the limiting direction $\bar{a}$ is zero. Clearly, the above argument, with minor modifications, applies when s decreases on approaching the point of zero velocity.

Thus a streamline approaches the point of zero velocity in such a way that if its unit tangent vector approaches a limiting value a, the angular velocity of a line element along $\bar{a}$ is zero. This theorem shows that the question of whether or not the streamline whirls around a point of zero velocity is directly related to the angular velocity of line elements.

The above results were obtained for use in subsequent sections of this paper. It should be pointed out, however, that since these results throw light on the connections between the rate of rotation of line and surface elements, vorticity, curvature, and torsion of streamlines in a general way, they have a broader significance than many other theorems in this paper.

The dynamical significance of the angular velocities can be gauged from the observation that the dissipation in a Newtonian fluid of constant properties cannot be expressed in terms of invariants of vorticity, but is proportional to the following invariant of rotation tensor:

$$(4R_{i:jk}\, R_{i:jk} - 3R_{i:jj}\, R_{i:kk})/6,$$

as can be verified by using Eq. (7).

GEOMETRY OF STREAMLINES IN PLANE FLOWS

We shall examine in this section closed or spiralling streamlines in the vicinity of a point with zero velocity, in terms of angular velocities of line elements. The discussion is confined to plane flows which are, by definition, flows in which the motion of the fluid takes place in parallel planes. The velocity is assumed to be differentiable. Let an inertial observer be at rest relative to a given fluid particle. With the z axis normal to the plane of motion, the equations of streamlines, which lie in the plane of motion, are

$$dx/dh = u, \quad dy/dh = v, \tag{22}$$

where the velocity components u and v relative to the observer depend on coordinates x, y z and time t. The behavior of streamlines can be easily described if the velocities are linear in x and y. From the results of ordinary autonomous equations (Hurewicz, in 1958, for example) (18), one can describe the streamline behavior in terms of

$$S = \left(\frac{\partial u}{\partial x}\frac{\partial v}{\partial y} - \frac{\partial u}{\partial y}\frac{\partial v}{\partial x}\right) - \frac{1}{4}\left(\frac{\partial u}{\partial x} + \frac{\partial v}{\partial y}\right)^2 \tag{23}$$

If $(\partial u/\partial x)\ (\partial v/\partial y) - (\partial u/\partial y)\ (\partial v/\partial x)$ is different from zero, the necessary and sufficient condition for closed or spiralling streamlines is that S be positive at the given particle. If, in addition, the flow satisfies the continuity equation of an incompressible fluid, the streamlines are closed. It may be noted that nonzero vorticity is necessary but not sufficient for positive S.

The kinematic meaning of S, which we shall call swirl, can be readily understood. The angular velocity of a line element in the plane of motion can be seen as parallel to the z axis from Eq. (8). It is given by

$$\frac{\partial v}{\partial x}\cos^2\phi + \left(\frac{\partial v}{\partial y} - \frac{\partial u}{\partial x}\right)\sin\phi\cos\phi - \frac{\partial u}{\partial y}\sin^2\phi$$

$$= \frac{1}{2}\left[\left(\frac{\partial v}{\partial x} - \frac{\partial u}{\partial y}\right) + \left(\frac{\partial v}{\partial x} + \frac{\partial u}{\partial y}\right)\cos 2\phi + \left(\frac{\partial v}{\partial y} - \frac{\partial u}{\partial x}\right)\sin 2\phi\right] \tag{24}$$

for an element inclined at an angle ϕ with the x axis. Its maximum and minimum values are then

$$\frac{1}{2}\left[\left(\frac{\partial v}{\partial x} - \frac{\partial u}{\partial y}\right) \pm \left\{\left(\frac{\partial v}{\partial x} + \frac{\partial u}{\partial x}\right)^2 + \left(\frac{\partial v}{\partial y} - \frac{\partial u}{\partial x}\right)^2\right\}^{1/2}\right] \tag{25}$$

Their product is the swirl, while their sum is the z-component of vorticity. Note that positive swirl is associated with maximum and minimum angular velocities of the same sign, and hence with the absence of any line element having zero angular velocity in the plane of motion.

To extend the results of the linear case, let a whirl point be defined as a point $\bar{x}_0$ of zero velocity which has a segment of a streamline $\bar{x} = \bar{x}(h)$, $h_1 \leq h \leq h_2$ in each of its neighborhoods, satisfying the following conditions:

1. For any given unit vector $\bar{t}$, there is a point $\bar{x}(h)$ on the segment so that $\bar{x}(h) - \bar{x}_0 = k\bar{t}$ for some positive k.

2. $\bar{x}_1 = \ell \bar{x}_2$ for some positive ℓ, where $\bar{x}_1$ and $\bar{x}_2$ are the ends of the segment.

3. The segment does not pass through $\bar{x}_0$.

The definition essentially describes what is generally meant by streamlines whirling around a point. The main result in this section, which is believed to be new, is the following theorem.

Theorem I: Any point of zero velocity where the swirl is positive is a whirl point. Conversely, the swirl cannot be negative at a whirl point.

Some preliminary results are required for its proof. Let the point of zero velocity be chosen as the origin. The equations of streamlines in cylindrical coordinates are

$$dr/dh = u_r, \quad rd\theta/dh = u_\theta \quad . \tag{26}$$

The conditions on the segment of the streamline for a whirl point are then that r does not vanish anywhere on it, that for any given α there is a point on it with the angular coordinate $\alpha + 2n\pi$, n being an integer, and that θ_1 and θ_2 at the ends differ by a multiple of $2n\pi$. One can also estimate the velocity components by using the mean value theorem

$$\frac{dr}{dh} = \left.\frac{\partial u_r}{\partial r}\right|_{r = r_m} r, \quad 0 \leq r_m \leq r \tag{27a}$$

and

$$r\frac{d\theta}{dh} = \left.\frac{\partial u_\theta}{\partial r}\right|_{r = r_m} r, \quad 0 \leq r_m \leq r \; . \tag{27b}$$

Note that $\partial u_r/\partial r$ and $\partial u_\theta/\partial r$ are the rate of deformation and the angular velocity of a radial line element.

Now one can prove the first part of the theorem. If a neighborhood of the point of zero velocity is specified, we can choose a circular neighborhood of radius R within the given neighborhood such that the swirl is positive in the circle. This is possible because the swirl given by Eq. (23) is a continuous function.

The streamline through any point in the circle, except the origin, can be continued until it approaches a point of zero velocity or the circumference,

since it is an integral curve of the differential equations in Eq. (22) (Hurewicz [18]). It will be shown in the next section of this paper that velocity in the two-dimensional region of positive swirl cannot vanish at two points. Hence the streamline through any point other than the origin can be continued until it approaches the origin or the circumference. Now we want to show that a point can be chosen within the circle so that the streamline through it turns around by 2π before it approaches the origin or the circumference. Such a streamline will clearly provide a segment satisfying the definition of a whirl point.

Since the rate of deformation and the angular velocity of any radial line element appearing in Eqs. (27a) and (27b) are continuous functions, they take maximum and minimum values, say d_1, d_2, w_1, and w_2, in the circle. Hence we have

$$d_1 \geq (dr/dh)/r \geq d_2, \tag{28a}$$

$$w_1 \geq d\theta/dh \geq w_2 \tag{28b}$$

at any point in the circle of radius R. Since the angular velocity of a line element cannot vanish in a region of positive swirl, w_1 and w_2 are of the same sign. One obtains from Eqs. (28a) and (28b)

$$A \geq (dr/d\theta)/r \geq B, \tag{29}$$

where A and B are equal to d_1/w_2 and d_2/w_1 if w_1 is positive, or to d_2/w_2 and d_1/w_1 if w_1 is negative. Hence for any point (r,θ) on a streamline through (r_1, θ_1) in the circle, we have

$$A(\theta - \theta_1) \geq \ell n(r/r_1) \geq B(\theta - \theta_1). \tag{30}$$

If A and B are zero, the streamlines are circles and the origin is a whirlpoint. If A is zero, the streamline through any point in the circle cannot cross the circle, because r cannot increase and B is zero, so that A cannot approach the origin.

Suppose A is not zero. Consider a point (r_1, θ_1) with $r_1 = Re^{-2\pi|A|}$ inside the circle. If the streamline through the point touches the circumference, Eq. (30) would require that for the point on the circumference, $A(\theta - \theta_1) \geq 2\pi|A|$, so that θ and θ_1 differ by more than 2π. Such a streamline can provide a segment meeting the requirements of the whirlpoint. If, on the other hand, the streamline approaches the origin, B is different from zero and there is an intermediate point where $r = r_1 e^{-2|B|}$. Then, from Eq. (30) we have

$$-2\pi|B| \geq B(\theta - \theta_1)$$

In this case, the streamline also would provide a segment required for the whirlpoint. If A is zero, but B is not, the above argument can be applied to any point $r_1 \leq R$. Thus, in any event, the point of zero velocity where the swirl is positive is a whirlpoint.

Suppose the swirl at a whirlpoint is negative. Let the radial line $\theta = 0$ be chosen to coincide with the direction of a line element at the origin that has extremum angular velocity. Then one can see from Eq. (24) that a normal element at the origin will also have an extremum value of angular velocity. Let these angular velocities be denoted by w_0 and $w_{\pi/2}$. They will have opposite signs, as the swirl is assumed to be negative. The differentiability of velocity permits us to choose a neighborhood where the derivatives of velocity occurring in Eq. (24) at any point differ from the corresponding derivatives at the origin by less than one-sixth of $\min(|w_0|, |w_{\pi/2}|)$. Then the angular velocity of a line element in the direction $\theta = 0$ situated at any point in the neighborhood differs from the angular velocity of a parallel element at the origin by less than one-half of $\min(|w_0|, |w_{\pi/2}|)$. Hence the angular velocity of any line element in the direction $\theta = 0$ has the same sign as w_0, and similarly the angular velocity of a normal line element has the same sign as $w_{\pi/2}$. Now consider the segment of streamline in the neighborhood of the whirlpoint. If θ increases from θ_1 to θ_2 as h increases from h_1 and h_2, θ changes from values in the first quadrant to those in the second at some intermediate point and from the second to those in the third at some other intermediate point. Clearly, $d\theta/dh$ cannot be negative at these points. One can see with the help of Eq. (27b) that neither w_0 nor $w_{\pi/2}$ can be zero, and hence that swirl at the origin, being the product of w_0 and $w_{\pi/2}$, cannot be negative. A similar argument can be made when θ decreases as h increases from h_1 to h_2. This contradiction leads to the required result.

Some light is thrown on the question of whether or not the swirl can be zero at a whirlpoint by the conclusion that $(\partial u/\partial x)(\partial v/\partial y) - (\partial u/\partial y)(\partial v/\partial x)$ must be different from zero there, provided that all of the derivatives in the expression do not vanish simultaneously. To see this, consider the segment of streamline satisfying the requirements of the definition in any neighborhood of the whirlpoint. Now for any given unit vector $\bar{t}$, there are two points $\bar{x}_3$ and $\bar{x}_4$ such that $\bar{x}_3 = k_3\bar{t}$, $\bar{x}_4 = -k_4\bar{t}$ for some positive k_3 and k_4, and as a result

$$\bar{x}_3 \cdot \bar{n} = \bar{x}_4 \cdot \bar{n} = 0$$

for a unit vector $\bar{n}$ normal to $\bar{t}$. Then, by the mean value theorem,

$$(d\bar{x}/dh) \cdot \bar{n} = 0$$

at an intermediate point. Hence, in any neighborhood of the whirlpoint, there is a particle whose velocity is normal to any specified unit vector $\bar{n}$.

Suppose $(\partial u/\partial x)(\partial v/\partial y) - (\partial u/\partial y)(\partial v/\partial x)$ is zero at a whirlpoint. Then there is a nontrivial solution (a,b) to the following simultaneous equations

$$(\partial v/\partial x)a - (\partial u/\partial x)b = 0$$

$$(\partial v/\partial y)a - (\partial u/\partial y)b = 0,$$

and for any values of x and y,

$$a[(\partial v/\partial x)x + (\partial v/\partial y)y] - b[(\partial u/\partial x)x + (\partial u/\partial y)y] = 0.$$

Hence as (x,y) approaches the origin, the ratio $u:v$ approaches $a:b$. But if we choose the unit vector $\bar{n}$ in the direction of the vector (a,b), we find that no matter how small a neighborhood we choose, there is always a point where velocity is normal to (a,b).

If the continuity equation for an incompressible equation fluid is used, a stronger result can be obtained. Let a vortex point be defined as a whirlpoint where the value of ℓ in the second requirement of the streamline segment is unity. This ensures closed streamlines.

Theorem II: In the plane flow of an incompressible fluid, any point of zero velocity where the swirl is positive is a vortex point, and conversely, the swirl at a whirlpoint is positive if all the derivatives $\partial u/\partial x$, $\partial u/\partial y$, $\partial v/\partial x$, and $\partial v/\partial y$ do not vanish simultaneously.

Consider any point of zero velocity where the swirl is positive: then it is a whirlpoint according to Theorem I. Suppose the value of ℓ in the second requirement of the streamline is different from one. Then we can consider the two-dimensional region bounded by the streamline segment and the radial segment joining the end points of the streamline. Since the flux across the radial segment is zero on account of incompressibility, the tangential component of velocity must be zero somewhere on the radial segment, and Eq. (27b) then implies that angular velocity must vanish somewhere. But the neighborhood can be chosen to be so small that swirl is positive everywhere and the angular velocity of a line element cannot vanish. Hence follows the first part of the theorem. The second part follows from Theorem I and the conclusion that $(\partial u/\partial x)(\partial v/\partial y) - (\partial u/\partial y)(\partial v/\partial x)$ cannot vanish at a whirlpoint when the velocity derivatives do not vanish simultaneously.

Consider the curvature of streamline at a point where velocity is different from zero. We see from Eq. (20) that if the curvature is zero, a line element tangential to the streamline has zero angular velocity. Hence the curvature of a streamline cannot vanish in a region of positive swirl.

The geometrical behavior of streamlines, then, is decisively influenced by the angular velocities of line elements. The dynamic implications of these kinematic results will become clear in the following section.

DEFINITION AND GENERAL PROPERTIES OF EDDIES

The formulation of a clear idea of an eddy is prerequisite to a systematic study of the properties of eddies. Since they are often identified in experimental investigations by closed or spiralling streamlines, it is but natural to seek a formulation in terms of the angular velocities of line and surface elements whose intimate relation with the streamline geometry has been pointed out in the previous sections. This approach differs from the prevailing approach in which eddies are regarded a priori as regions of concentrated vorticity and no attempt is made to formulate an unambiguous notion of an eddy.

A fluid particle in a plane flow may be regarded as being in an eddy, depending on whether or not the streamlines, relative to an inertial observer which is at rest with the particle, possess the whirling property in the particle's vicinity. Alternatively, we may decide whether or not a particle is in an eddy on the basis of positive swirl or the absence of a line element having zero angular velocity in the plane of motion. Note that any line element normal to the plane and any surface element parallel to the plane have zero angular velocity.

Generalization to arbitrary three-dimensional flow is facilitated by the theorem of Thomson (14) and others (see the section, Analysis of Rotation, which was presented earlier in this paper). The theorem asserts that there is at least one line and one surface element having zero angular velocity. Note also that in flow $u = Ay$, $v = 0$, and $w = Az$, the line elements parallel to the x or z axis have zero angular velocity, and that there are planes in which line elements with zero angular velocity are absent although the streamlines do not show any whirling property. Consequently, it is necessary to examine the line elements in a chosen plane. Hence the following definition:

> A fluid particle is said to be in an eddy at a given instant if, at that time, all the line elements, which are parallel to a surface element of zero angular velocity, have nonzero angular velocity.

Any particle in a region of positive swirl in a plane flow is certainly in an eddy. In particular, any particle in a rigidly rotating fluid or the core of a Rankine vortex is in an eddy. It will be shown later that no fluid particle in a plane Couette flow is in an eddy.

The advantages of the above definition are many. Since the properties given in this section include connections with streamline geometry, vorticity, and low-pressure spots, the definition pinpoints a characteristic property of the phenomena. Furthermore, it provides a basis for deduction of properties and interpretation of experimental data. Several qualitative observations about the flow with eddies can be readily explained, as will be seen later. The analytical content of the definition can also be readily extracted in the form of the following theorem:

> *Theorem III*: A fluid particle is in an eddy at a given instant, if and only if its whirlicity $4M^3 + 27N^2$ is positive.

The theorem of Thomson (14) and others, as was described earlier, ensures that there is at least one surface element of zero angular velocity. With the z-axis normal to such a surface element, V_{zx} and V_{zy} vanish according to Eq. (12), and the angular velocity of a line element in the x-y plane is parallel to the z axis and is given by

$$[(V_{yx} - V_{xy}) + (V_{yx} + V_{xy}) \cos 2\theta + (V_{yy} - V_{xx}) \sin 2\theta]/2, \qquad (31)$$

θ being the angle made by the element with the x axis. The swirl in the x-y plane, being a product of maximum and minimum velocities, is $\alpha - \beta^2$, where

$$\alpha = (V_{xx} V_{yy} - V_{xy} V_{yx}), \quad \beta = V_{zz}/2 = (V_{xx} + V_{yy})/2. \tag{32}$$

Since the invariants M and N are given by

$$\begin{aligned} M &= V_{xx} V_{yy} + V_{yy} V_{zz} + V_{zz} V_{xx} - V_{xy} V_{yx} = \alpha - 4\beta^2, \\ N &= V_{zz} (V_{xx} V_{yy} - V_{xy} V_{yx}) = 2\alpha\beta, \end{aligned} \tag{33}$$

the whirlicity can be expressed as

$$4M^3 + 27N^2 = 4 (\alpha - \beta^2) [(\alpha - \beta^2) + 9\beta^2]^2. \tag{34}$$

Hence the whirlicity is positive if, and only if, the swirl $\alpha - \beta^2$ is positive and the theorem follows.

Since the whirlicity is an invariant under Galilean transformations, an eddy in one inertial frame is also an eddy in any other.

Unlike vorticity, the whirlicity is nonlinear. Whereas the superposition of two irrotational flows always leads to an irrotational flow, flows with zero whirlicity behave differently. Two plane Couette flows in perpendicular directions ($u = Ay$, $v = w = 0$; $v = -Ax$, $u = w = 0$), when superposed, lead to rigid body rotation. It is to be expected then that an unstable flow with a wavelike disturbance may have eddies, although neither the streamlines of the flow nor those of the disturbance may display any whirling property. Many flows and disturbances analyzed in the hydrodynamic stability theory have this property.

It is known that the appearance of eddies transforms the flow in a marked way and that the dynamic and thermodynamic consequences of the transition are unmistakable, whereas the picture of concentrated vorticity does not give any clue to the difference in kind between the flows with eddies and those without them (the definition given above fills this lack). Let the z axis be chosen as in the proof of Theorem III. Now if the whirlicity is zero or negative at a point, there is a line element at the point in the x-y plane with zero angular velocity, and x the axis can be chosen in its direction. Then Eqs. (8) and (14) imply that $\partial v/\partial x$, $\partial w/\partial x$, and $\partial w/\partial y$ are zero, so that the convective part of acceleration can be written in the canonical form:

$$u\partial u/\partial x + v\partial u/\partial y + w\partial u/\partial z$$

$$v\partial v/\partial y + w\partial v/\partial z$$

$$w\partial w/\partial z.$$

If, on the other hand, we similarly examine a particle in an eddy, the form for the convective part of acceleration would be

$$u\partial u/\partial x + v\partial u/\partial y + w\partial u/\partial z$$

$$u\partial v/\partial x + v\partial v/\partial y + w\partial v/\partial z$$

$$w\partial w/\partial z.$$

Thus the inertia terms introduce a stronger coupling between the equations in the presence of eddies. This coupling offers an explanation for larger transfer of momentum and energy in the presence of eddies.

Consider a surface on which fluid velocity vanishes everywhere. Clearly, the angular velocity of an element of such a surface is zero, and so also is the angular velocity of a tangential line element. The arguments used in Theorem III lead to the conclusion that particles on such a surface cannot be in an eddy. The significance of the conclusion stems from the no-slip condition. If a stationary, impervious solid is introduced in an eddy, the fluid particles at the solid boundary would cease to be in the eddy and the value of whirlicity would decline in the neighborhood of the solid boundary. Notice that the viscosity of the fluid enters in the argument only through the no-slip condition and that the geometry of the surface does not enter the picture at all. Hence, it can be concluded that if a stationary, impervious, thin bar is introduced in an eddy of a fluid of low viscosity such as water, there will be a noticeable change in the flow, although the diameter of the rod may be very small in comparison with the diameter of the eddy. A crucial experiment to test this conclusion was made at the University of California, Berkeley. A steady draining vortex was generated in a vertical circular cylinder of 11-1/2 inches diameter, turning at 20 rpm and having an axial hole of one-inch diameter. The apparatus is sketched in Fig. 2 and was described by Einstein and Li in 1955 (19). The depression of the water surface indicates roughly the pressure distribution in a horizontal plane, as vertical accelerations are low. Low-pressure gradients in the horizontal plane are associated with small slopes of the free surface. If the introduction of a bar reduces the whirlicity and thereby constrains the whirling motion, its consequences on the free surface would be apparent. When a bar of 1/8-inch diameter was kept near the boundary of the drain hole, the depression in the water surface reduced by 70%, although the cross-sectional area of the bar was less than 3% of the area of the hole (Fig. 3). When it was placed at the axis of the hole, the depression was reduced by 30%. Comparable reductions were obtained with rectangular and square bars. Such noticeable effects of thin, solid members on eddies have also been observed in the wake of a bluff body (Roshko, 1954) (20) and in the leading-edge vortex from a delta wing (Harvey, 1962).

This constraining effect has to be taken into account in the interpretation of data obtained by small probes in eddies, and the interference of the flow may be considerably larger than what one would expect from the probe size. The constraining effect can also be used as an inexpensive and highly effective method of control of vortices near the outlets of reservoirs, or the intake chambers of pumps (J. P. Berge, 1966).

It is to be expected that vorticity cannot vanish in an eddy; for no line element has zero angular velocity in a particular plane, and hence the normal component of vorticity, being the average of the angular velocities of all such

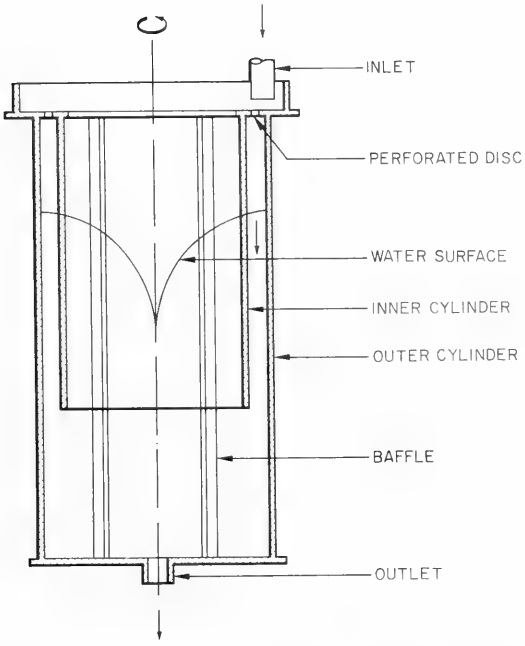

Fig. 2 - Apparatus for creating a draining vortex

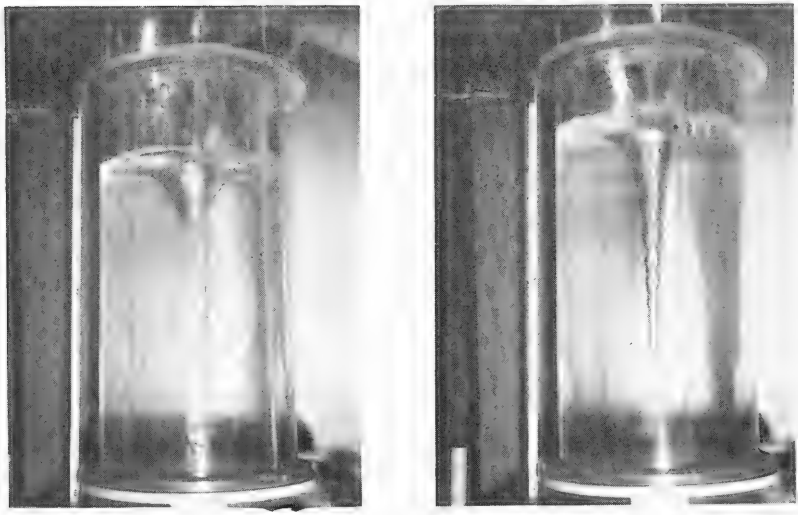

(a) Draining vortex

(b) The interference of a thin rod with the vortex

Fig. 3 - Draining vortex experiment

line elements, cannot be zero. Eddies may thus arise in a region of sensible vorticity such as the boundary layer or the wake of a body.

One may also expect that if the velocities in the vicinity of a particle are parallel, it cannot be in an eddy. With the z axis in the direction of the velocities, V_{xy}, V_{xz}, V_{yx}, and V_{yz} can be seen to be zero and so also whirlicity. Hence rectilinear flows, including plane Couette and Poisuelle flows, do not have any eddies.

It should be remarked in passing that an eddy is thought to be a connected set of particles of positive whirlicity. For the sake of definiteness, we will take it to be a maximal connected set. This avoids the possibility of intersection of eddies.

Consider the boundary of an eddy where whirlicity vanishes. The velocity of propagation normal to itself is then given by

$$\partial(4M^3 + 27N^2)/\partial t + c|\nabla(4M^3 + 27N^2)| = 0,$$

or

$$c = \frac{2M^2\,\partial M/\partial t + 9N\partial N/\partial t}{|(2M^2\nabla M + 9N\nabla N)|} \tag{35}$$

if the denominator is different from zero. Since this velocity will in general be different from fluid velocity, particles may enter or leave an eddy.

Now let us consider eddies of an incompressible fluid. The invariants M and N reduce to

$$M = -\nabla\bar{u} : \nabla\bar{u}/2 = -(\nabla \cdot \dot{\bar{u}})/2 , \tag{36a}$$

$$N = \det|\nabla\bar{u}| . \tag{36b}$$

Thus M is proportional to the divergence of acceleration, whereas N^2 is a local measure of three-dimensionality of the flow. If N is zero, there exists a non-zero vector $\bar{a}$ such that $(\nabla\bar{u})\bar{a}$ vanishes and the flow in the vicinity of the particle relative to an observer travelling with the particle is normal to $\bar{a}$. Note that three-dimensionality always favors the occurrence of eddies. This conclusion is compatible with the observations of more prevalent eddies in three-dimensional turbulent flows than in two-dimensional flows.

Since the equations of motion of a Newtonian fluid of constant properties are

$$\rho\dot{\bar{u}} = -\nabla p + \rho\bar{F} + \mu\nabla^2\bar{u} , \tag{37}$$

ρ, μ, p, and $\bar{F}$ being respectively, density, coefficient of viscosity, pressure, and body force, the invariant M can be calculated with the help of a continuity equation as

$$M = (\nabla^2 p - \rho\nabla\cdot\bar{F})/2 . \tag{38}$$

Hence the characteristic feature of the distribution of pressure and body force is such that $(\nabla^2 p - \rho \nabla \cdot \bar{F})$ is greater than a certain datum which is determined by the local three-dimensional character of the flow, i.e., $-3\rho(2N^2)^{1/3}$. The datum value can be readily calculated in certain flows such as plane flows and axisymmetric flows without tangential velocity, because elements of certain planes are known to have zero angular velocity. In any event, a fluid particle is in an eddy if $\nabla^2 p - \rho \nabla \cdot \bar{F}$ is positive. When gravitational force is the only body force, this sufficient condition reduces to positive $\nabla^2 p$. Regions where minimum pressure occurs will particularly have eddies. This is fully supported by observation.

Eddies in plane flows have interesting properties. Because a surface element parallel to the plane of motion has zero angular velocity, the characteristic kinematic property of an eddy is positive swirl or the absence of a line element in the plane of motion having zero angular velocity. The component of vorticity normal to the plane cannot be zero in an eddy, and the circulations along any two closed curves in the plane within an eddy have the same sign. this property can be used to distinguish a clockwise eddy from a counterclockwise eddy. Also, Theorem I implies that a point of zero velocity in an eddy is a whirlpoint. The results in the previous section of this paper further imply that the curvature cannot vanish in an eddy. The center of curvature of a streamline in an eddy remains on one side, as the curvature is continuous and finite if the velocity is differentiable and nonzero. Convex streamlines are thus to be expected in eddies. Indeed, the computations of Yih in 1959 and 1960 (21,22) and Michalke in 1964 (9) show such streamlines.

If velocity vanishes at two points in the plane of motion, $\partial v/\partial x$ vanishes at an intermediate point according to the mean-value theorem, the x axis being parallel to the line joining the points. The zero angular velocity of a line element at the intermediate point parallel to the line ensures zero or negative swirl. Hence if the two-dimensional cross section of the eddy is convex, velocity cannot be zero at two points in the cross section.

The intimate relation between the closed streamlines and plane eddies of an incompressible fluid is brought out by Theorem II. If a particle in an eddy has zero velocity, it is a vortex point. Conversely, a vortex point is in an eddy if the derivatives $\partial u/\partial x$, $\partial u/\partial y$, $\partial v/\partial x$, and $\partial v/\partial y$ do not vanish simultaneously.

The dynamic characteristic property of a plane eddy of a Newtonian fluid of constant properties is readily obtained from Eq. (38) and from the observation that N is zero everywhere. Thus a fluid particle in such flow is in an eddy if, and only if, $\nabla^2 p - \rho \nabla \cdot \bar{F}$ is positive. When gravity is the only body force, superharmonic character of pressure is then the essential feature. If pressure is minimum at a point within a region in the plane of motion, then there is an eddy in the region, because $\nabla^2 p$ is positive somewhere in the region. The optical method of identifying eddies by locating low-pressure spots in waterflows is justified by the above argument.

Eddies in axisymmetric flows without a tangential velocity component have analogous properties, although the different form of the continuity equation

$$\partial u_r/\partial r + u_r/r + \partial u_z/\partial z = 0 \tag{39}$$

introduces some differences. Since any element of a meridian plane has zero angular velocity, the positive value of swirl $\alpha - \beta^2$ is a characteristic property of an eddy where α and β as given by Eq. (32) can be expressed in the cylindrical coordinates

$$\alpha = (\partial u_r/\partial r)(\partial u_z/\partial z) - (\partial u_r/\partial z)(\partial u_z/\partial r),$$
$$\beta = -(\partial u_r/\partial r + \partial u_z/\partial z)/2 = u_r/2r. \tag{40}$$

Hence, from Eqs. (33) and (38),

$$\nabla^2 p - \rho \nabla \cdot \bar{F} = 2\rho(\alpha - \beta^2) - 6\rho\beta^2.$$

The characteristic dynamic property of such an eddy is then

$$\nabla^2 p - \rho \nabla \cdot \bar{F} > -3\rho (u_r/r)^2/2 \tag{41}$$

In particular, a particle at rest is in an eddy only if $\nabla^2 p - \rho \nabla \cdot \bar{F}$ is positive.

Since Theorems I and II can easily be extended for the axisymmetric case, all the kinematic properties, with minor modifications, are valid for axisymmetric situations.

CONCLUDING REMARKS

Mathematical representation for the angular velocity $\bar{W}$ of a fluid line element and of the angular velocity of a fluid surface element are derived here. These angular velocities are shown not to depend on expansion $u_{i,i}$. Vorticity, on the other hand, is shown to be three times the average of either velocity. The relation of curvature of the fluid line element, its velocity, and its angular velocity is derived, but to complete this fundamental relation it is necessary to develop the equivalent of Frenet's formula in terms of the Eulerian derivative. This has recently been obtained by Paul Lieber and his former student, Kirit Yajnik, on the basis of the work presented in this paper. The results bring out the differential-geometrical features of torsion of the fluid line element. The behavior of the line element in the vicinity of a singular point is decisively influenced by the angular velocity $\bar{W}$ of the line elements at the singular point. The new definition of an eddy given in the present paper and its relation to whirlicity as it is defined here, has been deduced. In Theorem 3, which gives the relation between whirlicity and eddy, we have considered whirlicity to be positive. However, by considering it to be zero and/or negative, interesting results have also been recently obtained by Lieber and his student, which evidently concern the development of secondary and turbulent flows. These recent results which rest incisively on the results of the present paper, will be published in due course, and will point up the significance of the results presented here.

ACKNOWLEDGMENTS

This investigation was carried out mostly at the University of California, Berkeley, for the Ph.D. dissertation of the first coauthor of this paper, under the supervision of the second (Yajnik, 1964) (17,23). The financial support provided by the Office of Naval Research is deeply appreciated. The experimental facilities provided by the Hydraulics Laboratory are also acknowledged. The authors would like to thank Professors John Wehausen and Hans Einstein, and Doctors Lyle Macros and Shrikant Desai for their assistance and discussions. The expression of swirl in Eq. (23) was constructed as an extension of a simpler one constructed by Lyle Macros in 1962 (24).

REFERENCES

1. von Kármán, T., Nachr. Akad. Wiss. Goettingen, Math. Physik. Kl., 509-517, 547-556 (1911, 1912); also, collected Werke 1, 324-330, 331-338

2. Taylor, G., Rept. Mem. Adv. Com. Aeron., No. 598 (1918); also Scientific Papers 2, 96-101, Cambridge, 1958

3. Oseen, C., Arkiv Math. Astron. Cch. Fysik 7 (1911)

4. Hamel, G., Jahrber. Deut. Math. Verein. 34 (1916)

5. Rott, N., ZAMP 9b, 543-553 (1958)

6. Küchman, D., J. Fluid Mech. 21, 1-20 (1965)

7. Moffatt, J. Fluid Mech. 18, 1-18 (1964)

8. Wille, R., Advan. Appl. Mech. 6 (No. 11), 273-287 (1960)

9. Michalke, A., J. Fluid Mech. 19, 543-556 (1964)

10. Hung, T.K. and Macagno, E., La Houille Blanche, 391-402 (1966)

11. Macagno, E. and Hung, T.K., J. Fluid Mech. 28, 43-64 (1967)

12. Cauchy, A.L., Ex. d'Abal. Phys. Math. 2, 302-330 (1841); also, Oeuvres 12 (2), 343-377

13. Truesdell, C., "The Kinematics of Vorticity," Indiana University Press, 1954

14. Thomson, W. and Tait, P., "Treatise on Natural Philosophy," Cambridge, 1867

15. Bertrand, J., C.R. Acad. Sci. 67, 1227-1230, Paris, 1868

16. Ericksen, J.L., J. Wash. Acad. Sci. 45, 65-66 (1955)

17. Yajnik, K., Ph.D. dissertation, University of California, Berkeley, 1964

18. Hurewicz, W., 1958 Lectures on Advanced Ordinary Differential Equations, MIT Press and Wiley

19. Einstein, H.A. and Li, H., La Houille Blanche 10 (No. 4), 483-496; also, Proc. Heat Trans. Fluid Mech. Inst. (1951)

20. Roshko, A., NACA Technical Note 3169 (1954)

21. Yih, C.S., J. Fluid Mech. 5, 36-40 (1959)

22. Yih, C.S., J. Fluid Mech. 9, 1961-1974 (1960)

23. Lieber, P. and Yajnik, K., Report MD-63-7, Institute of Engineering Research, University of California, Berkeley, 1964

24. Macros, L., Ph.D. dissertation, University of California, Berkeley, 1962

* * *

II—Aspects of the Principle of Maximum Uniformity: A New and Fundamental Principle of Mechanics

Paul Lieber
University of California
Berkeley, California

INTRODUCTION

A comparative study of the principles of classical mechanics has revealed that they are only conditionally equivalent, and that questions concerning their equivalence and completeness cannot be put with meaning, without naturally evoking a new concept pertaining to the existence in nature of categories of information (1). The emergence of this concept in this study, shows that the equivalence or nonequivalence of the principles of mechanics, considered as propositions about the world of mechanical expérience, should be decided according to the nature of the information which they do and can render explicit about it.

The observations and conclusions noted above, were developed by focusing attention on the principles of Newton, Gauss, and Hertz. In so doing, it was demonstrated that general and fundamental global information on the distribution of internal forces in many-body systems, which is rendered explicit and without integration by using the principles of Gauss and Hertz, at present appears inaccessible in terms of the principles of Newton (2). This information is obtained within the edifice of the principles of Gauss (3) and Hertz (4), by reintroducing and underlining therein the concept force, which they sought to eliminate as a primitive notion, by its geometrization in terms of geometrical constraints. This was done for a nontrivial class of mechanical systems which included the gas model used by Maxwell, by first establishing and then using a fundamental connection between nonholonomic, unilateral, geometrical constraints and the impenetrability of matter (Refs. 5 through 11). In so doing it was found that the primitive role ascribed by Newton to the concept force is linked with the primitive concept of the impenetrability of matter, conceived here as the physical basis for the geometrization of force in terms of the geometrical constraints as used by Gauss and Hertz. That is, the ultimate ontological, geometrical property by which matter evokes its being and thus its existence in space-time, is local impenetrability, and it is this property of matter and evidently only this property which can account for the existence in nature of stringent geometrical constraints. Impenetrability of matter is accordingly envisaged here as an

ontological-geometrical property of *position* (local property) rather than as a property of extension.*

The Principle of Maximum Uniformity was first established† in Ref. 2 by generalizing (to all classical mechanical systems) a theorem obtained on a global-positive definite measure of the internal forces for a particular class of mechanical systems. The conception of the principle of maximum uniformity ascribes to the force which is designated by the symbol $\overline{F}$ in Newton's propositions a much more fundamental and universal aspect in nature, than it does to the terms which pertain to the acceleration of a material particle upon which the force is impressed. Accordingly, the restricted covariance of the propositions of classical mechanics to Galilean frames, derives from the acceleration-dependent terms, and not from what is symbolically represented by $\overline{F}$ in Newton's law which expresses the total connection between a particle endowed with an inertia 'm' and the universe in which it exists.

This way of thinking about $\overline{F}$, ascribes to it the same role as does Mach's principle to the inertia of a material particle, and consequently bestows upon it an equal significance. This allows the reconciliation of a principle of universal correspondence with Bohr's correspondence principle, by ascribing all forces in nature, including those which emerge in the domain of classical mechanics to the immutable processes in nature from which the dimensional universal constants emanate. In this way, the principle of maximum uniformity is directly extended to every domain of natural phenomena (nonclassical and classical), and all forces in nature which are posited to sensation and sense-awareness are thus conceived as the manifestations of this principle.

The principle of maximum uniformity can be formulated in such a way that it embraces in addition to the equilibrium propositions of classical mechanics, a general stability principle which naturally accommodates chronological time and consequently implies historical commitment.

The concept of nonuniformity refers to strictly intensive properties of space-time structure. These have familiar manifestations which include asymmetry, nonhomogeneity, isotropy, structure, curvature, and the number of parameters necessary for the description of a phenomenon and the gradients of these parameters. Other examples include the impression of a fossil, printing, labelling, symbols, alphabet, and language. Force and information are of course outstanding examples. All of these are aspects of nonuniformity and would therefore be interconnected by a general proposition which pertains to, and conditions, a global measure of a fundamental aspect of nonuniformity in nature.

*This in effect establishes within the edifice of classical mechanics the impenetrability of matter as the physical foundation of force; and the geometrical constraints as an (geometrical) intermediary between force and impenetrability; and accordingly as a geometrical manifestation of their ontological connection.

†This principle was first established in (2) in a restricted sense and has since been generalized as it is presented in this paper.

As the concept nonuniformity refers to an intensive and general aspect of nature, it is not restricted to particular scales and therefore gives a basis for unifying phenomena that depend simultaneously on many scales. A principle which restricts a global measure of uniformity is therefore equivalent to a law that conditions, and thus connects, phenomena which are described and coordinated over a large range of space-time scales. Accordingly, the principle of maximum uniformity leads naturally to the concept of control centers which are seated in restricted space-time domains, and which control and organize the function of matter extending over much larger domains of space and time. The principle of maximum uniformity implies that these control centers are dominant sites of action in a global domain which it conditions.

To evolve concepts necessary for comprehending the nature and function of control centers and for formulating general propositions which condition nonequilibrium thermodynamical processes, it is necessary to find a way simultaneously to consider, condition, and thus connect natural phenomena which exist and which are coordinated over a large range of space-time scales. Only in this way can we expect to gain an insight into the nature of these centers which evidently are universal aspects of nature. They are of course phenomenologically and strikingly displayed in the performance of living materials, by their facility to structure, organize, and coordinate the functions of matter which extends over a large range of space-time scales. The principle of maximum uniformity conceived as a generalization of explicit information, obtained as a theorem on the distribution of internal forces for a class of dynamical systems, does provide a conceptual framework for unifying and thereby interconnecting phenomena coordinated over a large range of space and time scales. It also provides a basis for seriously attempting a formulation of propositions governing strongly nonequilibrium thermodynamical systems.

Finally, this paper will consider the principle of maximum uniformity as a basis for formulating a general proposition pertaining to nonequilibrium thermodynamics, by citing the correspondence between the mechanical concept 'force' and the thermodynamical concept 'availability,' each conceived here as particular manifestations of the principle of maximum uniformity. Certain hydrodynamical aspects of this principle and its role in the conception and application of variational principles in hydrodynamics will also be presented.

THEORETICAL CONSIDERATIONS

The present paper is the first of a series concerned with the identification of various aspects of evolution and their connection with a universal evolutionary process which emanates from irreducible and universal processes, identified here with the Dimensional Universal Constants of Nature. This paper is specifically concerned with the nature of force, equilibrium, nonuniformity, and stability, envisaged here as particular aspects of evolution which is conceived as a universal process that reconciles everywhere in nature, constancy, and change.

An outline will be given of the ideas and reasoning which led to the conception of a proposition that may prove to be a general law of nature, fundamentally

endowed with aspects of evolution. This proposition embraces the laws of classical mechanics, a general stability law, historical thrust and commitment, and information relevant to the formulation of a theory conditioning strongly non-equilibrium thermodynamical processes. The stability law so obtained bears the same kind of relation to stability, envisaged here as a general aspect of the performance of classical mechanical systems, as do the laws of classical mechanics to another equally general aspect of their performance — equilibrium.

The conception of the general proposition which embraces this stability law is inextricably linked with a conception of the nature of force. By this conception, force is the universal and most fundamental global aspect of nonuniformity posited in nature to sense perception and sense awareness, and from which all sensation, experience, information, and consequently knowledge ultimately originate. In the particular case of classical mechanics, force is here conceived of as the universal manifestation in sensation of global nonuniformity in nature, i.e., as the resultant of all nonuniform connections that exist between an inertial body instantaneously situated at a particular location and the universe in which it is contained. From these considerations it follows that the dynamical aspect of classical mechanics (more specifically, the kinematical aspect), which is based on a conception and description of processes ascribed to immutable bodies in motion, is significantly more restricted and consequently less fundamental than is the aspect of nature symbolically designated by $\overline{F}$ in Newton's propositions. I use the word designated, rather than represented in order to emphasize that this symbol, as it is used in classical mechanics, is not brought into correspondence with the anatomy and structure of nature's space-time manifold.

A critical examination of Newton's formulation and use of the known laws of classical mechanics does in fact suggest that he may have also tacitly conceived of force as an ultimate and global aspect of nature, and of his law of motion as a relationship between this ultimate aspect of nature and the motion of a body endowed with inertia. This point of view differs essentially from that taken by most of his followers as well as from a consensus among contemporary scientists who choose to interpret his law of motion as a definition of force. According to the ideas of this paper, force as designated by the symbol $\overline{F}$ in Newton's propositions, in fact dominates the established laws of classical mechanics which are here understood to express only some and consequently not all of its fundamental aspects in nature. According to this view $\overline{F}$ assumes the fundamental and dominant role in Newton's propositions. It dominates the dynamical term appearing in Newton's law of motion, which expresses only one of its particular manifestations within the domain of classical mechanics, and consequently does not define it. Indeed, by this symbol, Newton implicitly designated the resultant and thus total connection between a body endowed with inertia and the universe in which it exists. In so doing he implicitly assumed that this connection is independent of the frame of reference in which the motion of the body is described and calculated. This is tantamount to postulating by implication that the global aspect of nature symbolically designated by $\overline{F}$, and the connection it represents between a body and the universe, is covariant under all coordinate transformations. By treating force in this way Newton evidently displayed humility and wisdom. Humility, because he instinctively realized that the nature of the global connection between a body and the universe in which it exists is the most fundamental and least understood aspect of mechanics; and wisdom, by

treating force as primitive and thereby not imposing arbitrary restrictions on what is not understood of it. The interpretation given in the present paper to force as it appears in the propositions of classical mechanics is not presented in Newton's writings, but rather is inferred here from its usage and the way the symbol $\overline{F}$ is formally treated in his propositions. From the above considerations it follows that the global connection designated by $\overline{F}$ and called force, has the same stature in classical mechanics, as does inertia interpreted according to Mach's principle, according to which inertia is also a manifestation of a global connection between a body and the universe — a connection which however is characterized by a scalar, and is therefore intrinsically endowed with high uniformity.

What is strictly local in Newton's propositions is the kinematical content on which their dynamical aspect is based. It is this dynamical and local aspect which restricts their covariance to inertial frames and consequently limits their generality. From this it also follows that it is naive to interpret Newton's law of motion as a definition of force, as it is nonsense to define a fundamental aspect of nature that has unrestricted covariance, in terms of an aspect whose covariance is limited to inertial frames. We see here again, from this point of view, that force does in fact dominate the laws of classical mechanics.

These considerations show that in classical mechanics, the presence of a resultant force impressed by the universe on an inertial body which is consequently not free, implies a nonsymmetrical and thus nonuniform connection between the body and the universe. When the connection between an inertial body and the universe is symmetrical and thus uniform — in the particular sense that individually impressed forces cancel vectorially — the body is then said to be free according to the established laws of classical mechanics and consequently moves according to Galileo's principle. We shall show in the section titled 'Hierarchies of Uniformity' that there in fact exists a hierarchy of free bodies, i.e., bodies which can with meaning be distinguished as being more or less free, but all of which are equivalent and therefore not distinguishable by the established laws of classical mechanics.

These and other considerations concerning the nature of force made within the framework of classical mechanics are sufficient to demonstrate that *all forces* in nature may be conceived of as manifestations of the existence in nature's space-time manifold of nonuniform connections between inertial bodies and the universe. According to this thinking, forces that are revealed in the domain of classical mechanics emerge from the same ultimate and universal processes in nature as do all other forces. Force, thus conceived as the universal manifestation of nonuniformity in the space-time manifold posited to sense-perception and to inertial bodies embedded in this manifold, brings into universal correspondence the various domains of physical theory which we have by convention learned to distinguish as classical and modern. These ideas and considerations are particularly designed to point out the fundamental connection between nonuniformity in nature and in force, and to establish the thesis that force is the universal manifestation of these nonuniformities invoked in sensation and experience.

I shall now introduce the observations and ideas which led me to the conception of the principle of maximum uniformity in which force is conceived as the fundamental physical aspect of nonuniformity. The identification of a natural law is not an exercise in formal logic, nor is what its propositions assert, provable. General propositions about nature are testable only by experience — by what they predict and explain of it. In the present case the principle of maximum uniformity was discerned by fully generalizing explicit global information which was obtained as a theorem for a class of dynamical systems, by suitably modifying and using Gauss's and Hertz's formulations of the principles of classical mechanics (2). This information pertains to a global, positive, definite scalar measure of the internal forces generated at each instant within such a system. The modifications of the Gauss-Hertz variational principles of mechanics which render this general information explicit and without quadrature, consist of ascribing to force the dominant role in mechanics, and of identifying all forces in nature with an ontological-geometrical basis for the production of stringent geometrical constraints, which were in Refs. 2, 6, and 9 originally conceived to emerge from the impenetrability of matter understood as a property of position. This information, which bears directly on the fundamental problem of continuum mechanics, has not been made explicit, and as far as I see *cannot* be made explicit by Newtonian mechanics in which the only representation given to force in its propositions is vectorial. This means that in the significant sense of information-rendering, the various formulations of the principles of mechanics are only conditionally equivalent. This development led me inexorably to the concept of 'Categories of Information,' in terms of which questions concerning the equivalence and nonequivalence of various formulations of the principles of mechanics can be rationally examined and resolved. This led to identification of eleven distinct yet related categories of information, by examples derived from familiar as well as more sophisticated aspects of experience. Once cited, these examples invoke consensus (1).

The global information so explicitly obtained as a theorem on the distribution of internal forces, asserts that a positive, definite *scalar* measure of all the internal forces is *instantaneously* less for the actual motion, than it is for any other motion which satisfies the initial conditions and the geometrical constraints (as well as the external forces) which are instantaneously impressed upon the dynamical system. This theorem was established for a particular (nontrivial) class of dynamical systems. For this class, the scalar measure of the internal forces can be directly interpreted as a global measure of nonuniformity in momentum space.

The principle of maximum uniformity as it pertains to classical mechanics and classical continuum mechanics was obtained by (a) interpreting the information obtained from the above theorem as a particular aspect of a general law which holds in all mechanical systems, and (b) introducing the concept of conditionally stringent geometrical constraints and relating these to material properties through which they are implemented in nature. This brings the principle of maximum uniformity into correspondence with the thermodynamical aspects of the equations for the constitution of various materials, and relates the idea of conditionally stringent geometrical constraints to uncertainties in the initial conditions from which historical commitment, causality, and a general stability principle naturally emerge.

The phenomenological description of the performance of classical mechanical systems, reveals two general and mutually independent characteristics; equilibrium and stability. The known propositions of classical mechanics refer strictly to equilibrium, by invoking the condition that forces be instantaneously in equilibrium everywhere and for all time in the system. This is their information content. They report nothing of stability which is an equally general and fundamental aspect of the behavior of classical mechanical systems. The laws of mechanics give but limited expression to the principle of maximum uniformity by asserting that the forces acting everywhere in a system sum vectorially to zero in all directions. This restriction allows a multiplicity of directional and spatial distributions in the magnitude of the forces impressed upon a body, but without exercising a condition on preferred distributions which the stability principle presented here, in fact, does.

Concerning the Nature of Evolutionary Adaptation

The considerations noted above help demonstrate that force, equilibrium, and stability are particular manifestations of an overriding tendency in nature to increase a global measure of uniformity identified with the global structure of the space-time manifold. This process is envisaged here as universal and conditioned by the principle of maximum uniformity, with the following postulates: that force is the instrument for increasing uniformity in nature, or what is equivalent — the instrument for effecting reduction of global nonuniformity existing in the space-time manifold; that all forces in nature emerge from these global nonuniformities, and constantly act to reduce them; that forces are the universal manifestations of nonuniformities in nature insofar as they are directly posited to sensation.

Evolutionary adaptation is envisaged here as a universal aspect of all processes in nature; an aspect which reconciles constancy and change in all of their ramifications in natural phenomena. The thrust of evolutionary adaptation, so conceived, derives from the ultimate processes embedded in the space-time manifold, which drive and structure the manifold by irreversible connections that must necessarily exist between these ultimate processes and the manifold. The irreversible connections are implied by the immutability of these ultimate processes, called here the universals, as they are reflected in and revealed by the 'Dimensional Universal Constants of Nature,' with which they are here identified.

The universal adaptive process described above has been conceptually identified with and has emerged from a conceptual model of nature's space-time manifold that is endowed with certain essentially ontological features inferred from the dimensional universal constants (7). These ontological characteristics were independently discerned in a concurrent study initiated in 1947, which is based on Gauss's and Hertz's formulations of the principles of classical mechanics. Both Gauss and Hertz were motivated by a quest to understand the nature of force by attempting to establish force on a strictly geometrical foundation. This endeavor was initiated by Gauss in 1829 and culminated at the turn of the century in Hertz's last and monumental work entitled "Principles Of Mechanics." In this profound and beautiful work Hertz formally constructs a 6N

dimensional Euclidean manifold in which the motion and state of a classical mechanical system consisting of N bodies free of prescribed forces, are described and represented. Hertz restricts the admissible motions and states of the mechanical system, by formally subjecting the coordinates of its bodies to constraints which in the most general case are considered as nonintegrable and therefore nonholonomic. As the application of these geometrical constraints to a body restricts its freedom geometrically, these restrictions must emerge in the Newtonian scheme as forces.

The study based on the Gauss-Hertz formulations* has produced two results which bear on the conception of the principle of maximum uniformity and on the identification of a physical, i.e., of an ontological-geometrical basis for the production of actual, stringent, holonomic as well as nonholonomic constraints in nature's space-time manifold. This ontological-geometrical basis gives physical support and justification for the existence in nature of the geometrical restrictions which Hertz used to effect a formal reduction of force to geometry, and serves to identify the formal representations he gave to nonholonomic constraints, with experience and thus with nature.

The same study revealed that Hertz's construction, in which he formulated a general law governing the motion of forceless mechanical systems subjected to nonholonomic geometrical constraints, and which he showed renders valid all previously known formulations of the laws of classical mechanics, also accommodates the formulation of a new and general stability law cited above. This law which bears the same kind of general relation to stability as the established laws of classical mechanics do to equilibrium, is found to be independent of the known laws of mechanics and to embrace fundamental and general information not included in these laws. This information bears on historical thrust and commitment and derives from an adaptive-evolutionary process ascribed directly to the geometrical restrictions which impress nonuniformities on the space-time manifold, and from which all forces are understood here to emerge. This entails the identification and classification of holonomic and nonholonomic ontological-geometrical constraints into the following types: (a) Active Stringent Constraints, (b) Passive Stringent Constraints, and (c) Conditionally Stringent Passive Constraints. This classification led naturally to the idea that the annihilation of conditionally stringent passive constraints which are ascribed here to universal congruence restrictions impressed on the space-time manifold by the irreducible universals identified by the dimensional universal constants, constitutes a fundamental and general instrument of adaptation in the space-time manifold. It is this crucial instrument that allows one to conceive and posit a general stability law for classical mechanical systems and that affords, according to the principle of maximum uniformity, the mechanism which is essential for physically producing the required many-to-one mappings evident in biological systems.

The annihilation of conditionally stringent constraints is accompanied by consequent modifications of the forces emanating from the nonuniformities induced by them in nature's space-time structure. According to the observations

*Some results of this study are presented in Refs. 1 and 2.

and reasoning of this paper, the annihilation of conditionally stringent constraints is envisaged as an essential feature and instrument of adaptation, conceived here as a general and universal aspect of all processes in nature originating in the space-time manifold. This universal process of adaptation in nature and consequently the process of annihilation of conditionally stringent constraints upon which it incisively depends, follow, by the thesis of this paper, the principle of maximum uniformity.

Concerning Aspects of Uniformity and Nonuniformity

In this section, some significant aspects of uniformity and nonuniformity revealed in experience are cited. This is done to point up their universal role in natural phenomena, and as a consequence the strong implications they have for the principle of maximum uniformity which will be further examined in depth in a subsequent paper.

The Aspects of Uniformity include —

1. Symmetry
2. Equilibrium: local, global, spatial, and temporal
3. Stability: local, global, spatial, and temporal
4. Isotropy: a local aspect
5. Homogeneity: a global aspect
6. Constancy
7. Invariance
8. Covariance
9. Law
10. Correspondence
11. Element
12. Order
13. Reproducibility: the ultimate criterion and requirement of scientific investigation
14. Regularity.

Some Corresponding Aspects of Nonuniformity include —

1. The most fundamental and universal aspect of nonuniformity posited to sense-perception and sense-awareness is *force.*
2. Asymmetry
3. Information
4. Curvature

5. Symbol
6. Language
7. Anisotropy: a local aspect
8. Inhomogeneity: a global aspect
9. Gradient
10. Structure
11. Shear
12. Constraints
13. Uncertainty
14. Fluctuations
15. Disorder.

To each set of conditionally stringent constraints there corresponds a positive, definite, scalar measure of nonuniformity manifested in experience by the internal forces. The relaxation of such constraints increases uniformity, and the selection among a possible set of conditionally stringent constraints is made to maximize global uniformity in adherence with the principle of maximum uniformity, as amplified in the following section. The universal constants embrace constancy and process and thus both uniformity and nonuniformity. This is the synthesis they reveal in the elementary processes.

The process of reducing the nonuniformities in nature's space-time manifold is here envisaged to be the ultimate aspect of all adaptive phenomena in nature. Evolution becomes then a word to label this universal adaptive process. An aspect of evolution that is *both essential and universal*, is *force*, and its nature we evidently no more grasp in physics than in biology.

HIERARCHIES OF UNIFORMITY

We can interpret the resultant force posited to a nonfree body, as the vector sum of all nonuniform connections which exist between the body and the universe. Each force individually contributing to this sum, posits to the body a nonuniform aspect of the universe. In cases when the vector sum of these individually applied forces vanishes, we previously considered the body as free but not disjoined from the universe. Here the individual forces may be envisaged as existing in mirror-symmetric pairs, the forces in each pair being consequently equal in magnitude. However, according to the usual laws of classical mechanics, the definition of a free body does not demand that the magnitudes of the individually applied forces be uniform for all pairs.

From these considerations we learn that there exist hierarchies of free bodies, all of which are equivalent according to the known laws of classical mechanics and which are therefore not discernible nor identifiable by these laws. The hierarchies of free bodies may be identified and thus distinguished by the degree either of uniformity or nonuniformity of the magnitudes of the individual

forces which are the immediate manifestations immanent in experience of particular aspects of nonuniformity existing between a body and the universe. Since all free bodies which belong to these various hierarchies (of freedom) are equivalent according to the presently established laws of classical mechanics, these laws cannot, in principle, offer conditions which select from among the many actual possibilities these hierarchies afford at each instant a particular one that belongs to a particular hierarchy of freedom. The concept 'hierarchies of freedom' is a particular aspect of the concept 'hierarchies of uniformity.'

It is helpful to point out some other equivalent aspects of this concept, because it assumes a crucial role in the statement of a general principle of evolution which is in accord with the principle of universal correspondence, and which is consequently understood to operate universally in all natural phenomena, including those which belong to the domain of classical mechanics and hydrodynamics. Some equivalent and related aspects of the concept 'hierarchies of uniformity' include: 'hierarchies of symmetry,' 'hierarchies of certainty,' 'hierarchies of order,' 'hierarchies of information,' 'hierarchies of compatibility,' 'hierarchies of harmony,' 'hierarchies of forces,' and 'hierarchies of consistency.' Moreover, in all of these cases, it is important to distinguish between what in each case corresponds to the local aspects of uniformity and what to its global spatial-temporal aspects. It is clear that the established propositions of classical mechanics do not and cannot make such a distinction because the restrictions they impose on mechanical systems apply instantaneously and locally, everywhere as well as for all time. As the conditions they invoke, i.e., that forces be instantaneously in equilibrium everywhere and always, are constant and therefore uniform in space and time, they do not implicitly describe or define, nor do they condition the existence and the spatial-temporal evolution of local and global nonuniformity in their various hierarchies. For this reason, the known laws of classical mechanics are inherently devoid of historical thrust, causality, and evolutionary process.

It is the universal character of all forces in nature, and therefore in particular of those forces which in the classical domain are designated by the symbol $\overline{F}$, that facilitates invoking and applying the principle of evolution cited above, in the domain of classical mechanics. The established laws of classical mechanics, in all of their equivalent formulations, express a particular and restricted aspect of the principle of maximum uniformity, an aspect, which as was explained earlier is independent of location and time. These laws consequently express universal propositions, i.e., truths which are necessary in the strictly logical sense, and are therefore not contingent upon space and time. For the same reason, they are, in the sense of Liebniz, logically universal, i.e., necessary and analytic. It is important to emphasize in this regard, that these laws refer to a particular and restricted aspect of uniformity which is characterized and defined by the equilibrium of forces, and that they assert that this particular aspect of uniformity is constantly maintained at all locations and is therefore not contingent upon space or time. In other words, the laws of classical mechanics as well as the particular hierarchy of uniformity to which they refer, viz., the hierarchy characterized by the equilibrium of forces, and which, as laws, they report to be general aspects of nature, are *both constant* in space and time, and are thus both free of contingency. If we follow this way of thinking, the usual laws of classical mechanics may be conceived as developing in two

steps. The first consists of a definition of equilibrium, in which force is the aspect of nature to which the word equilibrium in the definition refers. The second uses this definition to express the universal law which asserts that equilibrium so defined is constantly maintained in nature, i.e., everywhere and at all times.

The existence in nature of hierarchies of uniformity which, as in the particular case of equilibrium, are all directly revealed in experience by forces, leads here naturally to the identification of a universal law that although free of contingencies in its assertion, nevertheless conditions aspects of nature which are contingent upon the evolution in space and time of distinct hierarchies of uniformity. The law does not in this case constantly refer to a particular hierarchy, but reports a universal proposition that governs a process of evolution which is contingent upon the emergence in space and time of the various hierarchies of uniformity. The usual laws of mechanics which are indeed embraced by this general law, are a very special case of it, insofar as the particular hierarchy of uniformity in terms of which they are expressed is always constant and therefore not contingent. This is precisely the reason why the established laws of mechanics are inherently and completely devoid of contingency in all aspects, and consequently of historical thrust, causality, stability criteria, and evolution. This is, of course, also true for all of the equivalent formulations of the laws of classical mechanics, and in particular for their formulation in terms of the principle of least action. I refer here particularly to the principle of least action because of its power and unifying role in physical theory. The power of this principle in the formulation given to it by Hamilton, is seen by the fact that not only the classical mechanics of particles and rigid bodies, but also elasticity and hydrodynamics, electromagnetism and all modern field theories connected with ultimate particles (electron, proton, and neutron) can be formulated with its help. All of the theories formulated with its help therefore share with Newton's laws of classical mechanics the important feature of being devoid of historical commitment, causality, and inherent stability criteria. In other words, all of these theories are free of historical content, and consequently essentially devoid of an evolutionary principle.

On A General Stability Principle

We have shown earlier that the formulation of the laws of classical mechanics may be conceived in two essentially distinct steps. The first is a definition of equilibrium, and in the second the proposition is made that equilibrium as defined by the first step holds constantly everywhere, and for all time. The notions of stability and equilibrium were both developed by observing and examining critically the phenomenological behavior of classical mechanical systems. As was explained in the case of equilibrium, a general operational definition based on forces was established on the basis of experience, and then used in the formulation of the known laws of mechanics, which inherently report nothing about stability for reasons already described. Whereas the notion of stability has been described by many definitions, these have led to various stability criteria which are statements of convention rather than of a general law that refers to stability in the same way as the laws of mechanics refer to equilibrium. I shall now endeavor to formulate a statement of a general stability law which will

refer to all of the hierarchies of uniformity and will have the same kind of general relation to them as the known laws of classical mechanics have to the particular hierarchy of uniformity characterized by the equilibrium of forces. For this purpose it is first necessary to identify and define descriptively the hierarchies of uniformity in terms of forces, which as explained above, are interpreted here as the most fundamental, universal, and direct manifestation in experience, of the nonuniform connections existing between the universe and the bodies contained within it.

We may start by considering in some detail the very special and fundamental hierarchy of uniformity to which the known laws of classical mechanics pertain. This special hierarchy is defined by characteristics such that the vector addition of all the nonuniform connections existing between a body and the universe which are posited in experience and which we designate by the name force, sums to zero. It is clear that there can exist a conceivably infinite number of distinct configurations of forces impressed on a material point, which individually designate the individual nonuniform connections between it and the universe, and all of which equally belong to the very special hierarchy of force equilibrium. It is the *differences* between these distinct but otherwise equivalent force configurations which I define as the hierarchies of uniformity. Figure 1 below illustrates how we can conceive of an infinite number of distinct force configurations, all of which belong to the hierarchy of uniformity defined by the equilibrium of forces, and which by their differences here define the hierarchies of uniformity. The figure shows various configurations of force equilibria, with uniformity increasing from left to right.

The hierarchies of uniformity, defined in terms of force fields, are now used to formulate a Principle of Maximum Uniformity, which includes virtually all the known laws of classical mechanics, as well as a general stability law. The principle of maximum uniformity asserts that: among all the force configurations, individually characterized by force equilibrium, which can be collectively and instantaneously accommodated in a finitely extended material domain that is nonuniformly connected to the universe by maintained forces, the particular set of force configurations which actually evolves and which satisfies the instantaneous and stringently exercized geometrical constraints, instantaneously maximizes a global positive, definite, scalar measure of uniformity obtained by summing the local measures of uniformity that depend on the local force configurations over the entire domain.

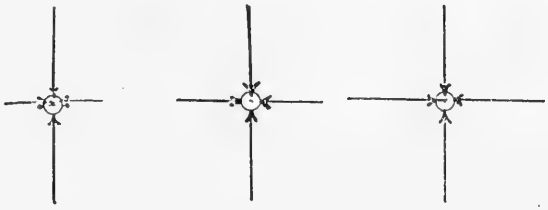

Fig. 1 - Configurations of force of the hierarchy of uniformity defined by the equilibrium of forces

This statement of the principle of maximum uniformity differs essentially from the statements of the established laws of classical mechanics. As explained above, the laws of classical mechanics are essentially a-temporal and a-causal, and consequently devoid of historical commitment and evolutionary process. The principle of maximum uniformity, though conceived here as a universal proposition, nevertheless refers to essentially contingent aspects of nature expressed in terms of hierarchies of uniformity which generally evolve nonuniformly in space-time. It is precisely because the universal and established laws of classical mechanics constantly refer to one, and only one, hierarchy of uniformity, that they are free of contingency in all respects, and are consequently amenable in principle to mathematical formulation; for all mathematically stateable propositions are essentially free of contingencies which refer to space-time and therefore in principle devoid of historical content.

The principle of maximum uniformity is indeed a *procedure* rather than a formally stateable proposition — it is the description of a process which is understood to operate universally. In this process the existence and operation in the space-time manifold of contingently stringent geometrical constraints, as well as absolutely stringent passive and active constraints, are among its essential features. The description and statement of the operation in nature of the principle of maximum uniformity cannot be completely subjected to mathematical formulation, because: (a) time is conceived of as duration rather than the times of events ordered as points on the real time line; (b) the ontological-geometrical ground for stringent, passive, geometrical constraints is ascribed here to the local impenetrability of matter; (c) force is the essential instrument in nature for effecting compatibility and excluding contradiction, by reconciling its universal and contingent aspects; and (d) the temporal and spatial contingencies are expressed by the space-time evolution of various and distinct hierarchies of uniformity.

This conclusion has a direct bearing on the questions concerning the nature of biological theory and the kind of laws we can expect it to produce. It also bears, of course, on the nature of physical theory and the fundamental implications inherent in the formal statements of its laws. It is precisely because these laws can be given mathematical expression, that they are in principle devoid of all contingency and consequently of historical content and thrust, inherent stability criteria, causality, and evolutionary process. Conversely, it is because the present laws of physics are essentially a-historical and a-causal, that they can be given mathematical formulation. The second law of thermodynamics is unique among the laws of physics. Whereas the other laws of physics do not take into account aging, and therefore history, the second law of thermodynamics does consider and compare earlier and later states of systems, but not how they evolve from the earlier to the later states.

We can sum up by saying that the physical laws as they are known are space-time invariant and thus not contingent, and that the aspects of nature to which they refer are devoid of the aging process. Laws of nature may however be space-time invariant and still refer to fundamental aspects of nature which are nevertheless contingent, and which therefore essentially include historical and evolutionary aspects. The principle of maximum uniformity appears to be such a law, and laws which we may expect to emerge in biological theory will be

essentially of this character. The principle of maximum uniformity will be considered in a larger context and in much more detail from the biological view in a later volume concerned with the constants of nature and biological theory, categories of information, and aspects of evolution, and in which it will assume a unifying role.

Stability, according to the present definition, is a characteristic of the instantaneous state of a system, just as is equilibrium; moreover, the stability so defined has both local and global aspects, which again correspond to the case of equilibrium. The instantaneously stable state is defined as the force configurations belonging to the highest hierarchy of uniformity which instantaneously satisfies all the conditions cited above in the statement of the principle of maximum uniformity. According to this definition, instantaneous *global* stability is defined as the collection of instantaneous locally stable force configurations. The definitions given here for hierarchies of uniformity and for stability are descriptive, pictorial, and conceptual, not analytic or quantitative in a mathematical sense. For this purpose it is natural to consider continuously extended material domains, in which the forces joining an element to the universe are characterized by a stress tensor. The principle of maximum uniformity and the general stability law that derives from it will be in part formulated in more analytical (terminology) language in another volume, in which it is planned to treat this subject in a more comprehensive manner, particularly its biological ramifications.

The principle of maximum uniformity is manifested in the domain of classical mechanics, as required by the principle of universal correspondence, by the evolution in time at different locations of various and distinct *force* configurations. Each of these force configurations belongs to the hierarchies of uniformity, and has in common a particular member of the hierarchy, which is defined here by the equilibrium of forces. The progressive evolution in time of the hierarchies of uniformity is revealed in all experience, and therefore in the classical domain in particular, by the progressive evolution of different force configurations, each of which may also be interpreted as a hierarchy of order. As noted earlier, all forces are understood here to give direct expression in experience to the universals, which are reflected by the Dimensional Universal Constants, and consequently to what is referred to in Ref. 7 as the domain of the domain of the universals. By this way of thinking, the operation in nature of the principle of maximum uniformity and the conception of its operation demand the existence, and the consideration of the relation between, and interaction of, the domain of the universals and what I call in Ref. 7, the domain of the observables. This, of course, applies equally to the operation in nature of the universal stability law manifested in every domain of experience, and which derives, as do the conventional laws of mechanics, from the principle of maximum uniformity.

The principle of maximum uniformity and the universal stability law attendant upon it, have been made operational within the realm of classical mechanics, i.e., have been exercised computationally in this realm by the development of an algorithm, by modelling certain aspects of the domain of universals by a potential theory. This model allows the formal description of the interaction between viscous flow fields which belong to the domain of the observables, and an ideal domain characterized by the potential theory from which according to

the algorithm, they emerge by what is analogous to a process of evolution. This has produced mathematical representations of viscous flow fields that evidently satisfy the fundamental partial differential equations of classical hydrodynamics and realistic boundary conditions.

The interaction between the domain of the universals and the observable domain brings necessarily under consideration multiple scales and the realization that they assume an essential role, especially their interrelationship, in the interaction between these domains. From the standpoint of classical mechanics, for example, such scales may be identified with temperature fluctuations in a heat bath which are related to the universal Boltzmann constant, and with the production of inelastic deformations in a solid subjected to forces impressed by the universe from the outside. These considerations, as well as the relationships between the principle of maximum uniformity, the stability law, the role of the constants of nature as the foundation of natural law and the development of biological theory; and the connection between these, and the existence in nature of Categories and Hierarchies of Information, all will be comprehensively examined together in a later volume more specifically directed at their ultimate biological aspects.

CONCERNING DEVELOPMENT OF HIERARCHIES OF UNIFORMITY IN CONTINUA ENDOWED WITH RHEOLOGICAL CHARACTERISTICS

In this section we will describe the spatial and temporal development of hierarchies of uniformity in classical continua, as a process, by presenting a procedure which gives operational expression to the principle of maximum uniformity through an algorithm in which potential theory assumes the fundamental role. This procedure and the algorithm which formally describes it have already been effectively used in the construction of analytical representations of viscous flow fields which satisfy the Navier-Stokes equation and which emerge from realistic boundary conditions. This procedure evidently has very broad applications, and consequently can be applied to physical continua endowed with various linear as well as nonlinear constitutive properties, provided they have rheological features.

In all such cases uniformity, or its counterpart nonuniformity, is directly manifested and in experience, in its various hierarchies, by stress fields, which are understood here to correspond to force fields, as considered previously in conjunction with particle mechanics. Accordingly, the same fundamental role and meaning is ascribed here to stress, as I have done earlier to force, in the case of particle mechanics. In other words, stress directly posits to experience both the uniform as well as the nonuniform universal connections that exist between an element of a continuously extended material domain and the entire universe to which it belongs.

Just as force has been shown above to dominate the propositions of classical mechanics, so correspondingly, stress dominates the laws that condition natural phenomena which transpire in continuously extended material domains.

The uniform connections are represented by what corresponds to a locally isotropic stress field, whereas the nonuniform connections may be represented symbolically by the stress deviator tensor.

The constitutive properties by which specific materials are conventionally identified, as well as their heat baths and thermal fluctuations, are all relevant in producing at each instant a manifold of actual possibilities, available for the selection at each instant, of a particular and preferred stress field as required and selected by the principle of maximum uniformity. Strictly speaking, according to this conception of the operation in nature of the principle of maximum uniformity, the so-called constitutive properties are not strictly constant, but may, according to this principle and the mental picture drawn above of its operation, undergo change, which is tantamount to a change of state or of mechanical phase. In actual and familiar cases, what I am describing here is manifested in the plastic yield of solids and in the turbulence in fluids.

With this background, we can present a statement of the principle of maximum uniformity as it pertains specifically to the domain of classical mechanical experience. An amplified statement of this principle will be given in a separate volume, in the broader context of a unifying evolutionary principle which may pertain to all aspects of nature and consequently to hydrodynamical and biological phenomena in particular. The principle of maximum uniformity asserts — that among the manifold of actual-possible stress fields which are immediately and instantaneously available for selection in a continuously extended and bounded material domain, and which accord with the following conditions and aspects of the domain: (a) the instantaneous constitutive properties of the domain; (b) the temperature field and its fluctuations; (c) the forces impressed and sustained at the boundaries and within the domain; (d) the established laws of classical mechanics; (e) the principle of conservation of energy; and (f) the appropriate equation of state — that the stress field which actually evolves, minimizes an integral of a positive measure of the shear stresses extending over the whole domain.

This is equivalent to maximizing a global measure of uniformity of the domain, since according to the ideas of the present paper the shear stress of a differential element of the material is the direct manifestation in experience of its nonuniform connections with the universe.

This statement of the principle of maximum uniformity, as applied to continuously extended rheological materials, neglects nonuniformities in the inertia forces as manifested by the nonhomogeneity in their spatial distribution. When these are significant, they must, of course, be included in the total measure of global nonuniformity. Indeed, in an application of the principle of maximum uniformity to stratified flows presented in a later part of these studies, the global measure of nonuniformity includes only pressures and inertia forces, as viscous forces may be neglected in comparison.

As this statement of the principle depends incisively on the idea of a manifold of actual-possible states of stress which are available for the selection of a particular member, it is necessary to consider this concept in some detail. For this purpose, we first introduce the concepts microstress and macrostress

states and fields. Microstress fields mean here fields of stress that extend over finite domains, but which have small magnitudes everywhere within these domains. A macrostress field instantaneously prevailing within a finite domain of a material body, is conceived here as a superposition of a collection of microstress fields, each of which instantaneously agree with (a) force equilibrium conditions, (b) the instantaneously prevailing geometrical constraints in all their categories, (c) with the condition of the universe as it is posited by forces imparted to the material domain, and (d) with the constitutive properties of the domain, which can be translated into certain of the categories of geometrical constraint; in particular, the categories of active and passive conditionally stringent constraints. At each instant, the macrostress field is sustained over duration, and thus constantly evolves into new states which are derived by the selection and development of one of the fields of microstress which belongs to the immediately preceding field of macrostress. The selection and development of a particular microstress field that belongs at a particular instant to a macrostress field is determined by the condition invoked by the principle of maximum uniformity. Each and every actual microstress field that belongs to the collection that instantaneously corresponds to an actual macrostress field, is what we may call here an actual-possible state, in the sense that each is an actual microstate and is endowed with the possibility of subsequently (in time) evolving, according to the principle of maximum uniformity, new states of macrostress. We see that the above statement of the principle of maximum uniformity accommodates the evolution in space and time of various and distinct micro- and macrostates of stress which reveal in experience the various hierarchies of uniformity. This principle, which is understood here to be universal and consequently not contingent, refers to a whole hierarchy of aspects of uniformity, rather than as in the case of force equilibrium, to a particular member belonging to the hierarchies of uniformity. From the present statement of the principle of maximum uniformity, we see that it accommodates the emergence in space and time of various members of the hierarchies of uniformity.

An Observation Concerning Turbulence

Turbulence, i.e., its evolution, appears from the hydrodynamical study cited above, to derive from an aspect of the principle of maximum uniformity which is not embraced in the propositions of classical mechanics, and consequently not by the Navier-Stokes equations.

In this sense, it follows that the information which can resolve the enigma of turbulence is not contained in the Navier-Stokes equations, and correspondingly, neither do the equations contain the information necessary to construct analytical solutions to them, which derive from realistic boundary conditions. One has to prescribe more information than the Navier-Stokes equations contain in the category of implicit information, in order to construct these solutions. This seems to be related to Gödel's theorem, which is here interpreted to be a particular aspect of a general law that concerns the accessibility and inaccessibility of information in its various categories.

Some fundamental aspects of the principle of maximum uniformity derive from an interpretation of force, which ascribes to all of the forces in nature

certain universal characteristics that unify them, and by which they in turn unify all natural phenomena. *All* of the forces in nature are accordingly understood to emanate from the universal and irreducible aspects of nature, and to join these directly with immediate experience. By this understanding, all of the forces in nature directly link what is most fundamental in nature with immediate experience. This is an aspect of nature which all forces have in common and through which they bear to each other a correspondence which is universal rather than asymptotic, as is, for example, the correspondence that exists between the classical and nonclassical physical theories invoked by Bohr's principle of asymptotic correspondence. Since this universal correspondence is an aspect of *all* of the forces in nature, it refers in particular to the forces which are manifested within the domains of experience that are now conditioned by the classical physical theories, and implies that through these forces the classical and nonclassical physical theories, in fact, bear to each other a much stronger correspondence than is demanded or revealed by Bohr's correspondence principle. It is through *the forces* that the classical and nonclassical physical theories, and the phenomena as well as the principles revealed in their respective experimental domains, are brought into complete correspondence. The principle of uncertainty, first identified in the experimental domain of quantum mechanics, is a case in point. By this concept, all experimental domains, i.e., all aspects of experience, are brought into mutual and total correspondence by forces. This is the experimental aspect of the Principle of Universal Correspondence.

The laws of classical mechanics have been and are still mistakenly construed to imply deterministic causal connections between mechanical phenomena. This misconception is largely based on a misunderstanding which claims that these laws define and consequently determine the aspect of nature, which is designated in Newton's propositions by the symbol $\overline{F}$. The force designated by this symbol is, in fact, not defined and consequently not determined by the known laws of mechanics; it simply expresses a relation between them. This simple relation between forces, which is invoked by known laws of classical mechanics as a general feature of all bodies and which is defined as equilibrium, also includes inertia forces in cases where equilibrium cannot be maintained statically.

The nature of the connections through which the ultimate aspects of nature, called here the universals, are joined to immediate experience, is, of course, a most fundamental and open question — a question that concerns the nature of force itself — because all forces in nature, as they are envisaged here, are precisely these connections. By this thinking, what is common to all forces in nature and from which they all derive their causal features and evolutionary thrust — features which the known laws of classical mechanics do not express — is a constantly sustained process of adaptation to the irreducible space-time structures irreversibly impressed by the universals embedded in nature's space-time manifold. These immutable and irreducible phenomena which are envisaged here as being endowed with a dynamism by which they internally drive the space-time manifold, by irreversible connections, are called universals because they were conceptually identified by and inferred from the Dimensional Universal Constants. The universals are thus conceived as constantly-regenerating immutable space-time structures which are embedded in the space-time manifold, and

which constantly impress irreducible nonuniformities within the manifold. These nonuniformities may be envisaged as active-stringent geometrical-temporal constraints.

The principle of maximum uniformity posits the constant evolution in nature of hierarchies of increasing uniformity and of their attendant forces, which constantly drive the space-time manifold towards states which are instantaneously and maximally compatible and thus maximally uniform with the irreducible universals of the space-time manifold.

These considerations are presented here as a foundation on which to base a new thesis — viz., that the universal correspondence understood here to exist between all forces and which is ascribed to their common origin in universals seated in the space-time manifold which have given them order, and structure and thereby irreversibly impart to them a constantly sustained nonuniformity — means that all natural phenomena are unified by these forces (since they all have a common source), phenomena which have been hitherto distinguished artificially as animate and inanimate. This means that the forces which, so to speak, drive the life process correspond in all their essential features to the forces which, for example, are designated by the symbol $\overline{F}$ in Newton's propositions — that they have a common ground and that they both originate from the universals as aspects of a universal process of evolution which operates equivalently in all natural phenomena, including those which we currently designate as inanimate. The present interpretation, that all forces in nature are the viable instruments of a process of evolution which extends and works equivalently in every aspect of nature, forces upon us the conclusion that those aspects of nature usually referred to as physical are fundamentally endowed with this universal evolutionary process, and therefore challenge us with the task of experimentally identifying this process in the laboratory within the domain of classical mechanical experience. For this purpose it is important to distinguish between physical reality and physical theory, the latter of which is only a way of looking at, describing, and conditioning particular aspects of physical reality. Indeed, the laws of physical theory, which with exception of the second law of thermodynamics, are distinguished by being mathematically formulated equations, are also distinguished by the absence of concepts which have historical content and which accordingly refer to historical development as an essential aspect of physical reality. My point is, that physical reality is in both its fundamental and comprehensive aspects essentially equivalent, and fully corresponds to aspects of reality which we currently refer to as biological. This total correspondence between biological and physical reality which derives from the universal correspondence between all of the forces in nature, does not mean however that biological reality is encompassed by physical theory as we presently know it. This complete correspondence does not therefore imply a reduction of biological reality to physical theory in the usual sense. Instead, the total correspondence claimed here as existing between biological and physical reality means that contemporary physical theory does not in fact describe or condition certain fundamental aspects of *physical reality*; i.e., those aspects which correspond to, and which are phenomenologically imminent in, biological phenomena as known by ordinary human experience — aspects that concern historical development and evolution.

The reason historical development and evolution have not previously been recognized as fundamental aspects of physical reality, is that physical theory, which is but a way of looking at certain phenomena which we by convention call physical, is based on a description of nature and concepts which are formulated in mathematical statements, called principles or laws, that are in principle devoid of historical content and information. If we look at biological reality from the point of view of physical theory, what we see is not different, and in principle cannot differ, from what we see by adopting the same point of view in examining phenomena which we arbitrarily call physical. According to the present work, which claims a total correspondence between all natural phenomena, and in particular therefore between phenomena which we have by convention designated as biological and physical, the evolutionary and historical aspects of nature should in fact emerge in what by convention is called physical reality, if we engage this reality directly by crucial experiments that are conceived to identify them. The expression, 'physical aspects of evolution' will be used in what follows in order to refer concisely to the particular aspects of evolution which we may be able to identify experimentally and theoretically, within the experimental domain that physical theory now purports to condition fully by its mathematically stated laws.

Whereas evolutionary and developmental processes are macroscopically imminent to us in certain materials which we have learned to call biological (and no doubt the reason for this is that we are made of these materials), aspects of evolution and of historical development emerge in materials which we have learned to call physical, on time scales that are either much larger or much smaller than the time scale in which, for example, the aging of a man or the development of an embryo can be discerned by direct observation — i.e., without requiring specially designed experiments. It is the attenuation in these materials of the immediately apparent phenomenological manifestations of evolution, which has given rise to the misconception that there exists a real and fundamental dichotomy between two aspects of reality, called physical and biological. This circumstance has, however, afforded man the important opportunity to identify experimentally in the nature of matter certain features that are constant in space and time and that are therefore maintained constant under the universal process of evolution, which is understood here to prevail and function equivalently in all matter and to be an equivalent aspect of all natural phenomena. These constant features of nature with which, according to the principles of universal correspondence, all matter is essentially endowed, but which were initially revealed in the behavior of so-called physical material, have been mathematically formulated by propositions which are now the established laws of physical theory. Again, by the principle of universal correspondence, it follows that the laws of physical theory are laws that condition *all* natural phenomena, and therefore in particular materials we now call biological. It also follows from the principle of universal correspondence, that physical theory does not give a complete description of or condition all of the essential aspects of physical reality, viz., its evolutionary aspects. The forces in nature *bridge* and thus reconcile the aspects of nature which according to the laws of physical theory are maintained constant in space and time, with the evolutionary aspects which manifest themselves by the historical development and thus change of natural phenomena in space and time. This conclusion, which bears fundamentally on the nature of force and which is therefore equally relevant to all forces in nature, implies that all forces are the universal instruments of evolutionary thrust

and historical development, with which all matter is endowed and by which all aspects of matter are joined to the immutably constant features of nature, i.e., the universals, and by which they are mutually unified. The origin of the universal process of evolution which constantly prevails in all matter and consequently in such materials which we have by convention tried to distinguish as biological and physical, resides in force. This means that the forces of evolution (and historical development) in living materials, as well as those which we identify with physical reality through the laws of physical theory, and to which we here ascribe evolution in physical reality, are one. All forces in nature are therefore essentially equivalent insofar as they are the essential causal connection between all historically developing events, which they motivate as aspects of a universal process of evolution. The motivating power of all forces is ascribed here to the constant and immutable dynamism with which the universals are innately endowed, and in which forces are understood to emerge. They are all equivalently endowed with evolutionary thrust and historical commitment; in a sense, therefore, the notion of *élan vital* pertains to all forces. Consequently, rather than suggesting an ambiguous and false distinction between inanimate and animate nature, its usage here emphasizes that all forces in nature are equally endowed with an innate dynamism derived from the universals, and that they are the basis of all causal relations that lead to historical development in all nature.

PHYSICAL ASPECTS OF EVOLUTION

The principle of maximum uniformity and the principle of universal correspondence jointly imply that force is the essential instrument that unifies nature in its various phenomenological manifestations and joins them with the universals which are the source of the power by which the forces jointly motivate a universal process of evolution. As stated in the previous section, this concept has motivated a search to identify, both conceptually and experimentally, aspects of the universal process of evolution revealed in natural phenomena which are now supposed to be fully accounted for by widely accepted physical theories. In this search, for conciseness, we shall cautiously refer to aspects of evolution which are revealed in such natural phenomena, as 'physical aspects of evolution.' We say cautiously, because in the previous section we concluded that physical reality bears a total correspondence to biological reality, and that therefore they are essentially and completely equivalent. We shall examine here certain examples of the physical aspects of evolution which concern the historical development of actual flow fields that evolve from real boundary conditions, i.e., flow fields actually produced in historical time. We also have the task of developing their analytical representations on the basis of the Navier-Stokes equations and realistic boundary conditions. We shall consider a fundamental geophysical aspect of the principle of maximum uniformity which led to the discovery of a primary seismic driving force, and to its identification with the earth's rotation. This primary seismic driving force extends throughout the earth and constantly motivates historical and thus evolutionary changes in its tectonic structure, in its figure, surface features, physical constitution, and distribution of internal forces.

Hydrodynamical Aspects of Evolution

The Navier-Stokes equations have long been considered and are still considered to contain all of the essential information relevant to the development of actual flow fields in materials well-modelled by the Newtonian fluid. In mathematical terms, this is equivalent to saying that the Navier-Stokes equations are supposed to imply this information mathematically, and consequently that it is, in principle, obtainable without requiring the explicit statement of additional information. The reason the fundamental problem of theoretical hydrodynamics has remained open for about a hundred years is that the Navier-Stokes equations do not contain, in principle, all the information which is necessary to obtain mathematically the kind of information which we so long expected of them; i.e., analytical representations of actual flow fields. This section of the paper endeavors to explain on the basis of ideas and conclusions developed in the preceding sections, why, in principle, this is so. We shall point out that it is necessary, in principle, to augment the information reported by the Navier-Stokes theory as general restrictions on actual flow fields, by statements which directly or indirectly pertain to the evolutionary development of such fields. The algorithm presented in the joint paper with S. M. Desai, included in the proceedings of this symposium, is not implied by the Navier-Stokes equations. It endeavors to give tacit operational expression to some information concerning actual flow fields contained in the principle of maximum uniformity — information which evidently is not included in the Navier-Stokes equations.

The Navier-Stokes equations formulate for a Newtonian fluid the law of classical mechanics, which invokes the equilibrium of forces as a general condition that applies to all elements of the fluid, and which is constantly maintained at all locations and for all time. The information content of the Navier-Stokes equations is therefore equivalent to the information content of this law of mechanics, which as explained earlier in this paper does not constitute a definition of force, and therefore does not, in principle, determine the space-time development of the forces between which this law expresses a simple relation — a relation which is in fact independent of space and time, and which is consequently devoid of historical information. The historical content and evolutionary aspect with which, by the present thesis, all forces are essentially endowed is not therefore implicitly or explicitly expressed by this law and consequently not by the Navier-Stokes equations. If the space-time structure of actual flow fields sustained by boundary conditions that are maintained constant with time depend on the historical process by which these boundary conditions are actually produced in nature, then it follows that their dependence on the historical development of the boundary conditions, i.e., on their evolution, is, in principle, not implied and therefore not predictable by the Navier-Stokes equations. If this is generally the case, as our work indicates, then it follows that actual flow fields cannot, in principle, be predicted by the complete Navier-Stokes equations without augmenting them with general and fundamental information about these fields which they do not imply, and which specifically concerns their evolution. This information is, I believe, contained in the principle of maximum uniformity. It was given only an approximate representation in the original formulation of the Principle of Minimum Dissipation (6), where it was introduced as a fundamental restriction on viscous flow fields, which augments at all Reynolds numbers the restrictions implied by the complete Navier-Stokes equations. Only in the

limiting case of very small Reynolds numbers are the restrictions implied by the Navier-Stokes equations and the principle of minimum dissipation essentially equivalent; at all finite Reynolds numbers, they are evidently complementary and consequently imply different restrictions on viscous flow fields. This thinking is consistent with the conclusions Ladyzhenskaya (1963) obtained in her work on the mathematical theory of the Navier-Stokes equations, which indicate that the Navier-Stokes equations are not sufficient to describe the motion of a viscous fluid for large Reynolds numbers.

The principle of minimum dissipation used in conjunction with the Navier-Stokes equations and its extension by a theorem obtained from a variational principle which we formulated in order to give more complete hydrodynamical expression to the principle of maximum uniformity (Lieber and Wan, 1957), imply that the structure of actual flow fields is restricted by linear differential relations, which are referred to as a linear substructure, and by a nonlinear compatibility equation that implies certain necessary connections between symmetry properties of actual flow fields and their time-dependent motion.

The work of Desai and Lieber reported in the proceedings of this symposium gives further, though indirect, hydrodynamical representation to the principle of maximum uniformity, through an algorithm which is implicitly endowed with a linear substructure that joins successive steps of an iteration procedure by which the algorithm is defined. The successive steps of this iteration procedure correspond to successive finite steps in the development of a viscous flow field, which are not generally separated by small perturbations but rather by finite changes that become arbitrarily small only when the flows obtained by successive steps virtually converge to a fixed pattern. S. M. Desai (1965) introduced the very significant idea of using the potential flow solutions which correspond to particular shapes of physical boundaries, as the base flow upon which to initiate the iteration procedure that defines the algorithm cited, and by which analytical representations of viscous incompressible flow fields are obtained on the basis of the complete Navier-Stokes equations and realistic boundary conditions. Each step of the iteration process is thus made compatible with the Navier-Stokes equations and then with the law of force equilibrium.

The potential flow on which the iteration is initiated has a fundamental linear substructure, in the sense that its kinematics is governed by Laplace's equation, and is intrinsically endowed with the maximum uniformity attainable from ideal (slip) boundary conditions. This is because potential flows are a subclass of flows governed by a direct hydrodynamical formulation of the principle of maximum uniformity in which the integral constructed in formulating this variational principle is a positive, definite measure of force. This force measure of nonuniformity bears therefore a direct connection with the fundamental scalar measure of force used in the conception and general statement of the principle of maximum uniformity. From these considerations, we envisage the potential flow on which the iteration procedure that defines our algorithm is initiated, as affording a formal representation within the framework of the algorithm, of the ideally maximum uniformity state toward which actual flow fields tend in their evolutionary development, in complying with the law governing their development — the principle of maximum uniformity. This, I believe, explains the fact that by only one iteration on the base potential flow, we obtain a

sophisticated hydrodynamical structure that includes qualitatively essentially all the observable structural features of actual flows (including zones of high dissipation and eddy structure), and also the fact that this viscous flow structure which strongly differs from the potential flow from which it is obtained by a single iteration, is connected to it by a *linear* relation. This relation is an aspect of the linear substructure noted above, which I believe is an intrinsic feature of all actual flows. Moreover, the agreement of the quantitative results obtained from the first iteration with the measurements is striking.

The application of higher order iterations directed toward improving agreement between quantitative results and measurements, necessarily calls for the inclusion of higher harmonics that correspond to the higher order terms of a Fourier series representation of the flow field. These higher harmonics assume a fundamental role in the development of eddy structure and become increasingly significant in our mathematical representation of the viscous flow fields as the Reynolds number increases. We envisage these higher harmonics as seeds of turbulence, which are highly attenuated in very low Reynolds number flows, but which must be used in increasingly refining flow fields at lower Reynolds numbers by successively applying increasingly higher order iterations. We may think of these higher harmonics as the grindstones on which the iteration process works and by which it progressively sharpens by higher iterations a finer hydrodynamical structural detail.

On the other hand, if higher order iterations are applied without correspondingly introducing higher harmonics, even at lower Reynolds numbers, then we cannot expect the higher iterations to improve the flow fields previously calculated by lower order iterations. As nonlinear effects grow in intensity, the higher order iterations become increasingly necessary, as do the higher harmonics to which they are applied, and these will increase in amplitude as the Reynolds number increases.

We are presently engaged in extending the application of our algorithm to the calculation of actual time-dependent viscous flow fields. In so doing we have come to realize that its application to the calculation of higher Reynolds number flows demands that we give explicit consideration, and representation in the actual calculation, to the historical process of their development.

The concepts and considerations presented here on the physical aspects of evolution displayed in classical hydrodynamical systems, has motivated the conception and design of simple hydrodynamical experiments, by which we expect to identify experimentally the process of evolution in hydrodynamics as a process which accords with, but is not implied by, the Navier-Stokes equations. The evolutionary aspects in classical hydrodynamical systems are strongly linked with the features of flows which we now try to examine from the standpoint of hydrodynamical stability theory, without taking cognizance of their historical development. Hydrodynamical stability theory is accordingly basically limited, because in its deeper meaning the stability of a hydrodynamical system is inextricably linked with the process of its historical evolution, and therefore cannot be separated from it. At higher Reynolds number the flow fields corresponding to a particular boundary condition which is maintained in space and time, depend not only on the Navier-Stokes equations, but also upon the way the boundary

conditions are actually made, i.e., historically developed. This is the deeper meaning of stability, in the sense that the flow field that actually develops by a particular historical process is the most stable among the flows admitted by the Navier-Stokes equations, which do not imply a unique flow, and the maintained boundary conditions. According to the thesis of the present paper, the evolution of stable flows accords with the principle of maximum uniformity.

Geophysical Aspects of Evolution

The search for a primary seismic driving force, i.e., a force that causally drives earthquakes on a global scale, is as old as the science of geophysics and has been a most important challenge to the mind. The mechanical aspects of geophysics have been and are being considered primarily from the standpoint of the established laws of classical mechanics which are supposed to be complete in their application to the mechanics of the earth, and thus to contain all the information necessary for answering all questions that concern the mechanical nature and behavior of the earth. This point of view has been applied equally in the search for a primary seismic driving force, and explains, I believe, why such a force has not been identified until comparatively recently. The reason is that such a force is a direct consequence of an evolutionary mechanical process, which it in part motivates, and the fact that the laws of classical mechanics as they are known, are in principle devoid of historical content and therefore of information that concerns evolution as a process in a mechanical system, such as the earth. Therefore, the answer to the question put at the beginning of this section is simply not contained in the laws of classical mechanics to which man turned for the answer. The answer is evidently in the principle of maximum uniformity. A primary seismic driving force was discovered by the author on the basis of this principle about two years ago, and was specifically identified with the earth's rotation, which provides its primary source of energy. The idea that led to its conception is simple, once the principle of maximum uniformity is brought into consideration. The rotation of the earth impresses a global nonuniformity on the earth, which is physically expressed by the nonuniformity in the local and global distribution of forces that its rotation produces in conjunction with the nonuniformities of the figure of the earth, of its mechanical constitution, and of the nonuniform spatial distribution of its inertial mass. A necessary condition required for the development of this primary seismic driving force is that the earth be inelastic and that it accordingly accommodate relaxation phenomena which may progressively lead to reduction of shear stress — shear stress being interpreted here as a local and fundamental aspect of local nonuniformity of the force field around an element of material. The states of stress produced in a fluid in hydrostatic equilibrium are free of shear stress and consequently are states in which uniformity is everywhere locally maximized. When the primary seismic-tectonic force presented here is considered in relation to a mechanical model of the earth's crust and mantle, which ascribes to the very upper mantle a thin layer of visco-elastic material of comparatively low viscosity and high mobility, then according to the principle of maximum uniformity, forces will develop that cause the material to flow with velocity components that are parallel as well as perpendicular to the surface of the earth. This motion in the layer induces horizontal forces on the ocean floor that would cause spreading of the continents; but since the direction of the

horizontal flow is away from the continents, the meeting of the streams near the center of the oceans will produce oceanic ridges there. According to the principle of maximum uniformity, the material in the thin layer of the model will constantly move to reduce everywhere its shearing stresses which are constantly imparted to it by the global nonuniformity impressed upon the earth by its rotation. It is this constant transfer of locally and globally nonuniform forces by the earth's rotation to the materials of the earth, which is enhanced by the geometrical nonuniformities of the figure of the earth and the nonuniformities in the physical constitution of its materials; and the rheological changes in the earth that constantly reduce these nonuniformities in accordance with the principle of maximum uniformity, which cause a constant redistribution of stresses in the earth that culminate in earthquakes. Since this process will continue indefinitely as long as the earth is rotating, nonuniform and nonisotropic stresses will be constantly imparted to its materials and their constant redistribution and concentration will produce earthquakes more or less indefinitely. A basic structural feature in the earth's crust which actively functions in the reduction and redistribution of shear stress as required by the principle of maximum uniformity is the geological fault.

CONCLUDING REMARKS AND DISCUSSION

The above concepts and considerations draw attention to the fact that the known laws of classical mechanism are dominated by the fundamental aspect of nature designated as force, and that these laws are expressed only in terms of a hierarchy of uniformity which is defined by the equilibrium of forces. This enables us to make a sharp distinction between the familiar laws of classical mechanics which (simply) express a simple relation between all the forces acting on and within a body, and the laws of force which are in principle and essentially independent of them. In other words, we must distinguish between the known laws of mechanics conceived and interpreted as invoking a particular but nevertheless general aspect of the principle of maximum uniformity, which is characterized by a definite connection between all the forces acting on a body defined as mechanical equilibrium, and the general as well as restricted laws of force which express the connections between particular types of forces and the space-time structure. These considerations, in part, reveal as well as emphasize the facts that: (a) the forces designated by the symbol $\overline{F}$ in the familiar laws of the classical mechanics of discrete particles dominate these propositions and are therefore, in principle, not defined or determined by them; (b) that this is tantamount to and is an aspect of a principle of indeterminacy exercised within the domain of classical mechanics; and (c) that this indeterminacy principle is explicitly revealed on two levels in the case of mechanical systems consisting of a very large number of particles. From these facts, three deductions may be made: the first concerns the fact already noted, that the known laws of mechanics do not in principle define and/or determine the forces; second, that even when the forces are prescribed by a force law, the task of computation easily exhausts all available capacities; third, in the case of the three-body problem, where the laws of mechanics are augmented by a law of force, i.e., the universal law of gravitation, the motion and consequent changes in configuration on which changes in the gravitational forces depend cannot, according to Poincare, in principle be determined analytically and precisely by mathematical procedures.

According to the thesis of the present paper, the known general force laws which refer to particular kinds of forces that are characterized phenomenologically and thus identified by particular experimental arrangements, are particular aspects of the principle of maximum uniformity. This is also the interpretation given here to constitutive relations, by which materials are identified and phenomenologically distinguished in classical mechanics, and which are also interpreted as restricted force laws emerging from the principle of maximum uniformity. In general, it is understood here that all forces in nature are linked with, and are the concrete instruments of, a universal process of evolution which develops according to the principle of maximum uniformity, and that the general laws of force which express certain constant and thus uniform relations between certain kinds of forces and space-time, are universal but nevertheless particular aspects of the principle of maximum uniformity.

In conclusion, it is significant to point out that the distinction between real forces, as compared to forces of reaction, is based on the idea that motivating forces are endowed with a causal aspect which is not expressed either implicitly or explicitly by the laws of classical mechanics; and that the laws of classical mechanics state a particular connection between forces which they define as equilibrium, but which in reality does not define them. This simple connection between forces acting on each and every material body in the universe, which is termed equilibrium, is a very special aspect of uniformity in nature, which according to these laws is a *constant* aspect of every material body in the universe of classical mechanics. The known laws of classical mechanics accordingly do not express the causal and, consequently, the historical and evolutionary aspect of force. This stems from the fact that what they report about forces does not in principle distinguish between motivating forces (the so-called real forces) and forces of inertia or forces of reaction, such as emerge, for example, from passive geometrical constraints when they are challenged by motivating forces, which, according to the principle of maximum uniformity, are in fact endowed with evolutionary thrust.

The use of the principle of maximum uniformity — i.e., the derivation of a process of evolution from it — calls for applying and maintaining over chronological time an agent which constantly impresses on the space-time manifold nonuniformities which are manifested in experience, and in bodies subjected to them, as forces. The nonuniformities so impressed on the space-time manifold may be envisaged as active-stringent geometrical constraints.

REFERENCES

1. Lieber, P., "Categories of Information," Office of Research Services, University of California, Berkeley, Nonr-222 (87) AM-65-13, Oct. 1965 (published in the Markus Reiner Honorary Volume, Elsevier Press, 1968)

2. Lieber, P., "A Principle of Maximum Uniformity Obtained as a Theorem on the Distribution of Internal Forces," Institute of Engineering Research,

University of California, Berkeley, Nonr-222 (87), MD-63-8, Apr. 1963 (published in the Israel J. Sci. Technol., Apr. 1968)

3. Gauss, C.F., "On a New General Fundamental Principle of Mechanics," Creele's J. Math. 4, 232 (1829) (also appears in Werke 5, 23)

4. Hertz, H., "Principles of Mechanics," Collected Works, Vol. II, New York: MacMillan, 1896

5. Lieber, P., "Points de Vue Nouveaux dans la Théorie de la Turbulence des Écoulements Gazeux," (initially presented in March 1954 at the Institute de Mécanique, University of Paris Faculté des Sciences, as an invited lecture)

6. Lieber, P. and Wan, K., "A Minimum Dissipation Principle for Real Fluids," Int. Congr. Mech., Proc. IX, Brussels, Belgium, 1957

7. Lieber, P., "Constants of Nature; Biological Theory and Natural Law," Proceedings of the First Serbelloni Conference on Theoretical Biology, University of Edinburgh Press, 1967

8. Lieber, P. and Wan, K., "A Proof and Generalization of the Principle of Minimum Dissipation," Air Force Office of Scientific Research Report TN 57-479, AD 136-471, Sept. 1957

9. Lieber, P. and Farmer, A., "Studies on Wave Propagation in Granular Media," Trans. Am. Geophys. Union 39 (No. 2), Apr. 1958

10. Lieber, P. and Wan, K., "An Integral Invariant of a Class of Steady-State Viscous-Incompressible Flows," Trans. Am. Geophys. Union 43 (No. 4), 444 (Dec. 1962)

11. Lieber, P., "The Mechanical Evolution of Clusters by Binary Elastic Collisions and Conception of a Crucial Experiment on Turbulence," Volume of the Proceedings of the Symposium on Second-Order Effects in Elasticity, Plasticity, and Fluid Dynamics, sponsored by the International Union of Theoretical and Applied Mechanics, Apr. 1962

* * *

III—Theoretical Aspects and Application of the Linear Substructure Underlying the Complete Navier-Stokes Equations

S. Desai and P. Lieber
University of California
Berkeley, California

ABSTRACT

In this paper the potential flows are shown to be fundamental as a basis leading to the construction of analytical representations of viscous incompressible flows by a process of iteration. This concept reveals the linear substructure underlying the Navier-Stokes equations as applied to the problem of a two-dimensional flow of a viscous incompressible fluid past a circular cylinder. This linear substructure is here understood as characteristic everywhere in the domain and for all Reynolds numbers. A viscous flow is regarded as a deviation, not necessarily small, for the basic potential flow. A theorem (Theorem I) is established on the basis of a principle of minimum dissipation, to the effect that for a large class of real flows the velocity field tends to become irrotational and hence derivable from a potential. Iterative equations representing the linear substructure are obtained, and it is shown that at least two iterations are necessary, and are to a large extent sufficient, to obtain with good approximation an analytical solution which corresponds to the flow field around a circular cylinder as observed in nature

On the basis of the linear substructure equations, an intimate relation between asymmetry and the time dependence of the flow field around the cylinder is shown to exist, and a symmetry theorem concerning them is proved. Experimental results are shown to be in accord with this theorem.

An idea of a physically infinite distance is introduced and applied to obtain solutions to the sets of equations governing the first two iterations for a steady flow. These solutions are obtained in power series expansions of $1/c \log_e r$ as well as $1/c \log_e (\log_e r + 1)$, where r is the radial distance in polar coordinates and c is a suitable scale factor, both having an infinite radius of convergence. It is shown that these two transformations, viz., $s = 1/c \log_e r$ and $s = 1/c \log_e (\log_e r + 1)$, belong to a group of transformations. However, only the analysis using the second transformation is presented here. The analysis using the first transformation is presented in Refs. 1 and 2. Information about the structure of vortices and the wake is implicit in these analytical solutions insofar as they give the complete streamline field around the circular cylinder.

Computer programs using double-precision arithmetic are developed and presented to evaluate these analytical solutions for any Re in the

range $0 < Re \leq 20$, where Re is the Reynolds number based on the cylinder radius. Corresponding to the two transformations, there are two sets of programs. Solutions are evaluated specifically for the following discrete values of Re: 0.05, 0.125, 0.1875, 0.25, 0.50, 0.75, 1.0, 2.0, 2.1, 2.3, 2.4, 2.5, 2.75, 4.00, 7.5, 10.0, 15.0, and 20.0. These yield meaningful results.

The computed results for solution constants Y1(J), drag, pressure distribution around the cylinder, and a measure of error in certain simplifying assumptions, are presented in a series of graphs. Plots of streamline fields for the above values of Reynolds number are obtained and they show that a vortex can be obtained as a sum of at least the first two harmonics in θ of the stream function, and hence need not be viewed as a singularity in the flow field. Further, the critical Reynolds number at which separation begins is found thereby to be $Re \cong 2.3$. These results are discussed in detail with reference to the existing theoretical and experimental work. They are shown to be in accord with the experimental work.

SYMBOLS

$\hat{}$	This superscript designates dimensional quantities
$\hat{r}$, r	Radial coordinate
$\hat{\theta}$, θ	Angular coordinate
$\hat{t}$, t	Time coordinate
$\hat{\psi}$, ψ	Stream function
$\hat{u}$, u	Radial velocity component
$\hat{v}$, v	Tangential velocity component
$\hat{\omega}$, ω	Vorticity field
$\hat{p}$, p	Pressure field
$\hat{h}$, h	Physically infinite distance for whole flow field
$\hat{\epsilon}_u$, ϵ_u	Error in measuring the radial velocity
$\hat{\epsilon}_v$, ϵ_v	Error in measuring the tangential velocity
$\hat{\epsilon}_p$, ϵ_p	Error in measuring the pressure
$\dot{E}$	Rate of energy dissipation
$\vec{\Omega}$	Vorticity vector
$\vec{V}$	Velocity vector

$\vec{n}$	Normal vector
Φ	Dissipation function
λ, μ	Coefficients of viscosity of the fluid
ρ	Density of the fluid
$\nu = \frac{\mu}{\rho}$	Kinematic viscosity
$\hat{U}_\infty$	Dimensional uniform velocity at infinity
$\hat{p}_\infty$	Dimensional constant pressure at infinity
$Re \equiv RE = \hat{u}_\infty a/\nu$	Reynolds number based on the radius of the cylinder
$\bar{s}$	Linear vector space
L, L_n	Linear differential operators
$\bar{L}$, $\bar{L}_0$	Nonlinear differential operators
S	Formal solution to the Navier-Stokes equations and associated boundary conditions, etc.
ψ_0	Potential flow stream function
u_0, v_0	Potential flow velocity components
p_0	Potential flow pressure field
ψ_n	Stream function corresponding to the nth iteration
u_n, v_n	Velocity components corresponding to the nth iteration
S_n	Formal solution corresponding to the nth iteration
$\hat{F}$	Force exerted by the fluid on the cylinder per unit length along the polar axis
$\hat{\sigma}_{\hat{r}\hat{r}}$, σ_{rr}	Radial stress
$\hat{\sigma}_{\hat{r}\hat{\theta}}$, $\sigma_{r\theta}$	Tangential stress
p_n	Pressure field corresponding to the nth iteration
A_n, B_n	Fourier coefficients of the stream function
C_n, D_n	Fourier coefficients of the stream function
$\mathfrak{A}_n$, $\mathfrak{B}_n$	Refer to definition in Eq. (2.4)

$\mathcal{C}_n$, $\mathcal{D}_n$	Refer to definition in Eq. (2.50)
h_i^*	The physically infinite distance for the iterative solutions
C_D - CD	Total drag coefficient
$C_{D_1} \equiv$ CD1	Total first iteration drag coefficient
C_{D_2} CD2	Total second iteration drag coefficient
$C_{DP_1} \equiv$ CDP1	First iteration pressure drag coefficient
$C_{DV_1} \equiv$ CDV1	First iteration viscous drag coefficient
$C_{DP_2} \equiv$ CDP2	Second iteration pressure drag coefficient
$C_{DV_2} \equiv$ CDV2	Second iteration viscous drag coefficient
s, s'	Space variables defined by $r = e^{cs} = e^{(e^{cs'}-1)}$
$B1_k^j$ = B1(K,J)	Constants in the power series expansion of $\mathcal{B}_1$
$B2_k^j \equiv$ B2(K,J)	Constants in the power series expansion of $\mathcal{B}_2$
$D1_k^j$ = D1(K,J)	Constants in the power series expansion of D_1
$D2_k^j \equiv$ D2(K,J)	Constants in the power series expansion of D_2
δ_k^j	Kronecker delta
$Y_j \equiv$ Y(J), $Y1_j \equiv$ Y1(J)	Constants involved in the first iteration solution
$Y2_j \equiv$ Y2(J)	Constants involved in the second iteration solution
PRET1 PREP1 PREC1 PRES1 PRET2 PREP2 PREC2 PRES2 PRESS	Fourier components of the pressure fields p_1 and p_2 as defined in Part 3 of this paper
PRESI	Potential flow pressure field
ER1, ER21, ER22	Measures of error due to the assumptions $B_n(r) \equiv 0$, $D_n(r) \equiv 0$, $n \geq 3$

$h \equiv H$ This is defined either by the transformation $h \equiv H \equiv 1/c \log_\epsilon h_i^*$, or by the transformation $h \equiv H \equiv 1/c' \log_e (\log_e h_i^* + 1)$

α Angle of separation

α_1 Angle of separation obtained without considering iterations higher than the first

INTRODUCTION AND THEORETICAL BACKGROUND

It is well known that there is a vast gap in our theoretical understanding of the flows around solid obstacles. At the extreme values, viz., $Re \to 0$ and $Re \to \infty$, of the characteristic flow parameter Re, the Reynolds number, we have some insight, but in the vast intermediate range our lack of knowledge is disquieting. The usual remarks about the difficulty of solving the highly nonlinear Navier-Stokes equations are, accordingly, quite challenging. The small perturbation theories which deal with flows with $Re \to 0$ set up a priori limitations to what is possible to investigate and then use a mathematical apparatus which is consistent with and circumscribed by these self-imposed limitations. Consequently, the possibility of being able to obtain a coherent and complete description is there abandoned at the beginning. For $Re \to \infty$, where the boundary layer theory has prevailed, no satisfying description and explanation of the evolution and structure of the wake region can be found, because the assumptions of that theory make it invalid for these regions. It is evident that without this knowledge and understanding of these regions, the mechanism of turbulence still remains an open question, as does its theoretical foundation.

During a period of more than a century, a large body of experimental work has accumulated. Thus information about the flows as they exist in nature is not lacking. Theoretical work and, wherever possible, its experimental confirmation on all aspects of fluid mechanics so far seem to indicate that the Navier-Stokes equations do contain implicitly all the essential information for the flows of a large class of fluids. It appears, therefore, that if mathematical knowledge about the theory of nonlinear partial differential equations, in particular the Navier-Stokes equations, were sufficiently advanced, we could have all the information about flow structures etc. in explicit and detailed form. The question then is, since we do not have this mathematical knowledge, how can we obtain it in the first place.

It is our belief that to make explicit any information from the Navier-Stokes equations, which are presumed to contain it implicitly, we must provide some prior information to initiate a process which leads to the information desired in explicit form. Evidently, the prior information to be provided must be consistent with the implicit information embodied in the Navier-Stokes equations. Therefore, an important question needs to be resolved first; i.e., what information should be provided and how can one be assured about its consistency with the implicit information embodied in the Navier-Stokes equations? Since we feel reasonably certain that the Navier-Stokes equations do represent the physical laws governing the behavior of a class of fluids and since we have a large

body of information on the flows as they exist in nature, it is evident that whatever information we seek to provide must not contradict experience; indeed, it must be taken from experience. Then we can be reasonably assured of its consistency with the implicit information presumed to be embodied in the Navier-Stokes equations.

A natural question which now arises is this: What is the common factor in all our experimental and theoretical experience? The answer seems to be the prominent place of potential flows. All real flows are always found to have some parts of their flow field potential under suitable conditions and, more significantly, they can be made increasingly potential by definite manipulations of the flow parameters. Impulsively started motions are always potential in the initial stages. All existing theories, e.g., the boundary layer theory; water waves theory; wing theory; and the subsonic, supersonic, and hypersonic flow theories etc., give a central place to the potential flows. This realization leads us to believe that the key information can be provided by the potential flows.

The next question to arise is: How shall we use the available explicit information about potential flows in the Navier-Stokes equations to make explicit the information about flows as observed in nature without imposing any restrictions on the flow parameters? It has been our conviction that one way to realize the evolution of a flow field characterized by nonlinear equations is through a process of iterations which yields a linear set of equations and that this process does not need to be assumed a priori to be valid for any specific range of the characteristic parameters that are not for any particular part of the flow domain. In fact, we think that this process is of fundamental importance in arriving at a mathematical solution of nonlinear partial differential equations, such as the Navier-Stokes equations, which contain information about physical phenomena.

It is a remarkable fact that a very few cases exist for which explicit information bearing on the motion of actual flows has been extracted from the Navier-Stokes equations by strictly mathematical procedures, i.e., without using explicit information obtained from extramathematical sources. In the context of this work, it is equally relevant to note and emphasize that when explicit analytical and experimentally verifiable information has been derived from the Navier-Stokes equations, in almost all such cases explicit information derived from extramathematical sources was employed. Such extramathematical information is usually introduced by making judicious simplifying assumptions based on the observation of phenomena and the critical examination of experiments for which they are appropriate. Accordingly, a good simplifying assumption is a way of explicitly stating information which is already implicitly contained in the Navier-Stokes equations, in such cases for which the simplifying assumption is valid. Indeed, we may regard this as a mathematical criterion for a simplifying assumption to be appropriate in a particular case. That is, if we could solve the Navier-Stokes equations for such a specific case, the solution obtained would support the simplifying assumption.

We should be open to the possibility that the reason we have been waiting so long for the mathematical apparatus which can render explicit useful information implicitly contained in the Navier-Stokes equations, is that the development

of this apparatus may require primitive notions yet to emerge. It is quite conceivable that such primitive ideas may, as they have in the past, emerge from extramathematical sources, and we believe that some of the results presented here may be of this nature.

The work presented here is part of a comprehensive exploration and study in classical mechanics and hydrodynamics which was started in 1947 by Lieber [3] and has been sustained and brought into sharper focus since then. This study was initially motivated by a search for ways of extracting useful information from the Navier-Stokes equations, which information until now has remained inaccessible in terms of strictly mathematical procedures. In the works of Lieber and Wan [4-7] can be found some attempts to materialize this desire by the introduction of several significant ideas.

In the course of the comprehensive study to which the work presented here belongs, it was seen by Lieber (class notes in Relativity), that there exist in nature distinct yet related categories of information. This came from the realization that the different known formulations of the principles of classical mechanics are only conditionally equivalent, and that questions concerning their equivalence cannot be meaningfully considered without invoking the idea that these categories exist in nature. It then became apparent that the task of extracting useful and testable information from the principles of classical mechanics is not strictly a mathematical endeavor, and that the feeding of explicit information obtained from one formulation of the principles of mechanics into another formulation can produce additional explicit information in analytical terms. These observations and ideas led Lieber to the formulation of a fundamental theorem on the global distribution of internal forces which was obtained on the basis of Gauss' principle of mechanics [8].

With the realization that this information should be implicitly contained in the Navier-Stokes equations, attempts were made by Lieber and Wan to formulate statements in terms of the parameters and functions appearing in the Navier-Stokes equations, in order to give this information formal representation in the framework of classical hydrodynamics. The dissipation mechanism of Ref. 3 was used to construct a theoretical bridge between the internal forces and the Rayleigh dissipation function, as it shows that dissipation is proportional to the internal forces for a comparatively large class of initial conditions. In this way a connection was established between the information obtained on the global minimization of internal forces and a statement of the minimum dissipation of energy in real fluids. The physical content of this statement is restricted by its mathematical formulation as given in Refs. 5 and 6, where a linear structure emerges for the governing equations.

A step to give it a less restricted formulation has been made by Lieber and Wan in Refs. 9 and 10 by postulating the existence of a fluid interface joining the rotational and irrotational flow regimes, into which the flow field is divided a priori. With the knowledge that the principle of minimum dissipation gives only approximate representation to the information obtained from the theorem on internal forces, they sought to give this information more complete representation by formulating another variational principle which maximizes a global

measure of uniformity. The results obtained from both of these variational principles share a common denominator, by showing:

1. That the velocity fields are conditioned by linear partial differential equations, thereby suggesting a linear substructure underlying solutions to Navier-Stokes equations for actual flows.

2. That there exist necessary connections between the global geometrical symmetry properties of a body and the production of time-dependent flows under time-independent boundary conditions.

3. That there is the necessity to postulate a fluid interface joining the rotational flow with a potential flow extending from the interface to infinity.

An hypothesis has come out of our work which is strongly related to the principle of minimum dissipation and to its basis as established in the theorem on the global distribution of internal forces, obtained by Lieber [8]. The hypothesis is that solutions to the Navier-Stokes equations for actual flows *tend everywhere*, as far as the actual boundary conditions permit, to approach asymptotically solutions for a class of ideal flows which satisfy the Navier-Stokes equations everywhere and a set of ideal boundary conditions at solid boundaries. The ideal flows of the Navier-Stokes equations are the class of potential flows which can dissipate only under very special conditions at fluid interfaces joining rotational-irrotational flow regimes [9,10]. Since these flows are kinematically determined by conditions expressed as linear partial differential equations, we may conjecture from the above hypothesis, that solutions to the Navier-Stokes equations for actual flows which are formally represented by an iterative process applied to a well-defined sequence of functions, must converge asymptotically toward, and are thus bounded by, functions which satisfy linear equations. Such is the theoretical background of our work.

In the present work, the iterative process is assumed to have a fundamental validity, and governing equations for successive iterations are obtained by asserting the fundamental role of the potential flow as a base flow that is valid in the *whole domain* for all flow conditions to start the process of iteration. This is done on the basis of physical and mathematical reasoning. A real flow is viewed as a deviation, not necessarily small, from the basic potential flow. The linear equations governing the iterations are called here linear substructure equations. It is shown that at least two iterations are necessary and are sufficient for the restricted range of Reynolds number to represent the flow field around a circular cylinder. Boundary conditions are discussed and an idea of a physically infinite distance is introduced.

Historically, starting with Boussinesq, various authors have used the potential solution with a conviction that the results so obtained describe flows which deviate only slightly from potential flows, thus ruling out, a priori, any consideration of the regions close to the cylinder and in the wake. The governing equation obtained by them, which has been recently called "Burger's equation" by Pillow, is formally equivalent to our base flow and first iteration equations taken together. The conceptual basis, motivation, and justification — mathematical and physical — of our work is, however, entirely different from theirs. This

difference is reflected in the fact that the continuation of the iteration procedure was not recognized as an instrument for constructing analytical representations of actual flows at higher Reynolds numbers, particularly if the higher order iterations are used in conjunction with higher harmonics as used in our representation of the stream function. Our algorithm consists of an analytical procedure, i.e., of a set of mathematically specified rules for constructing analytical representations of viscous incompressible flow fields which are based on the complete Navier-Stokes equations and on realistic boundary conditions which define solid bodies fixed in the flow field. This algorithm is free of the a priori restrictions used in the application of the small-perturbation theory for the construction of approximate solutions to the Navier-Stokes equations, and which, consistent with the reasoning underlying small-perturbation theories, have been severely limited by their authors (Oseen, Kaplun, Van Dyke, Lagerstrom, etc.) to a very restricted range of Reynolds numbers. Among these cases, in those in which solutions based on the potential flow theory are used as the basis for the application of the perturbations, it is either implicitly assumed or explicitly stated, that actual flows in general deviate strongly, i.e., significantly and thus finitely from potential flows, and that only in such cases where these deviations are *very* small, is it justifiable to use potential flow solutions as a basis for constructing analytical representations of viscous flows by a method of successive approximations. The theoretical basis of our work has freed us from these ad hoc restrictions by rendering a new interpretation and understanding of the nature of potential flows, which ascribes to them a fundamental and distinguished position in the development of actual flow fields and therefore necessarily endows them with a dissipation process. The insight which revealed in our work that potential flows are essentially and universally connected with the detailed development of actual flow fields at all locations in the field, was inspired by phenomenological considerations similar to those which reinforced the conceptual grounds on which we originally conceived the principle of minimum dissipation as a fundamental restriction on the development of viscous flow fields — a restriction not reported or implied by the Navier-Stokes equations. It is indeed the absence of the interpretation given here to potential flows and of an appreciation of their fundamental and universal role in the development of actual viscous-incompressible flow fields, which accounts for the fact that it was previously assumed that potential flows can only be used to calculate viscous flows which deviate from them only slightly, thus justifying the application of the methods of small perturbation. The algorithm presented here is defined by an infinite sequence of iterations, successive steps of which are connected by linear differential relations. These linear differential relations are understood to represent actual linear restrictions which constrain the development of actual flow fields. It is with this understanding that we assert that actual flow fields are essentially endowed with a linear substructure, and that this linear substructure frees the iteration procedure from restrictions adopted in the application of small-perturbation methods. These differences are further brought out in Part 1 of the paper, where our equations are formulated, and in Part 3, where the results of our work are discussed.

Subsidiary equations governing the coefficients of the Fourier expansions of the stream functions of the first two iterations are obtained in Part 2. Expressions for drag and pressure are obtained here in terms of these coefficients. An intimate relation, which has been discussed by Lieber and Wan in their work,

between asymmetry and the time dependence of the flow field is shown to exist from a consideration of solutions to these subsidiary equations, and a theorem concerning them is proven.

Steady motion is investigated in Part 2 of this paper. The governing subsidiary equations for the first two iterations are solved, and the solutions are obtained in the form of power series expansions of $1/c \log_e r$ as well as $1/c \log_e (\log_e r + 1)$, where r is the radial distance in polar coordinates and c is a suitable constant scale factor. As was previously mentioned, only the analysis using the second transformation is presented here; the analysis using the first transformation is contained in Refs. 1 and 2. Explicit expressions for drag and pressure are obtained with the help of these solutions. Streamline field and separation are also discussed; expressions are obtained for the angle of separation and the significance of streamline field is explained.

Finally, in Part 3, the computed results and streamline fields are presented in a series of graphs and discussed in detail, with reference to the existing body of literature in the field.

We may summarize the introduction to this paper by drawing the reader's attention to the salient results and conclusions, and which may be pursued in further detail by referring to Refs. 1 and 2.

1. In this work the class of potential flows assumes a fundamental physical as well as mathematical role in the construction of analytical representations of steady and unsteady viscous-incompressible flow fields, which accord with the Navier-Stokes equations and realistic boundary conditions. This is achieved by developing an algorithm defined by an infinite sequence of iterations, successive members of which are connected by linear differential relations, and by introducing a group of scale transformations that facilitate the numerical determination of the coefficients of the analytical representation of the flow by the boundary conditions, with increasing Reynolds number.

2. The fundamental and universal physical role, which according to the present paper potential theory assumes in the development of viscous incompressible flow fields in general and the linear differential relations connecting successive steps in the iteration procedure that defines our algorithm, are understood here to correspond physically to fundamental aspects incurred in the development of actual flows. These features free the application of the algorithm presented here from the a priori restriction used in the application of small-perturbation theories to the calculation of viscous incompressible flows at low Reynolds number.

3. The scale transformations introduced in the present work, to facilitate the application of the analytical representation of flow fields obtained from the algorithm to the numerical calculation of particular flow fields at increasing Reynolds number, are shown in the present theory to comprise a group. The group property of these scale transformations derives from the linear substructure cited above and plays a fundamental role in the present theory. Members of this group of transformations may therefore, in principle, be applied successively to the contraction of the scale of one of the space variables of the theory,

thereby facilitating the numerical calculation of higher Reynolds-number flow by available computer facilities.

4. Another important result of this work concerns the asymptotic behavior of the solutions obtained when the location of the surface joining the strictly potential outside flow with the rotational flow inside, and in terms of which Desai introduced his concept of physical infinity, is extended away from the cylinder. This is illustrated in the graphical presentation of the results of numerical calculation.

5. A fundamental and striking result obtained in the present work concerns a detailed field description of the evolution of flow fields with Reynolds number, including eddies distinguished by the closure of streamlines which obtains from the superposition of harmonics, in terms of which the solutions are here developed according to the linear substructure. This reveals the remarkable fact that the superposition of two harmonics of the solution produces eddy structure whose distinguishing feature is the closure of streamlines, a feature derived from the linear substructure, and which was anticipated though not analytically deduced from it.

6. Flow separation from the circular cylinder predicted by the present theory agrees favorably with available measurements.

7. Though the drag calculated here for Reynolds numbers greater than 5 differs from measurements, this discrepancy has helped us recognize that harmonics higher than the second must be included even at very low Reynolds numbers in order to apply effectively the higher order iterations needed to obtain increasing accuracy in the calculation of the flow field, and in particular, of the drag. This means that higher harmonics, which may be envisaged as representing the nuclei of turbulence which increase in strength with Reynolds number, are significant aspects of viscous flows, even at very low Reynolds number. Another reason for the discrepancy noted, is that for higher Reynolds number, we must locate the surface of physical infinity that joins the rotational and strictly potential regimes very close to the body, in order to work numerically within the limitations of the available computers. We can free ourselves of this restriction by applying another scale transformation. The close proximity of this interface (physical infinity) relative to the body in the cases where a discrepancy between calculated and measured drag was found, has the effect of artificially restricting and thus deforming the eddy structure of the rotational regime, thereby increasing the calculated drag over the actual value.

8. The analytical representation of flow fields developed here is also found to imply certain necessary relations between time-dependent motion and the symmetry properties of flow fields, and correspondingly to reinforce the principle of minimum dissipation by a theorem presented here.

9. A very detailed field description of the pressure is obtained here and presented for all Reynolds numbers for which actual flow solutions have been calculated.

10. The purpose of the numerical calculations is two-fold: (a) to test the theory as it is presented; and (b) to obtain information that corresponds to observables, but which extends significantly beyond available experimental information, and which bears on the details concerning the evolution of flow fields with increasing Reynolds number.

11. Concerning procedures for extending the application of the present theory to the calculation of actual flows at higher Reynolds number, we are continuing to examine two possibilities: (a) the continued reapplication of the scale transformation cited; and (b) the development of an integral representation of flow fields, instead of the present power-series representation.

A basic question which this effort will engage is whether or not the continued application of the scale transformation has a theoretical basis. If it does, this means that, in principle, we have an instrument for calculating actual flows at higher Reynolds numbers.

PART 1

SUBSTRUCTURE FORMULATION

In this section we shall formulate substructure equations for the flow of a Newtonian viscous incompressible fluid of density ρ and viscosity μ around a circular cylinder of radius 'a' such that the velocity of the fluid at the cylinder wall is zero for all time t, whereas the velocity at distances from the cylinder approaching infinity is uniform in direction and with a magnitude u_∞, which may be a constant or a function of time alone. The starting point is the set of Navier-Stokes equations and the continuity equation in two dimensions.

FUNDAMENTAL EQUATIONS IN TWO DIMENSIONS

The fundamental equations for the flow are the two-dimensional Navier-Stokes equations and the continuity equation. As the boundary of the cylinder is circular, it is natural to use a two-dimensional polar-coordinate system. The reference frame is fixed to the cylinder so that the orientation of the polar axis is parallel to the direction of the velocity vector in the flow field as the radius vector $\hat{r}$ approaches infinity. Figure A illustrates the reference coordinate system.

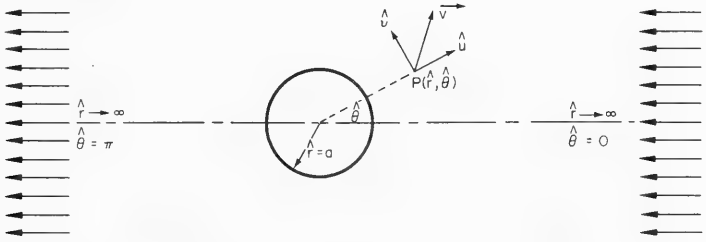

Fig. A - Reference coordinate system of a cylinder

Conservation of Momentum Equations (the Navier-Stokes Equations):

$$\frac{\partial \hat{u}}{\partial \hat{t}} + \hat{u}\frac{\partial \hat{u}}{\partial \hat{r}} + \frac{\hat{v}}{\hat{r}}\frac{\partial \hat{u}}{\partial \hat{\theta}} - \frac{\hat{v}^2}{\hat{r}} = -\frac{1}{\rho}\frac{\partial \hat{p}}{\partial \hat{r}} + \frac{\mu}{\rho}\left(\frac{\partial^2 \hat{u}}{\partial \hat{r}^2} + \frac{1}{\hat{r}}\frac{\partial \hat{u}}{\partial \hat{r}} - \frac{\hat{u}}{\hat{r}^2} + \frac{1}{\hat{r}^2}\frac{\partial^2 \hat{u}}{\partial \hat{\theta}^2} - \frac{2}{\hat{r}^2}\frac{\partial \hat{v}}{\partial \hat{\theta}}\right) \tag{1.1}$$

$$\frac{\partial \hat{v}}{\partial \hat{t}} + \hat{u}\frac{\partial \hat{v}}{\partial \hat{r}} + \frac{\hat{v}}{\hat{r}}\frac{\partial \hat{v}}{\partial \hat{\theta}} + \frac{\hat{u}\hat{v}}{\hat{r}} = -\frac{1}{\rho \hat{r}}\frac{\partial \hat{p}}{\partial \hat{\theta}} + \frac{\mu}{\rho}\left(\frac{\partial^2 \hat{v}}{\partial \hat{r}^2} + \frac{1}{\hat{r}}\frac{\partial \hat{v}}{\partial \hat{r}} - \frac{\hat{v}}{\hat{r}^2} + \frac{1}{\hat{r}^2}\frac{\partial^2 \hat{v}}{\partial \hat{\theta}^2} + \frac{2}{\hat{r}^2}\frac{\partial \hat{u}}{\partial \hat{\theta}}\right). \tag{1.2}$$

Conservation of Mass Equation (the Continuity Equation):

$$\frac{\partial \hat{u}}{\partial \hat{r}} + \frac{\hat{u}}{\hat{r}} + \frac{1}{\hat{r}} \frac{\partial \hat{v}}{\partial \hat{\theta}} = 0 \ . \tag{1.3}$$

The set of Eqs. (1.1), (1.2), and (1.3) can be conveniently reduced to a single equation of the fourth order by introducing a stream function, defined as follows:

$$\hat{\psi} = \hat{\psi}(\hat{r}, \hat{\theta}, \hat{t}) \ , \tag{1.4}$$

such that

$$\hat{u} = \hat{u}(\hat{r}, \hat{\theta}, \hat{t}) = + \frac{1}{\hat{r}} \frac{\partial \hat{\psi}}{\partial \hat{\theta}} \tag{1.5}$$

$$\hat{v} = \hat{v}(\hat{r}, \hat{\theta}, \hat{t}) = - \frac{\partial \hat{\psi}}{\partial \hat{r}} \ . \tag{1.6}$$

We observe that the stream function $\hat{\psi}$ is defined in such a way that the continuity Eq. (1.3) is identically satisfied. By differentiating Eq. (1.1) partially with respect to $\hat{\theta}$ and Eq. (1.2) partially with respect to $\hat{r}$ and then eliminating between them the common term $\partial^2 \hat{p} / \partial \hat{r} \partial \hat{\theta}$ in pressure, we obtain the Vorticity Transport Equation by using Eqs. (1.4), (1.5), and (1.6) to express $\hat{u}$ $\hat{v}$, and their derivatives in terms of $\hat{\psi}$ and its derivatives.

Vorticity Transport Equation:

$$\frac{\partial \hat{\nabla}^2 \hat{\psi}}{\partial \hat{t}} + \frac{1}{\hat{r}} \frac{\partial \hat{\psi}}{\partial \hat{\theta}} \frac{\partial \hat{\nabla}^2 \hat{\psi}}{\partial \hat{r}} - \frac{1}{\hat{r}} \frac{\partial \hat{\psi}}{\partial \hat{r}} \frac{\partial \hat{\nabla}^2 \hat{\psi}}{\partial \hat{\theta}} - \nu \hat{\nabla}^4 \hat{\psi} = 0 \ , \tag{1.7}$$

where the Laplacian Operator is

$$\hat{\nabla}^2 \equiv \frac{\hat{\partial}^2}{\partial \hat{r}^2} + \frac{1}{\hat{r}} \frac{\partial}{\partial \hat{r}} + \frac{1}{\hat{r}^2} \frac{\partial^2}{\partial \hat{\theta}^2} \ ,$$

the Biharmonic Operator is

$$\hat{\nabla}^4 \equiv \hat{\nabla}^2 (\hat{\nabla}^2)$$

and, by definition, the Vorticity Field is

$$\hat{\omega} \equiv \hat{\omega}(\hat{r}, \hat{\theta}, \hat{t}) \equiv \frac{1}{2} \left(\frac{\partial \hat{v}}{\partial \hat{r}} + \frac{\hat{v}}{\hat{r}} - \frac{1}{\hat{r}} \frac{\partial \hat{u}}{\partial \hat{\theta}} \right) = - \frac{1}{2} \hat{\nabla}^2 \hat{\psi} \ . \tag{1.8}$$

Using the definition of Eq. (1.8) of $\hat{\omega}$, Eq. (1.7) can be written as

$$\frac{\partial \hat{\omega}}{\partial \hat{t}} + \hat{u}\frac{\partial \hat{\omega}}{\partial \hat{r}} + \frac{\hat{v}}{\hat{r}}\frac{\partial \hat{\omega}}{\partial \hat{\theta}} = \nu \hat{\nabla}^2 \hat{\omega} \ , \tag{1.9a}$$

or, briefly,

$$\frac{D\hat{\omega}}{D\hat{t}} = \nu \hat{\nabla}^2 \hat{\omega} \ ,$$

where

$$\frac{D}{D\hat{t}} \equiv \frac{\partial}{\partial \hat{t}} + \hat{u}\frac{\partial}{\partial \hat{r}} + \frac{\hat{v}}{\hat{r}}\frac{\partial}{\partial \hat{\theta}} \ . \tag{1.9b}$$

The first term of Eq. (1.9a) represents local time change of vorticity. The second and the third terms represent the convective change of vorticity. Together they represent the total change of vorticity. The term on the right represents the rate of dissipation of vorticity due to internal friction. The form of Eq. (1.9a) clearly reveals the transport and the diffusion characteristics of a significant property of the flow, viz., the vorticity function.

DIMENSIONAL BOUNDARY CONDITIONS

Conditions at the Cylinder Wall

The boundary of a solid circular cylinder is characterized by two properties. First, it is impermeable except for adsorption effects. Second, it is virtually nondeformable with respect to the forces applied to it. By introducing the two ideas of impermeability and rigidity the cylinder boundary can be idealized for a simplified and yet representative mathematical formulation. The idea of impermeability ascribes this property to every point on the boundary of the cylinder.

The condition of impermeability requires that, for a fluid element indefinitely close to a surface element of the cylinder wall, their relative velocity along the surface normal be zero. Since the coordinate system is fixed to the cylinder, the normal and the tangential components $\hat{u}$ and $\hat{v}$ respectively of all the surface elements are zero for all time $\hat{t}$. Then the condition of impermeability is expressed as a kinematic condition

$$\hat{u}(a, \hat{\theta}, \hat{t}) = 0 \tag{1.10a}$$

for all fluid elements on the boundary of the cylinder.

The ideas of impermeability and rigidity lead to a condition on the normal velocity component $\hat{u}$, but not on the tangential component $\hat{v}$ at the cylinder wall [11,12]. To obtain a condition on $\hat{v}$, the following three hypotheses were considered during the 19th century:

1. The velocity at a solid wall is the same as that of the solid itself, and changes continuously in the fluid, which has everywhere the same properties.

2. There is slipping at a solid boundary and this slipping is resisted by a force proportional to the relative velocity.

3. A very thin layer of fluid remains completely attached to the walls and the rest of the fluid slips over it. If the walls are of the same material everywhere, the layer has a constant thickness, so that its surface presents to the current the same irregularities as those of the wall itself. The thickness of the layer is different for different liquids or different materials of the wall; and it depends on the curvature of the wall and on the temperature. Further, it is zero for liquids which do not wet the wall.

The above hypotheses are essentially quoted from volume II, pages 676-677 of Ref. 13.

Serious objections can be raised against the third hypothesis. It includes two assumptions about the thickness of the fluid layer which contradict each other. The first asserts that if the walls are of the same material everywhere, the layer has a constant thickness, so that its surface presents to the current the same irregularities as those of the wall itself. The second asserts that the thickness depends on the curvature of the wall.

To see how the above two assumptions involve a contradiction, let us suppose that we have a wall of the same material and that it has irregularities so that its cross section is as shown in Fig. B. Suppose Δ to be the maximum depth within which the surface irregularities are confined and that Δ is small enough compared to a representative dimension of the wall so that the surface variations within this depth can be considered as irregularities. Let us now construct a curve at a depth $\Delta/2$ such that part of the surface variations fall above it and part of them fall below it. This would be a continuous curve drawn along the centerline C/L shown in Fig. B. We draw it separately in Fig. C.

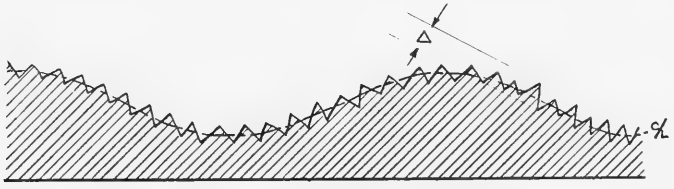

Fig. B - Cross section of a wall with irregularities

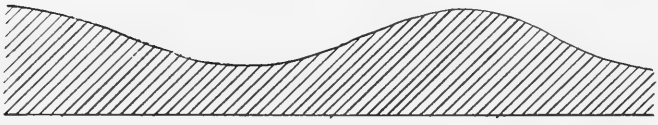

Fig. C - Curve with surface variations partly above and partly below Δ

Since the wall has the surface as shown in Fig. B, if we interpret 'the curvature of the wall' to mean the curvature of the surface of the wall at different points on the surface then this curvature must be different at its different points. In that case, according to the first assumption, the thickness must be the same everywhere, while according to the second it cannot be so. This is a contradiction. However, if we interpret 'the curvature of the wall' to mean the curvature of the surface at various points after the irregularities are neglected and a curve such as the one in Fig. C is considered, the contradiction appears in another way. The curvature changes from point to point on the curve in Fig. C. Consequently, the thickness of the layer of fluid adhering to it must change from point to point. The resulting shape of the outer surface of the layer, therefore, will be different from that of the wall when the irregularities are neglected. If we now superimpose the original irregularities on this shape of the outer surface of the layer, the final shape presented to the current will have irregularities which are oriented somewhat differently than before. Hence they cannot be regarded as the same irregularities as those presented by the wall itself. Thus we again reach a contradiction.

Looking at the two assumptions from another point of view, a deeper question arises. The thickness of the layer may vary from point to point and accordingly be a local attribute of the layer. Then how can it be influenced by the curvature of an imaginary surface obtained by neglecting the irregularities of the surface of the wall and not by the curvature of the actual surface of the wall which has these irregularities? Moreover, whether or not a surface variation can be regarded as a surface irregularity should also depend on the actual thickness of the layer as compared to the depth Δ. This would involve a serious investigation into the idea of the 'relative scales' of different aspects of an actual physical process.

Besides these questions there are other objections which Lighthill [14] has clearly presented as follows: "Supporters of this view do not seem to have discussed the dynamics of such a layer, or thought about the necessarily continuous variation of velocity across it which results from viscous action, or about the effect on the fluid in this layer of the pressure gradients to which it is subjected." It is then not difficult to see why this hypothesis has fallen into disfavor.

About the first hypothesis, Lighthill says:

> Stokes (1851), in his great paper "On Effect of the Internal Friction of Fluids on the Motion of Pendulums," had shown that the condition of zero relative velocity of the fluid at a solid surface both was the most physically tenable boundary condition for the equations of motion of a viscous fluid, and led to remarkable agreement with a wide range of experiments in that problem, as it had also in the capillary-tube resistance experiments of Poiseuille (1840) and Hagen (1839).

Three questions arise in relation to this statement. First, how can one decide that this condition is *the most physically tenable condition*? Second, in what way is it the most physically tenable condition *for the equations of motion of a viscous fluid*, i.e., can it be deduced from or can it be shown to be the only condition

compatible with the equations of motion? Third, did Stokes in fact answer these questions? Below we quote two relevant paragraphs from Stokes' [15, 16] papers, the first from the paper of 1845 and the second from the paper of 1851.

> The next case to consider is that of a fluid in contact with a solid. The condition which first occurred to me to assume for this case was, that the film of fluid immediately in contact with the solid did not move relatively to the surface of the solid. I was led to try this condition from the following considerations. According to the hypotheses adopted, if there was a very large relative motion of the fluid particles immediately about any imaginary surface dividing the fluid, the tangential forces called into action would be very large, so that the amount of relative motion would be rapidly diminished. Passing to the limit, we might suppose that if at any instant the velocities altered discontinuously in passing across any imaginary surface, the tangential force called into action would immediately destroy the finite relative motion of particles indefinitely close to each other, so as to render the motion continuous; and from analogy the same might be supposed to be true for the surface of junction of a fluid and solid. But having calculated, according to the conditions which I have mentioned, the discharge of long straight circular pipes and rectangular canals, and compared the resulting formulae with some of the experiments of Bossut and Dubuat, I found that the formulae did not at all agree with experiment. I then tried Poisson's conditions in the case of a circular pipe, but with no better success. In fact, it appears from experiment that the tangential force varies nearly as the square of the velocity with which the fluid flows past the surface of a solid, at least when the velocity is not very small. It appears however from experiments on pendulums that the total friction varies as the first power of the velocity, and consequently we may suppose that Poisson's conditions, which include as a particular case those which I first tried, hold good for very small velocities. I proceed therefore to deduce these conditions in a manner conformable with the views explained in this paper.
>
> For the purposes of the present paper there will be no occasion to consider the case of a free surface, but only that of the common surface of the fluid and a solid. Now, if the fluid immediately in contact with a solid could flow past it with a finite velocity, it would follow that the solid was infinitely smoother with respect to its action on the fluid than the fluid with respect to its action on itself. For, conceive the elementary layer of fluid comprised between the surface of the solid and a parallel surface at a distance h, and then regard only so much of this layer as corresponds to an elementary portion ds of the surface of the solid. The impressed forces acting on the fluid element must be in equilibrium with the effective forces reversed. Now conceive h to vanish compared with the linear dimensions of ds, and lastly let ds vanish. It is evident that the conditions of equilibrium will ultimately reduce themselves to this, that the oblique pressure

> which the fluid element experiences on the side of the fluid must be equal and opposite to the pressure which it experiences on the side of the fluid. Now if the fluid could flow past the solid with a finite velocity, it would follow that the tangential pressure called into play by the continuous sliding of the fluid over itself was no more than counteracted by the abrupt sliding of the fluid over the solid. As this appears exceedingly improbable a priori, it seems reasonable in the first instance to examine the consequences of supposing that no such abrupt sliding takes place, more especially as the mathematical difficulties of the problem will thus be materially diminished. I shall assume, therefore, as the conditions to be satisfied at the boundaries of the fluid, that the velocity of a fluid particle shall be the same, both in magnitude and direction, as that of the solid particle with which it is in contact. The agreement of the results thus obtained with observation will presently appear to be highly satisfactory. When the fluid, instead of being confined within a rigid envelope, extends indefinitely around the oscillating body, we must introduce into the solution the condition that the motion shall vanish at an infinite distance, which takes the place of the condition to be satisfied at the surface of the envelope.

These quotations show that in 1845 Stokes was inclined towards the first hypothesis but quite undecided about it and in fact tried Poisson's conditions which in essence represent the second hypothesis. The second hypothesis was deduced from the molecular hypothesis by Navier. However, in 1851, Stokes makes use of the first hypothesis. According to his remarks, the choice of this hypothesis seems to be governed by the following criteria.

1. Hueristic reasoning when applied to the conditions of equilibrium lead to a *conclusion which seems exceedingly improbable a priori*.

2. Mathematical simplification of the condition.

3. Experimental justification of the final results.

From these criteria it is seen that Stokes did not show that the so-called "no-slip condition" was physically the most tenable condition for the equations of the motion of a viscous fluid—not at least conceptually.

The second hypothesis includes, as a particular case, the first one. Lighthill's discussion [14], which is also based on molecular considerations, shows this to be the case. From this point of view the first hypothesis becomes a valid approximation under ordinary flow conditions. What happens under extreme conditions when thermodynamic equilibrium exists no longer is not so clear. The behavior of the superfluids also raises questions about the nature of this condition at a solid wall.

Conceptually, it seems that the question about the nature of this condition at a solid wall is an open one. A good discussion on this condition is given by Langlois [17]. We intend to use the "no-slip" condition as a hypothesis on the

basis of the criteria of (a) mathematical simplification and (b) experimental justification on the final results of the analysis.

The no-slip condition in the case of the flow under consideration is expressed as a kinematic condition

$$\hat{v}(a,\hat{\theta},\hat{t}) = 0 \qquad (1.10b)$$

for all fluid elements on the boundary of the cylinder.

The two conditions of Eqs. (1.10a) and (1,10b) together represent the continuity of the velocity vector at the interface of the two media, viz., the fluid and the solid cylinder. It should be noted that the conditions on $\hat{u}$ and $\hat{v}$ are obtained through the ideas of impermeability and no-slip and that the idea of rigidity is involved only as the particular form these conditions have taken here. *The continuity of the velocity vector at a boundary separating the two media does not require the boundary to be rigid.*

Condition at Infinity and the Idea of Physically Infinite Distance

Generally, this condition for the motion of a fluid around an obstacle is expressed by the statement that the velocity at infinity is uniform in direction and has a magnitude which is either constant or a function of time alone. Such a statement, in particular for a sudden relative motion which brings about a constant relative velocity from rest between a circular cylinder and an infinite mass of fluid, is expressed mathematically in either of the following two ways:

(i) At $\hat{r} = \infty$,

$$\hat{u}(\infty,\hat{\theta},\hat{t}) = 0 \qquad \hat{t} = 0$$

$$= -\hat{u}_\infty \cos\hat{\theta} \qquad \hat{t} > 0$$

$$\hat{v}(\infty,\hat{\theta},\hat{t}) = 0 \qquad \hat{t} = 0$$

$$= +\hat{u}_\infty \sin\hat{\theta} \qquad \hat{t} > 0$$

$$\hat{p}(\infty,\hat{\theta},\hat{t}) = \hat{p}_\infty, \quad \text{a constant.}$$

(ii) As $\hat{r} \to \infty$,

$$\hat{u}(\hat{r},\hat{\theta},\hat{t}) = 0 \qquad \hat{t} = 0$$

$$\to -\hat{u}_\infty \cos\hat{\theta} \qquad \hat{t} > 0$$

$$\hat{v}(\hat{r},\hat{\theta},\hat{t}) = 0 \qquad \hat{t} = 0$$

$$\to +\hat{u}_\infty \sin\hat{\theta} \qquad \hat{t} > 0$$

$$\hat{p}(\hat{r},\hat{\theta},\hat{t}) \to \hat{p}_\infty, \quad \text{a constant.}$$

These formulations of the condition at infinity are found in many books on fluid mechanics and in technical papers. In particular, references may be made to books by Milne-Thomson [11], Lamb [18], Schlichting [19], Rosenhead [20], and Landau and Lifshitz [21], and to papers by Kaplun [22, 23], Southwell and Squire [24], Bairstow, Cave, and Lang [25], and Hollingdale [26].

This manner of stating this condition is not entirely appropriate because it conceals a very significant point.

If we consider the ideas underlying such a condition we see that the condition stems from a feeling that the changes introduced in the flow field by an obstacle in an infinite body of fluid must be finitely extended. The principle of conservation of energy would imply that an infinite domain cannot be disturbed everywhere at finite amplitudes. It might be asked what we mean by an infinite body of fluid. Experiments show that for steady motion of a fluid around an obstacle the flow field significantly far away is essentially the same as when the obstacle was absent. What is actually and decisively observed is that the disturbances, the physical changes in the flow field, attenuate with distance away from the obstacle.

There are two categories of variables involved in the measurement and observation of a physical process. The first category is the geometric category, i.e., the category to which the coordinate variables $\hat{r}$, $\hat{\theta}$, and $\hat{t}$ belong. The second category is the dynamic category to which belong the variables $\hat{u}$, $\hat{v}$ and $\hat{p}$. There is a significant difference between the variables belonging to these two categories in relation to their measurements.

Let us consider a disturbance at some point in a body of homogeneous and isotropic fluid. Suppose there is some particular law of decay of this disturbance as it propagates outwards in the fluid from the source of disturbance. This law must be the same for all directions in the fluid because the fluid is assumed to be isotropic. However, the intensity of the disturbance at the source may be different in different directions. Now let us consider the measurement of the intensity of the propagated disturbance at some distance ℓ away from the source. Suppose the measurements are made in some suitable but definite system of units. The measured intensity at ℓ can be expressed as some multiple of the unit of measurement selected or as a percentage of the magnitude of the intensity in this direction at the source. If the law of decay is such that increasing the intensity at the source increases the intensity at ℓ linearly, the percentage which expresses the ratio of these two intensities will remain unchanged thereby. Hence, considering other directions in which the intensity of disturbance at the source may be different in magnitudes, we come to the conclusion that with such a law of decay this percentage will remain unchanged at a distance ℓ in all directions; i.e., the isopercentage surface will be spherical, considering the source to be at the center of the sphere. We can obtain an isopercentage surface even if the law of decay does not exhibit the property of linearty mentioned above. If the fluid is nonhomogeneous and nonisotropic, even then one can obtain isopercentage surfaces, though the law of decay will depend on the direction of propagation of the disturbance. In these cases the surface is not spherical. However, on an isopercentage surface the magnitudes of the intensity of disturbance will, in general, vary from point to point. Just as we can obtain an

isopercentage surface, we can obtain an isomagnitude surface on which, in general, the percentages are different.

When we want to say that a disturbance has died out in a domain of the fluid, we have two alternatives. We can say that beyond a certain isopercentage surface the disturbance is insignificant. Or we might say that beyond a certain isomagnitude surface the disturbance is insignificant. Now the construction of an isomagnitude surface involves measurement only at points in the flow field, and no knowledge of the disturbance at the source is required except insofar as the suitable selection of a system of units is concerned. On the other hand, the construction of isopercentage surfaces involves a detailed measurement and knowledge of the disturbance at the source, in addition to the measurement at points in the flow field. From the point of view of measurement, then, the isomagnitude surfaces are more appropriate. More significantly, however, the magnitudes and not the percentages based on the magnitude of the disturbance at the source represent the actual disturbance at a point. Hence, physically also, the isomagnitude surfaces are more appropriate to delineate the domains of the disturbed and the undisturbed field. For mathematical convenience, we may construct a spherical envelope which would enclose the isomagnitude surface within it, by taking the largest distance between the source and the isomagnitude surface as the radius of the envelope, and then using it in place of the isomagnitude surface.

Now we introduce the idea of a Physically Infinite Distance.

> *Definition:* Physically Infinite Distance in a certain direction is that smallest distance away from an obstacle at which the flow field is not *significantly* affected by the presence or absence of the obstacle. The word "significantly" is to be interpreted in relation to the degree of accuracy with which the field variables are measured.

Evidently, a change in the field variables in the dynamical category represents a disturbance. The magnitude of this change is the magnitude of the disturbance. It is a matter of convention to decide when a certain magnitude of this disturbance is negligible. Any magnitude which falls within the limits of accuracy of a measuring instrument, which is judiciously chosen so that the measurements made with it describe the physical conditions properly, may be considered negligible. Then this magnitude may be used to construct an isomagnitude surface. The smallest distance in a certain direction from the obstacle to this surface is the Physically Infinite Distance in that direction.

The Physically Infinite Distance will depend on the following:

1. The physical nature of the fluid
2. The intensity of the disturbance
3. The direction in which it is reckoned
4. The degree of accuracy of the measuring instruments.

Since disturbances may become, as they generally do, insignificant at mathematically finite distances, a physically infinite distance may be finite mathematically. Since a mathematically infinite distance embodies the idea of *indefinitely large distance*, it would then follow that a physically infinite distance will always be less than, or at the most equal to, a mathematically infinite distance, and hence that at a mathematically infinite distance also the physical disturbances should be insignificant in the sense of being immeasurable within a certain degree of accuracy.

In contrast to the idea of physically infinite distance, a mathematically infinite distance depends on none of the four points on which the physically infinite distance depends. Moreover, the mathematical idea of the point at infinity is based on the idea of limit and hence a material point cannot be uniquely associated with such a point at infinity. This is the essential difference between the abstract and the real. Herein lies both the strength and weakness of the mathematically infinite distance. Its strength lies in the fact that in most instances it leads to the possibility of a mathematical formulation which does not require the information demanded under the above-mentioned four points and yet can represent the corresponding physical process in essence. Its weakness is that in its reinterpretation in an actual situation, where the domain is always finite and hence the condition at infinity must be considered to apply at finite distances, one must necessarily resort to the idea of physically infinite distances. Since the choice of the idea of mathematical infinity is governed by the criteria of mathematical convenience, the idea of physically infinite distance may be used if it is found to be more convenient than the other. It will then have the dual advantage of being both convenient and realistic.

The idea of a physically infinite body of fluid involves two notions. One is that of the physically infinite distance and the other is that of an inexhaustible supply of fluid. Sources and sinks are devices by which the latter is accounted for in some cases. For the corresponding mathematical idea, the indefinite extension implied by the point at infinity is sufficient.

It might seem that before any use can be made of the idea of physically infinite distances one must necessarily possess the information about the nature of the fluid, the intensity of the disturbance, degree of accuracy of the instruments, etc. The nature of the fluid is adequately described by the knowledge of physical constants like density ρ and viscosity μ, as these are needed for any mathematical formulation. That the other information need not be known a priori for a mathematical formulation which makes use of the idea of physically infinite distances can be shown by considering the following examples.

The flow of an inviscid incompressible fluid around a circular cylinder of radius 'a' must satisfy the harmonic equation $\hat{\nabla}^2\hat{\psi}_0 = 0$, where $\hat{\psi}_0 = \hat{\psi}_0(\hat{r},\hat{\theta})$ is the stream function.

The solution of the above equation, which renders the flow at infinity uniform is given by

$$\hat{\psi}_0 = -\hat{u}_\infty\left(\hat{r} - \frac{a^2}{\hat{r}}\right)\sin\hat{\theta} \ .$$

The normal and the tangential components of velocity are given by

$$\hat{u}_0 = -\hat{u}_\infty \left(1 - \frac{a^2}{\hat{r}^2}\right) \cos \hat{\theta}$$

$$\hat{v}_0 = +\hat{u}_\infty \left(1 + \frac{a^2}{\hat{r}^2}\right) \sin \hat{\theta}\,, \quad \hat{u}_\infty = \text{a constant.}$$

The corresponding pressure is given by

$$\hat{p}_0 = \frac{1}{2} \rho \hat{u}_\infty^2 \frac{a^2}{\hat{r}^2} \left(2 \cos 2\hat{\theta} - \frac{a^2}{\hat{r}^2}\right) + \hat{p}_\infty\,,$$

where $\hat{p}_\infty$ is a constant.

As $\hat{r} \to \infty$,

$$\hat{u}_0 \to -\hat{u}_\infty \cos \hat{\theta}\,, \quad \hat{v}_0 \to +\hat{u}_\infty \sin \hat{\theta}\,, \quad \hat{p}_0 \to \hat{p}_\infty\,.$$

At $\hat{r} = a$,

$$\hat{u}_0 = 0\,, \quad \hat{v}_0 = 2\hat{u}_\infty \sin \hat{\theta}\,, \quad \hat{p}_0 = \frac{1}{2} \rho \hat{u}_\infty^2 (2 \cos 2\theta - 1) + \hat{p}_\infty\,.$$

We can construct Table 1, supposing $\hat{\theta} = 45°$. From the table it can be seen that the magnitudes of the components of the velocity vector evaluated at various finite distances along the line $\hat{\theta} = 45°$ and away from the cylinder approach very rapidly those evaluated at infinity. Even at a distance as close as $\hat{r} = 10a$ their difference is only 1% of the magnitudes at infinity. And at a distance $\hat{r} = 50a$ this reduces to only 0.04% of the magnitudes at infinity.

Table 1
Measurement of Physically Finite Distance, with $\theta = 45°$

$\frac{\hat{r}}{a}$	$\frac{a^2}{\hat{r}^2}$	$\hat{u}_0$	$\hat{v}_0$	$\hat{u}_0 - \lim_{\hat{r}\to\infty} \hat{u}_0$	$\hat{v}_0 - \lim_{\hat{r}\to\infty} \hat{v}_0$
10	0.0100	$-\frac{1}{\sqrt{2}}\hat{u}_\infty(1-0.0100)$	$+\frac{1}{\sqrt{2}}\hat{u}_\infty(1+0.0100)$	$+0.0100\frac{\hat{u}_\infty}{\sqrt{2}}$	$+0.0100\frac{\hat{u}_\infty}{\sqrt{2}}$
25	0.0016	$-\frac{1}{\sqrt{2}}\hat{u}_\infty(1-0.0016)$	$+\frac{1}{\sqrt{2}}\hat{u}_\infty(1+0.0016)$	$+0.0016\frac{\hat{u}_\infty}{\sqrt{2}}$	$+0.0016\frac{\hat{u}_\infty}{\sqrt{2}}$
50	0.0004	$-\frac{1}{\sqrt{2}}\hat{u}_\infty(1-0.0004)$	$+\frac{1}{\sqrt{2}}\hat{u}_\infty(1+0.0004)$	$+0.0004\frac{\hat{u}_\infty}{\sqrt{2}}$	$+0.0004\frac{\hat{u}_\infty}{\sqrt{2}}$
$\to\infty$	$\to 0$	$\to -\frac{1}{\sqrt{2}}\hat{u}_\infty$	$\to \frac{1}{\sqrt{2}}\hat{u}_\infty$	$\to 0$	$\to 0$

If now the velocity measuring instruments are such that they cannot measure accurately any quantities of the order of $0.0004\ \hat{u}_\infty/\sqrt{2}$ or smaller, then within this accuracy the boundary condition at infinity is met at a finite distance of 50a. Such a distance would here be called a physically infinite distance. In fact, we may assert that the flow becomes uniform at a finite distance of 50a. That it is 50a we concluded after looking at Table 1 and the accuracy of the instruments. Moreover, we made use of the solution obtained by the consideration of the condition at infinity.

We shall now show that for the same physical process described by the previous solution there is another mathematical procedure consistent with the physical ideas to determine physically infinite distance.

In this procedure we first make the assertion that there is a finite distance $\hat{h}$ at and beyond which the flow can be regarded as uniform. We may express this by the condition

$$\begin{aligned} \hat{u}_0(\hat{h},\hat{\theta}) &= -\hat{u}_\infty \cos\hat{\theta} + \hat{\epsilon}_u \cos\hat{\theta} \\ \hat{v}_0(\hat{h},\hat{\theta}) &= +\hat{u}_\infty \sin\hat{\theta} + \hat{\epsilon}_v \sin\hat{\theta} \\ \hat{p}_0(\hat{h},\hat{\theta}) &= \hat{p}_\infty + \hat{\epsilon}_p \ , \end{aligned} \tag{A}$$

where $\hat{u}_\infty$ and $\hat{p}_\infty$ are constant magnitudes of velocity and pressure recorded by the instruments and which may be regarded as known completely. The errors $\hat{\epsilon}_u$, $\hat{\epsilon}_v$ in velocity and $\hat{\epsilon}_p$ in pressure are to be regarded as unknown, but less than the error bounds of the instruments, which may be regraded as known.

Using the method of separation of variables, we obtain as a general solution of the harmonic equation

$$\hat{\psi}_0(\hat{r},\hat{\theta}) = (c_1 \sin\lambda\hat{\theta} + c_2 \cos\lambda\hat{\theta})(c_3 \hat{r}^{\lambda} + c_4 \hat{r}^{-\lambda}) + c_5\hat{\theta} \log_e \hat{r} + c_6\hat{\theta} + c_7 \log_e \hat{r} + c_8 \ ,$$

where $c_1, c_2, \ldots, c_8$ and λ are arbitrary constants. This satisfies $\hat{\nabla}^2\hat{\psi}_0 = 0$.

We may take $c_8 = 0$ because $\hat{\psi}_0$ is to be determined within an arbitrary constant. For periodicity in $\hat{\theta}$ we must have λ an integer, say n and c_5, c_6 equal to zero. Superposition for all n gives

$$\hat{\psi}_0(\hat{r},\hat{\theta}) = c_7 \log_e \hat{r} + \sum_{n=1}^{\infty} (c_{1n} \sin n\hat{\theta} + c_{2n} \cos n\hat{\theta})(c_{3n} \hat{r}^n + c_{4n} \hat{r}^{-n}) \ .$$

By differentiation we get

$$\hat{u}_0(\hat{r},\hat{\theta}) = \frac{1}{\hat{r}} \frac{\partial\hat{\psi}_0}{\partial\hat{\theta}} = 0 + \sum_{n=1}^{\infty} n (c_{1n} \cos n\hat{\theta} - c_{2n} \sin n\hat{\theta})(c_{3n} \hat{r}^{n-1} + c_{4n} \hat{r}^{-n-1})$$

$$\hat{v}_0(\hat{r},\hat{\theta}) = -\frac{\partial\hat{\psi}_0}{\partial\hat{r}} = -\frac{c_7}{r} - \sum_{n=1}^{\infty} n\,(c_{1n}\sin n\hat{\theta} + c_{2n}\cos n\hat{\theta})(c_{3n}\hat{r}^{n-1} - c_{4n}\hat{r}^{-n-1}) .$$

Thus at $\hat{r} = \hat{h}$ we must have

$$\sum_{n=1}^{\infty} n\,(c_{1n}\cos n\hat{\theta} - c_{2n}\sin n\hat{\theta})(c_{3n}\hat{h}^{n-1} + c_{4n}\hat{h}^{-n-1}) = -(\hat{u}_\infty - \hat{\epsilon}_u)\cos\hat{\theta}$$

$$-\frac{c_7}{h} - \sum_{n=1}^{\infty} n\,(c_{1n}\sin n\hat{\theta} + c_{2n}\cos n\hat{\theta})(c_{3n}\hat{h}^{n-1} - c_{4n}\hat{h}^{-n-1}) \equiv +(\hat{u}_\infty + \hat{\epsilon}_v)\sin\hat{\theta} .$$

Hence we must have $c_7 = 0$, $c_{2n} = 0$ for all n, since $n \neq 1$, c_{1n}, c_{3n}, c_{4n} must be zero. Writing $c_1 \equiv c_{11}\cdot c_{31}$, $c_2 \equiv c_{11}\cdot c_{41}$, we get

$$c_1 + c_2 h^{-2} = -\hat{u}_\infty + \hat{\epsilon}_u$$

$$c_1 - c_2 h^{-2} = -\hat{u}_\infty + \hat{\epsilon}_v .$$

Moreover, the kinematic condition that the normal component of velocity at $\hat{r} = a$ be zero requires that $c_1 + c_2/a^2 = 0$.

Now there are three conditions on two constants c_1 and c_2. In the evaluation of the previous solution where the condition of uniform flow was demanded as $\hat{r} \to \infty$ and $\hat{\epsilon}_u = \hat{\epsilon}_v = 0$, the first two of the above conditions reduce to a single condition that $c_1 = -\hat{u}_\infty$ because the term in c_2 drops out. c_2 is then obtained from the third condition. This condition of overdeterminacy is peculiar to the example chosen and is not generally obtained, as will be clear when the actual problem of the flow of a viscous fluid around a circular cylinder is considered. It is important to note that, in general, such constants like c_1, c_2 must be functions of $\hat{h}$, the distance at which this condition is applied.

The overdeterminacy determines $\hat{h}$ directly in the above case. c_1, c_2, and $\hat{h}$ which satisfy these conditions are given by

$$c_1 = -\hat{u}_\infty + \frac{\hat{\epsilon}_u + \hat{\epsilon}_v}{2} = -\hat{u}_\infty\left(1 - \frac{\hat{\epsilon}_u + \hat{\epsilon}_v}{2\hat{u}_\infty}\right)$$

$$c_2 = -\left(-\hat{u}_\infty + \frac{\hat{\epsilon}_u + \hat{\epsilon}_v}{2}\right)a^2 = +\hat{u}_\infty a^2\left(1 - \frac{\hat{\epsilon}_u + \hat{\epsilon}_v}{2\hat{u}_\infty}\right)$$

$$\hat{h}^2 = +\left(1 - \frac{\hat{\epsilon}_u + \hat{\epsilon}_v}{2\hat{u}_\infty}\right)\left(\frac{2\hat{u}_\infty a^2}{\hat{\epsilon}_u - \hat{\epsilon}_v}\right).$$

The corresponding stream function is given by

$$\hat{\psi}_0(\hat{r},\hat{\theta}) = -\left[\hat{u}_\infty\left(\hat{r} - \frac{a^2}{\hat{r}}\right)\sin\hat{\theta}\right]\left(1 - \frac{\hat{\epsilon}_u + \hat{\epsilon}_v}{2\hat{u}_\infty}\right). \qquad (B)$$

We can see from these expressions that as $\hat{\epsilon}_u + \hat{\epsilon}_v \to 0$, $\hat{\epsilon}_u - \hat{\epsilon}_v \to 0$, and $\hat{h} \to$ infinitely large distance, $\hat{\psi}_0$ reduces to the previous solution. Even though we happen to have a relation between $\hat{h}$, $\hat{\epsilon}_u$, and $\hat{\epsilon}_v$, $\hat{h}$ cannot be calculated because we do not know $\hat{\epsilon}_u$ and $\hat{\epsilon}_v$. In general, we do not have such an explicit relation. To see how c_1 and c_2 depend on $\hat{h}$ we may rewrite them as follows:

$$c_1 = -\hat{u}_\infty + \left(\frac{\hat{\epsilon}_u + \hat{\epsilon}_v}{\hat{\epsilon}_u - \hat{\epsilon}_v}\right)\left(1 - \frac{\hat{\epsilon}_u + \hat{\epsilon}_v}{2\hat{u}_\infty}\right)\left(\frac{2\hat{u}_\infty a^2}{\hat{h}^2}\right)$$

$$c_2 = +\hat{u}_\infty a^2 - \left(\frac{\hat{\epsilon}_u + \hat{\epsilon}_v}{\hat{\epsilon}_u - \hat{\epsilon}_v}\right)\left(1 - \frac{\hat{\epsilon}_u + \hat{\epsilon}_v}{2\hat{u}_\infty}\right)\left(\frac{2\hat{u}_\infty a^4}{\hat{h}^2}\right).$$

Since the actual nature of $\hat{\epsilon}_u$ and $\hat{\epsilon}_v$ is not known, we may assume that the ratio $\hat{\epsilon}_u + \hat{\epsilon}_v/\hat{\epsilon}_u - \hat{\epsilon}_v$ will generally be finite and that $\hat{\epsilon}_u + \hat{\epsilon}_v$ is definitely smaller than $2\hat{u}_\infty$, in view of the fact that they each are smaller than the error of the instruments. Hence c_1 and c_2 as functions of $\hat{h}$ approach asymptotically the values $-\hat{u}_\infty$ and $+\hat{u}_\infty a^2$ respectively as $\hat{h}$ becomes increasingly large.

The pressure field is given by $\hat{p}_0(\hat{r},\hat{\theta})$ such that

$$\hat{p}_0(\hat{r},\hat{\theta}) = \frac{1}{2}\rho\hat{u}_\infty^2\frac{a^2}{\hat{r}^2}\left(2\cos 2\hat{\theta} - \frac{a^2}{\hat{r}^2}\right)\left(1 - \frac{\hat{\epsilon}_u + \hat{\epsilon}_v}{2\hat{u}_\infty}\right)^2 + \hat{p}_\infty + \hat{\epsilon}_p . \qquad (C)$$

This also reduces to the pressure field as obtained before when $\hat{\epsilon}_u = \hat{\epsilon}_v = \hat{\epsilon}_p = 0$.

The stream function in Eq. (B) and the pressure field in Eq. (C) adequately represent the potential flow, though the conditions were applied at a finite distance $\hat{h}$.

The situation can now be generalized. We apply the conditions of uniform flow to the general solution of the equations of motion at a finite distance, say $\hat{h}$. We then obtain the constants of the solution as a function of the distance $\hat{h}$. If we find analytically or numerically that these constants are approaching limiting values as the distance at which the conditions of uniform flow are applied is increased, then we may take for solution that distance at which they approach the limiting values, and consequently the final solution does not change significantly as the Physically Infinite Distance for the problem. Since the solution does not change, the physical quantities like drag and pressure should also exhibit asymptotic behavior with increasing $\hat{h}$.

From the above, we can state the condition of uniform flow as follows:

At $\hat{r} = \hat{h}$,

$$\begin{aligned}
\hat{u}(\hat{h},\hat{\theta},\hat{t}) &= 0 && t = 0 \\
&= (-\hat{u}_\infty + \hat{\epsilon}_u)\cos\hat{\theta} && t > 0 \\
\hat{v}(\hat{h},\hat{\theta},\hat{t}) &= 0 && t = 0 \\
&= (+\hat{u}_\infty + \hat{\epsilon}_v)\sin\hat{\theta} && t > 0 \\
\hat{p}(\hat{h},\hat{\theta},\hat{t}) &= \hat{p}_\infty + \hat{\epsilon}_p, \quad \text{a constant.}
\end{aligned} \tag{1.10c}$$

$\hat{\epsilon}_u$, $\hat{\epsilon}_v$, and $\hat{\epsilon}_p$ are to be less than the errors of the instruments, so that the solution exhibits asymptotic behavior with increasing values of $\hat{h}$.

It was mentioned earlier that there is a significant difference between the geometric and the dynamic categories of the variables. This difference is that the variables $\hat{r}$, $\hat{\theta}$, and $\hat{t}$ are measured by instruments which have limitations of accuracy just as great as those instruments used for measuring velocities and pressure. Physically infinite distance, however, does not depend significantly on the accuracy with which the geometric variables are measured, but it does depend crucially on the accuracy with which the dynamic variables are to be determined.

Summing up, the dimensional boundary conditions are as follows:

At $\hat{r} = a$,

$$\begin{aligned}
\hat{u}(a,\hat{\theta},\hat{t}) &= 0 && \hat{t} \geq 0 \\
\hat{v}(a,\hat{\theta},\hat{t}) &= 0\,. && \hat{t} \geq 0
\end{aligned}$$

At $\hat{r} = \hat{h}$,

$$\begin{aligned}
\hat{u}(\hat{h},\hat{\theta},\hat{t}) &= 0 && \hat{t} = 0 \\
&= (-\hat{u}_\infty + \hat{\epsilon}_u)\cos\hat{\theta} && \hat{t} > 0 \\
\hat{v}(\hat{h},\hat{\theta},\hat{t}) &= 0 && \hat{t} = 0 \\
&= (+\hat{u}_\infty + \hat{\epsilon}_v)\sin\hat{\theta} && \hat{t} > 0 \\
\hat{p}(\hat{h},\hat{\theta},\hat{t}) &= \hat{p}_\infty + \hat{\epsilon}_p\,. && \hat{t} > 0
\end{aligned} \tag{1.10}$$

The condition at $\hat{r} = \hat{h}$ is to be interpreted as explained previously

NONDIMENSIONAL EQUATIONS AND BOUNDARY CONDITIONS

Let us introduce the following nondimensional variables, as it is convenient to work with them.

$$u = \frac{\hat{u}}{\hat{u}_\infty} \; ; \quad v = \frac{\hat{v}}{\hat{u}_\infty} \; ; \quad p = \frac{\hat{p} - \hat{p}_\infty}{\frac{1}{2}\rho \hat{u}_\infty^2}$$

$$\epsilon_u = \frac{\hat{\epsilon}_u}{\hat{u}_\infty} \; ; \quad \epsilon_v = \frac{\hat{\epsilon}_v}{\hat{u}_\infty} \; ; \quad \epsilon_p = \frac{\hat{\epsilon}_p}{\frac{1}{2}\rho \hat{u}_\infty^2} \; ; \quad h^* = \frac{\hat{h}}{a} \tag{1.11}$$

$$r = \frac{\hat{r}}{a} \; ; \quad \theta = \hat{\theta} \; ; \quad t = \hat{t}\,\frac{\hat{u}_\infty}{a} \; ; \quad \psi = \frac{\hat{\psi}}{a\hat{u}_\infty} \, .$$

The Reynold's number based on radius is $Re = \hat{u}_\infty a/\nu$. We note that $\hat{u}_\infty$ and $\hat{p}_\infty$ are constant magnitudes of velocity and pressure recorded by the instruments at and beyond some finite distance away from the cylinder. The symbol ∞ is retained in the sense of the idea of a physically infinite distance.

Using Eqs. (1.11), we get from Eqs. (1.1), (1.2), (1.3), and (1.7) the following nondimensional equations:

$$\frac{\partial u}{\partial t} + u\frac{\partial u}{\partial r} + \frac{v}{r}\frac{\partial u}{\partial \theta} - \frac{v^2}{r} = -\frac{1}{2}\frac{\partial p}{\partial r} + \frac{1}{Re}\left(\frac{\partial^2 u}{\partial r^2} + \frac{1}{r}\frac{\partial u}{\partial r} - \frac{u}{r^2} + \frac{1}{r^2}\frac{\partial^2 u}{\partial \theta^2} - \frac{2}{r^2}\frac{\partial v}{\partial \theta}\right) \tag{1.12}$$

$$\frac{\partial v}{\partial t} + u\frac{\partial v}{\partial r} + \frac{v}{r}\frac{\partial v}{\partial \theta} + \frac{uv}{r} = -\frac{1}{2r}\frac{\partial p}{\partial \theta} + \frac{1}{Re}\left(\frac{\partial^2 v}{\partial r^2} + \frac{1}{r}\frac{\partial v}{\partial r} - \frac{v}{r^2} + \frac{1}{r^2}\frac{\partial^2 v}{\partial \theta^2} + \frac{2}{r^2}\frac{\partial u}{\partial \theta}\right) \tag{1.13}$$

$$\frac{\partial u}{\partial r} + \frac{u}{r} + \frac{1}{r}\frac{\partial v}{\partial \theta} = 0 \tag{1.14}$$

$$\frac{\partial \nabla^2 \psi}{\partial t} + \frac{1}{r}\frac{\partial \psi}{\partial \theta}\frac{\partial \nabla^2 \psi}{\partial r} - \frac{1}{r}\frac{\partial \psi}{\partial r}\frac{\partial \nabla^2 \psi}{\partial \theta} - \frac{1}{Re}\nabla^4 \psi = 0 \, , \tag{1.15}$$

where

$$\nabla^2 \equiv \frac{\partial^2}{\partial r^2} + \frac{1}{r}\frac{\partial}{\partial r} + \frac{1}{r^2}\frac{\partial^2}{\partial \theta^2} \, ,$$

and

$$1 \le r \le \infty \, , \quad 0 \le \theta \le 2\pi \, .$$

The corresponding nondimensional boundary conditions obtained from Eqs. (1.10) are:

At $r = 1$,

$$u(1,\theta,t) = \left(\frac{1}{r}\frac{\partial\psi}{\partial\theta}\right)_{r=1} = 0 \quad \text{for all} \quad t$$

$$v(1,\theta,t) = \left(-\frac{\partial\psi}{\partial r}\right)_{r=1} = 0. \quad \text{for all} \quad t$$

At $r = h^*$,

$$\begin{aligned} u(h^*,\theta,t) &= \left(\frac{1}{r}\frac{\partial\psi}{\partial\theta}\right)_{r=h^*} = 0 \quad \text{for} \quad t = 0 \\ &= -(1-\epsilon_u)\cos\theta \quad \text{for} \quad t > 0 \\ v(h^*,\theta,t) &= \left(-\frac{\partial\psi}{\partial r}\right)_{r=h^*} = 0 \quad \text{for} \quad t = 0 \\ &= +(1+\epsilon_v)\sin\theta \quad \text{for} \quad t > 0 \\ p(h^*,\theta,t) &= \epsilon_p . \quad \text{for} \quad t > 0 \end{aligned} \tag{1.16}$$

ϵ_u, ϵ_v, and ϵ_p fall within the limits of accuracy of the measuring instruments and hence are not registered. For the purposes of calculations they are to be regarded as negliglble. The physically infinite distance is h^*, determined as discussed earlier.

It is interesting to note that the condition at h^* requires that $\partial\psi/\partial\theta$ be equal to zero, because h^* is a finite distance. The conventional boundary condition at infinity requires

$$\lim_{r\to\infty}\left(\frac{1}{r}\frac{\partial\psi}{\partial\theta}\right) = 0 .$$

This appears a much weaker condition on $\partial\psi/\partial\theta$ than the previous one. That this is not so can be seen when we take into consideration how the idea of a physically infinite distance h^* is based on the requirement that all physical disturbances should attenuate with distances away from the source of disturbances and on the manner in which it is to be found mathematically.

To complete the formulation of the problem, we should add to the boundary conditions an initial condition, depicting the state of the whole fluid at $t = 0$. If we neglect the initial and the boundary conditions at time $t = 0$ and look for a time-independent solution, the problem becomes simpler. The boundary conditions as stated correspond to the idealized problem of flow past a cylinder started impulsively from rest. The idealization consists in the discontinuous variation of the velocity at $t = 0$. A realistic formulation may need to alter this by allowing for a very rapid but continuous variation of the velocity at $t = 0$. In

principle, these conditions together with an initial condition permit an examination of the transient flow.

The choice of an initial condition is very important from the point of view of the progressive evolution of the flow structure. A critical examination of the governing questions reveals under what circumstances a flow can become time-dependent. This being the case, a condition which is mathematically simple and yet physically representative should be selected with care. In this work, the equations of motion for a time-dependent motion are carefully examined without attempting to solve them. Consequently, we have not formulated realistic initial conditions. The time-independent case for which the boundary conditions of Eqs. (1.16) suffice, is treated completely.

POTENTIAL FLOW SOLUTION

Let us consider the stream function

$$\psi_0 = \psi_0(r,\theta) = -\left(r - \frac{1}{r}\right)\sin\theta \ , \tag{1.17}$$

which leads to the velocity components

$$u_0 = u_0(r,\theta) = +\frac{1}{r}\frac{\partial\psi_0}{\partial\theta} = -\left(1 - \frac{1}{r^2}\right)\cos\theta \tag{1.18}$$

$$v_0 = v_0(r,\theta) = -\frac{\partial\psi_0}{\partial r} = +\left(1 + \frac{1}{r^2}\right)\sin\theta \ , \tag{1.19}$$

and the pressure field

$$p_0 = p_0(r,\theta) = \frac{1}{r^2}\left(2\cos 2\theta - \frac{1}{r^2}\right) . \tag{1.20}$$

These functions in Eqs. (1.17), (1.18), (1.19), and (1.20) satisfy the following equations:

$$\begin{aligned}
&\frac{\partial u_0}{\partial t} + u_0\frac{\partial u_0}{\partial r} + \frac{v_0}{r}\frac{\partial u_0}{\partial\theta} - \frac{v_0^2}{r} = -\frac{1}{2}\frac{\partial p_0}{\partial r} \\
&\frac{\partial v_0}{\partial t} + u_0\frac{\partial v_0}{\partial r} + \frac{v_0}{r}\frac{\partial v_0}{\partial\theta} + \frac{u_0 v_0}{r} = -\frac{1}{2r}\frac{\partial p_0}{\partial\theta} \\
&\frac{\partial u_0}{\partial r} + \frac{u_0}{r} + \frac{1}{r}\frac{\partial v_0}{\partial\theta} = 0 \ ,
\end{aligned} \tag{1.21}$$

and they are such that

$$\frac{\partial^2 u_0}{\partial r^2} + \frac{1}{r}\frac{\partial u_0}{\partial r} - \frac{u_0}{r^2} + \frac{1}{r^2}\frac{\partial^2 u_0}{\partial \theta^2} - \frac{2}{r^2}\frac{\partial v_0}{\partial \theta} \equiv 0$$

$$\frac{\partial^2 v_0}{\partial r^2} + \frac{1}{r}\frac{\partial v_0}{\partial r} - \frac{v_0}{r^2} + \frac{1}{r^2}\frac{\partial^2 v_0}{\partial \theta^2} + \frac{2}{r^2}\frac{\partial u_0}{\partial \theta} \equiv 0 \qquad (1.22)$$

$$\nabla^2 \psi_0 \equiv -2\omega_0 \equiv \frac{\partial^2 \psi_0}{\partial r^2} + \frac{1}{r}\frac{\partial \psi_0}{\partial r} + \frac{1}{r^2}\frac{\partial^2 \psi_0}{\partial \theta^2} \equiv 0 \ .$$

The boundary conditions satisfied by u_0, v_0 and p_0 are:

At $r = 1$,

$$u_0(1,\theta) = \left(\frac{1}{r}\frac{\partial \psi_0}{\partial \theta}\right)_{r=1} = 0$$

$$v_0(1,\theta) = \left(-\frac{\partial \psi}{\partial r}\right)_{r=1} = 0$$

$$p_0(1,\theta) = 2\cos 2\theta - 1 \ .$$

As $r \to \infty$,

$$\lim_{r\to\infty} u_0(r,\theta) = \left(\frac{1}{r}\frac{\partial \psi_0}{\partial \theta}\right)_{r\to\infty} = -\cos\theta$$

$$\lim_{r\to\infty} v_0(r,\theta) = \left(-\frac{\partial \psi_0}{\partial r}\right)_{r\to\infty} = +\sin\theta \qquad (1.23)$$

$$\lim_{r\to\infty} p_0(r,\theta) = 0 \ .$$

The set of Eqs. (1.21) consists of the Euler equations and the continuity equation in two dimensions. The Euler equations are equations of equilibrium for an idealized fluid which is assumed to be nonviscous. Historically, Eqs. (1.17), (1.18), (1.19), and (1.20) are obtained as solutions to Eqs. (1.21) and (1.23) when the flow is further assumed to be irrotational. However, in view of Eqs. (1.21) and (1.22), it follows that ψ_0, u_0, v_0, and p_0 as given by Eqs. (1.17), (1.18), (1.19), and (1.20) satisfy Eqs. (1.12), (1.13), (1.14), and (1.15) for a real viscous fluid. We emphasize that this is due to the condition of irrotationality which implies that the velocity field can be derived from a potential. A comparison of the kinematical conditions in Eqs. (1.23) with the conditions in Eqs. (1.16) shows that these solutions satisfy all but the no-slip condition for a real fluid.

POTENTIAL FLOW AS A BASE FLOW FOR AN ITERATIVE PROCESS IN ACTUAL FLOWS

We shall consider the significance of the potential flow solution given by Eqs. (1.17), (1.18), (1.19), and (1.20) from both the physical and mathematical points of view.

Let us write the Navier-Stokes Eqs. (1.12) and (1.13) as follows:

$$\frac{\partial u}{\partial t} + u\frac{\partial u}{\partial r} + \frac{v}{r}\frac{\partial u}{\partial \theta} - \frac{v^2}{r} + \frac{1}{2}\frac{\partial p}{\partial r} = \frac{1}{Re}\left(\frac{\partial^2 u}{\partial r^2} + \frac{1}{r}\frac{\partial u}{\partial r} - \frac{u}{r^2} + \frac{1}{r^2}\frac{\partial^2 u}{\partial \theta^2} - \frac{2}{r^2}\frac{\partial v}{\partial \theta}\right) \qquad (1.12a)$$

$$\frac{\partial v}{\partial t} + u\frac{\partial v}{\partial r} + \frac{v}{r}\frac{\partial v}{\partial \theta} + \frac{uv}{r} + \frac{1}{2r}\frac{\partial p}{\partial \theta} = \frac{1}{Re}\left(\frac{\partial^2 v}{\partial r^2} + \frac{1}{r}\frac{\partial v}{\partial r} - \frac{v}{r^2} + \frac{1}{r^2}\frac{\partial^2 v}{\partial \theta^2} + \frac{2}{r^2}\frac{\partial u}{\partial \theta}\right). \qquad (1.13a)$$

Here, the Reynolds number is $Re \equiv \hat{u}_\infty a/\nu$.

There are three ways by which the Eqs. (1.12a) and (1.13a) can be reduced to the Euler equations: (a) We may assume, *a priori*, the fluid to be nonviscous, in which case $1/Re \equiv \mu/\mu_\infty a\rho$ is identically equal to zero. Then the governing equations *for all such flow conditions* are the Euler equations. (b) We may consider the fluid to be viscous, but assume $1/Re$ to be so small that *in some domain* the right-hand sides of Eqs. (1.12a) and (1.13a) can be regarded as negligible and hence put equal to zero. In this case the Euler equations are the governing equations only when the *specific conditions* are met. (c) We may consider the fluid to be viscous, but assume the velocity field to be irrotational, in which case the terms in parentheses of Eqs. (1.12a) and (1.13a) are identically equal to zero. Here the Euler equations are the governing dynamic equations for a viscous fluid when the *flow is assumed to be irrotational.*

Possibilities (a) and (b), which are quite distinct, impose restrictions on the Reynolds number Re. Possibility (c) imposes a restriction on the nature of the flow. Historically, the Euler equations are derived through the first possibility (a).

The boundary layer theory assumes that, when the Reynolds number is very large, i.e., $1/Re$ is very small, a real flow is a *potential flow* except near a solid boundary; accordingly, it asserts that near a solid boundary the terms in parentheses of the right-hand sides of Eqs. (1.12a) and (1.13a) are significant, even though $1/Re$ may be made arbitrarily small. This theory, then, makes use of the second possibility (b). It has led to a widely held view that the potential flow is an approximation to the corresponding real flow only at very large Reynolds number. However, an alternative view, which is very significant in the present work, can be taken as shown by the following considerations.

First, we note that the possibilities (a), (b), and (c) show that when $1/Re$ is assumed to be zero the velocity field need not be assumed irrotational and, conversely, when the velocity field is assumed irrotational Re may have any finite value so that $1/Re$ differs significantly from zero. As we have already seen, the potential flow solution given by Eqs. (1.17), (1.18), (1.19), and (1.20) satisfies Eqs. (1.22) and thus satisfies the requirements of the third possibility (c).

Consequently, if the boundary conditions are not brought into consideration, this potential flow solution satisfies the Navier-Stokes equations for all Reynolds numbers, i.e., even though the solution is generally referred to as the solution for an inviscid fluid, it is in fact independent of the viscosity of a fluid.

Let S denote the actual solution which satisfies the Navier-Stokes equations, the continuity equation, and all the boundary conditions, and which, we assume, represents the flow field as observed in experiments. Let S_0 denote the potential flow solution given by Eqs. (1.17), (1.18), (1.19), and (1.20). Let the flow domain be denoted by M. The solution S, if substituted *in the Euler equations*, will not, in general, satisfy them everywhere in the domain M. However, it may satisfy them in some subdomain M_1 of M to a high degree of approximation. Let M_2 denote the remaining subdomain of M so that $M_1 + M_2 = M$. The solution S_0 satisfies the Navier-Stokes equations as well as the Euler equations everywhere in the domain M and consequently in the subdomain M_1, regardless of the viscosity of the fluid. Therefore, in the subdomain M_1 the actual solution S must be a close approximation to the potential flow solution S_0, but in the subdomain M_2 it may be significantly different from it. Now A is said to deviate from B under a variable set of conditions C if A changes with C while B does not, and A approaches B when the variable set of conditions C approach one or more fixed sets of conditions D, E, etc. *The actual solution* S *depends on the Reynolds number as a parameter and hence changes with it, whereas the potential solution* S_0, *being independent of the Reynolds number, remains constant for all Reynolds numbers.* Therefore we can identify S with A, S_0 with B, Re with the variable set of conditions C, and fixed limiting values of Re with the fixed sets of conditions D, E, etc. If then the subdomain M_1 happens to enlarge as the Reynolds number Re approaches any one of the fixed limiting values, this fact may be taken to mean that *the actual solution* S *deviates from the potential flow solution* S_0 *in the whole domain* M *and that this deviation decreases as the Reynolds number* Re *approaches any one of the fixed limiting values.* The observations at high values of Reynolds number show that the domain in which the real flow can be regarded as a potential flow does in fact increase with increasing Reynolds numbers. Similar observations at extremely low values of Reynolds numbers, e.g., for Hele-Shaw flows, show that the same is the case with decreasing Reynolds numbers. Consequently, if we assume that S does represent the real flow as observed, the foregoing conclusion becomes compulsive.

As we have shown, the potential flows satisfy the Navier-Stokes equations in a stricter sense than do the viscous flows, i.e., by leading to the vanishing of the separate parts of the governing equations whatever be the viscosity of the fluid—and this is all the more striking when the individual terms of the Vorticity Transport Equation are observed to vanish separately. *The irrotational character of the flow* is what leads to this remarkable behavior. This is here regarded to be of fundamental importance and consequently, for the present work, the third possibility (c) leading to the Euler equations is the meaningful one. In this light, *we may think of a real flow as a deviation from the corresponding potential flow,* made in order to satisfy the no-slip boundary conditions, and*

*By corresponding potential flow is meant here the flow which satisfies the N-S equations and all boundary conditions except the no-slip condition.

that this deviation need not necessarily be considered small in any sense. The subdomain M_1, may be a null domain for certain ranges of flow parameters, but for other ranges it may not be so and then the deviation would be small in it. This is to be considered incidental. *However, as a hypothesis which is later supported on the basis of the principle of minimum dissipation, this deviation for a given Reynolds number will be considered to be a minimum consistent with the governing equations and the actual boundary and flow conditions.* The potential flow then assumes the position of a base flow from which the deviations take place. This holds for all flow conditions and, in particular, for all Reynolds numbers.

In the immediately following pages we present an examination and critique of significant experiments and observations made by distinguished investigators which accord with and support the above hypothesis. We shall consider the beautiful experiments carried out in 1899 by Professor Hele-Shaw [27, 28]. It is helpful to quote here the following passages from his paper of 1899.

> If we take two sheets of glass, and bring them nearly close together, leaving only a space the thickness of a thin card or piece of paper, and then by suitable means cause liquid to flow under pressure between them, the very property of viscosity, which as before noted, is the cause of the eddying motion in large bodies of water, in the present case greatly limits the freedom of motion of the fluid between the two sheets of glass, and thus prevents not only eddying or whirling motion, but also counteracts the effects of inertia. Every particle is then compelled by the pressure behind and around it to more onwards without whirling motion, following the path which corresponds exactly with the stream-lines in a perfect liquid.
>
> * * *
>
> But at this stage you may reasonably enquire how it is that we are able to state, with so much certainty, that the artificial conditions of flow with a viscous liquid are really giving us the stream-line motion of a perfect one; and this brings me to the results which mathematicians have obtained.
>
> The view now shown represents a body of circular cross-section past which a fluid of infinite extent is moving, and the lines are plotted from mathematical investigation and represent the flow of particles. This particular case gives us the means of most elaborate comparison; although we cannot employ a fluid of infinite extent, we can prepare the border of the channel to correspond with any of the particular stream-lines, and measure the exact positions of the lines inside.
>
> By means of a second lantern, the real flow of a viscous liquid for this case is shown upon the second screen, and you will see that it agrees with the calculated flow around a similar obstacle of a perfect liquid. The diagram shown on the wall is the actual

figure employed for comparison and upon which the experimental case was projected. By this means, it was proved that the two were in absolute agreement.

* * *

Mathematicians, however, predicted with absolute certainty, that with stream-line motion the water should flow round and meet at the back, a state of things that, however slow we make the motion in the present case, does not occur owing to the effect of inertia. They have drawn with equal confidence the lines along which this should take place. We could either effect this result with the experiment you have just seen, by using a much more viscous liquid, such as treacle, or, what comes to the same thing, bringing the two sheets of glass nearly close together.

In these quoted passages we see that there are three controlling factors by which a real flow configuration is created so that its streamline field is exactly the same as that of a corresponding potential flow. These are (a) the pressure, (b) the viscosity, and (c) the distance separating the two plates.

Following Professor Hele-Shaw's experiments, Professor Stokes (1898) in his paper "Mathematical Proof of the Identity of the Stream-Lines Obtained by Means of a Viscous Film with Those of a Perfect Fluid Moving in Two Dimensions" [29], starts out with the equations for a creep motion in which the nonlinear inertia terms are neglected, and shows that, when the distance separating two plates is small, the stream function for the flow satisfies the harmonic equation and is uniquely determined by the condition that the boundaries shall be streamlines. And since a stream function for a potential flow meets these requirements, the identity is established. He continues: "It may be objected that the streamlines cannot be the same in the two cases, inasmuch as the perfect liquid glides over the surface of the obstacle, whereas in the case of the viscous liquid the motion vanishes at the surface of the obstacle. This is perfectly true, and forms the qualification above referred to; but it does not affect the truth of the proposition, which applies only to the limiting case of a viscid liquid confined between walls which are infinitely close. Any finite thickness of the stratum of liquid will entail a departure from the identity of the streamlines in the two cases, which, however will be sensible only to a distance from the obstacle comparable with the distance between the walls, and therefore capable of being indefinitely reduced by taking the walls closer and closer together."

In 1938, F. Riegels [30] carried out further experiments on Hele-Shaw flows and gave a theoretical representation of the same, based on an iterative scheme. As a starting point he takes a solution of the equations of creeping motion, which may be written as

$$u_1 = u_0(x,y)\left(1 - \frac{z^2}{h^2}\right)$$

$$v_1 = v_0(x,y)\left(1 - \frac{z^2}{h^2}\right)$$

$$w_1 = 0 ,$$

where $u_0(x,y)$ and $v_0(x,y)$ are the velocity components of the two-dimensional potential flow past a given body. The flow represented by the above equations has the same streamlines as the potential flow about the body, and the streamlines for all parallel layers z = constant are congruent. The condition of no-slip at the plates $z = \pm h$ is satisfied, but the same at the surface of the body is not satisfied [19].

Using the above solution to calculate the nonlinear inertia terms, he obtains a second approximation. For the case of a circular cylinder he gives the radial and tangential velocity components as

$$u_2 = \mathrm{Reh}^2\left[\left(\frac{\cos 2\theta}{r^3} - \frac{1}{r^5}\right)\left(-\frac{1}{21} + \frac{11}{35}\frac{z^2}{h^2} - \frac{1}{3}\frac{z^4}{h^4} + \frac{1}{15}\frac{z^6}{h^6}\right)\right]$$

$$v_2 = \mathrm{Reh}^2\left[\frac{\sin 2\theta}{r^3}\left(-\frac{1}{21} + \frac{11}{35}\frac{z^2}{h^2} - \frac{1}{3}\frac{z^4}{h^4} + \frac{1}{15}\frac{z^6}{h^6}\right)\right],$$

and the component in the z direction is given as

$$w_2 = \mathrm{Reh}^3\,\frac{1}{r^6}\left(\frac{4}{21}\frac{z}{h} - \frac{44}{105}\frac{z^3}{h^3} + \frac{4}{15}\frac{z^5}{h^5} - \frac{4}{105}\frac{z^7}{h^7}\right).$$

Here $\mathrm{Re} = UL/\nu$, where U is the maximum velocity of the stream in the center of the plate, ν is the kinematic viscosity of the fluid, and L is a characteristic dimension of the obstacle, which for a circular cylinder is taken as the radius.

It can be seen that u_2, v_2 and w_2 satisfy the no-slip boundary condition at the plate $z = \pm h$, but they do not satisfy it at the cylinder wall. What is interesting is that the normal component u_2 is also not zero at the cylinder wall. The total solution is given by the sums $u_1 + u_2$, $v_1 + v_2$, and w_2.

Since u_2 and v_2 depend on the number (Reh^2) and w_2 depends on the number (Reh^3), h being the nondimensional thickness of the fluid layer between the walls, Riegels introduces a characteristic Reynolds number for the flow configuration as

$$\Lambda = \mathrm{Re}\,\frac{h'^2}{R^2} = \frac{Uh'^2}{\nu R} \equiv \mathrm{Reh}^2 ; \quad h \equiv \frac{h'}{R} .$$

For w_2

$$\Lambda_1 = \mathrm{Re}\,\frac{h'^3}{R^3} = \frac{Uh'^3}{\nu R^2} \equiv \mathrm{Reh}^3 .$$

Thus for any obstacle, the characteristic Reynolds number is given by $Uh'^2/\nu L$, where L is a characteristic length of the obstacle and h' is the distance separating the two plates. Since Λ is proportional to h'^2, u_2, v_2, and w_2 all tend to zero as $h' \to 0$. Then, in the limit, the flow reduces to a two-dimensional flow with u_1 and v_1 as velocity components, w_1 being zero. This was the conclusion of Stokes and the experimental observation of Hele Shaw. Riegels' experiments, carried out up to about $\Lambda = 6$, show that for $\Lambda \leq 1$ there is no discernible deviation from the potential streamline field, but that for higher values of this parameter the deviation is noticeable.

The pressure field for a creeping flow satisfies the harmonic equation $\nabla^2 p = 0$ because the convective terms in the Navier-Stokes equations are completely neglected, but the velocity field does not satisfy the equation. On the other hand, the velocity field for a potential flow always satisfies the harmonic equation, but the pressure field does not and is in fact given by $\nabla^2 p = -\rho(\partial u_i/\partial x_j \, \partial u_j/\partial x_i)$. When the product term $\rho(\partial u_i/\partial x_j \, \partial u_j/\partial x_i)$ can be neglected, the pressure field of the potential flow is harmonic in the limit. Stokes has shown that the velocity field of a creep flow becomes harmonic in the limit. Hence in the limit, the velocity field and the pressure fields of a creep flow are potential. Thus these experiments and theoretical treatments show that there exists a three-dimensional real flow, which apparently satisfies the no-slip conditions, such that the streamline field due to it becomes identical with that due to a two-dimensional potential flow in the same space when the Reynolds number tends to become vanishingly small; and that this potential flow evidently does not satisfy the no-slip conditions.

There are two noteworthy points in these experiments of Hele-Shaw and Riegels: (a) the three-dimensional flow becomes two-dimensional; and (b) the velocity field attains a potential character, i.e., it becomes irrotational. Of these two, the first may be regarded as peculiar to the particular geometry under consideration, and hence incidental. The second point, however, may be regarded as an expression of a general truth, and hence fundamental, for the following reasons.

The rate at which energy E is dissipated in a body of fluid is given by the expression

$$\dot{E} = \mu \int_{(V)} \Omega^2 \, d\tau + 2\mu \int_{(S)} [\vec{\mathbf{n}} \cdot (\vec{\mathbf{V}} \times \vec{\Omega})] \, ds$$
$$-2\mu \int_{(S)} [\mathbf{V} \cdot (\mathbf{n} \cdot \text{grad}) \mathbf{V}] \, ds + \lambda \int_{(S)} (\text{div } \mathbf{V}) \, \mathbf{n} \cdot \mathbf{V} \, ds \,, \tag{1.24a}$$

where

Ω = Curl $\mathbf{V}$ = vorticity vector

$\mathbf{V}$ = Velocity vector with components u_i

$\mathbf{n}$ = Unit vector directed inwards along the normal to an element ds of the surface S bounding the fluid

λ, μ = coefficients of viscosity.

After transforming the surface integrals into volume integrals, the above expression may be rewritten as

$$\dot{E} = \int \Phi \, d\tau \, , \tag{1.24b}$$

where

Φ = Dissipation function

$$= \lambda \sum_i \left(\frac{\partial u_i}{\partial x_i} \right)^2 + \frac{\mu}{2} \sum_{i,j} \left(\frac{\partial u_i}{\partial x_j} + \frac{\partial u_j}{\partial x_i} \right)^2 . \tag{1.25}$$

From (1.25) we see that Φ and hence $\dot{E}$ are nonnegative. It is also clear that Φ and hence $\dot{E}$ can vanish only under the following two circumstances.

(i) $\lambda = 0$, $\mu = 0$, i.e., when the fluid is regarded as ideal.

(ii) $\partial u_i / \partial x_i = 0$, $\partial u_i / \partial x_j + \partial u_j / \partial x_i = 0$, i.e., when there is no deformation and the fluid moves as a rigid body.

For a real fluid for which $\lambda > 0$, $\mu > 0$, $\dot{E}$ can vanish only under the second condition and this is of little interest. We note that $\dot{E} = 0$ is the absolute minimum which this function can attain. Under circumstances other than the one noted there will always be some dissipation of energy. If we postulate that the flow evolves to minimize dissipation [2, 3, 4], this is tantamount to a principle.

PRINCIPLE OF MINIMUM DISSIPATION

For all real flows, the rate of energy dissipation assumes the lowest attainable value consistent with the conservation principles and the boundary conditions.

To see the implications of this principle, let us write Eq. (1.24a) in the following two groups:

$$\dot{E} = (I_1 + I_2) + (I_3 + I_4) \tag{1.24c}$$

$$= (I_1) + (I_2 + I_3 + I_4) \, , \tag{1.24d}$$

where

$$I_1 = \text{Volume integral} = \mu \int_{(V)} \Omega^2 \, d\tau$$

$$I_2 = \text{Surface integral} = 2\mu \int_{(S)} [\mathbf{n} \cdot (\vec{\mathbf{V}} \times \Omega)] \, ds$$

$$I_3 = \text{Surface integral} = -2\mu \int_{(S)} \mathbf{V} \cdot (\mathbf{n} \cdot \text{grad}) \mathbf{V} \, ds$$

$$I_4 = \text{Surface integral} = \lambda \int_{(S)} (\text{div } \mathbf{V}) \, \mathbf{n} \cdot \mathbf{V} \, ds$$

Let us consider the circumstances under which the sum $(I_2 + I_3 + I_4)$ of the surface integrals I_2, I_3, and I_4 vanishes. It would be a very special flow in which the surface conditions are such that the sum vanishes, but none of the integrals I_2, I_3, and I_4 vanishes. Further, the class of flows in which the conditions are such that these integrals vanish individually but their integrands are nonzero will also be a special one. The third possibility, when the integrands of I_2, I_3, and I_4 vanish identically, is the most important.

The integrands of I_2, I_3, and I_4 are zero when $\mathbf{V} = 0$ on S. Thus when the fluid is enclosed within fixed boundaries this condition is realized. Alternatively, the integrands of I_2, I_3, and I_4 vanish when $\mathbf{n} \cdot (\mathbf{V} \times \Omega) = 0$, $(\mathbf{n} \cdot \text{grad}) \mathbf{V} = 0$, and $\text{div } \mathbf{V} = 0$ respectively on S. In general, $\mathbf{n}$ will not be perpendicular to the direction of $\mathbf{V} = \Omega$. Hence $\mathbf{n} \cdot (\mathbf{V} \times \Omega)$ can vanish if $\mathbf{V} \times \Omega = 0$. But since $\mathbf{V} \neq 0$, this would require $\Omega = 0$. It is important to note that the vanishing of Ω on S does not imply that it vanishes everywhere in the fluid. Similarly, $\text{div } \mathbf{V} = 0$ on S does not imply that $\text{div } \mathbf{V} = 0$ everywhere. However, if the fluid is incompressible, $\text{div } \mathbf{V} = 0$ everywhere and, in particular, $\text{div } \mathbf{V} = 0$ on the surface S.

We may visualize the bounding surface S to be divided into the following parts:

(i) Part S_1 such that at least the condition $\mathbf{V} = 0$ holds.

(ii) Part S_2 such that $\Omega = 0$, $(\mathbf{n} \cdot \text{grad}) \mathbf{V} = 0$, and $\text{div } \mathbf{V} = 0$, but $\mathbf{V} \neq 0$.

(iii) Part S_3 such that $(\mathbf{n} \cdot \text{grad}) \mathbf{V} = 0$ and $\text{div } \mathbf{V} = 0$, but $\mathbf{V} \neq 0$ and $\Omega \neq 0$.

(iv) Part S_4 such that none of the above conditions hold.

It may happen that one or more of the above four parts are zero.

All fixed surfaces at which the no-slip boundary condition holds constitute the part S_1. Whenever the condition of uniform flow at infinity is valid, all the conditions $\Omega = 0$, $(\mathbf{n} \cdot \text{grad})\,\mathbf{V} = 0$, and $\text{div}\,\mathbf{V} = 0$ hold because they involve differentiation of the vector $\mathbf{V}$ which is constant when the flow is uniform. Hence the enveloping surface at infinity belongs to the class S_2. The external flows for which the bounding surface S is made up of fixed boundaries in the interior and an enveloping boundary at infinity where uniform flow conditions prevail, belong to the class of flows for which the surface integrals I_2, I_3, and I_4 are zero, no matter whether the fluid is compressible or incompressible. For internal flows where part of the enveloping surface is a fixed boundary and the inlet and outlet conditions are such that $(\mathbf{n} \cdot \text{grad})\,\mathbf{V} = 0$ and $\text{div}\,\mathbf{V} = 0$, but $\mathbf{V} \neq 0$ and $\Omega \neq 0$, the surface integrals I_3 and I_4 vanish. We then see that for external flows

$$\dot{E} = \mu \int_{(V)} \Omega^2 \, d\tau \,, \tag{1.24e}$$

and for internal flows

$$\dot{E} = \mu \int_{(V)} \Omega^2 \, d\tau + 2\mu \int_{(S_3)} [\mathbf{n} \cdot (\mathbf{V} \times \Omega)] \, ds \tag{1.24f}$$

are valid expressions for $\dot{E}$.

If we assert that the principle of minimum dissipation holds, then that would imply that the integrals in Eqs. (1.24e) and (1.24f) achieve their lowest attainable value consistent with conservation principles and the surface conditions. We note that these integrals depend on Ω, the vorticity field. If Ω vanishes or at least becomes insignificantly small in most parts of the flow field, the contribution to the volume integral would be reduced materially. From Eqs. (1.24e) and (1.24f) it is also clear that as $\Omega \to 0$, $\dot{E} \to 0$. Conversely, $\dot{E} \to 0$ should imply $\Omega \to 0$ because both the integrands are positive-definite. We observe that though for real fluids $\dot{E}$ cannot be zero in general, it must tend to zero according to the principle of minimum dissipation. Consequently, the validity of this principle would lead us to infer that $\Omega \to 0$. Since $\Omega = 0$ implies that the velocity field is irrotational and hence derivable from a potential, we can now state the following as a conclusion:

> *Theorem I:* For a large class of real flows, the velocity field tends to become irrotational and hence derivable from a potential.

The Hele-Shaw flows belong to the class of real flows for which the above statement holds. Hence the fact that, as $\Lambda \to 0$, the velocity field becomes potential can be viewed as the substantiation of the principle of minimum dissipation. That large parts of a flow field become derivable from a potential as the Reynolds number of the flow is increased in experimentally well established and forms the basis of the boundary layer theory. The streamline pattern of a creep

flow around a sphere reminds one of the streamline pattern of the corresponding potential flow.

A potential flow is thus seen to play a fundamental role at the lower as well as the higher ranges of the characteristic parameter, the Reynolds number, of the flow of a real fluid. This being the case, there seems no a priori reason why it should not play a fundamental role all through the range of this parameter. The principle of minimum dissipation, if assumed to hold, indicates that it should play such a role. Consequently, we may regard it as the fundamental base flow for all Reynolds numbers.

MATHEMATICAL CONSIDERATIONS

In the theory of linear differential operators, the operator and its domain are defined as in the following paragraphs [30].

First, the linear vector space $\bar{S}$ of functions on which the differential operator L, say of order n, operates is defined such that (a) the interval of the variable, (b) the nature of the functions, and (c) the scalar product are specified. The domain of the operator is the set of all functions u in $\bar{S}$ which have a piecewise continuous derivative of the order n, which satisfy n independent and linear conditions, and are such that Lu belongs to $\bar{S}$.

The differential equation $Lu = f$ does not have a unique solution unless the conditions to be satisfied by u are given. Different sets of conditions lead to different solutions. Hence for precise notation, a different symbol should be used for the operator each time the conditions are changed. For convenience, however, the same symbol is used for the differential operator under all conditions, but the conditions which the solution of $Lu = f$ is to satisfy are specified. Thus the operator is formally the same for all the solutions of $Lu = f$, but in fact is different for different solutions [30].

In solving linear boundary value problems with involved boundary conditions it is a common practice to consider the ultimate solution as made up of two or more parts, each part satisfying the governing equations completely, but the boundary conditions only partially so that when added together they satisfy the governing equations and all the boundary conditions due to the linearity of the operator. The number of parts into which the solution is divided is generally finite. For example, if u is the final solution of a second order differential equation $Lu = f$ such that it satisfies a set of conditions $B_1(u) = \alpha_1$, $B_2(u) = \alpha_2$ for specified values of the variable, it may be conceived as made up of two parts, u_1 and u_2, such that

$$Lu_1 = 0\,, \quad B_1(u_1) = \alpha_1\,, \quad B_2(u_1) = \alpha_2\,,$$

and

$$Lu_2 = f\,, \quad B_1(u_2) = 0\,, \quad B_2(u_2) = 0\,.$$

Due to linearity,

$$Lu = Lu_1 + Lu_2 = f$$

$$B_1(u) = B_1(u_1) + B_1(u_2) = \alpha_1$$

$$B_2(u) = B_2(u_1) + B_2(u_2) = \alpha_2 .$$

In general, therefore, we may write

$$Lu = Lu_1 + Lu_2 + \cdots + Lu_n = f , \tag{1.26}$$

where $u_1, u_2, \ldots, u_n$ satisfy different equations and boundary conditions. If we recall the precise notation, this should have been written

$$Lu = L_1u_1 + L_2u_2 + \cdots + L_nu_n = f , \tag{1.27}$$

where $L_1, L_2, \ldots, L_n$ are differential operators which are formally the same as L, but with different boundary conditions. The functions u_i, $i = 1$, and n may be required to be the solutions of the operator equations

$$L_iu_i = f_i \quad i = 1, \ldots, n \text{ (no summation)} , \tag{1.28}$$

where

$$\sum_{i=1}^{n} f_i = f$$

and f_i belong to $\bar{S}$. The functions f_i are suitably selected, depending on the problem.

Let us assume that in the case of a system of nonlinear differential equations, in particular the Navier-Stokes equations under consideration, there exists an infinite sum of functions

$$S_0 + S_1 + S_2 + S_3 + \cdots$$

of the space-time variables and the flow parameters such that it converges to the solution S, which satisfies the Navier-Stokes equations, the continuity equation, and the boundary conditions completely, in the sense that the partial sums

$$S_{pn} = S_0 + S_1 + S_2 + S_3 + \cdots + S_n$$

converge to the solution S; i.e., given $\epsilon > 0$, there exists an integer $N(\epsilon)$ such that

$$|S - S_{pn}| < \epsilon$$

for all $n > N$.

With the above assumption, we may write

$$
\begin{aligned}
u &= u_0 + u_1 + u_2 + u_3 + \cdots \\
v &= v_0 + v_1 + v_2 + v_3 + \cdots \\
p &= p_0 + p_1 + p_2 + p_3 + \cdots \\
\psi &= \psi_0 + \psi_1 + \psi_2 + \psi_3 + \cdots ,
\end{aligned}
\tag{1.29}
$$

where u, v, p, and ψ correspond to the solution S, while u_n, v_n, p_n, and ψ_n correspond to the function S_n.

Let us substitute Eqs. (1.29) in Eqs. (1.12), (1.13), (1.14), and (1.15). Assuming that a rearrangement and grouping of terms in these equations as made below is permissible, we get the following equations:

$$
\begin{aligned}
&\left[\left(\frac{\partial u_0}{\partial t} + u_0\frac{\partial u_0}{\partial r} + \frac{v_0}{r}\frac{\partial u_0}{\partial \theta} - \frac{v_0^2}{r}\right) + \frac{1}{2}\frac{\partial p_0}{\partial r}\right. \\
&\left. - \frac{1}{Re}\left(\frac{\partial^2 u_0}{\partial r^2} + \frac{1}{r}\frac{\partial u_0}{\partial r} - \frac{u_0}{r^2} + \frac{1}{r^2}\frac{\partial^2 u_0}{\partial \theta^2} - \frac{2}{r^2}\frac{\partial v_0}{\partial \theta}\right)\right] \\
&+\left\{\left[\frac{\partial u_1}{\partial t} + (u_0)\frac{\partial u_1}{\partial r} + \left(\frac{v_0}{r}\right)\frac{\partial u_1}{\partial \theta} + \left(\frac{\partial u_0}{\partial r}\right)u_1 + \left(\frac{1}{r}\frac{\partial u_0}{\partial \theta} - \frac{2v_0}{r}\right)v_1\right]\right. \\
&\left. + \frac{1}{2}\frac{\partial p_1}{\partial r} - \frac{1}{Re}\left(\frac{\partial^2 u_1}{\partial r^2} + \frac{1}{r}\frac{\partial u_1}{\partial r} - \frac{u_1}{r^2} + \frac{1}{r^2}\frac{\partial^2 u_1}{\partial \theta^2} - \frac{2}{r^2}\frac{\partial v_1}{\partial \theta}\right)\right\} \\
&+\left\{\left[\frac{\partial u_2}{\partial t} + (u_0+u_1)\frac{\partial u_2}{\partial r} + \left(\frac{v_0+v_1}{r}\right)\frac{\partial u_2}{\partial \theta} + \left(\frac{\partial u_0}{\partial r} + \frac{\partial u_1}{\partial r}\right)u_2\right.\right. \\
&\left.\left. + \left(\frac{1}{r}\frac{\partial}{\partial \theta}(u_0+u_1) - \frac{2}{r}(v_0+v_1)\right)v_2\right] + \frac{1}{2}\frac{\partial p_2}{\partial r}\right. \\
&\left. - \frac{1}{Re}\left(\frac{\partial^2 u_2}{\partial r^2} + \frac{1}{r}\frac{\partial u_2}{\partial r} - \frac{u_2}{r^2} + \frac{1}{r^2}\frac{\partial^2 u_2}{\partial \theta^2} - \frac{2}{r^2}\frac{\partial v_2}{\partial \theta}\right)\right. \\
&\left. + \left(u_1\frac{\partial u_1}{\partial r} + \frac{v_1}{r}\frac{\partial u_1}{\partial \theta} - \frac{v_1^2}{r}\right)\right\} + \left\{\left[\frac{\partial u_3}{\partial t} + (u_0+u_1+u_2)\frac{\partial u_3}{\partial r} + \left(\frac{v_0+v_1+v_2}{r}\right)\frac{\partial u_3}{\partial \theta}\right.\right. \\
&\left.\left. + \left(\frac{\partial u_0}{\partial r} + \frac{\partial u_1}{\partial r} + \frac{\partial u_2}{\partial r}\right)u_3 + \left(\frac{1}{r}\frac{\partial}{\partial \theta}(u_0+u_1+u_2) - \frac{2}{r}(v_0+v_1+v_2)\right)v_3\right]\right. \\
&\left. + \frac{1}{2}\frac{\partial p_3}{\partial r} - \frac{1}{Re}\left(\frac{\partial^2 u_3}{\partial r^2} + \frac{1}{r}\frac{\partial u_3}{\partial r} - \frac{u_3}{r^2} + \frac{1}{r^2}\frac{\partial^2 u_3}{\partial \theta^2} - \frac{2}{r^2}\frac{\partial v_3}{\partial \theta}\right)\right. \\
&\left. + \left(u_2\frac{\partial u_2}{\partial r} + \frac{v_2}{r}\frac{\partial u_2}{\partial \theta} - \frac{v_2^2}{r}\right)\right\} \\
&+ \cdots = 0 ;
\end{aligned}
\tag{1.30}
$$

$$\left[\left(\frac{\partial v_0}{\partial t} + u_0\frac{\partial v_0}{\partial r} + \frac{v_0}{r}\frac{\partial v_0}{\partial \theta} + \frac{u_0 v_0}{r}\right) + \frac{1}{2r}\frac{\partial p_0}{\partial \theta}\right.$$

$$\left. - \frac{1}{Re}\left(\frac{\partial^2 v_0}{\partial r^2} + \frac{1}{r}\frac{\partial v_0}{\partial r} - \frac{v_0}{r^2} + \frac{1}{r^2}\frac{\partial^2 v_0}{\partial \theta^2} + \frac{2}{r^2}\frac{\partial u_0}{\partial \theta}\right)\right]$$

$$+\left\{\left[\frac{\partial v_1}{\partial t} + (u_0)\frac{\partial v_1}{\partial r} + \left(\frac{v_0}{r}\right)\frac{\partial v_1}{\partial \theta} + \left(\frac{v_0}{r} + \frac{\partial v_0}{\partial r}\right)u_1 + \left(\frac{u_0}{r} + \frac{1}{r}\frac{\partial v_0}{\partial \theta}\right)v_1\right]\right.$$

$$\left. + \frac{1}{2r}\frac{\partial p_1}{\partial \theta} - \frac{1}{Re}\left(\frac{\partial^2 v_1}{\partial r^2} + \frac{1}{r}\frac{\partial v_1}{\partial r} - \frac{v_1}{r^2} + \frac{1}{r^2}\frac{\partial^2 v_1}{\partial \theta^2} + \frac{2}{r^2}\frac{\partial u_1}{\partial \theta}\right)\right\}$$

$$+\left\{\left[\frac{\partial v_2}{\partial t} + (u_0+u_1)\frac{\partial v_2}{\partial r} + \left(\frac{v_0+v_1}{r}\right)\frac{\partial v_2}{\partial \theta} + \left(\frac{v_0+v_1}{r} + \frac{\partial}{\partial r}(v_0+v_1)\right)u_2\right.\right.$$

$$\left.\left. + \left(\frac{u_0+u_1}{r} + \frac{1}{r}\frac{\partial}{\partial \theta}(v_0+v_1)\right)v_2\right] + \frac{1}{2r}\frac{\partial p_2}{\partial \theta}\right.$$

$$\left. - \frac{1}{Re}\left(\frac{\partial^2 v_2}{\partial r^2} + \frac{1}{r}\frac{\partial v_2}{\partial r} - \frac{v_2}{r^2} + \frac{1}{r^2}\frac{\partial^2 v_2}{\partial \theta^2} + \frac{2}{r^2}\frac{\partial u_2}{\partial \theta}\right)\right.$$

$$\left. + \left(u_1\frac{\partial v_1}{\partial r} + \frac{v_1}{r}\frac{\partial v_1}{\partial \theta} + \frac{u_1 v_1}{r}\right)\right\} + \left\{\left[\frac{\partial v_3}{\partial t} + (u_0+u_1+u_2)\frac{\partial v_3}{\partial r}\right.\right.$$

$$\left. + \left(\frac{v_0+v_1+v_2}{r}\right)\frac{\partial v_3}{\partial \theta} + \left(\frac{v_0+v_1+v_2}{r} + \frac{\partial}{\partial r}(v_0+v_1+v_2)\right)u_3\right.$$

$$\left.\left. + \left(\frac{u_0+u_1+u_2}{r} + \frac{1}{r}\frac{\partial}{\partial \theta}(v_0+v_1+v_2)\right)v_3\right] + \frac{1}{2r}\frac{\partial p_3}{\partial \theta}\right.$$

$$\left. - \frac{1}{Re}\left(\frac{\partial^2 u_3}{\partial r^2} + \frac{1}{r}\frac{\partial v_3}{\partial r} - \frac{v_3}{r^2} + \frac{1}{r^2}\frac{\partial^2 v_3}{\partial \theta^2} + \frac{2}{r^2}\frac{\partial u_3}{\partial \theta}\right) + \left(u_2\frac{\partial v_2}{\partial r} + \frac{v_2}{r}\frac{\partial v_2}{\partial \theta} + \frac{u_2 v_2}{r}\right)\right\}$$

$$+ \cdots = 0 \; ; \tag{1.31}$$

$$\left(\frac{\partial u_0}{\partial r} + \frac{u_0}{r} + \frac{1}{r}\frac{\partial v_0}{\partial \theta}\right) + \left(\frac{\partial u_1}{\partial r} + \frac{u_1}{r} + \frac{1}{r}\frac{\partial v_1}{\partial \theta}\right)$$

$$+ \left(\frac{\partial u_2}{\partial r} + \frac{u_2}{r} + \frac{1}{r}\frac{\partial v_2}{\partial \theta}\right) + \left(\frac{\partial u_3}{\partial r} + \frac{u_3}{r} + \frac{1}{r}\frac{\partial v_3}{\partial \theta}\right)$$

$$+ \cdots = 0 \; ; \tag{1.32}$$

and

$$\left(\frac{\partial \nabla^2\psi_0}{\partial t} + \frac{1}{r}\frac{\partial \psi_0}{\partial \theta}\frac{\partial \nabla^2\psi_0}{\partial r} - \frac{1}{r}\frac{\partial \psi_0}{\partial r}\frac{\partial \nabla^2\psi_0}{\partial \theta} - \frac{1}{Re}\nabla^4\psi_0\right)$$

$$+\left[\frac{\partial \nabla^2\psi_1}{\partial t} + \left(-\frac{1}{r}\frac{\partial \nabla^2\psi_0}{\partial \theta}\right)\frac{\partial \psi_1}{\partial r} + \left(\frac{1}{r}\frac{\partial \nabla^2\psi_0}{\partial r}\right)\frac{\partial \psi_1}{\partial \theta}\right.$$

$$\left.+\left(\frac{1}{r}\frac{\partial \psi_0}{\partial \theta}\right)\frac{\partial \nabla^2\psi_1}{\partial r} + \left(-\frac{1}{r}\frac{\partial \psi_0}{\partial r}\right)\frac{\partial \nabla^2\psi_1}{\partial \theta} - \frac{1}{Re}\nabla^4\psi_1\right]$$

$$+\left\{\left[\frac{\partial \nabla^2\psi_2}{\partial t} + \left(-\frac{1}{r}\frac{\partial}{\partial \theta}\nabla^2(\psi_0+\psi_1)\right)\frac{\partial \psi_2}{\partial r} + \left(\frac{1}{r}\frac{\partial}{\partial r}\nabla^2(\psi_0+\psi_1)\right)\frac{\partial \psi_2}{\partial \theta}\right.\right.$$

$$\left.+\left(\frac{1}{r}\frac{\partial}{\partial \theta}(\psi_0+\psi_1)\right)\frac{\partial \nabla^2\psi_2}{\partial r} + \left(-\frac{1}{r}\frac{\partial}{\partial r}(\psi_0+\psi_1)\right)\frac{\partial \nabla^2\psi_2}{\partial \theta} - \frac{1}{Re}\nabla^4\psi_2\right]$$

$$\left.+\left(\frac{1}{r}\frac{\partial \psi_1}{\partial \theta}\frac{\partial \nabla^2\psi_1}{\partial r} - \frac{1}{r}\frac{\partial \psi_1}{\partial r}\frac{\partial \nabla^2\psi_1}{\partial \theta}\right)\right\}$$

$$+\left\{\left[\frac{\partial \nabla^2\psi_3}{\partial t} + \left(-\frac{1}{r}\frac{\partial}{\partial \theta}\nabla^2(\psi_0+\psi_1+\psi_2)\right)\frac{\partial \psi_3}{\partial r} + \left(\frac{1}{r}\frac{\partial}{\partial r}\nabla^2(\psi_0+\psi_1+\psi_2)\right)\frac{\partial \psi_3}{\partial \theta}\right.\right.$$

$$\left.+\left(\frac{1}{r}\frac{\partial}{\partial \theta}(\psi_0+\psi_1+\psi_2)\right)\frac{\partial \nabla^2\psi_3}{\partial r} + \left(-\frac{1}{r}\frac{\partial}{\partial r}(\psi_0+\psi_1+\psi_2)\right)\frac{\partial \nabla^2\psi_3}{\partial \theta} - \frac{1}{Re}\nabla^4\psi_3\right]$$

$$\left.+\left(\frac{1}{r}\frac{\partial \psi_2}{\partial \theta}\frac{\partial \nabla^2\psi_2}{\partial r} - \frac{1}{r}\frac{\partial \psi_2}{\partial r}\frac{\partial \nabla^2\psi_2}{\partial \theta}\right)\right\}$$

$$+ \cdots = 0 \,. \qquad (1.33)$$

Eqs. (1.30), (1.31), (1.32), and (1.33) can be rewritten concisely as follows so that certain regular features stand out:

$$\left\{\left[\frac{\partial}{\partial t} - \frac{1}{Re}\left(\frac{\partial^2}{\partial r^2} + \frac{1}{r}\frac{\partial}{\partial r} - \frac{1}{r^2} + \frac{1}{r^2}\frac{\partial^2}{\partial \theta^2}\right)\right]u_0 + \left(\frac{2}{Re\,r^2}\frac{\partial}{\partial r}\right)v_0\right.$$

$$\left.+\left(\frac{1}{2}\frac{\partial}{\partial r}\right)p_0 + \left(u_0\frac{\partial u_0}{\partial r} + \frac{v_0}{r}\frac{\partial u_0}{\partial \theta} - \frac{v_0^2}{r}\right)\right\}$$

$$+\sum_{n=1}^{\infty}\left\{\left[\frac{\partial}{\partial t} + a_{1n}\frac{\partial}{\partial r} + b_{1n}\frac{\partial}{\partial \theta} + c_{1n} - \frac{1}{Re}\left(\frac{\partial^2}{\partial r^2} + \frac{1}{r}\frac{\partial}{\partial r} - \frac{1}{r^2} + \frac{1}{r^2}\frac{\partial^2}{\partial \theta^2}\right)\right]u_n\right.$$

$$\left.+\left(d_{1n} + \frac{2}{Re\,r^2}\frac{\partial}{\partial \theta}\right)v_n + \left(\frac{1}{2}\frac{\partial}{\partial r}\right)p_n + f_{1n}\right]\Bigg\} = 0 \,; \qquad (1.30a)$$

$$\left\{\left[\frac{\partial}{\partial t} - \frac{1}{Re}\left(\frac{\partial^2}{\partial r^2} + \frac{1}{r}\frac{\partial}{\partial r} - \frac{1}{r^2} + \frac{1}{r^2}\frac{\partial^2}{\partial \theta^2}\right)\right] v_0 - \left(\frac{2}{Re\, r^2}\frac{\partial}{\partial \theta}\right) u_0 + \left(\frac{1}{2r}\frac{\partial}{\partial \theta}\right) p_0 + \left(u_0 \frac{\partial v_0}{\partial r} + \frac{v_0}{r}\frac{\partial v_0}{\partial \theta} + \frac{u_0 v_0}{r}\right)\right\}$$

$$+ \sum_{n=1}^{\infty} \left\{\left[\frac{\partial}{\partial t} + a_{2n}\frac{\partial}{\partial r} + b_{2n}\frac{\partial}{\partial \theta} + c_{2n} - \frac{1}{Re}\left(\frac{\partial^2}{\partial r^2} + \frac{1}{r}\frac{\partial}{\partial r} - \frac{1}{r^2} + \frac{1}{r^2}\frac{\partial^2}{\partial \theta^2}\right)\right] v_n + \left(d_{2n} - \frac{2}{Re\, r^2}\frac{\partial}{\partial \theta}\right) u_n + \left(\frac{1}{2r}\frac{\partial}{\partial \theta}\right) p_n + f_{2n}\right\} = 0 \; ; \tag{1.31a}$$

$$\sum_{n=0}^{\infty} \left[\left(\frac{\partial}{\partial r} + \frac{1}{r}\right) u_n + \left(\frac{1}{r}\frac{\partial}{\partial \theta}\right) v_n\right] = 0 \; ; \tag{1.32a}$$

and

$$\left[\left(\frac{\partial \nabla^2 \psi_0}{\partial t} - \frac{1}{Re}\nabla^4 \psi_0\right) + \left(\frac{1}{r}\frac{\partial \psi_0}{\partial \theta}\frac{\partial \nabla^2 \psi_0}{\partial r} - \frac{1}{r}\frac{\partial \psi_0}{\partial r}\frac{\partial \nabla^2 \psi_0}{\partial \theta}\right)\right]$$

$$+ \sum_{n=1}^{\infty} \left[\left(\frac{\partial}{\partial t}\nabla^2 + a_{3n}\frac{\partial}{\partial r} + b_{3n}\frac{\partial}{\partial \theta} + c_{3n}\frac{\partial}{\partial r}\nabla^2 + d_{3n}\frac{\partial}{\partial \theta}\nabla^2 - \frac{1}{Re}\nabla^4\right) \psi_n + f_{3n}\right] = 0 \; . \tag{1.33a}$$

Where

$$a_{1n} \equiv \sum_{m=0}^{n-1} u_m \equiv a_{2n} \qquad n > 0$$

$$b_{1n} \equiv \sum_{m=0}^{n-1} \frac{1}{r} v_m \equiv b_{2n} \qquad n > 0 \; .$$

The expressions in the following Eq. (1.34) show that a_{1n}, b_{1n}, etc., are functions of space-time variables and the flow parameters:

$$c_{1n} \equiv \sum_{m=0}^{n-1} \frac{\partial}{\partial r} u_m \qquad n > 0$$

$$c_{2n} \equiv \sum_{m=0}^{n-1} \left(\frac{u_m}{r} + \frac{1}{r}\frac{\partial}{\partial \theta} v_m\right) \quad n > 0 \tag{1.34 (Cont.)}$$

$$
\begin{aligned}
d_{1n} &\equiv \sum_{m=0}^{n-1} \left(\frac{1}{r} \frac{\partial u_m}{\partial \theta} - \frac{2}{r} v_m \right) && n > 0 \\
d_{2n} &\equiv \sum_{m=0}^{n-1} \left(\frac{v_m}{r} + \frac{\partial v_m}{\partial r} \right) && n > 0 \\
f_{1n} &\equiv 0 && n = 1 \\
&\equiv u_{n-1} \frac{\partial u_{n-1}}{\partial r} + \frac{v_{n-1}}{r} \frac{\partial u_{n-1}}{\partial \theta} - \frac{v_{n-1}^2}{r} && n > 1 \\
f_{2n} &\equiv 0 && n = 1 \\
&\equiv u_{n-1} \frac{\partial v_{n-1}}{\partial r} + \frac{v_{n-1}}{r} \frac{\partial v_{n-1}}{\partial \theta} + \frac{u_{n-1} v_{n-1}}{r} && n > 1 \\
a_{3n} &\equiv \sum_{m=0}^{n-1} - \frac{1}{r} \frac{\partial}{\partial \theta} \nabla^2 \psi_m && n > 0 \\
b_{3n} &\equiv \sum_{m=0}^{n-1} \frac{1}{r} \frac{\partial}{\partial r} \nabla^2 \psi_m && n > 0 \\
c_{3n} &\equiv \sum_{m=0}^{n-1} \frac{1}{r} \frac{\partial}{\partial \theta} \psi_m && n > 0 \\
d_{3n} &\equiv \sum_{m=0}^{n-1} - \frac{1}{r} \frac{\partial}{\partial r} \psi_m && n > 0 \\
f_{3n} &\equiv 0 && n = 1 \\
&\equiv \frac{1}{r} \frac{\partial \psi_{n-1}}{\partial \theta} \frac{\partial \nabla^2 \psi_{n-1}}{\partial r} - \frac{1}{r} \frac{\partial \psi_{n-1}}{\partial r} \frac{\partial \nabla^2 \psi_{n-1}}{\partial \theta} && n > 1 \, .
\end{aligned}
\tag{1.34}
$$

From Eqs. (1.30a), (1.31a), and (1.32a) we see that the groups are so formed that, for $n > 0$, the n-th group involves only the linear terms in u_n, v_n and their derivatives with coefficients a_{1n}, b_{1n}, etc., depending on u_i, v_i and their derivatives $i = 1, 2, \ldots, n - 1$. For $n = 0$, the group involves nonlinear terms in u_0, v_0 and their derivatives. We could have arranged the terms so that this group for $n = 0$ also involved only the linear terms in u_0, v_0 and their derivatives by transferring the nonlinear terms to the $n = 1$ group so that

$$f_{11} = u_0 \frac{\partial u_0}{\partial r} + \frac{v_0}{r} \frac{\partial u_0}{\partial \theta} - \frac{v_0^2}{r}$$

$$f_{21} = u_0 \frac{\partial v_0}{\partial r} + \frac{v_0}{r} \frac{\partial u_0}{\partial \theta} + \frac{u_0 v_0}{r} .$$

Then the summation could have been taken from $n = 0$ onwards after defining $a_{10} = a_{20} = b_{10} = b_{20} = c_{10} = c_{20} = d_{10} = d_{20} = f_{10} = f_{20} = 0$. The reason for not doing so will become clear shortly.

These groups can be expressed symbolically in terms of the functions S, S_0, S_1, ..., S_n as

$$\bar{L}S = \bar{L}_0 S_0 + \sum_{n=1}^{\infty} (\bar{L}_n S_n + f_n) = 0 , \tag{1.35}$$

where $\bar{L}$ is a nonlinear differential operator and $\bar{L}_0$ is formally identical to $\bar{L}$. The operators $\bar{L}_n$ are linear differential operators which are not formally identical because the coefficients differ for different n, but they nevertheless belong to the same class of differential operators because their structures are similar. The remarkable thing about these operators $\bar{L}_n$ is that they depend on the knowledge of the functions S_i, $i = 1, 2, \ldots, n-1$. In Eq. (1.27) we noted that the operators L_i, $i = 1, \ldots, n$ were formally identical. Moreover, they do not depend on the knowledge of the solutions u_i in any way. Thus the linear differential operators L_i, $i = 1, \ldots, n$ being formally identical, and having the same structure and not depending on the functions u_i, $i = 1, \ldots, n-1$, form a subclass of the class of linear differential operators $\bar{L}_n$ which have the same structure and which depend in some way on the functions S_i, $i = 1, \ldots, n-1$. One may therefore view Eq. (1.35) as a generalization of Eq. (1.27) for a nonlinear case.

To find u_i in Eq. (1.27) a rule was prescribed in the form of Eqs. (1.28). The rule essentially states that not only the sum $\Sigma(L_i u_i - f_i) = (Lu - f)$ is zero, but that the individual elements of the sum are also zero. Analogously, we now prescribe the same rule for Eq. (1.35). This gives the equations

$$\bar{L}_0 S_0 = 0 \tag{1.36}$$

$$\bar{L}_n S_n + f_n = 0 , \quad n = 1 . \tag{1.37}$$

In the case of Eq. (1.27), it is proven that such a procedure will give u_i, the sum of which is the required solution. We have no such proof for (1.37), but the strong analogy intuitively leads us to believe that such may be the case. If we believe that our equations truly represent the physical processes, then the solution to these equations must represent the observed facts. Conversely, the observed facts can be regarded as describing the mathematical solution which is actually 'realized.' This gives us a possibility of a posteriori verification of our procedure by comparison of the solutions so obtained with observed facts. Indeed, the proof of the validity of such a procedure is here heuristic in nature.

As we have already noted in the Introduction, Eqs. (1.34) and (1.35) for $n = 1$ together are equivalent only formally to the so-called 'Burger's Equation' obtained by various authors. After assuming, a priori, that the flow deviates only slightly from potential flows, they set $u = u_0 + u_1$, $v = v_0 + v_1$, $\psi = \psi_0 + \psi_1$ and then argue that the nonlinear terms can be neglected to arrive at their governing equations. This procedure of obtaining a linear governing equation has no mathematical rationale except in the sense of a small-perturbation technique. On the other hand, the procedure outlined and argued by us assumes (a) the existence of an infinite sum of functions $S_0, S_1, S_2, \ldots, S_n, \ldots$ such that it converges to the solution S, and (b) that a rearrangement and grouping of terms with subsequent setting of each group individually equal to zero is permissible. The results of our work show that this procedure is valid in the whole domain and, at least, for the range of the Reynolds number investigated. Thus an essentially new mathematical justification of the assumptions involved in our procedure, which is here justified by comparison with experiments, must be sought eventually. However, one conclusion that emerges from this procedure and its heuristic justification is that no ideas of small-perturbation theory need be brought into picture.

There is an important difference in the set of Eqs. (1.28) and the set of Eqs. (1.36) and (1.37). The equations in Eqs. (1.28) may be solved in any order, because none of the operators L_i depend on the knowledge of the solutions to any of the equations in the set. Equations (1.36) and (1.37) must be solved in a definite order, progressing with n from $n = 0$ onwards, since the operator $\bar{L}_n$ is determined completely only when the preceding solutions S_i, $i = 1, 2, \ldots, n-1$ are determined. This defines an iterative process. We shall call the set of equations corresponding to a particular n the equations for n-th iteration.

For an iterative process, we must obtain a solution to Eq. (1.36) to start with. Consequently, it is important to choose the nature of this operator $\bar{L}_0$ carefully. Either $\bar{L}_0$ can be made formally identical to $\bar{L}$, or it can be made structurally similar to $\bar{L}_n$, $n \geq 1$. If a solution S_0 can be obtained to $\bar{L}_0 S_0 = 0$ with $\bar{L}_0$ formally identical to $\bar{L}$ such that it satisfies a maximum number of given conditions, then we may call it, by definition, a close solution to the exact solution which satisfies the equation and all the given conditions. The nonlinear effects which correspond physically to dynamical effects are then taken into account right from the beginning of the process of iteration. Because this is not the case with the second alternative, we should, if we can, make $\bar{L}_0$ formally identical to $\bar{L}$. Fortunately, a potential solution which satisfies all except the no-slip condition meets the requirements for being a close solution. Hence we select $\bar{L}_0$ such that it is formally identical to $\bar{L}$ and S_0 as the corresponding potential solution satisfying all except the no-slip condition to start the process of iteration.

If we took S_0 as a uniform flow through out the flow field, then it would satisfy the harmonic equation and hence the equation $\bar{L}_0 S_0 = 0$. The equations for the first iteration would then be Oseen's equations. But, with particular reference to external flows, we see that such a selection for S_0 would satisfy only the conditions at infinity and none at the wall—not even the condition that the normal velocity component vanish at the wall. Thus it satisfies one condition less than the corresponding potential solution which satisfies, in addition to

the conditions at infinity, the condition on the normal velocity component. It is therefore less close and therefore less appropriate than the latter. In fact, there cannot be any solution closer than the potential solution, because if it were otherwise then it would have to satisfy all the conditions, and that would make it the exact solution which we assume not to be the case.

Two solutions may be equally close from a mathematical point of view, i.e., they both satisfy the given equations and all except one of the given conditions, and yet be different because the conditions they do not satisfy may not be the same. If such is the case, then we have to decide upon the appropriateness of one with respect to the other. For the problems in fluid mechanics, all the conditions except the no-slip condition seem self-evident, and hence a solution satisfying them would seem to be more appropriate than the solution that does not satisfy one of them and satisfies instead the no-slip condition. If we adhere to this view, then the potential solution is the more appropriate.

There is another way in which the appropriateness can be meaningfully decided. That solution S_0 which, first, allows us to determine in some way the number of iterations necessary to secure sufficient convergence and, second, calls for a minimum number of these iterations would certainly be the most appropriate. As is shown later, for the problem of the flow around a circular cylinder the potential solution which satisfies all but the no-slip condition is the most appropriate according to this criterion.

If $\bar{L}_0$ were made structurally similar to $\bar{L}_n$, $n \geq 1$, then the equation $\bar{L}_0 S_0 = 0$ would represent the set of equations for a creeping motion. Stokes has obtained a solution to these equations for the case of a sphere which satisfies all the conditions on the flow. Other cases of axisymmetric bodies have been explored since then. But one cannot obtain, in all cases, nonsingular solutions to these equations which satisfy all the boundary conditions. The case of a cylinder is one such. However, what is interesting in this case is that the solution which Stokes obtains and discusses in Eq. 130 of Ref. [16] is one which satisfies the harmonic equation. A solution to the harmonic equation cannot satisfy all the conditions on the flow, and if one required all but the no-slip condition to be fulfilled, the streamline field will be identical to that for a potential flow. The pressure field found from the equations of creeping motion would appear constant everywhere, while that due to a potential flow is a function of space variables and evidently much closer to the actual pressure field in most of the flow field. This shows that the dynamics of the potential flow as compared to that of a creep flow is much closer to the actual—a strong reason for the selection of $\bar{L}_0$ such that it is formally identical to $\bar{L}$ and S_0 as the potential flow solution.

As noted earlier, any solution of the harmonic equation will satisfy the equation $\bar{L}_0 S_0 = 0$, where $\bar{L}_0$ is formally identical to $\bar{L}$. For the case of the flow around a circular cylinder, the appropriate general form of the stream function which satisfies the harmonic equation is the following:

$$\psi' = (Ar^{-1} + Br + Cr \log_e r + Dr^3) \sin\theta \,. \tag{1.38}$$

Then

$$u' = \frac{1}{r}\frac{\partial \psi'}{\partial \theta} = (Ar^{-2} + B + C \log_e r + Dr^2) \cos\theta \tag{1.39}$$

$$v' = -\frac{\partial \psi'}{\partial r} = (Ar^{-2} - B - C - C \log_e r - 3Dr^2) \sin\theta \,. \tag{1.40}$$

We have four conditions on the flow to consider.

$$u'\Big|_{r=1} = 0 \tag{1.41}$$

$$v'\Big|_{r=1} = 0 \tag{1.42}$$

$$\lim_{r\to\infty} u' = -\cos\theta \tag{1.43}$$

$$\lim_{r\to\infty} v' = +\sin\theta \,. \tag{1.44}$$

Evidently all these conditions cannot be fulfilled. We would like to obtain those solutions which satisfy at least three out of the four conditions. We have four cases to consider:

(i) $v'|_{r=1} \neq 0$: Applying the conditions of Eqs. (1.41), (1.43), and (1.44) to Eqs. (1.39) and (1.40), we get

$$A + B + D = 0$$

$$B + C(\infty) + D(\infty) = -1$$

$$-B - C(\infty) - C - 3D(\infty) = +1 \,.$$

This gives

$$B = -1, \quad A = +1, \quad C = D = 0 \,.$$

Consequently,

$$\psi' = -\left(r - \frac{1}{r}\right)\sin\theta$$

$$u' = -\left(1 - \frac{1}{r^2}\right)\cos\theta \tag{1.45}$$

$$v' = +\left(1 + \frac{1}{r^2}\right)\sin\theta \,.$$

(ii) $u'|_{r=1} \neq 0$: Applying the conditions of Eqs. (1.42), (1.43), and (1.44) to Eqs. (1.39) and (1.40), we get

$$A - B - C - 3D = 0$$

$$B + C(\infty) + D(\infty) = -1$$

$$- B - C - C(\infty) - 3D(\infty) = +1 \ .$$

This gives

$$B = -1 \ , \quad A = -1 \ , \quad C = D = 0 \ .$$

Consequently,

$$\psi' = - \left(r + \frac{1}{r} \right) \sin\theta$$

$$u' = - \left(1 + \frac{1}{r^2} \right) \cos\theta \qquad (1.46)$$

$$v' = + \left(1 - \frac{1}{r^2} \right) \sin\theta \ .$$

(iii) $\lim_{r\to\infty} u' \neq - \cos\theta$: Applying the conditions of Eqs. (1.41), (1.42), and (1.44) to Eqs. (1.39) and (1.40), we get

$$A + B + D = 0$$

$$A - B - C - 3D = 0$$

$$- B - C - C(\infty) - 3D(\infty) = +1 \ .$$

The last of these three conditions requires that $C = 0$, $D = 0$, and $B = -1$. But with $C = D = 0$, the first two demand that $A = 0$ and $B = 0$. Hence we conclude that there is no solution which can satisfy all three conditions of Eqs. (1.41), (1.42) and (1.44).

(iv) $\lim_{r\to\infty} v' \neq + \sin\theta$: Applying the conditions of Eqs. (1.41), (1.42), and (1.44) to Eqs. (1.39) and (1.40), we get

$$A + B + D = 0$$

$$A - B - C - 3D = 0$$

$$B + C(\infty) + D(\infty) = -1$$

The last of these three necessary conditions requires that $C = 0$, $D = 0$, and $B = -1$. But with $C = D = 0$, the first two demand that $A = B = 0$. Hence, in this case also there is no solution which can satisfy all three conditions of Eqs. (1.41), (1.42), and (1.44).

The conclusion is that Eqs. (1.45) and (1.46) are the only solutions of the harmonic equations which satisfy three out of the four given conditions. Depending

upon which of the two sets of equations leads to the least number of iterations necessary to secure sufficient convergence, we can now decide as to the appropriateness of one over the other.

Let us first write down explicitly the governing equations for iterations up to $n = 3$. We shall call equations for $n = 0$ the Base Equations. The sets of equations as written down below correspond to the symbolic Eqs. (1.36) and (1.37).

BASE EQUATIONS $(n = 0)$

$$\frac{\partial u_0}{\partial t} + u_0 \frac{\partial u_0}{\partial r} + \frac{v_0}{r}\frac{\partial u_0}{\partial \theta} - \frac{v_0^2}{r} = -\frac{1}{2}\frac{\partial p_0}{\partial r} + \frac{1}{Re}\left(\frac{\partial^2 u_0}{\partial r^2} + \frac{1}{r}\frac{\partial u_0}{\partial r} - \frac{u_0}{r^2} + \frac{1}{r^2}\frac{\partial^2 u_0}{\partial \theta^2} - \frac{2}{r^2}\frac{\partial v_0}{\partial \theta}\right)$$

$$\frac{\partial v_0}{\partial t} + u_0 \frac{\partial v_0}{\partial r} + \frac{v_0}{r}\frac{\partial v_0}{\partial \theta} + \frac{u_0 v_0}{r} = -\frac{1}{2r}\frac{\partial p}{\partial \theta} + \frac{1}{Re}\left(\frac{\partial^2 v_0}{\partial r^2} + \frac{1}{r}\frac{\partial v_0}{\partial r} - \frac{v_0}{r^2} + \frac{1}{r^2}\frac{\partial^2 v_0}{\partial \theta^2} + \frac{2}{r^2}\frac{\partial u_0}{\partial \theta}\right)$$

$$\frac{\partial u_0}{\partial r} + \frac{u_0}{r} + \frac{1}{r}\frac{\partial v_0}{\partial \theta} = 0 \; ; \qquad (1.21a)$$

$$\nabla^2 \psi_0 = 0 \; ; \qquad (1.22a)$$

where

$$u_0 = \frac{1}{r}\frac{\partial \psi_0}{\partial \theta}$$

$$v_0 = -\frac{\partial \psi_0}{\partial r} \; .$$

These are the equations for a potential flow. The first two equations are Euler's equations.

FIRST ITERATION EQUATIONS $(n = 1)$

$$\frac{\partial u_1}{\partial t} + (u_0)\frac{\partial u_1}{\partial r} + \left(\frac{v_0}{r}\right)\frac{\partial u_1}{\partial \theta} + \left(\frac{\partial u_0}{\partial r}\right)u_1 + \left(\frac{1}{r}\frac{\partial u_0}{\partial \theta} - \frac{2v_0}{r}\right)v_1 = -\frac{1}{2}\frac{\partial p_1}{\partial r} + \frac{1}{Re}\left(\frac{\partial^2 u_1}{\partial r^2} + \frac{1}{r}\frac{\partial u_1}{\partial r} - \frac{u_1}{r^2} + \frac{1}{r^2}\frac{\partial^2 u_1}{\partial \theta^2} - \frac{2}{r^2}\frac{\partial v_1}{\partial \theta}\right) \; ; \qquad (1.47)$$

$$\frac{\partial v_1}{\partial t} + (u_0)\frac{\partial v_1}{\partial r} + \left(\frac{v_0}{r}\right)\frac{\partial v_1}{\partial \theta} + \left(\frac{v_0}{r} + \frac{\partial v_0}{\partial r}\right)u_1 + \left(\frac{u_0}{r} + \frac{1}{r}\frac{\partial v_0}{\partial \theta}\right)v_1 = -\frac{1}{2r}\frac{\partial p_1}{\partial \theta}$$

$$+ \frac{1}{Re}\left(\frac{\partial^2 v_1}{\partial r^2} + \frac{1}{r}\frac{\partial v_1}{\partial r} - \frac{v_1}{r^2} + \frac{1}{r^2}\frac{\partial^2 v_1}{\partial \theta^2} + \frac{2}{r^2}\frac{\partial u_1}{\partial \theta}\right); \qquad (1.48)$$

$$\frac{\partial u_1}{\partial r} + \frac{u_1}{r} + \frac{1}{r}\frac{\partial v_1}{\partial \theta} = 0 ; \qquad (1.49)$$

$$\frac{\partial \nabla^2 \psi_1}{\partial t} + \left(\frac{1}{r}\frac{\partial \psi_0}{\partial \theta}\right)\frac{\partial \nabla^2 \psi_1}{\partial r} + \left(-\frac{1}{r}\frac{\partial \psi_0}{\partial r}\right)\frac{\partial \nabla^2 \psi_1}{\partial \theta} - \frac{1}{Re}\nabla^4 \psi_1 = 0 . \qquad (1.50)$$

SECOND ITERATION EQUATIONS (n = 2)

$$\frac{\partial u_2}{\partial t} + (u_0 + u_1)\frac{\partial u_2}{\partial r} + \left(\frac{v_0 + v_1}{r}\right)\frac{\partial u_2}{\partial \theta} + \left[\frac{\partial}{\partial r}(u_0 + u_1)\right]u_2$$

$$+ \left[\frac{1}{r}\frac{\partial}{\partial \theta}(u_0 + u_1) - \frac{2}{r}(v_0 + v_1)\right]v_2$$

$$+ \left(u_1\frac{\partial u_1}{\partial r} + \frac{v_1}{r}\frac{\partial u_1}{\partial \theta} - \frac{v_1^2}{r}\right) = -\frac{1}{2}\frac{\partial p_2}{\partial r}$$

$$+ \frac{1}{Re}\left(\frac{\partial^2 u_2}{\partial r^2} + \frac{1}{r}\frac{\partial u_2}{\partial r} - \frac{u_2}{r^2} + \frac{1}{r^2}\frac{\partial^2 u_2}{\partial \theta^2} - \frac{2}{r^2}\frac{\partial v_2}{\partial \theta}\right); \qquad (1.51)$$

$$\frac{\partial v_2}{\partial t} + (u_0 + u_1)\frac{\partial v_2}{\partial r} + \left(\frac{v_0 + v_1}{r}\right)\frac{\partial v_2}{\partial \theta} + \left[\frac{v_0 + v_1}{r} + \frac{\partial}{\partial r}(v_0 + v_1)\right]u_2$$

$$+ \left[\frac{u_0 + u_1}{r} + \frac{1}{r}\frac{\partial}{\partial \theta}(v_0 + v_1)\right]v_2 + \left(u_1\frac{\partial v_1}{\partial r} + \frac{v_1}{r}\frac{\partial v_1}{\partial \theta} + \frac{u_1 v_1}{r}\right) = -\frac{1}{2r}\frac{\partial p_2}{\partial \theta}$$

$$+ \frac{1}{Re}\left(\frac{\partial^2 v_2}{\partial r^2} + \frac{1}{r}\frac{\partial v_2}{\partial r} - \frac{v_2}{r^2} + \frac{1}{r^2}\frac{\partial^2 v_2}{\partial \theta^2} + \frac{2}{r^2}\frac{\partial u_2}{\partial \theta}\right); \qquad (1.52)$$

$$\frac{\partial u_2}{\partial r} + \frac{u_2}{r} + \frac{1}{r}\frac{\partial v_2}{\partial \theta} = 0 ; \qquad (1.53)$$

$$\frac{\partial \nabla^2 \psi_2}{\partial t} + \left(- \frac{1}{r} \frac{\partial \nabla^2 \psi_1}{\partial \theta} \right) \frac{\partial \psi_2}{\partial r} + \left(\frac{1}{r} \frac{\partial \nabla^2 \psi_1}{\partial r} \right) \frac{\partial \psi_2}{\partial \theta}$$

$$+ \left[\frac{1}{r} \frac{\partial}{\partial \theta} (\psi_0 + \psi_1) \right] \frac{\partial \nabla^2 \psi_2}{\partial r} + \left[- \frac{1}{r} \frac{\partial}{\partial r} (\psi_0 + \psi_1) \right] \frac{\partial \nabla^2 \psi_2}{\partial \theta} - \frac{1}{Re} \nabla^4 \psi_2$$

$$+ \left(\frac{1}{r} \frac{\partial \psi_1}{\partial \theta} \frac{\partial \nabla^2 \psi_1}{\partial r} - \frac{1}{r} \frac{\partial \psi_1}{\partial r} \frac{\partial \nabla^2 \psi_1}{\partial \theta} \right) = 0 \ . \tag{1.54}$$

THIRD ITERATION EQUATIONS (n = 3)

$$\frac{\partial u_3}{\partial t} + (u_0 + u_1 + u_2) \frac{\partial u_3}{\partial r} + \left(\frac{v_0 + v_1 + v_2}{r} \right) \frac{\partial u_3}{\partial \theta} + \left[\frac{\partial}{\partial r} (u_0 + u_1 + u_2) \right] u_3$$

$$+ \left[\frac{1}{r} \frac{\partial}{\partial \theta} (u_0 + u_1 + u_2) - \frac{2}{r} (v_0 + v_1 + v_2) \right] v_3 + \left(u_2 \frac{\partial u_2}{\partial r} \right.$$

$$\left. + \frac{v_2}{r} \frac{\partial u_2}{\partial \theta} - \frac{v_2^2}{r} \right) = - \frac{1}{2} \frac{\partial p_3}{\partial r} + \frac{1}{Re} \left(\frac{\partial^2 u_3}{\partial r^2} + \frac{1}{r} \frac{\partial u_3}{\partial r} - \frac{u_3}{r^2} + \frac{1}{r^2} \frac{\partial^2 u_3}{\partial \theta^2} - \frac{2}{r^2} \frac{\partial v_3}{\partial \theta} \right) ; \tag{1.55}$$

$$\frac{\partial v_3}{\partial t} + (u_0 + u_1 + u_2) \frac{\partial v_3}{\partial r} + \left(\frac{v_0 + v_1 + v_2}{r} \right) \frac{\partial v_3}{\partial \theta}$$

$$+ \left[\frac{v_0 + v_1 + v_2}{r} + \frac{\partial}{\partial r} (v_0 + v_1 + v_2) \right] u_3$$

$$+ \left[\frac{u_0 + u_1 + u_2}{r} + \frac{1}{r} \frac{\partial}{\partial \theta} (v_0 + v_1 + v_2) \right] v_3$$

$$+ \left(u_2 \frac{\partial v_2}{\partial r} + \frac{v_2}{r} \frac{\partial v_2}{\partial \theta} + \frac{u_2 v_2}{r} \right) = - \frac{1}{2r} \frac{\partial p_3}{\partial \theta}$$

$$+ \frac{1}{Re} \left(\frac{\partial^2 v_3}{\partial r^2} + \frac{1}{r} \frac{\partial v_3}{\partial r} - \frac{v_3}{r^2} + \frac{1}{r^2} \frac{\partial^2 v_3}{\partial \theta^2} + \frac{2}{r^2} \frac{\partial u_3}{\partial \theta} \right) ; \tag{1.56}$$

$$\frac{\partial u_3}{\partial r} + \frac{u_3}{r} + \frac{1}{r} \frac{\partial v_3}{\partial \theta} = 0 \ ; \tag{1.57}$$

$$\frac{\partial \nabla^2 \psi_3}{\partial t} + \left[-\frac{1}{r}\frac{\partial}{\partial \theta} \nabla^2(\psi_1 + \psi_2) \right] \frac{\partial \psi_3}{\partial r} + \left[\frac{1}{r}\frac{\partial}{\partial r} \nabla^2(\psi_1 + \psi_2) \right] \frac{\partial \psi_3}{\partial \theta}$$

$$+ \left[\frac{1}{r}\frac{\partial}{\partial \theta} (\psi_0 + \psi_1 + \psi_2) \right] \frac{\partial \nabla^2 \psi_3}{\partial r} + \left[-\frac{1}{r}\frac{\partial}{\partial r} (\psi_0 + \psi_1 + \psi_2) \right] \frac{\partial \nabla^2 \psi_3}{\partial \theta} - \frac{1}{Re} \nabla^4 \psi_3$$

$$+ \left(\frac{1}{r}\frac{\partial \psi_2}{\partial \theta}\frac{\partial \nabla^2 \psi_2}{\partial r} - \frac{1}{r}\frac{\partial \psi_2}{\partial r}\frac{\partial \nabla^2 \psi_2}{\partial \theta} \right) = 0 \ . \tag{1.58}$$

We observe that u, v, and p are physical quantities. They are the field variables in which we are interested. At any generic point P in the flow field these quantities should have a definite set of values at a given time. Since the choice of the zero direction for the polar axis from which θ is measured is arbitrary, and since after a complete rotation of the radius vector through an angle of 2π radians we arrive at the same geometrical point from which we started, any increase in θ by multiples of 2π should not affect the values of u, v, and p at any generic point in the field of any given time. This means that u, v, and p should be periodic functions of θ with a period of 2π radians. This *periodicity condition* is expressed as follows:

$$\begin{aligned} u(r,\theta,t) &= u(r,\theta + 2n\pi, t) \\ v(r,\theta,t) &= v(r,\theta + 2n\pi, t) \quad n = \pm 1, 2, \ldots \\ p(r,\theta,t) &= p(r,\theta + 2n\pi, t) \end{aligned} \tag{1.59}$$

Consequently, we can assume that the stream function $\psi(r, \theta, t)$ and hence the functions u_n, v_n, p_n, and ψ_n are also periodic functions of θ. Let us therefore assume the following Fourier representations for ψ_1, ψ_2, and ψ_3 respectively:

$$\psi_1(r,\theta,t) = \frac{A_0(r,t)}{2} + \sum_{n=1}^{\infty} A_n(r,t) \cos n\theta + B_n(r,t) \sin n\theta \tag{1.60}$$

$$\psi_2(r,\theta,t) = \frac{C_0(r,t)}{2} + \sum_{n=1}^{\infty} C_n(r,t) \cos n\theta + D_n(r,t) \sin n\theta \tag{1.61}$$

$$\psi_3(r,\theta,t) = \frac{E_0(r,t)}{2} + \sum_{n=1}^{\infty} E_n(r,t) \cos n\theta + F_n(r,t) \sin n\theta \ , \tag{1.62}$$

where A, B, C, D, E, and F stand for the coefficients of the Fourier representations.

We now impose suitable boundary conditions on the solutions of various iterations. Let the first iteration velocity components u_1 and v_1 be such that the sums $(u_0 + u_1)$ and $(v_0 + v_1)$ satisfy all the velocity conditions on the

flow. Thus the condition not satisfied by the base flow velocities u_0 and v_0 will be satisfied by the first iteration velocities u_1 and v_1. Let, for $n \geq 2$, $u_n = 0$ and $v_n = 0$ at both boundaries. From Eqs. (1.60), (1.61), and (1.62) we have by differentiation

$$u_1(r,\theta,t) = + \sum_{n=1}^{\infty} - \frac{nA_n(r,t)}{r} \sin n\theta + \frac{nB_n(r,t)}{r} \cos n\theta$$

$$v_1(r,\theta,t) = - \frac{A_0'(r,t)}{2} - \sum_{n=1}^{\infty} \left[A_n'(r,t) \cos n\theta + B_n'(r,t) \sin n\theta\right] ; \tag{1.63}$$

$$u_2(r,\theta,t) = + \sum_{n=1}^{\infty} - \frac{nC_n(r,t)}{r} \sin n\theta + \frac{nD_n(r,t)}{r} \cos n\theta$$

$$v_2(r,\theta,t) = - \frac{C_0'(r,t)}{2} - \sum_{n=1}^{\infty} \left[C_n'(r,t) \cos n\theta + D_n'(r,t) \sin n\theta\right] ; \tag{1.64}$$

$$u_3(r,\theta,t) = + \sum_{n=1}^{\infty} - \frac{nE_n(r,t)}{r} \sin n\theta + \frac{nF_n(r,t)}{r} \cos n\theta$$

$$v_3(r,\theta,t) = - \frac{E_0'(r,t)}{2} - \sum_{n=1}^{\infty} \left[E_n'(r,t) \cos n\theta + F_n'(r,t) \sin n\theta\right] ; \tag{1.65}$$

where prime denotes partial differentiation with respect to r.

Consider, first, ψ_0, u_0, and v_0 as given by ψ', u', and v' in Eq. (1.45). Since $v = 0$ at $r = 1$, we must have for this case

$$v_1\big|_{r=1} = -v'\big|_{r=1} = -2 \sin\theta ,$$

and

$$u_1\big|_{r=1} = u_2\big|_{r=1} = u_3\big|_{r=1} = v_2\big|_{r=1} = v_3\big|_{r=1} = 0 . \tag{1.66}$$

Applying Eqs. (1.66) to Eqs. (1.63), (1.64), and (1.65), we find that

$$\begin{aligned} &A_n(1,t) = 0 \quad , \quad B_n(1,t) = 0 \quad n = 1, 2, \ldots \\ &A_n'(1,t) = 0 \qquad\qquad\qquad\quad n = 0, 1, 2, \ldots \\ &B_1'(1,t) = +2 \, , \quad B_n'(1,t) = 0 \quad n = 2, 3, \ldots ; \end{aligned} \tag{1.67a}$$

$$C_n(1,t) = 0\,, \quad D_n(1,t) = 0 \quad n = 1,\ 2,\ \ldots$$
$$C_n'(1,t) = 0\,, \quad D_n'(1,t) = 0 \quad n = 0,\ 1,\ 2,\ \ldots\ ; \tag{1.67b}$$

$$E_n(1,t) = 0\,, \quad F_n(1,t) = 0 \quad n = 1,\ 2,\ \ldots$$
$$E_n'(1,t) = 0\,, \quad F_n'(1,t) = 0 \quad n = 0,\ 1,\ 2,\ \ldots\ . \tag{1.67c}$$

The conditions of Eqs. (1.67a), (1.67b), and (1.67c) imply that at $r = 1$ we have

$$\frac{\partial u_1}{\partial \theta} = 0\,, \quad \frac{\partial^2 u_1}{\partial \theta^2} = 0\,, \quad \frac{\partial u_1}{\partial r} = 2\cos\theta\,, \quad \frac{\partial v_1}{\partial \theta} = -2\cos\theta\,, \quad \frac{\partial^2 v_1}{\partial \theta^2} = +2\sin\theta$$

$$\frac{\partial u_2}{\partial \theta} = 0\,, \quad \frac{\partial^2 u_2}{\partial \theta^2} = 0\,, \quad \frac{\partial u_2}{\partial r} = 0\,, \quad \frac{\partial v_2}{\partial \theta} = 0\,, \quad \frac{\partial^2 v_2}{\partial \theta^2} = 0 \tag{1.68}$$

$$\frac{\partial u_3}{\partial \theta} = 0\,, \quad \frac{\partial^2 u_3}{\partial \theta^2} = 0\,, \quad \frac{\partial u_3}{\partial r} = 0\,, \quad \frac{\partial v_3}{\partial \theta} = 0\,, \quad \frac{\partial^2 v_3}{\partial \theta^2} = 0\,.$$

We also have

$$u_0 = \frac{\partial u_0}{\partial \theta} = 0$$

and (1.69)

$$\frac{\partial v_0}{\partial \theta} = 2\cos\theta\ .$$

All partial derivatives with respect to time are zero at the wall. The results of Eqs. (1.68) are a consequence of the periodicity condition. If we apply the conditions of Eqs. (1.66), (1.68), and (1.69) to Eqs. (1.47), (1.48), (1.51), (1.52), (1.55), and (1.56), we get $r = 1$ the following equations:

$$+8\sin^2\theta = -\frac{1}{2}\frac{\partial p_1}{\partial r}\bigg|_{r=1} + \frac{1}{\mathrm{Re}}\frac{\partial^2 u_1}{\partial r^2}\bigg|_{r=1} + \frac{6\cos\theta}{\mathrm{Re}} \tag{1.70a}$$

$$-4\sin^2\theta = -\frac{1}{2}\frac{\partial p_2}{\partial r}\bigg|_{r=1} + \frac{1}{\mathrm{Re}}\frac{\partial^2 u_2}{\partial r^2}\bigg|_{r=1} \tag{1.70b}$$

$$0 = -\frac{1}{2}\frac{\partial p_3}{\partial r}\bigg|_{r=1} + \frac{1}{\mathrm{Re}}\frac{\partial^2 u_3}{\partial r^2}\bigg|_{r=1}\ ; \tag{1.70c}$$

$$-8 \sin\theta \cos\theta = -\frac{1}{2}\left.\frac{\partial p_1}{\partial \theta}\right|_{r=1} + \frac{1}{Re}\left(\frac{\partial^2 v_1}{\partial r^2} + \frac{\partial v_1}{\partial r}\right)_{r=1} + \frac{4 \sin\theta}{Re} \qquad (1.71a)$$

$$+4 \sin\theta \cos\theta = -\frac{1}{2}\left.\frac{\partial p_2}{\partial \theta}\right|_{r=1} + \frac{1}{Re}\left(\frac{\partial^2 v_2}{\partial r^2} + \frac{\partial v_2}{\partial r}\right)_{r=1} \qquad (1.71b)$$

$$0 = -\frac{1}{2}\left.\frac{\partial p_3}{\partial \theta}\right|_{r=1} + \frac{1}{Re}\left(\frac{\partial^2 v_3}{\partial r^2} + \frac{\partial v_3}{\partial r}\right)_{r=1} . \qquad (1.71c)$$

The first terms on the left-hand sides of Eqs. (1.70a) and (1.71a) are the contributions of the linear convective terms in u_1 and v_1. The first terms on the left-hand sides of Eqs. (1.70b) and (1.71b) are the contributions of the nonlinear convective terms in u_1 and v_1 to the pressure p_2 of the second iterations. Similarly, the terms on the left-hand sides of Eqs. (1.70c) and (1.71c) are the contributions of the linear convective terms in u_3 and v_3 and the nonlinear convective terms in u_2 and v_2. These terms are zero. It is clear by comparison that the order of magnitude of the linear and nonlinear convective terms in u_1 and v_1 is the same. Because of this, the second iteration must make about the same order of magnitude contribution to the pressure field p as the first iteration, but of opposite sign, as Eqs. (1.70a), (1.70b), (1.71a), and (1.71b) indicate. Since there is no contribution to pressure from convective terms in Eqs. (1.70c) and (1.71c), the pressure field p_3 may be assumed to contribute very little to the total pressure p if we bear in mind that the boundary conditions require u_3 and v_3 to vanish at the wall as well as far away from the cylinder. Higher iteration pressure fields p_n will behave essentially as p_3, but with decreasing intensity. This discussion is based on the pressure around the cylinder and is not regarded here as rigorous. However, it is strongly indicative of the importance of the second iteration and the relative unimportance of the higher iterations. We may say that two iterations are sufficient in this case to give results close to the actual solution.

The case we have just discussed relates to the stream function ψ' as given by Eq. (1.45). This is, in fact, the potential flowstream function. Along similar lines we will now consider ψ_0, u_0, and v_0 to be given by ψ', u', and v' as in Eqs. (1.46). We then have at $r = 1$

$$u_1\big|_{r=1} = u'\big|_{r=1} = +2 \cos\theta$$

$$v_1\big|_{r=1} = u_2\big|_{r=1} = u_3\big|_{r=1} = v_2\big|_{r=1} = v_3\big|_{r=1} = 0 . \qquad (1.72)$$

Applying Eqs. (1.72) to Eqs. (1.63), (1.64), and (1.65), we find that in Eqs. (1.67a) instead of $B_1'(1,t) = +2$ and $B_1(1,t) = 0$ we should have $B_1'(1,t) = 0$ and $B_1(1,t) = 2$. These conditions imply that for this case

$$\frac{\partial u_1}{\partial \theta} = -2 \sin\theta, \quad \frac{\partial^2 u_1}{\partial \theta^2} = -2 \cos\theta, \quad \frac{\partial u_1}{\partial r} = -2 \cos\theta, \quad \frac{\partial v_1}{\partial \theta} = 0, \quad \frac{\partial^2 v_1}{\partial \theta^2} = 0, \tag{1.73}$$

which should replace the values given in Eqs. (1.68). We also have

$$v_0 = \frac{\partial v_0}{\partial \theta} = 0, \quad \frac{\partial u_0}{\partial \theta} = +2 \sin\theta = \frac{\partial v_0}{\partial r}, \quad \frac{\partial u_0}{\partial r} = 2 \cos\theta . \tag{1.74}$$

Using Eqs. (1.72), and Eqs. (1.73) with the rest of (1.68), and Eq. (1.74), we get for $r = 1$ the following equations from Eqs. (1.47), (1.48), (1.51), (1.52), (1.55), and (1.56):

$$+8 \cos^2\theta = -\frac{1}{2}\frac{\partial p_1}{\partial r}\bigg|_{r=1} + \frac{1}{Re}\frac{\partial^2 u_1}{\partial r^2}\bigg|_{r=1} - \frac{6\cos\theta}{Re} \tag{1.75a}$$

$$-4 \cos^2\theta = -\frac{1}{2}\frac{\partial p_2}{\partial r}\bigg|_{r=1} + \frac{1}{Re}\frac{\partial^2 u_2}{\partial r^2}\bigg|_{r=1} \tag{1.75b}$$

$$0 = -\frac{1}{2}\frac{\partial p_3}{\partial r}\bigg|_{r=1} + \frac{1}{Re}\frac{\partial^2 u_3}{\partial r^2}\bigg|_{r=1} ; \tag{1.75c}$$

$$(-2\cos\theta)\frac{\partial v_1}{\partial r}\bigg|_{r=1} + 4 \sin\theta \cos\theta = -\frac{1}{2}\frac{\partial p_1}{\partial \theta}\bigg|_{r=1} + \frac{1}{Re}\left(\frac{\partial^2 v_1}{\partial r^2} + \frac{\partial v_1}{\partial r}\right)_{r=1} - \frac{4\sin\theta}{Re} \tag{1.76a}$$

$$(+2\cos\theta)\frac{\partial v_1}{\partial r}\bigg|_{r=1} = -\frac{1}{2}\frac{\partial p_2}{\partial \theta}\bigg|_{r=1} + \frac{1}{Re}\left(\frac{\partial^2 v_2}{\partial r^2} + \frac{\partial v_2}{\partial r}\right)_{r=1} \tag{1.76b}$$

$$0 = -\frac{1}{2}\frac{\partial p_3}{\partial \theta}\bigg|_{r=1} + \frac{1}{Re}\left(\frac{\partial^2 v_3}{\partial r^2} + \frac{\partial v_3}{\partial r}\right)_{r=1} . \tag{1.76c}$$

The term $(+8 \cos^2\theta)$ of Eq. (1.75a) is the contribution of the linear convective terms in u_1, v_1 and their derivatives of the pressure gradient $\partial p_1/\partial r$ at $r = 1$. The term $(-4 \cos^2\theta)$ of Eq. (1.75b) is the contribution of the nonlinear convective terms in u_1, v_1 and their derivatives to the pressure gradient $\partial p_2/\partial r$ at $r = 1$. They are of the same order of magnitude, but have opposite signs. Similarly, the left-hand side of Eq. (1.76a) is the contribution of the linear convective terms in u_1, v_1 and their derivatives to the pressure gradient $\partial p_1/\partial \theta$ at $r = 1$, and the left-hand side of Eq. (1.76b) is the contribution of the nonlinear convective terms in u_1, v_1 and their derivatives to the pressure gradient $\partial p_2/\partial \theta$ at $r = 1$. Both of these terms involve

$$\left.\frac{\partial v_1}{\partial r}\right|_{r=1} ,$$

a quantity whose order of magnitude cannot be determined in advance. Consequently we cannot compare the orders of magnitude of the left-hand sides of Eqs. (1.76a) and (1.76b), although we recognize that these contributions have opposite signs insofar as the term involving

$$\left.\frac{\partial v_1}{\partial r}\right|_{r=1}$$

is concerned. The result is that we cannot know in advance the orders of magnitudes of these contributions to the total pressure field p. Since there is no contribution to pressure from convective terms in Eqs. (1.75c) and (1.76c), the pressure field p_3 may be assumed to contribute little to the total pressure field p if we bear in mind that u_3 and v_3 vanish at both boundaries. As argued before, higher iteration pressure fields p_n will behave essentially as p_3, but with decreasing intensity, and this indicates the relative unimportance of iterations higher than the second, which, on the contrary, is very significant.

A comparison of this case with the case previously considered shows that in both instances the third and higher iterations are relatively unimportant as compared to the first two iterations. In both cases, we may say that at least two iterations are necessary and that they are sufficient to take into account, to a large extent, the significant convective terms which are related to the curvature of the streamlines. In this respect both the solutions of Eqs. (1.45) and (1.46) are equally appropriate as base solutions. However, the solution of Eqs. (1.45) is more appropriate than the solution of Eqs. (1.46), because the former allows us to estimate the orders of magnitude of the linear and nonlinear convective terms in u_1, v_1 and their derivatives in advance, while the latter does not, because of the unknown magnitude of

$$\left.\frac{\partial v_1}{\partial r}\right|_{r=1} .$$

It is interesting to note that this comparison tempts us to say that

$$\left.\frac{\partial u_1}{\partial r}\right|_{r=1} = -2 \sin\theta ,$$

i.e., it almost leads us to information which we cannot have in advance without such a comparative study. Whether this information turns out to be correct or not, it is still true that Eqs.(1.45) is the more appropriate solution from the point of view of the a priori information that it provides.

From both the physical and the mathematical considerations we then see that the irrotational potential flow solution of Eq. (1.17) which satisfies all

except the no-slip boundary condition is the most appropriate base flow for the process of iteration. *The solutions* $S_1, S_2, \ldots, S_n$ *define a linear substructure to the solution* S, *and the equations* $L_n S_n + f_n = 0$, $n \geq 1$ *define a system of linear substructure equations underlying the Navier-Stokes equations.* The equations for the first three iterations as given by Eqs. (1.47) to (1.58) inclusive are the explicit expressions of these substructure equations for $n = 1, 2$, and 3. We emphasize that in this theory no idea of small perturbations about a given solution is involved and that there is no limitation imposed on the characteristic parameter, the Reynolds number, of the flow field. Consequently, this theory is not a small-perturbation theory.

The potential flow solution around a circular cylinder was used by Wilson (1904) [32], Boussinesq (1905) [33], Russel (1910) [34], and King (1914) [35] as a means of convecting away heat from the cylinder. Later Burgers (1921) [36], Zeilon (1926) [37], Southwell and Squire (1933) [24], Meksyn (1937) [38], and recently, Pillow (1964) [39] have used it in a spirit of refinement over Ossen's work. The conviction, at least tacitly shared by these authors, is that their work is inherently restricted to flows that deviate only slightly from potential flows. An immediate consequence of this convection is that these authors do not consider their work as applicable close to the cylinder or in the wake. There is, therefore, a conspicuous absence of the recognition of the crucial importance which we have assigned to the higher iterations, among which the second iteration equations appear to be of particular significance, as explained earlier. Further, only in Southwell and Squire's work is there a clear recognition of the validity of their equation for all Reynolds numbers. Burgers and Zeilon have considered the case of $\nu \to 0$, i.e., the case of large Reynolds numbers, and moreover, Zeilon has permitted convection by separated potential flows. Lewis [40], in his paper, states: "Of course, it is not at all obvious which irrotational motion is the one best suited in each particular case." Since the potential flow solution $\psi = -(r - 1/r) \sin\theta$ approaches the potential uniform flow solution $\psi = -r \sin\theta$ far away from a circular cylinder, there, if a real flow is viewed as a slight deviation from the uniform flow, it just as well can be viewed as a slight deviation from the potential flow given by $\psi = -(r - 1/r) \sin\theta$. Thus the dilemma stated by Lewis is natural when particular cases, in which some parts of the complete flow field can be viewed as deviating slightly from some irrotational flow field, are considered in a technical spirit. In the present work where an evolutionary point of view is taken, the potential flow $\psi = -(r - 1/r) \sin\theta$ plays a fundamental role, valid in the whole domain, as the base flow from which deviations, not necessarily small in any sense, take place to accommodate the no-slip boundary condition. In this sense we have ascribed a kind of reality to the potential flow solution under all flow conditions. Hence, even though all the studies just cited indeed lead to equations and conditions which are equivalent to our base flow and the first iteration equations and conditions, the conceptual basis, motivation, and justification of our work are entirely different from those other studies.

BOUNDARY CONDITIONS ON THE ITERATIONS

At the Cylinder Wall ($r = 1$)

First Iteration —

$$u_1(1,\theta,t) = \left(\frac{1}{r}\frac{\partial \psi_1}{\partial \theta}\right)_{r=1} = 0 \qquad \text{for all} \quad t \tag{1.77}$$

$$v_1(1,\theta,t) = \left(-\frac{\partial \psi_1}{\partial r}\right)_{r=1} = -2\sin\theta \qquad \text{for all} \quad t > 0\,. \tag{1.78}$$

Second Iteration —

$$u_2(1,\theta,t) = \left(\frac{1}{r}\frac{\partial \psi_2}{\partial \theta}\right)_{r=1} = 0 \qquad \text{for all} \quad t \tag{1.79}$$

$$v_2(1,\theta,t) = \left(-\frac{\partial \psi_2}{\partial r}\right)_{r=1} = 0 \qquad \text{for all} \quad t\,. \tag{1.80}$$

Higher Iterations ($n \geq 3$) —

$$u_n(1,\theta,t) = \left(\frac{1}{r}\frac{\partial \psi_n}{\partial \theta}\right)_{r=1} = 0 \qquad \text{for all} \quad t \tag{1.81}$$

$$v_n(1,\theta,t) = \left(-\frac{\partial \psi_n}{\partial r}\right)_{r=1} = 0 \qquad \text{for all} \quad t\,. \tag{1.82}$$

At Physically Infinite Distance ($r = h^*$)

We first note that according to Eq. (1.16) the actual flow field is such that it can be regarded as uniform beyond a certain distance h^*. The potential base flow also becomes uniform with increasing distance, and during the discussion on a physically infinite distance it was shown, with reference to Table 1, that $h^* = 50$ may be taken as the corresponding physically infinite distance. Now $u = u_0 + u_1 + u_2 + \cdots$ and $v = v_0 + v_1 + v_2 + \cdots$. Hence if u_n and v_n, $n \geq 1$ all become zero at some distance h_i^* evaluated in the sense of a physically infinite distance, the flow beyond h_i^* will be given by u_0, and the condition of uniform flow will be satisfied by u because it is satisfied by u_0. The distance h_i^* must be found so that the solutions u_n, $n \geq 1$ do not change significantly if the condition of their vanishing is applied at any other distance greater than h_i^*; i.e., h_i^* is to be the physically infinite distance for the iterative solutions. We note that this distance h_i^* must be the same for all iterations, because higher

iterations use lower iteration solutions which have already used a condition at this distance.

The domain within a radius h_i^* has viscous effects, whereas beyond h_i^* the potential flow represents the real flow. In this sense one may say that h_i^* is the thickness of a boundary layer surrounding the cylinder; indeed, this thickness may be several times the diameter of the cylinder for some values of the Reynolds number. However, we must expect this domain to become smaller, i.e., h_i^* to decrease, with increasing Reynolds number when the flow is time-independent. Even for a temporal flow we should expect the part of the domain close to the cylinder to become smaller with increasing Reynolds number.

Hence we have the following conditions to be satisfied by u_n and v_n, $n \geq 1$ at h_i^*:

First Iteration —

$$u_1(h_i^*, \theta, t) = \left(\frac{1}{r} \frac{\partial \psi_1}{\partial \theta} \right)_{r=h_i^*} = 0 \quad \text{for all} \quad t \tag{1.83}$$

$$v_1(h_i^*, \theta, t) = \left(- \frac{\partial \psi_1}{\partial r} \right)_{r=h_i^*} = 0 \quad \text{for all} \quad t \, . \tag{1.84}$$

Second Iteration —

$$u_2(h_i^*, \theta, t) = \left(\frac{1}{r} \frac{\partial \psi_2}{\partial \theta} \right)_{r=h_i^*} = 0 \quad \text{for all} \quad t \tag{1.85}$$

$$v_2(h_i^*, \theta, t) = \left(- \frac{\partial \psi_2}{\partial r} \right)_{r=h_i^*} = 0 \quad \text{for all} \quad t \, . \tag{1.86}$$

Higher Iterations ($n \geq 3$) —

$$u_n(h_i^*, \theta, t) = \left(\frac{1}{r} \frac{\partial \psi_n}{\partial \theta} \right)_{r=h_i^*} = 0 \quad \text{for all} \quad t \tag{1.87}$$

$$v_n(h_i^*, \theta, t) = \left(- \frac{\partial \psi_n}{\partial r} \right)_{r=h_i^*} = 0 \quad \text{for all} \quad t \, . \tag{1.88}$$

DRAG

The component of force exerted by the fluid on the cylinder per its unit dimensional length along the polar axis in the direction of the velocity $\hat{u}_\infty$ is given by

$$\hat{F} = \int_{\hat{z}=-1/2}^{\hat{z}=+1/2} \int_0^{2\pi} \left[\left(\hat{p} \cos\hat{\theta} - \hat{\sigma}_{\hat{r}\hat{r}} \cos\hat{\theta} + \hat{\sigma}_{\hat{r}\hat{\theta}} \sin\hat{\theta} \right) \hat{r} \right]_{\hat{r}=a} d\hat{\theta}\, d\hat{z} \ . \tag{1.89}$$

Since

$$\hat{z} = za \ , \quad \hat{p} = \frac{1}{2} \rho \hat{u}_\infty^2 p + \hat{p}_\infty \ , \quad \hat{\sigma}_{\hat{r}\hat{r}} = \rho \hat{u}_\infty^2 \sigma_{rr} \ ,$$

where

$$\sigma_{rr} = \frac{2}{Re} \frac{\partial u}{\partial r} \ ,$$

and

$$\hat{\sigma}_{\hat{r}\hat{\theta}} = \rho \hat{u}_\infty^2 \sigma_{r\theta}$$

and where

$$\sigma_{r\theta} = \frac{1}{Re} \left(\frac{1}{r} \frac{\partial u}{\partial \theta} + \frac{\partial v}{\partial r} - \frac{v}{r} \right) ,$$

the right-hand side of Eq. (1.67) can be rewritten:

$$\hat{F} = \rho \hat{u}_\infty^2 a^2 \int_0^{2\pi} \left(\frac{1}{2} p \cos\theta - \sigma_{rr} \cos\theta + \sigma_{r\theta} \sin\theta \right)_{r=1} d\theta \ ,$$

using

$$\int_0^{2\pi} \frac{\hat{p}_\infty}{\rho \hat{u}_\infty^2} \cos\theta \, d\theta = 0 \ .$$

The projected area per unit length of the cylinder is given by

$$\text{Area} = (2a) \times a = 2a^2 \ .$$

Hence the drag coefficient defined by $C_D \equiv \hat{F} / [1/2 (\rho \hat{u}_\infty^2)] \times$ projected area is given by

$$C_D = \int_0^{2\pi} \left(\frac{1}{2} p \cos\theta - \sigma_{rr} \cos\theta + \sigma_{r\theta} \sin\theta \right)_{r=1} d\theta = C_D(Re) \ . \tag{1.90}$$

Because the drag due to the potential flow is zero, we may write Eq. (1.90) as

$$C_D = \int_0^{2\pi} \left(\frac{1}{2} p_1 \cos\theta - \sigma_{rr_1} \cos\theta + \sigma_{r\theta_1} \sin\theta \right)_{r=1} d\theta$$
$$+ \int_0^{2\pi} \left(\frac{1}{2} p_2 \cos\theta - \sigma_{rr_2} \cos\theta + \sigma_{r\theta_2} \sin\theta \right)_{r=1} d\theta + \cdots, \tag{1.91}$$

where the first integral represents the drag contribution from the first iteration and the second integral represents that from the second iteration.

PART 2

CONSTRUCTION OF ANALYTICAL REPRESENTATION OF VISCOUS FLOWS AROUND A CIRCULAR CYLINDER

This part of the paper presents in outline some significant steps developed in the application of the theory of Part 1 to the construction of an analytical representation of viscous flows around a circular cylinder, based upon the complete Navier-Stokes equations and realistic boundary conditions.

Here, the subsidiary equations governing the coefficients $A_n(r,t)$, $B_n(r,t)$, $C_n(r,t)$, and $D_n(r,t)$ of the stream functions ψ_1 and ψ_2 as given by Eqs. (1.60) and (1.61) respectively are obtained from the sets of equations for the first and second iterations. Appropriate conditions at the two boundaries are respectively obtained for these functions and their derivatives, with respect to r, from the conditions of Eqs. (1.77) to (1.80), inclusive, and Eqs. (1.83) to (1.86), inclusive.

FIRST ITERATION

To obtain u_1, v_1, and p_1 which satisfy Eqs. (1.47), (1.48), and (1.49), and the boundary conditions of Eqs. (1.77), (1.78), (1.83), and (1.84), we solve Eqs. (1.50), together with the same boundary conditions, so as to obtain first ψ_1 and hence u_1 and v_1. Then, from Eqs. (1.47) and (1.48), by integration we will obtain p_1. Using Eqs. (1.18) and (1.19) in Eq. (1.50), we get

$$\nabla^4\psi_1 - \left[\frac{\mathrm{Re}}{r}\left(1+\frac{1}{r^2}\right)\sin\theta\right]\frac{\partial\nabla^2\psi_1}{\partial\theta} + \left[\mathrm{Re}\left(1-\frac{1}{r^2}\right)\cos\theta\right]\frac{\partial\nabla^2\psi_1}{\partial r} = \mathrm{Re}\,\frac{\partial\nabla^2\psi_1}{\partial t} \,. \tag{2.1}$$

Now, in Eq. (1.60) we have

$$\psi_1 = \frac{1}{2}A_0(r,t) + \sum_{n=1}^{\infty} A_n(r,t)\cos n\theta + B_n(r,t)\sin n\theta \,,$$

where A_0, A_n, and B_n are functions of r and t. These are the functions we wish to determine.

Using Eq. (1.60) and putting

$$\begin{aligned}
\mathcal{A}_0(r,t) &= \mathcal{A}_0''(r,t) + \frac{1}{r}\mathcal{A}_0'(r,t) \\
\mathcal{A}_n(r,t) &= \mathcal{A}_n''(r,t) + \frac{1}{r}\mathcal{A}_n'(r,t) - \frac{n^2}{r^2}\mathcal{A}_n(r,t) \\
\mathcal{B}_n(r,t) &= \mathcal{B}_n''(r,t) + \frac{1}{r}\mathcal{B}_n'(r,t) - \frac{n^2}{r^2}\mathcal{B}_n(r,t) \,,
\end{aligned} \tag{2.2}$$

we obtain, after some algebraic manipulation, the following governing equations for $\mathfrak{A}_n$ and $\mathfrak{B}_n$:

$$\frac{\mathfrak{A}_0''}{2} + \frac{1}{r}\frac{\mathfrak{A}_0'}{2} + \frac{Re}{2r}\left(1 + \frac{1}{r^2}\right)\mathfrak{A}_1 + \frac{Re}{2}\left(1 - \frac{1}{r^2}\right)\mathfrak{A}_1' = \frac{Re}{2}\frac{\partial \mathfrak{A}_0}{\partial t} \; ; \tag{2.3}$$

$$\mathfrak{A}_1'' + \frac{1}{r}\mathfrak{A}_1' - \frac{1}{r^2}\mathfrak{A}_1 + \frac{Re}{r}\left(1 + \frac{1}{r^2}\right)\mathfrak{A}_2 + \frac{Re}{2}\left(1 - \frac{1}{r^2}\right)\mathfrak{A}_2' + Re\left(1 - \frac{1}{r^2}\right)\frac{\mathfrak{A}_0'}{2} = Re\,\frac{\partial \mathfrak{A}_1}{\partial t} \; ; \tag{2.4}$$

$$\mathfrak{A}_n'' + \frac{1}{r}\mathfrak{A}_n' - \frac{n^2}{r^2}\mathfrak{A}_n + \frac{(n+1)\,Re}{2r}\left(1 + \frac{1}{r^2}\right)\mathfrak{A}_{n+1} - \frac{(n-1)\,Re}{2r}\left(1 + \frac{1}{r^2}\right)\mathfrak{A}_{n-1}$$
$$+ \frac{Re}{2}\left(1 - \frac{1}{r^2}\right)\mathfrak{A}_{n+1}' + \frac{Re}{2}\left(1 - \frac{1}{r^2}\right)\mathfrak{A}_{n-1}' = Re\,\frac{\partial \mathfrak{A}_n}{\partial t} \tag{2.5}$$

$$n = 2, 3, 4, \ldots \; ;$$

$$\mathfrak{B}_1'' + \frac{1}{r}\mathfrak{B}_1' - \frac{1}{r^2}\mathfrak{B}_1 + \frac{Re}{r}\left(1 + \frac{1}{r^2}\right)\mathfrak{B}_2 + \frac{Re}{2}\left(1 - \frac{1}{r^2}\right)\mathfrak{B}_2' = Re\,\frac{\partial \mathfrak{B}_1}{\partial t} \; ;$$

$$\mathfrak{B}_2'' + \frac{1}{r}\mathfrak{B}_2' - \frac{4}{r^2}\mathfrak{B}_2 - \frac{Re}{2r}\left(1 + \frac{1}{r^2}\right)\mathfrak{B}_1 + \frac{Re}{2}\left(1 - \frac{1}{r^2}\right)\mathfrak{B}_1' \tag{2.6}$$
$$+ \frac{3Re}{2r}\left(1 + \frac{1}{r^2}\right)\mathfrak{B}_3 + \frac{Re}{2}\left(1 - \frac{1}{r^2}\right)\mathfrak{B}_3' = Re\,\frac{\partial \mathfrak{B}_2}{\partial t} \; ; \tag{2.7}$$

$$\mathfrak{B}_n'' + \frac{1}{r}\mathfrak{B}_n' - \frac{n^2}{r^2}\mathfrak{B}_n - \frac{(n-1)\,Re}{2r}\left(1 + \frac{1}{r^2}\right)\mathfrak{B}_{n-1} + \frac{Re}{2}\left(1 - \frac{1}{r^2}\right)\mathfrak{B}_{n-1}'$$
$$+ \frac{(n+1)\,Re}{2r}\left(1 + \frac{1}{r^2}\right)\mathfrak{B}_{n+1} + \frac{Re}{2}\left(1 - \frac{1}{r^2}\right)\mathfrak{B}_{n+1}' = Re\,\frac{\partial \mathfrak{B}_n}{\partial t} \tag{2.8}$$

$$n = 3, 4, \ldots \; .$$

From Eq. (1.60) we have

$$u_1(r,\theta,t) = \frac{1}{r}\frac{\partial \psi_1}{\partial \theta}$$

$$= \sum_{n=1}^{\infty} -\frac{nA_n(r,t)}{r}\sin n\theta + \frac{nB_n(r,t)}{r}\cos n\theta$$

$$v_1(r,\theta,t) = -\frac{\partial \psi_1}{\partial r}$$

$$= -\frac{1}{2}A_0'(r,t) - \sum_{n=1}^{\infty}\left[A_n'(r,t)\cos n\theta + B_n'(r,t)\sin n\theta\right] \tag{1.63a}$$

The boundary conditions in Eqs. (1.77), (1.78), (1.83), and (1.84), when applied to the expressions of Eqs. (1.63) which result from the periodicity condition on u_1 and v_1, imply that the following conditions on the functions A_n and B_n should hold:

$$A_0'(1,t) = 0\,, \quad A_0'(h_i^*,t) = 0\,; \tag{2.9}$$

$$A_n(1,t) = 0\,, \quad A_n'(1,t) = 0\,, \quad A_n(h_i^*,t) = 0\,, \quad A_n'(h_i^*,t) = 0\,; \qquad n = 1, 2, 3, \ldots . \tag{2.10}$$

$$B_1(1,t) = 0\,, \quad B_1'(1,t) = +2\,, \quad B_1(h_i^*,t) = 0\,, \quad B_1'(h_i^*,t) = 0\,; \tag{2.11}$$

$$B_2(1,t) = 0\,, \quad B_2'(1,t) = 0\,, \quad B_2(h_i^*,t) = 0\,, \quad B_2'(h_i^*,t) = 0\,; \tag{2.12}$$

$$B_n(1,t) = 0\,, \quad B_n'(1,t) = 0\,, \quad B_n(h_i^*,t) = 0\,, \quad B_n'(h_i^*,t) = 0\,. \qquad n = 3, 4, \ldots . \tag{2.13}$$

For a steady flow, these boundary conditions together with the differential Eqs. (2.3), (2.19), and (2.8), suffice to determine the functions A_n and B_n. For a time-dependent flow, the nature of initial conditions also needs to be critically considered. Once the functions A_n and B_n are obtained uniquely, they determine uniquely the stream function ψ_1 and hence the first iteration velocity field u_1 and v_1.

In view of the harmonic structure of the stream function, the pressure field also has the same structure, which is described in detail in Refs. 1 and 2.

SECOND ITERATION

To obtain u_2, v_2, and p_2 which satisfy Eqs. (1.51), (1.52), and (1.53) together with the boundary conditions of Eqs. (1.79), (1.80), (1.85), and (1.86), we will solve, as in the case of the first iteration, Eq. (1.54) together with the conditions in Eqs. (1.79), (1.80), (1.85), and (1.86) to obtain first ψ_2 and then u_2 and v_2. Since ψ_2, like ψ_1, is a periodic function of θ and has a Fourier series representation, an examination of the terms in Eq. (1.54) reveals that we must here obtain a Fourier representation of terms involving the products of two Fourier series. For this purpose, we refer to the following two theorems.

Theorem II (Perseval's Theorem) [41]: If $f(x)$ and $F(x)$ are square integrable functions defined on $(-\pi, \pi)$, for which

$$f(x) = \frac{a_0}{2} + \sum_{n=1}^{\infty} (a_n \cos nx + b_n \sin nx)$$

$$F(x) = \frac{A_0}{2} + \sum_{n=1}^{\infty} (A_n \cos nx + B_n \sin nx) ,$$

then

$$\frac{1}{\pi}\int_{-\pi}^{\pi} f(x) F(x)\, dx = \frac{a_0 A_0}{2} + \sum_{n=1}^{\infty} (a_n A_n + b_n B_n) . \tag{2.14}$$

Theorem III [41]: Using Perseval's Theorem, we can show that if the product

$$f(x) \cdot F(x) \equiv \left[\frac{a_0}{2} + \sum_{n=1}^{\infty} (a_n \cos nx + b_n \sin nx)\right] \times \left[\frac{A_0}{2} + \sum_{n=1}^{\infty} (A_n \cos nx + B_n \sin nx)\right] \tag{2.15}$$

is represented by the Fourier series

$$f(x) \cdot F(x) = \frac{\alpha_0}{2} + \sum_{n=1}^{\infty} (\alpha_n \cos nx + \beta_n \sin nx) , \tag{2.16}$$

then the coefficients α_0, α_n, and β_n are given by the following expressions:

$$\alpha_0 = \frac{a_0 A_0}{2} + \sum_{n=1}^{\infty} (a_n A_n + b_n B_n)$$

$$\alpha_n = \frac{a_0 A_n}{2} + \frac{1}{2}\sum_{m=1}^{\infty} [a_m(A_{m+n} + A_{m-n}) + b_m(B_{m+n} + B_{m-n})] \tag{2.17}$$

$$\beta_n = \frac{a_0 B_n}{2} + \frac{1}{2}\sum_{m=1}^{\infty} [a_m(B_{m+n} - B_{m-n}) - b_m(A_{m+n} - A_{m-n})] ,$$

with the stipulation that

$$A_{-k} \equiv +A_k$$
$$B_{-k} \equiv -B_k . \tag{2.18}$$

Using Eqs. (1.18) and (1.19) and Theorems II and III, we obtain from Eq. (1.54)

$$\left\{\nabla^4\psi_2 + \mathrm{Re}\left[\left(1 - \frac{1}{r^2}\right)\cos\theta\right]\frac{\partial\nabla^2\psi_2}{\partial r} + \frac{\mathrm{Re}}{r}\left(\sum_{n=1}^{\infty} - nB_n\cos n\theta + nA_n\sin n\theta\right)\frac{\partial\nabla^2\psi_2}{\partial r}\right.$$

$$- \frac{\mathrm{Re}}{r}\left(\frac{1}{2}\mathfrak{A}'_0 + \sum_{n=1}^{\infty}\mathfrak{A}'_n\cos n\theta + \mathfrak{B}'_n\sin n\theta\right)\frac{\partial\psi_2}{\partial\theta}$$

$$- \frac{\mathrm{Re}}{r}\left[\left(1 + \frac{1}{r^2}\right)\sin\theta\right]\frac{\partial\nabla^2\psi_2}{\partial\theta} + \frac{\mathrm{Re}}{r}\left(\frac{1}{2}A'_0 + \sum_{n=1}^{\infty}A'_n\cos n\theta + B'_n\sin n\theta\right)\frac{\partial\nabla^2\psi_2}{\partial\theta} \tag{2.19}$$

$$+ \frac{\mathrm{Re}}{r}\left(\sum_{n=1}^{\infty} n\mathfrak{B}_n\cos n\theta - n\mathfrak{A}_n\sin n\theta\right)\frac{\partial\psi_2}{\partial r}$$

$$\left. - \frac{\mathrm{Re}}{r}\left[\frac{\alpha_0 - \gamma_0}{2} + \sum_{n=1}^{\infty}(\alpha_n - \gamma_n)\cos n\theta + (\beta_n - \delta_n)\sin n\theta\right]\right\} = \mathrm{Re}\,\frac{\partial\nabla^2\psi_2}{\partial t},$$

where

$$\mathfrak{A}'_{-k} \equiv \mathfrak{A}'_k\,, \quad \mathfrak{B}'_{-k} \equiv -\mathfrak{B}'_k\,; \tag{2.20}$$

$$\frac{\alpha_0}{2} \equiv \sum_{n=1}^{\infty}(nB_n\mathfrak{A}'_n - nA_n\mathfrak{B}'_n)\,; \tag{2.21}$$

$$\alpha_n \equiv \frac{1}{2}\sum_{m=1}^{\infty}[mB_m(\mathfrak{A}'_{m+n} + \mathfrak{A}'_{m-n}) - mA_m(\mathfrak{B}'_{m+n} + \mathfrak{B}'_{m-n})]\,; \tag{2.22}$$

$$\beta_n \equiv \frac{1}{2}\sum_{m=1}^{\infty}[mB_m(\mathfrak{B}'_{m+n} - \mathfrak{B}'_{m-n}) + m\mathfrak{A}_m(\mathfrak{A}'_{m+n} - \mathfrak{A}'_{m-n})]\,; \tag{2.23}$$

$$A'_{-k} \equiv A'_k\,, \quad B'_{-k} \equiv -B'_k\,; \tag{2.24}$$

$$\frac{\gamma_0}{2} \equiv \sum_{n=1}^{\infty}(n\mathfrak{B}_nA'_n - n\mathfrak{A}_nB'_n)\,; \tag{2.25}$$

$$\gamma_n \equiv \frac{1}{2}\sum_{m=1}^{\infty}[m\mathfrak{B}_m(A'_{m+n} + A'_{m-n}) - m\mathfrak{A}_m(B'_{m+n} + B'_{m-n})]\,; \tag{2.26}$$

$$\delta_n = \frac{1}{2}\sum_{m=1}^{\infty} [m\mathcal{B}_m(B'_{m+n} - B'_{m-n}) + m\mathcal{A}_m(A'_{m+n} - A'_{m-n})] \quad . \tag{2.27}$$

In Eq. (1.61) we have

$$\psi_2(r,\theta,t) = \frac{C_0(r,t)}{2} + \sum_{n=1}^{\infty} C_n(r,t)\cos n\theta + D_n(r,t)\sin n\theta \quad .$$

Putting

$$\begin{aligned}
\mathcal{C}_0(r,t) &\equiv C''_0(r,t) + \frac{1}{r}C'_0(r,t) \\
\mathcal{C}_n(r,t) &\equiv C''_n(r,t) + \frac{1}{r}C'_n(r,t) - \frac{n^2}{r^2}C_n(r,t) \\
\mathcal{D}_n(r,t) &\equiv D''_n(r,t) + \frac{1}{r}D'_n(r,t) - \frac{n^2}{r^2}D_n(r,t) \quad ,
\end{aligned} \tag{2.28}$$

and using Eq. (1.61) in Eq. (2.19), we obtain an equation which involves the trigonometric functions $\cos m\theta$ and $\sin m\theta$.

Since the terms in $\cos m\theta$ ($m = 0, 1, 2, \ldots$) and $\sin m\theta$ ($m = 1, 2, \ldots$) are linearly independent, Eq. (2.19) can be satisfied only if the coefficients of these terms are identically equal to zero. This gives the following equations connecting the functions C_n and D_n:

$$\begin{aligned}
&\frac{1}{2}\left(\mathcal{C}''_0 + \frac{1}{r}\mathcal{C}'_0\right) + \frac{Re}{2}\left(1 - \frac{1}{r^2}\right)\mathcal{C}'_1 - \frac{Re}{r}\left[\sum_{n=1}^{\infty} n(B_n\mathcal{C}'_n - A_n\mathcal{D}'_n)\right] \\
&- \frac{Re}{r}\left[\sum_{n=1}^{\infty} n(D_n\mathcal{A}'_n - C_n\mathcal{B}'_n)\right] + \frac{Re}{2r}\left(1 + \frac{1}{r^2}\right)\mathcal{C}_1 + \frac{Re}{r}\left[\sum_{n=1}^{\infty} n(\mathcal{D}_nA'_n - \mathcal{C}_nB'_n)\right] \\
&+ \frac{Re}{r}\left[\sum_{n=1}^{\infty} n(\mathcal{B}_nC'_n - \mathcal{A}_nD'_n)\right] - \frac{Re}{2r}(\alpha_0 - \gamma_0) = \frac{Re}{2}\frac{\partial\mathcal{C}_0}{\partial t} \quad ;
\end{aligned} \tag{2.29}$$

$$\begin{aligned}
&\left(\mathcal{C}''_1 + \frac{1}{r}\mathcal{C}'_1 - \frac{1}{r^2}\mathcal{C}_1\right) + \frac{Re}{2}\left(1 - \frac{1}{r^2}\right)\mathcal{C}'_0 + \frac{Re}{2}\left(1 - \frac{1}{r^2}\right)\mathcal{C}'_2 + \frac{Re}{r}\left(1 + \frac{1}{r^2}\right)\mathcal{C}_2 \\
&- \sum_{m=1}^{\infty}\frac{Re}{2r}[mB_m(\mathcal{C}'_{m+1} + \mathcal{C}'_{m-1}) - mA_m(\mathcal{D}'_{m+1} + \mathcal{D}'_{m-1})]
\end{aligned}$$

$$- \sum_{m=1}^{\infty} \frac{Re}{2r} [mD_m(\mathcal{A}'_{m+1} + \mathcal{A}'_{m-1}) - mC_m(\mathcal{B}'_{m+1} + \mathcal{B}'_{m-1})]$$

$$+ \sum_{m=1}^{\infty} \frac{Re}{2r} [m\mathcal{D}_m(A'_{m+1} + A'_{m-1}) - m\mathcal{C}_m(B'_{m+1} + B'_{m-1})]$$

$$+ \sum_{m=1}^{\infty} \frac{Re}{2r} [m\mathcal{B}_m(C'_{m+1} + C'_{m-1}) - m\mathcal{A}_m(D'_{m+1} + D'_{m-1})]$$

$$- \frac{Re}{r} (\alpha_1 - \gamma_1) = Re \frac{\partial \mathcal{C}_1}{\partial t} ; \qquad (2.30)$$

$$\left(\mathcal{C}''_n + \frac{1}{r}\mathcal{C}'_n - \frac{n^2}{r^2}\mathcal{C}_n\right) + \frac{Re}{2}\left(1 - \frac{1}{r^2}\right)(\mathcal{C}'_{n+1} + \mathcal{C}'_{n-1})$$

$$- \sum_{m=1}^{\infty} \frac{Re}{2r} [mB_m(\mathcal{C}'_{m+n} + \mathcal{C}'_{m-n}) - mA_m(\mathcal{D}'_{m+n} + \mathcal{D}'_{m-n})]$$

$$- \sum_{m=1}^{\infty} \frac{Re}{2r} [mD_m(\mathcal{A}'_{m+n} + \mathcal{A}'_{m-n}) - mC_m(\mathcal{B}'_{m+n} + \mathcal{B}'_{m-n})]$$

$$+ \frac{Re}{2r}\left(1 + \frac{1}{r^2}\right)[(n+1)\mathcal{C}_{n+1} + (n-1)\mathcal{C}_{n-1}]$$

$$+ \sum_{m=1}^{\infty} \frac{Re}{2r} [m\mathcal{D}_m(A'_{m+n} + A'_{m-n}) - m\mathcal{C}_m(B'_{m+n} + B'_{m-n})]$$

$$+ \sum_{m=1}^{\infty} \frac{Re}{2r} [m\mathcal{B}_m(C'_{m+n} + C'_{m-n}) - m\mathcal{A}_m(D'_{m+n} + D'_{m-n})]$$

$$- \frac{Re}{r} (\alpha_n - \gamma_n) = Re \frac{\partial \mathcal{C}_n}{\partial t} ; \qquad n = 2, 3, 4, \ldots \qquad (2.31)$$

$$\left(\mathcal{D}''_1 + \frac{1}{r}\mathcal{D}'_1 - \frac{1}{r^2}\mathcal{D}_1\right) + \frac{Re}{2}\left(1 - \frac{1}{r^2}\right)\mathcal{D}'_2 + \frac{Re}{r}\left(1 + \frac{1}{r^2}\right)\mathcal{D}_2$$

$$- \sum_{m=1}^{\infty} \frac{Re}{2r} [mB_m(\mathcal{D}'_{m+1} - \mathcal{D}'_{m-1}) + mA_m(\mathcal{C}'_{m+1} - \mathcal{C}'_{m-1})]$$

$$- \sum_{m=1}^{\infty} \frac{Re}{2r} [mD_m(\mathcal{B}'_{m+1} - \mathcal{B}'_{m-1}) + mC_m(\mathcal{G}'_{m+1} - \mathcal{G}'_{m-1})]$$

$$+ \sum_{m=1}^{\infty} \frac{Re}{2r} [m\mathcal{D}_m(B'_{m+1} - B'_{m-1}) + m\mathcal{C}_m(A'_{m+1} - A'_{m-1})]$$

$$+ \sum_{m=1}^{\infty} \frac{Re}{2r} [m\mathcal{B}_m(D'_{m+1} - D'_{m-1}) + m\mathcal{G}_m(C'_{m+1} - C'_{m-1})]$$

$$- \frac{Re}{r} (\beta_1 - \delta_1) = Re \frac{\partial \mathcal{D}_1}{\partial t} ; \tag{2.32}$$

$$\left(\mathcal{D}''_n + \frac{1}{r}\mathcal{D}'_n - \frac{n^2}{r^2}\mathcal{D}_n\right) + \frac{Re}{2}\left(1 - \frac{1}{r^2}\right)(\mathcal{D}'_{n+1} + \mathcal{D}'_{n-1})$$

$$- \sum_{m=1}^{\infty} \frac{Re}{2r} [mB_m(\mathcal{D}'_{m+n} - \mathcal{D}'_{m-n}) + mA_m(\mathcal{C}'_{m+n} - \mathcal{C}'_{m-n})]$$

$$- \sum_{m=1}^{\infty} \frac{Re}{2r} [mD_m(\mathcal{B}_{m+n} - \mathcal{B}_{m-n}) + mC_m(\mathcal{G}'_{m+n} - \mathcal{G}'_{m-n})]$$

$$+ \frac{Re}{2r}\left(1 + \frac{1}{r^2}\right)[(n+1)\mathcal{D}_{n+1} - (n-1)\mathcal{D}_{n-1}]$$

$$+ \sum_{m=1}^{\infty} \frac{Re}{2r} [m\mathcal{D}_m(B'_{m+n} - B'_{m-n}) + m\mathcal{C}_m(A'_{m+n} - A'_{m-n})]$$

$$+ \sum_{m=1}^{\infty} \frac{Re}{2r} [m\mathcal{B}_m(D'_{m+n} - D'_{m-n}) + m\mathcal{G}_m(C'_{m+n} - C'_{m-n})]$$

$$- \frac{Re}{r} (\beta_n - \delta_n) = Re \frac{\partial \mathcal{D}_n}{\partial t} . \quad n = 2, 3, 4, \ldots \tag{2.33}$$

The boundary conditions of Eqs. (1.79), (1.80), (1.85), and (1.86) imply

$$C'_0(1,t) = 0 , \quad C'_0(h_i^*,t) = 0 ; \tag{2.34}$$

$$C_n(1,t) = 0 , \quad C'_n(1,t) = 0 , \quad C_n(h_i^*,t) = 0 , \quad C'_n(h_i^*,t) = 0 ; \quad n = 1, 2, 3, \ldots \tag{2.35}$$

$$D_n(1,t) = 0\,, \quad D_n'(1,t) = 0\,, \quad D_n(h_i^*,t) = 0\,, \quad D_n'(h_i^*,t) = 0\,. \qquad n = 1,\ 2,\ 3,\ \ldots \tag{2.36}$$

Equations (2.29) to (2.33) inclusive, together with the homogeneous boundary conditions of Eqs. (2.34), (2.35), and (2.36), complete the formulation of the second iteration.

SIMPLIFYING CONSIDERATIONS

The sets of subsidiary equations and the boundary conditions in Eqs. (2.3) to (2.13) inclusive, for the first iteration, and Eqs. (2.29) to (2.36) inclusive, for the second iteration, are in their most general form consistent with the assumption of the existence of Fourier representations for the stream function ψ_1 and ψ_2. These equations and the boundary conditions can be simplified considerably.

The terms in $\cos n\theta$ and $\sin n\theta$ respectively represent an asymmetric and a symmetric flow pattern. If the initial flow conditions are such that they represent a symmetric flow pattern at the time $t = 0$, or if we are considering a steady flow problem such that A_n, B_n, C_n, and D_n are all assumed to be time-independent, then it is evident from Eqs. (2.3), (2.4), and (2.5) together with the boundary conditions of Eqs. (2.9) and (2.10) that $A_n(r,t) \equiv 0$, $(n = 0, 1, 2, \ldots)$ are admissible trivial solutions to these equations and conditions. Similarly, $C_n(r,t) \equiv 0$ are admissible trivial solutions to Eqs. (2.29), (2.30), and (2.33) together with the conditions of Eqs. (2.34) and (2.35). Since the set of Eqs. (2.3), (2.4), and (2.5) is a set of simultaneous linear differential equations with variable coefficients, they have unique solutions, if they exist, satisfying the conditions of Eqs. (2.9) and (2.10) and suitable initial conditions. The same is true of the set of Eqs. (2.6), (2.7), and (2.8) with the conditions of Eqs. (2.11), (2.12), (2.13), and suitable conditions for the functions B_n. Hence we can conclude that $A_n(r,t) \equiv 0$ are the only solutions. Then a similar argument shows that the set of Eqs. (2.29) and (2.30) with the conditions of Eqs. (2.35) and (2.36) has only $C_n(r,t) \equiv 0$ as the only solutions. The only nontrivial solutions are in B_n and D_n. And these correspond to symmetric terms in ψ_1 and ψ_2 respectively.

Since the equations for ψ_n, $n \geq 3$ are structurally similar to the equations for ψ_1 and ψ_2, and the conditions on the asymmetric parts of these stream functions ψ_n are the same as those on the asymmetric parts of the stream functions ψ_1 and ψ_2, we can conclude by induction that the solutions corresponding to the asymmetric parts of the stream functions ψ_n must be only the trivial ones. This leads to the following theorem.

> *Theorem IV* (Symmetry Theorem): If the initial flow conditions are such that they represent a symmetric flow pattern at time $t = 0$, or if the flow is steady, then the resulting flow pattern must be symmetric about the polar axis for all time t. Moreover, an asymmetric flow pattern must be time-dependent and can result only if an external disturbance at any time t or the initial flow conditions at time $t = 0$ introduce an asymmetry. However, a time-dependent flow is not necessarily asymmetric.

By introducing the principle of minimum dissipation as a hypothesis, Lieber and Wan [5] conclude that a two-dimensional flow field for a viscous incompressible fluid is governed by the Biharmonic Equation. Since, in addition, the flow must satisfy the conservation-of-momentum principle in the form of the Vorticity Transport Equation, they regard the vanishing of the convective part of this equation as a compatibility condition. A physical interpretation of this condition based on the consideration of odd and even parts of the stream function brings them essentially to the conclusion stated in the Symmetry Theorem. Our work shows that the flow field cannot be strictly governed by the biharmonic equation, and that the separate vanishing of the biharmonic and convective parts of the vorticity transport equation is not necessary to arrive at the Symmetry Theorem, which is here proved by induction on the basis of a consideration of the solutions of the linear sets of the differential equations and the boundary conditions etc. governing the successive iterations. However, what is significant in our work and the work of others is the clear recognition of the relation between symmetry and time-dependence in viscous flows. We believe that some such relation should hold for all viscous flows in general.

Using the Fourier representations of Eqs. (1.60), (1.61), (1.62), etc. for the stream functions ψ_n, $n = 1, 2, 3, \ldots$, together with the expression for ψ_0 in Eqs. (1.29), we get

$$\begin{aligned}\psi(r,\theta,t) = {} & \left[\frac{A_0(r,t) + C_0(r,t) + E_0(r,t) + \cdots}{2}\right] \\ & + [A_1(r,t) + C_1(r,t) + E_1(r,t) + \cdots]\cos\theta \\ & + \left[-\left(r - \frac{1}{r}\right) + B_1(r,t) + D_1(r,t) + F_1(r,t) + \cdots\right]\sin\theta \\ & + [A_2(r,t) + C_2(r,t) + E_2(r,t) + \cdots]\cos 2\theta \\ & + [B_2(r,t) + D_2(r,t) + F_2(r,t) + \cdots]\sin 2\theta \\ & + \sum_{n=3}^{\infty} [A_n(r,t) + C_n(r,t) + E_n(r,t) + \cdots]\cos n\theta \\ & + [B_n(r,t) + D_n(r,t) + F_n(r,t) + \cdots]\sin n\theta \,. \end{aligned} \tag{2.37}$$

When the stream function ψ is such that its streamline pattern is symmetric about the polar axis, the terms in $\cos\theta$, $\cos 2\theta$ and $\cos n\theta$ drop out, giving us

$$\begin{aligned}\psi(r,\theta,t) = {} & \left[-\left(r - \frac{1}{r}\right) + B_1(r,t) + D_1(r,t) + F_1(r,t) + \cdots\right]\sin\theta \\ & + [B_2(r,t) + D_2(r,t) + F_2(r,t) + \cdots]\sin 2\theta \\ & + \sum_{n=3}^{\infty} [B_n(r,t) + D_n(r,t) + F_n(r,t) + \cdots]\sin n\theta \,. \end{aligned} \tag{2.38}$$

Let us put, for brevity,

$$\bar{\psi}_1(r,\theta,t) = \left[-\left(r - \frac{1}{r}\right) + B_1(r,t) + D_1(r,t) + F_1(r,t) + \cdots \right] \sin\theta ; \quad (2.39)$$

$$\bar{\psi}_2(r,\theta,t) = [B_2(r,t) + D_2(r,t) + F_2(r,t) + \cdots] \sin 2\theta ; \quad (2.40)$$

$$\bar{\psi}_n(r,\theta,t) = [B_n(r,t) + D_n(r,t) + F_n(r,t) + \cdots] \sin n\theta . \quad n \geq 3 \quad (2.41)$$

Then we may rewrite

$$\psi(r,\theta,t) = \bar{\psi}_1 + \bar{\psi}_2 + \bar{\psi}_3 + \cdots \quad (2.42)$$

From Eq. (2.39) we see that the terms in $\sin\theta$, due to various iterations, combine with the corresponding term in the potential stream function ψ_0. Together they make it possible for the stream function ψ and its derivatives to satisfy the required conditions at the cylinder wall. This is achieved by a modification of the potential flow field. If the lines $\bar{\psi}_1$ = constant are plotted they will have two axes of symmetry, viz., (a) the polar axis and (b) the line at right angles to the polar axis at the origin. The polar axis itself is one of the lines $\bar{\psi}_1$ = constant, but the other axis is perpendicular to all the lines $\bar{\psi}_1$ = constant. Evidently the lines $\bar{\psi}_1$ = constant represent a streamline pattern markedly similar in structure to the potential streamline pattern. Similarly, if we plot the lines $\bar{\psi}_2$ = constant, they will have four axes of symmetry, two of which are the same as for $\bar{\psi}_1$ = constant. The other two axes of symmetry are mutually perpendicular lines making an angle of 45° with the polar axis. In this case, the polar axis as well as the line at right angles to it at the origin are the lines $\bar{\psi}_2$ = constant, while the other two lines are perpendicular to all the lines $\bar{\psi}_2$ = constant. If we write

$$\bar{u}_1 = \frac{1}{r}\frac{\partial\bar{\psi}_1}{\partial\theta} = \frac{1}{r}\left[-\left(r - \frac{1}{r}\right) + B_1 + D_1 + \cdots \right] \cos\theta$$

$$\bar{v}_1 = -\frac{\partial\bar{\psi}_1}{\partial r} = -\left[-\left(1 + \frac{1}{r^2}\right) + B_1' + D_1' + \cdots \right] \sin\theta ; \quad (2.43)$$

$$\bar{u}_2 = \frac{1}{r}\frac{\partial\bar{\psi}_0}{\partial\theta} = \frac{1}{r}(B_2 + D_2 + \cdots)\ 2\cos 2\theta$$

$$\bar{v}_2 = -\frac{\partial\psi_2}{\partial r} = -(B_2' + D_2' + \cdots)\sin 2\theta , \quad (2.44)$$

where prime denotes partial differentiation with respect to r, then we have

$$\bar{u}_1(\theta) = -\bar{u}_1(\pi - \theta)$$

$$\bar{v}_1(\theta) = +\bar{v}_1(\pi - \theta) ; \quad (2.45)$$

$$\bar{u}_2(\theta) = +\bar{u}_2(\pi - \theta)$$

$$\bar{v}_2(\theta) = -\bar{v}_2(\pi - \theta) \ . \qquad (2.46)$$

The relations of Eqs. (2.45) and (2.46) show that, if at any generic point $P(r,\theta)$ in the flow field the velocities $\bar{u}_1$, $\bar{v}_1$, $\bar{u}_2$, $\bar{v}_2$ have the same sign so that $\bar{u}_1 + \bar{u}_2$ and $\bar{v}_1 + \bar{v}_2$ represent a strengthened velocity field, then at a point $\Phi(r,\theta)$, which is the mirror-image of the point $P(r,\theta)$ about the line at right angles to the polar axis, the velocities $\bar{u}_1$ and $\bar{v}_1$ will have signs opposite to the velocities $\bar{u}_2$ and $\bar{v}_2$, and hence their sums $\bar{u}_1 + \bar{u}_2$ and $\bar{v}_1 + \bar{v}_2$ will represent a weakened velocity field. The streamline patterns for $\bar{\psi}_1$ = constant and $\bar{\psi}_2$ = constant are sketched roughly in Figs. D and E respectively. The arrows indicate the direction of the velocity vector, which is tangential to the streamlines, and hence the direction of the flow at any instant.

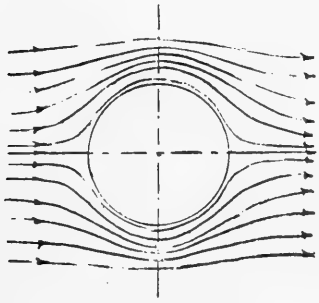

Fig. D - Streamline patterns for ψ_1 = constant

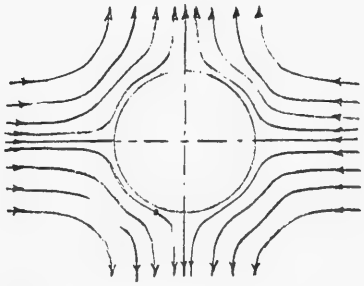

Fig. E - Streamline patterns for ψ_2 = constant

Let us consider the superposition of the two streamline patterns given in Figs. D and E due to $\bar{\psi}_1$ = constant and $\bar{\psi}_2$ = constant, wherein we have assumed that in front of the cylinder $\bar{u}_1$, $\bar{v}_1$, $\bar{u}_2$, and $\bar{v}_2$ are all positive. Whatever the relative magnitudes of $\bar{u}_1$, $\bar{v}_1$, $\bar{u}_2$, and $\bar{v}_2$, the resultant flow due to the superposition in front of the cylinder will be moving with higher velocities, and its appearance will be similar to that in Fig. D, but with the streamlines displaced outwards from the cylinder. Specifically, there cannot be any closed streamline in front of the cylinder. In the rear of the cylinder the resultant flow will be moving with lower velocities, and its appearance will depend on whether or not $|\bar{u}_1| > |\bar{u}_2|$ and $|\bar{v}_1| > |\bar{v}_2|$ everywhere. If $|\bar{u}_1| > |\bar{u}_2|$ and $|\bar{v}_1| > |\bar{v}_2|$ everywhere in the flow field, then the flow in the rear will resemble the flow pattern in Fig. D, but with very widely separated streamlines as indicated by lowered velocities. The streamlines, moreover, cannot be closed and there cannot be any separation. However, if in some velocity domain $|\bar{u}_1| < |\bar{u}_2|$ and $|\bar{v}_1| < |\bar{v}_2|$, then the flow in that part of the domain which is at the rear of the cylinder will resemble the flow pattern in Fig. E, and this region will be characterized by the appearance of closed streamlines and points of separation.

These considerations show that the terms in sin 2θ are the ones that account for the structure of the flow field in the wake of the cylinder. We conclude therefore that these terms in sin θ and sin 2θ which portray the essential features of the flow field and which completely account for the drag on the cylinder are the most important terms in the Fourier representations of the stream functions ψ and ψ_n, $n = 1, 2, 3, \ldots$. With this in mind, let us introduce the following simplifying assumption. Let

$$B_n(r,t) \equiv 0 , \quad n = 3, 4, \ldots . \tag{2.47}$$

Then Eq. (2.8) for $n = 4, 5, 6, \ldots$ and the conditions of Eqs. (2.13) are completely satisfied. The equations for $n = 1, 2$, and 3 are the following:

$$\mathcal{B}_1'' + \frac{1}{r}\mathcal{B}_1' - \frac{1}{r^2}\mathcal{B}_1 + \frac{Re}{r}\left(1 + \frac{1}{r^2}\right)\mathcal{B}_2 + \frac{Re}{2}\left(1 - \frac{1}{r^2}\right)\mathcal{B}_2' = Re\,\frac{\partial \mathcal{B}_1}{\partial t} ; \tag{2.48}$$

$$\mathcal{B}_2'' + \frac{1}{r}\mathcal{B}_2' - \frac{4}{r^2}\mathcal{B}_1 - \frac{Re}{2r}\left(1 + \frac{1}{r^2}\right)\mathcal{B}_1 + \frac{Re}{2}\left(1 - \frac{1}{r^2}\right)\mathcal{B}_1' = Re\,\frac{\partial \mathcal{B}_2}{\partial t} ; \tag{2.49}$$

$$- \frac{Re}{r}\left(1 + \frac{1}{r^2}\right)\mathcal{B}_2 + \frac{Re}{2}\left(1 - \frac{1}{r^2}\right)\mathcal{B}_2' = 0 . \tag{2.50}$$

Equations (2.48), (2.49), and (2.50) are a set of three equations for the two unknown functions B_1 and B_2. We observe that the Eq. (2.50) is a first order equation in $\mathcal{B}_2$, while Eqs. (2.48) and (2.49) are second order equations in $\mathcal{B}_1$ and $\mathcal{B}_2$ respectively. The set of Eqs. (2.50) and (2.51) together with the boundary conditions of Eqs. (2.11) and (2.12) form a well-defined boundary value problem when adjoined with a suitable initial condition, if the flow is considered time-dependent. If we solve this set to obtain unique solutions B_1 and B_2 and then find on substitution of these solutions into Eq. (2.14) that it is not violated to any significant degree in the domain, then we can conclude that these solutions are good approximations to the exact solutions to the set of Eqs. (2.6), (2.7), and (2.8), satisfying the conditions of Eqs. (2.11) to (2.13), inclusive. We therefore decide to verify this a posteriori and proceed to solve Eqs. (2.48) and (2.49), subject to the conditions of Eqs. (2.11) and (2.12), etc. We note here the intrinsic symmetry and the consequent beauty of these two equations which govern the most significant terms of the stream function ψ_1.

If we compare the set of equations for the first iteration with that of the second iteration we see that in the first set the equations governing the functions A_n and their derivatives do not contain the functions B_n and their derivatives and vice versa, whereas in the second set the equations contain C_n, D_n, and their derivatives all mixed together. This means that the functions A_n and B_n are not connected explicitly. However, they are connected implicitly through the time variable t; and this connection will be lost when the flow is assumed to be steady. The functions C_n and D_n are connected explicitly. If the body is geometrically asymmetrical about the polar axis, as would be the case if an elliptical cylinder were placed with its major or minor axis inclined at an angle to the flow direction, then again it can be shown that the resulting equations corresponding to Eqs. (2.3) to (2.8) connect the functions A_n, B_n, and their derivatives explicitly.

Let us consider Eqs. (2.29) to (2.33) inclusive, with the stipulation that $A_n(r,t) \equiv 0$ for all n, $B_n(r,t) \equiv 0$ for $n \geq 3$, and $B_n(r,t)$ for $n = 1$ and 2 are the solutions to Eqs. (2.48) and (2.49), satisfying the conditions of Eqs. (2.11) and (2.12), etc. In Eqs. (2.29), (2.30), and (2.31) all the terms which involve D_n and their derivatives drop out, thus leaving them as equations in C_n and their derivatives. On the other hand, in Eqs. (2.32) and (2.33) all the terms involving C_n and their derivatives drop out, thus leaving them as equations in D_n and their derivatives only. The essential effect is that the explicit connections between C_n and D_n are severed. These equations, then, deal with only one set of functions; either C_n or D_n.

Since Eqs. (2.29), (2.30), and (2.31) are a set of simultaneous linear-differential equations with variable coefficients, they have unique solutions, if they exist, satisfying the conditions of Eqs. (2.34) and (2.35) with a suitable initial condition when the above stipulations are taken into account. The trivial solutions $C_n(r,t) \equiv 0$ satisfy these equations and the required conditions of Eqs. (2.34) and (2.35). Hence, if the initial flow conditions are such that they represent a symmetric flow pattern, or if we are considering a steady flow problem, then it follows that $C_n(r,t) \equiv 0$ are the only solutions to these equations and conditions.

Now we made another simplifying assumption similar to as follows:

$$D_n(r,t) \equiv 0 \qquad n = 3, 4, \ldots . \tag{2.51}$$

As a result, we obtain the following equations governing the functions D_1 and D_2:

$$\mathfrak{D}_1'' + \left(\frac{1}{r} + \frac{Re}{r} B_2\right) \mathfrak{D}_1' - \left(\frac{1}{r^2} - \frac{Re}{2r} B_2'\right) \mathfrak{D}_1 + \frac{Re}{2} \left(1 - \frac{1}{r^2} - \frac{Re}{r} B_1\right) \mathfrak{D}_2'$$

$$+ \frac{Re}{r} \left(1 + \frac{1}{r^2} - B_1'\right) \mathfrak{D}_2 + \frac{Re}{r} (D_2 \mathfrak{B}_1' - D_1' \mathfrak{B}_2) + \frac{Re}{2r} (D_2' \mathfrak{B}_1 - D_1 \mathfrak{B}_2')$$

$$+ \frac{Re}{2r} (B_2' \mathfrak{B}_1 - B_1 \mathfrak{B}_2') + \frac{Re}{r} (B_2 \mathfrak{B}_1' - B_1' \mathfrak{B}_2) = Re \frac{\partial \mathfrak{D}_1}{\partial t} ; \tag{2.52}$$

$$\mathfrak{D}_2'' + \frac{1}{r} \mathfrak{D}_2' - \frac{4}{r^2} \mathfrak{D}_2 + \frac{Re}{2} \left(1 - \frac{1}{r^2} - \frac{B_1}{r}\right) \mathfrak{D}_1' - \frac{Re}{2r} \left(1 + \frac{1}{r^2} - B_1'\right) \mathfrak{D}_1$$

$$+ \frac{Re}{2r} (D_1' \mathfrak{B}_1 - D_1 \mathfrak{B}_1') + \frac{Re}{2r} (B_1' \mathfrak{B}_1 - B_1 \mathfrak{B}_1') = Re \frac{\partial \mathfrak{D}_2}{\partial t} ; \tag{2.53}$$

$$\left(r - \frac{1}{r} - B_1\right) \mathfrak{D}_2' - 2 \left(1 + \frac{1}{r^2} - B_1'\right) \mathfrak{D}_2 + (\mathfrak{D}_1 B_2' - 2 B_2 \mathfrak{D}_1')$$

$$+ (\mathfrak{B}_1 D_2' - D_1 \mathfrak{B}_2') + 2 (\mathfrak{B}_2 D_1' - D_2 \mathfrak{B}_1') + (\mathfrak{B}_1 B_2' - B_1 \mathfrak{B}_2') + 2 (\mathfrak{B}_2 B_1' - B_2 \mathfrak{B}_1') = 0 ; \tag{2.54}$$

$$(B_2 \mathfrak{D}_2' - B_2' \mathfrak{D}_2) + (D_2 \mathfrak{B}_2' - D_2' \mathfrak{B}_2) + (\mathfrak{B}_2 B_2' - \mathfrak{B}_2' B_2) = 0 . \tag{2.55}$$

As discussed in the case of Eqs. (2.48), (2.49), and (2.50), we regard Eqs. (2.52) and (2.53), which are of second order in $\mathcal{D}_1$ and $\mathcal{D}_2$, respectively as the governing equations for the functions D_1 and D_2, and consider Eqs. (2.54) and (2.55), which are one order lower than Eqs. (2.52) and (2.53), to represent, in a sense, the error involved in the assumption.

EQUATIONS AND CONDITIONS FOR STEADY FLOW

As explained above, we may put $A_n \equiv C_n \equiv 0$ in the expression for the stream functions ψ_1 and ψ_2 when the motion is considered to be time-independent. To simplify mathematical analysis, we assume here that $B_n \equiv D_n \equiv 0$ for 3, 4, ... = n. This enables us to reduce the stream functions ψ_1 and ψ_2 to the following:

$$\psi_1(r,\theta) = B_1(r) \sin\theta + B_2(r) \sin 2\theta \tag{2.56}$$

$$\psi_2(r,\theta) = D_1(r) \sin\theta + D_2(r) \sin 2\theta \ . \tag{2.57}$$

First Iteration

Governing Equations

$$\mathcal{B}_1'' + \frac{1}{r}\mathcal{B}_1' - \frac{1}{r^2}\mathcal{B}_1 + \frac{Re}{r}\left(1 + \frac{1}{r^2}\right)\mathcal{B}_2 + \frac{Re}{2}\left(1 - \frac{1}{r^2}\right)\mathcal{B}_2' = 0 \ ; \tag{2.58}$$

$$\mathcal{B}_2'' + \frac{1}{r}\mathcal{B}_2' - \frac{4}{r^2}\mathcal{B}_2 - \frac{Re}{2r}\left(1 + \frac{1}{r^2}\right)\mathcal{B}_1 + \frac{Re}{2}\left(1 - \frac{1}{r^2}\right)\mathcal{B}_1' = 0 \ ; \tag{2.59}$$

where

$$\mathcal{B}_1 \equiv B_1'' + \frac{1}{r}B_1' - \frac{1}{r^2}B_1 \ ; \tag{2.60}$$

$$\mathcal{B}_2 \equiv B_2'' + \frac{1}{r}B_2' - \frac{4}{r^2}B_2 \ . \tag{2.61}$$

Boundary Conditions

$$B_1(1) = B_2(1) = B_2'(1) = 0 \ , \quad B_1'(1) = +2 \ ; \tag{2.62}$$

$$B_1(h_i^*) = B_2(h_i^*) = B_1'(h_i^*) = B_2'(h_i^*) = 0 \ . \tag{2.63}$$

Error Equation

$$\left(r - \frac{1}{r}\right)\mathcal{B}_2' - 2\left(1 + \frac{1}{r^2}\right)\mathcal{B}_2 = 0 \ . \tag{2.64}$$

Second Iteration

Governing Equations

$$\mathcal{D}_1'' + \left(\frac{1}{r} + \frac{Re}{r} B_2\right) \mathcal{D}_1' - \left(\frac{1}{r^2} - \frac{Re}{2r} B_2'\right) \mathcal{D}_1 + \frac{Re}{2} \left(1 - \frac{1}{r^2} - \frac{1}{r} B_1\right) \mathcal{D}_2'$$

$$+ \frac{Re}{r} \left(1 + \frac{1}{r^2} - B_1'\right) \mathcal{D}_2 + \frac{Re}{r} (D_2 \mathcal{B}_1' - D_1' \mathcal{B}_2) + \frac{Re}{2r} (D_2' \mathcal{B}_1 - D_1 \mathcal{B}_2')$$

$$+ \frac{Re}{2r} (B_2' \mathcal{B}_1 - B_1 \mathcal{B}_2') + \frac{Re}{r} (B_2 \mathcal{B}_1' - B_1' \mathcal{B}_2) = 0 \; ; \tag{2.65}$$

$$\mathcal{D}_2'' + \frac{1}{r} \mathcal{D}_2' - \frac{4}{r^2} \mathcal{D}_2 + \frac{Re}{2} \left(1 - \frac{1}{r^2} - \frac{B_1}{r}\right) \mathcal{D}_1' - \frac{Re}{2r} \left(1 + \frac{1}{r^2} - B_1'\right) \mathcal{D}_1$$

$$+ \frac{Re}{2r} (D_1' \mathcal{B}_1 - D_1 \mathcal{B}_1') + \frac{Re}{2r} (B_1' \mathcal{B}_1 - B_1 \mathcal{B}_1') = 0 \; ; \tag{2.66}$$

where

$$\mathcal{D}_1 \equiv D_1'' + \frac{1}{r} D_1' - \frac{1}{r^2} D_1 \; ; \tag{2.67}$$

$$\mathcal{D}_2 \equiv D_2'' + \frac{1}{r} D_2' - \frac{4}{r^2} D_2 \; . \tag{2.68}$$

Boundary Conditions

$$D_1(1) = D_2(1) = D_1'(1) = D_2'(1) = 0 \; ; \tag{2.69}$$

$$D_1(h_i^*) = D_2(h_i^*) = D_1'(h_i^*) = D_2'(h_i^*) = 0 \; . \tag{2.70}$$

Error Equations

$$\left(r - \frac{1}{r} - B_1\right) \mathcal{D}_2' - 2 \left(1 + \frac{1}{r^2} - B_1'\right) \mathcal{D}_2 + (\mathcal{D}_1 B_2' - 2 B_2 \mathcal{D}_1') + (D_2' \mathcal{B}_1 - D_1 \mathcal{B}_2')$$

$$+ 2 (\mathcal{B}_2 D_1' - \mathcal{B}_1' D_2) + (\mathcal{B}_1 B_2' - B_1 \mathcal{B}_2') + 2 (\mathcal{B}_2 B_1' - B_2 \mathcal{B}_1') = 0 \; ; \tag{2.71}$$

$$(B_2 \mathcal{D}_2' - B_2' \mathcal{D}_2) + (D_2 \mathcal{B}_2' - D_2' \mathcal{B}_2) + (\mathcal{B}_2 B_2' - \mathcal{B}_2' B_2) = 0 \; . \tag{2.72}$$

TRANSFORMATIONS OF THE SPACE VARIABLE r

The radial coordinate r varies from r = 1 to r = ∞, where the symbol ∞ is used in the sense of the idea of a physically infinite distance. The solutions

of the preceding equations can be represented in the form of a power series. However, the power series solutions need not be expansions in powers of r. In fact, it is advantageous to use a transformation which affects a contraction in scale. We then have two advantages in the computation of these analytical expressions: the first is increased precision, and the second is that there is a less number of terms to compute for a given value of r, because of the increased convergence. The application of the boundary condition at the wall is simplified if the transformed coordinate varies from 0 to ∞ when r varies from 1 to ∞. The following class of transformations which affect a logarithmic contraction in scale has this property.

$$\begin{aligned} r &= e^{cs} \\ r &= e^{(e^{cs}-1)} \qquad 1 \le r \le \infty \\ r &= e^{[e^{(e^{cs}-1)}-1]} \qquad 0 \le s \le \infty \end{aligned} \tag{2.73}$$

and so on, c being a constant scale factor. At first, the transformation $r = e^{cs}$ was used, but when it was found that higher precision was needed in the calculation of the second iteration, the transformation $r = e^{(e^{cs}-1)}$ was used.

The results presented in this paper are obtained by using the later transformation $r = e^{(e^{cs}-1)}$. The equations obtained by using these transformations are contained along with relevant algebraic details in Ref. 2. These equations are then solved by expressing the solutions as sums of power series in the variable s. We thus obtain

$$B_1(s) = \sum_{j=1}^{4} Y_j^1 \left[\frac{e^{-2c}}{2} \left(e^{e^{cs}} \sum_{k=1}^{\infty} \frac{K1J_k^j}{K} s^k - e^{-e^{cs}} \sum_{k=1}^{\infty} \frac{K13_k^j}{K} s^k \right) \right]$$

$$+Y1_5 e^{e^{cs}} + Y1_6 e^{-e^{cs}} ; \tag{2.74}$$

$$B_2(s) = \sum_{j=1}^{4} Y1_j \left[\frac{e^{-2c}}{4} \left(e^{2e^{cs}} \sum_{k=1}^{\infty} \frac{M10_k^j}{K} s^k - e^{-2e^{cs}} \sum_{k=1}^{\infty} \frac{M14_k^j}{K} s^k \right) \right]$$

$$+ Y1_7 e^{2e^{cs}} + Y1_8 e^{-2e^{cs}} ; \tag{2.75}$$

$$D_1(s) = \sum_{j=1}^{8} Y2_j \left(\sum_{k=1}^{\infty} D1_k^j s^{k-1} \right) + \sum_{k=1}^{\infty} D1_k^q s^{k-1} ; \tag{2.76}$$

$$D_2(s) = \sum_{j=1}^{8} Y2_j \left(\sum_{k=1}^{\infty} D2_k^j s^{k-1} \right) + \sum_{k=1}^{\infty} D2_k^q s^{k-1} ; \tag{2.77}$$

where $Y1_j$ and $Y2_j$, $1 \le j \le 8$ are constants determined by the boundary conditions, while the constants $K11_k^j$, $K13_k^j$, $M14_k^j$, $D1_k^j$, $D2_k^j$, and $M10_k^j$, $1 \le j \le 8$, $1 \le k \le \infty$ are obtained by using the recurrence relations arising from the governing differential equations. These are explicitly defined, and the manner of obtaining them is described in detail in Ref. 2. On applying the boundary conditions to the general solutions in Eqs. (2.74), (2.75), (2.76), and (2.77), we obtain the following expressions for the stream functions:

$$\psi_0 = -\left[e^{(e^{cs}-1)} - e^{-(e^{cs}-1)}\right] \sin\theta \ ; \tag{2.78}$$

$$\psi_1 = -\psi_0 + \frac{e^{-2c}}{2}\left(e^{e^{cs}} \sum_{k=1}^{\infty} \frac{K11_k}{K} s^k - e^{-e^{cs}} \sum_{k=1}^{\infty} \frac{K13_k}{K} s^k\right) \sin\theta$$

$$+ \frac{e^{-2c}}{4}\left(e^{2e^{cs}} \sum_{k=1}^{\infty} \frac{M10_k}{K} s^k - e^{-2e^{cs}} \sum_{k=1}^{\infty} \frac{M14_k}{K} s^k\right) \sin 2\theta \ ; \tag{2.79}$$

$$\psi_2 = \left(\sum_{k=1}^{\infty} D1_k s^{k-1}\right) \sin\theta + \left(\sum_{k=1}^{\infty} D2_k s^{k-1}\right) \sin 2\theta \ ; \tag{2.80}$$

where

$$K11_k \equiv \sum_{j=1}^{4} Y1_j K11_k^j \ , \quad K13_k \equiv \sum_{j=1}^{4} Y1_j K13_k^j$$

$$M10_k \equiv \sum_{j=1}^{4} Y1_j M10_k^j \ , \quad M14_k \equiv \sum_{j=1}^{4} Y1_j M14_k^j$$

$$D1_k \equiv \sum_{j=1}^{9} Y2_j D1_k^j \ , \quad D2_k \equiv \sum_{j=1}^{9} Y2_j D2_k^j \ . \tag{2.81}$$

The constants $Y1_j$ and $Y2_j$ in Eqs. (2.81) are known values and $Y2_9$ is by definition taken as unity. Adding Eqs. (2.78), (2.79), and (2.80), we obtain

$$\psi = \left[\frac{e^{-2c}}{2}\left(e^{e^{cs}} \sum_{k=1}^{\infty} \frac{K11_k}{K} s^k - e^{-e^{cs}} \sum_{k=1}^{\infty} \frac{K13_k}{K} s^k\right) + \sum_{k=1}^{\infty} D1_k s^{k-1}\right] \sin\theta$$

$$+ \left[\frac{e^{-2c}}{4}\left(e^{2e^{cs}} \sum_{k=1}^{\infty} \frac{M10_k}{K} s^k - e^{-2e^{cs}} \sum_{k=1}^{\infty} \frac{M14_k}{K} s^k\right) + \sum_{k=1}^{\infty} D2_k s^{k-1}\right] \sin 2\theta . \tag{2.82}$$

As shown in Ref. 2, Eq. (2.82) can be rewritten in the following form:

$$\psi = [F(s) + G(s) \cos\theta] \, s^2 \sin\theta \ , \tag{2.83}$$

where $F(s)$ and $G(s)$ are known functions of s.

It can be seen from Eq. (2.83) that the cylinder boundary for which $s = 0$ is a streamline with $\psi = 0$. Also the lines of symmetry with $\theta = 0$ and $\theta = \pi$ are streamlines with $\psi = 0$. In other words, the streamline $\psi = 0$ has branch points at the front and rear stagnation points. Since streamlines are lines for which ψ has constant values, two streamlines having two different constant values cannot meet. Therefore, if a streamline does meet the cylinder boundary at any point it must be a branch of the streamline $\psi = 0$, and the point at which it meets the wall is then a branch point of the streamline $\psi = 0$. From Eq. (2.83) we see that ψ can be zero even if $s \neq 0$ and $\theta \neq \pi \neq 0$, when the terms in the brackets vanish. This is,

$$\cos\theta = -\frac{F(s)}{G(s)} . \tag{2.84}$$

Since $|\cos\theta| \leq 1$, it may happen that there are no points in the flow field which satisfy Eq. (2.84) if the right-hand side of the equation has an absolute value greater than one for all $s \geq 0$. Since the value depends on the Reynolds number of the characteristic flow parameter, the existence of a line satisfying Eq. (2.84) also depends on it.

Let us assume that the Reynolds number is such that a line the points of which satisfy Eq. (2.84) exists. Then, on this line, $\psi = 0$. Since $\cos\theta = \cos(-\theta)$, we conclude that the part of the streamline given by Eq. (2.84) is symmetric about the polar axis. We may regard it as consisting of two parts, each a mirror image of the other, about the polar axis. In other words, we may say that Eq. (2.84) gives two more branches of the streamline $\psi = 0$. Denoting the angle θ at $s = 0$ on these branches by α, we obtain the angle of separation

$$\alpha = \pi - \cos^{-1}\left[\frac{F(0)}{G(0)}\right] . \tag{2.85}$$

If we drop the terms corresponding to the second iteration from the functions $F(s)$ and $G(s)$, and denote the resulting functions by $F_1(s)$ and $G_1(s)$ respectively, we obtain separating streamlines due to the first iteration alone from the equation

$$\cos\theta = -\frac{F_1(s)}{G_1(s)} . \tag{2.86}$$

Defining α_1 as the corresponding first iteration angle of separation, we obtain

$$\alpha_1 = \pi - \cos^{-1}\left[\frac{F_1(0)}{G_1(0)}\right] . \tag{2.87}$$

PART 3

RESULTS, DISCUSSION, AND CONCLUSIONS

This part of the paper presents the results of computations of viscous flow fields around a circular cylinder based on the analytical representations obtained from the algorithm and its attendant linear substructure as they were applied in previous sections to complete the Navier-Stokes equations and boundary conditions. These results are discussed with reference to the existing body of literature which covers a range $0 < \mathrm{Re} \leq 20$ of Reynolds number based on the radius of the cylinder. Following the discussion, we present conclusions in the light of the results and discussion. Numerical information is given in Table 2 and in a series of plots which are placed at the end of this paper.

RESULTS

The first and second iteration solutions are computed for 18 discrete values of the Reynolds number. The results of the computation are presented concisely in Table 2. They are given in detail by plots contained in Figs. 1A through 34F. These plots are divided into two sections. Figures 1A through 20F give information about the drag, pressure, separation, and behavior of solutions with increasing Reynolds number and the radius at which the boundary conditions of Eqs. (2.62), (2.63), (2.69), and (2.70) are applied. Figures 21A through 34F give streamline plots showing the development of viscous flow fields with bound vortices as the Reynolds number is increased from 0.05 to 20.

In Fig. 1A the total drag coefficient CD is plotted against the Reynolds number on a linear scale. Tritten's (1959) experimental results are included for comparison. In Fig. 1B logarithms of total drag coefficient CD are plotted against the logarithm of the Reynolds number ($-1.5 \leq \log_{10} \mathrm{Re} \leq 1.5$), and the results of Bairstow, Cave, and Lang (1923), and of Tritton (1959) are included for comparison. Figure 1C is exactly the same as 1B, except that here the *least* values of the first iteration drag coefficient CD1 are plotted instead of the total coefficient CD. Figure 1D shows on a linear scale the plot of the second iteration drag coefficient CD2 against the Reynolds number Re. Figure 1E gives an enlarged portion of the plot of CD against Re together with the results of Lamb (1911), Kaplun (1957), and Tritton (1959) for comparison. Figure 2A gives plots of the ratios η, η_1, and η_2 of pressure drag to viscous drag against Re. Figure 2B gives plots of the angle of separation α_1 obtained by the first iteration and of the angle of separation α, obtained by the first and second iterations against Re. Figures 2C and 2D give, respectively, the plots of the stagnation pressures in front and at the rear of the cylinder against Re. In these figures we have plotted PRESS-PREC2 instead of the stagnation pressure PRESS which is the result of the first and second iterations together, because, due to its smallness, PREC2 could not be calculated accurately, and erroneous values were obtained for it due to lack of precision in computation at that stage. Figure 2E gives the plots of PREC1, $\mathrm{PRET1}_{max}$, and $\mathrm{PREP1}_{min}$ v/s Re. These quantities are the constant, the first harmonic, and the second harmonic amplitudes of the first iteration pressure field around the circular cylinder.

Figures 3A through 20F constitute eighteen sets of figures, each corresponding to one of the eighteen discrete values of the Reynolds number at which solutions are evaluated. Each of these sets is composed of six graphs. The number, such as 3 in Fig. 3A, refers to the set belonging to a particular Reynolds number, while the alphabetical characters A, B, C, D, E, and F refer to the six graphs in that particular set according to the following scheme.

Character A: Plots of Y1(J), J = 1, 2, 3, and 4 against r.

Character B: Plots of the drags CD1, CDP1, and CDV1 against r.

Character C: Plots of PRECI, PRETIM, and PREPIM against r. PRETIM = $PRET1_{max}$, PREPIM = $PREP1_{min}$, as defined earlier.

Character D: Plots of ER1 against S(H); $0 \leq S \leq H$. Here the symbol (H) is used to signify that the range of S depends on H.

Character E: Plots of PRES1, PRET1, PREP1, and PREC1 against θ.

Character F: Plots of PRESS-PREC2, PRES2-PREC2, PREP2, PRET2, PRES1, and PRESI against θ. The reason why PRESS-PREC2 and PRES2-PREC2 instead of PRESS, PRES2, and PREC2 are plotted is as explained earlier.

To examine salient features of these results, let us consider the set of plots corresponding to the Reynolds number Re = 0.05, viz., Figs. 3A through 3F. The plots in the first three are all against r. They show the effect on the first iteration solution for a given Re, here 0.05, of applying the boundary conditions at various distances from the cylinder. In Fig. 3A the constants Y1(J), J = 1, 2, 3, and 4 increase very rapidly in absolute magnitude below $r \cong 7$. In general, they may behave erratically below a certain value of r. From $r \cong 7$ to r = 300 all the four constants behave asymptotically and tend to a limiting set of values. However, the inherent numerical errors involved in computation with finite precision and a large number of operations cause the calculation to break down for r > 340. Since the drag coefficients depend explicitly on the constants Y1(1) and Y1(2), Fig. 3B displays a similar behavior. So also is the case with PRECI, PRETIM, and PREPIM in Fig. 3C. The numerical breakdown which occurs for r > 340 with a double-precision program using the transformation $r = e^{e^{cs'}-1}$, takes place for r > 22.198 with a double-precision program using the transformation $r = e^{cs}$, and for r > 11 with a single-precision program using the same later transformation. However, the distance $r \cong 7$ at which the values for the constants Y1(J) stop changing rapidly and start behaving asymptotically remains the same whatever precision program and transformation are used. In fact, the results of computation using the transformation $r = e^{cs}$ show that in this case, figures corresponding to 3A, 3B, and 3C have plots which remain the same up to r = 11 for both single- and double-precision computations. However, with a different transformation of values of Y1(J), the corresponding plots differ, as far as magnitude of the constants is concerned. Whereas the numerical breakdown occurs for r > 11 with a single-precision program, it is deferred to r > 22.198 by the use of a double-precision

program based on the same transformation $r = e^{cs}$. It is still further deferred to $r > 340$ by the use of a double-precision program based on the transformation $r = e^{e^{cs'}-1}$. This shows two things. First, the numerical breakdown can be deferred so that it occurs at some later stage by increasing precision as well as by using a transformation belonging to the group of transformations discussed in Part 2 of this paper. Second, the behavior of the solutions when the boundary conditions are applied at points for which r is less than 7 is not due to any numerical errors, but indicates that significant viscous effects cannot be restricted to a domain bound by $r < 7$. Consequently, the imposition of the boundary conditions in a domain bound by $r < 7$ is physically unrealistic and hence unacceptable mathematically. In other words, the domain bound by $r < 7$ is the smallest domain for Re = 0.05 in which the viscous effects must be considered extremely significant, and therefore the physically infinite distance h_i^* cannot be smaller than $r \cong 7$. We define the lower bound of h_i^* for a given Reynolds number as the number below which the value of h_i^* cannot be chosen. The asymptotic behavior is terminated for $r > 340$. Below and near this value of r, the solution for Re = 0.05 does not seem to change significantly with r. The distance $r = 340$ relates to the results of the first iteration computations. It can and does happen that at such a limiting distance the second iteration calculations involve numerical breakdowns. To obviate this, a distance such as $r = 275$ is chosen as h_i^* such that the second iteration calculations can be carried out successfully. In carrying these out with two or three other radii, it is seen that the second iteration solution retains the asymptotic behavior. Hence we take the physically infinite distance h_i^* as the distance 275 at which meaningful information is possible but beyond which the solution breaks down numerically. It should be noted that the value of the physically infinite distance then depends on the precision and transformation with which the computations are carried out. This, of course, is true up to a point. However, improved precision and new transformations simply extend the range in which the asymptotic behavior is obtained by shifting the point at which the numerical breakdown occurs. And if the extended portion of the range is such that no significant change occurs in the solution evaluated with $r = 275$, then improved precision and/or a new transformation are unnecessary. Otherwise, improved precision and/or a new transformation, if possible, are desirable. Herein lies the significance and the strength from a numerical point of view of the idea of a physically infinite distance. It should be noted that because h_i^* is selected so that no numerical breakdown takes place in either iterations, it is possible that the solution corresponding to this h_i^* may give a first iteration drag value CD1 which is higher than the least value indicated by figures such as 3B. Figure 3D gives for the solution evaluated at $r = 275$, a plot of ER1, the error involved in the simplifying assumption $B_n(r) \equiv 0$ for $n \geq 3$, against S, where $0 \leq S \leq H$ and $RT = h_i^* = e^{e^{CH}-1} = 275$, so that $H = 1/c \log (1 + \log h_i^*) = 0.9448$. Figures 3E and 3F show the harmonic components of the pressure fields due to first and second iterations respectively. The plot of PRESS-PREC2 in Fig. 3F shows the distribution of total pressure around the cylinder except for a constant term PREC2 which, due to numerical errors, could not be evaluated accurately. It is, however, a small value.

The same features displayed by the set of graphs for Re = 0.05 are also present in all the other sets of graphs for the remaining 17 values of Re. They

then hold for all Reynolds numbers in the range $0 < Re \leq 20$. Table 2 contains all of the significant information, a part of which is also presented in Figs. 1A through 2E.

Bearing in mind that there is some arbitrariness involved in the choice of RT $\equiv h_i^*$ and its lower bound for a given Reynolds number, the corresponding values from Table 2 for different Re show that even with increasing Re, the physically infinite distance h_i^* decreases, while its lower bound at first increases but ultimately decreases for the most part. *This means that viscous effects become increasingly localized near the cylinder as the Reynolds number is increased. And this, of course, is confirmed by experimental observations.* The existence of asymptotic behavior of the first and second iteration solutions for all Reynolds numbers considered is conclusive support of the validity of the idea of a physically infinite distance as applied to this problem. Figures 1A through 1E for drag, and Figs. 2C, 2D, and 2E for pressure, show that though the solutions for various Reynolds numbers are obtained by applying the conditions of Eqs. (2.62) and (2.63) at different distances h_i^*, in general, the corresponding points for drags and pressures when plotted against Re give smooth curves which behave asymptotically with increasing Re in the range $0 < Re \leq 20$. This further supports the validity of the idea of a physically infinite distance, for otherwise the curves would not be smooth. However, the values of drag plotted in these figures for $Re > 4$ could be lower than those shown if the physically infinite distance could be increased. This is indicated because, for $Re > 4$, the values of drag plotted lie close to the bend in the drag v/s r plots for a given Re and are not the asymptotically limiting values. This accounts for the discrepancy for $Re > 4$. It also indicates the need to take more harmonics into consideration.

Figure 3D shows that the second iteration drag for $Re > 4$ becomes positive. Referring to Table 2, we see that the viscous component CDV2 of this drag remains negative whereas the pressure component CDP2 becomes positive. Because of possible numerical errors arising from the application of boundary ditions at short distances, in order to avert numerical breakdown, it is not con conclusive that CDP2 and CD2 are indeed positive. If they remain positive after the possibility of computational inaccuracies is ruled out, in our opinion, this would support the conjecture that, even at very low Reynolds number, higher harmonics must be used in order to effectively apply higher order iterations to improve accuracy in numerical representations of flow fields.

Figures 21A through 34F give streamline plots for all the Reynolds numbers considered, except for Re = 2.1, 2.3, 2.4, and 2.5. There are two harmonics and two iterations. Both the harmonics and their sum are plotted for each iteration. Therefore, there are basically six plots for a given Reynolds number. However, when a vortex appears in the flow field, an enlarged plot of the vortex is added to the set. The only exception to this is the case of Re = 20, where the vortex in the flow field is not plotted. The reason is that the computer program had to be modified at this stage, to plot the vortex. Figures 22C and 22D for Re = 0.125 are the same, except that the latter shows a discontinuous behavior in the streamline pattern. The reason for this is that when the two harmonics are added together, due to the discontinuous behavior of the second harmonic at

$\theta = \pi/2$, the sum also displays this behavior. If more harmonics are taken into account this behavior will be smoothed out. In anticipation of this and for the sake of clarity, the discontinuous behavior in Fig. 22D is smoothed out by drawing tangential lines to opposite branches of the streamlines. Figures 22G and 22H, 23C and 23D, and 23G and 23H are also included to show that the discontinuous behavior takes place for all Reynolds numbers. Figure 28B and similar other plots of the second harmonic for higher Reynolds numbers show the streamlines intersecting each other near the $\pm 45^\circ$ lines. This is purely due to the fact that the points on the streamlines are obtained as intersections of the radial lines with the streamlines, and hence when these lines are more or less parallel to each other their intersections cannot be determined accurately. In short, this feature is attributable to the mode of obtaining points on the streamline, and is not a property of the streamlines.

Figure 27C shows a tiny vortex behind the cylinder for Re = 1.0. But this disappears when the second iteration contribution is added, and all that is left is a wake without a vortex. The same happens at Re = 2.0, except that the vortex in Fig. 28C is larger. However, at Re = 2.75, the vortex appears with both iterations; but the second iteration vortex is much smaller than the first iteration vortex. This shows that the effect of the second iteration is to delay the separation and also affect the size and structure of the vortex. The calculations for Reynolds numbers between Re = 2.0 and 2.75 show that the vortex begins to appear in the second iteration plots from Re = 2.3 onwards, i.e., the flow separation begins at Re = 2.3. The vortex structure does not show fully rounded contours, because only two harmonics are taken into account. There are three noteworthy features here. If we observe Figs. 29G and 29H we see that the gradients within the vortex are smaller than the outside flow field by some order of magnitudes. This means that in the initial stages of the development of a vortex its appearance may not be noticeable by the naked eye or even by a microscope, because its size as well as the movement within it are extremely small in the beginning. The experiments, therefore, must give a higher value of Re for separation than does the theory. Further, the velocities in a vortex such as in Fig. 31H are higher near the separation streamline and the cylinder wall than near the center, in contrast to the case with potential vortices. This is, of course, what is observed in real vortices. The vortex is here obtained as a result of the addition of two harmonics which are continuous functions of the space variables r and θ and hence must be represented by a continuous function. Therefore, a vortex need not be represented by or viewed as a singular structure in the flow field. With increasing Reynolds number the point of separation first moves forward on the cylinder wall, and then attains a limiting position as shown by the plots of the angles of separation α_1 and α in Fig. 2B. This agrees with what is observed in nature.

DISCUSSION

The existing explicit theoretical knowledge about flows of viscous fluids is, for the most part, obtained from the Navier-Stokes equations by the application of small-perturbation techniques [42]. Here we have attempted to depart from this thinking. Although we have used an iterative process for solving the

Navier-Stokes equations, no ideas of parameter or coordinate perturbations are invoked. Instead, a fundamental role for potential flows is, a priori, asserted and the iterative process is used as a method of obtaining solutions to the Navier-Stokes equations. In this, we differ fundamentally from the existing theories.

It has been our desire to understand the flow around a circular cylinder as it evolves, because the understanding gained would also be gained for flows around other obstacles as well. The existing theories do not shed light on the continuous evolution of a flow field. This means that we must abandon well-trodden paths and examine the nature of this flow with a fresh outlook. Well-chosen and critically performed experiments with actual flows provide information on which we are building a theoretical structure, an image of reality which is also a reflection of our understanding of it. This information has accumulated over a period of years, but there has been no theoretical structure which embraces all or even a large part of it. Experience with small-perturbation theories and comparison between them and actual experimental results lead us to believe that the Navier-Stokes equations contain implicitly essential theoretical information about flows of a class of actual fluids. Computer experiments [43,44,45,46] performed by using the Navier-Stokes equations vividly demonstrate that the equations do have this information implicitly. Consequently, the present work considers the Navier-Stokes equations as embodying the essential theoretical information implicitly and differs from other theories insofar as it endeavors to make explicit as large a part of this information as it can, without setting a priori limits to what is possible.

Because a steady-flow situation actually exists in nature and because from an analytical point of view it is the most appropriate one to study first, we have directed our efforts to obtain concrete results for this aspect of the flow field after obtaining the general information contained in the Symmetry Theorem about the conditions under which the flow can be time-dependent. Fromm and Harlow in their fine work [45] on the nonsteady problem of vortex street development have used numerical techniques based on a method of iterations. They have observed the following:

> All examples started at time $t = 0$, with the walls and fluid impulsively accelerated to this velocity, and the first cycle iteration procedure immediately adjusted the configuration to the nonviscous laminar flow solution. Advancement of the configuration through subsequent time cycles resulted in a gradual transition to the viscous steady-state solution whose most prominent feature is an eddy pair just behind the plate. Since the solution procedure preserves symmetry to approximately one part in 10^5, the steady solution persists for long times, even for large values of R. Thus we found it desirable to introduce a perturbation, accomplished by artificially increasing the value of ω by a small amount at three mesh points just in front of the plate; this was done at a time when the double eddy pattern was well established. In all cases, the perturbation was small enough that no immediate change was visible in the flow pattern; nevertheless, such a small perturbation was always effective in starting the vortex shedding process within a fairly short time, provided, of course, that R was

sufficiently large. For $R \leq 40$ we found that the steady-state flow pattern never visibly changed after introduction of the perturbation.

The above observation shows two things. One is that the evolution in time of a viscous steady-state configuration takes place from an initial nonviscous laminar flow configuration, i.e., a potential flow configuration. Consequently, the viscous steady-state configuration may naturally be conceived of as a deviation from a basic potential flow configuration. This is, indeed, the view basic in the present work. Second, is that the steady-state motion is preserved so long as symmetry is preserved, and it is destroyed only by the artificial introduction of small perturbations. This is exactly what the Symmetry Theorem asserts. Grove, Shair, Petersen, and Acrivos in their experimental work [47] observe the following: "By artificially stabilizing the steady wake, this system was studied up to Reynolds numbers R considerably larger than any previously attained, thus providing a much clearer insight into the asymptotic character of such flows at high Reynolds numbers." The first part of this statement is factual, whereas the second part is an interpretation of the significance of the first part. From the point of view of the present work, the significance of the factual part lies in the fact that it demonstrates the validity of the Symmetry Theorem. The wake was stabilized, i.e., made steady by them, by the introduction of a splitter plate along the line of symmetry in the wake. This device, in essence, forces a symmetry, with the result that from all possible configurations — symmetric and asymmetric — only a symmetric configuration emerges. This symmetric configuration is a steady-state configuration. Thus, with forced symmetry, a steady-state emerges — a result consistent with the Symmetry Theorem. That Allen and Southwell [48] could calculate through relaxation methods flow fields at $R = 100$ and $R = 1000$ which display steady-state configuration, is to be considered a consequence of the Symmetry Theorem, because they started with equations and conditions which do not involve time as a variable. However, for reasons which Kawaguti [49] has already pointed out, their streamline fields and the pressure distributions over the surface of the cylinder are suspect to some sort of error. Kawaguti and Apelt both find in their numerical solutions that steady-state solutions are possible for somewhat higher Reynolds number, even though they may not exist in nature. This is again consistent with the Symmetry Theorem.

Southwell and Squire [50] have used the potential solutions instead of a uniform-flow solution to obtain governing equations for the flow past a plate and a circular cylinder. They also point out that other authors, e.g., Zeilon, Burgers, Boussinesq, Russel, and King have worked along similar lines. This approach leads to their equation (no. 16) and conditions (no. 10) which naturally correspond to our base flow and first iteration equations and conditions taken together. However, their approach in obtaining the equations is technical in spirit and does not recognize or assert the fundamental role which we have assigned to the potential flow as a base flow that is valid in the whole domain, including, of course, the points near the wall and in the wake, for all Reynolds numbers. To show this is the case, we quote the following from their work. "Now we know from experiment that the undisturbed velocities u, v are approximately irrotational in parts of the field which are not very near to the solid

boundary or to the 'wake.' Hence, to replace them by irrotational velocities should be a closer approximation to the truth than to replace them by undisturbed velocities ... And we may conclude that (16) will be a satisfactory approximation to the exact form (11) of the governing equation throughout the whole of the speed-scale range, provided that α is the velocity potential function appropriate to a cylinder of the form which we are considering. For the experimental evidence (5) indicates that the actual flow pattern at high speeds does in fact approximate to irrotational flow pattern, except at points very close to the boundary of the cylinder and in the 'wakes'." These quotations show that although they have indicated that their equation (16) may be applicable to high value of Reynolds number, they have not attached any significance to the use of a potential solution as far as points very close to the cylinder and in the wake are concerned. In fact, the idea of deviation from a potential flow is absent. Their work differs in other respects also. The method adopted by them to solve their governing equation is quite different from ours. And consequently there are no equations in their work like the subsidiary equations which we have derived and used. The recognition that the results up to the first iteration must give a value of drag higher than that observed in actual experiments by a considerable margin, and that the second iteration is essential to account for this difference, is absent in their work. In fact, their drag formula for a circular cylinder gives a value which is less by 20% than Lamb's [18] and by 7% than Bairstow's when $R = 2$. In principle, this should be the same as our first iteration drag. But the value we have at Re = 1, i.e., at $R = 2$ since $R = 2Re$, is a little higher than Bairstow's, as can be seen from Table 2 and Fig. 1B. Since we have shown that the first iteration values are lowered by taking into account the second iteration, the discrepancy between their and our first iteration drags when $R = 2$ shows that their value cannot be accurate. In their approximate solutions to the governing equations they have applied the boundary condition at the wall in such a way that it is satisfied at only a discrete number of points. This is not the case with our method.

A central feature of all the works which use the potential flow solution is their use of the Boussinesq coordinate transformation from the Cartesian space coordinates to the velocity potential α-stream function β coordinates. Burgers neglects $\partial^2\omega/\partial\beta^2$, where $\omega = \nabla^2\psi$, in the differential equation for ω and hence works ultimately with an equation different from the one which corresponds to our base flow and the first iteration equation. Lewis, using Meksyn's analytical methods for obtaining Green's function for the stream function removes the limitations involved in the works of Southwell and Squire, and Burgers, but gives no specific information about drag, pressure, etc. Pillow's work treats flow past a parabola and uses similar techniques; consequently, a direct comparison between his and our work is not possible. However, to show the difference in basic ideas involved in his and our work we quote the following from his work.

> A construction is given for the general solution of the Burgers vorticity equation. Such a solution which satisfies the boundary conditions at infinity provides a general outer solution for real viscous flow past bodies, into which any inner solution must ultimately match.

> In any iterative procedure working inwards and based on a Burgers flow as a first approximation, it becomes important to construct particular solutions of the non-homogeneous form of the Burgers vorticity equation in which the successive estimates of the self-convection effect appear as perturbation terms on the right-hand side ...
>
> ... However, it must be clearly understood that boundary layer flow must inevitably dominate the inner flow region sufficiently far downstream. In such a region, non-linear self-convection effects become comparable with Burgers convection ...

These statements show that the ideas of inner and outer expansions are central in his work. Although the last quotation shows, in a sense, the recognition of the importance of our second iteration, it is used to refute the validity of the process of iteration for the whole domain consistent with the ideas of inner and outer expansions, as the following statement indicates: "... In its outer region, this solution merges with a suitable Burgers flow but, owing to the finite difference of displacement thickness, not the one one obtains by a naive application of linear theory right up to the boundary of the parabola. A blind iteration from such a linear solution fails ..." This statement shows the fundamental differences between his and our work.

Starting with Stokes' [16] treatment of the creeping motion of a sphere, which neglected the inertia terms completely, and Oseen's work [51,52,53] which by taking into account, to some measure, these inertia terms, aimed at resolving Whitehead's paradox [54], a large body of work has been based on their approach to the external flow problems for low values of Reynolds number. Lamb's solution [18], based on Oseen's equations for a circular cylinder, has provided a milestone for work on cylindrical objects. Stokes' paradox [16] in case of a circular cylinder is resolved in a sense by the use of Oseen's equations instead of Stokes' equations for creeping motion. It is also resolved, as Bairstow [55] has shown, by using Stokes' equations together with a flow field which is partially bounded at infinity. S. Goldstein [56] has given an exact analytical solution of Oseen's equation for the case of the steady flow of an incompressible viscous fluid past a sphere. For the case of a circular cylinder, Faxen [57] provided the solution. The solution given by Bairstow, Cave, and Lang [25] for a circular cylinder is based on an extension of Lamb's treatment. Tomotika and Aoi [58] have given similar solutions for a sphere and a circular cylinder along lines following Goldstein's work on a sphere. Both of these works have carried out calculations of drag for a circular cylinder in the range $0 < R \leq 23$, where R is based on the diameter of the cylinder. This is just a little more than half the range which we have examined in detail. As noted by Tritton [59], the results of Bairstow et al. and Tamotika and Aoi are essentially the same as far as the drag is concerned. Hence only the results of Bairstow et al. are plotted for comparison in Fig. 1B.

The methods of small perturbation in fluid mechanics are discussed in detail by Van Dyke [42]. Stokes' and Oseen's solutions are shown to be asymptotic expansions of the solutions of the Navier-Stokes equations for small values,

usually regarded as less than 1, of the Reynolds number. Two ideas generated by S. Kaplun have made it possible to extend methods in this field of asymptotic expansions. Lagerstrom [60] has stated them as: "(1) The discovery of suitable inner and outer limits; (2) An extension of the technique of matching between various expansions." The works of Lagerstrom and Cole [61], Kaplun and Lagerstrom [62], and Kaplun [22,23] in this field are quite significant. Kaplun has given a higher approximation solution than Lamb's for a circular cylinder that is valid for small Reynolds numbers. We have plotted Lamb's as well as Kaplun's results for drag in Fig. 1E. Lamb's expression for drag is as follows:

$$C_D = \frac{4\pi}{Re}\left(\frac{1}{0.5 - \gamma - \log_e \frac{Re}{4}}\right), \qquad \begin{aligned} Re &= \text{Reynolds number based on radius} \\ \gamma &= 0.5772157, \text{ Euler's constant.} \end{aligned}$$

Kaplun's expression for drag includes one more term than Lamb's. It is

$$C_D = \frac{4\pi}{Re}\left(\Delta_1 - 0.87\,\Delta_1^3\right),$$

where

$$\Delta_1 \equiv \frac{1}{0.5 - \gamma - \log_e \frac{Re}{4}}.$$

It is easy to see that both of these expressions become unbounded for $Re \cong 3.73$. For this value Lamb's expression becomes $+\infty$ and Kaplun's becomes $-\infty$, though the latter obviously tends to $-\infty$ faster than does Lamb's, which tends to $+\infty$ as $Re \to 3.73$. As noted by Van Dyke [42], all such higher approximations will have expressions for drag which are expansions in powers of Δ_1. Hence they cannot be meaningful beyond Re = 3.73, although their actual range of validity is successively increased within these limits $0 < Re < 3.73$.

By using ideas of inner and outer expansions and matching procedures, Proudman and Pearson [63] have also obtained higher approximations to the flow past a sphere and a circular cylinder than those represented by the solutions of Stokes and Oseen. The results are essentially same as Kaplun's for a circular cylinder. Proudman and Pearson as well as Van Dyke [42] regard the works of Bairstow et al. [25], Goldstein [56], and Tomotika and Aoi [58] as of limited value. Proudman and Pearson [63] remark that "there is no point in solving the linear equation (2.12) to a greater degree of approximation than that of the inertial terms neglected by substituting the Oseen equations for Navier-Stokes equations, and so the simple solution given by Lamb (1911) is as good an approximation as it is possible to obtain from the linearized equation." The equation (2.12) to which the remark refers is $(\nabla_r^2 - R\,\partial/\partial x)\,\nabla_r^2\psi = 0$. Van Dyke [42] states that the approximation is qualitatively as well as quantitatively invalid at high Reynolds number and, to support his view, gives the reason that Oseen's approximation gives boundary layers whose thickness is of the order R^{-1} rather than $R^{-1/2}$, as in Prendtl's correct theory. Moreover he points to Yamada's work [64] to invalidate qualitative results even at low Reynolds

number. We think that these views are not well justified. It is true that Kaplun's expression for drag represents a higher approximation than Lamb's expression to which, surely, the expressions of Bairstow et al. and Tomotika and Aoi reduce for the range of Reynolds number in which both Lamb's and Kaplun's expressions are meaningful. However the expressions due to Bairstow et al. and Tomotika and Aoi are asymptotic in nature with increasing Reynolds number and show no unboundedness, at least within the range they have investigated, whereas those due to Lamb and Kaplun are otherwise and become unbounded for Re = 3.73. The results that do not become unbounded are more of value, even if they are quantitatively somewhat different from the exact results produced by those expressions that do. This shows that expansions in terms of Re as a perturbation parameter, as obtained by Lamb and Kaplun, are not mathematically equivalent to the solutions obtained by Bairstow et al., Tomotika and Aoi, and others, except in a narrow range, for otherwise, they all should show unboundedness at Re $\cong$ 3.73. The range $0 < Re < 12$ which is the one investigated by Tomotika and Aoi as well as Bairstow and others is a range in which the assumptions of the boundary layer theory are invalid. Consequently, the thickness of the boundary layer argument cannot be applied to this range. For this range, then, these works cannot be invalidated totally on this count. As for Yamada's work [64], his results as shown in Fig. 3 of Ref. 64 do not seem to be correct. The reasons are as follows.

The experimental work of Thom shows that for $R = 3.5$ the maximum stagnation pressure in front of the cylinder is $p - p_0/(\rho v^2/2) \cong 2.3$. Figure 6 in his work shows that for higher values of R, this must be decreasing. Consequently for $R = 4$, the value must be less than 2.3. Since the pressure drag is somewhat directly related to, and has a value in excess of, that of the maximum stagnation pressure for this value of Reynolds number, we can also estimate what value this maximum pressure may possibly have. From Tritton's work [59] the value of total drag at $R = 4$ is about 4.85. According to Oseen's theory the pressure drag is half the total drag. This would give the pressure drag 2.425. On the other hand, if we take the pressure drag as 0.65 times the total drag as found by Kawaguti [65] and as can be roughly estimated from Fig. 8 in Thom's work [66], it turns out to be 3.152. In any case, then, the maximum pressure cannot be larger than 3.152. However, Fig. 3 in Yamada's work [64] shows this value obtained by considering the exact Navier-Stokes equations to be 5.2, which is much too large in comparison to the maximum estimated value 3.152 and the possible experimental value which may be less than 2.3. Hence we cannot but conclude that Yamada's results are in error. Consequently, Van Dyke's statement, which is based on Yamada's work, has to be discounted.

The method of inner and outer expansions has been utilized by Blair et al. [43], Brenner [67], Brenner and Cox [68], Caswell and Schwartz [69], Chester [70], and many other authors. But the limitations of the small-perturbation theories are too severe to help us understand the evolution of a flow field for the complete range of a characteristic parameter. Lagerstrom [60] rightly considers that the main importance of their work lies in the analysis of basic problems in asymptotic expansions.

The measurements of the drag on a circular cylinder made by Tritton are the most recent experiments and extend down to the lowest value — 0.416 — of the Reynolds number, based on diameter, as yet attempted. The results of Wieselsberger [71] and Relf [72] are in agreement with Tritton's. Those of Fage [73,74,75], Schiller and Linke [76], Roshko [77], and Humphreys [78] cover the range of high Reynolds numbers and hence are not useful for comparison with the present work. The results obtained by Thom [66], Kawaguti [65], and Apelt [79] by numerical integration of the exact Navier-Stokes equations are in agreement with Tritton's results. Allen and Southwell's [48], and Southwell and Squire's [24] results are somewhat higher than Tritton's. Since Tritton's paper gives a comparison of these other works with its own results, it is considered sufficient to compare our results with Tritton's. For this purpose, Tritton's drag v/s Re curve is plotted in Figs. 1A, 1B, and 1C. From them it can be seen that the first and second iteration results behave asymptotically in the same fashion as Tritton's, but that these curves for higher Re lie above those of Tritton's. The values of the first iteration drag are lowered by the negative contributions of the second iteration results for $Re \leq 4$. We expressly state that the second iteration drag results for $Re > 4$ are not very accurate and that they should be considered indicative of what the second iteration leads to rather than as conclusive.

Figure 2A shows that the ratio of the first iteration pressure drag to the viscous drag remains essentially equal to 1. The divergence with increasing Re may be an indication of decreasing accuracy of computation, though this has not been ascertained in the present work. By comparing these results with those which may be obtained by computation with multiple precision, we can decide on this issue. It is interesting that, like Oseen's theory, this ratio has turned out to be unity. However, this is not the ratio of the total pressure drag to the total viscous drag obtained by considering both the first and the second iterations together. The results of the second iteration show that the ratio will be different from unity. Kawaguti's [65] and Thom's work [66] show that this is indeed the case.

Definition of points of separation similar to the one we have given have been used by Van Dyke, Proudman and Pearson, and Yamada. These first two authors have correctly pointed out that the results of Tomotika and Aoi are seriously in error as far as the determination of points of separation is concerned. Figure 2B gives the angle of separation determined with first iteration as well as first and second iterations together. It shows the general behavior found in experiments by Grove et al. [47], Thom [66], Homann [80,81], and Taneda [82]. It shows asymptotic behavior with increasing Reynolds number. At $Re \cong 0.75$ the angle α_1 is zero, which implies that according to the results of the first iteration separation begins at Re = 0.75. On the other hand, α_2 is zero at $Re \cong 2.3$, showing that the separation begins at $Re \cong 2.3$ when two iterations are taken into account. Nisi and Porter [83,84] estimate the Reynolds number at which the separation begins to be 1.6. Homann [80,81] gives a value of 6.0. Taneda [82] estimates it to be 2.5, and this recent value is close to the theoretical $Re \cong 2.3$ predicted by the present work. Experimental values must be slightly higher than theoretical values, because a vortex and separation associated with the former cannot be discerned until after they have reached a finite size which can be observed. Theoretical values, on the other hand,

refer to the Reynolds number at which there is no vortex but above which separation begins and a vortex forms. Hence Taneda's value of 2.5, which is just above 2.3 of the present work, confirm the linear substructure theory.

Figures 2C and 2D give respectively the stagnation pressures in front and in the rear of a circular cylinder for a first iteration. The qualitative behavior of these curves is again the same as found by Grove et al. [47], Thom [66], and Homan [80,81]. The pressures behave asymptotically and tend to a constant value with increasing Re in the range investigated. This is one of the main observations of Grove et al. They [47] state: "First, that the rear pressure quickly reaches a limit of approximately -0.45 as the Reynolds number is increased; and second, that this limit is attained, for all practical purposes, at a Reynolds number as low as 25." From Fig. 2D it can be seen that the pressure becomes essentially constant from Re = 4, i.e., Re = 8 onwards. Thus there is complete qualitative agreement. Figures 3E, 3F, 4E, 4F, etc. give the distribution of total pressure, ideal pressure, first iteration pressure, second iteration pressure, and their harmonic components on the surface of the cylinder for different values of Re. The total pressure, as stated earlier, is given as the sum of the ideal pressure, the first iteration pressure, and the second iteration pressure. Figure 2E shows how the amplitudes of the harmonic components of the first iteration pressure varies with Reynolds number. It can be seen that the amplitude PRET1_{max} is at first very large, then decreases rapidly in a narrow range of the Reynolds number, and thereafter behaves asymptotically with increasing Re, tending to a constant value. The other two components, viz., the constant PREC1 and the amplitude PREP1_{min} also behave asymptotically with increasing Re, but they do not attain very high values like PRET1_{max} for small Re. This then means that, for small Re, the harmonic PRET1 in $\cos\theta$ dominates so that the total first iteration pressure PRES1 and hence the total pressure PRESS behaves essentially as this harmonic. On the other hand, for high Re, the harmonic PREP1 in $\cos 2\theta$ and the constant PREC1 make significant contributions to the pressure PRES1, and hence to the total pressure PRESS. The qualitative behavior in Figs. 3E, 3F, 4E, 4F, etc. is as observed in experiments.

Figures 3D, 4D, etc. give an idea of the error involved in the assumption that $B_n(r,t) \equiv 0$ for $n \geq 3$ for different values of Re. They show that ER1 takes extreme values at the two boundaries. Further, the absolute magnitudes of these extreme values which are at first small increase with increasing Re. However, bearing in mind that these curves are plotted against S and that the actual distance is given by $r = e^{ecs-1}$, we see that in most of the flow field the absolute magnitude of ER1 remains very small compared to the absolute magnitudes of these extreme values. The assumption seems to be justified, though these curves do give an indication that for larger values of Re one may have to introduce corrective measures for this error.

In the present work we have not gone into an investigation of the time-dependent motion. Consequently, the literature available on this aspect of the flow field is not discussed. The experimental works of Grove et al. [47], Gerrard [85], Roshko [86,87,88], Relf and Simmons [89], Tyler [90], Hollingdale

[26], and other authors are significant. Of particular importance is the work of Taneda [82]. When investigation is carried out for large values of Re, then the literature based on the boundary layer theory becomes significant. However, this latter literature cannot provide any understanding of the wake. The literature based on free-streamline theories which display infinite wake and on theories which lead to finite wakes or no wakes at all, show attempts to give the solutions to the Euler equations a central place. Boundary layer theory definitely gives an important place to the potential solution. In the present scheme we have attempted to unify the picture by asserting the fundamental role of the potential flow as a base flow for actual flows under all conditions.

CONCLUDING REMARKS

The conclusions based on the general aspects of the theory and investigation of the steady flow in the range $0 < \mathrm{Re} \leq 20$ are as follows:

1. The potential flow solution does play a fundamental role inasmuch as it has lead us to results which are in good agreement with the experimental results for $\mathrm{Re} \leq 4$, and which shed light on the evolution of the vortex structure. Moreover, a theoretical value of the Reynolds number at which separation begins is obtained, in agreement with experiments.

2. The results support the existence of a linear substructure underlying the Navier-Stokes equations in the present case.

3. The time-independent subsidiary equations and their solutions for the first and second iterations show by induction that the coefficients of the subsidiary equations for all iterations will be analytic with infinite radius of convergence, leading to corresponding solutions which also have infinite radius of convergence (Refs. 1 and 2).

4. The analytical solutions for the first two iterations contain implicitly all the information about the structure of vortices and the wake insofar as they give rise to the streamline field around the circular cylinder.

5. Nonsymmetric wakes and the evolution of vortices which are distinguished by closed streamlines are the result of *the same process* of superposition of the harmonics of the streamline field, and consequently one might view a vortex structure to be inherent in the flow field even at the smallest Reynolds numbers, although explicitly identifiable closed streamline structures may not be then manifest in the field.

6. The discrepancy in the drag at higher Reynolds numbers is attributable to the fact that in these cases the boundary at which the flow is assumed to become potential is situated close to the cylinder to avoid numerical breakdown of the computations. And to maintain this situation there, a highly rotational flow is required to be constrained within a smaller domain than is physically admissible.

7. The numerical calculations have served a twofold purpose; (a) to test the theory, and (b) to give information that corresponds to observations but extends significantly beyond available observed information and which bears on the details concerning the evolution of flow fields with Reynolds number.

8. The Symmetry Theorem is supported by the experimental evidence. It predicts the asymptotic behavior which was looked for and found independently by Grove et al., through experiments.

9. The results support the validity and the use of the idea of a physically infinite distance.

10. The presence and the behavior of a subdomain in which the viscous effects are very significant is demonstrated by the results.

ACKNOWLEDGMENTS

The authors gratefully acknowledge the support of the Fluid Mechanics branch of the Office of Naval Research, Washington, D.C. We thank the Computer Center at the University of California, Berkeley, for providing almost unlimited use of their facilities which has lead to the concrete numerical results presented in this series of reports. Also, we thank warmly Mrs. Etha Webster for her invaluable assistance in preparing this manuscript and Mrs. Dorathy Brohl for printing the reports on which it is based.

REFERENCES

1. Desai, S., "On a Linear Substructure Underlying the Navier Stokes Equations as Applied to the Problem of Flow of a Viscous Incompressible Fluid Past a Circular Cylinder," Ph.D. thesis, University of California, Berkeley, 1965

2. Desai, S., and Lieber, P., Reports AM-67-5, 9, 10, and 13, Parts I, II, III, and IV, Office of Research Services, University of California, Berkeley, 1967

3. Lieber, P., "A Dissipation Mechanism in Gas Flows and Similar Physical Systems," Trans. N.Y. Acad., Sci., Vol. II (No. 5), 175-181 (1949)

4. Lieber, P., Wan, K.S., and Anderson, O., "A Principle of Virtual Displacements for Real Fluids," Int. Congr. Mech., Proc. IX, Belgium, 1957 (Also issued as a Rensselaer Polytechnic Institute Research Division Report AFOSR TN 57-476, AD 136 468, under Air Force Contract AF 18(600)-1704, July 1957)

5. Lieber, P., and Wan, K.S., "A Minimum Dissipation Principle for Real Fluids," Int. Congr. Mech., Proc. IX, Brussels, Belgium, 1957 (Also issued by Rensselaer Polytechnic Institute, Troy, N.Y., as a Research Division Report AFOSR TN 57-477, AD 136 469, Aug. 1957, and released, Office of Scientific Research, USAF, as TN 57-477, under Contract AF 18(600)-1704, Aug. 1957

6. Lieber, P., and Wan, K., "A Proof and Generalization of the Principle of Minimum Dissipation," report under contract AF18 (600)-1704 (1957)

7. Wan, K.S., and Lieber, P., "Applications Based on Variational Principles for Real Fluids," report under contract AF18(600)-1704 (1957)

8. Lieber, P., "A Principle of Maximum Uniformity Obtained as a Theorem on the Distribution of Internal Forces," report MD-63-8, Nonr-222(87), Institute of Engineering Research, University of California, Berkeley, 1963

9. Lieber, P., and Wan, K.S., "A Study leading to the Boundary Conditions at a Free Surface Joining an Irrotational-rotational Flow Regime," report under contract AF18(600)-1704 (1957)

10. Wan, K.S., and Lieber, P., "Applications Based on Variational Principles for Real Fluids," Office of Scientific Research of USAF, TN 57-481, Sept. 1957 (Also issued by the Rensselaer Polytechnic Institute Research Division Report AFOSR TN 57-481, AD 136-473, under Contract AF 18(600)-1704, Sept. 1957)

11. Milne-Thomson, L.M., "Theoretical Hydrodynamics" 3rd ed., New York: MacMillan, 1955

12. Prandtl, L., and Tietjens, O.G., "Fundamentals of Hydro- and Aeromechanics," New York: Dover, 1934

13. Goldstein, S. (Editor), "Modern Developments in Fluid Dynamics," Vols. I and II, Oxford: Clarendon Press, 1938

14. Lighthill, M.J. (1963), "Introduction. Real and Ideal Fluids," from 'Laminar Boundary Layers,' ed. L. Rosenhead, Oxford, Fluid Motion Memoirs

15. Stokes, G.G., "On the Theories of the Internal Friction of Fluids in Motion, and of the Equilibrium and Motion of Elastic Solids," Cambridge Phil. Trans., Vol. VIII, 287 (1845); also, Math. and Phys. papers, Vol. I

16. Stokes, G.G., "On Effect of the Internal Friction of Fluids on the Motion of Pendulums," Cambridge Phil. Trans., Vol. IX, part II, p. 8 (1851)

17. Langlois, W.E., "Slow Viscous Flow," New York: MacMillan, 1964

18. Lamb, H., "Hydrodynamics," Dover Paperback, 6th ed., New York: Dover, 1932

19. Schlichting, H., "Boundary Layer Theory" (transl. Dr. J. Kestin), London: Pergamon Press, 1955

20. Rosenhead, L. (Editor), "Laminar Boundary Layers," Oxford Fluid Motion Memoirs, 1963

21. Landau, L.D., and Lifshitz, E.M., "Fluid Mechanics," Course of Theoretical Physics 6, Oxford: Pergamon Press, 1959

22. Kaplun, S., "The Role of Co-ordinate Systems in Boundary-Layer Theory," J. Appl. Math. Phys. (ZAMP) 1, 111-134 (1954)

23. Kaplun, S., "Low Reynolds Number Flow Past a Circular Cylinder," J. Math Mech. 6, 595-603 (1957)

24. Southwell, R.V., and Squire, R.B., "A Modification of Oseen's Approximate Equation for the Motion in Two Dimensions of a Viscous Incompressible Fluid," Phil. Trans. Roy. Soc. London, A 232, 27-64 (1933)

25. Bairstow, L., Cave, B.M., and Lang, E.D., "The Resistance of a Cylinder Moving in a Viscous Fluid," Phil. Trans. Roy. Soc. London, A 223, 383-432 (1923)

26. Hollingdale, S.H., "Stability and Configuration of the Wakes Produced by Solid Bodies Moving through Fluids," Phil. Mag., ser. 7, 29, 209-257 (1940)

27. Hele-Shaw, H.S., "Investigation of the Nature of Surface Resistance of Water and of Stream-line Motion under Certain Experimental Conditions," Trans. Inst. Naval Architects, Vol. XL, 21-46 (1898)

28. Hele-Shaw, H.S., "The Motion of a Perfect Liquid," Proc. Roy. Inst. 16, 49-64 (1899)

29. Stokes, G.G., "Mathematical Proof of the Identity of the Stream-lines Obtained by means of a Viscous Film with Those of a Perfect Fluid Moving in Two Dimensions," Math. and Phys. papers, Vol. V, 278-282 (1898)

30. Riegels, F., "Zur Kritik des Hele-Shaw-Versuchs," Z. Angew. Math. Mech., B. 18 (Heft 2), 95-106 (1938)

31. Friedman, B., "Principles and Techniques of Applied Mathematics," New York: Wiley, 1956

32. Wilson, H.A., "On Convection of Heat," Proc. Cambridge Phil. Soc. 12, 406-423 (1904)

33. Boussinesq, M.J., "Calcul de Pouvoir Refroidissant des Courants Fluides," J. Math. Pures Appl., ser. 6, 1, 285-332 (1905)

34. Russel, A., "The Convection of Heat from a Body Cooled by a Stream of Fluid," Phil. Mag., ser. 6, 20, 591-610 (1910)

35. King, L.V., "On the Convection of Heat from Small Cylinders in a Stream of Fluid," Phil. Trans. Roy. Soc. London, A 214, 373-432 (1914)

36. Burgers, J.M., "Stationaire Stroomingen door een Lichaam in een Vloeistof met Wrijving Teweeggebracht," Koninkl. Akad. Wetenschap. te Amsterdam, Deel XXIX, Part I, p. 835; Part II, p. 952, Verslag 1921

37. Zeilon, N., "Ein Allgemeines Hydrodynamisches Potential Problem," from 'Neure Methoden und Ergebnisse in der Hydrodynamik' by C.W. Oseen, Leipzig, 1927

38. Meksyn, D., "Solution of Oseen's Equation for an Inclined Elliptic Cylinder in a Viscous Fluid," Proc. Roy. Soc. London, A 162, 232-251 (1937)

39. Pillow, A.F., "Diffusion of Heat and Circulation in Potential Flow Convection," J. Math Mech. 13 (No. 4), 521 (1964)

40. Lewis, T., "Solutions of Oseen's Extended Equations for Circular and Elliptic Cylinders and a Flat Plate," Quart. J. Math., Oxford ser. 8-9, (1937-1938)

41. Tolstoy, G.P., "Fourier Series," translated from Russian by R.A. Silverman, Prentice Hall, 1962

42. Van Dyke, M., "Perturbation methods in fluid mechanics," New York: Academic Press, 1964

43. Blair, A., Metropolis, N., Neumann, J.v., Taub, A.H., and Tsingon, M., "A Study of a Numerical Solution to a Two-Dimensional Hydrodynamical Problem," Report LA-2165, Los Alamos Scientific Lab, University of California, Los Alamos, New Mexico, 1957

44. Fromm, J.E., "A Method for Computing Nonsteady, Incompressible Viscous Fluid Flows," Report LA-2910 UC-32, Mathematics and Computers TID-4500 (21st ed.), Los Alamos Scientific Lab., University of California, Los Alamos, New Mexico, 1963

45. Fromm, J.E., and Harlow, F.H., "Numerical Solution of the Problem of Vortex Street Development," Phys. Fluids 6 (No. 7), 975-982 (1963)

46. Harlow, F.H., and Fromm, J.E., "Computer Experiments in Fluid Dynamics," Sci. Am., Mar. 1965

47. Grove, A.S., Shair, F.H., Petersen, E.E., and Acrivos, A., "An Experimental Investigation of the Steady Separated Flow Past a Circular Cylinder," J. Fluid Mech. 19, Part 1, 60-80 (1964)

48. Allen, D.N., and Southwell, R.V., "Relaxation Methods Applied to Determine the Motion, in Two Dimensions, of a Viscous Fluid Past a Fixed Cylinder," Quart. J. Mech. 8, 129-145 (1955)

49. Kawaguti, M., "Note on Allen and Southwell's Paper 'Relaxation Methods Applied to Determine the Motion, in Two Dimensions, of a Viscous Fluid Past a Fixed Cylinder'," Quart J. Mech. **12**, 261-263 (1959)

50. Southwell, R.V., and Squire, R.B., "A Modification of Oseen's Approximate Equation for the Motion in Two Dimensions of a Viscous Incompressible Fluid," Phil. Trans. Roy. Soc. London, A **232**, 27-64 (1933)

51. Oseen, C.W., "Über die Stokessche Formel und über eine verwandte Aufgabe in der Hydrodynamik," Arkiv Math. Astron. Fysik **6**, No. 29 (1910)

52. Oseen, C.W., "Exakte Lösungen der hydrodynamischen Differentialgleichungen," I, Arkiv Math. Astron. Fysik **20A**, No. 14 (1927)

53. Oseen, C.W., "Neure Methoden und Ergebnisse in der Hydrodynamik," Leipzig Akademische Verlagszesellsehaft, M.B.H., 1927

54. Whitehead, A.N., "Second Approximations to Viscous Fluid Motion," Quart. J. Math. **23**, 143-152 (1899)

55. Bairstow, L., "The Two-dimensional Slow Motion of Viscous Fluids," Proc. Roy. Soc. London, A **100**, 394-413 (1921)

56. Goldstein, S., "The Steady Flow of a Viscous Fluid Past a Fixed Spherical Obstacle at Small Reynolds Numbers," Proc. Roy. Soc. London, A **123**, 225-235 (1929)

57. Faxen, H., "Exakte Lösung der Oseenschen Differential Gleichungen einer Zäher Flussigkeit fur den Fall der Translations Bewegung eines Zylinders," Nova Acta Regiae Societatis Scientiarum Upsaliensis, volumen extra ordinem, 1-55 (1927)

58. Tomotika, S., and Aoi, T., "The Steady Flow of Viscous Fluid Past a Sphere and Circular Cylinder at Small Reynolds Numbers," Quart. J. Mech. Appl. Math., Vol. III, 140-161 (1950)

59. Tritton, D.J., "Experiments on the Flow Past a Circular Cylinder at Low Reynolds Number," J. Fluid Mech. **6**, 547 (1959)

60. Lagerstrom, P.A., "Note on the Preceding Two Papers," J. Math. Mech., Vol. 6 (No. 5), 605-606 (1957)

61. Lagerstrom, P.A., and Cole, J.D., "Examples Illustrating Expansion Procedures for the Navier-Stokes Equations," J. Rat. Mech. Anal., Indiana University **4**, 817-882 (1955)

62. Kaplun, S., and Lagerstrom, P.A., "Asymptotic Expansions of Navier-Stokes Solutions for Small Reynolds Numbers," J. Math. Mech. **6**, 585-593 (1957)

63. Proudman, I., and Pearson, J.R.A., "Expansions at Small Reynolds Numbers for the Flow Past a Sphere and a Circular Cylinder," J. Fluid Mech. 2, 237-262 (1957)

64. Yamada, H., "On the Slow Motion of Viscous Liquid Past a Circular Cylinder," Rep. Res. Inst. Appl. Mech., Vol. III (No. 9), Kyushu University, Fukuoka, Japan, 1954

65. Kawaguti, M., "Numerical Solution of the Navier-Stokes Equations for the Flow around a Circular Cylinder at Reynolds Number 40," J. Phys. Soc. Japan 8, 747-757 (1953)

66. Thom, A., "The Flow Past Circular Cylinders at Low Speeds," Proc. Roy. Soc. London, A 141, 651-669 (1933)

67. Brenner, H., "The Oseen Resistance of a Particle of Arbitrary Shape," J. Fluid Mech. 11 (1961)

68. Brenner, H., and Cox, R.G., "The Resistance to a Particle of Arbitrary Shape in Translational Motion at Small Reynolds Numbers," J. Fluid Mech. 17 (1963)

69. Caswell, B., and Schwartz, W.H., "Creeping Motion of a Non-Newtonian Fluid Past a Sphere," J. Fluid Mech. 13 (1965)

70. Chester, W., "On Oseen's Approximation," J. Fluid Mech. 13 (1962)

71. Wieselsberger, C. von, "Neure Feststellungen über die Gesetze des Flüssigkeits- und Luftwiderstandes," Physik. Z., XXII (No. 11), 321-328 (1921)

72. Relf, E.F., "Discussion of the Results of Measurements of the Resistance of Wires, with Some Additional Tests on the Resistance of Wires of Small Diameter," Aero. Res. Council, London, R. and M. No. 102 (1914)

73. Fage, A., "Determination of the Pressure Distribution Round a Cylinder," Aero Res. Council, Londin, R. and M. No. 106 (1913)

74. Fage, A., "The Air Flow Around a Circular Cylinder in the Region, Where the Boundary Separates from the Surface," Phil. Mag. 7, 253 (1929)

75. Fage, A., and Falkner, V.M., "Further Experiments on the Flow Around a Circular Cylinder," Aero. Res. Council, London, R. and M. No. 1369 (1931)

76. Schiller, L., and Linke, W., "Druck und Reibungs Widerstand des Zylinders bei Reynoldschen Zahlen 5000 bis 40000," ZFM 24, 193 (1933); also, Tech. Memo. Net. Adv. Comm. Aero., Washington, D.C., No. 715

77. Roshko, A., "Experiments on the Flow Past a Circular Cylinder at Very High Reynolds Numbers," J. Fluid Mech. 10, 345 (1961)

78. Humphreys, J.S., "On a Circular Cylinder in a Steady Wind at Transition Reynolds Numbers," J. Fluid Mech. 9 (1960)

79. Apelt, C.J., "The Steady Flow of a Viscous Fluid Past a Circular Cylinder at Reynolds Number 40 and 44," Aero. Res. Council, London, R. and M. No. 3175 (1961)

80. Homann, F., "Einfluss Grösser Zähigkeit bei Strömung um Zylinder," Forsch. Ing. Wes. 7, 1-10 (1936)

81. Homann, F., "Der Einfluss Grösser Zähigkeit bei der Strömung um den Zylinder und um die Kugel," Z. Angew. Math. Mech. 6, 153-164 (1936)

82. Taneda, S., "Studies on Wake Vortices (II). Experimental Investigation of the Wake Behind Cylinders and Plates at Low Reynolds Numbers," Rep. Res. Int. Appl. Mech., Vol. IV (No. 14) Kyushu University, Fukuoka, Japan, 1955

83. Nisi, H., and Porter, A.W., "On Eddies in Air," Phil. Mag. ser. 6, 46, 754 (1923)

84. Nisi, H., "Experimental Studies on Eddies in Air," Japan. J. Phys. 4, 1 (1925)

85. Gerrard, J.H., "An Experimental Investigation of the Oscillating Lift and Drag of a Circular Cylinder Shedding Turbulent Vortices," J. Fluid Mech. 11 (1961)

86. Roshko, A., "On the Drag and Shedding Frequency of Two-Dimensional Bluff Bodies," Tech. Note Nat. Adv. Comm. Aero., Washington, D.C., No. 3169 (1953)

87. Roshko, A., "On the Development of Turbulent Wakes from Vortex Streets," Rep. Nat. Adv. Comm. Aero., Washington, D.C., No. 1191 (1954)

88. Roshko, A., "On the Wake and Drag of Bluff Bodies," J. Aeron. Sci. 22, 124 (1955)

89. Relf, E.F., and Simmons, L.F.G., "The Frequency of the Eddies Generated by the Motion of the Circular Cylinders through a Fluid," Aero. Res. Council, London, R. and M. No. 917 (1924)

90. Tyler, E., "Vortex Formation behind Obstacles of Various Sections," Phil. Mag., ser. 7, 11, 849-890 (1931)

* * *

Table 2
Summary of Numerical Results Based on an Analytical Representation of Viscous Flow Fields Around a Circular Cylinder

Reynolds Number Re	Exp. Drag Tritton (1959)	Lamb's Solution Drag	CD	CDP	CDV	$\eta = \frac{CDP}{CDV}$	CD1	CDP1	CDV1	$\eta_1 = \frac{CDP1}{CDV1}$	CD2	CDP2	CDV2	$\eta_2 = \frac{CDP2}{CDV2}$	First Iteration Angle of Separation α°	First and Second Iterations Angle of Separation α°	h_1^* RT	Scale Factor C	Minimum Value of CD1	RT Corresponding to $CD1_{min}$
0.05	-	58.38	63.832	31.919	31.902	1.000	65.590	32.796	32.794	1.000	-1.768	-0.877	-0.892	+0.983	-	-	275	2.0	65.59	275
0.125	-	29.668	32.560	16.254	16.205	1.003	33.927	16.965	16.961	1.000	-1.467	-0.711	-0.756	+0.940	-	-	135	2.0	33.927	135
0.1875	-	22.468	22.560	11.299	11.262	1.003	25.882	12.943	12.939	1.000	-3.322	-1.644	-1.677	+0.980	-	-	110	1.9	25.882	110
0.25	10.0 -17.5	18.649	20.09	10.094	10.005	1.009	21.626	10.816	10.810	1.000	-1.527	-0.722	-0.805	+0.890	-	-	85	1.9	21.626	85
0.50	10.5 -11.7	12.550	13.147	6.661	6.486	1.019	14.50	7.26	7.24	1.000	-1.353	-0.599	-0.754	+0.795	-	-	46	1.8	14.50	46
0.75	8.05- 9.30	10.493	10.415	5.031	5.284	1.000	11.768	5.897	5.87	1.004	-1.353	-0.8667	-0.586	+1.478	Incipient Separation	-	30	1.8	11.768	30
1.0	7.26-	9.59	9.52	4.933	4.587	1.075	10.282	5.166	5.115	1.010	-0.762	-0.2335	-0.528	+0.442	22°	-	20	1.7	10.243	25
2.0	4.91-	10.02	7.1576	3.871	3.286	1.178	7.5976	3.851	3.741	1.029	-0.440	+0.02	-0.460	-0.044	42°40'	-	12	1.6	7.555	19
2.1	-	10.50	6.996	3.79	3.206	1.185	7.436	3.770	3.666	1.013	-0.424	+0.037	-0.461	-0.0806	43°46'	-	12	1.6	7.371	21
2.3	-	11.40	6.8076	3.725	3.083	1.208	7.176	3.647	3.529	1.033	-0.368	+0.0782	-0.447	+0.1750	44°57'	Incipient Separation	11	1.4	7.084	20
2.4	4.2 -	12.0	6.6918	3.6743	3.0175	1.2177	7.0446	3.5801	3.4645	1.033	-0.353	+0.094	-0.447	-0.2106	44°12'	7.5°	11	1.4	6.988	20
2.5	-	12.75	6.5853	3.6281	2.9572	1.2269	6.9222	3.5180	3.4042	1.033	-0.337	+0.1101	-0.447	-0.406	48°35'	13°2'	11	1.4	6.886	17
2.75	3.99-	15.35	6.4009	3.559	2.842	1.253	6.6769	3.4047	3.2722	1.040	-0.276	+0.1546	-0.4306	-0.359	47 40'	18' 30'	10	1.4	6.355	19
4.00	3.33-	-40.6	5.4826	3.155	2.328	1.355	5.7797	2.9794	2.8003	1.064	-0.297	+0.1754	-0.4725	-0.3713	51 40'	26 40'	8	1.4	5.705	12
7.50	2.2 - 2.3	-	5.321	3.357	1.964	1.81	5.028	2.810	2.218	1.265	+0.2933	+0.5468	-0.2535	-2.1573	52 15'	35 45'	4	1.2	4.471	6.5
10.0	2.10-	-	5.0506	3.310	1.741	1.902	4.6439	2.6749	1,969	1.3585	+0.4067	+0.6352	-0.2285	-2.7799	53°30'	39°16'	3.5	1.1	4.003	8.0
15.0	1.6 -1.85	-	4.9384	3.429	1.510	2.272	4.4415	2.7254	1.6898	1.6129	+0.5232	+0.7036	-0.1803	-3.9012	53°10'	39°50'	2.75	1.0	3.306	5.5
20.0	1.5 -1.65	-	5.1513	3.738	1.413	2.645	4.6032	3.0526	1.5506	1.9687	+0.5481	+0.6854	-0.1372	-4.9939	52°20'	39°30'	2.25	0.9	3.015	4.5

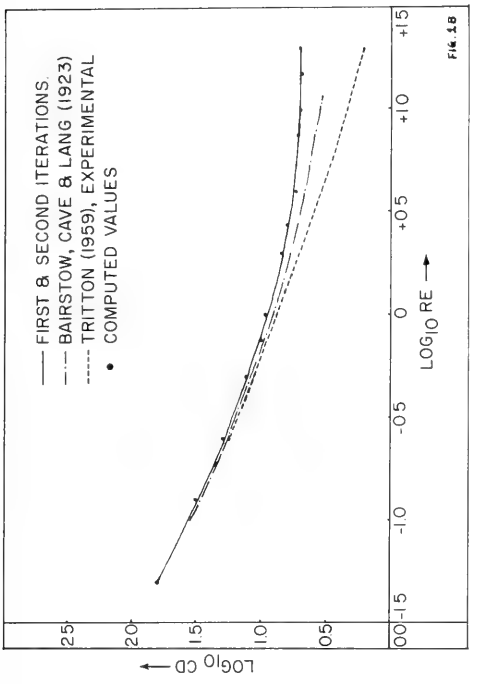
FIRST & SECOND ITERATIONS.
BAIRSTOW, CAVE & LANG (1923)
TRITTON (1959), EXPERIMENTAL
COMPUTED VALUES
LOG10 CD
LOG10 RE
Fig.1B

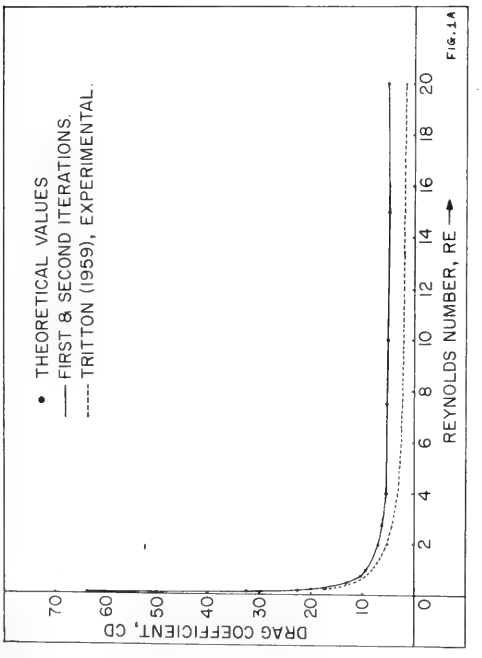
THEORETICAL VALUES
FIRST & SECOND ITERATIONS.
TRITTON (1959), EXPERIMENTAL.
DRAG COEFFICIENT, CD
REYNOLDS NUMBER, RE
Fig.1A

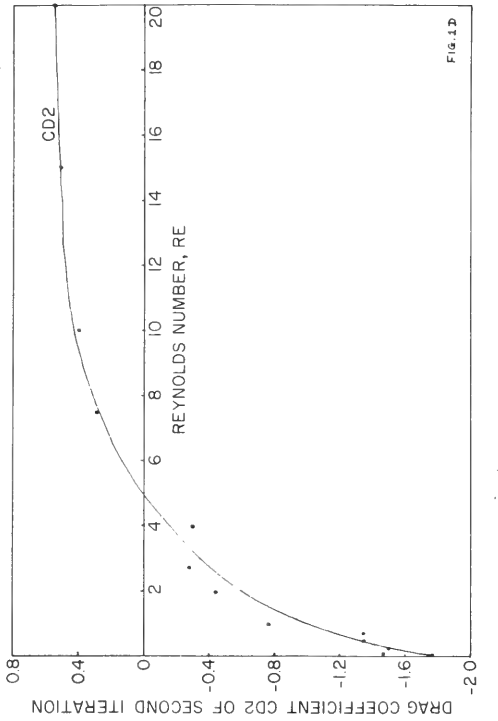
CD2
REYNOLDS NUMBER, RE
DRAG COEFFICIENT CD2 OF SECOND ITERATION
Fig.1D

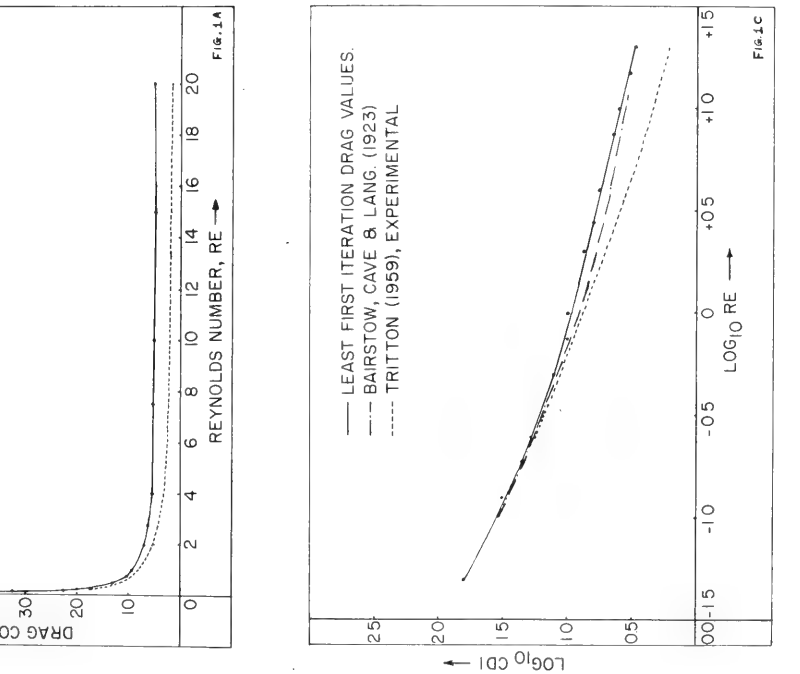
LEAST FIRST ITERATION DRAG VALUES.
BAIRSTOW, CAVE & LANG. (1923)
TRITTON (1959), EXPERIMENTAL
LOG10 CD1
LOG10 RE
Fig.1C

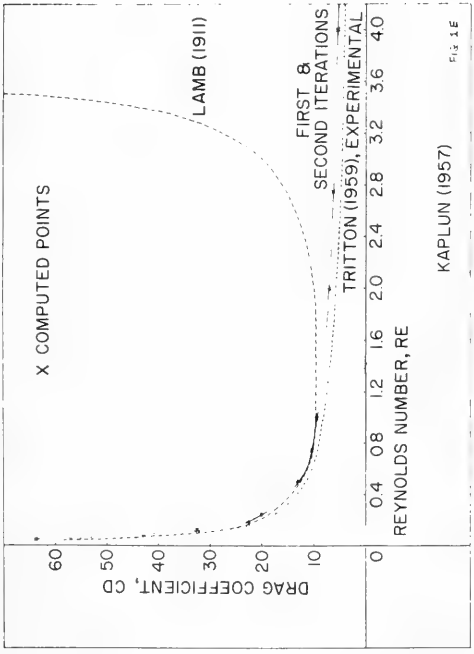

Fig 1E

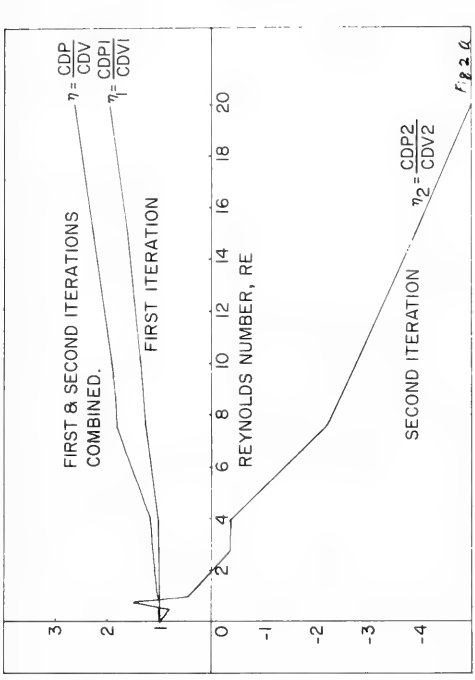

Fig 2A

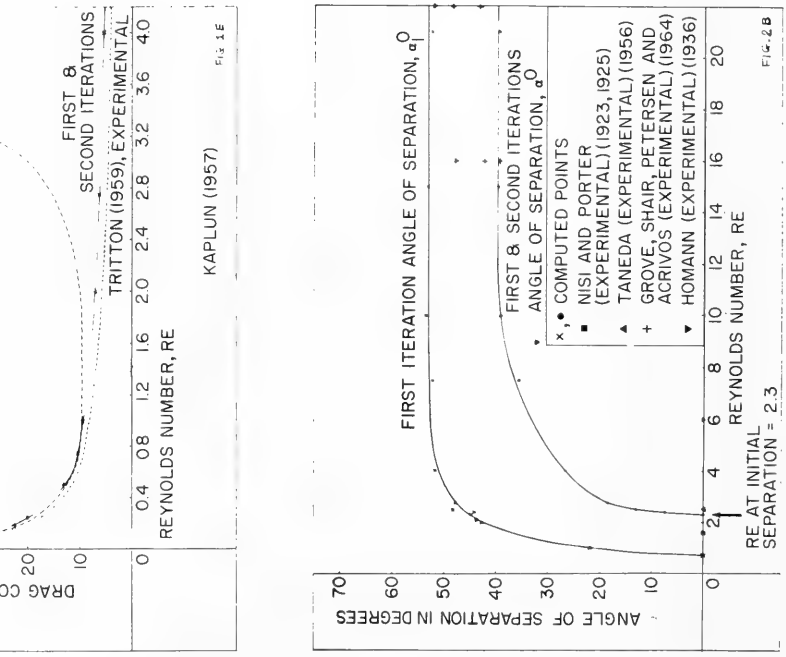

Fig 2B

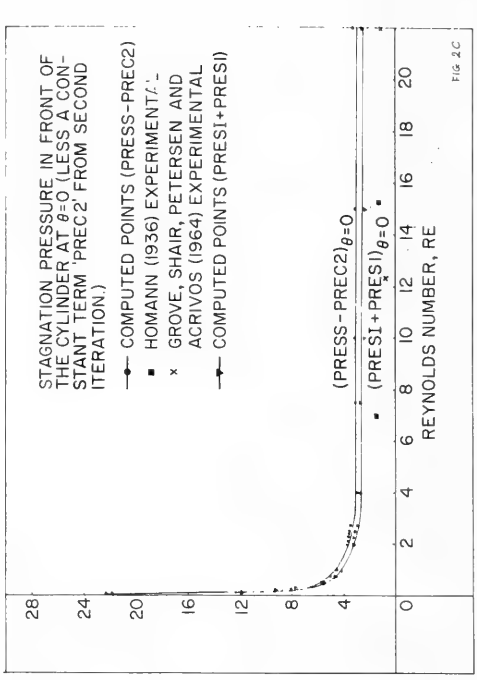

Fig 2C

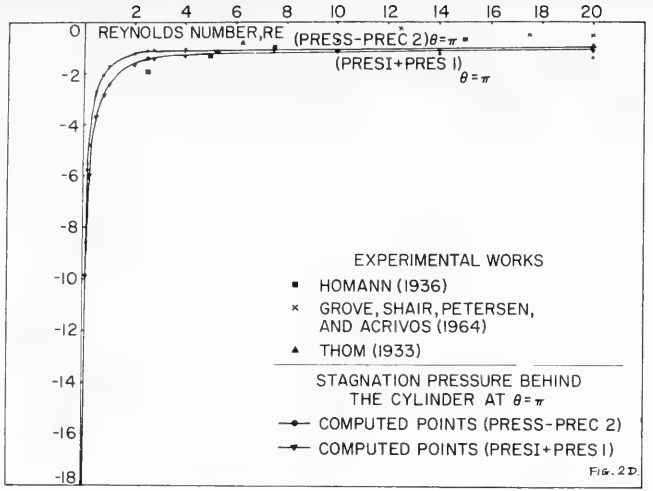

FIG. 2D.

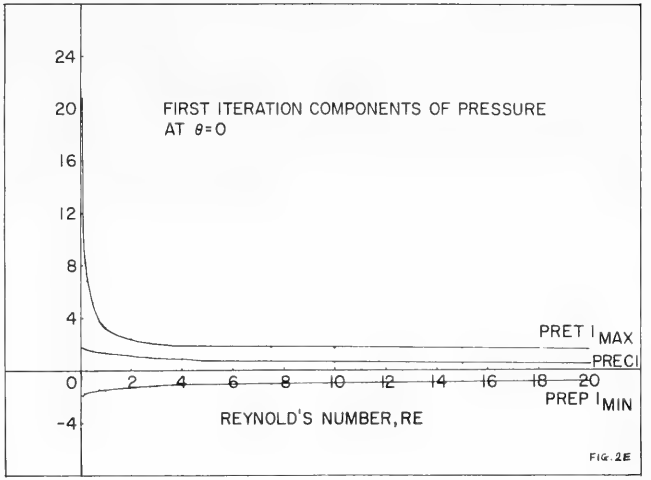

FIG. 2E

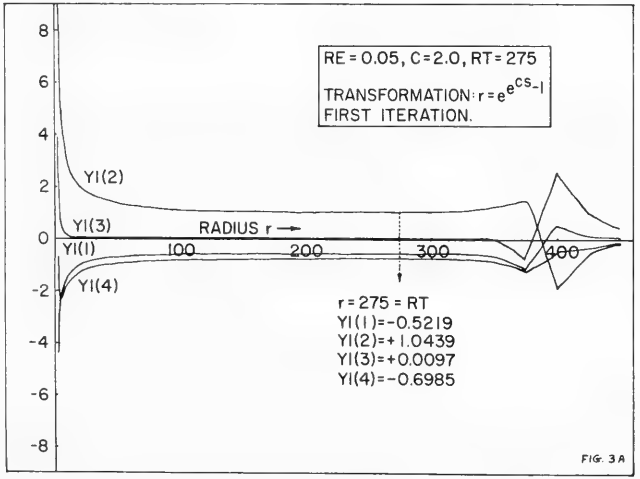

FIG. 3A

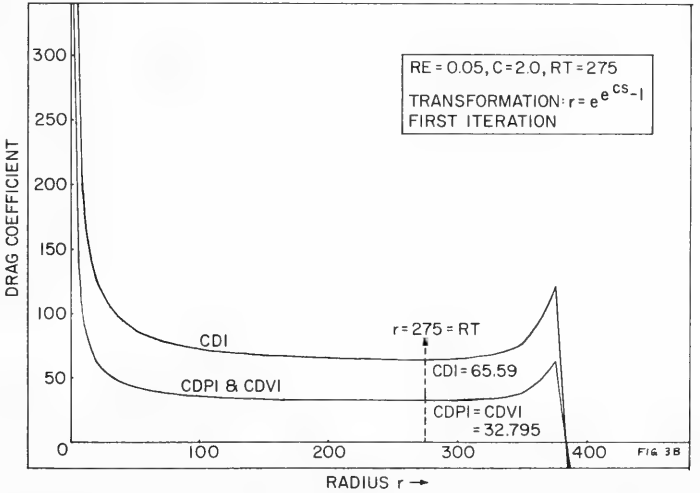

FIG. 3B

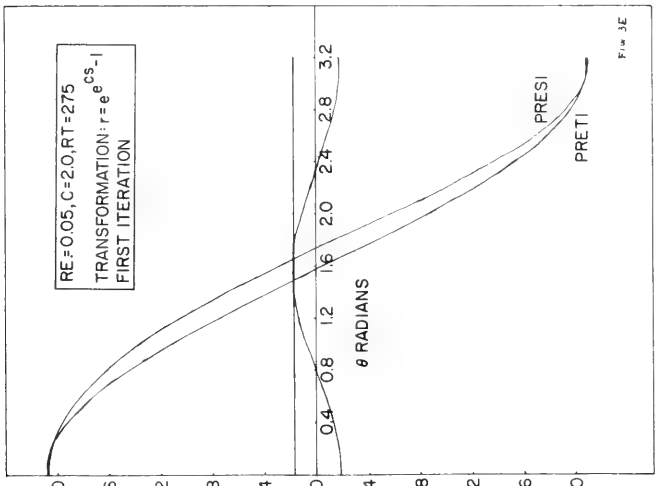
RE=0.05, C=2.0, RT=275
TRANSFORMATION: r = e^(cs) - 1
FIRST ITERATION
θ RADIANS
PRESI
PRETI
Fig 3E

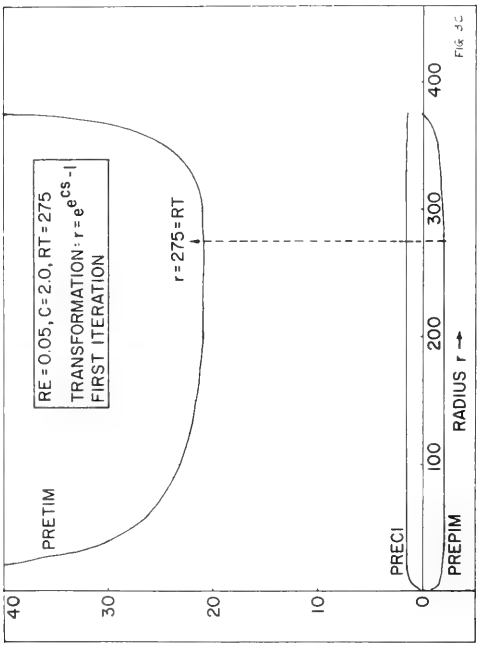
PRETIM
RE = 0.05, C = 2.0, RT = 275
TRANSFORMATION: r = e^(cs) - 1
FIRST ITERATION
r = 275 = RT
PRECI
PREPIM
RADIUS r
Fig 3C

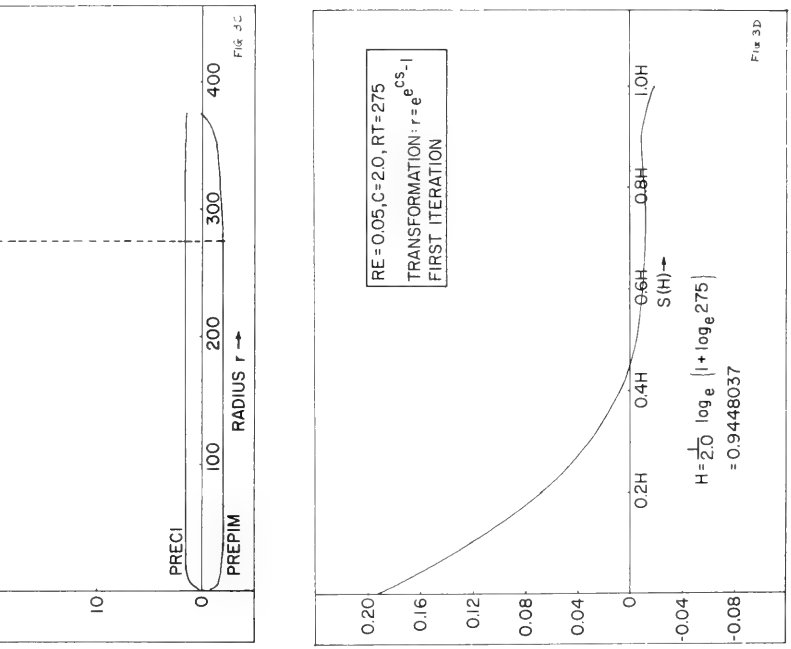
RE = 0.05, C = 2.0, RT = 275
TRANSFORMATION: r = e^(cs) - 1
FIRST ITERATION
ER
S(H)
H = 1/2.0 log_e |1 + log_e 275|
= 0.9448037
Fig 3D

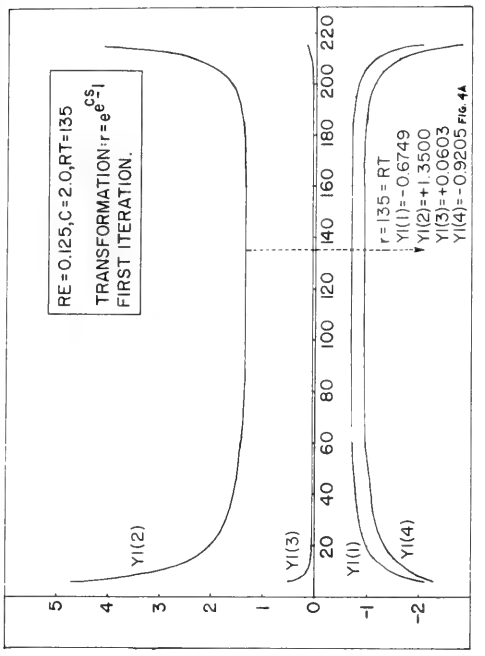
RE = 0.125, C = 2.0, RT = 135
TRANSFORMATION: $r = e^{cs} - 1$
FIRST ITERATION.
Y1(2)
Y1(3)
Y1(1)
Y1(4)
r = 135 = RT
Y1(1) = -0.6749
Y1(2) = +1.3500
Y1(3) = +0.0603
Y1(4) = -0.9205
FIG. 4A

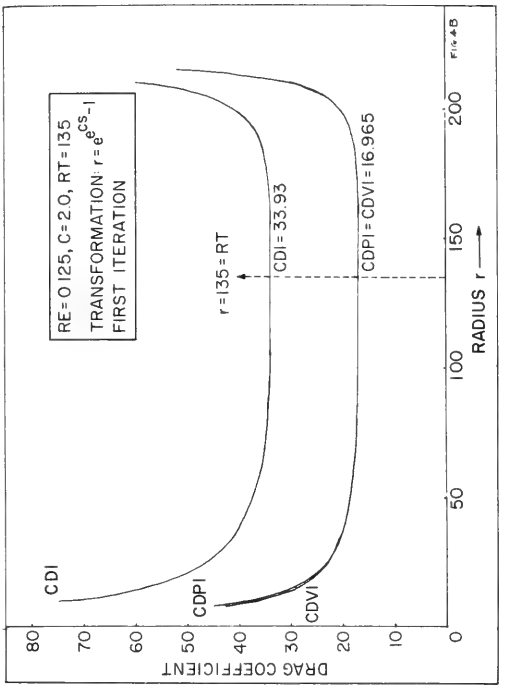
RE = 0.125, C = 2.0, RT = 135
TRANSFORMATION: $r = e^{cs} - 1$
FIRST ITERATION
CDI
CDPI
CDVI
r = 135 = RT
CDI = 33.93
CDPI = CDVI = 16.965
DRAG COEFFICIENT
RADIUS r
FIG. 4B

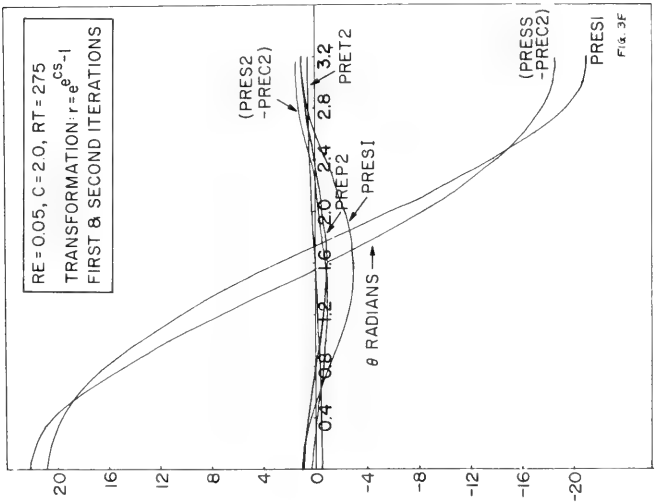
RE = 0.05, C = 2.0, RT = 275
TRANSFORMATION: $r = e^{cs} - 1$
FIRST & SECOND ITERATIONS
(PRES2 -PREC2)
PRET2
PREP2
PRES1
(PRESS -PREC2)
PRESI
θ RADIANS
FIG. 3F

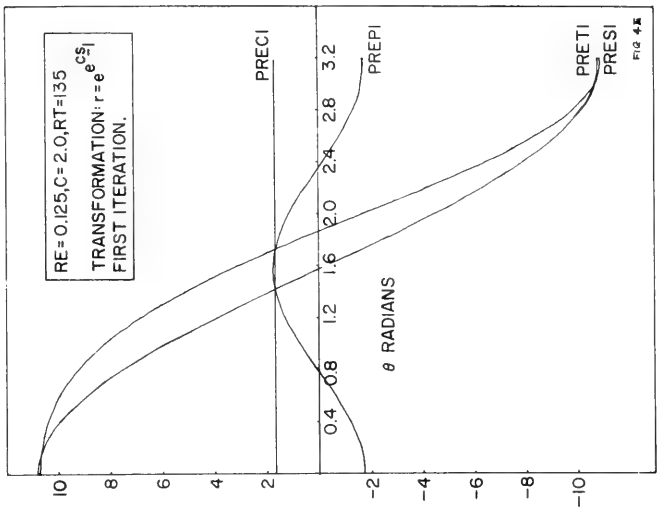
RE=0.125,C=2.0,RT=135
TRANSFORMATION: r=e^cs-1
FIRST ITERATION.
PRECI
PREPI
PRETI
PRESI
θ RADIANS
0.4
0.8
1.2
1.6
2.0
2.4
2.8
3.2
10
8
6
4
2
-2
-4
-6
-8
-10

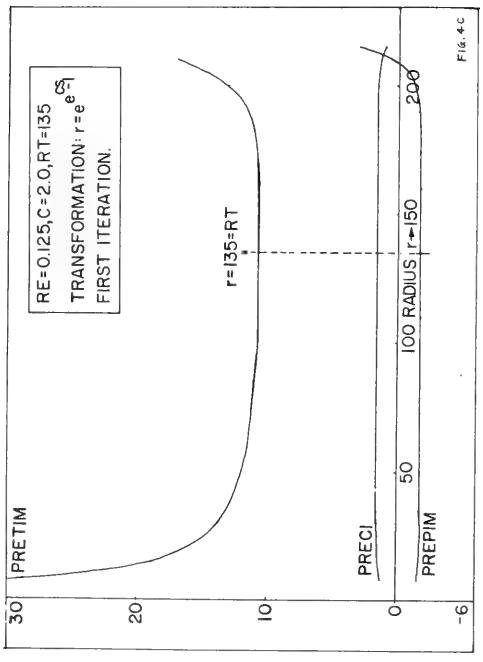
RE=0.125,C=2.0,RT=135
TRANSFORMATION: r=e^cs-1
FIRST ITERATION.
PRETIM
PRECI
PREPIM
r=135=RT
r=150
50
100 RADIUS
200
30
20
10
0
-6

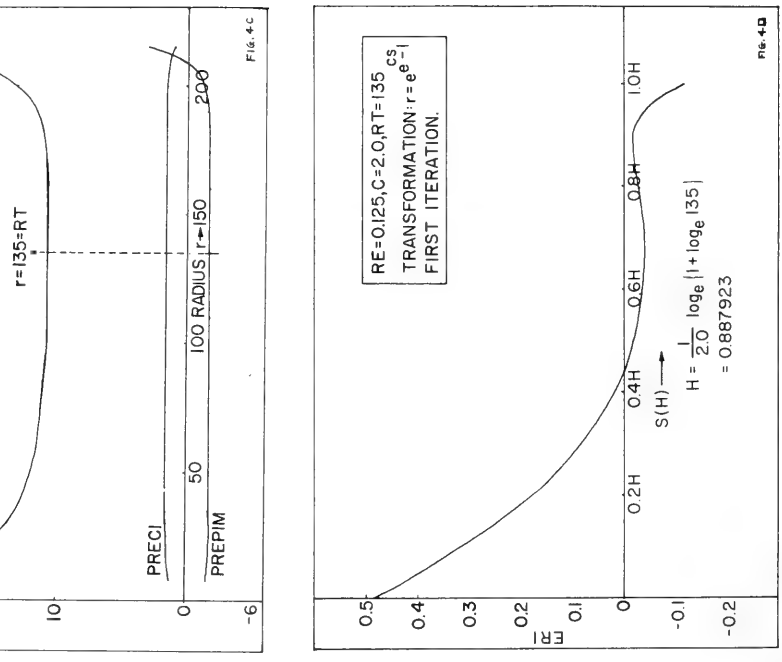
RE=0.125,C=2.0,RT=135
TRANSFORMATION: r=e^cs-1
FIRST ITERATION.
RI
S(H) ⟶
0.2H
0.4H
0.6H
0.8H
1.0H
H = 1/2.0 log_e |1+log_e 135|
= 0.887923
0.5
0.4
0.3
0.2
0.1
0
-0.1
-0.2

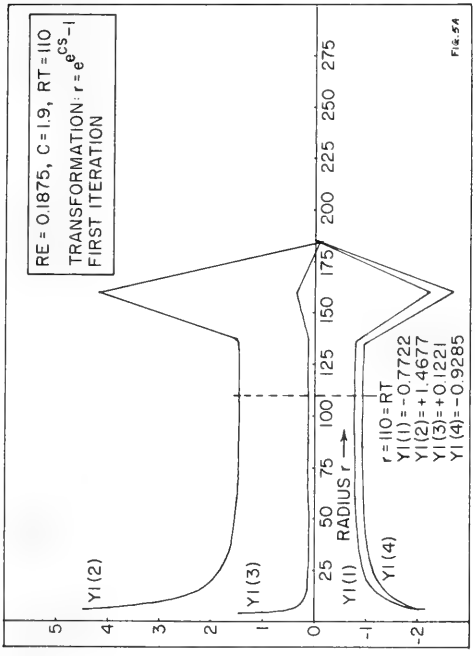
RE = 0.1875, C = 1.9, RT = 110
TRANSFORMATION: $r = e^{cs} - 1$
FIRST ITERATION
Y1(2)
Y1(3)
Y1(1)
Y1(4)
RADIUS r
r = 110 = RT
Y1(1) = -0.7722
Y1(2) = +1.4677
Y1(3) = +0.1221
Y1(4) = -0.9285
FIG 5A

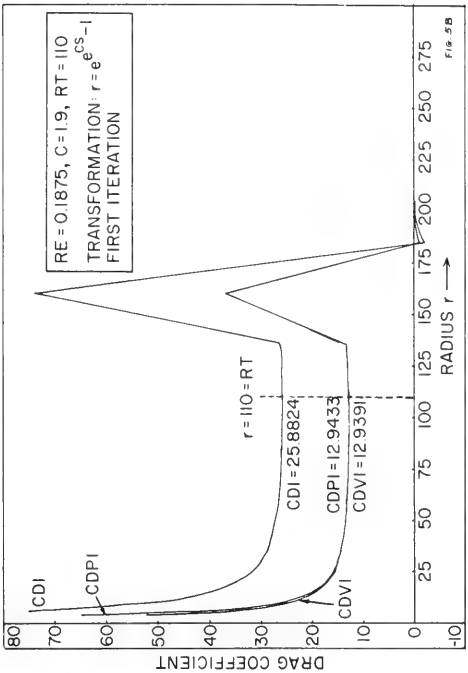
RE = 0.1875, C = 1.9, RT = 110
TRANSFORMATION: $r = e^{cs} - 1$
FIRST ITERATION
CDI
CDPI
CDVI
r = 110 = RT
CDI = 25.8824
CDPI = 12.9433
CDVI = 12.9391
DRAG COEFFICIENT
RADIUS r
FIG 5B

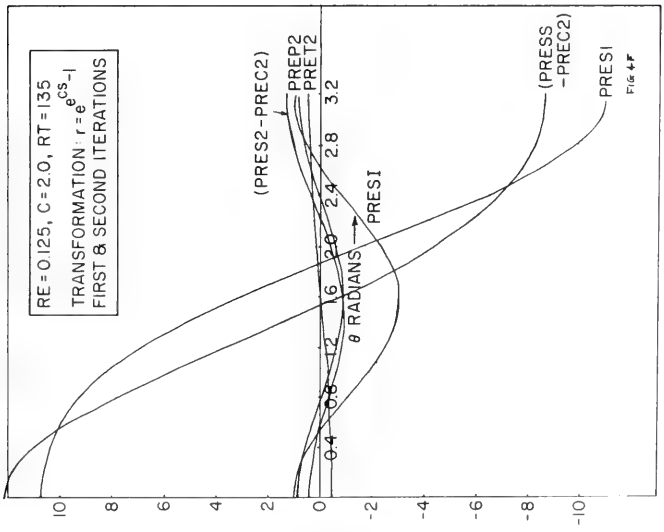
RE = 0.125, C = 2.0, RT = 135
TRANSFORMATION: $r = e^{cs} - 1$
FIRST & SECOND ITERATIONS
(PRES2-PREC2)
PREP2
PRET2
PRESI
θ RADIANS
(PRESS -PREC2)
PRESI
FIG 6A

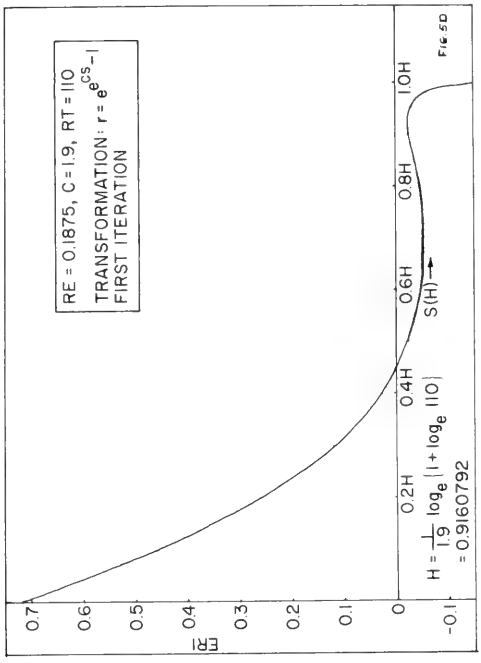
RE = 0.1875, C = 1.9, RT = 110
TRANSFORMATION: r = e^cs - 1
FIRST ITERATION
ER
0.7
0.6
0.5
0.4
0.3
0.2
0.1
0
-0.1
0.2H
0.4H
0.6H
0.8H
1.0H
S(H)
H = 1/1.9 log_e |1 + log_e 110|
= 0.9160792
FIG. 5D

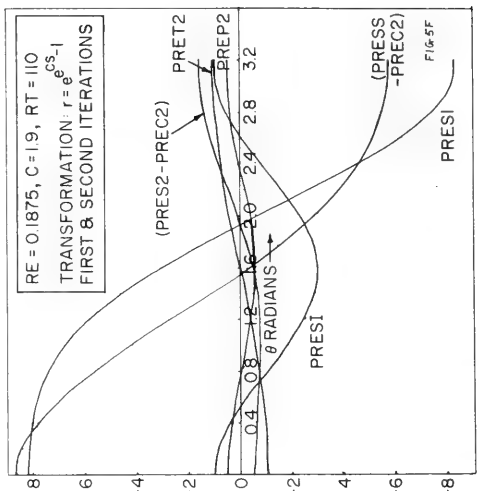
RE = 0.1875, C = 1.9, RT = 110
TRANSFORMATION: r = e^cs - 1
FIRST & SECOND ITERATIONS
(PRES2 - PREC2)
PRET2
PREP2
PRESI
θ RADIANS
(PRESS - PREC2)
FIG. 5F

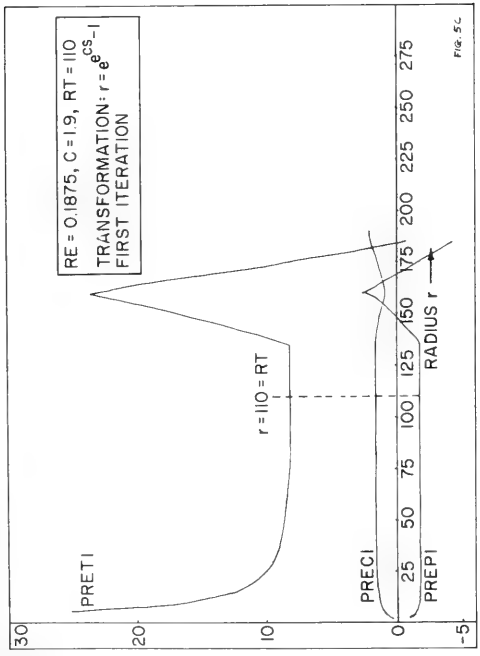
RE = 0.1875, C = 1.9, RT = 110
TRANSFORMATION: r = e^cs - 1
FIRST ITERATION
PRET1
r = 110 = RT
PRECI
PREP1
RADIUS r
FIG. 5C

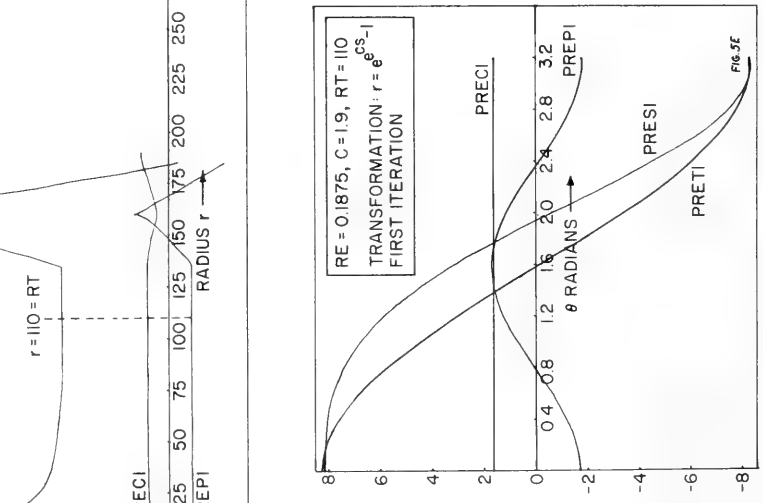
RE = 0.1875, C = 1.9, RT = 110
TRANSFORMATION: r = e^cs - 1
FIRST ITERATION
PRECI
PREP1
PRESI
PRET1
θ RADIANS
FIG. 5E

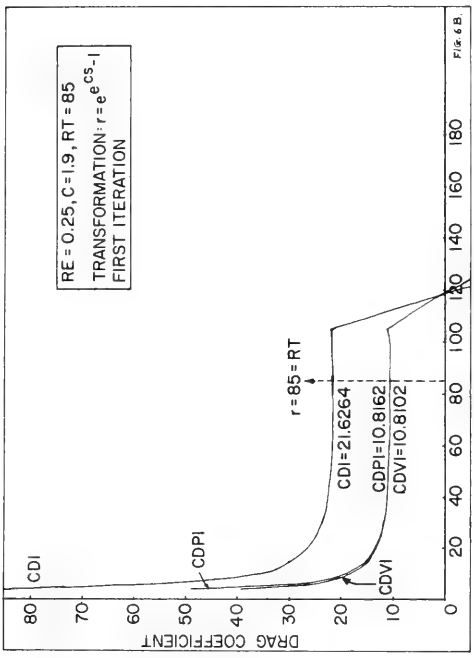
RE = 0.25, C = 1.9, RT = 85
TRANSFORMATION: r = e^(e^cs − 1)
FIRST ITERATION
CDI
CDPI
CDVI
CDI=21.6264
CDPI=10.8162
CDVI=10.8102
r = 85 = RT
DRAG COEFFICIENT
RADIUS r →
Fig. 6B.

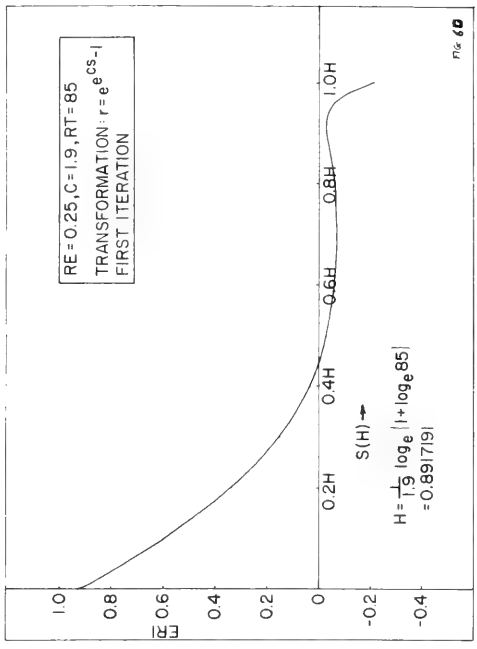
RE = 0.25, C = 1.9, RT = 85
TRANSFORMATION: r = e^(e^cs − 1)
FIRST ITERATION
ER
S(H) →
0.2H
0.4H
0.6H
0.8H
1.0H
H = 1/1.9 log_e |1 + log_e 85|
= 0.891719
Fig. 6C.

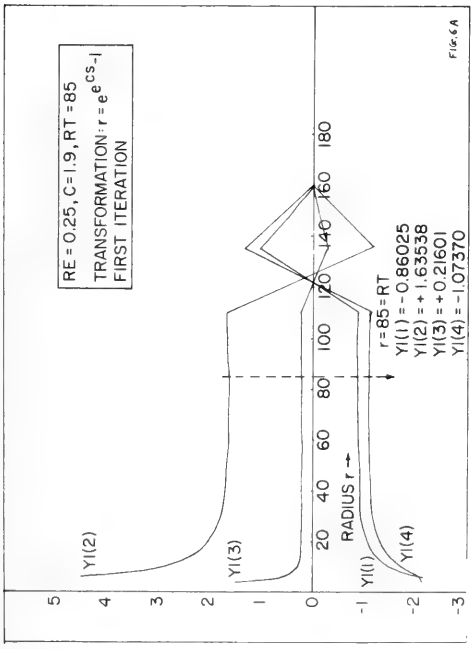
RE = 0.25, C = 1.9, RT = 85
TRANSFORMATION: r = e^(e^cs − 1)
FIRST ITERATION
Y1(2)
Y1(3)
Y1(1)
Y1(4)
r = 85 = RT
Y1(1) = −0.86025
Y1(2) = +1.63538
Y1(3) = +0.21601
Y1(4) = −1.07370
RADIUS r →
Fig. 6A

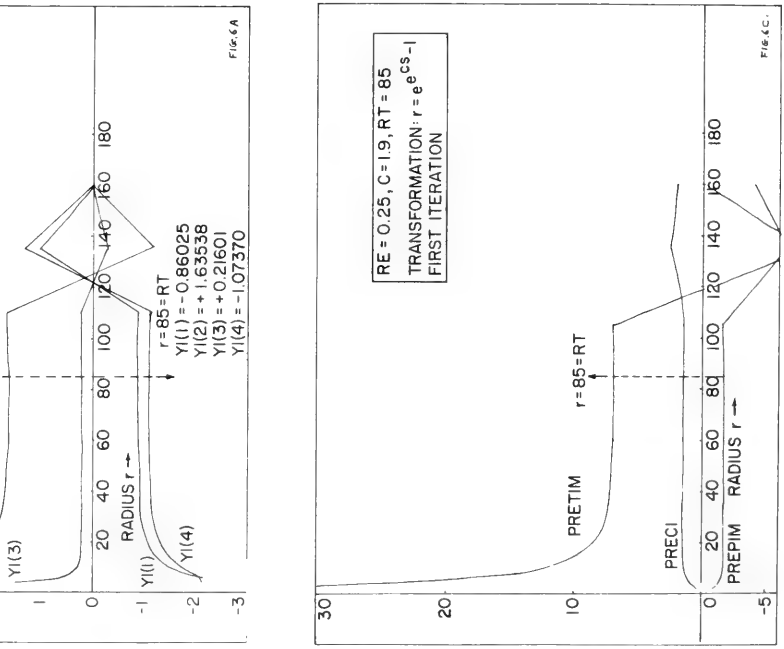
RE = 0.25, C = 1.9, RT = 85
TRANSFORMATION: r = e^(e^cs − 1)
FIRST ITERATION
PRETIM
PRECI
r = 85 = RT
PREPIM
RADIUS r →
Fig. 6C.

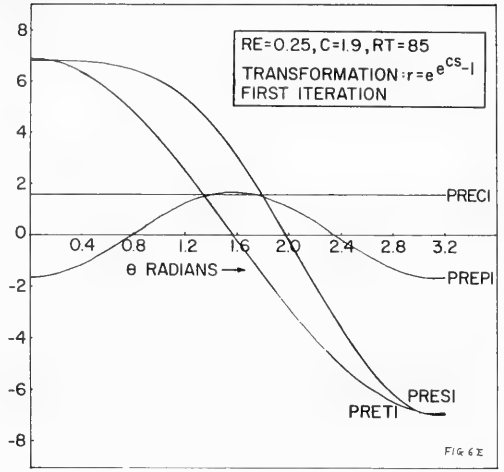
RE=0.25, C=1.9, RT=85
TRANSFORMATION: $r=e^{e^{CS}-1}$
FIRST ITERATION
PRECI
PREPI
PRESI
PRETI
θ RADIANS
FIG. 6E

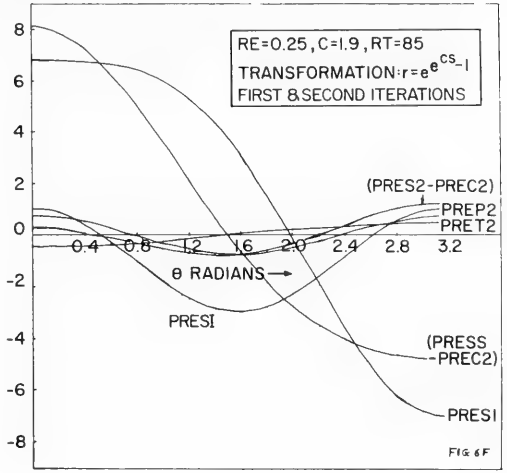
RE=0.25, C=1.9, RT=85
TRANSFORMATION: $r=e^{e^{CS}-1}$
FIRST & SECOND ITERATIONS
(PRES2-PREC2)
PREP2
PRET2
θ RADIANS
PRESI
(PRESS -PREC2)
PRESI
FIG. 6F

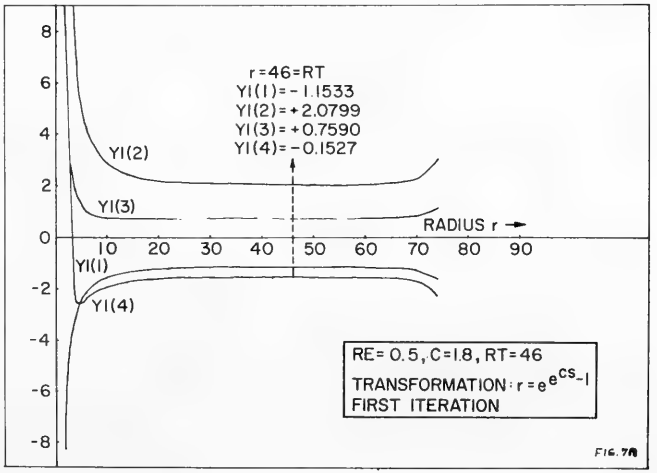
r=46=RT
YI(1)=-1.1533
YI(2)=+2.0799
YI(3)=+0.7590
YI(4)=-0.1527
YI(2)
YI(3)
YI(1)
YI(4)
RADIUS r
RE=0.5, C=1.8, RT=46
TRANSFORMATION: $r=e^{e^{CS}-1}$
FIRST ITERATION
FIG. 7A

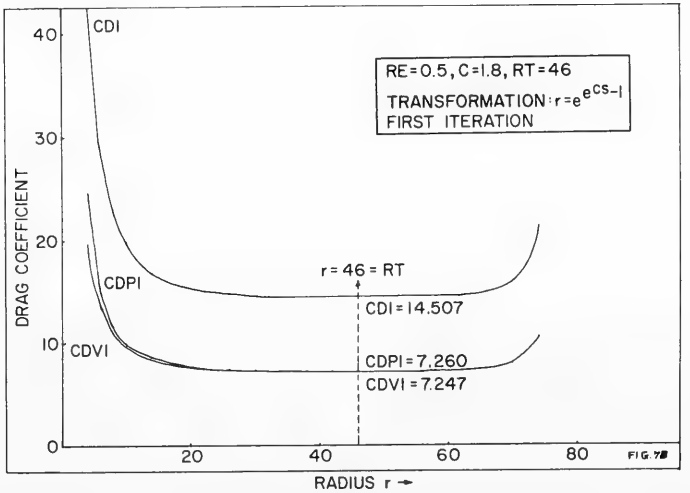
CDI
RE=0.5, C=1.8, RT=46
TRANSFORMATION: $r=e^{e^{CS}-1}$
FIRST ITERATION
DRAG COEFFICIENT
CDPI
CDVI
r=46=RT
CDI=14.507
CDPI=7.260
CDVI=7.247
RADIUS r
FIG. 7B

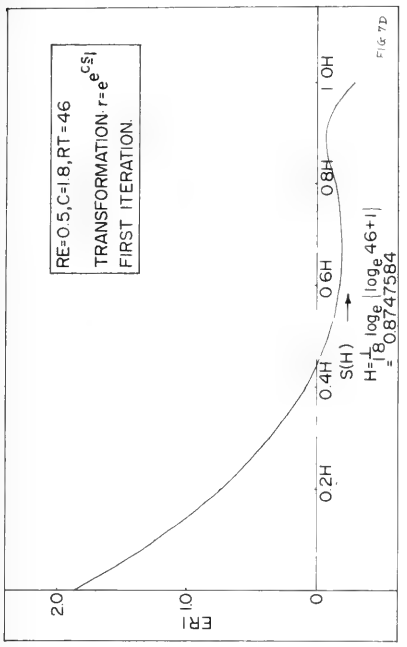

FIG 7D

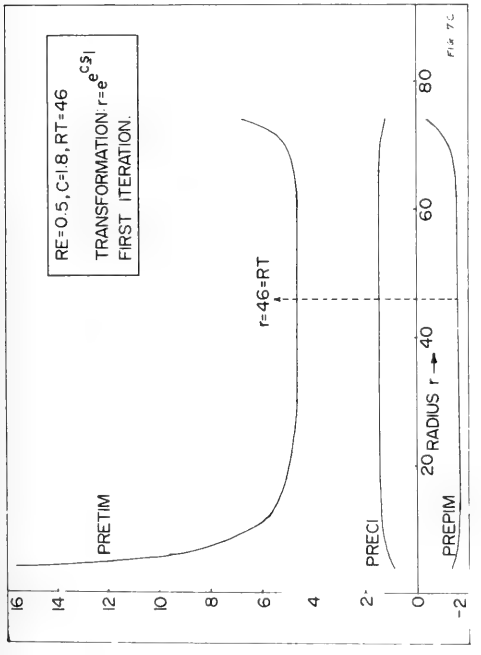

FIG 7C

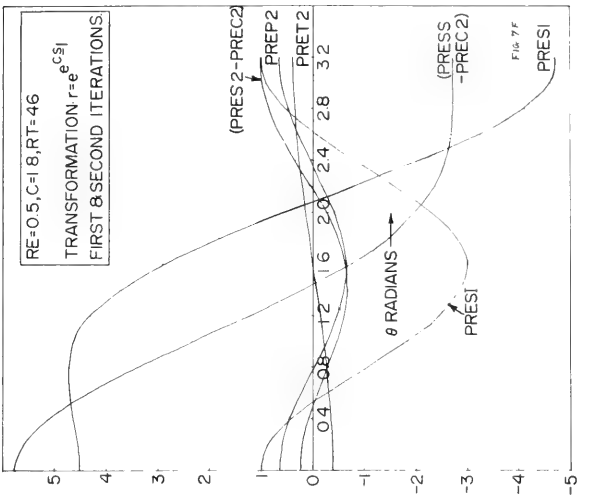

FIG 7F

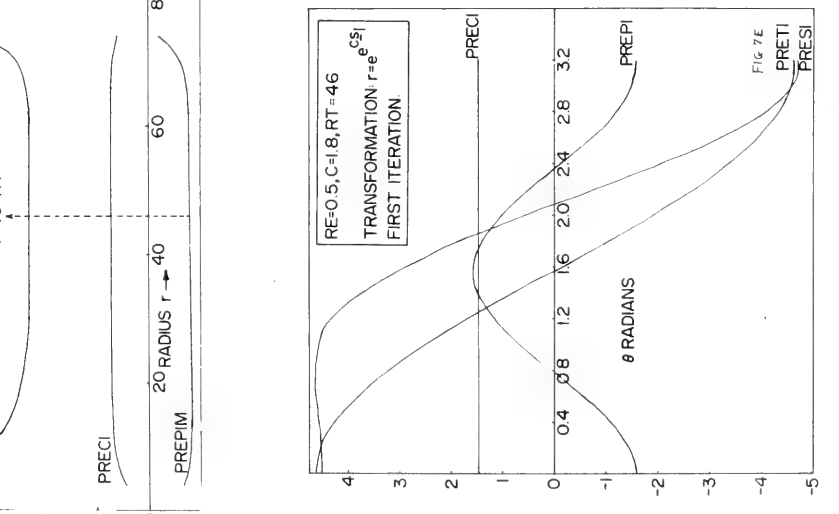

FIG 7E

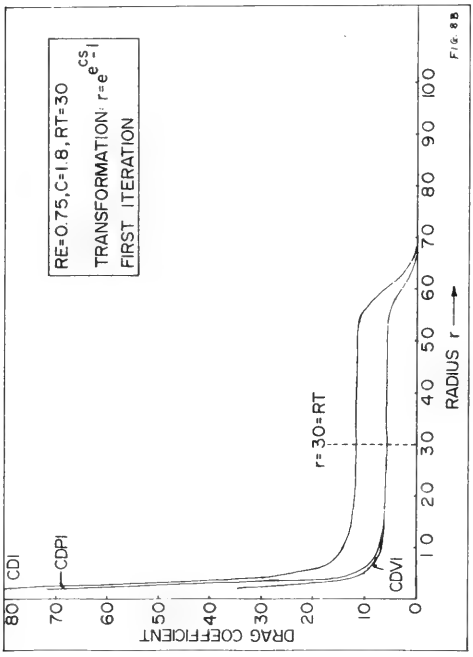
RE=0.75, C=1.8, RT=30
TRANSFORMATION: r=e^cs-1
FIRST ITERATION
CDI
CDPI
CDVI
r=30=RT
DRAG COEFFICIENT
RADIUS r
FIG. 8B

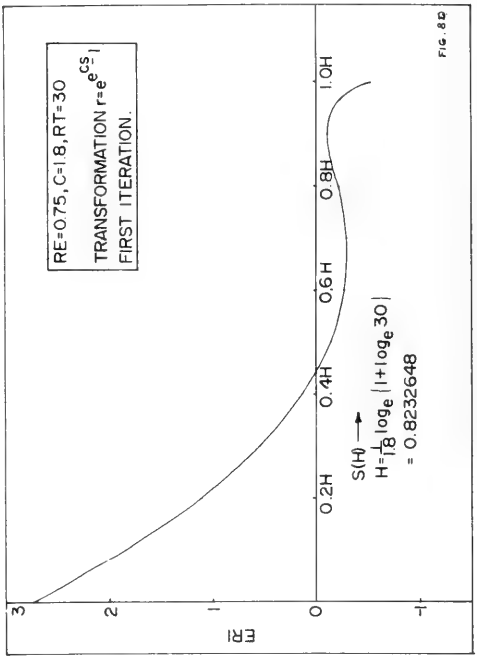
RE=0.75, C=1.8, RT=30
TRANSFORMATION r=e^cs-1
FIRST ITERATION.
ER
S(H) →
H=1/1.8 log_e |1+log_e 30|
= 0.8232648
FIG. 8D

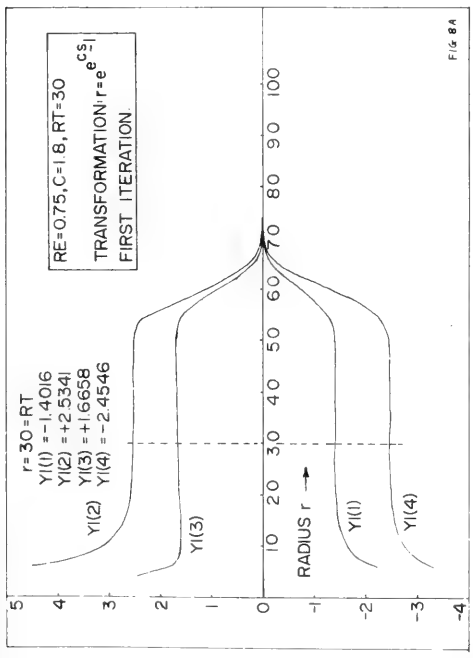
r=30=RT
Y1(1) =-1.4016
Y1(2) =+2.5341
Y1(3) =+1.6658
Y1(4) =-2.4546
RE=0.75, C=1.8, RT=30
TRANSFORMATION: r=e^cs-1
FIRST ITERATION
Y1(3)
Y1(1)
Y1(4)
RADIUS r
FIG. 8A

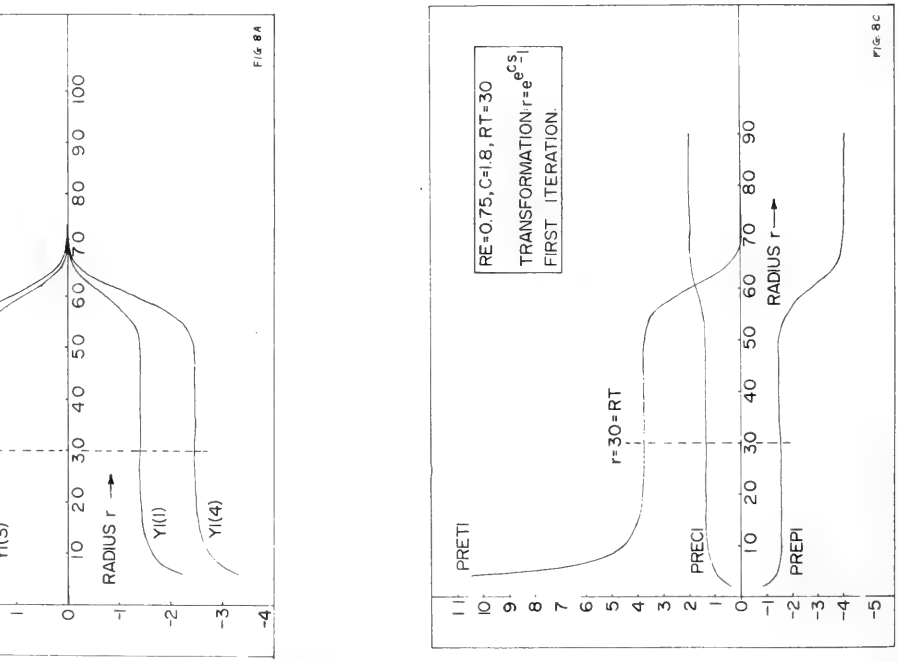
RE=0.75, C=1.8, RT=30
TRANSFORMATION r=e^cs-1
FIRST ITERATION.
PRETI
PRECI
PREPI
r=30=RT
RADIUS r
FIG. 8C

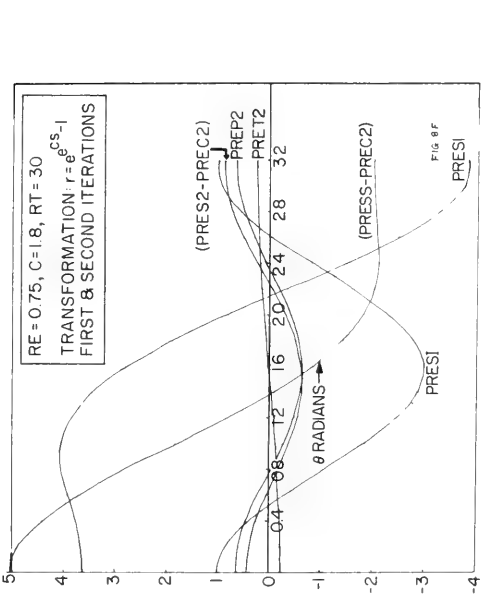
RE = 0.75, C = 1.8, RT = 30
TRANSFORMATION: r = e^(cs-1)
FIRST & SECOND ITERATIONS
(PRES2-PREC2)
PREP2
PRET2
(PRESS-PREC2)
PRESI
θ RADIANS
Fig 8F

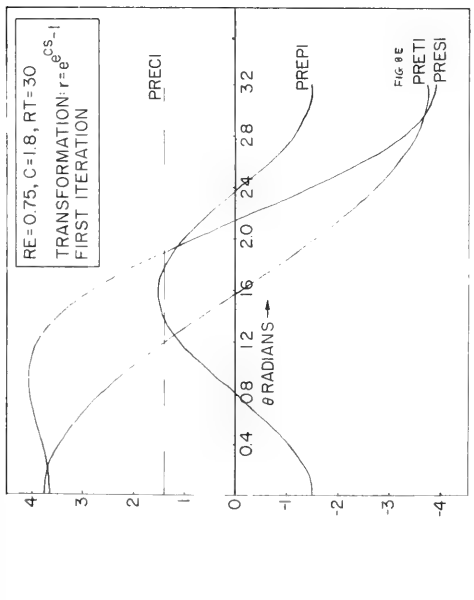
RE = 0.75, C = 1.8, RT = 30
TRANSFORMATION: r = e^(cs-1)
FIRST ITERATION
PRECI
PREPI
PRETI
PRESI
θ RADIANS
Fig 8E

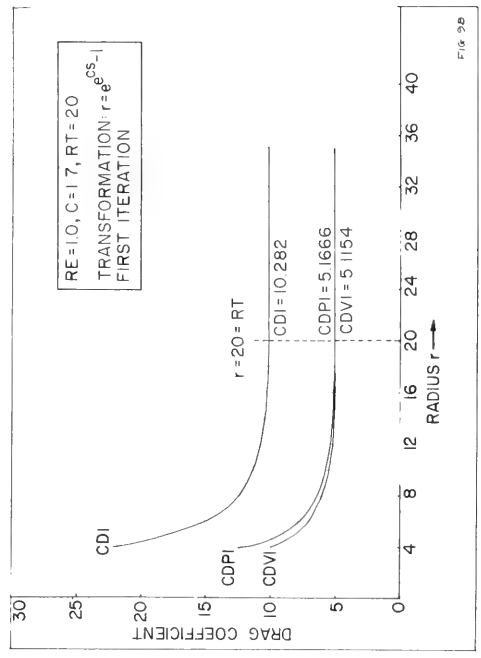
RE = 1.0, C = 1.7, RT = 20
TRANSFORMATION: r = e^(cs-1)
FIRST ITERATION
CDI
CDPI
CDVI
r = 20 = RT
CDI = 10.282
CDPI = 5.1666
CDVI = 5.1154
DRAG COEFFICIENT
RADIUS r
Fig 9B

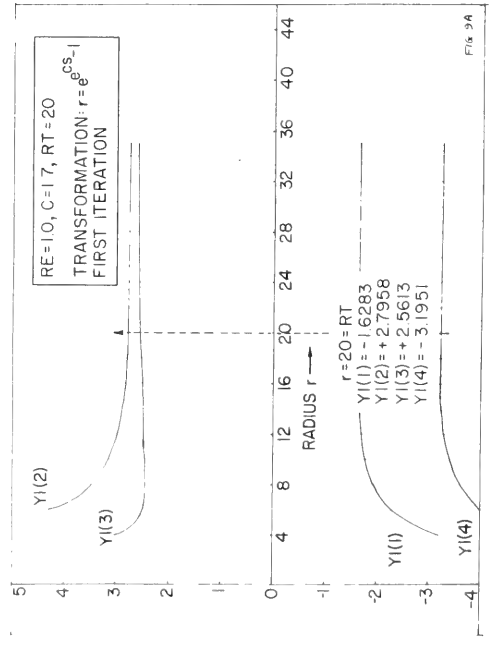
RE = 1.0, C = 1.7, RT = 20
TRANSFORMATION: r = e^(cs-1)
FIRST ITERATION
Y1(1)
Y1(2)
Y1(3)
Y1(4)
r = 20 = RT
Y1(1) = - 1.6283
Y1(2) = + 2.7958
Y1(3) = + 2.5613
Y1(4) = - 3.1951
RADIUS r
Fig 9A

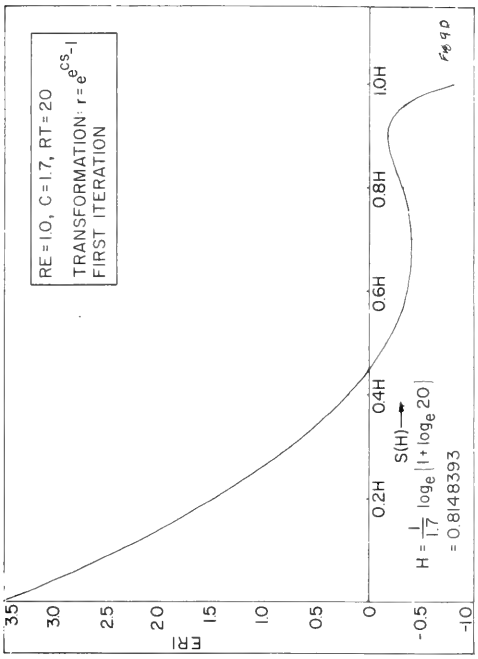
RE = 1.0, C = 1.7, RT = 20
TRANSFORMATION: r = e^cs - 1
FIRST ITERATION
RE
S(H) →
0.2H
0.4H
0.6H
0.8H
1.0H
H = 1/1.7 log_e |1 + log_e 20|
= 0.8148393
Fig 9D

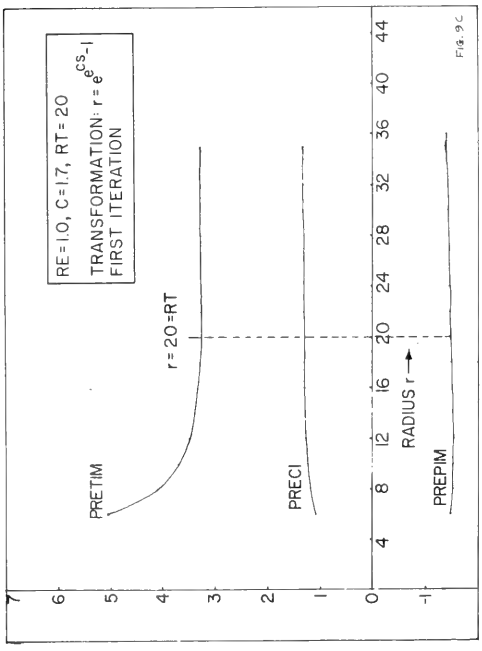
RE = 1.0, C = 1.7, RT = 20
TRANSFORMATION: r = e^cs - 1
FIRST ITERATION
PRETIM
r = 20 = RT
PRECI
PREPIM
RADIUS r →
Fig 9C

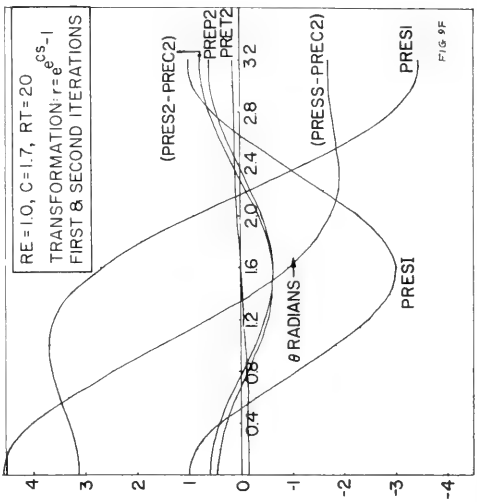
RE = 1.0, C = 1.7, RT = 20
TRANSFORMATION: r = e^cs - 1
FIRST & SECOND ITERATIONS
(PRES2 - PREC2)
PREP2
PRET2
(PRESS - PREC2)
PRESI
θ RADIANS →
Fig 9F

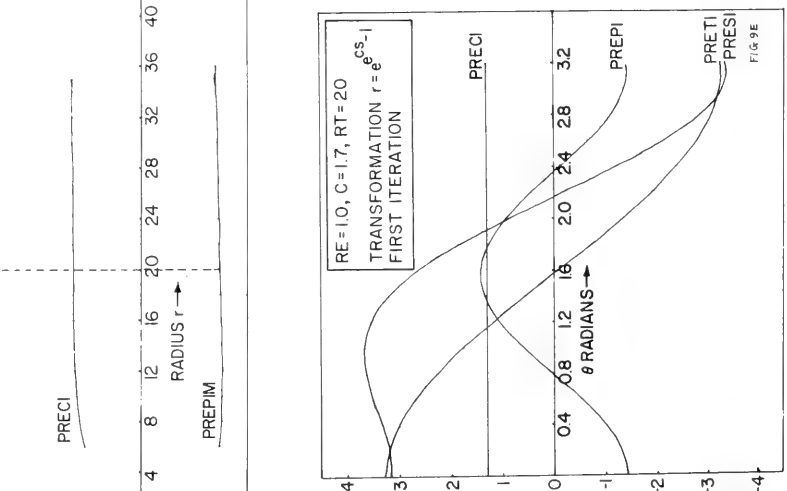
RE = 1.0, C = 1.7, RT = 20
TRANSFORMATION r = e^cs - 1
FIRST ITERATION
PRECI
PREPI
PRETI
PRESI
θ RADIANS →
Fig 9E

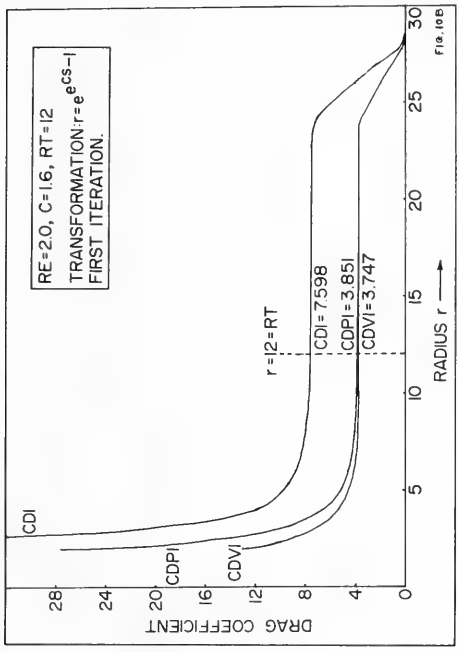
RE=2.0, C=1.6, RT=12
TRANSFORMATION: $r=e^{cs-1}$
FIRST ITERATION.
CDI
CDPI
CDVI
r=12=RT
CDI=7.598
CDPI=3.851
CDVI=3.747
DRAG COEFFICIENT
RADIUS r
Fig. 10B

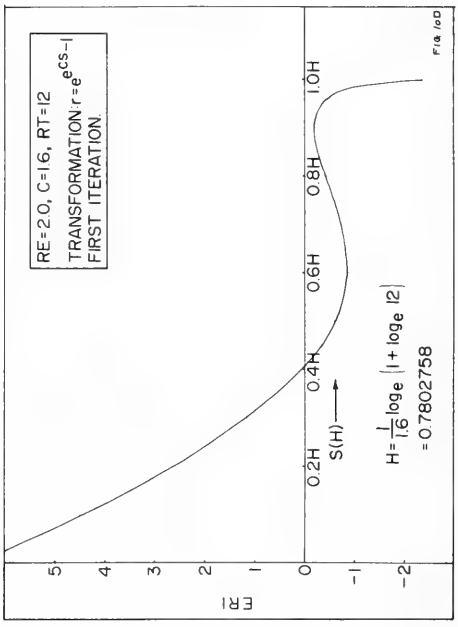
RE=2.0, C=1.6, RT=12
TRANSFORMATION: $r=e^{cs-1}$
FIRST ITERATION.
ER
S(H)
0.2H
0.4H
0.6H
0.8H
1.0H
$H=\frac{1}{1.6}\log_e|1+\log_e 12|$
$=0.7802758$
Fig. 10D

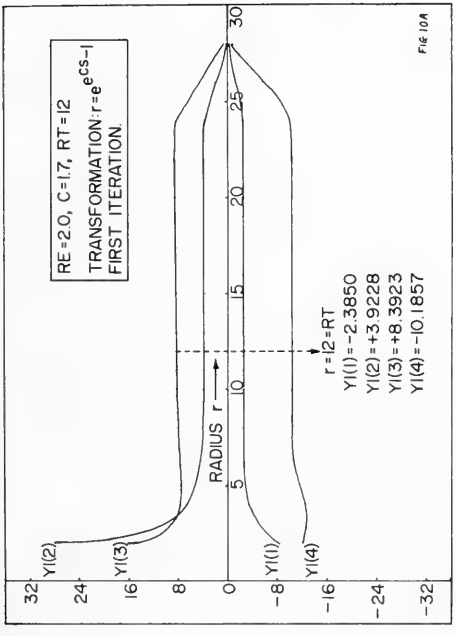
RE=2.0, C=1.7, RT=12
TRANSFORMATION: $r=e^{cs-1}$
FIRST ITERATION.
Y1(2)
Y1(3)
Y1(1)
Y1(4)
RADIUS r
r=12=RT
Y1(1)=-2.3850
Y1(2)=+3.9228
Y1(3)=+8.3923
Y1(4)=-10.1857
Fig. 10A

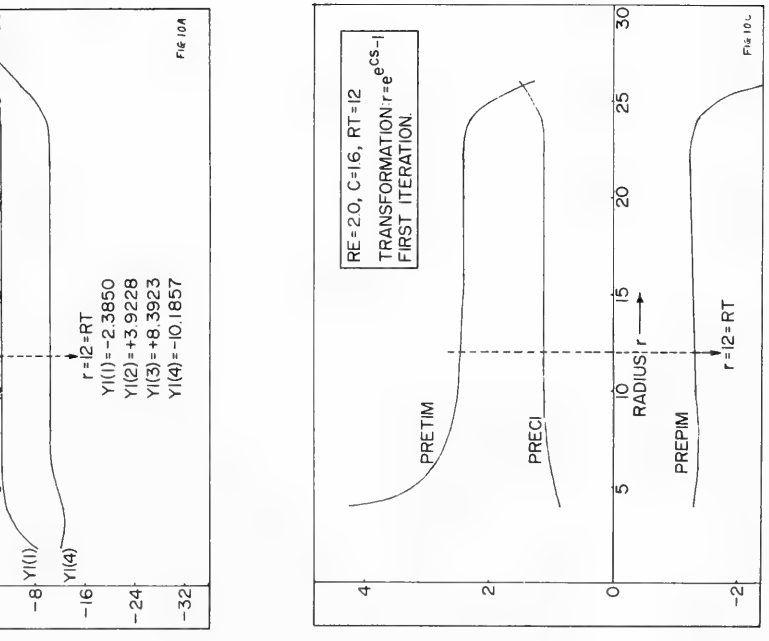
RE=2.0, C=1.6, RT=12
TRANSFORMATION: $r=e^{cs-1}$
FIRST ITERATION.
PRETIM
PRECI
PREPIM
RADIUS r
r=12=RT
Fig. 10C

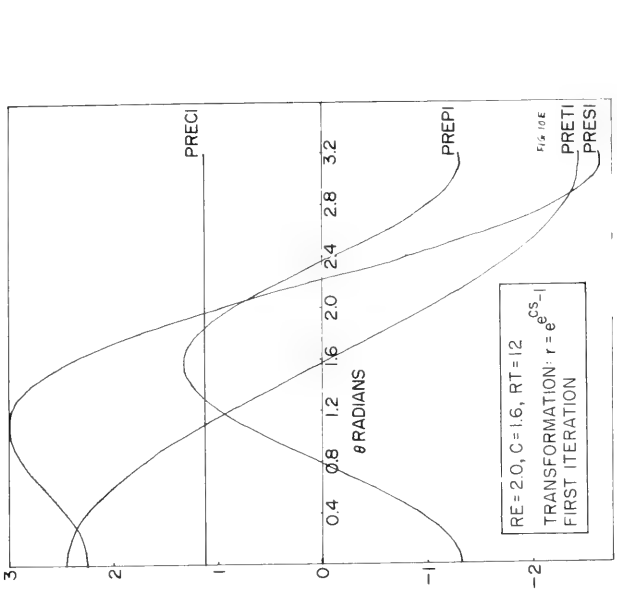
PRECI
PREPI
PRETI
PRESI
θ RADIANS
RE = 2.0, C = 1.6, RT = 12
TRANSFORMATION: r = e^(CS-1)
FIRST ITERATION

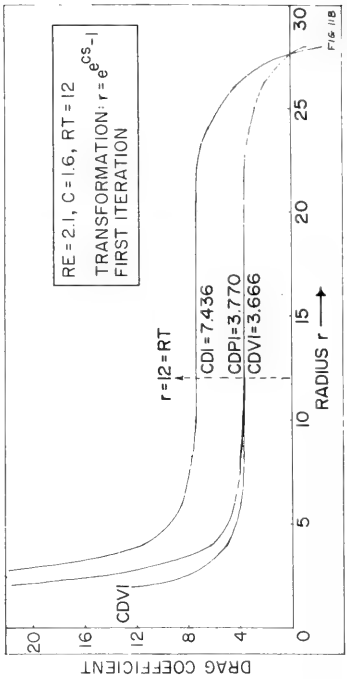
RE = 2.1, C = 1.6, RT = 12
TRANSFORMATION: r = e^(CS-1)
FIRST ITERATION
r = 12 = RT
CDI = 7.436
CDPI = 3.770
CDVI = 3.666
CDVI
DRAG COEFFICIENT
RADIUS r

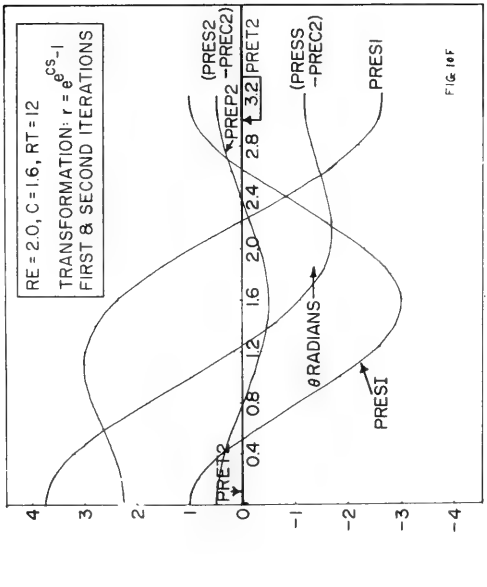
RE = 2.0, C = 1.6, RT = 12
TRANSFORMATION: r = e^(CS-1)
FIRST & SECOND ITERATIONS
(PRES2 -PREC2)
PREP2
(PRESS -PREC2)
PRET2
PRESI
θ RADIANS

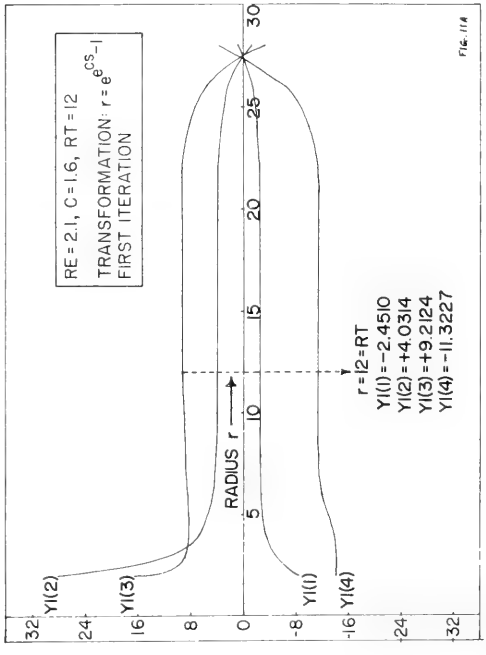
RE = 2.1, C = 1.6, RT = 12
TRANSFORMATION: r = e^(CS-1)
FIRST ITERATION
RADIUS r
r = 12 = RT
Y1(1) = -2.4510
Y1(2) = +4.0314
Y1(3) = +9.2124
Y1(4) = -11.3227

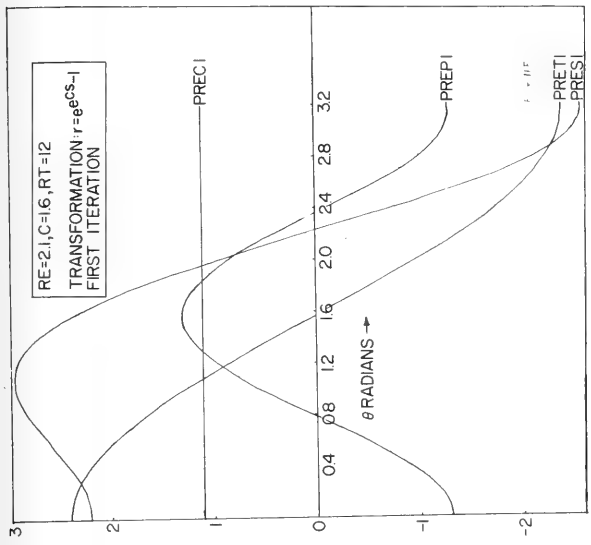
RE=2.1, C=1.6, RT=12
TRANSFORMATION r=e^{cs}-1
FIRST ITERATION
PRECI
PREPI
PRETI
PRESI
θ RADIANS →
04 08 12 16 20 24 28 32
3 2 1 0 -1 -2

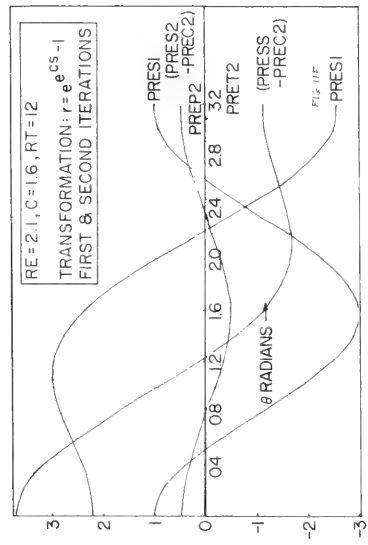
RE=2.1, C=1.6, RT=12
TRANSFORMATION: r=e^{cs}-1
FIRST & SECOND ITERATIONS
PRESI
(PRES2 -PREC2)
PREP2 -PREC2)
PRET2
(PRESS -PREC2)
PRESI
θ RADIANS →
04 08 12 16 20 24 28 32
3 2 1 0 -1 -2 -3

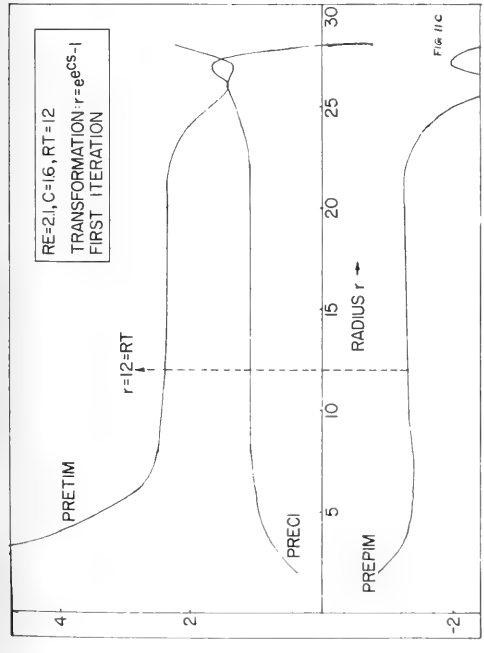
RE=2.1, C=16, RT=12
TRANSFORMATION: r=e^{cs}-1
FIRST ITERATION
PRETIM
PRECI
PREPIM
r=12=RT
RADIUS r →
5 10 15 20 25 30
4 2 -2

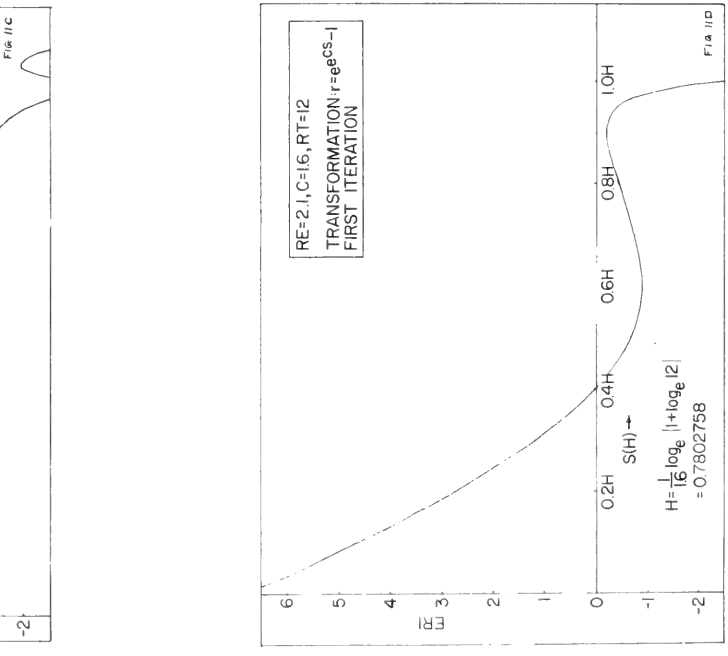
RE=2.1, C=16, RT=12
TRANSFORMATION: r=e^{cs}-1
FIRST ITERATION
E/R
S(H) →
0.2H 0.4H 0.6H 0.8H 1.0H
H=1/16 log_e |1+log_e 12|
=0.7802758
6 5 4 3 2 1 0 -1 -2

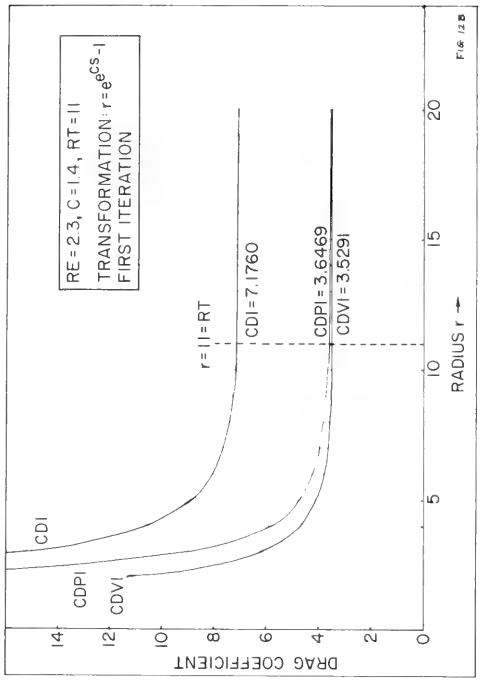

Fig. 12B

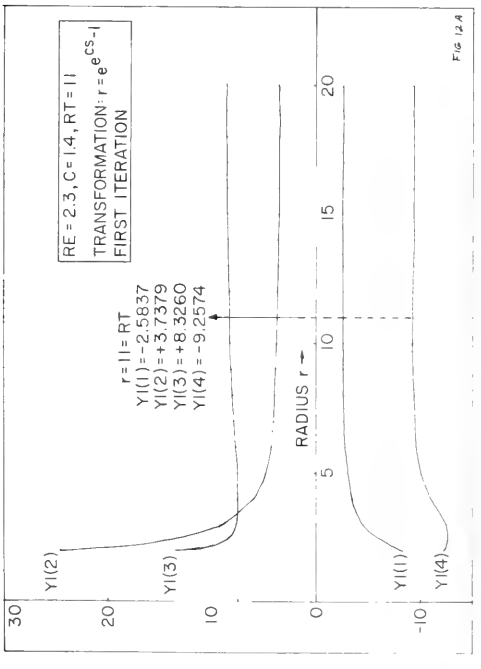

Fig. 12A

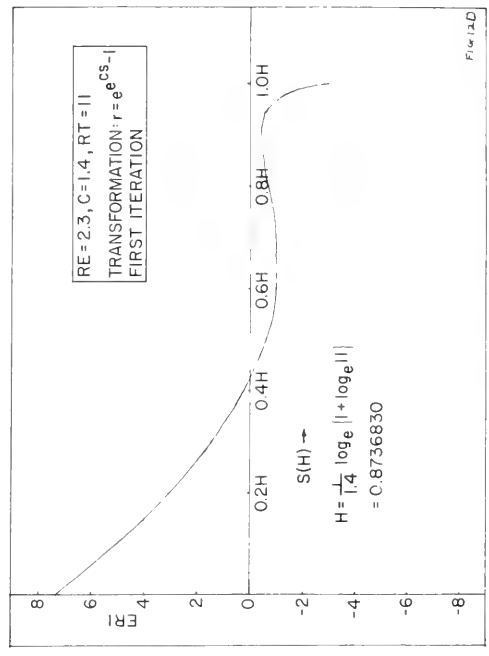

Fig. 12D

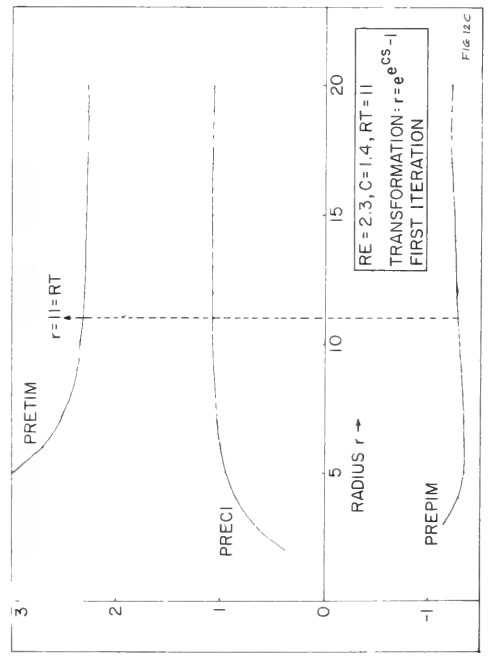

Fig. 12C

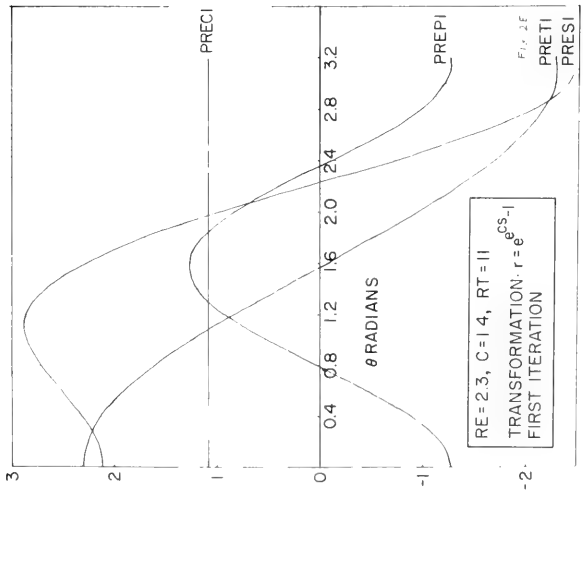
RE = 2 3, C = 1 4, RT = 11
TRANSFORMATION r = e^(CS-1)
FIRST ITERATION
PRECI
PREPI
PRETI
PRESI
θ RADIANS
0.4 0.8 1.2 1.6 2.0 2.4 2.8 3.2

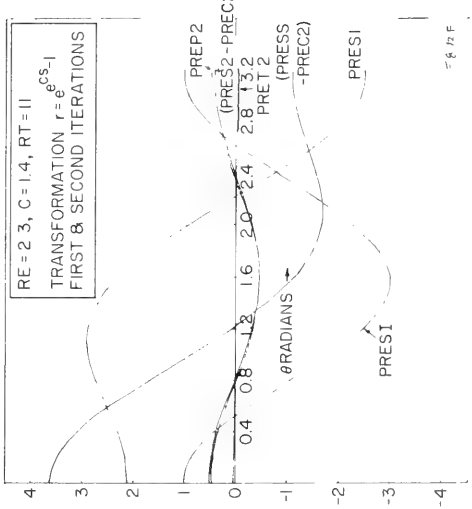
RE = 2 3, C = 1 4, RT = 11
TRANSFORMATION r = e^(CS-1)
FIRST & SECOND ITERATIONS
PREP2
(PRES2 - PREC2)
PRET 2
(PRESS - PREC2)
PRESI
θ RADIANS
0.4 0.8 1.2 1.6 2.0 2.4 2.8 3.2

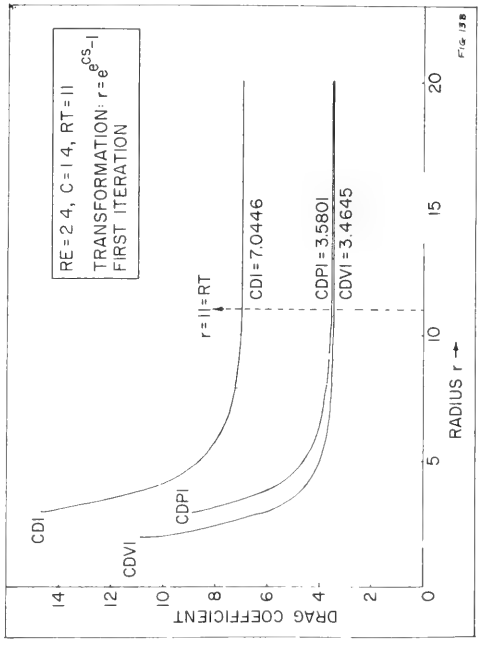
RE = 2 4, C = 1 4, RT = 11
TRANSFORMATION r = e^(CS-1)
FIRST ITERATION
CDI
CDVI
CDPI
r = 11 = RT
CDI = 7.0446
CDPI = 3.5801
CDVI = 3.4645
DRAG COEFFICIENT
RADIUS r →

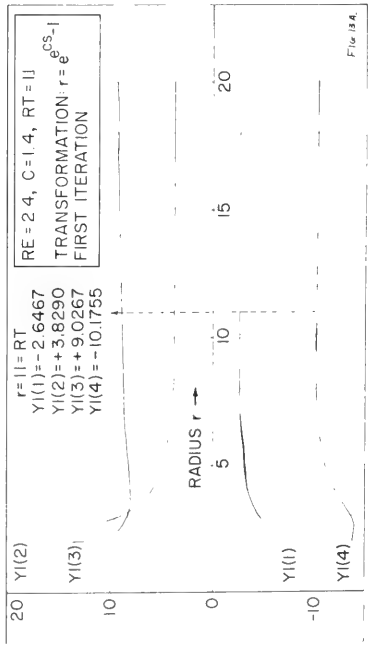
r = 11 = RT
Y1(1) = - 2.6467
Y1(2) = + 3.8290
Y1(3) = + 9.0267
Y1(4) = - 10.1755
RE = 2 4, C = 1 4, RT = 11
TRANSFORMATION r = e^(CS-1)
FIRST ITERATION
Y1(2)
Y1(3)
Y1(1)
Y1(4)
RADIUS r →

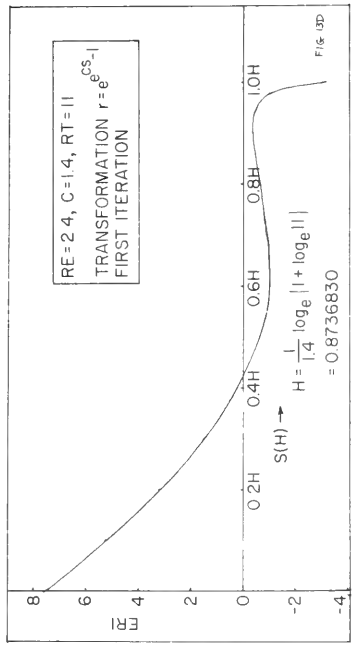

Fig. 13D

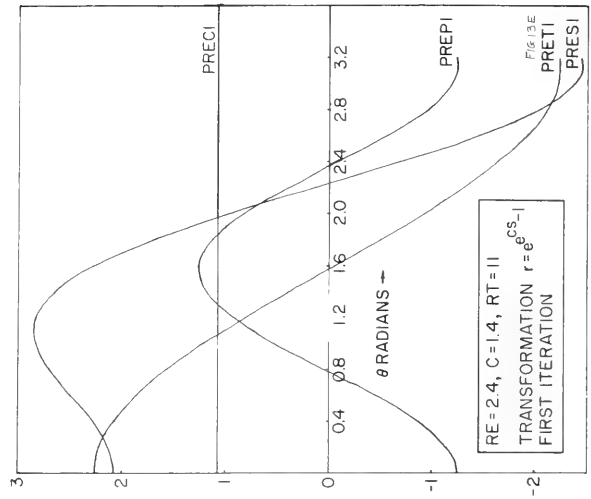

Fig. 13E

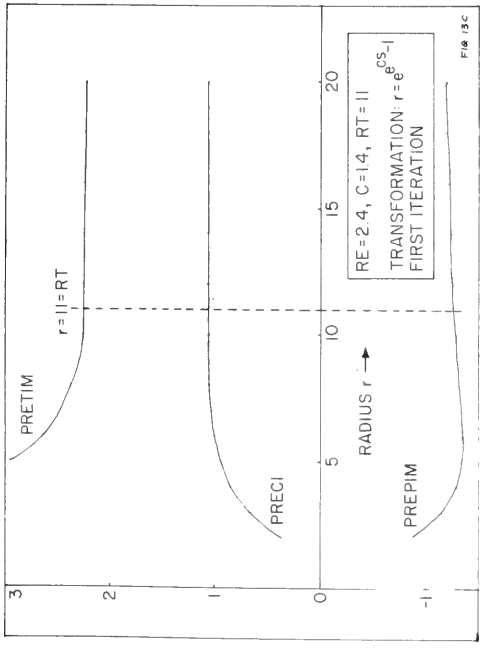

Fig. 13C

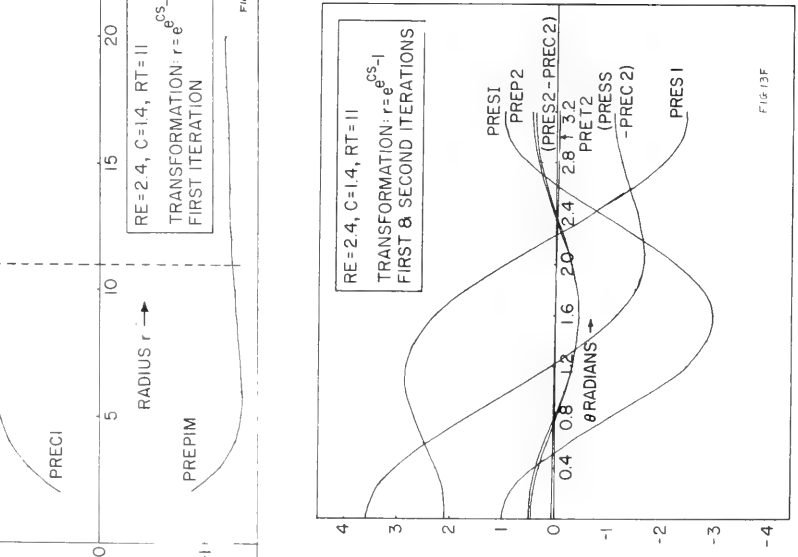

Fig. 13F

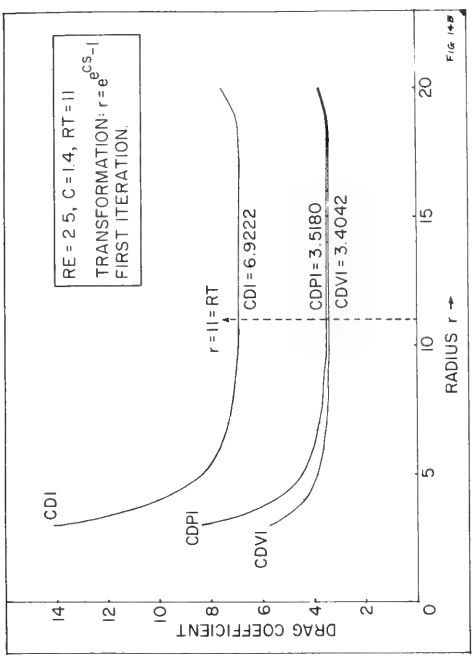
RE = 2.5, C = 1.4, RT = 11
TRANSFORMATION: r = e^(cs-1)
FIRST ITERATION
CDI
CDPI
CDVI
r = 11 = RT
CDI = 6.9222
CDPI = 3.5180
CDVI = 3.4042
DRAG COEFFICIENT
RADIUS r →
FIG. 14B

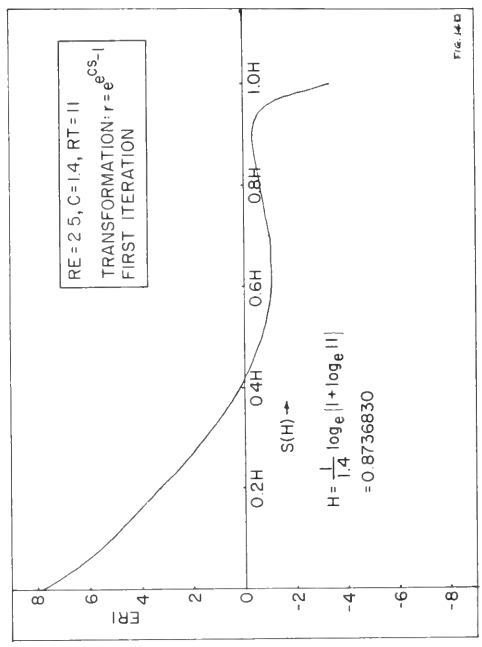
RE = 2.5, C = 1.4, RT = 11
TRANSFORMATION: r = e^(cs-1)
FIRST ITERATION
ER
S(H) →
0.2H
0.4H
0.6H
0.8H
1.0H
H = 1/1.4 log_e|1 + log_e 11|
= 0.8736830
FIG. 14D

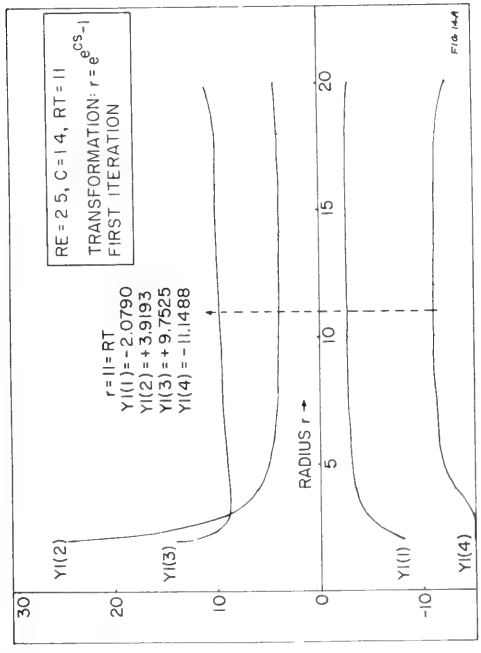
RE = 2.5, C = 1.4, RT = 11
TRANSFORMATION: r = e^(cs-1)
FIRST ITERATION
r = 11 = RT
Y1(1) = -2.0790
Y1(2) = +3.9193
Y1(3) = +9.7525
Y1(4) = -11.1488
Y1(2)
Y1(3)
Y1(1)
Y1(4)
RADIUS r →
FIG. 14A

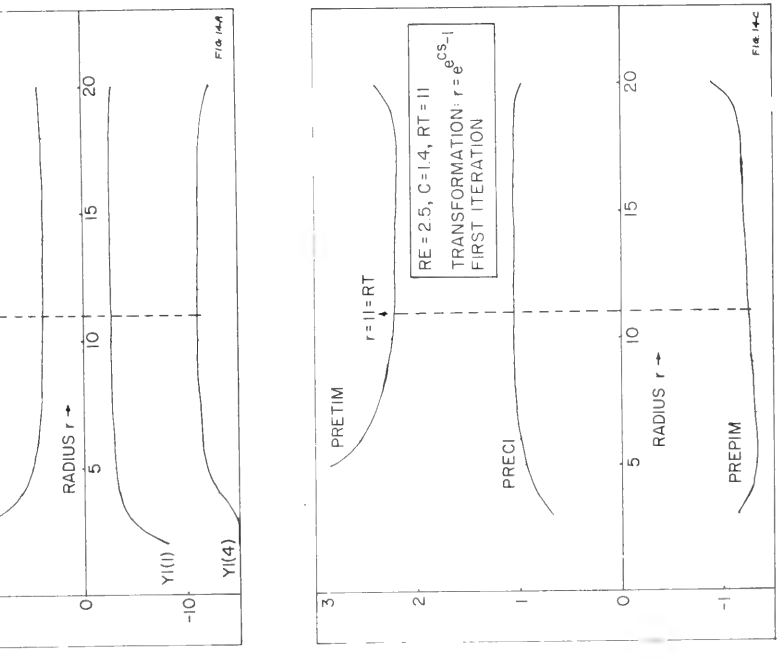
RE = 2.5, C = 1.4, RT = 11
TRANSFORMATION: r = e^(cs-1)
FIRST ITERATION
r = 11 = RT
PRETIM
PRECI
PREPIM
RADIUS r →
FIG. 14C

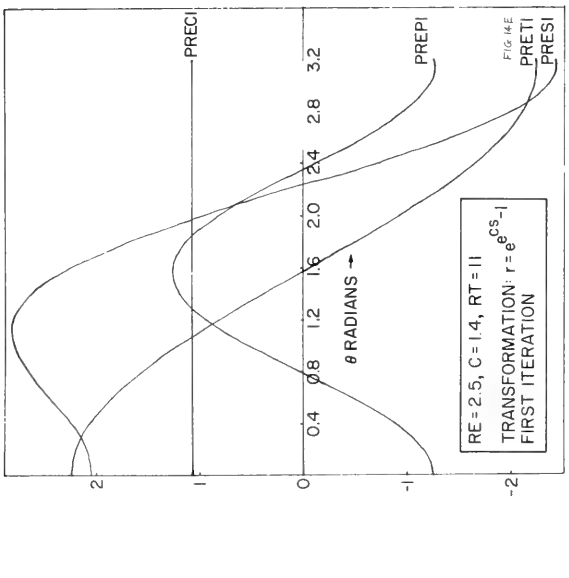
RE = 2.5, C = 1.4, RT = 11
TRANSFORMATION: r = e^cs − 1
FIRST ITERATION
PRECI
PREPI
PRETI
PRESI
θ RADIANS
FIG 14E

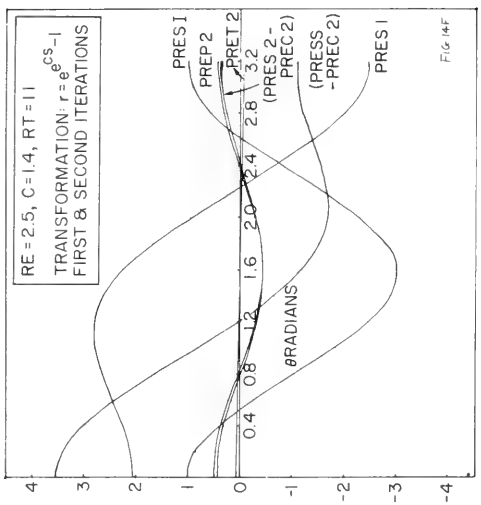
RE = 2.5, C = 1.4, RT = 11
TRANSFORMATION: r = e^cs − 1
FIRST & SECOND ITERATIONS
PRES I
PREP 2
PRET 2
(PRES 2 − PREC 2)
(PRESS − PREC 2)
PRES I
θ RADIANS
FIG 14F

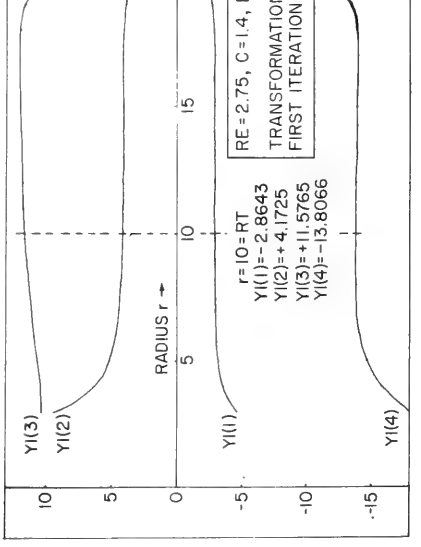
RE = 2.75, C = 1.4, RT = 10
TRANSFORMATION: r = e^cs − 1
FIRST ITERATION
CDI
CDPI
CDVI
r = 10 = RT
DRAG COEFFICIENT
RADIUS r →
FIG. 15B

RE = 2.75, C = 1.4, RT = 10
TRANSFORMATION: r = e^cs − 1
FIRST ITERATION
r = 10 = RT
Y1(1) = − 2.8643
Y1(2) = + 4.1725
Y1(3) = + 11.5765
Y1(4) = − 13.8066
Y1(1)
Y1(2)
Y1(3)
Y1(4)
RADIUS r →
FIG. 15A

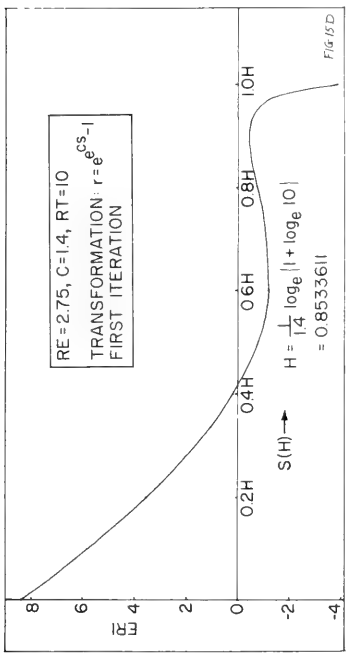
RE = 2.75, C = 1.4, RT = 10
TRANSFORMATION: r = e^cs - 1
FIRST ITERATION
S(H) → H = 1/14 log_e |1 + log_e 10|
= 0.8533611
0.2H 0.4H 0.6H 0.8H 1.0H
RE
FIG 15D

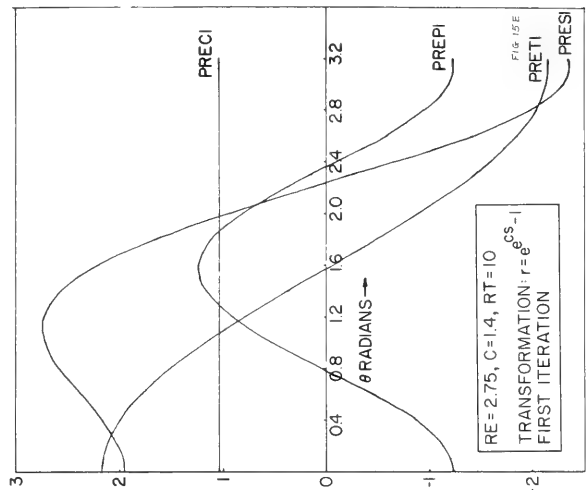
PRECI
PREPI
PRETI
PRESI
θ RADIANS →
RE = 2.75, C = 1.4, RT = 10
TRANSFORMATION: r = e^cs - 1
FIRST ITERATION
FIG 15E

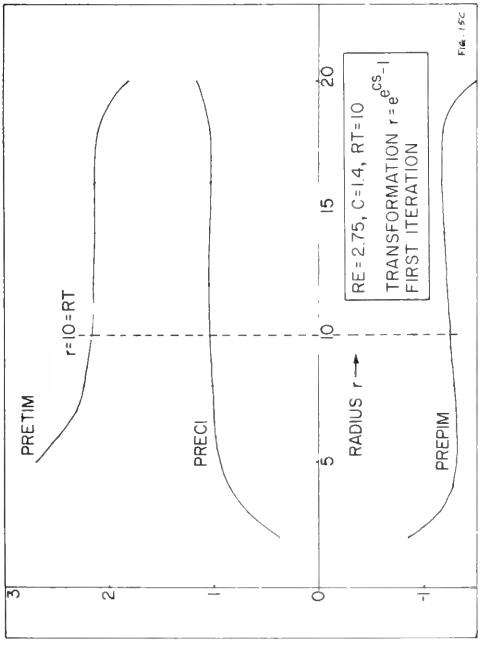
PRETIM
r=10=RT
PRECI
PREPIM
RADIUS r →
RE = 2.75, C = 1.4, RT = 10
TRANSFORMATION r = e^cs - 1
FIRST ITERATION
FIG. 15C

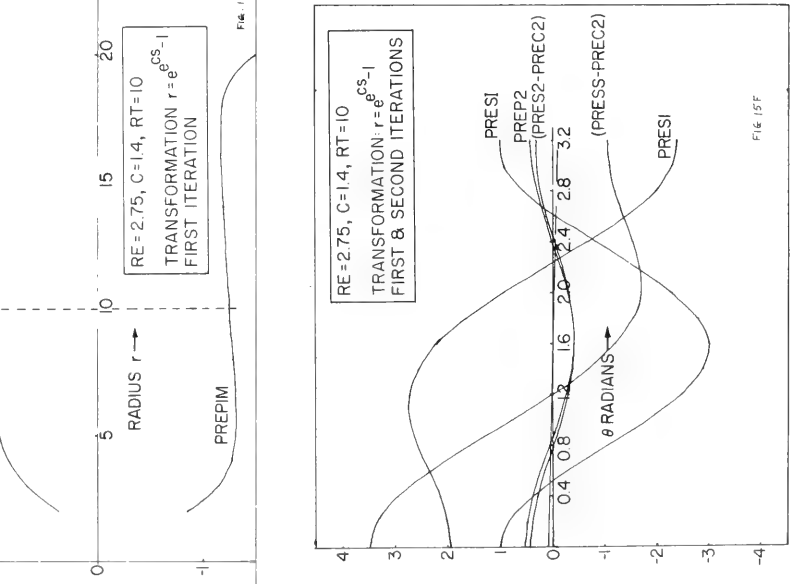
RE = 2.75, C = 1.4, RT = 10
TRANSFORMATION: r = e^cs - 1
FIRST & SECOND ITERATIONS
PRESI
PREP2
(PRES2-PREC2)
(PRESS-PREC2)
PRESI
θ RADIANS →
FIG 15F

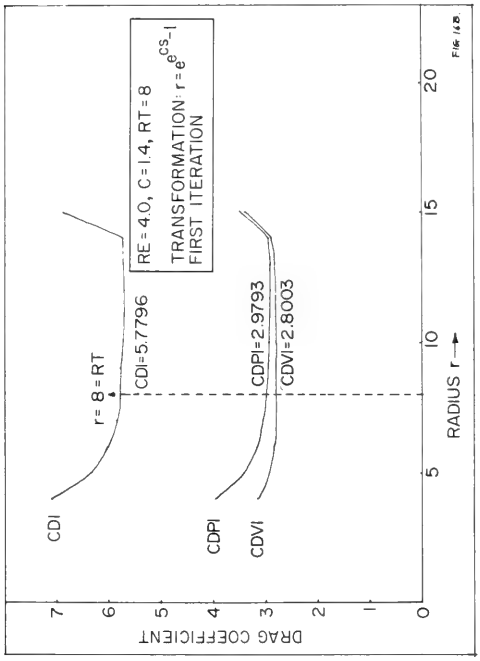

Fig. 14B

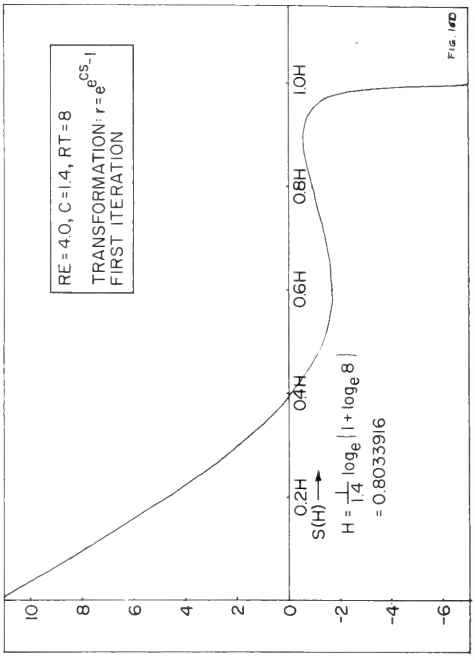

Fig. 14D

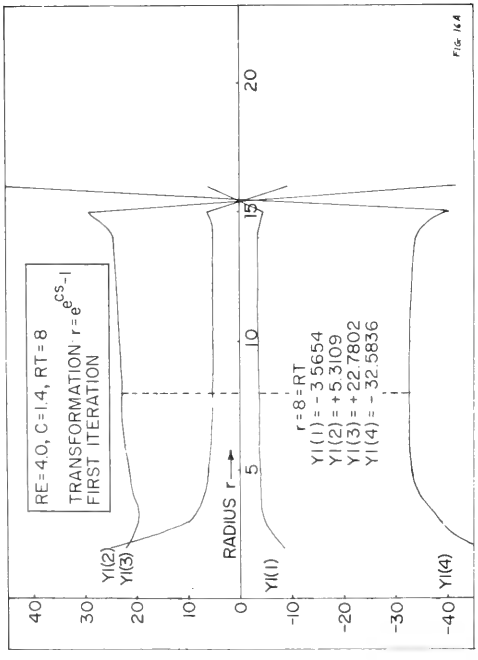

Fig. 14A

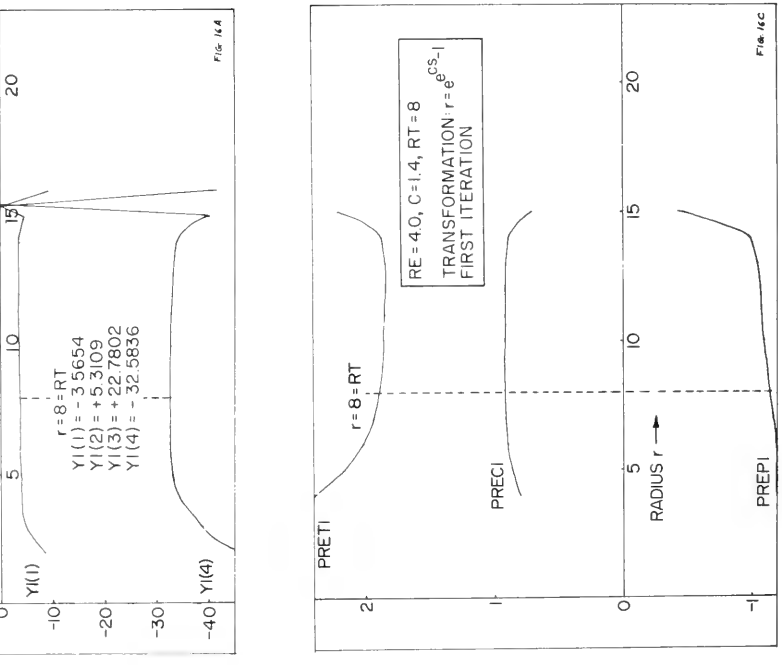

Fig. 14C

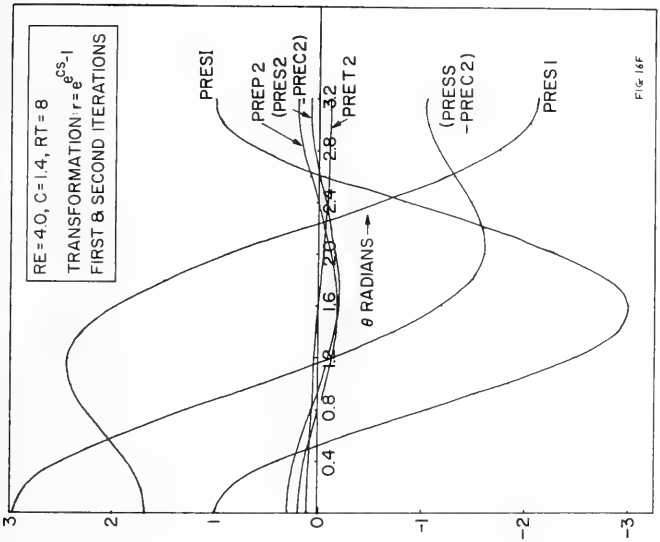
RE = 4.0, C = 1.4, RT = 8
TRANSFORMATION: r = e^(CS-1)
FIRST & SECOND ITERATIONS
PRESI
PREP 2
(PRES2
-PREC2)
PRET 2
(PRESS
-PREC2)
PRES I
θ RADIANS
FIG 16F

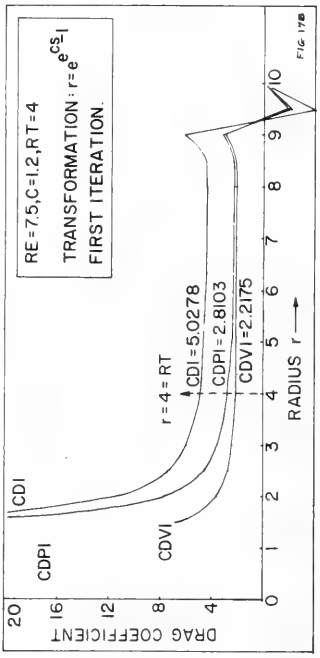
RE = 7.5, C = 1.2, RT = 4
TRANSFORMATION: r = e^(CS-1)
FIRST ITERATION.
CDI
CDPI
CDVI
r = 4 = RT
CDI = 5.0278
CDPI = 2.8103
CDVI = 2.2175
DRAG COEFFICIENT
RADIUS r
FIG 17B

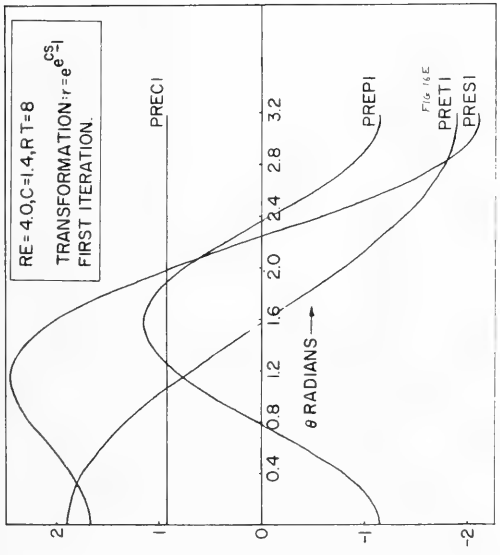
RE = 4.0, C = 1.4, R T = 8
TRANSFORMATION: r = e^(CS-1)
FIRST ITERATION.
PRECI
PREPI
PRETI
PRESI
θ RADIANS
FIG 16E

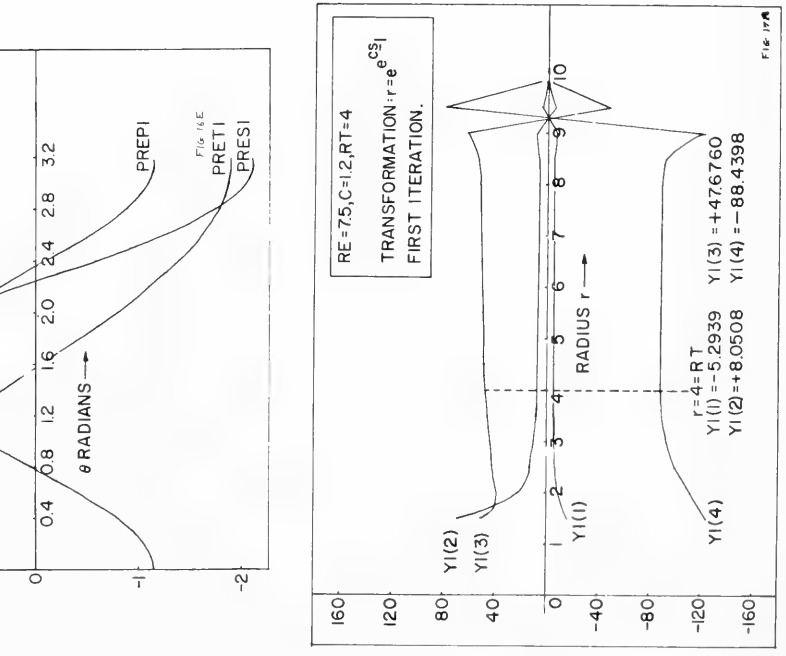
RE = 7.5, C = 1.2, RT = 4
TRANSFORMATION: r = e^(CS-1)
FIRST ITERATION.
Y1(1)
Y1(2)
Y1(3)
Y1(4)
r = 4 = R T
Y1(1) = -5.2939
Y1(2) = +8.0508
Y1(3) = +476760
Y1(4) = -88.4398
RADIUS r
FIG 17A

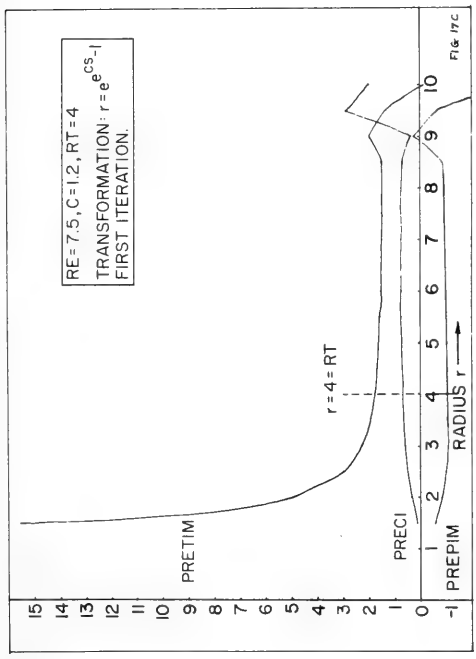
RE=7.5, C=1.2, RT=4
TRANSFORMATION: r=e^(cs-1)
FIRST ITERATION.
PRETIM
PRECI
PREPIM
r=4=RT
RADIUS r
FIG 17C

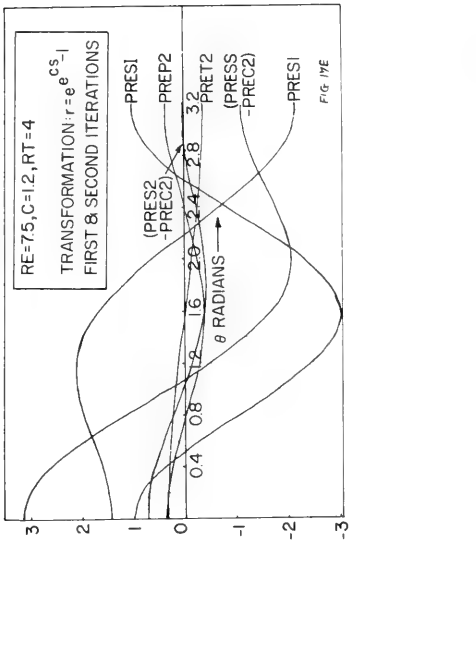
RE=7.5, C=1.2, RT=4
TRANSFORMATION: r=e^(cs-1)
FIRST & SECOND ITERATIONS
PRES1
PREP2
(PRES2 -PREC2)
PRET2
(PRESS -PREC2)
θ RADIANS
FIG 17E

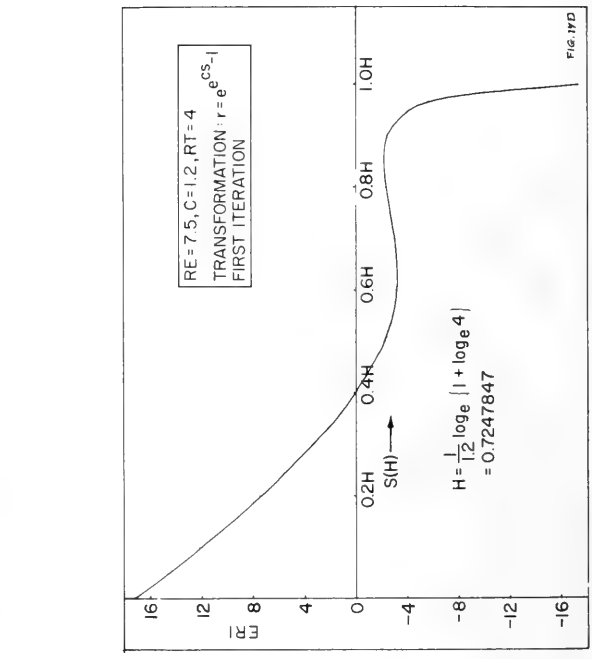
RE=7.5, C=1.2, RT=4
TRANSFORMATION: r=e^(cs-1)
FIRST ITERATION.
PRECI
PREPI
PRETI
PRESI
θ RADIANS
FIG 17F

RE=7.5, C=1.2, RT=4
TRANSFORMATION: r=e^(cs-1)
FIRST ITERATION
S(H)
H=1/1.2 log_e |1+log_e 4|
=0.7247847
FIG 17D

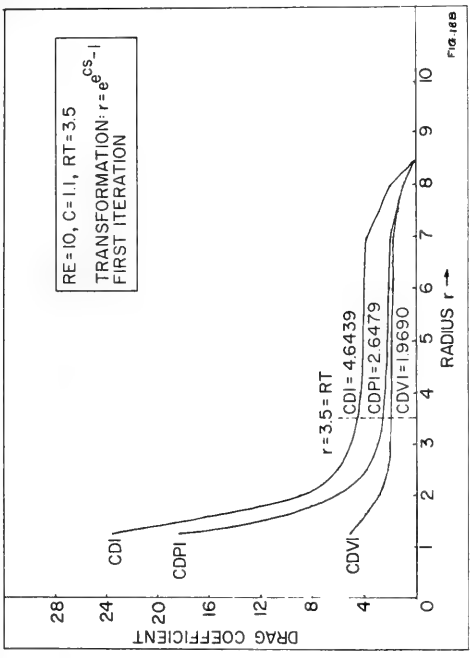
RE=10, C=1.1, RT=3.5
TRANSFORMATION: r=e^cs-1
FIRST ITERATION
DRAG COEFFICIENT
RADIUS r →
r=3.5=RT
CDI= 4.6439
CDPI=2.6479
CDVI=1.9690
CDI
CDPI
CDVI
FIG.18B

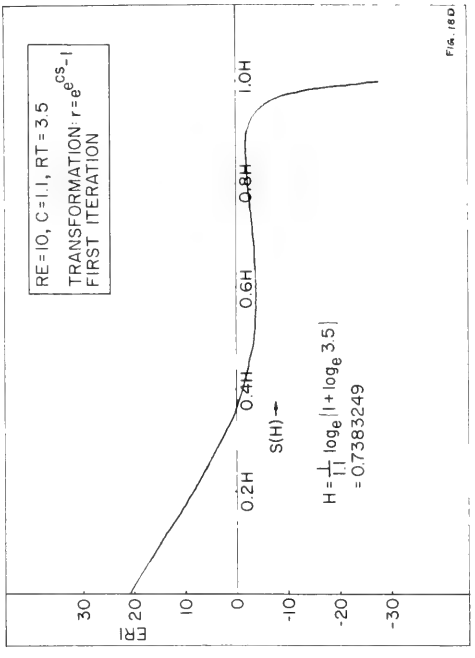
RE=10, C=1.1, RT=3.5
TRANSFORMATION: r=e^cs-1
FIRST ITERATION
ER
S(H) →
0.2H
0.4H
0.6H
0.8H
1.0H
H=1/1.1 log_e|1+log_e 3.5|
=0.7383249
FIG.18D

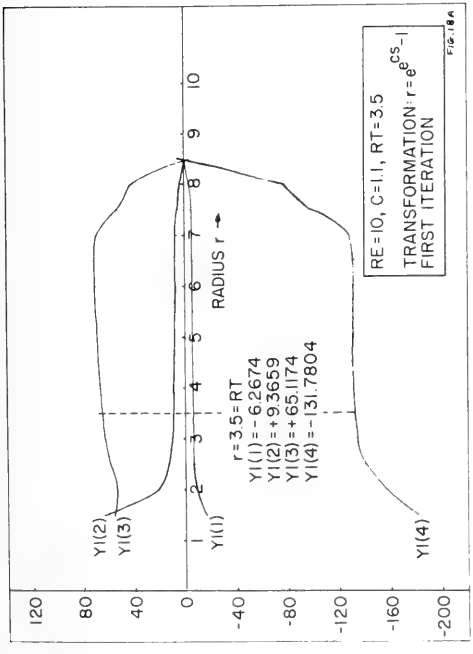
RE=10, C=1.1, RT=3.5
TRANSFORMATION: r=e^cs-1
FIRST ITERATION
RADIUS r →
r=3.5=RT
Y1(1) = -6.2674
Y1(2) = +9.3659
Y1(3) = +65.1174
Y1(4) = -131.7804
Y1(1)
Y1(2)
Y1(3)
Y1(4)
FIG.18A

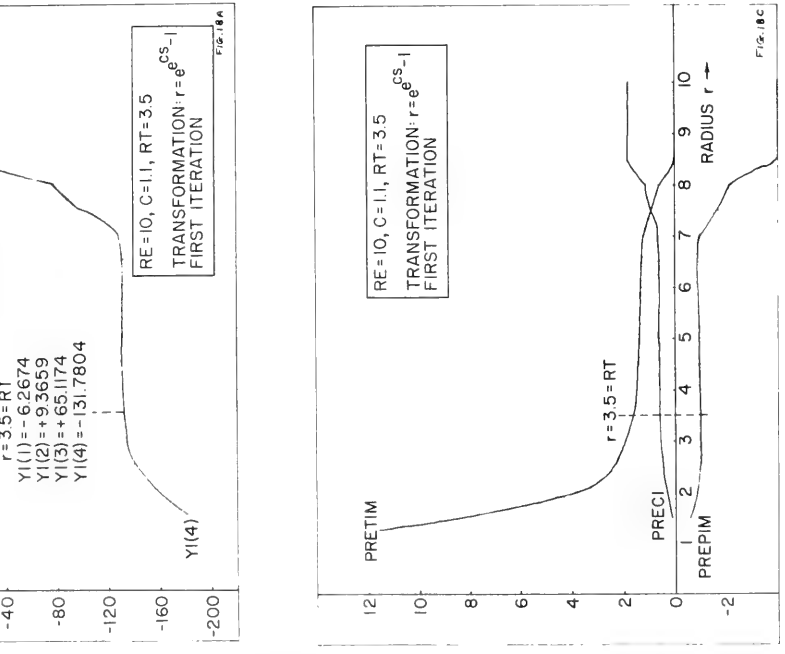
RE=10, C=1.1, RT=3.5
TRANSFORMATION: r=e^cs-1
FIRST ITERATION
PRETIM
PRECI
PREPIM
RADIUS r →
r=3.5=RT
FIG.18C

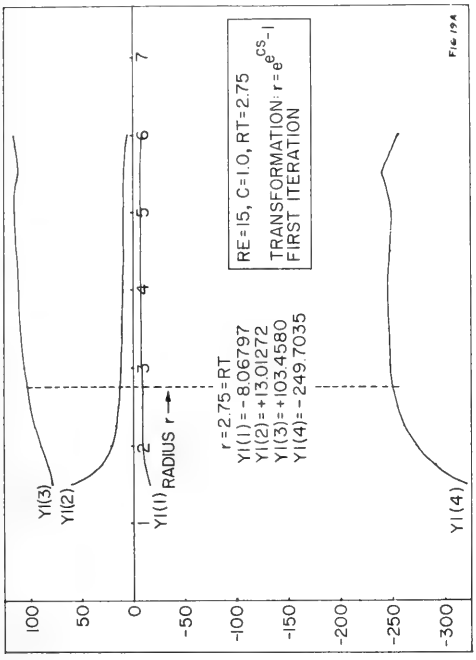

Fig 19A

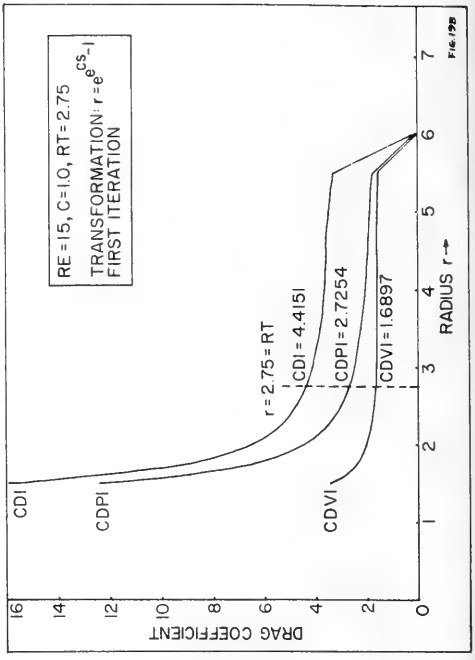

Fig 19B

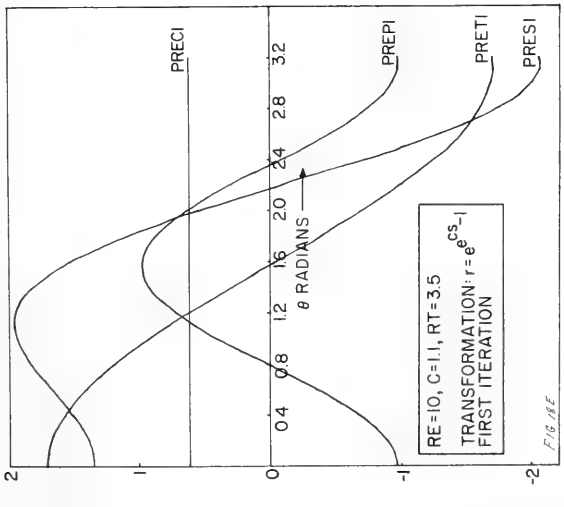

Fig 18E

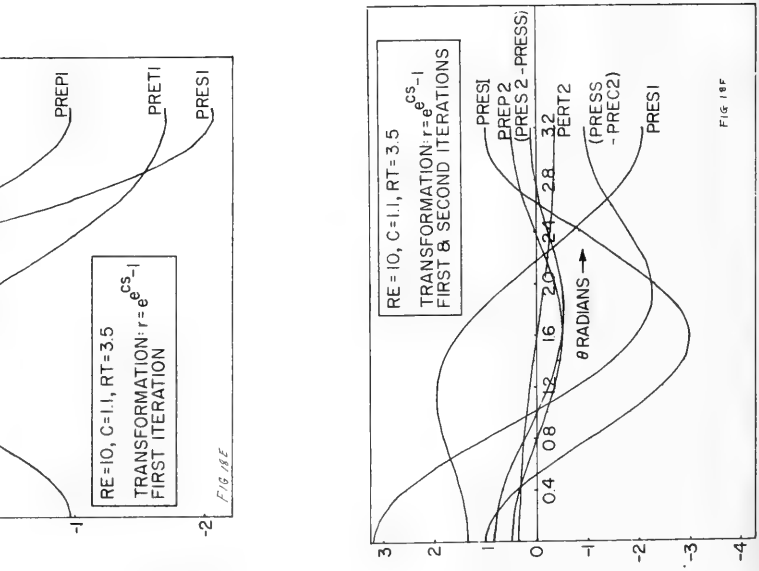

Fig 18F

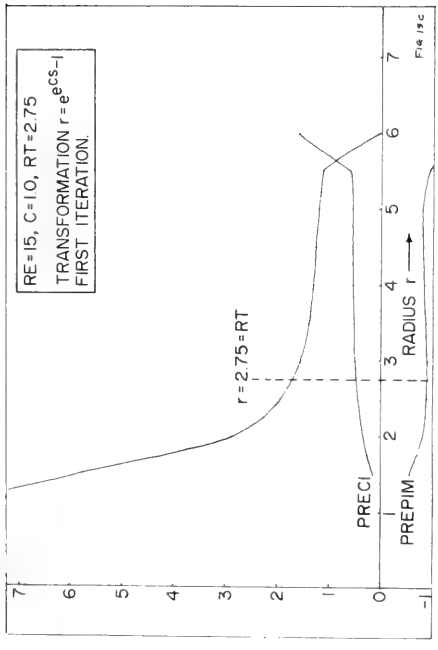
RE=15, C=1.0, RT=2.75
TRANSFORMATION r=e^(cs-1)
FIRST ITERATION
r=2.75=RT
PRECI
PREPIM
RADIUS r
Fig. 19c

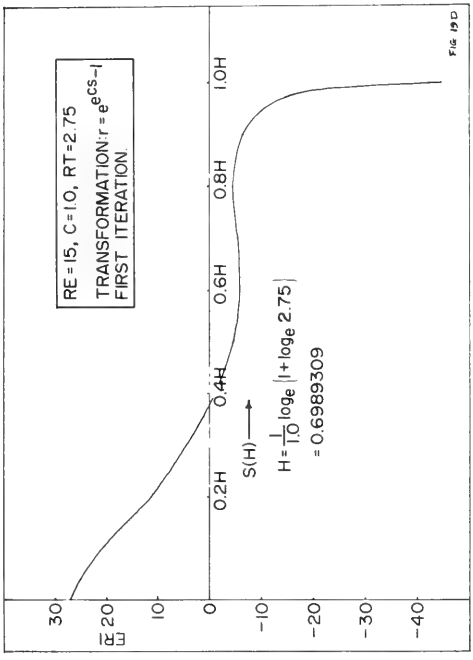
RE=15, C=1.0, RT=2.75
TRANSFORMATION r=e^(cs-1)
FIRST ITERATION
0.2H
0.4H
0.6H
0.8H
1.0H
S(H)
H=1/1.0 log_e |1+log_e 2.75|
=0.6989309
Fig. 19d

RE=15, C=1.0, RT=2.75
TRANSFORMATION r=e^(cs-1)
FIRST ITERATION
PRECI
PREPI
PRETI
PRESI
θ RADIANS
Fig. 19e

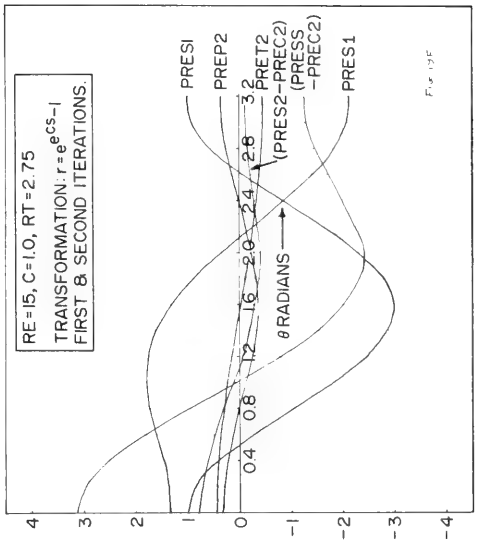
RE=15, C=1.0, RT=2.75
TRANSFORMATION r=e^(cs-1)
FIRST & SECOND ITERATIONS.
PRESI
PREP2
PRET2
(PRES2-PREC2)
(PRESS-PREC2)
PRES1
θ RADIANS
Fig. 19f

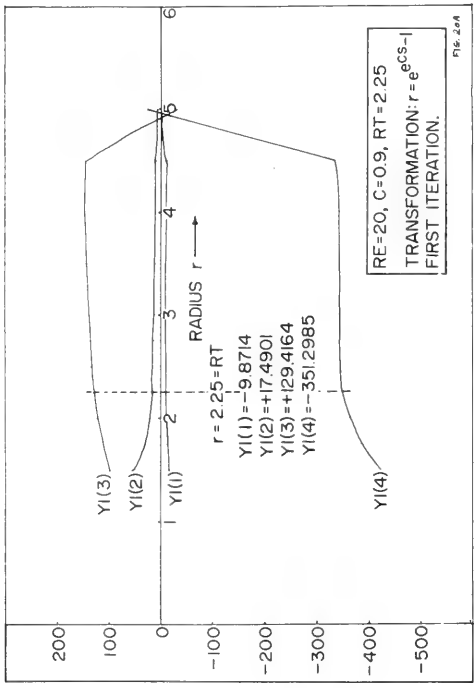

Fig. 2a

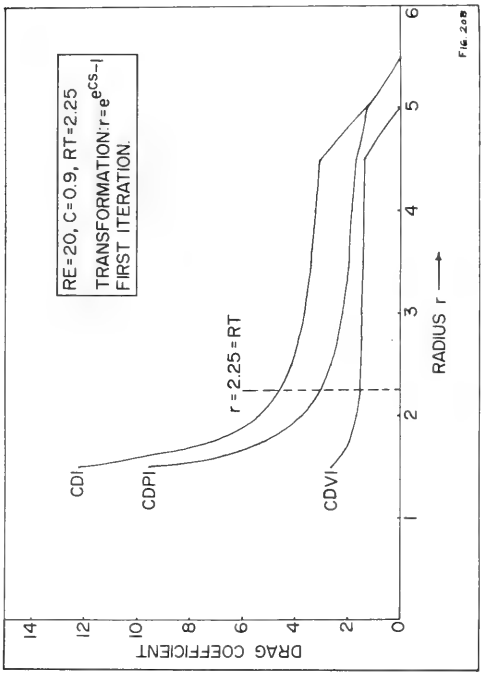

Fig. 2b

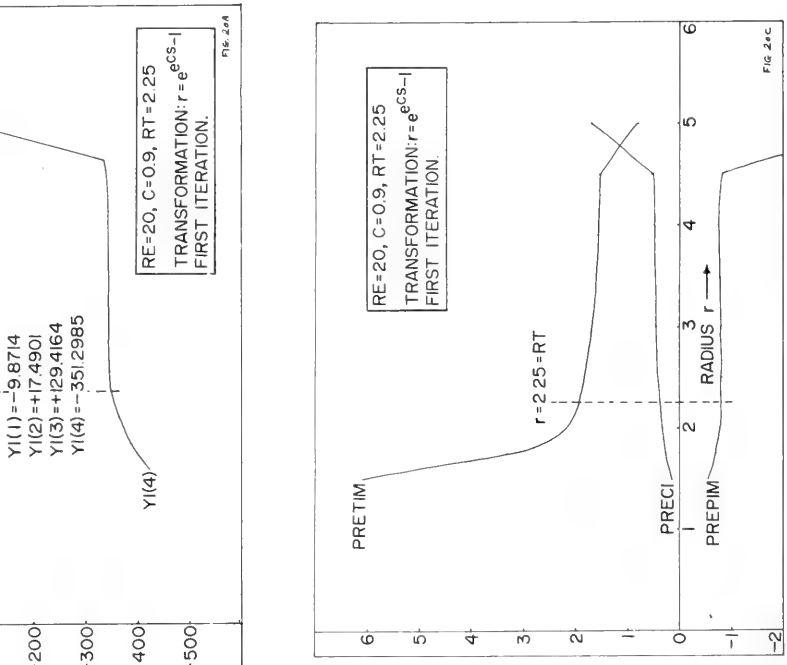

Fig. 2c

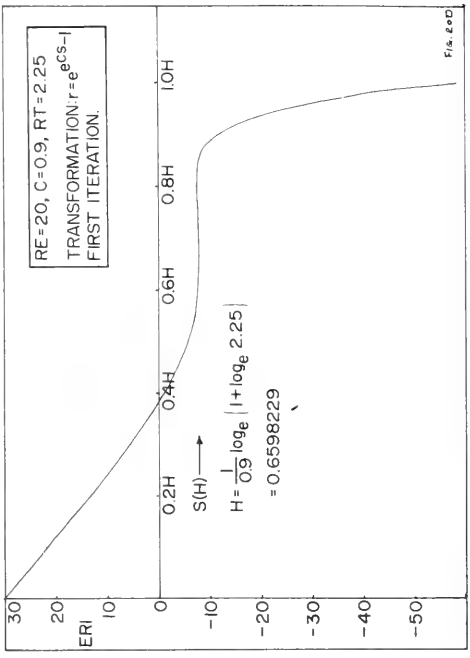

Fig. 2d

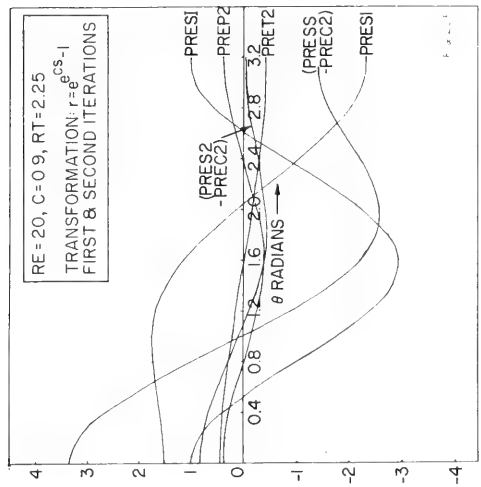
RE=20, C=0.9, RT=2.25
TRANSFORMATION: r=e^(cs-1)
FIRST & SECOND ITERATIONS
PRESI
PREP2
PRET2
(PRESS2 -PREC2)
(PRESS -PREC2)
PRESI
θ RADIANS
0.4
0.8
1.2
1.6
2.0
2.4
2.8
3.2
4
3
2
1
0
-1
-2
-3
-4

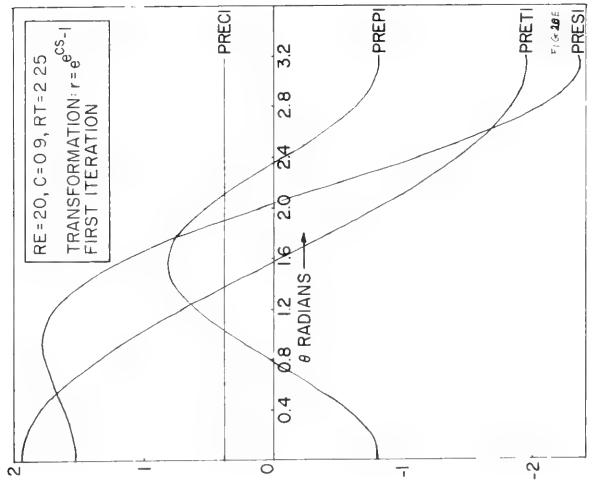
RE=20, C=0.9, RT=2.25
TRANSFORMATION: r=e^(cs-1)
FIRST ITERATION
PRECI
PREPI
PRETI
PRESI
θ RADIANS
0.4
0.8
1.2
1.6
2.0
2.4
2.8
3.2
2
1
0
-1
-2

VISCOUS STREAMLINE FIELD AROUND A CIRCULAR CYLINDER

RE= 0.0500 , C= 2.0 , RT=275

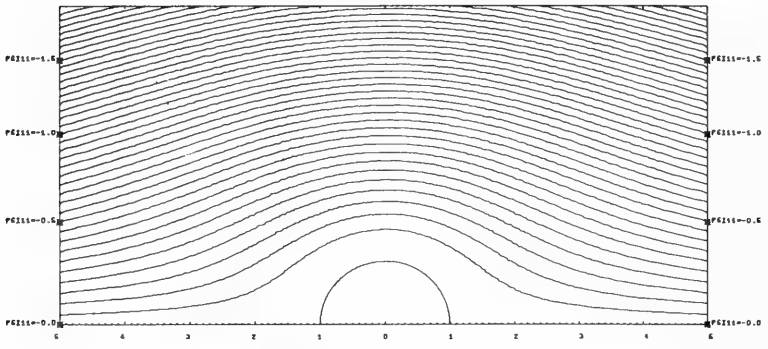

FIRST ITERATION, FIRST HARMONIC

FIG. 21A

RE= 0.0500 , C= 2.0 , RT=275

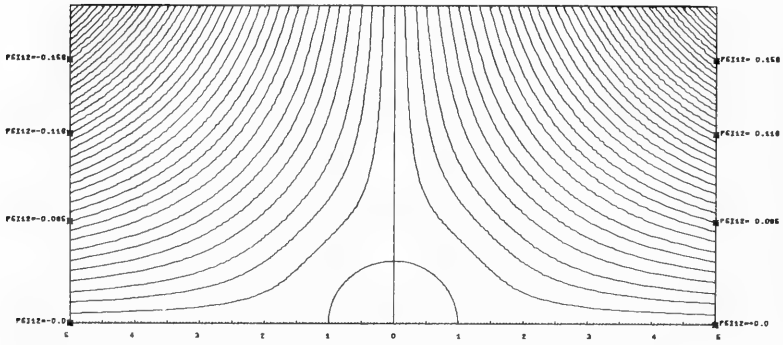

FIRST ITERATION, SECOND HARMONIC

FIG. 21B

RE= 0.0500 , C= 2.0 , RT=275

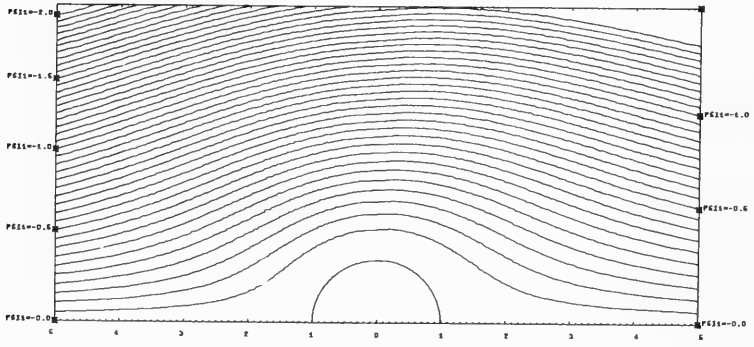

FIRST ITERATION, SUM OF HARMONICS

FIG. 21C

VISCOUS STREAMLINE FIELD AROUND A CIRCULAR CYLINDER

RE= 0.0500 , C= 2.0 , RT=275

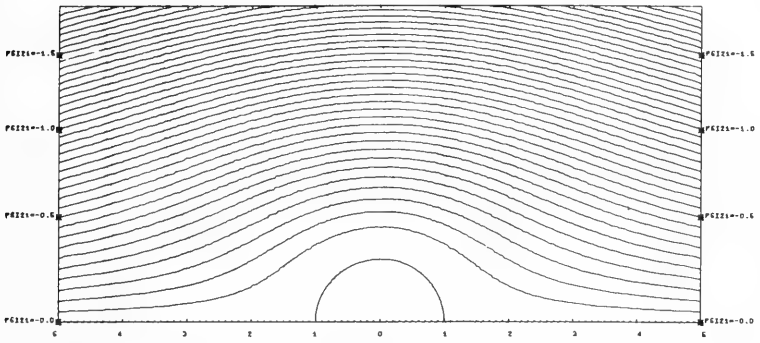

FIRST AND SECOND ITERATIONS, FIRST HARMONIC FIG 2ID

RE= 0.0500 , C= 2.0 , RT=275

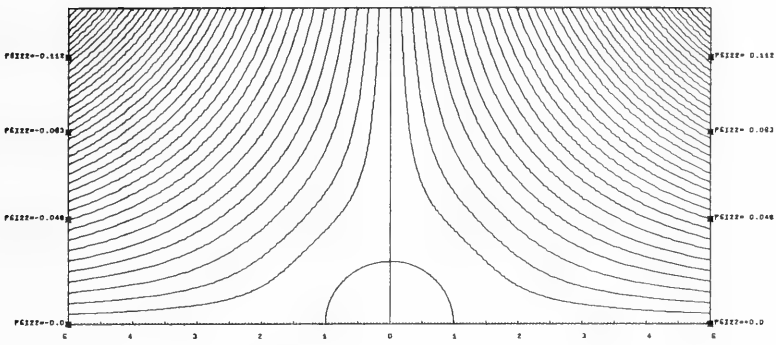

FIRST AND SECOND ITERATIONS, SECOND HARMONIC FIG 2IE

RE= 0.0500 , C= 2.0 , RT=275

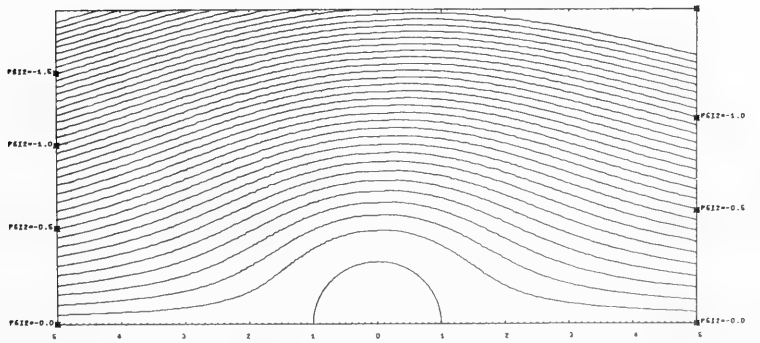

FIRST AND SECOND ITERATIONS, SUM OF HARMONICS FIG 2IF

VISCOUS STREAMLINE FIELD AROUND A CIRCULAR CYLINDER

RE= 0.1250 , C= 2.0 , RT=135

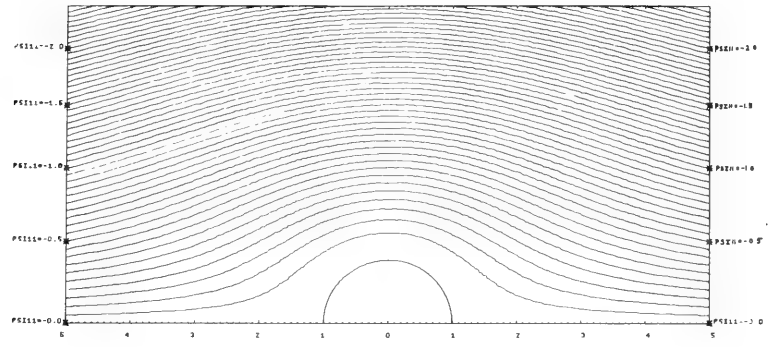

FIRST ITERATION, FIRST HARMONIC

FIG. 11A

RE= 0.1250 , C= 2.0 , RT=135

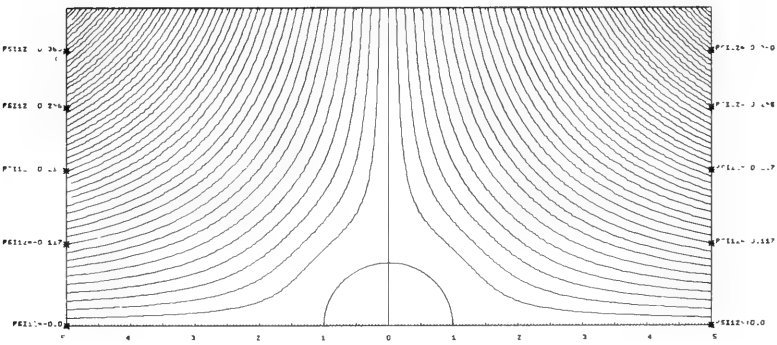

FIRST ITERATION, SECOND HARMONIC

FIG. 11B

RE= 0.1250 , C= 2.0 , RT=135

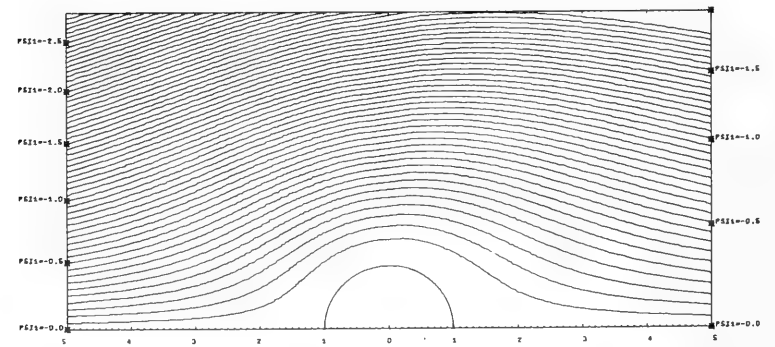

FIRST ITERATION, SUM OF HARMONICS

FIG. 11C

VISCOUS STREAMLINE FIELD AROUND A CIRCULAR CYLINDER

RE= 0.1250 , C= 2.0 , RT=135

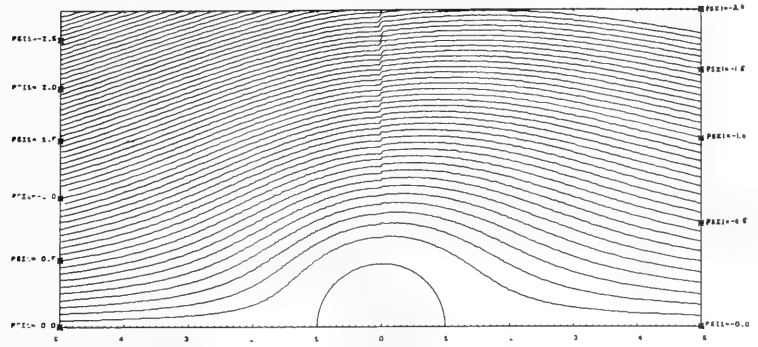

FIRST ITERATION, SUM OF HARMONICS

RE= 0.1250 , C= 2.0 , RT=135

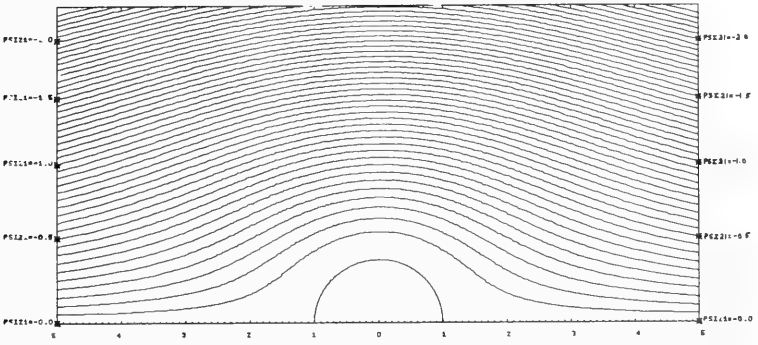

FIRST AND SECOND ITERATIONS, FIRST HARMONIC

RE= 0.1250 , C= 2.0 , RT=135

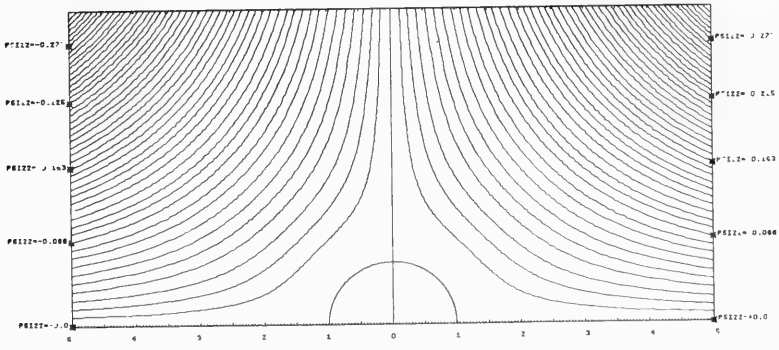

FIRST AND SECOND ITERATIONS, SECOND HARMONIC

VISCOUS STREAMLINE FIELD AROUND A CIRCULAR CYLINDER

RE= 0.1250 , C= 2.0 , RT=135

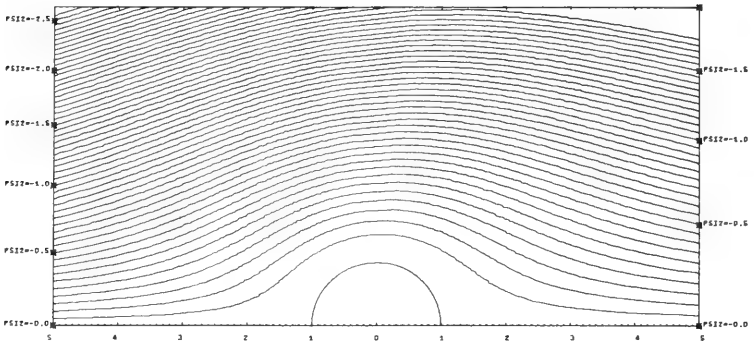

FIRST AND SECOND ITERATIONS, SUM OF HARMONICS FIG. 22G

RE= 0.1250 , C= 2.0 , RT=135

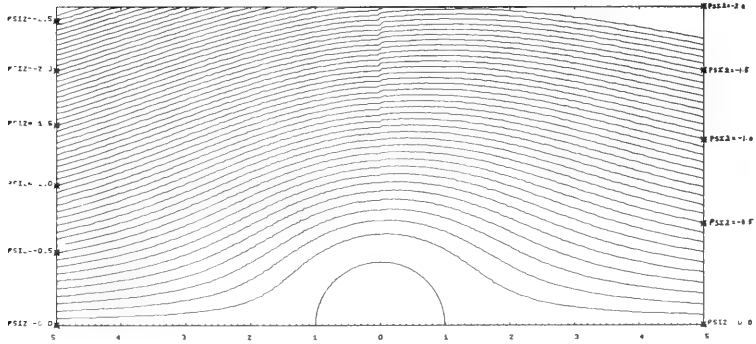

FIRST AND SECOND ITERATIONS, SUM OF HARMONICS FIG. 22H

VISCOUS STREAMLINE FIELD AROUND A CIRCULAR CYLINDER

RE= 0.1875 , C= 1.9 , RT=110

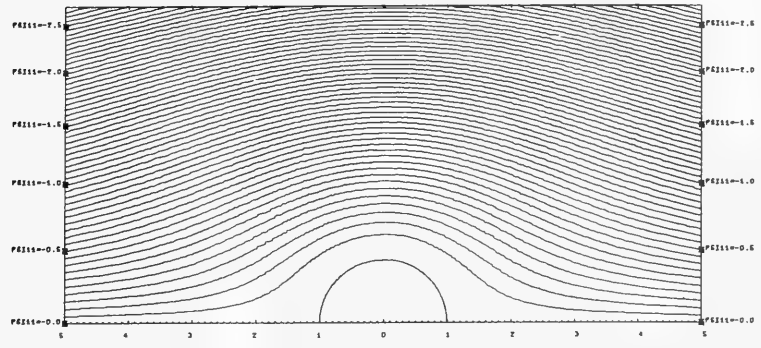

FIRST ITERATION, FIRST HARMONIC

FIG. 2.3A

RE= 0.1875 , C= 1.9 , RT=110

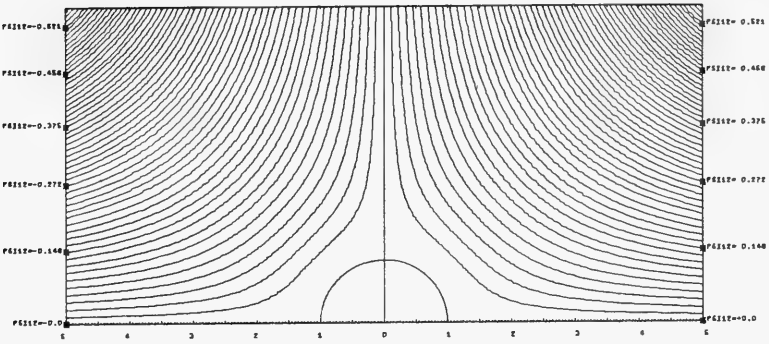

FIRST ITERATION, SECOND HARMONIC

FIG. 2.3B

RE= 0.1875 , C= 1.9 , RT=110

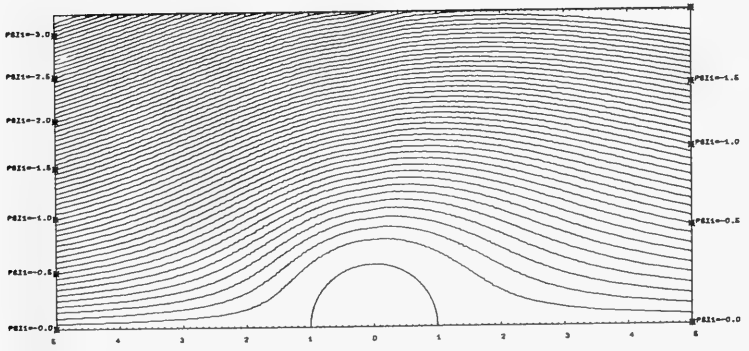

FIRST ITERATION, SUM OF HARMONICS

FIG. 2.3C

VISCOUS STREAMLINE FIELD AROUND A CIRCULAR CYLINDER

RE= 0.1875 , C= 1.9 , RT=110

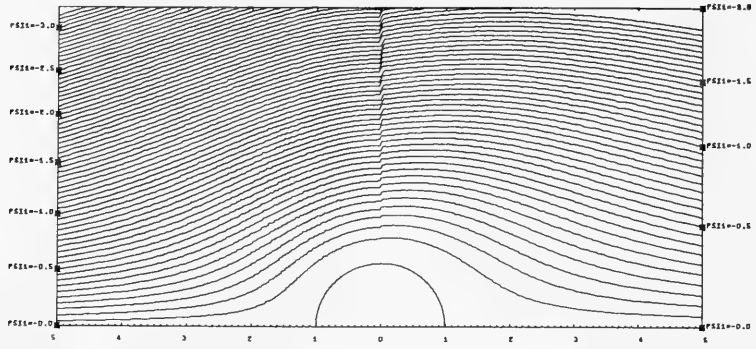

FIRST ITERATION, SUM OF HARMONICS FIG. 23D

RE= 0.1875 , C= 1.9 , RT=110

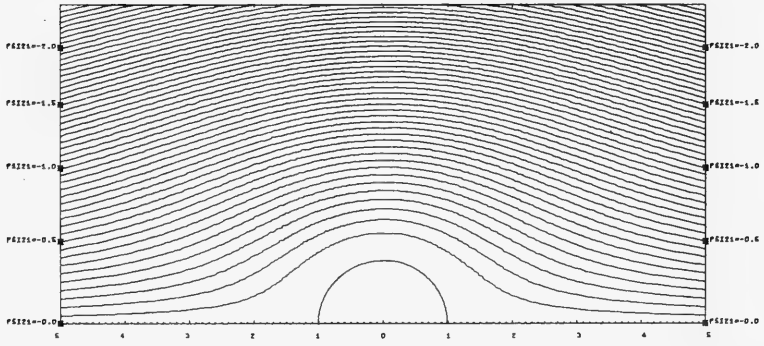

FIRST AND SECOND ITERATIONS, FIRST HARMONIC FIG. 23E

RE= 0.1875 , C= 1.9 , RT=110

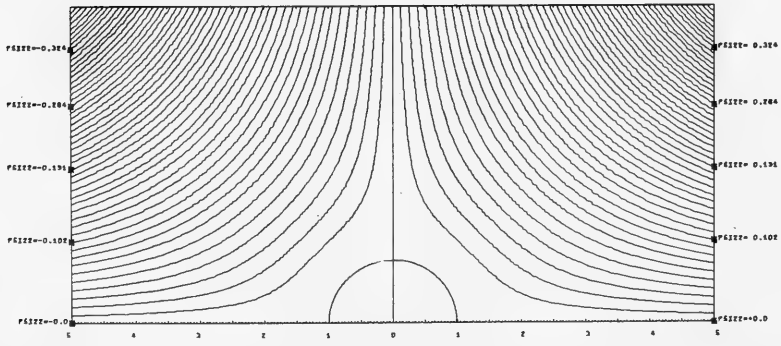

FIRST AND SECOND ITERATIONS, SECOND HARMONIC FIG. 23F

VISCOUS STREAMLINE FIELD AROUND A CIRCULAR CYLINDER

RE= 0.1875 , C= 1.9 , RT=110

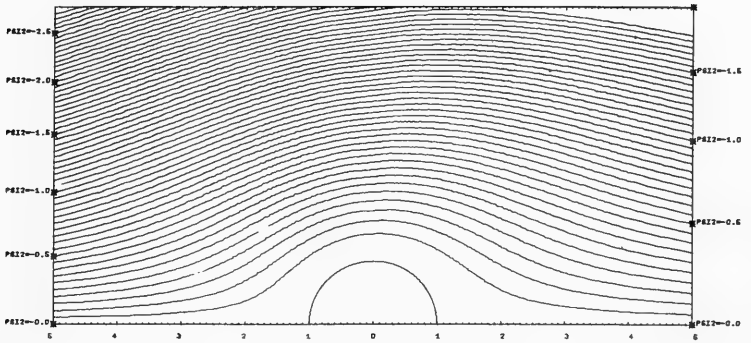

FIRST AND SECOND ITERATIONS, SUM OF HARMONICS FIG.23A

RE= 0.1875 , C= 1.9 , RT=110

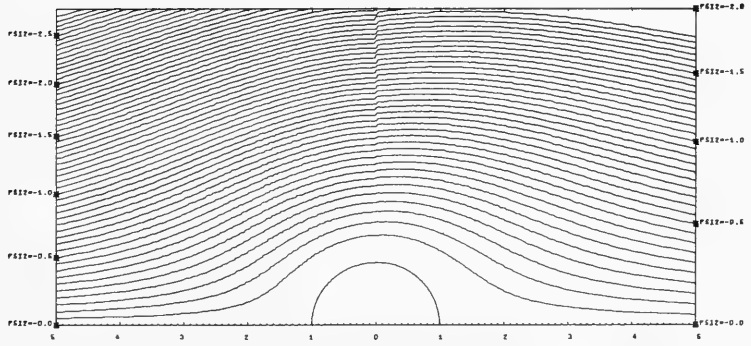

FIRST AND SECOND ITERATIONS, SUM OF HARMONICS FIG.23B

VISCOUS STREAMLINE FIELD AROUND A CIRCULAR CYLINDER

RE= 0.2500 , C= 1.9 , RT= 85

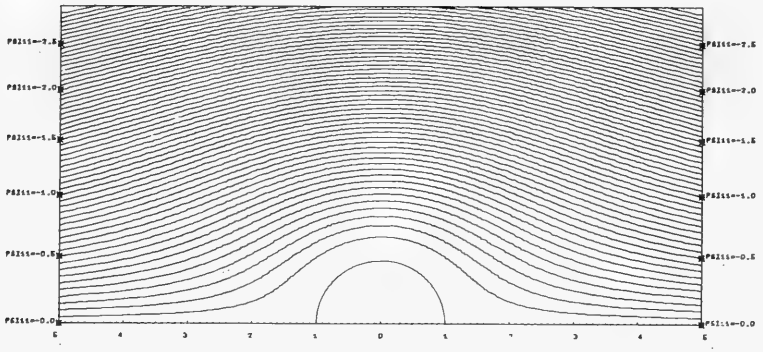

FIRST ITERATION, FIRST HARMONIC

RE= 0.2500 , C= 1.9 , RT= 85

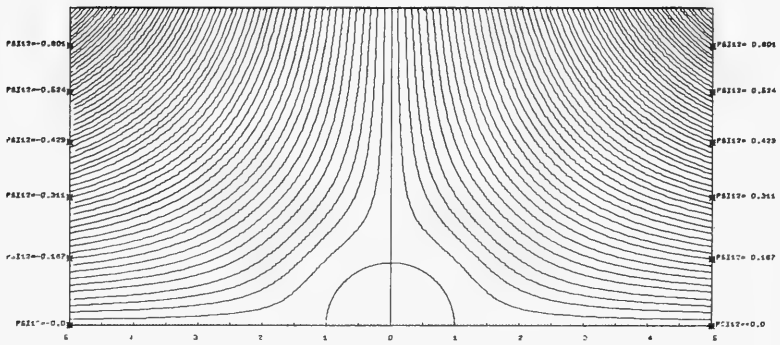

FIRST ITERATION, SECOND HARMONIC

RE= 0.2500 , C= 1.9 , RT= 85

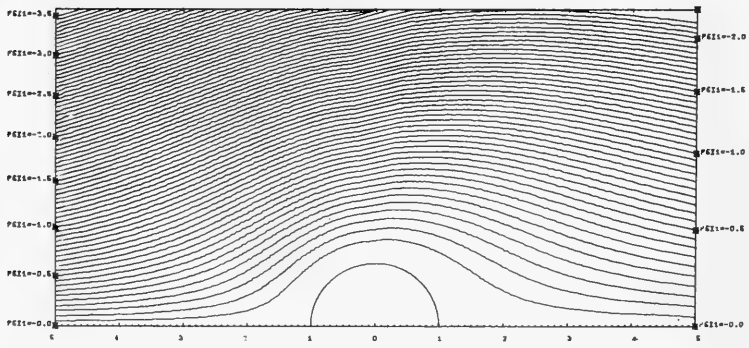

FIRST ITERATION, SUM OF HARMONICS

VISCOUS STREAMLINE FIELD AROUND A CIRCULAR CYLINDER

RE= 0.2500 , C= 1.9 , RT= 85

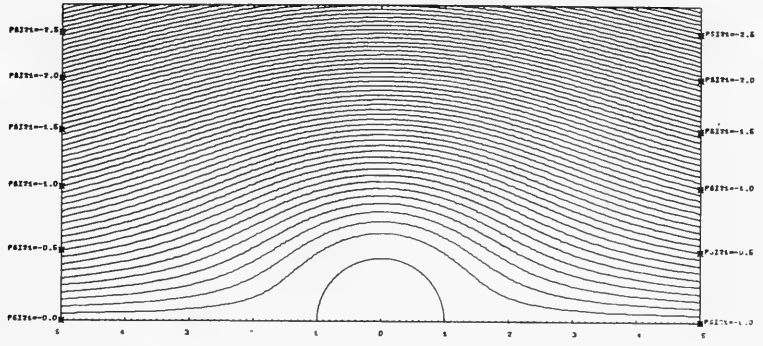

FIRST AND SECOND ITERATIONS, FIRST HARMONIC Fig. 24D

RE= 0.2500 , C= 1.9 , RT= 85

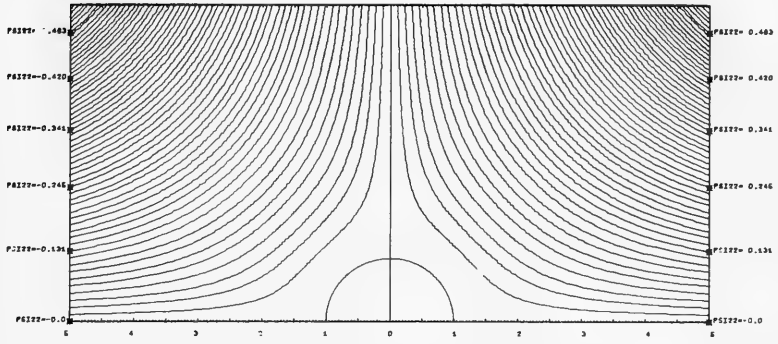

FIRST AND SECOND ITERATIONS, SECOND HARMONIC Fig. 24E

RE= 0.2500 , C= 1.9 , RT= 85

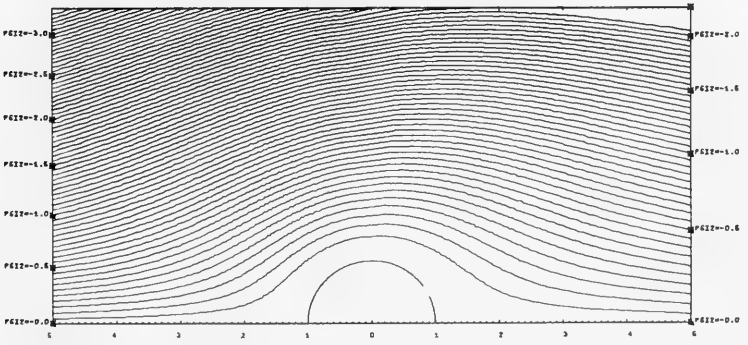

FIRST AND SECOND ITERATIONS, SUM OF HARMONICS Fig. 24F

VISCOUS STREAMLINE FIELD AROUND A CIRCULAR CYLINDER

RE= 0.5000 , C= 1.8 , RT= 46

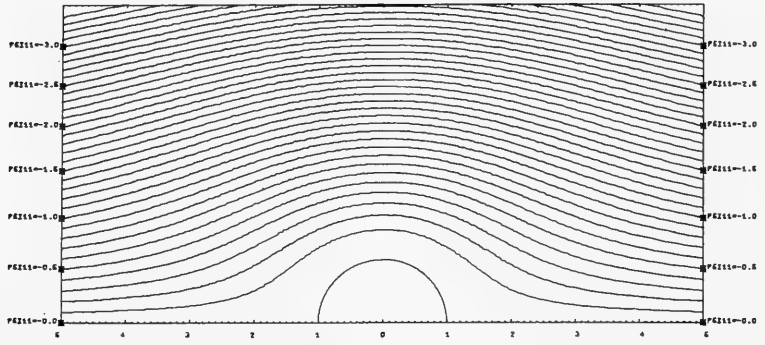

FIRST ITERATION, FIRST HARMONIC

FIG. 25A

RE= 0.5000 , C= 1.8 , RT= 46

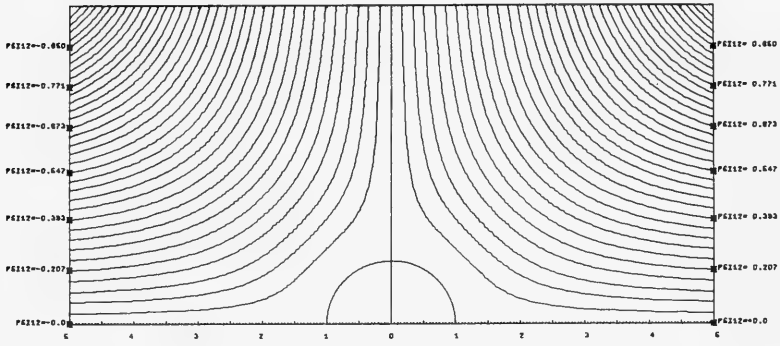

FIRST ITERATION, SECOND HARMONIC

FIG. 25B

RE= 0.5000 , C= 1.8 , RT= 46

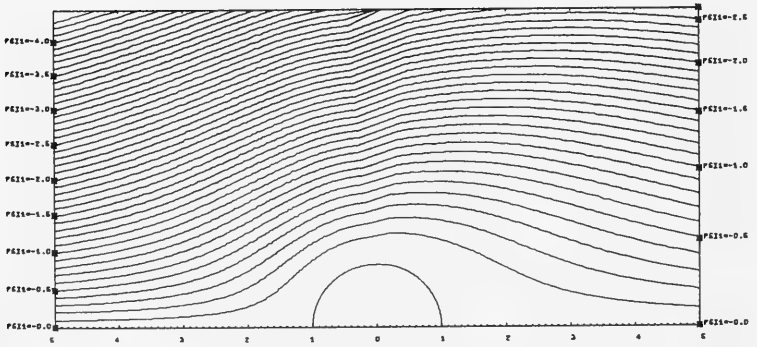

FIRST ITERATION, SUM OF HARMONICS

FIG. 25C

VISCOUS STREAMLINE FIELD AROUND A CIRCULAR CYLINDER

RE= 0.5000 , C= 1.8 , RT= 46

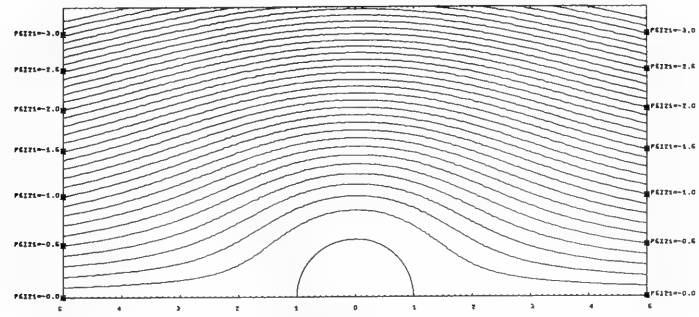

FIRST AND SECOND ITERATIONS, FIRST HARMONIC Fig. 14D

RE= 0.5000 , C= 1.8 , RT= 46

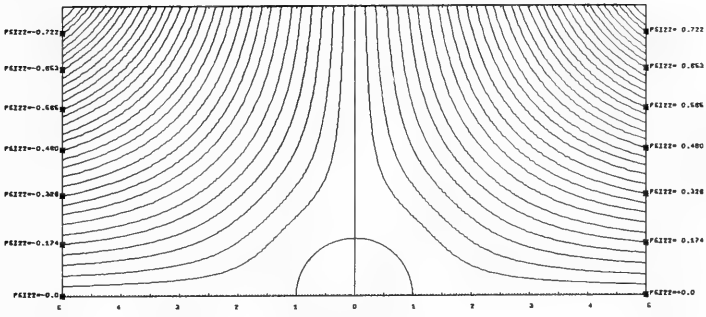

FIRST AND SECOND ITERATIONS, SECOND HARMONIC Fig. 15E

RE= 0.5000 , C= 1.8 , RT= 46

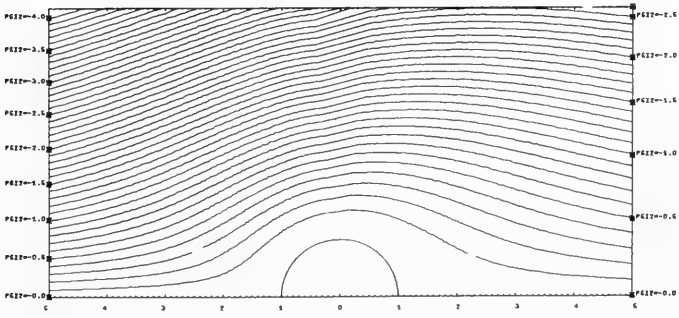

FIRST AND SECOND ITERATIONS, SUM OF HARMONICS Fig. 25F

VISCOUS STREAMLINE FIELD AROUND A CIRCULAR CYLINDER

RE= 0.7500 , C= 1.8 , RT= 30

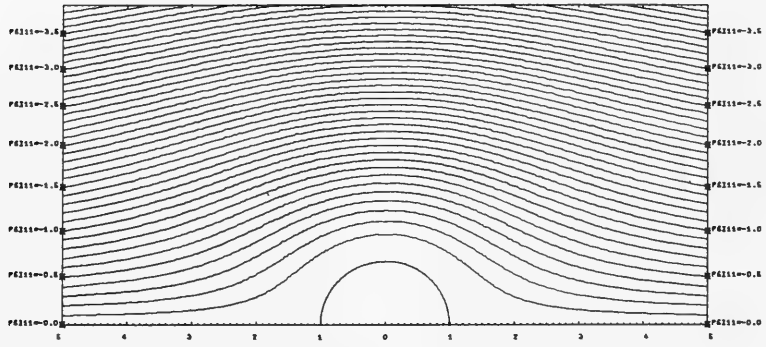

FIRST ITERATION, FIRST HARMONIC

RE= 0.7500 , C= 1.8 , RT= 30

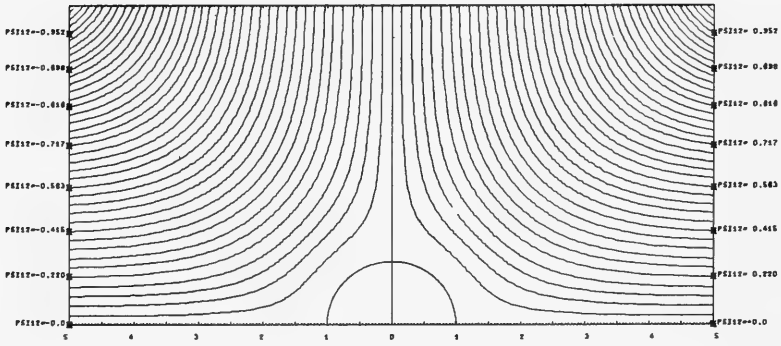

FIRST ITERATION, SECOND HARMONIC

RE= 0.7500 , C= 1.8 , RT= 30

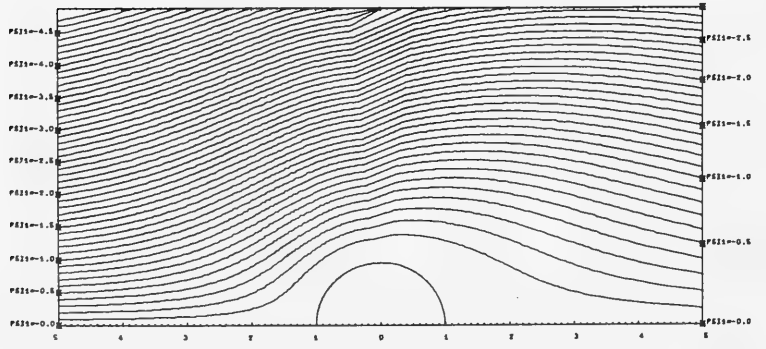

FIRST ITERATION, SUM OF HARMONICS

VISCOUS STREAMLINE FIELD AROUND A CIRCULAR CYLINDER

RE= 0.7500 , C= 1.8 , RT= 30

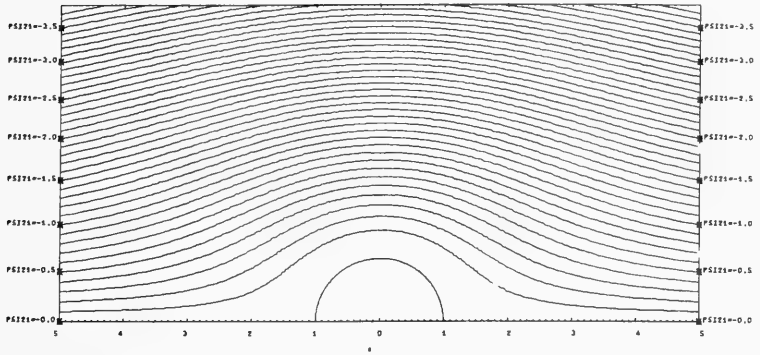

FIRST AND SECOND ITERATIONS, FIRST HARMONIC FIG. 24D

RE= 0.7500 , C= 1.8 , RT= 30

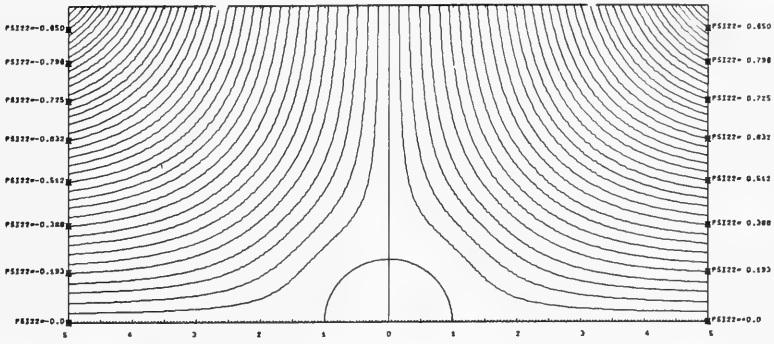

FIRST AND SECOND ITERATIONS, SECOND HARMONIC FIG. 24E

RE= 0.7500 , C= 1.8 , RT= 30

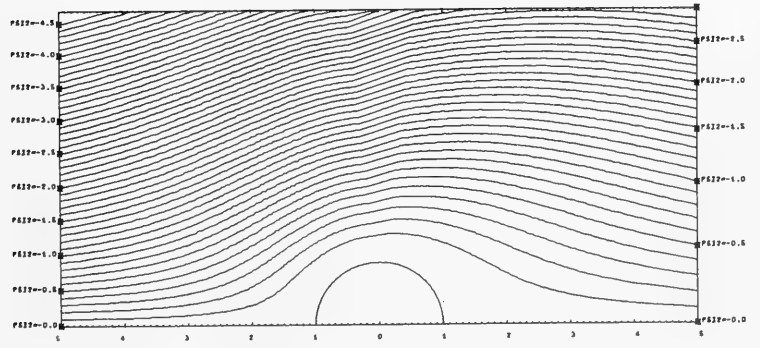

FIRST AND SECOND ITERATIONS, SUM OF HARMONICS FIG. 24F

VISCOUS STREAMLINE FIELD AROUND A CIRCULAR CYLINDER

RE= 1.0000 , C= 1.7 , RT= 20

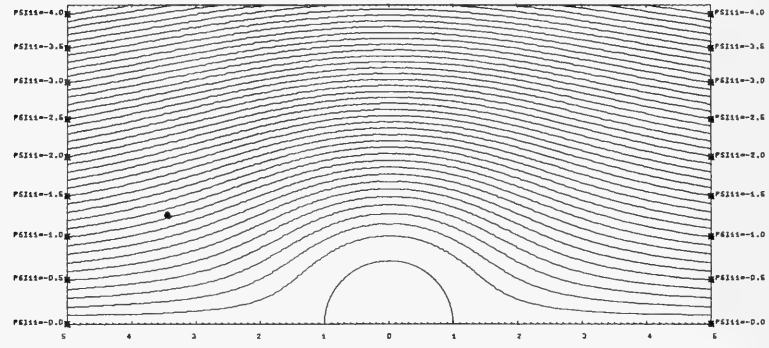

FIRST ITERATION, FIRST HARMONIC

Fig. 27A

RE= 1.0000 , C= 1.7 , RT= 20

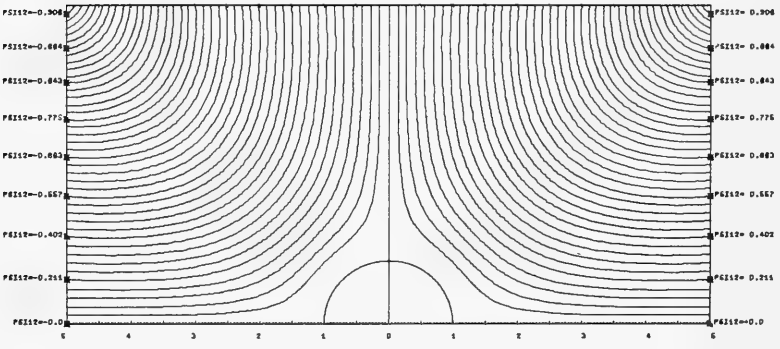

FIRST ITERATION, SECOND HARMONIC

Fig. 27B

RE= 1.0000 , C= 1.7 , RT= 20

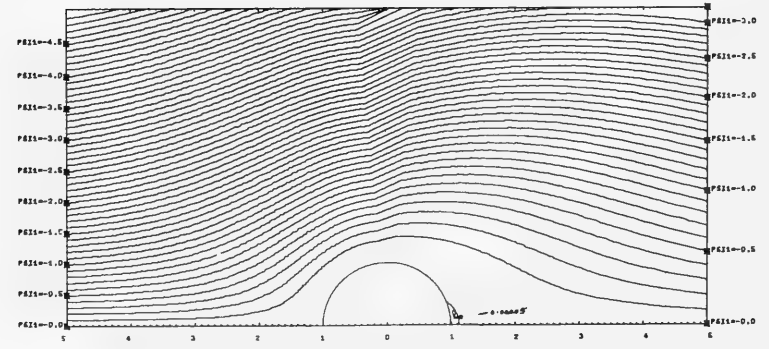

FIRST ITERATION, SUM OF HARMONICS

Fig. 27C

VISCOUS STREAMLINE FIELD BEHIND A CIRCULAR CYLINDER

RE= 1.0000 , C= 1.7 , RT= 20

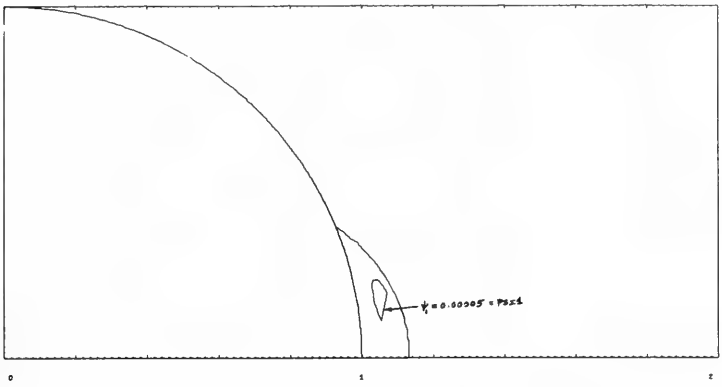

FIRST ITERATION, SUM OF HARMONICS

VISCOUS STREAMLINE FIELD AROUND A CIRCULAR CYLINDER

RE= 1.0000 , C= 1.7 , RT= 20

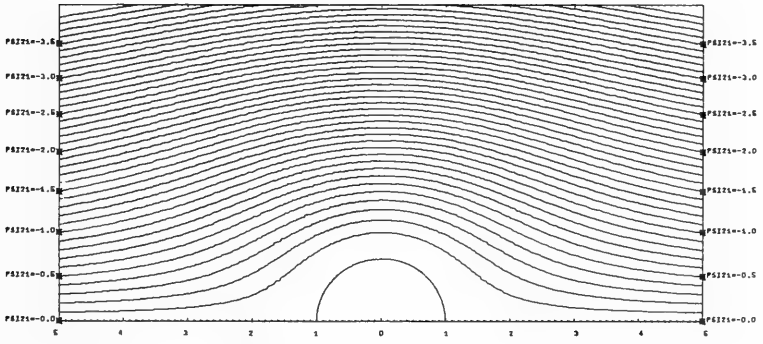

FIRST AND SECOND ITERATIONS, FIRST HARMONIC

VISCOUS STREAMLINE FIELD AROUND A CIRCULAR CYLINDER

RE= 1.0000 , C= 1.7 , RT= 20

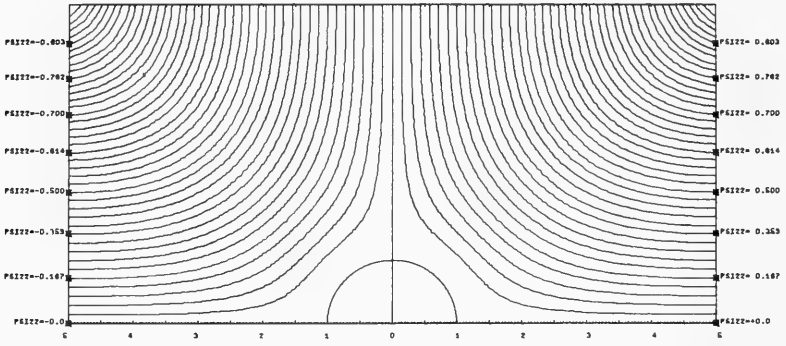

FIRST AND SECOND ITERATIONS, SECOND HARMONIC Fig. 27f

RE= 1.0000 , C= 1.7 , RT= 20

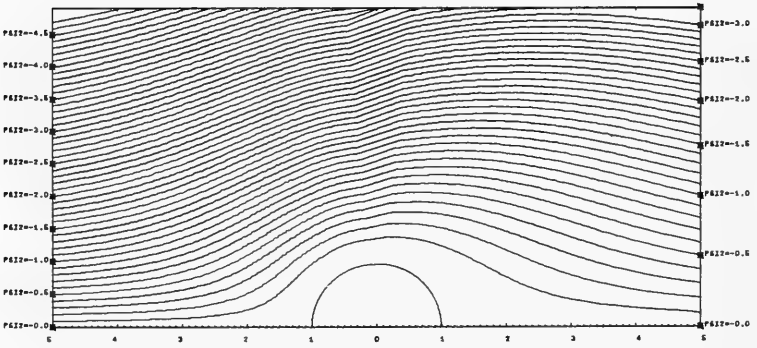

FIRST AND SECOND ITERATIONS, SUM OF HARMONICS Fig. 27g

VISCOUS STREAMLINE FIELD AROUND A CIRCULAR CYLINDER

RE= 2.0000 , C= 1.6 , RT= 12

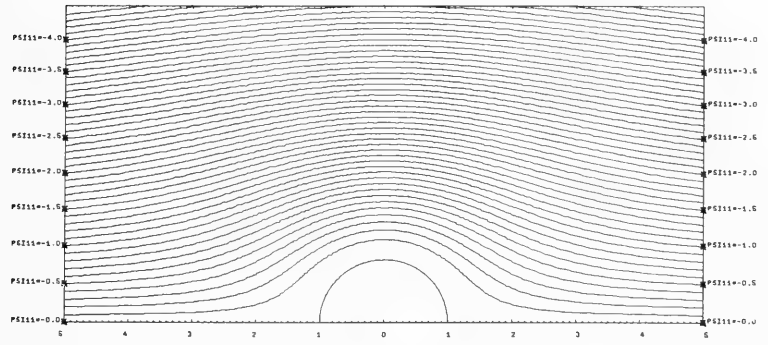

FIRST ITERATION, FIRST HARMONIC

Fig. 2A

RE= 2.0000 , C= 1.6 , RT= 12

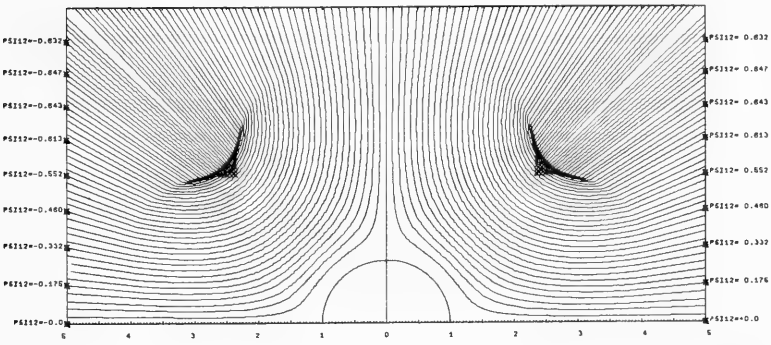

FIRST ITERATION, SECOND HARMONIC

Fig. 2B

RE= 2.0000 , C= 1.6 , RT= 12

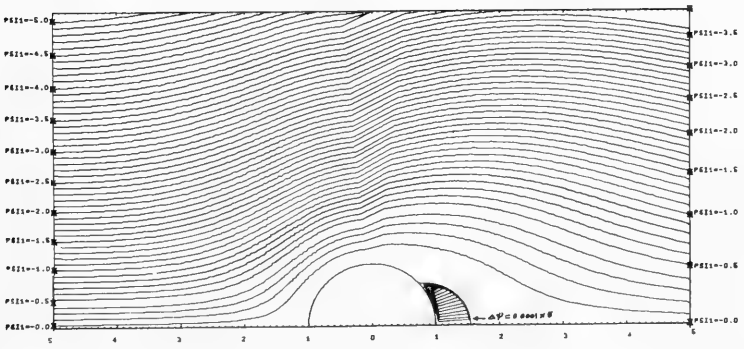

FIRST ITERATION, SUM OF HARMONICS

Fig. 2C

VISCOUS STREAMLINE FIELD BEHIND A CIRCULAR CYLINDER

RE= 2.0000 , C= 1.6 , RT= 12

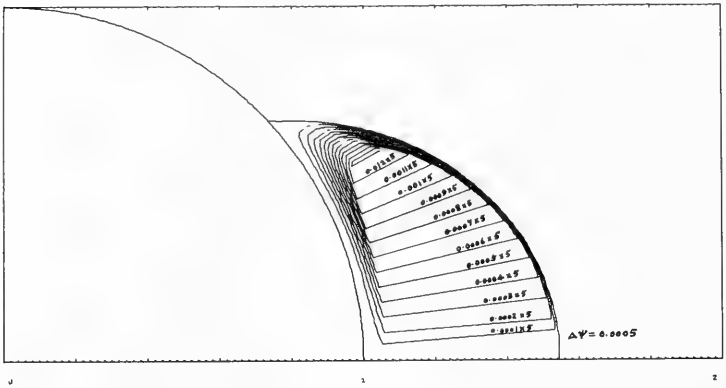

FIRST ITERATION, SUM OF HARMONICS

VISCOUS STREAMLINE FIELD AROUND A CIRCULAR CYLINDER

RE= 2.0000 , C= 1.6 , RT= 12

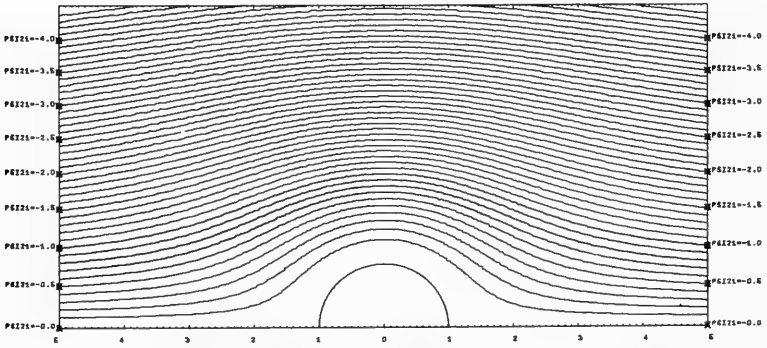

FIRST AND SECOND ITERATIONS, FIRST HARMONIC

VISCOUS STREAMLINE FIELD AROUND A CIRCULAR CYLINDER

RE= 2.0000 , C= 1.6 , RT= 12

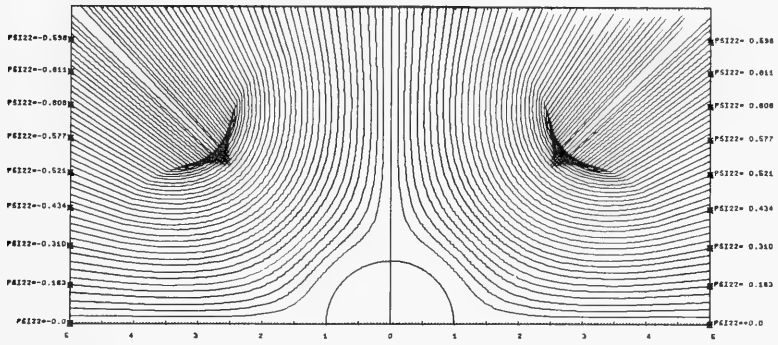

FIRST AND SECOND ITERATIONS, SECOND HARMONIC Fig. 28F

RE= 2.0000 , C= 1.6 , RT= 12

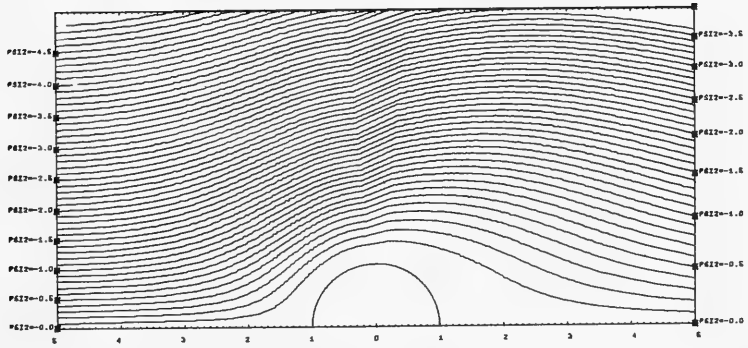

FIRST AND SECOND ITERATIONS, SUM OF HARMONICS Fig. 28G

VISCOUS STREAMLINE FIELD AROUND A CIRCULAR CYLINDER

RE= 2.7500 , C= 1.4 , RT= 10

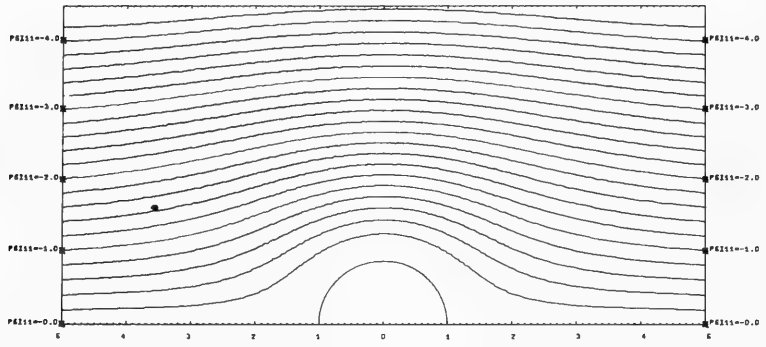

FIRST ITERATION, FIRST HARMONIC

FIG. 29A

RE= 2.7500 , C= 1.4 , RT= 10

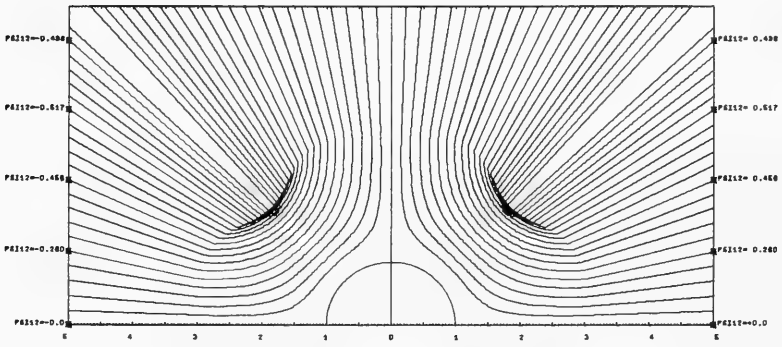

FIRST ITERATION, SECOND HARMONIC

FIG. 29B

RE= 2.7500 , C= 1.4 , RT= 10

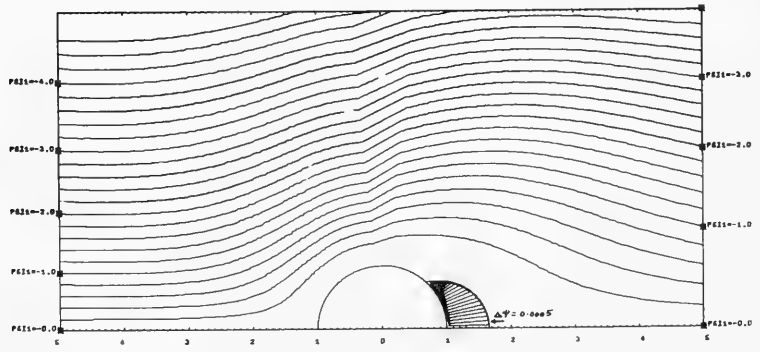

FIRST ITERATION, SUM OF HARMONICS

FIG. 29C

VISCOUS STREAMLINE FIELD BEHIND A CIRCULAR CYLINDER

RE= 2.7500 , C= 1.4 , RT= 10

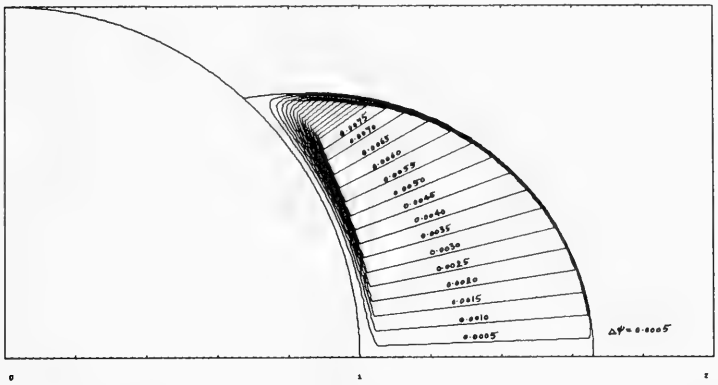

FIRST ITERATION, SUM OF HARMONICS Fig. 29D

VISCOUS STREAMLINE FIELD AROUND A CIRCULAR CYLINDER

RE= 2.7500 , C= 1.4 , RT= 10

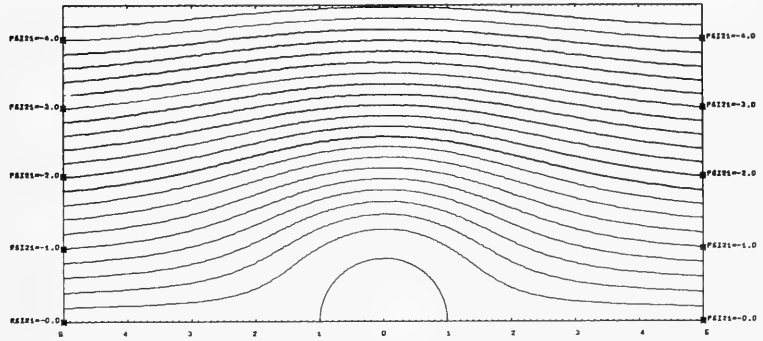

FIRST AND SECOND ITERATIONS, FIRST HARMONIC Fig. 29E

RE= 2.7500 , C= 1.4 , RT= 10

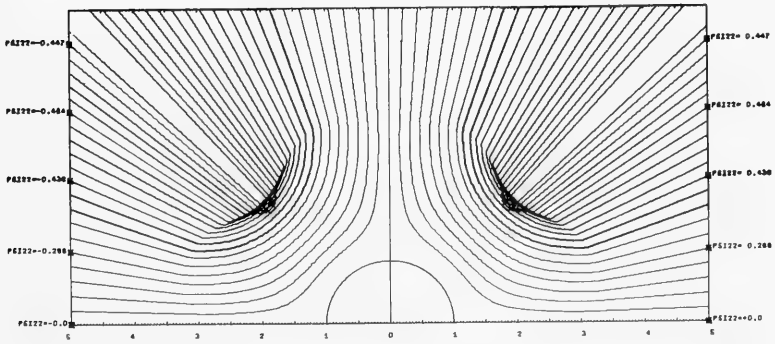

FIRST AND SECOND ITERATIONS, SECOND HARMONIC Fig. 29F

VISCOUS STREAMLINE FIELD AROUND A CIRCULAR CYLINDER

RE= 2.7500 , C= 1.4 , RT= 10

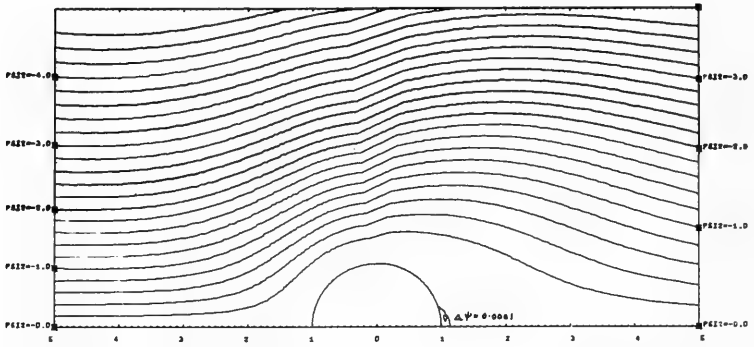

FIRST AND SECOND ITERATIONS, SUM OF HARMONICS

VISCOUS STREAMLINE FIELD BEHIND A CIRCULAR CYLINDER

RE= 2.7500 , C= 1.4 , RT= 10

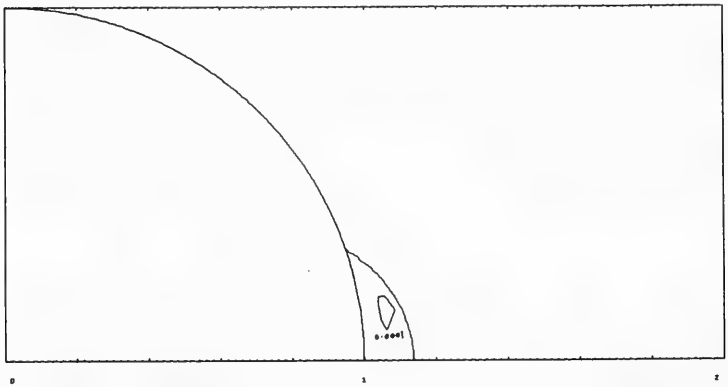

FIRST AND SECOND ITERATIONS, SUM OF HARMONICS

VISCOUS STREAMLINE FIELD AROUND A CIRCULAR CYLINDER

RE= 4.0000 , C= 1.4 , RT= 8

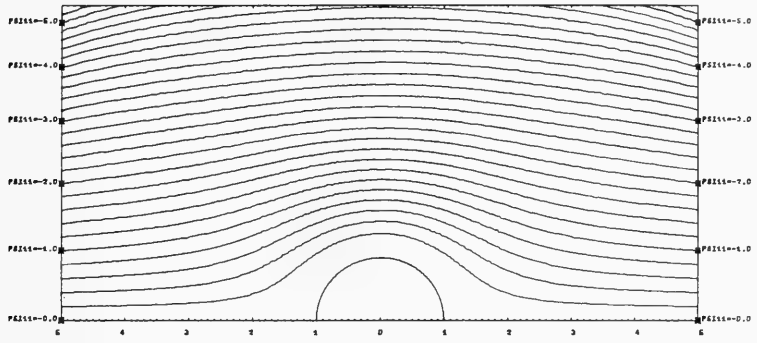

FIRST ITERATION, FIRST HARMONIC

RE= 4.0000 , C= 1.4 , RT= 8

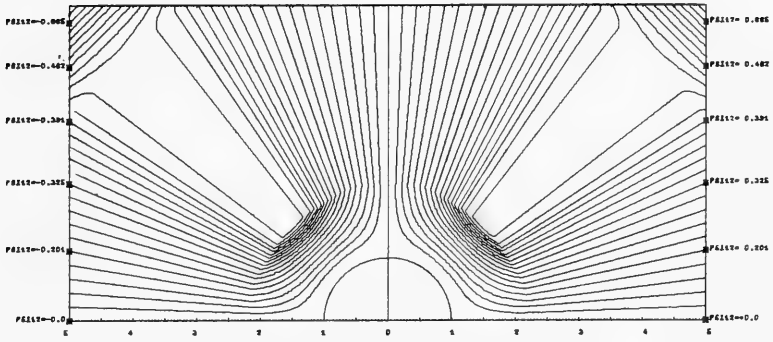

FIRST ITERATION, SECOND HARMONIC

RE= 4.0000 , C= 1.4 , RT= 8

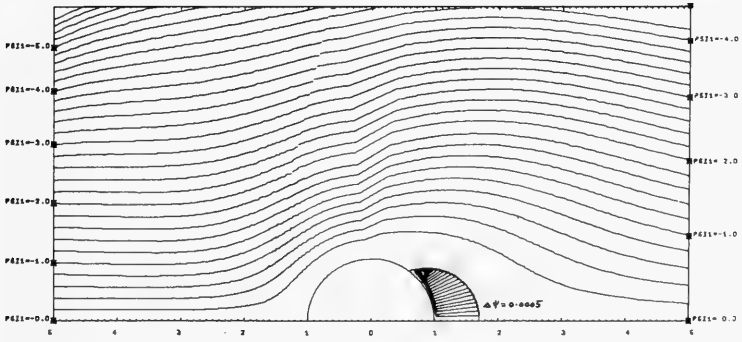

FIRST ITERATION, SUM OF HARMONICS

VISCOUS STREAMLINE FIELD BEHIND A CIRCULAR CYLINDER

RE= 4.0000 , C= 1.4 , RT= 8

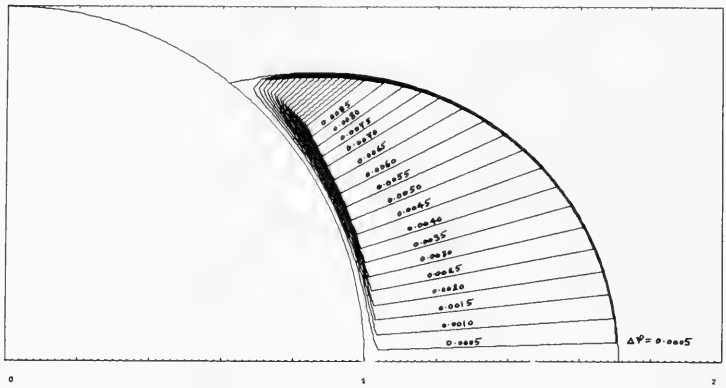

FIRST ITERATION, SUM OF HARMONICS Fig. 30D

VISCOUS STREAMLINE FIELD AROUND A CIRCULAR CYLINDER

RE= 4.0000 , C= 1.4 , RT= 8

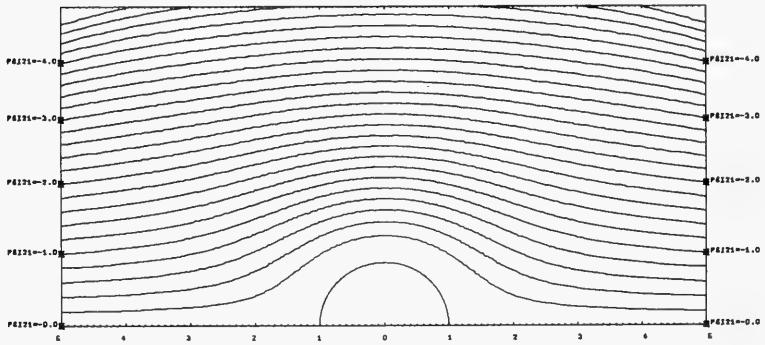

FIRST AND SECOND ITERATIONS, FIRST HARMONIC Fig. 30E

RE= 4.0000 , C= 1.4 , RT= 8

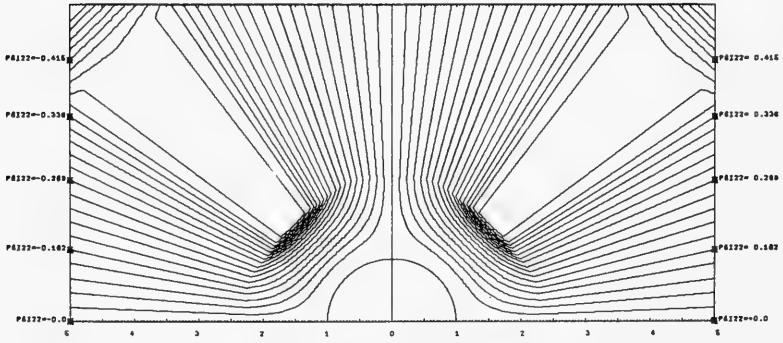

FIRST AND SECOND ITERATIONS, SECOND HARMONIC Fig. 30F

VISCOUS STREAMLINE FIELD AROUND A CIRCULAR CYLINDER

RE= 4.0000 , C= 1.4 , RT= 8

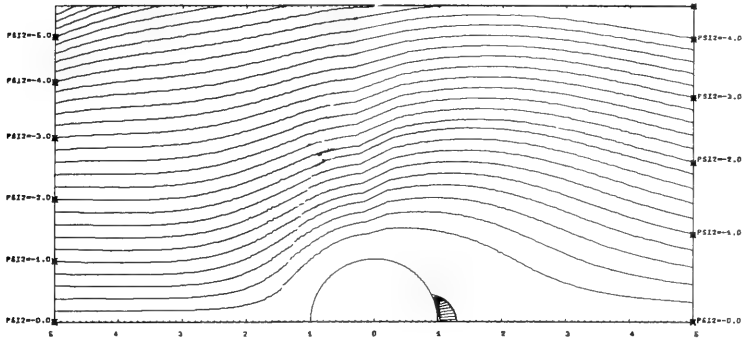

FIRST AND SECOND ITERATIONS, SUM OF HARMONICS Fig. 30a

VISCOUS STREAMLINE FIELD BEHIND A CIRCULAR CYLINDER

RE= 4.0000 , C= 1.4 , RT= 8

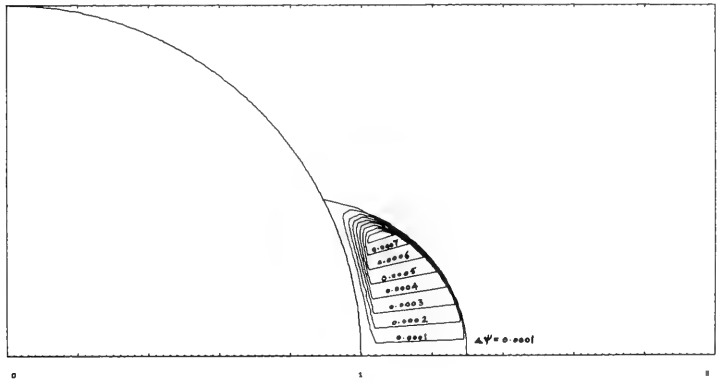

FIRST AND SECOND ITERATIONS, SUM OF HARMONICS Fig. 30b

VISCOUS STREAMLINE FIELD AROUND A CIRCULAR CYLINDER

RE= 7.5000 , C= 1.2 , RT= 4

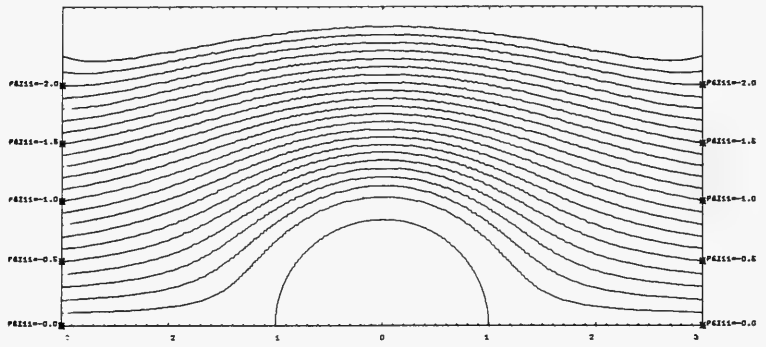

FIRST ITERATION, FIRST HARMONIC

Fig. 3.1A

RE= 7.5000 , C= 1.2 , RT= 4

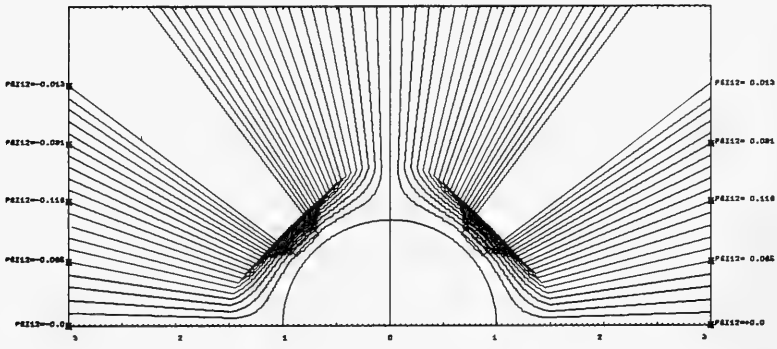

FIRST ITERATION, SECOND HARMONIC

Fig. 3.1B

RE= 7.5000 , C= 1.2 , RT= 4

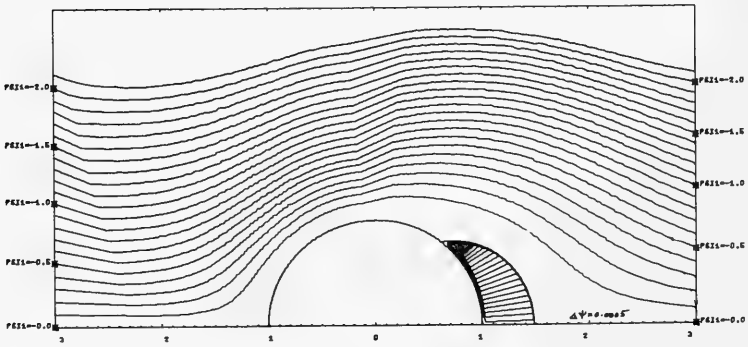

FIRST ITERATION, SUM OF HARMONICS

Fig. 3.1C

VISCOUS STREAMLINE FIELD BEHIND A CIRCULAR CYLINDER

RE= 7.5000 , C= 1.2 , RT= 4

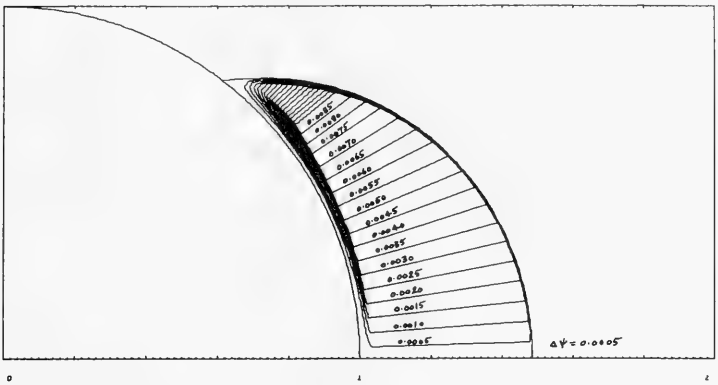

FIRST ITERATION, SUM OF HARMONICS FIG. 31D

VISCOUS STREAMLINE FIELD AROUND A CIRCULAR CYLINDER

RE= 7.5000 , C= 1.2 , RT= 4

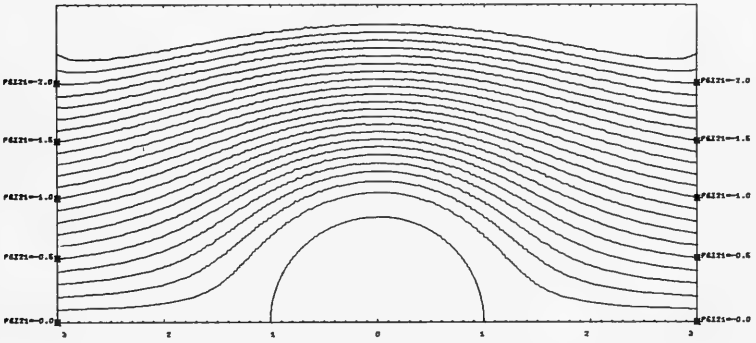

FIRST AND SECOND ITERATIONS, FIRST HARMONIC FIG. 31E

RE= 7.5000 , C= 1.2 , RT= 4

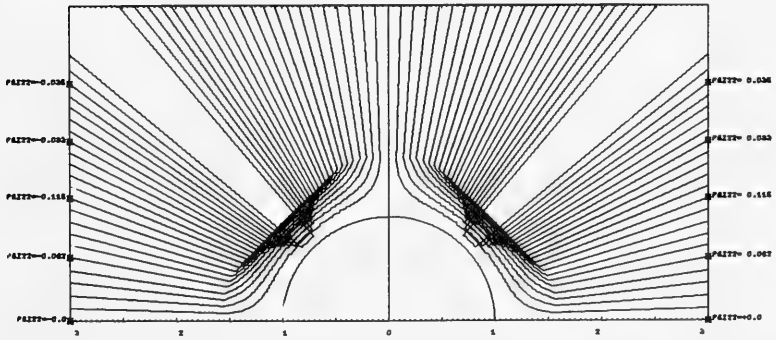

FIRST AND SECOND ITERATIONS, SECOND HARMONIC FIG. 31F

VISCOUS STREAMLINE FIELD AROUND A CIRCULAR CYLINDER

RE= 7.5000 , C= 1.2 , RT= 4

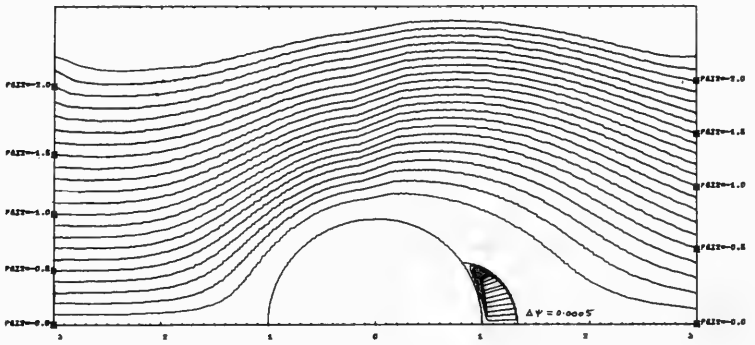

.FIRST AND SECOND ITERATIONS, SUM OF HARMONICS FIG3(6.

VISCOUS STREAMLINE FIELD BEHIND A CIRCULAR CYLINDER

RE= 7.5000 , C= 1.2 , RT= 4

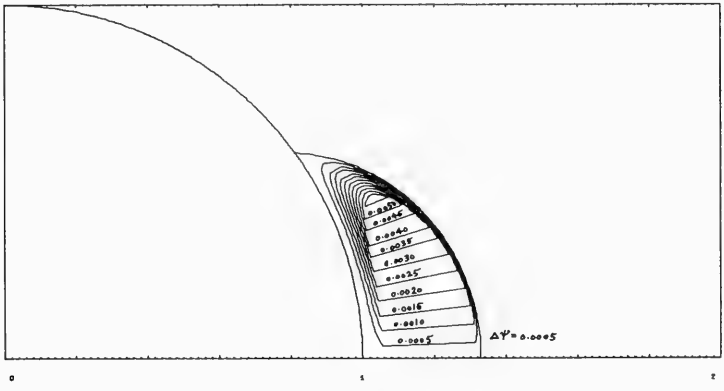

FIRST AND SECOND ITERATIONS, SUM OF HARMONICS FIG3(b)

VISCOUS STREAMLINE FIELD AROUND A CIRCULAR CYLINDER

RE= 10.000 , C= 1.1 , RT= 3.5

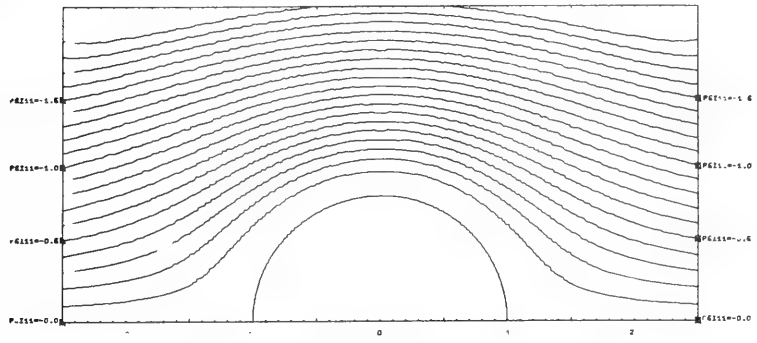

FIRST ITERATION, FIRST HARMONIC

Fig. 3.2A

RE= 10.000 , C= 1.1 , RT= 3.5

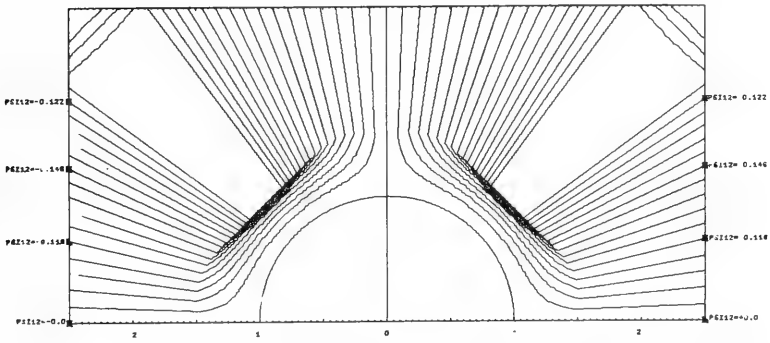

FIRST ITERATION, SECOND HARMONIC

Fig. 3.2B

RE= 10.000 , C= 1.1 , RT= 3.5

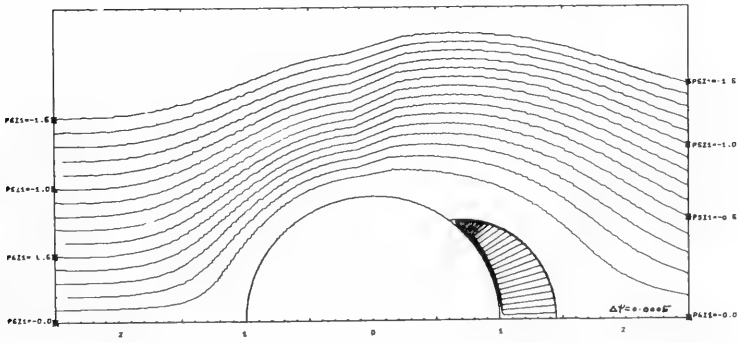

FIRST ITERATION, SUM OF HARMONICS

Fig. 3.2C

VISCOUS STREAMLINE FIELD BEHIND A CIRCULAR CYLINDER

RE= 10.000 , C= 1.1 , RT= 3.50

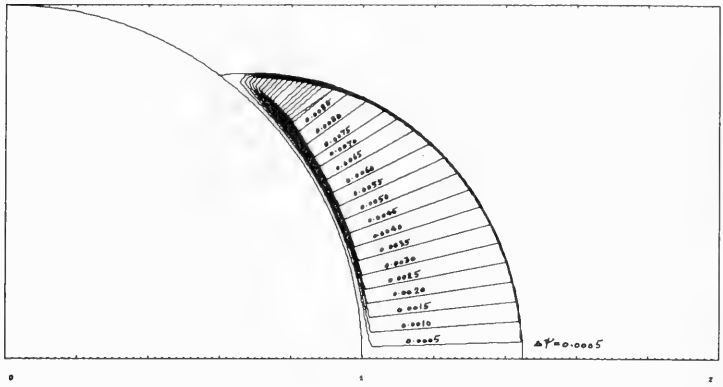

FIRST ITERATION, SUM OF HARMONICS Fig.33

VISCOUS STREAMLINE FIELD AROUND A CIRCULAR CYLINDER

RE= 10.000 , C= 1.1 , RT= 3.5

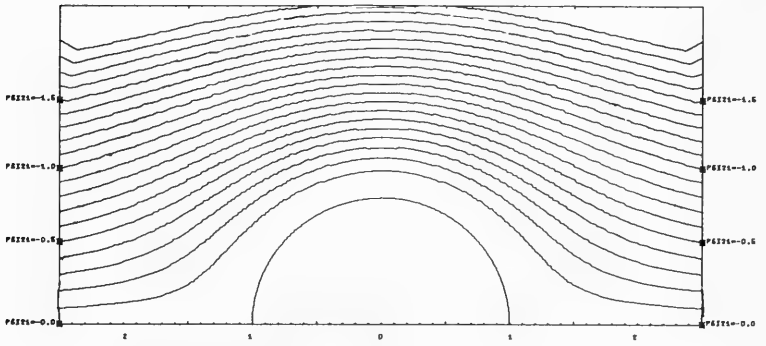

FIRST AND SECOND ITERATIONS, FIRST HARMONIC Fig.34E

RE= 10.000 , C= 1.1 , RT= 3.5

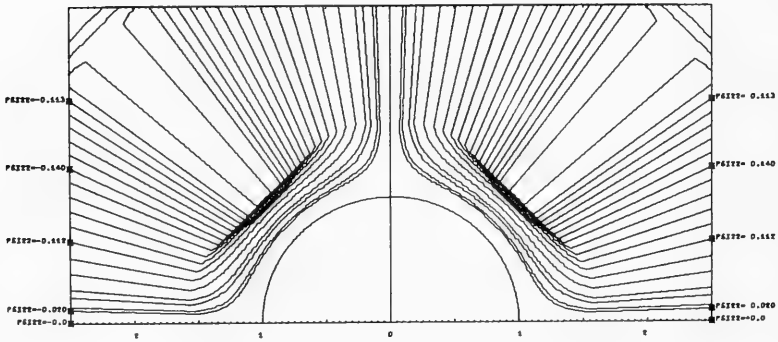

FIRST AND SECOND ITERATIONS, SECOND HARMONIC Fig.34F

VISCOUS STREAMLINE FIELD AROUND A CIRCULAR CYLINDER

RE= 10.000 , C= 1.1 , RT= 3.5

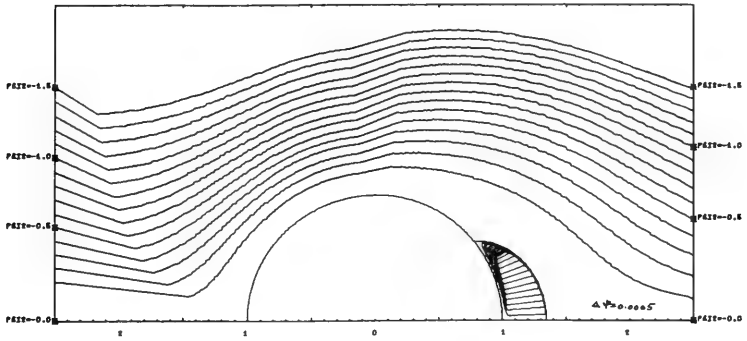

FIRST AND SECOND ITERATIONS, SUM OF HARMONICS FIG 33G

VISCOUS STREAMLINE FIELD BEHIND A CIRCULAR CYLINDER

RE= 10.000 , C= 1.1 , RT= 3.50

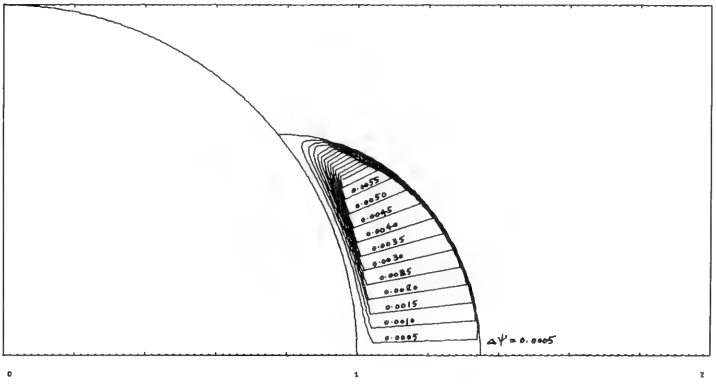

FIRST AND SECOND ITERATIONS, SUM OF HARMONICS FIG 33H

VISCOUS STREAMLINE FIELD AROUND A CIRCULAR CYLINDER

RE= 15.000 , C= 1.0 , RT= 2.75

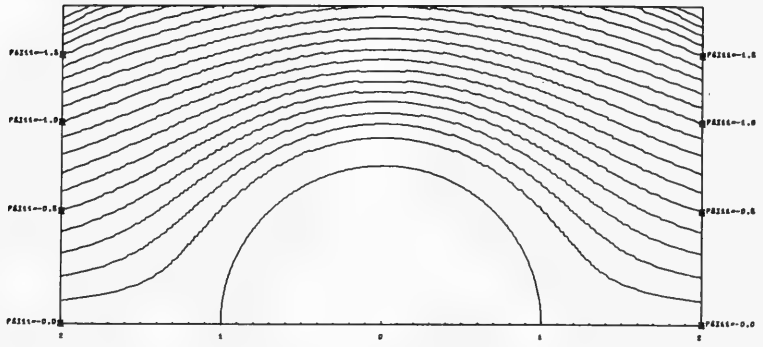

FIRST ITERATION, FIRST HARMONIC Fig. 3A

RE= 15.000 , C= 1.0 , RT= 2.75

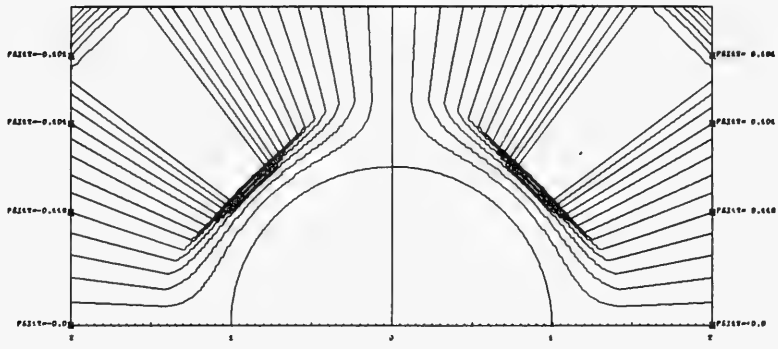

FIRST ITERATION, SECOND HARMONIC Fig. 3B

RE= 15.000 , C= 1.0 , RT= 2.75

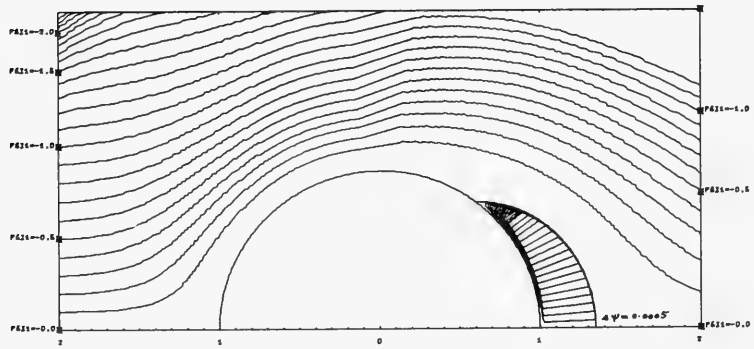

FIRST ITERATION, SUM OF HARMONICS Fig. 3C

VISCOUS STREAMLINE FIELD BEHIND A CIRCULAR CYLINDER

RE= 15.000 , C= 1.0 , RT= 2.75

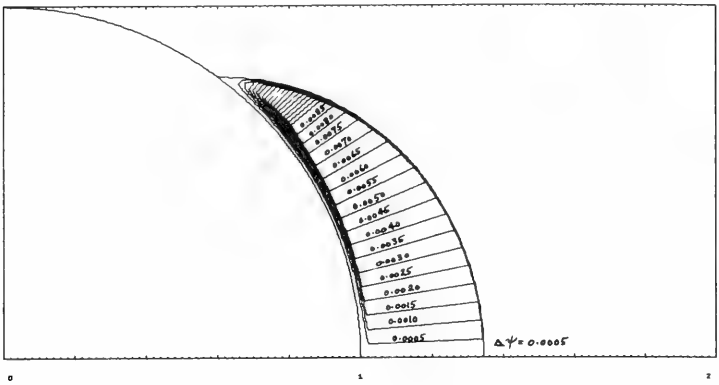

FIRST ITERATION, SUM OF HARMONICS FIG 33D

VISCOUS STREAMLINE FIELD AROUND A CIRCULAR CYLINDER

RE= 15.000 , C= 1.0 , RT= 2.75

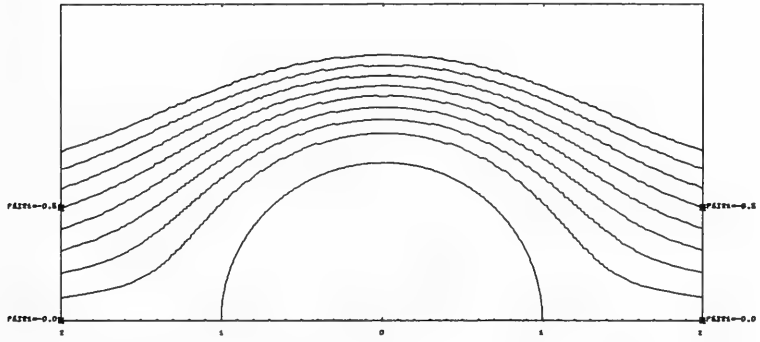

FIRST AND SECOND ITERATIONS, FIRST HARMONIC FIG 33E

E= 15.000 , C= 1.0 , RT= 2.75

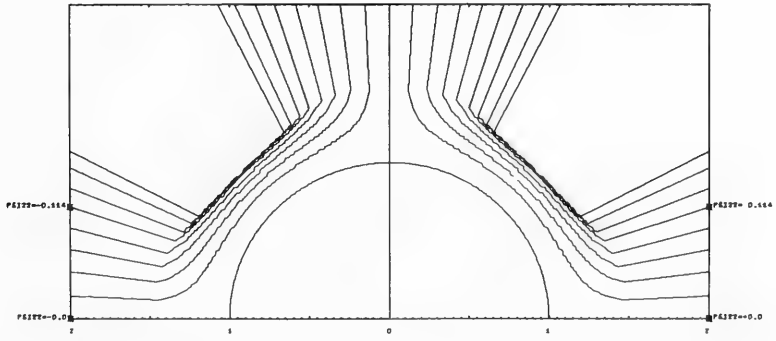

FIRST AND SECOND ITERATIONS, SECOND HARMONIC FIG 33F

VISCOUS STREAMLINE FIELD AROUND A CIRCULAR CYLINDER

RE= 15.000 , C= 1.0 , RT= 2.75

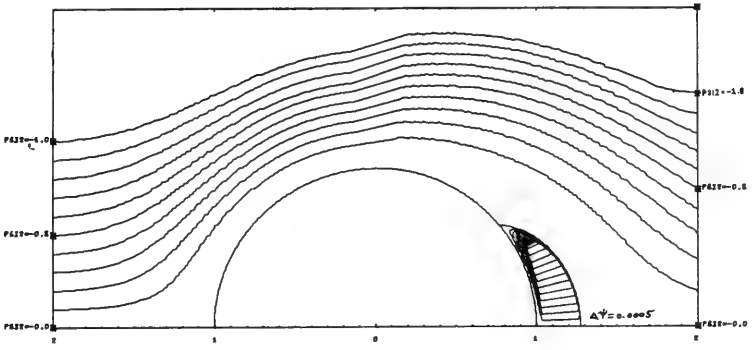

FIRST AND SECOND ITERATIONS, SUM OF HARMONICS FIG. 33C

VISCOUS STREAMLINE FIELD BEHIND A CIRCULAR CYLINDER

RE= 15.000 , C= 1.0 , RT= 2.75

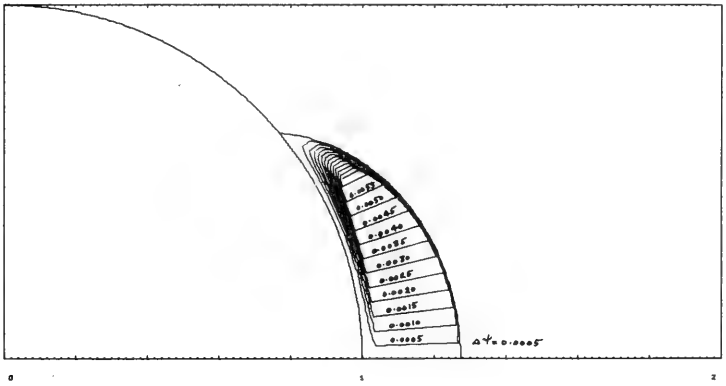

FIRST AND SECOND ITERATIONS, SUM OF HARMONICS FIG. 33H

VISCOUS STREAMLINE FIELD AROUND A CIRCULAR CYLINDER

RE= 20.000 , C= 0.9 , RT= 2.25

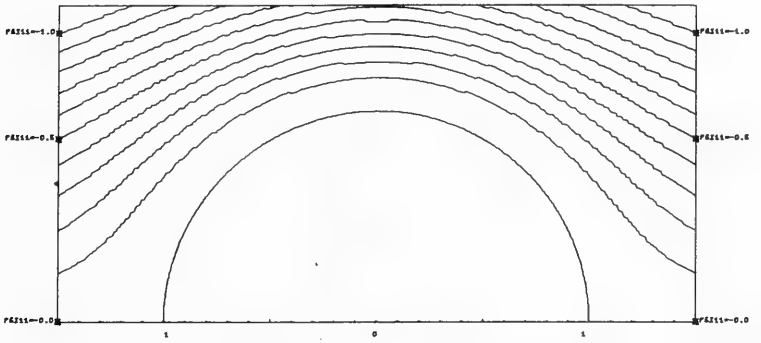

FIRST ITERATION, FIRST HARMONIC

Fig. 34A

RE= 20.000 , C= 0.9 , RT= 2.25

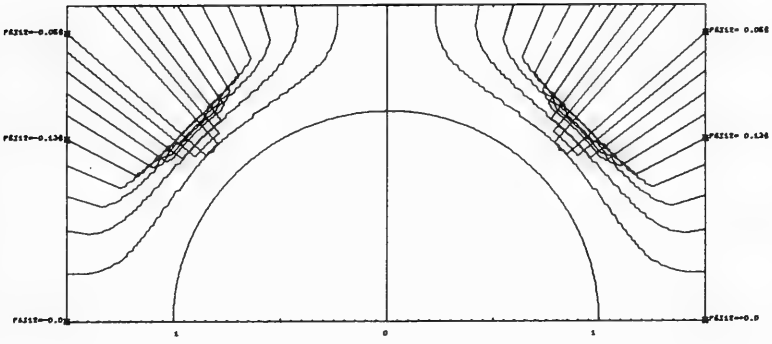

FIRST ITERATION, SECOND HARMONIC

Fig. 34B

RE= 20.000 , C= 0.9 , RT= 2.25

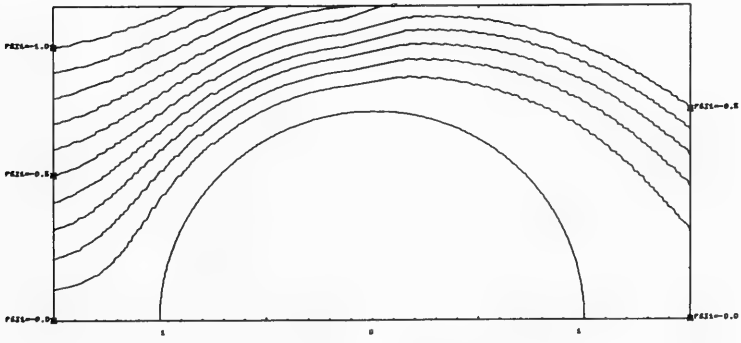

FIRST ITERATION, SUM OF HARMONICS

Fig. 34C

VISCOUS STREAMLINE FIELD AROUND A CIRCULAR CYLINDER

RE= 20.000 , C= 0.9 , RT= 2.25

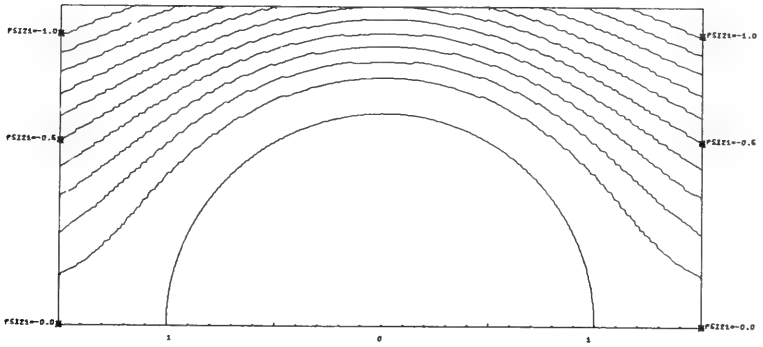

FIRST AND SECOND ITERATIONS, FIRST HARMONIC FIG.34D

RE= 20.000 , C= 0.9 , RT= 2.25

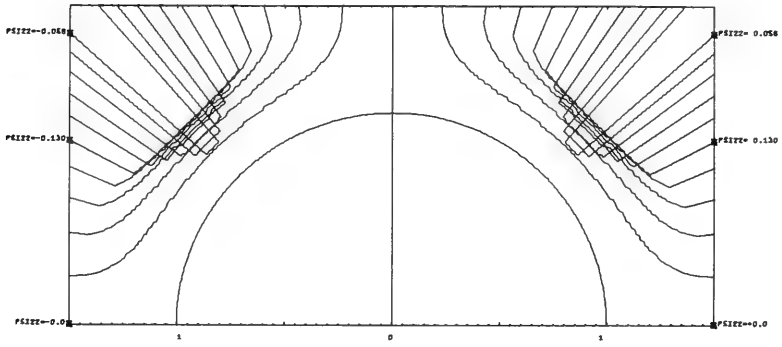

FIRST AND SECOND ITERATIONS, SECOND HARMONIC FIG.34E

RE= 20.000 , C= 0.9 , RT= 2.25

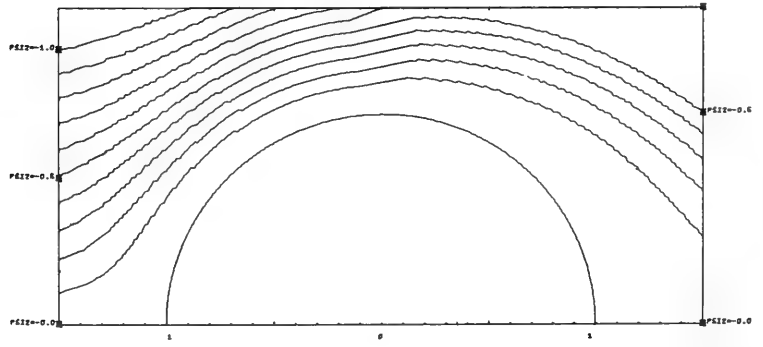

FIRST AND SECOND ITERATIONS, SUM OF HARMONICS FIG.34F

DISCUSSION

Dr. I. M. Schmiechen
Versuchsanstalt für Schiffbau
Hamburg, Germany

The approach of Prof. Lieber will undoubtedly be of great importance in the theory of viscous flows, and I congratulate him on the numerical results he has obtained so far. Actually, I tried to follow the same line on a smaller scale years ago. Coming from the thermodynamics of irreversible processes, I was wondering whether the principle of minimum entropy production might have any bearing in hydrodynamics. At that time I was involved in basic research on vortex streets in connection with the general theory of propulsion. The stability problem appeared to be most fundamental and at the same time most tractable. In fact, I derived a criterion of minimum instability for Kárman vortex streets, which is in better agreement with experiments than those derived in the customary fashion.

* * *

DISCUSSION

Dr. K. Wieghardt
Institut für Schiffbau der Universität Hamburg
Hamburg, Germany

A variational principle equivalent to the Navier-Stokes equations can be formulated when Lagrange's coordinates are used. Yet, the principle of minimum dissipation expressed in Eulerian coordinates corresponds to the Navier-Stokes equations only in some restricted cases. Why should it be correct in general?

* * *

REPLY TO DISCUSSION

Paul Lieber

I will first respond to Dr. M. Schmiechen's written discussion and refer to the materials presented therein in subsequently responding to the written comments of Professor K. Wieghardt. A self-contained bibliography is attached to facilitate the examination of the references cited in my response to the comments of the two discussants.

COMMENTS ON THE DISCUSSION OF DR. SCHMIECHEN

Dr. M. Schmiechen's encouraging written comments are very much appreciated, as they are evidently motivated by an exceptional insight into the nature of our work, which is concerned with the foundations of the theory of viscous flows, and by a grasp of its significance in producing an algorithm for constructing analytical representations of flow fields using the complete Navier-Stokes equations and realistic boundary conditions. We are especially grateful to Dr. Schmiechen, as his comments are somewhat characteristic of the encouraging response to this work which some colleagues kindly communicated to me in person during the symposium. Accordingly, the present reply affords the opportunity to also express here in writing my thanks to Professor R. Timman, Professor E. Laitone, Dr. H. H. Chen, and Dr. N. Francev in this regard.

Dr. Schmiechen's insight into our work no doubt stems partially from his researches concerned with the hydrodynamical implications of the thermodynamics of irreversible processes, and in particular with the principle of minimum entropy production, which he cites in his comments and from which he derives a very interesting criterion of minimum instability pertaining to the development of the Karman vortex street. The reported criterion of minimum instability appears highly significant in the context of our study, as it evidently bears a correspondence to and may be a particular aspect of a general stability principle which has emerged from our work. This stability principle and the conceptual background which lead to its identification are discussed in some detail in the paper appearing in the present studies with the title "Aspects of the Principle of Maximum Uniformity: a New and Fundamental Principle of Mechanics."

The theoretical basis of the materials presented in the six papers included in the present studies were originally and conceptionally motivated by information we obtained by using Carl Gauss's [1] and Heinrich Hertz's [2] formulations of the principle of classical mechanics, and by introducing and underlining therein the concept force which they, in fact, endeavored to completely eliminate in their formulations by formal representations of geometrical constraints.

This information which was obtained as a theorem on the distribution of internal forces for a hydrodynamically significant class of mechanical systems [3], and which was then generalized by hypothesis to be an aspect of all mechanical systems, was the theoretical basis for introducing the principle of minimum dissipation as a general restriction on realizable flow fields in nature [4]. This restriction was thus originally introduced in hydrodynamical theory with the understanding that it augments and compliments the restrictions imposed by the Navier-Stokes equations which were then and are still understood in our work to admit a larger class of flows than the class of realizable flows. However, when we originally introduced the principle of minimum dissipation in 1957 as a general condition on realizable flows, we did not realize, as we do now, that the Navier-Stokes equations do not in principle afford a criterion by which realizable flows are selected in nature from a larger class of admissible flows which also satisfy the physical principle expressed by the Navier-Stokes equations, but which do not in general satisfy a condition of realizability.

Although the theorem on the distribution of internal forces mentioned above was first established in 1953 and subsequently presented on numerous occasions in lectures, it was published in 1963 [3], and then, with modifications, in the 1968 issue of the Israel Journal of Science and Technology, with the title "A Principle of Maximum Uniformity Obtained as a Theorem of the Distribution of Internal Forces." The principle of minimum dissipation was conceived as a general restriction on the class of realizable flows, by identifying a relation between internal forces produced by binary collisions and a dissipation process according to which the energy dissipation was found to be proportional to these forces when the collisions are oblique. Consequently, for the class of oblique collisions that are responsible for dissipation in gas flows, we found that the principle of minimum dissipation may be used to give an approximate and indirect representation to the information obtained from the theorem on the distribution of internal forces cited above. The dissipation mechanism used for this purpose is presented in Ref. 5 and is further discussed and used in Ref. 6.

As previously noted, the principle of minimum dissipation was originally conjectured as a principle of realization from information we obtained by appropriately using the Gauss-Hertz principles of mechanics, and by interpreting this information as a particular and limited aspect of a general natural law, called here the principle of maximum uniformity. This principle evidently includes the established laws of classical mechanics, as well as a realization principle which is tantamount to a stability law. The evolutionary and historical content of the information expressed by this principle of realization is absent in the known laws of classical mechanics, and as far as I can see it is, in fact, not included in any of the known propositions of physical theory as they are written today. The principle of minimum dissipation is, in general, not implied by the Navier-Stokes equations and can be deduced from them only for a highly restricted class of viscous flows which are in fact endowed with unique solutions, because of the linearity of the Navier-Stokes equations by which they are conditioned and uniquely determined. Due to the linearity of the Navier-Stokes equations governing this restricted class of flows and the consequent uniqueness of their solutions, a principle of realization that would in general select a realizable member among multiple admissible solutions to the Navier-Stokes equations is redundant. For this very restricted class of flows the principle of realization, which is the principle of minimum dissipation in the present discussion, and the laws of mechanics as expressed by the Navier-Stokes equations, are equivalent.

Stability criteria which are based on various definitions of stability are essentially motivated by a search for realization criteria that augment and complement the conditions of force equilibrium expressed by the principles of mechanics. The laws of classical mechanics concern a particular aspect of uniformity characterized and defined by the equilibrium of forces. They accordingly express and assert the proposition that this aspect of uniformity, as characterized by the equilibrium of forces, is maintained for each and every body in nature everywhere and always. The notion of force equilibrium to which these laws refer is instantaneously associated with the states of the bodies governed by the laws of mechanics, as are all the other parameters by which the mechanical system is described in the statement of these laws.

We thus see that the information content of the classical laws of mechanics can be noted in two steps: the first consists of the definition of force equilibrium that characterizes a particular aspect of uniformity, and the second consists of a proposition that is based on the previous definition and which asserts that equilibrium so defined is a condition which is constantly and instantaneously maintained everywhere in the domain of classical mechanics. Neither in the definition nor in the proposition does the notion of perturbation appear, since all parameters and statements pertaining thereto are brought into correspondence with the instantaneous configuration of a mechanical system. In man's endeavor to grapple with the notion of stability, elucidate its nature, and grasp the phenomenon of stability as an aspect of nature, he has endeavored to comprehend it by couching it in definitions. This has produced in the literature many definitions of stability, each of which produces different stability criteria. All of these, however, seem to share the notion of a perturbation in terms of which various definitions of stability are formulated. Many of these endeavors inquire into the stability of a mechanical system by subjecting such a system to a perturbation and investigating the subsequent changes the system follows with the passing of time.

The principle of maximum uniformity identifies the stability of a particular member of a mechanical system with its instantaneous state, and correspondingly the global stability of a mechanical system with its instantaneous global state. As in the case of the propositions of classical mechanics, which are expressed in terms of force equilibrium and which assert that this aspect of uniformity is instantaneously and everywhere constantly maintained in classical mechanical systems, so correspondingly according to the principle of maximum uniformity all realizable states are instantaneously maximum-stable under the instantaneously prevailing forces and the constraints to which the system is instantaneously subjected. By this concept of stability there does not exist an instantaneously realizable unstable state, and this concept, like the concept of force equilibrium, does not appeal to the notion of a perturbation. I accordingly believe that Dr. Schmiechen's minimum stability criterion which he derived for the Karman vortex street may be an aspect of the stability principle cited here, and according to which all realizable flows are instantaneously maximum-stable.

When the principle of minimum dissipation was conceived and originally formulated in hydrodynamical terms as an approximate but reasonable representation of the restriction on realizable flows implied by the original and restricted version of the principle of maximum uniformity, we were cognizant of existing thermodynamical theories of weakly irreversible processes and of the principle of minimum entropy production. We were, however, interested in working within the framework of the description, parameters, and functions that are characteristic of classical hydrodynamics, and therefore were interested in formulating restrictions on realizable flows in terms of these, such as, for example, the dissipation function. Furthermore, by so doing we do not necessarily restrict the conditions of realization of actual flows which were introduced to augment the Navier-Stokes equations, to weakly reversible processes. In this regard it is interesting to note that Prigogine, who, I believe, established the principle of minimum entropy production as a theorem in 1947 for highly restricted conditions, has only recently considered and used the principle of

of minimum dissipation as a restriction on a development of viscous flows. As noted, we recognized from the beginning however that the principle of minimum dissipation does not give full expression in hydrodynamical terms even to the restricted version of the principle of maximum uniformity as presented in Ref. 3. For this reason we formulated in 1957 in hydrodynamical terms [7] a more comprehensive statement of the principle of maximum uniformity which in fact rendered the principle of minimum dissipation as a theorem for a more restricted class of viscous flows. In both of these formulations the integrands are expressed in terms of quantities which have the physical dimension of energy.

The extended version of the principle of maximum uniformity as discussed in the paper appearing in the present studies with the title "Aspects of the Principle of the Maximum Uniformity: a New and Fundamental Principle of Mechanics," gives increasing emphasis to the idea that the most fundamental aspects of nonuniformity in nature are directly manifested by forces rather than by energy. This subsequent theoretical development and an indeterminancy incurred in the application of the hydrodynamical variational principle presented in [7] accounts, in part, for the procedure which led to the algorithm presented in these studies for constructing analytical representations of viscous flows by using the complete Navier-Stokes equations — a procedure which gives tacit expression to the principle of maximum uniformity, i.e., without explicitly referring to a global force measure of nonuniformity. For the above reasons we have tried to formulate the extended version of the principle of maximum uniformity in mathematical terms for Newtonian fluids by constructing an appropriate global force measure. Concurrently, we have also endeavored to carry out the same program in developing a kinetic theory of gases with internal degrees of freedom in which the principle of maximum uniformity is formulated as a condition of realization of actual states. We have in both cases achieved some success. In the hydrodynamical case, we have formulated new hydrodynamical principles which may be effectively used for the numerical calculation of steady, inviscid, stratified flow fields. This is noted in the paper of the present studies entitled "Comparative Studies of Hydrodynamical Principles, Based on the Principle of Maximum Uniformity." These formulations are being extended, but with difficulty, to include viscous forces and time-dependent forces as well. We are doing this in two steps. First, the inclusion of time-dependent forces without viscous forces. This we have been able to carry out for a significant class of inviscid time-dependent flow fields by using a global force in the statement of the appropriate variational principles. We have considerable difficulty, however, in carrying out the second step, which will include viscous as well as time-dependent forces in the force functional of the variational principle which expresses hydrodynamically the condition of realization of actual flow fields as invoked by the principle of maximum uniformity.

Concerning the embodiment of the principle of maximum uniformity in a kinetic theory of gases and its application to specific situations, we have already obtained some encouraging results. In so doing, we find linear substructures underlying solutions to the nonlinear equations obtained from the application of the principle to the kinetic theory gases, that are analogous to the linear substructure of the complete Navier-Stokes equations on which the algorithm

used in the present volume to construct analytical representations of viscous incompressible flows is based.

In concluding my response to Dr. Schmiechen's obviously inspiring discussion, it is relevant to present here the conjecture that the question of statistical stability versus the stability of individual flows as noted by Professor R. Kraichnan may possibly be resolved, if we understand averaging to be an aspect of uniformity and therefore to offer implicitly a condition of realization for actual fields. This, in principle, is not included in the Navier-Stokes equations for the reasons given above, and which are given more extensively in some of the papers we present in these studies. It is also relevant to draw attention here to the possibility that the dramatic reduction of the friction coefficient obtained by the addition of minute quantities of certain polymers to turbulent flow may also be an aspect of the principle of maximum uniformity. We are trying to pinpoint the connection between them, with the guiding hypothesis that the polymer material physically produces sites of high nonuniformity in the viscous flow fields, and therefore as a consequence of the principle of maximum uniformity both assume the role of control centers that dominate the evolution of actual flow fields.

COMMENTS ON THE DISCUSSION OF DR. WIEGHARDT

First, in Ref. 8, we presented in 1957 a formulation of a hydrodynamical variational principle that gives the complete Navier-Stokes equations as the Euler-Lagrange condition expressed in terms of the Eulerian description of flows. As noted in the paper in the present studies entitled "Comparative Study of Hydrodynamical Variational Principles, Based on the Principle of Maximum Uniformity," this hydrodynamical variational principle has been successively applied by us and subsequently by others for the purpose for which it was invented.

I believe that an adequate response to the important question Dr. Wieghardt raises concerning the range of validity of the principle of minimum dissipation is contained in my response to Dr. Schmiechen's discussion and in the materials included in the six papers we present in these studies. It was this question which in part motivated my extended response to Dr. Schmiechen's remarks.

CONCLUDING REMARK

In responding above to the comments of Dr. Schmiechen and Dr. K. Wieghardt, a fundamental distinction is made between flow fields allowed by certain established laws of physics and flow fields that are realized. This distinction is grounded in the observation that the laws of classical mechanics are essentially devoid of evolutionary content and information and that a principle of realization is a principle of evolution, i.e., evolution is the process of realization.

REFERENCES

1. Gauss, C.F., "On a New General Fundamental Principle of Mechanics," Creele's J. Math. 4, 232 (1829)

2. Hertz, H., "Principles of Mechanics," Collected Works, Vol. II, New York: MacMillan, 1896

3. Lieber, P., "A Principle of Maximum Uniformity Obtained as a Theorem on the Distribution of Internal Forces," Institute of Engineering Research, University of California, Berkeley, Nonr-222 (87), MD-63-8, Apr. 1963 (Also published in the Israel J. Sci. Technol., Apr. 1968)

4. Lieber, P., and Wan, K.W., "A Principle of Minimum Dissipation for Real Fluids," Int. Congr. Mech., Proc. IX, Brussels, Belgium, 1957 (Also issued in August, 1957 by Rensselaer Polytechnic Institute, Troy, N.Y., as a Research Division Report AFOSR TN 57-477, AD 136-469, Aug. 1957, and released, Office of Scientific Research, USAF, as TN 57-477, under Contract AF 18(600)-1704, Aug. 1957)

5. Lieber, P., "A Dissipation Mechanism in Gas Flows and Similar Physical Systems," Trans. N.Y. Acad. Sci., Vol. II (No. 5), 175-181 (1949)

6. Lieber, P., "The Mechanical Evolution of Clusters by Binary Elastic Collisions and Conception of a Crucial Experiment on Turbulence," Volume of the Proceedings of Symposium on Second-Order Effects in Elasticity, Plasticity, and Fluid Dynamics, sponsored by the International Union of Theoretical and Applied Mechanics, Apr. 1962; edited by Prof. Markus Reiner, Holland: Elseview Press, 1968

7. Lieber, P., and Wan, K.S., "A Proof and Generalization of the Principle of Minimum Dissipation," issued by the Rensselaer Polytechnic Institute, Troy, N.Y., Sept. 1957; also released to the Office of Scientific Research, USAF, under contract AF 18 (600)-1704

8. Lieber, P., and Wan, K.S., "A Principle of Virtual Displacements for Real Fluids," Int. Congr. Mech., Proc. IX, Brussels, Belgium, 1957 (Also issued as a Rensselaer Polytechnic Institute Research Division Report AFOSR TN 57-476, AD 136 468, under Air Force Contract AF 18(600)-1704, July 1957

* * *

IV—Comparative Study of Hydrodynamical Variational Principles, Based on the Principle of Maximum Uniformity

Paul Lieber
University of California
Berkeley, California

In this paper I endeavor to communicate the salient features and results of a study originating in 1953, which has since then been committed to the conception and application of variational principles to flow fields conditioned by the complete Navier-Stokes equations.

At the beginning of this search, we formulated two distinct types of variational principles which were motivated by essentially different considerations and objectives. In one case we sought to formulate a statement as a variational principle which renders, according to a prescribed procedure for performing the variations, the complete Navier-Stokes equations, as its Euler-Lagrange differential equations. In so doing, the variational methods of Rayleigh-Ritz, Galerkin, and related methods, may be used to obtain approximate but nevertheless useful analytical representations of viscous flow fields, in a manner which is analogous to the application of these variational methods in the mechanics of solids, where the variational principles to which they are applied have already been known for some time. Such a variational principle was formulated and effectively applied by Lieber and Wan, and is presented in the Proceedings of the IX International Congress of Theoretical and Applied Mechanics, published in Brussels, Belgium, in 1957 [1]. Since then, it has been successfully applied by Wan and others (Prigogine and Shecter), with small modifications, to obtain useful approximate mathematical representations of viscous flow fields produced in nature. These successful applications of this variational principle attest to its power and practical value.

At this point, it is convenient and important to draw attention to the fundamental distinction that must be made between a variational principle and a variational method, a distinction which evidently is not understood even by individuals who write comprehensive papers on the search for variational principles [2].* A variational principle is a proposition that refers to and conditions

*Ref. (2) overlooks this distinction by not grasping the outstanding contribution of M.A. Biot.

natural phenomena — it is a statement of a natural law. A variational method is a mathematical scheme for deriving the analytical consequences from a statement that expresses the stationary quality of a certain functional, and in particular of a variational principle which is so formulated. In the case noted above, the information content of the variational principle which we formulated is essentially equivalent to that of the Navier-Stokes equations, which are its Euler-Lagrange equations. The Navier-Stokes equations express the proposition that all forces acting on each and every element of the materials in nature which are adequately modeled by a Newtonian fluid, are constantly in equilibrium, i.e., everywhere and for all time. The statement which formally defines a Newtonian fluid expresses a connection between force geometry and time, and is of the nature of a force law which is however restricted to, and thus identifies, certain macromechanical features of a class of natural materials. The known laws of mechanics which are statements of the equilibrium of forces, are not laws of force, but are instead propositions asserting certain necessary and constant connections that are maintained between all forces acting on any and every component of a classical mechanical system.

The particular simple connection between forces, by which mechanical equilibrium is defined, is a particular aspect of uniformity which according to the laws of classical mechanics is constantly maintained everywhere in space and always in time, for all material bodies. The fact that the known laws of mechanics do not determine the so-called motivating forces which are included in their formulation and which express a connection between them and the motion of material bodies, is made abundantly clear when we consider a substance continuously extended in space as a model for depicting the macromechanical characteristics of systems consisting of a very large number of discrete bodies. In so doing, we obtain, by applying the laws of mechanics, a set of three scalar equations which conditions the three components of acceleration, and the space derivatives of nine components of the stress tensor of each element of the material continuum. The resultant force externally applied to a characteristic element of such a material continuum depends on the stress tensor by which it is externally joined to the universe in which it is situated. By applying the laws of classical mechanics to such a model, we obtain a set of three scalar differential equations which relate the three components of acceleration of a characteristic element of the material, to the partial coordinate derivatives of the nine components of stress, which designate the resultant force by which such a characteristic element of the continuously extended material is externally joined to the universe. From a strictly mathematical viewpoint it is obvious that the nine components of stress in terms of which these forces are formally written are in principle not determined by the principles of mechanics. Indeed, from a mathematical point of view these stresses are highly *undetermined*, even if we ascribe very strong properties of continuity and differentiability to the material substratum. It is for this reason that it has been necessary to specify constitutive relations between stress, geometry, and time in order to obtain an equivalence between the number of relations and the number of parameters used to describe the mechanical features of the system.

The constitutive relations are tantamount to restricted force laws by which the macromechanical properties of particular classes of materials are characterized. Augmenting the laws of classical mechanics by general and/or restricted

force laws is necessary to obtain a physical theory which is determinate even in the strictly mathematical sense. We know from experience, of course, that actual materials cannot in general be mechanically characterized by a fixed constitutive relation that remains constantly appropriate for all physical environments of the material. It is therefore significant to recognize that in general the restricted force laws used to depict appropriately the macromechanical properties of actual materials, may change significantly as their physical environment changes. We are therefore given to consider the concept of the evolution of force fields, i.e., the idea that different kinds of force fields individually depicted by particular constitutive relations, may evolve as the environment of the material changes. We have familiar examples of marked changes in the macromechanical properties of solids when they yield plastically, and of fluids when turbulence develops in them.

The second type of variational principle which Wan and Lieber formulated in 1956 was motivated by an attempt to express and formulate in terms of the parameters of classical hydrodynamics, explicit and general information on the global distribution of internal forces in a many-body classical mechanical system, which Lieber obtained by using Gauss's and Hertz's formulation of the principles of mechanics. This was done with a fundamental modification, which reintroduces and underlines in their formulations the irreducible fundamental nature of force and its nonreducibility to purely abstract geometry [3].

It was the emergence of this fundamental theorem on the distribution of internal forces within the edifice of Gaussian-Hertzian mechanics, and the realization that this information is not rendered explicit without integration, by Newtonian mechanics, that led to the concept "Categories of Information" and to the realization that the various categories of information which were identified are aspects of nature that assume a fundamental role in scientific inquiry and in the development of mathematics [4]. Accordingly, it was realized that questions concerning the equivalence between various formulations of natural laws which pertain to a particular domain of experience and experimentation cannot be meaningfully considered and resolved without taking cognizance of the various categories of information which were identified.

These considerations become particularly relevant when there emerged in our work the question of augmenting the Navier Stokes equations by formal statements of the condition on flow fields purported to comply with the restrictions implied by the Navier-Stokes equations. More specifically, questions concerning consistency and redundancy arise, when we introduce statements of information augmenting the Navier-Stokes equations, as in the case when we formulate variational principles that indirectly express the global information on the distribution of internal forces which we have obtained as a theorem by using Gauss's and Hertz's formulation of the principles of classical mechanics. The question concerning the equivalence of the various known formulations of the principles of mechanics is particularly relevant at this point, because the Navier-Stokes equations are based on Newtonian mechanics, from which general information concerning the distribution of internal forces evidently cannot be derived in the category of explicit information.

The concept "Categories of Information" and the identification of the various categories give us insight into the nature of applied mathematics and have produced the realization that applied mathematics is an art that uses the various categories of information contrapuntally -- where, for example, the same information prescribed in more than one category of information does not in fact constitute a redundancy, but is instead a viable instrument for further rendering explicit information otherwise restricted to the category of implicit information. Specifically, introducing a simplifying assumption which, for example, is appropriate to and correctly reports a fact about a particular aspect of fluid flows, e.g., in the case of boundary layer theory, is tantamount to specifying information in the category of explicit information, which the Navier-Stokes equations purportedly already include in the category of implicit information. As is well known, this procedure is neither redundant nor sterile. It is, in fact, the very crux of applied mathematics and the only viable instrument which has so far rendered explicit, and thereby useful, information which the Navier-Stokes equations include in the category of implicit information.

It is with this understanding that we originally formulated the principle of minimum dissipation for viscous flows as a proposition which augments without contradiction and/or redundancy the Navier-Stokes equations, and which in fact rendered new and fundamental information about viscous flows which had not been previously obtained by studies restricted to the Navier-Stokes equations themselves. It was in this way that we first recognized that there exists a linear substructure underlying the Navier-Stokes equations; that the prominence of actual flows that tend to be potential over the principle part of a flow field, is an aspect of the principle of minimum dissipation; that the principle of minimum dissipation may be an aspect of a general stability principle according to which a particular flow configuration among multiple configurations equally admitted by the Navier-Stokes equations and boundary conditions is selected, thereby suggesting a correspondence between hydrodynamic stability and minimum dissipation.

This in turn suggested to us a connection between a generalization of the information first obtained as a theorem on the distribution of internal forces, and a new general and fundamental law of mechanics. This new law includes the propositions of classical mechanics as well as of a general stability principle which, in fact, gives expression to the evolutionary aspects and historical thrust of the motivating forces in nature -- aspects of force which the known laws of classical mechanics do not express or include in any category of information.

The realization that the principle of minimum dissipation gives only limited expression to the principle of maximum uniformity as it was originally conceived and formulated in terms of a positive, definite scalar measure of force, prompted us to give it a more complete hydrodynamical expression by formulating a new Hydrodynamical Variational Principle [6]. Although this variational principle does in part achieve this objective, it is nevertheless formulated in terms of an integral of a function of gradients of energy, rather than directly, in terms of a positive, definite, scalar force representation and measure of nonuniformity.

Both the principle of minimum dissipation as we originally formulated it in Ref. 5 and the hydrodynamical variational principle we subsequently formulated in Ref. 6, produced some fundamental information and implications for hydrodynamical fields. These were obtained by requiring that the restrictions these variational principles impose upon admissible flow fields be compatible with the restrictions imposed by the conservation laws, including, of course, the Navier-Stokes equations. It was in this way that we originally conceived the idea that actual hydrodynamical fields are subject to linear differential restrictions, which we now realize are not implied by the Navier-Stokes equations and which must be explicitly expressed by statements such as variational principles, or implicitly expressed by an analytical algorithm, which augment the Navier-Stokes equations. We refer to these linear differential restrictions as the linear substructure of actual hydrodynamical fields. Another result originally revealed by the application of the variational principles of Refs. 5 and 6, concerns necessary and evidently fundamental connections between spatial symmetry features of flow fields and their dependence upon time. The necessary connection between the time-dependent features of hydrodynamical fields and the symmetry properties of their space-dependent structures, was first revealed by the compatibility conditions obtained by formally requiring that the hydrodynamical variational principles cited above be compatible with the restrictions imposed by the Navier-Stokes equations.

We then endeavored to construct analytical representations of actual flow fields by jointly applying the linear differential restrictions on flow fields implied by the variational principles, in conjunction with the nonlinear compatibility equation which insures the compatibility of these linear restrictions with the nonlinear restrictions implied by the Navier-Stokes equations. In so doing, we restricted our attention and objective to the class of fully developed steady-state flows, which are maintained by boundary conditions that are fixed in time. Thus, by construction, we removed from our consideration the historical development of these fields and of the boundary conditions by which they are maintained, an aspect which we have since discovered to be fundamental and evidently essential for the production in nature of space-time-dependent flow fields. This ad hoc restriction which we used in trying to obtain actual steady-state flow fields from the hydrodynamical variational principles noted in conjunction with the Navier-Stokes equations, may explain the fact that in every case we were left with an arbitrary coefficient not determined by the formal statement of the problem -- a statement which omits the historical development of steady-state flows, as well as the historical development of the boundary conditions which maintain them. If this explanation is valid, then the fact that we were consistently left with an undetermined coefficient when certain essential historical aspects were excluded by the formal statement of the problem, is then indeed a positive and possibly important result. This conclusion obtains, because if the space-time structure of steady-state flows depend in fact upon their historical development, then obtaining an analytical representation of them without giving representation in the analysis to their historical development would be untenable.

When we originally conceived and applied the hydrodynamical variational principles used to augment the Navier-Stokes equations, we interpreted the linear differential restrictions on the actual flow field implied by them as corresponding to real linear restrictions which are understood to exist in actual

flows, and to which we refer as a linear substructure of flow fields. This idea, which led us to conjecture that all flow fields are essentially endowed with fundamental linear restrictions, was then reinforced by observing that in the class of potential flows, a linear substructure is preeminently distinguished by the fact that the velocity field is completely governed there, by a linear partial-differential equation. Moreover, this remains the case even though the force fields of potential flows remain conditioned in the absence of viscous forces, by nonlinear partial-differential equations.

During 1961, Lieber worked with Shrikant Desai to resolve the indeterminacy in a coefficient appearing in the analytical representation of flow fields obtained from the linear restrictions implied by the hydrodynamical variational principles, used in conjunction with the complete Navier-Stokes equations. The difficulties incurred encouraged us to conceive and develop a mathematical algorithm which has been effectively used in the construction of analytical representations of flow fields, based on the complete Navier-Stokes equations and realistic boundary conditions. In so doing, Desai gives particular emphasis in his Ph.D. dissertation to the idea that potential flows are fundamental in the development of actual viscous flows, and he incorporated this important idea in the algorithm cited above, thereby putting it to very practical use. The algorithm consists of an iteration procedure consisting of an infinite sequence of iterations applied to the complete Navier-Stokes equations, the successive steps of which are joined by linear differential relations. These relations are evidently an aspect of the fundamental linear substructure of actual flow fields, discussed earlier in this paper.

The application of this algorithm has produced analytical representations of steady flow fields around a circular cylinder for a range of Reynolds numbers extended from .015 to 20. These representations have been used to calculate flow fields which correspond to eighteen distinct values assigned to the Reynolds number. The calculations reveal, for the first time, fine detail and features of the structure of a real vortex formed behind a cylinder, and in particular that the outer boundary of such a vortex is like a membrane at which vorticity and dissipation are concentrated with relatively high intensity. These and other results which are presented in detail in a joint paper with Desai have been compared with experiments and generally supported by them.

When, however, we endeavor to construct analytical representations of time-dependent flow fields which naturally develop at higher Reynolds number, we find that it is evidently necessary in such cases to incorporate in the calculations, where the iteration procedure is actually applied, a model of the historical development of steady-state flows. Unless we do so, we cannot in principle proceed to calculate by the application of our algorithm space-time flows. This again supports the ideas and conjectures set forth in another related paper, which hold that hydrodynamical fields in general display, and are in general determined by, physical aspects of a universal process of evolution that follows a new and fundamental law.

Comparatively recently, Lieber formulated with L. Teuscher a new hydrodynamical variational principle based on the principle of maximum uniformity that is specifically designed for application to the calculation of steady-stratified

flows under the simplifying assumption that viscous forces are negligible. In the application of the principle of maximum uniformity to stratified flows, the integral of the hydrodynamical variational principle is expressed in a positive, definite, scalar measure of all the prevailing forces. This places it in direct correspondence with the scalar force measure used in the statement of the fundamental principle of maximum uniformity. We find that generalizing this new hydrodynamical variational principle for application to time-dependent stratified flows, again necessarily brings under consideration the idea that time-dependent flows and therefore turbulent flows in particular are necessarily strongly conditioned by the process of their historical development.

CONCLUDING REMARKS

In this paper I have tried to demonstrate the crucial and unifying role of the principle of maximum uniformity in revealing certain new and fundamental features of hydrodynamical fields, such as (1) an underlying linear substructure, (2) a hydrodynamical principle of minimum dissipation, (3) fundamental as well as necessary connections between spatial symmetry properties of actual flow fields and time-dependent motion, and (4) the concept and discovery that the space-time structures of hydrodynamical fields are in principle determined by their historical development, and furthermore that the evolutionary aspects of such fields are not in principle implied and therefore not mathematically determined by the Navier-Stokes equations. This puts in perspective the significance and role of various hydrodynamical variational principles which we have formulated in order to give at least partial representation to the principle of maximum uniformity in the context of classical hydrodynamics.

The theoretical ground of the algorithm and the linear relations that connect successive steps of an interaction process by which it is defined, are evidently also contained in the principle of maximum uniformity, which does indeed explain why potential flows are distinguished and fundamental in the development of viscous flows. The various formulations of hydrodynamical variational principles cited in this paper, with the exception of the first which was conceived with the object of rendering the Rayleigh-Ritz methods available to hydrodynamical theory, are particular and restricted aspects of the principle of maximum uniformity, formulated in the context of hydrodynamical theory. The hydrodynamical variational principle, by which we recently formulated the principle of maximum uniformity for stratified inviscid flows, bridges the two principle objectives which directed our original work concerned with the formulation of hydrodynamical variational principles. This new hydrodynamical variational principle achieves in part the two objectives simultaneously, because it does afford a viable instrument for using effectively and economically the Rayleigh-Ritz and Galerkin methods, for calculating with good approximation steady-stratified flow fields, and because this variational principle is based on a functional which represents a positive, definite, scalar measure of all the forces acting in the field. We find that the generalization of this variational principle to include viscous forces will necessarily require that we consider the flows as time- as well as space-dependent, and the historical aspects of their development.

In conclusion, we draw attention to our work on hydrodynamical stability which originated in 1955, and in which the question concerning the stability of hydrodynamical fields jointly subjected to multiple-maintained gradients in the state parameters was originally posed and brought under theoretical examination. Here also, the motivating concept for posing this question was the principle of maximum uniformity, and the idea that the response of a hydrodynamical system jointly subjected to multiple gradients maintained in the state variables is in general determined by the principle of maximum uniformity. A paper in these studies written with L. Rintel, demonstrates the ideas by which we originally attacked this problem from the standpoint of small-perturbation analysis. A direct connection between the principle of maximum uniformity and hydrodynamical stability is under examination in our work, and will take time to develop in a form suitable for presentation.

REFERENCES

1. Lieber, P., and Wan, K.S., "A Principle of Virtual Displacements for Real Fluids," Int. Congr. Mech., Proc. IX, Brussels, Belgium, 1957 (also issued as a Rensselaer Polytechnic Institute Research Division Report AFOSR TN 57-476, AD 136 468, under Air Force Contract AF 18(600)-1704, July 1957

2. Finlayson and Scriven, L.E., "On the Search for Variational Principles," J. Mass Transfer, 10, 799-821, Pergamon Press, 1967 (printed in Great Britain)

3. Lieber, P., "A Principle of Maximum Uniformity Obtained as a Theorem on the Distribution of Internal Forces," Israel J. Sci. Technol., Jerusalem: Weizmann Press, Apr. 1968; also published under same title as a technical report of the Institute of Engineering Research, University of California, Berkeley, Nov. 1968

4. Lieber, P., "Categories of Information," technical report of the Institute of Engineering Research, University of California, Berkeley, Oct. 1965; also published in Markus Reiner Honorary Volume, Pergamon Press, 1968

5. Lieber, P., and Wan, K.S., "A Principle of Minimum Dissipation for Real Fluids," Int. Congr. Mech., Proc. IX, Brussels, Belgium, 1957 (also issued by Rensselaer Polytechnic Institute, Troy, N.Y., as a Research Division Report AFOSR TN 57-477, AD 136-469, Aug. 1957, and released Office of Scientific Research, USAF as TN 57-477, under Contract AF 18(600)-1704, Aug. 1957)

6. Lieber, P., and Wan, K.S., "A Proof and Generalization of the Principle of Minimum Dissipation," issued by the Rensselaer Polytechnic Institute, Troy, N.Y., Sept. 1957; also released to the Office of Scientific Research, USAF under contract AF 18(600)-1704

* * *

V—General Symmetry Properties of Flows and Some Consequences

Paul Lieber
University of California
Berkeley, California

and

Kirit Yajnik
Indian Institute of Technology
Kanpur, India

ABSTRACT

Mathematical conditions are formulated for flows displaying symmetry and antisymmetry with respect to a plane. When homogeneous incompressible Newtonian fluids manifest such properties, the equations of motion restrict the distribution of the stresses. This report establishes that pressure is symmetrical in symmetrical flows. When the flow is antisymmetrical, the asymmetrical part of pressure is harmonic. Furthermore, each component of vorticity obeys the heat conduction equation in antisymmetrical flows. Thus the vorticity transport equations reduce to linear equations in antisymmetric flows. More than ten exact solutions of Navier-Stokes equations satisfy these linear equations. Finally, such antisymmetrical flows can be represented as a superposition of potential flow on a flow in which each component of velocity satisfies the heat conduction equation.

INTRODUCTION

Experiments on fluid flow often are designed so that the solid boundaries have properties of symmetry. The departure from symmetry occurring in these boundaries are reduced to a minimum. Yet the flow of fluids in a majority of cases does not enjoy the symmetry property. The wake of a circular cylinder placed symmetrically in a water channel or an air tunnel exhibits a Karman vortex street in a limited range of Reynolds numbers, and the flow in the wake is not symmetrical about the central plane of the channel or tunnel. When a water channel or air tunnel bifurcates into two, forming a Y-intersection, there is a regime where the flow takes place in one arm of the bifurcation. Here too the flow does not possess the symmetry of the boundaries. This lack of respect of fluid for symmetry is a striking and puzzling property.

Here we attempt to obtain some insight into the above problem by posing a slightly different question, viz., what are the general properties of symmetric and antisymmetric flows. The starting point of the present study is the formulation of conditions of symmetry and antisymmetry. Their application to the equations of motion immediately provides the information which was sought.

This study was in part motivated by a result relating to the existence of necessary connections between the geometrical symmetry characteristics of a boundary and the production of time-dependent motion under time-independent boundary conditions [1]. This result was obtained as part of a comprehensive study concerned with the formulation and application of variational principles in the study of viscous flows [6,7, 8,9,10].

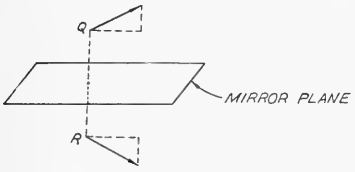

Fig. 1 - Velocity vectors about a mirror plane

Symmetry and Antisymmetry

Let Q and R in Fig. 1 be mirror images about a plane. Let the velocity vectors at Q and R be also mirror images of each other. Then the components of velocity parallel to the mirror plane must be equal and the components normal to the plane must be equal in magnitude, but opposite in direction. If the velocity vectors at any such image points about a mirror plane are images of each other, then the flow is here called symmetrical about the plane. If, on the other hand, the velocity vector at R is equal and opposite to the image of the velocity vector at Q, then such a situation would be an antithesis of the symmetrical flow. We may call a flow antisymmetrical if the velocity vector at the image point of any point is equal and opposite to the velocity vector at the point.

Let us leave the optical analogy aside and start with analytical definitions. If a flow satisfies the conditions

$$\begin{aligned} u_1(x_1, x_2, x_3, t) &= u_1(x_1, -x_2, x_3, t) \\ u_2(x_1, x_2, x_3, t) &= -u_2(x_1, -x_2, x_3, t) \\ u_3(x_1, x_2, x_3, t) &= u_3(u_1, -x_2, x_3, t) \end{aligned} \tag{1}$$

for all values of x_1, x_2, x_3, and t, the flow is said to be symmetrical about the plane $x_2 = 0$. Here x_1, x_2, and x_3 are Cartesian coordinates, t is time, and u_1, u_2, and u_3 are components of velocity parallel to the x_1, x_2, and x_3 axes. If, on the other hand, the flow satisfies

$$\begin{aligned} u_1(x_1, x_2, x_3, t) &= -u_1(x_1, -x_2, x_3, t) \\ u_2(x_1, x_2, x_3, t) &= u_2(x_1, -x_2, x_3, t) \\ u_3(x_1, x_2, x_3, t) &= -u_3(x_1, -x_2, x_3, t) \ , \end{aligned} \tag{2}$$

it is said to be antisymmetrical about the plane $x_2 = 0$.

It is easy to see (see the Appendix for illustration) with the help of the definition of partial derivatives that $u_{1,t}$; $u_{1,1}$; $u_{1,3}$; $u_{3,t}$; $u_{3,1}$; $u_{3,3}$; $u_{2,2}$; $\nabla^2 u_1$; and $\nabla^2 u_3$ are even functions of x_2 in the symmetrical flow and odd functions of x_2 in the antisymmetrical flow. Here, a comma followed by index 1, 2, 3, t means partial differentiation with respect to x_1, x_2, x_3, or t. $\nabla^2 f$ denotes $f_{,11} + f_{,22} + f_{,33}$. That is,

$$u_{1,t}(x_1, x_2, x_3, t) = u_{1,t}(x_1, -x_2, x_3, t) ,$$

if the flow is symmetrical, and

$$u_{1,t}(x_1, x_2, x_3, t) = -u_{1,t}(x_1 - x_2, x_3, t) ,$$

if the flow is antisymmetrical.

Similarly, $u_{2,t}$; $u_{2,1}$; $u_{2,3}$; $u_{1,2}$; $u_{3,2}$; and $\nabla^2 u_2$ are odd in the symmetrical flow and even in the antisymmetrical flow.

Now let us consider a homogenous incompressible Newtonian fluid. The flow obeys the equations

$$u_{i,t} + u_j u_{i,j} = -P_{,i} + \nu \nabla^2 u_i , \tag{3}$$

and

$$u_{i,i} = 0 . \tag{4}$$

Here P is the pressure divided by the density, and ν the kinematic viscosity. The body forces are assumed to be absent. It is now convenient to define

$$P^s(x_1, x_2, x_3, t) = \frac{1}{2} [P(x_1, x_2, x_3, t) + P(x_1, -x_2, x_3, t)] ,$$

and

$$P^a(x_1, x_2, x_3, t) = \frac{1}{2} [P(x_1, x_2, x_3, t) - P(x_1, -x_2, x_3, t)] .$$

Hence,

$$P^s(x_1, x_2, x_3, t) = P^s(x_1, -x_2, x_3, t) \tag{5}$$

$$P^a(x_1, x_2, x_3, t) = -P^a(x_1, -x_2, x_3, t) , \tag{6}$$

and

$$P^s + P^a = P . \tag{7}$$

Substituting Eq. (7) in Eq. (3), we obtain

$$u_{i,t} + u_j u_{i,j} = -P^s_{,i} - P^a_{,i} + \nu \nabla^2 u_i \ . \tag{8}$$

Consequences of Symmetry

Let us now consider symmetrical flow. The even and odd terms in Eq. (8) are indicated by e and o:

$$\underset{e}{u_{1,t}} + \underset{e}{u_1 u_{1,1}} + \underset{e}{u_2 u_{1,2}} + \underset{e}{u_3 u_{1,3}} = \underset{e}{+P^s_{,1}} - \underset{o}{P^a_{,1}} + \underset{e}{\nu \nabla^2 u_1} \ ;$$

$$\underset{o}{u_{2,t}} + \underset{o}{u_2 u_{2,1}} + \underset{o}{u_2 u_{2,2}} + \underset{o}{u_3 u_{2,3}} = \underset{o}{-P^s_{,2}} - \underset{e}{P^a_{,2}} + \underset{o}{\nu \nabla^2 u_2} \ ;$$

$$\underset{e}{u_{3,t}} + \underset{e}{u, u_{3,1}} + \underset{e}{u_2 u_{3,2}} + \underset{e}{u_3 u_{3,3}} = \underset{e}{-P^s_{,3}} - \underset{o}{P^a_{,3}} + \underset{e}{\nu \nabla^2 u_3} \ ;$$

$$\underset{e}{u_{1,1}} + \underset{e}{u_{2,2}} + \underset{e}{u_{3,3}} = 0 \ .$$

Since even and odd parts must vanish individually, we get

$$u_{i,t} + u_j u_{i,j} = -P^s_{,i} + \nu \nabla^2 u_i \tag{9}$$

$$P^a_{,i} = 0 \tag{10}$$

$$u_{i,i} = 0 \ . \tag{11}$$

Since P^a does not vary with x_i,

$$P^a(x_1, x_2, x_3, t) = P^a(x_1, -x_2, x_3, t) \ .$$

Hence, by virtue of Eq. (6), P^a vanishes everywhere. In other words,

$$P(x_1, x_2, x_3, t) = P(x_1, -x_2, x_3, t) \ .$$

Thus, pressure must be symmetrical in a symmetrical flow.

Consequences of Antisymmetry

Now let us consider antisymmetric flow. The even and odd terms are indicated below by e and o respectively:

$$u_{1,t} + u_1 u_{1,1} + u_2 u_{1,2} + u_3 u_{1,3} = -P^s_{,1} - P^a_{,1} + \nu\nabla^2 u_1 ;$$

$$u_{2,t} + u_2 u_{2,1} + u_2 u_{2,2} + u_3 u_{2,3} = -P^s_{,2} - P^a_{,2} + \nu\nabla^2 u_2 ;$$

$$u_{3,t} + u_1 u_{3,1} + u_2 u_{3,2} + u_3 u_{3,3} = -P^s_{,3} - P^a_{,3} + \nu\nabla^2 u_3 ;$$

$$u_{1,1} + u_{2,2} + u_{3,3} = 0 .$$

Consequently,

$$u_{i,t} = -P^a_{,i} + \nu\nabla^2 u_i , \tag{12}$$

$$u_j u_{i,j} = -P^2_{,i} , \tag{13}$$

and

$$u_{i,i} = 0 . \tag{14}$$

Let $w_i = e_{ijk} u_{k,j}$ be vorticity. Here e_{ijk} is the permutation symbol. Then, from Eq. (12),

$$\begin{aligned} w_{i,t} &= -e_{ijk} P^a_{,kj} + \nu e_{ijk} \nabla^2 u_{k,j} \\ &= \nu\nabla^2 (e_{ijk} u_{k,j}) \\ &= \nu\nabla^2 w_k . \end{aligned}$$

Thus,

$$w_{i,t} = \nu\nabla^2 w_k . \tag{15}$$

Each component of vorticity obeys the heat conduction equation in an anti-symmetrical flow. (A similar argument was previously given by Lieber and Wan in Ref. 1.)

Also from Eq. (13), we have

$$\begin{aligned} e_{ijk} u_j w_k &= e_{ijk} u_j e_{k\ell m} u_{m,\ell} \\ &= u_j u_{j,i} - u_j u_{i,j} \\ &= (1/2\, u_j u_j)_{,i} + P^s_{,i} \\ &= (P^s + 1/2\, u_j u_j)_{,i} . \end{aligned}$$

Let $H^s = P^s + 1/2(u_j u_j)$. Then

$$e_{ijk} u_j w_k = H^s_{,i} \quad . \tag{16}$$

It follows that

$$H^s_{,i} u_i = H^s_{,i} w_i = 0 \quad . \tag{17}$$

That is, the symmetrical part of the total head (H^s) does not vary along a streamline or a vorticity line. H^s is as a result constant in the surface of the streamline and the vorticity line. Further, from Eq. (16), we have

$$e_{imn}(e_{njk} u_j w_k)_{,m} = e_{imn} H^s_{,nm} = 0 \quad .$$

That is,

$$(u_\ell w_m)_{,m} - (u_m w_\ell)_{,m} = 0 \quad .$$

Since $u_{i,i} = w_{i,i} = 0$,

$$w_m u_{\ell,m} - u_m w_{\ell,m} = 0 \quad . \tag{18}$$

This means that the increase of the velocity vector u_ℓ along a vorticity line is equal to the increase of the vorticity vector w_ℓ along a streamline.

Examples of Antisymmetric Flow

The result wherein each component of vorticity obeys a heat conduction equation is severe. This leads us to believe that the hypothesis of antisymmetry is severe. A question naturally arises whether there are any flows which satisfy the hypothesis. The following two examples show that there are indeed flows where the conditions given by Eqs. (2) are met.

Rectilinear Flows -- In rectilinear flows, all particles move in parallel straight lines. Let the common direction of motion be chosen as the x_2 axis. Then

$$u_2 = u_2(x_1, x_2, x_3, t), \quad u_1 = u_3 = 0 \quad .$$

Continuity requires that

$$u_{2,2} = 0 \quad .$$

Thus, u_2 is independent of x_2. Consequently,

$$u_2(x_1, x_2, x_3, t) = u_2(x_1, -x_2, x_3, t) \quad .$$

Since u_1 and u_3 are identically zero, Eqs. (2) are satisfied.

Plane Axisymmetric Flows without Radial Velocity — In such flows, $u_1 = -qx_2$, $u_2 = qx_1$, $u_3 = 0$; where $q = q(r, x_3, t)$, and $r^2 = x_1^2 + x_2^2$. Such flows clearly satisfy Eqs. (2).

Let us list the known exact solutions of the Navier-Stokes equations which belong to the above two families:

Examples of Rectilinear Flows —

1. Steady flow between parallel plates
2. Steady flow in a circular pipe (more generally, of arbitrary section)
3. Flow in Stokes' first problem
4. Flow in Stokes' second problem
5. Pipe flow starting from rest
6. Flow between plates starting from rest.

Plane Axisymmetric Flow —

1. Rigid body rotation
2. Steady flow between concentric cylinders
3. Potential vortex
4. Vortex of Hamel and Oseen [7]
5. Vortex of Taylor [8]
6. Vortex of Rouse and Hsu [9].

Since the above examples refer to plane motion, a doubt lingers as to whether any three-dimensional motion satisfying Eqs. (2) is dynamically possible. To remove this doubt, we give a three-dimensional solution.

Flow through a Rotating Pipe —

$$u_1 = -Ax_2, \quad u_2 = Ax_1, \quad u_3 = B\left(1 - \frac{r^2}{R^2}\right),$$

where A, B, and R are constants, and $r^2 = x_1^2 + x_2^2$. If we put A equal to zero, the flow reduces to Poiseuille flow. If we take pressure P as $1/2\,[A^2(x_1^2 + x_2^2)] - 4(B/R^2)\nu x_3$, and substitute in Eq. (3), we have

$$u_{1,t} + u_1u_{1,1} + u_2u_{2,2} + u_3u_{1,3} = Ax_1(-A) \ ;$$

$$-P_{,1} + \nu\nabla^2 u_1 = -A^2 x_1 \ ;$$

$$u_{2,t} + u_1 u_{2,1} + u_2 u_{2,2} + u_3 u_{2,3} = -A x_2(A) \ ;$$

$$-P_{,2} + \nu\nabla^2 u_2 = -A^2 x_2 \ ;$$

$$u_{3,t} + u_1 u_{3,2} + u_2 u_{3,2} + u_3 u_{3,3} = 0 \ ;$$

$$-P_{,3} + \nu\nabla^2 u_3 = \frac{4B\nu}{R^2} - \frac{4B\nu}{R^2} = 0 \ ;$$

and

$$u_{1,1} + u_{2,2} + u_{3,3} = 0 \ .$$

Hence the above flow is dynamically possible. If we have a long pipe with reasonably smooth entrance conditions, the actual flow would approximate the above solution for low Reynolds numbers.

We have additional information. From Thom's work, we know that vortices behind a cylinder have approximately elliptical streamlines, and consequently stream function is approximately symmetrical about one diameter [10]. If this diameter is chosen as the x_2 axis,

$$\psi(x_1, x_2, x_3, t) \cong \psi(x_1, -x_2, x_3, t) \ .$$

Since $u_1 = -\psi_{,2}$ and $u_2 = \psi_{,1}$, u_1 is odd and u_2 is even in x_2. Equation (2) is satisfied approximately. We can thus expect that the vorticity satisfies the heat conduction equation. This was observed by Thom [10]. Thus we have correlated two observed features of a separated flow.

Integration of Equations of Motion for Antisymmetrical Flow

Having convinced ourselves about the physical significance of the family of antisymmetrical flows, let us proceed to the task of integration of the equations of motion. From Eqs. (12) and (14),

$$u_{i,it} + P^a_{,ii} - \nu\nabla^2 u_{i,i} = P^a_{,ii} = 0 \ . \tag{19}$$

Hence the antisymmetric part of the pressure is harmonic. Let

$$\phi = -\int P^a \, dt \ . \tag{20}$$

Then

$$\phi_{,it} = -P^a_{,i} \ . \tag{21}$$

Also

$$\phi_{,ijj} = -\int P^a_{,ijj}\, dt = 0 \ , \tag{22}$$

as P^a is harmonic. Substituting Eq. (21) in Eq. (12), we obtain

$$u_{i,t} = \phi_{,it} + \nu\nabla^2 u_i \ ,$$

or

$$(u_i - \phi_{,i})_{,t} = \nu\nabla^2 u_i \ .$$

On account of Eq. (22), we have

$$(u_i - \phi_{,i})_{,t} = \nu\nabla^2(u_i - \phi_{,i}) \ . \tag{23}$$

In other words, the flow can be decomposed into two parts. One part arises from a potential ϕ. The other is such that each component obeys the heat conduction equation. We then conclude that any antisymmetric flow obeying the Navier-Stokes equations can be written as

$$u_i = \phi_{,i} + u'_i \ , \tag{24}$$

where

$$\phi_{,ii} = 0 \ , \tag{25}$$

and

$$u'_i = \nu\nabla^2 u'_i \ , \tag{26}$$

and

$$u'_{i,i} = 0 \ . \tag{27}$$

Equation (18) imposes an additional condition on ϕ and u'. Let

$$w'_i = e_{ijk} u'_{k,j} \ . \tag{28}$$

Then

$$w_i = w'_i + e_{ijk}\phi_{,kj} = w'_i \ . \tag{29}$$

Substituting Eq. (28) in Eq. (18), we obtain

$$w'_m(\phi_{,nm} + u'_{n,m}) - (\phi_{,m} + u'_{,m})\, w'_{n,m} = 0 \ . \tag{30}$$

So the integration of the equations of motion amounts to finding a velocity field u_i [1] and a potential ϕ satisfying the following conditions:

$$\phi_{,ii} = 0 \tag{25}$$

$$u'_{i,i} = 0 \tag{27}$$

$$u'_i = \nu \nabla^2 u'_i \ , \tag{26}$$

and

$$w'_m(\phi_{,nm} + u'_{n,m}) - (\phi_{,m} + u'_{,m})\, w'_{n,m} = 0 \ . \tag{30}$$

CONCLUSIONS

1. When a flow is symmetrical about a plane, the pressure is also symmetrical.

2. When a flow is antisymmetrical about a plane, the antisymmetrical part of the pressure is harmonic. Also, such a flow of homogeneous incompressible Newtonian fluid can be written as

$$u_i = \phi_{,i} + u'_i \ ,$$

where

$$\phi_{,ii} = 0 \ ;$$

$$u'_{i,i} = 0 \ ;$$

$$u'_{i,t} = \nu \nabla^2 u'_i \ ,$$

and

$$w'_m(\phi_{,nm} + u'_{n,m}) - (\phi_{,m} + u'_{,m})\, w'_{n,m} = 0 \ .$$

3. Antisymmetrical solutions are available and are of physical interest. More than ten such solutions have been noted. There are steady and nonsteady, two-dimensional as well as three-dimensional flows in this category. Bound vortices behind a cylinder come close to enjoying this property.

REFERENCES

1. Lieber, P., and Wan, K.S., "A Principle of Minimum Dissipation for Real Fluids," Office of Scientific Research, USAFOSR, report TN57-477, p. 43 (1957)

2. Lieber, P., and Wan, K.S., "A Minimum Dissipation Principle for Real Fluids," Int. Cong. Mech., Proc. IX, 1957 (amplified in Rensselaer Polytechnic Institute and USAF Office of Scientific Research Report TN 57-477, AD 136 469, Aug. 1957) (See Ref. 1)

3. Lieber, P., Wan, K.S., and Anderson, O.L., "A Principle of Virtual Displacements for Real Fluids," Int. Congr. Mech., Proc. IX, 1957 (amplified in Rensselaer Polytechnic Institute and USAF Office of Scientific Research Report TN 57-476, AD 136 468, July 1957)

4. Lieber, P., and Wan, K.S., "A Proof and Generalization of the Principle of Minimum Dissipation," Rensselaer Polytechnic Institute and USAF Office of Scientific Research Report TN 57-479, AD 136 471 (Sept. 1957)

5. Wan, K.S., and Lieber, P., "Applications Based on Variational Principles for Real Fluids," Rensselaer Polytechnic Institute and USAF Office of Scientific Research Report TN 57-481, AD 136 473 (Sept. 1957)

6. Lieber, P., and Wan, K.S., "A Study Leading to the Boundary Conditions at a Free Surface Joining an Irrotational-Rotational Flow Regime," Rensselaer Polytechnic Institute and USAF Office of Scientific Research Report TN 57-480, AD 136 472 (Sept. 1957)

7. Schlichting, H., "Boundary Layer Theory," (transl. J. Kestin), McGraw Hill, 4th ed.

8. Taylor, G., "On Dissipation of Eddies," Rept. Mem. Adv. Com. Aeron., No. 598 (1918); also, Scientific Papers 2, 96-101, Cambridge, 1958

9. Rouse, H., and Hsu, H.C., "On the Growth and Decay of a Vortex Filament," 1st U.S. Nat. Congr. Appl. Mech., 741-746

10. Thom, A., "The Flow Past Circular Cylinders at Low Speeds," Proc. Roy. Soc. London, A 141, 651-669 (1933)

APPENDIX
THE DIFFERENTIABLE FUNCTIONS f AND g

Let $f(x,y,t)$ and $g(x,y,t)$ be two differentiable functions such that

$$f(x,y,t) = f(x,-y,t), \quad \text{and} \quad g(x,y,t) = -g(x,-y,t) . \tag{A1}$$

We then obtain

$$\frac{\partial f}{\partial y}(x,y,t) = \operatorname*{Lt}_{\Delta y \to 0} \frac{f(x,y+\Delta y,t) - f(x,y,t)}{y}$$

$$= \operatorname*{Lt}_{\Delta y \to 0} \frac{f(x,-y-\Delta y,t) - f(x,-y,t)}{y}$$

$$= \underset{(-\Delta y)\to 0}{\mathrm{Lt}} \frac{f(x,-y,-\Delta y,t) - f(x,-y,t)}{(-\Delta y)}$$

$$= -\frac{\partial f}{\partial y}(x,-y,t) \ ;$$

$$\frac{\partial f}{\partial x}(x,y,t) = \underset{\Delta x\to 0}{\mathrm{Lt}} \frac{f(x+\Delta x,y,t) - f(x,y,t)}{\Delta x}$$

$$= \underset{\Delta x\to 0}{\mathrm{Lt}} \frac{f(x+\Delta x,-y,t) - f(x,-y,t)}{\Delta x}$$

$$= \frac{\partial f}{\partial x}(x,-y,t) \ ;$$

$$\frac{\partial f}{\partial t}(x,y,t) = \frac{\partial f}{\partial t}(x,-y,t) \ .$$

We also obtain, by similar reasoning,

$$\frac{\partial g}{\partial y}(x,y,t) = \frac{\partial g}{\partial y}(x,-y,t) \ ;$$

$$\frac{\partial g}{\partial x}(x,y,t) = -\frac{\partial g}{\partial y}(x,-y,t) \ ;$$

$$\frac{\partial g}{\partial t}(x,y,t) = -\frac{\partial g}{\partial t}(x,-y,t) \ .$$

Thus $\partial f/\partial x$, $\partial f/\partial t$ and $\partial g/\partial y$ are symmetric, whereas $\partial g/\partial x$, $\partial g/\partial t$, and $\partial f/\partial y$ are antisymmetric.

Notice that fg is antisymmetric. Also, if $f + g$ vanishes at (x,y,t) and at $(x,-y,t)$, then

$$f(x,y,t) + g(x,y,t) + f(x,-y,t) + g(x,y,t) = 0 \ .$$

Hence f and g must vanish individually.

We shall make use of these properties of symmetric and antisymmetric functions.

* * *

VI—Convective Instability of a Horizontal Layer of Fluid with Maintained Concentration of Diffusive Substance and Temperature at the Boundaries

Paul Lieber
University of California
Berkeley, California

and

Lionel Rintel
William and Mary College
Williamsburg, Virginia

ABSTRACT*

The critical conditions for the convective instability of a horizontal layer of fluid which has constant gradients of temperature and concentration of a diffusive substance are derived. The parameter determining the stability is a sum of two dimensionless parameters of the form of Rayleigh numbers, one based on the quantities determining the molecular heat transfer across the layer, and the second based on those quantities determining the molecular transfer of the diffusive substance. For liquids, a strong stabilizing or destabilizing action of the molecular diffusion results, which depends on the sign of the gradient of the salt concentration. When the gradient of salt concentration stabilizes, overstable oscillations are found to provide the mechanism of the stabilization.

INTRODUCTION

Convective vortices in fluids are associated with unstable equilibria of forces which act on and/or are produced by the motion of the fluid. It has been found that a class of convection-causing agents, characterized by transfer

*This paper is based on a technical report issued under the same title by the Institute of Engineering Research, University of California, Berkeley, as Report Nonr 222(87), MD-63-6, in November 1963.

properties, interact in a simple way. The stability or instability of a fluid subjected to such forces, with respect to convective vortex perturbations, was found to depend on the value of an interaction number, defined as the sum of the parameters measuring the stabilizing or destabilizing action of the separate agents. As a typical example of such an interaction, the case of the stability of a nongravitating fluid confined between two cylinders rotating with different angular velocities and maintained at different temperatures, was conjectured (Lieber, 1957) and then initially treated analytically (Lieber, 1959). This treatment in which was originally projected the idea concerning the effect of simultaneously impressed gradients of macroscopic-state parameters on hydrodynamic stability, was restricted to a small gap between cylinders rotating with nearly equal velocity in the same direction. This result was extended in order to examine the effects of the gap as well as of angular velocities, differing both in magnitude and sign and reported in a doctoral dissertation (Rintel, 1961). The results of an approximate free-surface theory (Lieber and Rintel, 1965) for the case of counterrotating cylinders provided a basis for a unified presentation of the results. In all of these cases the interaction number is the sum of the Taylor and Rayleigh numbers, and its critical value is found to be independent of the kinematic parameters (Lieber and Rintel, 1962). These results are to be presented in a comprehensive paper accommodating some recent experimental results and in subsequent analytical investigations using the same ideas.

The phenomenon examined in this paper belongs to the same class of phenomena and can therefore be considered as another model of this class. The two agents interacting in this case are the buoyancy forces, generated by the gradient of temperature and the gradient of concentration of the diffusive substance. The simplicity of the present model facilitates a schematic representation of the stabilizing or destabilizing action of the various agents.

THE CRITICAL CONDITIONS

The differential equations associated with the problem are those of Navier-Stokes, the continuity and molecular transfer of heat, and the diffusive substance:

$$\begin{aligned} &\frac{d\mathbf{v}}{dt} + (\mathbf{v} \cdot \operatorname{grad})\ \mathbf{v} = \nu\nabla^2\ \mathbf{v} - \frac{1}{\rho}\operatorname{grad}\pi - \mathbf{k}g \\ &\operatorname{div}\ \mathbf{v} = 0\ , \\ &\frac{dT}{dt} + \mathbf{v} \cdot \operatorname{grad}\ T = k'\nabla^2 T\ , \\ &\frac{dc}{dt} + \mathbf{v} \cdot \operatorname{grad}\ c = k''\nabla^2 c\ . \end{aligned} \tag{1}$$

In these v designates the velocity vector, π the pressure, ρ the density, g the gravitational constant, T the temperature, c the concentration of diffusive substance, and ν, k', and k'' are respectively the coefficients of viscosity, molecular

transfer of heat, and diffusive substance. Equations (1) are interrelated by the equation of state, which for small variations in concentration and temperatures is:

$$\rho = \rho_0(1+\alpha'\delta T+\alpha''\delta c) \ , \quad \alpha' = \frac{1}{\rho_0}\frac{\partial \rho}{\partial T}, \alpha'' = \frac{1}{\rho_0}\frac{\partial \rho}{\partial c} \ . \tag{2}$$

The basic solution of Eqs. (1) is that of molecular transfer of heat and salinity across this layer of stationary fluid

$$\mathbf{v}_0 = 0 \ , \quad \pi_0 = g\int_0^z \rho \, dZ, \qquad T_0 = \beta' Z + \gamma' \ , \quad C_0 = \beta'' Z - \gamma'' \ , \tag{3}$$

where the constants γ' and γ'' and the gradients β' and β'' are determined by the boundary conditions. By superimposing the basic solution in Eqs. (3) on small perturbations, we have from Eqs. (1) and (2) the linearized equations for the perturbations

$$\begin{aligned}
&\text{(a)} \quad \frac{d\mathbf{v}_1}{dt} = \nu\nabla^2 \mathbf{v}_1 - \frac{1}{\rho_0}\operatorname{grad}\pi_1 - g(\alpha' T_1 + \alpha'' c_1)\,\mathbf{k} \\
&\qquad \operatorname{div}\mathbf{v}_1 = 0 \ , \\
&\text{(b)} \quad \frac{dT_1}{dt} = k'\nabla^2 T_1 - \beta'\omega_1 \ , \\
&\text{(c)} \quad \frac{dc_1}{dt} = k''\nabla^2 c - \beta''\omega_1 \ .
\end{aligned} \tag{4}$$

In Eqs. (4), in accordance with Boussinesq's equations (1904) as used by Rayleigh (1916), the small quantities which arise from variations of density are neglected, with the exception of those which represent the buoyancy force. Taking the divergence of Eq. (4a) by use of Eq. (4b), we obtain

$$\frac{1}{\rho_0}\nabla^2\pi_1 = -g\left(\alpha'\frac{\partial T_1}{\partial Z} + \alpha''\frac{\partial C_1}{\partial Z}\right) . \tag{5}$$

Elimination of π_1 from Eqs. (4) and (5) gives

$$\left(\frac{\partial}{\partial t} - \nu\nabla^2\right)\nabla^2\omega_1 = -g\nabla_1^2(\alpha' T_1 + \alpha'' c_1) \ , \tag{6}$$

where

$$\nabla_1^2 = \nabla^2 - \frac{\partial^2}{\partial Z^2} = \frac{\partial^2}{\partial x^2} + \frac{\partial^2}{\partial y^2} \ .$$

For considering stability with respect to convective vortices, the standard form of the perturbations in dimensionless form is (Pellew and Southwell, 1940):

$$\omega_1 = \frac{\nu}{h} e^{\sigma t} f(\xi,\eta)\, \omega^*(\zeta) ,$$

$$T_1 = \Delta T\, e^{\sigma t} f(\xi,\eta)\, \tau^*(\zeta) , \tag{7}$$

$$C_1 = \Delta C\, e^{\sigma t} f(\xi,\eta)\, C^*(\zeta) , \quad \xi = \frac{x}{h_1} , \quad \eta = \frac{y}{h} , \quad \zeta = \frac{Z}{h} ,$$

where f is the solution of the membrane equation for the particular form of horizontal periodicity of the perturbations

$$\frac{\partial^2 f}{\partial \xi^2} + \frac{\partial^2 f}{\partial \eta^2} + k^2 f = 0 ,$$

ΔT is a characteristic temperature difference, ΔC is a characteristic difference of concentration, and h is the depth of the fluid layer. The constant k arises from the separation of variables and depends on the particular geometry of periodicity of the perturbations. This geometry is not specified in the present investigation, so that the result is valid for hexagonal cellular vortices as well as for longitudinal rolls arising when a small shear is applied to the fluid. Equations (4) and (6) then reduce to

$$\left[\sigma - \frac{k'}{h^2}(D^2 - k^2)\right] \tau^* = \frac{\nu}{h\Delta T} \beta' \omega^* ,$$

$$\left[\sigma - \frac{k''}{h^2}(D^2 - k^2)\right] C^* = \frac{\nu}{h\Delta C} \beta'' \omega^* ,$$

$$\frac{\nu}{h}\left[\sigma - \frac{\nu}{h^2}(D^2 - k^2)(D^2 - k^2)\omega^*\right] = k^2 g(\alpha' \Delta T_{\tau *} - \alpha'' CC^*) , \tag{8}$$

$$D = \frac{d}{d\xi} .$$

By construction, the stability or instability of the basic solution of Eqs. (3) is determined by the sign of the real part of σ. Thus the margin of instability will be characterized by the vanishing of the real part of σ. Concerning the imaginary part, two possibilities are considered: (a) the marginal instability is characterized by the principle of exchange of stabilities, i.e., the imaginary part of σ also vanishes for the state of transition; and (b) overstable oscillations characterized by the nonvanishing imaginary part of σ are relevant to the instability. By using a method developed by Chandrasekhar (1963), Mr. H. Weinberger (1962) has shown that in the case considered here overstability can be the first kind of instability to evolve. However, experiments performed

by Goroff (1960) have shown that overstable oscillations do not result in significant changes of heat transfer (and thus presumably no significant changes in the transfer of diffusive substance). He also found that for the critical value of the characteristic parameter predicted by the use of the principle of exchange of stabilities, there evolves convective motion, which is superimposed on the overstable oscillations. Since this convective motion is accompanied by transfer properties and is therefore of more interest, in terms of Goroff's observation we simplify the analysis by using the principle of exchange of stability. Consequently, according to the present notation, and consistent with Eddington's motivation for introducing the notion, overstability is here considered as a case of stability, although in the formal mathematical sense it is a case of instability. Subsequently we will show that the overstable oscillations indeed provide the stabilizing mechanism as a case of stability. The differential equations for the state of transition to convective motion are

$$\text{(a)} \quad (D^2 - k^2)\omega^* = -k^2 \frac{gh^3}{\nu^2} (\alpha' \Delta T \tau^* + \alpha'' \Delta C \cdot C^*) ,$$

$$\text{(b)} \quad (D - k^2)\tau^* = - \frac{h\nu}{k' \Delta T} \beta' \omega^* , \tag{9}$$

$$\text{(c)} \quad (D - k^2)C^* = \frac{h\nu}{k'' \Delta C} \beta'' \omega^* .$$

Operating by $(D^2 - k^2)$ on Eq. (9a) after elimination of C^* and τ^* by use of the remaining Eqs. (9), we obtain

$$(D^2 - k^2)\omega^* = k^2 R_a \omega^* , \tag{10}$$

where

$$R_a = R'_a + R''_a , \quad R'_a = \frac{h^4 g \alpha' \beta'}{k' \nu} \qquad R''_a = \frac{h^4 g \alpha'' \beta''}{k'' \nu} \tag{11}$$

is the generalized Rayleigh number. In terms of a virtual temperature gradient

$$\frac{d\theta}{dz} = \beta' + \frac{\alpha''}{\alpha'} \frac{k'}{k''} \beta' ,$$

this Rayleigh number can be represented as

$$R_a = \frac{h^4 g \alpha'}{k' \nu} \frac{d\theta}{dz} . \tag{12}$$

Since Eq. (10) differs from Rayleigh's equation determining the convective instability of a layer of fluid heated from below only by a virtual temperature gradient as defined by Eq. (12), critical conditions are (Pellew and Southwell, 1940):

Two rigid boundaries	$R_{a_{cr}} = 1708$	
Upper boundary free from tangential stresses and boundary rigid	$R_{a_{cr}} = 1100$	(13)
Two free boundaries	$R_{a_{cr}} = 658$	

CONCLUSIONS

The critical conditions of Eqs. (13) are valid both for gases and liquids; in the latter case the diffusive substance is dissolved salts. For this case, since $\alpha_1 < 0$ and $\alpha_2 > 0$, the following situations are possible:

(a) $\beta' > 0$, $\beta'' < 0$ Both gradients, that of the temperature and that of the concentration of the dissolved salts, are destabilizing.

(b) $\beta' > 0$, $\beta'' > 0$ The temperature gradient destabilizes, while that of concentration of salts stabilizes.

(c) $\beta' < 0$, $\beta'' < 0$ The gradient of salt concentration destabilizes, while that of temperature stabilizes.

(d) $\beta' < 0$, $\beta'' > 0$ The basic solution of Eqs. (2) is stable with respect to convection.

Moreover, the stabilization or destabilization of the gradients of concentration of salts and temperature are respectively weighted by the reciprocals of k' and k''. Since for common salts the numerical value of k' is two orders of magnitude larger than that of k'', in case (b) above a very small gradient of concentration of salts can stabilize a much larger adverse temperature gradient and, vice versa in case (c) a very small decrease in salt concentration with depth can destabilize a fluid layer with density increasing with depth. This particular case has been considered in detail by Stern (1960). For case (b) the result can be interpreted as follows:

Convection is a mechanism of heat transfer by means of vortices of finite dimensions. The heat into (from below) and out of (from above) the convective vortices is supplied by the molecular diffusion. In the case of gradients of temperature and concentration of salts, the convective vortex transfers salts and heat upward, as represented schematically in Fig. 1.

In state 1 of the figure, salts and heat are diffusing into the vortex at point *a* and out of it at point *b*. The resulting buoyancy forces cause the

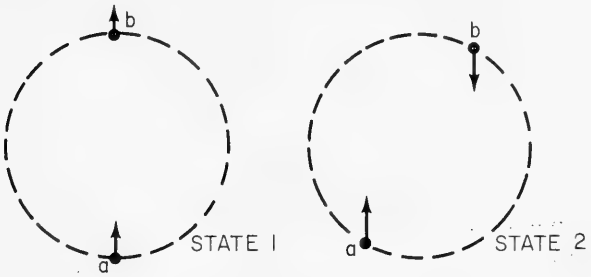

Fig. 1 - Schematic representation of stabilization by the molecular diffusion of salts

vortex to rotate and transfer the heat and salts upward. After completing the rotation to state 2, part of the heat and salts which diffused into point *a* in state 1 are transmitted upward, while new quantities of heat and salts diffuse into point *b*. However, because of the much smaller numerical value of the coefficient of diffusion of salts as compared to that of diffusion of heat, an excess of the quantity of salts as compared with the quantity of heat will be present at point *a*. For the same reason, the quantity of heat diffused in *b* will exceed the quantity of salts at the same point. Consequently, because of the buoyancy, a restoring momentum arises, turning the convective vortex in a direction opposite to that of its original rotation. In this way, the delay of the molecular diffusion of salts inhibits the rotation of the convective vortex and causes an oscillating motion. Indeed, Mr. H. Weinberger (1962), has shown analytically that in case (b) above, overstability can precede the convective instability.

As noted, case (c) has been considered in detail (Stern, 1960). It is interesting to note the reversal of the phenomenon: as reported by Stern, in case (c) internal gravity waves are inhibited in favor of convective instability, while as shown here in case (b) convective instability is inhibited by means of overstable oscillations. The present theory may explain some interesting observations concerning the antarctic Lake Vanda. In the lower part of the lake (Wilson and Wellman, 1962), from 170-ft depth down to the bottom of the lake, a stable-stratified solution with gradients of salinity and temperature is observed. Between 50 ft and 120 ft depth no gradients of temperature and salinity are observed, and this part of the lake is most probably in a state of turbulent convection. In the remaining two parts of the lake, from a depth of about 125 ft down to 165 ft, and from 45-ft depth up to the ice level, starting at about 10 ft, a small gradient of salinity seems to be stabilizing a larger temperature gradient. Abnormally hot saline water has also been found in the red sea (Swallow, 1965). However, from the limited data reported in this case, it is not possible to distinguish regions of overstability.

An attempt to investigate the results concerning case (c) in the laboratory has not been successful (Turner and Stommell, 1964). This may be ascribed to difficulties in simulating a virtually unbounded horizontal domain, with

respect to salinity, in a laboratory. Therefore the presence of vertical boundaries produced currents resembling the ones first observed in vertical tubes and incisively interpreted in the literature (Taylor, 1954).

In the 38th Guthrie Lecture delivered in 1954, Sir G. I. Taylor examined conditions for convection of a fluid contained in a vertical column (tube) and subjected to a gradient in the concentration of a diffusive substance. His purpose was to determine the effect of gravity on dispersion in a vertical tube as an adjunct of his comprehensive study on "Diffusion and Mass Transport in Tubes," inspired by a physiological problem. In so doing, Taylor established on theoretical grounds that equilibrium becomes stable and that vertical currents stop when the vertical gradient in concentration, dc/dz, becomes less than 67.94. $D\mu/g\rho\alpha a^4$, where $2a$ is the diameter of the tube, D is the coefficient of diffusion, g the acceleration of gravity, and μ the viscosity.

When we set $\beta' = 0$ in the present work, we obtain a result that corresponds to the results obtained in 1954 by Taylor for diffusion in a vertical tube of radius a. For if we define $X = a/h$ and identify our K'' with Taylor's symbol D for the coefficient of diffusion, the result of Eq. (12) reduces, when use is made of the relation in Eqs. (3), to

$$\frac{dc_0}{dz} = (R_a X^4) \frac{D\mu}{g\rho\alpha a^4} , \tag{14}$$

which corresponds to Taylor's result

$$\frac{dc_0}{dz} = 67.94 \frac{D\mu}{g\rho\alpha a^4} . \tag{15}$$

Thus the fact of the proportionality of dc_0/dz to $D\mu/g\rho\alpha a^4$ is found to be the same in both works. We may rewrite Eq. (14) as

$$\frac{dc_0}{dz} = \epsilon_1 \frac{D\mu}{g\rho\alpha a^4} , \tag{16}$$

and Eq. (15) as

$$\frac{dc_0}{dz} = \epsilon_2 \frac{D\mu}{g\rho\alpha a^4} , \tag{17}$$

where $\epsilon_1 = R_a X^4$ in the present work and ϵ_2 is given numerical value 67.94 in Taylor's work. If we regard the upper and lower boundaries to be free, then we may take $R_a = 658$, which makes $\epsilon_1 = 658\ X^4$.

If now we require that $\epsilon_1 = \epsilon_2$, then this would mean that

$$\epsilon_2 = 658\ X^4 . \tag{18}$$

In considering the numerical value 67.94 assigned by Taylor to ϵ_2, there can be two alternative interpretations of the relation in Eq. (18):

(i) $X = a/h$ is a constant with a definite value $(67.94/658)^{1/4}$ which is nearly equal to ϵ_2.

(ii) ϵ_2 is a function of X and hence its numerical value will be different, in general, from 67.94.

The first case would imply that the solute as described in Taylor's experiments should penetrate to a depth equal to twice the radius of the tube, irrespective of the nature of the solute. If on the other hand the depth of penetration is found to be different from the diameter of the vertical tube, then the numerical value of ϵ_2 must, in general, vary.

Furthermore, *if* the present theory is appropriate to the experiments described by Taylor, then we can obtain from Eq. (14) by writing $dc_0/dz = c_0/z$ (following Taylor),

$$D = \frac{1}{658} \frac{c_0 g \rho \alpha z^3}{\mu} , \qquad (19)$$

where c_0 is the concentration of the solute at top of the tube and z is the depth of penetration of the solute.

Equation (19) can then be used, following Taylor's reasoning, to determine the diffusion coefficient D experimentally, whatever the depth of penetration z. In the above expression we have used $R_a = 658$. If, however, rigid-free boundaries are more representative of a particular experimental arrangement, then $R_a = 1100$ is appropriate. It remains to be decided experimentally whether Eq. (18) holds in nature, and if so, by which of the two possibilities noted above as cases (i) and (ii).*

ACKNOWLEDGMENT

The present paper is part of an overall investigation concerning the effects of simultaneously impressed gradients of macroscopic-state parameters on hydrodynamic stability, which originated under the support of the General Electric Co. MSVD (Lieber, 1957, 1959). The present work was initiated under support of the National Research Council of Israel (Rintel, 1962) and completed with the support of the Fluid Mechanics Branch of the Office of Naval Research. We are also indebted to Dr. A. T. Wilson of Victoria University, Wellington, New Zealand for sending us unpublished measurements of temperatures and salinity in Lake Vanda.

*The senior author (P. Lieber) is entirely responsible for this interpretation of the correspondence between Sir G. I. Taylor's work and a limiting case of the present theory. This matter was first brought to his attention by personal communication with Sir Geoffrey.

BIBLIOGRAPHY

Boussinesq, J., 1904. Theorie Analytique de la Chaleur. Vol. 2, p. 172. Paris: Gauthie-Villars

Chandrasekhar, S., 1953. Proceedings of the Royal Society, London, Series A, Vol. 217, pp. 306-327

Goroff, I.R., 1960. Proceedings of the Royal Society, London, Series A, Vol. 254, pp. 537-541

Lieber, Paul, 1957. A survey and observation relating to thermal turbulence. Thermodynamics Technical Memo No. 79, September 25, 1957. MSVD, General Electric Co., Philadelphia

Lieber, Paul, 1959. On interaction of shear flow and thermal turbulence in curvilinear flow. Aerophysical Engineering Technical Memo No. 128, February 19, 1959. MSVD, General Electric Co., Philadelphia

Lieber, Paul, and Rintel, Lionel, 1962. The stability of viscous flow between rotating cylinders in the presence of radial temperature gradient. Transactions of AGU, Vol. 43, p. 444. (Also, Institute of Engineering Research, University of California, Berkeley, Report Nonr 222 (87), No. MD-623-5

Lieber, Paul, and Rintel, Lionel, 1965. Memorial volume for Prof. Edwin Schwerin. Amsterdam, Holland: Elsevier Publishing Co.

Pellew, A., and Southwell, R.V., 1940. Proceedings of the Royal Society, London, Series A, Vol. 176, pp. 312-343

Rayleigh, Lord, 1916. Philosophical Magazine, Vol. 32, p. 529

Rintel, Lionel, 1961. Doctoral thesis. Technion, Israel Institute of Technology

Rintel, Lionel, 1962. The Negev Research Institute, Israel. Solar Pond Project, Report No. 117, March 1962, and Report No. 129, August 1962

Lieber, Paul, and Rintel, Lionel, 1963. Convective instability of a horizontal layer of fluid with maintained concentration of diffusive substance and temperature at the boundaries. Institute of Engineering Research, University of California, Berkeley, Report H MD-63-6, Nonr-222 (87), November 1963

Stern, M., 1960. Tellus, Vol. 12, pp. 172-175

Swallow, J.S., 1965. Oceanus, Vol. 11, No. 3, pp. 3-5

Turner, J.S., and Stommel, H., 1964. Proceedings of the National Academy of Sciences, Vol. 52, pp. 49-53

Taylor, G.I., 1954. Proceedings of the Physics Society, London, Series B, Vol. 67, pp. 857-869

Weinberger, H., 1962. Stability criteria for a liquid system with temperature and salt concentration gradients. National Physics Laboratory of Israel, July 1962

Wilson, A.T., and Wellman, H.W., 1962. Nature, Vol. 196, pp. 1171-1173

* * *

A Contribution to the Theory of Turbulent Flow Between Parallel Plates

A. S. Iberall
General Technical Services, Inc.
Upper Darby, Pennsylvania

INTRODUCTION

The study of the stability of motion of a viscous fluid was begun by Reynolds to determine those conditions under which laminar flow might no longer persist. Theory and background are presented by Lin [1]. In this report, an alternative study is undertaken of conditions under which stable nonlinear limit cycles might persist at Reynolds number well beyond the laminar flow limit. The case of turbulent, low-Mach-number flow between parallel plates is discussed. Since the turbulent field beyond the critical Reynolds number appears to be stable and marked by a stationary though stochastic spectrum of fluctuations, there is considerable reason for attempting to identify the suggestive nonlinear behavior with limit cycles. Since sustained oscillations in a distributed field are associated with propagation, one type of which is concerned with compressible waves, compressibility is retained. While an apparent added complexity, if it is not needed in any particular hydrodynamic problem, it should drop out naturally as negligible. Actually, it will be shown to be needed to establish limit cycles in parallel-plate flow. Turbulence in that problem is thereby traced to a coupling of acoustic waves with the hydrodynamic field.

EQUATIONS FOR TURBULENCE

In Cartesian tensor form, the continuum equations of hydrodynamics for a fluid, which is not concerned with mass diffusion, body forces, or radiation, are:

Momentum equation

$$\rho \frac{DV_i}{Dt} = -p_{,i} + \left[\mu(V_{i,j} + V_{j,i})\right]_{,j} - \left[\left(\frac{2}{3}\mu - \lambda\right) V_{i,j}\right]_{,j} ,$$

Energy equation

$$\rho T \frac{DS}{Dt} = -\left[kT_{ij}\right]_{,j} + \mu\left[V_{i,j} + V_{j,i}\right] V_{j,i} - \left[\frac{2}{3}\mu - \lambda\right]\left[V_{j,j}\right]^2 , \qquad (1)$$

Equation of continuity

$$\frac{D\rho}{Dt} = -\rho V_{j,j} ,$$

Thermodynamic relations (valid for near-equilibrium fields), one of which is the relation of state

$$d\rho = \frac{\gamma}{C^2} dp - \alpha\rho dT ,$$

$$dS = \frac{C_p}{T} dT - \frac{\alpha}{\rho} dp ,$$

A relation of compatibility

$$\alpha T = \frac{\gamma - 1}{\alpha} \frac{C_p}{C^2} .$$

Symbols are identified in the section on nomenclature.

By examining their derivation within a modern statistical mechanical framework [2], it is possible to determine the following limits [3,4] for their applicability to continuous phenomena:

$$\beta[1 + \lambda/\mu] < 0.001 << 1 ,$$

$$\Gamma[1 + \lambda/\mu] < 0.1 << 1 ,$$

where

$\beta = \nu/Ch$ (a spatial continuum parameter — the ratio of mean free path to dimensions),

$\Gamma = \nu\Omega/C^2$ (a temporal continuum parameter — the ratio of molecular relaxation time to shortest fluctuating period).

In any hydrodynamic field, whether laminar or turbulent, in which these conditions are met, the molecular ensemble will not manifest their fluctuations. Any fluctuations that do exist must arise from the macroscopic dynamics that are fully represented by Eq. (1).

In this development for one elementary form of turbulent phenomena, that induced by pressure gradients, attention will be restricted to small compressibility effects by assuming that the square of the Mach number is not significantly large compared to unity. Since there may still remain other sources of turbulence, typically induced by heat transfer, rotation, or other relative wall motions, the set is specialized for fields that only show small density changes and little temperature changes. This may be represented by the following nonlinear

set, in which the derivatives of density and entropy have been eliminated by use of the thermodynamic relationships:

$$\rho_{oo}\frac{DV_i}{Dt} = -p_{,i} + \mu_{oo}[V_{i,jj} + V_{j,ij}] - \left[\frac{2}{3}\mu_{oo} - \lambda_{oo}\right]V_{i,jj} ,$$

$$\rho_{oo}C_{p_{oo}}\frac{DT}{Dt} - \alpha_{oo}T_{oo}\frac{Dp}{Dt} = k_{oo}T_{,jj} + \mu_{oo}[V_{i,j} + V_{j,i}]V_{j,i} - \left[\frac{2}{3}\mu_{oo} - \lambda_{oo}\right]\left[V_{j,j}\right]^2 , \quad (2)$$

$$\frac{\gamma_{oo}}{C_{oo}^2}\frac{Dp}{Dt} - \alpha_{oo}\rho_{oo}\frac{DT}{Dt} = -\rho_{oo}V_{j,j} .$$

The parameters with oo subscripts are now constant. It is this set involving five variables, three components of velocity, one of pressure, and one of temperature, that will be explored subject to the boundary conditions for parallel-plate flow.

Solutions for the linear (small-amplitude) set were explored earlier [5,6,7] for flow in a tube. Their validity (the solutions representing both laminar flow and all modes of propagation) over the entire frequency range of possible convergence of the Navier-Stokes (NS) equations was quite sharply tested by Greenspan [3]. The question now arises whether a second nonlinear solution, other than the small-amplitude set, can exist.

First, transforming the equations into dimensionless form:

Momentum equation

$$\frac{DR_i}{D\tau} = -\Box P + (R_{i,jj} + R_{j,ij}) - \left(\frac{2}{3} - \frac{\lambda_{oo}}{\mu_{oo}}\right)R_{i,jj} ,$$

Energy equation

$$\frac{D\mathcal{T}}{D\tau} - (\gamma_{oo} - 1)\frac{DP}{D\tau} = \varepsilon_{oo}(R_{i,j} + R_{j,i})R_{j,i} + \frac{1}{\sigma_{oo}}\Box^2\mathcal{T} , \quad (3)$$

Continuity equation

$$\beta_{oo}^2\left[\frac{D\mathcal{T}}{D\tau} - \gamma_{oo}\frac{DP}{D\tau}\right] = R_{j,j} .$$

Incompressibility may be invoked by letting β_{oo} approach zero. This lowers the order of the combined equation set. Such a procedure is quite dangerous in a nonlinear set. It leads to defects that are already suggested by the small-amplitude linear solution. For the NS equations to be valid, β must be small (in tube or plate experiments in the laboratory with normal air it will be about 10^{-6}). The parameter $\Gamma = \beta^2\omega$ must also be small. (The parameter ω is a dimensionless frequency.) However, $\beta\omega$ is not very restricted, and, in fact, the small-amplitude equations show that low-loss acoustic resonances are possible. (In the turbulent field, the magnitude of $\beta\omega$ may range from 0 to 10 or more.)

Thus, it is not ruled out that near resonances may be excited into a turbulent field. It is only by satisfying all boundary conditions that one can determine what propagation modes are permitted by the field. Nonlinear excitation of elastic modes cannot be dismissed in any material medium even though their amplitude may not be considered to be of any importance.

The nonlinear problem will be examined under the assumption that a turbulent field exists with an unknown mean velocity distribution whose maximum value is sufficiently removed from zero that fluctuating propagative modes persist. Decomposed into a time-dependent (1 subscript) and time-independent (0 subscript) set, they are

$$\mathbf{R} = \mathbf{R}_0(x,y,z) + \sum \mathbf{R}_1(x)\, e^{j(\omega\tau+\alpha y+\delta z)} = \mathbf{R}_0 + \mathbf{R}_{(1)} ,$$

$$P = P_{oo} + P_0(x,y,z) + \sum P_1(x)\, e^{j(\omega\tau+\alpha y+\delta z)} = P_{oo} + P_0 + P_{(1)} ,$$

$$\mathcal{T} = \mathcal{T}_{oo} + \mathcal{T}_0(x,y,z) + \sum_{\omega} \mathcal{T}_1(x)\, e^{j(\omega\tau+\alpha y+\delta z)} = \mathcal{T}_{oo} + \mathcal{T}_0 + \mathcal{T}_{(1)} ,$$

in which the propagation constants ω, α, δ are assumed to be real. They are here indexed in the primitive form of traveling waves. (The vector indices i have been omitted for clarity.)

The justification for the search in this form may be considered to be Poincaré's concept of characteristic exponents. As Whittaker's "Mechanics" states, in discussing stability of types of motion of dynamical systems, "Hence a necessary condition for stability of the periodic orbit is that all the characteristic exponents must be purely imaginary."

The solution technique is basically also known as the describing-function technique. Even though the fluctuating components sought are trapped into oscillation by the nonlinearity of the overall process, their amplitudes are assumed to be small. Thus, they will be assumed to contribute, in the quadratic terms, to the time-independent processes, but the fluctuating components arising from difference frequencies in the quadratic terms will be neglected. As a first-order theory for the fluctuating components, it can only furnish necessary conditions for the existence of nonlinear limit cycles. Intuitively, one expects that if the fluctuating components possess small amplitude, the technique should be reliable. The decomposed equation sets are:

For the mean state:

$$\mathbf{R}_0 \cdot \Box\mathbf{R}_0 + \overline{\mathbf{R}_{(1)} \cdot \Box\mathbf{R}_{(1)}} = -\Box P_0 + \Box^2\mathbf{R}_0 + q\Box(\Box\cdot\mathbf{R}_0) ,$$

$$\mathbf{R}_0 \cdot \Box\mathcal{T}_0 + \overline{\mathbf{R}_{(1)} \cdot \Box\mathcal{T}_{(1)}} - (\gamma_{oo} - 1)\left[\mathbf{R}_0 \cdot \Box P_0 + \overline{\mathbf{R}_{(1)} \cdot \Box P_{(1)}}\right] \tag{4}$$

$$= \varepsilon_{oo}\left[R_{0\,i,j} + R_{0\,j,i}\right] R_{0\,j,i} + \varepsilon_{oo}\overline{\left[R_{(1)\,i,j} + R_{(1)\,j,i}\right] R_{(1)\,j,i}} + \sigma_{oo}^{-1}\Box^2\mathcal{T}_0 ,$$

$$\beta_{oo}^2\left[\gamma_{oo}\left(\mathbf{R}_0 \cdot \Box P_0 + \overline{\mathbf{R}_{(1)} \cdot \Box P_{(1)}}\right) - \left(\mathbf{R}_0 \cdot \Box\mathcal{T}_0 + \overline{\mathbf{R}_{(1)} \cdot \Box\mathcal{T}_{(1)}}\right)\right] = -\Box\cdot\mathbf{R}_0 ,$$

where time-averaged quantities are under a bar, vectors are in black type, and

$$q = 1/3 + \lambda_{oo}/\mu_{oo}$$

For the fluctuating state:

$$\frac{\partial}{\partial\tau}\mathbf{R}_1 + \mathbf{R}_0 \cdot \square\mathbf{R}_{(1)} + \mathbf{R}_{(1)} \cdot \square\mathbf{R}_0 = -\square P_{(1)} + \square^2\mathbf{R}_{(1)} + q\square(\square \cdot \mathbf{R}_{(1)}),$$

$$\left[\frac{\partial}{\partial\tau}\mathcal{T}_{(1)} + \mathbf{R}_0 \cdot \square\mathcal{T}_{(1)} + \mathbf{R}_{(1)} \cdot \square\mathcal{T}_0\right] - (\gamma_{oo} - 1)$$

$$\times \left[\frac{\partial}{\partial\tau}P_{(1)} + \mathbf{R}_0 \cdot \square P_{(1)} + \mathbf{R}_{(1)} \cdot \square P_0\right] = \varepsilon_{oo}[R_{0i,j} + R_{0j,i}]\, R_{(1)j,i} \qquad (5)$$

$$+ \varepsilon_{oo}[R_{(1)i,j} + R_{(1)j,i}]\, R_{0j,i} + \sigma_{oo}^{-1}\square^2\mathcal{T}_{(1)},$$

$$\beta_{oo}^2\left[\left(\frac{\partial}{\partial\tau}\mathcal{T}_{(1)} + \mathbf{R}_0 \cdot \square\mathcal{T}_{(1)} + \mathbf{R}_{(1)} \cdot \square\mathcal{T}_0\right)\right.$$

$$\left. - \gamma_{oo}\frac{\partial}{\partial\tau}P_{(1)} + \mathbf{R}_0 \cdot \square P_{(1)} + \mathbf{R}_{(1)} \cdot \square P_0\right] = R_{(1)j,j}.$$

BOUNDARY CONDITIONS

The following boundary conditions are assumed for one-dimensional long-channel flow between parallel plates. For the fluctuating field components, let

$$\mathbf{R}_{(1)} = (\mathbf{i}U_{(1)} + \mathbf{j}V_{(1)} + \mathbf{k}W_{(1)}) = \Sigma(\mathbf{i}U + \mathbf{j}V + \mathbf{k}W)\, e^{j(\omega\tau + \alpha y + \delta z)}$$

represent the components of the fluctuating flow;

$\mathbf{R}_{(1)} = 0$ at $x = \pm 1$ (velocity zero at the walls),

$\mathcal{T}_{(1)} = 0$ at $x = \pm 1$ (temperature deviations zero at the walls).

For the mean field components, let

$$\mathbf{R}_0 = k R_0(x) = k R_{oo}[1 - \varphi(x)]$$

represent the undetermined form of the mean velocity;

$R_0(x) = 0$ at $x = \pm 1$,

$P_0(z) = -gz$.

g is assumed to be constant independent of x;

$$\mathcal{T}_0(x) = 0.$$

Because of the low Mach number and the long isothermal wall system, the effects of any minor cross-channel temperature distribution will be disregarded.

The boundary condition commonly invoked — see, for example, Laufer [8] — relates the pressure gradient to the shearing stress at the wall. Typically, this is achieved by integration of the appropriate NS momentum equation written in the form of Reynolds stresses. Assuming, for parallel-plate flow, that the mean values of the quadratic terms involving the fluctuating components have no axial variation, it is first shown that the pressure gradient g has no cross-channel variation and then that the first integral of the equation of motion is

$$g x + \frac{dR_0}{dx} = \overline{U_{(1)} W_{(1)}} \ .$$

Thus, at the walls,

$$\pm g = - \frac{dR_0}{dx} \quad \text{at } x = \pm 1 \ .$$

In addition, there is a second condition which is not commonly noted. The mean momentum equation in the z direction is

$$g + \frac{d^2 R_0(x)}{dx^2} = \overline{\left[U_{(1)} \frac{\partial}{\partial x} + V_{(1)} \frac{\partial}{\partial y} + W_{(1)} \frac{\partial}{\partial t} \right] W_{(1)}} \ .$$

Thus, a second boundary condition is

$$g + \frac{d^2 R_0}{dx^2} = 0 \quad \text{at } x = \pm 1 \ .$$

Laufer demonstrates quite satisfactorily (Ref. [8], Figs. 8 and 19) that the shear stress obtained from the velocity gradient and the pressure gradient are in accord with the first boundary condition, and consistent with the known deviations near the wall of the von Kármán logarithmic velocity law ([8], Fig. 7). The relation

$$u^+ = y^+$$

is approached at the wall (the common normalization based on the friction velocity which is computed from the wall shear). Another experimental study [9] presents more detail on the flow field near the wall.

Consistent with Laufer's data and the universal von Kármán curves, Fig. 1 depicts the character of the mean velocity distribution near the wall in terms of the properties of φ, φ', and φ'' in an attempt to clarify the boundary conditions.

This may be transformed into the more familiar parameters of the logarithmic presentation. In terms of the variables of this paper, the variation near the wall was estimated to be

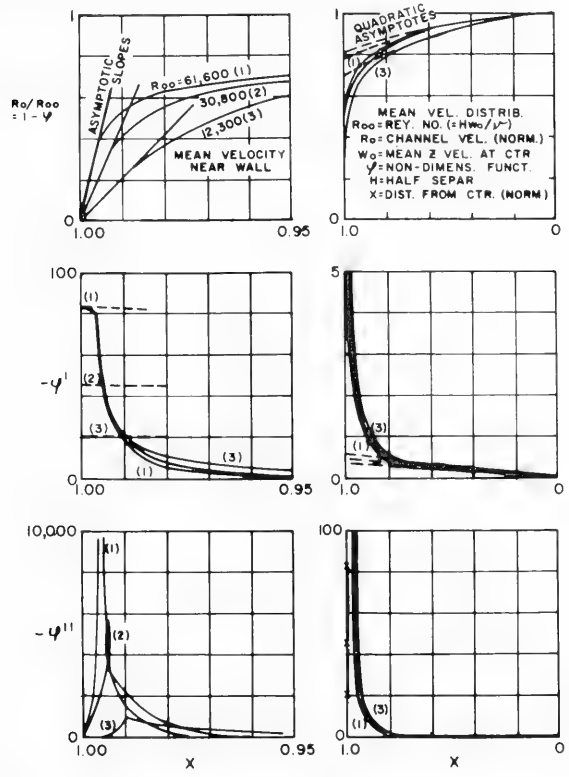

Fig. 1 - Properties of the mean velocity distribution for one-dimensional flow between parallel plates driven by a constant pressure gradient (data from Laufer (8))

$$R_{oo} = 12,300:$$

$$\frac{h^2}{W_0}\frac{d^2W}{dx^2} = 21 + 10,000\ (1 - x/h)\ , \qquad \text{to } 1 - x/h = 0.0095$$

$$\frac{h}{W_0}\frac{dW}{dx} = -21 + 21\ (1 - x/h) + 5,000\ (1 - x/h)^2\ ,$$

$$\frac{W}{W_0} = 21\ (1 - x/h) - 10.5\ (1 - x/h)^2 - 1,670\ (1 - x/h)^3\ ;$$

$$R_{oo} = 30,800:$$

$$\frac{h^2}{W_0}\frac{d^2W}{dx^2} = 46 + 300,000\ (1 - x/h)\ , \qquad \text{to } 1 - x/h = 0.0065$$

$$\frac{h}{W_0}\frac{dW}{dx} = -46 + 46\,(1 - x/h) + 150{,}000\,(1 - x/h)^2 \ ,$$

$$\frac{W}{W_0} = 46\,(1 - x/h) - 23\,(1 - x/h)^2 - 50{,}000\,(1 - x/h)^3 \ ;$$

$$R_{oo} = 61{,}600:$$

$$\frac{h^2}{W_0}\frac{d^2W}{dx^2} = 83 + 600{,}000\,(1 - x/h) \ , \quad \text{to } 1 - x/h = 0.0035$$

$$\frac{h}{W_0}\frac{dW}{dx} = -83 + 83\,(1 - x/h) + 300{,}000\,(1 - x/h)^2 \ ,$$

$$\frac{W}{W_0} = 83\,(1 - x/h) - 41.5\,(1 - x/h)^2 - 150{,}000\,(1 - x/h)^3 \ .$$

In terms of the logarithmic presentation (using Laufer's nomenclature),

$$U_r = \sqrt{\frac{\tau_0}{e}} \ ,$$

$$\tau_0 = -h\frac{dp}{dx} = \mu\left(\frac{du}{dy}\right)_{y=0} \ ,$$

$$u^+ = \frac{u}{U_r} \ ,$$

$$y^+ = \frac{U_r}{\nu}\,y \ ,$$

$$\frac{g}{R_{oo}} = \frac{R_{oo}}{2}\,\frac{h}{\left(\frac{1}{2}\right)\rho U_0^2}\frac{dp}{dx} = \frac{h}{u_0}\left(\frac{du}{dy}\right)_{y=0} \ ,$$

so that

$$u^+ = \frac{R_{oo}}{\sqrt{g}}\,\frac{W}{W_0} \ ,$$

$$y^+ = \sqrt{g}\,(1 - x/h) \ ,$$

transforms our variables to Laufer's;

$$R_{oo} = 12,300 ,$$

$$u^+ = (y^+) - 0.99 \times 10^{-3}(y^+)^2 - 0.91 \times 10^{-3}(y^+)^3 ,$$

$$0 \leq y^+ < 4.8 ;$$

$$R_{oo} = 30,800 ,$$

$$u^+ = (y^+) - 4.2 \times 10^{-4}(y^+)^2 - 7.7 \times 10^{-4}(y^+)^3 ,$$

$$0 \leq y^+ < 7.7 ;$$

$$R_{oo} = 61,600 ,$$

$$u^+ = (y^+) - 2.2 \times 10^{-4}(y^+)^2 - 2.4 \times 10^{-4}(y^+)^3 ,$$

$$0 \leq y^+ < 7.9 .$$

It is impossible to detect the graphic difference from $u^+ = y^+$ for this "boundary-layer" region. Since experimental data (e.g., [8] or [9]) show no deviation from $u^+ = y^+$ over a range y^+ up to 7 or 8, Fig. 1 derived from Laufer [8] is a more sensitive presentation of the boundary layer. However, what Fig. 1 succeeds in doing is to show quite explicitly the existence of a boundary-layer region (namely, the region in which φ' is nearly constant).

Intercomparison with [9], the logarithmic law, and the form of φ' and φ'' provides some measure of the so-called laminar sublayer. In agreement with [9], a sublayer may be identified below $y^+ = 6$, more probably below $y^+ = 4$. It is not surprising that a simple linear gradient is found only within the range up to $y^+ = 1.6$.

It thus appears safe to infer that there is a region — typically $x = 0.998 - 1$ (or $y^+ = 0 - 1.5$) — in which the variation in φ' is essentially small; and a region — typically $x = 0 - 0.8$ (or y^+ above 500) — in which the variation in φ' is again small. In this report this transition zone will be considered very cursorily. The complexity arises from the rapidly changing magnitude of φ''.

In a preliminary report of this work [10], the form

$$R_0/R_{oo} = 1 - a_0 x^2 - (1 - a_0)\, x^{2N}$$

had been used, a two-parameter form, consistent with the same proposal by Pai [11]. The form is not satisfactory at the wall. It cannot satisfy all the φ boundary conditions. A basic conclusion drawn from [10] was that trapping limit cycle in parallel-plate flow was sensitive both to the mean flow in the core and its form in the boundary layer. Thus, a more suitable form for the mean flow must be selected.

In order to avoid the mass of algebraic detail that arises when the problem is not treated as an eigenvalue problem, the suggestion of a mathematical colleague was accepted of breaking the field into two parts, a core and a layer near the wall. The simplest form to take for φ is then

over the core region:

$$1 - \varphi = 1 - a_0 x^2 \approx 1 , \quad \text{for } x^2 < 1$$

$$\varphi' \approx 0 ,$$

$$\varphi'' \approx 0 ,$$

in the boundary layer

$$1 - \varphi = \frac{g}{2R_{oo}} (1 - x^2) , \quad \text{for } x^2 \approx 1$$

$$\varphi' = \frac{g}{R_{oo}} x ,$$

$$\varphi'' = \frac{g}{R_{oo}} .$$

WORKING EQUATIONS FOR BOUNDARY LAYER AND CORE

Let

$$\psi = \omega + \delta R_0$$

$$= \omega + \delta R_{oo}(1 - \varphi) ,$$

$$M_0 = \omega + \delta R_{oo} .$$

The working form of the fluctuating equations may be represented by

$$\begin{aligned}
[D^2 - \lambda - j\psi] U + qD [DU + j\alpha V + j\delta W] - DP &= 0 , \\
[D^2 - \lambda - j\psi] V + j\alpha q [DU + j\alpha V + j\delta W] - j\alpha P &= 0 , \\
[D^2 - \lambda - j\psi] W + j\delta q [DU + j\alpha V + j\delta W] + R_{oo}\varphi' U - j\delta P &= 0 , \\
\sigma^{-1} [D^2 - \lambda - j\sigma\psi] \mathcal{T} - 2\varepsilon j\delta R_{oo}\varphi' U - [2\varepsilon R_{oo}\varphi' D + (\gamma - 1) g] W + (\gamma - 1) j\psi P &= 0 , \\
[DU + j\alpha V + j\delta W] - \gamma\beta^2 g W + \gamma\beta^2 j\psi P - \beta^2 j\psi \mathcal{T} &= 0 ,
\end{aligned} \tag{6}$$

where

$$\lambda = \alpha^2 + \delta^2 \quad \text{and} \quad D = \frac{d}{dx} .$$

The variables U, V, W, P, and $\mathcal{T}$ represent the fluctuating amplitudes, indexed by the harmonic ω. They are as yet undetermined functions of x and ω. (The subscripts oo have been dropped from the constants.)

It is convenient to utilize one component X of the vorticity (vorticity may be identified by variables X, Y, Z appropriate to each coordinate):

$$\alpha X = \alpha W - \delta V \ .$$

Eliminating W,

$$\begin{aligned}
&[D^2 - \lambda - j\psi]\, U + qD\,[DU + (j\lambda/\alpha)\, V + j\delta X] - DP = 0 \ , \\
&[D^2 - \lambda - j\psi]\, V + j\alpha q\,[DU + (j\lambda/\alpha)\, V + j\delta X] - j\alpha P = 0 \ , \\
&[D^2 - \lambda - j\psi]\, X = -R_{oo}\varphi' U \ , \\
&\sigma^{-1}\,[D^2 - \lambda - j\sigma\psi]\, \mathcal{T} - 2\varepsilon j\delta R_{oo}\varphi' U - [2\varepsilon R_{oo}\varphi' D + (\gamma - 1)\, g]\, X \\
&\quad = \frac{\delta}{\alpha}\,[2\varepsilon R_{oo}\varphi' D + (\gamma - 1)\, g]\, V + (\gamma - 1)\, j\psi P = 0 \ , \\
&[DU + (j\lambda/\alpha)\, V + j\delta X] - \gamma\beta^2 gX - (\gamma\delta/\alpha)\,\beta^2 gV + \gamma\beta^2 j\psi P - \beta^2 j\psi \mathcal{T} = 0 \ .
\end{aligned} \tag{7}$$

This set may be decomposed

over the core:

$$\begin{aligned}
&[D^2 - \lambda - jM_0]\, U + qD\,[DU + (j\lambda/\alpha)\, V + j\delta X] - DP = 0 \ , \\
&[D^2 - \lambda - jM_0]\, V + j\alpha q\,[DU + (j\lambda/\alpha)\, Y + j\delta X] - j\alpha P = 0 \ , \\
&[D^2 - \lambda - jM_0]\, X = 0 \ , \\
&\sigma^{-1}\,[D^2 - \lambda - j\sigma M_0]\, \mathcal{T} + (\gamma - 1)\, jM_0 P - (\gamma - 1)\, gX - (\gamma - 1)\,(\delta g/\alpha)\, V = 0 \ . \\
&[DU + (j\lambda/\alpha)\, V + j\delta X] + \gamma\beta^2 jM_0 P - \beta^2 jM_0 \mathcal{T} - \gamma\beta^2 gX - (\gamma\delta\beta^2 g/\alpha)\, V = 0 \ .
\end{aligned} \tag{8}$$

for the region near the wall ($x = \pm 1$):

$$\begin{aligned}
&[D^2 - \lambda - j\omega]\, U + qD\,[DU + (j\lambda/\alpha)\, V + j\delta X] - DP = 0 \ , \\
&[D^2 - \lambda - j\omega]\, Y + j\alpha q\,[DU + (j\lambda/\alpha)\, V + j\delta X] - j\alpha P = 0 \ , \\
&[D^2 - \lambda - j\omega]\, X = \mp gU \ , \\
&\sigma^{-1}\,[D^2 - \lambda - j\sigma\omega]\, \mathcal{T} \mp 2\varepsilon j\delta gU - g\,[\pm 2\varepsilon D + \gamma - 1]\, X - (\delta g/\alpha)\,[\pm 2\varepsilon D + \gamma - 1]\, V + (\gamma - 1)\, j\omega P = 0 \ , \\
&[DU + (j\lambda/\alpha)\, V + j\delta X] + \gamma\beta^2 j\omega P - \beta^2 j\omega \mathcal{T} - \gamma\beta^2 gX - (\gamma\delta/\alpha)\,\beta^2 gV = 0 \ .
\end{aligned} \tag{9}$$

CHARACTERISTIC FUNCTIONS

These equations may be independently solved in terms of four independent modalities (characteristic functions) within each region. Because of the assumption of small compressibility, results will only be sought to first order in β^2.

Core Solutions

Modes I and II (available at a glance from the core equations as independent solutions $X \neq 0$, and $X = 0$). $e^{\pm jb_1 x}$; $b_1 = \sqrt{-jM_0 - \lambda}$ (a repeated root):

$$U = j\alpha^2 b_1 \mathcal{A}_1 e^{jb_1 x} - jM_0 [(1-\sigma)\lambda + j(\gamma-\sigma) q\lambda\beta^2 M_0 + j(\gamma-\sigma)\delta\beta^2 g] \mathcal{B}_1 e^{jb_1 x} ,$$

$$V = -j\alpha b_1^2 \mathcal{A}_1 e^{jb_1 x} + j\alpha M_0 b_1 [(1-\sigma) + j(\gamma-\sigma) q\beta^2 M_0] \mathcal{B}_1 e^{jb_1 x} ,$$

$$X = j\delta b_1^2 \mathcal{A}_1 e^{jb_1 x} ,$$

$$\mathcal{T} = \sigma(\gamma-1)\delta g b_1 \mathcal{B}_1 e^{jb_1 x} ,$$

$$P = j(\gamma-\sigma) q\delta\beta^2 M_0 g b_1 \mathcal{B}_1 e^{jb_1 x} .$$

These modes represent viscous diffusion.

Mode III (The mode is in the vicinity of $D^2 \equiv -j\sigma M_0 - \lambda$ from the $\mathcal{T}$ equation. It is the thermal diffusive mode. If $\beta^2 = 0$, the solutions would be "exact." The solutions presented are valid to first order in β^2.)

$e^{\pm jb_3 x}$; $b_3 = \sqrt{-j\sigma M_0 - \lambda + \beta^2 [(\gamma-1)(1-\sigma-\sigma q) M_0^2 - j(\gamma-1)\delta g]}$:

$$U = j\beta^2 b_3 \mathcal{C}_1 e^{jb_3 x} ,$$

$$V = j\alpha\beta^2 \mathcal{C}_1 e^{jb_3 x} ,$$

$$X = 0 ,$$

$$\mathcal{T} = \sigma \mathcal{C}_1 e^{jb_3 x} ,$$

$$P = -j(1-\sigma-\sigma q)\beta^2 M_0 \mathcal{C}_1 e^{jb_3 x} .$$

Mode IV (This is the elastic mode of propagation of pressure.)

$e^{\pm d_4 x}$; $d_4 = \sqrt{\lambda - \beta^2 M_0^2 + j\delta\beta^2 g + j[(\gamma-1)/\sigma + 1 + q]\beta^4 M_0^3}$:

$$U = -j d_4 [\sigma M_0 - j(\lambda - d_4^2)] \mathcal{D}_1 e^{d_4 x} ,$$

$$V = \alpha [\sigma M_0 - j(\lambda - d_4^2)] \mathcal{D}_1 e^{d_4 x} ,$$

$$X = 0$$

$$\mathcal{T} = -\sigma(\gamma-1)[M_0^2 - j(1+q)(\lambda - d_4^2) M_0 - j\delta g] \mathcal{D}_1 e^{d_4 x} ,$$

$$P = j[\sigma M_0 - j(\lambda - d_4^2)][jM_0 + (1+q)(\lambda - d_4^2)] \mathcal{D}_1 e^{d_4 x} .$$

Wall Solutions

Mode I

$$e^{\pm j a_1 x} \; ; \quad a_1^2 = -\lambda - j\omega \; ; \quad a_1 = \sqrt{\frac{\omega}{2}} \left[\left(1 - \frac{\lambda}{2\omega} \right) - j \left(1 + \frac{\lambda}{2\omega} \right) \right] :$$

$$x = 1$$

$$U = 0 \; ,$$

$$V = -\alpha\omega \left[(1-\sigma)\,\delta - 2\varepsilon\sigma\beta^2 g a_1 \right] A_1 e^{j a_1 x} \; ,$$

$$X = \omega \left[(1-\sigma)\,\lambda - 2\varepsilon\sigma\delta\beta^2 g a_1 \right] A_1 e^{j a_1 x} \; ,$$

$$\mathcal{T} = -j\sigma\alpha^2 g \left[2\varepsilon j a_1 + \gamma - 1 \right] A_1 e^{j a_1 x} \; ,$$

$$P = j q \alpha^2 \beta^2 \omega g \left[2\varepsilon\sigma a_1 - j(\gamma - \sigma) \right] A_1 e^{j a_1 x} \; .$$

$$x = -1$$

$$U = 0 \; ,$$

$$V = -\alpha\omega \left[(1-\sigma)\,\delta - 2\varepsilon\sigma\beta^2 g a_1 \right] A_3 e^{-j a_1 x} \; ,$$

$$X = \omega \left[1 - \sigma \right) \lambda - 2\varepsilon\sigma\delta\beta^2 g a_1 \right] A_3 e^{-j a_1 x} \; ,$$

$$\mathcal{T} = -j\sigma\alpha^2 g \left[2\varepsilon j a_1 + \gamma - 1 \right] A_3 e^{-j a_1 x} \; ,$$

$$P = j q \alpha^2 \beta^2 \omega g \left[2\varepsilon\sigma a_1 - j(\gamma - \sigma) \right] A_3 e^{-j a_1 x} \; .$$

Mode II (Neglected terms are of the order of $\beta^2\omega$)

$$x = 1$$

$$e^{(\delta g/2\omega)x} e^{\pm c_2 x} \; ; \quad c_2 = \sqrt{j\omega} \left[1 + \frac{\lambda}{2j\omega} - \frac{\varepsilon\sigma\beta^2 g^2}{(1-\sigma)\,j\omega} - \frac{3}{2j\omega} \left(\frac{\delta g}{2\omega} \right)^2 \right] :$$

$$U = g^{-1} \left[j\omega(1-\sigma) + \frac{\delta g}{\omega} \sqrt{j\omega} \right] \left[\sqrt{j\omega} + \frac{\delta g}{2\omega} \right] \left[-\frac{\delta g}{\omega} \sqrt{j\omega} + \frac{1}{2} \left(\frac{\delta g}{\omega} \right)^2 + \frac{2\varepsilon\sigma\beta^2 g^2}{1-\sigma} \right] B_1 e^{(\delta g/2\omega)x} e^{c_2 x} \; ,$$

$$V = g^{-1} \left[j\omega(1-\sigma) + \frac{\delta g}{\omega} \sqrt{j\omega} \right] j\alpha \left[-\frac{\delta g}{\omega} \sqrt{j\omega} + \frac{1}{2} \left(\frac{\delta g}{\omega} \right)^2 + \frac{2\varepsilon\sigma\beta^2 g^2}{1-\sigma} \right] B_1 e^{(\delta g/2\omega)x} e^{c_2 x} \; ,$$

$$X = \left[j\omega(1-\sigma) + \frac{\delta g}{\omega} \sqrt{j\omega} \right] \left[\sqrt{j\omega} + \frac{\delta g}{2\omega} \right] B_1 e^{(\delta g/2\omega)x} e^{c_2 x} \; ,$$

$$\mathcal{T} = \sigma g \left[2\varepsilon j\omega + \left(\gamma - 1 + 2\varepsilon \frac{\delta g}{\omega} \right) \sqrt{j\omega} \right] B_1 e^{(\delta g/2\omega)x} e^{c_2 x} \; ,$$

$$P = g^{-1}\left[j\omega(1-\sigma) + \frac{\delta g}{\omega}\sqrt{j\omega}\right]\left[\left(\frac{2\varepsilon\sigma q\beta^2 g^2}{1-\sigma} - \left[\frac{\delta g}{\omega}\right]^2\right) j\omega + \left(\frac{(\gamma-\sigma)\,q + 2\varepsilon\sigma q + 2\varepsilon\sigma(2+q)\,\frac{\delta g}{\omega}}{1-\sigma}\beta^2 g^2 + \left[\frac{\delta g}{\omega}\right]^3\right)\sqrt{j\omega}\right] B_1 e^{(\delta g/2\omega)x} e^{c_2 x} \,.$$

$x = -1$

$e^{-(\delta g/2\omega)x} e^{\pm c_2 x}$:

$$U = g^{-1}\left[j\omega(1-\sigma) + \frac{\delta g}{\omega}\sqrt{j\omega}\right]\left[-\sqrt{j\omega} - \frac{\delta g}{2\omega}\right]\left[\frac{\delta g}{\omega}\sqrt{j\omega} - \frac{1}{2}\left(\frac{\delta g}{\omega}\right)^2 - \frac{2\varepsilon\sigma\beta^2 g^2}{1-\sigma}\right] B_3 e^{-(\delta g/2\omega)x} e^{-c_2 x} \,,$$

$$V = g^{-1}\left[j\omega(1-\sigma) + \frac{\delta g}{\omega}\sqrt{j\omega}\right] j\alpha\left[\frac{\delta g}{\omega}\sqrt{j\omega} - \frac{1}{2}\left(\frac{\delta g}{\omega}\right)^2 - \frac{2\varepsilon\sigma\beta^2 g^2}{1-\sigma}\right] B_3 e^{-(\delta g/2\omega)x} e^{-c_2 x} \,,$$

$$X = \left[j\omega(1-\sigma) + \frac{\delta g}{\omega}\sqrt{j\omega}\right]\left[-\sqrt{j\omega} - \frac{\delta g}{2\omega}\right] B_3 e^{-(\delta g/2\omega)x} e^{-c_2 x} \,,$$

$$\mathcal{T} = \sigma g\left[-2\varepsilon j\omega - \left(\gamma - 1 + 2\varepsilon\,\frac{\delta g}{\omega}\right)\sqrt{j\omega}\right] B_3 e^{-(\delta g/2\omega)x} e^{-c_2 x} \,,$$

$$P = g^{-1}\left[j\omega(1-\sigma) + \frac{\delta g}{\omega}\sqrt{j\omega}\right]\left[-\left(\frac{2\varepsilon\sigma q\beta^2 g^2}{1-\sigma} - \left[\frac{\delta g}{\omega}\right]^2\right) j\omega - \left(\frac{(\gamma-\sigma)\,q + 2\varepsilon\sigma q + 2\varepsilon\sigma(2+q)\,\frac{\delta g}{\omega}}{1-\sigma}\beta^2 g^2 + \left[\frac{\delta g}{\omega}\right]^3\right)\sqrt{j\omega}\right] B_3 e^{-(\delta g/2\omega)x} e^{-c_2 x} \,.$$

Mode III (terms of order $\beta^2\omega$ are neglected)

$$e^{\pm j a_3 x} \;;\quad a_3^2 = -j\sigma\omega - \lambda + \beta^2\left[(\gamma-1)(1-\sigma-\sigma q)\,\omega^2 - \frac{2\varepsilon\sigma g^2}{1-\sigma}\right],$$

$$a_3 = \left[\left(1 + \frac{\beta^2\left[(\gamma-1)(1-\sigma-\sigma q)\,\omega^2 - \frac{2\varepsilon\sigma g^2}{1-\sigma}\right] - \lambda}{2\sigma\omega}\right) - j\left(1 - \frac{\beta^2\left[(\gamma-1)(1-\sigma-\sigma q)\,\omega^2 - \frac{2\varepsilon\sigma g^2}{1-\sigma}\right] - \lambda}{2\sigma\omega}\right)\right]\sqrt{\frac{\sigma\omega}{2}} :$$

$$x = 1$$

$$U = j(1-\sigma)\beta^2\omega a_3 C_1 e^{ja_3x} ,$$

$$V = j(1-\sigma)\alpha\beta^2\omega C_1 e^{ja_3x} ,$$

$$X = \beta^2 g a_3 C_1 e^{ja_3x} ,$$

$$\mathcal{T} = \left[\sigma(1-\sigma)\omega + \frac{\delta g a_3}{\omega}\right] C_1 e^{ja_3x} ,$$

$$P = j\beta^2\left[-(1-\sigma)(1-\sigma-\sigma q)\omega^2 + q\delta g a_3\right] C_1 e^{ja_3x} .$$

$$x = -1$$

$$U = -j(1-\sigma)\beta^2\omega a_3 C_3 e^{-ja_3x} ,$$

$$V = j(1-\sigma)\alpha\beta^2\omega C_3 e^{-ja_3x} ,$$

$$X = \beta^2 g a_3 C_3 e^{-ja_3x} ,$$

$$\mathcal{T} = \left[\sigma(1-\sigma)\omega + \frac{\delta g a_3}{\omega}\right] C_3 e^{-ja_3x} ,$$

$$P = j\beta^2\left[-(1-\sigma)(1-\sigma-\sigma q)\omega^2 + q\delta g a_3\right] C_3 e^{-ja_3x} .$$

Mode IV

$$e^{c_4x} ; \quad c_4^2\left[1 + j\left(1+q+\frac{\gamma-1}{\sigma}\right)\beta^2\omega - 2j\frac{\varepsilon\beta^2 g^2}{\omega}\right] + c_4\left[\frac{\delta g}{\omega} + j\frac{\beta^2 g^2}{\omega} + j\frac{\delta\lambda g}{\omega^2}\right.$$

$$\left. + j\delta\beta^2 g(q+\psi\varepsilon)\right] - \left[\lambda - \beta^2\omega^2 + j\delta\beta^2 g + j\left(1+q+\frac{\gamma-1}{\sigma}\right)\lambda\beta^2\omega\right] = 0 :$$

$$x = 1$$

$$U = \omega c_4 D_1 e^{c_4x} ,$$

$$V = j\alpha\omega D_1 e^{c_4x} ,$$

$$X = -\frac{jgc_4}{i - j\dfrac{\lambda - c_4^2}{\omega}} D_1 e^{c_4x} ,$$

$$\mathcal{T} = -j(\gamma-1)\omega^2\left[1 + j\left(\frac{1}{\sigma} - 1 - q\right)\frac{\lambda - c_4^2}{\omega} + \frac{j\delta g}{\omega^2}\left(q - \frac{4\varepsilon}{(\gamma-1)}\right)c_4 + \frac{2\varepsilon j g^2 c_4^2}{(\gamma-1)\omega^3}\right.$$

$$\left. + \frac{jg^2c_4}{\omega^3} - \frac{j\delta g}{\omega^2}\right] D_1 e^{c_4x} ,$$

$$P = -j\omega^2\left[1 + (1+q)\frac{\lambda - c_4^2}{j\omega} + \frac{jq\delta g c_4}{\omega^2}\right] D_1 e^{c_4x} .$$

$x = -1$

$$U = -\omega C_4 D_3 e^{-c_4 x} ,$$

$$V = j\alpha\omega D_3 e^{-c_4 x} ,$$

$$X = \frac{-jgc_4}{1 - j\dfrac{\lambda - c_4^2}{\omega}} D_3 e^{-c_4 x} ,$$

$$\mathcal{T} = -j(\gamma - 1)\omega^2 \left[1 + j\left(\frac{1}{\sigma} - 1 - q\right)\frac{\lambda - c_4^2}{\omega} + \frac{j\delta g}{\omega^2}\left(q - \frac{4\varepsilon}{\gamma - 1}\right) c_4 + \frac{2\varepsilon j g^2 c_4^2}{(\gamma - 1)\omega^3} - \frac{jg^2 c_4}{\omega^3} - \frac{j\delta g}{\omega^2} \right] D_3 e^{-c_4 x} ,$$

$$P = -j\omega^2 \left[1 + (1+q)\frac{\lambda - c_4^2}{j\omega} + \frac{jq\delta g c_4}{\omega^2} \right] D_3 e^{-c_4 x} .$$

Note: Building these solutions requires some a priori estimate of relative magnitudes of various parameters, typically the following:

parameters large compared to unity — ω, g, R_{oo}, M_0, $\sqrt{\omega}$ (It is not likely that ω is less than 100.),

parameters small compared to unity — β, $\beta^2\omega$, $\beta^2 g$, $\beta^2 R_{oo}$,

parameters that are quite bounded — λ, δ, α, $\delta R_{oo}/\omega$, βg, $\beta\omega$ (It is not likely that $\beta\omega$ is greater than 100.].

However, there are some parameters, such as ω/g, whose bounded magnitude is uncertain. Also, in developing coefficients in series, while use can be made of the small magnitude of β, $\beta^2\omega$, $\beta^2 g$ to permit rapid cutoff of such sequences, this may not be done with regard to the square root of such magnitudes, e.g., $\sqrt{\beta}$, $\sqrt{\beta^2\omega}$, $1/\sqrt{\omega}$. Thus, sequences must be carried forward at least to such terms, i.e., all series must be imagined in terms of such half-power expansions.]

SECULAR EQUATION — SELF-GENERATED PROPAGATION

The vanishing of the secular determinant emerges from satisfying boundary conditions $U = V = W = X = \mathcal{T} = 0$, at $x = \pm 1$ with these primitives.

A preliminary result can illustrate how limit cycles are generated. A secular determinant may be obtained first from the core solutions, which assesses the nonlinear contribution of a substantial mean velocity (Reynolds number) over

the central region of the tube. It does not assess the contribution of curvature of the mean velocity field near the wall. Letting the dual set of even and odd core solutions vanish at $x = \pm 1$ leads to the following conditions:

$$\mathcal{G}_1,\ \mathcal{G}_2 = 0$$

(both even and odd solutions for the vorticity vanish independently)

$$d_4^2 = 0 ,$$

from which

$$\lambda = \beta^2 M_0^2 \approx \beta^2 \omega^2 ,$$

and $\delta\beta^2 g$ is small.

The eigenvalues hereby obtained for self-generated propagation are instructive but not necessarily complete or correct. Instead of the vorticity actually vanishing, a weak generation of vorticity may develop. Most interesting is the expectation that the "mean" propagation is likely to be an elastic wave ($\alpha^2 + \delta^2 = \beta^2\omega^2$).

Returning to satisfying boundary conditions with the wall solutions, it can be shown that the leading-order terms for these solutions are the following:

$$U = \omega(1-\sigma)\left[\delta - \frac{2\varepsilon\sigma\beta^2 g\omega}{(1-\sigma)\sqrt{j\omega}}\right] Be^{\pm(\delta g/2\omega)x} e^{\pm c_2 x} \pm j(1-\sigma)\beta^2\omega a_3 Ce^{\pm j c_3 x} \pm \omega c_4 De^{\pm c_4 x}$$

$$V = -\alpha\omega[(1-\sigma)\delta - 2\varepsilon\sigma\beta^2 g a_1] Ae^{\pm j a_1 x} + j\alpha\omega De^{\pm c_4 x}$$

$$X = \omega[(1-\sigma)\lambda - 2\varepsilon\sigma\delta\beta^2 g a_1] Ae^{\pm j c_1 x} \pm j\omega(1-\sigma)\sqrt{j\omega}\ Be^{\pm(\delta g/\omega)x} e^{\pm c_2 x}$$

$$\mathcal{T} = \sigma(1-\sigma)\omega Ce^{\pm j a_3 x} - j(\gamma-1)\omega^2 De^{\pm c_4 x}$$

Invoking the conditions for a nonzero set of coefficients A, B, C, D, the vanishing of the determinant

$$\begin{vmatrix} 0 & \omega(1-\sigma)\left[\delta - \dfrac{2\varepsilon\sigma\beta^2 g\omega}{(1-\sigma)\sqrt{j\omega}}\right] & \pm j(1-\sigma)\beta^2\omega a_3 & \pm\omega c_4 \\ -\alpha\omega[(1-\sigma)\delta - 2\varepsilon\sigma\beta^2 g a_1] & 0 & 0 & j\alpha\omega \\ \omega[(1-\sigma)\lambda - 2\varepsilon\sigma\delta\beta^2 g a_1] & \pm j\omega(1-\sigma)\sqrt{j\omega} & 0 & 0 \\ 0 & 0 & \sigma(1-\sigma)\omega & -j(\gamma-1)\omega^2 \end{vmatrix} = 0$$

leads to the following secular equation:

$$[\omega c_4] = \frac{[j\alpha\omega]\left[\omega(1-\sigma)\left(\delta - \frac{2\varepsilon\sigma\beta^2\omega g}{(1-\sigma)\sqrt{j\omega}}\right)\right][\omega\lambda(1-\sigma) - 2\varepsilon\sigma\delta\beta^2 g\omega a_1]}{[\alpha\omega\delta(1-\sigma) - 2\varepsilon\sigma\beta^2 g\alpha\omega a_1][j\omega(1-\sigma)\sqrt{j\omega}]}$$

$$- \frac{[j(\gamma-1)\omega^2][j(1-\sigma)\beta^2\omega a_3]}{[\sigma(1-\sigma)\omega]} .$$

(The brackets preserve the source of each factor.) Thence

$$c_4 = \frac{(1-j)}{\sqrt{2\omega}}\left[\lambda + \frac{\gamma-1}{\sqrt{\sigma}}\beta^2\omega^2\right] ,$$

which when coupled with the quadratic equation for c_4, leads to two equalities from the real and imaginary parts.

From the real part:

$$\lambda\left[1 - \frac{\delta g}{\omega\sqrt{2\omega}} = \frac{\beta^2 g^2}{\omega\sqrt{2\omega}}\right] = \beta^2\omega^2\left[1 + \frac{\gamma-1}{\sqrt{\sigma}}\frac{\delta g}{\omega\sqrt{2\omega}} + \frac{\gamma-1}{\sqrt{\sigma}}\frac{\beta^2 g^2}{\omega\sqrt{2\omega}}\right].$$

From the imaginary part:

$$-\frac{\delta g}{\omega}\sqrt{\frac{\omega}{2}}\left(\frac{\lambda}{\beta^2\omega^2} + \frac{\gamma-1}{\sqrt{\sigma}}\right) - \beta^2\omega^2\left(\frac{\lambda}{\beta^2\omega^2} + \frac{\gamma-1}{\sqrt{\sigma}}\right)^2 - \frac{\delta g}{\omega} - \left(1 + q + \frac{\gamma-1}{\sigma}\right)\lambda$$

$$\pm\left(1 + \frac{\gamma-1}{\sqrt{\sigma}}\right)\frac{\beta^2 g^2}{\sqrt{2\omega}} = 0 ,$$

$$\frac{\delta g}{\omega} \approx \beta^2 g^2\sqrt{\frac{2}{\omega}}\left[\frac{-\left(\frac{\omega}{g}\right)^2\left[\left(1 + \frac{\gamma-1}{\sqrt{\sigma}}\right)^2 + \left(1 + q + \frac{\gamma-1}{\sigma}\right)\right] + \frac{1 + \frac{\gamma-1}{\sqrt{\sigma}}}{\sqrt{2\omega}}}{1 + \frac{\gamma-1}{\sqrt{\sigma}} + \sqrt{\frac{2}{\omega}}}\right].$$

The secular equation thus finally leads to the pair (to the order of $1/\sqrt{\omega}$ terms)

$$\lambda = \alpha^2 + \delta^2 = \beta^2\omega^2$$

$$\frac{\delta g}{\omega} = -\beta^2 g^2\sqrt{\frac{2}{\omega}}\frac{\left(\frac{\omega}{g}\right)^2\left[\left(1 + \frac{\gamma-1}{\sqrt{\sigma}}\right)^2 + \left(1 + q + \frac{\gamma-1}{\sigma}\right)\right] - \frac{1 + \frac{\gamma-1}{\sqrt{\sigma}}}{\sqrt{2\omega}}}{1 + \frac{\gamma-1}{\sqrt{\sigma}} + \sqrt{\frac{2}{\omega}}} .$$

One may note that of the two roots possible for the fourth mode, only one could satisfy the boundary conditions (namely, that it should nearly vanish along a particular complex path). This root leads to a propagative system, the elastic wave given by

$$\lambda = \alpha^2 + \delta^2 = \beta^2\omega^2 .$$

While the same result might have been suspected from the core equations just by assuming a mean velocity in the core, it now appears intrinsically excited. Beyond this, the mean velocity characteristics near the wall determine the dispersion of the wave system.

[The following comments may help to "explain" the process of satisfying the boundary conditions that lead to the final secular equation. Corresponding to the primitive $e^{j(\alpha y+\delta z+\omega\tau)}$ (δ negative), expressing a temporarily coherent traveling wave system traveling downstream, there is really a dual set, approaching and reflecting from the walls. This dual set must satisfy the boundary conditions. The viscous and thermal diffusive modes have leading terms $e^{\pm\sqrt{j\omega}x}$, $e^{\pm\sqrt{j\sigma\omega}x}$, over the entire cross section. The outgoing system of waves grows large in the face of the local pressure gradient, while the incoming wave is highly damped. This suggests that the boundary condition need be satisfied by only one of the two wave systems, namely, the outgoing one which has resulted from the excited pressure mode moving also in the downstream direction. Near the wall, the mean gradient is sufficient, by perturbation, to split the two viscous diffusive modes into two with slightly different propagative velocities. (In the laminar – small velocity amplitude -- case one clearly can see the source of the two viscous diffusive modes, which Kovasznay [12] refers to as vorticity modes. They are eigenvalues for two components of the vector velocity potential – the solenoidal components that give rise to vorticity. The two unsplit repeated roots are seen clearly in the core solutions, associated with $X = 0$, and $X \neq 0$.) It is their interaction with the pressure gradient in the boundary layer that turns the waves over into an eddy, and thus provides a source of radiated acoustic eddies that emerge from the wall region. Further, only one of the two propagation constants – say, $c_{4,1}$ – can satisfy the boundary conditions. What emerges is that neither an upstream propagated system (δ positive), nor $c_{4,2}$, the second possible "elastic" mode can satisfy the boundary conditions. It is rapidly attenuated or absorbed.

Actually, it is the inability of the second mode $c_{4,2}$ to provide a trapped self-generated vortical filament that is crucial. (It could very well have been that the first mode might not have been able to, also, or that some other mode – given other boundary conditions – might have been the source.) There then emerges linear combinations of the other diffusive modes which provide trapped limit cycle structures. Here the outward radiated "acoustic" components are exhibited.

While some added nonlinear distortion may visually deform the local field even further, the intrinsic modal interaction should essentially persist as shown in this elementary derivation.]

More globally, these results may be interpreted as follows: There may be many waves that can be excited. For any e^{kg}, say, there will be a possible $e^{\ell z}$. The nondenumerable class of all such waves forms a complex stochastic system that fits Kraichnan's allusions to the inordinately complex picture of a turbulent field. (This was a salient point in Kraichnan's keynote address at the 10th Annual Meeting of the Fluid Mechanics Division of the American Physical Society, Lehigh U., November, 1967.) With the existence of such a complex picture, we would concur. However, practically all of the waves are dissipated.

Among all the possible waves, we have selected those systems that may persist (not indefinitely, but as a sample of these waves that are not dissipated). They do not represent all the waves, but they represent a potential wave system which deterministically can provide ever-present fluctuations and which perhaps can account for the mean dissipative losses. Namely, it is this system that the pressure gradient generates and which also represents the source of drag. The others are evanescent. Thus what we propose is that there is an extensive distribution of systems that may satisfy the equation set. We chose as representative of this distribution, the one in which nondecaying modes exist and all decaying modes are zero. This is one feasible set, and in our view a "typical" one which should give good "typical" measures, i.e., measures near the mean. Others scatter around in a suitable phase space. These waves represent a dispersive "plane" system that is self-excited. Actually, they are not really plane, but curve with changing curvature in the mean field. Here we are locating the asymptotic system within the boundary layer.

SPECTRAL RANGE ASSOCIATED WITH PROPAGATION

As the first step, we can examine these first propagation results for consistency with the spectrum of turbulence.

(i) The coupled results for δ and λ lead to a finite cutoff for ω. Let this be represented by ω_0. Since, by inspection, δ grows with ω, let it take on its maximum value $\delta^2 = \delta_0^2$. $\alpha_0^2 = 0$. Then

$$\lambda = \delta_0^2 = \beta^2\omega_0^2 = \frac{2\beta^4\omega_0^5}{g^2}\left[\frac{\left(1 + \frac{\gamma - 1}{\sqrt{\sigma}}\right)^2 + \left(1 + q + \frac{\gamma - 1}{\sigma}\right)}{\left(1 + \frac{\gamma - 1}{\sqrt{\sigma}}\right)}\right]^2 ,$$

whence

$$\omega_0 = \left[\frac{\frac{1}{\sqrt{2}}\left(1 + \frac{\gamma - 1}{\sqrt{\sigma}}\right)}{\left(1 + \frac{\gamma - 1}{\sqrt{\sigma}}\right)^2 + \left(1 + q + \frac{\gamma - 1}{\sigma}\right)}\right]^{2/3} \left(\frac{g}{\beta}\right)^{2/3} \approx \left(\frac{g}{\beta}\right)^{2/3} .$$

We can make use of Laufer's data [8], in particular his $R_{oo} = 30{,}800$ data, because of its completeness. We may adapt for his experiments air flow, nominally normal (20°C) temperature.

$\nu = 0.150 \text{ cm}^2/\text{sec}$

$\rho = 1.206 \times 10^{-4} \text{ gr/cm}^3$

$\mu = 1.81 \times 10^{-4}$ poise

$h = 6.35$ cm

$C = 3.43 \times 10^4$ cm/sec

$W_0 = 728$ cm/sec (maximum mean velocity, from R_{oo})

$$\frac{h}{1/2\,(\rho W_0^2)}\,\frac{\Delta p}{\Delta z} = 0.00295 \text{ (from [8], Fig. 19)}$$

$$\frac{R_{oo}}{2}\,\frac{\Delta p}{1/2\,(\rho W_0^2)\,\Delta(z/h)} = \frac{h}{W_0}\,\frac{dW}{dx} = 45.5 \text{ (from [8], Fig. 19; Fig. 8).}$$

$\gamma = 1.400$

$\sigma = 0.709$

$q = 0.33$

Derived dimensionless parameters:

$R_{oo} = 30{,}800$

$\beta = \nu/Ch = 0.69 \times 10^{-6}$

$g/R_{oo} = 45.5$

$q = 1.40 \times 10^6$

$\omega = \frac{h^2(2\pi f)}{\nu} = 1120\ f$ (this relates ω to frequency f - Hz)

Laufer (Fig. 27 [8]) shows the frequency spectrum reproduced as Fig. 2.

We would estimate a high-frequency cutoff at

$\omega_0 = 65 \times 10^6$

$f_0 = 58{,}000$ Hz

As indicated in Fig. 2 (dotted lines), this is not inconsistent with Laufer's data.

An added "validation" for the high-frequency cutoff is the question of the smallest size "eddies" that might be associated with the turbulent field.

Let us consider the "wavelength" ℓ associated with the high-frequency cutoff. Because of the vector magnitude of $\lambda = \alpha^2 + \delta^2$, one would expect approximately

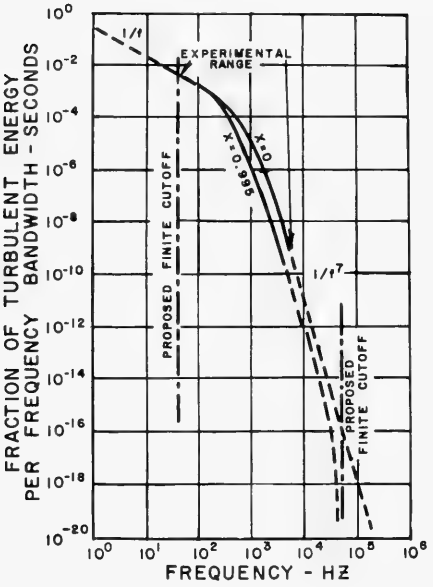

Fig. 2 - Frequency spectrum for velocity fluctuations parallel to mean flow

$$\ell = \frac{h}{\sqrt{\lambda}} = \frac{h}{\beta\omega_0}$$

$$= 0.14 \text{ cm } (\doteq 0.06 \text{ in.}) .$$

A query by private communication to Laufer ("In your 1951-2 parallel plate work, your spectral data (at R = 30,800) show significant observations at f = 3,000 Hz. In terms of the plate separation of 5 in., what is the size or scale of 'instantaneous' waves or eddies associated with this frequency level?") elicited the response that the eddy size corresponding to 300 Hz was about 0.1 in. We cannot help but feel that this minimal propagative "wavelength" (which appears in all field components including its vorticity) and the minimal eddy size that Laufer identifies by instrument inspection, are related, i.e., the field has a limited graininess. We propose that it has a corollary limiting frequency response.

(ii) We may also attempt an approximate estimate of the low-frequency cutoff for this experiment.

One may note that downstream propagation may vanish (e.g., $\delta = 0$, $\omega = \omega_1$) when

$$\left(\frac{\omega_1}{g}\right)^2 \left[\left(1 + \frac{\gamma - 1}{\sqrt{\sigma}}\right)^2 + \left(1 + q + \frac{\gamma - 1}{\sigma}\right)\right] = \frac{1 + \frac{\gamma - 1}{\sqrt{\sigma}}}{\sqrt{2\omega}} ,$$

i.e., when the numerator in δ vanishes.

(This may be checked independently by letting $\delta = 0$ in the solutions. The result is the same.)

Thence,

$$\omega_1 = \left[\frac{\left(1 + \frac{\gamma - 1}{\sqrt{\sigma}}\right) g^2}{\sqrt{2}\left(\left[1 + \frac{\gamma - 1}{\sqrt{\sigma}}\right]^2 + \left[1 + q + \frac{\gamma - 1}{\sigma}\right]\right)}\right]^{2/5} \approx g^{4/5}$$

$$= 4.8 \times 10^4 ,$$

$$f = 43 \text{ Hz} .$$

It is impossible, at the present state of development, to assign a precise meaning to this estimate. It marks the end at which a mechanism for the self-generated formation of eddies can be found. In magnitude, their size is of the order of the characteristic dimension. One suggestive connection may be proposed between the low-frequency cutoff and the onset of nonlinear phenomena found in the von Kármán vortex street.

Goldstein [13], (Fig. 149, Vol. II) represents the von Kármán vortex frequency for a circular cylinder in a wind tunnel by its Strouhal number, as a function of increasing Reynolds number. It is clear that a "noise" spectrum, associated with turbulence, appears "suddenly" at a critical Reynolds number (near "the" critical Reynolds number). As an approximation, it then appears that the Strouhal number is essentially constant. For the cylinder in a wind tunnel, it is experimentally shown that

$$S = \frac{Df}{W_0} = 0.16 ,$$

$$D = \text{cylinder diameter} .$$

If the two walls in parallel plate flow were similarly viewed as alternating sources of vorticity then a Strouhal number of nominal magnitude

$$\frac{2hf}{W_0} = 0.16$$

might be correspondingly assigned. This leads to

$$f = 92 \text{ Hz} .$$

We suggest these as two related estimates of a limit cycle fluctuation which represents a near "maximum" for low-frequency noise as a relaxation process by which a system of fluctuation is maintained from wall to wall.

We will attempt a more compelling estimate, namely, we will attempt to estimate a "critical" Reynolds number. The following crude scheme is used.

From the small-amplitude linear theory [5,7], we found that the transition from an overdamped (Rayleigh damping) wave for the tube to an underdamped (organ pipe) wave for the tube took place over the range $\omega = 1 - 100$.

We will obtain a result in two ways:

First, from $\omega_1 = 100$,

$$g = \left[\frac{\sqrt{2}\left(\left[1 + \frac{\gamma - 1}{\sqrt{\sigma}} \right]^2 + \left[1 + q + \frac{\gamma - 1}{\sigma} \right] \right)}{\left(1 + \frac{\gamma - 1}{\sqrt{\sigma}} \right)} \right]^{1/2} \qquad \omega_1^{5/4} = 625 \ .$$

For turbulent flow, approximately

$$g = a \, R_{oo}^{1.75} \ .$$

Fitted with Laufer's point, $g/R_{oo} = 45.5$ at $R_{oo} = 30{,}800$, the experimentally fitted result is

$$g = 0.0196 \, R_{oo}^{1.75} \ .$$

For $g = 625$, $R_{oo} = 370$.

Second, we propose that "all of a sudden," as Reynolds number increases, the underdamped frequency can become entrained. Thus, as before, from the Strouhal number

$$f = \frac{0.16}{2} \frac{W_0}{h} = \frac{0.16}{2} \frac{\nu}{h^2} R_{oo} \ ,$$

$$\omega_1 = 100 = 1120 \ f$$

$$f = 0.089 \text{ Hz} \ .$$

$$R_{oo} = 300 \ .$$

These values 370 and 300 (based on the half separation), may be compared with the standard value of 400 - 700 for the critical Reynolds number for parallel plates (on the basis of mean velocity and half-plate separation — see, for example, Sec. 146 [11]). The estimate is not bad.

SUGGESTIONS FOR FURTHER DEVELOPMENT

In this paper the problem is not completed. Instead, this section offers some ideas for further development.

Solutions Near The Wall

Returning now to the solutions within the boundary layer, we can evaluate the constants of integration to obtain the following primitives that satisfy wall boundary conditions.

$$x = \pm 1$$

$$U = \mp \frac{(1+j)}{\sqrt{2\omega}} \left[(1-\sigma)\,\delta - 2\varepsilon\sigma\beta^2 g a_1\right] \beta^2\omega^2 A \left[\frac{e^{\pm(\delta g/2\omega)x}\, e^{\pm c_2 x}}{e^{\delta g/2\omega}\, e^{c_2}} + \frac{\gamma-1}{\sqrt{\sigma}} \frac{e^{\pm j a_3 x}}{e^{j a_3}} - \left(1 + \frac{\gamma-1}{\sqrt{\sigma}}\right) \frac{e^{\pm c_4 x}}{e^{c_4}} \right],$$

$$V = \alpha \left[(1-\sigma)\,\delta - 2\varepsilon\sigma\beta^2 g a_1\right] A \left[\frac{e^{\pm j a_1 x}}{e^{j a_1}} - \frac{e^{\pm c_4 x}}{e^{c_4}} \right],$$

$$X = -(1-\sigma)\,\beta^2\omega^2 A \left[\frac{e^{\pm j a_1 x}}{e^{j a_1}} - \frac{e^{\pm(\delta g/2\omega)x}\, e^{\pm c_2 x}}{e^{\delta g/2\omega}\, e^{c_2}} \right],$$

$$\mathcal{T} = -(\gamma-1)\,\omega A \left[(1-\sigma)\,\delta - 2\varepsilon\sigma\beta^2 g a_1\right] \left[\frac{e^{\pm j a_3 x}}{e^{j a_3}} - \frac{e^{\pm c_4 x}}{e^{c_4}} \right],$$

$$P = \omega \left[(1-\sigma)\,\delta - 2\varepsilon\sigma\beta^2 g a_1\right] A \left[\frac{e^{\pm c_4 x}}{e^{c_4}} \right],$$

where

$$a_1 = (1-j)\sqrt{\frac{\omega}{2}}, \quad c_2 = (1+j)\sqrt{\frac{\omega}{2}}, \quad a_3 = (1-j)\sqrt{\frac{\sigma\omega}{2}},$$

$$c_4 = \frac{(1-j)}{\sqrt{2\omega}} \left[1 + \frac{\gamma-1}{\sqrt{\sigma}}\right] \beta^2\omega^2,$$

$$\alpha^2 + \delta^2 = \beta^2\omega^2, \quad \delta = -\beta^2 g \sqrt{2\omega} \left[\frac{\left[\left(1 + \frac{\gamma-1}{\sqrt{\sigma}}\right)^2 + \left(1 + q + \frac{\gamma-1}{\sigma}\right)\right]}{\left[1 + \frac{\gamma-1}{\sqrt{\sigma}}\right]} \left(\frac{\omega}{g}\right)^2 - \frac{1}{\sqrt{2\omega}} \right].$$

While δ is restricted to its nonpositive domain, there are the conjugate sets $e^{\pm j(\pm\alpha y + \delta z + \omega\tau)}$.

What we have derived is a primitive system of self-generated traveling wavelets in the boundary layer that act as a source of "acoustically" derived

vorticity for the main stream whose frequency components are coexistent with the frequency spectrum of turbulence. Whether we can proceed into the main stream may be regarded as conjecture (it is main-stream energy that has been captured to develop and sustain these piece-wise "coherent" elements; the net effect of the capture is that the layer radiates a structure of acoustic eddies back into the main stream. This is suggested as the energy budget at the wall).

We continue with a tentative scheme along the following crude path:

In the core, the main terms are likely to be

$$U = j\alpha^2 b_1 \mathcal{A} e^{jb_1 x} - j(1-\sigma)\lambda b_1 \mathcal{B} e^{jb_1 x} - jd_4 \mathcal{D} e^{d_4 x}$$

$$V = -\alpha M_0 \mathcal{A} e^{jb_1 x} + \alpha(1-\sigma) M_0 \mathcal{B} e^{jb_1 x} + \alpha \mathcal{D} e^{d_4 x}$$

$$X = \delta M_0 \mathcal{A} e^{jb_1 x}$$

$$\mathcal{T} = -j\sigma(\gamma-1)\delta g \mathcal{B} e^{jb_1 x} + \sigma \mathcal{C} e^{jb_3 x} - (\gamma-1) M_0 \mathcal{D} e^{d_4 x}$$

$$P = - M_0 \mathcal{D} e^{d_4 x}$$

$$W = \delta(1-\sigma) M_0 \mathcal{B} e^{jb_1 x} + \delta \mathcal{D} e^{d_4 x}$$

where

$$b_1 = (1-j)\sqrt{\frac{M_0}{2}}, \quad b_3 = (1-j)\sqrt{\frac{\sigma M_0}{2}},$$

$$d_4 = \beta \sqrt{\delta R_{oo}\omega + \sqrt{\delta^2 R_{oo}^2 \omega^2 + \frac{\left(1 + \frac{\gamma-1}{\sigma} + q\right)}{4} \beta^4 \omega^6}} + \frac{j\left(1 + \frac{\gamma-1}{\sigma} + q\right)\beta^3\omega^3}{2\sqrt{\delta R_{oo}^2 \omega + \sqrt{\delta^2 R_{oo}^2 \omega^2 + \frac{\left(1 + \frac{\gamma-1}{\sigma} + q\right)}{4} \beta^4 \omega^6}}}.$$

Strictly speaking, it is necessary that the form of φ be developed over a series of layers so as to match solutions, particularly the rapidly changing velocity solutions, through the transition zone layer by layer. However, we propose to only deal with the very crude two-zone approximation. We can only perform a very crude match.

(i) We will assume that the pressure fluctuations are continuous across the transition layer. In particular at small Mach number (so that d_4 is definitely quite small),

$$P = -\omega \mathcal{D} e^{d_4} \approx -\omega \mathcal{D} = -E$$

so that the core is flooded by a small excitation E.

(ii) We will assume that the temperature fluctuations are continuous across the transition layer. Thus,

$$0 = -j\sigma(\gamma - 1)\,\delta g\,\mathcal{B}\,e^{jb_1} + \sigma\,\mathcal{C}\,e^{jb_3} - (\gamma - 1)\,E\,,$$

from which $\mathcal{C}$ can be evaluated. Thus, the set remaining in the core is

$$U = j\alpha^2 b_1\,\mathcal{A}\,e^{jb_1 x} - j(1-\sigma)\lambda b_1\,\mathcal{B}\,e^{jb_1 x} - j\,\frac{d_4}{\omega}\,E$$

$$V = -\alpha\omega\,\mathcal{A}\,e^{jb_1 x} + \alpha\omega(1-\sigma)\,\mathcal{B}\,e^{jb_1 x} + \frac{\alpha}{\omega}\,E$$

$$W = \delta\omega(1-\sigma)\,\mathcal{B}\,e^{jb_1 x} + \frac{\delta}{\omega}\,E$$

$$X = \delta\omega\,\mathcal{A}\,e^{jb_1 x}\,.$$

Mean-Flow Equations

Except for eliminating two more constants of integration, we are up to a critical point — how to satisfy the mean-flow equations, say, by determination of a spectral density function.

While there are five equations, two involve terms of lower order of magnitude than the others, and so may be dropped in a first-order approximation. Instead they are replaced by the following lemmas.

(iii) The mean flow at low Mach number essentially behaves as if it were an incompressible, in the present instant, one-dimensional flow.

In the fifth mean-flow equation, the left-hand side can contribute only negligible residue, so that

$$\square \cdot \mathbf{R}_0 = 0$$

itself represents the fifth mean-flow equation.

(iv) The isothermal injection of fluid with isothermal boundaries at the same temperature, at low Mach number, creates a mean flow field which behaves essentially as if it were isothermal.

Similarly in the fourth mean-flow equation, other terms contribute negligibly, so that

$$\Box^2 \mathcal{T}_0 = 0 ,$$

and in fact

$$\mathcal{T}_0 = 0 .$$

(v) We are left with the three momentum equations

$$\overline{\left(U_{(1)} \frac{\partial}{\partial x} + V_{(1)} \frac{\partial}{\partial y} + W_{(1)} \frac{\partial}{\partial z}\right) U_{(1)}} = 0 , \quad \text{x momentum}$$

$$\overline{\left(U_{(1)} \frac{\partial}{\partial x} + V_{(1)} \frac{\partial}{\partial y} + W_{(1)} \frac{\partial}{\partial z}\right) V_{(1)}} = 0 , \quad \text{y momentum}$$

$$\overline{\left(U_{(1)} \frac{\partial}{\partial x} + V_{(1)} \frac{\partial}{\partial y} + W_{(1)} \frac{\partial}{\partial z}\right) W_{(1)}} = g , \quad \text{z momentum}$$

to satisfy throughout the core. At present we do not have a satisfactory program for this end game. (The end game probably requires determination of a spectral density function by means of an integral equation, summed over states $\omega_1 \leq \omega \leq \omega_0$, $\pm\alpha$, odd and even, of Fourier or Laplace form.) However, we can illustrate very crudely that our amplitude functions do possess a valid order of magnitude.

Laufer shows that the rms fluctuations in the cross-channel and lateral direction are essentially equal and not greatly different (by about a factor of 2 or 3) from the axial rms fluctuation. We will disregard this fact and imagine that the first two momentum equations are satisfied identically by each traveling wave system, namely, by letting both U and V approach zero. Specifically, we will consider that both

$$\alpha^2 \mathcal{A} = (1-\sigma)\lambda \mathcal{B} ,$$

$$\mathcal{A} = (1-\sigma)\mathcal{B} ,$$

are true and that the excitation E is small. Thus there only remains the z momentum

$$\overline{\frac{DW_{(1)}}{D\tau}} = \overline{W_{(1)} \frac{\partial W_{(1)}}{\partial z}} = g$$

(what is essential is that both W and X not vanish, i.e., that neither $\mathcal{A}$ nor $\mathcal{B}$ vanish. The lesser magnitude of X compared to g momentum suggests that the better condition may be $\mathcal{A} = (1-\sigma)\mathcal{B}$.)

Further we will imagine that there is only one frequency component ω_0, corresponding to the high-frequency eddy size.

Imagine now the standing wave system given by

$$W_{(1)} = a\, e^{\pm j(b_1 x \pm \alpha y - \delta_0 z \pm \omega_0 \tau)} , \quad (\alpha = 0)$$

then

$$\overline{\frac{DW_{(1)}}{D\tau}} = \frac{\delta_0 a^2}{2}$$

$$= \frac{\beta\omega_0 a^2}{2} = |g| ,$$

$$a = 250 .$$

Since the velocity

$$W = W_0 + W_{(1)}$$

and in the core this is given by

$$W = R_{oo} + W_{(1)}$$

a fluctuating amplitude of 250 compared to the Reynolds number of 20,800 is of the proper order of magnitude for the rms fluctuation found in the core. Illustrated in an average sense, such acoustic fluctuations, thus, can account for the momentum discrepancy in turbulent channel flow.

We can demonstrate further that this is no accident by the following: The "complete" z momentum equation is

$$\overline{[U_{(1)}\partial/\partial x + V_{(1)}\partial/\partial y + W_{(1)}\partial/\partial z]W_{(1)}} = g + d^2R_0/dx^2$$

$$= g - R_{oo}\varphi'' .$$

Drop $U_{(1)}$ and $V_{(1)}$ as before. Now consider this equation at the "end" of the boundary layer, i.e., where φ'' has its peak. In particular, apply this to Laufer's $R_{oo} = 30{,}800$ data. Whereas $|g/R_{oo}|$ has the value of about 45.5, $|\varphi''|$ has a value of about 6000, at least a hundred times larger. Thus,

$$\beta\omega_0 a^2/2 = |g - R_{oo}\varphi''|$$

or

$$a = 250\sqrt{R_{oo}\varphi''/g}$$

$$= 2800 .$$

This represents a peak amplitude of about 10% of the mean flow in the center. This is the magnitude of the peak rms fluctuation that Laufer shows at about the same location in his Fig. 11. This stresses the need for considerable attention to a theory for d^2R_0/dx^2 $(= -R_{oo}\varphi'')$, or φ''.

ACKNOWLEDGMENTS

Grateful acknowledgment is due Ralph Cooper and to the office of Naval Research for their singular willingness to support this effort; also to the author's colleague Don Young for a continued dialectic on the mathematical issues, and to Dr. D. P. Johnson and Dr. Harry Soodak for reviewing the mathematical-physical questions.

NOTATION

Operators, Indices, Coordinates

x, y, z = Cartesian coordinates. In any particular context they may have dimensions or be dimensionless (normalized by half separation of the parallel plate channel). When specialized for channel flow, x = the cross-channel coordinate, y = the lateral coordinate, z = the axial coordinate parallel to the mean flow.

t = time

i = Subscript representing the Cartesian coordinates. When an index is repeated in a term, it is summed by tensor convention.

$,i$ = Covariant derivative ($= \partial/\partial x_i$)

$\mathbf{V}$ = Alternatively, boldface is used to denote a vector V.

$\mathbf{i}, \mathbf{j}, \mathbf{k}$ = Unit vectors

D = Derivative with respect to x ($= d/dx$)

$\frac{D}{Dt}[\ \ ] = \frac{d}{dt}[\ \ ] + V_j[\ \ ]_{,j}$ = total derivative

V_i = i-th component of velocity

$j = \sqrt{-1}$

$\frown$ = Time average of the expression spanned by the symbol.

oo = A subscript that denotes parameters which are constant throughout the field.

0 = A subscript that denotes time averaged terms.

(1) = A subscript that denotes fluctuating terms.

$\square$ = Dimensionless del operator ($= h\nabla$).

Symbols (some with dimensions, some dimensionless) — in order of first use

ρ = density

p = pressure

μ, λ = shear viscosity, dilatational viscosity

T = temperature

S = entropy

k = thermal conductivity

γ = ratio of specific heats (dimensionless)

C = Laplacian velocity of sound

α = thermal coefficient of volume expansion

C_p = specific heat at constant pressure

h = half separation of the parallel-plate channel

ν = kinematic viscosity

Ω = any harmonic frequency in the field (e.g., rad/sec)

f = frequency (Hz)

β = spatial continuum parameter — ratio of mean free path to dimensions ($= \nu/Ch$ — dimensionless)

ω = dimensionless frequency ($= h^2\Omega/\nu$)

Γ = temporal continuum parameter — ratio of molecular relaxation time to the period of a fluctuation ($= \nu\Omega/C^2 = \beta^2\omega$ — dimensionless)

R_i = dimensionless velocity components ($= hV_i/\nu_{oo}$)

τ = dimensionless time ($= \nu_{oo}t/h^2$)

P = dimensionless pressure ($= h^2p/\mu_{oo}\nu_{oo}$)

ε = dimensionless thermal parameter ($= \alpha C^2/Cp$)

$\mathcal{T}$ = dimensionless temperature ($= \varepsilon_{oo}h^2C_{poo}T/\nu_{oo}^2$)

σ = Prandtl number ($= \mu Cp/k$)

$\mathbf{R}_0$ = dimensionless vector velocity, time averaged

R_0 = the z component of the time-averaged velocity (the only component in one-dimensional channel flow), dimensionless

R_{oo} = the magnitude of the time-averaged velocity in the center of the channel (dimensionless, and thus the Reynolds number of the flow field, based on half-plate separation and maximum velocity)

$P_{oo} + P_0$ = the time-averaged dimensionless pressure

$P_{oo} - gz$ = its form for one dimensional flow in a long channel

P_{oo} = the level of mean pressure in the field

g = the constant dimensionless pressure gradient in the field $[= -(dP_0/dz)]$

$\mathcal{T}_{oo} + \mathcal{T}_0$ = the time-averaged dimensionless temperature

$\mathcal{T}_{oo}$ = the level of temperature (assumed for the source, as an infinite reservoir, and for the long channel walls, as so thermostatted)

$\mathcal{T}_0$ = mean temperature deviations in the channel (assumed negligible)

$\varphi(x)$ = the form of the time-averaged z velocity in channel flow, expressed as a deviation from its value in the center of the channel (i.e., $R_0 = R_{oo}(1 - \varphi)$)

$\mathbf{R}_{(1)}$ = dimensionless vector velocity, instantaneous fluctuating component

$U_{(1)}, V_{(1)}, W_{(1)}$ = dimensionless fluctuating velocity components

$\omega\tau + \alpha y + \delta z$ = the dimensionless propagation phase for a fluctuation indexed by ω as a harmonic.

α = the dimensionless y propagation constant

δ = the dimensionless z propagation constant

$\lambda = \alpha^2 + \delta^2$

$\mathbf{R}_1$ = the dimensionless vector amplitude for a particular fluctuation indexed by ω.

$\mathcal{T}_{(1)}$ = dimensionless fluctuating temperature

$P_{(1)}$ = dimensionless fluctuating pressure

$\mathcal{T}_1$ = dimensionless temperature amplitude indexed by ω (when written in fluctuation equation sets, the 1 subscript may be omitted but is understood)

P_1 = dimensionless pressure amplitude indexed by ω (when written in fluctuation equation sets, the 1 subscript may be omitted but is understood)

U, V, W = the dimensionless x, y, z velocity amplitudes for a particular fluctuation indexed by ω.

$q = 1/3 + \lambda_{oo}/\mu_{oo}$

u^+, y^+ = dimensionless variables based on the friction velocity

ψ = a functional form $(= \omega + \delta R_o)$

M_0 = a constant indexed by ω $(= \omega + \delta R_{oo})$

a = indifferently used to represent a constant

X, Y, Z = dimensionless amplitudes representing the fluctuating components of vorticity, indexed by ω.

b_1, b_2, b_3, d_4 = characteristic functions in the core (dimensionless — e^{jb_1x}, e^{jb_2x}, e^{jb_3x}, e^{d_4x})

$\mathfrak{A}, \mathfrak{B}, \mathcal{C}, \mathfrak{D}$ = amplitudes for core solutions

a_1, c_2, a_3, c_4 = characteristic functions in the boundary layer (dimensionless — e^{ja_1x}, e^{c_2x}, e^{ja_3x}, e^{c_4x})

A, B, C, D = amplitudes for boundary-layer solutions

ℓ = wavelength

S = Strouhal number

APPENDIX — SOME FINAL COMMENTS

Since a number of readers were satisfied with the results obtained in the secular equation, but did not consider the argument by which boundary conditions were satisfied only for a single set at each wall (namely, for the incoming wave system, and not the dual incoming and outgoing system) fully transparent, it seems desirable to suggest how the result may be obtained by functions which are continuous across the entire section. This requires a suitable open form

for the mean flow. A simple form has finally been found. While not perfect, it may be considered one further element in a sequence of open forms. Expand the mean velocity distribution

$$R_0 = R_{oo}[1 - \varphi]$$

as

$$R_0 = R_{oo}[1 - a_2 x^2 - a_{2M} x^{2M} + a_{2M+2} x^{2M+2}] \ ,$$

a four parameter family (except for R_{oo}, which is given) with boundary conditions

$$\varphi = 1 \qquad \text{for} \quad x = \pm 1 \quad (R_0/R_{oo} = 0)$$

$$\varphi = 0 \qquad \text{for} \quad x = 0 \quad (R_0/R_{oo} = 1)$$

$$\varphi' = \pm g/R_{oo} = \pm N \quad \text{for} \quad x = \pm 1 \left(\frac{1}{R_{oo}} \frac{dR_0}{dx} = \mp N \right)$$

$$\varphi'' = g/R_{oo} = +N \quad \text{for} \quad x = \pm 1 \left(\frac{1}{R_{oo}} \frac{d^2R_0}{dx^2} = -N \right) .$$

It can be shown that the solution is

$$R_o + R_{oo}\left[1 - \left(1 - \frac{N-2}{M-1}\right)x^2 - \frac{M+1}{M-1}\frac{N-2}{2}x^{2M} + \frac{N-2}{2}x^{2M+2}\right]$$

$$N = \frac{g}{R_{oo}} \ .$$

(The earlier form used in [10] led to an erroneous value for the propagation constant δ — not for λ — since the result is sensitive to the velocity distribution in the boundary layer.)

This equation is a three-parameter representation of the mean flow, containing R_{oo} the Reynolds number, g the pressure gradient, and an arbitrary but large constant M.

We know M is large (i.e., the boundary layer is thin) because we found a high peak in R_0'' near the wall.

By setting $R_0''' = 0$, we can note where this peak occurs. It is found at

$$x^2 = \frac{2M-1}{2M+1} \approx 1 - \frac{1}{M} \ ,$$

i.e., near the wall, if M is large.

However, we also know that the coefficient of the x^2 term is small compared to unity in turbulent flow. (As may be found in Laufer's data, it is an appreciable fraction, such as 0.2, 0.3. Thus for more precise perturbations, it may not be neglected. However, at the present stage of theory, we may disregard it.) Thus as an approximation, we may let the coefficient vanish

$$N - 2 = M - 1 ,$$

so that a simpler two-parameter result may be obtained.

$$R_0 + R_{oo}\left[1 - \frac{N}{2}\, x^{2(N-1)} + \frac{N-2}{2}\right] x^{2N}$$

$$N = \frac{g}{R_{oo}} .$$

At the present, this is the simplest relation that has been found that satisfies the boundary conditions and yet is capable of fairly reasonable representation of the mean flow. Thus it is a good starting perturbation for a self-consistent field study.

Note that this relation contains only two constants, the "given" Reynolds number R_{oo} of the field, and an as-yet-undetermined parameter g, which is to be determined finally as a function of R_{oo}. As such, this relation has the very minimum number of constants. More complicated self-consistent expressions will have to determine additional constants. What is specifically involved at this point, is how much detail a priori can be involved in describing the boundary layer.

For example, the form is "wrong" when compared with experimental data. It suggests that the "end" of the boundary layer, as marked by φ''', occurs at

$$1 - x = \frac{1}{2N} .$$

Laufer's three points suggest, more nearly,

$$1 - x = \frac{1}{4N} .$$

Also, it suggests that the maximum value of φ'' is about $0{,}8\ N^2$; Laufer's data suggest $2.5\ N^2$. However, what seems quite satisfactory in this form is the proper dependence on the power of $N\ (= g/R_{oo})$ and the emergence of a correct order-or-magnitude estimate of boundary-layer parameters.

Obtaining results from such self-consistent field theories (i.e., assume an n-parameter open form for the time-independent solutions, then use them in the inhomogeneous time-dependent equations to get the ω indexed fluctuating components, and then compute the undetermined parameters of the time-independent solutions) is sensitive to the form of the time-independent solution assumed — here, the mean velocity distribution. Even the slightly extended form

$$1 - \varphi = 1 - ax^{2M} + bx^{2P}$$

is not satisfactory. It can satisfy the φ boundary conditions, but it is not a completely accurate enough description of the φ function.

The salient characteristics of the φ function beyond its boundary conditions — to be noted experimentally — are the magnitude, location, and width of the very high impulse in φ'', and possibly even its slope at $x = \pm 1$. For this there is no theory, none at least in a self-consistent sense. This is no trivial observation.

Kraichnan, in private criticism of this work, called attention to the possible pertinence of the work of Landahl. Landahl pointed out the differences in our motivation and purpose, and kindly supplied material that he considered relevant from his work [14]. He makes therein an important point. He points up, validly, that the Orr-Sommerfeld theory, essentially obtained by eliminating pressure between the incompressible set of the Navier-Stokes equation and continuity, leading (in his terminology) to a result like

$$(U - C)(\varphi'' - K^2\varphi) - U''\varphi + i/\alpha R(\varphi'''' - 2K^2\varphi'' + K^2\varphi) = 0 \quad \text{[his Eq. (30]}$$

cannot or has not been correctly applied to turbulent fields. The essence of the matter, he states, is that in stability theory U'' (our R_0'') is assumed to be of order unity. This is fine for the laminar flow field, but far from true in turbulence. He points up that the results depend on U'', and that values of U'' run up to the thousands, (on the basis of boundary-layer thickness). Thus, Orr-Sommerfeld stability theory is only valid for the transition from laminar flow. In the turbulent field, it is not correct. In order to be applicable, it must deal with the form and boundary conditions for U'' as well as U. However, this difficulty is intensified in Orr-Sommerfeld theory. Actually the Orr-Sommerfeld theory is embedded in the theory herein developed as part of the equation set. However, we do not "eliminate" any variables, such as pressure. It is this elimination, by differential operations, that introduced U'' (or our φ''). The original inhomogeneous linear equation set does not contain terms higher than first order in φ'. It is here that the theory of linear equations is not complete. A mathematical colleague pointed out that the results in Poole and other books on linear differential equations are not complete for inhomogeneous linear sets; that it is moot whether derivatives higher than the coefficients that appear in the original equation set appear in the solution. The standard theoretical course is the discussion of the transformed set of first order equations. To avoid related difficulties, the earlier treatment [10] stumbled on a valid path, purely by necessity.

The elimination of all of the variables but one (i.e., the reduction to one higher-order equation), in addition to possible ambiguities, leads to thousands of coefficients for the much higher ordered equation set for compressible flow. It was only in desperation that Frobinius-type series solutions were elected for exploration. It was quickly realized that the solution of the five-equation set is arrived at by a "relaxation" of terms in the power series one at a time, by cycling through the equation set, with quite a few being developed before a cycle of repetition could be obtained. The second method, having then found these series summable essentially into modalities, was to then derive solutions by

"relaxations," equation by equation. (Find a solution that relaxes each equation at least one order in β^2, and then continue to find higher-order relaxations. It was realized that it was essential to expand the perturbations in half powers, say of 1, $1/\sqrt{\omega}$, $1/\omega$, ... ; 1, $\sqrt{\beta^2\omega}$, ... ; 1, $\sqrt{\beta}$, ... since otherwise compensating zeros might arise.) This mathematically was satisfactory. It avoids the very difficult question of straining one's detailed knowledge of φ'' other than its boundary condition.

It is certain that the rigorous iterative task is best left to mathematicians. Thus, only crude but suggestive ideas have been thrown into our developments.

The minimal requirement is to satisfy the φ' and φ'' boundary conditions on φ. The second is to avoid stirring up too much trouble over the φ'' impulse. One perhaps may achieve this by a selected sequence of open forms ordered by a single parameter, i.e., the maximum value of φ''. Let this be φ_0'', and assume this to be large, located at x_0, nearly 1. One might regard this as a fifth boundary condition on φ (with the requirement that it be estimated self-consistently).

Proceeding now to the task of building solutions, we may then take for the form of ψ, the following

$$\begin{aligned}\psi &= \omega + \delta R_0 \\ &= \omega + \delta R_{oo}\left[1 - g/2R_{oo}\, x^{2(g/R_{oo}-1)} + g/R_{oo} - 2/2\, x^{2g(R_{oo}}\right] \\ &= M_0 - \delta g/2\, x^{2(g/R_{oo}-1)} + \delta(g - 2R_{oo})/2\, x^{2g/R_{oo}} \\ &= M_0 - \delta R_{oo}\varphi\,.\end{aligned}$$

(Note: Since $g \approx 0.02\ R_{oo}^{1.75}$ is the required result, $g/R_{oo} = 0.02/R^{0.75}$ has a value of approximately 2 and 4 for $R_{oo} = 500$ and 1000. Thus, it is not sufficiently larger than 1 or 2 to permit disregarding $2R_{oo}/g$ in the last term.)

The working equation set [from Eqs. (6)] becomes, letting $W = X + \delta/\alpha\, V$,

$$[D^2 - \lambda - j\psi]U + qD\,[DU + j\lambda/\alpha\, V + j\delta X] - DP = 0\,,$$

$$[D^2 - \lambda - j\psi]V + j\alpha q\,[DU + j\lambda/\alpha\, V + j\delta X] - j\alpha P = 0\,,$$

$$[D^2 - \lambda - j\psi]X = -R_{oo}\varphi' U\,,$$

$$[DU + j\,\lambda/\alpha\, V + j\,\delta X] - \gamma\beta^2 gX - \gamma\delta\beta^2 g/\alpha\, V + \gamma\beta^2 j\psi P - \beta^2 j\psi T = 0\,,$$

$$1/\sigma\,[D^2 - \lambda - j\sigma\psi]\,T - 2\varepsilon j\delta R_{oo}\varphi' U - [2\varepsilon R_{oo}\varphi' D + (\gamma - 1)\,g]X - \delta/\alpha\,[2\varepsilon R_{oo}\varphi' D + (\gamma - 1)\,g]\,V + (\gamma - 1)\,j\psi P = 0\,,$$

$$\psi = M_0 - \delta R_{oo}\varphi\ ;\quad M_0 = \omega + \delta R_{oo}\ ;\quad \varphi = \frac{N}{2}\,x^{2(N-1)} - \frac{N-2}{2}\,x^{2N}$$

$$N = g/R_{oo}\,.$$

We lose very little — for the present purposes — to neglect the difference between $[D^2 - \lambda - j\omega]$ and $[D^2 - \lambda - jM_0]$ and $[D^2 - \lambda - jM_0 + j\delta R_{oo}\varphi]$. Thus, we will assume ($a^2 = -j\omega - \lambda$). (The difference is first order in (low) Mach number.)

$$[D^2 + a^2]U + qD[DU + j\lambda/\alpha V + j\delta X] - DP = 0 ,$$

$$[D^2 + a^2]V + j\alpha q[DU + j\lambda/\alpha V + j\delta X] - j\alpha P = 0 ,$$

$$[D^2 + a^2]X = -R_{oo}\varphi' U ,$$

$$[DU + j\lambda/\alpha V + j\delta X] - \gamma\beta^2 gX - \gamma\delta\beta^2 g/\alpha V + \gamma\beta^2 j\omega P - \beta^2 j\omega T = 0 ,$$

$$1/\sigma[D^2 + a^2 + j(1-\sigma)\omega]T - 2\varepsilon j\delta R_{oo}\varphi' U - [2\varepsilon R_{oo}\varphi' D + (\gamma - 1)g]X$$

$$-\delta/\alpha[2\varepsilon R_{oo}\varphi' D + (\gamma - 1)g]V + (\gamma - 1)j\omega P = 0 ,$$

i.e., we will consider that the only salient perturbation comes from φ'. Examine this.

In the Core ($\varphi' \approx 0$)

$$[D^2 + a^2]U + qD[DU + j\lambda/\alpha V + j\delta X] - DP = 0 ,$$

$$[D^2 + a^2]V + j\alpha q[DU + j\lambda/\alpha V + j\delta X] - j\alpha P = 0 ,$$

$$[D^2 + a^2]X = 0 ,$$

$$[DU + j\lambda/\alpha V + j\delta X] - \gamma\beta^2 gX - \gamma\delta\beta^2 g/\alpha V + \gamma\beta^2 j\omega P - \beta^2 j\omega T = 0 ,$$

$$1/\sigma[D^2 + a^2 + j(1-\sigma)\omega]T - (\gamma - 1)gX - \delta/\alpha(\gamma - 1)gV + (\gamma - 1)j\omega P = 0 .$$

Except for the indifferent replacement of M_0 by ω, this is the same as Eqs. (8).

Thus (to first order — anticipating the final results) two independent symmetry solutions emerge:

$$U_{10} = j\alpha^2 A_0 \sin ax + \lambda(1-\sigma)\omega B_0 \sin ax - \beta^2 d\, C_0 \sin dx + jbD_0 \sinh bx ,$$

$$V_{10} = -\alpha a A_0 \cos ax + j(1-\sigma)\alpha a\omega B_0 \cos ax + j\alpha\beta^2 C_0 \cos dx - \alpha D_0 \cosh bx ,$$

$$X_{10} = \delta a A_0 \cos ax ,$$

$$T_{10} = \sigma(\gamma - 1)\delta ag B_0 \cos ax + \sigma C_0 \cos dx + (\gamma - 1)\omega D_0 \cosh bx$$

$$P_{10} = jq(\gamma - \sigma)\delta ag\beta^2\omega B_0 \cos ax - j(1 - \sigma - \sigma q)\beta^2\omega C_0 \cos dx + \omega D_0 \cosh bx$$

$$U_{20} = -j\alpha^2 A_1 \cos ax - \lambda(1-\sigma)\omega\beta_1 \cos ax + \beta^2 dC_1 \cos dx + jbD_1 \cosh bx$$

$$V_{20} = -\alpha a A_1 \sin ax + j(1-\sigma)\alpha a\omega B_1 \sin ax + j\alpha\beta^2 C_1 \sin dx - \alpha D_1 \sinh bx$$

$$X_{20} = \delta a A_1 \sin ax$$

$$T_{20} = \sigma(\gamma-1)\delta ag B_1 \sin ax + \sigma C_1 \sin dx + (\gamma-1)\omega D_1 \sinh bx$$

$$P_{20} = jq(\gamma-\sigma)\delta ag\beta^2\omega B_1 \sin ax - j(1-\sigma-\sigma q)\beta^2\omega C_1 \sin dx + \omega D_1 \sinh bx$$

$$a^2 \approx -j\omega - \lambda, \quad d^2 \approx -j\sigma\omega - \lambda, \quad b^2 \approx \lambda - \beta^2\omega^2 + j\delta\beta^2 g + j\left(1 + \frac{\gamma-1}{\sigma} + q\right)\beta^4\omega^3.$$

These solutions are essentially the same as the previous core solutions.

In the boundary layer ($\varphi' = \pm N$, $x = \pm 1$)

$$[D^2 + a^2]U + qD[DU + j\lambda/\alpha\, V + j\delta X] - DP = 0$$

$$[D^2 + a^2]V + j\alpha q[DU + j\lambda/\alpha\, V + j\delta X] - j\alpha P = 0$$

$$[D^2 + a^2]X = \mp gU$$

$$[DU + j\lambda/\alpha\, V + j\delta X] - \gamma\beta^2 gX - \gamma\delta\frac{\beta^2 g}{\alpha}V + \gamma\beta^2 j\omega P - \beta^2 j\omega T = 0$$

$$\frac{1}{\sigma}[D^2 + a^2 + j(1-\sigma)\omega]T \mp 2\varepsilon j\delta gU - g[\pm 2\varepsilon D + \gamma - 1]X - \frac{\delta}{\alpha}g[\pm 2\varepsilon D + \gamma - 1]V + (\gamma-1)j\omega P = 0.$$

This is the same as Eqs. (9). The solutions were previously written in terms of exponentials as independent boundary-layer solutions.

The first solution set should be transformable into the second solution set by perturbation. The present purpose would be to relate the constants for the core solution to the boundary-layer solutions, and second to derive, if possible, an explicit perturbation theory.

In accord with [10], we can surmise that a convergent perturbation is of the form

$$V = V_0 \cos F' + V_1 \sin F' + V_2 \cos F', \quad \text{etc.}$$

an in-phase perturbation (V_2 cos — where V_2 is even when V_0 is even) and an out of phase perturbation (V_1 sin — where V_1 is odd when V_0 is even). The functions V_1, V_2, F' will depend on φ and its derivatives, to first order in a first-order theory. (While the decomposition into F', V_1 and V_2 is not unique F' is chosen for convenience, e.g., if

$$[D^2 + a^2 + j\delta R_{oo}\varphi]\ V = 0$$

$$V = A\,[1 + C_0\varphi + C_2\varphi'' + \ldots]\ \cos\left[ax + j\delta\,\frac{R_{oo}}{2a}\int\varphi\right]$$

$$+A\,[D_1\varphi' + D_3\varphi''' + \ldots]\ \sin\left[ax + j\delta\,\frac{R_{oo}}{2a}\int\varphi\right]$$

$$+B\,[1 + E_0\varphi + E_2\varphi'' + \ldots]\ \sin\left[ax + j\delta\,\frac{R_{oo}}{2a}\int\varphi\right]$$

$$+B\,[F_1\varphi' + F_3\varphi''' + \ldots]\ \cos\left[ax + j\delta\,\frac{R_{oo}}{2a}\int\varphi\right] .$$

It will be found, as in [10], that the solutions separate into odd and even solutions, and that both cannot satisfy the boundary conditions because of the irreducibility of cosh c_4x. (Only sinh c_4x can relax the secular determinant to zero.)

Further, the large magnitude of a_1, and a_3 make

$$\sin a_{1,3} = -j \cos a_{1,3}$$

because of the large complex magnitude of the arguments. Thus, the independent even and odd solutions are proportional to each other, except for the fourth mode. It is this relation which ultimately results in each of the two families of waves incoming to the wall vanishing independently.

The program has not yet been carried through completely, so that the constants of integration for the core have not been fully related to the boundary-layer constants. However, the independence of the two solutions of different symmetry is clarified.

Another task that had been neglected was the demonstration of a second "stable" branch for turbulence, namely, a law of mean flow other than the $g = AR_{oo}$ law of laminar flow.

This can be obtained crudely as follows.

Roughly, the boundary-layer thickness is of the order of the limiting eddy size. Our theory says

$$\ell = h/\beta\omega_0 .$$

If we use the new expression for $1 - \varphi$ this had a peak in R_o'' at $R_o''' = 0$. Whence $x^2 = 2N - 3/2N - 1$ or $1 - |x| = 1/2N$. (Laufer's data show $1 - x = 1/4N$ instead.)

$$\ell/h = 1/\beta\omega_0 = 1 - |x| = 1/2N$$

so that

$$\beta\omega_0 = 2N ,$$

but

$$\omega_0 \approx (g/\beta)^{2/3} ,$$

thus

$$g \approx \frac{\beta}{8} R_{oo}^3$$

or

$$g \approx 10^{-7} R_{oo}^3 .$$

This is not $g = 0.02\ R_{oo}^{7/4}$, but it shows that the deviation from g proportional to Re, the laminar flow branch (1) can come from a limiting frequency, and (2) can come from an elastic parameter $\beta \neq 0$.

One may note that the estimate of critical Reynolds number

$$g \approx \omega_1^{5/4}$$

did not *explicitly* depend on compressibility, whereas now the turbulent branch does. This is consistent with the concept that it is not impossible for a critical transition to take place over a range rather than at one critical Reynolds number.

Finally, with regard to intermittency: The essential matter is the fourth mode. It has two independent forms -- $\sinh(c_4 x)$ or $\cosh(c_4 x)$. The two independent secular determinants of differing symmetries must be made to vanish for a continuous range of ω. This was accomplished by letting c_4 approach zero, leading to the specific secular result used. Another possibility has suggested itself.

The inquiry in this paper dealt with the question: Does there exist a set for the fluctuating components of the field that represents stationary limit cycles? These were probed at by a describing function technique in the form $e^{j(\alpha y+\delta z+\omega\tau)}$, α, δ, ω real. An affirmative answer was supplied, and a set was demonstrated. *The equation set cannot support any other stationary fluctuating systems.*

But turbulence is not made up of stationary fluctuations — it is locally episodic. It is only in the mean that the field is a stationary stochastic one. How are the episodic fluctuations to be found? (So far we have a family whose phase are stochastic, not the frequencies or amplitudes.) We propose a new answer. It is related to the discarded solution set of opposite symmetry.

It is true that the second set cannot exist as a stationary set. It cannot satisfy the boundary conditions except by null amplitudes, basically because $\cosh c_4 x \neq 0$.

$$c_4^2 = \lambda - \beta^2\omega^2 + [\text{an imaginary part}] .$$

However, another possibility exists. The first family has produced a stationary fluctuating set marked by α, δ, ω. These wavelets — radiating from each wall in a certain "regular" manner (actually stochastic in phase, which really makes each subsequent chunk stochastic) — then can act as coupled sources for the second set. However, for this set α, δ, ω are not unchanged.

We may assume that α and δ are unchanged (the size of the radiating element has been fixed by a scale) but that a complex ω_2

$$\omega_2 = \omega \pm Kj$$

is developed. Thus, the second family becomes $e^{j(\alpha y+\delta z+\omega\tau)\pm K\tau}$, with the previous amplitudes (via reflection). This new instantaneously nonstationary field (since it has attenuating and growing components) represents a stochastic field that "fluctuates" around the mean fluctuations. Namely, this is a clue to the theory of the fluctuation band width associated with each "stationary" limit cycle system that crosses through the field. This family instantaneously can create the horribly complex picture of the turbulent field.

Note this field cannot come into existence except as it is created by the stable limit cycle field. Thus our inquiry is "justified." By this verbal "picture," however, we have shown how the three components of the turbulent field can be arrived at by a decomposition: namely a mean field; stationary limit cycles; and a fluctuating band width for each spectral line. I believe that many other nonlinear field quantizations arise by related mechanisms.

In conclusion: Thus we have shown

(1) Frequency limits to the spectrum of turbulence.

(2) A better than order of magnitude estimate of the fluctuating amplitude.

(3) Rough estimable form for the mean velocity distribution.

(4) Estimate of the critical Reynolds number.

All consistent with this self-generated standing and wave system, I have suggested a "reason" for the apparent random nature for the fluctuating field, rather than this estimated "stationary" field (albeit with the "same" spectral characteristics).

In this crude but suggestive fashion, a deterministic nonlinear theory for turbulence has thereby been proposed.

SUMMARY

The compressible equations of hydrodynamics are investigated for conditions under which self-sustained propagative primitives would persist for the particular boundary value problem of turbulent flow between parallel plates under a constant pressure gradient. This requires assuming a form for the mean velocity distribution that satisfies the boundary condition. It is shown that an extra condition other than the equality of pressure gradient and viscous shear (proportional to the velocity gradient) at the wall is required. As in

laminar flow, the gradient and the second derivative must be related. This dual defines a region near the wall that can be identified as a boundary layer. (Approximately out to $y^+ = 2$ in the von Kármán logarithmic presentation.) It is in this region that vorticity is developed in the form of "acoustic" eddies that radiate into the core region. The frequency range for these eddies can be estimated by both a low frequency cut-off and a high frequency cut-off. The frequency range seems to fit Laufer's measured spectrum of turbulence for parallel plates. The high-frequency end seems compatible with his limiting eddy size, and the low-frequency seems to fit what might be considered loosely to be von Kármán vortices, namely, an alternative relaxation, shedding, or intermittency measure for the flow field. Turned around to estimate the critical Reynolds number, a value of about 750 is computed, based on the plate separation and center mean velocity. A magnitude of fluctuation velocity amplitude in the range 1 - 10 percent is crudely computed. It is believed that some preliminary modelling of processes pertinent to turbulence in such a field has been achieved. Further, it would appear that the method of attack could be extended to other turbulent fields.

* * *

REFERENCES

1. Lin, C., *The Theory of Hydrodynamic Stability*, Cambridge, 1966

2. Rossini, F., *Thermodynamics and Physics of Matter*, Princeton, 1955

3. Greenspan, M., "Combined Translational and Relaxational Dispersion of Sound in Gases," J. Acoustic Soc. Amer. **26**, 70, 1954; "Propagation of Sound in Five Monatomic Gases," ibid. **28**, 644, 1956; "Rotational Relaxation in Nitrogen, Oxygen, and Air," ibid. **31**, 155, 1959

4. Iberall, A., "Contributions Toward Solutions of the Equations of Hydrodynamics. Part A: The Continuum Limitations of Fluid Mechanics." Contractors Report to Office Naval Research, Wash. D.C., Dec. 1963

5. Iberall, A., "Attenuation of Oscillatory Pressures in Instrument Lines," J. Res. Nat'l. Bur. Stands., **45**, 85, 1950

6. Brown, F., "The Transient Response of Fluid Lines," J. Basic Eng. **84**, 547, 1962

7. Watts, G., "An Experimental Verification of a Computer Program for the Calculation of Oscillatory Pressure Attenuation in Pneumatic Transmission Lines," Los Alamos LA-3199-MS, Clearinghouse Fed. Sci. Tech. Info. Dept. Commerce, Springfield, Va., Feb. 1965

8. Laufer, J., "Investigation of Turbulent Flow in a Two-Dimensional Channel," NACA Rep. 1953, 1951

9. Popovich, A., Hummel, R., "Experimental Study of the Viscous Sublayer in Turbulent Pipe Flow," AIChE, 13, 854, 1967

10. Iberall, A., "Contributions Toward Solutions of the Equations of Hydrodynamics. Part B: Primitive Solutions for the Fluctuating Components of Turbulent Flow Between Parallel Plates," Contractors Report to Off. Nav. Res., Wash. D.C., Oct. 1965

11. Pai, S., "On Turbulent Flow Between Parallel Plates," J. Appl. Mech., 1953

12. Kovasznay, L., "Turbulence in Supersonic Flow," J. Aero. Sci. 20, 657, 1953; Chu, B., Kovasznay, L., "Non-Linear Interactions in a Viscous Heat Conducting Compressible Gas," J. Fl. Mech. 3, 494, 1958

13. Goldstein, S., *Modern Developments in Fluid Dynamics*, 2 Vols., Oxford, 1938

14. Landahl, M., "A Wave-Guide Model for Turbulent Shear Flow," J. Fl. Mech. 29, 441, 1967

DISCUSSION

K. Wieghardt
Institut für Schiffbau der Universität Hamburg
Hamburg, Germany

Experimentally the same critical Reynolds number has been found for water and air. Are you sure that your theory would also give critical Reynolds numbers independent of the speed of sound if no experimental data were used?

* * *

REPLY TO DISCUSSION

A. S. Iberall

Yes. In fact one of the self-consistent and thereby validating facets of this theory is that the compressibility relation involving water leads to the same results for air. In other words, we are predicting something about how frequency results for air and water are transformed for comparable Reynolds number determined turbulent states.

In the paper, two estimates are made of the critical Reynolds number. One uses no experimental data for the estimate, the other does.

(1) Estimate from $\omega_1 = 100$:

$$g(\approx \omega_1^{5/4}) = 625 .$$

This result, based on the low-frequency cutoff, emerges as a pressure gradient condition ($g = fRe^2$ where f = the friction factor). Since the friction factor is the same function of Reynolds number in incompressible and compressible flow, in nonsupersonic flow, then the gradient similarly is the same function of Reynolds number. Thus, by this argument there is no difference between the results for compressible and incompressible flow. The result did not depend on experimental data.

More fundamentally, where does the $\omega_1 = 100$ criterion come from? The parameter ω itself made its appearance in the small-amplitude theory as a *damping parameter*, even though proportional to frequency. As one attempts to push the fluid back and forth at increasing frequency (or rate), one finds a propagation parameter that is at first attenuative. It depends on viscosity. At sufficiently high rate, an elastic "resonance" can come into existence. This is true whether for gas or liquid. There is a critical value of ω (= 100, where $\omega = h^2\Omega/\nu$ depends on geometry -h-, viscosity -ν-, and frequency -Ω-, but *not* on the velocity of propagation) at which the propagation is elastic. It does not matter how high the propagation velocity is, as long as it is finite.

(2) Crude estimate from the Strouhal number S. As an approximation, we wrote

$$Re = \frac{\omega}{2S} ,$$

where the number 2 depends on the method of modelling equivalence among fields of different geometries. We assume that the sudden appearance of a sustained Strouhal number as Reynolds number is increased is associated with the appearance of a von Kármán-like vortex street shedding patchily from wall to wall into the core. By assigning a numerical value (from wind tunnel data — assuming that the *same* Strouhal number would be found for water tunnels) then the critical Reynolds number at which $\omega_1 = 100$ would occur simultaneously gives the critical Reynolds number.

The assumption here is that the critical Strouhal number does not depend on the velocity of propagation.

* * *

Tuesday, August 27, 1968

Afternoon Session

FUNDAMENTAL HYDRODYNAMICS

Chairmen: Dr. I. Stakgold

Office of Naval Research Branch Office
London, England

and

Dr. K. Wieghardt

Institut für Schiffbau der Universität Hamburg
Hamburg, Germany

NUMERICAL EXPERIMENTS ON CONVECTIVE FLOWS IN GEOPHYSICAL FLUID SYSTEMS

Steve A. Piacsek
University of Notre Dame
Notre Dame, Indiana

INTRODUCTION

In the last two decades meteorologists, oceanographers, and astrophysicists have been turning increasingly to the use of model experiments, both theoretical and in the laboratory. In analogy with the wind tunnel modeling of aerodynamicists, they hope to simulate the complicated motions exhibited by planetary and stellar fluid systems by studying flows on a reduced scale, but being governed by the same nondimensional parameters. These parameters depend on the properties of the fluid, the imposed density contrasts, rotation of the container corresponding to that of a planet or star, dimensions and shape of the container, and, in the case of electrically conducting fluids, imposed magnetic fields corresponding to planetary and stellar fields.

The advantages of model experiments are the strict control that can be exercised over the parameters determining the flow, and the possibility of isolating the several concurring processes in order to study each separately. The disadvantages include working with fluids that do not approximate well some of the natural systems, rigid boundaries that exert considerable control over the flow but often have no counterpart in the geophysical processes, and the inability to produce a spherical gravitational field in the laboratory. Furthermore, experimental observations on flow details can be obtained only with difficulty, particularly in the boundary layers. Visual studies using injected dyes and dye crystals, and the use of interferometers and hot-wire probes give in many instances only a qualitative or semiquantitative information on the velocity fields, particularly in the case of liquids. Though reasonably accurate temperature measurements have been obtained using thin thermocouples, even in the boundary layers, the flow is known to be disturbed to various degrees by such probes or array of probes. And because of the highly nonlinear nature of the governing equations, purely analytical approaches have been made only with great difficulty, and only for a limited range of the relevant nondimensional parameters. To overcome these disadvantages, geophysicists have begun to rely more and more on numerical experiments, made possible by the advent of large and extremely fast digital computers.

Initial efforts in modeling fluid motions in geophysics were discussed at a symposium at the Johns Hopkins University in 1953 (proceedings edited by R. Long); at this meeting, no numerical experiments were discussed as yet. At a

recent colloquium at the National Center for Atmospheric Research in Boulder, Colorado, several numerical experiments modeling some aspect of geophysical fluid dynamics were presented [proceedings edited by G. M. Hidy (1966)]. In addition, in the last few years many articles have been published on numerical experiments concerned with specific model problems, or with specific numerical methods appropriate to such flow problems.

The model experiments that numerical experiments have so far been mostly concerned with may be divided into four groups:

1. Convection between parallel vertical surfaces that are maintained at different temperatures, in the absence or presence of rotation;

2. Convection between parallel horizontal surfaces that are maintained at different temperatures;

3. Convection inside cumulus clouds;

4. Wind-driven ocean circulations.

The results of previous studies on these problems will be discussed in the section below, where recent numerical results for a few specific problems are also presented. A review of studies on numerical methods, mostly centered on two-dimensional incompressible flows, will be given in the concluding section.

RESULTS FOR SPECIFIC MODEL EXPERIMENTS

A. Thermal Convection in a Rotating Cylindrical Annulus

This problem considers the convective flow of a liquid contained in a vertical cylindrical annulus, and undergoing rotation about the cylinder's axis and having differential heating in the horizontal. The temperature contrast is applied by maintaining the vertical cylindrical walls, assumed to be perfect conductors, at different but uniform temperatures. The bottom surface of the container and the free top surface of the liquid are considered to be thermal insulators.

The annulus experiments were introduced by Hide (1952, 1953) in the hope of leading to a better understanding of convection in the earth's liquid core and the related generation of the earth's magnetic field. The resultant flow phenomena resembled those obtained in a rotating dishpan by Fultz (1953), whose experiments were designed to simulate atmospheric motions. In both cases the observed flow patterns appeared to have their counterparts in the general atmospheric circulation, and to have similar physical processes among their causes. Thus, the axisymmetric flow seemed to resemble a Hadley cell, proposed by Hadley (1735) to explain the general trade winds, and to be due to deflection by Coriolis forces of the north-south convection currents into zonal (east-west) motion. The nonaxisymmetric flow regime seemed to resemble a Rossby (1949) wave pattern in which finite amplitude waves propagated about

the axis, similar to the Rossby waves found superposed on the zonal atmospheric circulation. The causes for both the laboratory and atmospheric waves are the growing perturbations due to baroclinic instability, as discussed by Lorenz (1955), Eady (1949), and Charney (1947). Recently, similar phenomena have been observed in the circulation of the solar atmosphere by Ward (1965), adding astrophysical significance to these modelling experiments.

Hide (1958), Fultz (1959), and Fowlis and Hide (1965) have studied the transition between the symmetric and wave regimes, and found that below a certain rotation rate no waves can occur. Above this critical rotation rate the flow is symmetric for very small or very high temperature contrasts, with waves forming for intermediate values. The value of the critical rotation rate and the range of temperature contrasts for which waves occur depends on the geometry of the container and the properties of the fluid; the latter also depend on the actual rotation rate. They also found that the number of lobes forming the wave increased with increasing rotation, but decreased with increasing heat contrast. Theoretical studies to predict the stability curve in parameter space has been performed by Brindley (1960), Lorenz (1962), Barcilon (1964), and Merilees (1967). Although they obtained a general qualitative agreement with the experimental curve, a quantitative agreement left much to be desired.

A detailed laboratory study of the temperature field and heat transfer, along with qualitative velocity measurements, has been performed by Smith (1958), Bowden and Eden (1965), and Eden and Piacsek (1968), for the upper symmetric regime of flow (large heat contrast). These studies showed that the flow set up strong boundary layers and a strong, stabilizing, vertical temperature gradient. The isotherms were found to be horizontal in the interior for the case of small or vanishing rotation rate, and to slope upward to the cold wall for high rotation rate. There was a noticeable transition from stratification-controlled flow to rotation-controlled above a critical rotation rate. A reversal occurred in the radial temperature gradient near the cylindrical walls, and this effect disappeared gradually for increasing rotation rates. At any given radial distance from the walls, the temperature deviation from the respective wall temperature was found to be an exponential function of height over a major portion of the flow, including the boundary layers. This variation with depth was different for the high and low rotation cases, indicating the transition between flow regimes, and also in the upper and lower regions of the fluid, indicating the possible existence of two convective cells. The experiments also revealed the strong effect that the cylindrical geometry has on the flow: the height at which the mean isotherm traversed the gap was found to occur close to the bottom, and the heat transfer varied with rotation as $\log (1/\Omega^{3/2})$.

To obtain a quantitative picture of the velocity field and the extent to which the different transport processes contribute in the various regions of the flow, Piacsek (1966, 1968), Quon (1967), and Williams (1967) independently have carried out a series of numerical experiments in the axisymmetric regime of flow. All of Quon's results and all but two of Williams' applied to flows with a rigid lid in contact with the top surface of the liquid. Since the above laboratory experiments were performed with a free top surface, only the relevant cases of Piacsek and Williams will be discussed.

The relevant equations of momentum and heat transport are formulated in accordance with the following assumptions:

1. The z axis of the cylindrical coordinate system coincides with the axis of the cylindrical walls.

2. The rotation vector Ω is assumed to point in the positive z direction, and the gravitational acceleration g in the negative z direction.

3. The boundaries of the annulus are defined by the cylindrical surfaces $r = a$ and $r = b$, and by the horizontal surfaces $z = 0$ and $z = d$, respectively.

4. The motion is described in a rotating system, so that all velocities represent motion with respect to the cylinders.

5. Only small rotation rates are considered, so that centrifugal body forces may be neglected.

6. Only small temperature contrasts are considered, so that the variation of the coefficients of viscosity and heat conductivity with temperature may be neglected, and the usual Boussinesq approximation concerning the density of an incompressible fluid in natural convection may be applied, i.e., density variations are neglected everywhere except in the gravitational body force term, giving rise to buoyancy effects.

Taking the cylindrical coordinates (r, φ, z) with the corresponding unit vectors $\hat{r}$, $\hat{\varphi}$, $\hat{z}$, and a velocity vector $\mathbf{u} = (u, v, w)$, we may write the equations of state, continuity and momentum, and heat transport as:

$$\rho = \rho_0[1 - \alpha(T - T_0)] = \rho_0(1 - \alpha T_1) \tag{1}$$

$$\nabla \cdot \mathbf{u} = 0 \tag{2}$$

$$\frac{\partial u}{\partial t} + u\frac{\partial u}{\partial r} + v\frac{\partial u}{\partial \varphi} + w\frac{\partial u}{\partial z} = \nu\left(\nabla^2 u - \frac{u}{r^2}\right) - \frac{1}{\rho_0}\frac{\partial p}{\partial r} + v\left(\frac{v}{r} + 2\Omega\right) \tag{3a}$$

$$\frac{\partial v}{\partial t} + u\frac{\partial v}{\partial r} + \frac{v}{r}\frac{\partial v}{\partial \varphi} + w\frac{\partial v}{\partial z} = \nu\left(\nabla^2 v - \frac{v}{r^2}\right) - \frac{1}{\rho_0 r}\frac{\partial p}{\partial \varphi} - u\left(\frac{v}{r} + 2\Omega\right) \tag{3b}$$

$$\frac{\partial w}{\partial t} + u\frac{\partial w}{\partial r} + \frac{v}{r}\frac{\partial w}{\partial \varphi} + w\frac{\partial w}{\partial z} = \nu(\nabla^2 w) - \frac{1}{\rho_0}\frac{\partial p}{\partial z} + \alpha g T_1 \tag{3c}$$

$$\frac{\partial T_1}{\partial t} + u\frac{\partial T_1}{\partial r} + \frac{v}{r}\frac{\partial T_1}{\partial \varphi} + w\frac{\partial T_1}{\partial z} = \kappa\nabla^2 T_1 \ , \tag{4}$$

where T_1 is defined by Eq. (1), T_0 is the "mean" temperature $(T_b + T_a)/2$ and ρ_0 the corresponding density, and p is the dynamic pressure (total minus hydrostatic).

Since the experiments were performed on axisymmetric types of flow only, $\partial/\partial\varphi$ of all quantities vanishes. Then the equation of continuity, Eq. (2), reduces to

$$\frac{1}{r}\frac{\partial}{\partial r} ru + \frac{\partial w}{\partial z} = 0 , \tag{5a}$$

and we can introduce a stream function ψ defined by the relations

$$ru = \frac{\partial \psi}{\partial z} , \quad rw = -\frac{\partial \psi}{\partial r} , \tag{5b}$$

Cross-differentiating the first and third component of Eqs. (3) to eliminate p, and introducing the azimuthal component of the vorticity

$$\xi = \frac{\partial u}{\partial z} - \frac{\partial w}{\partial r} , \tag{6}$$

we obtain

$$\frac{\partial \xi}{\partial t} + \frac{\partial}{\partial r}(u\xi) + \frac{\partial}{\partial z}(w\xi) = \nu\alpha(\xi) + \frac{\partial}{\partial z}\left(\frac{v^2}{r} + 2\Omega v\right) - \alpha g \frac{\partial T_1}{\partial r} , \tag{7}$$

where we used the equation of continuity to obtain the left-hand side, and α is a cylindrical diffusion operator defined by

$$\alpha(\xi) = \frac{\partial}{\partial r}\frac{1}{r}\frac{\partial}{\partial r} r\xi + \frac{\partial^2 \xi}{\partial z^2} . \tag{8}$$

Furthermore, we may note that

$$\xi = \alpha(\psi) . \tag{9}$$

We may introduce the following scaling now:

$$\begin{aligned} r &= (b-a)\, r' \\ z &= d \cdot z' \\ T_1 &= (T_b - T_a) \cdot T' = \Delta T \cdot T' \\ (u, v) &= [\alpha g \Delta T d / 2\Omega (b-a)] \cdot (u', v') . \end{aligned} \tag{10}$$

Then, from (5a),

$$w = \frac{d}{(b-a)} \cdot \frac{u}{u'} \cdot w' . \tag{11}$$

Equations (4), (8), and the second component of Eqs. (3) may then be written

$$\frac{\partial \xi}{\partial t} + \Theta\left[\frac{\partial}{\partial r}(u\xi) + \frac{\partial}{\partial z}(w\xi)\right] = \epsilon\alpha(\xi) + \frac{\partial}{\partial z}\left(\Theta\frac{v^2}{r} + v\right) - \frac{\partial T}{\partial r} \tag{12}$$

$$\frac{\partial v}{\partial t} + \Theta \cdot \left(u\frac{\partial v}{\partial r} + w\frac{\partial v}{\partial z}\right) = \epsilon \cdot \left(\nabla^2 v - \frac{v}{r^2}\right) - \left(\Theta\frac{v}{r} + 1\right)u \tag{13}$$

$$\frac{\partial T}{\partial t} + \Theta \cdot \left(u\frac{\partial T}{\partial r} + w\frac{\partial T}{\partial z}\right) = \frac{\epsilon}{\sigma}\nabla^2 T\ , \tag{14}$$

where

$$\Theta = \frac{\alpha g \Delta T \cdot d}{4\Omega^2 (b-a)^2}\ , \quad \epsilon = \frac{\nu}{2\Omega(b-a)^2}\ , \quad \sigma = \frac{\nu}{\kappa}\ , \tag{15}$$

and the operator α includes the geometric aspect ratio

$$\alpha = \frac{\partial}{\partial r}\frac{1}{r}\frac{\partial}{\partial r}r + \lambda^2 \cdot \frac{\partial^2}{\partial z^2}\ , \quad \lambda = \frac{d}{b-a}\ . \tag{16}$$

The boundary conditions on the system are taken as follows:

1. At the rigid walls of the container all velocities vanish; hence both the normal and tangential derivatives of ψ vanish, as does v.

2. At the top free surface the normal velocity w and all stresses vanish. This is equivalent to a "frictionless lid" approximation, and is designed to eliminate external gravity waves and centrifugal effects on the surface.

3. On the conducting cylindrical surfaces, the temperature is assumed to be uniform; on the horizontal surfaces no heat flow is assumed.

4. Since there is no in- or outflow into the annular cavity, the stream function ψ may be set equal to zero on all surfaces.

Before we write down the final set of equations that was programmed for the computer, we must note that the advective term involving ξ is written as $\nabla \cdot \mathbf{u}\xi$, whereas those involving v and T are written as $(\mathbf{u}\cdot\nabla)v$ and $(\mathbf{u}\cdot\nabla)T$, respectively. The former is referred to in numerical weather forecasting as a "conservative" or "divergent" form, because its integral over r and z will reduce to integrations on the boundaries only; furthermore, its finite difference analogue preserves this property with respect to summation over the lattice of gridpoints. In order to throw the remaining advective terms into a "conservative" form, we multiply through Eq. (13) by r^2, and Eq. (14) by r, respectively, and obtain

$$\frac{\partial m}{\partial t} + \Theta\,\nabla \cdot \mathbf{u}m = \epsilon P(m) - ur^2 \tag{17a}$$

$$\frac{\partial \tilde{T}}{\partial t} + \Theta\,\nabla \cdot \mathbf{u}\tilde{T} = \frac{\epsilon}{\sigma} S(\tilde{T})\ , \tag{17b}$$

where $m/r = vr$ is the angular momentum about the cylinder's axis and $\tilde{T} = Tr$. P and S are cylindrical diffusion operators defined by

$$P = \frac{\partial}{\partial r} r^3 \frac{\partial}{\partial r} \frac{1}{r^3} + \lambda^2 \frac{\partial^2}{\partial z^2} \tag{18a}$$

$$S = \frac{\partial}{\partial r} r \frac{\partial}{\partial r} \frac{1}{r} + \lambda^2 \frac{\partial^2}{\partial z^2} . \tag{18b}$$

Finite difference versions of Eqs. (9), (13), and (17a,b) were programmed for a digital computer; the appropriate numerical schemes for differencing the individual terms and for iterating the resulting system of nonlinear algebraic equations are discussed in the concluding section.

The results are displayed in Figs. 1, 2, and 3, and are for the case of $\Theta = 1.75$, $\epsilon = 1.0 \times 10^{-3}$, $\lambda = 2$, $\sigma = 7$, and $a' = a/(b - a) = .67$. Figure 1 shows a cross section of the annulus, Fig. 2 the streamlines, isotherms, and isolines of the zonal velocity, and Fig. 3 the behavior of the temperature deviation from the hot-wall temperature, as a function of height at the radial midpoint.

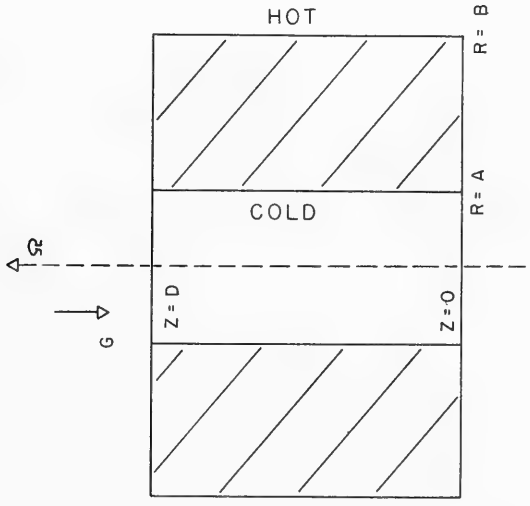

Fig. 1 - Cross section of the annulus

In general, the results agree with the experimental results. Figure 3 clearly shows the exponential behavior of the quantity $\delta T = T_b - T(r, z)$ in the upper region of the flow, and a comparison with the isotherms in Fig. 2(b) shows that this region coincides with the large isothermal region above the $T = .6$ line, approximately. The curved portion plots to a straight line on

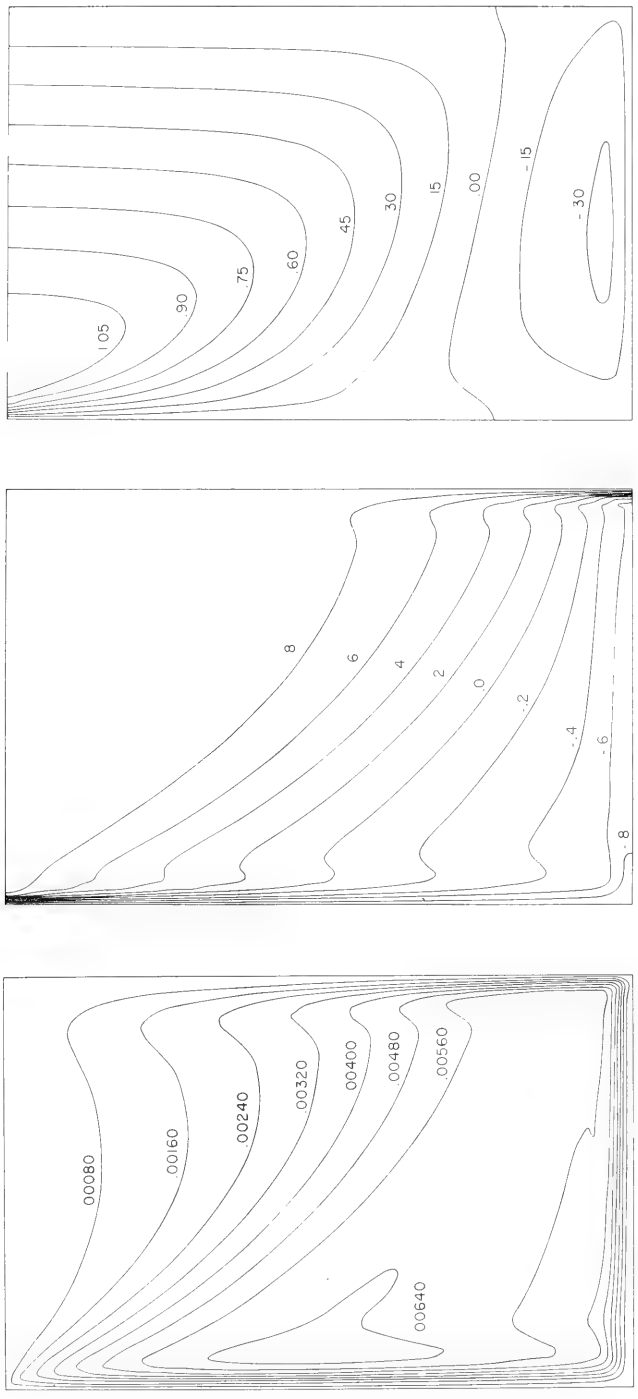

Fig. 2 - Experiment A: (a) streamlines; (b) isotherms; and (c) isolines of zonal velocity

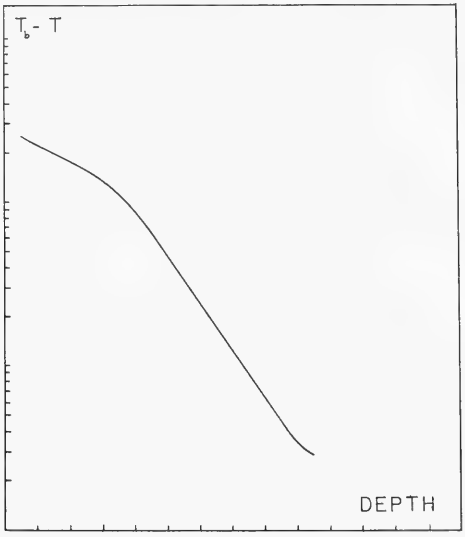

Fig. 3 - Plot of log $(T_b - T)$ vs. z at the radial midpoint of the annular gap

ordinary graph paper, and corresponds to the central "bundle" of isotherms between $0 \leq T \leq .6$. For lower rotation the central "bundle" occupies a considerably larger portion of the interior region, confining the exponential region to a smaller region near the top; for higher rotation, the bundle becomes narrower and steeper. Both the cylindrical geometry and rotation contribute to this behavior of the temperature field, the former being responsible for the strong asymmetry and the latter for the bundle formation. The isotherms and streamlines are parallel only in certain regions of the flow, indicating that thermal conduction is important throughout the gap. The isotherms display clearly the "humps" found in the laboratory experiments, and even bigger humps are found in the streamlines, indicating a weak reverse flow outside the boundary layers. If we denote by d_1 and d_2 the distances from the top and bottom, respectively, at which the mean isotherm $\bar{T} = 0$ crosses the radial midpoint, we find that their ratio has the value $d_1/d_2 = 3.3$. This is considerably higher than the ratio $b/a = 2.5$ that may be shown from simple geometrical arguments to be the required value of d_1/d_2. For larger rotation rates this value is indeed approached, but for lower rotation rates it becomes much higher. An inspection of Fig. 2(c) shows that the zonal velocity reverses at some depth in order to conserve torques about the axis. Furthermore, most of the shear in the v field is concentrated at the upper part of the inner cylinder and the rigid bottom, influencing strongly the entrainment into the sidewall layers.

The theory of stratification-controlled flow in a nonrotating cavity has been worked out by Gill (1966), and for a rotating annulus by McIntyre (1967). A simple theory for the existence of the humps in the isotherms, their variation with rotation, and the large value of the ratio d_1/d_2 has been put forward by

Eden and Piacsek (1968) for the case of small rotation rates. It may be shown that the reversals in the boundary layer temperature gradient are related to the curvature of the vertical velocity profile, such that its points of inflection occur where the temperature equals the horizontally averaged temperature at that height, i.e., where the "relative buoyancy" vanishes. For increasing rotation, the Coriolis force deflects any radial motion into zonal motion and sets up a vertical pressure gradient opposing the buoyancy force, so that the convective flux decreases in the boundary layer and fluid particles eject sooner. The net result is greater warming and cooling by conduction near the cylindrical walls, and a shrinking of the isotherms to a "bundle." So far, no satisfactory explanation has been found for the exponential behavior of the temperature with height, nor for the peculiar dependence of the convective heat transfer on rotation; for $.1 \leq \Omega \leq .9$ rad/sec the quantity $N - 1$ is found to be $\sim \log(1/\Omega^{3/2})$, N being the Nusselt number (Eden and Piacsek, 1968, Piacsek, 1968), whereas for $1.3 \leq \Omega \leq 2.1$ rad/sec it is found to be $\sim 1/\Omega$ (Williams, 1967). The large ratio of d_1/d_2 is attributed to the different entrainment rates into the cold and hot boundary layers.

The strong boundary layer seen on the bottom surface is due to the squeezing of the radial motion out of the core region by the rotation to boundaries where friction enables the fluid to convert zonal into radial motion again. This layer is similar to the Ekman layer found near the top of wind-driven ocean currents, and to those found during spin-up time near a rotation disc. For a discussion of these layers, the reader is referred to Barcilon (1964) and McIntyre (1967).

B. Convection in a Semi-Infinite Fluid Cooled from Above: Penetrative Convection

This problem considers the convection currents that arise in unstable fluid layers that are bounded below by either positively or neutrally stable layers. In the former case, the stable layers are penetrated to a certain extent by the rising or descending thermal columns in the unstable regions, but they themselves remain stable, on the whole. In the latter case, the convection currents will sooner or later involve all of the accessible fluid volume.

Many phenomena in nature exhibit a similar process — atmospheric thermals and cumulus towers impinging on stably stratified layers above, including inversions and the tropopause; evaporation-driven ocean currents penetrating into lower regions stably stratified by solar radiation, or seasonal cooling effects reaching down to the thermocline; convection in the sun and stars in layers where radiation causes a superadiabatic temperature gradient, bounded both below and above by stable layers. Often the penetration currents are coupled to larger-scale general circulations, and their mutual interaction is of great interest to geo- and astrophysicists.

Ball (1954) and Ewing (1960) have studied the difference between the radiation temperature of the ocean's surface and the temperature of the water below the surface. Ball has found a difference of $\sim .25°C$ in the top cm or so of the surface layer; Ewing and McAlister found $\sim .60°C$ in about 15 cm. In addition,

the latter have observed that when the surface was disturbed the radiation temperature rose to that of the lowered thermistor, but it returned to its normal value in about 5 seconds. From this cooling rate they estimated that the cold layer must be ~1 mm thick.

Since observations on such a small-scale phenomenon are difficult to carry out at sea (because of waves, instrumentation, etc.), several workers have attempted to isolate the phenomenon in the laboratory. Spangenberg and Rowland (1961) studied evaporative cooling by taking schlieren photographs simultaneously from the top and side of a tank of water. They found that the cooled surface layer collects along lines, producing thickened regions which become unstable and plunge in vertical sheets. These lines appeared to have no fixed dimensions or geometric pattern, and their number per unit area appeared to depend on the cooling rate rather than on the depth of the container. From the experimentally observed nonlinear temperature profiles with depth, they have deduced a local Rayleigh number of 1193 when convective circulation was started, and a Rayleigh number (see the next subsection in this paper) of 102 for maintaining an established circulation. The cells were always changing their shape and size, with some drifting about, some fading away, and others replacing them, suggesting some kind of turbulent behavior. The circulation in the cells was primarily two-dimensional and appeared to be independent of the depth of the water layer for depths greater than 1 cm. However, some temperature deviations were measured as low as 4 cm below the surface. Foster (1965a) performed similar experiments in which he measured the top surface temperature by an infrared radiometer, and the onset of convective behavior by visual observations of a thin layer of ink at the bottom of the water. He found that at large Rayleigh numbers the time needed for the commencement of convection and the horizontal wave number of the disturbances amplified most are independent of the depth of the fluid layer. The convection cells appeared as roughly circular or polygonal white spots in the ink layer, underneath descending columns of water. Berg, Boudart, and Acrivos (1966) performed an elaborate study on natural convection in pools of evaporating liquids. They found certain patterns to be due to surface-tension-driven instability, and others due to buoyancy-driven motion. Water behaved differently from all the other fluids investigated; no convection at all was observed until the depth of the layer reached 1 cm, and then it occurred in sheets only. This anomalous behavior was attributed mostly to surface contamination by surface-active agents which always seem to be present in water. Foster (1965b) has performed a theoretical analysis of the stability of an initially homogeneous layer of fluid which is cooled uniformly from above, and found that the onset time of the convection and the horizontal wave-number amplified most are independent of the depth, but depend on the Prandtl number and the cooling rate, thereby agreeing with the experimental results.

Whitehead and Chen (1967) have studied the stability and finite amplitude motion of a thin, thermally unstable fluid layer, bounded above by a rigid surface and below by a stably stratified body of fluid. Observations made by top and side shadowgraph views showed that the flow consists of intermittent jets and sheets plunging downward. For stronger cooling rates, more sheets were seen, similar to Spangenberg and Rowland's results. Gribov and Gurevich (1957) have made a theoretical investigation of instabilities in a fluid layer that is bounded above and below by stable fluid regions, but into which the

disturbances were free to propagate. They have found that the value of the critical Rayleigh number in this case is 6.5 times smaller than the value obtained in the usual case. Veronis (1963) has also studied penetrative convection in a case where an unstable layer of liquid was bounded above by a stable region. He found that a finite amplitude instability sets in at values of the Rayleigh number below critical (given by the linear theory). He argued that any finite amplitude motion which mixes liquid above and below the upper boundary of the unstable layer would create a deeper layer that would be gravitationally more unstable than if it were in a conduction state only.

In view of the two-dimensional nature of the penetrating sheets, the numerical experiments were confined to two-dimensional flows only. The relevant system of equations were left in dimensional form. They may be obtained from Eqs. (7), (4), (9), and (5a) by neglecting curvature and putting $\Omega = v = 0$:

$$\frac{\partial \xi}{\partial t} + \frac{\partial}{\partial x}(u\xi) + \frac{\partial}{\partial z}(w\xi) = \nu \nabla^2 \xi - \alpha g \frac{\partial T}{\partial x} \tag{19}$$

$$\frac{\partial T}{\partial t} + \frac{\partial}{\partial x}(uT) + \frac{\partial}{\partial z}(w\xi) = \kappa \nabla^2 T \tag{20}$$

$$\xi = \nabla^2 \psi \ , \quad u = \frac{\partial \psi}{\partial z} \ , \quad w = -\frac{\partial \psi}{\partial x} \tag{21}$$

$$\frac{\partial u}{\partial x} + \frac{\partial w}{\partial z} = 0 \ , \tag{22}$$

where we used Eqs. (22) to put the left-hand side of Eqs. (20) into conservative form. The volume of the fluid is assumed to be contained between the surfaces $x = 0$ and L, and $z = 0$ and D. The results presented here were designed for the following cases:

1. An initially homogeneous rectangular volume of fluid is subject to constant heat loss at its top surface. The dimensions of the volume are so chosen that a semi-infinite region is simulated: the lateral dimensions are such as to allow two to four cells to develop, and the vertical dimensions are anywhere from 10 to 50 times the boundary layer thickness at the cooling surface. All the boundaries are assumed to be "frictionless lids" (i.e., at which only the normal velocity vanishes), and all except the top surface are assumed to be thermal insulators. Based on the results of laboratory experiments, cooling rates are so chosen that the thickness of the thermal boundary layer at the top is small compared to the total depth of the fluid.

2. A situation similar to that described above, but with the bottom surface cooled at the same rate as the top, to set up a stable layer near the bottom.

The procedure was to solve the equation of thermal conduction until the cooling effect penetrated to a depth judged to be sufficient to support convection. Then the temperature field had a perturbation added to it of the form

$$T(x,z) = A \cdot \cos(2\pi nx/L) \cdot (1 - e^{-z/H}) \qquad (23)$$

to start the convection. The scale height H is so chosen that the perturbation is strongest where the fluid is most unstable. The relations between the time elapsed in cooling and the amplitude of the perturbations on the one hand, and the growth rate and the final form of the convection cells on the other, have not yet been worked out.

The results for Case 1 are displayed in Fig. 4(a) and 4(b) and Fig. 5, for $L = 3$ cm, $D = 1.5$ cm, $\partial T/\partial Z|_{z=D} = 1.5°C/cm$, and water as the working fluid ($\nu = 1.0 \times 10^{-2}$ cm^2/sec and $\kappa = 1.4 \times 10^{-3}$ cm^2/sec). A time of 16 seconds elapsed before a perturbation of $n = 1$, $A = .001$, and $H = 1.5$ cm was applied. It was found that the isotherms are a much more sensitive indicator of the convective motions than the streamlines; this is not surprising if we consider that the diffusion coefficient of friction is ~7 times that of heat, so that it will take ~7 times longer for all thermal fluctuations to die out than for the velocities. Similarly, the temperature field is concentrated into narrower regions, for the small thermal diffusion is ineffective in smearing it out.

Figures 4(a) and 4(b) represent the time development of the temperature pattern when conduction gives way to convection. The times elapsed between frames are listed in the figure captions. The last two frames for temperature and streamline in Fig. 4(b) are taken at $t = 454$ seconds. All six frames of isotherm development in this figure had the same (visible) streamline pattern associated with them (shown in the bottom frame). At the onset, a heavy blob of cold fluid forms which penetrates to the bottom and is reflected by the rigid surface. When the reflected upward-moving thermals join the top layer again, a strong "finger" of cold fluid forms which again descends to the bottom and is reflected; however, at this time, two weaker fingers develop also at the sidewalls, and the streamline pattern shows that at this time the two-cell pattern breaks into a four-cell pattern. After this time there are three descending and two ascending columns. The foregoing pattern is repeated many times, with the "finger" growing weaker after each cycle until the pattern shown in the final frame eventually emerges. It was also observed that the period of the oscillations increased steadily; this can be understood if we assume the oscillations to be some form of internal gravity waves whose frequency depends on the average vertical temperature gradient. The total kinetic energy and absolute vorticity have converged to four significant figures, yet small but nevertheless visible changes occurred in the isotherms. Though a truly steady state in this problem can never be achieved as the mean temperature of the system decreases linearly, the location of this temperature becomes a constant and the horizontally averaged temperature as a function of depth also becomes a constant. Thus a "quasi-steady" state is possible in the system, but one has to iterate a very long time to damp out the thermal fluctuations.

Figure 5 shows the vertical variation of the horizontally averaged temperature. In a significant portion of the flow the temperature gradient is reversed: this can be traced to the impinging cold stream on the bottom and its consequent spreading. Because of the relatively weak nature of the upward-moving compared to the descending columns, a fluid particle spends a greater time in the former regions and achieves its highest temperature only on the upward passage.

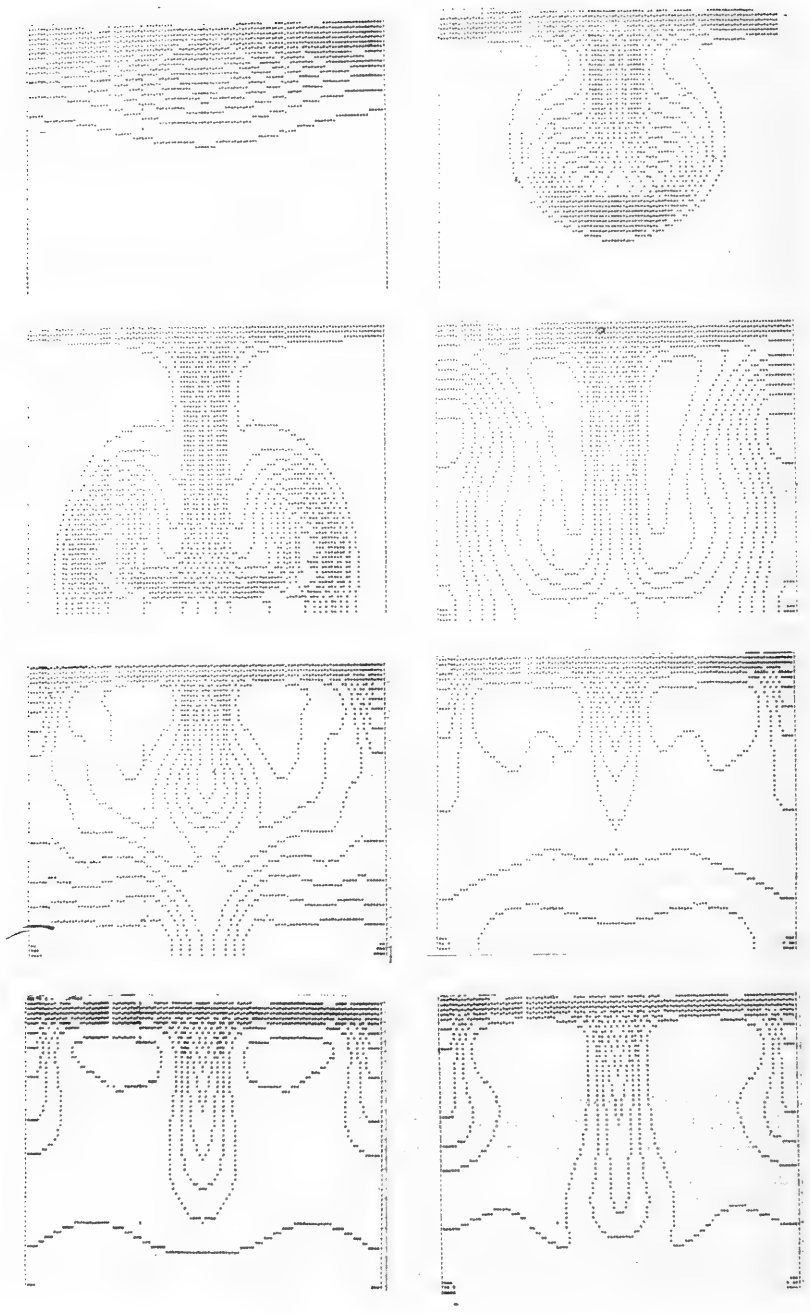

Fig. 4(a) - Time development of experiment B (read from left to right and down); frames for the isotherms at t = 8, 12, 14, 18, 24, 44, 54, and 62 seconds

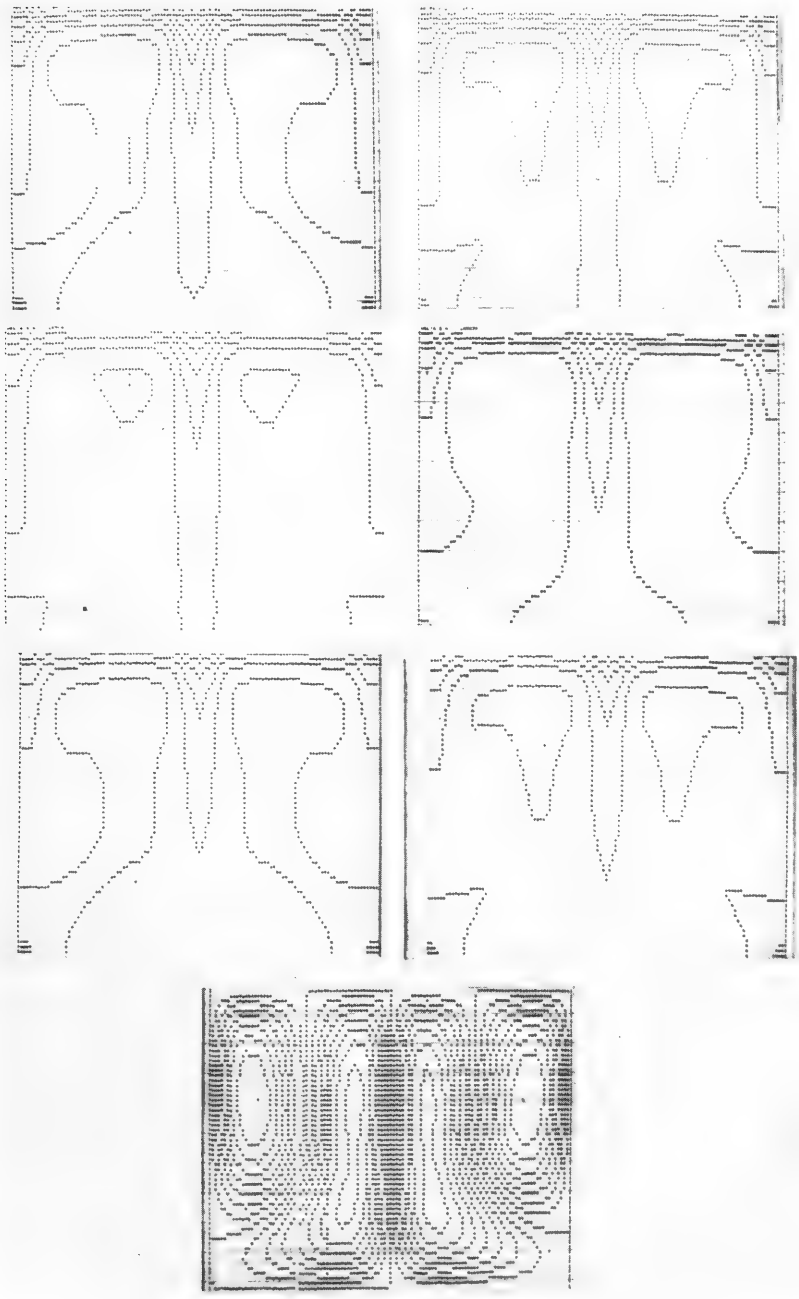

Fig. 4(b) - Frames for the isotherms at t = 134, 142, 178, 230, 330, and 454 seconds

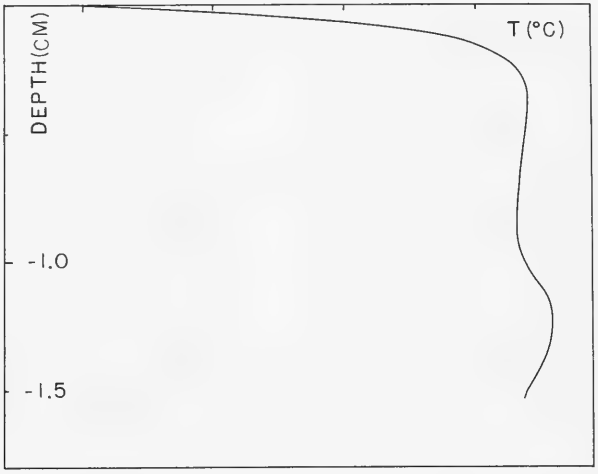

Fig. 5 - Variation of horizontally averaged temperature with depth for experiment B

The results for Case 2 are presented in Figs. 6 and 7, for L = 3 cm, D = 4.5 cm, $\partial T/\partial z|_{z=D}$ = 3.0°C/cm, and water as the working fluid. The perturbation was applied only after 2 seconds, and had n = 1, A = .001°C, and H = 1.5 cm. Since this is a much deeper system and has a stable layer forming on the bottom, the transient convection pattern is very different, although the final state is not that much. Only one noticeable period of oscillation was carried out by the fluid, and the latter again came to a steady state after ~180 seconds. The downward-moving initial blobs had weakened long before they reached the stable layer: they seemed to consist of wide but weak "tongues" with a "finger" growing inside them. Eventually the tongues retracted and formed fingers in the steady state. The maximum depression of the top of the stable layer came when the tongues were already in the retracting stage, indicating that the temperature profiles are a poor indicator of the actual fluid motion, for the reasons mentioned in discussing Case 1. A further evidence of this was the almost symmetrical pattern in the streamlines (not shown), indicating that the strength of the up- and downward-moving columns is not greatly different. One must bear in mind that the fluid particles continue to gain heat from the time they leave the top until they return to it, so that in this type of convection the temperature field is not at all reliable to assess local circulation strengths, though it may be used to study the geometry of cell patterns, as the schlieren photographs have shown.

Figure 7 shows the vertical variation of the horizontally averaged temperature field, which again shows that in a substantial portion of the flow the temperature gradient is reversed, for the same reasons as in Case 1.

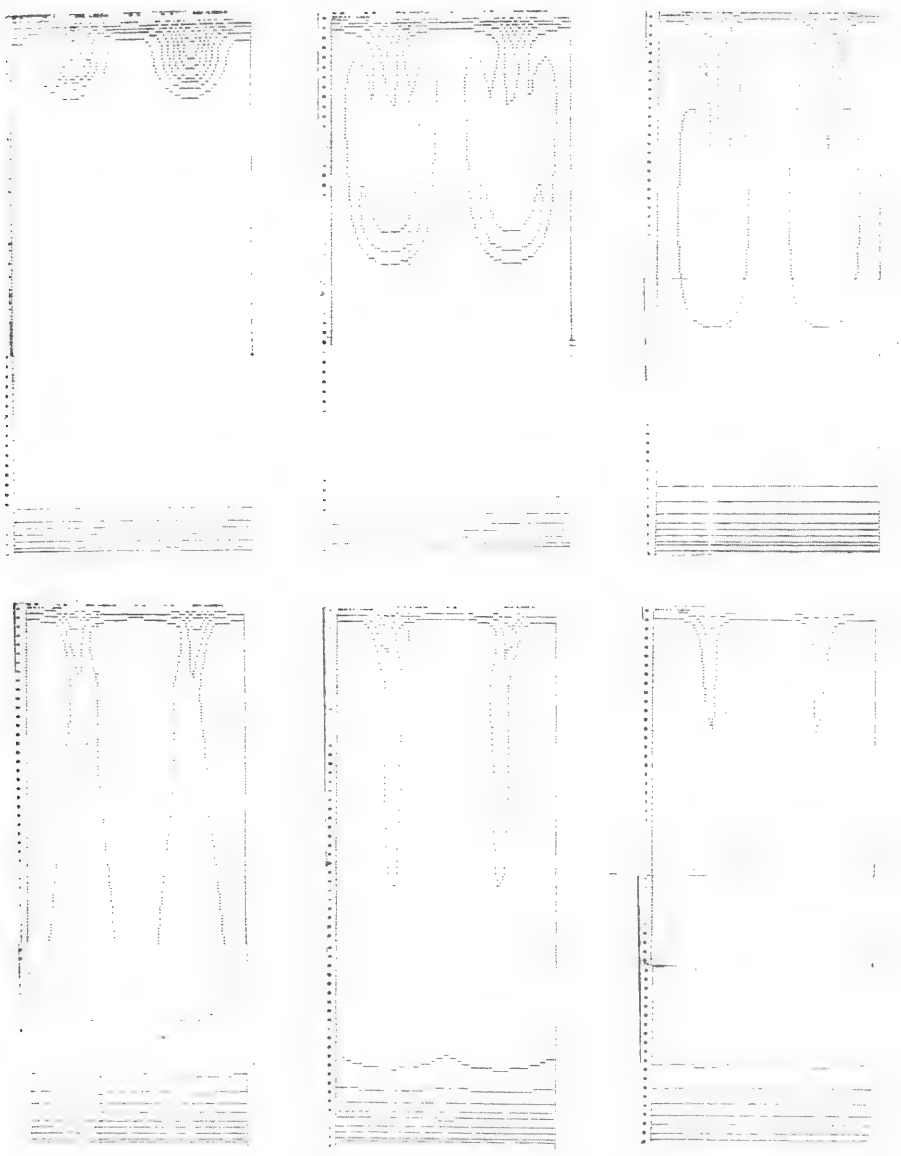

Fig. 6 - Time development of experiment C (read from left to right and down); frames for the isotherms at t = 45, 60, 75, 90, 105, and 165 seconds

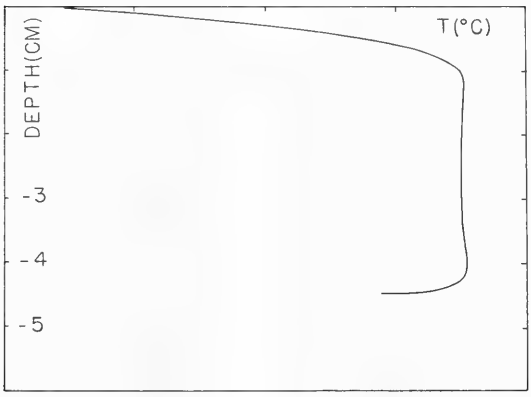

Fig. 7 - Variation of horizontally averaged temperature with depth for experiment C

C. Wave-Number Selection in Finite Amplitude Benard Convection

This problem considers the convection flow that arises in a thin horizontal layer of fluid when a steady and uniform temperature contrast is maintained across it. In particular, a determination of the horizontal cell dimensions is sought when the motions may be considered to be two-dimensional. Both the experimental results of Rossby (1966), Koschmieder (1966), and Chen and Whitehead (1968), and the theoretical results of Schluter, Lortz, and Busse (1965), have indicated that in the case of rigid-rigid boundaries almost all the laminar flow range exhibits two-dimensional behavior in the form of "rolls." The object of the present study was to determine the preferred horizontal length of such rolls and the mechanisms or principles that are responsible for the selection.

Equations (19) through (22) are also applicable here. They may be put in nondimensional form, by choosing

$$z = dz' \,, \quad w = \frac{\kappa}{d} \cdot w' \,, \quad t = \frac{d}{w} \cdot t' \,, \quad T = \Delta T \cdot T' \,, \quad x = a \cdot x' \,, \tag{24}$$

to obtain (dropping the primes)

$$\frac{1}{\sigma}\left[\frac{\partial \xi}{\partial t} + \frac{\partial}{\partial x}(u\xi) + \frac{\partial}{\partial z}(w\xi)\right] = \nabla^2 \xi - Ra \cdot \frac{\partial T}{\partial x} \tag{25}$$

$$\frac{\partial T}{\partial t} + \frac{\partial}{\partial x}(uT) + \frac{\partial}{\partial z}(wT) = \nabla^2 T \tag{26}$$

$$\xi = \gamma^2 \nabla^2 \psi , \quad \nabla^2 = \frac{1}{\gamma^2} \frac{\partial^2}{\partial x^2} + \frac{\partial^2}{\partial z^2} \tag{27}$$

$$Ra = \frac{\alpha g \Delta T d^3}{\nu \kappa} , \quad \sigma = \frac{\nu}{\kappa} , \quad \gamma = \frac{a}{d} , \tag{28}$$

where d is the depth of the fluid, α the coefficient of thermal expansion, and ΔT the applied temperature contrast. The boundary conditions are $u = w = 0$ at $z = 0$ and 1, and $T = 1$ at $z = 0$, and $T = -1$ at $z = 1$. The lateral extension of the system, though infinite in principle, must be restricted for computational purposes. Since this dimension influences the horizontal wavelengths admitted by the system, we will discuss below the special conditions assumed in connection with the instability problem.

The final dominant mode is expected to depend on the Rayleigh number Ra, the Prandtl number σ, and the geometry of the container. Furthermore, because in finite amplitude flows the various horizontal wave numbers interact in a nonlinear fashion, the final mode will also depend on the amplitude of the total initial perturbation, the relative amplitudes of the various constituent harmonics, and the initial state of the system. The complete examination of this problem is a long and tedious task; in this paper only token results are presented that, in the author's opinion, serve to illustrate some of the interesting and difficult aspects of this problem.

An excellent review of most analytical studies on Benard convection appears in a recent article by Brindley (1967). Rayleigh (1916) has shown that in the case of rigid-rigid boundaries convection will only occur if the value of Ra exceeds 1708; below this, friction is able to overrule the weak destabilizing temperature gradient. The preferred horizontal wavelength at the onset of convection was predicted by Pellew and Southwell (1940), based on linearized theory. A summary of all linearized work appears in Chandrasekhar (1961). For two-dimensional rolls, the nondimensional wavelength is $\lambda' = \lambda/d = 2.016$. Later workers included nonlinear effects in several ways. Malkus and Veronis (1958), Palm and Øiann (1960), Segel and Stuart (1962), Segel (1965a,b), Schluter, Lortz, and Busse (1965), and Busse (1967), have included the nonlinear interaction of many harmonics by working with finite amplitude flows; many workers have included the variation of viscosity with temperature. Most of the studies have been based on expansion in a small parameter ϵ, being $\sim Ra - Ra_c$, so that the results are valid only for Ra not too much larger than the critical value. Near Ra_c, hexagonal shapes were predicted, and for higher Ra two-dimensional rolls.

Roberts (1965) has used a different approach: he assumed a simple sinusoidal variation in time, $e^{i\sigma t}$, and in the horizontal direction, $\sin n\pi x$, and searched for the eigenvalues of the resulting system of nonlinear ordinary differential equations in z. The criterion in determining the critical wave number used was to find the value of λ' for which $d\sigma/d\lambda' = 0$. In this manner, he found the optimum wavelengths for Ra up to 5000; at $Ra = 4000$ a value of $\lambda' = 2.004$ was found, slightly smaller than the critical value. The behavior of λ' with increasing Ra showed a monotonic decrease.

Recently, Chen and Whitehead (1968) have performed a careful laboratory study of Benard convection by introducing small controlled perturbations prior to the onset of motion, producing two-dimensional rolls of arbitrary width-to-depth ratio. The conditions employed corresponded to the finite-amplitude stability problem for a constant viscosity, large Prandtl number, Boussinesq fluid with rigid, conducting boundaries. They found that two-dimensional cells with width-to-depth ratios close to unity are stable at all Ra investigated ($Ra_c \leq Ra \leq 2.5\ Ra_c$), whereas for moderately too large or too small values they tend to undergo size adjustments toward a preferred value of 1.1. Snyder (1967) has performed experimental studies on wave-number selection of finite amplitude between differentially rotating cylinders (the "Taylor" problem). He showed that a finite-amplitude secondary flow may have any wavelength within a range which depends on the amplitude. The reason is that the problem is inherently time-dependent, and that the actual wavelength selected is determined by the initial conditions of the problem. He has experimentally found hysteresis effects similar to the ones reported here. Meyer (1967) has performed a somewhat similar numerical experiment on preferred wavelengths in the nonlinear region of Taylor flow. He made a big box of two complete cells and determined the preferred length by varying the box length until the ratio of energy contained in the even harmonics to that of the odd harmonics was a maximum.

Numerical experiments have been performed on Benard convection by Deardorff (1964, 1965) and Fromm (1965), but only for perturbations of $\lambda' = 2$ and horizontal (nondimensional) width $\gamma = 2$, 4, 8, and 20.

The present investigation consists of two approaches. One purpose is to determine the wavelength that transports the maximum heat, and then find if that is the preferred wavelength. To this end, a single roll was considered, for $Ra = 20000$ and $\gamma = \lambda'/2 = 1.00$. The latter value was chosen because it lies very near the analytically predicted value of 1.002 by Roberts (1965), for $Ra = 4000$. The circulation in each roll in two-dimensional convection is in the opposite sense from that of its neighbors, and such that within each unidirectional vortex there is symmetry about a diagonal. Furthermore, each is symmetrical with respect to its neighbors; hence the cell boundaries can be defined as "surfaces of symmetry." Such a definition was used by Chandrasekhar (1961) and Stuart (1964) in their treatment of the Benard problem. It is sufficient, therefore, to find the flow fields in only a half cell or single vortex, and from that one may construct the whole circulation (see Fig. 8). The boundary conditions on these surfaces become the following: no mass or heat flow may cross the cell wall, and no stress may act upon it, i.e., they become frictionless, insulating lids. It is of interest to note that heretofore these boundary conditions have not been used in numerical work on Benard convection. Both Fromm (1965) and Deardorff (1964) have assumed either rigid lateral boundaries or periodic conditions on them. The present conditions enable us to deal with half-cells only.

The flow was started by assuming a linear temperature profile due to conduction only, with the temperature contrast already at its final value, and applying a temperature perturbation of the form $A \cdot \cos \pi x \cdot \sin \pi z$. The finite-difference versions of Eqs. (24) to (27) were iterated in time until a fully developed steady-state convective flow was obtained. The aspect ratio γ was then incremented (or decremented) in steps of $\Delta\gamma = .2$, always using the previous steady

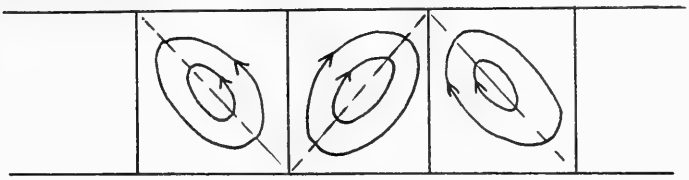

Streamlines

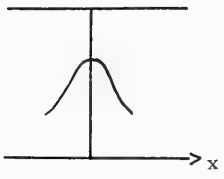

Vertical Velocity

$\left(\frac{\partial w}{\partial x} = 0\right)$

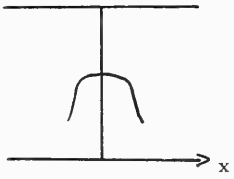

Temperature

$\left(\frac{\partial T}{\partial x} = 0\right)$

Fig. 8 - Symmetry sketch of Benard cells

state as input for the next case, to see how far a single cell could be "stretched" without breaking up into multiple vortices of opposite circulation. So far a value of 2.8 has been reached with no real sign of a breakup; a lower limit to γ has not been reached as yet. The heat transfer variation with γ is tabulated below (N = Nusselt number):

γ	N
.80	3.084
1.00	3.028
1.20	2.941
1.68 (a)	2.736
1.68 (b)	2.808
1.68 (c)	2.978
2.10	2.534
2.80	2.208

According to the above results, the γ of maximum heat transfer must be $<.8$. Work is under way to find its value as closely as possible.

The runs denoted by (a), (b), and (c) for $\gamma = 1.68$ (illustrated in Fig. 9) comprise the second approach in this investigation. Here it was sought to find the largest and smallest value of γ' for which a perturbation of given amplitude and containing only the γ' harmonic can come to steady state in a fluid volume

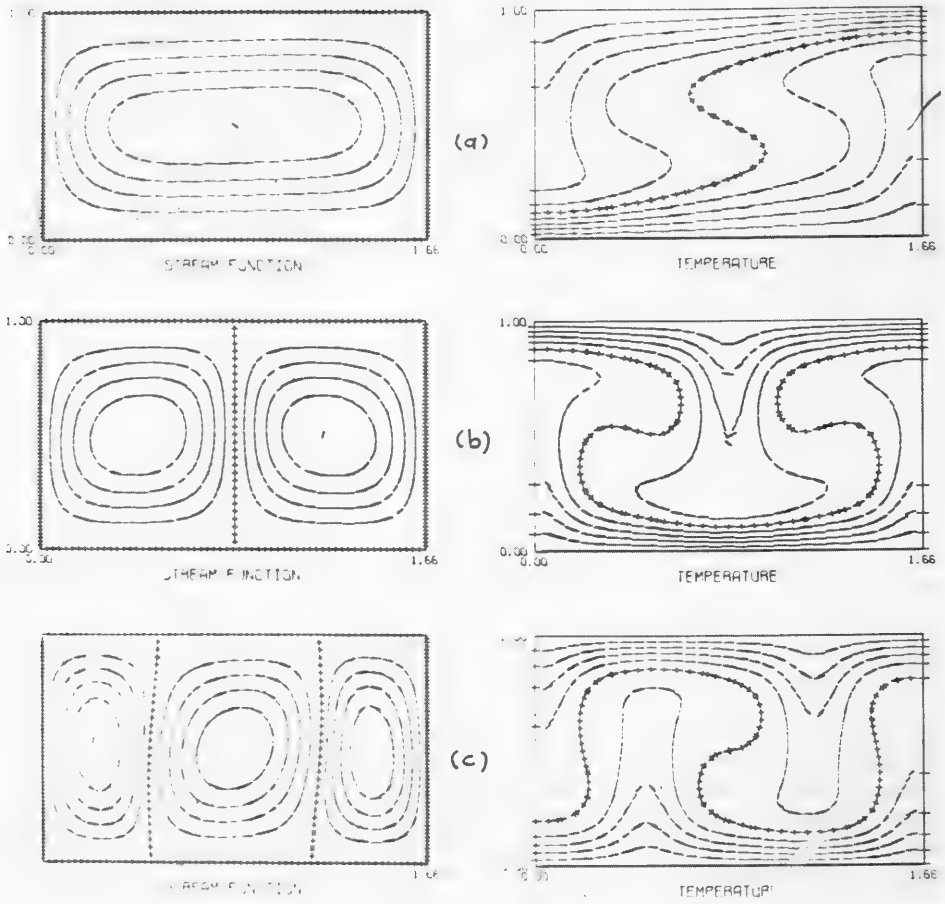

Fig. 9 - Steady-state streamlines (left) and isotherms (right) for Benard convection with $\gamma = 1.68$: (a) stretching of a $\gamma = 1.00$ cell; (b) initial perturbation cos $2\pi x$; and (c) initial perturbation sin $2\pi x$

of aspect ratio γ. The curious result found was that a perturbation of form cos $2\pi x$ (run (b))will lead to a 2-roll steady state, whereas a sin $2\pi x$ (run (c)) will lead to a 3-roll behavior. Run (c) corresponds to the $\gamma = 1.00$ cell adiabatically "stretched" to a $\gamma = 1.68$ cell. The answer appears to lie in the fact that the sin $2\pi x$ mode does not naturally satisfy the temperature boundary conditions, but is forced to do so at the gridpoints adjacent to the boundary, by the numerical procedure. This causes the temperature profile to have a point of inflection near the boundary and to develop regions of buoyancy opposite to that of the interior region adjacent to it. These appear to be the cause of the formation of the smaller cells on the sides. The highest heat transfer is associated with mode (c), i.e., the one exhibiting the largest number of upward-moving columns per unit area. This agrees with the Nusselt number's dependence on γ, where the largest heat transfer occurs for the smallest width-to-depth ratio.

REVIEW OF NUMERICAL METHODS IN CONVECTIVE FLOWS

The systems of partial differential equations governing two-dimensional or three-dimensional axisymmetric flows in natural convection divide into two groups: those involving the time-derivative called "forecast" equations, describing the transport of vorticity, temperature, and angular momentum; and a Poisson equation relating the stream function to vorticity. The first group contains equations that are of mixed parabolic-hyperbolic type, although, due to the nonlinearities, these terms must be used in a loose sense only. It is possible for the system to be parabolic in one region of the flow and not in another, or at one time during its evolution and not at another. The Poisson equation is, of course, elliptic. An extensive review of numerical methods used in geophysical fluid dynamics up to 1962 was given by Miyakoda (1962), and a more recent survey was made by Lilly (1965). Since then, still more progress has been made in this field, some in adapting existing methods to the Navier-Stokes equations and some in developing new ones.

We will first discuss the methods used to solve the Poisson equation $\nabla^2\psi = \xi$. The most common and easily programmed technique is the optimum overrelaxation [Frankel (1950); Forsythe and Wasow (1960), p. 242; Varga (1962), p. 105; Miyakoda (1962), p. 98]. The scheme for rectangular coordinates $x = i \cdot \Delta$ and $z = j \cdot \Delta$ with centered space differencing is given by

$$\psi_{ij}^{n+1} = \psi_{ij}^{n} + \frac{r}{4}\left(\psi_{i+1,j}^{n} + \psi_{i-1,j}^{n+1} + \psi_{i,j+1}^{n} + \psi_{i,j-1}^{n+1} - 4\psi_{ij}^{n} - \xi_{ij} \cdot \Delta^2\right) , \tag{29}$$

where the superscript n denotes the iteration cycle, and r is the relaxation coefficient or acceleration parameter. The mesh is swept in the order $j = 1$, $i = 1, 2, \ldots I$; $j = 2$, $i = 1, 2, \ldots I$, etc. so that the scheme is explicit. The constant r depends on the mesh size, and its variation with grid size is given by the authors cited above. Experience shows that, to decrease an initial error by a factor of 10^3, the matrix must be swept $\sim 3/4\sqrt{I^3}$ times. The total number of arithmetic operations would then be $\sim 9 \times 3/4 \times \sqrt{I^3}$. The fastest iterative technique for the solution of Poisson's equation in a rectangular region is a variant of the Peaceman-Rachford (1953) method, in which there is relaxation alternatively on rows and columns of the mesh and changes in the acceleration parameter from cycle to cycle. These methods are also known as the alternating-direction implicit or simply ADI methods. If the number of iteration cycles is chosen as a power of 2, say 2^k, then the acceleration parameters may be predetermined in advance and will obtain maximum convergence [Varga (1962), p. 226; Gary (1967)]. The scheme may be written

$$(r_k + 2)\psi_{ij}^{n+1/2} - \psi_{i+1,j}^{n+1/2} - \psi_{i-1,j}^{n+1/2} = (r_k - 2)\psi_{ij}^{n} + \psi_{i,j+1}^{n} + \psi_{i,j-1}^{n} \tag{30a}$$

$$(r_k + 2)\psi_{ij}^{n+1} - \psi_{i,j+1}^{n+1} - \psi_{i,j-1}^{n+1} = (r_k - 2)\psi_{ij}^{n+1/2} + \psi_{i+1,j}^{n+1/2} + \psi_{i-1,j}^{n+1/2} , \tag{30b}$$

where the sequence of parameters r_k is given by

$$r_k = \beta\delta^{(17-2k)} , \quad k = 1, 2, \ldots 8 ; \quad \beta = \mu\left(\frac{\pi}{I}\right)^2 ; \quad \delta = \left(\frac{4}{\beta}\right)^{1/16} , \tag{31}$$

and μ is adjusted to obtain most rapid convergence. The remaining values of r_k are defined modulo 8, i.e., $r_9 = r_1$, $r_{10} = r_{11}$, etc. Each row iteration, Eq. (30a), or column iteration, Eq. (30b), is implicit, in that all the values on the respective row or column must be found simultaneously. Since there are only three unknowns in each equation, the resulting coefficient matrix becomes tri-diagonal: the only nonzero elements are on the diagonal and two adjacent lines. For this type of matrix there is a special inversion algorithm that is very efficient; a detailed formulation is given by Varga (1962), p. 195, and Richtmeyer and Morton (1967), p. 200.

The ratio of the asymptotic rate of convergence for the overrelaxation to that of the ADI method decreases as the number of gridpoints increases, so that for large meshes the ADI method is far superior. This is particularly so in the case of Neumann boundary conditions for which the overrelaxation is extremely slow in converging. A detailed comparison of the two methods for Dirichlet and Neumann boundary conditions and for various ratios of the grid spacings $\Delta x/\Delta z$ may be found in Gary's (1967) article.

When the boundaries in one or both of the directions are "frictionless lids," where $\psi = \xi = 0$, the Fourier inversion method becomes very suitable particularly when the respective dimension is much shorter than the other. In this method, ψ_{ij} and ξ_{ij} are both expanded in discrete Fourier series in the respective direction, say z:

$$\psi_{ij} = \sum_{n=1}^{J} a_i^n \cdot \sin(n\pi j\Delta), \quad \xi_{ij} = \sum_{n=1}^{J} b_i^n \cdot \sin(n\pi j\Delta), \tag{32}$$

and the resulting J ordinary difference equations

$$(a_{i+1}^n + a_{i-1}^n - 2a_i^n)/\Delta^2 - n^2\pi^2 a_i^n = b_i^n \tag{33}$$

are solved by the tri-diagonal algorithm mentioned above. Here practically all the computation is spent in finding the b_i^n from decomposing ξ_{ij}, and the ψ_{ij} from superposing the a_i^n, which is $\sim 5IJ^2$ calculations. If $J \ll I$, the ratio of computational work in this method to that of overrelaxation is $\sim 20/27 \cdot \sqrt{J/I}$.

Recently, two ingenious simplifications were introduced by Hockney (1965) into this method. He noted that if a suitable number is chosen for J (such as 12, 24, 48), the symmetry in the sine functions may be used to reduce the computing time to about a tenth of the above estimate. Furthermore, the two-cyclic nature of the difference Eqs. (33) allows one to replace the original equations involving all the points in the net to a set of $IJ/2$ slightly more complex equations involving only the points on the even lines of the mesh. The set of revised equations could also be solved by the Fourier method. The final program led to a solution time 1/10 that of the ADI and 1/60 that of the overrelaxation method, on a mesh size 48 x 48.

On noting that the values of the vorticity on the boundary are actually not needed to solve the finite-difference version of the Poisson equation, the

Fourier inversion method was used for all three experiments. In experiment A, the expansion was made in the z-direction, and the resulting ordinary difference equations had variable coefficients in the radius r. In experiments B and C expansion was made in the horizontal x-direction.

We must turn now to solutions of the "forecast" equations, where one marches forward in time and finds the new values of ξ, T, and m at a later time step from their values at earlier time steps. Each transport equation may be put in the general form

$$\frac{\partial \varphi_i}{\partial t} = -\nabla \cdot \mathbf{u}\varphi_i + c_i \nabla^2 \varphi_i + F_i\left(\varphi_1, \varphi_2, \ldots; \frac{\partial \varphi_1}{\partial x}, \ldots; \frac{\partial \varphi_1}{\partial z}, u, r, \ldots\right) . \quad (34)$$

In cases B and C, $F_1 = -Ra \cdot \partial T/\partial X$ and $F_2 = 0$; in case A, $F_1 = (1/r^2) \cdot (2\Theta m/r^3 + 1) \cdot \partial m/\partial z - \partial T/\partial r$, $F_2 = -r^2 \cdot u$, $F_3 = 0$, and ∇^2 is replaced by the more complicated diffusion operators α, P and S (see Eqs. (16 - 18)). Suppose the time coordinate has been discretized as $t = n \cdot \Delta t$ and the iteration has progressed through step n; we would like to compute the next values at $t = (n + 1)\Delta t$. In general, the time iteration methods may be divided into two classes: explicit methods, in which all terms on the right-hand side of Eq. (34) are evaluated at previous time steps n, $n - 1$, etc.; and implicit methods, in which some terms may be evaluated at the step $n + 1$ to be computed. In the latter case an iterative procedure is required to find the values at all grid-points; for, in general, these become coupled in Eq. (34). In all the numerical experiments the author has seen, the terms F_i are evaluated at the step n, and the time derivatives as $\partial\varphi/\partial t = (\varphi_i^{n+1} - \varphi_i^{n-1})/\Delta t$ or $(\varphi_i^{n+1} - \varphi_i^{n})/\Delta t$.

Lilly (1965) has given a summary of the more widely used time iteration methods in geophysical fluid dynamics. Both he and Henrici (1962) have shown that weak instabilities are associated with some of the multistep methods (i.e., involving more than two time levels), due to the fact that the difference equation admits spurious solutions that are not present in the original equation. In fact, the solution may become decoupled on odd and even time levels. In addition, strong instabilities may arise if care is not taken in differencing the advective formas, or if too large a time step is used in the explicit schemes.

The existence of "aliasing errors," due to misrepresentation of the shorter waves because of the inability of the finite grid to properly resolve them, may lead to computational instability. It may occur due to the nonlinear advective terms; but it may also occur in linear equations with nonconstant coefficients. Arakawa (1966) has shown that by a proper form of space-differencing the advective terms the nonlinear instability may be overcome. He presented several schemes which simulate several important properties of continuous fluids, such as conservation of vorticity, kinetic energy, mean-square vorticity, and constraint on the spectral distribution of energy.

In two-dimensional incompressible flow, the expression $\nabla \cdot \mathbf{u}\varphi = (\mathbf{u} \cdot \nabla)\varphi$ may be written as

$$\frac{\partial \psi}{\partial z} \cdot \frac{\partial \varphi}{\partial x} - \frac{\partial \psi}{\partial x} \cdot \frac{\partial \varphi}{\partial z} = \frac{\partial(\psi, \varphi)}{\partial(x, z)} = \mathfrak{J}(\psi, \varphi) . \quad (35)$$

Since the contributions from the advection terms in vorticity equations were generally small, and in the case of rotation completely negligible, the finite difference form of the Jacobian was used that conserves only kinetic energy and vorticity. In all cases the total absolute value of the vorticity converged to four or more significant figures, so there was no need to use a scheme which also conserves mean-square vorticity; such a scheme is the superposition of two differently differenced Jacobians and represents twice the computer time. The scheme used is given by

$$\mathfrak{J}(\psi,\varphi) = [(\psi_{i+1,j+1} - \psi_{i+1,j-1})\xi_{i+1,j} - (\psi_{i-1,j+1} - \psi_{i-1,j-1})\xi_{i-1,j} - (\psi_{i+1,j+1} - \psi_{i-1,j+1})\xi_{i,j+1} - (\psi_{i+1,j-1} - \psi_{i-1,j-1})\cdot\xi_{i,j-1}]\frac{1}{\Delta X\cdot\Delta z\cdot 4}. \quad (36)$$

Three schemes were used in evaluating the advective and diffusive terms during the model experiments:

$$\text{I.}\quad \frac{\varphi^{n+1} - \varphi^{n-1}}{2\Delta t} = c(\nabla^2\varphi)^n + \mathfrak{F}(\psi,\varphi)^n + F^n \quad (37)$$

$$\text{II.}\quad \frac{\varphi^{n+1} - \varphi^{n-1}}{2\Delta t} = c\left[\frac{\left(\varphi^n_{i+1,j} + \varphi^n_{i-1,j} - \varphi^{n+1}_{ij} - \varphi^{n-1}_{ij}\right)}{(\Delta x)^2} + \frac{(\ldots)}{(\Delta z)^2}\right] + \mathfrak{J}(\psi,\varphi)^n + F^n . \quad (38)$$

The combination of the time-derivative evaluated at levels $n+1$ and $n-1$ with the advective terms evaluated at level n is called the "leap-frog" procedure. The particular way of differencing the diffusive terms in Scheme II is the well-known DuFort-Frankel method (for a detailed description of this and other schemes for the diffusion terms, the reader is referred to Richtmeyer and Morton (1967), p. 189). Scheme III is described below and is given essentially by Eqs. (41). Based on linearized stability analysis (see Richtmeyer and Morton (1967)), Scheme I has a limit on the time step for the case $\Delta x = \Delta z$ given by

$$\Delta t \le \frac{\Delta^2}{8c + (|u| + |w|)\cdot\Delta}, \quad (39)$$

while the stability of Scheme II is not affected by the diffusion terms, but is

$$\Delta t \le \frac{\Delta}{|u| + |w|}. \quad (40)$$

The truncation errors of the two schemes are $0(\Delta t + \Delta x^2)$ and $0(\Delta t/\Delta X)^2$, so that the gain in computer time is slightly offset by the poorer accuracy of Scheme II. Nevertheless, in the cases considered, the truncation error could be kept the same and still gain a factor of 10 in the allowable time step.

After noting that a cycle of iteration for elliptic partial differential equations is analogous to a time step in parabolic equations such as the diffusion equation, Douglas and Rachford (1956) devised an ADI method for the diffusion

equation that was applicable to three-dimensional problems. In this case, however, no set of acceleration parameters was found. Later, Douglas (1961, 1962) has extended the method to nonlinear parabolic equations of the type $\partial\varphi/\partial t = \nabla^2\varphi + F(\varphi, x, z)$. The scheme is as follows:

$$
\begin{aligned}
(\varphi^{n+1/4} - \varphi^n)/(\Delta\tau/2) &= \frac{1}{2}\left(\frac{\partial^2\varphi}{\partial x^2}^{n+1/4} + \frac{\partial^2\varphi}{\partial x^2}^{n}\right) + \frac{\partial^2\varphi}{\partial z^2}^{n} + F^n , \\
(\varphi^{n+1/2} - \varphi^{n+1/4})\ (\Delta\tau/2) &= \frac{1}{2}\left(\frac{\partial^2\varphi}{\partial z^2}^{n+1/2} - \frac{\partial^2\varphi}{\partial z^2}^{n}\right), \\
(\varphi^{n+3/4} - \varphi^n)\ (\Delta\tau/2) &= \frac{1}{2}\left(\frac{\partial^2\varphi}{\partial x^2}^{n+3/4} + \frac{\partial^2\varphi}{\partial x^2}^{n}\right) + \frac{\partial^2\varphi}{\partial z^2} + F^{n+1/2} , \\
(\varphi^{n+1} - \varphi^{n+3/4})\ (\Delta\tau/2) &= \frac{1}{2}\left(\frac{\partial^2\varphi}{\partial z^2}^{n+1} - \frac{\partial^2\varphi}{\partial z^2}^{n}\right).
\end{aligned}
\tag{41}
$$

It consists of two pairs of row-column iterations with a correction for the nonlinear term sandwiched in between, and has a truncation error of $0(\Delta t^2 + \Delta x^2)$. Subject to the condition that $|\partial F/\partial\varphi|$ is bounded for all times, the scheme has unconditional stability regarding the time steps. In view of the high order of truncation error and the unlimited stability, it is most promising for application to the Navier-Stokes equations, at least for flows in which the nonlinear terms are not larger by orders of magnitude than the diffusive terms. It must be noted that the column iteration involves only the second derivative in the z-direction, so that the additional arithmetic due to row-column iteration is minimal. Although the advective terms in the Navier-Stokes equations are not exactly of the form $F(x, z, \varphi)$, they can be taken care of in several ways. One way is to iterate more frequently in the predictor-corrector fashion of Eq. (41) for the advective terms, and with each of such iterations solve the Poisson equation for the stream function. The other method, as introduced by Wilkes and Churchill, is to include the $u \cdot d/dx$ and $w \cdot d/dz$ terms into joint operators $d^2/dx^2 + u \cdot d/dx$ and $d^2/dz^2 + w \cdot d/dz$, respectively, and then proceed as in Eq. (41), with F^n now including only the buoyancy and Coriolis terms.

A sure way of extending the Douglas method to the Navier-Stokes equations is to regard the nonlinear terms as the only ones giving rise to limitations on the time step. Thus, instead of unlimited stability we recover that of Scheme II, given by Eq. (40). This is justified, because with respect to the nonlinear term the scheme is a simple explicit one, and because unconditional stability holds for the pure diffusion terms. It is to overcome even this limitation on the time step that Wilkes and Churchill (1966) have evaluated the nonlinear terms implicitly. Aziz and Hellums (1967) have successfully used this method in a three-dimensional convection problem.

The general scheme for the whole numerical procedure, therefore, is as follows:

1. Forecast new values of the vorticity on interior gridpoints.

2. Solve the Poisson equation for the stream function, and if there are any rigid boundaries, find the values of the vorticity on them. On the frictionless lid surfaces, both ξ and ψ vanish.

3. Forecast new values of T and m, using the newly found stream function in the Jacobians. Start all over in 1.

Since the Poisson equation for the stream function must be solved at every time step and is a relatively lengthy procedure compared to the evaluation of the right-hand side of the transport equations, the use of implicit methods and fewer time steps almost always resulted in a large saving of computer time.

ACKNOWLEDGMENTS

This work was supported in part by the Office of Naval Research. The generous amount of computer time donated by the computing centers of the University of Notre Dame and the National Center for Atmospheric Research is gratefully acknowledged. The author would also like to thank Professors Raymond Hide and Norman Phillips of MIT and Paul Roberts of the University of Newcastle-upon-Tyne; also, Dr. Frank Eden of Arthur D. Little, Inc., and Dr. Gareth Williams of the Geophysical Fluid Dynamics Laboratory of ESSA for many valuable discussions and advice.

BIBLIOGRAPHY

Arakawa, A., 1966. J. Comput. Phys. **1**, p. 119

Aziz, K., and Hellums, J.D., 1967. Phys. Fluids **10**, p. 314

Ball, K.F., 1954. Australian J. Phys. **7**, p. 649

Barcilon, V., 1964. J. Atmospheric Sci. **21**, p. 291

Berg, J.C., Boudart, M., and Acrivos, A., 1966. J. Fluid Mech. **24**, p. 721

Brindley, J., 1960. Phil. Trans. Roy. Soc. London, Ser. A **253**, p. 1

, 1967. J. Inst. Math. Appl. **3**, p. 313

Bowden, M., and Eden, H.F., 1965. J. Atmospheric Sci. **22**, p. 185

Busse, F.H., 1967. J. Fluid Mech. **30**, p. 625

Chandrasekhar, S., 1961. Hydrodynamic and Hydromagnetic Stability. Oxford University Press

Charney, J.G., 1947. J. Meteorol. **4**, p. 135

Chen, M.M., and Whitehead, J.A., 1968. J. Fluid Mech. 31, p. 1

Chorin, J., 1968. J. Comput. Phys. 2

Deardorff, J.W., 1964. J. Atmospheric Sci. 21, p. 419

_____, 1965. J. Fluid Mech. 23, p. 337

Douglas, J., and Rachford, H.H., 1956. Trans. Am. Math. Soc. 82, p. 421

Douglas, J., 1961. Numer. Math. 3, p. 92

_____, 1962. Numer. Math. 4, p. 41

Eady, E.T., 1949. Tellus 1, p. 33

Eden, H.F., and Piacsek. S.A., 1968. Submitted for publication

Ewing, G., and McAlister, E.D., 1960. Science 131, p. 1374

Forsythe, G.E., and Wasow, W.R., 1960. Finite-Difference Methods for Partial Differential Equations. Wiley

Fowlis, W.W., and Hide, R., 1965. J. Atmospheric Sci. 22, p. 541

Foster, D.T., 1965(a). Phys. Fluids 8, p. 1770

_____, 1965(b). Phys. Fluids 8, p. 1249

Frankel, S.P., 1950. Math. Tables and Aids to Comput. 4, p. 65

Fromm, J.E., 1965. Phys. Fluids 8, p. 1757

Fultz, D., 1953. *In* Fluid Models in Geophysics, ed. R. Long. (See ref.)

_____, 1959. Meteorol. Monographs 4, p. 1

Gary, J., 1967. Math. Comput. 21, p. 220

Gill, A.E., 1966. J. Fluid Mech. 26, p. 515

Gribov, V.N., and Gurevich, L.E., 1957. Soviet Phys. JETP 4, p. 720 (Engl. trans.)

Hadley, G., 1735. Phil. Trans. Roy. Soc. London 39, p. 58

Henrici, P., 1962. Discrete Variable Methods in Ordinary Differential Equations. Wiley

Hide, R., 1952. Quart. J. Roy. Meteorol. Soc. 79, p. 161

_____, 1953. *In* Fluid Models in Geophysics, ed. R. Long. (See ref.)

_____, 1958. Proc. Roy. Soc., Ser. A 250, p. 441

Hidy, G.M., 1966. Bull. Am. Meteorol. Soc. 48, p. 143

Hockney, R.W., 1965. J. Assoc. Comput. Mach. 12, p. 95

Koschmieder, E.L., 1966. Beitr. Phys. Atmos. 39, p. 1

Lilly, D.K., 1965. Monthly Weather Rev. 93, p. 11

Long, R., ed., 1953. Fluid Models in Geophysics. U.S. Government Printing Office

Lorenz, E.N., 1955. Tellus 7, p. 157

_____, 1962. J. Atmospheric Sci. 19, p. 39

Malkus, W.V.R., and Veronis, G., 1958. J. Fluid Mech. 4, p. 225

McIntyre, M.E., 1967. Ph.D. thesis, Cambridge University

Merilees, P.E., 1967. Florida State University, Department of Meteorology, Technical Report 67-8

Meyer, K., 1967. Phys. Fluids 10, p. 1874

Miyakoda, K., 1962. Japan. J. Geophys. 3, p. 75

Palm, E., and Øiann, H., 1960. J. Fluid Mech. 19, p. 353

Peaceman, D. W., and Rachford, H.H., 1953. J. Soc. Ind. Appl. Math. 3, p. 28

Pellew, A., and Southwell, R.W., 1940. Proc. Roy. Soc., Ser. A 176, p. 312

Piacsek, S.A., 1966. Ph.D. thesis, MIT

_____, 1968. University of Notre Dame, Department of Aerospace Engineering, Technical Report UNDAS-TR-668

Rayleigh, Lord, 1916. Scientific Papers 6, p. 432

Richtmeyer, F.D., and Morton, K.W., 1967. Difference Methods for Initial Value Problems. Interscience Publ.

Roberts, P.H., 1965. *In* Non-equilibrium Thermodynamics, Variational Techniques, and Stability, ed. Prigogine. University of Chicago Press

Roberts, K.V., and Weiss, N.O., 1966. Math. Comput. 20, p. 272

Rossby, C.G., 1949. Quart. J. Roy. Meteorol. Soc. 66, Suppl. 68

Rossby, T., 1966. Ph.D. thesis, MIT

Quon, C., 1967. Ph.D. thesis, Cambridge University

Schluter, A., Lortz, D., and Busse, F., 1965. J. Fluid Mech. 23, p. 129

Segel, L.A., and Stuart, J.T., 1962. J. Fluid Mech. 13, p. 289

Segel, L.A., 1965(a). J. Fluid Mech. 21, p. 345

_____, 1965(b). J. Fluid Mech. 21, p. 359

Smith, A., 1958. Ph.D. thesis, Cambridge University

Snyder, H.A., 1967. Paper No. G2, Fluid Dynam. Symp., Am. Phys. Soc., Lehigh University

Spangenberg, W.G., and Rowland, W.R., 1965. Phys. Fluids 4, p. 743

Stuart, J.T., 1964. J. Fluid Mech. 18, p. 481

Varga, R.S., 1962. Matrix Iterative Analysis. Prentice Hall

Veronis, G., 1963. Astrophys. J. 137, p. 641

Ward, F., 1965. Astrophys. J. 141, p. 534

Whitehead, J.A., and Chen, M.M., 1967. Paper No. G8, Fluid Dynam. Symp., Am. Phys. Soc., Lehigh University

Wilkes, J.O., and Churchill, S.W., 1966. Proc. Am. Inst. Chem. Eng. J. 12, p. 161

Williams, G.P., 1967. J. Atmospheric Sci. 24, p. 162

* * *

DISCUSSION

A. S. Iberall
General Technical Services, Inc.
Upper Darby, Pennsylvania

The Bowen ratio (the hydrometric constant) approaches equilibrium for larger bodies of water in about 3 weeks. Thus, what systems in stability is Mr. Piacsek investigating?

* * *

REPLY TO DISCUSSION

Steve A. Piacsek

The Bowen ratio is the ratio between the amount of heat given off to the atmosphere as sensible heat and that used for evaporation. (Sverdrup, H.U., Johnson, M.W., and Fleming, R.H., "The Oceans," p. 117, Prentice-Hall.) For large bodies of water this indeed takes a long time to reach a steady value. However, the numerical experiments were concerned only with the stability of the top few centimeters near the ocean's surface, with a characteristic overturning time in the convection cells of a few minutes. During this time the mean air and water temperatures change very little, and the Bowen ratio may be considered to be a constant.

* * *

SOME PROGRESS IN TURBULENCE THEORY

Robert H. Kraichnan
Dublin, New Hampshire

ABSTRACT

A review is made of efforts to deduce the quantitative properties of turbulence from the Navier-Stokes equation, without the introduction of mixing lengths or other arbitrary parameters, by means of the direct-interaction family of statistical approximations. The direct-interaction results for turbulent dispersion, isotropic turbulence, and Boussinesq turbulent convection are compared with laboratory and computer experiments. The nature of expansions for statistical functions is discussed, together with techniques for the estimation of errors and the systematic refinement of the direct-interaction predictions. Finally, the numerical methods appropriate to the direct-interaction equations are discussed.

INTRODUCTION

Turbulence is a contradictory phenomenon which simultaneously exhibits both order and disorder. The combination has proved hard to analyze and predict successfully. The random aspect of turbulence arises from the rich variety of instabilities accessible to high-Reynolds-number flows. When a laminar flow breaks down into turbulence, so many different degrees of freedom can be excited that the detailed, point-to-point, causal dependence of the resulting turbulent velocity field on the initial disturbance field is impossible to unravel. The turbulent velocity field is intricate and irregular in appearance.

Measurements on a variety of sustained turbulent flows show that the probability distribution of the velocity measured as a function of time at any point within the fully turbulent region is close to a normal distribution. However, the joint probability distribution of the velocity at two or more points is significantly nonnormal. A snapshot of the velocity field at any instant would show an abundance of well-defined local features: filaments and streets of high vorticity separated by relatively quiescent regions.

The intricacy, irregularity, and nonreproducibility of individual turbulent flows make it natural to use a statistical description in which averages over space, time, or an ensemble of realizations of the flow are sought. In contrast to the instability of an individual turbulent flow, laboratory results suggest that appropriate statistical averages are relatively stable and reproducible. The transport properties of turbulent flows are naturally described by averages.

There are two general ways in which predictions of turbulence averages may be attempted with the Navier-Stokes equation as a starting point. The more straightforward is direct computer simulation of a turbulent flow, or ensemble of flows, followed by averaging. This involves numerical integration of the Navier-Stokes equation forward in time for each flow, individually. The second way is to seek dynamical equations for the statistical averages themselves. These latter equations then are solved numerically. There are advantages and disadvantages to each approach, and the two methods should be regarded as complements rather than competitors. Direct integration of the Navier-Stokes equation offers pictures of individual flow structures which are impossible to recover from statistical equations. On the other hand, statistical theory can exhibit more clearly some of the physics of the transport processes that characterize turbulence, and, equally important, can result in less demanding numerical computations. Direct computer simulation of turbulent flows has been limited, in the past, to two-dimensional flows, because of computer limitations. However, continuing advances in the speed and capacity of computers, together with numerical techniques like the Cooley-Tukey fast Fourier transform, appear to be changing this situation rapidly. As we shall discuss later in this paper, useful three-dimensional calculations already seem to be feasible [1].

The present paper reports on a family of statistical approximations, the "direct-interaction" approximation and its relatives, which the author and his colleagues have explored during the past ten years. The unique feature of the direct-interaction approximation is that it is an exact description of a model dynamical system, in addition to being an approximation to turbulence dynamics. The model system has the same expression for energy as the Navier-Stokes system, together with other common properties. This assures important internal consistency properties of the approximation.

The direct-interaction approximation and its variants have been applied to isotropic turbulence decay, turbulent dispersion, convection of scalar contaminants by turbulence, random solutions of Burgers' equation, hydromagnetic turbulence, turbulence in a Vlasov plasma, and buoyant turbulent convection. In the sections which follow, the nature of the approximation is reviewed, and brief reports are given on some of these applications, including comparisons of the results with laboratory and computer experiments. The paper concludes with discussions of error estimates, higher approximations which reduce errors systematically, and, finally, the numerical techniques called for by the direct-interaction equations.

THE NATURE OF DYNAMICAL EQUATIONS FOR STATISTICAL QUANTITIES

The simplest statistical field variables are the mean velocity $\bar{v}_i(\mathbf{x}, t) = \langle v_i(\mathbf{x}, t)\rangle$ and the velocity covariance tensor $U_{ij}(\mathbf{x}, t; \mathbf{x}', t') = \langle u_i(\mathbf{x}, t)u_j(\mathbf{x}', t')\rangle$, where $v_i(\mathbf{x}, t)$ is the velocity field in an individual realization of the flow, $\langle\ \rangle$ denotes the average over an ensemble of realizations, and $u_i(\mathbf{x}, t) = v_i(\mathbf{x}, t) - \bar{v}_i(\mathbf{x}, t)$ is the departure of the velocity field, in a realization, from the ensemble mean. We use ensemble averages here and in what follows because they are always applicable, while space or time averages are appropriate only if the flow exhibits statistical homogeneity or stationarity.

The dynamical equations obeyed by $\bar{v}$ and U differ fundamentally from the underlying Navier Stokes equation for $v(x, t)$. The latter is a vector differential equation which can be integrated forward in time once the initial values $v(x, 0)$ and the boundary conditions are specified. In contrast, there is no closed-form dynamical equation which can be integrated to generate $\bar{v}$ and U from their initial values. The equations for $\bar{v}$ and U can be formulated in several ways [2,3], but, always, an infinite sequence or series of some sort arises. In one formulation, there is an infinite set of coupled equations which determines simultaneously $\bar{v}, U$, and the infinite set of higher moments $\langle u_i(x, t)u_j(x', t')u_m \times (x'', t'')\rangle$, ... In a second formulation, $\bar{v}$ and U are expanded in an infinite perturbation series, with a characteristic Reynolds number of the flow serving as the expansion parameter. A third formulation yields integrodifferential equations for $\bar{v}$ and U which contain, within them, infinite series in $\bar{v}$ and U themselves. Finally, the infinite set of equations for $\bar{v}$, U, and higher-order moments can be replaced by an equivalent, single, functional equation for the probability-distribution characteristic functional [4,5]. All these ways of formulating the statistical equations require as input information the initial values of all moments of all orders. This infinite set of initial values replaces, in the statistical description, the initial values of the velocity field in all the individual members of the ensemble. The dynamical coupling of moments of different order comes from the nonlinearity of the Navier-Stokes equation; that is, from the advection term $(v\cdot\nabla)v$.

In order to compute $\bar{v}$ and U from the statistical equations, it is necessary to find an approximating algorithm which replaces the infinite dynamical equations by something integrable in a finite number of operations. Grave difficulties have been encountered here, because in all the formulations the infinite sequences or series are divergent [2]. At the time of writing (December 1968), no known scheme guarantees converging approximations to the correct values of $\bar{v}$ and U. Here is a sharp contrast to the original Navier-Stokes equation, which, with reasonable assurance, can be integrated with any desired accuracy, in any given realization, by taking a sufficiently fine grid in space and time.

In view of the preceding paragraph, what valid motivation is there for pursuing statistical turbulence theory instead of simply integrating the Navier-Stokes equation for representative turbulent flows? There are two principal reasons. First, equations for the statistical quantities themselves, even if approximate and mathematically difficult in their final usable form, can exhibit the important physics of turbulence more clearly than the Navier Stokes equation. Statistical equations can provide a bridge to intuitive ideas about turbulence, such as eddy viscosity and mixing lengths. Second, approximate statistical equations, required as an end result of moderately accurate numerical predictions for averages of interest, demand, in some cases at least, enormously less computation time than integration of the Navier-Stokes equation for representative flows. This is because the statistical functions $\bar{v}$ and U are smooth functions of their arguments and can be specified adequately by fewer numbers than the jaggedly varying velocity field of a typical realization. This is particularly true when there are statistical symmetries, such as isotropy or stationarity. Statistical equations can also be much more stable for machine computation than the Navier-Stokes equation.

DIRECT-INTERACTION APPROXIMATION FOR TURBULENT DIFFUSION

Turbulent diffusion by a random velocity field provides an example, simpler than Navier-Stokes turbulence, for introducing the direct-interaction statistical equations. We shall suppose that the mean velocity $\bar{v}$ vanishes, and that $u_i(\mathbf{x}, t)$ is incompressible and has a multivariate-normal statistical distribution over the ensemble of realizations of the flow. Suppose that a scalar quantity, e.g., temperature $T(\mathbf{x}, t)$, is passively convected according to

$$\left(\frac{\partial}{\partial t} - \eta\nabla^2\right) T(\mathbf{x}, t) = -u_i(\mathbf{x}, t) \frac{\partial T(\mathbf{x}, t)}{\partial x_i} , \tag{1}$$

where η is the molecular diffusivity. If the initial temperature field $T(\mathbf{x}, 0)$ is the same in all realizations $[T(\mathbf{x}, 0) = \bar{T}(\mathbf{x}, 0)]$, then the mean temperature field $\bar{T}(\mathbf{x}, t) = \langle T(\mathbf{x}, t)\rangle$ at later times is

$$\bar{T}(\mathbf{x}, t) = \int G(\mathbf{x}, t; \mathbf{y}, 0)\, \bar{T}(\mathbf{y}, 0)\, d^3y , \tag{2}$$

where $G(\mathbf{x}, t; \mathbf{x}', t')$ is the mean Green's function for the temperature field; i.e., $G(\mathbf{x}, t; \mathbf{x}', t') = T(\mathbf{x}, t)$ for the special initial condition $T(\mathbf{x}, t') = \partial^3(\mathbf{x} - \mathbf{x}')$.

From Eq. (1) and the assumption of normality of $\mathbf{u}$, an infinite-series integrodifferential equation for $G(\mathbf{x}, t; \mathbf{x}', t')$ can be developed in the following form:

$$\left(\frac{\partial}{\partial t} - \eta\nabla^2\right) G(\mathbf{x}, t; \mathbf{x}', t') = \frac{\partial}{\partial x_i} \int_{t'}^{t} ds \int d^3y\, G(\mathbf{x}, t; \mathbf{y}, s) \cdot U_{ij}(\mathbf{x}, t; \mathbf{y}, s) \frac{\partial G(\mathbf{y}, s; \mathbf{x}', t')}{\partial y_j} + \cdots , \tag{3}$$

$$G(\mathbf{x}, t'; \mathbf{x}', t') = \partial^3(\mathbf{x} - \mathbf{x}') .$$

The higher terms in Eq. (3), indicated by the dots, are an infinite series of increasingly complicated multiple integrals with G and U in the integrands. For the derivation and detailed analysis of Eq. (3), the reader is referred to the original papers [3,6,7]. In brief, the starting point for Eq. (3) is an iteration expansion in which the right-hand side of Eq. (1) is treated as a perturbation on the left-hand side. The iteration expansion is then reworked by partial summation to all orders, to yield Eq. (3).

Equation (3) is a formally exact equation for G. The direct-interaction approximation consists of dropping all the terms indicated by the dots. Equations (2) and (3) yield

$$\left(\frac{\partial}{\partial t} - \eta\nabla^2\right) \bar{T}(\mathbf{x}, t) = \frac{\partial}{\partial x_i} \int_0^t ds \int d^3y\, G(\mathbf{x}, t; \mathbf{y}, s)\, U_{ij}(\mathbf{x}, t; \mathbf{y}, s)$$

$$\frac{\partial \bar{T}(\mathbf{y}, s)}{\partial y_j} + \cdots , \tag{4}$$

and, again, the direct-interaction approximation is obtained by dropping the higher terms.

The most striking difference between Eqs. (1) and (4) is that the former is a differential equation, local in space and time, while the latter involves integrals over space and time and cannot be reduced to a differential equation. The nonlocalness of Eq. (4) is an analytical embodiment of some simple and widely held intuitive ideas about eddy transport phenomena. The effective range of the space integral in Eq. (4) is the correlation *length* of U_{ij}, or the characteristic eddy size, and the effective range of the time integral is the correlation *time* of U_{ij}, or the typical eddy circulation time, whichever is shorter. Thus, the nonlocalness of Eq. (4) is that which is intrinsic to the description of a mixing process on space and time scales, i.e., the order of the effective mean free path and intercollision time.

In the appropriate limit, Eq. (4) reduces to a local form in which an effective eddy-diffusivity tensor appears. Suppose that $T(\mathbf{x}, t)$ varies so gradually with its arguments that

$$\frac{\partial \bar{T}(\mathbf{y}, s)}{\partial y_j} \approx \frac{\partial T(\mathbf{x}, t)}{\partial x_j}$$

for $\mathbf{y}$ and s, where $G(\mathbf{x}, t; \mathbf{y}, s) U_{ij}(\mathbf{x}, t; \mathbf{y}, s)$ is large enough to contribute appreciably to the integral. Then Eq. (4) reduces to

$$\left(\frac{\partial}{\partial t} - \nu \nabla^2\right) \bar{T}(\mathbf{x}, t) = \frac{\partial}{\partial x_i} \left[\kappa_{ij}(\mathbf{x}, t) \frac{\partial \bar{T}(\mathbf{x}, t)}{\partial x_j} \right], \tag{5}$$

where

$$\kappa_{ij}(\mathbf{x}, t) = \int_0^t ds \int d^3y \, G(\mathbf{x}, t; \mathbf{y}, s) \, U_{ij}(\mathbf{x}, t; \mathbf{y}, s) \tag{6}$$

is the eddy-diffusivity tensor. It can be shown (as confirmed by the numerical results to follow) that the elements of κ_{ij} have the typical order of magnitude ℓv_0, where ℓ is the correlation length and v_0 is the root-mean-square turbulent velocity component. If, instead of making the direct-interaction approximation, the full series Eqs. (3) and (4) are retained, the eddy-diffusivity limit of Eq. (5) still emerges, but with an infinite series of higher-order integrals over G and U added to Eq. (6).

To provide a clean numerical test of the direct-interaction approximation, the prediction for eddy diffusivity was compared with the results of computer realizations of turbulent dispersion in statistically homogeneous and isotropic velocity fields. Homogeneity and isotropy imply that $\kappa_{ij}(\mathbf{x}, t)$ has the form $\kappa_{ij}(\mathbf{x}, t) = \delta_{ij} \kappa(t)$.

In the limits where η is very large or the correlation time of U_{ij} is very small compared to the typical eddy circulation time, Eq. (6) can be shown to be asymptotically exact [8]. Therefore, the most critical test is provided by taking $\eta = 0$ and making $\mathbf{u}(\mathbf{x}, t)$ a random time-independent field in each realization. The choice $\eta = 0$ also makes the computer realization easier, because instead of solving the field Eq. (1), we can equivalently [9] trace the motion of fluid particles in a Monte Carlo calculation. The eddy diffusivity then is expressed by

$$\kappa(t) = \frac{1}{3} \langle x_i(t)\ v_i(t) \rangle, \tag{7}$$

where, in each realization, $\mathbf{x}(t)$ and $\mathbf{v}(t)$ are the position and velocity of the fluid element which starts at $\mathbf{x} = 0$ at time $t = 0$.

To perform the numerical experiment economically, the velocity field in each realization was constructed only along the particle trajectory, by synthesis from stored Fourier amplitudes. A set of N-complex, vector Fourier coefficients was chosen, by use of pseudorandom numbers, from a normal probability distribution such that the synthesized velocity field was incompressible and, for $N \to \infty$, the spectrum function [10]

$$E(k) = \frac{1}{\pi} \int_0^\infty U_{ii}(\mathbf{x}, t; \mathbf{x}', t)\, kr \sin(kr)\, dr \tag{8}$$

where $r = |\mathbf{x}-\mathbf{x}'|$

took an assigned functional form. For the two forms of $E(k)$ which were investigated, $N = 100$ was found to give good statistics:

$$E(k) = 16\sqrt{\frac{2}{\pi}}\, v_0^2 \frac{k^4}{k_0^5} \exp\left[-2 \left(\frac{k}{k_0} \right)^2 \right], \tag{9a}$$

$$E(k) = \frac{3}{2} v_0^2\, \delta(k-k_0). \tag{9b}$$

Here, k_0 denotes the peak k and $3v_0^2/2$ is the kinetic energy per unit mass. In each realization, the fluid element was started off at $\mathbf{x} = 0$, its initial velocity synthesized, then the successive positions of the particle were found, and the velocity synthesized all along the trajectory. A simple predictor-corrector scheme was used for the integration. The average of Eq. (7) was taken over ensembles of approximately 20,000 realizations.

The direct-interaction equations were also Fourier-transformed before integration. The transforms of Eqs. (3) and (6) when the velocity field is time-independent, homogeneous, and isotropic are

$$\frac{\partial G(k,t)}{\partial t} = -\frac{k^2}{2}\int_0^t ds \int_0^\infty pdp \int_{|k-p|}^{k+p} E(q)\,\sin^2(q,k)\,G(p,t-s)\,G(k,s)\,\frac{dq}{q} + \ldots\,,\quad G(k,0) = 1 \tag{10}$$

$$\kappa(t) = \frac{2}{3}\int_0^\infty dq \int_0^t E(q)\,G(q,s)\,ds\,, \tag{11}$$

where $\sin(q,k)$ is the sine of the interior angle between q and k in a triangle with sides k, p, q, and $G(k, t-t')$ is the Fourier transform of $G(\mathbf{x}, t; \mathbf{x}', t')$ with respect to $\mathbf{x} - \mathbf{x}'$. Equation (10) was discretized and truncated in k, discretized in time, and integrated forward by a simple predictor-corrector scheme. Finally, $\kappa(t)$ was computed from Eq. (11). Variation of step sizes and truncated limits, interpreted by extrapolation techniques, was used to verify that numerical-integration errors were negligible.

Figure 1 compares $\kappa(t)$ as found [11] from the numerical experiment and from the direct-interaction approximation for the spectrum choice in Eq. (9b), wherein the accuracy of the direct-interaction approximation was found to be poorer. In the present case of dispersion by a statistically stationary velocity field, the Lagrangian velocity correlation (correlation of a fluid particle's current velocity with its initial velocity) is easily shown to be $U^L(t) = 1/3\,\langle v_i(0)\,v_i(t)\rangle = d\kappa(t)/dt$. Figure 2 compares the curves of $U^L(t)$ obtained from the numerical experiment and from the direct-interaction results.

ISOTROPIC TURBULENCE DECAY

The direct-interaction equations for the decay of isotropic turbulence are similar in general appearance to those for turbulent dispersion; but they are also more complicated because the Navier-Stokes equation is a vector equation, nonlinear in the unknown dynamical variables, in contrast to the linear scalar equation for $T(\mathbf{x}, t)$. The final equations of the approximation comprise an energy balance equation which determines the spectrum function $E(k, t)$, an equation for the time correlation $U(k; t, t')$ of the Fourier amplitude at wavenumber k, and an equation for the mean response $G(k; t, t')$ of Fourier amplitude k to infinitesimal perturbations. These equations are (G and T are unrelated to previous G and T) [12]:

$$\left(\frac{\partial}{\partial t} + 2\nu k^2\right) E(k,t) = T(k,t),\quad T(k,t) = 4\pi k^2 S(k;t,t) \tag{12}$$

$$\left(\frac{\partial}{\partial t} + \nu k^2\right) U(k;t,t') = S(k;t,t') \tag{13}$$

$$\left(\frac{\partial}{\partial t} + \nu k^2\right) G(k;t,t') = H(k;t,t'),\quad G(k;t',t') = 1 \tag{14}$$

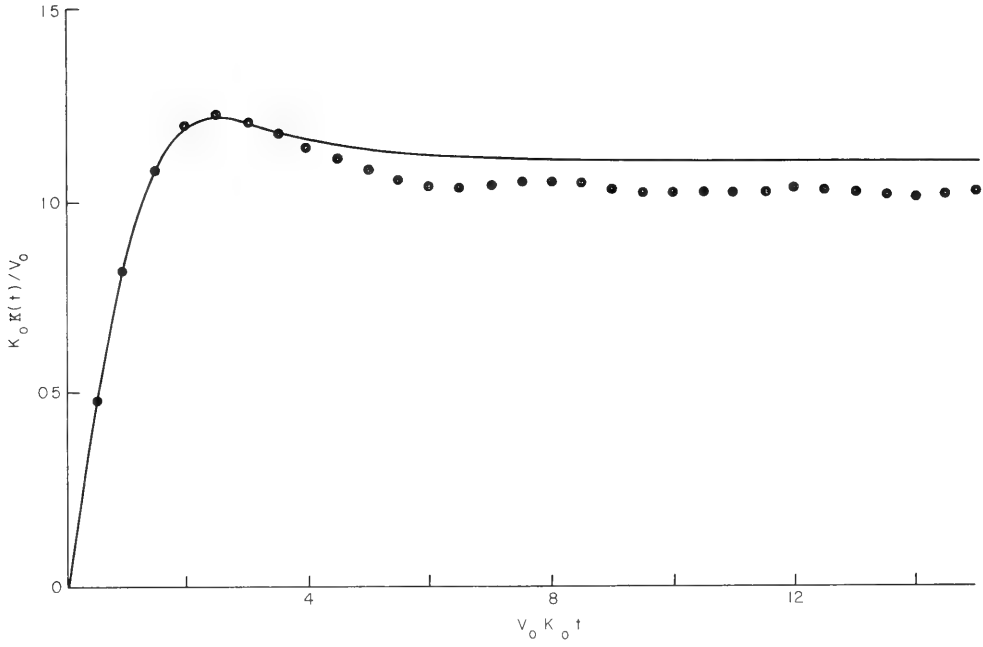

Fig. 1 - Eddy diffusivity found from numerical experiment (dots) and the direct-interaction approximation (solid curve) for the energy spectrum of Eq. (9b)

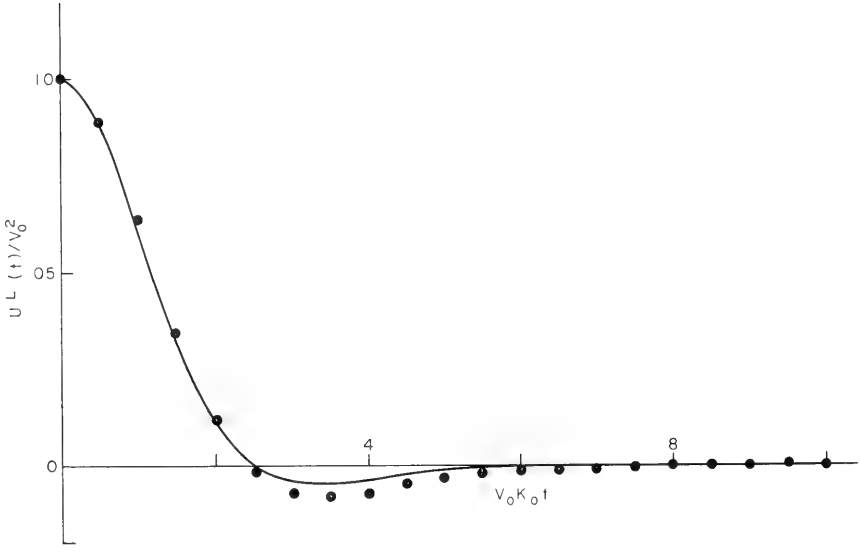

Fig. 2 - Lagrangian velocity correlation found from numerical experiment (dots) and the direct-interaction approximation (solid curve) for the energy spectrum of Eq. (9b)

$$S(k;t,t') = \pi k \iint_{\Delta} pqdpdq \left[\int_0^{t'} a_{kpq}\, G(k;t',s)\, U(p;t,s)\, U(q;t,s)\, ds \right. \tag{15}$$

$$\left. - \int_0^{t} b_{kpq}\, U(k;t',s)\, G(p;t,s)\, U(q;t,s)\, ds \right]$$

$$H(k;t,t') = -\pi k \iint_{\Delta} pqdpdq\, b_{kpq} \int_{t'}^{t} G(k;s,t')\, G(p;t,s)\, U(q;t,s)\, ds \ . \tag{16}$$

Here

$$a_{kpq} = \frac{1}{2}(1-xyz-2y^2\ z^2),\quad b_{kpq} = \frac{p}{k}(xy+z^3)\ ,$$

where x, y, z are the cosines of the interior angles opposite k, p, q, respectively, in a triangle with the latter numbers as sides. The integration $\iint_{\Delta}$ extends over all regions of the (p,q) plane where this triangle can be formed. Kinematic viscosity is ν. These equations are a complete set which determines $E(k,t)$, $U(k;t,t')$, and $G(k;t,t')$ for $t \geq 0$, $t' \geq 0$, if the initial spectrum $E(k,0)$ is given. The spectrum and correlation functions are related by $E(k,t) = 2\pi k^2\, U(k;t,t)$. The kinetic energy per unit mass at time t is

$$\int_0^{\infty} E(k,t)\, dk\ .$$

Also, $U(k;t,t') = U(k;t';t)$, while $G(k;t,t')$ vanishes for $t < t'$.

The equations above share, with the direct-interaction equations for dispersion, the property of nonlocalness, both in the present Fourier representation and if they are transformed back into physical space. As before, this expresses the finite length and time scales of the eddy-transport process.

The direct-interaction equations preserve some important properties of the exact turbulence dynamics. Equations (12) and (15) yield

$$\int_0^{\infty} T(k,t)\, dk = 0\ , \tag{17}$$

which expresses conservation of kinetic energy by the nonlinear processes. Moreover, and equally important, the equations guarantee the realizability of $U(k;t,t')$. This means that a vector random process can be constructed for which $U(k;t,t')$, as found from the direct-interaction equations, actually is the covariance scalar. This implies an infinite set of realizability inequalities, the simplest and most important of which is

$$E(k,t) \geq 0,\quad |U(k;t,t')|^2 \leq U(k;t,t)\, U(k;t',t')\ . \tag{18}$$

Whereas energy conservation follows identically from the expressions for a_{kpq} and b_{kpq}, realizability is deduced from a remarkable property of the direct-interaction equations which is not obvious from their final form. Although these equations are only an approximation for actual turbulence, they are exact for a model dynamical system that has the same energy integral as the Navier-Stokes system, but different dynamical equations for the Fourier amplitudes. The model system, which has been discussed in detail [3,7,13], is obtained by combining, with random phase factors, the elementary conservative interactions of triads of Fourier modes which characterize the Navier-Stokes system.

The representation by a conservative model system also implies that the direct-interaction equations yield a tendency toward absolute statistical equilibrium. It can be verified directly from Eqs. (12) - (16) that, if $\nu = 0$, the equipartition relation $U(k; t, t') \propto G(k; t, t')(t \geq t')$ is consistent with the equations [12]. Although the direction of energy transfer in Eq. (12) is toward establishing the equipartition solution, the latter is never actually achieved from physically admissible initial conditions. The tendency toward equipartition has been verified by numerical integrations for $\nu = 0$ [12].

So far, there have been no computer experiments on isotropic turbulence decay which would give a clean test of the direct-interaction equations, similar to the test for turbulent dispersion described in the previous section. Such experiments now appear to be imminent [1]. Meanwhile, it is possible to compare, behind grids, direct-interaction predictions with laboratory results on decay. This comparison is not so clean for several reasons, the most important of which are the difficulty of matching laboratory initial conditions, and the uncertainties about the degree of anisotropy and instrumental error present in the measurements. The most reasonable comparisons would appear to be those of properties associated with the high-wave-number end of the energy spectrum, where short intrinsic dynamical times should lead relatively rapidly to a state that is insensitive to initial conditions.

Numerical integrations of Eqs (12) - (16) have been carried out for a variety of initial conditions [12]. Figures 3 through 8 show some typical results. Figures 3 through 5 show the evolution of the energy spectrum, viscous dissipation (or mean-square-vorticity) spectrum, and transfer spectrum $T(k, t)$ for the initial condition

$$E(k,0) = 16\sqrt{\frac{2}{\pi}}\, v_0^2\, \frac{k^4}{k_0^5} \exp\left(-\frac{2k^2}{k_0^2}\right). \tag{19}$$

$L(0)$ is the initial value of the integral scale, a length characteristic of the size of the energy-containing eddies, while $u(0) = v_0$ is the initial root-mean-square value of the velocity along any axis. The Reynolds number $R_\lambda(t) = \lambda(t)u(t)/\nu$, where $u(t)$ is the root-mean-square velocity component at time t and $\lambda(t)$ is the Taylor microscale [10], decreased from 35 to 17 over the time interval shown.

Figures 6 and 7 depict the evolution from a less peaked initial spectrum,

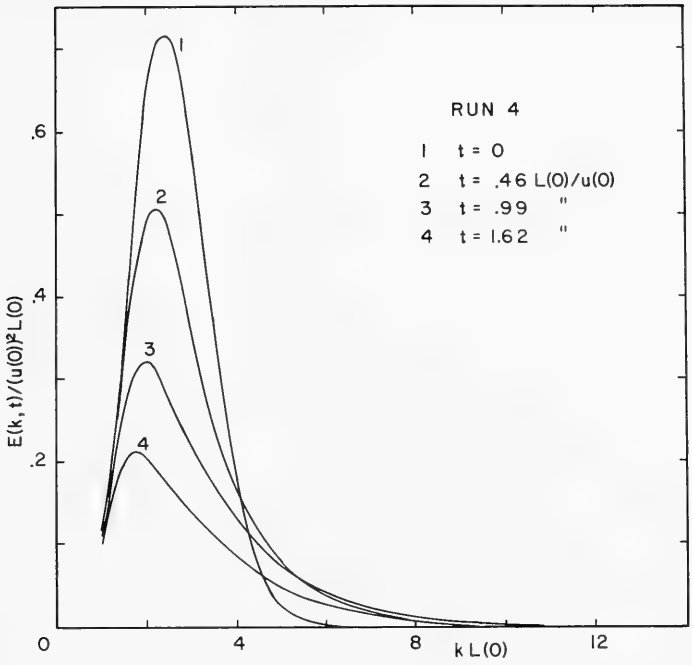

Fig. 3 - Evolution of the energy spectrum from the initial values of Eq. (19) (initial $R_\lambda = 35$)

$$E(k,0) = \frac{3}{2} v_0^2 \frac{k}{k_0^2} \exp\left(-\frac{k}{k_0}\right). \tag{20}$$

In contrast to the previous case, the energy spectrum here is nearly self-preserving, particularly at the higher wave numbers, with very little change of R_λ during decay. Figure 7 shows the dissipation, energy transfer, and vorticity-production spectra near the end of the time interval covered in Fig. 6.

The normalizing parameter k_d used in Fig. 7 is a characteristic dissipation-range wave number of the direct-interaction solutions [12,14]. It is related to λ by $k_d = (15\,R_\lambda)^{1/3}/\lambda$. The numerical integrations for a number of different shapes of initial spectra have been found to lead to evolved dissipation-range spectra which are nearly independent of initial conditions, and only weakly dependent on R_λ. This is true whether λ or k_d is used for normalization, in the range $R_\lambda < 50$ covered by the integrations.

Figure 8 shows the evolution of the skewness factor [10]

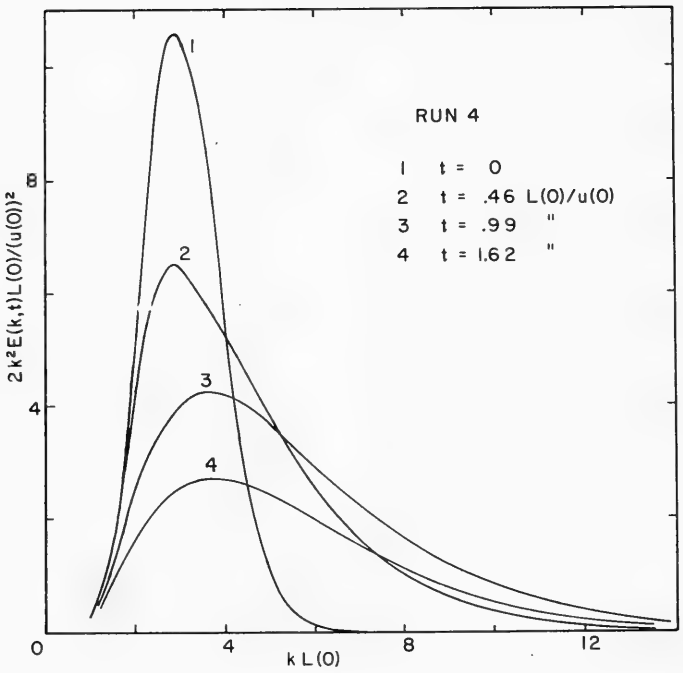

Fig. 4 - Evolution of the dissipation spectrum for the run shown in Fig. 3

$$S(t) = -\frac{\left\langle\left[\frac{\partial u_1(x,t)}{\partial x_1}\right]^3\right\rangle}{\left\langle\left[\frac{\partial u_1(x,t)}{\partial x_1}\right]^2\right\rangle^{3/2}} = \frac{2}{35}\left[\frac{\lambda(t)}{u(t)}\right]^3 \int_0^\infty k^2\, T(k,t)\, dk\,, \tag{21}$$

obtained from a variety of initial spectra, ranging in form from a very concentrated spectrum (all initial excitation confined to a single 1/4 octave k-band, Run 11) to the nearly self-preserving spectrum of Eq. (20), Run 10. The initial values of R_λ range from 16 to 47. Note that, after a transient behavior which is strongly dependent on initial conditions $S(t)$ settles down to a value ~ 0.4 which is insensitive to initial conditions. This value agrees well with laboratory measurements of $S(t)$ in the same range of R_λ [10], subject to some uncertainty because only crude estimates of wire-length corrections to the measurements can be made. The insensitivity of $S(t)$ to initial conditions makes this a comparatively well-posed comparison with experiment. Equation (21) shows that $S(t)$ is

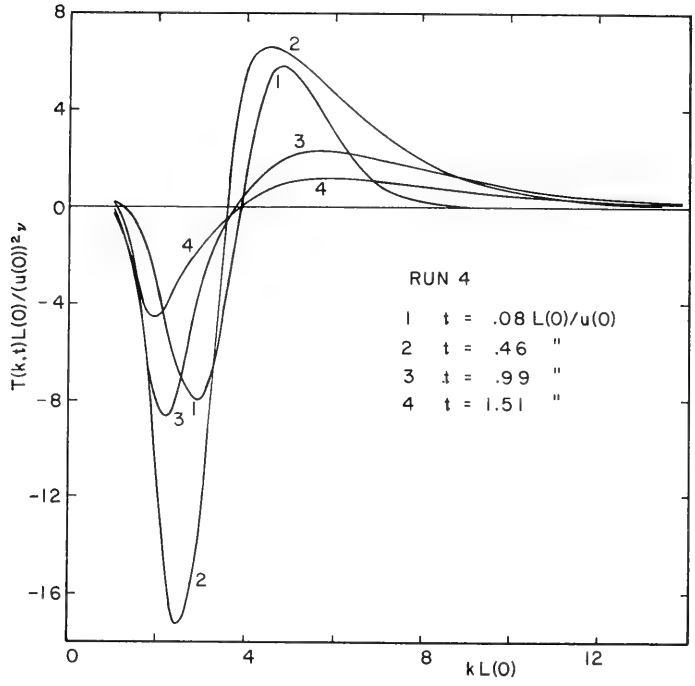

Fig. 5 - Evolution of the transfer spectrum for the run shown in Fig. 3

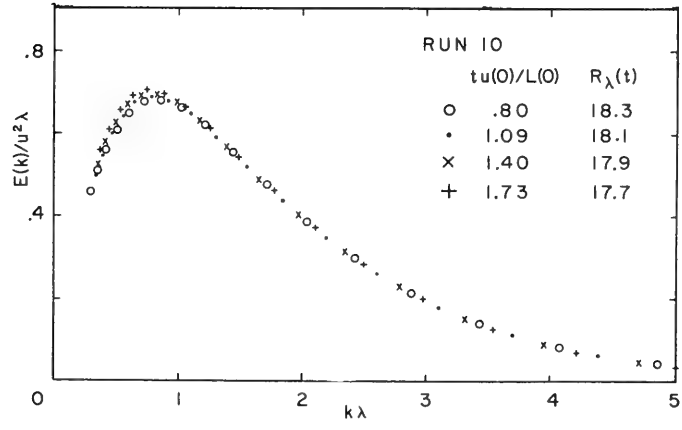

Fig. 6 - Evolution of the energy spectrum from the initial values of Eq. (20) (initial $R_\lambda = 19$)

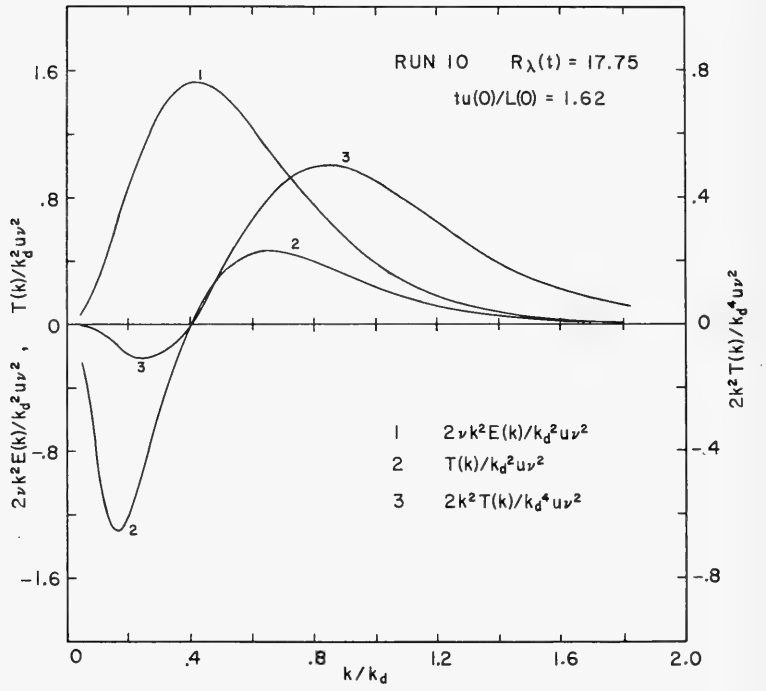

Fig. 7 - Comparison of the dissipation spectrum (1), transfer spectrum (2), and vorticity-production spectrum (3) for the run shown in Fig. 6

proportional to the instantaneous rate of vorticity production, normalized by the instantaneous dissipation rate, and thereby is an important measure of the nonlinear transfer processes.

Figures 9 and 10 compare the one-dimensional dissipation spectrum from the nearly self-preserving run depicted in Figs. 6 and 7 with spectra obtained by Stewart and Townsend [15] from measurements of decay behind grids. Again, there appears to be semiquantitative agreement, which is actually within the limits of experimental uncertainties.

The apparently satisfactory performance of the direct-interaction approximation at the moderate Reynolds numbers discussed above deteriorates at higher Reynolds numbers. At very high Reynolds numbers, the direct-interaction equations yield an inertial range spectrum $E(k) \propto k^{-3/2}$ instead of the $k^{-5/3}$ spectrum predicted by Kolmogorov [10] and supported by experiment [16]. The reasons for this deficiency, and the modifications of the approximation which correct it, are discussed in the Lagrangian Direct-Interaction Approximation section of this paper.

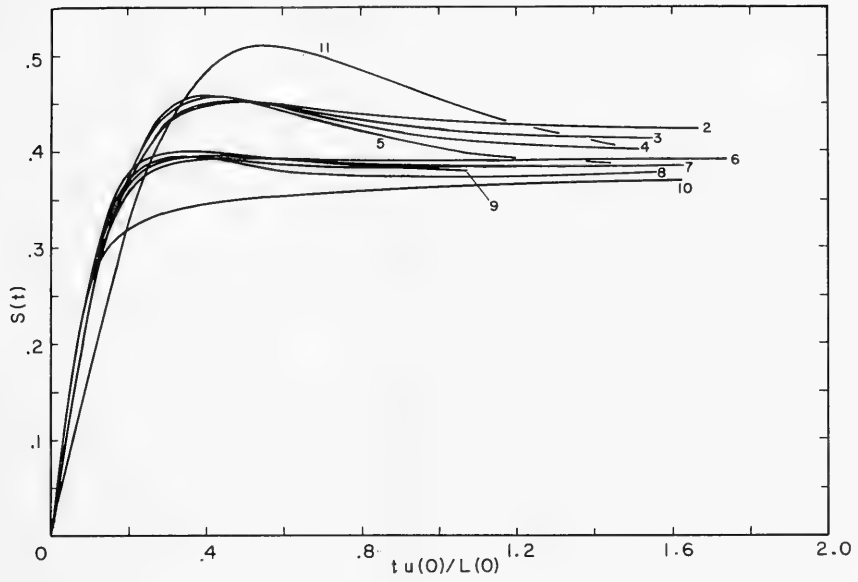

Fig. 8 - Evolution of skewness for a variety of initial conditions. Curve 4 is for the run shown in Figs. 3-5; curve 10, for the run shown in Figs. 6 and 7. (See Ref. 12 for full details.)

More definitive and detailed tests of the direct-interaction solutions for isotropic turbulence decay at moderate Reynolds numbers probably must come from computer simulation of the flows. Such computer experiments now seem feasible at the R_λ values cited above, and it is to be hoped that they will be carried out in the near future.

In the absence of these computer experiments at the present time, it is of interest to report a test of direct-interaction results against computer simulation for a simpler dynamical problem with the same kind of nonlinearity, viz., the interaction of a small, discrete set of shear waves [17]. The equations of motion here are obtained by writing the Navier-Stokes equation in Fourier form and then deleting all terms that refer to wave numbers outside a small set. The computer experiment is performed by integrating the equations of motion for an ensemble of initial conditions, and then averaging. Figure 11 shows a typical result for the interaction of a set of three shear waves confined to two dimensions. In this run, all of the energy was initially contained in two of the waves. Curves 1, 3, and 5 show the evolution of the energy in the three waves according to the computer experiment. Curves 2, 4, and 6 show the corresponding evolution according to the direct-interaction equations.

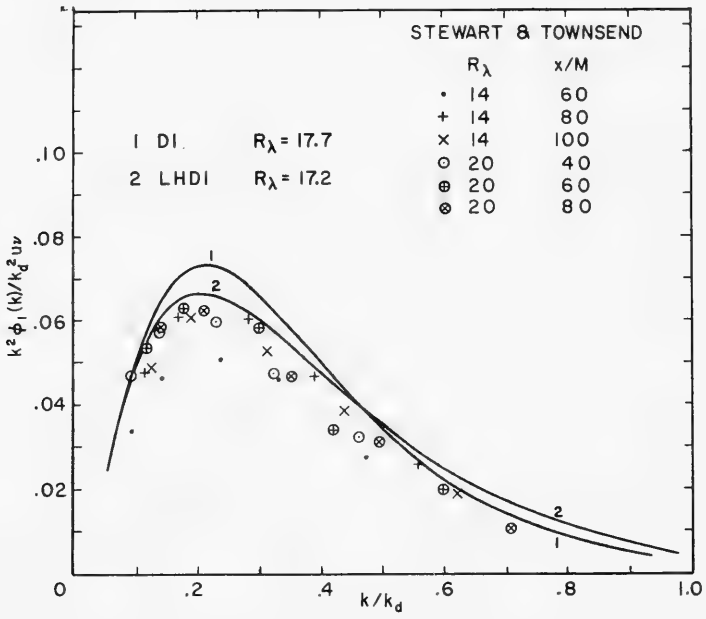

Fig. 9 - Comparison of direct-interaction results from the run of Figs. 6 and 7 (curve 1) with experimental dissipation spectra (Ref. 15). The quantity $\phi_1(k)$ is the one-dimensional spectrum. Curve 2 shows the result from the abridged LHDI equations (see the Lagrangian Direct-Interaction Approximation section of this paper) for the same initial spectrum.

ADDITIONAL APPLICATIONS OF THE DIRECT-INTERACTION APPROXIMATION

The direct-interaction equations have also been formulated for the evolution of the spectrum of scalar contaminants convected by turbulence [18,19], stochastic solutions of Burgers' equation [20], hydromagnetic turbulence [21,22], turbulence in a Vlasov plasma [23], buoyant convection in a Boussinesq fluid [24], and second-order chemical reactions in a turbulent fluid [25 - 27]. Further applications, for example to visco-elastic turbulence, are feasible. We shall give here only a brief report on the application to Boussinesq convection, which is the only one in which quantitative comparisons with experiment (computer experiment in this case) are available at the time of writing.

The equations for turbulent Boussinesq convection are substantially more complicated than those for isotropic turbulence, although they present the same general appearance, because there is reduced spatial symmetry and an additional field variable, the temperature field. We refer the reader to Ref. 24 for a full description. Numerical results so far have only been obtained for the case

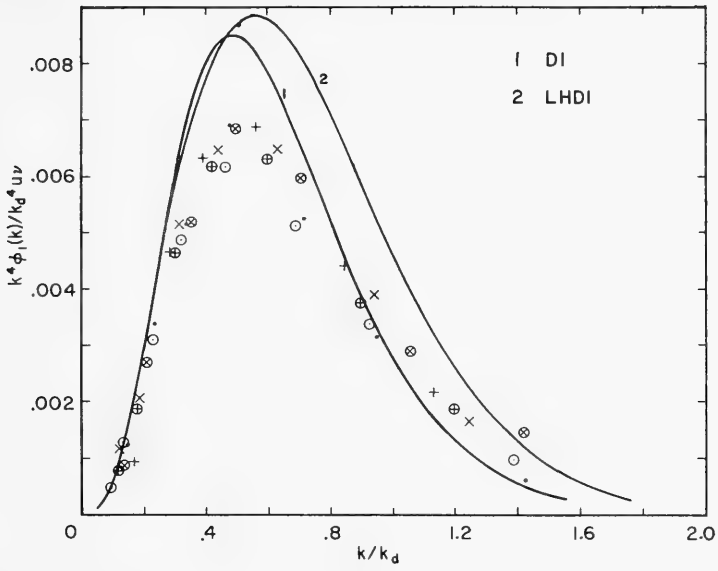

Fig. 10 - The direct-interaction and LHDI results of Fig. 9 compared with Stewart and Townsend measurements of $k^4\phi_1(k)$ (Ref. 15)

of infinite Prandtl number, a rather inhospitable limit in which to test a turbulence theory because laboratory experiments have found strong evidence of a tendency toward ordered motion in this limit. Extension of this work to lower Prandtl numbers is in progress.

Figures 12 and 13 illustrate the results for convection in a horizontally infinite layer of fluid contained between slippery, infinitely conducting boundaries, at a Rayleigh number of 3000. In both the computer experiment and the direct-interaction equations, only the gravest three Fourier modes of temperature fluctuation in the vertical z-direction were retained in combination with all horizontal wave vectors whose x and y components fell within a chosen octave. Cyclic boundaries were taken in the horizontal such that the numerical experiment involved usually 76 distinct wave-vector projections in the horizontal, and averages were performed over an ensemble of ten realizations. The initial conditions were zero velocity everywhere, with Gaussian-distributed temperature fluctuation. The direct-interaction equations were integrated with an initial temperature fluctuation spectrum corresponding to the distribution used in the numerical experiment.

Figure 12 shows the evolution of Nusselt number (the ratio of mean heat transfer across the layer to what the transfer would be without convection) according to the numerical experiment and the direct-interaction equations. Also shown are the results of two other statistical approximations, the quasilinear

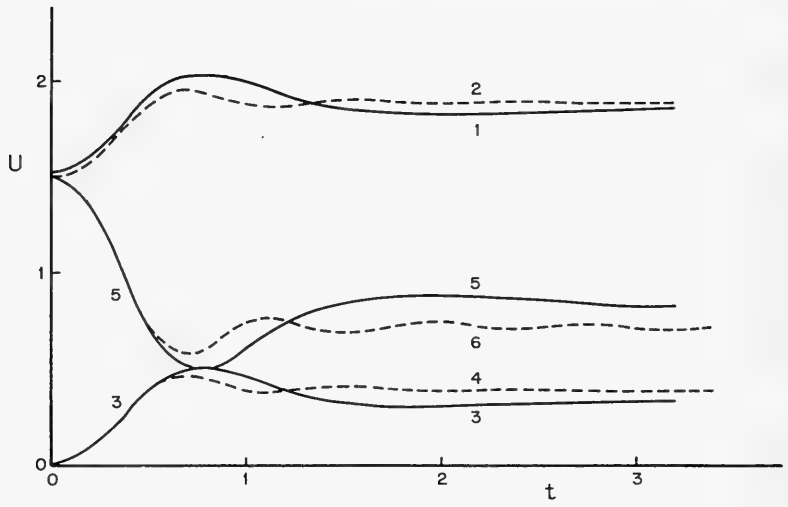

Fig. 11 - Comparison of direct-interaction and computer-experiment results for evolution of the energy in three interacting shear waves (Ref. 17). Curves 1, 3, and 5 show the energy in the three waves according to the computer experiment, while curves 2, 4, and 6 show the respective direct-interaction results.

and quasinormal approximations [24]. Herring estimates that statistical uncertainties in the numerical experiment curve, due to the finite density of modes in the horizontal and finite ensemble size, amount to about 3% where they are maximum, while the numerical error in the integration of the direct-interaction equations is smaller. The graph therefore suggests the excellent performance of the direct-interaction approximation.

The truncation in wave-number space to three vertical modes and a single octave in the horizontal is physically artificial (although not seriously so at the Rayleigh number taken), but this does not weaken the test of the direct-interaction equations, since the same truncation is used in both the numerical experiment and the statistical approximation.

Figure 13 shows the evolution of the spectrum of temperature fluctuations in the gravest vertical mode as a function of horizontal wave number. Again the direct-interaction results seem to agree excellently with the numerical experiment. Here, however, the comparison is less sharp, because the statistical fluctuations in the numerical experiment show up more prominently in the spectrum results than in the Nusselt number curve.

Numerical results from the work at lower Prandtl numbers and higher Rayleigh numbers and also for non-slip boundary conditions are expected in

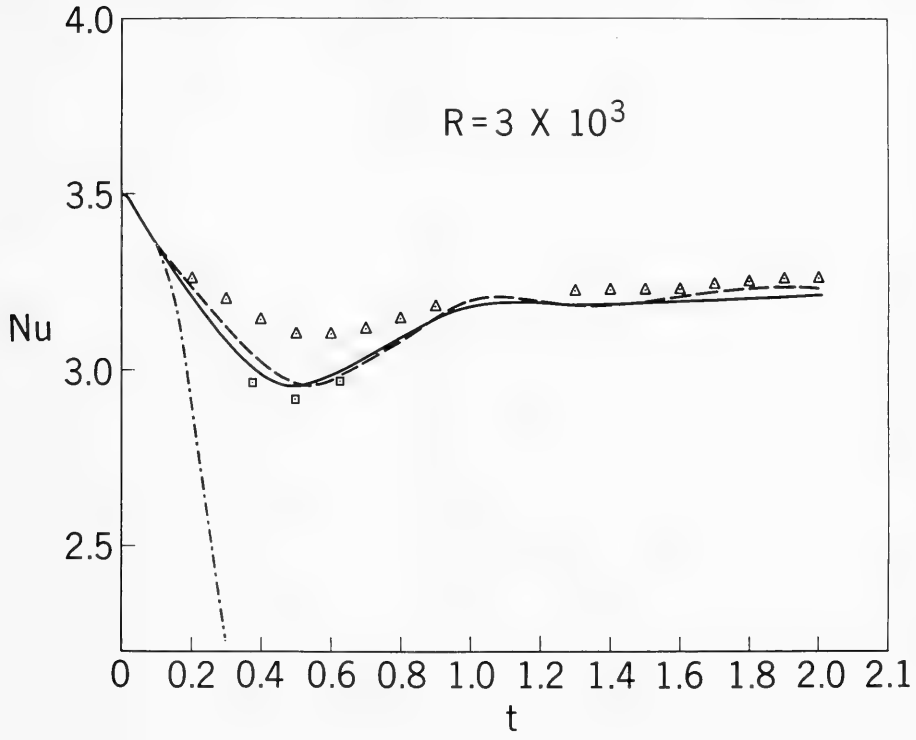

Fig. 12 - Comparison of direct-interaction and computer-experiment results for the evolution of Nusselt number at infinite Prandtl number, Rayleigh number = 3000. The solid curve is the numerical experiment; the dashed curve, the direct-interaction approximation; the triangles are the quasilinear approximation; and the dot-dash curve is the quasinormal approximation. The squares show points from another numerical experiment, with 124 horizontal wave vectors, and give a measure of the statistical error at the time of evolution, when that error was found to be maximum. (See Ref. 24 for further detail and for normalization.)

the near future. This should permit meaningful comparison with laboratory as well as computer experiment.

LAGRANGIAN-HISTORY DIRECT-INTERACTION APPROXIMATION

We noted in the section on Isotropic Turbulence Decay that the direct-interaction equations for isotropic turbulence failed to give the Kolmogorov $k^{-5/3}$ inertial-range spectrum, yielding instead a $k^{-3/2}$ spectrum. The trouble here can be traced back to a deep-lying cause: the use of Eulerian description. The principal idea behind Kolmogorov's theory is that eddies of large size convect eddies of

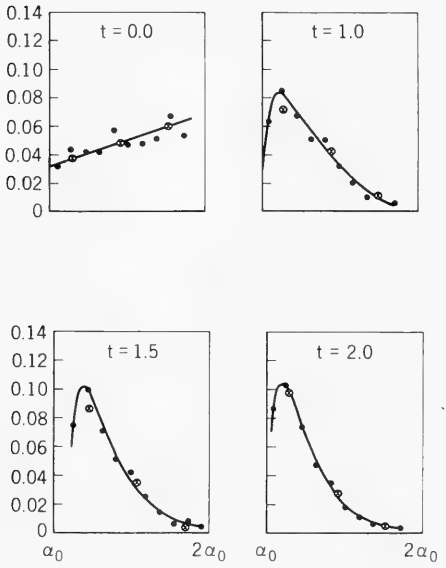

Fig. 13 - Comparison of direct-interaction and computer-experiment results for spectrum as a function of horizontal wave number for the case shown in Fig. 12. The dots are the numerical experiment; the crosses in circles, the direct-interaction approximation. The horizontal wave number plotted horizontally is the spectrum level vertically.

small size in a random fashion, but do not distort the small eddies appreciably. In the Fourier representation, this means that the excitation at wave numbers in the energy-containing range does not affect the dynamics of energy transfer at high wave numbers.

The direct-interaction approximation for energy transfer, as given by Eqs. (12) and (16), expresses the transfer as an integral over the past history of the fluid. The function $U(k; t', s)$ in Eq. (15) is an Eulerian time-correlation for wave number k. If the equations are Fourier-transformed back to physical space, the time integrals may be interpreted as tracing the velocity correlations back in time at fixed points in space. However, the Eulerian time correlations at high wave numbers (small spatial separations) are strongly affected by the distortionless random convection of small eddies by large eddies. $U(k; t, s)$ does not convey sufficient information to tell whether or not the decorrelation at high wave numbers is due to convection without energy transfer, or to the internal

distortion of the small eddies associated with energy transfer. This is why the direct-interaction approximation is inadequate in the inertial range. It confuses the two processes and makes the convection decorrelation time the effective decorrelation time for energy-transferring triple correlations built up by interactions among the inertial-range wave numbers [28].

In order to correct this situation, the direct-interaction equations have been modified so that the integral over the past history is taken along particle trajectories, instead of at fixed points in space. This transforms away the spurious effects of convection on energy transfer. The change requires an initial reformulation in terms of generalized Lagrangian velocities. The resulting equations, called the Lagrangian-History Direct-Interaction (LHDI) approximation, yield Kolmogorov's form of the inertial-range spectrum, and provide a unified dynamical description of both Eulerian and Lagrangian flow statistics [29].

A simplified formulation, called the abridged LHDI approximation, has been integrated numerically in considerable detail, yielding numerical predictions for Kolmogorov's constant, for the dissipation range spectrum of isotropic turbulence at high Reynolds numbers, and for a number of Lagrangian statistics [30]. At moderate Reynolds numbers, the abridged LHDI equations yield an isotropic turbulence decay which is similar to that obtained from the original direct-interaction approximation. Figures 9 and 10 illustrate the moderate-Reynolds-number comparison in the dissipation range, where the differences are largest.

Figures 14 and 15 compare the abridged LHDI predictions for inertial range and dissipation range at high Reynolds numbers with the measurements in sea water by Grant, Stewart, and Moilliet [16]. Here ϵ is the rate of dissipation by viscosity per unit mass, $k_s = (\epsilon/\nu^3)^{1/4}$ is the Kolmogorov dissipation wave number, and $\phi_1(k)$ is the one-dimensional energy spectrum. It should be noted that these comparisons are absolute in the sense that there are no adjustable scaling parameters in the abridged LHDI equations.

The LHDI and abridged LHDI approximations have also been applied to several other problems: relative dispersion of two particles by turbulence [31], spectrum of scalar fluctuations convected by turbulence [31,32], spectrum evolution of random solutions of Burgers' equation [20], turbulence in a Vlasov plasma [33], and second-order chemical reactions in a turbulent fluid [34]. In these varied applications, the LHDI equations have had substantial success in differentiating among qualitatively different kinds of dynamical behavior. Thus the same approximation which yields the Kolmogorov $k^{-5/3}$ law in isotropic incompressible turbulence, yields Richardson's law in two-particle dispersion [31], a $k^{-5/3}$ law for the inertial-convective spectrum range of a passive scalar [31], a k^{-2} inertial range for Burgers' equation [20], the k^{-1} viscous-convective-range law of Batchelor for the spectrum of a passive scalar at very high wave numbers [32], and a $k^{-3/2}$ inertial-range law for hydromagnetic turbulence [22,35]. However, where quantitative accuracy has been assessable in these applications, it appears mostly to be poorer than in the case of the Kolmogorov inertial and dissipation range for isotropic Navier-Stokes turbulence.

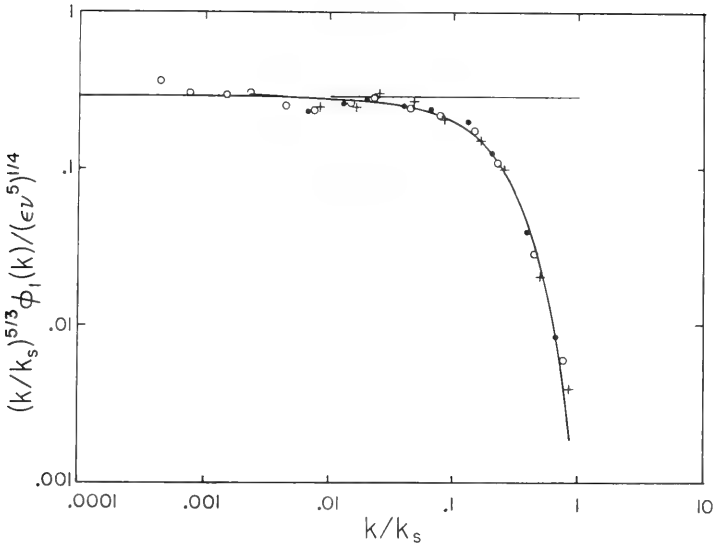

Fig. 14 - Logarithmic plot of the inertial and dissipation range spectrum from abridged LHDI approximation, compared with the data of Grant, Stewart, and Moilliet (Ref. 16)

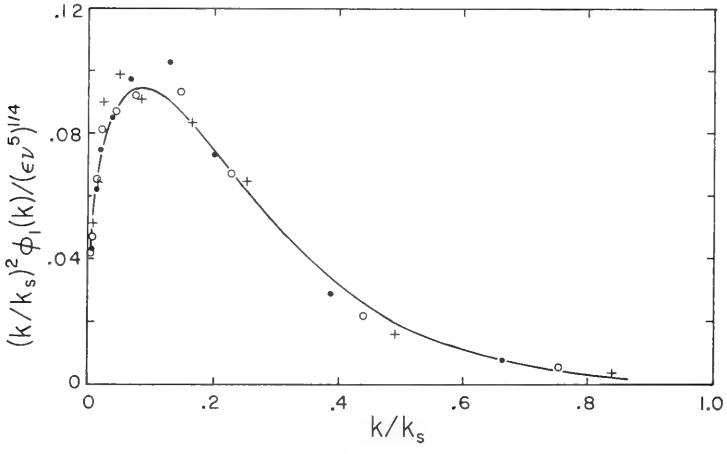

Fig. 15 - Linear plot of the data in Fig. 14

HIGHER APPROXIMATIONS AND ESTIMATION OF ERRORS

The comparisons with laboratory and computer experiments outlined above suggest that the direct-interaction family of statistical equations provide

reasonably satisfactory first approximations to a wide variety of turbulence phenomena, yielding qualitatively correct behavior, with quantitative errors of the order of 10% in favorable cases (e.g., the eddy diffusivity found in the section on Approximation for Turbulent Diffusion). Two questions arise at this point. Can the errors be bounded, or estimated, analytically, without recourse to experimental comparisons? Can a convergent sequence of higher approximations to desired statistical functions be constructed, with the direct-interaction as a base? Incomplete investigations, which we report briefly below, suggest that the answer to both questions is yes, with the qualification that the estimates and higher corrections may be difficult to extract and evaluate numerically.

In the section on Dynamical Equations for Statistical Quantities, it was stated that all known techniques for forming dynamical equations for the statistical functions lead to divergent, infinite series or sequences of some kind. In particular, there is a divergent series of integrals on the right-hand side of Eq. (3), the dynamical equation whose truncation yields the direct-interaction approximation for turbulent dispersion by a random velocity field. As an aid to understanding the nature of the divergence, its significance, and how to cope with it, we shall consider a simpler case of a divergent series. Suppose that $f(\lambda)$ is defined by the integral

$$f(\lambda) = \int_0^\infty \frac{e^{-a}\, da}{1 + a\lambda^2} . \tag{22}$$

If the integrand is expanded in a power series in λ, and the integration is performed, the result is

$$f(\lambda) = 1 - \lambda^2 + 2!\, \lambda^4 - 3!\, \lambda^6 + \ldots , \tag{23}$$

a strongly divergent series.

Although Eq. (23) is divergent, it is not meaningless. A power-series expansion of a function may be considered a kind of encoding. In the case of a convergent series, the decoding process can be simple summation. This no longer is possible for divergent series, but the code may nevertheless be unambiguously soluble, given some qualitative information about the function. In the case of Eq. (23), rapidly converging approximants to $f(\lambda)$ are yielded by the Padé table [36]. This is an array of functions, each the ratio of two polynomials, chosen so that, for polynomials of given orders in numerator and denominator, the power-series expansion of the approximating function reproduces as many coefficients of Eq. (23) as possible.

The Padé technique may be stated in a more intuitive form, which brings out better its broad significance. Suppose we know, or have reason to believe, that an unknown function $f(\lambda)$ has a representation of the form

$$f(\lambda) = \int_0^\infty \frac{\rho(a)\, da}{1 + a\lambda^2} . \tag{24}$$

The coefficients of the power-series expansion of $f(\lambda)$ are then the moments

$$\int_0^\infty \rho(a)\, a^n\, da\ .$$

The Padé table approximates the unknown $\rho(a)$ by a weighted sum of δ-functions, $\Sigma_i\, \rho_i\, (a - a_i)$, such that, as we go higher in the table, more and more moments are reproduced correctly [36]. Expansion of a function in δ-functions is a special case of expansion in a complete set of orthogonal functions, and Eq. (24) is a special case of an integral representation of the form

$$f(\lambda) = \int_0^\infty \rho(a)\, g(a\lambda^2)\, da\ ,$$

where $g(a\lambda^2)$ has a power-series expansion. Thus a number of generalizations of the Padé approximants are possible.

If ρ in Eq. (24) is nonnegative, a case which includes Eq. (22), then the approximants on the diagonal of the Padé table yield successively improving upper bounds on $f(\lambda)$, while a set of approximants off the diagonal yield successively improving lower bounds. It should be noted that the approximation to $f(\lambda)$, obtained by substituting a sum of δ-functions for $\rho(a)$, is a smooth function.

The technique of Padé approximation, and its generalizations, can be applied formally to the infinite expansions of turbulence theory by regarding the latter as a power series in a parameter. In the case of perturbation expansion of turbulence functions about purely viscous decay values, the ordering parameter is the Reynolds number. In the case of Eq. (3), we can form the power series by multiplying the successively higher terms on the right-hand side by powers of λ^2, and, at the end, taking $\lambda = 1$. Here λ is a formal ordering parameter without immediate significance.

To justify such manipulations, we must establish that appropriate forms of integral representation exist for the functions of interest. Only a start at this has been made at the time of writing. The plausibility of representations like Eq. (24) perhaps is enhanced by the nature of turbulence functions as averages over an ensemble of realizations, with ρ playing the role of probability distribution for an actual or effective parameter. Then large values of "a" would correspond to contributions from the fringes of the probability distribution, which have little effect on the final values of the functions of interest but which affect strongly the higher terms in the divergent power series.

The Padé technique, and some generalizations, has been tried out with apparent success on several turbulence problems, including a detailed application to Eq. (10) [37]. The theory of successive approximations for the Laplace transform of $G(k, t)$ has been worked out fully in the limit of high k, and the Padé approximants have been shown to yield bounds on errors, as well as improving approximations in this limit. The theory is in less complete shape for general k, but comparison with the computer experiments show that improvement over the direct-interaction results is obtained at all k, with a reduction of about 50% in

the error of the prediction for the long-time eddy-diffusivity $\kappa(\infty)$ coming in the first diagonal Padé approximation. Extension of the Padé technique to isotropic turbulence dynamics and turbulent flow in pipes and channels is underway. The outlook is favorable, but with insufficient work done to make any definite statements.

NUMERICAL INTEGRATION OF THE DIRECT-INTERACTION EQUATIONS

We noted earlier that although statistical equations like the direct-interaction equations are much more complicated than the original Navier-Stokes equation, they can be less troublesome to solve numerically, because the solutions of the statistical equations, being averages, are smoother and more stable than the velocity fields of individual flow realizations.

To illustrate, consider the isotropic turbulence decay discussed in the section on Isotropic Turbulence Decay. Recent numerical techniques, using the Cooley-Tukey fast Fourier transform, make it possible to integrate a flow represented by $32 \times 32 \times 32$ Fourier modes (i.e., 32 values for each component of wave vector), by direct solution of the Navier-Stokes equation in a computation time of about one minute per time step on an IBM 390/95 computer [1]. This is sufficient Fourier resolution to describe fairly well the energy-containing and dissipation-range wave numbers in isotropic turbulence decay at $R_\lambda \sim 20$. In order to follow the evolution for a time equivalent to the evolution times of the direct-interaction solutions of section of this paper just mentioned, the order of 100 time steps would be needed, giving a total computation time per realization of the order of an hour. An ensemble of perhaps 10 members would probably give acceptable statistics at the higher wave numbers where the number of similar modes is large.

In contrast, the direct-interaction solutions illustrated in the above-mentioned section require less than a minute per run on the same computer. This time is based on a numerical scheme for the direct-interaction equations which involves logarithmic steps in wave number and linear steps in time [12]. The favorable properties of the statistical functions are exploited several ways in this scheme. First, the spatial symmetries, homogeneity and isotropy, have already been used in writing Eqs. (12) - (16), since the unknown functions are scalar functions of scalar wave number. The use of logarithmic steps in wave number (about 20 to cover the entire k range) is possible because of the smooth dependence of $U(k; t, t')$ and $G(k; t, t')$ on k. Finally, a time step about five times larger than permissible for the straight computer simulation is permissible because of the high stability of the direct-interaction equations.

It should be noted that the isotropy and homogeneity properties are no help in the computer experiment, except possibly in reducing the number of realizations needed to get good statistics. It still is necessary to follow the complex vector amplitude of each of the $32 \times 32 \times 32$ Fourier modes. On the other hand, if no use of symmetry and smoothness had been made in integrating the direct-interaction equations, the machine time for the latter would have been staggering. In this case, a tensor function of two vector arguments, of the form

$U_{ij}(k, k', t, t')$ would replace $U(k; t, t')$. If the direct-interaction equations were then integrated using point-to-point integration on the $32 \times 32 \times 32$ grid, and the same time step as for the computer experiment, the number of multiplications required would be billions of times greater than for integration of the Navier-Stokes equation for a realization.

The saving in computation time over direct simulation offered by the direct-interaction equations rises with Reynolds number. Consider a steady-state turbulent flow. Here logarithmic steps in both wave number and frequency can be used with the direct-interaction equations, with the result that computation time rises only as the logarithm of Reynolds number. With direct simulation, on the other hand, the number of Fourier modes must go up as the cube of ratio-of-dissipation wave number to energy-containing wave number, while the permissible time step gets smaller.

Further marked reductions in the integration time for the direct-interaction equations can be achieved through the use of more economical representations of the statistical functions than by (linear or nonlinear) grids in k. The integrations illustrated in the section on Isotropic Turbulence Decay used about twenty logarithmic steps in k. However, the resulting functions are so smooth that they could be represented adequately by two or three coefficients in an aptly chosen representation by orthogonal functions (e.g., Laguerre functions). Savings of this kind become of increasing value in nonisotropic problems, such as turbulent flow in a pipe, where the loss of symmetry raises the dimensionality of the final statistical equations.

Increased dimensionality also makes the Monte-Carlo evaluation of multiple integrals attractive for reducing computation time. The use of Monte-Carlo methods was what made feasible the evaluation of the higher-order corrections to the direct-interaction dispersion equations, discussed in the previous section. The use of representation by well-chosen orthogonal functions, coupled with Monte-Carlo evaluation of integrals, makes integration of the direct-interaction equations for simple shear flows [38], such as a flow in an infinite pipe or channel, appear practicable with presently available computers. Work toward this end is in progress.

The use of Monte-Carlo methods for evaluating the statistical equations is of theoretical as well as of practical interest, and leads to a point of view in which direct simulation and representation by statistical approximation appear as intimately related complements. Let us again take isotropic turbulence as an example. Suppose an initial spectrum is prescribed, with initial, multivariate, Gaussian statistical distribution. Suppose first that the initial R_λ is low enough that only a few modes need be retained in the computer simulation. Integration time per realization is then small, and solution for a sizable ensemble of realizations is feasible. For $R_\lambda \sim 40$, however, the order of 10^5 to 10^6 Fourier modes must be retained, and the computation task becomes onerous. Apart from the cost of computer time, the direct simulation seems fundamentally inefficient at this stage. Most of the effort goes into handling the large number of high k modes, whose behavior is statistically redundant. We would like to handle only a few of these modes, which then would typify the others. This is not possible with direct simulation. If a sizable fraction of the high k modes are

simply omitted from the dynamical equations, statistical weights are altered, and the faithfulness of the solution destroyed. Moreover, there is no way to interpolate between selected high k modes, because of the jagged variation of amplitude from mode to mode, which, although unpredictable, incorporates elaborate dynamically created statistical correlations.

Suppose, on the other hand, we deal with statistical equations: the direct-interaction approximation and a sequence of (presumed valid) higher approximations built upon it after the fashion of that described in the previous section. Here the smoothness of the statistical functions does permit interpolation at high wave numbers. If these equations are solved by Monte-Carlo evaluation of multiple k-space integrals, we are, in effect, sampling just a few of the high k modes, and interpolating — which is what we wanted to do and could not with the computer simulation. If only the direct-interaction equations, without higher corrections, are solved, a semiquantitative solution (errors in spectrum on the order of 10% - 20%) emerges with great computational economy. As higher corrections are admitted, a more accurate solution is obtained (if the proposals of the previous section are valid), at the expense of evaluating more elaborate multiple k-space integrals. This means that the Monte-Carlo sampling involves longer sample chains of interacting Fourier modes.

If a prediction of only the energy spectrum is desired, the sequence of statistical approximations appears to offer greater economy at moderate Reynolds numbers. Suppose, however, that a more elaborate statistical function were desired — say, the joint-probability distribution of the velocity at three points, or the flatness factor of some probability distribution. A formulation of the statistical equations to yield such functions with acceptable accuracy could be expected to be very elaborate and to require, ultimately, the sampling of very long chains of interacting Fourier modes in very complicated equations. Here it would likely be more economical to work with direct simulation, where all sets of Fourier-mode interactions are explicitly calculated from the outset.

ACKNOWLEDGMENT

This work was supported by the Office of Naval Research under Contract N00014-67-C-0284. I am grateful to Dr. J. R. Herring for permission to reproduce Figs. 12 and 13.

REFERENCES

1. Orszag, S.A., "Numerical Methods for the Simulation of Turbulence," Proc. Int. Symp. on High-Speed Computing in Fluid Dynamics, Monterey, California, 1968

2. Kraichnan, R.H., "Invariance Principles and Approximation in Turbulence Dynamics," *in* Dynamics of Fluids and Plasmas, ed. S.I. Pai, New York: Academic Press, 1966

3. Kraichnan, R.H., "The Closure Problem of Turbulence Theory," Proc. Symp. Appl. Math. **13**, 199 (1962)

4. Hopf, E., "Statistical Hydromechanics and Functional Calculus," J. Rational Mech. Anal. **1**, 87 (1952)

5. Lewis, R.M., and Kraichnan, R.H., "A Space-Time Functional Formalism for Turbulence," Comm. Pure and Appl. Math. **15**, 397 (1962)

6. Roberts, P.H., "Analytical Theory of Turbulent Diffusion," J. Fluid Mech. **11**, 257 (1961)

7. Kraichnan, R.H., "Dynamics of Nonlinear Stochastic Systems," J. Math. Phys. **2**, 124 (1961)

8. Kraichnan, R.H., "Small-Scale Structure of a Scalar Field Convected by Turbulence," Phys. Fluids **11**, 945 (1968)

9. Batchelor, G.K., "The Effect of Homogeneous Turbulence on Material Lines and Surfaces," Proc. Roy. Soc. (London) Ser. A, **213**, 349 (1952)

10. Batchelor, G.K., "The Theory of Homogeneous Turbulence, Cambridge University Press, 1953

11. Kraichnan, R.H., submitted to Phys. Fluids

12. Kraichnan, R.H., "Decay of Isotropic Turbulence in the Direct-Interaction Approximation," Phys. Fluids **7**, 1030 (1964)

13. Kraichnan, R.H., "A Theory of Turbulence Dynamics," in "Second Symposium on Naval Hydrodynamics: Hydrodynamic Noise and Cavity Flow," Office of Naval Research, Department of the Navy, ACR-38, 1958

14. Kraichnan, R.H., "The Structure of Isotropic Turbulence at Very High Reynolds Numbers," J. Fluid Mech. **5**, 497 (1959)

15. Stewart, R.W., and Townsend, A.A., "Similarity and Self-Preservation in Isotropic Turbulence," Phil. Trans. Roy. Soc. London, Ser. A, **243**, 359 (1951)

16. Grant, H.L., Stewart, R.W., and Moilliet, A., "Turbulence Spectra from a Tidal Channel," J. Fluid Mech. **12**, 241 (1962)

17. Kraichnan, R.H., "Direct-Interaction Approximation for a System of Several Interacting Simple Shear Waves," Phys. Fluids **6**, 1603 (1963)

18. Lee, J., "Decay of Scalar Quantity Fluctuations in a Stationary, Isotropic, Turbulent Velocity Field," Phys. Fluids **8**, 1647 (1965)

19. Lee, J., "Comparison of Closure Approximation Theories in Turbulent Mixing," Phys. Fluids **9**, 363 (1966)

20. Kraichnan, R.H., "Lagrangian-History Statistical Theory for Burgers' Equation," Phys. Fluids **11**, 265 (1968)

21. Kraichnan, R.H., "Irreversible Statistical Mechanics of Incompressible Hydromagnetic Turbulence," Phys. Rev. **109**, 1407 (1958)

22. Kraichnan, R.H., "Inertial-Range Spectrum of Hydromagnetic Turbulence," Phys. Fluids **8**, 1385 (1965)

23. Orszag, S., and Kraichnan, R., "Model Equations for Strong Turbulence in a Vlasov Plasma," Phys. Fluids **10**, 1720 (1967)

24. Herring, J.R., "The Statistical Theory of Thermal Convection at Large Prandtl Number," Phys. Fluids (to be published)

25. O'Brien, E.E., "Closure Approximations Applied to Stochastically Distributed Second-Order Reactants," Phys. Fluids **9**, 1561 (1966)

26. Lee, J., "Isotropic Turbulent Mixing under a Second-Order Chemical Reaction," Phys. Fluids **9**, 1753 (1966)

27. O'Brien, E.E., "Quantitative Test of the Direct-Interaction Hypothesis," Phys. Fluids **11**, 2087 (1968)

28. Kraichnan, R.H., "Kolmogorov's Hypotheses and Eulerian Turbulence Theory," Phys. Fluids **7**, 1723 (1964)

29. Kraichnan, R.H., "Lagrangian-History Closure Approximation for Turbulence," Phys. Fluids **8**, 575 (1965)

30. Kraichnan, R.H., "Isotropic Turbulence and Inertial-Range Structure," Phys. Fluids **9**, 1728 (1966)

31. Kraichnan, R.H., "Dispersion of Particle Pairs in Homogeneous Turbulence," Phys. Fluids **9**, 1937 (1966)

32. Kraichnan, R.H., "Small-Scale Structure of a Scalar Field Convected by Turbulence," Phys. Fluids **11**, 945 (1968)

33. Orszag, S.A., "Theory of Strong Plasma Turbulence," Proc. Symp. on Turbulence of Fluids and Plasmas, New York, April 1968

34. O'Brien, E.E., "Lagrangian-History Direct-Interaction Approximation for Isotropic Turbulent Mixing under a Second-Order Chemical Reaction," Phys. Fluids **11**, 2328 (1968)

35. Kraichnan, R.H., and Nagarajan, S., "Growth of Turbulent Magnetic Fields," Phys. Fluids **10**, 859 (1967)

36. Baker, G.A., "The Theory and Application of the Padé Approximant Method," Advan. Theoret. Phys. **1**, 1 (1965)

37. Kraichnan, R.H., "Convergents to Infinite Series in Turbulence Theory," Phys. Rev. 174, 240 (1968)

38. Kraichnan, R.H., "Direct-Interaction Approximation for Shear and Thermally Driven Turbulence," Phys. Fluids 7, 1048 (1964)

* * *

STRIP THEORY AND POWER SPECTRAL DENSITY FUNCTION APPLICATION TO THE STUDY OF SHIP GEOMETRY AND WEIGHT DISTRIBUTION INFLUENCE ON WAVE BENDING MOMENT

Sergio Marsich
Genoa University
Genoa, Italy

and

Franco Merega
Registro Italiano Navale
Genoa, Italy

FOREWORD

In this paper, research is described which was carried out by means of a large electronic computer with the aim of detecting which parameters affect the wave bending moment of a ship and thereafter to evaluate their quantitative influence.

The present research may have some importance especially for ships as bulk-carriers and tankers for which there is actually a trend to larger and larger sizes and for which the influence of certain parameters, weight distribution, for instance, may be of paramount importance from the point of view of the longitudinal strength in confused sea. For this reason the choice of the types of hulls and weight distributions adopted for this study was oriented to such kinds of ships.

The work is based upon the theory of Korvin-Kroukovsky (KK) and the absolute values obtained for bending moment are obviously comprised between the accuracy limits of the above theory, which can be deemed sufficient in most of practical cases. However, at least from a qualitative point of view, the parameter identification remains valid, as well as the exclusion of the influence of other parameters, that have also been taken into consideration.

The results of the work are reported in the first part, while in the second the procedure adopted and the justification of the assumptions made are given in detail.

In the third part the formulas are given in the form used for the calculation, slightly modified in respect to the original ones of KK with the purpose of simplifying the numerical evaluation of certain quantities.

The complete program is also reported, worked out in FORTRAN 2, together with the input data formats and the output tables.

Note that the application of a known hydrodynamic theory has permitted finding a solution of practical utility of one of the most serious problems related to the study of ship's strength, leading to results given in general form, which it otherwise, given the present state of knowledge, would not have been possible to achieve.

1. DETERMINATION OF WAVE BENDING MOMENT

1.1 Parameters Affecting the Phenomenon

As is known, the wave bending moment is essentially due to:

(a) local hydrostatic pressure variations produced by:

  (1) height of wave profile in way of each hull transverse section;

  (2) vertical shift of each section owing to pitching and heaving motions;

(b) inertial forces variable from time to time and from section to section;

(c) hydrodynamic forces variable as well during the time and along the hull and which can be divided as follows:

  (1) exciting forces due to the vertical velocity of water particles;

  (2) forces due to the vertical velocity of hull sections;

  (3) exciting forces due to modifications induced by the hull presence on the velocity potential.

In the static method of wave bending moment calculation, according to which the hull is considered in balance on a wave, only the factors listed under (a) are taken into consideration, and therefore the calculation is referred to a position where the rotation due to pitching is zero.

Methods deriving from Froude-Krilov hypotheses lead one to neglect the factors listed in (2) and (3) of (c) above and therefore not to take properly into account the hydrodynamic influence.

According to the KK method instead (as well as those of Haskind and Watanabe) all listed factors are taken into account, and therefore such a method may be considered adequate for practical purpose.

Many authors have compared theoretical results based on KK theory with the experimental data and have achieved in every case an acceptable agreement. For this reason, it has been deemed acceptable to adopt the KK method as a basis for this study, assuming that the results obtained from its application be satisfactorily in accordance with the real behavior, and the influence of the different parameters has been investigated, systematically applying this method.

As is known, the KK method allows one to know at any time, and for whatever station along the hull, the value of the wave bending moment when the ship is sailing at constant speed in regular waves. Therefore solving the equation that provides the bending moment values in regular waves corresponding to different stations along the hull at different times, the envelope of the peak values along the hull could be determined and the peak value of the envelope curve then selected.

The bending moment value that would be obtained in this way, however, is not the most dangerous obtainable, even though, as a basis for the calculation, the regular wave of the highest value that the ship may encounter during its life is assumed with an acceptable probability. It can easily be demonstrated, in fact, with energetic considerations, that the most probable peak value of the bending moment that can be obtained as a response to a confused sea spectrum is, as absolute value, greater than the peak value that can be obtained in regular waves.

Therefore in this study the most probable peak value of the bending moment over 10^4 cycles has been taken into account, when the ship is sailing against a long-crested confused sea induced by a 60-knot wind, choosing for any ship the transverse section where the bending moment also reaches its peak value along the hull.

The main parameters that may affect the bending moment are: length, breadth, draft, speed, weight distribution along the hull, hull volumes distribution along the hull, waterline shape, and sea spectrum.

While the first four parameters are uniquely determined, for the rest it was necessary to carry out preliminary investigation with the aim of detecting which quantities are suitable for providing a quantitative as well as qualitative definition of the exposed concepts.

To the purpose of characterizing the *weight distribution*, different parameters have been considered (for instance, area, moment of inertia, and abscissa of the center of gravity of the weight curve, adequately reduced to certain formulas).

After some investigation, (see Sec. 2.4), a strict correlation was discovered between the wave bending moment and the quantity

$$p = 2 \frac{D_{AV} X_{AV} + D_{AD} X_{AD}}{DL},$$

where

D = displacement,

D_{AV} = displacement portion lying forward of ship's center of gravity,

D_{AD} = displacement portion lying aft of ship's center of gravity,

X_{AV} = distance between ship's center of gravity and D_{AV}'s center of gravity,

X_{AD} = distance between ship's center of gravity and D_{AD}'s center of gravity,

L = waterline length.

Thereafter, the quantity p has been assumed as representing the weight distribution along the hull.

When considering the *hull volume distribution* and the *waterline shape*, the following factors were to be assessed:

(a) the independent effect of the two parameters, each separately considered, and

(b) the reciprocal influence of the two parameters.

Some systematic calculations have been carried out, assuming the same hull volume, first maintaining the same waterline shape and systematically modifying the area curve, then maintaining the same area curve and modifying the waterline shape. It has been found that the wave bending moment is much more affected by waterline shape modifications than by area curve, in agreement with what had been clearly stated by Swaan (see Sec. 2.2).

Therefore, the waterline coefficient has been kept as only significant parameter and as a matter of fact the consequent errors are even more negligible than could be expected at first, owing to the fact that generally a certain correspondence exists between block coefficient and waterline fineness coefficient, it being extremely unlikely that full ships have low-fineness waterlines or that fine ships have full waterlines.

When considering *sea spectrum* it was decided to adopt Scott's formula, which allows one to write the equation as a function of frequency, when wind speed is known. In Table 1 the above formula is reported, together with the expressions for significant height, peak frequency, and mean wave period. Figure 1 shows spectra corresponding to wind speeds of 20, 40, and 60 knots, while in Fig. 2 diagrams are drawn of significant height, peak frequency, and mean wave period, as a function of wind speed.

Table 1
Scott's Formula (See text)

$$F(\omega_o) = 0.214 H^2 e^{-\left[\frac{(\omega_o-\omega_p)^2}{0.065(\omega_o-\omega_p+0.26)}\right]^{1/2}} \qquad \omega_{min} < \omega_o < \omega_{max}$$

$$F(\omega_o) = 0 \qquad \text{otherwise}$$

F = Power spectral density function (m^2/sec)	g = Gravity acceleration (m/sec^2)
ω_o = Frequency (1/sec)	$H = 0.25W - 1.77$
H = Significant wave height (m)	$\omega_p = \frac{3.15}{T_v} + \frac{8.98}{T_v^2} = \frac{1}{0.0984H + 1.35}$
ω_p = Peak frequency (1/sec)	$\omega_{min} = \omega_p - 0.26$
λ^* = Maximum energy wavelength (m)	$\omega_{max} = \omega_p + 1.65$
T_v = Mean wave period (sec)	$\lambda^* = \frac{2\pi g}{\omega_p^2}$
W = Wind speed (knots)	

W	H	T_v	ω_p	ω_{min}	ω_{max}
10	0.73	6.45	0.703	0.443	2.353
15	1.98	6.88	0.647	0.387	2.297
20	3.23	7.30	0.600	0.340	2.250
25	4.48	7.72	0.558	0.298	2.208
30	5.73	8.14	0.522	0.262	2.172
35	6.98	8.55	0.491	0.231	2.141
40	8.23	8.96	0.463	0.203	2.113
45	9.48	9.37	0.438	0.178	2.088
50	10.73	9.78	0.416	0.156	2.066
55	11.98	10.19	0.395	0.135	2.045
60	13.23	10.60	0.377	0.117	2.027
65	14.48	11.00	0.360	0.100	2.010
70	15.73	11.40	0.345	0.085	1.995

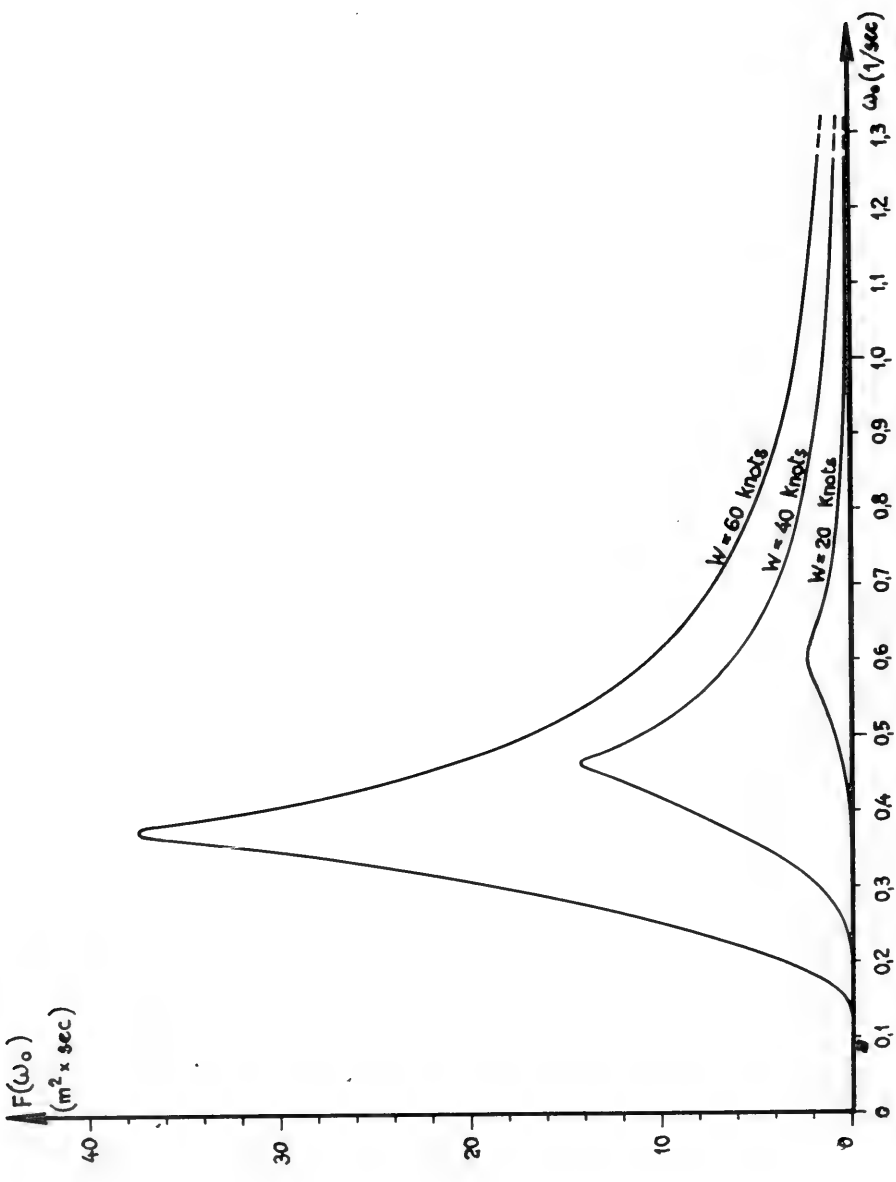

Fig. 1 - Sea Spectra

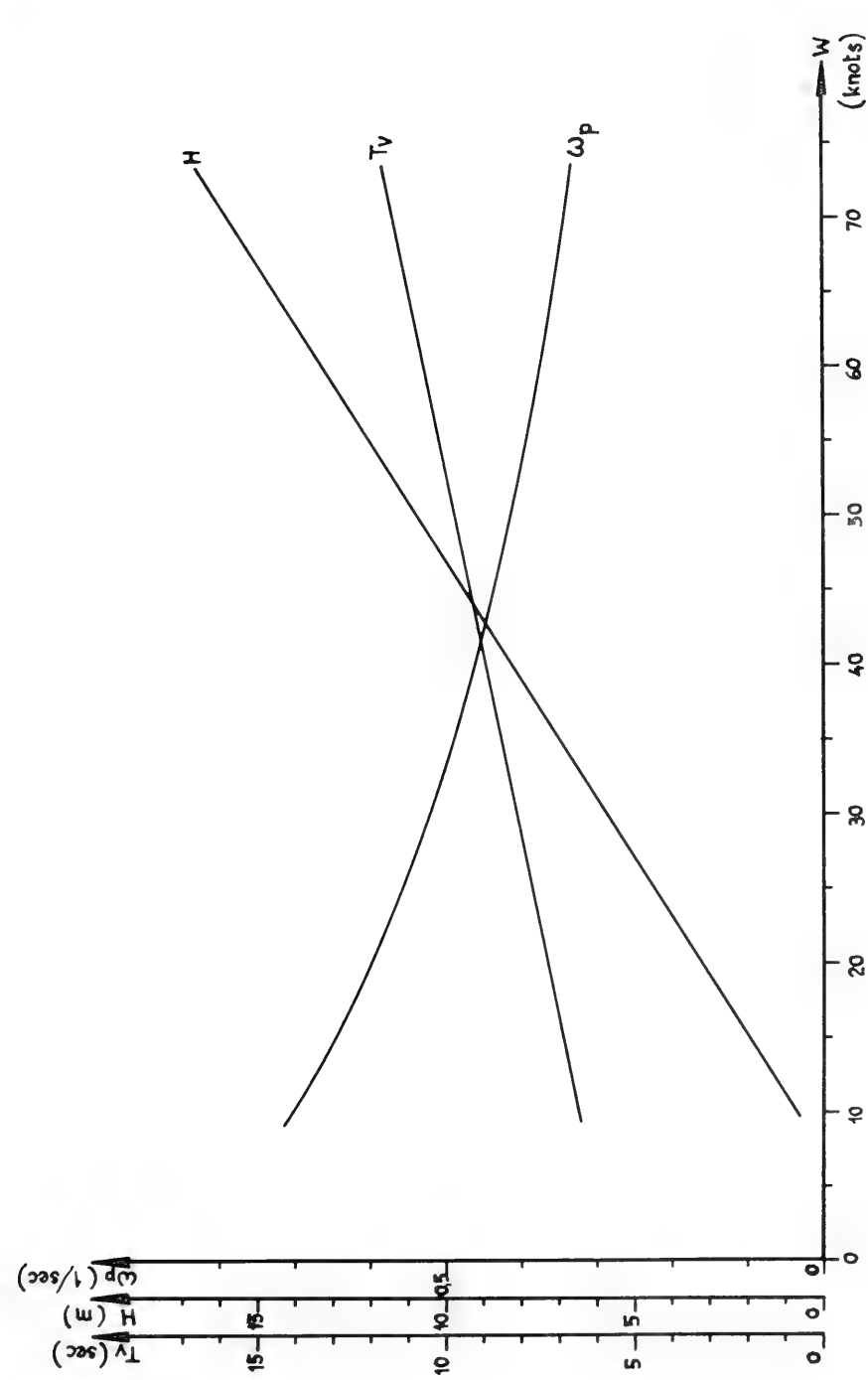

Fig. 2 - Significant height, peak frequency, and mean wave period as a function of wind speed

1.2 Parameters Selected as Characteristic

As a result of what has been stated in the preceding paragraphs, the following nondimensional parameters were selected as fundamental for describing the phenomenon under investigation:

Wave bending moment $c_m = \frac{M}{\rho g B L^3}$

Ship's breadth $\frac{L}{B}$

Draft $\frac{L}{i}$

Ship's speed $Fr = v/\sqrt{Lg}$ (Froude number)

Weights distribution $p = 2\frac{D_{AV}\, X_{AV} + D_{AD}\, X_{AD}}{DL}$

Hull volumes distribution and waterline shape $C_w = \frac{A}{LB}$

Ship's length $R = \frac{L}{\lambda^*}$

where, in addition to symbols already defined in Sec. 1.1,

M = wave bending moment (t × m),

B = ship's breadth (m),

i = mean draft (m),

A = waterline surface (m^2),

ρ = seawater density ($t \times sec^2/m^4$).

To the purpose of systematically analyzing the influence on wave bending moment of all these parameters, first the response operators were obtained for 1008 combinations of the following values:

4 values of L/B	7.00	7.25	7.50	7.75			
7 values of L/i	16.00	17.50	19.00	23.75	28.50	30.00	31.50
3 values of Fr	0.0	0.05	0.10				
4 values of C_w	0.804	0.836	0.872	0.900			
3 values of ρ	0.345	0.404	0.448				

A first investigation was carried out calculating the response corresponding to a sea spectrum relevant to a wind speed of 60 knots for a ship 200 meters in length (see tables in Appendix).

Subsequently, the result analysis allowed one to reduce the operators number:

(a) reducing to one the number of L/B values, because this parameter does not practically affect the phenomenon;

(b) reducing to three the number of L/i values, the influence of which can be notwithstanding easily studied; and

(c) reducing to two the number of p values, which affects the phenomenon according to an approximately linear law (see Sec. 2.4).

As a consequence, the combination of the following parameters values have been finally investigated:

1 value of L/B 7.00

3 values of L/i 17.50 23.75 30.00

3 values of Fr 0.00 0.05 0.10

4 values of C_w 0.804 0.836 0.872 0.900

2 values of p 0.345 0.448

Finally, the response spectra were calculated corresponding to spectra relevant to wind speeds of 45, 50, 55, and 60 knots for ship's lengths of 180, 200, 220, 240, 260, 280, 300, 320, and 340 m. Each of these 36 cases can be identified by means of a value of the ratio L/λ^* given in Table 2.

Table 2
L/λ^* Values

Wind speed (kn)		45	50	55	60
Peak wave length (m)		321	357	394	433
Ship lengths (m)	180	0.560	0.504	0.457	0.415
	200	0.623	0.561	0.507	0.462
	220	0.685	0.617	0.558	0.508
	240	0.747	0.673	0.609	0.554
	260	0.809	0.729	0.660	0.600
	280	0.872	0.785	0.710	0.646
	300	0.934	0.841	0.761	0.692
	320	0.996	0.897	0.812	0.738
	340	1.058	0.953	0.862	0.784

In short: In the first investigation 1008 cases were examined, studying the influence of the different parameters on a ship of 200 m in length, assuming a spectrum corresponding to 60 kn; in the subsequent investigation the influence

was studied of the same parameters, assuming however several sea spectra and several ship's lengths, so considering altogether 2592 cases (72 of which already considered during the preceding investigation).

Obviously the response operators have been calculated only once, and the influence of sea spectrum and ship's length have been obtained by means of a simple integration (see Sec. 2.5).

1.3 Results of Systematic Calculations

Results of systematic calculations are partially reported in tables contained in the attached appendix and in Figs. 3 through 6.

The result analysis leads to the following general conclusions for the types of ships and conditions investigated:

(a) bending moment coefficient c_m does not depend appreciably upon ship's breadth; i.e., the wave bending moment is a linear function of ship's breadth;

(b) C_w, L/i and Fr being the same, c_m is a linear function of p;

(c) the slope of the straight line $c_m = f(p)$ is mainly and substantially affected by L/i and Fr, while variations of the parameter C_w only produce parallel shifting of the same straight line;

(d) although c_m is not a linear function of C_w, for values $0.80 \leq C_w \leq 0.90$ it may be approximately assumed that the variation remains linear, provided that p, L/i, and Fr are kept constant. This may be accepted owing to the flex point corresponding to $C_w = 0.85$ shown by all curves;

(e) the function $c_m = f(C_w)$ is therefore practically a straight line, the slope of which depends only upon L/i, while variations of Fr and p produce parallel shiftings of the same line;

(f) c_m increases for increasing values of L/i, according to a law very close to a hyperbole, so that c_m is substantially a linear function of the ratio i/L;

(g) when increasing Fr, keeping C_w constant, c_m increases for low p values and decreases for high p values.

As far as sea spectrum and ship's length influence is concerned, it was discovered that the bending moment coefficient depends only upon the ratio $R = L/\lambda^*$ and not separately and independently upon sea spectrum and ship's length (see Sec. 2.5).

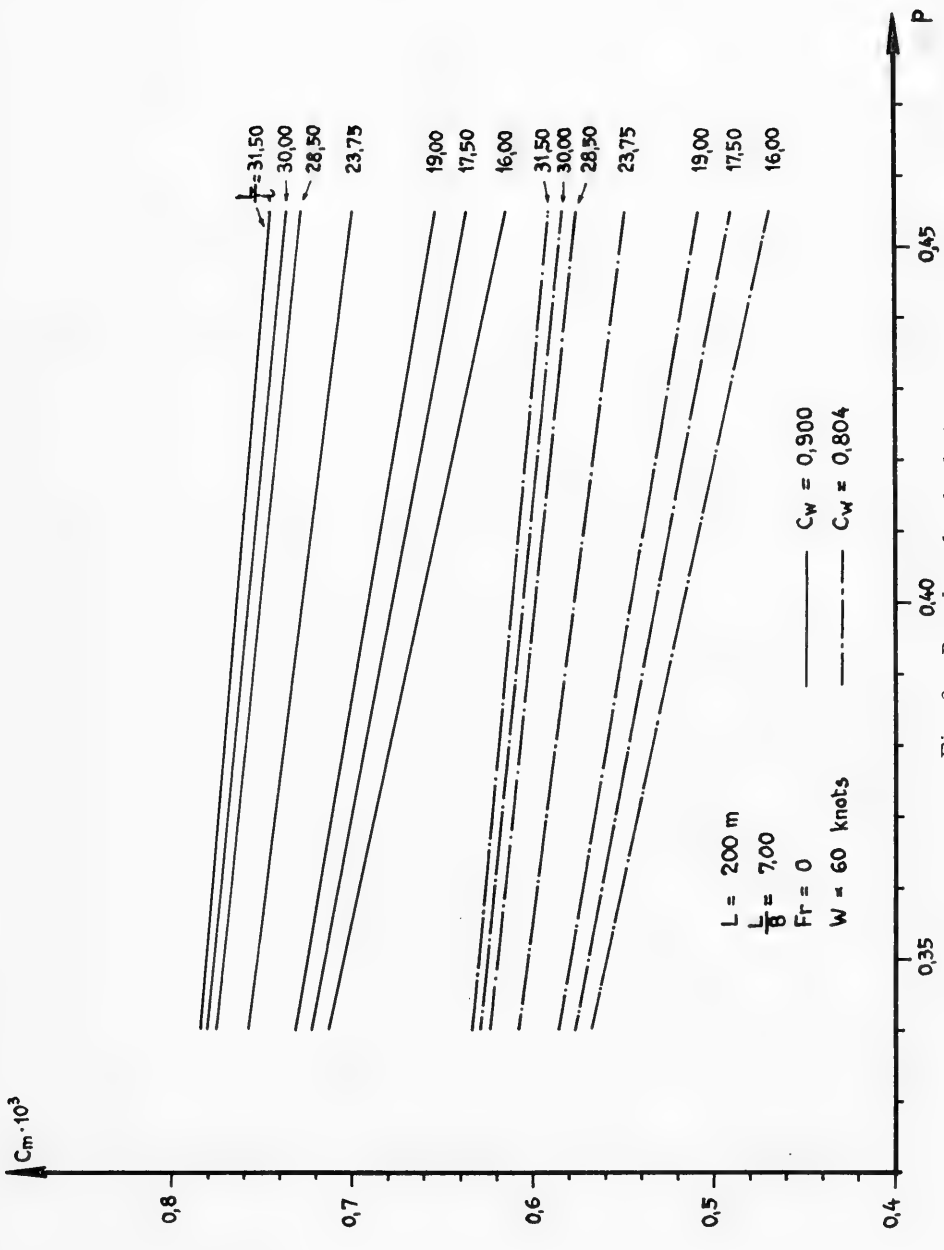

Fig. 3 - Results of calculations

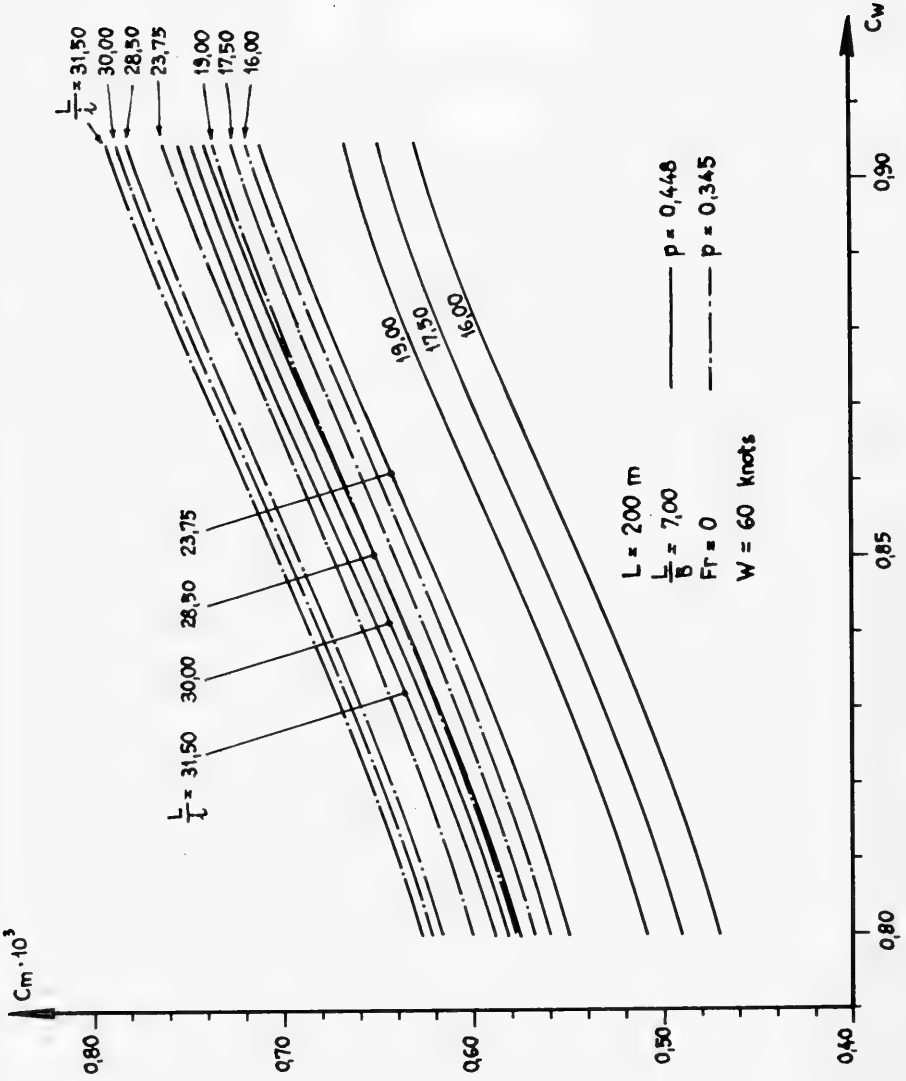

Fig. 4 - Results of calculations

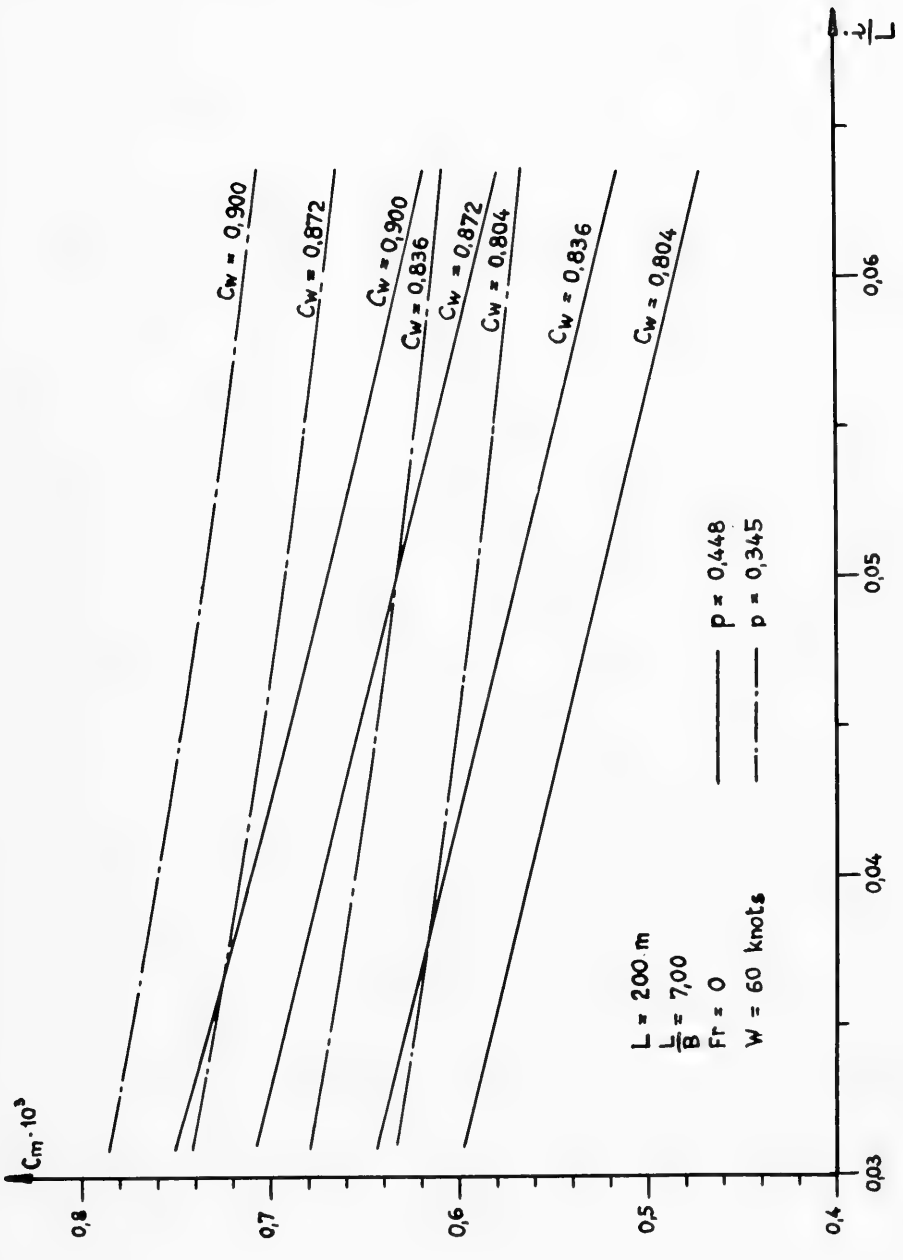

Fig. 5 - Results of calculations

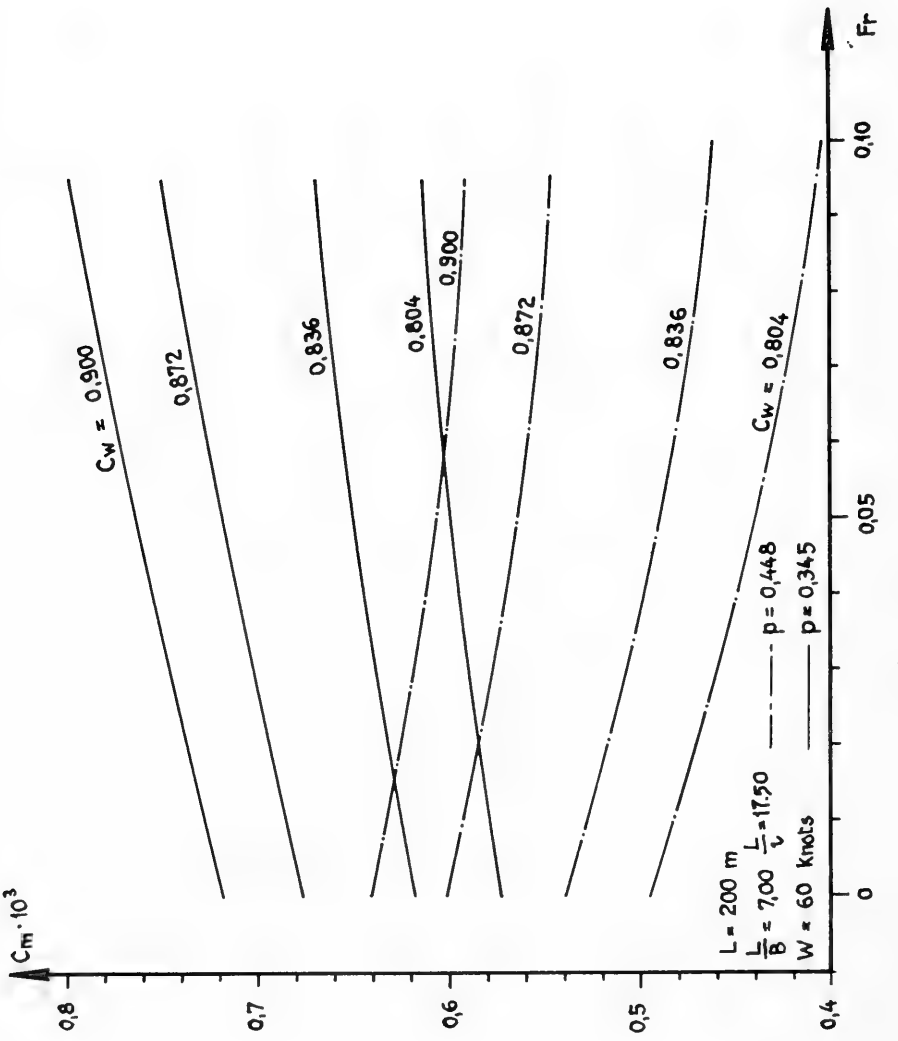

Fig. 6 - Results of calculations

1.4 Formula for Determining the Wave Bending Moment

From the analysis of the total set of results, a formula was produced which seems to cover all possible cases:

$$c_m = 10^{-3}\left[(3.38 + 11.20\,\bar{\lambda})\,C_w + (1.94 - 71.63\,\bar{\lambda} - 21.38\,Fr)\,p - (1.91 - 12.45\,\bar{\lambda} - 8.15\,Fr)\right]\frac{1 - 0.3\,R}{1 + 2\,R},$$

where $\bar{\lambda} = {}^{i}/_{L}$.

Hence, the wave bending moment can be immediately deduced as

$$M = c_m \times \rho\, g\, BL^3 .$$

By a comparison between the values given by the above formula and those calculated, it can be noted that the differences distribution follows with sufficient accuracy the Gauss law, with a mean value equal to zero and variance $\sigma^2 \sim 1.5$. The error probability is given by Table 3.

Table 3
Error Probability

Error	Probability
±1.5%	68.3%
±3.0%	95.4%
±4.5%	99.7%

Consequently, it would seem entirely justified to use, in any actual case of maximum wave bending moment calculations, the values provided by the above formula in lieu of those obtained according to the KK method; it is not, in fact, expected that the difference between the values obtained according to the KK method and the real values on the actual ship may be restricted within limits more narrow than those above. It is however, to be well kept in mind that the validity limits of the formula lie within the field of the values selected for the systematic calculation, particularly as far as Froude number and sea state are concerned.

The preceding formula can be written in the form:

$$c_m = K_1\, K_2 \times 10^{-3} ,$$

where

$$K_1 = f\,(\bar{\lambda},\ C_w,\ Fr,\ p)$$

and

$$K_2 = f(R) .$$

Figures 7 and 8 show the curves having K_1 = constant, while in Fig. 9 the curve $K_2 = f(R)$ is drawn.

These diagrams may be utilized for determining c_m by means of simple linear interpolations, avoiding the numerical evaluation of the above formula, and we hope they may be of some help to the ship designer.

1.5 Examples of Formula Application to Existing Ships

As an example the comparison between the results from the above formula and from a direct calculation according to the KK method is given in Table 4 for nine ships having typical characteristics of oil tankers and bulk carriers.

The differences found for these ships are representative of a large set of ships calculated to check the validity of the formula.

Table 4
Comparison of Formula and KK Method (v = 60 knots; Fr = 0.05)

Case	L(m)	B(m)	i(m)	C_w	p	$c_m \times 10^3$ (Form.)	$c_m \times 10^3$ (KK)	Difference (%)
1	242.80	32.25	12.75	0.864	0.380	0.581	0.558	4.16
2	242.80	32.25	12.94	0.864	0.427	0.525	0.514	2.15
3	188.50	25.00	9.40	0.828	0.443	0.550	0.541	1.62
4	188.50	25.00	9.40	0.828	0.374	0.636	0.627	1.48
5	221.51	28.00	11.63	0.860	0.389	0.602	0.587	2.70
6	178.26	23.20	10.00	0.857	0.389	0.676	0.676	0
7	232.80	32.25	7.78	0.862	0.456	0.588	0.588	0
8	210.91	28.00	7.07	0.834	0.461	0.580	0.600	-3.23
9	171.66	23.20	5.50	0.811	0.484	0.609	0.598	1.20

2. THE RESEARCH METHOD

2.1 General

In the first part of this paper, the results have been exposed of an investigation on the wave bending moment in confused sea. The aim of the second part is to explain the procedure followed during the investigation, so that the readers have the possibility of appraising the reliability of the obtained results. To this purpose it is necessary that some considerations be premised about selected hulls and weight distribution diagrams adopted for calculation.

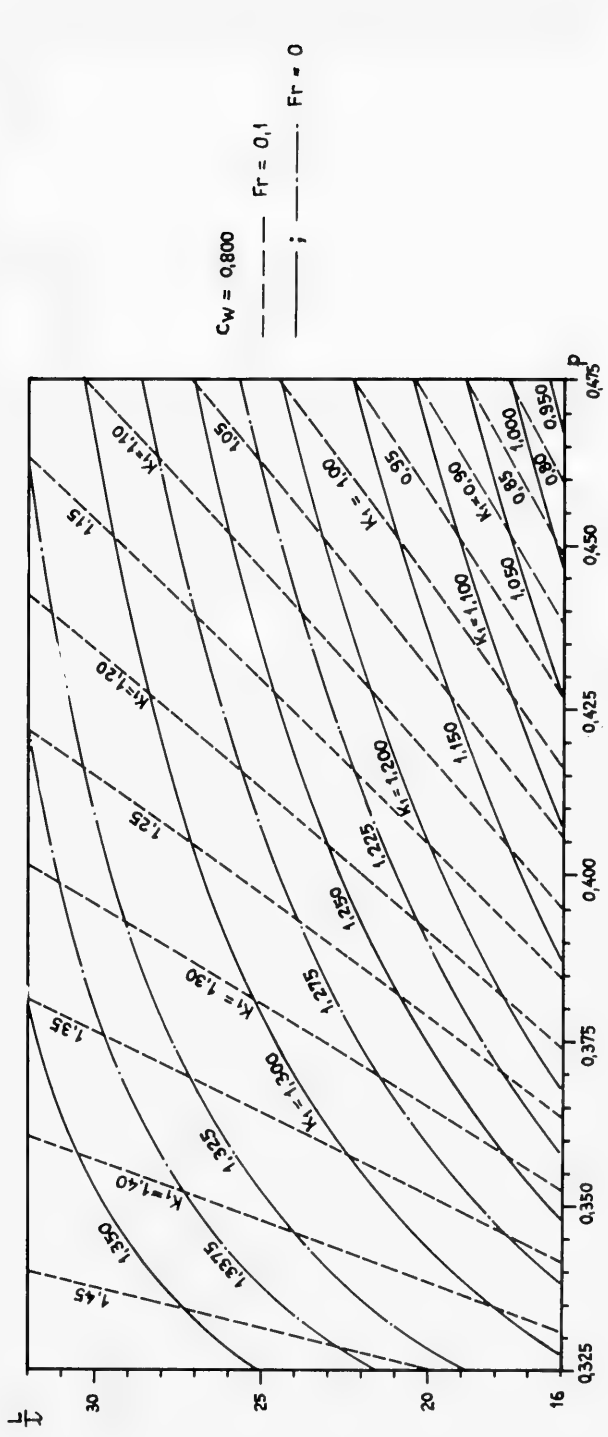

Fig. 7 - Family of curves $K_1 = f(\bar{\lambda}, C_w, Fr, p)$

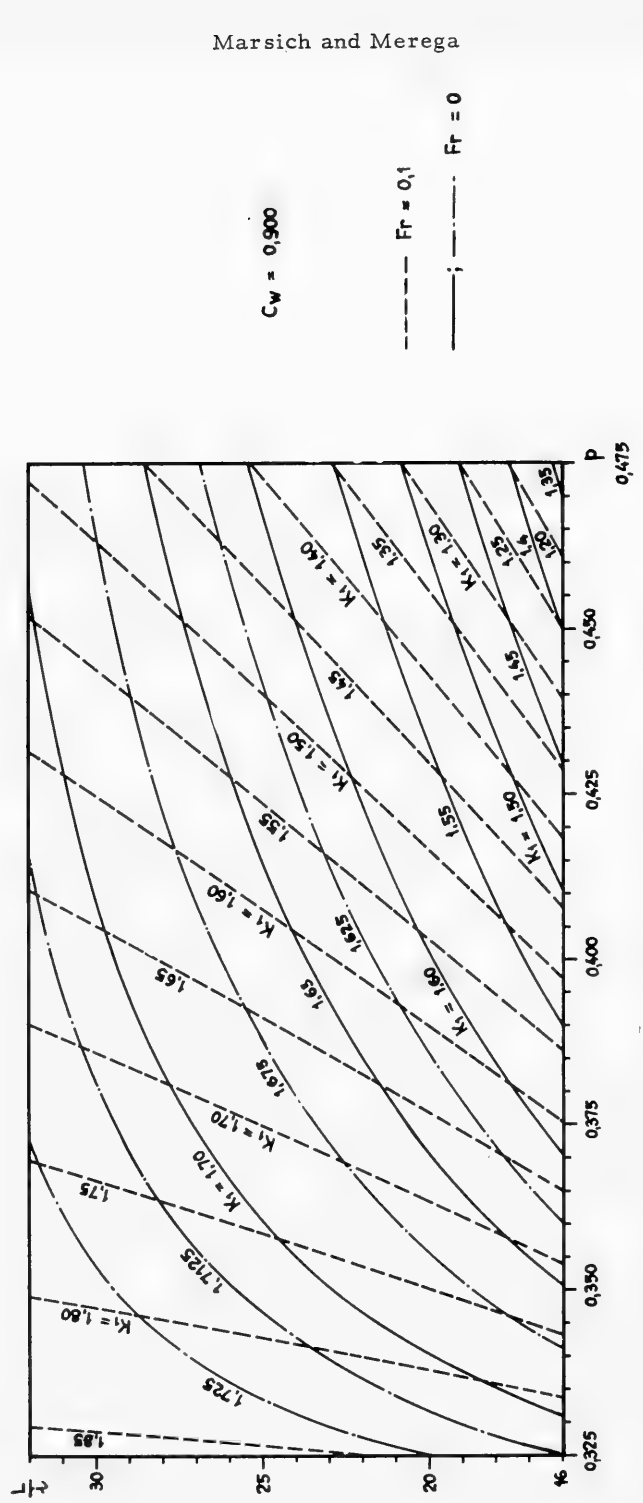

Fig. 8 - Family of curves $K_1 = f(\bar{\lambda}, C_w, Fr, p)$

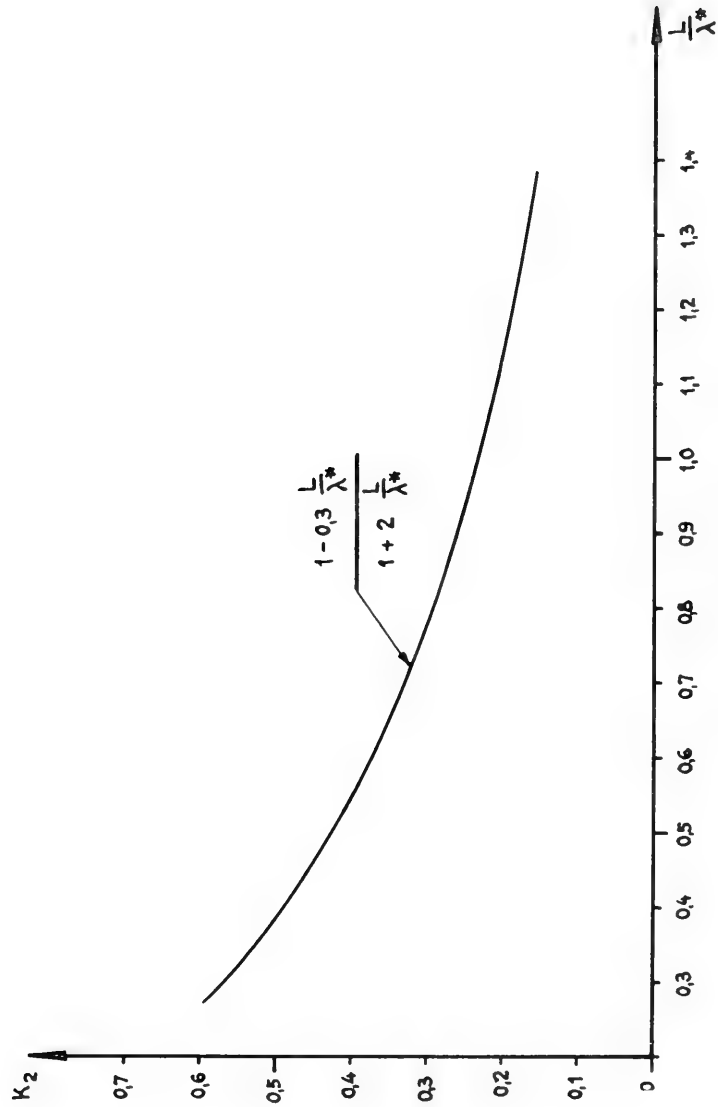

Fig. 9 - The curve $K_2 = f(R)$

2.2 Selected Hulls

Some Todd's hulls have been selected, which may be considered typical for tankers and bulk carriers. The principal parameters characterizing these hulls are reported in Tables 5 and 6, where the following symbols are used (It is to be noted that in Table 6 values of B_x/B and A_x/A correspond to equally spaced transverse cross sections of body plan, so that section 0 corresponds to aft perpendicular and section 20 to fore perpendicular.):

L = waterline length

L_{pp} = length between perpendiculars

B = maximum waterline breadth

i = draft (from base line)

A = maximum surface of immersed transverse cross section (up to waterline)

B_x = breadth (at waterline level) of actual transverse cross section x

A_x = surface of actual immersed transverse cross section x

C_B = block coefficient

C_w = waterplane area coefficient

C_x = midship section area coefficient

X_G = center of buoyancy, from aft perpendicular

Table 5
Selected Hulls

C_B	0.728	0.766	0.806	0.842			
C_w	0.804	0.836	0.872	0.900			
C_x	0.988	0.991	0.994	0.996			
L/B	7.00	7.25	7.50	7.75			
L/i	16.00	17.50	19.00	23.75	28.50	30.00	31.50
X_G/Lpp	0.525						

The choice of the hull parameters appearing in the tables has been suggested by the following partial results, obtained from a preliminary calculation worked out before planning the systematic calculation, which does not appear necessary to expose here in complete detail:

Table 6
Selected Hulls

Section	C_B = 0.728		C_B = 0.766		C_B = 0.806		C_B = 0.842	
	B_x/B	A_x/A	B_x/B	A_x/A	B_x/B	A_x/A	B_x/B	A_x/A
0	0.024	0.004	0.053	0.009	0.085	0.014	0.115	0.020
1	0.324	0.128	0.400	0.159	0.490	0.216	0.612	0.305
2	0.572	0.310	0.647	0.373	0.717	0.442	0.802	0.561
3	0.763	0.501	0.815	0.583	0.863	0.648	0.912	0.744
4	0.889	0.667	0.921	0.752	0.947	0.805	0.972	0.877
5	0.956	0.806	0.976	0.876	0.990	0.913	0.999	0.958
6	0.986	0.908	0.997	0.951	1.000	0.975	1.000	0.990
7	0.998	0.966	1.000	0.985	1.000	0.997	1.000	0.999
8	1.000	0.998	1.000	0.997	1.000	1.000	1.000	1.000
9	1.000	0.998	1.000	1.000	1.000	1.000	1.000	1.000
10	1.000	1.000	1.000	1.000	1.000	1.000	1.000	1.000
11	1.000	1.000	1.000	1.000	1.000	1.000	1.000	1.000
12	1.000	1.000	1.000	1.000	1.000	1.000	1.000	1.000
13	1.000	0.999	1.000	1.000	1.000	1.000	1.000	1.000
14	0.999	0.987	1.000	0.998	1.000	1.000	1.000	1.000
15	0.982	0.950	0.999	0.980	1.000	0.997	1.000	1.000
16	0.923	0.870	0.971	0.930	0.993	0.972	1.000	0.993
17	0.790	0.724	0.888	0.810	0.950	0.902	0.990	0.950
18	0.572	0.496	0.680	0.605	0.800	0.750	0.910	0.823
19	0.280	0.241	0.355	0.302	0.480	0.438	0.630	0.540
20	0.000	0.000	0.000	0.000	0.000	0.000	0.000	0.000

(1) Being C_B equal, the shape of the transverse section area diagram has an almost negligible influence on wave bending moment in confused sea; the same may be said, being C_w equal, for the shape of the waterline. Therefore the location of the center of buoyancy has a scarce influence, so that it may be assumed as a constant for the systematic calculation.

(2) In tanker or bulk-carrier-type hulls, a nearly constant relationship has been found among all fineness coefficients, so that it has been decided not to investigate any longer, for instance, the influence of C_w, being C_B equal, because these variations are very slight in practice.

In the systematic calculation, all values of C_w (i.e., C_B and C_x) have been associated to each couple of values $L/_B$ and $L/_i$, totaling 112 combinations of nondimensional parameters.

Note that the selected values of L/i are not uniformly spread, but are concentrated around the mean values relevant to "full load" and "ballast" conditions; only one intermediate value ($L/i = 23.75$) grants a sufficient linkage between the two aforesaid conditions.

2.3 Weight Diagrams

The criterion adopted in choosing the weights distributions is appreciably in accordance with weights diagrams of tankers and bulk-carriers. In fact these types of ships are often characterized by weight distributions very different from those relevant to evenly distributed load along all holds; loading conditions with empty holds are met and even more complex cases, especially when high-density cargos are carried. Besides, the weight distributions in ballast conditions are not to be forgotten, which may cause very different situations to arise from ship to ship and even for the same ship.

The actual weight diagram has here been considered as the sum of three separate diagrams (see Fig. 10):

(A) weight of ship's section aft of the forward bulkhead of engine room and forward of the collision bulkhead;

(B) evenly distributed load between the above bulkheads;

(C) weights and loads unevenly distributed between the above bulkheads.

As far as portion (A) is concerned, three distributions have been selected, shown in Table 7, named, respectively, types A_1, A_2, and A_3 (the meaning of the symbols of Table 7 is clearly stated in Fig. 10).

Table 7
Distributions Selected for Portion A in Fig. 10

	Type A_1	Type A_2	Type A_3
H_{AD}	$0.1487\ D/L_f$	$0.2897\ D/L_f$	$0.4307 D/L_f$
K_{AD}	$0.6800\ D/L_f$	$0.8210\ D/L_f$	$0.9621\ D/L_f$
H_{AV}	$0.3050\ D/L_f$	$0.6609\ D/L_f$	$1.0168\ D/L_f$
K_{AV}	$0.0753\ D/L_f$	$0.4311\ D/L_f$	$0.7868\ D/L_f$
D_{AD}	$0.0816\ D$	$0.1094\ D$	$0.1372\ D$
D_{AV}	$0.0168\ D$	$0.0848\ D$	$0.0799\ D$

Configuration A_1 is considered to be in good agreement with standard full-load conditions of tankers and bulk carriers, while configurations A_2 and A_3 are more suitable for representing ballast conditions.

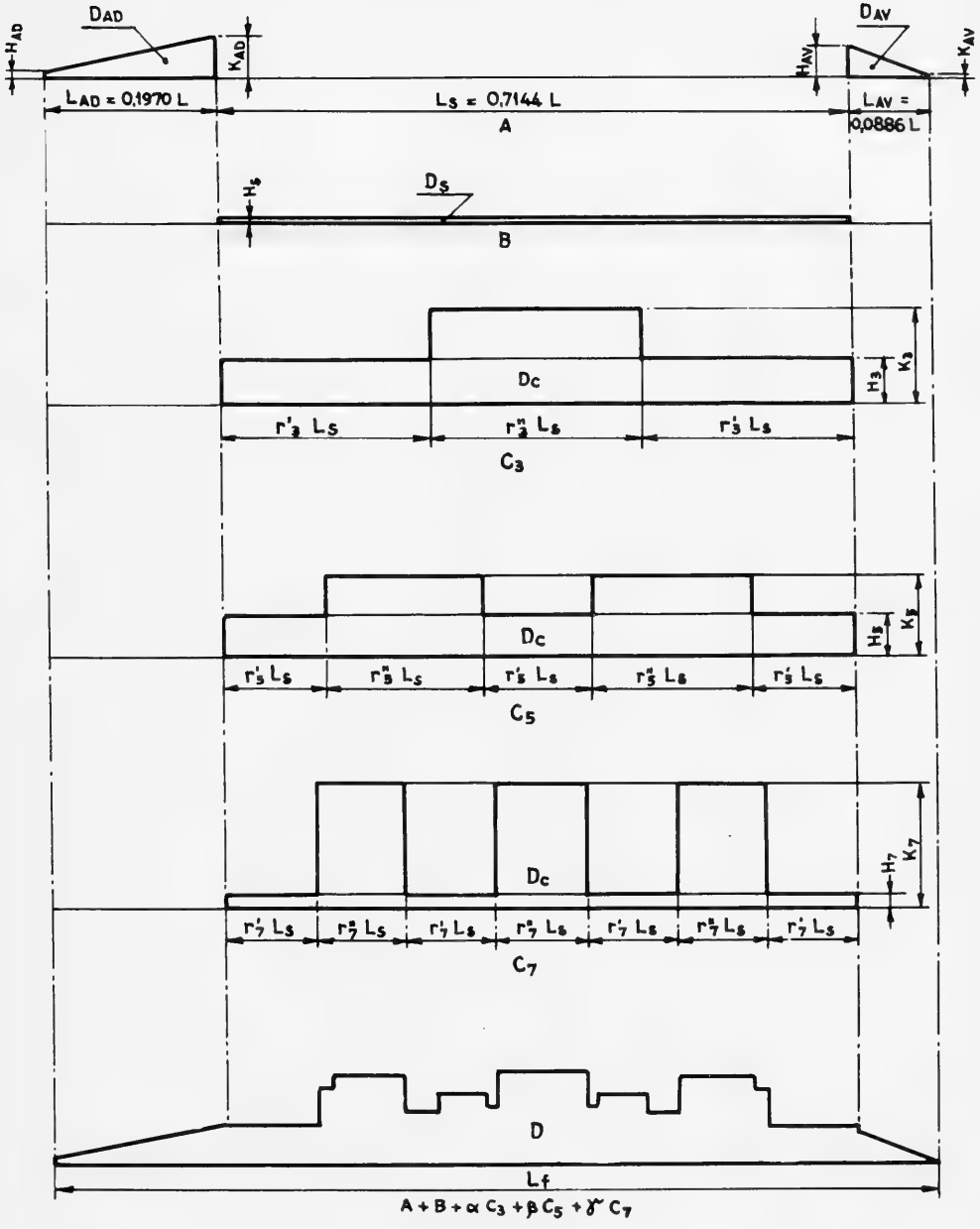

Fig. 10 - Weight diagram

As far as portion (B) is concerned, the three configurations reported in Table 8 have been selected, named, respectively, type B_1, B_2, and B_3. Configuration B_1 may properly represent the standard hull weight distribution between engine-room bulkhead and collision bulkhead.

Table 8
Configurations Selected for Portion B in Fig. 10

	Type B_1	Type B_2	Type B_3
H_s	0.1661 D/L_f	0.0830 D/L_f	0
D_s	0.1187 D	0.0593 D	0

As far as portion (C) is concerned, that obviously represents hold cargo, it consists of three parts, C_3, C_5, and C_7, respectively; these parts correspond to noncontinuous distribution along holds length L_s divided into 3, 5, or 7 holds, having the following characteristics:

even holds of equal length;

odd holds of equal length;

equal loading heights in even holds;

equal loading heights in odd holds.

The definition of distribution type C is given in Tables 9 and 10, where reference is made to symbols of Table 11. In case that in particular $r_i = 1$ ($i = 3, 5, 7$), values of h_j and k_i will become as simplified, as in Table 12.

The final distribution is given by relationships reported in Table 13, where, it is proper to underline, C_3, C_5, and C_7 are distributions characterized by the same equatorial moment of inertia J_c, previously assumed.

In conclusion, to the aim of defining a weights distribution it is necessary to fix the following values

(A) H_{AD}, K_{AD}, H_{AV}, K_{AV}

(B) H_S

(C) r_3, r_5, r_7, α, β, γ, j

For instance, in the case of Fig. 10, the following values were assumed:

(A) type A_1

(B) type B_1

(C) $r_3 = 1$; $r_5 = 1.5$; $r_7 = 1$; $\alpha = 1/3$; $\beta = 1/3$; $\gamma = 1/3$; $j = 0.73$

Table 9
Distribution Type C_i
(Continued in Tables 10 through 13)

H_i	$h_i \; D_S/L_S \quad (h_i \geq 0)$
K_i	$k_i \; D_S/L_S \quad (k_i \geq 0)$
D_c	$D - (D_{AD} + D_S + D_{AV}$

Table 10
Continuation of Table 9

$h_i = \dfrac{j - X_{i,r}}{1 - X_{i,r}}$	$k_i = 1 + r_i \dfrac{i+1}{i-1}(1-h_i)$
$X_{i,r} = \dfrac{4}{[(i+1)\,r_i + (i-1)]^2}\left[1 + 3(i-3)^2 \dfrac{(1+r_i)^2}{i-1}\right]$	
$j = \dfrac{12\,J_c}{D_S L_S^2}$	$r_i = \dfrac{l_{io}}{l_{ie}}$
$l_{io} = r_i^{1}\,L_S$	$l_{ie} = r_i^{11}\,L_S$
$r_i^{1} = \dfrac{2\,r_i}{(i+1)\,r_i + (i-1)}$	$r_i^{11} = \dfrac{2}{(i+1)\,r_i + (i-1)}$
$i = 3, 5, 7$	

Table 11
Continuation of Tables 9 and 10

D	Ship's displacement
L_f	Ship's length
J_c	Moment of inertia of "c" distribution
I_{io}	Odd holds length
I_{ie}	Even holds length
i	Number of holds

Table 12
Values for $r_i = 1$ ($i = 3, 5, 7$)

$h_3 = \frac{9}{8} j - \frac{1}{8}$	$k_3 = \frac{13}{4} - \frac{9}{4} j$
$h_5 = \frac{25}{12} j - \frac{13}{12}$	$k_5 = \frac{33}{8} - \frac{25}{8} j$
$h_7 = \frac{49}{16} j - \frac{33}{16}$	$k_7 = \frac{61}{12} - \frac{49}{12} j$

Table 13
Final Distribution

Weight distribution $= A + B + \alpha C_3 + \beta C_5 + \gamma C_7$	
$\alpha + \beta + \gamma = 1$	$\alpha, \beta, \gamma \geq 0$

2.4 Weight Parameter

A first systematic calculation, results of which have not been reported in the first part of this paper, has been carried out to the aim of determining which and how many parameters are necessary to characterize a weight distribution in respect with their influence on wave bending moment in confused sea (highest value along the hull).

To this purpose, weight distributions 1 to 36 of Table 14 have been chosen in association with a hull having: length 200 m, $L/B = 7$, $L/i = 17.50$, $C_W = 0.804$ and ship's speeds corresponding to $Fr = 0, 0.05, 0.10$.

It was found that, being Fr equal, values of coefficient c_m are uniquely correlated to values of p (as defined in part 1 of this paper) reported in the last column of Table 14, although loading conditions were different. The unique relationship between p and c_m is shown as an example in Fig. 11, for one value only of Fr. From this figure it can easily be seen that the interdependence between the two variables may be assumed as linear.

It is to be noted, in order to establish the limits of accuracy of the assumption, that this relationship remains linear and unique up to Fr values not much higher than 0.10. There are instead no limitations for hull dimensional parameters.

Table 14
Weight Distributions

No.	A type	B type	r_3	r_5	r_7	α	β	γ	j	p
1									0.675	0.350
2									0.750	0.362
3									0.825	0.375
4									0.900	0.387
5*						0.20	0.00	0.80	1.000	0.404
6									1.075	0.416
7									1.150	0.429
8									1.225	0.441
9									0.675	0.357
10									0.750	0.368
11									0.825	0.379
12	A_1	B_1			1	0.10	0.50	0.40	0.900	0.390
13									1.075	0.415
14									1.150	0.425
15									1.225	0.436
16									0.675	0.365
17									0.750	0.374
18									0.825	0.383
19			1	1			1.00	0.00	0.900	0.392
20									1.075	0.413
21									1.150	0.422
22									1.225	0.431
23	A_2	B_2							1.000	0.426
24					0.5				0.760	0.363
25						0.00			1.360	0.467
26									0.673	0.345
27*	A_1				1				1.000	0.404
28									1.245	0.448
29					2				0.603	0.333
30		B_3					0.00	1.00	1.149	0.432
31									0.673	0.380
32	A_2								1.000	0.434
33					1				1.245	0.475
34									0.673	0.413
35	A_3								1.000	0.464
36									1.245	0.502

*Same distribution.

The linear relationship between c_m and p allowed to plan a second systematic calculation aiming to determine the influence of hull parameters taking into account only three loading conditions (exactly, Nos. 26, 27, and 28) and therefore only three p values, as may be seen in result tables reported in the Appendix.

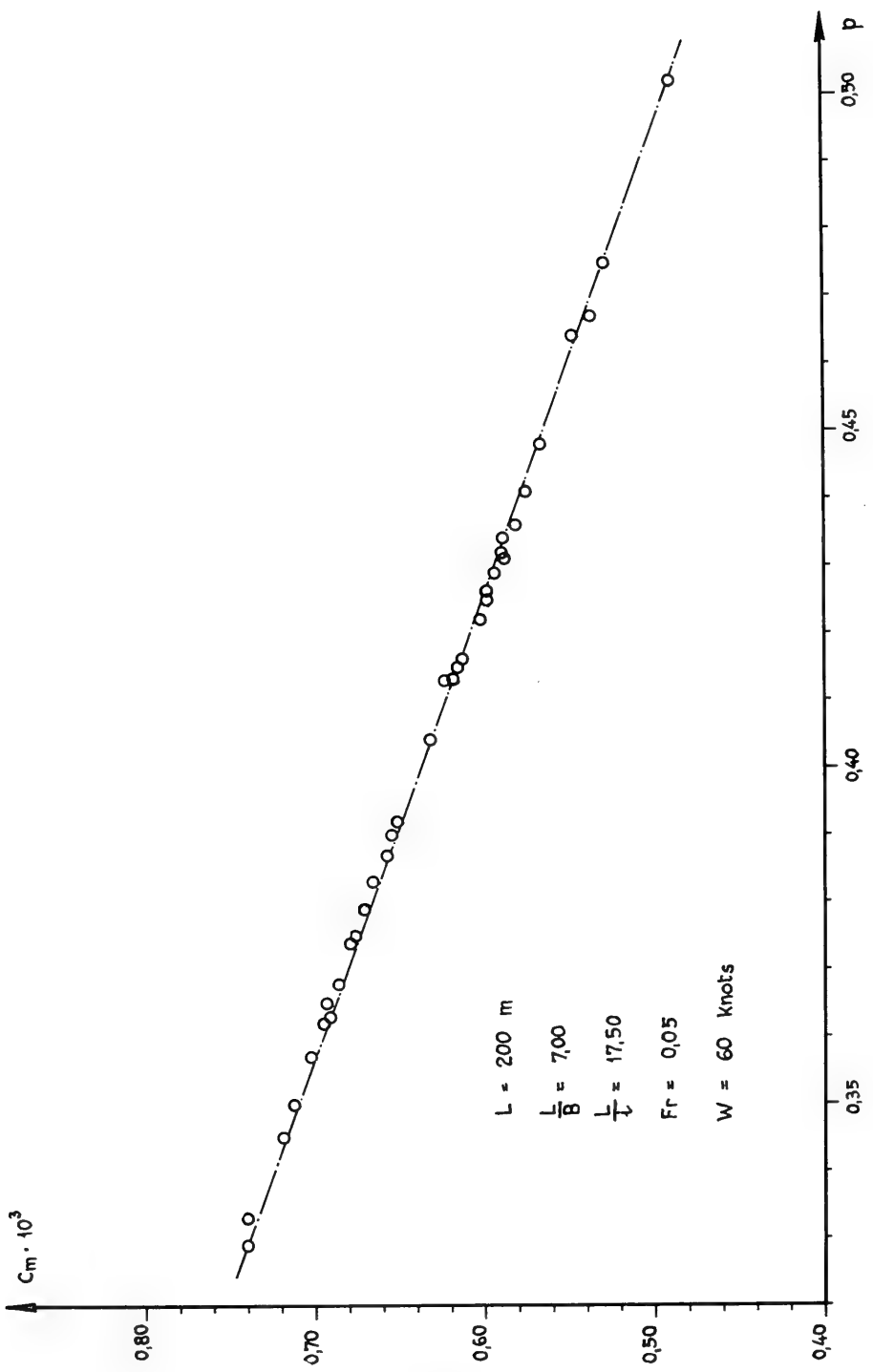

Fig. 11 - Correlation of c_m to p

2.5 Influence of Ship's Length and Sea Spectrum

After having systematically investigated the influence of parameters L/B, L/i, c_w, and Fr on the moment coefficient c_m for a ship of 200 m length crossing a confused sea generated by a 60-knot wind, it was decided to study the influence of ship's length and sea state. That was achieved without using the calculation program shown in the last section of the present paper, because the calculation had already furnished the response operators in regular waves for certain λ/L values. Considering that these response operators, when in nondimensional form, are not functions of L, but only of the ratio λ/L, it was possible to use such response operators in order to carry out the investigation, simply by applying the superposition principle, on different ship's lengths and different conditions of sea state (expressed by means of wind speed).

In so doing the following very important fact was detected; the variation law of bending moment coefficient c_m as a function of ship's length and of sea state is in practice not affected by selected weights distribution, hull type, and ship's speed and can be represented as a function of the only parameter L/λ^*, where λ^* is the maximum energy wavelength for each given sea state (therefore λ^* is a function of only the parameter W).

This fact is emphasized in Fig. 12, which is self-explanatory, where also a curve is drawn, having the simple algebraic expression written at the end of Section 1.4.

The discovered characteristic allowed one to easily extend the investigation to other W and L values; the results given above were found to be fully acceptable, for W not much lower than 45 kn.

3. CALCULATION PROGRAM

3.1 Summary of the KK Theory

The KK theory for the investigation of ship's motions and of loads acting on a ship in a regular sea formulates and solves the differential equations of motion taking into account the phase relationship between ship's and wave motions and the coupling effect of heaving and pitching. As this theory is well-known, it seems here advisable to recall only formulas that are used in the calculation program; reference is made to symbols collected in Table 15, where the numbers are shown of the formulas in Table 16 defining the relevant quantities. The coordinate-system choice is shown in Fig. 13, which is self-explanatory.

3.2 Description of the Calculation Program

The program "Ship motions, shear, and bending moment in regular waves and a confused sea" is written in FORTRAN 2 and processed on an IBM 7090 computer. It evaluates, for each hull and for each loading condition, shear and still-water bending moment along the hull and besides heaving and pitching motions in regular waves in head sea, for eight wave lengths and eight ship's

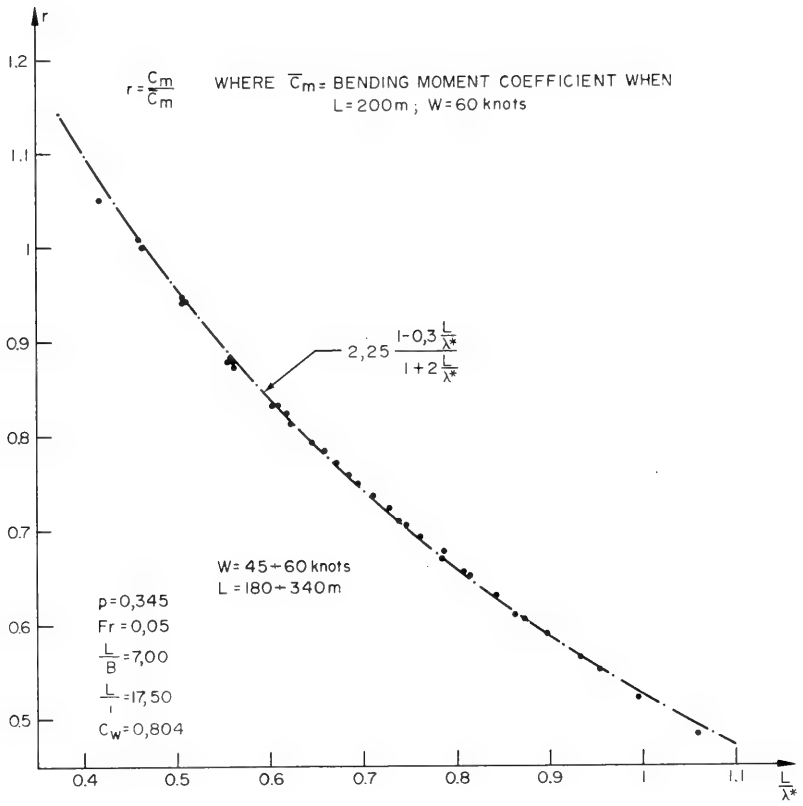

Fig. 12 - Relation between c_m and L/λ^*

Table 15
Definitions and Dimensions of Symbols in the Formulas
Used in the Calculation Program

Symbol	Formula	Dimension	Definition
A	(29)	$[ML^2]$	Coefficient of differential equation of ship's motions
$\bar{a}$	(23)	$[M]$	Coefficient of differential equation of ship's motions
B	(30)	$[ML^2T^{-1}]$	Coefficient of differential equation of ship's motions
$\bar{b}$	(24)	$[MT^{-1}]$	Coefficient of differential equation of ship's motions
C	(31)	$[ML^2T^{-2}]$	Coefficient of differential equation of ship's motions
c_x	—	—	Sectional area coefficient at x: $c_x = s_x/(2y_w i_x)$
$\bar{c}$	(25)	$[MT^{-2}]$	Coefficient of differential equation of ship's motions
D	(32)	$[ML]$	Coefficient of differential equation of ship's motions
$\bar{d}$	(26)	$[ML]$	Coefficient of differential equation of ship's motions
dm	—	$[M]$	Mass loading on a unit length at x
E	(33)	$[MLT^{-1}]$	Coefficient of differential equation of ship's motions
e	—	—	2,7182818...
$\bar{e}$	(27)	$[MLT^{-1}]$	Coefficient of differential equation of ship's motions
F_c	(35)	$[MLT^{-2}]$	Cosine amplitude of total exciting force
F_s	(36)	$[MLT^{-2}]$	Sine amplitude of total exciting force
F_t	—	$[MLT^{-2}]$	Total force: $F_t = \int_L \left(\frac{dF_1}{dx} + \frac{dF_2}{dx} + \frac{dF_3}{dx} \right) dx$
F_1	(13)	$[MLT^{-2}]$	Total exciting force
F_2	(14)	$[MLT^{-2}]$	Hydrodynamic force

(Table continues)

Table 15 (Continued)

Symbol	Formula	Dimension	Definition
F_3	(15)	$[MLT^{-2}]$	Hydrostatic force
f	(44)	$[MLT^{-2}]$	Total force, including inertial force
f_c	(46)	$[MLT^{-2}]$	Cosine amplitude of f
f_s	(47)	$[MLT^{-2}]$	Sine amplitude of f
G	(34)	$[MLT^{-2}]$	Coefficient of differential equation of ship's motions
g	—	$[LT^{-2}]$	Acceleration of gravity
$\bar{g}$	(28)	$[MLT^{-2}]$	Coefficient of differential equation of ship's motions
h	(4 and 5)	$[L]$	Surface elevation of waves
h_0	—	$[L]$	Wave amplitude
i_m	—	$[L]$	Section mean draft at x: $i_m = c_x i_x$
i_x	—	$[L]$	Section draft at x
J_0	—	$[ML^3T^{-2}]$	Moment of inertia of the ship
K	—	$[L^{-1}]$	$K = 2\pi/\lambda$
L	—	$[L]$	Ship's length
M_c	(37)	$[ML^2T^{-2}]$	Cosine amplitude of total exciting moment
M_s	(38)	$[ML^2T^{-2}]$	Sine amplitude of total exciting moment
M_t	—	$[ML^2T^{-2}]$	Total moment: $M_t = \int_L \left(\frac{dF_1}{dx} + \frac{dF_2}{dx} + \frac{dF_3}{dx}\right) x\, dx$
M_x	(49)	$[ML^2T^{-2}]$	Wave bending moment amplitude at x
P_0	—	$[MLT^{-2}]$	Ship's weight: $P_0 = \int_L dm\, dx$
P_1	(10)	$[ML^{-1}]$	Sectional added mass at x
P_2	(11)	$[ML^{-1}T^{-1}]$	Sectional damping coefficient at x
P_3	(12)	$[ML^{-1}T^{-2}]$	Sectional hydrostatic coefficient at x
s_x	—	$[L^2]$	Sectional area at x
T_x	(48)	$[MLT^{-2}]$	Wave shear amplitude at x
t	—	$[T]$	Time
v	—	$[LT^{-1}]$	Ship's speed

(Table continues)

Table 15 (Continued)

Symbol	Formula	Dimension	Definition
X	—	[L]	Longitudinal coordinate fixed to the space
x	—	[L]	Longitudinal coordinate fixed to the ship
Y	—	[L]	Transverse coordinate fixed to the space
y	—	[L]	Transverse coordinate fixed to the ship
y_w	—	[L]	Half of waterline breadth at x
Z	—	[L]	Vertical coordinate fixed to the space
Z_G	—	[L]	Vertical elevation of ship's center of gravity
z	—	[L]	Vertical coordinate fixed to the ship
α_ζ	(42)	—	Heaving phase angle
α_φ	(43)	—	Pitching phase angle
ζ	(6)	[L]	Heaving
ζ_c	(39)	[L]	Cosine heaving amplitude
ζ_s	(39)	[L]	Sine heaving amplitude
ζ_0	(40)	[L]	Heaving amplitude
η	(16)	[L]	Vertical motion at x
λ	—	[L]	Wave length
π	—	—	3,1415...
ρ	—	$[ML^{-3}]$	Sea water density
φ	(7)	—	Pitching
φ_c	(39)	—	Cosine pitching amplitude
φ_s	(39)	—	Sine pitching amplitude
φ_0	(41)	—	Pitching amplitude
χ_1	—	—	First hydrodynamic coefficient: $\chi_1 = f'(C_W, \omega_e^2 y_w/g, 2y_w/i_x)$
χ_2	—	—	Second hydrodynamic coefficient: $\chi_2 = f''(C_W, \omega_e^2 y_w/g, 2y_w/i_x)$
ω_e	—	$[T^{-1}]$	Frequency of encounter: $\omega_e = \omega_0 + kv$
ω_0	—	$[T^{-1}]$	Wave frequency: $\omega_0 = (2\pi g/\lambda)^{1/2}$

Table 16
Formulas

1.	$X = x + v\,t$	Coordinate system transformation
2.	$Y = y$	
3.	$Z = Z_G + z + x\varphi$	
4.	$h = h_o \cos(kx + \omega_o t)$	Surface elevation of waves
5.	$h = h_o \cos(kx + \omega_e t)$	
6.	$\xi = \xi_o \cos(\omega_e t + \alpha_\xi)$	Heaving and pitching motions
7.	$\varphi = \varphi_o \cos(\omega_e t + \alpha_\varphi)$	
8.	$\frac{P_o}{g}\ddot{Z} = F_t$	Differential equations of ship's motion
9.	$\frac{J_o}{g}\ddot{\varphi} = M_t$	
10.	$P_1 = \frac{\pi\rho\, Y_w^2}{\chi_i^2}$	Sectional added mass
11.	$P_2 = \frac{\rho g^2}{\omega_e^3}\chi_2$	Sectional damping coefficient
12.	$P_3 = 2\rho g\, y_w$	Sectional hydrostatic coefficient
13.	$\frac{dF_1}{dX} = \left[P_i \ddot{h} + \left(P_2 - v\frac{dP_1}{dx}\right)\dot{h} + P_3 h\right] e^{-Ki_m}$	Exciting force distribution
14.	$\frac{dF_2}{dX} = P_1\ddot{\eta} - \left(P_2 - v\frac{dP_i}{dx}\right)\dot{\eta}$	Hydrodynamic force distribution
15.	$\frac{dF_3}{dX} = P_3\,\eta$	Hydrostatic force distribution
16.	$\eta = \xi + x\varphi$	Vertical displacement, velocity, and acceleration of a ship's transverse section at a distance x from LCG
17.	$\dot{\eta} = \dot{\xi} + x\dot{\varphi} - v\varphi$	
18.	$\ddot{\eta} = \ddot{\xi} + x\ddot{\varphi} - 2v\dot{\varphi}$	

(Table continues)

Table 16 (Continued)

19. $\dot{h} = -h_o \omega_o \sin(kx + \omega_e t)$

20. $\ddot{h} = -h_o \omega_o^2 \cos(kx + \omega_e t)$

Vertical velocity and acceleration of water in wave

21. $\bar{a}\ddot{\xi} + \bar{b}\dot{\xi} + \bar{c}\xi + \bar{d}\ddot{\varphi} + \bar{e}\dot{\varphi} + \bar{g}\varphi = F_c \cos \omega_e t - F_s \sin \omega_e t$

22. $A\ddot{\varphi} + B\dot{\varphi} + C\varphi + D\ddot{\xi} + E\dot{\xi} + G\xi = M_c \cos \omega_e t - M_s \sin \omega_e t$

Differential equations of ship's motion

23. $\bar{a} = \frac{P_0}{g} + \int_L P_1 \, dx$

24. $\bar{b} = \int_L P_2 \, dx$

25. $\bar{c} = \int_L P_3 \, dx$

26. $\bar{d} = \int_L P_4 \, x \, dx$

27. $\bar{e} = \int_L P_2 \, x \, dx - v \int_L P_1 \, dx$

28. $\bar{g} = \int_L P_3 \, x \, dx - v \int_L P_2 \, dx$

29. $A = \frac{J_0}{g} + \int_L P_1 \, x^2 \, dx$

30. $B = \int_L P_2 \, x^2 \, dx$

31. $C = \int_L P_3 \, x^2 \, dx - v \int_L P_2 \, x \, dx - v^2 \int_L P_1 \, dx$

32. $D = \int_L P_1 \, x \, dx$

33. $E = \int_L P_2 \, x \, dx - v \int_L P_1 \, dx$

34. $G = \int_L P_3 \, x \, dx$

Coefficients of differential equations of ship's motions

(Table continues)

Table 16 (Continued)

35. $$F_c = h_0\left[\int_L e^{-ki_m}(P_3 - \omega_0\omega_e P_1)\cos kx\,dx - \omega_0\int_L e^{-ki_m}P_2\sin kx\,dx\right]$$

36. $$F_s = h_0\left[\int_L e^{-ki_m}(P_3 - \omega_0\omega_e P_1)\sin kx\,dx + \omega_0\int_L e^{-ki_m}P_2\cos kx\,dx\right]$$

37. $$M_c = h_0\left[\int_L e^{-ki_m}(P_3 - \omega_0\omega_e P_1)\,x\cos kx\,dx - \omega_0\int_L e^{-ki_m}(P_2 x + vP_1)\sin kx\,dx\right]$$

38. $$M_s = h_0\left[\int_L e^{-ki_m}(P_3 - \omega_0\omega_e P_1)\,x\sin kx\,dx + \omega_0\int_L e^{-ki_m}(P_2 x + vP_1)\cos kx\,dx\right]$$

Total exciting forces and moments acting on the ship

39. $$\begin{bmatrix} \bar{c} - \omega_e^2\bar{a} & -\omega_e\bar{b} & \bar{g} - \omega_e^2\bar{d} & -\omega_e\bar{e} \\ \omega_e b & \bar{c} - \omega_e^2\bar{a} & \omega_e\bar{e} & \bar{g} - \omega_e^2\bar{d} \\ G - \omega_e^2 D & -\omega_e E & C - \omega_e^2 A & -\omega_e B \\ \omega_e E & G - \omega_e^2 D & \omega_e B & C - \omega_e^2 A \end{bmatrix} \times \begin{bmatrix} \xi_c \\ \xi_s \\ \varphi_c \\ \varphi_s \end{bmatrix} = \begin{bmatrix} F_c \\ F_s \\ M_c \\ M_s \end{bmatrix}$$

Linear system of 4 equations to solve the differential equations of motion

(Table continues)

Table 16 (Continued)

40. $\xi_0 = (\xi_c^2 + \xi_s^2)^{1/2}$

41. $\varphi_0 = (\varphi_c^2 + \varphi_s^2)^{1/2}$

42. $\alpha_\xi = \arctan(\xi_s/\xi_c)$

43. $\alpha_\varphi = \arctan(\varphi_s/\varphi_c)$

} Heave and pitch amplitudes and phase angles

44. $$\frac{df}{dX} = -dm(\ddot{\xi} + x\ddot{\varphi}) - P_1(\ddot{\xi} + x\ddot{\varphi} - 2v\dot{\varphi}) - \left(P_2 - v\frac{dP_1}{dx}\right)(\dot{\xi} + x\dot{\varphi} - v\varphi) - P_3(\xi + x\varphi) + \frac{dF_1}{dX}$$

45. $$\frac{df}{dX} = \frac{df_c}{dX}\cos\omega_e t - \frac{df_s}{dX}\sin\omega_e t$$

46. $$\frac{df_c}{dX} = \left[(dm + P_1)\omega_e^2 - P_3\right](\xi_c + x\varphi_c) + \left(P_2 - v\frac{dP_1}{dx}\right) \times \left[(\xi_s + x\varphi_s)\omega_e + v\varphi_c\right] - 2v\omega_e P_1\varphi_s + h_0 e^{-ki_m} \times \left[(P_3 - \omega_0^2 P_1)\cos kx - \omega_0\left(P_2 - v\frac{dP_1}{dx}\right)\sin kx\right]$$

47. $$\frac{df_s}{dX} = \left[(dm + P_1)\omega_e^2 - P_3\right](\xi_s + x\varphi_s) - \left(P_2 - v\frac{dP_1}{dx}\right) \times \left[(\xi_c + x\varphi_c)\omega_e - v\varphi_s\right] + 2v\omega_e P_1\varphi_c + h_0 e^{-ki_m} \times \left[(P_3 - \omega_0^2 P_1)\cos kx + \omega_0\left(P_2 - v\frac{dP_1}{dx}\right)\cos kx\right]$$

} Longitudinal distribution of total forces acting on the ship

48. $$T_x = \left[\left(\int_x \frac{df_c}{dX}\,dx\right)^2 + \left(\int_x \frac{df_s}{dX}\,dx\right)^2\right]^{1/2}$$

49. $$M_x = \left[\left(\iint_x \frac{df_c}{dX}\,dx\,dx\right)^2 + \left(\iint_x \frac{df_s}{dX}\,dx\,dx\right)^2\right]^{1/2}$$

} Shear amplitude and bending moment amplitude at a distance x from LCG

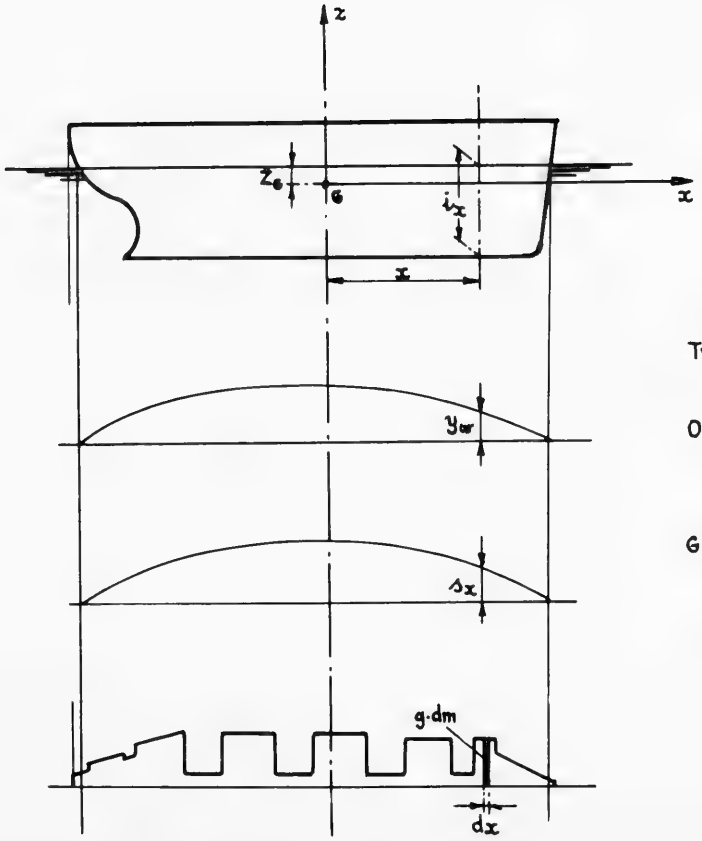

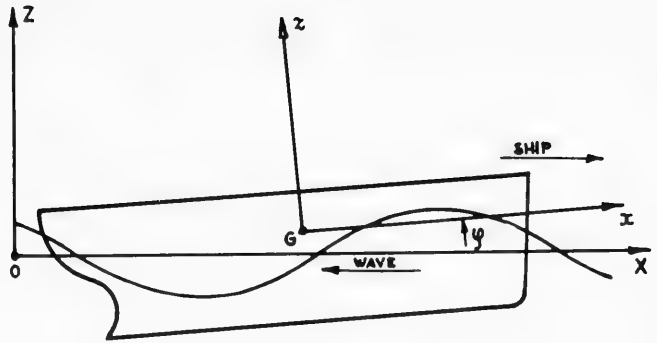

Two sets of co-ordinate axes are used.

O-XYZ : fixed to the space

XY plane coincides with the still water surface and Z axis is directed upward.

G-xyz : fixed to the ship

origin is located in the centre of gravity and, when the ship is in still water, x y z are respectively parallel to XYZ.

Fig. 13 - Coordinate system

speed. Moreover, shear and bending moment amplitude are calculated in way of 19 transverse sections (spaced L /20 from each other).

Besides in the above specified sections shear and wave bending moment maximum most probable amplitudes are evaluated, which ship under consideration will undergo in case she encounters, during 10^4 cycles, one-dimension head sea generated by a 60-kn wind.

In Fig. 14 the block diagram is shown, together with the input-output flow chart, while input data are shown in Table 16, with respective formats and directions for data collection.

Hydrodynamic coefficients χ_1 and χ_2 are gathered, in their input format, in Tables 18 and 19. Table 18 contains coefficient χ_1, and Table 19 contains coefficient χ_2.

In each line there are, after an order number, 16 values corresponding to values of $\omega_e^2 y_w/g$ 0 - 1.5, spaced 0.1. Each block of 11 lines (6 blocks refer to χ_1, 6 blocks to χ_2) corresponds to c_x values 0.5 - 1.0, spaced 0.1.

Each line of each 11 lines block corresponds to values $2 y_w/i_x$ 0.4 - 4.4, spaced 0.4.

Output forms are shown in Figs. 15 and 16. The program list follows Fig. 16.

Table 17
Input Data for the Program

Card type	Specification	Col.	Data	Unit	Format
I	General data	01-03	Hull code	-	13, 6F8.3, 13
		04-11	Length between perpendiculars	m	
		12-19	Ship's breadth	m	
		20-27	Aft draft (at Aft. Pp.)	m	
		28-35	Forward draft (at Fwd. Pp.)	m	
		36-43	Wave amplitude	m	
		44-51	Sea water density	$Kg \cdot s^2/m^4$	
		52-54	Transverse section number (*)	-	
II	Transverse sections data (1 card each section)	01-08	Section abscissa from Aft Pp (†)	m	3F8.3, 13
		09-16	Waterline breadth	m	
		17-24	Transverse section area (up to water plan)	m^2	
		25-27	Section order number	-	

(Table continues)

Table 17 (Continued)

Card type	Specification	Col.	Data	Unit	Format
III	Ship's speeds	01-03 04-11 12-19 ... 73-80	Ship's speed number (‡) 1st ship's speed 2nd ship's speed ... 8th ship's speed	- m/sec m/sec ... m/sec	13, 8F8, 3
IV	Wave lengths	01-03 04-11 12-19 ... 73-80	Wavelength number (§) 1st wavelength 2nd wavelength ... 8th wavelength	- m m ... m	13, 8F8.3
V	Weights (¶) (1 card each 8 section)	01-10 11-20 ... 71-80	Weight per length unit in 1st section (1st card), in 9th section (2nd card), ... Weight per length unit in 2nd section (1st card), in 10th section (2nd card),... ... Weight per length unit in 8th section (1st card), in 16th section (2nd card),...	kg/m kg/m ... kg/m	8F10.0
VI	Weight index	01-03 04-06 07-09	Weight codes NSTR 1 (**) NSTR 2 (**)	- - -	313

(*) The maximum allowable transverse section number is 80
(†) Sections are not generally equally spaced
(‡) The maximum allowable speed number is 8
(§) The maximum allowable wavelength number is 8
(¶) Two transverse sections shall be always located in way of each weights diagram lack of continuity, spaced not more than 5 cm

(**) NSTR 1: { = 0 in case actual card deck is the last one for ship under examination
= 1 otherwise

NSTR 2: { = 0 in case preceding card deck refers to a calculation at the same displacement, moment of inertia and gravity center location
= 1 otherwise or in case actual card deck is the first one for the ship under examination

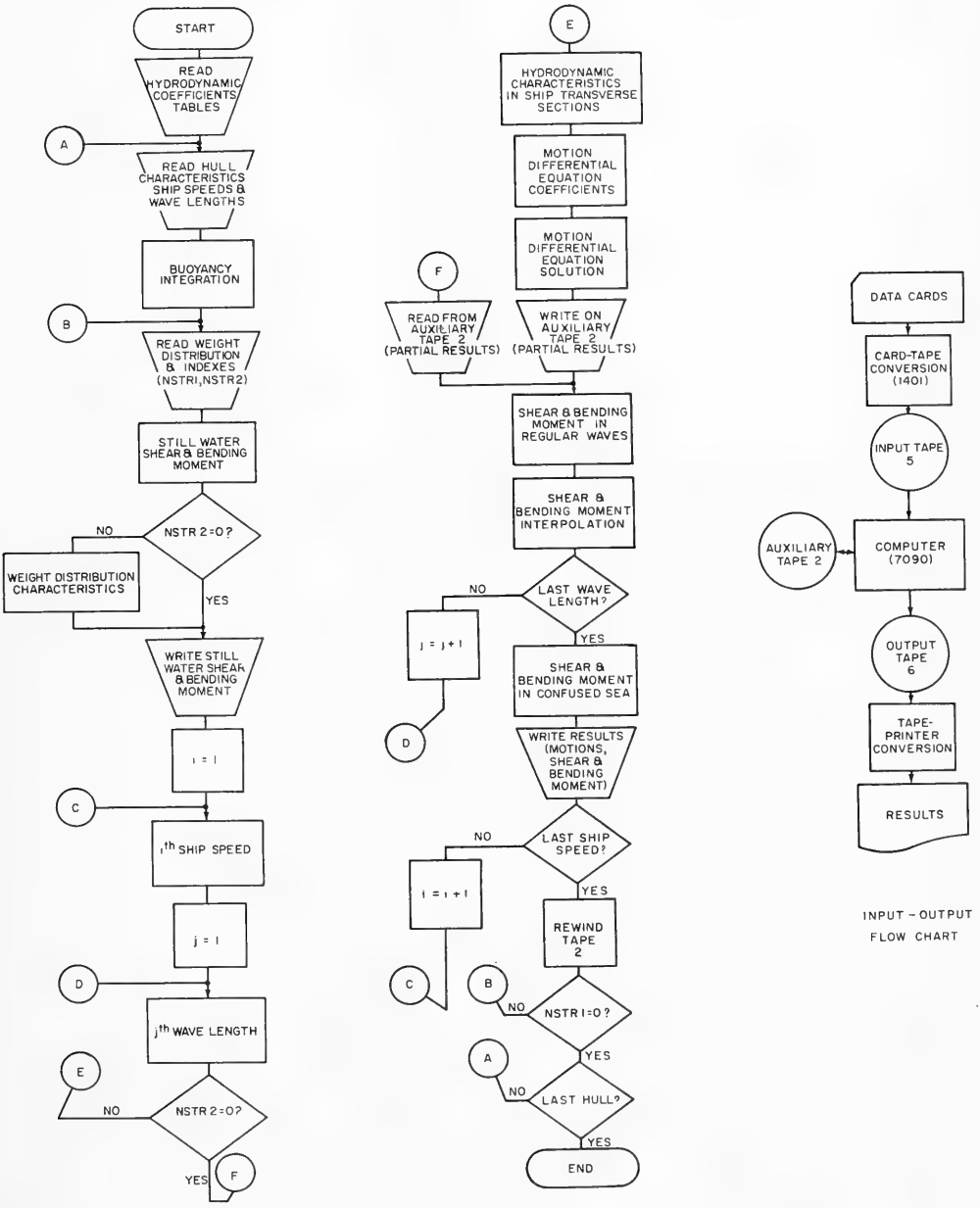

Fig. 14 - Block diagram of the program (ship motions, shear, and bending moment in regular waves and a confused sea)

Hull code		Weight code	

Length		Displacement	
Breadth		C. of gravity posit.	
Mean draft		Radius of gyration	

Section n.	Still water Shear	Still water Bending Moment
1		
2		
3		
4		
5		
6		
7		
8		
9		
10		
11		
12		
13		
14		
15		
16		
17		
18		
19		

Fig. 15 - First-output form

Hull code	Weight code	Ship's speed

λ								
ω_o								
ζ_c								
ζ_s								
φ_c								
φ_s								

	CONFUSED SEA		REGULAR WAVES															
	Sh.	B.M.	Sh.	B.M.	Sh.	B.M.	Sh.	B.M.	Sh.	B.M.	Sh.	B.M.	Sh.	B.M.	Sh.	B.M.	Sh.	B.M.
1																		
2																		
3																		
4																		
5																		
6																		
7																		
8																		
9																		
10																		
11																		
12																		
13																		
14																		
15																		
16																		
17																		
18																		
19																		

Fig. 16 - Second-output form

Table 18
Hydrodynamic Coefficient X_1 in the Input Form

1	042	184	285	333	324	286	256	234	218	205	194	185	178	172	168	165
2	042	100	152	201	244	270	280	280	277	270	261	250	238	227	218	210
3	042	081	115	147	175	198	217	228	236	241	243	243	242	240	236	232
4	042	073	099	122	143	162	177	190	200	208	212	215	217	217	216	215
5	042	070	090	110	127	142	155	166	174	181	186	190	192	194	195	196
6	042	067	086	104	119	132	142	150	158	164	169	173	177	180	183	184
7	042	064	082	098	111	123	132	141	148	154	159	163	166	168	170	171
8	042	062	078	094	107	118	127	134	140	146	150	154	158	161	163	164
9	042	060	076	091	104	114	122	128	134	139	143	147	151	154	156	157
10	042	058	074	088	101	111	118	125	130	135	139	143	146	149	151	152
11	042	057	072	086	098	108	115	121	126	130	134	138	141	144	146	147

12	040	220	323	333	296	257	228	208	194	183	174	168	162	159	157	156
13	040	108	172	233	270	283	278	264	250	239	227	219	208	200	193	187
14	040	080	125	163	193	215	228	238	239	238	233	227	221	215	210	207
15	040	074	106	135	160	179	193	203	209	213	214	214	212	210	207	204
16	040	070	096	119	139	154	167	178	185	191	194	196	196	196	195	194
17	040	067	090	111	127	140	151	160	167	173	178	180	181	182	182	182
18	040	065	086	104	118	130	140	148	155	160	164	167	170	172	172	172
19	040	063	082	099	113	124	133	141	148	152	156	160	162	164	165	166
20	040	061	079	095	108	119	128	135	142	146	150	154	156	157	158	159
21	040	059	076	092	104	115	124	131	137	141	145	149	151	153	154	155
22	040	057	074	089	101	111	120	127	132	137	141	144	147	149	151	152

(Table continues)

Table 18 (Continued)

23	045	227	286	251	217	192	174	162	153	147	142	139	136	134	133	132
24	045	119	181	234	248	237	223	208	196	184	174	167	162	158	156	155
25	045	093	135	168	195	210	217	216	212	205	198	190	183	176	170	164
26	045	083	114	141	164	182	191	195	196	195	194	191	188	184	179	174
27	045	078	103	125	145	160	171	178	182	184	185	184	183	181	179	177
28	045	074	095	115	132	146	157	164	169	173	174	175	175	175	175	175
29	045	071	091	108	124	137	147	154	160	164	166	167	168	169	170	170
30	045	069	087	104	119	130	139	146	152	156	159	160	161	162	163	164
31	045	067	084	100	114	125	133	140	145	149	152	154	156	157	158	159
32	045	065	082	097	110	121	128	135	140	144	147	149	151	152	153	154
33	045	063	080	094	107	118	124	131	136	140	142	144	146	147	148	149
34	080	170	201	182	150	132	124	118	114	111	109	107	106	105	105	105
35	063	105	169	185	187	175	160	149	140	132	127	122	119	117	115	115
36	058	097	134	164	178	181	175	166	156	148	142	138	134	132	130	128
37	056	086	113	138	158	167	169	169	167	164	160	155	149	145	142	140
38	055	080	104	125	142	154	162	165	166	164	160	155	153	152	150	150
39	054	075	096	114	130	143	152	158	160	160	158	155	153	152	152	152
40	053	071	090	109	124	137	146	151	154	155	154	153	152	152	152	152
41	052	069	086	104	119	131	140	146	149	151	151	151	151	151	151	151
42	051	067	083	100	114	126	135	141	145	147	149	150	150	150	150	150
43	049	065	081	097	110	121	130	136	141	143	146	147	147	147	147	147
44	047	063	079	094	106	116	125	132	137	140	143	144	145	145	145	145

(Table continues)

Table 18 (Continued)

45	109	137	127	110	097	091	087	085	083	082	081	080	080	080	080	080
46	057	108	133	135	128	119	111	104	099	095	093	091	089	088	088	088
47	054	093	119	133	139	136	128	121	116	111	107	103	101	099	098	097
48	052	083	108	126	135	139	138	132	127	122	118	114	111	108	106	105
49	051	078	100	118	130	137	138	137	133	130	126	123	119	116	114	113
50	050	074	094	111	125	134	138	138	137	135	132	128	125	122	120	119
51	054	072	090	106	120	130	135	137	137	135	132	130	129	127	126	125
52	053	070	087	102	116	126	132	135	135	133	132	131	130	129	128	128
53	052	068	084	099	112	123	129	132	133	132	131	131	131	130	130	130
54	050	066	082	097	109	120	126	130	132	132	131	131	131	131	131	131
55	048	064	080	095	107	117	124	128	131	131	131	131	131	131	131	131

56	110	094	080	072	067	064	062	061	060	060	060	060	060	060	060	060
57	074	088	095	091	084	079	075	071	069	067	066	065	065	065	065	065
58	062	080	095	101	098	092	087	083	079	077	075	073	072	071	071	071
59	057	076	093	103	106	102	097	093	088	085	083	081	080	079	078	077
60	053	073	091	103	110	110	108	103	100	096	093	090	088	086	085	084
61	049	070	088	102	110	113	113	111	108	105	102	098	096	094	092	091
62	046	067	085	100	110	114	115	114	112	109	107	105	103	101	100	099
63	043	065	083	098	109	114	116	116	115	114	112	110	108	107	106	105
64	041	063	081	096	107	114	117	118	118	117	116	114	112	111	110	109
65	039	061	079	094	105	113	117	119	120	120	119	117	116	115	114	114
66	037	059	077	093	104	113	118	120	121	121	121	120	119	118	117	117

Table 19
Hydrodynamic Coefficient X_2 in the Input Form

67	000	016	025	031	035	036	037	036	035	034	033	032	030	028	026	024
68	000	017	027	037	045	052	058	061	064	066	068	070	071	072	073	073
69	000	017	029	040	051	059	066	073	079	083	087	091	095	099	101	104
70	000	019	032	042	052	062	070	078	085	091	097	103	108	113	117	121
71	000	019	032	043	053	063	072	080	088	096	103	109	115	120	125	129
72	000	019	032	043	054	065	074	083	091	099	106	113	119	125	131	136
73	000	019	032	043	054	065	074	083	092	100	108	116	123	129	135	140
74	000	019	032	045	056	066	076	085	093	101	109	117	125	131	137	142
75	000	019	032	045	056	066	076	085	093	102	110	118	126	133	139	143
76	000	019	032	045	056	066	076	085	094	103	111	119	127	134	140	145
77	000	019	032	045	056	066	076	085	094	103	112	120	128	135	141	147

78	000	016	022	026	027	028	027	026	024	023	022	021	020	019	018	017
79	000	016	029	037	043	048	052	054	056	057	058	058	058	058	057	057
80	000	017	030	040	048	056	062	067	072	076	078	080	082	084	085	086
81	000	017	030	041	052	060	068	075	080	085	090	094	097	100	103	106
82	000	017	031	043	053	063	071	079	085	091	096	101	106	111	115	118
83	000	018	031	043	053	063	072	080	088	095	101	107	112	117	122	126
84	000	018	032	043	054	064	074	082	090	098	104	110	116	122	128	133
85	000	018	032	045	055	065	075	083	091	099	106	113	119	125	131	136
86	000	018	032	045	055	065	075	084	092	100	108	115	121	127	133	138
87	000	018	032	045	056	066	076	085	093	101	109	116	123	129	135	140
88	000	018	032	045	056	066	076	086	094	102	110	117	124	130	136	141

(Table continues)

Table 19 (Continued)

89	000	015	020	022	023	022	021	019	017	016	014	013	011	010	008	007
90	000	016	026	034	038	042	044	045	046	045	044	044	043	042	041	040
91	000	016	028	039	046	052	056	060	062	064	066	067	068	068	068	068
92	000	017	030	040	049	057	063	069	073	077	080	082	084	086	087	088
93	000	017	030	042	051	060	068	074	079	084	089	092	095	098	100	102
94	000	018	031	042	052	061	070	077	084	089	094	099	103	107	110	112
95	000	018	031	042	052	062	072	080	086	092	098	104	108	112	116	120
96	000	018	031	043	054	065	074	081	088	095	101	107	112	117	121	125
97	000	018	031	043	054	065	074	082	090	097	103	109	115	120	125	130
98	000	019	032	044	055	066	075	083	091	099	105	111	117	123	128	133
99	000	019	032	044	055	066	075	084	092	100	107	113	119	125	131	136

100	000	014	017	019	018	017	016	014	012	010	008	006	004	003	002	001
101	000	017	026	032	034	036	037	037	036	035	034	032	030	028	026	024
102	000	017	028	037	043	047	050	052	053	054	054	053	052	051	050	048
103	000	018	030	040	047	054	059	062	065	066	068	069	069	069	069	068
104	000	018	030	041	050	058	064	068	072	075	078	080	082	083	083	083
105	000	019	031	041	051	060	067	072	077	082	085	088	091	093	095	096
106	000	019	031	042	052	062	069	076	082	087	091	095	098	101	103	105
107	000	020	032	043	053	063	071	078	084	090	094	098	102	106	109	112
108	000	020	032	044	054	064	072	080	086	092	097	102	107	111	115	119
109	000	020	033	045	055	065	073	081	088	095	100	105	110	115	119	123
110	000	020	033	045	055	065	074	082	090	097	103	108	113	118	122	126

(Table continues)

Table 19 (Continued)

111	000	012	016	015	013	011	009	007	005	003	002	001	002	003	004	003
112	000	015	024	028	030	030	030	027	025	022	020	017	015	013	011	010
113	000	016	026	033	038	040	041	041	041	040	040	037	035	032	030	027
114	000	017	027	036	042	047	051	053	054	054	053	052	051	050	048	046
115	000	018	028	038	046	051	056	060	063	065	066	065	065	064	063	062
116	000	019	030	040	048	054	060	065	070	073	075	076	076	076	075	074
117	000	020	032	042	050	057	064	070	075	079	081	082	083	084	085	085
118	000	020	032	042	051	059	066	073	078	082	086	088	090	091	092	092
119	000	020	032	042	051	060	068	075	080	085	090	093	096	098	100	101
120	000	020	032	042	052	061	070	077	083	088	093	097	100	103	105	107
121	000	020	032	042	053	062	071	079	085	091	096	100	104	107	110	112

122	000	010	012	011	007	005	003	001	000	002	003	004	005	006	006	006
123	000	014	020	022	022	021	019	016	013	010	007	004	002	001	002	004
124	000	014	025	030	032	033	032	030	028	025	022	019	016	013	010	007
125	000	015	025	032	037	040	041	041	040	038	035	032	029	026	023	020
126	000	015	026	036	042	046	049	050	050	050	049	047	045	042	039	036
127	000	015	026	037	045	050	054	056	058	059	058	057	055	053	051	049
128	000	016	030	039	047	054	059	062	064	066	067	067	066	064	062	060
129	000	016	030	039	048	056	062	066	069	071	073	074	074	073	072	070
130	000	016	030	040	050	058	064	069	073	076	079	080	081	081	081	080
131	000	016	030	040	050	059	066	072	076	080	083	085	087	088	088	088
132	000	016	030	041	051	060	068	074	079	084	087	090	092	094	095	095

```
C     ***************************************************************
C                  SHIP MOTIONS, SHEAR AND BENDING MOMENT
C                    IN REGULAR WAVES AND IN CONFUSED SEA
C     ***************************************************************
C
      DIMENSION KZ(2112),CG(10,80),VE(8),CN(8),A(80),B(80),CC(3,4),DIST(
     180),AA(2,2),ZZ(2,2),XA(2,2),XB(2,2),BB(2,2),TS(6,80),C(80),CRD(80)
     2,SS(2,19),SH(8,19),BM(8,19),CME(8),SPC(2,8),SPETT(2,19),TAB(8),VCM
     3(4,8),CA(3,80),GG(80),ESP(8),DFT(80),PRIS(80),SECS(80),PRIP(80),TR
     4AN(2,80),UIL(2,19)
C
      REWIND 2
C
C     READ HYDRODYNAMIC COEFFICIENTS TABLES
C
      INDX=0
      DO 2 IL=1,2112,16
      IN=IL+15
      READ INPUT TAPE 5,201,IND,(KZ(J),J=IL,IN)
      INDX=INDX+1
      IF(INDX-IND)1,2,1
    1 PRINT 202
      PAUSE
    2 CONTINUE
C
C     READ HULL CHARACTERISTICS,SHIP SPEEDS AND WAVE LENGTHS
C
    3 READ INPUT TAPE 5,203,KODC,UVE,AVE,DFTAD,DFTAV,CAMP,RO,K
      DFTAM=0.5*(DFTAD+DFTAV)
      DO 5 J=1,K
      READ INPUT TAPE 5,204,(CA(I,J),I=1,3),KSK
      DFT(J)=DFTAD+(DFTAV-DFTAD)*CA(1,J)/UVE
      IF(J-KSK)4,5,4
    4 PRINT 205
      PAUSE
    5 CONTINUE
      READ INPUT TAPE 5,206,NVEL,(VE(I),I=1,NVEL)
      READ INPUT TAPE 5,206,NCND,(CN(I),I=1,NCND)
C
C     BUOYANCY INTEGRATION
C
      DO 81 J=1,K
      A(J)=CA(1,J)
   81 B(J)=0.00981*RO*CA(3,J)
      KDEF=K
      INDEF=10
      GO TO 301
   82 DO 83 J=1,K
      PRIS(J)=C(J)
   83 B(J)=C(J)
      INDEF=11
      GO TO 301
   84 DO 85 J=1,K
   85 SECS(J)=C(J)
C
C     READ WEIGHT DISTRIBUTION AND INDEXES
C
    6 READ INPUT TAPE 5,207,(CG(6,J),J=1,K)
```

```
C
   55 WRITE OUTPUT TAPE 6,210,KODC,KODP
      WRITE OUTPUT TAPE 6,211,UVE,DIS
      WRITE OUTPUT TAPE 6,212,AVE,FG
      WRITE OUTPUT TAPE 6,213,DFTAM,RGI
      WRITE OUTPUT TAPE 6,209
      DO 94 I=1,19
   94 WRITE OUTPUT TAPE 6,224,I,UIL(1,I),UIL(2,I)
C
C     SHIP SPEED AND WAVE LENGTH VARIATION
C
   14 DO 54 IV=1,NVEL
      V=VE(IV)
   15 DO 47 IC=1,NCND
      CLUN=CN(IC)
      IF(NSTR2)33,33,16
C
C     HYDRODYNAMIC CHARACTERISTICS IN SHIP TRANSVERSE SECTIONS
C
   16 FO=7.849/SQRTF(CLUN)
      F1=FO+6.28*V/CLUN
      DO 19 J=1,K
      GG(J)=CA(3,J)/CA(2,J)
      X=GG(J)/DFT(J)
      Y=CA(2,J)/DFT(J)
      Z=CA(2,J)*F1**2 /19.62
      INIZ=0
      KR=1
      GO TO 401
   17 CG(4,J)=0.3927*RO*CA(2,J)**2 /F
      INIZ=66
      KR=2
      GO TO 401
   18 CG(5,J)=96.2361*RO*F**2 /F1**3
   19 CONTINUE
      DO 20 J=1,K
      CG(3,J)=EXPF(-6.28*GG(J)/CLUN)
   20 CG(2,J)=9.81*RO*CA(2,J)
C
C     MOTION DIFFERENTIAL EQUATION COEFFICIENTS
C
      DO 21 J=1,K
   21 A(J)=CG(1,J)
      KDEF=K
      INDEF=4
      DO 24 L=1,3
      LL=(7*L-L*L-2)/2
      DO 24 J=1,3
      DO 22 I=1,K
   22 B(I)=CG(LL,I)*CG(1,I)**(J-1)
      GO TO 301
   23 CG(J,L)=DEF
   24 CONTINUE
      DO 29 L=1,2
      DO 25 I=1,K
      PI=6.28*CG(1,I)/CLUN
      AA(1,I)=COSF(PI)
      AA(2,I)=-SINF(PI)
```

```
      AA(1,2)=-AA(2,1)
      AA(2,2)=AA(1,1)
      B(I)=CAMP*CG(3,I)*(AA(1,L)*(CG(2,I)-FC*F1*CG(4,I))+FC*AA(2,L)*CG(5
     1,I))
      CG(L+6,I)=B(I)
   25 CG(L+8,I)=-CAMP*V*FC*CG(3,I)*CG(4,I)*AA(2,L)
      INDEF=5
      GO TO 301
   26 ZZ(1,L)=DEF
      DO 27 I=1,K
      PI=6.28*CG(1,I)/CLUN
      AA(1,1)=SINF(PI)
      AA(1,2)=-COSF(PI)
   27 B(I)=B(I)*CG(1,I)-CAMP*CG(3,I)*V*FC*CG(4,I)*AA(1,L)
      INDEF=6
      GO TO 301
   28 ZZ(2,L)=DEF
   29 CONTINUE
C
C     MOTION DIFFERENTIAL EQUATION SOLUTION
C
      DO 30 I=1,2
      K1=5-2*I
      PI=2-I
      PJ=2*I-3
      XA(1,I)=F1**2 *(CC(K1,4)+CC(K1,2))-CC(K1,1)+PI*V*(CC(2,3)+V*CC(1,2
     1))
      XA(2,I)=F1*CC(K1,3)
      XB(1,I)=F1**2 *CC(2,2)-CC(2,1)+PI*V*CC(1,3)
   30 XB(2,I)=F1*(CC(2,3)+PJ*V*CC(1,2))
      DO 31 J=1,2
      KK=3-J
      DO 31 I=1,2
      K1=3-I
      PI=2*I-3
   31 BB(J,I)=XA(1,J)*ZZ(J,I)-PI*XA(2,J)*ZZ(J,K1)-XB(1,J)*ZZ(KK,I)+PI*XB
     1(2,J)*ZZ(KK,K1)
      PI=XA(2,1)*XA(2,2)-XA(1,1)*XA(1,2)+XB(1,1)*XB(1,2)-XB(2,1)*XB(2,2)
      PJ=XA(1,1)*XA(2,2)+XA(2,1)*XA(1,2)-XB(1,1)*XB(2,2)-XB(2,1)*XB(1,2)
      DLT=PI*PI+PJ*PJ
      DO 32 J=1,2
      DO 32 I=1,2
      K1=3-I
      D1=3-2*I
   32 ZZ(J,I)=(PI*BB(J,I)+D1*PJ*BB(J,K1))/DLT
      DO 56 IM=1,4
      KM=(IM+1)/2
      KN=(IM-1)/2
      KP=IM-2*KN
   56 VCM(IM,IC)=ZZ(KM,KP)
C
C     WRITE (READ) ON (FROM) AUXILIARY TAPE 2 (PARTIAL RESULTS)
C
      WRITE TAPE 2,((CG(J3,J4),J3=1,5),J4=1,K),((CG(J5,J6),J5=7,10),J6=1
     1,K),ZZ,FC,F1,(VCM(J7,IC),J7=1,4)
      GO TO 34
   33 READ  TAPE 2,((CG(J3,J4),J3=1,5),J4=1,K),((CG(J5,J6),J5=7,10),J6=1
     1,K),ZZ,FC,F1,(VCM(J7,IC),J7=1,4)
```

```
      READ INPUT TAPE 5,208,KCDP,NSTR1,NSTR2
C
C     STILL WATER SHEAR AND BENDING MOMENT
C
      DO 86 J=1,K
      A(J)=CA(1,J)
   86 B(J)=0.001*CG(6,J)
      KDEF=K
      INDEF=12
      GO TO 301
   87 DO 88 J=1,K
      PRIP(J)=C(J)
   88 SECS(J)=C(J)
      INDEF=13
      GO TO 301
   89 DO 90 J=1,K
      TRAN(1,J)=PRIP(J)-PRIS(J)
   90 TRAN(2,J)=C(J)-SECS(J)
      IMPOL=2
      DO 93 J=1,2
      DO 91 I=1,K
      DIST(I)=CA(1,I)
   91 COD(I)=TRAN(J,I)
      DO 93 I=1,19
      F=I
      UV=0.05*F*UVE
      GO TO 501
   92 UIL(J,I)=USC
   93 CONTINUE
      DO 57 J=1,K
   57 CG(6,J)=CG(6,J)/9.81
      IF(NSTR2)55,55,7
C
C     WEIGHT DISTRIBUTION CHARACTERISTICS
C
    7 DO 8 J=1,K
      A(J)=CA(1,J)
    8 B(J)=CG(6,J)
      KDEF=K
      INDEF=1
      GO TO 301
    9 CC(1,4)=DEF
      DO 10 J=1,K
   10 B(J)=B(J)*A(J)
      INDEF=2
      GO TO 301
   11 FG=DEF/CC(1,4)
      DO 12 J=1,K
      CG(1,J)=CA(1,J)-FG
      A(J)=CG(1,J)
   12 B(J)=CG(6,J)*A(J)**2
      INDEF=3
      GO TO 301
   13 CC(3,4)=DEF
      DIS=0.00981*CC(1,4)
      RGI=100.*SQRTF(CC(3,4)/CC(1,4))/UVE
C
C     WRITE STILL WATER SHEAR AND BENDING MOMENT
```

```
C
C      SHEAR AND BENDING MOMENT IN REGULAR WAVES
C
   34 DO 35 I=1,K
   35 GG(I)=F1**2 *(CG(6,I)+CG(4,I))-CG(2,I)
      DO 36 J=1,2
      PI=3-2*J
      K1=3-J
      DO 36 I=1,K
      PJ=F1*(ZZ(1,K1)+CG(1,I)*ZZ(2,K1))+PI*V*ZZ(2,J)
      TS(J,I)=GG(I)*(ZZ(1,J)+CG(1,I)*ZZ(2,J))+PI*CG(5,I)*PJ-PI*V*F1*CG(4
     1,I)*ZZ(2,K1)+CG(J+6,I)
   36 CG(J+8,I)=CG(J+8,I)-PI*V*CG(4,I)*PJ
      DO 41 L=1,2
      K1=L+8
      DO 37 I=1,K
      A(I)=CG(1,I)
   37 B(I)=TS(L,I)
      KDEF=K
      INDEF=7
      GO TO 301
   38 DO 39 I=1,K
      C(I)=C(I)+CG(K1,I)
      B(I)=C(I)
   39 TS(L+2,I)=C(I)*C(I)
      INDEF=8
      GO TO 301
   40 DO 41 I=1,K
   41 TS(L+4,I)=C(I)*C(I)
      DO 42 J=1,2
      K1=2*J+1
      DO 42 I=1,K
   42 TS(J,I)=(SQRTF(TS(K1,I)+TS(K1+1,I)))/1000.
C
C      SHEAR AND BENDING MOMENT INTERPOLATION
C
      IMPOL=1
      DO 45 J=1,2
      DO 43 I=1,K
   43 ORD(I)=TS(J,I)
      DO 45 I=1,19
      F=I
      UV=0.05*F*UVE
      GO TO 501
   44 SS(J,I)=USC
   45 CONTINUE
      DO 46 I=1,19
      SH(IC,I)=SS(1,I)
   46 BM(IC,I)=SS(2,I)
C
C      SHEAR AND BENDING MOMENT IN CONFUSED SEA
C
   47 OME(IC)=FC
      DO 48 I=1,NOND
      A(I)=OME(I)
   48 ESP(I)=-SQRTF((A(I)-0.377)**2 /(0.065*(A(I)-0.117)))
      KDEF=NOND
      DO 52 KSEZ=1,19
```

```
      DO 49 I=1,NOND
      SPC(1,I)=SH(I,KSEZ)**2 *37.45*EXPF(ESP(I))
   49 SPC(2,I)=BM(I,KSEZ)**2 *37.45*EXPF(ESP(I))
      DO 52 J=1,2
      DO 50 I=1,NOND
   50 B(I)=SPC(J,I)
      INDEF=9
      GO TO 301
   51 SPETT(J,KSEZ)=3.044*SQRTF(DEF)
   52 CONTINUE
C
C     WRITE RESULTS (MOTIONS,SHEAR AND BENDING MOMENT)
C
      WRITE OUTPUT TAPE 6,214
      WRITE OUTPUT TAPE 6,215,KODC,KODP,V
      WRITE OUTPUT TAPE 6,216,(ON(I),I=1,NOND)
      WRITE OUTPUT TAPE 6,217,(OME(I),I=1,NOND)
      WRITE OUTPUT TAPE 6,218,(VOM(1,I),I=1,NOND)
      WRITE OUTPUT TAPE 6,219,(VOM(2,I),I=1,NOND)
      WRITE OUTPUT TAPE 6,220,(VOM(3,I),I=1,NOND)
      WRITE OUTPUT TAPE 6,221,(VOM(4,I),I=1,NOND)
      WRITE OUTPUT TAPE 6,222
      DO 53 I=1,19
   53 WRITE OUTPUT TAPE 6,223,I,(SPETT(JO,I),JO=1,2),(SH(J,I),BM(J,I),J=
     11,NOND)
   54 CONTINUE
      REWIND 2
      IF(NSTR1)3,3,6
C
C     INTEGRATION SUBPROGRAM
C
  301 Q=A(2)-A(1)
      C(1)=0.
      DO 306 INT=2,KDEF
      P=Q
      Q=-1.
      IF(KDEF-INT)304,304,302
  302 Q=A(INT+1)-A(INT)
      IF(P-0.05)304,304,303
  303 IF(Q-0.05)304,304,305
  304 C(INT)=C(INT-1)+0.5*P*(B(INT)+B(INT-1))
      IF(Q)307,307,306
  305 R=P/Q
      G=0.1666667*P/(1.+R)
      S=R*R
      C(INT)=C(INT-1)+G*(B(INT-1)*(3.+2.*R)+B(INT)*(3.+4.*R+S)-S*B(INT+1
     1))
  306 CONTINUE
  307 DEF=C(INT)
      GO TO (9,11,13,23,26,28,38,40,51,82,84,87,89),INDEF
C
C     HYDRODYNAMIC COEFFICIENTS TABLES INTERPOLATION SUBPROGRAM
C
  401 KK=1
      IF(X-0.5)402,403,403
  402 I=1
      GO TO 404
  403 I=10.*X-4.
```

```
  404 IF(Y-0.4)405,406,406
  405 JJ=1
      GO TO 407
  406 JJ=2.5*Y
  407 KK=1.+10.*Z
      K1=KK
      IF(6-I)408,408,409
  408 I=5
  409 IF(11-JJ)410,410,411
  410 JJ=10
  411 IF(16-KK)412,412,413
  412 KK=15
  413 NBL1=11*(I-1)+JJ+INIZ-1
      KK=KK+16*NBL1
      DO 417 MU=1,4
      IF(MU-2)414,414,415
  414 JCTA=16*(MU-1)
      GO TO 416
  415 JCTA=16*(MU+8)
  416 KAPPA=KK+JCTA
      TAB(MU)=KZ(KAPPA)
      KAPPA=KK+JCTA +1
  417 TAB(MU+4)=KZ(KAPPA)
      DO 418 JE=1,8
  418 TAB(JE)=0.001*TAB(JE)
      VMI=I
      VMJ=JJ
      VMK=K1
      DX=X-(0.4+0.1*VMI)
      DY=Y-0.4*VMJ
      DZ=Z-0.1*(VMK-1.)
      F11=10.*(TAB(3)-TAB(1))
      F22=2.5*(TAB(2)-TAB(1))
      F33=10.*(TAB(5)-TAB(1))
      F12=25.*(TAB(1)-TAB(2)-TAB(3)+TAB(4))
      F13=100.*(TAB(1)-TAB(3)-TAB(5)+TAB(7))
      F23=25.*(TAB(1)-TAB(2)-TAB(5)+TAB(6))
      F123=250.*(-TAB(1)+TAB(2)+TAB(3)-TAB(4)+TAB(5)-TAB(6)-TAB(7)+TAB(8
     1))
      F=TAB(1)+F11*DX+F22*DY+F33*DZ+F12*DX*DY+F13*DX*DZ+F23*DY*DZ+F123*D
     1X*DY*DZ
      GO TO (17,18),KR
C
C     SHEAR AND BENDING MOMENT INTERPOLATION SUBPROGRAM
C
  501 DO 502 IL=1,K
      DFR=DIST(IL)-UV
      IF(DFR)502,503,504
  502 CONTINUE
  503 USC=ORD(IL)
      GO TO(44,92),IMPOL
  504 USC=DFR*(ORD(IL)-ORD(IL-1))/(DIST(IL)-DIST(IL-1))
      USC=ORD(IL)-USC
      GO TO(44,92),IMPOL
C
C     INPUT/OUTPUT FORMAT
C
  201 FORMAT(I3,1X,16I4)
```

```
202 FORMAT(32HSCHEDE TABELLE FUORI ORDINAMENTO)
203 FORMAT(I3,6F8.3,I3)
204 FORMAT(3F8.3,I3)
205 FORMAT(31HSCHEDE CARENA FUORI ORDINAMENTO)
206 FORMAT(I3,8F8.3)
207 FORMAT(8F10.0)
208 FORMAT(3I3)
210 FORMAT(1H1,46X,11HCODICE NAVE,I4,9X,11HCODICE PESI,I4)
211 FORMAT(1X//37X,14HLUNGHEZZA  (M),F8.2,6X,18HDISLOCAMENTO   (T),F11
   1.0)
212 FORMAT(1X/37X,14HLARGHEZZA  (M),F8.2,6X,18HASC.BARICENTRO (M),F11.
   12)
213 FORMAT(1X/37X,14HIMM. MEDIA (M),F8.2,6X,18HRAGGIO GIRAZ.  ($),F11.
   12)
209 FORMAT(1X////48X,11HTAGLIO  (T),13X,13HMOMENTO (T*M))
224 FORMAT(1X/37X,I2,7X,F10.0,16X,F10.0)
214 FORMAT(1H1,90X,30HCOD.NAVE    COD.PESI   VELOCITA)
215 FORMAT(1X/93X,I3,8X,I3,F12.2)
216 FORMAT(1X//3X,17HLUNGHEZZA ONDA    ,8(3X,F7.2,4X))
217 FORMAT(1X/3X,17HFREQUENZA ONDA    ,8(3X,F7.4,4X))
218 FORMAT(1X/3X,17HSUSSULTO   COS    ,8(3X,F7.4,4X))
219 FORMAT(1X/3X,17HSUSSULTO   SEN    ,8(3X,F7.4,4X))
220 FORMAT(1X/3X,17HBECCHEGGIO COS    ,8(3X,F7.4,4X))
221 FORMAT(1X/3X,17HBECCHEGGIO SEN    ,8(3X,F7.4,4X))
222 FORMAT(1X//3H NO,3X,1HT,6X,1HM,6X,8(3X,1HT,6X,1HM,3X))
223 FORMAT(1X/I3,F6.0,F9.0,2X,8(F7.1,F7.0))
    END
```

APPENDIX. Tables of $c_m \times 10^6$ values for L = 200 m and W = 60 kn.

Table A1a
Values of $c_m \times 10^6$ for L = 200 m, W = 60 knots,
P = 0.345, C_w = 0.804, and Fr = 0.00

L/B \ L/i	16.00	17.50	19.00	23.75	28.50	30.00	31.50
7.00	564	573	583	606	621	627	632
7.25	567	576	586	608	623	629	634
7.50	569	578	588	610	625	631	636
6.75	572	581	590	613	628	634	639

Table A1b
Values of $c_m \times 10^6$ for L = 200 m, W = 60 knots,
P = 0.345, C_w = 0.804, and Fr = 0.05

L/B \ L/i	16.00	17.50	19.00	23.75	28.50	30.00	31.50
7.00	597	599	601	610	624	629	633
7.25	599	601	603	613	626	631	635
7.50	601	603	605	616	628	633	638
7.75	603	606	608	618	631	636	640

Table A1c
Values of $c_m \times 10^6$ for L = 200 m, W = 60 knots,
P = 0.345, C_w = 0.804, and Fr = 0.10

L/B \ L/i	16.00	17.50	19.00	23.75	28.50	30.00	31.50
7.00	611	614	619	629	633	636	639
7.25	613	616	621	632	635	638	641
7.50	615	619	623	634	638	641	643
7.75	618	621	625	637	640	643	646

Table A2a
Values of $c_m \times 10^6$ for L = 200 m, W = 60 knots,
P = 0.404, C_w = 0.804, and Fr = 0.00

L/B \ L/i	16.00	17.50	19.00	23.75	28.50	30.00	31.50
7.00	514	530	543	575	597	604	610
7.25	517	533	546	579	600	607	613
7.50	520	536	549	582	603	610	616
7.75	523	539	552	585	606	613	619

Table A2b
Values of $c_m \times 10^6$ for L = 200 m, W = 60 knots,
P = 0.404, C_w = 0.804, and Fr = 0.05

L/B \ L/i	16.00	17.50	19.00	23.75	28.50	30.00	31.50
7.00	489	507	522	558	584	691	598
7.25	492	511	525	562	587	594	601
7.50	496	514	529	565	590	597	604
7.75	499	517	532	569	593	600	607

Table A2c
Values of $c_m \times 10^6$ for L = 200 m, W = 60 knots,
P = 0.404, C_w = 0.804, and Fr = 0.10

L/B \ L/i	16.00	17.50	19.00	23.75	28.50	30.00	31.50
7.00	474	486	501	540	567	574	581
7.25	477	490	504	543	570	577	584
7.50	480	493	507	547	574	580	587
7.75	483	496	511	550	577	583	590

Table A3a
Values of $c_m \times 10^6$ for L = 200 m, W = 60 knots,
P = 0.448, C_w = 0.804, and Fr = 0.00

L/B \ L/i	16.00	17.50	19.00	23.75	28.50	30.00	31.50
7.00	475	496	514	554	580	587	594
7.25	479	500	517	557	583	590	597
7.50	483	504	520	560	586	593	600
7.75	486	508	523	564	589	596	603

Table A3b
Values of $c_m \times 10^6$ for L = 200 m, W = 60 knots,
P = 0.448, C_w = 0.804, and Fr = 0.05

L/B \ L/i	16.00	17.50	19.00	23.75	28.50	30.00	31.50
7.00	413	440	463	518	553	562	571
7.25	416	443	467	522	556	566	574
7.50	420	447	470	526	559	569	578
7.75	423	450	474	530	563	573	582

Table A3c
Values of $c_m \times 10^6$ for L = 200 m, W = 60 knots,
P = 0.448, C_w = 0.804, and Fr = 0.10

L/B \ L/i	16.00	17.50	19.00	23.75	28.50	30.00	31.50
7.00	385	403	422	478	518	528	538
7.25	388	406	426	482	521	531	542
7.50	391	409	429	485	525	534	545
7.75	394	412	432	488	528	538	549

Table A4a
Values of $c_m \times 10^6$ for L = 200 m, W = 60 knots,
P = 0.345, C_w = 0.836, and Fr = 0.00

L/B \ L/i	16.00	17.50	19.00	23.75	28.50	30.00	31.50
7.00	609	618	628	651	669	673	678
7.25	612	621	631	654	672	676	680
7.50	614	623	634	657	674	678	683
7.75	617	626	636	660	677	681	686

Table A4b
Values of $c_m \times 10^6$ for L = 200 m, W = 60 knots,
P = 0.345, C_w = 0.836, and Fr = 0.05

L/B \ L/i	16.00	17.50	19.00	23.75	28.50	30.00	31.50
7.00	649	650	650	657	671	675	680
7.25	652	653	653	660	674	678	683
7.50	654	655	655	663	677	681	686
7.75	657	658	658	665	679	683	689

Table A4c
Values of $c_m \times 10^6$ for L = 200 m, W = 60 knots,
P = 0.345, C_w = 0.836, and Fr = 0.10

L/B \ L/i	16.00	17.50	19.00	23.75	28.50	30.00	31.50
7.00	670	671	673	679	683	684	686
7.25	673	674	676	682	686	687	689
7.50	675	676	678	684	689	690	691
7.75	678	678	681	687	691	692	694

Table A5a
Values of $c_m \times 10^6$ for L = 200 m, W = 60 knots,
P = 0.404, C_w = 0.836, and Fr = 0.00

L/B \ L/i	16.00	17.50	19.00	23.75	28.50	30.00	31.50
7.00	559	574	588	621	644	650	657
7.25	562	578	592	624	647	653	660
7.50	565	581	595	628	650	656	663
7.75	568	584	598	631	653	659	666

Table A5b
Values of $c_m \times 10^6$ for L = 200 m, W = 60 knots,
P = 0.404, C_w = 0.836, and Fr = 0.05

L/B \ L/i	16.00	17.50	19.00	23.75	28.50	30.00	31.50
7.00	542	558	571	605	631	638	644
7.25	546	562	575	609	634	641	647
7.50	549	565	579	612	637	644	651
7.75	553	569	582	616	641	648	654

Table A5c
Values of $c_m \times 10^6$ for L = 200 m, W = 60 knots,
P = 0.404, C_w = 0.836, and Fr = 0.10

L/B \ L/i	16.00	17.50	19.00	23.75	28.50	30.00	31.50
7.00	537	547	559	592	617	623	629
7.25	541	551	562	595	620	626	632
7.50	544	554	566	598	623	630	636
7.75	548	558	569	602	627	633	639

Table A6a
Values of $c_m \times 10^6$ for L = 600 m, W = 60 knots,
P = 0.448, C_w = 0.836, and Fr = 0.00

L/B \ L/i	16.00	17.50	19.00	23.75	28.50	30.00	31.50
7.00	520	541	559	599	626	634	641
7.25	524	545	562	603	628	637	644
7.50	528	549	566	607	631	640	647
7.75	532	553	570	610	634	643	650

Table A6b
Values of $c_m \times 10^6$ for L = 600 m, W = 60 knots,
P = 0.448, C_w = 0.836, and Fr = 0.05

L/B \ L/i	16.00	17.50	19.00	23.75	28.50	30.00	31.50
7.00	465	491	513	565	600	609	617
7.25	469	495	517	569	604	613	621
7.50	473	498	521	573	608	617	625
7.75	476	502	524	577	612	621	629

Table A6c
Values of $c_m \times 10^6$ for L = 600 m, W = 60 knots,
P = 0.448, C_w = 0.836, and Fr = 0.10

L/B \ L/i	16.00	17.50	19.00	23.75	28.50	30.00	31.50
7.00	444	462	480	530	568	578	587
7.25	448	466	484	534	571	581	590
7.50	451	469	488	538	575	585	594
7.75	455	473	491	541	579	590	598

Table A7a
Values of $c_m \times 10^6$ for L = 200 m, W = 60 knots,
P = 0.345, C_w = 0.872, and Fr = 0.00

L/B \ L/i	16.00	17.50	19.00	23.75	28.50	30.00	31.50
7.00	668	677	687	711	729	735	741
7.25	670	679	690	714	732	737	743
7.50	673	682	693	718	734	740	745
7.75	676	685	696	721	737	742	748

Table A7b
Values of $c_m \times 10^6$ for L = 200 m, W = 60 knots,
P = 0.345, C_w = 0.872, and Fr = 0.05

L/B \ L/i	16.00	17.50	19.00	23.75	28.50	30.00	31.50
7.00	720	717	714	719	732	737	742
7.25	723	720	717	722	735	740	745
7.50	726	723	720	725	738	743	748
7.75	729	726	723	728	741	746	751

Table A7c
Values of $c_m \times 10^6$ for L = 200 m, W = 60 knots,
P = 0.345, C_w = 0,872, and Fr = 0.10

L/B \ L/i	16.00	17.50	19.00	23.75	28.50	30.00	31.50
7.00	745	746	746	746	748	749	751
7.25	748	749	749	749	751	752	754
7.50	751	752	752	752	754	755	757
7.75	754	755	755	756	757	758	760

Table A8a
Values of $c_m \times 10^6$ for L = 200 m, W = 60 knots,
P = 0.404, C_w = 0.872, and Fr = 0.00

L/B \ L/i	16.00	17.50	19.00	23.75	28.50	30.00	31.50
7.00	619	634	649	682	706	713	720
7.25	623	638	653	686	709	716	723
7.50	627	642	656	690	712	719	726
7.75	630	645	660	694	715	722	730

Table A8b
Values of $c_m \times 10^6$ for L = 200 m, W = 60 knots,
P = 0.404, C_w = 0.872, and Fr = 0.05

L/B \ L/i	16.00	17.50	19.00	23.75	28.50	30.00	31.50
7.00	617	629	639	669	694	702	709
7.25	621	633	643	673	697	705	712
7.50	625	637	647	676	701	708	716
7.75	628	640	650	680	704	712	719

Table A8c
Values of $c_m \times 10^6$ for L = 200 m, W = 60 knots,
P = 0.404, C_w = 0.872, and Fr = 0.10

L/B \ L/i	16.00	17.50	19.00	23.75	28.50	30.00	31.50
7.00	621	630	638	664	685	691	698
7.25	625	634	642	668	688	694	701
7.50	628	638	646	672	691	697	704
7.75	632	641	649	675	695	701	709

Table A9a
Values of $c_m \times 10^6$ for L = 200 m, W = 60 knots,
P = 0.448, C_w = 0.872, and Fr = 0.00

L/B \ L/i	16.00	17.50	19.00	23.75	28.50	30.00	31.50
7.00	583	603	621	661	689	697	705
7.25	588	608	624	665	692	700	708
7.50	592	612	629	669	695	703	711
7.75	596	616	633	673	698	707	714

Table A9b
Values of $c_m \times 10^6$ for L = 200 m, W = 60 knots,
P = 0.448, C_w = 0.872, and Fr = 0.05

L/B \ L/i	16.00	17.50	19.00	23.75	28.50	30.00	31.50
7.00	544	565	584	632	666	675	684
7.25	548	569	588	636	670	679	688
7.50	552	573	592	640	674	683	692
7.75	556	577	596	644	678	687	696

Table A9c
Values of $c_m \times 10^6$ for L = 200 m, W = 60 knots,
P = 0.448, C_w = 0.872, and Fr = 0.10

L/B \ L/i	16.00	17.50	19.00	23.75	28.50	30.00	31.50
7.00	526	545	562	602	639	649	658
7.25	530	549	566	606	643	653	662
7.50	534	552	570	610	647	657	665
7.75	537	556	574	614	651	661	669

Table A10a
Values of $c_m \times 10^6$ for L = 200 m, W = 60 knots,
P = 0.345, C_w = 0.900, and Fr = 0.00

L/B \ L/i	16.00	17.50	19.00	23.75	28.50	30.00	31.50
7.00	710	718	728	755	773	778	783
7.25	713	721	731	758	776	781	786
7.50	716	724	734	761	779	784	789
7.75	719	727	737	764	782	788	793

Table A10b
Values of $c_m \times 10^6$ for L = 200 m, W = 60 knots,
P = 0.345, C_w = 0.900, and Fr = 0.05

L/B \ L/i	16.00	17.50	19.00	23.75	28.50	30.00	31.50
7.00	764	763	760	764	776	780	785
7.25	768	767	763	767	779	783	788
7.50	772	771	767	770	783	787	792
7.75	775	774	770	773	787	791	796

Table A10c
Values of $c_m \times 10^6$ for L = 200 m, W = 60 knots,
P = 0.345, C_w = 0.900, and Fr = 0.10

L/B \ L/i	16.00	17.50	19.00	23.75	28.50	30.00	31.50
7.00	797	794	793	793	793	794	795
7.25	801	798	797	797	797	798	799
7.50	805	801	801	801	801	801	803
7.75	808	805	804	804	804	805	806

Table A11a
Values of $c_m \times 10^6$ for L = 200 m, W = 60 knots,
P = 0.404, C_w = 0.900, and Fr = 0.00

L/B \ L/i	16.00	17.50	19.00	23.75	28.50	30.00	31.50
7.00	659	674	689	725	749	756	762
7.25	662	678	692	729	752	759	765
7.50	666	682	696	732	756	763	769
7.75	669	685	699	736	759	766	773

Table A11b
Values of $c_m \times 10^6$ for L = 200 m, W = 60 knots,
P = 0.404, C_w = 0.900, and Fr = 0.05

L/B \ L/i	16.00	17.50	19.00	23.75	28.50	30.00	31.50
7.00	661	673	683	712	737	744	751
7.25	665	677	687	716	741	748	755
7.50	669	681	691	720	745	752	759
7.75	673	685	694	724	749	756	763

Table A11c
Values of $c_m \times 10^6$ for L = 200 m, W = 60 knots,
P = 0.404, C_w = 0.900, and Fr = 0.10

L/B \ L/i	16.00	17.50	19.00	23.75	28.50	30.00	31.50
7.00	670	677	685	710	729	734	740
7.25	674	681	689	714	733	738	744
7.50	678	685	692	718	737	742	748
7.75	682	689	696	722	741	746	752

Table A12a
Values of $c_m \times 10^6$ for L = 200 m, W = 60 knots,
P = 0.448, C_w = 0.900, and Fr = 0.00

L/B \ L/i	16.00	17.50	19.00	23.75	28.50	30.00	31.50
7.00	621	642	659	704	732	739	747
7.25	625	647	663	708	735	743	751
7.50	629	651	667	712	739	747	755
7.75	633	655	670	715	743	751	759

Table A12b
Values of $c_m \times 10^6$ for L = 200 m, W = 60 knots,
P = 0.448, C_w = 0.900, and Fr = 0.05

L/B \ L/i	16.00	17.50	19.00	23.75	28.50	30.00	31.50
7.00	586	608	626	674	708	717	726
7.25	590	612	630	679	712	721	730
7.50	594	616	634	683	717	726	734
7.75	598	620	638	687	721	730	739

Table 12c
Values of $c_m \times 10^6$ for L = 200 m, W = 60 knots,
P = 0.448, C_w = 0.900, and Fr = 0.10

L/B \ L/i	16.00	17.50	19.00	23.75	28.50	30.00	31.50
7.00	572	590	606	649	682	691	700
7.25	576	594	610	654	686	695	704
7.50	580	598	614	658	691	700	708
7.75	584	602	618	662	695	704	713

* * *

DISCUSSION

G. Aertssen
University of Ghent
Ghent, Belgium

This work of Prof. Marsich and Dr. Merega on bending moments is undoubtedly one of the investigations which should be made. I have, however, two remarks, both related to the sea aspect the authors have selected for their calculations. In their Table 1, they refer to wind speeds of 60, 65, and 70 knots and corresponding wave heights of 13, 14, and 16 m, but nevertheless the calculations are made for a 60-knot wind and the corresponding wave height of 13.23 m. However, significant wave heights of 16 m have in fact been reported. I confess that this wave height of 16 m was recorded near Iceland and that the usual track of a 200-m ship is not in this area.

My second remark concerns energy distribution in waves. The authors assumed what they in Sec. 1.1 called a long-crested confused sea. There was a contradiction in this sea description. If the sea is long-crested the superposition principle fully applies. For a confused sea you have to assume a directional energy spread, and this, according to experiment, gives you a longitudinal moment which is 10 to 20% less. Actually, in these extreme seas energy is spread, and so it happens that the 20% loss in bending moments because of a significant wave height taken too low is counterbalanced by the 20% gain made by the authors where they ignored directional spread. There is also the question of Froude number. For a ship 200 m in length a Froude number 0.1 corresponds to a speed of 9 knots. I hardly imagine a ship, even one so large as 200 m, sailing at a speed of 9 knots ahead in waves Beaufort 11. I would also raise the point of wave frequency, but here again the authors are on the pessimistic side. Altogether, it is a satisfactory approach to the problem.

* * *

DISCUSSION

H. Volpich
Brown Bros. & Co. Ltd.
Edinburg, Scotland

The authors have selected for their important and valuable investigation the Series-60 Todd hull forms and given for them the appropriate parameters in the paper. Since the modern trend for large bulk-carriers and tankers consists of hull forms having large ram bulbs, it is suggested they include in any future study at least one form with a heavy ram bulb, because this may show up in the resulting bending moments and would give some idea of any possible deviations from the Todd Series 60, when the calculations are applied to bulbous hull forms.

It is stated in the paper that the investigation was carried out in a confused sea generated by a 60-knot wind and with given wavelengths. For comparative purposes it would have been advisable for the authors to have used a standard, internationally accepted spectrum, say, the Moskowitz one, which is nowadays available for confused seas at various wave slopes and Beaufort numbers.

* * *

REPLY TO THE DISCUSSION

S. Marsich and F. Merega

We thank Prof. Aertssen and Mr. Volpich for the favorable comments forwarded. As regards the remarks by Prof. Aertssen, we reply that our assumptions are justified by the aim to which our study was intended, not to furnish results valid as absolute values but to furnish only figures suitable for presenting evidence on the dependence of wave bending moment on different parameters characterizing hull form and weight distribution.

As regards the comments by Mr. Volpich, we want to assure him that we intend to extend our research both by considering bulbous hulls and examining the influence of different sea spectra.

* * *

Thursday, August 29, 1968

Morning Session

UNCONVENTIONAL PROPULSION

Chairmen: Prof. E. Castagneto

Instituto di Architettura Navale, University of Naples
Naples, Italy

Vice Adm. R. Brard

Bassin d'Essais des Carènes
Paris, France

and

M. P. Tulin

Hydronautics, Inc.
Laurel, Maryland

PROSPECTS FOR UNCONVENTIONAL MARINE PROPULSION DEVICES

A. Silverleaf

National Physical Laboratory
Teddington, England

ABSTRACT

This paper is intended as a general review of some of the factors which influence the development of propulsion devices for ships and other marine craft.

First, some general points are examined, and an attempt made to define criteria which help the designer to choose the propulsion system. Although there are few rules which apply to all classes or types of ship, the simplest useful parameter is the speed-displacement ratio; as this increases, so does the specific power (or power per ton-knot), and thus the power-weight characteristic of the propelling machinery becomes more important. Generally, at low and at high values of the speed-displacement ratio, the choice of main machinery and propulsion device is fairly clear; difficulties occur at intermediate values. However, high absolute power requirements also make choice more difficult.

Next, the principal features of the main types of propulsion device are outlined, and their potentialities and limitations considered. The long-established, orthodox open marine propeller is still a most efficient device for converting rotational energy into propulsive thrust, but its range of application is not unlimited. To extend the range of efficient operation, other types of screw propeller have been developed; these include ducted, controllable pitch, contrarotating, and fully cavitating propellers. Paddle wheels and vertical axis propellers, waterjets, and airscrews have also been used for marine purposes, while air-blown ramjets and magnetohydrodynamic devices have also been proposed.

Finally, some of the hydrodynamic, engineering, and operational factors affecting particular ship types are considered in more detail. Tankers and bulk carriers, high-speed container ships and other cargo liners, passenger liners and ferries, and very-high-speed foilcraft and hovercraft—all these have different needs and raise distinctive problems. Throughout it is stressed that the choice and design of a propulsion system for a ship must not be considered as a series of separate units, but as an integral whole in which the characteristics of main machinery, propulsion device, shafting or other connections, and needs for auxiliary power must be closely related.

INTRODUCTION

This paper is intended as a general review of some of the factors which influence the development of propulsion devices for ships and other marine craft. During the past twenty years there have been many remarkable changes in the

merchant and naval fleets of the world; major changes in the dimensions, speeds, and powers of conventional merchant ships have been accompanied by equally significant changes in naval vessels, and by other spectacular, and perhaps technically more challenging, innovations in high-speed marine craft, of which the most dramatic has been the birth of the hovercraft or waterborne air-cushion vehicle. Largely because of these striking and somewhat unexpected developments, there has been growing activity in exploring the value of propulsion devices which could supplement the long-established conventional marine screw propeller. These devices cover a very wide range of types and possible applications; some, like ducted, controllable-pitch, and contrarotating propellers, have been in regular, if limited, use for many years; others, like fully-cavitating propellers and waterjet systems, have undergone considerable engineering development in prototype installations; a third group, which includes air-blown ramjets and magnetohydrodynamic devices, are still in the early stages of laboratory investigation and are, in some cases, little more than "ideas in principle."

Faced with this diversity of possible propulsion devices, and by a barrage of technical and other literature extolling the virtues of each one, the designer of even a relatively conventional ship is faced with a difficult choice; for the designer of an unorthodox, advanced marine craft, the choice is often bewildering, and is not made easier by the apparently different standards and criteria used by the advocates of many of these propulsion devices. The principal aim of this paper is to suggest some general criteria, not all of which can readily be quantified, which can help in making the best choice of propulsion devices for ships and marine craft of many different types.

There are several recent papers which ably summarize and compare technical features of different marine propulsion devices (Refs. (1, 2, and 3) are examples), and many papers, including those at the present Symposium to follow this review, which discuss individual devices in considerable detail. For this reason, among others, this review will not contain new information about devices which are used for marine propulsion, or are proposed for such purposes. However, many papers about marine propulsion devices tend to emphasize selected aspects of their performance, generally concentrating on hydrodynamic efficiency, sometimes including cavitation susceptibility and associated noise generation, but frequently say little or nothing about engineering and operational features, which are often more decisive in the choice both of power plant and propulsion device. While such hydrodynamic studies are necessary, they are far from sufficient; indeed, high efficiency is but one factor among many, and reliability, liability to cause vibration, compactness, simplicity, low first cost and low direct and indirect maintenance costs, are generally of more importance in arriving at the techno-economic balance which determines the final choice.

Thus, in assessing the prospects for the widespread use of any unconventional marine propulsion device, it is essential to recognize that the choice and design of a propulsion system for a ship must not be considered as a series of separate and isolated units, each selected to have maximum component efficiency, but as an integrated whole in which the characteristics of main machinery, propulsion device, shafting or other connections, and needs for auxiliary power must be closely related. Finally, it is also desirable to recognize that

while unconventional devices are the only practical means of propelling some marine vehicles, for the overwhelming majority of conventional ships and for most marine craft—even some relatively unorthodox vessels—the conventional open marine screw propeller is both practical and highly efficient; it is not easy to beat.

GENERAL CONSIDERATIONS

Basis of Comparison

Efficiency and other criteria which can be expressed in direct numerical terms are seldom decisive in determining the choice of propulsive device for a particular ship or other marine craft. This choice should be made as part of an overall system design, in which the real target is minimum total operating cost to carry a specified payload over a stated range at optimum speed. The payload may be either a deadweight cargo such as oil, a light-weight load of passengers, or a weapons system or other mixed weight and volume load. The range is generally an independent operational variable, but optimum speed, though often treated as another independent factor, should more properly be regarded as a derived variable, depending on payload and range. Since total operating costs include both direct costs for fuel, crew, and maintenance, and also indirect costs which reflect initial capital expenditure, any attempt to minimize total costs will ensure that the most efficient ship has the most suitable propulsion system. The power plant and the propulsion device themselves affect the principal characteristics of the ship; dimensions, shape and displacement to carry a fixed payload will vary with the required power output and with the power-weight ratio and specific fuel consumption of the primary mover. For these reasons realistic comparisons of different propulsion devices should, in principle, form part of complete design studies for particular vessels, but clearly this is not practicable here.

A more limited, but reasonably realistic, basis of comparing different types of propulsion device is to consider their application to ships with total displacement, speed, and range all fixed. The emphasis is then placed on the propulsive efficiency of the device and the corresponding engine power required; the overall weight of the propulsion system and of the necessary fuel will then depend primarily on the primary mover selected, and this will in turn affect the available payload, which can be expressed, if desired, as a transport efficiency criterion. Although far from entirely satisfactory, such an approach is better than comparisons which consider different propulsion devices in isolation, without taking any serious account of their interaction with the ship which is to be propelled. On this basis of comparison, some efficiency criteria can be used to give general guidance about the likely prospects for unconventional marine propulsion devices.

Propulsive Efficiency

In the past, many accounts of novel propulsion devices have claimed advantages based on inadequate or even incorrect efficiency criteria. Fortunately, recent papers comparing different devices have adopted more realistic and correct criteria, but it is still important to stress that the definition and usage of

propulsive efficiency must be uniform, comprehensive, and unambiguous if it is to have value in comparisons between different systems.

The hydrodynamic performance of a marine propulsion device operating in isolation can be defined by its thrust efficiency, which is the ratio of the power output based on the effective thrust from the device, to the power input to the device. If the inflow velocity is taken as the mean velocity in the nonuniform flow conditions in which the device operates when propelling the ship, then this thrust efficiency is equal to the "behind" efficiency used in conventional ship-powering analyses, as defined in Ref. (4) and elsewhere.

When the device is part of the propulsion system of a ship, it has to be physically linked to the hull; this generally requires some external appendages, such as shaft supports or water inlets, and their net drag may increase the total resistance of the ship above that of the bare or naked hull. The flow induced by the propulsion device generally further increases the resistance of the hull, and the propulsive thrust must overcome this augmented resistance; there is a further interaction effect because in these conditions the mean inflow velocity to the device is less than the speed of the ship. The flow interaction effects between hull and propulsion device can be expressed as a single factor linking the thrust efficiency of the device alone to its propulsive efficiency when part of the propulsion system; this hull interaction factor is identical to the hull efficiency customarily used in ship powering analyses and cannot be ignored in assessing the relative merits of different types of propulsion device in real operating conditions.

The overall efficiency of the complete propulsion system, including prime mover, is the ratio of the useful power to the power output of the engine. In conventional ship powering analyses it is customary to consider that this useful power is the effective or tow-rope horsepower of the hull including any external propulsion appendages. However, the ship designer is primarily interested in the power required to propel the bare hull, and the power absorbed in overcoming the drag or resistance of external appendages directly associated with the propulsion device should not be regarded as useful output; consequently in comparing the efficiencies of different propulsion devices, the useful power should be related to the resistance of the naked hull alone. This gives a useful propulsive efficiency defined by the ratio of the effective horsepower for the naked hull to the power output of the prime mover.

Thrust Efficiency and Its Components

Although the thrust efficiency η_T alone is not a sound index for comparing the performance of different propulsion devices, it is a useful part of such an index, and it can also be resolved into components which have some value. Almost all practicable marine propulsion devices are of the reaction-screw-type, in which thrust is developed by a rotating pump or rotor, which imparts energy to accelerate a jet of water. The ideal or maximum efficiency η_I of such an a accelerated jet system can be readily derived by simple axial momentum or actuator disk theory which ignores viscous effects and other losses such as those due to flow rotation. The realizable thrust efficiency η_T is then obtained by applying a pump or hydraulic efficiency factor η_P to take account of these losses in the rotor. Some propulsion devices, such as water-jet systems,

enclose the rotor in a long duct which does not develop thrust; it is then convenient to introduce a further factor η_S to allow for the ducting and other losses in the system apart from those at the rotor itself. The factor for the system losses can be combined with the ideal jet efficiency to give a "real" jet propulsive efficiency η_J, and these different factors are by definition directly related thus:

$$\eta_T = \eta_P \eta_I \eta_S \quad \text{and} \quad \eta_J = \eta_I \eta_S \, .$$

Although the real jet propulsive efficiency η_J has been much used, particularly in analyses of waterjet systems, it is a convenience which does not have physical coherence, since it combines an ideal fluid jet efficiency with a factor dominated by viscous losses in ducting, while the corresponding losses in the rotor are included in the pump factor η_P.

The ideal jet efficiency η_I depends only on the ratio of the mean jet inlet velocity to the velocity at the nozzle or jet exit, decreasing sharply as this jet velocity ratio k increases. The real jet efficiency η_J depends on the head loss in the system (excluding pump losses) as well as on the jet velocity ratio; as this loss tends to zero $\eta_J \rightarrow \eta_I$. Two further coefficients are useful in comparative analyses; these are the thrust and power loading coefficients C_T and C_P, respectively, in which the thrust and the power are related to the disk area at the rotor and the speed of advance. The thrust loading coefficient C_T is directly related to the jet velocity ratio, so that the ideal jet efficiency η_I can be expressed either in terms of thrust loading C_T or jet velocity ratio k. Further, when consistent units are used throughout, these loading coefficients are related to the thrust efficiency η_T thus:

$$\eta_T = C_T / C_P \, .$$

It is often convenient to separate the power losses in the transmission between engine and propulsion device from the other losses in the system; this leads to a quasi-propulsive coefficient which conventionally is related to the effective horsepower of the hull with appendages, but which should more properly be related to the useful propulsion power based on the resistance of the naked hull alone. However, the overall efficiency is a more comprehensive index of relative performance than the quasi-propulsive coefficient; since alternative propulsion devices may necessarily have different transmission systems, such as geared or direct drives, it can be misleading to ignore the transmission losses in comparing the real efficiencies of different propulsion devices.

Table 1 summarizes these factors which affect the assessment of propulsive efficiency, and emphasizes the differences between the conventional efficiency factors and those proposed here.

The principal conclusions of this analysis are:

(a) The thrust efficiency η_T of a propulsion device defines its performance only in unreal isolated conditions. Hence, comparisons of the hydrodynamic efficiency based on thrust efficiency are inadequate and can be misleading.

Table 1
Propulsive Efficiency and its Assessment

Coefficient	Conventional	Proposed
Overall propulsive efficiency	$\eta = P_E/P_B$	$\eta_N = P_N/P_B = k_A\eta$
Quasi propulsive coefficient	$\eta_D = P_E/P_D$	$\eta_{DN} = P_N/P_D = k_A\eta_D$
Transmission efficiency	$\eta_t = P_D/P_B$	
Thrust efficiency	$\eta_T = P_T/P_D$	
Hull interaction effect	$\eta_D = \eta_T\eta_H$	$\eta_{DN} = k_A\eta_T\eta_H$

(b) Comparisons based on the conventional quasi-propulsive coefficient η_D take account of most interaction effects between the hull and the propulsion device, and thus give a far better indication than thrust efficiency η_T of relative hydrodynamic efficiencies. However, the quasi-propulsive coefficient does not penalize losses due to the drag of appendages associated with the propulsion device, and these can vary significantly for different devices.

(c) The most satisfactory basis for comparing hydrodynamic efficiencies is a qualified propulsive efficiency η_{DN} based on the useful propulsion power P_N related to the resistance of the naked hull. Although it may not always be easy to identify unambiguously and acceptably the resistance of the appendages defining the factor k_A in the relation $\eta_{DN} = k_A\eta_D$, this should always be attempted.

(d) The thrust and propulsive efficiencies of a propulsion device are linked by a hull interaction factor η_H, and the relation $\eta_D = \eta_T\eta_H$ provides a useful way of separately comparing the direct and the interaction effects of different propulsion devices.

(e) Transmission efficiency should be included in any complete performance comparison of propulsion devices; the overall factor η or η_N is a more comprehensive index of relative propulsive efficiency than any hydrodynamic efficiency criterion alone.

These relations between the thrust efficiency η_T and its components are summarized in Table 2, and Fig. 1 gives values of real jet efficiency η_J for the wide ranges of thrust loading C_T and head loss coefficient K_L over which marine propulsion devices are now required to operate.

Specific Power and its Implications

All the propulsive efficiencies considered here are based on a useful power output directly related to the resistance overcome. While this can be logically justified, it is irrelevant to the ship designer for whom hydrodynamic efficiency is more usefully defined by the power required to propel a specified displacement at a stated speed. This can be simply demonstrated by the not-infrequent

Table 2
Thrust Efficiency and its Components

Thrust efficiency	$\eta_T = \eta_P \eta_I \eta_S = C_T/C_P$
Real jet efficiency	$\eta_J = \eta_I \eta_S = \frac{2(k-1)}{(k^2-1)+K_L} = \frac{2[(1+C_T)^{1/2}-1]}{C_T+K_L}$
Ideal jet efficiency	$\eta_I = \frac{2}{k+1}$
System head loss coefficient	$K_L = H_L \Big/ \frac{V_A^2}{2g}$
	$\eta_J \to \eta_I$ as $K_L \to 0$
Thrust loading coefficient	$C_T = T \Big/ \frac{\rho}{2} A V_A^2 = P_T \Big/ \frac{\rho}{2} A V_A^3$
Power loading coefficient	$C_P = P_D \Big/ \frac{\rho}{2} A V_A^3$

situation in which, at constant displacement, a change in propulsion device leads to an increase in ship resistance (R or R_N) and a proportionately smaller increase in propulsion power P_D; then, though propulsive efficiency as measured by η_D or η_{DN} will increase, the designer will not consider it an advantage that a higher power is required.

Specific power is a parameter which can give guidance in such circumstances. Defined in engineering units as horsepower per ton-knot, it is related to an equivalent nondimensional parameter thus:

$$\text{Specific Power} = \frac{P}{\Delta V} = \frac{6.88\ R/\Delta}{\eta} ,$$

in which power P is in hp, speed V in knots, and displacement Δ and resistance R are in tons; if desired, the resistance-displacement ratio R/Δ can be replaced by the reciprocal of the familiar lift-drag ratio L/D. When the power P is taken as engine output P_B, then the overall efficiency η should be used if R is taken as total ship resistance, and η_N if the naked resistance R_N is the basis. Similarly, if the power is taken as the dhp P_D, then either η_D or η_{DN} should be used, as appropriate, in calculating the specific power.

It has been found useful to relate specific power $P/\Delta V$ to a speed coefficient such as $V/\Delta^{1/6}$ which does not involve more than ship speed and displacement. Figure 2 is a plot of specific power in terms of such a speed coefficient; the data, partly derived from published information which may not be precisely defined and partly from other sources, are for a very wide range of types of ships and other marine craft, including large tankers, passenger liners, high-speed patrol craft, hydrofoil ships, and amphibious and nonamphibious hovercraft. Plots such as this show that in general, as expected, specific power increases with speed coefficient, and also suggest that, for each speed coefficient, there is a minimum specific power corresponding to the "best" performance yet achieved.

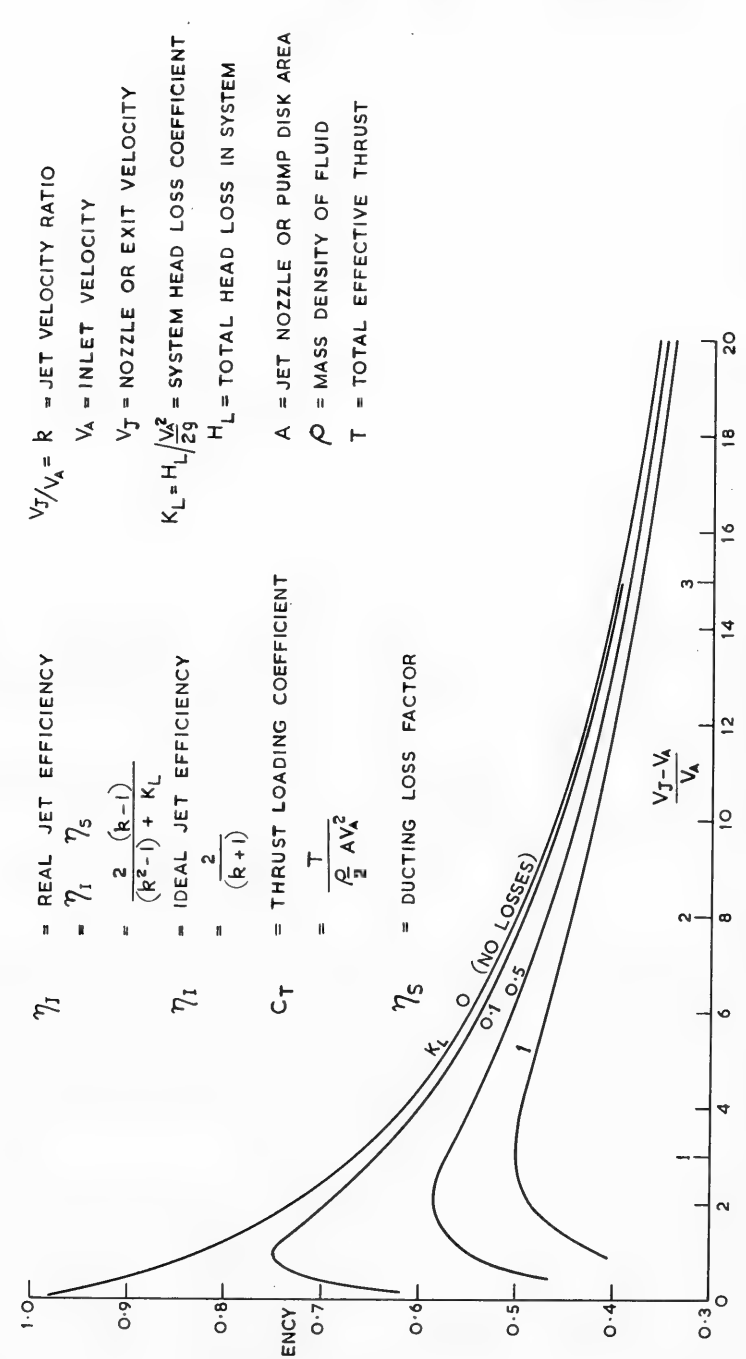

Fig. 1 - Real jet efficiency: effect of thrust loading and system losses

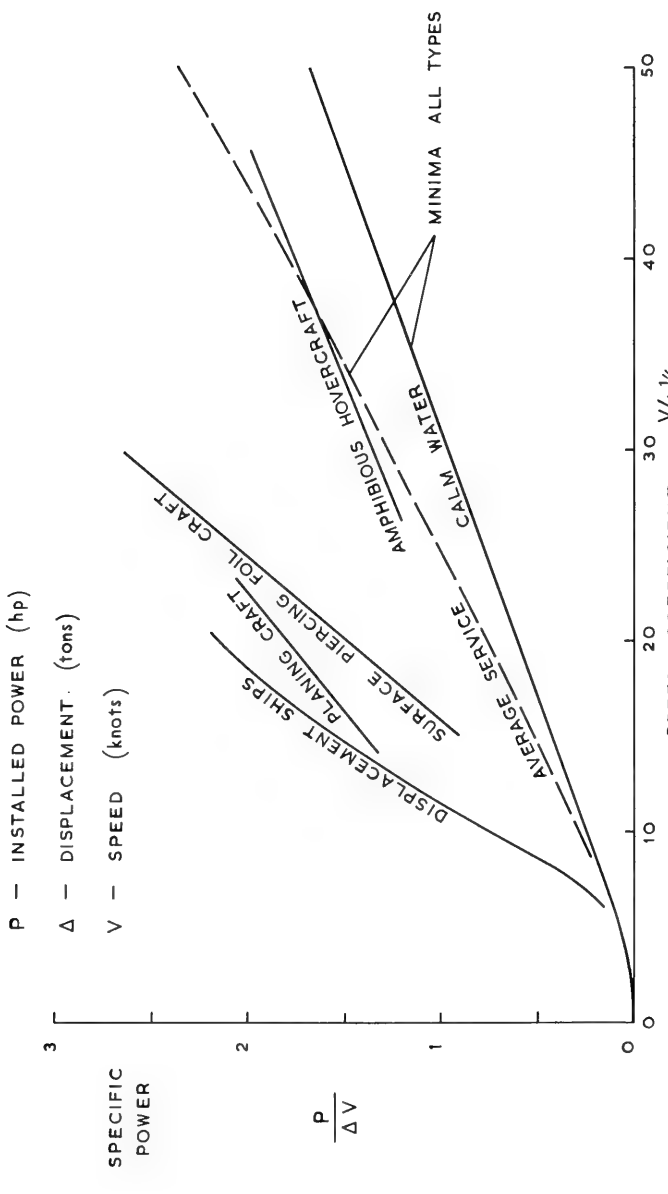

Fig. 2 - Specific power requirements

The resulting "minimum" curve indicates that, for a given speed-displacement ratio, there is often one type of marine craft with a significantly better hydrodynamic performance than others and gives an estimate of the minimum power required by such a craft. It also demonstrates the penalties in power incurred by design constraints or by a decision not to adopt the most favorable type of craft. Some simple diagrams illustrate the general guidance which can be directly derived in this way. Thus, Fig. 3 shows that the minimum values of P/Δ (hp per ton displacement or all-up weight) rise steeply with speed but fall steadily as displacement increases, while Fig. 4 shows the rapid rise in minimum power needed as either speed or displacement are increased; since Fig. 2 shows that for many high-speed displacement craft the power requirements are between two and three times the minimum, it is clear that there are serious limitations on speed-displacement values which are likely to be achieved in practice, and that even significant improvements in propulsive efficiency, however obtained, can have little effect in raising the practical speed-displacement boundaries.

The concept of specific power is also useful in assessing the prospects of different types of propulsion plant and propulsion device. Figure 5 illustrates the dependence of the ratio M/Δ on specific power and on speed; here M is the total weight of the propulsion system, and typical, reasonably representative values of 15 hp/ton and 20 hp/ton have been taken for diesel and steam turbine installations respectively (Ref. (5)), and 300 hp/ton taken for gas turbine installations based on mean values for known installations. Figure 6 shows the minimum values of the machinery weight ratio M/Δ for a range of speeds and displacements, corresponding to the minimum specific power values in Figs. 2 and 4.

It is also useful to examine fuel requirements in a similar general way. Figure 7 demonstrates the dependence of fuel weight ratio (F/Δ) on specific power and on range, while Fig. 8 is a guide to the minimum values of F/Δ needed for any given displacement and speed for a fixed range of operation.

Cavitation and Vibration

Almost all marine propulsion devices, particularly those dependent on screw propellers or pumps to impart energy to the fluid, are affected by cavitation or similar fluid-flow phenomena. Almost invariably, cavitation has two undesirable effects: It produces radiated noise, and it causes erosion of rotor blades and other parts of the propulsion device. Further, extensive cavitation may adversely affect the hydrodynamic performance of a propulsion device unless positive steps are taken to prevent this.

Many different criteria have been proposed and used to define the likelihood of cavitation occurrence and its extent; in general these can be divided into those which take account only of the ahead speed of the device, and those which also take some account of the rotational speed of the rotor or pump blade. The simple forms of cavitation index such as σ_A, which involve only ahead speed and depth of immersion, can be misleading and are almost always more inadequate than those, such as σ_R, which attempt to take account of blade resultant velocity.

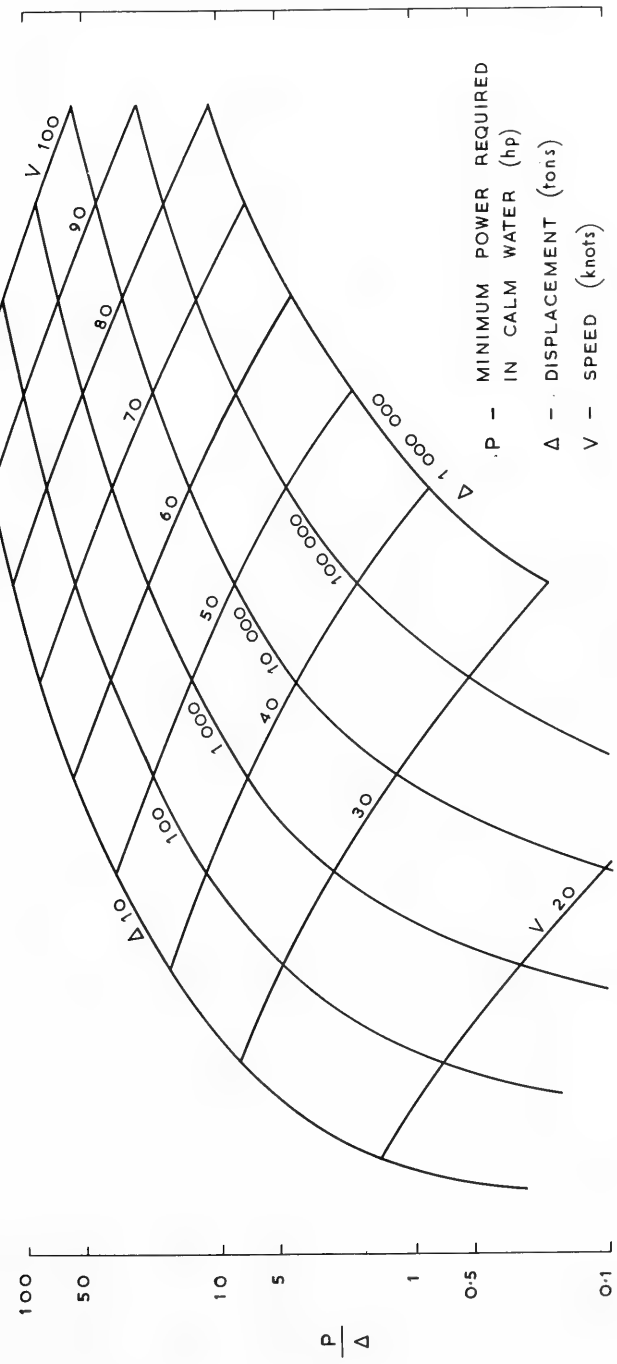

Fig. 3 - Power-displacement ratio: derived from present minimum values of specific power for ships and marine craft

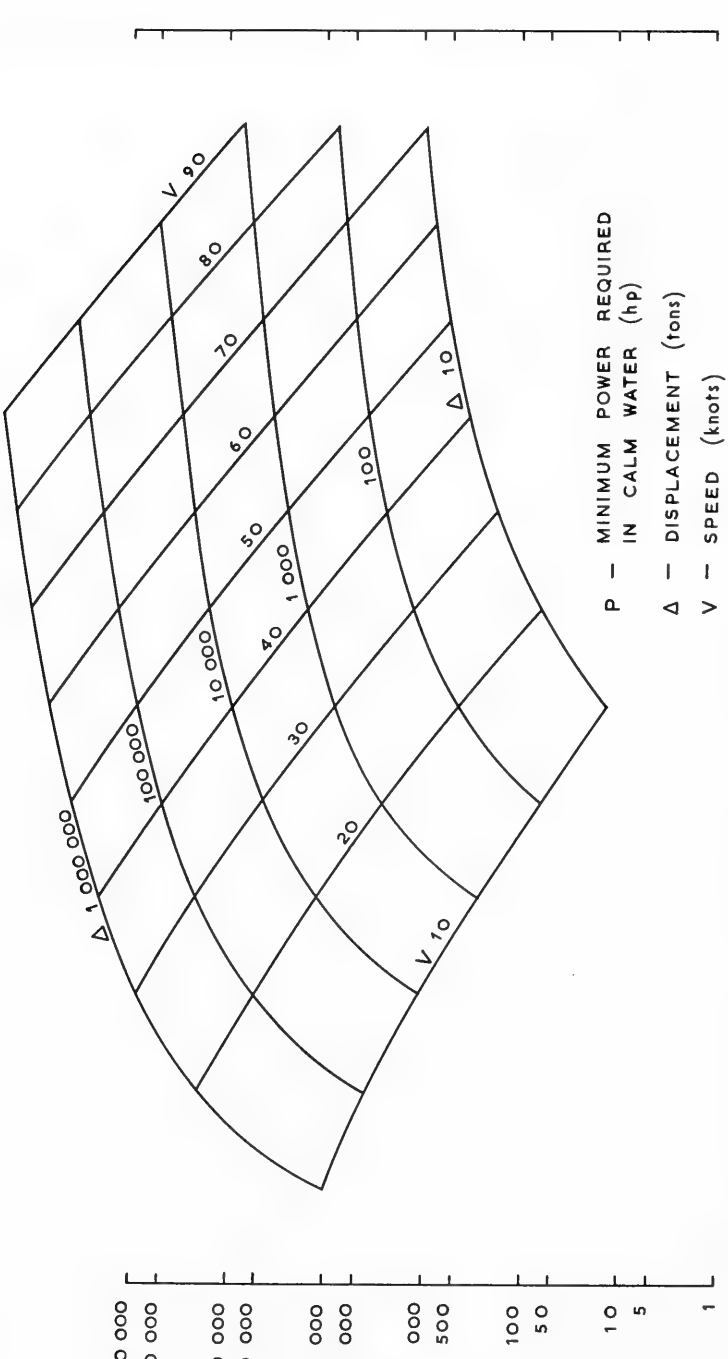

Fig. 4 - Power requirements: derived from present minimum values of specific power for ships and marine craft

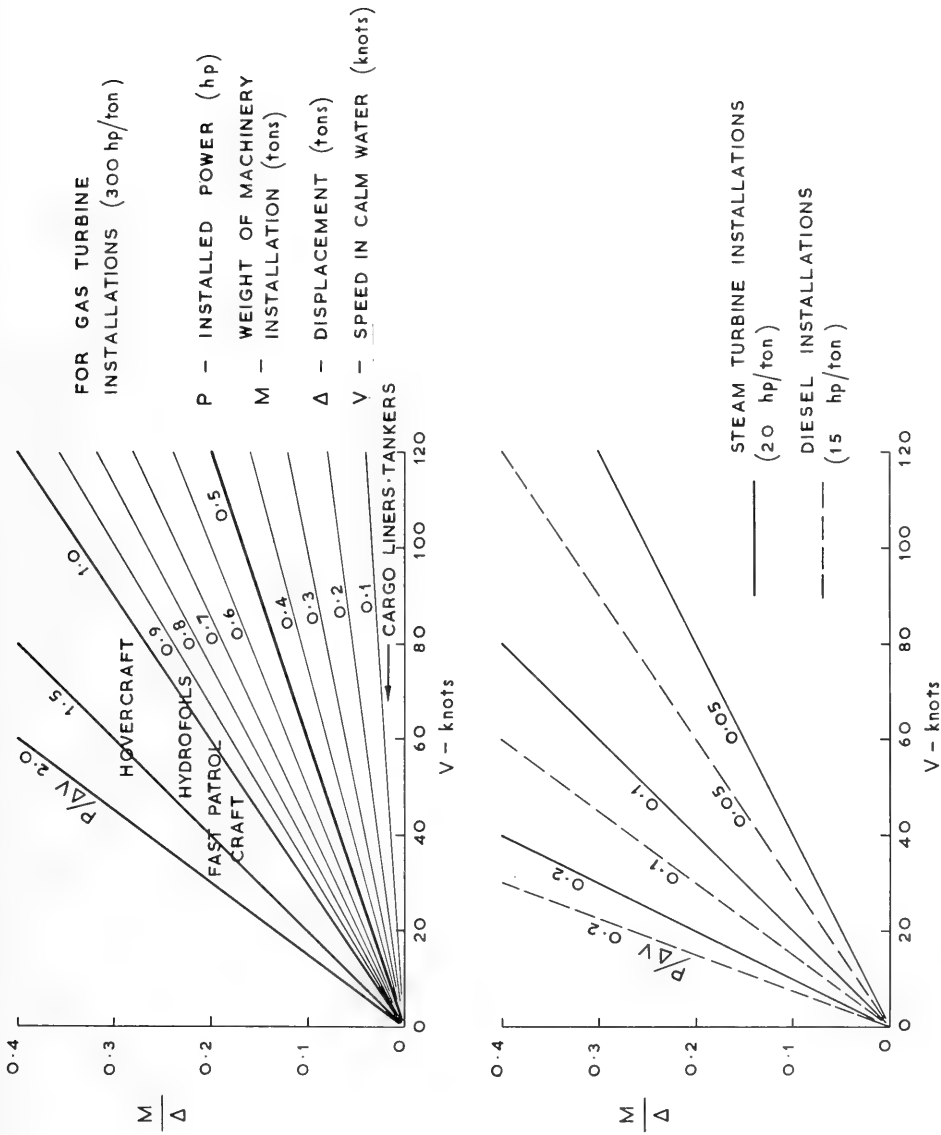

Fig. 5 - Machinery weight ratio: general

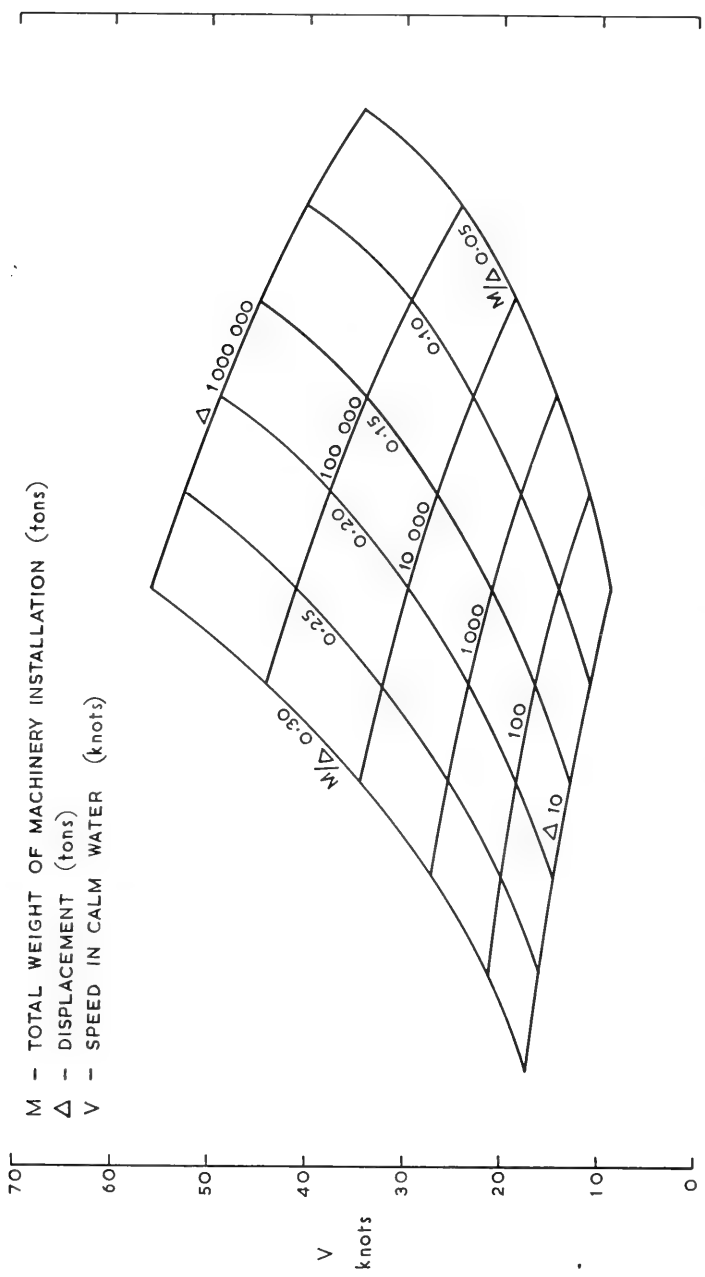

Fig. 6a - Machinery weight ratio: derived from present minimum values of specific power for steam turbine installations (assumed 20 hp/ton)

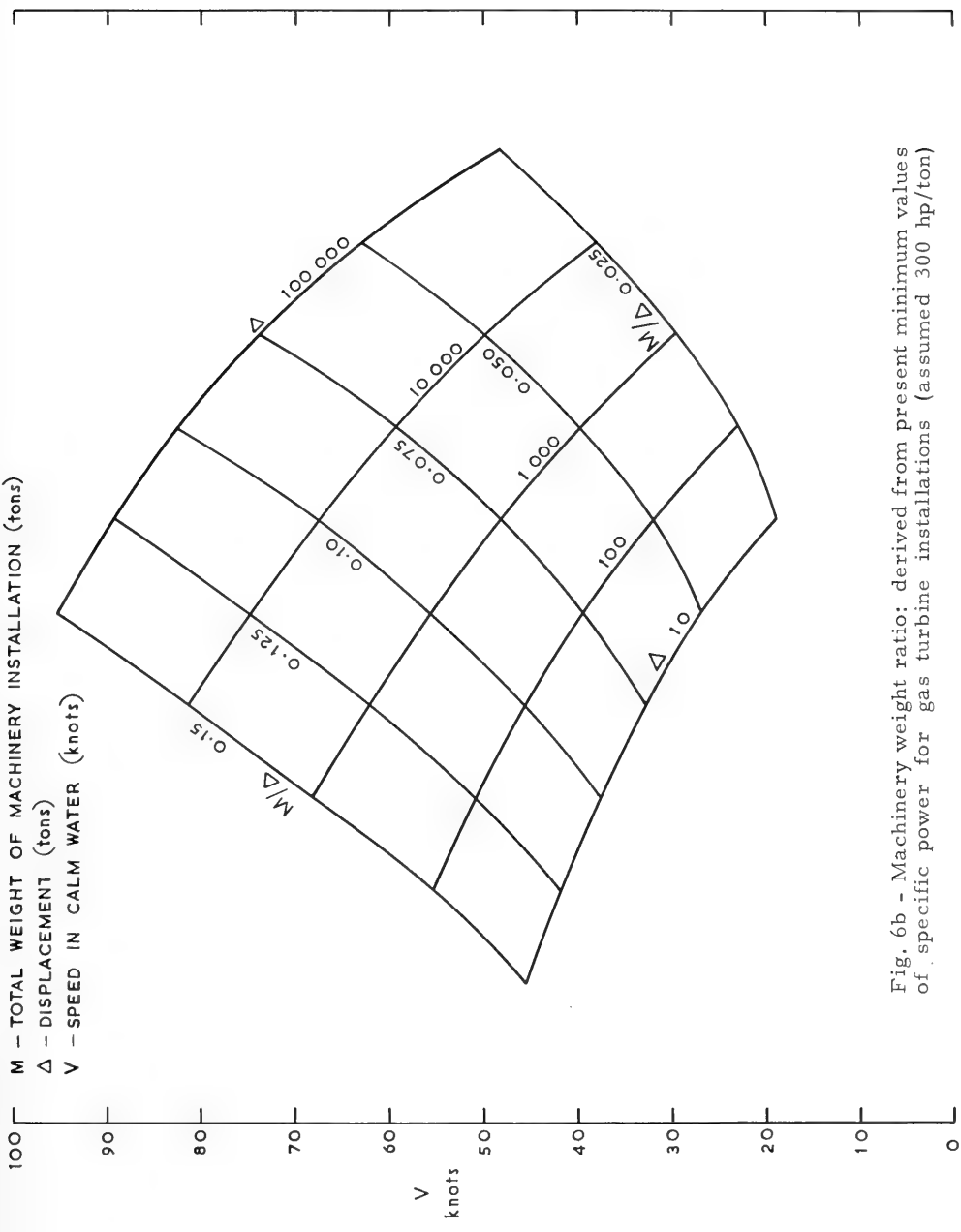

Fig. 6b - Machinery weight ratio: derived from present minimum values of specific power for gas turbine installations (assumed 300 hp/ton)

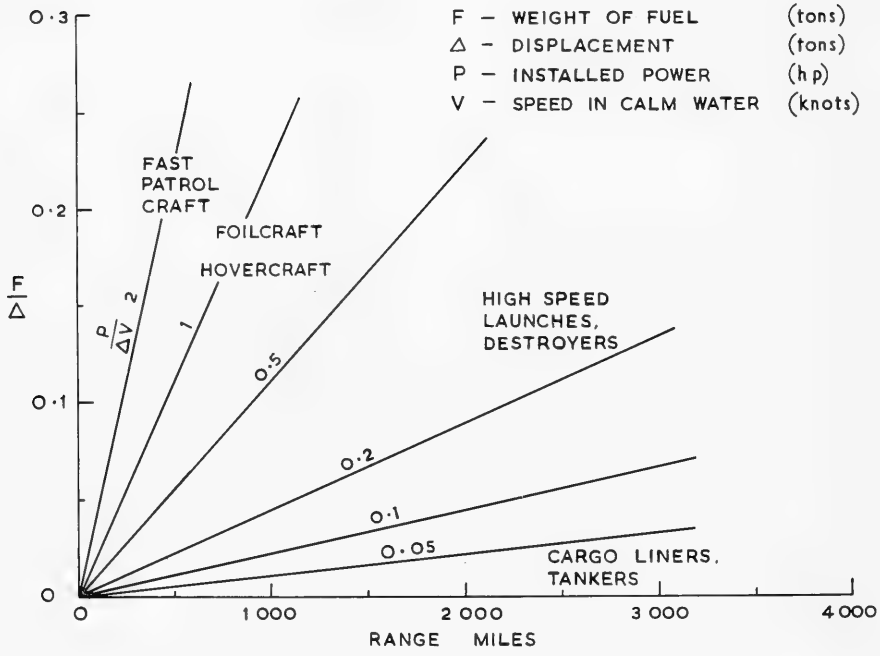

Fig. 7 - Fuel-displacement ratio: general (for fuel consumption of 0.5 lb/hp-hr)

Since most ship propulsion devices operate in a nonuniform inflow, the likelihood of propeller-excited vibration, or its equivalent, is an important factor in choosing the most appropriate device. As the thrust or power loading coefficient increases, so the likelihood of blade-excited vibration also increases, while growing nonuniformity of inflow naturally aggravates the situation even more.

Typical Values of Propulsion Parameters

Table 3 gives typical values of loading factors and other propulsion parameters for different types of ship and marine craft; these values show that:

(i) The thrust loading coefficient C_T is generally less than 1.5 for all types of vessel except large full-form tankers and bulk carriers for which much higher values are now common; in consequence, the ideal jet efficiency η_I is also generally greater than 0.8 except for these large low-speed ships, for which much lower values are the best that can now be achieved.

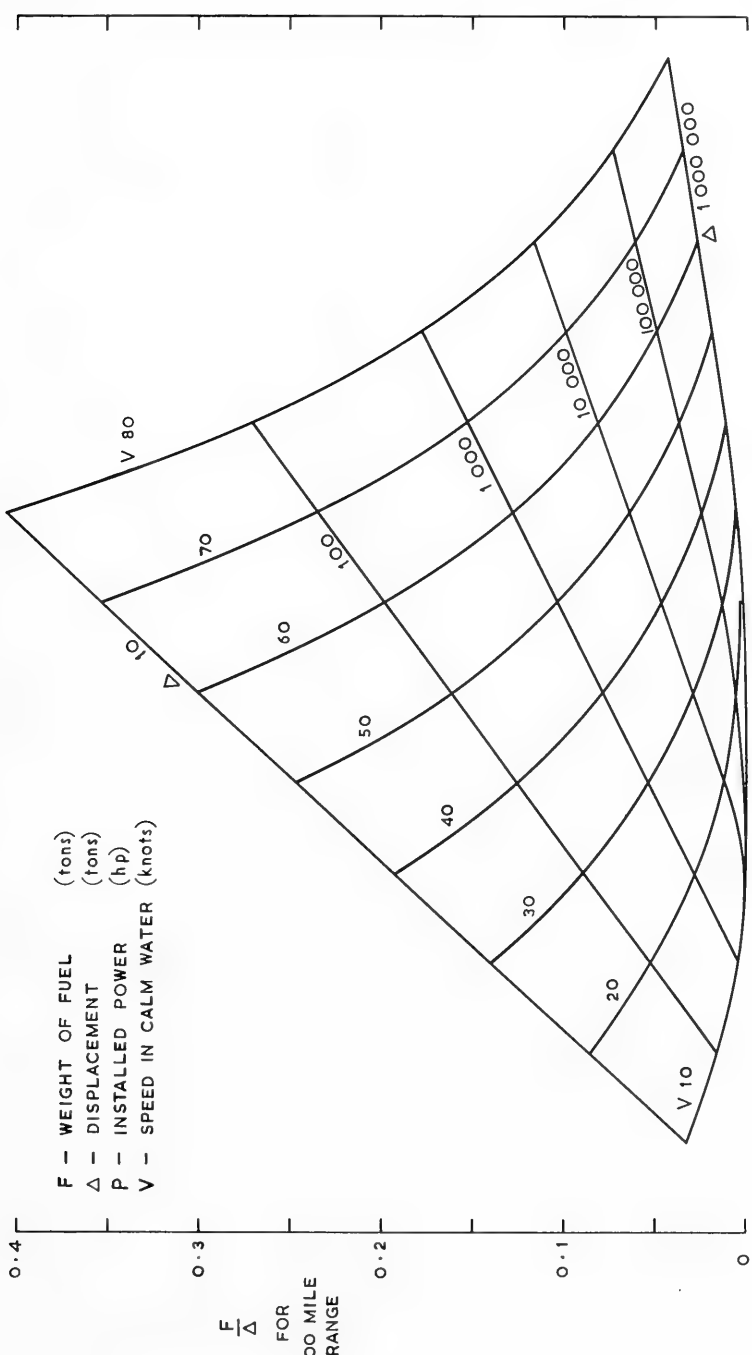

Fig. 8 - Fuel-displacement ratio: corresponding to present minimum values of specific power for ships and marine craft (for fuel consumption of 0.5 lb/hp-hr)

Table 3
Propulsion Parameters: Typical Values

Ship Type	Loading Factors					Specific Power	
	C_T	C_P	η_I	η_D	σ_R	$V/\Delta^{1/6}$	$P/\Delta V$
Tanker or Bulk Carrier:							
Mammoth (Δ 600,000: TS)	2	3	0.73	0.55	0.75	1.6	<0.01
Large (Δ 250,000: SS)	8	15	0.50	0.60	0.6	2.0	0.01
Medium (Δ 30,000: SS)	1.5	2.5	0.77	0.70	0.5	2.7	0.03
Trawler	1.2	2	0.80	0.63	0.4	4.0	0.08
Cargo Liner:							
Single Screw	1.2	1.8	0.80	0.70	0.5	4.1	0.05
Twin Screw	0.4	0.6	0.91	0.70	0.7	4.2	0.05
Vehicle Ferry	0.75	1.1	0.85	0.70	0.35	4.2	0.07
Passenger Liner	0.7	1.1	0.86	0.65	0.30	4.5	0.06
Destroyer	0.4	0.7	0.91	0.55	0.15	8	0.35
Patrol Craft	0.6	1.2	0.88	0.5	0.25	20	2.0
Foilcraft	0.5	1.0	0.89	0.5	0.05	20	1.0
Sidewall Hovercraft	0.5	1.0	0.89	0.5	0.1	20	1.0
Amphibious Hovercraft	1.4	2	0.78	0.7	—	30	1.2

(ii) Similarly, the power loading coefficient C_P is less than 2 except for such extreme ship types, although foilcraft in the take-off condition also have high values of both C_T and C_P.

(iii) The quasi-propulsive coefficient η_D generally has lower values for high-speed craft than for larger ships of all types, although its value is not directly associated with either C_T or C_P.

(iv) The speed-displacement ratio $V/\Delta^{1/6}$ is a parameter of major importance for almost all conventional ships it rarely exceeds 4, but for unconventional high-speed craft in calm water it may have a value as high as 50. As this speed coefficient increases, the specific power $P/\Delta V$ increases sharply and thus the power-weight characteristic of the propelling machinery becomes more important. Further, as the speed-displacement ratio increases the cavitation index σ_R decreases significantly, indicating the much greater importance of cavitation effects on propulsion devices for high-speed craft.

For these reasons the speed-displacement ratio may be regarded as the simplest single parameter which is of use in defining the desirable overall characteristics of the propulsion system. Some useful guidance affecting the development of marine propulsion devices can be obtained from Table 3 and Figs. 2-8. Thus:

(i) At low speed-displacement values, corresponding to those for most merchant ships, power-displacement ratios are low, and machinery and fuel weight ratios are not high enough to justify expensive light-weight propulsion systems. Equally, even where propulsive efficiency and low power requirements are important, they are seldom dominant factors in determining the type of propulsion system.

(ii) At high speed-displacement values, corresponding to those for high-speed marine craft, it is essential to minimize machinery power and weight if reasonable range and payload are to be obtained.

(iii) At intermediate speed-displacement values, corresponding to those for destroyers and similar craft, it is difficult to choose the power plant unequivocally. Improvements in propeller efficiency are desirable but unlikely to have a major effect on design criteria.

TYPES OF MARINE PROPULSION DEVICES

General Classification

In addition to the marine propulsion devices which already exist, there are many other possible types. These can be classified in several ways and, as suggested in Table 4, it is perhaps most convenient to divide them into the two main classes of reaction-screw-type devices and pure jet devices.

Reaction-screw-type devices may have many variants. Indeed, it is possible in principle to specify well over two hundred apparently different types of device since:

(a) The blade section shapes of rotating or fixed parts may be either fully wetted, fully cavitating, base vented, or airscrews may be used.

(b) The axis of rotation of the propeller or pump may be either longitudinal, vertical, or transverse.

(c) Single- or multi-stage pumps or propellers may be used.

(d) The pitch of the blades may be either fixed or controllable.

(e) The rotor may be either open (unshrouded), or enclosed in a duct or shroud which may be either long or short.

Table 4
Types of Marine Propulsion Devices

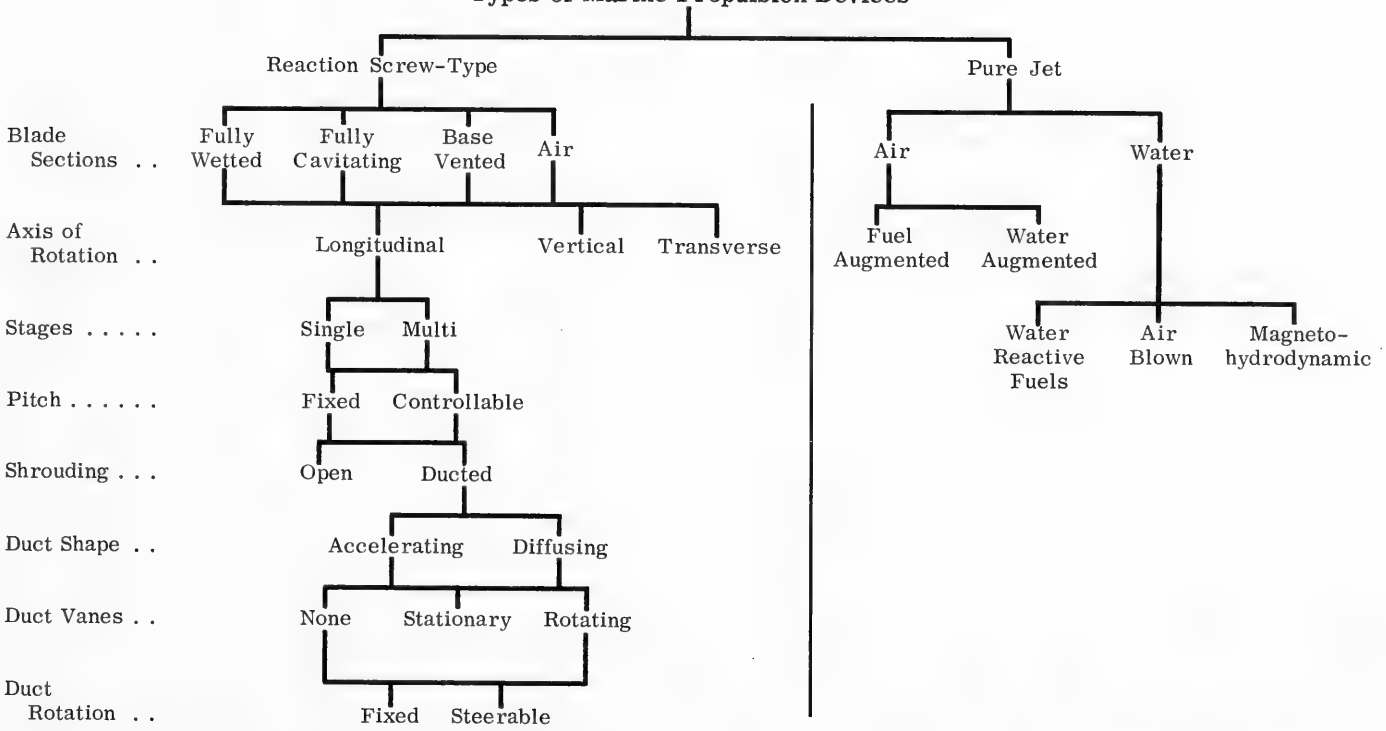

(f) For ducted or shrouded propellers the duct may have an accelerating or a diffusing nozzle, and may either be clear of vanes or have stationary or rotating inlet or exit guide vanes.

(g) Finally, the duct may be fixed in position, or be steerable so that it can be used as a rudder or control surface as part of the propulsion device.

Most commonly used screw-type propulsion devices have a fore-and-aft axis of rotation; conventional open marine propellers, ducted propellers, controllable pitch, contrarotating, tandem, and most waterjet systems are of this type. However, vertical-axis propellers are not uncommon; the well-known Voith-Schneider propeller, and the Flettner rotor, are examples of this type. Paddle wheels are the most common form of device with a transverse axis, but in principle the centrifugal pump in a waterjet system should be included in this group.

Pure jet types of propulsion device may be subdivided thus:

(a) Air jets: these may be like those used for aircraft (as in the "Lucy Ashton" experiments), or water-augmented to increase the density of the fluid at jet exit and thus increase the thrust.

(b) Underwater jets: in principle these may be of three types:

(i) Water as a working medium with water-reactive fuels
(ii) Air-blown ramjet or other hydropneumatic device
(iii) Magnetohydrodynamic devices.

Pure jet types have not yet been used for marine craft except in a very limited experimental way.

Need For Unconventional Devices

The conventional open unshrouded marine screw with fully wetted sections is a simple, efficient, reliable, cheap, and well-proven propulsion device, and considerable research effort has been expended in its development, particularly during the past twenty years. Why then should it be necessary to develop unconventional propulsion devices for ships?

Research on propulsion devices has shown that this cannot be isolated from research on hull forms and, in fact, the stern form, propulsion device, transmission, and steering system must be regarded as a whole. If there are no restrictions on the size and weight of the propulsion device, and on its operating rate of rotation, then in general the best performance will be achieved by a slow-running screw propeller of large diameter. Restrictions on diameter are always likely to be imposed by draught limitations, but restrictions due to difficulty of manufacture are likely to be overcome. Restrictions on revolutions are imposed by an insistence on using diesel engines as a primary mover with a direct drive to the propeller, but the wider adoption of geared drives, either with diesel engines or steam turbines, allows greater freedom of choice in propeller

revolutions. These points are important in considering the development of propulsion devices, other than conventional open propellers, because such devices often only have advantages where restrictions exist, and selection of the most profitable research topics therefore involves prediction of the likely trend in removing these restrictions.

The principal reasons for investigating the possible usefulness of unconventional marine propulsion devices can thus be summarized as:

(i) An attempt to maintain, at higher thrust and power loading coefficients (C_T, C_P) and lower cavitation values (σ_R), the high efficiencies which can be achieved with conventional open marine screws under less onerous operating conditions.

(ii) At lighter loadings to improve still further the efficiency obtainable and to reduce liability to cavitation damage.

(iii) To minimize vibration due to propeller excitation resulting from operation in a nonuniform inflow or through the free-space oscillating pressure field.

Comparative Features of Some Unconventional Devices:

Table 5 attempts to summarize some of the principal features which are important in any realistic comparison of practicable marine propulsion devices. Some comments on these comparisons may be helpful:

1. Open (unshrouded) propellers:

(a) Controllable pitch — These are so well established that it is doubtful whether they should be considered as unconventional devices. However, although they have advantages from the point of view of the engine builder in providing a better match between powerplant characteristics and changing thrust requirements, there is still considerable reluctance to adopt controllable-pitch propellers, even though they are now available for fairly high power outputs. In a recent paper (Ref. (6)) this reluctance has been primarily ascribed to the much higher capital cost of C_p propellers, which may be as much as 33% of the main engine cost compared with 8% for a fixed pitch propeller; a secondary reason is doubt about the realiability of any propulsion device which involves a special actuating mechanism.

(b) Fully cavitating propellers — Intensive efforts have been made, particularly in the past decade, to develop fully cavitating propellers primarily for high-speed craft. The emphasis has been on high efficiency under extreme cavitation conditions, and in consequence the present use of fully cavitating propellers has been limited to operating conditions in which both high speed and high rate of rotation are either necessary or desirable, as implied in Fig. 9, which is derived from Ref. (7). However, there is some indication that fully cavitating propellers give a much better propeller-hull interaction than conventional fully

Table 5
Marine Propulsion Devices: Comparative Features

Type	Open				Ducted		Vertical Axis	Paddle Wheel	Airscrew
	Controllable Pitch	Fully Cavitating	Contra-Rotating	Tandem	Nozzle	Pumpjet			
Characteristic features	Pitch variable in action	Complete cavity over blade back	Co-axial contra-turning shafts	Two screws on single shaft	Accelerating duct	Diffusing duct	Blade pitch variation with rotation	Large wheel on transverse axis	Air as propulsion fluid
Principal purpose	High efficiencies at varying loading	Good performance at high speeds	Reduce screw loading Regain rotational energy	Reduce loading on each screw	Increase η by part T on duct, so reducing T on rotor	Reduce C_T Raise cavitation-inception speed	Varying direction of thrust	Operation in shallow waters	Avoidance of water contact
Relative to equivalent conventional propeller η_T	Very slight reduction	Almost equal at very low σ and high V	Up at low C_T Down at high C_T	Slight reduction	Gain, increasing with C_T		As much as 30% reduction	Generally η_T does not exceed 0.5	Some gain for above 50
η_H	Unchanged	Perhaps better ($t \rightarrow 0$)	Down at low C_T Up at high C_T	Slight increase	Reduced			Probably about 0.97	Close to 1
η_D	Almost unchanged	Can be better at low σ, high V	Up at most C_T Best at low C_T (~10%)	Little change	Increase less than in η_T Best at high C_T (~ 10%)	Probably reduced	Much reduced	Generally η_D does not exceed 0.45	Some gain for V above 50
Advantages	Better matching of engine and hull	High T at high V, N Less blade erosion	Torque balance Diameter reduction possible	Higher thrust and power possible on single shaft	Rotor diameter and weight reduced Inflow more uniform	Noise reduction	Steering and stopping at constant N and at low V	Simplicity Easy repair	Amphibious capability
Disadvantages	Higher capital cost Complexity? Reliability?	Strength difficulties Off-design performance	Much higher cost Mechanical complexity	Higher cost	Duct weight Increased cost Tip clearance	Duct weight and drag	Low efficiency Higher cost	Affected by draught variations Low efficiency	Noise Affected by wind and power variations
Likely applications	Ships with varying operating conditions (tugs, trawlers, ferries)	High speed craft Ventilated sections for lower-speed ships?	Torpedoes High-speed cargo liners?		Tugs Trawlers Large tankers	Naval vessels	Tugs, Ferries; Vessels for crowded waters	Craft for shallow rivers in remote areas	Amphibious hovercraft up to 400 tons AUW

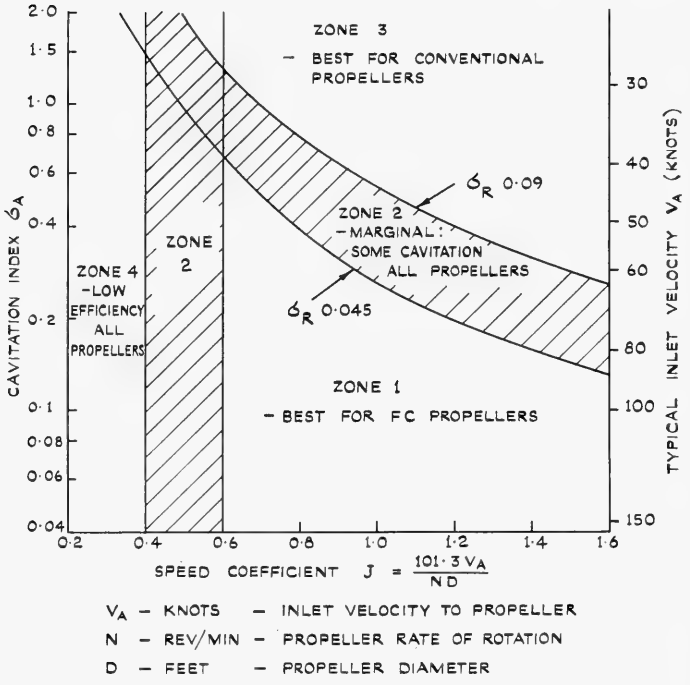

Fig. 9 - Useful range for fully cavitating propellers

wetted propellers, and this, coupled with the possible elimination of some transmission gearing, may open the way to the wider use of FC propellers for ships of lower speed than those for which they have been used until now, although there are still numerous practical difficulties to overcome before this becomes accepted practice.

(c) Contrarotating propellers — These offer a way of increasing the power which can be handled in cases of restricted diameter while retaining the basic single "line of shaft" configuration, and under some conditions these propellers can show considerable benefits. Full-scale application is at present limited by the mechanical engineering problems involved in producing a completely reliable transmission system, and by the very considerable increase in initial cost compared with the conventional single propeller.

(d) Tandem propellers — The use of two screws fixed to a single shaft is strangely reminiscent of very early attempts to make effective use of the output characteristics of steam turbines. Tandem propellers do not seem to have any marked disadvantages and they may well find unexpected applications.

2. Ducted propellers:

For ship propellers operating at high loading conditions, as in tugs when towing or fishing vessels when trawling, the advantages of enclosing the propeller in a duct which accelerates the inflow have been appreciated for many years. However, the operating conditions of some large tankers and bulk carriers are now in the range where propellers in such nozzles may be useful. More recently it has appeared that there might be advantages in enclosing a rotating impeller external to the hull in a duct or long shroud ring in which the inlet flow is decelerated before reaching the impeller blades. Operating conditions in which these two types of ducted propeller are of advantage are indicated in Fig. 10, while a comparison between efficiencies of an open unducted propeller, are one in an accelerating duct, is shown in Fig. 11; this also indicates how unloading part of the total thrust onto the duct makes it possible to reduce the diameter of the rotor compared with that of an open screw. The performance and efficiency of ducted propellers are sensitive to the clearance between the rotor tip and the shroud ring, as indicated in Fig. 12, and the need for a small clearance ratio can impose quite severe engineering and operational difficulties. Figs. 10-12 are taken from Ref. 8.

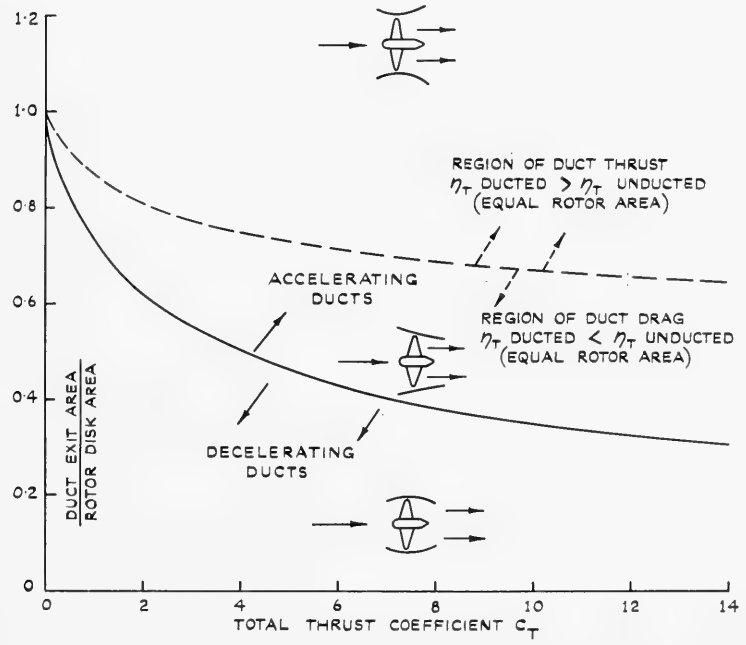

Fig. 10 - Ducted propellers: conditions for accelerating and decelerating ducts

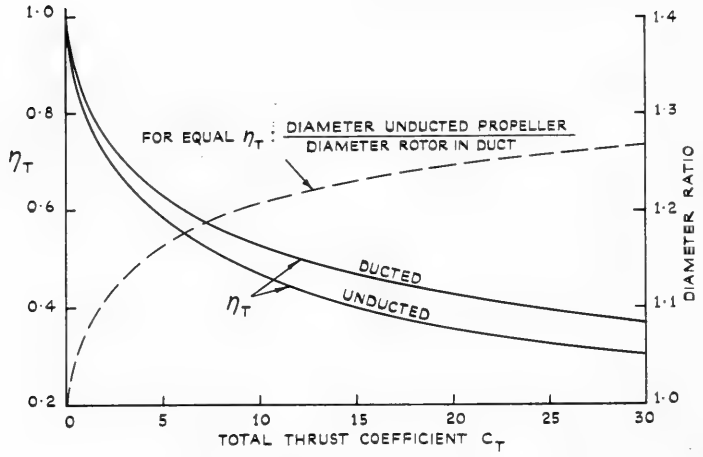

Fig. 11 - Ducted and unducted propellers: comparison of efficiencies and diameters

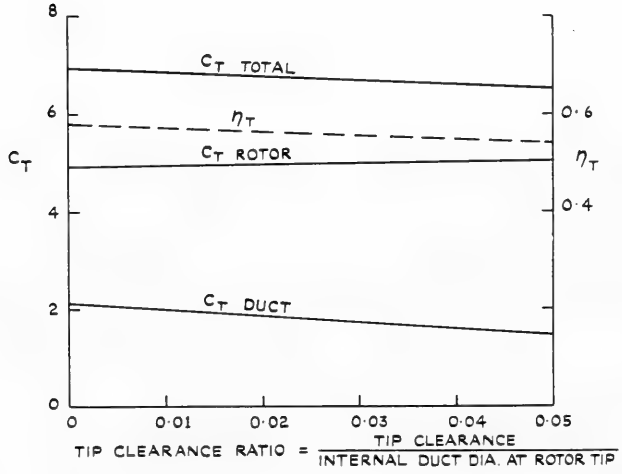

Fig. 12 - Effect of tip clearance on ducted propeller efficiency (calculated for a constant power coefficient C_P 12)

3. Vertical-axis propellers:

The much lower propulsive efficiency of vertical axis propellers makes it clear that the main reason for using such propellers is the very considerable advantage they give in providing a large steering power at low ship speeds. However, engineering developments have so far limited the total

power of such devices to about 2,000 hp, and even so for craft requiring less than 1,000 hp the use of vertical axis propellers has recently been severely challenged by other propulsion devices, such as the steerable open propeller and the Pleuger activated rudder, which also have good maneuvering qualities.

4. Paddle wheels:

These again scarcely rank as unconventional propulsion devices, but recent intensive studies of their performance suggest that they may not yet be entirely dead. Their value in remote areas in less developed countries indicates the importance of engineering simplicity and reliability in the overall choice of propulsion system.

5. Airscrews:

While airscrews have often been proposed as propulsion devices for marine craft they have only been used for this purpose since the advent of the amphibious hovercraft, for which they are obviously well suited. However, experience has shown that the performance of an open unducted airscrew is much more strongly affected by wind, wave, and power variations than a marine propeller. Further, limitations in propeller size may well limit their application to fairly small craft, quite apart from other factors such as noise.

6. Pure jet devices:

Most pure jet devices have very low propulsive efficiencies in any operating conditions resembling those for present or projected marine craft. However, theoretical studies of an air-blown ramjet (Ref. 9) have suggested that reasonable propulsive efficiencies, perhaps exceeding 40%, might be obtained, though these values have so far not been confirmed by experiment. If further work shows that reasonable propulsive efficiencies can be achieved then the simple air-blown ramjet might be employed as a booster unit, if not as the main propulsion device, for some high speed craft. It should be added that the effective thrust loading coefficient C_T for which reasonable efficiencies might be achieved is low, probably not much exceeding 0.15.

SHIP TYPES AND THEIR PROPULSION REQUIREMENTS

General Criteria

For ship propulsion systems, of which the propulsion device forms a critical part, the order of priority for design criteria is different for merchant ships and for naval ships; Table 6 shows these priorities as summarized in Ref. (5). It will be seen that reliability rates highly in all applications, but that low capital cost disappears from the naval list as a primary aim, while low weight and compactness become more important. Further, fuel consumption is judged on a weight basis for naval applications and on a cost basis for the Merchant Navy.

Table 6
Ship Propulsion Systems:
Order of Priority for Design Criteria

Ranking	Merchant	Naval
1	Low capital cost	Reliability
2	Reliability	Rapid maneuverability and ease of operation
3	Low fuel cost	Compactness
4	Ease of operation	Low weight
5	Ease of maintenance	Low fuel consumption
6	Compactness	Ease of maintenance
7	Low weight	Silence and shock resistance

Several important conclusions are implicit in this statement of priorities. For example, for most merchant ships it strongly suggests that, unless an unconventional propulsion device gives such an increase in propulsive efficiency that the consequent reduction in required power can be reflected in the capital cost of the machinery installation (including the propulsion device itself), then it is very unlikely to be regarded favorably, since the simple open marine propeller is clearly superior so far as all the other criteria are concerned. On this basis it is not unreasonable to suggest that the minimum reduction in required power due to adopting an unconventional marine propulsion device must be not much less than 10% to justify its widespread adoption; further, the attainable power reduction should increase with the complexity of the device, so that the improvement in performance needed to justify a mechanically complex contra-rotating system must be greater than that to justify the relatively simple single propeller in a short duct or nozzle, although even this may well have significant disadvantages in maintenance and total weight. For naval ships the emphasis on rapid maneuverability and ease of operation creates a more favourable climate for the adoption of propulsion devices which may not show any significant gain in propulsive efficiency or in overall power required; thus, waterjet systems may have advantages from this point of view, particularly if they can be designed to operate more quietly than unshrouded open marine screws. Because of the wide differences in the requirements for differnet classes of ship it is necessary to consider each main type separately.

Low-Speed Merchant Ships

Tankers and bulk carriers now dominate the world merchant fleet and so clearly their propulsion needs should be paramount in any civil research and development programs. The typical values of propulsion parameters in Table 3

show that large low-speed tankers and bulk carriers operate at thrust and power loadings much higher than those for all other merchant ships, except tugs. This means that only those devices which operate well at high loadings need be considered as alternatives to the conventional open propeller. Indeed, only devices which offer significant advantages in propulsive efficiency, without any accompanying disadvantage of complexity or liability to damage, can be seriously considered, and merchant-ship studies have already shown that a substantial gain in a thorough techno-economic assessment is an essential prerequisite to a departture from the conventional open marine propeller; indeed, there is even a reluctance to move away from single-screw systems. The ducted propeller is clearly the most obvious alternative for large, low-speed ships, but the need for a small tip clearance to obtain the best performance may be an inhibiting factor.

High-Speed Merchant Ships

There has been a great deal of discussion about high-speed cargo liners and similar apparently novel merchant ships. However, even though the diameter of propellers for such ships may be severely restricted by draft limitations, the thrust and power loadings at which they operate are not high; thus, conventional open propellers can still serve very efficiently. The main problem may well be that the higher absolute powers for such vessels may lead to more severe propeller excited vibration. Thus, while devices such as contrarotating propellers may show appreciable gains in propulsive efficiency, their increased mechanical complexity and much higher capital cost suggests that their adoption, except on an experimental basis, is unlikely unless they also appreciably reduce propeller-excited vibration.

Very-High-Speed Marine Craft

Foilcraft, hovercraft, and very-high-speed displacement craft clearly need unconventional propulsion devices, since the conventional open marine screw cannot be developed to perform efficiently under the extreme speed and cavitation conditions at which these vessels operate. For such craft it is particularly important not to consider the propulsion device in isolation but as part of the overall propulsion system. When this is done it would seem from information presently available that the overall efficiencies of fully cavitating propellers, and of current waterjet installations, are not sufficiently different to be decisive. Further, almost all present and projected very-high-speed merchant ships of this kind are not intended for long-range operation, and thus fuel consumption and cost are less important in the overall assessment of priorities. Equally, it must be recognized that such craft represent only a very small part of the whole world merchant and naval fleets, and this is most unlikely to change for many years. Development of propulsion devices for high-speed marine craft can easily absorb a disproportionate part of the total effort available for such activities.

Underwater Bodies

Marine propulsion devices are required for bodies other than ships. For torpedoes and other underwater bodies, including weapons, quite different considerations apply. Propulsive efficiency may not be at all significant and the sheer ability to reach a high speed at whatever cost may be decisive.

Future Possibilities

The significant progress made during the past decade in developing fully cavitating, contrarotating, and ducted propellers, and waterjet propulsion systems, show that much can be achieved if the effort and the will are there. Consequently, it would be wise to assume that the only limits to the further development of unconventional propulsion devices are those imposed by basic physical factors. However, for those of us who live in restricted economies in which the principle of "either/or" must be recognized, it is essential to make the right choice and not to dissipate research and development effort too widely. For those who are apparently fortunate enough to live in "as well" economies such a hard choice is, superficially at least, less necessary. However, it is a valuable discipline in itself. Some of the factors which must inevitably determine the emphasis in future research and development effort on marine propulsion devices are:

(a) The economic importance of the ships to which they might be applied.

(b) The engineering and operational difficulties associated with their use.

(c) The likely gains compared with those which can be achieved in other ways, particularly by improving other parts of the propulsion system.

(d) The relative importance of improvements in propulsion compared with improvements which may be obtained in quite different ways, such as by reducing crew costs and turn-around times or by increasing the useful payload.

It is a bold man who would venture a clear forecast in such circumstances.

NOMENCLATURE

A	Area of jet nozzle, pump disk, or equivalent
$C_P = P_D \frac{\rho}{2} A V_A^3$	Power loading coefficient
$C_T = T \frac{\rho}{2} A V_A^2$	Thrust loading coefficient

D	Drag
F	Weight of fuel
H_L	Total head loss in system excluding pump
$k = V_J / V_A$	Jet velocity ratio
k_A	Appendage resistance factor
$K_L = H_L \frac{V_A^2}{2g}$	System head loss coefficient
L	Lift
M	Weight of machinery installation
N	Propeller or rotor rate of rotation
p	Static pressure at axis of propulsion device
p_c	Static pressure in cavity
P	Power in general
P_B	Power output of propulsion machinery
P_D	Power delivered to propulsion device
$P_E \propto RV$	Useful or effective power based on ship resistance including appendages
$P_N \propto R_N V$	Useful or effective power based on ship resistance without appendages
$P_T \propto TV_A$	Thrust power from propulsion device
R	Resistance of ship including propulsion appendages
$R_N = k_A R$	Resistance of ship without propulsion appendages
t	Thrust deduction fraction
$T = R/(1-t)$	Effective thrust from propulsion device
V	Speed of ship
$V_A = V(1-w)$	Inlet velocity to propulsion device
V_J	Nozzle or exit velocity

V_R	Resultant velocity of propeller or rotor blade from ahead and rotational components
$w = (V-V_A)/V$	Wake fraction (Taylor)
Δ	Displacement
$\eta = P_E/P_B$	Overall propulsive efficiency
$\eta_D = P_E/P_D$	Quasi-propulsive efficiency or coefficient
$\eta_{DN} = P_N/P_D$	Qualified quasi-propulsive efficiency or coefficient
$\eta_H = (1-t)/(1-w)$	Hull interaction factor
η_I	Ideal jet efficiency
η_J	Real jet efficiency
$\eta_N = P_N/P_B$	Qualified overall propulsive efficiency
η_P	Hydraulic efficiency of propeller or pump
η_S	Ducting loss factor
$\eta_t = P_D/P_B$	Transmission efficiency
$\eta_T = P_T/P_D$	Thrust efficiency of propulsion device
ρ	Mass density of fluid
$\sigma_A = (p-p_c)/\frac{\rho}{2} V_A^2$	Cavitation index based on ahead velocity of propulsion device
$\sigma_R = (p-p_c)/\frac{\rho}{2} V_R^2$	Cavitation index based on resultant velocity of rotor blade

REFERENCES

1. Hadler, J.B., Morgan, W.B., and Meyers, K.A., Advanced Propeller Propulsion for High-Powered Single-Screw Ships. Trans. SNAME 1964, Vol. 72, p. 231.

2. Thurston, S. and Amsler, R.C., A Review of Marine Propulsive Devices. Am. Inst. Aero. & Astro. Second Annual Meeting, July, 1965.

3. Brandau, J.H., Aspects of Performance Evaluation of Waterjet Propulsion Systems and a Critical Review of the State-of-the-Art. AIAA-SNAME Advance Marine Vehicles Meeting, May, 1967.

4. Standard Procedure for Resistance and Propulsion Experiments with Ship Models. NPL Ship Division Report No. 10 (revised), 1960.

5. Yarrow, Sir E. and Norton E., Turbine Propelling Machinery. Trans. Instn. Engrs. Shpbldrs. in Scotland, 1966-67, Vol. 110, p. 1.

6. Smit, J.A., Considerations of Propeller Layout from the Enginebuilders point of view. Trans. Instn. Engrs. Shpbldrs. in Scotland, 1967-68, Vol. 111, p. 230.

7. Tachmindji, A.J. and Morgan, W.B., The Design and Estimated Performance of a Series of Supercavitating Propellers. Second Symposium on Naval Hydrodynamics, ONR, US Navy 1958, p. 489.

8. English, J.W., One-Dimensional Ducted Propeller Theory: Influence of Tip Clearance on Performance. NPL Ship Division Report 94, 1967.

9. Gadd, G.E., Some Experiments with an Air-blown Water Ramjet. NPL Ship Division Tech. Memo. 103, 1965.

PRINCIPLES OF CAVITATING PROPELLER DESIGN AND DEVELOPMENT ON THIS BASIS OF SCREW PROPELLERS WITH BETTER RESISTANCE TO EROSION FOR HYDROFOIL VESSELS "RAKETA" AND "METEOR"

I.A. Titoff, A.A. Russetsky, and E.P. Georgiyevskaya
Kryloff Ship Research Institute
Leningrad, U.S.S.R.

It has been found that appreciable erosion develops when cavities collapse on screw propeller blades, the area of collapse shifting in the course of revolution along the blade chord because of the nonuniformity of the velocity field. At high flow velocities characteristic for screw propellers, the intensity of the erosion process is so great that it is useless to attempt prevention of failure of the material by improving its mechanical properties. Accordingly, to decrease or fully eliminate erosion damage it is necessary to provide for a suitable form of cavity development, i.e., collapse outside the blade.

In principle, cavitation may occur on both the suction and pressure sides of the blade. The latter form of cavitation, however, is observed only when the adopted curvature of the blade section is excessive or the edge pitch is too small. Thus, the conditions required for the design of a propeller may be stated as (a) the absence of cavitation on the pressure side, and (b) the collapse of cavities beyond the trailing edge of the blades. The first of these conditions is mainly provided for by choosing reasonable blade sections, and the second by choosing the blade area ratio.

The collapse of cavities beyond the blades cannot be obtained for all speeds. There inevitably exists some range of speeds within which the cavities will collapse directly on the blades.

It is well known, however, that the intensity of erosion is proportional to approximately the sixth power of the flow velocity. Consequently, the erosion in this range of speeds will develop much slower than at full speed, should a similar form of cavitation exist under the latter condition. Moreover, fast ships, especially hydrofoil vessels, are for the most part operated at speeds approximating full speed, and hence the amount of intermediate speeds in the total period of operation is insignificant. Accordingly, it is more advantageous in attempting to decrease erosion damages that the conditions under which partial cavitation of the blades may occur should be observed at the lowest possible speeds, and hence the value of the blade area ratio should be as small as possible.

It is known, however, that the maximum value of the thrust coefficient, given the cavitation number and the advance coefficient of a cavitating propeller, is primarily a function of the blade area ratio and depends to a lesser extent on the pitch. Hence the lowest permissible value of the blade area ratio should be such as to secure the prescribed value of the thrust coefficient. For this purpose one may use the diagram in Fig. 1 on which the value C_{Ln} of the conventional lift factor is plotted as a function of the local cavitation number at the conventional radius $\bar{r} = r/R = 0.7$, which factor corresponds to the maximum value of the thrust coefficient k_T with a given blade area ratio. The value C_{LN} can be determined from the following relation

$$C_{Ln} = \frac{8K_T}{\pi \frac{A}{Ad} (\lambda_\rho^2 + \pi^2 \bar{r}^2) \cos \beta}$$

Solving this equation for A/Ad, the needed value of blade area ratio can be calculated from the values of K_T and C_L given in Fig. 1. For hydrofoil vessels, the needed value is usually defined not on a full-speed basis, but so as to ensure the defeat of drag hump.

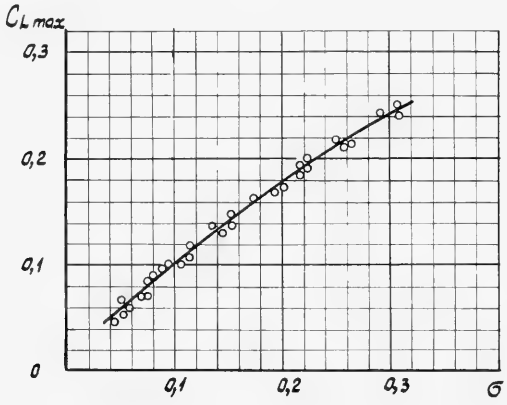

Fig. 1 - Conventional lift factor C_{Ln} as a function of the local cavitation number for the maximum value of the thrust coefficient K_T with a given blade area ratio

As noted above, the absence of cavitation on the pressure side of the blade is provided for by choosing the proper blade sections. For this purpose it is necessary first to calculate the induced velocity field of a cavitating propeller.

The propeller-induced velocities may be considered as the sum total of the velocities generated by the vortices of a propeller with infinitely thin blades and the velocities which are due to the thickness effect of the blades. For a subcavitating propeller, the former component prevails, which makes it possible in most cases to neglect the velocities associated with the thickness effect of the blades.

Such an assumption will lead to considerable errors, if applied to cavitating propellers whose hydraulic sections are blocked up by blade cavities rather than by the blades themselves.

We now turn to the methods of calculating the components of the velocities induced by the cavitating propeller. Theoretical principles for calculating the vortex component of the induced velocity were presented in 1948 by N.N. Polyakhov, who demonstrated, for the case of a developed cavitation, the relations existing between the lift and the circulation on a subcavitating section. This made it possible to apply the basic relations of the vortex theory to the design of the vortex component of the cavitating propeller velocity. The difference in the design formulas is that the lift coefficient proves to be the function of one more parameter, viz., the cavitation number, and the incident angle $dC_y/d\alpha$ is taken to be less than that for a subcavitating section. In the case of propeller design, the propeller is also considered as being optimum, according to Betz; such an assumption in the case of the finite length of cavities can be made to an accuracy of the magnitude of cavity drag. This approach is widely used both in the USSR and in other countries.

Practical calculations in which account is taken only for the vortex component of the velocity are, however, in bad agreement with the experiment, i.e., the pitch ratios and blade section curvatures prove to be underestimated.

This circumstance gave impetus to a number of investigations aimed at solving the problem of blade flow for a cavitating propeller, taking into account the finiteness of cavities which develop on the blades. Such a solution, based on using the acceleration potential, has been obtained by V.M. Lavrentiev. According to this solution, given the distribution of pressures over the suction side and the load, the distribution of singularities (sources) defining the configuration of the blade and cavity is due to the solution of Fredholm's integral equation of the first kind. A similar problem was later solved by G. Cox (1).

Unfortunately, the design diagrams based on these methods have found no practical application as yet, and accordingly consideration is given below to approximate methods of making allowance for cavities in the design of a screw propeller.

If we now turn to the performance of the cavitating propeller as shown in Fig. 2, we can see that the blocking up of the hydraulic section by cavities brings about (a) a decrease in the mean velocity of fluid inflow to the propeller disk, and (b) an increase in the flow velocity in between the cavities (blades).

The first of these circumstances can be taken into account for solving a three-dimensional problem of cavitating propeller performance, and the second for the flat-plate theory, considering the blade cascade at various relative radii.

In the practical design of decelerating the flow before the propeller, a solution found by V.F. Bavin (2) for an ideal cavitating propeller is used, by assuming that the cavity sizes are predetermined. To define the induced velocities in the way of the blades, it is assumed that cavities are responsible only for additional axial velocities which can be calculated by the equation for the uniformity of flow through the hydraulic section of the cascade. Hence, the local velocity

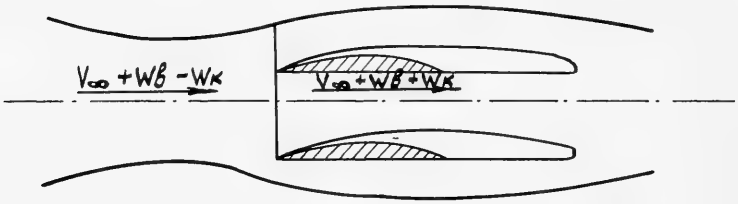

Fig. 2 - Cavitating propeller performance

characterizing the streamline shape in the way of the blades will be defined as the sum total of the velocities W_{aB} and W_{tB} induced by the vortices and the velocity W_{aK} which is due to the thickness effect of cavities (Fig. 3). Since the velocity W_{aK} increases from the leading edge in the direction of flow, an additional bending of the streamline takes place. On the basis of the assumptions made above, the calculation of the streamline shape enables us to obtain initial data for the deflection of the blade element section.

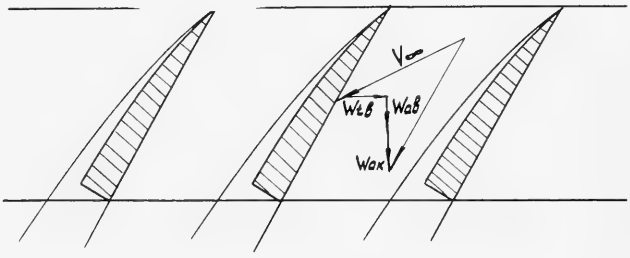

Fig. 3 - Local velocity of a blade streamline

The above method can be applied, if we know the thickness and the increase of thickness law for cavities developing on the blades.

It has been shown by analysis and checking the calculation that using data on the thicknesses of cavities for separate sections does not yield satisfactory results, and this apparently is attributable to the effect of the blades. That is why theoretical calculation was subsequently made only for the law of cavity increase, while the value of thickness was taken from the results of measurements conducted on propeller models.

Systematic measurements carried out by E.A. Fisher have made it possible to obtain the thickness of a cavity on the trailing edge versus the nominal angle of attack at infinity for various geometrical elements of the blade (e.g., curvature, shape of blade section, etc.). A diagram of such a measurement is given in Fig. 4. When using experimental diagrams, the use of the method of successive approximations is considered necessary; however, this does not involve

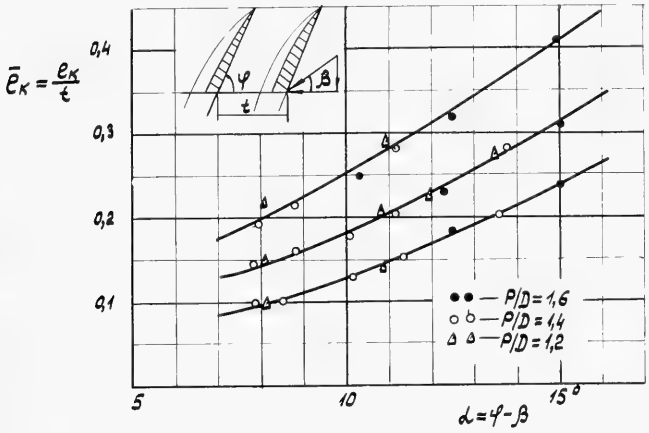

Fig. 4 - Thickness of a cavity on the trailing edge of a blade versus nominal angle of attack at infinity for various geometrical elements of the blade

much difficulty, because the convergence of process is rapid enough, provided the first approximation is reasonably chosen.

Following the determination of the flow parameters in way of the blades, one could proceed directly to choosing blade-section elements. It is clear that the curvature and the nominal angle of attack should be chosen so as to provide a prescribed value of the lift coefficient c_L for the element in two-dimensional parallel flow; subsequently, these values should be corrected, with allowance for the curvature of flow. Generally, the solution is not unequivocal, since one and the same value of c_L can be obtained with various relations between the blade curvature on the pressure face and the nominal angle of attack.

It is easily shown that the deceleration of flow before the propeller due to the presence of cavities involves a decrease in propeller inductive efficiency which is the greater, the greater the thickness of the cavities. The design losses will also increase with the increase of cavity thickness, and the latter will result in the deterioration of the hydrodynamic quality of the sections.

Thus, to ensure the maximum efficiency of a cavitating propeller, it is essential that the relation between the curvature and the angle of attack should be such as to reduce the cavity thickness to a minimum. An additional requirement restricting the greatest value of the pressure-face curvature is the absence of cavitation on this side of the blade.

Accordingly, the section elements are defined from two equations:

$$\alpha_K = f(\delta_2, C_L, \sigma) ,$$

$$\alpha_K = f(\delta_2, \delta, \sigma) ,$$

where

σ = local cavitation number,

δ = thickness of the section,

δ_2 = pressure-face curvature,

α_K = nominal angle of attack.

The form of these equations and hence the absolute values of curvature and pitch will vary according to the initial shape of the sections to be used for the construction of the blade.

Wedge-shaped sections with the pressure-face deflection shifted to the trailing edge make it possible to realize large absolute values of curvature and provide for high propeller efficiency in the design conditions. In a number of cases, however, the necessity of providing high efficiency values under transient conditions, when cavitation is underdeveloped, makes it necessary to use ordinary segmental or compromise sections.

It should be noted that, in spite of grave assumptions, the calculation method enables us to obtain fairly reliable data. Figure 5 shows performance curves for a propeller so designed; the small circle in the diagram characterizes the initial design conditions.

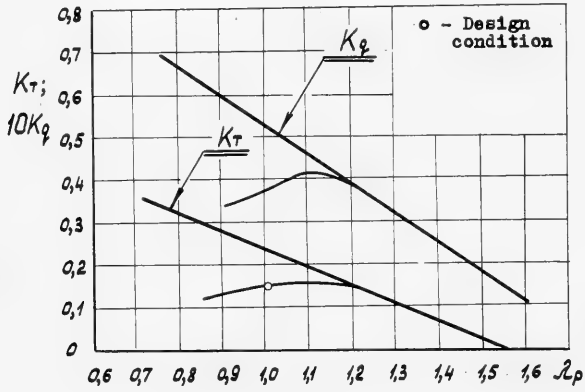

Fig. 5 - Performance curves of a propeller in relation to the initial design condition

The above procedure for determining the pressure-face curvature and the blade-element pitch suggests that the propeller will operate in the uniform velocity field. This is essentially true in the case of a propeller operating behind the strut, where the radial nonuniformity of the velocity field is the determining factor and the circumferential nonuniformity insignificant. When the propeller

operates in oblique flow, however, the circumferential nonuniformity, especially in the way of the root sections, is so substantial that it will inevitably give rise to outbreaks of cavitation on the pressure face, should the propeller be designed in the manner mentioned above. These outbreaks of cavitation may cause cavitation erosion. To avoid this phenomenon, the design of a propeller suitable for operation in oblique flow is carried out as follows. The propeller is first designed as described above, with the design speed range determined by the value of the mean pitch, and the coefficient K_T is made larger to allow for its subsequent decrease in the oblique flow. Then, using the known relation

$$\lambda_{max} = \frac{\lambda_\rho \cos\phi}{1 - \frac{\lambda_\rho}{\pi \bar{r}} \sin\phi},$$

the maximum instantaneous advance is calculated for the sections at different relative radii. After this the curvature is determined by assuming that pressure-face cavitation does not occur with this value of advance.

For the curvature so adopted the element pitch is defined so that with the mean advance of the propeller a prescribed thrust coefficient should be provided. As an illustration, Fig. 6 shows a comparison of curvature and pitch distributions for two propellers with equivalent thrust, one being designed for axial flow and the other for oblique flow inclined by 12°. From this comparison it can be seen that the greatest difference in the elements is observed in the way of the root sections. The reduced curvature and increased pitch will obviously result in the deterioration of propeller efficiency. Performance tests show that with the inclination of flow by 10 to 12° the loss of efficiency due to nonoptimal propeller elements ranges from 6 to 8%.

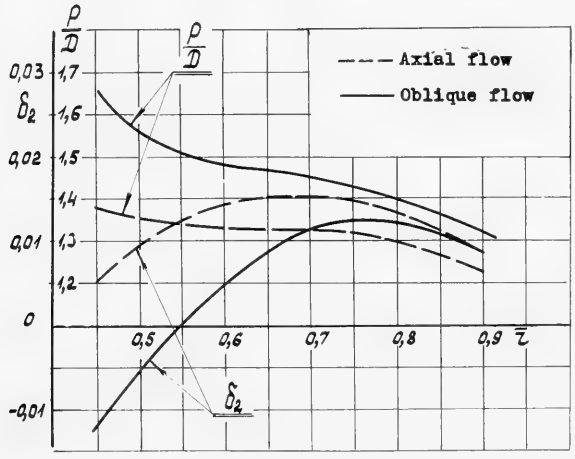

Fig. 6 - Comparison of curvature and pitch distributions for two propellers, one designed for axial flow and the other for oblique flow inclined by 12°

For vessels whose speed is not very high (35-40 knots), use is often made of the propeller design method that is based on drawing an analogy between the elements of cavitating and subcavitating propellers. According to this method, developed by O.V. Rozhdestvensky (3), the elements of the optimal subcavitating propeller designed for the prescribed K_T and λ_ρ (Fig. 7) are close to the elements of the cavitating propeller designed for K_T^* and λ_ρ.

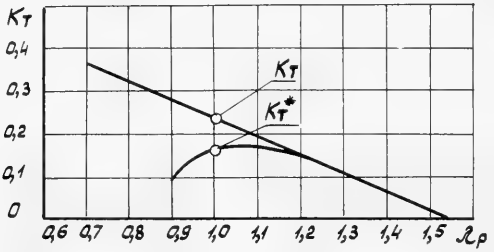

Fig. 7 - Analogy between the design elements of a subcavitating (K_T) and cavitating (K_T^*) propeller

With the value K_T^* being given, the first stage of calculation consists in the determination of the value K_T. This is effected by means of diagrams based on systematic model tests. Subsequent calculation is the same as for the ordinary cavitating propeller. The comparison made between the elements of propellers designed for cavitation and those based on the above analogy shows that the method mentioned above gives somewhat lower values of curvature, the difference being the greater, the smaller the assumed cavitation number.

The efficiency of the above design methods has been proven in the development of propellers for the hydrofoil vessels "Raketa" and "Meteor." The original variants of propellers for these vessels were subject to intensive erosion, as a result of which 10-to-12mm-deep cavities developed on the pressure side of the blade by the end of the navigation season.

Figure 8 illustrates a propeller after 500 hours of operation. The analysis of operating conditions and assumed propeller elements has shown that the cavitation erosion was caused by excessive curvature of the pressure face. The distribution of curvature over the radius of the propeller blades of "Raketa," as adopted in the original variant of the propeller, is correlated in Fig. 9 with that calculated with allowance for the inclination of the flow (4).

On the basis of the above calculations, new variants of propellers were designed for these vessels. Their blades are fully free from cavitation erosion after 6000 hours of operation, i.e., after three navigation seasons.

Fig. 8 - Cavitation erosion on a propeller after 500 hours of operation

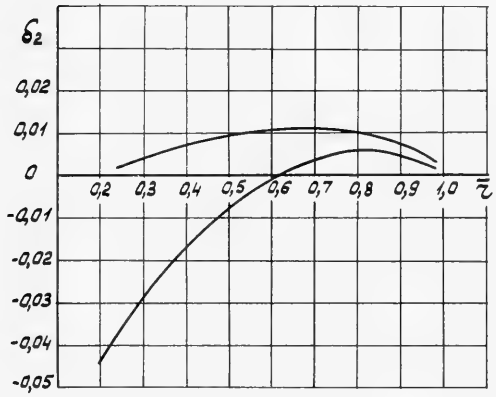

Fig. 9 - Comparison of the curvature distribution over the radius of the propeller of "Raketa," in the original variant and with allowance for the inclination of flow

REFERENCES

1. Cox, G.G., "The Derivation of Induced Velocity Equations and Formulation of Initial Design Procedure," Report 2166 DTMB, 1966

2. Bavin, V.F., and Miniovich, I.Ya., "Theory and Design of Screw Propellers," Sudpromgiz, 1963

3. Russetsky, A.A., "Hydrodynamics of Controllable-Pitch Propellers," Sudostroyenie Publishers, 1968

4. Georgiyevskaya, E.P., "Erosion on Propellers of Hydrofoil Passenger Ships," J. Sudostroyenie, No. 7, 1966

* * *

DISCUSSION

C.G. Cox

The authors have earned the appreciation of those concerned with the design of propellers for high-speed applications. They do not neglect to indicate where the state of the art lies today, and describe logically-derived, empirical approaches to allow for those aspects of design procedure which cannot, as yet, be mathematically determined with precision. They draw attention to the design problem caused by high shaft inclinations—a common feature of many high-speed craft. Anyone who has observed the severe root erosion that can be caused by large flow inclinations has no doubt as to the severity of the problem. If possible, such propellers should always be designed and tested to allow for this effect.

* * *

SUPERCAVITATING PROPELLER THEORY— THE DERIVATION OF INDUCED VELOCITY

Geoffrey G. Cox
Naval Ship Research and Development Center
Washington, D.C.

ABSTRACT

The determination of induced velocity components is the central problem of propeller design theory. Induced velocity equations -- together with a pressure equation -- are derived for a lifting-surface representation of a supercavitating propeller, where blade loading is represented by bound and free vorticity, and blade cavities by pressure-source distributions. Particular attention is paid to a tentative lifting-line model analogous to previous development of subcavitating propeller design theory.

1. INTRODUCTION

The increasing availability of digital computers during recent years has provided the necessary stimulus to improve propeller design methods. It is now relatively straightforward to perform the extensive numerical calculations based upon adequate mathematical models, to represent the complicated hydrodynamic action of subcavitating propellers. Although further efforts continue to be necessary with regard to refinement and improved accuracy of numerical calculation procedures, contemporary design theories for the propulsion performance of light to moderately loaded subcavitating propellers in inviscid flow can be considered satisfactory. The same situation however, does not apply to the case of supercavitating propeller design theory. Tulin, in an excellent paper presented at the Fourth ONR Symposium on Naval Hydrodynamics [1] drew attention to the work carried out in several countries, which led to an understanding of the operating characteristics and mechanism of operation for supercavitating propellers. He emphasized that the effects of the blade cavities must be recognized at all stages of the design process. Prior to this time, published design methods [2,3] had -- paraphrasing Tulin -- "essentially grafted two-dimensional supercavitating section theory or experimental data onto subcavitating design theory."

Recently, English formulated a supercavitating propeller theory [4], based on an extension of Goldstein's work for a subcavitating finite-bladed propeller [5], and modified the boundary conditions to allow for the effect of the cavities. Also Malavard and Sulmont devised a rheoelectric analogy method for performing supercavitating propeller design calculations [6].

Basically, there are five separate phases to the design of any propeller, namely:

(a) preliminary powering analysis to determine the design parameters for which the propeller is to be designed, i.e., thrust loading coefficient C_T, advance ratio λ, number of blades Q, etc., such that the propeller is compatible with the craft, installed propulsion machinery and transmission;

(b) determination of the relationship between propeller performance and design parameters in viscous and inviscid flow. This procedure is necessary since, essentially, the basic design process is concerned with behavior in inviscid flow;

(c) determination of desired blade radial lift distribution together with radial induced hydrodynamic pitch angle (hence thrust and torque distribution), for operation in inviscid flow;

(d) determination of blade shape and area; camber, pitch, and thickness distribution to *actually* achieve the desired requirements of (c);

(e) a strength check.

For a subcavitating propeller it is necessary to augment (d) with the requirement for freedom from cavitation erosion and thrust breakdown at the design condition. For a supercavitating propeller it is necessary to augment (a), (b), and (d) by the following:

for (a) — ensure that the design parameters are chosen to permit the blades to operate effectively in a supercavitating regime;

for (b) — although blade cavity-pressure drag is an inviscid flow parameter, it is best to consider it in association with blade viscous drag. Hence for design purposes inviscid flow performance is defined to omit blade cavity-pressure drag;

for (d) — ensure freedom from blade pressure-side (face) cavitation, and that the blade thickness lies within the upper cavity boundary. If necessary, due to blade thickness requirements or circumferential wake variations, an operating angle of attack is selected for the blade at the design condition.

The importance of preliminary design analysis cannot be overstressed, but will not be considered here, since it involves many aspects of naval architecture not concerned with detailed propeller design theory. It is, of course, intimately concerned with the theoretically predicted [7], or experimentally measured [8], performance for systematic series of propellers. Likewise, the subject of propeller blade strength can be considered independently of a particular theoretical design procedure, although use is made of intermediate results determined in the basic design process. Hence, the main emphasis of theoretical propeller design is usually considered to be concerned with phases (b), (c), and (d). It is important to realize that phases (b) and (c) are concerned with

forecasting required radial characteristics to meet prescribed design conditions, whereas phase (d) is concerned with the practical achievement of these characteristics, recognizing that the blades possess finite chord length. For inviscid flow calculations, the blade can be represented mathematically by a lifting line for phase (c), whereas a lifting-surface representation is required for phase (d). As already intimated for the supercavitating propeller phases (c) and (d) should adequately recognize the self and mutual interference effects of the blade cavities.

The purpose of this paper is to derive and assemble the necessary equations for supercavitating propeller design theory, such that cavity interference effects can be adequately accounted for at all stages of the design process. The major task is to derive the necessary equations for the induced velocity components, since they are directly or indirectly involved in every aspect of propeller design calculations. The problem is formulated in Appendix A, and the approach used is somewhat similar to that of Widnall [9] for the three-dimensional supercavitating hydrofoil, but considers the more complicated case of the screw propeller. Linearized equations of motion are used to define the existence of a perturbation velocity potential and perturbation pressure, i.e., acceleration potential, which satisfy the Laplace equation. Green's theorem and linearized boundary conditions for the blades and cavities are used to define a mathematical model, which consists of a distribution of pressure doublets over the linearized blade surfaces to represent loading, and a distribution of pressure sources over the linearized blades and cavity surfaces to represent the cavities. Lifting-surface equations are obtained for the induced velocity components and pressure at any point relative to axes rotating with the propeller.

Section 2 presents the lifting-surface equations for pressure and induced velocity components at any point on the blade surface. The pressure doublets are transposed into the more usual and convenient bound and free vorticity distribution. In conformity with normal practice for subcavitating propeller theory, the radial component of induced velocity is ignored and a nonlinear refinement is incorporated into the pitch of the lifting surface, so as to extend consideration to the case of moderate propeller loading. The solution of the lifting-surface equations is discussed briefly, and it is pointed out that effective computation to determine axial and tangential induced velocities, as for the subcavitating propeller case, requires a knowledge of lifting-surface pitch and loading, i.e., induced advance ratio and bound vorticity distribution, respectively. Finally it is hypothesized that for uniform propeller inflow, there appears to be little advantage in not assuming a constant-pitch lifting surface.

Section 3 discusses the necessity of specifying a simplified mathematical model, i.e., lifting line, for a propeller blade. Such a model is required for two purposes, first for prediction of supercavitating propeller performance, and secondly to provide necessary information for lifting-surface calculations. Induced velocity and pressure equations are defined for such a model and detailed consideration given to the case of uniform inflow and constant induced advance ratio. The simplification of the definite integrals which arise in the solution of the lifting-line equations is discussed in Appendix B.

Section 4 gives a brief outline of initial design procedure together with the necessary equations. As already mentioned, it is considered justifiable to account for section pressure drag along with viscous drag when determining thrust loading and power coefficients.

2. LIFTING SURFACE – INDUCED VELOCITIES

Lifting surface equations for pressure and induced velocity components at any position (x^*, r^*, θ^*) relative to the propeller, are derived in Appendix A, i.e., Eqs. (A9), (A10), (A11), and (A12), respectively. They are obtained by use of the inviscid linearized equations of motion for which the acceleration potential (or pressure) is a solution of the Laplace equation. In addition, by use of Green's theorem and linearized boundary conditions, the blade loading and cavity are represented by pressure doublet and source distributions, respectively.

In propeller theory it is usual and convenient to replace the pressure doublet strength $\Delta p(r,\theta)$ by a bound vortex strength $\gamma(r,\theta)$ per unit length, where $\gamma(r,\theta)$ is nondimensionalized by $2\pi U$. By use of the Kutta-Joukowski theorem it is possible to obtain the linearized relationship

$$\Delta p(r,\theta) = \gamma(r,\theta)\,\frac{(r^2+\lambda^2)^{1/2}}{\lambda}\,. \tag{1}$$

It should also be noted that the radial distribution of advance ratios $\lambda(r)$ are usually replaced by induced advance ratios $\lambda_i(r)$ in the equations referred to above. Strictly speaking this is a nonlinear refinement to the pitch of the lifting surface which allows consideration to be extended from light to moderate propeller loading. In addition, it is usual to neglect the effect of the radial component of induced velocity $u_r(x^*, r^*, \theta^*)$ for moderately loaded propellers. Thus, it is only necessary to consider axial and tangential components, i.e., $u_a(x^*, r^*, \theta^*)$ and $u_t(x^*, r^*, \theta^*)$, respectively. By the same token, it is then sufficient to put

$$M = r^2 + \lambda_i^2 + (r\theta\lambda_{i_r})^2 \simeq r^2 + \lambda_i^2\,.$$

Hence, by applying the transformation

$$-\tau = \frac{(\nu - x^*)}{\lambda_i} + \theta^*$$

the axial and tangential velocity Eqs. (A10) and (A12)[1] become

[1]Note a change in definition: Nondimensional axial and tangential induced velocities, i.e., u_x and u_θ, respectively, in Appendix A, are henceforth defined as u_a and u_t.

$$u_a(x^*, r^*, \theta^*) = \frac{1}{2} \sum_{q=1}^{Q} \left\{ \int_{r_h}^{1} \int_{\theta_L}^{\theta_E} S(r,\theta) \lambda_i \left[\int_{\theta-\theta^*}^{\infty} \frac{[x^* - \lambda_i(\tau + \theta^*)]\, d\tau}{R_\tau^3} \right] M^{1/2}\, d\theta dr \right.$$

$$- \int_{r_h}^{1} \int_{\theta_L}^{\theta_T} \gamma(r,\theta)(r^2 + \lambda_i^2)^{1/2} \frac{r^* \sin \Phi}{R_\Phi^3}\, d\theta dr \qquad (2)$$

$$\left. + \int_{r_h}^{1} \int_{\theta_L}^{\theta_T} \gamma(r,\theta)(r^2 + \lambda_i^2)^{1/2} \left[\frac{\partial}{\partial r} \int_{\theta-\theta^*}^{\infty} \frac{r(r - r^* \cos \psi)\, d\tau}{R_\tau^3} \right] d\theta dr \right\}$$

and

$$u_t(x^*, r^*, \theta^*) = \frac{1}{2} \sum_{q=1}^{Q} \left\{ - \int_{r_h}^{1} \int_{\theta_L}^{\theta_E} S(r,\theta) \lambda_i \left[\int_{\theta-\theta^*}^{\infty} \frac{r \sin \psi\, d\tau}{R_\tau^3} \right] M^{1/2}\, d\theta dr \right.$$

$$+ \int_{r_h}^{1} \int_{\theta_L}^{\theta_T} \gamma(r,\theta)(r^2 + \lambda_i^2)^{1/2} \frac{[(r^* - r\cos\Phi)\theta\lambda_{i_r} - (x^* - \theta\lambda_i)\cos\Phi]}{R_\Phi^3}\, d\theta dr \qquad (3)$$

$$+ \int_{r_h}^{1} \int_{\theta_L}^{\theta_T} \gamma(r,\theta)(r^2 + \lambda_i^2)^{1/2}$$

$$\left. \times \left[\frac{\partial}{\partial r} \int_{\theta-\theta^*}^{\infty} \frac{\{\lambda_i(r^* - r\cos\psi) + [x^* - \lambda_i(\tau + \theta^*)]\, r \sin\psi\}\, d\tau}{R_\tau^3} \right] d\theta dr \right\},$$

where

$$R_\tau = [\{x^* - \lambda_i(\tau + \theta^*)\}^2 - 2rr^* \cos\psi + r^2 + r^{*2}]^{1/2},$$

$$R_\Phi = [(x^* - \lambda_i\theta)^2 - 2rr^* \cos\Phi + r^2 + r^{*2}]^{1/2},$$

$$\psi = \tau + \sigma_q, \quad \Phi = \theta - \theta^* + \sigma_q,$$

and $\theta_L(r)$, $\theta_T(r)$, and $\theta_E(r)$ define the blade leading edge, trailing edge, and cavity, respectively.

In Eqs. (2) and (3) the three contributions to the induced velocity components can be recognized as due to pressure sources, bound and free vorticity, respectively, i.e.,

$$u = u_{ps} + u_{bv} + u_{fv}.$$

The free vorticity contribution can be expressed in the more convenient form

$$u_a(x^*, r^*, \theta^*)_{fv} = \frac{1}{2} \sum_{q=1}^{Q} \left\{ \oint_{S_b} \gamma(r,\theta)(r^2 + \lambda_i^2)^{1/2} \left[\int_{\theta-\theta^*}^{\infty} \frac{r(r - r^* \cos\psi)\, d\tau}{R_\tau^3} \right] d\theta \right.$$

$$\left. - \int_{r_h}^{1} \int_{\theta_L}^{\theta_T} \frac{\partial}{\partial r} [\gamma(r,\theta)(r^2 + \lambda_i^2)^{1/2}] \left[\int_{\theta-\theta^*}^{\infty} \frac{r(r - r^* \cos\psi)\, d\tau}{R_\tau^3} \right] d\theta dr \right\}, \tag{4}$$

$$u_t(x^*, r^*, \theta^*)_{fv} = \frac{1}{2} \sum_{q=1}^{Q} \left\{ \oint_{S_b} \gamma(r,\theta)(r^2 + \lambda_i^2)^{1/2} \right.$$

$$\times \left[\int_{\theta-\theta^*}^{\infty} \frac{\{\lambda_i(r^* - r\cos\psi) + [x^* - \lambda_i(\tau + \theta^*)]\, r \sin\psi\}\, d\tau}{R_\tau^3} \right] d\theta$$

$$- \int_{r_h}^{1} \int_{\theta_L}^{\theta_T} \frac{\partial}{\partial r} [\gamma(r,\theta)(r^2 + \lambda_i^2)^{1/2}] \tag{5}$$

$$\left. \times \left[\int_{\theta-\theta^*}^{\infty} \frac{\{\lambda_i(r^* - r\cos\psi) + [x^* - \lambda_i(\tau + \theta^*)]\, r \sin\psi\}\, d\tau}{R_\tau^3} \right] d\theta dr \right\}.$$

In order to obtain the induced velocity at various positions (x^*, r^*, θ^*) on the reference blade, i.e., $q = 1$, it will be necessary to take $x^* = \theta^* \lambda_i^* + \epsilon$ on that blade initially and consider the limit as $\epsilon \to 0$. For $q \neq 1$ it will be adequate to take $x^* = \theta^* \lambda_i^*$ immediately.

For the pressure equation (A9), see Fig. A2,

$$p_{S_b^-} = p_{S_c} = -\frac{\sigma}{2}, \tag{6}$$

where

$$\sigma = \frac{p_{-\infty} - e}{\frac{1}{2}\rho U^2}.$$

Thus

$$p(\theta^*\lambda_i^* - \epsilon, r^*, \theta^*) = \frac{1}{2}\sum_{q=1}^{Q}\left\{\int_{r_h}^{1}\int_{\theta_L}^{\theta_E} S(r,\theta)\,\frac{M^{1/2}}{R_\Phi}\,d\theta dr + \int_{r_h}^{1}\int_{\theta_L}^{\theta_T}\gamma(r,\theta)\,\frac{(r^2+\lambda_i^2)^{1/2}}{\lambda_i}\,\frac{N}{R_\Phi^3}\,d\theta dr\right\}, \tag{7}$$

where

$$N = r(x^* - \theta\lambda_i) + \lambda_i r^* \sin\Phi + r\theta\lambda_{i_r}(r - r^*\cos\Phi)$$

$$p(\theta^*\lambda_i^* - \epsilon, r^*, \theta^*) = -\frac{\sigma}{2}, \quad \theta_L(r) \le \theta^* \le \theta_T(r), \quad q = 1$$

$$p(\theta^*\lambda_i^* \mp \epsilon, r^*, \theta^*) = -\frac{\sigma}{2}, \quad \theta_T(r) \le \theta^* \le \theta_E(r), \quad q = 1$$

and consideration of ϵ is similar to that already discussed. Considerable care has to be exercised when Eqs. (2), (3), and (7) are evaluated numerically for the reference blade, since the integrands become singular for $r = r^*$, $\theta = \theta^*$ [9,10,11].

In order to use the lifting-surface equations (2), (3), and (7) for the purpose of design, i.e., to determine the blade face shape, it is assumed that $\lambda_i(r)$ and $\gamma(r,\theta)$ are known. After solving Eq. (7) for $S(r,\theta)$, the axial and tangential induced velocity components can be computed at desired positions (r^*, θ^*) on the blade, using Eqs. (2) and (3). Hence, the normal induced velocity components $u_n(r^*, \theta^*)$ can be obtained using

$$u_n(r^*,\theta^*) \simeq \frac{r^* u_a(r^*,\theta^*) - \lambda_i(r^*)\,u_t(r^*,\theta^*)}{(r^{*2}+\lambda_i^{*2})^{1/2}}. \tag{8}$$

Integration of the normal induced velocity components in a chordwise direction will give the blade face shape at any desired radial position r^* relative to the helical line pitched at angle $\beta_i(r^*) = \tan^{-1}(\lambda_i^*/r^*)$.

In the solution of Eq. (7), $S(r,\theta)$ should be represented by suitable modes possessing unknown coefficients, so that the problem reduces to the determination of these unknown coefficients. Attention is directed to the work of Widnall which includes a useful discussion of the problem [9], including the influence of various cavity closure conditions. As regards the prediction of lift force on a supercavitating hydrofoil, Widnall concludes that an approximate representation is adequate for $S(r,\theta)$ and that the cavity closure condition and closure location is not important, provided that the cavity is sufficiently long. Parkin's work [13] on linearized two-dimensional supercavitating hydrofoils operating at nonzero cavitation number indicates exact chordwise modes for $S(r,\theta)$ and $\gamma(r,\theta)$, where the designer has the choice of either designing for an angle of attack or shock-free entry with a prescribed cavity thickness at the trailing edge.

Finally, if the propeller is assumed to operate in homogeneous inflow, there appears to be little advantage in not assuming a constant induced advance ratio λ_i. This will permit some simplifications of the lifting-surface equations.

3. PROPOSED LIFTING LINE – INDUCED VELOCITIES

Prior to the use of lifting-surface theory, it is necessary to determine the induced advance ratio $\lambda_i(r)$ and bound vorticity $\gamma(r,\theta)$. The determination of $\gamma(r,\theta)$ is dependent on the total radial circulation distribution $\Gamma(r)$, where

$$\Gamma(r) = \int_{\theta_L(r)}^{\theta_T(r)} \gamma(r,\theta)\, d\theta \ ,$$

since the chordwise spreading of $\gamma(r,\theta)$ is a matter of choice. For a finite-bladed subcavitating propeller this information, including the lift distribution $C_L(r)[c(r)/D]$, is obtained using the lifting-line concept for a propeller blade. This is a simplification which ignores chordwise effects. Its major purpose is to adjust radial circulation for the effect of a finite number of blades. Likewise, the use of this concept is required for supercavitating propeller design, but recognizing the effect of the blade cavities.

In order to assist the design problem, and in analogy with the lifting-line concept for subcavitating propellers [14], the blades will be represented by lifting lines to account for loading. In other words, as a tentative first step, an initial procedure will be formulated where the mathematical model for each blade is considered to be a lifting line with associated free trailing vortices, together with a pressure source distribution on the trailing vortex sheet to represent the cavity.

By the use of the Dirac delta function, $\gamma(r,\theta)(r^2+\lambda_i^2)^{1/2}$ is replaced by $\Gamma(r)\,\delta(\theta)$ in Eqs. (2), (3), (4), and (7). In addition, θ^* is equated to zero in all but Eq. (7), since the induced velocity components are only required at the lifting line. For an unskewed blade, it should also be noted that $\theta_L(r) = 0$ for the pressure source integrals. Hence,

$$u_a(\epsilon, r^*, 0) = \frac{1}{2}\sum_{q=1}^{Q}\left\{\int_{r_h}^{1}\int_{0}^{\theta_E} S(r,\theta)\lambda_i(r^2+\lambda_i^2)^{1/2}\left[\int_{\theta}^{\infty}\frac{(\epsilon-\lambda_i\tau)\,d\tau}{R_\tau^3}\right]d\theta\,dr\right.$$

$$-\left[\Gamma(r)\int_{0}^{\infty}\frac{r(r-r^*\cos\psi)\,d\tau}{R_\tau^3}\right]_{r=r_h} \qquad (9)$$

$$\left.-\int_{r_h}^{1}\frac{d\Gamma(r)}{dr}\left[\int_{0}^{\infty}\frac{r(r-r^*\cos\psi)\,d\tau}{R_\tau^3}\right]d\tau\right\},$$

$$u_t(\epsilon, r^*, 0) = \frac{1}{2}\sum_{q=1}^{Q}\left\{-\int_{r_h}^{1}\int_{0}^{\theta_E} S(r,\theta)\,\lambda_i(r^2+\lambda_i^2)^{1/2}\left[\int_{\theta}^{\infty}\frac{r\sin\psi\,d\tau}{R_\tau^3}\right]d\theta dr\right.$$

$$-\left[\Gamma(r)\int_{0}^{\infty}\frac{\{\lambda_i(r^*-r\cos\psi)+(\epsilon-\lambda_i\tau)\,r\sin\psi\}\,d\tau}{R_\tau^3}\right]_{r=r_h} \qquad (10)$$

$$\left.-\int_{r_h}^{1}\frac{d\Gamma(r)}{dr}\left[\int_{0}^{\infty}\frac{\{\lambda_i(r^*-r\cos\psi)+(\epsilon-\lambda_i\tau)\,r\sin\psi\}\,d\tau}{R_\tau^3}\right]dr\right\},$$

where

$$R_\tau = [(\epsilon-\lambda_i\tau)^2 - 2rr^*\cos\psi + r^2 + r^{*2}]^{1/2},$$

$$\psi = \tau + \sigma_q,$$

$$\theta_E = \theta_E(r).$$

Here it should be noted that $u_{bv} = 0$ for the induced velocity components due to bound vorticity, i.e.,

$$\lim_{\epsilon\to 0} u_a(\epsilon, r^*, 0)_{bv} = -\frac{1}{2}\sum_{q=1}^{Q}\int_{r_h}^{1}\frac{\Gamma(r)\,r^*\sin\sigma_q\,dr}{R_{\sigma_q}^3} = 0,$$

$$\lim_{\epsilon\to 0} u_t(\epsilon, r^*, 0)_{bv} = -\frac{1}{2}\sum_{q=1}^{Q}\int_{r_h}^{1}\frac{\epsilon\Gamma(r)\cos\sigma_q\,dr}{R_{\sigma_q}^3} = 0,$$

where

$$R_{\sigma_q} = \left[\epsilon^2 - 2rr^*\cos\sigma_q + r^2 + r^{*2}\right]^{1/2}.$$

For the pressure equation (7),

$$\sigma = -\sum_{q=1}^{Q}\left\{\int_{r_h}^{1}\int_{0}^{\theta_E}\frac{S(r,\theta)(r^2+\lambda_i^2)^{1/2}\,d\theta dr}{\left[(\epsilon+\theta\lambda_i-\theta^*\lambda_i^*)^2 - 2rr^*\cos\Phi + r^2 + r^{*2}\right]^{1/2}}\right. \qquad (11)$$

$$\left.+\int_{r_h}^{1}\frac{\Gamma(r)}{\lambda_i}\,\frac{[r(\theta^*\lambda_i^*-\epsilon) - r^*\lambda_i\sin(\theta^*-\sigma_q)]\,dr}{\left[(\theta^*\lambda_i^*-\epsilon)^2 - 2rr^*\cos(\theta^*-\sigma_q) + r^2 + r^{*2}\right]^{3/2}}\right\},$$

where $0 \le \theta^* \le \theta_E(r)$.

If the propeller is assumed to operate in uniform inflow, there appears to be little advantage in not assuming λ_i independent of r. Therefore, the theory will be developed for uniform inflow and constant hydrodynamic pitch, i.e., U and $\pi\lambda_i$ independent of radius r.

A major difference between subcavitating and supercavitating lifting-line theory for constant induced advance ratio is that while the normality condition holds for the subcavitating case provided that $\Gamma(r_h) = 0$, i.e.,

$$u_t(r^*) = -\frac{\lambda_i}{r^*} u_a(r^*) ,$$

this condition no longer holds for the supercavitating case, see Fig. 1.

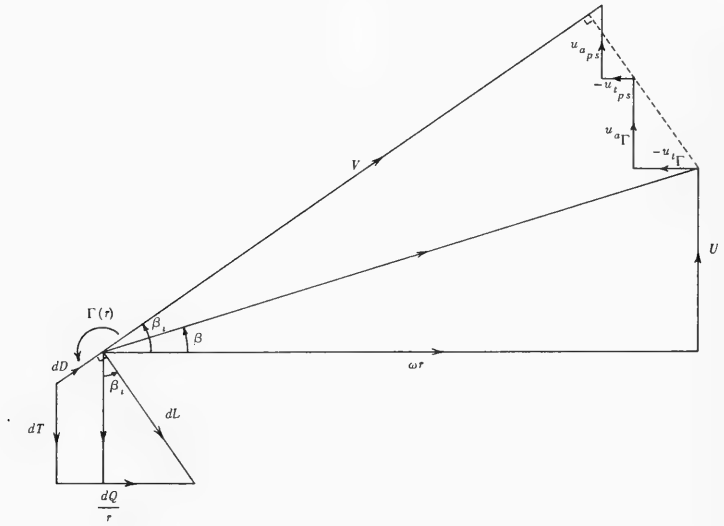

Fig. 1 - Velocity and force diagram

The mathematical model used to represent each supercavitating blade consists of:

(i) a lifting line at $\theta = \sigma_q$, $r_h \le r \le 1$ with associated trailing vorticity laid out on a helicoidal surface of pitch ratio $\pi\lambda_i$, downstream of the lifting line to represent loading;

(ii) a pressure source distribution laid out on the trailing vortex sheet at $\sigma_q \le \theta \le \sigma_q + \theta_E$, to represent the cavity.

If $\epsilon \rightarrow 0$, then the induced velocity and pressure equations (9) - (11) can be expressed:

$$u_a(0, r^*, 0) = u_a(r^*) = u_a(r^*)_\Gamma + u_a(r^*)_{ps} \ , \tag{12}$$

$$u_t(0, r^*, 0) = u_t(r^*) = u_t(r^*)_\Gamma + u_t(r^*)_{ps} \ , \tag{13}$$

and

$$\sigma = \sigma(r^*, \theta^*)_\Gamma + \sigma(r^*, \theta^*)_{ps} \ . \tag{14}$$

It should be noted that the normality condition still applies for the loading contribution to induced velocity. This can be shown easily, since

$$\frac{r - r^* \cos\psi}{R_\tau^3} = - \frac{\partial}{\partial r}\left(\frac{1}{R_\tau}\right) ,$$

and

$$\frac{(r^* - r\cos\psi) - r\tau \sin\psi}{R_\tau^3} = \frac{1}{r^*}\left[\frac{1}{R_\tau} + \tau \frac{\partial}{\partial \tau}\left(\frac{1}{R_\tau}\right) + r \frac{\partial}{\partial r}\left(\frac{1}{R_\tau}\right)\right]$$

with

$$\int_0^\infty \tau \frac{\partial}{\partial \tau}\left(\frac{1}{R_\tau}\right) d\tau = \left[\frac{\tau}{R_\tau}\right]_0^\infty - \int_0^\infty \frac{d\tau}{R_\tau} = \frac{1}{\lambda_i} - \int_0^\infty \frac{d\tau}{R_\tau} \ .$$

Thus,

$$u_a(r^*)_\Gamma = \frac{1}{2} \int_{r_h}^1 r \frac{d\Gamma(r)}{dr}\left[\sum_{q=1}^{Q} \frac{\partial}{\partial r} \int_0^\infty \frac{d\tau}{R_\tau}\right] dr \ , \tag{15}$$

and

$$u_t(r^*)_\Gamma = - \frac{\lambda_i}{r^*} u_a(r^*)_\Gamma \ . \tag{16}$$

Considerable simplification is also possible for the induced velocity components due to the cavities since

$$\frac{1}{r^*} \frac{\partial}{\partial \tau}\left(\frac{1}{R_\tau}\right) = - \frac{\lambda_i^2}{r^*} \frac{\tau}{R_\tau^3} - \frac{r \sin\psi}{R_\tau^3} \ .$$

Thus,

$$u_t(r^*)_{ps} = -\frac{\lambda_i}{r^*}\left[u_a(r^*)_{ps} + I(r^*)\right] , \tag{17}$$

where

$$u_a(r^*)_{ps} = -\frac{\lambda_i^2}{2}\int_{r_h}^{1}\int_{0}^{\theta_E} S(r,\theta)\left(r^2+\lambda_i^2\right)^{1/2}\left[\sum_{q=1}^{Q}\int_{\theta}^{\infty}\frac{\tau d\tau}{R_\tau^3}\right] d\theta dr \tag{18}$$

and

$$I(r^*) = \frac{1}{2}\sum_{q=1}^{Q}\int_{r_h}^{1}\int_{0}^{\theta_E}\frac{S(r,\theta)\left(r^2+\lambda_i^2\right)^{1/2} d\theta dr}{\left[\lambda_i^2\theta^2 - 2rr^*\cos(\theta+\sigma_q) + r^2 + r^{*2}\right]^{1/2}} . \tag{19}$$

The components of pressure Eq. (14) are

$$\sigma(r^*,\theta^*)_\Gamma = -\sum_{q=1}^{Q}\int_{r_h}^{1}\frac{\Gamma(r)\left[r\theta^* - r^*\sin(\theta^*-\sigma_q)\right] dr}{\left[r^2 - 2rr^*\cos(\theta^*-\sigma_q) + r^{*2} + \theta^{*2}\lambda_i^2\right]^{3/2}} , \tag{20}$$

$$\sigma(r^*,\theta^*)_{ps} = -\sum_{q=1}^{Q}\int_{r_h}^{1}\int_{0}^{\theta_E}\frac{S(r,\theta)\left(r^2+\lambda_i^2\right)^{1/2} d\theta dr}{\left[\lambda_i^2(\theta-\theta^*)^2 - 2rr^*\cos\Phi + r^2 + r^{*2}\right]^{1/2}} , \tag{21}$$

where $0 \le \theta^* \le \theta_E(r)$.

Hence, it can be seen that

$$I(r^*) = -\frac{1}{2}\sigma(r^*,0)_{ps} ,$$

where $\sigma = \sigma(r^*, 0)_{ps}$, since $\sigma(r^*, 0)_\Gamma = 0$; thus

$$I(r^*) = -\frac{\sigma}{2} . \tag{22}$$

It is interesting to observe from Eqs. (16), (17), and (22) that normality applies for $\sigma = 0$.

Referring to Fig. 1, it can be seen that

$$\frac{\lambda_i}{r^*} = \frac{1 + u_a(r^*)}{\frac{r^*}{\lambda} + u_t(r^*)} . \tag{23}$$

Hence, using Eqs. (16), (17), (22), and (23),

$$u_a(r^*) = \frac{\left(\frac{\lambda_i}{\lambda} - 1 + \frac{\lambda_i^2}{r^{*2}}\frac{\sigma}{2}\right) r^{*2}}{(r^{*2} + \lambda_i^2)}, \tag{24}$$

$$u_t(r^*) = -\frac{\left(\frac{\lambda_i}{\lambda} - 1 - \frac{\sigma}{2}\right) r^* \lambda_i}{(r^{*2} + \lambda_i^2)}. \tag{25}$$

The problem for numerical solution is to solve Eqs. (12) or (13) and (14) simultaneously for $\Gamma(r)$, assuming a known λ_i. This involves suitable representation of $\Gamma(r)$ and $S(r,\theta)$ in terms of unknown coefficients, so that the equations can be expressed as a set of linear algebraic equations to be solved for the unknown coefficients. The terms associated with the unknown coefficients are definite integrals, which have to be suitably arranged or simplified to enable their evaluation, see Appendix B. According to Widnall's supercavitating hydrofoil calculations [9], foil force prediction is not very sensitive to precise $\theta_E(r)$ values or a particular cavity closure condition. In addition, a reasonably simple representation of $S(r,\theta)$ appeared to suffice. Hence, θ_E can be assumed independent of radius and determined by use of a convenient closure condition at one representative radius. It may even suffice to use an estimate of cavity length based on Parkin's two-dimensional supercavitating foil theory [13], or some such similar reference.

A suitable representation of radial circulation $\Gamma(r)$ is

$$\Gamma(x) = (1-x)^{1/2} \sum_{m=1}^{M} A_m x^{m+1}, \tag{26}$$

where

$$x = \frac{r - r_h}{1 - r_h}. \tag{27}$$

The pressure source distribution $S(r,\theta)$ can be represented by

$$S(r,\theta)(r^2 + \lambda_i^2)^{1/2} = \sum_{m=1}^{M} B_m h(r, r_{m-1}, r_m)\,\delta(\theta) + (r^2 + \lambda_i^2)^{1/2} \sum_{m=1}^{M}\sum_{n=1}^{N} C_{mn} h(r, r_{m-1}, r_m)\, h(\theta, \theta_{n-1}, \theta_n), \tag{28}$$

where

$$(1 - r_h) = M\Delta r\,, \quad r_0 = r_h\,, \quad r_m = r_{m-1} + \Delta r\,, \quad r_M = 1$$

$$\theta_E = N\Delta\theta\,, \quad \theta_0 = 0\,, \quad \theta_n = \theta_{n-1} + \Delta\theta\,, \quad \theta_N = \theta_E$$

$$h(r, r_{m-1}, r_m) = 0 \quad , \quad r < r_{m-1}\,, \quad r > r_m$$

$$= 1 \quad , \quad r_{m-1} \le r \le r_m$$

$$h(\theta, \theta_{n-1}, \theta_n) = 0 \quad , \quad \theta < \theta_{n-1}\,, \quad \theta > \theta_n$$

$$= 1 \quad , \quad \theta_{n-1} \le \theta \le \theta_n\,.$$

Or, following Widnall,

$$S(r,\theta)(r^2 + \lambda_i^2)^{1/2} = \sum_{m=1}^{M} B_m h(r, r_{m-1}, r_m)\,\delta(\theta) + (r^2 + \lambda_i^2)^{1/2} \sum_{m=1}^{M} \sum_{n=0}^{N} C_{mn} h(r, r_{m-1}, r_m)\, g_n \tag{29}$$

where

$$g_0 = -\frac{\theta}{\Delta\theta} + 1 \quad , \quad 0 \le \theta \le \theta_1$$

$$\left.\begin{aligned} g_n &= \frac{\theta}{\Delta\theta} - (n-1) \quad , \quad \theta_{n-1} \le \theta \le \theta_n \\ &= -\frac{\theta}{\Delta\theta} + (n+1)\,, \quad \theta_n \le \theta \le \theta_{n+1} \end{aligned}\right\} n = 1, 2, \cdots, (N-1) \tag{30}$$

$$g_N = \frac{\theta}{\Delta\theta} - (N-1) \quad , \quad \theta_{N-1} \le \theta \le \theta_N\,.$$

The use of Widnall's modes in Eq. (30), i.e., g_n, provides piecewise continuity in the chordwise direction and Eq. (29) could be preferable to Eq. (28) as a representation of $S(r,\theta)$. However, Eq. (29) necessitates the evaluation of more definite integrals than (28) for the terms associated with the unknown coefficients.

4. OUTLINE OF APPLICATION TO PROPELLER DESIGN THEORY

Analogous to an initial design theory for subcavitating propellers [14], it is necessary to obtain an estimate for the induced advance ratio λ_i, and the radial bound circulation $\Gamma(r)$, to meet prescribed design conditions.

It has to be assumed that:

(a) Thrust loading coefficient C_T (or power coefficient C_P), advance ratio λ, free-stream cavitation number σ, and number of blades Q are known.

(b) The design conditions for the propeller are such that it can operate effectively as a supercavitating propeller.

In an actual theoretical design procedure, it is necessary to solve the Eqs. (12) or (13) and (14) of Sec. 3 for prescribed values of induced advance ratio λ_i to determine the bound circulation $\Gamma(r^*)$ and hence lift coefficient $C_L(r^*)$, using

$$C_L(r^*)\,\frac{c(r^*)}{D} = \frac{2\pi\Gamma(r^*)\,\cos\beta_i(r^*)}{\dfrac{r^*}{\lambda} + u_t(r^*)}\,, \tag{31}$$

where $\cos\beta_i(r^*) = r^*/(r^{*2} + \lambda_i^2)^{1/2}$ and $c(r^*)/D$ are assumed known. Once drag-to-lift ratios $\epsilon(r^*)$ have been assessed, it is possible to calculate the thrust loading coefficient C_T, or power coefficient C_P, from

$$C_T = 4Q\int_{r_h}^{1}\Gamma(r^*)\left[\frac{r^*}{\lambda} + u_t(r^*)\right]\left[1 - \frac{\lambda_i}{r^*}\,\epsilon(r^*)\right]dr^*\,, \tag{32}$$

$$C_P = \frac{4Q}{\lambda}\int_{r_h}^{1} r^*\Gamma(r^*)\,[1 + u_a(r^*)]\left[1 + \frac{r^*}{\lambda_i}\,\epsilon(r^*)\right]dr^*\,, \tag{33}$$

see Fig. 1.

An iteration or interpolation process is necessary to meet the desired design value of C_T or C_P. Once this has been achieved, it is possible to estimate propeller efficiency η from

$$\eta = \frac{C_T}{C_P}\,. \tag{34}$$

For the purposes of design it appears easier to account for section cavity pressure-drag coefficient $C_D(r^*)_p$ along with viscous drag coefficient $C_D(r^*)_f$, i.e.,

$$C_D(r^*) = C_D(r^*)_p + C_D(r^*)_f \tag{35}$$

when considering section drag-to-lift ratios $\epsilon(r^*) = C_D(r^*)/C_L(r^*)$. Hence, both drag contributions are accounted for on a strip-theory basis when determining thrust loading coefficient C_T and power coefficient C_P. Hence, $C_D(r^*)$ is obtained from experimental or theoretical two-dimensional data. This data, especially for cavity pressure drag, should conform as closely as possible to the propeller-blade-section design details such as chordwise loading, lift

coefficient $C_L(r^*)$, local cavitation number σ_ℓ, and operating angle of attack (if any). If theoretical estimates are used, the work of Parkin [13] may prove especially convenient for estimation of $C_D(r^*)_p$.

Finally, having decided the chordwise distribution of bound circulation $\gamma(r,\theta)$, the lifting-surface induced velocity components can be obtained from Eqs. (4), (5), and (7) of Sec. 2 (thus permitting determination of blade pressure side shape).

CONCLUSIONS

1. Lifting-surface and lifting-line equations have been derived which properly account for cavity interference effects. It should be noted that for $S(r,\theta) = 0$, i.e., no cavities, the equations revert to those for the subcavitating case, where blade thickness effects are neglected.

2. Although the derived equations have been nondimensionalized on the basis of uniform inflow to the propeller, only straightforward modifications are necessary to account for radially varying inflow.

3. The proposed lifting-line model is regarded as tentative and subject to modification, until exploratory calculations have been carried out. In particular, it will be necessary to ascertain the sensitivity of the induced velocity components to assumed cavity lengths, in order to formulate adequate cavity length criteria. These criteria will obviously be dependent on the design choice made about the nature of the blade section cavity, i.e., shock-free entry, with prescribed cavity thickness condition, or prescribed angle of attack.

4. Supercavitating lifting-line theory for the case of constant hydrodynamic pitch $\pi\lambda_i$, indicates dependency between axial and tangential induced velocity components. When the free-stream cavitation number is zero, this dependency is equivalent to that for the subcavitating case, i.e., the so-called normality condition.

ACKNOWLEDGMENTS

Appreciation is expressed to the Hydrofoil Development Project Office and the Hydromechanics Laboratory of the Naval Ship Research and Development Center for encouragement in the preparation of this paper. Thanks are due to Dr. W. B. Morgan, who reviewed the paper and made many helpful suggestions. Grateful thanks are due to Shirley Childers, Mary F. Gotthardt, and Terry Gilleland, for the painstaking efforts in the preparation of the manuscript.

NOTATION

A_m, B_m, C_{mn}	Unknown coefficients

$C_D(r)$ Section total drag coefficient, i.e., $\frac{dD}{\frac{\rho}{2} c(r) V^2}$

$C_D(r)_f$ Section viscous drag coefficient

$C_D(r)_p$ Section cavity pressure drag coefficient

$C_L(r)$ Section lift coefficient, i.e., $\frac{dL}{\frac{\rho}{2} c(r) V^2}$

C_P Power coefficient, i.e., $\frac{P}{\frac{\rho}{2} \pi R^2 U^3}$

C_T Thrust loading coefficient, i.e., $\frac{T}{\frac{\rho}{2} \pi R^2 U^2}$

$c(r)$ Section chord

D Propeller diameter

e Cavity pressure

$i(r^*, r)$ Induction factor

n Normal to linearization surface

$p_{-\infty}$ Freestream pressure

p Perturbation pressure

$\hat{p}$ Perturbation acceleration potential, i.e., $\frac{p}{\rho}$

$\Delta\hat{p}$ Pressure doublet strength per unit area, i.e., $\hat{p}^+ - \hat{p}^-$

$\left\langle \frac{\partial \hat{p}}{\partial n} \right\rangle$ Pressure source strength per unit area, i.e., $\frac{\partial \hat{p}^+}{\partial n} - \frac{\partial \hat{p}^-}{\partial n}$

P Power

Q Number of blades, (also torque)

R Propeller radius

R_Φ Linear distance between (x^*, r^*, θ^*) and $(x, r, \theta + \sigma_q)$, i.e., $[(x^* - x)^2 + r^2 + r^{*2} - 2rr^* \cos \Phi]^{1/2}$

r Radial cylindrical coordinate

S Surface consisting of cavity surface and propeller blade surface

$S(r,\theta)$ Pressure source strength, i.e., $\frac{1}{2\pi}\left\langle\frac{\partial \hat{p}}{\partial n}\right\rangle$

T Thrust

U Freestream velocity

$u(u_x, u_r, u_\theta)$ Perturbation flow velocity

u_n Normal induced velocity

V Resultant velocity

$v(v_x, v_r, v_\theta)$ Flow velocity

x Axial cylindrical coordinate

β_i Induced flow angle, i.e., $\tan^{-1}\left(\frac{\lambda_i R}{r}\right)$

$\gamma(r,\theta)$ Bound vorticity strength per unit length

$\Gamma(r)$ Bound circulation

$\delta(\theta)$ Dirac delta function

ϵ Small increment

$\epsilon(r)$ Drag to lift ratio

η Propeller efficiency

θ Angular cylindrical coordinate

λ Advance ratio, i.e., $\frac{U}{\omega R}$

λ_i Induced advance ratio

ν Dummy variable

ρ Fluid mass density

σ Freestream cavitation number, i.e., $\dfrac{p_{-\infty} - e}{\frac{\rho}{2} U^2}$

σ_ℓ Local section cavitation number, i.e., $\dfrac{p_{-\infty} - e}{\frac{\rho}{2} V^2}$

σ_q $\dfrac{2\pi}{Q}(q-1), \quad q = 1, 2, \cdots, Q$

τ $-\dfrac{(v - x^*)}{\lambda_i} - \theta^*$

Φ $\theta - \theta^* + \sigma_q$

ϕ Perturbation velocity potential, i.e., $\mathbf{u} = \nabla\phi$

ψ $\tau + \sigma_q$

ω Propeller angular velocity

Superscripts

$*$ Refers to reference point

$+$ Refers to face side of linearized blade and cavity surface

$-$ Refers to back side of linearized blade and cavity surface

Subscripts

a Refers to axial direction, i.e., x direction

t Refers to tangential direction, i.e., θ direction

x, r, θ Refer to x, r, θ directions

0 Refers to fixed-axes system

b Refers to blade

c Refers to cavity

h	Refers to hub
L	Refers to blade leading edge
r	Differentiation with respect to r
T	Refers to blade trailing edge
E	Refers to cavity trailing edge
ps	Refers to pressure source contribution
fv	Refers to free vorticity contribution
bv	Refers to bound vorticity contribution
Γ	Refers to lifting-line contribution

Nondimensionalizing Parameters

$x,\ x^*,\ r,\ r^*,\ r_h,\ \nu$	Nondimensionalized by R
$\hat{p}$	Nondimensionalized by U^2
$\left\langle \frac{\partial \hat{p}}{\partial n} \right\rangle$	Nondimensionalized by $\frac{U^2}{R}$
ϕ	Nondimensionalized by RU
u	Nondimensionalized by U
$\gamma(r,\theta)$	Nondimensionalized by $2\pi U$
$\Gamma(r)$	Nondimensionalized by $2\pi RU$

REFERENCES

1. Tulin, M.P., "Supercavitating Propellers — History, Operating Characteristics and Mechanics of Operation," Proceedings of the Fourth ONR Symposium on Naval Hydrodynamics, U.S. Government Printing Office, August 1962

2. Tachmindji, A.J., and Morgan, W.B., "The Design and Estimated Performance of a Series of Supercavitating Propellers," Proceedings of the Second ONR Symposium on Naval Hydrodynamics, U.S. Government Printing Office, August 1958

3. Venning, E., and Haberman, W.L., "Supercavitating Propeller Performance," Trans. SNAME, Vol. 70, 1962

4. English, J.W., "An Approach to the Design of Fully Cavitating Propellers," ASME Symposium on Cavitation in Fluid Machinery, November 1965

5. Goldstein, S., "On the Vortex Theory of Screw Propellers," Proc. Roy. Soc., Vol. 123, 1929

6. Malavard, L., "Theory Calculation and Design of Supercavitating Propellers," Bureau D'Analyse et de Recherche Appliquées, Final Report on ONR Contract F61052.67.C0107, 1968

7. Caster, E.B., "TMB 2-, 3-, and 4-Bladed Supercavitating Propeller Series," David Taylor Model Basin Report 1637, January 1963

8. Newton, R.N., and Rader, H.P., "Performance Data of Propellers for High-Speed Craft," Trans. RINA, Vol. 103, 1961

9. Widnall, S.E., "Unsteady Loads on Hydrofoils including Free Surface Effects and Cavitation," MIT Fluid Dynamics Research Laboratory Report 64-2, June 1964

10. Sparenberg, J.A., "Application of Lifting Surface Theory to Ship Screws," Koninki. Ned. Akad. Wetenschap. Proc. Ser. B, Vol. 62, No. 5, 1959

11. Tsakonas, S., and Jacobs, W.R., "Unsteady Lifting Surface Theory for a Marine Propeller of Low Pitch Angle with Chordwise Loading Distribution, SIT Report 994, January 1964

12. Lerbs, H.W., Alef, W., and Albrecht, K., "Numerische Auswertungen zur Theorie der Tragenden Flache von Propellern," Jahrb. Schiffbautechn. Ges., Vol. 58, 1964

13. Parkin, B.R., "The Inverse Problem of the Linearized Theory of Fully-Cavitating Hydrofoils," Rand Corporation Report RM-3566-PR, September 1964

14. Lerbs, H.W., "Moderately Loaded Propellers with a Finite Number of Blades and an Arbitrary Distribution of Circulation," Trans. SNAME, Vol. 60, 1959

15. Cox, G.G., "Supercavitating Propeller Theory – Part I. The Derivation of Induced Velocity Equations and Formulation of an Initial Design Procedure," David Taylor Model Basin Report 2166, February 1966

16. Moriya, T., "On the Integration of Biot-Savart's Law in Propeller Theory," J. Soc. Aeronaut. Sci., Japan, Vol. 9, No. 89, September 1942

17. Morgan, W.B., and Wrench, J.W., "Some Computational Aspects of Propeller Design," Methods in Computational Physics, Vol. 4, Academic Press, 1965

18. Pien, P.C., and Strom-Tejsen, J., "A General Marine Propeller Theory," Seventh ONR Symposium on Naval Hydrodynamics, 1968

APPENDIX A

FORMULATION OF THE PROBLEM [15]

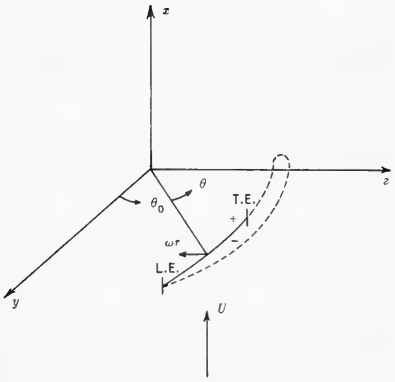

Fig. A1 - The coordinate system

Consider a propeller blade with no translation velocity, rotating with angular velocity ω in a fluid whose free-stream velocity is $U(r)$, see Fig. A1. Perturbation velocities u_x^*, u_r^*, $u_{\theta_0}^*$ are defined such that

$$v_x^* = U + u_x^*, \quad v_r^* = u_r^*, \quad v_{\theta_0}^* = u_{\theta_0}^* ,$$

while for upstream, i.e., $x^* \rightarrow -\infty$, $0 \leq r^* \leq \infty$,

$$v_x^* = U, \quad v_r^* = v_{\theta_0}^* = 0 .$$

The linearized equations of motion with respect to fixed axes are

$$\frac{\partial \mathbf{u}^*}{\partial t} + U \frac{\partial \mathbf{u}^*}{\partial x^*} = -\nabla^* \frac{p^*}{\rho} , \qquad \text{(A1)}$$

where $\mathbf{u}(u_x^*, u_r^*, u_{\theta_0}^*)$ is the perturbation velocity vector and p^* the perturbation pressure [9,10,11]. A perturbation velocity potential ϕ^* exists such that

$$\mathbf{u}^* = \nabla^* \phi^* ,$$

hence, taking the divergence for both sides of Eq. (A1), it can be shown that an acceleration potential $\hat{p}^* = p^*/\rho$ exists. Provided that dU/dr is a second-order term, Eq. (A1) can be written as

$$\frac{\partial \phi^*}{\partial t} + U \frac{\partial \phi^*}{\partial x^*} = -\hat{p}^* , \qquad \text{(A2)}$$

which possesses a solution

$$\phi(x^*, r^*, \theta_0^*, t) = -\frac{1}{U}\int_{-\infty}^{x^*-x} \hat{p}\left(\nu + x, r^*, \theta_0^*, t + \frac{\nu - x^* + x}{U}\right) d\nu , \tag{A3}$$

making use of the boundary condition that $\hat{p}^* = 0$ at $x^* = -\infty$.

Green's theorem for the case of a propeller with Q equally spaced blades gives

$$\hat{p}(x^*, r^*, \theta_0^*, t) = \frac{1}{4\pi}\sum_{q=1}^{Q}\left\{\iint_{S_0} \hat{p}(x, r, \theta)\frac{\partial}{\partial n_0}\left(\frac{1}{R_{\Phi_0}}\right) dS_0 - \iint_{S_0}\frac{1}{R_{\Phi_0}}\frac{\partial}{\partial n_0}[\hat{p}(x, r, \theta)]\, dS_0\right\} , \tag{A4}$$

where

$$R_{\Phi_0} = [(x^* - x)^2 + r^2 + r^{*2} - 2rr^*\cos\Phi_0]^{1/2} ,$$

$$\Phi_0 = \theta_0 - \theta_0^* + \sigma_q ,$$

$$\sigma_q = \frac{2\pi}{Q}(q - 1) .$$

The control point, considered fixed in space, is (x^*, r^*, θ_0^*) and $(x, r, \theta_0 + \sigma_q)$ is a point on the moving surface S_0. S_0 is the enclosed surface which, for the supercavitating propeller, consists of the face and cavity boundaries of a blade. In Eq. (A4) the direction of the normal is into the fluid.

In accordance with linearization procedure S_0 is assumed to be a surface composed of helical lines possessing a continuously varying pitch angle $\tan^{-1}(R\lambda(r)/r)$ in the r direction, see Fig. A2.

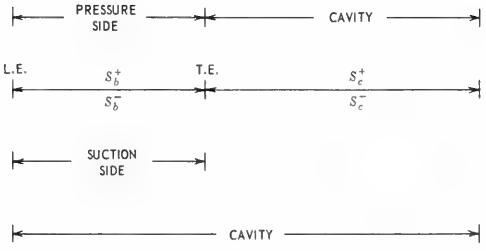

Fig. A2 - The linearization surface

If

$$\Delta\hat{p} = \hat{p}^{+} - \hat{p}^{-} ,$$

$$\left\langle \frac{\partial p}{\partial n} \right\rangle = \frac{\partial p^{+}}{\partial n} - \frac{\partial p^{-}}{\partial n} , \tag{A5}$$

where $n = n^{-}$, Eq. (A4) becomes

$$\hat{p}(x^*, r^*, \theta_0^*, t) = \frac{1}{4\pi} \sum_{q=1}^{Q} \left\{ \iint_{S_b + S_c} \left\langle \frac{\partial p}{\partial n} \right\rangle \frac{1}{R_{\Phi_0}} dS_0 - \iint_{S_b} \Delta\hat{p} \frac{\partial}{\partial n_0} \left(\frac{1}{R_{\Phi_0}} \right) dS_0 \right\} . \tag{A6}$$

From Eq. (A6) it is seen that $(\partial\hat{p}/\partial n)$ and Δp are pressure source and doublet strengths per unit area, respectively. Furthermore it is clear that the pressure doublet strength is only nonzero on the blade surface S_b.

If the surface of a blade is considered to be composed of helical lines with varying pitch in the r direction, the surface can be defined as

$$x - \theta_0 R\lambda(r) = 0 .$$

Hence,

$$dS_0 = [r^2 + R^2\lambda^2 + (r\theta_0\lambda_r)^2]^{1/2} \, d\theta_0 \, dr ,$$

where

$$\lambda(r) = \frac{U(r)}{\omega R} , \qquad \lambda_r = \frac{d\lambda}{dr} ,$$

and

$$\frac{\partial}{\partial n_0} = - \frac{r \frac{\partial}{\partial x} - r\theta_0 R\lambda_r \frac{\partial}{\partial r} - \frac{R\lambda}{r} \frac{\partial}{\partial \theta_0}}{\left[r^2 + R^2\lambda^2 + (r\theta_0 R\lambda_r)^2 \right]^{1/2}} ,$$

since the normal is defined in the n^{-} direction. Thus,

$$\frac{\partial}{\partial n_0} \left(\frac{1}{R_{\Phi_0}} \right) = - \frac{r(x^* - x) + R\lambda r^* \sin\Phi_0 + r\theta_0 R\lambda_r (r - r^* \cos\Phi_0)}{\left[r^2 + R^2\lambda^2 + (r\theta_0 R\lambda_r)^2 \right]^{1/2} R_{\Phi_0}^3} . \tag{A7}$$

Now $\theta_0 = \theta - \omega t$, where θ_0 refers to axes fixed in space and θ refers to a rotating axes system fixed with respect to the propeller. Hence if Eq. (A3) is applied to Eq. (A6) and time t is subsequently equated to zero, i.e., the time at which the two axes systems are assumed to instantaneously coincide,

$$\phi(x^*, r^*, \theta^*) = -\frac{1}{2}\sum_{q=1}^{Q}\left\{\iint_{S_b+S_c} S(r,\theta)\left[\int_{-\infty}^{x^*-\theta\lambda}\frac{d\nu}{R_\nu}\right]M^{1/2}\,d\theta dr + \iint_{S_b}\Delta p(r,\theta)\left[\int_{-\infty}^{x^*-\theta\lambda}\frac{N_\nu}{R_\nu^3}\,d\nu\right]d\theta dr\right\}, \tag{A8}$$

where x, x^*, r, r^*, ν are nondimensionalized by propeller radius R, ϕ by RU, $\hat{p}$ by U^2 and written p, $\Delta\hat{p}$ by $2\pi U^2$ and written Δp, $(\partial\hat{p}/\partial n)$ by $2\pi U^2/R$ and written $S(r,\theta)$.

Also,

$$M = r^2 + \lambda^2 + (r\theta\lambda_r)^2 ,$$

$$N_\nu = r\nu + r^*\lambda\sin\psi - \frac{r}{\lambda}(\nu - x^*)\lambda_r(r - r^*\cos\psi) ,$$

$$\psi = -\frac{1}{\lambda}(\nu - x^*) - \theta^* + \sigma_q ,$$

$$R_\nu = [\nu^2 + r^2 + r^{*2} - 2rr^*\cos\psi]^{1/2} .$$

Likewise, Eq. (A6) becomes

$$p(x^*, r^*, \theta^*) = \frac{1}{2}\sum_{q=1}^{Q}\left\{\iint_{S_b+S_c} S(r,\theta)\frac{M^{1/2}}{R_\Phi}\,d\theta dr + \iint_{S_b}\Delta p(r,\theta)\frac{N}{R_\Phi^3}\,d\theta dr\right\}, \tag{A9}$$

where

$$N = r(x^* - \theta\lambda) + r^*\lambda\sin\Phi + r\theta\lambda_r(r - r^*\cos\Phi) ,$$

$$R_\Phi = [(x^* - \theta\lambda)^2 + r^2 + r^{*2} - 2rr^*\cos\Phi]^{1/2} ,$$

$$\Phi = \theta - \theta^* + \sigma_q .$$

Now $u_x(x^*, r^*, \theta^*) = \partial\phi/\partial x^*$, $u_r(x^*, r^*, \theta^*) = \partial\phi/\partial r^*$, and $u_\theta(x^*, r^*, \theta^*) = (1/r^*)(\partial\phi/\partial\theta^*)$, hence the induced velocities nondimensionalized by U are

$$u_x(x^*, r^*, \theta^*) = -\frac{1}{2}\sum_{q=1}^{Q}\left\{-\iint_{S_b+S_c} S(r,\theta)\left[\int_{-\infty}^{x^*-\theta\lambda}\frac{\nu d\nu}{R_\nu^3}\right]M^{1/2}\,d\theta dr + \iint_{S_b}\Delta p(r,\theta)\left[\int_{-\infty}^{x^*-\theta\lambda}\left(\frac{r}{R_\nu^3} - \frac{3\nu N_\nu}{R_\nu^5}\right)d\nu\right]d\theta dr\right\}, \tag{A10}$$

$$u_r(x^*, r^*, \theta^*) = -\frac{1}{2}\sum_{q=1}^{Q}\left\{-\iint_{S_b+S_e} S(r,\theta)\left[\int_{-\infty}^{x^*-\theta\lambda}\frac{(r^*-r\cos\psi)\,d\nu}{R_\nu^3}\right]M^{1/2}\,d\theta dr\right.$$

$$+\iint_{S_b}\Delta p(r,\theta)\left[\int_{-\infty}^{x^*-\theta\lambda}\left(\frac{\lambda\sin\psi+\frac{r}{\lambda}(\nu-x^*)\lambda_r\cos\psi}{R_\nu^3}\right.\right. \tag{A11}$$

$$\left.\left.-\frac{3N_\nu(r^*-r\cos\psi)}{R_\nu^5}\right)d\nu\right]d\theta dr\Bigg\},$$

$$u_\theta(x^*, r^*, \theta^*) = -\frac{1}{2}\sum_{q=1}^{Q}\left\{\iint_{S_b+S_e} S(r,\theta)\left[\int_{-\infty}^{x^*-\theta\lambda}\frac{r\sin\psi\,d\nu}{R_\nu^3}\right]M^{1/2}\,d\theta dr\right.$$

$$+\iint_{S_b}\Delta p(r,\theta)\left[\int_{-\infty}^{x^*-\theta\lambda}\left(\frac{-\lambda\cos\psi+\frac{r}{\lambda}(\nu-x^*)\lambda_r\sin\psi}{R_\nu^3}\right.\right. \tag{A12}$$

$$\left.\left.+\frac{3N_\nu\, r\sin\psi}{R_\nu^5}\right)d\nu\right]d\theta dr\Bigg\}.$$

APPENDIX B

SIMPLIFICATION OF DEFINITE INTEGRALS

Simplification of $u_a(r^*)_\Gamma$

From Lerbs [14], Moriya [16], and others, Eq. (34) can be expressed as

$$u_a(r^*)_\Gamma = \frac{1}{2}\int_{r_h}^{1}\frac{d\Gamma(r)}{dr}\,\frac{i_a(r^*,r)}{(r^*-r)}\,dr \tag{B1}$$

by defining an induction factor $i_a(r^*, r)$, where

$$i_a(r^*,r) = r(r^*-r)\sum_{q=1}^{Q}\frac{\partial}{\partial r}\int_0^\infty\frac{d\tau}{R_\tau}. \tag{B2}$$

The induction factor integral, summed over all blades, can be expressed as an infinite series of products of modified Bessel functions of the first and second kind. By the use of Nicholson's asymptotic formulas for the modified Bessel functions, the numerical computation of the induction factor is rendered straightforward. A very full description of the process is given by Morgan and Wrench who offer refinements to Nicholson's approximation [17].

By applying Eq. (26) to Eq. (B1) and using the transformation (27)

$$u_a(r^*)_\Gamma = \frac{1}{2(1-r_h)} \sum_{m=1}^{M} A_m \left\{ (m+1) \int_0^1 \frac{x^m (1-x)^{1/2} i_a(x^*,x)}{(x^*-x)} \, dx \right.$$

$$\left. - \frac{1}{2} \int_0^1 \frac{x^{m+1} i_a(x^*,x)}{(1-x)^{1/2}(x^*-x)} \, dx \right\} . \tag{B3}$$

The integrals of (B3) can be made suitable for straightforward numerical computation by subtracting out the singularity at $x = x^*$, and eliminating the square-root singularity at $x = 1$ by applying the transformation $w = (1-x)^{1/2}$.

Hence,

$$u_a(r^*)_\Gamma = \frac{1}{2(1-r_h)} \sum_{m=1}^{M} A_m \left\{ -(m+1) \int_0^1 x^m (1-x)^{1/2} G(x,x^*) \, dx \right.$$

$$\left. + \frac{1}{2} \int_0^{\bar{x}} \frac{x^{m+1} G(x,x^*)}{(1-x)^{1/2}} dx + \int_0^{\bar{w}} (1-w^2)^{m+1} G(w,x^*) \, dw + J_m(x^*) \cos \beta_i(r^*) \right\} , \tag{B4}$$

where

$$G(x,x^*) = \frac{i_a(x,x^*) - i_a(x^*,x^*)}{(x-x^*)} ,$$

$$i_a(x^*,x^*) = \cos \beta_i(r^*) ,$$

$$J_m(x^*) = \frac{x^{*m}}{(1-x^*)^{1/2}} [(2m+3)\, x^* - 2(m+1)] \ln \left[\frac{1 + (1-x^*)^{1/2}}{x^{*1/2}} \right]$$

$$+ (2m+3) \sum_{s=1}^{m+1} \frac{[2^{s-1}(s-1)!]^2}{(2s-1)!} x^{*m+1-s}$$

$$- 2(m+1) \sum_{s=1}^{m} \frac{[2^{s-1}(s-1)!]^2}{(2s-1)!} x^{*m-s} .$$

Simplification of $u_a(r^*)_{ps}$ and $\sigma(r^*, \theta^*)_{ps}$

By applying Eq. (28) to Eq. (18)

$$u_a(r^*)_{ps} = -\frac{\lambda_i^2}{2} \sum_{q=1}^{Q} \left\{ \sum_{m=1}^{M} B_m \int_{r_{m-1}}^{r_m} \left[\int_0^\infty f(r, r^*, \sigma_q, \tau)\, d\tau \right] dr \right. \tag{B5}$$

$$\left. + \sum_{m=1}^{M} \sum_{n=1}^{N} C_{mn} \int_{r_{m-1}}^{r_m} (r^2 + \lambda_i^2)^{1/2} \int_{\theta_{n-1}}^{\theta_n} \left[\int_\theta^\infty f(r, r^*, \sigma_q, \tau)\, d\tau \right] d\theta dr \right\},$$

where

$$f(r, r^*, \sigma_q, \tau) = \frac{\tau}{\left[\lambda_i^2 \tau^2 - 2rr^* \cos\psi + r^2 + r^{*2}\right]^{3/2}},$$

and

$$\psi = \tau + \sigma_q .$$

The integral associated with B_m can be integrated with respect to r to give

$$\int_0^\infty \frac{\tau}{(\lambda_i^2 \tau^2 + r^{*2} \sin^2\psi)} \left\{ \frac{(r_m - r^* \cos\psi)}{\left[\lambda_i^2 \tau^2 - 2r_m r^* \cos\psi + r_m^2 + r^{*2}\right]^{1/2}} \right. \tag{B6}$$

$$\left. - \frac{(r_{m-1} - r^* \cos\psi)}{\left[\lambda_i^2 \tau^2 - 2r_{m-1} r^* \cos\psi + r_{m-1}^2 + r^{*2}\right]^{1/2}} \right\} d\tau .$$

For the integral associated with C_{mn},

$$\int_{\theta_{n-1}}^{\theta_n} \left[\int_0^\infty f(r, r^*, \sigma_q, \tau)\, d\tau \right] d\theta = \Delta\theta \int_{\theta_n}^\infty f(r, r^*, \sigma_q, \theta)\, d\theta \tag{B7}$$

$$+ \int_{\theta_{n-1}}^{\theta_n} (\theta - \theta_{n-1})\, f(r, r^*, \sigma_q, \theta)\, d\theta$$

after integration by parts. Although the integrations with respect to r can be solved analytically as elliptic integrals, it may be more straightforward to simplify $f(r, r^*, \sigma_q, \theta)$ such that integrations with respect to θ can be performed analytically [18]. For the integral with finite limits, this can be achieved by replacing θ with $\theta_{n-1} + \alpha$ and substituting $\cos\alpha \simeq 1 - (\alpha^2/2)$, $\sin\alpha \simeq \alpha$. Hence,

$$\lambda_i^2\theta^2 - 2rr^* \cos(\theta+\sigma_q) + r^2 + r^{*2} \simeq E_{n-1}\,\alpha^2 + 2F_{n-1}\,\alpha + H_{n-1}\,, \qquad \text{(B8)}$$

where

$$E_{n-1} = \lambda_i^2 + rr^* \cos(\theta_{n-1}+\sigma_q)\,,$$

$$F_{n-1} = \lambda_i^2\theta_{n-1} + rr^* \sin(\theta_{n-1}+\sigma_q)\,,$$

$$H_{n-1} = r^2 + r^{*2} - 2rr^* \cos(\theta_{n-1}+\sigma_q) + \lambda_i^2\theta_{n-1}^2\,.$$

The integral with an infinite upper limit can be dealt with in a similar manner after transposing it into an infinite sum of integrals, each with limits 0 and $\Delta\theta$. This is reasonable because the terms involved soon become negligible as θ increases.

By applying Eq. (28) to Eq. (21),

$$\sigma(r^*,\theta^*)_{ps} = -\sum_{q=1}^{Q}\left\{\sum_{m=1}^{M} B_m \int_{r_{m-1}}^{r_m} \frac{dr}{\left[r^2 - 2rr^*\cos(\theta^*-\sigma_q) + r^{*2} + \lambda_i^2\theta^{*2}\right]^{1/2}}\right.$$

$$+ \sum_{m=1}^{M}\sum_{n=1}^{N} C_{mn} \int_{r_{m-1}}^{r_m} \left(r^2+\lambda_i^2\right)^{1/2}$$

$$\left.\times \int_{\theta_{n-1}}^{\theta_n} \frac{d\theta}{\left[\lambda_i^2(\theta-\theta^*)^2 - 2rr^*\cos(\theta-\theta^*+\sigma_q) + r^2 + r^{*2}\right]^{1/2}}\, dr\right\}.$$

The integral associated with B_m can be integrated to give

$$\ln\left\{\frac{\left[r_m^2 - 2r_m r^*\cos(\theta^*-\sigma_q) + r^{*2} + \lambda_i^2\theta^{*2}\right]^{1/2} + r_m - r^*\cos(\theta^*-\sigma_q)}{\left[r_{m-1}^2 - 2r_{m-1} r^*\cos(\theta^*-\sigma_q) + r^{*2} + \lambda_i^2\theta^{*2}\right]^{1/2} + r_{m-1} - r^*\cos(\theta^*-\sigma_q)}\right\} \qquad \text{(B9)}$$

The simplification of the integral associated with C_{mn} is similar to that already discussed for $u_a(r^*)_{ps}$.

* * *

DISCUSSION

V. F. Bavin
Kryloff Ship Research Institute
Leningrad, U.S.S.R.

The author has indeed done a most valuable job by deriving equations for supercavitating propeller design theory which take into account the cavity thickness effect. It is fully recognized now that this is the only possible way to get the correct solution of the problem. I hope we will have the first numerical results in the near future.

I would like to note that the same approach to the problem was made in the U.S.S.R. by Dr. V. M. Lavrentjev and later by V. M. Ivchenko. The outline of Ivchenko's theory is given in the book titled "Problems and Methods of Hydrodynamics of Hydrofoils and Propellers," published in Kiev in 1966.

When making numerical computations at the Kiev Institute of Hydrodynamics, they came to the conclusion that for thin cavities, which are typical for the design conditions, the effect of cavity thickness can be estimated approximately by making use of two-dimensional theory. It would be most interesting to know the author's opinion on this subject.

* * *

DISCUSSION

J. W. English
National Physical Laboratory
Felthan, England

I would like to endorse the importance that is attached to obtaining numerical results from the work of Dr. Cox. The problem he had in attacking it is truly the heart of the fully cavitating propeller problem.

Could I ask the author if he has any ideas as to how he might allow for the known nonlinear effects that occur with the growth of the cavities that arise with increasing loading and reduced cavitation number. Does he consider, for example, that it might be necessary to resort to some empiricism, or might it be possible to allow for this growth by establishing an approximate mathematical technique to be used after his initial linear theory calculations.

* * *

DISCUSSION

C. Kruppa
Technische Universität, Berlin

I stated in a lecture series held at Michigan University last year that, in my opinion, *all* fully cavitating propellers, designed so far, have to be regarded as designed on an empirical or at least semiempirical basis. This statement does not, of course, deny that fully cavitating propellers have been designed in the past which have met certain design specifications and performed more or less satisfactorily in service. It simply means that, for fully cavitating propellers, no design method exists which can be compared with the lifting-surface

theory for moderately loaded noncavitating propellers and as such would make use of adequate singularity distributions, to represent not only blade loading but also cavity thickness.

The author's paper must therefore be regarded as a most welcome step towards producing the basis for a more rational approach to the design problem of propellers which are to operate under fully cavitating conditions. I am particularly looking forward to the numerical results that eventually will be obtained by this method. With the fairly comprehensive model-test data, that nowadays exist for fully cavitating propellers, one should easily be in a position to judge the relative merits of the various assumptions that have been made by the author in the process of deriving the expressions for the induced velocities.

It is in this context that I would like to put a question to the author: Having carried out cavitation-tunnel tests for a number of fully cavitating propellers, which were based on the so-called Newton-Rader series, I feel that the assumption of a basically cylindrical propeller race may well be justified under operating conditions when the angle of attack of the propeller blade sections is just high enough to ensure absence of face cavitation. However, at low advance ratios the expansion of the cavity-filled propeller race and the retarded inflow to the propeller disc are well-known features. Does the author expect that his theoretical work can also be used for analyzing the off-design performance of fully cavitating propellers, as encountered at the take-off point in hydrofoils or at the shallow-water hump in surface-effect ships? In asking this question it is, of course, realized that propeller lifting surface theory for fully wetted propellers can nowadays be regarded as an adequate method for analyzing the off-design performance of noncavitating propellers.

* * *

REPLY TO DISCUSSION

Geoffrey G. Cox

The author is grateful for the encouraging remarks of Mr. Bavin, Dr. English and Professor Kruppa. Their common desire to see numerical design data, based on the presented theory, is shared by the author. Work is presently being carried out at NSRDC to achieve this goal.

It is interesting to hear from Mr. Bavin that a similar approach to the supercavitating propeller design problem is being developed in the U.S.S.R. His suggestion regarding the use of two-dimensional supercavitating hydrofoil thickness data, as an approximation, appears to be plausible for the design condition. For this condition, the cavities will be relatively long and thin, and precision regarding cavity shape, especially for the trailing portion of the cavities, is not necessary. In any event strip-theory methods are necessary when allowing for friction and cavity pressure drag effects.

Dr. English and Professor Kruppa both draw attention to the important question of need for "off-design" prediction, such as applies to the "take-off" condition for craft which possess a resistance hump. For such "off-design" conditions, there will be high blade loading with large section angle of attack and cavity thickness. Under such conditions the propeller possesses relatively poor efficiency, but the major concern is to ensure an adequate reserve of power to "take-off" for a propeller designed for a cruise or top-speed condition. No really satisfactory *subcavitating* propeller theoretical performance analysis method exists, as yet, for such extreme "off-design" conditions. In the case of a supercavitating propeller, the problem is even more difficult, due to the influence and behavior of thick cavities. As such, the theoretical method proposed in the paper for the design problem is highly unlikely to prove a suitable basis for the "off-design" prediction purposes, without the incorporation of empirical information based on prior experimental test data.

* * *

THE EVOLUTION OF A FULLY CAVITATING PROPELLER FOR A HIGH-SPEED HYDROFOIL SHIP

B.V. Davis
The De Havilland Aircraft of Canada Limited
Ontario, Canada

and

J.W. English
Ship Division, National Physical Laboratory
Feltham, England

SUMMARY

A description is given of the work that has been conducted in producing the main, foilborne, fully cavitating propellers for the 200-ton Canadian Armed Forces hydrofoil ship HMCS *Bras d'Or*.

Designed for an all-weather antisubmarine role in the Atlantic, severe thrust loadings are experienced by the screws in both the takeoff and flying conditions, and model testing was essential to aid in design and confirm the predicted performance. The high thrust loadings produce difficult structural problems, and some testing was conducted to clarify this aspect of design.

The joint programme of work was sponsored by the De Havilland Aircraft of Canada, the prime contractors in designing and building the vessel. Broadly, the hydrodynamic design and water-tunnel testing were conducted at Ship Division NPL, while the structural analysis and testing were conducted at De Havilland, Canada. The programme has evolved a fully-cavitating propeller design with good hydrodynamic and structural characteristics over a wide range of speeds and thrusts. Water-tunnel testing is continuing for the purpose of further developing the design.

A brief review of some future alternative methods of propulsion is included in the paper, together with a résumé of future development prospects for fully cavitating and ventilated propellers.

INTRODUCTION

The HMCS *Bras d'Or* hydrofoil ship, designated FHE 400 by the Canadian Armed Forces, represents the fruition of a long Canadian Navy interest in such craft, an interest dating back as far as 1911. It was in 1960, however, following a review of the Naval Research Establishment's (now DREA) proposals, that the

decision was made to conduct a feasibility and engineering study based on the NRE proposals. This study was conducted by the De Havilland Aircraft of Canada, and later, in 1963, the same company was selected as the prime contractor for the design and construction of the vessel—a 200-ton ship intended for an all-weather antisubmarine role in the Atlantic.

The vessel has already been described on several occasions (Refs. 1, 2, and 3), and therefore the brief description given here relates mainly to the propulsion system that has been employed.

Figure 1 is an artist's impression of the vessel operating at high speed. The foil arrangement used is of the canard type, in which about 90 percent of the weight is carried by the after surface-piercing, noncavitating, main foil assembly, the remaining 10 percent being carried by the forward foil system which is designed to operate in the fully-cavitating condition. The power trains are contained within the main foil assembly. Figure 2 shows the propulsion system configuration that has been adopted, while Table 1 and Fig. 3 give the principal characteristics of the ship.

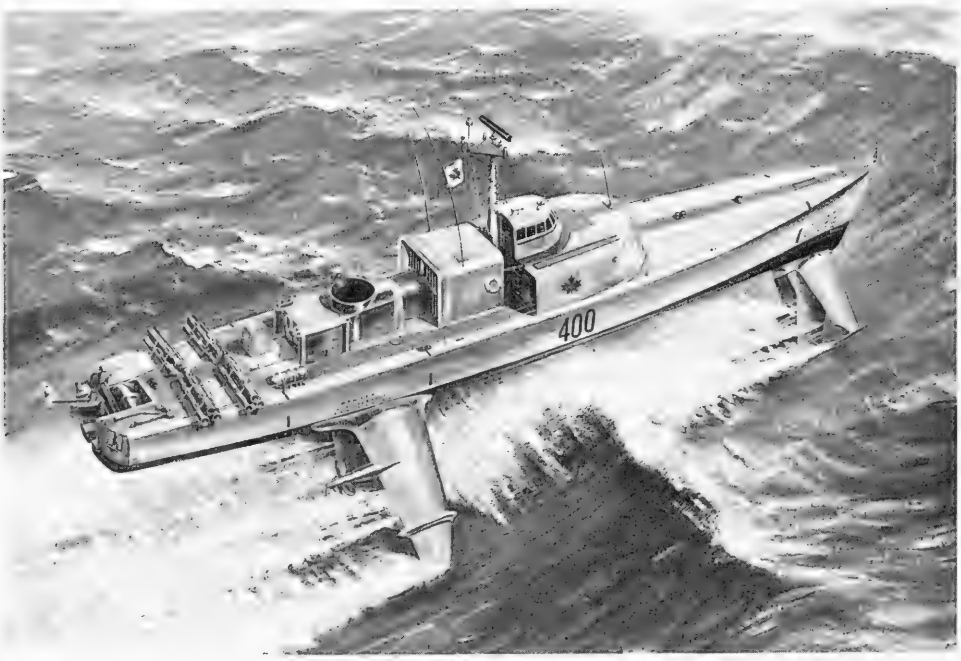

Fig. 1 - Artist's impression of HMCS Bras d'Or

The drive to the controllable pitch propellers is through the anhedral foils as shown in Fig. 2, while the shafting for the fully cavitating propellers passes down through the main struts to the propulsion pods situated at the intersection of the main foil and dihedral foils.

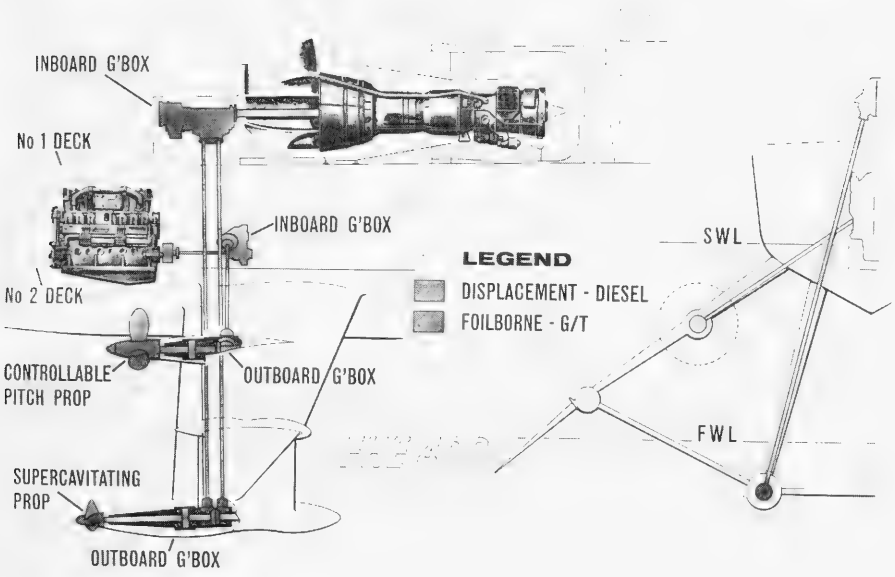

Fig. 2 - Layout of propulsion system

Table 1
Principal Specifications of the *Bras d'Or*

Length:	150 ft-9 in, Hull Beam: 21 ft-6 in, Foil Span: 66 ft
Weight:	200-250 tons (according to fuel carried)
Speed:	Foilborne - 60 knots, calm water 50 knots, sea state 5
Range:	Several hundred miles foilborne. More than 2000 miles at 12 knots hullborne.
Power:	Foilborne - P & W FT 4 gas turbine, 25,000 shp continuous. Driving two fully cavitating propellers.
	Hullborne - Davy Paxman 16 YJCM diesel, 2000 bhp continuous. Driving two controllable pitch propellers of KMW design.

The power transmission system for the fully cavitating propellers has been developed by the General Electric Company of the USA, the pioneer of hydrofoil 'Z' drives. The power output from the turbine passes into an inboard gearbox where the speed is increased from 4000 rpm maximum to 8000 rpm, to reduce the torque and hence shaft diameters to fit within the struts. The main drive is

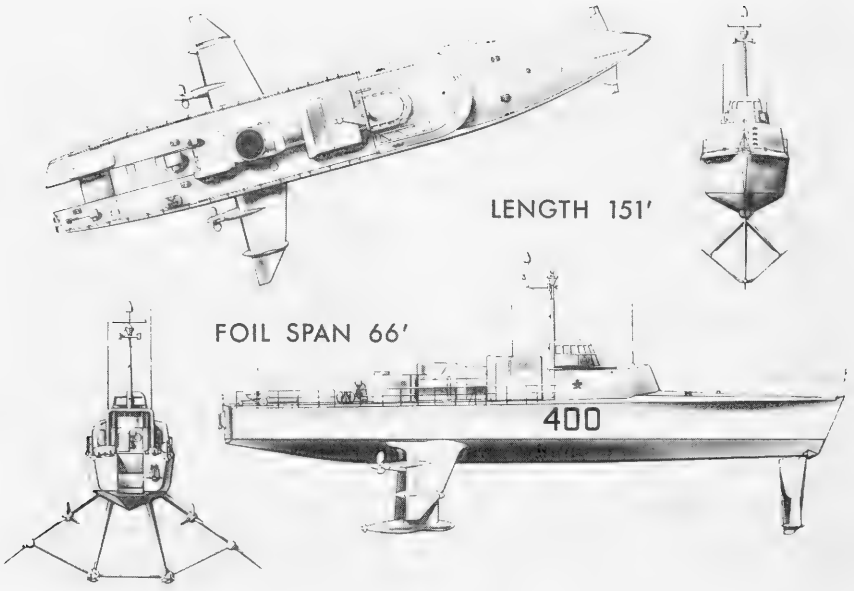

Fig. 3 - Main particulars of the FHE 400

split between two shafts in each strut, for the same purpose. Within the propulsion pods the drives are regrouped and reduced to the propeller shaft speed by means of compound star gears. It will be appreciated that this gearing system is very sophisticated, and yet it is only one of the many new developments that have been necessary in the production of this ship.

Early experience obtained with fully cavitating propellers of similar powering on the hydrofoil ship *Denison* were disappointing (Ref. 3). Fatigue failures occurred until thicker screws were used, and eventually titanium was employed as a material to avoid this difficulty. With this foreknowledge, De Havilland decided upon an extensive hydrodynamic and structural test programme, in an effort to develop efficient screws that would have adequate structural integrity.

SCOPE OF HYDRODYNAMIC DESIGN AND TESTING

Hydrofoil ships, like other types of high-speed craft, usually exhibit resistance characteristics, with a maximum occurring at the transition from the displacement mode to the flying mode. Once the speed at which the maximum resistance occurs has been passed, the resistance decreases before beginning to rise again at the high-flying speeds. Any propulsive device must, therefore, be capable of producing the required thrust over a widely varying range of operating conditions. Fixed-pitch noncavitating propellers, such as those used on trawlers, have a remarkable capacity for accommodating a large range of

loading, although minor compromises, largely due to engine characteristics at the extreme thrust and rpm conditions, are necessary for this. Fortunately, fully cavitating propellers behave reasonably well in this respect, when compared with other propulsion devices such as present-day water jets. This requirement is essential for hydrofoil ships when, in addition to the calm-water resistance variation, extra loads may be imposed because of high sea states and variable depth sonar (VDS) towing requirements.

Much has been done in recent years towards producing a design method for fully cavitating propellers, and the work at NSRDC (Refs. 4 and 5) may be cited, together with the interesting qualitative observations of Tulin in Ref. 6. Much still remains to be done, however, in the field of fully cavitating propeller theory to put it on an equal footing with noncavitating propeller theory. Steps in this direction are being taken, and numerical results from the work by Cox (Ref. 7) are awaited with interest, while at NPL evaluation of the proposals made in Ref. 8 are continuing. At NPL, considerable emphasis is given to obtaining a detailed quantitative physical insight into the flows created by fully cavitating and ventilated propellers, and partly for this purpose the instrumentation described in Ref. 9 has been built.

The design situation with highly loaded, fully cavitating propellers, as may occur in the hydrofoil ship takeoff condition, is more difficult than for the moderately loaded case, since there is a dearth of empirical information at off-design advance ratios. Consequently, model testing is even more essential for an actual fully cavitating propeller design. With this in mind, therefore, the approach used in designing the *Bras d'Or* screws has been to consider the flying condition first, following this with tests on propeller models over a wide range of loading and cavitation number to determine if the other critical conditions were satisfied.

In parallel with the specific design work for the *Bras d'Or* screws, a number of additional experiments were conducted at NPL on a model screw made to the T95 design described in Ref. 8. This screw was used mainly for convenience and because information was required before the design for the *Bras d'Or* was finalised. These tests were undertaken to determine the importance of some design features on performance, and included the observation of the cavity heights above the backs of the blade surfaces in the vicinity of the leading edges over a range of operating conditions, the effect of leading edge thickness on performance, and the determination of stress levels in a region near the leading edges. Attention was given to these aspects of design, since it was recognised from the experience of others that leading edge geometry is a crucial factor in the production of a reliable, full-scale, fully cavitating propeller.

MEASUREMENT OF WAKE CONDITIONS AND SIMULATION IN THE WATER TUNNEL

The *Bras d'Or* screws are of the pusher type and are mounted at the stern of the propulsion pods. Considerable care was taken in designing the propulsion pods and the junctions with the struts, the main foil, and dihedral foils, in order to minimise the irregular wakes created by these components. The method of streamline contouring was used for this purpose. Nevertheless, it was considered

necessary to measure these wakes on a 1/8th-scale mainfoil model in the towing tank. This was done to determine the flow irregularity and also to obtain information with which to design a wake simulator for the water-tunnel tests. As will be seen later, it was found essential to conduct the water-tunnel tests in the presence of the wake simulator.

The rig for measuring the wakes is shown in Fig. 4, where it is seen that a five-hole probe was mounted at the aft end of the port pod with a crank arm for altering the angular setting. The experiments were conducted at a speed of 30 ft/sec, the probe having been calibrated at this speed previously. In the tests, the attitude of the foil assembly was varied over a considerable range of pitch and yaw to cover the ranges likely to be encountered by the ship in service conditions. However, in order to conduct the tests within a reasonable time, the wakes were measured at the 0.7 propeller radius only.

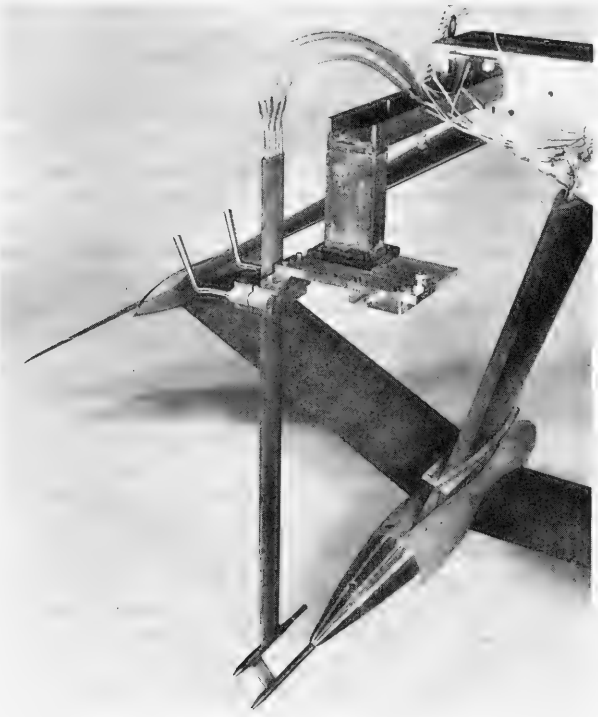

Fig. 4 - Rig for wake measurement

The wake measurements showed variations with pod attitude, but on the whole these variations were not large and the results obtained at the zero yaw and pitch setting, which are shown in Fig. 5, can be considered representative of the complete tests. From these results the wake shadows cast by the pod attachments are evident, the main foil wake being the greatest. The results are

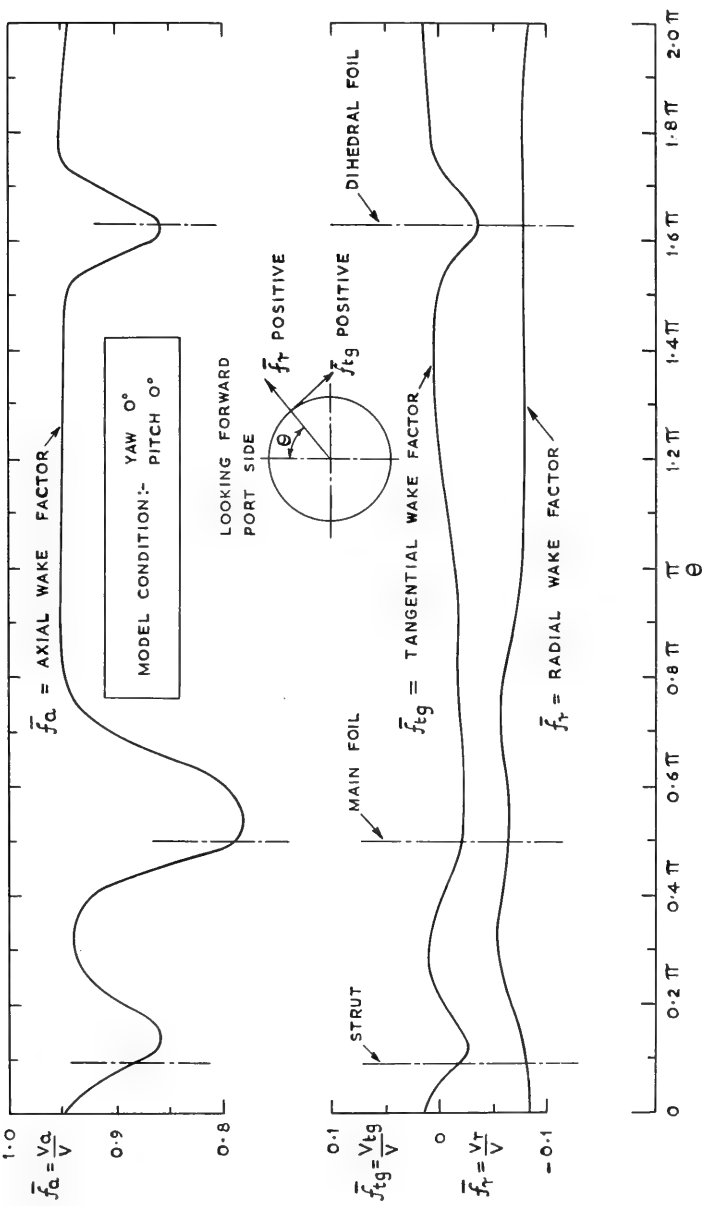

Fig. 5 - One-eighth scale model wake traverse results

all given in terms of wake factors which are the local axial, tangential, and radial velocities divided by the ship speed, or

$$\bar{f}_a = \frac{V_a}{V}, f_{tg} = \frac{V_{tg}}{V} \text{ and } f_r = \frac{V_r}{V}.$$

When considering the fluctuating forces and moments that might be produced by the screw operating in a nonuniform flow, the inflow angle β is highly significant, since this angle incorporates both variations in axial and tangential velocities. This angle is defined as,

$$\tan \beta = \frac{\bar{f}_a V}{\Omega r + \bar{f}_{tg} V} = \frac{\bar{f}_a}{\frac{x\pi}{J} + \bar{f}_{tg}}$$

for an anticlockwise-turning propeller looking forward, and using the sign convention for f_{tg} shown in Fig. 5. The variation of β at the zero-pitch zero yaw attitude of the pod is shown in Fig. 6, while Fig. 7 shows the results of harmonically analysing this β variation. Clearly, the amplitude of the third harmonic, which could be of significance in producing undesirable vibration at blade passage frequency with a three-blader, is relatively low, lower in fact than the sixth harmonic and only slightly larger than the ninth harmonic. Thus the attempt at minimising the harmonic content of the wake corresponding to multiples of the blade number has been quite successful and should ensure freedom from serious thrust and torque fluctuations. The second and fourth harmonics, which are important in relation to the production of fluctuating shaft bending moments and which must be withstood by the shaft bearings, are higher than the third harmonic. However, from the magnitude of the wake distribution there is no reason to suspect serious excitation from this source.

The wake simulator used in the No. 1 water tunnel was of simple construction and is shown mounted upstream of a fully cavitating screw in Fig. 8. Due to limitations imposed by the size of the tunnel, the simulator had to be contracted in the length dimension; but nevertheless a reasonable simulation of the axial flow was found possible, as may be seen from Fig. 9. Adjustments to the intensities and widths of the wakes shed by the arms of the simulator were made by adding wire gauze to the arms. The intensity of the main foil wake could not be reproduced before the arm of the simulator began to cavitate, and therefore this particular wake shadow was not sufficiently intense.

DESIGN STAGES AND PERFORMANCE CHARACTERISTICS

The initial diameter chosen for the *Bras d'Or* screws was 3.67 ft. This was based mainly on satisfying the requirements in the full-power high-speed condition, and on the desire to keep the screws as small as possible in order to obtain high rpm and hence a moderate gear cartridge and pod diameter. Little propeller data were available in the early stages from which the estimates of full-power low-speed operation could be made, but as the project progressed and more models were tested it became clear that it would be necessary to increase the diameter to 4.0 ft to meet the low-speed high-thrust requirement at takeoff and the VDS body towing requirement at foilborne speeds.

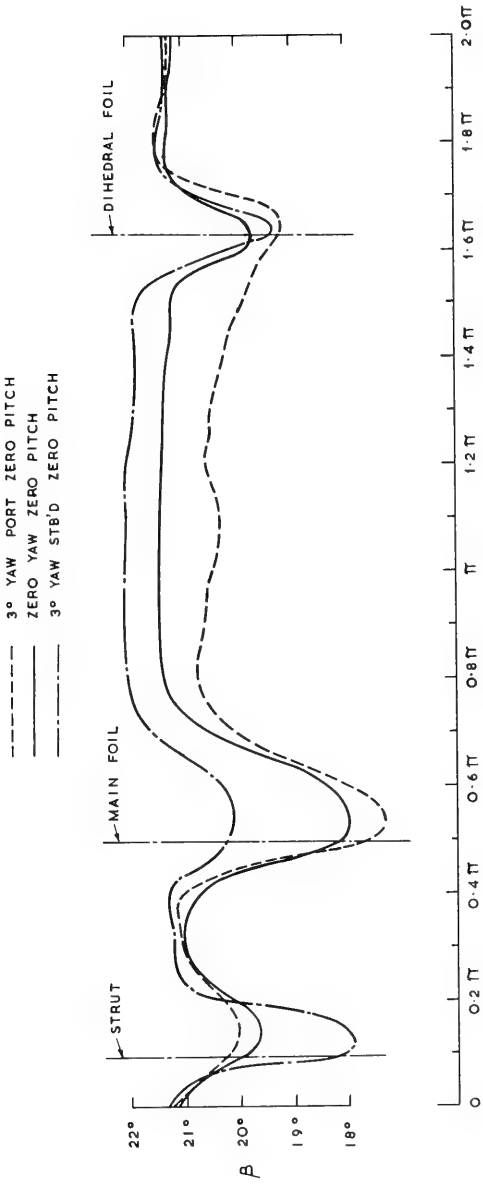

Fig. 6 - One-eighth scale model wake traverse results, β variation

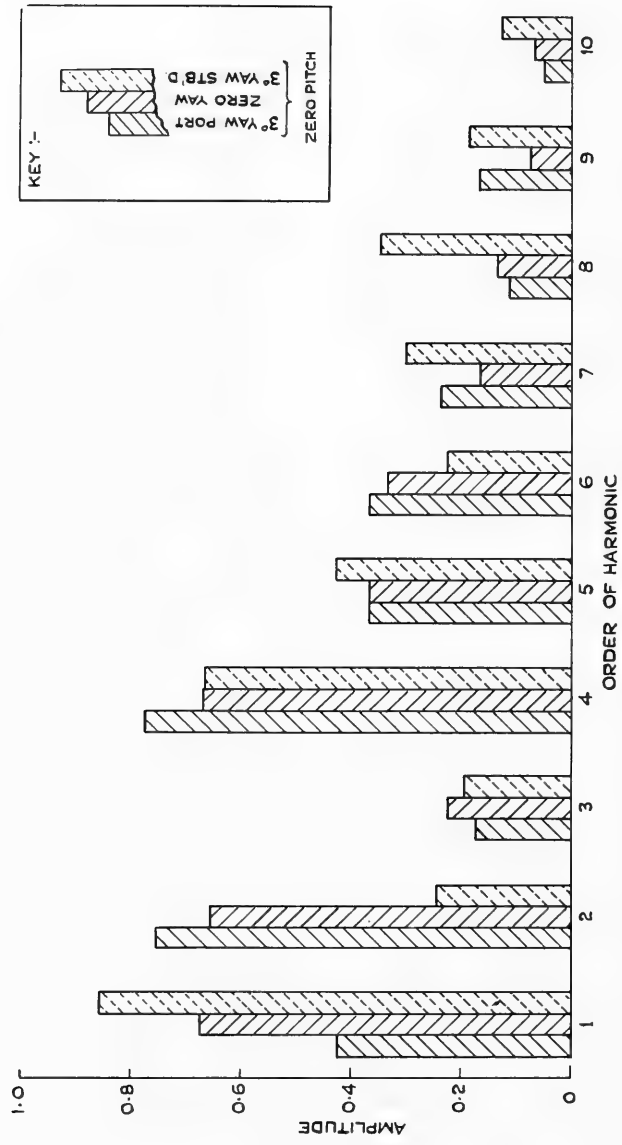

Fig. 7 - One-eighth scale wake traverse results; harmonic analysis of β variation

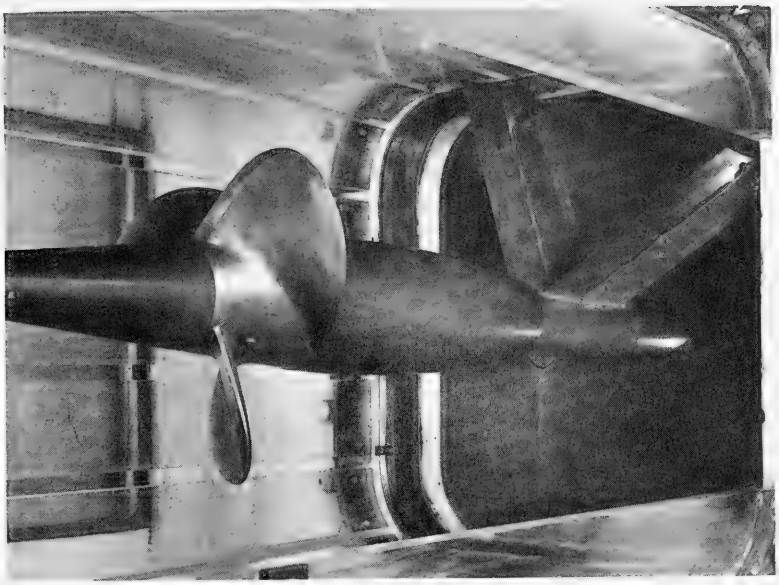

Fig. 8 - Screw and wake simulator in tunnel

For reasons of brevity it is not proposed to discuss the details of all the screws that have been tested in the course of this project, but since the final design has been built on the results of the earlier testing it is informative to summarise the conclusions drawn from this work. A summary of the various models that have been tested is given in Table 2.

In the early design procedures the most important hydrodynamic features of the screws, apart from diameter, i.e., the pitch and camber of the wetted faces of the cylindrical sections, were designed using a mixture of momentum theory, in which an appropriate allowance was made for the presence of the cavities in the wake, and noncavitating propeller theory. The camber shape adopted for the wetted faces of the sections was of circular-arc form, mainly because of the availability of Wu's nonlinear theory for calculating the flow around isolated fully cavitating foils at nonzero cavitation numbers (Ref. 10). Also, it is possible to calculate accurately the position of the back cavity relative to the wetted faces—a factor that was considered highly important in the early design stages for minimising section cavitation drag, i.e., ensuring that the cavity runs clear of the back of the section.

In retrospect, it would now appear that while the above approach gave a satisfactory pitch distribution, the section cambers predicted by the method were underestimated. This led to a propeller which, although highly efficient, would not absorb the full engine power and hence did not produce sufficient thrust at the high-speed design point or the takeoff condition. Modifications were then made to the propeller geometry in order to increase the load-carrying capacity. These consisted of increasing the amount of circular-arc cambers

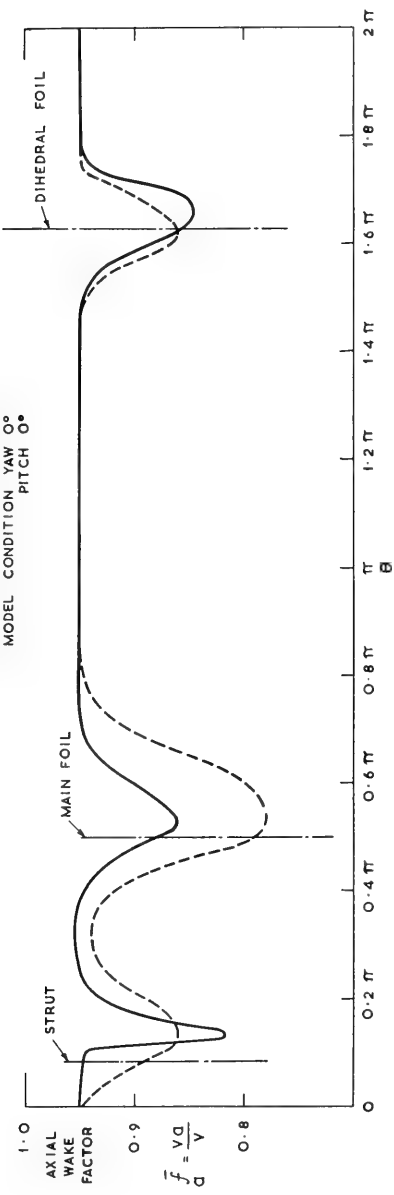

Fig. 9 - Axial flow factors produced by wake simulator and one-eighth scale model of main foil assembly

Table 2
Models Tested During the Development of the FHE 400 Propellers

(All of the following propellers are 3-bladed.
All models are 10 inches in diameter.)

NPL Designation	Full-Scale Diameter (ft)	Pitch Diameter Ratio	Camber m/c at .7R	B.A.R. Wetted	Maximum Thrust -20 knots, 2 props (lbf)	Maximum Thrust -40 knots, 2 props (lbf)	Maximum Efficiency, 40 knots (%)	Maximum Efficiency, 50 knots (%)
T95	Bronze model	1.369	.0177	.535	Development Model			61.5
T95a	Epoxy resin	1.369	.0177	.535	Hydroelastic Model			60.5
W252	3.67	1.157	.0086	.492	51,000	50,000	64.3	59.0
W253	3.67	1.24	.0150	.483	54,500	59,000	56.5	54.8
W253	4.0	Identical Model						
		1.24	.0150	.483	68,500	76,000	56.5	54.8
W257	4.0	1.232	.0204	.467	72,000	80,000	55.5	55.0
W264	4.0	1.157	.0263	.492	90,000	92,000	64.0	62.0

NOTES: (a) The propellers manufactured for the FHE-400 hydrofoil ship are precise scaled-up replicas of Model W257. (b) The driving face of Model W264 has a mixture of 3-term cambers and circular arc cambers. All other models have circular arc cambers. (c) Model T95 was not specifically designed for the FHE-400, and therefore cannot be directly compared with the W-series propellers. (d) Maximum efficiencies are not necessarily the best guide to propeller performance, as the propeller is not normally run at the corresponding J Condition for maximum η. In general, propeller W257 gives better results than its predecessors for cruising conditions, but is inferior to Model W264.

installed in the sections and, because isolated two-dimensional hydrofoil theory indicates that a positive incidence of the chord of the wetted face is necessary with this type of section in order that cavitation shall not occur on the face, an incidence or pitch increase was also incorporated.

The model screw employing circular-arc cambered faces that came nearest to satisfying all the design requirements is designated model No. W257, and Fig. 10 is a drawing of the 4-ft diameter ship screw. The features of this screw that are worthy of comment are the relatively large root chord lengths and the amount of leading edge sweepback. In addition, it will be seen that the large-diameter hub has a significant amount of taper which is necessary to fair in with the pod shape. These features are common to all the screws that have been considered for propelling the *Bras d'Or*, the particular chordal distribution and the sweepback being incorporated for structural reasons in an attempt to keep the leading edge stresses within reasonable limits in accordance with the results of the De Havilland's structural testing and analysis. The amount of skew or sweepback is specifically calculated to minimise torsional deflections of the blades.

The operating characteristics of this screw, as determined from the NPL No. 1 water tunnel with the wake simulator, are given in Figs. 11, 12, and 13, where it will be seen that the peak efficiency at the low cavitation numbers typical of high-speed operation is about 55 percent. This value of efficiency was considered to be lower than might be achieved, and it was therefore decided to continue the development programme in an attempt to improve the performance. Before describing the remainder of this test programme, however, it is pertinent to digress and explain the reasons for the relatively low efficiency, and describe some relevant work that has been conducted at NPL on a screw not directly intended for the *Bras d'Or*.

Johnson has shown in Ref. 11 that practical, fully cavitating, two-dimensional circular-arc sections, in which an allowance for the structural thickness of the foil is made, are, in terms of the lift-to-drag ratio, almost as efficient as the best alternative section, viz., the 5-term section. This is sufficient justification for using a circular-arc section, provided other factors such as structural strength are not impaired. Clearly, in the propeller design process the simple relationships between c_L and camber, and c_L and incidence, that hold in two dimensions require adjustment when propeller sections are being considered. This adjustment is analogous to the lifting surface corrections required in noncavitating propellers, but it also includes the effect due to the presence of the cavities. In the absence of any numerical information on the magnitude of the corrections that should be applied to the two-dimensional data, it has been necessary to employ a purely empirical correction obtained from a simple analysis of previous test results. This correction was then applied as a factor to both the basic two-dimensional camber and to the incidence values. This led to propeller sections with a moderate amount of circular-arc face camber, viz., about 2 percent of the chord at 70 percent radius, together with a relatively large incidence, giving a pitch-diameter ratio of about 1.26 at the same radius. Limited evidence from the operating characteristics of a number of fully cavitating screws now suggests that this method of applying the correction equally to the basic camber and incidence has led to screw W257 having a deficiency of camber and possibly an excess of incidence, and that it would have been more appropriate to apply

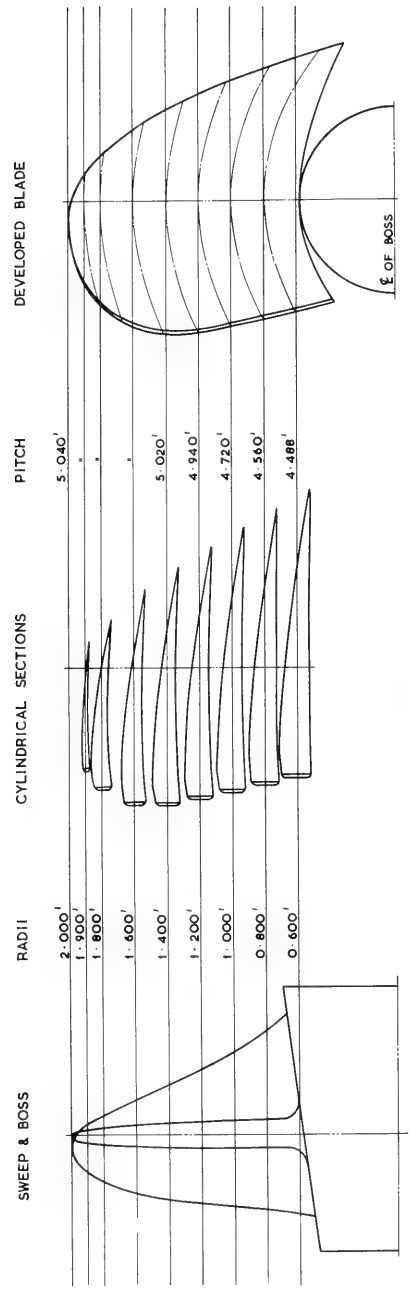

DIAMETER	4·00 ft.
Nº OF BLADES	3 (R.H)
BLADE AREA RATIO TOTAL	0·477
" " " WETTED SURFACE	0·467
MEAN FACE PITCH RATIO	1·232

Fig. 10 - Drawing of propeller W257

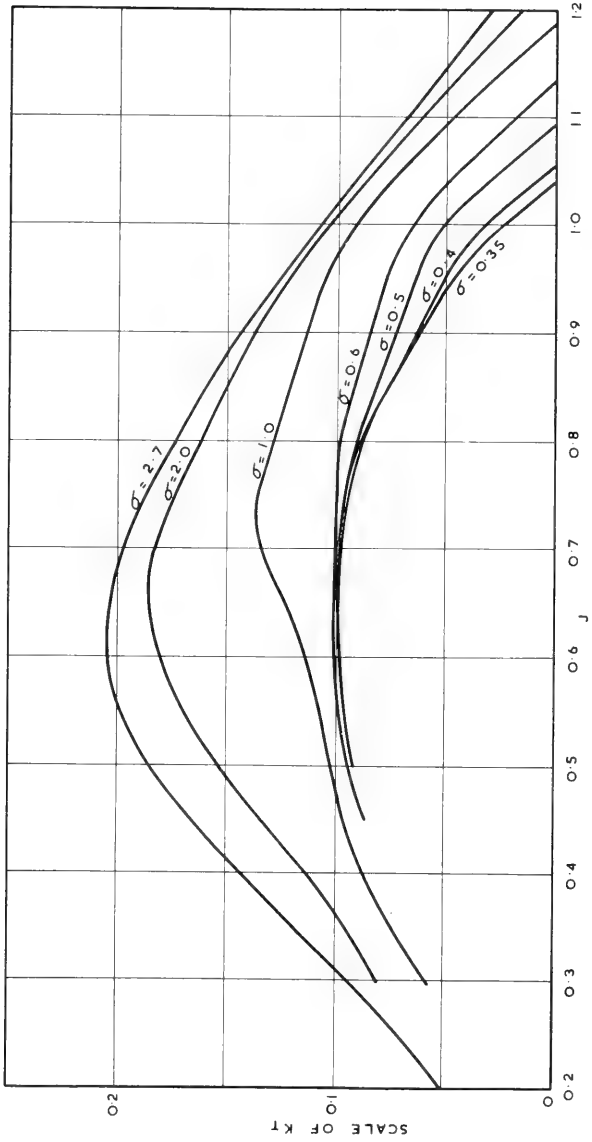

Fig. 11 - K_T performance curves of propeller W257

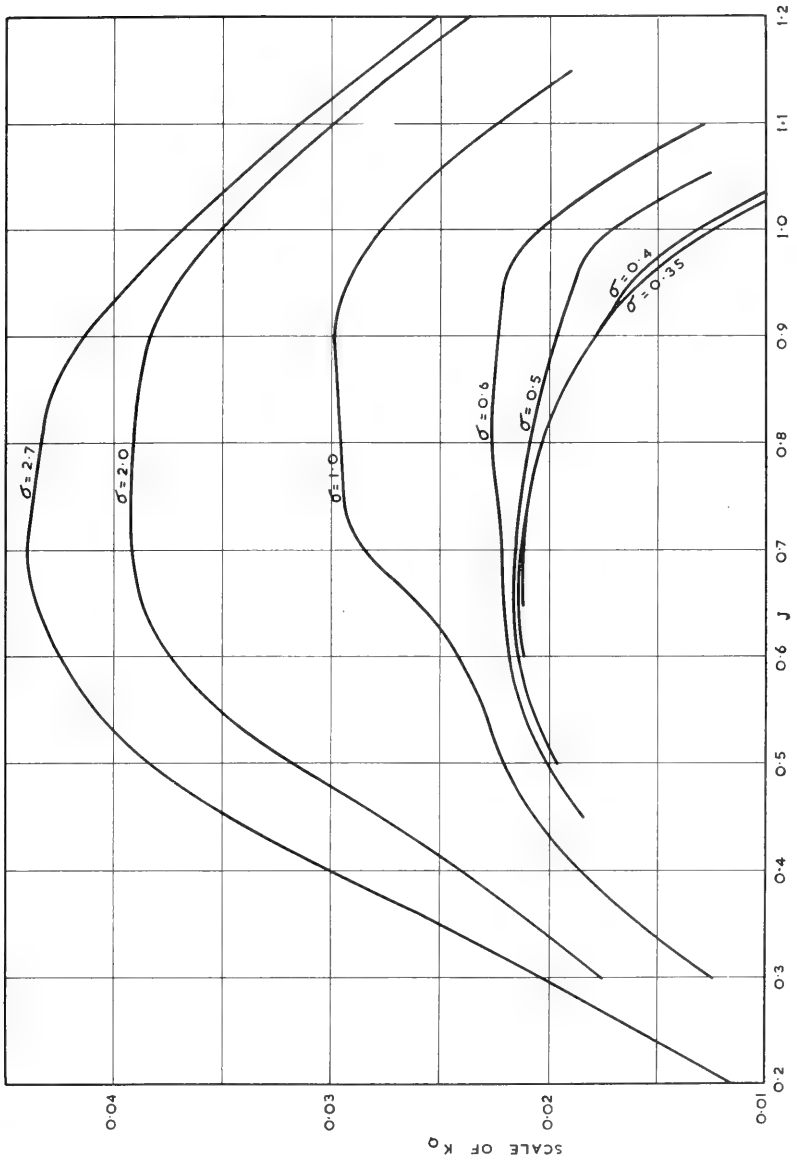

Fig. 12 - K_Q performance curves of propeller W257

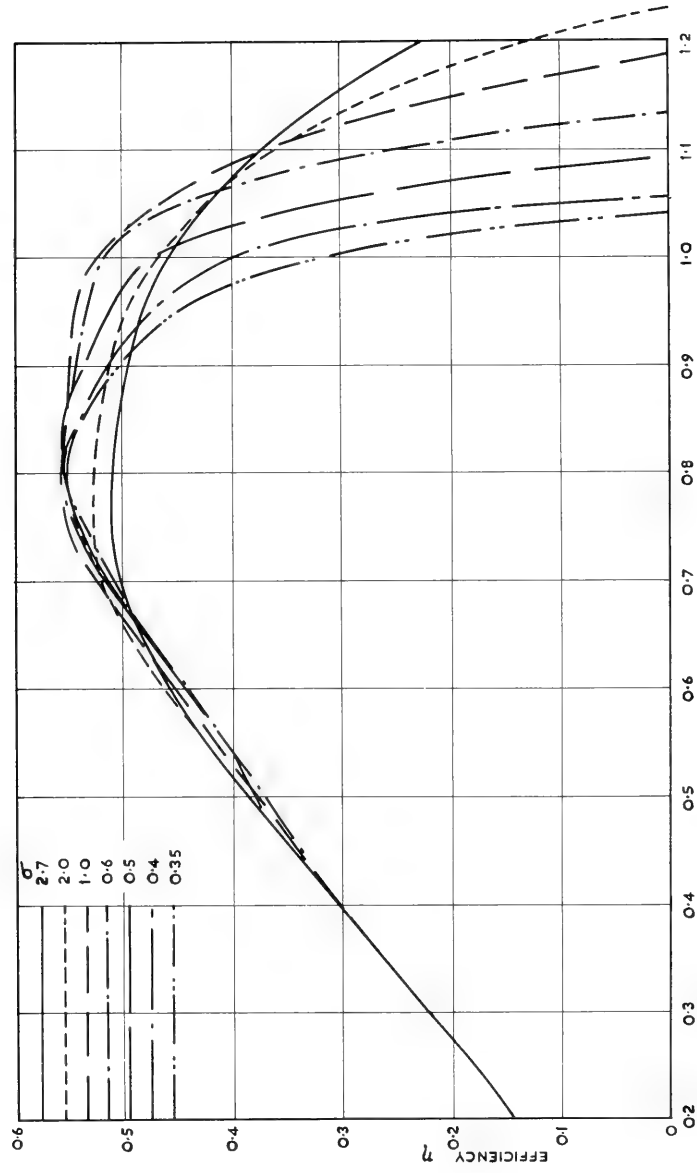

Fig. 13 - η performance curves of propeller W257

the correction to the camber only. This reasoning is endorsed by the work of Ōba in Ref. 12, where he has shown that in the case of a two-dimensional cascade of fully cavitating foils, the minimum incidence required to ensure clearance between the back cavity and the face of the section is less than that required in the case of the isolated hydrofoil. Tulin's description of the advantage to be gained by using high camber in fully cavitating propellers, given in Ref. 6, reinforces this conclusion.

A further factor that was instrumental in producing large angles of attack in these circular-arc face screws was the manner in which allowance was made for the structural thickness of the sections themselves. This was done by specifying a control thickness at 20 percent of the chord from the leading edge of each section, and then installing the initial incidence (and camber), before applying the aforementioned corrections, so that the back cavity would clear this point. This procedure led to relatively large values of incidence being installed. The cavity height calculations used in this approach were made using Wu's theory, and are given in Ref. 13.

Up to the time of the W257 experiments, the extreme leading edges of the fully cavitating screws designed at NPL were made relatively sharp, the structural thickness being controlled at the 20 percent chord position as previously described. Because this region of these propellers is so critical from the strength and vibration standpoints, it was decided to conduct a few simple experiments to determine the effect of increasing the extreme leading edge thickness. The screw used for these experiments was T95, as described in Ref. 8. The leading edges were initially sharp and were thickened for these experiments by adding soft solder to the backs of the blades in the leading edge vicinity. The leading edge roundings had a diameter of one-half percent of the local chords and the solder was then faired in to zero thickness at a postion 20 percent of the chord length from the leading edges. The modified screw was then rerun and the results compared with those obtained earlier. This comparison is shown in Figs. 14, 15, and 16, where it is seen that in the normal operating range the effect of the thickened leading edges is mainly manifested as a reduction in thrust. The effect on efficiency is small—the efficiency with the thickened leading edges being about 97-1/2 percent of that with sharp edges. Clearly, the small loss in efficiency and thrust arising from this modification is worth incurring for the added strength that will result.

A further experiment was conducted on the modified T95 screw with the object of gauging the heights of the cavities above the backs of the blades. For this purpose three pins, each of different length, were attached to the blades, one to each blade at 70 percent radius and 20 percent of the chord length from the leading edge. The arrangement is similar to the method used by Johnson in Ref. 11 on a three-dimensional hydrofoil in a tank. The relative positions of the back cavities on the propeller were then observed under stroboscopic lighting, leading to the results given in Table 3.

A reasonable J value for the high-speed operating condition of this screw would be in the range 0.9 to just over 1.0, i.e., at $\sigma = 0.3$, $J = 1.0$, then $\eta = 0.59$ and $K_T = 0.09$. In this case the height of the cavity above the blade surface is about one and one-half percent of the chord and, therefore, the thickness of the blade at this position could be increased by this amount without adversely

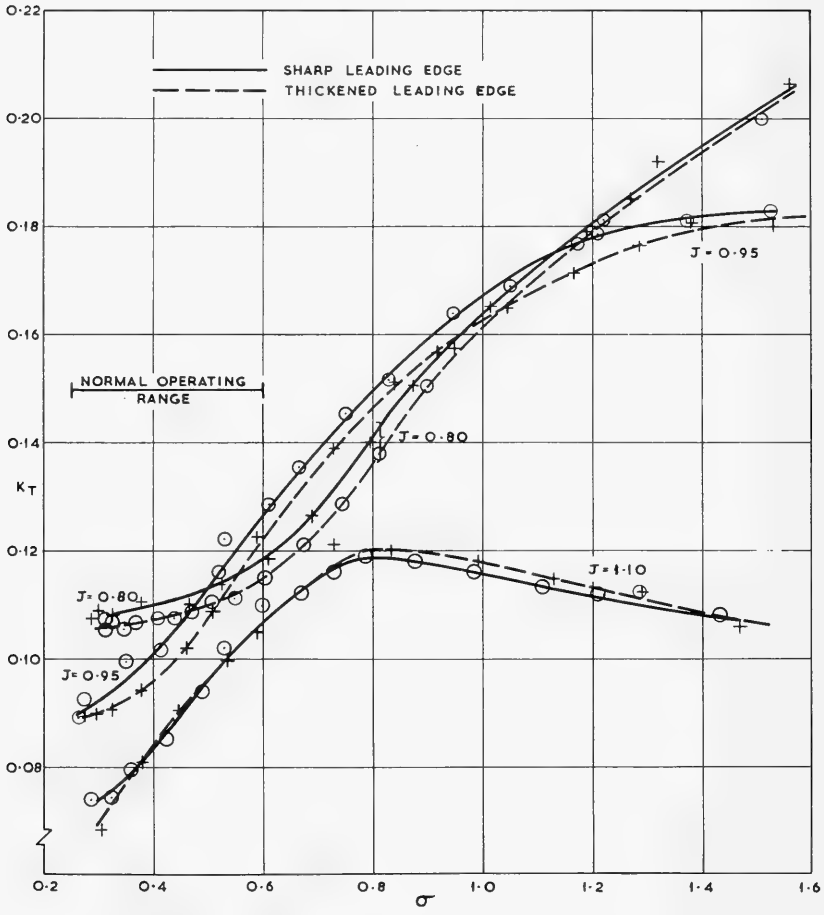

Fig. 14 - Thrust comparison--effect of thickened leading edges--screw T95

affecting the performance. These results suggest that for screws with circular-arc faces, at least, there should be no difficulty in installing sufficient material in the leading edges to secure structural integrity without seriously impairing the efficiency.

Since screw T95 is untypical of the *Bras d'Or* requirements with respect to blade sweepback and hub size and shape, it was considered desirable and expedient to confirm the effect of increasing camber and leading edge thickness on a typical screw before proceeding to the final screw design. This was done by simply modifying an existing screw. The blade faces were recut to provide the increased camber and the backs were thickened over the leading edge region with solder, giving a leading edge thickness of one-half percent chord. The additional camber was provided in the form of a Johnson 3-term camber as given

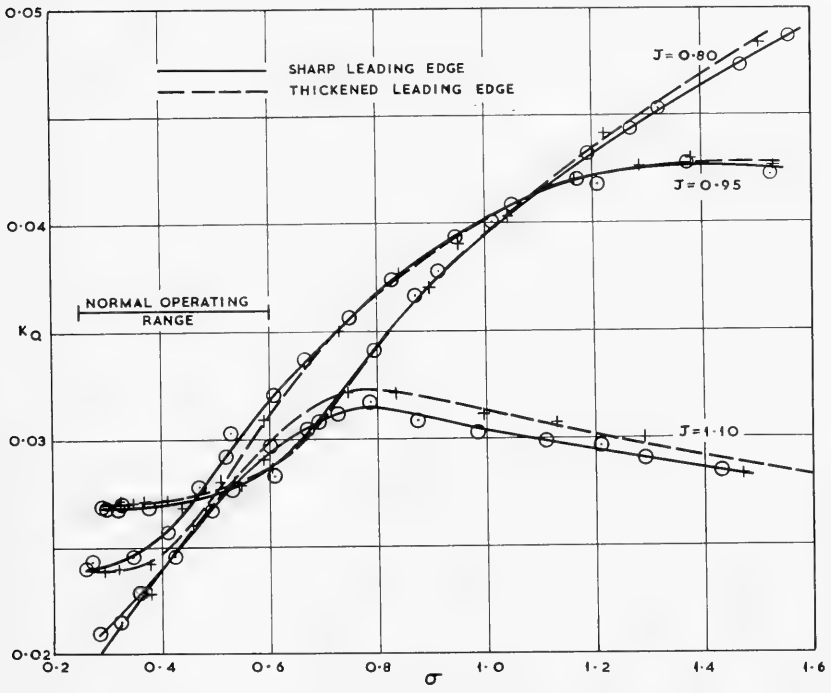

Fig. 15 - Torque comparison--effect of thickened leading edges--screw T95

in Ref. 11, such that the section cambers comprised about one-third circular-arc camber and two-thirds 3-term camber. Since the geometric incidence of the chord of the two-dimensional 3-term section is close to zero, no pitch adjustment was made when installing this camber. The modified screw was designated W264 and is shown in Fig. 17, while the results obtained with it are given in Figs. 18, 19, and 20. The improvements obtained with the W264 as compared with the W257 are quite large, giving approximately 17 percent more thrust at a considerably higher efficiency in the flying condition, with attendant improvements in the takeoff condition.

The ship will be fully operational in the 200-ton load condition with screws made to the W257 design. A speed of 60 knots will be attainable in the calm water condition, while adequate thrusts are also available in the higher resistance conditions when operating in high sea states at speeds up to 50 knots, and with a towing load at lower speeds. The improvements offered by screws according to the W264 design are mainly in additional thrust margins at the higher loads and increased range through the higher efficiency.

A typical fully cavitating propeller model of the type fitted to the *Bras d'Or* is shown in Fig. 21 operating at simulated high speed in the No. 2 water tunnel at NPL.

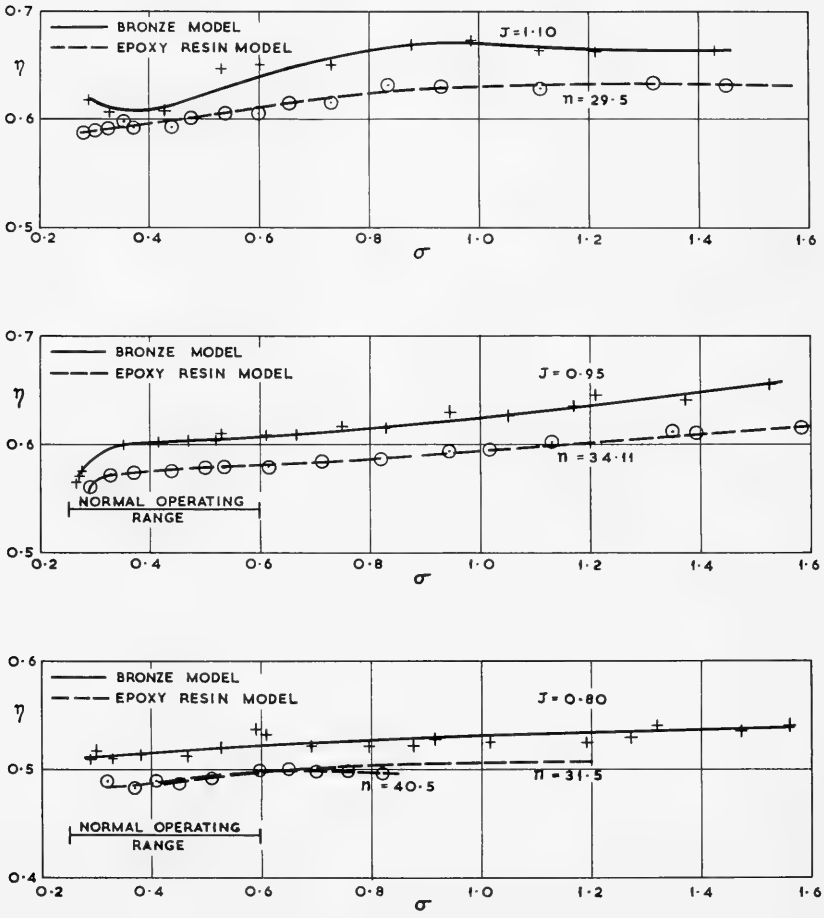

Fig. 16 - Comparison of efficiencies between bronze and epoxy resin models--screw T95

Table 3
Screw T95 (Leading Edge Thickness—1/2% Chord),
Height of Cavity Above Back of Blade Surface,
Measurement Position: 70% Radius, 20% Chord from Leading Edge

J	σ			
	0.30	0.40	0.5	0.6
0.8	← Greater than 2-1/2% chord →			
0.95	← Nearly 2-1/2% chord →			
1.05	← About 1-1/2% chord →		Less than 1-1/2% Greater than 1/2%	Results uncertain due to striations from leading edge
1.10	← Not fully cavitating—all pins visible →			

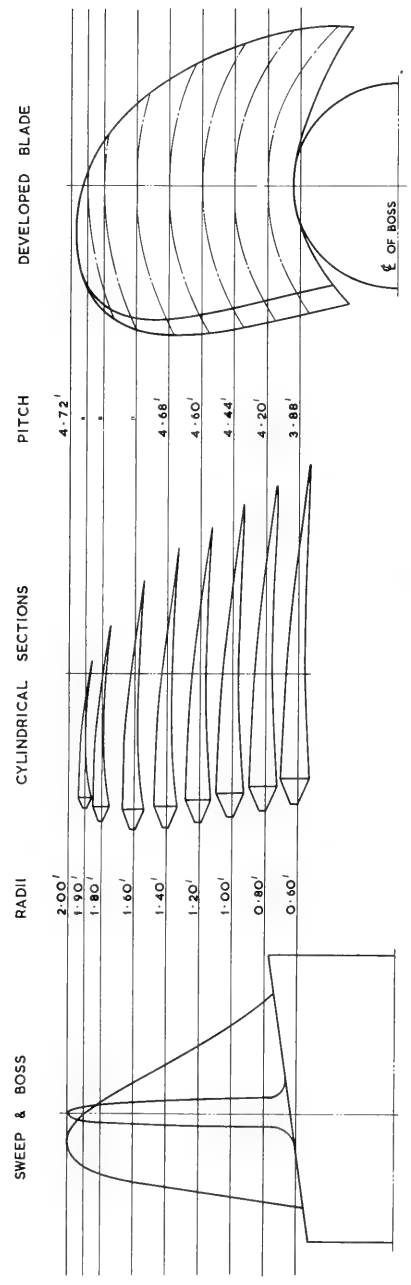

Fig. 17 - Drawing of propeller W264

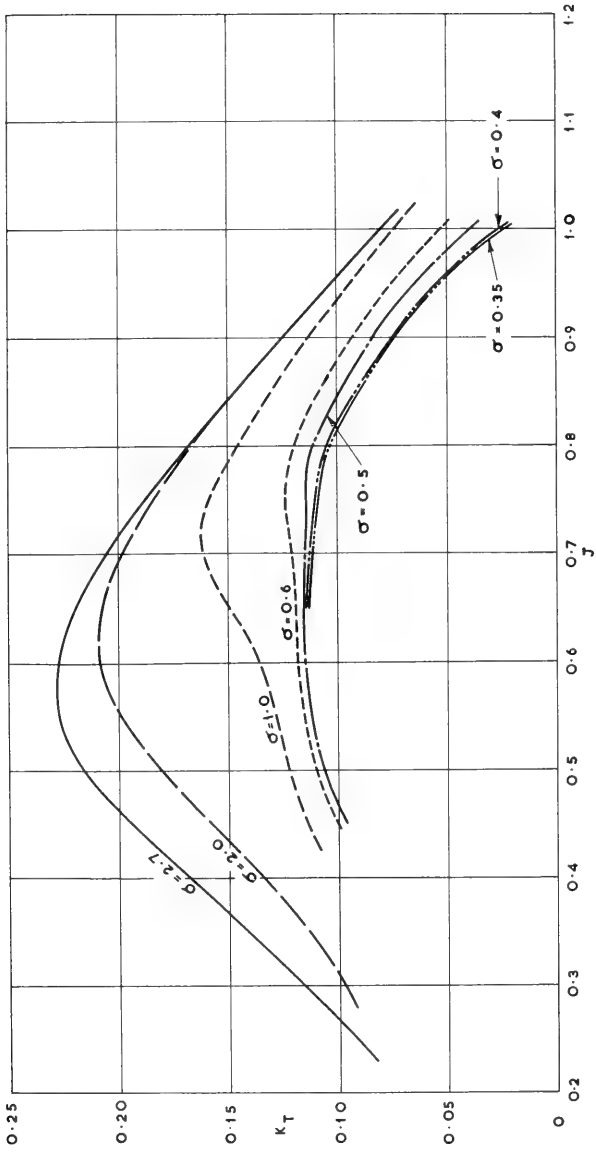

Fig. 18 - K_T performance curves of propeller W264

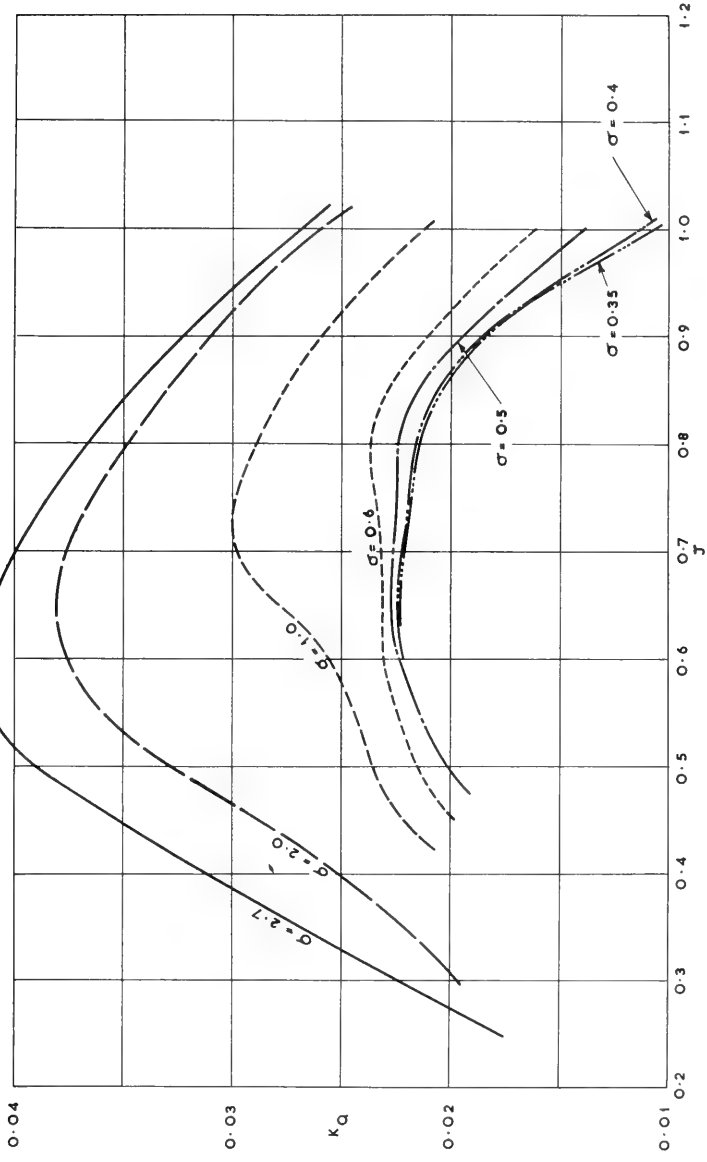

Fig. 19 - K_Q performance curves of propeller W264

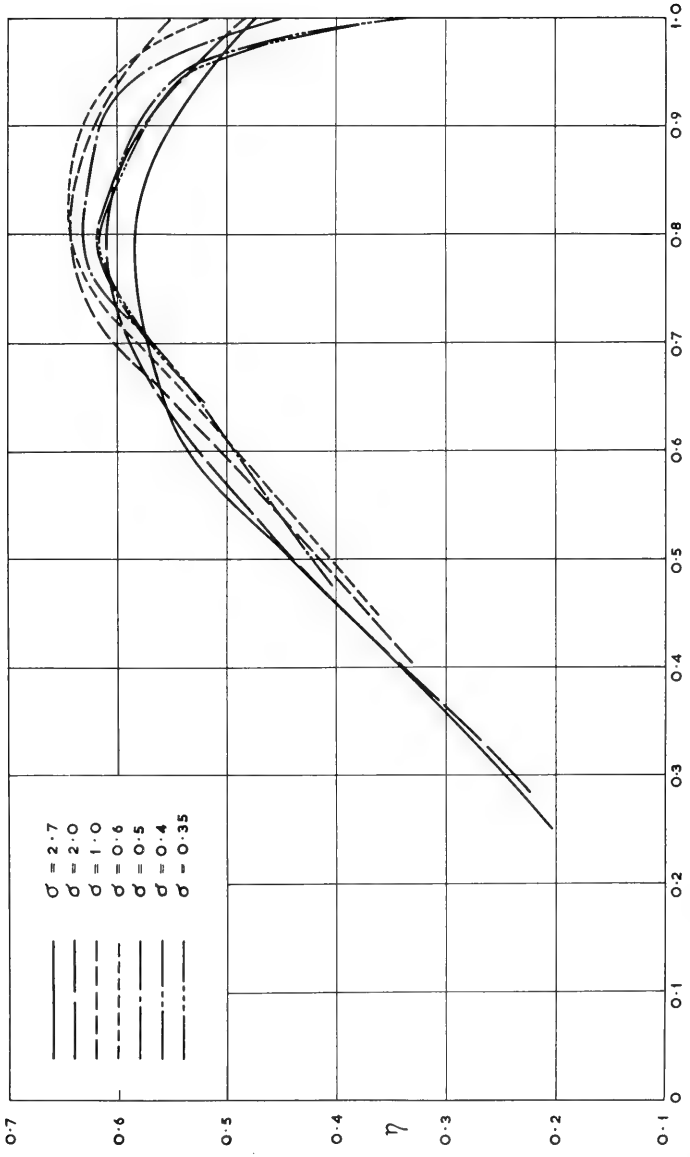

Fig. 20 - η performance curves of propeller W264

Fig. 21 - Moderately loaded, fully cavitating propeller

The development of fully cavitating propellers is being continued, and proposals for additional design studies and tunnel testing have been made. An immediate objective is to produce a propeller with an efficiency comparable to that of screw W264 mentioned earlier, but in which the structural integrity is increased by thickening the blades. For this purpose an additional model with thickened blades has been made and partially tested. However, these results indicate that wetting of the back surfaces occurs, and therefore a modification is necessary.

Further testing is required to establish the optimum camber and the optimum relationship between camber and incidence or pitch, and to this end it is hoped that a further test series of a family of fully cavitating propellers can be initiated in the near future.

STRUCTURAL CONSIDERATIONS

The hydrodynamic requirement for relatively thin leading edges in fully cavitating screws, together with the high powers that are transmitted and the difficult operating environment, give rise to severe structural problems which must be considered in the design stage. The blades must be made sufficiently strong to withstand the maximum steady stresses likely to be experienced, in addition to the fluctuating stresses that will occur when operating in the wakes of the pod attachments. Further, the deflections of the blades under load should be as small as possible.

In order to combat these onerous operating conditions it is necessary to employ a strong propeller material possessing high resistance to erosion and cavitation damage, combined with high values of fatigue strength and elastic

modulus. Several materials were considered for the *Bras d'Or* application, including titanium, beryllium nickel, and various steels. The eventual choice, however, was for forged billets of a high nickel chromium alloy known as Inconel 718. This material possesses excellent physical properties; its main disadvantage is that it is difficult to fabricate, since it is an extremely tough alloy. Its main advantages over titanium are its higher elastic modulus which is nearly double that of titanium and its superior fatigue life characteristics, particularly in sea water. A screw made from Inconel 718 would therefore deflect about half as much as a similar screw in titanium and would presumably last longer.

In line with the choice of an exotic material for the propeller construction, the blades have been made separate from the hub and are retained by bolts, thus enabling a blade to be changed without a complete screw replacement in the event of damage.

It was essential that the propeller blades were forged separately, as it would be impossible to forge a single propeller of this size in this alloy, i.e., 4-ft. diameter and weighing 1000 lbf finished. Thus the blades are bolted to the hub using special Inco 718 bolts. This method of construction therefore has some merit from both the manufacturing and blade replacement points of view.

Structural Testing on Static Models

Structural testing has been conducted at De Havilland by Mr. S. Morita (Refs. 14 and 15), to explore the effects of blade geometry and external blade loading on the stresses and deflections induced in the blades. The experiments were performed in two stages, the first of which employed simple plane models without pitch, while the second used a more representative model in which pitch was included. In both cases static models of single blades were used and hence centrifugal effects were not included. Only a brief survey of the experiments and the results is given here.

The simple models were used to aid in the rapid production of results and to permit a large coverage of parameters to be made relatively easily. These models consisted of cantilevered, trapezium-shaped aluminum specimens representing the blade under test. Pitch was not incorporated in these specimens. The specimens had a common radial distribution of chord widths, but three values of leading edge sweepback were covered, while two variations in section shape were used. The sections were either or triangular shape with blunt trailing edges or triangular apart from a trailing edge chamfer on the back. Camber was not included in the sections. The radial blade loading was the same in all the tests, but two chordwise loading distributions were used in which the centre of pressure position was at 39 percent and 25 percent of the chord from the leading edges.

In all the experiments the external load was applied using rubber pads bonded to the specimen and loaded in tension through a system of cables, pulleys, and "whiffle trees" by a single hydraulic jack. Such a system is commonly used in the aircraft industry, and Fig. 22 shows the test setup employed. Strain measurements were made using strain gauges attached to the "wetted" side of the blades, while blade deflections were made with dial gauges.

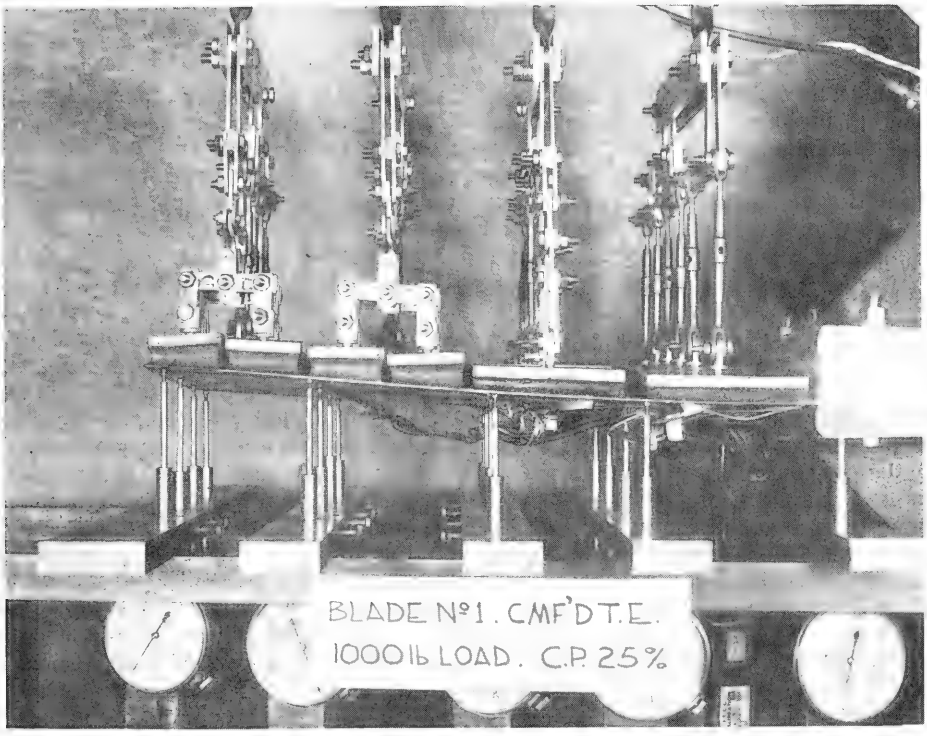

Fig. 22 - Test setup used in structural tests

The principal conclusions resulting from the work on the simple blade shapes were as follows:

1. Blade sweepback has a significant effect on the stress levels in the blades, and a judicious choice of sweepback can be made to minimise the stress levels in critical areas of the blade or, alternatively, the sweepback can be chosen to produce a reasonable stress distribution across the entire chord. Too much sweepback is undesirable, however, since this can lead to an increase in stresses in parts of the blade. The choice of sweepback is affected by the chordwise pressure distribution.

2. Blade sweepback reduces blade deflections appreciably when compared with unswept blades. However, introducing large sweepback for this purpose can have an adverse effect on the blade stresses.

3. Blade stress distribution and deflections are influenced by the chordwise pressure distribution, as might be expected. The closer the section centre of pressure is to the leading edge the higher are the stresses and deflections.

4. Reasonable correlation exists between measured and calculated stress distributions when simple bending theory is used.

The tests on the simple blade shapes at De Havilland were followed by a similar test on a more realistic blade in which the pitch of the sections was incorporated. At about the same time, some further tests were being conducted at NPL on hydroelastically sealed model propellers in the water tunnel. Ideally it would have been desirable for the same blade geometry to have been tested in both establishments, but this was not possible due to the tight time schedule. As a consequence, while the two sets of test results can be compared, too close a correlation of the results cannot be expected since the blade shapes and thicknesses were different. The two sets of tests are described separately therefore, commencing with the static tests conducted at De Havilland.

The blade used for the static tests had sections with circular-arc wetted face cambers, as shown in Fig. 23, and an appreciable amount of leading edge sweepback or skew. The test setup was similar to the one used earlier, apart from the extra complication introduced because of the pitch of the blade, and is shown in Fig. 24. The test blade was made from aluminum to limit the external load necessary to produce easily measurable surface strains and deflections. For the purposes of simulating and distributing the external hydrodynamic load this load was split into 28 discrete elements and applied through rubber pads bonded to the back of the blade and loaded in tension. Deflections and surface strains were measured on the blade face. In the absence of any measured blade pressure distributions which could be used as a basis for distributing the external load, reliance had to be placed on an estimated distribution. From these estimates the radial distribution of lift coefficient was almost inversely proportional to radius, while the chordwise loading was taken as similar to that produced by a fully cavitating flat plate hydrofoil at incidence where the pressure is concentrated towards the leading edge and the centre of pressure occurs at the 25 percent chord position. In this respect, fully cavitating propeller theory is not considered sufficiently refined to justify attempts at producing a more realistic load distribution. It is probable, however, that the particular load distribution used produced larger stresses in the critical regions of the leading edge and blade root than would be experienced in an actual propeller, since a substantial part of the total load was situated towards the tip and leading edge regions.

The blade strains were measured with strain gauge rosettes at sixteen positions, thus enabling principal stresses and directions to be derived. The maximum principal stresses deduced from this work have been scaled to correspond to a 44-inch diameter propeller developing 40,000 lbf thrust. These stresses are shown in Fig. 25, where it will be seen that they always fall well below a value of 40,000 lbf/in^2 which is the stipulated maximum steady stress level allowable for Inconel 718 when fatigue is a factor to be considered. It will be observed from these stresses that despite the incorporation of a considerable amount of sweepback the stress level in the leading edge vicinity at the 70 percent radius is higher than anywhere else in the blade. The directions of these principal stresses are given in Fig. 26 and show how significant the chordwise loading can become, since at the 90 percent radius the maximum principal stress direction approaches the chordwise direction.

From the above discussion it might be expected that the simple Engineer's Beam Theory, commonly used for estimating stresses in propellers, could not predict reliable stresses throughout the blade. This has been found to be the

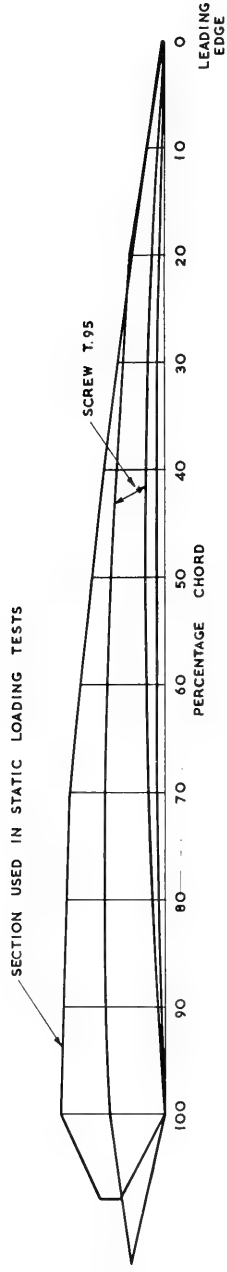

Fig. 23 - Comparison of screw sections tested structurally

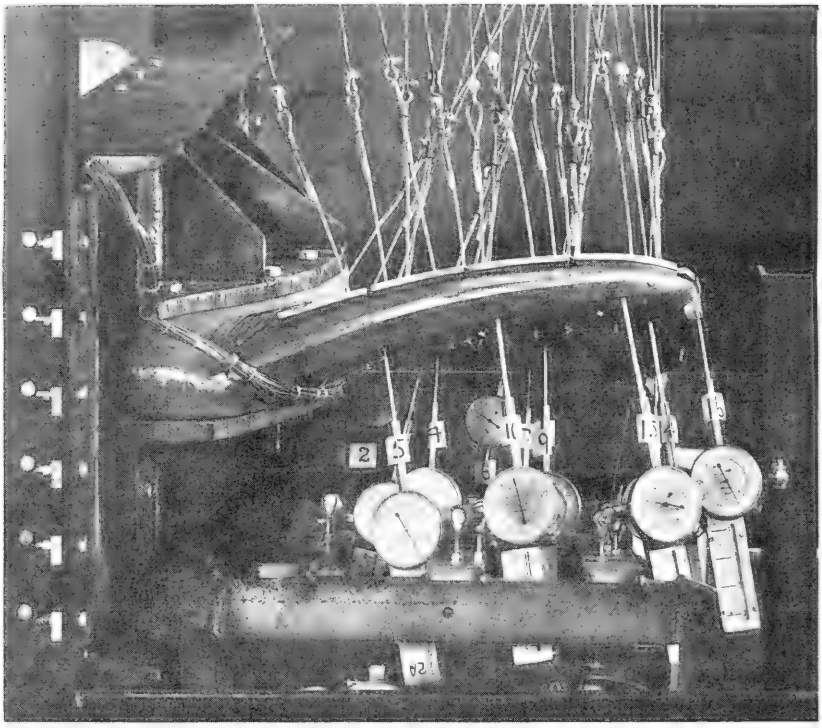

Fig. 24 - Test setup used in structural tests

case by Morita in Ref. 15. For example, Fig. 27 shows a comparison of the stresses calculated using the Beam Theory with the measured stresses, vividly illustrating this point.

Two further points should be mentioned in connection with these stress measurements. First, centrifugal effects have not been considered, but the direct stresses from this cause will increase the tensile stresses given in Fig. 25. This increase is expected to be small (less than 10 percent of the maximum plotted value) at 70 percent radius, becoming a maximum at the root section. In neither case is it expected to increase the stress level to 40,000 lbf/in^2 however. Centrifugal stresses were, of course, considered in the final screw design, as they are of considerable magnitude towards the blade root. The second factor to be considered is the screw diameter, since in the *Bras d'Or* application the screw diameter was increased to 48 inches. This effect would then reduce the stresses in Fig. 25 by about 19 percent assuming the thrust remained at 40,000 lbf.

The measurements of the blade deflections indicated that the largest deflections occurred at the outer radii and leading edge positions, as might be expected. The deflection of the sections was such as to reduce the installed face cambers and slightly increase the section incidences. This would be expected

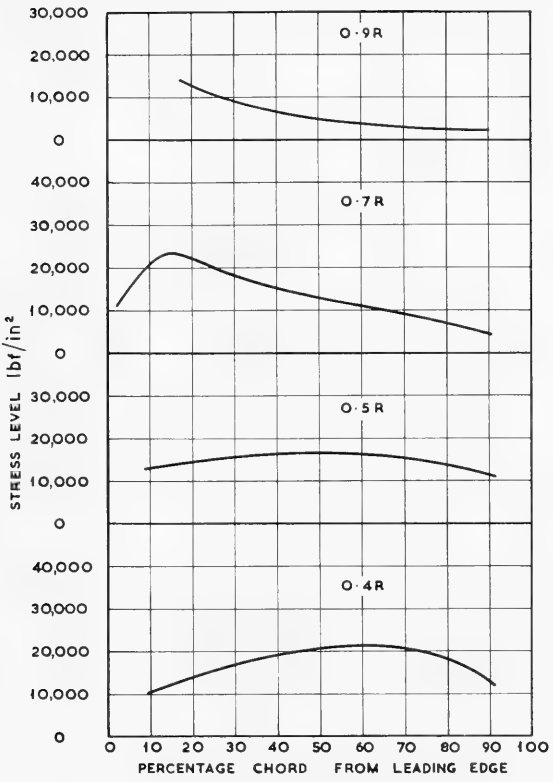

Fig. 25 - Chordwise distribution of maximum principal tensile stresses

to lead to a reduced thrust and an increased torque as a consequence of the higher section drag and lower propeller efficiency.

Hydroelastic Model Tests

The NPL tests on hydroelastically scaled models were performed simply for the purpose of obtaining general background information on the effect of blade deflection on fully cavitating propeller performance and to obtain steady-strain measurements on an operating propeller. It was not intended that the models should be used to predict the dynamic behaviour of the blades from the vibration standpoint. Again, since this work was planned early in the experiment programme and before the *Bras d'Or* screws were finalised, the tests were conducted on the T95 design.

The conditions that must be satisfied when testing hydroelastically scaled model propellers, based on the assumption that the blades behave as thin plates

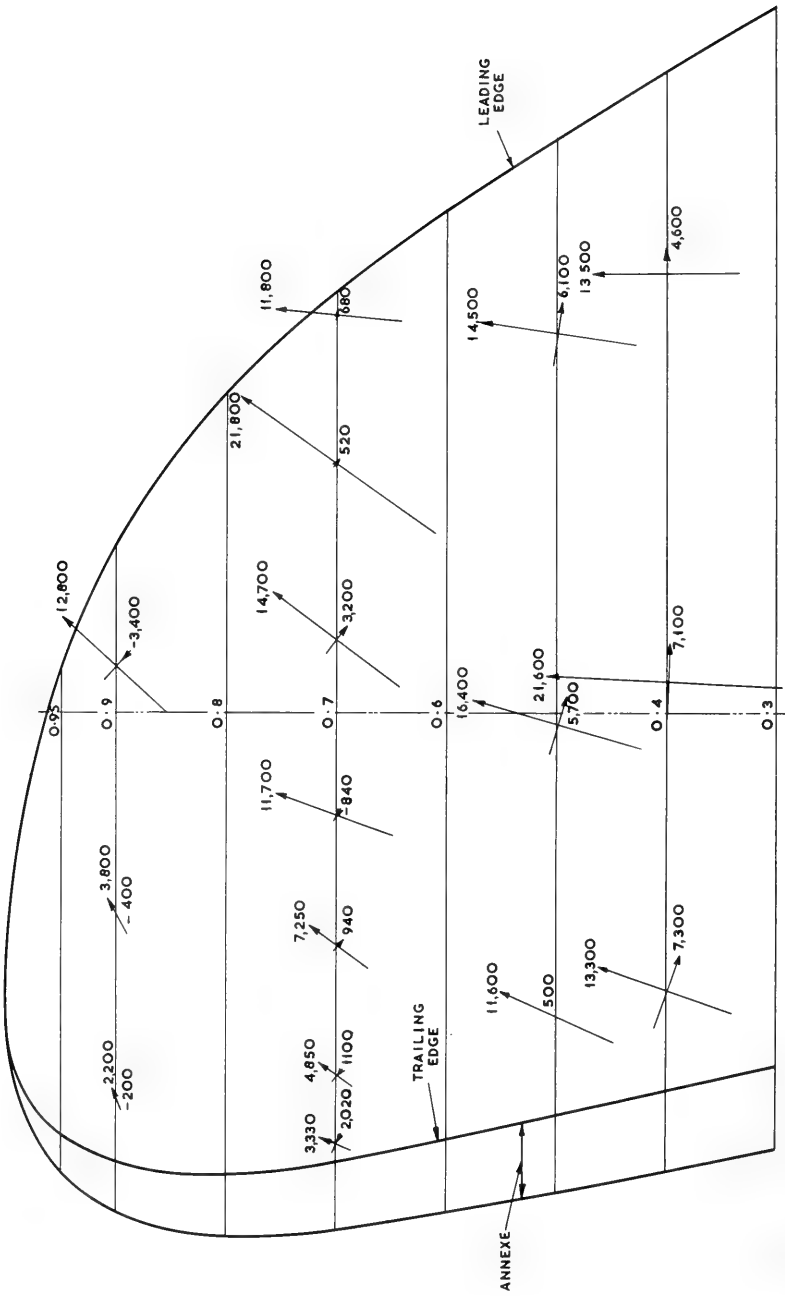

Fig. 26 - Directions of principal stresses

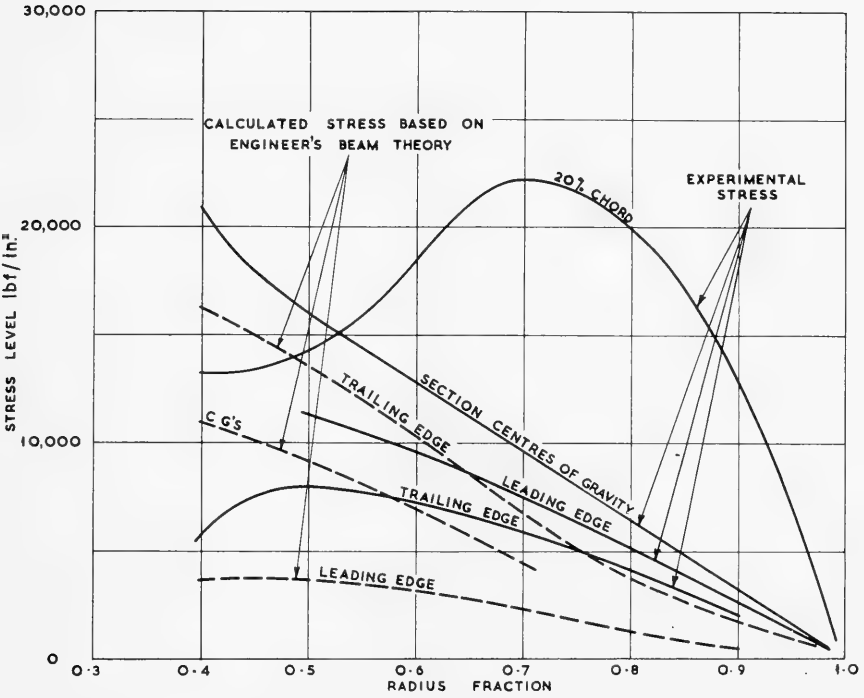

Fig. 27 - Comparison of calculated and measured stresses

subject to bending, has been fully described by Acum in Ref. 16. When referred to fully cavitating propellers tested in a water tunnel, one of the two additional structural similarity parameters that must be the same for the model and prototype is

$$S = n^2D^2 \frac{(1 - \sigma^2)}{E},$$

where E is the elastic modulus and σ is Poisson's ratio for the propeller material. This ensures the equivalence of blade stresses and deflections between model and prototype when they are caused by steadily applied hydrodynamic loads. Then, with this similarity, the stresses vary as $\rho\, n^2D^2$ and deflections vary directly as the scale.

When it is necessary to scale stresses and deflections due to inertia forces such as derived from rotation (centrifugal force) and nonsteady hydrodynamic loads, the further requirement of equal densities in model and prototype is also necessary. It is usually impossible to satisfy these two similarity conditions simultaneously, due to restrictions arising from the tunnel operating conditions, model scale, and the limited choice of materials from which models can be made. A means of complying with these conditions is sometimes adopted in structural experiments where the model material and density are kept the same

as that of the prototype, but the model is weakened by cuts to reduce effectively its elastic modulus. Very complicated model construction can result from using this technique, however, and in the experiments described here it was decided to ignore the condition for the equivalence of stresses and deflections induced by inertia forces. This neglect is probably not very important, since the tests were conducted in uniform flow in which the hydrodynamic loads were nominally steady. Further, the direct centrifugal stresses are usually small when compared with the bending stresses due to the hydrodynamic loading, and the centrifugal bending stresses depend mainly on the rake of the blades which in the case of the T95 design was only five degrees aft. Blade skew and the unsymmetrical distribution of material about a radial generator line will also influence the centrifugal stresses, but since there is no skew in T95 the effects due to these features will also be small.

Two hydroelastic model propellers were made from epoxy resin loaded with fibre glass. These 10-inch diameter screws were initially formed at De Havilland, Canada and then cut to the T95 design at NPL. This particular material was chosen mainly because of its elastic modulus (1.8×10^6 lbf/in^2), as this together with the screw scale and tunnel conditions enabled model tests to be conducted at values of $n^2D^2 (1 - \sigma^2)/E$ applicable to the prototype screw.

The first hydroelastic model was run in a similar manner to the bronze screw, but at particular values of rotational speed to obtain the desired values of the parameter $n^2D^2 (1 - \sigma^2)/E$. If it is assumed that the deflection of the bronze screw was negligible, a reasonable assumption according to Ref. 17, then the difference between the results from the hydroelastic screw and the bronze screw are due to the deflection of the former, apart from small differences that arise from experimental scatter in the results. The results obtained from the two screws are compared in Figs. 28, 29, and 30, where it is clear that both the thrust and torque of the hydroelastic screw have increased above the values for the bronze screw. Also, since the torque increase is greater than that of the thrust, the efficiency of the hydroelastic model is less than that of the bronze screw, and further this reduction in efficiency is fairly significant in this case. As an example, in a typical high-speed operating condition the efficiency of the screw with deflected blades is about 95 percent of the undeflected value. Similar results to these were also found in the takeoff conditions. It may be noted however, that because the T95 blades are thinner than those used in the *Bras d'Or* application the T95 results exaggerate the effects of deflection on these screws.

The second hydroelastic model of the T95 design was used for measuring blade surface strains under fully cavitating conditions and then deducing stress levels. For this purpose small foil strain gauges were attached to the wetted surface of each blade at a number of positions. The leads for energising the gauges and conducting the output signals passed down the blades and through the hollow shaft to slip-rings outside the tunnel where they were transferred to the external instrumentation. The gauges were attached to the wetted surface in order to ensure temperature stability which might have been difficult with gauges attached to the backs of the blades and within the cavities. Temperature-compensating gauges were attached to a piece of epoxy resin and situated in the reservoir of the working section. The gauges and leads on the blades were coated with a thin covering of epoxy resin for insulation purposes. This coating

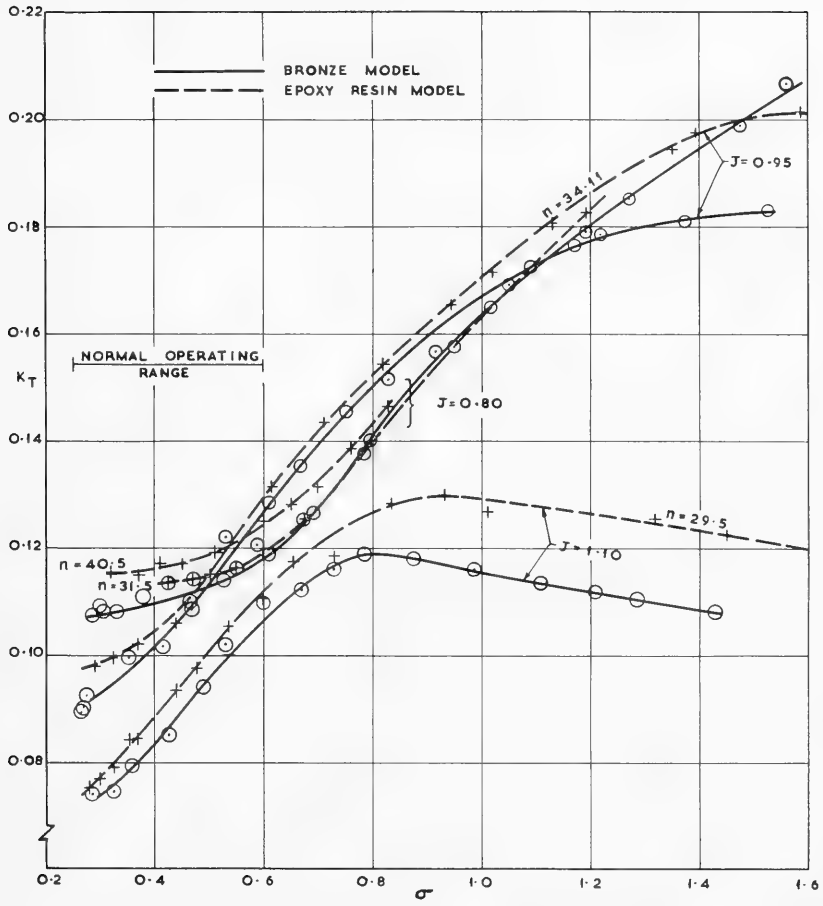

Fig. 28 - Comparison of thrust between bronze and epoxy resin models--screw T95

had to be thin to avoid changing the blade shape and increasing the structural stiffness. At the same time the leads could not be let into the blades, as this would also have altered the local structural stiffness.

Considerable difficulty was experienced in maintaining a high resistance between the gauges the blade wiring and the tunnel water, and after a relatively short period of immersion this resistance began to fall. It became necessary therefore to halt the experiments after the earth resistance had fallen appreciably and allow time for the equipment to dry out before proceeding. This difficulty, on top of the initial waterproofing problems, made these experiments very time-consuming and it became necessary to restrict the scope of the measurements to the gauges situated at the 20 percent chord position only.

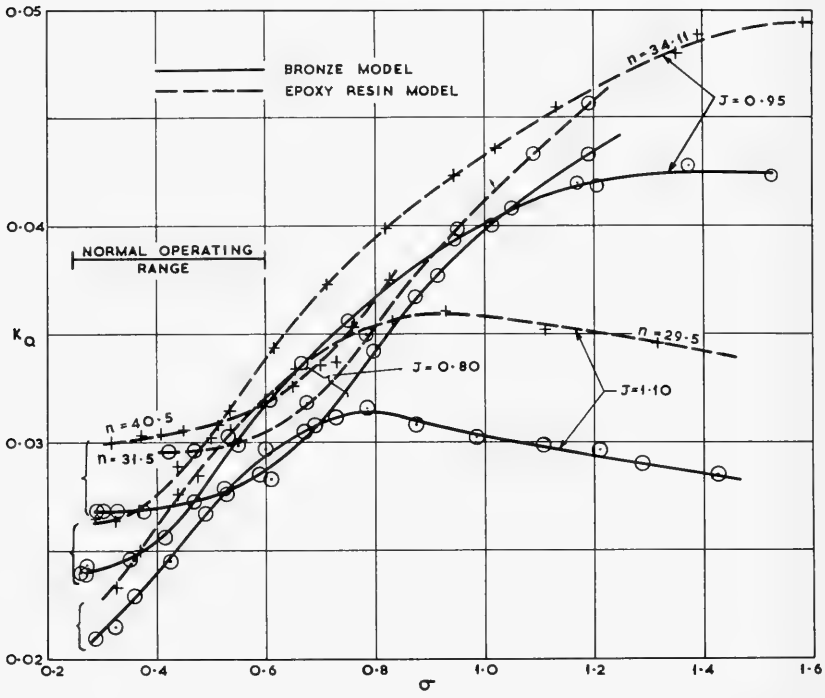

Fig. 29 - Comparison of torque between bronze and epoxy resin Models--screw T95

The gauge rosettes were mainly of the star type with 120-degree separation between the arms, and were orientated with an arm of each rosette on a cylindrical section and pointing towards the leading edge. Rosettes were positioned at 0.5, 0.65, 0.8, and 0.9 of the propeller radius and 20 percent of the local chord from the leading edge on the blade in question. Some of the rosettes and blade wiring can be seen in Fig. 31 before the waterproofing was applied.

The recorded strain levels were reduced to principal stress values for a full size screw assumed to be 44 inches in diameter and rotating at a speed of 1700 rpm. The elastic modulus of the prototype was taken as 30×10^6 lbf/in^2 and Poisson's ratio was assumed to be the same for model and prototype with a value of 0.3. Graphs showing the results of these experiments are given in Figs. 32, 33, 34, and 35 where the maximum and minimum tensile principal stresses and the maximum shear stresses are plotted against the radius fraction for the 20 percent chord position. Stress directions are given in Figs. 36 and 37. The results are plotted for a range of advance coefficients and two cavitation numbers which can be considered typical of the takeoff and flying conditions for a craft employing 44-inch diameter propellers.

In both conditions the maximum principal stress at the 20 percent chord position occurs around the 60 to 65 percent radius. The stress increases with

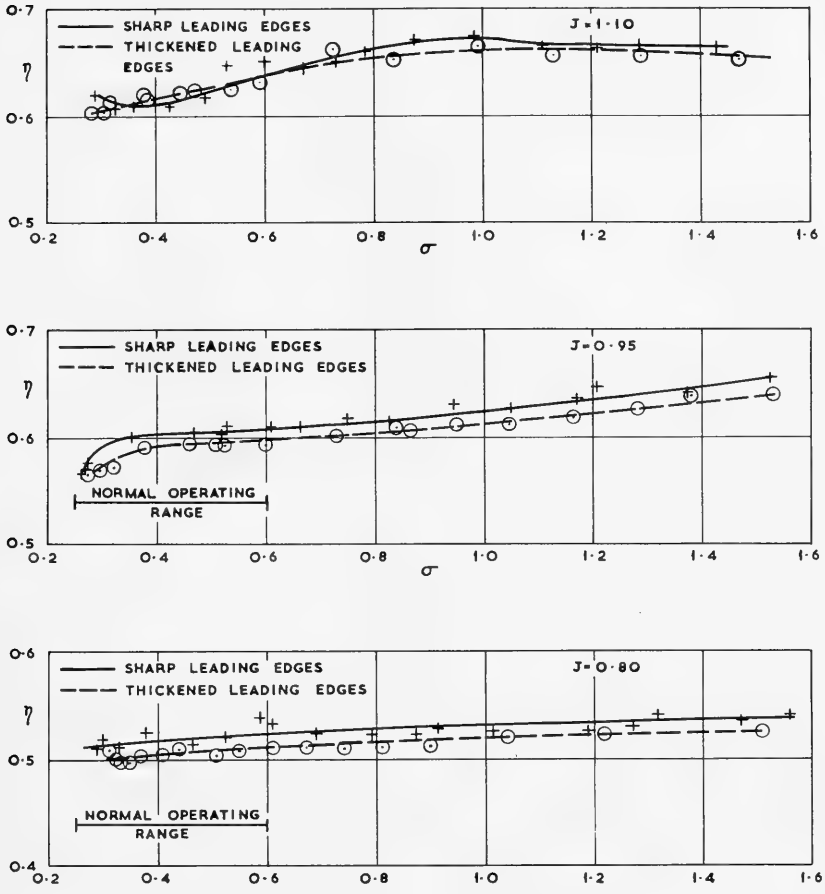

Fig. 30 - Efficiency comparison--effect of thickened leading edges--screw T95

thrust and torque, as might be expected, since thrust increases with decreasing advance coefficient in the flying conditions, Fig. 32, and reduces with decreasing advance coefficient in the takeoff conditions, Fig. 33. Although the structural design of screw T95 differs appreciably from the screw blade tested at De Havilland it seems worthwhile attempting to correlate the results at the 20 percent chord position as far as possible. For example, if in Fig. 32 an advance coefficient of 0.95 is taken as the flying condition, then the thrust developed by a 44-inch diameter propeller is 29,200 lbf and the peak maximum principal stress is 19,800 lbf/in^2. If we now assume that the thrust of screw T95 can be increased to 40,000 lbf by increasing the camber, say, without appreciably affecting the structural properties, then we can scale the stress directly as thrust. This then produces a stress of 27,100 lbf/in^2 for a 40,000 lbf thrust as compared with about 22,000 lbf/in^2 from De Havilland's tests. Further, if we assume the

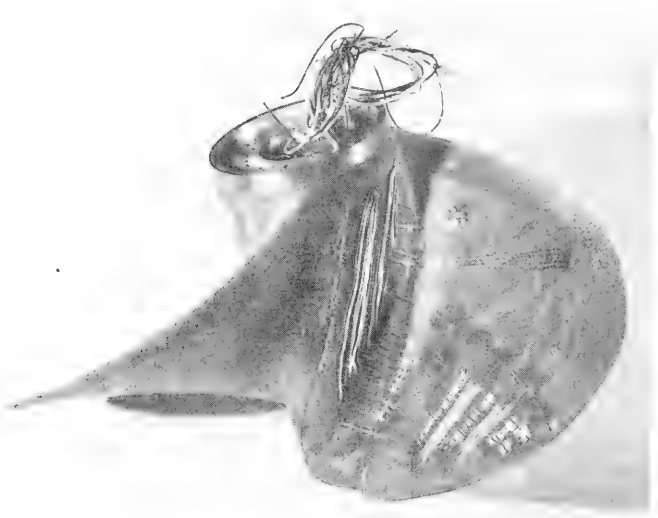

Fig. 31 - Strain-gauged hydroelastic propeller

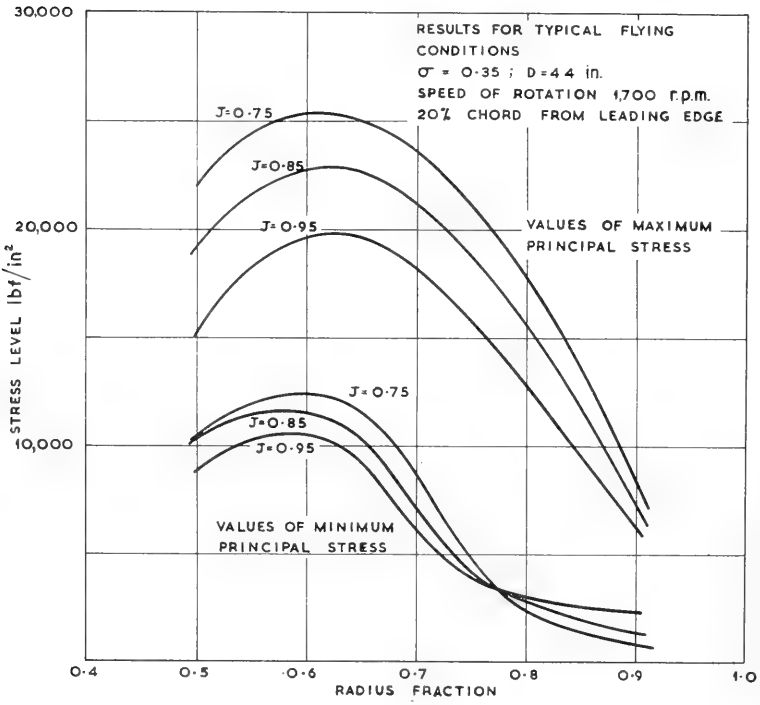

Fig. 32 - Values of maximum and minimum tensile principal stresses, typical flying conditions--screw T95

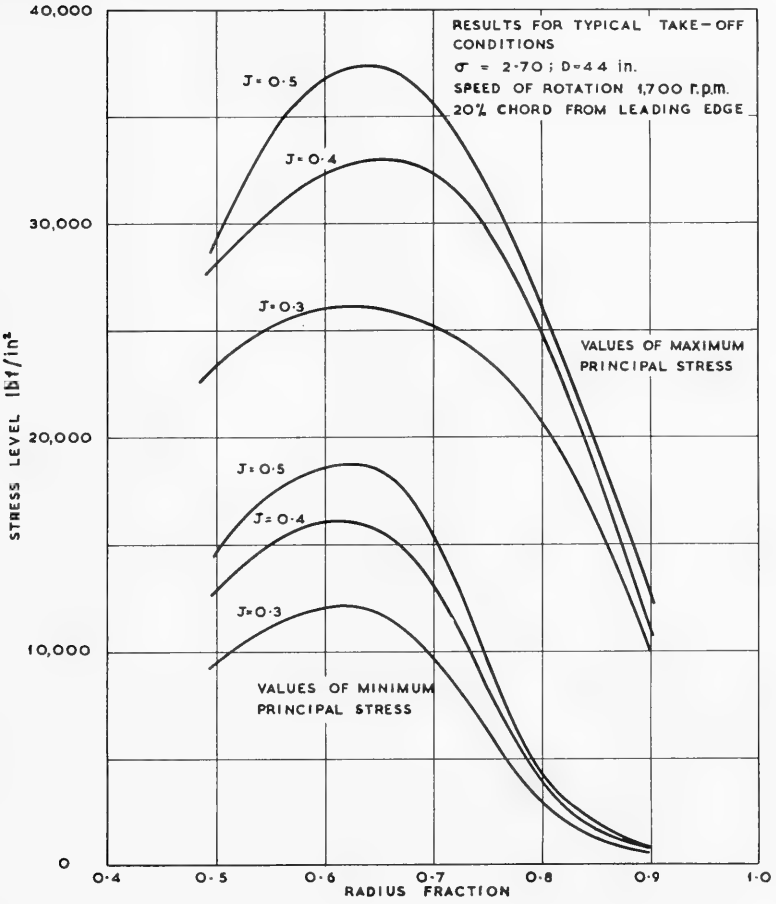

Fig. 33 - Values of maximum and minimum tensile principal stresses, typical takeoff conditions--screw T95

stress at the 20 percent chord position and that the 65 to 70 percent propeller radius arises primarily because of the local bending of the leading edge, then in accordance with the simple beam theory the stress may be taken as inversely proportional to the blade thickness squared. A correction to account for the difference in the thickness of the two blades can then be made by multiplying the T95 stresses by a value of 0.7. This then approximates to the stresses that would be experienced in the T95 blades if the thickness at 20 percent chord were made the same as that used in the De Havilland test. Applying this correction reduces the T95 stress to about 19,000 lbf/in^2 compared with 22,000 lbf/in^2 from the static loading tests.

In a similar manner, if the takeoff condition is taken as that occurring at an advance coefficient of 0.4 in Fig. 33, then a stress of 33,000 lbf/in^2 results when

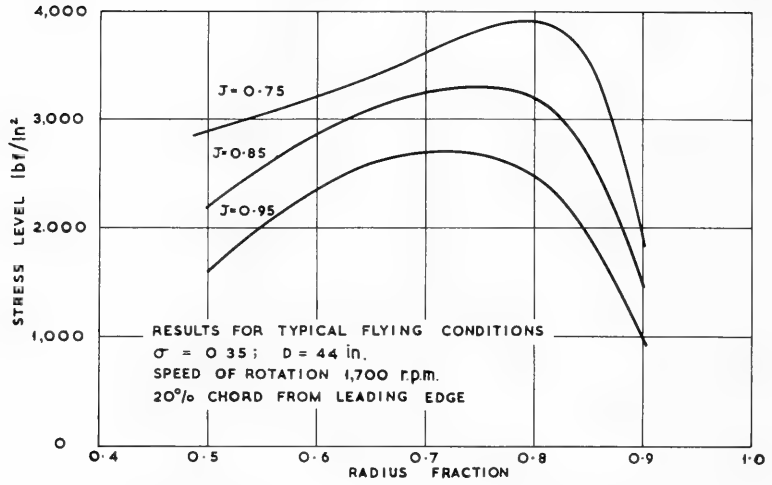

Fig. 34 - Values of maximum shear stress, typical flying conditions--screw T95

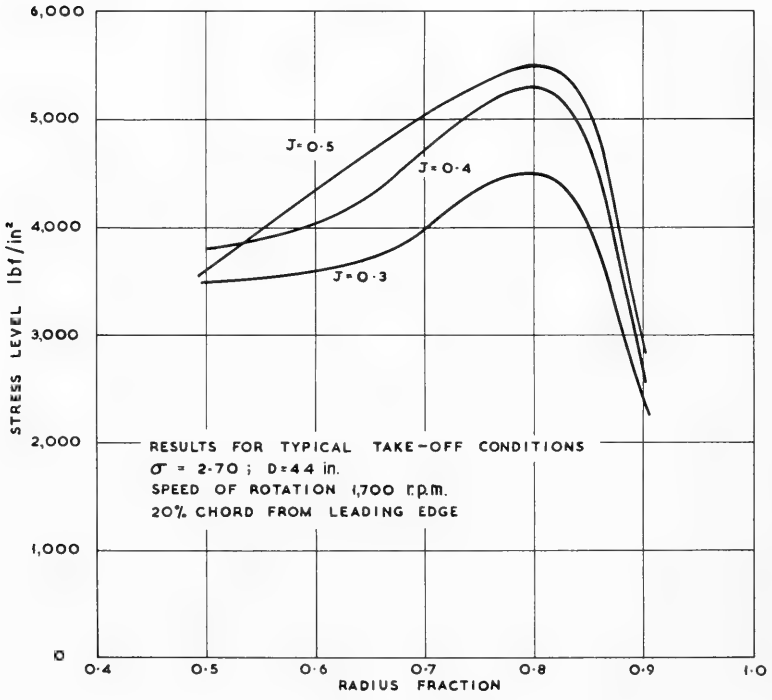

Fig. 35 - Values of maximum shear stress, typical takeoff conditions--screw T95

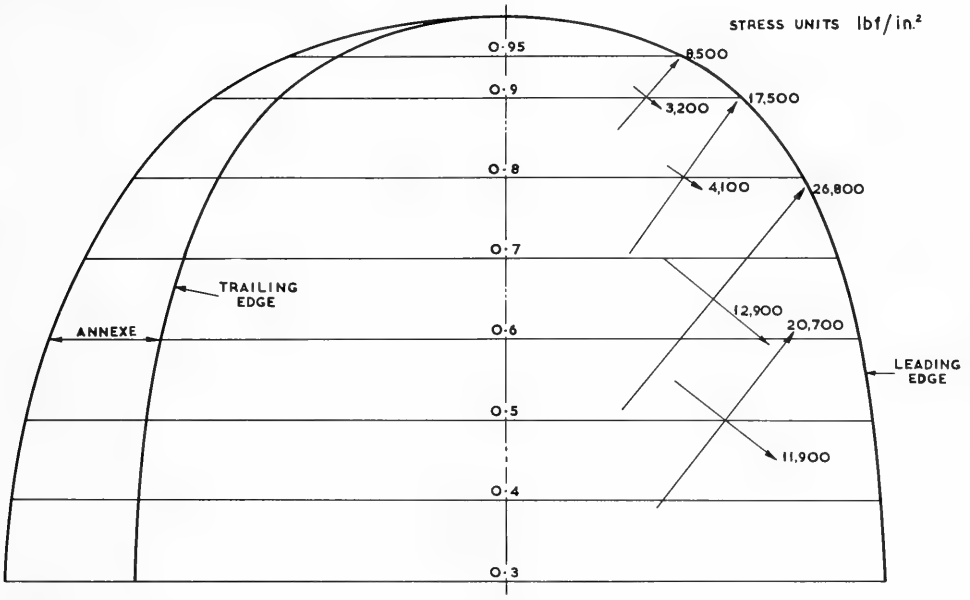

Fig. 36 - Principal stress vectors on expanded blade, typical flying condition--screw T95

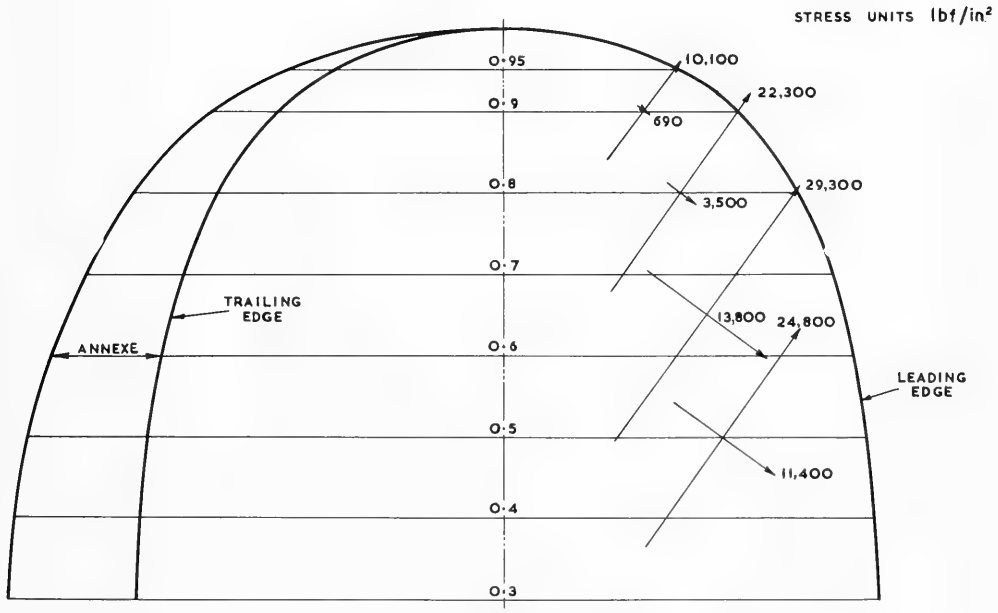

Fig. 37 - Principal stress vectors on expanded blade, typical takeoff condition--screw T95

developing 45,100 lbf thrust. Scaling this stress directly with thrust then gives 29,200 lbf/in^2 for 40,000 lbf thrust as compared with 22,000 lbf/in^2 from the De Havilland static tests. Again applying the thickness correction reduces the T95 stress to 24,400 lbf/in^2 as compared with 22,000 lbf/in^2. This comparison is slightly closer than that in the flying condition, as might be expected, since the static load distribution used was more appropriate to the takeoff condition. The closeness of this T95 result and the static test result then tends to confirm the view that leading edge sweepback is not as highly effective in reducing the steady stress level in the leading edge vicinity as predicted in the earlier simple static tests on the plane blades. It is noticeable from the NPL tests that the stresses in the takeoff condition are higher than those in the flying conditions by nearly 30 percent.

In concluding this section on structural considerations, it would appear that blades with relatively thick leading edges are essential not only for ensuring structural integrity but also for reducing the leading edge deflection and the attendant efficiency loss. High values of the elastic modulus of the propeller material are also desirable for this purpose. Blade-root stresses can also be high, but it is relatively easier to control these by thickening the blades. With a fixed diameter the additional factors that influence the leading edge deflection and stress levels are the blade pressure distribution and to some extent the geometrical blade shape, although it appears that a large improvement due to sweepback is not evident. In the calm-water flying condition when the sections should be operating at relatively low values of incidence, the advantage of the rearward centre of pressure position of the Johnson 3-term section, say, over the circular-arc section is desirable. However, in the takeoff and more heavily loaded flying conditions when the incidences are relatively large, this advantage will diminish in value.

In the *Bras d'Or* application when 4-ft diameter screws developing thrusts of about 40,000 lbf are used, it is expected that steady maximum principal stresses no greater than 25,000 to 30,000 lbf/in^2, including centrifugal effects, will be experienced. It is also anticipated that due to the relatively moderate wake caused by the strut/foil assembly, the fluctuating stresses liable to cause fatigue will also be well within the capabilities of the material being used. Fluctuating propeller loading assumptions as used for design purposes are shown in Table 4.

CONSIDERATION OF FUTURE METHODS OF PROPULSION

In 1963, at the time when it was decided to proceed with the design and construction of the *Bras d'Or*, the only practical means of propelling the vehicle in the foilborne mode was by means of fully cavitating propellers. Despite the advances that have been made with alternative means of propulsion in the intervening period, it is doubtful if a different decision would be made today, since the system that has been adopted has required the least development effort in return for a relatively high propulsive efficiency.

The propulsion system may be divided into the three components—the engine, the Zed drive transmission, and the propeller. Considerable operational experience has been obtained with marinised gas turbines, but the requirement

Table 4
FHE-400 Estimates of Fluctuating Fully Cavitating Propeller Loads
for a Five-Year Period in the North Atlantic

Condition	Foilborne Time		RPM	Frequency Hz	Thrust Lbf T	Torque Ft Lbf Q	ΔT% ±	Δ Q% ±	Δ X Lbf ±	ΔQ Ft Lbf ±	ΔM_y Ft Lbf -	Δ Y/Δ Z Lbf ±
	%	Hours										
Takeoff	10	300	1,800	90	60,000	38,000	10	10	6,000	3,800	7,700	3,000
Maximum												
Minimum												
Cruise	76	2,300	1,800	90	30,000	30,000	5	5	1,500	1,500	1,900	1,200
Maximum												
Minimum												
Turns	10	300	2,000	100	50,000	35,000	10	10	5,000	3,500	6,400	2,700
Maximum												
Minimum												
Broaching	3.3	33.3	1,800	90	30,000	30,000	10	10	3,000	3,000	3,800	2,400
Maximum		33.3	1,800		20,000	20,000	50	50	10,000	10,000	12,800	8,000
Minimum		33.3	1,800		10,000	10,000	100	100	10,000	10,000	12,800	8,000

ΔM_y = Couple due to alternating thrust. Positive nose-down.
ΔZ^y = Transverse load on propeller, any direction, but mainly sideload or upload.
Propeller Diameter = 3.666 ft.
Effective Radius for point application of forces is .7r = 0.35D = 1.282 ft.

to transmit 25,000 hp through two Zed drives in the struts has required considerable development effort by the General Electric Company of the USA. Rather similar drive systems of comparable complexity have been used in the US on the hydrofoil ships *Denison* and *Plainview* (AGEH-1) (Refs. 3 and 18), and no doubt the complexity expense, and vulnerability of this particular component, more than any other factor, has motivated the search for alternative means of propulsion. However, in the authors' opinion it is extremely unlikely that a more efficient means of propulsion will be found.

The point is frequently made (Refs. 19 and 20, for example) that the efficiency of the propulsion device is not the only factor to be considered when selecting a method of propulsion for a hydrofoil ship, and that when all the relevant factors are considered, preference for an alternative device with a lower propulsive efficiency may result. It might be expected that the overall system efficiency obtainable with the alternative device will be higher, but even this is not an essential prerequisite if the alternative is more reliable and requires less maintenance. At the present time, however, and in relation to the *Bras d'Or* power requirement, no alternative propulsion system can be said to provide a satisfactory alternative to gas-turbine-driven fully cavitating propellers. Nevertheless, it might be of interest to make a brief assessment of the possible future means of propulsion.

In basic terms, hydrofoil ship propulsion, as with all ships, requires the rearward acceleration of fluid, whether it be water or air, or a mixture of both. This requires the generation of energy onboard, the transmission of this energy, and finally the transference of the energy to the fluid used for propulsion. Some methods of propulsion such as rockets, both above and below water, do not require the transmission and transference stages, but these fall outside the scope of devices that accelerate the ambient mass of fluid to obtain propulsion. Other devices such as jet engines without additional equipment only utilise the first and last stages, omitting the energy transmission stage. They lead to a mechanically simple system, but unfortunately, due to the high jet velocities, the efficiencies are much too low. In fact, all forms of air propulsion, including air propellers, can be excluded on the grounds that the efficiency will be too low or the device will be too large.

The possibility of extending air propulsion by mixing water with airjets after the compression stages as described in Ref. 21 appears very attractive. This would increase the density of the fluid being accelerated and reduce its jet velocity, leading to an increase in efficiency over that of the plain airjet. The performance of such a device depends largely on the effectiveness with which the water particles can be accelerated and the air decelerated in the energy transference stage, and also on the efficiency of this transference. It seems to the authors that this method of propulsion will fail in the context of the *Bras d'Or* requirements precisely on these grounds, although this statement is based on the performance of the airblown ramjet and airlift pumps, and not on hard facts obtained from a water-augmented airjet. The airblown ramjet itself (Refs. 22, 23 and 24), appears doomed to failure on the grounds that the efficiency is too low or the device will be too large. Also, auxiliary starting is required and acceleration is poor.

In connection with devices employing air/water mixtures, it appears that the efficiency and effectiveness with which energy can be transferred from gas to water, using the natural mixing process, is considerably less than that achieved when energy is transferred to water with the blades of propellers or pumps, where, for example efficiencies in the range of 80 to 90 percent are commonplace. If in the mixing process the efficiency of energy transference is only in the range of 20 to 40 percent, then this is too large a deficiency to make up by factors which have a second-order influence on the overall efficiency.

Water propulsion is the only alternative method and this must be accomplished by means of rotodynamic machines such as propeller-type devices or pumps. The principal difference in the application of these two types of device is that the propeller type, i.e., fully cavitating screws or ducted propellers of the so-called pump-jet type (Ref. 25), must be submerged beneath the surface, whereas those employing pumps, e.g., waterjets, may be installed within the hull. When mechanical power transmission is used, then pumps installed within the hull possess the obvious practical engineering advantage of a simpler mechanical drive system, and this weighs heavily in their favour. Also the question of the vulnerability of complicated underwater equipment such as screws, ducts, gears, etc., must be considered, and while this is of secondary importance in the case of oceangoing vehicles such as the *Bras d'Or*, it may be of primary importance in vehicles employed on coastal and inland routes.

Clearly then, the future choice of a propulsion device will depend largely on the role of the vehicle and on any developments that occur in power transmission systems. In the authors' opinion, any advances in geared or possibly hydraulic transmissions will strengthen the case for the fully cavitating propeller, on account of its relatively high efficiency and ability to accommodate a wide range of loading without additional complications.

Ducted propellers, similar to the type described in Ref. 25, in which the noncavitating screw or impeller is situated within a decelerating duct that is either base-ventilated or surface-ventilated on the external surface, could be contenders in the future. Mounted on the aft end of propulsion pods similar to those of the *Bras d'Or*, the device would employ a mechanical shaft drive, and the overall complication would be slightly greater than that with fully cavitating propellers. However, the presence of the duct and a support strut may enable more flexible alternative drives to be considered, e.g., hydraulic or pneumatic drives, in which the strut and duct are utilised for the power transmission, possibly to the tips of the rotor instead of the axis. With a device of this type it is conceivable that the duct could replace the propulsion pod and the strut and foils could then be attached to it.

Finally, the waterjet is another alternative, although in many respects it can be considered as a particular type of ducted propeller. Intense interest has been shown in these devices over the past few years, and the work mainly sponsored by the US Navy Department, Bureau of Ships, has given fresh impetus to this subject. The current position and thoughts in relation to waterjet propulsion are contained in the numerous papers that have been published recently, for example, Refs. 19, 26, 27, 28, 29 and 30. While some advanced proposals have been made, most of the component testing appears to have been conducted on pumps of established and proven design. A number of troublesome design areas

in the overall system have been highlighted. These are associated with the avoidance of cavitation erosion of the pump impeller, particularly in the takeoff condition, avoidance of inlet cavitation with fixed inlets and cavitation in the bends, ducting and elevation losses, and the weight of the system, including the water in the ducting. Suggestions for alleviating these difficulties include installing variable geometry intakes and nozzles and using inducers to enable the pumps to operate at lower suction specific speeds. However, the engineering development required with variable geometry intakes and their installation are added complications; also, the efficiency of present-day inducers is too low for the large hydrofoil ship application. As regards the future, therefore, the introduction of these items can only be viewed with uncertainty. In the meantime, the progress of the US Navy's *Tucumcari*, Ref. 18, fitted with a gas-turbine-driven waterjet system is observed with great interest, although it will be appreciated that the *Bras d'Or* power requirement is about six times that of the *Tucumcari*.

Perhaps the only firm prophecy that can be made regarding future hydrofoil ship propulsion systems is that they will employ gas turbine power units. Their high power-to-weight ratio, the flexibility of the free-power turbine, and the large amounts of power that can be developed make them invincible for this application. The aeronautical requirement will also ensure a high level of development in the future. Developments in the marinised versions will possibly take place, and the interesting suggestion mentioned by Waldo in Ref. 31 of separating the free-power turbine from the gas generator and considering the ducted gases as a replacement for the mechanical drive arouse interesting speculations. For example, possibly alternative engine arrangements could be devised to enable simpler geared drives to be used for propellers, even including the possibility of inclined shaft drives. The relative simplicity of the inclined drive makes it an attractive proposition for use with fully cavitating and ventilated propellers, both of which offer good prospects for reliable, efficient propulsion.

While fully cavitating propellers have received considerable attention in the past, ventilated propellers have been virtually ignored up to now, although considerable benefits are envisaged with this type of propeller since the problems of cavity collapse, cavitation erosion, and particularly underwater noise propagation should be greatly reduced. Further this type of propulsion, in which the venting air or gas is delivered through support struts which may be of the base-vented type, will also have application to high-speed displacement ships such as destroyers or frigates and hovercraft of both the sidewall and peripheral-skirted types, in addition to hydrofoils employing either noncavitating or fully cavitating foil systems.

The structural problems associated with these propellers, such as providing adequate strength and resistance to fatigue and cavitation erosion, may be relieved with the new materials that are emerging from the laboratory; for example, the boron or carbon-filament reinforced composite materials employing metallic or polymeric matrices may provide a better solution than either Inconel 718 or titanium. Also, these materials may be more easily fabricated than Inconel and titanium, thereby eliminating the very costly forging and machining procedures currently employed.

ACKNOWLEDGMENTS

The work described in this paper was conducted at the De Havilland Aircraft of Canada Ltd., and the National Physical Laboratory, England. It forms part of the work sponsored by the Canadian Armed Forces in the development of the hydrofoil ship H.M.C.S. *Bras d'Or*.

At De Havilland, Mr. S. Morita was responsible for most of the structural design and testing, and his advice is gratefully acknowledged. Also, Mr. P.D. Hedgecock provided valuable advice and recommendations on structural materials. The De Havilland programme was carried out under the direction and guidance of Mr. R.W. Becker—Project Engineer Hydrofoil, Mr. J.P. Uffen—Chief Aerodynamicist, and Mr. F.W. Buller—Chief Designer.

At NPL, Mr. A. Silverleaf together with the authors formulated the initial programme of work, while Mr. K. Poulton and Mr. M.S. Loveday performed most of the NPL experiments.

NOMENCLATURE

C_L Lift coefficient

D Screw diameter

E Elastic Modulus

$\bar{f}_a$ Axial wake factor $= \frac{V_a}{V}$

$\bar{f}_{tg}$ Tangential wake factor $= \frac{V_{tg}}{V}$

$\bar{f}_r$ Radial wake factor $= \frac{V_r}{V}$

J Screw advance ratio $= \frac{V}{nD}$

K_T Screw thrust coefficient $= \frac{T}{\rho n^2 D^4}$

K_Q Screw torque coefficient $= \frac{Q}{\rho n^2 D^5}$

n Screw speed of rotation

p Static pressure

p_v Vapour pressure

Q Screw torque

r Radius

R Screw radius

S Structural similarity parameter $= n^2D^2 \frac{(1 - \sigma^2)}{E}$

T Screw thrust

V Ship speed

V_a Axial wake velocity

V_{tg} Tangential wake velocity

V_r Radial wake velocity

x Radius fraction $= \frac{r}{R}$

β Inflow angle tan $\beta = \frac{\bar{f}_a}{\frac{x\pi}{J} + \bar{f}_{tg}}$

η Screw efficiency $= \frac{J}{2\pi} \cdot \frac{K_T}{K_Q}$

Ω Angular rate of rotation

ρ Mass density

σ Cavitation number $\frac{p - p_v}{\frac{1}{2}\rho V^2}$ or Poisson's ratio

REFERENCES

1. Monteith, R.G., and Becker, R.W., "Development of the Canadian Anti-submarine Hydrofoil Ship," Canadian Congress of Engineers, Montreal, June 1967

2. Milman, J.W., and Fisher, R.E., "The Canadian Hydrofoil Programme," Trans. R.I.N.A. 108 (1966)

3. Lacey, R.E., "A Progress Report on Hydrofoil Ships," Trans. R.I.N.A. 107 (1965)

4. Tachmindji, A.J., and Morgan, W.B., "The Design and Estimated Performance of a Series of Supercavitating Propellers," "Second Symposium on

Naval Hydrodynamics; Hydrodynamic Noise and Cavity Flow," Office of Naval Research, US Department of the Navy, ACR-38, Aug. 1958

5. Venning, E., and Haberman, W.L., "Supercavitating Propeller Performance," Trans. SNAME 70 (1962)

6. Tulin, M.P., "Supercavitating Propellers History, Operating Characteristics, Mechanism of Operation," Hydronautics Technical Report 127-6, June 1964

7. Cox, G.G., "Supercavitating Propeller Theory—Part I. The Derivation of Induced Velocity Equations and Formulation of an Initial Design Procedure," D.T.M.B. Report 2166, Feb. 1966

8. English, J.W., "An Approach to the Design of Fully Cavitating Propellers," Symposium: Cavitation in Fluid Machinery, ASME, Nov. 1965

9. English, J.W., "Instrumentation for the Detailed Evaluation of Propeller Performance," Symposium on Testing Techniques in Ship Cavitation Research, Skipsmodelltanken, Norway, May 1967

10. Wu, T.Y., "A Free Streamline Theory for Two-Dimensional Fully Cavitated Hydrofoils," J. Math and Phys. XXXV, Oct. 1965

11. Johnson, V.E., "Theoretical and Experimental Investigation of Supercavitating Hydrofoils Operating Near the Free Water Surface," NASA Technical Report R-93 (1961)

12. Ōba, R., "Theory on Supercavitating Cascade Flow for Arbitrary Form Hydrofoils," Symposium: Cavitation in Fluid Machinery, ASME, Nov. 1965

13. English, J.W., "Characteristics of Fully Cavitating Hydrofoils Having Circular Arc Faces, from Wu's Theory," Ship Division Report 67/65, NPL

14. Morita, S., "Model Propeller Blade Structure Test to Determine Optimum Sweepback Angle," De Havilland Aircraft of Canada Ltd. Report HF1-S-G-3/1, July 1966

15. Morita, S., "Full Scale Supercavitating Propeller Blade Structure Test," De Havilland Aircraft of Canada Ltd. Report HF1-S-G-3/2, July 1966

16. Acum, W.E.A., "Note on the Use of Elastic Models in Marine Propeller Testing," Ship Division TM 136, NPL, June 1966

17. Berry, L.W., and Steele, B.N., "Deflection Measurements on a Propeller Rotating Under Load," Ship Division Report 40/66, NPL

18. Ellsworth, W.M., "The U.S. Navy Hydrofoil Development Program—A Status Report," Paper 67-351, AIAA/SNAME Advance Marine Vehicles Meeting, May 1967

19. Traskel, J., and Woodrow, E.B., "Waterjet Propulsion for Marine Vehicles," J. Aircraft 3 (No. 2) Mar.-Apr. 1966

20. Berg, D.J., Jones, W.S., and Marron, H.W., "Why Waterjets?," Naval Engineers Journal, Oct. 1967

21. Muench, R.K., and Keith, T.G., "A Preliminary Parametric Study of a Water-Augmented Air-Jet for High-Speed Ship Propulsion," U.S. Navy Marine Engineering Lab R&D Report 358/66, Annapolis, Feb. 1967

22. Gadd, G.E., "A Note on Air-Blown Ramjets," Ship Division TM 51, NPL, Apr. 1964

23. Gadd, G.E., "Some Experiments with an Air-Blown Water Ramjet," Ship Division TM 103, NPL, Nov. 1965

24. Pierson, J.D., "An Application of Hydropneumatic Propulsion to Hydrofoil Craft," J. Aircraft 2 (No. 3), May-June 1965

25. Thurston, S., and Evanbar, M.S., "Ducted Propellers for High-Speed Underwater Propulsion," Paper 67-460, AIAA 3rd Propulsion Joint Specialist Conference, Washington, D.C., July 1967

26. Johnson, V.E., "Water-Jet Propulsion for High-Speed Hydrofoil Craft," AIAA Paper 64-036, Washington, D.C., June 1964

27. Brandau, J.H., "Aspects of Performance Evaluation of Waterjet Propulsion Systems and a Critical Review of the State of the Art," Paper 67-360, AIAA/SNAME Advance Marine Vehicles Meeting, May 1967

28. Arcand, K., and Connolli, C.R., "Waterjet Propulsion for High-Speed Ships," Paper 67-350, AIAA/SNAME Advance Marine Vehicles Meeting, May 1967

29. Contractor, D.N., and Johnson, V.E., "Waterjet Propulsion," Paper 67-361, AIAA/SNAME Advance Marine Vehicles Meeting, May 1967

30. Garnett, J.H., "Preliminary Design of Water-Jet Propulsion Systems for 4000-ton Captured Air Bubble (CAB) Ship," U.S. Navy Marine Engineering Lab R&D Report 41/67, Mar. 1967

31. Waldo, R.D., "Some Special Problems in Surface Effect Ships," Paper 67-346, AIAA/SNAME Advance Marine Vehicles Meeting, May 1967

32. Morgan, W.B., "The Testing of Hydrofoils and Propellers for Fully-Cavitating or Ventilated Operation," Appendix IV, Cavitation Session, 11th International Towing Tank Conference, Tokyo, Oct. 1966

APPENDIX

WATER TUNNEL TESTING TECHNIQUES

All the hydrodynamic testing for this project has been conducted in the No. 1 water tunnel in the Ship Division, NPL, and in the course of testing a number of factors have come to light which are considered worthy of comment. These mainly refer to the corrections that have been applied to the raw measured data in order to determine the predicted ship values. Because it is not customary to use water tunnel results when predicting conventional displacement ship propulsion from models, these corrections assume a greater importance in the model testing of fully cavitating propellers where tunnel testing is necessary.

WATER SPEED MEASUREMENT

The largest single factor affecting the results has arisen through the use of the upstream wake simulator. In order to set the water speed in the tunnel working section, the flow downstream of the wake simulator was first measured with a pitot rake and then this volumetric mean flow was plotted against the pressure drop occurring in the upstream contraction. Subsequently, when the screws were being tested the tunnel water speeds were set by using this calibration.

At any early stage in the test programme one of the fully cavitating propellers was tested both with and without the wake simulator. When tested without the simulator, the upstream bluff end of the screw hub was shielded from the oncoming flow by attaching a fairing cone to the hub which rotated with the screw. This procedure is customary when testing propellers with a downstream drive shaft. However, in this case, due to the large amount of hub taper which is necessary to fair in with the pod shape, the upstream fairing cone was necessarily ill-shaped in order to keep it of reasonable length. Testing the screw in this manner gave quite large differences compared with the results of testing behind the wake simulator, the thrust without the simulator being less than when it was tested with it. This was considered to be due to the large pre-swirl in the direction of the screw rotation caused by the rotating fairing cone, a view that was supported by the nature of the slight amount of cavitation that occurred on the upstream cone. Subsequently, no further tests were conducted without the presence of the wake simulator.

SHAFT PULL CORRECTION

A correction to the measured values of thrust has been necessary due to the differential pressures acting on the ends of the downstream drive shaft. One end of the shaft is in atmospheric air, while the other end is in the low pressure of the working section. Normally, without a wake simulator, the pressure acting on the propeller end of the shaft is taken to be the water tunnel working section pressure. However, with the wake simulator that was used, it was necessary to measure the actual pressure between the upstream end of the rotating screw and the stationary downstream end of the wake simulator. The arrangement tested

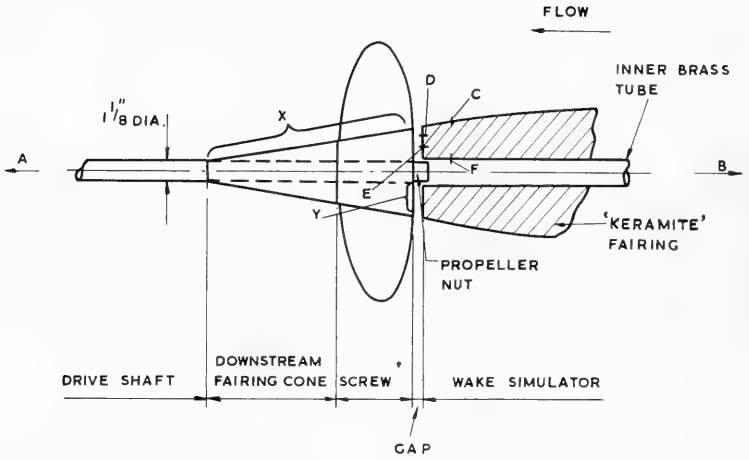

Fig. A-1 - Diagrammatic arrangement of fully cavitating screw with wake simulator

is sketched in Fig. A-1, and two sample sets of pressure measurements are given below.

(i) $J = 0.80$; $\sigma = 0.35$

Tunnel water speed = 27.0 ft/sec
Screw rate of rotation = 40.5 rps
Vapour pressure = 44 lbf/ft^2

Pressure tap position →	A (Atmospheric)	B (Upstream static)	C	D	E	F
Absolute pressure lbf/ft^2 →	2120	314	129	151	178	169

(ii) $J = 0.3$; $\sigma = 2.7$

Tunnel water speed = 10.5 ft/sec
Screw rate of rotation = 42.0 rps
Vapour pressure = 47 lbf/ft^2

Pressure tap position →	A (Atmospheric)	B (Upstream static)	C	D	E	F
Absolute pressure lbf/ft^2 →	2120	339	48	79	129	125

In the first case the pressure at F, which was used in the pull correction, was considerably different from the upstream static pressure at B which would have been used in making the pull correction in uniform flow. For these results

the pull correction would amount to 13.5 lbf for a 1.1/8-inch diameter shaft, which is highly significant when compared with the total force measured on the dynamometer, which in this case was just over 100 lbf. Since the pressure at the tunnel end of the shaft is always low with low cavitation numbers, the pull correction does not vary too much; but it becomes a relatively large proportion of the total force at the higher J values when the thrust approaches zero.

It can be inferred from the above pressure measurements at C and B, and from the fact that the difference between them is greater than the pressure drop across the simulator, that the inflow velocity to the screw at point C is greater than the upstream velocity, i.e., the inflow at this point *is* accelerated. While this may not be the case at the outer radii, it does not confirm the statement that it is possible for decelerated inflows to accompany fully cavitating propeller operations.

Referring again to Fig. A-1, it can be seen that the axial forces P_x and P_y on the surfaces of the hub and downstream fairing cone X, and the annular area of the upstream hub surface Y, have also been included in the measured shaft force or thrust, and the net propulsive force arising from these pressure forces is given by $(P_x - P_y)$. In considering this force, it may be noted that whereas the flow, and hence the pressure forces over the hub, downstream fairing, and outer surfaces of the simulator near the propeller, are correctly produced on the model in relation to the ship, there exists a little doubt as to the relative magnitude of the force P_y in the model tests. This arises because the conditions in the gap between the propeller hub and wake simulator could not be correctly produced in the model arrangement when using a downstream shaft.

A few tests were made on a model screw in which the gap between the screw and the simulator was varied from about 0.6 to 3 percent of the screw diameter, and it was found that the shaft axial force was unaffected while the gap was small but began to fall off when the gap reached 3 percent of the screw diameter. Subsequently, all tests were conducted with a gap varying from about 0.6 percent to 1.5 percent of the diameter, and in this range the thrust did not vary with gap size.

Finally, in connection with the measured tunnel thrust, the pull correction, and the pressure forces acting over the hub, it should be pointed out that the resistance of the craft should include the flow over the pods as far downstream as the propellers, plus the pressure forces acting over the pod surfaces in the propeller-pod gaps, both, of course, being determined with the propellers operating.

TUNNEL WALL EFFECT

No corrections have been made to the results to account for the constraint imposed on the flow by the presence of the tunnel walls. The tunnel used in these experiments had a slotted-wall working section and, like an open jet tunnel, this is expected to reduce the corrections from this source to small values as it does with noncavitating propellers. Reference 32 summarises the existing data on fully cavitating propellers in relation to wall effects, but the results are obscure and could not be used for making corrections.

It may be noted that in these experiments the lowest cavitation numbers attainable were limited to some extent by the tunnel circuit cavitating in addition to the cavitation produced by the propeller itself. It was also necessary to perform the tests at relatively low values of air content in order to prevent free air from recirculating around the tunnel circuit, and to enable the lowest working section pressures to be obtained. Throughout the tests the air content was kept approximately within the range of 3.5 to 7.0 parts per million by weight.

REYNOLD'S NUMBER OF TESTS

To achieve the low cavitation numbers required, the experiments had to be run at high speeds, and this led to high values of Reynold's number. Based on the relative flow and the blade chord lengths at the 70 percent radius, the Reynold's number of the tests was about 2×10^6 compared with 30×10^6 for the ship.

* * *

DISCUSSION

W.B. Morgan

Naval Ship Research and Development Center
Washington, D. C.

This extensive paper shows the amount of work necessary to develop a high-speed propeller for a particular application. An accounting of the details gone through in such a development is most welcomed.

I have two questions which involve the strength analysis. The first question concerns the use of the simple beam theory for making the stress analysis. The stresses obtained by the authors experimentally indicate that the direction of the principal stresses toward the blade tip deviate considerably from that normally assumed for airfoil-shaped sections, i.e., normal to the nose-tail line. I would like to know, in the use of the simple beam theory, whether or not the principal stresses were considered as normal to the nose-tail line. It should be possible to calculate the location of the principal axis and take into account its true position.

My second question is whether or not a section with a large annex was considered for strength purposes.

* * *

REPLY TO DISCUSSION

B.V. Davis

I am indebted to Mr. S. Morita, who has provided the following answers to Mr. W.B. Morgan's questions:

1. The methods applied to analyse the hydrofoil propeller blades included the simple beam theory for determining spanwise bending stresses, and torsional stress analysis of the noncircular blade sections. The combination of bending and shear stresses can give principal stresses in directions which are not normal to the section nose-to-tail line. This feature was clearly demonstrated during extensive structural testing of a full-scale aluminum blade model.

2. With regard to the need for a large annex to the blade section, this was considered for early versions of the design. It was found that when applying the simple beam theory, the section modulus at the leading edge was reduced in spite of the increase in the moment of inertia. This is due to rotation of the principal axes, giving rise to increased fibre distance at the leading edge. The conclusion was that an annex at the trailing edge does not always provide a reduction in the peak stress levels, and has the disadvantage of additional weight and hence higher centrifugal stresses.

(Author's Note) — For the final design it was found necessary to trim off the upper rear section surfaces, to obtain small tension stresses in the thin blade leading edges, i.e., by rotating the section principal axis slightly above the section leading edge. A computer programme was used to obtain section properties at various blade stations, and a trial and error method used by removing trailing edge upper surface material until the desired principal axis orientation was obtained.

* * *

THEORETICAL AND EXPERIMENTAL STUDY ON THE DYNAMICS OF HYDROFOILS AS APPLIED TO NAVAL PROPELLERS

E. Castagneto
Istituto Architettura Navale
Naples, Italy

and

P. G. Maioli
Centro Esperienze Idrodinamiche
Rome, Italy

ABSTRACT

The transformation of a hydrodynamic field into an actual propulsive device follows a method which, although being derived from theory, is based upon simplifications and approximations. Up till now no univocal procedure has been proved by experience.

The main reasons for this unsatisfactory situation seem to be: (a) differences between hydrofoils' theoretical and actual performances; (b) the effect of flow curvature in wide-bladed propellers.

Since the hydrofoil's performance is one of the basic elements for the majority of naval propulsive systems, conventional or not, it is intended in this report to present some theoretical analyses and experimental results dealing with the dynamics of hydrofoils. At the same time some practical consequences of the effect of flow curvature are pointed out.

1. INTRODUCTION

In the design of a naval propeller based on the vortex theory two main phases may be considered: the evaluation of the hydrodynamic field for a limited number of radial stations, that is, the computation of both the velocity diagrams and the products, lift coefficient x chord length $(C_L \cdot c)$; and the shaping of the related cylindrical blade sections in such a manner as to be able to produce the desired lift without cavitation.

The first phase follows a theoretical formulation, by now universally adopted, which does not require any further comment; on the contrary, the second one, in which the hydrodynamic field turns into an actual propulsive device,

This work has been supported by the "Consiglio Nazionale delle Ricerche."

is derived from theory but contains unavoidable approximations, simplifications and empirical evaluations which do not yet lead to a univocal procedure well proved by experience (1, 2).

The basic reasons for such discrepancies seem to be:

(a) the considerable differences between the true performance in real fluid of the hydrofoils normally used in the design of a naval propeller, and their theoretical performance, as deduced by conformal mapping, in ideal flow; and

(b) the effects due to the blade width; because the blade, in naval propellers, is better represented by a vortex lifting surface rather than by a lifting line.

The aim of this report is to present some theoretical analyses and to refer to some experimental results dealing with the above-mentioned topics.

Studies on the dynamics of lifting foils are considered to be a topical question, because the hydrofoil is the basic element for the majority of naval propulsive systems, conventional or not.

2. THE HYDROFOIL'S ACTUAL PERFORMANCE

2.1 Lift Coefficient in Ideal Flow

In designing the blades of a naval propeller, extensive use is made nowadays of foils with thickness distribution NASA 16 or NASA 66 mod. (the NASA 66 is less often used because of its thinness at the trailing edge), cambered according to the mean lines NASA a = 1, NASA a = 0.8, and NASA 65, and operating at an angle of attack α, measured between the chord and the direction of the undisturbed flow.

Tables 1 and 2 show the geometry of the above-mentioned section foils and mean lines, taken from the NASA Report 824. Theoretical values of the velocity increments for the basic thickness forms and mean lines considered and for a wide range of thickness ratios are tabulated in that report for each particular station along the chord, namely:

(a) $\Delta V_t = \Delta' V_t V$ = function of the thickness ratio of a particular hydrofoil, and proportional to the velocity of the undisturbed flow V;

(b) $\Delta V_f = \Delta' V_f V \frac{f_m}{c}$ = function of a particular mean line, and proportional both to the velocity V and to the camber ratio f_m/c; and

(c) $\Delta V_a = \Delta' V_a V C_{L\alpha}$ = function of the thickness ratio t_m/c, of a particular thickness form, and directly proportional, for each thickness ratio, to the velocity V and to the lift coefficient $C_{L\alpha}$, depending on the angle of attack.

Table 1
Half Ordinates—NASA 16-66-66 Mod

% C	$t/2t_m$ NASA 16	$t/2t_m$ NASA 66	$t/2t_m$ NASA 66 mod
0	0	0	0
1.25	0.1077	0.1155	0.1155
2.50	0.1504	0.1530	0.1530
5.00	0.2091	0.2095	0.2095
7.50	0.2527	0.2540	0.2540
10	0.2881	0.2920	0.2920
15	0.3450	0.3530	0.3530
20	0.3887	0.4002	0.4002
30	0.4514	0.4637	0.4637
40	0.4879	0.4952	0.4952
50	0.5000	0.4975	0.4962
60	0.4862	0.4592	0.4653
70	0.4391	0.3860	0.4035
80	0.3499	0.2572	0.3110
90	0.2098	0.1108	0.1877
95	0.1179	0.04367	0.1143
100	0.0100	0.0000	0.0333

If direction is disregarded, the velocity increments are the same both on the face and on the back, at each particular station along the chord. By applying Bernoulli's equation between any couple of symmetrical points M and M' on the foil surface, at which the pressure is assumed to be p_b and p_f, the following relation is obtained:

$$\frac{p_f - p_b}{\frac{1}{2}\rho V^2} = 4(1 + \Delta' V_t)\left(\Delta' V_f \frac{f_m}{c} + \Delta' V_a C_{La}\right) \qquad (1)$$

Table 2
Mean Lines a = 1-a = 0.8-NASA 65

% C	f/f_m NASA a = 1	f/f_m NASA a = 0.8	f/f_m NASA 65
0	0	0	0
1.25	0.097	0.091	0.049
2.50	0.169	0.159	0.098
5.00	0.286	0.271	0.190
7.50	0.384	0.366	0.277
10	0.468	0.448	0.360
15	0.610	0.588	0.510
20	0.721	0.705	0.640
30	0.882	0.865	0.840
40	0.970	0.962	0.960
50	1.000	1.000	1.000
60	0.970	0.980	0.960
70	0.882	0.890	0.840
80	0.721	0.703	0.640
90	0.610	0.359	0.360
95	0.468	0.171	0.190
100	0.384	0.000	0.000

and by integrating along the whole chord:

$$C_L = \frac{f_m}{c}\frac{4}{c}\int_0^c \Delta' V_f \, dc \left[1 + \frac{\left(\int_0^c \Delta' V_f \, \Delta' V_t \, dc\right)}{\left(\int_0^c \Delta' V_f \, dc\right)}\right] + C_{L\alpha}\int_0^c \frac{4}{c}\left(1 + \Delta' V_t\right)\Delta' V_a \, dc \quad . \qquad (2)$$

According to relation (2), the lift coefficient consists of two main parts: the first one, C_{Lf}, produced by curvature, depends upon the camber ratio f_m/c of a particular mean line and upon the thickness ratio t_m/c of a particular thickness

form; the second, $c_{L\alpha}$, produced by the angle of attack, depends upon the incidence and upon the thickness ratio of a particular thickness distribution. See Fig. 1.

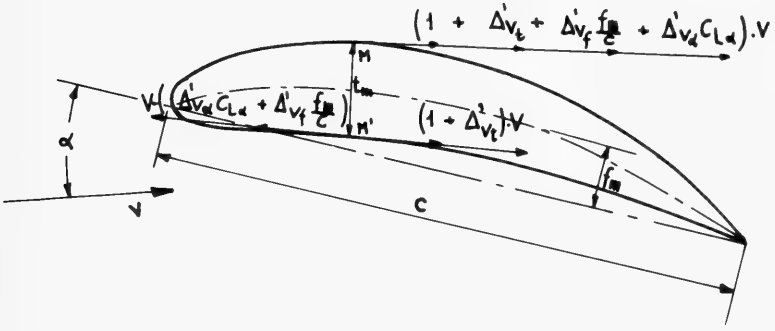

Fig. 1 - Velocity increments

Assuming

$$\frac{4}{c}\int_0^c \Delta' V_f \, dc = K_f \tag{3}$$

and

$$\frac{\int_0^c \Delta' V_f \, \Delta' V_t \, dc}{\int_0^c \Delta' V_f \, dc} = K_t' \tag{4}$$

it follows that

$$C_{Lf} = K_f \frac{f_m}{c}(1 + K_t') \, . \tag{5}$$

If the structure of the two formulas (3) and (4) is considered, it is easily recognized that the coefficient K_f depends only upon the mean line, and that K_t', in practice, even though not in theory, depends almost only upon the thickness distribution and the thickness ratio.

In Figs. 2-7, values of C_{Lf} versus t_m/c and f_m/c are given for several combinations of thickness forms and mean lines. The values shown have been calculated by A. Silvestro (3), integrating numerically the velocity increments tabulated in NASA Report 824.

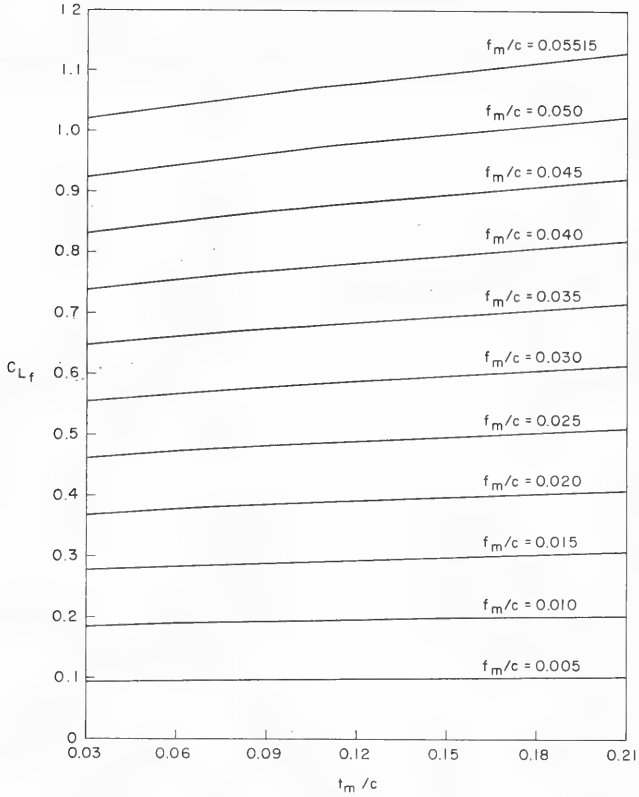

Fig. 2 - Lift coefficient at shock-free entry conditions versus f_m/c and t_m/c.

The same results can be very closely approximated (the error is no more than 0.5% for the ratios of t_m/c normally used) by

$$C_{Lf} = K_f \frac{f_m}{c}\left(1 + K_t \frac{t_m}{c}\right), \tag{6}$$

K_f and K_t being as shown in Table 3.

In the practical design of naval propellers, an average value of $K_t = 0.75$ may be assumed for all cases, if preferred, thanks to the very low values of the thickness ratio used.

From a former work (4), a value of $K_t = 1.55$ for Karman-Treffts profiles with NASA-65 mean line has been derived. This value is very far from those listed above, which refer, in general, to the foils by now normally used in naval construction, and, in particular, to those employed in the design of the blade

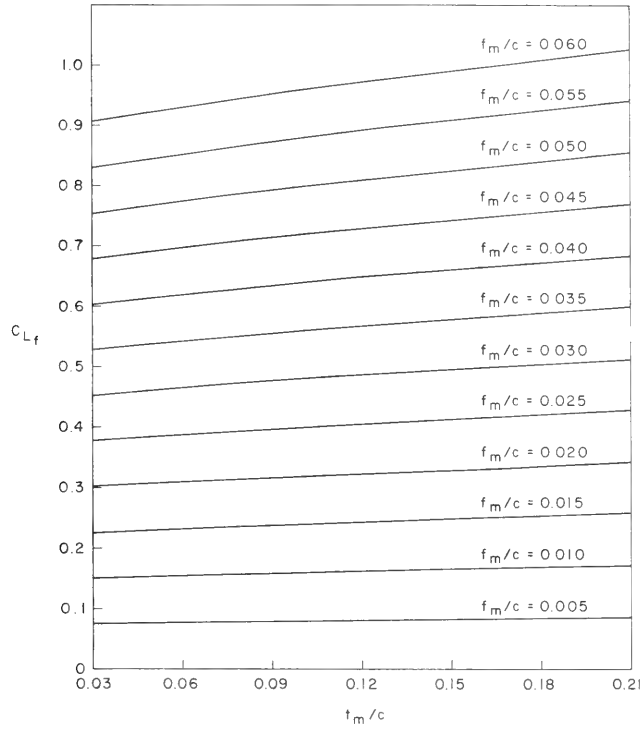

Fig. 3 - Lift coefficient at shock-free entry conditions versus f_m/c and t_m/c.

Table 3
Values of K_f and K_t

		Mean line		
		a = 1	a = 0.8	NASA 65
Values of K_f		18.15	14.75	12.50
Values of K_t	NASA 16	0.725	0.88	0.77
	NASA 66	0.65	0.82	0.70
	NASA 66 mod.	0.65	0.82	0.70

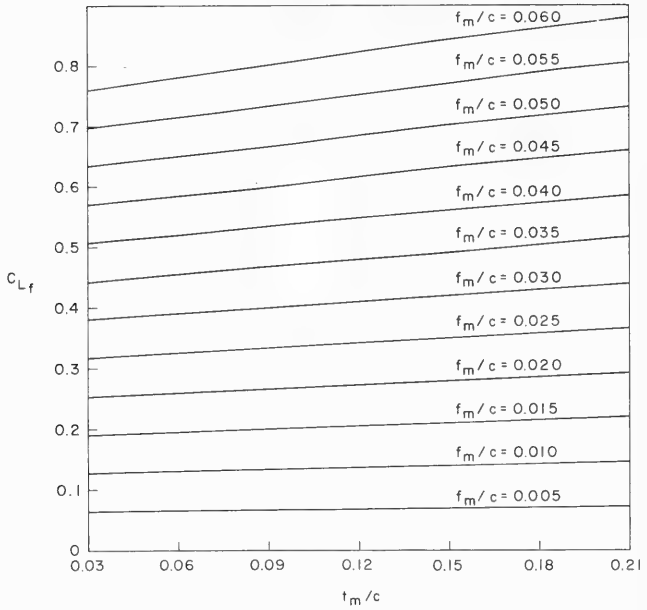

Fig. 4 - Lift coefficient at shock-free entry conditions versus f_m/c and t_m/c.

sections of naval propellers. In the case of an ideal foil of zero thickness, operating at shock-free entry conditions, relation (6) becomes

$$C_{Lf} = K_f \frac{f_m}{c} , \tag{7}$$

and as such is commonly used in drawing the so-called "incipient cavitation diagrams" (5), (6), (7).

It must be noted, however, that the approximation involved in formula (7) is too wide (errors made in evaluating C_{Lf} may reach 15% or more), and the authors who use it themselves suggest a consequent pitch correction. On the other hand, the reading of such cavitation charts does not appear easier than the numerical calculation involved in the relation suggested above, (6).

The last term in Eq. (2) clearly leads to the conclusion

$$\int_0^c \frac{4}{c} (1 + \Delta' V_t) \, \Delta' V_\alpha \, dc = 1 . \tag{8}$$

In the NASA Report 824 a definite dependence of the velocity increments upon the angle of attack has not been shown; this means that the relation

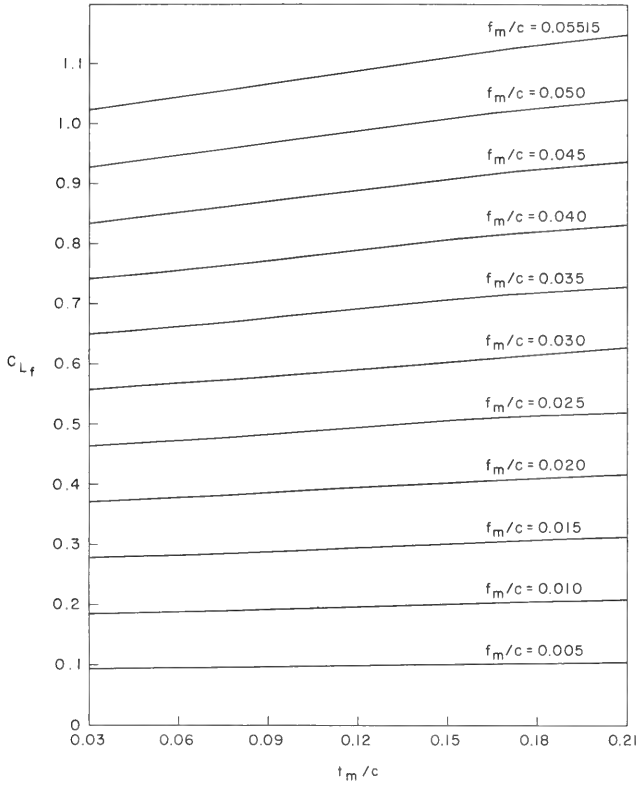

Fig. 5 - Lift coefficient at shock-free entry conditions versus f_m/c and t_m/c.

$$C_{L\alpha} = \rho \left(\alpha, \frac{t_m}{c} \right)$$

cannot be put into an explicit form. In other words, it is not possible to isolate the individual influence exerted upon the lift coefficient $C_{L\alpha}$ by the angle of attack and by the thickness ratio, respectively.

There is consequently no possibility of building up an expression of the same form as relation (6)

$$C_{L\alpha} = K_\alpha \, \alpha \left(1 + K_t'' \frac{t_m}{c} \right),$$

in which both the values of K_α and K_t'' may be evaluated. Theoretically, the following relation holds good:

$$C_{L\alpha} = 2\pi\alpha \, , \tag{9}$$

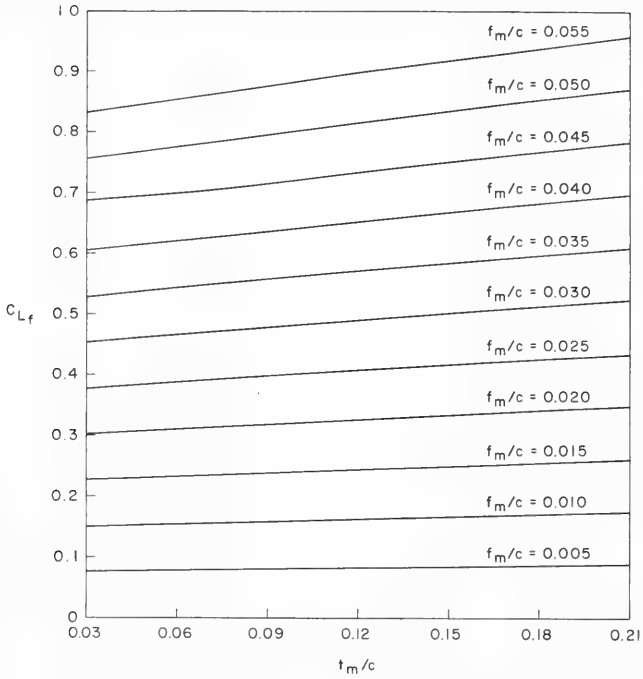

Fig. 6 - Lift coefficient at shock-free entry conditions versus f_m/c and t_m/c.

but in this simple equation the lift coefficient, caused by incidence, does not depend on thickness ratio.

However, the values of $\Delta' V_\alpha$ do depend on thickness, as is shown by relation (8), which, taken as a whole, always has to be equal to one; but this does not mean that

$$\frac{4}{c}\int_0^c \Delta' V_\alpha \, dc = 1 \quad \text{and} \quad \frac{4}{c}\int_0^c \Delta' V_\alpha \, \Delta' V_t \, dc = 0 \ .$$

The dependence of $\Delta' V_t$ and of $\Delta' V_\alpha$ on thickness is not linear, especially in the proximity of the leading edge. Most authors realize the required lift coefficient only by camber, that is, at shock-free entry condition; therefore there is no question, whatever expression be used for $c_{L\alpha}$, but, as will be shown later on, it is advantageous to operate both with camber and with a little amount of incidence as well.

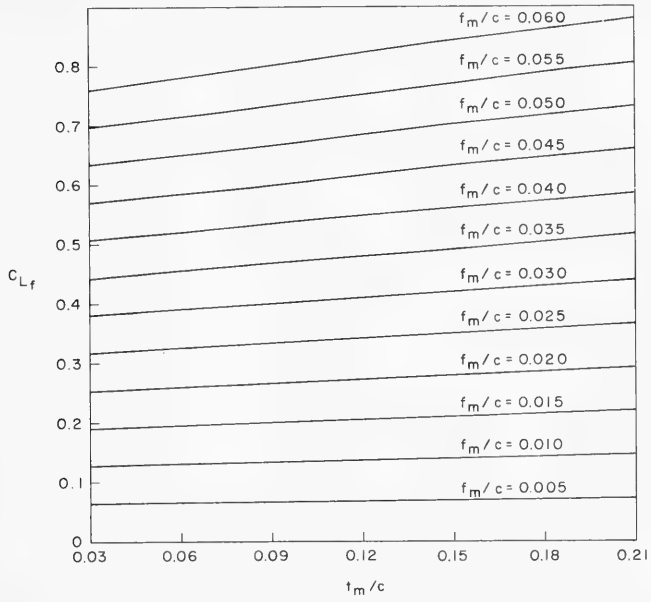

Fig. 7 - Lift coefficient at shock-free entry conditions versus f_m/c and t_m/c.

Suction-Side Maximum Depression in Ideal Flow

In operating conditions, the maximum value of the depression at a typical point M on the suction side of a foil (see Fig. 1) may be easily obtained by means of Bernoulli's equation,

$$\frac{\Delta p}{\frac{1}{2}\rho V^2} = \frac{\Delta p}{q} = \left(1 + \Delta' V_t + \Delta' V_f \frac{f_m}{c} + \Delta' V_\alpha C_{L\alpha}\right)^2 - 1 , \tag{10}$$

and substituting the value of f_m/c obtained by the relation (6):

$$\frac{\Delta p}{q} = \left(1 + \Delta' V_t + \frac{\Delta' V_f}{K_f} \frac{C_{Lf}}{1 + K_t \frac{t_m}{c}} + \Delta' V_\alpha C_{L\alpha}\right)^2 - 1 . \tag{11}$$

For the basic thickness forms and mean lines considered in this report, when lift coefficients and thickness ratios fall in the range of those normally involved in the design of a naval propeller (generally $C_L c/t_m < 6$), the point of maximum depression on the suction side occurs at 60% of the chord from the leading edge, whenever the required lift coefficient is obtained completely by camber or 90% by camber and 10% by the angle of attack. From the basic data tabulated in the NASA Report 824, the values of the various coefficients in relation (11), shown in Table 4 are easily obtained for that point. Substituting the

Table 4
Values of $\Delta' V_t$, $\Delta' V_a$, $\Delta' V_f / K_f$

	NASA 16	NASA 66	NASA 66 mod
$\Delta' V_t$	$1.132 \frac{t_m}{c}$	$1.27 \frac{t_m}{c}$	$1.27 \frac{t_m}{c}$
$\Delta' V_a$	0.131	0.130	0.130
Mean line			
	a = 1	a = 0.8	NASA 65
$\frac{\Delta' V_f}{K_f}$	0.25	0.278	0.31

foregoing values in Eq. (11), the pressure coefficient at 60% of the chord, for various combinations of thickness forms and mean lines, becomes those shown in Table 5.

Table 5
Pressure Coefficient at 60% Chord Length on the Suction Side, for Some Combinations of Basic Thickness Forms and Mean Lines

Foil	Mean Line	Formulas
NASA 16	a = 1	$\frac{\Delta p}{q} = \left(1 + 1.132 \frac{t_m}{c} + 0.250 \frac{C_{Lf}}{1 + K_t \frac{t_m}{c}} + 0.131 C_{L\alpha}\right)^2 - 1$
NASA 16	a = 0.8	$\frac{\Delta p}{q} = \left(1 + 1.132 \frac{t_m}{c} + 0.278 \frac{C_{Lf}}{1 + K_t \frac{t_m}{c}} + 0.131 C_{L\alpha}\right)^2 - 1$
NASA 16	NASA 65	$\frac{\Delta p}{q} = \left(1 + 1.132 \frac{t_m}{c} + 0.310 \frac{C_{Lf}}{1 + K_t \frac{t_m}{c}} + 0.131 C_{L\alpha}\right)^2 - 1$
NASA 66 NASA 66M	a = 1	$\frac{\Delta p}{q} = \left(1 + 1.270 \frac{t_m}{c} + 0.250 \frac{C_{Lf}}{1 + K_t \frac{t_m}{c}} + 0.130 C_{L\alpha}\right)^2 - 1$
NASA 66 NASA 66M	a = 0.8	$\frac{\Delta p}{q} = \left(1 + 1.270 \frac{t_m}{c} + 0.278 \frac{C_{Lf}}{1 + K_t \frac{t_m}{c}} + 0.130 C_{L\alpha}\right)^2 - 1$
NASA 66 NASA 66M	NASA 65	$\frac{\Delta p}{q} = \left(1 + 1.270 \frac{t_m}{c} + 0.310 \frac{C_{Lf}}{1 + K_t \frac{t_m}{c}} + 0.130 C_{L\alpha}\right)^2 - 1$

These simple relations represent the cavitation index, which appears in the "incipient cavitation diagrams" referred to before, in a precise, analytical way. At the same time, this analytical solution amplifies and corrects the meaning of the cavitation charts both in that it includes the possibility of realizing lift partially by camber and partially by incidence, and in that the evaluation of the lift coefficient produced by camber takes into adequate account the influence of the thickness.

The same relations show the convenience of realizing a certain amount of lift, that is, 10%, as suggested previously, by incidence, and the remaining amount by camber. Introducing these percentages into the above relations, and also eventually neglecting the term $K_t \; t_m/c$ which causes small differences to arise for thicknesses less than 0.05, the same relations can be further simplified; the first, for instance, becomes:

$$\frac{\Delta p}{q} = \left(1 + 1.132 \; \frac{t_m}{c} + 0.238 \; C_L\right)^2 - 1 \; .$$

The analytical layout also offers the advantage of a direct determination of the minimum chord length required to avoid cavitation, without iterative processes and without further readings of the "charts." If it is desired, the strength requirements may also be introduced directly by means of a specified series of the products $t_m^2 \, c$ for each section, or by means of the appropriate values for the root section.

All this clearly facilitates the preparation of electronic computer programs.

2.3 Chordwise Load and Pressure Distribution

An ideal foil, such as that shown in Fig. 8, without thickness and incidence and cambered according to the mean line a = 1, has a uniform load distribution all along the chord, a constant negative pressure coefficient on the suction side

$$-\frac{\Delta p_b}{q} = 0.5 \; C_{Lf} + (0.25 \; C_{Lf})^2$$

and a constant positive pressure coefficient on the face

$$\frac{\Delta p_f}{q} = 0.5 \; C_{Lf} - (0.25 \; C_{Lf})^2$$

However, when the foil considered is no longer ideal, but thick, the chordwise load distribution still remains more or less constant, but the pressure distribution changes considerably.

Figure 9 shows the pressure distribution on both sides of a section foil at shock free entry conditions, with mean line a = 1, thickness ratio 0.18, and camber ratio 0.05515. This figure clearly reveals that at least from a theoretical point of view and as far as cavitation is concerned it is advisable to load the extremities of an actual section foil more heavily, when hydrodynamically possible. In the inlet area this loading is achieved precisely by realizing a given part

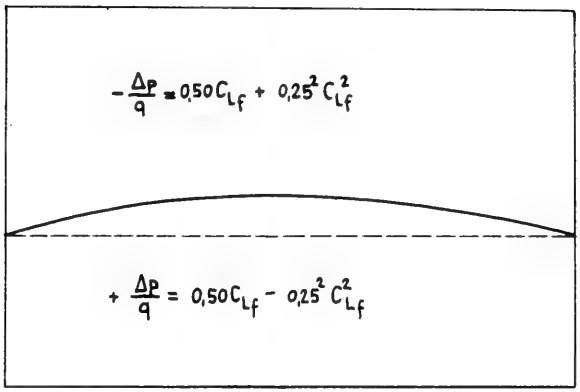

Fig. 8 - Chordwise pressure distribution upon the pressure and suction sides of and ideal foil with a NASA a = 1 mean line

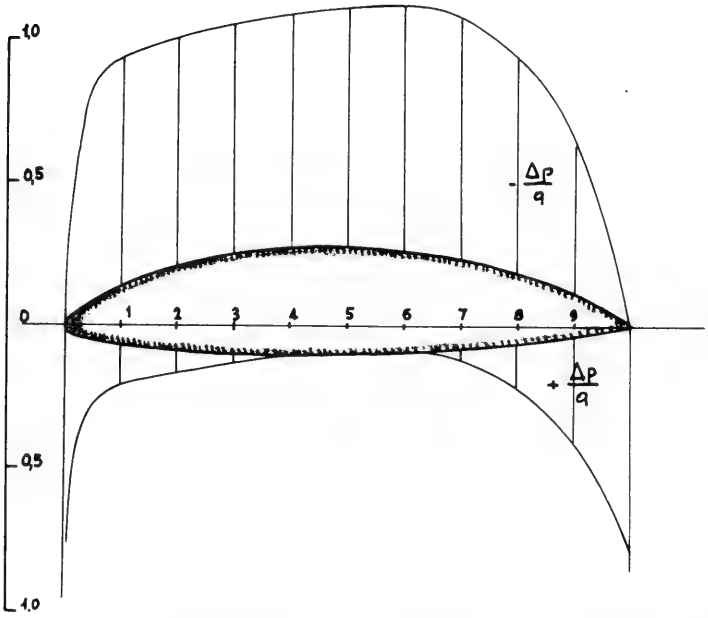

Fig. 9 - Chordwise pressure distribution for a section foil: $t_m/c = 0.18$, a = 1, $C_{Lf} = 1$

of the lift coefficient by incidence, as is shown in Fig. 10, which refers to a profile NASA 16, a = 1, $t_m/c = 0.06$, $C_L = 0.314$, $C_{Lf} = 0.9\, C_L$, $C_{L\alpha} = 0.1\, C_L$.

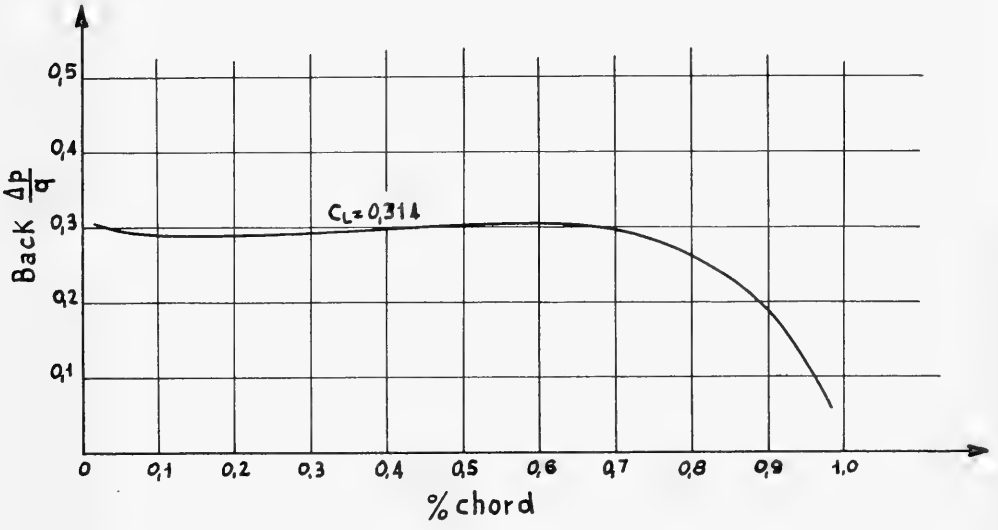

Fig. 10 - Depression distribution on the suction side of a section foil NASA 16 a = 1, $t_m/c = 0.06$, $C_L = 0.314$, $C_{L\alpha} = 0.1\, C_L$, $C_{Lf} = 0.9\, C_L$.

2.4 Performance in Actual Flow

In actual flow the hydrodynamic characteristics of hydrofoils change quite considerably. The experimental data available are rather scarce, doubtful, and poorly correlated. As far as the foils considered in the present study are concerned, these data refer only to experiments in air at a Reynold's number (referring to the chord) between 3 and 9 x 10^6, and with thickness ratio $t_m/c \geq 0.06$, notably larger than the smallest ones used in the design of naval propellers (and which are usually of more interest with regard to cavitation effects).

For this reason, systematic, experimental research in water would be very welcome. Such research should include the two thickness forms NASA 16 and 66 mod, the three mean lines a = 1, a = 0.8, and NASA 65, and should cover a range of thickness ratios from 0.03 to 0.2, while the angle of attack should vary between 0° and 5°.

In the following paragraphs several average values are reported as they resulted out of an examination and interpretation of the experimental data of NASA Report 824. For want of something more precise, these data may be employed in naval propeller design.

(a) *Lift coefficient due to incidence.*

$$\text{Mean line NASA 65} \quad C_{L\alpha} = 6.10\,(1 - 0.15\ t_m/c)\,\alpha$$

$$\text{Mean lines} \begin{cases} a = 1 \\ a = 0.8 \end{cases} \quad C_{L\alpha} = 5.80\,(1 + 0.25\ t_m/c)\,\alpha$$

As can be seen, the thickness effect on the mean line NASA 65 leads in the opposite direction to that on the mean lines a = 1 and a = 0.8.

When the thickness ratio ranges between 3% and 10% of the chord, it can be more easily assumed in both cases that

$$C_{L\alpha} = 6.00\ \alpha = 0.105\ \alpha^0$$

where α and α^0, expressed respectively in radians and degrees, represent the angle of attack with reference to the chord.

(b) *Lift coefficient due to camber.* Designating the lift produced by camber by the symbol $|C_{Lf}|_i$ [as can be deduced from relation (6) for operation in ideal flow], the same coefficient $|C_{Lf}|_r$, for operation in actual flow, can be calculated as follows:

$$|C_{Lf}|_r = 0.75 \quad |C_{Lf}|_i \quad \text{for mean lines} \begin{cases} a = 0.8 \\ \text{NASA 65} \end{cases}$$

$$|C_{Lf}|_r = 0.675 \quad |C_{Lf}|_i \quad \text{for mean line} \quad a = 1.$$

(c) *Zero lift angle of attack.* It can be assumed with sufficient accuracy that

$$\alpha_0 = \frac{|C_{Lf}|_r}{6}$$

in radians.

(d) *Pressure distribution along the surfaces of the foils.* An experimental result obtained with a NASA-16 section foil, a = 1, $t_m/c = 0.06$, and $f_m/c = 0.011$, at shock-free entry, is shown in Fig. 11. The values of the pressure distribution on the surface, as they resulted from experiments, are compared with the theoretical values which were calculated on the basis of the methodology previously discussed, by employing the velocity increments tabulated in NASA Report 824 for several stations along the chord.

The experimental data were measured in a cavitation tunnel, with a test section of 60cm x 60cm, by means of thirty pressure holes drilled at appropriate intervals on the surface of a profile (with a chord of 20cm and a span of 60cm), connected with the same number of mercury manometers. In order to avoid difficulties arising from the effect of finite span and correction for support interference, the span of the foil was made equal to the width of the test section.

The theoretical lift coefficient for this foil, as calculated by integrating the velocity increments along the chord, results at the value of 0.2076, that is, very close to the value 0.208 obtainable by means of relation (6). The experimental value of the lift coefficient, as given by the integration of the measured pressures diagram, closely approaches 0.151.

The loss in lift seems to be largely attributable to the positive pressure fall which occurs all along the face of the foil, but especially in the vicinities of the leading and trailing edges. On the contrary, the depression on the back, for the entire width of the foil, practically matches that calculated theoretically; a fact which could lead to the conclusion that viscosity has little or no influence on this particular aspect of the phenomenon.

The verification of such a result is of obvious importance from the cavitation point of view. In any case the subject needs to be gone into more thoroughly, and this emphasizes the usefulness mentioned earlier of appropriate, systematic research.

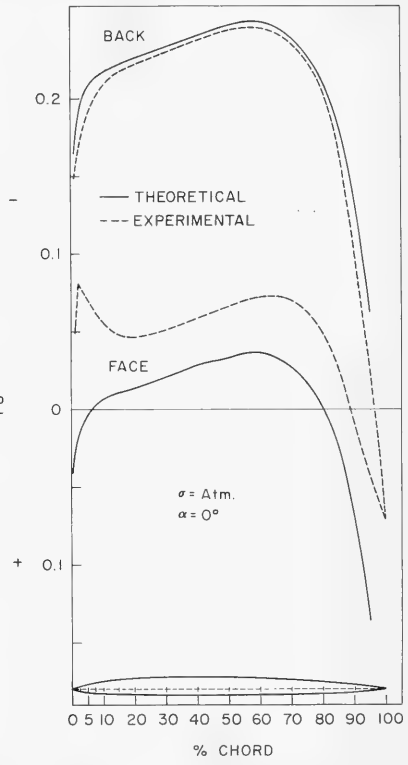

Fig. 11 - NASA 16-206: experimental and theoretical results

It should be noted, though, that during the tests the onset of cavitation always took place, as far as could be seen, at values of the cavitation index 20-25% higher than those evaluated by theory. This could explain the usual practice of reducing the cavitation index by the same percentage both when designing a naval propeller, and when evaluating the results of water tunnel experiments.

However, one should remember the difficulties of establishing the exact moment in which cavitation takes place, either by natural observation or by using stroboscopic light, and one should also remember the error involved in substituting the critical value of the pressure by the vapour pressure at test temperature.

3. EFFECTIVE PERFORMANCE OF THE PROPELLER

3.1 Propeller Models

The difference between the performance of a hydrofoil in ideal fluid and its performance in actual fluid has already been mentioned, and the reduction coefficients 0.675, 0.75, and 0.75 have been suggested for the mean lines $a = 1$, $a = 0.8$, and NASA 65, respectively.

In order to evaluate the accuracy of these coefficients in propeller design and at the same time to measure as far as possible the effect of the blade width (the second cause of difference given in the introduction) an experimental test was carried out using the following models:

case A: A propeller for fast, military craft, with a high value of expanded blade area ratio and a low value of thrust coefficient (Table 6), constructed in three models with identical design data and identical radial thickness distribution, but according to three different geometrical solutions:

E.973 mean line a = 1 lift 90% by camber and 10% by incidence,

E.1065 mean line a = 0.8 lift by camber and by angle of attack associated with the mean line, and

E.1030 mean line NASA 65 lift by camber alone.

Table 6
Design Data of Real Propeller

	Case *A*	Case *B*
T	6500 Kg	146,000 Kg
n	16.28 g/sec	1.83 g/sec.
D	1.10 m	7 m
d_m	0.204 m	1.4 m
z	4	3
H	12.063 m H_2O	17 m H_2O
Calculated Hydrodynamic Data		
V_A	20.56 m/sec	5,684 m/sec
λ	0.3654	0.14101
C_T	0.3097	2.24736
C_{Ti}	0.3337	2.28274
η_i	0.8521	0.621
K_T	0.1603	0.17318
J	1.148	0.443
σ	0.546	9.93

case B: A propeller for cargo boats, with a low value of expanded blade area ratio and a high value of thrust coefficient (Table 6), constructed, as case *A*, with identical design data and identical radial thickness distribution, but according to the three solutions:

E.1031 mean line a = 1 lift by camber alone,

E.1066 mean line a = 0.8 lift by camber and by angle of attack associated with the mean line,

E.997 mean line NASA 65 lift by camber alone.

case C:

E.997 as above (basic model)

E.998 camber reduced by 50% with reference to the basic model,

E.999 camber increased by 50% with reference to the basic model.

The mean line NASA 65 was adopted for each of the three models, and the thickness distribution and chord length were identical in each case.

The aim of investigations *A* and *B* was to check the effect of the mean line and of the blade width; the aim of *C* was to emphasize the effect of the camber. The hydrodynamic calculation for cases *A* and *B* was carried out on the basis of the vortex theory, involving, in particular:

optimum circulation distribution;

ideal efficiency as illustrated by Shultz in the DTMB Report 1148;

Goldstein factors reported by Tachmindji in the DTMB Report 1141;

theoretical lift coefficients and pressure coefficients on the suction side as for the numerical expressions and coefficients referred to in Secs. 2.1 and 2.2;

real fluid reduction coefficient 0.75 for all mean lines;

lift coefficient for angel of attack $C_{L\alpha} = 0.1\alpha^0$;

corrections for camber and angle of attack according to Ludwieg-Ginzel.

The thickness distribution NASA 16 was adopted for all the models. Theoretical performances for models E.998 and E.999 were determined by means of a "reverse calculation"; this allows an evaluation of the hydrodynamic characteristics to be made for any desired advance coefficient (in this case that of the basic model E.997) when the geometry of the propeller is given in its entirety.

Such a "reverse procedure" is based upon the equality of the conditions imposed by the hydrodynamic calculation, which can be expressed, section by section, by the well-known relation

$$C_L = \frac{4\pi D}{z\,c} \times \chi \sin(\beta_i) \tan(\beta_i - \beta)$$

and upon the equality of the conditions imposed by the geometry of each single section, which, according to the notations and relations presented in the preceding paragraphs, are expressed by

$$C_L = 0.75\, K_f \frac{f_m}{c}\left(1 + K_t \frac{t_m}{c}\right) + 6.00\,\alpha\ ,$$

where 0.75 is the coefficient of reduction from perfect to viscous fluid.

The equation of equality is an implicit function only of the hydrodynamic angle of advance β_i, which can be evaluated for each separate section together with the ideal efficiency η_i. In this way it is possible to deduce the values of the thrust T_i, of the ideal moment Q_i, and of the corresponding quantities in actual fluid; the latter with the introduction of an appropriate value of the drag-lift ratio ϵ (in this case equal to 0.035). Table 6 gives the design and the calculated hydrodynamic data for cases *A* and *B*; Table 7 for the three models in case *C*.

Table 7
Camber and Pitch Ratios of Models
E.997 (Basic)-E.998-E.999

Case *C*				
X	$f_{g/c}$			P/D
	E.997	E.998	E.999	
0.2	0.0277	0.0138	0.0414	0.7131
0.3	0.0470	0.0235	0.0705	
0.4	0.0542	0.0271	0.0813	
0.5	0.0545	0.0272	0.0816	
0.6	0.0514	0.0257	0.0771	
0.7	0.0460	0.0230	0.0690	
0.8	0.0394	0.0197	0.0591	
0.9	0.0320	0.0160	0.0480	

The tolerances of the models resulted as follows:

mean pitch	± 0.3%
thickness on inner radii	± 1.8%
thickness on outer radii	± 0.9%

3.2 Experimental Results

The final results of the tests carried out in a cavitation tunnel, at constant velocity and variable revolutions, are reported in Table 8. Experimental data have been corrected for wall effect according to the formula

$$\frac{V}{V_E} = 1 + \frac{a}{2}\left(\sqrt{1 + C_T - 1}\right),$$

in which

V = velocity of the water in the tunnel, measured by a venturimeter;

V_E = advance velocity of the propeller in open water at the same thrust constant C_T;

a = propeller disk area/tunnel test section area.

3.3 Comments and Conclusions

An examination of the results presented in Table 8 gives rise to the following comments and conclusions:

(a) The actual performance of propellers with a low expanded blade area ratio (equal to or less than 0.45) matches the expected data very well when the mean lines a = 0.8 and NASA 65 are adopted (propeller models E.1066, E.997, E.998 and E.999), and when the hydrofoil coefficients suggested in Sec. 2. are used.

When the mean line a = 1 is employed, performance is about 10% lower. This reconfirms the advisability, already mentioned in previous pages, of adopting a reduction coefficient equal to 0.675 for viscous flow (instead of 0.75 as used in designing the models in question) when employing the mean line a = 1.

(b) Propellers with a high expanded blade area ratio are subject to a further drop in performance (valuable at 10% when $A_D/A_0 > 1.00$). Such a conclusion has been reached by other authors, and the problem has given rise to many thorough, theoretical and experimental investigations (8), (9), (10), (11).

Table 8
Results

Case	A			B			C		
Propeller	E.973	E.1065	E.1030	E.1031	E.1066	E.997	E.997 (Basic)	E.998	E.999
Hydrofoil	NASA 16	NASA 16	NASA 16	NASA 16	NASA 16	NASA 16	NASA 16	NASA 16	NASA 16
Mean line	a = 1	a = 0.8	NASA 65	a = 1	a = 0.8	NASA 65	NASA 65	NASA 65	NASA 65
A_E/A_0	1.00	1.06	1.11	0.36	0.38	0.41	0.41	0.41	0.41
z	4	4	4	3	3	3	3	3	3
C_T des.	0.3097	0.3097	0.3097	2.247	2.247	2.247	2.247	1.7725	2.7508
P/D	1.359	1.355	1.347	0.713	0.733	0.713	0.713	0.713	0.713
f_m/c 0.7R	0.0148	0.0178	0.0198	0.0358	0.0429	0.0460	0.0460	0.0230	0.0690
Load distribution	90% 10%	$f + \alpha i$	f	f	$f + \alpha i$	f	f	$f + \alpha i$	$f + \alpha i$
σ des.	0.546	0.546	0.546	9.93	9.93	9.93	9.93	9.93	9.93
ϵ des.	0.0800	0.0860	0.0910	0.0280	0.0310	0.0345	0.0345	0.0345	0.0345
J des.	1.148	1.148	1.148	0.443	0.443	0.443	0.443	0.443	0.443
K_T des.	0.160	0.160	0.160	0.173	0.173	0.173	0.173	0.0366	0.212
K_T exp.	0.130	0.145	0.145	0.153	0.180	0.179	0.179	0.138	0.215
ΔK_T	-19%	-9.5%	-9.5%	-11.5%	+4%	+3.5%	+3.5%	+1.5%	+1.4%
η_e des.	0.698	0.696	0.688	0.567	0.562	0.555	0.555	0.596	0.518
η_e exp.	0.690	0.692	0.692	0.566	0.560	0.553	0.553	0.583	0.487
$\Delta\eta_e$	-0.3%	-0.6%	+0.6%	-0.18%	-0.35%	-0.54%	-0.54%	-2.7%	-6%
Tip vortex	Yes	Yes	Yes	Yes	Yes	Yes	Yes	Yes	Yes
Hub vortex	Yes	Yes	Yes	Yes	Yes	Yes	Yes	Yes	Yes
Back cavitation	No	No	No	No	No	No	No	No	Yes Face
R_N {0.7R J des.	1.95×10^6	2.1×10^6	2.2×10^6	1.46×10^6	1.57×10^6	1.65×10^6	1.65×10^6	1.65×10^6	1.65×10^6

Rough approximations and the inadequacy of the Ludwieg-Ginzel method of correcting flow curvature (based only on the induced velocity at one point half way along the chord) account for the differences encountered.

(c) The preceding deductions and in general the reliability of the procedure followed are supported by the reverse calculation, even though the experimental results contain unavoidable inaccuracies of measurement and the reverse calculation was used only in connection with nonoptimum free-running propellers.

REFERENCES

1. Castagneto, E., Maioli, P.G., Servello, A., and Spinelli, F.S., "La Conservazione Delle Eliche Navali," La Tecnica Italiana, March 1968

2. Johnsson, C.A., "Comparison of Propeller Design Techniques," Fourth Symposium on Naval Hydrodynamics, Aug. 1962, Washington, D.C.

3. Silvestro, A., "Considerazioni sui Profili Alari NASA per Determinare Alcune Formule di uso Pratico," Note di Ingegneria Navale, Fasc. LXII° del Ministero Difesa Marina

4. Van Manen, J.D., "Fundamentals of Ship Resistance and Propulsion," Publication of N.S.M.B. No. 132

5. Saunders, H.E., "Hydrodynamics in Ship Design," Part II SNAME, 1957

6. Eckhardt, M.K., and Morgan, W.B., "A Propeller Design Method," Trans. SNAME, 63, 1955

7. Morgan, W.B., and Milam, A.B., "Section Moduli and Incipient Cavitation Diagrams for a Number of NACA Sections," D.T.M.B. Report 1177, October 1957

8. Pien, P.C., "The Calculation of Marine Propellers Based on Lifting-Surface Theory," J. Ship Res., Sept. 1961

9. Cheng, H.M., "Hydrodynamic Aspect of Propeller Design Based on Lifting Surface Theory-Uniform Chordwise Distribution," Part I, D.T.M.B. Report 1802, Sept. 1964

10. Cheng, H.M., "Hydrodynamic Aspect of Propeller Design Based on Lifting-Surface Theory-Arbitrary Chordwise Load Distribution," Part II, D.T.M.B. Report 1803, June 1965

11. Murray, M.T., "Propeller Design and Analysis by Lifting-Surface Theory," Intern. Ship. Progr. 160

* * *

DISCUSSION

Wm. B. Morgan
Naval Ship Research and Development Center
Washington, D.C.

I would like to emphasize the authors' remarks concerning the NACA a = 1.0 and the NACA a = 0.8 mean lines. It is our experience at NSRDC that the theory for design of moderately loaded propellers is *adequate* provided that certain important steps are made.

(1) The NACA a = 0.8 load distribution is used and not the constant load distribution, because due to viscosity the a = 1.0 distribution cannot be realized in practice.

(2) Lifting-surface corrections from modern computer programs are used. These correction factors must include a camber correction, an ideal angle of attack correction, an angle correction for skew (if used), and an angle of attack correction for thickness.

A paper presenting extensive tables of correction factors will be presented at the 1968 Annual Meeting of the Society of Naval Architects and Marine Engineers.

* * *

DISCUSSION

C. Kruppa
Technische Universität
Berlin, Germany

I would like to supplement the data on foil section characteristics presented by the authors, and refer to some hitherto unpublished work which I carried out in the Vosper cavitation tunnel (Portsmouth, England), some years ago. The main scope of this work was to assess the cavitation-free angle of attack (or lift coefficient) ranges of two-dimensional foil sections, consisting of elliptic-parabolic thickness distributions, cambered with the NACA a = 1.0 mean line. In total, eight different foil sections were tested, covering thickness-chord ratios $0.03 \leq t/c \leq 0.12$ and design lift coefficients $0 \leq c_{L_i} \leq 0.56$. The work was sponsored by the British Admiralty. Copies of the report should be obtainable through AEW-Haslar by referring to Vosper Report No. 115 ("Methodical Cavitation Tests on Blade Sections—Three Component Factors and Cavitation Patterns").

The experimental results obtained in the cavitation tunnel were compared with theoretical results, using the superposition method referred to by the authors as well as the rigorous method of conformal mapping.

The experimental data showed indeed that for the NACA a = 1.0 mean line, viscous flow effects resulted in an 25% shift in zero lift angle of attack, towards smaller values. If satisfactory agreement between theoretical predictions of cavitation-free angle of attack ranges and experimental data was to be obtained, the viscous flow corrections had to be incorporated both in camber and angle of attack.

At present, an experimental program has been started in the cavitation-tunnel laboratory of Berlin Technical University where the cavitation-free angle of attack ranges are to be assessed for oscillating foil sections. The latter consist of NACA 16 thickness distributions cambered with the a = 0.8 mean line. In total, 25 different foil sections will be tested in a two-dimensional test section, over a wide range of cavitation numbers and reduced frequencies, covering thickness-chord ratios $0.03 \leq t/c \leq 0.18$ and design lift coefficients $0 \leq c_{Li} \leq 0.5$.

* * *

DISCUSSION

C.-A. Johnsson
Swedish State Shipbuilding Experimental Tank
Göteborg, Sweden

I should like to support Dr. Morgan when he claims that the lifting-surface theory in its present stage is adequate for design purposes for conventional propellers in most cases. In his answer to Dr. Morgan, Dr. Castagneto refers to some comparisons between calculations and experiments, reported recently by me, where he has found, in some cases, very large differences between the calculated number of revolutions and those obtained in open-water tests. Regarding those two cases, where such discrepancies could be noticed, it can be clearly seen in the report that they are characterized by very small values of the advance ratio J. Thus, the reason for the discrepancies is most likely that these cases are outside the range within which the theory of moderately loaded propellers can be applied. As this range is difficult to determine accurately enough, low J values have to be considered with care, which, of course, is a limitation of the applicability of the theory. Bearing this in mind, however, the lifting-surface theory seems to be adequate for design purposes as long as the NACA a = 0.8 mean line is used. Very good agreement between calculated and measured number of revolutions can be expected without adding any empirical corrections, provided the thickness effect is included.

* * *

REPLY TO DISCUSSION

E. Castagneto and P.G. Maioli

The authors would like to thank all those who took part in the discussion for their precious contributions.

The main aim of our paper was to present simple and practical mathematical relations [formula (6) and Table 5], which would permit the evaluation of some dynamic characteristics of hydrofoils as applied to naval propellers in ideal flow. At the same time the paper emphasized the necessity of using suitable coefficients to take the effect of viscous flow into account.

With regard to the hydrodynamic characteristics of hydrofoils in actual flow, we are very glad to learn from Dr. Kruppa's communication that something has already been done (at the Vosper cavitation tunnel), and is being done at present (at the Berlin Technical University), to fill in the gap of which we complained in our paper and which interests not only propellers but also other design particulars such as rudders, stabilizers, etc.

Dr. Morgan and Dr. Johnnson have emphasized that the design theory of moderately loaded propellers operating under incipient cavitation conditions can nowadays be considered as adequate, provided that NACA = 0.8 load distribution and lifting-surface corrections are used. The authors take note of this with much satisfaction. Undoubtedly it represents an important achievement, even if the problem still remains open for other types of load distribution, and certainly it justifies the further research which is being done on the dynamics of hydrofoils in viscous flow, the results of which, once obtained, we hope can be presented in such a plain and simple way as to be easily utilizable by all naval designers, whether of propellers or not.

* * *

WATERJET PROPULSION

Virgil E. Johnson, Jr.
Hydronautics, Inc.
Laurel, Maryland

INTRODUCTION

Although waterjet propulsion is certainly not a new type of propulsion, it has become of increasing interest in the past decade. In the late 1950's, waterjet propulsion received considerable publicity as the method of propulsion for sports craft of the future—probably because the glamour of *jet*-propelled aircraft appealed to the small sports craft owner. Most of this type of appeal has worn off now, and the rush to waterjet-propelled small sports craft has not yet materialized. The facts are that at the present speed of most small craft (35 knots or less), the efficiency of the conventional screw propeller is considerably higher than that achievable by waterjet systems. Consequently, except in those cases where very shallow craft or a completely protected impeller is required (regardless of efficiency), waterjet propulsion is not likely to take over in the small sports craft field.

At higher speeds, say, greater than 45 knots, the conventional screw propeller suffers because of cavitation. The substitute for the conventional screw propeller at these higher speeds is the "supercavitating" propeller. Such propellers have been successfully designed and built for numbers of planing and hydrofoil craft in the speed range less than 60 knots. Much higher speeds are achieved in racing craft using supercavitating propellers.

The great increase in interest in waterjet propulsion in the past five years has been brought about because of the need to propel high-speed craft (45-100 knots) such as hydrofoils and surface-effect ships. Although the supercavitating propeller is a logical candidate for propulsion of these higher-speed craft, the supercavitating propeller does experience serious performance degradation at low advance ratios and thus has difficulty producing the large thrust required at hump speed. In those configurations using a "Z" drive, the bevel gears required in the pod to supply power to the supercavitating propeller tax the state of the gear design art.

Waterjet propulsion offers a substitute for supercavitating propellers at high speeds. Waterjet propulsion systems eliminate the gearbox problem, and it should be possible to design waterjet systems with "hump" thrust characteristics superior to those of supercavitating propellers. Of course, it is generally nature's way that solutions to existing problems introduce new problems—so it is with waterjet propulsion. This paper presents no new information related to waterjet propulsion, but rather highlights the present state of the art. For a more comprehensive state-of-the-art report, including an extensive and up to date bibliography, see Ref. (1).

EFFICIENCY

In Ref. (2), expressions are derived for the efficiency of waterjet propulsion systems strictly on the basis of momentum theory. No account is taken of (1) the wake inflow to the inlet (inflow is assumed to be uniform at the velocity of the craft), (2) the effect of the inlet on the resistance of the craft, and (3) the additional drag of the craft that may be attributed to the additional weight requirements of a waterjet system. Typical waterjet systems are schematically shown in Fig. 1.

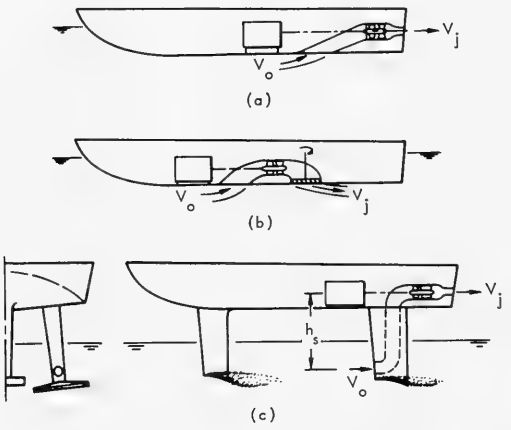

Fig. 1 - Geometric configuration of waterjets

As derived in Ref. (2), the ratio of propulsive efficiency η to pump efficiency η_p is presented in Fig. 2 as a function of the parameter $H^* = 2gH/V_0^2$, where H is the head added by the pump and V_0 is the forward speed of the craft. The various curves shown in Fig. 2 are for different values of the parameter K, where the internal losses h_e (inlet, internal diffusion, ducting and nozzle) are defined as $h_e = K V_0^2/2g$. The important point to note from Fig. 2 is that an optimum value for H^* exists for each value of K.

Physically, Fig. 2, points out that for a given value of K, the efficiency is less than optimum for $H^* < H^*_{opt}$, because excess energy is used in overcoming the internal losses; whereas operation at values of $H^* > H^*_{opt}$ results in decreased efficiency because of excess kinetic energy expended in the jet. It is important to recognize that operation at increasing values of H^* means increased jet velocity and consequently, for a given thrust requirement, decreased discharge. Thus, operation at higher values of H^* means smaller inlets, ducts, pumps, and nozzles, and thus less weight for a given thrust. This fact, as is pointed out in several Refs. (1 - 4), generally leads the designer to select $H^* > H^*_{opt}$ in order to achieve a system which requires less power to propel a given payload, even though the "momentum" efficiency as presented in Fig. 2 is less than optimum.

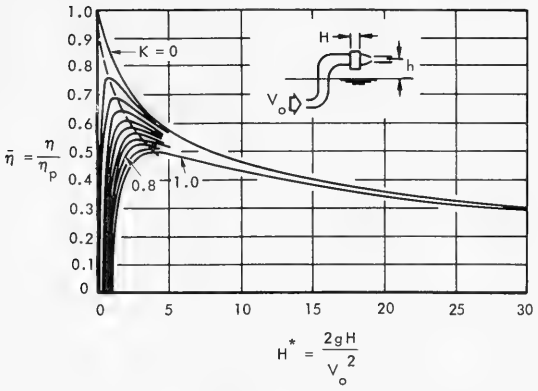

Fig. 2 - Hydrodynamic characteristics of waterjet propulsion systems

In fact, the final or "best" design of a waterjet propulsion system is achieved only after a very sophisticated examination of all the factors which influence achieving maximum payload/unit horsepower as payload/unit cost for a prescribed mission. This inability to compare waterjet systems with conventional or supercavitating propellers on the simple basis of η or even P.C. is a serious difficulty that has not yet been universally resolved. It is important that the lack of a simple comparitive "figure of merit" does not exist; however, those who design systems for a specific requirement do recognize that it is indeed "cost effectiveness" that selects the superior system. The problem is discussed in some detail in Refs. (1) and (3), and the general problem is treated further in the following paragraphs.

Figure 3 illustrates the important factors the designer must treat in establishing an optimum design. These factors are: (1) the influence of the wake approaching the inlet, (2) the effect of the inlet and fairing on the "bare hull" resistance of the craft, and (3) the machinery, structure, fuel, and propulsor weight are all dependent on the actual power required for the ship's mission, and this power in turn depends on minimizing these weights. Clearly many engineering compromises are required to achieve a final "optimum" design. An example of the results of a study (Ref. (4)), which attempts to compare various propulsion systems over the speed range up to 100 knots, is presented in Fig. 4. The value of P.C. presented as the ordinate does take into account most of the factors previously discussed. Although the results presented in Fig. 4 are generally comprehensive, and the results of such a study are extremely valuable in pointing out possibilities not previously appreciated, much more detailed studies are required for a specific mission to definitely establish the superiority of one propulsion system over another.

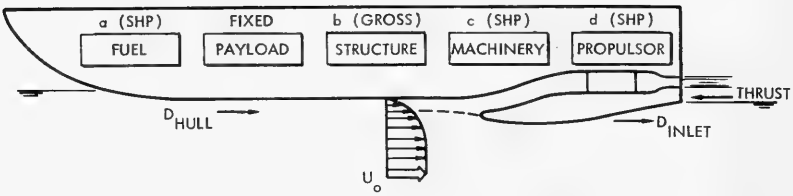

Fig. 3 - Factors influencing optimum propulsor selection

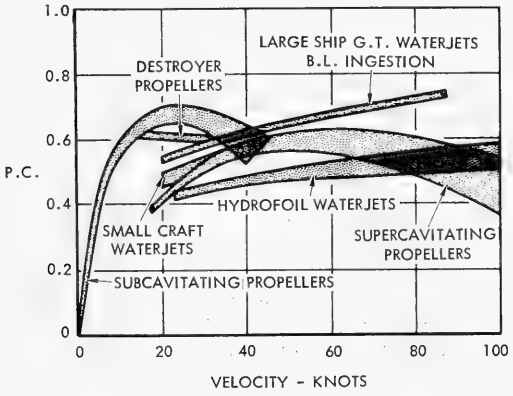

Fig. 4 - Design propulsor comparisons (Ref. 4)

INLETS

The two most important problem areas in the design of water-jet propulsion systems are the inlet and the pump.

The inlet must be designed to operate cavitation-free at cruise speed. Such cavitation-free operation in uniform, zero-incidence operation should be straightforward, but the inflow is generally nonuniform and there is always some incidence as the craft moves through rough water or maneuvers even in smooth water. Furthermore, the optimum flow rate through the system varies with the speed and thrust requirements of the boat, so that the inlet must be capable of operating over a wide range of inlet velocity/forward speed ratios or must be designed with special features, such as variable area. There is, at present, a great lack of experimental data concerned with the cavitation characteristics and efficiency of head recovery of inlets suitable for waterjet propulsion systems. Reference (5) does present a procedure for the design of two-dimensional, base-vented inlets for various inlet velocity ratios.

PUMPS

The principal requirements of pumps for waterjet propulsion systems are that they be cavitation-free and light-weight. As usual, these requirements are not compatible.

The most severe conditions for cavitation-free operation exist at the low-speed "hump" situation. At this condition large thrusts are demanded at low suction heads. If the pump is designed to operate nearly cavitation-free at the hump condition, the additional suction head obtained from ram recovery is more than adequate to prevent pump cavitation at cruise.

A detailed discussion of the pump selection problem is given in Ref. (2). Figure 5 (taken from Ref. (2)) illustrates the type of pump required for a typical hydrofoil craft as a function of speed and size of craft (as indicated by the static lift parameter h). This figure assumes that the pump is single-stage and is noncavitating at the hump speed (taken as one-half the cruise speed). The ordinate of Fig. 5 is the specific speed $n_s = \text{rpm}(\text{gpm})^{1/2}\,(\text{ft})^{3/4}$. This parameter is indicative of the type of pump required. For example, Fig. 5 illustrates that, at high speeds, the pumps should be centrifugal.

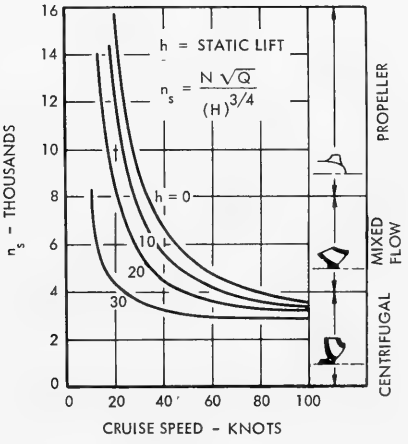

Fig. 5 - Single-stage non-cavitating pump types for waterjet propulsion systems

It is also explained in Ref. (2) that pump sizes can be reduced for a given requirement by dividing the total discharge required into a number of parallel units. Double-suction centrifugal pumps are examples of a simple division of the total flow into two equal parts. Figure 6 (taken from Ref. (2)) illustrates the use of multiple, parallel, double-suction, centrifugal pumps. The Boeing Company has utilized this scheme in the design of the pumps for the U.S. Navy Patrol Craft "Tucumcari" (Fig. 7), shown in Fig. 8 prior to installation in the craft.

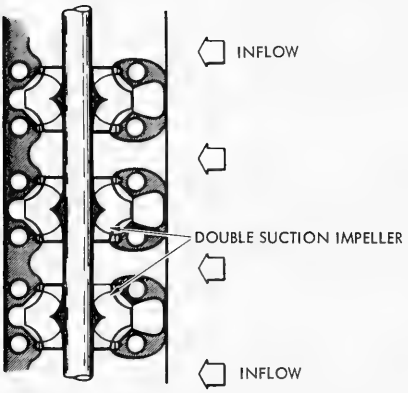

Fig. 6 - Multiple impeller double-suction pump

Fig. 7 - The waterjet-propelled hydrofoil craft Tucumcari (designed and constructed by the Boeing Company for the U.S. Navy)

Another approach to achieving light-weight pumps has been described in Ref. (3). In this approach, very-high-solidity axial or mixed flow pumps are proposed and, in fact, have been tested and operated. The pumps generally operate with rather severe cavitation at the hump condition, but Ref. (4) suggests that, by properly designing the rotor, cavitation damage can be alleviated. An example of the high-solidity rotor is shown in Fig. 9. Figure 10 is a photograph

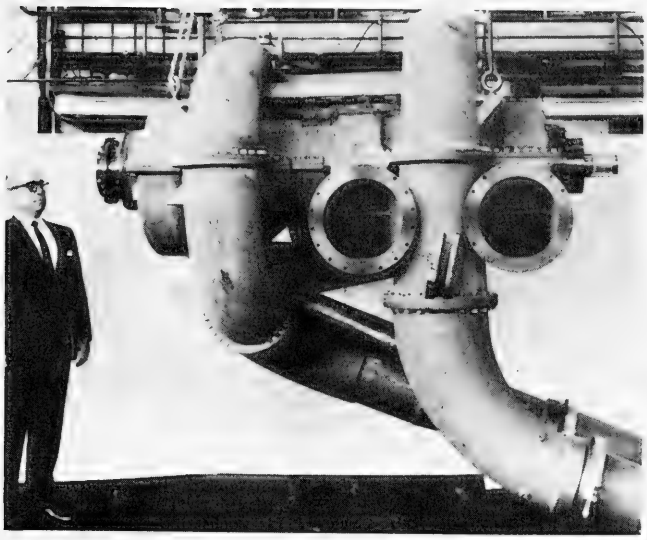

Fig. 8 - Parallel double suction pumps used in the Tucumcari

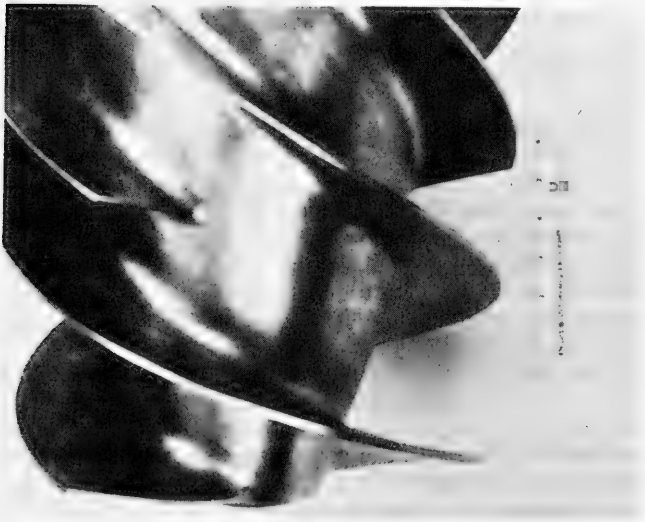

Fig. 9 - High-solidity rotor used in the Pratt and Whitney waterjet system Sea Jet-6

Fig. 10 - The planing craft Thunderbird propelled by the Pratt and Whitney Sea Jet-6 waterjet system

of the Pratt and Whitney planing craft "Thunderbird," propelled with a waterjet system using the high solidity-rotor.

TEST APPARATUS FOR WATERJET SYSTEMS

The "physics" of waterjet propulsion are well understood. No new theoretical analyses other than those of an engineering nature are required. Further development of optimum systems must be made through model and full-scale experimentation. An example of such a model test and the experimental apparatus used is given in Ref. (6). The tests described in Ref. (6) were carried out in the Hydronautics, Inc. High-Speed Channel. The test rig is shown schematically in Fig. 11. The entire inlet-diffuser-pump-nozzle combination was supported as an isolated section of the tunnel roof. This section was supported on linear bearings, so as to be free in the direction of flow. Power was supplied to the pump through a thrust-torque dynamometer so that thrust on the entire system could be measured along with the power supplied. The characteristics of the waterjet system were obtained for a variety of forward speeds, pump rpm, jet velocities, and discharges. Since the facility has a variable pressure capability, the effect of cavitation number may also be readily studied. Experiments with the inlet closed provided tares for the thrust produced and velocity surveys forward of the inlet and within the jet, provided deduced measurements of the thrust breakdown; that is, drag added by the inlet. Complete details of the studies carried out are presented in Ref. (5).

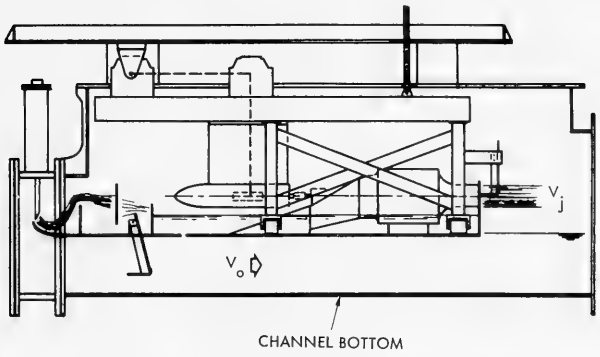

Fig. 11 - Experimental apparatus for testing waterjet systems in the hydronautics high-speed channel

CONCLUDING REMARKS

In conclusion, it may be stated that, particularly at high speeds, waterjet propulsion promises to be competitive with the supercavitating propeller. However, before the promise is fulfilled, considerable work remains to be done. This work is principally engineering design and experimental development. The most urgent research needs are:

(1) Light-weight cavitation-free pumps, including the influence of nonuniform inflow.

(2) Inlet hydrodynamics, including nonzero incidence:

a. boundary-layer ingestion

b. ram recovery

c. external drag

d. cavitation characteristics

e. air ingestion

f. off-design performance—variable area.

ACKNOWLEDGMENTS

The author gratefully acknowledges the provision of Figs. 7 and 8 by C. T. Ray of the Boeing Co. and Figs. 9 and 10 by L. Arcand of the Pratt and Whitney Co.

REFERENCES

1. Brandau, John H., "Aspects of Performance Evaluation of Waterjet Propulsion Systems and A Critical Review of The State-of-the-Art," Journal of Hydronautics (AIAA), April 1968.

2. Johnson, V.E., Jr., "Waterjet Propulsion for High-Speed Hydrofoil Craft," AIAA, Journal of Aircraft, March-April 1966.

3. Traskel, J., and Beck, W.E., "Waterjet Propulsion for Marine Vehicles," AIAA Journal of Aircraft, March-April 1966.

4. Arcand, L., and Comolli, C.R., "Waterjet Propulsion for High-Speed Ships," AIAA/SNAME Advanced Marine Vehicles Meeting, Paper No. 67-350, May 1967.

5. Hsieh, T., "Linearized Theory for a Two-Dimensional, Base-Vented Strut with an Inlet in the Leading Edge," Hydronautics, Inc. Technical Report 463-8, Nov. 1966.

6. Contractor, D.C., "Experimental Investigation of a Water Jet Propulsion System for Shallow Draft Boats," Hydronautics, Inc. Technical Report 516-a, May 1966.

* * *

DISCUSSION

Pier Giacomo Maioli and Giovanni Venturini
Ministero Difesa Marina
Rome, Italy

In a recent paper we have prepared with Cdr. Maioli, we have tried to work out an expression of what we called "total propulsive efficiency," defined as the ratio of the effective horsepower of a "basic" hull and the brake power of the primary mover. The basic hull is an ideal hull, complete in every part with the exception of its propulsive devices and those parts which are connected to the propulsive devices.

If the missing parts are added, though the value of design speed is kept the same, hull resistance increases, both because of the increase in weight and because of the presence of additional elements in the water.

In this way external efficiency may be defined as the ratio between the resistance of the basic hull and the resistance of the complete hull.

Moreover, if we define as internal efficiency the ratio between the ideal and the real head of the pump, the total propulsive efficiency assumes the following general expression:

$$\eta_T = \eta_{ideal} \cdot \eta_{internal} \cdot \eta_{pump} \cdot \eta_{external} ,$$

where, for the free jet,

$$\eta_i = \frac{2}{1 + r} ,$$

$$\eta_{int} = \frac{r^2 - 1}{r^2(1 + K_u) + (K_i - 1) + \Sigma K \beta_i^2 + 2\frac{ghu}{V_0^2}} ,$$

$$\eta_p = \text{constant} ,$$

$$\eta_{ext} = \frac{T_B}{T} ,$$

while for the jet on wake,

$$\eta_i = \frac{2(r - \chi_i)}{r^2 - \chi_2} ,$$

$$\eta_{int} = \frac{r^2 - \chi_2}{r^2(1 + K_u) + (K_i - \chi_2) + \Sigma \beta_i^2 + 2\frac{ghu}{V_0^2}} = \eta_p = \eta_{ext} .$$

In the above equations we have assumed

$$\Delta_p = B \cdot Q \text{ and } T - T_B = \Delta_c \cdot \epsilon + \Delta_p \cdot \epsilon + \frac{1}{2} \rho A_i V_0^2 C_D$$

and we use the following symbols:

V_0 = design speed

V_i = speed at the inlet

V_u = speed at the nozzle. rel. V_0

r = V_u/V_0

K_i = free-stream head loss coefficient, rel. V_0

K_u = outlet head loss coefficient, rel. V_u

ΣK = sum of suction duct head loss coefficient, rel. V_i

β_i = V_i/V_0

h_u = elevation of the nozzle

T = total thrust at design speed

T_B = basic thrust at design speed

A_i = inlet area

C_0 = resistance coefficient

Q = flow rate

B = constant for the weight of the pump

R = range

F_c = specific fuel consumption

L_c = duct length

ω_0 = correlation factor

Δ_p = weight of the pump

Δ_A = weight of propulsion device (wet) and its installation

ϵ = any parameter able to express resistance per unit displacement weight, as D/Δ or D/L

Δ_n = weight at disposal for optimization

$\Delta'_n = \Delta_n + \Delta_u$

As you can see, two cases are considered above: the free jet, that is, the jet the inlet of which does not lie in the boundary layer, and the jet on wake, that is, the jet the inlet of which does lie in the boundary layer.

The effect of mounting the propulsion device on board is expressed by the term $T-T_b$, which may be divided into three parts, the first of which considers the effect of weight increase, the second the effect of additional elements in the water, and the third the effect borne on resistance by a particular weight, that is, the pump.

For the subsequent elaboration of the basic formulas we have considered the weight of the pump as a linear function of the flow rate. This, of course, is not really the case, as the weight of the pump depends on several different elements, as it is well known. But if we calculate the value of the constant B, having in mind a particular type of pump the flow rate of which lies at some point between 70% and 140% of the flow rate of the actual design, the above-said assumption may hold good with sufficient accuracy.

In the optimization process two methods may be used, for we can either (see Table A1):

(i) choose a value of the inlet area and so accept an established amount of external losses, thereby minimizing the sum of E + U + I; or

(ii) choose a value of the inlet velocity ratio and so accept an established amount of internal losses. In this case we minimize the sum of E + U + P.

Table A1
Optimization Procedures

E = residual jet energy

I = energy due to the internal losses in suction duct

U = energy due to the internal losses in discharge duct

P = energy due to the parasitic drag

Total thrust method	Basic thrust method
A_i = constant $P\sim$ = constant β_i = variable $\beta_i^2 = \left(\frac{T}{\rho A_i V_0^2 (r - X_1)}\right)^2$ The sum E + U + I is minimized	β_i = constant $I\sim$ = constant A_i = variable The sum E + U + P is minized
How the value of the optimum velocity ratio may be found	
(a) *Prefixed displacement* Minimum Power directly Maximum Payload directly Maximum Range iterative process Fuel Economy iterative process	(a) *Prefixed displacement* Minimum Power directly Maximum Payload directly Maximum Range directly Fuel Economy directly
(b) *No prefixed displacement* Minimum Power iterative process Maximum Payload iterative process Maximum Range iterative process Fuel Economy iterative process	(b) *No prefixed displacement* Minimum Power directly Maximum Payload directly Maximum Range iterative process Fuel Economy iterative process

The optimization procedures can be carried out with different objectives in mind, that is, either the minimum power, the maximum payload with a fixed range, the maximum range with a fixed payload, or the best utilization of fuel per mile.

If the above-mentioned assumptions are made, the value of the optimum velocity ratio can be found either directly or by means of an iterative process. We have been able to derive it directly in the cases illustrated in Table A1 (see Table A2).

The formulas are valid for all cases of free jets. In the case of the jet on wake they are valid only if χ_1 and χ_2 are considered, as an approximation, as independent of the inlet area or the inlet velocity ratio.

Table A2
Direct Evaluation of the Optimum Velocity Ratio

Formulas	Value of the Constants
A. *Total thrust method — prefixed displacement*	$C = K_i + 1 + \Sigma k\beta_i^2 + \dfrac{2gh_u}{V_0^2}$
Minimum power	$C_2 = \dfrac{2gh_u}{V_0^2} - (\chi_2 - K_i)$
$r_{opt} = \chi_1 + \sqrt{\dfrac{\chi_1^2(1+K_u) + C_2\sqrt{\left[\chi_1^2(1+K_u) + C_2\right]^2 + 12C_3(1+K_u)}}{2(1+K_u)}}$	$C_3 = \Sigma K\left(\dfrac{T}{\rho A_i V_0^2}\right)^2$
Maximum payload	$C_4 = (\rho g A_i L_c \omega_0)\,\epsilon + \dfrac{1}{2}\rho C_D A_i V_0^2$
$r_{opt} = \chi_1 + \sqrt{\dfrac{\chi_1^2(1+K_u) + C_2 + C_5\sqrt{\left[\chi_1^2(1+K_u) + C_2 + C_5\right]^2 + 12C_3(1+K_u)}}{2(1+K_u)}}$	$C_5 = \dfrac{2\eta_p B}{\rho V_0 R F_c}$
B. *Basic thrust method — Prefixed displacement*	$C_6 = \chi_1 + \dfrac{\rho L_c \omega_0 \epsilon}{\beta_i V_0^2} + \dfrac{B\epsilon}{\rho V_0} + \dfrac{1}{2}\dfrac{C_D}{\beta_i}$
Minimum power	$\bar{C}_6 = \chi_1 + \dfrac{1}{2}\dfrac{C_D}{\beta_i}$
$r_{opt} = \bar{C}_6 + \sqrt{\bar{C}_6^2 + \dfrac{C}{1+K_u}}$	$C_7 = \dfrac{P_c R T_B}{2\eta_p}$
Maximum payload	$C_8 = \dfrac{T_B}{\rho V_0}\left(B + \dfrac{\omega_0 L_c \rho g}{\beta_i V_0}\right)$
$r_{opt} = \bar{C}_6 + \sqrt{\bar{C}_6^2 + \dfrac{C}{1+K_u} + \dfrac{C_8}{C_7(1+K_u)}}$	$C_9 = \dfrac{2\eta_p \Delta_N}{F_c \cdot T_B}$
Maximum range	$\bar{C}_9 = \dfrac{2\eta_p \Delta'_N}{F_c T_B}$
$r_{opt} = \bar{C}_6 + \dfrac{C_{10}}{C_9} + \sqrt{\left(\bar{C}_6 + \dfrac{C_{10}}{C_9}\right)^2 + \dfrac{C}{1+K_u}}$	$C_{10} = \dfrac{2\eta_p}{\rho F_c V_0}\left(\dfrac{\rho g L_c \omega_0}{\beta_i V_0} + B\right)$
Fuel economy	
$r_{opt} = \bar{C}_6 + \dfrac{C_{10}}{\bar{C}_9} + \sqrt{\left(\bar{C}_6 + \dfrac{C_{10}}{\bar{C}_9}\right)^2 + \dfrac{C}{1+K_u}}$	
C. *Basic thrust method — no prefixed displacement*	
Minimum power	
$r_{opt} = C_6 + \sqrt{C_6^2 + \dfrac{C}{1+K_u}}$	
Maximum payload	
$r_{opt} = C_6 + \sqrt{C_6^2 + \dfrac{C}{1+K_u} + \dfrac{C_8}{C_7(1+K_u)}}$	

* * *

ON THE THEORY OF ONE TYPE OF AIR-WATER JET (MIST-JET) FOR SHIP PROPULSION

Earl R. Quandt
Naval Ship Research and Development Center
Annapolis, Maryland

ABSTRACT

Vehicles which operate on an air-water interface may use as the thrust medium either phase separately or any mixture of phases. One inherently amphibious combination which utilizes a water-augmented air-jet (Mist-Jet) principle has been studied. To analyze this concept, one-dimensional conservation equations for mass, momentum, and energy have been written and solved to define overall propulsive coefficient as well as two-phase nozzle shape and size. It is concluded that the concept is practical, provided that reasonably efficient scoops, injectors, and two-phase nozzles can be developed.

INTRODUCTION

Among transportation vehicles, ships occupy a unique position in the sense that they operate at the interface between a liquid and a gas of greatly different densities. Because of the availability of either phase for the generation of thrust, it becomes of interest to examine which phase is most suitable for propulsion, and whether some advantages might not also be possible using mixtures of air and water. Certainly, one conceptual advantage of an air-water mixture is the potential for having a thrust medium of widely and continuously variable density. Also, in principle, it should be possible to apply the propulsive power to either fluid or to any mixture, depending upon convenience or the engineering advantages of alternate arrangements.

Although these considerations are not original, past attempts to apply two-phase propulsion systems to ships have not been notably successful. In 1947, Anderson et al. (1) reported on a study of a hydro-ramjet system powered by compressed air. Although the arrangement was simple in design, propulsive efficiency was too low for practical utilization. Similar conclusions have been reached more recently by Mottard and Shoemaker (2) and by Pierson (3), although improved engineering techniques have raised efficiency considerably. Shuster et al. (4) describes comparable German investigations as well as mentioning work on a pulsating air-water ramjet using expanding combustion air to accelerate the water. Such a scheme is attractive because it permits the fuel energy to work directly on the thrust medium without any intervening machinery. Unfortunately, however, if the hot gas and cold water phases are allowed to mix,

considerable heat transfer and poor combustion result, thus giving low thermodynamic efficiency.

In the past several years interest has developed in continuous air-water jets for ship propulsion. Muench and Keith (5) describe the results of an analysis of propulsive efficiencies possible with augmentation of a basic air jet and conclude that reasonable efficiencies are predictable at higher speeds. Davidson and Sadowski (6) discuss similar computations directed toward modification of a particular aircraft turbofan engine for ship propulsion. These detailed analyses have been made possible through the development of a large body of data and analytical techniques suitable for predicting the behavior of enclosed two-phase systems. For example, Quandt (7) has developed a rational method of predicting natural flow patterns which control the heat, mass, and momentum-transfer characteristics of these mixtures. Levy (8) has provided a basis for computing friction losses and mean density in dispersed flows, while Elliott (9) has reported a satisfactory analytical description for predicting liquid droplet acceleration in an expanding gas stream.

The purpose of this paper is to assemble some of the more recent theoretical and experimental techniques required to understand the gas-phase-continuous two-phase jet system. The development will be that needed to predict thrust performance for a water-droplet-air-jet system, and is similar to that of Muench and Keith (8). It is intended that this paper will serve to illustrate a formal basis for the analysis of air-water jets and to suggest the potential of these variable density fluids as ship propulsion media.

THEORY

In order to satisfactorily construct a two-phase thrust device, it is necessary to ingest each phase, add energy to one or both phases, form the mixture, and eject it in the rearward direction. Significant differences arise in the analysis techniques used for the nozzle description in a single- and two-phase systems because in the latter the separate phases do not generally flow with the same velocity. This velocity difference or "slip" between the phases has a significant effect upon mixture density, momentum flux, energy transfer efficiency, and consequently the size of apparatus needed to produce a given thrust. This section will follow a development based upon separate ingestion and energy addition to each phase, since this may be accomplished with existing components and analysis techniques. A two-phase analysis will be developed for the mixing and ejection nozzle stages to predict thrust augmentation, thrust intensity, and propulsive efficiency. Certain simplifying assumptions will be made to facilitate a first-order solution, so that the essential features of the two-phase jet may be illustrated.

Figure 1 presents a schematic of the air-water thrust system to be analyzed. Here, the water-handling component is characterized by a simple scoop, duct, and injection nozzle station capable of delivering dispersed liquid to the two-phase nozzle area at a velocity slightly less than the forward speed of the ship. Air is taken in through a compressor, which, in this example, adds the energy required to accelerate both the air and water phases. This air is ducted to the vicinity of the water injection nozzles and mixed with the water, and the

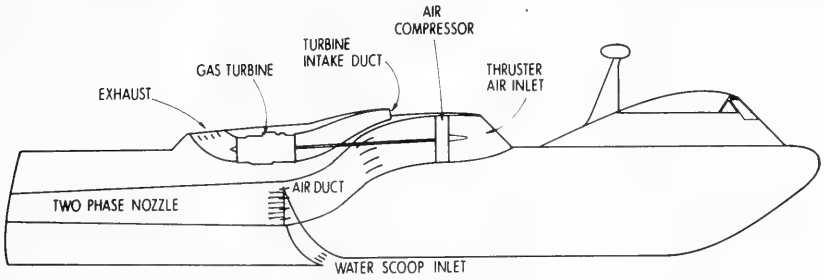

Fig. 1 - Schematic drawing of Mist-Jet installation in high-speed ship

mixture is allowed to expand to the atmosphere. At the mixing zone the air velocity, pressure, and quantity may be varied to give a range of mixture velocities at the nozzle exit and consequently to make a larger or smaller unit.

In order to compute the gas and liquid velocities at the nozzle exit from the inlet conditions and nozzle shape it is necessary to couple the mass, momentum, and energy conservation equations for each phase. To accomplish this analysis the one-dimensional gas-liquid dynamic equations will be written for a differential length control volume as shown in Fig. 2. It will be assumed that the gas properties are transversely uniform and that this phase obeys the ideal gas equation of state.

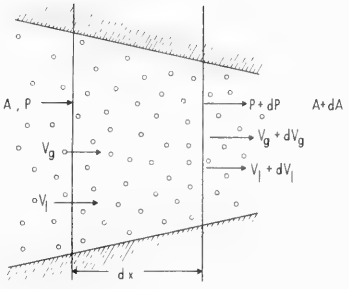

Fig. 2 - Control volume for two-phase nozzle analysis

Conservation Equations

Mass Conservation:

Gas $W_g = \rho_g V_g A_g = \text{Constant}$

Liquid $W_\ell = \rho_\ell V_\ell A_\ell = \text{Constant}$

Total $W_T = W_g + W_\ell$

Axial Momentum Conservation:

$$\text{Gas} \qquad \frac{W_g}{g_c}\, dV_g = A_g\, dP - dF - \tau_w\, \pi D_e\, dx$$

$$\text{Liquid} \qquad \frac{W_\ell}{g_c}\, dV_\ell = -A_\ell\, dP + dF$$

The frictional drag force dF from the gas to the liquid droplets may be analyzed using Fig. 3. At this point, and in further analysis, the axial pressure gradient force on the droplets will be neglected, since it is small in comparison to the frictional drag. It will further be assumed in this analysis that the gas phase has a higher velocity than the liquid droplets. Hence, for a single droplet,

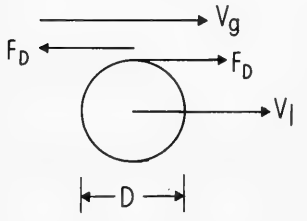

Fig. 3 - Droplet drag force model

$$F_D = C_D \frac{\pi D^2}{4} \rho_g \frac{(V_g - V_\ell)^2}{2g_c}$$

The number of droplets in a differential length is

$$dN = \frac{6A_\ell\, dx}{\pi D^3} = \frac{6A_\ell\, dx}{\pi D^3} ,$$

hence the differential drag force between the phases is

$$dF = F_D\, dN = 3C_D \frac{\rho_g (V_g - V_\ell)^2\, A_\ell}{4g_c\, D}\, dx$$

$$\text{Total:} \quad \frac{W_g}{g_c}\, dV_g + W_\ell \frac{dV_\ell}{g_c} = -A\, dP - \tau_w \pi\, D_e\, dx .$$

Energy Conservation:

$$\text{Gas} \qquad W_g \left(Cp_g\, dT_g + \frac{dV_g^2}{2g_c J} \right) = -dQ ,$$

$$\text{Liquid} \qquad W_g \left(Cp_\ell\, dT_\ell + dP/\rho_\ell + \frac{dV_\ell^2}{2g_c J} \right) = dQ .$$

The heat transfer between the phases may be analyzed similarly to the drag force to yield

$$dQ = h_{g\text{-}\ell} (T_g - T_\ell) \frac{6A_\ell}{D}\, dx .$$

Again a tacit assumption here is that evaporation of the liquid phase is negligible. Consideration of the temperature distribution between phases shows that the gas will be hotter than the liquid at the point of mixing due to the work of

compression. The rate of temperature decay is given by combining the gas energy equation with the particle heat-transfer equation

$$\frac{dT_g}{dx} = - \frac{h_{g-\ell} (T_g - T_\ell)}{D \, Cp_g \, \rho_\ell \, V_\ell} \frac{W_\ell}{W_g} .$$

For many cases of interest, the initial decrease in gas temperature is so rapid that the gas quickly approaches the liquid temperature. Expansion will therefore occur at almost constant temperature as the liquid resupplies energy to the gas during the drop in pressure along the nozzle. Hence, it will be assumed, conservatively, that the nozzle expansion is isothermal at the liquid temperature. This results in a certain loss in available compressor work, and may be thought of as an inherent loss in gas-liquid systems where the energy is added primarily to the gas phase. Figure 4 shows the fraction of isentropic work that may be recovered from a gas which expands isothermally at ambient temperature for a range of pressure ratios. This approximation to the energy efficiency may be written in general as

$$\frac{q_T}{q_s} = \frac{\gamma - 1}{\gamma} \left[\frac{\ln \nu}{\nu \dfrac{\gamma - 1}{\gamma} - 1} \right] .$$

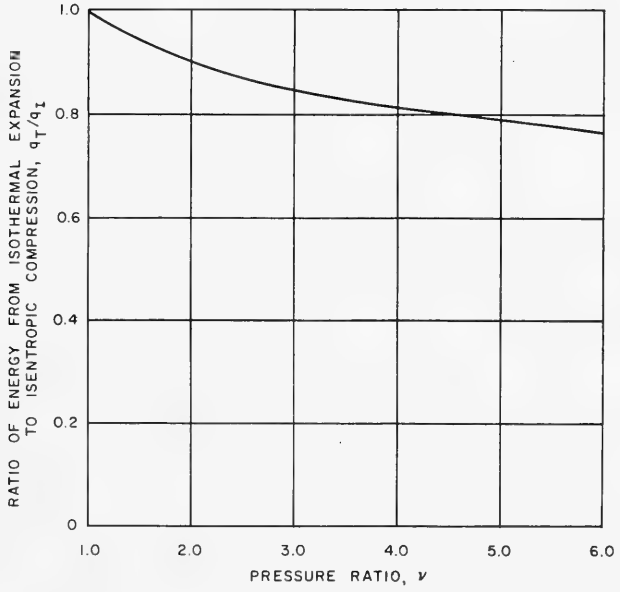

Fig. 4 - Fraction of isentropic work that may be recovered from a gas which expands isothermally at ambient temperature for a range of pressure ratios

Approximate Solution to Nozzle Equations

Examination of the energy equations revealed that over the range of air-water mixtures of interest it is permissible to approximate the expansion as isothermal at the liquid temperature. Additionally it will be assumed that nozzle friction is associated with the gas phase and will depend upon the total momentum flux. With these assumptions the total momentum equation becomes

$$\frac{W_T}{g_c} d\tilde{V} = -AdP - \tau_w \pi D_e \, dx \ ,$$

where a momentum average velocity is defined as

$$\tilde{V} = \frac{W_g}{W_T} V_g + \frac{W_\ell}{W_T} V_\ell \ ,$$

$$\tilde{V} = \frac{1}{1 + r} V_g + \frac{r}{1 + r} V_\ell \ ,$$

$$\tilde{V} = V_g \frac{1 + r\sigma}{1 + r} \ ,$$

where the slip ratio is defined as

$$\sigma = V_\ell / V_g \ .$$

Using the mass continuity equation allows definition of a liquid-gas area ratio as

$$A = A_g(1 + A_\ell / A_g) = A_g(1 + \alpha) \ ,$$

where

$$\alpha = A_\ell / A_g = \frac{W_\ell}{W_g} \frac{\rho_g}{\rho_\ell} \frac{V_g}{V_\ell}$$

or, more simply,

$$\alpha = \frac{r}{\sigma} \frac{\rho_g}{\rho_\ell} \ ,$$

from which it may be seen that α is very small for σ near one and r less than ten.

Now, the gas area may be related to pressure through the ideal gas equation

$$A_g = \frac{W_g}{V_g \rho_g} = \frac{W_g RT}{V_g PM} \ .$$

Substituting α, r, and σ into the total momentum equation yields

$$\frac{(1+r)^2}{(1+r\sigma)}\,\tilde{V}\,\frac{d\tilde{V}}{g_c} = -\frac{RT}{M}(1+\alpha)\frac{dP}{P} - \frac{\tau_w \pi D_e\, dx}{\rho_g A_g}$$

as the differential equation relating momentum velocity to pressure and distance in a two-phase expansion nozzle.

Looking next at the particle momentum equation, and rearranging gives

$$\frac{W_\ell}{g_c}\,dV_\ell = \frac{3}{4}C_D\,\frac{\rho_g V_g^2 (1-\sigma)^2}{g_c D}\,A_\ell\,dx\,,$$

$$\frac{dV_\ell}{V_\ell} = \frac{3}{4}\frac{C_D}{D}\frac{\rho_g}{\rho_\ell}\frac{(1-\sigma)^2}{\sigma^2}\,dx\,.$$

But

$$\frac{dV_\ell}{V_\ell} = \frac{dV_g}{V_g} + \frac{d\sigma}{\sigma}$$

and

$$\frac{dV_g}{V_g} = \frac{d\tilde{V}}{\tilde{V}} - \frac{r\sigma}{1+r\sigma}\frac{d\sigma}{\sigma}\,,$$

so that the particle equation can be rewritten as

$$\frac{d\tilde{V}}{\tilde{V}} + \frac{1}{1+r\sigma}\frac{d\sigma}{\sigma} = \frac{3}{4}\frac{C_D}{D}\frac{\rho_g}{\rho_\ell}\frac{(1-\sigma)^2}{\sigma^2}\,dx\,.$$

There are now two equations for momentum mean velocity for the two-phase nozzle which give $\tilde{V}$ in terms of pressure, distance, and slip ratio. For the purposes of this analysis it will be assumed that the slip ratio is constant along the nozzle length. This is not meant to be a requirement for such nozzles, but it does permit straightforward integration of the momentum equations.

Taking first the total momentum equation, it may be reasonably assumed that $\alpha << 1$ for a Mist-Jet type nozzle, thus

$$A = A_g\,, \quad \text{and} \quad \tau_w \approx f\,\frac{\bar{\rho}\,\tilde{v}_e^2}{8 g_c}$$

so that, upon integration,

$$\tilde{V}_e^2 - \tilde{V}_i^2 = -\frac{2(1+r\sigma)}{(1+r)^2}(C_T)^2 \ln(P_e/P_i) - \frac{f(r+1)}{2}\,\tilde{V}_e^2\,\frac{L}{D_e}\,,$$

or

$$\left(1 + \frac{f(r+1)}{2}\,\frac{L}{D_e}\right)\frac{\tilde{V}_e^2}{\tilde{V}_i^2} - 1 = -2\,\frac{(1+r\sigma)}{(1+r)^2}\left(\frac{C_T}{\tilde{V}_i}\right)^2 \ln(P_e/P_i)\,.$$

Integrating the particle equation at constant σ, ρ_g, C_D, and D yields

$$\ln\left(\tilde{V}_e/\tilde{V}_i\right) = \frac{3}{4}\frac{C_D}{D}\frac{\overline{\rho}_g}{\rho_\ell}\frac{(1-\sigma)^2}{\sigma^2}L$$

or

$$\frac{\tilde{V}_e}{\tilde{V}_i} = \rho^{L/\lambda} ,$$

where

$$L/\lambda = \frac{3}{4}\frac{C_D}{D}\frac{\overline{\rho}_g}{\rho_\ell}\frac{(1-\sigma)^2}{\sigma^2} .$$

Combining these equations to eliminate nozzle length allows calculation of momentum mean velocity increase for given r, σ, and ν. Results of this calculation are shown in Fig. 5. Figure 6 illustrates the variation of pressure and velocity with distance along the nozzle for a pressure ratio of 1.4 with $\sigma = 0.85$. Figure 7 shows the axial variation of nozzle area ratio with length for $\nu = 1.4$; $\sigma = 0.85$; and r = 5, 10, and 20. Here it can be seen that the proper nozzle shpae may be converging, converging-diverging, or diverging, depending upon the water-to-air mixture ratio.

Nozzle Thrust

Using the law of conservation of axial momentum it is possible to compute an ideal propulsion system thrust by taking a control volume around the entire ship. In that case, neglecting free-stream diffusion for the moment,

$$\theta = \frac{W_g}{g_c}\left(V_{g_\rho} - V_s\right) + \frac{W_\ell}{g_c}\left(V_{\ell_\rho} - V_s\right) .$$

The major losses in this system are those associated with the water scoop, duct, and nozzles. Internal flow losses such as friction drag, area, or form losses and discharge losses will be lumped into one loss coefficient based on craft speed. Therefore, the liquid static pressure after injection into the air stream is given by

$$P_i = P_0 + \frac{\rho_\ell}{2g_c}\left(V_s^2 - V_i^2\right) - K\frac{\rho_\ell V_s^2}{2g_c} .$$

When the nozzle pressure ratio is specified this equation is used to compute an effective injection velocity for use in the thrust analysis:

$$V_i^2 = V_s^2(1-K) - P_0(\nu - 1)\frac{2g_c}{\rho_\ell} .$$

It is of interest to note here that the scoop system being analyzed will always operate with a free-stream compression because of internal losses.

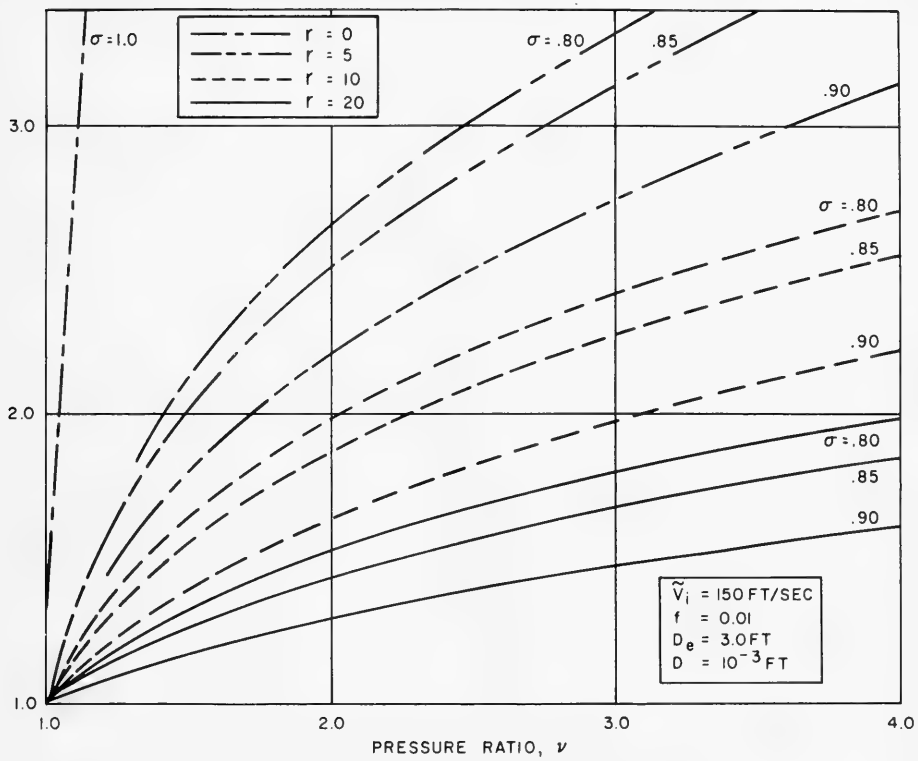

Fig. 5 - Results of calculation of momentum mean velocity increase for given r, σ, and ν

The other significant scoop loss to be considered is that of profile drag, which may be defined in terms of a drag coefficient, C_{D_s}. The thrust deduction from the propulsion system may be written as

$$\theta_s = C_{D_s} A_s \rho_\ell \frac{V_s^2}{2g_c}$$

and rearranged to a more convenient form by accounting for the free-stream compression,

$$\theta_s = \frac{C_{D_s}}{2g_c} W_\ell V_s \frac{A_s}{A_0} .$$

Subtracting water scoop drag from the total thrust equation provides an expression for net thrust from the two-phase system:

$$\theta_N = \frac{W_g}{g_c} \left| (1+r)(\tilde{V}_e - V_s) - \frac{1}{2} r C_{D_s} \frac{A_s}{A_0} V_s \right| .$$

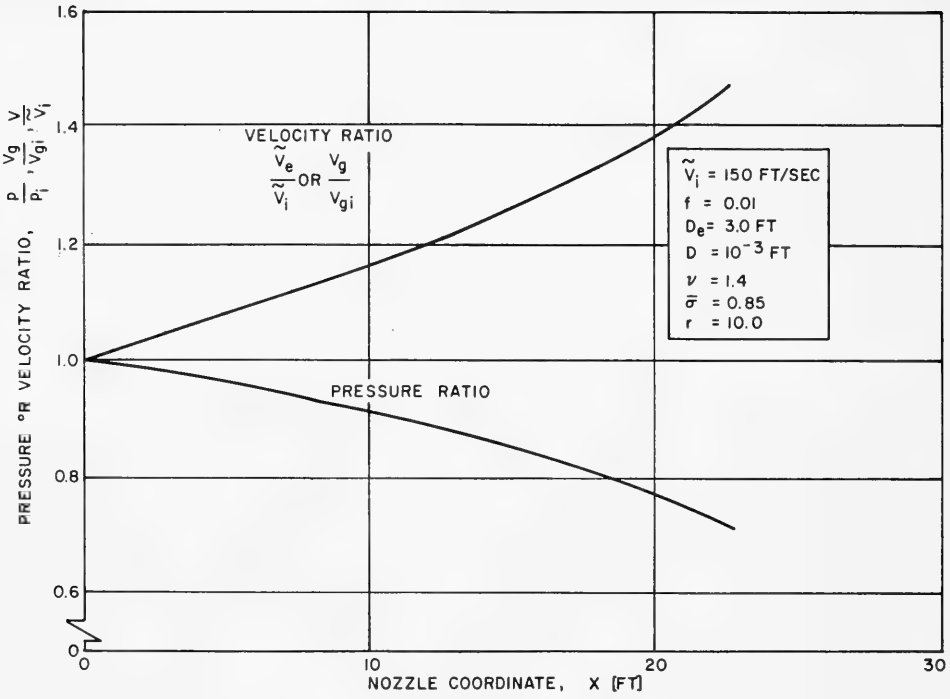

Fig. 6 - Variation of pressure and velocity with distance

Here, the total thrust is reduced directly by effective appendage drag and indirectly by the lower $\tilde{V}_e$ resulting from internal losses. For illustration, Fig. 8 shows predicted thrust per unit mass flow of air as a function of water-to-air mass flow ratio for several nozzle pressure ratios. Alternatively, Fig. 9 shows the variation of specific thrust with ship speed for several pressure and mass augmentation ratios. Another important characteristic of two-phase jets is presented in Fig. 10, which shows thrust intensity (thrust per unit exit area) versus nozzle pressure ratio for various augmentation ratios. Also shown on this plot is overall propulsion efficiency defined as

$$\eta_0 = \frac{\theta_N V_s}{\text{Compressor Work}} = \eta_c \frac{\left[(1+r)(\tilde{V}_e - V_s) V_s - \frac{1}{2} r C_{D_s} \frac{A_s}{A_0} V_s^2\right]}{C_P T_0 \left(\nu \frac{r-1}{r} - 1\right)} .$$

For the performance shown in Figs. 8-10, the following loss coefficients and system constants have been assumed:

$$K = 0.20$$

$$C_{D_s} \frac{A_s}{A_0} = 0.15$$

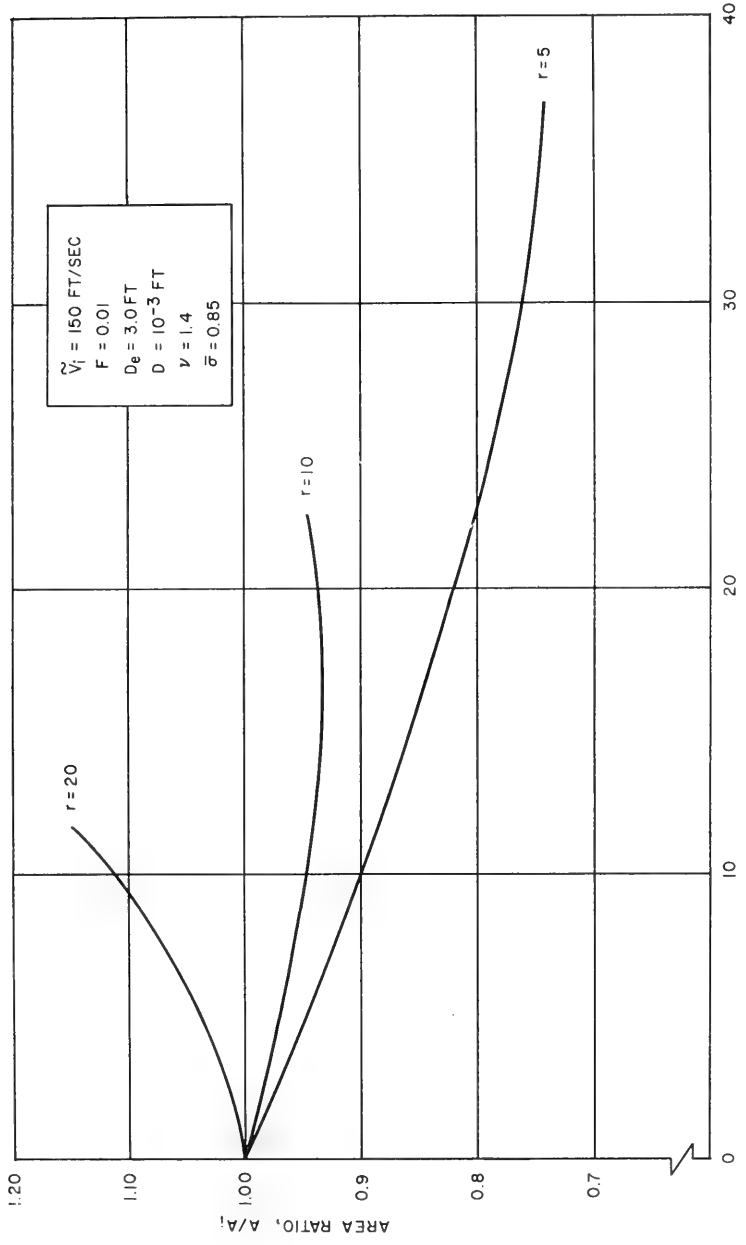

Fig. 7 - Axial variation of nozzle area ratio with length

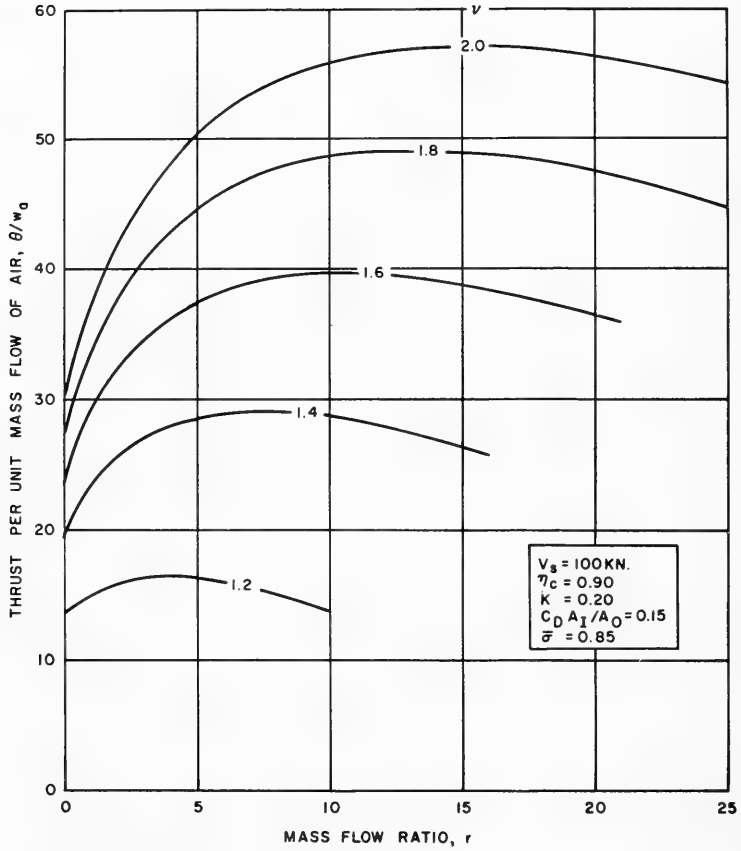

Fig. 8 - Predicted thrust per unit mass flow of air as a function of water-to-air mass ratio for several nozzle pressure ratios

$\eta_c = 0.90$

$f = 0.01$

$\bar{\sigma} = 0.85$

$D = 10^{-3}$ ft

$T = 60°F$

It is felt that these are representative of achievable values, but may be improved somewhat depending upon a particular design requirement.

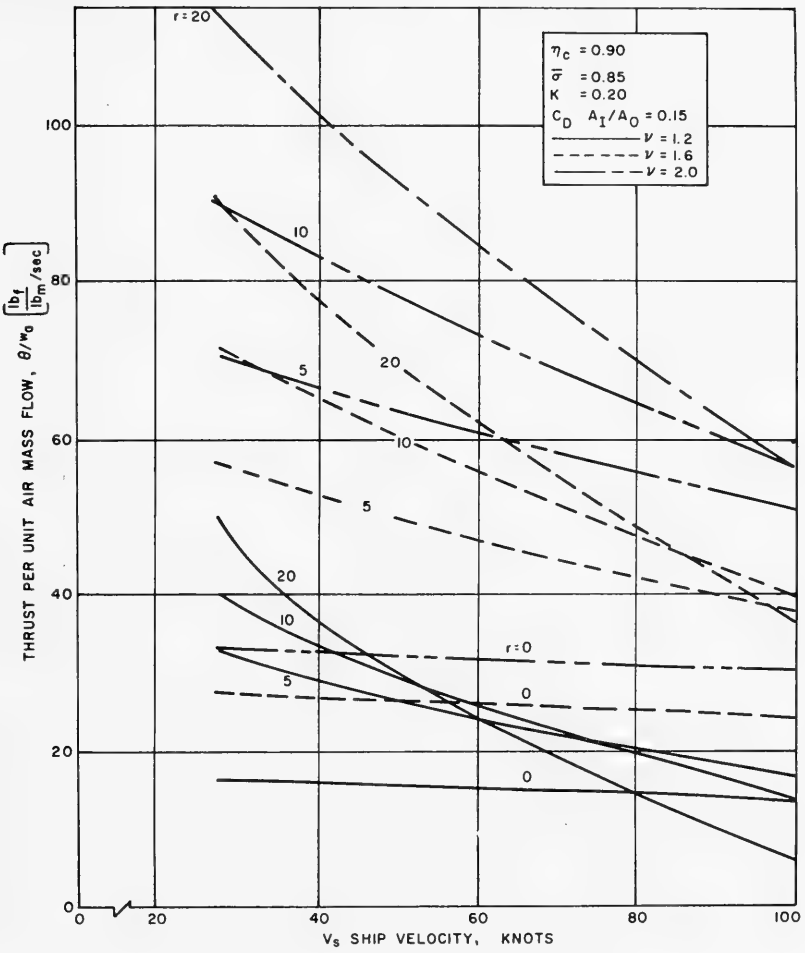

Fig. 9 - Variation of specific thrust with ship speed

DISCUSSION

The preceding two-phase nozzle analysis has established a basis for the evaluation of the propulsion effectiveness of one class of air-water systems, i.e., the water-augmented air-jet (Mist-Jet). It appears from this and many previous studies that the derived equations are satisfactory for an initial understanding of the major properties needed to evaluate a propulsion device. Of course, more detailed analyses and experiments are required to refine these calculations with regard to:

(i) water scoop inlet losses and cavitation behavior,

(ii) water injection nozzle size, droplet size and spray distribution,

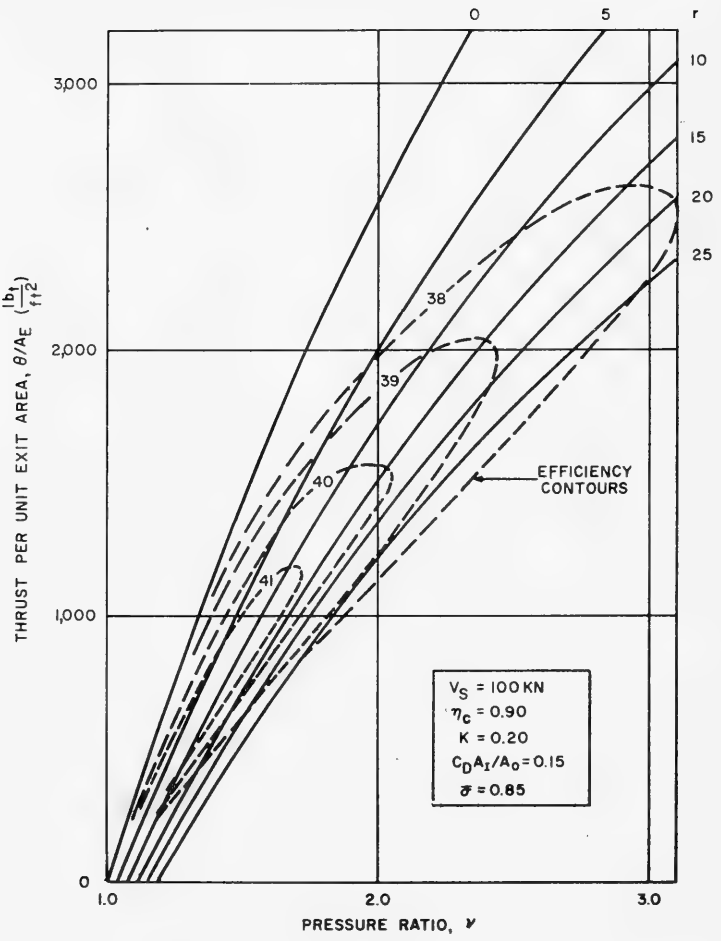

Fig. 10 - Thrust intensity versus nozzle pressure ratio

(iii) optimization of two-phase nozzle shape based upon computed particle slip, and

(iv) refinement of heat and mass transfer rates, duct friction and axial pressure distribution.

However, since the results to date of the more detailed analyses differ only slightly from those of the present study, it is considered that the essential characteristics of Mist-Jet-type systems may be seen from the present work.

One of the first considerations for any propulsive device is that of fuel economy or more particularly propulsive efficiency. In this study propulsive efficiency has been defined as total thrust less appendage drag times ship

velocity divided by shaft power into the air compressor for the given total thrust. Figures 11-13 show typical computed levels of propulsion efficiency versus pressure ratio, ship speed, and water-to-air mass flow ratio, respectively. It can be seen that for the range of loss coefficients assumed herein the propulsive efficiency tends to peak slightly below a value of 0.50. Furthermore, it is apparent that air system pressure ratios less than 1.5 atm are desirable and would require water-to-air mass flow ratios from 5 to 20 depending upon ship speed. It may be recalled that the large difference in density between air and water results in a very disperse mixture even at the higher mass flow ratios. Figure 13 shows that overall efficiency is quite sensitive to average phase slip, so that a considerable effort is required to assure a satisfactory slip ratio σ in practical cases. In summary, it appears that propulsion efficiencies up to 50% may be achieved for Mist-Jet systems at pressure ratios from 1.2 to 1.5 and water mass augmentation ratios near 10. It should be noted that at these high mass augmentation ratios virtually all the system thrust is developed by rearward acceleration of the liquid phase. Hence, the air phase is acting much as a pump or propeller would. Of course, one conceptual difference between the air system and a water pump is that the air system will deliver about half thrust in the absence of any water, thus making the propulsion system inherently amphibious.

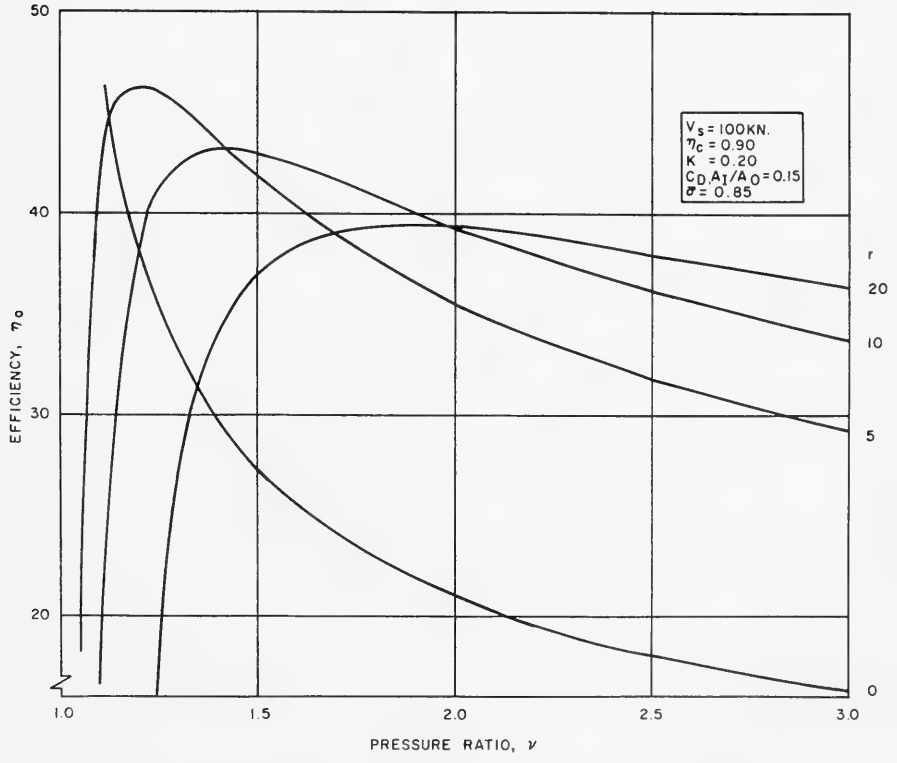

Fig. 11 - Propulsion efficiency versus pressure ratio

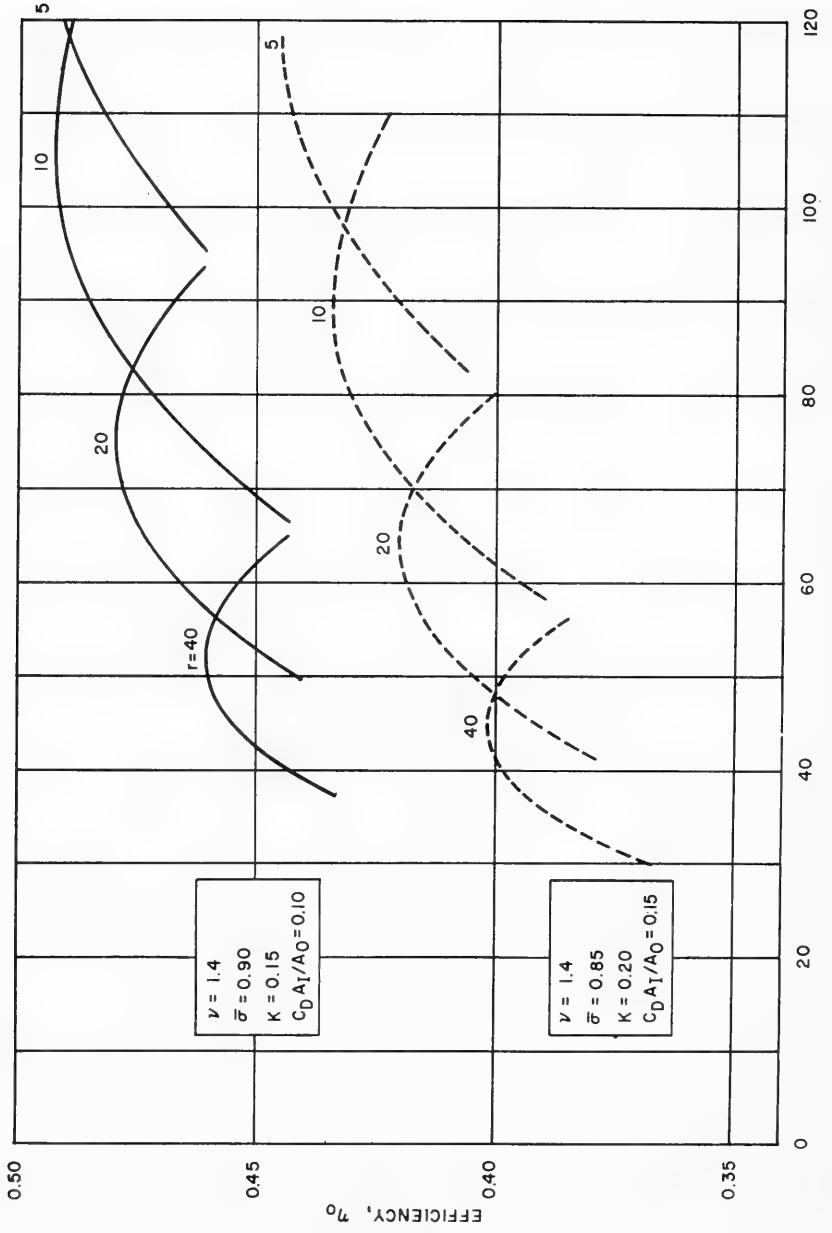

Fig. 12 - Propulsion efficiency versus ship speed

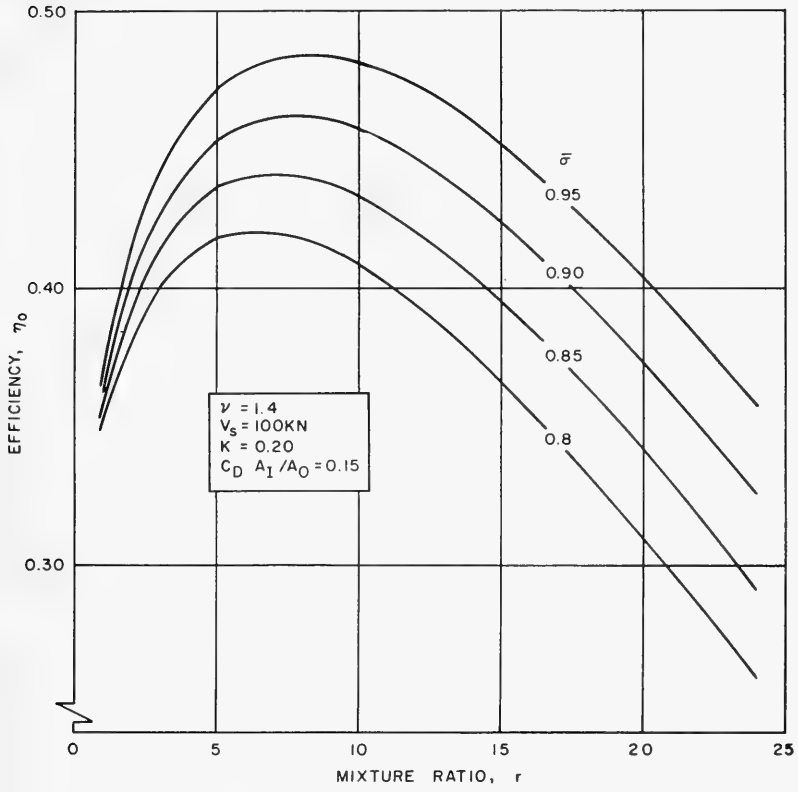

Fig. 13 - Propulsion efficiency versus water-to-air mass flow ratio

Another characteristic of a propulsion device is system volume, which is directly related to thrust density. Figures 8 and 9 show thrust per unit mass of air versus mass augmentation ratio and ship speed, respectively. It can be seen that for any ship speed and pressure ratio there is an optimum water-to-air augmentation ratio. The thrust used here is net thrust, which accounts for losses, both internal and external, arising from adding the liquid phase. These figures show the normal decrease in thrust per unit energy added with increase in speed and also indicate that net thrust increases of more than a factor of two may result from water-augmentation of an air jet. Figure 10 illustrates the variation of thrust intensity, i.e., thrust per unit exit area versus nozzle pressure ratio. Here it can be seen that for a given thrust intensity there is an optimum pressure ratio and mass augmentation ratio combination resulting in highest overall efficiency. It is this information that can be used in vehicle design where size and weight are balanced against system efficiency. Generally it can be seen that a nozzle thrust intensity of 1000 lb/ft^2 is a reasonable upper value for the practical range of propulsive efficiencies.

Although the water augmented air jet may be somewhat less efficient than the all-water systems, this is not of great significance for smaller ships because these tend to be more sensitive to machinery weight than fuel weight (10). Perhaps one of the more critical application problems for any of the ship propulsion systems appears to be satisfactory passage through the low speed hump condition. For a Mist-Jet design, this consideration is made more or less significant depending upon desired top speed capability because of the availability of the air-only thrust at all speeds. Additionally, as mentioned earlier, water augmented air jets have the inherent amphibious capability and furthermore may also have sufficient air flow to augment lift fans at the hump condition so that not as great a horizontal thrust need be supplied.

CONCLUSIONS

The significant conclusions of this analytical and experimental investigation of two-phase air-water ship propulsion systems are:

(i) There exist analytical techniques for predicting performance of the two-phase components with first-order confidence.

(ii) These analyses are being improved through more detailed descriptions as well as by comparison with selected experimental data.

(iii) Overall propulsion coefficients of 50% are predictable for high-speed ship applications of water-augmented air-jets.

(iv) This efficiency is achievable with a bulky but light propulsion plant.

(v) Air-water jets are inherently amphibious, and also offer certain design flexibilities for craft using air-support concepts.

ACKNOWLEDGMENTS

The work reported herein has been sponsored by the Independent Exploratory Development program of the Naval Ship Research and Development Center. Additionally, the author particularly wishes to acknowledge John H. Garrett, Rolf K. Muench, and Allen E. Ford for their efforts on this program and for their work in performing some of the computations for this paper.

NOMENCLATURE

Symbol	Description	Units
A	Flow area in nozzle	ft^2
A_s	Flow area in water scoop	ft^2
A_0	Flow area in free stream	ft^2

Symbol	Description	Units
C_D	Droplet drag coefficient	-
C_{DS}	Water scoop drag coefficient	-
C_T	Isothermal acoustic velocity	ft/sec
D	Droplet diameter	
D_e	Nozzle equivalent diameter	
F_D	Drag force on droplet	poundal
F	Drag force between phases	poundal
f	Friction factor	-
g_c	Mass-to-force conversion	lb ft/poundal sec^2
$h_{g-\lambda}$	Gas-to-liquid heat-transfer coefficient	$\frac{\text{BTU}}{\text{sec ft}^2\ ^\circ\text{F}}$
J	Mechanical equivalent of heat	BTU/ft poundal
K	Water scoop internal loss coefficient	-
L	Nozzle length	ft
M	Molecular weight	$\frac{\text{lb}}{\text{lb mole}}$
N	Number of droplets	-
P	Pressure	poundal/ft^2
P_i	Inlet pressure	poundal/ft^2
P_e	Nozzle exit pressure	poundal/ft^2
P_0	Free-stream static pressure	poundal/ft^2
Q	Heat flow	BTU/sec
q_T	Energy for isothermal compression	BTU/lb
q_s	Energy for isentropic compression	BTU/lb
R	Gas constant	$\frac{\text{ft poundal}}{\text{lb}_{\text{mole}}\ ^\circ\text{R}}$
r	Water-to-air mass flow ratio	-

Symbol	Description	Units
T	Absolute temperature	°R
T_0	Ambient temperature	°R
V	Velocity	ft/sec
V_s	Ship velocity	ft/sec
$\tilde{V}$	Momentum mean velocity	ft/sec
W	Mass flow rate	lb/sec
X	Distance along nozzle	ft
α	Liquid-to-gas volume ratio	-
γ	Ratio of specific heats	-
η_c	Compressor efficiency	-
η_0	Propulsive efficiency	-
λ	Characteristic length for droplet acceleration	ft
ν	Pressure ratio	-
ρ	Density	lb/ft^3
σ	Liquid-to-gas velocity ratio	-
τ_w	Wall frictional shear stress	$poundal/ft^2$
θ_N	Net propulsion system thrust	poundal
θ_s	Water scoop drag	poundal
θ	Thrust	poundal

Subscripts

ℓ	Liquid
g	Gas
i	inlet
e	exit

REFERENCES

1. Anderson, R.G., Rush, C.W., Jr., and McClellan, T.R., "Development of a Hydroduct," Thesis, Guggenheim Aeronautical Lab., California Institute of Technology, 1947

2. Mottard, E.J., and Shoemaker, C.J., "Preliminary Investigation of an Underwater Ramjet Powered by Compressor Air," NASA Report TND-991, Dec. 1961

3. Pierson, John D., "An Application of Hydropneumatic Propulsion to Hydrofoil Craft," AIAA J. Aircraft, 2, No. 3, pp. 250-254, May-June, 1965

4. Schuster, S., Schwannecke, H., et al., "Über Probleme des Wasserstrahlantriebs," J. Schiffbautechn. Ges., Springer-Verlag, 1961

5. Muench, R., and Keith, T., "A Preliminary Parametric Study of a Water-Augmented Air-Jet for High-Speed Ship Propulsion," U.S. Navy Marine Engineering Laboratory R&D Report 358/66, Feb. 1967

6. Davison, W.R., and Sadowski, J., "A Water-Augmented Turbofan Engine for High-Speed Ship Propulsion," AIAA J. Hydronaut., 2, No. 1, pp. 14-21, Jan. 1968

7. Quandt, E., "Two-Phase Flow Patterns," A.I.Ch.E. Symposium Series, Heat Transfer—Boston, 1963

8. Levy, S., "Prediction of Two-Phase Pressure Drop and Density Distribution From Mixing Length Theory," ASME Paper 62-HT-6, Heat Transfer Conference, Houston, Texas (1962)

9. Elliott, D.G., "Analysis of the Acceleration of Lithium in a Two-Phase Nozzle," Proceedings of the High-Temperature Liquid-Metal Heat-Transfer Technology Meeting, pp. 353-380, Dec. 1964

* * *

DISCUSSION

V. Kostilainen
Finland Institute of Technology
Otaniemi, Finland

First of all I must thank Dr. Quandt for this interesting paper. Some five years ago there existed very few papers which dealt with two-phase propulsion. Now the research in this area is largely increased.

One point of view I would like to emphasize here, is the effect of gravity. I see that Dr. Quandt has excluded gravity effects and considers the flow in this propeller steady and homogeneous. I am afraid that, at least with lower speeds and higher water-to-air mass flow ratios, the flow will be unsteady.

For the past two years we have been studying a two-phase propeller which is based on the effect of gravity and which possibly can be used for the propulsion of slow and medium-speed ships. A model having a WL-length of 1.6 m was made and tested. It was observed among other things that at least in this case the two-phase flow was very unsteady. Results of these first tests will be reported in ISP September issue.

To study the scale effect of this propulsion we have built this spring another geometrically similar model which has a WL-length of 6.4 m and total length of 10 m. This larger model was tested in open sea. It can be seen from Fig. D-1 that unsteadiness of this two-phase propeller even dominates the stern wave system.

Fig. D1 - Test boat equipped with two-phase propulsion; waterline length 6.4 m, displacement 6 tons

Wärtsilä shipyard in Helsinki has also started research of this propulsion and they have concentrated on the application of this propulsion to the lateral thrust units. As a result of this research, a car ferry now under construction in Finland will be equipped with two-phase bow-propeller.

* * *

DISCUSSION

R. Pallabazzer
Istituto di Fisica Tecnica e Macchine, Politecnico
Milan, Italy

I have a few remarks to make about this paper. The first question is about the values for the drag coefficient C_D and the heat transfer h_e for the droplet motion. I would like to know whether, as it appears, the Stokes flow hypothesis was assumed. If this was the case, I would like to point out that the real motion of the particle is probably not in the Stokes range, because of the high local turbulant speed, which especially affects the heat transfer. It is obvious, in fact, that the very low value of the components of the relative speed in the axial direction $(V_g - V_e)$ is not an index for the heat transfer, when a Brownian motion is present.

A second remark relates to the analysis of the mixing phase. The inlet conditions in the nozzle have been assumed as reference or as a datum; in the propulsor, actually, they are not known, because we know the flow conditions just at the inlet of the propulsor. It seems to me that the mixing phase, which occurs in the chamber, is highly unpredictable but it strongly affects the flow parameters at the nozzle inlet. Therefore, I think that the exactness of the particle-flow analysis developed here instead of an homogeneous two-phase flow analysis can be useless when the initial flow conditions are not well known.

Finally, I would like to observe that it is the hypothesis of a constant slip ratio which determines the shape of the nozzle. This fact was clearly observed by Kliegel in some papers he presented, I think, about ten or fifteen years ago, on gas-solid particle flow. In his works, the only one of which I can now remember was entitled "Two-Phase Gas-Particle Flow," Kliegel developed a particle flow analysis which is quite the same as that developed by Dr. Quandt, but for application to rocket exhaust gases.

* * *

REPLY TO DISCUSSION

E. R. Quandt

Both discussers have raised some interesting questions concerning the fundamental nature of the homogeneity and internal transport characteristics of two-phase flows. Taking first Dr. Kostilainen's question, I would like to recommend Ref. (7) of my paper as one approach to determining whether or not gravity effects are important. In low-velocity flow, such as encountered in natural circulation, gravity does prove controlling. However, in the applications I have considered, i.e., thrust devices for high-speed ships, the axial acceleration

forces are severe enough so that the phases will be rather uniformly mixed and performance independent of gravitational orientation.

Professor Pallabazzer, on the other hand, assumes that the flow pattern will be more or less homogeneous, but questions the best approach to describing the internal transport properties of turbulent air-water mixtures. With regard to the heat transfer and particle drag coefficient values used in the paper, I wish to say that I believe them to be consistent and conservative for the purposes of this analysis. In my opinion only experimental data will be able to resolve the proper magnitude. Concerning the initial conditions for the particle-gas flow analysis, it is possible to create a spectrum of initial velocity and pressure conditions by varying water spray nozzle and air duct areas. It is also possible to control the homogeneity of the initial mixture by variations in design of the injection station. Although it may seem desirable to design for an initially homogeneous air-water mixture, cases may be conceived where some controlled maldistribution of air and water would actually improve thrust augmentation. Finally, I appreciate the information concerning the earlier work by Kliegel on a particle-gas flow analysis.

* * *

Thursday, August 29, 1968

Afternoon Session

UNCONVENTIONAL PROPULSION

Chairmen: Prof. E. Castagneto

Instituto di Architettura Navala, University of Naples
Naples, Italy

Vice Adm. R. Brard

Bassin d'Essais des Carènes
Paris, France

and

M. Tulin

Hydronautics, Inc.
Laurel, Maryland

PERFORMANCE CRITERIA OF PULSE-JET PROPELLERS

Michael Schmiechen
Versuchsanstalt für Wasserbau und Schiffbau
Berlin, Germany

ABSTRACT

Starting from the fundamental concepts and principles of hydrodynamics component efficiencies of pulse-jet propellers are defined, which may be directly compared for various propulsion devices. Some of the problems encountered in the evaluation of the criteria defined are discussed and the problem of propeller-hull-interaction is treated as far as possible.

1. INTRODUCTION

With the recent interest in jet propulsion of ships, the lack of clear-cut concepts and generally adopted procedures to define and evaluate performance criteria of propulsion devices has often been felt; Brandau, 1967. The conceptual and experimental difficulties to overcome this situation are considerable not only in the field of conventional and pump-jet propulsion, but even more in the field of pulse-jet propulsion.

Due to his engagement in various projects concerning pulse-jet propellers at the Berlin Towing Tank, the author had the opportunity to tackle the problems encountered in performance evaluation from different points of view. Some of the ideas and procedures that have evolved from this work and may be useful in a wider range of applications will be presented here in a systematic account.

In fact, the aim of the present paper is to reconstruct some well-known concepts of the theory of propulsion, to the effect that they may be applied to any type of propulsion device. For this reason the model considered and the concept formulation will be as general as necessary right from the beginning. Starting with the extremely specialized model of the actuator disk would, in this context, not be adequate. Although periodically acting propellers will be considered in general the case of steadily acting propellers will be included as a limiting case.

The method of presentation adopted will be axiomatic, but the exposition will not be formalized. The main interest rests on the logical consequences of the principles and the link-up of the various concepts introduced, the knowledge of which should be the basis of any discussion and work in the field. Though there is a strong demand for orientation towards easily measurable integral magnitudes as far as the evaluation is concerned, this cannot be the only guideline

in developing the conceptual framework for the definition of the performance criteria looked for.

Propulsion devices considered as subsystems of complex systems, i.e., vehicles, may be described by their representative points in multidimensional spaces of performance criteria, the definition of the appropriate criteria depending on the contexts of the particular types of vehicles. In cases where all relevant definitions are established and a best-practice envelope may be determined accordingly, it is easy to judge on the merits of any propulsion device, especially those newly proposed as compared with the state-of-the-art.

In this paper only few aspects of propeller performance will be considered. In view of the multidimensionality of the parameter space, it should be kept in mind that optimizing with respect to the aspects considered will in general not result in an optimum overall system. It is this point that is often rightly stressed by inventors claiming simplified power plants, etc., for their devices as compared with conventional propulsion.

2. PRINCIPLES OF PROPULSION

Although the basic principles have been stated over and over again, a short review is presented here for ready reference.

Any propulsion device of the type to be considered may be defined as a mechanical system, parts of which consist of the surrounding fluid; see Fig. 1. The latter will be considered as incompressible here, having the mass density ρ. The construction of the boundary of the system is in general undoubtedly one of the basic problems, to which many other problems may be reduced; see Sec. 5.2.

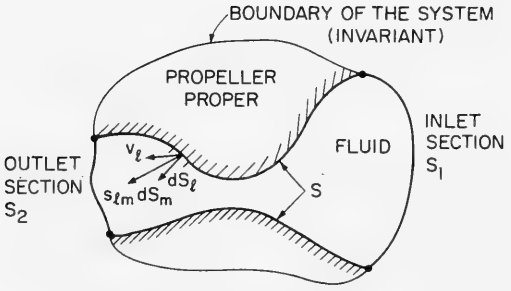

Fig. 1 - Propeller: a mechanical system

In any case, there exists in the system a dividing surface S between the propeller proper and the surrounding fluid. While the relative velocities v_ℓ of the elements dS_ℓ of this surface with respect to the invariant boundaries of the system characterize the kinematics of the propeller, the stresses $s_{\ell m}$ at these

elements characterize its dynamics. For many purposes a rather detailed knowledge of both distributions spatial as well as temporal will be necessary.

In the present context however we may introduce the mean thrust

$$T_\ell = f \int_{1/f} \int_S - S_{\ell m} \, dS_m \, dt \tag{1}$$

and the mean power

$$P = f \int_{1/f} \int_S v_\ell \, S_{\ell m} \, dS_m \, dt \tag{2}$$

of the propeller acting as the frequency f as the basic measures of its overall performance.

Introducing further the propeller translation advance speed V_ℓ in the fluid, we may immediately establish the principle

$$T_\ell \, V_\ell < P \tag{3}$$

for the reaction power of the propeller due to the velocity field induced by the propeller at its own location. Once again we are facing a serious problem, since it is in general apparently difficult to define the advance speed in question.

The part of the system's boundary passing through the fluid may now be divided into two parts S_1 and S_2, the inlet and the outlet section, respectively, the definition of the dividing line being another problem to be solved in any particular case. With the appropriate choice of normals the mean volume flows

$$Q_i = f \int_{1/f} \int_{S_i} v_\ell \, dS_\ell \, dt \tag{4}$$

through the sections are both positive and, according to the principle of conservation of matter, equal:

$$Q_\ell = Q_1 = Q \, . \tag{5}$$

The general conservation principle for any quantity included in the boundary of the system may be put in the form

$$FL_2 - FL_1 = FL + PR \tag{6}$$

expressing the fact that the mean net outflow of the quantity over the fluid boundaries equals its mean inflow FL over the other part of the boundary and its mean production PR in the boundary of the system, the mean storage in the boundary being zero due to the periodicity, see Fig. 2.

Application of this prinicple to the momentum flows

$$M_{i\ell} = f \int_{1/f} \int_{S_i} (\rho \, v_\ell \, v_m + S_{\ell m}) \, a S_m \, dt \tag{7}$$

results in the momentum principle

$$M_{2\ell} - M_{1\ell} = T \, , \tag{8}$$

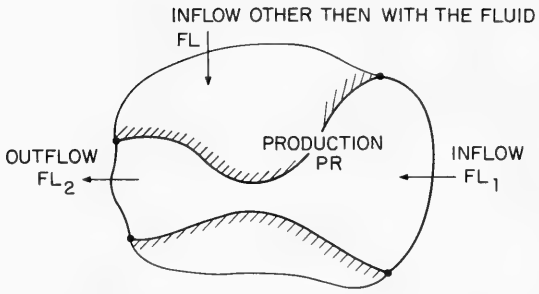

Fig. 2 - General conservation principal

while the energy principle reads

$$E_{\ell} - E_1 < P \ , \tag{9}$$

due to the dissipation of mechanical energy in the system, the energy flows being defined as

$$E_i = f \int_{1/f} \int_{S_i} [\rho(e_{kin} + e_{pot}) v_{\ell} + t_{\ell}] \, dS_{\ell} \, dt \tag{10}$$

e_{kin}, e_{pot}, and t_{ℓ} denoting the mass-specific kinetic and potential energies and the diffusive energy transport, respectively.

Further on only integral magnitudes will be dealt with and, as we are mainly interested in the principles, the tensor notation will be dropped.

3. DEFINITIONS OF EFFICIENCIES

3.1 Propeller Efficiency

From the basic concepts introduced, various performance parameters may be derived, in particular if a reference length L and cross section A of the propeller are introduced. The definitions of the advance number

$$J = V/(fL) \ , \tag{11}$$

the thrust number

$$K_T = T/(\rho f^2 L^2 A) \ , \tag{12}$$

and the power number

$$K_P = P/(\rho f^3 L^3 A) \ , \tag{13}$$

according to the rules of dimensional analysis are very similar to those known for screw propellers; Schmiechen, 1960. If one set of parameters is defined it may be transformed into any other suitable set.

Due to the ambiguity in the choice of the reference magnitudes the parameters so defined are in general not comparable for various propulsion devices, except for those parameters not containing geometrical reference magnitudes at all. Examples of comparable parameters, i.e., criteria proper, are efficiencies, provided the boundaries of the systems are correctly chosen in any case.

From the principle of reaction power we may directly define the overall propeller efficiency

$$\eta_{PROP} = TV/P \ . \tag{14}$$

Taking into account the momentum and the energy principles we may write this as the product

$$\eta_{PROP} = \eta_{EXT} \ \eta_{INT} \tag{15}$$

of the external efficiency

$$\eta_{EXT} = (M_2 - M_1) \ V/(E_2 - E_1) \tag{16}$$

and the internal efficiency

$$\eta_{INT} = (E_2 - E_1)/P \ . \tag{17}$$

Introducing the mean mass-specific momenta

$$m_i = M_i/(\rho Q) \ , \tag{18}$$

energies

$$e_i = E_i/(\rho Q) \ , \tag{19}$$

and energy jump

$$e = P/(\rho Q) \ , \tag{20}$$

we have the external efficiency

$$\eta_{EXT} = (m_2 - m_1) \ V/(e_2 - e_1) \tag{21}$$

and the internal efficiency

$$\eta_{INT} = (e_2 - e_1)/e \tag{22}$$

in terms of these magnitudes.

It should be noted here that the mean mass-specific quantities m_i and

$$r_i = \sqrt{2 e_i} \ , \tag{23}$$

the momentum and energy velocities, respectively, are clearly distinct from the ordinary mean mass or volume velocity

$$v_i = Q/A_i \ , \tag{24}$$

A_i denoting some cross section. The situation is very similar to that encountered in boundary-layer theory, where displacement, momentum and energy thicknesses have to be distinguished. In this case the definition of the different velocities, rather than cross-sections, has proved to be more promising.

3.2 External Efficiency

The external efficiency itself may be considered as the product

$$\eta_{EXT} = \eta_{IDEAL} \, \eta_{JET} \tag{25}$$

of the ideal and jet efficiencies

$$\eta_{IDEAL} = 2m_1/(m_2 + m_1) \tag{26}$$

and

$$\eta_{JET} = (m_2^2 - m_1^2)/2(e_2 - e_1) \tag{27}$$

respectively. The ambiguity in the definition of the ideal efficiency, i.e., the efficiency of dynamically equivalent ideal propellers, due to the propeller advance speed (undefined up to now), has been removed by the convention

$$V = m_1 \tag{28}$$

so that the efficiency is exactly the same as that of an actuator disk,,with the important qualification, that all relevant velocities are momentum velocities. Later on it will be seen that this choice is actually not the only and best one; see Sec. 5.2.

With the momentum ratio

$$u = M_1/M_2 = m_1/m_2 \ , \tag{29}$$

the ideal efficiency becomes

$$\eta_{IDEAL} = 2/(1 + 1/\mu) \ . \tag{30}$$

Either the momentum ratio or the ideal efficiency itself may serve as universal propeller advance criteria. Actually, any function rising with increasing values of these criteria may serve the same purpose, while functions falling may be considered as loading criteria, e.g., the load factor

$$C_{TO} = 4/\eta_{IDEAL} \, (1/\eta_{IDEAL} - 1) \tag{31}$$

based on the maximum propeller cross-section.

In the following, the ideal efficiency will be chosen as advance criterion, while the hydraulic efficiency

$$\eta_{HYD} = \eta_{PROP} / \eta_{IDEAL} \quad (32)$$

will be considered as performance criterion proper, i.e., the propeller performance will be characterized by the function

$$\eta_{HYD} = h(\eta_{IDEAL}) \quad (33)$$

see Fig. 3.

The advantage of this presentation of performance data, as compared with the older one

$$\eta_{PROP} = g\ (C_{TO}) \quad (34)$$

(Gutsche, 1937), is due to the facts that, on the one hand the ideal efficiency, contrary to the load factor, is restricted to values between zero, for the towing condition, and unity, for the idling condition, and on the other hand the hydraulic efficiency, i.e., the degree of approximation towards the ideal is, contrary to the propeller efficiency, a reasonable performance criterion over the whole range of working conditions including the towing condition.

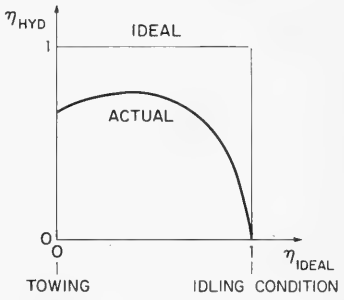

Fig. 3 - Performance characteristic

Concerning the detailed analysis of the hydraulic efficiency, we may write

$$\eta_{HYD} = \eta_{JET}\ \eta_{INT} \quad , \quad (35)$$

the jet efficiency accounting for the nonuniformities of the inflow and outflow in space and time. Introducing the inflow and outflow efficiencies

$$\eta_{INF/OUTF} = m^2_{1/2}/2e_{1/2} \quad , \quad (36)$$

we have for the jet efficiency

$$\eta_{JET} = (1 - \mu^2)/(1/\eta_{OUTF} - \mu^2/\eta_{INF}) \quad , \quad (37)$$

or, in terms of the energy ratio,

$$\epsilon = E_1/E_2 = e_1/e_2 = \eta_{OUTF}\ \mu^2/\eta_{INF} \quad , \quad (38)$$

$$\eta_{JET} = (\eta_{OUTF} - \eta_{INF}\ \epsilon)/(1 - \epsilon) \quad . \quad (39)$$

This efficiency may apparently not be split up into factors accounting for the inflow and outflow separately.

3.3 Internal Efficiency

The second factor of the hydraulic efficiency, the internal efficiency may either be considered at a pump efficiency or, in the presence of a ducting system, as the product

$$\eta_{INT} = \eta_{DUCT}\, \eta_{PUMP} \tag{40}$$

of the duct efficiency and the pump efficiency proper.

Introducing the energy flows E_{10} and E_{20} across some appropriately chosen internal fluid surfaces S_{10} and S_{20}, respectively, we may define the mean mass-specific energies

$$e_{10} = E_{10}/\rho Q \ , \tag{41}$$

the inlet efficiency (see Sec. 4.2)

$$\eta_{INL} = E_{10}/E_1 = e_{10}/e_1 \ , \tag{42}$$

and the outlet efficiency

$$\eta_{OUTL} = E_2/E_{20} = e_2/e_{20} \ . \tag{43}$$

In terms of these magnitudes, the duct efficiency

$$\eta_{DUCT} = (e_2 - e_1)/(e_{20} - e_{10}) \tag{44}$$

becomes

$$\eta_{DUCT} = (1 - \epsilon)/(1/\eta_{OUTL} - \eta_{INL}\, \epsilon) \ , \tag{45}$$

and the pump efficiency is defined as

$$\eta_{PUMP} = (e_{20} - e_{10})/e \ . \tag{46}$$

After all our basic performance criterion may be rendered in the form

$$\eta_{HYD} = \eta_{PROP}/\eta_{IDEAL} = \eta_{JET}\, \eta_{DUCT}\, \eta_{PUMP} \tag{47}$$

with the flow efficiency

$$\begin{aligned} \eta_{FLOW} &= \eta_{JET}\, \eta_{DUCT} \\ &= (1 - \mu^2)/(1/\eta_{OUTF}\, \eta_{OUTL} - \eta_{INL}\, \mu^2/\eta_{INF}) \ , \end{aligned} \tag{48}$$

showing the link-up of the various component efficiencies introduced. Once again, neither the duct nor the flow efficiency may be split into factors accounting for the inflow and outflow separately.

All the component efficiencies will in general be functions of the ideal efficiency. The problem in any particular case is to evaluate the mean mass-specific quantities displayed in the energy diagram (Fig. 4) as far as possible and determine the various ratios and efficiencies according to their appropriate definitions.

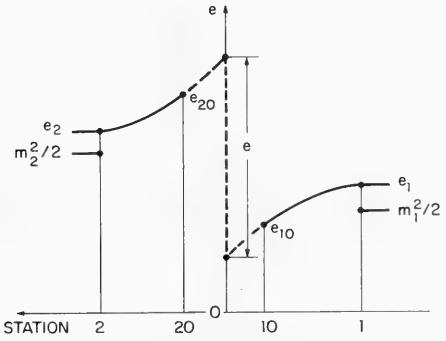

Fig. 4 - Specific energy diagram

4. FREE-RUNNING PROPELLERS

4.1 Conventional Procedures

The first case to be considered is a free-running propulsion device advancing in an otherwise undisturbed fluid with constant speed V. The volume, momentum, and energy velocities at the inlet section of the boundary of the system in this case are by convention

$$V_1 = V \ , \tag{49}$$

$$m_1 = V \ , \tag{50}$$

and

$$r_1 = V \ , \tag{51}$$

respectively, and the inflow efficiency is therefore

$$\eta_{INF} = 1 \ . \tag{52}$$

The inflow section of the fluid boundary may be imagined as a large surface around the propeller leaving an appropriate hole for its jet to pass. Due to the convention adopted, no further details have to be specified.

Provided now that the mean thrust and power of the propeller are measured, how far may we proceed in the evaluation of the performance criteria

introduced? Apparently only the overall propeller efficiency may be determined as a function of an arbitrary advance ratio, of some reference length is introduced. This situation changes when either the maximum cross section A_0 or the outlet cross section A_2 of the propeller is introduced, which ever may be typical for the dynamically equivalent ideal propeller. Now, the load factor

$$C_{TI} = 2T/(\rho V^2 A_i) \tag{53}$$

may be defined and consequently the universal advance ratio

$$\eta_{IDEAL} = 2/(1 + \sqrt{1 + C_{T_0}}) \tag{54}$$

or

$$\eta_{IDEAL} = 4/(3 + \sqrt{1 + 2C_{T_2}}) \ . \tag{55}$$

This again is a conventional procedure circumventing the difficult measurement of the mass flow. In the case of unducted propellers it appears to be the only possible procedure.

From the propeller efficiency and the ideal efficiency so determined, the basic performance characteristic, the hydraulic efficiency, may be derived, i.e., actually from the data usually at hand; Schmiechen, 1966.2. In case these are provided in terms of the nondimensional parameters (11)-(13) the load factor may be determined according to the formula

$$C_{T_i} = 2K_{T_i}/J^2 \ . \tag{56}$$

Although the whole procedure appears to be rather straightforward its application is often hampered by the ambiguity in the choice of the appropriate cross section. While the selection of the maximum cross section may (e.g., for shrouded propellers) at least for the larger area ratios

$$\alpha = A_2/A_0 \tag{57}$$

result in hydraulic efficiencies exceeding unity this difficulty does not arise, if the outlet cross section is selected as reference.

The reason for this effect is simply, that in the first case the geometrically equivalent ideal propeller is referred to, while in the second case the dynamically equivalent reference propeller is chosen. Unless no appropriate criterion for the space requirement of a propeller has been defined the usual, oversimplified comparison of shrouded and unshrouded propellers does not make much sense; Saunders, 1957, and predecessors.

4.2 Further Analysis

The analysis may be carried on following the lines indicated, if further information is provided, e.g., the mass flow through a ducted system. From the momentum principle, the momentum outflow

$$M_2 = \rho QV + T$$

may be determined and accordingly the corresponding momentum velocity

$$m_2 = V + T/\rho Q \ , \tag{58}$$

the ideal efficiency, and the basic performance characteristic.

Further on the volume velocity

$$V_2 = Q/A_2 \tag{59}$$

may be determined, which will in general differ from the momentum velocity, while the conventional procedure implies the equality

$$V_2 = m_2 \ , \tag{60}$$

due to the lack of relevant information.

From the definitions of the various velocities, which may be rendered in the forms

$$V_i = Q/A_i = f/A_i \int_{1/f} \int_{A_i} v \, dA \, dt \ , \tag{61}$$

$$m_i = M_i/(\rho Q) = f/Q \int_{1/f} \int_{A_i} v^2 \, dA \, dt \ , \tag{62}$$

or

$$2e_i = 2E_i/\rho Q = f/Q \int_{1/f} \int_{A_i} v^3 \, dA \, dt \ , \tag{63}$$

the approximate relation

$$e_i \approx 3/2 \, m_i v_i - v_i^2 \tag{64}$$

may be derived.

This relation however crude the approximation provides at least a first estimate of the specific energy at the outlet and consequently of the outflow efficiency and the jet efficiency from measured integral values. Theoretical values may be obtained according to the same rule; Schiele, 1967.

For propellers discharging above the free fluid surface the analysis may be even more refined due to the fact, that the momentum outflow may be determined directly by means of a balance struck by the jet; Fig. 5. In this case it appears reasonable to treat the resistance

$$R = M_2 - \rho QV - T \tag{65}$$

separately, as the ducting system will in general serve as strut.

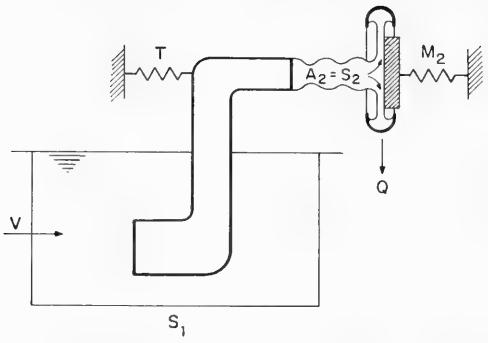

Fig. 5 - Free-discharge device

The other possibility would be to determine the inflow momentum velocity

$$m_1 = (M_2 - T)/\rho Q \tag{66}$$

differing from the advance speed, i.e., the propeller would have to be considered acting in its own wake. Although nothing would be wrong with that concept, it would not fit into our picture of a free-running propeller.

As far as the intake efficiency is concerned performance data are conveniently presented in terms of the nondimensional pressure drop

$$\zeta = (e_1 - e_{10})/v_{10}^2 \tag{67}$$

as a function of the velocity ratio

$$\nu = V/v_{10} \ . \tag{68}$$

According to the former definitions, the inlet efficiency is now

$$\eta_{INL} = 1 - 2\zeta/\nu^2 \ . \tag{69}$$

As it may assume very large negative values, the modified inlet efficiency

$$\bar{\eta}_{INL} = 1/(2 - \eta_{INL}) \tag{70}$$

avoiding this inconvenience may be used as inlet performance criterion.

5. PROPELLER-HULL INTFRACTION

5.1 Uniform Inflow

In order to reconstruct the basic ideas concerning the interaction between a propeller and the vehicle to be propelled, let us first consider the case of

uniform inflow to the propeller, although this is not likely to occur in practice. As basic model we may imagine a propulsion device of advance speed V with respect to a large body of fluid but the propeller acting in a wide stream of velocity wV in that fluid, no matter how this stream may be generated. Actually this model excludes interaction phenomena proper. We are still considering free-running propellers changing only the reference conditions; the propeller does not change the stream it is acting in.

To account for this change we have to distinguish between the propulsive efficiency and the propeller efficiency as defined earlier. As the case of a fluid stream generated by a ship hull, i.e., a wake, w denoting the wake fraction, is of particular interest, the propulsive efficiency

$$\eta_{EFF} = RV/P \ , \tag{71}$$

i.e., the effective efficiency of the propeller, R denoting the resistance of the vehicle equal to the net thrust of the propeller delivered under service conditions, whatever the definitions of both magnitudes may be.

With the thrust deduction

$$1 - t = R/T \tag{72}$$

and the hull efficiency

$$\eta_{HULL} = (1 - t)/(1 - w) \ , \tag{73}$$

the effective or propulsive efficiency is obtained in the conventional form

$$\eta_{EFF} = \eta_{HULL} \, \eta_{PROP} \ . \tag{74}$$

For specified uniform wakes the thrust deduction, and therefore the hull and the effective efficiencies, may be determined theoretically, if the thrust deduction due to friction is neglected in a first approximation, when practical application is concerned.

While for wakes w_0 of the same pressure, i.e., the same potential energy, as the surrounding fluid, the hull efficiency is simply

$$\eta_{HULL} = 1/(1 - w_0) \ ; \tag{75}$$

in any other case a thrust deduction has to be taken into account. It may be determined from a comparison of the actual propeller with a dynamically equivalent propeller outside the regime of modified pressure, i.e., outside the near-field of the ship, both producing the same race far downstream, supposing that such a propeller may be constructed. The conditions of equivalence are the equalities of mass flows encountered and power transmitted to the wake at the one and the other pressure level, explicitly,

$$Q_0 = Q \tag{76}$$

and

$$(E_2 - E_1)_0 = E_2 - E_1 \ . \tag{77}$$

As a consequence, the general relation

$$1 - t = \frac{1/\mu_0 - 1}{\varphi(1/\mu - 1)} \tag{78}$$

for the thrust deduction may be derived, where

$$\varphi = \frac{1 - w}{1 - w_0} \tag{79}$$

denotes the wake ratio. The additional condition for the determination of the momentum ratio of the equivalent propeller may be rendered in the simplified form

$$1/\mu_0^2 = \varphi^2(1/\mu^2 - \eta_{OUTF}) - \eta_{OUTF} \tag{80}$$

if the condition

$$(\eta_{INF})_0 = \eta_{INF} = 1 \tag{81}$$

and the approximation

$$(\eta_{OUTF})_0 = \eta_{OUTF} \tag{82}$$

are introduced.

In terms of the load factor, the inverse momentum ratio of the propeller itself is either

$$1/\mu^2 = 1 + C_{T_0} \tag{83}$$

or

$$1/\mu^2 = 1 + C_{T_2} + \sqrt{1 + 2C_{T_2}}\,, \tag{84}$$

which ever applies. Accordingly, the thrust deduction may be determined as a function of the wake ratio, the load factor, and the outflow efficiency. Apart from the generalization the basic concepts as well as the details of the present reasoning differ considerably from those proposed by Dickmann, 1939.

The notion that the thrust deduction does not affect the power balance may be illustrated by the consideration of a ducted system, only the intake of the duct taking part in the interaction; Fig. 6. The suction at the hull and the thrust of the duct, being effected by the same pressure, vary in the same way for various configurations without any overall effect. The higher nozzle thrust results apparently only in higher frictional losses and the necessity of a stronger support.

5.2 Nonuniform Inflow

We have dealt so far with essentially free-running propulsion devices, the evaluation of performance criteria being based on measured integral values, no problems arising in the appropriate choice of the boundaries of the propulsion

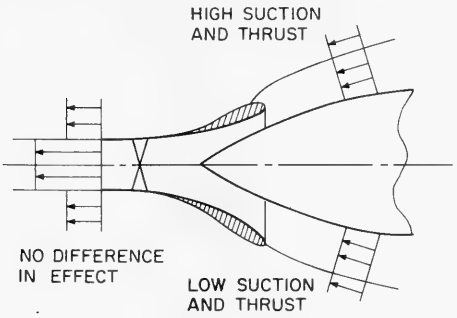

Fig. 6 - Propeller-hull interaction

system. The situation changes completely, when devices in nonuniform wake and built-in devices are under consideration.

The standard procedure of performance evaluation based on measured integral values as practiced in conventional propulsion where ever possible has often been felt inadequate; Prohaska et al., 1966. Attempts to resolve the inherent logical difficulties of the procedure, e.g., concerning the determination of the "correct" wake fraction, are neither satisfactory nor generally applicable; Horn, 1964. In many cases, neither resistance nor free-running tests, if feasible at all, furnish meaningful results.

The evaluation according to the general definitions established does not suffer from the drawbacks mentioned, but depends on the choice of the propeller boundary and the measurement of local values, which as a standard procedure is apparently not very convenient. When the wake fraction

$$w = 1 - m_1/V \tag{85}$$

and anything else has been determined, the thrust deduction may be estimated according to the same relations as before, when the outflow efficiency is replaced by the ratio of the out and inflow efficiencies.

In view of the final aim, the whole procedure is actually not very straightforward. Due to various reasons, not the least of which is the ambiguity in the choice of the propeller boundary, the concept of thrust as a propulsive force and a measure of performance turns out to be rather meaningless, however useful and necessary it may be for design and model-test purposes, etc. For the evaluation of the propulsive efficiency, only the net thrust under service conditions is of interest.

In the present context, this magnitude may be defined as

$$R = M_2 - \rho QV - F \tag{86}$$

in terms of magnitudes to be determined in propulsion tests alone, M_2 denoting the momentum outflow from the propeller outside the near field of ship and propeller, and F denoting a towing force, if any. For propellers discharging above the free surface, the measuring procedure is particularly simple; see Sec. 4.2.

In order to avoid the difficulties encountered in the determination of the propeller inflow details depending on the choice of the propeller boundary the following procedure is suggested. Instead of the hull, ideal, and jet efficiencies as defined before in terms of the inflow momentum velocity, we may introduce the effective efficiencies

$$\eta^*_{HULL} = \frac{(m_2 - V)\, V}{(m_2 - r_1)\, r_1} \tag{87}$$

$$\eta^*_{IDEAL} = \frac{2r_1}{m_2 + r_1} \tag{88}$$

and

$$\eta^*_{JET} = \frac{m_2^2/2 - e_1}{e_2 - e_1} \tag{89}$$

in terms of the inflow energy velocity.

This description of the propulsive performance in terms of energy rather than momentum has particular advantages. It avoids not only explicit, but even implicit references to the interaction forces between propeller and hull, however they may be defined. Further on the value of the mass-specific energy, e.g., is only weakly dependent on the location of the propeller boundaries and consequently the same holds for the effective efficiencies (87)-(89) and the effective performance characteristic

$$\begin{aligned} \eta^*_{HYD} &= \eta_{EFF}/(\eta^*_{HULL}\ \eta^*_{IDEAL}) \\ &= h^*\ (\eta^*_{IDEAL})\ . \end{aligned} \tag{90}$$

6. CONCLUSIONS

This outline of ideas and procedures concerning the definition and evaluation of performance criteria of pulse-jet propellers will not be complete without due reference to further extensions and generalizations.

As the basic principles are not restricted to propulsion systems, the deductions are euqally valid for reaction motors and brakes, if the quantities introduced are considered as algebraic. Two major disadvantages of a unified exposition, which has been envisaged, are that the efficiencies defined would assume any positive and negative value and that the word-language would be extremely clumsy.

While in a completely formalized presentation, making use of some sort of operational notation, these drawbacks may be fully compensated for by the advantages gained, they are prohibitive in the present context. The disadvantage of the suggestive language chosen is certainly that it may suggest exactly the

wrong thing. But as in any case a complete definition is provided, no difficulties should arise.

In order to render this presentation as systematic as necessary in view of the various concepts involved, the corresponding symbols and terms are not in any case in accordance with the ITTC Standard Symbols (1965), which as a collection of signs and words rather than a language proper, do not lend themselves readily for systematic work; Schmiechen, 1966.1.

The aim of this paper, the reconstruction of some concepts of the theory of propulsion in view of a wider application, has been achieved by deduction from the basic principles of hydrodynamics, resulting in consistent sets of performance parameters and criteria for any type of propulsion device, and thus, it is hoped, throwing new light on various problems, even in conventional propulsion.

The paper does not provide a review of the state-of-the-art concerning pulse-jet propellers and their possible applications elsewhere, but rather some concepts and procedures currently under consideration or applied at the Berlin Towing Tank.

This work is dedicated to Professor F. Horn. The partial support by the Deutsche Forschungsgemeinschaft, the Fraunhofer Gesellschaft fuer angewandte Forschung, the Max Kade Foundation, and the Massachusetts Institute of Technology is gratefully acknowledged.

NOTATION

The numbers after the definitions are those of the sections wherein the quantity is first mentioned or defined.

Magnitudes

A	cross sections, 3.1
C_T	load factors, 3.2
e	mass-specific energies, 2., 3.1
E	energy flows, 2.
f	frequency, 2.
F	towing forces, 5.2
FL	flows in general, 2.
J	advance number, 3.1
K	performance parameter, 3.1

L	length, 3.1
m	mass-specific momenta, 3.1
M	momentum flows, 2.
P	power, 2.
PR	production in general, 2.
Q	volume flow, 2.
r	energy velocities, 3.1
R	resistance, net thrust, 5.1
s	stresses, 2.
S	surfaces, 2.
t	time, 2., thrust deduction, 5.1
T	thrust, 2.
υ	local velocities, 2.
v	volume velocities, 3.1
V	speed, 2.
w	wake fraction, 5.1
α	area ratio, 4.1
ϵ	energy ratios, 3.2
ζ	nondimensional pressure drop, 4.2
η	efficiencies, 3.
η^*	effective efficiencies, 5.2
μ	momentum ratios, 3.2
ν	velocity ratio, 4.2
ρ	density, 2.

Indices

σ	maximum, 4.1., reference, 5.1
1	propeller inlet, 2.
2	propeller outlet, 2.
10	pump inlet, 3.3
20	pump outlet, 3.3
ℓ m	operational indices, 2.
DUCT	duct, 3.3
EFF	effective, propulsive, 5.1
EXT	external, 3.1
FLOW	flow, 3.3
HYD	hydraulic, 3.2
IDEAL	ideal, 3.2
INF	inflow, 3.2
INL	inlet, 3.3
INT	internal, 3.1
JET	jet, 3.2
OUTF	outflow, 3.2
OUTL	outlet, 3.3
PROP	propeller, 3.1
PUMP	pump, 3.3

REFERENCES

Brandau, J.H.: Aspects of Performance Evaluation of Waterjet Propulsion Systems and a Critical Review of the State-of-the-Art.

Washington: NSRDC, Oct. 1967; Rep. 2250.

Dickmann, H.E.: Wechselwirkung zwischen Propeller und Schiff unter besonderer Berueecksichtigung des Welleneinflusses.

STG 40 (1939) pp. 234-291.

Gutsche, F.: Die Entwichklung der Schiffsschraube im Licht des neuzeitlichen Stroemungslehre.

VDI-Z.81 (1937) No. 26, pp. 745-753.

Horn, F.: Ermittleing des Mittelwerts des Mitstroms aus Propulsions- und Freifahrtversuch.

Schiffstechnik 11 (1964) No. 59, pp. 131-136.

Prohaska, C.W.: Open discussion: Propeller session.

11.ITTC (1966) p. 327 f.

Saunders, H.E.: Hydrodynamics in Ship Design.

New York: SNAME, 1957, I, pp. 508 ff.

Schiele, O.: Ein Beitrag zur Theorie instationär und periodisch arbeitender Propulsionsorgane.

Karlsruhe: TH, 1961; Dissertation.

Schmiechen, M.: Theoretische Ansätze.

STG 54 (1960) pp. 208-217.

Schmiechen, M.: Open discussion: Presentation session.

11.ITTC (1966) p. 593.

Schmiechen, M.: Formal discussion: Paper by Grim.

STG 60 (1966).

ITTC Standard Symbols.

Feltham: NPL, Sept. 1965; Ship Rep. 77.

DESIGN ANALYSIS OF GAS-TURBINE POWERPLANTS FOR TWO-PHASE HYDROPROPULSION

Rodolfo Pallabazzer
Politecnico di Milano
Milan, Italy

INTRODUCTION

Marine propulsion is probably one of the most contradictory fields of engineering research. Many propulsive systems and problems are in fact developed in detail, but we do not have an exact idea of what kind of system would be the optimum beyond the speed range in which we now operate. There are no uncertainties about hydrodynamic problems, because the hydrodynamic phenomena are uniquely determined by the motion itself; besides, the solutions until now proposed to delay hydrodynamic problems are hydrodynamically corrected and can be easily shared; therefore, hydrodynamic problems are in a refinement and improving phase for some time to come.

This cannot come true for propulsive problems; any new speed field or environment yields special exigencies, related to the achievement of high propulsive performances, such as low fuel consumption, low weight, large range, mechanical simplicity, reliability, governing, control stability, and low additional drag induced by the propulsor on the base vehicle.

Such a collection of disparate and often contradictory problems needs not only lengthy and specialized research but also a wide-ranging tentative activity, by means of which one could evaluate the availability of new solutions and achieve exact ideas about the real exigencies of the operative field one wants to penetrate.

One must admit that this kind of lengthy research is very poor, in marine propulsion, especially when compared to aerospace propulsion. Few solutions have been proposed and developed as advanced propulsors, apart from the well-known supercavitating propeller and the water jet, and no solution has been proposed for the powerplant but the classical mechanical connection between a gas turbine and the propulsor. [Since the only jet propulsor sufficiently developed for marine propulsion is the water-jet (or pump-jet) system, in the following it will be also the fundamental term of comparison for other jet devices.]

A new kind of propulsor has been proposed by Foa [1,2,3,4] based on non-steady (cryptosteady) energy exchange between two fluids; this idea has been not sufficiently developed for underwater propulsion to approach the expected

performances. A turbofan whose thrust can be augmented by water injection has been recently presented [5,6], but the results were too concise to achieve an exact idea of the characteristics.

A propulsive ejector driven by compressed air was projected some years ago [7,8], without later being developed. Apparently the interruption of the project was due to the actual performances of the propulsor.

As will be outlined later, while the energetic efficiency of the ejector can be sufficiently high, being increased by the velocity, the thrust performances can be very poor, showing strong collapse at increasing speed. It will appear that cold air expressly compressed for powering an ejector is not the best generator for this purpose; besides, new ejector designs can raise the thrust performances.

The reasons for studying the ejector as a means of propelling a body in or on water, in spite of the aforementioned limitations, depend on the fundamental simplicity of such a propulsive device whose merits are weight, maintenance, failure and noise, no mechanical transmission, no water deadweight on board, no inlet clog risk, brief internal duct length and reduction of internal losses with regard to water-jet ducts, and availability of underwater instead of surface jet. The gain of weight by itself is a sufficient merit of a two-phase propulsor compared to a water-jet system.

For example, if we figure substituting the propulsor of the Boeing water-jet hydrofoil PG-H(2) with an ejective device, the gain of weight is of 1.78 tons, which means 53% of the power apparatus (turbine + pumps + water) and 3.5% of the net displacement (50 tons).

These reasons are sufficiently valid to require an exhaustive analysis of the ejector as a device for two-phase propulsion. This analysis has to be developed in two directions: (a) powerplant investigation of the gas generator and its connection with the ejector, with the purpose of identifying the configurations which allow the best propulsive performances; this analysis can be initially developed by means of some idealizations about the two-phase exchange phenomena; (b) a theoretical-experimental investigation of propulsive ejectors, which allows identification of the most correct analytical idealization of the exchange and the optimum geometrical configurations of the ejector with regard to propulsive performances.

At the Istituto di Macchine, Politecnico di Milano, the first investigation has been widely developed, and its results are presented here, while the second investigation is just beginning at a two-phase tunnel which has been recently realized.

TWO-PHASE JET PROPULSION: STATUS OF ART AND BASES OF THE PRESENT STUDY

The working principle of an ejector is well known: In a propulsive device (Fig. 1), a secondary water stream, which arrives at the propulsor chamber

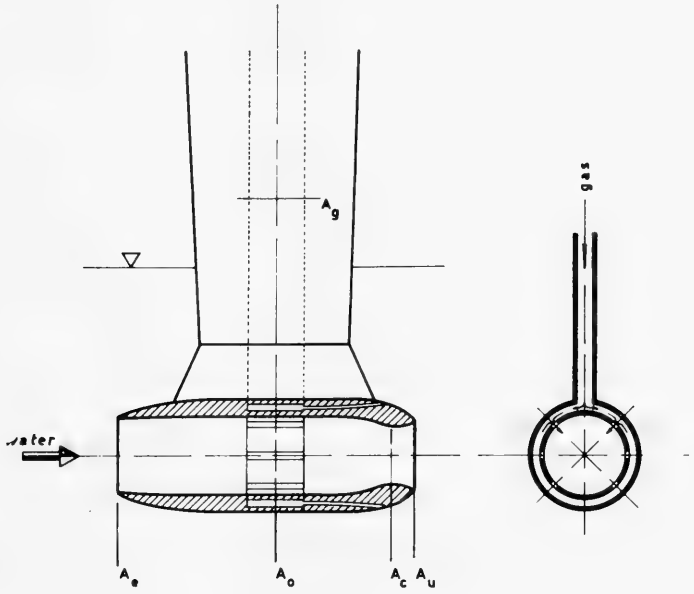

Fig. 1 - The Hydrojector: schematic cutway

owing to the free-stream velocity, is accelerated by a high-energy low-rate primary gas jet (supposed in the figure as injected from the chamber walls). The chamber can present a rectangular [8] or a circular [7] cross section. In an ideal propulsor there is no dissipation, since the water enters the chamber at same (high) pressure and (low) velocity of the gas. The basic effect consists in the production of a high-density two-phase compressible fluid, which can be accelerated in the nozzle to high speed. The drag effect is important just because it avoids slip, not because it accelerates water. In the hypothesis of no slip effect there will be no momentum exchange between water and gas, and the only phenomena in which we will be interested are the total amount of energy and the direct energy exchange. The slip effect can be very low in a two-phase mixture when operating at high-flow-rate ratios of water to gas (that is, in "bubble" flow). However, the slip effect can be differently strong, depending on the jet shattering into the water and on the bubble diameter, that is, on injection technique and on chamber design. An injection coaxial with the water stream (see, e.g., Ref. [9]) will provide a gas axial momentum recovery but also a strong slip effect with large bubbles mean diameter, while a radial injection [7] will destroy the axial momentum, producing small bubbles mean diameter and lower slip effect.

It is beyond the purpose of this work to investigate the methods of optimizing the ejector performances, and later an idealization will be done about its behavior.

As previously outlined, such an optimization can result only from a theoretical-experimental analysis restricted to the propulsive ejector. On the other hand, no extensive works appear to have been developed on this subject, and no exact indications are available about the validity of the hypotheses that can be done.

Besides, one must have in mind that the most delicate and uncertain phase of the two-phase flow is the first mixing phase, which takes place soon after the gas injection; it is generally a very turbulent phenomenon on a macroscopic scale, where the bubbles' path is random and analytically unforseeable. In this phase, only statistical, experimental data are available, reducing the overall merit of more exact analysis of the successive quasi-homogeneous nozzle flow.

Generally speaking, a wide bibliography on two-phase flow was published recently by Gouse [10].

More pertinent works on propulsive-type ejectors are listed in Refs. [7,9,11,12], while the theoretical bases of the most logical hypotheses are available in Refs. [7,9,13,14]. The only actual projects of two-phase propulsor appear to be those reported in Refs. [8,15,16,17]. In Ref. [18], a preliminary analysis of two-phase powerplant with a turbine as gas generator was developed, while in Ref. [19] a liquid-metal-water reactor was studied as a gas generator for two-phase underwater propulsion.

From another point of view, a propulsor based on cryptosteady energy exchange [1,2] can be ideally considered as a combination of a pump with an ejector, because of the mixing energy exchange phase which follows the pressure exchange phase. This means that, as compared with a shrouded propeller, the propulsor offers the ideal advantages of no cavitation, no mechanical connection or mixing contribution, while as compared with an ejector it offers the advantage of a highly efficient pressure energy exchange preceding the mixing phase. From a power-plant point of view, it will be immaterial how any performances can be actually obtained by a propulsor, when the propulsor behavior is idealized and when there are experimental confirmations of these performances.

On the basis of the previous considerations, several power plant-propulsor configurations have been analyzed by a simplified model of ejector behavior. Such an analysis allows a comparison either among configurations which have been studied under the same hypotheses or among configurations which require different kinds of hypotheses, when experimental data can confirm their validity under the same order of approximation. Some of these hypotheses can be considered as rather questionable because insufficiently confirmed by experimental data available at present. However, they represent a compromise between the exigencies of trustworthiness and simplification. While in fact a particle analysis of the two-phase exchange can be, and really was, already developed under a lower manifold of hypotheses [9,12] for studies regarding the propulsor alone, this kind of analysis would be absolutely impossible when evaluating the powerplant performances, because of the exceedingly high number of variables one should have to consider for an exhaustive investigation.

Therefore, as already outlined, two kinds of analysis must be developed: With the first one, the general powerplant has to be considered with a simplified analytical model of ejector to evaluate the most efficient configuration and its absolute performance with sufficient approximation; the second kind of investigation requires a particle-exchange analysis of the pure ejector, from both the theoretical and the experimental points of view, to identify the best propulsor design and mixing technique.

3 PROPULSOR ANALYSIS

3.1 Description

Actual hydrojet (IG) configurations are represented in Fig. 2. Cases (a) and (b) refer to surface vehicles (pump jets) and case (c) refers to an underwater vehicle (ducted propeller). No detailed configurations of propulsive ejectors are available in the literature, but appropriate configurations can be easily represented (Figs. 1 and 3). Figure 3 is deduced from the Marjet [8], where the chamber is obtained between two separated parallel foils, while Fig. 1 considers a circular chamber. This propulsor, where the water stream is accelerated just by the gas (which has been sometimes called "water ramjet") will be designated here as hydrojector (IR). No example exists of hybrid systems (that is, a pump associated with an ejector) apart from the Foa propulsor (Fig. 4a), where a gas pseudoblade takes the place of the conventional pump, being followed by a mixing phase. However, new types of hybrid propulsor with mechanical pump can be easily imagined (Fig. 4b, 4c). This kind of propulsor will be designated as pump-jector (IB). The most general fluid-dynamic model of the propulsor is presented in Figs. 5 and 6. In Fig. 5 the propulsor is axially symmetric and rectilinear. This model can be applied to underwater propulsors. In Fig. 6 an S-propulsor model is shown which can be applied to surface (water-air) propulsion.

The water stream velocity V_∞ is slowed down partially outside and partially inside the diverging inlet to the chamber value V_i. Here the water is first compressed by the pump at constant velocity, then accelerated by the mixing at quasi-constant pressure to the value V_0 at the nozzle inlet, where a two-phase homogeneous compressible flow enters, expanding to the external pressure at the exit. [The cylindrical shape of the chamber is not a statement; the experimental analysis must recommend the best shape. Therefore section (o) can be considered just as a reference.]

In underwater models, this pressure is equal to the free-stream one, while in S-models the exit pressure is the atmospheric one. In underexpanded nozzles, the pressure depends on the internal flow.

In the following, a simplified analysis of the propulsor is developed under the hypotheses of one-dimensional, homogeneous, ideal flow.

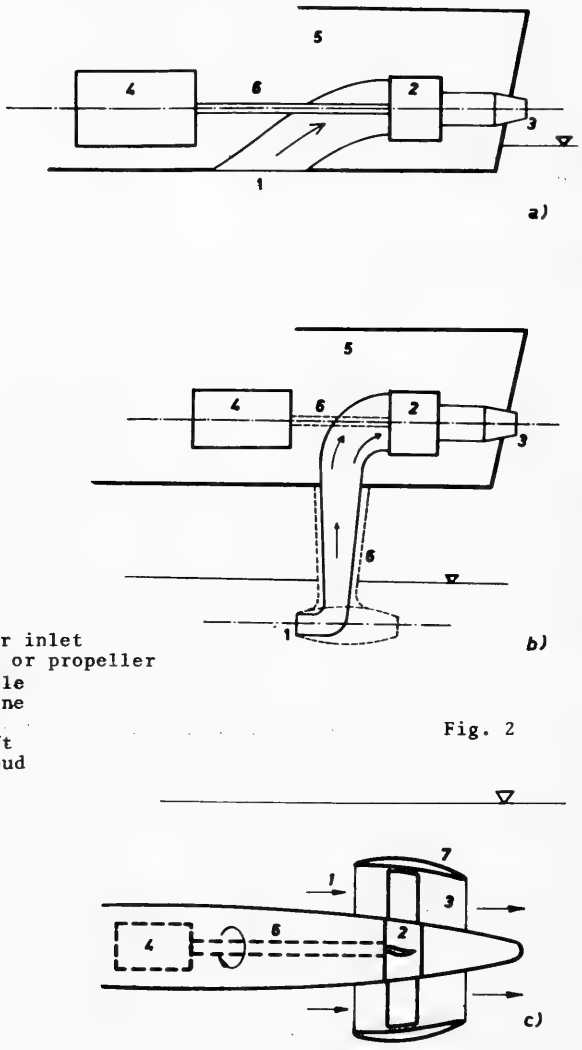

1 Water inlet
2 - Pump or propeller
3 - Nozzle
4 - Engine
5 - Hull
6 - Shaft
7 - Shroud

Fig. 2

Fig. 2 - Water-jet propulsive systems: (a) motorboat installation; (b) hydrofoil installation; (c) underwater ducted propeller

3.2 Fundamental Hypotheses

We will outline the hypotheses necessary for the analysis. All these hypotheses have been generally adopted in the literature (Refs. [7,8,9,11,12,13, 14,17]), but they will be briefly justified here too.

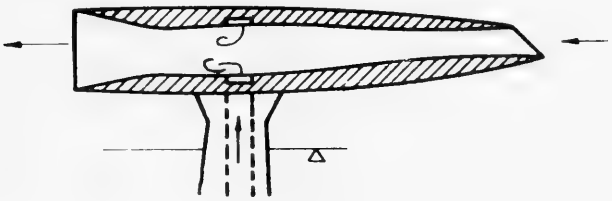

Fig. 3 - Planar hydrojector (Marjet)

(a) The motion is treated as one dimensional.

(b) The analysis will concern design performances.

(c) Water and gas enter the chamber at the same pressure p_i;

(d) The velocity V_i will be expressed by the *diffusion coefficient*,

$$\psi = 1 - \left(\frac{V_i}{V_\infty}\right)^2 , \tag{1}$$

the significance of which is clearly discussed in Ref. [20]. Here ψ is a design coefficient which is fixed on the ground of several exigencies (external and internal cavitation, losses, and flow rate).

(e) The internal pressure drag losses ΔH_a will be expressed by an overall *losses coefficient*

$$\xi = \frac{\Delta H_a}{V_\infty^2/2g} . \tag{2}$$

This is also a design coefficient, meaning that ξ can be considered as a constant only when the analysis refers to design performances.

(f) The two-phase flow is homogeneous. There will be no slip effects between water and gas, that is, water and gas move at same speed. The gas density ρ_g is negligible in comparison with the water density ρ_H, and the same thing happens for the mass flow rates, that is, the *mixing mass ratio* $\epsilon << 1$.

(g) The gas momentum will at the chamber inlet be neglected; this corresponds to the hypothesis of a complete viscous dissipation. The gas energy amount will be taken into account in the form of total enthalpy.

(h) The gas is perfect and ideal, but its nature will be taken into account by means of different thermodynamic coefficients.

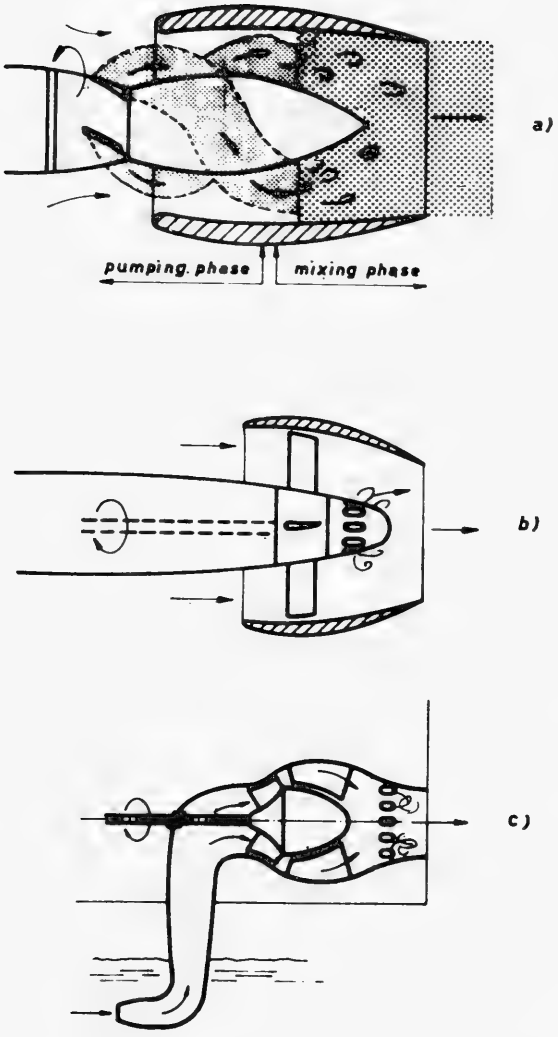

Fig. 4 - Pumpjector devices: (a) cryptosteady system; (b) underwater hybrid system; (c) hydrofoil hybrid system

(i) The gas expansion is adiabatic. This hypothesis is the most critical one, because it is surely not true. As a matter of fact, in one-dimensional homogeneous analysis one must assign the gas-expansion law, and the only other hypothesis which has also often been made (Ref. [8]), that is, an isothermal (at the water temperature) expansion, seems to be less valid than an adiabatic expansion, when the gas is at high temperature. It is obvious that the actual law will depend on the gas permanence time and contact

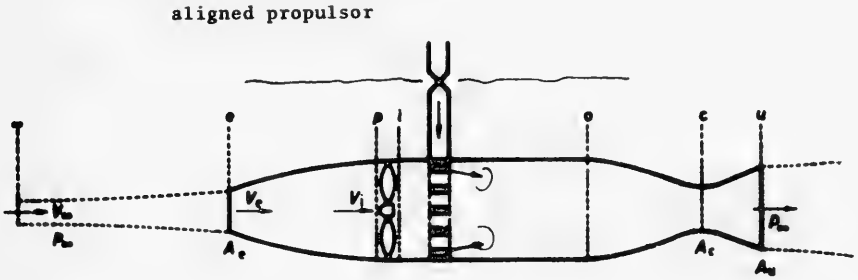

Fig. 5 - Fluid flow for aligned propulsor (a.p.)

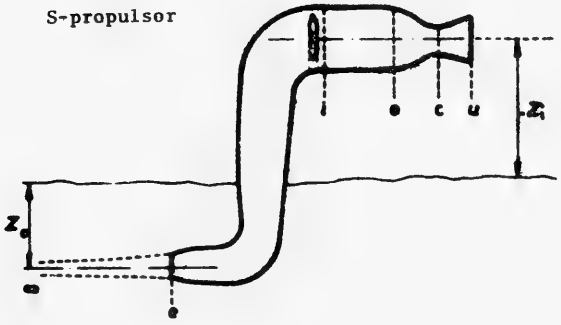

Fig. 6 - Fluid flow for S-propulsor (S.p.)

surface, that is, on the mixing technique, on the bubble dimensions, and on the propulsor length. Therefore, at present only experimental observations can suggest more exact ideas about the expansion law.

(j) No water evaporation is considered.

3.3 Basic Equations

With reference to Figs. (5) and (6), when the Bernoulli equation is applied between sections (∞) and (i) there results

$$p_i = p_a + g\rho_H z_i + g\rho_H H_p + \frac{\rho_H}{2}(V_\infty^2 - V_i^2) - g\rho_H \Delta H_a \ . \qquad (3)$$

Symbols are listed at the end of the paper; the z-coordinate is positive downwards. By means of dimensionless parameters, Eq. (3) can be written as:

$$\left.\begin{aligned} \beta'_e &= \frac{p_i}{p_a} = \beta_e(1+\beta_{ho}) = 1 + \beta_{hi} + \beta_p + \beta_o(\psi - \xi) \ , \\ \beta_e &= \frac{p_i}{p_\infty} = \beta_h(1+\beta_m) \ . \end{aligned}\right\} \tag{4}$$

The total energy balance between section (i) and the current section, which are aligned, can be written as

$$\dot{m}_H\left(\frac{p_i}{\rho_H} + \frac{V_i^2}{2}\right) + jg\dot{m}_g h_i = \dot{m}_H\left(\frac{p_i}{\rho_H} + \frac{V^2}{2}\right) + \dot{m}_g\left(jgh + \frac{V^2}{2}\right) .$$

This equation can be developed, by means of definitions and of thermodynamical relations, as

$$\frac{V_i^2}{2} + \frac{1}{\phi}\frac{p_i}{\rho_{gi}}\left(\epsilon + \phi\frac{\rho_{gi}}{\rho_H}\right) = \frac{V^2}{2} + \frac{1}{\phi}\frac{p}{\rho_g}\left(\epsilon + \phi\frac{\rho_g}{\rho_H}\right) , \tag{5}$$

where $\epsilon = \dot{m}_g/\dot{m}_H$ is the *mixing mass ratio.* The isentropic law furnishes

$$gj\,(h_i - h) = \frac{p_a(1+\beta_{ho})}{\phi}\,\frac{\beta_e}{\rho_{gi}}\,(1 - \beta_i^{-\phi}) \ . \tag{6}$$

Therefore, by means of Eqs. (4), Eq. (5) becomes

$$1 + \beta_{hi} + \beta_p + \beta_0(1-\xi) - (1+\beta_{ho})\frac{\beta_e}{\beta_i} - \frac{\rho_H}{p_a}\frac{V^2}{2} + \epsilon\frac{\rho_H}{\phi}(1+\beta_{ho}) \tag{7}$$

$$\times \frac{\beta_e}{\rho_{gi}}(1 - \beta_i^{-\phi}) = 0 \ .$$

Thus,

$$1 + \beta_n - \beta_h\frac{\beta_e}{\beta_i} - \frac{\rho_H}{p_a(1+\beta_{hi})}\frac{V^2}{2} + \frac{1}{\phi}\epsilon\frac{\rho_H}{\rho_{gi}}\beta_h\beta_e(1-\beta_i^{-\phi}) = 0 \ , \tag{7'}$$

which gives

$$V = \left[\frac{2\,p_a(1+\beta_{hi})}{\rho_H}\left(1 + \beta_n - \beta_h\frac{\beta_e}{\beta_i} + \frac{1}{\phi}\epsilon\frac{\rho_H}{\rho_{gi}}\beta_h\beta_e(1-\beta_i^{-\phi})\right)\right]^{1/2} . \tag{8}$$

Now let us define the *mixing volume ratio* λ:

$$\lambda = \frac{\dot{m}_g/\rho_g}{\dot{m}_H/\rho_H} = \frac{\rho_H}{\rho_g}\epsilon \ . \tag{9}$$

Different from ϵ, λ is not a constant but depends on local conditions. Denoting by $\lambda_i = \epsilon\rho_H/\rho_{gi}$ the volume ratio in the chamber, the previous equations become

$$1 + \beta_n - \beta_h \frac{\beta_e}{\beta_i} - \left(\frac{V}{V_r}\right)^2 + \frac{\beta_h}{\phi} \lambda_i \beta_e (1 - \beta_i^{-\phi}) = 0 \ , \qquad (7'')$$

$$V = V_r \left(1 + \beta_n - \beta_h \frac{\beta_e}{\beta_i} + \frac{\beta_h}{\phi} \lambda_i \beta_e (1 - \beta_i^{-\phi})\right)^{1/2} \ . \qquad (8')$$

It will be useful to apply Eq. (8') at the nozzle exit for evaluating the exit velocity V_u in two particular cases:

(i) *aligned propulsor* (Figs. 1, 3, 4a, 4b, 5):
It results $z_i = z_o$, $\beta_{hi} = \beta_{ho}$; $\beta_n = 1$. The external pressure is p_∞, and therefore $\beta_{iu} = p_i/p_\infty = \beta_e$. Therefore,

$$V_u = V_r \left(\beta_n + \frac{1}{\phi} \lambda_i \beta_e (1 - \beta_e^{-\phi})\right)^{1/2} \ . \qquad (10)$$

(ii) *S-propulsor* (Figs. 2a, 2b, 4c, 6):
It is $\beta_{ho} > o$ and $\beta_{hi} < o$, while the external pressure is now p_a, and therefore $\beta_{iu} = p_i/p_a = \beta_e'$:

$$V_u = V_r \left[1 + \beta_n - \frac{1}{1 + \beta_{hi}} + \frac{\beta_h}{\phi} \lambda_i \beta_e (1 - \beta_e'^{-\phi})\right]^{1/2} \ , \qquad (10')$$

and, for the waterjet ($\lambda_i = 0$),

$$V_u = \frac{V_r}{(1 + \beta_{hi})^{1/2}} \left[\beta_{ho} + \beta_p + \beta_o (1 - \xi)^{1/2}\right] \ . \qquad (10'')$$

It appears from the previous equations that the flow inside the ejector depends just on the volume ratio instead of on the actual conditions of the gas injected. Besides, the solution will not depend on the compressibility of the two-phase mixture. On the other hand, it will be useful to introduce the compressibility into the flow equations, by the two-phase *pseudo-Mach number*. In the following an analysis will be outlined which was already developed partially in Refs. [7,14,21]. Let us define a *mean density* of the mixture (this is valid owing to the hypothesis of no slip) as

$$\rho = \frac{\rho_H A_H + \rho_g A_g}{A} = \rho_g + \frac{A_H}{A} (\rho_H - \rho_g) \simeq \rho_g + \frac{A_H}{A} \rho_H \ ,$$

where A is the local cross section, and A_H and A_g are the fraction of A occupied respectively by water and gas ($A = A_H + A_g$). On the other hand, we have $\lambda = A_g/A_H$. Therefore

$$\rho = \rho_g + \frac{\rho_H}{1+\lambda} = \frac{\rho_H + \lambda\rho_g}{1+\lambda} = \frac{\rho_H}{1+\lambda} = \frac{1}{\frac{\epsilon}{\rho_g} + \frac{1}{\rho_H}}. \tag{11}$$

By means of the water continuity between sections (i) and (o) (where $A_i = A_o$), we obtain the water acceleration as

$$\frac{V_o}{V_i} = \frac{A_o}{A_{Ho}} = 1 + \lambda_o . \tag{12}$$

Therefore $(1+\lambda)$ measures the water acceleration just due to the mixing at constant section. Let us now define the *pseudosonic velocity* of the mixture as

$$\frac{1}{c^2} = \frac{d\rho}{dp} = \frac{\frac{\epsilon}{\rho_g^2}\frac{d\rho_g}{dp} + \frac{1}{\rho_H}\frac{d\rho_H}{dp}}{\left(\frac{\epsilon}{\rho_g} + \frac{1}{\rho_H}\right)^2} = \frac{1}{c_g^2}\,\epsilon\,\frac{\rho_H^2}{\rho_g^2}\,\frac{1 + \frac{1}{\epsilon}\left(\frac{\rho_g}{\rho_H}\right)^2\left(\frac{c_g}{c_H}\right)^2}{\left(\epsilon\frac{\rho_H}{\rho_g} + 1\right)^2}.$$

A comparison between the orders of magnitude of the terms in the numerator allows us to neglect the second one, provided that

$$\epsilon >> 10^{-6} .$$

In this case, we have

$$c^2 = c_g^2\,\frac{(1+\lambda)^2}{\lambda}\,\frac{\rho_g}{\rho_H}, \tag{13}$$

which can be accepted as valid in the range

$$10^{-4} \le \epsilon \le 10^{-2} , \tag{14}$$

which is a practical operating range of our propulsor. By using the isentropic expansion law of the gas, and the definition

$$\frac{p_\infty}{p_a} = 1 + \beta_{ho} ,$$

Eq. (13) furnishes the following expression of the local pseudosonic velocity:

$$c^2 = K_1\,\frac{\beta_e}{\beta_i^\tau}\,\frac{(1+\lambda_i\,\beta_i^m)^2}{\lambda_i}, \tag{15}$$

where

$$K_i = \frac{k\,p_a(1+\beta_{ho})}{\rho_H} .$$

At the exit, Eq. (15) becomes

(a) *aligned propulsor* ($p_u = p_\infty$; $\beta_i = \beta_e$):

$$c_u^2 = K_1 \beta_e^{-m} \frac{(1+\lambda_i \beta_e^m)^2}{\lambda_i} . \tag{16}$$

(b) *S-propulsor* ($p_u = p_a$; $\beta_i = \beta_e'$):

$$c_u^2 = \frac{K_1}{(1+\beta_{ho})^\tau} \beta_e^{-m} \frac{(1+\lambda_i \beta_i'^m)^2}{\lambda_i} . \tag{16'}$$

The local *pseudo-Mach number M* is defined as

$$M = V/c . \tag{17}$$

It will be useful to identify the pseudosonic conditions, which can be obtained by equalizing Eq. (8') to Eq. (15). The corresponding value of $\beta_i = \beta_c$ is the critical expansion ratio

$$1 + \beta_n - \beta_h \frac{\beta_e}{\beta_c} + \frac{\beta_h}{\phi} \lambda_i \beta_e (1 - \beta_c^{-\phi}) = \frac{k}{2} \beta_h \frac{\beta_e}{\beta_c^\tau} \frac{(1+\lambda_i \beta_c^m)^2}{\lambda_i} . \tag{18}$$

By numerical procedure it will be possible to deduce β_c from Eq. (18). The exit pseudo-Mach number can be obtained from Eqs. (10) [or (10')], (16) [or (16')], and (17). The equations cannot show any useful solutions for the water-jet in terms of M, because of the limits (14). The previous equations define all the parameters necessary to the flow solutions when λ_i or ϵ are fixed.

In the present work we will, on the contrary, assign an exit value (M_u), and the values of λ_i or ϵ which are consistent with such exit value will be determined. By matching Eqs. (10) [or (10')], (16) [or (16')], and (17), one obtains the following equation:

$$B_1 \lambda_i^2 - B_2 \lambda_i - B_3 = 0 , \tag{19}$$

where

$$B_1 = \frac{\beta_e^m}{2_\phi} [2(\beta_e^\phi - 1) - M_u^2 (k-1)] \qquad \text{(aligned propulsor)}$$

$$= \frac{\beta_e^m}{2_\phi} [2(1+\beta_{ho})^\tau (\beta_e^\phi - 1) - M_u^2 (k-1)] , \qquad \text{(S-propulsor)} \tag{19'}$$

$$B_2 = kM_u^2 - \frac{\beta_p + \beta_o(1-\xi)}{1+\beta_{hi}} \qquad \text{(aligned propulsor)}$$

$$= kM_u^2 - (1+\beta_{ho})^m [\beta_{hi} + \beta_p + \beta_o(1-\xi)] , \quad \text{(S-propulsor)} \tag{19'}$$

$$B_3 = \frac{k}{2} M_u^2 \beta_e^{-m} .$$

Equation (9) furnishes two values of λ_i, both of which have physical meaning:

$$\lambda_i = \frac{B_2 \pm \sqrt{B_2^2 + 4B_1B_3}}{2B_1} = \frac{B_2 \pm \Delta^{1/2}}{2B_1} . \tag{20}$$

An analysis of the solutions allows us to observe that λ_i^+ is positive everywhere; $\lambda_i^+(M_u)$ is a monotonic function (Fig. 7), the asymptote of which corresponds to the condition $B_1 = 0$, that is, to (The following relationships are deduced for aligned propulsor.)

$$(B_1 = 0) \quad M_u'' = \left(\frac{2}{k-1} (\beta_e^{\phi} - 1) \right)^{1/2} \tag{21}$$

only up to a speed $\bar{V}_\infty$ where it happens simultaneously $B_1 = B_2 = 0$, that is,

$$\beta_n = \frac{2k}{k-1} (\beta_e^{\phi} - 1) , \tag{22}$$

for which $\bar{V}_\infty$ can be obtained numerically. Up to the same speed λ_i^- is always negative. Above $\bar{V}_\infty$, λ_i^- is positive above M_u'' and both solutions merge in a maximum at the condition where $\Delta = 0$, that is, at

$$M_u' = \frac{\beta_n}{\left[2k \left(\beta_n - \frac{\beta_e^{\phi} - 1}{\phi} \right) \right]^{1/2}} . \tag{21'}$$

In this range, λ_i^- shows the same asymptote at $M_u = M_u''$. Therefore, there is a range of M_u where two values of λ_i are possible at $V_\infty > \bar{V}_\infty$, and M_u shows a maximum, but this does not represent an indetermination because λ_i is the physical datum, while M_u, which has been selected as a datum in the numerical procedure, is actually a physical effect. In any case, that is, at any speed, there is a maximum M_u which cannot be exceeded (it will be M_u'' at $V_\infty < \bar{V}_\infty$ and M_u' at $V_\infty > \bar{V}_\infty$). It can be interesting to observe that in any case for $\lambda_i \to \infty$ $M_u \to M_u''$, which is the Mach number of the gas, as it would have to be. Another significant pseudo-Mach number is the one corresponding to $B_2 = 0$, that is,

$$M_u'' = (\beta_n/k)^{1/2} , \tag{21''}$$

since the speed $\bar{V}_\infty$ is obtained at $M_u'' = M_u''$'. All these conditions differently represent physical limits.

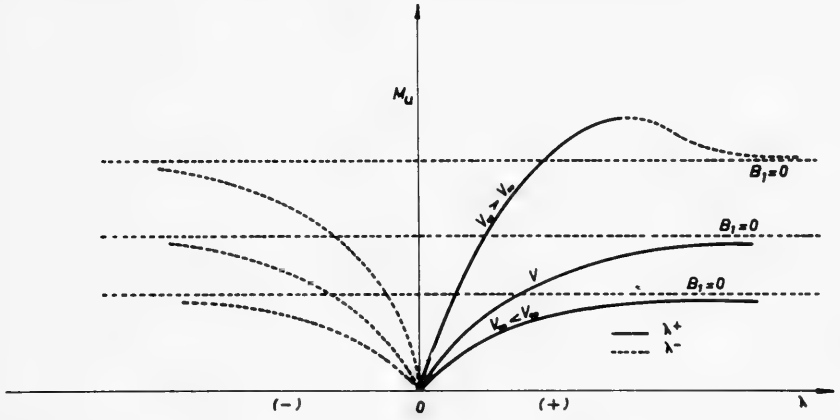

Fig. 7 - Qualitative variation of the discharge pseudo-Mach number M_u with chamber volumic flow ratio λ_i

In Fig. (8), $\bar{V}_\infty$ is represented for the aligned propulsor as a function of β_p, together with the corresponding pseudo-Mach number $\bar{M}_u$; in Fig. (9), the limit pseudo-Mach numbers M', M'', M''' are shown as a function of V_∞ for some values of β_p, while in Fig. (10) the same has been done for λ_i' (corresponding to $\Delta = 0$). All these functions have been calculated for $k = 1.35$ (exhaust gas) $z_o = z_i = 1$ m, $\xi = 0.2$, and $\psi = 0.9$ (these values will be discussed later), while in Fig. (9) the effect of changing ψ to $\psi = 0.6$ is shown.

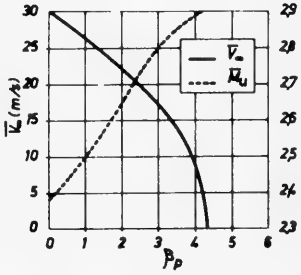

Fig. 8 - Variation of the transition velocity and discharge pseudo-Mach number $\bar{V}_\infty$ and $\bar{M}_u$ with β_p

From Eq. (11) one can deduce the cross section ratio A/A_H:

$$\frac{A}{A_H} = \frac{\rho_H}{\rho - \rho_g} = 1 + \lambda \ ,$$

$$\frac{A_o}{A_{Ho}} = \frac{\rho_H}{\rho_i - \rho_{gi}} = 1 + \lambda_o \ ,$$

and therefore

$$\frac{A}{A_o} = \frac{A_H}{A_{Ho}} \frac{\rho_i - \rho_{gi}}{\rho - \rho_g} = \frac{A_H}{A_{Ho}} \frac{1 + \lambda}{1 + \lambda_o} \ .$$

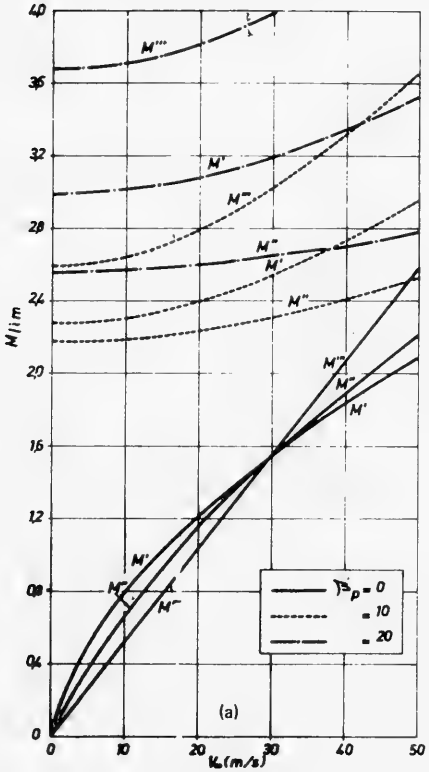

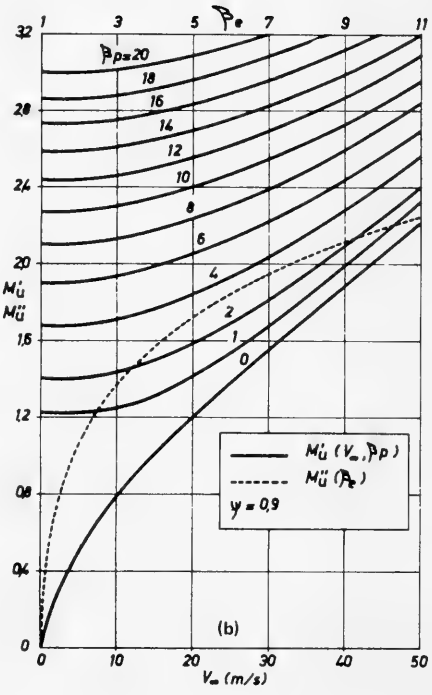

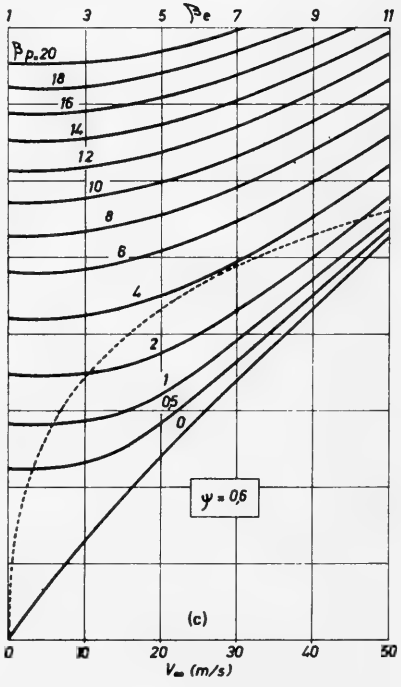

Fig. 9 - Variation of the limit pseudo-Mach number M'_u, M''_u, M'''_u with V_∞ and β_p, for ψ = 0.9 and for ψ = 0.6

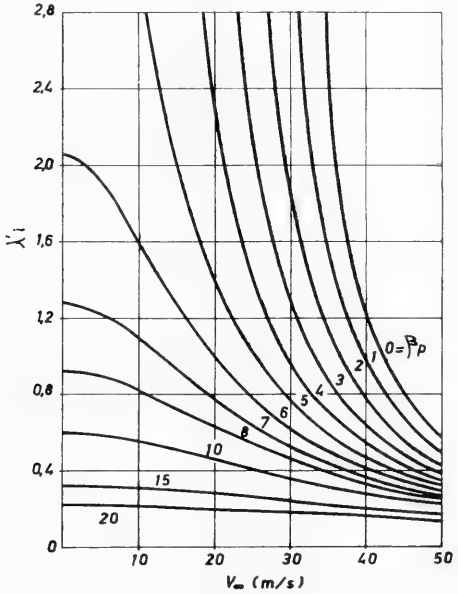

Fig. 10 - Variation of the transition volumic ratio λ'_i

By means of the water continuity and by Eq. (12) one obtains

$$\frac{A}{A_o} = \frac{V_i}{V}\left(1 + \epsilon\frac{\rho_H}{\rho}\right) = \frac{V_i}{V}(1+\lambda) = \frac{V_o}{V}\frac{1+\lambda}{1+\lambda_o},$$

which can be written as

$$\left.\begin{aligned} \frac{A}{A_o} &= \frac{A_i}{V}\theta \\ \theta &= 1 + \lambda = 1 + \lambda_i \beta_i^m \end{aligned}\right\}. \qquad (23)$$

By means of Eq. (23) it will be possible to calculate the local cross section, particularly the throat and discharge sections. In Fig. (11) the discharge ratios A_u/A_o are represented for a few values of β_p; for $\beta_p = 0$ the critical ratio A_c/A_o is represented too.

It is useful to remark that from Eq. (23) the continuity equation for the two-phase flow can be written as

$$\frac{AV}{1+\lambda} = \frac{AV}{1+\lambda_1\beta_i^\phi} = \frac{A_oV_o}{1+\lambda_o} = \text{const}. \qquad (23')$$

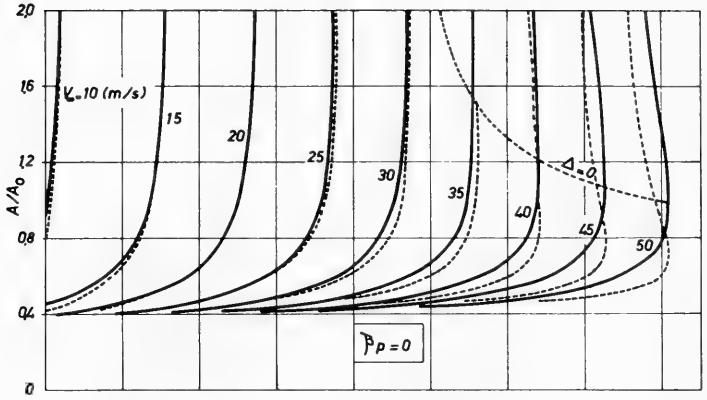

(a)

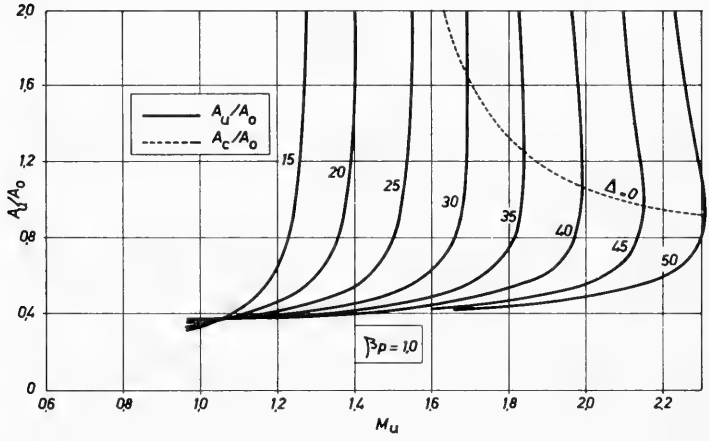

(b)

Fig. 11 - Variation of the exit (A_u/A_o) and of the critical (A_c/A_o) cross-section ratios with M_u for some values of β_p (ψ = 0.9, a.p.)

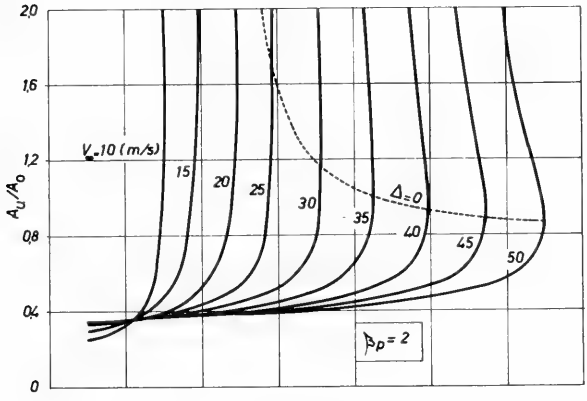

(c)

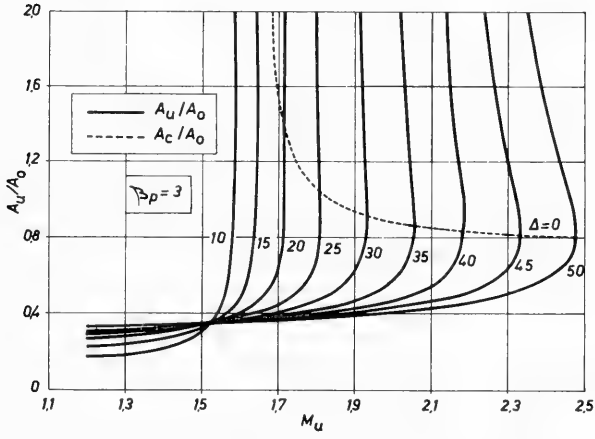

(d)

Fig. 11 - Variation of the exit (A_u/A_o) and of the critical (A_c/A_o) cross-section ratios with M_u for some values of β_p (ψ = 0.9, a.p.) (Continued)

It appears also that $A/A_o \rightarrow \infty$ when $\lambda_i \rightarrow \infty$, meaning that during the expansion the gas dilates more than the two-phase mixture. In Fig. (12), σ is plotted against A_u/A_o, and in Fig. (13), λ_i is represented as a function of V_∞, M_u, and β_p.

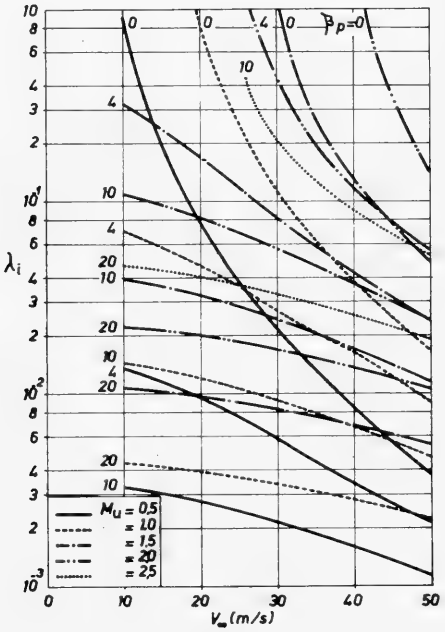

Fig. 12 - Variation of λ_i as a function of V_∞ for some values of M_u and β_p(ψ = 0.9, a. p.)

To sum up, the following remarks can be made:

(a) There is a typical velocity $\bar{V}_\infty$, below which any positive value of λ_i is obtained asymptotically; the pseudo-Mach number at the exit has a limit at $M_u = M_u''$, where λ_i becomes infinite. There are no physical but just sonic limits. At a velocity above $\bar{V}_\infty$, a maximum in the pseudo-Mach number is reached at $\lambda_i = \lambda_i'$, but λ_i still increases asymptotically as M_u decreases to M_u''.

(b) $\bar{V}_\infty$ corresponds to 30 m/s for $\beta_p = 0$ (that is for the *hydrojector*), while it decreases strongly at increasing β_p and becomes zero for $\beta_p = 4.3$. This means that the hydrojector at a speed above 30 m/s will tend to be unsuitable for reaching the highest performances; at increasing β_p the physical threshold advances but the value of λ_i' decreases at increasing β_p and at increasing speed (Fig. 10), becoming insensitive to the speed at the highest β_p.

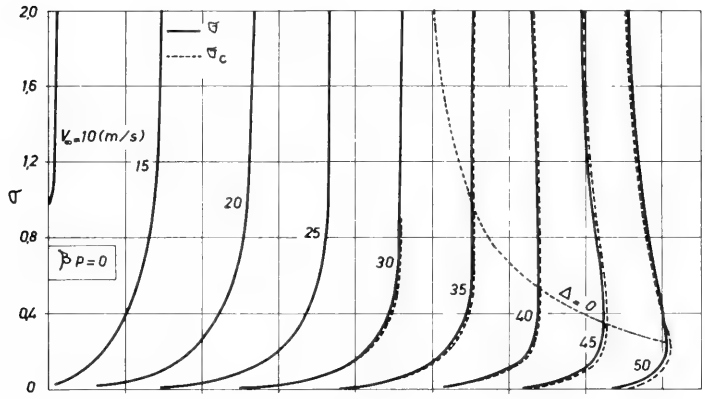

(a)

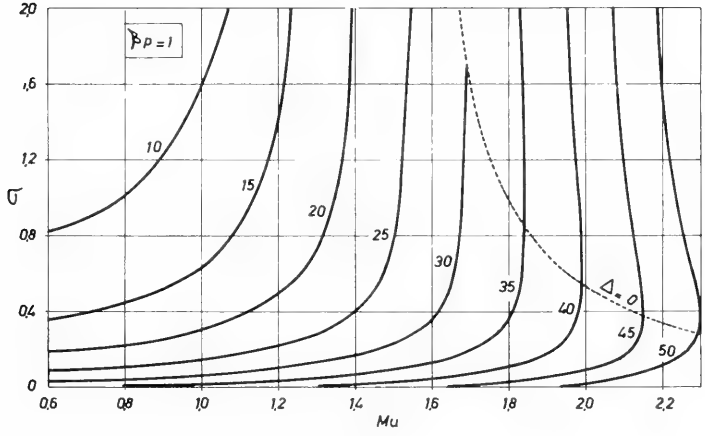

(b)

Fig. 13 - Variation of the specific thrust σ and its value σ_c corresponding to throat truncation (ψ = 0.9, a.p.)

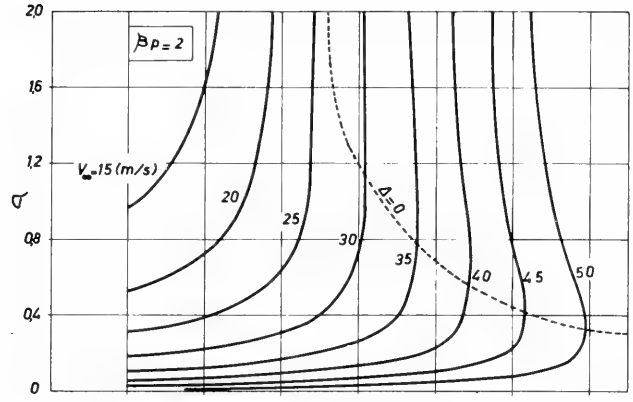

(c)

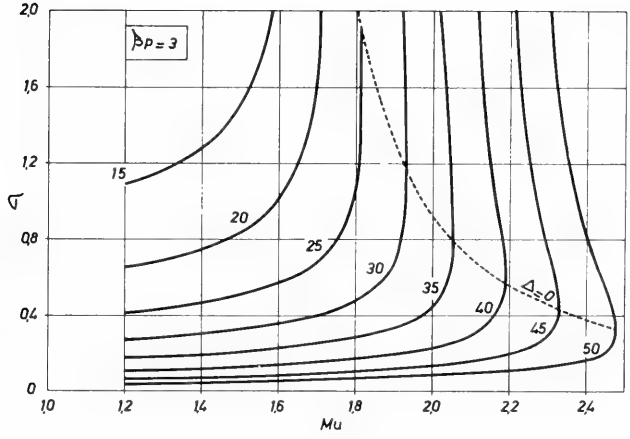

(d)

Fig. 13 - Variation of the specific thrust σ and its value σ_c corresponding to throat truncation (ψ = 0.9, a.p.) (Continued)

It already appears from these remarks that the hydrojector at moderately low speed seems to promise higher efficiency than the pumpjector and, by extrapolation, than the water jet.

(c) The functions λ_i, M_u', M_u'', M_u''', $\bar{V}_\infty$, $\bar{M}_u$, V_u, β_c, A_u/A_o, and A_c/A_o are independent of the actual conditions of the gas, which are expressed by the chamber density ρ_{gi}; they depend just on the parameters V_∞, β_p, and M_u, besides on the gas thermodynamical nature. On the contrary, the mass ratio ϵ will depend on ρ_{gi}, that is, on the engine powerplant configuration.

(d) The area ratios A/A_o present a strong increase in proximity of the discharge limits M_u'. It can often be $A/A_o > 1$, depending on the "dilatation" of the gas during the expansion, as was noted.

4 DEFINITION OF THE PERFORMANCE PARAMETERS

4.1 Thrust

For an adapted nozzle, the net thrust S will be

$$S = \dot{m}_H(V_u - V_\infty) + \dot{m}_g' V_u = \dot{m}_H V_\infty \left(\frac{V_u}{V_\infty} - 1 \right) . \tag{24}$$

Let us define a *specific thrust* as

$$\sigma = \frac{S}{\dot{m}_H V_\infty} = \frac{S}{\rho_H A_o V_\infty^2 (1 - \psi)^{1/2}} = \frac{V_u}{V_\infty} - 1 . \tag{25}$$

This is a fundamental figure of merit for comparison among propulsors of same design and advance velocity. On the other hand, the *thrust coefficient* c_s

$$c_s = \frac{S}{\frac{1}{2} \rho_H A_o V_\infty^2} = 2\sigma (1 - \psi)^{1/2} \tag{26}$$

depends on the frontal diameter of the propulsor instead of the overall design coefficient $A_o(1 - \psi)^{1/2}$; it will be especially useful in comparisons among propulsors of different shapes.

If the nozzle is truncated during supersonic flow (underexpanded nozzle), the thrust S_t will be

$$S_t = \dot{m}_H(V_u - V_\infty) + A_u(p_u - p_\infty) . \tag{24'}$$

In the present work we will take into consideration the case of nozzles which have been truncated at throat, that is, at the critical pressure p_c. The corresponding thrust is

$$S_c = \dot{m}_H(V_c - V_\infty) + A_c(p_c - p_\infty) , \tag{24''}$$

which can be written in dimensionless form as

$$\sigma_c = \frac{V_c}{V_\infty} - 1 + \frac{A_c}{A_o}(1+\beta_{ho})\frac{\beta_e/\beta_c - 1}{2\beta_o(1-\psi)^{1/2}} \qquad (25')$$

and accordingly

$$c_{sc} = 2\sigma_c(1-\psi)^{1/2} .$$

In Ref. [22] the feasibility of truncated nozzles for underwater propulsion was presented, showing that practically ideal performances can be actually obtained.

4.2 Efficiency

As can be seen from the literature, the efficiency of a propulsor in marine environment is the most discussed parameter, because of the difficulty of taking into account so many variables. In this work, two efficiencies have been introduced, that is, (a) the conventional *propulsive efficiency* η_p:

$$\eta_p = \frac{S V_\infty}{\frac{1}{2}\dot{m}_H(V_u^2 - V_\infty^2)} = \frac{2}{1 + \frac{V_u}{V_\infty}} = \frac{2}{2+\sigma} , \qquad (27)$$

where the gas contribution has been neglected. Its value for a truncated nozzle is

$$\eta_{pc} = \frac{2\sigma_c}{\frac{V_c^2}{V_\infty^2} - 1} . \qquad (27')$$

(b) an *overall efficiency* η_g, defined as the ratio between the propulsive power SV_∞ and the chemical energy inflow $\Delta E_c = jg\dot{m}_a(\alpha' + \alpha'' + \alpha_1\delta)\, H_i$ (α', α'' and $\alpha_1\delta$ are the fuel rate fractions)

$$\eta_g = \frac{SV_\infty}{\Delta E_c} = \frac{\sigma V_\infty^2}{jg\gamma(\alpha' + \alpha'' + \alpha_1\delta)\, H_i} . \qquad (28)$$

Since for underexpanded nozzles all the quantities at denominator cannot change because of the supersonic flow, the value of η_g for truncated nozzles is

$$\eta_{gc} = \frac{\sigma_c V_\infty^2}{jg\gamma(\alpha' + \alpha'' + \alpha_1\delta)\, H_i} = \eta_g \frac{\sigma_c}{\sigma} . \qquad (28')$$

This efficiency is the only one which could permit a comparison among completely different propulsive devices, such as the water jet and the hydrojector, since any mechanical power is excluded from the performances.

It is obviously impossible in such an analysis to take into account the effect of the external drag on the net thrust and on the efficiencies, and only qualitative considerations can be made about the additional drag induced by the propulsor and its appendages. Typical behavior of σ is showed in Figs. 14 and 13 for a few values of β_p, while in Fig. 14 σ is plotted against A/A_o. All these functions have been calculated for exhaust gas and for $\psi = 0.9$, as already mentioned. In Figs. 13 and 15, the values of σ_c for an underexpanded nozzle are reported for $\beta_p = 0$ (hydrojector).

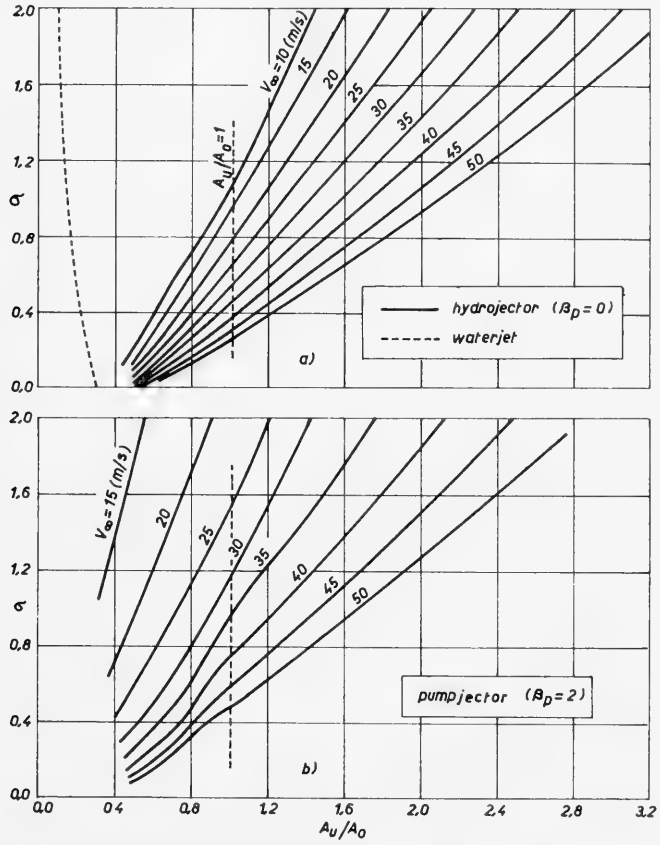

Fig. 14 - Variation of σ as a function of A_u/A_o for: (a) hydrojector ($\beta_p = 0$) and water jet; (b) pumpjector ($\beta_p = 2$) ($\psi = 0.9$, a.p.)

By means of the condition $\lambda_i = 0$ the previous equations get solved for the pure water jet. A plot of diagrams have been reported on Figs. 14, 16, 17, and 18 for the following data: $\psi = 0.9$, $\xi = 0.3$, $z_o = 1$ m, $z_i = -3$ m. In Fig. 19,

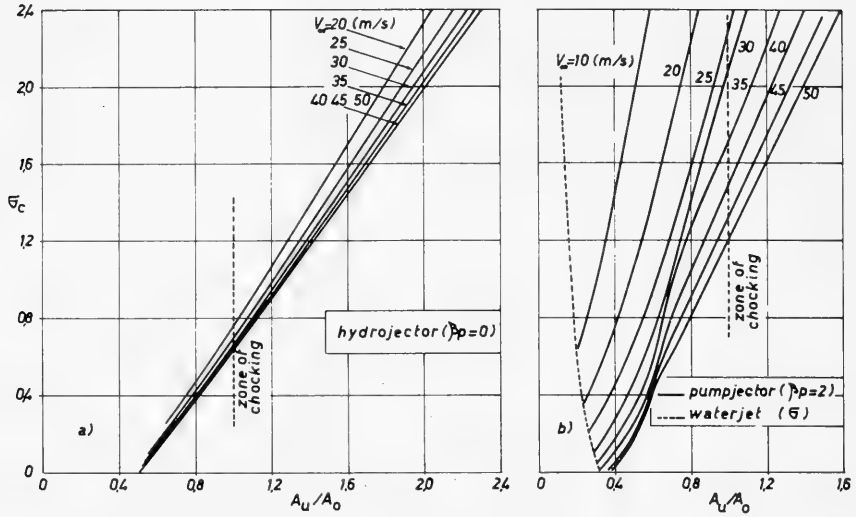

Fig. 15 - Variation of σ_c with A_u/A_o for: (a) hydrojector; (b) pumpjector ($\beta_p = 2$) compared with the water jet's σ

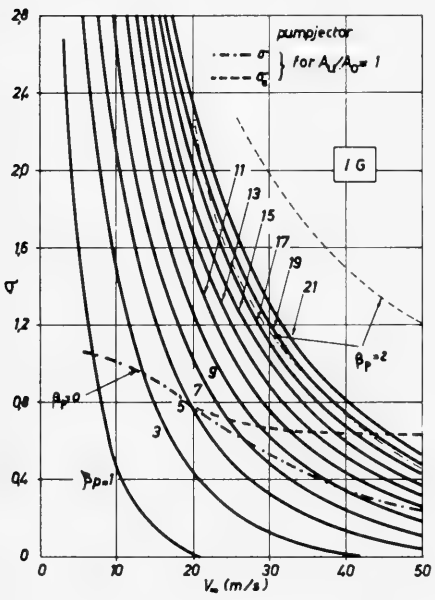

Fig. 16 - Variation of σ for a water jet with V_∞ and β_p (ψ = 0.9, S.p.), compared with the hydrojector (β_p = 0) and pumpjector (β_p = 2) values of σ and σ_c corresponding to A_u/A_o = 1 (ψ = 0.9, a. p.)

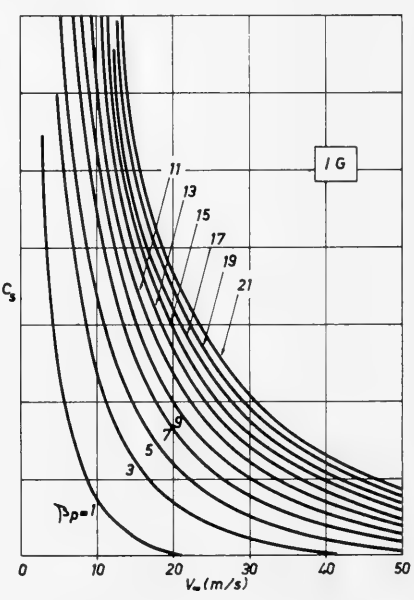

Fig. 17 - Variation of the thrust coefficient c_s for water jet (ψ = 0.9, S.p.)

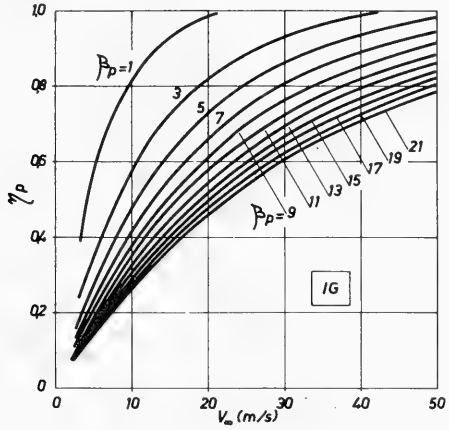

Fig. 18 - Variation of the propulsive efficiency η_p for waterjet (ψ = 0.9, S.p.)

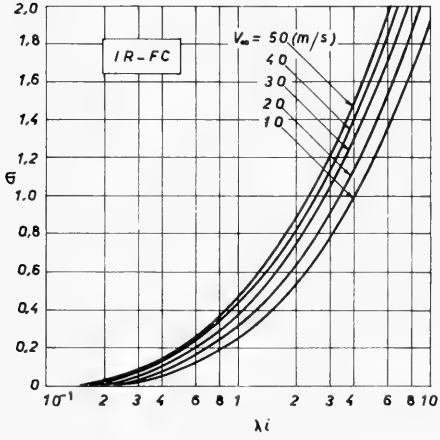

Fig. 19 - Variation of σ with λ_i, for a hydrojector (ψ = 0.9, a. p.)

20, and 21, σ, c_s and η_p as functions of λ_i have been diagrammed for an exhaust-gas ejector and for ψ = 0.9.

Finally, to evaluate the overall efficiency η_g, the solution of the powerplant equations will be necessary. It is possible to make the following remarks about the pure propulsive performances:

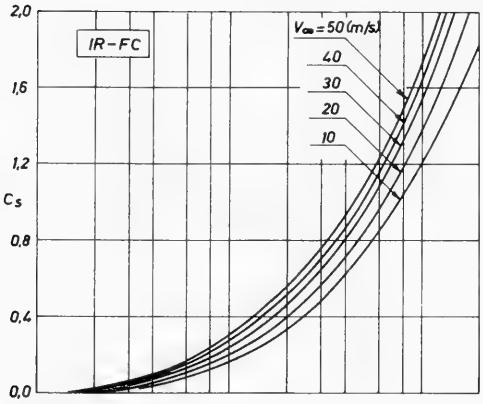

Fig. 20 - Variation of c_s with λ_i, for a hydrojector (ψ = 0.9, a. p.)

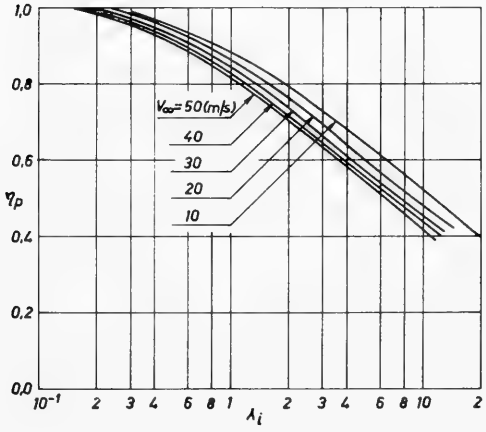

Fig. 21 - Variation of η_p with λ_i, for a hydrojector (ψ = 0.9, a. p.)

(a) In a range of λ_i of practical interest (this corresponds to a range of $10^{-4} < \epsilon < 10^{-2}$, which is both a valid solution of the equations and of practical interest), the hydrojector can provide higher specific thrust than the water jet at the same speed. While the increase of β_p becomes less and less efficient at higher values (Fig. 16), the effect of increasing λ_i is more and more efficient (Fig. 19); values of σ higher than 1 can be obtained at $\lambda_i > 2$.

From the equation of state and from Eq. (9) it can be seen that at given pressure and given ϵ, λ_i is proportional to the gas temperature. This means, for example, that the substitution of cold air at $T = 288°K$ with hot gas

at $T = 1150°K$ about quadruples λ_i and, from Fig. (19), triples or quadruples σ at same speed V_∞ and same flow rate ratio ϵ. Such comparison will appear clearly in the following part, where σ will be calculated. It is also noteworthy that η_p decreases while σ increases with λ_i.

This behavior, which is well known, will be pointed out later in comparison with the behavior of the overall coefficient, to stress the fact that the analysis of the propulsive efficiency can suggest completely wrong conclusions.

(b) A propulsive comparison among hydrojectors, pumpjectors, and water jets can be made only in terms of actual propulsive feasibility. Since the hydrojector and the pumpjectors can provide any thrust and any propulsive efficiency, two other design parameters must be examined, that is, the inflow ratio $\gamma = \dot{m}_a/\dot{m}_H$ and the cross-section ratio A_u/A_o. However, the parameter γ depends on the actual powerplant, and it will be discussed in the following paragraphs; here only a discussion on the cross-section ratio can be developed. As has been pointed out, the specific thrust of the water jet is really limited, but there are no problems about the exit cross section, because it will always be $A_u/A_o < 1$ (Fig. 14); that is, the chamber cross section is actually the significant propulsor cross section. It will be not so for two-phase propulsors, as can be seen from Figs. (11) and (14), because A_u/A_o often becomes >1; nay, the highest thrust is always obtained at $A_u/A_o > 1$. If one decides to function at A_u/A_o not higher than 1, a design limit on σ immediately descends. At $A_u/A_o = 1$ and $V_\infty = 50$ m/s, the hydrojector is poorer than water jets at $\beta_p > 11$, at $V_\infty = 30$ m/s this happens for water jets at $\beta_p > 9$. This means, for example, that the PG-H(2)-type water jet, which provides an advance speed of 26 m/s with $\beta_p = 17$ (see Ref. [23]) shows a thrust of $\sigma = 1.4$, while the hydrojector which has been limited by $A_u/A_o = 1$ offers $\sigma = 0.62$ at the same speed.

In Fig. (14) the behavior of σ (hydrojector) corresponding to $A_u/A_o = 1$ has been represented.

(c) In Figs. (13) and (15) the graph of σ_c, the thrust obtained by truncation of a supersonic nozzle at the throat, is also plotted. It is remarkable that a very faint decrease of thrust is associated with a strong decrease of the discharge cross section, which is now A_c. This behavior is emphasized in Fig. (16), where the curve of σ_c for $A_u/A_o = 1$ is plotted. It appears that now the thrust available for $A_u/A_o = 1$ is increased especially at high speed, where the thrust produced by hydrojector can be higher than that produced by water jet. It is also noteworthy (Fig. 15) that σ_c becomes practically insensitive to the velocity V_∞, for any given value of A_u/A_o.

(d) The presence of a pump strongly improves performance [Figs. (14) and (15)]. A pumpjector at $\beta_p = 2$ and $A_u/A_o = 1$ provides a specific thrust comparable with the one produced by a $\beta_p = 18$ water jet. If the nozzle is truncated at $A_c/A_u = 1$, the thrust can be more than double that for a $\beta_p = 21$ water jet (Fig. 16). On the other hand, a $\beta_p = 2$ water jet moving at $V_\infty = 15$ m/s (Fig. 14) shows $\sigma = 0.47$ with $A_u/A_o = 0.22$. If the same nozzle (that is the same A_u/A_o) is adopted in such a way that the exit cross section could represent a critical section for two-phase flow (Fig. 15b) a thrust of 0.64 can

be obtained. Therefore the pumpjector provides thrust improvement with regard to both water jet and hydrojector.

5 POWERPLANT ANALYSIS

5.1 Description

As already mentioned, three different kinds of connection between propulsor and powerplant have been studied:

(a) the *hydrojector* (Figs. 22 and 23), where a purely gas-dynamical connection is realized;

(b) the *water jet* (Fig. 24), with a purely mechanical connection;

(c) the *pumpjector* (Figs. 25 and 26) which can be realized either with both mechanical and gas-dynamical connections (Figs. 4b and 4c) or with a purely gas-dynamical connection which acts by both pressure and mixing exchange (Fig. 4a). This propulsor can be considered as either a change of previous propulsors or a completely new design; it can be seen as a device similar to the afterburner of a turbojet engine, both on thermodynamical and on performance point of view.

For all the powerplants a gas turbine was considered as the basic engine, whose behavior was suitably idealized. The gas turbine therefore will supply high-temperature high-pressure gas or mechanical power, or both, to the propulsor, as shown in the diagrams.

The fundamental powerplant configurations which have been analyzed are:

(i) a gas-turbine cycle provided by single or double combustion;

(ii) a turbine with three possible points for gas extraction: just before the turbine, at a suitable point during the turbine expansion, and just after the afterburner. The powerplant shown in Fig. (22d) or (25d) is the most general one, because cases (a), (b), and (c) can be obtained by regulation of scheme (d).

(iii) The gas for the ejector can be supplied by the secondary cycle of a bypass turbine or of a driven compressor (Figs. 23 and 26), with or without secondary combustion.

The thermodynamical cycles are represented in Figs. (27a and 27b). The constraints the powerplant must satisfy are:

(a) *hydromechanical constraint*, represented by the equality of the turbine net power and the pump or propeller power;

(b) *gas-dynamical constraints*, represented by the equality of the gas-extraction pressure, the chamber pressure, and the overall gas flow-rate continuity.

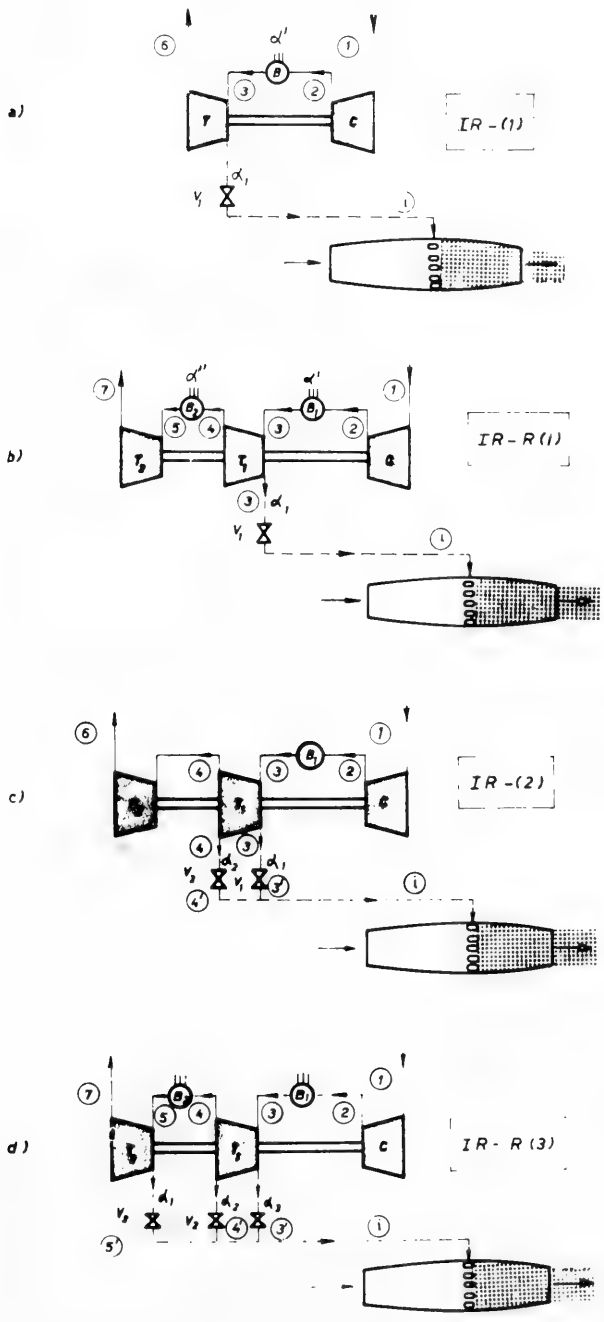

Fig. 22 - Hydrojector conventional powerplants

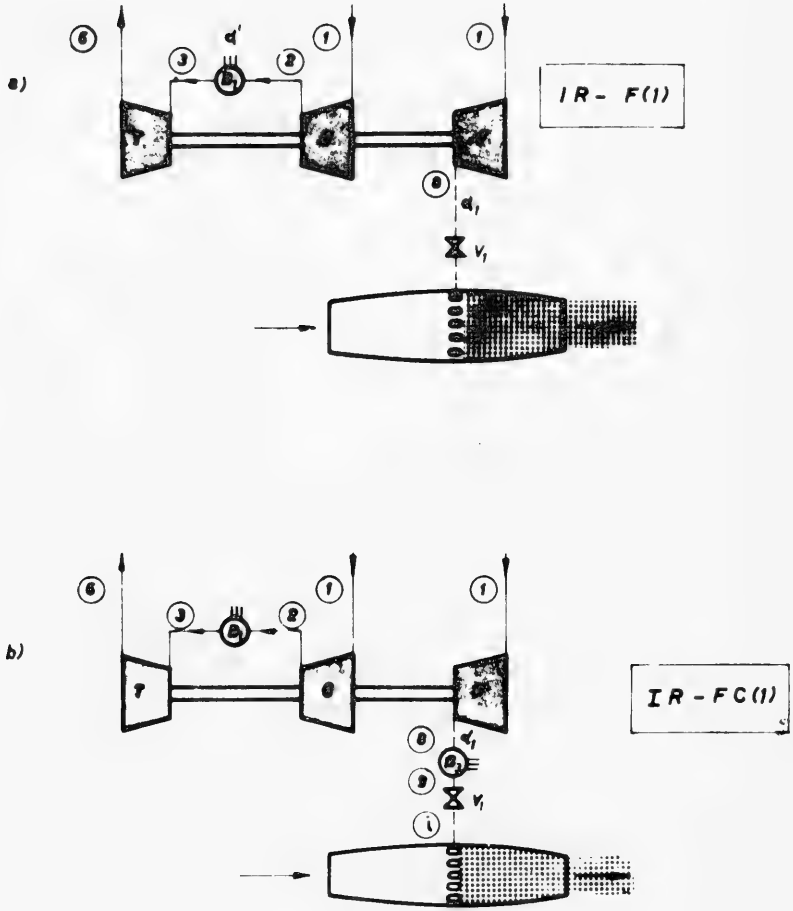

Fig. 23 - Hydrojector bypass powerplants

A pressure loss $\delta\beta$ is taken into account at the valves V_i of the powerplant. In the aforementioned figures, the abbreviations of the configurations which have been studied are given too.

4.2 Criticism

Here we will expound the reasons which led us to conceive and to analyze the previous configurations. As mentioned, the pure hydrojector was fairly well studied and designed in the literature, and its general advantages have been already emphasized, but what we would investigate was the overall effect on the propulsive performance of using hot, high-pressure, partially exhaust gas, instead of a cold gas (compressed air). The partially exhaust gas can provide

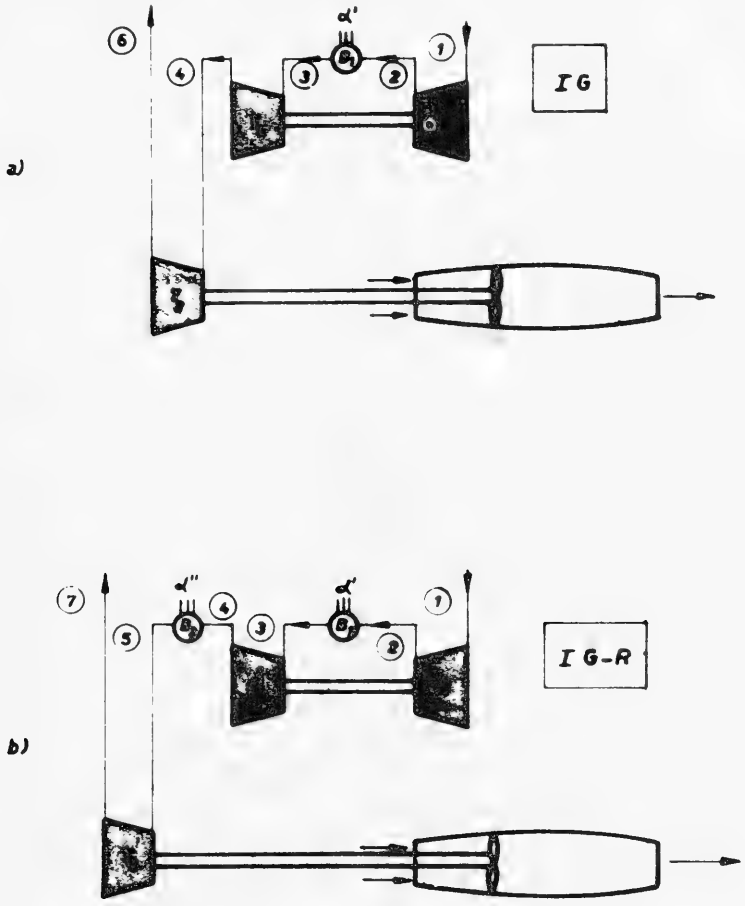

Fig. 24 - Water-jet powerplants

two kinds of advantages: (a) higher effect of the volume ratio λ_i at same mass ratio ϵ [as shown, the propulsive performances (σ, β_p, A/A_o, etc.) are increasing functions of λ_i; therefore an improvement of the performances could be expected when hot instead of cold gas is used], and (b) an improvement of the overall efficiency could also be expected when the gas was extracted from the turbine after partial expansion, because of the net work contribution given to the mechanical balance.

Therefore it seemed reasonable to analyze: (a) a conventional turbine with several possible points of gas extraction, and (b) a bypass turbine (or turbocompressor) to yield either cold compressed air or hot compressed gas (this being produced by secondary or auxiliary gas burner). The analysis of a cold-air ejector was introduced for sake of comparison, since this scheme corresponds to the Marjet propulsor, which has already been mentioned (Refs. [8,15,16]).

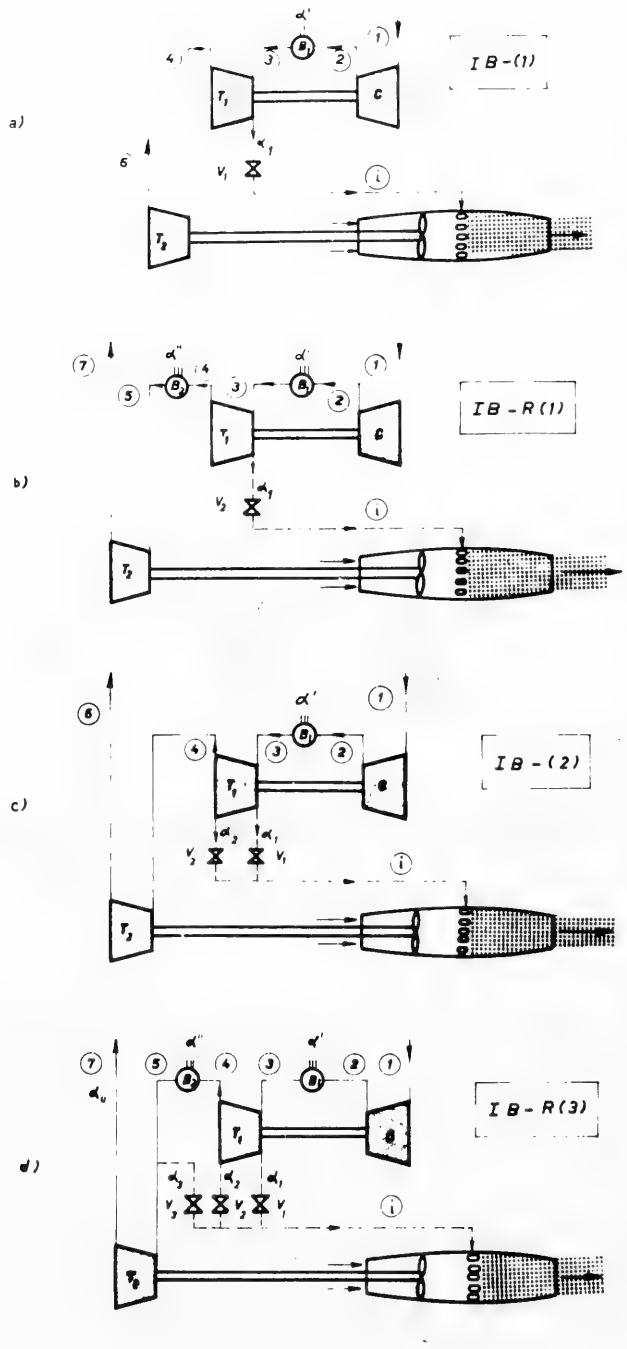

Fig. 25 - Pumpjector conventional powerplants

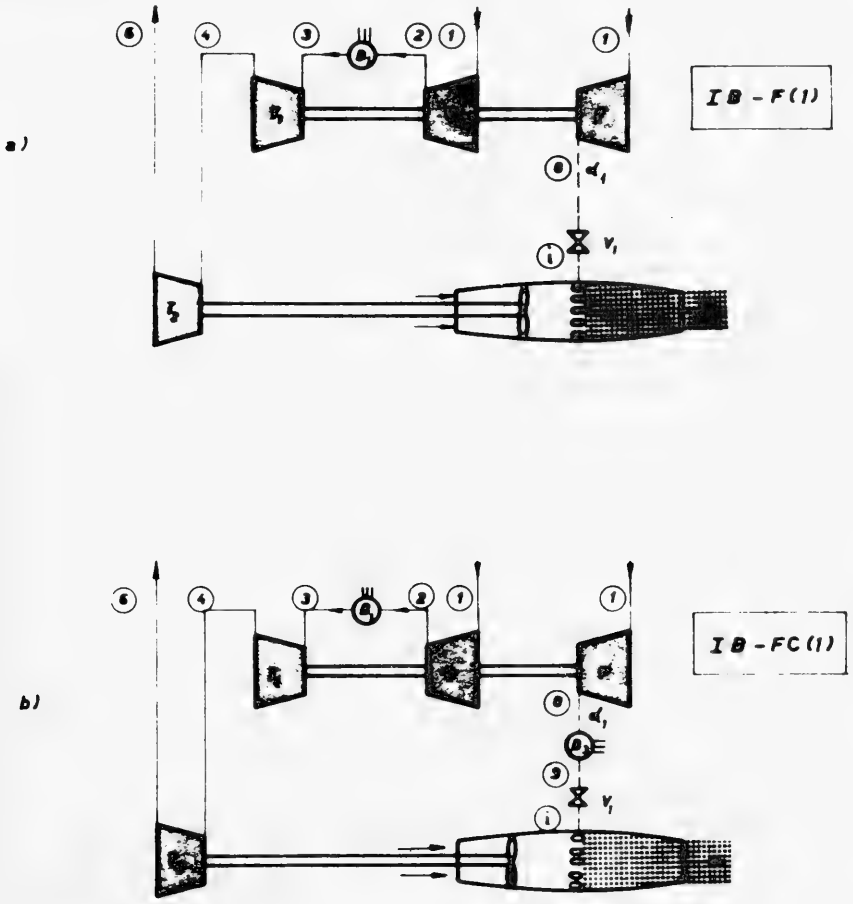

Fig. 26 - Pumpjector bypass powerplants

The foreseeable profit of hybrid propulsors, which could be imagined as either a conventional power system or a schematisation of a cryptosteady exchanger or an emergency auxiliary system for thrust augmentation was also noted. It was expected that its performances were a compromise between the water jet and the hydrojector.

The analysis of a water jet was also introduced to allow an internal means of comparison. Finally, afterburner systems were considered as conventional systems of thrust augmentation.

4.3 Powerplant Equations

It would be exceedingly time consuming to expound in detail the systems of equations which solve the fourteen powerplant configurations studied, even

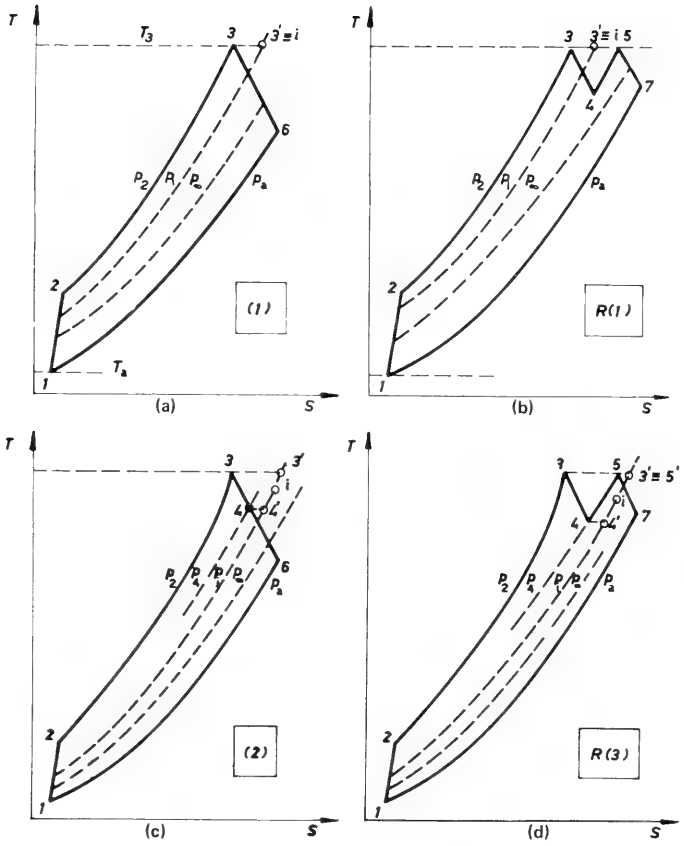

(a) Conventional powerplants

Fig. 27 - Thermodynamical cycles

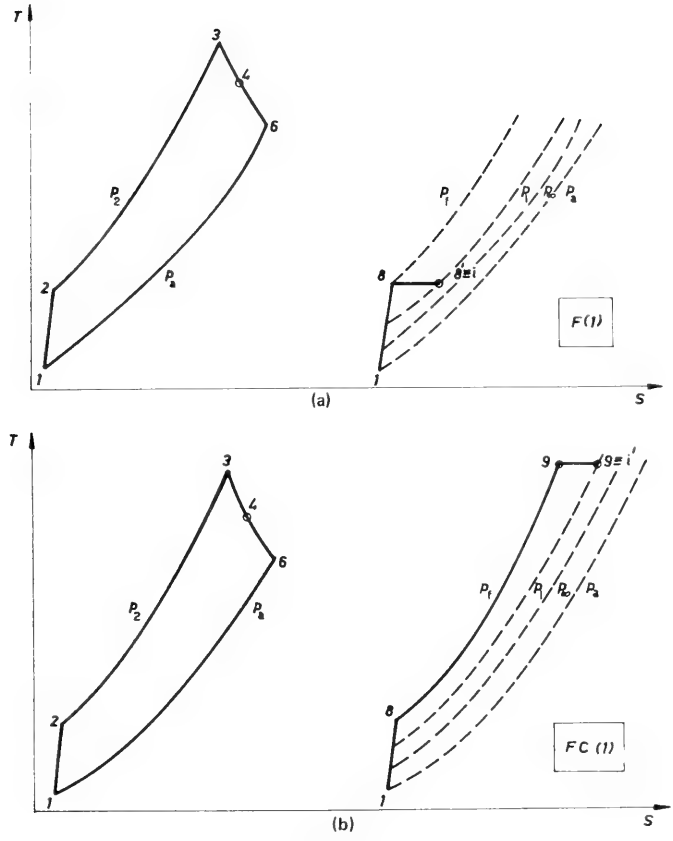

(b) Bypass powerplants

Fig. 27 - Thermodynamical cycles (Continued)

though no new hypothesis is involved with the equations. We will just recall the expression of the single terms which appear in the equations, so that the degree of idealization made will also be clear. All the quantities are defined for unit air flow rate entering the turbine.

(a) *Work of compression:*

$$L_c = \frac{c_{pa}}{\eta_{mc}} (T_2 - T_1) \quad , \quad \text{(turbine compressor)}$$

$$L_f = \frac{c_{pa}}{\eta_{mf}} \alpha_1 (T_8 - T_1) \quad , \quad \text{(bypass compressor)} \quad . \tag{29}$$

(b) *Work of expansion:*

$$L_t = (1 + \alpha' - \alpha_1)\, c_{pg}\, \eta_{mt} (T_3 - T_6) \quad , \quad \text{(one turbine)}$$

$$L_{tf} = (1 + \alpha')\, c_{pg}\, \eta_{mt} (T_3 - T_6) \quad , \quad \text{(one bypass turbine)}$$

$$L_{th} = (1 + \alpha' - \alpha_1)\, c_{pg}\, \eta_{mt} (T_3 - T_4) \quad , \quad \text{(high-pressure turbine)} \tag{30}$$

$$L_{tl} = \alpha_u\, c'_{pg}\, \eta_{mt} (T_4 - T_6) \quad , \quad \text{(low-pressure turbine)}$$

$$L_{tl,b} = \alpha_u\, c'_{pg}\, \eta_{mt} (T_5 - T_7) \quad , \quad \text{(low-pressure reburning turbine)} \quad .$$

(c) *Pumping work:*

$$L_p = \frac{H_p/\gamma}{\eta_p\, \eta_{mp}} \quad , \tag{31}$$

where $\gamma = \dot{m}_a/\dot{m}_H$ is the *inflow mass ratio*

By equating separately the previous work, one obtains the mechanical equilibrium at the compressor axle (*mechanical constraint*) and at the *pump axle* (*hydromechanical constraint*). The other balances are:

(d) *Energy balance at the burners:*

$$(1 + \alpha')\, c_{pm} (T_3 - T_2) = \alpha'\, \eta_b H_i \quad , \quad \text{(first burner B1)}$$

$$(1 + \alpha' + \alpha'' - \alpha_1 - \alpha_2)\, c'_{pm} (T_5 - T_4) = \alpha''\, \eta_b H_i \quad , \quad \text{(afterburner B2)} \tag{32}$$

$$(1 + \delta)\, \alpha_1\, c_{pm} (T_9 - T_8) = \delta \alpha_1\, \eta_b H_i \quad , \quad \text{(auxiliary burning B3)} \quad .$$

(e) *Mass balance:*

$$\begin{aligned} &1 + \alpha' + \alpha'' - (\alpha_1 + \alpha_2 + \alpha_3) - \alpha_u = 0 \ , \quad \text{(conventional turbine)} \\ &\left.\begin{aligned} 1 + \alpha' + \alpha'' - \alpha_u &= 0 \ , \\ \alpha'(1+\delta) - \alpha_f &= 0 \ , \end{aligned}\right\} \quad \text{(bypass turbine)} \ . \end{aligned} \tag{33}$$

(f) *Pressure balance (first gas-dynamical constraint):*

$$\begin{aligned} \beta_a = \beta'_e &= 1 + \beta_{hi} + \beta_p + \beta_o(\psi - \xi) \ , \\ \beta'_e + \delta\beta &= \beta \quad \text{(one-extraction turbine)} \\ &= \beta_2 \quad \text{(multiple-extraction turbine)} \\ &= \beta_f \quad \text{(bypass turbine)} \ . \end{aligned} \tag{34}$$

(g) *Definitions:*

$$\begin{aligned} \epsilon &= (\alpha_1 + \alpha_2 + \alpha_3)\,\gamma \ , \quad \text{(second gas-dynamical constraint)} \\ \beta &= \beta_1\beta_2 \ . \end{aligned} \tag{35}$$

The previous balance equations, which have been written in thermal form, can be more usefully written in baric form, that is, in terms of the pressure ratios, by making use of the isentropic laws and of the equation of state, for perfect gases; the one real parameter introduced is the c_p, to which different constant values have been given in different ranges. For the matching of the powerplant and propulsor solutions, which are independent, it will be necessary to evaluate the density ρ_{gi} of the gas injected at the chamber pressure p_i. By means of the hypotheses previously made, one obtains

$$\begin{aligned} \rho_{gi} &= \frac{\rho'_3(\alpha_1 + \alpha_3) + \rho'_4\alpha_2}{(\alpha_1 + \alpha_2 + \alpha_3)} \ , \quad \text{(conventional turbine)} \\ &= K_2 \frac{\beta_a}{1 + \dfrac{1}{\eta_f}(\beta_f^{\phi} - 1)} \ , \quad \text{(bypass turbine)} \end{aligned} \tag{36}$$

where:

$$\begin{aligned} \rho'_3 &= \rho_3 \frac{p_i}{p_3} = K_3\beta_a \ , \\ \rho'_4 &= \rho_4 \frac{p_i}{p_4} = \frac{\rho_3\beta_a}{\beta_1^{m''}\beta_2} = K_3 \frac{\beta\beta_a}{\beta_1^{m''}\beta_2} \ , \\ K_2 &= \frac{p_a}{g_j R_a T_a} \ , \quad K_3 = \frac{p_a}{g_j R_g T_3} \ . \end{aligned} \tag{37}$$

The previous equations allow the complete solution when some of the parameters are given. V_∞, β_p, M_u have generally been chosen as fundamental parameters (the choice of M_u, which appeared very useful from the point of view of the numerical procedure, turned out to be very ineffective from the point of view of the physical meaning) and $\beta_i \beta_f$, α_2 as auxiliary parameters for the powerplant solution.

6 NUMERICAL DATA AND SOLUTIONS

The parametric range chosen was

V_∞ = 0 to 50 m/s, (0 to 97 knots)
β_p = 0 to 21, (0 to 210 m water)
M_u = 0.4 to 3,
β = 1 to 20,
α_2 = 0 to 1.

Moreover, the dimensionless valve pressure loss of $\delta\beta$ was

$$\delta\beta = 0 , \quad 1 .$$

All the hydrojectors and pumpjectors have been studied in the aligned configuration ($z_i = z_o = 1$ m), while the water jet was analyzed in the S configuration ($z_o = 1$ m, $z_i = -3$ m). To the loss coefficient ξ there was assigned a mean value of 0.2 for all the aligned propulsors and of 0.3 for the S propulsors; these values were deduced from similar cases (Refs. [7,8,20,23]). The coefficient ψ was everywhere assumed equal to 0.9, but some attempts were made with different values. All other fundamental numerical coefficients are listed in Table 1.

On the basis of the previously examined equations and of the numerical coefficients which have been listed, the fourteen powerplants represented in Figs. 23 - 26 were analyzed; the most significant results are plotted in Figs. 28 - 40 for the power-plants which proved to be the most interesting. The fundamental functions which have been mostly represented are the overall efficiency η_g and the inflow mass ratio γ; the last one is, in fact, the ratio between air and water flow rates; it represents the air flow rate which can involve the unit water flow rate and therefore it is an important figure of merit among powerplants, because it represents the water driving availability of the turbine.

Since the specific thrust σ indicates the thrust which can be obtained at a fixed speed by the unit water flow rate, this information is completed by the necessary knowledge of how large an air flow rate can drive the unit water flow rate, that is by γ. In other words, γ provides information about the turbine potentiality which is needed to provide the thrust σ. (In such powerplants the turbine potentiality can never be represented by the net power but by the air inflow rate.)

Table 1
Numerical Coefficient Adopted

$\eta_t = 0.88$	thermodynamical turbine efficiency
$\eta_c = 0.84$	thermodynamical compressor efficiency
$\eta_{mt} = \eta_{mc} = 0.98$	mechanical efficiencies
$\eta_p = 0.8$	hydrodynamical pump efficiency
$\eta_{mp} = 0.95$	mechanical pump efficiency
$\eta_b = 0.96$	combustion efficiency
$c_{pa} = 0.24$	specific heat at constant pressure — air(kcal/kg°K)
$c_{pg} = 0.275$ $c'_{pg} = 0.26$	idem, exhaust gas
$c_{pm} = 0.26$ $c'_{pm} = 0.27$	idem, mean values air-gas
$k_a = 1.4$ $k_g = 1.35$	specific heat ratios, for air and for gas
$R_a = 6.854 \times 10^{-2}$	gas constant — air(kcal/kg°K)
$R_g = 6.86 \times 10^{-2}$	gas constant — exhaust gas
$p_a = 1.033 \times 10^4$	atmospheric pressure (kg/m^2)
$T_a = 288$	atmospheric temperature (°K)
$T_3 = 1150$	maximum turbine temperature (°K)
$\rho_H = 102$	water density (kg s^2/m^4)
$z_o = 1$	water inlet depth (m)
$z_i = -3$	water-jet chamber depth (m)
$\xi = 0.2, 0.3$	overall losses coefficient
$\psi = 0.9$	speed diffusion coefficient

In Figs. 28 - 34, the results for the hydrojector configurations have been plotted, while in Figs. 35 - 38 some of the results for the pumpjectors are shown. Finally, in Fig. 39 the water-jet results are represented, while in Figs. 40 - 42 some auxiliary diagrams are reported. (It can be observed that sometimes it was necessary to change the references as abscissas and as parameters, because of plotting difficulties.)

7 ANALYSIS OF THE RESULTS FOR THE POWERPLANT

We briefly examine the implications of the numerical results which have been presented. The purpose of this discussion is to compare the four fundamental kinds of powerplants which have been examined: the hot-gas hydrojector,

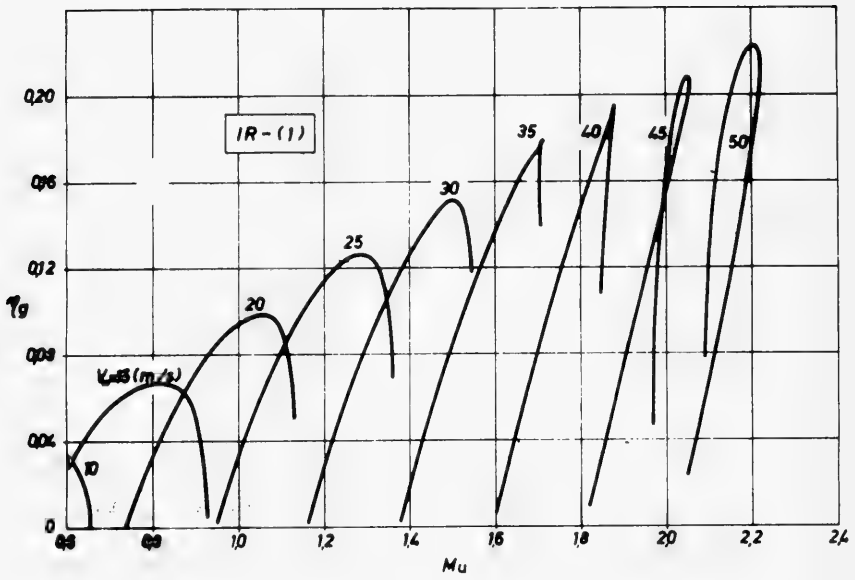

(a) overall efficiency η_g

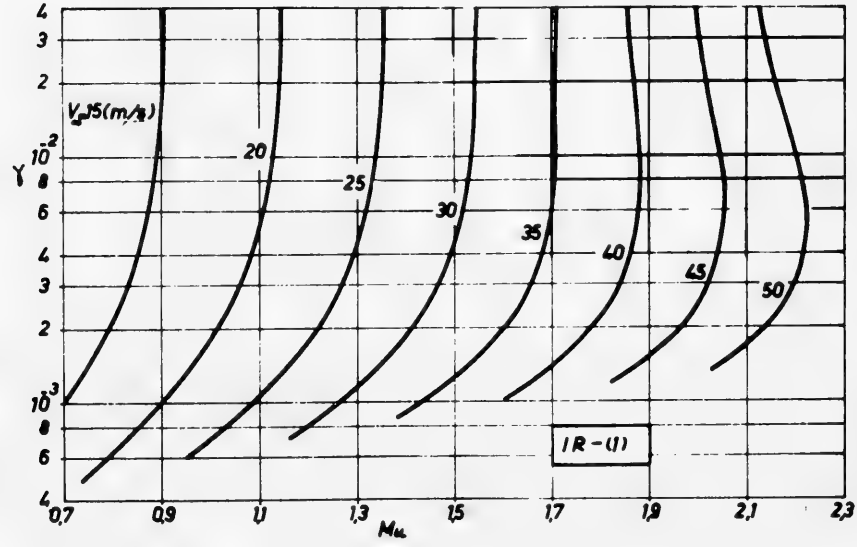

(b) inflow mass ratio γ

Fig. 28 - IR-(1) powerplant performances

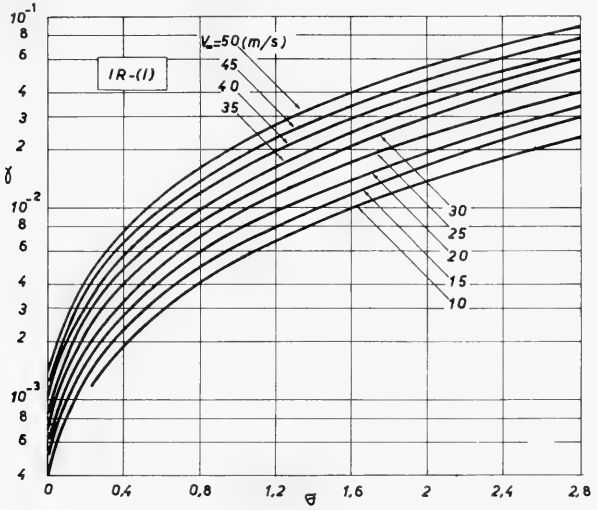

(c) the same, as a function of σ (ψ = 0.9, β = 12, a.p.)

Fig. 28 - IR-(1) powerplant performances (Continued)

the hot-gas pumpjector, the cold-air hydrojector, and the water jet. The last two systems have been introduced just with the aim of comparison, because actually realized (see Sec. 2).

In Sec. 4, the pure propulsive performances (σ, η_p, A_u/A_o, etc.) were discussed, while here the powerplant performances (η_g, γ, ϵ) will be considered; however, some of the results of Sec. 4 will be reviewed here.

(a) On the whole, all the hot-gas powerplants showed very close peak performances. It was already shown that the thrust σ and all the other propulsive parameters do not depend on the powerplant configuration; it can be seen now that both hydrojector and pumpjector powerplants are able to provide a peak over-all efficiency of about 22%, and the only difference consists in the advance speed range, where that efficiency is available, or in the discharge pseudo-Mach number and consequently in the thrust and in the discharge cross section which need it.

IR-(2) provides overall efficiency above 0.21 at a speed comprised between 25 m/s and 40 m/s, by regulating α_u between 0.2 and 0.6, but no solutions are available above 40 m/s. However, since IR-(1) and IR-(2) actually are the same powerplant (the IR-(2) chamber pressure has been imposed equal to the H.P. turbine discharge pressure (also when $\alpha_2 = 0$), while the IR-(1) chamber pressure is equal to the highest powerplant pressure; this configuration can be obtained by cutting out the mean-pressure extraction), operating ranges up to 50 m/s can be obtained by IR-(1) configuration at same efficiency.

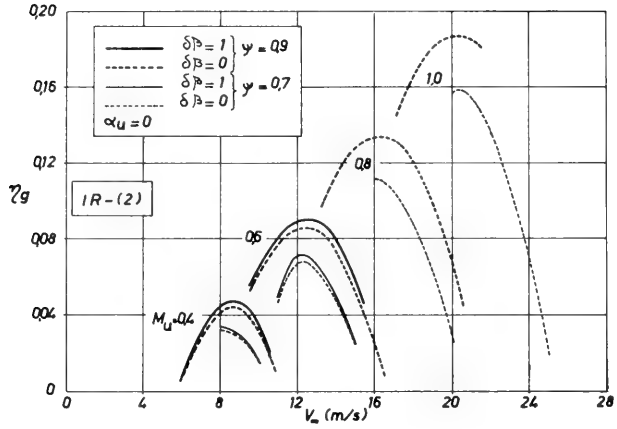

(a) η_g, for some values of α_u and for: $\psi = 0.9$ and $\psi = 0.7$ ($\beta = 12$, a.p.)

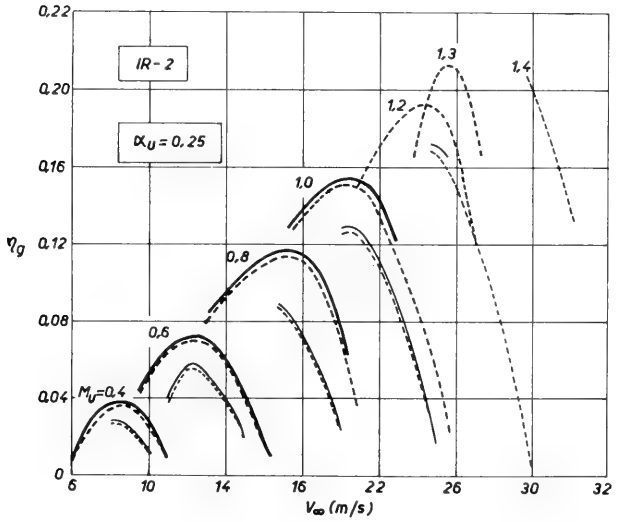

(b) η_g, for some values of α_u and for: $\psi = 0.9$ and $\psi = 0.7$ ($\beta = 12$, a.p.)

Fig. 29 - IR-(2) powerplant performances

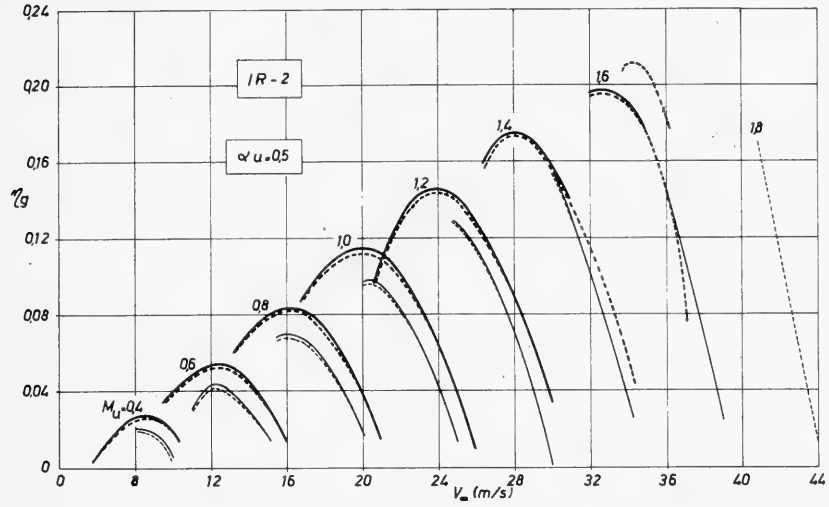

(c) η_g, for some values of α_u and for: $\psi = 0.9$
$\psi = 0.7$ ($\beta = 12$, a.p.)

Fig. 29 - IR-(2) powerplant performances (Continued)

This efficiency appears to be surprisingly high when compared with the water jet's, which does not reach 0.16. An improvement of 35% is sufficiently large to include a margin for the inaccuracy due to the higher unforeseeability of two-phase flow with respect to water flow; that is, a hot-gas hydrojector can be expected as actually competitive with water jets as for efficiency. On the other hand, the observation of the propulsive performances allows control if the efficiency peaks are reached at values of discharge cross sections not higher than 1, especially when truncated nozzles are adopted.

Another advantage as regards to water jets is obtained in terms of γ (that is, in terms of turbine flow rate for given water flow rate), since the values of γ which correspond to the efficiency peaks for the hydrojector are considerably lower than for the water jet. For example, at $\alpha_u = 0.6$, $V_\infty = 35$ m/s, $M_u = 1.72$ for the IR-(2) system we find $\eta_g = 0.18$, $\gamma = 5.7 \times 10^{-3}$, and $\sigma = 0.96$; the water jet which could provide the same value of σ at the same speed has $\beta_p = 19$, where it is $\gamma = 1.3 \times 10^{-2}$ and $\eta_g = 0.15$. The advantages in terms of γ are higher when the operating range is very close to the limits at $\Delta = 0$; also, however, far from this condition lower advantages can be always obtained.

Figures (29), (30) and (33) show the effect of changing the flow rate fractions: An increase of α_u causes an increase of efficiency peak speed. Since α_i are independent of M_u, a change of their distribution does not change σ, but (Fig. 30) it changes the inflow ratio γ; therefore, as was obvious, a change in the turbine air flow rate $\dot{m}_a$ as well in the flow rate fractions α_i will be required to change the advance speed.

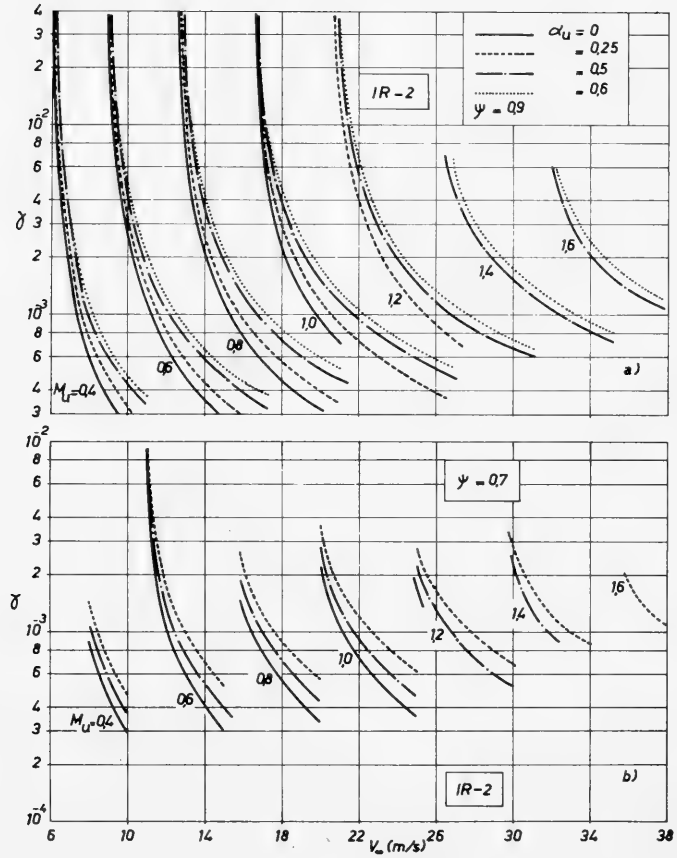

Fig. 30 - IR-(2) ψ performances: (a) ψ = 0.9; (b) ψ = 0.7 (β = 12, a.p.)

It is also remarkable that the effect of the valve losses $\delta\beta$ is very small on the performances, but it is large on the operating limits, because at increasing $\delta\beta$ the maximum speed which can be operated decreases. Besides, in terms of efficiency, the decrease of ψ from 0.9 to 0.7 which has been tried is quite unfavorable.

(b) The cold-air bypass powerplant (Figs. (31), (42)] appeared to be very ineffective from any point of view: The specific thrust can be two or three times less than for a hot-gas hydrojector, the efficiency about two times less, and the inflow ratio also about two times higher. These parameters are very poor also when compared with the water jet's ones.

The overall efficiency is too low to permit economically convenient running, and the thrust could propel just a proportionately light vehicle. It is

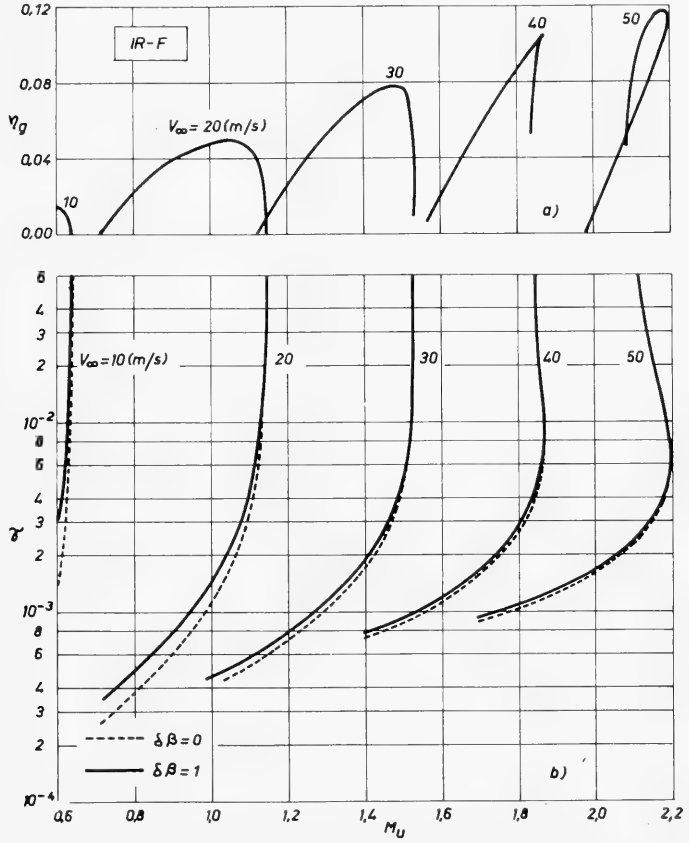

Fig. 31 - IR-F powerplant performances: (a) η_g; (b) (ψ = 0.9, β = 12, a. p.)

only apparently surprising how the combustion of fuel into the compressed air (that can be realized without any mechanical complexity) could raise strongly the performances, since a qualitative argument in this way was the base of the present work.

(c) The increase of the turbine compression ratio β moderately improves the efficiency in the range of interest (Fig. 34), and this improvement is magnified at higher speed. The values plotted in all the other diagrams correspond to β = 12, which can be considered a good compromise between performances and simplicity, but it is easy to ensure that values to β = 8 do not change the performances sensibly.

(d) The pumpjector is operatively poor in the configuration IB-(1) (Fig. 37), since the operative speed field is very restricted, because the chamber

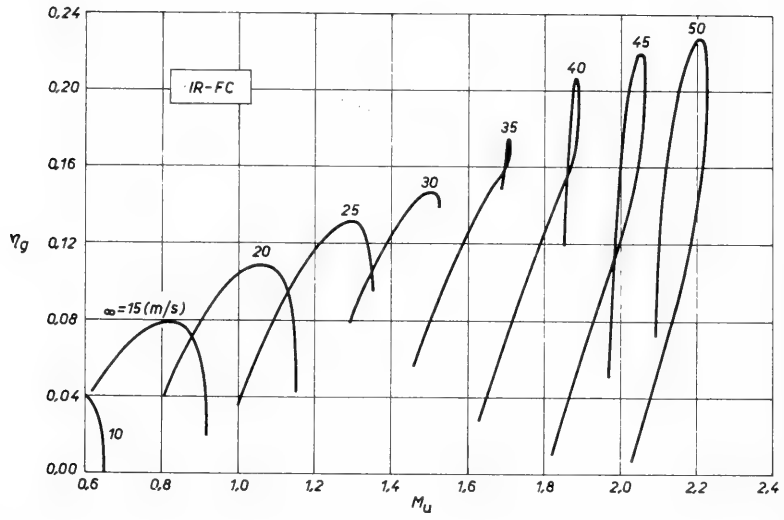

(a) η_g

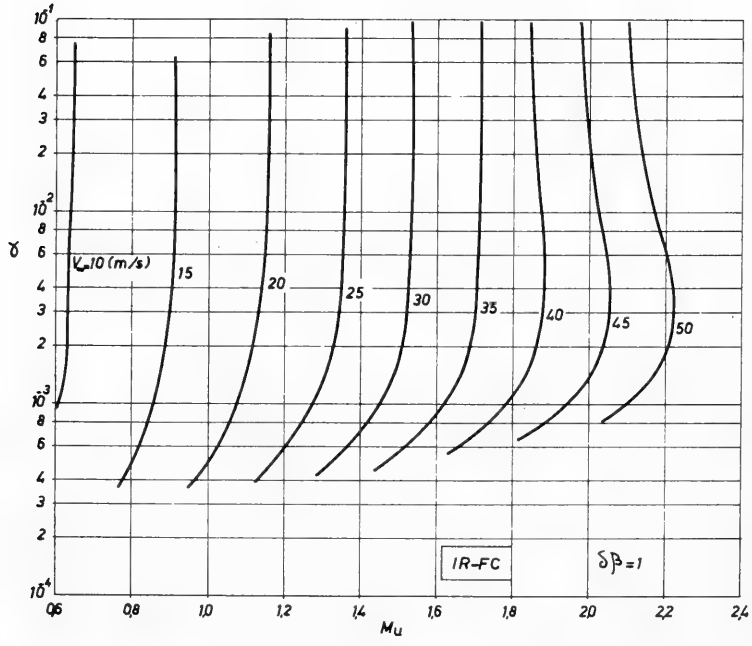

(b) γ

Fig. 32 - IR-FC powerplant performances

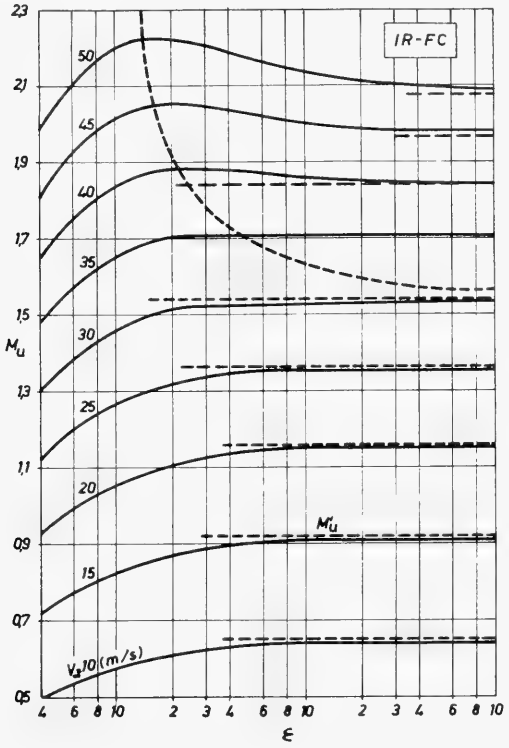

(c) M_u as a function of ϵ (ψ = 0.9, β = 12, a.p.)

Fig. 32 - IR-FC powerplant performances--Cont'd.

pressures that can be reached by the turbine mean pressure are somewhat low. On the contrary, good performance can be obtained by the configuration IB-(2) (Fig. 35); the efficiency is very high (up to 0.2) and no speed limits were found up to 50 m/s. Higher exit pseudo-Mach numbers are required at higher β_p, because of the shifting in the maxima. No solutions at the highest speed can be obtained at $\beta_p > 3$, because of the exceedingly high chamber pressure compatibility with the turbine pressure ratio $\beta = 12$.

In Fig. (41) the maximum speed $V_{\infty\ max}$ which can be obtained at variable β_p and at fixed β is shown. This diagram indicates the operative fall of a turbine-fed system; it can be used for any powerplant, and β must represent the lowest pressure (that is, β_2 in IR-(2) and IB-(2) plants).

It appears that, with a (β = 12)-turbine, a speed not higher than 54 m/s at β_p = 2 and not higher than 37.5 m/s at β_p = 4 can be achieved.

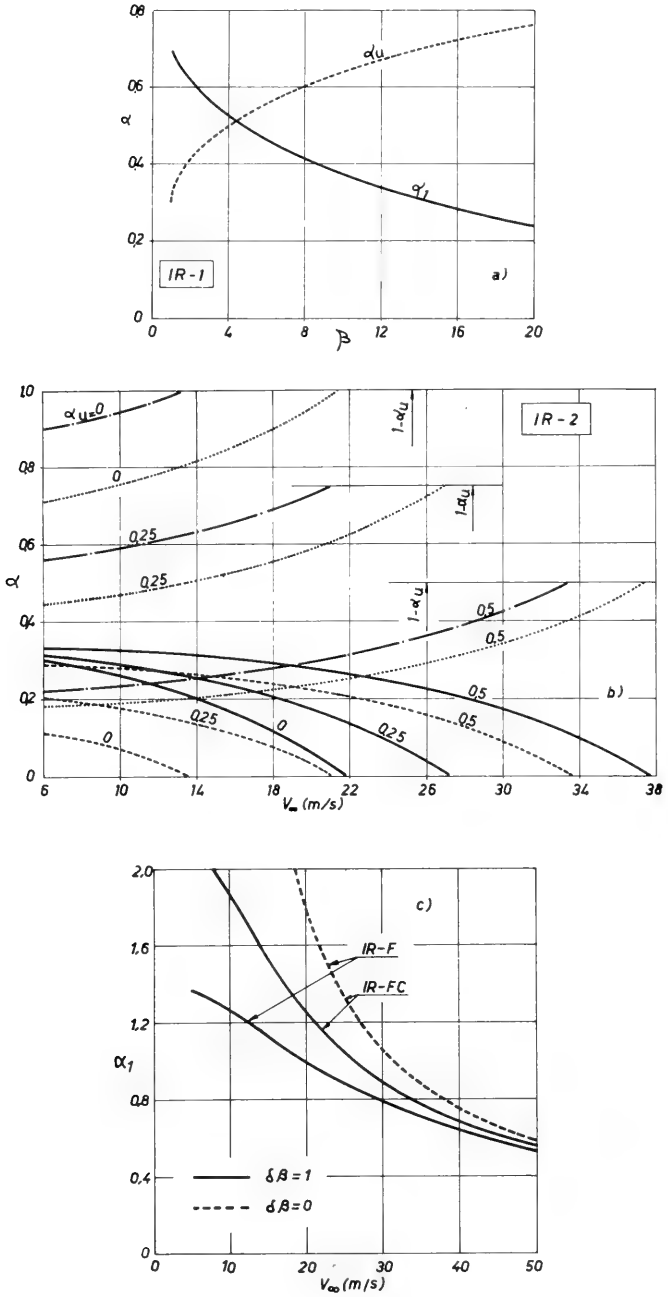

Fig. 33 - Variation of the mass flow ratios α_i for several hydrojector power-plants (ψ = 0.9, β = 12, a.p.)

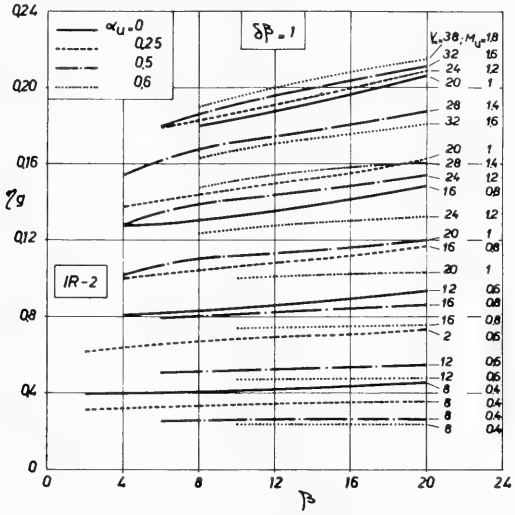

Fig. 34 - IR-(2) performances: variation of η_g with the compressor pressure ratio β (ψ = 0.9, a.p.)

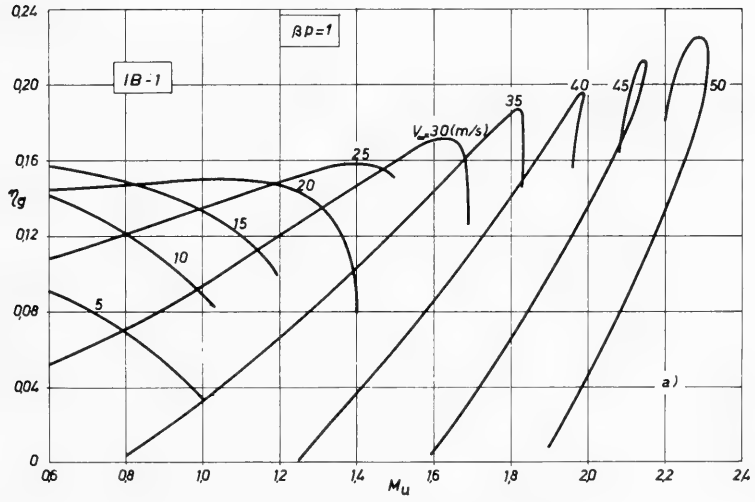

Fig. 35(a)

Fig. 35 - IB-(1) powerplant: variation of η_g for some values of β_p (ψ = 0.9, β = 12, a.p.)

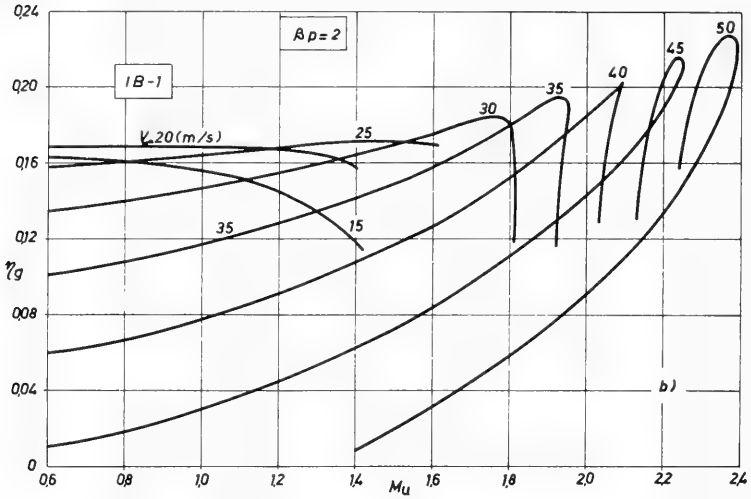

Fig. 35(b)

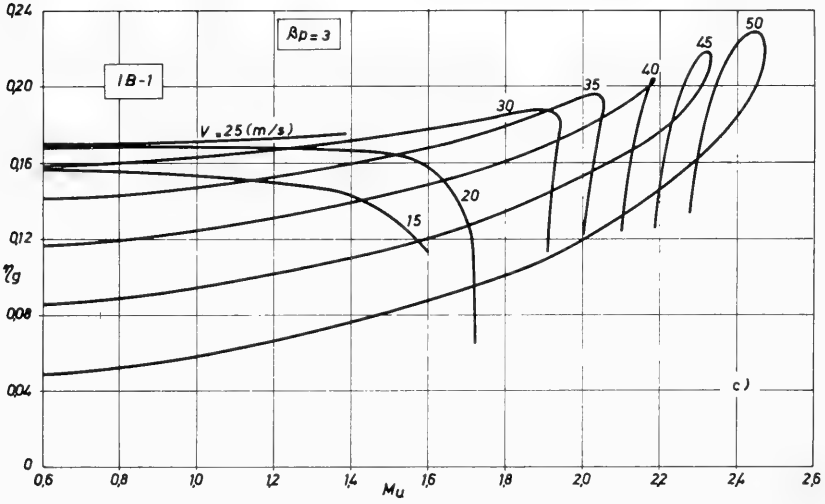

Fig. 35(c)

Fig. 35 - IB-(1) powerplant: variation of η_g for some values of β_p (ψ = 0.9, β = 12, a. p.) (Continued)

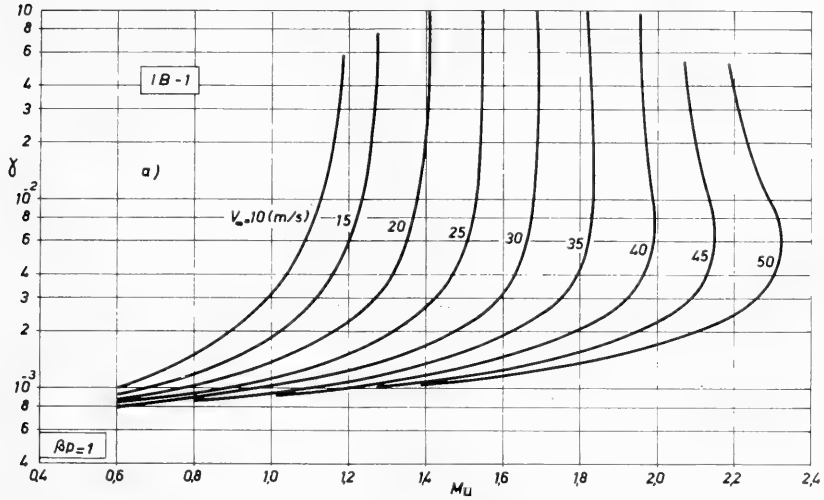

Fig. 36(a)

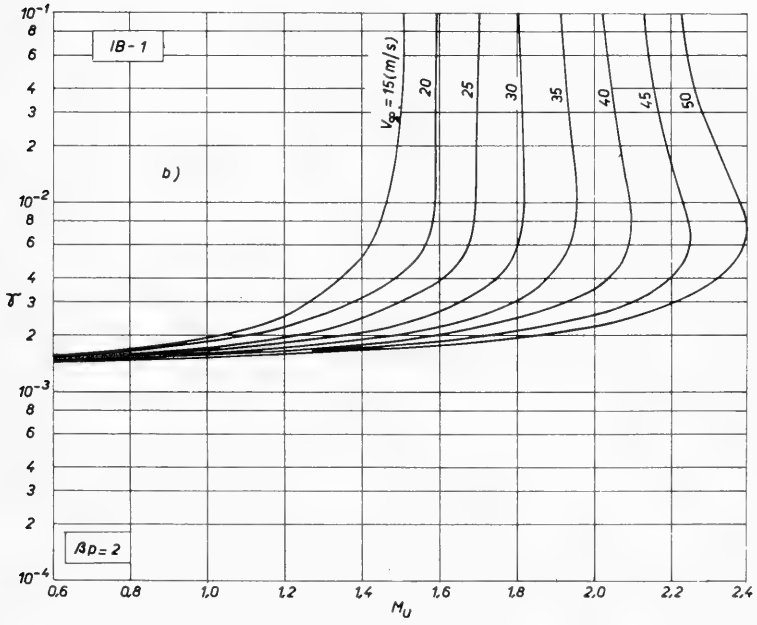

Fig. 36(b)

Fig. 36 - IB-(1) powerplant: variation of γ for some values of β_p (ψ = 0.9, β = 12, a. p.)

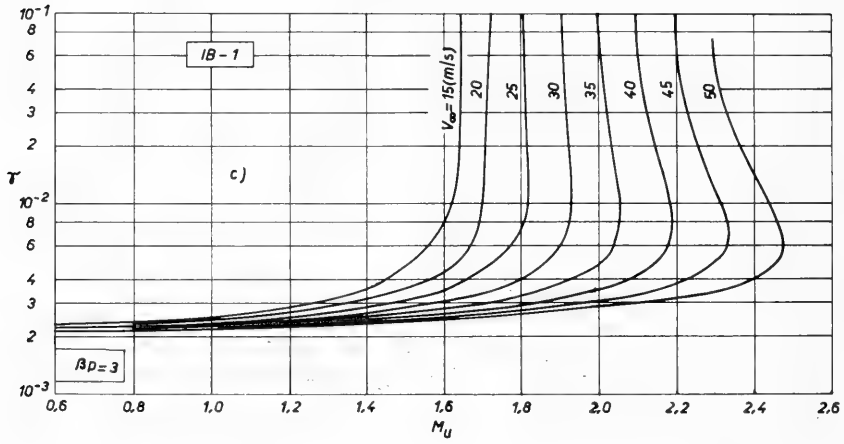

Fig. 36(c)

Fig. 36 - IB-(1) powerplant: variation of γ for some values of β_p (ψ = 0.9, β = 12, a. p.) (Continued)

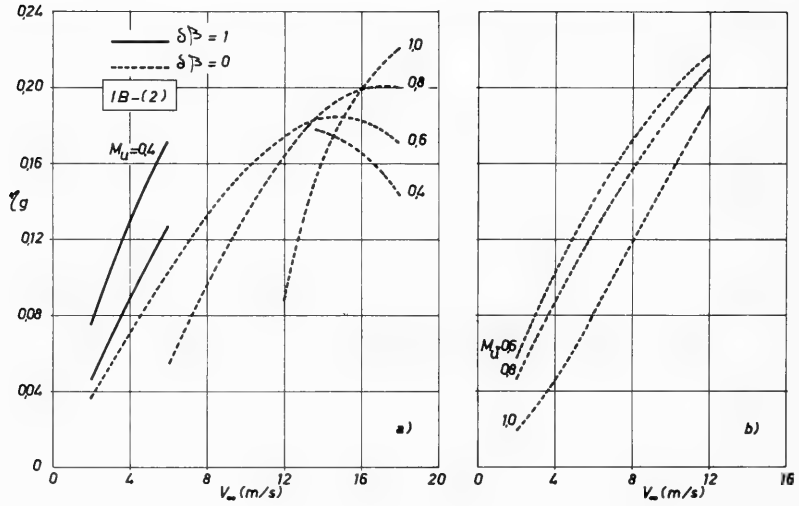

Fig. 37 - IB-(2) powerplant: η_g for a few values of β_p (no solution is available above) (ψ =0.9, β = 12, a. p.)

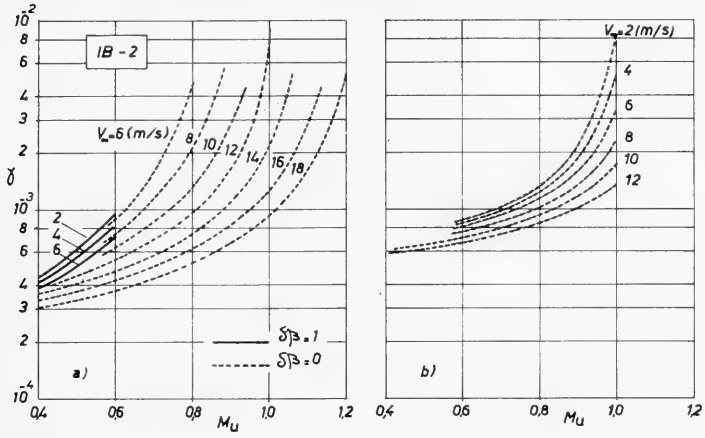

Fig. 38 - IB-(2) powerplant: γ for a few values of β_p (no solution above) (ψ = 0.9, β = 12, a. p.)

This limit is imposed if the gas injection must be made possible. On the other hand, a pure water jet can offer higher limits, imposed by the condition of no thrust (see Figs 17 and 41, dashed line) or by the condition of maximum efficiency (Fig. 41). The last condition is actually comparable with the pumpjector's, since the limit of this corresponds roughly to maximum efficiency. Therefore, it appears that a (β = 12)-pumpjector allows higher advance speeds than the water jet up to β_p = 7, while above this β_p the water jet allows higher speeds of maximum efficiency than the pumpjector. The inflow ratio γ required by a pumpjector is increased by β_p and it approaches the water jet values.

The previous considerations confirm the idea that a system of gas injection as modification of the water jet either design or operation is possible, and it accomplishes a large improvement of the performances.

(e) For the hydrojector the condition of maximum efficiency does not allow high thrust (Fig. 41); the σ corresponding to η_{gmax} is about 0.45, that is, a somewhat low value. Higher thrust can be obtained at lower efficiency, but the actual problem in the hydrojector design is the discharge cross section. In Fig. 41 a line at A_u/A_o = 1 for a conventional nozzle is shown; the zone at its right is not practicable if a discharge cross section higher than the chamber one must be avoided. This limitation practically does not affect the efficiency range, but it is very restrictive for the thrust, especially at high speed.

Better results can be obtained with a truncated nozzle. In this case, the condition A_u/A_o = 1 provides a specific thrust which can be 0.64 at V_∞ = 50 m/s. (It must be observed that the condition A_u/A_o = 1 for a nozzle truncated at throat means that the chamber mixture speed coincides with its critical speed. Therefore, conditions at $A_u/A_o > 1$ are physically not available, because it would correspond to choking in the chamber.)

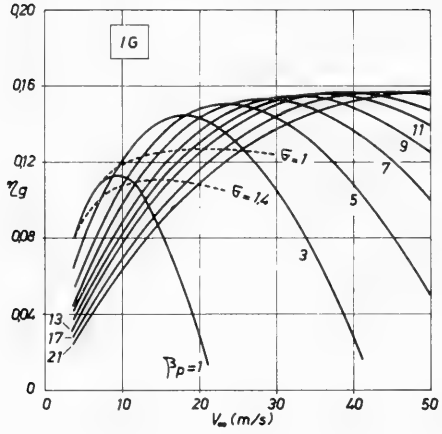

Fig. 39(a) - η_g

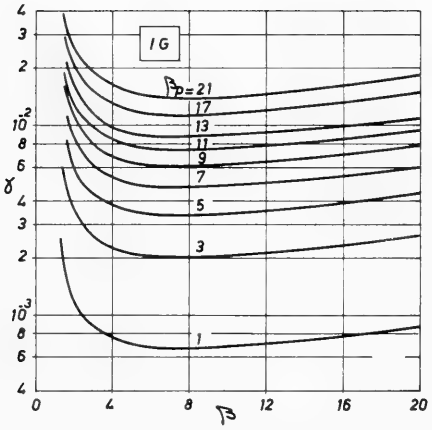

Fig. 39(b) - γ

Fig. 39 - Waterjet (IG) performances

Finally, one can observe (Fig. 41) that the values of ϵ, which provide good performances, are very close (between 0.001 and 0.03). They are remarkably lower than the values of a cold-air hydrojector (Fig. 42 and Refs. [7] and [8]), which reach and exceed 0.01.

(f) No remarkable results derived from the analysis of powerplants where aftercombustion was realized. On the contrary, however, no numerical analysis was developed about it. It is noteworthy to consider the possibility that

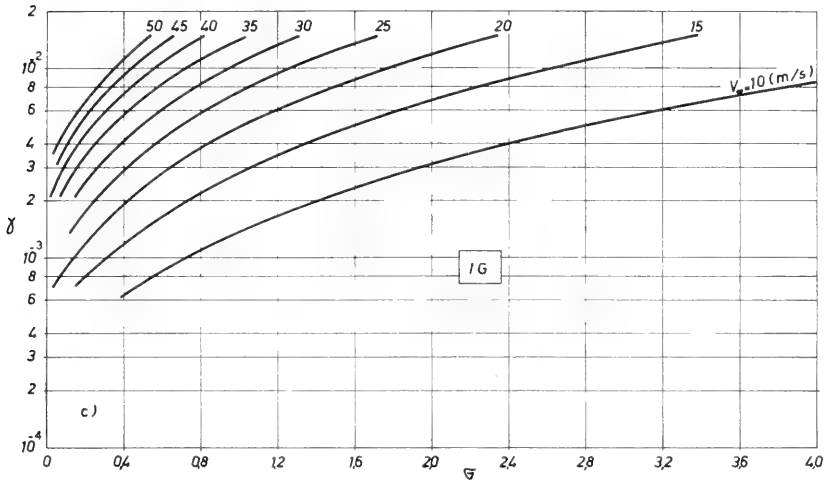

Fig. 39(c) γ as a function of σ (ψ = 0.9, β = 12, S. p.)

Fig. 39 - Water-jet (IG) performance (Continued)

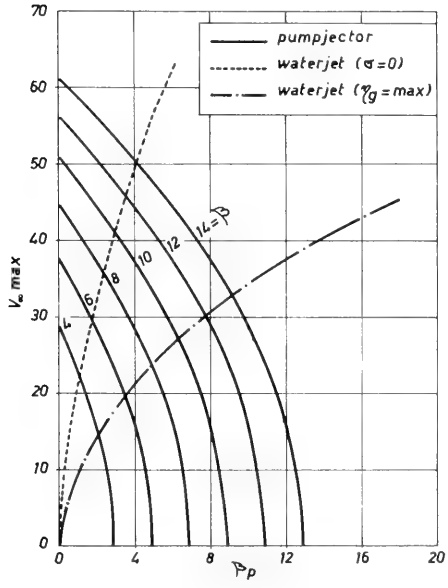

Fig. 40 - Operative limits for hydrojectors, pumpjectors (ψ = 0.9, a. p.) and water jets (ψ = 0.9, β = 12, S. p.)

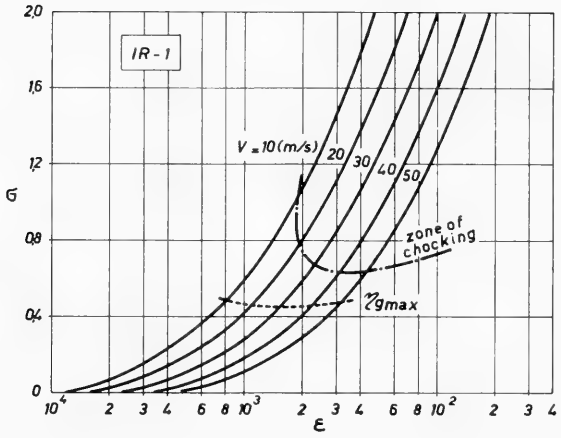

(a)

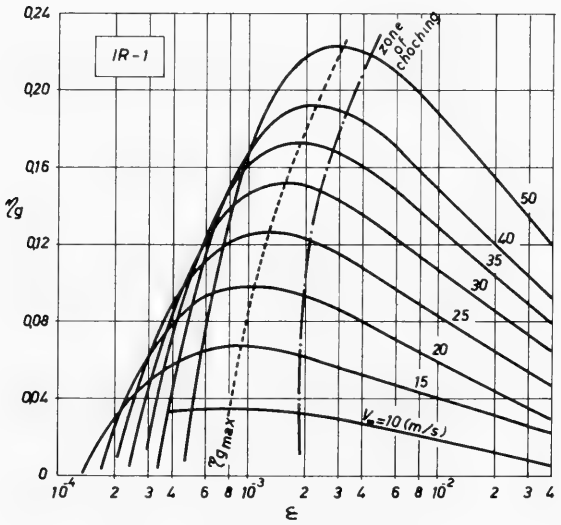

(b)

Fig. 41 - Variation of σ and η_g with ϵ for IR-(1) powerplant (ψ = 0.9, β_1 = 12, a.p.)

the heating of the gas in the IR FC powerplant (but the same thing can be realized for any hot-gas powerplant) could be partially supplied by the turbine exhaust in a heat recuperator. This practice would not provide any thrust improvement, but it would surely improve the efficiency.

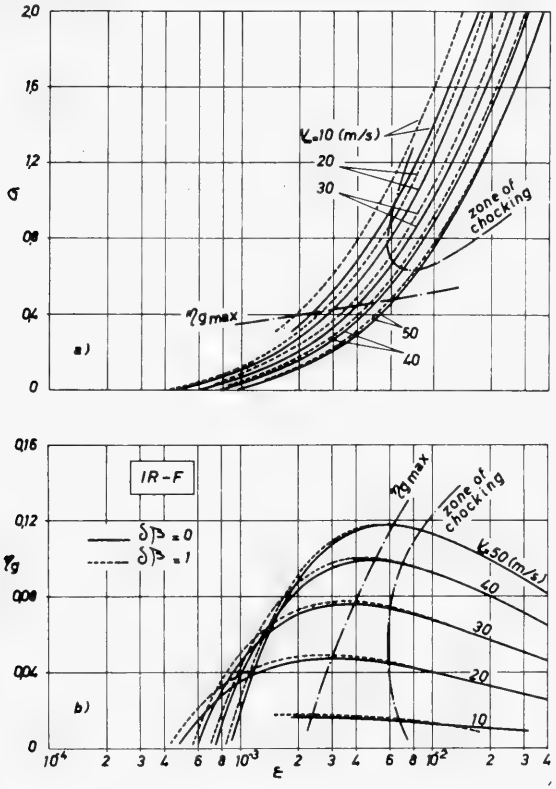

Fig. 42 - Variation of σ and η_g with ϵ for IR-F powerplant (ψ = 0.9, β = 12, a.p.)

8 CONCLUSIONS

The analysis of four basic powerplants for marine propulsion, that is, hot-gas hydrojector, hot-gas pumpjector, cold-air hydrojector, and water jet, allows the fundamental conclusion that a propulsive jet device powered by compressed hot gas can be actually competitive with water jets, both in the pure ejector configuration (hydrojector) and in the hybrid pump-ejector configuration (pumpjector).

When powered by cold air, the same device provides very poor and non-competitive performance, its performance being strongly improved by the gas temperature or specific volume.

The pumpjector can be seen as a useful change of the water jet, the thrust of which can be so improved without efficiency decrease. Essentially, the comparison between water jets and hydrojectors is favorable to the latter for the

low weight of the propulsive system (about 50% less than a water jet's propulsive weight), simplicity, easy maintenance, higher efficiency, and less powerful turbine. Its disadvantage is the lower thrust obtainable which in turn needs larger propulsors and therefore higher external drag. However the efficiency advantage can allow an operating range where the thrust ineffectiveness could be minimized and the lower propulsive weight allows a moderate increase in drag. On the other hand, until now the hydrojector appears to be the only propulsive device which does not fall at the highest speed as the water jet does both for propulsive and for cavitation reasons.

NOMENCLATURE

A	local cross section (m^2)
A_g	part of A occupied by gas
A_H	part of A occupied by water
A_c	nozzle critical (throat) cross section (m^2)
B_1, B_2, B_3	functions defined by Eq. (19')
c	velocity of sound, for the two-phase mixture (m/s)
c_g	the same, for gas
c_H	the same, for water
c_{pa}	specific heat at constant pressure, for air (kcal/kg °K)
c_{pg}	c_p, for gas, (mean in the H.P. turbine)
c'_{pg}	c_p, gas (L.P. turbine)
c_{pm}	c_p, mean air-gas at the principal burner B1
c'_{pm}	c_p, mean air-gas at the afterburner B2
c_s	thrust coefficient [Eq. (26)]
g	gravity acceleration (m/s^2)
H_i	fuel heat of combustion (kcal/kg)
h	gas total enthalpy (kcal/kg)
H_p	pump head (m)
j	mechanical equivalent of heat (=426.9 kcal/kg m)

k	specific heat ratio
K_1	coefficient [Eq. (15)]
K_2, K_3	coefficients [Eq. (37)]
$\dot{m}_a$, $\dot{m}_g$, $\dot{m}_H$	mass flow rate, air, gas, water (kg s/m)
m	$1/k$
M	pseudo-Mach number of the two-phase mixture
p	pressure (kg/m^2)
p_a	atmospheric pressure
S	thrust (net of internal losses) (kg)
T	temperature (°K)
V	velocity (m/s)
V_r	reference velocity $[=(2p_\infty\beta_n/\rho_H)^{1/2}]$
V_∞	advance velocity of the vehicle
z	depth (positive downwards) (m)
α_1, α_2, α_3	turbine flow rate drawing fractions (referred to $\dot{m}_a$)
α_u	turbine flow rate discharge fraction (referred to $\dot{m}_a$)
α', α''	turbine flow rate fuel fractions (referred to $\dot{m}_a$)
β	overall turbine compression ratio
β_1	H.P. turbine pressure ratio
β_2	L.P. turbine pressure ratio
β_f	bypass compression ratio
β_o	stream dimensionless dynamic pressure $(=\gamma_H V_\infty^2/2gp_a)$
β_{hi}	dimensionless chamber depth $(=\gamma_H z_i/p_a)$
β_{ho}	dimensionless water inlet depth $(=\gamma_H z_o/p_a)$
β_p	dimensionless pump head $(=\gamma_H H_p/p_a)$
β_i	local expansion ratio $(=p_i/p)$

β_e overall expansion ratio for underwater nozzle ($=p_i/p_\infty$)

β'_e overall expansion ratio for surface nozzle ($=p_i/p_a$)

β_c critical expansion ratio ($=p_i/p_c$)

β_a ratio of chamber pressure to atmospheric pressure ($=p_i/p_a = \beta'_e$)

β_h $(1 + \beta_{ho})/(1 + \beta_{hi})$

β_n $\beta_p + \beta_o (1 - \xi)/(1 + \beta_{hi})$

β_m $\beta_p + \beta_o (\psi - \xi)/(1 + \beta_{hi})$

γ inflow mass ratio ($=\dot{m}_a/\dot{m}_H$)

γ_H water specific weight (kg/m^3)

δ turbine flow rate fuel fraction at the bypass burner (referred to $\alpha_1 \dot{m}_a$)

Δ discriminant [Eq. (20)]

ΔH_a internal losses (m)

$\delta\beta$ dimensionless pressure loss at the valves ($=\Delta_p/p_a$)

ϵ mixing mass ratio ($=\dot{m}_g/\dot{m}_H$)

η_t, η_c, η_f thermodynamical efficiencies (turbine, compressor, and bypass compressor)

η_{mt}, η_{mc}, η_{mf} mechanical efficiencies, for the above

η_b combustion efficiency

η_p propulsive efficiency [Eq. (27)]

η_{pc} the same, for truncated nozzle

η_g overall powerplant efficiency [Eq. (28)]

θ cross-section augmentation coefficient [Eq. (23)]

λ mixing volume ratio (Eq. (9)]

λ_i chamber value of λ

ξ overall internal losses coefficient [Eq. (2)]

ρ mixture density (kg s^2/m^4)

ρ_g gas density

ρ_H water density

σ specific thrust [Eq. (25)]

σ_c the same, for truncated nozzle [Eq. (25')]

τ $(k + 1)/k$

ϕ $(k - 1)/k$

ψ diffusion coefficient [Eq. (1)]

When not otherwise specified, the subscripts $( )_o$, $( )_i$, $( )_\infty$, and $( )_u$ refer to the corresponding stream cross sections [Figs. (5) and (6)], while $( )_g$, $( )_H$ and $( )$ refer to gas, water, and two-phase mixture properties.

REFERENCES

1. Foa, J.V.: "Crypto-Steady Pressure Exchange" Rensselaer Polytechnic Institute, TR AE 6202, March 1962

2. Foa, J.V.: "A Method of Energy Exchange" ARS Journal, Sept. 1962

3. Sarro, C.A., and Kosson, R.L.: "Theoretical Analysis of the Foa Propulsor with Gas Primary and Liquid Secondary Fluids"; Grumman Aircraft Eng. Corp., Rep. No. ADR 01-09-64-1, Aug. 1964

4. Hoenemser, K.H.: "Flow Induction by Rotary Jets" J. Aircraft, Vol. 3 No. 1, Jan. 1966

5. Poole, D.M.: "Water-Augmented Turbofan for the Propulsion of High-Speed Surface Vessels" United Aircraft Research Laboratories, Rep. UAR-E116, June 1966

6. Davison, W.R., and Sadowski, T.J.: "Water-Augmented Turbofan Engine" J. Hydronautics, Vol. 2 No. 1, Jan. 1968

7. Mottard, E.J., and Shoemaker, C.J.: "Preliminary Investigation of an Underwater Ramjet Powered by Compressed Air" NASA-TN D-991, Dec. 1961

8. Pierson, J.D.: "An Application of Hydropneumatic Propulsion to Hydrofoil Craft", J. Aircraft, Vol. 2, No. 3, May-June 1965

9. Muir, J.F., and Eichorn, R.: "Compressible Flow of an Air-Water Mixture through a Vertical, Two-Dimensional Converging Nozzle" Proc. 1963 Heat Transfer and Fluid Mech. Inst., June 1963

10. Gouse, S.W., Jr.: "An Index to the Two-Phase Gas-Liquid Flow Literature" M.I.T. Rep. No. 9, 1966

11. Gouse, S.W., Jr., Kemper, C.A., Brown, G.A., and Miguel, J.: "Heat Mass and Momentum Transfer in a Condensing Ejector Mixing Section" AIAA Paper 67-420, AIAA III Propulsion Joint Specialist Conference, July 1967

12. Vogrin, J.A., Jr.: "An Experimental Investigation of the Two-Phase Two-Component Flow in a Horizontal Converging-Diverging Nozzle" ANL-6754 Rep., July 1963

13. Heinrich, G.: "The Equation of Flow of Liquid-Gas Mixture" Z.A.M., Vol. 22, No. 2, 1942

14. Tangren, R.F., Dodge, C.H., and Seifert, H.S.: "Compressibility Effects in Two-Phase Flow" J. Appl. Phys., Vol. 20, No. 7, July 1949

15. "Marjet Feasibility Study 500 ton Hydrofoil Ship-Final Report" Martin Co., Rep. ER 12392 (April 1962)

16. "Marjet Design Data Development 500-ton Hydrofoil Ship-Final Report" Martin Co., Rep. ER 13298 (April 1964)

17. Rosen, G.: "Design of a Nuclear-Powered Water Ramjet" ARS Journal, pp. 1403 - 1404, Sept. 1962

18. Pallabazzer, R.: "Preliminary Analysis of a Mixed-Cycle Power-Plant" (in Italian) C.N.P.M.-NT 42 (1966)

19. Montevecchi, F.M., Pallabazzer, R.: "A Liquid-Metal Hydropropulsive Engine" (in Italian) C.N.P.M.-NT 43 (1966)

20. Gongwer, C.A.: "The Influence of Duct Losses on Jet-Propulsion Devices" Jet Propulsion, pp. 385 - 386, Nov.-Dec. 1954

21. Bursik, J.W.: "Pseudosonic Velocity and Pseudo-Mach Number Concepts in Two-Phase Flows" NASA-TN D-3734, Dec. 1966

22. Gongwer, C.A.: "Some Aspects of Underwater Jet-Propulsion Systems" ARS Journal, pp. 1148 - 1151, Dec. 1960

23. "Study and Design of a Waterjet Propulsor for Hydrofoil" (in Italian) Advanced Marine System – Alinavi SpA Rep., Rome, 1967

* * *

DISCUSSION

W. van Gent
Netherlands Ship Model Basin
Wageningen, Netherlands

Our main comments on this interesting paper are referred to the analysis of the propulsor, presented in Sec. 3. In this section, first an adiabatic gas expansion in the nozzle is assumed. This causes an overestimation of the efficiency of hot gas injection and, in addition, an underestimation of the efficiency of gas injection at water temperature. Whereas this assumption is physically more or less acceptable, next, another assumption on the mixing process is made, which, however, is physically unacceptable, because it violates the energy balance.

It is stated in Sec. 3.1 that during the mixing process the water is accelerated at quasi-constant pressure and stated following Eq. (12) that the mixing section has a constant cross-sectional area. The increase in velocity of the water phase is derived from the equation of continuity, but there is no check on the energy equation. The energy balance given above Eq. (5) shows that, at constant pressure, the increase in kinetic energy can only be supplied by a decrease in enthalpy of the gas, but there is no mechanism by which energy transfer can take place. The gas will not expand, but will even contract in consequence of heat losses. Thus, especially at high bulk gas-water ratios, this assumption gives a very unrealistic picture of the mixing process.

Fortunately, it seems that this assumption has not influenced the calculations of efficiency and specific thrust, defined in Sec. 4. In calculating the efficiency and the thrust, the correct energy balance is used and the specific thrust is the thrust per unit area of the undisturbed water flow cross section. However, the thrust coefficient, defined in Sec. 4 as the thrust per unit area of the largest cross section of the propulsor, is much too high, because the cross-sectional area of the mixing section cannot be constant.

In our opinion this area must increase in such a way that the water is not accelerated during gas injection. Energy transfer can only take place after complete mixing. Our own experiments have shown that a higher efficiency is achieved when the cross-sectional area of the mixing chamber is enlarged after gas injection.

* * *

DISCUSSION

Earl Quandt
Naval Ship Research and Development Center
Annapolis, Maryland

Professor Pallabazzer has, in my opinion, presented commendable ideal component and system analysis of several liquid-phase, continuous air-water jet-propulsion arrangements. However, because of the assumptions concerning

(a) Isentropic gas expansion in the presence of large amounts of cold liquid, and

(b) No relative slip between the gas and liquid phases,

I would caution those who might interpret these results with too much optimism.

* * *

REPLY TO THE DISCUSSION

Rodolfo Pallabazzer

I wish very much to thank Mr. Van Gent because his intervention allows me to clear up a passage which appears to be questionable. The question arises from the expressions mentioned by Mr. Van Gent about a quasi-constant pressure mixing and a constant-section chamber, which obviously are inconsistent. As a matter of fact, the first expression was never an assumption, that is, the pressure was never set as a constant in the chamber; the expression about a quasi-constant pressure mixing is purely qualitative and arises from the fact that some quick checks showed only small pressure decreases. Therefore, the equations appear not to be influenced by the constant-pressure assumption, because this assumption was never made.

As regards the constant-cross-section chamber, this also has not the meaning of a statement but just of a reference; indeed, as Mr. Van Gent kindly emphasizes, only an experimental analysis can suggest the shape of the chamber. In a purely theoretical analysis like the present one, there is no effect of the shape of the chamber; therefore, it can be supposed cylindrical without any difference in the discharge results. A difference appears if the discharge data are referred to the chamber cross section, which happens here for the thrust coefficient only. Since its expression [Eq. (26)] depends on the diffusion coefficient ψ, the reference cross section is that where the flow velocity is $V_\infty (1 - \psi)^{1/2}$; this can be not the largest cross section if the chamber is actually divergent. In practice one must pay for this inaccuracy until the shape of the chamber cannot be specified. For this reason in this paper a large emphasis

has not been given to the thrust coefficient, in opposition to the current methods, and an analysis based on the specific thrust has been preferred.

Finally, as regards the hypothesis of an adiabatic gas expansion and its consequences of overestimation of the efficiency of hot-gas injection and underestimation of the efficiency of cold-gas injection, I think the best one could expect from a theoretical provisional analysis is just to provide a couple of limit conditions between which all practical cases take place. As I emphasized in this paper, its aim is not to furnish exact solutions of the problem but just a provisional comparative evaluation from which one could estimate the competitive availability of a two-phase propulsor.

The same reply can be addressed to the first remark of Dr. Quandt; one must add also that the energy exchange between hot gas and water is not a standard phenomenon, since it can be strongly influenced and shifted by a geometry which must be studied purposely to reduce heat transfer.

As regards the slip in a bubble flow, its effect is very feeble, in opposition to the droplet flow, which has been considered by Dr. Quandt in his paper, where the slip effect can be very strong.

* * *

FLUID MECHANICS OF SWIMMING PROPULSION

T. Yao-tsu Wu
California Institute of Technology
Pasadena, California

ABSTRACT

In this paper the fluid mechanics of swimming propulsion of objects of various sizes is discussed for the cases of both large and small values of the Reynolds number. Several problems of current interest will be examined. The content is partly a review of the literature and partly presentation of some new results.

INTRODUCTION

Swimming objects propelling themselves in water or in other liquid media span a wide range in their sizes and speeds. Large cetaceans, such as whales and porpoises, have lengths from 6 to 90 ft, and can swim with cruising speeds from 14 to 20 knots. Microscopic organisms as small as turbatrix (vinegar worm) and spermatozoa — ranging from 0.2 to 0.005 cm in length with length-diameter ratio from 20 to 100 — swim with speeds from 0.05 to 0.002 cm/sec. In between these two extremes there are many species of fish of various sizes. If ℓ is some characteristic length of a body moving with velocity U in a liquid of kinematic viscosity ν, the Reynolds number $R = U\ell/\nu$ measures the relative magnitude of inertial stress to viscous stress. The value of R is of order 10^8 for the most rapid cetaceans, 10^6 for migrating fishes, $10^4 - 10^3$ for a great variety of fishes, about 10^2 for tadpoles, down to about 10^{-2} for turbatrix and 10^{-3} or less for spermatozoa. Thus, the Reynolds number R covers practically the entire range of interest known to hydrodynamicists. Although R may vary greatly from case to case, the swimming motions of these different biological objects have been observed to differ very little from a vibrating motion of the body, in a wave form propagating along the body. In this kind of body motion, the stresses arise from the reaction between the waving surface and the surrounding fluid, and the propulsive thrust is derived from the resultant of these surface forces.

The hydrodynamics of swimming motion has been recently investigated for both large and small values of the Reynolds number. For the case of large Reynolds number, the swimming propulsion depends primarily on the inertial effect, since the flow outside a thin boundary layer next to the body surface is irrotational. The viscous effect is relevant only in its role of determining the vorticity shed into the wake, and of producing a skin friction at the body surface. Although in principle the latter problem can be evaluated separately, it

involves the difficult problem of unsteady boundary-layer and hydrodynamic stability theory. This general subject remains as an important and crucial problem. The mechanism of swimming motion has been elucidated based on the potential flow theory by von Karman and Burgers (1943) for the simple case of a rigid plate in transverse oscillation and rotation. Swimming of slender fish has been treated by Lighthill (1960); and the swimming of a two-dimensional waving plate has been calculated by Wu (1961).

In the other extreme, movements of microscopic bodies always correspond to small Reynolds numbers. The propulsion in this range depends almost entirely on the viscous stresses, since the inertial forces are then extremely small, except possibly for motions at very high frequencies. Oscillatory motion in a viscous fluid was discussed as early as 1851 by Stokes. Various studies of the swimming of microscopic organisms have been led by Taylor (1951, 1952a,b), who discussed the propulsion of a propagating, monochromatic, transverse wave along a sheet immersed in a very viscous fluid, and later evaluated the action of waving cylindrical tails of microscopic organisms. Further studies in this field have been contributed by Hancock (1954), Gray and Hancock (1955), Reynolds (1965), and by Tuck (1968).

Apart from the mode of propagating transverse waves, which a great majority of swimming creatures adopt as the principal means of propulsion, there are still other kinds of body motions, such as (a) actually ejecting a liquid, as employed by squids, shrimps, and lobsters, (b) propagating waves along fringe belts as used by some flat fishes, and waving motion produced by bending a large number of dense tassels underneath a starfish, and (c) squirming motion by changing the body shape of a tailless object in slow motion through a viscous fluid. Problem (a) has been discussed by Siekmann (1963), and (c) has been analyzed by Lighthill (1952). The problem of self-propulsion of a deformable body in a perfect fluid has been treated by Saffman (1967).

Hydrodynamics of swimming is only a part of the whole problem. From the viewpoint of bioengineering, the entire process begins with the biochemical energy stored in the swimming being, which can be converted, with efficiency η_1, into mechanical energy for maintaining the body motion, the latter is in turn transformed, with efficiency η_2, into hydrodynamic energy for swimming. A part (fraction η_3, say) of the hydrodynamic energy is spent as the useful work done by the thrust, which balances the work done by frictional drag, and the remaining part becomes the energy lost, or dissipated, in the flow wake.

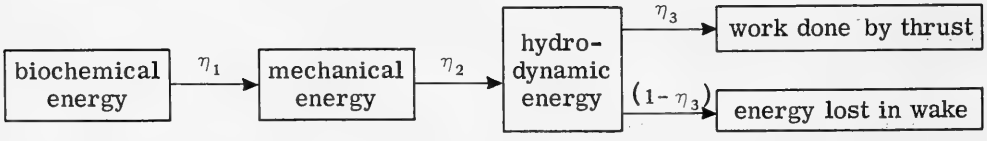

It is in the effort of making a self-contained balance of energy that some apparently astonishing observations have been reported. For example, Johannessen and Harder (1960) reported several impressively high speeds (about 20 to 22 knots) attained by porpoises, killer whales, and black whales. The

boundary layer over a rigid, smooth surface of a similar body in this Reynolds-number range is definitely turbulent. If the skin friction is evaluated on this basis, then the power required to maintain such high speeds would violate severalfold the rule of thumb in biology that a pound of strong muscle can deliver only up to 0.01 horsepower. More recently, the speed of porpoises has been investigated carefully, under well-controlled conditions, by Lang (1962, 1963). Another interesting study is that of migratory salmon by Osborne (1960). According to this careful investigation, a detailed estimate again led to one of the two conclusions: either (1) these creatures have a much smaller drag than could be achieved with similar, rigid bodies, or (2) the power output per gram of muscle is much larger than observed from physiological experiments on warm-blooded animals — these being known as the paradox of Gray (1948, 1949). These puzzling conclusions have stimulated fluid dynamicists to explore various other possibilities, such as the effect of compliant skin and the effects of mucous surface and additives on frictional drag, the studies of the former being so far inconclusive.

The purpose of this paper is to discuss some of the hydrodynamic aspects of swimming propulsion. No attempt is made here to venture beyond this scope. It may well be that only after some extensive efforts are made in basic research can the final chapter be written of this most interesting story.

I. SWIMMING MOTION AT LARGE REYNOLDS NUMBERS

When the Reynolds number R is large, the swimming motion depends primarily on the inertial effects which can be evaluated based on the potential theory. Viscosity of the fluid is unimportant, except in its role of determining the vorticity shed into the wake, and of producing a thin boundary layer, and hence a skin friction at the body surface. A large number of swimming objects employ in propelling themselves the commonly observed mode of body motion which can be characterized by a wave of lateral displacement moving down the body from head to tail. As the body attains a forward momentum, the propulsive force pushes the fluid backward with a net total momentum equal and opposite to that of the action, while the frictional resistance of the body gives rise to a forward momentum of the fluid by entraining some of the fluid surrounding the body. The momentum of reaction to the inertia forces is concentrated in the vortex wake due to the small thickness and amplitude of the undulatory trailing vortex sheet; this backward jet of fluid expelled from the body can however be counterbalanced by the momentum in response to the viscous drag. When a self-propelled body is cruising at a constant speed, the forward and backward momenta exactly balance; they can nevertheless be evaluated separately.

THRUST; ENERGY BALANCE

In order to visualize why a waving form of the body motion is desirable for swimming propulsion, we consider the energy balance for the typical case of a planar flexible body of negligible thickness, performing a general unsteady motion of small amplitude, achieving a forward velocity $U(t)$, which may

depend on the time t, through a fluid which is otherwise at rest. We choose a Cartesian coordinate system (x,y,z) fixed at the body, with the stretched plan form of the body lying in the $y = 0$ plane and with the free-stream velocity $U(t)$ pointing in the positive x direction. The body motion can be written generally as

$$y = h(x,z,t), \quad (x,z \in S) \tag{1}$$

where S is the stretched plan form of the body (when h vanishes identically), h is an arbitrary function of x, z, and t, with $|\partial h/\partial t|$ and swimming velocity U assumed to be small (compared with the speed of sound in the fluid) so that the flow may be regarded as incompressible, and with $|\partial h/\partial x|$ and $|\partial h/\partial z|$ assumed also small enough to justify the linear theory.

The Reynolds number $R = U\ell/\nu$, based on the velocity U and body length ℓ (in the streamwise direction), is taken to be so large that the boundary layer is thin and the inertial effects can be evaluated with the inviscid flow assumption. Then the boundary condition requiring the normal component of velocity relative to the solid surface to vanish provides the y component of the flow velocity at the planar surface

$$v(x,\pm 0,z,t) \equiv V(x,z,t) = \frac{\partial h}{\partial t} + U\frac{\partial h}{\partial x}, \quad (x,z \in S) . \tag{2}$$

The planar body may admit of sharp leading edges and sharp trailing edges. When the latter kind is present, we shall impose, as usual, at such edges the Kutta condition that the velocity is required to be finite, and hence the pressure continuous at a sharp trailing edge. The following discussion can also be applied to plane flows, say, in the xy plane, in which case the dependence on z simply drops out, and all the quantities will then refer to a unit span in the z direction.

The thrust (positive when directed in the negative x direction) acting on the body, based on the inviscid linear theory, results from the integration of the pressure component in the forward direction,

$$T = T_p + T_s = \int_S (\Delta p)\frac{\partial h}{\partial x}\,dS + \int_{L.E.} F_s(x,z,t)\,dz , \tag{3}$$

where (Δp) denotes the pressure difference across the flexible plate, $\Delta p = p(x,-0,z,t) - p(x,+0,z,t)$, F_s is the singular force per unit arc length along the leading edge due to the leading edge suction, and the last integral is evaluated along the leading edge $z = b(x)$. The power required to maintain the motion is equal to the time rate of work done against the reaction of the fluid in the direction of the lift,

$$P = -\int_S (\Delta p)\frac{\partial h}{\partial t}\,dS . \tag{4}$$

In this inviscid flow the mechanical energy imparted to the fluid per unit time is equal to the time rate of work done by the pressure over the body surface, or

$$W = -\int_S (\Delta p)\, V(x,z,t)\, dS - T_s U \,. \tag{5}$$

These quantities, of course, satisfy the principle of conservation of energy, which asserts that the power input P is equal to the rate of work done by the thrust TU, plus the kinetic energy W lost to the fluid in unit time, that is,

$$P = TU + W \,. \tag{6}$$

If the viscous effects are further taken into account, then the thrust T must include the viscous drag due to skin friction and the energy loss must contain the viscous dissipation.

On physical grounds, it can be inferred that W is non-negative in several cases of broad interest. One of such cases is the periodic body movement with constant forward velocity,

$$U = \text{const.}\,, \quad h(x,z,t) = \mathrm{Re}\,[h_1(x,z)\, e^{j\omega t}]\,, \quad (x,z \in S) \tag{7}$$

where $j = \sqrt{-1}$ is the imaginary unit for the periodic time motion, $h_1(x,z)$ may generally be complex with respect to j, and Re denotes the real part. After the transient stage is over, it is clear that the kinetic energy imparted to the fluid is largely confined in the wake which contains the trailing vortex sheet and is lengthening at the rate U. Therefore, W cannot be negative. [A mathematical proof of this statement has been given for the case of plane flows, see Eq. (39).] Another example is when the body starts to swim from a state of rest,

$$U = U(t)\,, \quad h = h(x,z,t)\,, \quad (t > 0) \tag{8}$$

while U, h, and (u,v,w) are all zero for $t \le 0$, where u, v, and w are the components of the perturbation velocity. In this case any disturbance generated in the flow must correspond to a gain of kinetic energy of the fluid.

The following discussion will be based on the presumption $W \ge 0$. Under this condition we have, by (6),

$$P \ge TU \quad \text{if} \quad W \ge 0 \,. \tag{9}$$

P, however, may not be positive definite. When P is negative, energy is transferred out of the fluid (such as by a turbine). In such case $T < 0$, indicating that there must be an inertial drag acting on the body. Forward swimming is possible only when the thrust $T > 0$, large enough to overcome the viscous drag; then $P > 0$, and hence a power is required to maintain the motion. Now, from (3) it is seen that a positive thrust is assured if Δp and $\partial h/\partial x$ are everywhere of the same sign, since the suction force F_s depends only on the instantaneous local condition and is never negative. In view of the inequality (9) and the expression

(4), Δp and $\partial h/\partial t$ cannot be also of the same sign everywhere. Suppose, as a qualitative picture, that $\partial h/\partial x$ and $\partial h/\partial t$ are everywhere opposite in sign, then a propagating wave toward the tail is clearly indicated (see Fig. 1).

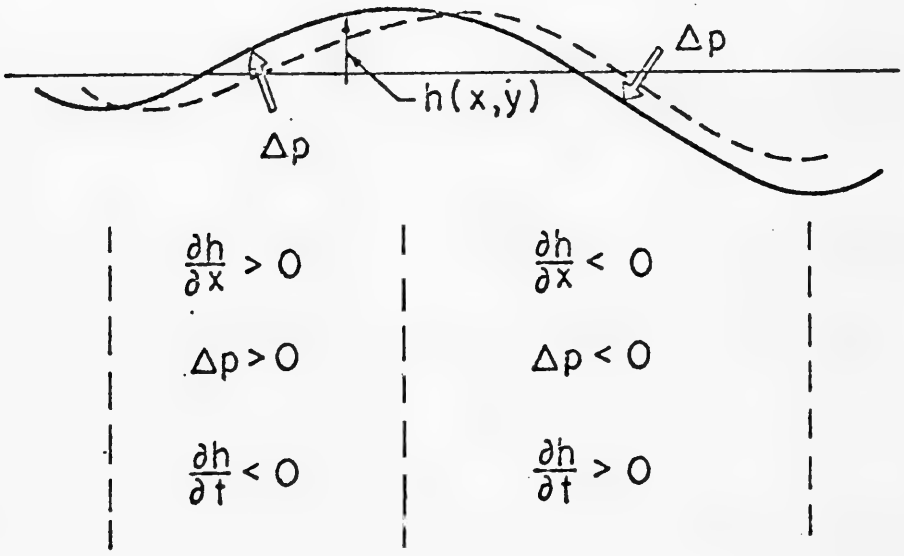

Fig. 1 - Wave propagating toward the tail

To investigate further the qualitative features of such periodic waving motions, it suffices to consider the case of simple harmonic form (7), since for arbitrary time dependence all linear effects, such as the pressure, lift, and moment, can be obtained by the Fourier synthesis and as for the quadratic effects such as T, P, and W, it can be seen that in their time averages, the components with different multiple frequencies are not coupled. In fact, consider two functions:

$$g(\mathbf{x},t) = \mathrm{Re}\left[\sum_n g_n(\mathbf{x})\, e^{j\omega_n t}\right], \quad h(\mathbf{x},t) = \mathrm{Re}\left[\sum_n h_n(\mathbf{x})\, e^{j\omega_n t}\right]. \tag{10}$$

The time average of gh is

$$\overline{gh} \equiv \lim_{T\to\infty} \frac{1}{T}\int_0^T g(\mathbf{x},t)\, h(\mathbf{x},t)\, dt = \frac{1}{2}\,\mathrm{Re}\left[\sum_n g_n(\mathbf{x})\, h_n^*(\mathbf{x})\right], \tag{11}$$

where h^* is the complex conjugate of h (with respect to j). This result is readily extended to the integral form when g, h are expressed by integrals over a continuous spectrum.

Returning to the waving motion, we consider the fundamental form

$$y = \mathrm{Re}\,[h_1(x,z)\,e^{j(\omega t - kx)}]\ , \quad (x,z \in S) \tag{12}$$

which represents a simple wave propagating along the planar body in the streamwise direction with phase velocity $c = \omega/k$ and amplitude $h_1(x,z)$. Substituting (12) in (3) and (4), and taking the time average, we obtain

$$\bar{T}_p = \frac{k}{2}\,\mathrm{Re}\int_S (\Delta p_1)\left(j h_1 + \frac{1}{k}\frac{\partial h_1}{\partial x}\right) e^{jkx}\,dS\ , \tag{13a}$$

$$\bar{P} = \frac{\omega}{2}\,\mathrm{Re}\int_S (\Delta p_1)\,(j h_1)\,e^{jkx}\,dS\ , \tag{13b}$$

where (Δp_1) is the time-independent part of (Δp), $\Delta p = (\Delta p_1)\exp(j\omega t)$ as a result of the linearized theory. Since the thrust T_s due to the leading-edge suction is always non-negative, it follows from the inequality (9) that

$$\bar{P} \geq U\bar{T} \geq U\bar{T}_p \tag{14}$$

provided $\bar{W} \geq 0$. Consequently, if $\partial h_1/\partial x = 0$ (the amplitude h_1 is independent of x), or when $|\partial h_1/\partial x| \ll |k h_1|$, then from (13) and (14) we immediately have

$$c = \omega/k \geq U\ . \tag{15}$$

This result shows that not only is a progressive wave desirable, but also its phase velocity must be greater than U (under the stated conditions) in order to achieve a given swimming velocity U. This qualitative feature remains true for a wide class of amplitude function $h_1(x,z)$, particularly when additional thrust is required to overcome the viscous drag.

SWIMMING OF A TWO-DIMENSIONAL WAVING PLATE

Although the flow around swimming fish is certainly three-dimensional, the theory of two-dimensional swimming motion has received more attention, partly because the analysis is relatively less complicated. We review in the following the main features of swimming in plane flows.

Here we consider the incompressible plane flow of an inviscid fluid past a flexible plate of zero thickness, spanning from $x = -1$ to $x = 1$, and performing a waving motion of the general form

$$y = h(x,t), \quad (-1 < x < 1, \ t > 0) \qquad (1')$$

h again being arbitrary and assumed to be always small. The motion starts at $t = 0$ from a uniform state; the free-stream velocity $U(t)$ may depend on t. Let u and v again denote, respectively, the x and y components of the perturbation velocity. We introduce the Prandtl acceleration potential

$$\phi(x,y,t) = (p_\infty - p)/\rho \ , \qquad (16)$$

where p_∞ is the pressure at infinity, and ρ is the fluid density. An harmonic function $\psi(x,y,t)$ conjugate to ϕ may be defined by $\phi_x = \psi_y$, $\phi_y = -\psi_x$, where the subscripts x and y denote differentiations. By virtue of the incompressibility and irrotationality, the complex acceleration potential $f = \phi + i\psi$ and the complex velocity $w = u - iv$ are analytic functions of the complex variable $z = x + iy$ for all real t. (We borrow the notation w and z for this different purpose in this section.) By neglecting the nonlinear terms of all the small quantities, Euler's equation of motion is linearized to give

$$\frac{\partial f}{\partial z} = \frac{\partial w}{\partial t} + U(t)\frac{\partial w}{\partial z} \ . \qquad (17)$$

The linearized boundary conditions are:

$$v(x,0_\pm,t) = V(x,t) = h_t + Uh_x \ , \quad (-1 < x < 1) \qquad (18)$$

$$-\frac{\partial \psi}{\partial x} = \left(\frac{\partial}{\partial t} + U\frac{\partial}{\partial x}\right)^2 h \ , \quad (y = 0_\pm \ , \ |x| < 1) \qquad (19)$$

$$\phi(x,0,t) = 0 \ , \quad (|x| > 1) \qquad (20)$$

$$|f(1,t)| < \infty, \quad \text{for all } t \qquad (21)$$

$$f(z,t) \to 0 \ \text{ as } \ |z| \to \infty; \quad w(z,t) \to 0 \ \text{ as } \ z \to -\infty \ . \qquad (22)$$

Here, condition (19) is obtained by applying (18) to the imaginary part of (17); condition (20) follows from that ψ is even, and hence ϕ is odd in y; (21) is the Kutta condition for the flow at the trailing edge $z = 1$. Condition (22) for w may also be specified as $|z| \to \infty$, $|\arg z| > 0$, i.e., as $z \to \infty$ in the region excluding the trailing vortex sheet.

Integration of (17) to obtain the boundary value of ψ on the plate can be done by using the method of characteristics. However, with variable $U(t)$, it is more convenient to make use of the Laplace-transform method. We first introduce the variable

$$\tau(t) = \int_0^t U(t)\,dt \qquad (23)$$

and assume that its inverse function $t = t(\tau)$ is unique, so that $U = U(t(\tau))$ is a one-valued function of τ. Regarding w and f as functions of z and τ, (17) becomes

$$\frac{\partial F}{\partial z} = \frac{\partial w}{\partial \tau} + \frac{\partial w}{\partial z} , \tag{24}$$

where

$$F(z,\tau) = f(z,\tau)/U(\tau) = \Phi(x,y,\tau) + i\Psi(x,y,\tau) . \tag{25}$$

Application of the Laplace transform

$$\tilde{F}(z,s) = \int_0^\infty e^{-s\tau} F(z,\tau)\, d\tau \quad (\mathrm{Re}\ s > 0) \tag{26}$$

to (24), under zero initial conditions, yields

$$\frac{d\tilde{F}}{dz} = \left(\frac{d}{dz} + s\right) \tilde{w} .$$

Integrating this equation from $z = -\infty$, using conditions (22), and expressing $\tilde{F}$ in terms of $\tilde{w}$, and vice versa, we obtain its imaginary part at $y = 0$ as

$$\tilde{\Psi}(x,0_\pm,s) = -\tilde{v}(x,0_\pm,s) - s \int_{-\infty}^{x} \tilde{v}(x_1,0_\pm,s)\, dx_1 , \tag{27}$$

or

$$\tilde{v}(x,0_\pm,s) = -\tilde{\Psi}(x,0_\pm,s) - s \int_{-\infty}^{x} e^{s(x_1-x)} \tilde{\Psi}(x_1,0_\pm,s)\, dx_1 \tag{28}$$

for all x. On the plate, $\tilde{v}(x,0_\pm,s) = \tilde{V}(x,s)$, which is the Laplace transform of (18), we have

$$\tilde{\Psi}(x,0_\pm,s) = \tilde{\Psi}_1(x,s) + \tilde{A}_0(s) , \quad (|x| < 1) \tag{29a}$$

where

$$\tilde{\Psi}_1(x,s) = -\left(\frac{\partial}{\partial x} + s\right) \int_{-1}^{x} \tilde{V}(x_1,s)\, dx_1 \quad (|x| < 1) \tag{29b}$$

and

$$\tilde{A}_0(s) = -s\int_{-\infty}^{-1} \tilde{v}(x,0_\pm,s)\,dx = s\int_{-\infty}^{-1} e^{s(x+1)}\tilde{\Psi}(x,0,s)\,dx \quad . \tag{29c}$$

Thus, $\tilde{\Psi}$ is known except for an additive constant term $\tilde{A}_0(s)$. Furthermore, from (20) it follows that

$$\tilde{\Phi}(x,0_\pm,s) = \mathrm{Re}\,\tilde{F}(x \pm i0,s) = 0\,, \quad (|x| > 1)\,. \tag{30}$$

This Riemann-Hilbert problem, specified by (29), (30) and conditions (21) and (22) can be readily solved, giving

$$\tilde{F}(z,s) = \frac{1}{\pi i}\left(\frac{z-1}{z+1}\right)^{1/2}\int_{-1}^{1}\left(\frac{1+\xi}{1-\xi}\right)^{1/2}\frac{\tilde{\Psi}(\xi,0,s)}{\xi - z}\,d\xi\,,$$

in which the function $(z-1)^{1/2}(z+1)^{1/2}$ is defined with a branch cut from $z = -1$ to $z = 1$ so that this function tends to 1 as $|z| \to \infty$. The leading-edge singularity can be separated out in the above solution by suitable integrations while using (29a), giving

$$\tilde{F}(z,s) = i\tilde{A}_0(s) - \frac{i}{2}\tilde{a}_0(s)\left(\frac{z-1}{z+1}\right)^{1/2} + \frac{1}{\pi i}\int_{-1}^{1}\left(\frac{z^2-1}{1-\xi^2}\right)^{1/2}\frac{\tilde{\Psi}_1(\xi,s)}{\xi - z}\,d\xi\,, \tag{31a}$$

where

$$\frac{1}{2}\tilde{a}_0(s) = \tilde{A}_0(s) + \frac{1}{\pi}\int_{-1}^{1}\frac{\tilde{\Psi}_1(\xi,s)}{(1-\xi^2)^{1/2}}\,d\xi\,. \tag{31b}$$

Now, substituting the value of $\tilde{\Psi}(x,0,s)$ [for $x < -1$, which can be readily deduced from (31a)] into the second-integral representation of (29c), then after some appropriate integrations by parts, using the identity

$$(x^2-1)^{-1/2}\frac{\partial}{\partial\xi}\frac{(1-\xi^2)^{1/2}}{\xi - x} = (1-\xi^2)^{-1/2}\frac{\partial}{\partial x}\frac{(x^2-1)^{1/2}}{\xi - x}\,,$$

we determine the coefficient $\tilde{a}_0(s)$ as

$$\tilde{a}_0(s) = \frac{2}{\pi}\int_{-1}^{1}[\xi - \tilde{G}(s)(1+\xi)]\frac{\tilde{V}(\xi,s)}{(1-\xi^2)^{1/2}}\,d\xi\,, \tag{32a}$$

where

$$\tilde{G}(s) = \frac{K_1(s)}{K_0(s) + K_1(s)} \tag{32b}$$

and K_0 and K_1 are modified Bessel functions of the second kind.

Finally, we note that after the inverse transform the solution of ϕ on the body surface is $\phi^+(x,t) = \phi(x,0+,t) = -\phi(x,0-,t) = -\phi^-(x,t)$,

$$\phi^+(x,t) = \frac{1}{2} U(t)\, a_0(\tau) \left(\frac{1-x}{1+x}\right)^{1/2} + \frac{1}{\pi} \int_{-1}^{1} \left(\frac{1-x^2}{1-\xi^2}\right)^{1/2} \frac{\psi(\xi,0,t)}{\xi - x}\, d\xi , \quad (|x| < 1) \tag{33}$$

$$a_0(\tau) = \int_0^{\tau} [\lambda_0(\tau_1) + \lambda_1(\tau_1)]\, G(\tau - \tau_1)\, d\tau_1 - \lambda_1(\tau) , \tag{34}$$

$$\lambda_n(\tau) = -\frac{2}{\pi} \int_{-1}^{1} \frac{V(x,t) \cos n\theta}{(1-x^2)^{1/2}}\, dx , \quad (x = \cos\theta , \quad n = 0, 1, \cdots) \tag{35}$$

$$G(\tau) = \frac{1}{2\pi i} \int_{b-i\infty}^{b+i\infty} e^{s\tau} \tilde{G}(s)\, ds . \tag{36}$$

The coefficient $a_0(t)$ gives the strength of the leading edge singularity, which is the first term on the right-hand side of (33); the integral term is regular wherever ψ is continuous. The pressure difference (Δp) defined previously is, by (16),

$$\Delta p = 2\rho\phi^+(x,t) , \quad (|x| < 1) . \tag{37}$$

The following cases have been developed earlier:

Simple Harmonic Time Motion; Constant Swimming Speed

The motion is prescribed by Eq. (7) (with the third coordinate z omitted, and S given by $|x| < 1$). It has been shown by Wu (1961) that

$$a_0 = [(\lambda_0 + \lambda_1)\, \mathcal{C}(\sigma) - \lambda_1] , \quad (\sigma = \omega/U) \tag{38a}$$

$$\mathcal{C}(\sigma) = K_1(j\sigma)/[K_0(j\sigma) + K_1(j\sigma)] = \mathcal{F}(\sigma) + j\mathcal{G}(\sigma) , \tag{38b}$$

in which λ_0 and λ_1 are still given by (35), now having the time factor $\exp(j\omega t)$. $\mathcal{C}(\sigma)$ is the Theodorsen Function, $\mathcal{F}$ and $\mathcal{G}$ being its real and imaginary parts, and σ is the reduced frequency based on half-chord (which is taken to be unity).

The time average of the quadratic quantities T, P, and W, can be readily obtained by substituting the solution (33), (37) into (13) giving

$$\bar{W} = \frac{\pi}{4} \rho U |\lambda_0 + \lambda_1|^2 \{\mathcal{F} - (\mathcal{F}^2 + \mathcal{G}^2)\} , \tag{39}$$

$$\bar{P} = \frac{\pi}{4} \rho U^2 \sigma \, \mathrm{Re} \{(\lambda_0 + \lambda_1) [j\mathcal{C}(\sigma) \beta_0^* + j(1 - \mathcal{C}(\sigma)) \beta_1^*]\} , \tag{40}$$

where

$$\beta_n = \frac{2}{\pi} e^{j\omega t} \int_{-1}^{1} \frac{h_1(x) \cos n\theta}{(1 - x^2)^{1/2}} \, dx , \quad (x = \cos\theta , \quad n = 0, 1, \ldots) . \tag{41}$$

Finally, the average thrust $\bar{T}$ follows from (6), $\bar{T} = (\bar{P} - \bar{W})/U$. The result (39) shows that $\bar{W} \geq 0$, since it is known from $\mathcal{C}(\sigma) = \mathcal{F} + j\mathcal{G}$ that $\mathcal{F} \geq (\mathcal{F}^2 + \mathcal{G}^2)$ for $\sigma \geq 0$ and the equality holds only if $\sigma = 0$. Thus, $\bar{W} \geq 0$ in general, $\bar{W} = 0$ only when $\sigma = 0$ or $\lambda_0 + \lambda_1 = 0$. The first special case $\sigma = 0$ is the trivial steady motion, whereas the second case corresponds to the condition that the circulation around the plate remains zero for all t and hence no trailing vortex sheet is shed from the body, since the strength of the vortex sheet at the trailing edge is

$$\gamma(1, t) = -\pi \, \mathrm{Re} \left\{ \frac{\lambda_0 + \lambda_1}{K_0(j\sigma) + K_1(j\sigma)} e^{j(\omega t - \sigma)} \right\} . \tag{42}$$

When no vortex is shed, $\lambda_0 + \lambda_1 = 0$, it is seen from (39) and (40) that $\bar{W}$, $\bar{P}$, and hence $\bar{T}$ all vanish, even though the plate may still be waving. For any other unsteady motion ($\sigma > 0$) we must therefore have the inequality (14). When $\bar{T}$ is positive, we may define the hydrodynamic efficiency as

$$\eta = U\bar{T}/\bar{P} = 1 - \bar{W}/\bar{P} . \tag{43}$$

The principal features of the solution may be seen from the following specific example:

$$h(x, t) = \frac{1}{16} (x + 1) \cos (kx - \omega t) \quad (|x| < 1) . \tag{44}$$

The thrust coefficient $C_T = \bar{T}/[(1/4)\pi\rho U^2]$ is plotted versus the reduced frequency $\sigma = \omega\ell/2U$ (ℓ being the chord) for $\kappa = (1/2)\, k\ell = \pi$ in Fig. 2, in which the experimental results of Kelly (1961) are also shown for comparison (these data include the skin-friction drag). The theoretical result shows that C_T is positive for $\sigma > \kappa$, or when the wave velocity

$$c = \omega/k = (\sigma/\kappa) U \tag{45}$$

is greater than the swimming speed U, and C_T is negative for $0 < c < U$, or $\sigma < \kappa$. This qualitative feature has already been predicted earlier.

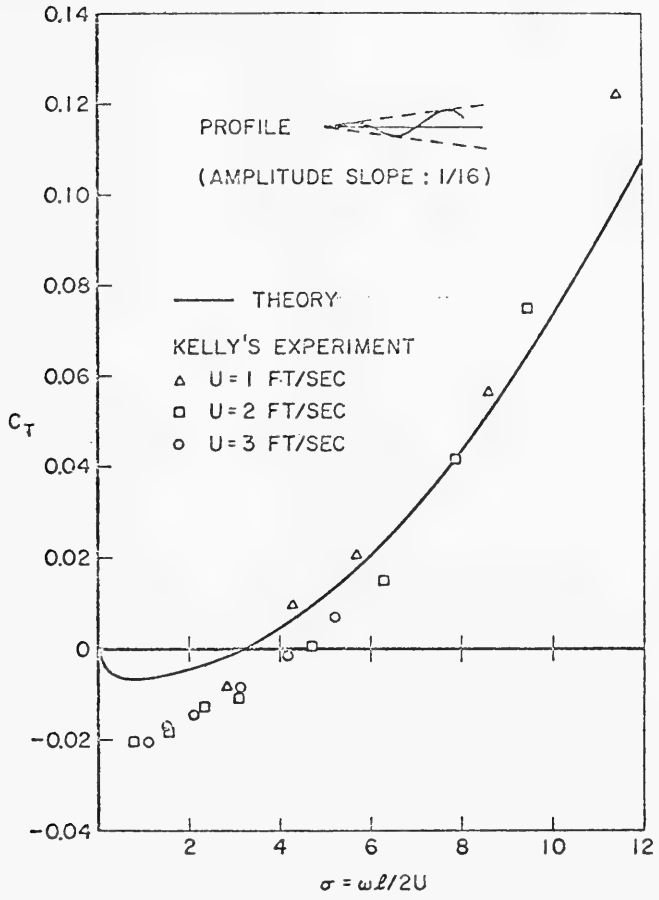

Fig. 2 - Thrust coefficient C_T versus reduced frequency σ for $\kappa = 1/2\ k\ell = \pi$

Another approach towards analyzing the mechanism of swimming is based on the principle of action and reaction. Considering the inertial forces alone in this inviscid approximation (i.e., leaving out the viscous effects of the boundary layer and the viscous wake for a separate account), we find that the flow momentum at large distances is concentrated in the vortex wake, as should be expected in view of the trailing vortex sheet shed to the rear being thin, resulting in a jet of fluid which is expelled from the plate. This mechanism can be seen as follows. In the motion prescribed by (44), the tail (at $x = 1$) reaches the uppermost position at $t = \kappa/\omega + 2n\pi$ $(n = 0, 1, \ldots)$, and the lowest position at $t = \kappa/\omega + (2n + 1)\pi$. After some calculation, it can be found from (42) that if $c > U$ (or $\sigma > \kappa$), vorticity shed from the plate is negative (or in counterclockwise sense) when the tail is at the highest position, and increases monotonically,

as the tail moves downward, to a positive maximum (in clockwise sense) when the tail is at the lowest position. The velocity field due to this vortex system is clearly in the form of a jet moving in the positive x direction, as depicted in Fig. 3. By the principle of action and reaction, the plate therefore experiences a positive thrust. For the same reason, the thrust is negative if $c < U$, since the shed vorticity is reversed in sense. In the case of a self-propelling body, however, the backward momentum due to inertial forces and the forward momentum due to the skin friction exactly balance in steady swimming.

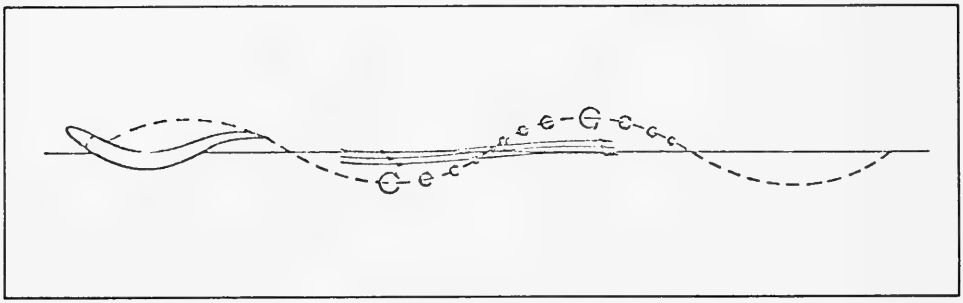

Fig. 3 - Jet moving in the positive x direction

The effect of body thickness in sinusoidal motion has been discussed by Uldrick and Siekmann (1964).

Starting Stage of a Forward Swim

A typical starting motion has been considered by Wu (1962), with the plate starting with a constant acceleration from at rest,

$$U(t) = at\,, \quad (a > 0)$$

and with $h(x,t)$ assuming a polynomial of degree 3 in x. The small time behavior of the solution has been evaluated with the assumption of small lift and moment, in order to minimize the body recoil in lateral and spinning motions. The result shows that the thrust is generated at the time of order t^2, whereas the power is already required at the time of $0(t)$, the initial power being positive definite for arbitrary transverse motion $h(x,t)$. When a high efficiency is required in addition, the body profile appears in an S shape, with a maximum and minimum of h at $x = -0.564$ and $x = 0.295$ approximately.

SWIMMING OF SLENDER FISH

Lighthill (1960) treated the problem of swimming of slender fish, at sufficiently large Reynolds number, by applying an inviscid slender-body

approximation. The body, when stretched straight, lies in between $x = 0$ and $x = \ell$; its cross section is small in dimension compared to ℓ. The free stream has a constant velocity U in the x direction. The motion of the curve passing through the centroids of the cross section of the body remains in the xz plane, and is prescribed as

$$z = h(x,t) \quad (0 < x < \ell) \tag{47}$$

with the same qualification for h as before.

The flow has two components: One is the steady flow around the stretched straight body, which gives no resultant force or moment for symmetric bodies, and the other is the cross flow due to the displacement $h(x,t)$, which has, in the cross-flow plane, the velocity $V(x,t)$ as given by (18). This latter component alone determines the lift, moment, thrust, and other relevant quantities. The cross-flow momentum is $\rho A(x)V(x,t)$, where $\rho A(x)$ is the virtual mass corresponding to the transverse unsteady flow and $A(x)$ can be readily determined for given cross sections. The instantaneous lift acting on a section of length dx at x is equal and opposite to the rate of change of momentum in cross flow (or equivalently, it can be obtained by integrating p over the boundary of the body cross-section), that is,

$$L(x,t)\,dx = -\rho\left(\frac{\partial}{\partial t} + U\frac{\partial}{\partial x}\right)[A(x)V(x,t)]\,dx\ . \tag{48}$$

The rate of work done by the body in making the displacement h in the direction of lift is therefore

$$P = -\int_0^\ell h_t L(x,t)\,dx = \rho\frac{\partial}{\partial t}\int_0^\ell \left(AVh_t - \frac{1}{2}AV^2\right)dx + \rho U\,[Ah_t V]_{x=\ell} \tag{49}$$

Alternatively, this expression is obtained by replacing $(\Delta p)\,dS$ in (4) by $L(x,t)\,dx$ over $0 < x < \ell$. The kinetic energy imparted to the fluid due to the lateral motion in unit time is

$$W = \int_0^\ell \left(\frac{\partial}{\partial t} + U\frac{\partial}{\partial x}\right)\left(\frac{1}{2}\rho AV^2\right)dx = \frac{1}{2}\rho\frac{\partial}{\partial t}\int_0^\ell AV^2\,dx + \frac{1}{2}\rho U\,[AV^2]_{x=\ell} \tag{50}$$

The time average of P and W are clearly

$$\bar{P} = \rho UA(\ell)\,\overline{[h_t V]}_{x=\ell} = \rho UA(\ell)\,\overline{[h_t + Uh_x)]}_{x=\ell}\ , \tag{51}$$

$$\bar{W} = \frac{1}{2}\rho UA(\ell)\,\overline{V^2}_{x=\ell} = \frac{1}{2}\rho UA(\ell)\,\overline{(h_t + Uh_x)^2}_{x=\ell}\ . \tag{52}$$

The physical significance of these results is clear. $\bar{P}$ is equal to the average of the product of the lateral velocity h_t and the rate of shedding lateral

momentum $(\rho VA)U$ at the tail; $\bar{W}$ is equal to the shedding of the average kinetic energy $(\rho AV^2/2)$ at the rate U. Finally, from (6) it follows that the average thrust is

$$\bar{T} = \frac{1}{2}\rho A(\ell)\,\overline{[h_t^2 - U^2 h_x^2]}_{x=\ell} \ . \tag{53}$$

Obviously, $\bar{W} \geq 0$, as should be expected from the general argument stated before. When $\bar{T}$ is positive, the hydrodynamic efficiency of swimming is defined, as before, by (43).

Lighthill reasoned that high efficiency can be achieved if $V \ll h_t$, but V and h_t must be positively correlated, i.e., $\overline{h_t V} > 0$ (for otherwise, $\bar{P} < 0$, hence $\bar{T}$ is also negative). Furthermore, there are two side conditions that the inertial lift and moment of the body (with known mass distribution) must balance, respectively, the hydrodynamic lift and moment in order to free the body from any recoil.

Two specific examples have been given by Lighthill. When the body motion is a standing wave, the efficiency is always <0.5. If the body motion is a progressive wave,

$$h(x,t) = b(x)\cos\omega(t - x/c) \ ; \tag{54}$$

then

$$\bar{T} = \frac{1}{4}\rho A(\ell)\left[\omega^2 b^2\left(1 - U^2 b'(\ell)^2\right)\right] \ , \tag{55}$$

$$\bar{P} = \frac{1}{2}\rho U A(\ell)\omega^2 b^2(1 - U/c) \ . \tag{56}$$

An estimate shows that η can be as high as 0.9 at $c = 1.25U$ provided that the slope of the amplitude profile is negligible at the tail. We observe that $\bar{T}$ cannot be positive unless $c > U$, which is a general feature as expected.

It should be noted that for this category of slender-body motion, it is essential that the fish must have a tail edge structure so that $A(\ell) > 0$, since $\bar{T}$, $\bar{P}$, and $\bar{W}$ are all proportional to $A(\ell)$. In reality, however, typical body shapes of fishes, aside from being slender, usually are rather planar and have side edges that may be regarded as sharp. In such cases, the vortex sheet shed from the sharp trailing edges will considerably modify the flow field, so that the thrust and energy balance will no longer depend only on the flow at the tail section $x = \ell$.

OPTIMUM SHAPE OF WAVING PLATE

An interesting problem concerning swimming propulsion is to find the optimum shape of the body motion. The special case of the two-dimensional

waving plate has been treated by Wang (1966), who adopted a discretized Fourier representation of the body motion. For the simple harmonic motion given by

$$h(x,t) = \mathrm{Re}\,[h_1(x)\, e^{j\omega t}] \,, \quad (|x| < 1) \tag{57}$$

let h_1 be represented by an $(N+1)$-term Fourier series

$$h_1(x) = \frac{1}{2}\beta_0 + \sum_{n=1}^{N} \beta_n \cos n\theta \,, \quad (x = \cos\theta) \tag{58}$$

where β_n is given by (41) with the time factor deleted. Then the coefficients λ_0 and λ_1 can be expressed in terms of β_n's. Let $\beta_n = \beta_n' + j\beta_n''$, β_n' and β_n'' being both real, and we define the vector

$$\vec{\beta} = (\beta_0', \beta_0'', \beta_1', \beta_1'', \ldots, \beta_N', \beta_N'') \,, \tag{59}$$

in which β_0'' may always be set equal to zero as the reference phase. Then the thrust and power coefficient can be written as

$$C_T = \vec{\beta}^t \mathcal{Q} \vec{\beta} \,, \quad C_p = \sigma \vec{\beta}^t \mathcal{P} \vec{\beta} \tag{60}$$

where $\vec{\beta}^t$ is the transpose of $\vec{\beta}$, and $\mathcal{Q}$ and $\mathcal{P}$ are $(2N+1) \times (2N+1)$ symmetric real matrices. $\mathcal{Q}$ is nonsingular and has real eigenvalues of both signs for $N > 1$ and for all $\sigma > 0$, implying that the origin $\vec{\beta} = 0$ is a saddle point of C_T. Also, $\mathcal{P}$ has eigenvalues of both signs for all $\sigma > 0$.

We consider the problem of maximizing C_T, which is required to be positive, under one of the two constraints

$$(C-1): \quad \bar{C}_p \le \bar{P}_0 \tag{61a}$$

or

$$(C-2): \quad C_p(t) \le P_0 \,, \quad (0 < t < t_1) \tag{61b}$$

where P_0 and $\bar{P}_0$ are specified positive constants. This constrained optimization problem is equivalent to that of maximizing a new function

$$C_T^* = C_T - \lambda(\sigma \vec{\beta}^t \mathcal{P} \vec{\beta} - \bar{P}_0) \,, \tag{62}$$

where λ is a Lagrange multiplier. Setting the derivatives C_T^* with respect to all components of $\vec{\beta}$ to zero yields

$$\mathcal{Q}(\sigma)\vec{\beta} = \lambda\sigma\mathcal{P}(\sigma)\vec{\beta} \,. \tag{63}$$

Let $\vec{\beta}^\circ$ denote the optimum solution; then, since $\mathcal{Q}$ is nonsingular, $\vec{\beta}^\circ$ satisfies

$$\sigma\mathcal{Q}^{-1}(\sigma)\mathcal{P}(\sigma)\vec{\beta}^\circ = \lambda^{-1}\vec{\beta}^\circ \,. \tag{64}$$

The corresponding optimum value of C_T is

$$C_T^{\circ} = \lambda\sigma(\vec{\beta}^{\circ})^t \mathcal{P}(\sigma)\,\vec{\beta}^{\circ} . \tag{65}$$

Upon using the constraints

$$\sigma(\vec{\beta}^{\circ})^t \mathcal{P}(\sigma)\,\vec{\beta}^{\circ} = \bar{P}_0 , \tag{66}$$

(65) reduces to

$$C_T^{\circ} = \lambda\,\bar{P}_0 , \tag{67}$$

which signifies this λ as the maximum hydrodynamic efficiency under these conditions. Consequently, C_T is maximized when

$$\lambda^{-1} = \lambda^{+}_{min}[\sigma\mathcal{Q}^{-1}(\sigma)\,\mathcal{P}(\sigma)] , \tag{68}$$

the minimal element of the set of all positive eigenvalues of $[\sigma\mathcal{Q}^{-1}\mathcal{P}]$ for a given $\sigma > 0$, whose corresponding eigenvector $\vec{\beta}^{+}$ satisfy $(\vec{\beta}^{+})^t\mathcal{P}\vec{\beta}^{+} > 0$. The optimum solution $\vec{\beta}^{\circ}$ is an eigenvector corresponding to $\lambda^{+}_{min}[\sigma\mathcal{Q}^{-1}\mathcal{P}]$ satisfying condition (67).

Numerical calculation of the result has been carried out by Wang (1966) for the simplest case of a flat plate with average power limitation constraint (61a) for the motion having $\vec{\beta} = (\beta_0', \beta_1', \beta_1'')$, which corresponds to a rigid plate in plunging and pitching oscillations. The numerical results of the optimum efficiency for the subspaces:

$$(M-1)\,S_1 = \{\vec{\beta}:\beta_1' = \beta_1'' = 0\} \quad \text{and} \quad (M-2)\,S = \{\vec{\beta}:\beta_1' = 0\}$$

are shown in Fig. 4.

SKIN-FRICTION DRAG OF CETACEAN

Recently a series of hydrodynamic experiments with several specimens of different species of porpoises (Tursiops gilli, Stenella attenuata) have been performed by Lang and co-workers (1963, 1966a,b,c) under more carefully controlled conditions. The test results with a Pacific bottlenose porpoise (Tursiops gilli) compare closely with highest predictions based upon rigid-body drag calculations, the same power output per unit body weight as for athletes, and a propulsive efficiency of 85%. The maximum power output of Stenella attenuata, per unit body weight, was, however, 50% greater than for human athletes; and the measured drag coefficient was approximately the same as that of an equivalent rigid body with a near-turbulent boundary layer. Thus, in general, no unusual hydrodynamic or physiological performance was observed. Also, it has been pointed out that Gray's paradox can be largely resolved by consideration of duration; Gray's analysis was based on the power output of humans for a 15 minute period and this figure can be raised several times if based on a shorter period, such as a few seconds.

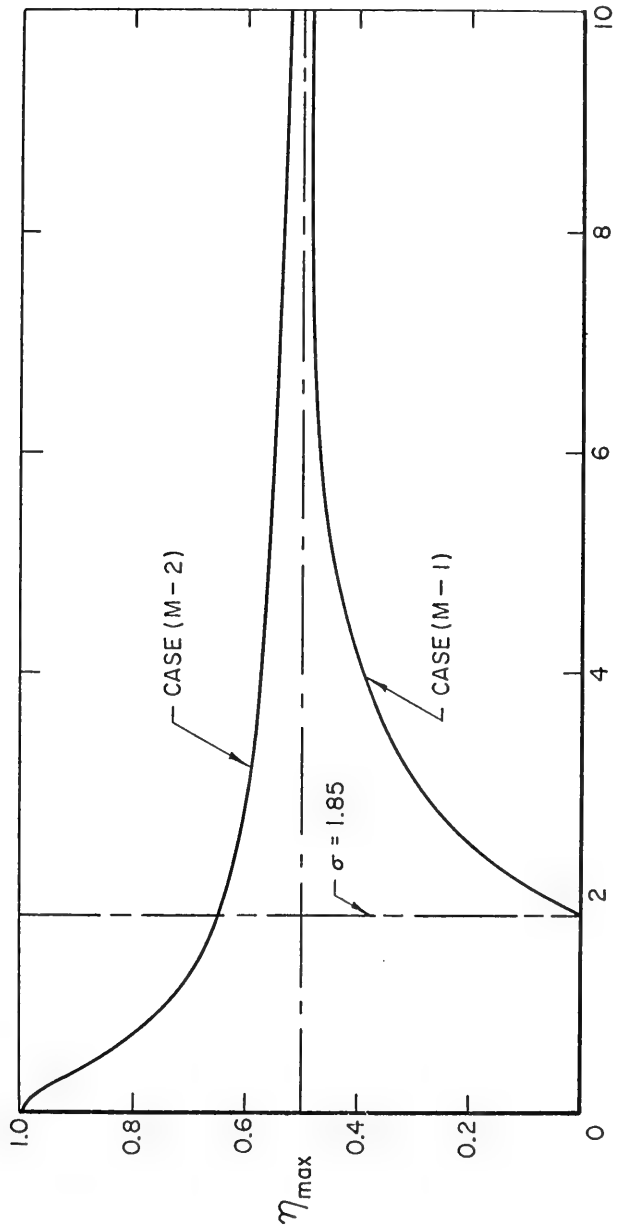

Fig. 4 - η_{max} for cases (M-1) & (M-2)

While these results have put the whole picture in a much improved aspect, a closer examination of the experimental data as shown in Fig. 5 indicates that there are still cases in which the laminar flow was maintained over a considerably greater percent point of the porpoise skin than for an equivalent rigid body. A number of hypotheses have been proposed in an effort to explain the observed low drag. One of the likely effects is attributed to a favorable pressure gradient over a well-shaped streamline body, as indicated by van Driest and Blumer (1963) for laminar flows up to $R = 10^8$. Another possibility is by means of boundary-layer control, such as the compliant skin discovered by Kramer (1960). Subsequent theoretical studies of this effect by Betchov (1959), Benjamin (1960), and Landahl (1961) have indicated that the increases in critical Reynolds number obtainable with passive flexible surfaces are too modest to support this effect on the basis of simple stability theory alone. Even though the possibility of activated flexible surfaces have been proposed, the structural complexity of such skin seems to be biologically infeasible.

A fairly certain explanation for low drag on fish is the effect on the boundary layer produced by the addition of long-chain molecules, as reported by Fabula, Hoyt, and Crawford (1963). The mucous exuded by fish is composed of a similar type of long-chain molecules and has been found by Hoyt (private communication) to bear significantly the same effect. Still another possible explanation, which seems to be really the principal one to this author, is the unsteady flow effects, due to body undulations, on the hydrodynamic stability.

SELF-PROPULSION IN A PERFECT FLUID

The previous theories are concerned with the swimming of bodies in fluids of small, but not zero viscosity. Recently, Saffman (1967) raised the interesting question: can a fish swim in a perfect fluid whose viscosity is identically zero (as in a superfluid)? It has been shown that the classical paradox of D'Alembert for steady flows of a perfect fluid does not apply to the general unsteady flows past a deformable body and that a fish could indeed swim in a perfect fluid.

The momentum equation for the rectilinear motion of a deformable body in a perfect fluid can be written

$$[M + m(t)]\, W = -MU(t) - I_D(t) , \tag{69}$$

where M is the mass and $m(t)$ the virtual mass of the body, $W(t)$ is the velocity of the geometric centroid, $U(t)$ the velocity of the center of mass of the body, and I_D is the component of the fluid impulse due to the change in body shape relative to an instantaneously identical rigid body moving with velocity W. The quantities m, U, and I_D are functions only of the shape and structure of the deformable body and are independent of W. It is clear that an arbitrary displacement can be effected without a permanent or net deformation of the body if m, U, and I_D can be made to vary periodically with t in such a way that W has a nonzero time average

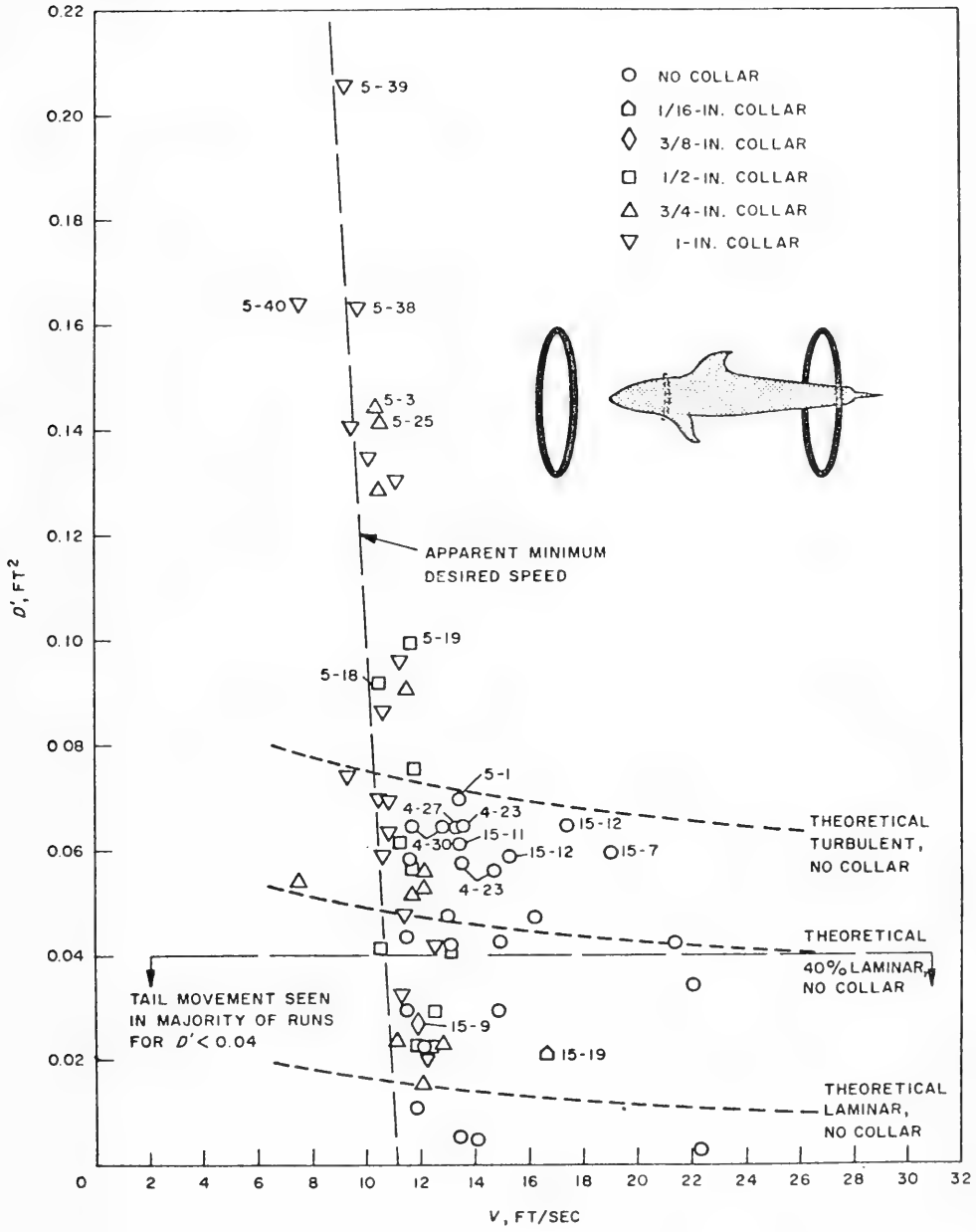

Fig. 5 - Drag area versus velocity

$$\int_0^t W(t')\,dt' \to \bar{W}t \quad \text{as} \quad t \to \infty \ (\bar{W} \neq 0) \ . \tag{70}$$

Saffman described two different ways in which this can be accomplished, one for heterogeneous and the other for a homogeneous body.

For a heterogeneous body, we can have $U = 0$, and it is simplest to suppose that the surface deformation has fore and aft symmetry so that $I_D \equiv 0$. Then $\bar{W}$ is positive if $U(t)$ and $m(t) - m(0)$ oscillate periodically in phase or with an in-phase component. The physical explanation of the propulsion mechanism in this case is clear. There is a hydrodynamic force on a body whenever the body accelerates, which is described by the virtual mass. Now, if the center of mass is moved backwards, the recoil will send the shell forward. If then the resistance or virtual mass is less when the shell goes forward than it is when the reverse recoil is moving the shell backwards, the distance covered during the forward motion exceeds that covered during the backwards motion and there is a net forward displacement during each cycle. Note that there is no continuing transfer of momentum between the body and the fluid; the momentum of the body oscillates about a nonzero mean while the oscillating deformation continues. There is of course a transfer of energy between body and fluid, but this is loss-free.

II. SWIMMING MOTION AT SMALL REYNOLDS NUMBERS

Propulsion of microscopic organisms always corresponds to a small Reynolds number and depends almost entirely on the viscous stresses. Although the body motions of some minute biological creatures bear a close resemblance to those of fish, in that they also send waves of lateral displacement from its head down a thin, long tail (or flagellum), the mechanics of the fluid is however greatly different from the case of large R. The effect of viscous stresses in steady flows at small R extends over a wide range, such that the body tends to drag along a very large volume of the surrounding fluid. The vorticity in steady flows is well diffused, leaving practically no wake near the body. Oscillation of the body reduces the amount of fluid moving with the body with increasing frequency, as was discussed by Stokes (1851). The mechanics of swimming in this case obeys, nevertheless, the basic principle of action and reaction, so that the total time rate of production of momentum is zero for a self-propelling body at a constant forward speed.

IMPORTANT FLOW PARAMETERS

A wide class of unsteady flows of an incompressible, viscous fluid past an oscillating body of arbitrary shape can be adequately described by the linearized Navier-Stokes equations, or Oseen's equations,

$$\frac{\partial \mathbf{u}}{\partial t} + U\frac{\partial \mathbf{u}}{\partial x} = -\frac{1}{\rho}\nabla p + \nu\nabla^2\mathbf{u} + \mathbf{F} \ , \tag{71}$$

$$\text{div } \mathbf{u} = 0 \ , \tag{72}$$

where $\mathbf{u}$ is the perturbation flow velocity, U is the free-stream velocity directed along the x axis, and $\mathbf{F}$ stands for the external force and may include surface force acting on the fluid by the moving body. The conditions necessary for this linearization to be valid have been well understood for the case of rectilinear and steady motions. The corresponding conditions for oscillatory motions can be examined as follows.

When a body, either rigid or flexible, of a characteristic length ℓ, undergoes an oscillation with frequency ω and amplitude a, the flow motion is characterized by the following dimensionless parameters:

$$R = U\ell/\nu \ , \quad S = \left(\frac{\ell}{\delta}\right)^2 \equiv \ell^2\omega/\nu \ , \quad \lambda = a/\ell \ . \tag{73}$$

The rectilinear Reynolds number R measures the relative importance of the translational inertial force and the viscous stresses; the oscillatory Reynolds number S gives the ratio of the body length ℓ to the depth of penetration of the vorticity, $\delta = (\nu/\omega)^{1/2}$. The relative magnitudes of these parameters give rise to the following principal regimes of interest:

(i) $R \ll 1$, $S \ll 1$, λ arbitrary. This is the case of low-frequency oscillation with the amplitude not necessarily small. Consequently, the flow field varies only slowly with time, and the problem may be treated as quasisteady, such that the terms on the left-hand side of (71) can be neglected.

(ii) $S \gg 1$, $\lambda \ll 1$, R arbitrary. This is the case of rapid oscillation with amplitude small compared with the body dimension, and hence the unsteady and viscous effects are of equal importance. The depth of penetration of the vorticity is now small compared with the body length; consequently, there exists an unsteady boundary layer, outside of which the flow is inviscid and irrotational. The nonlinear effect is still unimportant in this case, since the amplitude a is small. The Reynolds number R, however, need not be small.

(iii) $S \gg 1$, $\lambda = O(1)$. This case represents rapid oscillations with amplitude comparable to, or larger than the body dimension. The effects of unsteadiness, viscosity, and nonlinearity are now of equal importance, consequently the nonlinear terms of the Navier-Stokes equations must be restored, which will give rise to the phenomenon of nonlinear streaming. Two boundary layers are therefore anticipated in the motion, one due to the unsteady effect and the other due to the nonlinearity.

SWIMMING OF A WAVING PLATE IN A VISCOUS FLUID

In order to investigate the mechanism of swimming of microorganisms, Sir Geoffrey Taylor (1951) took as his first model a doubly-infinite sheet,

flexible but inextensible, which is propelling itself by small transverse progressive waves. Taylor considered a wave of displacement $y = b \sin(kx - \omega t)$ propagating in the $+x$ direction with phase velocity $c = \omega/k$, and found that this motion induces a velocity in the fluid at infinity of

$$U_\infty = \left[\frac{1}{2}(kb)^2 + O(kb)^4\right] c \ , \tag{74}$$

also in the $+x$ direction. A limitation of Taylor's analysis is that the Reynolds number $R = \omega/\nu k^2$ must be small enough for the application of Stokes's equations. This limitation was removed by A. J. Reynolds (1965), but his result is incorrect. This has been pointed out by Tuck (1968), who provided the correct result as

$$U_\infty = c\left[\frac{1}{2}(kb)^2 \frac{1 + F(R)}{2F(R)} + O(kb)^4\right] \ , \tag{75}$$

where

$$F(R) = \left[\frac{1 + (1+R^2)^{1/2}}{2}\right]^{1/2} \ , \tag{76}$$

a function which increases monotonically from unity at $R = 0$, tending to infinity like $R^{1/2}$ as $R \to \infty$. Thus, the effect of inertia appears to be to decrease (rather than to increase, according to Reynolds) the propulsion velocity above that found by Taylor at $R = 0$.

The analysis has been somewhat simplified by Tuck. We use a stream function ψ satisfying $u = \psi_y$, $v = -\psi_x$, $\zeta = -\nabla^2\psi$, and the Navier-Stokes equation

$$\nu\nabla^2\zeta - \frac{\partial \zeta}{\partial t} = u\zeta_x + v\zeta_y \ . \tag{77}$$

The boundary conditions (Taylor, 1951) are

$$\begin{aligned} u &= b^2 k\omega \cos(2kx - 2\omega t) + O(b^4) \ , \\ v &= -\omega b \cos(kx - \omega t) + O(b^3) \ , \end{aligned} \tag{78}$$

on the moving surface

$$y = b \sin(kx - \omega t) \ .$$

We now make the expansion

$$\psi = \Re\left[\psi_1(y)\, e^{-ikx+i\omega t}\right] + \Psi_2(y) + \Re\left[\psi_2(y)\, e^{-2ikx+2i\omega t}\right] + O(b^3) \ , \tag{79}$$

where the first term of (79) is $O(b)$ and satisfies a linearized version of the Navier-Stokes equation (77), while the remaining second-order terms are

divided into a "D.C." part $\Psi(y) = O(b^2)$ independent of t and x, and a "second-harmonic" part which varies sinusoidally in t and x, and with which we shall not be concerned.

The solution for the linearized flow is obtained by inspection, with the result

$$\psi_1 = -\nu b\ell(\ell + k)\left[\frac{e^{-\ell y}}{\ell} - \frac{e^{-ky}}{k}\right], \quad \ell = \left(k^2 + \frac{i\omega}{\nu}\right)^{1/2} . \tag{80}$$

The equation satisfied by the "D.C." second approximation is

$$\nu \frac{d^4\Psi_2}{dy^4} = -\langle u_1\zeta_{1x} + v_1\zeta_{1y}\rangle , \tag{81}$$

where $\alpha = k + \bar{\ell}$, $\gamma = \ell + \bar{\ell} = 2\Re(\ell)$. The solution for Ψ_2 which corresponds to a velocity U_∞ at $y = \infty$ is

$$\Psi_2 = U_\infty y + \frac{1}{2}\omega b^2|\alpha|^2\Re\left[\frac{\ell}{\alpha^3}e^{-\alpha y} - \frac{k}{\gamma^3}e^{-\gamma y}\right] . \tag{82}$$

The boundary condition to be satisfied on $y = 0$ is obtained by substitution of the expansion (79) into the boundary conditions (78), resulting in (75) and (76).

HIGH-FREQUENCY MOTION OF MICROSCOPIC ORGANISMS

The asymptotic limit of large S has been evaluated by Wu (1966) for the swimming of a slender microscopic body, of length ℓ and a circular cross section of radius a ($a \ll \ell$). The body motion is again given by

$$y = b(x)e^{i(\omega t - kx)}, \quad (0 < x < \ell) . \tag{83}$$

We shall assume ω to be sufficiently large, and kb ($b = \max|b(x)|$) sufficiently small, that

$$a^2\omega > \nu, \quad kb < 1 . \tag{84}$$

The first condition implies that $\delta = O(a)$, which is small compared to body length ℓ for slender bodies; the second condition means that the flow field does not vary rapidly with respect to x. As the first approximation, we may therefore regard the flow as consisting of two components: One is the cross flow due to the lateral oscillations, and the other is the longitudinal flow along the mean (stretched straight) position of the body. The transverse component gives rise to lateral force, thrust, etc., and the longitudinal component produces the friction drag.

We first evaluate the cross flow by using a slender-body approximation. At a station x ($0 < x < \ell$) the cross section of the body is taken to be fixed at the

origin of the yz plane. (The acceleration associated with such a moving origin is small, since $(\mathbf{q}\cdot\nabla)\mathbf{q}$ has been assumed to be negligible under the present condition.) The free-stream velocity of the cross flow is

$$V(x,t) = -\left(\frac{\partial}{\partial t} + U\frac{\partial}{\partial x}\right)h(x,t) = V_0(x)\,e^{i\omega t}\ , \tag{85}$$

pointing in the direction of y increasing. The cross-flow velocity in the yz plane will be denoted by $v = (0, v_2, v_3)$, which is required to tend to $(0, V(x,t), 0)$ as $y^2 + z^2 \to \infty$. The vorticity of the cross flow, $\zeta = \partial v_3/\partial y - \partial v_2/\partial z$, satisfies the equation

$$\zeta_t = \nu\Delta_2\zeta = \nu(\zeta_{yy} + \zeta_{zz})\ . \tag{86}$$

In terms of the stream function ψ of the cross flow, defined by $v_2 = \partial\psi/\partial z$, $v_3 = -\partial\psi/\partial y$, ζ may be written as

$$\zeta = -\Delta_2\psi\ . \tag{87}$$

Noting that ψ has a time factor $\exp(i\omega t)$, we obtain for ψ the equation

$$(\Delta_2 - \beta^2)\,\Delta_2\psi = 0\ , \quad (\beta = (i\omega/\nu)^{1/2})\ . \tag{88}$$

The solution satisfying the condition at infinity and no-slip conditions at the cylinder is found to be

$$\psi = V(x,t)\,f(r)\,\sin\theta\ , \quad (r > a) \tag{89}$$

with

$$f(r) = r + AaK_1(\beta r) - B\frac{a^2}{r}\ , \tag{90}$$

$$A = \frac{2}{\beta a\,K_0(\beta a)}\ , \quad B = 1 + \frac{2\,K_1(\beta a)}{\beta a\,K_0(\beta a)}\ , \tag{91}$$

where (r,θ) are the polar coordinates defined by $y = r\cos\theta$, $z = r\sin\theta$, and $K_n(\beta r)$ denote the modified Bessel functions of the second kind. The instantaneous lift acting on a section of length dx at x, $L(x,t)\,dx$, positive in the direction of y increasing, due to the forces of the cross flow, is

$$L(x,t) = \pi\mu V\sigma^2 W(\sigma)\ , \tag{92}$$

where

$$W(\sigma) = i(2B-1) = i\left[1 + \frac{4\,K_1(\beta a)}{\beta a\,K_0(\beta a)}\right] = F(\sigma) + iG(\sigma)\ , \tag{93}$$

$$\sigma = (a^2\omega/\nu)^{1/2} = |\beta a|\ . \tag{94}$$

Here, F and G are, respectively, the real and imaginary parts of the function $W(\sigma)$. $F(\sigma)$ is always >0. For $\sigma \ll 1$, or as $\omega \to 0$, the asymptotic value of L is

$$L \sim 4\pi\mu V \left[\frac{1}{2} \log \left(\frac{4\nu}{\omega a^2} \right) - \gamma + \frac{\pi}{4} i \right]^{-1} , \tag{95}$$

where $\gamma = 0.5772$; and for $\sigma \gg 1$

$$L \sim \pi\rho a^2 \frac{dV}{dt} + \pi a \rho V (2\omega\nu)^{1/2} . \tag{96}$$

The first term in this expression is due to the apparent mass in potential flow past a cylinder, while the second gives the limit of the dissipative force.

It can be shown that favorable values of thrust can be achieved if

$$c = \omega/k > U , \quad b = \text{const.} \tag{97}$$

Under this condition we obtain

$$\overline{T} = \pi\mu\ell\sigma^2 F(\sigma)(c-U)(kb)^2 , \tag{98}$$

$$\overline{W} = (c-U)\overline{T} , \tag{99}$$

so that

$$\eta = U/c , \quad (\text{for} \quad c > U) \tag{100}$$

which is simply the ratio of the swimming speed to wave speed.

REFERENCES

Benjamin, T.B. (1960) J. Fluid Mech. **9**, 513 - 532

Betchov, R. (1959) Douglas Aircraft Co. Rept. ES-29174

Fabula, A.G., Hoyt, J.W., and Crawford, H.R. (1963) Am. Phy. Soc. Meeting, Buffalo, N.Y.

Gray, J. (1948) Nature, London, **161**, 199 - 200

Gray, J. (1949) Nature, London, **164**, 1073 - 1075

Gray, J., and Hancock, G.J. (1955) J. Exp. Biol. **32**, 802 - 814

Hancock, G.J (1954) Proc. Roy. Soc. A **217**, 96 - 121

Karman, Von T., and Burgers, J.M. (1943) General Aerodynamic Theory — Perfect Fluids, Div. E, Vol. II, "Aerodynamic Theory" (edited by W.F. Durand) 304 - 310

Kelly, H.R. (1961) Fish Propulsion Hydrodynamics, "Developments in Mechanics" (ed. J.E. Lay and L.E. Malvern) Plenum Press, Vol. I, 442 - 450, New York

Kramer, M.O. (1960) J. Am. Soc. Naval Engr. 25 - 33

Landahl, M.T. (1961) J. Fluid Mech. **13**, 609 - 632

Lang, T.G., and Daybell, Dorothy A. (1963) NAVWEPS Rept. 8060; NOTS Tech. Publ. 3063

Lang, T.G. (1966a) Science, **151**, 588 - 590

Lang, T.G. (1966b) Science, **152**, 531 - 533

Lang, T.G. (1966c) Hydrodynamic analysis of cetacean performance, in "Whales, Dolphins, and Porpoises" (edited by K.S. Norris) Univ. California Press, Berkeley, Calif.

Lighthill, M.J. (1960) J. Fluid Mech. **9**, 305 - 317

Lighthill, M.J. (1952) Commun. Pure Appl. Math. **5**, 109 - 118

Osborne, M.F.M. (1960) J. Exp. Biol., **38**, 365 - 390

Reynolds, A.J. (1965) J. Fluid Mech. **23**, 241 - 260

Saffman, P.G. (1967) J. Fluid Mech.

Siekmann, J. (1963) J. Fluid Mech. **15**, 399 - 418

Stokes, G.G. (1851) Trans. Camb. Phil. Soc. **9**, 8 - 106

Taylor, G.I. (1951) Proc. Roy. Soc. A **209**, 447 - 461

Taylor, G.E. (1952a) Proc. Roy. Soc. A **211**, 225 - 239

Taylor, G.I. (1952b) Proc. Roy. Soc. A **214**, 158 - 183

Tuck, E.O. (1968) J. Fluid Mech. **31**, 305 - 308

Van Driest, E.R., and Blumer, C.B. (1963) North Amer. Aviation, Inc., Rept. SID 63-390

Uldrick, J.P., and Siekmann, J. (1964) J. Fluid Mech. **20**, 1 - 33

Wang, P.K.C. (1966) IEEE Trans. Automatic Control, AC-**11**, 645 - 651

Wu, T.Y. (1961) J. Fluid Mech. 10, 321 - 344

Wu, T.Y. (1962) Accelerated swimming of a waving plate, Proc. Fourth Symp. on Naval Hydrodynamics, 457 - 473, ONR/ACR-92, Washington, D.C.

Wu, T.Y. (1966) The mechanics of swimming, in "Biomechanics" (edited by Y.C. Fung) Proc. Symp. on Biomechanics, Amer. Soc. Mech. Engr., New York, New York

* * *

DISCUSSION

J. D. van Manen
Netherlands Ship Model Basin
Wageningen, Netherlands

At the request of Professor Wu, I give in this discussion some results of tests which were performed at the Netherlands Ship Model Basin with Dutch swimmers.

With a resistance dynamometer on the towing carriage, we have determined the resistance of the towed body of swimmers. During the tests the swimmer kept his hands on a bar of the resistance dynamometer just above the water. The resistance curve of a swimmer is given in Fig. D1.

The circumstances for the second type of tests were identical to those for the resistance tests; however, the swimmer was now swimming with his legs only. With the resistance dynamometer, the total force developed by the swimmer (that is resistance and the leg thrust) corresponding with a certain type of stroke (breast, dolphine, or crawl stroke) was measured over a large speed range. The results of these tests are also presented in Fig. D1.

Finally, the free-running speed of the swimmer with arms and legs moving was determined for the different types of strokes. An intersection between these speeds and the resistance- and leg-thrust curves is made in Fig. D1.

For the breast stroke, it was amazing to conclude that the legs were practically doing nothing. For dolphine and crawl strokes, the contribution by the legs to propel the body is much more favorable. Up till now, these tests have been carried out with only two persons, so the results of these tests must be considered with caution. More tests must be carried out before final conclusions can be drawn.

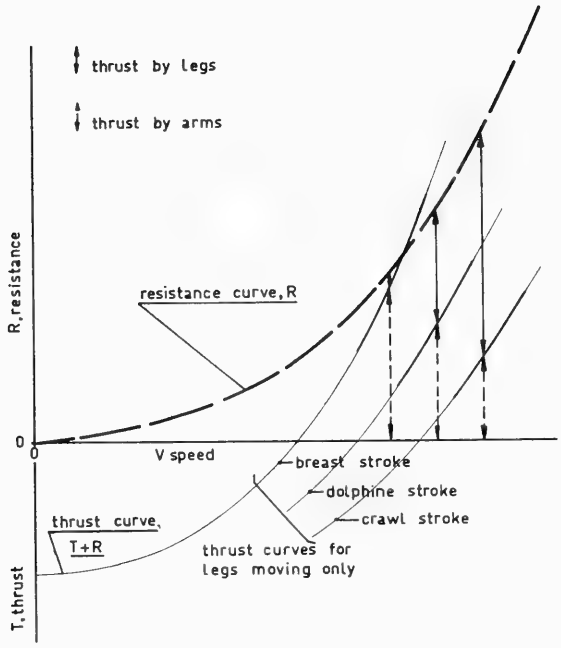

Fig. D1 - Results of tests on swimmers

* * *

DISCUSSION

H. Schwanecke
Versuchanstalt für Schiffbau
Hamburg, Germany

The paper presented by Professor Wu is excellent, as we could expect. May I refer to the problem of fish propulsion. It has been discussed many times if there is any mechanical propulsion device by which an arbitrary sea vehicle can be driven at a relatively high speed and at a high propulsive efficiency as it is with certain kinds of fishes. Moreover, this device should not be too complicated in order to obtain a high mechanical efficiency.

Some years ago, a propulsive device named "well-propeller" was proposed by Schmidt. Schmidt has also performed some experiments in air on this device. Unfortunately, I received the experimental results too late to refer to them. The well-propeller is a combination of two foils. One performs a translatory motion in such a way that every point of it describes a circle with the

radius R (see Fig. D2), while the second foil is fixed in the downwash of the oscillating foil. By this arrangement the vorticity in the unsteady downwash is reduced and the efficiency of the system is enlarged.

Applying the results obtained by Schiele for alternating vortex streets, the axial efficiency in ideal flow foil can be estimated. In Fig. D2, the efficiency is plotted against the induced axial velocity nondimensionalized by the speed of the undisturbed flow. The nondimensionalized angular velocity of the oscillating foil is taken as a parameter, and represents a reduced freeway. As can be seen from the figure, the free-running efficiency is unfavorable even for light loading.

When the propeller is placed behind a vehicle of similar configuration as the propeller, for example, a vehicle as shown in Fig. D3, the total efficiency in ideal flow can be considerably enlarged. The curves in Fig. D3 are obtained by applying Weinig's interaction theory, and are valid for a total ideal efficiency equal to unity. As can be seen from the diagram also at medium loadings a high total efficiency can be obtained supposing the frequency of oscillation is favorably chosen and the flow interaction resistance is of sufficient value.

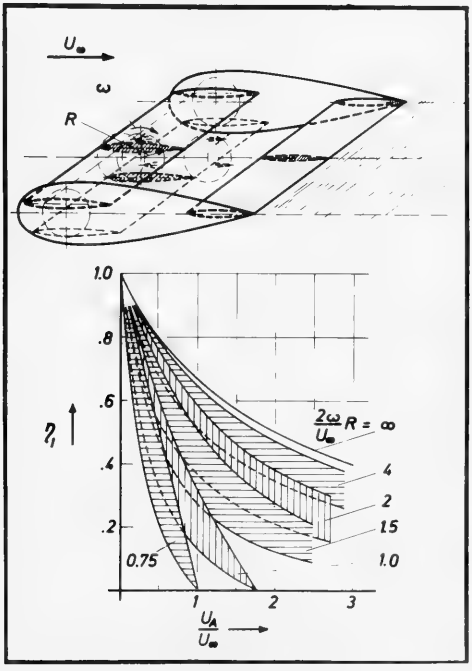

Fig. D2 - The well-propeller in the free-running condition

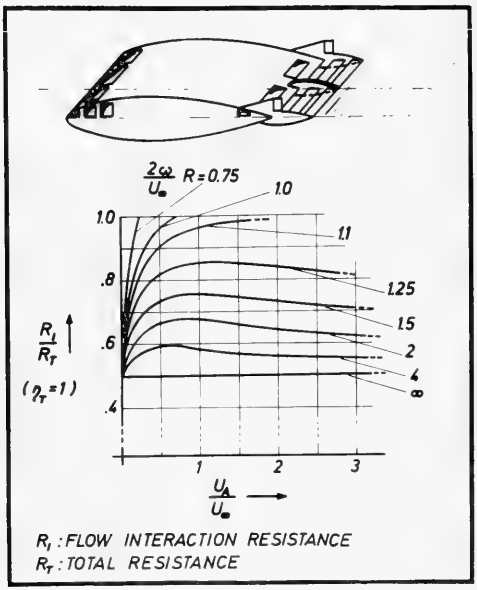

Fig. D3 - The well-propeller in the optimum behind condition (R_1, the flow interaction resistance, equals the resistance caused by those fluid particles which will be used for propelling afterward)

* * *

REPLY TO DISCUSSION

T. Y. Wu

I wish to thank Professor van Manen and Dr. Schwanecke for their interesting comments. Dr. Schwanecke pointed out several promising propulsive devices that have been innovated with ingeneous applications of the underlying fluid dynamical principles. In this respect, I may also mention the theoretical studies of A. A. Fejer, of H. R. Kelley, and some full-scale experiments of Glen Bowles. Their studies are concerned with the swimming motion of three hinged plates in two-dimensional oscillations, for which the optimum six degrees of freedom can be evaluated. In this kind of inventive attempts, I think one can be duly rewarded if the efforts are directed towards extraction of the basic physical principles underlying the phenomenon, rather than imitating nature to the very last detail. From bird flying came the innovation of airplanes, which has evolved through decades to supersonic flights, a regime already highly transcending the original level. An effective application of the swimming

principle has, however, so far remained a good challenge. The previous attempts brought forth by Dr. Schwanecke will shed light to stimulate further developments.

I am particularly grateful to Professor van Manen for his contribution of some yet unpublished results. His experiments with Dutch swimmers are most intriguing, in that a method of separating the thrust from the resistance is proposed. I certainly agree with him that these results should be viewed with caution since swimming is one of those physical motions in which the quantities of interest, such as the thrust or the viscous resistance, when considered separately, can hardly be observed without disturbing the phenomenon under observation. This is a kind of "uncertainty principle" that makes the problem interesting and the solution difficult. The quantitative results of Professor van Manen are nevertheless extremely enlightening.

* * *

Friday, August 30, 1968

Morning Session

UNCONVENTIONAL PROPULSION

Chairmen: Dr. W. E. Cummins

Naval Ship Research and Development Center
Washington, D. C.

and

Dr. H. Edstrand

Swedish State Shipbuilding Experimental Tank
Göteborg, Sweden

THEORY OF THE DUCTED PROPELLER— A REVIEW

Johannes Weissinger and Dieter Maass
Institut für Angewandte Mathematik
Universität Karlsruhe
Karlsruhe, Germany

ABSTRACT

This review is concerned mainly with the theory of ducted propellers in incompressible, nonviscous, steady flow. Emphasis is laid on theories which try to determine the complete flow field and which have been developed in the last 12 years. A brief survey of the development before 1955, which was covered in a review presented by Sacks and Burnell in 1959, is given.

The main part starts with the theory of the duct alone (ring airfoil) in axial and nonaxial flow. The numerical methods which form the basis for the theory of the ducted propeller are outlined briefly, and some of the basic assumptions are considered critically. The effects of camber (including taper) and thickness of the profile and of a central body are treated.

This theory is easily extended to a theory of the ducted actuator disk of constant load without tip clearance in axial flow. Some linear terms usually neglected in linear theories are shown to have a considerable influence.

The theory of the actuator disk with tip clearance treated next builds the link to the theory of the ducted propeller with a finite number of blades. The main problem is the determination of the velocity induced by the free vortices shed from the propeller blades. This can be solved only by a priori assumptions on the form of the vortex surface. These can be checked and improved to some extent by iteration. In nonaxial flow, the propeller produces an unsteady field, which, so far, can be treated only by very rough methods. In this case, the duct experiences not only a lift, but also a side force.

The emphasis of the review is on analysis, not on design. The underlying models (vortex configurations, etc.), the numerical methods, and the numerical results are the main subject.

1. INTRODUCTION

1.1 A Brief Historical Survey

By choosing the proper type of duct, the velocity at a propeller can be increased ("Kort nozzle") or decreased ("pump-jet"). The Kort nozzle is used for increasing the efficiency of heavily loaded propellers, e.g., in S/VTOL

aircrafts. In a pump-jet propeller, cavitation is delayed or compressibility effects are decreased. Noise can also be influenced by shrouding the propeller.

We can discern two trends in the development of theories, one aiming at most simple results and formulas which can be used in design without much additional computation, the other trying to predict the whole field under most general assumptions. The price to be paid in the first case is a loss in numerical accuracy and a restriction in general applicability, because special assumptions such as small chord/diameter ratio or special singularity distributions are introduced. Aside from the fact that theories of the second kind require an expert to understand them, their main disadvantage is the need of a big computer to perform the numerical evaluations. Naturally, theories of the first kind were developed first. So, we may distinguish two periods, one (ca. 1940-1955) in which the first trend dominates, while after 1955 more efforts were exerted in developing theories of the second kind. A "pioneer" period (ca. 1927-1940) preceded both during which the idea was born and first applications, experiments and theoretical considerations were made.

First Period: It seems that L. Stipa (84) in 1927 was the first to propose the shrouding of the propeller by using the fuselage of an airplane as a duct. There is also a Russian paper (82) claiming the concept for the Russian scientist C.A. Bracks back to 1887. In 1934 Kort proposed the "Kort-nozzle" for heavily loaded marine propellers.

Second Period: During World War II a group of Göttingen (Küchemann, Weber, Krüger) began a systematic theoretical and experimental investigation of the ducted propeller. Here, some of the basic ideas were conceived for all further theoretical work. After the war, a group in Berlin (Horn, Dickmann, Amtsberg) improved the theory and developed a design procedure based on representing the duct by a vortex distribution and the propeller by a sink distribution. A similar concept was applied by Lerbs (46). Stewart (83) and Ribner (75) developed a theory for ring airfoils with small chord/diameter ratio based on a lifting line theory. The papers of Helmbold (28, 29), which are not so well known because of their restricted distribution, also contain some fundamental ideas. Unfortunately, a limited distribution is the rule rather than the exception for most reports on ducted propellers.

Third Period: The paper of Dickmann and Weissinger (101) was the starting point for the investigations of a group working at Karlsruhe (Dickmann, Weissinger, Wiedemer, Bollheimer, Brakhage, Maass, Rautmann). In (101) the shape of the (thin) duct represented by the sum of a constant and an elliptic distribution of ring vortices was determined by a linearized theory under the assumption of a constant pressure jump at the propeller plane. Dickmann also proposed the use of semiempirical knowledge from turbomachines and pumps for the propeller design, a line of thinking also followed by Bussler (8) and van Manen. The theory was confirmed by experiments of Finkeldei (116). Using the vortex model of (101) completed by ring sources, Weissinger developed a theory for ring airfoils (without duct) of a given shape in axial flow, including effects of profile thickness, struts, and central bodies. This theory was generalized for ducted propellers with constant pressure jump in axial flow by Bollheimer, who included some effects of profile thickness neglected in other theories.

The model and some of the basic mathematical ideas used at Karlsruhe were also used by two other groups, working at THERM (Ordway, Ritter, Greenberg, Hough, Kaskel, Lo, Sluyter, Sonnerup) and at NSRDC (Morgan, Caster, Chaplin, Voigt). Though there are differences in mathematical details (e.g., representation of kernel functions by elliptic or by Legendre functions, different methods for a numerical solution of the integral equations, etc.), the numerical results of all three groups, in so far as the same problems were treated, coincide because a common model is used. At THERM and NSRDC the theory was extended to finite-bladed propellers with tip clearance. At THERM the steady part of the forces caused by nonaxial flow was also computed.

The numerical analysis of THERM culminated in the presentation of work sheets for the numerical evaluation of shroud performance for finite-bladed ducted propellers in axial flow at cruise velocity (151). For specified values of blade number, axial propeller position, tip clearance ($\neq 0$), ratio of propeller radius to shroud reference radius, propeller advance ratio, the geometric parameters of NACA 4, 5, and 6 digit profiles and arbitrary values of propeller thrust coefficient and chord line incidence, tables are presented such that the shroud sectional radial force and moment coefficients and center of pressure, the shroud thrust coefficient, the net shroud pressure coefficients, and the outer and inner shroud surface pressure coefficients can easily be computed by hand on the worksheets. Configurations other than those given by the specified parameter values can be handled by interpolation or extrapolation. On the propeller blade an otpimum circulation is assumed. An addendum (156) contains worksheets for the calculation of shroud-induced axial velocity. Knowing this velocity, the blade geometry required to produce the assume dcirculation can be determined by classical methods. The THERM tables can also be used for other purposes, e.g., two-dimensional profile theory.

The theory developed at NSRDC was condensed in a FORTRAN program for the IBM-7090 high-speed computer (134). The input for the duct consists mainly of the section camber and thickness ordinates, the section angle of attack, and the chord-diameter ratio. There are options whereby the ideal angle of attack of the duct section can be determined in the presence of the propeller. The propeller input consists of the propeller diameter, propeller speed in revolutions per second, design thrust (or propeller shaft horsepower), ship speed, number of blades, inflow velocity, and circulation (or pitch distribution). If the propeller is to be designed using the LERBS optimum pitch distribution, only an estimate of the propeller ideal efficiency is given as input, instead of the circulation or pitch distribution. The output consists of the propeller design characteristics and performance, as well as the duct thrust and pressure distribution. The results can normally be obtained in approximately 27 minutes of computer time. Consequently, features which are not included in the THERM approach include the following:

(1) Any shape can be considered for the duct.

(2) The ducted propeller can be designed for a given thrust or horsepower.

(3) The design and predicted performances of the propeller can be obtained.

(4) An option in the computer program allows calculations of the ideal angle of attack of the duct section in the presence of a propeller.

In (132), a computer program and results are presented for the inverse problem, where the duct shape is computed once the duct pressure distribution has been specified.

Perhaps the most comprehensive investigations of ducted propellers have been made by VIDYA (Nielsen, Kriebel, Mendenhall, Sacks, Spangler). For example, they include duct stall interference in tandem configurations or interference with hulls and also experimental investigations. The price for the comprehensiveness is a simplification of the theoretical models. So, to some extent, these theories may be placed into the first category of theories characterized above. The basic model is shown in Fig. 1 (164). The propeller annulus is divided into a number (≤ 10) of equal-area annuli in each of which blade element theory is used to describe local propeller-blade performance. The bound propeller circulation is constant within each annulus, and a cylinder of ring vortices is assumed to be shed from each annulus and to extend downstream. Centerbody-induced velocities are neglected. The duct may have both thickness and camber, the chord/diameter ratio is not restricted to small values. The propeller is specified by the number of blades and by the radial distribution of chord and pitch. From the above model, relations are derived by which, at a specified advance ratio, duct loading and propeller loading can be calculated from a given inflow profile. From the loading distributions an improved inflow profile is determined. The iteration converges rapidly. A digital computer program, presented in (164), takes one minute on the IBM 7094. A second program (164) for the design of uniformly loaded propellers takes the same time. A rough estimate of the influence of the angle of attack is also possible.

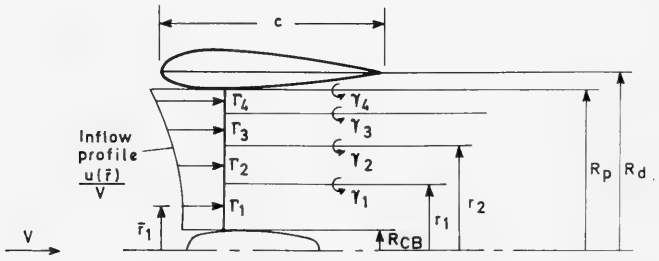

Fig. 1 - Flow model used in (164)

Last but not least in this enumeration of institutes and major research groups, the name of van Manen and the Netherlands Ship Model Basin should not be omitted. Their work, though mainly experimental and therefore not pertaining to the subject of this review, has also contributed to the theory and gives very valuable advice for design, based on theory and the results of extensive, systematic series of experiments.

1.2 Program of This Review

This review will be concerned only with incompressible, nonviscous, and, primarily, steady flow. Some hints referring to other problems can be found in the list of references, e.g., cavitation (Tulin, Chen), boundary layer (Nickel), compressibility (Zierep, Laschka).

Since the development in the first two periods is well covered by the review of Sacks and Burnell (78), where emphasis has been placed on theories of the first kind, this review will be restricted to theories of the second kind developed during the third period. Papers and reports published before 1955 are listed in the references only insofar as they are referred to in the text. This is also true for publications concerned mainly with experiments.

The presentation is guided by a systematic and not by a historical point of view. Emphasis is placed on the analysis of the phenomena and not on design methods. Because of the complexity of the mathematical apparatus, we cannot always give mathematical formulas in detail. Instead, we shall describe the underlying models and the basic assumptions, characterize the numerical methods used for the solution, and state the main theoretical results. We will concentrate our attention on the theories developed at Karlsruhe, THERM, and NSRDC.

In aerodynamics and hydrodynamics two kinds of problems are distinguished. In the "direct" problem the geometry is given and the flow field or special characteristics such as lift or pressure distribution are sought, vice versa in the "inverse" problem. Something inbetween is the case where a mathematical singularity distribution is given and the corresponding geometry and/or flow field is to be determined. If the mathematical relations between the singularity distribution and the geometry as well as the induced flow are known, it is purely a question of mathematical skill to solve the direct or inverse problem by elimination of the singularity distribution. Of course, this can usually be done by numerical methods.

The problem of the ducted propeller is a problem of interference, of interaction between two bodies, the duct and the propeller. From the four possible direct/inverse combinations we shall choose the mixed one with given duct geometry and propeller distribution. From the solution of this problem, the propeller geometry can be determined by slight modifications (128, 134) of well-known methods (48).

Problems of interference can often be solved by an iteration scheme in the following manner. First, one has to find a method for determining the flow field of each separate body in a very general (nonuniform) flow. Then, starting with an arbitrary field, this field is modified by the presence of the first body, the new field is modified by the second body, this field again by the first body, and so on.

Following this line of thought, we deal first with the duct alone (Sec. 2), i.e., we solve the direct problem for the ring airfoil in fairly general flows. These contain also the case where a jet is emitted out of the ring airfoil by an actuator disk of constant pressure jump. This case (Sec. 3) can be considered as the

most simple model of a ducted propeller and shows many of the relevant features. Next we must consider the propeller field. The blade circulation being given, the main problem is the determination of the shape of the vortex sheets shed from the blades and of the field induced by these sheets. Then, the interference problem can be attacked. The most important result of Sec. 5 is that the steady part of the flow through a finite-bladed ducted propeller is the same as the flow for the same configuration but with an infinite blade number. This problem, simplified to constant radial distribution of propeller circulation, is treated in Sec. 4.

So far, axial flow is assumed. In the case of nonzero incidence, which is considered next (Sec. 6), there does not exist a system of coordinates in which the field is time independent. Obviously, this problem is very complex and only rough approximate solutions have been found. As a matter of fact, only the steady part of the solution has been determined.

Before starting this program we will have a brief look at the two-dimensional theory in order to clear some of the basic ideas.

1.3 Two-Dimensional Considerations

(A) *Infinitely thin airfoils* (Fig. 2). Assuming small camber and small curvature of the profile, the linearized boundary condition is fulfilled by putting on the chord a vortex distribution $\gamma(\xi) = v_g(\xi)$ which satisfies the Kutta condition and the integral equation

$$v_g = \frac{1}{2\pi}\int_{-1}^{1} \frac{g(\xi')}{\xi - \xi'}\, d\xi' = -\alpha(\xi), \quad -1 \le \xi \le 1, \quad \gamma(1) = 0 \tag{1.1}$$

or, written with the "Glauert operator" G in operator form,

$$Gg = \alpha . \tag{1.2}$$

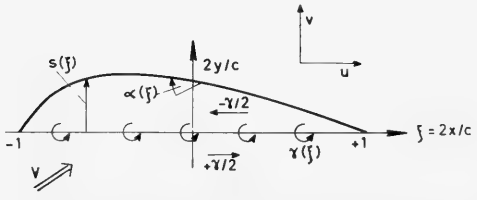

Fig. 2 - Two-dimensional airfoil theory. The infinitely thin cambered airfoil. (Actually, for this configuration the vortices rotate in the opposite direction.)

The solution is known to be

$$g(\xi) = G^{-1}(\alpha) = \frac{2}{\pi}\sqrt{\frac{1-\xi}{1+\xi}}\int_{-1}^{1}\frac{\alpha(\xi')}{\xi-\xi'}\sqrt{\frac{1+\xi'}{1-\xi'}}\,d\xi' \,. \tag{1.3}$$

The integral can be evaluated by means of the formula

$$\int_0^{\pi}\frac{\cos n\theta'}{\cos\theta' - \cos\theta}\,d\theta' = \pi\frac{\sin n\theta}{\sin\theta} \qquad n = 0,\ 1,\ 2,\ \ldots \tag{1.4}$$

and the Fourier expansion

$$\alpha(\xi) = \frac{a_0}{2} + \sum_{\nu=1}^{\infty} a_\nu \cos\nu\theta\,, \quad \xi = -\cos\theta\,. \tag{1.5}$$

The result is the Birnbaum series

$$g = -a_0\cot\frac{\theta}{2} + 2\sum_{\nu=1}^{\infty} a_\nu \sin\nu\theta\,. \tag{1.6}$$

Another method (114) of solving the integral equation

$$\frac{1}{2\pi}\int_0^{\pi}\frac{g(\theta')\sin\theta'}{\cos\theta' - \cos\theta}\,d\theta' = -\alpha(\theta)\,, \quad 0 \le \theta \le \pi \tag{1.7}$$

which is equivalent to (1.1), is a collocation method based on the quadrature formula

$$\int_0^{\pi}\frac{f(\theta')}{\cos\theta' - \cos\theta_i}\,d\theta' = \frac{\pi}{N}\sum_{k=0}^{N}\delta_k\frac{f(\theta_k')}{\cos\theta_k' - \cos\theta_i}\,, \quad i = 1,\ \ldots,\ N$$
$$\theta_i = \frac{(2i-1)\pi}{2N}\,, \quad \theta_k' = \frac{2k\pi}{2N}\,, \quad \delta_k = \begin{cases} 1 & \text{for } k = 1,\ \ldots,\ N-1 \\ \frac{1}{2} & \text{for } k = 0,\ N\,. \end{cases} \tag{1.8}$$

This formula is exact if $f(\theta)$ is a cosine polynomial of degree $\le 2N$, i.e., the accuracy has Gaussian character. Formally, it cna be interpreted as the application of the rectangular rule on the singular integral (1.8). To obtain the high accuracy, the collocation points θ_i must be the midpoints of the subintervals of length π/N. Applying (1.8) with $f(\theta) = g(\theta)\sin\theta$ and introducing the Kutta condition, the integral equation (1.7) is transformed into a set of linear equations

$$\frac{\pi}{N}\sum_{k=0}^{N-1}\delta_k\frac{\bar{g}_k}{\cos\theta_k' - \cos\theta_i} = -\alpha(\theta_i)\,, \quad i = 1,\ \ldots,\ N \tag{1.9}$$

for the N finite unknowns $\bar{g}_k = g(\theta_k)\sin\theta_k$. These values coincide with the exact ones if $\alpha(\theta)$ is a cosine polynomial of degree $\le 2N-1$.

The tangential velocity induced by γ is

$$u_\gamma = \mp V g/2 \ . \tag{1.10}$$

(B) *Moderately thick airfoils* (see Fig. 3). At zero incidence the boundary condition can be satisfied approximately by putting a source distribution of strength

$$q(\xi) = 2 \frac{d}{d\xi} [V t(\xi)] \tag{1.11}$$

on the chord. This relation can be found immediately from continuity considerations and, in this form, is also correct for more general flows where V depends on ξ. The tangential velocity induced at the chord is

$$u_q = \frac{1}{2\pi} \int_{-1}^{1} \frac{q(\xi')}{\xi - \xi'} \, d\xi' \ . \tag{1.12}$$

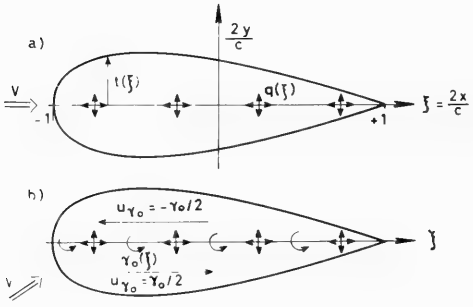

Fig. 3 - Two-dimensional airfoil theory. Symmetrical airfoil at (a) zero incidence, (b) nonzero incidence [actually, for the configuration in (b) the vortices rotate in the opposite direction].

If the profile is cambered and at incidence, $u = u_g + u_q$ is very often considered as the induced surface velocity. Near the leading edge, this is not very accurate because u_γ becomes infinite. If the velocity vector $(V \cos \alpha + u, 0)$ is multiplied by the surface tangent, a better approximation

$$\frac{1}{\sqrt{1 + [y'(\xi)]^2}} \{V \cos \alpha_0 + u_\gamma + u_q\} \ , \quad y(\xi) = s(\xi) \pm t(\xi) \ , \tag{1.13}$$

is obtained for the surface velocity.

With $\cos \alpha_0 \simeq 1$, this is a consequent linearization if α_0, (ξ), $t(\xi)$ (and the derivatives) are considered small. But it might be advisable in certain cases not to neglect the product of quantities proportional to γ and t, respectively. If one looks at the symmetrical profile in Fig. 3b, where the vortex- and source-distribution of the strict linear theory is placed on the chord, one sees that there remains a normal component $\gamma_0 t'/2$ on the surface. Another component comes from the first-order term in the Taylor expansion of the vertical component induced by γ_0

$$v_{\gamma_0}(\xi, \pm t) = v_{\gamma_0}(\xi, 0) \pm \frac{\partial}{\partial \eta} v_{\gamma_0}(\xi, 0)\, t \tag{1.14}$$

$$= v_{\gamma_0}(\xi, 0) \mp \frac{\partial}{\partial \xi} u_{\gamma_0}(\xi, 0)\, t = v_{\gamma_0}(\xi, 0) + \gamma_0' t/2 \ .$$

The sum of both normal components is $d/d\xi\ (\gamma_0 t)/2$. Since it is continuous through the chord, it must be annihilated by a vortex distribution γ_t satisfying

$$v_{\gamma_t} = \frac{1}{2\pi} \int_{-1}^{1} \frac{\gamma_t(\xi')}{\xi - \xi'}\, d\xi' = -\frac{d}{d\xi}(\gamma_0 t)/2 \ . \tag{1.15}$$

Putting $\gamma = \gamma_0 + \gamma_t$, the surface velocity is then given by (1.13). In this manner one obtains a theory which is linearized in t, but not in α_0. For elliptic profiles the surface velocity is exact. Riegels (76) first introduced the thickness-influences vortex distribution based on ideas of conformal mapping theory. But the idea is more general and can be applied to rotational flows (123), too. A theory in which γ_t is neglected will be called a "strictly" linearized theory.

For thick airfoils with small camber, the camber-induced velocity is usually superposed linearly.

(C) *The biplane* (Fig. 4). Aside from profile geometry, the configuration is characterized by the "chord/diameter" ratio c/D and the inclination of the chord relative to the axis. In order to avoid the second parameter in the kernels of the integral equations, the singularity distributions are put on a "reference chord," e.g., the projection of the profile on a line parallel to the axis through the leading edge. Obviously, the vertical velocity v_γ induced at one profile by the vortex distribution γ located on both (reference) chords has the form

$$v_\gamma = G\gamma + K\gamma \ , \tag{1.16}$$

where G is the Glauert operator and K an integral operator with a continuous kernel depending on c/D. The term $K\gamma$ represents the velocity $\bar{v}_\gamma$ induced by the vorticity of the opposite profile. Similarly, the source-induced velocity is

$$v_q = \pm q/2 + \bar{v}_q \ , \tag{1.17}$$

where $\bar{v}_q$ is the source-induced velocity from the opposite profile. The (strictly) linearized boundary condition

$$v_\gamma + v_q = -V\alpha(\xi) \tag{1.18}$$

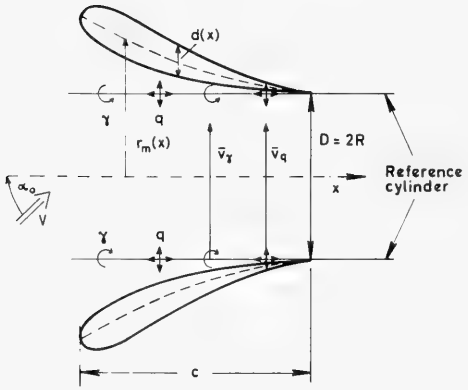

Fig. 4 - The biplane in two-dimensional theory and the cross section of a ring airfoil

can be split into the two equations

$$q = 2 \frac{d}{d\xi} [V t(\xi)] , \tag{1.19}$$

$$G\gamma + K\gamma = -V\alpha(\xi) - \bar{v}_q . \tag{1.20}$$

Since the right-hand side is known after evaluating the integral for $\bar{v}_q$ by means of (1.19), an integral equation of the form

$$Gg + Kg = f \tag{1.21}$$

remains to be solved for g, where f is a known function, G the Glauert operator, and K a regular operator.

The integral equations to be solved in the theory of ring airfoils and ducted propellers are of the same type. Essentially, the following four methods have been applied for solving (1.21). The first two were used at Karlsruhe, the third at THERM, and the fourth at NSRDC.

(1) If the kernel of K is developed into a double cosine Fourier series with respect to the variable θ, and if the Birnbaum series (1.6) for g is introduced, the left-hand side of (1.21) can be expressed as a cosine series with coefficients that are linear combinations of the Birnbaum coefficients c_ν. Equating these coefficients with the Fourier coefficients of f, one obtains an infinite system of linear equations exactly equivalent to (1.21). This is solved approximately by truncation to a finite system and Gauss elimination.

(2) This method (114) is a generalization of the above collocation method for solving the Glauert equation $Gg = \alpha$ by (1.8). Since Kg is a regular integral the same rectangular rule applied above to Gg can be used for the approximate

evaluation and again a system of linear equation for the unknown values $\bar{g}_k = g(\theta'_k) \sin\theta'_k$ is obtained. That the accuracy in this evaluation of Kg is not as high as that for the singular integral Gg does not matter very much, because usually, i.e., if c/D is not too large, Kg is small compared with Gg. Compared with the other three methods, this method has the advantage that no Fourier expansions are needed for constructing the system of linear equations. Essentially, the matrix is immediately equal to the matrix of kernel values $G + K$ at the points $(\xi_i, \xi'_k) = -(\cos\theta_i, \cos\theta'_k)$. Therefore, the programming will be easier. The disadvantage consists in the fact that the accuracy in the numerical evaluation of Kg is coupled with the number N of unknowns. In our experience this methid is superior to the first—and probably to the other ones—with respect to computation time.

(3) Let g_0 be the solution of the Glauert equation

$$Gg_0 = f \ . \tag{1.22}$$

The Birnbaum coefficients of g_0 are essentially (i.e., apart from factors such as -2) equal to the Fourier coefficients of f. Then (1.21) is equivalent to

$$g = g_0 + \bar{K}g \ , \quad \bar{K} = -G^{-1}K \ , \tag{1.23}$$

where the kernel of $\bar{K}$ is known because G^{-1} is known. Then the solution g is given by the Neumann series

$$g = \{I + \bar{K} + \bar{K}^2 + \cdots\} \, g_0 \tag{1.24}$$

and can be found by the iterative scheme

$$g_{\nu+1} = g_0 + \bar{K}g_\nu \ , \quad \nu = 0, 1, \ldots \ . \tag{1.25}$$

This operator equation can be approximated by a matrix equation if the vector of the first N Birnbaum coefficients is substituted for g and, for $\bar{K}$, a matrix P which is connected in a simple way with the Fourier coefficients of K.

(4) Equation (1.21) is written in the form

$$g - \bar{K}g = \bar{f} \ , \quad \bar{K} = -G^{-1}K \ , \quad \bar{f} = G^{-1}f \ . \tag{1.26}$$

If $\bar{K}$ is represented approximately by a truncated double Fourier series, one obtains a Fredholm integral equation of the second kind with a degenerate kernel. This equation can be transformed into a system of linear equations by classical methods.

2. THE RING AIRFOIL

We assume that the profile satisfies the conditions of linearized two-dimensional theory and that the angle between profile chord and axis is small enough so that the surface formed by the chords can be approximated by a circular cylinder. Then the boundary condition (zero normal velocity on the surface) can be satisfied within the limits of linear approximation by putting

distributions of ring vortices and ring sources on a reference cylinder of radius R. If the vortex strength varies with the azimuthal angle, straight vortices must also be placed on the cylinder.

We introduce cylinder coordinates (x, r, ϕ) and define the nondimensional coordinates

$$\xi = \frac{2x}{c}, \quad \rho = \frac{2r}{c} \quad \text{or} \quad \bar{r} = \frac{r}{R} \tag{2.1}$$

and the chord/diameter ratio

$$\lambda = \frac{c}{2R}. \tag{2.2}$$

The induced axial, radial, and azimuthal velocities are denoted by u, v, and w, respectively. If the arithmetic mean of the values of a function at the outer and inner point of the cylinder is denoted by a bar, we can write for the velocities induced at the cylinder by a vortex distribution γ or a source distribution q

$$u_\gamma = \mp \frac{\gamma}{2} + \bar{u}_\gamma, \quad v_\gamma = \bar{v}_\gamma, \tag{2.3}$$

$$u_q = \bar{u}_q, \qquad v_q = \pm \frac{q}{2} + \bar{v}_q, \tag{2.4}$$

where the upper (lower) sign refers to the outer (inner) surface of the cylinder.

Then the (strictly) linearized boundary condition can be written in the form

$$v_\gamma \pm \frac{q}{2} + \bar{v}_q + V_n = 0, \tag{2.5}$$

where V_n denotes the normal component of the given flow on the airfoil surface. For zero thickness this reduces to

$$v_\gamma + V_n = 0. \tag{2.6}$$

For an axisymmetric ring airfoil the surface can be described by

$$r(x) = R + r_m(x) \pm \frac{d(x)}{2} \tag{2.7}$$

or, in nondimensional form,

$$\rho(\xi) = \frac{1}{\lambda} + \rho_m(\xi) \pm t(\xi), \tag{2.8}$$

$$\rho_m(\xi) = \frac{2r_m(x)}{c}, \quad t(\xi) = \frac{d(x)}{c}. \tag{2.9}$$

For brevity we shall call $\rho_m'(\xi) = d\rho_m/d\xi$ the camber of the ring airfoil, although—interpreted as local angle of attack—it also includes the incidence of the profile chord.

Then, for parallel flow with angle of attack α_0, V_n is obtained by linear approximation as

$$V_n = \mp V t'(\xi) - V\rho_m'(\xi) + V\alpha_0 \cos\phi \ , \tag{2.10}$$

and putting

$$q = Vq_t \ , \quad \gamma = V(g_c + g_t + \alpha_0 g_\alpha \cos\phi) \tag{2.11}$$

Eq. (2.5) splits into

$$q_t = 2t'(\xi) \ , \quad T_0 g_c = \rho_m'(\xi) \ , \quad T_0 g_t = -\bar{v}_{q_t} \ , \quad T_1 g_\alpha = -1 \ , \tag{2.12}$$

where T is an integral operator that transforms a vortex distribution into the radial velocity induced by it. It follows that the effects of thickness (q_t, g_t) can be obtained by considering the ring airfoil without camber $(\rho_m' = 0)$ in axial flow, the effect of camber from the infinitely thin ring airfoil in axial flow and the effect of angle of attack from the infinitely thin cylinder at angle of attack. Addition of these separate effects gives the entire distribution. From these the surface velocity is determined by

$$\frac{1}{\sqrt{1 + [t'(\xi)]^2}} (v + u_q + u_\gamma) \ . \tag{2.13}$$

The continuous part of V_n can be considered as the first terms of the more general Fourier series

$$V_n = V\left\{\sum_{m=0}^{\infty} a_m(\xi) \cos m\phi + \sum_{m=1}^{\infty} b_m(\xi) \sin m\phi\right\} . \tag{2.14}$$

This happens when the ring airfoil is not exactly axisymmetric or if there is an interaction with a nonaxisymmetric velocity field. Then the distribution of ring vortices has the form

$$\gamma = V\left\{\sum_{m=0}^{\infty} g_m(\xi) \cos m\phi + \sum_{m=1}^{\infty} h_m(\xi) \sin m\phi\right\} . \tag{2.15}$$

The Fourier coefficients $g_m(\xi)$ and $h_m(\xi)$ which satisfy the Kutta condition are determined by the equations

$$T_m g_m = a_m \ , \quad T_m h_m = b_m \ , \tag{2.16}$$

with the integral operator T_m defined by

$$T_m g = \frac{1}{2\pi} \int_{-1}^{1} \frac{g_m(\xi')}{\xi - \xi'} d\xi' + \frac{\lambda}{2\pi} \int_{-1}^{1} g_m(\xi') U_m(\eta) d\xi' + \frac{m\lambda}{4} \int_{-1}^{1} g_m(\xi') d\xi' \ . \tag{2.17}$$

The kernels $U_m(\eta)$ are antisymmetric continuous functions of the argument

$$\eta = \lambda(\xi - \xi') = \frac{x - x'}{R} \,. \tag{2.18}$$

So, all these integral equations are of the type (1.21) and can be solved by the methods described in Sec. 1.3.

The most important of these operators is T_0, defined as

$$v_g = T_0 g = \frac{\lambda}{2\pi} \int_{-1}^{1} K_0(\xi, \xi')\, g(\xi')\, d\xi' \,, \tag{2.19}$$

$$K_0(\xi, \xi') = \frac{k^3 \eta}{4} G_1(k^2) = \frac{\operatorname{sgn} \eta}{2k'} \left[(1 + k'^2) E(k) - 2k'^2 K(k)\right]$$
$$= -\frac{\eta}{2} \frac{d}{d\omega} \left[Q_{1/2}(\omega) + Q_{-3/2}(\omega)\right] \,, \tag{2.20}$$

$$k^2 = \frac{4}{\eta^2 + 4} \,, \quad k'^2 = 1 - k^2 \,, \quad \omega = 1 + \frac{\eta^2}{2} \,, \tag{2.21}$$

where

$$G_m(k^2) = (-1)^m \int_0^{\pi/2} \frac{\cos 2m\vartheta}{(1 - k^2 \sin^2\theta)^{3/2}}\, d\theta \,, \quad \text{(Riegels function)} \tag{2.22}$$

$$Q_{m-1/2}(\omega) = \int_{-\pi/2}^{\pi/2} \frac{\cos 2m\vartheta}{[2(\omega - 1) + 4 \sin^2\theta]^{1/2}}\, d\theta \,, \quad \text{(Legendre function)} \tag{2.23}$$

$$K(k) = \int_0^{\pi/2} \frac{d\theta}{(1 - k^2 \sin^2\theta)^{1/2}} \,, \quad E(k) = \int_0^{\pi/2} (1 - k^2 \sin^2\theta)^{1/2}\, d\theta \,. \tag{2.24}$$

Formulas and numerical tables for the kernels of the operators T_m have been presented by means of Riegels functions at Karlsruhe (102, 103) and by means of Legendre functions at THERM (135, 137, 138, 139).

The basic ideas of lifting-line theory and of generalized lifting-line theory ("three-quarter-point method") can also be applied to the ring airfoil (102), thus obtaining very simple formulas, e.g., for the lift. For the latter theory the agreement with the exact results is very good over the whole range of λ, $0 \le \lambda < \infty$; lifting-line theory is valid only for small values of λ.

In Karlsruhe, ring airfoils with central bodies have also been investigated (110). The axisymmetric body is assumed to be slender and to have a small maximal radius r_m, such that it can be represented by an axial distribution of sources and doublets. To satisfy the boundary conditions at the body and the ring airfoil, only the leading terms in the Taylor expansion with respect to $\rho_m = r_{max}/R$ are retained. For geometry and notation see Fig. 5.

In (110), emphasis is placed on the net characteristics such as the lift and the moment of the body and of the ring airfoil. But essentially the theory can also be used to calculate the entire flow field. Numerical results are presented for four families of bodies: (1) (infinite) cylinder, (2) ellipsoid, (3) a body with a blunt nose and a sharp tail, and (4) the same body reversed (sharp nose, blunt tail). In what follows we shall mention only a few of the theoretical and numerical results.

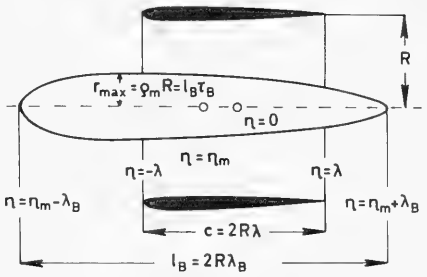

Fig. 5 - (See (106)) Ring airfoil with central body

The lift and the moment of the wing are determined by the first-order Fourier coefficient $g_1(\xi)$ of the wing vortex distribution (2.15) (if $\phi = 0$ corresponds to the "lowest" point on the circumference), otherwise there may be a change of sign and/or g_1 must be replaced by h_1. $g_1(\xi)$ is determined by the integral equation

$$(T_1 + T_{1B})\, g_1 = \alpha_0 - 2F_B(\xi)\,\alpha_0\,, \quad -1 \le \xi \le 1 \tag{2.25}$$

where T_1 is the basic first-order operator and T_{1B} is defined by

$$T_{1B}g_1 = -\frac{\lambda}{2} F_B(\xi) \int_{-1}^{1} g_1(\xi')\, d\xi' + \frac{\lambda}{2} \int_{-1}^{1} B(\xi,\xi')\, g_1(\xi')\, d\xi'\,. \tag{2.26}$$

The function

$$F_B(\xi) = \tau_B^2\, \bar{F}_B(\eta_m - \lambda\xi) \tag{2.27}$$

and the kernel $B(\xi,\xi')$ are continuous functions that depend only on the geometry of the configuration.

The lift coefficient of the body (referred to the same area $2\pi Rc$ as the lift coefficient C_{LW} of the wing) can be expressed in the form

$$C_{LB} = -\frac{1}{2} \int_{-1}^{1} F_B(\xi')\, g_1(\xi')\, d\xi'\,. \tag{2.28}$$

The moment coefficient can be written in a similar manner.

The function $\bar{F}_B(t)$ is plotted in Fig. 6 for three ellipsoidal bodies with different values of $\lambda_B = l_B/(2R)$. For a cylindrical body the kernel $B(\xi,\xi')$ can be written in the form $B(\lambda\xi - \lambda\xi') = B(\bar{\eta}) = B(-\bar{\eta})$; this is plotted in Fig. 7.

The lift ratio L_{W+B}/L_W of the wing-body combination and the (cylindrical) wing alone is shown in Fig. 8 for an ellipsoidal body in several axial positions and for the cylindrical body and several values of λ in Fig. 9. The lift ratio has been plotted over the whole range $0 \le \rho_m \le 1$ of ρ_m, although the theory assumes

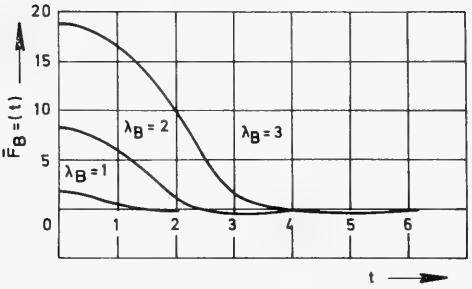

Fig. 6 - (See (106)) The function $\bar{F}_B(t)$ for ellipsoidal bodies

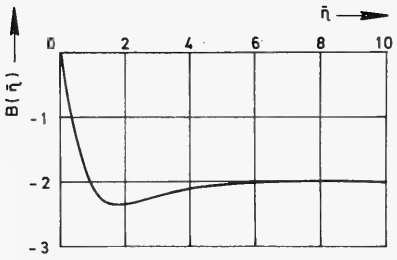

Fig. 7 - (See (106)) The kernel $B(\bar{\eta}) = -B(-\bar{\eta})$, $\bar{\eta} = \lambda(\xi - \xi')$

ρ_m to be small. Nevertheless, the value of zero obtained for $\rho_m = 1$ is exact for the cylindrical body because there is no lift when the wing and the cylindrical body coincide. Most of the results shown in these figures have been obtained by the three-quarter-point method. It can be seen that they agree fairly well with the results derived from the "exact" (linearized) theory. No example of results for the moment will be shown here.

The numerical results of (110) may be used immediately for determining the influence of a hub on the lift and moment of a ducted propeller at angle of attack by means of a "superposition model" as described in Sec. 6. The general framework of the theory may also be used for a more thorough solution of this problem. These remarks may be true also for the theory developed in (109) on the influence of struts.

3. THE DUCTED ACTUATOR DISC WITH CONSTANT PRESSURE JUMP

3.1 Linear Theory

The simplest model of a ducted propeller is a ring airfoil with a constant pressure jump Δp at a cross section $x = x_p$ (the "disk"). Of course, this can be used only for axisymmetric flows. It can be interpreted as the representation of a ducted propeller with many blades and with the swirl neglected or cancelled either by a counterrotating propeller or by guide vanes.

Since the disk does not produce vorticity, we have two regions of potential (irrotational) flow: the propeller slipstream and the rest. The slipstream is bounded by the disk, part of the duct and a free surface beginning at the trailing

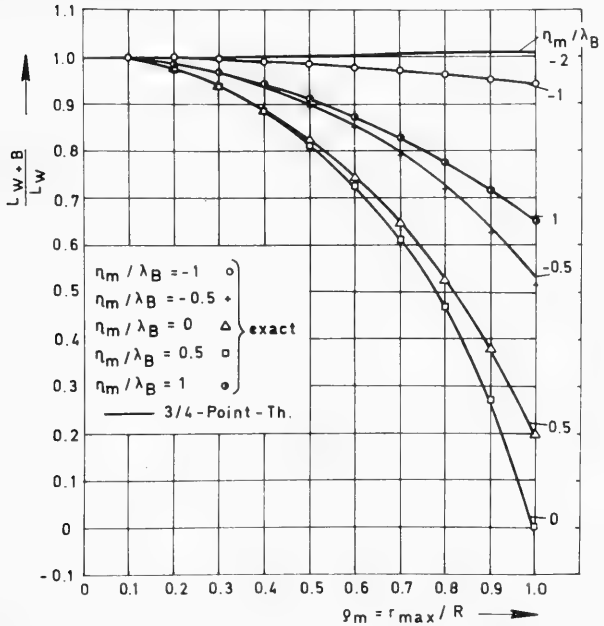

Fig. 8 - (See (106)) The lift ratio L_{W+B}/L_W, i.e., of (wing + body) to wing without body for a cylindrical wing ($\lambda = 0.5$) and an ellipsoidal body $[\lambda_B = l_B/(2R) = 2]$ in several axial positions, plotted against $\varrho_m = r_{max}/R$

edge of the duct. At this surface a jump in the tangential velocity v_t must exist in order to cancel the jump Δp in total pressure such that the static pressure as determined from the Bernoulli equation is continuous. If the velocity jump is represented by a distribution γ_f of ring vortices on the free surface, and if the mean tangential velocity is denoted by $\bar{v}_t$ this condition is expressed in the form

$$\rho \bar{v}_t \gamma_f = \Delta p \quad (\rho = \text{density}) . \qquad (3.1)$$

Obviously, the resulting velocity field does not depend on the location of the disk in the duct.

In the linear theory, the duct is represented by a distribution of vortex rings and

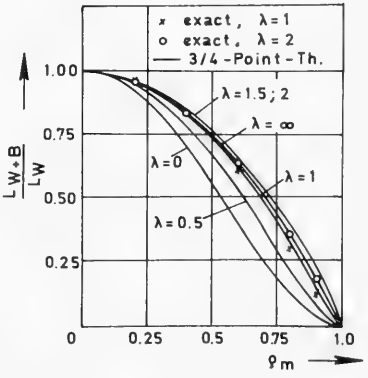

Fig. 9 - (See (106)) The lift ratio L_{W+B}/L_W for cylindrical wings and cylinder bodies plotted over the diameter ratio ϱ_m

source rings on the cylinder used in ring-airfoil theory. The free vortex rings are placed on the same cylinder (extended to $x = \infty$) and their strength γ_f is assumed to be constant. Since the velocity field must be continuous everywhere with the exception of the jump at the slipstream boundary, the value of the free vorticity γ_f must be equal to that of the bound vorticity γ_T at the trailing edge. Then the boundary condition (3.1) can be satisfied in one cross section only, which will be taken here at the trailing edge. These simplifications are reasonable because one is usually interested in the flow near the duct and this flow is influenced mainly by the behaviour of the slipstream in the neighbourhood of the duct.

Using the propeller thrust coefficient

$$c_{T_p} = 2\Delta p/(\rho V^2) , \tag{3.2}$$

the boundary condition (3.1) is simplified to

$$c_{T_p} = 2\left(1 + \frac{\bar{u}_T}{V}\right) g_T , \quad g_T = \gamma_T/V , \tag{3.3}$$

where $\bar{u}_T$ is the mean induced axial velocity at the trailing edge.

Now we consider the most simple case of an infinitely thin cylinder of length c as a duct. The constant free vorticity γ_f must be extended continuously to a bounded vorticity on the duct such that the radial velocity v_{γ_s}, induced by the sum γ_s of free and bounded vorticity, is zero. This can be achieved in the following manner.

The constant vorticity γ_f of the slipstream is extended continuously on the duct, e.g., by a linear distribution γ_1 that vanishes at the leading edge of the duct. The radial velocity $v_{\gamma_f+\gamma_1}$ induced at the duct can be calculated explicitly in terms of complete elliptic integrals of the first and second kind. On the duct, a vortex distribution γ_b satisfying the Kutta-Joukowski condition is then determined from the integral equation

$$T_0\gamma_b = -v_{\gamma_f+\gamma_1} . \tag{3.4}$$

Thus, γ_s is the superposition of the two bounded distributions γ_1, γ_b and the free distribution γ_f. From now on we shall consider only the entire distribution γ_s. All further distributions will be confined to the duct and must satisfy the Kutta-Joukowski condition. We put

$$\gamma_s = V g_T g_s^* . \tag{3.5}$$

In a theory that is linearized with respect to all singularity distributions, the distributions of the strictly linearized airfoil theory can be added to γ_s in order to obtain the solution for the ducted disk. This is dome essentially in all the theories developed at NSRDC and THERM. But, for small V and heavy propeller loading, the axial velocity u_{γ_s} induced by γ_s can have the same order of magnitude as V and should not be neglected in a consistent theory.

In order to show clearly the distinct efforts, we put, according to Bollheimer (116, 120, 122, 125),

$$\gamma = V\{g_c + g_t + g_T[g_s^* + g_c^* + g_t^*]\} \ , \tag{3.6}$$

$$q = V\{q_t + g_T q_t^*\} \ . \tag{3.7}$$

Here, g_c, g_t, and q_t give the distributions of the ring airfoil and are determined from the equations

$$q_t = 2t'(\xi) \ , \quad T_0 g_c = \rho_m'(\xi) \ , \quad T_0 g_t = -\bar{v}_{q_t} \ . \tag{3.8}$$

Similarly, from the mean axial velocity $\bar{u}_{\gamma_s} = V g_T \bar{u}_{g_s^*}$ we obtain

$$q_t^* = 2\frac{d}{d\xi}[\bar{u}_{g_s^*} t] \ , \quad T_0 g_c^* = \bar{u}_{g_s^*} \rho_m'(\xi) \ . \tag{3.9}$$

Finally, a vortex distribution is required to cancel $\bar{v}_{q_t^*}$ and the component arising from the interaction of strong vorticity with thickness as described by (1.15). So, g_t^* must satisfy

$$T_0 g_t^* = -\bar{v}_{q_t^*} - \frac{d}{d\xi}\left(\frac{g_s^*}{2} t\right) \ . \tag{3.10}$$

The operator of the four integral equations is the basic operator T_0 of thin ring airfoil theory. Of course, one can determine the sums $g_c + g_t$ and $g_c^* + g_t^*$ from one equation. Numerical methods have been discussed in Sec. 1.3. To solve the last three ("starred") equations, one has to determine g_s^* first and, from this, $\bar{u}_{g_s^*}$ by numerical integration. These two functions depend only on the parameter λ. All equations can be approximated by relations between matrices and vectors composed of Birnbaum and Fourier coefficients. These have been tabulated by Bollheimer (116, 120) for several values of λ.

So far, the value of the propeller thrust coefficient has not been used. This value is needed to determine g_T. First, the mean axial velocity $\bar{u}_T$ induced by γ and q at the trailing edge can be computed from (3.6) and (3.7) as a linear function of g_T. Insertion of $\bar{u}_T$ into (3.3) gives a quadratic equation for g_T. The coefficients of this equation can be easily computed by means of the vectors t tabulated by Bollheimer. Finally, the velocity distribution on the duct surface is the sum of V and the axial velocity induced by γ and q on the reference cylinder, multiplied by the Riegels factor $\{1 + [\rho_m'(\xi) \pm t'(\xi)]^2\}^{-1/2}$. In our notation the distributions having a subscript c or t are zero if the camber ρ_m' or the thickness are zero, respectively.

Obviously, the static case $V = 0$ is contained in this theory. Putting

$$\gamma = g_T[g_s^* + g_c^* + g_t^*] \ , \quad q = g_T q_t^* \ , \tag{3.11}$$

g_T is obtained by virtue of (3.1) from

$$\rho\left(\bar{u}_{q_s^*} + \bar{u}_{g_c^*} + \bar{u}_{g_t^*} + \bar{u}_{q_t^*}\right)_T g_T^2 = \Delta p \ , \tag{3.12}$$

if Δp is prescribed.

In Fig. 10, the factor g_T as a function of c_{T_p} is shown for a duct with a symmetrical Joukowski profile of relative thickness $\tau = 0.15$, chord/diameter ratio $\lambda = 0.5$, and zero chord incidence $[\rho'_m(\xi) \equiv 0]$. The two functions g_t and g_t^* are proportional to the thickness parameter τ of the Joukowski profile. Their values, divided by τ, are plotted over the chord in Fig. 11. Multiplication of g_t and g_t^* by V and V_{g_T}, respectively, gives the two vortex distributions γ_t and γ_t^* due to thickness. One sees that γ_t^* has at least the same order of magnitude as γ_t if c_{T_p} is of order 1 or greater. So, it does not seem consistent to neglect γ_t^* and take into account γ_t as is done in most theories.

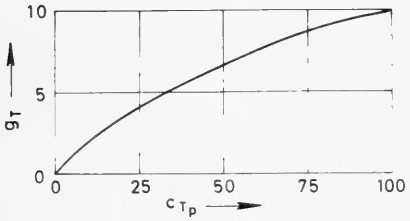

Fig. 10 - (See (122)) Nondimensional vortex strength g_T at the trailing edge of a ducted actuator disc ($\lambda = 0.5$, $\rho'_m = 0$) with a symmetric Joukowski profile of relative thickness $\tau = 0.15$ plotted against the propeller thrust coefficient c_{T_p}

3.2 Nonlinear Theory

The only consistent nonlinear theory for ducted propellers has been given by Chaplin (130). The duct is assumed to have zero thickness. The exaxt problem is to find a harmonic stream function ψ having a constant value $\psi = \psi_0$ on the boundary $B = D + S$ formed by the duct D and the slipstream surface S. On S, the condition for continuous pressure $\bar{v}_t \Delta v_t = \text{const.}$, where $\bar{v}_t$ denotes the mean (tangential) velocity and Δv_t the jump of the velocity at S, must also be satisfied. If the induced flow is produced by a distribution γ of ring vortices on B, the pressure condition on S can be written as $\bar{v}_t \gamma = \text{const.}$ The problem is solved if γ on B and the shape of S are determined. Then, the stream function, the velocity field, and other characteristics can be found by numerical integration. Special emphasis is placed on the evaluation of the slipstream contraction ratio

$$\Phi = (R_\infty / R_T)^2 \ , \tag{3.13}$$

where R_T and R_∞ denote the radius of the duct at the trailing edge and of the slipstream far away from the duct, respectively.

At present a mathematical theory of existence and uniqueness does not exist. No exact analytical solutions are known, not even for special cases. Nevertheless, there are strong reasons, based on analogy and numerical experience, to believe that the results of the method developed by Chaplin for use on high-speed computer are exact in a numerical sense.

The boundary conditions are made discrete in the following manner.

(1) The boundary surface B is approximated by $N + M$ cone frustum segments such that the midpoint of the N-th segment coincides with the trailing edge of the duct (see Fig. 12). The $(N + M)$-th segment is assumed to be

cylindrical. In other words, the generating curve of B is approximated by a continuous, piecewise linear graph. The approximate surface S is determined by M–1 radii r_i.

(2) Corresponding to this approximation, γ is approximated by a continuous, piecewise linear function, which is constant on the cylindrical part of S. For numerical reasons γ is written as the sum of triangular distributions (see Fig. 12). The first segment is loaded with a distribution which has a square-root singularity at the leading edge. The function γ is determined by N + M parameters $\bar{\gamma}_i$, i=1, ..., N+M.

(3) With these approximations, the boundary condition $\psi = \psi_0$ is satisfied at the leading edge and at the midpoints of the segments, with the exception of the last cylindrical one. The pressure condition is satisfied at the trailing edge and the following M - 1 midpoints. For a specified value ψ_0 this affords N + 2M - 1 equations for the N + 2M - 1 unknown values $\bar{\gamma}_i$, r_i.

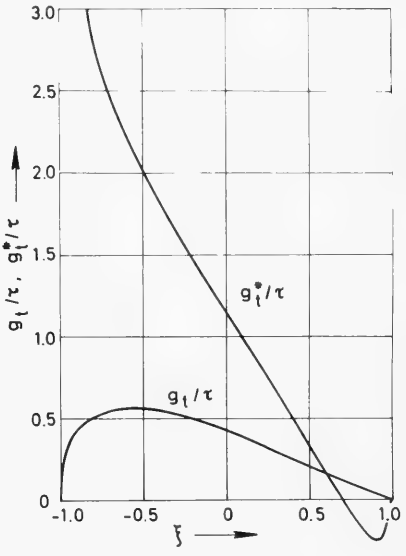

Fig. 11 - (See (122)) Nondimensional vortex distributions g_t and g_t^* due to interaction of thickness with the free-stream and the slipstream vorticity, respectively, for a ducted actuator disc ($\lambda = 0.5$, $\rho_m' = 0$) with symmetrical Joukowski profile

Since ψ and the induced axial and radial velocity can be expressed as linear combinations of the $\bar{\gamma}_i$, the unknowns $\bar{\gamma}_i$ appear in a fairly simple way in the equations. But the "influence coefficients" of the $\bar{\gamma}_i$ contain the unknown radii in a very complex manner, so that the system of equations is highly nonlinear and has to be solved by iteration.

The iteration starts by putting the values r_i, $\bar{\gamma}_i$ on S as constants (equal to the trailing-edge value) into the equations. Then, in the first cycle the equations are solved for the unknowns $\bar{\gamma}_i$ on D. This first approximation must coincide exactly with the results obtainable by the linear theory for cylindrical shrouds or by the somewhat more general theory developed by Bollheimer (116) for the static case. Then, the resulting error in the boundary conditions on S is evaluated and from this by certain rules, improved estimates of the γ_i, r_i on S are obtained. From the improved r_i, a better approximation of the boundary conditions can be calculated by means of improved influence coefficients. Then the second cycle starts by solving the improved equations for the $\bar{\gamma}_i$ on D.

Contrary to most other theories, the basic aerodynamic input parameter is not the pressure jump (or some other thrust parameter), but the value ψ_0, i.e., essentially the mass flow. Without loss of generality, by appropriate choice of units one can take ψ_0 as an arbitrary fixed value ($\psi_0 = 0.5$ in (130)). The cylinder approximation of S begins at a distance $4R_T$ from the leading edge. It

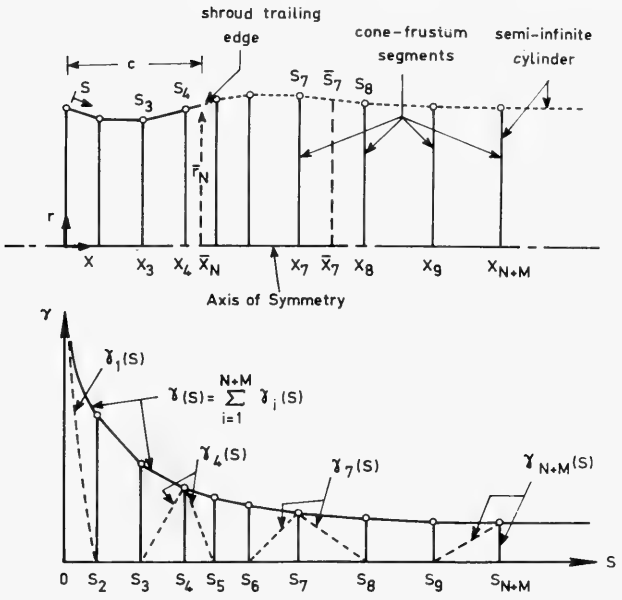

Fig. 12 - (See (130)) Approximation of the vortex distribution on a shroud and its slipstream by a vortex distribution on a system of cone-frustum segments

has been checked numerically that this gives an adequate representation. The contraction ratio is not determined from the resulting value r_{N+M} of the cylinder, but, in a more accurate way, from the constant boundary value $\bar{v}_t\gamma$. One general result of all numerical examples (cylindrical, conical, and parabolically cambered ducts, $0 \leq \lambda \leq 1$) is that the value of $\bar{v}_t\gamma$ and therefore of Φ and of other net characteristics does not change much during the iteration (see Fig. 13). That is a strong indication that the linear theory affords good results for these characteristics.

The number of segments chosen for the computations is $N = 24$ on the duct, $M = 41$ on the slipstream. A check has shown that smaller numbers will also give sufficient accuracy (see Fig. 14).

Unfortunately, the report does not present enough results to deduce general conclusions about the accuracy of pressure distribution, etc., computed from the linear theory. The only example presented extensively is the cylindrical duct with chord/diameter ratio $\lambda = 0.1$ in the static case. Fig. 15 shows that the vortex distributions computed by both linear and nonlinear theories agree rather well. Probably, with increasing λ and/or V (for noncylindrical ducts) the agreement would even be better.

Two other attempts to take into account nonlinear effects may be mentioned. Bollheimer (116) developed a theory in which the ring vortices representing the

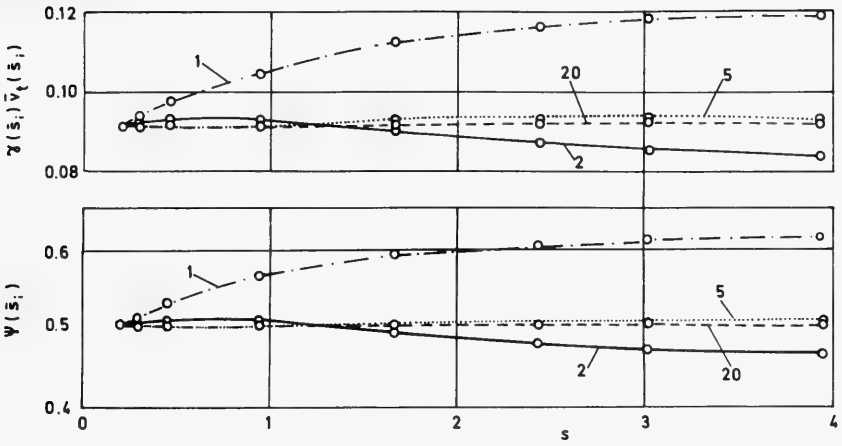

Fig. 13 - (See (130)) Approximation of slipstream boundary conditions at various stages of a twenty-iterative-cycle calculation. Cylindrical shroud: $1/\bar{r}_N = 0.2$, $U = 0$

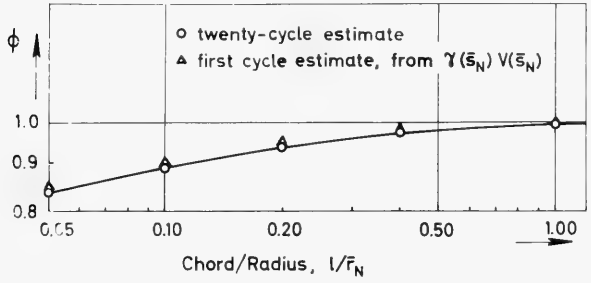

Fig. 14 - (See (130)) Slipstream contraction ratio for cylindrical shrouds

duct are placed not on a cylinder but on a cone; otherwise linear theory is applied. He found that the results do not depend very much on the choice of the approximating cone and agree sufficiently well with the usual linear theory.

Wiedemer (113) improved the results of Dickmann and Weissinger (102) by an interative procedure. In (102), duct profiles (with zero thickness) have been obtained by determining the streamlines through the trailing edge that are induced by certain vortex distributions placed on a reference cylinder. In each iteration cycle, Wiedemer places the (unchanged) vortex distribution of the duct on the profile obtained in the previous cycle and calculates the next profile approximation. One example is shown in Fig. 16, where a remarkable difference between the Dickmann-Weissinger profile and the Wiedemer profile can be seen. For lower values of c_{T_p} the difference is smaller. A method similar to that of

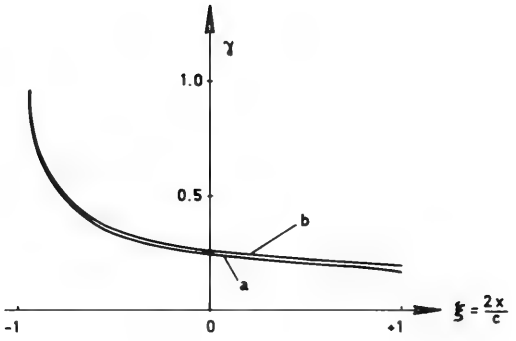

Fig. 15 - Vortex distribution on a cylindrical duct ($\lambda = 0.1$) in the static case as determined by (a) linear theory and (b) nonlinear theory (130)

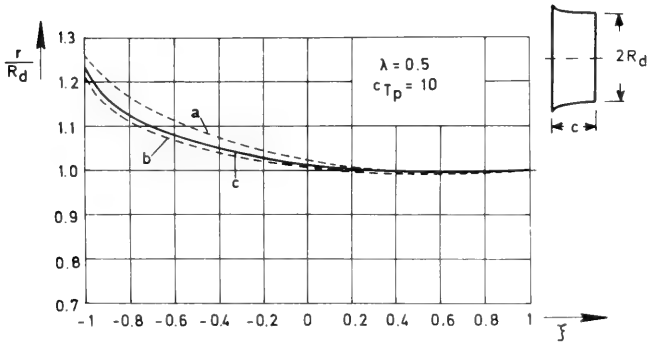

Fig. 16 - (See (113)) Duct profile corresponding to a specified vortex distribution as determined by (a) the linear theory (102), (b) the first iteration of a partially nonlinear theory (113), and (c) the second iteration

Chaplin has been used by Hunt (35) for determining the flow from a circular orifice.

4. THE UNIFORMLY LOADED DUCTED PROPELLER WITH AN INFINITE NUMBER OF BLADES IN AXIAL FLOW

For the rest of this paper each propeller blade will be represented by a radial vortex with a circulation distribution $\Gamma(r)$. From each element (r, dr) a helical vortex with strength $-\Gamma'(r)\,dr$ is shed. In an exact theory the radius and the pitch of the helix will naturally depend on the axial coordinate x. In linearized theory the radius is assumed constant and in most theories also the pitch, i.e., the helix is assumed as a regular helix of radius r and pitch $j(r)$. The pitch has to be determined. See Fig. 17.

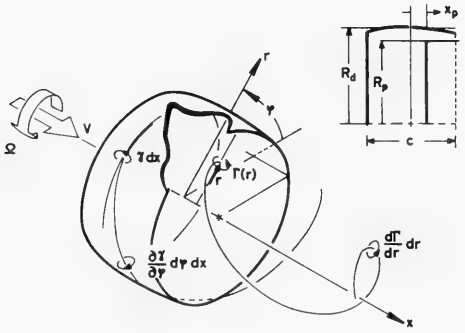

Fig. 17 - (See (142)) Vortex system and geometry for ducted propeller configuration

In this section is is assumed that $\Gamma(r) = \Gamma = \text{const}$. Then the shed helical vortices have strength Γ and lie on a cylinder of radius R_p = propeller radius. On the axis lies a vortex, and "hub vortex," extending from $x = x_p$ (= axial location of the propeller) with strength $N\Gamma$, where N denotes the number of propeller blades. It is assumed that N becomes infinite, such that

$$N\Gamma = \Gamma_0 \tag{4.1}$$

is a finite constant. In practice, it can be expected that the following theory can be applied for blade numbers as low as 3 or 4.

In this model, the slipstream cylinder $r = R_p$, $x \geq x_p$ is covered with a continuous and constant distribution of helical vortices. Taking orthogonal components, this distribution can be split into a distribution of ring vortices and of

straight axial vortices, each having constant strength γ_ϕ and γ_x, respectively. Since the circulation outside the slipstream is zero, the total strength of the axial vortices on the cylinder must be $-\Gamma_0$. Therefore, the axial vorticity is

$$\gamma_x = -\frac{\Gamma_0}{2\pi R_p} . \tag{4.2}$$

If the velocity components corresponding to cylindrical coordinates (x, r, ϕ) are denoted by $u, v, w,$ then the vortex system without the ring vortices induces

$$\begin{aligned} &u = v = w = o , && \text{outside the slipstream} \\ &u = v = o , \quad w = \frac{\Gamma_0}{2\pi r} && \text{inside the slipstream} . \end{aligned} \tag{4.3}$$

If w is considered small in comparison with the angular rotational propeller speed Ω, we have constant pressure jump

$$\Delta p = \rho \frac{\Omega}{2\pi} \Gamma_0 \tag{4.4}$$

at the propeller disk. That gives the propeller thrust

$$T_p = \pi R_p^2 \Delta p . \tag{4.5}$$

Putting

$$\tilde{\Gamma}_0 = \frac{\Gamma_0}{\Omega R_p^2} , \quad \tilde{\gamma}_x = \frac{\gamma_x}{\Omega R_p} = -\frac{\tilde{\Gamma}_0}{2\pi} , \quad \tilde{\gamma}_\phi = \frac{\gamma_\phi}{\Omega R_p} , \tag{4.6}$$

one obtains the propeller thrust coefficient

$$c_{T_p} = \frac{T_p}{\frac{\rho}{2}(\Omega R_p)^2 \pi R_p^2} = \frac{\tilde{\Gamma}_0}{\pi} = -2\tilde{\gamma}_x . \tag{4.7}$$

Now, if the propeller is ducted, we have almost the same model as that treated in Sec. 3.1. The only difference is that there is a contribution $\rho w^2/2$ to the pressure jump at the slipstream surface. But this can be neglected for the same reasons as was done at the propeller disk. So, given the propeller thrust or pressure jump, this problem can be solved by the methods discussed in Sec. 3.1. The important fact that the results do not depend on the location of the propeller in the duct remains true.

If there is a "tip clearance" (with respect to the reference cylinder), measured by the parameter

$$\mu = R_p/R_d \quad (\mu \leq 1) \tag{4.8}$$

one has to determine the strength γ_ϕ of the ring vortices from the pressure condition on the slipstream surface, the radial velocity v_{γ_ϕ} induced on the duct and a ring vortex distribution γ on the duct from the integral equation

$$T_0\gamma = -v_{\gamma_\phi} \tag{4.9}$$

or

$$T_0\tilde{\gamma} = -v_{\tilde{\gamma}_\phi}, \quad \tilde{\gamma} = \frac{\gamma}{\Omega R_p} . \tag{4.10}$$

If the duct is not cylindrical, the influence of camber and thickness can be taken into account by superposing the singularity distributions of ring-airfoil theory (within the framework of strict linearization).

By satisfying the pressure condition far away from the duct, where the duct-induced velocities are zero, one obtains

$$\tilde{\gamma}_\phi = \frac{c_{T_p}}{J + \sqrt{J^2 + c_{T_p}}}, \quad J = \frac{V}{\Omega R_p} . \tag{4.11}$$

Therefore, the pitch j of the helical vortices is given by

$$j = -\tilde{\gamma}_x/\tilde{\gamma}_\phi = \frac{1}{2}\left(J + \sqrt{J^2 + c_{T_p}}\right), \tag{4.12}$$

and we can write

$$\tilde{\gamma}_\phi = \frac{c_{T_p}}{2j} . \tag{4.13}$$

The velocity induced by a semi-infinite cylinder of ring vortices with constant strength can be expressed by means of the Legendre functions $Q_{1/2}$. So, one obtains

$$v_{\tilde{\gamma}_\phi} = -\frac{\sqrt{\mu}}{2\pi}\,\tilde{\gamma}_\phi Q_{1/2}(\sigma) = -\frac{\sqrt{\mu}}{4\pi j}\,c_{T_p} Q_{1/2}(\sigma) , \tag{4.14}$$

$$\sigma = 1 + \frac{(1-\mu)^2 + (\bar{x} - \bar{x}_p)^2}{2\mu}, \quad \bar{x} - \bar{x}_p = (x - x_p)/R_d , \tag{4.15}$$

and the integral equation

$$T_0\tilde{\gamma} = \frac{\sqrt{\mu}}{4\pi j}\,c_{T_p} Q_{1/2}(\sigma) . \tag{4.16}$$

Putting

$$Q_{1/2}(\sigma) = q_0 - \sum_{n=1}^{\infty} q_n \cos n\theta , \quad \bar{x} = -\lambda \cos\theta , \tag{4.17}$$

$$\tilde{\gamma} = c_0 \cot \frac{\theta}{2} + \sum_{n=1}^{\infty} c_n \sin n\theta \ , \qquad (4.18)$$

and introducing the coefficient vectors

$$\{q\} = \{q_0, q_1, \cdots\} \ , \quad \{c\} = \{c_0, c_1, \cdots\} \ ,$$

the solution can be expressed as

$$\{c\} = \frac{\sqrt{\mu}}{2\pi j} c_{T_p} [0]\{q\} \ , \qquad (4.19)$$

with a matrix $[0]$ which depends only on λ and which has been tabulated in (153) as a 7x7 matrix for $\lambda = 0.25, 0.5, 0.75$. For small λ the matrix is close to the unit matrix. Interpolation for λ may be possible. The vector q has also been tabulated for several values of λ, x_p/c, and $\mu (0.9 \leq \mu \leq 1)$. Similarly, the continuous part $\bar{u}_{\tilde{\gamma}} = \pm\tilde{\gamma}/2 + u_{\tilde{\gamma}}$ of the axial velocity $u_{\tilde{\gamma}}$ induced by $\tilde{\gamma}$ at the duct is expressed by a Fourier series whose coefficients can be calculated as a vector $[S]\{c\}$ with a tabulated matrix $[S]$. Then, the total axial velocity at the duct and the pressure coefficient can easily be calculated by means of Legendre functions.

For $\mu = 1$, the ring vortex distributions γ_d on the duct is given by $\gamma_d = \gamma + \gamma_\phi$ with $\gamma_\phi = 0$ for $-c/2 \leq x < x_p$ and $\gamma_\phi = \text{const.} \neq 0$ for $x_p < x \leq c/2$. Since the induced velocities must be continuous inside the duct, the jump of γ_ϕ at $x = x_p$ must be cancelled by a jump of γ equal to $-\gamma_\phi$. Therefore, the Birnbaum series (4.18) of γ converges very slowly, corresponding to a slow convergence of the Fourier series (4.7) for the discontinuous function $Q_{1/2}(\sigma)$. Therefore, for $\mu = 1$ the procedure requires a large number of Fourier coefficients q_n, and a tabulation to $n = 12$ as given in (153) may not be sufficient. Probably, as indicated above, the methods of the first part of Sec. 3. should be preferred.

Of course, slow convergence will also occur if the tip clearance is very small, i.e., if μ is close to unity. In this case the logarithmic singularity of v_{γ_ϕ} [or $Q_{1/2}(\sigma)$] is replaced by a sharp peak at $x = x_p$. The peak is still present for fairly large tip clearance, as can be seen in Fig. 18 ($J = 0$, $c_{T_p} = 0.1$, $\lambda = 0.5$, $\mu = 0.9$), at $x = x_p = 0$ for a cylindrical duct. The corresponding vortex distribution is shown in Fig. 19, together with the distribution for the propeller located at $x_p = -0.25c$. At $x = x_p$, an indication of the jump occurring for $\mu = 1$ can be observed. The corresponding pressure distributions are shown in Fig. 20. The distributions on the outer surface are practically independent of the axial propeller position. The inner duct surface pressure decays almost to zero immediately behind the propeller plane. The duct-to-propeller thrust ratios c_{T_d}/c_{T_p} for the two cases are 0.683 and 0.706 for $x_p = -0.25c$ and $x_p = 0$, respectively. Even in this case of large tip cleraance this ratio is almost independent of x_p; for $\mu = 1$ it is totally independent.

In (153), the influence of an improved determination of the pitch is also investigated. The new pitch $j_1 = j_1(x)$ is defined by $j_1 = J + \tilde{u}$ where $\tilde{u}$ is the mean axial velocity on the slipstream surface induced by $\tilde{\gamma}$ and $\tilde{\gamma}_\phi$. Then, from (4.13), an improved slipstream distribution $\tilde{\gamma}_\phi^{(1)}$ is obtained and the induced radial velocity $v_{\tilde{\gamma}_\phi^{(1)}}$ is introduced in the right-hand side of the integral

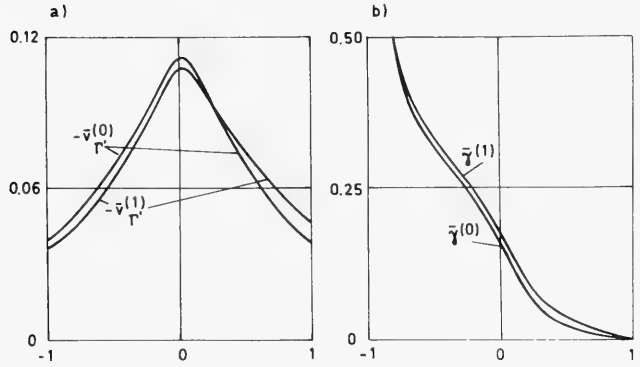

Fig. 18 - (See (153)) Uniformly loaded ducted propeller with infinite blade number at zero incidence. Cylindrical duct, $\lambda = 0.5$, $x_p = 0$, $\mu = 0.9$, $J = 0$, $c_{T_p} = 0.1$. (a) Radial velocity induced by the propeller slipstream on the duct; (b) ring vortex distribution on the duct. Suffix (0) refers to constant pitch of helical vortices, (1) to pitch improved by one iteration.

equation (4.10), from which an improved duct distribution $\tilde{\gamma}^{(1)}$ is then determined. This procedure can be iterated. Because the pitch $j(x)$ varies, the induced velocities, e.g., $v_{\tilde{\gamma}_\phi}^{(1)}$, must be calculated by numerical integration (over an infinite interval) which makes the computations much more cumbersome. For the example discussed above, the effect of axial pitch variation is shown in Fig. 18. Qualitatively, the effect is a shift of the "effective" propeller plane rearward by approximately 2% of the chord length. The corresponding duct thrust coefficients differ also by 2%. From this example it may be concluded that the small differences in the final results do not justify the additional computational effect of the iteration procedure.

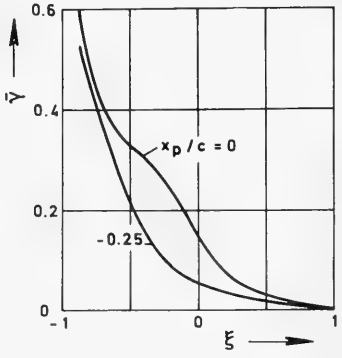

Fig. 19 - (See (153)) Duct vortex distribution for two propeller locations and other parameters as in Fig. 18

5. THE FINITE-BLADED DUCTED PROPELLER IN AXIAL FLOW

If a propeller-fixed system of cylinder coordinates (x, r, ϕ) is introduced, the flow that is unsteady is shroud-fixed coordinates will be steady and periodic in ϕ with a period $2\pi/N$. Because of the rotational symmetry of the duct, no additional normal velocity is introduced on the duct surface by the rotation.

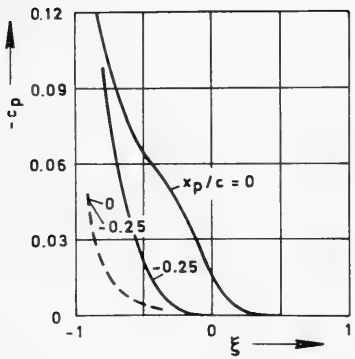

Fig. 20 - (See (153)) Duct pressure distribution for two propeller locations and other parameters as in Fig. 18

——— inner surface
----- outer surface

As described in the first paragraph of Sec. 4, the propeller is represented by N radial vortices with equal distribution $\Gamma(r)$ of circulation. The helical vortices with strength $-\Gamma'(r)$ shed from a blade form a quasi-helical surface with pitch $j(r)$. Assuming a moderately loaded propeller, the axial pitch dependence can be neglected. From theory and experiment it is known that a hub of usual shape does not affect the duct distributions very much. Therefore, it will at first be considered as nonexistent. $\Gamma(r)$ is considered as a known function with $\Gamma(0) = 0$ and $\Gamma(R_p) = 0$. Only if the distance between propeller tip and duct surface is practically zero do we have $\Gamma(R) \neq 0$. The meaning of "practically zero" is a question of boundary-layer theory.

As in the theories of Secs. 3 and 4, the duct is represented by a distribution γ of ring vortices and for nonzero thickness, by a distribution q of sources, both lying on a reference cylinder of radius R_d. The main feature now is that, obviously, γ depends on ϕ as well as on x. Therefore, from each ring element γdx free vortices of strength $\partial\gamma/R_d\partial\phi\, dx$ are shed. These are not straight lines, as in the case of the ring airfoil at angle of attack but rather are of helical shape. They are assumed to be regular helices with constant pitch $j_d = V/\Omega R_d$. This assumption excludes the static case. It yields a reasonable approximation for the case of moderately loaded propellers in cruise condition. It will easily be perceived that the theory of this section and the computational labour involved are not changed essentially by the choice of another constant value for j_d.

If, within the framework of strict linearization—contrary to the more general Bollheimer theory described in Sec. 3.1, the interaction between the propeller slipstream and both profile camber and thickness are neglected, then the duct distributions due to camber and thickness can be calculated separately by ring-airfoil theory. These have to be added to the distributions induced by the propeller and its slipstream on a cylindrical duct, which shape will be assumed for the rest of this section. As a practical choice for the duct radius R_d, the radius of the shroud camber line at the propeller plane is proposed in (147).

Because of the helical shape of the vortices shed from the duct, the radial velocity induced by the duct vortex system at the duct cannot be expressed by the integral operators T_n used in ring-airfoil theory. But the main interest is in the circumferential average

$$\gamma_0(x) = \frac{1}{2\pi}\int_0^{2\pi} \gamma(x,\phi)\, d\phi \qquad (5.1)$$

because this, evidently, is the steady part of the solution γ as referred to a duct-fixed system of coordinates. This can be determined by the ideas of the foregoing section.

Obviously, $\gamma_0(x)$ is that part of γ that must cancel the average radial velocity induced by the propeller vortex system, and the average velocity is the same as the velocity induced by the average vortex system, which is equivalent to the propeller with an infinite number of blades. With respect to the model considered in Sec. 4 the only difference lies in the dependence of Γ on r. This difficulty can be overcome by integrating the pertinent formulas of Sec. 4 with respect to r in the following manner.

The sought radial velocity v_p is written as

$$v_p = \int_0^{R_p} dv_p \ , \tag{5.2}$$

where dv_p is the radial velocity induced by an annular part of the slipstream of radius $r \leq R_p$ and width dr. By (4.14) we have

$$dv_p = -\frac{1}{2\pi}\sqrt{\frac{r}{R_d}}\,\gamma_\phi\, Q_{1/2}(\sigma)\, dr \ , \quad \sigma = 1 + \frac{(r-R_d)^2 + (x-x_p)^2}{2rR_d} \ , \tag{5.3}$$

and

$$\gamma_\phi = -\gamma_x / j(r) \ , \tag{5.4}$$

where $j(r)$ is the pitch of the helical vortices lying on the cylinder of radius r and where γ_ϕ and γ_x denote their azimuthal and axial components, respectively. Since

$$\gamma_x = -\frac{N}{2\pi r}\frac{d\Gamma}{dr} \ , \tag{5.5}$$

we obtain the integral equation

$$T_0\gamma_0 = -v_p \tag{5.6}$$

with

$$v_p = \frac{-N}{4\pi^2}\int_0^{R_p} \frac{1}{j(r)\sqrt{rR_d}}\frac{d\Gamma}{dr}\, Q_{1/2}(\sigma)\, dr \ . \tag{5.7}$$

If the propeller-shed vortices are assumed to be convected with the free stream, then

$$j(r) = \frac{V}{\Omega r} = J\frac{R_p}{r} \ , \quad J = \frac{V}{\Omega R_p} \ , \tag{5.8}$$

and the integral equation (5.6) can be written in the form

$$T_0\gamma_0 = \frac{N}{4\pi^2 J R_p} \int_0^{R_p} \sqrt{\frac{r}{R_p}} \frac{d\Gamma}{dr} Q_{1/2}(\sigma)\, dr \tag{5.9}$$

with the standard operator T_0.

Equations (5.6) and (5.9) can be solved by the methods of Sec. 2, after numerical evaluation of the right-hand side integrals for a given function $\Gamma(r)$. If $\Gamma(R_p) \neq 0$, the right-hand side includes an explicit term similar to that of (4.16).

By both the THERM work sheets (151) and the NSRDC computer program (134) only the steady part of the distributions can be calculated. In (151), γ_0 is determined from (5.9) with $\Gamma(r)$ specified as the optimum propeller circulation of Betz, including a tip correction for wall effects derived by Goodman (22). In (134), Eq. (5.6) is solved with an arbitrary distribution $\Gamma(r)$. The tangent of the propeller hydrodynamic pitch angle determined by Lerbs' theory of moderately loaded propellers (48) is used for $j(r)$, i.e., the propeller-induced velocity is taken into account in determining $j(r)$ (to some extent), while the velocity induced by duct and hub is neglected. These are neglected in (151), too.

The program (134) includes also a design program based on an iterative procedure with three steps in each cycle. First, $\Gamma(r)$ is determined for the unducted propeller from a slight modification of Lerbs' theory. Because of the modification, small additional axial and azimuthal velocities such as those induced by a duct can be taken into account. Second, the steady radial (Eq. (5.7)) and axial velocity components induced on the duct by the propeller are computed. Then, (5.6) and the corresponding equations of ring-airfoil theory, as far as camber and thickness are concerned, are solved and the velocity induced at the propeller by these duct distributions computed. Then the next cycle can be started. The computation starts with the determination of $\Gamma(r)$ for the unducted propeller. The iteration is repeated until the inflow velocity at the propeller converges to four significant figures. Usually, this accuracy can be obtained in less than six cycles.

The propeller can be designed on the basis of thrust or shaft horsepower and for a prescribed blade circulation or pitch distribution. The viscous effects of the propeller are taken into account by giving as input the blade-section drag coefficient and the propeller blade outline. The viscous drag on the duct, which includes both the skin-friction and pressure drag, can also be calculated on the computer. The frictional drag on the duct is computed by giving as input the frictional drag as presented by Gertler (20), where the Reynolds number is based on the duct length. The computer program calculates the pressure drag on the duct according to the method developed by Granville (23).

At THERM (139, 142) and NSRDC (128, 129), similar theories have been developed for determining the unsteady part of γ, too, i.e., the harmonics of nonzero order in the expansion

$$\gamma(x,\phi) = V\left\{g_0 + \sum_{m=1}^{\infty} [g_m(x) \cos mN\phi + h_m(x) \sin mN\phi]\right\} . \tag{5.10}$$

Only the terms of order mN are left in the general Fourier series because the flow must be periodic with a period $2\pi/N$. Evidently, Vg_0 is identical with γ_0 in the foregoing steady-part theory.

It turns out that the two-dimensional integral equation, which equates the radial downwash of the duct vortex system and the radial velocity induced by the propeller at the duct, is equivalent to an infinite system $(m=1, 2, \cdots)$ of coupled integral equations for g_m and h_m. According to (142), these equations can be written in the form

$$\int_{-\lambda}^{\lambda} g_m K'_m \, d\bar{x}' - \frac{mN}{J\mu} \int_{-\lambda}^{\lambda} h_m K_m \, d\bar{x}' = B_{\Gamma' m} \ , \tag{5.11}$$

$$\int_{-\lambda}^{\lambda} h_m K'_m \, d\bar{x}' + \frac{mN}{J\mu} \int_{-\lambda}^{\lambda} g_m K_m \, d\bar{x}' = A_{\Gamma m} + A_{\Gamma' m} \ . \tag{5.12}$$

Here, $VA_{\Gamma' m}$ and $VB_{\Gamma' m}$ are the coefficients of the mN-th sine and cosine harmonics, respectively, in the Fourier expansion of the radial velocity induced on the duct by the helical vortices shed from the blades. Similarly, $VA_{\Gamma m}$ is the sine coefficient of the contribution due to the propeller blades. For the rather complex formulas see (139, 142).

The kernel K_m is defined by

$$K_m = \frac{1}{4\pi} \{S_{mN}(\omega) - G_{mN}(\Delta\bar{x}')\} \qquad \omega = 1 + (\Delta\bar{x}')^2/2 \ , \quad \Delta\bar{x}' = (x - x')/R \ , \tag{5.13}$$

$$S_n(\omega) = Q_{n+1/2}(\omega) + Q_{n-3/2}(\omega) \ , \tag{5.14}$$

$$G_n(\Delta\bar{x}') = n \int_0^{\infty} \{2J^2\mu^2 Q_{n-1/2}(\tilde{\omega}) + S_n(\tilde{\omega})\} \sin\mu\tau \, d\tau \ , \tag{5.15}$$

$$\tilde{\omega} = 1 + (\Delta\bar{x}' - J\mu\tau)^2/2 \ .$$

K'_m denotes the derivative of K_m with respect to $\Delta\bar{x}'$ and has the well-known Cauchy singularity.

The pair of integral equations (5.11) and (5.12) can be solved simultaneously by methods similar to those used in the preceding sections. In (139, 142), a method of decoupling the equations has been described. There, it is also indicated that there may exist nontrivial solutions of the homogeneous equations. The physical interpretation of these distributions is not clear. Evidence for the existence of such periodic eigensolutions can be deduced also from theories of Ludwieg (50, 51) and Rautmann (118, 120).

As $J \to \infty$, the helical trailing vortices of the duct become straight lines, i.e., one obtains the vortex model of the thin-ring airfoil with deviations in shape from axisymmetry such that γ depends on ϕ also. So, one gets the uncoupled equations of ring-airfoil theory with the integral operators T_n. The decoupling for $1/J = 0$ can be observed immediately in (5.11) and (5.12). On the

right-hand side in (5.11), the $B_{\Gamma'_m}$ become zero. Therefore, putting $g_m = 0$, the first equation of each pair drops out from the computation. The expressions for $A_{\Gamma m} + A_{\Gamma' m}$ can be simplified.

So far, numerical results have been presented only for the steady part of the solution. This is the most important part because it yields the time average of all linear quantities in linearized theory such as the distribution of velocity and pressure on the duct, the radial sectional force, etc. On the other hand, the duct thrust is a nonlinear quantity and depends not only on the coefficient of zero order, which is used in the usual computations, but on all Fourier coefficients.

6. THE DUCTED PROPELLER AT ANGLE OF ATTACK

The problem of this section is much more difficult than the previous ones, because, for a propeller at angle of attack, a system of coordinates in which the flow is time independent does not exist. Therefore, in its present state, the theory is more rough than those presented in the previous sections.

The first rough approximation is based on the so-called "superposition model," in which the time dependence is eliminated. The flow is determined by superposing the flow of the ducted propeller at zero incidence and the flow of a cylindrical ring airfoil at angle of attack. Both flows can be determined separately by the theory of Secs. 5 and 2, respectively. Essentially, this model was first used by Kriebel (160). The gross forces resulting from this model are the thrust due to the ducted propeller at zero incidence and a lift force due to the ring airfoil at incidence.

The most important result of the following theory developed at THERM (157) is that it shows the existence of a mean net force due to the time-dependent part of the flow which, in turn, produces a side force that can be as great as 20% or more of the lift. Approximately one half results from the propeller and the other half from the duct. A decrease in shroud lift of about 10% is also predicted by the interaction model, although it is approximately balanced by a lift force on the propeller. A typical example ($N = 3$, $x_p/c = -0.219$, $d/R_p = 0.213$, $\lambda = 0.5$, $\mu = 0.956$, $J = 0.344$) is shown in Table 1. The coefficients of lift and side forces and the corresponding pitching and yawing moments are tabulated separately for the duct and the propeller. The moments are referred to the leading edge with the nose-up and nose-right directions taken as positive. The positive direction of the side force is oriented to the left (Fig. 21).

The problem to be solved may be stated as follows: Given the geometry of the configuration and the mean propeller blade circulation $\Gamma(r)$ (design circulation), determine the duct source distribution q and the steady part of the bound duct vortex distribution such that the tangent-flow condition is satisfied at the reference cylinder $r = R_d$ and the Kutta condition, at the trailing edge.

A duct-fixed system of coordinates (x, r, ϕ) is used, as shown in Fig. 21. If γ and Γ denote the duct and propeller distributions of the superposition model, then the corresponding distributions of the interaction model are taken to be $\gamma + \tilde{\gamma}$ and $\Gamma + \tilde{\Gamma}$. The trailing vortices of the duct $-\partial(\gamma + \tilde{\gamma})/\partial\phi$ are

Table 1
Comparison of Predictions of Two Models

		Quantity	Superposition Model	Interaction Model
Duct	Lift	$dC_L/d\alpha$	3.074	2.701
	Side force	$dC_S/d\alpha$	0	-0.242
	Pitching moment	$dC_M/d\alpha$	-0.682	-0.624
	Yawing moment	$dC_N/d\alpha$	0	0.013
Propeller	Lift	$dC_L/d\alpha$	0	0.219
	Side force	$dC_S/d\alpha$	0	-0.207
	Pitching moment	$dC_M/d\alpha$	0	-0.192
	Yawing moment	$dC_N/d\alpha$	0	0.203

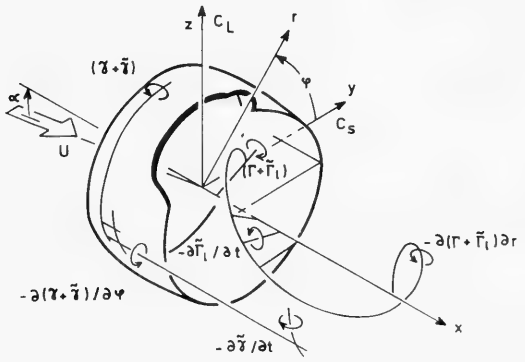

Fig. 21 - (See (157)) Vortex system of the ducted propeller at angle of attack

assumed to convect downstream with speed V. Each bound ring vortex, therefore, contributes a semi-infinite cylinder of straight trailing vortices. The corresponding shed vortices $\partial\tilde{\gamma}/\partial t$ constitute a similar cylinder composed of ring vortices. The trailing vortices from the 1-th propeller blade $-\partial(\Gamma+\tilde{\Gamma}_1)/\partial r$ are also assumed to convect downstream with speed V, forming regular helices with advance ratio $U/\Omega r$. The shed vortices $-\partial\tilde{\Gamma}_1/\partial t$ emitted from each blade fall on these helices and are perpendicular locally to the trailing vortices. The

steady radial wash v may be expressed accordingly as the superposition of the individual contributions or

$$v = v_q + v_\gamma + v_{\gamma'} + v_\Gamma + v_{\tilde{\Gamma}'} + [v_{\tilde{\gamma}} + v_{\tilde{\gamma}'} + v_{\dot{\tilde{\gamma}}} + v_\Gamma + v_{\tilde{\Gamma}} + v_{\dot{\tilde{\Gamma}}}] \quad . \tag{6.1}$$

The expression in the bracket turns out to be zero.

Putting

$$\gamma = \gamma_0 + \gamma_1 , \quad \gamma_0 = Vg_0(x) , \quad \gamma_1 = V[A(x) \sin\phi + B(x) \cos\phi] , \tag{6.2}$$

one finds easily that q and γ_0 are the distributions of the ducted propeller at zero incidence, which account for the effects of thickness and camber. So we are left with the condition

$$v_{\gamma_1} + v_{\gamma_1'} = -V\alpha \sin\phi - v_{\tilde{\Gamma}'} . \tag{6.3}$$

The left-hand side, corresponding to the model of ring-airfoil theory, can be written as $V \sin\phi \; T_1 A + V \cos\phi \; T_1 B$ by means of the operator T_1.

Since only the first harmonic is present in either the case of the ring airfoil at incidence or that of the propeller at incidence, the distribution $\tilde{\Gamma}$ will turn out to vary sinusoidally with Ωt such that, from Biot-Savart integration, is found

$$v_{\tilde{\Gamma}'} = V[F(x) \sin\phi + G(x) \cos\phi] . \tag{6.4}$$

The functions $F(x)$ and $G(x)$ involve complicated double integrals over the amplitude and phase angle of $\tilde{\Gamma}(r)$ which must be determined by solving the unsteady-propeller problem explicitly.

If $F(x)$ and $G(x)$ are known, Eq. (6.3) splits into the two equations

$$T_1 A = -\alpha - F , \quad T_1 B = -G , \tag{6.5}$$

which can be interpreted as the equation for a ring airfoil at incidence with a modified ϕ-dependent camber and can be solved by the numerical methods described in Secs. 1 and 2.

The distribution $\tilde{\Gamma}(r)$ is determined in the following manner. At each propeller blade the unsteady axial velocity component due to γ_1 and the unsteady tangential component due to both the incidence cross flow and the duct trailing vortices γ_1' are calculated. The component of this velocity vector taken perpendicular to the effective free stream composed of V and Ωr gives the unsteady downwash at the propeller blade. This downwash has a sinusoidal distribution over the blade chord. Now, at a representative radius $r = r_0$ (e.g., $r_0 = 0.7 R_p$) the solution of Kemp (41) for the sinusoidal gust problem gives a value $\tilde{\Gamma}(r_0)$ that depends on a phase angle and an amplitude factor, both of which can be expressed by Bessel and Hankel functions of the reduced frequency $\Omega d/(2\sqrt{V^2 + \Omega^2 r_0^2})$ (d = propeller chord length). The application of Kemp's two-dimensional theory implies that the blade interference can be neglected, i.e., that the blade number N is small.

In a further simplification, it is assumed that $\tilde{\Gamma}(r)$ is constant: $\tilde{\Gamma}(r) = \tilde{\Gamma}(r_0)$. Then $v_{\tilde{\Gamma}'}$ is produced by concentrated helical vortices trailing from each of the N blade tips and can be expressed by integrals of Legendre functions over an infinite interval in a way similar to that in the previous section.

Three typical distributions of F/α and G/α are shown in Fig. 22. Since their importance is determined by their magnitude relative to unity, we see that the duct-propeller coupling is, in fact, large enough to account for a significant improvement over the simple superposition model but not large enough to discredit the superposition model as a reasonable first approximation. A typical pressure distribution is shown in Fig. 23.

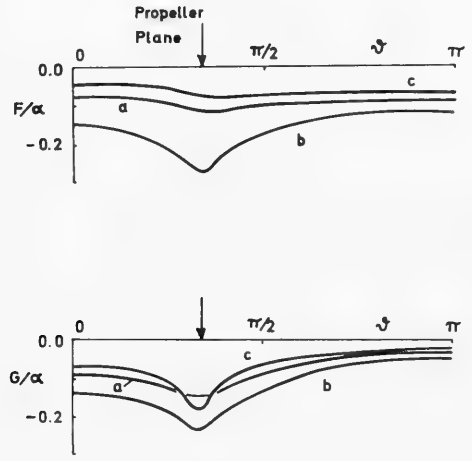

Fig. 22 - (See (157)) Camber functions for ducted propeller at angle of attack (N = 3, μ = 0.95, d/R_p = 0.2, x_p/c = -0.25)

(a) λ = 0.5, J = 0.5
(b) λ = 0.5, J = 0.25
(c) λ = 1.0, J = 0.5

7. FINAL REMARKS

The theory of ducted propellers as presented in this review has reached a first goal. Based on linearizations which have been successfully used for a long time in propeller and airfoil theory, a consistent and complete theory has been developed for axial, nonviscous, incompressible flow. To some extent, the basic linear assumptions have been checked by nonlinear theories; the linearization does not affect the relevant results gravely. Insofar as the effects of viscosity, compressibility, and cavitation can be determined separately, the theory should now afford a reliable tool for predicting design and performance.

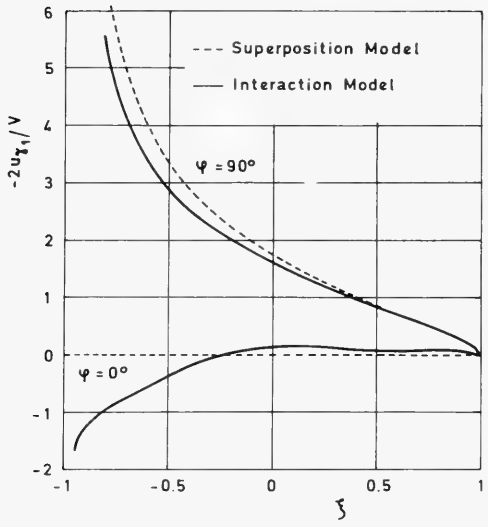

Fig. 23 - (See (157)) Angle of attack contribution to net shroud pressure coefficient ($N = 3$, $\mu = 0.956$, $d/R_p = 0.213$, $x_p/c = -0.219$, $\lambda = 0.5$, $J = 0.344$)

Of course, there remain problems, even within the framework of the linear theory. For example, the problems connected with the higher harmonics of the finite-bladed propeller might be investigated more thoroughly. It might be desirable to drop the assumption of slenderness for the propeller blades and to investigate the flow in the neighbourhood of the propeller (supplemented, perhaps, by guide vanes) by a lifting-surface theory. Also problems of interference or of free surface might be sought. An important problem, though transcending the realm of nonviscous theory, is a practical determination of the propeller tip clearance for use in the above theory.

For the ducted propeller at angle of attack, the rough theory of Sec. 6 should be refined, at least for checking this comparatively simple theory.

Finally, two problems will be mentioned which are beyond the scope of this review. The first one arises from the fact that a ducted propeller does not usually operate in a uniform stream. As a matter of fact, the NSRDC computer program includes the possibility of a radial dependence of the inflow. One might also include the higher harmonics induced by a ship as analysed in (4). Isay (40) developed a theory for ducted propellers in a wake based on two-dimensional theory with three-dimensional corrections. But, by the methods discussed in this review, the problem had to be solved by the methods of potential theory, though the flow in a wake usually is not a potential flow. This leads to the problem of nonviscous nonpotential flow (Euler equations), which has been treated only rarely in comparison with the extensive literature concerned with solutions

of the Laplace equation or the Navier-Stokes equations. A first study of a ring airfoil in a nonuniform flow has been presented by Maass (122).

Another problem, perhaps more important in practice, is the boundary layer on ring airfoils and ducted propellers. At angle of attack, the ring airfoil yields a comparatively simple model for investigations in three-dimensional boundary-layer theory which is interesting in itself (109, 113).

Lastly, one should not forget, that—from the point of view of pure mathematics—almost nothing has been proven rigorously in the three-dimensional theory of airfoil and propellers, not even in the linear theory. There is a wide field of open problems.

From a practical point of view, the dominating task is to check the existing theory by carefully designed experiments in order to find out if and where improvements are desirable. But this is not the concern of this review.

NOTATION

c	Duct (chord) length
$c_L = L/(\rho V^2 \pi R c)$	Lift coefficient
$c_{T_p} = 2T_p/(V^2 \pi R_p^2)$	Propeller thrust coefficient [In Sec. 4, $c_{T_p} = 2T_p/(\rho \pi R_p^4 \Omega^2)$]
G	Glauert integral operator
$g = \gamma/V$	Nondimensional vortex distribution
$g_n(\xi)$	n-th order Fourier coefficient of g
$h_n(\xi)$	
$J = V/\Omega R_p$	Propeller advance ratio
j, $j(r) = -\gamma_x/\gamma_\phi$	Pitch of helical vortices
L	Lift
N	Number of propeller blades
p	Static pressure
q	Source distribution
R	Radius of reference cylinder (usually = R_d)
R_d	Duct radius
R_p	Propeller radius

r	Radial coordinate
$r_m(x)$	Mean camber line
T	Thrust
T_p	Propeller thrust
$T_0, T_1, \ldots, T_m, \ldots$	Basic integral operators of ring-airfoil theory
$t(\xi)$	Nondimensional thickness distribution [thickness $= c \cdot t(\xi)$]
u, v, w	Axial, radial, and azimuthal induced velocity
V	Free-stream velocity
V_n	Normal component of free-stream velocity at profile
x	Axial coordinate
x_p	Axial propeller location
α_0	Angle of attack
$\alpha(\xi)$	Local angle of attack
$\Gamma, \Gamma(r)$	Circulation of propeller blades
γ	Ring vortex distribution
γ_x, γ_ϕ	Axial and azimuthal components of helical vortices
Δp	Pressure jump at propeller disk and slipstream surface
$\eta = \lambda(\xi - \xi') = (x - x')/R$	Argument of kernels in ring-airfoil theory (also $\eta = x/R$, see Fig. 5)
θ	"Glauert variable," $\xi = -\cos\theta$
$\lambda = c/(2R)$	Chord-diameter ratio of duct
$\mu = R_p/R_d$	Propeller tip clearance with respect to reference cylinder
$\xi = 2x/c$	Nondimensional axial coordinate; $\xi = -1(+1)$: leading (trailing) edge
ρ	Mass density
$\rho_m(\xi) = 2r_m(x)/c$	Nondimensional mean camber line

$\rho_m'(\xi) = \frac{d}{d\xi}\rho_m(\xi)$	"Camber" distribution
$\Phi = (R_\infty/R_T)^2$	Contraction ratio of propeller slipstream
Ω	Angular velocity of propeller

Subscripts

q, γ, g, ...	Induced by q, γ, g, ...
c, t	Due to camber, thickness
B, W	Referring to body, wing
T	At trailing edge
p, d	Referring to propeller, duct

A bar (e.g., $\bar{u}$) denotes the average of the limiting values at a jump discontinuity.

REFERENCES

General

1. Bagley, J.A., Kirby, N.B., and Mercer, J.P., "A Method of Calculating the Velocity Distribution on Annular Airfoils in Incompressible Flow," Aeronautical Research Council Tech. Report R&M 3146 (1961)

2. Barna, P.S., "Preliminary Aerodynamic Design Considerations of Axial Flow Fans," Engineering Experiment Station, Auburn University, Auburn, Alabama, Bulletin 50 (April 1965)

3. Borisov, B.I., "Determination of the Profile of Least Resistance of an Annular Wing," Foreign Tech. Division, Translation 63-397 Wright-Patterson Air Force Base, Ohio (June 1963)

4. Breslin, J.P., and Odenbrett, C.L., "Blade Frequency Harmonic Content of the Potential Wake of Single Screw Ships," Stevens Institute of Technology, Davidson Laboratory, Report 956 (April 1963)

5. Buehning, P.G., "On the Selection of Propeller Diameter and RPM for Optimum Performance of Nozzle Propellers," Accurate Products Co., Hillside, New Jersey, Misc. No. 1 (Nov. 1960)

6. Buehning, P.G., "Design of Nozzle Propellers," Accurate Products Co., Hillside, New Jersey, Contract NONR-2812(00), Technical Report 31 (April 1967)

7. Buhtz, P., "Vergleich zwischen freien Propellern und mit Kort-Düsen ummantelten Schiffsschrauben bei Dieselschleppern," of Hanse-Schiffahrt-Schiffbau-Hafen, No. 20 (1962)

8. Bussler, M., "Berechnung optimaler Schiffsdüsen nach der Theorie von Dickmann und Weissinger," Veröffentlichungen der Schiffbautechnischen Fakultät der Universität Rostock (1960)

9. Cahn, M.A., "The Design and Performance of Shrouded Propellers," Society of Automotive Engineers (Oct. 1962)

10. Castles, W., Jr., and Gray, R.B., "An Investigation of an Approach to the Problem of Determining the Optimum Design of Shrouded Propellers," Georgia Institute of Technology, TCREC 60-44 (May 1960)

11. Chen, C.F., "Final Study on the Feasibility Study of Supercavitating Propellers in Kort Nozzles," Hydronautics Inc. Tech. Note 005-5 (Sept. 1961)

12. Chen, C.F., "Feasibility Study of Supercavitating Propellers in Kort Nozzles—Phase II," Hydronautics Inc. Tech. Note 005-3 (April 1961)

13. Chen, C.F., "Shrouded Supercavitating Propellers," Fourth Symposium on Naval Hydrodynamics (Aug. 1962)

14. Chung, H.W., "A General Theory of 3-Dimensional Flow in Subsonic and Supersonic Turbomachines of Axial, Radial, and Mixed Flow Types," NACA TN 2604 (Jan. 1952)

15. Crater, W.D., and Mikelson, F.D., "Recent Development in the Propulsion of Surface Ships and Submarines by Means of Axial Flow Pumpjets," Mgt. Technology Inc. (Los Angeles), Operations Research Inc. (Santa Monica)

16. Cumming, J.D., "Research on Annular Nozzle Type Ground Effect Machine Operating Over Water Surface Configuration," University of California, Series 187, Issue 3 (Sept. 1963)

17. Dickmann, H.E., "Grundlagen zur Theorie ringförmiger Tragflügel (frei umströmte Düsen)," Ing. Arch. 11 (1940), pp. 36-52

18. Dyne, G., "A Method for the Design of Ducted Propellers in a Uniform Flow" (Publ. No. 62 of the Swedish State Shipbuilding Experimental Tank)

19. Dyne, G., "Dyspropellrar," Statens Skeppsprovningsanstalt, Allman Report No. 16 (1966)

20. Gertler, M., "The Prediction of the Effective Horsepower of Ships by Methods in Use at the David Taylor Model Basin," David Taylor Model Basin Report 567 (Dec. 1947)

21. Ginzel, I., "The Ducted Propeller," Admiralty Research Laboratory, Teddington, England, Report No. ARL/R5/G/HY/71 (May 1963)

22. Goodman, T., "The Tip Correction for Wind-Tunnel Tests of Propellers," J. Aeron. Sci. 23 (1956), pp. 1094-1098

23. Granville, P.S., "The Calculations of the Viscous Drag of Bodies of Revolution," David Taylor Model Basin Report 849 (July 1953)

24. Gutsche, F., "Düsenpropeller in Theorie und Experiment," Jahrb. Schiffbautechn. Ges., Vol. 53 (1959)

25. Hacques, G., and Malavard, P., "Problemes de la Surface Portante Annulaire Traités Par la Methode des Analogies Rheoelectriques," Scientifiques et Techniques de l'Air, No. 358 (March 1960)

26. Hale, M.R., "The Design of Ducted Impellers using a Vortex Line Analysis and an Optimizing Computer Technique," University of Adelaide, Report 65/2 (March 1965)

27. Hansen, E.O., and Cumming, R.A., "Experimental Pressure Distribution on the Duct of an ERG Pumpjet," David Taylor Model Basin Report 2133 (Jan. 1966)

28. Helmbold, H.B., "Range of Application of Shrouded Propellers," Fairchild Aircraft Division, Hagerstown, Maryland, Engineering Report No. 221-011 (1955)

29. Helmbold, H.B., "Compressibility Effect on a Shrouded Propeller," Fairchild Aircraft Division, Hagerstown, Maryland, Engineering Report No. R 221-012 (1955)

30. Henderson, R.E., MacMahon, J.F., and Wislicenus, G.F., "The Design of Pumpjets," State University of Pennsylvania, Naval Ordnance Research Lab. (July 1963)

31. Henderson, R.E., MacMahon, J.F., and Wislicenus, G.F., "A Method for the Design of Pumpjets," Pennsylvania State University, Ordnance Research Laboratory, Report No. NOw 63-0209-c-7 (May 1964)

32. Hoehne, V.O., and Monical, R.E., "A Method of Design of Shrouded Propellers," University of Wichita Report 213-8 (Oct. 1959)

33. Horn, F., "Beitrag zur Theorie ummantelter Schiffsschrauben," Jahrb. Schiffbautechn. Ges., Vol. 41 (1940)

34. Horn, F., and Amtsberg, H., "Entwurf von Schiffsdüsensystemen (Kortdüsen)," Jahrb. Schiffbautechn. Ges., Vol. 44 (1950)

35. Hunt, B.W., "Numerical Solution of an Integral Equation for Flow from a Circular Orifice," J. Fluid Mech. Vol. 31 (1968), pp. 361-377

36. Isay, W.H., "Der Schraubenpropeller nahe der freien Wasseroberfläche und im Flachwasser," Ing. Arch., Vol. 31 (1962), pp. 194-213

37. Isay, W.H., "Propellertheorie, Hydrodynamische Probleme," Kapitel II. Ringflügel und Düsenpropeller, Berlin-Göttingen-Heidelberg (1964)

38. Isay, W.H., "Zur Theorie Schräg Angeströmter Düsenpropeller," Schiffstechnik, Vol. 14 (1967), pp. 15-18

39. Isay, W.H., "Theoretische Grundlagen der Hydroakustik des Schraubenpropellers," Ing. Arch., Vol. 35 (1967), pp. 382-400

40. Isay, W.H., "Der Schraubenpropeller im Nachstrom eines Schiffsrumpfes," Schiffstechnik. Vol. 5 (1958), pp. 157-168

41. Kemp, N.H., "On the Lift and Circulation of Airfoils in Some Unsteady Flow Problems," J. Aero. Sci., Vol. 19 (1952), pp. 713-714

42. Küchemann, D., and Weber, J., "Aerodynamics of Propulsion," McGraw-Hill Book Co. (1963)

43. Kobylinski, L., "The Calculation of Nozzle Propeller Systems Based on the Theory of Thin Annular Airfoils with Arbitrary Circulation Distribution," International Shipbuilding Progress, Vol. 8 (Dec. 1961)

44. Kramer, J.J., Stockmann, N.O., and Bean, R.J., "Nonviscous Flow Through a Pump Impeller on a Blade-to-Blade Surface of Revolution," NASA TN D-1108 (Feb. 1962)

45. Laschka, B., "Über die Potentialtheorie von zylindrischen rotationssymmetrischen Flügeln (Ringflügeln) in kompressibler instationärer Unterschallströmung," Z. Flugwiss. 12 (1964), pp. 205-211

46. Lerbs, H.W., "Theoretical Considerations on Shrouded Propellers," David Taylor Model Basin Report C-543 (June 1953)

47. Lerbs, H.W., "Moderately loaded Propellers with a Finite Number of Blades and an Arbitrary Distribution of Circulation," Trans. SNAME 60 (1952), 73-177

48. Lerbs, H.W., "Ergebnisse der angewandten Theorie des Schiffspropellers," Jahrb. der Schiffbautechn. Ges., Vol. 49 (1955), pp. 163-206

49. Levine, P., "Incompressible Potential Flow About Axially Symmetric Duct Bodies," Wright Air Development Center Aeronautical Research Lab., WADC Tech. Note 57-287 (Aug. 1957)

50. Ludwieg, H., "Stabilität der Strömung in einem zylindrischen Ringraum," Z. Flugwiss. 8 (May 1960), pp. 135-140

51. Ludwieg, H., "Ergänzung zu der Arbeit: Stabilität der Strömung in einem zylindrischen Ringraum," Z. Flugwiss. 9 (1961), pp. 359-361

52. van Manen, J.D., "Ergebnisse systematischer Versuche mit Schiffsdüsensystemen," Jahrb. Schiffbautechn. Ges., Vol. 47 (1953) [also International Shipbuilding Progress 1 (1954)]

53. van Manen, J.D., "Recent Research on Propellers in Nozzles," Journal of Ship Research, Vol. I (July 1957)

54. van Manen, J.D., "Neuere Fortschritte in der Forschung über Düsenpropeller," Schiff und Hafen (1957), pp. 101-122

55. van Manen, J.D., and Superina, A., "The Design of Screw Propellers in Nozzles," International Shipbuilding Progress, 6 (March 1959)

56. van Manen, J.D., "Der Entwurf von Düsenschrauben," Schiff und Hafen, Jahrg. 11, Heft 2 (Feb. 1959)

57. van Manen, J.D., "Effect of Radial Load Distribution on the Performance of Shrouded Propellers," Royal Institute of Naval Architects, Vol. 104 (1962)

58. van Manen, J.D., and Oosterveld, M.W.C., "Analysis of Ducted Propeller Design," Transactions of the Society of Naval Architects and Marine Engineers, Vol. 74 (1966), pp. 522-562

59. Manontov, I.N., "Diagrammy dla Opredelenia Efpktivnosti Ustanovki Napravlauschikh Nasadok i Rascheta Grebnykh Vintov," Sudostroenie, No. 8 (Aug. 1959), pp. 9-11

60. Martensen, E., "Numerische Auflösung der Integralgleichung des Robinschen Problems für eine torusartige Berandung," Symposium, Provisional International Computation Centre (1960), pp. 131-150

61. Martensen, E., "Über eine Methode zum räumlichen Neumannschen Problem mit einer Anwendung für torusartige Berandungen," Acta Math., Vol. 109 (1963), pp. 76-135

62. McCormick, B.W., and Eisenhuth, J.J., "The Design and Performance of Propellers and Pumpjets for Underwater Propulsion," Rocket Society Meeting (Fall 1962)

63. McNay, D.E., "Study of Effects of Various Propeller Configurations on the Flow about a Shroud," Mississippi State College, Research Report 14 (Feb. (1958)

64. Meyerhoff, L., and Finkelstein, A.B., "On the Theories of the Ducted Shape for a Ducted Propeller," Polytechnic Institute of Brooklyn Dept. of Aeronautical Engineering and Applied Mechanics, PIBAL Report 484 (Aug. 1958)

65. Michalke, A., "Theoretische und experimentelle Untersuchung einer rotationssymmetrischen laminaren Düsengrenzschicht," Ing. Arch., Vol. 31 (1962)

66. Morgan, W.B., and Wrench, J.W., Jr., "Some Computational Aspects of Propeller Design," Methods in Computational Physics, Vol. 4, Academic Press, Inc., New York (1965), pp. 301-331

67. Moser, H.H., and Livingston, C.L., "Experimental and Analytic Study of the Ducted Fan and Fan-in Wing Hovering and Forward Flight," Massachusetts Institute of Technology Report 79-1 (ASTIA Doc. 201398) (Jan. 1959)

68. Pabst, O., "Calculation of Ducted Propellers," Focke-Wolfe Rep. G. DV. 09020 (1942)

69. Patraulea, N.N., "Annular Wings with Jet Flap," Aeromecanique, Published in Studii Si Crecetari de mecanica aplicata, Acad. R.P.R. (1961)

70. Pivko, S., "The Annular Aerofoil with Central Body and Propeller," Aerotechnical Inst., Beograd-Zarkovo, Yugoslavia (Nov. 1957)

71. Plaskowski, Z., "Concerning Ring Airfoils," Institute for Aerodynamics, ETH, Zurich (1953)

72. Rains, D.A., "Tip Clearance Flows in Axial Flow Compressors and Pumps," California Institute of Technology Report, Misc. 3 (June 1954)

73. Raspet, A., "The Ducted Propeller," Presented at the Aviation Conference, Dallas, Texas, 5-9 June 1960, of the American Society of Mechanical Engineers, Paper 60-AV-11

74. Reynolds, J.F., "Lifting-Surface Theory Applied to Isolated Ring Wings at Angle of Attack," Underwater Ordnance (Nov. 1963)

75. Ribner, H.S., "The Ring Airfoil in Nonaxial Flow," Journal of Aeronautical Sciences, Vol. 14 (1947), pp. 529-530

76. Riegels, F., "Die Strömung um schlanke, fast drehsymmetrische Körper," Mitteilungen des Max-Planck-Instituts für Strömungsforschung No. 5 (1952)

77. Roberts, A., "Annular Wings Simple Cowl and Fan," Aerodynamics Department, British Aircraft Corporation, MA-Rep. 4 (Sept. 1966)

78. Sacks, A.H., and Burnell, J.A., "Ducted Propellers — A Critical Review of the State-of-the-Art," Progr. in Aeronaut. Sci., Vol. 3 (1962), Pergamon Press, New York

79. Schatte, E., "Eine Methode zur Berechnung von Düsenpropellers," Schiff und Hafen (1956)

80. Siekmann, J., "Analysis of Ring Aerofoils of Elliptic Cross Section, Part 1: General Theory," J. Soc. Indust. Appl. Math., Vol. 11 (Dec. 1963)

81. Sinacori, J., and Lange, A., "Theoretical Investigation of Ducted Propeller Aerodynamics," TCREC Tech. Report 61-120, Vol. III (prepared by Republic

Aviation, Farmingdale, Long Island, for U.S. Army Transportation Research Command) (Sept. 1961)

82. Soloviev, U.I., and Churmack, D.A., "Marine Propulsion Devices," published by Military Publishing House, Ministry of Armed Forces, Moscow, USSR (1948). Translated by Rose Jermaier, Sci. Transl. Serv., University of Alabama, STS-101 (March 1951) (BuShips TR408)

83. Stewart, H.J., "The Aerodynamics of a Ring Airfoil," Quarterly of Applied Mathematics, Vol. II, No. 2 (1944), pp. 136-141

84. Stipa, L., "Experiments with Intubed Propellers," NACA TM-665 (Aug. 1931)

85. Tachmindji, A.J., "The Potential Problem of the Optimum Propeller with Finite Number of Blades Operating in a Cylindrical Duct," David Taylor Model Basin Report 1228 (July 1958)

86. Theodorsen, T., "Theoretical Investigation of Ducted Propeller Aerodynamics," prepared by Republic Aviation Corporation, Farmingdale, Long Island, for U.S. Army Transportation Research Command (Aug. 1960)

87. Theodorsen, T., and Nomicos, G., "Theoretical Investigation of Ducted Propeller Aerodynamics," TCREC Tech. Report 61-119, Vol. III (prepared by Republic Aviation, Farmingdale, Long Island, for U.S. Army Transportation Research Command) (Sept. 1961)

88. Tsakonas, St. and Jacobs, W.R., "Unsteady Lifting Surface Theory for a Marine Propeller of Low Pitch Angle with Chordwise Loading Distribution," Stevens Institute of Technology, Davidson Laboratory, Report 994 (Jan. 1964)

89. Tulin, M.P., "Supercavitating Propellers — Momentum Theory," Hydronautics Inc. Technical Report 121-4 (Sept. 1964)

90. Tulin, M.P., "Supercavitating Propellers History, Operating Characteristics, Mechanism of Operation," Hydronautics Inc. Technical Report 127-6 (June 1964)

91. Turbal, V.K., "Effect of the Clearance Between the Blade and the Nozzle Wall on the Efficiency of the System and the Optimum Contour of the Propeller Blade," Sbornik Statey po Gidrodinamike Sudna (Symposium of Articles on Ship Hydrodynamics) — Part II, Sudostroyeniye, Publishing House (1965), pp. 55-74

92. Vollbrecht, E., "Betrachtungen über Methoden zum Entwurf optimaler Düsenschrauben," Schiffstechnik, Vol. 6 (1959)

93. Weissinger, J., "Einige Ergebnisse aus der Theorie des Ringflügels in incompressibler Strömung," International Series on Aeronautical Sciences and Space Flight, Vol. 2 (1958)

94. Whittley, D.C., "Simplified Mechanics of the Lifting Fan," Aircraft Engineering, Vol. 34, No. 398 (April 1962)

95. Wiegel, et al., "Research on Annular Nozzle Type Ground Effect Machine Operating over Water — Operation over Waves," University of California, Series 197, Issue 7 (1963)

96. Wislicenus, G.F., "The Design of a Pumpjet for a Coaxial Body of Revolution," State University of Pennsylvania, Ordnance Research Laboratory TM-5.2410-13 (Dec. 1961)

97. "An Investigation of a Digital Computer Method of Determining the Optimum Design Parameter of Shrouded Propellers," TCREC Tech. Report 61-124 (Oct. 1961)

98. "Survey of Propulsive Devices for Merchant Marine Application," Stevens Institute of Technology Report 874 (Oct. 1961)

99. "On the Aerodynamic Design of Propellers and Duct Systems for Ground Effect Vehicles" (prepared by Kellet Aircraft), ASTIA Doc. No. 174159 (Jan. 1962)

100. "Determination of Optimized Propellers for Ground Effect Machines," Transportation Research Command, TRECOM. Tech. Report 63-16 (Aug. (1963)

101. Zierep, J., "Auftrieb und Widerstand langer Ringflügel in Überschallströmung," Jahrb. d. WGL (1957), pp. 83-88

Publications from Karlsruhe University

102. Dickmann, H.E., and Weissinger, J., "Beitrag zur Theorie optimaler Düsenschrauben (Kortdüsen)," Jahrb, Schiffbautechn. Ges. 49 (1955), pp. 253-305

103. Weissinger, J., "Zur Aerodynamik des Ringflügels. I. Die Druckverteilung dünner, fast drehsymmetrischer Ringflügel in Unterschallströmung," DVL-Bericht No. 2 (1955)

104. Weissinger, J., "Zur Aerodynamik des Ringflügels. II. Die Ruderwirkung," DVL-Bericht No. 39 (1957)

105. Weissinger, J., "Zur Aerodynamik des Ringflügels. III. Der Einfluss der Profildicke," DVL-Bericht No. 42 (1957).

106. Weissinger, J., "Zur Aerodynamik des Ringflügels. IV. Ringflügel mit Zentralkörper," DVL-Bericht No. 140

107. Weissinger, J., "The Ring Airfoil Deflected Control Surface in Steady Incompressible Flow," Contract AF 61 (514)-904, European Office, ARDC, ASTIA Doc. No. 115097 (Jan. 1957)

108. Weissinger, J., "The Influence of Profile Thickness on Ring Airfoils in Steady Incompressible Flow," Contract AF 61(514)-904, European Office, ARDC (Jan. 1957)

109. Weissinger, J., "Remarks on Ring Airfoil Theory," Contract AF 61(514)-1207, European Office, ARDC, ASTIA Doc. No. 154127 (Jan. 1958)

110. Weissinger, J., "Ring Airfoil Theory (Problems of Interference and Boundary Layer)," Contract AF 61(514)-1207, European Office, ARDC, ASTIA Doc. No. 211809 (Jan. 1959)

111. Weissinger, J., "Einige Ergebnisse aus der Theorie des Ringflügels in inkompressibler Strömung," Advan. Aeron. Sci. 2 (1959), pp. 798-831

112. Weissinger, J., "Theoretical Investigations on Ring Airfoils," Contract AF 61(514)-1207, European Office, ARDC (Jan. 1960)

113. Wiedemer, K., "Ein Beitrag zur Theorie der Düsenschrauben (Kortdüsen)," Diss. Techn. Hochschule Karlsruhe, 1960

114. Nickel, K., "Über driedimensionale Grenzschichten an Ringflügeln," ZAMM 40 (1960), pp. T142-T143

115. Brakhage, H., "Bemerkung zur numerischen Behandlung und Fehlerabschätzung bei singularen Integralgleichungen," ZAMM 41, Sonderheft der GAMM-Tagung (1961), pp. T12-T14

116. Bollheimer, L., "Bestimmung von Zirkulationsverteilung, Durchflusszahl und Düsensogziffer unendlich dünner Düsenschrauben," DVL-Bericht No. 186 (1962)

117. Finkeldei, H., "Experimentelle Untersuchungen an Düsenschrauben," Diss. Techn. Hochschule Karlsruhe, 1963

118. Wiedemer, K., "Der Düsenpropeller bei veränderlicher Belastung," Schiffstechnik 10 (1963), pp. 1-7

119. Rautmann, R., "Ein Existenz- und Eindeutigkeitssatz für ein nichtlineares Randwertproblem der Turbinentheorie," Diss. Techn. Hochschule Karlsruhe, 1964. Abstract in Z. Ang. Math. Mech. 44 (1964), pp. 56-61

120. Bollheimer, L., "Ein Verfahren zur Berechnung der Durchflusszahl, der Düsensogziffer sowie der Geschwindigkeitsverteilung an der Kontur mässig dicker Düsenschrauben," DVL-Bericht No. 277 (1964)

121. Rautmann, R., "Strenge Lösungen eines Strömungsproblems in Axialturbinen," Z. Ang. Math. Mech. 45 (1965), pp. 167-171

122. Bollheimer, L., "Neuere Beiträge zur Theorie des Düsenpropellers," Diss. Techn. Hochschule Karlsruhe, 1966

123. Maass, D., "Zur Theorie des Ringflügels bei ungleichförmiger Anströmung," Diss. Techn. Hochschule Karlsruhe, 1967

124. Weissinger, J., "Theorie des Tragflügels in exponentieller Scherströmung," to appear in Ing. Arch. 1968. Condensed from: Nonuniform steady flow of an ideal fluid past airfoils, Part I: Report No. 515, Part II: Report No. 536, Part III: Report No. 571, Mathematics Research Center, U.S. Army, Madison, Wisconsin (1964-1965)

125. Bollheimer, L., "Ein Beitrag zur Theorie der Düsenpropeller," to appear in Schiffstechnik, Vol. 15 (1968)

Publications from NSRDC

126. Chaplin, H.R., "Theory of the Annular Nozzle in Proximity to the Ground," David Taylor Model Basin Report Aero 923 (July 1957)

127. Chaplin, H.R., "Effect of Jet Mixing on the Annular Jet," David Taylor Model Basin Report Aero 953 (Feb. 1959)

128. Morgan, W.B., "Theory of Ducted Propeller with a Finite Number of Blades," University of California, Institute of Engineering Research, Berkeley (May 1961)

129. Morgan, W.B., "Theory of the Annular Airfoil and Ducted Propeller," Fourth Symposium on Naval Hydrodynamics (Aug. 1962)

130. Chaplin, H.R., "A Method for Numerical Calculation of Slipstream Contraction of a Shrouded Impulse Disc in the Static Case with Application to Other Axisymmetric Potential Flow Problems," David Taylor Model Basin Report 1857 (June 1964)

131. Morgan, W.B., and Caster, E.B., "Prediction of the Aerodynamic Characteristics of Annular Airfoils," David Taylor Model Basin Report 1830 (Jan. 1965)

132. Morgan, W.B., and Voigt, R.G., "The Inverse Problem of the Annular Airfoil and Ducted Propeller," David Taylor Model Basin Report 225i (Sept. 1966)

133. Voigt, R.B., "On a Numerical Solution of an Integral Equation with Singularities," Mathematics of Computation (Jan. 1966)

134. Caster, E.G., "A Computer Program for Use in Designing Ducted Propellers," Naval Ship Research and Development Center Report 2507 (Nov. 1967)

Publications from THERM

135. Sonnerup, B.U.O., "Expression as a Legendre Function of an Elliptic Integral Occurring in Wing Theory," THERM, Inc., TAR-TN 59-1 (Nov. 1959)

136. Megrue, J., "A Brief Survey of Ducted Propeller Literature," THERM, Inc., TAR-MEMO 59-2 (Nov. 1959)

137. Sluyter, M.M., "A Computational Program and Extended Tabulation of Legendre Functions of Second Kind and Half Order," THERM, Inc., TAR-TR 601 (Aug. 1960)

138. Supplement to TAR-TR 601, "Table of Legendre Function of Second Kind and Half Order $Q_{-1/2}(z)$."

139. Ordway, D.E., Sluyter, M.M., and Sonnerup, B.U.O., "Three-Dimensional Theory of Ducted Propellers," THERM, Inc., TAR-TR 602 (Aug. 1960)

140. Ritter, A., and Ordway, D.E., Editors, Proceedings of the Seminar on "General Airscrew Applications to VTOL Propulsion," Ithaca, N.Y., May 16 and 17, 1961; see also, J. Am. Helicopter Soc., Vol. 7 (July 1962), pp. 3-8

141. Hough, G.R., "A Feasibility Study on the Measurement of the Time-Dependent Shroud Pressure of a Ducted Propeller," THERM, Inc., TAR-TR 612 (Aug. 1961)

142. Ordway, D.E., and Greenberg, M.D., "General Harmonic Solutions for the Ducted Propeller," THERM, Inc., TAR-TR 613 (Aug. 1961)

143. Ritter, A., and Ordway, D.E., "Ducted Propeller and Related Airscrew Studies at TAR," THERM, Inc., TAR-TR 614 (Aug. 1961)

144. Ordway, D.F., Hough, G.R., and Kaskel, A.L., "The Method of Computing Performance of a Ducted Propeller With Finite Blading and Viscosity Effects," THERM, Inc., TAR-TR 623 (March 1962)

145. Ritter, A., and Ordway, D.E., "Some Results of Finite-Bladed Ducted-Propeller Theory for VTOL," Aerospace Engineering, Vol. 21 (July 1962), pp. 54-55

146. Ordway, D.E., "Ad Hoc Committee Meeting Report on Shrouded Propeller Design," Fourth Symposium on Naval Hydrodynamics, Washington, D.C., Aug. 27-31, 1962

147. Ordway, D.E., Hough, G.R., and Kaskel, A.L., "Three-Dimensional Aerodynamics of Ducted Propellers," Fifth European Aeronautical Congress, Venice, Italy, Sept. 12-15, 1962

148. Erickson, J.C., Hough, G.R., Kaskel, K.L., Ordway, D.E., and Ritter, A., "The Calculation of the Propeller Inflow for a Specific Ducted Propeller," THERM, Inc., TAR-TR 6210 (Oct. 1962)

149. Hough, G.R., "The Aerodynamic Loading on Steamlined Ducted Bodies," THERM, Inc., TAR-TR 625 (Dec. 1962); see also, Proceedings of the Eighth Midwestern Mechanics Conference, Cleveland, Ohio, April 1-3, 1963, "Developments in Mechanics," Pergamom Press, pp. 340-357, 1965

150. Hough, G.R., "Ducted Propeller Performance Calculations for X-22A VTOL Research Aircraft," THERM, Inc., TAR-TR 634 (Aug. 1963)

151. Kaskel, A.L., Ordway, D.E., Hough, G.R., and Ritter, A., "A Detailed Numerical Evaluation of Shroud Performance for Finite-Bladed Ducted Propellers," THERM, Inc., TAR-TR 639 (Dec. 1963)

152. Hough, G.R., and Ordway, D.E., "The Generalized Actuator Disk," THERM, INC., TAR-TR 6401 (Jan. 1964); see also, Proceedings of the Second Southeastern Conference on Theoretical and Applied Mechanics, Atlanta, Georgia, March 5-6, 1964, "Developments in Theoretical and Applied Mechanics," Vol. II, Pergamom Press, pp. 317-336, 1965

153. Greenberg, M.D., and Ordway, D.E., "The Ducted Propeller in Static and Low-Speed Flight," THERM, Inc., TAR-TR 6407 (Oct. 1964); see also, "Low-Speed Aerodynamics of the Ducted Propeller," Zietschrift für Flugwissenschaften (May 1965)

154. Hough, G.R., and Ordway, D.E., "The Steady Velocity Field of a Propeller with Constant Circulation Distribution," J. Am. Helicopter Soc., Vol. 10 (April 1965), pp. 27-28

155. Ordway, D.E., "Summary of Recent Ducted Propeller Developments at TAR, Inc.," Comments made at Discussion Session on Aerodynamics of Ducted Propellers, CAST Annual General Meeting, Vancouver, Canada, May 17 and 18, 1965

156. Kaskel, A.L., and Greenberg, M.D., "A Detailed Numerical Evaluation of Shroud Performance for Finite Bladed Ducted Propellers, Addendum: Computation of Shroud-Induced Axial Velocity," THERM, Inc., TAR-TR 6508 (Oct. 1965)

157. Greenberg, M.D., Ordway, D.E., and Lo, C.F., "A Three-Dimensional Theory for the Ducted Propeller at Angle of Attack," THERM, Inc., TAR-TR 6509 (Dec. 1965)

158. Hough, G.R., and Kaskel, A.L., "A Comparison of Ducted Propeller Theory with Bell X-22A Experimental Data," THERM, Inc., TAR-TR 6510 (Oct. 1965)

Publications from VIDYA

159. Kriebel, A.R., Sacks, A.H., and Neilsen, J.N., "Theoretical Investigation of Dynamic Stability Derivatives of Ducted Propellers," Vidya Research and Development, Palo Alto, Calif., Vidya-Report No. 63-95 (1963)

160. Kriebel, A.R., "Theoretical Investigation of Static Coefficients, Stability Derivatives and Interference for Ducted-Propellers," Vidya Research and Development, Palo Alto, Calif., Vidya Report No. 112 (1964)

161. Kriebel, A.R., "Interference between a Hull and a Stern-Mounted Ducted Propeller," Vidya Research and Development, Palo Alto, Calif., Vidya Report No. 161 (1964)

162. Kriebel, A.R., and Mendenhall, M.R., "Interference Between a Hull and a Stern-Mounted Ducted Propeller," Vidya Report 204 (Oct. 1965)

163. Kriebel, A.R., and Mendenhall, M.R., "Predicted and Measured Performance of Two Full-Scale Ducted Propellers," ITEK Corporation, Palo Alto, Calif. (prepared for Ames Research Center), NASA Contractor Report 578 (Sept. 1966)

164. Mendenhall, M.R., Kriebel, A.R., and Spangler, S.B., "Theoretical Study of Ducted Propeller Blade Loading, Duct Stall, and Interference," Vidya Report 229 (Sept. 1966)

Addendum

Worobel, R., and Peracchio, A.A., "Shrouded Propeller Test Program Method Development," Hamilton Standard Engineering Report No. HSER 4776, Jan. 1968

* * *

DISCUSSION

Gilbert Dyne
The Swedish State Shipbuilding Experimental Tank
Gothenburg, Sweden

The authors are to be commended for giving a very systematic and thorough review of the theories of ducted propellers, within the limitations imposed. I would, however, like to make some comments concerning some details of the theories described.

In all theories reviewed by the authors, the duct shape (or the source and vortex distributions of the duct) is determined by satisfying the boundary condition at the duct. When we started to design ducted propellers six years ago at the tank in Gothenburg, we also used this method. After some time, however, we discovered, that the boundary-condition method in some cases could lead to very unrealistic results. This was especially true for heavily loaded ducted propellers, when the slipstream deviated from the cylindrical form, and the blade circulation was zero at the blade tips. The reason was found to be that a

radial velocity component was lost, when the ring vortices representing the propeller slipstream were placed along cylinders with constant radii and not along the real streamtubes. Since the constant-radii assumption influences the propeller-induced axial velocities only in a slight degree, we now prefer to use the continuity law, when we determine the shape of the duct.

Figure D-1 shows that the difference between the two methods can be considerable. The four ducted propellers in Fig. D-1 all have the same design total thrust $C_T \cong 4$, while the duct thrust is varied systematically between 0 and 45%.

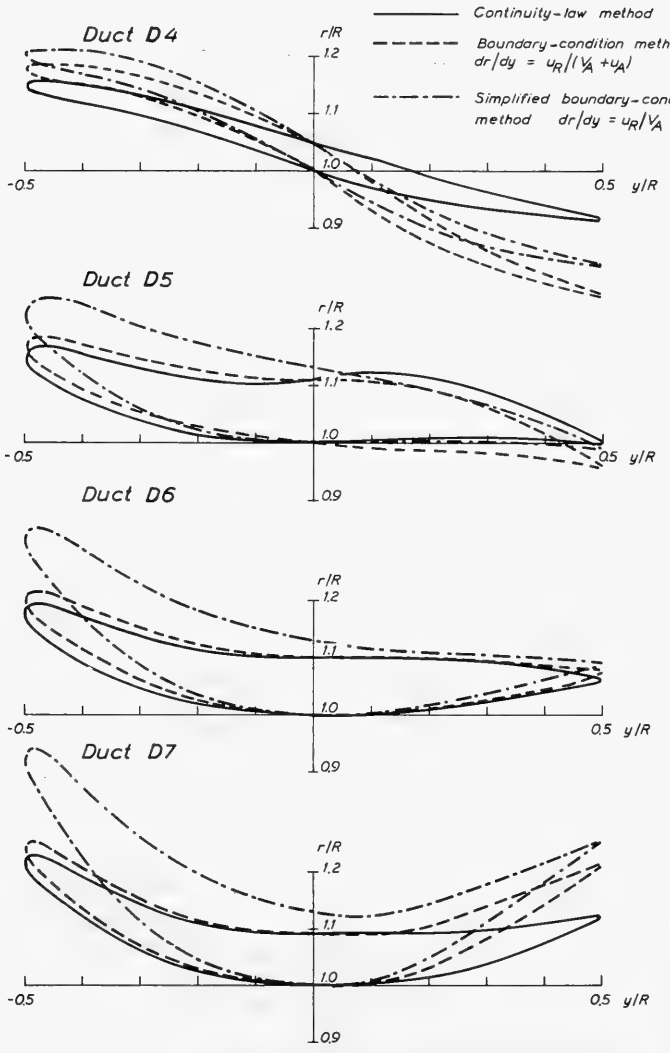

Fig. D-1 - The shape of the duct calculated by different methods

In the fore part of the duct, the difference is about the same for all ducts. In the rear part, however, where the influence of the propeller wake is considerable, very large differences are obtained. Duct No. D4 is neutral, which means that it coincides with the mean slipstream of a conventional propeller. The radius of the slipstream must in this case decrease continuously from 1.0 at the propeller to 0.86 in the ultimate wake, where the propeller-induced velocities are about twice that at the propeller. If the continuity law is used to determine the shape of the duct the radius of duct D4 will be 0.92 at the trailing edge, while corresponding value obtained with the boundary condition method is 0.80 — a quite unrealistic result.

Figure D-1 also illustrates a fact enforced by the authors — that it is not advisable to ignore the induced axial velocity in comparison to the advance velocity, when satisfying the boundary condition. As seen quite different camber and thickness distributions are obtained with the complete and the simplified boundary condition equations.

The authors state in their final remarks that "it might be desirable to drop the assumption of slenderness for the propeller blades." As described in SSPA publication no. 62/18/, our design method includes also lifting surface calculations. Figure D-2 shows an example of the results obtained. Starting from the effective camber distribution, the camber correction due to the propeller is calculated according to the method by Pien. An additional correction caused by the mean vorticity of the duct is then determined. In the present case the camber correction due to the duct generally counteracts the correction caused by the propeller.

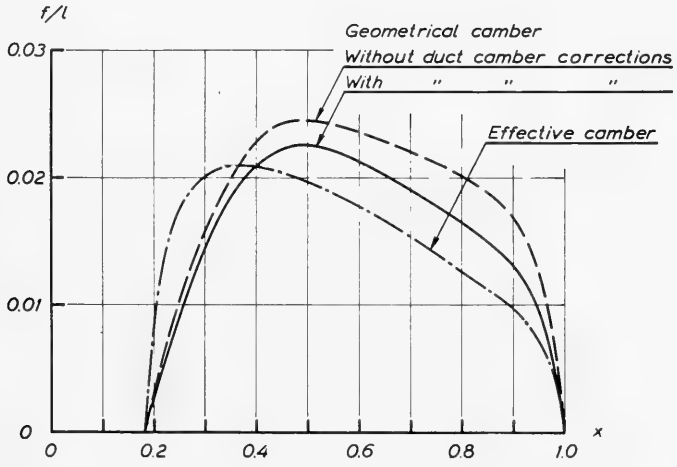

Fig. D-2 - Radial distribution of maximum camber of blade profiles. Ducted propeller P1315 D6 (SSPA publication No. 63)

* * *

REPLY TO THE DISCUSSION

J. Weissinger and D. Maab

Similar difficulties (e.g., crossing of streamlines) in using the boundary-condition method have also been observed by Dickmann and Weissinger during their computations. Therefore, in (102), the figures showing the streamlines inside the duct were calculated by means of the stream function which expresses the law of continuity. If an iteration procedure is applied, both methods should give the same results. An iterated-boundary-condition method has been used by Wiedemer (113), and Fig. 16 above shows that the duct profile can be changed considerably by iteration.

It does seem to be a question if the changes are also as great in the direct problem, i.e., if the flow field has to be determined for a given duct shape. From Bollheimer's results (116), there is some indication that the location of the ring vortices does not matter so much, at least for the over-all characteristics.

As long as we do not know bounds for the errors caused by the approximations (and they are unknown even in two-dimensional airfoil theory), we must rely on intuition and numerical experience in judging the accuracy of a method. The experience brought forward in the discussion is highly appreciated by the authors.

* * *

STUDIES OF THE APPLICATION OF DUCTED AND CONTRAROTATING PROPELLERS ON MERCHANT SHIPS

Hans Lindgren, C.-A. Johnsson and Gilbert Dyne

The Swedish State Shipbuilding Experimental Tank (SSPA)
Göteborg, Sweden

ABSTRACT

The paper starts with a survey of the trends in the development of modern merchant ships and how these trends have influenced propeller loadings and propulsive characteristics. Earlier studies on the application of ducted and contrarotating propellers are summarized and some of the SSPA research activities in these fields are presented. The SSPA design methods for ducted and contrarotating propellers are outlined and some experimental verifications in uniform flow are discussed. Optimum propeller efficiencies, diameters and essential geometric properties are given for different propeller loadings.

Results of comparisons between conventional, ducted and contrarotating propellers applied to a 150 000 TDW tanker as well as conventional and contrarotating propellers on a 12 000 TDW container vessel project are reported. The comparisons are based on open-water and self-propulsion tests as well as on cavitation tunnel tests in uniform flow and irregular wake distributions. Some concluding remarks and a scheme for further investigations are given at the end of the paper.

1. INTRODUCTION

The recent, explosive development of ship size, speed, and engine power available for the powering of merchant ships, has been accompanied by increased propulsion problems. Questions concerning efficiency, cavitation, and vibration have become highly important. About 15 years ago there was a clear trend towards single-screw propulsion with diesel engines of low number of revs. The development during the last 10 years has caused increased interest in very high engine powers and thus actualized multiple-engine arrangements and, for large tankers, still lower number of revs. In this connection also, different, for merchant-ship propulsion, less conventional propeller arrangements have been discussed. Below are presented the results of an investigation of the application of conventional, ducted, and contrarotating propellers on merchant ships, carried out at the Swedish State Shipbuilding Experimental Tank (SSPA).

The development for tanker ships has been characterized primarily by increased size, increased block coefficient, and diminishing length-draught ratio. The speed has essentially remained unaltered. For dry cargo ships, the size has not changed so radically, and the block coefficient has tended to decrease.

The maximum speed has increased considerably. For both types of ships, engine power has been doubled many times over.

For propellers, this development has caused remarkable changes in loading conditions and cavitation numbers (Fig. 1). The upper left corner of the diagram indicates the cavitation-free region for SSPA 5.60 propellers (1) in homogeneous flow. For tanker-ship propellers the danger for cavitation problems has increased due to increased load coefficients

$$\left(K_T/J^4\right)^{1/4} = \left(T\, n^2/\rho V_A{}^4\right)^{1/4} ,$$

while for dry-cargo-ship propellers decreased cavitation numbers have increased the cavitation problems. The trend towards higher propeller load for the tankers means decreased propeller efficiency, while for cargo-ship propellers limited draft, and thus limited propeller diameter, may cause similar effects. Figure 2 exemplifies the situation. In this diagram a scale of B_p is also included.

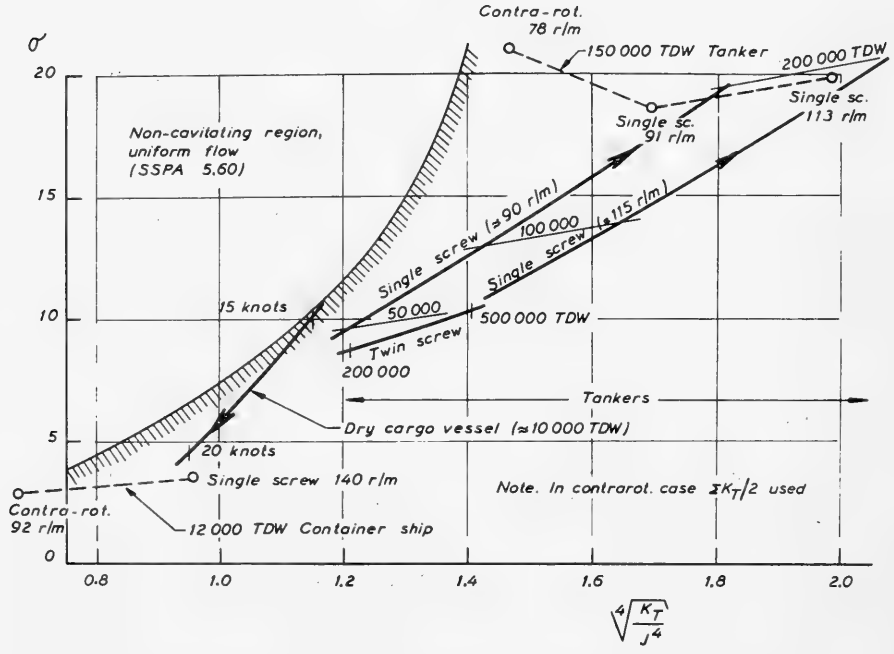

Fig. 1 - Cavitation number for propellers. Trend curves.

2. EARLIER SELF-PROPULSION STUDIES

A great number of reports and papers presented in different modern publications deal with the propulsion of merchant ships with contrarotating and ducted

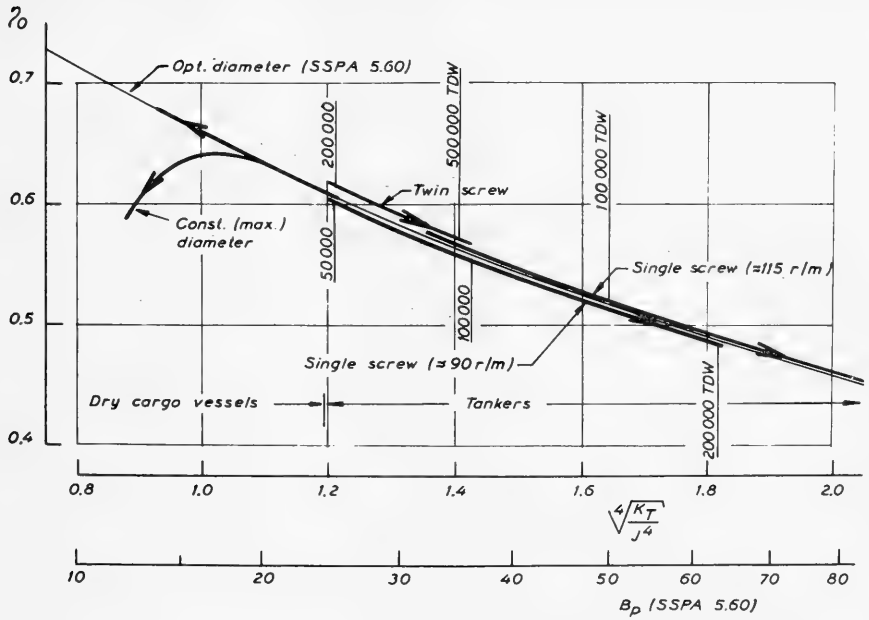

Fig. 2 - Propeller open-water efficiency. Trend curves.

propellers. It is interesting to note that only a very few of these reports include results based on self-propulsion experiments.

In most cases only theoretical hypotheses are presented, and in some cases open-water test results are included. Due to the complexity of the problem and to the difficulty in defining and separating different propulsive factors, complete self-propulsion experiments are, however, required for a final comparison between different propeller alternatives.

2.1. Contrarotating Propellers

Very extensive experiments with alternative propulsive arrangements have been carried out with the American 106 000 TDW tanker project "Manhattan" (2, 3). The investigation includes conventional single- and twin-screw propulsion, tandem propellers, and overlapping propellers. It also includes the only complete experiments with contrarotating propellers hitherto published. These self-propulsion test results have been condensed in Fig. 3, where the propeller shaft power for the different propeller arrangements has been plotted against propeller rate of revolutions. For reference, an approximate line representing conventional single-screw propulsion at different number of revs. has been calculated. The results indicate that for this project the contrarotating alternative is the most favourable, whilst the extreme 9-bladed propeller required the highest shaft power. The gain in shaft power obtained with the contrarotating system

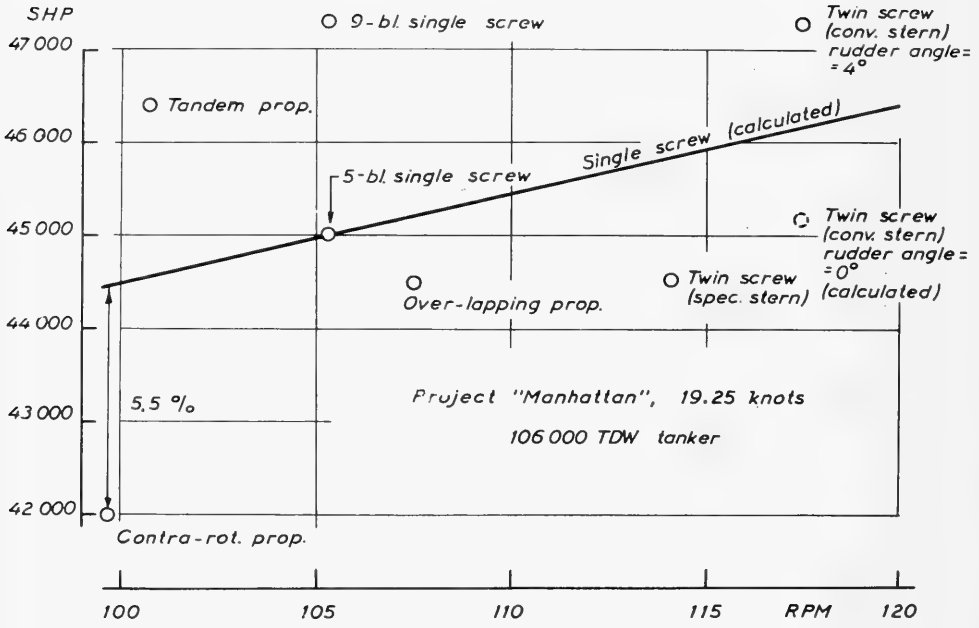

Fig. 3 - Condensed results from self-propulsion tests with "Manhattan" (2)

was about 5.5%, compared with a conventional single-screw arrangement at the same number of revs. It should be mentioned that the load coefficient $(K_T/J^4)^{1/4}$ for the contrarotating case was about 1.0, which is a fairly low value for a tanker project.

In this connection it is necessary to state that it is at present impossible to make any quite fair comparison between different propeller alternatives. Such a comparison must be based in some cases on constant propeller diameter and in some cases on constant number of revs. or something between. This will be discussed in Sec. 6. The most important problem is, however, that a fair comparison requires that for all propellers the margin against different disadvantages due to cavitation is the same and that in no case are dangerous vibratory forces introduced. Lack of reliable criteria for cavitation erosion for different kinds of propellers as well as criteria for dangerous vibratory forces makes the comparisons questionable in most cases.

Some of the self-propulsion test results with contrarotating propellers presented in Sec. 6 have been reported earlier (4). These preliminary tests indicated that the contrarotating propeller arrangement in some cases was very favourable from the point of view of efficiency, especially for slender types of ships.

2.2. Ducted Propellers

Results of self-propulsion tests with ducted propellers on large merchant ships have been presented by van Manen from NSMB, Wageningen (5), Minsaas from SMT, Trondheim (6) and English from NPL, Feltham (7).

At NSMB, tests have been carried out with three different tanker ship projects, 32,500 TDW, 48,500 TDW, and 90,000 TDW (5) For each project a conventional stern arrangement fitted with conventional propellers was compared with a Hogner-type stern arrangement fitted with ducted propellers. The results indicated that, for all the cases, the ducted propeller alternative was superior from the point of view of efficiency. The shaft power reduction was about 5%, 3%, and 6%, respectively, for the three projects in loaded conditions at a speed corresponding to trial speed.

In (8) van Manen has presented a diagram based on the results of self-propulsion tests with about 15 tanker models and results of systematic open-water tests with ducted propellers. This diagram indicates that, for 30 000 SHP and 100 RPM, the power reduction due to the introduction of ducted propellers is

4 - 7% for 50 000 TDW,
7 - 9% for 100 000 TDW,
9 - 12% for 150 000 TDW.

At Skipsmodelltanken in Trondheim, an extensive program of tests with ducted propellers on large tankers is under way. Some preliminary tests (6) with a 100 000 TDW tanker resulted in a power reduction of about 12% at 110 RPM, compared with a conventional propeller with the same number of revs.

Some tests with a 150,000 TDW tanker, fitted with a ducted propeller, carried out at NPL, have been presented in (7). Unfortunately, the report does not include any comparison with a ship with conventional propulsion. It is only stated that "the results show that a very high propulsive performance (QPC) has been achieved. This is similar to the findings of van Manen...."

Common to all the reports mentioned above is that no attempt has been made to analyse the results nad present components of the propulsive factors.

3. CONTRAROTATING PROPELLERS, THEORETICAL BACKGROUND AND EXPERIMENTAL VERIFICATION

3.1. Design Method

The results with contrarotating propellers, included in the present report, have all been obtained with propellers designed according to the same method. This method is essentially the same as that of (9) and (10), i.e., a development of Lerbs' method. Below are listed in the main differences between the method used in the present investigation and the original method of Lerbs (9) and the refinements according to Morgan, outlined in (10).

(1) Morgan and Lerbs use the pitch distribution for an equivalent propeller as input data and calculate the circulation distribution. In our scheme the circulation distribution for the equivalent propeller is used as input data.

(2) Morgan and Lerbs use Lerbs' induction-factor method when calculating the relation between the circulation and the induced velocities. In our scheme the modified induction factor method proposed in (11) is used. The pitch angles assumed for the free vortices, when determining the induction factors, are those of an equivalent propeller, as defined in (10).

(3) The interference velocities between the propellers are defined in (9) and (10) as

$$u_{ai1} = u_{as2} \quad f_{a2} \ (1 - g_{a2}) \ ,$$

$$u_{ti1} = 0 ,$$

$$u_{ai2} = u_{as1} \quad f_{a1} \ (1 + g_{a1}) \ ,$$

$$u_{ti2} = 2u_{ts1} \ f_{t1} \ (1 + g_{t1}) \ ,$$

where u_{as} and u_{ts} are axial and tangential self-induced velocities, f_a and f_t are factors for obtaining circumferential average of interference velocities, and g_a and g_f are factors for obtaining effect of axial distance on interference velocities.

By using Stokes' law, Lerbs derived

$$f_{t1} = \frac{G}{2x \ \frac{u_t}{V_A}} \qquad (1)$$

and introduced the following approximation:

$$f_{a1} \cong f_{a2} \cong f_{t1}$$

In our scheme the additional approximation

$$f_{t1} \cong \mathcal{K} \ (x, \ \lambda_i) \ ,$$

where $\mathcal{K}$ = Goldstein factor has been used in order to facilitate the procedure of convergence. If Eq. (1) is used instead, very large values are obtained for small values of u_t, which tends to upset the calculation procedure.

For g_a, Lerbs obtained values by replacing each propeller by a uniformly loaded sink disk. Tachmindji (12) later derived new values by replacing the propellers by a succession of ring vortices, whose strength varies with propeller

radius, thereby assuming optimum circulation distribution. These values were used by Morgan. In our scheme Lerbs' original values have been used, as the improvement obtained by using the values of Tachmindji seemed to be doubtful for the circulation distributions normally used in our calculations. Instead, a modified version of the computer program, which is now under work, will contain a calculation of these factors for arbitrary circulation distributions.

(4) The calculations are carried out for corresponding radii for the forward and aft propellers as defined by Lerbs:

$$r_2 = r_1(1 - \delta_r) \ , \tag{2}$$

where r_1 is the local radius of the forward propeller, r_2 is the corresponding local radius for aft propeller, and δ_r is the contraction of streamline.

For calculating the contraction δ_r Lerbs applied the equation of continuity to each annular element. By introducing Eq. (2) and neglecting second-order terms, a linear differential equation was obtained for δ_r, the solution of which is a definite integral (see (9) or (10)). According to the authors' experience, this way of calculating the contraction is not accurate enough and in our scheme the contraction is obtained by direct numerical integration. Thereby no simplifications are necessary. The diameter D_2 of the aft propeller is determined, as by Lerbs and Morgan, by the relation

$$D_2 = D_1(1 - \delta_1) \ , \tag{2a}$$

where D_1 is the diameter of forward propeller and $\delta_1 = \delta_r$ at the blade tips.

(5) What has been said above applies to the lifting-line calculations. After the completion of these calculations lifting-surface calculations are carried out according to a method based on Pien's approach (13, 14), giving corrections on camber and pitch. Finally, an approximate correction of the pitch for thickness effect is added (14). In the lifting-surface calculations and the calculations of the thickness effect, the mutual interference of the propellers is neglected.

3.2. Systematic Series of Contrarotating Propellers

For checking the design method and providing figures of the possible efficiencies, a systematic series consisting of four sets of contrarotating propellers was designed, manufactured, and tested in open-water condition in the SSPA cavitation tunnel. The propellers were fitted with adjustable blades. Some of the important design data of the propellers are given in Table 1, together with the pitch ratios investigated with the different sets. Further, the blade form, pitch distributions, and radial distributions of maximum camber of the blade sections of the propellers are shown in Figs. 4-6. The results of the open-water tests with the four propeller sets at the design pitch are compared with the computed propeller characteristics for the design point in Table 2. In Fig. 7 the difference of number of revs. between calculation and experiment are shown for the four propeller sets, together with the corresponding results obtained

Table 1
Important Design and Test Data for Systematic Series of Contrarotating Propellers

Common design data								
Design value of ΣK_T				ΣK_T = 0.38				
Number of blades, forward propeller				z = 4				
Number of blades, aft propeller				z = 5				
Blade area ratio, forward propeller				A_D/A_0 = 0.4				
Blade area ratio, aft propeller				A_D/A_0 = 0.5				
Hub diameter (forward propeller)				x_H = 0.186				
Mean line of blade sections				NACA a = 0.8				
Thickness distribution of blade sections				NACA 16				
Diameter of forward model propeller				D = 0.25 m				
	Forward	Aft	Forward	Aft	Forward	Aft	Forward	Aft
Propeller No.	P1254	P1255	P1358	P1359	P1356	P1357	P1252	P1253
No. in diagrams	1		2		3		4	
Design J	0.35		0.5		0.7		1.02	
Diam. reduct. of aft prop. in %	10.9		8.8		6.5		4.2	
Design pitch ratio P/D at 0.7R. (D = forward and aft prop. diam., respectively)	0.893	1.192	0.972	1.199	1.104	1.275	1.360	1.465
Additional pitch ratios tested	0.893	1.310	0.972	1.32	1.104	1.400	1.360	1.610
	.893	1.070	.972	1.08	1.104	1.150	1.360	1.320
			.893	1.192	1.360	1.465		
					.972	1.199		
					.893	1.192		

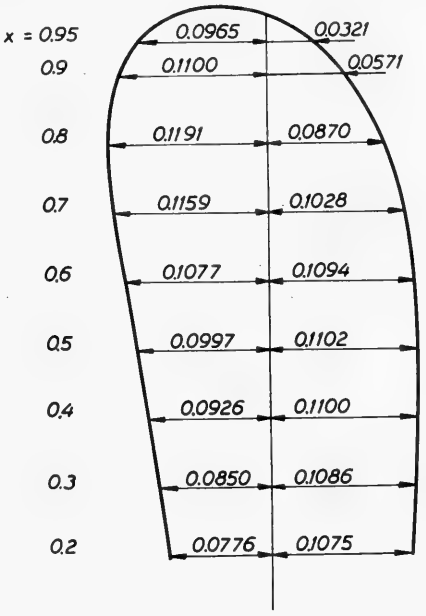

Fig. 4 - Family of contrarotating propellers. Blade form. Figures give 1/D.

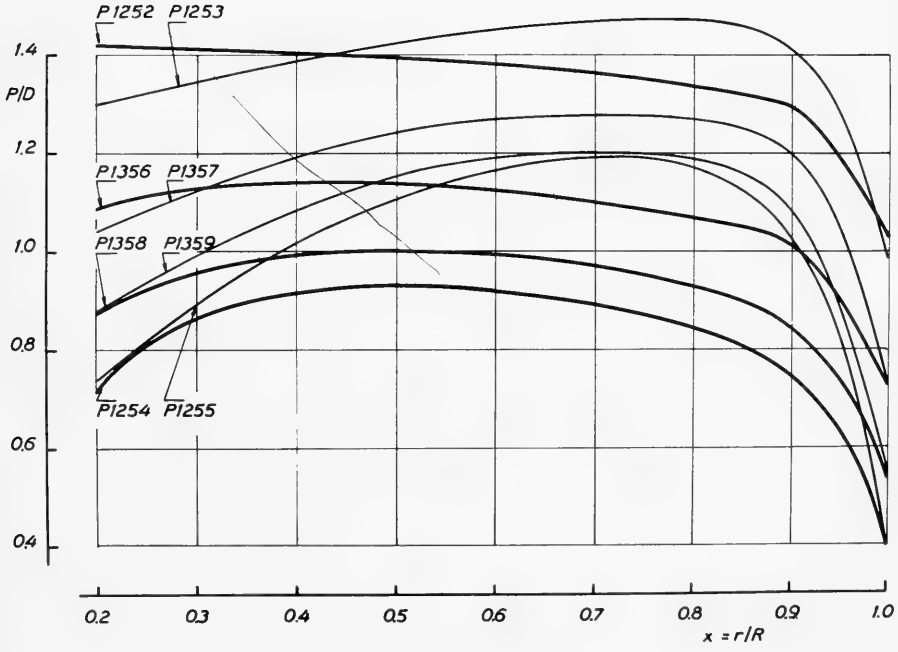

Fig. 5 - Family of contrarotating propellers. Radial distributions of pitch. See further Table 1 (D = forward and aft propeller diameter, respectively).

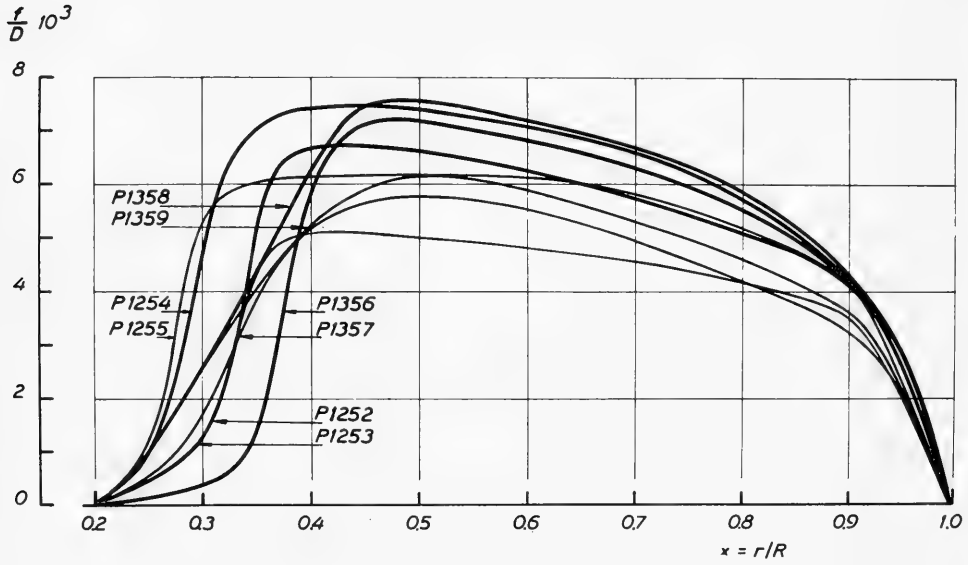

Fig. 6 - Family of contrarotating propellers. Radial distributions of maximum camber of blade sections. See further Table 1 (D = forward and aft propeller diameter, respectively).

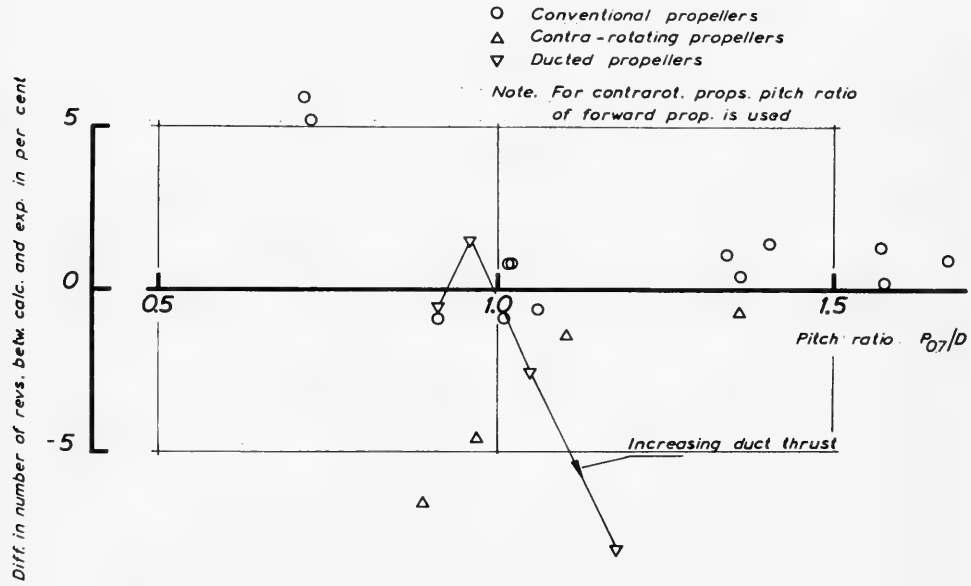

Fig. 7 - Difference in number of revs. between calculations and open-water tests for different types of propellers

Table 2
Contrarotating Propellers. Comparison Between Computed and Measured Propeller Characteristics at the Design Point. Design Value $\Sigma K_T = 0.38$.

Propeller No., Forward/Aft . . .		P1254/P1255	P1358/P1359	P1356/P1357	P1252/P1253
Design value K_T/J^2		3.118	1.528	0.784	0.362
Advance ratio J	Design	0.35	0.50	0.70	1.02
	Measured	0.373	0.523	0.708	1.027
	Deviation in % . .	+6.6	+4.6	+1.1	+0.7
Efficiency η_0	Calculated	0.378	0.498	0.617	0.729
	Measured	0.392	0.500	0.615	0.713
	Deviation in % . .	+3.7	+0.4	-0.3	-0.2
$(K_{TF}/K_{TA} - 1) \cdot 100$ % calc.		+16.8	+11.6	+7.0	+1.9
$(K_{TF}/K_{TA} - 1) \cdot 100$ % meas. . . .		+34.7	+24.9	+16.8	+0.0
$(K_{QF}/K_{QA} - 1) \cdot 100$ % calc.		+0.7	+0.3	+0.3	-0.7
$(K_{QF}/K_{QA} - 1) \cdot 100$ % meas. . . .		+4.2	+6.3	+5.4	+4.4

with conventional and ducted propellers, calculated according to analogous methods (see (14)).

From Table 2 it is evident that for the contrarotating propellers the torque balance and propeller efficiency is predicted with good accuracy by the calculations. Figure 7 shows, however, that the propellers designed for low values of the advance ratio J are overpitched in comparison with the calculations. This is in contrast to what is the case for conventional propellers, designed according to an analogous method. One of the reasons for this discrepancy could be that the use of the pitch of an equivalent propeller when determining the induction factors is not accurate enough.

In Fig. 8 the efficiency η_0 at the design value $K_T = 0.38$ is shown on the basis of the advance ratio J for the four sets of propellers, at the design pitch ratio as well as at other pitch ratios tested. Also the torque balance is shown in the diagram. From the diagram it is evident that the influence of pitch distribution and torque balance on efficiency is very small.

4. DUCTED PROPELLERS: THEORETICAL BACKGROUND AND EXPERIMENTAL VERIFICATION

4.1. Design Method

The ducted propellers are designed in accordance with a method which has been developed at SSPA (15). This method is an improvement of the theory of Dickmann and Weissinger (16). Thus, the distribution of blade circulation is arbitrary, the number of propeller blades is finite, and the thickness of the duct is considered. The method is analogous to the design method for conventional propellers in use at SSPA. This implies that also cavitation and strength calculations are included.

The calculations start from known values of total thrust, number of revolutions, propeller diameter, number of blades and blade form, distribution of blade circulation, duct vorticity, minimum cavitation margin, etc. The method determines blade area, propeller efficiency, duct thrust, shape of duct, and pitch, camber, and thickness of the propeller blade sections.

When calculating the shape of the duct and the thrust of the propeller and the duct, the actual propeller is replaced by an equivalent infinite-bladed propeller, represented by continuous radial distributions of ring vortices and rectilinear vortices. The strength of the vortices is determined by the conditions in the ultimate wake. The duct is replaced by systems of ring vortices and ring sources, which simulate the acceleration (deceleration) and the thickness of the duct, respectively. The hub is replaced by a source distribution along the axis. If the hub is cylindrical and the thickness distribution of the duct is prescribed, the source distributions of the hub and the duct, respectively, are determined by the local axial velocity. The definite strength of the vortex systems of the propeller and the duct and the hub is determined by an iteration process in such a way that the desired total thrust is obtained. The total thrust is calculated according to the momentum theorem and the thrust of the propeller according to.

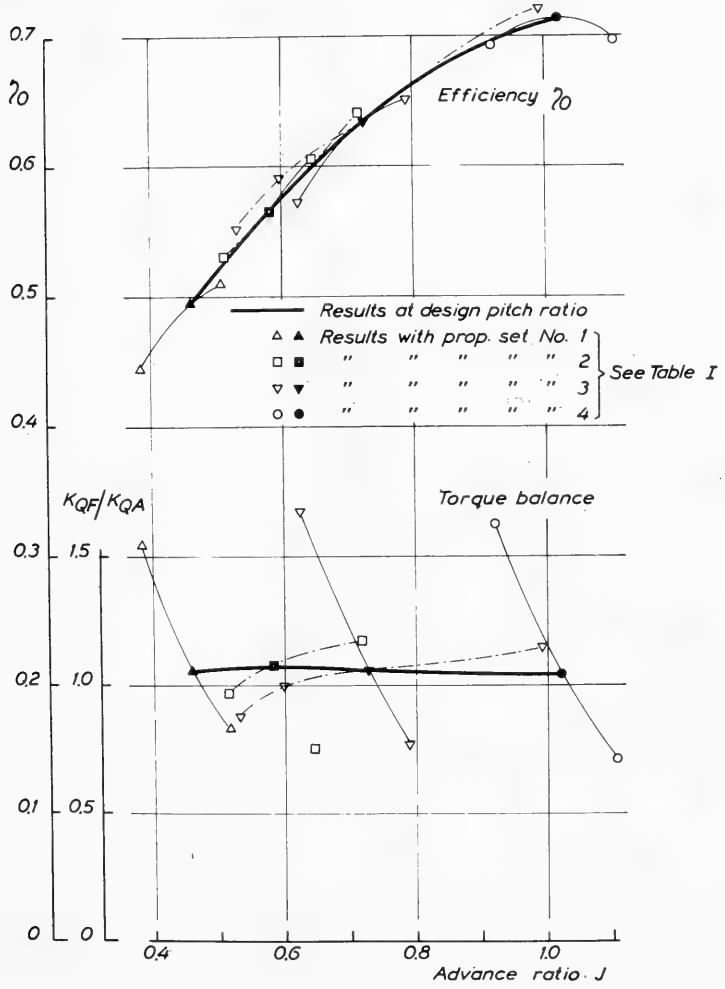

Fig. 8 - Contrarotating propeller family. Efficiency and torque balance at different pitch ratios.

the law of Bernoulli. Allowance is made for the drag of the propeller blades and the duct.

The shape of the duct can be determined either by applying the continuity law on the flow inside the duct or by satisfying the boundary condition at the duct.

Since the singularities representing duct and propeller are placed upon cylinders with constant diameters and not on the real streamsurfaces, the two methods give different results. The decisive factor on the boundary-condition method is the radial velocity induced by the propeller. When calculating this

velocity, however, errors can arise due to the simplified representation of the propeller. Since corresponding disadvantages have not been found in the calculations of the axial velocity, the continuity-law method is preferred when the shape of the duct is determined.

A method is presented which makes it possible to adjust the shape of the duct, if the first calculations give a shape that is not satisfactory from a practical point of view. The corrections applied do not influence the velocities at the propeller disk directly, and the first calculations need therefore hardly be repeated.

In the propeller calculations the number of blades is assumed to be finite. Starting from the propeller thrust as obtained above, the velocities induced by the propeller are determined by a conventional lifting line method. The pitch of the helical vortices is assumed to be determined by the velocities in the ultimate wake. Due to the finite number of blades, the velocities induced by the duct and the hub at the blades deviate from the circumferential mean values, especially near the blade tips. No allowance is so far made for this fact when the pitch of the propeller blades is determined.

Due to the relatively great blade widths generally used for ship propellers, the axial variation of the induced velocities makes camber and pitch corrections necessary. Besides the ordinary corrections, calculated by some lifting-surface method, additional corrections have to be introduced, primarily due to the vorticity of the duct.

Pitch corrections due to viscosity and blade thickness are calculated in the same way as for a conventional propeller.

4.2. Experimental Verification

In order to obtain an experimental verification of the design method, a series of open-water tests with four heavily loaded, ducted propellers has been carried out in the SSPA cavitation tunnel. The design value of the total thrust was in all cases the same, while the theoretical thrust of the duct was varied systematically.

The important design and test data of the ducted propellers are given in Table 3. The blade form and distribution of blade circulation were the same as for a conventional propeller. The shapes of the ducts are given in Fig. 9.

The experimental results are described in (17). A comparison between computed and measured ducted propeller characteristics is also given in Table 4 and in Figs. 7 and 10. As long as no flow separation occurred, the agreement between the theoretical and experimental values of total thrust at the design advance ratio was very good. The duct thrust was found to be slightly too large for small duct vorticity, while the opposite condition was valid when the theoretical vorticity of the duct was large. The efficiency of the ducted propellers was somewhat lower than that predicted by the theory (see Fig. 10).

Table 3
Important Design and Test Data for Ducted Propellers

Common design data				
Total thrust coefficient			K_{TT}	= 0.278
Advance ratio			J	= 0.412
Number of blades			z	= 5
Hub diameter			x_H	= 0.186
Mean line of blade sections			NACA a	= 0.8
Thickness distribution of blade section			NACA 16	
Model propeller diameter			D	= 0.186 m
Cavitation margin			c	= 30%
Ducted propeller No.	P1313 D4	P1314 D5	P1315 D6	P1316 D7
Duct thrust K_{TD}/K_{TT}	0.01	0.15	0.30	0.45
Blade area ratio A_D/A_0	0.68	0.65	0.64	0.69
Pitch ratio P/D at x = 0.7	0.92	0.96	1.04	1.18
Camber f_g/l of the blade sections at x = 0.7	0.033	0.024	0.019	0.014

Hence the design method seems to function satisfactorily under the conditions tested, as long as no separation phenomena occur.

The most extreme ducted propeller, which theoretically should have given a duct thrust of K_{TD}/K_{TT} = 0.45, suffered from flow separation inside the rear part of the duct, which decreased K_{TD}/K_{TT} to 0.29. The separation was detected in a series of flow visualization studies, which were carried out using a quartz lamp illuminating small air bubbles in the flow through a narrow slit.

To investigate the sensitivity of the co-operation between duct and propeller, some of the ducts were also tested together with propellers originally designed for other ducts. At the design K_{TT}/J^2 both the duct thrust and the propeller efficiency were decreased considerably, if the pitch ratio of the propeller was lower and the camber of the blade section higher than the design values, see Fig. 10. In one case of two this was also true when the pitch ratio was higher and the camber lower than the design values. The flow visualization studies indicated that the probable reason was flow separation inside the rear part of the duct.

Flow separation outside the ducts was recorded only at values of K_{TT}/J^2 lower than the design value.

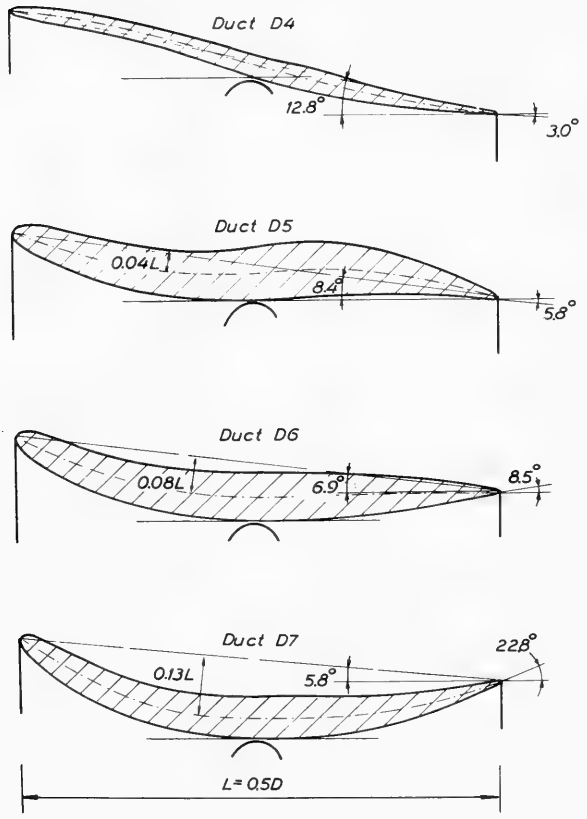

Fig. 9 - The shapes of the four ducts testsd

Table 4
Comparision Between Computed and Measured Ducted Propeller Characteristics at the Design Point $K_{TT}/J^2 = 1.64$

Ducted propeller No.		P1313 D4	P1314 D5	D1315 D6	P1316 D7
Advance ratio J	Design	0.412	0.412	0.412	0.412
	Measured	0.414	0.406	0.422	0.443
	Deviation in %	+0.5	-1.5	+2.4	+7.5
Efficiency η_0	Calculated	0.491	0.520	0.552	0.580
	Measured	0.477	0.499	0.529	0.530
	Deviation in %	-2.9	-4.0	-4.2	-9.4
Duct thrust $\frac{K_{TD}}{K_{TT}}$	Design	0.01	0.15	0.30	0.45
	Measured	0.11	0.20	0.29	0.29

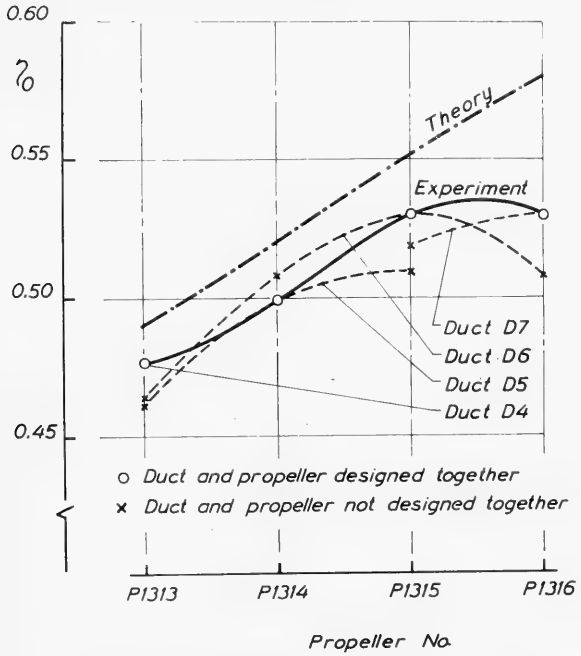

Fig. 10 - Efficiency of the different ducted propellers at the design value of K_{TT}/J^2. For geometrical data of propellers and ducts, see Table 3 and Fig. 9.

5. CALCULATION OF OPTIMUM PROPELLER EFFICIENCIES AND DIAMETERS

5.1. Contrarotating Propellers

Below diagrams showing the optimum relations between speed, number of revolutions, thrust, and diameter will be given for contrarotating propellers. It might, however, be of interest to look first into the reasons sometimes given why better efficiency should be expected with a set of contrarotating propellers than with the corresponding single propeller of the same diameter, developing the same thrust at the same number of revs. The main reasons for an improvement in efficiency should be:

(1) The load is distributed over two propellers instead of one.

(2) The rotational losses from the forward propeller are more or less nullified by the aft propeller (tangential interference).

These conditions are illustrated in Fig. 11. This figure shows the calculated values of the propeller efficiency at the design advance ratio for the four sets of propellers mentioned in Sec. 3. From the diagram in Fig. 11 it is evident that

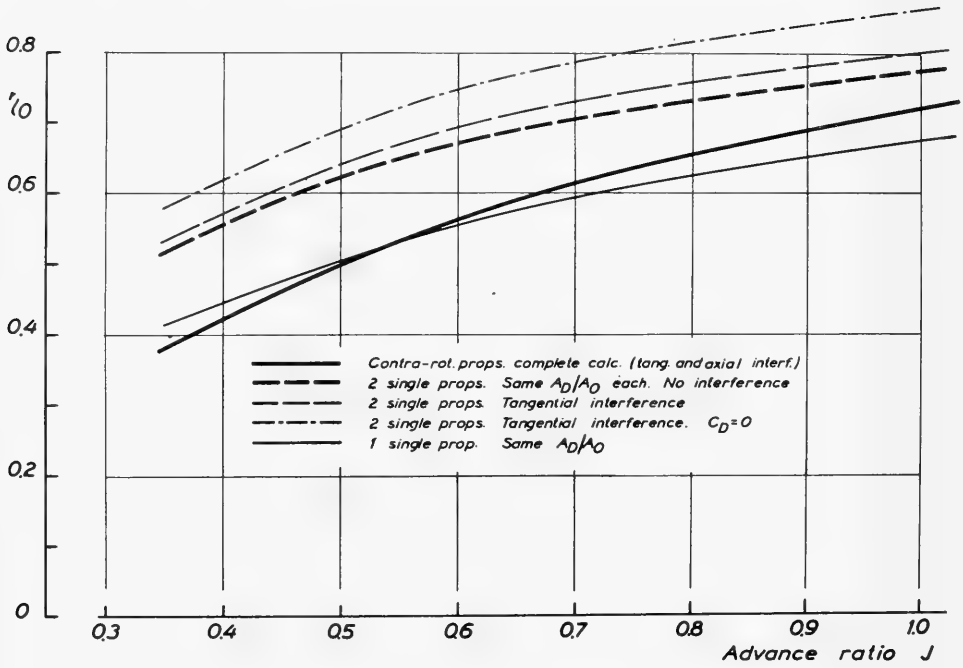

Fig. 11 - Different approximations when calculating the propeller efficiency for contrarotating propellers

the factor (1) above should be the most important reason for an improvement. From Fig. 11 it is, however, also evident that, when the propellers are placed behind each other, the beneficial influence of the factors mentioned above are to a large extent compensated by the axial interference between the propellers. Thus, the open-water efficiency of the contrarotating propeller set is only slightly better than that of the corresponding single propeller.

In Fig. 12 open water test results of the four sets of contrarotating propellers, described in Sec. 3, are given. Based on this material, curves giving the open water-efficiency and advance ratio for optimum propellers are presented in Figs. 13 and 14, together with the corresponding values for conventional propellers. The results for the conventional propellers have been reproduced from (1). In Fig. 13 the comparison is based on $\Sigma K_T/J^2$, i.e., equal diameter for the same load, while Fig. 14 gives the same comparison on the basis of $\left(\sqrt[4]{\Sigma\ K_T/J^4}\right)$, i.e., at the equal number of revs. for the same load. From the diagrams the following conclusions can be drawn:

(1) Compared with a conventional propeller at the same number of revs., about 20% smaller optimum diameter is obtained with the contrarotating propeller set. The open-water efficiency is about the same in the two cases, or slightly lower for the contrarotating case.

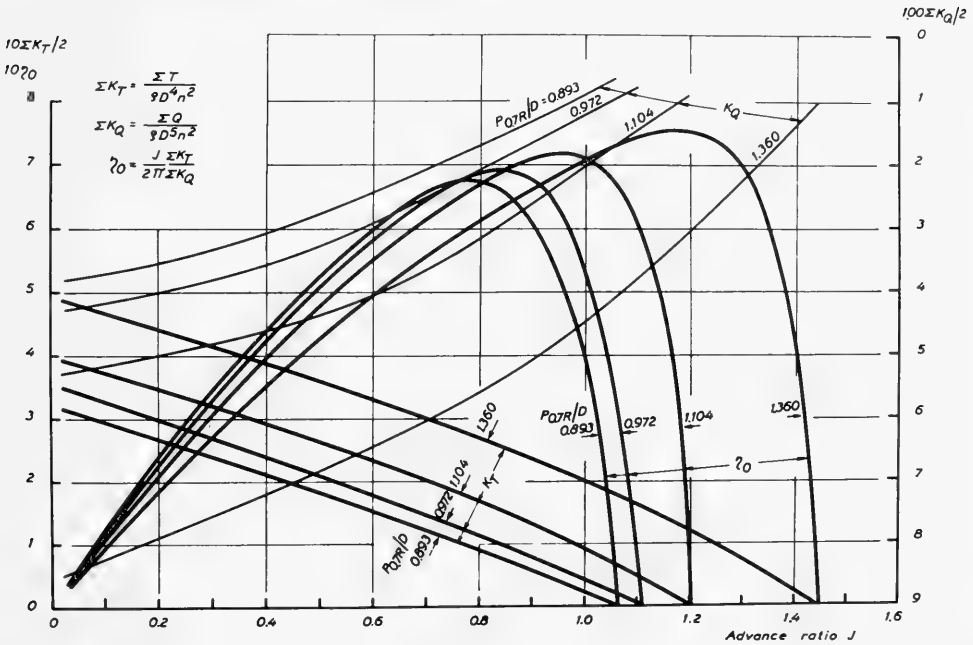

Fig. 12 - Results of open-water tests with contrarotating propeller family

(2) Compared with a conventional propeller at the same diameter, about 35% lower optimum number of revs. is obtained with the contrarotating propeller. A gain in open-water efficiency of the order of 5-7% is obtained with contrarotating propellers under these conditions.

5.2. Ducted Propellers

On merchant ships the duct is introduced primarily to increase the propeller efficiency. To obtain this, the duct must be formed in such a way that the axial velocity at the propeller disk is increased, which means that the duct is taking over some part of the thrust from the propeller. If the duct vorticity, which determines the duct-induced velocity, is increased too much, however, the diffusor angle at the rear part of the duct internal surface becomes so large that the flow separates and the efficiency decreases. Thus, for a given total thrust, there exists a certain duct vorticity which gives maximum values of duct thrust and propeller efficiency.

In the experiments mentioned in Sec. 4.2., the total thrust was kept constant, while the thrust of the duct was varied systematically. Maximum values of duct thrust and propeller efficiency was obtained with duct D6 (see Figs. 9 and 10), which had a diffusor angle of about 8.5°. The calculated ratio between the wake area A_∞ and the disk area A_0 was $A_\infty/A_0 = 1.086$.

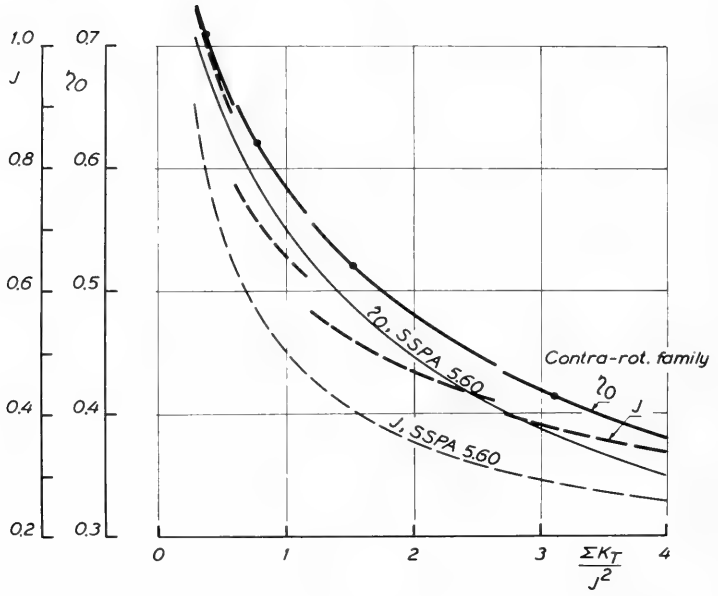

Fig. 13 - Comparison between optimum efficiencies and diameters of contrarotating and conventional propellers. $\Sigma\ K_T/J^2$ as basis.

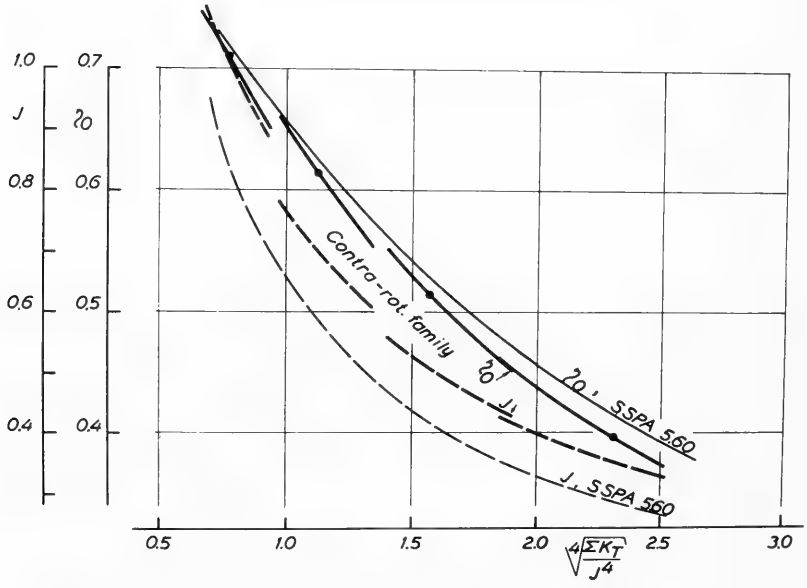

Fig. 14 - Comparison between optimum efficiencies and diameters of contrarotating and conventional propellers. $\sqrt[4]{\Sigma\ K_T/J^4}$ as basis.

On basis of these experimental results, a series of "optimum" ducted propellers has been calculated for loads which can be of interest for merchant ships. At the optimum advance ratio J_{opt}, the total thrust coefficient was found to be the same, $K_{TT} = 0.246$ for all ducted propellers. The ducts had a length $L/D = 0.5$ and a maximum thickness $t_D/L = 0.14$. The thickness distribution was similar to NACA 0015. The ratio A_∞/A_0 was 1.10, which means a diffusor angle of about 8.5°. The results of the calculations are given in Table 5.

Table 5

$\left(\sqrt[4]{K_{TT}/J^4}\right)$	K_{TT}/J^2	J_{opt}	K_{TD}/K_{TT}	η_0	α_D	f_D/L
0.77	0.28	0.92	0.17	0.692	4.5°	0.03
1.13	0.63	0.63	0.23	0.634	5.7°	0.05
1.57	1.22	0.45	0.28	0.559	7.7°	0.07
2.24	2.50	0.31	0.33	0.468	9.6°	0.09

α_D and f_D are defined in Fig. 15.

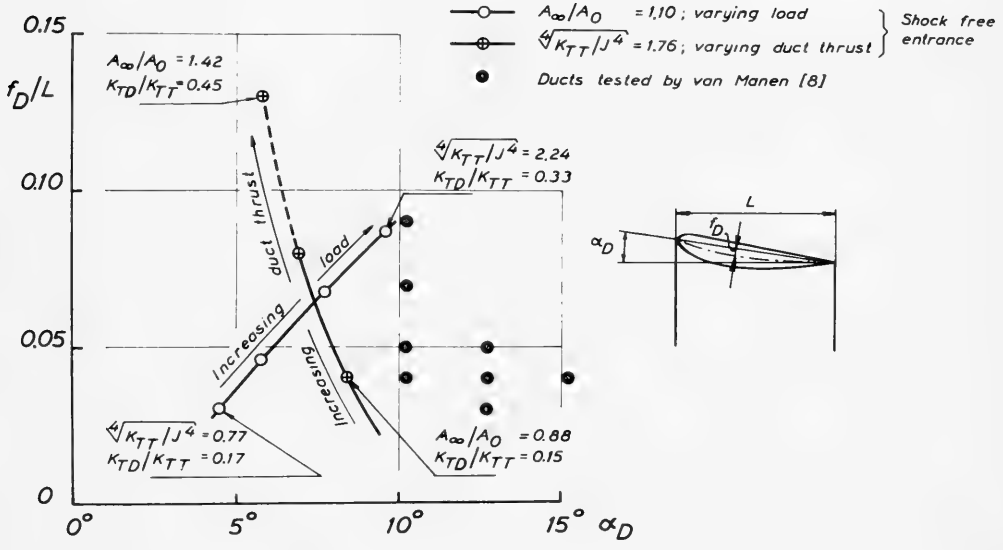

Fig. 15 - Different relations between camber and geometrical angle of attack for duct profiles

For the same number of revolutions, the optimum propeller diameter was 7% less, and the maximum diameter of the duct 7-15% greater than the optimum diameter of a conventional propeller.

The calculated efficiency of ducted propellers with $A_\infty/A_0 = 1.10$ ("optimum") and $A_\infty/A_0 = 1.00$ (smaller diffusor angle) is given in Fig. 16, where a comparison

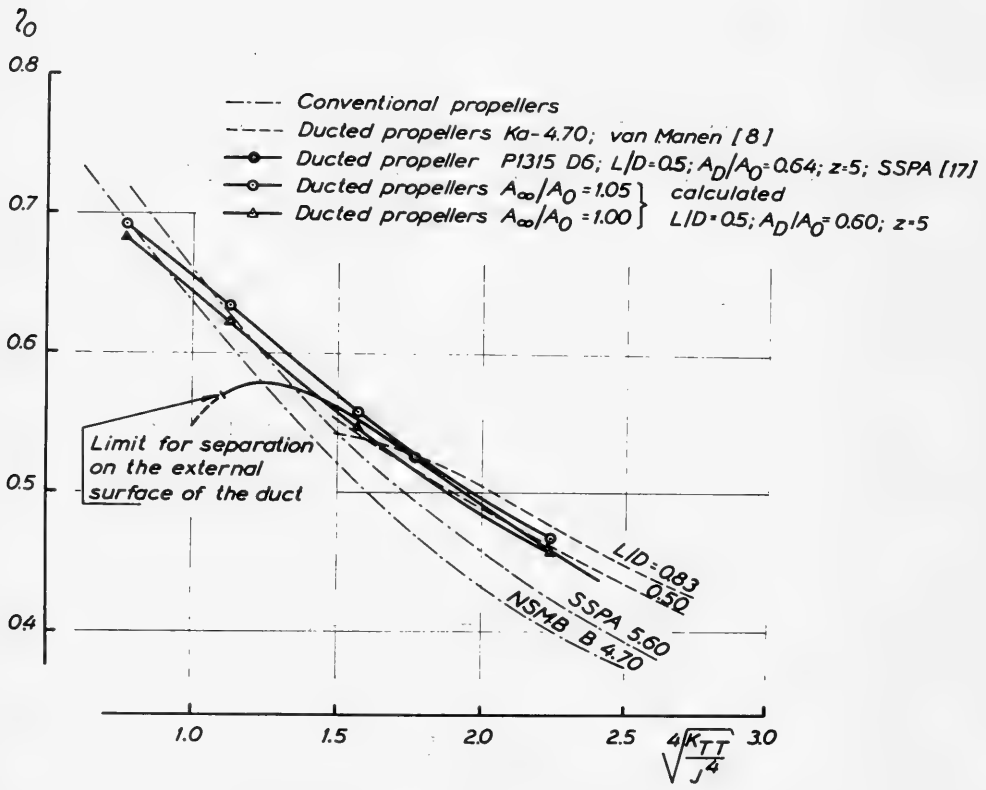

Fig. 16 - Comparison between optimum efficiencies of ducted and conventional propellers

with conventional propellers can be made. The experimental efficiencies of SSPA ducted propeller P1315 D6 (see (17)), and of ducted propellers tested by van Manen (8) are also given. From Fig. 16 the following conclusions can be drawn:

(1) It seems to be possible to design ducted propellers with higher efficiency than conventional propellers, also at low loads. For the "optimum" ducted propellers the lower limit for efficiency gain is

$$\sqrt[4]{K_{TT}/J^4} \cong 1.1 \ ,$$

which means $B_u \cong 16$ or $B_p \cong 20$.

(2) The gain in efficiency due to the duct increases with increasing load. Unfortunately it is not yet possible to make a fair comparison based upon equal strength, vibration, and cavitation characteristics between different propulsion systems. However, a comparison has been made with the conventional propeller series SSPA 5.60 and NSMB B.4.70 in Fig. 16.

(3) If A_∞/A_0 is decreased from 1.10 to 1.00, which means that the diffusor angle decreases from 8.5° to 3°, a loss in efficiency of about 2% is obtained.

(4) On heavily loaded ducted propellers, higher efficiency is obtained for large duct lengths. This is probably due to the fact that larger values of A_∞/A_0 can be used with longer ducts.

(5) If a ducted propeller is tested at loads considerably lower than the design load, the flow separates from the duct external surface and the efficiency decreases.

All the ducts calculated at SSPA are intended to have a shock-free entrance at the design point. The angle α_D between nose-tail line of duct profile and propeller shaft and the camber f_D/L of the different ducts are shown in Fig. 15. Corresponding values for the ducts tested by van Manen (8) are also given.

It is interesting to note that the angle α_D is larger for the ducts tested by van Manen than those designed at SSPA. If, for a given total load, α_D of the duct is larger than the value valid for shock-free entrance, a peak of low pressure is developed on the external surface of the fore part of the duct. Since this low pressure must be followed by a pressure increase for a flow-accelerating duct, too-large values of α_D mean an increasing risk for separation on the external surface of the duct [compare point (5) above].

6. PROPULSIVE COEFFICIENTS

6.1. Projects Investigated

Most of the results discussed in this section have been obtained from self-propulsion tests with models for two projects, one tanker of about 150 000 tons DW and one fast container vessel of about 12 000 tons DW. Main dimensions of these two projects are given in Table 6. In the case of the tanker two conventional propellers, calculated for different numbers of revs., were tested as well as three sets of contrarotating and six different ducted propellers. In the case of the container vessel only two conventional propellers, designed for the same number of revs., and two sets of contrarotating propellers were tested. The different stern arrangements of the tanker and the container vessel are shown in Figs. 17 and 18. From the figures it can be seen that in both cases conventional afterbody shapes were used.

Table 6

Project	Displ.	Length L_{pp}	L_{pp}/B	B/T	Speed	Approx. shaft power	Model Scale Factor α
	m^3	m			knots	HP	
Tanker	180,000	283	6.3	2.6	16.5	30,000	38.6
Container	19,000	156	6.6	2.7	23.0	25,000	24.0

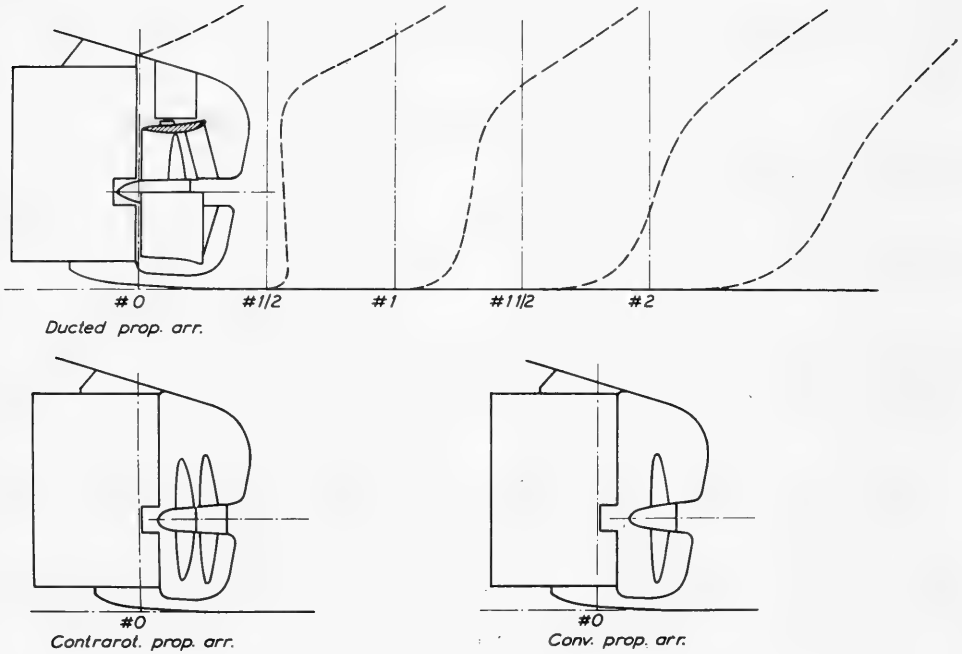

Fig. 17 - Tanker project. Stern arrangements.

6.2. Tanker Project

The results of the self-propulsion tests, carried out with the tanker model are given in Table 7 and in Fig. 19. A certain caution is recommended when examining the results for two reasons:

(1) From earlier studies the optimum diameter of a conventional propeller in behind condition was known approximately, and the diameters of the two conventional propellers were determined with this in mind. It is difficult to judge, however, if the diameters of the contrarotating and ducted propellers tested were optimum.

(2) Due to the large scale factor, the advance velocity of the propellers is low and thus the thrust and torque values recorded are small. This may influence the accuracy of the measurements, particularly in the case of the torque of the contrarotating propellers.

Bearing this in mind the following conclusions can be drawn from Fig. 19 and Table 7:

(1) The gain in efficiency for the best set of contrarotating propellers P1250-P1251 is about 6% compared to a conventional propeller at the same number of revs.

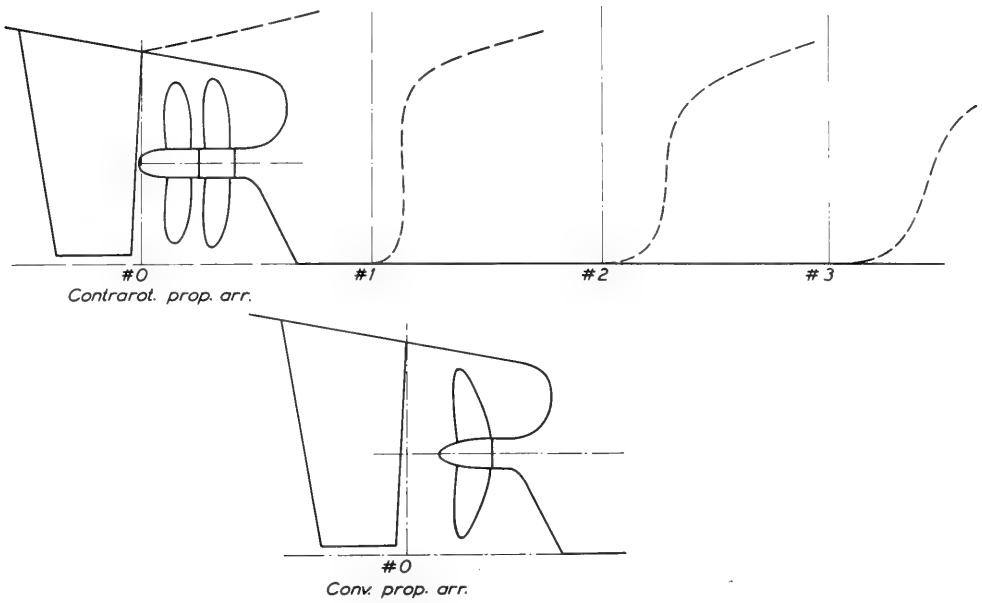

Fig. 18 - Container vessel project. Stern arrangements.

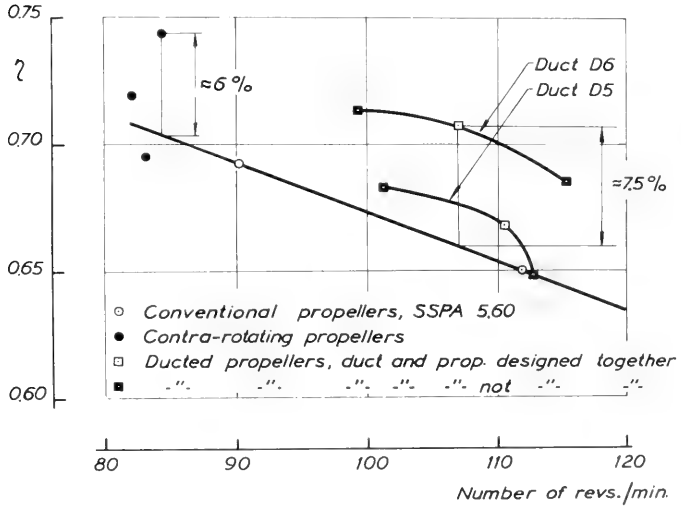

Fig. 19 - Tanker project. Results of self-propulsion tests.

Table 7
Tanker Project. Propulsive Coefficients.

Prop. type		Conv. props.		Contrarot. props.			Ducted props. Duct D6			Ducted props. Duct D5		
Prop. No.		P1123	P1172	P1250 P1251	P1248 P1249	P1370 P1371	P1314	P1315	P1316	P1313	P1314	P1315
Diameter (m)		8.29	7.51	8.20	7.90	7.52	7.00	7.00	7.00	7.00	7.00	7.00
$P_{0.95}/P_{0.7}$		1.00	1.00	0.99 0.92	0.84 0.80	0.69 0.71	0.75	0.86	0.97	0.67	0.75	0.86
N r/m		90.2	111.8	84.4	82.1	83.1	115.2	106.8	99.2	112.6	110.5	101.1
η		0.693	0.651	0.744	0.720	0.695	0.686	0.708	0.714	0.649	0.668	0.684
t		0.222	0.222	0.232	0.250	0.251	0.254	0.238	0.251	—	—	—
Thrust identity	w_T	0.527	0.552	0.572	0.557	—	0.524	0.511	0.535	—	—	—
	η_H	1.65	1.74	1.79	1.69	—	1.57	1.56	1.61	—	—	—
	η_R	1.01	1.02	1.11	1.08	—	1.05	1.01	1.05	—	—	—
	η_0	0.417	0.368	0.375	0.392	—	0.415	0.450	0.423	—	—	—
Torque identity	w_Q	0.512	0.541	0.468	0.459	—	0.497	0.493	0.454	—	—	—
	η_H	1.60	1.70	1.44	1.39	—	1.52	1.47	1.37	—	—	—
	η_R	1.01	1.02	1.24	1.12	—	1.04	1.05	1.12	—	—	—
	η_0	0.428	0.377	0.440	0.465	—	0.436	0.459	0.465	—	—	—
K_{TD}/K_{TT}							0.33	0.33	0.35	—	—	—
A_D/A_0		0.60	0.60	0.36 0.42	0.40 0.47	0.40 0.50	0.65	0.64	0.69	0.68	0.65	0.64

(2) The other sets of contrarotating propellers are comparable with the conventional propeller. The main difference between P1250-P1251 and the other contrarotating propellers is a larger diameter (see Table 7). The results seem to indicate that the optimum diameter in behind condition is larger than in open water. Compare Figs. 14 and 19. Another difference is, however, that the propellers P1250-P1251 have a circulation distribution, which gives more load near the blade tips, i.e., a larger value of $P_{0.95}/P_{0.7}$. Further, the blade area ratio is smaller.

(3) The gain in efficiency for the best ducted propeller P1315 D6 is about 7.5%, compared to a conventional propeller at the same number of revs.

(4) The relation between the efficiencies of the different ducted propellers is approximately the same, when tested in open water (Fig. 16) and in the behind condition (Fig. 19). Thus, duct D5 gives lower efficiency than duct D6 and for the same duct the propeller, which is designed together with the duct, generally has the best efficiency.

The different propulsive coefficients calculated by established methods are given in Table 7. By way of comparison the effective wake fraction and associated factors are determined, assuming thrust as well as torque identity. As shown, great differences between the two methods are obtained, both for the contrarotating and the ducted propellers. A comparison with the results of the conventional propellers indicates that the thrust-identity method generally gives more consistent results.

A comparison of Fig. 19 with Fig. 14 shows that, for contrarotating propellers, a great part of the final gain in efficiency, which is obtained at the self-propulsion tests, must be attributed to improvement of the propulsive coefficients η_H (i.e., w and t) and η_R. If the thrust-identity assumption is used, both η_H and η_R are larger than for a conventional propeller, in spite of the slightly higher thrust deduction factor $\underline{t}$. See Table 7.

The reason for the slightly higher thrust deduction factor $\underline{t}$ in the contrarotating case might be the fact that the thrust coefficient K_T/J^2 is smaller in this case than for the corresponding single-propeller case.

Also on the relative rotative efficiency η_R of the contrarotating propellers an influence of the thrust coefficient can be noticed, working in the direction that η_R increases as the thrust coefficient decreases. This might be one of the explanations of the fact that the optimum diameter in behind condition seems to be larger than in open water.

The gain in efficiency for the ducted propellers compared with a conventional propeller at the same number of revs. (Fig. 19) was lower than could be expected from the open water tests, Fig. 16 [$(K_{TT}/J^4)^{1/4} = 2.3$]. The main reason for this is lower values of the hull efficiency η_H (lower wake fraction w_T and higher thrust deduction factor $\underline{t}$). The relative rotative efficiency η_R was similar to that of a conventional propeller, and the thrust of the duct K_{TD}/K_{TT} was about the same as in the open-water tests.

Further self-propulsion tests may show if it is possible to improve the hull efficiency of a ducted propeller arrangement by introducing some kind of Hogner stern, as proposed by van Manen (5).

6.3. Container-Vessel Project

The results of the self-propulsion tests, carried out with the container-vessel model, are given in Table 8 and in Fig. 20.

Table 8
Container-Vessel Project. Propulsive Coefficients.

Prop. type		Conventional propellers		Contrarotating propellers	
Prop. No.		P1241	P1032	P1319 P1348	P1252 P1253
Diam. m		6.0	6.0	6.0	6.0
Blade area ratio		0.63	0.60	0.41 0.41	0.40 0.50[1]
$P_{0.95}/P_{0.7}$		0.99	1.0	0.92 0.92	0.87 0.88
N, r/m		128.3	139.2	84.2	94.1
η		0.674	0.690	0.755	0.763
t		0.189	0.194	0.211	0.211
Thrust identity	w_T	0.254	0.257	0.253	0.246
	η_H	1.09	1.09	1.06	1.05
	η_R	1.02	1.01	1.08	1.06
	η_0	0.611	0.631	0.661	0.686
Torque identity	w_Q	0.248	0.255	0.197	0.207
	η_H	1.08	1.08	0.98	1.00
	η_R	1.02	1.01	1.12	1.09
	η_0	0.613	0.632	0.689	0.706

[1] Five-bladed aft propeller

The diagram in Fig. 20 shows that the gain, when using contrarotating propellers, is in this case about 12%, compared to the single propeller, intended to be used for the project. Compared to a stock propeller, having too-short outer blade sections from the point of view of cavitation, the gain is about 10%. In contrast to what was the case for the tanker model, the scale factor is in this case not very large and the advance velocity of the propellers not particularly low. Thus, the accuracy of the measurements can be expected to be better and the results more reliable. The reasons for the gain in efficiency, obtained in the present case, are somewhat different from those mentioned in connection with the case of the tanker. In the present case, the diameter of the propeller was limited to 6 m. Thus, the comparison with the single propeller is one, based on constant K_T/J^2. Figure 13 shows that under such circumstances a gain

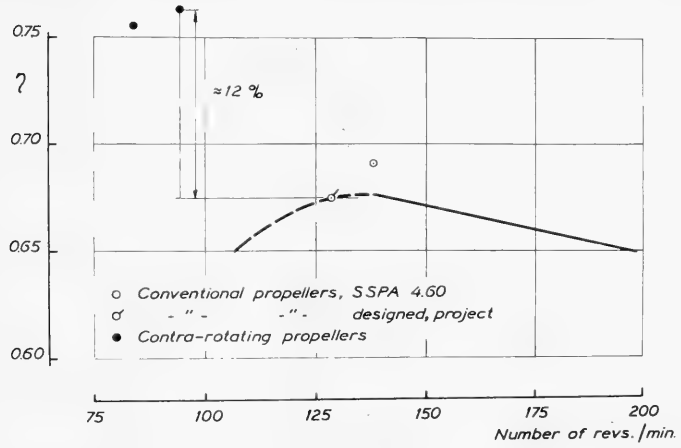

Fig. 20 - Container-vessel project. Results of self-propulsion tests.

in open-water efficiency of the order of 5-7% can be expected. This gain, together with the better value of the relative rotative efficiency, makes the improvement as large as 12% in the present case, in spite of the lower value of the hull efficiency.

7. CAVITATION AND VIBRATION STUDIES

As mentioned above, in addition to the efficiency it is also necessary to discuss cavitation and vibration properties when comparing the merits of different propeller arrangements. Although these questions have not been finally treated in connection with the investigation mentioned above, some preliminary experiments have been carried out in order to illustrate the situation. The experiments include cavitation studies in uniform flow with all the propellers, cavitation experiments in irregular flow distributions with some of the contrarotating propellers and introductory studies of local pressure variations on the afterbody, induced by contrarotating propellers.

7.1. Cavitation Inception in Uniform Flow

Some indication about the danger for cavitation with different propellers might be obtained from the studies of incipient cavitation.

Tanker project. For the tanker project three different sets of contrarotating propellers have been tested, as mentioned in Sec. 6. They differ primarily with regard to diameter, radial pitch distribution, and blade area ratio (see Table 7). Curves for incipient cavitation phenomena, including tip vortex, back, and face cavitation, are presented in Fig. 21. All the curves are fairly favourable in comparison with corresponding curves for conventional SSPA 5.60

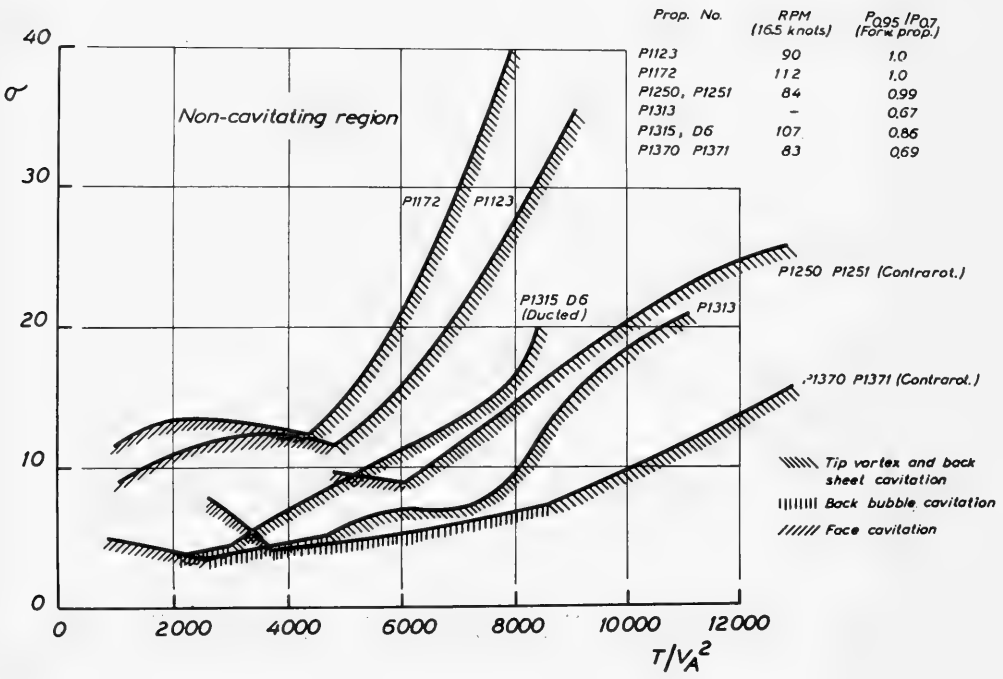

Fig. 21 - Tanker project. Incipient cavitation curves.

propellers, P1172 and P1123. The advantage in decreasing the load near the tip is, however, obvious, i.e., the radial circulation distribution appears to be the most important parameter.

A great number of ducted propeller configurations have been tested for the same project (see also Sec. 6). The cavitation test results are described in more detail in (17). It is concluded that most of these propellers are comparable with the conventional propellers with regard to cavitation properties.

In Fig. 21, also, the best ducted propeller from an efficiency point of view, P1315 D6, is compared with the other types of propellers with regard to incipient cavitation. A curve representing a conventional propeller, designed by use of the vortex theory, P1313, is included for comparison. Both P1315 D6 and P1313 have considerably better cavitation properties than the SSPA 5.60 propellers.

Container-vessel project. For the container project only contrarotating and conventional propellers have been investigated. Curves of incipient cavitation for a conventional SSPA 4.60 propeller and the contrarotating set of propellers from the systematic series, described in Sec. 3, have been presented in Fig. 22, together with a set of wake-adapted, contrarotating propellers, P1319, P1348. Also in this case a slight advantage with contrarotating propellers was obtained in comparison with the SSPA 4.60 propeller.

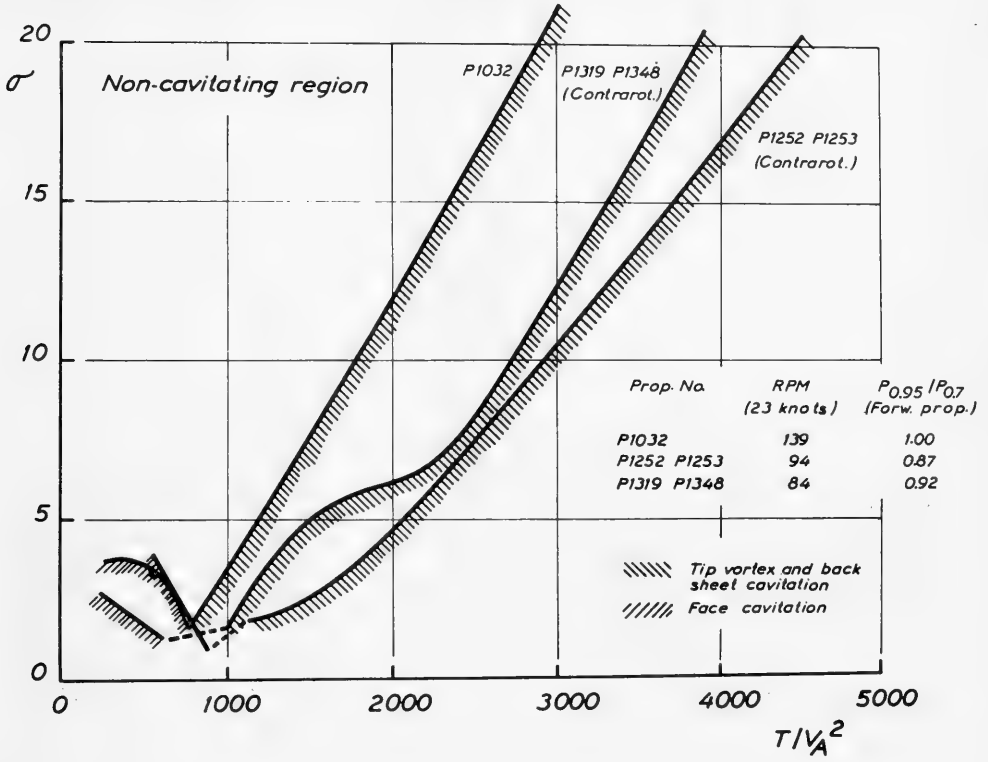

Fig. 22 - Container vessel project. Incipient cavitation curves.

7.2. Cavitation in Irregular Flow

Most of the contrarotating propellers used in connection with the tanker and container projects have been tested in two different wake distributions in the cavitation tunnel. The model wake for the two projects was simulated by the aid of a combination of transverse wire meshes and a longitudinal centre line plate.

The results of the experiments are exemplified in Figs. 23 and 24, representing the tanker and container vessel projects respectively. In both figures, the cavitation patterns of the set of contrarotating propellers having the best efficiency are compared with those obtained with a conventional propeller from the SSPA propeller family. From these studies it can be concluded that no bubble cavitation or any other kind of cavitation, which is supposed to cause erosion, was observed on any of the propellers. The only exception is the cavitation which occurs where the tip vortex from the forward propeller hits the aft propeller. Other studies in the cavitation tunnel have shown that this may cause serious problems. It seems to be necessary to eliminate this risk, either by a further decrease of the diameter of the aft propeller in relation to the forward propeller, or by further unloading of the propeller tips of the forward propeller.

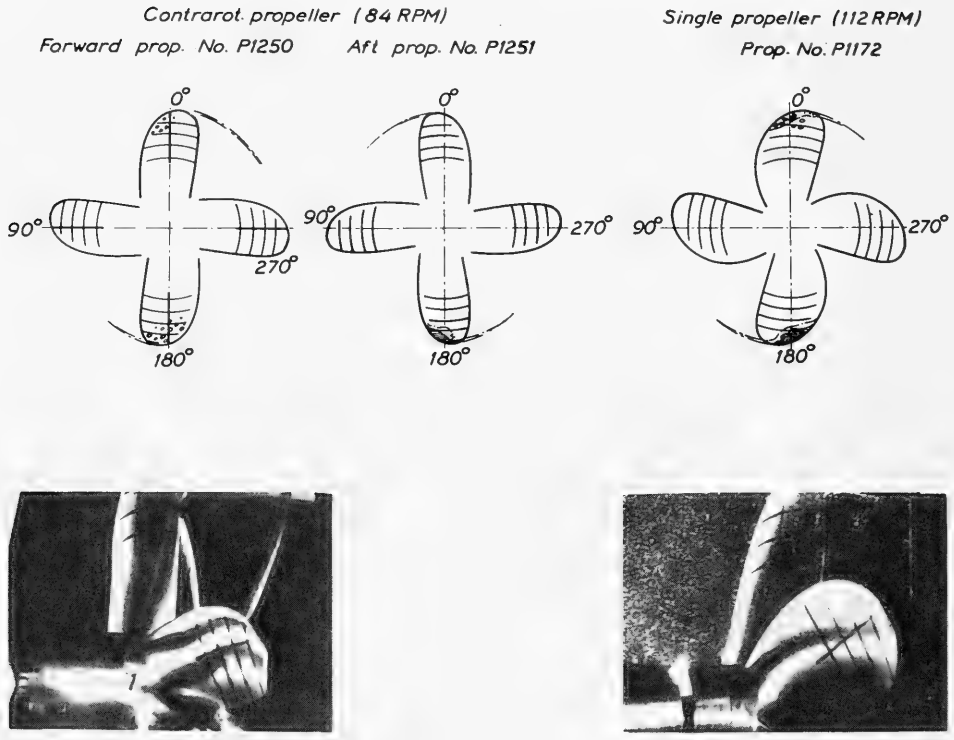

Fig. 23 - Tanker project. Results of cavitation tests in irregular flow.

7.3. Local Pressure Fluctuations Induced on the Afterbody by Conventional and Contrarotating Propellers

In many cases studies have been carried out at SSPA in order to determine the pressure fluctuations on the afterbody induced by the propeller. Unfortunately, experiments of this kind have not yet been carried out with the two projects discussed above. To throw some light on these problems, two diagrams are, however, presented, Figs. 25 and 26. The first diagram illustrates the influence of the number of propeller blades on the pressure fluctuations at some critical spots in the aperture. This influence is obvious. Thus an increase from 4 to 6 blades decreases the amplitude by more than half of the original. From Fig. 26 it is evident that the pressure amplitudes from the contrarotating propellers are somewhat lower than those from a conventional, single propeller. With the conventional twin-screw arrangement still lower amplitudes were recorded.

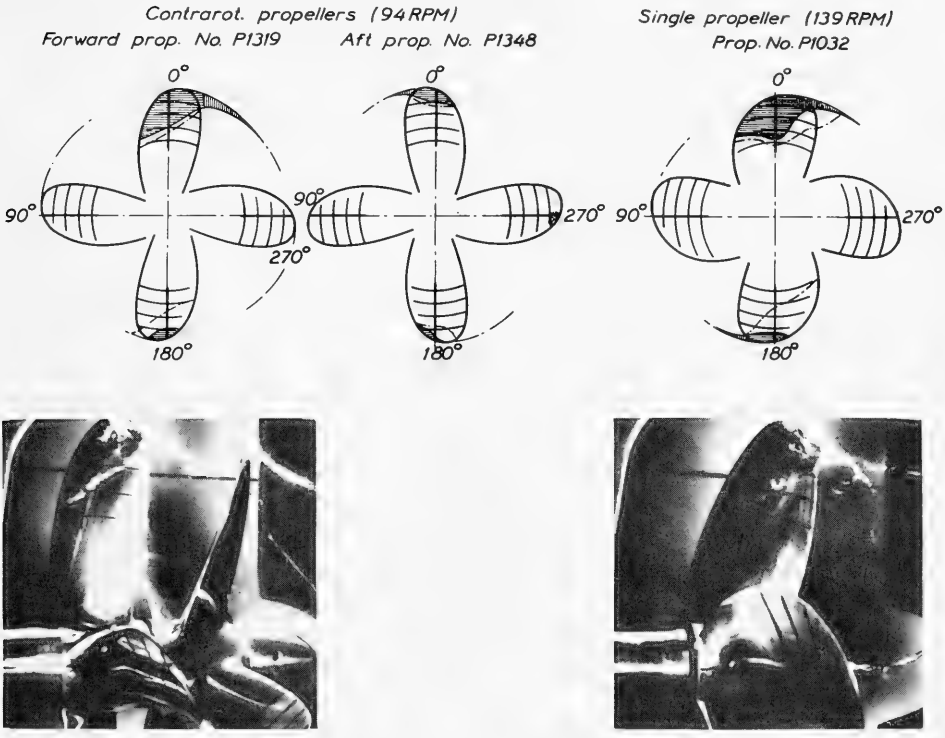

Fig. 24 - Container-vessel project. Results of cavitation tests in irregular flow.

8. CONCLUSIONS AND FURTHER INVESTIGATIONS

From the results presented above it may be concluded that:

(1) The contrarotating propellers of this investigation show slightly lower values of open-water efficiency than the conventional propellers, when the comparison is based on the same number of revs. and optimum propeller diameter is assumed in both cases. (See Fig. 14.) In the case of a 150 000 TDW tanker a corresponding comparison in behind condition resulted, however, in a gain in propulsive efficiency of about 6% for the contrarotating propellers (see Fig. 19). The main reason seems to be more favourable values of η_H and η_R. (See Table 7.)

(2) If the diameter is limited for some reasons (see Fig. 18) but optimum number of revs. can be used, the comparison between different types of propellers must be based on the same value of K_T/J^2. Under these conditions a gain in open water efficiency of about 5-7% was obtained for contrarotating propellers, compared to conventional propellers (see Fig. 13). In the case of a 12 000 TDW container vessel, a corresponding comparison in behind condition

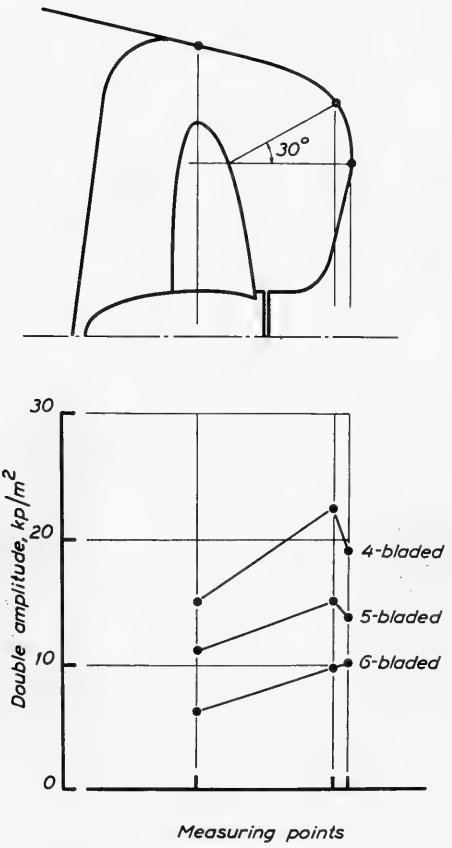

Fig. 25 - Pressure amplitudes.
Influence of number of blades.

resulted in a gain in propulsive efficiency of about 12%, in spite of a slightly lower value of η_H. (See Table 8.)

(3) The ducted propellers generally had higher open-water efficiency than the conventional propellers at the same number of revs. The gain in efficiency increased with increasing thrust coefficient (see Fig. 16). In the case of a 150,000 TDW tanker a corresponding comparison in behind condition resulted, however, in a gain in propulsive efficiency of only 7.5%, which is less than could be expected from the open-water tests. The main reason seems to be a lower hull efficiency η_H.

(4) There is no doubt that further work on the afterbody lines, in order to improve the propeller-hull interaction, is of the utmost importance, particularly for ducted propeller arrangements. Thus, tests carried out by van Manen with ducted propellers in combination with different types of Hogner sterns have given promising results (5).

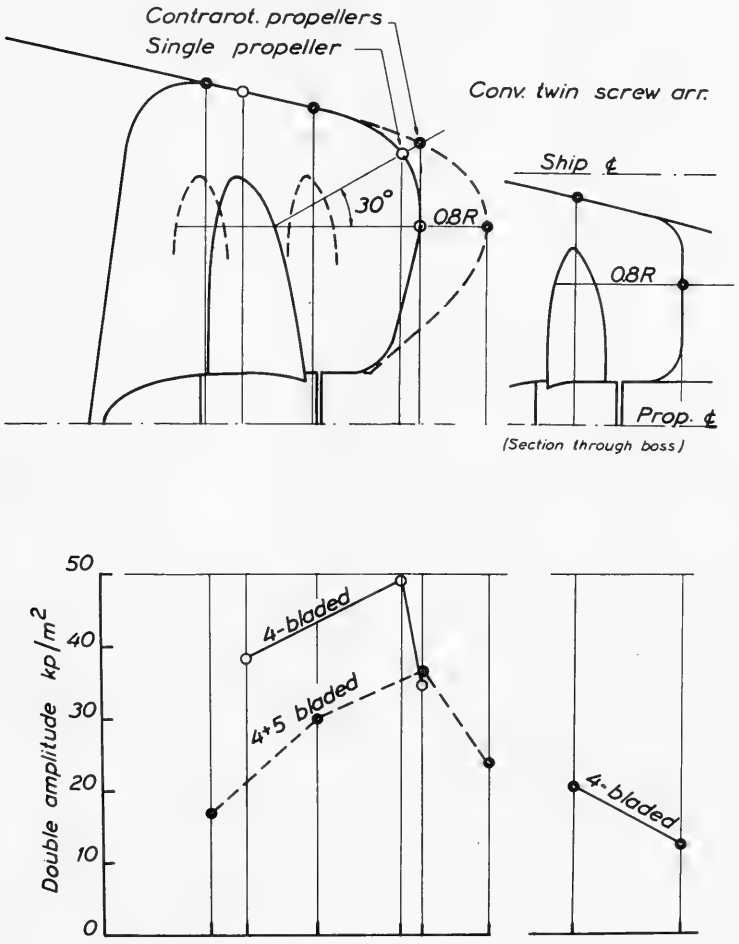

Fig. 26 - Pressure amplitudes. Comparison between different propeller arrangements.

(5) The conventional way of splitting up the propulsive coefficients appears to be less suitable for unconventional propulsive devices.

(6) The cavitation properties of contrarotating and ducted propellers seem to be similar to or better than those of the corresponding conventional propellers. In the contrarotating case, however, there is a risk that the cavitating tip vortex from the forward propeller might cause erosion on the aft propeller.

(7) The investigations with ducted propellers have to be completed with further cavitation-tunnel experiments.

(8) A series of "optimum" ducted propellers analogous to the family of contrarotating propellers, will be manufactured and tested (see Table 5).

(9) The questions concerning vibratory forces, maneuverability, and stopping and backing ability require further studies.

ACKNOWLEDGMENTS

The authors wish to express their gratitude to the Swedish Council for Applied Research for sponsoring the present investigation.

The authors are indebted to Dr. Hans Edstrand, Director General of the Swedish State Shipbuilding Experimental Tank, for the opportunity to undertake this study, as well as for the interest he has shown.

Thanks are also due to Mr. Eric Bjärne for his assistance with the analysis of the material and to other members of the staff for their assistance in various stages of the work.

LIST OF SYMBOLS

$A_0 = \frac{\pi D^2}{4}$ = propeller disk area

A_∞ = ultimate wake area

A_D = developed blade area

B = beam of hull

$B_p = 33.48 \sqrt{\frac{K_Q}{J^5}}$

$B_u = 13.36 \sqrt{\frac{K_T}{J^4}}$

} Taylor variables (salt water)

D = propeller diameter

f = camber of blade sections

f_D = camber of duct profile

$G = \frac{\Gamma}{\pi D V_A}$ = non dimensional blade circulation coefficient

$J = \frac{V_A}{D \cdot n}$ = advance ratio

$K_Q = \frac{Q}{\rho D^5 n^2}$ = torque coefficient

$K_T = \frac{T}{\rho D^4 n^2}$ = thrust coefficient

l = length of blade section

L = length of duct

L_{pp} = length of hull between perpendiculars

n = number of revolutions

p = static pressure at propeller shaft

p_v = vapour pressure

P = propeller pitch

Q = torque

r = radius

$R = \frac{D}{2}$ = propeller radius

R_T = total resistance

$t = \frac{T - R_T}{T}$ = thrust deduction factor

T, T_T = total thrust

T_D = duct thrust

T = draught of hull

W_Q, $W_T = \frac{V - V_A}{V}$ = Taylor wake fraction determined from torque and thrust identity, respectively

V = speed of model

V_A = speed of advance of propulsion system

$x = r/R$

x_H = nondimensional hub radius

z = number of blades

a = scale factor

α_D = angle between nose-tail line of duct profile and propeller shaft

Γ = circulation

η = propulsive coefficient

η_0 = open water efficiency

η_H = hull efficiency

η_R = relative rotative efficiency

ρ = mass density of water

$\sigma = \frac{p - p_v}{\frac{1}{2} \rho V_A^2}$ = cavitation number

As Index

F = forward

A = aft

T = total

D = duct

REFERENCES

1. Lindgren, H., Bjärne, E., "The SSPA Standard Propeller Family. Open Water Characteristics," Publ. No. 60 of the Swedish State Shipbuilding Experimental Tank, Göteborg, 1967.

2. Hadler, J.B., Morgan, W.B., Meyers, K.A., "Advanced Propeller Propulsion for High-Powered Single-Screw Ships," Trans. SNAME, Vol. 72, pp. 231-293 (1964).

3. Pien, P.C., Strom-Tejsen, J., "A Proposed new Stern Arrangement," Naval Research and Development Center, Report 2410 (1967).

4. Lindgren, H., "Hydrodynamiska aspekter på motroterande propellrar," The Swedish State Shipbuilding Experimental Tank (SSPA), General Report 24

(1967) (In Swedish). See also "Hydrodynamic Aspects of Contra-Rotating Propellers," Shipping World and Shipbuilder, Nov. 1967.

5. van Manen, J.D., Oosterveld, M.W.C., Witte, J.H., "Research on the Manoeuverability and Propulsion of Very Large Tankers," Trans. 6th Naval Hydrodynamics Symposium, Washington (1966).

6. Minsaas, K., "Large Tanker Propulsion Research," Shipping World and Shipbuilder, p. 832, June 1967.

7. English, J.W., Grant, S., Poulton, K., "Mammoth Tanker Propulsion with a Ducted Propeller System. Experiment Results," National Physical Laboratory, Ship T.M. 121, March 1966.

8. van Manen, J.D., Oosterveld, M.W.C., "Analysis of Ducted-Propeller Design," Trans. SNAME, Vol. 74, pp. 522-562 (1966).

9. Lerbs, H.W., "Contra-Rotating Optimum Propellers Operating in a Radially Non-Uniform Wake," DTMB Report 941, May 1955. [See also "Uber gegenläufige Schrauben geringsten Energieverlustes in radialen ungleichförmigen Nachstrom," Forschungsheft für Schiffstechnik, Heft 9, April (1954)].

10. Morgan, W.B., "The Design of Counterrotating Propellers Using Lerbs' Theory," Trans. SNAME Vol. 68 (1960).

11. Johnsson, C.-A., "Comparison of Propeller Design Techniques," Fourth Symposium on Naval Hydrodynamics, Washington, D.C., 1962. (ONR. ACR-92) See also Publ. No. 52 of the Swedish State Shipbuilding Experimental Tank, Göteborg, 1963.

12. Tachmindji, A.J., "The Axial Velocity Field of an Optimum Infinitely Bladed Propeller," DTMB Report 1294, Jan. 1959.

13. Pien, P.C., "The Calculations of Marine Propellers Based on Lifting-Surface Theory," Journal of Ship Research, Vol. 5 (1961).

14. Johnsson, C.-A., "On Theoretical Predictions of Characteristics and Cavitation Properties of Propellers," Publ. No. 64 of the Swedish State Shipbuilding Experimental Tank, Göteborg, 1968.

15. Dyne, G., "A Method for the Design of Ducted Propellers in a Uniform Flow," Publ. No. 62 of the Swedish State Shipbuilding Experimental Tank, Göteborg, 1967.

16. Dickmann, H.E., Weissinger, J., "Beitrag zur Theorie optimaler Düsenschrauben (Kortdüsen), Jahrbuch STG, Bd. 49 (1955).

17. Dyne, G., "An Experimental Verification of a Design Method for Ducted Propellers," Publ. No. 63 of the Swedish State Shipbuilding Experimental Tank, Göteborg, 1968.

* * *

DISCUSSION

M.W.C. Oosterveld

Netherlands Ship Model Basin
Wageningen, Netherlands

The investigations presented in the paper under discussion are a valuable contribution to the attempts of providing merchant ships with superior propulsion devices. I would like to make a comparison between the ducted propeller work given in the paper and performed at the N.S.M.B..

Extensive investigations performed by van Manen at the N.S.M.B. concerning ducted propellers with nozzles of the accelerating-flow type have led to the development of a standard nozzle (nozzle no. 19A) which meets a number of practical requirements. It has an axial cylindrical part on the inner side of the nozzle at the location of the screw, the outside of the nozzle is straight, and the nozzle has a relatively thick trailing edge. In addition, screw series especially for use in this nozzle, were developed (the K_a screw series). The screws of this series have wide blade tips (attractive with regard to cavitation), uniform pitch, and flat face sections. Experimental investigations have shown that this screw type is as good as theoretically calculated screws with regard to efficiency and cavitation. Besides, they have reasonable stopping qualities.

The open-water test results of nozzle no. 19A in combination with the K_a 4-55 screw series are given in Fig. D1. It can be seen from this diagram that at a design coefficient $C_T = 4.17$ (corresponding with the design loading of the ducted propellers given in the paper), the optimum ducted propeller with regard to efficiency has an efficiency $\eta_p = 0.53$, an impeller thrust total thrust ratio $\tau = 0.72$, while the impeller has a pitch ratio $P/D = 0.88$. The values of η_p and τ are of the same magnitude as found for the best nozzle of the series given in the paper under discussion.

Not clearly given in the paper is the way in which for given speed and thrust the optimum impeller diameter or rpm with regard to efficiency of the ducted propellers were determined. For instance, if for a systematic series of nozzles, the diameters of the impellers are chosen equal, then the optimum rotation speeds with regard to efficiency will certainly not be equal. In the paper, all the ducted propeller systems have equal impeller diameters and rpm's, and, consequently, these systems will not be optimum. This fact has also been shown in Fig. 10 of the paper. From this diagram it can be seen that only duct D6 and screw P1316 form more or less an optimum combination from the standpoint of efficiency.

The conclusion in Sec. 5.2 of the paper that the N.S.M.B. nozzles suffered from flow separation at the exterior surface of the nozzle at low screw loads, due to the relatively large angle α_D (between nose-tail line of the nozzle profile and the propeller shaft), must be considered with caution. The risk of flow separation on the nozzle depends on the *complete* shape of the nozzle profile determined by α_D, the camber ratio, the location of the maximum camber, and the

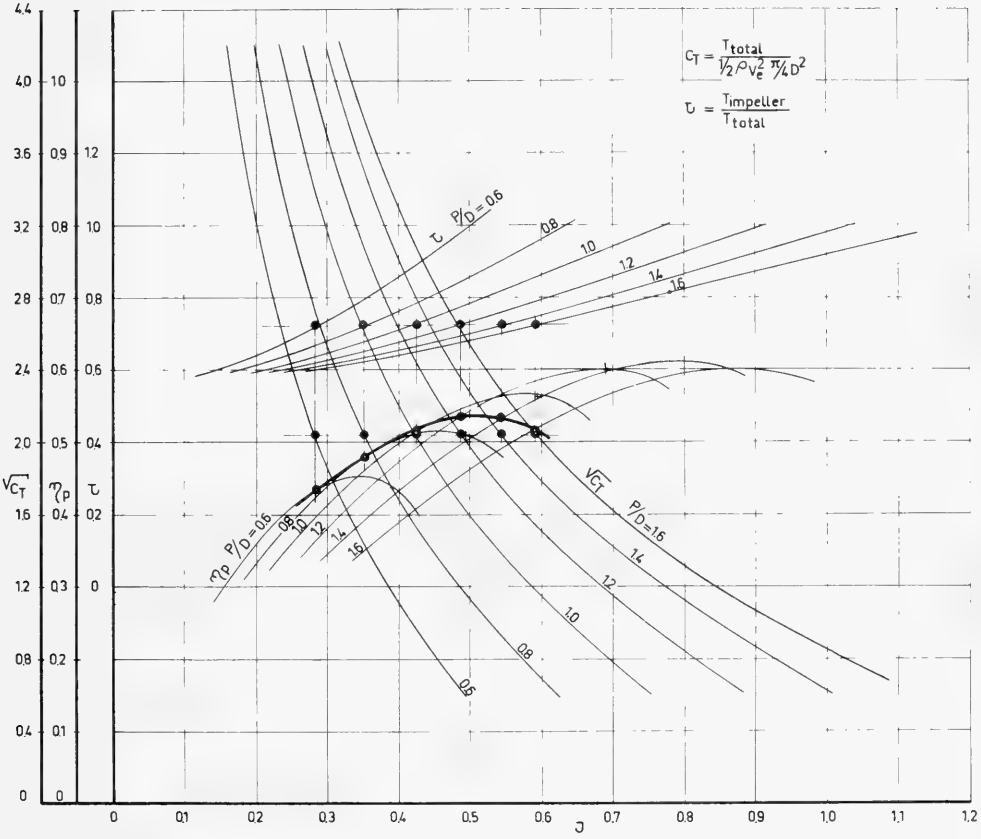

Fig. D1 - Open water test results of K_a 4-55 screw series in nozzle No. 19A

thickness ratio, and thickness distribution of the nozzle profile. The optimum relationship between the efficiency η_p and the thrust coefficient $(K_T/J^4)^{1/4}$ is shown in Fig. 2 for the N.S.M.B. nozzle no. 19A and the SSPA duct D6. In addition the nozzle shapes are presented in this diagram. From Fig. D2 it can be seen that the standard nozzle no. 19A of the N.S.M.B. has better characteristics at low screw loads than the SSPA duct, in spite of a larger angle α_D.

For a propeller operating in the wake of a ship, the intake velocity will be lower in the upper part of the screw disk than in the lower part. Consequently, the propeller is relatively more heavily loaded in the upper part of the screw disk. The inflow velocity can be made more constant over the screw disk by surrounding the propeller by a *noncylindrical* nozzle which is adapted to the wake distribution and the flow direction as occur behind the ship. A view of the stern of a tanker equipped with a noncylindrical ducted propeller is given in Fig. D3. The noncylindrical nozzle is at the inside of the nozzle still cylindrical

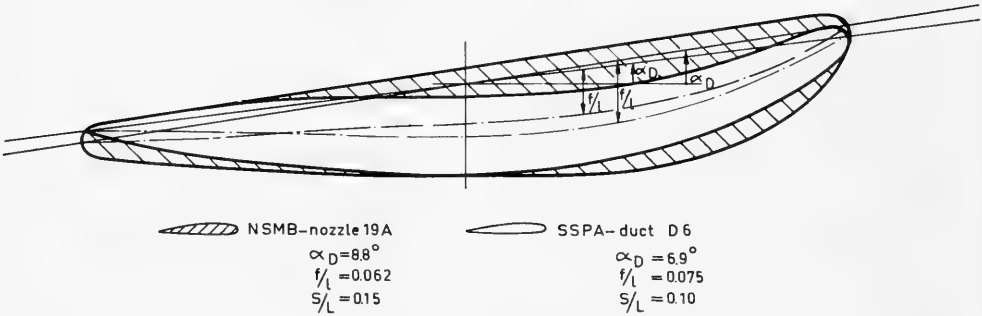

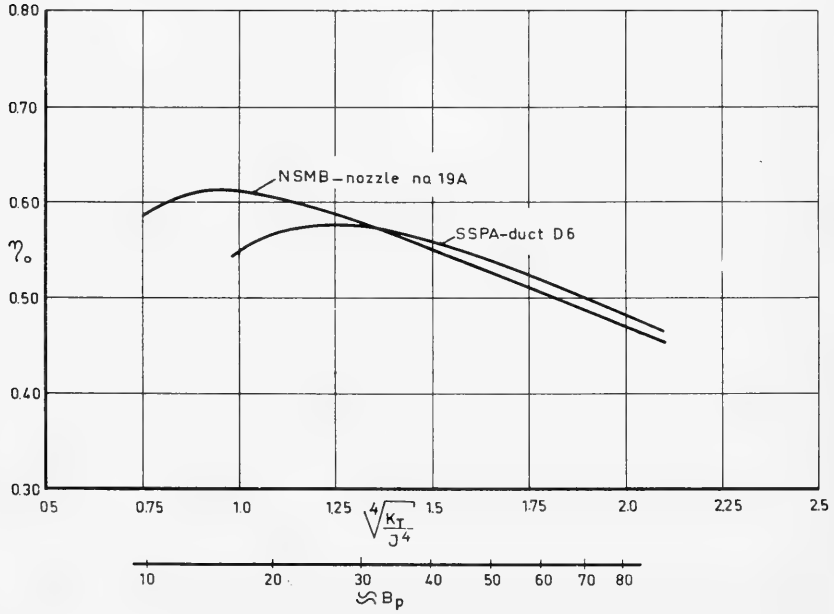

Figure D2

from the leading edge of the nozzle to the impeller, only the aft part of the nozzle is made noncylindrical. The outside of the nozzle is straight.

Tests performed at the N.S.M.B. with tanker models equipped with noncylindrical ducted propellers have shown that with this arrangement reductions in SHP can be obtained for a conventional afterbody which are of the same order as found for a Hogner type stern with cylindrical nozzle. The noncylindrical ducted propeller offers a definite means of minimizing propeller-induced vibration and cavitation problems due to the homogenizing effect of the noncylindrical nozzle on the inflow velocity of the propeller.

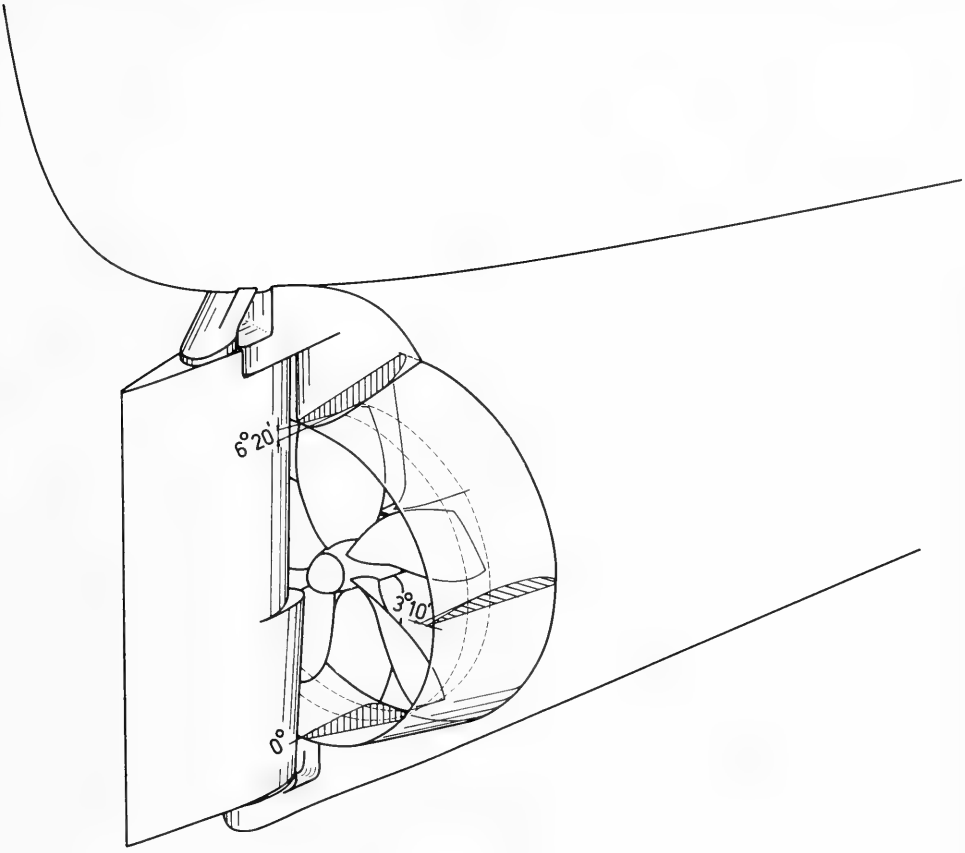

Fig. D3 - View of stern of tanker with non-cylindrical ducted propeller

Finally, it may be noted that application of the noncylindrical ducted propeller also offers a means of improving the propulsion characteristics of already existing ships without expensive alterations of the hull shape. There is no doubt that further work on noncylindrical ducted propellers for tankers is of utmost importance.

* * *

DISCUSSION

A. Emerson

University of Newcastle-on-Tyne
Newcastle, England

I would like to add to the list of references on contrarotating-propeller results and then make one or two comments.

For the high-speed cargo ship, particularly the container ship, the change from single- to twin-screw propulsion leads to considerable loss of cargo space and requires a different, bigger ship. For this reason, Stone Manganese Marine investigated the engineering and hydrodynamic problems of contrarotating-propeller drive. The result for a ship similar to that described by the authors was given before a meeting of the Institute of Marine Engineers in January of this year (L. Sinclair and A. Emerson, "The design and development of propellers for high-powered merchant ships"). The model self-propulsion results were given in the discussion by Mr. C.A. Lister of Vickers St. Albans Tank, because they designed the excellent model instrumentation for S.M.M. and carried out the experiments. Briefly, a set of contrarotating propellers replaced the single propeller on a recently completed 22.5-knot cargo vessel, changing only the size of aperture. They showed a 10% increase in propulsive efficiency above the excellent result obtained with the single propellers. The diameter of the forward propellers was maintained the same as for the single, and the design used optimum rpm. The contrarotating pair was designed using a method devised by Glover; the results showed the calculated improvement of 12% in efficiency of the propeller, but the increased aperture size caused a small increase in thrust-deduction fraction. Cavitation-tunnel observations suggested that the area of the propeller could be reduced; there are other alterations that are being investigated.

Turning now to the comments: We are used to the scaling differences between the propeller results from the towing tank at relatively low Reynolds number and the results in the cavitation tunnel. But for contrarotating propellers with critical balancing of power between the forward and aft propellers, the question of designing for the model experiments and then redesigning for the ship becomes a very real one.

A second observation from tunnel experiments is designing for a particular condition.

Thirdly, in related experiments with tandem propellers on a tanker model, we have obtained consistent values when the total result is used, but the individual thrust and torque results show peculiarities. Have the authors any comments?

* * *

DISCUSSION

V. Silovic

Hydro-og Aerodynamisk Laboratorium
Lyngby, Denmark

At Lyngby, we use Cheng's development of Pien's theory for lifting-surface-effect calculations. To my knowledge, the authors use a simplified 0.8 mean-line representation. My question would be: What is their experience as to the comparison of the two?

* * *

REPLY TO THE DISCUSSION

H. Lindgren, C.-A. Johnsson, and G. Dyne

After having listened to the discussion, the authors have come to the conclusion that one of the most important results of the paper might be that it has initiated activities in different laboratories and brought a great deal of interesting material to common knowledge. In the case of the Dutch Tank, these activities have been so intense that they went two days ahead of us in the end of the race by reading a similar paper without any advance announcement.

With regard to the oral discussion by Dr. English and Mr. Minsaas, the results they have presented are of the utmost interest and we regret that they have not given their discussion in a written form. We look, forward, however, to seeing their material published.

Mr. Oosterveld raises the interesting question about the relation between the ducted propellers designed in accordance with the SSPA design method and the systematic series of ducted propellers tested by van Manen. The number of unknown factors influencing the efficiency and the cavitation characteristics of a ducted propeller is of course much greater than for a conventional propeller. This means that the empirically based systematic series must be very extensive to ascertain that all factors have been considered. With the aid of a reliable design method it is possible to come to a good result much faster and in a more controlled way. The influence of a number of factors can be clarified purely theoretically, and the experiments can be concentrated to investigate such difficult problems as, for example, duct flow separation behind the propeller. In connection with this question, it is interesting to note that the values of geometrical angle of attack ($\alpha_D = 8.8°$) and camber ratio ($f_D/L = 0.062$) of NSMB nozzle no. 19A is much closer to the theoretical values for shock-free entrance than the earlier NSMB ducts plotted in Fig. 15.

As pointed out by Mr. Oosterveld, the optimum diameter of the different ducted propellers in our investigation must be different. Calculations carried out show, however, that the deviation from the optimum diameter means a loss in efficiency of less than about 2%.

The authors agree with Mr. Oosterveld that the risk for flow separation on the duct depends also on the thickness of the duct profile. The reason why ducted propeller P1315 D6, which has a higher efficiency than NSMB nozzle at the design point, is less effective at lower loads is certainly its more slender duct profile.

Since the wake behind a ship is nonuniform, it seems, at a first glance, to be natural to use noncylindrical ducts. The question is, however, how to design the duct shape in this case. A local increase of the low velocities in the upper part of the screw disk will certainly make the inflow velocity more uniform, but this does not necessarily mean an increased propulsive efficiency. However, the NSMB tests with the noncylindrical ducts are very interesting, and we hope that there will appear a more detailed description of the investigation in a near future.

Turning to Mr. Silovic's question, it is true that we use a simplified representation of the 0.8 mean line for our lifting-surface calculations. As described in Ref. (14), a constant distribution over 90% of the chord length is used, starting from the leading edge. Comparison with results of calculations using the true 0.8 mean-line distribution show very good agreement, and this is the reason why we have not yet used our limited programmer staff for completing the program in this respect.

Mr. Emerson's summary of the Stone Manganese Marine investigation on contrarotating propellers is valuable, and it is interesting to note that the improvements obtained with regard to propulsion efficiency and cavitation properties are in good agreement with the results presented by the authors.

The authors are not convinced that the balancing of power between the forward and aft propellers represents a critical problem. As a matter of fact, our results indicate an astonishingly small influence of the relation of power between the two propellers, as could be seen, for instance, in Fig. 8. However, no doubt the scale-effect problem including Reynolds-number effects is very difficult, and there are still many confusing problems to be solved. In connection with our experiments with the tanker, we tested one pair of contrarotating propellers designed for the model case and one pair designed for the ship case. At the conventional self-propulsion experiments the "model" pair was superior, but when we tried to carry out experiments at a J value corrected for wake scale effects the "full-scale" pair gave better results. The scale effects are, however, not known with sufficient accuracy and, furthermore, it is impossible to copy the full-scale case on a model in a quite true way.

As mentioned in our paper, we have no experience of our own with regard to the application of tandem propellers. Furthermore, we do not know of any measurements that include individual thrust and torque readings.

* * *

COMPARISON OF THEORY AND EXPERIMENT ON DUCTED PROPELLERS

Wm. B. Morgan and E. B. Caster
Naval Ship Research and Development Center
Washington, D. C.

ABSTRACT

The adequacy of the various theories in predicting the performance of annular airfoils and ducted propellers is discussed. Force data and pressure distributions are presented and conclusions are drawn as to the limitations of the theories. In general, the available theories can give an adequate prediction of the forces and the pressure distribution if no separation occurs on the annular airfoil and, in addition for ducted propellers, if a sufficient mathematical model of the propeller is used.

INTRODUCTION

Many studies have been made during the past few years of annular airfoils and of the use of annular airfoils as shroud rings around propellers. These studies have been both theoretical and experimental and have been directed toward application in both air and water. An extensive summary of this work was made by Burnell and Sacks (1) in 1960.

Ducted propellers of two types have been investigated: (1) where the duct accelerates the flow at the propeller, and (2) where the duct decelerates the flow at the propeller. The first type is used for thrust augmentation; the second has been suggested for increasing the limiting Mach number of the propeller in air and for increasing the cavitation inception speed of the propeller in water. For these applications, the annular foil, or duct, is an integral part of the propulsor, and a theoretical treatment must consider the interaction between the propeller and duct. Because of the complexity of the problem, this interaction is considered by an iterative procedure.

The results of the various experimental studies have direct application to either air or water, providing the Mach number is not too high for the studies in air and cavitation does not occur for the studies in water. The theoretical studies, of course, have application to any fluid, i.e., providing the mathematical model gives a reasonable approximation to the real flow. It is the purpose of this paper to discuss the adequacy of the various theories in predicting the actual performance of annular airfoils and ducted propellers. Are the various theories adequate to predict the pressure distribution on the duct or to predict the duct and propeller forces? What are the shortcomings of either the theories or experiments and where does additional work need to be done? These questions will be considered in the subsequent discussion. It is not the intent of this paper to present new data, but to synthesize comparisons already made.

In the following sections of the paper, the theory of annular airfoils and ducted propellers will be discussed first, then the experimental data available for use in making comparisons will be presented. The review of the theory will be very brief, as Weissinger's review (2) gives the details of the various theories. Theoretical-experimental comparisons will be made for pressure distributions and forces, and from these comparisons conclusions will be drawn as to the adequacy or inadequacy of the theory.

DISCUSSION OF THE THEORY

Theoretical investigation of the ducted propeller has concentrated to a large extent on linearized theory. Some investigations have been made, however, where the annular airfoil, or duct, is treated in a less restrictive manner. In general, the following assumptions are made regarding the mathematical model of the annular airfoil and the duct of a ducted propeller:

(a) The fluid is inviscid and incompressible, and no separation occurs on the duct.

(b) Body forces such as gravity are neglected.

(c) The free-stream flow is, in general, axisymmetric but may have a small cross-flow component. The free-stream velocity is, of course, zero for the static case.

(d) The annular airfoil is axisymmetric and of finite length. Although, Siekmann (3) has considered annular airfoils of elliptic cross-section.

For the linearized theory, the following two additional assumptions are made:

(e) The annular airfoil can be represented mathematically by a distribution of ring vortices and ring sources along a cylinder of constant diameter. This implies that the boundary conditions are linearized, i.e., the perturbation velocities are small in relation to the free-stream velocity (in calculating the pressure distribution, the Bernoulli equation without linearization is often used) and the boundary condition (normal velocity zero) is satisfied on the cylinder rather than on the foil surface.

(f) The trailing vortex system of the annular airfoil, if one exists, has the constant diameter of the annular airfoil and extends from the annular airfoil to infinity.

These foregoing assumptions apply only to the duct. Assumptions for the propeller are usually more restrictive, and the propeller is often considered as a crude approximation. Various mathematical models of the propeller have been used, some of which are: [1] momentum theory (4), [2] variable-load actuator disk (5), and [3] lifting-line theory (6). In the design process, the propeller and duct are treated separately, and a process of iteration is used to obtain

the mutual interaction. This means that for practical purposes we can discuss each separately.

In general, the linearized theories of the duct are based on the so-called Dickmann-Weissinger mathematical model, i.e., a distribution of ring vortices and ring sources lie on a cylinder of a diameter representative of the duct diameter and a length equal to the duct length. Some pertinent references are (7 - 17). In the various references quoted, the theory of the annular airfoil is essentially the same but with differences in numerical approach. Generally, two problems have been considered: [1] the direct problem, and [2] the inverse problem. The direct problem of the annular airfoil is: Given the annular airfoil shape, determine the pressure distribution and forces (7 - 12). The inverse problem is: Given the pressure distribution, determine the annular airfoil shape (13). Both the direct and inverse problems require the solution of a singular integral equation, the first for the ring vortex distribution and the second for the ring source distribution. Another version of the inverse problem is to assume the ring vortex strength and, if the effect of thickness is considered, to assume either the thickness or source distribution (14 - 17). The shape and pressure distribution of the annular airfoil are then calculated. For the purposes of this paper, any approach is pertinent as long as the theoretical and experimental data are for the same shape.

Some of the previously mentioned references considered the annular airfoil at an angle of incidence (8, 10 - 12). In the linearized theory, the effect of the angle of incidence on the pressure distribution, forces and moments are independent of the actual duct section shape, except for a small moment component, and only dependent on the chord-diameter ratio. This means that the angle-of-incidence effect is that of a circular cylinder at an angle of attack with a length-diameter ratio equal to the chord-diameter ratio of the duct.

As stated previously, various mathematical models of the propeller have been added to the theory of the annular airfoil. In some cases, a constant pressure jump with no clearance has been used to represent the propeller (17 - 19) and in others, a variable-load actuator disk (16, 20, 21), or lifting-line theory (9, 10). The use of a pressure jump at the propeller location would not appear to represent a realistic flow, as this would imply that a pressure jump could occur on the inner surface of the duct at the plane of the propeller (13). For the normal number of blades used in ducted propellers and an adequate tip clearance, it would not be possible to maintain a pressure jump on the duct surface. A more realistic approach, it would seem, would be to use an actuator disk which does not have a constant pressure jump or to assume a small tip clearance (5). In any case, the propeller induces a radial velocity on the duct which, for the inverse problem, causes a change in the duct shape (13).

When the lifting-line theory is used as the mathematical model for the propeller, the finite blade effect causes the ring vortex strength to vary in the circumferential direction and free vortices are shed from the duct. The vortex strength is steady with respect to the rotating propeller but unsteady with respect to a coordinate system fixed in the duct. The finite blade effect can only be considered for the direct problem as in this case, the pressure distribution can fluctuate with the rotation of the propeller, but the finite blade effect in the

inverse problem would imply the physical impossibility that the duct shape could change with the rotation of the propeller.

For the design of a ducted propeller it may be necessary to consider the effect of the finite number of blades, but this effect hasn't been completely investigated. The principal interference with the duct is the average velocity induced on the duct by the propeller. The form of the equation of this average component is identical with the actuator disk solution with the same average radial load, but the induced velocity differs somewhat because of the fact that the propeller pitch changes with the number of blades and that the viscous drag of the blades changes with the propeller blade area, i.e., if viscous effects are considered, the theoretical thrust of the propeller must be increased to account for this additional drag.

A few investigations of the nonlinear theory of ducted propellers have been made. In these cases the nonlinear theory was applied to the duct only and not to the propeller. A nonlinear approximation, based on second-order airfoil theory, has been given by Morgan (10), but more exact theories have been given by Chaplin (18) and Meyerhoff (22). Chaplin places a distribution of ring vortices on the surface of the duct and downstream along the slipstream of the wake. The slipstream boundary is not known a priori but is obtained by an iteration procedure. The pressure distribution and duct forces are obtained once the slipstream location is known. Meyerhoff uses a finite-difference approach (iteration and relaxation) and calculates the stream functions, and streamlines, for a known duct shape. Both the Chaplin and Meyerhoff treatments of the theory are mathematically correct, but certain numerical approximations must be made in each. Also, both treat the propeller as a pressure jump, which means that the mathematical model of the propeller is less sophisticated than that of Ordway et al. (9) or Morgan (10). As with numerical approximations of the type used by Chaplin and Meyerhoff, some difficulty is encountered in obtaining solutions for arbitrary shapes.

Besides the work of Chaplin and Meyerhoff on the nonlinear theory, the calculation procedure developed by Douglas Aircraft Division for the solution of the Neumann problem has been applied to the calculation of pressure distributions on the forward part of a ducted propeller (23). In the use of the computer program, the duct must be treated as semi-infinite, which means that only the pressures calculated near the leading edge are meaningful and no duct forces can be determined. Here again, the propeller is treated as a pressure jump.

The theoretical approaches discussed have generally been for the case of the ducted propeller moving at a constant velocity. However, there have been some investigations of the static condition, i.e., zero forward velocity. Linearized theories for this condition have been developed by Kriebel (24) and Greenberg et al. (25). Also, the Chaplin development of the nonlinear theory was carried out mainly to obtain a solution for the static case (18). In the linearized theory of the static case, the axial perturbation velocity cannot be assumed small, as in the free-running case. Both Kriebel and Greenberg neglect the slipstream contraction behind the duct even though the ducted propeller is heavily loaded. On the other hand, Chaplin, in his nonlinear treatment of the duct in the static condition, concentrates mainly on calculating this contraction.

In addition to these studies, some work has been done on the ducted propeller system at an angle of incidence, Kriebel (24) and Greenberg et al. (26). In both these approaches, the mathematical model is similar to the linearized theory discussed previously. As a first approximation, both Kriebel and Greenberg et al. showed that the ducted propeller may be regarded as a superposition of the ducted propeller at zero incidence plus a cylindrical duct at a given incidence. This approximation, however, does not account for the side forces and moments which occur on a propeller at an angle of attack (27). Greenberg et al. refined the approximation by taking into account the cyclic variation of the blade loading and these additional forces appear in the solution.

Some theoretical work has been done on the effect of blade tip clearance on performance. Both Kopeyetskiy (28) and Tachmindji (29) have considered the case of a finite-bladed propeller in an infinite cylinder. Lifting-line theory was utilized by both and the theories are essentially the same although different numercial solutions are utilized. Turbal carried out a theoretical and experimental investigation utilizing the previous theories (30), while English (31) and Gearhart (32) have utilized one-dimensional analysis to obtain the effect of blade tip clearance. Gearhart and Turbal considered the viscosity of the fluid in their analyses.

In the next section, comparisons will be made between pertinent theoretical and experimental results.

THEORETICAL AND EXPERIMENTAL COMPARISONS

Criteria for Comparison

Determination of whether a theory is adequate for predicting experimental performance is highly subjective. To offset this problem to some extent, criteria for the adequacy of the comparisons will be established on the basis of the use of the data. Two types of measurements will be analyzed in the following sections; pressure or velocity distributions and forces and moments. The pressure or velocity distributions will be both those on the annular airfoil surface and those within the flow field of the airfoil. Knowledge of the pressure distribution on the airfoil, or duct, is necessary: [1] for estimation of the critical Mach number in air or the critical cavitation number in water, [2] for estimation of the probable boundary-layer characteristics such as separation, and [3] for making structural analyses. *Satisfactory* prediction will be taken to mean that the predicted pressure distribution is generally within experimental accuracy and that the pressure distribution is adequate for determining the foregoing items. *Unsatisfactory* prediction will be taken to mean that the predicted pressure distribution is not adequate for determining these items. For many comparisons the prediction will be *marginal*, in that the pressure distribution is adequate for determining only some of these items.

Knowledge of the velocity field of the annular airfoil, or duct, is necessary: [1] for design of the propeller, stator and guide vanes (if used), [2] for predicting improvement in cavitation performance of the propeller, and [3] for determining the interaction of the duct with a centerbody (hub) or other bodies in the

flow field. Satisfactory, unsatisfactory, and marginal will be defined in a similar manner to that for the pressure distribution on the surface of the annular airfoil.

Knowledge of the forces and moments is necessary: [1] for estimating the system performance, [2] for design of a system to produce a given force, [3] for determination of the stability of a particular craft, and [4] for making structural analyses. Satisfactory will be taken to mean that the particular force or moment being discussed is, in general, within experimental accuracy, and unsatisfactory will be taken to mean that it is not within experimental accuracy. When discussing the thrust, or drag, on the duct of a ducted propeller however, the adequacy will be based on a comparison of the total thrust of the system, since the total force is the important parameter.

These criteria serve as a basis for making comparisons, however, the establishment of the experimental accuracy of the various tests is not straightforward. If no information is available on the experimental accuracy of a particular set of data, the following accuracy will be assumed: (1) for the pressure, or velocity, coefficients ± 5 percent, and (2) for force and moment coefficients ± 2 percent. The accuracy of the pressure measurements may very well be less than ± 5 percent and more than ± 10 percent for small values of the pressure coefficient.

Annular Airfoil Pressure Distributions

Experimental and theoretical pressure distributions are presented for several annular airfoils (ducts) which typify some of the duct shapes used for ducted propeller systems. Two ducts were tested in a wind tunnel at NSRDC and reported in Ref. (33). Duct I typifies a shape used for accelerating velocities at the propeller (Kort nozzle type). This duct has a NACA 0010 thickness distribution, a NACA 250 mean line with a camber-chord ratio of -0.0375, a chord-diameter ratio of 0.8, and a section angle of attack α, of 6°.

The measured pressure coefficients C_p, along with the theoretical predicted values from linearized theory with a nonlinear approximation (33) are plotted in Fig. 1 for this duct at a zero angle of incidence($\alpha_r = 0$). The symbols used are described in the Notation Section of this paper. Two sets of theoretical curves are shown on this figure; one using the linearized Bernoulli equation (shown by a solid line) and the other using the Bernoulli equation without linearization (shown by a dashed line). Figure 1 shows that the theoretical prediction of the pressure distribution on the inside of the duct is satisfactory. While on the outside of the duct boundary layer separation* occurs near the leading edge of this duct and

*Two regions of separation may occur on an annular airfoil; one is laminar separation near the leading edge and the other is turbulent separation near the trailing edge. The occurrence of separation depends on the gradient of the chordwise pressure distribution and will always occur if the annular airfoil has a sufficiently high angle of incidence. For ducts which are very thick, it would be expected that turbulent separation would occur near the duct trailing edge at angles of incidence lower than for which laminar separation would occur near the leading edge. For ducts of conventional thickness, laminar separation would be expected at lower angles of incidence than for which turbulent separation would occur. At high angles of incidence, both regions of separation would be expected to be present and at sufficiently high angles, the regions merge and stall of the annular airfoil occurs. These various flow regions on annular airfoils have been investigated in detail by Eichelbrenner et al. (34).

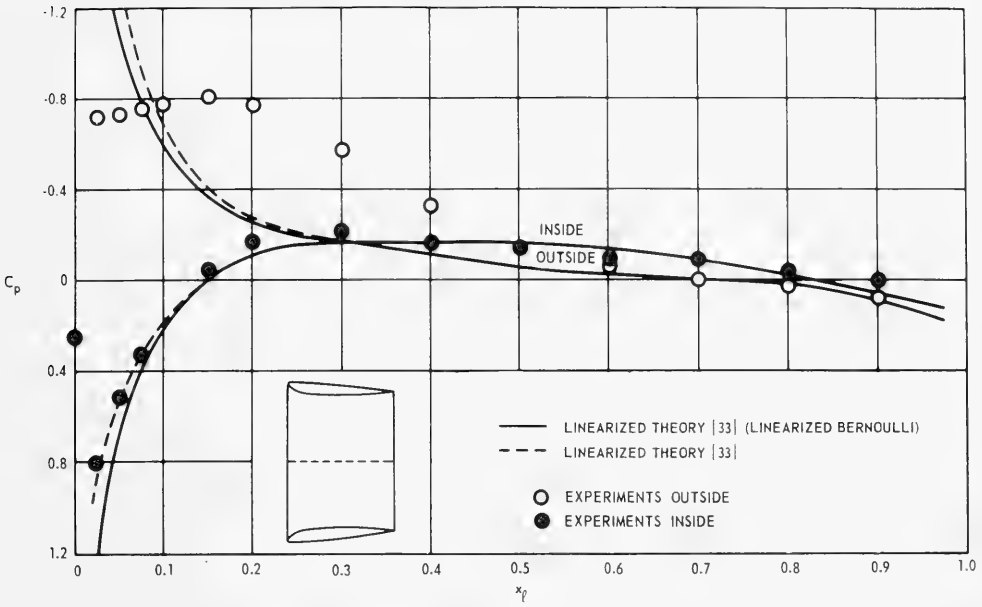

Fig. 1 - Pressure distribution on NSRDC duct I at zero angle of attack ($\alpha_r = 0$)

the flow is distorted so that the theoretical pressures are not valid. The difference in results from the two forms of Bernoulli equation is small, with the complete form giving slightly better results.

The separation occurring near the leading edge of this duct is undoubtedly laminar separation and Fig. 1 indicates that the flow reattaches itself probably near the transition region. This type of separation is, in general, predictable (34) and was predicted for this duct from the theoretical pressure distribution. Thus, for predicting separation this pressure distribution was satisfactory.

The experimental and theoretical pressure distributions on Duct I when this duct is at a 6° angle of incidence are shown in Fig. 2 for an angular position $\phi = 0$ and in Fig. 3 for an angular position of $\phi = 180°$. The angular position $\phi = 0$ refers to the duct section at the uppermost point of the duct and at a duct incidence angle of 6°, the local section angle to the flow is 12°. The angular position $\phi = 180°$ refers to the duct section at the lowermost point of the duct and at a duct incidence angle of 6° the local section angle to the flow is 0°. As before, two forms of the Bernoulli equation were used for the theoretical calculations. Figure 2 shows that $\alpha_r = 6°$, $\alpha = 12°$, the theoretical predictions are unsatisfactory on both the inside and outside of the duct. Flow separation covers more of the duct for this position and incidence than for zero incidence and apparently is severe enough to affect the pressure distribution on the inside of the duct. On the other hand, Fig. 3 shows that at $\phi = 180°$, $\alpha = 0°$, the theoretical predictions are generally satisfactory near the leading edge but only

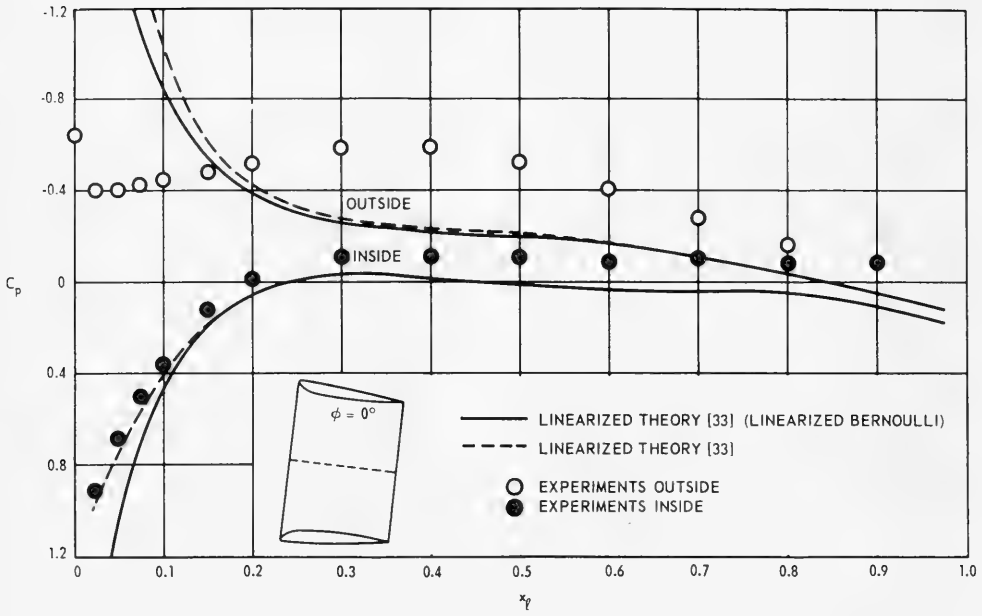

Fig. 2 - Pressure distribution on NSRDC duct I, α_r = 6 degrees and ϕ = 0 degrees

marginal toward the middle and trailing edge of the duct on both the inside and outside. Again, the form of the Bernoulli equations has only a small effect.

Duct II typifies a shape used to decelerate the velocity inside the duct. This duct has a NACA 66 modified thickness distribution with a thickness-chord ratio of 0.10, a NACA $\frac{a}{}$ = 0.8 mean line with a camber-chord ratio of 0.04, a chord-diameter ratio of 0.8, and a 0° section angle of attack. The measured pressure coefficients C_p along with the theoretical predicted values (33) for this duct at zero angle of incidence are plotted in Fig. 4. Also shown in Fig. 4 is the theoretical pressure distribution calculated from the nonlinear theory of Chaplin (18) and the nonlinear approximation of Morgan (10). All the theoretical predictions are generally satisfactory, with the nonlinear theory of Chaplin (18) giving the best prediction. The prediction using the linearized theory (using the linearized Bernoulli equation) gives a somewhat lower pressure on the outside of the annular airfoil near the leading edge than measured.

The experimental and theoretical pressure distributions on Duct II when this duct is at an 8° angle of incidence are shown in Fig. 5 for an angular position of ϕ = 0 and in Fig. 6 for an angular position of ϕ = 180°. Figure 5 shows that at the position ϕ = 0°, α = 8°, the comparison between theory and experiment is generally satisfactory. The linearized Bernoulli equation gives a slightly better prediction on the outside of the duct and the other form gives a better prediction on the inside. Figure 6 shows that at the position ϕ = 180°, α = -8°, the

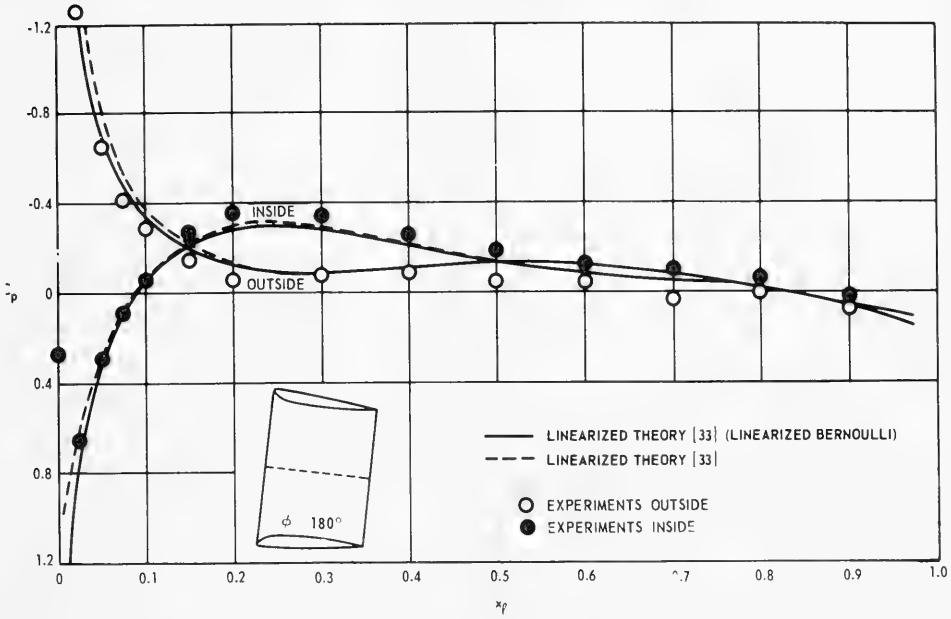

Fig. 3 - Pressure distribution on NSRDC duct I, α_r = 6 degrees and ϕ = 180 degrees

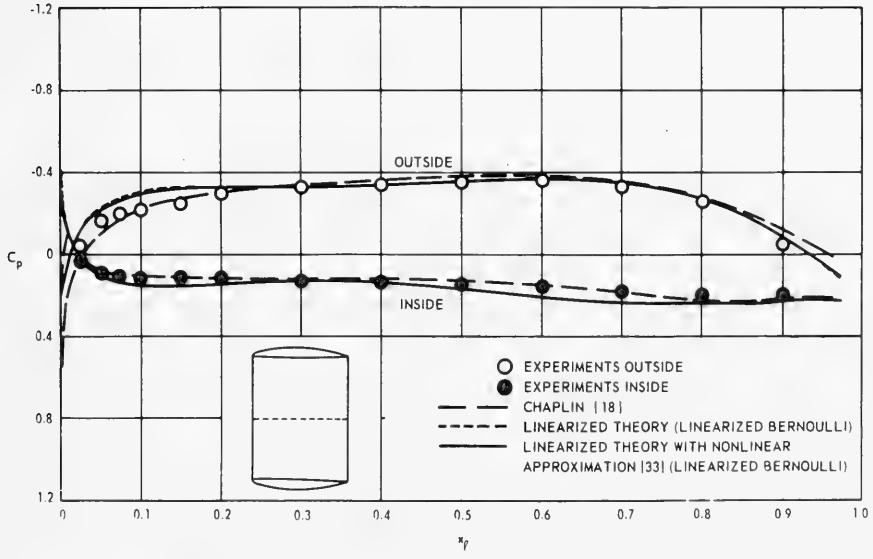

Fig. 4 - Pressure distribution on NSRDC duct II at zero angle of attack (α_r = 0)

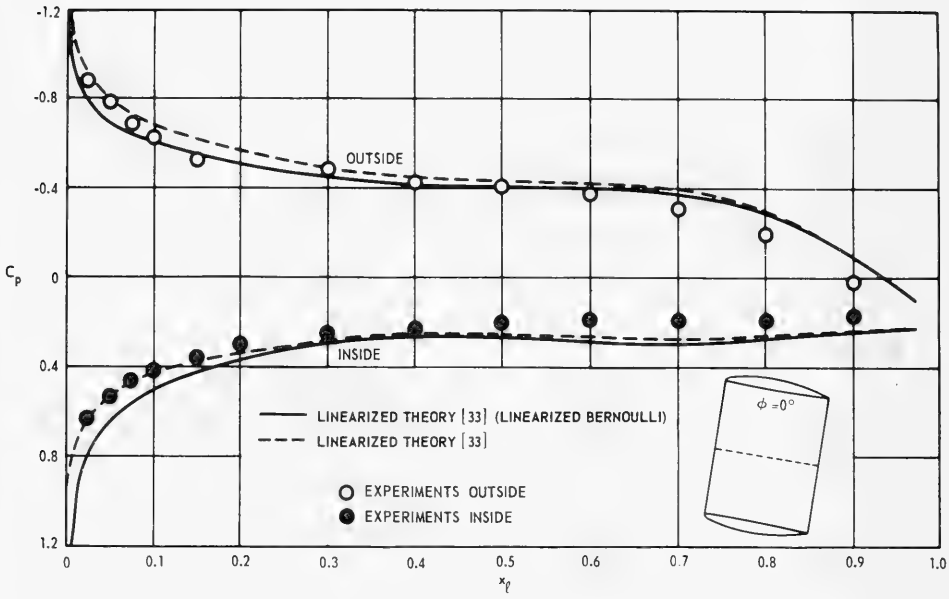

Fig. 5 - Pressure distribution on NSRDC duct II, α_r = 8 degrees and ϕ = 0 degrees

theoretical predictions from linearized theory are unsatisfactory but do give the right general shape. The difference in the results from the two forms of the Bernoulli equation is small. Apparently at an angle of incidence of 8°, this duct has started to separate at the position ϕ = 180°. Separation was apparent at this position when the angle of incidence was 10° (33).

Another duct (BTZ duct) for which extensive data is available is one designed and tested by the Bureau Technique Zborowski (12). This duct has a NACA 66-006 thickness distribution, zero camber, zero section angle of attack and a chord-diameter ratio of 0.96. The measured pressure distribution C_p, along with the theoretical predicted values from linearized theory with a nonlinear approximation (33), are plotted in Fig. 7 for the duct at a zero angle of incidence. The predicted pressure distribution for this duct is very satisfactory indeed. Experiments were conducted on this duct at angles of incidence but the data are not presented here, as they show the same trends as for Duct I and Duct II. The BTZ duct did show separation on the inside at the position ϕ = 180° at an angle of incidence of 12°. The prediction is given by both forms of the Bernoulli equation.

Pressure distribution tests on annular airfoils were also made at the Admiralty Research Laboratory (35). These ducts all had NACA 0006 thickness distributions, slightly thickened at the trailing edge for structural reasons, and a chord-diameter ratio of 0.75. Ducts B1, B2, and B3 have maximum camber

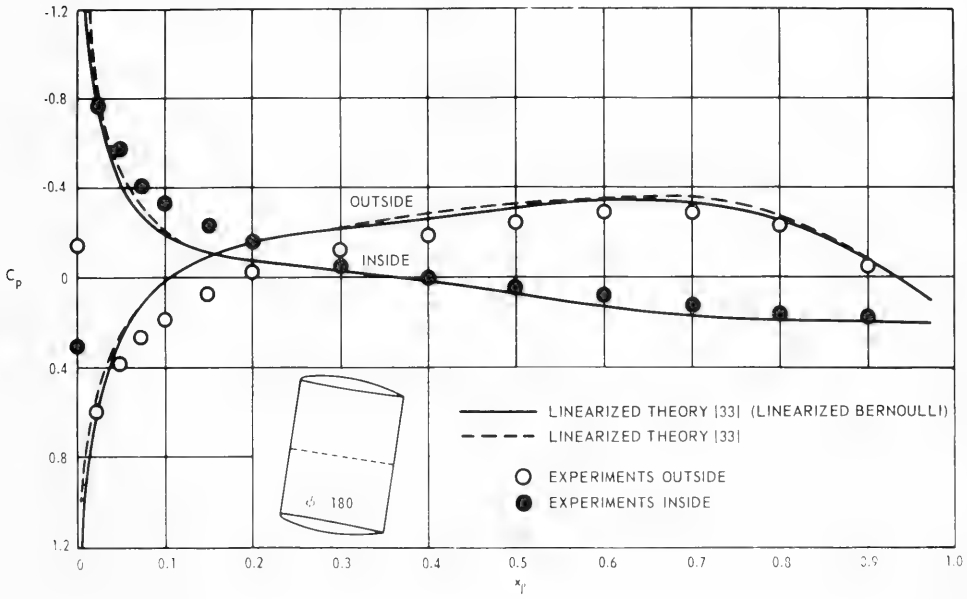

Fig. 6 - Pressure distribution on NSRDC duct II, α_r = 8 degrees and ϕ = 180 degrees

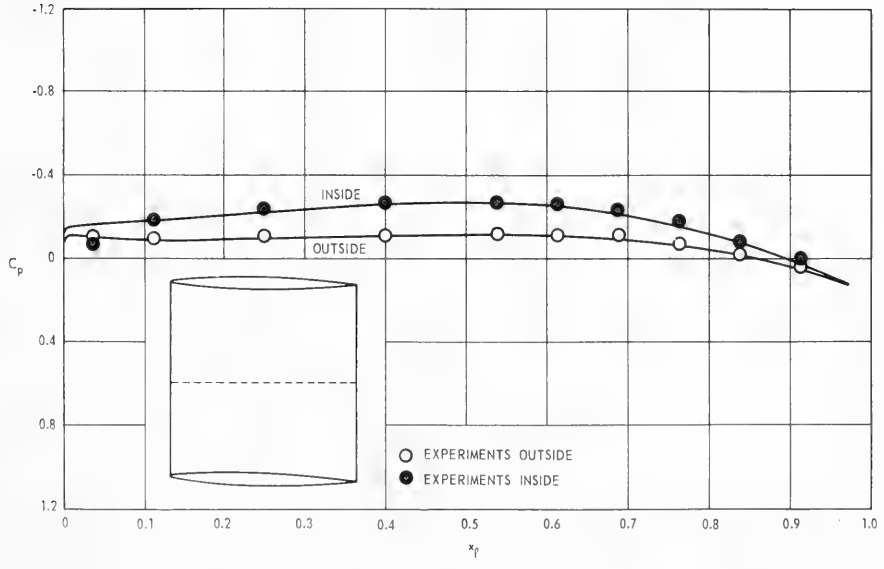

Fig. 7 - Pressure distribution on BTZ duct at zero angle of attack (α_r = 0) (12, 33)

ratios of 0.065, 0.025, and -0.022, respectively. Each of the ducts were designed to have a constant chordwise circulation distribution.

The experimental pressure distribution, along with two sets of theoretical values from linearized theory, are shown in Figs. 8, 9, and 10 for these ducts at zero angle of incidence. The solid lines are the theoretical results from Ryall et al. (35), who assumed that a constant chordwise circulation distribution produces only 74% of its theoretical loading. They based this assumption on the fact that in two dimensions the constant chordwise circulation distribution (NACA $\underline{a}$ = 1.0 mean line) produces only 74% of its predicted lift (36). Thus, in determining the pressure distributions shown by the solid lines in Figs. 8, 9, and 10, only 74% of the contribution from the ring vortices was used in calculating the pressure distribution. The dashed lines on these figures are the theoretical pressure distribution calculated by the linearized theory of Ref. (33) with a nonlinear correction. All the predictions shown in these figures were made using the Bernoulli equation without linearization.

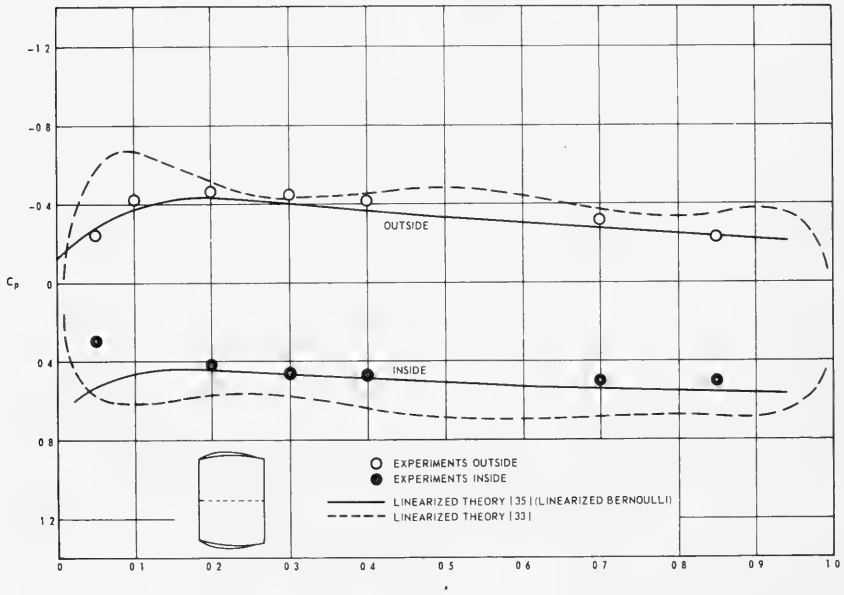

Fig. 8 - Pressure distribution on ARL duct B1 at zero angle of attack (α_r = 0)

The theoretical predictions for this set of tests are quite inconclusive. The predicted pressure distribution for duct B1, decelerating type, is satisfactory except near the leading edge if 74% of the contribution from circulation is used in the calculation (35), Fig. 8. For duct B3, accelerating type, the prediction is unsatisfactory on the inside of the duct using the same procedure, Fig. 10. On

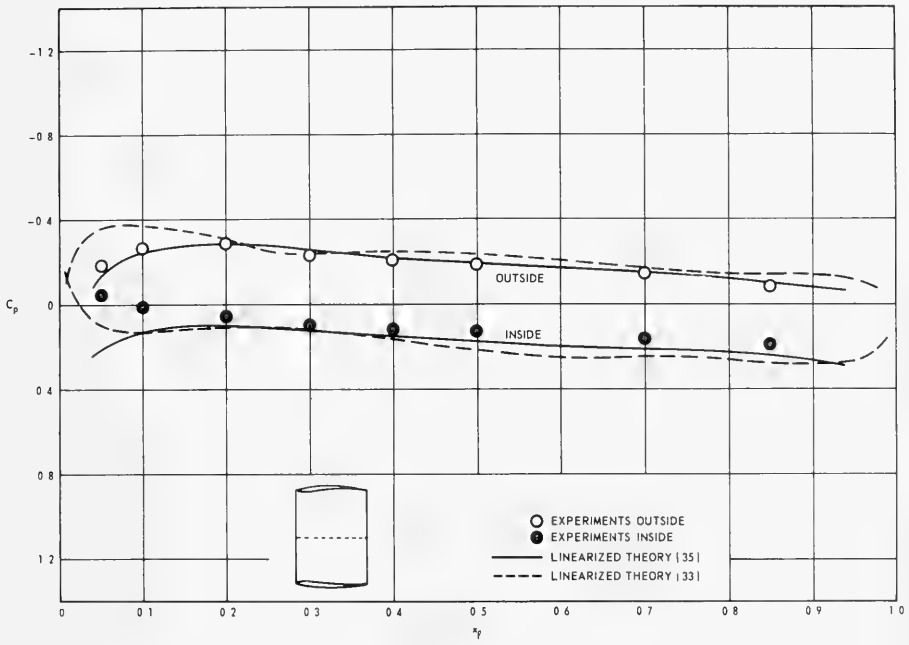

Fig. 9 - Pressure distribution on ARL duct B2 at zero angle of attack ($\alpha_r = 0$)

the other hand, for this duct the prediction is generally satisfactory using the method of Ref. (33) with no reduction in circulation. For duct B2, both approaches generally give a satisfactory prediction, Fig. 9. Both prediction methods are, in general, marginal to unsatisfactory near the leading edge. The method of Ref. (35) shows more of a deviation on the inside of duct B1 and B2 and on the outside of duct B3 near the leading edge, since a nonlinear correction for the velocity is not used (10). The results of the comparison for this series are very interesting for two reasons: (1) the sizeable viscous effect on the circulation distribution, and (2) the need for judicious choosing of the load distribution to minimize these effects.

In summary, the data reviewed show that the linearized theory gives a generally satisfactory prediction of the pressure distribution (both forms of the Bernoulli equation) on a duct when leading-edge laminar separation does not occur and other viscous effects are small. The nonlinear approximation (10) improves the prediction toward the leading edge and eliminates the theoretical prediction of infinite pressures at the leading edge. The nonlinear theory of Chaplin (18) gives a better prediction of the pressure distribution than the linearized theory. It should be pointed out that the duct shapes did not deviate markedly from a cylinder so that the good comparisons obtained might be

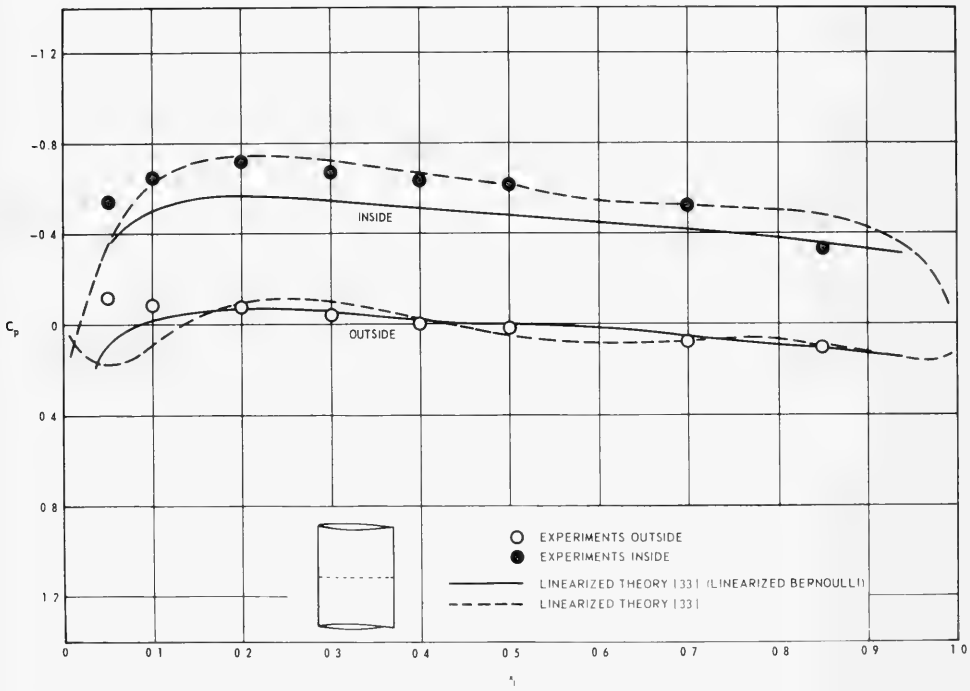

Fig. 10 - Pressure distribution on ARL duct B3 at zero angle of attack ($\alpha_r = 0$)

misleading if extreme shapes were used. On the other hand, separation might occur on extreme shapes which would void the comparisons anyway. The main shortcoming of the theory is the inability to predict the pressure distribution when separation occurs.

Annular Airfoil Forces

When annular airfoils are at a zero angle of incidence to the flow, the only net force is that due to viscous drag. Each section of the duct will be subject to forces and moments, however, which balance out. At an angle of incidence, the forces and moments do not balance out, and there are lift, moment, and induced drag forces acting on the duct in addition to the viscous drag. These forces and moments, except for a moment arising from horizontal forces, are independent of the section shape in linearized theory, and depend only on the chord-diameter ratio of the annular airfoil. Figure 11 shows the theoretical lift-curve slope for a range of chord-diameter ratios. Also plotted on this curve are the test spots from Ducts I and II, BTZ duct, and results obtained by Fletcher (37). The ducts tested by Fletcher had Clark-Y sections with a thickness-chord ratio of 0.117. As can be seen from this figure, the theory gives a satisfactory prediction even

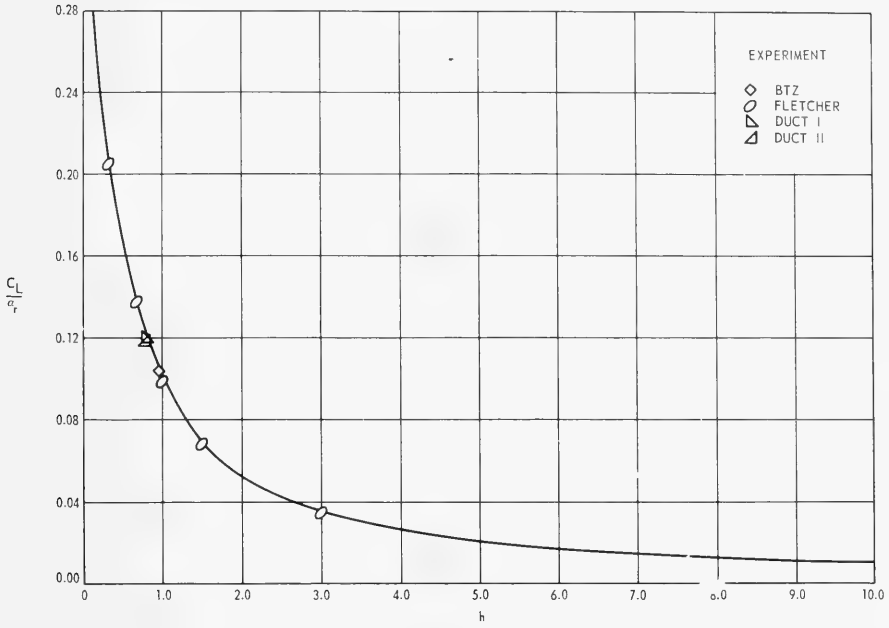

Fig. 11 - Lift curve slope as function of chord-diameter ratio (33)

though some of the ducts had laminar separation. When stall occurs, the prediction would not be satisfactory.

The theoretical lift coefficient C_L, drag coefficient C_D, and moment coefficient C_M, along with measured values are plotted in Fig. 12 for Duct II (33). This figure shows that the theoretical predictions are generally satisfactory. Results for the other ducts mentioned previously show similar trends.

The drag coefficient shown in this figure is the sum of the profile drag, i.e., drag at zero incidence, and the induced drag calculated theoretically (33). The profile drag can be approximated, for instance, by the method discussed by Granville (38) for predicting the drag of axisymmetric bodies. This procedure gives reasonable drag predictions when no separation occurs on the duct, e.g., the measured drag coefficient for Duct II at zero incidence was 0.07, while the drag predicted by the Granville method was 0.077. However, for Duct I, on which separation occurred, the measured drag coefficient was 0.48 at zero incidence, while the drag predicted by the Granville method was 0.413. At the higher angles of attack (positive or negative) where separation begins, the drag prediction starts to deviate from the measured value, Fig. 12. Ryall et al. (35) indicated in their investigation that the profile drag of one of their ducts increased by a factor of about 1.8 when the angle of incidence was changed from 0 to 10°.

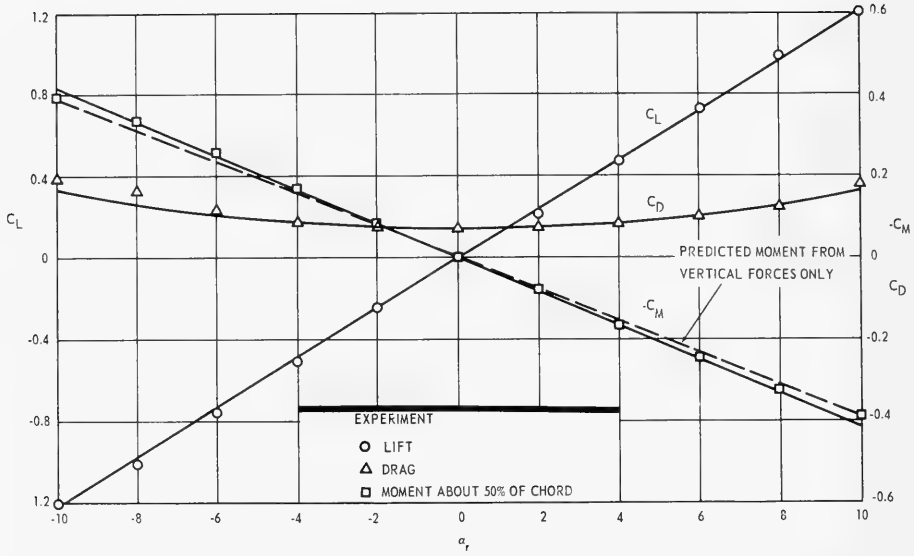

Fig. 12 - Lift, drag, and moment coefficients for NSRDC duct II (33)

The theoretical moment shown in Fig. 12 consists of two parts: one part from the vertical forces (lift) and one part from the horizontal forces (drag). The solid line is the theoretical moment including both of these parts, while the dashed line is the moment due to the vertical forces only, which is the dominant part.

In summary, the linearized theory gives a satisfactory prediction of the lift, induced drag, and moment for angles of incidence up to where separation influences the results. The first effect of laminar separation at the leading edge is on the drag force. This separation does not have much of an influence on the lift and moment when it first begins, but as the separation region increases in size, stall of the annular airfoil will occur (see footnote in previous Sec.).

It appears that the profile drag (viscous) of the annular airfoil can be estimated with some degree of confidence. However, if separation occurs on the duct, this drag may be underestimated by a significant amount. Because of the detrimental influence of separation, it would seem worthwhile to attempt to predict separation during the design stage of an annular airfoil. References (12) and (34) indicate that this has been done with some success.

Annular Airfoil Axial Induced Velocities

Axial induced velocities were measured at a number of locations inside several ducts tested at ARL (35). Figure 13 presents the axial induced velocities measured at the midchord for Ducts A1, A2, and A3 along with the theoretical predictions obtained using Ref. (35). Figure 14 presents similar results for

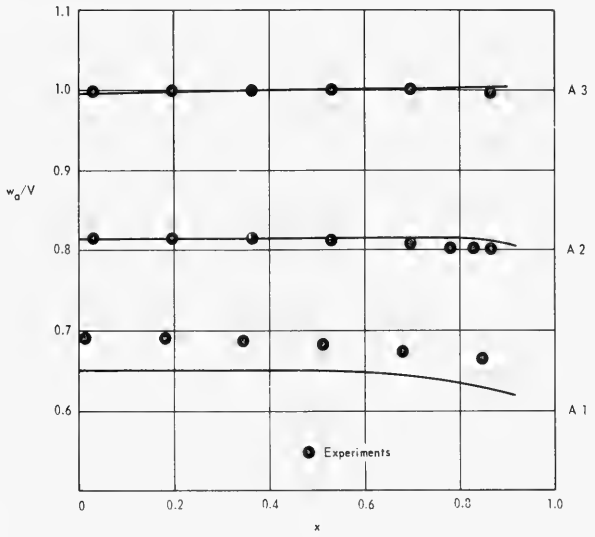

Fig. 13 - Radial variation of the axial induced velocity distributions in midplane of ARL ducts A1, A2, and A3 (35)

Ducts B1, B2, and B3. ARL ducts A1, A2, and A3 all have chord-diameter ratios of 1.0, a section angle of attack of zero, and a NACA 0006 thickness distribution. The maximum camber ratios for these ducts are 0.0659, 0.0385, and 0.0118, respectively. Ducts B1, B2, and B3 were described in a previous section.

In Fig. 13 the theoretical predictions for A2 and A3 are within experimental error and therefore, satisfactory; whereas for Duct A1, which has the largest camber ratio, the prediction is unsatisfactory. In Fig. 14, satisfactory predictions are obtained for Duct B2; Duct B1 is marginal, whereas for Duct B3 (accelerating-type duct) the prediction is unsatisfactory.

It should be noted that the velocities were predicted by Ryall et al. (35) on the basis of using only 74% of the contribution from the vortex distribution. As discussed previously, the stated reason for this reduction (35) was to correct for viscous flow effects. Even though the comparison between theory and experiment for the majority of ducts was satisfactory, it is difficult to draw general conclusions as to the applicability of the linearized theory from these data. Additional experimental results are needed for duct shapes for which the viscous effects would be expected to be small.

Ducted-Propeller Pressure Distribution

In this section, experimental and theoretical pressure distributions on ducts when a propeller is operating on the inside will be presented for a number of

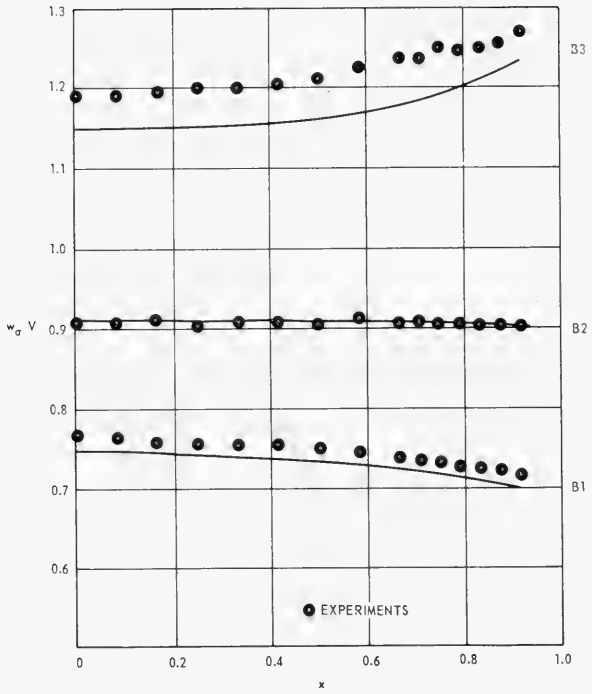

Fig. 14 - Radial variation of the axial induced velocity distribution in midplane of ARL ducts B1, B2, and B3 (35)

different ducted-propeller systems. Pressure measurements were made on a duct for various propeller loadings (Model 3650) in the David Taylor Model Basin (20, 39). This duct has a maximum camber ratio of 0.067, at approximately 67% of the duct chord from the leading edge, and a maximum thickness ratio of 0.045, at approximately 63% of the duct-chord length. Each duct section has an angle of attack of 3.9° and the chord-diameter ratio of the duct is 1.57. A five-bladed propeller with a hub radius of 0.4 was located at 28% of the duct-chord length from the leading edge and six stator vanes were located aft of the propeller at approximately 54% of the duct-chord length.

The experimental and theoretical pressure distributions on the duct of Model 3650 are shown in Fig. 15 at the design speed of advance, J, of 1.27. It is apparent from Fig. 15 that the predicted pressure distribution using linearized theory with a nonlinear approximation (20) gives a slightly better prediction on the outside of the duct than on the inside. This is also true for the Meyerhoff nonlinear theory (22) of the duct. The nonlinear theory gives a slightly better prediction than the linearized theory on the outside of the duct and on the inside of the duct forward of the propeller. In general, both predictions are satisfactory. The assumed pressure jump due to the propeller

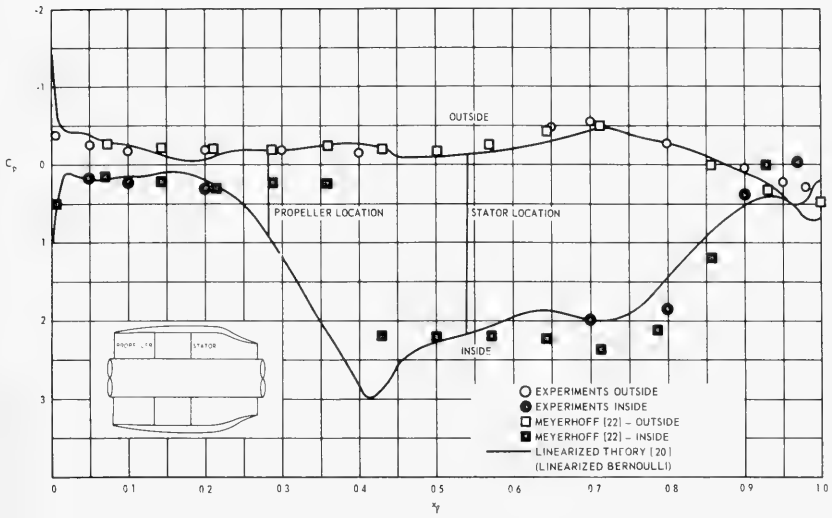

Fig. 15 - Pressure distribution on NSRDC duct model 3650 for $J = 1.27$, $C_{TP} = 1.330$

appears in the predictions by Meyerhoff (22), and the more realistic treatment of the propeller in the linearized theory is apparent. Theoretical predictions of the duct pressure distributions have been made at off-design conditions using both the nonlinear and the linearized theory. The comparisons, especially on the inside of the duct, are not as good as the data presented in Fig. 15 for higher propeller loadings. Part of the problem at these conditions may be due to the inaccuracy involved in estimating the effect of the stator vanes. This may also be the reason the predicted pressure distribution on the inside of the duct was not as good as on the outside for the design speed coefficient (22).

The most extensive duct pressure distributions have been measured on the Bell X22A ducted propeller system. This system consists of a duct with a chord-diameter ratio of 0.525 and a maximum thickness ratio of 0.172, of a three-bladed, controllable-pitch propeller, and of six streamlined support struts aft of the propeller. A one-third scale model of this system was tested in the 8 x 10-foot subsonic wind tunnel at NSRDC (40). Data were recorded for zero as well as a number of other angles of incidence at several forward flight speeds. Tests of a full-scale system were conducted at the NASA Ames Research Center in their 40 x 80-foot wind tunnel (41). Experimental pressure distributions are presented in Figs. 16 and 17 at two operating conditions for the full-scale model only, since the one-third scale test results were similar.

The theoretical predictions shown on Fig. 16 were calculated by Kriebel and Mendenhall (19) and those shown on Fig. 17 by Hough and Kaskel (21). The methods used by both were similar, except that Kriebel and Mendenhall used a nonlinear approximation to correct the duct velocity distribution and they used a

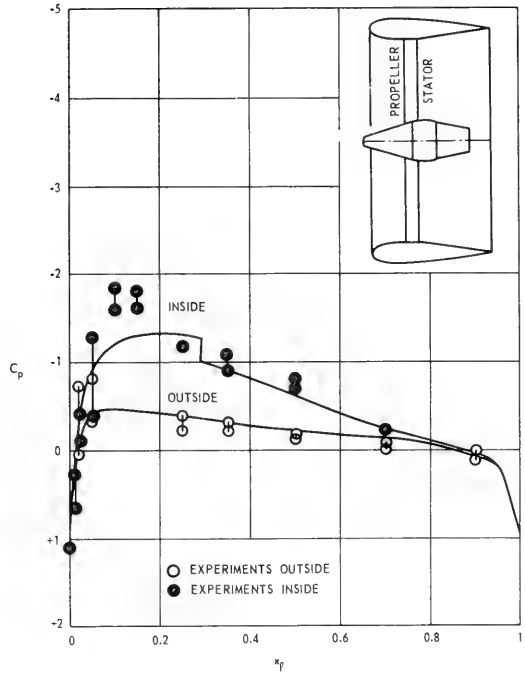

Fig. 16 - Pressure distributions on the X22a duct for $J = 0.617$, $C_{TT} = 0.220$ (19)

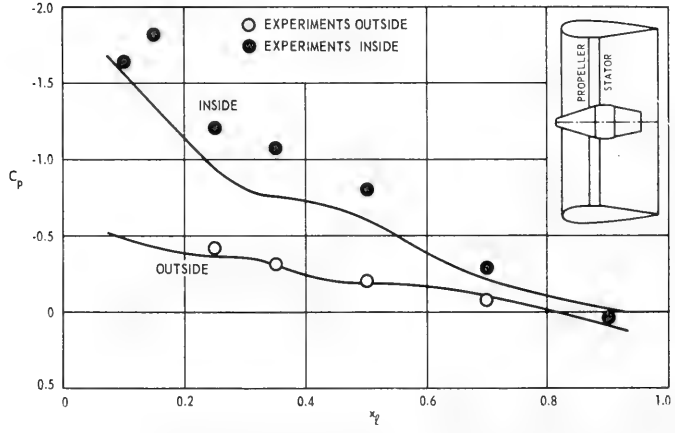

Fig. 17 - Pressure distribution on the X22A duct for $J = 0.628$, $C_{TP} = 0.276$ (21)

pressure jump to represent the propeller. The experimental scatter shown in Fig. 16 was also present in the data for Fig. 17, but only the average value is plotted in this figure.

Figure 16 presents the theoretical and experimental duct pressure distributions for a propeller thrust coefficient C_{T_p} of 0.220 and a speed coefficient J of 0.617, and Fig. 17 presents data for $C_{T_p} = 0.276$ and $J = 0.628$. Generally, the agreement between theory and experiment is satisfactory for the outside of the duct but not satisfactory for the inside. This conclusion also holds for other speeds of advance for this ducted system (19, 21). The calculations of Mendenhall and Kriebel give a slightly better prediction on the inside of the duct than those of Hough and Kaskel. It can be observed in Fig. 16 that the nonlinear correction to the duct surface velocity used by Mendenhall and Kriebel overcorrects the velocities on the inside of the duct forward of the propeller. Hough and Kaskel observed in making their calculations (21) that a better prediction could be made if a different cylinder diameter were used for the inside of the duct from that used for the outside.

For the ducted propeller in static operation, experimental and theoretical pressure distributions are presented in Fig. 18 as obtained by Hess and Smith (23), using a nonlinear theory. This figure compares calculated and experimental distributions on the forward portion of the duct only, as the pressure distributions behind the propeller cannot be calculated by the Douglas method (23). The predicted pressures are very satisfactory indeed. Kriebel and Mendenhall (19) have made theoretical predictions of duct pressure distribution for a ducted propeller in static operation which was a model of the Doak V2-4DA ducted system. This unit consists of a duct with a chord-diameter ratio of 0.608 and a profile-thickness ratio of 0.158, an eight-bladed propeller with pitch of 15° at the tip, a set of seven inlet guide vanes, and a set of nine stators aft of the propeller. At the static condition, the pressure distribution predictions from linearized theory (19), Fig. 19, are very satisfactory for the outside of the duct, are marginal for the inside of the duct forward of the propeller, and are unsatisfactory aft of the propeller. It is apparent that the contributions of the propeller, guide vanes, and stator blades are not adequately considered.

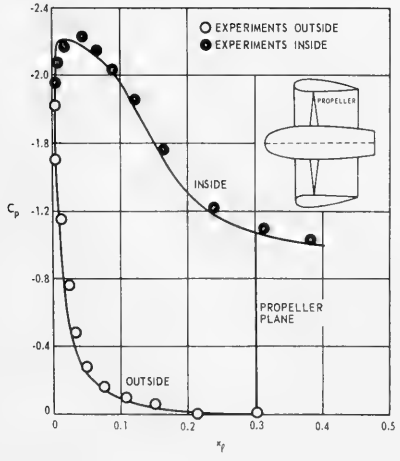

Fig. 18 - Pressure distribution on the Douglas duct for the static condition (23)

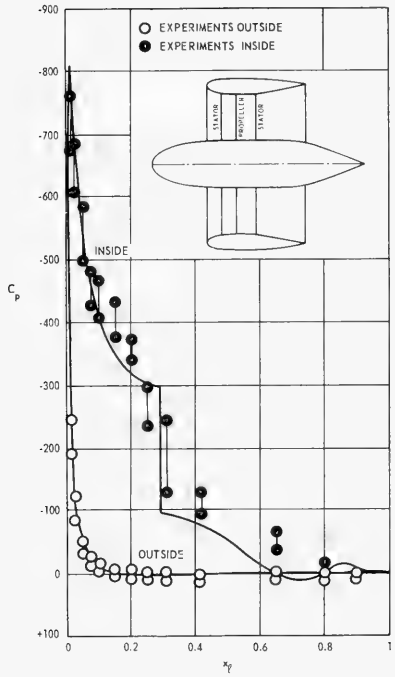

Fig. 19 - Pressure distribution on the Doak duct for the static condition (19)

Mention should be made of the pressure distribution on ducts when the ducted system is at an angle of incidence. Kriebel and Mendenhall (19) have made comparisons between theory and experiment for the full-scale X22A ducted propeller system, discussed previously, for angles of attack of up to 80°. These comparisons are not presented here, but it is obvious that significant improvements in theory are needed before reasonable predictions of the duct pressure distributions on the inside can be made for ducted systems at the high angles of attack investigated.

In summary, the prediction of the duct pressure distribution when a propeller is operating within the duct is satisfactory on the outside of the duct but varies between marginal and unsatisfactory on the inside of the duct. This poorer prediction than for the duct by itself is most probably related to the fact that the pressure contributed by the propeller is not properly determined. For instance, none of the experimental data reviewed showed a pressure jump at the propeller

position, as is sometimes assumed in the theoretical calculations. Also, the finite blade chord and blade thickness may produce considerably different induced velocities, even on an average, than given by an actuator-disk model. An example of this difference is the steady axial and radial induced velocities presented in Table 1, which were calculated from actuator-disk theory and propeller lifting-surface theory. These data are for a three-bladed marine propeller for $J = 0.833$ and $C_{T_p} = 0.578$. The lifting-surface calculations, which contain both effects of loading and thickness, generally give slightly greater values for the axial induced velocities and considerably different values for the radial induced velocities, as compared to the lifting-line calculations. The lifting-surface calculations smooth out the radial velocities in the vicinity of the blade tip. Since these induced velocities are different from those obtained from the actuator-disk model, it is not possible to say whether the linearized theory of the duct is adequate or not in the presence of the propeller. Quite clearly the mathematical model used for the propeller in the pressure distribution data presented must be improved.

Table 1
Average Propeller-Induced Velocities from Lifting-Line and Lifting-Surface Theory at $R_d/R = 1.05$

$x\ell/D$	Lifting Line		Lifting Surface	
	w_a	w_r	w_a	w_r
1.0	-0.0082	-0.0018	-0.0093	-0.0044
0.750	-0.0118	-0.0034	-0.0132	-0.0077
0.625	-0.0144	-0.0048	-0.0159	-0.0105
0.500	-0.0179	-0.0067	-0.0193	-0.0147
0.375	-0.0226	-0.0096	-0.0235	-0.0214
0.250	-0.0287	-0.0153	-0.0283	-0.0328
0.125	-0.0277	-0.0917	-0.0296	-0.0541
0.0625	-0.0166	-0.1023	-0.0229	-0.0699
0	0	-0.1091	-0.0033	-0.0807
0.0625	0.0166	-0.1023	0.0173	-0.0730
0.125	0.0277	-0.0917	0.0261	-0.0588
0.250	0.0287	-0.0153	0.0278	-0.0374
0.375	0.0226	-0.0096	0.0243	-0.0248
0.500	0.0179	-0.0067	0.0205	-0.0170
0.625	0.0144	-0.0048	0.0171	-0.0121
0.750	0.0118	-0.0034	0.0142	-0.0088
1.0	0.0082	-0.0018	0.0101	-0.0049

Ducted Propeller Forces

Considerably more force data (measured ducted propeller thrust) than pressure distribution data are available on ducted propellers. However, theoretical predictions have not been made for most of available force data.

For NSRDC Model 3650 ducted propeller system, the theoretical and measured ducted forces are presented in Table 2 (20). These results show satisfactory agreement between measured and theoretical results. In making these calculations, the stator thrust was determined from the measured propeller and duct plus stator thrust and the calculated duct thrust. For this reason, the comparison may not be truly representative of the accuracy of the calculations.

Table 2
Theoretical and Measured Thrust Coefficients for a Pumpjet and Kort Nozzle Type Ducted Propeller (20)

Ducted Propeller	J	C_{Tp}	C_{Td}	C_{Tsv}	$C_{Td} + C_{Tsv}$	C_{TT}
Theory — Pumpjet	2.260	0.270*	-0.309	0.142*	-0.167	0.103
Measured — Pumpjet	2.260	0.270	-	-	-0.170	0.100
Theory — Pumpjet	1.270	1.330*	-0.638	0.354*	-0.284	1.046
Measured — Pumpjet	1.270	0.330	-	-	-0.280	1.050
Theory — Kort Nozzle	0.40	2.75*	0.425	-	-	3.175
Measured — Kort Nozzle	0.40	2.75	0.40	-	-	3.150

*Input. Nomenclature: J = speed coefficient, C_{Tp} = propeller thrust coefficient, C_{Td} = duct thrust coefficient, C_{Tsv} = stator thrust coefficient, C_{TT} = total thrust coefficient ($C_{Tp} + C_{Td} + C_{Tsv}$).

The second set of data shown in Table 2 is for a Kort nozzle type ducted propeller (20), and the agreement is also satisfactory. In this case, the theory over-predicts the duct thrust by about 6% and the total thrust by about 1%.

Theoretical and measured duct forces for the X22A ducted system are shown in Table 3 (19). On the basis of the total thrust, the theoretical predictions are satisfactory for a speed coefficient of 0.22 and higher. The theory over-predicts the duct forces for speed coefficients below 0.22 and slightly under-predicts the duct forces at the higher speed coefficients. The maximum deviation is at a speed coefficient of zero where the predicted duct thrust is 10% high and the total thrust 5.5% high. This unsatisfactory comparison may be due to separation occurring on the inside of the duct.

Dyne (42) has also made comparisons between theoretical and experimental ducted propeller forces. Results presented in Table 4 show generally satisfactory agreement between theory and experiment for three ducted systems but unsatisfactory agreement for one of the four. This unsatisfactory agreement is probable due to separation that occurred on the duct.

Figure 20 shows the ratio of propeller thrust to total system thrust for a range of thrust coefficients as presented by Weissinger (43). The experimental curve shown in this figure is from the work of Finkeldei (44) and the theoretical curve from the work of Bollheimer (11). The agreement between theory and experiment is very satisfactory.

Table 3
Measured and Predicted Thrust Coefficients for the Doak Ducted Propeller (19)

J	C_{TT} Measured	C_{T_p} Measured	C_{Td} Measured	C_{Td} Theory
0.541	0.890	0.766	0.186	0.186
0.471	1.530	1.150	0.403	0.360
0.419	2.250	1.620	0.671	0.625
0.342	4.150	2.740	1.390	1.380
0.220	12.700	7.520	5.030	5.450
0.178	19.400	10.800	7.980	8.700
0	306.000	142.000	147.000	164.000

Table 4
Performance of Four Ducted Propeller Systems According to Dyne (42)

Propeller	Duct	C_{Td}/C_{TT}		J		$\eta\%$	
		Theory	Expt.	Theory	Expt.	Theory	Expt.
P1313	D4	0.01	0.11	0.412	0.414	49	48
P1314	D5	0.15	0.20	0.412	0.406	52	50
P1315	D6	0.30	0.29	0.412	0.422	55	53
P1316	D7	0.45	0.29	0.412	0.443	58	53

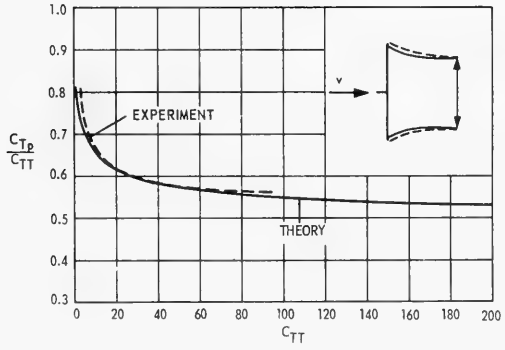

Fig. 20 - Comparison of ducted propeller thrust by Weissinger (43)

The most extensive experimental investigation on ducted propellers has been conducted by the Netherlands Ship Model Basin (NSMB). Oosterveld (17) and (45) has made theoretical-experimental comparisons for three ducts designed for decelerating the flow at the propeller. These data are shown in Table 5. The theoretical predictions, which did not include the viscous drag, are generally satisfactory for two of the ducts, nozzles 30 and 31, and unsatisfactory for nozzle 32. Including the viscous drag would have improved the prediction for nozzle 30 only, and would probably have made the prediction for nozzle 31 unsatisfactory.

Table 5
Measured and Predicted Thrust Coefficients
According to Oosterveld (45)

Ducted Propeller	J	C_{TT}	C_{Td}
Theory — Nozzle 30	1.0	0.950	0
Measured — Nozzle 30	1.0	0.930	-0.027
Theory — Nozzle 31	1.0	0.950	-0.143
Measured — Nozzle 31	1.0	0.973	-0.120
Theory — Nozzle 32	1.0	0.950	-0.285
Measured — Nozzle 32	1.0	1.021	-0.214

In addition to the theoretical-experimental comparisons for the free-running condition, comparisons have been made at the static condition by Kriebel and Mendenhall (19), Table 3; comparisons were also made by Greenberg and Ordway (25). Their predictions under-predicted the measured value of the duct thrust by 30%, whereas Kriebel and Mendenhall (19) over-predicted the thrust. Both predictions were unsatisfactory.

A few theoretical-experimental comparisons of force and moment data have been made for ducted propellers at an angle of incidence by Kriebel and Mendenhall (19). Data for both the Bell X22A and Doak VZ-4DA systems have been compared. The variations of lift, duct thrust, and drag coefficients with propeller thrust and angle of incidence are shown in Figs. 21, 22, and 23, respectively, for the Doak system. The theoretical predictions are, in general, greater than the measured results. Prediction of the lift, except for small thrust coefficients, was unsatisfactory while the prediction of duct thrust and pitching moment was marginal. The theoretical predictions of the lift and pitching moment for the Bell X22A system were lower than measured (19) and varied between marginal and satisfactory.

In summary, the predicted ducted propeller thrust is generally satisfactory, except at the static condition, if separation does not occur on the duct. For the ducted propeller at an angle of attack, the prediction of thrust and pitching moment was marginal, while the prediction of lift was unsatisfactory in one case and marginal to satisfactory in another. In calculating the duct thrust, some of the methods used the measured propeller thrust rather than a theoretical value. Consequently, the predictions may not be as good as the data indicate if all the

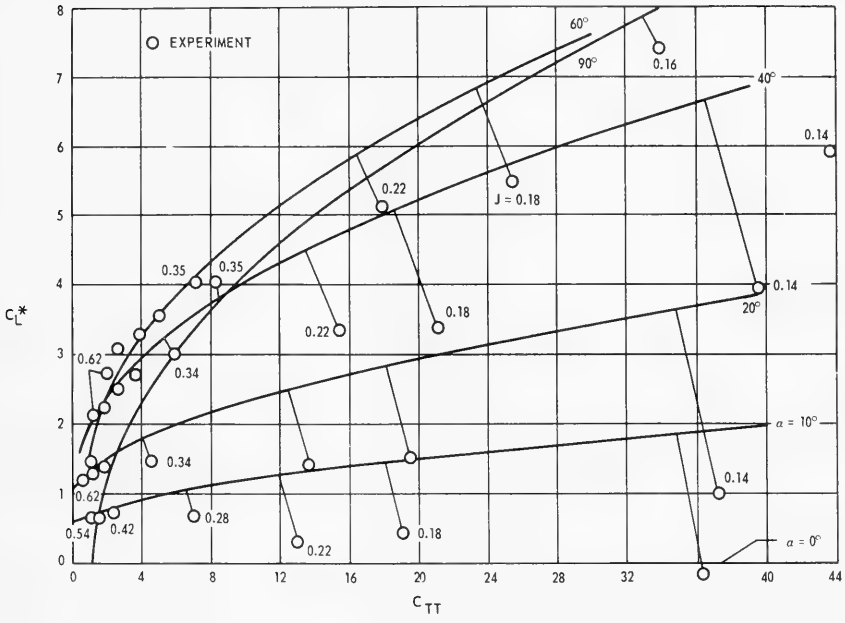

Fig. 21 - Lift of the Doak ducted propeller at angles of incidence (19)

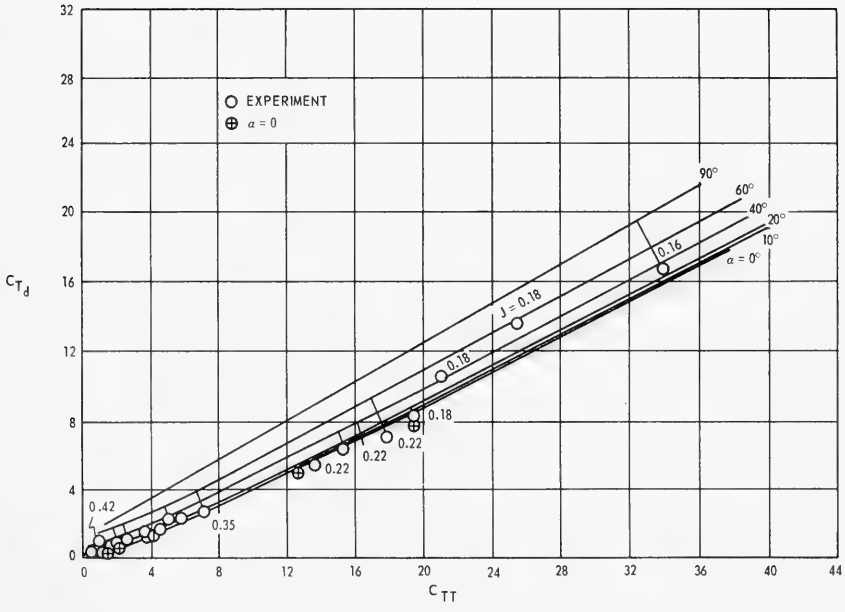

Fig. 22 - Duct thrust of the Doak ducted propeller at angles of incidence (19)

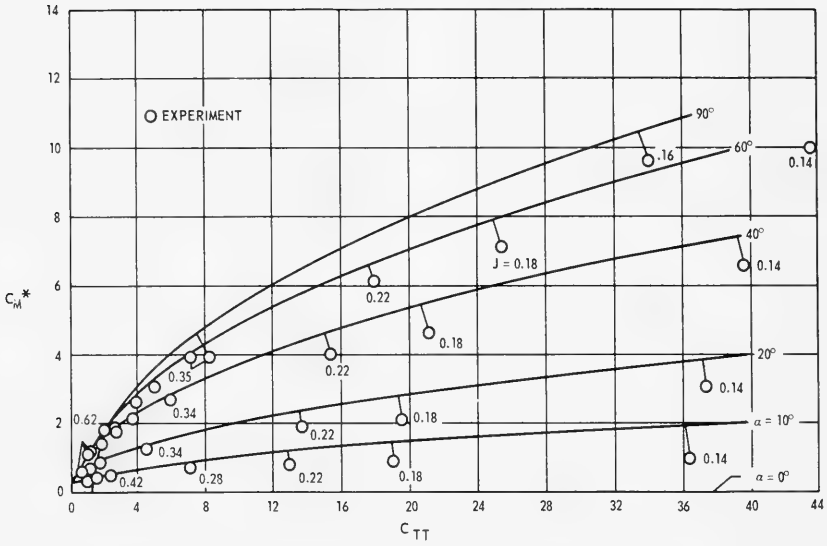

Fig. 23 - Pitching moment of the Doak ducted propeller at angles of incidence (19)

comparisons were based on predicting the total system thrust. It can be concluded that a more complete mathematical treatment is required for the propeller, stator vanes, and guide vanes to be able to predict all the forces satisfactorily. Also, more complete experimental data are required where the forces on the various components are measured separately, especially for an angle of incidence.

Tip Clearance

Several investigations have been made of the effect of tip clearance on the performance of ducted propellers, e.g., Refs. (28 - 32). Results of a theoretical-experimental comparison made by English (31) are shown in Fig. 24. The basic conclusions of this work is that, for increasing tip clearance, the duct thrust decreases and the propeller thrust increases, while the net effect is a small reduction in efficiency. The theoretical predictions of English slightly underpredict the change in efficiency with tip clearance. The comparisions made by Turbal (30) show similar results. In summary, the comparisons show that the theory indicates the trends of the experimental data.

CONCLUSIONS

The following conclusions as to the adequacy of the theory are based on a limited number of geometric shapes. Consequently, general applicability of the conclusions may be limited.

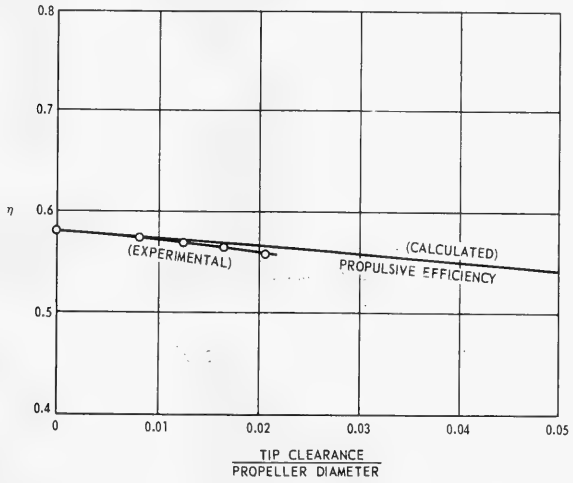

Fig. 24 - Variation of thrust and efficiency with tip-clearance by English (31)

(1) The comparison of the theoretical and experimental pressure distributions on the annular airfoil show that the theoretical prediction is satisfactory if no separation occurs on the duct and other viscous effects are small. The linearized theory, of course, does not give as good a prediction as the nonlinear theory.

(2) The linearized theory predicts annular airfoil forces and moments satisfactorily if no separation occurs on the airfoil.

(3) The linearized theory gives a satisfactory prediction of the velocities in the annular airfoil if the pressure distribution on the airfoil is satisfactorily predicted.

(4) The prediction of the duct pressure distribution when a propeller is operating within the duct is satisfactory on the outside of the duct but varies between marginal and unsatisfactory on the inside of the duct.

(5) The predicted ducted propeller thrust appears to be generally satisfactory, except at the static condition, if separation does not occur. However, because of the procedures used, this conclusion is probably optimistic.

(6) The predicted propeller forces and moments for an angle of attack are marginal.

(7) The linearized theory of the duct with suitable nonlinear corrections appears to be generally satisfactory if separation does not occur on the duct.

(8) The importance of separation should be emphasized, and, if predictions are to be reasonable, the duct must be designed so that boundary-layer separation does not occur.

(9) Lifting-surface theory of the propeller should be used in predicting the interaction between the propeller and duct and for the propeller design. This mathematical model of the propeller would have the same linearized boundary conditions as presently used for the duct.

(10) Adequate consideration must be given to the influence of the guide vanes and stator vanes.

ACKNOWLEDGMENTS

We wish to express our appreciation for the encouragement received from the management of the Naval Ship Research and Development Center in the preparation of this paper. The permission of the Admiralty Research Laboratory for the use of their ducted propeller data is gratefully acknowledged. We wish to express our appreciation to Mr. Geoffrey G. Cox for review of this paper and his numerous suggestions, to Mrs. Shirley Childers for preparation, and to Mrs. Mary Dickerson for review of the manuscript.

NOTATION

$\underline{a}$ Duct-chord length

C_D Drag coefficient, $\dfrac{D_r}{\frac{1}{2}\rho a R_d V^2}$

C_L Lift coefficient, $\dfrac{L}{\frac{1}{2}\rho a R_d V^2}$

C_L^* Lift coefficient, $\dfrac{L}{\frac{1}{2}\rho \pi R_d V^2}$

C_M Moment coefficient, $\dfrac{M}{\frac{1}{2}\rho \pi R_d^2 V^2}$

C_M^* Moment coefficient, $\dfrac{M}{\frac{1}{2}\rho \pi R_d^3 V^2}$

C_p Pressure coefficients on outside and inside of duct,

$$\frac{[p(x_d, x_\ell) - p_0]}{\frac{1}{2}\rho V^2}$$

C_{ps}	Power coefficient, $\frac{P_s}{\frac{1}{2}\rho\pi R^2V^3}$
C_T	Thrust coefficient, $\frac{T}{\frac{1}{2}\rho\pi R^2V^2}$
D	Propeller diameter
D_r	Drag
h	Chord-diameter ratio of duct
J	Propeller speed coefficient, V/nD
L	Lift
M	Moment
n	Propeller rps
P_s	Shaft power
$p(x_d, x_\ell)$	Local pressure on duct
P_0	Free-stream static pressure
R	Propeller radius
R_d	Duct radius
T	Thrust
V	Free-stream velocity
w_a	Axial induced velocity
w_r	Radial induced velocity
x	Nondimensional radius
x_d	Ratio of duct radius to the propeller radius
x_ℓ	Axial distance from leading edge of duct nondimensionalized by the duct chord
Z	Number of blades
α	Duct section angle of attack with reference to section nosetail line
α_r	Relative duct angle of incidence

η	Efficiency of ducted propeller system, $\frac{C_{TT}}{C_{ps}}$
ρ	Mass density
ϕ	Angular position of a duct section

Subscripts

d	Duct
P	Propeller
sv	Stator vanes
T	Total

REFERENCES

1. Burnell, J.A., and Sacks, A.H., "Ducted Propellers—A Critical Review of the State of the Art," Progress in Aeronautical Sciences, Vol. 3, Pergamon Press, New York, 1962, pp. 85-135.

2. Weissinger, J., "The Theory of the Ducted Propeller—A Review," Seventh Symposium on Naval Hydrodynamics, Office of Naval Research, Aug. 1968.

3. Siekman, J., "Analysis of Ring Aerofoils of Elliptic Cross Section, Part 1: General Theory," Journal Society of Industrial Applied Mathematics, Vol. II, No. 4, Dec. 1963, pp. 941-963.

4. Kuchemann, D., and Weber, J., "Aerodynamics of Propulsion," McGraw-Hill, New York, 1953.

5. Hough, G.R., and Ordway, D.E., "The Generalized Actuator Disc," Developments in Theoretical and Applied Mechanics, Vol. II, Pergamon Press, New York, 1965, pp. 317-336.

6. Morgan, W.B., and Wrench, J.W., Jr., "Some Computational Aspects of Propeller Design," Methods in Computational Physics, Academic Press, New York, Vol. 4, 1965, pp. 301-331.

7. Dickmann, H.E., "Grundlagen zur Theorie Ringförmigen Tragflügel (frei umströmte Düsen)," Ingenieur-Archiv, Vol. II, 1940, pp. 36-52.

8. Weissinger, J., "Einige Ergebnisse aus der Theorie des Ringflügels in Inkompressibler Strömung," Advances in Aeronautical Sciences, Vol. 2, Pergamon Press, New York, 1959, pp. 798-831.

9. Ordway, D.E., Sluyter, M.M., and Sonnorup, B.O.U., "Three-Dimensional Theory of Ducted Propellers," Therm, Inc., Report TAR-TR 602, Aug. 1960.

10. Morgan, W.B., "Theory of the Annular Airfoil and Ducted Propeller," Fourth Symposium on Naval Hydrodynamics, Office of Naval Research ACR-73, 1962, pp. 151-197.

11. Bollheimer, L., "Neure Beitrage zur Theorie des Düsenpropellers," Institute fur Angewandte Mathematik der Technischen Hochschule Karlsruhe Report 48, 1966.

12. "Theoretical Investigation and Examination by Measuring Tests in What a Degree the Economy of Flying Vehicles is Influenced by Pre-Cambered Skeletons of Airfoils Closed in Themselves," Bureau Technique Zborowski Report under Contract DA-91-508-EUC-393, August 1959.

13. Morgan, W.B., and Voigt, R.G., "Inverse Problem of the Annular Airfoil and Ducted Propeller," David Taylor Model Basin Report 2251, September 1966.

14. Lerbs, H.W., "Theoretical Considerations on Shrouded Propellers," David Taylor Model Basin Report C-543, June 1953.

15. Dickmann, H.E., and Weissinger, J., "Beitrag zur Theorie optimaler Düsenschrauben (Kortdüsen)," Jahrbuch der Schiffbautechnischen Gesellschaft, Vol. 49, 1955.

16. Dyne, G., "A Method for the Design of Ducted Propellers in a Uniform Flow," Statens Skeppsprovningsanstalt Report 62, 1967.

17. Oosterveld, M.W.C., "Series of Model Tests on Ducted Propellers," Netherlands Ship Model Basin Report N62558-4555, Oct. 1967.

18. Chaplin, H.R., "A Method for Numerical Calculation of Slipstream Contraction of a Shrouded Impulse Disk in the Static Case with Application to Other Axisymmetric Potential Flow Problems," David Taylor Model Basin Report 1857, Jan. 1964.

19. Kriebel, A.R., and Mendenhall, M.R., "Predicted and Measured Performance of Two Full-Scale Ducted Propellers," National Aeronautics and Space Administration Contractor Report CR-578, Sept. 1966.

20. Caster, E.B., "A Computer Program for Use in Designing Ducted Propellers," Naval Ship Research and Development Center Report 2507, October 1967.

21. Hough, G.R. and Kaskel, A.L., "A Comparison of Ducted Propeller Theory with Bell X22A Experimental Data," Therm, Inc., Report TAR-TR 6510, Dec. 1965.

22. Meyerhoff, L., Discussion to paper by van Manen, J.D. and Oosterveld, M.W.C., "Analysis of Ducted-Propeller Design," Transactions Society of Naval Architects and Marine Engineers, Vol. 74, 1966, pp. 549-550.

23. Hess, J.L., and Smith, A.M.O., "Calculation of Potential Flow about Arbitrary Body Shapes," International Symposium on Analog and Digital Techniques Applied to Aeronautics. Liege, Belgium, Sept. 1963.

24. Kriebel, A.R., "Theoretical Stability Derivatives for Ducted Propellers," Journal of Aircraft, Vol. 1, No. 4, July-Aug. 1964, pp. 203-210.

25. Greenberg, M.D., Ordway, D.E., "The Ducted Propeller in Static and Low-Speed Flight," Therm Advanced Research, Inc., TAR-TR 6407, Oct. 1964.

26. Greenberg, M.D., Ordway, D.E., and Lo, C.F., "A Three-Dimensional Theory for the Ducted Propeller at Angle of Attack," Therm, Inc., Report TAR-TR 6509, Dec. 1965.

27. Glauert, H., "Airplane Propellers," Aerodynamic Theory, Vol. IV, edited by W.F. Durand, Dover Publications, Inc., New York, 1963, pp. 351-357.

28. Kopeyetskiy, V.V., "Gidrodinamika Vista v Trube Krugovogo Secheniya," (Hydrodynamics of a Screw in a Tube with a Round Cross-Section), Sudpromgiz, 1956.

29. Tachmindji, A.J., "The Potential Problem of the Optimum Propeller with a Finite Number of Blades Operating in a Cylindrical Duct," J. Ship Research 2, No. 3, 1958.

30. Turbal, V.K., "Effect of the Clearance Between the Blade and the Nozzle Wall on the Efficiency Coefficient of the System and the Optimum Contour of the Propeller Blade," Symposium of Articles on Ship Hydrodynamics, Part II, Sudostroyenige Publishing House, 1965, pp. 55-74.

31. English, J.W., "One-Dimensional Ducted Propeller Theory—Influence of Tip Clearance on Performance," National Physical Laboratory, Ship Division Report 94, May 1967.

32. Gearhart, W.S., "Tip Clearance Cavitation in Shrouded Underwater Propulsors," Journal of Aircraft, Vol. 3, No. 2, Mar.-Apr. 1966, pp. 185-192.

33. Morgan, W.B., and Caster, E.B., "Prediction of the Aerodynamic Characteristics of Annular Airfoils," David Taylor Model Basin Report 1830, Jan. 1965.

34. Echelbrenner, E.A., Angiolotti, S., Grellier, Y.M., and Hellerstrom, R.S., "Theoretical Investigation and Control by Measuring Tests on the Behavior of the Three-Dimensional Turbulent Boundary Layer in an Annular Wing at Various Incidences," Bureau Technique Zborowski Report under Contract ONR N62558-3514, Sept. 1963.

35. Ryall, D.L., and Collins, I.F., "Design and Test of a Series of Annular Airfoils," Admiralty Research Laboratory, Teddington, Middlesex, Report A.R.L./R3/G/AE/2/5, ARL/G/R6, March 1965.

36. Abbott, I.H., and von Doenhoff, A.E., "Theory of Wing Sections," Dover Publications, Inc., New York, 1959.

37. Fletcher, H.S., "Experimental Investigation of Lift, Drag, and Pitching Moment of Five Annular Airfoils," National Advisory Committee for Aeronautics TN 4117, 1957.

38. Granville, P.S., "The Calculation of the Viscous Drag of Bodies of Revolution," David Taylor Model Basin Report 849, July 1953.

39. Hansen, E.O., and Cumming, R.A., "Experimental Pressure Distribution on the Duct of an ERG Pumpjet," David Taylor Model Basin Report 2133, Jan. 1966.

40. Boone, J.R., "Wind Tunnel Test Data Report for the 1/3-Scale Powered Duct Model," Bell Aerosystems Co., Report 2127-921003, Mar. 1964.

41. Hesby, A., and Sherman, E.W., Jr., "Wind Tunnel Test Data Report for the Full-Scale Powered Duct Model," Bell Aerosystems Co., Report 2127-921007, Aug. 1965.

42. Dyne, Gilbert, "An Experimental Verification of a Design Method for Ducted Propellers," American Society of Mechanical Engineers Symposium on Pumping Machinery for Marine Propulsion, Philadelphia, May 1968, pp. 58-83.

43. Weissinger, J., Discussion to paper by van Manen, J.D. and Oosterveld, M.W.C., "Analysis of Ducted Propeller Design," Transactions Society of Naval Architects and Marine Engineers, Vol. 74, 1966, pp. 558-561.

44. Finkeldei, H., "Experimentelle Untersuchungen an Düsenschrauben," dissertation, Karlsruhe Polytechnic Institute, 1963.

45. Oosterveld, M.W.C., "Model Tests with Decelerating Nozzles," American Society of Mechanical Engineers Symposium on Pumping Machinery for Marine Propulsion, Philadelphia, May 1968, pp. 17-41.

* * *

DISCUSSION

V. Silovic
Hydro- og Aerodynamisk Laboratorium
Lyngby, Denmark

The interaction between the ship and the propulsive unit plays an important part in the case of a partial duct. In this case, the open-water results and available theories are of little help. Do the authors have any comments?

* * *

DISCUSSION

Gilbert Dyne
The Swedish State Shipbuilding Experimental Tank (SSPA)
Gothenburg, Sweden

This is a very interesting paper and it illustrates in a striking way how astonishingly few the experimental verifications of the theories are, especially for ducted propellers. In fact, a closer examination shows that the stringent verifications are still fewer than what they first seem to be. I would like to make some comments on this fact.

The results from two different theoretical approaches to the problem have been described in the paper. These approaches are set forth in Table D1. It is common to all theories mentioned that the total thrust (or propeller thrust) and the advance ratio are given, while the duct thrust and the pressure distribution along the duct are determined.

Table D1

Problem	Given	Desired
Direct-inverse	Duct shape and radial distribution of circulation or ideal pitch angle	Propeller shape
Inverse-inverse	Duct vortex distribution and radial distribution of circulation or ideal pitch angle	Shapes of duct and propeller

A stringent verification of these theories means that

(1) the ducted propellers are designed according to the theory (experiments carried out after the calculations);

(2) the comparison between theory and experiment are made only at the design point.

As far as I know, these requirements are fulfilled only by

(1) the four ducted propellers tested at SSPA (42),

(2) one of the ducted propellers tested at Karlsruhe (44), and possibly

(3) some of the ducted propellers tested at NSMB (45).

In many of the ducted propeller investigations described, however, the calculations have been carried out after the tests. Since, so far, no stringent theory has been presented for this direct-direct approach of the problem, the theories used must involve some more or less satisfactory approximations. The authors have mentioned some of them in their paper, for example, the pressure jump at the propeller assumed in Refs. (19, 21, 22), but it would be valuable to get some information also about the more reliable method used in (20). The paper seems to indicate that the authors use the measured propeller thrust rather than a theoretical value. If, instead, one starts from the pitch and camber distributions of the propeller and not from the measured propeller thrust, how large will the difference between the experimental and theoretical values of propeller thrust be for the three ducted propellers described in (20)?

* * *

DISCUSSION

George Rosen
Hamilton Standard Division of United Aircraft Corp.
Windsor Locks, Connecticut

The authors should be complimented on an excellent contribution toward the improving technology on ducted propellers. It is from this type of continuing correlation of advanced theoretical and experimental work that the necessary refinements in design criteria must come.

At the Ducted Propeller Panel meeting I described some extensive wind-tunnel tests conducted by Hamilton Standard on a series of systematic ducted propeller configurations. Unfortunately, the results of these tests were not available in time for the authors to include them in the studies reported in this paper. I hope that they will have the opportunity to do this in the near future.

I would like to make the following two comments on this paper:

(1) Shroud static pressure distribution measurements made under the shrouded propeller research wind-tunnel program conducted by Hamilton Standard and reported in HSER 4048 indicate a definite pressure jump at the propeller plane particularly at low forward speeds. The tip clearance was 0.25 percent of the diameter. This appears to be inconsistent with the views expressed in this paper.

(2) The generally favorable comparison of the theoretical and experimental pressure distribution reported in this paper is in agreement with similar comparisons made with shrouded propeller performance method developed from the Therm-Ordway theory by Hamilton Standard reported in HSER 4776 and the test data of HSER 4348. However, in these latter comparisons the pressure distributions inside as well as outside of the duct were quite accurately predicted by the calculation method.

* * *

REPLY TO DISCUSSION

Wm. B. Morgan and E. B. Caster

We wish to thank the discussers for contributing to the paper by their taking time to make pertinent comments. The problem posed by Dr. Silovic is a difficult one, both from the standpoint of the interaction and from the fact that the duct operates partially in the boundary layer of the ship. One way of approaching this problem is to design the unit as if the duct is whole, then multiply the duct force (thrust or drag) by the ratio of circumference of the partial duct to the complete duct. This method should give the approximate effect of the duct on the propeller and vice versa. The partial duct on a ship also gives a lift force; whether its direction is up or down depends on the duct shape, and the effect of this force should be considered, since the ship trim could be changed enough to affect the ship's resistance.

Dr. Dyne discussed what we found to be one of the most distrubing aspects of the comparisons, i.e., there were little data available where the duct and propeller were designed and compared by the same method. In fact, only for the duct by itself were we able to find such data which included experimental pressure distributions. Some of the data presented were for a more or less exact solution in inviscid flow (18, 22) of the duct, but the propeller was treated as a pressure jump. References (18, 22) give no method for doing the direct propeller problem. The linearized procedure given in Ref. (20) can start with either the propeller thrust or total thrust. The calculations for the theoretical data given in Ref. (20) for the pumpjet-type ducted propeller when operated at two propeller loading conditions started with the measured propeller thrust, and, for

the Kort nozzle-type ducted propeller, the theoretical data were the design data for the ducted system. We don't know of any theoretical calculations for ducted propellers where the starting point was the pitch and camber distributions of the propeller. We can only guess that such comparisons would not be very satisfactory.

We wish to thank Mr. Rosen for reference to work on ducted propellers at Hamilton Standard and supporting comments. We were aware that this work was going on but did not receive a copy of the report of this work until after completion of the paper. In our paper we said that none of the experimental results that we knew about showed a pressure jump at the propeller, and, in general, we were referring to the free-running case. Hamilton Standards's results do show a pressure jump at the static condition and at very low speed coefficients, and due note should be taken of these results, but this does not change our conclusion about the pressure jump at the higher advance coefficients.

* * *

THE BLADELESS PROPELLER

Joseph V. Foa
Rensselaer Polytechnic Institute
Troy, New York

ABSTRACT

The mechanism of cryptosteady pressure exchange is discussed, with particular attention to its applications to propulsion. The available theoretical and experimental information is briefly reviewed, and pertinent problem areas are identified.

NOMENCLATURE

Symbols

A	Cross-sectional area
c	Flow velocity in "relative" frame of reference
h, h^0	Static, stagnation specific enthalpy
H	Total head
$\dot{m}$	Mass flow rate
p, p^0	Static, stagnation pressure
r	Radial distance from axis of rotation
s	Specific entropy
t	Time
T, T^0	Static, stagnation temperature
u	Flow velocity in a space-fixed frame of reference
V	Transverse or peripheral velocity of primary discharge orifice
β	Azimuthal flow angle
β_{1i}	Spin angle

$\beta_{1i'} = \tan^{-1}\left(\frac{V}{u_1'}\right)$ Equivalent spin angle

λ Entrainment coefficient

$\mu = \dot{m}_2/\dot{m}_1$

ρ Density

ϕ Thrust augmentation ratio

Subscripts

0 Free stream

1 Primary

2 Secondary

i Merger station

d End of deflection phase

f End of interaction

Superscripts

A prime (') denotes the conditions of the primary flow when expanded isentropically to pressure p_0.

INTRODUCTION

The simplest thrust augmenters are those in which the transfer of mechanical energy from the driving "primary" to the induced "secondary" flow takes place directly, i.e., through the work of mutually exerted forces at the interfaces between the two flows.

With the exception of the conventional ejector, where the energy transfer is effected through the work of shear forces, all devices of this class operate on the basis of nonsteady flow processes. In these devices the transfer is effected in whole or in part through "pressure exchange," i.e., through the work of interface pressure forces; and this requires that the flow be nonsteady, because no work is done by pressure forces acting on a stationary interface.

The conventional steady-flow ejector is simple, but inefficient and bulky. Its effectiveness as a thrust augmenter is low and deteriorates rapidly with increasing forward speed (Ref. 1). Nonsteady-flow thrust augmenters—e.g., the pulsating-flow ejector (Fig. 1)—are capable of higher energy transfer efficiencies

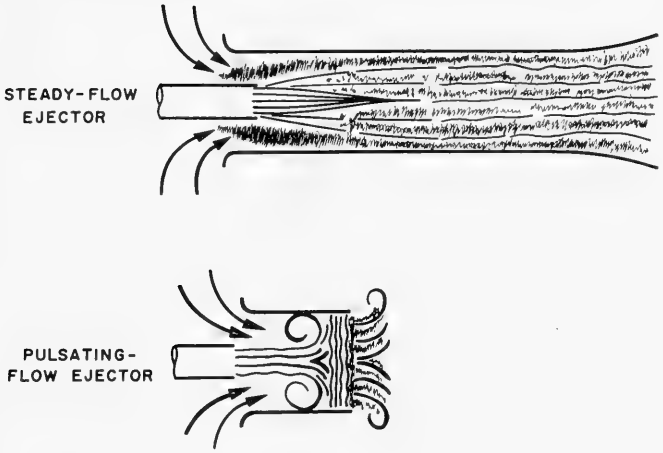

Fig. 1 - Steady-flow and pulsating-flow ejectors (from Ref. 2)

with greatly reduced interaction lengths (Fig. 2 and Ref. 2). However, their performance normally depends very critically on the timing of the wave processes on which their operation is based. Furthermore, if the primary flow is initially steady, its conversion to nonsteadiness for the purpose of utilizing pressure exchange may be accompanied by losses large enough to offset the entire thrust increment that is produced in the augmenter (Ref. 3).

These drawbacks and difficulties are largely eliminated in a pressure exchanger whose flow processes admit a frame of reference in which they are steady. This device, which has been variously referred to as the "bladeless" or "pseudobladed" propeller, promises to combine an attractive efficiency with advantages of compactness and simplicity.

This paper will discuss the principle of operation of the bladeless propeller and briefly review the available theoretical and experimental information that relates to its performance as a thrust augmenter.

THE PRINCIPLE

Euler's equation and the definitions of total head H and specific stagnation enthalpy h^0 yield for a fluid element, in the absence of body forces,

$$\frac{DH}{Dt} = \frac{\partial p}{\partial t} + \bar{u} \cdot \bar{f} \quad \text{(if incompressible)} ,$$

and

$$\frac{Dh^0}{Dt} = \frac{1}{\rho} \frac{\partial p}{\partial t} + T \frac{Ds}{Dt} + \frac{1}{\rho} \bar{u} \cdot \bar{f} \quad \text{(if compressible)} ,$$

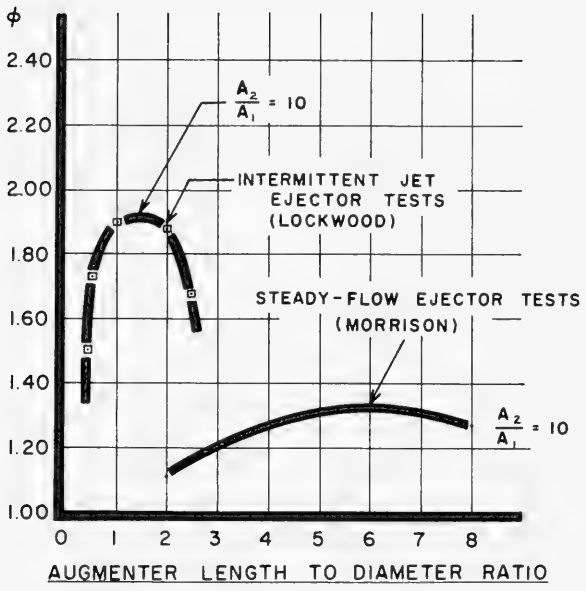

Fig. 2 - Comparison of static performance of steady-flow and pulsating-flow ejectors (from Ref. 2)

where p, ρ, and T are the static pressure, density, and temperature, respectively, s is the specific entropy, $\bar{u}$ the local velocity, $\bar{f}$ the force per unit volume due to surface viscous stresses, and t the time. These equations show that a reversible transfer of mechanical energy within a flow system is possible only in regions where the local derivatives $\partial p/\partial t$ are not zero, i.e., in regions of nonsteady flow.

From this it must also be concluded that a transfer of mechanical energy from one flow to another can be nondissipative only if both flows are nonsteady. This conclusion is supported by the observation that the only known steady-flow mechanism of direct exchange of mechanical energy between two flows is that of the conventional ejector, where the exchange is entirely effected through irreversible transport processes, whereas considerably higher efficiencies can be achieved through nonsteady flow induction.

Of special interest, among the methods of nonsteady flow induction, is a method that does not require that the interacting flows be nonsteady in *all* frames of reference. As demonstrated in Ref. 4, a nonsteady process that admits a frame of reference with respect to which it is steady over certain regions in space and intervals of time will be said to be *cryptosteady* over these space and time domains.

A flow which is steady and isoenergetic in a frame of reference F_s is neither steady nor isoenergetic in any other frame of reference F unless it is

uniform in the direction of the velocity $\bar{V}$ of F relative to F_s. Indeed, since the pressure is constant at any point fixed in F_s, at points fixed in F the pressure varies with time at the rate $\partial p/\partial t = -\bar{V}\cdot\nabla_p$. Therefore, except when ∇p is zero or normal to $\bar{V}$, the flow in F is nonsteady — more precisely, cryptosteady — and the energy level of its particles undergoes nondissipative changes that are absent in F_s. Similarly, whereas two contiguous streams will exchange energy only by irreversible transport processes in a frame of reference F_s in which they are both steady, they will exchange energy also by pressure exchange in every other frame of reference. This additional transfer of mechanical energy is essentially nondissipative. It is, as in all forms of pressure exchange, equal to the work done by the pressure forces which the interacting flows exert on one another at their interfaces. This work is zero in F_s, where the interfaces are stationary. In every other frame of reference the interfaces move and energy is transferred from one flow to the other by pressure exchange. The special merit of cryptosteady interactions is that they can be generated, controlled, and analyzed as steady-flow processes in F_s, while retaining the potential advantages of nonsteady interactions in the frame of reference in which they are utilized.

In the following discussion, the frame of reference F_s will be referred to as the "relative" frame, and the velocities in it as "relative velocities," whereas the frame of reference F, in which the sought energy transfer is to be effected and utilized, will be referred to as the "absolute" frame, and the velocities in it will be called "absolute velocities."

Consider, in the absolute frame, the interaction schematically described in Fig. 3, between two flows at different energy levels — that of a "primary" fluid I and that of a "secondary" fluid II, both inviscid. Upstream of the interaction region, the two flows are separated from one another by an infinitely thin containing wall, extending to infinity in the $\pm y$ direction. At infinity upstream, the velocity is uniform and constant in each flow and both velocities are parallel to the x axis.

The primary fluid enters the interaction space through an orifice in the containing wall. This wall moves in the $+y$ direction at the constant velocity $\bar{V}$, but since the wall is infinitely thin and the fluid is inviscid, no momentum in the y direction is imparted by the moving orifice on the primary fluid: the area of emergence of this fluid moves at the velocity $\bar{V}$, but the primary fluid particles themselves emerge through it at a velocity U_{1_i} which is parallel to the x axis. Because of the stipulated absence of viscosity, no work is required to sustain the motion of the containing wall; nor is any energy otherwise exchanged between the double-flow system considered and its surroundings.

In the frame of reference fixed to the orifice — the relative frame — the two flows are both steady. Therefore, the flow system is cryptosteady in the absolute frame.

In contrast to the absolute velocities $\bar{u}$ of the two flows, their relative velocities $\bar{c}$ upstream of their merger station are not parallel. On the other hand, in the relative frame the streamlines of the two flows must be parallel to one another at their interfaces, because the latter are stationary. Thus, as they come in contact, the interacting flows must deflect each other, in the relative

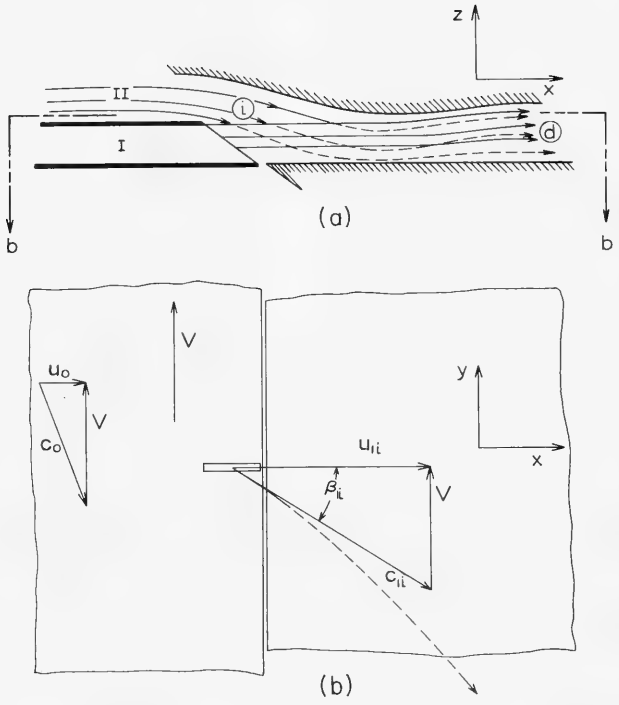

Fig. 3 - Plane-flow cryptosteady pressure exchange

frame, to common orientations at their interfaces. If the primary stream spans the whole width of the interaction space (as in the situation of Fig. 3), the entire flow is deflected in pressure exchange to a common orientation in the relative frame. Under these conditions, and if the mutual deflection is assumed to be completed before any appreciable mixing takes place across the interfaces, the process can be analyzed in the relative frame as an interaction between steady isoenergetic flows. The resulting modification of the flow is described by the velocity vector diagram of Fig. 4 for a situation in which the final pressure p_d is equal to the static pressure p_0 of the undisturbed secondary flow. The velocities of the deflected flows in the relative frame are $\overline{c_{1d}}$ and $\overline{c_{2d}}$, and the corresponding "absolute" velocities are $\overline{u}_{1d}$ and $\overline{u}_{2d}$. It can be seen, from the relative magnitudes of these vectors at the beginning and at the end of the interaction, that in this process the secondary flow gains mechanical energy, in the absolute frame, at the expense of the primary flow.

The "deflection phase" just described is normally followed by further interactions. A second phase of pressure exchange takes place if the two flows, following the deflection phase, are subjected together to Coriolis or other accelerations normal to their interfaces, as in a rotating flow field or in a passage of varying cross section. Heat transfer and mixing also start as soon as the two

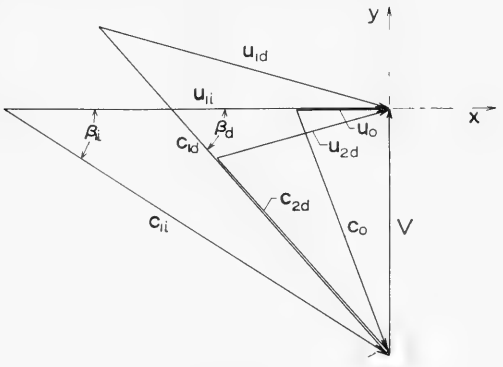

Fig. 4 - Velocity vector diagram

flows come in contact, i.e., simultaneously with the start of the pressure exchange phases, but can be expected to proceed at a slower rate. In an extreme idealization, mixing can be regarded as the third and last phase of the interaction.

It is possible, and sometimes desirable, to separate the two fluids after pressure exchange, before mixing between them has progressed too far. One obvious way to do this is to extract them from the interaction zone through separate ports suitably arranged in fixed positions in the relative frame. Another way is suggested by the observation that $\bar{u}_{1d}$ and $\bar{u}_{2d}$ have different orientations. If the exit from the interaction zone is made up of two sets of stationary passages, one with the orientation of $\bar{u}_{1d}$ and the other with the orientation of $\bar{u}_{2d}$, then a predominant portion of each of the two fluids will flow out through that set of passages which matches the orientation of its motion.

The simplest embodiments of the cryptosteady pressure exchange concept are those in which frame F_s rotates at a constant angular velocity relative to frame F. Figures 5 and 6 show two such arrangements. The primary fluid is discharged into the interaction space through skewed orifices on the periphery of a rotor. If no external torque is applied to the rotor — i.e., if the rotor spins freely, with negligible friction, and is solely driven by the reaction of the issuing jets — and if no prerotation is imparted on the flows by fixed vanes or by other external means, then the deflection phase of the interaction takes place essentially in the manner discussed above.

At every instant, the primary fluid which has emerged during a brief and immediately preceding time interval from each rotating orifice, occupies in space a spiral or helical region which rotates about the same axis and at the same angular velocity as the rotor. Although the fluid particles within this region do not follow the same motion, its boundaries are the interfaces separating the primary from the secondary fluid, and their relation to the flow of this secondary fluid is therefore substantially the same as that of blade or vane surfaces of the same shape, rotating at the same angular velocity. Thus the driving fluid forms a cascade of "pseudoblades," the action of which on the driven fluid

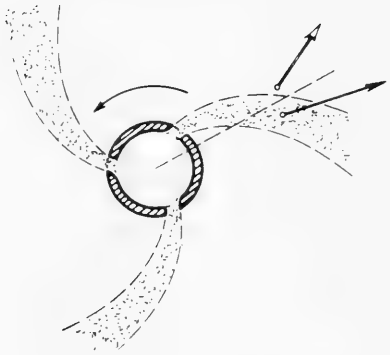

Fig. 5 - Radial-flow crypto-steady pressure exchanger

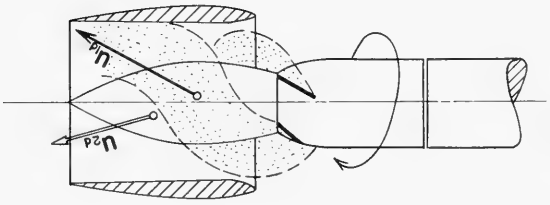

Fig. 6 - Axial-flow cryptosteady pressure exchanger

is somewhat similar to that of fan or propeller blades. Similarly, the effect of the interface pressure forces on the primary flow is essentially the same as the energy-extracting action of a turbine. Figure 7 is a flash photograph of these pseudoblades. Here water was used as the primary fluid, for the purpose of visualization. The flow of water is parallel to the interfaces in F_s but not in F, as shown by the streaks, which are particle path lines in F.

THE BLADELESS PROPELLER — AVAILABLE THEORIES

Figure 8, which is taken from Ref. 5, shows a schematic section view of a typical thrust augmenter utilizing this mode of energy exchange — a "bladeless propeller" — and identifies the angles that, following Hohenemser's terminology, will hereafter be referred to as the "spin angle" and the "coning angle."

The first analysis of the operation of this device (Ref. 6) dealt numerically with a variety of specific cases, involving plane interactions between compressible or incompressible flows, with or without separation of the two flows after

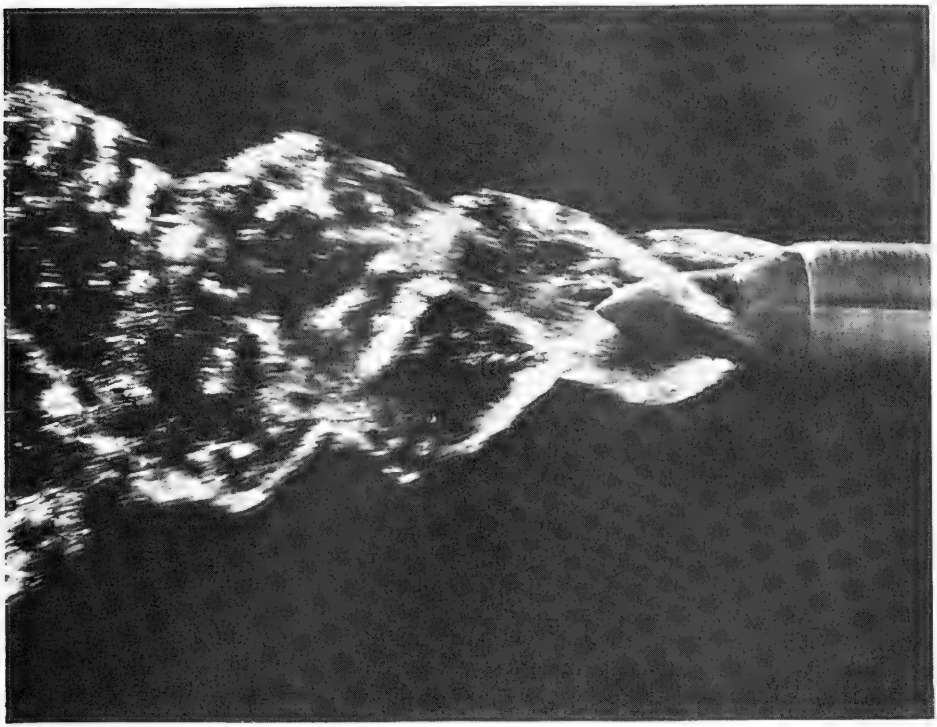

Fig. 7 - Water pseudoblades in air (streaks are particle path lines)

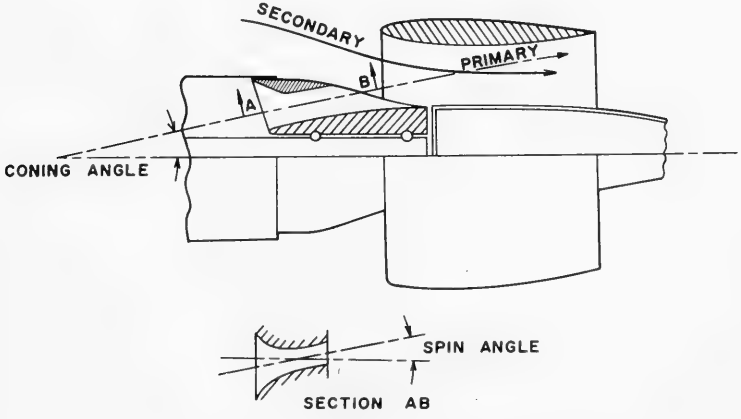

Fig. 8 - Schematic of bladeless propeller

the pressure exchange phase, and with or without a subsequent mixing phase. Similar but generalized treatments were developed in Refs. 5, 7, and 8. These analyses considered situations in which the coning angle was zero and the width of the interaction space was constant and very small compared to its mean radius, so that the flows could again be treated as two-dimensional in the interaction region. Heat transfer and mixing effects were neglected. Under these conditions, the effect of the interaction could again be described by a velocity vector diagram like that of Fig. 4 and the thrust augmentation ratio could be calculated as

$$\phi = \frac{(U_{1d} + \mu\, U_{2d})\, \cos \beta_d - (1+\mu)\, U_0}{U_1' - U_0}$$

The analysis of Ref. 8, which was limited to the case of an interaction duct of constant cross-sectional area, revealed the necessity of velocity nonuniformities at the merger station — a necessity reflecting the implictly assumed irrotationality of both flows in the deflection phase. Thus, the absolute velocities of the secondary fluid particles have different orientations at the merger station, although the overall transverse momentum of this flow is, of course, still zero at this station in the absolute frame. The results of this analysis, for static operation and for two values of the secondary-to-primary density ratio, are presented in Figs. 9 and 10. Here, as in subsequent performance charts, A_1 and A_2 denote the cross-sectional areas of the primary and of the secondary flow, respectively, at the merger station. These figures show that an increase of the secondary-to-primary density ratio has a very favorable effect on the thrust augmentation obtainable with the bladeless propeller (whereas it has the opposite effect on the performance of the ejector). It should be noted that, because of the specified absence of mixing, the bladeless propeller considered in this analysis does not, for $\beta_{1i} = 0°$, reduce to an ejector: instead, it is reduced to a totally ineffective device, for which $\phi = 1.0$ throughout.

An elegant generalization of this analysis was developed by Hohenemser in Ref. 5, through the introduction of an "equivalent spin angle," defined as $\beta_{1i}' = \tan^{-1}(V/u_1')$. Use of this parameter in lieu of the actual spin angle made it possible to bypass the axial momentum equation, and hence to bypass consideration of the shape of the interaction duct. Except for cases involving very large density differences between the two fluids, equivalent and actual spin angles were found to differ relatively little from one another. In fact, the results of the two-dimensional analyses of Refs. 5 and 8 are practically identical.

A further refinement of the theory was introduced by Hohenemser, also in Ref. 5, through a strip approach similar to the strip concept of propeller theory. Here, the primary jet is assumed to be thin in comparison with the width of the interaction space and is further assumed to penetrate this space at a coning angle small enough to make it permissible to neglect primary velocity components normal to the direction of the secondary flow. The interaction is then treated as an infinite succession of infinitesimal steps, in each of which the primary jet and the elemental layer of secondary flow which it penetrates deflect each other to a common direction. Coriolis and centripetal accelerations are again neglected, as if these secondary flow layers were plane rather than annular. The resulting axial velocity distribution at the shroud exit is nonuniform,

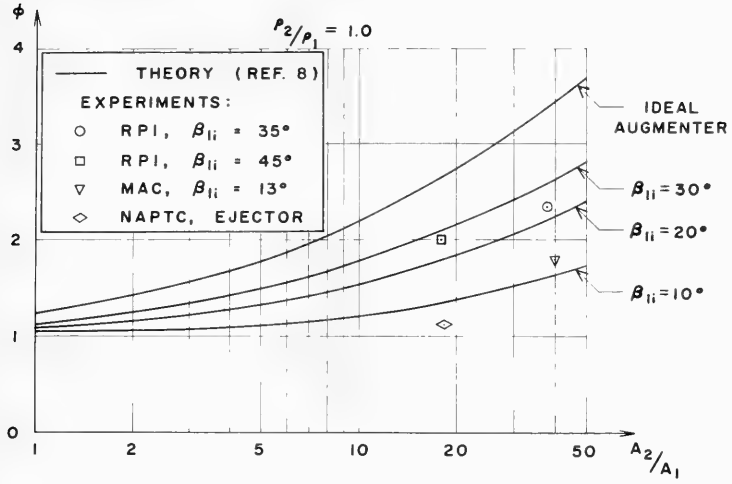

Fig. 9 - Static performance of an axial-flow bladeless propeller

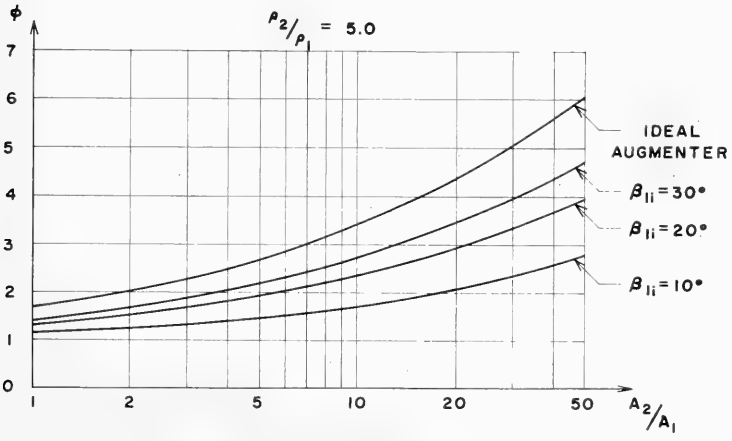

Fig. 10 - Static performance of an axial-flow bladeless propeller

and the calculated thrust augmentation ratio is lower than that predicted by the two-dimensional theory. Furthermore, the strip theory predicts for each area ratio an optimum spin angle. The discrepancy between the two theories increases as the density ratio increases. A comparison of the results of the two theories for a density ratio of 1.0 is presented in Fig. 11. It should be noted that neither of the two theories accounts for the adverse effect of mixing during the deflection phase. Although in remarkably good agreement with experimental

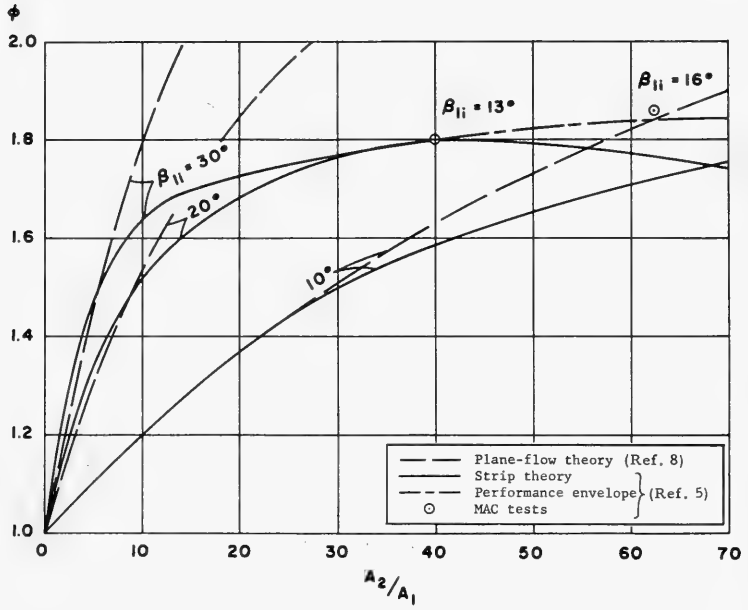

Fig. 11 - Static performance of a bladeless propeller for $\rho_2/\rho_1 = 1.0$

results, the thin-jet-strip theory is probably overly pessimistic as a basis for prediction of potential performance. If the primary jet were of sufficient radial width to span the entire interaction space, the upper limit of performance would (apart from the effect of mixing during deflection) be that predicted by the two-dimensional theory.

In the analysis of Ref. 9, a constant-area mixing phase is added to the deflection phase, which is again treated as a plane-flow interaction. With this addition, the analytical model reduces to the ideal constant-area ejector when the spin angle is zero. Typical results of this analysis, for static operation with an area ratio of 15, a ratio of primary total pressure to ambient static pressure of 2.8, and two primary-to-secondary stagnation temperature ratios, are presented in Fig. 12. These results confirm that the superiority of the bladeless propeller over the ejector increases as the primary-to-secondary temperature ratio — or the secondary-to-primary density ratio — is increased.* They also show that the effect of mixing following the deflection phase may be favorable or unfavorable, depending on the spin angle and on the temperature ratio.

*As the spin angle is increased from 0° (ejector) to 20°, the calculated energy transfer efficiency (ratio of mechanical energy gained by the secondary to mechanical energy lost by the primary) increases from .40 to .53 if the temperature ratio is 1.0; whereas it increases from .22 to .55 if the temperature ratio is 4.0.

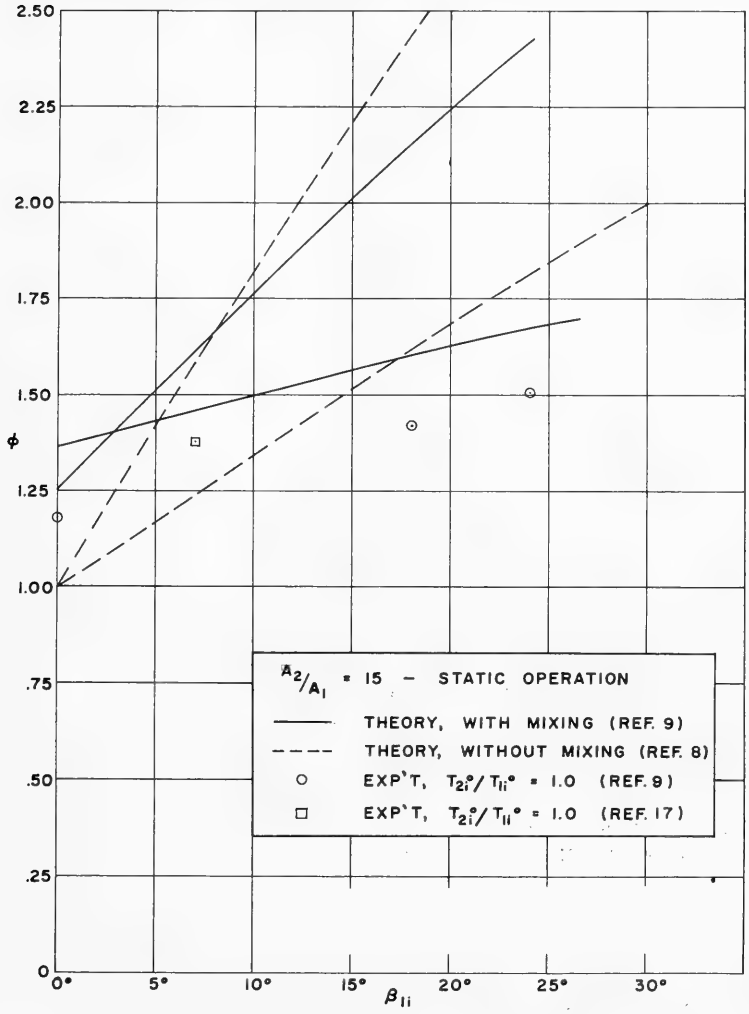

Fig. 12 - Static performance of a bladeless propeller with and without constant-area mixing following the deflection phase

When the coning angle is large, Coriolos and centripetal accelerations can no longer be neglected. These accelerations, first accounted for in the two-dimensional analyses of Ref. 10 and 11, have a marked and favorable effect on performance (Fig. 13).

Coriolis effects are incorporated in the analysis of Ref. 12, where, in addition, (a) the deflection phase is treated by the strip method of Ref. 5, (b) consideration is given to the effect of partial mixing during the deflection phase, and

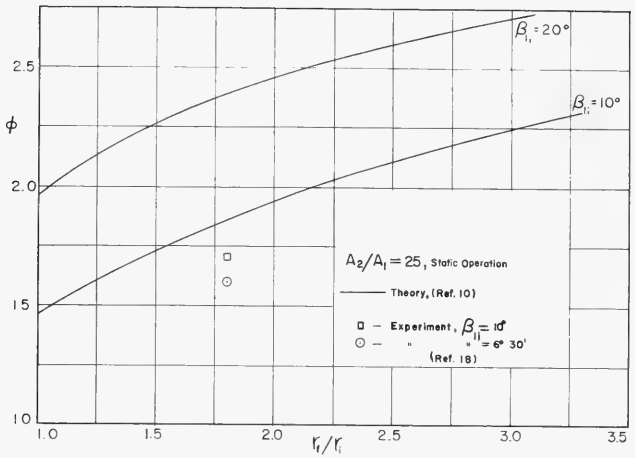

Fig. 13 - Performance of a bladeless propeller with a large coning angle

(c) a constant-area mixing phase is added, as in Ref. 9. The primary gas particles are assumed to move, during the deflection phase, along the surface of the cone defined by the initial coning angle of the nozzle axes. Of particular interest here is the effect of mixing during the deflection phase. Jet cascade tests by Palmieri at R.P.I. (Ref. 13) and velocity surveys in jet injection tests at the McDonnell Propulsion Laboratory (Ref. 5) have shown that the mutual deflection of the two flows can be completed before mixing has made substantial progress. This, however, has yet to be accomplished in the actual operating conditions of the bladeless propeller, mainly because mixing is promoted by the curl components which are introduced in both flows by the rotation of F_s. Mixing in the deflection phase is described in Ref. 12 as a mass transfer which is assumed to progress at a constant rate per unit length of the primary jet. The mass transferred from the secondary to the primary flow during the deflection phase is related nondimensionally to the length of the primary jet through an "entrainment coefficient" λ, the value of which varies from zero (for the case of no mixing) to 0.05 for the worst condition considered. Some of the numerical results of the analysis of Ref. 12 are shown in Fig. 14. The adverse effect of entrainment increases, as expected, with increasing spin angles. An increase of primary-to-secondary stagnation temperature ratio (hence of secondary-to-primary density ratio) is again found to increase the augmentation ratio and to decrease the optimum spin angle for any given area ratio.

Special attention to the interaction of a gaseous primary with a liquid secondary fluid has been given in recent years at Grumman Aircraft Engineering Corp. in an extensive study of underwater propulsion applications of the bladeless propeller (Refs. 14 and 15). In such interactions, the collision angle between the two flows is generally very much larger than the spin angle, and the Grumman study has revealed that the best performance is obtained, as a consequence, with very small spin angles. In Refs. 14 and 15 the deflection phase is

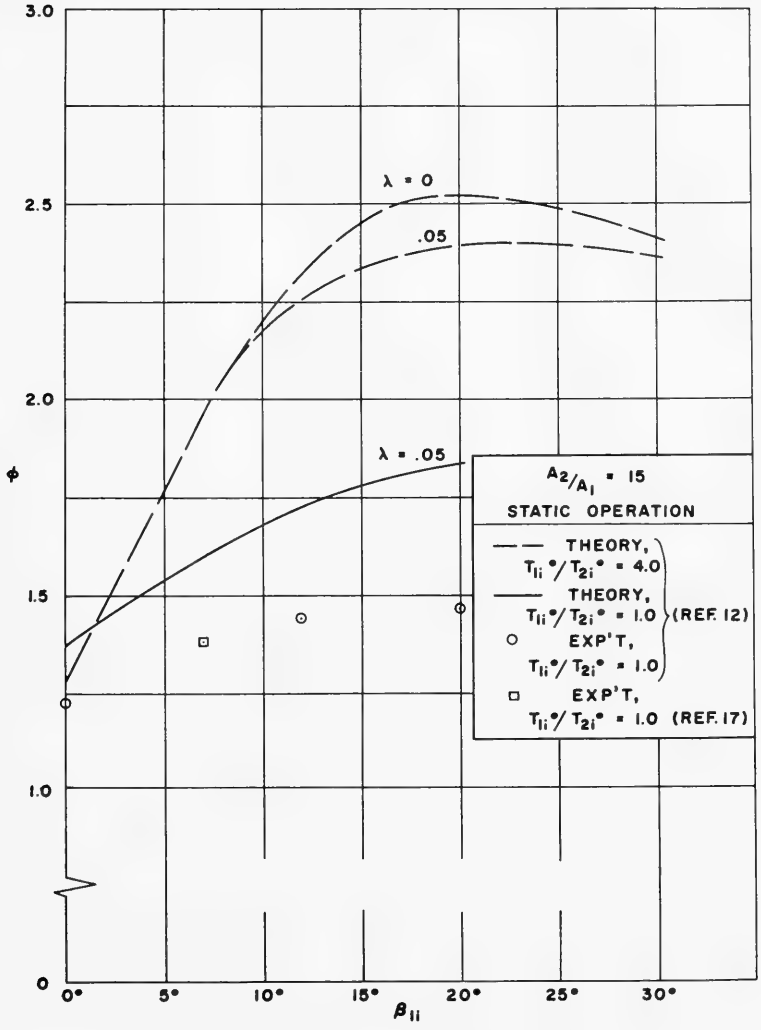

Fig. 14 - Effect of mixing during the deflection phase

analyzed by the strip approach, but with consideration of meridional deflections of the primary jet. In addition, these analyses stipulate the presence of (a) secondary prerotation guidevanes for the purpose of obtaining radial uniformity of energy transfer, hence radial dynamic equilibrium, (b) exit straightening vanes for the purpose of turning the secondary flow, after the interaction, everywhere to the axial direction, and (c) a separator for the extraction of the deflected primary flow, which is then also turned to the axial direction and discharged isentropically to ambient pressure. Numerical results of these analyses, for a

noncondensing primary, are presented in Figs. 15 and 16. The thrust augmentation ratios predicted by the Sarro-Kosson strip theory for very low spin angles and disc loadings are considerably higher than those predicted for the same conditions by the two-dimensional theory. This is primarily due to the fact that the analytical model considered in the latter theory makes no provision for the recovery of the transverse momentum of the two flows after the deflection phase. Work on the theory of the bladeless propeller with a condensing primary is in progress at R.P.I. and at Grumman, but no numerical result is yet available at this writing.

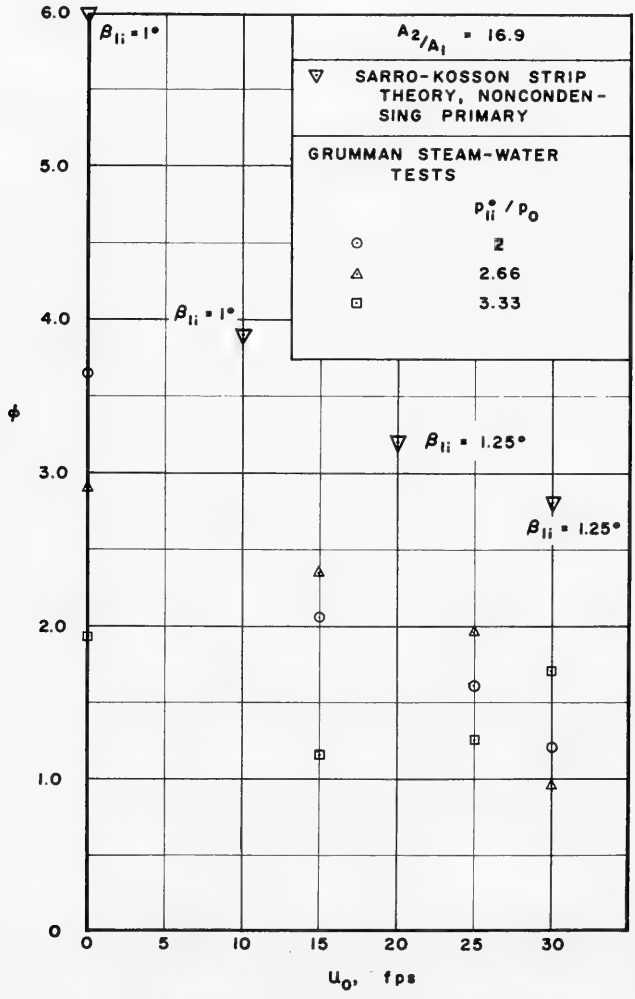

Fig. 15 - Comparison of the Sarro-Kosson strip theory with the results of the Grumman steam-water tests, for a noncondensing primary (Refs. 14 and 15)

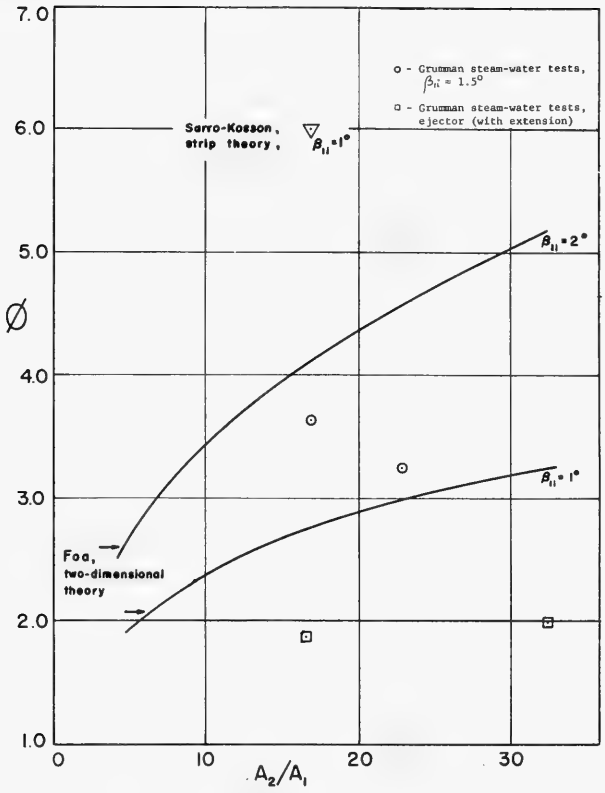

Fig. 16 - Static performance of two-phase bladeless propeller, Grumman steam-water tests

EXPERIMENTAL RESULTS

The first experiments on a bladeless propeller were conducted by this writer in 1952, using an unshrouded model with a large afterbody. The tests (air-to-air) were conducted in a free jet simulating a forward speed of 300 ft/sec. Thrust augmentation ratios as high as 1.2 were measured, but the results were considered inconclusive because it could not be ascertained whether the apparent increase of thrust was not in part a decrease of drag such as might be caused by delayed flow separation on the afterbody. Following some work on pumping applications, thrust augmentation experiments were resumed at R.P.I. by Vennos in 1959 (Ref. 16). These experiments were conducted on a variety of water-water models, the most successful of which had zero coning angle, a spin angle of 35° (Fig. 17), a secondary-to-primary area ratio of 37.6, and a shroud length-to-diameter ratio of about 1. Two of the test points are shown in Fig. 9. Not shown are the test points corresponding to the highest augmentation ratios measured in these experiments, because they were obtained under test conditions

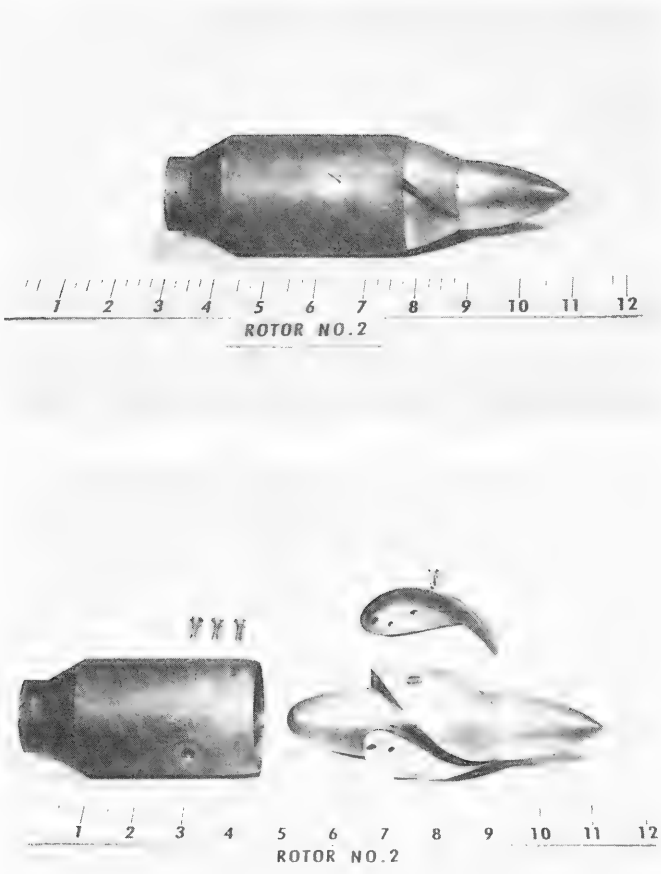

Fig. 17 - Rotor No. 2 of the Vennos water-water test series (Ref. 16)

that left some room for error (Ref. 16). It was found in these and subsequent tests that apparently minor modifications of external shape or internal ducting in these models could produce major changes of performance.

Also plotted in Fig. 9 is an air-to-air test point reported by Hohenemser in Ref. 5. Finally, for the purpose of direct comparison with the conventional ejector, there is also shown a typical constant-area ejector test point (Ref. 17).

Results of air-to-air experiments conducted by Hohenemser (Ref. 5) are compared in Fig. 11 with the predictions of the two-dimensional theory and of the strip theory. The experimental points fall very close to the performance envelope according to the strip theory. However, as has already been noted,

this agreement should not be interpreted as an indication that the upper limit of performance has already been attained. Indeed, the theoretical prediction, being based on an analysis that does not account for the finite thickness of the primary jets, is likely to be pessimistic except for very small area ratios.

Measurements made at McDonnell Aircraft (Ref. 9) have shown that rotary jet mixing can be accomplished within rather short mixing duct lengths. This observation appears to be confirmed by the results of an experimental program recently reported by Palcza (Ref. 17). Less is known about the extent to which mixing progresses during the deflection phase. Comparison of theoretical and experimental results in Figs. 12 and 14 seems to indicate that the actual entrainment coefficient may exceed the estimated value.

Air-to-air models with large coning angles have been extensively tested by Avellone (Ref. 18). These models had an externally-driven, thin-walled rotor with sharp-edged orifices, incapable of imparting a significant tangential momentum to the primary fluid. Thus, the spin angle could be varied continuously by just varying the rotor speed. Typical results of these tests are shown in Fig. 13, where they can be compared with the theoretical predictions of Ref. 10.

Two-phase underwater propulsion tests have recently been reported by Avellone and Sarro (Ref. 19). The model used was of the axial-flow type and had an externally-driven, thin-walled rotor for continuous spin angle control in the same manner as the Avellone air-to-air model. In all tests the optimum spin angle was found to be between 1° and 2°. Some of the reported test points are plotted in Figs. 15 and 16. Direct comparison of the experimental results with those of the available theories for two-phase interactions is not yet possible in this case, because the primary fluid used in these tests was steam, whereas numerical results of the theories are available only for the case of a noncondensing primary. It will also be noted that, whereas the theory (Ref. 14) predicts a decrease of thrust augmentation with increasing pressure ratio, the experimental results are still inconclusive in this respect. Clearly, there is a great need for further research in this area, particularly since it is evident from Figs. 15 and 16 that the possibility still exists for vast improvements in the performance of two-phase bladeless propellers.

CONCLUSIONS

1. The bladeless propeller has the distinct advantages of efficiency and compactness over the conventional steady-flow ejector, and the distinct advantages of simplicity, ruggedness, and flexibility of operation over existing nonsteady-flow thrust augmenters.

2. The superiority of the bladeless propeller over the ejector increases as the secondary-to-primary density ratio is increased, all other conditions being equal.

3. For each spin angle there exists a secondary-to-primary area ratio that produces the maximum augmentation; and, similarly, there exists for each area ratio an optimum spin angle. These optima depend on the density ratio, the

thickness of the primary jet, and the secondary-flow entrainment during the deflection phase.

4. Jet dissipation during the deflection phase has an adverse effect on performance under all conditions (in the limit, if the two streams were to mix instantly at merger, the performance of the bladeless propeller would be reduced to that of the conventional ejector).

5. The effect of mixing after the deflection phase can be favorable or unfavorable, depending on the spin angle and the temperature ratio.

6. An increase of coning angle can have a markedly beneficial effect on performance.

7. Marine applications of two-phase bladeless propellers appear to be very promising.

Further study is needed in several areas, including:

(a) a means of inhibiting jet dissipation during the deflection phase;

(b) the operation of bladeless propellers with large spin angles and/or large area ratios;

(c) the operation of bladeless propellers with large density ratios;

(d) the operation of bladeless propellers at high forward speeds;

(e) utilization of two-phase interactions, with a condensable or noncondensable primary gas;

(f) the determination of criteria for rotor and shroud contouring, the design of internal ducting, and the selection of primary orifice shapes;

(g) utilization of rotating stall through a stationary cascade for the generation of cryptosteady interactions; and

(h) optimization of thrust generators in which cryptosteady pressure exchange is compounded with other energy transfer mechanisms for the purpose of augmentation.

REFERENCES

1. Johnson, J.K., Jr., Shumpert, P.K., and Sutton, J.F., "Steady-Flow Ejector Research Program," Lockheed-Georgia Company ER-5332 (AD-263180), Sept. 1961

2. Lockwood, R.M., "Energy Transfer from an Intermittent Jet to an Ambient Fluid," Hiller Aircraft Co., Summary Report ARD-238, 30 June 1959

3. Lockwood, R.M., and Patterson, W.G., "Energy Transfer from an Intermittent Jet to Secondary Fluid in an Ejector-Type Thrust Augmenter," Hiller Aircraft Co., Interim Report ARD-305, 30 June 1962

4. Foa, J.V., "Elements of Flight Propulsion," Wiley, 1960

5. Hohenemser, K.H., "Preliminary Analysis of a New Type of Thrust Augmenter," Proceedings of the 4th U.S. National Congress of Applied Mechanics (ASME, New York, 1962), pp. 1291-1299

6. Foa, J.V., "A New Method of Energy Exchange Between Flows and Some of Its Applications," Rensselaer Polytechnic Institute Tech. Rept. TR AE 5509, Dec. 1966

7. Foa, J.V., "Energy Transfer Rates in Axial-Flow Cryptosteady Pressure Exchange," Rensselaer Polytechnic Institute Tech. Rept. TR AE 6102, Feb. 1962

8. Foa, J.V., "Cryptosteady Energy Exchange," Rensselaer Polytechnic Institute Tech. Rept. TR AE 6202, Mar. 1962

9. Hohenemser, K.H., "Flow Induction by Rotary Jets," J. Aircraft 3 (No. 1), pp. 18-24, Jan.-Feb. 1966

10. Foa, J.V., "A Method of Energy Exchange," Am. Rocket Soc. J. 32 (No. 9), pp. 1396-1398, Sept. 1962

11. Foa, J.V., "A Vaneless Turbopump," AIAA Journal 1 (No. 2), pp. 466-467, Feb. 1963

12. Hohenemser, K.H., and Porter, J.L., "Contribution to the Theory of Rotary Jet Flow Induction," J. Aircraft 3 (No. 4), pp. 339-346, July-Aug. 1966

13. Project Tubeflight. Phase I. Feasibility Study, Rensselaer Polytechnic Institute (Clearinghouse No. PB 174-085), Sept. 1966

14. Sarro, C., and Kosson, R., "Theoretical Analyses of the Foa Propulsor with Gas Primary and Liquid Secondary Fluids," Grumman Advanced Development Report ADR 01-09-61.1, Aug. 1964

15. Avellone, G., and Sarro, C., "Extended Theoretical Study of the Pseudoblade Propulsor Concept," Grumman Research Department Report RE-302, Aug. 1967

16. Vennos, S.L.N., "Experiments with Water-Water Bladeless Propellers," Rensselaer Polytechnic Institute Tech. Rept. TR AE 6106, May 1961

17. Palcza, J.L., "Effect of Mixing Length on Rotary Flow Inductors," Department of the Navy, Naval Air Propulsion Test Center, Trenton, N.J., Tech. Rept. NAPTC-ATD 147, June 1968

18. Avellone, G., "Theoretical and Experimental Investigation of the Direct Exchange of Mechanical Energy Between Two Fluids," Grumman Research Department Memorandum RM-365, June 1967

19. Avellone, G., and Sarro, C., "Experiments with a Steam-to-Water Pseudo-blade Propeller for Marine Application," Grumman Research Department Report RE-235, Dec. 1965

* * *

ON PROPULSIVE EFFECTS OF A ROTATING MASS

Prof. Alfio Di Bella
Instituto di Architettura Navale
University of Genoa
Genoa, Italy

ABSTRACT

This paper is dedicated to the study of particular rotatory motions of masses in space.

It is demonstrated experimentally that, within certain limits, small motions in the desired direction of a vehicle can be obtained by placing within it a mass that is kept rotating by a motor. The devices that were used are described and a full summary of the results that were obtained is given.

We have pointed out what, with certain difficulties overcome, will probably be the most important application of these devices: on certain types of ships, to give them forward or backward motions, lateral and evolution motions, at low speeds; in automobiles, to create in them lateral motions which would be useful for parking, in forward and backward motions, and in changes of the direction of motion.

DESCRIPTION OF THE TESTED DEVICES

In January 1962, we proposed to initiate a study on the rotatory movement of a mass in space, to see if the dynamic actions produced by it could make way for possible applications in the field of propulsion. We decided to begin by considering the rotatory motion of a mass around a point.

The device indicated in Fig. 1 immediately appeared useful to our study. It executes the motion of a point on a hemisphere. With simple mechanisms, it was possible to have an arm $AP = R$, rotating around a point O, having the extremity A coincide with O, and the extremity P free to move on the hemisphere. A mass m was concentrated in P.

As a matter of interest, it is recalled that the trajectory described by P belongs to the hypopedes family, studied in astronomy by Eudoxus, a contemporary of Plato. More precisely, the trajectory represents the window of Viviani, a pupil of Galilei, who posed the problem of tracing four windows of maximum area on a hemisphere. (The solution of the problem, given by Gauss, requires

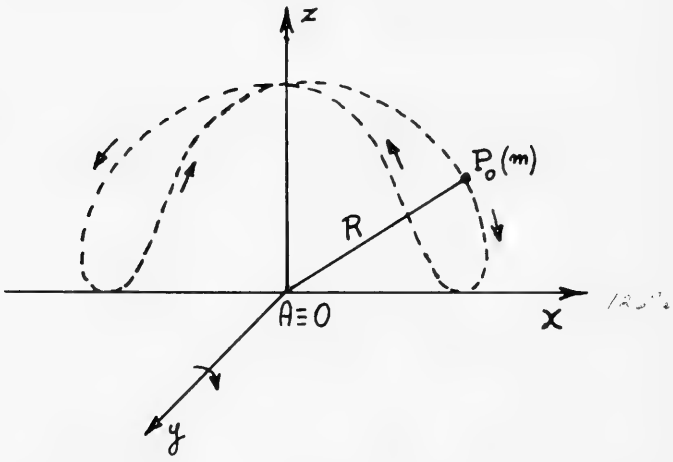

Fig. 1 - Rotatory motion of a mass around a point

that each window have as its contour the trajectory described by P, which is also the intersection of a hemisphere with a cylinder of circular section, having the ray of the sphere as its diameter.)

The device was tested extensively on the ground and on the surface of the water with satisfying results on the whole.

Continuing our study, we thought it suitable to release the extremity of arm A from the center O and to insert between A and O an arm $r = 0A$. Thus we obtained the device indicated in Fig. 2 which represents a mass that turns around an axis, with the latter rotating around another axis. The mass moves on a sphere of ray $R_1 = (R^2 + r^2)^{1/2}$. The device, which may be considered the basis of the present paper, is formed as follows.

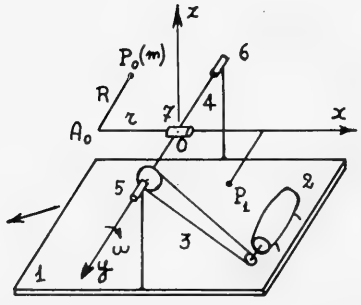

Fig. 2 - Rotation of a mass around an axis, with the latter rotating around another axis

On a light base (1) posed on a horizontal plane, a motor is placed (2) which, by means of a transmission (3), turns the horizontal shaft (4) that is held up by two supports (5) and (6) attached to the base. The shaft has a collar (7) within which can rotate an arm $0A_0 = r$, which has welded in A_0 at 90° another arm $A_0 P_0 = R$, at whose extremity P_0 is concentrated a mass m. There are also two toothed conical wheels of equal diameter (not designated in the figure), one connected to arm $0A_0$ and the other connected to one of

the supports. Thus, when the motor, and therefore the shaft, are in rotation, the collar makes arm $0A_0$ rotate around the shaft (4), while the two toothed wheels make it rotate around itself. Therefore, m rotates around $0A_0$ that, in turn, rotates around the shaft (4).

If the weights of all the rotating parts are negligible with respect to the weight (p) of the mass(m) and if the two arms are of equal length ($R = r$), then this peculiar fact is proved experimentally: when m reaches point P_1 the device behaves as if it were struck by an external force passing through P_1. The force is transmitted to the base (1) by means of the arms, the shaft, and the supports; the base is thus forced to undergo a small displacement on the plane of support in the direction indicated by the arrow. The same thing is not repeated for P_0, symmetrical to P_1, nor for the other points. It follows from this that the device, at each turn of the shaft (4), acquires a small displacement in only one direction. And if the shaft rotates with continuity, the device completes a succession of small jerks, and therefore, a forward motion on the supporting plane.

Thus, the rotatory motion of the mass corresponds to a forward motion of the device on the supporting plane.

The experiment also demonstrates that the displacement occurs when the angular speed (ω) of the motor shaft (4) is adapted to the dimensions of the device. In fact, if ω is relatively low, the thrust brought about by the mass is not sufficient to overcome the friction resistance from the contact of the base (1) with the supporting plane, and the device remains motionless; if, instead, ω is relatively high, the device undergoes strong vibrations, and hops about on the supporting plane in a disorderly fashion.

The experiment demonstrates, finally, that the propulsive effect of the rotating mass can also be obtained without making a complete 360° rotation of the shaft. In fact, if it leaves P_1 and is made to rotate the shaft a few degrees, first in one direction and then in the other, each time m passes through P_1 we observe the formation of a force that displaces the device on the supporting plane always in the same direction.

The motion of the mass can be related to the system of orthogonal axes 0, x, y, and z fixed with the device and having the origin on the point of intersection of the axis of the shaft (4) with the arm along r; x parallel to the base (1) of the device; y coinciding with the axis of the shaft (4); and z perpendicular to the base. If point P_0 belonging to the plane xy is assumed as the origin of the motion, then point P_1 is also found on plane xy, but rotated 180° in respect to P_0; i.e., from P_0 it passes to P_1, making the shaft (4) rotate 180°.

The device accomplishes, as has already been said, a propulsive effect for each turn of the shaft (4). If, however, (Fig. 3) we add an arm r' equal to r, we weld to A_0' an arm R' equal to arm R, and we place in P_0' a mass m' equal to the mass m placed in P_0, we get as a result a device with two masses, which, in one turn of the shaft, generates two propulsive effects. In fact, let us assume point P_0 as the origin of the motion. For a rotation of 180°, the mass from P_0 passes to P_1 and generates a propulsive effect there. In the

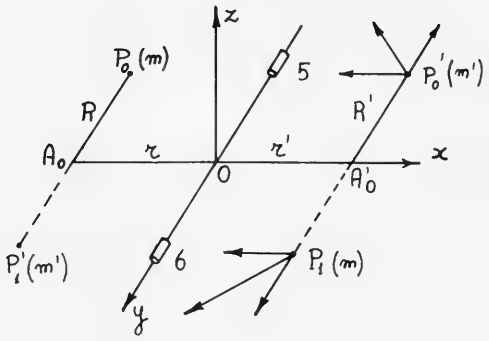

Fig. 3 - Expansion of Fig. 2 to two rotating masses with two propulsive effects in a single shaft revolution

same instant, mass m' is at P_1' and after a successive rotation of 180° it passes to P_0' and generates its propulsive effect there.

The arrangement of the device with three toothed wheels (one fixed and two mobile) and two rotating masses, indicated in Fig. 4, allows two propulsive effects to be executed for each turn of the motor shaft: one is generated by m when it is at P_1 and the other is generated by m' when, after a 180° rotation of the motor shaft, it is at point P_1.

If, instead, the two rotating masses are arranged as indicated in Fig. 5, then the device, for each turn of the motor shaft, generates at the same instant two propulsive effects, symmetrical in respect to the y axis: one is generated by m at the moment in which it is at P_1 and the other is generated by m' which at the same moment is at P_1'. This description shows how effectively the motion of the devices has been observed, and can be verified by arranging the same devices on a horizontal plane and setting them in motion.

EQUATIONS OF THE MOTION OF THE MASS WITH DEVICES FIXED TO THE SUPPORTING PLANE

It seems rather difficult to be able to write the general equations for the motion of the tested devices; first, because the cause of the forward motion in a desired direction, instead of a back-and-forth motion, is not very clear; second, because the motion of the devices is accompanied by strong vibrations, depending on the number and weight of the rotating masses, the rotatory speed of the motor shaft, the reactions of the support, etc.

Consequently, we can do nothing but limit ourselves to the case in which the bases of the devices are not free to move on the supporting plane, but are fixed rigidly to this plane. Likewise, for simplicity, we have to suppose that the mass is concentrated in one point, that the arms of length R and r and the

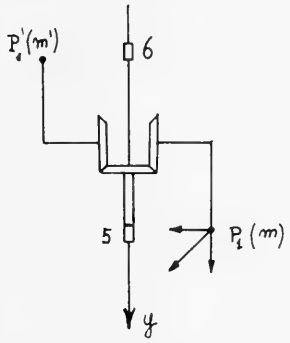

Fig. 4 - Arrangement of the device in Fig. 3 to include one fixed and two mobile toothed wheels

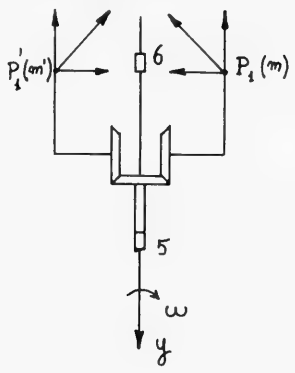

Fig. 5 - Arrangement of the device in Fig. 3 so that the two propulsive effects at one shaft turn are both symmetrical to the y axis

toothed wheels have a negligible weight in respect to the weight of the mass m, and finally that the passive resistances are null. With these simplifications, we can write equations for the motion of the mass and obtain useful results.

Let us begin with the case of the basic device indicated in Fig. 6, which, as has already been mentioned, executes a rotatory motion of a mass around an axis, with the latter rotating in turn around another axis. Let us refer the motion of the mass to the system of axes 0, x, y, and z as previously indicated. Let us assume the point P_0 as the origin of the motion on the xy plane corresponding to the angle of rotation $\theta = 0$. At time t the two arms are turned by θ; therefore, from $0A_0P_0$ we pass to 0AP. If P' is the projection of P on the plane z0x, we have $AP' = AP \sin\theta = R \sin\theta$. The coordinates of P then are:

$$\begin{aligned} x &= AC - AB = AP' \sin\theta - r\cos\theta = R\sin^2\theta - \cos\theta \\ y &= -R\cos\theta \\ z &= DC + CP' = 0A\sin\theta + AP'\cos\theta = (R\cos\theta + r)\sin\theta \,. \end{aligned} \tag{1}$$

These expressions represent a trajectory whose projections on the three coordinate planes have the forms indicated in Fig. 7. In P_1 we have a checkpoint. If the angular speed and acceleration are indicated with $\dot{\theta} = \omega$ and $\ddot{\theta} = \epsilon$, the components of the speed and those of the acceleration assume the form

$$\begin{aligned} v_x &= (R\sin 2\theta + r\sin\theta)\omega \\ v_y &= R\sin\theta\,\omega \\ v_z &= (R\cos 2\theta + r\cos\theta)\omega \,, \end{aligned} \tag{2}$$

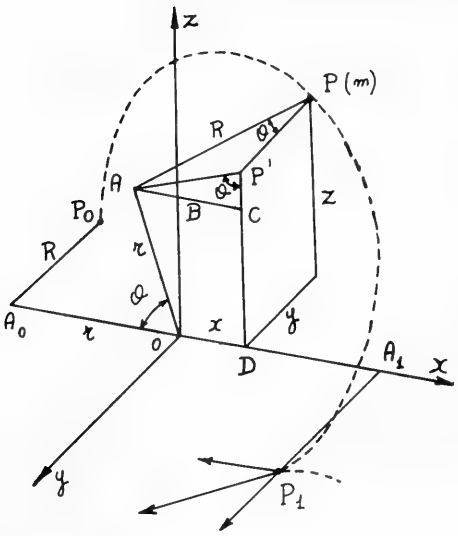

Fig. 6 - Arrangement of the device in Fig. 3, with $\theta = 0$ as the angle of rotation, for determination of the coordinates of P

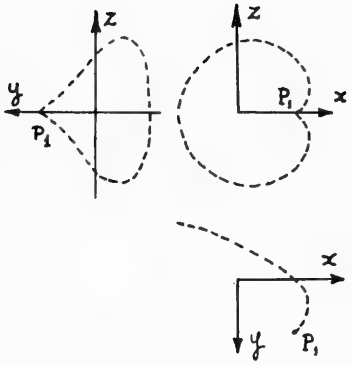

Fig. 7 - Trajectory projections of the three coordinates of P

$$a_x = (2R \cos 2\theta + r \cos\theta)\,\omega^2 + (R \sin 2\theta + r \sin\theta)\,\epsilon$$

$$a_y = R \cos\theta\,\omega^2 + R \sin\theta\,\epsilon \qquad (3)$$

$$a_z = -(2R \sin 2\theta + r \sin\theta)\,\omega^2 + (R \cos 2\theta + r \cos\theta)\,\epsilon \,.$$

The speed of the mass becomes

$$v = \left(v_x^2 + v_y^2 + v_z^2\right)^{1/2} = \left[R^2 (1 + \sin^2\theta) + r^2 + 2Rr \cos\theta\right]^{1/2} \omega \,. \qquad (4)$$

For $R = r$ and $\theta = \pi$, i.e., in P_1, we have $v = 0$.

In the study of the dynamics of the point, the principle of the conservation of energy is often used. If we suppose that in the system we are considering the energy remains constant, we can derive an expression that may give us an indication about the way of varying ω and ϵ to the varying of the angle θ. For this expression we can write:

$$E = \frac{1}{2} mv^2 + \frac{1}{2} J\omega^2 + pz = \text{const.} \,, \qquad (5)$$

where $1/2\ mv^2$ is the kinetic energy of the mass m, $1/2\ J\omega^2$ is the kinetic energy of the remaining masses that rotate around the y axis and in respect to which the moment of inertia equals J, and pz is the energy of the vertical motion of the weight p.

Equations (5), (4), and the third equation of Eqs. (1) yield

$$E = \frac{1}{2} m\ [R^2(1+\sin^2\theta) + r^2 + 2Rr\cos\theta]\ \omega^2 + \frac{1}{2} J\omega^2 + p(R\cos\theta + r)\sin\theta\ .$$

If we put $h = J/mR^2$, we obtain

$$\omega = \left\{ \frac{E - P(R\cos\theta + r)\sin\theta}{\frac{1}{2} m\ [R^2(1+\sin^2\theta) + r^2 + 2Rr\cos\theta + hR^2]} \right\}^{1/2} . \tag{6}$$

Differentiating Eq. (5) with respect to the time t, we obtain ϵ. To determine the value of E necessary for the calculation of ω, we can resort to the mean value of the number of revolutions $\bar{N}$. In fact, from $d\theta = \omega dt$, using Eq. (6), we obtain the period

$$T = \int_0^T dt = \int_0^{2\pi} \frac{d\theta}{\omega} = \int_0^{2\pi} \left\{ \frac{\frac{1}{2} m\ [R^2(1+\sin^2\theta) + r^2 + 2Rr\cos\theta + hR^2]}{E - P(R\cos\theta + r)\sin\theta} \right\}^{1/2} d\theta = \frac{1}{\bar{N}} . \tag{7}$$

To deduce E from this expression, we can proceed graphically, choosing arbitrary values $E_1, E_2, E_3, \ldots$, calculating the integral and determining the corresponding values $T_1, T_2, T_3, \ldots$. Entering in graphs having E as a function of T with the value of $1/\bar{N}$, we can obtain the value of E.

By applying the procedure used for the device indicated in Fig. 3 to other devices, the corresponding expressions can be obtained.

It is particularly useful for what will be said to consider the device indicated in Fig. 5.

The coordinates of points P_1 and P_2 in which the masses are concentrated are:

$$x_1 = R\sin^2\theta - r\cos\theta \qquad x_2 = -R\sin^2\theta + r\cos\theta$$

$$y_1 = -R\cos\theta \qquad y_2 = -R\cos\theta$$

$$z_1 = (R\cos\theta + r)\sin\theta \qquad z_2 = -(R\cos\theta + r)\sin\theta\ .$$

With $R = r$ and putting $m_1 = m_2 = M/2$, the coordinates of the center of gravity G of the two masses are

$$x_G = 0\ , \quad y_G = -R\cos\theta\ , \quad z_G = 0\ .$$

This means that, instead of the two masses which are symmetrical every moment in respect to the y axis, a single mass M may be adopted which moves with a well-timed back-and-forth motion along the y axis. The quantities of motion and their derivatives are:

$$Q_x = 0 \qquad \dot{Q}_x = 0$$

$$Q_y = MR \sin\theta \qquad \dot{Q}_y = MR\,(\cos\theta\omega^2 + \sin\theta\epsilon)$$

$$Q_z = 0 \qquad \dot{Q}_z = 0\ .$$

The energy of the system is:

$$E = \frac{1}{2} m_1 v_1^2 + \frac{1}{2} m_2 v_2^2 + \frac{1}{2} J\omega^2 = \text{const.}$$

Continuing these calculations, using $h = J/MR^2$, we obtain

$$E = MR^2\,[\sin^2\theta + 2(1+\cos\theta) + h]\,\omega^2\ , \tag{8}$$

and thus,

$$\omega = 1/R\,(E/M)^{1/2}\,[\sin^2\theta + 2(1+\cos\theta) + h]^{-1/2} = d\theta/dt\ . \tag{9}$$

From this expression, it follows

$$T = \int_0^T dt = R\left(\frac{M}{E}\right)^{1/2} \int_0^{2\pi} [\sin^2\theta + 2(1+\cos\theta) + h]^{1/2}\, d\theta = \frac{1}{\bar{N}}\ . \tag{10}$$

With this expression we can obtain E. By substituting in Eq. (9), E is obtained, and thus by deriving from Eq. (8), we have

$$\epsilon = \frac{\sin\theta\,(1-\cos\theta)\,E^2}{[\sin^2\theta + 2(1+\cos\theta) + h]^2}\ .$$

The expression of $\dot{Q}_y$ becomes therefore:

$$\dot{Q}_y = MRE^2\,\frac{1 + (2+h)\cos\theta + \cos^2\theta}{[\sin^2\theta + 2(1+\cos\theta) + h]^2}\ . \tag{11}$$

If we plot $\dot{Q}_y$ against t, we obtain a graph of the type indicated in Fig. 8.

RESULTS OF THE TESTS

The described devices were submitted to a long series of tests to establish what concrete results could be obtained for propulsive purposes by a mass

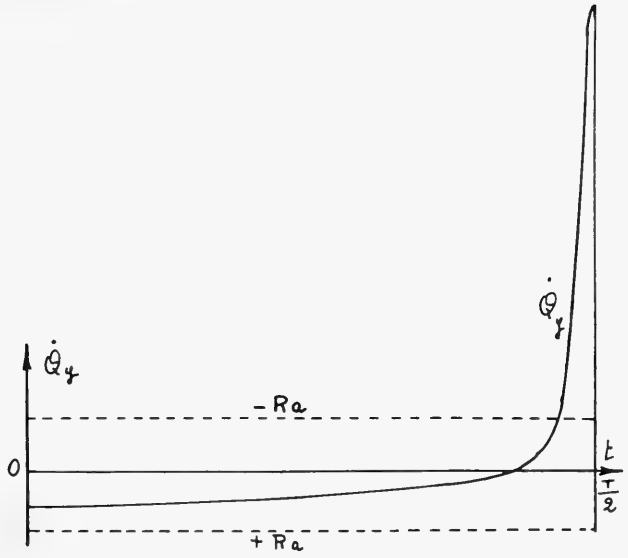

Fig. 8 - Graph plot of $\dot{Q}_y$ against t

rotating in space. We studied above all the device with two masses indicated in Fig. 3. The tests were carried out on land, in the water, and in the air, with no saving of time. We can now report the most important results of these tests.

Land Tests

These tests were carried out on the floor, on horizontal tables, and on inclined planes.

Figure 9 shows a device with two masses placed at the front extremities of two sets of longitudinal poles, one of which is attached to two transverse poles which rest on the floor by means of four heels. The device weighs 30 kg; the two masses consist of two pieces of lead each weighing 200 grams, and are driven by an electric motor.

In Fig. 10 the results of the tests are shown; in the abscissa we have the speed with which the device moves on the floor, and in the ordinate the gross motor power absorbed by the apparatus. Since it was a small motor and since we did not have at our disposal any torque meter qualified to calibrate these motors, we cannot effectively say what the net power absorbed by the device is. If, in the case we are considering, we assume that the efficiency is 0.25 for the motor and the transmission, we may deduce that at the maximum speed of 0.41 m/sec the net power measured on the motor shaft is 50 watts.

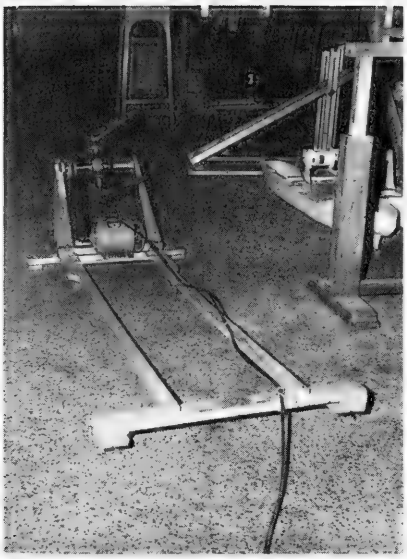

Fig. 9 - Land-tested device weighing 30 kg, with two masses consisting of two pieces of lead weighing 200 grams each

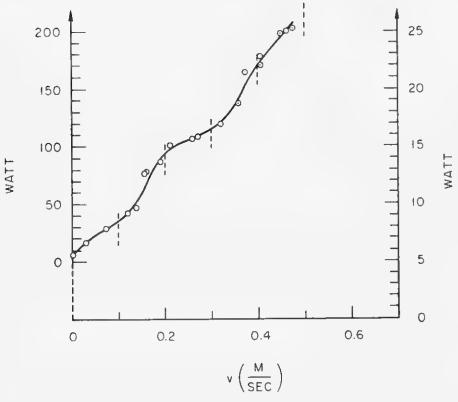

Fig. 10 - Results of tests on the device in Fig. 9

With a device having two masses of the same type, but with a weight of 450 grams and with two pieces of lead weighing 20 grams each, we obtained the results shown in Fig. 11. If we assume the efficiency of the electric micromotor and the transmission to be equal to 0.20 at the maximum speed of 0.61 m/sec, the absorbed power measured on the motor shaft is 4.6 watts. The device advances toward the right or toward the left, according to the way in which the rotating masses are oriented.

Figure 12 shows a device placed on four wooden heels covered with soft rubber. It weighs 1,275 grams and climbs a sheet of glass, inclined at 59° on a horizontal plane.

Figure 13 shows one of the different curves obtained to measure the efficiency of a device that climbs a table inclined at an angle β on a horizontal plane. Different values of β were assumed, and for each value the height of the climb (h) and the time of the climb (t) of the device were measured. By multiplying the weight p of the device by the h/t we obtained the power rendered by the device. It can be deduced from the figure that the device renders the greatest power when it climbs a table inclined at an angle β given by $\text{tg } \beta = 0.41$.

Figure 14 shows a device placed on the back part of a wooden frame 2 meters long and 1 meter wide and having four automobile wheels. The device, with two masses of 3 kg each, put in motion by a 12-volt battery of an automobile, turns the frame around vertical axes. The front part of the frame remains substantially in the same position, while the back part moves sideways to the right or left, according to the direction of rotation of the two masses.

Figure 15 shows a Fiat 1100 automobile. On the lower face of the bottom of the trunk a device with two masses is placed, turned toward the road surface. The weight of each mass is 6 kg, and the motor of the device, put in motion by the automobile battery, absorbs a power of 220 watts.

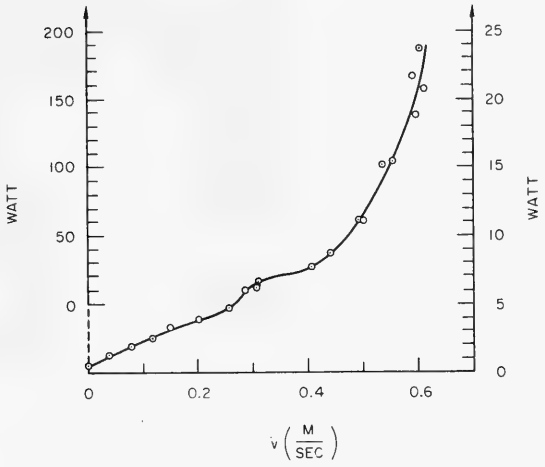

Fig. 11 - Results of tests on the same type of device as in Fig. 9, but with a total weight of 450 grams and having two pieces of lead weighing 20 grams each

The phenomenon shown in the preceding case is repeated here; i.e., the back part of the car moves sideways toward the right or toward the left, according to the direction of rotation of the masses. In about 40 seconds, the back part of the car moves sideways about 2 meters. This means that if the car is approaching to park at a pavement and its longitudinal plane forms an angle of 30° with the pavement itself, a device with two masses is able to bring all of the car to the pavement in a short time. By changing the direction of rotation of the two masses, the car is brought back to the position of arrival.

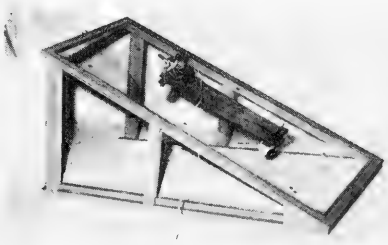

Fig. 12 - Device having four rubber-covered heels and weighing 1275 grams, climbing a sheet of glass inclined at 59°

An indication of the efficiency of the device can be obtained in the following way. Let us assume an automobile weight of 800 kg, and let us distribute 500 kg on the front wheels and 300 kg on the back wheels. If we assume a friction coefficient between wheels and pavement equal to 0.60, the force necessary to move the back part of the car sideways is equal to $300 \times 0.6 = 180$ kg. Since the lateral displacement of 2 meters happens in about 40 seconds, the useful power is $180 \times 2/40 \times 75 = 0.12$ hp. The ratio of the powers is 0.80.

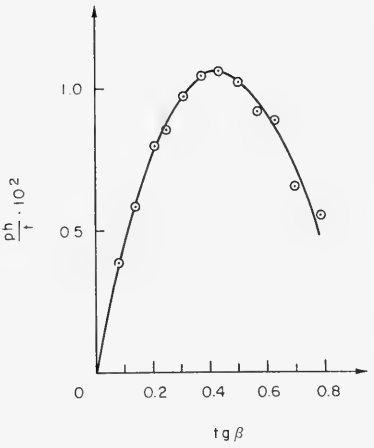

Fig. 13 - Curve measuring the efficiency of a device that climbs a table inclined at an angle β

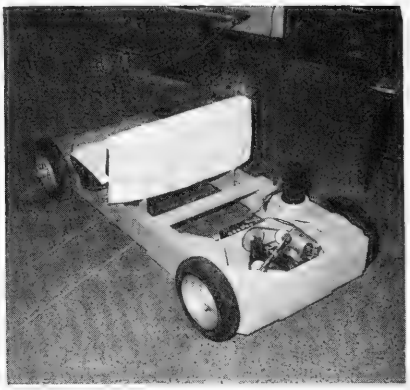

Fig. 14 - Device on back part of a wooden frame set on four automobile wheels, consisting of two masses of 3 kg each. The masses are put in motion by a 12-volt automobile battery and move the back part of the frame sideways, in the direction of rotation

Tests on the Surface of Water

We devoted a great deal of time to tests on the surface of water. We tested models of merchant and military ships, pontoons, catamarans, and wooden and plastic containers. We shall report here some of the results.

Figure 16 shows a device with hyppopedes placed on the forward part of a ship model 1.60 meters long and weighing 15 kg. The model advances at low speed on the surface of the water, with a rectilinear motion.

Figure 17 shows a float with a flat bottom and vertical sides. Length L is 4 meters, width l is 0.74 meters, and displacement d is 77 kg. It has a two-mass device, each mass having a weight p_1 of 4.900 kg. Arms R = r are 0.16 meters long. The relation of the weight of the two masses to the displacement is $2p_1/d = 2 \times 4.90/77 = 0.127$. The relation of double the length of the arms to the length of the hull is $2r/L = 2 \times 0.16/4 = 0.08$. The float moves at a speed of 0.36 m/sec.

Another float similar to the preceding one, 1.60 meters long, and with $2p_1/d = 2 \times 0.300/4.20 = 0.142$ and $2r/L = 2 \times 0.04/1.60 = 0.05$, has a speed v of 0.22 m/sec. Since the scale of the models is $\lambda = 4.00/1.60 = 2.5$, the results of the tests indicate that the functioning of the devices can be regulated in such a way as to satisfy the relation $V = v(\lambda)^{1/2}$.

With another hull having a flat bottom and vertical sides, and with $2p_1/d = 2 \times 0.30/24.90 = 0.02$ and $2r/L = 2 \times 0.10/4 = 0.05$, we obtained the speed of

0.085 m/sec. If this hull were extended proportionally, to the length of 160 meters, it would be able to reach a speed $V = v(\lambda)^{1/2} = 0.085/0.514 \times (160/4)^{1/2} = 1.04$ knots. The device would occupy $5/100 \times 160 = 8$ meters of the length of the hull, and 2% of the displacement. The hull of Fig. 17, on the other hand, if lengthened to 160 meters would be able to reach a speed $V = 0.36/0.514(40)^{1/2} = 4.45$ knots. The device would occupy $8/100 \times 160 = 12.8$ meters of the length of the hull, but 12.7% of the displacement.

Figure 18 shows the hull indicated in Fig. 17 tested in the port of Genoa. The wave produced by the lateral displacements of the hull is quite visible.

Figure 19 shows a very light hull, 1.40 meters long, with a flat bottom, driven by a device with two masses. The hull can advance in any direction. It completes a rotation of 360° in 30 seconds.

Indicated in Fig. 20 is a model destroyer with $2p_1/d = 0.062$ and $2r/L = 0.039$. In a surface of water of 10.5 square meters, it turns in a short time.

Figure 21 shows a long device having $R = r = 0.80$ meters. It will be tested in the sea as soon as a suitable small ship is found. In such a way we hope to see what can be achieved on a ship in normal navigation on the open sea.

Fig. 15 - Trunk of a Fiat 1100 with a device consisting of two masses at 6 kg each and having the same effect on the back part of the car, after being set in motion, as the device in Fig. 14

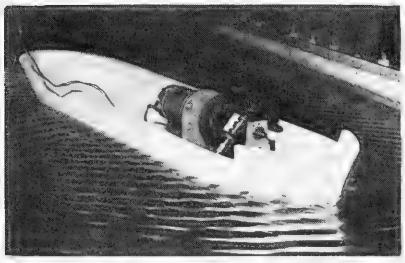

Fig. 16 - Device with hyppopedes on forward part of a ship model 1.60 meters long, 15 kg weight, advancing at low speed and having rectilinear motion

It should be pointed out that very little force is needed to move a float on an absolutely calm surface of water. For example, the model of the destroyer indicated in Fig. 20, which weighs 24 kg can be moved by applying a force of 1 gram to it. Since, as we have seen, the tested device has the capacity to move a float, it follows from this that the device generates a propulsive effect even when the resistance is very low.

Fig. 17 - Float with flat bottom and vertical sides, 4 meters long, 0.74 meters wide, 77 kg displacement, having a 2-mass device and moving at 0.36 m/sec

Fig. 18 - Hull of float in Fig. 17, showing the wave produced by its lateral displacements

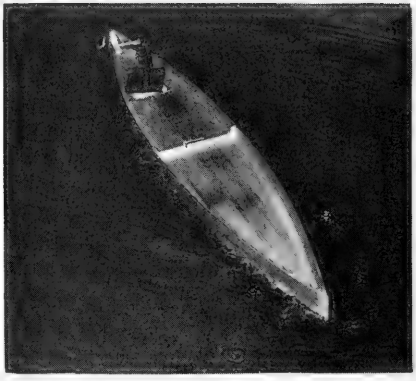

Fig. 19 - Very light hull, 1.40 meters long, flat bottom, driven by a device with two masses

Tests in Immersion

These tests were carried out by placing a two-mass device on a completely immersed hull, 3.10 meters long and 0.48 meters wide, with $2p_1/d = 2 \times 4.90/470 = 0.208$ and $2r/L = 0.18/3.10 = 0.116$. The resulting speed was very low, but it was sufficient to demonstrate that the device functions even when placed on a hull that is completely immersed. However, because of the excessive dimensions of the device, its weight, and its very low speed, it cannot at presence have practical applications for navigation in immersion.

We must add that the immersion tests are rather difficult and that we have dedicated very little time to them. To the study of navigation in immersion we must return at another time.

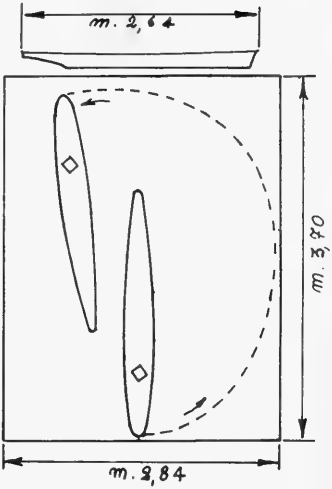

Fig. 20 - Diagram of the turn of a model destroyer

Tests in Air

The tests were carried out by placing a small two-mass device on two hydrogen-filled balloons enclosed within a frame of very light wood. The tests were performed in a closed room with the air absolutely still.

A device (Fig. 4) placed at one end of the two balloons with the y axis horizontal, made the balloons turn around vertical axes. With the device rotating 180° around the y axis, the balloons rotated in the opposite direction. The device has the capacity to impart a forward motion to the balloons, but at a very low speed.

These tests were also very difficult. We had to avoid the formation of air currents, eliminate the vibrations of the two balloons, reduce to a minimum the propulsive effect of the apparatus which stirs up the air, and limit the weight of the apparatus as much as possible.

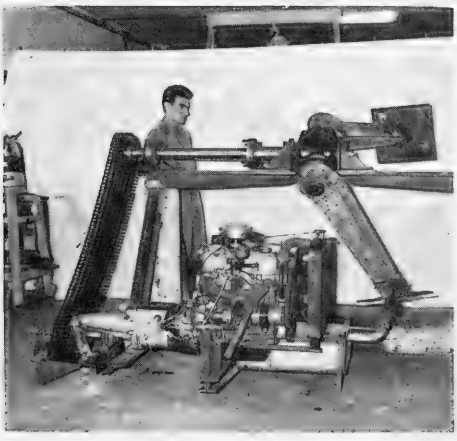

Fig. 21 - Long device having $R = \tau = 0.80$ meters for navigation testing on the open sea

The results of these tests do not allow us to predict the immediate practical applications of the devices for air navigation, since here also we dedicated a rather limited amount of time to the tests.

Tests in Rarefied Air

These tests were carried out with the aim of observing the influence of air on the functioning of the device. We set up an airtight iron case, in the form of a cube, each side 60 cm long. The vacuum within the case was created with a pump, and was measured by means of a column of mercury. A vertical pole with a metallic tip was attached to the bottom of the case. Around it could rotate a horizontal pole, carrying a device at one end and electric piles at the other. The center of gravity G of the device-transversal-piles complex falls on the vertical w passing through the tip (Fig. 22).

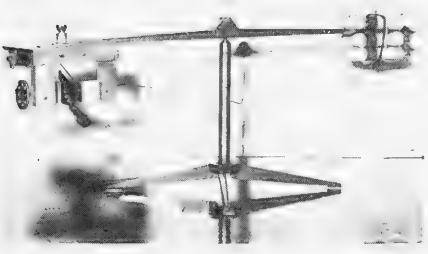

Fig. 22 - Transversal-piles device for rarefied air tests

The result of the tests was that the device was not influenced by the absence of air. In fact, the device, at the same motor power, made the horizontal pole rotate the same number of turns (24 at first) with atmospheric pressure as with a 98.4% vacuum.

In place of the device we substituted a small propeller with dimensions equal to those of the device. We found that the propeller, with its motor power used for the device, makes the pole rotate at 74 rpm with atmospheric pressure; but in the vacuum indicated above, the propeller acquires a very high number of revolutions without generating thrust, and the pole remains still.

The device makes the pole rotate, even if the center of gravity G does not fall on the vertical w. In fact, if Y_G is the distance of G from w, the pole for Y_G = 0, 0-1, 6-3, and 2 cm completes 31, 31, and 26 rpm respectively.

The maximum number of revolutions reached with the pole was 61 rpm. Since the distance of the device from the axis of rotation was 0.25 meters, it follows that the maximum speed reached by the device was 1.6 m/sec.

Tests With the Device Suspended from a Thread

Figure 23 shows the horizontal pole t having a device (A_1) and the piles (A_2). A vessel R having a circular section contains water in which is placed a float G, which also has a circular section. A thin thread f suspends the pole to the float. By operating the motor of the device, the pole begins to rotate, and by means of the thread, also sets the float rotating. In such a way both the pole and the float turn slowly in the same direction with continuity.

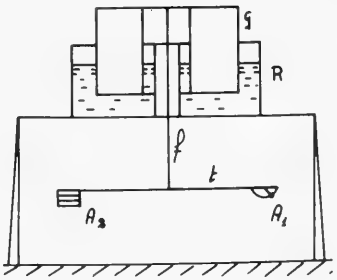

Fig. 23 - Diagram of a test with the device suspended from a thread

Tests on Dry Ice Moving on a Horizontal Smooth Slate

As it is known according to the principles of mechanics, a body not subjected to any force either remains at rest or moves at a uniform speed. In practice, it happens that a body put into motion by an initial thrust, slows its own motion gradually because of friction, and stops. However, if the friction is very small, the body is able to maintain a constant speed for quite a long time.

In order to create in the laboratory a motion with very low friction, we resorted to small pieces of smooth dry ice on a horizontal slate that was likewise accurately smoothed. The friction derived from it is, in effect, very low. In fact, a piece of dry ice pushed by a light puff of air, can run the length of the slate at a uniform speed. Glass is less suitable than slate, because the ice, which melts little-by-little, sticks to the glass very easily.

The friction coefficient for dry ice in motion on a smoothed slate, according to experiments specifically carried out by us, is equal to about 0.001. As may be recalled, the coefficient of friction for steel on ice, as given by the manuals, is 0.01.

A device with two masses, with an overall weight of 140 grams, was posed, by means of a light wooden frame, on four small pieces of dry ice placed on an accurately smooth slate 3.20 meters long and 0.50 meters wide. Numerous tests of systematic type were carried out, with the device running over the slate in all directions. The tests were repeated with another device weighing 120 grams. The final result of these tests was that the device-frame-ice complex, according to the way in which the device is oriented on the slate, (a) advances on the slate with rectilinear and uniform motion, (b) turns to the right, (c) turns to the left, and (d) launched at low speed from extremity A to the other extremity B of the slate, at a certain point stops and returns backwards. As is apparent, a friction resistance that is of the order of thousandths of grams does not impede the functioning of the apparatus.

It should be noted that in the last case, both the dynamic action of the rotating masses that brings the frame back again and the friction resistance are headed in the same direction: from B toward A.

Graph of the Forward Motion of the Device

A large sheet of paper was laid out on the floor, and on it the device (Fig. 9) was made to advance, carrying a penpoint for writing on the paper. The penpoint was more or less in correspondence to the vertical passing through the

center of gravity of the device. The device was tested with one mass and with two masses, at different numbers of revolutions. The trajectory described by the penpoint in the various cases is shown in Fig. 24. We have:

(1) one arm and N = 150
(2) one arm and N = 200
(3) one arm and N = 224
(4) one arm and N = 318
(5) two arms and N = 132
(6) two arms and N = 170
(7) two arms and N = 210
(8) two arms and N = 250

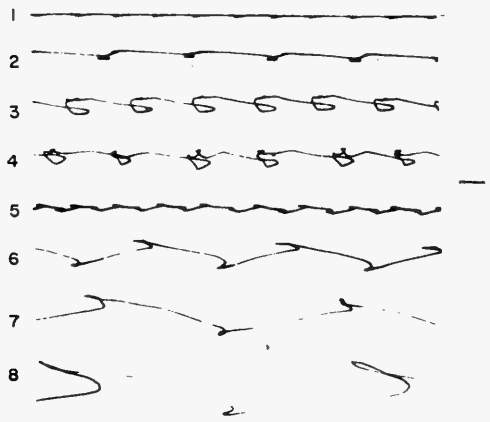

Fig. 24 - Trajectories described by penpoint for various tests on the forward motion of a device

It is clearly noted that for each revolution of the motor shaft, we have a forward motion (s_1) and a backward motion (s_1') of the device. The second is much smaller than the first. For example, we have:

s_1'/s_1 = 0.10 for N = 200 and a device with one arm
s_1'/s_1 = 0.25 for N = 224 and a device with one arm
s_1'/s_1 = 0.27 for N = 250 and a device with two arms.

Graph Using the Oscillograph

In order to complete the series of experiments, it was considered suitable to have a graph of the variation of N and of the motor power during a 360° rotation of the motor shaft. Siemens oscillographs were used, and altogether there were carried out eighty graphs of tension, current, and N on devices with one mass or two masses.

Figure 25 shows one of these graphs. It was carried out on the device indicated in Fig. 9 fixed to the floor, and having a single rotating mass. In the

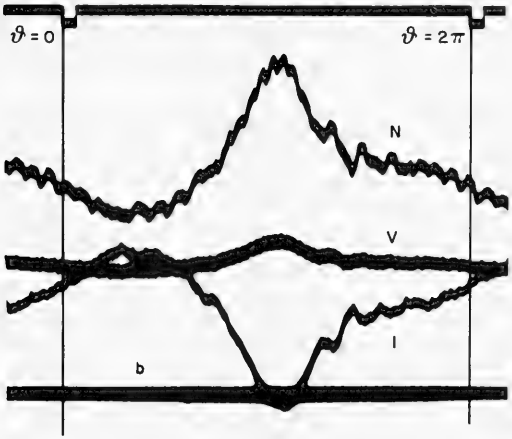

Fig. 25 - Oscillograph of the performance of the device indicated in Fig. 9

abscissa we have the angle of rotation θ of the motor shaft and in the ordinate N, the voltage V and the current I, measured on the terminals of the motor. In order to pass from the input power VI to that measured on the shaft in Eq. (4), it was necessary to remove from VI the power absorbed by all the passive resistances and to multiply the power that remained by the efficiency of the motor. The power absorbed by the passive resistance was 9 watts.

For $\theta = 0$ and for $\theta = 2\pi$ we have V = 26 v, I = 0.46 amp, and VI = 11.96 w. The corresponding power on the device is 2.96 w.

In the points $\theta = 0$ and $\theta = 2\pi$ we have N = 1.42/sec and at the maximum 2.22/sec. The mean value measured by a tachymeter during the test was $\bar{N}$ = 95/min = 1.58/sec. The corresponding period is T = 0.6316/sec.

With this value of T, Eq. (7) gives E = 0.1828 kg-m. Having had in the device R = 0.20 m, r = 0.15 m, p = 0.200 kg, and h = 2.15, it was possible to calculate with Eq. (6) the angular speed ω. In Fig. 26 the values of ω obtained during the test are indicated with (+), and those calculated with Eq. (6) are indicated with (o).

We wanted to see the contribution given by pz and by $1/2\ J\omega^2$ to the values of E and of ω. In Eq. (6), placing pz = 0 produces a curve indicated by (·), and placing h = 0 gives the curve indicated by (△). The values of E are 0.1666 kg-m in the first case, and 0.0927 kg-m in the second.

For R = r, h = 0, $\theta = 180°$, from Eq. (6) we obtain $\omega = \infty$.

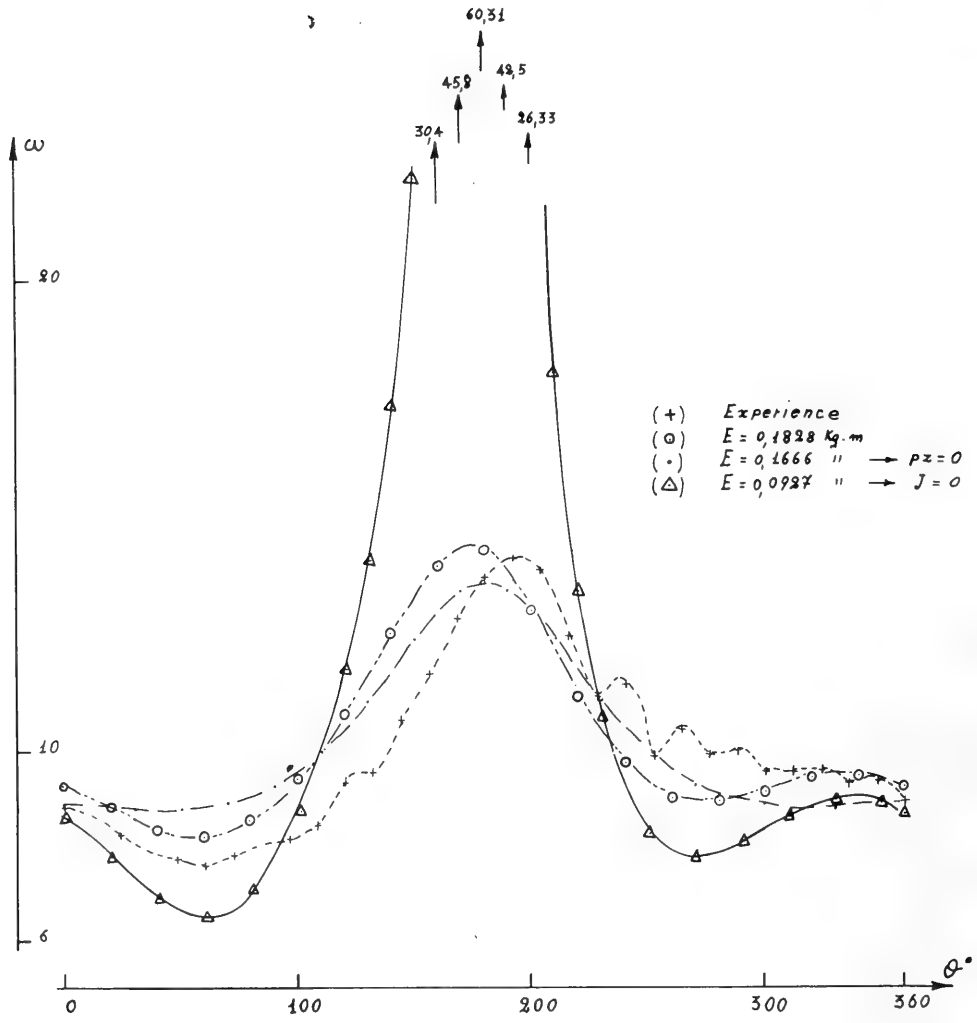

Fig. 26 - Comparison of values of ω obtained from tests with those obtained from Eq. (6)

CONSIDERATION OF TESTED DEVICES

The device which first produces the greatest interest is the one indicated in Fig. 5. In fact, it is perfectly balanced, moves forward on the floor, and climbs an inclined plane. A small device of this kind, held in the hand, gives evident proof of the possibility it has for generating a substantial propulsive thrust for each turn of the motor shaft.

However, this device does not function in either water or air, nor when suspended from a thread, nor even on small blocks of dry ice that are free to move on a horizontal slate. When the device is placed on a model of a ship, for example, it makes the model go forward and backward, while the center of gravity of the model remains in the same position. The device, therefore, functions only if a suitable value of friction resistance exists; if this resistance is too low or nonexistent, the device does not function.

In order to give an explanation of this, it is necessary to consider only the derivative of the quantity of motion (Fig. 8). Since the area of this diagram is zero, it follows that, if there is no friction, the device goes back and forth; if there is friction, linear or not, the device acquires a forward motion.

In fact, if the friction resistance is represented by lines $+R_a$ and $-R_a$ as indicated in Fig. 8, then the device advances and does not go back. This is so because the diagram of force that thrusts the device back is always inferior to the friction resistance, while in the meantime the point of the diagram of force that thrusts the device forward is superior to the friction resistance. The device, in correspondence to this point, undergoes a forward jerk. If instead the friction resistance is very low, the two lines $+R_a$ and $-R_a$ that represent it come very close to the t axis, so that the two areas of the diagram remain substantially equal between them, and the device does not advance. The device thus remains defined, in both its functioning and its limited practical applications.

This conclusion cannot be extended to the devices indicated in Figs. 2 and 3. They, in fact, function even with a very low friction, as can be seen in the tests in water and on dry ice. On the other hand, if we analyze the trajectory of the forward motion of the device (Fig. 27) deduced from Fig. 24, it is clearly indicated that when the mass reaches point P_1 and remains there motionless, the device is displaced of $+s_1$; when the mass is in the remaining points of the trajectory, the device goes forward and backward; when the mass returns to P_1 there is the $+s_1$ displacement again; and thus it goes on. The trajectory of the motion of the device is therefore composed of two parts: one closed, in which the device completes a back-and-forth motion, and the other open, giving proof of the forward motion of the device. It seems very difficult to give an explanation for this forward motion. On the one hand, we have definite proof that the device advances, even in the presence of an extremely small amount of friction; on the other, we have the theorem of the motion of the center of gravity, which excludes the possibility of the device advancing, unless there is a friction resistance. No "internal" muscular force and no "internal" mechanism, simple or complex, can influence the motion of the center of gravity.

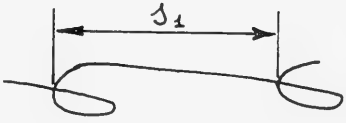

Fig. 27 - Trajectory of devices (Figs. 2 and 3) that function with very low friction

The explanation of the forward movement will eventually be found. What is necessary is a thorough examination of the functioning of the device, both from

the theoretical and experimental point of view. As to the theoretical viewpoint, it will be necessary to be able to form the general equations for the motion of the device, to find again the trajectory indicated in Fig. 27, and to demonstrate that the displacement $+s_1$ ceases to exist if there is effected a lack of friction resistance because of the contact of the device with the surface of the support. As to the experimental viewpoint, it is a question of finding a laboratory test in which the friction resistance is small enough to remove the possibility that the device might move.

For now, we have established the fact that a vehicle, by means of an "internal" mechanism, can move in the presence of very little friction.

CONCLUSIONS

During the tests that were made, the best results were obtained with the device indicated in Fig. 3; thus, we intend to refer to this device in our final summary considerations.

1. The device, as has been mentioned, does not generate a continuous thrust, as happens for example in the case of the propeller, but produces two propulsive effects for each turn of the motor shaft. Meanwhile, in the interval between one propulsive effect and the other, the device undergoes the reaction of the vehicle that it must thrust. It follows from this that the functioning of the device depends upon the type of vehicle, and on the point and way in which it is placed on the vehicle.

2. The number of turns of the motor cannot be notably increased, because beyond a certain value the device begins to jump around on the supporting plane, and the absorbed power is thus dispersed in vibrations.

3. Up to the present time, it has not been possible to combine more than two rotating masses in such a way as to be able to have more than two propulsive effects for each turn of the motor shaft. Even after having recognized the great importance that the resolution of this problem would have, we have only been able to devote rather limited time to it.

4. The device generates vibrations that may be tolerable on ships and floats in general, but rather unpleasant in land vehicles. It is necessary to foresee an arrangement of mechanisms that can absorb the vibrations. In the case of automobiles, if the device is attached to the axis of the rear wheels, it is necessary to anticipate an arrangement of shock-absorbers that will prevent the vibrations from passing from the axis of the wheels to the chassis.

5. The weight and dimensions of the device may constitute a serious obstacle for its use on ships. It depends on the speed it has to reach. If it is limited to the minimum speed needed to move a ship in port, with a calm sea and without wind, then the weight and the dimensions of the device may be tolerable. Numerical indications concerning this problem will be obtained only after having made tests on some ships.

6. We did not run any tests of devices placed on hulls in motion to see if a device produces its forward motion even when the hull has the propeller in action, or if it produces its turning motion even when the hull has the propeller alone or the propeller and the rudder in action. These are tests that would be of great interest for the practical application of the device. If the outcome of the tests were satisfactory, the use of the device could become useful even if just for the contribution it would make in support of the rudder. These tests should be carried out, naturally, on a ship under normal navigation conditions.

7. It was not possible for us to conduct research on trajectories different from those indicated previously; for example, trajectories that are less cumbersome and more efficient.

Having seen from the first that, even with determined limitations, there existed the possibility of moving a vehicle in a desired direction, by making a mass rotate within it, we dedicated ourselves solely to the execution of a vast series of tests with the goal of giving a definite proof of the existence of this possibility.

We are of the conviction that what is of interest is mainly the construction of evidence for a given phenomenon. If it appears useful for practical applications, the necessary modifications can always be found in order to execute the phenomenon in the best possible way.

Finally, we should like to state that the present paper is original and that the devices described in it are patented.

* * *

DISCUSSION

Prof. M. Poreh
Technion-Israel Institute of Technology
Hafia, Israel

The propulsion effect of certain unsteady motions of a mass within a closed system with rigid boundaries seems, at first, surprising and contradictory to physical laws. The phenomenon is not new, however. The "Mexican jumping bean" is just one example of a motion due to polarized acceleration. Friction is the dominating factor in all of Prof. DiBella's experiments. In some of them, the friction coefficient is very small indeed, but so is the power necessary to maintain the motion.

* * *

REPLY TO DISCUSSION

Prof. Alfio Di Bella

I should like to thank Prof. Poreh for his contribution to the discussion and to write down here some of my considerations.

To show that results of tests of my devices are in agreement with the principles of mechanics it is not necessary to draw an analogy with larval insects; it is enough to remember these principles.

The chapter concerning the motion of any material system in Appell's classical treatise on Rational Mechanics states that: "Le centre de gravitè du système se meut comme un point matériel, qui aurait pour masse la masse totale du système, et auquel seraient appliquées des forces égales et parallèles aux forces extérieures." We can see therefore that any force conditions are acceptable, as long as they are "external."

The test results of my devices were obtained in the presence of external forces. In fact:

- In tests on dry ice, friction resistance is the dominating factor; it is very little (practically negligible), but not strictly zero.

- In tests in water the water pressure acting against the hull is the dominating factor.

- In tests in air the pressure against the balloon on which the device is placed is the dominating factor.

For these reasons the working of the devices follows the classical mechanical principles, and the dominating factor in my experiments is not the friction coefficient alone.

However, it would be interesting to know the minimum values of the external forces which are necessary to prevent the device from working. Theoretically, this could be done by writing the motion equations of the device; and in a practical way, by carrying out tests in the presence of external forces that gradually decrease to zero.

As far as the power absorbed by the device is concerned, it has not been possible to find out experimentally if the power diminishes with the external forces. The 140-gram device works with the same small battery both on dry ice and on a wood table. We should remember, however, that the device is subject to vibrations and shocks on the supporting plain.

At present, it is difficult to say how power absorbed by the device is distributed.

* * *

THE AERODYNAMICS OF SAILS

Jerome H. Milgram
Massachusetts Institute of Technology
Cambridge, Massachusetts

INTRODUCTION

The general nature of the aerodynamics of sails is similar to that of low-speed aircraft, for the most part. However, there are a few significant differences. It is the purpose of this paper to discuss the fundamentals of these differences and, to a limited extent, how these differences affect the design of sails. As in the case of aircraft, the best starting point here is the lifting line theory for a single lifting line. One difference between the lifting line theory for sails and the lifting line theory in an unbounded free stream is that there is a boundary beneath the lifting line in the sail problem which represents the hull and the sea. Another difference is that sails operate in a wind gradient that is significant over the entire span of a sail, whereas on most aircraft the wind gradient is usually significant only near the root of a wing.

For a vessel carrying two sails, much can be learned from the theory of two interacting lifting lines. This is, of course, similar to the biplane theory for aircraft, and some generalizations drawn from aircraft theory can be applied to a sailing rig. Because of the various limitations of the biplane theory, however, as well as the fact that, for sails, the lifting lines are skewed to each other if one of the sails is set on a stay, detailed results from the theory of two lifting lines must be obtained by numerical methods.

When boundary layer effects are examined, the situation relating to sails is much more complicated than most other applications, because, for the most part, sails operate at relatively large lift coefficients. For example, a typical wing or propeller blade might have a lift coefficient of about 0.4, whereas a typical sail would have a lift coefficient of about 1.4. Most boundary layer effects are determined by the chordwise pressure distribution, since the flow is usually almost wholly chordwise. This is shown in Fig. 1 which is a photograph of sails having tufts to indicate the flow direction in a wind tunnel. Two other frequent effects are also indicated. These are the local leading-edge separation on the mainsail near the head of the jib due to a poor match between the sails, and the local trailing-edge separation near the head of the mainsail due to the large local lift coefficient in this region.

LIFTING LINE THEORY FOR A SINGLE SAIL

Two of the main differences between the aerodynamics of sails and the aerodynamics of most other low-speed lifting surfaces are that a sail operates in a

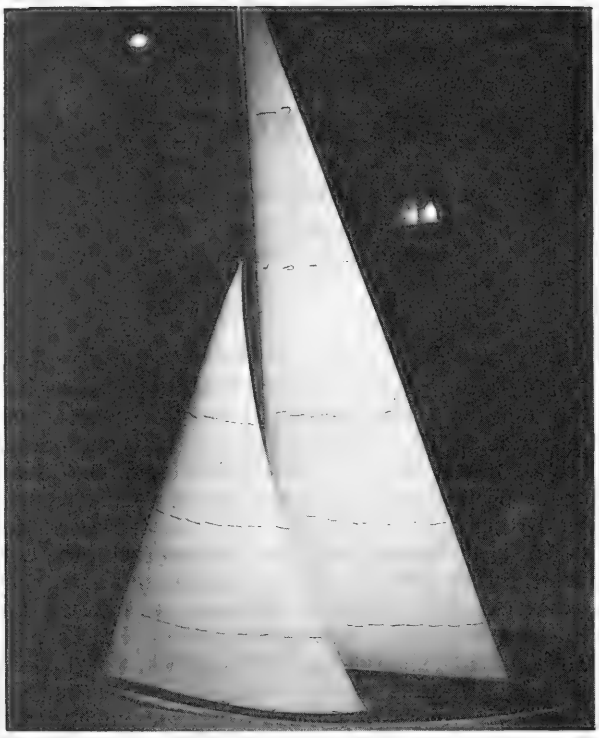

Fig. 1 - Model sails with tufts in a wind tunnel

velocity gradient and that it has a solid boundary beneath it formed by the hull and the sea surface. The effects due to these differences can be determined from the lifting line theory. The actual design of sail shapes must be carried out by the lifting surface theory (see, e.g., Milgram, 1968). However, for the linearized problem the lifting line theory and the lifting surface theory yield identical flows in the Trefftz plane. Hence gross quantities such as lift, induced drag, and heeling moment can be calculated by the lifting line theory.

Consider a steady, incompressible, inviscid flow in the presence of a heeled lifting line. The flow is taken to be irrotational except on the lifting line and its trailing vortex sheet. The boundary conditions beneath the lifting line are approximated by a plane parallel to the sea surface lying somewhere between the deck of the hull and the sea surface. To satisfy the boundary condition of no-flow through this plane, henceforth called the image plane, the method of images is used as shown in Fig. 2. The free stream velocity is approximated by a linearly varying function of height having the value U_0 at midspan and a slope of K. The direction of the free stream is taken to be constant in this development, whereas on an actual sailing vessel the incident stream direction is not constant. This occurs because the incident wind is the vector sum of the

true wind velocity whose magnitude increases with height, and the negative of the velocity of the vessel. This small effect is neglected in this analytical development, but is taken into account in the numerical calculations of the next section.

The lifting line problem is formally posed as follows. Determine the flow field and associated lift, and the induced drag and heeling moment for a lifting line of length b perpendicular to an incident, x-directed, shear flow and inclined to the vertical by an angle ϕ. An infinite horizontal plane is located at a distance h below the lifting line, and the variation of free stream velocity depends only on height in a linear fashion such that its speed is given by

$$U = U_0 + Ky \ . \tag{1}$$

The origin of the coordinates is at the midspan of the lifting line (Fig. 2). Calling the disturbance velocity potential by ϕ and the disturbance velocity components by u', v', and w', the boundary conditions are:

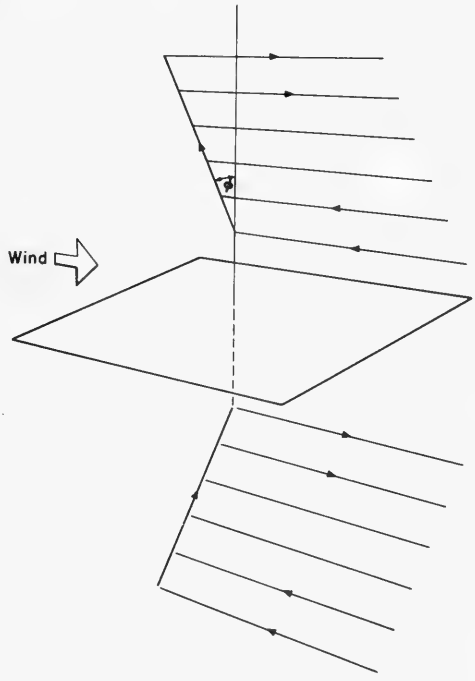

Fig. 2 - The geometry for a heeled lifting line in the presence of an image plane

$$\phi_y\Big|_{y=-b/2-h} = 0 \tag{2}$$

$$\lim_{y\to\pm\infty} \nabla\phi = 0 \tag{3}$$

$$\lim_{z\to\pm\infty} \nabla\phi = 0 \tag{4}$$

$$\lim_{x\to-\infty} \nabla\phi = 0 \tag{5}$$

$$\lim_{x\to\infty} \nabla\phi < \infty \ . \tag{6}$$

The method of solution is similar to that used by Glauert (1948) for an unbounded airfoil in a uniform stream. The circulation must vanish at the ends of the lifting line to satisfy Eq. (6). This is because a nonzero value of circulation at an end of the lifting line would necessitate a trailing vortex of nonzero strength, since the vortex field is solenoidal. The circulation strength on the lifting line is expanded in a Fourier series, each term of which vanishes at the ends of the span. First the angular variable ψ is defined by the relation

$$y = -\frac{b}{2}\cos\psi \tag{7}$$

with the simple Jacobian

$$\frac{dy}{d\psi} = \frac{b}{2}\sin\psi \ . \tag{8}$$

Then the circulation can be expanded as

$$\Gamma[y(\psi)] = 2\,U_0\,b\sum_{n=1}^{\infty} A_n \sin n\psi \ , \tag{9}$$

where the A_n's are dimensionless. The usual relation for the lift distribution holds;

$$\ell\,[y(\psi)] = \rho U(y)\Gamma(y) \ , \tag{10}$$

which gives

$$\ell(\psi) = [2\rho U_0^2 b - \rho U_0 K b^2 \cos\psi]\sum_{n=1}^{\infty} A_n \sin n\psi \ . \tag{11}$$

Since the vortex field is solenoidal and Kelvin's circulation theorem is valid, there must be a trailing vortex sheet of strength equal to the negative of the spanwise derivative of the circulation:

$$\gamma\,[y(\psi)] = -\frac{\partial\Gamma}{\partial y} \tag{12}$$

and in terms of ψ ,

$$\gamma(\psi) = \frac{-4\,U_0\sum_{n=1}^{\infty} n A_n \cos n\psi}{\sin\psi} \ . \tag{13}$$

The solution of this problem is carried out by use of the method of images as shown in Fig. 2, where the sign of the image of any vortex element is opposite to the sign of the element in order to satisfy the boundary condition on the image plane. The perturbation velocity is taken as the velocity induced by the system of vorticity comprised of the lifting line and its trailing vortex sheet as well as the image system. There is another source of velocity alteration. This alteration occurs whenever the system of vorticity induces velocity parallel to the direction in which the free stream speed varies. Because of the vertical variation of free stream velocity, such induced flow convects fluid of a given stream velocity to a region where the undisturbed stream velocity has a possibly different value. For wind gradients commonly encountered in normal sailing

craft, this effect is very small and will not be taken into account in the following theory.

It is shown in appendix A that the effect of heeling on sail aerodynamics is negligible. Hence, the following developments will be carried out for zero heel. The dominant effects of heeling can then be accounted for by proper resolution of forces. The lift and heeling moment are determined by the circulation distribution on the lifting line and the free stream velocity distribution. These independent variables, along with the induced velocity component w', determine the induced drag to the first order in the velocity ratio.

We can now determine w'. From the law of Biot and Savart,

$$w'(y) = \frac{1}{4\pi} \int_{-b/2}^{b/2} \frac{\gamma(\eta)}{y - \eta} \, d\eta - \frac{1}{4\pi} \int_{-b/2}^{b/2} \frac{\gamma(\eta)}{y + b + 2h + \eta} \, d\eta \, . \tag{14}$$

The negative sign occurs on the second term because the sign of the image vortex system is the negative of the sign of the lifting line and trailing vortex sheet system.

Let

$$\eta = -\frac{b}{2} \cos \psi' \quad \text{on the lifting line} \tag{15}$$

$$\eta = -\frac{b}{2} \cos \phi' \quad \text{on the image line} \, , \tag{16}$$

and, as before,

$$y = -\frac{b}{2} \cos \psi \, . \tag{17}$$

In terms of the variables ψ, ψ', and ϕ', $w'(y)$ is given by

$$w'(y) = \frac{1}{4\pi} \sum_{n=1}^{\infty} -4 U_0 \, n \, A_n \left\{ \int_0^{\pi} \frac{\cos n\psi' \, d\psi'}{\cos \psi - \cos \psi'} - \int_0^{\pi} \frac{\cos n\phi' \, d\phi'}{2 + 4h/b - (\cos \psi + \cos \phi')} \right\} . \tag{18}$$

The first integral was evaluated by Glauert (1948) as

$$\int_0^{\pi} \frac{\cos n\psi' \, d\psi'}{\cos \psi' - \cos \psi} = \pi \frac{\sin n\psi}{\sin \psi} \, . \tag{19}$$

The second integral is evaluated in appendix B as

$$\int_0^{\pi} \frac{\cos n\phi' \, d\phi'}{2 + \frac{4h}{b} - (\cos\psi + \cos\phi')} = \pi \frac{\left[Q(\psi) - \sqrt{Q^2(\psi) - 1}\right]^n}{\sqrt{Q^2(\psi) - 1}} \tag{20}$$

where

$$Q(\psi) = 2 + \frac{4h}{b} - \cos(\psi) \, . \tag{21}$$

Using Eqs. (19) and (20), the expression for the downwash becomes

$$w'(y) = - U_0 \sum_{n=1}^{\infty} n A_n \left\{ \frac{\sin n\psi}{\sin\psi} - \frac{\left[Q(\psi) - \sqrt{Q^2(\psi) - 1}\right]^n}{\sqrt{Q^2(\psi) - 1}} \right\} . \tag{22}$$

In the linearized theory the induced angle, $\alpha_d(y)$, is given by

$$\alpha_d(y) = - \frac{w'(y)}{U(y)} \, , \tag{23}$$

and the induced drag distribution $d_i(y)$ is

$$d_i(y) = \ell(y) \, \alpha_d(y) \, . \tag{24}$$

Hence,

$$d_i(y) = \rho \Gamma(y) w'(y) \, . \tag{25}$$

The total induced drag is

$$D_i = \int_0^{\pi} - \rho \Gamma(\psi) \, w'(\psi) \, \frac{b}{2} \sin\psi \, d\psi \, . \tag{26}$$

Using Eqs. (9) and (22) and carrying out the integration for the part of the downwash due to the trailing vortex sheet gives

$$D_i = \rho U_0^2 \, b^2 \left\{ \sum_{n=1}^{\infty} n A_n^2 \frac{\pi}{2} - \sum_{n=1}^{\infty} \sum_{m=1}^{\infty} n A_n \, A_m \int_0^{\pi} \sin m\psi \, \sin\psi \, \frac{\left[Q(\psi) - \sqrt{Q^2(\psi) - 1}\right]^n}{\sqrt{Q^2(\psi) - 1}} \, d\psi \right. . \tag{27}$$

Using the notation

$$I_{mn} = \int_0^{\pi} \sin m\psi \, \sin\psi \, \frac{\left[Q(\psi) - \sqrt{Q^2(\psi) - 1}\right]^n}{\sqrt{Q^2(\psi) - 1}} \, d\psi \, , \tag{28}$$

then

$$D_i = \rho U_0^2 \, b^2 \sum_{n=1}^{\infty} n A_n \left(\frac{\pi}{2} A_n - \sum_{m=1}^{\infty} A_m \, I_{mn} \right) . \qquad (29)$$

Values of I_{mn} for various values of h/b are shown in Table 1. This table indicates that I_{mn} decreases rapidly as m or n increases. For practical purposes, negligible error is introduced in the induced drag calculation by neglecting the effect of all terms in the double sum for m or n greater than eight, except possibly for the case of h equal to zero.

Table 1
I_{mn} for Various Values of h/b (gap/span)

h/b = 0. m \ n	1	2	3	4	5	6	7	8	9	10
1	.429	.192	.100	.060	.039	.027	.020	.015	.012	.010
2	.383	.237	.150	.099	.069	.050	.038	.030	.024	.019
3	.301	.225	.163	.118	.087	.066	.052	.041	.033	.028
4	.238	.198	.157	.123	.097	.076	.061	.050	.041	.034
5	.195	.172	.146	.121	.099	.081	.067	.056	.047	.040
6	.164	.150	.133	.115	.098	.083	.070	.060	.051	.044
7	.141	.133	.121	.107	.094	.082	.071	.062	.054	.047
8	.124	.118	.110	.100	.090	.080	.070	.062	.055	.049
9	.110	.106	.100	.093	.085	.077	.069	.062	.055	.050
10	.099	.096	.092	.086	.080	.073	.067	.061	.055	.050
h/b = .050 m \ n	1	2	3	4	5	6	7	8	9	10
1	.358	.139	.061	.029	.015	.008	.005	.003	.002	.001
2	.277	.151	.080	.044	.025	.014	.008	.005	.003	.002
3	.182	.121	.075	.046	.028	.017	.010	.006	.004	.003
4	.117	.088	.061	.040	.026	.017	.011	.007	.005	.003
5	.076	.061	.046	.033	.023	.015	.010	.007	.005	.003
6	.050	.042	.034	.025	.018	.013	.009	.006	.004	.003
7	.033	.029	.024	.019	.014	.011	.008	.005	.004	.003
8	.022	.020	.017	.014	.011	.008	.006	.004	.003	.002
9	.015	.014	.012	.010	.008	.006	.005	.004	.003	.002
10	.011	.010	.009	.007	.006	.005	.004	.003	.002	.002
h/b = .100 m \ n	1	2	3	4	5	6	7	8	9	10
1	.317	.113	.045	.019	.009	.004	.002	.001	.001	.000
2	.227	.114	.056	.028	.014	.007	.004	.002	.001	.001
3	.135	.084	.048	.027	.015	.008	.004	.002	.001	.001
4	.078	.055	.036	.022	.013	.008	.004	.003	.001	.001
5	.045	.035	.024	.016	.010	.006	.004	.002	.001	.001
6	.026	.021	.016	.011	.008	.005	.003	.002	.001	.001
7	.015	.013	.010	.008	.005	.004	.002	.002	.001	.001

(Table continues)

Table 1 (Continued)

h/b = .100 m \ n	1	2	3	4	5	6	7	8	9	10
8	.009	.008	.007	.005	.004	.003	.002	.001	.001	.001
9	.006	.005	.004	.003	.002	.002	.001	.001	.001	.000
10	.003	.003	.003	.002	.002	.001	.001	.001	.000	.000
h/b = .150 m \ n	1	2	3	4	5	6	7	8	9	10
1	.286	.096	.035	.014	.006	.003	.001	.001	.000	.000
2	.192	.091	.042	.019	.009	.004	.002	.001	.000	.000
3	.106	.063	.034	.017	.009	.004	.002	.001	.001	.000
4	.056	.038	.023	.013	.007	.004	.002	.001	.001	.000
5	.030	.022	.015	.009	.005	.003	.002	.001	.001	.000
6	.016	.013	.009	.006	.004	.002	.001	.001	.000	.000
7	.009	.007	.005	.004	.002	.002	.001	.001	.000	.000
8	.005	.004	.003	.002	.002	.001	.001	.000	.000	.000
9	.003	.002	.002	.001	.001	.001	.000	.000	.000	.000
10	.001	.001	.001	.001	.001	.000	.000	.000	.000	.000
h/b = .200 m \ n	1	2	3	4	5	6	7	8	9	10
1	.262	.083	.029	.011	.004	.002	.001	.000	.000	.000
2	.166	.075	.032	.014	.006	.003	.001	.001	.000	.000
3	.086	.049	.025	.012	.006	.003	.001	.001	.000	.000
4	.042	.028	.016	.009	.005	.002	.001	.001	.000	.000
5	.021	.015	.010	.006	.003	.002	.001	.000	.000	.000
6	.010	.008	.005	.003	.002	.001	.001	.000	.000	.000
7	.005	.004	.003	.002	.001	.001	.000	.000	.000	.000
8	.003	.002	.002	.001	.001	.000	.000	.000	.000	.000
9	.001	.001	.001	.001	.000	.000	.000	.000	.000	.000
10	.001	.001	.000	.000	.000	.000	.000	.000	.000	.000
h/b = .250 m \ n	1	2	3	4	5	6	7	8	9	10
1	.241	.073	.024	.008	.003	.001	.000	.000	.000	.000
2	.145	.063	.026	.010	.004	.002	.001	.000	.000	.000
3	.071	.039	.019	.009	.004	.002	.001	.000	.000	.000
4	.033	.021	.012	.005	.003	.001	.001	.000	.000	.000
5	.015	.011	.007	.004	.002	.001	.001	.000	.000	.000
6	.007	.005	.004	.002	.001	.001	.000	.000	.000	.000
7	.003	.003	.002	.001	.001	.000	.000	.000	.000	.000
8	.002	.001	.001	.001	.000	.000	.000	.000	.000	.000
9	.001	.001	.000	.000	.000	.000	.000	.000	.000	.000
10	.000	.000	.000	.000	.000	.000	.000	.000	.000	.000

(Table continues)

Table 1 (Continued)

h/b = .300 m \ n	1	2	3	4	5	6	7	8	9	10
1	.224	.065	.020	.007	.002	.001	.000	.000	.000	.000
2	.129	.054	.021	.008	.003	.001	.000	.000	.000	.000
3	.060	.031	.015	.006	.003	.001	.000	.000	.000	.000
4	.026	.016	.009	.004	.002	.001	.000	.000	.000	.000
5	.012	.008	.005	.003	.001	.001	.000	.000	.000	.000
6	.005	.004	.002	.001	.001	.000	.000	.000	.000	.000
7	.002	.002	.001	.001	.000	.000	.000	.000	.000	.000
8	.001	.001	.001	.000	.000	.000	.000	.000	.000	.000
9	.000	.000	.000	.000	.000	.000	.000	.000	.000	.000
10	.000	.000	.000	.000	.000	.000	.000	.000	.000	.000
h/b = .350 m \ n	1	2	3	4	5	6	7	8	9	10
1	.209	.058	.017	.005	.002	.001	.000	.000	.000	.000
2	.116	.046	.017	.006	.002	.001	.000	.000	.000	.000
3	.051	.026	.012	.005	.002	.001	.000	.000	.000	.000
4	.022	.013	.007	.003	.001	.001	.000	.000	.000	.000
5	.009	.006	.003	.002	.001	.000	.000	.000	.000	.000
6	.004	.003	.002	.001	.000	.000	.000	.000	.000	.000
7	.022	.001	.001	.000	.000	.000	.000	.000	.000	.000
8	.001	.000	.000	.000	.000	.000	.000	.000	.000	.000
9	.000	.000	.000	.000	.000	.000	.000	.000	.000	.000
10	.000	.000	.000	.000	.000	.000	.000	.000	.000	.000

The problem of determining the conditions needed for minimum induced drag, with fixed lift, of a lifting line in an unbounded fluid with the free stream speed being dependent on the position in the plane perpendicular to the stream direction, was solved by Von Karman and Tsien (1945). The result is that minimum induced drag occurs when the induced angle is constant over the span, which reduces to the well-known case of constant downwash when the stream speed is independent of position. When the method of Von Karman and Tsien is applied to a lifting line over and normal to an infinite plane, the condition for minimum induced drag is the same as before — constant induced angle. However, the circulation distribution needed to cause a constant induced angle over the span depends on the distance from the base of the lifting line to the infinite plane. Table 2 shows the values of the first ten A_n's divided by A_1 needed to result in a constant induced angle for various values of h/b. The values in this table were determined by inversion of Eq. (22), subject to the condition of constant induced angle.

The total lift L is given by

$$L = \int_{-b/2}^{b/2} \ell\,(y)\,dy \,. \tag{30}$$

Table 2
Values of the First Ten A_n's for Minimum Induced Drag for Various Values of h/b and $Kb/2U_0$

A_1	A_2	A_3	A_4	A_5	A_6	A_7	A_8	A_9	A_{10}
h/b = 0.010	Kb/2U = 0.000								
1.0000	0.1165	0.0667	0.0362	0.0221	0.0143	0.0098	0.0069	0.0128	0.0091
h/b = 0.010	Kb/2U = 0.100								
1.0000	0.0957	0.0658	0.0356	0.0217	0.0141	0.0097	0.0068	0.0125	0.0090
h/b = 0.010	Kb/2U = 0.200								
1.0000	0.0749	0.0648	0.0351	0.0214	0.0138	0.0095	0.0065	0.0123	0.0088
h/b = 0.010	Kb/2U = 0.300								
1.0000	0.0539	0.0639	0.0345	0.0210	0.0136	0.0093	0.0065	0.0121	0.0086
h/b = 0.010	Kb/2U = 0.400								
1.0000	0.0329	0.0629	0.0339	0.0206	0.0133	0.0092	0.0064	0.0119	0.0085
h/b = 0.050	Kb/2U = 0.000								
1.0000	0.0943	0.0420	0.0205	0.0108	0.0060	0.0035	0.0021	0.0023	0.0014
h/b = 0.050	Kb/2U = 0.100								
1.0000	0.0742	0.0415	0.0202	0.0106	0.0059	0.0034	0.0020	0.0023	0.0014
h/b = 0.050	Kb/2U = 0.200								
1.0000	0.0540	0.0410	0.0199	0.0105	0.0058	0.0034	0.0020	0.0022	0.0014
h/b = 0.050	Kb/2U = 0.300								
1.0000	0.0337	0.0404	0.0196	0.0103	0.0057	0.0033	0.0020	0.0022	0.0013
h/b = 0.050	Kb/2U = 0.400								
1.0000	0.0133	0.0399	0.0194	0.0101	0.0056	0.0032	0.0019	0.0021	0.0013
h/b = 0.100	Kb/2U = 0.000								
1.0000	0.0756	0.0304	0.0133	0.0062	0.0030	0.0015	0.0003	0.0007	0.0004
h/b = 0.100	Kb/2U = 0.100								
1.0000	0.0550	0.0300	0.0131	0.0061	0.0030	0.0015	0.0008	0.0007	0.0004
h/b = 0.100	Kb/2U = 0.200								
1.0000	0.0343	0.0296	0.0129	0.0060	0.0029	0.0015	0.0008	0.0007	0.0004
h/b = 0.100	Kb/2U = 0.300								
1.0000	0.0136	0.0292	0.0127	0.0059	0.0029	0.0015	0.0008	0.0006	0.0003
h/b = 0.100	Kb/2U = 0.400								
1.0000	-0.0072	0.0289	0.0125	0.0058	0.0028	0.0014	0.0008	0.0006	0.0003

(Table continues)

Table 2 (Continued)

A_1	A_2	A_3	A_4	A_5	A_6	A_7	A_8	A_9	A_{10}
h/b = 0.150	Kb/2U = 0.000								
1.0000	0.0634	0.0235	0.0094	0.0040	0.0018	0.0008	0.0004	0.0003	0.0001
h/b = 0.150	Kb/2U = 0.100								
1.0000	0.0424	0.0232	0.0093	0.0040	0.0018	0.0008	0.0004	0.0008	0.0001
h/b = 0.150	Kb/2U = 0.200								
1.0000	0.0213	0.0230	0.0092	0.0039	0.0017	0.0008	0.0004	0.0003	0.0001
h/b = 0.150	Kb/2U = 0.300								
1.0000	0.0002	0.0227	0.0090	0.0038	0.0017	0.0008	0.0004	0.0003	0.0001
h/b = 0.150	Kb/2U = 0.400								
1.0000	-0.0209	0.0224	0.0089	0.0038	0.0017	0.0008	0.0004	0.0003	0.0001
h/b = 0.200	Kb/2U = 0.000								
1.0000	0.0544	0.0189	0.0071	0.0028	0.0012	0.0005	0.0002	0.0001	0.0000
h/b = 0.200	Kb/2U = 0.100								
1.0000	0.0331	0.0187	0.0070	0.0027	0.0011	0.0005	0.0002	0.0001	0.0000
h/b = 0.200	Kb/2U = 0.200								
1.0000	0.0113	0.0185	0.0069	0.0027	0.0011	0.0005	0.0002	0.0001	0.0000
h/b = 0.200	Kb/2U = 0.300								
1.0000	-0.0096	0.0183	0.0068	0.0027	0.0011	0.0005	0.0002	0.0001	0.0000
h/b = 0.200	Kb/2U = 0.400								
1.0000	-0.0311	0.0180	0.0067	0.0024	0.0011	0.0005	0.0002	0.0001	0.0000
h/b = 0.250	Kb/2U = 0.000								
1.0000	0.0475	0.0156	0.0055	0.0020	0.0008	0.0003	0.0001	0.0000	0.0000
h/b = 0.250	Kb/2U = 0.100								
1.0000	0.0260	0.0154	0.0054	0.0020	0.0008	0.0003	0.0001	0.0000	0.0000
h/b = 0.250	Kb/2U = 0.200								
1.0000	0.0044	0.0152	0.0053	0.0020	0.0008	0.0003	0.0001	0.0000	0.0000
h/b = 0.250	Kb/2U = 0.300								
1.0000	-0.0173	0.0151	0.0053	0.0019	0.0007	0.0003	0.0001	0.0000	0.0000
h/b = 0.250	Kb/2U = 0.400								
1.0000	-0.0390	0.0149	0.0052	0.0019	0.0007	0.0003	0.0001	0.0000	0.0000

This can be written in terms of the angular variable ψ by use of Eqs. (8) and (10):

$$L = \rho U_0 \, b^2 \int_0^{\pi} \sum_{n=1}^{\infty} A_n \, U_0 \sin n\psi \sin\psi - \frac{Kb}{4} \sin 2\psi \sum_{n=1}^{\infty} A_n \sin n\psi \; d\psi \; . \tag{31}$$

Carrying out the indicated integration gives

$$L = \rho U_0 \, b^2 \frac{\pi}{2} \left(U_0 \, A_1 - \frac{Kb}{4} A_2 \right) . \tag{32}$$

The heeling moment about the midspan is called M_c, and is given by

$$M_c = \int_{-b/2}^{b/2} \ell \, (y) \, y \, dy \; . \tag{33}$$

Using Eqs. (7), (8), and (11),

$$M_c = - \frac{\rho U_0 \, b^3}{4} \sum_{n=1}^{\infty} A_n \int_0^{\pi} \left[U_0 \sin n\psi \sin 2\psi - \frac{Kb}{4} (\cos\psi - \cos 3\psi) \sin n\psi \right] d\psi \; , \tag{34}$$

which reduces to

$$M_c = - \frac{\rho U_0 \, b^3}{8} \left[A_2 \, U_0 \, \pi - 2Kb \sum_{n=1}^{\infty} A_{2n} \left(\frac{n}{4n^2-1} - \frac{n}{4n^2-9} \right) \right] . \tag{35}$$

The heeling moment about the base of lifting line is

$$M_b = M_c + L \frac{b}{2} \; . \tag{36}$$

For the relative values of Kb and U_0 commonly encountered, the dominant terms contributing to the heeling moment are the lift itself which are found in the second term in Eq. (36) and the first term of Eq. (35).

Conclusions from the Theory of a Single Lifting Line

The second term of Eq. (32) represents the effect of the nonuniform strength of the incident wind on the lift. For the case of a constant windspeed gradient considered here, the lift is affected through the second term in the Fourier series representation for the circulation distribution. Different forms of nonuniformity would affect the lift through other terms in the series. It should be noted that the ratio of the part of the lift generated by the nonuniform part of the wind to the lift generated by the uniform part of the wind is small. This ratio can be obtained from Eq. (32) as

$$\frac{L_{non\text{-}uniform}}{L_{uniform}} = \frac{Kb}{4U_0}\,\frac{A_2}{A_1} \quad . \tag{37}$$

Typical values of $Kb/4U_0$ are on the order of 0.03.

The condition for minimum induced drag at fixed lift is constant induced angle. As shown in Table 2, the circulation distribution needed to result in constant induced angle under normal conditions has only the first four terms of its Fourier series representation in Eq. (9) significantly different from zero. For a fixed value of the lift, the strength of the second term needed for minimum induced drag is the quantity most affected by the presence of the image plane and the wind gradient. Under normal conditions these effects oppose each other (Table 2). The fact that the wind strength increases with height reduces A from its value in a uniform wind for minimum induced drag. The presence of the image plane increases A from its value on an unbounded airfoil for minimum induced drag. For most cases the image-plane effect slightly outweighs the velocity gradient effect, and A_2 is small and positive for minimum induced drag.

For a fixed lift, the largest effect on the heeling moment is that due to A_2. Furthermore, the way to alter the load distribution from that giving minimum induced drag, such that the heeling moment is changed the most for the least increase in induced drag, is to alter A_2. The above facts coupled with the fact that most sails can support more circulation over their lower portions than over their upper portions, because of differences in local chord length, indicate a general scheme for the design of vertical load distributions. This is to choose A_1 to give the desired amount of lift, and A_2 to prevent excessive heeling moment and excessive local lift coefficients near the head of the sail. All the other An's should be almost zero.

THE THEORY OF TWO LIFTING LINES AS APPLIED TO SAILS

Within the limits of linearized theory, the lift, induced drag, and heeling moment of a system of staggered airfoils are independent of the stagger. This is a consequence of Munk's (1918-1921) equivalence theorem for stagger which states that the total induced drag of a lifting system is unaltered if any of the lifting elements are translated parallel to the free stream direction. This theorem is true because such a translation causes no change in the flow in the Trefftz plane. By the same theorem, airfoils can be contracted to lifting lines for purposes of determining lift, drag, and heeling moment. Therefore, the lift, drag, and heeling moment for a sloop-rigged vessel can be determined by contracting the mainsail to the mast and the jib to the jibstay. The problem is then that of a pair of skewed lifting lines.

The drag of a sailing rig is dominated by the induced drag. Therefore, sloop rigs can be evaluated by determining the lift and induced drag, and the resulting forward force, side force, and heeling moment for the pair of skew lifting lines representing the mainsail and jib. A computer program has been prepared to do this in the presence of an image plane and a linear velocity profile. The program has been checked with known analytical results, and forces obtained by the two methods vary by about one percent.

As an example of the use of this program, a rig evaluation of a sloop-rigged offshore cruising boat is carried out. The vessel chosen is the New York "32", a vessel for which the results of model tests are available. Figure 3 shows three rigs which are analyzed for this vessel; the original seven-eights rig, and two masthead rigs. Tables 3a through 3f show the analysis of these rigs based on the theory of two interacting lifting lines. The speeds predicted by model tests for the resulting forces and moments are shown in each table. The course with respect to the direction of the true wind is taken as 42.5° and the wind strength considered is 18 ft/sec at the midspan of the mainsail, with a velocity profile slope of 0.12 per second. Table 3a shows the results for the original seven-eights rig with lift coefficients of 2.0 based on the true windspeed on both main and jib. Note the relatively high value used for the second Fourier coefficient in the circulation series on the jib. This is necessary to keep the local lift coefficient near the jib head at an attainable value, because the chord lengths in this region are so small. The problem is not as severe on the mainsail because of the headboard and the roach. Another reason for keeping the circulation at the jib head small on a seven-eights rig is that this region is near the mainsail. If the jib circulation does not taper to zero gradually enough as the jib head is approached from below, the mainsail shape will have to vary greatly in passing from regions below the jib head to regions above the jib head, if the mainsail is to attain an efficient load distribution. Table 3b shows the results for conditions as above, except that the mainsail lift coefficient is increased by 15 percent. Note the decrease in the drag factor, which shows that this is a better relative distribution than the preceding one, provided that the mainsail lift coefficient is not too large to be attained.

Table 3c shows the results of the rig calculation for the lower of the masthead rigs shown in Fig. 3. The lift coefficient based on the true wind is 2.0 for both sails, and the sail area is reduced from its value on the seven-eights rig. The increase in resulting boat speed over that for the case shown in Table 3b is apparent. The improved load distribution is also revealed by a reduction in drag factor, which is the ratio of the drag coefficient to the square of the lift coefficient. Since, according to linear theory, this ratio is unchanged by multiplying the lift coefficients by a factor, it is a measure of the efficiency of the rig geometry and relative load distribution. An increase in mainsail lift coefficient of 10 percent increases the boat speed and leaves the drag factor unaffected (Table 3d). Since the jib is taller than the mainsail, it should and does carry more lift than the mainsail as shown in Tables 3c and 3d. It does so even though it has a smaller lift coefficient than the mainsail, because it has more area (Fig. 3). Increasing the jib lift coefficient by 10 percent so that both the jib sails and the mainsails have lift coefficients of 2.2 increases the boat speed further, as shown in Table 3e. An increase in rig height of 3 feet while maintaining the same sail area as before improves performance, as shown in Table 3f.

Conclusions from Numerical Examples

The example just described indicates the beneficial effect of an increase in span, as long as the heeling moment does not become excessive. It is instructive to take note of the magnitude of the induced drag of a sailing rig. For example of Table 3f, the rig producing the highest speed of all the rigs considered

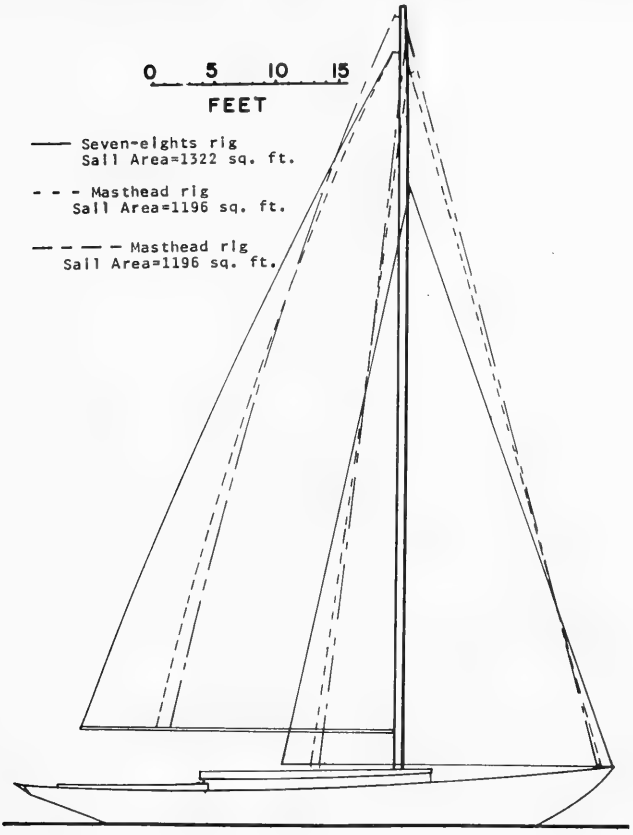

Fig. 3 - Comparative rigs for the New York "32"

for the New York "32", the mean lift coefficient is 1.26 and the mean induced drag coefficient is 0.225. The following section will show that the skin friction drag coefficient is on the order of 0.03, and when the effect of parasitic drag of masts and stays is included in the sail skin friction drag, the friction drag coefficient is on the order of 0.05. Hence, the induced drag is typically about four times as large as the remaining air drag.

BOUNDARY LAYER EFFECTS ON THIN, HIGHLY LOADED LIFTING SURFACES

The major effect of viscosity on most airfoils having lift coefficients less than 0.5 is the production of skin friction drag. The boundary layer on such airfoils is quite thin, and a very accurate prediction of the pressure distribution is obtained by solving for the potential flow about the airfoil. When the airfoil is relatively thin, the lift can be easily obtained by the thin airfoil theory

Table 3
Sailplan Calculations for the New York "32"

(a) Seven-Eights Rig

BB = 55.00	CH = 24.80	JBB = 47.50	JCH = 26.70	HH = 6.00
HI = 3.00	CL = 2.000	JCL = 2.000		
A(1) = .146	A(2) = .029	A(3) = 0.	A(4) = 0.	
J(1) = .184	J(2) = .074	J(3) = 0.	J(4) = 0.	

Forces and Coefficients -- Boat speed = 7.03 knots

	Jib	Main	Total
Forward	206.538	237.250	443.788
	.351	.374	.363
Side	712.433	790.644	1503.077
	1.209	1.248	1.229
Lift	720.625	813.317	1542.942
	1.238	1.283	1.262
Drag	133.662	141.144	274.806
	.227	.223	.225
Drag factor	.148	.135	.141
Moment	13531.864	21806.493	35338.356
	.967	1.128	.947

NOTES:
The following have their respective indicated value the same throughout Table 3:
β, the angle between wind and course = .740; θ, the momentum thickness = .300; VV, the windspeed = 18.00 ft/sec; KK, the wind gradient = .10 ft/sec/ft; VB, the approximate boat speed = 11.00 ft/sec; MM, the JMM ratio of the 2nd to 1st circulation series coefficients = .200; MMM, the same as for JMMM, but for 4th coefficients = 0; JMM = .400; JMMM = 0; CR and CRL = 0.

The following symbols, included in the tables, are defined as:
BB = the main span; CH = boom length (for finding area only); JBB = jib span; JCH = jib foot length (for finding area only); HH = distance from main foot to image plane; HI = distance from mainsail foot to jib foot; A's and J's = circulation series coefficients.

The heeling moments and coefficients are about the jibtack. Nondimensional length is from jibtack to midspan of jib for jib column, and to midspan of main for main and total columns.

All forces are in pounds and all computed coefficients are based on the apparent wind at the midspan of the mainsail. The nominal input coefficients CL and JCL are based on the true wind.

(Table continues)

Table 3 (Continued)

(b) Seven-Eights Rig with More Mainsail Load and Less Jib Load than in Case (a)

BB = 55.00	CH = 24.80	JBB = 47.50	JCH = 26.70	HH = 6.00
HI = 3.00	CL = 2.300	JCL = 1.600		
A(1) = .168	A(2) = .034	A(3) = 0.	A(4) = 0.	
J(1) = .147	J(2) = .059	J(3) = 0.	J(4) = 0.	

Forces and Coefficients -- Boat speed = 7.09 knots

	Jib	Main	Total
Forward	177.647	276.520	454.167
	.302	.436	.371
Side	572.756	912.427	1485.182
	.972	1.440	1.214
Lift	591.763	939.810	1531.573
	1.004	1.483	1.252
Drag	97.077	160.446	257.523
	.165	.253	.211
Drag factor	.163	.115	.134
Moment	10914.981	25264.003	36178.983
	.780	1.307	.970

(c) The Lower of the Two Masthead Rigs Considered

BB = 55.00	CH = 19.00	JBB = 58.00	JCH = 23.20	HH = 6.00
HI = 3.00	CL = 2.000	JCL = 2.000		
A(1) = .112	A(2) = .022	A(3) = 0.	A(4) = 0.	
J(1) = .132	J(2) = .053	J(3) = 0.	J(4) = 0.	

Forces and Coefficients -- Boat speed = 7.10 knots

	Jib	Main	Total
Forward	267.667	187.104	454.771
	.428	.385	.409
Side	773.484	612.954	1386.438
	1.237	1.263	1.248
Lift	811.561	631.949	1443.511
	1.298	1.302	1.300
Drag	106.264	106.584	212.849
	.170	.220	.192
Drag factor	.101	.130	.113
Moment	18032.782	17143.011	35175.793
	.995	1.158	1.038

(Table continues)

Table 3 (Continued)

(d) As in (c), But with More Mainsail Load

BB = 55.00	CH = 19.00	JBB = 58.00	JCH = 23.20	HH = 6.00
HI = 3.00	CL = 2.200	JCL = 2.000		
A(1) = .123	A(2) = .025	A(3) = 0.	A(4) = 0.	
J(1) = .132	J(2) = .053	J(3) = 0.	J(4) = 0.	

Forces and Coefficients — Boat speed = 7.12 knots

	Jib	Main	Total
Forward	265.767	201.058	466.825
	.425	.414	.420
Side	774.257	675.465	1449.721
	1.239	1.391	1.305
Lift	811.403	694.106	1505.509
	1.298	1.430	1.356
Drag	108.309	122.041	230.350
	.173	.251	.207
Drag factor	.103	.123	.113
Moment	18055.765	18890.349	36946.114
	.996	1.276	1.091

(e) As in (c), But with More Load on Both Sails

BB = 55.00	CH = 19.00	JBB = 58.00	JCH = 23.20	HH = 6.00
HI = 3.00	CL = 2.200	JCL = 2.200		
A(1) = .123	A(2) = .025	A(3) = 0.	A(4) = 0.	
J(1) = .145	J(2) = .058	J(3) = 0.	J(4) = 0.	

Forces and Coefficients — Boat speed = 7.14 knots

	Jib	Main	Total
Forward	283.907	194.511	478.418
	.454	.401	.431
Side	852.037	676.790	1528.827
	1.363	1.394	1.377
Lift	889.090	692.365	1581.455
	1.422	1.426	1.424
Drag	126.847	128.489	255.336
	.203	.265	.230
Drag factor	.100	.130	.113
Moment	19845.283	18917.212	38762.495
	1.095	1.278	1.144

(Table continues)

Table 3 (Continued)

(f) The Taller of the Two Masthead Rigs Considered

BB = 58.00	CH = 18.00	JBB = 61.00	JCH = 22.00	HH = 6.00
HI = 3.00	CL = 2.200	JCL = 2.200		
A(1) = .110	A(2) = .022	A(3) = 0.	A(4) = 0.	
J(1) = .131	J(2) = .052	J(3) = 0.	J(4) = 0.	

Forces and Coefficients — Boat speed = 7.19 knots

	Jib	Main	Total
Forward	292.380	206.992	499.372
	.469	.427	.450
Side	850.933	672.756	1523.689
	1.365	1.387	1.375
Lift	891.889	694.335	1586.224
	1.431	1.432	1.431
Drag	118.773	115.522	234.295
	.191	.238	.211
Drag factor	.093	.116	.103
Moment	20881.878	19722.493	40604.372
	1.098	1.271	1.145

(Prandtl, 1919; Glauert, 1943). Although experimental data is in abundance for sections of moderate camber and thickness, very little data is available for very thin, highly cambered sections. The small amount of such data that is available indicates that the lift predicted by the thin airfoil theory is in poor agreement with experiment. Figure 4 shows data obtained by Wallis (1961) and by the author for thin, circular-arc sections with camber ratios of 0.10. The difference between experimental results and the theoretical solution for potential flow about the section lies in the effect of the boundary layer. Under the assumption of the boundary layer theory (Schlichting, 1955) that the pressure associated with flow outside the boundary layer is conducted across the layer to the body, the correct pressure should be obtained by calculating the potential flow about the shape formed by the airfoil and the displacement thickness of the boundary layer. The displacement thickness of the boundary layer and the external pressure are interdependent, so that an iterative scheme must be used to determine the solution.

The Use of Semi-Empirical Boundary Layer Theories

An exact solution to the boundary layer equations is impossible for the turbulent boundary layer, so that a semi-empirical theory must be used to determine the boundary layer parameters. There are a large number of these semi-empirical theories in existence and of these, four have been investigated by the

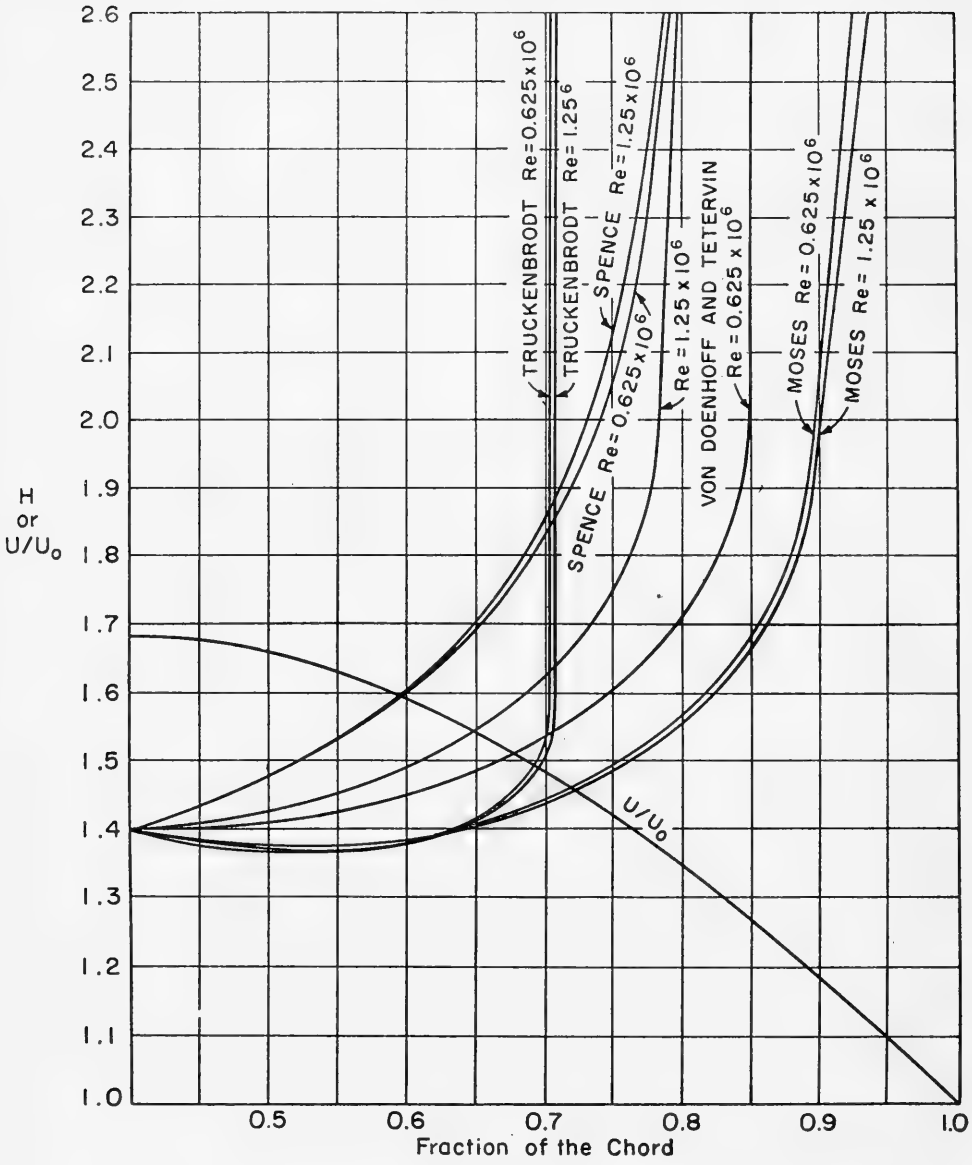

Fig. 4 - Calculations from four semi-empirical boundary layer theories

author. They are those of Von Doenhoff and Tetervin (1943), Truckenbrodt (1955), Spence (1956), and Moses (1964). For all of these semi-empirical theories, a skin friction law must be used and a number of investigators have deemed the Ludwieg-Tillman Law (1950) to be the most reliable of these laws. This law

relates the skin friction coefficient to the Reynolds number based on momentum thickness and H, the ratio of displacement thickness to momentum thickness, as

$$C_f = 0.246\ R_\theta^{-0.266}\ 10^{-0.678H} \quad . \tag{38}$$

This law has been used in connection with a number of existing semi-empirical theories. Moses (1964) has supplied a computer program for his semi-empirical theory. He uses a skin friction law where the skin friction coefficient is dependent only on R_θ in order to compensate for some approximations in his theory.

In almost all cases the presentations of the semi-empirical theories include a comparison with experiment, and the semi-empirical results are shown to be in excellent agreement. However, when a number of the theories are applied to a given experimental situation, there is often a significant discrepancy between their various predictions. For example, Fig. 4 shows results from the four theories investigated for a normalized chordwise velocity distribution given by

$$\frac{U'}{U_0} = A\left[(1-e^{-Kx}) - (1-e^{-K})x\right] , \tag{39}$$

where the chord is taken as the line $0 \leq x \leq 1$. K is chosen to locate the point of maximum u' 40% of the chord length aft of the leading edge. A is chosen to correspond to a lift coefficient of 1.8. The predominating influence on separation is the velocity gradient. The velocity distribution is also shown in Fig. 4. The semi-empirical theories predict separation points between 71 and 92 percent of the chord. The normalized velocities at these two points are 1.45 and 1.06, respectively. This range is too large to accept the accuracy of all of the theories, and accordingly an examination of them has been carried out to determine which one, if any, is likely to be accurate. The experimental comparisons considered by Von Doenhoff and Tetervin (1943), Truckenbrodt (1955), and Spence (1956) were for airfoils on which it is quite difficult to make accurate pressure measurements. Furthermore, there are three-dimensional effects affecting the entire flow field, and there is no way to determine the results of these effects. The experiments of Moses (1964) were carried out in an annular chamber with axial flow in which the axial pressure distribution could be varied by varying the leakoff on the outer wall. Boundary layer growth was studied on the inner wall. It is less difficult to make accurate pressure measurements on such a device than on an airfoil. Three-dimensional effects are minimized, since the purely axisymmetric effects can be accounted for.

Almost all section data (Abbott and Von Doenhoff, 1959) indicates that raising the Reynolds number results in an increase in lift coefficient and a decrease in drag coefficient, indicating that the separation point moves aft when the Reynolds number is increased. The semi-empirical theories of Spence and of Von Doenhoff and Tetervin (Fig. 4) indicate the reverse of this. This is always the case with the theory of Von Doenhoff and Tetervin and occurs on some pressure distributions with the theory of Spence. Spence and Truckenbrodt present

relatively little experimental data, whereas Moses presents a considerable amount for a variety of pressure distributions which is in excellent agreement with his semi-empirical theory.

The Design of a Chordwise Pressure Distribution for High Lift

The dominating effect on boundary layer growth in an adverse pressure gradient is the work done against the force of the adverse gradient by the fluid in the boundary layer. To minimize this work, the maximum pressure on the suction side of the airfoil should be made as small as possible. The lift coefficient is given by

$$C_L = \frac{1}{\rho U_0^2} \int_0^c \Delta P(x) \frac{dx}{c} , \tag{40}$$

where the suction side pressure is $\Delta P/2$ for a very thin airfoil. Clearly, the way to minimize the strength of the peak suction while retaining a given lift coefficient is to make $\Delta P(x)$ constant. However, just ahead of and just behind the airfoil the pressure must be equal to free stream pressure, but streamwise pressure jumps are not realizable. Furthermore, it has been found that if the approach of the pressure to free stream pressure at the trailing edge is faster than linear, separation is likely. Most experiments indicate that the value of H for turbulent flow just following transition is 1.4 (see, e.g., Von Doenhoff and Tetervin, 1943). In an adverse pressure gradient, H rises with increasing downstream position. Since separation is avoided by keeping H small and since transition from laminar to turbulent flow occurs just aft of the point of maximum suction, it seems desirable to have the point of maximum pressure difference relatively far aft. Putting the above facts together indicates that a pressure distribution giving relatively high lift without separation might have the form shown in Fig. 5. The results of the boundary layer calculation, by the theory of Moses (1964) with a lift coefficient of 1.9, on this pressure distribution are shown in Fig. 6. The maximum attainable lift coefficient without flow separation is about 1.9. The section shape needed to attain this pressure distribution in two-dimensional flow with a lift coefficient of 1.9 has been calculated by use of the thin airfoil theory and is shown in Fig. 7.

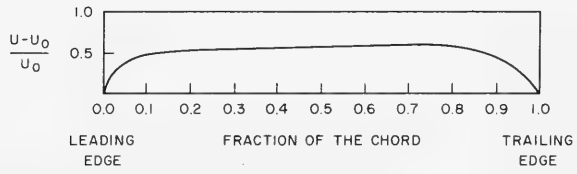

Fig. 5 - Pressure distribution for a high-lift section

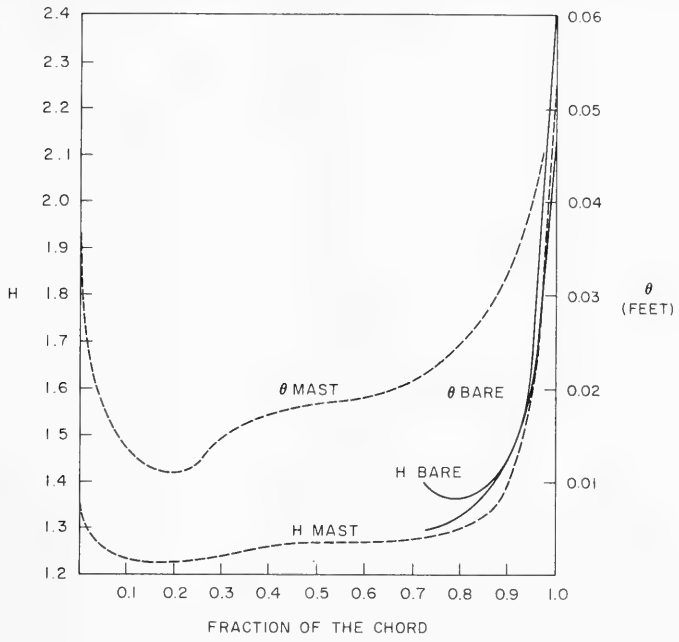

Fig. 6 - Shape factor and momentum thickness for a high-lift section with a lift coefficient of 1.9

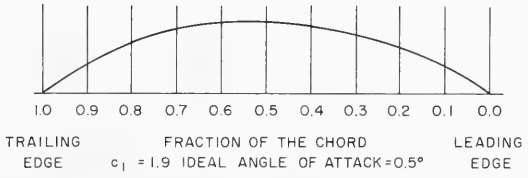

Fig. 7 - Shape of a high-lift section

The Effect of a Mast

The flow over a section with an unfaired leading edge spar is shown schematically in Fig. 8. The mast acts as a turbulence stimulator. The region on the suction side of the section just aft of the mast has a negative (favorable) pressure gradient which accelerates the boundary layer. Measurements on boundary layers in negative pressure gradients aft of the turbulence stimulators were made by Launder (1963). He found that for the range of Reynolds numbers and pressure gradients of interest here, the semi-empirical boundary layer of Spence (1956) gave good agreement with his experiments which showed a very strong thinning of the boundary layer in the favorable pressure gradient. When

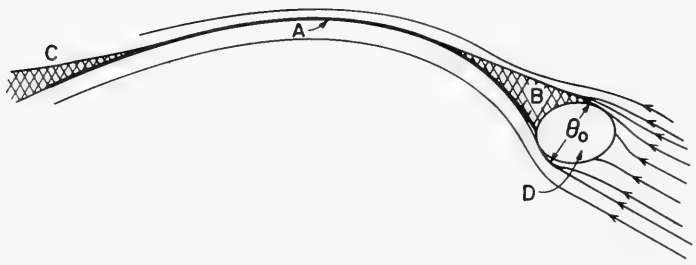

Fig. 8 - Schematic view of the outer edge of the boundary layer on the suction side of a section with a mast (A-Airfoil, B-Turbulent region behind the mast, C-Thickening of the boundary layer near the trailing edge, D-Mast)

semi-empirical boundary layer theory is applied to the region behind a mast, there is no set place to begin the integration and no set values to choose for θ and H at this point. Launder (1963) shows that H attains a value between 1.4 and 1.5 a short distance aft of his turbulence grid. The momentum thickness is less certain, as it increases rapidly with downstream distance. For the estimates made here the integration is started at the leading edge with H equal to 1.4 and the momentum thickness equal to the width of the projected thickness of the mast perpendicular to the local flow direction. Figure 6 shows the results of the boundary layer calculations on a high-lift section with and without a mast. The mast reduces the tendency for flow separation. This effect is found on all pressure distributions.

The Boundary Layer Thickness Correction

As shown by Van Dyke (1964), the effect of a thin boundary layer on the flow around a body is to yield pressures on the body associated with the potential flow around a shape defined by the body plus the displacement thickness of the boundary layer. In the case of an airfoil treated within the framework of linearized theory, the flow can be decomposed into components due to thickness and components due to camber (see, e.g., Ashley and Landahl, 1965). The flow associated with the thickness yields no lift. For an infinitely thin airfoil all the thickness is due to the displacement thickness of the boundary layer, and the camber is the mean line between the section and the line representing the displacement thickness of the boundary layer. For sections without a mast the displacement thickness will be significant only near the trailing edge, whereas for sections with a mast there will be significant displacement thickness effects near the leading edge and near the trailing edge. In the design of a section for a given pressure distribution, each point must be moved to windward from the shape calculated by the thin airfoil theory by an amount equal to half the displacement thickness of the boundary layer at that point.

Experiments on Thin, Highly Cambered, Two-Dimensional Sections

Although vast amounts of data have been taken for sections common to airplane wings (Abbott and Von Doenhoff, 1959), very little data has been taken for thin, highly cambered sections. Data for circular arc sections with camber ratios between 0.02 and 0.10 were taken and reported by Wallis (1961). His sections were of uniform thickness, with a thickness-to-chord ratio of 0.02. The lift was measured on a circular arc section with a camber ratio of 0.10 by the author. This section had a thickness ratio of 0.04 and a faired thickness form with sharp edges. The data for this foil and the 10 percent foil of Wallis is shown in Fig. 9. Thin airfoil theory predicts an ideal angle of attack of zero degrees with a lift coefficient of 1.25 for these sections. At zero degrees Wallis measured a lift coefficient of 0.90 and the author measured 0.94. The discrepancy is due to boundary layer thickness near the trailing edge. When this is taken into account, theory predicts an ideal angle of attack of 1.8° and a lift coefficient of 1.07 at this angle. This is in excellent agreement with the experiments. The drag measurements of Wallis show the profile drag coefficient to be 0.022 at ideal angle of attack.

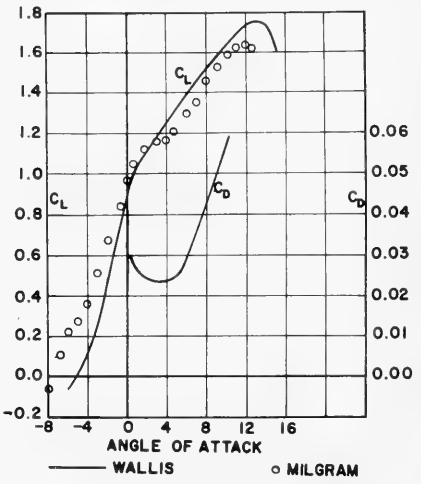

Fig. 9 - Experimental results for a thin section with a camber ratio of 0.10 (Reynolds number = 3×10^5)

A series of four highly cambered sections were tested with and without masts by Herreshoff (private communication). His sections are shown in Fig. 10 and his results are shown in Figs. 11a through 11d. The figures show the ideal angle of attack and lift coefficient at this angle predicted by the thin airfoil theory in the absence of boundary layer effects. In the cases without a mast, the flow separates, so that the thin airfoil theory cannot be used for a lift prediction. With a mast, however, the effect of the displacement thickness forward reduces the effective camber and lift sufficiently to prevent flow separation. Taking the boundary layer into account, the thin airfoil theory predicts an ideal angle of attack of 1.76° with a lift coefficient of 0.85, for Herreshoff's Number One foil with a mast. This is in good agreement with experiment. It is worth noting that at ideal angle of attack the measured drag coefficients were about 0.05 without a mast and 0.06 with a mast. The drag coefficients measured by Herreshoff are higher than those representative of the sections, because there were many structural members protruding from the pressure sides of the airfoils.

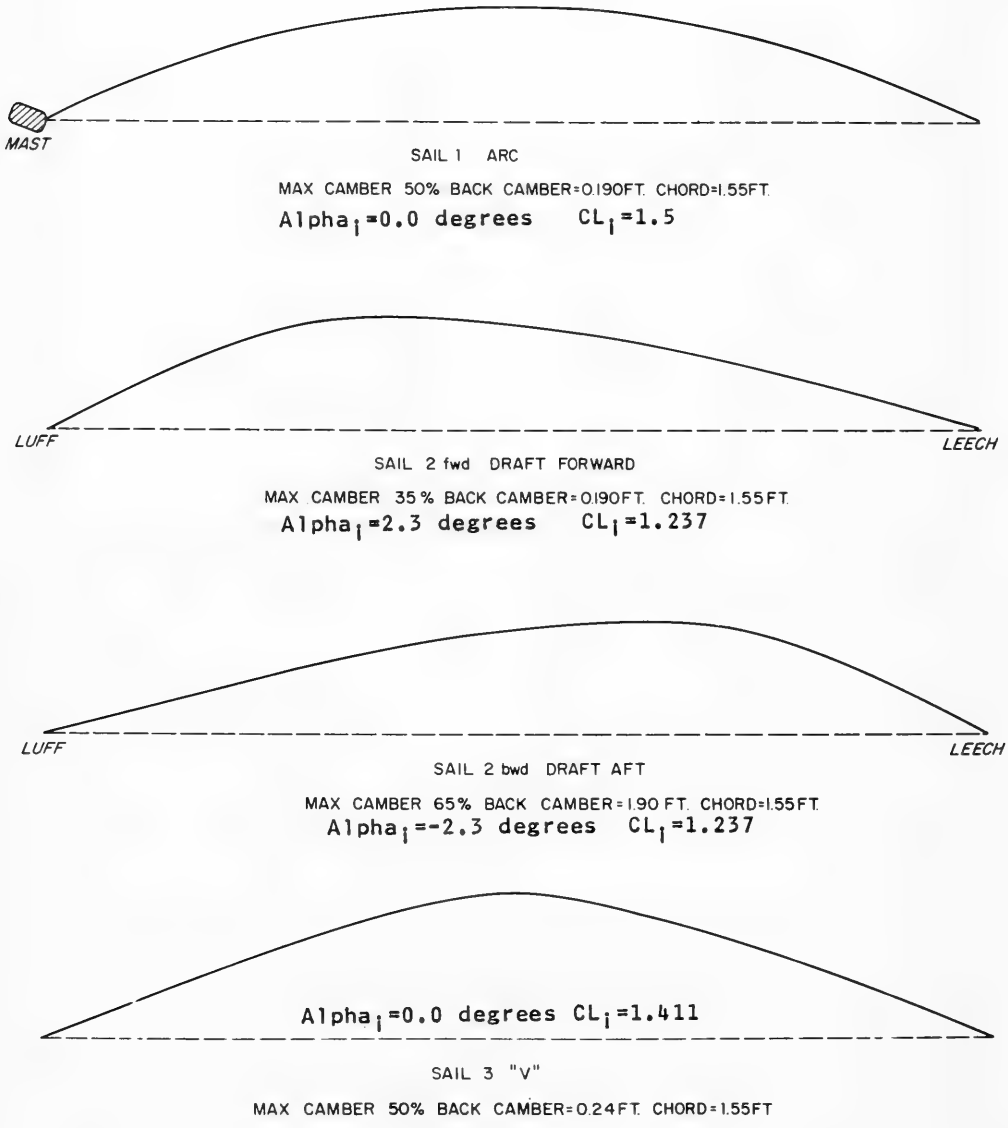

Fig. 10 - Two-dimensional sections tested by Herreshoff

CONCLUSIONS

Because sails operate at unusually high lift coefficients and in the presence of a lower boundary and a spatially varying incident wind, there are some important differences between the aerodynamics of sails and those of most other

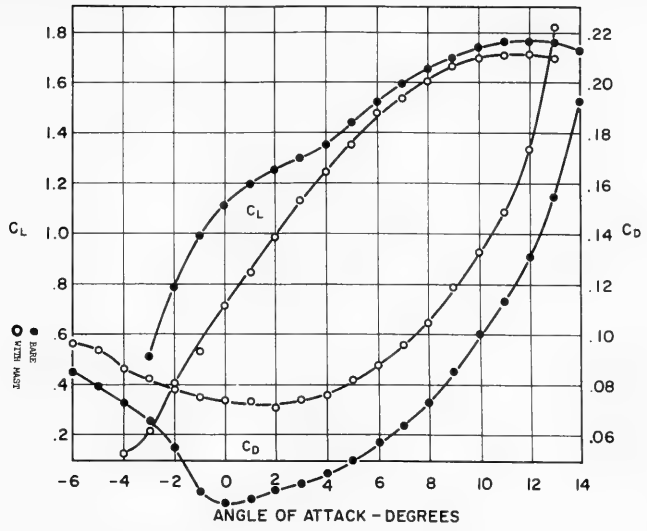

Fig. 11a - Herreshoff Number One section

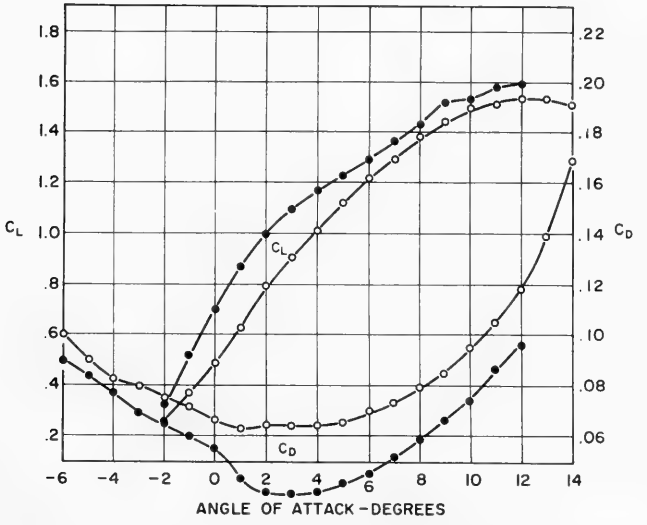

Fig. 11b - Herreshoff Number Two section--
draft forward

lifting surfaces. Because of the constraints of the maximum of heeling and pitching moments that can be resisted by a given hull, there is a limit on usable sail spans. These constraints, coupled with the large lift coefficients, result in large coefficients of induced drag. The major effect of the lower boundary is a

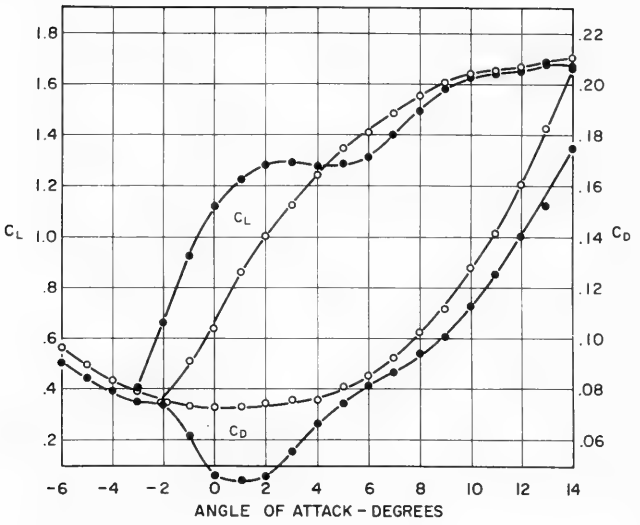

Fig. 11c - Herreshoff Number Two section--draft aft

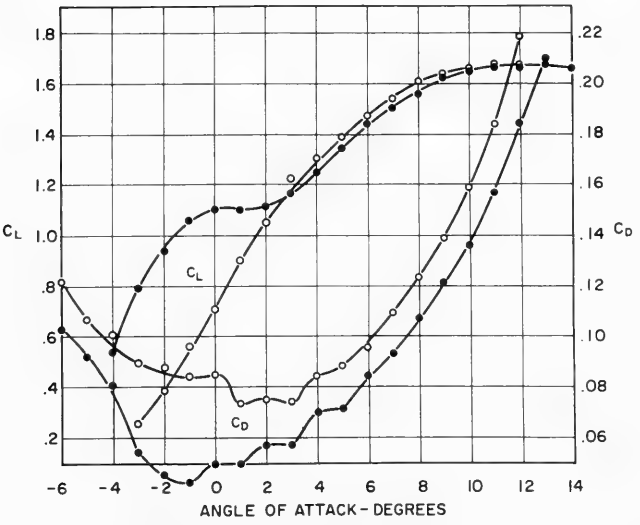

Fig. 11d - Herreshoff Number Three section

small reduction in the induced drag that would exist in the absence of the boundary. The effect of the increase in wind strength with height is that minimum induced drag occurs with more loading on the upper parts of the sails than that

loading which would produce minimum induced drag in a uniform wind. This is of little practical importance, since the loading must usually be relatively higher in the lower parts of the sails than that loading which would result in minimum induced drag because of limitations on pitching and heeling moment.

The effect of the unusually high lift coefficients of sails results in large alterations of the suction side pressure due to boundary layer effects. In some cases these effects are restricted to a thickening of the boundary layer, and in others they result in flow separation. Recently, some analytical methods have been devised to handle partially separated flows. A presentation of this subject is currently being prepared by the author.

ACKNOWLEDGMENTS

The author wishes to thank the sponsors of this research for their help in making the work possible. Some of the work was carried out under ONR contract N00014-67-A-0204-0022. The remainder of the work was supported by the kind contributions of Mr. Benjamin Gilbert and Mr. Ernest Fay.

SYMBOLS

A	Multiplicative constant or coefficient
b, B, BB	Sail span
JB	Span of a jib
C	Chord length
C_D	Drag coefficient
C_L	Lift coefficient
d_i	Induced drag per unit span
D_i	Total induced drag
h	Gap from bottom or mainsail to image plane
H	Boundary layer shape factor, the ratio of displacement thickness to momentum thickness
HI	Vertical distance from foot of jib to foot of mainsail
ℓ	Lift per unit span
L	Total lift
M_b	Heeling moment about the foot of a sail

M_c	Heeling moment about the midspan of a sail
p	Pressure
Δp	Pressure difference
R_e	Reynolds number based on chord length
R_θ	Reynolds number based on momentum thickness
U	Apparent wind
U_0	Apparent wind at midspan
u', v', w'	Perturbation velocity components
x, y, z	Coordinate axes moving with vessel; x is in the apparent wind direction or in the plane containing the three corners of a sail, z is positive in the direction to which the wind is blowing, y is positive upward
X	Forward force – in the direction of the course of a vessel
Y	Side force
α_i	Induced angle
β	Angle between a vessel's course and the true wind
γ	Vortex sheet strength
Γ	Circulation
η	Dummy linear variable
Φ	Heel angle; velocity potential
ψ, ψ', Φ	Dummy angular variables
ρ	Density of air

BIBLIOGRAPHY

Abbott, I.A., and Von Doenhoff, A.E., 1959. Theory of Wing Sections. New York: Dover Publications

Ashley, H., and Landahl, M., 1965. Aerodynamics of Wings and Bodies. Reading, Massachusetts: Addison Wesley Publishing Co., Inc.

Glauert, H., 1948. The Elements of Aerofoil and Airscrew Theory. 2nd. Ed., Cambridge, England: The University Press

Launder, B.E., 1963. The turbulent boundary layer in a strongly negative pressure gradient. MIT Gas Turbine Laboratory, Cambridge, Massachusetts, Report No. 71

Ludwieg, H., and Tillmann, W., 1950. Investigation of the wall shearing stress in turbulent boundary layers. NACA Technical Memorandum No. 1285

Milgram, J.H., 1962. The design and construction of yacht sails. MIT MS thesis, Department of Naval Architecture and Marine Engineering, Cambridge, Massachusetts

Milgram, J.H., (to be presented). The analytical design of sails, Transactions of the Society of Naval Architects and Marine Engineers, New York

Moses, H., 1964. The behavior of turbulent boundary layers in adverse pressure gradients. MIT Gas Turbine Laboratory, Cambridge, Massachusetts, Report No. 73

Munk, M., 1921. Isoperimetrische Ausgaben aus der Theorie des Fluges. Gottingen dissertation; translated as NACA Report No. 121

Prandtl, L., 1919. Tragflügel Thorie. Gottingen, Nachrichten

Schlichting, H., 1955. Boundary Layer Theory. Pergamon Press

Spence, D.A., 1956. The development of turbulent boundary layers. Journal of the Aeronautical Sciences, Vol. 23, No. 1

Truckenbrodt, E., 1955. A method of quadrature for the calculation of the laminar and turbulent boundary layer in the case of plane and rotationally symmetric flow. NACA Technical Memorandum No. 1379

Von Doenhoff, A.E., and Tetervin, N., 1943. Determination of general relations for the behavior of turbulent boundary layers. NACA Report No. 772

Van Dyke, M., 1964. Perturbation Methods in Fluid Mechanics. New York: Academic Press

Wallis, R.A., 1961. Axial Flow Fans. London: William Clowes and Sons, Ltd.

Appendix A

THE EFFECT OF HEELING ON THE AERODYNAMICS OF SAILS

The aerodynamic effect of heeling will be considered for lifting-line theory inasmuch as almost identical results are obtained for lifting-surface theory. Consider the lifting line and image system of vorticity shown in Fig. 2. The problem is to determine w' on the lifting line. For a given circulation distribution, the value of w' induced by the lifting line and its trailing vortex sheet is independent of the heel angle ϕ. Therefore, only the velocity induced by the image system of vorticity will be considered. Since the line representing the direction of w' and the image of the lifting line are coplanar, there is no w'-directed induced velocity on the lifting line due to the image of the lifting line. Hence, only the image-trailing vorticity need be considered. Calling the w'-directed induced velocity at the lifting line by the image-trailing vorticity by w',

$$w_T'(y,\eta) = \frac{1}{4\pi}\int_{-b/2}^{b/2} \frac{\gamma(\eta)\cos(\phi+\alpha)\,d\eta}{\sqrt{(y+\eta+2b+h)^2\cos^2\phi + (\eta-y)^2\sin^2\phi}}, \tag{A1}$$

where

$$\alpha = \tan^{-1}\left(\frac{\eta-y}{y+b+2h+\eta}\tan\phi\right). \tag{A2}$$

The integrand of Eq. (A1) can be written as

$$I(y,\eta) = \frac{\gamma(\eta)}{y+b+2h+\eta}\left[\frac{\cos\alpha - \sin\alpha\tan\phi}{\sqrt{1+\dfrac{(\eta-y)^2\tan^2\phi}{(y+b+2h+\eta)^2}}}\right], \tag{A3}$$

where the term outside the brackets is what the integrand would be if the heel angle were zero. The bracketed term can be interpreted as a weighting function due to heel. The difference between the weighting function and unity increases with increasing heel angle and decreasing lower-end gap, h. Under normal circumstances, the largest heel angle of most boats does not exceed 30°. Values of the weighting function for various values of y and η, with ϕ equal to 10, 20, and 30° and the gap, h, equal to five percent of the span are shown in Table A1. This table shows that the weighting function is positive and differs significantly from unity only when the heel angle is large, and even then only for values of y near the lower end of the lifting line and values of η near the lower end of the image of the lifting line; i.e., for points on the lifting line near the image plane and points on the image of the lifting line far from the image plane. The influence of the image vorticity is least for large values of η, as shown in Table A2 which is a table of values of the integrand of the integral in Eq. (A1) divided by $\gamma(\eta)$.

Table A1

The Weighting Function on the Integral of Eq. (A1) due to Heel (Tabulated values are given by bracketed term of Eq. (A3) for h = 5% of b. For zero heel, the weighting function is unity.)

Percent of the Span of the Lifting Line (Zero is closest to the image plane)	Percent of the Span of the Image of the Lifting Line (Zero is closest to the image plane)										
	00	10	20	30	40	50	60	70	80	90	100
	Heel = 10.000000 degrees										
0.	1.000	.977	.966	.960	.956	.954	.952	.950	.949	.948	.947
10.00	1.008	1.000	.990	.983	.977	.972	.969	.966	.964	.962	.960
20.00	1.007	1.006	1.000	.994	.989	.984	.980	.977	.974	.972	.969
30.00	1.006	1.007	1.004	1.000	.996	.992	.988	.985	.982	.979	.977
40.00	1.005	1.008	1.006	1.003	1.000	.997	.993	.990	.988	.985	.983
50.00	1.004	1.008	1.007	1.005	1.003	1.000	.997	.994	.992	.990	.987
60.00	1.004	1.007	1.008	1.007	1.005	1.002	1.000	.998	.995	.993	.991
70.00	1.003	1.007	1.008	1.007	1.006	1.004	1.002	1.000	.998	.996	.994
80.00	1.003	1.006	1.008	1.008	1.007	1.005	1.004	1.002	1.000	.998	.996
90.00	1.003	1.006	1.007	1.008	1.007	1.006	1.005	1.003	1.002	1.000	.998
100.00	1.003	1.006	1.007	1.008	1.007	1.007	1.006	1.004	1.003	1.001	1.000
	Heel = 20.000000 degrees										
0.	1.000	.904	.861	.838	.824	.815	.808	.803	.799	.795	.793
10.00	1.032	1.000	.959	.927	.904	.886	.872	.861	.852	.844	.838
20.00	1.028	1.025	1.000	.974	.952	.933	.917	.904	.893	.883	.875
30.00	1.023	1.031	1.018	1.000	.981	.964	.949	.935	.924	.913	.904
40.00	1.020	1.032	1.027	1.014	1.000	.985	.972	.959	.947	.937	.927
50.00	1.017	1.031	1.030	1.023	1.012	1.000	.988	.977	.966	.956	.946
60.00	1.015	1.030	1.032	1.027	1.020	1.010	1.000	.990	.980	.971	.962
70.00	1.013	1.028	1.032	1.030	1.025	1.017	1.009	1.000	.991	.983	.974
80.00	1.012	1.026	1.032	1.031	1.028	1.022	1.015	1.008	1.000	.992	.985
90.00	1.011	1.025	1.031	1.032	1.030	1.026	1.020	1.014	1.007	1.000	.993
100.00	1.010	1.023	1.030	1.032	1.031	1.028	1.024	1.013	1.012	1.006	1.000
	Heel = 30.000000 degrees										
0.	1.000	.769	.677	.632	.604	.586	.574	.564	.557	.551	.546
10.00	1.077	1.000	.898	.823	.769	.730	.700	.677	.659	.644	.632
20.00	1.065	1.061	1.000	.936	.881	.836	.799	.769	.744	.723	.706
30.00	1.053	1.076	1.046	1.000	.953	.911	.874	.842	.814	.790	.769
40.00	1.044	1.077	1.066	1.036	1.000	.963	.929	.898	.870	.845	.823
50.00	1.038	1.074	1.075	1.057	1.030	1.000	.970	.941	.915	.890	.868
60.00	1.033	1.069	1.077	1.068	1.049	1.025	1.000	.975	.950	.927	.905
70.00	1.029	1.065	1.077	1.074	1.061	1.043	1.022	1.000	.978	.956	.936
80.00	1.026	1.060	1.075	1.077	1.069	1.055	1.038	1.020	1.000	.980	.961
90.00	1.024	1.056	1.073	1.077	1.073	1.064	1.050	1.034	1.017	1.000	.983
100.00	1.022	1.053	1.070	1.077	1.076	1.069	1.059	1.046	1.031	1.016	1.000

Table A2
Relative Contributions to the Downwash due to Various Regions of the Image of the Lifting Line (Tabulated values are given by $I(y,\eta)/\gamma(\eta)$ as defined by Eq. (A3))

Percent of the Span of the Lifting Line (Zero is closest to the image plane)

	Percent of the Span of the Image of the Lifting Line (Zero is closest to the image plane)										
	00	10	20	30	40	50	60	70	80	90	100
Heel = 0. degrees											
0.	10.000	5.000	3.333	2.500	2.000	1.667	1.429	1.250	1.111	1.000	.909
10.00	5.000	3.333	2.500	2.000	1.667	1.429	1.250	1.111	1.000	.909	.833
20.00	3.333	2.500	2.000	1.667	1.429	1.250	1.111	1.000	.909	.833	.769
30.00	2.500	2.000	1.667	1.429	1.250	1.111	1.000	.909	.833	.769	.714
40.00	2.000	1.667	1.429	1.250	1.111	1.000	.909	.833	.769	.714	.667
50.00	1.667	1.429	1.250	1.111	1.000	.909	.833	.769	.714	.667	.625
60.00	1.429	1.250	1.111	1.000	.909	.833	.769	.714	.667	.625	.588
70.00	1.250	1.111	1.000	.909	.833	.769	.714	.667	.625	.588	.556
80.00	1.111	1.000	.909	.833	.769	.714	.667	.625	.588	.556	.526
90.00	1.000	.909	.833	.769	.714	.667	.625	.588	.556	.526	.500
100.00	.909	.833	.769	.714	.667	.625	.588	.556	.526	.500	.476
Heel = 10.000000 degrees											
0.	10.000	4.884	3.220	2.400	1.912	1.589	1.359	1.188	1.054	.948	.861
10.00	5.039	3.333	2.476	1.965	1.628	1.389	1.211	1.073	.964	.874	.800
20.00	3.356	2.515	2.000	1.657	1.412	1.230	1.089	.977	.885	.810	.746
30.00	2.514	2.015	1.674	1.429	1.245	1.102	.988	.895	.818	.753	.698
40.00	2.010	1.680	1.438	1.254	1.111	.997	.903	.825	.760	.704	.655
50.00	1.674	1.439	1.259	1.117	1.003	.909	.831	.765	.709	.660	.617
60.00	1.434	1.259	1.120	1.007	.913	.835	.769	.713	.664	.621	.583
70.00	1.254	1.119	1.008	.916	.838	.772	.716	.667	.624	.586	.552
80.00	1.114	1.006	.916	.840	.774	.718	.669	.626	.588	.555	.524
90.00	1.003	.915	.840	.775	.719	.671	.628	.590	.556	.526	.499
100.00	.911	.838	.775	.720	.672	.629	.592	.558	.528	.501	.476
Heel = 20.000000 degrees											
0.	10.000	4.519	2.870	2.095	1.648	1.358	1.154	1.003	.887	.795	.721
10.00	5.160	3.333	2.397	1.855	1.506	1.266	1.090	.957	.852	.768	.698
20.00	3.426	2.562	2.000	1.624	1.360	1.166	1.019	.904	.811	.736	.673
30.00	2.558	2.062	1.697	1.429	1.227	1.071	.949	.850	.770	.702	.646
40.00	2.039	1.720	1.467	1.268	1.111	.985	.883	.799	.729	.669	.618
50.00	1.695	1.473	1.288	1.136	1.012	.909	.823	.751	.690	.637	.591
60.00	1.450	1.287	1.147	1.027	.927	.842	.769	.707	.653	.607	.566
70.00	1.266	1.142	1.032	.936	.854	.782	.721	.667	.620	.578	.541
80.00	1.124	1.026	.938	.860	.791	.730	.677	.630	.588	.551	.518
90.00	1.011	.931	.859	.794	.736	.684	.638	.596	.559	.526	.497
100.00	.918	.853	.702	.737	.687	.643	.602	.566	.533	.503	.476
Heel = 30.000000 degrees											
0.	10.000	3.846	2.258	1.579	1.209	.977	.820	.705	.619	.551	.497
10.00	5.385	3.333	2.245	1.646	1.282	1.043	.876	.753	.659	.585	.526
20.00	3.548	2.653	2.000	1.560	1.258	1.045	.888	.769	.677	.603	.543
30.00	2.632	2.152	1.743	1.429	1.192	1.012	.874	.765	.678	.608	.549
40.00	2.088	1.795	1.523	1.295	1.111	.963	.845	.748	.669	.604	.549
50.00	1.729	1.534	1.343	1.174	1.030	.909	.808	.724	.653	.593	.542
60.00	1.475	1.336	1.197	1.068	.954	.855	.769	.696	.633	.579	.532
70.00	1.286	1.183	1.077	.976	.884	.802	.730	.667	.611	.563	.520
80.00	1.140	1.060	.977	.897	.822	.754	.692	.637	.588	.545	.506
90.00	1.024	.960	.894	.829	.767	.709	.656	.608	.565	.526	.491
100.00	.929	.877	.823	.769	.717	.668	.623	.581	.543	.508	.476

It then appears that the effect of heeling on sail aerodynamics is small. To provide further confirmation of this fact, the downwash on a lifting line with an end gap of five percent of the span of the lifting line was calculated for 0° heel and 30° heel. These results are shown in Fig. A1. The difference in downwash between 0 and 30° of heel is discernable only near the bottom of the lifting line, and the maximum difference is 4.5 percent of the value of the local downwash. Therefore, accurate prediction and analysis of sailing rigs in the heeled condition can be carried out by proper resolution of forces and moments determined in the non-heeled case.

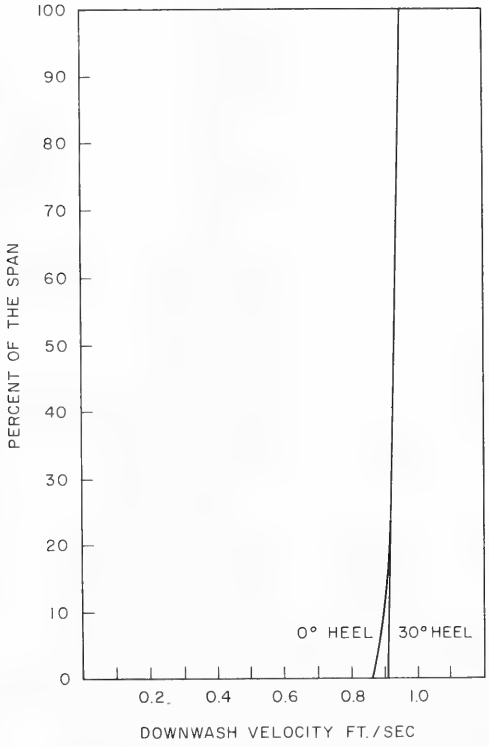

Fig. A1 - Downwash on a lifting line with an elliptical circulation distribution at zero and 30° of heel (gap from the base of the lifting line to the image plane is five percent of the span of the lifting line)

Appendix B
EVALUATION OF LIFTING-LINE IMAGE INTEGRALS

This section contains the evaluation of the set of integrals

$$I_n = \int_0^{\pi} \frac{\cos n\phi \, d\phi}{2 + \frac{4h}{b} - (\cos\psi + \cos\phi)} \quad . \tag{B1}$$

Let

$$Q = 2 + \frac{4h}{b} - \cos\psi > 1 \tag{B2}$$

Then,

$$I_n = \int_0^{\pi} \frac{\cos n\phi}{Q - \cos\phi} d\phi \quad . \tag{B3}$$

A difference equation for the I_n's will now be derived.

$$I_{n+1} + I_{n-1} = \int_0^{\pi} \frac{\cos (n+1)\phi + \cos (n-1)\phi}{Q - \cos\phi} d\phi \quad . \tag{B4}$$

This can be written as

$$I_{n+1} + I_{n-1} = \int_0^{\pi} \left[\frac{2Q \cos n\phi}{Q - \cos\phi} - 2 \cos n\phi \right] d\phi \quad . \tag{B5}$$

Since the integrated value of the second term of Eq. (B5) is zero,

$$I_{n+1} + I_{n-1} = 2 QI_n \quad . \tag{B6}$$

The solution of Eq. (B6) contains two constants which can be determined by equating the solution to I_n for two different values of n. I_0 and I_1 can be determined by simple integration, giving

$$I_0 = \frac{\pi}{\sqrt{Q^2 - 1}} \tag{B7}$$

and

$$I_1 = \frac{QI_0}{\sqrt{Q^2 - 1}} - \pi \ . \tag{B8}$$

With these two requirements, the solution of Eq. (B6) is

$$I_n = \frac{\pi \left(Q - \sqrt{Q^2 - 1}\right)^n}{\sqrt{Q^2 - 1}} \ . \tag{B9}$$

* * *

DISCUSSION

Hans Thieme
Institut für Schiffbau der Universität Hamburg
Hamburg, Germany

I think Professor Milgram's lecture here is a long step forward in theoretical calculation of sail forces. Hoping he will proceed in his work, I may only add some additional information on experimental work.

At the Shipbuilding Institute of the University of Hamburg a lot of wind-tunnel tests are performed. Most of the results are not published yet, but it is possible to have the reports open for your future use. A list of the reports is given below. They comprise our investigations on single sails of different profile and shape, fundamental sail combinations, and complete rigs for three types of vessels. The best results for the cruiser yacht, 7KR-YACHT, the oldtime four-masted barque, PAMIR, and the six-masted square-rigger, 6M-DYNA, developed by Mr. Prölss of Hamburg, are compared in the figure here (Fig. D1). I think the figure also shows quite clearly the possibility of increasing the efficiency of sail propulsion. The last report in the list comprises some information on the blockage effect of large sail areas and other superstructure lateral areas on the forces measured in the wind tunnel by means of so-called "silhouette tests."

REPORTS OF THE INSTITUT FÜR SCHIFFBAU
DER UNIVERSITÄT HAMBURG

No. 107 (1962). Wagner, B.: Preliminary wind-tunnel tests with full-rigged masts.

No. 122 (1964). Wagner, B.: Wind-tunnel tests with cambered plate section sails on a square-rigger mast of elliptic cross section and new cantilever design.

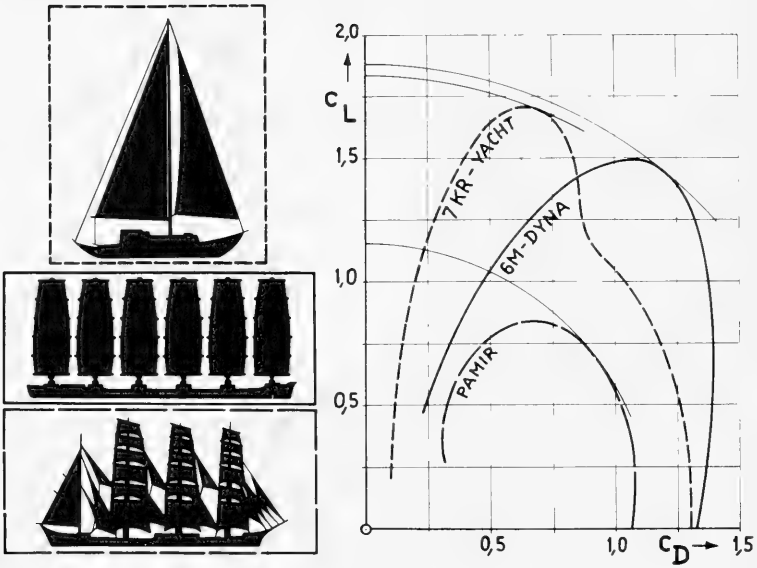

Fig. D1 - Comparison of wind-tunnel tests on sail performances of 7KR-YACHT, 6M-DYNA, and PAMIR at at the Institut für Schiffbau, Hamburg

No. 123 (1964). Wagner, B.: Wind-tunnel tests for a square-rigger mast of elliptic cross section with a cambered plate at different adjustments of studding sails.

No. 132 (1967). Wagner, B.: Calculation of speed for sailing vessels.

No. 171 (1966). Wagner, B.: Wind-tunnel tests with cambered plate sails, with single rigged masts, and with plate sails in multimasted arrangements.

No. 172 (1966). Wagner, B.: Wind-tunnel tests with the rigging model of a four-masted barque.

No. 173 (1967). Wagner, B.: Wind-tunnel tests for a six-masted sailing vessel of Prölss-design.

No. 207 (1968). Wagner, B., and Boese, P.: Wind-tunnel tests with a sailing yacht model at different sail settings.

* * *

REPLY TO DISCUSSION

Jerome H. Milgram

I wish to thank Mr. Thieme for his comments and valuable references. Some interesting results can be obtained by comparing theory with the data presented in Mr. Thieme's discussion. For given normalized load distributions and lift coefficients, theory predicts that the coefficient of induced drag is proportional to the area of the lifting surfaces divided by the square of the span. This ratio is 0.30 for the 7KR YACHT, 1.70 for PAMIR, and 1.92 for DYNA. The fact that the drag coefficients for DYNA are less than those for PAMIR attests to the high efficiency of her rig which has equal sail areas on spans of equal height.

* * *

MAGNETOHYDRODYNAMIC PROPULSION FOR SEA VEHICLES

E. L. Resler, Jr.
Cornell University
Ithaca, New York

Any propulsion mechanism, internal or external to the vehicle structure, is ultimately a pump that imparts momentum to the fluid medium in the direction opposite the vehicle's direction of motion. The thrust on the vehicle is the reaction force and is equal and opposite the force on the fluid. For magnetohydrodynamic (MHD) type propulsion, the general features are the same; however, some of the reaction forces may act via the electromagnetic fields on magnetic pole pieces or current elements producing the magnetic field. Although many different arrangements are possible, the general features of such propulsion systems are most easily discussed and examined for a simple duct flow with constant area.

Consider a simple propulsive duct or MHD-type pump, as depicted in Fig. 1. This type of pump is usually referred to as a crossed fields pump, as the electric and magnetic fields are at right angles to one another. The details of the sources of the electromagnetic fields will not be discussed, but our purpose is to explore their interaction with the fluid in the propulsive duct.

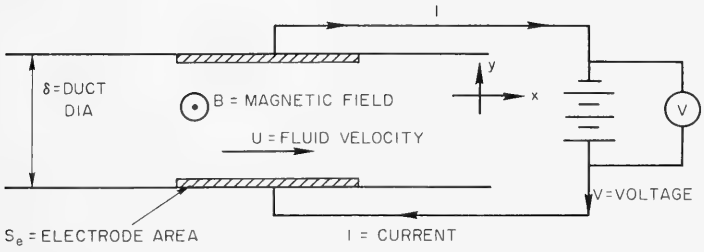

Fig. 1 - MHD propulsive duct, B field towards the reader

In this discussion we will neglect the internal resistance of the source of current I, and the fluid in the duct will have a conductivity σ. The resistance the fluid offers to the current flow in Fig. 1 is then $R = \delta / \sigma S_e$. The applied

voltage is V and the current is determined by this voltage, the back emf (electromotive force) generated by the fluid motion, and the resistance R in accord with Ohms law, and is:

$$I = \frac{V - UB\delta}{R} = \frac{V - UB\delta}{\frac{\delta}{\sigma Se}} = \sigma Se \left(\frac{V}{\delta} - UB\right) . \tag{1}$$

Consider a constant area duct. Then for incompressible fluids the velocity U will be constant through the duct. The force $IB\delta$ will act on the fluid to increase its pressure in going through the duct. The MHD duct serves as a pump without blades or vanes, the force on the fluid being a direct body force acting throughout the flow where the electrical currents flow in the presence of the magnetic field B. The work done on the fluid per unit time (P_P) is the $IB\delta$ force multiplied by the velocity U or

$$P_P = (IB\delta)U = \sigma Se\ BU\delta \left(\frac{V}{\delta} - UB\right) . \tag{2}$$

The power supplied by the source of current is just IV, so the pumping efficiency, the ratio of work done on the fluid to the power supplied by the source, is:

$$\eta = \text{efficiency} = \frac{IB\delta U}{IV} = \frac{UB}{\frac{V}{\delta}} = \frac{U}{\frac{V}{\delta B}} . \tag{3}$$

The efficiency is therefore the ratio of the electric field induced by the motion (UB) to the applied electric field V/δ or, alternatively, the velocity of the fluid U divided by the velocity $(V/\delta)/B$. The choice of voltage for the power source thus determines the efficiency of the pumping action and is under the operator's control. Using Eq. (3) to eliminate the voltage V from the equation for P_P, Eq. (2) gives

$$P_P = (\sigma US)\ (U)\ (B^2Se) \left(\frac{1 - \eta}{\eta}\right) . \tag{4}$$

The expression for P_P has been written as the product of four terms, each enclosed in parentheses. The first term is the so-called magnetic Reynolds number $Rm = \sigma U\delta$ and is a measure of how efficiently the electromagnetic forces are coupled to the fluid. The second term is the fluid velocity U, the useful power P_P being the force acting multiplied by this velocity. The term B^2Se is the magnetic pressure B^2 multiplied by the area Se, in a certain sense the maximum force expected. The last term involving the efficiency is controlled by proper choice of voltage V. The force on the fluid supplied by the forces in the propulsive duct or MHD pump is then

$$F = (\sigma U\delta)\ (B^2Se)\ \frac{1 - \eta}{\eta} . \tag{5}$$

Consider the MHD pump or propulsive duct integrated into a thrust-producing propulsive unit, as shown in Fig. 2. The vehicle and propulsive unit will be considered moving with constant speed V. The propulsive duct will be considered as square and therefore of area δ^2. Ae is the exit area for the fluid jet and Ue is the exit velocity. For steady motion, the thrust of the propulsion unit must equal the drag on the vehicle. If w is the mass flow per unit time through the unit, the thrust is ($w = \rho Ue\, Ae$), so that

$$\text{Thrust} = T = \text{Drag} = w\,(Ue - V)\ . \tag{6}$$

The drag can be expressed in terms of the wetted area of the vehicle S_w and the drag coefficient C_D as Drag $= (1/2)\,\rho V^2\, C_D S_W$ so that Eq. (6) becomes

$$C_D S_W = 2Ae\,\frac{Ue}{V}\left(\frac{Ue}{V} - 1\right). \tag{7}$$

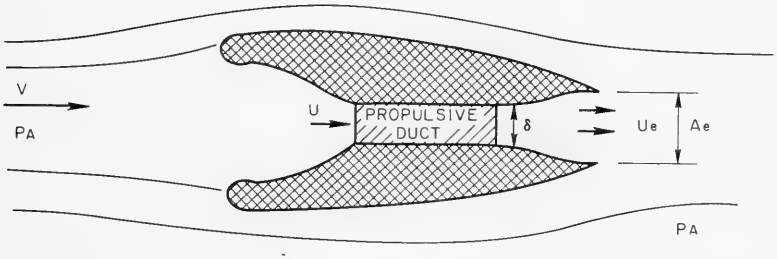

Fig. 2 - Propulsion unit with propulsive duct

For a given vehicle of known C_D and S_W, the velocity ratio Ue/V is determined once the exit area of the propulsive unit is chosen. The propulsive efficiency of the unit η_P is determined by this velocity ratio

$$\eta_P = \frac{2}{1 + \dfrac{Ue}{V}} \tag{8}$$

Equation (7) could just as conveniently be written in terms of the propulsive efficiency, or

$$C_D S_W = 4Ae\,\frac{(2 - \eta_P)\,(1 - \eta_P)}{\eta_P^2} \tag{9}$$

As mentioned above, although the velocity does not change through the duct, the pressure does. The fluid enters the duct with a Bernoulli constant equal to

that in the free stream, namely $\mathcal{P}_A + (1/2)\rho V^2$, where $\mathcal{P}_A$ is the ambient pressure. At the exit of the propulsion unit the Bernoulli constant is $\mathcal{P}_A + (1/2)\rho u_e^2$. These two Bernoulli constants differ by the pressure rise across the propulsive duct which is equal to F, Eq. (5), divided by the duct area δ^2, so

$$\Delta\mathcal{P}_{MHD} = \frac{F}{\delta^2} = \frac{1}{\delta^2}(\sigma US)(B^2 Se)\left(\frac{1-\eta}{\eta}\right). \tag{10}$$

In accordance with the above discussion,

$$\mathcal{P}_A + \frac{1}{2}\rho V^2 + \frac{F}{\delta^2} = \mathcal{P}_A + \frac{1}{2}\rho Ue^2 . \tag{11}$$

The fluid is incompressible, so the velocities Ue and V are related by the continuity equation as

$$UeAe = U\delta^2 . \tag{12}$$

Using Eqs. (10) and (12) in Eq. (11) gives

$$\sigma V\delta\left(\frac{Ae}{\delta^2}\right)\left(\frac{Se}{\delta^2}\right)\left(\frac{B^2}{\frac{1}{2}\rho V^2}\right)\frac{1-\eta}{\eta} = \left(\frac{Ue^2}{V^2} - 1\right)\left(\frac{Ue}{V}\right)^{-1} . \tag{13}$$

Equation (7) can be solved for Ue/V, giving

$$\frac{Ue}{V} = \frac{1}{2}\left[1 + \sqrt{1 + \frac{2C_D S_W}{Ae}}\right]. \tag{14}$$

Using Eq. (14), Eq. (13) can be alternatively written

$$\sigma V\delta\left(\frac{Ae}{\delta^2}\right)\left(\frac{Se}{\delta^2}\right)\left(\frac{B^2}{\frac{1}{2}\rho V^2}\right)\frac{1-\eta}{\eta} = \frac{\frac{C_D S_W}{Ae} + \sqrt{1 + \frac{2C_D S_W}{Ae}} - 1}{1 + \sqrt{1 + \frac{2C_D S_W}{Ae}}} . \tag{15}$$

Equation (15), which is general, can be rearranged to be used to compute the required magnetic field B to propel a vehicle, giving for B:

$$B = \left[\left(\frac{1}{2}\rho V^2\right)\frac{\eta}{1-\eta}\left(\frac{\delta^2}{Ae}\right)\left(\frac{\delta^2}{Se}\right)\frac{1}{\sigma V\delta}\left\{\frac{\frac{C_D S_W}{Ae} + \sqrt{1 + \frac{2C_D S_W}{Ae}} - 1}{1 + \sqrt{1 + \frac{2C_D S_W}{Ae}}}\right\}\right]^{1/2} . \tag{16}$$

Suppose we now use Eq. (16) to estimate the magnetic field necessary for the described propulsion system. Some of the parameters will be taken from the paper "Prospects for the Electromagnetic Submarine," by S. Way and C. Devlin, presented at the AIAA 3rd Propulsion Joint Specialist Conference in Washington, D.C., in July, 1967 (AIAA paper 67-432). The system they designed and tested is reported there and may be referred to for actual design details. Their measured value of σ for sea water was $\sigma = 4.5$ mho/m or $\sigma = .045$ mho/cm. A typical drag coefficient will be taken as $C_D = .004$. In Eq. (16) if we wish B in gauss, then ρV^2 must be expressed in dynes/cm^2 and rms $= 10^{-9}\sigma V\delta$, if σ is in mhos/cm, V in cm/sec, and δ in cm. Putting V in knots and δ in meters for convenience (1 knot = 51.4 cm/sec),

$$B = 1.6 \times 10^4 \left[\frac{V}{\sigma\delta} \frac{\eta}{1-\eta} \left(\frac{\delta^2}{Ae}\right) \left(\frac{\delta^2}{Se}\right) \left\{ \frac{\frac{C_D S_W}{Ae} + \sqrt{1 + \frac{2C_D S_W}{Ae}} - 1}{1 + \sqrt{1 + \frac{2C_D S_W}{Ae}}} \right\} \right]^{1/2}, \quad (17)$$

where B~ gauss, V~ knots, σ~ mho/cm, and δ~ meters.

Consider a typical case. For a submarine shape, the wetted area, if the length is L and its maximum diameter D, is about $S_W = \pi DL$. Suppose Ae, the exit area of the propulsion unit, is about $1/5\,(\pi D^2/4)$. Then $C_D S_W/Ae = C_D \pi DL \,/\, 1/5\pi D^2/4 = (20)\, C_D L/D$. If $L/D = 10$ and $C_D = .004$, then $C_D S_W/Ae = 0.8$. In this case, $\sqrt{1 + 2C_D S_W/Ae} = \sqrt{2.6} = 1.613$, so $Ue/V = 1.31$ and the propulsive efficiency $\eta_P = 86.5\%$, and

$$B = 1.18 \times 10^4 \left[\frac{V}{\sigma\delta} \frac{\eta}{1-\eta} \left(\frac{\delta^2}{Ae}\right) \left(\frac{\delta^2}{Se}\right) \right]^{1/2}. \quad (18)$$

In Eq. (18) the term δ^2/Ae is the area of the propulsive duct divided by the exit area. If this term is small, B is small, because the velocity in the duct gets larger, increasing the fluid coupling with the electromagnetic fields. The fluid attains its maximum value of velocity there, however, and care must be taken to avoid cavitation. For our purposes here, assume $\delta^2 = 1/2$ Ae. Also assume the propulsive duct length λ is half the length of the vessel, so the electrode area might be $\delta\lambda = \delta(L/2)$. Then, if $\sigma = .045$ mho/cm,

$$B = 5.56 \times 10^4 \left[\left(\frac{V}{L}\right) \frac{\eta}{1-\eta} \right]^{1/2}, \quad (19)$$

where B~ gauss, L~ meters, and V~ knots.

For a submarine tanker with L about 200 meters and V = 20 knots and with $\eta = 0.5$, a field of 1.76×10^4 or 17,600 gauss is required. This is not a difficult field to produce in small volumes, but generally does require heavy equipment. Of course, with superconducting magnets the prospects are much better, but the engineering details are indeed challenging.

I would like to discuss now some variations of the propulsion system which would allow smaller fields. In the preceding discussion we have assumed that the magnetic field must necessarily act on the sea water and also that the electric field came from a battery-type source or possibly a generator. We also assumed that we would use electrodes, always a source of possible difficulty in MHD-type devices.

Consider first the possibility of avoiding the electrodes. To operate without electrodes the currents would have to close in the fluid, but then the electric field would have to be induced in the fluid. If the fluid flow was in an annulus the electric field could be induced by a coil and the fluid in the annulus would act like the secondary of a transformer. More appropriate for our purposes, consider a coil surrounding an annulus, a conducting fluid in the annulus, and a single-turn coil moving with speed V_P, carrying a current and thus producing a magnetic field, as depicted in Fig. 3. The radial component of the magnetic field B passing through the fluid at a relative velocity $V_P - U$ will induce a circumferential electric field proportional to B and the relative velocity. So in this case V/δ in our formula is

$$V/\delta \propto (V_P - U)\, B \,. \tag{20}$$

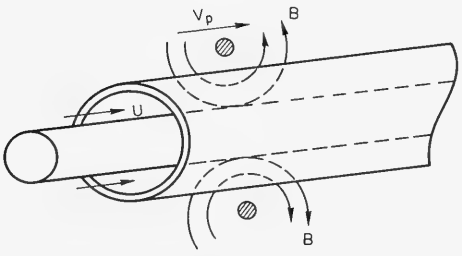

Fig. 3 - Magnetic field of a conducting fluid in an annulus

The moving magnetic field can be likened to a screen that is dragged through the fluid. The higher the conductivity of the fluid the less porous the screen. The field tends to drag the fluid with it, and the interaction is the same as already described except for the reinterpretation of the electric field term. Of course, it is possible to energize a solenoidal winding electrically so that a magnetic field configuration will travel along the winding, thus making it unnecessary to move the coil physically. In this case, V_P would be the phase velocity of the electromagnetic configuration along the winding.

To propagate magnetic fields of the size of 20,000 gauss and larger along the coil is not at all practical, so that to use this scheme a fluid of larger conductivity is required. Consider for a moment other fluids such as the liquid metals which possess conductivities from 10^4 to 10^5 mho/cm. If σ were 10^4 in our example instead of 0.045, the required field would be reduced by

$(10^4/.045)^{\frac{1}{2}} = 471$, or B need only be 37.4 gauss. Fields this size can easily be arranged to travel along coils. It is unfortunate that the sea does not have such an enhanced conductivity. Liquid metal pumps of this type, however, can operate with very reasonable fields.

Since pressure forces are conveniently created in liquid metals, consider the possibility of using electromagnetic fields to pump a liquid metal which then pumps the sea water. One needs the liquid metal to transfer the momentum from the electromagnetic fields to the sea water. Consider a flexible elastic tube filled with a liquid metal. It is well known that a pressure pulse in such a system will be propagated as a wave along the tube. Consider the possibility of pushing a solid ring along the tube with the pulse, the pulse being driven and sustained if necessary by our traveling electromagnetic wave. The device might resemble that depicted in Fig. 4.

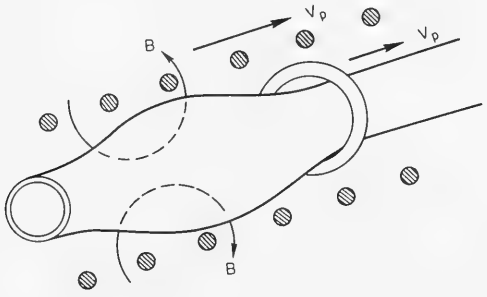

Fig. 4 - Electromagnetic wave propagation along plastic tube filled with liquid metal (ring is propelled forward by the pulse)

Of course, the elastic properties of the tube wall must be chosen so that the wave velocity and the phase velocity V_P are the same, or nearly so. The magnetic field B drives the pressure pulse in the liquid metal ahead of it. Now consider the possibility of replacing the solid ring by sea water. The water would, unfortunately, flow around the bulge if it were not prevented from doing so. The sea water to be pumped can be prevented from flowing around the bulge by providing another wall or sealing surface. The whole propulsion configuration might then look as in Fig. 5. In Fig. 5 the radial position of the water "ring" and liquid metal have been interchanged.

The magnetic field traveling along the coil will tend to deform the liquid metal so as to conform to the field configuration. How successful it is in doing this is governed by the magnetic Reynolds number previously discussed. The magnetic pressure is transformed to fluid pressure in the liquid metal, and the pressure is transmitted to the sea water across the flexible diaphragm. The pressure pulse will also propagate along the interface, and the whole system is designed so that the magnetic field configuration, the pulse in the material, and

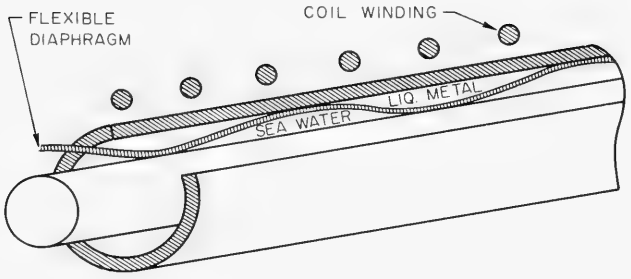

Fig. 5 - Use of sea water as the "ring" of Fig. 4

the water move together. This combination makes use of the good coupling, because of the high electrical conductivity of the liquid metal, and retains the general features of MHD propulsion.

Note that these electromagnetic devices work successfully, in that the currents flow in such a manner as to realize the magnetic pressure as a fluid pressure. We have discussed above mostly dynamic systems. Magnetic pressure can be realized in yet another manner. It is possible to fabricate a fluid with ferromagnetic properties by suspending very small ferromagnetic particles, say magnetite, in a fluid such as kerosene. These fluids tend to deform with the magnetic fields, much as conducting fluids. This is another way that magnetic pressure can be materialized in a fluid. Such a ferromagnetic fluid can be used in the device shown schematically in Fig. 5, and would replace the liquid metal. This fluid would also be more compatible with sea operations. A number of papers that describe such a fluid appear in the bibliography that follows. The theory outlined at the outset is not directly applicable to ferromagnetic fluids, but the phenomena are similar to those described.

A brief presentation of the principles governing direct magnetohydrodynamic propulsion has been discussed and typical operating conditions outlined. Other indirect schemes, seemingly more convenient, have also been discussed. It seems fair to conclude that the versatility of MHD propulsion makes worthwhile the further exploration of its possibilities.

BIBLIOGRAPHY

Way, S., and Devlin, C., Prospects for the electromagnetic submarine. AIAA 3rd Propulsion Joint Specialist Conference, AIAA Paper 67-432, July 17-21, 1967

Resler, E.L., Jr., and Rosensweig, R.E., Magnetocaloric power. AIAA Journal 2 (No. 8) pp. 1418-1422, (1964)

Rosensweig, R.E., Magnetic fluids. Int. Sci. Technol., pp. 48-57, July 1966

Neuringer, J.L., and Rosensweig, R.E., Ferrohydrodynamics. Phys. Fluids 7 (No. 12) pp. 1927-1937, (1964)

Resler, E.L., Jr., and Rosensweig, R.E., Regenerative thermomagnetic power. J. of Engineering for Power, Paper 66-WA/Ener-1, pp. 1-7 (1966)

* * *

Friday, August 30, 1968

Afternoon Session

UNCONVENTIONAL PROPULSION

Chairmen: Dr. E. W. Cummins

Naval Ship Research and Development Center
Washington, D. C.

and

Dr. H. Edstrand

Swedish State Shipbuilding Experimental Tank
Göteborg, Sweden

PERFORMANCE OF PARTIALLY SUBMERGED PROPELLERS

J. B. Hadler and R. Hecker
Naval Ship Research and Development Center
Washington, D. C.

ABSTRACT

Open-water experiments have been conducted on 2 three-bladed and 1 two-bladed supercavitating propellers operating in the partially submerged condition. Thrust, torque, and rpm have been measured over a wide range of advance ratios. The results have been compared with existing experiments made with the propellers fully submerged, both cavitating and noncavitating. A geosim of one of the three-bladed propellers has been further tested over a wide range of advance ratios at various speeds of advance. Besides the thrust, torque, and rpm, the vertical and horizontal components of the transverse forces have been measured as well as the location of the center of thrust. The latter measurements have been made with a four-component dynamometer that measures the bending moments imposed by the propeller.

The results have been analyzed to ascertain the hydrodynamic origin of the various forces and how they change with different advance ratios and different speeds of advance. Through this analysis, identification of major problem areas is attempted with the hope that viable research goals can be established.

HISTORICAL BACKGROUND

Since the 1850's, the screw propeller has been the dominant form of marine propulsion. Its advantages over the paddle wheel, which it replaced, were its light weight, its relatively high rotative speed, and its insensitivity to change in submergence. As a consequence of its success, much inventive and research effort has gone into improving performance or devising specialized applications, using the screw-propeller principle. One of the specialized offshoots was the partially submerged propeller. Initially, this propeller was viewed as another means besides the paddle wheel for achieving shallow-draft propulsion in sheltered waters. The first U.S. patent was issued about one hundred years ago (1869) to C. Sharp of Philadelphia (Pa.). His patent was quite ingenious, in that he yawed the propeller to the flow to reduce the transverse force, used multiblades to reduce unsteady forces, cupped or, in current terminology, cambered the blades to improve their effectiveness, and used high pitch for maximum efficiency. Figure 1 shows some of the sketches contained in his patent grant.

As engine developments progressed and higher boat speeds became practical, the emphasis as shown by the patents shifted from low-speed shallow-draft

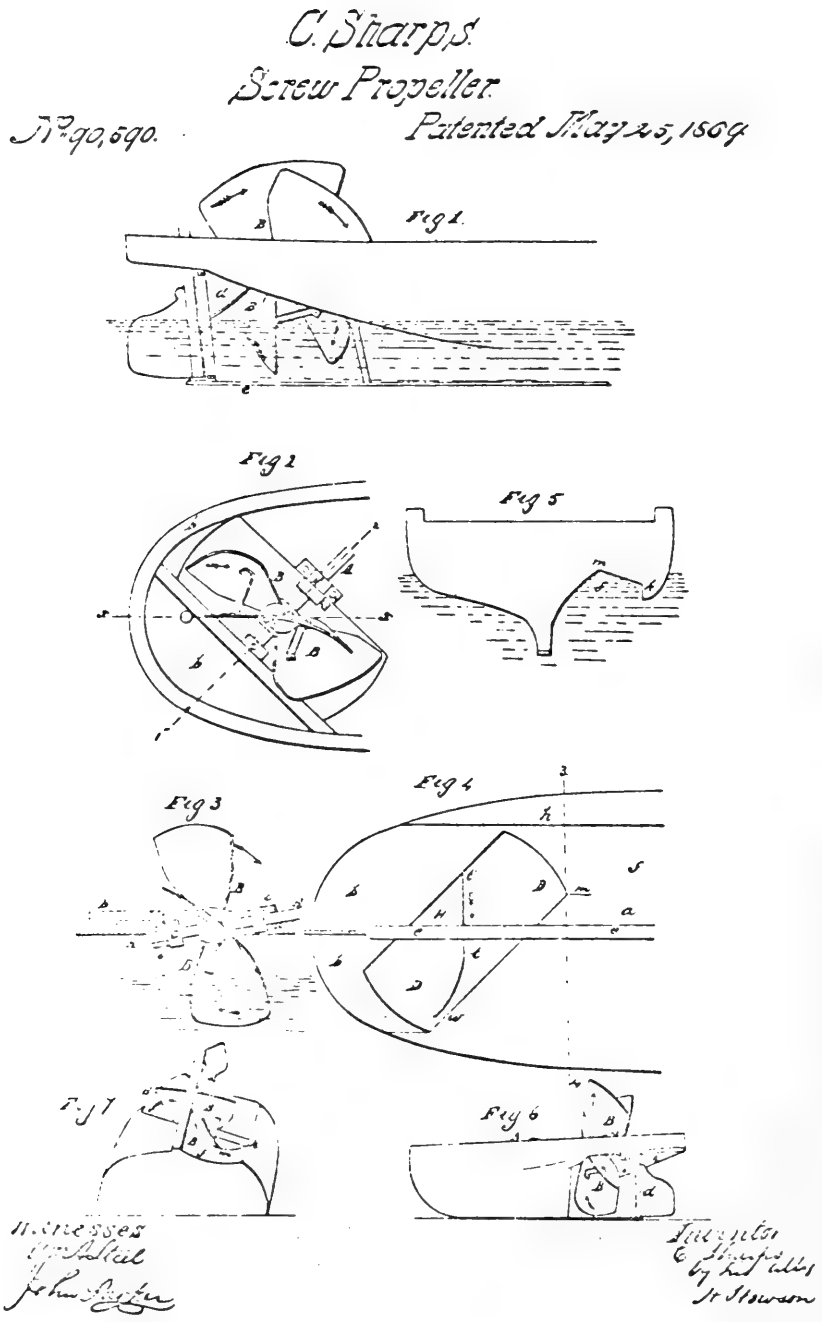

Fig. 1 - Patent sketches of C. Sharp (1869)

displacement ships to hydroplane boats, where a fixed-water surface existed at the stern. Typical of these developments was a patent issued in 1914 to W. H. Farber for a hydroplane boat having two large surface propellers, Fig. 2. During and immediately after World War I, Albert Hickman, of Sea Sled fame, employed "surface" propellers on a sea-sled torpedo boat and on a 55-mph sea-sled airplane carrier he developed for the U.S. Navy. Throughout these developments Hickman had the active support of Adm. D. W. Taylor. It was at this time that the first known model tests [1] were run both in open water and self-propelled on a propeller designed to operate in the partially submerged condition for a high-speed vessel. The propeller used in these tests was three-bladed, with semiogival sections having a flat pressure face and sharp leading edge. The test results showed high efficiency, comparable to those fully submerged, but significantly reduced thrust and torque. The self-propulsion tests brought forth the prime design difficulty with this type of propeller, that of developing adequate thrust at the "hump" resistance speed to assure successful operation of the craft over the desired speed range.

Among the list of subsequent inventions was a patent granted in 1927 to Gebers of the Model Basin in Vienna, Austria. He recognized that the partially submerged propeller was limited to a relatively narrow range of load variations. Thus, for application to displacement vessels it was necessary to provide some means for operating at low speed or during heavy loads by incorporating a combination of small fully submerged propellers with minimal appendages and large "semisubmerged" high-pitch propellers as shown in Fig. 3.

Insofar as practical applications of the partially submerged propeller are concerned, they have, so far, been limited to the racing high-speed hydroplane, which evolved into the well known "prop riders." The key developments occurred in the period just before and immediately after World War II and resulted, in 1948, in the pace-setting hydroplane Slo-Mo which increased the unlimited speed record from 141.7 to 183 mph. The propellers employed are two-bladed with wedge-type sections and are high-pitched. Besides being highly efficient, these propellers also provide a lift, thus, to a point, establishing the magnitude of their submergence; hence, the name prop riders.

Much of the development previously recounted was carried out without the benefit of model or "scientific" investigation, but was largely the result of "cut and try" in actual applications. Laboratory research work on partially submerged propellers has largely been confined to the problem of air drawing of the normal displacement ship-screw propeller when the ship is ballasted, so that part of the propeller is partially out of water. Osborne Reynolds was one of the first to study this problem in a paper entitled "On the Effects of Immersion on Screw Propellers" [2] in Transactions Institute of Naval Architecture 1874. Since then, the results of a number of investigations have been published. The publication by H. Shiba of Japan [3] provided the most thorough analysis, using the widest range of experiments, and gave the most complete bibliography. He tested 28 propellers in which area ratio, pitch ratio, number of blades, section form, plan form, pitch distribution, and skewback were varied. In his experiments he varied the tip emergence from 0 to 20% of the propeller diameter. Most of the blade sections were of the airfoil type, but he did include a circular arc section with a flat pressure face and sharp leading edge and noted the

W. H. FAUBER.
HYDROPLANE BOAT.
APPLICATION FILED NOV. 25, 1912.

1,121,006. Patented Dec. 15, 1914.

6 SHEETS—SHEET 6.

Fig. 22.

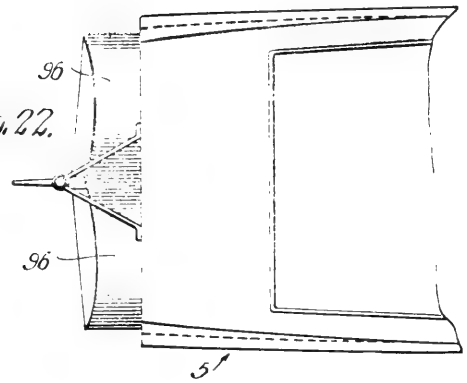

Fig. 23.

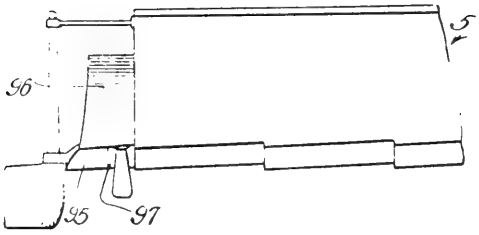

Fig. 24.

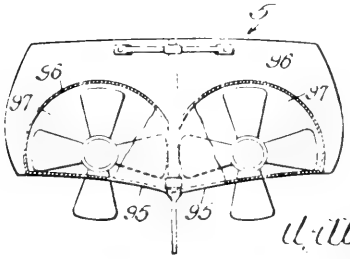

Witnesses
[illegible]
[illegible]

Inventor
William H. Fauber
by Poole & Crowe Attys

Fig. 2 - Patent sketches of W. H. Farber (1914)

May 17, 1927. 1,628,837

F. GEBERS

PROPELLING MECHANISM FOR SHIPS

Filed July 3. 1924 2 Sheets-Sheet 1

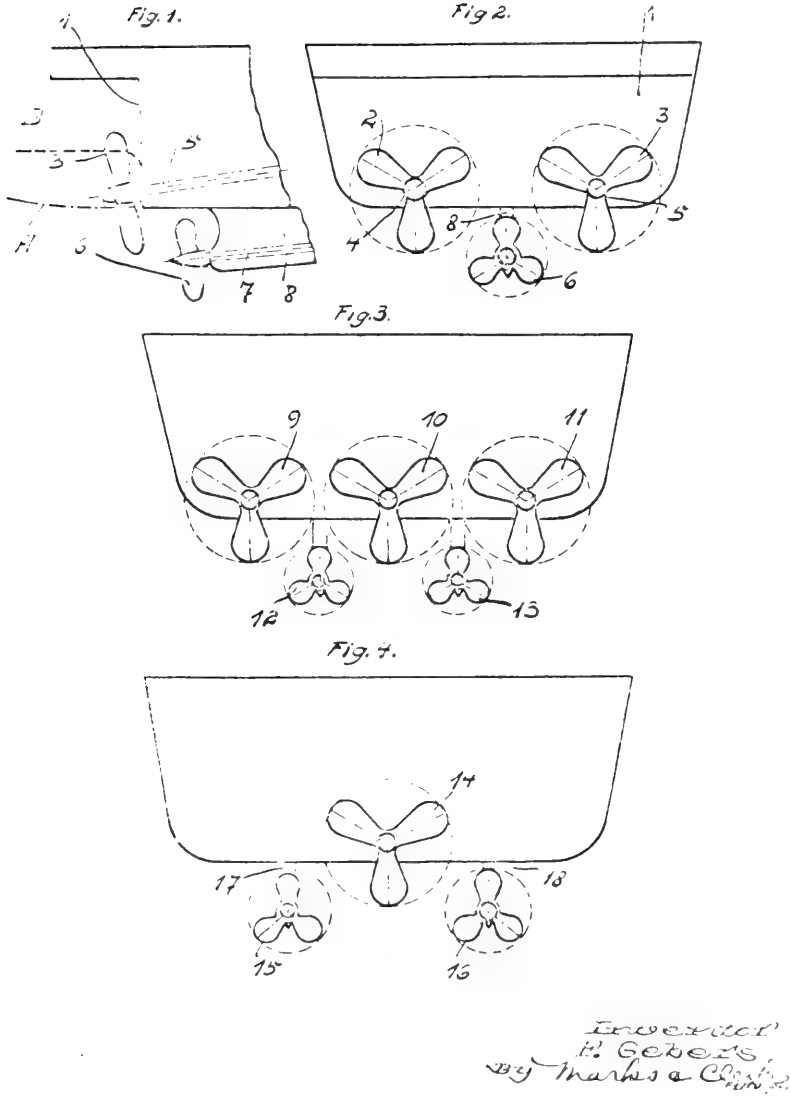

Fig. 3 - Patent sketches of F. Gebers (1927)

difference in the performance curves. Besides the wide range of experimental information, he established, through the hydrodynamic equations of motion, the law of similarity as it related to the air drawing of a partially submerged propeller.

The most recent work on this problem was that by Gutsche in East Germany [4]. He tested eight propellers, covering a wider range of blade-area ratios over a slightly wider range of submergences. Since he used airfoil sections, his results were similar to those of Shiba.

The tests on the circular arc sections in Refs. [1] and [3] clearly show different characteristic curves than do those with airfoil sections. Although all partially submerged propellers show a reduction in thrust and torque coefficient with reduction in advance ratio, those with the airfoil sections show a more precipitous drop at a critical advance ratio than do sections employing flat or cambered pressure-face sections.

The other recent noteworthy work was that of the Russians Yegorov and Sadovnikov, Ref. [5], who were concerned with applying this type of propulsion to hydrofoil craft operating in protected water such as rivers.

INTRODUCTION

With the growing interest in high-speed high-performance craft, the Naval Ship Research and Development Center has undertaken the task of developing more effective means of propelling these vehicles. Most schemes of propulsion involve fully submerged supercavitating propellers with appropriate appendages to house the shafting. These appendages, unfortunately, impose drag penalties which become quite severe at high speed (Ref. [6]), hence, the interest in examining other means of propulsion. The partially submerged propeller with its low appendage drag appears to offer a possible solution for high efficiency, provided performance is not unduly jeopardized in solving the vibration and strength problems arising from the cyclic loading and unloading of the blades.

Since preceding work, Refs. [1] and [3], had shown that the circular arc section with flat faces and sharp leading edge had efficiencies comparable to those for the fully submerged condition and had more desirable thrust characteristics than propellers with airfoil sections, it was decided to start this investigation utilizing propellers with supercavitating-type sections. The availability of a number of supercavitating propellers from previous research programs made this approach quite attractive and provided a large data base for comparison of performance between partially submerged, fully wetted, and supercavitating operation, Refs. [7] and [8].

The initial investigation was made on three propellers in which the major differences were the P/D ratios and number of blades. The objective of these tests was to investigate the steady-state power performance, i.e., torque, thrust, and propeller efficiency over a wide range of advance coefficients. Subsequently, measurements were made on a geosim of one of the preceding propellers over a wide range of advance coefficients and test speeds. As well as the usual measurements of thrust, torque, and rpm, measurements were also made of the force in

the transverse plane and the shaft-bending moments with a dynamometer especially designed for this purpose.

It is the objective of this paper to present the results of the experiments on the four propellers and to make comparisons with their performance when fully submerged, both cavitating and noncavitating. An analysis will be attempted, albeit somewhat heuristically, of the hydromechanical sources of the force generated by partially submerged propellers so that guidance can be obtained for future research, both theoretical and experimental. There will be many questions raised which at this point are incompletely answered. It is hoped that these questions will stimulate other investigators into examining this form of propulsion, which holds potential for the efficient propulsion of high-speed vehicles.

EXPERIMENTAL PROCEDURES

The objective of the initial set of experiments was to determine the efficiency and thrust characteristic of partially submerged supercavitating propellers and to compare these with the fully submerged performance.

For this phase three propellers were used from the NSRDC supercavitating-propeller library, Propellers 4002, 3820, and 3767. Table 1 lists the characteristic coefficients for these propellers. Figures 4-6 show the geometry and photographs of the three propellers. As may be noted, only the camber shape of the sections was common to all three propellers. All of the sections had blunt trailing edges, except the tip 20% of Propeller 3767. The primary differences sought in selecting these propellers were number of blades and pitch ratio.

Measurements of thrust, torque, and rpm were made in open water at two submergences, semisubmerged, and with the shaft centerline 2 in. above the

Table 1
Propeller Characteristics

Propeller	Diameter (in.)	(P/D) 0.7R	Number of Blades	EAR	BTF	Camber Line
4002	12.00	1.319	2	0.304	0.019	Modified 2-term.
3820	15.50	1.628	3	0.505	0.027	do
3767	16.00	1.180	3	0.506	0.022	do
3768*	10.00	1.180	3	0.506	0.022	do

*Propellers 3768 and 3767 are different-sized models of the same propeller.

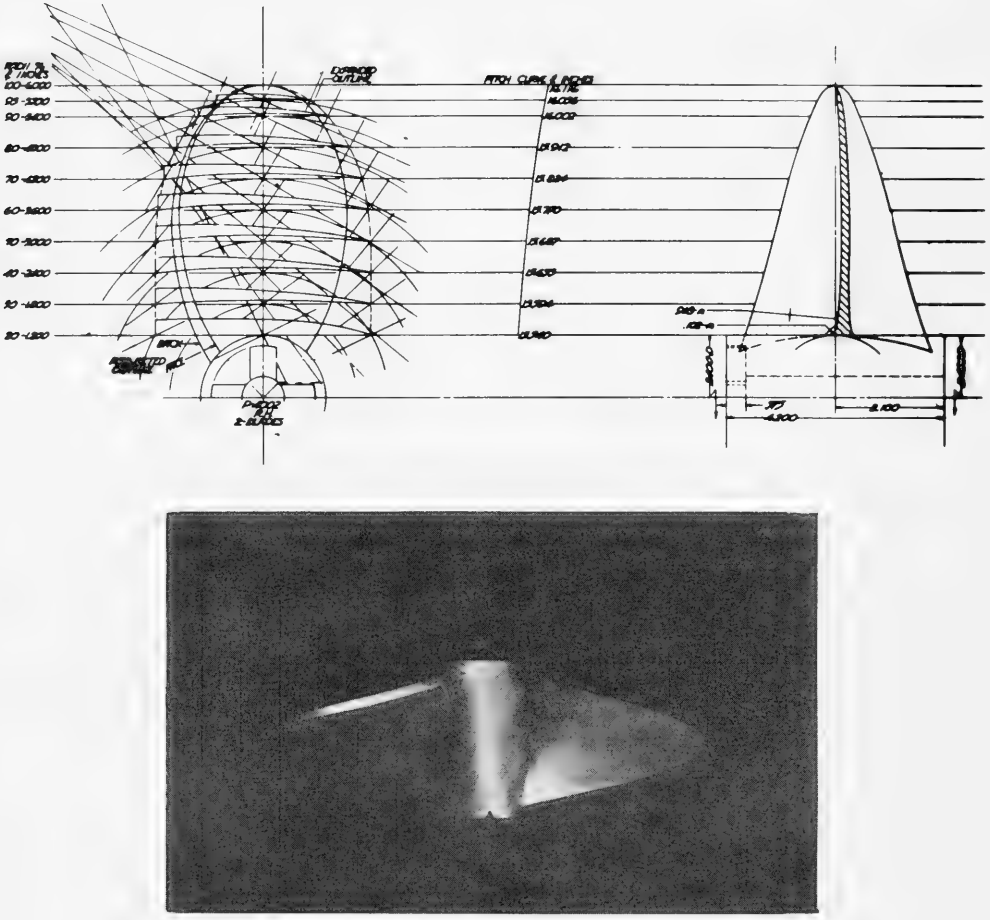

Fig. 4 - Drawing of propeller 4002

water surface. Normal open water-test procedures were used, i.e., the rpm was held constant and the forward velocity ranged from 0 to about 12 fps. Test conditions are tabulated in Table 2. A three-to-one elliptical fairwater was used in front of the propeller. It was noted in the semisubmerged condition that a film of water came over the fairwater into the propeller disk. Comparisons of the spray patterns in both the semisubmerged and hub-out conditions did not seem to indicate any effect from this thin film of water. It was also noted in running these tests at the low advance coefficients that the propeller and its hub were generating a wave train which appeared to modify the submergence.

The objective of the second phase of the experimental program was a more detailed examination of all of the steady forces generated by a partially submerged propeller for a number of speeds of advance. For this phase, Propeller

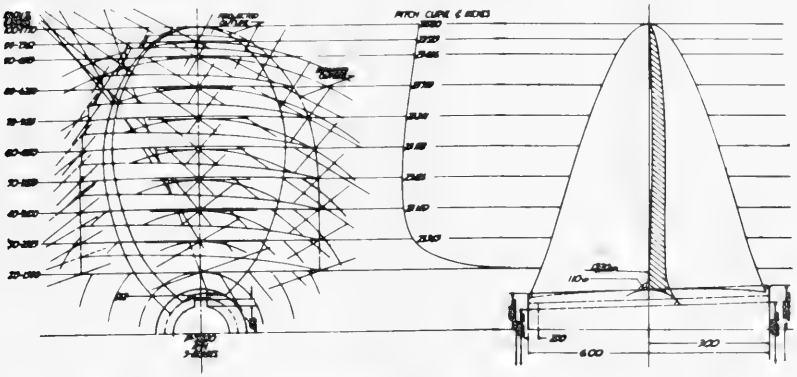

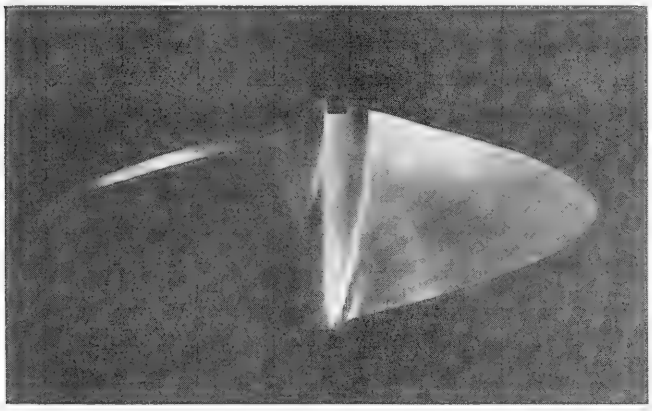

Fig. 5 - Drawing of propeller 3820

3768, a geosim of Model 3767, the most thoroughly tested of all the supercavitating propellers available at the Center, was used.

The experiments in this phase were carried out somewhat differently, as the effect of speed of advance upon performance was an objective. Hence, the tests were run at a constant forward velocity, and the rpm's were varied. This limited the lowest advance coefficient to the maximum torque attainable with the propulsion dynamometer and removed the problem of the wave train at low advance coefficients. Table 2 lists the conditions tested. During these tests visual observations were made of the flow variations.

In order to minimize the effect of the elliptical fairwater on performance, it was replaced by a 60° cone. This seemed to help in reducing the thickness of the film of water.

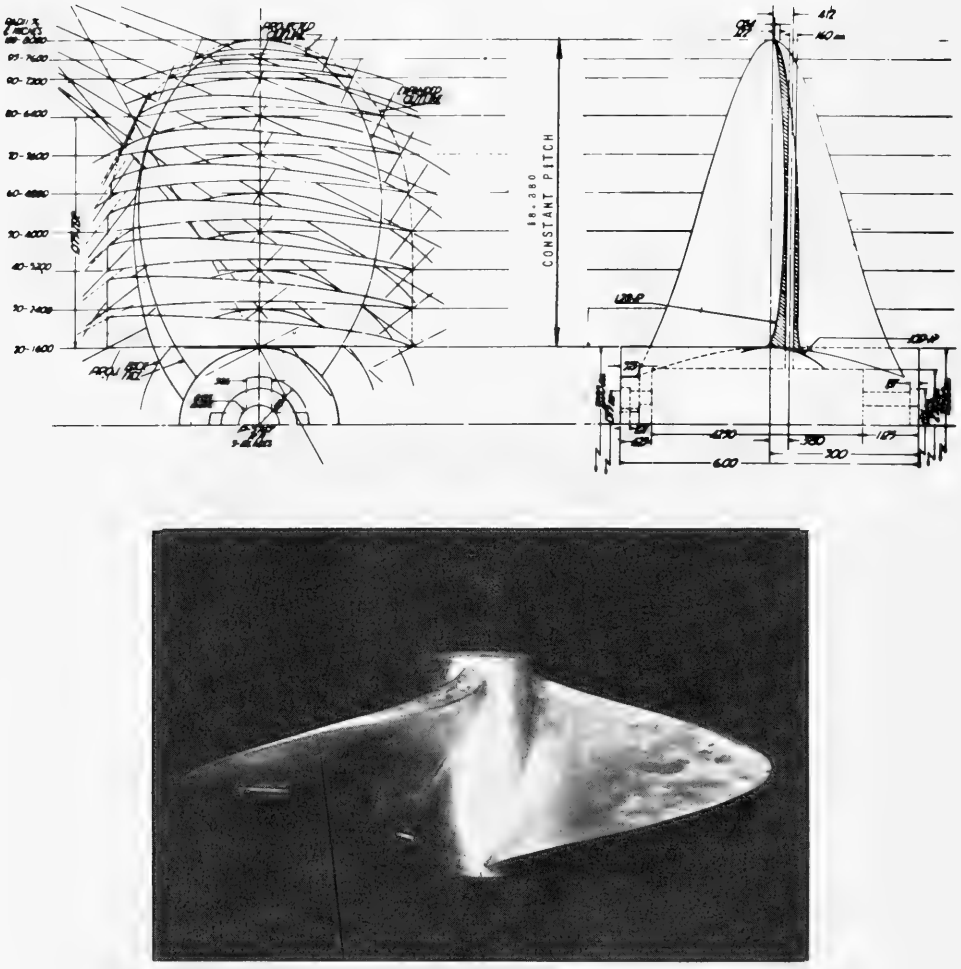

Fig. 6 - Drawing of propeller 3767

Since the center of thrust is well below the shaft axis, the propeller generates large bending moments in the shaft. Correspondingly the unbalanced torque force during 1 revolution also generates a large force in the transverse plane. To determine the shaft-bending moments arising from the thrust eccentricity and magnitude and direction of the transverse force, a special dynamometer which measures the bending moment in the shaft at two points was used. The dynamometer was designed to measure these moments in both the horizontal and vertical planes on the propeller shaft housing. Thus, identification of the various components of the steady propeller force is possible with this dynamometer in conjunction with the thrust and torque measured by a conventional propulsion dynamometer. A detailed description of the dynamometer and the calibration is given in Appendix A.

Table 2
Summary of Test Conditions

Propeller	Submergence (% of diameter)	Advance coefficient	rpm	Speed (fps)
4002	50	0 - 1.4	840	Vary
	33.3	0 - 1.4		
3820	50	0 - 1.6	600	Vary
	35.9	0 - 1.6		
3767	50	0 - 1.4	420	Vary
	37.5	0 - 1.4		
3768	50	0.3 - 1.4	Vary	5.18
		0.3 - 1.4		7.77
		0.4 - 1.4		10.35
		0.6 - 1.4		15.53
		0.8 - 1.4		20.71
	40	0.3 - 1.4		5.18
		0.3 - 1.4		7.77
		0.3 - 1.4		10.35
		0.5 - 1.4		15.53
		0.8 - 1.4		20.71
	60	0.4 - 1.4		10.35
		0.8 - 1.4		15.53
		0.9 - 1.4	Vary	20.71

PRESENTATION OF EXPERIMENTAL RESULTS

The results of the experiments of the first phase are presented in Figs. 7 - 12 as propeller efficiency η, thrust coefficient K_T, and torque coefficient K_Q versus advance coefficient J. The thrust and torque coefficients of all these propellers show a characteristic increase, a maximum, and then a decrease as the advance coefficient is decreased — similar to those of supercavitating propellers working under cavitating conditions. Propeller 3820 in Figs. 9 and 10 also shows a definite discontinuity in the performance curves. This discontinuity will be discussed in detail in a later section.

The results of the second-phase experiments on Propeller 3768 are presented in Figs. 13 - 15. The vertical e_v and horizontal e_h locations of the center of thrust from the shaft axis, expressed as a function of propeller diameter are also included. In addition to the normal propeller coefficients, the horizontal and vertical transverse force coefficients are included in Figs. 16 - 18, which are defined as follows:

$$K_{F_H} = \frac{F_H}{\rho n^2 D^4} ,$$

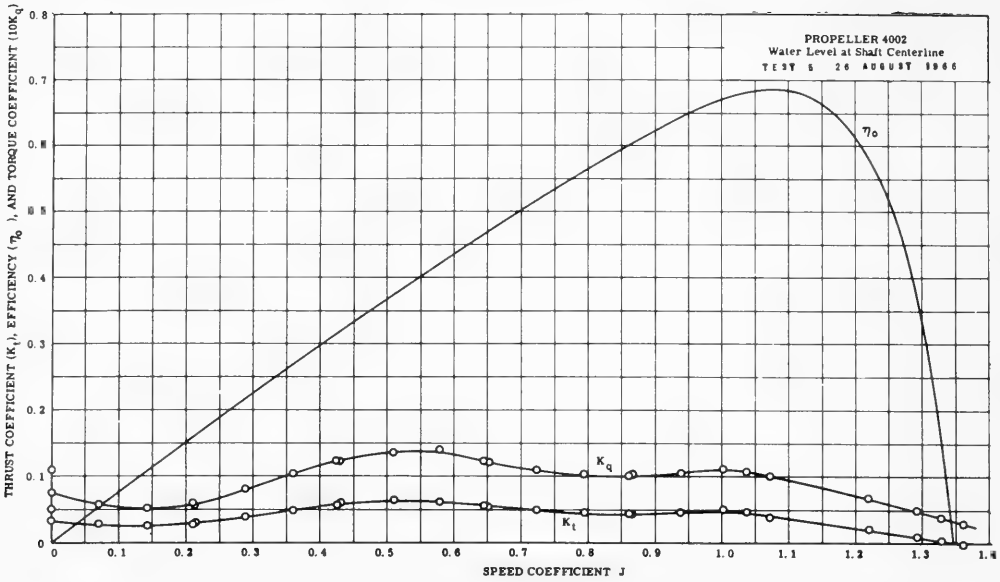

Fig. 7 - Performance characteristics of propeller 4002 50% submerged

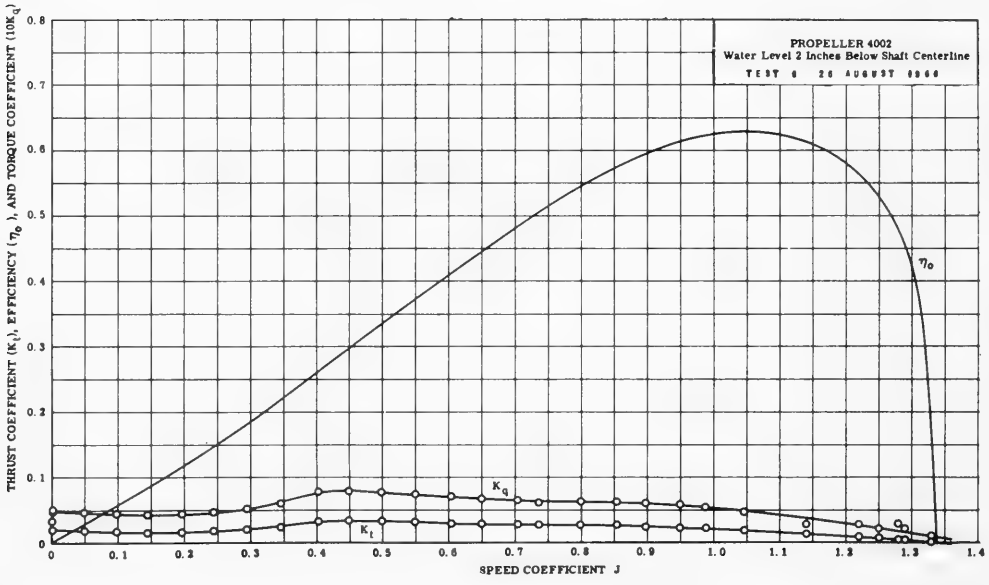

Fig. 8 - Performance characteristics of propeller 4002 33.3% submerged

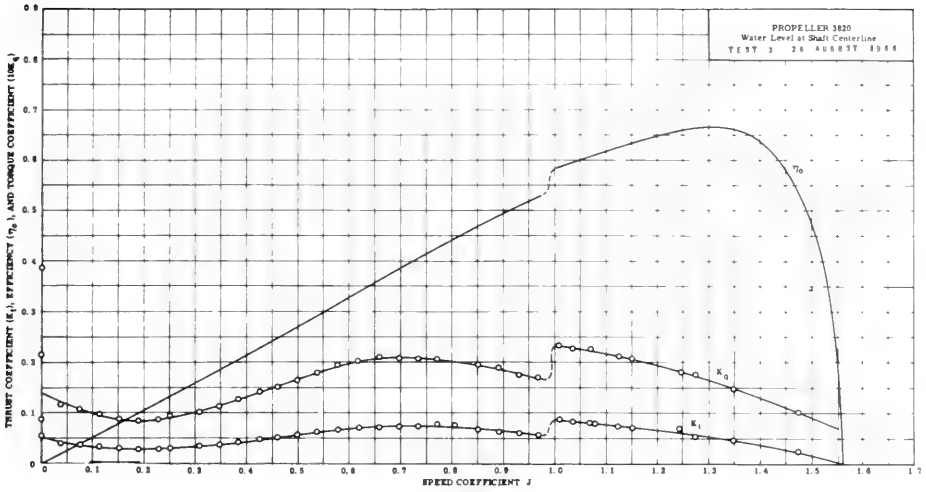

Fig. 9 - Performance characteristics of propeller 3820 50% submerged

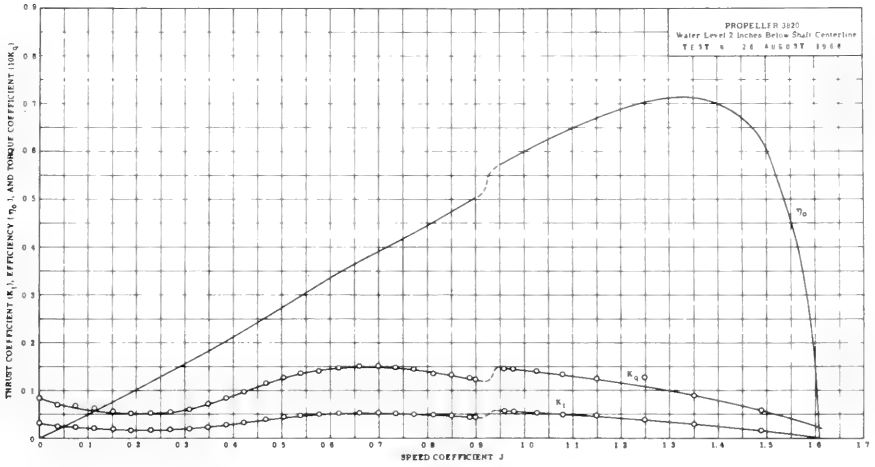

Fig. 10 - Performance characteristics of propeller 3820 35.9% submerged

$$K_{F_v} = \frac{F_v}{\rho n^2 D^4} .$$

All of these quantities are presented as a function of the advance coefficient J. The results at one submergence are presented together to show the effect of advance speed upon the results.

It may be noted that the thrust and torque curves show a discontinuity, not obtained in the first set of tests upon the prototype Propeller 3767. Part of the

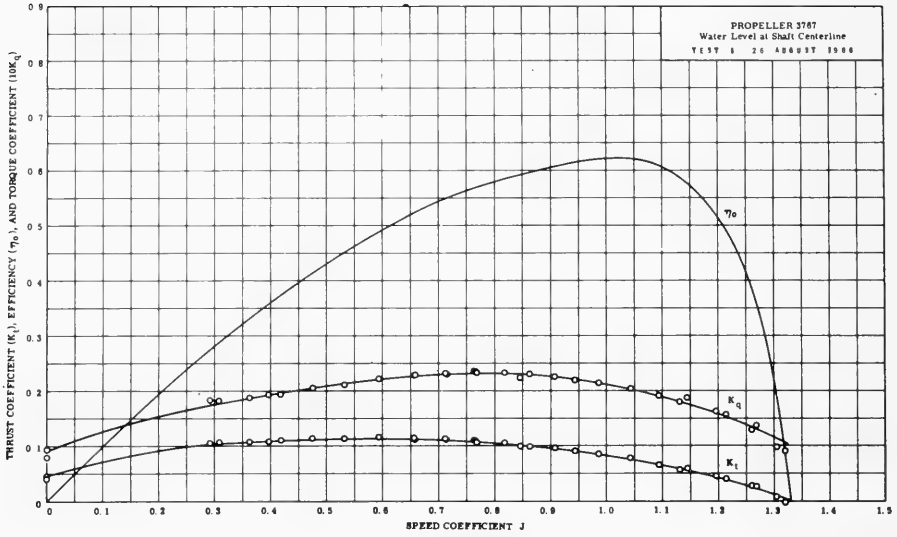

Fig. 11 - Performance characteristics of propeller 3767 50% submerged

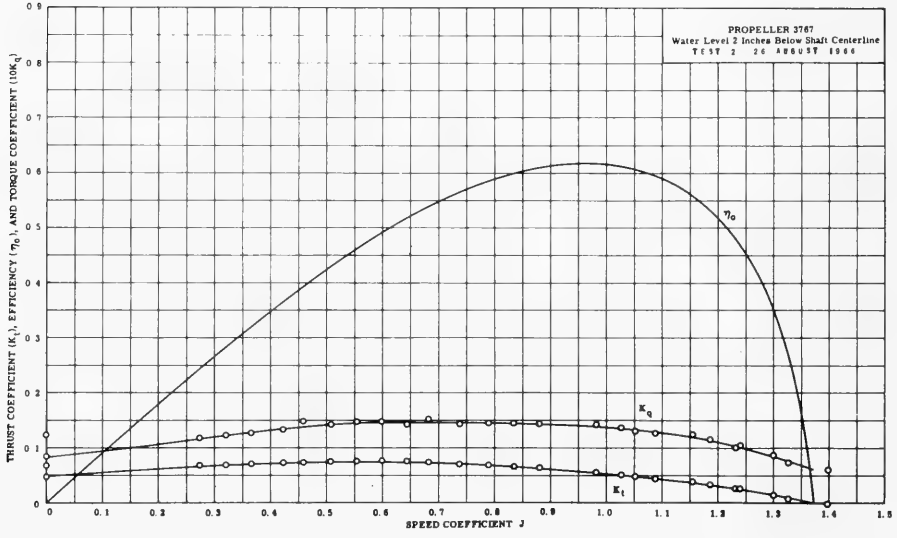

Fig. 12 - Performance characteristics of propeller 3767 37.5% submerged

objective of the second set of experiments was to look for any discontinuity in the performance curves. The discontinuity was most easily found by observing the change in spray pattern and then making several measurements in that region.

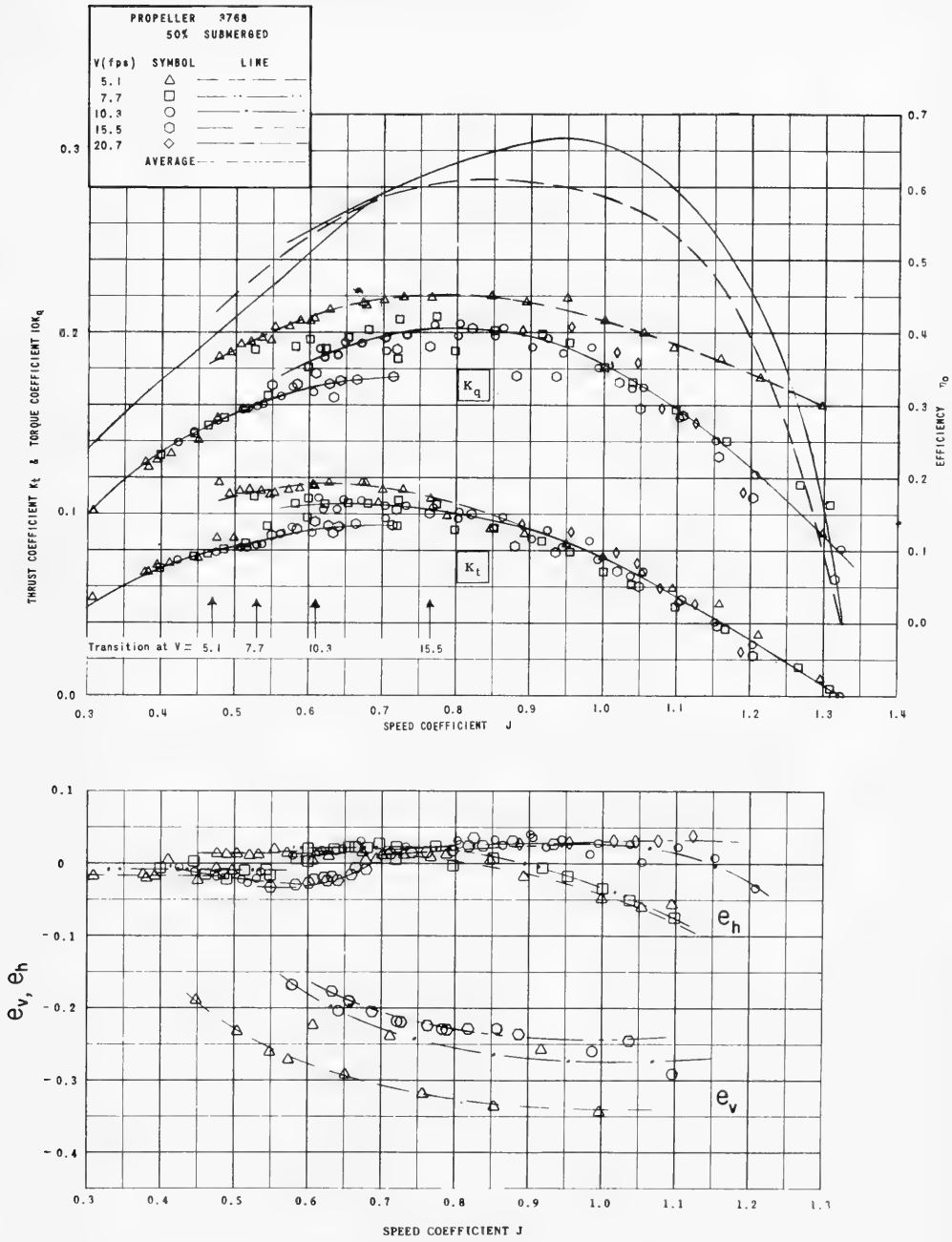

Fig. 13 - Performance characteristics of propeller 3768 50% submerged at several Froude numbers

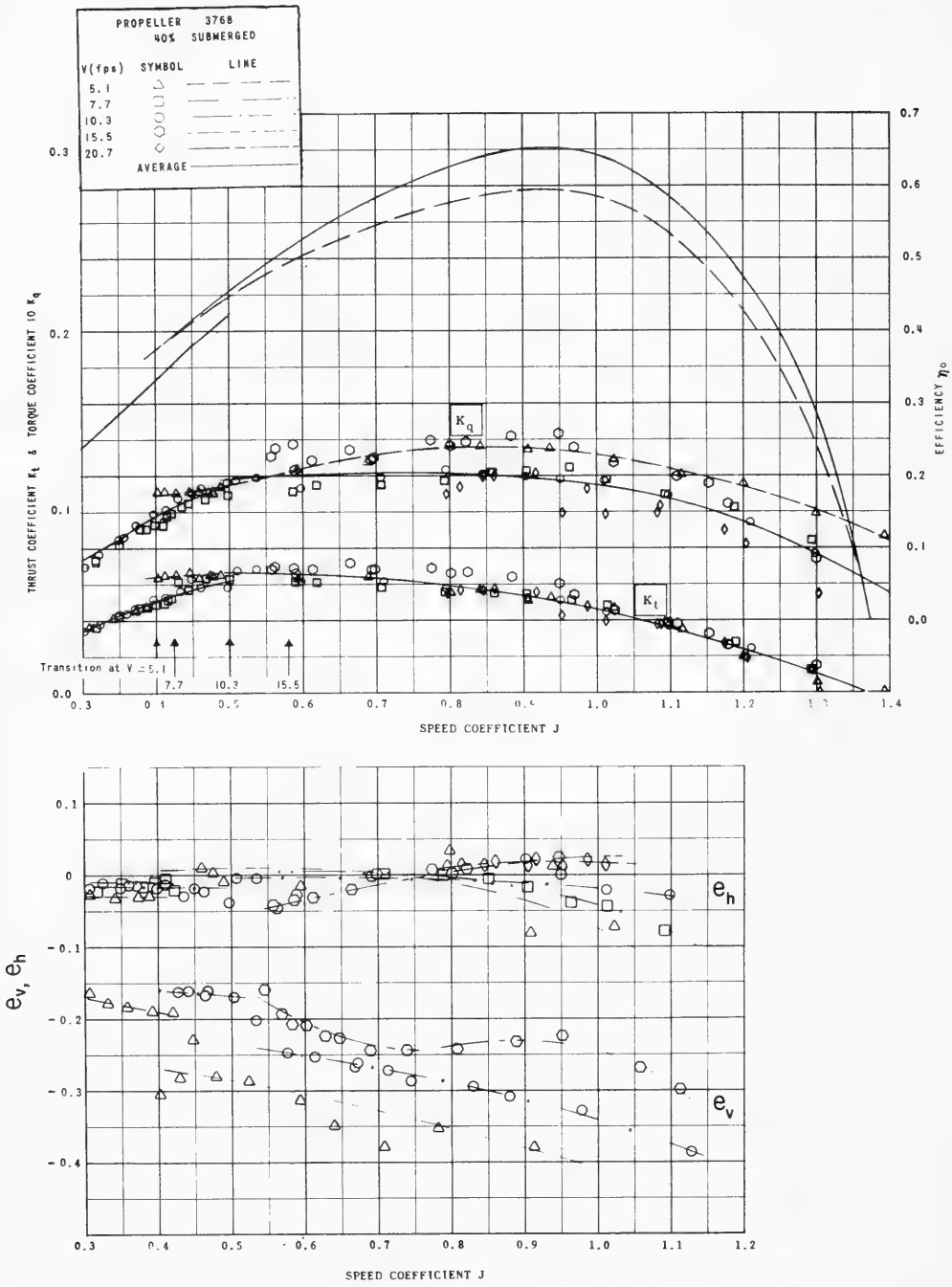

Fig. 14 - Performance characteristics of propeller 3768
40% submerged at several Froude numbers

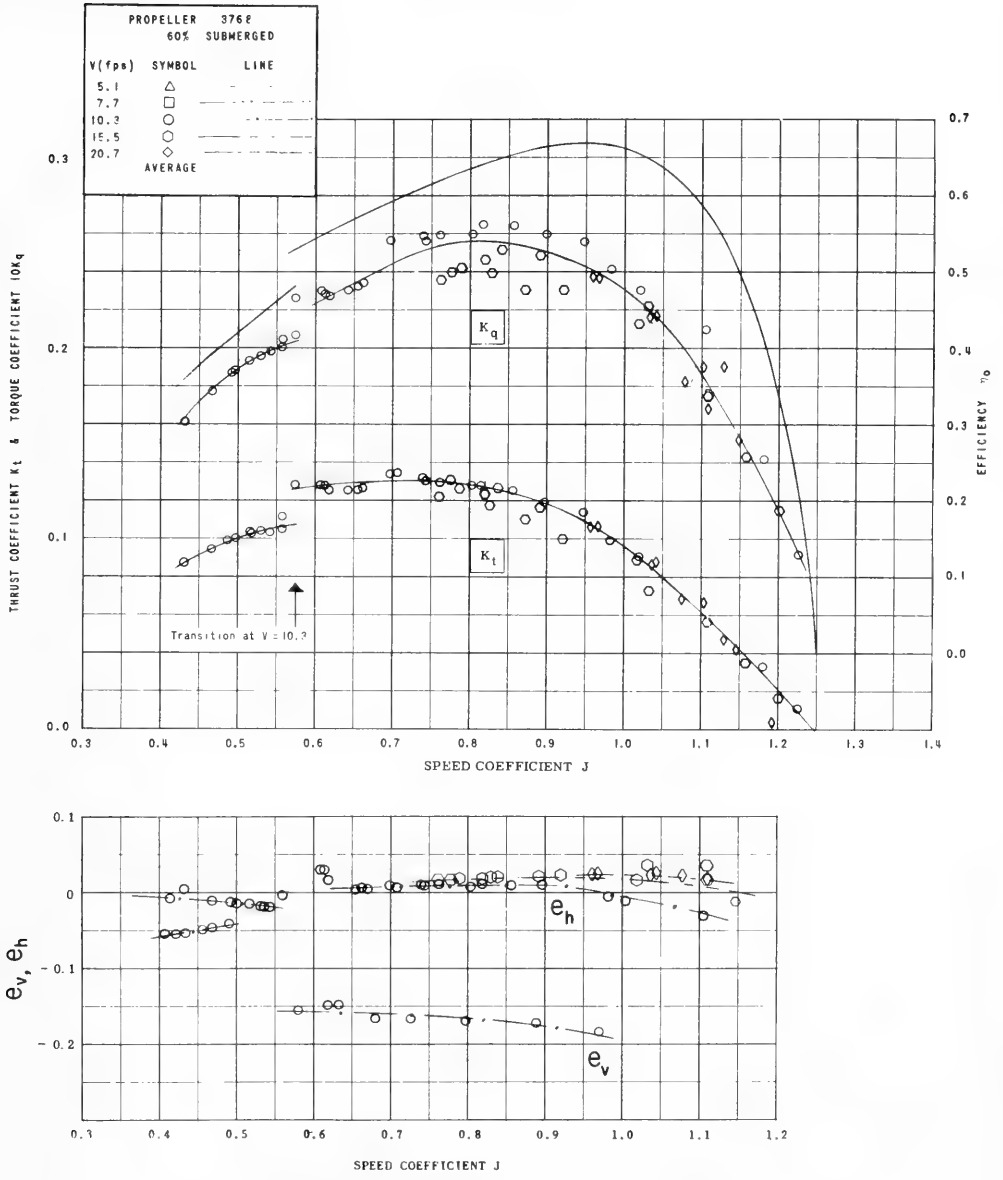

Fig. 15 - Performance characteristics of propeller 3768 60% submerged at several Froude numbers

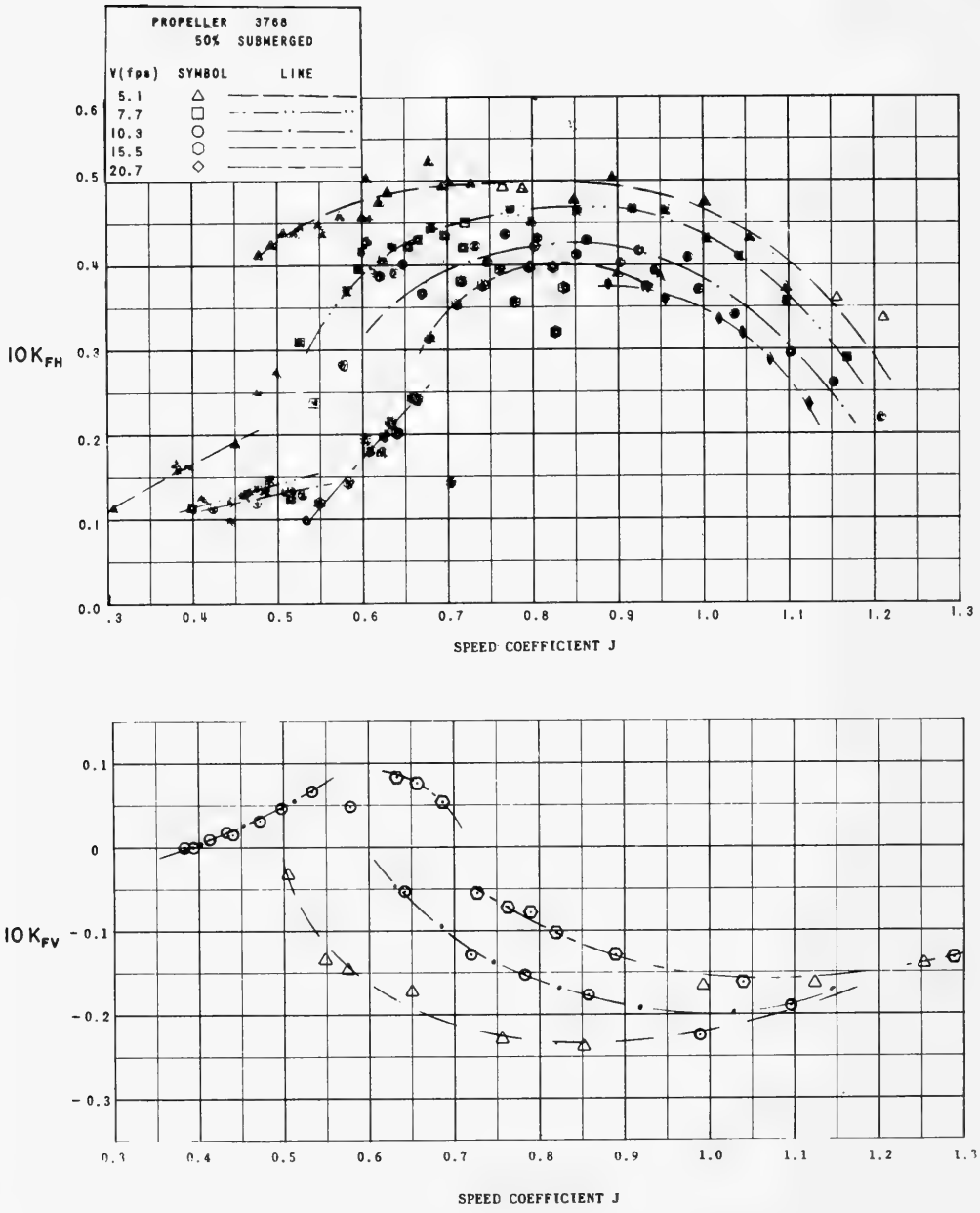

Fig. 16 - Transverse force coefficients of propeller 3768 50% submerged

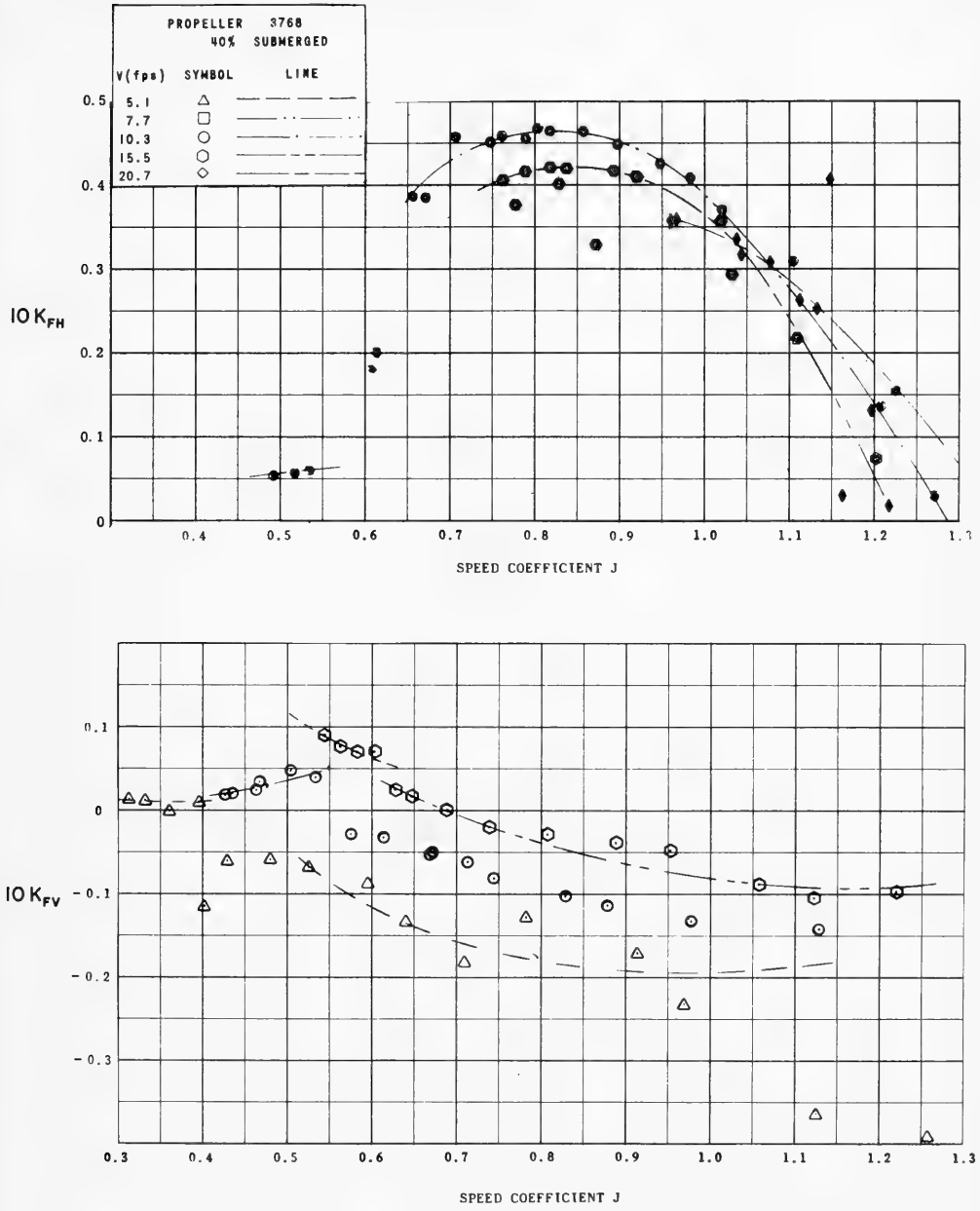

Fig. 17 - Transverse force coefficients of propeller 3768 40% submerged

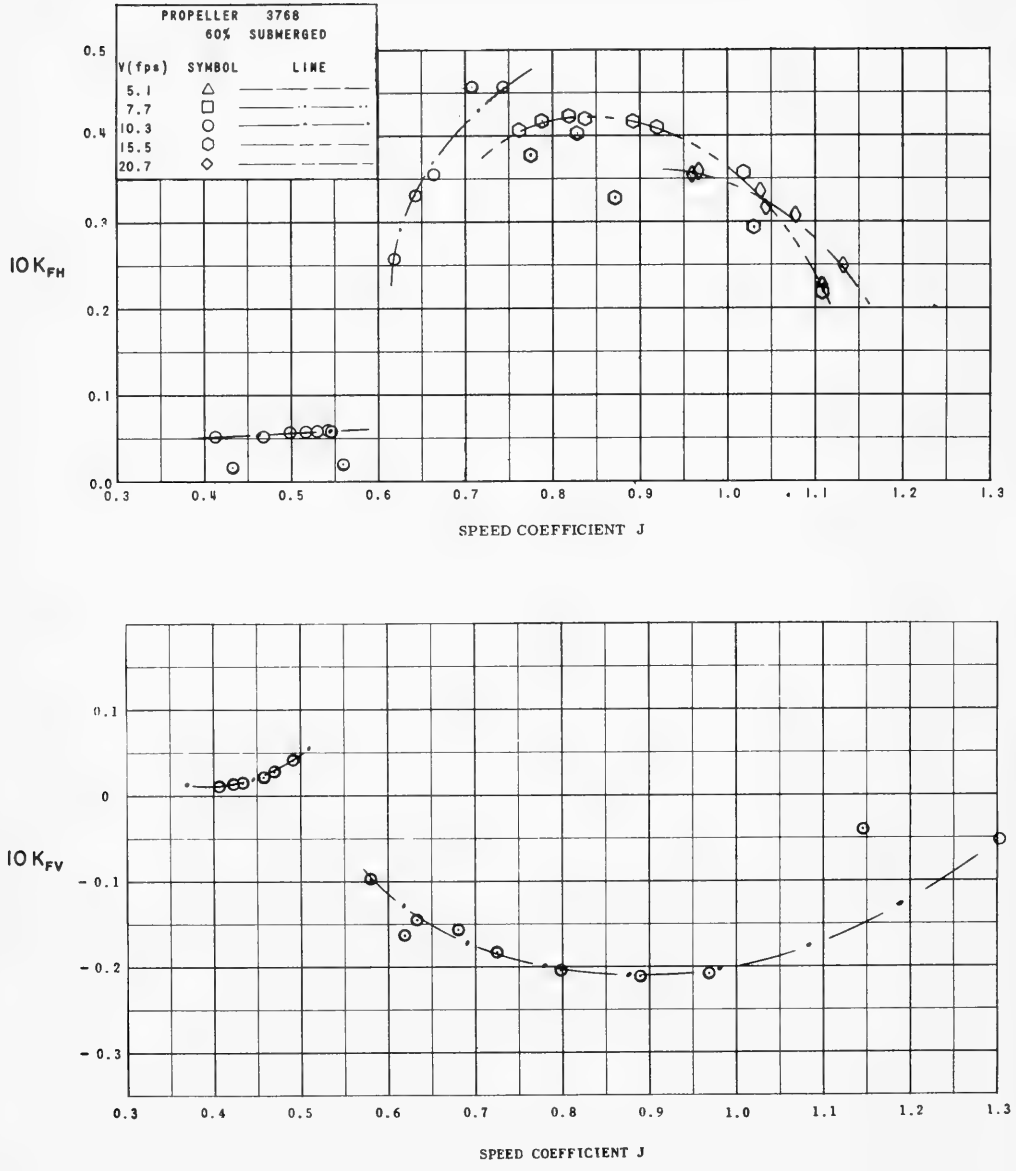

Fig. 18 - Transverse force coefficients of propeller 3768 60% submerged

It is common practice to present the results of open-water propeller tests in the K_T, K_Q, J system of coefficients. This system has limitations when comparisons of the performance of the propeller at different submergence levels or when comparisons with fully submerged operation are being attempted, either

fully wetted or cavitating. More effective comparisons can be made by presenting n_0 and J as a function of the thrust coefficient

$$C_T' = \frac{T}{(\rho/2)\ A_0'\ V^2},$$

where A_0' is the submerged disk area, V is velocity, and T is thrust. Figures 19 - 22 present the results of these comparisons. In Figs. 19 and 20 the results of the partially submerged tests are compared with the supercavitating tests of Propeller 3767 presented in Refs. [7] and [8]. Figure 23 shows the fully submerged data of Propeller 3767 over a range of cavitation numbers which may be compared to Fig. 21, showing the performance of the same propeller at three partially submerged conditions.

VISUAL OBSERVATIONS

Visual observation of the flow around Propeller 3768 indicates, at the high J values prior to transition, that the spray is relatively low to the water surface

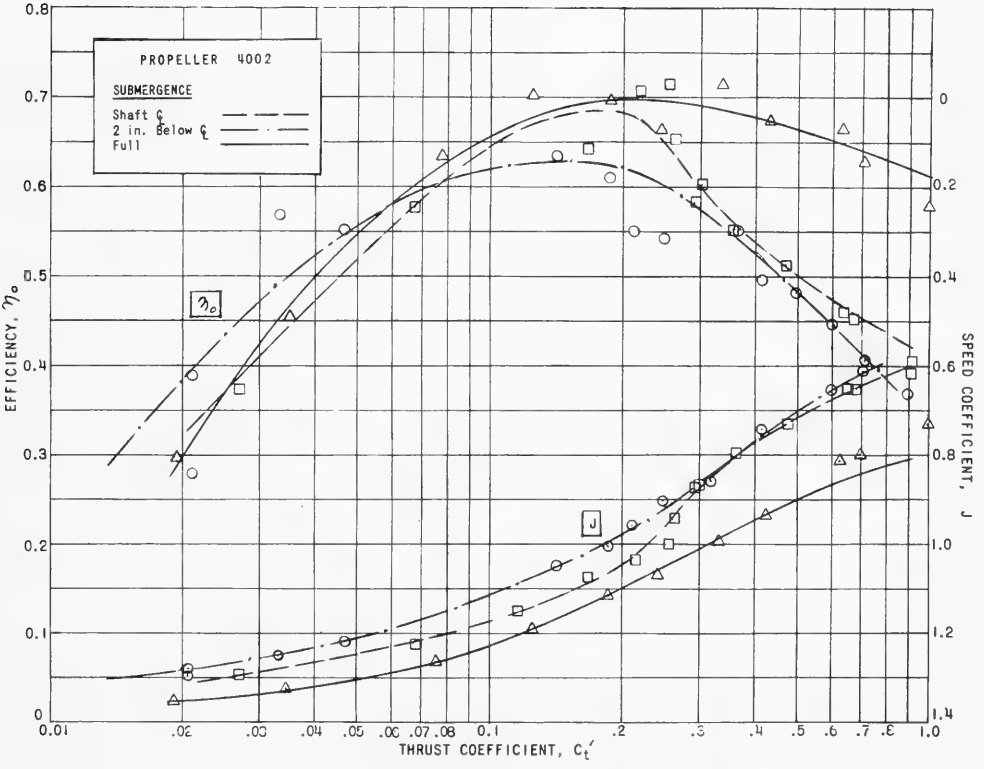

Fig. 19 - C_T' - η_0 - J diagram of propeller 4002 partially submerged

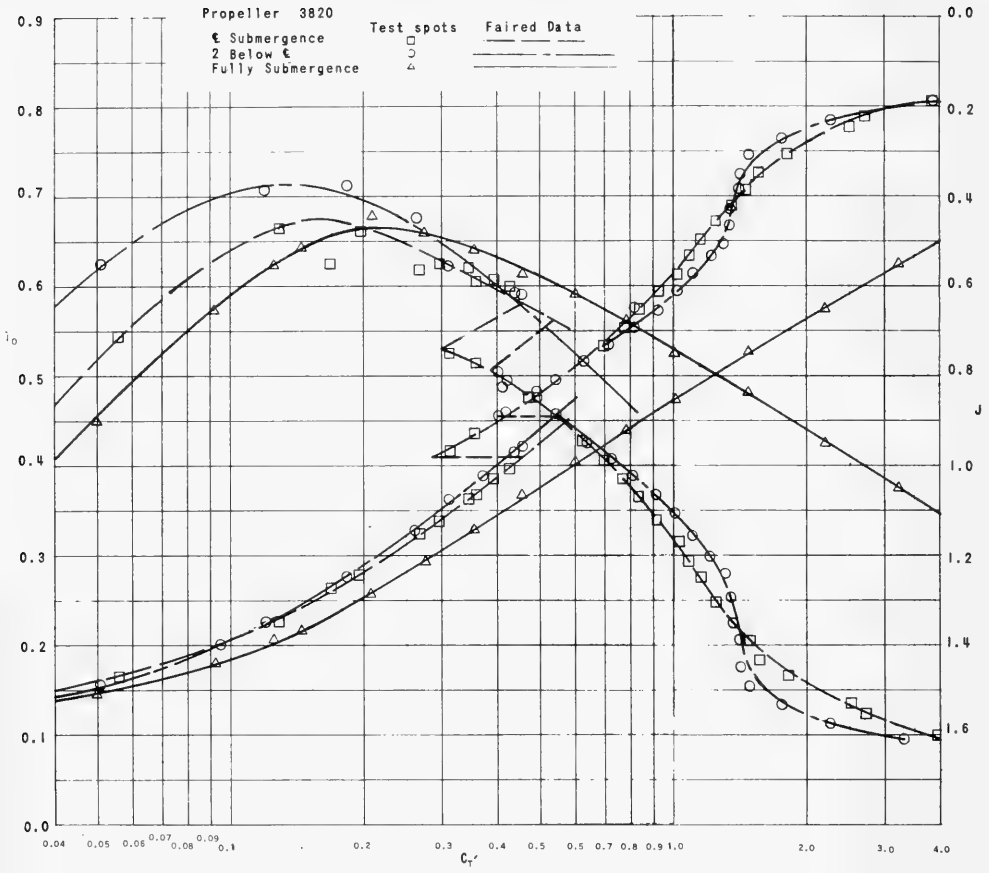

Fig. 20 - C_T' - η_0 - J diagram of propeller 3820 partially submerged

and comes largely from the exit side of the propeller. In this flow regime, as the advance coefficients were reduced toward the transition regime, there seemed to be a cavity starting from the leading edge on the suction face as the blade entered the water surface which became slightly larger as the advance coefficient was reduced. In this regime there did not appear to be any change of water-level flow into the propeller, except at the very lowest test speed of 5.18 ft/sec, where there appeared to be an actual lowering of the water surface — suggesting that there may have been a wave effect.

At transition there was a very marked change in the flow pattern. The spray became much more intense and extended considerably higher into the air. The intensification seemed to be most marked on the entry side of the propeller. It was noted on most tests that in the region of transition there was strong forced vibration of the propeller and propeller shaft.

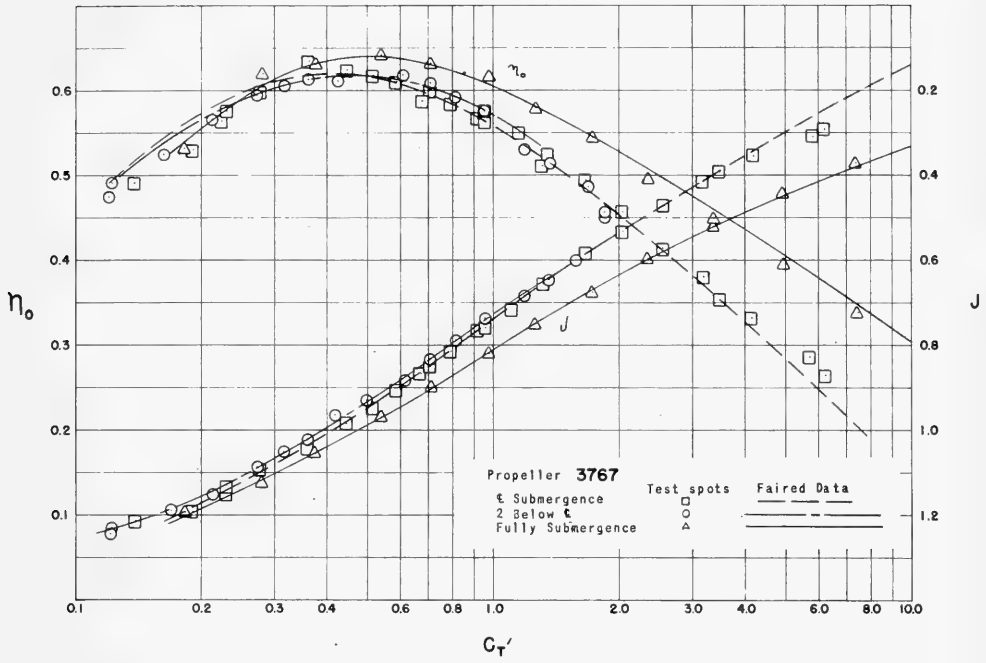

Fig. 21 - C_T' - η_0 - J diagram of propeller 3767 partially submerged

At the low advance coefficients, after transition, the flow pattern remained similar to that at transition, except that the amount of spray increased in quantity and amplitude as the advance coefficient was reduced. Forward of the propeller it was noted that the water surface increased in elevation, the amount varying inversely with the advance coefficient. At one point the increase just before entry into the propeller was more than 1 in., thus indicating a blockage of flow and a positive pressure field forward of the propeller. It was also noted that there was an extensive amount of spray extending forward of the propeller.

In conjunction with these observations a special test was made at 1-knot intervals from 1 to 9 knots, when the propeller rpm at transition was recorded. During the measurements it was noted that just as transition occurred there was a sudden increase in the rpm, which made it difficult to obtain a consistant value for the transition advance coefficient.

ANALYSIS OF PERFORMANCE

Before undertaking an interpretation of the test results for the guidance they can offer in predicting the performance of a partially submerged propeller, it is helpful to examine the flow regime around a supercavitating-type section under ventilated flow conditions. To assist there is a small but growing body of information on hydrofoils with ventilated flows of which Refs. [9] and [10] are most

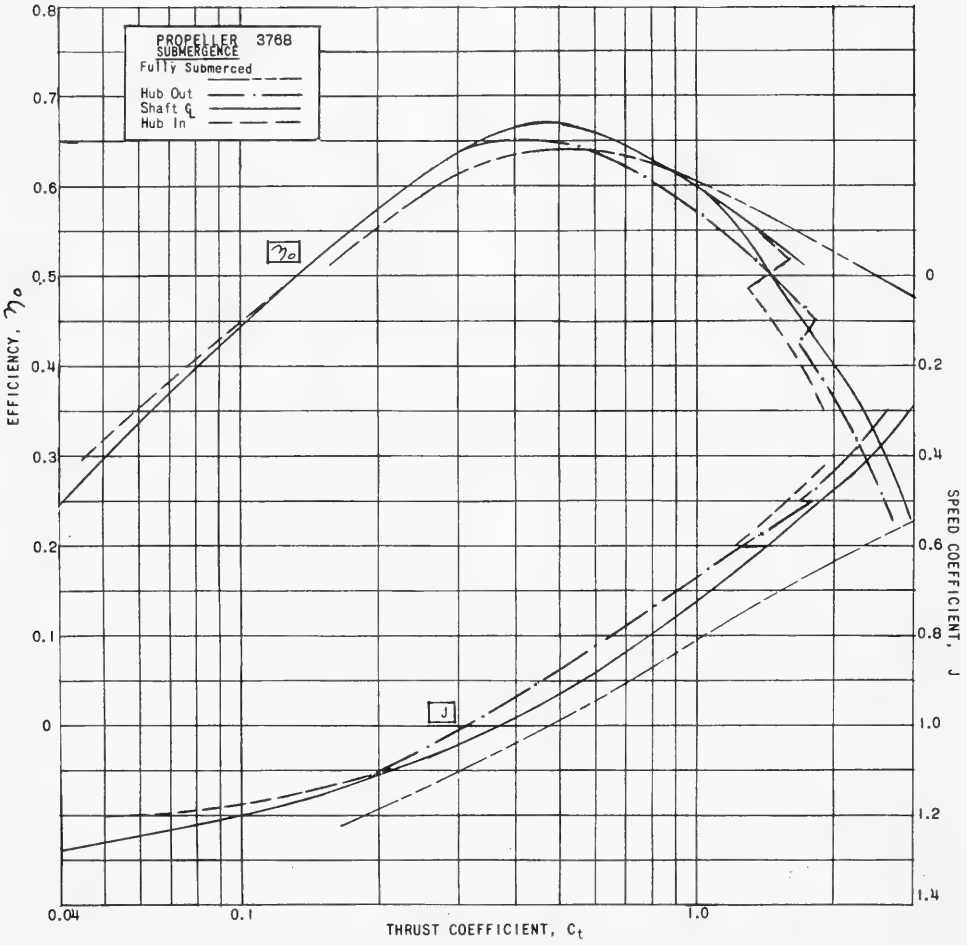

Fig. 22 - C_T' - η_0 - J diagram of propeller 3768 partially submerged

helpful. Three flow regions are distinguishable for surface ventilated foils as follows:

Base-Vented Region. In this regime the cavity springs from the blunt trailing edge of the foil and trails aft. At this condition the foil develops its approximate design lift. This is also the condition in which the foil develops its highest lift-to-drag ratio. If the foil has some reduction in thickness at the trailing edge the ventilation probably starts from a separation point near the point of maximum thickness.

Partially Cavitating Region. In this regime a vapor cavity of less than one chord length exists on the suction side of the foil. At this condition the foil force and moment coefficients are usually unsteady.

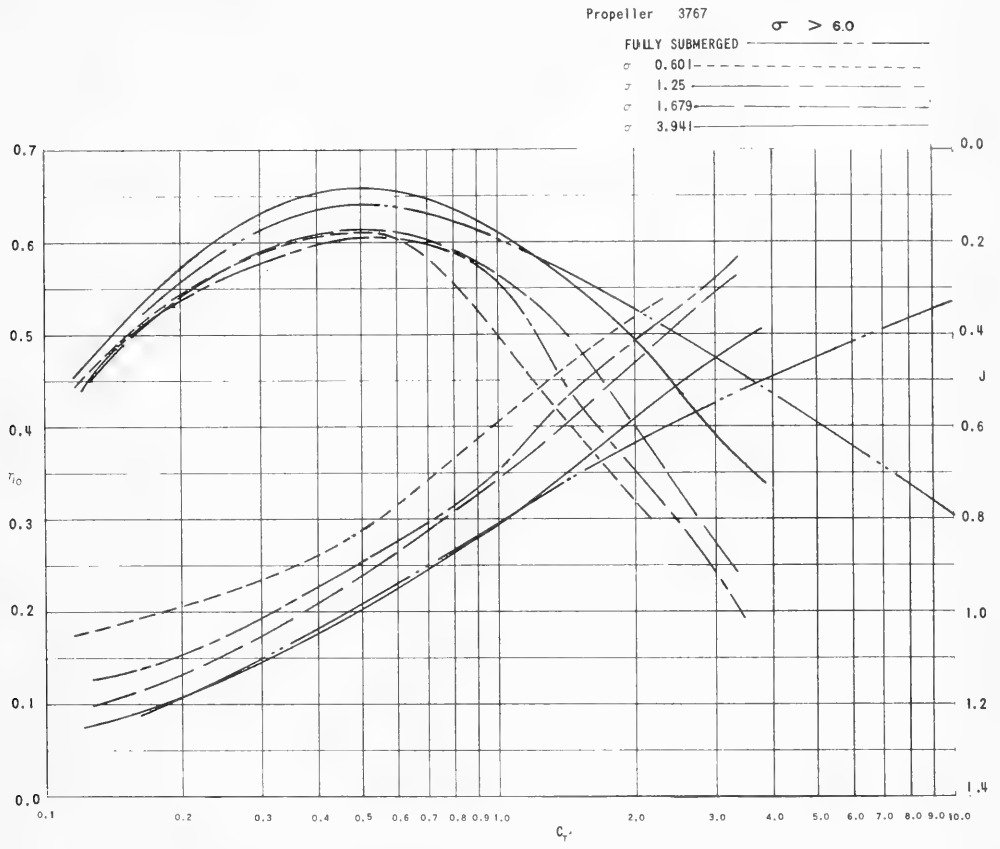

Fig. 23 - C_T' - η_0 - J diagram of propeller 3767 fully submerged

Fully Vented Region. In this regime a cavity greater than one chord length exists on the suction side starting from the leading edge, thus the suction side and the base of the foil are fully vented to atmospheric pressure. At this condition there is a drop in lift coefficient when compared to base-vented regions and a corresponding drop in lift-to-drag ratio.

The results of these flow regimes may be readily summarized on the following force diagrams as a function of angle of attack, Fig. 24. The forces are shown in the usual convention — lift and drag coefficients parallel and normal to the flow. The break in the lift curve is the transition point from the partially cavitating to the fully vented region. This transition is accompanied by violent oscillation in the forces identified as buffeting. The angle of attack where the transition takes place, as well as its magnitude, is a function of a number of variables, most of which are dependent upon the section geometry. Increasing the base thickness-to-chord ratio tends to increase the transition angle of attack and results in a larger shift in the lift coefficient. The details of the suction surface, particularly

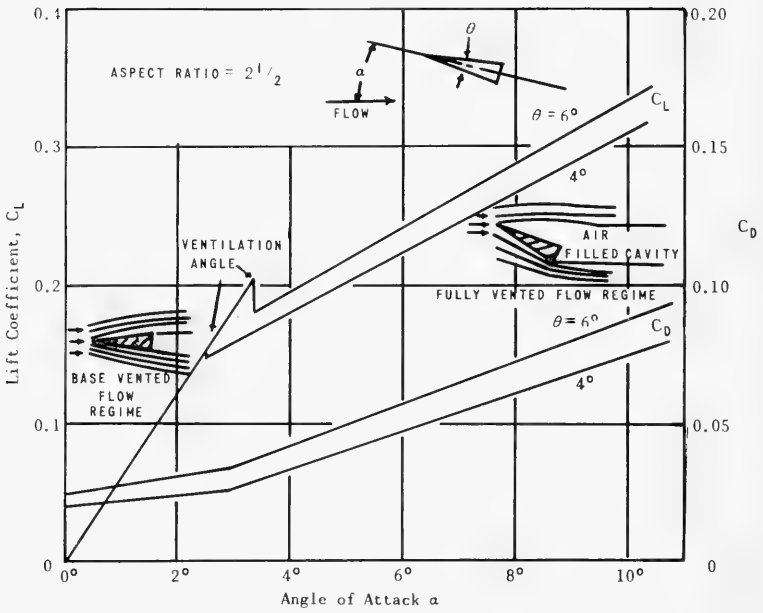

Fig. 24 - Lift and drag coefficients of wedges in various flow regimes

the leading edge, can have a marked effect. Flattening or blunting the leading edge reduces both the transition angle of attack and the magnitude of the shift of the lift coefficient. Reducing the hydrofoil-aspect ratio increases the transition angle of attack.

The absolute speed of a given hydrofoil also has a marked effect. Increasing speed tends to reduce the transition angle of attack and reduces the magnitude of the change in lift, even at a Reynolds number well above the laminar-turbulent transition region.

With this background we are now better able to analyze the action of the propellers tested. Figure 25 shows Propeller 3768 operating semisubmerged in the Hydronautics variable-pressure channel, Ref. [11]. The $J = 0.75$ condition is base-vented, whereas the $J = 0.35$ condition is fully vented. The differences in both the spray and cavity patterns may be noted for those two operating conditions.

The abrupt shifts in the K_T and K_Q coefficients noted on Propellers 3820 and 3768 are quite clearly the points at which transition occurs from base-vented to fully vented operation. As could be expected the efficiency drops when the sections become fully ventilated. The drop in lift-to-drag ratio accounts for this.

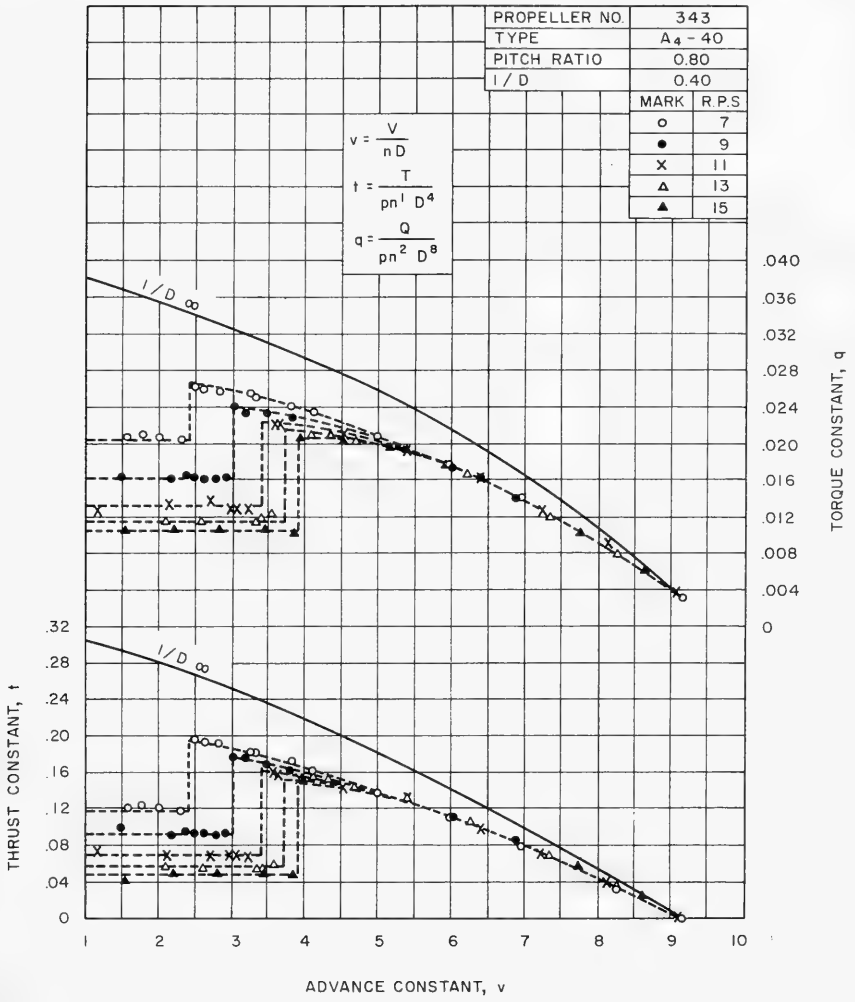

Fig. 25 - Performance characteristics of partially submerged propeller (Ref. 3)

The clear transition point noted on Propeller 3820 at relatively high advance ratio is a result of the greater thickness-to-chord ratio on this propeller. The difference in the J value at which transition occurred between the two submergences was probably due to the lower aspect ratio of the blade at the smaller submergence.

In presenting the K_T and K_Q results for Propeller 3768, a single curve has been faired through each of these quantities for all of the speeds tested except

for the lowest speed of 5.18 ft/sec. The low-speed test clearly shows a significantly larger torque coefficient and a small increase in the thrust coefficient in the base-vented flow regime. A close examination of the torque results indicates that there is a possible difference for each test speed but this is largely masked by the experimental scatter. An estimate of the propeller blade drag shows that the base drag is quite large for the low speed test due to the relatively low blade velocity, hence, the high torque values measured. Since the base drag coefficient decreases as a function of the local velocity squared, it becomes quite small at the highest test speed. This points to the importance on this type of propeller experimentation of scaling the section σ values.

A comparison between the K_T and K_Q versus J curves for propellers with airfoil sections shows marked difference from those with supercavitating-type sections. Figure 26 from Ref. [3] is typical. It may be noted that at the high advance coefficients the K_T and K_Q values are independent of test rpm but as J is reduced, the higher-rpm tests start to show a decrease; ultimately, there is the transition point where there is a large drop in K_T and K_Q, the magnitude of which is sensitive to the test rpm. To explain the differences we should know how ventilation develops on an airfoil-type section. At the higher advance coefficients the foil is at a low enough angle of attack that it is fully wetted, thus K_T and K_Q are independent of test speed. As the advance coefficient is reduced, a vented cavity probably forms from a point near the maximum thickness. Eventually the advance coefficient will be reduced to the point that a fully vented cavity forms from the leading edge. It is at this point that there is a rapid change in the lift, which results in the drop in the K_T and K_Q values. The large drop in lift observed on the airfoil section can be accounted for by noting that when a fully vented cavity develops on an airfoil section it acts as a supercavitating section with negative camber. Unpublished measurements of side forces on wedgelike and ogival surface-piercing struts show much more radial change in side-force coefficients for those struts with convex curvature on the pressure face. The preceding comparison points rather clearly to the desirability of using section shapes that do not result in convex curvature when operating fully vented and that have a minimum tendency towards cavitation inception at the leading edge.

COMPARISON OF TEST RESULTS

So that comparisons can be more easily made between the performance of the propeller at different test conditions, the system of n_0 and J versus C_T' have been used in Figs. 19-22. The thrust coefficient C_T' is based on the submerged-disk area. These curves rather clearly show that the maximum efficiencies in the partially submerged condition are comparable to those for the fully wetted condition. The lift-to-drag ratio of base-vented sections is greater than when fully wetted, but the blade entry and exit losses must reduce their efficiency to the point where they are comparable. It should also be noted that the range of C_T' value over which a given propeller can operate efficiently is much narrower than for the fully submerged condition. The extent of the operating range is comparable to that of the supercavitating propeller.

These curves, particularly those on Propellers 3767 and 3768 show that for the base-vented condition there is partial collapse of the data for the range of

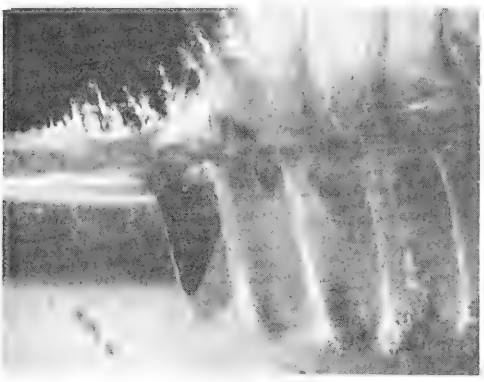

J = 0.75

Fig. 26 - Photographs of propeller 3768 partially submerged

submergence tested, and that for estimating purposes it would be possible to make a tentative prediction of the performance at any submergence based upon the results of tests at one submergence.

It was noted in comparing the efficiency curve of Propellers 3767 and 3768 at the semisubmerged condition that the efficiency of 3768 was somewhat higher. This was because the test speeds of 3767 were quite low; thus, the base drag of the blade sections was relatively high.

The collapse for the two tests conducted on Propeller 3820 is not as good but the region of greatest variation is the low C_T's where the small amount of data that exist are of questionable accuracy and where there is a fairly large base-drag component. The coincidences demonstrated from Propellers 3767, 3768, and 3820 do not hold for 4002. It may be noted that the test data are

considerably more scattered. Because this is a two-bladed propeller, the unsteady forces are quite large. At the smaller submergence the thrust will vary from nearly zero to the maximum developable by one blade.

The results of the cavitation tests in a variable pressure water tunnel on Propeller 3767, Ref. [7], have been presented on the same type of diagram, Fig. 22, for purposes of comparison with partially submerged operation, Fig. 21. As may be noted in Fig. 22, the curves change their character with decreasing σ, indicating in particular a reduction in the favorable operating range of thrust coefficient. The only region of comparability between cavitating and partially submerged operation is when full ventilation has occurred for the latter. In this region the n and J values are somewhat similar to those of the cavitating propeller when operating at low σ values.

ANALYSIS OF TRANSVERSE FORCES AND THRUST ECCENTRICITY

The fully submerged propeller, when operating in a uniform flow field, develops a net thrust and torque which acts at the axis of rotation. If the propeller operates in an asymmetric flow field, the forces no longer occur at the exact center of rotation nor do they appear as a simple steady force (thrust) and moment (torque). Usually these asymmetries in the flow are not large enough to be of concern as far as the thrust eccentricity and transverse forces are concerned. This is no longer possible in the case of the partially submerged propeller, which may be viewed as a limiting case of asymmetry in the flow field, i.e., a step-function velocity field which is symmetrical about a vertical plane through the propeller axis.

Before undertaking an analysis of the results of the measurements of the side force and the thrust eccentricity, it is helpful to examine the force on the propeller as it enters and exits through the air-water interface. There is a modest amount of literature derived from seaplane dynamics and hydroballistics on the air-water entry of bodies and more recently on water exit of missiles. The most applicable literature is that derived from seaplane dynamics, which is concerned with impact forces of wedgelike bodies. The work was intended for the deadrise angle of seaplane floats rather than the knife-edge shapes of propellers; however, extensions have been made using the same assumptions as for the larger vertex angles, Ref. [12].

There are three phases recognized in the air-water entry of a rigid body, Ref. [13], which might be considered applicable to a propeller blade; sequentially these are as follows:

Shock Phase. This regime covers the initial, extremely brief period of water contact where compressibility is the important effect. Since this phase lasts only microseconds, and the leading edge of the blade is "sharp," the pressure is localized on an extremely small area; thus, any imposed drag force on the blade is probably negligible.

Flow-Forming Phase. In this regime the water around the blade is set into motion, and the entry cavity is initiated. It is during this phase that there is a

considerable exchange of energy taking place which can give rise to large impulse forces. On a partially submerged propeller the time duration of the impulse force can be relatively large when considered in relation to the time of one revolution. For the root sections of Propeller 3768 when operating in a semisubmerged condition, the impulse phase lasts as long as one-fourth of a revolution, and its duration is approximately one-third of the time the blade is in the water. Even at the 0.7 radius the duration is more than 20% of the time the blade is in the water.

Open-Cavity Phase. This phase occurs when the blade proceeds beyond the flow-forming phase, and an open cavity grows outward from the region of flow separation, either base-vented or fully vented, depending upon the advance coefficient of the propeller. This phase is the dominant regime of the propeller action and has been discussed in the previous section on performance.

Considerably less knowledge exists on the water-exit regime of rigid bodies such as missiles, which geometrically are far from similar to a rotating propeller blade. It is known from this work that the amount of entrained water exiting with the body is equivalent to 7 - 12% of the body volume. This tends to reduce the vertical force on the propeller. This is also the source of much of the spray generated by the propeller when operating in the base-vented regime.

We can now examine the results of the measurements made of thrust eccentricity and transverse force on Propeller 3768 as shown in Figs. 13 - 18. The test results for horizontal thrust eccentricity e_h show that the center of thrust in the base-vented condition is a small distance, less than 5% of the propeller diameter to the right, or starboard, for a right-hand-turning screw; whereas for the fully vented condition it is almost the same amount to the left, or port. This implies for the base-vented condition that more blade lift is developed on the entry half of the revolution, while for the fully vented condition more blade lift is developed on the exit half of the revolution.

The vertical position of the center of thrust is obviously a function of submergence of the propeller, the less the submergence the larger the eccentricity e_v. The most marked effect is in the magnitude of the shift between base-vented and fully vented operation. The implication of these results is that there is a very large shift of the center of loading towards the root in the change from base-vented to fully vented operation. The reason for this is not clear.

The results of the transverse-force measurements, Figs. 16 - 18, show significant vertical force as well as the expected strong horizontal force. As noted before there is a marked difference in the magnitude of these forces for the two flow regimes, the base-vented condition producing the larger forces. The horizontal force coefficient for the fully vented condition appears to be independent of the test speed. Just the opposite is true for the base-vented condition, where the force coefficient varies significantly with test speed. This is not unexpected, as both the base and viscous components of the blade drag decrease with increasing speed. It would be expected that smaller differences would have been obtained at the higher test speeds. This again points to the necessity for proper modeling of the section σ if successful predictions are to be made.

The vertical force coefficient for the base-vented regime is dependent upon both test speed and submergences. The force is upward, implying that the impact forces are significant and that more blade lift is developed during the entry half of the revolution than during the exit half. This is consistent with the thrust-eccentricity measurements.

The vertical force coefficient for the fully vented condition, just as for the horizontal force coefficient, appears to be independent of test speed. It also appears to be independent of depth of submergence. In this regime the net force is downward, implying that more blade lift is being developed on the exit half of the revolution and that this net force is greater than the impact force upon entry. This again is consistent with the thrust-eccentricity measurements, where the center of thrust is located in the exit half of the propeller disk.

The generation of the spray upon blade entry and exit represents a loss of energy to the system. It would be expected that this would have a significant effect upon the efficiency of the propeller. It is probable that these losses account, in the case of Propeller 3768, for the gains made in the L/D ratio when operating in a base-vented as compared to the fully wetted condition; hence the reason for the comparable efficiencies when being operated as either a fully wetted or a partially submerged propeller.

SCALING

The dominant scaling problem is associated with maintaining the proper value on the propeller blade sections to ensure achieving similarity of flow. Since the cavities are vented to the atmosphere at all times, with the possible exception of a small leading-edge vapor cavity just before transition from base-vented to fully vented flow, the static pressure is equal to the atmospheric pressure. The pressure differential is

$$\Delta\rho = \gamma h \ ,$$

where γ is the density of water, and h is the depth of water at the propeller blade section; thus

$$\sigma_h = \frac{\Delta\rho}{\frac{1}{2}\rho U^2} = \frac{\gamma h}{\frac{1}{2}\rho V^2\left[1 + \left(\frac{\pi x}{J}\right)^2\right]} \ ,$$

where U is the inflow velocity to the propeller-blade section. This relationship can also be expressed in terms of a depth Froude number:

$$\sigma_h = \frac{2}{F_h^{\,2}} \ ,$$

where $F_h = U/gh$. Since σ_h is a function of Froude number, the condition for similarity of flow is that the speed of advance of the model and full-scale propellers should be in accordance with the Froude law of comparison; thus

$$n_m = n_s \lambda^{1/2}$$

and

$$V_m = \frac{V_s}{\lambda^{1/2}} ,$$

where λ is the linear ratio of full-scale to model propeller.

In the open-water testing of fully submerged propellers it is not necessary to observe the Froude law of comparison; hence, the practice of running these tests at constant rpm just high enough to achieve an adequate local Reynolds number to ensure turbulent flow (usually greater than 5×10^5 at the 0.7 radius).

It would appear from these tests that the same minimum-Reynolds-number requirements will have to be maintained for the open-water testing of partially submerged propellers. In addition there is the requirement of σ (or Froude) scaling. Fortunately, the base drag coefficient decreases as the square of the velocity; thus, there must be some σ value beyond which any further increase in test speed is unwarranted. Some of the low advance coefficient data at the higher test speeds in this series has σ_h values, based upon tip velocity, of less than 0.005 (root section σ values were considerably larger). The good collapse of test results in this region adds support to such a suggestion.

The advance coefficient of transition from base-vented to fully vented operation is also subject to σ scaling as demonstrated by the speed dependency shown in Table 3. These results along with the transition value obtained from the tests have been plotted as a function of σ_h, based upon the propeller-tip velocity in Fig. 27. Above and to the right of the line is the base-vented region, and below and to the left is the fully vented region. An extrapolation of these results to a lower σ value would indicate that there is a probable maximum J value at which transition would occur. If σ is one of the dominant scaling laws then it would be expected that geosims would provide a comparable curve. At this writing a similar test has not yet been made on Propeller 3767 to check the validity of this hypothesis.

Assuming that this is the proper relationship for scaling transition, the results of the lowest test spots from Propeller 3767 are shown in this same figure; hence, it becomes apparent why transition was not achieved on the tests on this propeller.

SUMMARY

As stated in the introduction, the results of these experiments tended to raise as many questions as they answered. It must also be remembered that the experiments represent the results of only three propellers, all with similar-type sections and all with a small number of blades; hence, the conclusions should be construed as tentative, pending a wider base of experimental and theoretical knowledge.

Summarized below are the major findings from these experiments.

Table 3
Tabulation of Transition Advance Coefficients
for Propeller 3768

Speed (knots)	J for 40% Submergence	J for 50% Submergence
1.0	Unattainable	Unattainable
2.0	0.267	0.363
3.0	0.365	0.486
4.0	0.452	0.525
5.0	0.534	0.564
6.0	0.541	0.613
7.0	0.566	0.635
8.0	0.598	0.667
9.0	0.610	0.668

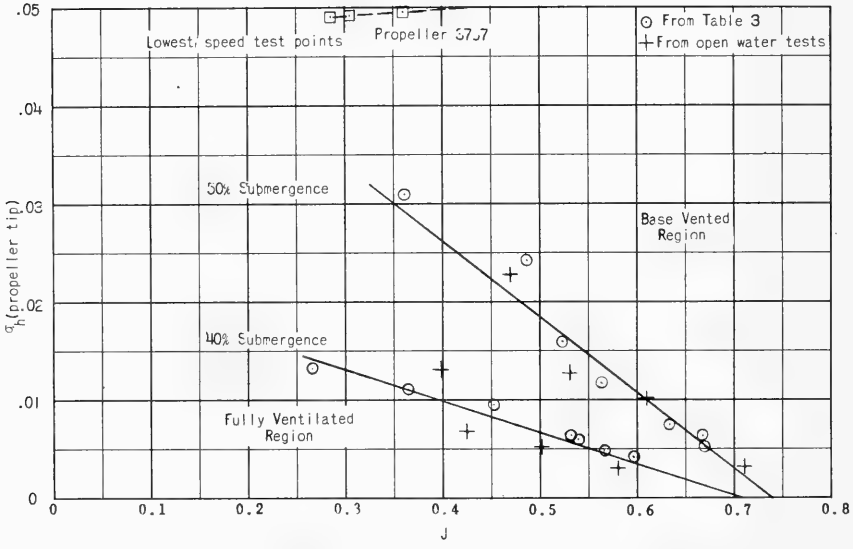

Fig. 27 - Transition curves for propeller 3768

1. There are two flow regimes in which the propeller operates, one where the blades are base-vented, and the other where the blades are fully vented with the cavity springing from the leading edge.

2. The propeller has inherently a higher efficiency in the base-vented regime because of the higher L/D ratio of the blades.

3. The advance ratio at which the propeller changes from fully vented to base-vented flow is subject to scale effects.

4. During the period that the propeller blade is entering the water, impact forces are developed which contribute to the vertical force generated by the propeller and, in the fully vented regime, contribute significantly to the generation of the spray.

5. During the period that the propeller blade is exiting, entrained water is carried into the atmosphere, creating much of the spray, particularly for the base-vented regime and contributing a downward component to the vertical force.

6. Propulsive efficiencies in partially submerged operation comparable to fully submerged noncavitating operation can be achieved, in spite of the losses mentioned in 4 and 5 above.

7. The partially submerged propeller has a narrower range of thrust loadings over which it can operate efficiently than it does when operating fully submerged.

8. It appears for the base-vented condition, at least within engineering needs, that the results of tests at various depths of submergence can be normalized on a thrust coefficient, C_T', which is based upon submerged area.

9. The center of thrust is near the vertical center plane of the propeller shifting from the starboard side to the port side for a right-hand-turning propeller when the flow changes from base-vented to fully vented.

10. The vertical center of thrust is reduced significantly when the flow changes from base-vented to fully vented.

11. The vertical component of the transverse force is upward for the base-vented regime shifting to downward in the fully vented regime.

12. The horizontal component of the transverse force is to starboard for a right-hand-turning propeller and the force coefficient is much larger in magnitude for the base-vented than for the fully vented regime.

13. The appearance and intensity of the spray pattern changes significantly when the flow changes from base-vented to fully vented.

14. The supercavitating-type section shows a much smaller drop in thrust than does a propeller with airfoil section when operating fully vented.

15. The condition for similarity of cavity flow pattern on ventilated partially submerged propellers requires that the speed of advance of the model full-scale propeller should be in accordance with Froude's law of comparison.

RECOMMENDATIONS

The results of the experiments presented in this paper are only the beginning of a long chain of research which must be accomplished before this type of propeller can be applied to high-speed high-performance vehicles. Some of the most important of these are listed below.

1. Scaling of the point of transition from base to fully vented flows must be examined and a method for prediction developed.

2. High-speed photographs should be taken of the flow at the suction side of the leading edge of the blade as it enters the water in both base-vented and fully vented operating conditions to help guide the development of the theory.

3. Develop theory for the force and moments on a propeller blade as it enters and emerges from the air-water interface.

4. Measure the time history of lift, drag, and moment on an individual blade, so that we can better understand the forces experienced by the blade and the results can be used to check theory.

5. Develop a rational hydrodynamic theory for designing this type of propeller comparable to that for propellers operating fully submerged.

6. Examine the vibratory forces produced by a propeller which is experiencing both cyclic loading and unloading and impact force upon water entry.

7. Blade strength and fatigue must be investigated for their effect upon performance.

8. Details of blade section shape should be investigated to obtain sections of adequate strength which will have minimum drag under base-vented condition, reduced magnitude of drop in lift coefficient when fully vented, and will produce minimum impact force when entering the water.

9. The explanation for the large radial shift in center of loading towards the root when the propeller changes from base-vented to fully vented should be ascertained.

10. It is necessary to be able to predict the pressure field ahead of the propeller in both of its two operating modes so that interaction forces with the vehicle can be estimated.

ACKNOWLEDGMENTS

The authors wish to record their appreciation for the valuable assistance rendered by F. W. Puryear, C. E. Shields, and D. E. Crown for their participation in the experimental work and to D. E. Crown and J. G. Peck for their assistance in preparing the graphs and curves. We also wish to express our appreciation to the Technical Directorate, particularly, Dr. W. E. Cummins, Head of the Hydromechanics Laboratory, for its support. Grateful thanks are due to Mrs. L. Greenbaum for the careful preparation of the manuscript.

Appendix A
MEASUREMENT OF TRANSVERSE FORCES

DESCRIPTION

As previously discussed in this paper, propellers which operate partly out of the water cause the effective center of thrust to be applied below the shaft centerline. The imbalance of the torque force results in a transverse force in the plane of the propeller. In order to determine the resultant force and moment, a four-component dynamometer was designed and built. The four components were the horizontal and vertical components of the resultant moment and the horizontal and vertical components of the transverse force.

In principle, the dynamometer acts as a cantilever beam of hollow cross section with a concentrated load at the free end. Two reduced-area sections, designated Plane A and Plane B, are strain gaged. The strain gages are wired into 4 four-arm Wheatstone bridges. Each bridge is wired so that it reacts to the bending moment at a given plane in a given direction. For example the vertical moment at Plane A is proportional to the signal produced by a Wheatstone bridge where one side (two legs) measures the strains in the top of the flexure while the other two legs measure the strains in the lower sides of the flexures. Hence, the output is the difference between a compressive and a tensile force in the material. Figure A1 shows a schematic of the dynamometer, and Fig. A2 shows the dynamometer assembly and the strain-gage wiring diagram.

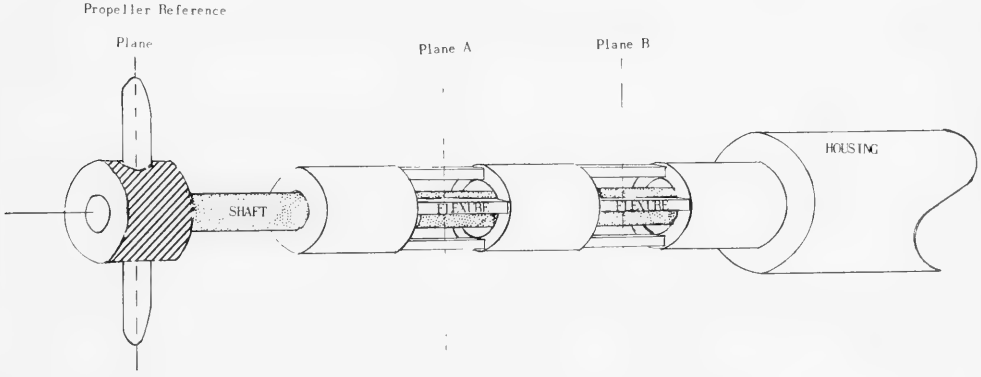

Fig. A1 - Schematic diagram of four-component dynamometer

PRINCIPLE OF OPERATION

Consider a coordinate system where the shaft is coincident with the x axis, the positive y axis is vertically upward, and the positive x axis is horizontally

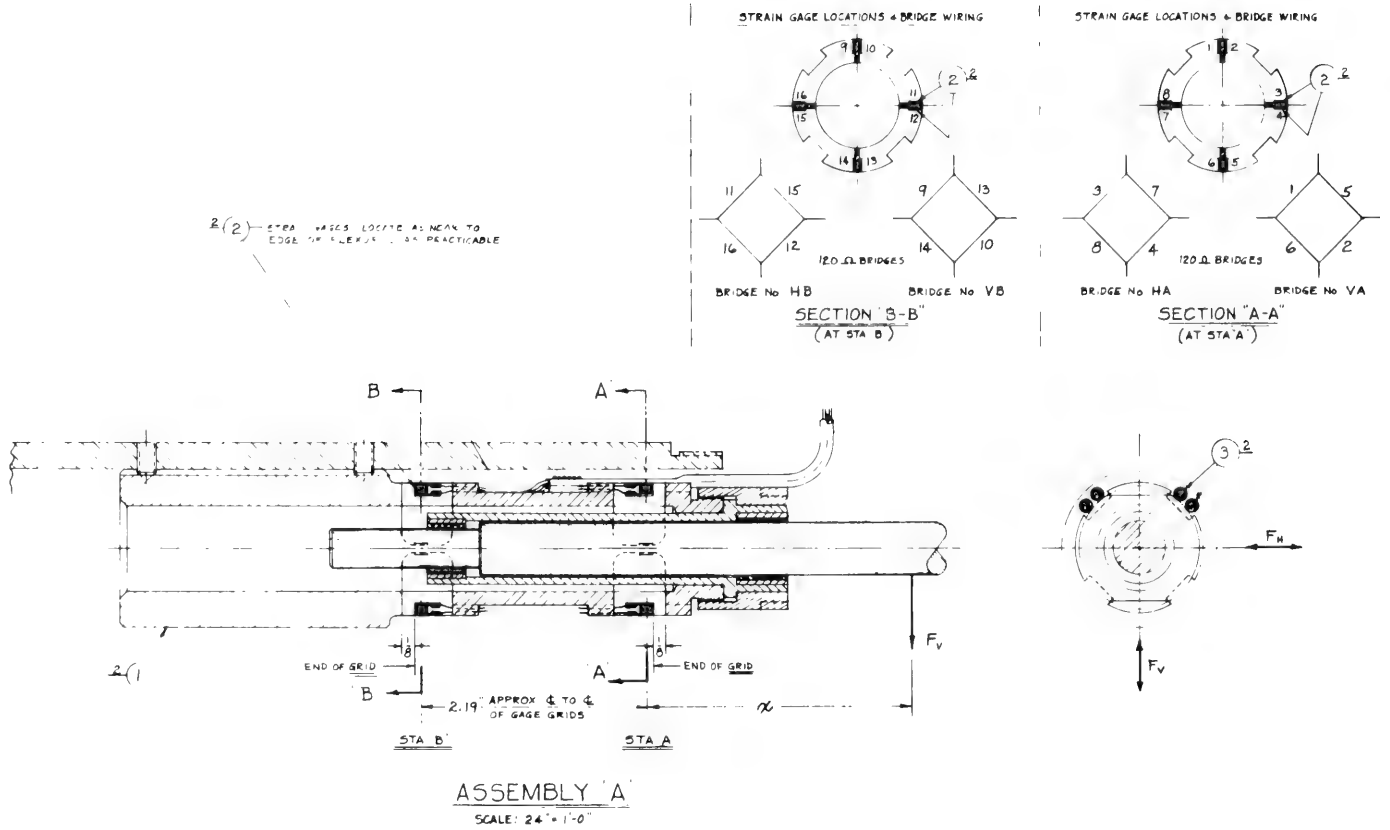

Fig. A2 - Dynamometer assembly

to the right, facing forward. The origin is at the intersection of the shaft axis with the transverse propeller plane. The coordinate system is shown in the upper part of Fig. A3. Arrowheads indicate the positive x, y, and z directions. Also included for reference are the positive direction of rotation n and speed v for a right-hand propeller.

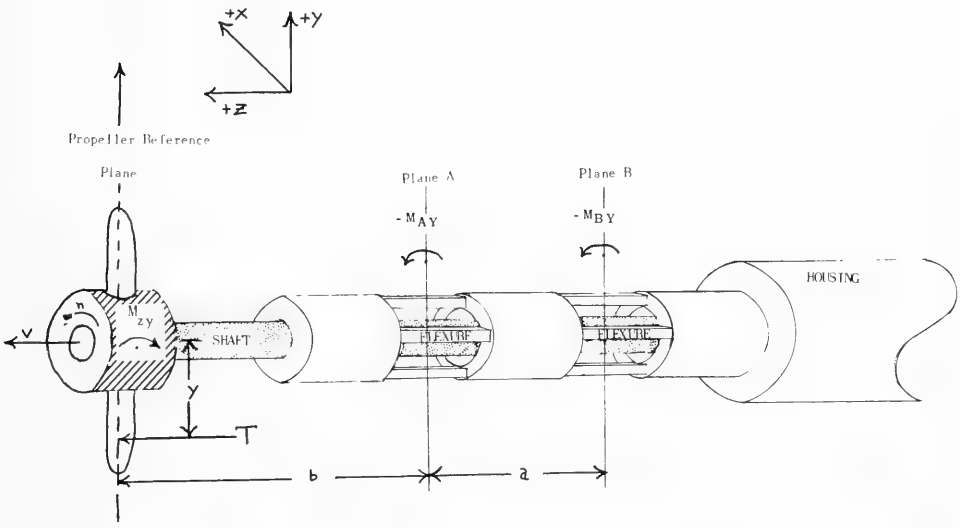

Fig. A3 - Coordinate system and force diagram

Eccentric application of the thrust force T at a distance y below the shaft produces a moment $M = Ty$. This moment can be represented by a pure moment in the vertical plane ($Z = 0$), M_{zy} and a vertical force F_v applied to the shaft in the same transverse reference plane, see Fig. A3. Resisting moments are generated at Plane A and Plane B, respectively:

$$- M_{AY} = M_{ZY} - F_v\, b \ ,$$

$$- M_{BY} = M_{ZY} - F_v\, b - F_v\, a \ .$$

From these relationships, the force F_v is

$$F_v = (M_{BY} - M_{AY})/a$$

and the moment M_{Zy} is

$$- M_{ZY} = [(a+b)\, M_{AY} - b\, M_{BY}]/a \ .$$

Similarly, the horizontal force and moment coefficients are

$$F_H = (M_{BX} - M_{AX})/a,$$

$$- M_{ZX} = [(a + b) M_{AX} - b M_{BY}]/a.$$

If the moments are divided by the thrust, the x and y distances to the point of application are obtained. These distances are nondimensionalized with respect to the propeller diameter, thus

$$e_h = M_{ZX}/T.D.,$$

$$e_v = M_{ZY}/T.D.$$

CALIBRATION PROCEDURE

From the foregoing description it is seen that the force and moment in either the vertical or horizontal plane can be computed if the moments in Planes A and B are known. Hence, the calibration procedure must relate these moments to the output of the strain-gage bridge circuits. The calibrations involve two steps, first, the exact axial location of each strain gage must be established, and, second, the slope of the calibration curve is established.

Establishing the center of the strain-gage grids was done by mounting a calibrating arm on the shaft with the short leg in the plane of the propeller and the long leg extending back past Planes A and B (see Fig. A4).

With the calibrating arm in place, but no additional weight, the two gages in the same transverse plane (either horizontal or vertical) are zeroed. A nominal force, or weight (5 lb.) is then imposed on the long leg of the calibrating arm. The weight is then moved toward Plane A until the output of the A gage is zero. This location is then marked as the center of the gage grid at Plane A. The output of gage B is also recorded.

Plane B is then established by moving the weight until the output of gage B is zero. The location of Plane B is then marked, and the output of gage A is recorded.

Note 1. If the outputs of gages A and B are not identical, the gage sensitivity is adjusted until the outputs are the same. This may require going through the above procedure two or three times.

Note 2. The same procedure is then followed for the horizontal gages but the weight is hung from a "frictionless" pulley.

The described procedure has established the dimension as indicated in Fig. A2. For this dynamometer, a = 2.19 in. Dimension b is then measured from Plane A to the point of application of the transverse force. For the calibration this was 2.62 in.

The actual calibrations are then performed by applying a known force (weight) at a given point simultaneously with a pure moment. The force and moments are varied independently. Outputs of all four gages are recorded as various weights are imposed on the systems. The same range of weights is then calibrated with different moments to assure that there are no coupling effects. A typical calibration curve is shown as Fig. A5. The line has a slope which is the arithmetic average of the data over the range of interest. The error of any reading is within 1.5%; hence, data acquisition with this dynamometer is considered to be about 3%.

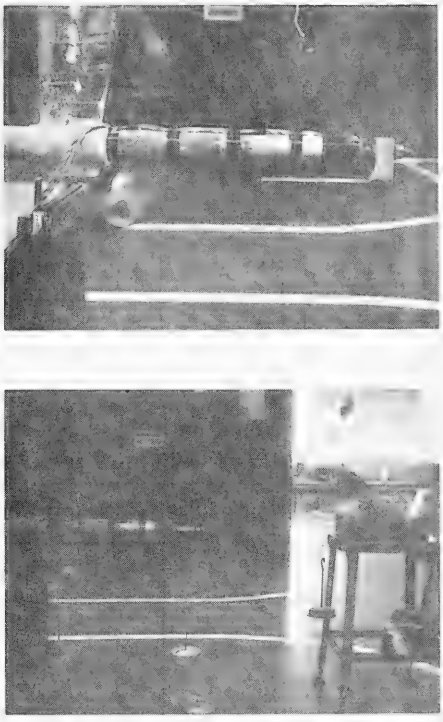

Fig. A4 - Photograph of dynamometer calibrations

Since the dimension b enters into the calculation of the moment, it is necessary to establish the point of application of the transverse forces in the plane of the propeller. For Propeller 3768 the design reference plane, located at the mid-chord length, was used (b = 3.31 in.). The center of lift on the blade varies depending upon the flow regime. A check on the error introduced by inaccuracy in determination of the magnitude of b shows that if the error was as large as 1.0 in. there would be less than 1% error introduced into the determination of the eccentricity.

NOMENCLATURE

A	Area
A_0	Disc area ($\pi D^2/4$)
A_0'	Submerged disc area
B_{TF}	Blade thickness fraction
C_D	Drag coefficient $\left(D_F/\frac{1}{2}\rho AV^2\right)$
C_L	Lift coefficient $\left(L/\frac{1}{2}\rho AV^2\right)$
C_T	Loading coefficient $\left(T/\frac{1}{2}\rho A_0V^2\right)$
C_T'	Loading coefficient $\left(T/\frac{1}{2}\rho A_0'V^2\right)$

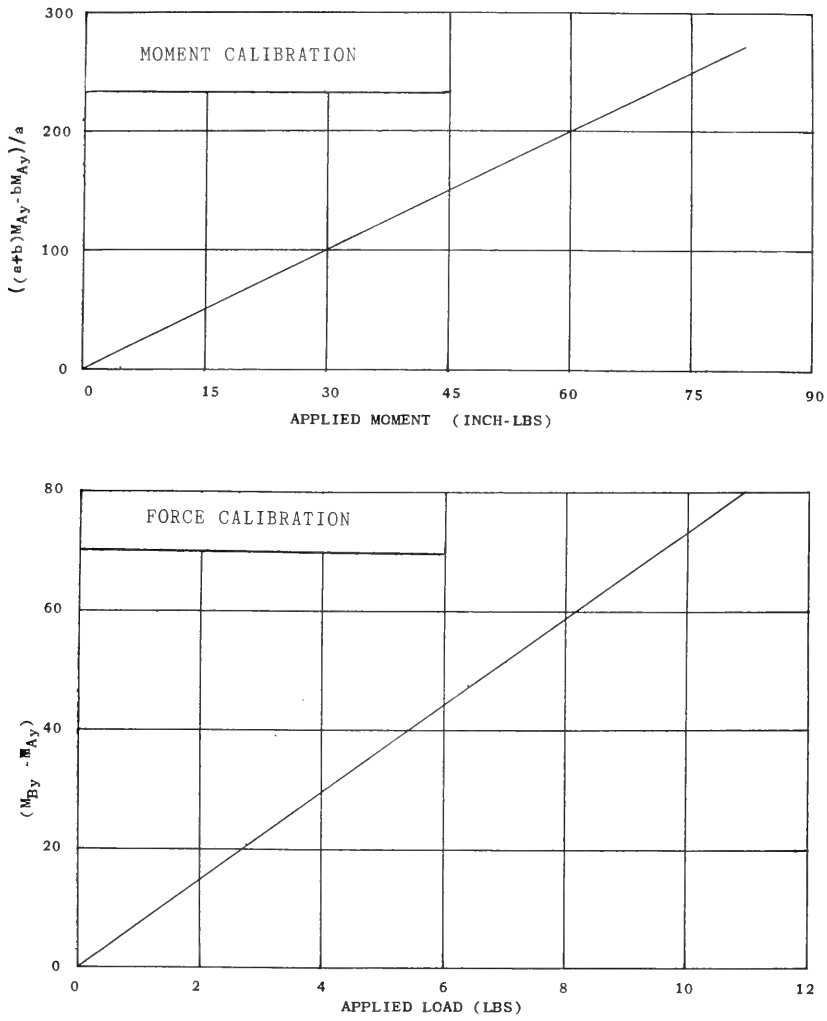

Fig. A5 - Typical calibrations

$c_{0.7}$ Chord length at 70% R

c Chord

D Propeller diameter

D_F Drag

E_{AR} Expanded-Area ratio

e_h	Horizontal thrust eccentricity/diameter
e_v	Vertical thrust eccentricity/diameter
F_H	Transverse horizontal force
F_V	Transverse vertical force
F_h	Depth Froude Number $(U/\sqrt{ghE})$
g	Acceleration due to gravity
h	Depth of submergence of a propeller blade section
J	Advance coefficient (V/nD)
K_{F_H}	Horizontal force coefficient $(F_H/\rho n^2D^4)$
K_{F_V}	Vertical force coefficient $(F_V/\rho n^2D^4)$
K_Q	Torque coefficient $(Q/\rho n^2D^5)$
K_T	Thrust coefficient $(T/\rho n^2D^4)$
L	Lift
L/D_F	Lift-Drag ratio
M_H	Moment in horizontal plane
M_V	Moment in vertical plane
n	Revolutions per unit time
P/D	Pitch-Diameter ratio
Q	Torque
R	Propeller radius $(D/2)$
R_n	Reynolds number $(V_{0.7}\ c_{0.7}/\nu)$
T	Thrust
U	Inflow velocity to blade section = $V[1 + (\pi x/J)^2]^{1/2}$
V	Velocity
x	Nondimensional propeller radius
z	Number of blades

γ	Density
η_0	Propeller efficiency in open water $(TV/2\pi Qn)$
λ	Linear ratio of full-scale to model propeller
ν	Kinematic viscosity
ρ	Mass density
σ	Cavitation number
σ_h	Local blade cavitation number based upon h

Subscripts

m	Model
s	Ship

REFERENCES

1. "Tests of Partially Submerged Propellers of the Sea-Sled Type," U.S. Experimental Model Basin Report R-132, April 1919

2. Reynolds, Osborne, "On the Effect of Immersion on Screw Propellers," Transactions Institute of Naval Architecture, 1874

3. Shiba, H., "Air-Drawing of Marine Propellers," Transportation Technical Research Institute, Japan — undated

4. Gutsche, F., "Einflub der Tauchung auf Schub und Wirkungsgrad von Schiffspropellern," Schiffbauforschung, Vol. 6, No. 516, 1967, pp. 256 - 277

5. Yegorov, I.T., and Sadovnikov, Y.M., "Effect of Instability on Hydrodynamic Characteristics of a Propeller Cutting the Water Surface," Sudostroyenige No. 1 (1961), pp. 15 - 17

6. Cheng, H.M., Hadler, J.B., Bernaertz, J., and Bader, J., "Analysis of Right-Angle Drive Propulsion System," Diamond Jubilee SNAME, June 1968

7. Hecker, R., Peck, J.G., and McDonald, N.A., "Experimental Performance of TMB Supercavitating Propellers," DTMB Report 1432, Jan. 1964

8. Venning, E., and Haberman, W.L., "Supercavitating Propeller Performance," Trans. SNAME Vol. 70, 1962

9. Dobay, G.F., "Hydrofoils Designed for Surface Ventilation -- An Experimental Analysis," SNAME, May 1965

10. Hoerner, S.F., "Fluid Dynamic Drag," published by the author, Midland Park, N.J., 1965

11. Lindenmuth, W.T., and Barr, R.A., "Study of the Performance of a Partially Submerged Propeller," Hydronautics Incorporated Technical Report 760-1, July 1967

12. Ward, L.W., "Methods for Estimating Impact Forces on Ship Appendages," Davidson Laboratory Report No. 616, Dec. 1956

13. Burt, F.S., "New Contributions to Hydroballistics," Advances in Hydroscience, Vol. 1, 1964

* * *

DISCUSSION

H. Volpick
Brown Bros. & Co. Ltd.
Edinburgh, Scotland

In the historical introduction of this very interesting paper, the authors have remarked on the use of partially submerged propellers years ago on rivers and lakes. As a former member of the Denny Ship Model Basin in Dumbarton (Scotland), which was liquidated in 1963 -- at least in name -- with the entire firm of Denny, I should like to mention that already in the 1920's ship propulsion of this type for specific river application in India and Burma was evolved by Denny. After extensive model tests, the first experimental vessel, the Meccano, was built, and full-scale experiments were continued. One of the first commercial vessels, the Chuchow, of about 100-ft length had two large, slightly submerged propellers, or "vane wheels" as they were called, at the stern, turning at about 60 rpm through a gearbox. Before this vessel was finally shipped out East, further extensive tests were carried out on the River Clyde at different immersions of the vane wheels, which were four-bladed, of large area, and with ordinary circular back sections. These trials showed that the predictions from the model tests were reasonable, and that the optimum propulsive efficiency coincided with an immersion coefficient (i.e., immersion of wheel/diameter) of between 0.30 and 0.35 falling off rapidly with higher immersion, due to increased drag. This peak efficiency was over 0.45, which did not compare unfavorably with the figure of 0.50 - 0.55 for customary paddle propulsion.

The largest vessel of this type built by Denny was the M. V. Stanley, a river cargo vessel which operated from 1929 onward on the Congo river. With the advent of high-speed Diesels and directly coupled, fast-turning, small, fully immersed propellers, vane-wheel propulsion went out of use. However, the

Denny Ship Model Basin was going to reactivate this system for a specific proposal for India in 1963 and commence a new series of experiments in the light of modern propeller design, when the firm's liquidation put an end to this proposed program.

* * *

DISCUSSION

S. G. Bindel
Bassin d'Essais des Carenes
Paris, France

When the submergence of a propeller is not sufficiently large, a ventilation may occur when the ship is stopping, since the rotation of the propeller is reversed while the motion of the ship is still forward. This ventilation leads to a decrease of the thrust, and thus to an increase in the stopping length. It is speculated that this unfavorable effect may also be severe on the partially submerged propeller.

I should like to ask Mr. Hadler if tests were carried out to investigate these unusual working conditions.

* * *

DISCUSSION

C. Kruppa
Technische Universität
Berlin, Germany

I would like to congratulate the authors on the presentation of a paper that undoubtedly will have to be looked upon as the first piece of fundamental information on the performance of partially submerged high-speed propellers. I think we all are aware of the fact that partially submerged propellers have been used for some time in racing craft and record-breakers, and have performed more or less successfully, due largely, no doubt, to the reduction of appendage drag. However, nobody has so far been able to quote efficiencies or account, on a rational basis, for possible advantages that this type of propulsion device may offer under certain circumstances.

The authors have already outlined what they think should be done in the future on a theoretical basis and experimentally, in order to arrive at a better understanding of the hydrodynamic phenomena in partially submerged propellers and to derive the basis for a design method, if possible. To their 10 recommendations for future investigations, however, I would like to add a further one, which

is concerned with the number of blades in partially submerged propellers. Although this aspect is directly linked to the question of vibratory output in partially submerged propellers, I think there is a strong need for testing partially submerged propellers with larger numbers of blades than commonly in use in fully submerged propellers. In fact, I am quite certain that in more sophisticated installations the partially submerged propellers will only stand a chance, from the vibration point of view, if the number of blades is sufficiently high.

I would like to ask the authors whether they share this point of view.

Finally, I would like to mention that at Berlin Technical University an experimental investigation into the performance of partially submerged propellers will be carried out in the near future. The tests will be conducted in the free-surface cavitation tunnel of the cavitation laboratory. All together, 8 propellers will be tested in the first phase of the program, among them propellers of the Newton-Rader series that have successfully been used for fully submerged propellers in the fully cavitating mode, but do not make use of blunt trailing edges. It is planned to extend the program eventually to measuring the fluctuating forces on individual blades and to investigate possible advantages of skew-back. The paper presented by the authors provides extremely valuable guidance for this work.

* * *

DISCUSSION

K. Suhrbier
Vosper Ltd.
Portsmouth, England

The authors presented an interesting and stimulating paper, which contains very useful information on this subject.

We have recently carried out some limited experiments with three supercavitating propellers on a race boat (described in the panel discussion on Planing Craft by Cdr. Du Cane). All propellers were designed for the same boat and had about the same characteristics in the fully submerged condition; they were:

1. a wedge-type SC propeller (P. Rolla, Switzerland), designed for semi-submerged condition;

2. a wedge type SC propeller, designed for fully submerged condition;

3. a Newton-Rader SC propeller (modified airfoil section), designed for fully immersed condition.

In the semisubmerged mode, good performance could be achieved with the first two propellers; the hump was no problem — in particular with Propeller 1,

which also gave by far the best overall performance. However, with the third propeller it was not possible to get on the plane (i.e., over the resistance hump), although this type has proved to be very successful in normal applications on many planing craft.

As already stated by the authors, the blade shape is very important and our experience seems to confirm that airfoil-type sections are not suitable for this working condition. For race boats, where the propeller is more deeply immersed at lower speeds, the vertical forces generated by the propeller have probably also some effect on the overall performance (trim).

From some tests with Propeller 3 in the Vosper Cavitation Tunnel, run with free surface at atmospheric pressure, the fully ventilated condition could be studied at low advance coefficients to simulate the acceleration phase in the hump region. The cavities were so large that hardly any water could be accelerated; only very small thrust (and torque) was measured.

* * *

REPLY TO DISCUSSION

J. B. Hadler and R. Hecker

Mr. Volpich has added significantly to the historical aspects of this paper. It should be noted that Mr. Volpich's comments pertain to the low-speed shallow-draft application of this type of propeller, where little or no ventilation occurs on the blade.

Captain Bindel requested performance information for the backing condition with the ship going forward. To our knowledge no work has been done in this area as yet. It certainly must be investigated before engineering application can be made on an operating vehicle.

Professor Kruppa's remarks pertain largely to possible vibration problems on partially submerged propellers. Our paper was concerned primarily with steady-state performance, and thus we have not treated the problem of vibratory forces. We most certainly would agree with Professor Kruppa that significantly increasing the number of blades offers one of the best means for reducing the vibratory forces to an acceptable level. To this end we are conducting ongoing research on an eight-bladed propeller to establish the effects of high number of blades upon performance both steady-state as well as vibratory.

Mr. Suhrbier notes the difference in performance at low advance coefficients for similar propellers with different types of blade sections. His experiences help point out the fact that little is known about interference effects of the cavities between propeller blades, particularly at low advance coefficients. We must obtain considerably more knowledge in this area if successful designs are to be achieved for the propulsion of sophisticated, high-performance craft which have a marked resistance hump to traverse in the process of achieving their design speeds.

* * *

OSCILLATING-BLADED PROPELLERS

S. Bindel
Bassin d'Essais des Carènes
Paris, France

SUMMARY

Due to the inclination of shaft on the flow coming along the hull, the angle of attack of the sections of a propeller blade is variable with the position of the blade. The performances in cavitation are reduced especially for the sections near the hub.

In order to decrease these drawbacks, it is proposed to oscillate the blades at the frequency of rotation of the shaft.

The results obtained in cavitation for one propeller model do not seem as promising as expected; however, further experiments are required in order to form a valuable estimate of this type of propeller.

SYMBOLS

D	Diameter of the propeller
$J = V/n\,D$	Advance ratio of the propeller
n	Number of revolutions of the propeller
R	Radius of the propeller
r	Radius of a blade element
r_H	Radius of the hub
x	Reduced radius of a blade element
x_H	Reduced radius of the hub
u_a, u_t	Induced velocities
V	Velocity of the flow
V_t	Transverse component of the flow velocity
W	Amplitude of the transverse flow variations

α_1, α_2	Maximum variations of the angle of attack
γ	Oscillation amplitude
θ	Inclination of the flow on the propeller shaft
φ	Longitude of a blade element
ψ	Phase of the oscillation relative to the incidence variation
σ	Cavitation parameter (based on the velocity V).

INTRODUCTION

The flow coming to a ship propeller is often inclined on the shaft, particularly in the case of multiscrew fast ships such as destroyers or torpedo boats. As a consequence, the relative flow is unsteady, even if the wake of the hull is uniform, with the corresponding drawbacks: vibrations and premature cavitation.

There may also be severe erosion near the propeller hub. In some cases it is possible to prevent this erosion by modifying the shape of the blade sections [1], but in other cases this procedure seems to be insufficient [2].

Thus, among the solutions that may be considered, one consists in adjusting the pitch of each blade to the local conditions encountered, so that the variations of the relative flow become as small as possible: this would constitute an oscillating-bladed propeller. This solution may be also considered for a propeller operating in the wake of the hull (the case of a single-screw ship, for example), but the law of pitch variation is here generally less simple.

It was initially planned to evaluate this idea by experiments on several propeller models, but, due to a lack of time, it was not possible to test more than one model. The present paper gives the results of this experiment and the tentative conclusions that can be drawn concerning oscillating-bladed propellers.

VARIATION OF THE INCIDENCE ON THE BLADE ELEMENT DUE TO THE INCLINATION OF THE SHAFT

Let V be the velocity of the flow and θ the angle of inclination of the flow on the propeller shaft (Fig. 1). The axial flow component is then $V \cos \theta$ and the transverse component $V \sin \theta$.

Assume that the hub is an infinite cylinder of radius r_H; the transverse flow is then the well-known two-dimensional potential flow around a circle (at least out of the viscous wake of the shaft). At a given point of radius r and longitude φ (the angle between the radius and the velocity at infinity), the component of the relative velocity normal to the radius (the transverse component V_t) is given by the formula:

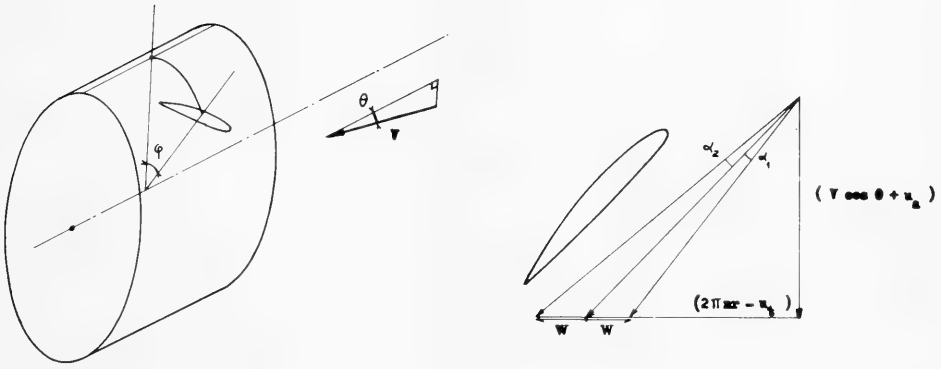

a b

Fig. 1 - Definitions

$$V_t = V \left[1 + \left(\frac{r_H}{r}\right)^2\right] \sin\theta \sin\varphi .$$

The variations of V_t with φ are sinusoidal. For a noninfinite hub, a correcting factor of 1/2 may be applied [3] and the tangential component of the velocity be written as:

$$V_t = V \left[1 + \frac{1}{2} \left(\frac{r_H}{r}\right)^2\right] \sin\theta \sin\varphi = W \sin\varphi .$$

This tangential component is to be added to the relative velocity due to the rotation of the propeller n in order to have the angle of attack of the blade element during its rotation. Supposing that the induced velocities (u_a, u_t) are constant, the maximum variations α_1 and α_2 of the angle of attack are then given by:

$$\operatorname{tg}\alpha = \operatorname{tg}\theta \frac{1 + \frac{1}{2}\left(\frac{x_H}{x}\right)^2}{1 + \frac{\pi x}{J \cos\theta}\left\{\frac{\pi x}{J \cos\theta} \pm \operatorname{tg}\theta \left[1 + \frac{1}{2}\left(\frac{x_H}{x}\right)^2\right]\right\}}$$

(with the sign - for α_1 and + for α_2). Here $x = r/R$ is the reduced radius ($R = D/2$ is the radius of the propeller), x_H is the reduced hub radius and $J = V/nD$ the advance ratio of the propeller. Figures 2a through 2d give the variations of α_1 and α_2 for two values of x_H and two values of θ.

For a given J, α_1 and α_2 decrease rapidly with x, i.e., the sections near the hub are more subject to premature cavitation than the outer sections of the

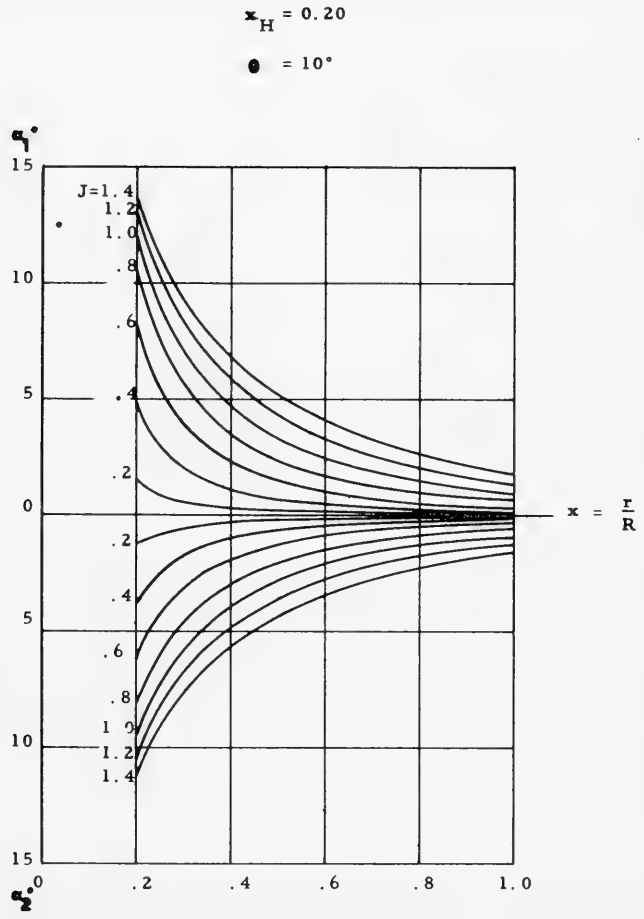

Fig. 2a - Variation of incidence on the blade element due to shaft inclination, $x_H = 0.20$ and $\theta = 10°$ (supposing $u_a = u_t = 0$)

blade. This is in accordance with common experience; however, it must be noted that for consideration of strength, the thickness ratio of the sections near the hub is larger and therefore less sensitive to incidence variations than the sections farther from the axis.

The incidence variations increase with J, i.e., large-pitch propellers are more sensitive to the phenomenon involved than low-pitch propellers. The incidence variations increase also, of course, with θ. It is thus normal that fast ships, such as torpedo boats for example, which have generally large-pitch propellers and for which θ is also large are the ships suffering the most severe erosion near the hub (for this type of ship, θ is approximately the angle between the shaft and the hull; it may be of the order of 15°).

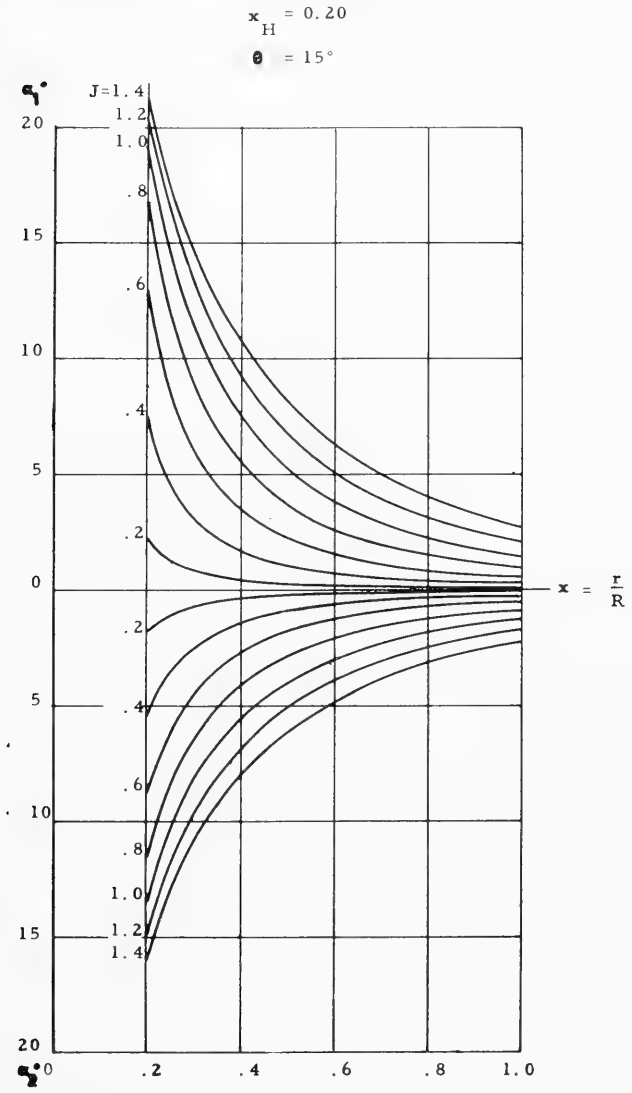

Fig. 2b - Variation of incidence on the blade element due to shaft inclination, $x_H = 0.20$ and $\theta = 15°$ (supposing $u_a = u_t = 0$)

It must be noted that the calculations made above do not take into account the length of the sections. In fact, if this length is not small relative to the "wavelength" $2\pi r$, a sophisticated theoretical approach can take into account not only the mean incidence at each position of the blade but also the camber of the relative flow. In addition, the variations of the induced velocities u_a and u_t are probably not negligible.

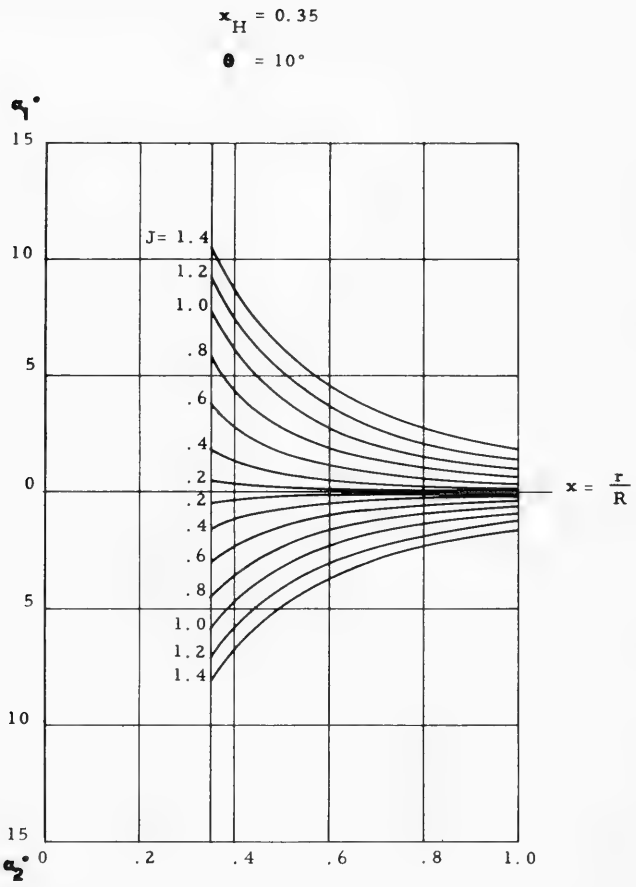

Fig. 2c - Variation of incidence on the blade element due to shaft inclination, $x_H = 0.35$ and $\theta = 10°$ (supposing $u_a = u_t = 0$)

THE OSCILLATING-BLADED PROPELLER

The principle of this system is simple: each blade is oscillated separately, the angle of oscillation being a function of the position of the blade, determined to avoid or delay the type of cavitation considered as the most dangerous — in the present case the cavitation near the hub.

But the problems to be solved are not simple. First, as shown above, the variations of the incidence due to the inclination of the shaft are not sinusoidal if θ is finite: α_1 is larger than α_2. However, from a practical point of view, it is sufficient to adopt for the oscillation a sinusoidal law which is simpler to apply.

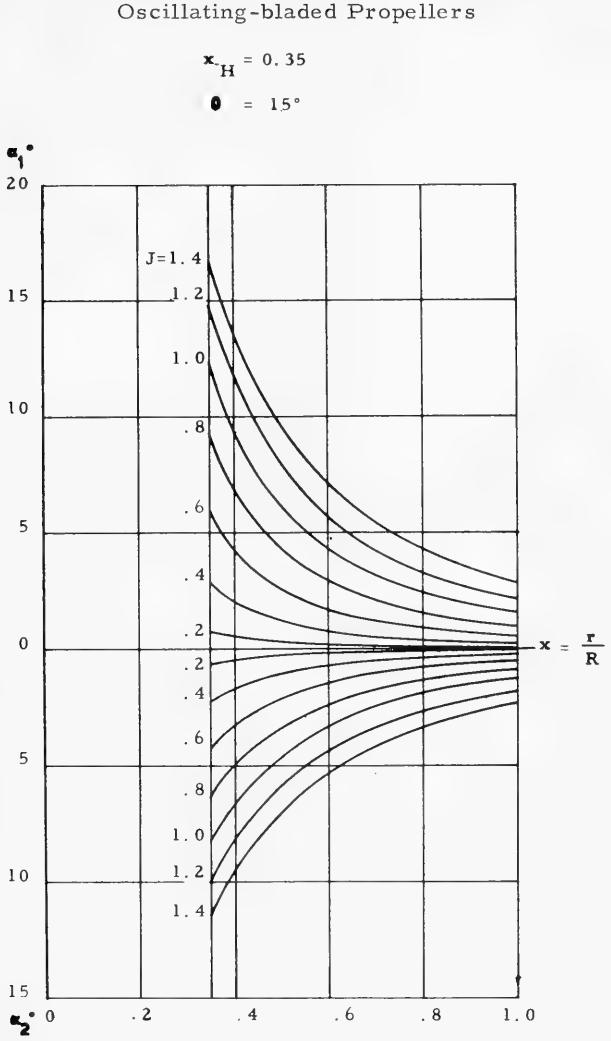

Fig. 2d - Variation of incidence on the blade element due to shaft inclination, $x_H = 0.35$ and $\theta = 15°$ (supposing $u_a = u_t = 0$)

Second, the variations of the incidence due to the inclination of the shaft are not constant with the radius of the section, but the oscillation of the blade is necessarily the same for all the sections. This leads to a difficult problem. If the amplitude of the oscillation is small (for example equal to the amplitude of the incidence variation at the tip), the resultant incidence on all the sections is reduced, but, due to the very important difference between the hub and tip sections, the incidence near the hub remains too large. On the other hand, if the amplitude of the oscillation is large, a favorable effect may be expected as regards the cavitation near the hub, but the incidence variations near the tip are

reversed and have a greater amplitude than without oscillation of the blades, thus leading to increased drawbacks. Finally, the choice of the amplitude γ is a compromise resulting from the estimation of the various dangers encountered by the propeller.

Third, as stated above, if the length of the sections is not negligible (which is generally the case for the propellers concerned), the sections are sensitive not only to the mean incidence of the flow but also to its camber, i.e., to the incidence of the flow along all the sections. In particular, it is not evident that the oscillation of the blade ought to be in phase with the variation of the flow incidence at the mean station of the section.

Regarding the application, the oscillating-bladed propellers raise some problems which it is not our purpose to deal with in this paper. However, we shall notice that the hub diameter ratio is necessarily larger than in the case of fixed-bladed propellers, due to the necessity of housing the oscillation mechanism system. Likewise, the shape of the blade root will resemble that of the controllable pitch.

CONDITIONS OF THE EXPERIMENTS

Initially, it was planned to test several propellers of different types, but, due to a lack of time, it was unfortunately not possible to test more than one propeller.

This propeller, number 2133, a photograph of which is given in Fig. 3, is the propeller of an escort vessel. It was chosen because it was originally a controllable-pitch propeller, although its nominal pitch was not high. Its characteristics are the following:

- Number of blades: 4
- Hub diameter ratio: 0.345
- Blade area ratio: 0.628
- Effective pitch in nominal conditions: 0.89
- Diameter of the model: 0.200.

It was tested in the cavitation tunnel of Bassin d'Essais des Carènes under the following conditions:

- Inclination θ of the shaft: 10° and 15°
- Amplitude of oscillation γ of the blades: 0 and ±3°
- Phase ψ of the oscillation relative to the incidence variation at the mean line of the blade: 0 and +30° (oscillation in advance)
- Speed of the flow in the tunnel: 3 m/sec
- Air-content ratio of the water at atmospheric pressure: 0.3.

For each condition of inclination of the shaft, and of amplitude and phase of the oscillation, visual observations were made first in order to determine the curves (σ versus J, where σ is the cavitation parameter based on the velocity V) of inception of the different types of cavitation encountered, and secondly,

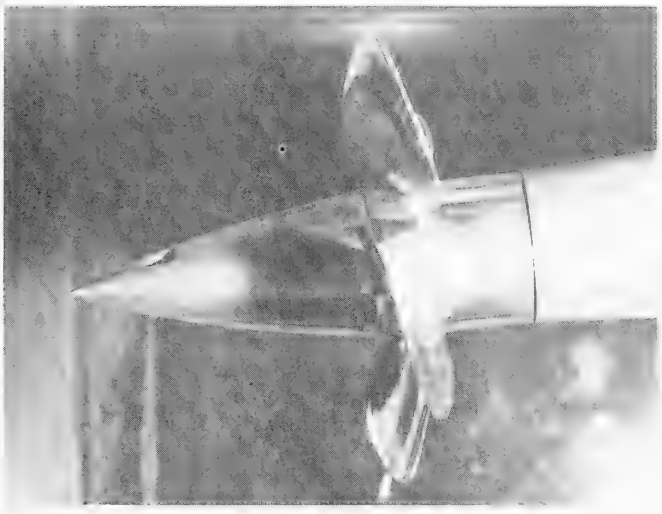

Fig. 3 - Fitting of propeller 2133
in the cavitation tunnel

to determine the cavitation patterns for given values of J and σ. At this effect, three values of J were selected: J = 0.65, corresponding to normal conditions of loading; J = 0.50 and J = 0.75, corresponding to overloaded and underloaded conditions.

EXPERIMENTAL RESULTS

Fixed-Bladed Propeller (γ = 0)

Types of Cavitation Observed — Figures 5a through 8a, and Fig. 10a show the cavitation patterns for different values of θ, J, and σ. According to the value of J, six different types of cavitation can be observed:

1. Bubbles on the back near the hub
2. Bubbles on the back for $x > 0.6$ at the inception
3. Sheet on the leading edge prolonged by a tip vortex
4. Tip vortex
5. Hub vortex
6. Sheet on the face leading edge near the hub.

Figures 4a and 9a give the inception curves (σ versus J) for θ = 10° and 15° respectively.

Influence of the Longitude φ — As expected from the analysis made in the section on variation of incidence on the blade element due to inclination of the shaft, the longitude has a considerable influence on the back and face cavitations.

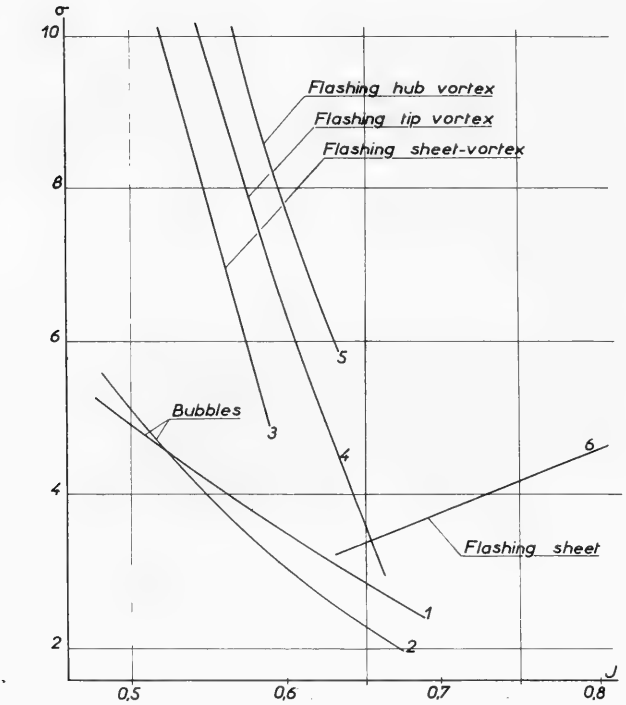

Fig. 4a - Cavitation inception curves for fixed-bladed propeller, $\theta = 10°$

The back cavitation is more developed when the blade is going down ($0 < \varphi < 180°$), especially the bubble cavitation near the hub, the tip vortex cavitation depending only slightly on φ. Conversely, the face cavitation is more developed when the blade is going up ($180° < \varphi < 360°$).

Influence of the Inclination of the Shaft – The cavitation patterns are similar for $\theta = 10°$ and 15°, as can be seen from the comparison between Figs. 7a and 10a. This is the reason for which the pattern schemes relative to $\theta = 15°$ were limited to one figure.

As expected, the cavitation appears earlier for $\theta = 15°$ than for $\theta = 10°$. The difference is small for bubble cavitation in the upper part of the back (second type) and for the sheet-vortex cavitation (third type).

Oscillating-Bladed Propeller with Oscillation In-Phase ($\gamma = \pm 3°$; $\psi = 0$)

According to Figs. 2b and 2c, an oscillation amplitude of ±3° could practically remove the cavitation near the hub and, on the other hand, strengthen the

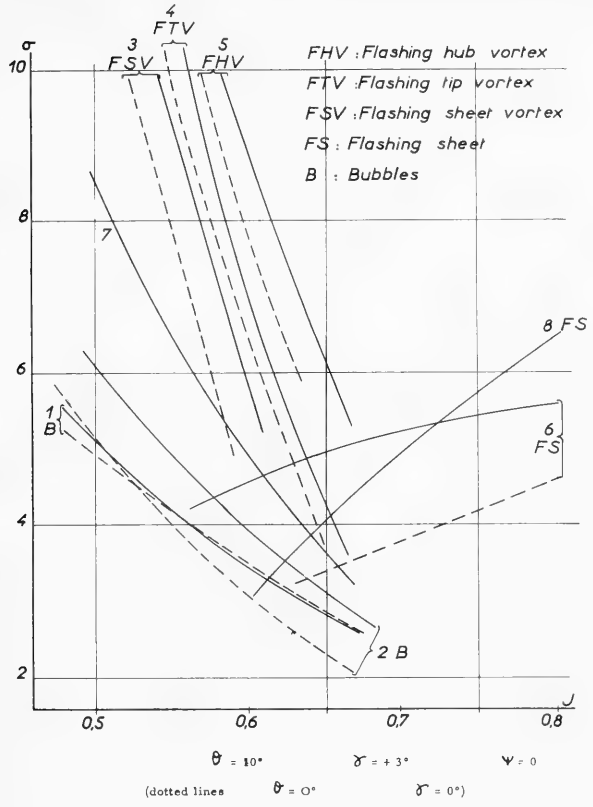

Fig. 4b - Cavitation inception curves for oscillating-bladed propeller, $\theta = 10^{\circ}$

other types of cavitation (except, of course, the hub-vortex cavitation, which integrates the behavior of all the blades) with an inverted effect of φ.

Cavitation Patterns — The cavitation patterns (Figs. 5b through 7b and Fig. 10b) are more complicated than for the fixed-bladed propeller. First, according to the longitude φ, the bubbles on the upper part of the back appear either amid the section (type 2; $\varphi \sim 180^{\circ}$), or near the leading edge (type 7; $\varphi \sim 0^{\circ}$).

Second, there can exist a sheet cavitation along the face leading edge, eventually prolonged by a vortex (type 8).

As in the case of the fixed-bladed propeller, the cavitation patterns are very similar for $\theta = 10^{\circ}$ and $\theta = 15^{\circ}$.

Influence of the Longitude φ — The influence of φ is less clear than in the case of the fixed-bladed propeller. The cavitation near the hub (back or face) seems to appear for about the same values of φ. As for the other types (bubbles, sheet vortex, tip vortex), they depend less upon φ than in the case of the

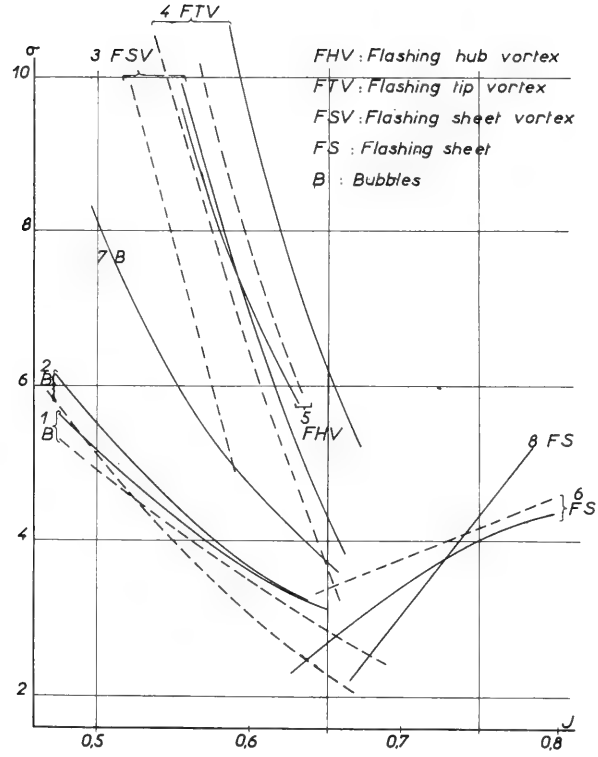

Fig. 4c - Cavitation inception curves for oscillating-bladed propeller, with oscillation in advance, θ = 10°

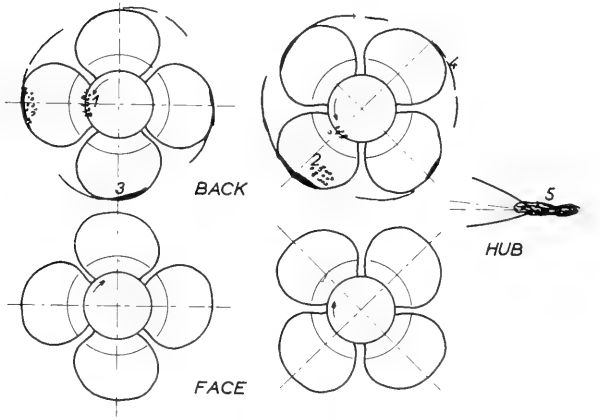

Fig. 5a - Cavitation patterns for fixed-bladed propeller, γ = 0, θ = 10°, J = 0.50, σ = 5

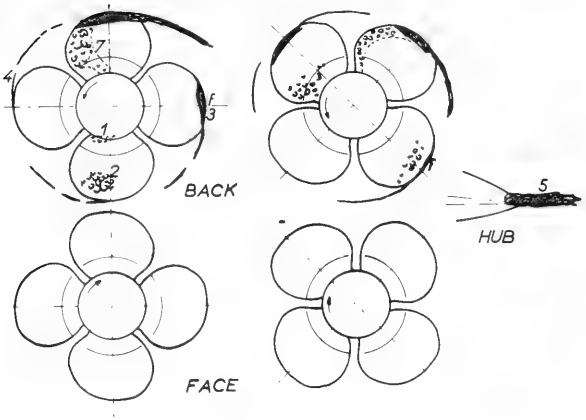

Fig. 5b - Cavitation patterns for oscillating-bladed propeller, $\gamma = \pm 3°$, $\psi = 0$, $\theta = 10°$, J = 0.50, $\sigma = 5$

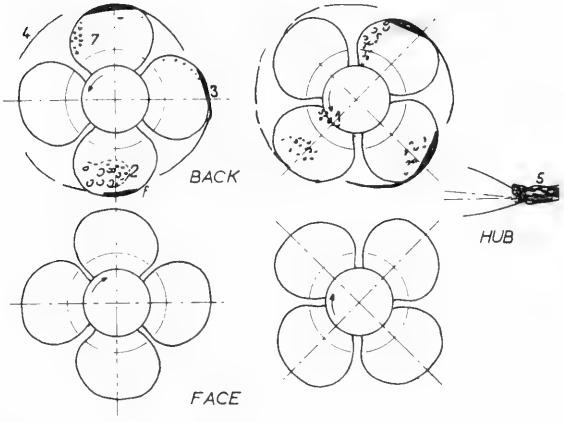

Fig. 5c - Cavitation patterns for oscillating-bladed propeller, with oscillation in advance, $\gamma = \pm 3°$, $\psi = 30°$, $\theta = 10°$, J = 0.50, $\sigma = 5$

fixed-bladed propeller, the inverted effect seemingly sensitive only for sheet-vortex and tip-vortex cavitations. As already noted, according to φ there exist two types of bubble cavitation in the upper part of the back.

Inception of Cavitation — Figures 4b and 9b allow an evaluation of the influence of oscillation on the inception of the different types of cavitation. The oscillation is beneficial as regards the bubble cavitation on the back near the

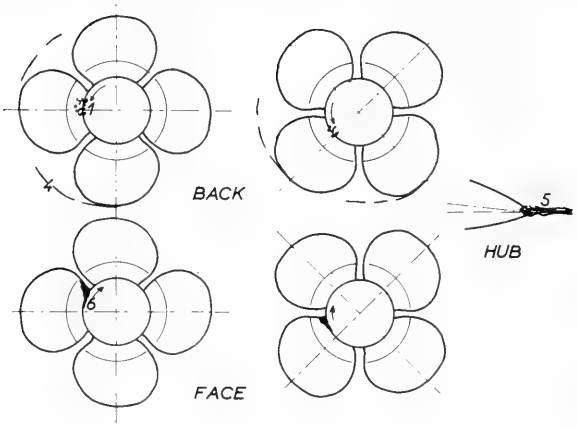

Fig. 6a - Cavitation patterns for fixed-bladed propeller, $\gamma = 0$, $\theta = 10°$, $J = 0.65$, $\sigma = 3$

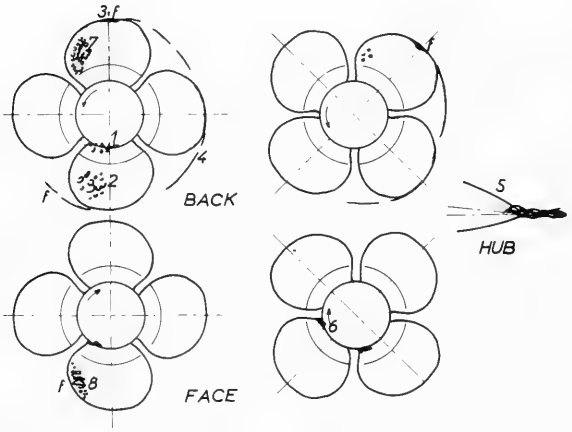

Fig. 6b - Cavitation patterns for oscillating-bladed propeller, $\gamma = \pm 3°$, $\psi = 0$, $\theta = 10°$, $J = 0.65$, $\sigma = 3$

hub (at least for $\theta = 15°$). But, on the other hand, there is a substantial loss as regards the sheet cavitation on the face leading edge.

For the other types of cavitation, there is a loss, especially for bubble and sheet-vortex cavitation, independent of the existence of new types of cavitation.

On the whole, the combination $\gamma = \pm 3°$, $\psi = 0$ has a negative effect.

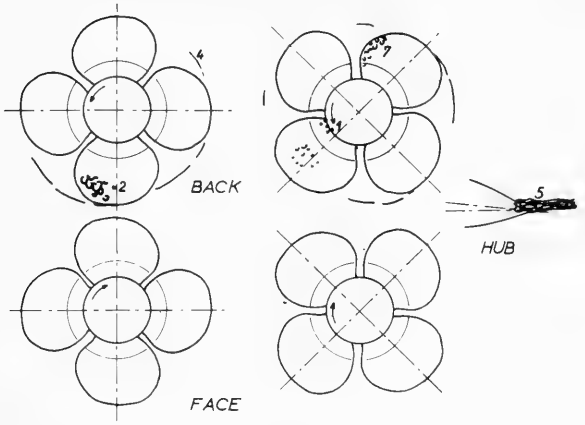

Fig. 6c - Cavitation patterns for oscillating-bladed propeller, with oscillation in advance, $\gamma = \pm 3°$, $\psi = 30°$, $\theta = 10°$, J = 0.65, $\sigma = 3$

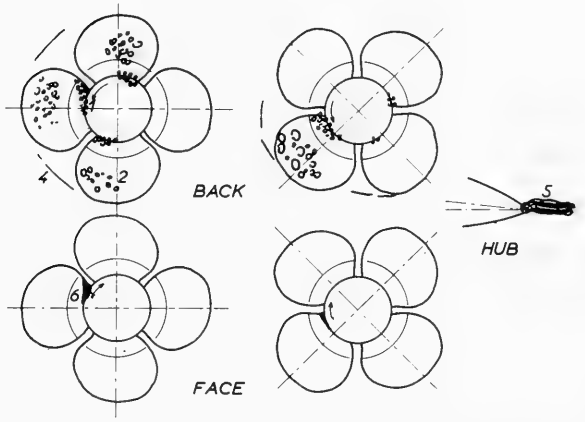

Fig. 7a - Cavitation patterns for fixed-bladed propeller, $\gamma = 0$, $\theta = 10°$, J = 0.65, $\sigma = 2$

Oscillating-Bladed Propeller with Oscillation in Advance ($\gamma = \pm 3°$; $\psi = +30°$)

Cavitation Patterns – The same remarks may be made as for $\psi = 0$ regarding the existence of two types of bubble cavitation on the upper part of the back, and of a sheet cavitation along the face leading edge. The same remarks also may be made regarding the influence, not so clear, of the longitude φ.

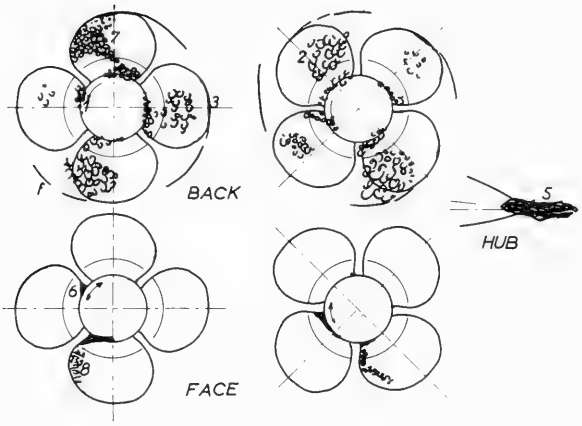

Fig. 7b - Cavitation patterns for oscillating-bladed propeller, $\gamma = \pm 3°$, $\psi = 0$, $\theta = 10°$, $J = 0.65$, $\sigma = 2$

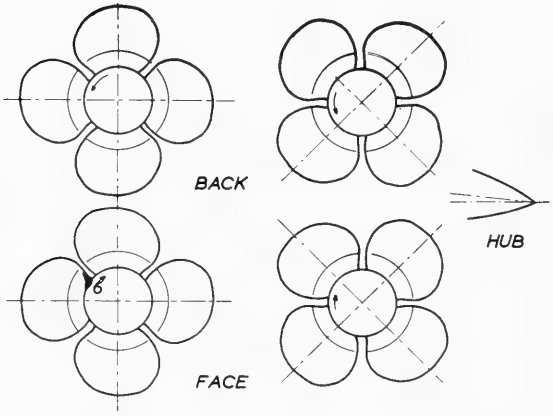

Fig. 8a - Cavitation patterns for fixed-bladed propeller, $\gamma = 0$

A great difference exists, however, for the cavitation near the hub. Relative to the fixed-bladed propeller, the bubble cavitation on the back is strengthened for $\theta = 10°$, while the sheet cavitation on the face leading edge is substantially reduced, especially for $\theta = 15°$.

The influence on the other types of cavitation is of the same order as for $\psi = 0$, except for the sheet cavitation along the face leading edge, which is much lower for $\psi = +30°$ than for $\psi = 0$.

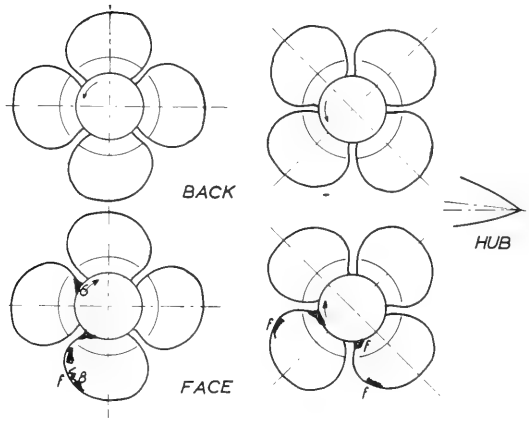

Fig. 8b - Cavitation patterns for oscillating-bladed propeller, $\gamma = \pm 3°$, $\psi = 0$

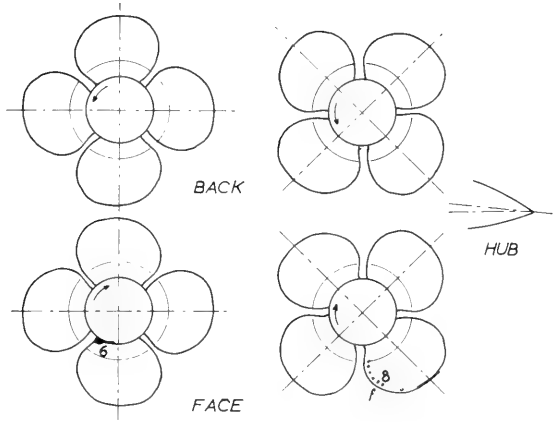

Fig. 8c - Cavitation patterns for oscillating-bladed propeller, with oscillation in advance, $\gamma = \pm 3°$, $\psi = 30°$, $\theta = 15°$, $J = 0.75$, $\sigma = .4$

On the whole, dephasing in advance the oscillation relative to the incidence is beneficial as regards the face cavitation, but causes a loss as regards the back cavitation near the hub.

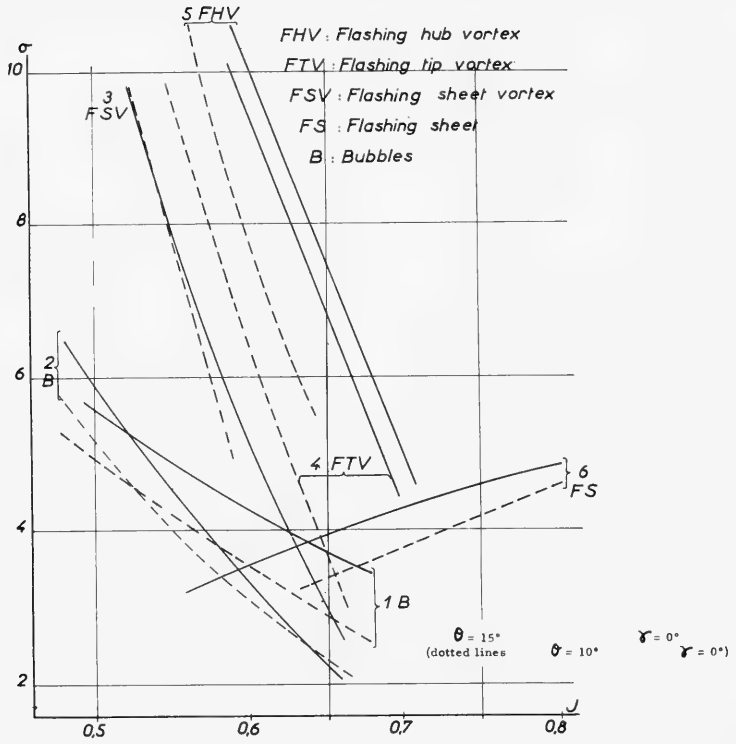

Fig. 9a - Cavitation inception curves for fixed-bladed propeller, $\theta = 15°$

CONCLUSIONS

1. The experiments carried out on a propeller model in inclined flow confirm, when the blades are fixed, the calculated influence of the longitude on the inception and development of cavitation, especially as regards the cavitation near the hub (bubbles on the back, sheet on the face leading edge).

2. For this propeller, the oscillation of the blades can delay the cavitation near the hub (back cavitation for the oscillation in phase with the incidence, face cavitation for the oscillation in advance of 30°), but the cavitation far from the hub is strengthened and even new types of cavitation can appear.

3. If the results obtained with this propeller do not seem as a whole very promising, a valuable conclusion regarding the oscillating-bladed propellers cannot be drawn without further experiments, especially with large-pitch propellers.

4. The influence of the amplitude and of the phase of the oscillation should also be investigated more thoroughly. For example, when two types of cavitation

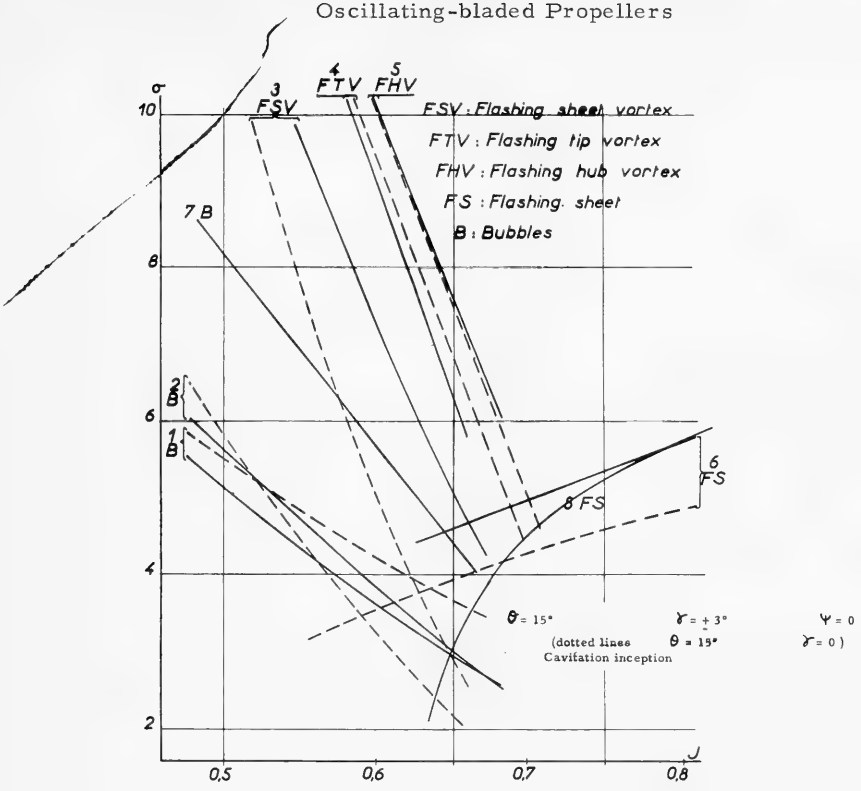

Fig. 9b - Cavitation inception curves for oscillating-bladed propeller, $\theta = 15°$

could take place near the hub (in the case of the propeller tested), better results would perhaps be obtained with a nonsinusoidal oscillation, the oscillation being successively in phase with the variation of incidence in order to delay cavitation near the mean line of the propeller, and in advance of phase to delay cavitation on the leading edge. Of course, the oscillation mechanism system would then be more complicated.

5. A sophisticated theory, taking into account the blade width and the variations of the induced velocities, seems also necessary for a better understanding of the phenomenon.

ACKNOWLEDGMENT

The author is greatly indebted to V. Adm. Brard, director of Bassin d'Essais des Carènes, for having supported this investigation, and to Mr. Riou for having carried out the tests.

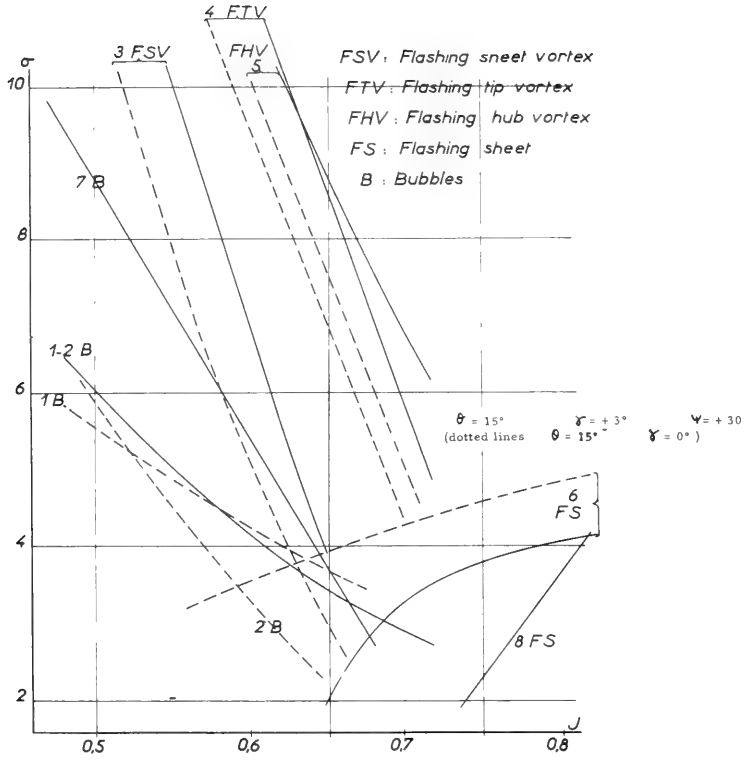

Fig. 9c - Cavitation inception curves for oscillating-bladed propeller, with oscillation in advance, $\theta = 15°$

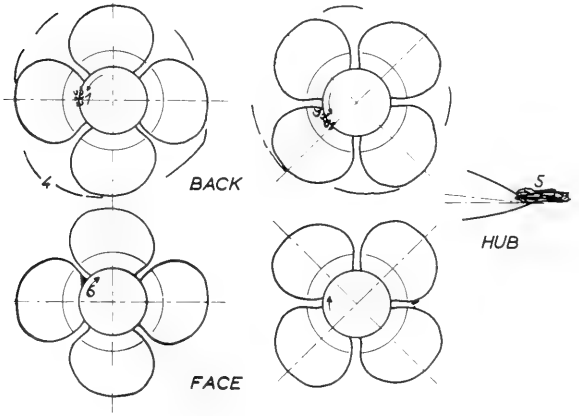

Fig. 10a - Cavitation patterns for fixed-bladed propeller, $\gamma = 0$, $\theta = 15°$

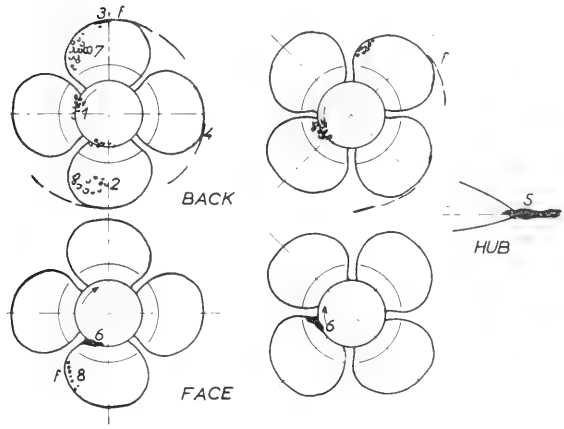

Fig. 10b - Cavitation patterns for oscillating-bladed propeller, $\gamma = \pm 3°$, $\psi = 0$, $\theta = 15°$

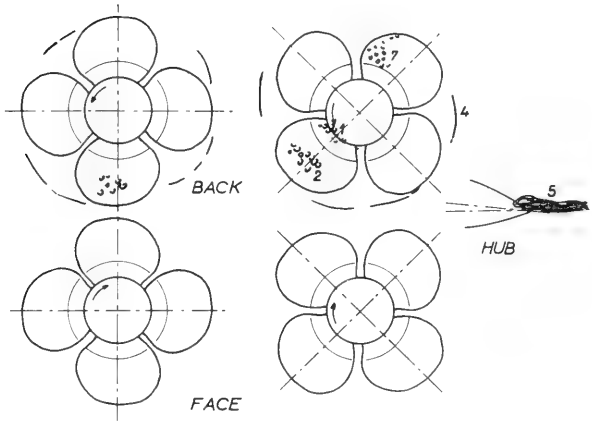

Fig. 10c - Cavitation patterns for oscillating-bladed propeller, with oscillation in advance, $\gamma = \pm 3°$, $\psi = 30°$, $\theta = 15°$, J = 0.65, $\sigma = 3$

REFERENCES

1. Taniguchi, K., and Chiba, N., "Investigation into the Propeller Cavitation in Oblique Flow," ONR Contract 4214 (00)

2. Maioli, P.G., "Cavitazione delle Eliche nella Zona del Raccordo," Ministero della Difesa, Comitato per i Progretti delle Navi, 5 (1966)

3. Johnson, V.E., Barr, R.A., Thiruvengadam, A., and Goodman, A., "Ship Cavitation Research at Hydronautics, Inc.," Symposium on Testing Techniques in Ship Cavitation, Trondheim, Norway, 31 May - 2 June 1967, Skipmodelltanken Pub. 99, Dec. 1967

* * *

DISCUSSION

G. G. Cox
Naval Ship Research and Development Center
Washington, D. C.

The author's paper on the effects of shaft inclination deals with a very important problem for high-speed ships, whether subcavitating or supercavitating propellers are used. Incidentally, the problem, although usually transient, is identical to the propeller in yawed flow, as during a turn.

Although the author has confined his investigation to the use of oscillating blades in an attempt to overcome the root erosion problem, there are other important aspects to the problem. For instance, a normal force and yawing moment arise about the normal axis through the propeller disc. These are in addition to the usual thrust and torque along and about the shaft line. At the 9th ITTC meeting, Newton [1] presented test results for a model destroyer propeller at zero and 10 degrees shaft inclination. These results indicated that all forms of blade cavitation inception occurred much earlier. In its turn, this cavitation tended to reduce thrust and increase torque for a wide range of advance coefficients. This is in contradistinction to the noncavitating inclination effects which tend to indicate an increase in thrust.

Lerbs and Rader [2] presented an interesting analysis method to determine the effective angle of attack for a blade section based on the concept of effective aspect ratio. This method can be useful in predicting cavitation inception characteristics for a propeller in inclined flow.

Finally, I would like to put a question to the author. In view of the results obtained from tests on one propeller with oscillating blades, does he really consider it worthwhile to continue with the full test program indicated in his paper?

REFERENCES

1. Newton, R.N., "Effect of Inclination of Shaft on Propeller Performance," Trans. 9th ITTC, p. 415 (1960)

2. Lerbs, H., and Rader, H.P., "Uber den Auftriebsgradienten von Profilen in Propellerverband," Schiffstechnik, 1962

* * *

DISCUSSION

L. A. Van Gunsteren
Lips Propeller Works
Drunen, The Netherlands

I would like to make two comments.

1. In my opinion, the value of the paper would be improved if Mr. Bindel would provide a description of the test arrangement. In other words, by which kind of mechanism did he obtain the desired motion of the propeller blades? This could give an indication about the efforts required for the realization of this device in practice. Also, a sketch of the hub-form would be appreciated, as this is an essential point with regard to blade-root cavitation.

2. We considered the oscillating-bladed propeller some years ago with regard to the wake-field of single-screw ships. We dropped the idea because of the continuous energy losses due to mechanical friction in the actuating mechanism. This, despite the fact that field-wake irregularity of single-screw ships is practically unavoidable. The nonuniformity of flow due to shaft inclination, however, can be avoided by simply placing the shaft in the direction of flow. In order to achieve this, the propeller shaft could be connected to the inclined shaft by some special kind of coupling, or by a gearing of two wheels with conical teeth. Such a device seems to be more attractive than any hub mechanism required for the oscillation of blades.

* * *

DISCUSSION

Prof. L. Mazarredo
Asociacion de Investigacion de la Construccion Naval
Madrid, Spain

Although these results don't appear to be very promising, I don't think this idea should be rejected at once. The cavitation which appears with oscillating blades may be due to the curvature of the relative flow, since it is stronger in the leading and trailing halves of chords at $\pm 90^\circ$ from the "longitude" where the root cavitation has been eliminated. If the movement was sinusoidal the rotation speed of the blades and the corresponding flow curvature would be maximum at that position.

We have also planned to carry out tests with oscillating blades, but in a tanker model. The arrangement consists in providing the rotating blades with pins which slide on a groove inside a cylinder fixed astern. Although this device introduces undue friction, I hoped that the improvement of the efficiency would balance this loss, since not only the change of angle of attack but also the lengthening of the hub will provide (as shown by Dr. Castagneto some years ago) such an improvement.

Even if the system is not used, this type of test may load to a better understanding. In this case, it may be interesting, for instance, to see whether an improvement of the propulsive coefficient is attained as a result of lowering the load in front of the stern post.

* * *

REPLY TO DISCUSSION

S. Bindel

In reply to the question of Dr. Cox, I should say that the test program indicated in the paper is a general outline of some possibilities among which it would be necessary to choose. It seems to me, at this time, that the best option would be to consider one or several "desperate" cases, for which the other methods revealed themselves ineffective (cf., for example, Ref. 2 of my paper), and to see if oscillating the blades may lead to an acceptable solution. If so, it would be desirable to cover all aspects of the investigation; if not, the system ought to be rejected, at least for inclined propellers.

I did not give the description of the mechanism used because the paper was primarily concerned with the hydrodynamic aspect of the problem; but the way to build the mechanism is important, of course, as underlined by Mr. Van Gunsteren. On the model, two opposite blades were actuated by a lever connected with a piece turning around a fixed cylinder, the axis of which was crossing the axis of the propeller. This system was simple; however, I do not think that its complete description would give valuable information on the efforts required for a full scale propeller, due to the fact that the real system would probably be different.

I agree with Mr. Van Gunsteren that from a hydrodynamic point of view it would be better to place the shaft in the direction of the flow, but in this case the coupling would have to transmit all the propulsive torque, whereas the torque necessary to oscillate the blades is much smaller and the mechanism may be located inside the hub.

I agree with the suggestion of Mr. Van Gunsteren and Prof. Mazarredo, that the oscillating-bladed propellers would perhaps be best utilized in the case of single screws working in nonuniform flow. I also thought of this application, but so far I have had no time to make any investigation in this direction.

Finally, I thank very much the contributors for their supplementary information, their remarks, and their questions.

* * *

UNUSUAL TWO-PROPELLER ARRANGEMENTS

T. Munk and C. W. Prohaska
Hydro- og Aerodynamisk Laboratorium
Lyngby, Denmark

INTRODUCTION

Many of the problems connected with the screw propulsion of ships originate from the irregularity of the wake of the ship. When a propeller is working in an irregular wake, the change of the inflow velocity and the angle of incidence may give rise to cavitation or vibrations.

These difficulties are less pronounced when twin-screw propulsion is used, but then only a small part of the energy in the friction wake is utilized and this causes a decrease in the hull efficiency. In many cases this decrease will not be fully compensated for by the increase in propeller efficiency due to the reduced loading of the two propellers.

THE INTERLOCKING PROPELLER ARRANGEMENT

The difficulties here are thoroughly treated by P. C. Pien and J. Strøm-Tejsen in Ref. 1 which discusses several stern arrangements with regard to total efficiency and the ability to reduce cavitation and vibration. In addition, a new stern arrangement is proposed.

In this arrangement, the two propellers of a normal twin-screw system are moved aft to the longitudinal position of a normal single-screw propeller and inward until the distance between the shafts is less than the diameter of the propellers, which therefore overlap in the centerline zone. This should combine the advantages of the twin-screw system, which are high propeller efficiency due to the reduced propeller load and minimal generation of cavitation and vibration due to the smooth wake field, with those of the ordinary single-screw system, which are low appendage resistance and high hull efficiency due to the high viscous wake just behind the ship.

Tests were carried out with the system mounted on a tanker model and the results compared with results from previous tests with other propulsion systems on the model. It was evident that the interlocking propeller arrangement offers great advantages.

THE AUXILIARY PROPELLER ARRANGEMENT

Another propeller arrangement which may reduce the risk of cavitation and vibrations was developed at the Hydro- and Aerodynamics Laboratory (HyA) at Lyngby, Denmark. It consists of a normal single-screw propeller and a small auxiliary propeller placed in the high-wake zone between the upper part of the main propeller and the stern. The auxiliary propeller will accelerate the water behind the stern and thereby smooth out the wake at the position of the main propeller. The primary effect is the higher safety against cavitation and vibrations, but a minor increase in propeller efficiency should also be expected.

PRACTICAL POSSIBILITIES

In practice, both systems may be adopted in ships without any technical difficulties. In the case of interlocking propellers the two shafts are geared together and driven by a single propulsion unit. The cost of the gear and the extra shaft will be modest in comparison to the gain in total efficiency of the system, and the gear will permit an optimum number of revolutions to be chosen.

Separate drives of the two shafts may be adopted if the two overlapping propellers are placed clear of each other in the longitudinal direction. This arrangement corresponds to a twin-screw ship with an abnormally low distance between the two shafts at the tail end.

In the auxiliary propeller system, the small propeller may be driven in any number of ways: by gear, chain-drive, or electric motor. The power required will only be about 10 percent of the total power.

Even a combination of the two systems might be advantageous, e.g., a three-propeller system with two interlocking and one auxiliary propeller, all driven by a single propulsion unit.

TESTING OF THE SYSTEMS

At HyA the results from Ref. 1 were found to be of the greatest interest, and as no further treatment of interlocking propeller arrangements was available, it was decided to carry out supplementary tests with this system in order to confirm the results of Ref. 1, and to obtain more knowledge of the interaction between propellers. It was considered of special interest to know how the vibration-generating variation of the forces on a propeller blade would compare with the variation on a normal single screw, and how the wake of one propeller is influenced by the induced velocities from the other propeller, since this would be of importance in the design of interlocking propellers.

The problems connected with the auxiliary propeller system are similar, and it was therefore decided also to carry out tests with this arrangement.

The two systems should be of particular interest for large tankers and bulk-carriers, which usually have a high and very irregular wake, and where the diameter of the propeller often is kept small on account of the relatively high number of revolutions of diesel marine engines for large ships. The two propulsion systems were therefore tested on a model of a tanker in the fully loaded condition and in a ballasted condition. The model fitted with interlocking propellers is shown in Fig. 1, with auxiliary propeller in Fig. 2, and with ordinary twin screws in Fig. 3. The principal data of model and ship fully loaded and ballasted are stated in Table 1.

Fig. 1 - Interlocking propeller arrangement

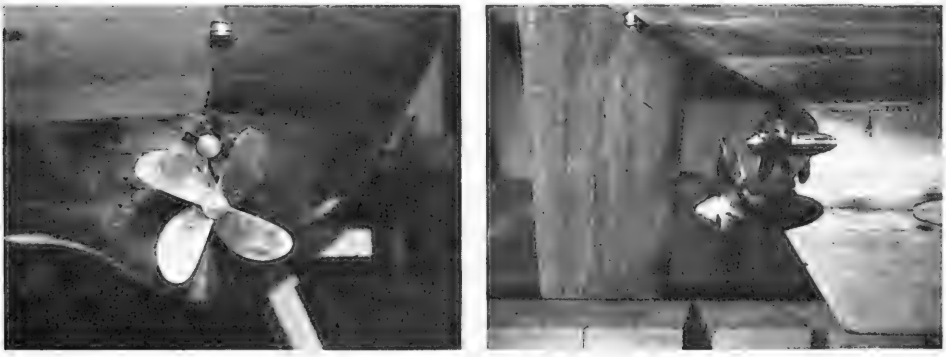

Fig. 2 - Auxiliary propeller arrangement

The interlocking propeller arrangement was tested with three different distances between the propeller axes and with the propellers turning both inwards and outwards.

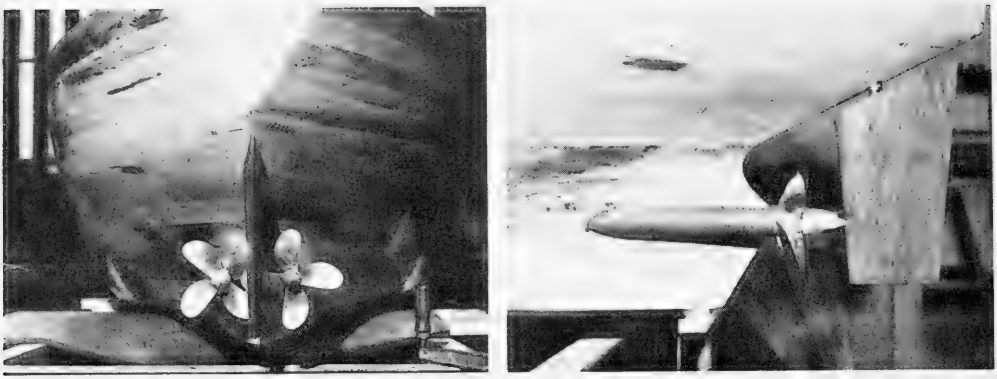

Fig. 3 - Ordinary twin-screw arrangement

Table 1
Data of Model and Ship Ballasted and Fully Loaded

(Scale = 1:35)

	Ballasted		Fully Loaded	
	Model	Ship	Model	Ship
Length, perpendicular — L_{pp} (m)	7.200	252.000	7.200	252.000
Length, vertical — L_{v1} (m)	7.000	245.000	7.321	256.235
Breadth — B_m (m)	1.114	38.990	1.114	38.990
Draught forward — d_f (m)	0.214	7.490	0.382	13.37
Draught aft — d_a (m)	0.229	8.015	0.382	13.37
Mean draught — d_m (m)	0.221	7.752	0.382	13.37
Displacement — V (m^3)	1.398	59951.8	2.523	108176.9
Wetted surface — S (m^2)	9.146	11203.4	11.582	14188.0
Block coefficient	0.810		0.810	
Prismatic coefficient	0.820		0.813	
Midship section coefficient	0.988		0.996	
Waterline coefficient	0.867		0.879	
$L_{v1}/V^{1/3}$	6.26		5.375	
B/d	5.029		2.916	
L/B	6.284		6.57	
Longitudinal center of buoyancy aft of $L_{pp}/2$ — LCB (%)	-2.405		-1.702	

In order to get an impression of the influence of the induced velocity from one propeller on the wake at the position of the other propeller, nearly all the

tests were repeated with only one propeller working and the other removed and compensated for by a tow-rope force.

The auxiliary propeller arrangement was tested with a right-hand as well as a left-hand auxiliary propeller in combination with a right-hand main propeller.

For comparison, self-propulsion tests were also carried out with a normal single screw and with normal twin screws turning outwards.

The stress at the root of one propeller blade was measured in a number of the tests.

In Table 2 a list is given of the total number of tests carried out until May 1968. Further tests, however, are underway.

Stock propellers were used for all the tests. The diameter of the single-screw propeller was chosen as optimum for a number of revolutions for the ship in agreement with that of large slowly running diesels. The diameter of the interlocking propellers was taken as 0.9 times that of the single-screw propeller. This diameter gave an optimum number of revolutions somewhat below that of the single-screw propeller, but this was found permissible, as a gear in any case is necessary for the connection of the two shafts, and some reduction of the number of revolutions will then be natural.

Two sets of stock propellers were used as interlocking propellers. Both had pronounced rake and were therefore not quite suitable for the purpose.

In the auxiliary propeller system the stock propeller with the smallest diameter was used as an auxiliary propeller. This propeller was not very suitable, since the diameter was too large and the pitch ratio and the developed blade area ratio were too high.

Data for the propellers are given in Table 3.

TESTING METHODS

The resistance tests were carried out in the normal way.

The self-propulsion tests were carried out with a tow-rope force according to the Hughes friction line for a form factor of 1.36 for fully loaded condition and 1.28 for ballasted condition, and with $C_A = 0.15 \cdot 10^{-3}$.

Except for the auxiliary propeller arrangement, torque and thrust were measured by mechanical dynamometers. In the two-propeller cases the two dynamometers were connected to one motor to ensure uniform running of the propellers.

The stress at the root of one propeller blade was measured by means of strain gauges. These were placed on each side of the propeller blade to prevent signals caused by temperature expansion. The strain gauges were wired through a hollow shaft to a unit which was placed on the shaft inside the model and which consisted of the remaining resistances of a Wheatstone's bridge, an

Table 2
Tests Carried Out with Different Propulsion Systems

Test No.	Type of Test	Propulsion System	Prop No.	Condition
1, 2	Resistance			Fully loaded and ballasted
3, 4	Self-propulsion	2 interlocking props, inward rotation. Distance between axes = 0.9 · D	6137	Fully loaded and ballasted
5, 6	Self-propulsion	1 interlocking prop, inward rotation. Distance between axes = 0.9 · D	6137	Fully loaded and ballasted
7, 8	Self-propulsion	2 interlocking props, inward rotation. Distance between axes = 0.8 · D	6137	Fully loaded and ballasted
9, 10	Self-propulsion	1 interlocking prop, inward rotation. Distance between axes = 0.8 · D	6137	Fully loaded and ballasted
11, 12	Self-propulsion	2 interlocking props, inward rotation. Distance between axes = 0.7 · D	6137	Fully loaded and ballasted
13, 14	Self-propulsion	1 interlocking prop, inward rotation. Distance between axes = 0.7 · D	6137	Fully loaded and ballasted
15	Self-propulsion	2 interlocking props, inward rotation. Distance between axes = 0.68 · D	5915	Fully loaded
16, 17	Self-propulsion	2 interlocking props, outward rotation. Distance between axes = 0.77 · D	5915	Fully loaded and ballasted
18, 19	Self-propulsion	1 interlocking prop, inward rotation. Distance between axes = 0.77 · D	5915	Fully loaded and ballasted
20	Self-propulsion	2 interlocking props, inward rotation. Distance between axes = 0.68 · D	5915	Fully loaded
21, 22	Self-propulsion	twin-screw props, inward rotation	5915	Fully loaded and ballasted
23, 24	Self-propulsion	single-screw props, inward rotation	6507	Fully loaded and ballasted
25	Self-propulsion	auxiliary prop, small prop, right-hand	6507+6109	Fully loaded
26	Self-propulsion	auxiliary prop, small prop, left-hand	6507+6109	Fully loaded

Table 3
Propeller Data

Propeller Number	6507	6137	5915	6109
Diameter, model (mm)	201.9	180	186.4	88.9
Diameter, ship (mm)	7050	6300	6520	3110
Number of blades	4	4	4	3
Pitch ratio	0.754	0.963	1.27	1.335
Developed blade area ratio	0.458	0.524	0.43	0.794
Rake (deg.)	6	8	15	0
Purpose	single-screw	interlocking prop	interlocking prop, twin-screw	auxiliary prop

amplifier for amplification of the signals from the bridge, and an accumulator for feeding the amplifier. The measuring circuit was fed by an accumulator through slip rings, and the amplified signal was led through slip rings to an oscilloscope and a direct-recording ultraviolet oscillograph with a sensibility enabling it to follow the variation of the stress through a revolution (Fig. 4).

Electronic dynamometers were used in the self-propulsion tests with the auxiliary propeller system, and each propeller was driven by a separate motor. At each tested speed, the numbers of the revolutions of the two propellers that would minimize the stress variations in the main propeller blade were found by

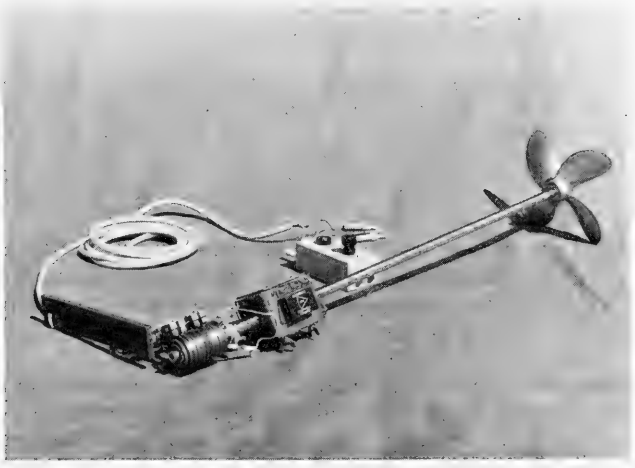

Fig. 4 - Shaft equipment for measuring of the stress at the propeller blade root

successive changes of the revolutions of the auxiliary propeller, adjusting in each case the revolutions of the main propeller until the model was self-propelled.

ANALYSIS OF THE RESULTS

The resistance tests were extrapolated to ship scale by using the Hughes method and a form factor of 1.36 for fully loaded condition and 1.28 for ballasted condition, and a C_A value of $0.15 \cdot 10^{-3}$. The self-propulsion tests were analyzed by the method described in Ref. 2, which method normally is used at HyA. The analysis work was done on the HyA-GIER computer.

The wake coefficient corrections used in the different cases are given in Table 4.

Table 4
Wake Coefficient Corrections Used for Analysis of the Self-Propulsion Tests

(Ship wake coefficient = model wake coefficient - wake coefficient correction)

Propulsion Arrangement	Wake Coefficient Correction*
Ordinary single-screw	0.140
Ordinary twin-screw	0.010
Interlocking propellers, distance between axes = 0.7 · D	0.097
Interlocking propellers, distance between axes = 0.8 · D	0.086
Interlocking propellers, distance between axes = 0.9 · D	0.074
Auxiliary propeller system, main prop	0.140
Auxiliary propeller system, small prop	0.180

*The wake correction is calculated as the difference between the velocity in the boundary layer integrated over the propeller disk for model and for ship.

The results of the stress measurements were given by the recorder in the form of curves showing the stress caused by the bending moment on the blade as a function of time or of blade position, a mark being placed on the paper every time the blade was in the upper position.

The blade stress is proportional to the bending moment, and after calibration the curves therefore represent the bending moment at the blade root as a function of the blade position. The bending moment is a function of the resultant force on the blade normal to the section where the stress is measured, hereafter called the normal force, and of the distance of the center of pressure from the root,

which may be assumed to be nearly constant. The stress, consequently, in the first approximation is proportional to the normal force. The normal force is a function of the inflow velocity vector, which is the vector sum of the ship speed, the circumferential velocity, and the wake speed. Only the last is not constant. Therefore, the variation of the curves gives an impression of the variation of the wake during one revolution.

TEST RESULTS

The results of the test series are given graphically in Figs. 5 through 12.

Figures 5 through 9 give the required propeller horsepower for the tested propulsion systems as a function of the ship speed, and the corresponding numbers of revolutions are given in Fig. 10.

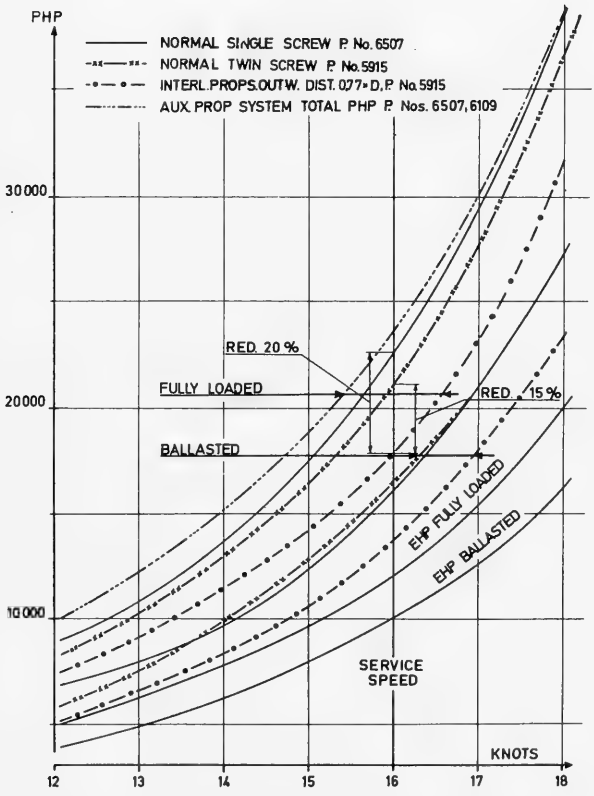

Fig. 5 - Comparison between the required propeller horsepowers for the different propeller arrangements

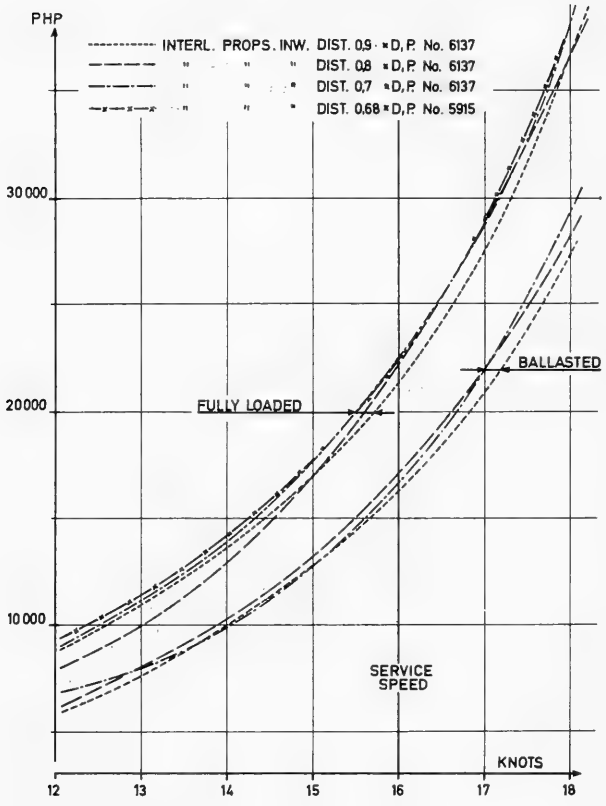

Fig. 6 - Propeller horsepowers from tests with inward-turning interlocking propellers

The model torque wake coefficients for all the tests are given graphically as a function of the speed in Fig. 11. The thrust deduction coefficients and the relative rotative efficiencies varied little and not systematically and were of the order of 0.29 and 1.00 respectively for a fully loaded ship, and 0.27 and 1.00 for a ballasted ship.

The results of the stress measurements are shown in Figs. 12a through 12h. For the interlocking propellers the distance between the axes is $0.7 \cdot D$.

DISCUSSION OF THE RESULTS

Interlocking Propellers

It is seen from Fig. 5 that the interlocking propeller system with the propellers turning outward is the most favorable one as regards total efficiency,

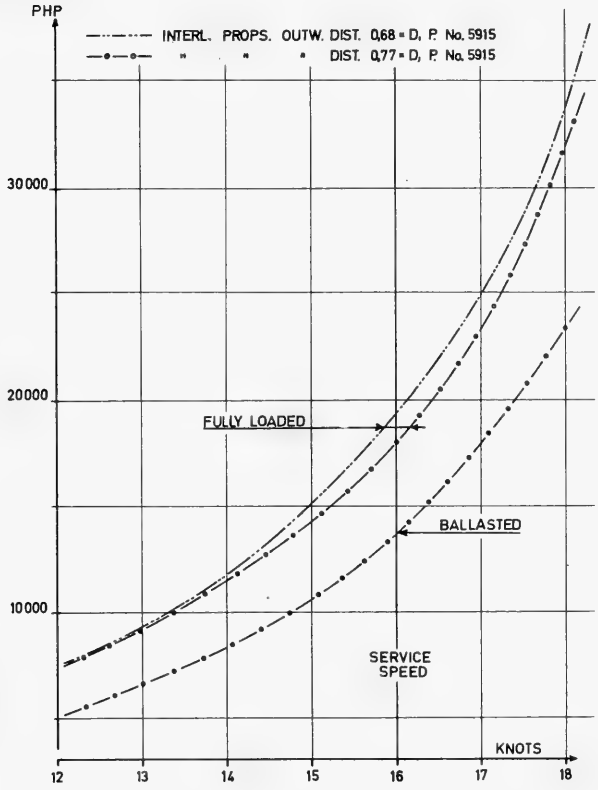

Fig. 7 - Propeller horsepowers from tests with outward-turning interlocking propellers

while the inward-rotating propellers give almost the same result as the normal single-screw. None of the propellers were optimum propellers. For instance, at 16 knots the optimum number of revolutions for the single-screw and for the outward-turning interlocking propellers were 106 and 94 respectively, while the actual numbers of revolutions in the self-propulsion tests were 115 and 74.

From Fig. 11 it is seen that the mean wake is higher when the propellers are turning outward than when they are turning inward, and that the mean wake for each interlocking propeller is decreased by the action of the other, especially for the inward-rotating propellers. The differences in total efficiency are caused by the differences in wake, a higher wake giving a lower propeller efficiency, but a higher hull efficiency.

A small shaft distance is not advantageous. As the propellers are moved inward the wake and thrust deduction increases, but the interaction of the propellers will increase also and decrease the resulting wake. This additional inflow velocity is dependent on the propeller load, and as the resulting wake

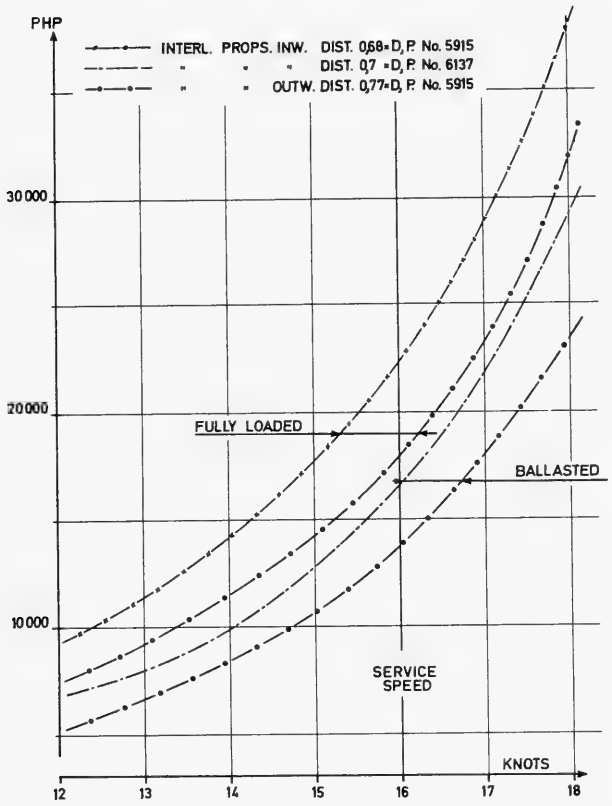

Fig. 8 - Comparison between best results from tests with inward- and outward-turning interlocking propellers

has a great influence on the total efficiency, the optimum distance between the propeller axes must be a function of the propeller load. A general optimum distance, therefore, cannot be given at present. For cases considered most important, shaft distance is clearly the best.

The differences corresponding to inward- and outward-rotating interlocking propellers are due to the wake components in the propeller disk plane. It is possible to get an impression of this component if the normal force on a blade in a certain position is compared to the normal force on the blade in the same position, but with the propeller turning in the opposite direction. The difference between the normal forces is due to the differences between the tangential velocities as shown in the velocity diagram, Fig. 13. The tangential wake velocity, w_t, is seen to change the resulting inflow velocity from v_1 to v_2, when the direction of rotation is altered, and this largely influences the normal force.

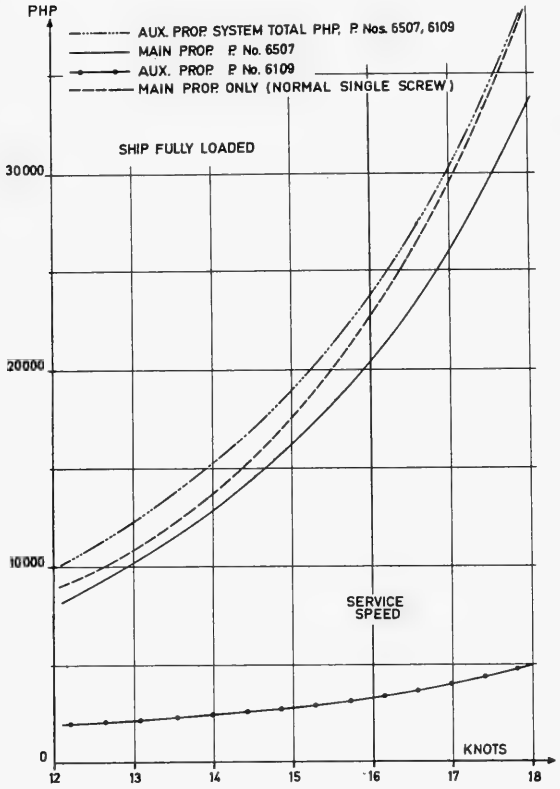

Fig. 9 - Propeller horsepowers from tests with the auxiliary propeller system

If the stress curve is looked upon as a curve of normal force, as mentioned earlier, and the curve for the normal right-hand single screw is copied upside down, the copy will give the normal force for a left-hand propeller. When the two curves are placed together as shown in Fig. 14, their mean value represents the normal force in the case of no tangential wake component, and the difference between the mean curve and one of the other curves gives the additional normal force caused by the tangential wake component. Figure 14 then indicates that wake components are present as shown in Fig. 15.

The stresses measured in the cases where one of the interlocking propellers was removed, are compared in the same way in Fig. 16, which shows the curves representing mean normal force and additional normal force. The transverse wake components are indicated in Fig. 15. The normal force is at the same speed, but the number of revolutions is higher for an outward- than for inward-rotating propeller. When the model is self-propelled, this difference will result in a lower number of revolutions and a higher wake for the outward-rotating propeller, in accordance with what is well known from ordinary twin-screw ships.

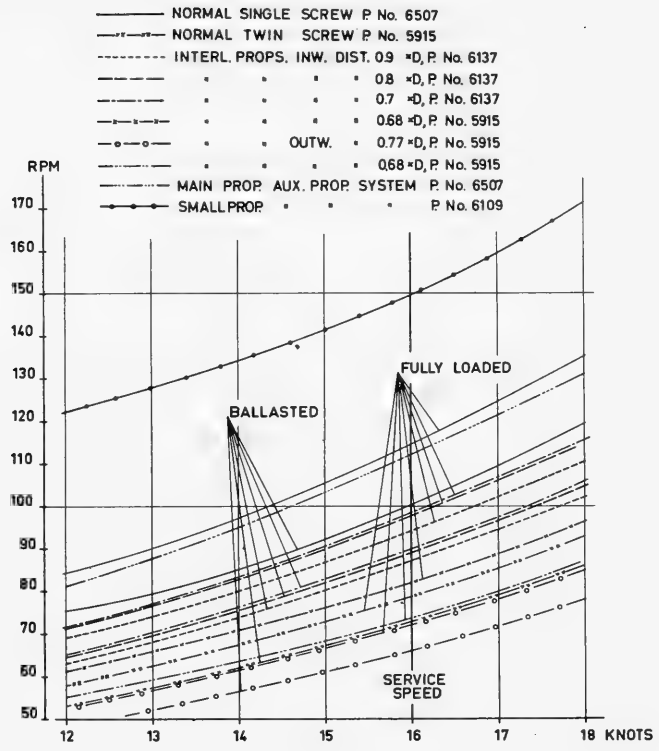

Fig. 10 - Revolutions versus speed for the propellers

The rest of the difference between the wake for inward- and outward-rotating interlocking propellers may be explained by the velocity diagrams for a blade in the overlapping position, rotating inward and outward, as given in Fig. 17. The figure shows that the induced velocity from one propeller is much higher for the inward-rotating propeller and therefore the wake for the other propeller is much reduced.

This is in good accordance with the result of a comparison of the stress curves for a propeller rotating inward and outward when it is working alone and when the other propeller is also working. It can be seen from Fig. 18 that the influence from the other propeller is much greater for an inward-rotating than for an outward-rotating propeller.

The results of the stress measurements on single-screw and on interlocking propellers are scaled to the same mean normal force in Fig. 19 to show the relative stress variations. The comparison is, however, not quite correct because the wake-scale effect is not taken into account and because the distance between the shafts here is the smallest distance, and not the one which gave the best propulsion result.

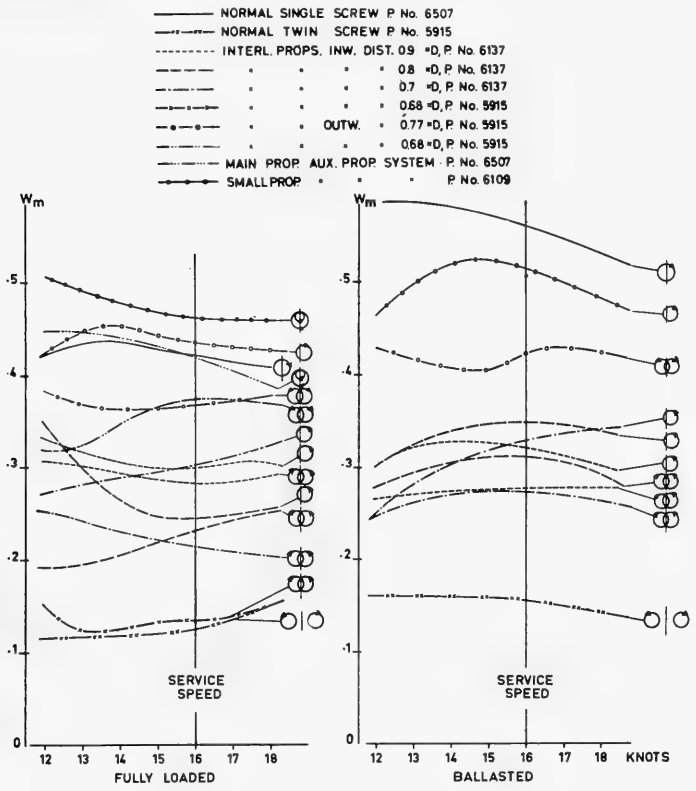

Fig. 11 - Model torque wake coefficients

The Auxiliary Propeller System

In this case the auxiliary propeller system does not yield favorable results from the point of view of efficiency, but it must be remembered that the small propeller is too large and works at a poor value of the advance coefficient. The results from the stress measurements are nevertheless interesting.

As mentioned earlier, it was possible to find on an oscilloscope the best number of revolutions for the small propeller. A good result was obtained within rather wide limits, but it was also seen that it was not possible to remove all of the high-stress peak for the upper position of the blade. A further increase in the number of revolutions for the small propeller only gave a decrease of the stress in front of the remaining stress peak as shown in Fig. 12d. It must therefore be expected that on account of the tangential wake component a position of the axis of the auxiliary propeller slightly outside the center line will be optimum. It must also be expected that an additional auxiliary propeller below the main propeller axis will almost completely smooth out the stress curve.

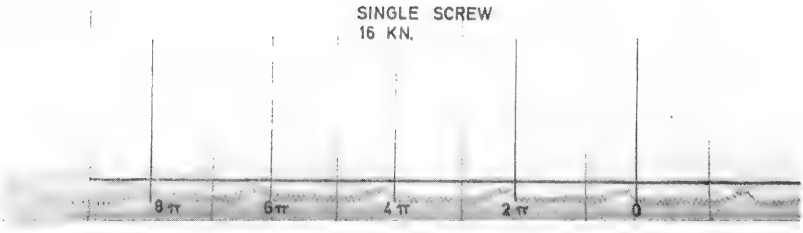

a

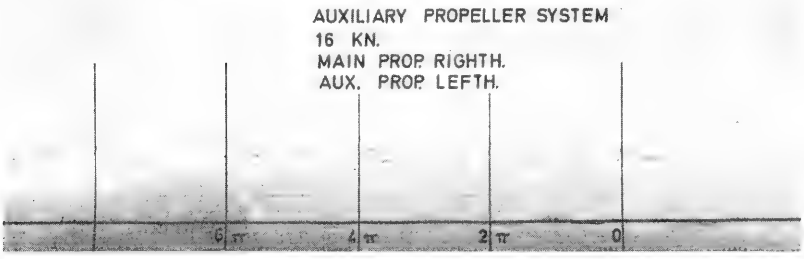

b

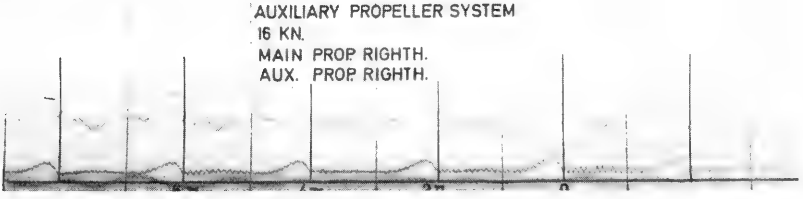

c

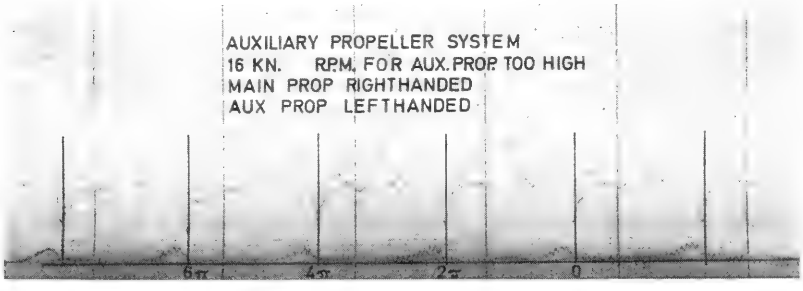

d

Fig. 12 - Propeller blade stress recordings

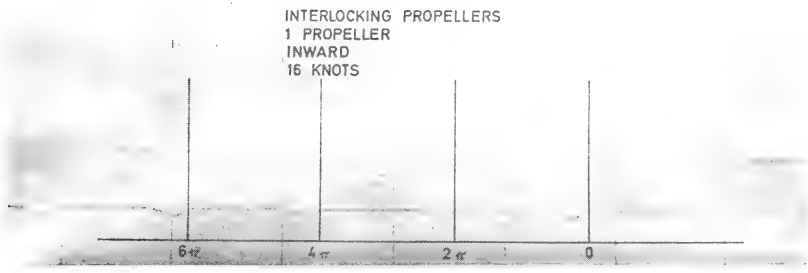

e

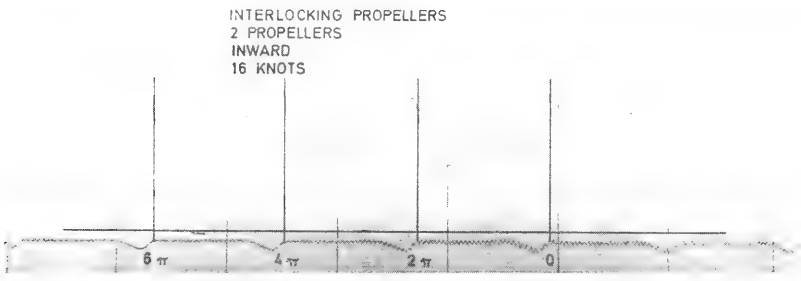

f

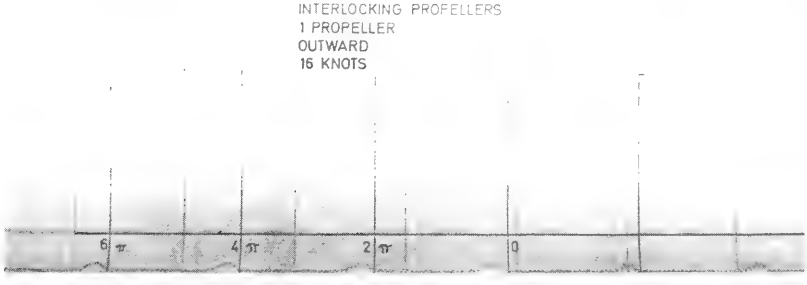

g

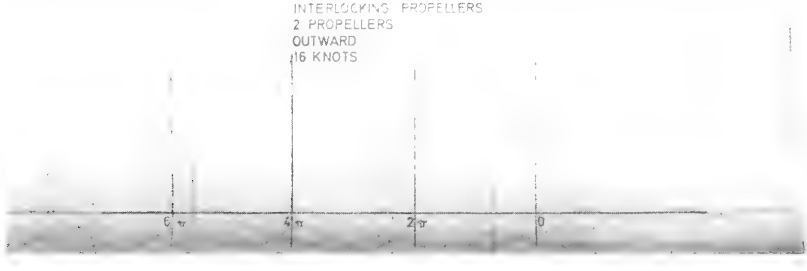

h

Fig. 12 - Propeller blade stress recordings (Continued)

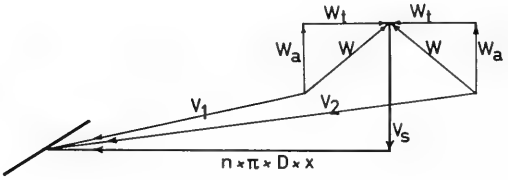

Fig. 13 - Velocity diagram showing the influence of the tangential wake component

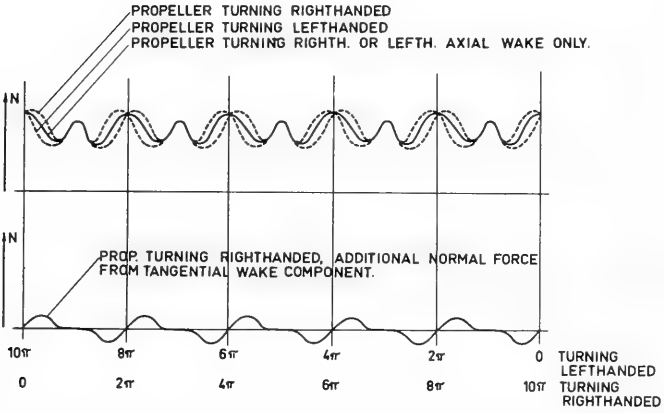

Fig. 14 - Normal force curves for right-hand and left-hand single screws

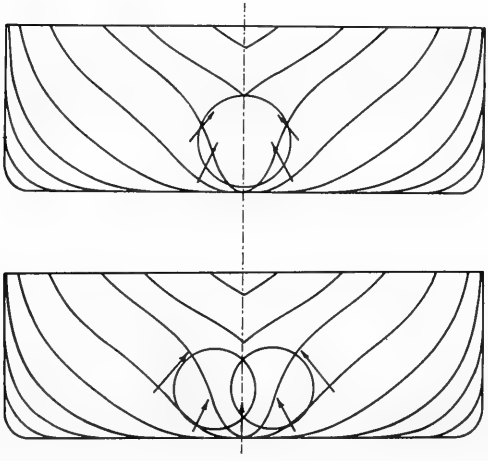

Fig. 15 - Wake components in the propeller disk plane

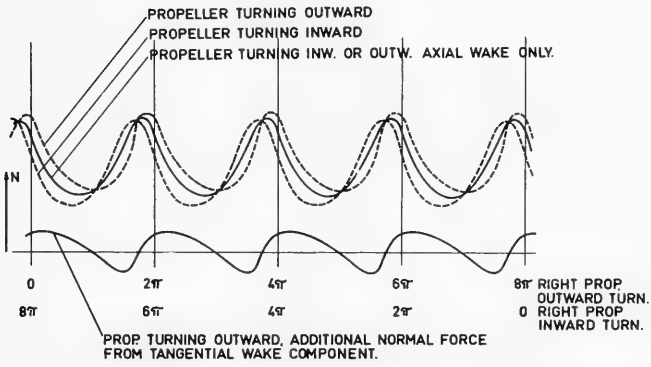

Fig. 16 - Normal force curves for only one interlocking propeller, inward- and outward-rotating

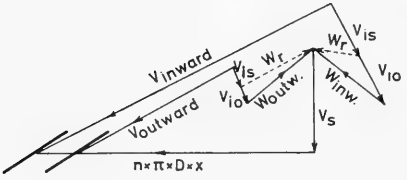

Fig. 17 - Velocity diagram for a propeller blade in the interlocking zone, inward- and outward-rotating

CONCLUSION

The results of the test series show that from a propulsion point of view both of the new arrangements may be used with advantage.

In the case of interlocking propellers, a higher total efficiency is obtained than for the normal single-screw and twin-screw systems. However, the direction of rotation of the propellers has a great influence on the results, and it is obvious that the wake components in the plane of the propeller disk must be taken into account, as they are a part of the mean wake.

The auxiliary propeller arrangement has in this case shown a decrease and not an increase in the total efficiency in comparison with the normal single-screw arrangement. However, the tests with the system were primarily carried

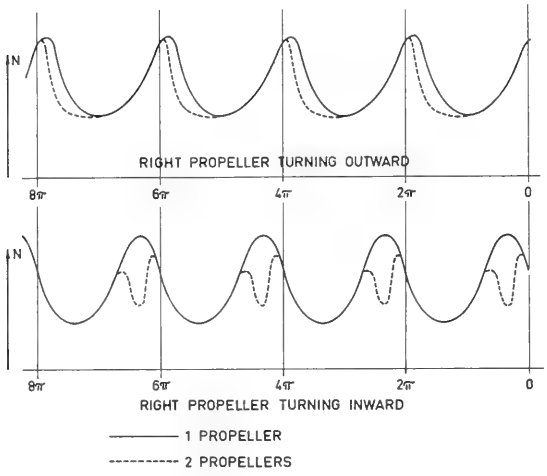

Fig. 18 - Normal force curves for an interlocking propeller working alone and in combination with the other propeller

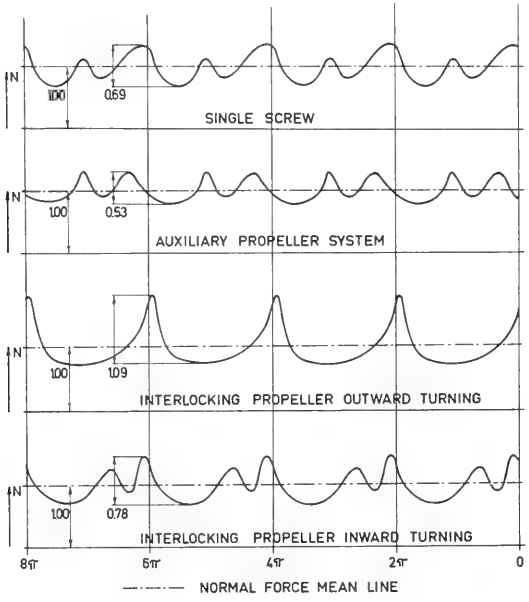

Fig. 19 - Comparison between normal force curves for the different propulsion systems

out to examine the possibility of reducing the high wake peak just behind the stern, and the results indicate that this may be done. If so, the developed blade area may be reduced, and a higher propeller efficiency for the main propeller will be obtained. This, together with a specially designed auxiliary propeller, should give a higher total efficiency. Yet the main reason for using this arrangement should still be the reduction of the risk of vibrations and cavitation on the main propeller.

The stress measurements give no direct information on the reduced risk of cavitation. It must be expected that a smooth stress curve is an expression of a smooth wake field, for which it is easy to design a cavitation-free propeller, but only cavitation tunnel tests will give the final information.

At zero speed, stress measurements were taken at full power and showed for both propulsion systems greater variations than normally found on single-screw ships. In the case of interlocking propellers, it is expected that these stresses will be reduced considerably for greater shaft distances. This problem will be studied carefully in coming experiments. For the auxiliary propeller system, it is obvious that the remedy will be to make arrangements permitting this type of propeller to be coupled in only when a certain forward speed has been obtained.

NOMENCLATURE

D	Propeller diameter
x	Nondimensional radius
W	Wake
W_r	Resultant wake
W_t	Tangential wake component
W_a	Axial wake component
n	Number of revolutions per second
V_s	Ship speed
V	Inflow velocity
V_{is}	Velocity induced by the propeller itself
V_{io}	Velocity induced by the other interlocking propeller
N	Resultant force normal to the blade-root section
EHP	Effective horsepower

PHP Propeller horsepower

C_A Additional resistance coefficient

REFERENCES

1. Pien, P.C., and Strøm-Tejsen, J., "A Proposed New Stern Arrangement," Naval Ship Research and Development Center, Washington, D.C., Report 2410, May 1967

2. Prohaska, C.W., "Analysis of Ship Model Experiments and Prediction of Ship Performance," Hydro- and Aerodynamics Laboratory, Lyngby, Denmark, Report Hy-1, Dec. 1960

APPENDIX A
FURTHER TESTS WITH INTERLOCKING PROPELLERS

A supplementary test with outward-rotating interlocking propellers with a distance between the shafts of about 0.9 • D was carried out after the completion of the paper, and the results are given in Fig. A1 (refer to Fig. 7).

The results confirm that a distance between the shafts of about 0.8 • D still gives the lowest propeller horsepower at the service speed.

Supplementary stress measurements were also carried out for outward-rotating propellers with a distance between the shafts of about 0.8 • D and 0.9 • D. The results at service speed were nearly the same as earlier found for a distance of 0.7 • D. At zero speed, the stress variations proved to be smaller, and thus can be judged as of no importance.

APPENDIX B
OVERLAPPING PROPELLERS

Test No. 18 with interlocking propellers, which gave the lowest propeller horsepower, was repeated with the propellers placed clear of each other, in longitudinal direction. The distance between the propeller shafts was about 0.8 • D and the longitudinal distance about 0.2 • D. The shafts were still coupled together and the propellers therefore ran at the same number of revolutions.

This modification of the arrangement did not give rise to any measurable difference in the total horsepower. The wake coefficient for the forward propeller was increased by 0.06, and for the aft propeller decreased by 0.04. The

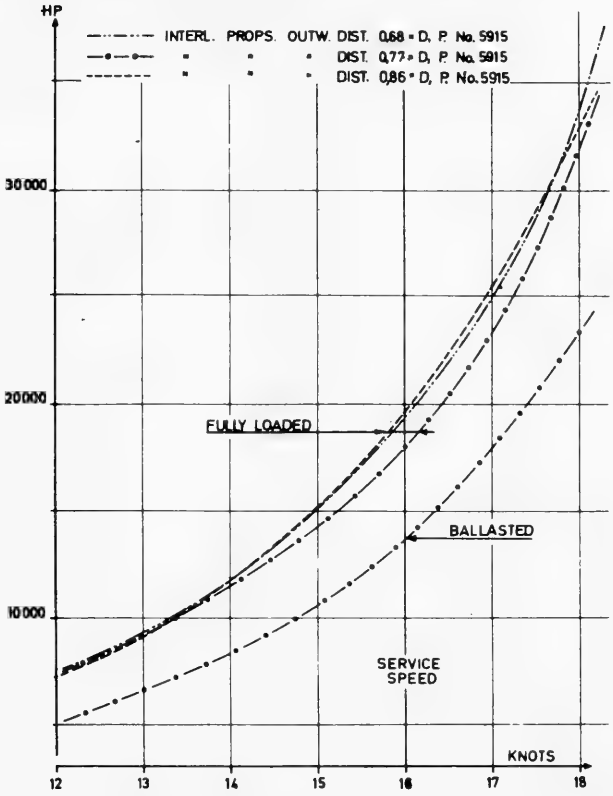

Fig. A1 - Propeller horsepowers from tests with outward-turning interlocking propellers

two propeller loadings were therefore different. If this arrangement should be preferred to interlocking propellers, the two propellers should have different diameters and pitch.

Stress measurements were carried out on both propellers running at the same number of revolutions as well as at different numbers of revolutions. The stresses were nearly the same as for interlocking propellers (Fig. 18). The influence of the aft propeller on the stresses of the forward propeller was extremely small, but the influence of the latter on the stresses of the former was, as could be expected, more pronounced.

* * *

DISCUSSION

Dr. P. C. Pien
Naval Ship Research and Development Center
Washington, D. C.

This paper by Professor Prohaska and Mr. Munk is very interesting. At the Naval Ship Research and Development Center we have been experimenting with the overlapping propeller stern arrangement for the last couple of years. The authors use the term "interlocking propellers." Six models with such an arrangement have been tested for powering performances. In each case, a large saving in power requirements has been achieved as compared with a conventional twin-screw arrangement. At several other towing tanks, similar experiments have been conducted. All the available experimental results are quite comparable with those given in the paper.

Despite the simplicity and the high hull efficiency of a single-screw stern arrangement, there are many cases where such an arrangement cannot be used. In most cases a conventional twin-screw arrangement has been chosen as an alternative. In the light of the results given in this paper, as well as other published and unpublished test results, it can be stated that the overlapping propeller stern arrangement is a better alternative. Besides saving power, another advantage is the possibility of using with it either a single or a twin powerplant. If two powerplants are chosen, an overlapping propeller arrangement is simply a matter of installing the propellers in the proper locations to a single-screw ship hull. Two shafts are inclined to have propellers overlapping each other. By choosing a different number of blades between the two propellers, each propeller is essentially independent of the other as far as the hull vibration problem is concerned. Since the power absorbed by each propeller is only one-half of the total, the risk of propeller cavitation and propeller-induced vibration would be greatly reduced.

In view of this discussion and their own experience with the overlapping propeller stern arrangement, what reservations would the authors have in recommending such a stern arrangement to the shipping industry?

* * *

DISCUSSION

J. Strøm-Tejsen
Naval Ship Research and Development Center
Washington, D. C.

I would like to congratulate the authors on a most interesting paper, and in particular on their measurements of the fluctuating-blade bending forces, which to my knowledge are the first measurements of this kind carried out for the

overlapping-propeller arrangement. The tests indicate that there should be no reason to anticipate problems due to the close proximity of the two propellers to each other. In comparison with a single-screw arrangement, vibration and cavitation problems should be greatly reduced, since the loading carried by each propeller in the overlapping arrangement would be only half of the load to be carried by the propeller in a single-screw arrangement.

The authors have considered the application of the overlapping system to a large tanker, and the test results show that the system would be most attractive due to the reduction in the horsepower requirement. Another typical application would be the fast cargo ship, where, in particular, vibration problems might become serious for a single-screw arrangement. Consequently, a contrarotating system might be considered. In this case, however, the overlapping arrangement would seem to have an advantage over the contrarotating system, since there should be no particular mechanical problems in comparison with those to be faced in developing the shaft arrangement for the contrarotating system.

In the analysis of the test results, the authors have introduced a correction of the wake coefficient due to scale effects. This correction makes a twin-screw arrangement more favorable, whereas the single-screw is penalized. As a result of this analysis technique, the optimum distance between the propeller shafts in the overlapping-propeller arrangement is somewhat larger than in the case where no scale-effect correction is applied. The correction, however, is very small, and it seems that the difference in the method of analysis would give only an insignificant difference in the optimum shaft distance. I should like to know if the authors share this view.

* * *

REPLY TO DISCUSSION

C. W. Prohaska

It has been a great pleasure for the authors to have the comments of Dr. Pien and Dr. Strøm-Tejsen, who originally drew attention to the subject treated in the present paper.

Dr. Pien mentions that a further series of tests with overlapping propellers have been carried out at the Naval Ship Research and Development Center and that the results are quite comparable with those of this paper. The authors are glad to learn this, as the advantages of the new propeller arrangements regarding total efficiency are thus further confirmed.

The authors agree with Dr. Pien that the interlocking or overlapping propellers should be a superior alternative to the heavily loaded single-screw and to twin-screws. Until now, however, only a very full hullform has been tested at HyA, and our experience is therefore limited; but for this type of ship nothing has been found which could justify a rejection of the new systems.

Dr. Strøm-Tejsen points out that the new systems should also be an alternative to the contrarotating propeller system. This is also the opinion of the authors, as the reduction of required horsepower for the rather simple overlapping or interlocking propeller systems in relation to the other propulsion systems was of the same order as the reduction which might be expected for contrarotating propellers, where the technical difficulties are unpredictable.

Finally, Dr. Strøm-Tejsen mentions the correction of the wake for scale effect. This correction is used to reproduce the conditions of the trial trip, and the test results in this paper are therefore only valid for this case. If no correction had been used, the wake and consequently the other results found by the tests would correspond to some undefined service condition for the ship a year or two out of dock.

The wake correction is largest for the single-screw propulsion system. Part of the gain in total efficiency obtained by using overlapping or interlocking propellers instead of a single screw is therefore due to this correction. This part is, in the present case, about one-fourth of the total gain.

The difference in the wake correction for the three different distances between the shafts of the interlocking propellers is small, and only of minor importance for the comparison. The optimum distance between the shafts, as mentioned in the paper, is determined by the propeller loading and the strength of the tangential wake component, rather than by the use of the wake correction. It is therefore difficult to give a general optimum distance between the shafts.

* * *

DISCUSSIONS

Monday, August 26, 1968, 5 p.m.

PANEL DISCUSSION—WAVE RESISTANCE

Nonlinear and Viscous Effects in Wave Resistance

J. N. Newman, Panel Chairman
Massachusetts Institute of Technology
Cambridge, Massachusetts 02139

INTRODUCTION

In recent years there has been increasing evidence of the shortcomings in existing techniques for predicting the wave resistance of surface ships. Theory, as represented by the classical approach of Michell, and experiments carried out with the Froude hypothesis, have been known to be in poor agreement, especially at low Froude numbers. But the main impact of recent investigations, and particularly the direct experimental measurements of viscous and wave drag, has been to suggest that the fault may rest with *both* the theoretical and experimental techniques. This premise has now led to a broad questioning of the classical assumptions that wave resistance could be considered entirely as an inviscid mechanism and theoretically analyzed using the linearized theory of water waves. Relaxing either assumption involves a compounding of the analytical complexities, so that progress has been slow, and we must not expect any major breakthroughs to occur in the next few years, but sufficient advances have recently been made that it is timely to discuss and report on our progress at this time.

The following brief summaries are categorized under the three headings Nonlinear Effects, Viscous Effects, and Miscellaneous. Acknowledgment is due to the participants in the panel discussion on wave resistance. Of necessity, their contributions have been severely abbreviated in this report.

NONLINEAR EFFECTS

The classical Michell theory assumes that the ship hull is geometrically thin, and the boundary conditions both on the hull and on the free surface are linearized with only the leading (first) order terms retained. For many years the relative importance of these two linearizations has been discussed, and some investigations were aimed at the more tractable extension of including nonlinear effects from the hull boundary condition. The work of Sizov (1961) has stimulated several investigations of the complete second-order solution. These have included the two-dimensional treatments of submerged cylinders by Tuck (1965) and Salvesen (1966), and in three dimensions the analysis of the submerged sphere by Kim (1968), the spheroid by Chey (1968), and the parabolic strut by Eng (1968). All of these references contain actual calculations, and in some cases experimental confirmation is included as well; the importance of

nonlinear free-surface effects is emphasized, especially at low Froude numbers.

The second-order theory for thin surface ships was outlined by Wehausen (1963) and subsequently has been studied extensively by Eggers (1966), Yim (1968), and Wehausen (1968). In principle, the numerical calculations of wave resistance are tractable, but as yet these have not been completed.

Salvesen (1968) and Newman (1968) have considered certain aspects of the third-order theory, from different viewpoints. Salvesen showed that third-order effects were negligible for the submerged two-dimensional cylinder, thus validating the second-order truncation. Newman showed that no resonant nonlinear energy exchange mechanisms exist in the third-order solution of the three-dimensional free-wave distribution, as opposed to the opposite conclusion reached in the case of wind-generated wave spectra by Phillips and others.

The above-mentioned work is all based upon the Eulerian description (with the notable exception of Wehausen (1968) who has formulated the thin-ship problem in Lagrangian coordinates) of the fluid motion and the asymptotic expansion in terms of a suitable, small parameter such as the ship's beam or the wave elevation. The leading-order contribution to the asymptotic expansion is the classical linear solution associated with Kelvin's ship-wave pattern and Michell's wave-resistance integral. Second- and third-order contributions can be regarded as approximations to the nonlinear effects, although solutions obtained in this manner are, at each successive order of approximation, associated with *linear* boundary value problems. An entirely different and inherently nonlinear approach to wave problems is that developed by Whitham and others, in which the wave system is assumed to be of large amplitude but slowly varying in amplitude and wave number, so that it is in essence a perturbation of the exact nonlinear solution for purely periodic unidirectional wave motion. (Various papers describing and using this method are contained in the Proceedings of the Royal Society of London, Series A, Vol. 299, No. 28, 1967.) This method has been applied to the study of ship waves by Howe (1967, 1968) with striking nonlinearities along a "cusp" line where, in effect, a shock wave is formed. So far, however, this study has been restricted to a system of diverging waves only, since the assumption of slowly varying wave numbers does not permit the simultaneous existence (and interaction) of diverging and transverse wave systems. The interrelationship between the Whitham technique and the Eulerian perturbation approach has been examined in a recent paper by Hoogstraaten (1968).

Gadd (1968) has proposed a second-order correction for the hull boundary condition which is similar to the earlier technique of Guilloton. A computer program has been written which incorporates this correction and which is claimed to give realistic estimates of the wave resistance of fairly fine hull forms. (The free-surface nonlinearities were neglected after initial investigations showed that they required excessive computer time.)

VISCOUS EFFECTS

One only need observe the flow in the wake behind a ship's stern to realize that viscous effects, and especially separation, affect the ship's waves and

wave resistance. The converse effect of the waves on the viscous flow is more difficult to observe but no less surprising.

The earliest work in this area was Havelock's inclusion of the displacement thickness on the effective beam which led, from Michell's integral, to an estimate of the effects of viscosity on the wave resistance. Wu (1963) included the effects of the wave-field pressure gradient on the boundary layer for the case of a flat plate, and with wake effects ignored. Experimental investigations of this theory are in progress. Webster and his collaborators (1967) used a boundary-layer formulation, in conjunction with Guilloton's method, to compute the separation point on the hull as a function of Froude and Reynolds numbers.

It seems likely that, for reasonably full ships where the disagreement between theory and experiment is most severe, the effects of separation will dominate those of the relatively thin boundary layer upstream of the separation point. With this in mind Milgram (1968) has recently used Michell's integral, with empirical values of the wake geometry, to determine the wave resistance of a simple hull form. Generally speaking, the computed values of the wave resistance are decreased by the presence of the wake, at those speeds where the wave resistance is a decreasing function of the Froude number, and unaffected by the wake at other Froude numbers.

The effects of the wake can be idealized, from another viewpoint, by considering the characteristics of wave propagation in a shear flow. This problem has been considered by van Wijngaarden (1968), as well as in the earlier papers by Brooke-Benjamin (1959) and Kolberg (1958).

If the Reynolds number is sufficiently small and the body streamlined, so that laminar attached flow can be assumed, it is possible to attack the boundary-value problem for the solution of the Navier-Stokes equations, including the free-surface boundary condition. This has been done by Dugan (1968) for the restricted case of a submerged two-dimensional horizontal plate, moving at sufficiently low velocities that the Oseen linearization of the Navier-Stokes equations can be made. With the additional assumption that the plate is deeply submerged, the following equation is obtained for the drag coefficient:

$$C_D = \frac{4\pi/R + 6/R^2F^4d^3}{\gamma - 1 + \ell n(R/16)} \quad .$$

Here, R and F are the Reynolds and Froude numbers based on the chord length of the plate, d is the ratio of the depth of submergence to the chord length, and γ is Euler's constant. This result is valid for large values of F and d, and is asymptotic to the non-free-surface results when $F^4d^3 \to \infty$.

The interaction of waves and viscous wakes has been considered by Lurye (1968), using the Oseen equations and the linear free-surface conditions. A particular "singularity" solution is obtained, and more general flows can be generated by superposition. The Oseen equations have also been used by Nikitin and Gruntfest (1966) to find the wave resistance of a moving pressure distribution in a viscous fluid. (I am indebted to Professor Weinblum for calling attention to this work, and also to the subject of propeller and rudder effects on wave

resistance.) The latter problem was also treated in two dimensions, but including surface tension, in the earlier work of Wu and Messick (1958).

MISCELLANEOUS

One of the most important experimental developments, which has brought us to our present state of inquiry, is the determination of wave resistance from analysis of wave records. Several different methods exist for performing this analysis, and none can be regarded as "exact," but the results are fairly consistent and seem likely to be at least as reliable, for their stated purpose, as the Froude or Michell approaches are for theirs. However, the wave analysis techniques are still being examined critically, and Sabuncu (1968) has examined the effects of the local disturbance which are neglected in the usual free-wave analysis, and has also proposed the use of the wave-height measurements to determine the "equivalent body shape" which is the source of the disturbance. This appears to be an interesting scheme for experimentally finding the effective hull shape, including the displacement effects of the boundary layer and the separated wake. (The same scheme has been employed by Hogben (1967, 1968), who has demonstrated its success in the case of a parabolic model.)

Inui and Kajitani (1968 a,b) have investigated the bow wave system of a Wigley model and have compared the experimentally measured waves with corresponding theoretical predictions. It is found that good agreement results for wave angles $20^\circ < \theta < 60^\circ$, but that for smaller or larger angles the theoretical prediction of wave amplitude is substantially greater than that which is measured. For wave angles greater than 60° (i.e., very short wavelengths), this discrepancy is attributed to nonlinear effects, associated with the high values of the wave steepness in this region. For the angles less than 20°, the discrepancy is attributed to sheltering effects of the hull. Correcting empirically for the sheltering effect improves the experimental agreement considerably and also appears to lead to a superior approach for the investigation of low-resistance hull forms.

A recent experiment of fundamental significance has been performed by Sharma (1968), which might be conveniently described as a modern version of the Weinblum-Kendrick-Todd friction plank experiment. Sharma towed a wall-sided parabolic strut, of length 2.0 m, beam 0.1 m, and draft 0.3 m, at Froude numbers ranging from 0.2 to 1.0. Measurements were made of the free-wave spectrum using a longitudinal cut, and the wave resistance was computed from these data and also from Froude's method using the Prandtl-Schlichting frictional drag estimate and a constant form factor $C_v/C_F = 1.15$. The results of both experimental methods show quite good agreement with each other and with Michell's integral over the entire Froude-number range. Some significant discrepancy was found in the phase of the free waves at low Froude numbers, which Sharma attributes to nonlinear wave effects. (The satisfactory agreement achieved for this model, and for the parabolic hull discussed by Shearer and Cross (1965), is the principal evidence to suspect the importance of separation and nonlinear effects.)

Since attention has been focused on the low-Froude-number regime by the practical speeds of merchant ships and by the lack of satisfactory theories and

experimental predictions in this domain, it seems natural to seek a theory for the *slow* ship in the sense of a systematic perturbation expansion. This idea is not new, but attempts to exploit it have been abandoned in early stages when difficulties were encountered. In recent work Ogilvie (1968) has sought a fresh approach, in which the slow motion of a submerged body is treated as a perturbation about the exact zero-Froude-number, or rigid-free-surface, flow field. This approach seems more likely to succeed, although the subsequent extension to surface vessels is not trivial.

REFERENCES

Brooke-Benjamin, T., 1959, "Shearing Flow Over a Wavy Boundary," J. Fluid Mech., Vol. 6, p. 161

Chey, H., 1968, "Second-Order Wave Resistance of a Submerged Spheroid," Dissertation, Stevens Institute of Technology

Dugan, J.P., 1968, "On the Viscous Drag of Bodies Moving Near a Free Surface" (to be published)

Eggers, K.W.H., 1966, "Second-Order Contributions to Ship Waves and Wave Resistance," Proceedings of the Sixth Symposium on Naval Hydrodynamics, Washington, D.C., p. 649

Eng, King, 1968, "Development and Evaluation of a Second-Order Wave Resistance Theory," Dissertation, Stevens Institute of Technology

Gadd, G.E., 1968, "On Understanding Ship Resistance Mathematically," J. Inst. Maths. Applics., 4, 43

Gruntfest, R.A., and Nikitin, A.K., 1966, "On Wave Resistance in a Viscous Fluid," Izv. Akad. Nauk SSR, Mech. Fluids and Gases, No. 4, pp. 118-126

Hogben, N., 1967, "A Computer Program for Correlating Measured Wave Patterns with Theoretical Source Arrays," Ministry of Technology, National Physical Laboratory, Ship Division, T. M. 189

Hogben, N., 1968, "A New Method of Correlating Measured Wave Patterns with Theoretical Source Arrays," Ministry of Technology, National Physical Laboratory, Ship Division, T. M. 224

Hoogstraaten, N.W., 1968, "Dispersion of Nonlinear Shallow Water Waves," J. of Eng. Math., Vol. II, No. 3, pp. 249-273

Howe, M.S., 1967, "Nonlinear Theory of Open-Channel Steady Flow Past a Solid Surface of Finite-Wave-Group Shape," J. Fluid Mech., Vol. 30, pp. 497-512

Howe, M.S., 1968, "Phase Jumps," J. Fluid Mech., Vol. 32, pp. 779-790

Inui, T., and Kajitani, H., 1968a, "Bow Wave Analysis of a Simple Hull Form," J. Japanese Soc. Nav. Archs. (in press)

Inui, T., and Kajitani, H., 1968b, "Wavemaking Mechanism of Ship Hull Forms, Generated from Undulatory Source Distributions," J. Japanese Soc. Nav. Archs. (in press)

Kim, W.D., 1968, "Nonlinear Free Surface Effect on a Submerged Sphere," Davidson Lab Report 1271

Kolberg, F., 1958, "Untersuchung des Wellenwiderstandes von Schiffen auf flachem Wasser bei gleichformig scherender Grundstromung," ZAMM, Bd. 39, Heft 7/8, pp. 253-279

Lurye, J.R., 1968, "Interaction of Free-Surface Waves with Viscous Wakes," Phys. Fluids, Vol. 11, No. 2, pp. 261-265

Milgram, J.H., 1969, "The Effect of a Wake on the Wave Resistance of a Ship," (to be published in the J. Ship Res.)

Newman, J.N., 1968, "Third-Order Interaction in Kelvin Wave Systems" (to be published)

Ogilvie, T.F., 1968, "Wave Resistance: The Low Speed Limit," University of Michigan, DNAME, Report No. 002

Sabuncu, T., 1968, "Determination of the Equivalent Form and Wave Making Resistance of a Submerged Slender Body Moving in a Channel by Transversal Wave Profile Measurements" (to be published)

Salvesen, Nils, 1966, "Second-Order Wave Theory for Submerged Two-Dimensional Bodies," Proceedings of the Sixth Symposium on Naval Hydrodynamics, Washington, D.C., p. 595

Salvesen, Nils, 1968, "Higher-Order Wave Theory for Submerged Two-Dimensional Bodies" (to be published)

Sharma, S.D., 1968, "Some Results Concerning the Wavemaking of a Thin Ship," HSVA Report

Shearer, J.R., and Cross, J.J., 1965, "The Experimental Determination of the Components of Ship Resistance for a Mathematical Model," Trans. RINA

Sizov, S.G., 1961, "On the Theory of the Wave Resistance of a Ship on Calm Water," Izv. Akad. Nauk SSR, Otd. Tekh. Nauk, Mekh. i Mashinostr., No. 1, pp. 75-85 (Bureau of Ships Translation No. 887)

Tuck, E.O., 1965, "The Effect of Non-Linearity at the Free Surface of Flow past a Submerged Cylinder," J. Fluid Mech., Vol. 22

Webster, W., 1965, Hydronautics Proposal to SNAME, Hydrodynamics Committee

Wehausen, J.V., 1963, "An Approach to Thin-Ship Theory," Proceedings, International Seminar on Theoretical Wave-Resistance, Ann Arbor

Wehausen, J.V., 1968, "Use of Lagrangian Coordinates for Ship Wave Resistance (First- and Second-Order Thin-Ship Theory)," J. Ship Res. (to be published)

van Wijngaarden, L., 1968, "On the Propagation of Gravity Waves on a Flow with Nonuniform Velocity Distribution," Twelfth Congress of Applied Mechanics, Stanford

Wu, T.Y., and Messick, R.E., 1958, "Viscous Effect on Surface Waves Generated by Steady Disturbances," Calif. Inst. of Tech., Eng. Div., Report No. 85-8

Wu, T.Y., 1963, "Interaction between Ship Waves and Boundary Layer," Proceedings, International Seminar on Theoretical Wave-Resistance, Ann Arbor

Yim, B., 1968, "Higher-Order Wave Theory of Ships," J. Ship Res., 12, 3, pp. 237-246

* * *

An Evaluation of the Wave Flow Around Ship Forms with Application to Second-Order Wave Resistance Calculations

K. Eggers
Institut für Schiffbau der Universität Hamburg
Hamburg, Germany

ABSTRACT

For a class of shiplike bodies, a procedure is established for the calculation of first-order flow components including the local wave field. A second-order correction flow field then is defined, using an iteration procedure based on Green's formula. However, under introduction of an "inverse flow principle," the first- and second-order wave resistance can then be calculated directly from first-order flow components.

Numerical results show that the corrections to first-order wave resistance, both from free-surface singularities and from improvement of the body-boundary condition, are negative for Froude numbers ≤ 0.31, as was to be expected from experimental information. For higher Froude numbers, the correction due to free-surface effects becomes positive. However, mainly due to increasing influence of corrections

due to flow at the ship's bottom, the ship-surface corrections remain negative and large. This is in contrast to experimental evidence as well as to results from a slender-body-theory approach. Tentative calculations support the conclusion that at high Froude numbers the first-order approximation should be constructed according to slender-body theory (this would even imply a reduction of the computational effort) with less flow intensity at the ship's bottom area, and then improved by the iteration method developed.

It is found that the procedure developed is not affected by singular behavior of the first-order flow at the bow, stern, and keel, resulting from that part of the flow which would persist at zero Froude number, if appropriate methods of quadrature are selected and if the flow is evaluated on the hull rather than on the centerplane. This is considered to be even more pertinent for analytical reasons.

The second-order corrections found explain a significant part of the discrepancies between experimental wave resistance and predicted values from first-order theories. The rest must be attributed either to viscous wave interactions or to resistance components of still higher order. At least in the range of Froude numbers larger than 0.2, where the present investigations were performed (mostly for reasons of economy), it is felt that the computational effort is moderate, once a computer program has been established, and attempts to apply the method to more conventional forms should be encouraged.

* * *

Wave-Resistance Calculations for Practical Ships

G. E. Gadd
Ship Division, National Physical Laboratory
Feltham, England

A computer program has been written which appears to give fairly realistic estimates of the wave-making of practical ship hulls which are not too bluff. Kelvin sources are distributed over the vertical plane of symmetry of the hull, which is divided into a grid of rectangular panels, the hull shape being defined by the lateral offsets corresponding to the grid intersection points. The source density is assumed uniform over each of the panels in the computation of the downstream waves, but for computing local effects near the hull the cruder approximation is made of replacing each source panel by a concentrated source of equal flux output at its center.

Source strengths are calculated using second-order corrections as described by the author (J. Inst. Maths. Applics. Vol. 4, p. 43, 1968). The free-surface pressure distribution, which should be imposed (K. W. H. Eggers, Proceedings of the Sixth Symposium on Naval Hydrodynamics, p. 649) to compensate for linearization errors in the free-surface boundary condition, is neglected. This pressure distribution was computed for the simple case of a single submerged point source, but so much computer time was involved that it was judged

impracticable to incorporate such corrections in routine wave-resistance calculations.

Calculations of the wave pattern generated by practical ship hulls reveal several discrepancies between theory and experiment. In the bow-wave region, the main discrepancy is that the observed waves lie outboard of the predicted ones. It is not thought likely that inclusion of the free-surface pressure correction, if it were thought practicable, would remedy this defect, which probably springs from a nonlinear effect on the propagation speeds of the waves that increased their rate of lateral spreading. However, crudely speaking, the effect is as if the model were upstream of its true position, and therefore, as far as the computation of the wave resistance from downstream wave pattern goes, it may not be very important to remedy this defect of the theory. More significant is the fact that the stern-wave system is greatly overestimated in amplitude by the theory. This seems likely to be mainly a frictional effect. Theory predicts that a large wave crest exists just behind the stern, similar to the bow crest on the hull. Whereas the fluid entering the bow crest has been very little influenced by viscosity, however, the fluid just behind the stern has traveled through the hull boundary layer, and it is doubtful whether it could negotiate the steep slope of the forward face of a wave crest there such as theory predicts. It is not surprising, therefore, that in practice the stern-crest amplitude is often greatly attenuated. This could lead to the radiated stern waves being much smaller in practice than in theory.

Such effects would obviously be very difficult to treat theoretically. A seemingly useful empirical approach is as follows: The total downstream wave pattern is written as $= \zeta_B + \zeta_S$, where ζ_B represents a system centered on the bow and ζ_S a stern-centered system. Numerical estimates of ζ are obtained from the theory incorporating second-order hull source corrections; ζ is decomposed into ζ_B and ζ_S in such a way that the amplitude functions of ζ_B and ζ_S are as smooth as possible, to give the most "natural" subdivision into bow and stern waves. The stern-centered system ζ_S is then multiplied by the empirical reducing factor k and recombined with ζ_B to give the total wave pattern, and hence the wave resistance. For a typical 0.60-block-coefficient ship, an appropriate value of k is 0.5, and fairly realistic estimates of downstream wave pattern and wave resistance are then obtained.

* * *

Derivation of Source Arrays from Measured Wave Patterns

N. Hogben
Ship Division, National Physical Laboratory
Feltham, England

INTRODUCTION

In Refs. [1] and [2], a method for deducing theoretical source arrays from measured waves by solving linear simultaneous equations, is described.

Experience in analyzing experimental results has revealed some difficulties, and Ref. [3] describes a new method of solution which overcomes these. This new method uses Fourier analysis to solve the equations and is particularly effective in absorbing measured results covering a wide range of speeds. A practical example of a successful application to experiments by Everest on a fine model (Ref. [4]), is discussed in Ref. [3].

SKETCH OF NEW METHOD

The simultaneous equations relating source strength M_r and positions $(x_r, 0, z_r)$ with measured free-wave amplitude (according to linear theory for deep water) are

$$\sum_r \frac{M_r}{v} e^{-z_r \alpha_n^2/k} \cos(\alpha_n x_r) = \frac{b}{16\pi} \left(2 - \frac{k^2}{\alpha_n^2}\right) A_n ,$$

$$\sum_r \frac{M_r}{v} e^{-z_r \alpha_n^2/k} \sin(\alpha_n x_r) = \frac{b}{16\pi} \left(2 - \frac{k^2}{\alpha_n^2}\right) B_n , \qquad (1)$$

where

v is the speed of travel of the array,

x_r are longitudinal coordinates,

z_r are vertical coordinates,

$\alpha_n = k \sec \theta_n$,

$k = g/v^2$,

θ_n = Angle of propagation of nth wave component,

b = Tank width,

A_n, B_n are measured wave amplitudes.

Let (1) be rewritten as

$$\sum_r \left(\frac{M_{+r}}{v} + \frac{M_{-r}}{v}\right) \cos\left[\left(\frac{\pi r}{\Delta\alpha}\right)\alpha\right] = f_0(\alpha) = \frac{b}{16\pi} \left(2 - \frac{k^2}{\alpha^2}\right) A_n e^{z_m \alpha^2/k} ,$$

$$\sum_r \left(\frac{M_{+r}}{v} - \frac{M_{-r}}{v}\right) \sin\left[\left(\frac{\pi r}{\Delta\alpha}\right)\alpha\right] = f_s(\alpha) = \frac{b}{16\pi} \left(2 - \frac{k^2}{\alpha^2}\right) B_n e^{z_m \alpha^2/k} , \qquad (2)$$

where

z_m is a mean depth,

$f_0(\alpha)$, $f_s(\alpha)$ are functions which are invariant with speed if the linear theory is valid,

$\Delta\alpha$ is a range of α defined by

$$x_r = \frac{\pi r}{\Delta\alpha} = -x_{-r} \ . \tag{3}$$

From (2) it may be shown that

$$\begin{aligned} \frac{M_{+r}}{v} &= \frac{1}{2\Delta\alpha} \int_{-\Delta\alpha}^{+\Delta\alpha} \left\{ f_0(\alpha) \cos \left[\left(\frac{\pi r}{\Delta\alpha} \right) \alpha \right] + f_s(\alpha) \sin \left[\left(\frac{\pi r}{\Delta\alpha} \right) \alpha \right] \right\} d\alpha \ , \\ \frac{M_{-r}}{v} &= \frac{1}{2\Delta\alpha} \int_{-\Delta\alpha}^{+\Delta\alpha} \left\{ f_0(\alpha) \cos \left[\left(\frac{\pi r}{\Delta\alpha} \right) \alpha \right] + f_s(\alpha) \sin \left[\left(\frac{\pi r}{\Delta\alpha} \right) \alpha \right] \right\} d\alpha \ , \end{aligned} \tag{4}$$

with

$$f_0(\alpha) = f_0(-\alpha) \ ,$$

and

$$f_s(\alpha) = -f_s(-\alpha). \tag{5}$$

Figure 1 shows the results of applying this method to wave measurements by Everest (Ref. [4]) behind a model defined by

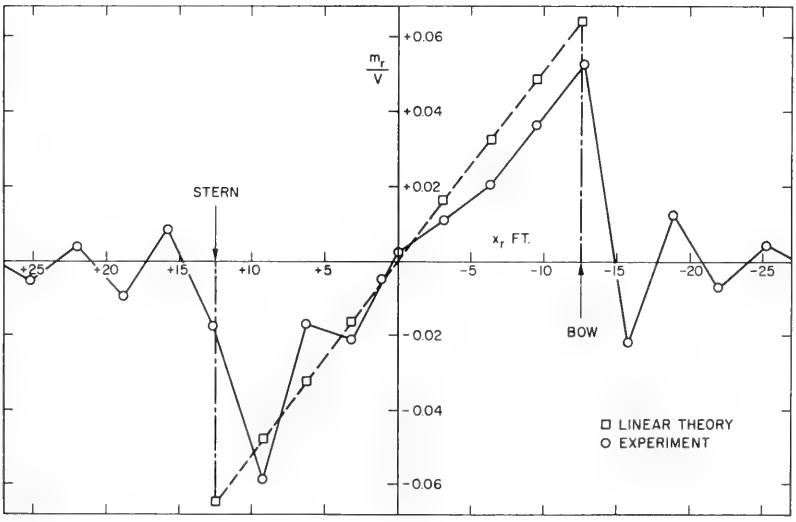

Fig. 1 - Source distribution

length L = 25 feet,

breadth B = 1.25 feet,

draft d = 1.5625 feet,

and an equation of form

$$\frac{y}{\frac{1}{2}B} = \left[1 - \left(\frac{x}{\frac{1}{2}L}\right)^2\right]\left[1 - \left(\frac{z}{d}\right)^2\right].$$

Measurements over the range of Froude number 0.3-0.55 were analyzed.

REFERENCES

1. Hogben, N., "A Note on the Relation of a Wave Pattern and a Source Distribution," Ship Div. TM No. 76 Dec. 1964

2. Hogben, N., "A Computer Program for Correlating Measured Wave Patterns with Theoretical Source Arrays," Ship Div. TM No. 189 Sept. 1967

3. Hogben, N., "A New Method of Correlating Measured Wave Patterns with Theoretical Source Arrays," Ship Div. TM No. 224 (in preparation)

4. Everest, J.T., "Measurements of the Wave Resistance of a Series of Mathematical Models including Comparison with Theoretical Estimates," Ship Div. Rep. No. 120 (in preparation)

* * *

Interaction of Free-Surface Waves with Viscous Wakes

Jerome R. Lurye
Control Data Corporation, TRG Division
Melville, New York

ABSTRACT

A method of investigating the interaction of free-surface waves with viscous wakes is described. The method consists in constructing a viscous-wake solution to the Oseen equations that satisfies the three linearized free-surface conditions appropriate to a viscous fluid. The solution is characterized by a singularity which simulates approximately the effect of a body. More general flows of the same type can be formed by superposition. The solution obtained is believed to be the first one to represent explicitly a viscous wake in the presence of a free surface.

* * *

Recent Developments on Bulbous Bows at Hydronautics, Inc.

M. Martin
Hydronautics, Inc.
Laurel, Maryland

It has been well known that a bulb at the bow reduces the bow wave height, and thus the wave resistance is decreased. (Inui, 1962; Yim, 1963). A simple analytical representation of a bulb is the flow due to a point doublet located at the stem of a ship bow. For a given polynomial representation of a Michell's ship source distribution, the optimum strength of the doublet or the approximate size of bulb at a given position located on the stem was given for low Froude numbers $Fr < 0.3$ by Yim (1965).

An approximate simple image system for a bulbous ship was also given (Yim, 1966c), and plotting streamlines of a bulbous ship can easily be done. However, when we plot the streamlines of a ship with a point-doublet bulb, the bulb is seen to have a narrow neck and is therefore susceptible to separation. Therefore, it has been customary to fair the waterlines so that separation can be avoided even though the fairing was not very scientific.

Yim (1964) has found an optimum source type of bulb for appropriate waterlines. These do not have any neck to induce flow separation. This type of bulb has been investigated by Maruo (1964) both theoretically and experimentally with good results. Pien (1964) also made use of the source type of bulb whenever his optimum ship waterline had negative-cosine bow waves. However, the source-type bulb needs the consideration of sinks in order to close the body and the ship shape which needs a purely source-type bulb is not too practical. Thus, this idea is useful only when we consider a total ship with proper attention to both the bow, the stern, and the shoulder.

At Hydronautics, Inc., a simple cylindrical bulb with a spherical head horizontally oriented at the bow was designed for a given ship and tested at the Naval Ship Research and Development Center (formerly David Taylor Model Basin) (Yim et al., 1966). Although the ship waterlines had been analyzed and it was found to need a strong source-type bulb in addition to a doublet-type bulb, a further important reason for taking the bulb to be a cylinder was its easy fabrication.

In this report, an optimum ship form for a given cylindrical bulb horizontally oriented at a ship bow is analyzed. A basic mathematical form for the ship is assumed based on the concept of a double model ship (Inui, 1957) and Michell's ship. Considering a point-doublet bulb and the optimum ship form from the theory already developed (Yim, 1965), many such bulbous ships were superposed, so that the bulb would fill in the given cylinder. A typical model was selected and tested in the Netherlands Ship Model Basin with good results.

THEORETICAL CONSIDERATIONS

The mechanism of bulbs at a ship bow has been studied quite extensively (Wigley, 1936; Inui, 1962; Yim, 1963). The wave resistance is known to be due to the regular waves which carry out energy far away. The regular waves consist of bow waves, stern waves, and possibly shoulder waves, all of which can be considered to originate from the discontinuities of a function representing the hull shape of a ship. These waves are a composition of sine waves and cosine waves propagating in all directions from the originating point and are called elementary waves (Havelock, 1934). In particular the bow waves of a sine ship; i.e., one represented by the source distribution

$$m(x_1) = a_0 \cos(\pi x_1) = a_0 \sum_{n=0}^{n=\infty} \frac{(\pi x_1)^{2n}}{2n!}$$

in

$$0 < x_1 < 1; \quad y = 0 \quad \text{and} \quad 0 < z_1 < 1$$

consists only of positive sine waves originating from the bow. The regular waves due to a point doublet below the free surface are known to be negative sine waves. Since the point doublet can be represented by an approximately spherical bulb, such bulbs, properly selected, can cause cancellations of the bow waves. Yim (1964) determined, for various Froude numbers, the optimum radii r_b of point-doublet bulbs located at various depths at the stem of sine ships. For low Froude numbers, it was shown that the same results applied to any general ship (Yim, 1965). This theory was applied to a practical bulb design with reasonable success (Yim et al., 1966). However, in practice, such bulbs must be made roughly cylindrical in order to avoid separation due to necking down of the bulb. This can be expected to reduce the bulb effectiveness.

In connection with problem, Yim (1967) has proposed a simple method for constructing an approximate source distribution and corresponding doublet distributions for an optimum ship with a cylindrical bulb. He assumes that for the ship with a cylindrical bulb, represented by the source distribution for the ship and the doublet distribution for the bulb, the volume of ship is the linear superposition of the volume of the ship without the bulb and that of isolated bulbs which would be produced by the doublet in an infinite medium. He considers a cross section of the ship with a cylindrical bulb whose center is located at $y = 0$, $z = -H$ in Fig. 2. Using the notation in Fig. 2 the area inside the circle of the given radius r and outside the cross section of the ship model is

$$A = \pi r^2 - \left(\frac{\pi y^2}{2} + r^2\theta + yr \cos\theta \right) ,$$

where θ is in radians. In Fig. 2 the Michell ship assumption (Michell, 1898) has been made insofar as the waterlines are taken to be given by $dy/dx = 2\pi m(x_1)$. Actual stream surface calculations (Yim, 1966c) show that the Michell assumption does not give the correct ship sectional shape. However, since the influence of draft is small at the low Froude numbers considered here, the simple attachment of a semicircular section to the bottom as shown in Fig. 2 has

been assumed to provide a sufficiently realistic shape for the present purpose.

If we use an approximate relation

$$y = \alpha x$$

for a short interval of x, we can find the volume inside the cylindrical column and outside the original ship hull between $x = a$ and $x = b$ by an integration of $A(x)$

$$V_b = \int_a^b A(x)\, dx$$

$$= \left[\pi r^2 x - r^2 \left(x \sin^{-1} \frac{\alpha x}{r} + \frac{1}{\alpha} \sqrt{r^2 - \alpha^2 x^2} - \frac{\pi}{6} \alpha^2 x^3 + \frac{1}{3\alpha} \sqrt{(r^2 - \alpha^2 x^2)^3} \right) \right]_{a_1}^{b_1},$$

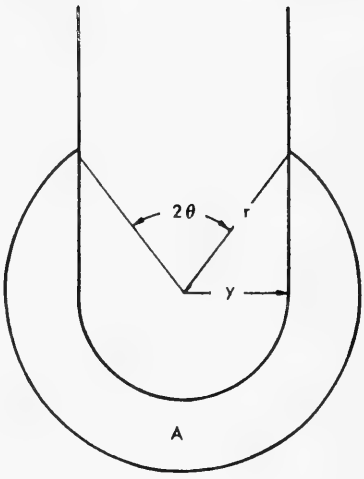

Fig. 2 - Cross section of a ship with cylindrical bulb

where a_1 and b_1 are values corresponding to a and b due to the approximation $y = \alpha x$, or $a_1 = y(a)/\alpha$ and $b_1 = y(b)/\alpha$. Since the volume of a sphere with the radius r_b is $4\pi r_b^3/3$, using the radius-strength relation of doublet bulb we can add a proper doublet to fill in V_b at a proper position, say, $z = -H$, $y = 0$, $x = d$. Then this would produce another negative sine wave which can be reduced by adding a sine ship which has the bow stem at the position of the doublet. Thus, for this sine ship the original Froude number F will be increased to

$$F_1 = F \sqrt{\frac{L}{L-d}}$$

if the stern position is kept the same for each elementary ship. Thus, r_b and F are known. Therefore one can obtain the optimum a_0 from the optimum relation mentioned before for r_b, F, and a_0.

For a given radius of cylindrical bulb r, we took

$$d = \frac{4}{3} nr \equiv d(n), \quad n = 0, 1, 2, 3, \ldots, N$$

$$a = \left(\frac{2}{3} + \frac{4}{3} n \right) r \equiv a(n), \quad b = \left\{ \frac{2}{3} + \frac{4}{3} (n+1) \right\} r \equiv a(n+1),$$

$$n = 0, 1, 2 \ldots N,$$

where N is such that V_b is always positive. Thus, $N + 1$ is equal to the number of point doublets distributed. Although the idea behind the choice of d, a, and b is that a cylindrical column whose radius is r and whose volume is the same as

that of a sphere of radius r has a column length equal to $4r/3$, any other finer choice of intervals is suitable. We note that, for

$$a(n) < x < a(n+1) ,$$

$$y(x) = 2 \sum_{n=0}^{n} a_0(n) \sin\{\pi[x-d(n)]\} ,$$

$$\alpha(x) = \frac{dy_0}{dx} = 2\pi \sum_{n=0}^{n} a_0(n) \cos\{\pi[x-d(n)]\} .$$

By the above procedure many waterlines for many different Froude numbers $F = V/\sqrt{gL}$, length-draft ratios L/H, and radii of cylinder r/H were obtained. A few of these are shown in Figs. 3 and 4 for $L/H = 32$.

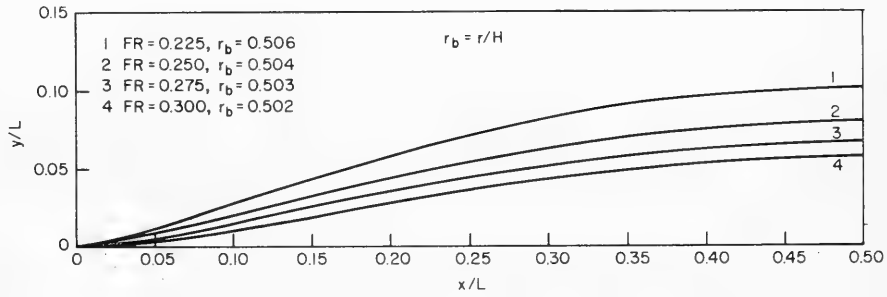

Fig. 3 - Waterlines for cylindrical bulbs -L/H = 32

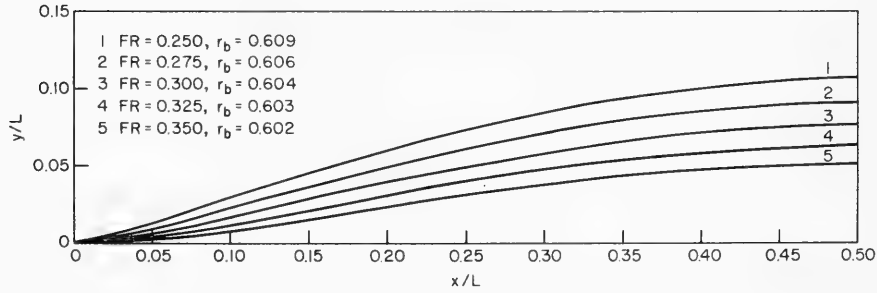

Fig. 4 - Waterlines for cylindrical bulbs -L/H = 32

MODEL TESTS

To determine the effectiveness of the above procedure, Hydronautics, Inc. had model resistance tests made for the case of $L/H = 32$, $r/H = 0.604$, $F = 0.3$.

The calculated waterline is shown in Figs. 5 and 6. The model was built in the Netherlands Ship Model Basin, with its body plane shown in Fig. 7. The results are shown in Figs. 8 and 9 in scales of CGS and feet-pound, respectively. The plottings of EHP (test)/EHP (Taylor) for the ship model with and without bulb are shown in Fig. 10. At the design point of $F = 0.3$, it is seen that a reduction in EHP of almost 20% was realized.

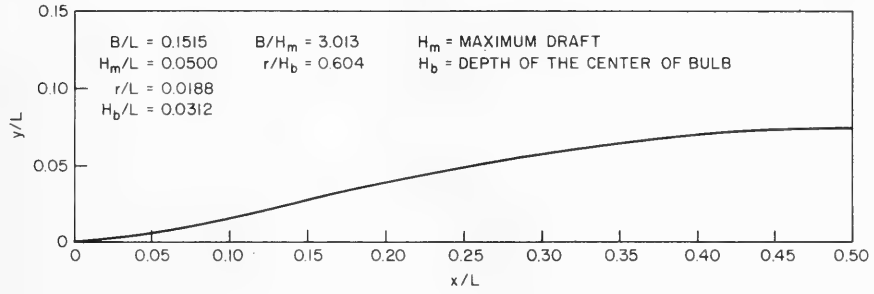

Fig. 5 - Waterline of a ship with a cylindrical bulb (tested)

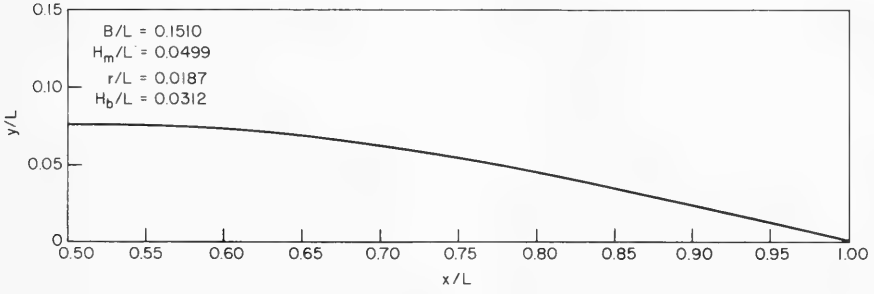

Fig. 6 - Waterline of a ship with a cylindrical bulb (tested)

CONCLUSIONS

The encouraging results of the model tests seems to support the theoretical approach proposed here for reducing ship wave resistance. This approach would be applicable not only to the determination of a good bulbous ship but also to the design of a bulb to an existing ship. If one can find a superposition of elementary sine ships for an existing ship, the optimum bulb for the given ship could be built up of the superposition of optimum bulbs for each elementary ship.

For the stern of a ship a separate treatment will be necessary. However, if the modification of the stern improves the efficiency of the ship without the bulb,

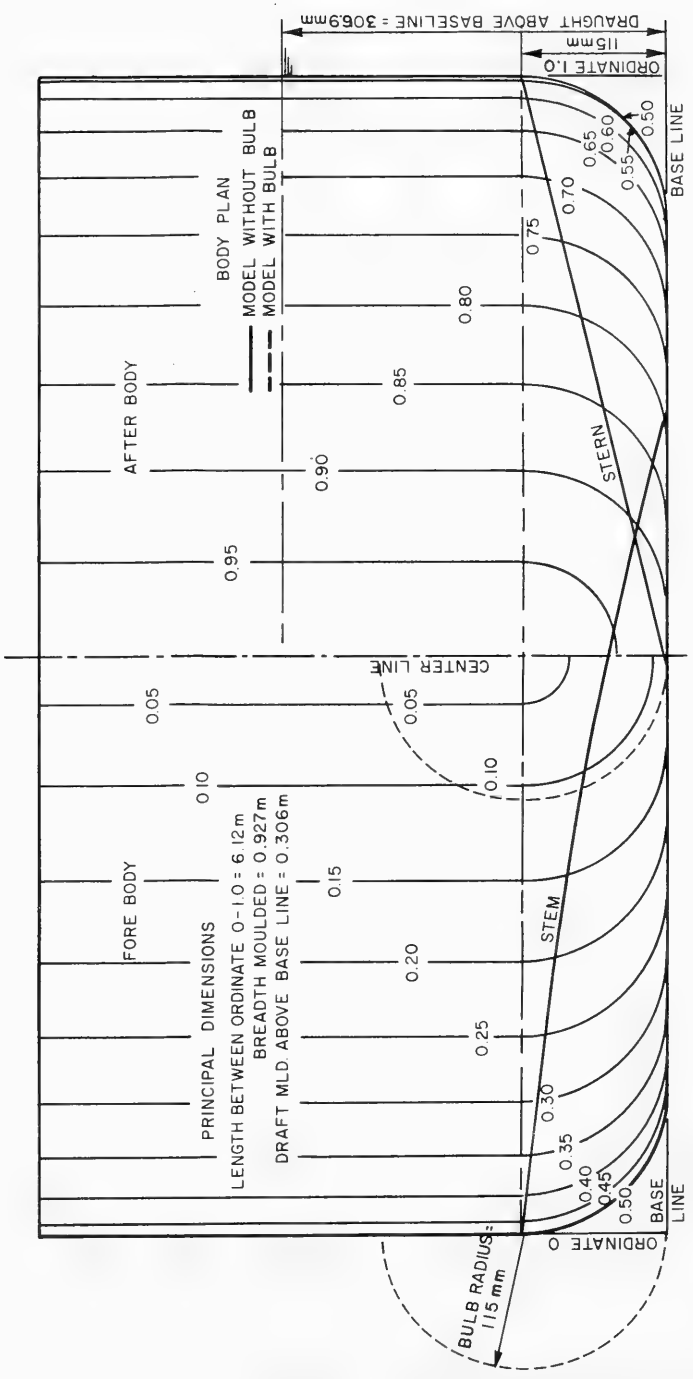

Fig. 7 - Body plan

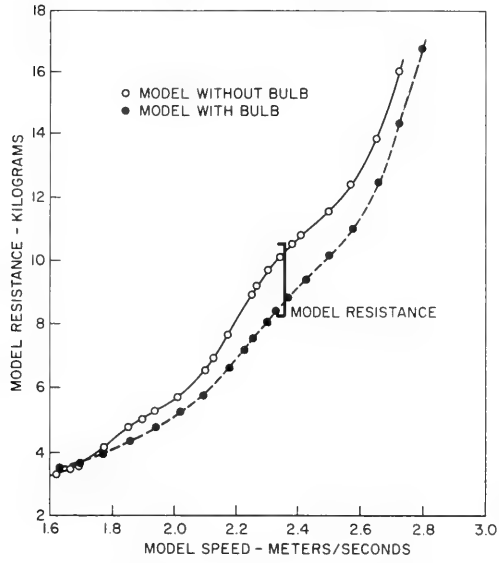

Fig. 8 -Results of resistance tests

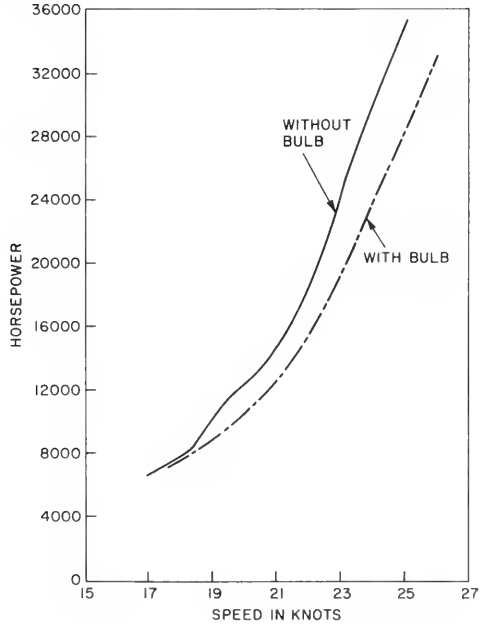

Fig. 9 - Curves of effective horsepower for a ship model

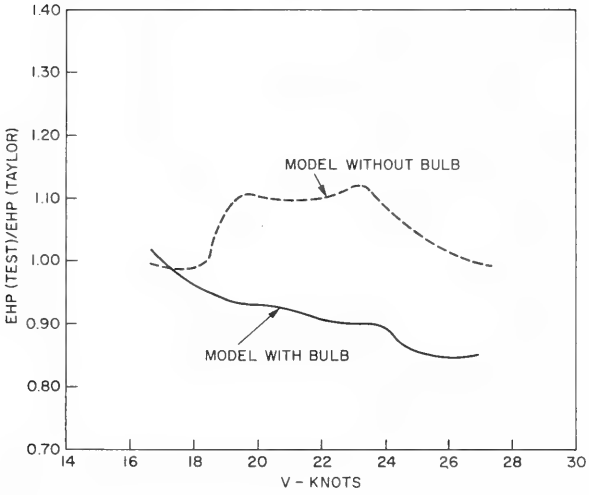

Fig. 10 - EHP (test)/EHP (Taylor) for ship models with and without bulbs

it will be safe in general to expect almost the same amount of improvement due to the stern in the ship with a bulb.

For ships of higher Froude numbers ($f > 0.35$) the method of analysis in this report may not be used. It would be rather more appropriate to use a modified slender-ship theory (Yim, 1967 or Maruo, 1962).

NOTATION

H is the ship draft in the Michell ship sense,

L is the ship length,

m is the source strength per unit area,

x_1 is the longitudinal distance aft from the bow nondimensionalized by dividing by L,

z_1 is the vertical coordinate from the mean free surface nondimensionalized by dividing by H,

x, y, z is a rectangular coordinate system with origin on the mean free surface, x in the direction of uniform flow at infinity and z positive upward.

REFERENCES

Havelock. T.H., "Wave Patterns and Wave Resistance," TINA Vol. 76, 1934, pp. 430-443

Inui, T., "Wave Making Resistance of Ships," Trans. SNAME, Vol. 70, 1962, pp. 283-353

Inui, T., "Study on Wave-Making Resistance of Ships," 60th Anniversary Series, Vol. 2, SNAJ, 1957

Maruo, H., "Problems Relating to the Ship Form of Minimum Wave Resistance," Fifth Symposium on Naval Hydrodynamics, ONR, Department of the Navy, 1964, p. 1019

Maruo, H., "The Calculation of the Wave Resistance of Ships the Draught of Which is Small as the Beam," Soc. of Nav. Arch. of Japan, 1962

Michell, J.H., "The Wave Resistance of a Ship," Philosophical Magazine, 45, 1898, pp. 106-122

Pien, P.C., "The Application of Wave-Making Resistance Theory to the Design of Ship Hulls with Low Total Resistance," Fifth Symposium on Naval Hydrodynamics, ONR, Department of the Navy, 1964, p. 1109

Wigley, W.C.S., "The Theory of Bulbous Bow and its Practical Application," Trans. N.E.C.I.E.S., Vol. L11, 1936, pp. 65-88

Yim, B., "Singularities on the Free Surface and Higher-Order Wave Height Far Behind a Parabolic Ship," Hydronautics, Inc. Technical Report 503-2, 1966a.

Yim, B., "Higher-Order Wave Theory on Slender Ships," Hydronautics, Inc. Technical Report 503-1, 1966b

Yim, B., "On Ships with Zero and Small Wave Resistance," International Seminar on Theoretical Wave-Resistance, University of Michigan, 1963

Yim, B., "Analyses on Bow Waves and Stern Waves and Some Small-Wave Ship Singularity Systems," Sixth Symposium on Naval Hydrodynamics, ONR, Department of the Navy, 1966c

Yim, B., "Some Recent Developments in Theory of Bulbous Ships," Fifth Symposium on Naval Hydrodynamics, ONR, Department of the Navy, 1964, p. 1065

Yim, B., "Analyses on Spherical Bulbs," Hydronautics, Inc. Technical Report 117-8, 1965

Yim, B., "A Ship with a Cylindrical Bulb Horizontally Oriented at the Bow," Hydronautics, Inc. Technical Report 117-10, 1967a

Yim, B., "Analyses on Waves and the Wave Resistance Due to a Ship with Transom Stern," Hydronautics, Inc. Technical Report 117-11, 1967b (in print)

Yim, B., Miller, E., and Kirkman, K., "Bulbous Bows for the Moore-McCormack Container/Ro-Ro Cargo Vessel Design No. 2568, for J.J. Henry, Co., Inc.," Hydronautics, Inc. Technical Memo 624-5

* * *

PANEL DISCUSSION—PROPELLER DESIGN

1. Introduction, J. D. van Manen, Chairman (Netherlands Ship Model Basin, Wageningen).

2. Selection of a Propeller's Principal Characteristics from Standpoint of Cavitation, Wm. B. Morgan (Naval Ship Research and Development Center, Washington, D.C.).

3. On the Optimum Cavitation-Free Lift Coefficient Range of Propeller Blade Sections, H. P. Rader (Versuchsanstalt fur Schiffbau, Hamburg).

4. On Selection of Propeller Type and Main Dimensions when Considering the Effect of Vibration, C. A. Johnsson (Swedish State Shipbuilding Experimental Tank, Göteborg).

5. Discussion on Dynamic Propeller Phenomena, R. Wereldsma (Netherlands Ship Model Basin, Wageningen).

6. Contribution on Stopping Abilities, M. C. Jourdain (Institut de Recherches de la Construction Navale, Paris).

7. Contribution on Stopping Abilities, H. Lackenby (The British Ship Research Association, London).

8. Statistical Properties of Powering Characteristics in Waves, M. K. Ochi (Naval Ship Research and Development Center, Washington, D.C.).

9. A Note on Propulsive Performance in Waves, J. Gerritsma (Delft Technical University, Shipbuilding Laboratory, Delft).

10. Propeller Design in View of the Maneuverability, S. Motora (University of Tokyo, Tokyo).

11. Some Considerations on the Influence of Propeller Surface Roughness, F. Gutsche (Berlinische Schiffbau Versuchsanstalt, Berlin).

12. Blade Control of Controllable-Pitch Propellers by Means of Ventilation, L. A. van Gunsteren (Lips Propeller Works, Drunen).

13. Prediction of Supercavitating Propeller Performance, R. A. Barr (Hydronautics, Inc., Laurel, Maryland).

14. High-Speed Propellers, G. Rosen (Hamilton Standard Division of United Aircraft Corp., Windsor Locks, Connecticut).

15. Design of Supercavitating Propellers on the Basis of Lifting-Surface Theory, T. S. Luu (Centre du Calcul Analogique, Chatillon sous Bagneux) and P. Sulmont (École Nationale Supérieure de Mécanique, Nantes).

16. A Propeller Design Method, A. Melodia (Cantieri Navali del Tirreno e Rinuiti, Genoa).

17. A Method to Determine the Efficiencies of Propellers, E. A. Schatté (Supramar, Lucerne).

18. Discussions on Cavitation Erosion Resistance of Propeller and Hydrofoil Structural Materials, J. Z. Lichtman (U.S. Naval Applied Science Laboratory, Brooklyn, New York).

In these proceedings only the introduction by Professor Van Manen has been printed. For the contributions to the Panel Discussion, see "International Shipbuilding Progress," March and April 1969.

Introduction

J. D. van Manen, Chairman
Netherlands Ship Model Basin
Wageningen, Netherlands

A propeller design can be divided into two parts:

1. the selection of propeller type;

2. the determination of the main dimensions, such as diameter, rpm, and number of blades.

In solving these two questions special attention should be paid to the following requirements:

1. high efficiency or minimum required shaft horsepower;

2. minimum danger of cavitation erosion;

3. minimum propeller-excited vibratory forces;

4. good stopping abilities;

5. good behaviour in a seaway;

6. favorable interaction with the rudder, to improve maneuverability.

In the selection of a propeller type all these hydrodynamic aspects of a ship propeller play an important role. Besides the dependability, minimum vulnerability and low initial and maintenance costs has to be taken into consideration.

The conventional ship screw with fixed blades designed for noncavitating condition has been for a period longer than 100 years the most applied type of ship propeller.

The ducted propeller (screw and nozzle or pumpjet) has shown its advantages for ship types where the propeller load is high or the cavitation danger is serious. Tugs, trawlers, and minesweepers are frequently outfitted with a ducted propeller. Coastal vessels and frigates are other ship types where the ducted propeller shows its favorable characteristics. Results of model tests show that application of ducted propellers to large tankers will be realized in the very-near future. The demand for a cigar-shaped afterbody, if a nozzle were applied to a tanker, is eliminated by the recent introduction of nozzle shapes adapted to both wake distribution and flow direction at the stern. At this moment it can be stated that sufficient theoretical and systematic experimental data are at hand for any design of a ducted propeller.

Contrarotating propellers form a type of propulsion that might be a serious competitor of the conventional ship screw on large container ships with such high speeds that the required power cannot be developed by one screw. Gradually, more design information becomes available for this propeller type. The selection of the blade number of fore and aft screws is of particular importance for the control of the propeller-induced vibratory forces and also for the transmission solution between propulsion plant and propeller.

The number of controllable-pitch propeller applications has increased very rapidly during the last years. Improvement of the dependability and minimum vulnerability and a reduction of the initial and maintenance costs are not the only reasons for this growth in controllable-pitch propeller applications. The solution of mechanical and technological difficulties and the development of suitable control systems have pushed the controllable-pitch propeller forward to application to frigates and even now to tankers. Shaft horsepowers up to 30,000 have successfully been absorbed by controllable-pitch propellers. The supreme qualities of controllable-pitch propellers with respect to stopping (for tankers) and accelerating (for frigates) promise a continuing growth in the application of this propeller type. The reduction and control of the blade spindle torque by advanced techniques such as ventilation or jet flaps might be a promising field for investigation.

The paddle wheel, before 1850 the most-applied ship propeller, is still one of these special-purpose propellers, which deserves our special attention for transport in very shallow waterways. In that case, it happens that the screw diameters which can be realized are seriously restricted, and the efficiency of

the paddle wheel is clearly superior. During the last 15 years, sufficient design information has been published on this particular type of propeller.

The vertical-axis propeller is a propeller type with outstanding maneuvering capabilities. Ferries, tugs, and supply vessels are examples of ship types where successful application of the vertical-axis propeller has frequently been realized. In solving problems of dynamic positioning of any vehicle at sea, the vertical-axis propeller has its own advantages. At very high speeds, in which case the blade motions will resemble the motion of a fish, some promises for the future may be hidden in further developments of the vertical-axis propeller.

The range where the conventional ship screw has never realized itself as a sufficient means of propulsion is that of very-high ship speeds. High-speed vehicles, such as hydrofoil boats, hovering crafts, and hydroskimmers (c.a.b. vehicles), are means of transportation where selection of the propeller type has a dominating effect on the whole design configuration.

Fully or supercavitating propellers with fixed or adjustable blades have shown successful operation at speeds up to about 50 knots, despite the problems of inclined shafts and partial immersion. Design methods for fully cavitating propellers are approaching a quality where the design requirements may already be satisfied by a first propeller design. Ventilation techniques have improved the off-design characteristics of this propeller type considerably. Strength problems have been attacked successfully by proper material selection and original ideas about the geometry of the blade profiles.

Pulse-jet propulsion and air propulsion are examples that underline our insufficient knowledge to solve the problems of high-speed propulsion in a satisfactory way. In this respect it is worthwhile to mention the development of two-phase hydrojets (water-ramjets) in the U.S.A., the Netherlands, and Italy. This type of high-speed propeller may become the most valuable contribution of all our extensive research activities in the field of high-speed propulsion.

A final remark on the selection of the propeller type may be on a way of representation of the propulsive efficiency which is suitable for comparison purposes. It may occur that for a certain propeller type the usual advance coefficient J, the ratio between advance and rotational speed of the propeller cannot be determined, for instance, due to the fact that there is no rotational speed. In that case it is recommended to plot against the Froude number based on displacement, the ratio between the required power and the product of displacement and ship speed:

$$\frac{SHP}{\Delta \times V_s} \text{ versus } \frac{V_s}{\sqrt{\Delta}}$$

In fact, this last ratio is the resistance per ton displacement divided by the total propulsive coefficient and is, as such, qualitative for the propulsion abilities of any ship or vehicle.

In the second part of my introduction to the panel discussion, I should like to emphasize some points with respect to the requirements already mentioned, i.e.,

1. selection of optimum diameter and rpm from the viewpoint of efficiency;

2. cavitation criteria, based on systematic experimental data;

3. the effect of cavitation on propeller-excited vibratory forces;

4. data for analyzing stopping maneuvers;

5. variations of propeller load in a seaway;

6. the effect of rpm variations on the interaction between rudder and propeller.

In Fig. 1 the effect of rpm on the efficiency has been illustrated by the result of a number of calculations for a 16-knot tanker with a 30,000-hp propulsion machinery. The calculations have been carried out both for conventional four- and seven-bladed screw propellers and for ducted propellers. Some conclusions can be drawn from this figure:

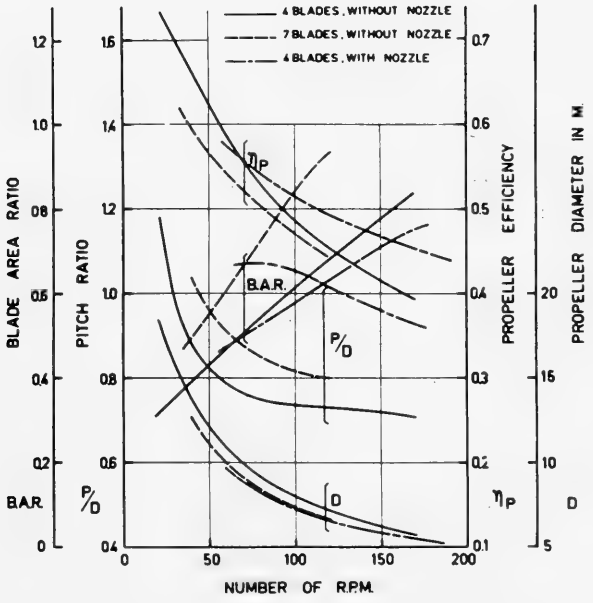

Fig. 1 - Effect of rpm on screw diameter and efficiency of a single-screw tanker having an engine power of 30,000 DHP and a speed of 16 knots

1. The seven-bladed screws are worse from an efficiency point of view than the four-bladed screws. Even at equal diameter and a corresponding difference in rpm this is the case.

2. The ducted propeller is better from an efficiency point of view than the four-bladed screw propeller, although at decreasing rpm this improvement in efficiency decreases and even disappears because of the smaller propeller load due to the larger screw diameter.

3. However, the most interesting point is a further decrease in rpm from that which is now usual. If the rpm be decreased from 80 to 50, then the screw diameter will increase in this case from 9 m to 12 m. The manufacturers of large screw propellers consider a screw propeller with a diameter of 12 m within their technological capabilities.

The improvement in efficiency, consequently, reduction in required SHP, amounts to more than 20 per cent. Such savings in SHP force us to consider the consequences for reduction gears and propeller shafts at these extremely low rpm values in order to approach an economical optimum. Attention should also be paid to diesel engines with relatively high rpm combined with reduction gears. In addition to these conclusions it is interesting to note that at the N.S.M.B. recently developed asymmetric nozzles have delivered an average reduction of SHP from 3 to 5% with respect to the results of conventional nozzles as indicated in Fig. 1. These asymmetric nozzles have been adapted both to the wake distribution and the flow direction at the stern. This asymmetric nozzle has the advantage that the conventional shape of afterbody can be maintained. The extra initial costs of such an asymmetric nozzle are more than compensated for by the reduction in required SHP.

Preliminary studies on the reduction of the resistance increase of large tankers as a consequence of course keeping indicate that an improvement may be expected by an enlargement of the nonrotatable rudder surface (deadwood). This can even be done by a reduction of the rotatable rudder surface. Another solution to this problem might be the application of nozzles outfitted with maneuvering devices.

In Fig. 2, results of identical calculations, as shown in Fig. 1, are indicated. In this case the ship is a fast cargo liner with a speed of about 25 knots and a propulsion plant of 30,000 hp. The calculations have been carried out for four- and seven-bladed screw propellers and for contrarotating propellers. In most cases it is usual that the propeller specialist has to design a ship propeller for a required speed, a given rpm and SHP; the propulsion machinery has already been selected and the propeller has yet to be designed. For these design conditions we see from Fig. 2 that contrarotating propellers deliver a 4 - 5% higher efficiency than the comparable four-bladed screw propellers. By a more favorable interaction between ship and propeller this increase in efficiency can be enlarged by about 3% with respect to required SHP. It may be that the engine power becomes so large that application of the conventional ship screw is only reliable as a twin-screw arrangement. This leads to an increase of required SHP of about 8%. So in the future contrarotating propellers may lead to reductions in SHP of 15 - 16% compared to the twin-screw arrangement of

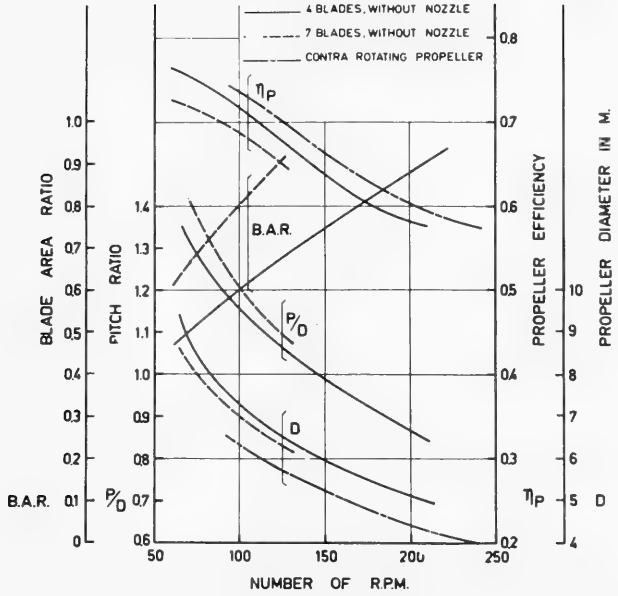

Fig. 2 - Effect of rpm on screw diameter and efficiency of a single screw cargo liner having an engine power of 30,000 DHP and a speed of 25 knots

conventional propellers. These percentages make it desirable to calculate the comparative costs for the two types of propulsion system. So far our remarks concern contrarotating propellers at equal rpm (identical propulsion plant).

Our design considerations will lead to quite different conclusions if we start our propeller design for these fast cargo liners from an equal maximum allowable propeller diameter for the propeller types in question. At a diameter of 6.30 m the rpm of the conventional four-bladed screw amounts to 130 and for contrarotating propellers to 90. The improvement in efficiency at equal diameter is in this case for the contrarotating propellers more than 10% (at equal rpm this increase in efficiency is, as mentioned, 4 - 5%). For the up-to-date fast cargo liners it is very desirable to make calculations for the two described alternatives, i.e., a ship with the conventional ship screw and a ship with contrarotating propellers of the same diameter as the conventional screw propeller. The consequences of the difference in rpm of the propulsion plants have, of course, to be taken into account.

In Figs. 3a and 3b, examples have been given of the results of systematic cavitation tests with the Wageningen B-screw series. On base of the screw load C_T,

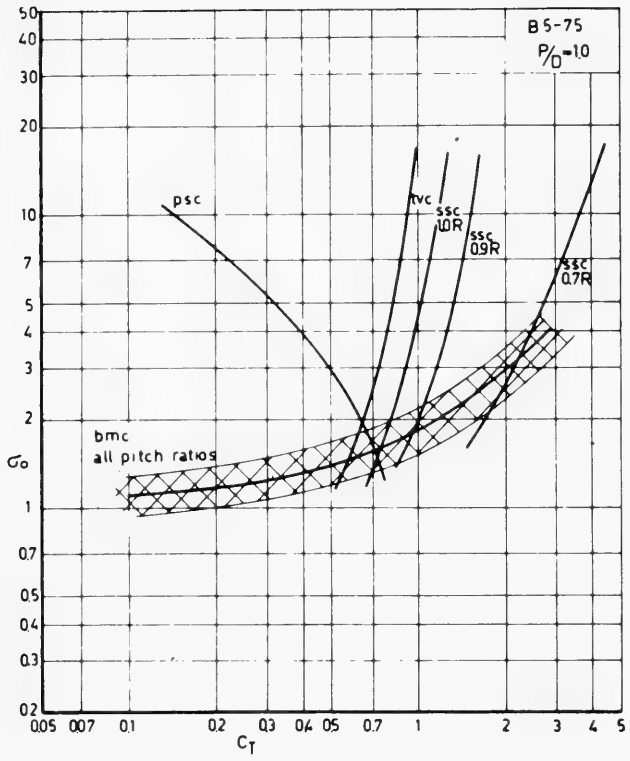

Fig. 3a - Curves of incipient cavitation phenomena of screw of the B 5-75 series

$$C_T = \frac{T}{\frac{1}{2}\rho V_a^2 \times \frac{\pi}{4} D^2},$$

the various characteristic curves for the onset of the different types of cavitation have been indicated: bubble cavitation midchord (bmc), sheet cavitation at the suction side (ssc), sheet cavitation at the pressure side (psc) and the visible tip vortex (tvc).

In Fig. 4, a part of the large N.S.M.B. cavitation tunnel is shown schematically with a measuring arrangement designed for the investigation of the effect of cavitation on the propeller-induced vibratory forces.

In Fig. 5, pressure distributions of a two-dimensional screw blade profile have been reproduced for various cavitation numbers at constant angle of incidence. From this figure, the effect of cavitation on the under-pressure peak at the leading edge is clear; cavitation reduces this peak strongly.

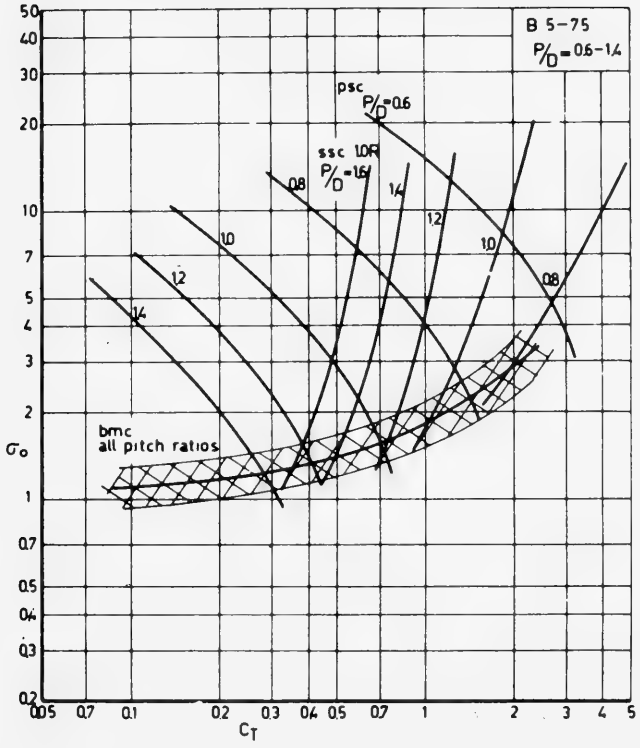

Fig. 3b - Curves of incipient cavitation phenomena of screw of the B 5-75 series

Propulsion tests with ship models in a towing tank are carried out under atmospheric pressure (thus, a relatively high pressure). The consequence is that during a propulsion test in a towing tank no cavitation occurs as it does in reality. The arrangement as indicated in Fig. 4 forms the first part of a research on the consequences of neglecting of cavitation during propulsion tests in a towing tank. The effect of cavitation on propeller-hull interaction and on propeller-induced dynamic transverse forces will form the most important research items of ship propulsion in the coming years. It might be that the results of this research will prove that the results of a propulsion test in a conventional towing tank are inadequate both for quantitative predictions and qualitative selections.

In Fig. 6. an example has been given of an extension of the "open-water" screw diagrams of the Wageningen B-series. This extension refers to the so-called "four-quadrant" measurements. The thrust coefficient C_T and the torque coefficient C_Q are given for the following conditions:

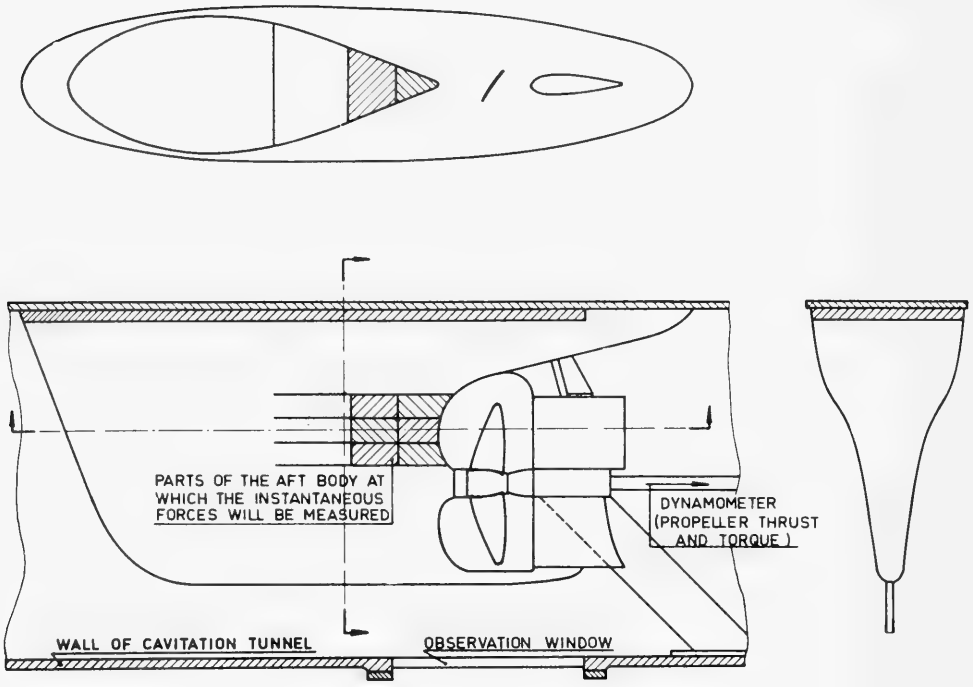

Fig. 4 - Arrangement in cavitation tunnel for the determination of the effect of propeller cavitation on the vibratory forces on the afterbody of a ship

Speed ahead, rpm ahead	(α = 0° - 90°),
Speed ahead, rpm backing	(α = 90° - 180°),
Speed astern, rpm backing	(α = 180° - 270°),
Speed astern, rpm ahead	(α = 270° - 360°).

The part for α = 0° to about 30° indicates the "normal" "open-water" screw diagram. From Fig. 6 the effect of the width of blade chord, also of B.A.R., on thrust coefficient and torque coefficient in the ranges where separation of flow occurs is clear. This type of diagram is of importance for the analysis of stopping maneuvers of ships.

A research area of increased interest is that of the behavior of the propeller in a seaway. Besides the dynamic load on the shaft and the afterbody induced by the propeller, the behavior of the propeller in a seaway with respect to cavitation plays a role. Diagrams as indicated in Fig. 3 may be of great value, when we analyze the danger of psc and ssc starting from the design condition (known c_T and given cavitation index σ_0) if we should know the load variations of the propeller in a seaway. From test results with ship models in waves, it has appeared that the load variations of the propeller are built up on an average power increase due to seaway. These load variations are the same order of magnitude

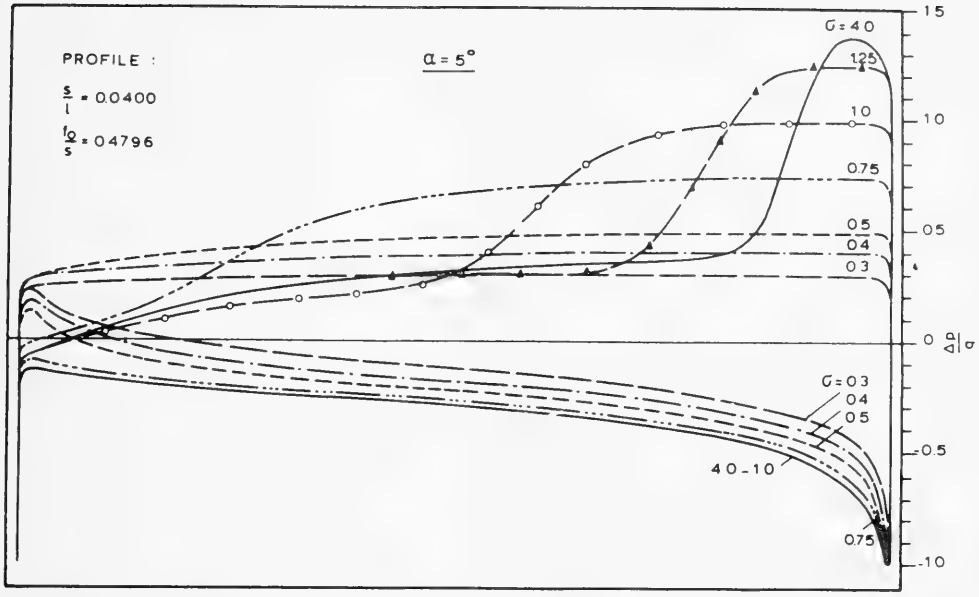

Fig. 5 - Pressure distribution on a blade section for different cavitation numbers

as the average power increase in the case of head seas. In that case, the risk of ssc will increase considerably. This type of cavitation has least risk of damage due to the cavitation. The chance of psc will remain equal or decrease.

Data for the behavior of the propeller in quartering seas are still lacking. It might be expected from the data as represented in Fig. 3, that in quartering seas, and as a consequence a power decrease, an increased risk of psc occurs. As a rule, psc must be qualified as very unfavorable from a view point of cavitation damage.

Figure 7 illustrates clearly that propeller and rudder must be considered as a closed system when solving maneuvering problems. The results shown in Fig. 7 refer to a 65,000-t.d.w. tanker. This is a ship type with low SHP/displacement ratio. Starting from equal speed (2.60 m/sec) and equal rudder angle (20°), the effect of an increase in rpm from 28.8 to 48 on the path of the ship appears already to be considerable; the ship speed only increasing slightly.

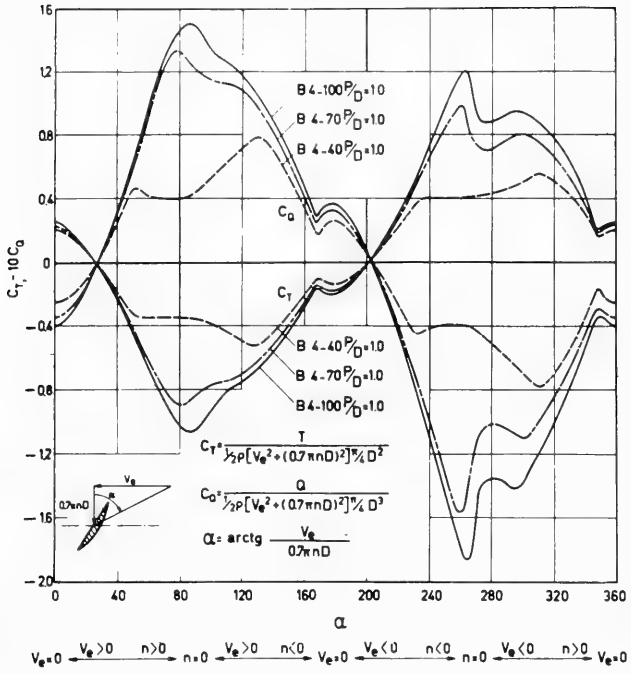

Fig. 6 - Some results of the four quadrant open-water tests with the B-screw series

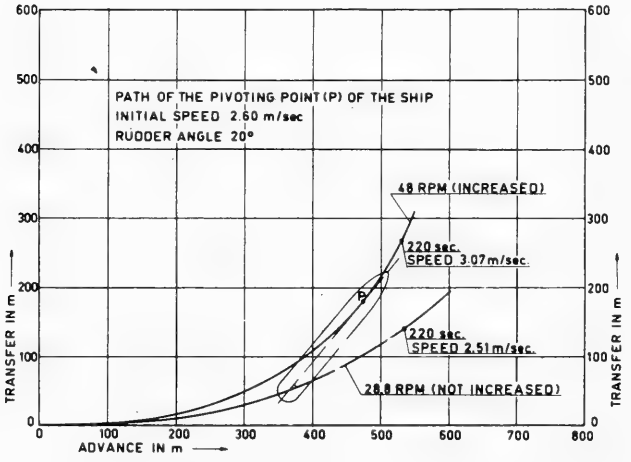

Fig. 7 - Effect of increased rpm on the maneuver of a 65,000 TDW tanker

* * *

PANEL DISCUSSION ON AIR CUSHION VEHICLES, HOVERCRAFT, AND SURFACE EFFECT SHIPS

Edited By

James L. Schuler, Chairman
Naval Ship Systems Command
Washington, D.C.

PANEL DISCUSSION—AIR CUSHION VEHICLES, HOVERCRAFT, AND SURFACE EFFECT SHIPS

James L. Schuler, Panel Chairman

The Chairman opened the meeting by stating the purpose, introducing the major participants, and briefly outlining the general areas to be discussed. The purpose of the meeting was to exchange ideas, concepts, and opinions on air cushion vehicles, hovercraft, and surface effect ships. The large number of attendees precluded general discussion. However, the leading participants were requested to make a few introductory remarks designed to provoke questions and dialogue. A summary of the remarks is as follows.

The first problem in defining a vehicle is defining the mission, size, speed, and payload to perform the required tasks. Once these are known, the technical problems concern (a) structure, arrangement, power, thrust, and lift and (b) control and stability. The technical areas of most interest to the hydrodynamicist are (a) propulsion, thrust, and drag, (b) internal flows, and (c) stability and control.

A full-cushion craft is quite accurately represented as a moving pressure field. This theoretical treatment is more representative of reality than using a moving pressure field to represent a displacement ship. The theoretical drag must then be corrected for appendages, if applicable. The major difficulty is how to realistically treat the degradation of performance in a seaway with the attendant wave impacting and spray drag.

Comparing the sidewall craft to the nonsidewall craft introduces new problems concerning frictional resistance of the sidewalls, possible cavitation, and control dynamics. Sidewalls should improve directional stability but could complicate steering. Sidewalls should reduce lift power requirements but could introduce surge in the air supply system due to wave-pumping action.

Following the preceding remarks, Mr. House was asked to present some comments and lead a discussion on some aspects of machinery selection. He made several important points (see Tables 1 and 2 and Fig. 1). One is that the use of lightweight power plants leads naturally to consideration of marine gas turbines. These machines are costly and require long development cycles. This leads the vehicle designer to select proven prime movers and this (to some extent) tends to yield craft designed around one or more existing machines. Recent developments, such as blade cooling techniques, will improve the performance of existing machines as we move forward in time.

Table 1
Propulsor Efficiencies at 70 to 80 knots

Propulsor	Usable Ideal Propulsive Efficiency (%)	Propulsor Efficiency (%)	Gearing and Power Plant Installation (%)	Appendage Drag Efficiency (%)	Total Propulsion Efficiency (%)
Amphibious					
Turbojet	16	95	100	98	15
Turbofan	25	95	100	98	23
Blower/fan	65	70/90	95	96	41/47
Water Craft					
Submerged SC propeller	97	64/70	95	75	44/48
Partly submerged SC propeller	97	64/70	95	98	58/63
Waterjet ram inlet	86	78	95	75	48
Waterjet flush inlet	86	78	95	97	62

Table 2
Overall (From Fuel to Clean Hull) Efficiency

Propulsor	Total Propulsion Efficiency (%)			η_T (%)			Overall Efficiency (%)		
	Today	Early 1970s	Someday	Today	Early 1970s	Someday	Today	Early 1970s	Someday
Turbojet	15	15	—	26	36	—	3.9	5.4	—
Turbofan	23	23	—	26	36	—	6.0	8.0	—
Blower/fan	44	46	48	26	36	55	10.7	16.6	26
Submerged SC propeller	46	48	—	26	36	—	12.0	17.3	—
Partly submerged SC propeller	60	63	65	26	36	55	15.5	22.6	35.7
Waterjet ram inlet	48	50	—	26	36	—	12.5	18.0	—
Waterjet flush inlet	62	64	66	26	36	55	16.1	23.0	36.3

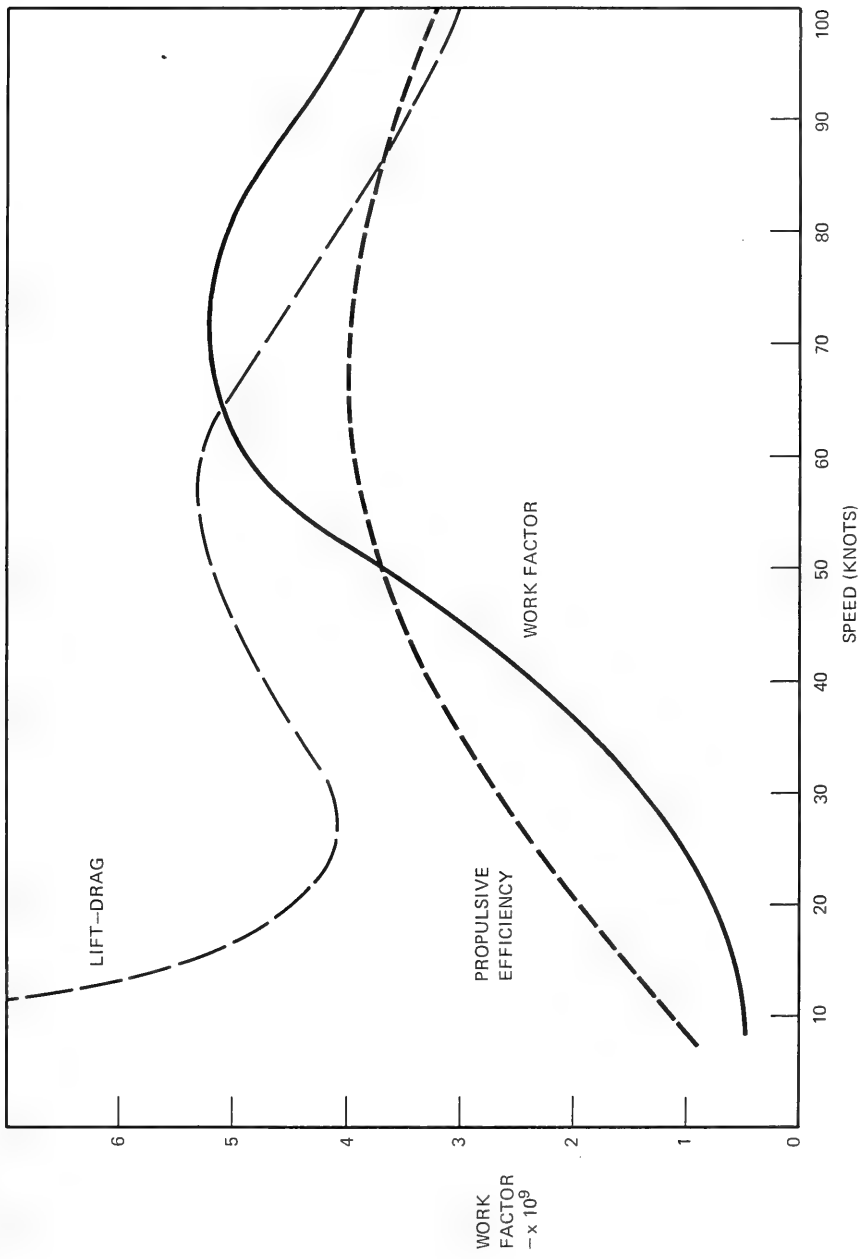
LIFT–DRAG
PROPULSIVE EFFICIENCY
WORK FACTOR
SPEED (KNOTS)
WORK FACTOR – x 10⁹
0
1
2
3
4
5
6
10
20
30
40
50
60
70
80
90
100

Figure 1

Possible propulsion systems include turbojets and turbofans, which are clearly suited to amphibious craft. Fully submerged or partially submerged supercavitating propellers as well as waterjets with flush or ram inlets can be used on nonamphibious types. The pure turbojet has an exhaust velocity which makes it unsuited for even fast craft speeds. The engine efficiency is further diluted with duct losses, gear losses, and drag induced by appendages. Putting these factors together gives some measure of efficiency. The actual numbers change with time as new developments appear.

Mr. House presented an example showing that a specific 500-ton sidewall craft does the greatest amount of work when operating in the 70 to 80 knot region. The example showed the interrelation among power plant efficiency, lift/drag ratio, and tons per mile per year with a constant 2000 hours of utilization. The percentage of operating time spent at each speed as well as the assumed sea conditions also affect the results. He also concluded that at these speeds waterjet propulsion seemed to be the best choice. Mr. House answered Dr. St. Denis that blade cooling and better materials would probably account for improved turbine performance rather than the use of regenerative cycles.

Mr. House assured Mr. Weller that his lift/drag calculations included the lift power requirements. He noted that the seaway places an upper limit on cushionborne performance.

Mr. House informed Dr. Quant that the tradeoff between propulsion system weight and propulsive efficiency depends heavily on how much time is spent at the various operating speeds. His final point was that the conclusions are very sensitive to the details of the specified mission.

Mr. House suggested, in reply to Dr. Wang, that speeds of 150 to 200 knots would give better propulsion efficiencies if you could build a craft to take it.

Dr. Sheets then presented some comments on three new subjects: fan design, propulsion, and load and structures.

The fan design characteristics govern the cushion characteristics, which in turn affect speed, degradation in a seaway, and bubble leakage. He has studied centrifugal and axial flow fans with variations in speed of rotation and pressure/quantity relationships plotted against horsepower. Craft of 100 tons, 500 tons, and 4000 tons have been analyzed. In some cases, the propeller and fan are driven by the same prime mover.

On the subject of propulsion, Dr. Sheets agreed with the problems as stated by Mr. House. Dr. Sheets compared his results with those of Fielding and Stanton-Jones to show that these vehicles fall in an unoccupied area in the Gabrielli/Von Karman line.

On the subject of loading criteria and structural analysis, Dr. Sheets demonstrated an approach using computer calculations and tank tests to assess the validity of a structural model. A large number of loads and loading conditions were included. He mentioned hogging, sagging, and torsional loads as well as unusual loads caused by docking, towing, and hoisting.

In reply to Dr. St. Denis, Dr. Sheets said that his treatment did not include nonsteady-state phenomena such as hydrodynamic impact because of the short time available in the panel discussion. Dr. Sheets also noted that larger ships may require greater flexibility.

The craft must have variable flexibility with hard structures to carry loads and a soft cushion of air connected by semirigid structures.

Dr. Wang asked if the data indicated that we could look forward to ships of 100 knots from a drag point of view. Dr. Sheets acknowledged that the curves he showed were cut off above hump speed. Above hump speed it is a third-power curve.

Dr. Skolnick then presented a contribution to the effect that bold ventures such as the surface effect ship (SES) were needed to galvanize the marine community into action. If the marine community did not heed the challenge, it would be accepted by the aerospace industry.

Mr. Weller asked how this related to the traditional marine concept of providing low-cost transport. Dr. Skolnick agreed that the SES case has not yet been adequately made.

Dr. Wang asked if the systems approach to SES had a clear objective. Dr. Skolnick stated that the SES program has a clear objective.

Dr. St. Denis lamented the emphasis on studies which can cost large amounts of time and money and hoped we would not suffer from "paralysis of analysis." Mr. Calkins asked if part of the problem could be the kind of training given to naval architects. Dr. Skolnick concurred that this added to the problem.

Mr. Christopher Hook raised the problem of the "rogue" wave. Dr. Skolnick was sure that such problems should not be overlooked — neither should they be overemphasized.

Mr. J. B. van den Brug presented some clear exposition of recent model tests including films and outlined a straightforward method for deriving lift fan requirements. He noted that in some cases the model acted as if it had a "negative added mass." That is to say, it has precisely the effect on damping. In reply to a question from Dr. Skolnick, he noted that their open water tests were not yet complete.

Mr. Everett asked if the behavior was different with upward motion than with downward motion. Mr. van den Brug stated that their tests centered on stability and therefore focused on small deviations from equilibrium.

Dr. Savitsky asked how the vehicle natural frequencies compared to the natural frequency of encounter with the waves. Mr. van den Brug stated that he would answer the question with data after the session.

Mr. T. K. S. Murthy presented some work he has done on the motions of craft in a wind-generated irregular seaway.

Dr. St. Denis felt that sea state defined in terms of wind and fetch was appropriate for oceanography, but he felt that the naval architect prefers sea state defined in terms of wave heights.

The chairman then closed the session. Copies of the actual transcript are available on request from the chairman.

* * *

PANEL DISCUSSION

Tuesday, August 27, 1968, 5 p.m.

PANEL DISCUSSION—LIFTING-SURFACE THEORY

R. Timman, Panel Chairman
Delft Institute of Technology
Consultant Netherlands Ship Model Basin

The discussion mainly consisted of three parts: (a) mathematical methods and foundation of the theory, (b) experimental verification, and (c) applications, in particular to sails and design of propellors.

Timman: The aim of this lifting-surface panel is an appraisal of the theory, a discussion on its physical foundation, a general outline of mathematical methods, and considerations on its applicability to practical problems.

The origin of lifting-surface theory dates back a long time. The Birnbaum series is from 1923. In the old days nobody ever tried to solve the two-dimensional integral equation because of the formidable amount of work required. For this reason airplane wings and ship propellors were calculated by lifting-line methods, based on Prandtl's formulation. Now, "exact" lifting surface theories are available, "exact" meaning a two-dimensional, linearized, nonviscous lifting-surface theory.

First is mentioned the theory of Tsakonas, and its counterpart, developed by Verbrugh (a joint effort of N.S.M.B. and Hydronautics-Europe). The theory of Tsakonas is a rather complete: Starting from the two-dimensional integral equation for the acceleration potential a numerical method is developed where the wake is simplified by taking stepwise constant distributions of free vortices, whereas Verbrugh's report, based on Sparenberg's theory, contains helicoidal wake vortices. Both methods use chordwise series of Birnbaum type and derive spanwise integral equations for the coefficients. Both require a special treatment of the Hadamard singularity in the integral equation, but Tsakonas makes a more extensive use of expansions in special functions, whereas Verbrugh uses more direct numerical methods.

Verbrugh's report dates from April 1968, but is not published because of administrative difficulties; Tsakonas' latest publication is in the April issue of the Journal of Ship Research. It will be of great interest to correlate the two theories. Since the starting points are the same, discrepancies must be due to numerical deviations.

Now it is proposed to discuss the value of these theories. Suppose they agree; (if they do not agree, it is only a matter of time before these differences are eliminated) we have available an accurate method for the solution of the linearized nonviscous integral equation. The computing time is about 40 minutes on the TR4 (somewhat less on a IBM 7090) and probably shorter on a third-generation computer.

The questions which now rise are

1. What is the use of this computer program for design purposes?

2. What kind of improvement is desirable for improvement of its applicability and which effects would be expected to be included in the near future?

Professor Weissinger (Technische Hochschule Karlsruhe) gives a contribution on the improvement of the treatment of the singularity in lifting-surface theory. [M. Borja and H. Brakhage, Z.F.W. 16 (1968), pp. 349-356]:

$$\alpha(x,y) = \frac{1}{4\pi V} \iint_F \frac{-1}{(y-y')^2} \left(1 + \frac{x-x'}{(x-x')^2 + (Y-y')^2}\right) k(x',y')dx'dy' ,$$

where $\alpha(x,y)$ is the local angle of attack and k the vorticity on the lifting surface. Through partial integration, the equation is transformed into

$$\alpha(x,y) = \frac{1}{4\pi V} \iint_F \frac{(x-x') + [(x-x')^2 + (y-y')^2]^{1/2}}{(x-x')\,(y-y')} k_{y'}(x',y')dx'dy' ,$$

where the form for the kernel

$$\frac{K_o(x,x'xy,y')}{(x-x')\,(y-y')}$$

is essential for the method.

Introducing Glauert coordinates $x'_j = -\cos\vartheta'_j$, $x_i = -\cos\vartheta_i$,

$$\vartheta_j' = \frac{(2j-1)\pi}{N} , \quad \vartheta_i = 2i\,\frac{\pi}{N} , \quad n = \left[\frac{N+1}{2}\right] , \quad j = 1(1)n, \quad i = 1(1)n-1$$

or

$$\vartheta_j' = \frac{(2j-2)\pi}{N} , \quad \vartheta_i = (2i-1)\,\frac{\pi}{N} , \quad n = \left[\frac{N+2}{2}\right] ,$$

where the first set of points are pivot points and the second set are collocation points.

These configurations give the approximation formulas

$$\frac{1}{\pi} \int_{-1}^{+1} \frac{u(x')}{x_i - x'} \frac{dx'}{\sqrt{1-x'^2}} \approx \frac{2}{N} \sum_{j=1}^{n_1} \frac{u(\xi_j')}{\xi_i - \xi_j'} ,$$

$$\frac{1}{\pi} \int_{-1}^{+1} u(x') \frac{dx'}{\sqrt{1-x'^2}} \approx \frac{2}{N} \sum_{j=1}^{n_1} u(\xi_j') ,$$

which are exact for polunomials of degree N - 1 viz., N. They correspond to *Gaussian* integration, giving a great improvement in accuracy. For unsteady motions a special treatment for the infinite wake is needed. The improvement in integration time as compared to a conventional method (e.g., Truckenbrodt) is about a factor of 10.

Coming back to the problem of applicability, viz., the alternative of using exact theories in design or faster approximation methods, which are checked or corrected by lifting-surface theory.

Pien (NSRDC, Washington, D.C.) remarks that we can predict rpm and thrust quite accurately. The main problem is to predict loading over the propeller blade with relation to the cavitation problem and secondly to predict vibratory force accurately. The question is the accuracy of the theory.

Theories have two purposes understanding the physical problem, this is already reached in history, but in order to reach quantitative predictions we cannot modify the problem too much in order to reduce computing time, we have to come as close to the problem as is possible.

The main point is geometry of the slipstream, we have very nonuniform inflow and the free vorticity has to follow this flow. This is a drawback of the vortex representation of the propellor. Going back to acceleration theory we either know the loading or assume the loading and go back to the history of the blade and bypass the helical sheet.

We have to reach the stage of high loading and nonuniform flow, which seems difficult on present computers.

Timman remarks that for this purpose two ways are open much more complicated calculations or simplified models which simulate special features. In his opinion the formulation of linearized lifting-surface theory contains.

Pien's time history: Going from the acceleration potential to the velocity potential requires an integration over the wake, which is essentially the same as in integration over the time history, since the free vortices in the wake carried along with the flow with the strength they have when they were generated.

For results as accurate in the nonlinear case as in the linear case it is necessary to put on more effort, but is it important to include some effects and leaving out others. It would be of interest to know whether it is contemplated to work on lifting surface theory with cavitation.

Weissinger asks whether in Dr. Pien's method the calculation of the shape of the wake vortices would give regular helices. There are some linearization assumptions in the theory, and it could be that the improvement is essentially an improvement in computing time.

Pien remarks that his theory bypasses the free vorticity and only calculates dq/dt at the time the propellor blade passes.

Timman, as a reply on a question on Tsakonas' staircase approximation, replies that in his experience the detailed structure of the wake in oscillating flow is not very crucial. The vortex strength oscillates and there is, at some distance, a cancelling effect of neighbouring vortices of opposite strength. This does not hold in the near slipstream, which is, however, always poorly represented by theory.

Probably there will be a reasonably close agreement between Tsakonas' theory and a more exact theory (5%). The problem of comparison with experiments is raised.

Laitone (Berkeley) reports on experiments on airfoils at low Reynolds numbers. From NACA data it was known that at Re < 200,000 in this case the lift curve slope is higher than at high Reynolds number. Experiments on rectangular wings to check these effects. The effects are either due to a separated wake or the formation of vortices at the leading edge. At Re > 200,000 and an aspect ratio of 6 results in $de_1/dx = 0.075$ Re > 200,000, and a lift-drag ratio of 20 at Re < 50,000 aspect ratio 6 result gives $de_1/dx = 0.085$ even greater than 2π. For a ring airfail a vortex is actually formed. For diameter/chord≈12 the data went along quite well, at high Re, but below 50,000 de_1/dx is about 15% higher than the theoretical value.

To check profiles, 5, 10, 20% thick wings gives a strong vortex at the leading edge.

Thieme (Hamburg) reports on experiments with similar results NACA profiles 12% thick 1958 and flat plates with different leading edges, and elementary ship forms with aspect ratio 0, 1 at Re 10^6. Not only lift coefficients, but also moments showed a remarkable increase at the low Reynolds numbers. The only explanation is the bubble at the leading edge.

Laitone tested several profiles for gliders and found that for flat plates at Re < 50,000 at 6 degrees is very linear and drops off at 45 degree. Max C_1 of 1.2 were found; the paper gliders optimize design at that Reynolds number.

Timman remarks that from a mathematical point of view classical theory uses the Kurta condition to fix the vorticity at the trailing edge, but at the leading edge there must be additional empirical conditions to fix the location and strength of the vortex. For ship propellors the leading edge vortex sheet is replaced by a cavity.

Weissinger remarks that for delta wings a theory is developed which assumed free vortices everywhere on the lifting surface.

Milgram (M.I.T.) reports on work on sails as an application of lifting-surface theory. The chief advantage of the kernel-function method is on the unsteady case. In the steady case Falkner's vortex lattice theory (1943) is very successful. It gives a prescription for the numerical computation, which avoids the trouble.

Referring to Cunningham's papers, which were carried out for rectangular and delta wings and no camber. A sail has a different shape and camber and a

high aspect ratio. Calculations by these methods, for an elliptic loading give a parabolic shape and linear down wash. For high aspect ratio and camber apparently numerical discrepancies arrive. Next problem regards the flow behind the blade, for according to D. Cummins the wake rolls up quite rapidly and within the framework of linear theory it is possible to predict this rolling up. But the next blade will meet this rolled up vortex sheet, which gives rise to a correction. For sails the leading edge vortex, as mentioned by Dr. Laitone, the separation from the top surface will be accompanied by separation from the bottom surface which gives a low lift, while the lift slope is very high.

Pien remarks that for a sail the camber is caused by the loading, because the sail is flexible the camber is different for different angles of attack.

Thieme refers to a thesis of Dr. Feltz (Braunschweig), with Prof. Schlichting. Here a flexible plate is considered between two small cylinders and the pressure distribution is calculated on the plate for several values of the parameters. This problem is similar to the problem mentioned. (Z.A.M.M.).

Barakat remarks that essentially the determination of the shape of the sail is essentially an eigenvalue value problem. (Thwaites, Nielson) The sail can assume different shapes under similar circumstances. For a porous sail the problem is changed somewhat.

Weissinger remarks that for a swept delta wing the downwash cannot be expected to be linear because of three-dimensional effects.

(Admirally) wrote a program for the design of propellors by lifting-surface theory.

A number of features are still lacking: the difference of the hub, there is not only an effect due to contraction due to nonlinear effects, there is also a contraction due to the absence of the hub.

Moreover boundary-layer effects are not included. For a section with large boundary-layer development the sheet would be wrong. The design by lifting-surface theory cannot yet compete with the design by an experienced designer in particular with respect to cost.

Pien remarks that at NSRDC Dr. Morgan's group is developing a program for taking account of the hub.

* * *

PANEL DISCUSSION—DUCTED PROPELLERS

D. E. Ordway, Panel Chairman
Therm Advanced Research, Inc.
Ithaca, New York

The objectives established for discussion were to determine what applications are of current interest for the ducted propeller, to review the analytical and experimental results that are available to meet the needs for these applications, and to recommend the future work required if any gaps are found. Representatives from many different countries participated and, in view of their diverse backgrounds, we hoped that such broad objectives could be achieved in a realistic and comprehensive fashion.

With regard to current interest in the ducted propeller, the response was very enthusiastic and a number of applications were cited. These included propulsion for hovercraft, hydrofoil boats, ocean-going merchant ships and liners, and several other high-speed craft. One specific suggestion was to consider some kind of a ducted propeller for the Sidewall Craft Program sponsored by the Joint Project Office of the U.S. Navy and Maritime Service. Design speeds here range from 80 to 100 kt for sizes from 100 tons up. It turned out that work along these lines is underway by Sogréah on what is called a "water-jet propeller." This was reported on briefly.

At the low-speed end, reference was made to V/STOL aircraft, such as the Bell X-22A for carrier operation, and variable geometry for off-design performance, to the classical tug-boat application or Kort nozzle, to dynamic positioning of research vessels and drilling and dredging rigs, and to lateral or bow thrusters. Bow thrusters are really not ducted propellers but more of a conduit propeller. Much interest was expressed in this area for stopping and emergency braking, as well as maneuvering and stabilizing big cargo and passenger ships, supertankers, ferries, cutters, and other vessels. Efforts here to date have been limited to low speeds, but attention has now been turned to higher speeds. Another variation from the normal ducted propeller configuration of interest touched upon was the noncylindrical nozzle to compensate for nonuniform inflow.

Simultaneous with the above discussions, the associated advantages of the ducted propeller for the different applications were reviewed in some depth. Since most of these advantages are well known, e.g., compactness, efficiency, static thrust increase, inlet flow control, etc., they will not be elaborated on.

The second objective for discussion concerned the analytical and experimental results that are available to meet different applications. In view of the thorough coverage by J. Weissinger and D. Maass from Karlsruhe, W. B. Morgan and E. B. Caster from NSRDC, and G. Dyne, C. A. Johnsson, and H. Lindgren from SSPA that was scheduled for the *Session On Unconventional*

Propulsion later, we shortened this discussion somewhat. However, related material which had been submitted in prepared communications was presented by G. Rosen from Hamilton Standard and J. Duport and J. Renard from Sogréah. This included a short description of the very extensive study recently completed by Hamilton Standard and the numerical programs used by Sogréah for high-speed inlet conditions. A new 1200 m. towing tank under construction in France with a fast gas-turbine-driven carriage was also mentioned. Several other participants made supporting remarks and clearly indicated the wealth of data available from NSMB to NPL, from Skipsmodeltanken of Norway to the São Paulo Towing Tank, for most ship applications, if ". . . we can find an owner prepared to fit one."

We finally addressed ourselves to the third and last objective, namely, to recommend the future work required in general ducted-propeller technology. Without order or preference, the following possibilities were suggested:

> Refine the mathematical model(s) for conditions at or near zero forward speed and lower rotational speeds.
>
> Incorporate more exact analyses for the effect of the hub, with special attention to larger hub-to-shroud-diameter ratios.
>
> Improve the existing analyses for the case of angle of attack and nonuniform or angular variations in inflow.
>
> Study ways and means to avoid separation/cavitation on duct and center body.
>
> Complete the analytical efforts to formulate an optimum ducted-propeller design, analogous to the Goldstein optimum for the free propeller, cf., J. A. Sparenberg, and confirm the design by experiment.
>
> Develop test facilities suitable for large-scale (10 m.) cavitation tests. Such facilities would also fulfill many other needs.
>
> Work on application of lateral thrusters to large ships at cruise speeds.
>
> Investigate the use of lifting-surface theory for the propeller in the calculation of propeller-shroud interaction. Also, include propeller thickness.
>
> Continue to refine the state of the art of ducted-propeller design procedures and narrow the differences between these procedures and measurements.

These recommendations were by no means unanimous. Some felt, in particular, that with respect to the first three recommendations, emphasis should be placed on the nonlinear but potential flow aspects. Others felt that, when linear theory

fails, the flow is no longer potential flow and viscous effects must be considered. All agreed, though, that an *importance factor* should be assigned to each recommendation and priority given accordingly.

* * *

PANEL DISCUSSION—HYDROFOIL CRAFT

J. P. Breslin, Panel Chairman
Stevens Institute of Technology
Hoboken, New Jersey

INTRODUCTION

The session was opened by a plea from the chairman for active participation from all and a dictum that this meeting was not to be reduced to a succession of prepared presentations. All prepared material was to be abstracted, leaving a maximum of time for airing of diverse opinions.

It was also arbitrarily announced that discussion would be largely limited to three aspects of hydrofoils with the hope that some answers to basic questions in each of these subtopics might be achieved. These aspects and questions were:

(1) Application of hydrofoil craft -- what are the future size and speed prospects for military and commercial vessels?

(2) Research in all hydrofoil-related phenomena -- are the results of past research of use to designers and what kinds of investigations should be conducted in the future?

(3) Current features of hydrofoils -- what are the expected trends in hydrofoil technology, particularly in regard to control and propulsion?

TOPIC 1

Topic 1 was initiated by J. Weller (Director of the NATO ASW Research Center at La Spezia), who virtually cast a bomb at all hydrofoil enthusiasts when he concluded that hydrofoils would prove to be too slow and too range-limited to be effective as a countermeasure for future high-speed submarines. To the dismay of the chairman, there was no hue and cry to this dramatic challenge, in spite of the presence of representatives of nearly all of the firms and agencies involved with current hydrofoil craft development and operation! W. Carl (Grumman Aircraft, Bethpage, N.Y.) suggested that certain studies were underway which might allow hydrofoils to listen for submarines while foil-borne at high speed. Weller brushed this aside by stating he knew of no way of solving that problem and retired uncontested from the podium! Reluctantly, the chairman introduced the second topic, hydrofoil-connected research.

TOPIC 2

A detailed presentation by J. Z. Lichtman (Naval Applied Science Laboratory, Brooklyn, N.Y.) was given in connection with cavitation erosion, resistance of propeller and hydrofoil structural materials. Lichtman presented several graphs showing the relative performance of samples of Titanium 621, 17-4 PH(1025) steel, HY 130, Cunisibe 18, Mn-Ni bronze, Mn bronze and HY 80, as well as the effectiveness of elastomeric coatings. He concluded that the resistance to cavitation erosion of several propeller and hydrofoil structural materials has been determined using high-velocity (rotating disk) and vibratory (magnetostriction) apparatuses. The materials were rated on the basis of their relative resistance. None of the structural materials were as resistant as high-strength elastomeric coatings, inlays or overlays, suggesting the use of elastomeric patches in local areas where erosion of structural materials occurs. The erosion of non-corrosion-resistant ferrous alloys was increased significantly in sea water, in comparison with fresh-water exposure due to electrochemical (corrosion) effects in the former liquid. The use of a sacrificial zinc-anode cathodic protection system decreased the erosion of these alloys to values within the range associated with fresh-water exposure. (Further details should be sought directly from the Naval Applied Science Laboratory.)

There were no discussers of this vital topic, which is so essential to the operation of transcavitating hydrofoils.

Professor T. Y. Wu (California Institute of Technology) abstracted a development of a quasi-steady planing of delta wings by R. K. DeLong and A. J. Acosta. Professor Wu pointed out that this study was indeed new, in that heretofore a nonstationary flow theory had not been attempted for planing craft. Agreement between measurements and theory was found to be good for angles of attack up to 10°. Agreement would be better at larger angles if the nonlinear terms could be doubled. The influence of reduced frequency was noteworthy. Out-of-phase forces were well predicted, but in-phase forces were lower than measured.

D. Savitsky (Stevens Institute of Technology, Hoboken, N.J.) asked if there were any physical interpretation of the in-phase lift results at very low reduced frequencies. He noted that analysis of experimental planing data for cases of slowly applied vertical velocity could not be analyzed simply as a change in trim or angle of attack, but, rather, it is necessary to calculate a higher effective forward or planing velocity to explain the large increase in lift due to a vertical velocity component. In contradistinction to wings, the planing body not only changes angle of attack with heave velocity, but also its wetted length. At low reduced frequencies, these two effects can be accounted for by calculating a higher steady-state planing speed.

Professor Wu generally deferred answers to the questions to the authors who were not in attendance and offered some copies of the paper to any who may be interested.

Next, a description was given of a new high-speed water-tunnel facility and hydrofoil tests in cavitating conditions at the Centre d'Etudes Aerodynamiques et Thermiques de Poitiers in France. This prepared work, read by Professor

R. Goethals, was entitled Research on High-Speed Hydrofoils. The abstract of this presentation is as follows:

> On March 1966 a blow-down water tunnel was started by the CEAT for research sponsored by the "Direction des Recherches et Moyens d'Essais". This research deals with supercavitating hydrofoils, submarine propulsion, and air-cushion vehicles over water. In our facility, water is driven out by compressed air from a tank and runs in free surface channels (cross area 1-2 dm^2) with a maximum velocity of 50 m./sec. The facility gets all the necessary equipment for pressure and force measurements.
>
> The first research work was a theoretical and experimental study of wall effect on force measurements. Especially for a test without wall correction, we designed a bottom with parallel slots. Research has been done on experimental studies of a hydrofoil family of finite aspect ratio in supercavitating flow. We have studied some hydrofoil groups corresponding to the same aspect ratio with various planforms.
>
> We have initiated the study in unsteady range of two-dimensional hydrofoils. We use the method of forced oscillations, and we are looking for the rotary derivatives.
>
> Further, along with the "Centre de Calcul Analogique," we have studied the design of a hydrofoil according to a given lifting pressure distribution. The control tests are under way.

Again, in spite of encouragement from the panel chairman, no discussion of hydrofoil experimentation was offered, save a question by M. Tulin (Hydronautics, Inc., Laurel, Md.) who inquired if this new facility at CEAT had been employed to study flutter problems as it possessed the unique advantage of high speeds. The answer was no.

M. Tulin next presented a summary of work done by Dr. M. Martin in surveying methods for study of hydrofoil flutter. The conclusions reached were as follows:

> It appears to be abundantly clear from the preceding survey that the hydro-elastic behavior of hydrofoils in the low mass density range is extremely sensitive to small changes in system parameters.
>
> Continuing research into obtaining a better understanding of viscous and nonlinear effects on the unsteady forces and moments on oscillating lifting surfaces is needed. Careful observations with the aid of dyes, motion pictures, and other flow visualization techniques, of the flow field around oscillating hydrofoils should provide some of the necessary ingredients for a lifting theory which corrects for the nonsatisfaction of the Kutta condition, for nonplanar wake effects, etc.

Additional, carefully planned, experimentation is needed to provide force, moment, and flutter data which would be useful in connection with the theoretical investigations in progress on aspect ratio, Froude number, and cavitation effects.

From the structural point of view, we have seen that, though in some cases it was possible to obtain conservative estimates of the flutter speed of swept, low-μ hydrofoils by taking a sufficiently large number of modes, in others the estimates were seriously under-conservative. Though insufficient knowledge of the hydrodynamics may account for much of this discrepancy, there is some evidence that in the low-μ range, additional insight into the problem might be obtained from the application of the differential-equation method of analysis and from correlations of careful observations of flutter mode shapes with theory. In the latter connection, motion pictures appear to be an extremely useful tool.

Since it appears that many strut-pod-foil systems operate in an effective mass density ratio range which is higher than the asymptotic value, the effects of sweep at moderate sweep angles may be small for such systems, and therefore simplifications in the analysis may be possible.

As far as actual hydrofoil configurations are concerned, it appears that, where hydroelastic stability is a source of serious concern, scale-model tests are a necessary ingredient in any analysis of the hydroelastic properties of the structure. In this connection, it appears to be a matter of the highest priority to develop techniques for the design and construction of realistic flutter models of strut-pod-hydrofoil prototype configurations.

Dale Calkins (Naval Undersea Warfare Center, San Diego, Calif.) asked if there were any instances of operational hydrofoils which suffered damage attributable to flutter. Tulin felt that the answer had to be no, but probably because of the limited number of craft that have been built and the preponderance of those being of relatively low speed. He went on to emphasize the dramatic failures due to flutter that have been obtained in model scale.

Next C. Elata (Hydronautics, Inc.) reported upon the principal findings of a study entitled "Choking of Strut-Ventilated Foil Cavities." He concluded that the ventilated cavity would be choked or starved of air for submergence-Froude numbers given by

$$F_h \leq 5\sqrt{\frac{C_D A}{t^2}}\sqrt{\frac{\rho_a}{\rho_w}},$$

where

C_D is the drag coefficient of the foil,

A is the foil area,

t is the strut thickness,

ρ_a is the mass density of air,

ρ_w is the mass density of water.

Dr. Breslin said that he would expect a considerable scale effect in such empirical determinations, since the spray sheets from the strut are continuous in model scale, causing an early closure of the ventilated cavity, as compared to full scale, where the spray sheets break up near the leading edge into disconnected droplets, allowing air to flow nearly unobstructed into the cavity at the base of the strut. Elata surmised that such effects would only change the constant in his inequality.

TOPIC 3

The third category, viz., current features of hydrofoils now under development, was opened by W. Carl (Grumman Aircraft, Bethpage, N.Y.) who showed an impressive film taken of the PGH-1 while operating during deck-gun firing. This craft cruises at 50 knots in six-foot waves. Carl pointed out that at Grumman the prospects of flutter are considered real and that both by design and experiment, they have managed to avoid flutter. This vessel is propelled by a KaMeWa controllable pitch propeller giving greater range and efficiency than the water-jet propulsion of the competing design developed by Boeing.

Dr. M. Kinoshita (Hitachi Shipbuilding Co., Osaka) gave a detailed analysis of data from commercial craft operating between the islands of Japan. He showed that suspension of service due to rough seas is a vital factor which could be reduced by research on the seakeeping characteristics of hydrofoils. This analysis was very thorough but, unfortunately, the unprepared charts could not be effectively projected.

Dr. Breslin asked if Dr. Kinoshita had established a relationship between the foilborne clearance and the wave height at which service had to be curtailed. No definitive answer was secured, although Dr. C. Hook (Hydrofin Design Centre, Bosham, England) allowed as how the relationship also depends upon speed. "The faster you go, the higher you must stand."

Baron H. W. Von Schertel (Supramar, Lucerne) showed slides and a motion picture. The slides depicted a new large car-carrying ferry. His new craft employ a pneumatic scheme to reduce lift by allowing air to be sucked by the lower pressure areas on the foils. The air supply is controlled by a valve, which is activated in response to pitch angle, roll angle, and roll angular rate. High reliability is claimed for this control system, which, when applied to only one foil (after) in conjunction with a surface-piercing foil forward, gives a smooth ride. The film showed an experimental craft with fully submerged foils employing the controlled ventilation principle. This craft was built for the U.S. Navy. The operation of this craft, as could be ascertained from the movie, was certainly impressive.

Dr. Hook gave an interesting account of the development of mechanical incidence control of hydrofoils. There were no discussers.

A movie of the water-jet propelled Boeing PGH-2 was shown. This vessel displays remarkable maneuverability and had, to that time, displayed a high degree of continuous reliability of the entire propulsion system.

The panel session was concluded on the note that, although answers to our arbitrarily posed questions were not obtained, we were all brought up to date on many aspects of hydrofoil research and development, particularly in the realms of new propulsion and control systems which are now being put to trial.

* * *

PANEL DISCUSSIONS

Thursday, August 29, 1968, 5 p.m.

Panel Discussion—Numerical Solutions

L. Landweber, Panel Chairman
Institute of Hydraulic Research, The University of Iowa
Iowa City, Iowa

INTRODUCTION

There were approximately two dozen participants in the Panel on Numerical Solutions. The following subjects were presented and discussed:

1. "Growth of Eddies in a Flow Expansion," by E. O. Macagno and T. K. Hung; presented by J. F. Kennedy.

2. "Laminar Boundary Layer on a Flat Plate in a Flow with Disturbances," by O. F. Vasiliev and I. V. Pushkareva; presented by O. F. Vasiliev.

3. "Some Problems in the Numerical Solution of Three-Dimensional, Incompressible Fluid Flows," by S. Piacsek.

4. "Numerical Solutions of the Two-Dimensional Navier-Stokes Equations," by M. Gauthier.

5. "Parametric Equations of Ship Forms by Conformal Mapping of Ship Sections," by L. Landweber.

6. "Computations of Ship Boundary Layers," by M. Martin; presented by L. Landweber.

* * *

Growth of Eddies in a Flow Expansion

Enzo Macagno
Institute of Hydraulic Research, The University of Iowa
Iowa City, Iowa

and

Tin-Kan Hung
Carnegie-Mellon University
Pittsburgh, Pennsylvania

presented by

J. F. Kennedy
Institute of Hydraulic Research, the University of Iowa
Iowa City, Iowa

The basic equations for this calculation of the laminar flow establishment at a two-dimensional abrupt flow expansion were the vorticity-transport equation

$$\frac{\partial \zeta}{\partial t} + u \frac{\partial \zeta}{\partial x} + v \frac{\partial \zeta}{\partial y} = \frac{1}{R} \left(\frac{\partial^2 \zeta}{\partial x^2} + \frac{\partial^2 \zeta}{\partial y^2} \right) \quad (1)$$

and the relation between vorticity and the stream function

$$\frac{\partial^2 \psi}{\partial x^2} + \frac{\partial^2 \psi}{\partial y^2} = - \zeta \ . \quad (2)$$

These equations are dimensionless with reference to the mean velocity U_0 and the spacing D_0 of the upstream portion of the nonuniform conduit, and the density of the fluid. The vorticity is denoted by ζ, and the stream function by ψ. (i, j) denote spatial coordinates in discrete form, n is a superscript which counts the time intervals in the following finite-difference equations which were established as counterparts of Eq. (1) and (2):

$$\zeta_{i,j}^{n+1} = \left(\frac{4}{h^2} + \frac{R}{2\delta t} \right)^{-1} \left\{ \frac{R}{2\delta t} \zeta_{i,j}^{n-1} + \frac{1}{h^2} \left(\zeta_{i+1,j}^{n} + \zeta_{i-1,j}^{n} + \zeta_{i,j+1}^{n} + \zeta_{i,j-1}^{n} \right) + \frac{R}{4h^2} \left[\left(\psi_{i+1,j}^{n} - \psi_{i-1,j}^{n} \right) \left(\zeta_{i,j+1}^{n} - \zeta_{i,j-1}^{n} \right) - \left(\psi_{i,j+1}^{n} - \psi_{i,j-1}^{n} \right) \left(\zeta_{i+1,j}^{n} - \zeta_{i-1,j}^{n} \right) \right] \right\} ,$$

$$\psi_{i,j}^{n+1} = \frac{1}{4} \left(\psi_{i-1,j}^{n+1} + \psi_{i,j-1}^{n+1} + \psi_{i,j+1}^{n+1} + \psi_{i+1,j}^{n+1} + h^2 \zeta_{i,j}^{n+1} \right) .$$

Boundary conditions (for example the nonslip condition) were also expressed by means of finite-difference schemes in the form of inward expansions. The functions ζ and ψ were expanded by means of Taylor series from the walls inwards.

Because the computational technique is based on calculating the distribution of the stream function during one of the steps, and subsequently that of the vorticity function, expressions in difference form are necessary to calculate ζ in terms of ψ at the boundaries (the expressions at inner points have the standard form for the Laplacian in two dimensions). One of the expressions used at the boundaries, which can be considered as a typical one, is

$$\zeta_B = \frac{3}{h^2} (\psi_B - \psi_{B+1}) - \frac{1}{2} \zeta_{B+1} + \frac{h^2}{8} (\zeta_{xx} + \zeta_{yy})_B \ .$$

Here, B is a point at the wall and $B+1$ is a point one mesh inside.

To begin the calculation we assumed that the flow would be started impulsively and that at the time 0^+ the flow would be irrotational. Thus, the initial values of ψ were given by irrotational flow without separation.

The results given in Fig. 1 show how an eddy forms initially at the entrant corner, and how it grows. Two eddies form at a certain time, but one is

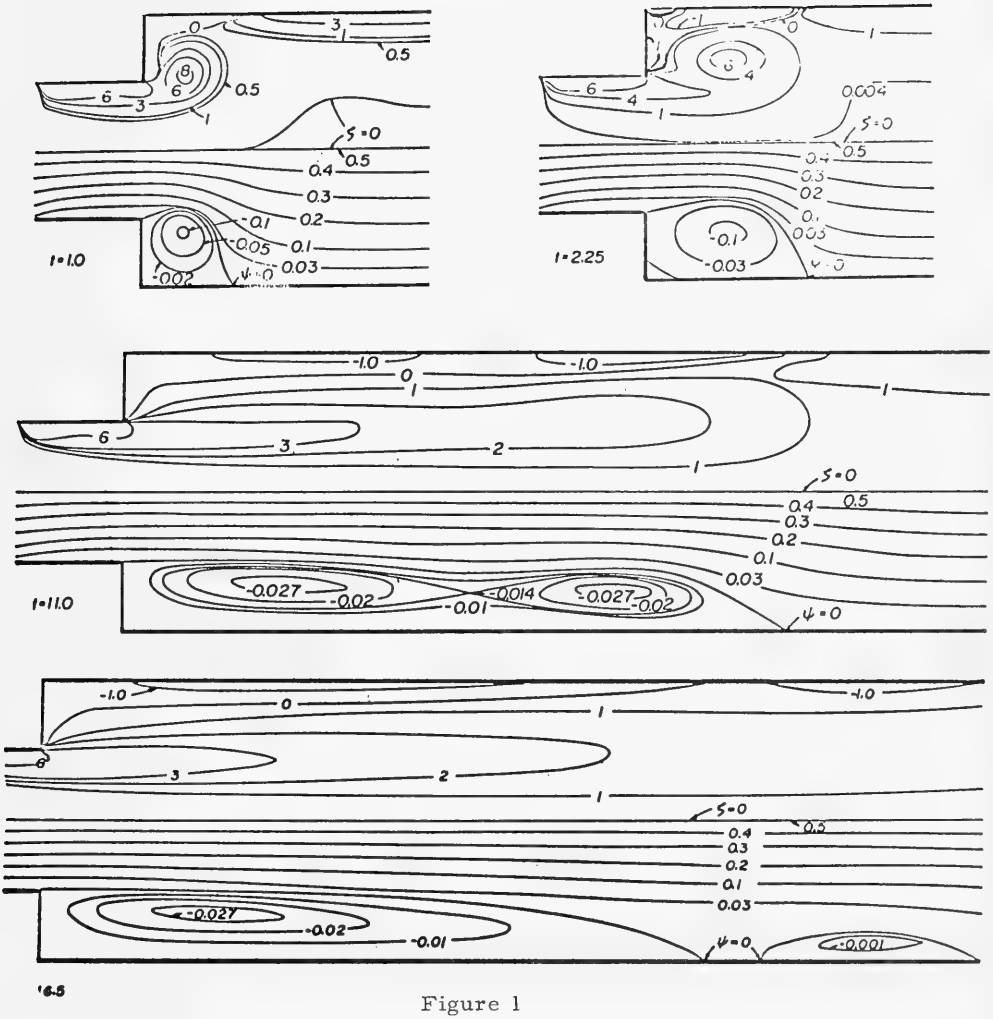

Figure 1

predominant (the closer to the expansion) and the other is finally eliminated. The Reynolds number for this flow, based on U_0, D_0, and ν was 200. We have calculated steady annular eddies for higher Reynolds numbers (see J. Fluid Mech., 1967, Vol. 28, Part 1), using equations including the local acceleration. In a way this also gives an example of a transient flow.

Computational Instability

The numerical calculations were based on an explicit finite-difference scheme, which has the advantage of being very simple to formulate and to treat numerically. It has the disadvantage of becoming unstable outside a region

bounded by a limiting curve of R versus D/h (Reynolds number versus ratio of spacing D to mesh size; D/h is actually the number of meshes across the channel in its upstream section).

As a means of verifying the accuracy of the difference scheme used (which was checked at each step by iterating until the discrepancies were reduced to a prescribed value), and also as a means of testing the stability of the scheme before applying it to the long calculations for the unsteady problem under investigation, the finite-difference system was applied to a disturbed uniform flow, i.e., a flow within parallel straight boundaries for which the vorticity distribution had been initially prescribed to be quite different from the one for uniform steady flow. The entire system of equations, including those for the boundary conditions, was used in calculating the transient flow that should lead from the disturbed flow to the steady uniform flow. Were the scheme unstable, it was reasoned, the disturbed flow would fail to return to the original uniform flow; were the scheme stable, but still convergent to a different solution, this would also be discovered. Figure 2 shows what happens when a calculation for uniform flow becomes unstable: Such rapidly expanding oscillations with a wave length directly related to the mesh size are quite typical of numerical instability as opposed to hydrodynamically originated instability. Figure 3 shows the result of a study of instability in the case of a two-dimension expansion. The effects of iterating in different ways are also shown (the influence of the paths of iteration is not great, but a less biased distribution of errors results from sweeping the field diagonally, N.W. to S.E., N.E. to S.W., S.E. to N.W., and S.W. to N.E.).

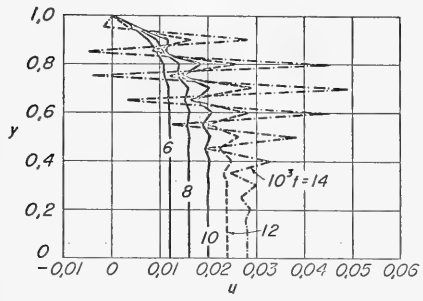

Figure 2

The exact position of the neutral line was not sought, because the process is time-consuming.

DISCUSSION

In reply to an inquiry by A. M. O. Smith (Douglas Aircraft Co., Long Beach, Calif.) whether the results obtained had been compared with other similar work, a recent study by a graduate student at the University of Notre Dame was mentioned by S. Piacsek (University of Notre Dame, Ind.). In this investigation a uniform stream parallel to a wall with a step was treated, and similar results were found.

Another comment was that symmetry of boundary geometry does not ensure flow symmetry, as is assumed in the present work. A calculation at Reynolds numbers from 100 to 200 of flow in an axisymmetric conduit which yielded non-axisymmetric flow was cited.

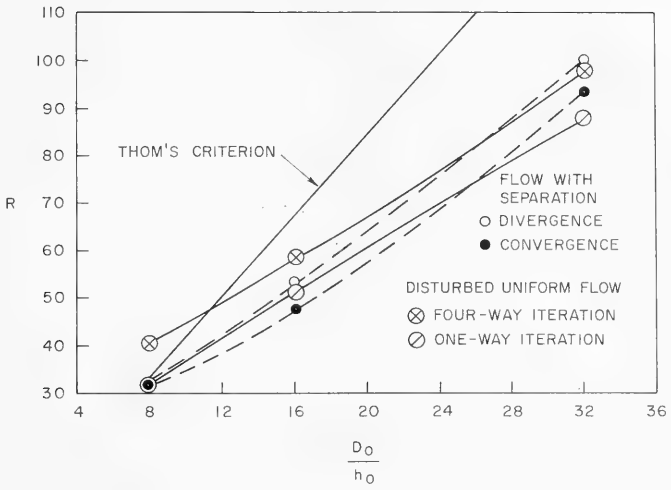

Figure 3

Several comments pertained to the stability of the calculations. One suggestion, by P. Fink (University of New South Wales, Australia), based on Dr. Hirt's paper in the session on Fundamental Hydrodynamics (paper No. 11 of these Proceedings), was that the mesh size for stability could be investigated analytically, rather than empirically by numerical trial, by carrying additional terms in the Taylor-series expansions used to express the Navier-Stokes equations in finite-difference form. Another suggestion, based on numerical calculations of flow about a cylinder, was that the results are sensitive to the assumed upstream and downstream boundary conditions. This is contrary to the experience of Macagno and Hung in the case of an abrupt expansion, who found that the development of the vortex structure was insensitive to the assumed upstream velocity profile, a uniform stream in one case and parabolic velocity profile in another; furthermore they found that the downstream flow pattern eventually became parabolic without the necessity of any assumption. It appears that the sensitivity of the computed flow to the assumed boundary conditions depends on the boundary geometry.

* * *

Laminar Boundary Layer on a Flat Plate in a Flow with Disturbances

O. F. Vasiliev and I. V. Pushkareva
Institute of Hydrodynamics
Siberian Department of the U.S.S.R. Academy of Sciences
Novosibirsk, U.S.S.R.

presented by

O. F. Vasiliev

The work is devoted to the theoretical analysis of the behavior of the two-dimensional laminar boundary layer along a flat plate when the free-stream approach flow of an incompressible fluid has disturbances. The influence both of periodic disturbances of two types and of random disturbances of the simplest type are treated.

At first the boundary-layer velocity distribution is studied when the outside stream $u(x,t)$ has periodic disturbances imposed on a constant velocity flow u_0. As mentioned, this problem is treated in two variants. In the first case,

$$u(x,t) = u_0 \left[1 + \lambda \cos \omega\left(\frac{x}{u_0} - t\right)\right]$$

(the disturbances are carried by the mean flow).
In the second case,

$$u(t) = u_0 \ (1 + \lambda \cos \omega t)$$

(the x axis is directed along the plate, t is the time).

The assumption of the relative smallness of the disturbance amplitude λ permits one to construct the solution in the form of an expansion in power series of the small parameter λ. The coefficients of the first three terms of this series were found. Because of a special choice of the nondimensional variables, the problem is reduced to the determination of universal functions.

Next the boundary-layer velocity fluctuations were studied, assuming that, upon the free flow with the constant velocity u_0 are superimposed stochastic disturbances u', carried by the free stream with the approach velocity u_0,

$$u(x,t) = u_0 + u'(\tau), \quad \tau = t - \frac{x}{u_0}.$$

It is thereby assumed that the flow velocity fluctuations are represented by a stationary random function of τ and that the relative intensity of turbulence in the free flow is small:

$$\epsilon = \sqrt{\frac{\overline{u'^2(\tau)}}{u_0^2}} \ll 1$$

The latter assumption permits one to construct the solution in the form of a power series of the small parameter ϵ.

In all cases the coefficients of the expansions are defined by systems of partial differential equations. These systems of equations were solved numerically by application of implicit difference schemes.

From the analysis of the behavior of the solutions obtained in this manner, some qualitative conclusions were reached in regard to the properties of the flows studied. For example, with increase of the parameter $\zeta = \omega x/u_0$ the influence zone of outer disturbances is displaced closer to the edge of the boundary layer in the first case, but closer to the place surface in the second case.

In the case of the random disturbances, the free-stream velocity fluctuations permeate the boundary layer most of all at the relatively large values of the scale of turbulence. In this case the velocity fluctuations within the boundary layer may exceed those which occur outside.

DISCUSSION

K. Wieghardt (Universität Hamburg, Germany) asked whether the term $\partial^2 u/\partial x^2$, which is neglected in the derivation of the boundary-layer equations, remains small in the presence of the assumed disturbances, as could easily be verified by examining the resulting solutions. It was stated, in reply, that the derived coefficients were examined for their variation with frequency and downstream distance x, but it would be necessary to examine the paper in detail to determine when $\partial^2 u/\partial x^2$ became large.

* * *

Some Problems in the Numerical Solution of Three-Dimensional, Incompressible Fluid Flows

S. A. Piacsek
University of Notre Dame, Indiana

Current attempts at numerical calculations of three-dimensional, incompressible flows on digital computers may be divided into two categories:

1. *Velocity-Pressure Approach:* In this method one uses the time-dependent Navier-Stokes equations to find the velocity components from a time iteration, and the pressure is found from a Poisson equation that one obtains by

taking the divergence of the Navier-Stokes equations. The relevant equations in Cartesian coordinates are

$$\frac{\partial u_i}{\partial t} + (\mathbf{u} \cdot \nabla)\, u_i = -\frac{1}{\rho_0}\frac{\partial p}{\partial x_i} + \nu \nabla^2 u_i \,, \tag{1}$$

$$\nabla^2 p = -\rho_0 \nabla \cdot (\mathbf{u} \cdot \nabla)\, \mathbf{u} = F(u_i) \,, \tag{2}$$

where ν and ρ are assumed constant for this discussion. Since neither the pressure nor its normal gradient are known at a rigid wall, the application of the boundary conditions becomes an integral part of the iteration process. The exact procedure is as follows: One forecasts new values of u_i at time level $n+1$, say, using their values (and that of p) at levels n and $n-1$, depending on the scheme employed. Then one finds p to order $n+1$ by iterating (2), using the values of the normal derivative $\partial p/\partial n$ on the boundaries and the source function F evaluated at time level $n+1$. The boundary values of $\partial p/\partial n$ at level $n+1$ are obtained from (1) upon substitution of the u_i^{n+1} into all the terms.

2. *Vorticity-Stream Function Approach:* In this method one introduces a vector potential ψ and a vorticity vector ζ. Defining $\mathbf{u} = \nabla \times \psi$ and $\zeta = \nabla \times \mathbf{u}$, one obtains the following set of equations:

$$\frac{\partial \zeta_i}{\partial t} + (\mathbf{u} \cdot \nabla)\, \zeta_i - (\zeta \cdot \nabla)\, u_i = \nu \nabla^2 \zeta_i \,, \tag{3}$$

$$\nabla^2 \psi_i = -\zeta_i \,, \tag{4}$$

where the condition $\nabla \cdot \psi = 0$ is put on the vector potential. The numerical procedure is similar to the previous one, though the boundary conditions are again troublesome. The components of the vorticity vector parallel to a rigid surface are not known, whereas the corresponding stream functions and their normal derivatives are known. It is clear that we cannot use both sets of conditions in solving (4), because then the problem becomes over-determined. Rather, one uses the boundary values of ψ_i to solve (4), and the boundary values of $\partial \psi_i/\partial n$ to find the vorticities ζ_i at the wall from a Taylor-series expansion. The exact iteration procedure is then as follows: One forecasts new values of ζ_i at time level $n+1$ on all interior mesh points and then finds ψ_i by iterating Eq. (4). Finally, the boundary values of ζ_i are found from a Taylor-series expansion of the stream function values on mesh points adjacent to the wall, about values on the wall, and utilizing the fact that, at a rigid wall, any parallel component of vorticity is given by $\zeta_i = \partial^2 \psi_i/\partial n^2$ evaluated at the wall. An alternative procedure would be to forecast ζ_i on the wall itself, using one-sided spatial differences and ensuring that the total forecast procedure remains conservative; however, this procedure has not met with much success.

In 1966, a paper appeared by Arakawa that showed how to difference the advective terms in two-dimensional, incompressible flow that conserves vorticity, mean-square vorticity, and kinetic energy. An analog of this procedure for Eq. (3) has not yet been found.

The author is not aware of any published works relying on the velocity-pressure approach, though recently successful use of it has been reported by

Orszag (1968) and Williams (1967). The vorticity approach has been used successfully by Aziz and Hellums (1967).

SOLUTION OF POISSON'S EQUATION ON THREE-DIMENSIONAL GRIDS

The standard iterative techniques that have been developed for the two-dimensional Poisson equation, such as the successive over-relaxation (SOR) and the alternating-direction implicit (ADI) cannot be carried over directly to three dimensions. Two alternative approaches are being employed at present to solve (2) with $\partial p/\partial n$ given or (4) with ψ_i given on the boundaries.

(A) One regards the Poisson equation as the steady-state version of the time-dependent parabolic diffusion equation

$$\frac{\partial \psi_i}{\partial t} = \nabla^2 \psi_i + \zeta_i \ , \tag{5}$$

in which ζ_i is a known source function, and uses any of the techniques developed for iterating (5) in three space dimensions. Among the successful techniques that have been used by the author with good success are the DuFort-Frankel (1953), Douglas-Rachford (1956), Douglas (1962), and Saul'ev (1957) schemes. In any of these methods, if the spectrum of the initial error is known in advance, one can choose a sequence of time steps such that each extinguishes a particular harmonic. By repeating this sequence several times one can obtain very good convergence; e.g., on a 10^3 mesh, four sweeps of a five-time-step sequence resulted in decreasing the error by a factor of 10^{-3}.

(B) If the boundary conditions are either periodic or of the "dynamically free" kind (no stress and no normal velocity) at one or two pairs of opposing boundaries, one can expand both the components ψ_i and ζ_i parallel to these surfaces in a sine or a sine/cosine series, as the case may be. Equation (4) may in general be reduced to a system of N^2 ordinary differential equations of the type

$$\frac{d^2 a_{mn}}{dz^2} - (m^2 + n^2)\, \pi^2 \cdot a_{mn} = b_{mn} \ , \tag{6}$$

where the a_{mn} and the b_{mn} are the Fourier coefficients of ψ and ζ in the x-y expansion. The finite-difference version of (6) can be solved easily by a special algorithm devised for tri-diagonal matrices (see Varga, p. 195).

Most of the computer time in approach b is spent in finding the coefficients b_{mn} and superimposing the a_{mn} to find ψ. For Fourier synthesis of functions with complex values, a very efficient algorithm exists if the number of grid points has a particular value, say, $N = 2^n$, as shown by Cooley and Tukey (1965). This approach, however, has as yet no known counterpart in the case of real functions (e.g., sines alone). Hockney (1965) devised a related method utilizing the symmetry of the sine functions and a cyclic reduction technique on grids of size $N = 3 \cdot 2^n$, but his technique was applied to two dimensions only. Studies are being made to extend the method to three dimensions.

REFERENCES

Arakawa, A., (1966), J. Comp. Phys. 1, 119

Cooley, J.W. and Tukey, J.W., (1965), Math. of Comput. 19, 297

Douglas, J., (1962), Numer. Mathem. 4, 41

Douglas, J. and Rachford, H.H., (1956), Trans. Am. Math. Soc. 82, 421

Hockney, R.W. (1965), J. Assoc. Comp. Mach. 12, 95

Orszag, S.A., (1968), International Symposium on High-Speed Computers in Fluid Dynamics, Monterey, Calif., Aug. 1968

Varga, R.S., (1962), "Matrix Iterative Analysis," Prentice-Hall

Williams, G.P., (1967), Geophysical Fluid Dynamics Lab., ESSA, Washington, D.C., private communication

DISCUSSION

R. Barakat (Itek Corp., Lexington, Mass.) has stated that, to his knowledge, an algorithm similar to that of Cooley-Tukey has been developed by Lanczos (1943) for real sine functions. The author replied that he has not read that paper, but will look into it. Barakat also questioned whether the Fourier-transform method would be accurate for functions which do not vanish outside a certain region. Piacsek indicated that his procedure was of the nature of "curve-fitting" by means of a discrete set of Fourier harmonics, so that the criticism did not apply.

* * *

Numerical Solutions of the Two-Dimensional Navier-Stokes Equations

M. Gauthier
Société Sogréah
Grenoble, France

I shall discuss briefly two numerical problems we have met for the solution of the Navier-Stokes (NS) equations for the two-dimensional case.

SOLUTION OF THE POISSON EQUATION

To solve the NS equation we have to solve at each step a Poisson equation which consumes much computing time. It would be very useful to have a systematic study of all the algorithms to solve this problem. According to our own experience, however, it is preferable to use iterative methods to solve a problem with a free surface. For fixed boundaries we have had better success by using properties of symmetric band matrices. Actually, we plan to use a modified algorithm based on chain-matrix properties.

NUMERICAL DIFFUSION OF TRANSPORT EQUATION

The problem of numerical treatment of transport terms is a very difficult one. We tested about twelve different schemes in both one- and two-dimensional cases. Because of the numerical diffusion we found it necessary to retain second-order terms in the time scheme. The use of staggered mesh gives rather good results but introduces difficulties with the boundary conditions.

We have also studied nonanalytical algorithms which give very good results, in particular for steady flow. This fact has facilitated the solution of the steady case even for high-Reynolds-number turbulent flow.

DISCUSSION

S. Piacsek inquired about the details of the staggered-mesh procedure in the numerical treatment of the transport equation and the coupling of solutions at odd and even time levels. The author emphasized that the major difficulty encountered is with the boundary conditions, because there are two different expressions of these conditions for the two levels. It is necessary to couple the two levels because otherwise there would be a discrepancy between the two solutions, as was discussed in a 1966 paper.

* * *

Parametric Equations of Ship Forms by Conformal Mapping of Ship Sections

L. Landweber

INTRODUCTION

In a previous paper [1], a modification of the Bieberbach method of conformal mapping has been applied to obtain added masses of ship sections. When a note by Kerczek and Tuck [2] appeared, suggesting that the coefficients of the mapping functions could be made to yield parametric equations of the entire ship hull, an attempt was made to apply the Bieberbach method for this purpose.

When the results were tested by comparing the computed ship sections with the original, it was found that the agreement was excellent for all but one of 20 sections, but was very bad, showing double points and poor agreement at the ends, in the one case of failure. The reasons for this failure will be discussed in a following section.

Another method of conformal mapping, which has been studied by many investigators, is that of the Gershgorin integral equation. This method is thoroughly treated by Gaier [3] from both the theoretical and practical point of view. Nevertheless, other investigators have found [4] that odd-shaped forms can be successfully mapped by means of the Gershgorin equation only if extreme care is taken in expressing the integrals by quadrature formulas.

The purpose of this note is to present our experience and recommendations for mapping pathological double ship sections, i.e., sections with inflection points and corners at the free surface and keel. Since it is intended to use the resulting mathematical representation in integral equations for potential flow about ship forms, economy of numerical evaluation is an important consideration.

BIEBERBACH METHOD

Let

$$z = \zeta + \frac{a_1}{\zeta} + \frac{a_3}{\zeta^3} + \frac{a_5}{\zeta^5} + \cdots , \tag{1}$$

$$\zeta = z + \frac{b_1}{z} + \frac{b_3}{z^3} + \frac{b_5}{z^5} + \cdots , \tag{2}$$

be a transformation and its inverse which map a double ship section in the complex z plane into a circle about the origin in the ζ plane. Here, $a_1, a_3, \cdots$ and $b_1, b_3, \cdots$ are real and only the coefficients with odd indices appear because of the symmetry of the section about the vertical and horizontal axes. The Bieberbach method is based on the property that, among the closed curves in the ζ plane obtained from the given section in the z plane by the transformation (2) for various values of $b_1, b_3, \cdots$, the circle will bound the maximum area. Thus, if the series in (2) is truncated, and the condition of maximizing the area is applied to each of the b's, one obtains a set of linear equations for determining them (Ritz procedure), as is elaborated in [1]. Finally, Eq. (2) is inverted to yield (1), since it is usually the a's that are of interest.

Since both (1) and (2) are infinite series, we must be concerned with their convergence. For (1) we can state that the series converges in the exterior of the unit circle and gives a one-to-one mapping of the given profile into the unit circle. For (2), however, we can only say that the series in (2) converges in the exterior of the smallest circle in the z plane which circumscribes the given profile. Actually, the radius of the inner circle of convergence may be reduced until the radius of the singularity of the mapping function closest to the circumscribing circle. Thus, (2) will give a one-to-one convergent transformation of the profile into the unit circle if and only if no singularities of the transformation (2) lie between the inscribed and circumscribed circles.

One sees then that the Bieberbach method, which necessarily operates with the inverse transformation (2), cannot be assured of success. Furthermore, a corollary of the foregoing discussion is that the probability of success is much higher for a nearly circular section than for an elongated one. This indicates the desirability of a preliminary transformation of the Joukowsky type, such as that used in the Theodorsen method of conformal mapping, which first maps the given profile into a near circle.

BRANCH-POINT TRANSFORMATIONS

Consider a ship section which intersects the free surface at an angle α at A and the vertical centerplane at an angle β at B. The double ship section will then have corners of angle 2α at A and 2β at B. We wish to transform the contour of this double section into one without corners.

A transformation which eliminates the corners at A and its image in the y axis is [5]

$$\frac{z - a}{z + a} = \left(\frac{z' - 1}{z' + 1}\right)^p, \quad p = 2\left(1 - \frac{\alpha}{\pi}\right), \quad 1 < p < 2 . \tag{3}$$

This transforms the point B to a point B in the z plane with coordinates $(0, b')$, where

$$b' = \cot\frac{\gamma}{p}, \quad \frac{b}{a} = \cot\gamma . \tag{4}$$

Since the point A is transformed into a point A' with coordinates $(1, 0)$, we see that

$$\gamma' = \frac{\gamma}{p} \tag{5}$$

is the angle O'B'A', where O' denotes the origin in the z' plane. Then we have $\gamma' < \gamma$.

Next, we wish to eliminate the corner at B' in the z' plane. Put

$$\frac{z' - ib'}{z' + ib'} = \left(\frac{z'' - i}{z'' + i}\right)^q, \quad q = 2\left(1 - \frac{\beta}{\pi}\right), \quad 1 < q < 2 . \tag{6}$$

In the z'' plane, the points A and B are now transformed into A'' and B'' with coordinates $(a'', 0)$ and $(0, 1)$, where

$$a'' = \tan\gamma_1'', \quad \gamma_1'' = \frac{\gamma}{pq} + \frac{\pi}{2}\left(1 - \frac{1}{q}\right) . \tag{7}$$

Here, γ'' is the angle O''B''A'' in the t plane.

If the corner at B were removed first, and that at A second, the resulting angle in the z'' plane could be obtained from (7) by replacing γ and γ_1'' by their complements and q by p. Thus we would obtain

$$\gamma_2'' = \frac{\gamma}{pq} + \frac{\pi}{2p}\left(1 - \frac{1}{q}\right). \tag{8}$$

Comparison of (7) and (8) shows that $\gamma_2'' < \gamma_1''$. Since, in general, mapping into a circle is accomplished more readily for nearly circular sections, it would be desirable to select that order which makes γ'' closer to $\pi/4$. For example, if $\gamma = \pi/8$ $(a/b = 0.445)$, $\alpha = \pi/4$, and $\beta = 3\pi/8$, we have $p = 3/2$, $q = 5/4$, and then, from (7) and (8), we obtain $\gamma_1'' = \pi/6$ and $\gamma_2'' = 2\pi/15$. In this case the original order appears to be preferable. The difference between (7) and (8) is independent of γ_1, viz.,

$$\gamma_1'' - \gamma_2'' = \frac{\pi}{2}\left(1 - \frac{1}{p}\right)\left(1 - \frac{1}{q}\right). \tag{9}$$

Let us combine the transformations (3) and (6). Put

$$Z = \frac{z - a}{z + a}, \quad Z'' = \frac{z'' - i}{z'' + i}. \tag{10}$$

We then also have, putting $z = x + iy$,

$$Z = \frac{x^2 + y^2 - a^2 + 2iay}{(x + a)^2 + y^2} \tag{11}$$

and, with $Z'' = \sigma + i\tau$,

$$z'' = i\,\frac{1 + Z''}{1 - Z''} = -\frac{2\tau + i\,(\sigma^2 + \tau^2 - 1)}{(\sigma - 1)^2 + \tau^2}. \tag{12}$$

Solving both (3) and (6) for z' gives

$$z' = \frac{1 + Z^{1/p}}{1 - Z^{1/p}} = ib'\,\frac{1 + Z''^{q}}{1 - Z''^{q}}$$

and then, by (4),

$$Z'' = \left[\frac{e^{i\frac{\gamma}{p}} - Z^{\frac{1}{p}}\, e^{-i\frac{\gamma}{p}}}{Z^{\frac{1}{p}}\, e^{i\frac{\gamma}{p}} - e^{-i\frac{\gamma}{p}}}\right]^{1/q}. \tag{13}$$

From (11) - (13) we can compute the real and imaginary parts of a point z'' from the coordinates of a point z.

If, in accordance with the foregoing discussion, it is preferable to reverse the order of the transformations, this can effectively be accomplished by rotating the given profile through an angle of $\pi/2$ rad, by

$$z_1 = e^{i\frac{\pi}{2}} z \tag{14}$$

and then substituting z_1 for z in the above formulas.

JOUKOWSKY TRANSFORMATION

We shall now transform the profile in the z'' plane to one in which the ratio of the principal dimensions is unity. Put

$$z'' = c\zeta + \frac{d}{\zeta} \tag{15}$$

and select the coefficients c and d so that the principal dimensions in the ζ plane are each unity. Then we have, from (15),

$$c + d = a'', \quad c - d = 1 , \tag{16}$$

where "a" is given in (7), and hence

$$c = \frac{1}{2}(a'' + 1), \quad d = \frac{1}{2}(a'' - 1) . \tag{17}$$

Set

$$z'' = \mu + i\nu, \quad \zeta = \lambda e^{i\psi} . \tag{18}$$

Then from (15) we obtain

$$\mu = \left(c\lambda + \frac{d}{\lambda}\right) \cos\psi , \tag{19}$$

$$\nu = \left(c\lambda - \frac{d}{\lambda}\right) \sin\psi . \tag{20}$$

Eliminating λ between (13) and (14) yields

$$\mu^2 \sec^2\psi - \nu^2 \csc^2\psi = 4cd ,$$

or

$$4cd \sin^4\psi + (\mu^2 + \nu^2 - 4cd) \sin^2\psi - \nu^2 = 0 , \tag{21}$$

a quadratic equation in $\sin^2\psi$. From its solutions one can obtain the corresponding values of λ from (19) or (20).

GERSHGORIN INTEGRAL EQUATION

We now wish to transform the profile in the ζ plane into a unit circle about the origin in the w plane,

$$w = e^{i\theta} . \tag{22}$$

Polar coordinates in the ζ plane have been designated as (λ,ψ) in (18). Arc length along the contour will be denoted by s, with $s = 0$ at A''' and increasing in the counterclockwise sense of traversing the contour. We shall also require the polar coordinates of the chord directed from a point P at arc length s to a point Q at arc length t along the contour,

$$\overline{PQ} = r_{st}\, e^{i\varphi_{st}} \tag{23}$$

in complex notation. In particular, the chord $\overline{A'''P}$ would have the polar coordinates $(r_{os},\ \varphi_{os})$.

The Gershgorin integral equation [3] may be written in the form

$$\theta(\psi) = \int_0^{2\pi} K(\psi,\psi')\,\theta(\psi')\,d\psi' + 2\varphi_{os}\ , \tag{24}$$

where $\overline{O'''P} = \lambda e^{i\psi}$, $\overline{O'''Q} = \lambda' e^{i\psi'}$;

$$\begin{aligned} K(\psi,\psi') &= -\frac{1}{\pi}\frac{\partial\varphi_{st}}{\partial\psi'} \\ &= \frac{\lambda'\,[\lambda' - \lambda\cos(\psi-\psi')] - \lambda\dfrac{d\lambda'}{d\psi'}\sin(\psi-\psi')}{\lambda^2 + \lambda'^2 - 2\lambda\lambda'\cos(\psi-\psi')}\ , \end{aligned} \tag{25}$$

$$\varphi_{os} = \arcsin\left(\frac{\lambda}{r_{os}}\sin\psi\right), \tag{26}$$

$$r_{os} = [\lambda_0^2 + \lambda^2 - 2\lambda_0\lambda\cos\psi]^{1/2},\ \lambda_0 = \lambda(0)\ . \tag{27}$$

When $\psi' = \psi$, the expression for $K(\psi,\psi')$ in (25) is indeterminate. Although the limit can be readily obtained, it is preferable to avoid this difficulty by writing (24) as

$$\theta(\psi) = \frac{1}{2}\int_0^{2\pi} K(\psi,\psi')\,[\theta(\psi') - \theta(\psi)]\,d\psi' + \varphi_{os}\ , \tag{28}$$

which is equivalent to (24), since, by (25),

$$\int_0^{2\pi} K(\psi,\psi')\theta(\psi)\,d\psi' = -\frac{\theta(\psi)}{\pi}\int_0^{2\pi}\frac{\partial\varphi_{st}}{\partial\psi'}\,d\psi' = -\theta(\psi)\ . \tag{29}$$

The integral equation (28) can be solved approximately by reducing it to a set of linear equations in a discrete number of values of ψ and θ. Because of the double symmetry, (28) can be collected so that the range of integration extends from zero to $\pi/2$. Mappings were computed for $\psi = 1°, 2°, 3°, \cdots, 89°$ and the resulting values of θ also range between 0 and 90°. It is assumed that $\theta = 0$ when $\psi = 0$ and $\theta = 90°$ when $\psi = 90°$.

Finally, we wish to obtain the coefficients $a_1, a_2, \cdots$ of the mapping functions

$$z = Aw + \frac{a_1}{w} + \frac{a_3}{w^3} + \frac{a_5}{w^5} + \cdots . \tag{30}$$

Express the original profile in polar coordinates (Fig. 1),

$$z = r(\varphi)e^{i\varphi} ,$$

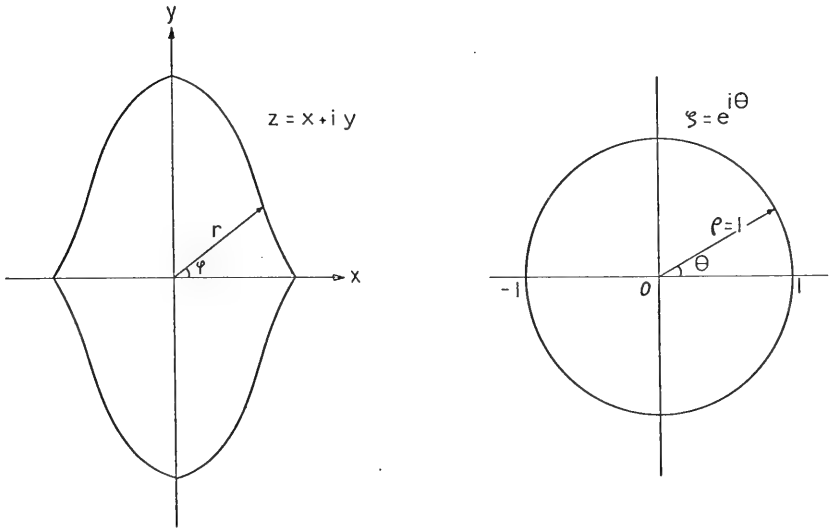

Figure 1

and since $w = e^{i\varphi}$, (30) becomes

$$re^{i\varphi} = Ae^{i\theta} + a_1e^{-i\theta} + a_3e^{-3i\theta} + \cdots .$$

Then

$$A = \frac{1}{2\pi}\int_0^{2\pi} r(\varphi)e^{i(\varphi-\theta)}\,d\theta = \frac{1}{2\pi}\int_0^{2\pi} r(\varphi)\cos(\varphi-\theta)\,d\theta \tag{31}$$

and

$$a_{2n-1} = \frac{1}{2\pi}\int_0^{2\pi} r(\varphi)\cos[\varphi + (2n-1)\theta]\,d\theta, \quad n = 1, 2, \cdots . \tag{32}$$

The ranges of integration in (31) and (32) can also be reduced to $0 - \pi/2$ by taking advantage of symmetry. The number of coefficients that can be computed with accuracy from (32) depends upon the number and distribution of the values of θ. For example, if nine values of θ in a half cycle of the oscillating integrand in (32) are considered to be necessary for the numerical evaluation of the integral, the series should be truncated at a_{19} when intervals of 1° are used in the calculations.

From (30) we now have the parametric equations of the ship section:

$$x = (A + a_1) \cos \theta + a_3 \cos 3\theta + a_5 \cos 5\theta + \cdots , \tag{33}$$

$$y = (A - a_1) \sin \theta - a_3 \sin 3\theta - a_5 \sin 5\theta - \cdots . \tag{34}$$

How well a given section can be represented by these equations is shown in Fig. 2. Results are shown for various combinations of mappings from the section into the unit circle. It is seen that the poorest representation is obtained from a direct application of the Gershgorin integral equation, with no intervening transformations. Preliminary branch-point transformations, or a preliminary Joukowsky transformation for transforming the section into one of unit height-to-breadth ratio, followed by the Gershgorin transformation, considerably improve the representation. Best of all is the result obtained by the succession of branch-point, Joukowsky, and Gershgorin transformations.

REFERENCES

1. Landweber, L. and Macagno, M., "Added Masses of Two-Dimensional Forms by Conformal Mapping," J. Ship Res., Vol. 11, No. 2, June 1967

2. von Kerczek, C. and Tuck, E.O., "The Representation of Ship Hulls by Conformal Mapping Functions," David Taylor Model Basin, Hydromechanics Laboratory Technical Note 58, September 1966

3. Gaier, D., "Konstruktive Methoden der Konformen Abbildung," Springer Tracts in Natural Philosophy, Vol. 3, Springer-Verlag, Berlin, 1964

4. Becker, E.B., Wilson, H.B., and Parr, C.H., "Further Developments of Conformal Mapping Techniques," Rohm & Haas Co., Report No. S-43, July 1964

5. "Advanced Mechanics of Fluids," edited by H. Rouse, Wiley-Interscience, New York, 1959

DISCUSSION

In reply to a question by R. Barakat, the author clarified the procedure for representing the entire ship hull in parametric form. If 20 sections were used,

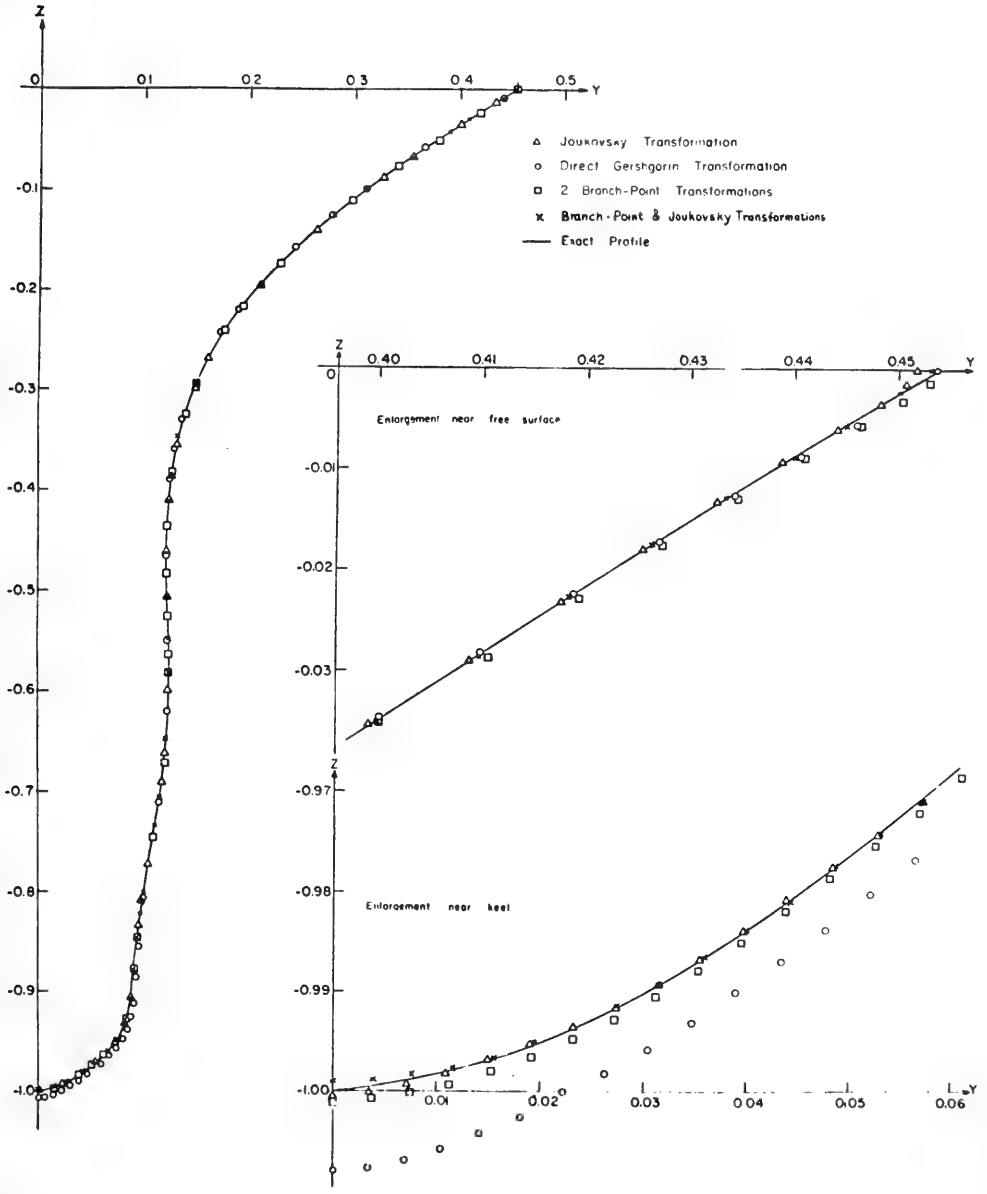

Figure 2

there would be 20 sets of a's. Each a would be treated as a function of longitudinal distance, and a curve would be fitted to the 20 values of a. Barakat suggested that Chebycheff polynomials might be well suited for this purpose, and

further inquired whether constraints on the coefficients are needed to represent ship sections. The author replied that advantage had already been taken of the symmetry of the ship sections, as a consequence of which only odd powers and real coefficients occurred in the series form of the transformation, and that, because the series was convergent, the only restriction on the number of terms was that of numerical accuracy.

Dr. Timman (Delft Technological University, Netherlands) asked whether the high degree of accuracy sought in the representation was desired for the purpose of laying out ship lines or for use in calculating added mass and damping coefficients. The author agreed that, for the latter purpose, high accuracy of representation is not required, but wavemaking resistance is sensitive to small variation in form.

Since the parametric form consists essentially of expansions in Fourier series, Dr. Eggers (Universität Hamburg, Germany) was concerned that slopes might not be accurately reproduced. The author's experience is that appreciable deviations occur only near corner points which are necessarily rounded by a truncated Fourier series. He felt, however, that it was preferable to accept a slight rounding of corners than to include the mathematical form of the branch-point transformations in the equations of the ship hull.

Finally Dr. Barakat described his recent work on the heaving of a semi-immersed cylinder of arbitrary section on a free surface in water of finite depth in which the added mass and damping coefficients were determined in the presence of an incident wave. He found that the modified values of these coefficients, the so-called dynamical added-mass and damping coefficients, make a tremendous difference in the ship response. Thus, contrary to the previous discussion on the insensitivity of the added mass and damping coefficients, the dynamical response of a cylinder is quite sensitive to the shape of section.

* * *

Panel Discussion

Computations of Ship Boundary Layers

M. Martin
Hydronautics, Inc.
Laurel, Maryland

presented by

L. Landweber

INTRODUCTION

The present study uses the available tools of the linearized potential flow about a ship and the three-dimensional integral turbulent boundary-layer equations to study the characteristics of the boundary-layer on ship forms. The method of Guilloton, as presented by Korvin-Kroukovsky, was used to compute the streamlines and pressures about the ship. Solutions of the boundary-layer equations were obtained using a nonslip boundary condition in the ship surface and the velocity and pressure distributions given by the potential theory as the "outer" conditions. The set of boundary-layer equations was integrated along the streamline using a Runge-Kutta-type technique and, as a result, the momentum thickness, shape parameter, and the angle of the boundary-layer flow to the outer flow were calculated.

The numerical results for series 60/.60 and 60/.80 ships of different lengths at various Froude numbers were presented.

THREE-DIMENSIONAL TURBULENT BOUNDARY-LAYER EQUATIONS

The following set of nondimensional boundary-layer equations were derived by Webster and Huang [1] from the three-dimensional turbulent boundary-layer equations presented by Cooke [2]

$$\frac{\partial \bar{\Omega}}{\partial \bar{s}} + \frac{\bar{\Omega}(1+n)}{2}\left[\frac{1}{g}\frac{\partial g}{\partial \bar{s}} + \frac{2}{u}\left(\frac{\delta \bar{u}}{\delta \bar{x}} + \frac{\delta \bar{w}}{\delta \bar{z}}\right)\right] = (1+n)\,\frac{\alpha(H)}{2}\,u^{(nH+H+1)}, \tag{1}$$

$$\frac{\partial \bar{\beta}}{\partial \bar{s}} + \frac{\bar{\beta}}{2}\left\{\frac{1}{g}\frac{\partial g}{\partial \bar{s}} + \frac{2}{u}\left(\frac{\delta \bar{u}}{\delta \bar{x}} + \frac{\delta \bar{w}}{\delta \bar{z}}\right) + \frac{(H^2+H)\,u^{(nH+H+1)}}{\bar{\Omega}}\right\} = \frac{1+H}{u^{H+2}}\frac{\partial u}{\partial \bar{m}}, \tag{2}$$

$$\frac{\partial H}{\partial \bar{s}} + \Phi(H)\,\frac{1}{u}\frac{\partial u}{\partial \bar{s}} + \bar{\psi}(H)\,\frac{u^{(nH+H+1)}}{\bar{\Omega}} = 0, \tag{3}$$

*This is a summary of part of the research carried out at Hydronautics, Inc. by Dr. W. C. Webster and T. T. Huang, between the years 1964 and 1967, on ship boundary layer research. The work was sponsored by the Society of Naval Architects and Marine Engineers under Purchase Order No. 400.

where

$$\bar{\Omega} = \left[\left(\frac{\theta}{L}\right)\left(\frac{U\theta}{\nu}\right)^{n} u^{(nH+H+1)}\right] ,$$

$$\bar{\beta} = \frac{2\beta}{(H-1)(H+2)u^{H+1}}$$

$$\delta = \int_0^\infty \left(1 - \frac{u_m}{U}\right) d\zeta = \text{boundary-layer thickness,}$$

ζ = distance measured normal to surface,

u_m = resultant velocity in the boundary parallel to surface,

$$\theta = \int_0^\infty \frac{u_m}{U}\left(1 - \frac{u_m}{U}\right) d\zeta = \text{boundary-layer momentum thickness,}$$

$$H = \frac{\delta}{\theta} ,$$

and

n is related to the local friction formula, i.e.,

$$c_\tau = \tau_{01} \Big/ \frac{1}{2}\rho U^2 = \alpha(H)\left(\frac{\theta U}{\nu}\right)^{-n} . \tag{4}$$

The solution to these equations will lead to the determination of θ, the boundary-layer momentum thickness, β the angle between the limiting streamlines at the wall and the external streamlines, and H the shape parameter. It is clear that $\bar{\Omega}$, $\bar{\beta}$ and H are determined from two sets of variables. The first set of quantities are dependent on the Reynolds number and are, for instance, n and $\alpha(H)$. The second set of quantities are dependent on the "outer" flow quantities, which are determined by obtaining the potential flow on the ship surface. These are dependent on the Froude number and the ship geometry, and are, for instance, u, $\bar{u}$, $\bar{w}$ as a function of $\bar{s}$, $\bar{m}$, $\bar{x}$, $\bar{z}$.

By comparing the empirical relation of Ludwieg and Tillman [4] for the local friction coefficient in a pressure gradient with Eq. (4) the following values of $\alpha(H)$ and n are determined:

$$\alpha(H) = 0.246 \times 10^{-0.678H} ,$$
$$n = -0.268 . \tag{5}$$

However, this relationship, when used to obtain c_τ for flat plates, with H determined from the comprehensive analysis of Landweber (3), gives poor agreement with the Schoenherr friction curve at Reynolds number corresponding to

large-scale ships. Webster and Huang [1] have therefore proposed the following relationship, which is a proposed extension of the Schoenherr curve to flow with a pressure gradient:

$$\alpha(H) = 0.019 \times 10^{\left[0.678\left(\frac{0.46\ \ell n(R_\theta)}{0.46\ \ell n(R_\theta - 1)} - H\right)\right]}, \qquad (6)$$

$$n = -0.256 + 0.004\ \ell n(R_\theta) .$$

This result is based on the assumption that at a given R_θ the ratio of c_τ without and with a given pressure gradient by Ludwieg and Tillman and by Schoenherr are the same.

The initial condition for the differential equations (1)-(3) is: At station 1/2 (that is, 5% aft from the bow), $\beta = 0$, θ and H are chosen to be identical to that which would exist on a flat plate of the same length between stations 0 and 1/2. These approximations may be sufficient for computing the boundary-layer characteristics at the stern section of the ship but not for that near the bow.

POTENTIAL FLOW ABOUT THE SHIP

The potential flow about the ship will be determined under the assumption that thin-ship theory of Michell [5] is valid. With this assumption, it is possible to write down formulas for the streamlines, free-surface elevation, and pressures on the hull of the ship (for instance, see Wehausen, [6]). The formulas for these quantities would be exceedingly tedious to evaluate. The improper integrals involved in these expressions converge so slowly that, even with today's high-speed computers, their computation is not an insignificant task. For the purposes of this study, the method of Guilloton [7], as presented by Korvin-Kroukovsky in [8], was adopted. This technique is ideally suited for digital-computer application, since the difficulties with the improper integrals are concentrated into universal functions, which have been tabulated in this reference.

In the Guilloton method, the hull is represented as a summation of simple geometric wedge shapes. Thin-ship theory is used to compute the flow about an elemental wedge; the functions which describe the constant-pressure lines and the streamlines of this flow comprise the aforementioned Guilloton functions. The flow about the given ship is then found by the summation of the flows about the wedges which make up the ship. This operation is valid because the velocity potential and the first-order thin-ship boundary conditions are all linear. The errors incurred by approximating the exact hull shape by the Guilloton wedge system appear to be quite small [7, 9, and 10].

A recapitulation of the details of the derivation of the Guilloton method will not be given here, but the reader is referred to the detailed exposition given in [8]. For the purposes of this boundary-layer study, none of the somewhat questionable second-order corrections to the theory, introduced in this reference have been adopted. The tables given in the reference have been punched on

cards, and a computer program has been written to use these tables, in connection with the ship offsets to determine the projections on the ship's centerplane of:

(a) Three lines of constant pressure on the ship's hull. The uppermost of these lines is the line of zero pressure or the free surface. The bottom two lines correspond to the locus of points such that the local piezometric head equals 0.5H and H, where H is the draft of the ship at rest.

(b) Three streamlines on the ship's hull. The uppermost streamline also corresponds to the free surface and thus is identical to the uppermost constant-pressure line. The bottom two streamlines correspond to streamlines at a depth of 0.5H and H at upstream infinity.

Since Guilloton's method yields only three streamlines and three constant piezometric-head lines, several additional streamlines were interpolated. With these results it was possible to obtain the variation of the velocity vector along the streamlines as required to permit integration of Eqs. (1)-(3).

NUMERICAL RESULTS AND DISCUSSION

The numerical computation was performed on the Hydronautics, Inc. IBM 1130 computer. Two typical ships, series 60/.60 and series 60/.80 were used in the present computation. Five speed-length ratios of 0.75, 0.80, 0.85, 0.90, and 0.95 corresponding to Froude numbers 0.224, 0.237, 0.252, 0.268, and 0.283, respectively, were used for each ship. Each Froude number covers five ship lengths – 800, 500, 200, 20, and 5 feet. Typical results of the cross-flow angle β, shape parameter H, and momentum thickness θ, along streamlines are shown in Figs. 1 and 2. The cross-flow angles are shown only along the stern section of these ships since the results are more reliable there.

Cooke's criterion is that separation occurs when the cross flow is 90°. It is important to note that within the range of present computation no separation is found before station 19 for the series 60/.60 ship model as well as its prototype (Fig. 1, for example). However, flow separation occurs at the shoulder of series 60/.80 model ships at low Froude numbers in the present calculation (Fig. 2, for example). The tendency toward separation at shoulder of a series 60/.80 ship is stronger for the model ship than that of the prototype; for the model ship, separation occurs only near the free surface. It is to be noted that the exact potential field near the bow is not known and the initial conditions used at station 1/2 are only the first approximations. Thus, the present results on separation at the shoulder may at best be considered as indicating the trend. The exact prediction is understood to be beyond the scope of the present study.

The cross-flow angle is larger near the stern of the ship model than that of the prototype for both ships of all Froude numbers calculated. Thus, separation is more likely for the ship model if it would occur after station 19. The present results indicate that the values of θ/L and H at a given station of the ship is much larger for the model ship than that of the prototype.

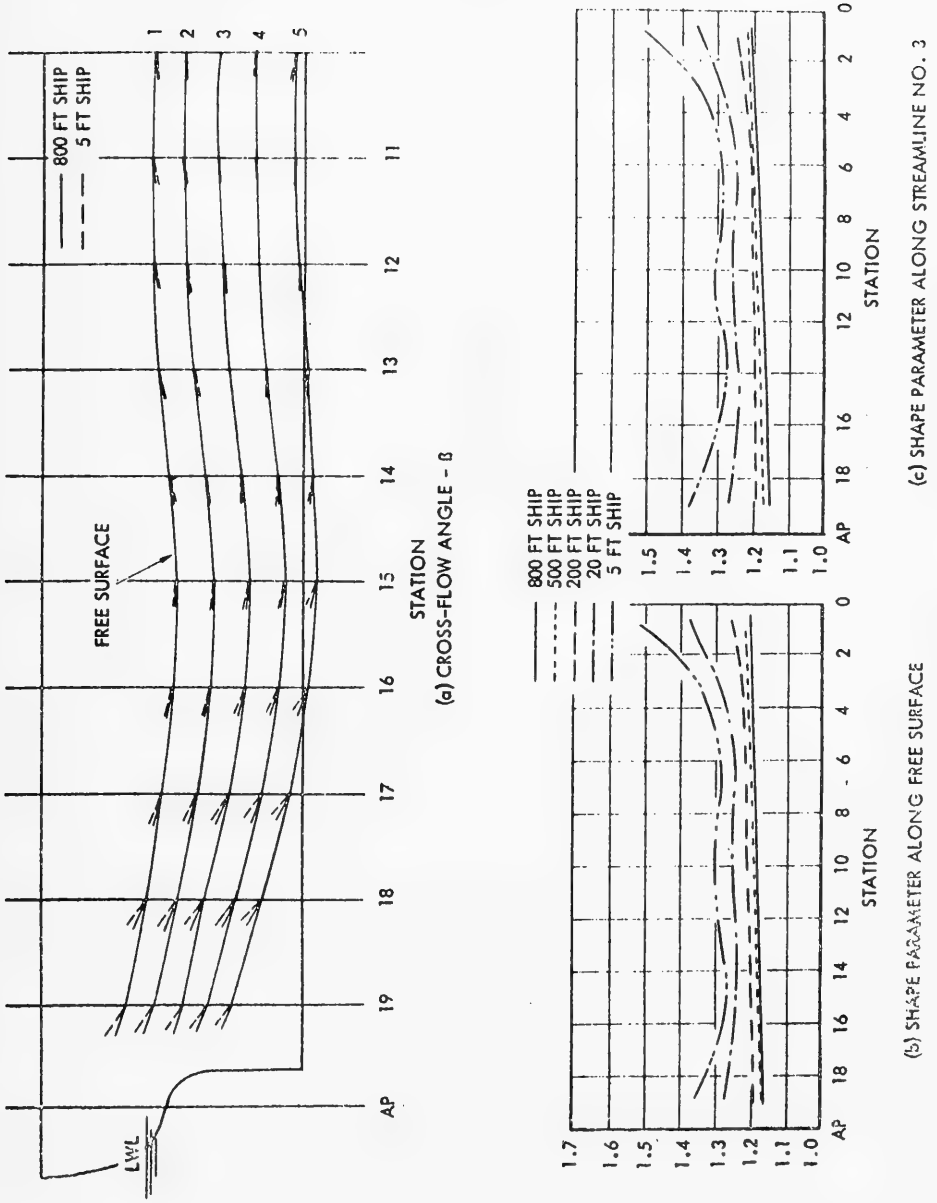
800 FT SHIP
5 FT SHIP
FREE SURFACE
LWL
AP
19
18
17
16
15
14
13
12
11
1
2
3
4
5
STATION
(a) CROSS-FLOW ANGLE - β
800 FT SHIP
500 FT SHIP
200 FT SHIP
20 FT SHIP
5 FT SHIP
1.7
1.6
1.5
1.4
1.3
1.2
1.1
1.0
AP 18 16 14 12 10 8 6 4 2 0
STATION
(b) SHAPE PARAMETER ALONG FREE SURFACE
AP 18 16 12 10 8 6 4 2 0
STATION
(c) SHAPE PARAMETER ALONG STREAMLINE NO. 3

Figure 1

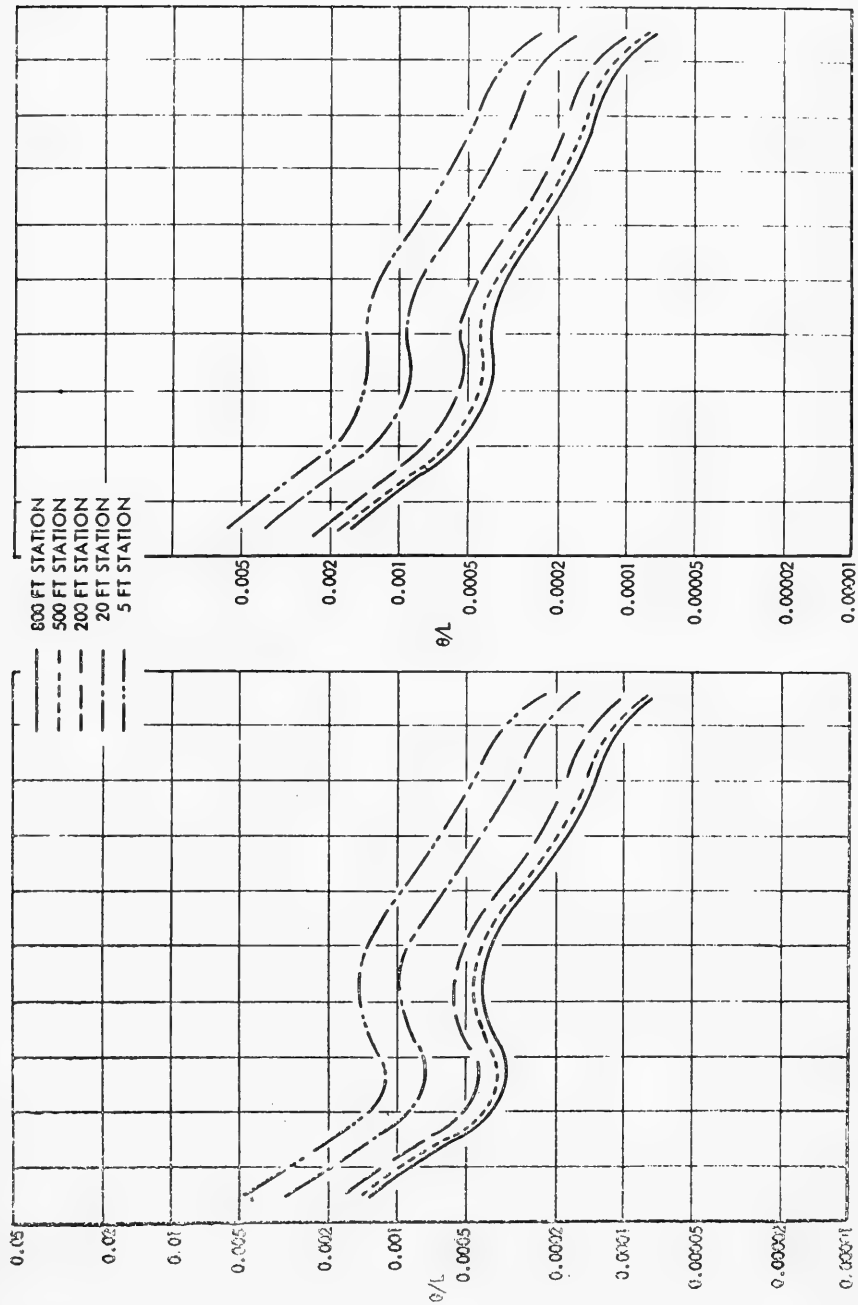

(d) MOMENTUM THICKNESS ALONG FREE SURFACE

(e) MOMENTUM ALONG STREAMLINE NO. 3

Figure 1 (Continued)

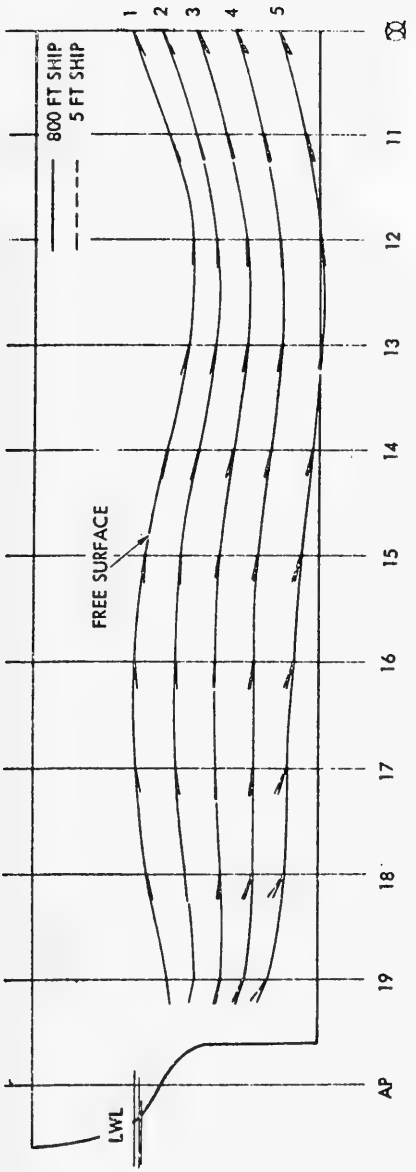

(a) CROSS-FLOW ANGLE - θ

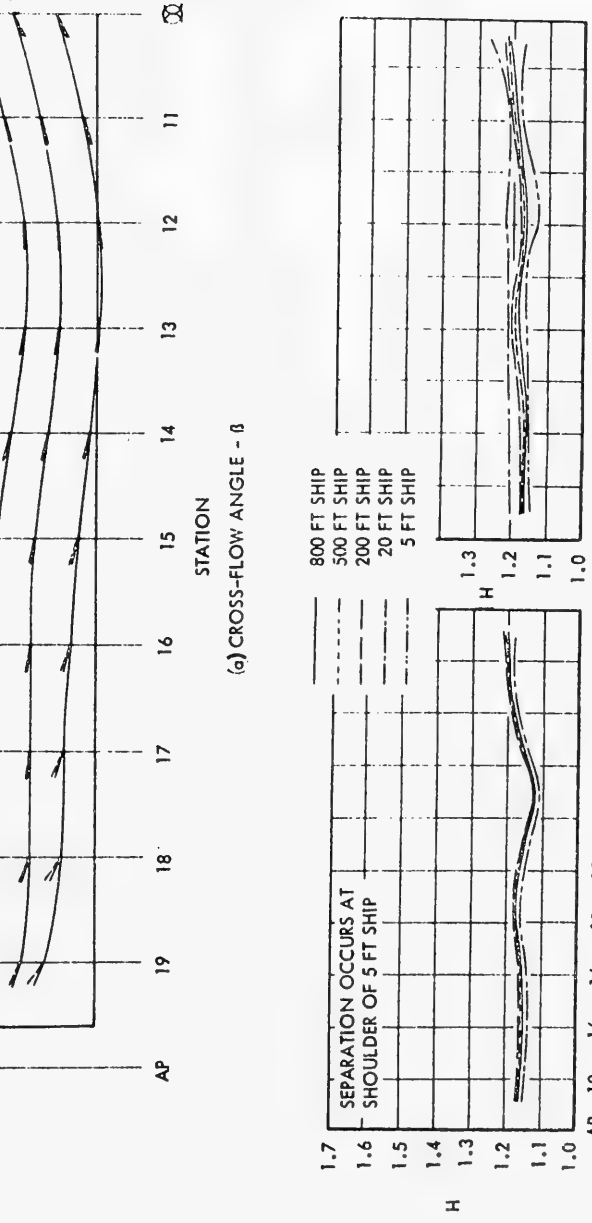

(b) SHAPE PARAMETER ALONG FREE SURFACE

(c) SHAPE PARAMETER ALONG STREAMLINE NO. 3

Figure 2

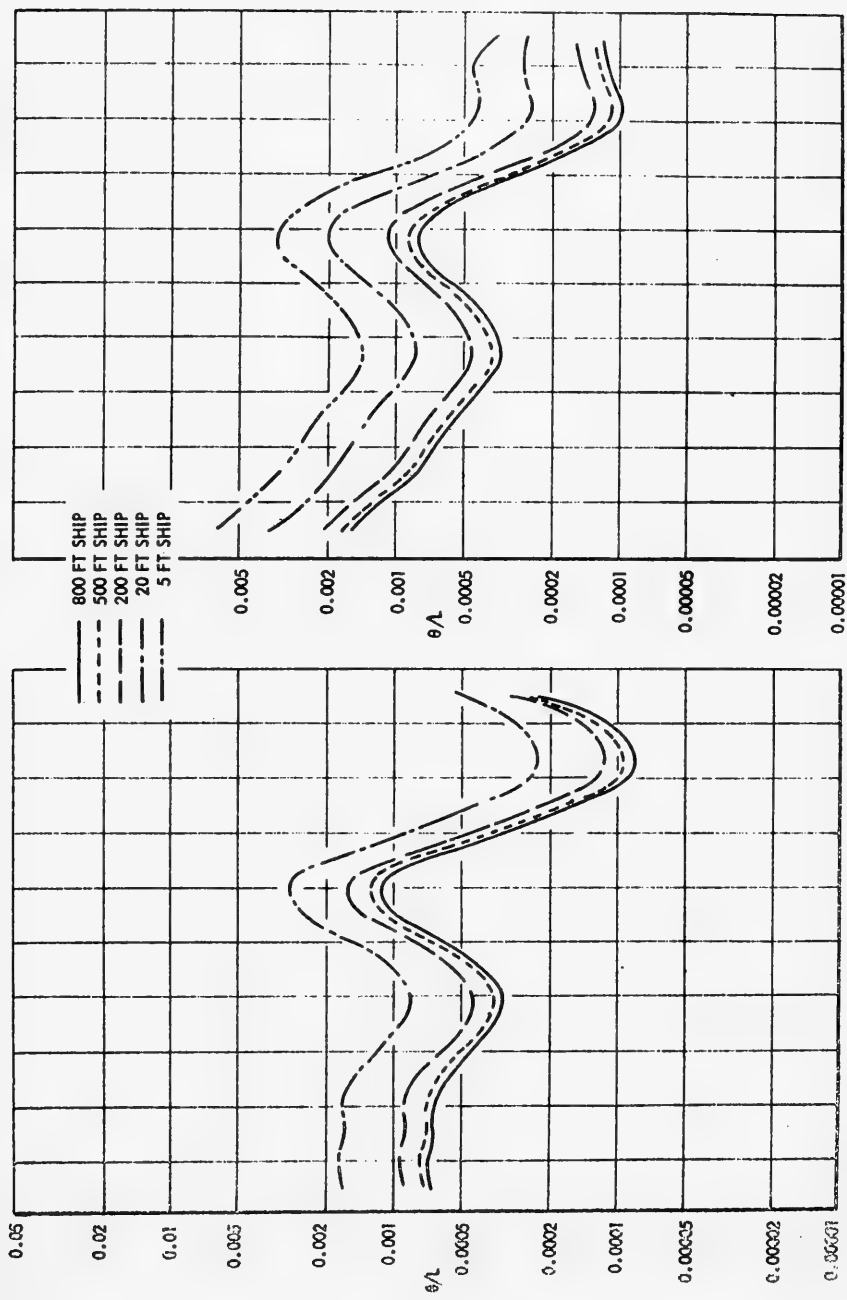

Figure 2 (Continued)

As can be seen from Fig. 2, for series 60/.80 ships, the momentum thickness oscillates considerably along the streamlines, which is due to the effect of the large pressure gradient generated by the large waves.

The average momentum thickness at station 19 of series 60/.60 is shown in Fig. 3. There exists a maximum at $F = 0.252$ at which the wave height is also maximum at this station.

It is to be understood that the present results, like the theories from which they are derived, bear only a qualitative resemblance to the complicated real situation. Much is to be done in order to develop a reliable theoretical technique for predicting the boundary-layer characteristics on ship forms.

NOTATION

c = Constant forward velocity of the ship

$c_\tau = \dfrac{\tau_{01}}{\frac{1}{2}\rho U^2} = \alpha(H)\left(\dfrac{\theta U}{\nu}\right)^{-n}$

$g = 1 + f_x^2 + f_z^2$, where the ship hull $y = \pm f(x,y)$

$H = \delta/\theta$ = Shape parameter

$H_0(R_\theta)$ = Shape parameter along a flat-plate boundary layer in zero pressure gradient

L = Ship length

$\bar{m} = m/L$

$R_\theta = \theta U/\nu$

$\bar{s} = s/L$

s, m, ζ = Arc lengths along streamline coordinates with s along streamline and ζ normal to the ship surface

$\bar{U}, \bar{V}, \bar{W}$ = External velocity components parallel to axes x, y, z

U, W = External velocity components parallel to and perpendicular to streamlines

$u = U/c$

$\bar{u} = \bar{U}/c$

u_m = Resultant velocity in the boundary layer parallel to surface

$\bar{w} = \overline{W}/c$

$\bar{x} = x/L$

$\bar{y} = y/L$

$\bar{z} = z/L$

x, y, z = Cartesian ship coordinates, x forward, y to port, z up

β = Angle between limiting streamlines and external streamlines; limiting value of ϵ at wall

$$\bar{\beta} = \frac{2\beta}{(H-1)(H+2)u^{H+1}}$$

δ = Boundary-layer thickness

θ = Boundary-layer momentum thickness

ϵ = Angle between flow direction in the boundary layer and external streamlines

$\bar{\zeta} = \zeta/L$

μ = Coefficient of viscosity

ν = Kinematic viscosity

ρ = Density

τ_{01}, τ_{02} = Components of the skin friction along and perpendicular to the external streamlines

$\Phi(H) = 9.524\ (H - 1.21)\ (H - 1)$

$\bar{\psi}(H) = 0.00307\ (H - 1)^2$

$$\bar{\Omega} = \left[\frac{\theta}{L}\left(\frac{U\theta}{\nu}\right)^n u^{(nH+H+1)}\right]$$

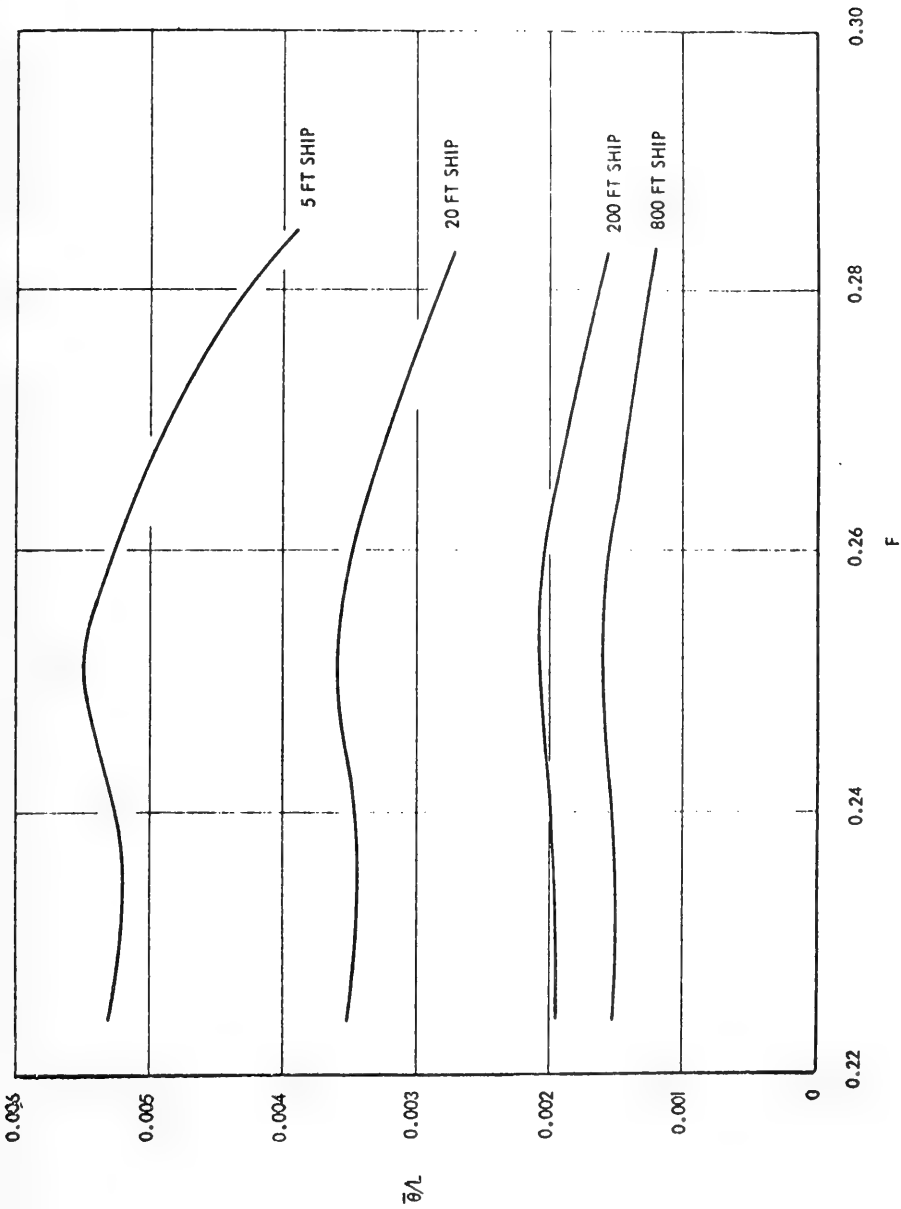
5 FT SHIP
20 FT SHIP
200 FT SHIP
800 FT SHIP
0.005
0.004
0.003
0.002
0.001
0
0.22
0.24
0.26
0.28
0.30
F
θ̄/L

Figure 3

REFERENCES

1. Webster, W.C. and Huang, T.T., "Study of the Boundary Layer on Ship Forms," Hydronautics, Inc. Technical Report 608-1, Jan. 1968

2. Cooke, J.C., "A Calculation Method for Three-Dimensional Turbulent Boundary Layers," Aeronautical Research Council, R. and M. No. 3199, Oct. 1958

3. Landweber, L., "The Frictional Resistance of Flat Plates in Zero Pressure Gradient," The Society of Naval Architects and Marine Engineers, Transactions Vol. 61, pp. 5-32, 1953

4. Ludwieg, H. and Tillmann, W., "Investigations of the Wall-Shearing Stress in Turbulent Boundary Layer," NACA TM 1285, May 1950

5. Michell, J.H., "The Wave Resistance of a Ship," Philosophical Magazine, London, Vol. 45 (1898), p. 106

6. Wehausen, J.V., "Wave Resistance of Thin Ships," First Symposium on Naval Hydrodynamics, Washington, D.C., 1956

7. Guilloton, R., "Potential Theory of Wave Resistance of Ships with Tables for its Calculation," The Society of Naval Architects and Marine Engineers, Transactions Vol. 59, 1951

8. Korvin-Kroukovsky, B.V. and Jacobs, W.R., "Calculation of the Wave Profile and Wave Making Resistance of Ships of Normal Commercial Form by Guilloton's Method and Comparison with Experimental Data," The Society of Naval Architects and Marine Engineers, Technical and Research Bulletin No. 1-16, Dec. 1954

9. Wigley, W.C.S., "L'Etat Actuel des Calculs de Resistance de Vagues," Association Technique Maritime Aeronautique, Paris, Vol. 48 (1949)

10. Timman, R. and Vossers, G., "The Linearized Velocity Potential Round a Michell-Ship," Rapport 1, Technische Hogeschool Laboratorium Voor Scheepsbouwkunde, Delft, Netherlands, April 1953

DISCUSSION

In his presentation of this contribution, the chairman referred to the remarkable agreement between the analytical prediction of J. D. Lin, who had preceded Webster and Huang in working on this problem at Hydronautics, and the experimental result of S. K. Chow at the University of Iowa, that, if separation occurred near a free surface, it would occur farthest forward at a Froude number of about 0.25. Also mentioned was the phenomenon of a generation of secondary flows in the boundary layer at a wave crest, and resultant separation at a depth below the free surface, observed in Chow's experiments.

Dr. Wieghardt inquired about the variation of boundary-layer characteristics around the girth of a section. Reference to Figs. 1 and 2 of the text indicated that the shape parameter and momentum thickness varied little with depth.

* * *

PANEL DISCUSSION—PROPELLER-HULL INTERACTION

F. H. Todd, Panel Chairman
Office of Naval Research Branch Office
London, England

The chairman, in opening the discussion, pointed out that the subject of propeller-ship interaction involved many different aspects of our disciplines. A balanced design for a ship needs not just an optimum hull shape from a resistance point of view and a propeller with the highest open-water efficiency, but requires that we have the optimum combination of the two. It is not always the case that the best hull and the best open propeller together lead to the best combination, this last being a function of the interaction between the propeller and the ship, the subject of this panel discussion.

The chairman went on to outline the principal headings under which the panel members might wish to contribute their ideas. The first of these is the *wake*, because a propeller behind the hull is not operating under open-water conditions but in the somewhat confused flow field that exists behind the ship and, therefore, a knowledge of the wake distribution is an essential factor in the interaction between hull and propeller. The second factor is the *resistance augment or thrust deduction* due to the effect of the propeller in accelerating the water ahead of it, which can have a number of effects on the hull—it reduces the pressure over the stern compared with that in the towed condition, thus increasing the resistance; it can cause an increase in the skin friction, because a greater part of the afterbody is subject to higher-velocity flow; also, by moving any point of separation aft, it may result in a decrease of separation resistance. A third heading is the *propeller performance*. Model propellers are standardized in open water, but when operating in the wake behind the hull the efficiency is in general different from that realized in open water. The variable wake will also induce *cavitation* at an earlier stage than that at which it will occur in open water. The operation of the propeller behind the hull also gives rise to *propeller forces*. Each blade as it rotates has a pressure field around it, and as this pressure field passes the hull, rudder, or bossings, the varying pressure gives rise to forces both on the propeller shaft and on the hull surface—forces referred to as bearing forces and surface forces, respectively. In addition, the pressure fields are themselves varying, due to the effect of the wake, which in turn modifies the transmitted forces. These forces can excite hull and shaft vibration, and it is desirable that they be kept as small as possible.

For many of the items mentioned, difficulties arise in applying model results to a ship because of scale effect, and Dr. Todd suggested that the panel might well discuss our present knowledge on scale effect upon the propulsive factors, and the overall problem of extrapolation from model to ship in which these factors play a most important part. Other items suitable for attention were the effect of fully cavitating propellers on thrust deduction and the relative

scale effects on different kinds of appendages. The treatment of the latter in different tanks differs quite materially, and leads to anomalous results in the predictions of ship powers.

Lastly, the chairman said it would be interesting to have from panel members their views on what research should be pursued in the future to resolve some of these problems and to improve the design of the optimum hull-propeller combination. In this connection, he read an extract from a written contribution from Professor E. V. Lewis, of the Webb Institute of Naval Architecture (who was unable to be present at the Symposium), because it summarized the general state of our knowledge and pointed to a definite objective. Professor Lewis wrote:

> I would like to pose the following question for discussion at the panel meeting: Is it possible to coordinate the design of hull and propulsive device in such a way as to obtain a significant advantage in overall propulsive efficiency over a good hull with an optimum propeller? Many experts, including the late Professor Burrill, have thought otherwise. Professor Horn long ago pointed out the fallacy of "wake gain," and aircraft designers have generally striven to put propellers well ahead of wing or fuselage. A little-noticed paper by Professor Troost in 1957 tends to confirm the negative view by adopting the idea of a "substitute propeller." As you know, this involves considering a propeller completely clear of the hull as a standard of comparison.
>
> Professor Troost's point is simply that what one gains in hull efficiency, he generally loses in propeller efficiency. Perhaps it would be worthwhile to make a broad survey of different types of ships and the various relevant factors, such as ship speed, limitations on propeller diameter and RPM, and thrust requirements, to see if there are any circumstances under which one could expect to improve hull efficiency more than the loss in propeller efficiency.

Dr. J. P. Breslin (Stevens Institute of Technology) opened the panel meeting with an account of theoretical work he had carried out to find the force on a cylinder caused by both the loading and thickness effects of a propeller operating in a wake, the propeller shaft being parallel to the axis of the cylinder. He showed that the force can be simply obtained from the fields induced by the propeller alone, being due to the sum of the pressures induced by all the loading components and by the blade thickness, and he deduced expressions for the total pressures and forces arising on the hull. From these it was concluded that the dominant contribution to the hull force arises from the $(m - 1)$th harmonic of the wake, where m is the number of blades, and it may be expected that the vertical hull force on a ship will be large when the $(m - 1)$th wake harmonic is large.

Increasing the tip clearance from 20 to 30% of the propeller diameter only reduced the hull force due to the blade loading by 8%, and the larger the hull relative to the propeller the less sensitive the force to clearance. The reduction of the force due to blade thickness was more responsive to clearance.

Means for achieving reductions in the hull force will be studied by further detailed evaluations of theory.

H. Lackenby (British Ship Research Association) said that his organization had not been directly involved in work on propeller-hull interaction, but had sponsored a great deal of systematic model testing over the years and, of course, this had involved the determination of the usual hull interaction factors such as wake and thrust deduction fractions, hull efficiency, etc. Some recent tests on a very full model of an 0.85 block-coefficient tanker form had shown some very interesting trends, which he thought worth reporting to the panel. These referred to the effects on the hull factors of systematically varying the longitudinal position of the center of buoyancy (LCB) over a range of 0.5% forward of midships to 2.5% forward, as shown in Fig. 1. The various hull interaction factors are plotted there on a base of longitudinal position of the center of buoyancy. The Taylor wake fraction, the second curve from the bottom, stays remarkably constant over the range; the bottom curve is the thrust deduction fraction, and unlike the wake fraction it is reduced quite significantly in going from 0.5% forward to 2.5% forward. This is somewhat unusual, because experience generally shows that any wake gain is quite often offset by a corresponding disadvantage in increased thrust deduction, and the hull efficiency generally remains much the same. But not in this case—the wake fraction stays constant, thrust deduction fraction goes down, and the effect on the hull efficiency is shown in the top curve. As the LCB moves from 0.5% to 2.5% forward, the hull efficiency goes from about 1.07 to about 1.22, a change of about 15%. And, of course, this is reflected in the quasi-propulsive coefficient, where, in going over that LCB range, there is again an increase in QPC of something like 18%. On the other hand, the relative rotative efficiency remains sensibly constant. It is a very simple case of some systematic experiments and there is a hull-interaction gain of 18% in moving the LCB over that range. Lackenby pointed out that it is not roses all the way, however, because as the LCB is moved forward of about 1.5% the resistance begins to go up, which begins to offset the gain in the propulsive effect. The overall effect of LCB, including both the resistance and this hull interaction effect, is shown in Fig. 2, where the delivered horsepower coefficient is plotted, again on the same base of LCB position, and it is seen that the optimum position of LCB is about 2% forward. The practical $V/\sqrt{L}$ for a form of this kind must be around 0.56, and when the LCB gets further than 2% forward the curve begins to rise again due to the increase in resistance offsetting this very favorable hull interaction effect. Nevertheless, the results are very striking, and if we could maintain this very favorable interaction without losing out on the resistance side it would be very attractive indeed.

Professor G. Aertssen (University of Ghent) first gave the results of the correlation between the calculated and measured two-node vertical natural hull frequency for a large ore-carrier, the Min Seraing, having a length of 218 m (715 ft). He had made a voyage on the ship from Chile to Antwerp, in the loaded condition, and in very smooth water in the Cape Verde Islands, where the ship called, had been able to do an anchor-drop test in deep water. The ship was instrumented with strain gages on the main deck amidships, which recorded the stresses and the two-node vertical natural hull frequency. The latter was very well defined, and therefore a full integral calculation was made for the two-node vertical frequency. The ship length was divided into 115 parts to give a correct distribution of hull weights, and the distribution of cargo was also known quite accurately. The added mass of water was calculated by the Lewis-Todd method, and amounted to 76,912 tons on a loaded displacement of 66,130 tons. A reduction factor of 0.97 was applied to the transverse moment of inertia of each

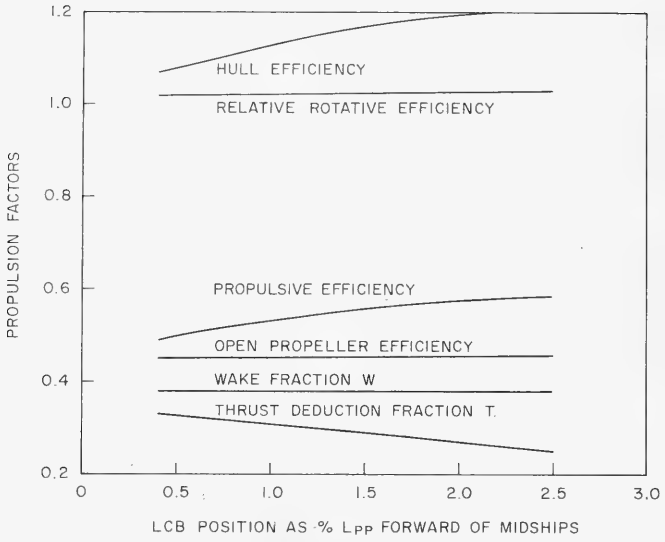

Fig. 1 - LCB position as % L_{pp} forward of midships; propulsion factors

section to allow for the effect of shearing stresses on deck and double bottom. The iteration necessary in the calculation was carried out on an IBM 360 computer. The calculated frequency was 45.3 per minute as compared with the measured value of 44 per minute. The effect of shear deflection on the total deflection was 15%.

Professor Aertssen's second point dealt with the problem of wake scale effects. There has been much discussion about a 1 or 2% reduction of ship rpm due to wake scale effect between model and ship. There is some evidence that this allowance on rpm is correct for a welded ship of about 200-250 m in length with the hull in best trial condition on the measured mile. When, however, the power allowance necessary on model-test results increases due to fouling or the state of the sea is not calm but moderate, this 1 or 2% allowance on rpm may disappear. The fouling is a result, for instance, of the ship going on trials (and this occurs frequently) a fortnight or even more after undocking. Hull fouling resulted in an increase of wake on the "Lubumbashi," where thrust was carefully measured. Professor Aertssen believed she is the only fouled ship where thrust has been measured carefully, and the measurements of thrust were good. On the "Lubumbashi" the wake was deduced from these thrust measurements, the increase being 0.027 after six months service. The corresponding increase in power, due to fouling, was 9%.

On large ships with high block coefficients, a substantial scale effect on wake has been found. The ore-carrier "Min Seraing," 218 m in length, with a block coefficient of 0.80 in loaded condition, at a speed of 16.5 knots at sea in the newly built condition, had a wake of 0.345 for the ship as compared with

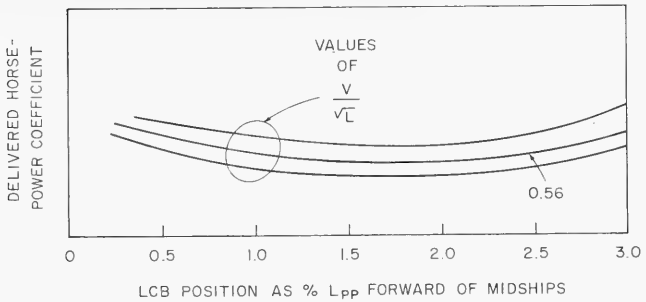

Fig. 2 - LCB position as % L_{pp} forward of midships; delivered horsepower coefficient

0.398 for the model, which results in a value of 0.92 for the ratio $(1 - W_m)/(1 - W_s)$. In ballast condition, the wake on the ship was 0.335. Unfortunately, the model test did not allow the wake to be estimated in the ballast condition.

Dr. Ing. A. Melodia (Cantieri Navali del Tirreno e Riuniti, Genoa) proposed a criterion for the analysis of the performance of a propeller behind a hull. The classical methods for the analysis of the performance of the propeller behind a hull follow two different criteria: the thrust identity and the torque identity. Such an analysis required the introduction of the relative rotative efficiency concept and gives different results for both wake and propeller efficiency. In consequence, the analysis gives different values for the relative rotative efficiency too. In order to eliminate the ambiguity of analysis, it is usual to assume as wake value the arithmetic mean of the values resulting from the application of the two different criteria.

Dr. Melodia, for many years (see Papers of the Collegio degli Ingegneri Navali e Meccanici, Genoa 1954), had adopted for the study of propeller performance a criterion of analysis which eliminates the ambiguity of the relative rotative efficiency by introducing the concept of the relation of tangential wake to the number of propeller revolutions, a concept which is similar, physically, to the one of relating axial wake to speed of advance.

Assuming that the operating point of the propeller is the one for which the same power corresponds to the same generated thrust, the comparison coefficient between open and behind propeller is no longer either K_t or K_q, but the K_0 coefficient, given from the relation

$$K_0 = K_t^3/K_q^2 = [(2\pi/75)^2 S^3]/\rho D^2 P^2 .$$

As K_0 is independent both of the propeller revolutions and the advance speed, entering into open-water propeller diagrams with the K_0 value, determined by self-propulsion tests, gives the corresponding values of J_0 and η_0, by which it is possible to calculate the axial wake factor

$$(1 - w_0) = V_0/V ,$$

the tangential wake factor

$$(1 - \mu_0) = n_0/n , ,$$

the advance speed

$$V_0 = 75\ \eta P/S\ ,$$

and the effective revolutions

$$n_0 = V_0/J_0\ D\ .$$

The fundamental efficiencies equation is thus satisfied without the necessity of any corrective factor:

$$\frac{1 - t}{1 - w_0}\eta_0 = \frac{75RV}{75\ S\ V_0}\ \eta_0 = \frac{RV/75}{SV_0/75\ \eta_0} = \frac{ehp}{dhp}\ .$$

Two typical examples of the practical application of simultaneous thrust and power identity criteria are presented in Fig. 3. In the first example, the case of a central propeller, the axial wake factor obtained has a lower value than that obtained by applying either the thrust identity or the torque identity criteria. The tangential wake factor is slightly less than unity.

In the second example, which refers to the case of propulsion with two lateral propellers (outward-rotating), the axial wake factor, on the contrary, is higher than those determined by the two classical identity criteria, while the tangential wake factor is slightly higher than unity.

As this result recurs qualitatively for all the cases examined, it seems possible to reach the conclusion that the overall inflow to the propeller is endowed with a rotating component in the same direction as the propeller in the central-propeller case and with a rotating component in the opposite direction to the propeller in the outward-rotating lateral-propeller case. In this regard, it may be observed that, independent of the identity criterion adopted, it is essential that the available open-water tests are carried out at a Reynolds number high enough to ensure that the performance of the propeller is surely turbulent and, therefore, comparable with the behind flow. If this is not so, it is advisable to correct the open results by the well-known Lerbs method (J.A.S.N.E. 1951). As the application of this method implies, at equal advance coefficient, a reduction of the torque coefficient, while the thrust coefficient remains practically unchanged, the K_0 coefficient will be too high.

To sum up, both the J_0 and J_q advance coefficients would tend to approach to the intermediate J_t value in the central-propeller case, while in the lateral-propeller case they would both tend to move away from the J_t value.

Therefore it seems that if the analysis is carried out with open-water diagrams deduced from turbulent-flow tests (or corrected for turbulent flow), instead of with diagrams deduced from experiments in flow which is not entirely turbulent, the rotating component in the inflow would be of a lower intensity in the central-propeller case and of a higher intensity in the lateral, outward-turning-propeller case. A possible explanation of this different behavior may be the following: For a central propeller it is possible to consider the inflow as divided into two equal symmetrical fields; for a lateral propeller,

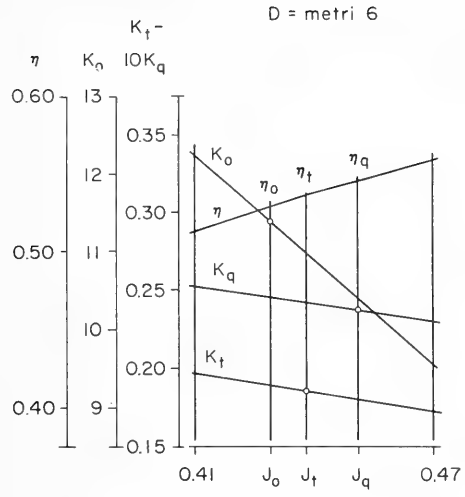

V = 17 nodi
N = 120.3 al 1'
S = 101000 Kg
DHP = 13000 Cv

IDENTITA:		K_t=0.185 K_t	K_q=0.0237 K_q	K_o=11.37 K_o
J	=	0.438	0.451	0.429
η	=	0.535	0.544	0.527
1-w	=	0.603	0.620	0.582
$1-\mu_o$	=	1	1	0.986
η_r	=	1.020	1.033	1

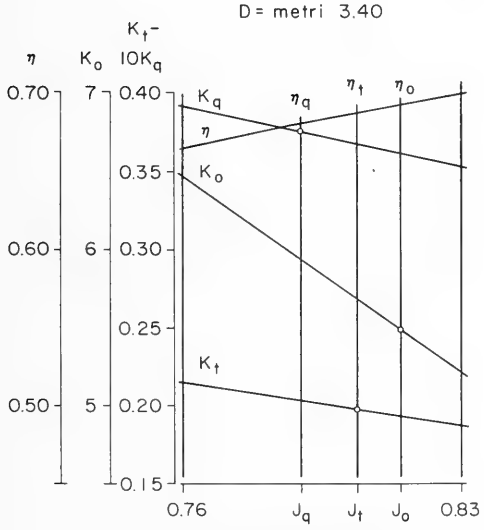

V = 22 nodi
N = 221.0 al 1'
S = 75000 Kg (tot.)
DHP = 14950 Cv (tot.)

IDENTITA:		K_t = 0.198 K_t	K_q = 0.0376 K_q	K_o = 5.483 K_o
J	=	0.804	0.790	0.815
η	=	0.687	0.680	0.692
1-w	=	0.890	0.874	0.914
$1-\mu_o$	=	1	1	1.014
η_r	=	0.981	0.973	1

Fig. 3 - Application of simultaneous thrust and power identity criteria. See text

however, this possibility does not exist, because of the asymmetric position of the propeller with respect to the hull.

The application of the thrust and power identity criteria of analysis allows one to point out, and to evaluate the intensity of, the rotating inflow component and therefore to have a more complete knowledge of the action which the hull and its appendages exercise on the propeller performance.

Professor J. D. van Manen (Netherlands Ship Model Basin) discussed the effects of cavitation on propeller-hull interaction, a subject on which he said very little is known. It is certain, however, that the change in the chord-wise pressure distribution on the propeller blade with cavitation will have a marked effect on the propeller-hull interaction factors as we determine them now in our conventional towing tanks, on the surface forces, and on the bending moments on the propeller shaft. Dr. van Manen said that one of the very few publications on the subject is from Russia, and was reported at the International Towing Tank Conference in London in 1963, which showed that in a towing tank with a ventilated propeller the thrust deduction was reduced by 50%. That would mean for big tankers a reduction in thrust deduction factor of 50% due to the effect of cavitation and about 10% change in power. That would be a very important effect in all our correlation thinking, and maybe if we have to test in the near future 500,000-ton tankers and have no experience to predict the power to install in the ship to get the speed, it might mean a mistake of about 6,000 horsepower, which is not too nice for the shipyard that has to build that ship. Dr. Todd asked Professor van Manen if he meant that there could be a 50% change in thrust deduction factor on a large tanker? Professor van Manen said that that was his estimate, but it could be wrong. If the thrust deduction measured without cavitation was 0.2, it would come down to perhaps 0.1. In addition to the effects of cavitation on thrust deduction, on correlation, on power prediction, on blade-spindle torque, and thus on the bending moments in the shafts, there is another aspect. If a conventional propeller and a ducted propeller, or a contrarotating propeller, are tested in a towing tank we may come to the conclusion that there is an improvement with the ducted propeller, but it might be that the effect of cavitation in one propeller type is quite different from that in another propeller type. It can be expected that the effect of cavitation on thrust deduction in a conventional propeller is larger than in a ducted propeller. That means that the reduction in the required shaft horsepower for the ducted propeller would be smaller, due to the effect of cavitation, which we neglect in our present towing tanks. Professor van Manen was of the opinion that there is a very great need for evacuated or reduced-pressure towing tanks and said that the preliminary design for such a facility at the NSMB was ready and the money problem informally already solved. In the design of an evacuated towing tank it is necessary to start with the model propeller, which cannot have a diameter less than 24 cm. This means that for the very big tankers the models will be 12 m or more in length. With such models a very big tank is needed, for instance, 175 m long, 18 m wide, and 8 m in depth. This is the line being considered at NSMB at this moment. Professor van Manen also referred to the small reaction to E. V. Lewis' remarks in his contribution about optimum hull, optimum propeller, and now the optimum hull and propeller combination, as read out by the chairman. In the last two years NSMB had adopted the duct design to nonuniform flow. That is normally done with the conventional propeller, too, but with the ducted propeller there is a chance to adopt the duct to the flow direction. There is an upward flow at the stern, and if the duct is designed in such a way that the flow into the propeller is horizontal, that means a lot to the propeller efficiency, and for a ducted propeller it is always favorable to change the stern shape to achieve such flow. With such a flow-directed nozzle, giving horizontal flow at the stern, NSMB succeeded in the case of three tankers in getting the same shaft horsepower reduction as for the Hogner stern, some 8-10%. Another example of the use of these ducted propellers might be with inclined shafts, where the control of the flow

with a pumpjet or ducted propeller might be very important for delaying the inception of cavitation.

Dr. M. Kinoshita (Hitachi Shipbuilding and Engineering Co. Ltd.) had some remarks to make on H. Lackenby's statement about the effect of LCB position on ship power. He understood from Lackenby's report that the position of the longitudinal center of buoyancy must be chosen as far forward from the midship section as possible as far as propeller interaction factors and vibration problems are concerned. He felt quite agreeable to this opinion so long as the ships' sizes and speeds are moderate. But as regards very large tankers, with a deadweight of more than 200,000 tons, the conditions change, and he hesitated to agree with this conclusion, and would like to recommend to designers of such large tankers selection of a longitudinal position of center of buoyancy not so far forward. The reason for such hesitation is that recently there have been occasions, on the speed trials of large oil tankers with a deadweight of more than 200,000 tons, when the measured speed has fallen short of the value predicted from the model experiments. Since the beginning of this year his company had started a very productive study to solve the probable difficulties to be encountered in the course of designing and building a large tanker with a deadweight of 400,000 tons. In these studies, the problem of discrepancies between the results of tank experiments and the results of speed trials is included as one of the important items, and has been carried out under Dr. Kinoshita's supervision. As to the cause of these discrepancies, we must examine both sides—model-experiment and sea-trial. In his personal opinion, however, the latter must be examined more carefully, and he considered that there were three main causes for these discrepancies. One of the three is concerned with the matter which Lackenby pointed out. In consequence of the expansion of the ship size, the length increases but the speed of tankers has kept nearly constant, so that the optimum longitudinal position of the center of buoyancy has a tendency to be chosen more and more ahead of midships, as he recommended. Furthermore, the value of the L/B ratio has become smaller and smaller and finally has reached a value less than 6.0. All of these above-mentioned factors lead to the so-called Kempf phenomenon, not only on a straight course during a service voyage but also at the important time of the speed trials. Dr. Kempf's phenomenon is the small yawing, long-period, snake action of the ship under straight-course sailing, which leads to increased resistance. It also happens sometimes—not always, but sometimes—that the ship loses its course stability slightly, and even on the maiden voyage of such newly built large tankers the expected speed cannot always be obtained for such ships. The ship designers also have a tendency to make the stern aperture and cut-up as large as possible for such tankers with large values of block coefficient to avoid vibration problems and to get a smaller value of thrust deduction, and this further reduces the course stability. In conclusion, Dr. Kinoshita emphasized that for all these very, very large vessels the location of the longitudinal position of center of buoyancy must be chosen carefully, not only from the point of view of the tank tests, but also to keep good course stability features.

Professor C. W. Prohaska (Hydro- og Aerodynamisk Laboratorium, Denmark) said that H. Lackenby had shown a most interesting diagram, from which it appeared that the position of the LCB had an enormous, and in some respects rather unexpected, influence on some of the propulsion factors. Professor Prohaska pointed out that this result necessarily must be a function of the method

of analysis used by the British tanks, and wondered if the Danish tank on the same set of experiments would have got the same results--he was positive that they would not. At HyA, they used for model-ship correlation a combination of the Hughes' method of extrapolation of the viscous resistance, together with a wake scale-effect allowance. In using this combination, they got, they believed, more constant C_A values than could be obtained by any other method. With respect to ship size and ship type, loaded or light condition, they could use the same value of C_A for ship predictions and believed that they obtained good results. If this method had been used for the analysis of the experiments made by the British tank, then the results probably would have looked different. This is because a change of LCB position from 0.5 to 2.5% forward certainly will influence the form effect, the factor $(1 + k)$, and if that is taken into account, the thrust deduction figures will be completely changed and probably would not have the trend shown in the figure. This is mentioned here, not as a criticism of Lackenby's contribution, which obviously is very valuable and which will be studied with great interest, but just to point out that we must, in our profession, be very careful when comparing results from other tanks, because they have been analyzed and arrived at in quite different ways. And, unless the raw figures are available for the actual model resistance and thrust, etc., and all details about the loading of the propeller during the measurements, it is not possible to compare them. One brief remark also on the figures given by Professor Aertssen, who gave some results for a special case where he showed the presence of wake scale effect. The Danish tank could give a very great number of these from all the trial trips that have been performed, and, generally, for a new ship of average size compared with a model of normal size, say, 7 m, wake scale effects of the order of 0.10-0.12 are obtained. These figures are largely in excess of those shown by Professor Aertssen, and they are found both for loaded and for light conditions, but not necessarily the same in each condition. They should be substantiated on trial trips wherever possible, when horsepower and revolutions are determined accurately. However, one must remember that the wake scale effect on the trial trip is there on that day but disappears after a period of time. It will decrease with time--it will even become negative--and an original wake scale effect of say 0.12 might, after five years, have changed to -0.05, a total change of 0.17 in wake. This will occur with a ship which has been regularly docked and cleaned, and is only due to deterioration of the hull. It is thus necessary to distinguish between the wake scale effect for a new ship and for an old ship. Also, for a new ship, there will, of course, be cost differences according to the paint applied.

V. F. Bavin (Kryloff Shipbuilding Research Institute, Leningrad) commented on the remarks by Dr. van Manen, in which he had made reference to the Russian work presented at the London ITTC Meeting, and suggested that a reduction of about 50% in thrust deduction factor would be possible for a large tanker. Bavin did not think that this would be so, because the influence of cavitation on thrust deduction factor was due to the cavity thickness effect, and he did not believe that supercavitating propellers would be used on super-tankers, even in the future. So the reduction, if any is possible, will be much less. The second point Bavin discussed was concerned with wake-adapted nozzles. In his institution, also, experiments have been made with such nozzles and a reduction of bending moment on the blade of the propeller of about 200% was found, i.e., it became about one-third of that with the propeller operating in a conventional

nozzle for a single-screw ship. There was also a reduction in thrust deduction fraction with the propeller operating in the wake adapted nozzle.

Dr. J. W. English (National Physical Laboratory, England) referred to the remarks of H. Lackenby and the comments on them by Professor Kinoshita and Professor Prohaska. An NPL tanker model has confirmed Professor Kinoshita's remarks about directional stability and at the same time refutes the remarks of Professor Prohaska regarding the British method of analysis. This particular tanker had its LCB well forward and it was directionally unstable, but it is believed that there is a physical explanation of why a large hull efficiency was obtained in this case. Like all modern tankers, it had a very large beam/draft ratio and at the stern the flow outside the boundary layer was predominantly upwards. This had the effect of turning the inner boundary layer upwards at the outside, and in fact, as has been pointed out at the last ITTC, swirling areas of flow can be seen. It is probably incorrect to call them vortices. Rather, they are a collection of the boundary-layer material from further upstream which is passed through the stern in the vicinity of the propeller disk. As a consequence of this, the wake is abnormally high and, one ends up with a high hull efficiency. The flow has now been studied by five-hole Warden tubes and flow visualization tuft techniques, etc., and the flow clearly has a downward component near the center line and an upward one further out.

Dr. Todd reminded Dr. English that he wished to comment upon Professor Prohaska's remarks about the method of analysis. Dr. English said that Professor Prohaska had implied that the methods of analysis used in British tanks gave different results, but he did not believe this to be true. There is a large wake fraction, there is a large hull efficiency, what Lackenby has shown is correct, and there is a physical explanation for them.

H. P. Rader (Hamburg Model Basin, Germany) described some work being done for the ITTC Cavitation Committee. The wake scale effect has not only a great bearing on the scaling of the shaft speed, but also on the local wake distribution for determining the cavitation patterns and the effect of the latter on thrust and torque variations in a nonuniform velocity field. Now, there are two ways of studying this effect. One is to consider it as a boundary-layer problem, and the other is to consider it as a wake problem far behind the ship. In between, one can interpolate (or make some guesses) with a polynomial of high order. It can be assumed that an essential part of the wake of model and ship consists of boundary-layer material which has been subjected to a pressure increase. Velocity distributions in accelerated and retarded turbulent flows can be described to a good approximation by the universal relation

$$\frac{u}{U} = \left(\frac{y}{\delta}\right)^{1/n} , \qquad (1)$$

where

u = the local velocity inside the boundary layer,

U = the undisturbed velocity outside the boundary layer,

y = the distance from the wall,

and

δ = the thickness of the boundary layer measured to the point where $u = 0.99\,U$.

The power coefficient n depends on the pressure gradient or on a form factor H_{12}, which is the ratio between the displacement thickness δ_1 and momentum thickness δ_2 of the boundary layer, where $\delta_1/\delta_2 = (2+n)/n$. The thickness of the boundary layer can be calculated approximately by the relation

$$\delta = \ell \frac{C}{Rn^{0.2}}, \tag{2}$$

where

ℓ = the length of the boundary flow,

C = a constant depending on the pressure gradient or on the form factor H_{12},

and

Rn = the Reynolds number $\ell U/\nu$.

For the flat plate without pressure gradient, n is about 7, and C is about 0.37. Substituting the value of δ in the first expression,

$$\frac{u}{U} = \left(\frac{y}{\ell} \frac{Rn^{1/5}}{C} \right)^{1/n}.$$

Using the subscripts M and S for the model and ship, respectively, an equation like this can be written for model and ship. Usually, n will be a little larger on the full scale, and little is known about the values of C_M and C_S. Assuming that n and C are the same for model and ship, then approximately the velocity ratios at equal relative positions y/ℓ in the propeller plane of ship and model are related as follows:

$$\frac{u_S}{U_S} = \frac{u_M}{U_M} \left(\frac{Rn_S}{Rn_M} \right)^{0.2/n_M},$$

By Froude's relation, $Rn_S/Rn_M = \lambda^{3/2}$, where λ is the scale ratio between ship and model, so that

$$\frac{u_S}{U_S} = \frac{u_M}{U_M} (\lambda)^{0.3/n_M}.$$

For a flat plate, if n is 7 and the scale ratio λ is 30, the value of the ratio u_S/U_M is 1.16; for λ equal to 40, it is 1.17. If n is less than 7 (say, 5) these ratios become 1.23 and 1.25.

The program for the cavitation committee is to do a test first in the uncorrected wake field and then to determine the value of n from a model test at various water lines and correct the wake field for the scale ratio. The new wake field would then be simulated in the cavitation tunnel and the cavitation pattern studied. The same methods will be used to calculate the thrust and

torque fluctuations, and it is hoped to report about this in a year's time, when the ITTC meets in Rome in 1969. This relation, of course, holds only as long as u_s / U_S is smaller than unity. This means also that the foregoing observations do not allow any direct conclusions regarding the scale effect on the volumetric mean value of the wake. But this can be easily obtained by integrating over the disk area.

If the scale effect is considered as a wake problem, it is found that the maximum wake behind a strut or shaft bracket on the ship is approximately equal to the maximum wake on the model, which can be measured, times the ratio of the drag coefficient C_{DS} for the ship appendage to the drag coefficient C_{DM} of the model appendage, to the power of 1/2. This is shown in books on boundary-layer theory, such as Vol. 3 of Durand's "Aerodynamic Theory" in Division G — The Mechanics of Viscous Fluids. Now, this would not be very serious if the two drag coefficients had near enough the same value, but it can happen that the Reynolds number of the model appendage is of the order of 8×10^4 and the Reynolds number of the ship appendage may be about 10^6. For a shaft strut with a thickness-chord ratio of 20% (which is a little high, perhaps) the drag coefficient of the model strut could be 0.07 and the drag coefficient of the full-scale strut about 0.01, which means a ratio of seven to one. The appendage drag is thus very sensitive to scale effect, and is very often overestimated. (This is a very important matter and the effects can be estimated from the diagrams given in Figs. 4 and 5.)

The chairman announced that there were no other written contributions whose authors were present and declared the meeting open for anyone to talk about any aspect of propeller-hull interaction. He was sure that many questions in this field had come up in the past, and here was an opportunity to voice them and hear what other people think about them.

H. B. Lindgren (The Swedish Tank, Gothenburg) said he would like to come back once more to the question raised by Dr. van Manen a while ago dealing with, in his opinion, the very important question of the possible scale effect on the thrust deduction factor. His reaction was very similar to the one previously expressed by Bavin. He had a strong feeling that Dr. van Manen must have overestimated the importance of this question. In this connection, he did not think it necessary to build such an extremely big new cavitation laboratory to find the solution to this problem. In Gothenburg they were just now finishing a new cavitation tunnel in which it was possible to install a complete ship model of a little more than 8 m in length, and in that it will be possible to study the propeller effects behind this big ship model. The Swedish Tank has been carrying out tests for a long while with models in the existing cavitation laboratory, and if there were such very big influences of cavitation on the thrust deduction factor, Lindgren was quite sure that they would have been detected when carrying out those experiments, because they were made under atmospheric pressure as well as under cavitating conditions.

The chairman believed that there was still a lot of vagueness about the thrust deduction. A great deal of model work done in the past has had very contradictory findings. The work on the Victory ship models at the Wageningen Tank showed a very large scale effect on thrust deduction t, increasing quite materially and rapidly with increase in size of model, and this continued right up to the 72-ft

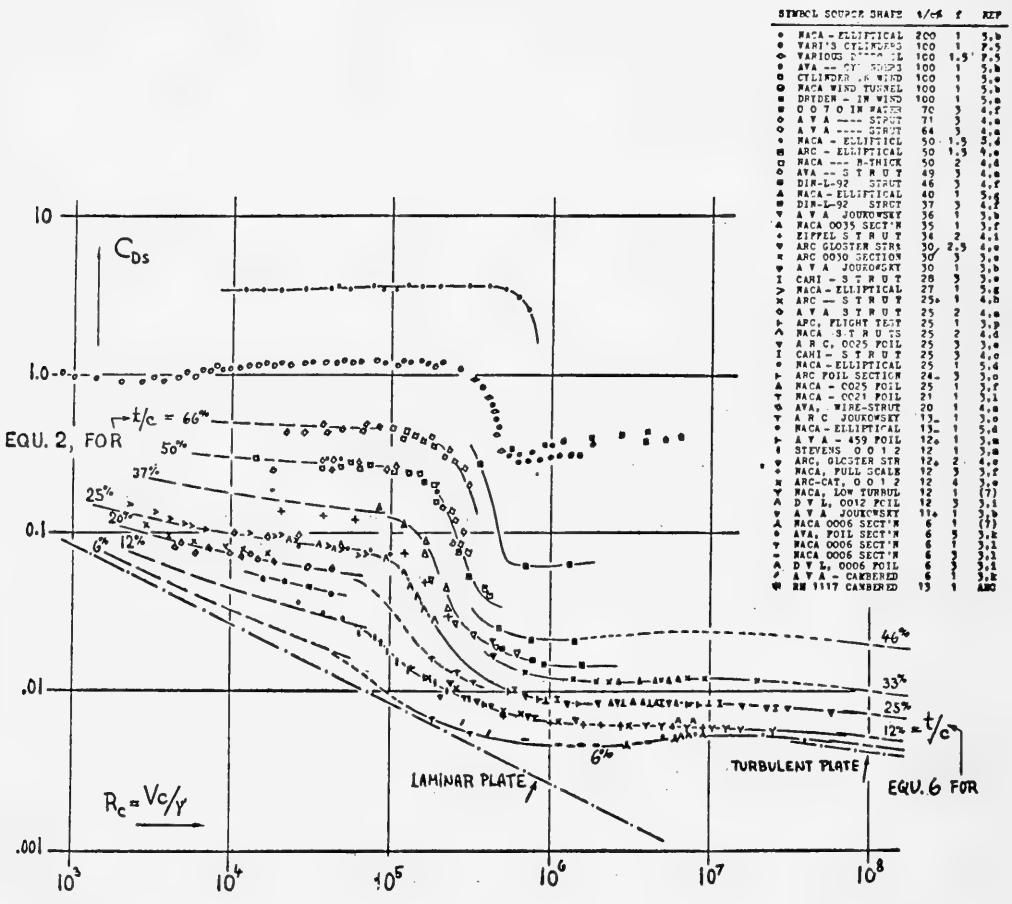

Fig. 4 - Data on sectional drag (at = zero lift) of streamline foil- and strut-sections. Many of the experimental results are obtained by wake-survey technique; in others, drag of blunt wing tips has been subtracted from the original values. Drag coefficients at subcritical R' numbers are as indicated by equation 24 (using $C_f = 2.66\ \sqrt{R}$); at very high R' numbers as given by equation 28 (using C_f as indicated by the Schoenherr equation in Chapter II)

"ship" which they built. The U.S. Navy found almost exactly the same rate of increase of t in the case of submarine Albacore. The Germans have run tests on a series of tanker models and they again found an increase in t with size. On the other hand, the Series-60 Models that were run at the Taylor Model Basin were later repeated at the Michigan tank on a smaller scale, and in this case the opposite effect was found — the bigger model had a smaller thrust deduction coefficient. He believed that something should be done about this question and invited any thoughts or opinions on the situation.

Dr. W. B. Morgan (Naval Ship Research and Development Center) also made a brief remark about the comments by van Manen. So far, only one paper had

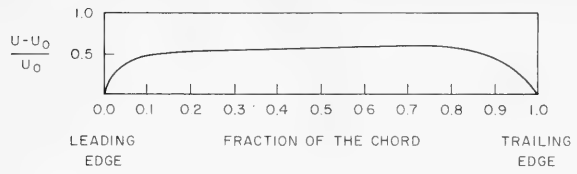

Fig. 5 - Selected results on the drag of rotationally symmetric bodies (no corrections applied)

been referred to on this problem, but he knew of at least five. In 1955 there was a Symposium held in Russia on ship hydrodynamics at which Bavin contributed two articles. These are quite extensive, one giving the theoretical treatment of the problem, the other the experimental. These were both very good pieces of work. Also, research has been done at the Naval Ship Research and Development Center by Beveridge on thrust deduction with a fully cavitating propeller, and by Nelson at Naval Weapons Center. It seems very clear with the fully cavitating propeller, at least, that the apparent change in thrust deduction is due to the increase in cavity size. It acts like a thickness effect, and there is some retarding of the flow ahead of the propeller. Dr. Morgan found it difficult to believe that the small amount of cavitation probably present on a large tanker would have such a big effect as stated by Dr. van Manen.

Dr. Morgan next referred to scale effect on propeller efficiency. The usual procedure for making powering predictions is to assume that the propeller efficiency does not change between model and full scale. This is obviously incorrect and does affect the magnitude of the correlation factors as well as giving a scale effect on rpm. The statement is made without regard to whether or not the flow is turbulent. For the blade sections normally used on propellers and for the conditions for which they normally operate, the viscous drag is for all practical purposes all frictional drag, i.e., no form drag. It would be expected for the usual condition that the frictional drag of the full-scale propeller would be about one-half that of the model which would lead to efficiency changes of between 4 and 8%, depending on the particular conditions. This difference in drag could be greater if the Reynolds number is low and if the flow remains turbulent. It would seem reasonable to include the changes in propeller performance, because of frictional drag, in our prediction procedures. Theoretical calculation methods should be sufficient for this purpose, although confirming experimental results are needed.

In regard to thrust deduction, Dr. Morgan felt that the discussion of any substantial scale effect on thrust deduction should be dismissed in the light of recent work by Beveridge at the Naval Ship Research and Development Center. In this regard, it is necessary to remember that thrust deduction is the difference between two large numbers and subject to considerable error. It has been possible to calculate the thrust deduction quite accurately on a body of revolution and a slow-speed cargo ship (the Simon Bolivar). The results of the calculations are shown in the following table.

	Potential t	Frictional t	Total t	Measured t
Body of revolution	0.069	0.015	0.084	0.09
Body of revolution (with appendages)	0.159	0.015	0.174	0.15
Simon Bolivar	0.232	0.015	0.247	0.24

It was his contention that since the thrust deduction can be calculated with such good accuracy there can be little scale effect on thrust deduction per se. Since most of the thrust deduction comes from the potential part of the problem, the scale effect must be small as only the frictional part can be affected. This is assuming, of course, that the propeller loading on the model is the same as the full-scale loading.

Apparent scale effect on thrust deduction could arise if the radial loading of the propeller is radically different between model and full scale or if the propeller action changes the separation point at the ship stern or the ship trim. The loading effect could come about by differences in the radial wake distributions. Calculations show that the radial load on the propeller can affect the thrust deduction to some extent. However, this effect is not large and in any case, it is not a true scale effect on thrust deduction. Also, changes in ship resistance by change in separation point or trim, even though the effect could be large, should be considered more rationally and not lumped in as part of the thrust deduction.

The chairman asked if these calculated values of t were done for the model size. Dr. Morgan said they were all model values. Similar calculations could be done for the full scale if it were possible to measure the full scale wake. What are called scale effects are really indications that there is something going on that is not understood.

Dr. M. Schmiechen (Berlin Towing Tank, West Berlin) said he had actually touched on this problem that morning and had given a set of equations for the thrust deduction in terms of thrust loading, wake ratio, which is the ratio of the total wake to the frictional wake, and the known uniformity of the propeller jet. This set of equations was derived upon the assumption that the frictional thrust deduction is zero. The work is based on that of Dickman, which is apparently completely forgotten (and is not even mentioned in the new Principles of Naval Architecture). In 1939 he presented a paper on this subject, but in his work there was a slip, and Dr. Schmiechen had tried to find out what the error was and so come up with the proper set of equations by putting the frictional component equal to zero, and saying that the thrust deduction is a function of the thrust loading, of the wake ratio and the known uniform thrust of the propeller jet.

L. A. Van Gunsteren (Lips Propeller Works, Holland) referred to Lindgren's earlier remarks, in which he said that the Swedish tank was building a test facility for models of 8 m in length. Van Gunsteren pointed out that that was about the length of the models employed at the NSMB. For the large tankers

his firm had made quite a few propellers weighing about 50 tons and costing $120,000, a serious matter for the customers. They found lower efficiencies with these very large ships and also that the propellers had a lower efficiency in the tank compared with the computer design. Tests at the NSMB at different Reynolds numbers showed that this effect could be fully explained by the low Reynolds number at which the propellers were tested in open water. Van Gunsteren believed that the ship models were too short for the large tankers, and that to get a correct prediction the model must be certainly larger than 8 m, giving a scale ratio of more than 1 to 50 for the propeller.

Lindgren agreed that this was a problem and also with the need of higher Reynolds numbers for the big tanker models. The philosophy at Gothenburg was that with the new cavitation laboratory it will be possible to study the influence of Reynolds number up to appreciably higher values than at present because there will be no free water level in the cavitation tunnel. On the other hand, he would like to know a little more about what Van Gunsteren meant about this scale effect due to low Reynolds number. Did he mean that laminar separation is present when carrying out propulsion experiments or does he mean that laminar flow occurs around the propeller profile? What was his hypothesis?

Van Gunsteren replied that conditions are under-critical if there is laminar flow at the root sections, and referred to a diagram given in the famous work of Troost, Van Lammeren, and Van Manen. Dr. Gutsche proposed a critical Reynolds number based on propeller diameter and revolutions. If the propellers for models of very large tankers are plotted in this diagram, it will be found that they are in the region where, based on this Reynolds number, the flow is going from turbulent to laminar. So the propellers are in the under-critical condition. Moreover, the effect is not the same for all types of propellers. If another kind of section or a different type of propeller is used, open water tests in such a critical range may show that one propeller is better than another, while behind a ship both propellers might be equal or the relative efficiencies may even be reversed.

Lindgren said that the Gutsche under-critical Reynolds number means that there is laminar separation on the profiles and is related to the performance in homogeneous flow in the open-water condition. He did not think that the Reynolds number in the open condition could be compared with that calculated using the wake fraction in the behind condition. They are operating in quite another degree of turbulence. What that really means is not known but it must have a very marked influence on the performance.

Dr. Morgan wished to make one point about the scale or Reynolds number effect on propellers. There seemed to be some confusion here and it might be as well to point out that the work that Gutsche did for propellers in uniform flow does not apply to the entirely different conditions behind the model. The friction coefficient variation with Reynolds number is something like that shown in Fig. 6 with a transition from laminar to turbulent flow. This transition on a propeller blade of airfoil section is roughly about 5×10^5 at 0.7 radius. However, if the propeller is operating in turbulent flow or is rough, it falls upon the upper turbulent line. The friction coefficients on model propeller blades may be three times higher than those on the full scale, and it is necessary to be very careful in analyzing the data when comparing different propellers. Such a problem was

met with in work done some years ago at NSRDC on the model of the tanker Manhattan when trying to compare a nine-bladed propeller with a five-bladed propeller of roughly the same blade-area ratio. The Reynolds number of the nine-bladed propeller was about 1.5×10^5, and that of the five-bladed propeller was about 5.0×10^5. It is clear from Fig. 6 that this would give rise to a considerable difference in the performance, whereas at full scale both propellers operate in the rather flat area and should not show any significant difference. Actually the comparison between the five-bladed and the nine-bladed models would indicate that the nine-bladed was not as efficient relatively as it actually would be full scale. Dr. Morgan came upon this problem when he was well along in developing a design technique for propellers. He discovered that on a couple of propellers, especially the nine-bladed, the performance was not as expected, and the theory did not match the experiment results. In the theoretical calculations it was assumed that the drag coefficient was 0.008, but reference to airfoil data showed that the drag coefficient in fully turbulent flow would have been 0.012, or 50% higher. By assuming this value, the theoretical and experimental results matched on the model, but the difficulty is to know whether the flow is fully turbulent, and this is a very important point in doing analysis.

Lackenby made a brief reply to Dr. Kinoshita, Professor Prohaska, and Dr. English. In regard to Dr. Kinoshita's remarks, he pointed out that the results given were essentially a resistance and propulsion investigation on a methodical series, and he agreed entirely that if these results were used on an actual design there might well be restraints on the movements of the LCB due to vibration and directional stability considerations. As to how this sort of behavior might apply to very large tankers, this work was done some time ago and was aimed at a tanker of about 75,000 tons. Certainly in a 250,000 tonner, the propeller today would be proportionally less in diameter in relation to the draft and the behavior might be somewhat different. Again, of course, as time goes on, the tendency will be to have slower-rotating propellers of much bigger diameter, but this trend may not be sufficient to overcome the effects just mentioned. In regard to the question of loading, raised by Professor Prohaska, the same loading was used throughout all the five model tests. In Lackenby's opinion, the peculiar changes with LCB position were a function of the shape of the sections. Some other results for a model of the same block coefficient of 0.85 in which a somewhat similar variation in LCB position was made, but where the section

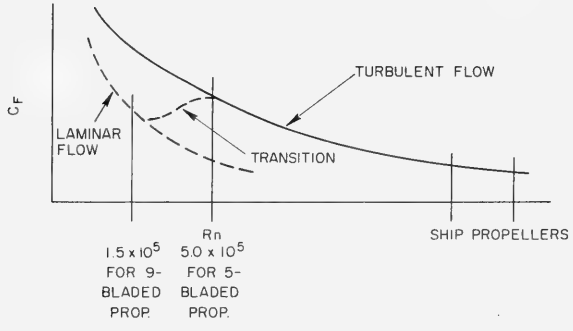

Fig. 6 - Variation of the friction coefficient with Reynolds number

shapes were different, showed that there was practically no change in hull efficiency as the LCB moved forward, while in a third model the hull efficiency decreased slightly. All these models were analyzed in the same way and Lackenby believed that the changes are essentially an effect of the ship form and the propeller interaction.

Dr. Todd recalled that in the analysis of the Series-60 models some peculiar shapes were found for some of these propulsion factor curves, which it was not possible to explain in a logical way.

J. Leaper (Admiralty Research Laboratory, Teddington, England) said that this propeller-hull interaction was not his specialty, but until Dr. Morgan spoke he had been very surprised by the complete absence of any mention of attempts to predict these factors theoretically, because it would seem that such a capability would be useful in itself and could possibly give an understanding of scale effects at the same time. The panel would be interested to know that at ARL one of his colleagues had started a program to compare theoretical predictions of hull efficiency elements with experimental measurements. Initially these experiments deal with a series of axisymmetrical hulls and behind the hull he has a simulated propulsion unit. He can also vary the actual spacing between hull and propulsor. This work is going to be done in a large wind tunnel, and he is going to measure drag, pressure distribution on the hull, pressure distribution on his simulated propulsor, and the mass flow through the propulsor. The measurements will be made on quite a series of hull shapes that have been theoretically derived. Some account will also be taken of the viscous effects and the boundary layer. The hope is that if these experiments on a wide range of body shapes give good agreement with theory, then an effort will be made to extend the theory to the case of the nonaxisymmetric body. Even if the theory is not confirmed, the work should show in what respect it is deficient, and in any case it will give a fairly large amount of systematic data.

Dr. Schmiechen said that the last speaker mentioned that naval architects had never considered the case of the theoretical prediction of t. He disagreed, and pointed out that a lot of work in this field had been done by the Berlin School under Professor Horn and Professor Dickman, and then by Professor Amtsberg and his pupils, the last work appearing from this school being that by Novaki. This research has covered a great many of the problems previously mentioned. Dr. Todd also pointed out that a great deal of work had been done on this subject by many people. A number of problems had been uncovered in the discussion, and a number of suggestions had been made as to what might be done to solve some of them in the future. He believed that at the ATTC Meeting in Ottawa in June a proposal was discussed to build an 80-ft craft -- call it a model or a ship — in order to get some line on the scale effect on wake and thrust deduction and other propulsion factors. Such a proposal has been discussed many times at Taylor Model Basin and by BSRA, but it has never got far because of expense. Dr. Todd said he had been one of the people who have for years advocated such full-scale trials, but he did not feel enthusiastic about an 80-ft model because he believed at the end it would still be necessary to run a fairly large ship. A 72-ft Victory model had been made at Wageningen and a 75-ft model of a tanker in Germany, and although they extended the geosim range quite appreciably, they probably created as many or more problems than they solved. In the Wageningen work, for instance, considering the range from the small models

of (1/50)-th scale of the Victory ship up to the size normally used in a towing tank – say, 23 ft – there is not too much wrong with the pattern. In fact, it is the 75-ft craft that really leads things astray. So he did not know whether a model of that length would really solve the problems. We had a feeling that, if we built it and spent a lot of money in testing it, when we were finished the experiments we would feel the need to extend them to a full-scale ship. It's a question of whether such an intermediate one is really worth the money. It is a remarkable fact that in all the history of ship research there has never been a good and comprehensive set of full-scale data. The nearest approach was the BSRA tests on the Lucy Ashton, but although they gave probably the most reliable resistance measurements ever made on a ship, the fact that the ship could not be propelled meant that no information was obtained about scale effects on the propulsion factors. The money that BSRA put into the Lucy Ashton provided an end spot on a geosim series, but in fact all that was really obtained was a roughness allowance for the Lucy Ashton with different hull surfaces, without any information on propulsion problems. This is in strange contrast to the money that is spent on other forms of transport, such as aircraft or hovercraft. It is strange that ever since powered ships were built there has never been a single vessel devoted solely to research, in which all the model tests could be repeated full scale. Instead, we have to put up with a few odd hours that some generous and forward-looking shipowner is willing to provide. Perhaps the main lesson to be learned from this panel discussion is the need for full-scale trials to investigate the problems of propeller-hull interaction.

Rader mentioned that in Germany they were in the fortunate position of having a large research vessel, the Meteor. The ship is about 90 m long and, this summer, wake surveys have been done, the ship being propelled by aircraft jet engines on deck. The data will be presented at the autumn meeting of the S.T.G. in Germany. Unfortunately, the vessel is relatively slow, but the trials should provide some data about wake scale effect, thrust deduction, etc. Unfortunately, the ship is mostly used by oceanographers.

Dr. Todd said that again the tests were restricted to what can be done in the time that is made available from the ship's other duties. Rader agreed, and said that sometimes they had to wait two years before time was allocated to do trials on the ship. Dr. Todd welcomed the good news that a research ship was available, even on an intermittent basis. Rader had said that if the panel had any suggestions as to work that could be done with the Meteor, the people concerned would be glad to see if they could be worked into the program.

* * *

PANEL DISCUSSION—PLANING CRAFT

Daniel Savitsky, Panel Chairman
Stevens Institute of Technology
Hoboken, New Jersey

INTRODUCTION

The currently increasing number of, and utilization of, planing craft in both naval and commercial applications has brought into sharp focus the relative dearth of small-boat hydrodynamic technology available to the naval architect. For the most part, the planing-boat designer has borrowed from the scientific literature on water-based aircraft and displacement ships, seasoned this with his own ingenuity, and produced a variety of successful and unsuccessful hull forms. The existing literature has now been extracted to exhaustion, making it essential to develop a program of hydrodynamic research tailored to the unique problems of small high-speed craft. Almost every phase of planing-craft technology is requiring of research -- i.e., hull hydrodynamics, propulsion, seakeeping, maneuverability and stability, shallow-water water effects, structural loads, and model-full-scale correlation, to name just a few. Many of these important problems have not been considered in past research programs. Fortunately, it now appears that an integrated program of small-boat research is being considered by the U.S. Navy. If so, it is eagerly awaited by the design community. It is hoped that the present panel discussion (which reports the first instance of separate consideration of planing craft in all seven Symposia on Naval Hydrodynamics) represents the start of a continuing series of technical seminars concerned with the varied hydrodynamics of planing craft.

The deliberations of the panel were well attended, and some fifteen formal contributions were presented. This large number of prepared statements precluded the possibility of arranging for general informal discussions on planing hulls and necessitated the presentation of the prepared material followed by discussions from the attendees. The material presented was grouped into the following three categories:

1. Innovations in Planing-Craft Design;

2. Model Test Procedures for Planing Hulls

3. Recent Test Results for Planing Hulls

The specific formal contributions to each of these categories, along with the associated discussions, are discussed below.

1. INNOVATIONS IN PLANING-CRAFT DESIGN

Commander P. DuCane of Vospers, Ltd. described the application of a "surface" propeller to a deep-veed racing boat of the international R1 class. It might be explained that in a "surface" propeller the axis of the propeller is so placed that only about one-half the disc is immersed. This is necessary to avoid propeller blade cavitation by allowing the propeller to break the water surface and thus ventilate the negative pressure side of the blade. Further, no appendages excepting a rudder will be under the boat, thereby eliminating the appendage drag arising from shaft and propeller strut. The propeller itself was a three-bladed supercavitating type with blunt trailing edge. In full-scale trials, other conditions being essentially identical, the fully submerged propeller drove the boat at 54.8 mph and the surface propeller drove the boat at 60 mph. Subsequent discussions indicated general interest in the application of a surface propeller to shallow-draft planing hulls and surface-effects ships.

D. F. Calkins of the U.S. Naval Undersea Warfare Center, discussed the design features and model test results for a three-point ram-wing hydroplane intended for unlimited hydroplane racing. This unique hull, which is a concept developed jointly by D. F. Calkins and B. Bryant, consists of two parallel planing surfaces that provide lateral stability and are located forward of the center of gravity; an NACA 4406 wing section between the planing surfaces and central hull operating in ground effect, and the vertical component of propeller thrust. The planing surfaces are extended aft along the wing tip chord to act as wing fences, thus creating a ram-wing hydroplane. The intent is to design a vehicle which has the C.G. forward of wing aerodynamic center and thus provide for longitudinal stability of the craft – conventional hydroplanes suffer from a lack of longitudinal stability at high speed. Tow-tank tests were conducted on a model of the ram-wing configuration up to model speeds of 60 fps. These tests, which were conducted at the Marine Technology Center, General Dynamics, showed that at 100 mps (full-scale equivalent) the lift-drag ratio of the ram-wing design was approximately twice that of the conventional hydroplane designs which generally consist of two sponsons (connected to a center hull) planing on their aft extremities and the lift of a "surface" propeller. Further, the test results showed that the trim of a conventional hull increases with speed up to the point that it literally flies from the water surface, whereas the trim of the ram-wing hull decreased with increasing speed in the high-speed range. Work is now proceeding on optimizing the configuration.

A report was presented on the work of E. P. Clement of NSRDC on the dynaplane boat concept. This is a stepped planing hull where most of the lift is provided by a cambered planing lifting surface of moderately high aspect ratio located just forward of the center of gravity with an adjustable lifting surface at the stern providing balance, stability, and control of trim. The large portion of superfluous wetted area of the conventional unstepped planing boat is eliminated by this approach and a drag decrease results from this fact together with the more favorable value of aspect ratio. Model tests at NSRDC showed that for boats of 100,000 pounds gross weight, the dynaplane design requires 10% more horsepower than the conventional unstepped design at a speed of 25 knots and 50% less horsepower at speeds of 55 knots. The respective values of lift to drag ratio at 55 knots are 6.2 for the conventional design and 12.5 for the dynaplane design.

A contribution was received from F. R. Miller and S. N. Gyves of Hydronautics on tests of a self-propelled 1/2 scale model (20 ft long) of a high-speed inverted V or sea-sled-hull amphibious vehicle. All tests were conducted in Chesapeake Bay and measurements were made of resistance, trim, and wave impact acceleration in various sea conditions up to upper 3 (significant wave height = 2.5 ft). In addition, self-propulsion tests were conducted on a 1/6 scale wood model at the National Physical Laboratory, England. Full-scale tests were conducted by the Marine Corps Landing Force Development Center, Camp Pendleton, California. The correlation between model and full-scale data varies from excellent to a maximum difference of 15% lower full-scale SHP in the speed range from 15 to 20 knots. Data were presented on the motions and impact accelerations of the sea-sled and qualitative comparisons were made with V bottom hulls.

2. TESTING PROCEDURES FOR PLANING-HULL MODELS

Professor C. Falkemo of Chalmers University of Technology described a new outdoor facility for model tests in calm water, regular waves, and also at sea in natural waves. The test basin is 300 ft long, 45 ft wide, and 15 ft deep. It is formed by a natural crevice which has been dammed and blown out. Planing boats can also be tested in full-scale on measured miles in sheltered water and outside the belt of rocks.

J. T. Everest and D. Bailey of National Physical Laboratory, England, described experiments made to determine the total power requirements of a systematic series of high-speed displacement craft. Measurements were made of the total resistance and wavemaking resistance by the method of Eggers based on wave-pattern analysis. Tests were limited to a maximum speed of 15 ft/sec, which, in turn, limited the wave-pattern measurements to a maximum Froude number based on water depth ($V/\sqrt{gd}$) of approximately 0.55. The measured values of wave drag formed well-defined curves, although there was a discontinuity at a ship Froude number of approximately 0.53. At this speed, a tumbling wave existed at the stern of the craft falling on to the transom — it is speculated that this effect could likely cause the discontinuity in wave-resistance measurements and also invalidate the assumptions made by Eggers in his method of estimating wave drag. Viscous drag was estimated using the ITTC formulation and measured wetted areas with an allowance for a form factor. It was found that the summation of wave drag and estimated friction drag was as much as 40-50% less than the measured total drag. Several possible reasons for this large discrepancy are discussed, and it is suggested that the complete lack of pressure recovery at the stern caused by complete flow separation at the transom is the most significant effect.

Consideration is also given by the author to wavemaking resistance of high-speed catamaran hulls. The estimation of this resistance was based upon the linear superposition of experimental wave-pattern data for a single hull in order to calculate the wave pattern and, hence, the wave resistance of multi-hulled ships. The results show that wave interference effects between hulls can be of some importance for Froude numbers less than 0.5, although adverse influences exceeding 25-30% are unusual. Some slight beneficial influence is

predicted at a Froude number of 0.4; the apparent absence of interaction for Froude numbers in excess of 0.5 was striking.

J. B. Hadler of NSRDC presented some comments on trim measurements of "free-to-trim" resistance tests on planing craft. Referring to the work of Sottorf and Schmidt (1933, 1937) on the comparison of geosims with full-scale seaplane floats, the expected scale effect on the viscous drag were observed, but the running trim for the geosims was larger than full-scale trim — which is opposite to what was expected. Tests at DTMB on models of the PT8 ranging in size from 11.1 ft to 5.6 ft also showed that the smallest models ran at higher trim angles for $V/\sqrt{L} > 1.75$, but that there was good agreement between the various size models at $V/\sqrt{L} < 1.75$. Mr. Hadler suggests that a research program be undertaken to explain this difference. The chairman suggested that, if the chine edges of the smallest models were not made with exaggerated sharpness, the flow separation would be delayed in the aft regions of the small model, which could result in slightly higher running trim angles. The practice at the Davidson Laboratory, Stevens Institute of Technology, is to sharpen the chines and recess the model walls immediately above the chine line in order to ensure proper ventilation and flow separation from the sides. It was suggested that consideration be given to adapting a standard for model construction which would provide for sharp chines.

R. Lofft of AEW, Hasler, also reported on "Effect of Scale on Running Trim and Resistance of Planing Forms." Tests were made of 1/6, 1/8, 1/12, and 1/20 scale models of a fast patrol boat (model beams of 3.52 ft, 2.78 ft, 1.39 ft, and 0.84 ft). An interesting side investigation was to determine the effect of model construction material on the test results. The 1.39-ft-beam and 2.78-ft-beam models were constructed in both wood and wax. Unfortunately, the smallest-scale model was only built of wood. From the test results, Lofft concludes that there is no scale effect for the 1/6-, 1/8-, and 1/12-scale models. The smallest-scale wooden model (1.20) had a lower resistance relative to the larger wooden models, and this was attributed to lack of artificial turbulence stimulation in the small model. The smallest model also ran at a slightly higher trim than the other models. Lofft attributes this high trim angle of the smallest model to its wooden construction. He found that for the other scales, the wood models ran at approximately 1/4° to 1/2° higher than the wax model.

E. Amble of the Norwegian Ship Model Basin reported on tests to investigate scale effects which arise when testing longitudinally stepped planing-hull models. A test program was carried out in Trondheim using four geometrically similar models where, for the same test Froude number for each model, the Reynolds number varied from 9.275×10^5 to 4.950×10^6. A surface-piercing turbulence strut towed ahead of the models was effective in obtaining satisfactory conformity in results. From the test results, Amble concludes that the drag-to-lift ratio for the largest model of the stepped hull ($B = 391$ mm) was 10% less than for the unstepped hull, while, for the smallest model tested ($B = 128$ mm), there was little difference between stepped and unstepped configurations. Further, Amble states that tank tests of longitudinally stepped planing hulls are much more exposed to scale effect influence than are tests with conventional, unstepped planing designs. It was suggested from the audience that the sharpness of the edges of longitudinal steps for the smallest model may have been insufficient to assure flow separation and that, further, perhaps, the introduction of

artificial ventilation in the way of the longitudinal steps would modify the flow. It was pointed out that, in seaplane model tests, the afterbody area just aft of the transverse step is open to the atmosphere to assure proper ventilation and flow separation – particularly if there is a shallow depth of step in the design.

3. RECENT TEST RESULTS FOR PLANING HULLS

Professor A. Nutku of I.T.U. described model tests in the Turkish tank with systematically varying hull forms to study the effect of geometric form, dynamic planing conditions, and loading on the performance and resistance of planing hulls. Geometric variations included flat bottom and constant deadrise prismatic hulls; varying deadrise surfaces; models with longitudinal variation in beam, and slope of buttock lines. In addition, hard-chine and round-bottom sections were tested. Professor Nutku has planned an extensive systematic model study of planing – however, his presentation at the panel discussion was limited to a presentation of only some of the test results collected to date. Many interesting performance characteristics were evident from the 13 data plots which were presented. Unfortunately, limited space does not permit the reproduction of those test results in this summary, and a discussion and interpretation of these data cannot be adequately accomplished without these plots. The attendees at the symposium expressed great interest in Professor Nutku's experiments and eagerly await publication of his work.

A. C. Conolly of the Marine Technology Center of General Dynamics discussed a procedure to predict the performance of stepped planing boats from model tests on a standard series of flying-boat hulls. The systematic seaplane model data were obtained by the Davidson Laboratory, Stevens Institute of Technology and by General Dynamics. Conolly refers to the work of Saunders-Roe in England in collapsing this data and making it easily usable by the designer for pre-design purposes. The work of F. W. S. Locke, Jr., is also referred to in this regard. Using these collapsed seaplane data, Conolly predicts the performance of a stepped planing boat with a plum stabilizer which had been model-tested. He finds that the resistance was overestimated throughout the speed range by about 15%, but the resultant resistance curve was of the same form as the model and the predicted hump resistance occurred at the same model speed. Seaplane data indicated a hump trim of 5.0°, whereas 5.8° was measured on the model. At planing speeds both seaplane data and model data agreed.

Dr. J. J. van den Bosch of Delft presented the results of a brief study on the linearity of motions of planing craft in head seas. Two models were tested. One was the series-62 type developed by Clement and Blount. The other was derived from this model by increasing the deadrise angle. For test speed coefficients up to $F_{\nabla} = 3.5$, it is shown that, considering the pitch and heave motions, the derivation from linearity were small at wave lengths approximately equal to the hull length, but that the derivations increased for longer wavelengths, especially for $F_{\nabla} > 2.5$. The accelerations were distinctly nonlinear for all wave and speed conditions. Heave and pitch response amplitude operators obtained from irregular and regular waves were compared at a $F_{\nabla} = 2.7$. The agreement was satisfactory for the high-frequency (short-wave) part of the spectrum but poor for the low-frequency (long-wave) part. Dr. van den Bosch speculates that the low-frequency part is not trustworthy because of the reflection of the very

long wave components involved. The chairman described some of the results from a systematic series of planing-hull tests in rough water currently underway at the Davidson Laboratory, Stevens Institute of Technology. The results showed that for speed-length ratios larger than approximately 2, the pitch, heave, accelerations, and added resistance are significantly nonlinear and that these nonlinearities increased with increased speed up to a maximum test speed-length ratio of 6.0. Further, it was found that wavelength had a significant effect on nonlinear behavior. For wavelengths of the order of hull length, linear relations for motions were observed at all speeds. Deviations from linearity increased as wavelength increased and reached a maximum for wavelengths approximately three times the hull length. For longer wavelengths, the trend to linearity in motions increased until, at a wavelength approximately five times the hull length, linear motion relations were observed at all speeds. The accelerations and added resistance were strongly nonlinear at all test speeds and wavelengths. These Davidson Laboratory results were obtained from regular wave tests, where, for a given test wavelength, the wave height was varied and from tests in two irregular sea states.

Dr. Graff of the Ship Model Tank at Duisburg made some general comments on operating regimes for round- and vee-bottom hulls. Quantitative information on this subject must await publication of his work.

G. Rosen of United Aircraft completed the session with a sound movie on full-scale operation of high-speed planing hulls driven by lightweight gas turbine engines.

* * *

INDEX

☆ U. S. GOVERNMENT PRINTING OFFICE : 1971 O - 413-016